ALOP

Alentejo: sistemas de Observação e Previsão

(Projecto ALT20-03-0145-FEDER-000004))

Relatório Final

Março de 2020

(Atualizado em Outubro de 2023)

Índice

1. Introdução....4

2. Equipa e funcionamento do Projeto....4

2.1 Pessoal com contrato com a Universidade de Évora e com o Instituto Politécnico de Évora. .5

2.2 Investigadores Contratados....5

2.3 Consultores....6

2.4 Equipamento adquirido....7

2.5 Reuniões de Projetos....9

2.6 Reuniões com Agentes....10

2.7 Sinergias com outros projetos....11

3. Atividades de Observação e recolha de dados....12

3.1 Equipamento instalado para medições contínuas....12

a) Plataforma Alqueva-Montante....12

b) Plataformas Alqueva-Mourão, Alqueva-Captação e Lucefecit....15

c) Estações meteorológicas de Barbosa e Cid Almeida....15

3.2 Saídas de campo....18

2.3 Observações em altitude....29

3.4 Observatório de Física da Atmosfera do ICT....30

3.5 Detecção remota a partir de satélite....30

3.6. Avaliação dos parâmetros físico-químicos, biológicos, perfis em profundidade e das concentrações de pesticidas e metais potencialmente tóxicos na água e sedimentos....31

Caracterização dos parâmetros de suporte na coluna de água e nos sedimentos....33

Mapa e características das estações meteorológicas existentes na Região Alentejo....34

4. Organização de eventos de formação avançada e de divulgação....40

4.1 Cursos de Verão....40

4.2 Outros cursos....48

4.2 Seminários....54

5. Resultados....55

5.1 Artigos em revistas de circulação internacional com arbitragem científica....56

5.2 Dissertações.....61

5.3 Patentes.....61

6. Disseminação dos resultados.....62

6.2 Desenvolvimento do sítio da Internet do ALOP e partilha de dados.....62

6.2 Comunicações em encontros científicos nacionais.....65

6.3 Comunicações em encontros científicos internacionais.....68

6.4 Sessão de Apresentação dos Resultados.....70

7. Indicadores.....79

Anexo A Publicações científicas.....80

1. Introdução

O Projeto ALOP teve início formal a 25 de Maio de 2016 e terminou a 31 de dezembro de 2019. Neste relatório final procuramos dar conta das atividades efetuadas e principalmente dos resultados obtidos. A tarefa está facilitada pois o projeto, em conjunto com as sinergias geradas com outros projetos e as colaborações nacionais e internacionais dos vários membros da equipa permitiram a publicação de um invejável número de publicações científicas: 45 (dado de Outubro de 2023). Por esse motivo, anexamos neste relatório cópia de todas estas publicações, prescindido de um relato exaustivo dos resultados que já estão publicados.

Para além dos resultados científicos, o projeto consolidou uma equipa de investigação na área da observação e previsão da água e da Atmosfera no Alentejo, envolvendo investigadores da Universidade de Évora e do Instituto Politécnico de Beja. Esta equipa continua a trabalhar, tendo alguns dos seus investigadores mais jovens encontrado emprego sob a forma de contratos da Universidade de Évora, alguns apoiados pelo Programa de Recursos Altamente Qualificados para o Alentejo. A equipa continua a trabalhar neste domínio com suporte em novos projetos e prestações de serviços. A experiência e as metodologias aprendidas e desenvolvidas no decorrer do projeto tem também sido postas ao serviço de outros projetos e da resolução de outros problemas. Destaca-se em particular o trabalho realizado pelo Laboratório da Água de OVID utilizando o equipamento de PCR financiado pelo ALOP. Uma parte da equipa está hoje a trabalhar em projetos ligados à prevenção e combate aos fogos florestais, em resultado de sinergias criadas no desenvolvimento do projeto.

Como previsto, o Projeto ALOP contribuiu para a formação avançada, tendo permitido a organização de Cursos de Verão, Seminários Técnicos e outros Seminários, como se documenta no presente relatório.

Last but not least, o ALOP permitiu a submissão de duas patentes, dando o seu contributo ao aumento das patentes na região Alentejo.

2. Equipa e funcionamento do Projeto

O Projeto ALOP contou com o envolvimento de Professores, investigadores e técnicos da Universidade de Évora e do Instituto Politécnico de Beja, mas assentou grande parte do seu trabalho nos investigadores contratados especificamente para o efeito.

2.1 Pessoal com contrato com a Universidade de Évora e com o Instituto Politécnico de Évora

Universidade de Évora

Nome	Grau Académico	Posição
Ana Cláudia Saúde	Lic.	Técnica de Laboratório
Ana Maria Silva	PhD	Prof. Associada c/ agregação (apos.)
Ana Rodrigues Costa	PhD	Prof. Auxiliar
Anabela Rosado	Master	Técnica de Laboratório
António Heitor Reis	PhD	Prof. Catedrático
Carlos Miranda Rodrigues	PhD	Prof. Auxiliar
Célia Antunes	PhD	Prof. Auxiliar
Daniele Bortoli	PhD	Inv. Principal
Eduardo Morales Luizaga	PhD	Bolseiro pós-doc
Joel Barrenho	Lic.	Técnico de Informática
Josué Figueira		Técnico de Laboratório
Madalena Moreira	PhD	Prof. Auxiliar
Manuela Morais	PhD	Prof. Auxiliar
Maria Inácia Mira	Master	Technician
Maria João Costa	PhD	Prof. Auxiliar
Marta Pereira		Técnica administrativa
Miguel Potes	PhD	Bolseiro pós-doc
Paulo Canhoto	PhD	Prof. Auxiliar
Rui Salgado	PhD	Prof. Auxiliar
Samuel Bárias		Técnico de Laboratório
Sergio Aranha		Técnico de Laboratório
Susana Nunes	Master	Técnico de Laboratório

Nome	Grau	Posição
Adelaide Almeida	PhD	Prof. Adjunta
Alexandra Tomaz	PhD	Prof. Adjunta
Anabela Durão	PhD	Prof. Adjunta
António Floro	Lic.	Técnico de Laboratório
Maria Ivone Castanheira	Lic.	Técnico de Laboratório
Patrícia Palma	PhD	Prof. Adjunta
Paula Alvarenga	PhD	Prof. Adjunta

2.2 Investigadores Contratados

Nome			data início	data fim
Maria Alexandra Marchã Penha	UE	pós-doc	11/10/2016	31/07/2019
Maria Helena Batista Costa Guerreiro Novais	UE	pós-doc	15/05/2017	31/12/2019
Gonçalo Correia da Fonseca Rodrigues	UE	Investigação	01/12/2016	31/12/2019
Sofia Fialho	IPBeja	Investigação		
Ana Filipa Lima ?	IPBeja			
Maksim Iakunin	UE	pós-doc	01/01/2017	31/12/2019
Ana Catarina Galveias Jorge	UE	Investigação	02/09/2019	31/12/2019
Jessica Cristina Almeida Carvalho	UE	Investigação	02/09/2019	31/12/2019
Ana Carolina Rodrigues da Purificação	UE	Investigação	02/09/2019	31/12/2019

Para além dos 5 bolseiros contratos para toda execução do projeto, nos últimos 4 meses foram contratados mais 3 bolseiros para apoiar a conclusão do projeto.

A Doutora Alexandra Penha foi contratada como técnica superior pela Universidade de Évora a 1/08/2019, no quadro do programa PREVPAP, pelo que continuou a participar na equipa do projeto ALOP, mas deixando o seu salário de ser imputado ao orçamento do projeto.

Após o termino do projeto, a investigadora Helena Novais foi contratada no âmbito de outros projetos, sendo atualmente investigadora contratada ao abrigo do projeto de Recursos Humanos Altamente Qualificados para o Alentejo, o mestre Gonçalo Rodrigues, continuou a sua atividade de investigação na Universidade de Évora, tendo obtido uma bolsa de doutoramento da FCT. O Investigador Maksim Iakunin continuou a trabalhar em Évora no âmbito de outros projetos. A Ana Carolina da Purificação valorizou o trabalho desenvolvido tendo posteriormente concluído a sua tese de mestrado.

Para além da equipa de trabalho, o projeto beneficiou do trabalho de outros estudantes da Universidade de Évora e do Instituto Politécnico de Beja que por sua vez beneficiaram dos dados recolhidos durante o projeto, do seu ambiente de investigação e das colaborações que foram criadas e desenvolvidas.

2.3 Consultores

O Projeto ALOP beneficiou e permitiu consolidar colaborações internacionais mantidas por membros da equipa de investigação. Em particular, o projeto beneficiou das seguintes estadas de consultores:

Veronique Ducrocq, Directora do grupo de investigação em Mesoscala do Centro Nacional de Investigação Meteorológica (CNRM, Head of the the mesoscale research Group of the National Meteorological Research Center) deslocou-se à Universidade de Évora, Portugal, de 5 a 8 de Julho de 2016, enquanto consultora do projecto ALOP. Veronique Ducrocq deu uma lição no Short Summer School on Atmospheric Physics, no dia 6 de Julho de 2016 na Universidade de Évora,

sobre precipitação intensa no Mediterrâneo. Além da participação no curso, debateu com membros da equipa o desenvolvimento do projeto, nomeadamente dando sugestões no que se refere à modelação atmosférica e hidrológica.

Juan Luis Rascado, Professor/Investigador do Centro Andaluz de Medio Ambiente, da Universidade de Granada. deslocou-se à universidade de Évora de 3 a 9 de Julho de 2016, enquanto consultor ALOP. Juan Luis Rascado deu uma lição no Short Summer School on Atmospheric Physics, no dia 4 de Julho de 2016 na Universidade de Évora, sobre "Aerosol profiling and the Atmospheric Boundary Layer", e participou activamente na campanha de observações OBservation of Evora boundary Layer Intensive eXperiment - OBELIX II, que decorreu de 4 a 6 de Julho de 2016 - OBELIX II. A sua estadia permitiu ainda discutir trabalhos conjunto em curso sobre observações atmosféricas que se inserem no âmbito da Task 3 do projecto.

Christine Lac, investigadora responsável pela equipa Meso-NH do grupo de investigação em Mesoscala do Centro Nacional de Investigação Meteorológica (CNRM) deslocou-se à Universidade de Évora, de 6 a 9 de Novembro de 2016, enquanto consultora do Projecto ALOP. Christine Lac, é especialista em modelos de previsão do tempo. foi a principal docente do curso "Meso-NH Tutorial", que decorreu na Universidade de Évora de 7 a 9 de Novembro. Este curso foi importante para formar alguns membros da equipa do ALOP, na utilização do modelo Meso-NH que tem sido extensivamente utilizado.

Victor Stepanenko, Investigador Sénior do Departamento de Meteorologia e Climatologia da Universidade Estatal Lomonosov de Moscovo. Especialista em modelação numérica de lagos. Desloca-se à Universidade de Évora a convite e como consultor do projecto ALOP entre 10 a 16 de Maio de 2018, para ajudar a equipa na Tarefa 2: Modelação e previsão da qualidade da água em Albufeiras, vindo dar formação na utilização de um modelo de lago e realizar conjuntamente simulações numéricas.

Florence Habets, directora de investigação do Centre National de Research Scientific (CNRS) no laboratório METIS (Milieux Environnementaux, Transferts et Interactions dans les Hydrosystèmes et les Sols). efectuou uma visita científica à Universidade de Évora e a Alqueva, de 19 a 21 de Junho de 2018, enquanto consultora do projecto ALOP. Florence Habets deu uma lição no 2nd Alqueva Summer School on Atmospheric and Inland Water Sciences. Além da participação no curso, debateu com membros da equipa o desenvolvimento do projeto, nomeadamente dando sugestões no que se refere à modelação hidrológica.

Gianpaolo Balsamo, Cientista Principal do Centro Europeu de Previsão do tempo a Médio Prazo (ECMWF) deslocou-se à Universidade de Évora e a Alqueva de 19 a 21 de Junho de 2018, enquanto consultor ALOP. Gianpaolo Balsamo deu uma lição no 2nd Alqueva Summer School on Atmospheric and Inland Water Sciences. Além da participação no curso, debateu com membros da equipa o desenvolvimento do projecto, nomeadamente dando sugestões no que se refere à modelação atmosférica.

2.4 Equipamento adquirido

Em 26/08/2016 foi adquirido um sensor de pressão para o instrumento EC100 (nota encomenda 2926).

Em 28/10/2016 foi adquirido um sensor submersível de concentração de CO_2 para utilização subaquática (Habilitação - Proc. n.º 116/DF-GCP/2016).

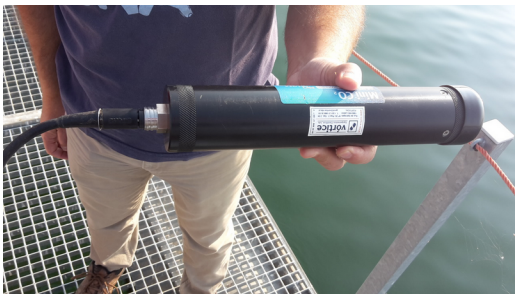

Em 14/03/2017 foi renovado o contracto 380210 para duas garrafas de gás comprimido para calibração do instrumento IRGASON (nota encomenda 1403).

O Instituto Politecnico de Beja, no âmbito do projecto ALOP adquiriu uma sonda multi-paramétrica WTW930-pH/FDO®/COND, e uma camara fitoclimática FITOCLIMA 600 BIO da ARALAB.

CFX96 Touch™ Real-Time PCR Sistema de deteção, para deteção e quantificação de ácidos nucleicos, Laboratórios Bio-Rad

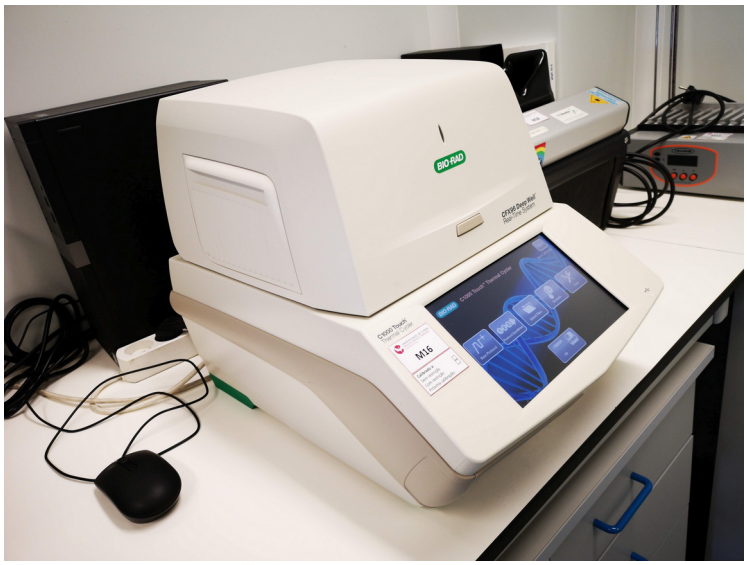

Arca Ultracongeladora (-86 ºC) para conservação de amostras, Interface.

2.5 Reuniões de Projetos

Reuniões de toda a equipa do projeto:

13 de Maio de 2016, 13 de Maio, às 10H na sala 138 do CLV da UE	0. Apresentação da equipa 1. Apresentação geral do projecto 2. Equipamento a adquirir 3. Plano de observações 4. Contratação de bolseiros 5. Patentes 6. Short course on Atmospheric Physics 7. Reunião com os actores regionais 8. Aspectos de gestão do projecto
27 de Junho, 14H na Escola Agrária do IPBeja	Programação da campanha de observações Apresentação sobre o modelo SWAT
3 de fevereiro 2017 às 10 H na sala 128 do CLV da UE	0. Apresentação dos novos membros da equipa 1. Questões financeiras e administrativas (participação da Dra Valentina Castro) 2. Balanço de Actividades 3. Campanha de observações e objectivos científicos 4. Publicações, participação em conferências e patentes 5. Reunião(ões) com agentes 6. Outros assuntos
17 de Janeiro de 2018 às 16:30 às 10 H na sala	- Curso de Verão

128 do CLV da UE	- Ponto da situação de publicações - Patentes - Reuniões com agentes - Próximas saídas de campo.

15 de Maio 2019	- Ponto da situação das actividades científicas e identificação do que nos falta fazer para cumprir o plano
	- Ponto da situação dos indicadores:
	  - Publicações;
	  - Patentes
	- Base de dados ALOP
	- Marcação de reunião / jornadas de apresentação de resultados com Agentes
	- Situação financeira; eventuais acertos ao orçamento

12 Dezembro de 2919, Anfiteatro da Escola Superior Agrária do IPBeja	Reunião de apresentação dos resultados do projeto às instituições e agentes regionais. (Ver Ponto específico)

2.6 Reuniões com Agentes

Foram realizadas reuniões e contactos com diversos agentes (stakeholders). Destacam-se pela importância as seguintes instituições:

IPMA: 15/07/2016

EDIA: 10/03/2017 e 6/2/2018

Associação Portuguesa do Ambiente: 20/03/2017

Conselho da Região Hidrográfica Do Alentejo: 15/11/2017

União de Freguesias de Amieira e Alqueva: 02/1018

Para a Sessão final para apresentação dos resultados (ver ponto próprio), realizada a 12 de Dezembro na Escola Superior Agrária de Beja foram convidados muitos agentes, públicos e privados, tendo estado presentes:

Administração de Região Hidrográfica (ARH) Alentejo

Administração de Região Hidrográfica (ARH) Tejo

Comunidade Intermunicipal do Alto Alentejo - CIMAA

Comunidade Intermunicipal do Baixo Alentejo CIMBAL

Câmara Municipal de Mourão

Câmara Municipal de Évora

Câmara Municipal da Vidiueira

Instituto de Ciências Agrárias e Ambientais Mediterrânicas - ICAAM

Administração Regional de Saúde (ARS) do Alentejo

Instituto Nacional de Investigação Agrária e Veterinária INIAV

Associação Terras Dentro

Instituto da Conservação da Natureza e das Florestas ICNF

Agência de Desenvolvimento Regional do Alentejo ADRAL

Agência Portuguesa do Ambiente (APA)

Instituto Português do Mar e da Atmosfera (IPMA)

Aquagri

Empresa Municipal de Água e Saneamento de Beja - EMAS

2.7 Sinergias com outros projetos

Existiram sinergias com outros projetos de investigação, nomeadamente:

Projeto DNI-A (ALT20-03-0145-FEDER-000011): Medição e avaliação da radiação solar directa no Alentejo: a sua interação com efeitos locais e respetivas implicações no mapeamento regional deste recurso energético. Coordenado por Paulo Canhoto, ICT, Universidade de Évora

Como o ALOP também tinha entre os seus objetivos melhorar a caracterização do recurso solar no Alentejo e como havia desde logo alguns membros da equipa que eram comuns aos dois projetos, foi possível articular estratégias de observação, partilhar dados e concluir trabalhos em conjunto que se traduzem em várias publicações. O conjunto de investigadores e bolseiros contratados e beneficiaram desta colaboração entre os dois projetos. Em termos de modelação numérica foi lançado um programa de simulação com um modelo atmosférico que permitiu ao mesmo tempo estimar os efeitos da albufeira no Clima e mapear a radiação solar direta no Alentejo.

Projeto ZOM3D (ALT20-03-0145-FEDER-000028): Modelos Metalogénicos 3D da Zona de Ossa-Morena – Valorização dos Recursos Minerais do Alentejo.

Coordenado por Pedro Nogueira, ICT, UEVORA. Fizeram-se ações comuns no âmbito da divulgação científica, da formação avançada.

CILIFO (Interreg /POCTEP 0753_CILIFO_5_E): Centro Ibérico para la Investigación y Lucha contra incêndios Forestales.

Coordenado localmente por Rui Salgado. O último ano do Projeto ALOP coincidiu com o primeiro ano do projeto CILIFO, um grande projeto interreg tendo por objetivo investigar e combater os incêndios florestais. Neste período foram possíveis colaborações no âmbito destes dois projetos, através da partilha de equipamento e dados de observação da atmosfera, bem como em termos de modelação atmosférica.

TOMAQAPA ((FCT reference PTDC/CTA-MET/29678/2017): Técnicas de Observações Multi-espectrais para a Avaliação da Qualidade da Água e Poluição do Ar

A colaboração com este projeto traduziu-se na partilha de equipamento de observação e na colaboração num estudo conjunto sobre o impacto de Alqueva no clima regional

Ações COST

COST CA15113: Science and Management of Intermittent Rivers & Ephemeral Streams (http://www.smires.eu/)

COST ES1404: "A European network for a harmonised monitoring of snow for the benefit of climate change scenarios, hydrology and numerical weather prediction" (http:/harmosnow.eu)

O envolvimento de investigadores da equipa ALOP nestas ações permitiu aumentar a internacionalização dos trabalhos efetuados no âmbito do projeto ALOP, estabelecer novos contactos e beneficiar de estadias de investigadores estrangeiros que participaram em atividades do projeto.

3. Atividades de Observação e recolha de dados

3.1 Equipamento instalado para medições contínuas

As coordenadas dos locais onde estão equipamentos em medições contínuas e medições pontuais podem ser consultadas na tabela abaixo.

Local	Latitude (ºN)	longitude (ºW)
Cid Almeida	38.21639	-7.45454
Barbosa	38.22755	-7.47076
Alqueva-Montante	38.223542	-7.459495
Alqueva-Mourão	38.398633	-7.387551
Alqueva-Captação	38.338446	-7.573441
Lucefecit	38.555283	-7.299137

a) Plataforma Alqueva-Montante

Nesta plataforma foi montada uma estação meteorológica em 11/04/2017 na qual constam os seguintes equipamentos:

Alqueva-Montanbe	Marca	Modelo	Nº Série
Data Início			
11-04-2017			
Tripode			1
Solar Panel 1	BP Solar	BP 380J - 80 W	I 2020306 2040330
Solar Panel 2	BP Solar	BP 380J - 80 W	AA0408263156709
Solar Panel 3	SolarWorld	SW 85 poly RNA/D	1312022807 46
Power Regulator	Steca	Solarix PRS 1515	739.389
Battery 1	Autosil	Série BE - 12 V - 100 Ah - C20	
Battery 2	Lucas	60 Ah	027 / 562-059
Battery 3	Lucas	44 Ah	068/ 544-065
Ambiental Box 1	Campbell Scientific	ENC 14/16	
Ambiental Box 2	Campbell Scientific	ENC 16/18	
Sonic Controlator	Campbell Scientific	EC100.07.01	1443
3D Sonic, CO2 & H2O	Campbell Scientific	IRGASON	1086
Datalogger	Campbell Scientific	CR3000 Std.28.02	8944
Memory Module	Campbell Scientific	CFM100	10896
Multiplexer	Campbell Scientific	AM 16/32B	E7266
Telemetry	Wismo within	Wavecom WMOD2	
Temp Probes 14	Campbell Scientific	107	
CO2 in water	Pro-Oceanus	Mini CO2 Analog Outuput	37-392-19
Albedometer	Kipp & Zonen	CM7B	920049
Pyrradiometer	Philipp Schenk	8111	8417
CO2 & H2O Analyzer	LICOR	LI-7210	
Flow Module	LICOR	7200-101	
Analyzer Interface Unit	LICOR	LI-7550	

de 13/06/2017 a xxxx esteve instalada na plataforma um equipamento de colegas da Universidade de Helsínquia,- Finlandia para a realização de um experiência de intercomparação de fluxos de vapor de água e dióxido de carbono.

Em Junho de 2018 foi instalado a sonda multi-paramétrica para medição em contínuo de:

Para além das estações meteorológicas, foram também instalados substratos artificiais (peças de cerâmica não tratada, de dimensão 5 x 7.5 cm) para estudo das comunidades de diatomáceas ao longo da coluna de água. Estes substratos foram colocados a diferentes profundidades, desde a superfície até ao fundo da albufeira (superfície, 1m, 2m, 3m, 5m, 10m, 15m, 20m, 25m, 30m, 35m, 40m, 45m, 50m, 55m, 60m), 3 peças em cada profundidade. As dificuldades na manutenção dos substratos artificiais colocados directamente na plataforma (Fig. X), conduziram à sua colocação em locais ligeiramente afastados das plataformas e devidamente identificados (Fig. X). O objectivo da colocação destes substratos é relacionar as comunidades e índices de contaminação orgânica, riqueza e diversidade de diatomáceas com os parâmetros meteorológicos e físico-químicos da coluna de água.

b) Plataformas Alqueva-Mourão, Alqueva-Captação e Lucefecit

Nas plataformas de Alqueva-Mourão, Alqueva-Captação e Lucefécit foram também instalados substratos artificiais, iguais aos colocados em Alqueva-Montante, para estudo das comunidades de diatomáceas em profundidade (à superfície, 1m, 2m, 3m, 5m, 10m, 15m, 20m em Lucefécit, até aos 25m em Alqueva-Captação e até aos 45m em Alqueva-Mourão).

c) Estações meteorológicas de Barbosa e Cid Almeida

A estação da herdade da Barbosa foi instalada em 24/02/2017 na margem Norte relativamente à plataforma de Alqueva-Montante.

Barbosa	Marca	Modelo	Nº Série
DataInício			
24/02/2017			
Tripode	Campbell Scientific	CM 10/3	
Ambiental Box	BRES	BRES54	
Solar Panel	Suoyang	Monocristalino - 20W	40104
Datalogger	Campbell Scientific	CR1000	E16188
Power Regulator	Campbell Scientific	PS12E-LA	E1052
Temp/Humidity	Campbell Scientific	CS215	E3537
WindSonic	Gill Instruments	Option 1 – 1405-PK-021	13450015
Ground Temp	Campbell Scientific	107	

A estação da herdade de Cid Almeida foi instalada em 17/02/2017 na margem Sul relativamente à plataforma de Alqueva-Montante.

Cid Almeida	Marca	Modelo	Nº Série
DataInício			
17/02/2017			
Tripode	Campbell Scientific	CM 10/3	
Ambiental Box	BRES	BRES54	
Solar Panel	SOLAREX	7.5 W	
Datalogger	Campbell Scientific	CR10	
Module	Campbell Scientific	SM716 KB	
Power Regulator	?	?	
Battery	DiaMec	12 V - 7 Ah	
Telemetry	Wavecom	Fast Tracker Supreme	
Temp/Humidity	Thies Clima	1.1005.51.512	0492006
Wind Speed	Vector Instruments	A100R	10108
Wind Direction	Vector Instruments	W200P	51061
Ground Temp	Campbell Scientific	107	
Udometer	Campbell Scientific	ARG 100	88021
Albedometer	Philipp Schenk	8104	5128

ALOP
DANGER

3.2 Saídas de campo

Data	Actividade
19/02/2016	Realizámos medições de irradiância em profundidade, medições com a sonda multiparamétrica, medições de irradiância fora de água em Amieira, Montante, Estrela e Monsaraz. Dia de céu limpo e muito vento. Fiz ~210 kms. **Não fiz reflectância!**
07/04/2016	Realizámos medições de irradiância em profundidade, disco de Secchi, medições de irradiância fora de água e de reflectância de superfície em Montante, Campinho e Mourão. Em Montante havia nuvens altas e nos outros dois locais céu limpo. **No Campinho a segunda medição irradiância a 1.5 m profundidade apresentou um aumento súbito**. **Fiz 2 séries de 25 reflectâncias em Mourão porque parece-me que a 1ª começou antes de estar a apontar para a água.** Fiz ~200 kms.
02/05/2016	Realizámos medições de irradiância em profundidade, disco de Secchi, perfil com sonda multiparamétrica, medições de irradiância fora de água e de reflectância de superfície em Montante, Estrela, Mourão e Monsaraz. Céu limpo e vento moderado. Fiz ~210 kms. **Atenção que a hora do PC não estava em UTC mas sim em LocalTime**. Montante2_300 tem 3 ficheiros a mais, ver quais os correctos (0,1,2)
03/06/2016	Realizámos medições de irradiância em profundidade, disco de Secchi, perfil com sonda multiparamétrica, medições de irradiância fora de água e de reflectância de superfície (só consegui em Montante, **porquê????**) em Montante (algumas nuvens altas), Estrela (nuvens altas), Mourão (céu limpo) e Monsaraz (céu limpo). Fiz ~210 kms. **Atenção que os ficheiros de ALQUEVALINE_IRR e REF deste dia só têm 15 espectros. ESTRELA_000 a 025 foram para o lixo, ficam os perfis ESTRELA2 e ESTRELA3** **Repetimos a sonda num dos locais, qual?? Ver as horas do ficheiro e ver a partir daí.**
14/06/2016	Reunião ALOP em Beja. RS, MJ, MP com Patrícia e Anabela
04 a 06/07/2016	Short Summer School
21/07/2016	Fui com no barco da EDIA com o Valter fazer medições de irradiância em profundidade e perfil com sonda em 4 locais entre o paredão e a Estrela. No segundo ponto o protótipo virou para baixo do barco a meio do perfil (Valter estava a segurar). Havia algumas nuvens altas nas duas primeiras medições.
26/07/2016	Fui com o Samuel realizar um ciclo diário ao Centro Náutico de Monsaraz. Fizemos das 9h às 16h. Pelas 14h30 apareceram algumas nuvens altas.
17/11/2016	Realizámos medições de irradiância em profundidade, disco de Secchi, perfil com sonda multiparamétrica, medições de irradiância fora de água e de reflectância de superfície em Montante, Estrela (nuvens

	altas), e Monsaraz. Fiz ~210 kms.
13/12/2016	Saída ao Alqueva para prospecção de locais para amostragens ALOP. Eu, Rui, Gonçalo, Josué, Alexandra, Patrícia, Sofia, Manuela Ruivo, Valter.
21/12/2016	Seminário do recém-chegado bolseiro Gonçalo Rodrigues sobre o seu trabalho passado enquanto bolseiro do IPMA.
29/12/2016	Realizámos medições de irradiância em profundidade, disco de Secchi, perfil com sonda multiparamétrica, medições de irradiância fora de água e de reflectância de superfície em Montante, Estrela e Monsaraz. Fiz ~210 kms.
09/01/2017	1º dia ALOP Janeiro (**C1**). Fomos às plataformas de Lucefecit, Mourão e Montante e às ribeiras de Lucefecit e Álamos.
10/01/2017	2º dia ALOP Janeiro (**C1**). Fomos às plataformas de Alqueva-Montante e Alqueva-Captação e às ribeiras de Amieira e Zebro.
23/01/2017	Realizámos medições de irradiância em profundidade, disco de Secchi, perfil com sonda multiparamétrica, medições de irradiância fora de água e de reflectância de superfície em Montante, Estrela e Monsaraz. Fiz ~210 kms.
03/02/2017	Reunião ALOP em Évora com membros de Évora e Beja. Bolseiros novos presentes: Alexandra, Gonçalo e Maxim. Faltou a Sofia de Beja. Prof. Salgado e Profa. Morais Grupo do Lab. Água e da Atmosfera fizeram uma breve apresentação.
16/02/2017 a 22/02/2017	O albedómetro que vai para CidAmeida esteve em calibração na Mitra com o master.
17/02/2017	Instalámos a estação da **CidAlmeida** que **ficou a funcionar sem o albedómetro**.
24/02/2017	Instalámos a estação da **Barbosa** que **ficou a funcionar**. Fomos à CidAlmeida instalar o albedómetro já calibrado. A plataforma de Montante estava fora do sitio em direcção a Norte.
06/03/2017	1º dia ALOP Março (**C2**). Fomos às plataformas de Lucefecit, Mourão e Montante e às ribeiras de Lucefecit e Álamos.
07/03/2017	2º dia ALOP Março (**C2**). Fomos às plataformas de Alqueva-Montante e Alqueva-Captação e às ribeiras de Amieira e Zebro.
13/03/2017	Realizámos medições de irradiância em profundidade, disco de Secchi, perfil com sonda multiparamétrica, medições de irradiância fora de água e de reflectância de superfície em Montante e Estrela. Muita onda em Montante. Estrela só conta a descida (a subida tinha nuvens), poucas ondas. Monsaraz só fizemos Secchi porque havia nuvens. Fiz ~210 kms no carro do Gonçalo.
24/03/2017	Fui à CidAlmeida resolver o problema de falta de comunicação. Era o Modem que estava bloqueado. Ficou a funcionar e fiz BackUp dos dados. O módulo de armazenamento dá para 9 dias e meio de dados.
31/03 a 04/04 2017	Montagem "a seco" da estação que vai para a plataforma Alqueva-Montante aqui no observatório do ICT. Está tudo a funcionar

	correctamente. OS Version EC100.07.01 (built on 30/08/2016). Gas Head Serial Number: SN1086, 21/01/2017; CC; by sp. Sonic Anemometer Head Serial Number: SN1086, 10/02/2017. OS Version CR3000.Std.28.02.
10/04/2017	**Os 4 MB do CR1000 de Barbosa dão para 34 dias** de dados com esta frequência temporal (1min) e com este número de sensores!
11/04/2017	Montagem da estação na plataforma Alqueva-Montante. **Ficou tudo a funcionar!** 2 Painéis da EDIA de 80W cada, a nossa bateria de 100 Ah e o nosso regulador de 15A porque o da EDIA (de 20A) está estragado. Na estação da Barbosa substituímos o CR850 (emprestado do projecto DNI) pelo CR1000 que comprámos através na nota de crédito da Campbell UK devido à reparação do IRGASON ter sido feita como se estivesse em garantia (embora tivesse chegado em Outubro de 2013!); substituímos também o escudo solar do termo-higrómetro por um com 10 "lamelas" em vez do de 6 que lá estava (mais apropriado para as 107); retirámos a telemetria e colocámos na plataforma, ficou a funcionar!
21/04/2017	Em CidAlmeida trocamos o modem e fizemos manutenção. Na Barbosa (**snake station**!!) tirámos dados, trocamos mastro do anemómetro sónico e fizemos a manutenção. Em Alqueva-Montante troquei de cartão de memória, ficou o de 8 GB, enviei programa novo com IEEE4 e signal strength, trocámos o mastro dos radiómetros e colocamos espias, **fizemos perfil CO2 que começou às 12:38 UTC** (valores de 1400 ppm aos 45 m!!), tirámos medidas dos painéis para calcular ângulo, **deixamos o CO2 preso ao mastro de ferro que estava nos radiómetros e fizemos a manutenção**. Quando chegámos a plataforma estava virada uns 90° para a esquerda, para oeste, ±270°.
15/05/2017	1º dia ALOP Maio (**C3**). Fomos às plataformas de Lucefecit, Mourão e às ribeiras de Lucefecit e Álamos.
16/05/2017	2º dia ALOP Maio (**C3**). Fomos à plataforma de Alqueva-Montante e às ribeiras de Amieira e Zebro. Em CidAlmeida fizemos a manutenção. Em Barbosa tirámos dados e fizemos manutenção. Em Alqueva-Montante fizemos a manutenção e verifiquei o OS do EC100 e confirma-se que é a última versão EC100.07.01 de 30/08/2016. Troquei o cartão de memória, ficou o de 4 GB. Há uma série de parâmetros que se podem alterar ligando-se via USB ao EC100 e ligado ao "Device Config Utility" do Loggernet, a explorar. **Não fizemos perfil de CO2**. A sonda estava solta do mastro de ferro onde tinha ficado presa, nós já estávamos desconfiados porque num gráfico havia um aumento súbito de concentração. A sonda estava com limos e a abraçadeira ferrugenta. Prendemo-la ao novo tubo de PVC que levei, ficou a 70 cm. **A seguir furei o barco!!!**
24/05/2017	Fomos à plataforma dos Álamos e fizemos medições de reflectância.
07/06/2017	Realizámos medições de irradiância em profundidade, disco de Secchi, medições de irradiância fora de água e de reflectância de superfície em Montante, Estrela e Monsaraz. A sonda multiparamétrica continua avariada. Fomos no carro do Gonçalo!
08/06/2017	Fomos à Barbosa tirar dados e fazer a manutenção. Em Alqueva-

	Montante troquei de cartão de memória, ficou o de 2 GB. Instalámos mais 1 painel solar nosso (85 W) e 2 baterias da geofísica (60 e 44 Ah) para recebermos o equipamento LICOR do Ivan na próxima semana. **A montagem do CO2 dentro de água estava solta porque a cola PVC e a borracha não aguentaram, o CO2 estaria a cerca de 1.5 m**. Quando chegámos a plataforma estava virada uns 90° para a esquerda, para oeste, ±270°. NOTA: não levei carro, mas disse que levei para cobrir a despesa da ficha para pressão do EC100 (23€).
13/06/2017	Fomos a Alqueva-Montante instalar o aparelho closed-path da LICOR com os colegas Finlandeses. Troquei de cartão de memória, ficou o de 8 GB. Quando estávamos a fazer um perfil de CO2 reparámos que os valores estavam excessivamente baixos e quando (em Évora) analisámos a série reparámos que de dia 11 para 12 os valores foram gradualmente caindo de 400 para 40 PPM. Quando chegámos a plataforma estava virada uns 45° para a direita, para este, ±45°. NOTA: não levei carro, mas disse que levei para cobrir a despesa de ir buscar Ivan ao aeroporto (~50€).
20/06/2017	Fomos a Alqueva-Montante melhorar o ângulo dos painéis solares que estão a ~14º para ~20º. Enviei novo programa para o IRGASON ficar a calcular logo a concentração de CO2 com a fast temperature (output 13 from the EC100 instruction using output mode 2). Troquei de USB stick dos Finlandeses (são ambas as pens de 16 GB) e trocámos de cartão de memória, ficou o de 4 GB. **Retirámos o aparelho de CO2 inwater**. Fizemos medições de reflectância na plataforma e também em Álamos. Quando chegámos a plataforma estava virada uns 15° para a esquerda, para oeste, ±345°. NOTA: não levei carro, mas disse que levei para cobrir a despesa de gasóleo da carrinha do Bento (28.13€).
04/07/2017	Realizámos medições de irradiância em profundidade, disco de Secchi, medições de irradiância fora de água, reflectância de superfície e perfis com a sonda TROLL em Montante, Estrela e Monsaraz. A sonda multiparamétrica continua avariada!? Fomos no carro do Gonçalo!
12/07/2017	Fiz medição em paralelo com o ASD e TRIOS no observatório ICT. Céu limpo.
13/07/2017	Fiz medição em paralelo com o ASD e TRIOS na piscina. Céu limpo ao início, mas nuvens altas para o meio e fim.
14/07/2017	Fomos à Barbosa tirar dados e fazer manutenção. Fomos à Cid Almeida fazer a manutenção (retirar a precipitação falsa!). Fomos a Alqueva-Montante realizar a manutenção e retirar dados, ficou o de 4 GB. Fizemos medição de reflectância espectral de superfície e perfil de irradiância com o ASD e com o TRIOS até ao fundo. Quando chegámos a plataforma estava virada uns 15° para a esquerda, para oeste, ±345°. NOTA: não levei carro, mas comprei de pilhas tamanho D para sonda TROLL e cabo laranja para radiómetros TRIOS (7.08€).
17/07/2017	1º dia ALOP de Julho (**C4**). Fomos às plataformas de Lucefecit, Mourão e Montante e às ribeiras de Lucefecit e Álamos. Fiz medição de irradância espectral com o TRIOS em mourão mas estava nublado.
18/07/2017	2º dia ALOP de Julho (**C4**). Fomos à plataforma de Alqueva-Captação e às ribeiras de Amieira (seca com apenas algumas zonas com poças) e Zebro. Deixámos o

	barco na Póvoa porque o "bendix" do motor de arranque estava a prender outra vez. O Sr. Joaquim Condeça diz que estava empenado 30 centésimos de milímetro.
19/07/2017	Fiz medição em paralelo com o ASD e TRIOS no observatório ICT. Céu nublado.
27/07/2017	Fui aos Jacintos com o Josué.
03/08/2017	O GR, JF e MY foram à Barbosa tirar dados e fazer manutenção. Não foi à Cid Almeida fazer a manutenção (estava muito calor já). Foi a Alqueva-Montante realizar a manutenção e retirar dados, ficou o de 8 GB. A plataforma estava virada para o sítio certo.
25/08/2017	Fui com a Lena a Mourão e Lucefecit deixar os tijolos afastados da plataforma. Bloom de cianobactérias em Lucefecit??? Sim!! Disco secchi de 0.40 m!!
31/08/2017	Fui com o JF a Montante, Barbosa e CidAlmeida fazer a manutenção e tiragem de dados. A plataforma estava virada para o sítio certo. Ficou o cartão de 4 GB.
08/09/2017	**Fui com o RS e GR a Montante deixar o CO2 inwater.** Caiu à água a peça de união do cabo ao aparelho!!!!! Pusemos tape vulcanizadora e deixamos essa ficha fora de água, aparelho ficou a 20 cm de profundidade. Enviei novo programa com nova constante de calibração do CO2, troquei de cartão, ficou o de 4GB. Fizemos medições de reflectância na plataforma. A plataforma estava bem posicionada.
19/09/2017	MP e GR realizaram medições de irradiância em profundidade, disco de Secchi, medições de irradiância fora de água, reflectância de superfície e recolha de água em garrafa para turbidez em Montante, Estrela e Monsaraz. Fomos no carro do Gonçalo!
26/09/2017	1º dia da saída ALOP Setembro (**C5**). Com a equipa toda. MP e RS foram de 4L para CidAlmeida fazer a manutenção e depois o JF foi-nos buscar de barco lá para irmos para a plataforma e Barbosa. Na Barbosa tiramos dados e fizemos manutenção. Em Alqueva-Montante realizamos a manutenção e retirar dados, ficou o de 8 GB. Trocámos o filtro de partículas do LICOR (2 um) e os valores voltaram ao normal. **A pen do LICOR não tinha sido limpa antes de colocar e perdemos dados: o dia 25/9 quase todo e até às 8:30 do dia 26/9!!!** A plataforma estava virada para o sítio certo. Gastei 10€ para fazer a matrícula para a carrinha do Bento.
27/09/2017	2º dia da saída de campo ALOP de Setembro (**C5**). Lucefecit e Mourão.
03/10/2017	MP e GR foram a Alqueva-Montante realizar a manutenção e retirar dados, ficou o de 4 GB. Colocámos a peça de união do cabo com o aparelho de CO2 que chegou do Canadá e fizemos um perfil. A plataforma estava virada para o sítio certo quando chegámos, mas durante os trabalhos virou-se para a direita, quando saímos deixámo-la virada para o sítio certo. Fizemos reflectância e perfil de irradiância dentro de água na plataforma e ao pé da Barbosa. Fizemos Secchi e levámos água em G4, G3, G2 e Ancoradouro. Levei a carrinha SH, fiz + ou – 200 kms. Gastei 5€ em gasolina do barco.
27/10/2017	MP, GR, JF e MY foram a Alqueva-Montante realizar a manutenção e retirar dados, ficou o de 8 GB. Desmontámos o equipamento LICOR

	porque já não há capacidade solar para alimentar a estação. Limpámos as sondas de temperatura em profundidade e colocámos um tubo PVC de 110 mm para protecção solar das mesmas (até aos 3 m e com furos de 10 em 10 cms) e fizemos um perfil de CO2 onde pela primeira vez esperámos que a concentração estabilizasse em cada nível. Fomos também realizar a manutenção e recolha de dados das estações de CidAlmeida, Barbosa. A plataforma estava virada para o sítio certo. Gastei 5.95€ no tubo PVC.
29/10/2017	Mudança para hore de Inverno às 02:00 LT passou para 01:00 LT. Agora LT == UTC.
31/10/2017	**MP, JF e SB foram à plataforma de Montante para resolução de um problema nas medições de CO2 e H2O, os valores de calibração do zero estavam erradas, ficou o de 4 GB**. A plataforma estava virada para o sítio certo quando chegámos, mas durante os trabalhos virou-se para a direita, quando saímos deixámo-la virada para o sítio certo.
10/11/2017	MP e GR foram com o Válter e equipa da EDIA aos jacintos e nenúfares no troço do "meio". Depois de almoço fomos ao Guadiana em Badajoz à margem do clube de canoagem fotografar e medir reflectâncias in situ de nenúfares. Fui na minha carrinha SH e fiz aproximadamente 225 kms.
13/11/2017	MP e GR realizaram medições de irradiância em profundidade, disco de Secchi, medições de irradiância fora de água, reflectância de superfície e recolha de água em garrafa para turbidez em Montante, Estrela e Mourão. Depois fomos ao Guadiana em Badajoz perto da última saída da autoestrada fotografar e medir reflectâncias in situ de jacintos. Fomos no carro do Gonçalo!
16/11/2017	MP e SB foram à mitra experimentar o router do Eng. Godinho naquela estação.
20/11/2017	1º dia da saída ALOP Novembro (**C6**). Com a equipa toda. MP, SB, GR, MY, JF e 4 meninas foram a montante. Fizemos limpeza e recolha de dados das estações Barbosa, Cid Almeida e Montante. Instalámos o router do Eng. Godinho na plataforma (ficou a funcionar bem embora com pouco sinal) e trocámos o CFM100 pelo NL116 da Mitra porque tem porta ethernet (ficou a funcionar). Fui na minha carrinha SH para a Cid Almeida.
22/11/2017	2º dia da saída ALOP Novembro (**C6**). JF e 3 meninas que foram a Lucefecit e Mourão.
24/11/2017	Samuel desligou o GSM de Montante. E vai criar um mecanismo de transmissão e backup de dados através do computador ESTACOES2.
06/12/2017	MP, SB e JF fomos à plataforma de Alqueva-Montante, para realização de manutenção e recolha de dados, alteração no router e no programa e recolha do aparelho de medição de CO2 inwater para calibração (0-4000 PPM). Foi também realizada a manutenção e recolha de dados nas estações de Cid Almeida e Barbosa.
14/12/2017	Foi a equipa toda (menos AP) a Beja ao jantar de Natal ALOP.
21/12/2017	MP e GR realizaram medições de irradiância em profundidade, disco de Secchi, medições de irradiância fora de água, reflectância de superfície e recolha de água em garrafa para turbidez em Montante,

	Estrela e Monsaraz. Fomos na carrinha SH.
04/01/2018	MP e GR foram retirar dados a Montante, CidAlmeida e Barbosa. Fomos de carro e no barco da EDIA.
08/01/2018	Alterei a recolha de dados de CidAlmeida para apenas 1 vez por dia às 12:10 para ser na altura com maior voltagem de bateria. Para tentar reduzir a fatura das comunicações.
26/01/2018	Fui aos Jacintos com o Josué ou Gonçalo.
29/01/2018	1º dia da saída ALOP Janeiro (**C7**). Com a equipa toda. MP, GR, RS, 3 meninas de laboratório e o Eduardo e a Célia, 3 meninas de Beja foram a Montante e Álamos. Fizemos limpeza e recolha de dados das estações Barbosa, Cid Almeida e Montante. Fui na minha carrinha SH para a Cid Almeida. Fomos com carro e barco da ARH com o Rui Ramos.
30/01/2018	2º dia da saída ALOP Janeiro (**C7**). Com MP, MY 3 meninas de laboratório e o Eduardo e a Ana, 3 meninas de Beja que foram a Lucefecit e Mourão.
23/02/2018	MP, JF e GR foram retirar dados a Montante, CidAlmeida e Barbosa. Fomos na carrinha do Laboratório da Água e no barco do AlquevaTours. Voltámos a instalar o CO2 que não chegou a ir a calibrar (0-4000PPM) e os valores já tinham baixado! Ou seja perdemos o momento que as concentrações voltaram a descer. Fizemos disco de secchi e coeficiente de extinção em montante, estrela e Mourão. Fomos a Mourão à tarde deixar os tijolos da Lena.
13/03/2018	MP, JF e GR foram retirar dados a Montante, CidAlmeida e Barbosa. **Uma das amarras estava rasgada, deixamos a plataforma presa apenas com 2 amarras em lados opostos. Ficou o Irgason virado a Sul**. Fomos no meu carro e no barco do AlquevaTours.
27/03/2018	MP e GR realizaram medições de irradiância em profundidade, disco de Secchi, medições de irradiância fora de água, reflectância de superfície e recolha de água em garrafa para turbidez em Montante, Estrela e Monsaraz. Fomos na carrinha RX.
09/04/2018	1º dia da saída ALOP Abril (**C8**). (era para ser em Março mas passou para inicio de por indisponibilidade de alguns membros da equipa) Com a equipa toda. Montante e Álamos. MP, GR, 3 meninas de laboratório e o Eduardo, Sofia e Patrícia de Beja foram a Montante e Álamos. Fizemos limpeza e recolha de dados das estações Barbosa, Cid Almeida e Montante. Fomos na carrinha do laboratório. Fomos com carro e barco da ARH com o Rui Ramos.
16/04/2018	2º dia da saída ALOP Abril (**C8**). (era para ser em Março mas passou para inicio de por indisponibilidade de alguns membros da equipa) Com a equipa toda. Lucefecit e Mourão. MP, MY, 3 meninas de laboratório, Sofia e Ana Filipa de Beja foram a Lucefecit e Mourão. Fomos na carrinha do laboratório. Fomos com carro e barco da ARH com o Rui Ramos.
04/05/2018	SB, JF e GR foram retirar dados a Montante, CidAlmeida e Barbosa. Os tijolos da Lena foram colocados. O Samuel instalou o UVB30 e tentou reparar o que lá estava sem sucesso e tentou pôr a funcionar o

	RV50 sem sucesso também. Funcionava no portátil mas não no CR3000. Pode ser um problema na NL116 ou outra coisa. Foram na carrinha do Lab. Água e no barco da EDIA. Eu vou dizer que fui para cobrir a despesa que tive com o relay para o heater do UV (21.6€).
30/05/2018	MP, SB, JF e GR foram a montante com o barco do lab.da Água que foi reparado mas continua a meter água, o Sr. Condeça diz que o PVC do barco não permite uma boa colagem. **Foi também o Sr. Humberto e o Hélder colocar a poita e amarração**. Nós retirámos o tubo da APA com cerca de 20 metros que continha as sondas de temperatura, e que tinha as 2 amarrações e o nosso cabo+sondas bastante enroladas. Retirámos o Irgason para calibração. O Samuel conseguiu colocar o router RV50 a funcionar na plataforma.
04/06/2018	1º dia da saída ALOP Junho (**C9**). Lucefecit e Mourão. Com a equipa toda. JF, GR, 2 meninas de laboratório+EM, Sofia e Ana Filipa de Beja (?). Fomos no barco do Lab. da Água.
05/06/2018	2º dia da saída ALOP Junho (**C9**). Montante e Álamos. MP, MY, 2 meninas de laboratório+EM, Sofia e Patrícia de Beja. Colocámos o Irgason de volta. Fizemos perfil de CO2. Fomos no barco do Lab. da Água.
15/06/2018	MP e GR realizaram medições de irradiância em profundidade, disco de Secchi, medições de irradiância fora de água, reflectância de superfície e recolha de água em garrafa para turbidez em Luz, Estrela e Monsaraz. Fomos no carro do Gonçalo.
18/06/2018 a 21/06/2018	Equipa toda ALOP organizou a 2ª Summer School. Levei a carrinha SH. Usámos o barco da APA com o Rui Ramos. No dia 20/06 realizamos um perfil de CO2 (não sei do registo de horas!! Mas fui eu que o fiz!!!)
03/07/2018	MP e GR foram a montante com o barco do lab. da Água que foi reparado novamente, agora está bom. Fizemos perfil com a sonda **multiparamétrica** e depois deixamo-la **instalada na plataforma**. Fizemos a manutenção e recolha de dados da Barbosa e de Montante. Levámos a carrinha SH.
24/07/2018	1º dia da saída ALOP Julho (**C10**). Montante e Álamos. JF, GR, MY, 2 meninas de laboratório, Sofia e Filipa de Beja. **Retiramos o CO2.** Fomos no barco do Lab. da Água.
25/07/2018	2º dia da saída ALOP Julho (**C10**). Barco avariou o cabo Mourão. JF, GR, 2 meninas de laboratório, Sofia e Ana Filipa de Beja. Fomos no barco do Lab. da Água.
30/07/2018	MP, GR e AP fomos a Montante e estações de terra. Verificação da sonda multiparamétrica. barco do lab. da Água.
04/08/2018	MP, AP, LN, MM e EM fomos a Lucefecit acabar o trabalho da campanha de Julho. **Dia mais quente do Ano**. barco do lab. da Água

09/08/2018	MP e SA (sérgio aranha) fomos a Álamos colocar os tijolos da Lena e a Montante, Cid Almeida e Barbosa tirar dados e fazer a manutenção. Colocámos o CO2 outra vez. Levei a carrinha SH. barco do lab. da Água.
06/09/2018	MP, GR e AP fomos a Montante fazer a verificação da multiparamétrica e quickcall do pH, conductividade, ORP, turbidez. Fizemos manutenção e recolha de dados de Montante, Cid Almeida e Barbosa. Retiramos o CO2 que estava outra vez a dar valores muito elevados. Fomos na carrinha e barco do Lab. Água.
24/09/2018	1º dia da saída ALOP Setembro (**C11**). Montante e Álamos. JF, GR, RS, Ana Costa, 2 meninas de laboratório, Sofia e Filipa de Beja. **Retiramos a multiparamétrica porque a de Beja avariou**. Alteramos a posição dos painéis solares e a inclinação. Fomos no barco do Lab. da Água. Levei a SH.
25/09/2018	2º dia da saída ALOP Setembro (**C11**). Lucefecit e Mourão. JF, MY, Célia Antunes, 2 meninas de laboratório, Sofia e Ana Filipa de Beja. Fomos no barco do Lab. da Água.
01/10/2018	MP e GR foram a Montante **instalar a multiparamétrica**, CO2, inclinar os painéis solares e **retirar o IRGASON. Levámos o barco do Nixon pela primeira vez**, **oferta esta viagem**. Levei a RX.
05/10/2018	MP e Fred foram a Montante buscar o EC100 que me esqueci no dia 1. Levei a RX. Fomos na RX. **Levámos o barco do Nixon, era para ser a primeira viagem a pagar mas como ele não tem a vistoria e seguro feitos e por isso não vai cobrar até ter.**
12/10/2018	MP, SB, PC e ES foram a Montante montar uma bateria extra de 80 Ah e os 2 IRGASON's. **Início da Campanha de Intercomparação.** Levámos o barco do Nixon. Fomos na carrinha do Lab. Água.
19/10/2018	MP, JF, ES e Carolina foram a Montante, Barbosa e CidAlmeida fazer manutenção e recolha de dados. Adicionámos outra bateria de 80 Ah. Levámos o barco do Nixon. Fomos na RX.
25/10/2018	MP, JF, ES e Sara Pereira foram a Montante fazer manutenção e recolha de dados. Retirámos o Irgason da Elena – **Fim da Campanha de Intercomparação**. Levámos o barco do Nixon. Fomos na carrinha do Lab. Água mas disse que fui na minha por causa da pilha do PC do ASD (pôr 30€).
19/11/2018	1º dia da saída ALOP Novembro (**C12**). Montante e Álamos. MP, JF, GR, RS, CP, Ana Costa, 2 meninas de laboratório, Sofia e Filipa de Beja. **Retiramos a multiparamétrica porque a de Beja continua avariada**. Fomos no barco da APA e na carrinha do Laboratório. Levei a SH também.
20/11/2018	2º dia da saída ALOP Setembro (**C12**). Lucefécit e Mourão. A plataforma de Mourão não foi feita porque havia muito vento. JF, MY, GR, 2 meninas de laboratório, Sofia e Ana Filipa de Beja.

	Fomos no barco da APA e na carrinha do Laboratório.
11/12/2018	Foi feita a plataforma de Mourão (**C12**). Não havia draga.
14/12/2018	MP, GR e CP foram a Montante, CidAlmeida e Barbosa. **Não instalámos a sonda porque não encontramos o tubo protector**, a plataforma estava com 1 amarração partida e fixámos uma amarração de cada lado, ficou com os painéis para Este. Trocámos o Albedómetro de Cid porque o antigo estava a dar erros no Downwelling. Fomos no barco do Humberto. Levei a minha carrinha.
21/12/2018	MP e GR foram colocar a poita nova. **Instalámos também a sonda multiparamétrica**. Tirámos as sondas de temperatura para limpeza, quando voltámos a colocar na água reparámos que a T11 (20m) estava a dar mais um grau do que as outras todas (deve estar avariada). A plataforma ficou firme para o sítio certo. Levei a minha carrinha e fomos de boleia no barco do Humberto.
10/01/2019	MP e GR realizaram medições de irradiância em profundidade, disco de Secchi, medições de irradiância fora de água, reflectância de superfície e recolha de água em garrafa para turbidez em Monsaraz, Estrela e Montante. Fomos no carro do Gonçalo.
15/01/2019	MP, GR, SB e JF foram a Montante, CidAlmeida e Barbosa no barco do Humberto e na carrinha do laboratório. **Trocámos os ThermoHigrometro e ventos e loggers das 2 estações de terra**; **montámos o visibilímetro e a tina de evaporação em CidAlmeida**; montámos uma sonda de temperatura "nova" e em paralelo aos 20 metros (T11).
06/02/2019	MP, GR, SB, CP e JF foram a Montante, CidAlmeida e Barbosa no barco do Humberto e na carrinha do laboratório. Instalámos a telemetria de Portel em Barbosa. Trocámos os dataloggers das 2 estações de terra (CidAlmeida cr1000 por cr1000x e barbosa cr10 por cr10x); calibrámos o visibilímetro e a tina de evaporação em CidAlmeida; tentamos fazer perfil em montante, mas por falha de comunicação do PC com a sonda ficámos pelos 30 metros aproximadamente; retirei medições de temperatura da sonda por cerca de ¾ minutos aos 6 e aos 20 metros para comparar com as sondas 107. Vou dizer que levei carro para cobrir a despesa da antena Konig (45€).
11/02/2019	MP, SB e JF fomos à Barbosa resolver o problema da alimentação, era o cabo da bateria para o regulador que estava solto, foi soldado e trocámos a bateria. Fomos a CidAlmeida onde o Josué cortou a piorneira e limpou o zambujeiro. No dia 7/2 tentámos enviar um programa via GSM e bloqueámos a estação, tivemos que reiniciar o logger. **Ficou a funcionar**. Fomos na minha carrinha.
21/02/2019	Fomos à mitra (terceira vez nos últimos 7 dias) retirar o albedómetro e pirradiómetro que estavam em calibração para irem para Cabo Verde. Fomos à CidAlmeida resolver o problema do visibilímetro: fizemos o ground e retirámos o ThermoHigrometro do CS125 para garantir que há sempre T e RH. Enterrámos o cabo do painel e fixámos o painel com um varão roscado. Enchemos a tina até aos 20.1cm aproximadamente. Reparámos que um dos cabos do regulador estava apertado na manga e não no cabo o que poderá justificar os problemas na bateria. **Alterámos o multiplier do albedómetro que estava errado desde 15/01/2019.** Fomos na minha carrinha.

01/03/2019	MP, GR e CP foram a barbosa, cid e montante. Desliguei os dew heaters do visibilímetro. Fizemos perfil em montante em duas vezes. **Disco de Secchi de 7 metros** em Montante e no Ancoradouro!! Fomos no barco do Humberto e na minha carrinha.
29/03/2019	MP e CP foram a barbosa, cid e montante. Fomos no barco do Humberto e no meu carro. **Primeira viagem a pagar**!! **Tivemos 9 viagens à borla à conta da vistoria e seguro do barco!!** Liguei os heaters do CS125 e alterei o formato de output para incluir o código METAR e também o mínimo de bateria.
03/04/2019	MP e SB foram a CidAlmeida alterar a alimentação 12v do CS125 (visibilímetro). Ficou com alimentação à parte 50Wp+18Ah. O dataloggers e restantes equipamentos ficaram com 15Wp+12Ah. Fomos na minha carrinha.
16/04/2019	MP, CP e GR foram às 3 estações no barco do Humberto e no carro do Gonçalo. Retirámos a sonda multiparamétrica porque ficou bloqueada durante o perfil aos 30 m. Voltámos a colocar todos os equipamentos de Cid com a alimentação original para ver se aguenta, com um barramento do Samuel. Enchemos a tina.
03/05/2019	MP e AP foram a montante à entrevista RTP. Fomos no meu carro e no barco do Nixon. Tirámos o IRGASON para verificação de gases.
07/05/2019	MP e CP foram a Barbosa, Montante e Cid. Colocámos de volta o IRGASON e retirámos o painel e bateria extra de Cid. Fomos no meu carro e no barco do Nixon. Enchemos a tina.
21/05/2019	MP e GR fomos a Barbosa, CidAlmeida e Montante no barco do Humberto. Foram também a Maria Ilhéu e outra Professora de Pintura com 10 alunos para aula de Limnologia. Fomos no carro do Gonçalo. Enchemos a tina.
31/05/2019	Enchemos a tina? Gonçalo?
13/06/2019	MP, GR e CP foram a Barbosa, CidAlmeida e Montante no barco do Humberto. Fizemos perfil e quando a sonda estava no fundo perdeu o contacto e ficou a reiniciar-se como antigamente. Quando ligamos ao logger começou a trabalhar bem mas não dava O2 nem Turb. Decidimos deixar estar porque ela uns meses antes recuperou sozinha. Fomos no carro do Gonçalo. Enchemos a tina.
05/07/2019	MP e GR foram a Barbosa, CidAlmeida e Montante no barco do Humberto. Retirámos a sonda e enviámos para a Vórtice que vai enviar para fábrica nos USA para reparar sob garantia. Começámos a colocar o BioKill (Kill-Bill) a partir deste dia. Fomos na carrinha Defender da Ecologia para acertar contas do dia 21/5. Enchemos a tina.
23/07/2019	GR foi a CidAlmeida encher a tina.
29/07/2019	MP, JF, GR e CP foram a Barbosa, CidAlmeida e Montante no barco do Humberto. Fomos no meu carro. Enchemos a tina.
16/08/2019	GR foi a Cidalmeida encher a tina e explicar ao sr. Como se faz.
30/08/2019	MP, SB, GR e CP foram a Barbosa, CidAlmeida e Montante no barco do Humberto (**9/15 viagens**). Instalamos o array novo de temperaturas (CS225). Fomos no meu carro. Enchemos a tina.
18/09/2019	Enchemos a tina. GR?
03/10/2019	MP e JF foram a Montante no barco do Humberto (**10/15 viagens**). Desinstalamos o array antigo de temperaturas (107) e o Irgason para calibração. Fomos na minha carrinha.

08/10/2019	MP, MJ, JF, GR e CP foram a Barbosa, CidAlmeida e Montante no barco do Humberto (**11/15 viagens**). Instalamos de novo o Irgason e sonda multiparamétrica Troll600. Fomos no meu carro. Enchemos a tina.
17/10/2019	MP e GR foram a Oeiras a uma reunião com o António Ramos da Aquagri.
18/10/2019	MP e JFontiela foram a CidAlmeida e Montante no barco do Humberto (**12/15 viagens**). Colocámos as lonas, a caixa azul, fizemos o zero wind offset (não funcionou-muito vento) e ligámos a Troll600 ao relay. Fomos no meu carro.
14/11/2019	MP, SB, GR foram ao edifício do CIMAC na zona industrial ver se era possível retirar a estação meteorológica. Não foi possível porque está num terraço a 8 metros. Fomos na carrinha Nissan 08-10-OL.
15/11/2019	MP, SB, JF, GR foram a CidAlmeida instalar o router com o cartão 3G novo. Não foi possível ir a Montante nem barbosa devido ao vento forte e ondulação. Fomos na carrinha Nissan 08-10-OL. Enchemos a tina.
18/11/2019	MP, SB, JF, GR foram a Barbosa, CidAlmeida e Montante no barco do Humberto (**13/15 viagens**). Em Montante colocámos o novo router com cartão 3G a funcionar com elevação solar > 25º através de um relay; retirámos a sonda Troll600. Em CidAlmeida colocámos a alimentação do router na porta SW12_1 para funcionar com elevação solar > 25º. Fomos na carrinha Nissan 08-10-OL.
17/12/2019	MP, CP, JF, GR foram a Barbosa, CidAlmeida e Montante no barco do Humberto (**14/15 viagens**). Em Montante retirámos a alimentação dos UV's porque a estação está com problemas de alimentação (valores a ir aos 12V de madrugada) e inclinámos os painéis solares para 55º. Em CidAlmeida desligámos o visibilímetro porque a estação esteve com problemas de alimentação e esteve desligado de dia 15 a 17. Em Barbosa não conseguimos retirar os dados do módulo de armazenamento (4MB) e por isso retiramo-lo e fazemos isso em laboratório. Conseguimos apenas tirar os dados do CR10X, cerca de 2 dias em meio. Fomos na carrinha Nissan 08-10-OL.
18/12/2019	MP e SB tiraram os dados do módulo 4MB em laboratório. Dá para cerca de 71 dias.
19/12/2019	MP e JF foram a Barbosa instalar o módulo 4 MB. Fomos a CidAlmeida instalar novamente alimentação secundária: 15Wp+12Ah para o datalogger e 50Wp+18Ah para o visibilímetro e os restantes equipamentos. Fomos na carrinha Nissan 08-10-OL.

2.3 Observações em altitude

No âmbito do projecto ALOP foi realizada uma campanha intensiva enquadrada na Escola de Verão: "2nd Alqueva Summer School on Atmospheric and Inland Water Sciences"

Data	Hora de	Variáveis	Altitude máxima

		Altitude, pressão atmosférica, temperatura do ar, Humidade, velocidade do vento	

3.4 Observatório de Física da Atmosfera do ICT

O Observatório de Física da Atmosfera do ICT encontra-se totalmente equipada, sendo único em Portugal e um dos poucos no Sul da Europa, oferecendo a possibilidade de manter e alargar as observações atmosféricas e interface água / atmosfera na região e, especificamente, para a área do Alqueva. As observações disponíveis incluem, entre outras: a radiação solar e atmosférica em várias regiões espectrais, qualidade do ar, variáveis meteorológicas, fluxos turbulentos, concentração, distribuição de tamanho e tipo de aerossóis e as concentrações de gases; cobertura de nuvens; vários sistemas de detecção remota estão disponíveis (Lidar, ceilometer, radiómetro de microondas (perfis atmosféricos), espectrofotómetros e espectrorradiómetros), bem como medidor de campo eléctrico e contadores de iões no ar.

Foram asseguradas durante este segundo ano de projecto as medições efectuadas neste observatório e que dão suporte aos estudos levados a cabo no âmbito do projecto ALOP.

Fig. – Observatório de Física da Atmosfera do ICT situado na Universidade de Évora, Colégio Luís A. Verney em Évora.

3.5 Detecção remota a partir de satélite

3.6. Avaliação dos parâmetros físico-químicos, biológicos, perfis em profundidade e das concentrações de pesticidas e metais potencialmente tóxicos na água e sedimentos

As amostragens (colheita de água e sedimentos) foram realizadas em 4 locais da albufeira de Alqueva: Lucefecit (Lf), Álamos-Captação (Al), Alqueva-Montante (Mn) e Alqueva-Mourão (Mr); e 4 Afluentes à Barragem: Ribeira da Amieira; Ribeira do Zebro; Ribeira dos Álamos; Ribeira de Lucefécit.

O programa de avaliação decorreu no período de Janeiro de 2017 a Dezembro de 2018. A amostragem apresenta uma periodicidade bimestral, contabilizando no total 12 campanhas. No entanto, a amostragem de fitobentos – diatomáceas teve início na campanha de Maio (C3),. Os meses de recolha das amostras são Janeiro (Jn), Março (Mr), Maio (M), Julho (Jl), Setembro (St), Novembro (Nv). O período húmido integra os meses de Outubro a Março, e o período seco de Abril a Setembro.

Em cada local de amostragem, antes de se proceder às medições e às colheitas de água, sedimentos e diatomáceas, foram registadas as informações relativas ao local de amostragem, às condições atmosféricas durante a amostragem e as condições da água e do troço amostrado (nas ribeiras afluentes) (ficha de campo).

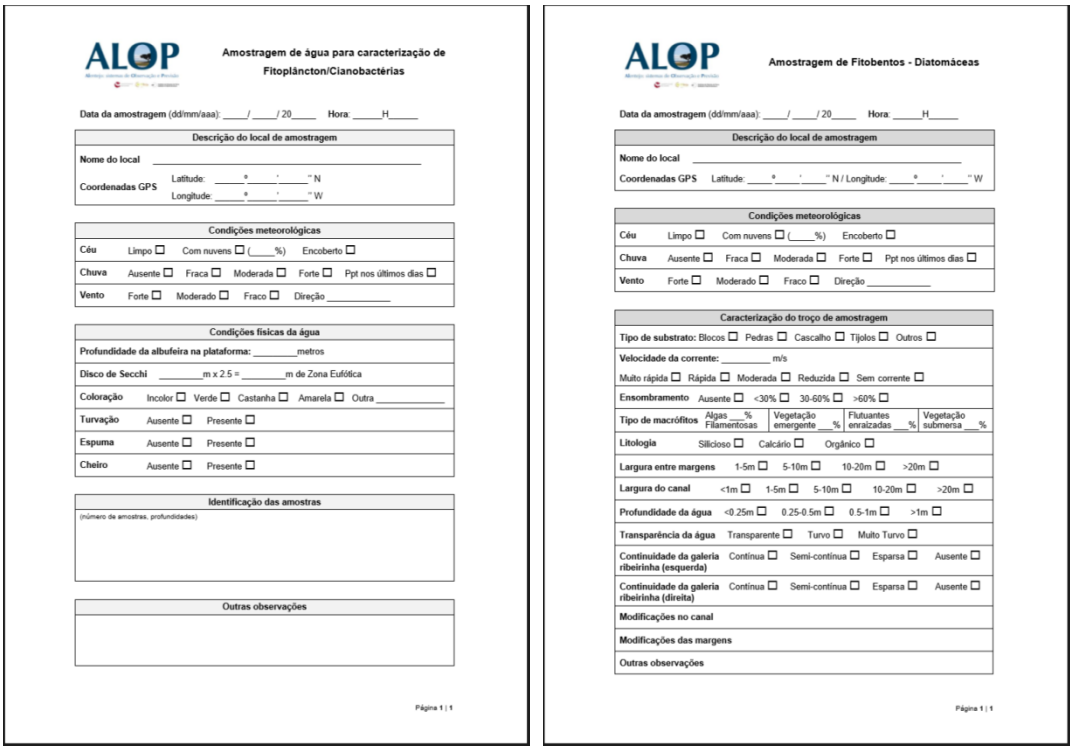

ALOP

Amostragem de água para caracterização de Fitoplâncton/Cianobactérias

Data da amostragem (dd/mm/aaa): ____/____/20____ **Hora:** _____H_____

Descrição do local de amostragem	
Nome do local	_____
Coordenadas GPS	Latitude: _____°_____'_____" N Longitude: _____°_____'_____" W

Condições meteorológicas					
Céu	Limpo ☐	Com nuvens ☐ (____%)	Encoberto ☐		
Chuva	Ausente ☐	Fraca ☐	Moderada ☐	Forte ☐	Ppt nos últimos dias ☐
Vento	Forte ☐	Moderado ☐	Fraco ☐	Direção _____	

Condições físicas da água	
Profundidade da albufeira na plataforma: _____metros	
Disco de Secchi	_____m x 2.5 = _____m de Zona Eufótica
Coloração	Incolor ☐ Verde ☐ Castanha ☐ Amarela ☐ Outra _____
Turvação	Ausente ☐ Presente ☐
Espuma	Ausente ☐ Presente ☐
Cheiro	Ausente ☐ Presente ☐

Identificação das amostras
(número de amostras, profundidades)

Outras observações

Página 1 | 1

ALOP

Amostragem de Fitobentos - Diatomáceas

Data da amostragem (dd/mm/aaa): ____/____/20____ **Hora:** _____H_____

Descrição do local de amostragem	
Nome do local	_____
Coordenadas GPS	Latitude: ____°____'____" N / Longitude: ____°____'____" W

Condições meteorológicas					
Céu	Limpo ☐	Com nuvens ☐ (____%)	Encoberto ☐		
Chuva	Ausente ☐	Fraca ☐	Moderada ☐	Forte ☐	Ppt nos últimos dias ☐
Vento	Forte ☐	Moderado ☐	Fraco ☐	Direção _____	

Caracterização do troço de amostragem				
Tipo de substrato: Blocos ☐ Pedras ☐ Cascalho ☐ Tijolos ☐ Outros ☐				
Velocidade da corrente: _____ m/s Muito rápida ☐ Rápida ☐ Moderada ☐ Reduzida ☐ Sem corrente ☐				
Ensombramento Ausente ☐ <30% ☐ 30-60% ☐ >60% ☐				
Tipo de macrófitos	Algas ___% Filamentosas	Vegetação emergente ___%	Flutuantes enraizadas ___%	Vegetação submersa ___%
Litologia	Siliciosa ☐	Calcário ☐	Orgânico ☐	
Largura entre margens	1-5m ☐	5-10m ☐	10-20m ☐	>20m ☐
Largura do canal	<1m ☐	1-5m ☐	5-10m ☐	10-20m ☐ >20m ☐
Profundidade da água	<0.25m ☐	0.25-0.5m ☐	0.5-1m ☐	>1m ☐
Transparência da água	Transparente ☐	Turvo ☐	Muito Turvo ☐	
Continuidade da galeria ribeirinha (esquerda)	Contínua ☐	Semi-contínua ☐	Esparsa ☐	Ausente ☐
Continuidade da galeria ribeirinha (direita)	Contínua ☐	Semi-contínua ☐	Esparsa ☐	Ausente ☐
Modificações no canal				
Modificações das margens				
Outras observações				

Página 1 | 1

Figura 1. *Modelo das fichas de campo para amostragem de água para caracterização de Fitoplâncton/Cianobactérias*

No local foram realizados: (i) perfis de medições dos parâmetros oxigénio dissolvido; temperatura; pH e condutividade, recorrendo a uma sonda multiparamétrica (WTW930-pH/FDO®/COND, ou TROLL 9500); e (ii) profundidade do disco de Secchi para o cálculo da profundidade da zona eufótica. Em cada estação de amostragem foram recolhidas: (i) amostras pontuais a 50 cm de profundidade: 3 L de água para a realização das análises físico-químicas; 250 mL em garrafas de cor âmbar para a análise dos pesticidas; 15 L de água para os ensaios ecotoxicológicos; (ii) amostras de água, recorrendo a uma garrafa de Van Dorn, a diferentes profundidades – superfície, 1m, 2m, 3m, meio da zona eufótica, fim da zona eufótica, meio da albufeira e fundo da albufeira, para avaliação do fitoplâncton e respetiva caracterização molecular. Para cada profundidade foi recolhida 1L de água. A amostragem da água foi efetuada segundo o "Manual para a Avaliação da Qualidade Biológica da Água em Lagos e Albufeiras, de acordo com a Diretiva Quadro da Água - Protocolo de amostragem e análise para o Fitoplâncton."; INAG, 2002); (iii) foram também recolhidas 1L de água à superfície, meio e fundo da albufeira para avaliação dos parâmetros físico-químicos da água segundo a legislação em vigor (INAG, 2009 e Decreto-Lei 236/1998 de 1 de Agosto); (iv) 1,5 L sedimento superficiais; e (v) diatomáceas amostradas nos substratos artificiais e nas ribeiras. As amostras foram acondicionadas em malas térmicas com temperaturas entre 0 e 4ºC até à chegada ao laboratório.

Os parâmetros físico-químicos foram realizados de acordo com os protocolos descritos no Standard Methods for the Examination of Water and Wastewater (APHA, 22nd Ed, 2012).

Os parâmetros analíticos, determinados na coluna de água, as metodologias utilizadas e respectivas unidades, foram os seguintes: Carência Química de Oxigénio (Método do dicromato de potássio; mg O_2/l); Carência Bioquímica de Oxigénio (Método manométrico; mg O_2 L^{-1}); Cloretos (Cromatografia Iónica; mg Cl^- L-^{1}); Nitritos (Cromatografia Iónica; mg NO_2^- L^{-1}); Nitratos (Cromatografia Iónica; mg NO_3^- L^{-1}); Azoto Kjeldahl (Método do Kjeldahl; mg N L-1); Azoto Amoniacal (Cromatografia Iónica; mg NH4 L-1); Fósforo total (Espectrometria de absorção no visível; mg P L^{-1}).

Nos sedimentos foram determinados os parâmetros: pH e condutividade eléctrica da fase intersticial (sonda de pH e condutividade); matéria seca (método gravimétrico)); % (g amostra/ 100 g amostra)); matéria orgânica (método da calcinação; % (peso seco)); Azoto Kjeldahl (Método do Kjeldahl; % N (g N/ 100g amostra)); Fósforo total (Espectrometria de absorção molecular; % P (g P/ 100g amostra)).

A amostragem das diatomáceas nos substratos artificiais consistiu na raspagem (com escova de dentes) do biofilme aderido às 3 peças de cerâmica a cada profundidade, lavagem com água destilada (ca. 100mL de amostra por local), e conservação com solução de formaldeído (4% v/v). Nas ribeiras, a amostragem das diatomáceas seguiu o protocolo nacional (INAG, 2008), que consiste na colheita de pelo menos 5 pedras, em zona de corrente e bem iluminada (sempre que possível), que são raspadas com escova de dentes, lavadas e conservadas com solução de formaldeído (4% v/v). Em laboratório, todas as amostras são oxidadas para remoção da matéria

orgânica, com peróxido de hidrogénio (35%) e ácido clorídrico (37%) e as preparações definitivas são montadas com Naphrax. Posteriormente, as diatomáceas presentes na amostra são identificadas (a nível específico ou sub-específico) e quantificadas em microscopia óptica, para determinação das abundâncias relativas de cada taxon.

Caracterização dos parâmetros de suporte na coluna de água e nos sedimentos

O objectivo desta sub-tarefa é avaliar a dinâmica dos parâmetros físico-químicos mais relevantes que suportam os elementos de qualidade biológica e química na água, a fim de caracterizar a sua variabilidade. De acordo com o documento de classificação das massas de água superficiais (INAG, 2009), os elementos físico-químicos de suporte aos elementos biológicos integram a avaliação das condições gerais dos cursos de água, através dos quais se avaliam as condições de oxigenação, o estado de acidificação e as condições relativas a nutrientes de uma massa de água.

Mapa e características das estações meteorológicas existentes na Região Alentejo

4. Organização de eventos de formação avançada e de divulgação

4.1 Cursos de Verão

Short Summer School on Atmospheric Physics, Universidade de Évora, Évora, 4 a 6 de julho de 2016.

Contou com lições dos seguintes investigadores: Joan Cuxart (JC) João Teixeira (JT), Juan Luis Rascado (JLR), Maria João Costa MJC), Rui Salgado (RS), Véronique Ducrocq (VD). O calendário foi o seguinte:

	Monday, July 4	Tuesday, July 5	Wednesday, July 6
09:00 – 11:00 11:20 – 13:20	Aerosol profiling and the Atmospheric Boundary Layer JLR	Turbulence, Clouds and Climate JT	Heavy Precipitation in Mediterranean VD
LUNCH			
14:30 – 16:00	Atmospheric Remote sensing MJC	Surface-Atmosphere Interactions RS	Impact of surface heterogeneities in the Atmospheric Boundary-Layer JC
16:00 – 17:00	Field Campaign	Field Campaign	Public Seminar: O Aquecimento Global e a Previsão de Clima JT
18:00			Field trip
20:00			Social Dinner

Mais informações em: http://www.alop.ict.uevora.pt/summerschool

No âmbito deste curso foi organizado um seminário publico com o apoio da Câmara Municipal de Évora que teve como orador João Teixeira, investigador da NASA, e que teve divulgação própria:

SEMINÁRIO
O AQUECIMENTO GLOBAL
E A PREVISÃO DE CLIMA
6 JULHO 2016 . 16h00 . Palácio D. Manuel, Évora
JOÃO TEIXEIRA
Investigador do Jet Propulsion Laboratory (JPL) / NASA
UNIVERSIDADE DE ÉVORA
ESCOLA DE CIÊNCIAS E TECNOLOGIA
ICT
Instituto de Ciências da Terra
Institute of Earth Sciences
CÂMARA MUNICIPAL
DE ÉVORA
ORGANIZAÇÃO
Projeto ALOP (ALENTEJO 2020, referência: ALT20-03-0145-FEDER-000004)
Comissão de Curso do 3.º ciclo em Ciências da Terra e do Espaço, Universidade de Évora
Comissão de Curso do 2.º ciclo em Ciências e Tecnologias da Terra, da Atmosfera e do Espaço, Universidade de Évora
Cofinanciado por:
ALENTEJO 2020
PORTUGAL 2020

2nd Alqueva Summer School on Atmospheric and Inland Water Sciences , Alqueva, 19 – 21 June 2018

Figura 2: cartaz da escola de Verão de Alqueva

Esta Escola de Verão cobriu um conjunto de tópicos avançados em ciências da atmosfera e da água, foi dirigido a jovens cientistas e estudantes de pós graduação em Ciências da Terra e do Ambiente, Física, Química, Biologia ou em Engenharias interessados em aprofundar os seus conhecimentos nos domínios das interacções entre a atmosfera e e as albufeiras, o clima e os recursos hídricos. A escola incluiu 3 dias de cursos intensivos, com professores de vários países e a participação em

atividades de uma campanha de observações meteorológicas e de qualidade da água. Contou com o apoio dos programas doutorais da Universidade de Évora e de Lisboa, do Instituto de Ciências da Terra e do Instituto Dom Luís, da Universidade de Évora e do Instituto Politécnico de Beja e da União de Freguesias de Alqueva e Amiera.
Não foi cobrada nenhuma taxa pela matrícula e frequência do curso. As aulas decorreram no Centro Cultural de Alqueva, na aldeia de Alqueva. Os estudantes ficaram alojados no Alqueva Hostel.

Participaram 24 estudantes, cuja lista se encontra na tabela

Name	Institution	
Gonçalo Rodrigues	Universidade de Évora	PhD Student
Giulia Sent	Universidade de Lisboa	Master Student
Masud Rana Rashel	University of Evora	PhD Student
Ana Caldeirinha	Instituto Dom Luiz / FCUL	PhD Student
Virgílio Bento	Instituto Dom Luiz / FCUL	PhD Student
Stevens David	Instituto Dom Luiz / FCUL	PhD Student
Daniela Lima	IDL / FCUL	PhD Student
Manuel Nascimento	FCUL/IDL	PhD Student
João António Martins Careto	Instituto Dom Luiz	Other
Marianne Moraes	Faculdade de Ciências e Tecnologia	Master Student
amandine pastor	ce3c, universidade de lisboa	Postdoc Researcher
Carolina Purificação	Universidade de Évora	Master Student
Inês de Castro da Silva Oliveira	Centro de Ciências do Mar e do Ambiente	Master Student
Inês Cristina Violante Mavioso	Lab. da Água Universidade de Évora	Master Student
Ana Filipa Costa Duarte Lima	Escola Superior Agrária de Beja	Researcher or teacher
João Pedro Andrade Marques	MARE - Universidade de Évora	Researcher or teacher
Sofia Fialho	IPBEJA	Researcher or teacher
Inês Martins	Escola Superior Agrária de Beja	Master Student
Sara Sofia Rego da Silva	Universidade de Évora	Researcher or teacher
Mariana Patanita		Master Student
Ana Galveias	University of Evora	PhD Student
Rute Arriegas	ICT- Évora	PhD Student
Maksim Iakunin	ICT- Universidade de Évora	Pos-doc researcher
Samuel Fernandes	Universidade de Évora	PhD Student

O programa foi o seguinte:

AGENDA	***Escola de Verão de Alqueva em Ciências da Atmosfera e da Água***
19 Junho	
9:00 - 10:00	Rui Salgado, Miguel Potes and Manuela Morais ***Sessão de Boas Vindas: Introdução à 2ª Escola de Verão e à campanha de observações ALOP***.
10:00 - 11:30	José da Silva, FCUP ***Deteção Remota de satélite sobre superfícies de água***

AGENDA	*Escola de Verão de Alqueva em Ciências da Atmosfera e da Água*
12:00 - 13:00	António Chambel**,** *UE* ***Interação águas superficiais-águas subterrâneas***
13:00 - 14:30	Almoço
14:30 - 16:00	Eduardo Morales and Helena Novais, ICT ***Algas e produtividade primária em albufeiras***
16:00 - 19:00	***Campanha de Observações***
19:30 - 21:00	Jantar
20 de Junho	
7:00	Lançamento de Balão Meteorológico
9:00-10:00	Pedro Soares, IDL ***Modelação climática regional e o clima do futuro***
10:00 - 11:00	Rita Cardoso, IDL ***Acoplamento Superfície-atmosfera e os extremos climáticos***
11:30 - 13:00	Patrícia Palma, IPB ***Avaliação de risco ambiental de pesticidas em albufeiras do Sul de Portugal***
13:00 - 15:00	Almoço Portugal – Marrocos
15:30 - 16:30	Alexandre Araújo, UE ***A Falha de Alqueva: Uma estrutura tectónica activa?***
16:30– 19:30	***Campanha de Observações***
20:00	Jantar da Escola de Verão e actividade social
21 de Junho	
7:00	Lançamento de balão meteorológico
9:00 – 10:30	Florence Habets, CNRS, França ***Hydrological modeling: integrating the impact of the groundwater and anthropogenic effect at the basin scale.***
11:00 - 12:00	Gianpaolo Balsamo, Centro Europeu de Previsão do Tempo, ECMWF ***Land surface modelling: representing heterogeneity***
	Gianpaolo Balsamo, Centro Europeu de Previsão do Tempo, ECMWF ***Land surface modelling: coupling to atmosphere***

AGENDA	*Escola de Verão de Alqueva em Ciências da Atmosfera e da Água*
12:00 - 13:00	***Almoço***
14:30 - 15:30	Célia Antunes, UE **Metodologias para Monitorização e Caracterização de Bioaerossóis: o papel dos lagos na constituição do ar**
15:30 - 19:00	***Campanha de Observações***

Earth surface modelling:
representing heterogeneity
ECMWF

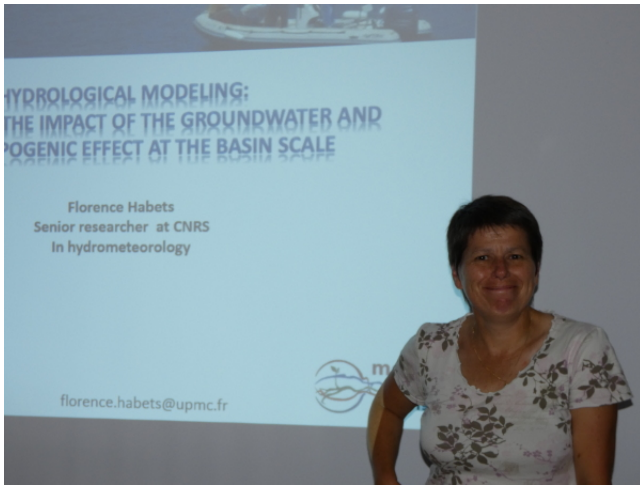
HYDROLOGICAL MODELING:
THE IMPACT OF THE GROUNDWATER AND
OGENIC EFFECT AT THE BASIN SCALE
Florence Habets
Senior researcher at CNRS
In hydrometeorology
florence.habets@upmc.fr

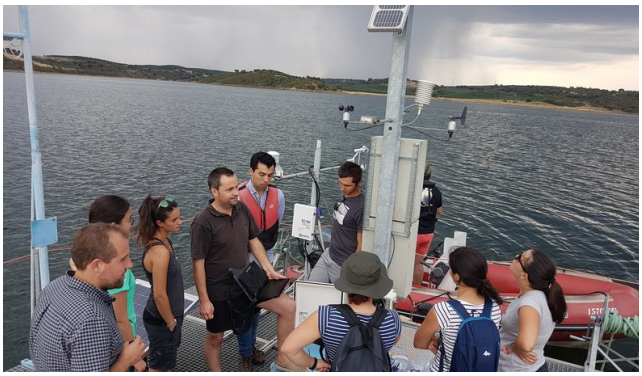

4.2 Outros cursos

Meso-NH Tutorial, University of Évora, 7-9 Novembro 2016

Calendário**:**

	9:00 – 9:30	9:30 – 10:30	11:00 – 12:30	14:00 – 15:30	15:45 – 18:00
					Practical Class
Monday 7	Welcome – Practical info (R. Salgado + C.Lac)	Atmospheric Modelling with Meso-NH (C. Lac)	Model Dynamics (C. Lac)	Environment, Files, Tools (C. Lac + R. Salgado)	Preparation of physiographic and initialization files (C. Lac + R. Salgado)
					Practical Class
Tuesday 8		Model Physics (C. Lac)	Surface – Atmosphere Interactions (SURFEX) (R. Salgado)	Diagnostics (C. Lac)	Real Case Simulations Filling the namelists (C. Lac + R. Salgado)
Wednesday 9		*Practical Class* Launch of students own simulations			

(R. Salgado)

Formadores: Christine Lac (CNRM / Météo France) e Rui Salgado (U. Évora)

1º Workshop on Taxonomy and Ecology of Cyanobacteria", Universidade de Évora, 10-14th September 2018a

First Workshop "Taxonomy and Ecology of Cyanobacteria"

September 10-15, 2018

Main Facilitators

Prof. Célia Leite Sant'Anna

Instituto de Botânica, Núcleo de Pesquisa em Ficologia, São Paulo, SP, Brasil

Prof. Jeffrey R. Johansen

Department of Biology, John Carroll University, University Heights, Ohio, USA

Invited speakers:

Prof. Dr. Vitor O. Manuel Vasconcelos

CIIMAR, Interdisciplinary Centre of Marine and Environmental Research of the University of Porto

Prof. Dr. Vitor Ramos

CIIMAR, Interdisciplinary Centre of Marine and Environmental Research of the University of Porto

Prof. Dr. Margarida P. Reis

Universidade do Algarve, UALG · Centro de Investigação Marinha e Ambiental (CIMA)

Prof. Dr. Fernando Bellém

Clinical Analyses and Public Health, Lisbon School of Health Technology

UNIVERSIDADE DE ÉVORA
ESCOLA DE CIÊNCIAS E TECNOLOGIA
DEPARTAMENTO DE BIOLOGIA

Laboratório da Água

ICT

IPBeja
INSTITUTO POLITÉCNICO DE BEJA

ALOP

JUSTIFICATION

With increased eutrophication and effects of climate change on aquatic systems, cyanobacterial blooms have increased in frequency and intensity with adverse consequences on ecosystems and their biota, including man. The risk is not only for organisms living in water, but also for those in the proximities of affected waterbodies. In recent years, southern Portugal has also seen an increase in cyanobacterial blooms. Scientists in the Instituto de Ciências da Terra, University of Évora (Atmospheric Sciences, Water and Climate-Group 1), have observed several blooms both in the field and by satellite imagery. Some of these proliferations are in fact toxic, but studies thus far have concentrated on planktonic blooms. Little is known on benthic cyanobacteria, which are also toxic, or on the aerial transport of these organisms and their toxins. Studies on subterranean waters, heavily relied upon in the region for human use, are also lacking, but they need attention as suggested by recent studies. The present workshop is a first step to the construction of databases containing taxonomical and ecological information on cyanobacteria, their toxins, and a cross-reference with health-related databases. Such information is required in order to develop standards for different water uses (e.g., drinking, irrigation, produce and wine industry uses, etc.), not only for human consumption as treated in the existing Portuguese legislation.

SCOPE

The workshop is open to biology, ecology, botany, microbiology, phycology or other applied biological or health related branch of biological studies. Professionals and graduate students planning to work, or already working, on cyanobacteria and willing to expand their knowledge on these organisms are especially welcome. All university students are also welcome, but preference will be given to those toward the end of their careers and with a desire to further continue their studies on cyanobacteria.

MATERIAL AND EQUIPMENT

Participants are welcome to bring their own material as long as it is safely transported, appropriately fixed and readily available for analysis during the extended laboratory sessions. The Water Lab will also provide local material for analysis, so, there will be plenty of organisms to identify and study. The laboratory will be equipped with a microscope per a pair of students and will count with proper safety installations, sink, glassware and other minor materials. Participants must bring their own lab coats!

REGISTRATION FEE

There is a unique fee of 250.00 Euros charged for the workshop. This fee will cover expenses of materials (lab and desk), coffee breaks, various other services, and transportation to Alqueva.

UNIVERSIDADE DE ÉVORA
ESCOLA DE CIÊNCIAS E TECNOLOGIA
DEPARTAMENTO DE BIOLOGIA

Laboratório da Água

ICT

IPBeja

ALOP

ACCOMMODATION AND FOOD

Évora is a UNESCO World Heritage city and therefore there is plenty of accommodations, food and facilities related to tourism. A simple Google search for hotels and hostels will yield quite a number of attractive hits. Participants will be on their own for lunch; there are plenty of places to eat entrees, soups, typical; and more international dishes. There is also a small market nearby where fruit, vegetables, bread and curated products can be purchased. The university also has a snack bar where coffee, tea and a general lunch menu, some types of sandwiches and other minor items can be found.

AGENDA

Monday 10

9:00-9:30 Welcome and organization of the workshop

9:30-10:30 Cyanoprokaryota - What is a species? (J. Johansen)

10:30-10:45 Coffee break

10:45-12:00 Cyanobacterial ecology (C. Sant'Anna)

12:00-14:00 Lunch

14:00-18:00 Laboratory session (led by C. Sant'Anna and J. Johansen, with coffee break)

Tuesday 11

9:00-10:00 Studies on cyanobacteria in Portugal, state of the art and future perspectives (Vitor Vasconcelos, open title)

10:00-10:15 Coffee break

10:15-12:30 Taxonomy and phylogeny lecture (C. Sant'Anna (coccoids), with 15 min intermission)

12:30-14:00 Lunch

14:00-18:00 Laboratory session (led by C. Sant'Anna and J. Johansen, with coffee break)

Wednesday 12

9:00-10:00 The study of cyanobacteria in southern Portugal, what has been done and what remains to be done (Margarida Reis, open title)

10:00-10:15 Coffee break

10:15-12:30 Taxonomy and phylogeny lecture (J. Johansen (Synechococcales) with 15 min intermission)

12:30-14:00 Lunch

14:00-18:00 Laboratory session (led by J. Johansen and C. Sant'Anna, with coffee break)

Thursday 13

9:00-10:00 Cyanobacteria and human health in Alentejo, is it really that bad? (Fernando Bellém, open title)

10:00-10:15 Coffee break

10:15-12:30 Taxonomy and phylogeny lecture (J. Johansen (Oscillatoriales and Nostocales) with 15 min intermission)

12:30-14:00 Lunch

14:00-18:00 Laboratory session (led by C. Sant'Anna and J. Johansen, with coffee break)

Friday 14

9:00-10:00 The use of molecular techniques for the study of cyanobacteria with special focus on toxic species (Vitor Ramos, open title)

10:00-10:15 Coffee break

10:15-12:30 Taxonomy and phylogeny lecture (J. Johansen (Nostocales concluded) with 15 min intermission)

12:30-14:00 Lunch

14:00-18:00 Laboratory session (led by C. Sant'Anna and J. Johansen, with coffee break)

Saturday 15

9:00-10:00 Ecological data compilation/summary of workshop (C. Sant'Anna)

10:00-11:00 Taxonomical phylogeny compilation/summary of workshop (J. Johansen)

11:00-11:30 Coffee break and Workshop close up

11:30-16:00 Lunch in Monsaraz Castle/Visit to Alqueva

HOSTS

The Water Laboratory, University of Évora

Biology Department, University of Évora

Alentejo Observation and Prediction Systems - ALOP project

Institute of Earth Sciences (Évora Pole)-ICT

Science and Technology School, University of Évora

Polytechnic Institute of Beja

ORGANIZING COMMITTEE

Eduardo A. Morales, Manuela Morais, Orlando Lopes, Monica Lima, Maria Helena Novais, Alexandra Penha, Rui Salgado, Célia Antunes, Ana Costa, Patricia Palma.

UNIVERSIDADE DE ÉVORA
ESCOLA DE CIÊNCIAS E TECNOLOGIA
DEPARTAMENTO DE BIOLOGIA

Laboratório da Água

ICT

IPBeja

ALOP

4.2 Seminários

Ivan Mammarela, Universidade de Helsinquia: Biosphere-Atmosphere Interactions. Universidade de Évora, 14 de Junho de 2017 ([link])

Maxim Yakunin, ICT: Retrieving absorbed solar energy by the surface using satellite data. Universidade de Évora, 22 de Fevereiro de 2017

Gonçalo Rodrigues, ICT: Desenvolvimento de um produto de vapor de água precipitável com base em estimativas GNSS e atividades realizadas no âmbito do risco meteorológico de incêndio florestal. Universidade de Évora, 21 de Dezembro 2016

Christine Lac, CNRM / Météo France: Atmospheric Modelling with Meso-NH. Universidade de Évora, 7 de Novembro de 2016

Elena Shevnina, Finnish Meterological Institute, Helsinki, Finland: *"Water balance and probabilistic hydrological models: from observations to forecasts"*; 24 de Outubro de 2018, às 14:00 horas, Universidade de Évora, Colégio Verney, Sala 138

Victor Stepanenko, Moscow State University: "Numerical simulation of coupled thermodynamic and biogeochemical processes in inland water bodies". 16 de Maio de 2018 às 14:30 horas, Universidade de Évora, Colégio Verney, Sala 134

Juan Luis Guerrero Rascado, Universidad de Granada, Espanha: "Lidar remote sensing". 10 de Janeiro de 2018, 14:30, Anfiteatro 1 (CLAV)

Maria José Monteiro , Instituto Português do Mar e da Atmosfera : A Assimilação de dados atmosféricos em previsão numérica operacional".29 de Novembro de 2017, 14:30 - Sala 138 do CLAV

Carlos Hiroo Saito, Centro de Desenvolvimento Sustentavel e Departamento de Ecologia/Instituto de Ciencias Biologicas, Universidade de Brasilia, Brasil: "*Educação Ambiental, Divulgação Científica e Visão Interdisciplinar*", 25 de Outubro de 2017, 10h30 - Sala 138 CLV

5. Resultados

Os resultados do projeto estão bem patentes nas 45 publicações em revistas científicas de circulação internacional e arbitragem científica, referenciadas na base Scopus. Por essa razão, em vez de se relatarem aqui os resultados obtidos, resolvemos anexar (Anexo A) as 45 publicações científicas que resultaram do projetos e que incluem, todas elas, a referência ao financiamento obtido no quadro do projeto ALOP. Listam-se de seguida, em publicações científicas, todos os artigos publicados. Os mesmos encontram-se impressos no Anexo A. Muitos dos resultados foram igualmente apresentados e discutidos em conferências técnicas e científicas. A listagem, não completa, das comunicações técnico-científicas encontra-se listada no capítulo sobre a disseminação de resulados.

Para além das o projeto apoiou a realização de Dissertações (ver ponto próprio) e a submissão de duas patentes (ver ponto próprio)

5.1 Artigos em revistas de circulação internacional com arbitragem científica

A versão integral de todos os artigos está contida no anexo A, seguindo a mesma ordem cronológica.

1. Obregón , M. A., M. J. Costa, A. Silva, A. Serrano, 2017, Thirteen Years of Aerosol Radiative Forcing in Southwestern Iberian Peninsula. Aerosol and Air Quality Research. DOI: 10.4209/aaqr.2017.05.0159.

2. Potes, M. Salgado, R., Costa M.J., Morais, M., Bortoli, D., Kostadinov, I. and Mammarella, I.(2017). Lake–atmosphere interactions at alqueva reservoir: a case study in the summer of 2014. Tellus A 2016, 00, 1272787, http://dx.doi.org/10.1080/16000870.2016.1272787

3. Salgueiro, V., Maria João Costa, Ana Maria Silva, Christian Lanconelli & Daniele Bortoli (2017) Cloud parameter retrievals from Meteosat and their effects on the shortwave radiation at the surface, International Journal of Remote Sensing, 38:4, 1137-1161, DOI: 10.1080/01431161.2017.1280630

4. Policarpo, C., Salgado, R**.** and Costa, M. J. (2017): Numerical Simulations of Fog Events in Southern Portugal. Advances in Meteorology, vol. 2017, Article ID 1276784, 16 pages, 2017. doi:10.1155/2017/1276784

5. Perdigão, J., Salgado, R., Magarreiro, C., Soares, P.M.M., Costa, M.J., Dasari. H.P., 2017: Iberian climatology of solar radiation obtained from WRF regional climate simulations for 1950–2010 period. Atmospheric Research, Volume 198, 151-162, doi: 10.1016/j.atmosres.2017.08.016

6. Conceição, R., H. G. Silva, A. Bennett, R. Salgado, D. Bortoli, M. J. Costa, M. Collares Pereira, 2018, High Frequency response of the Atmospheric Electric Potential Gradient under Strong and Dry Boundary Layer Convection. Boundary-Layer Meteorol. DOI: 10.1007/s10546-017-0298-2. https://link.springer.com/.

7. Nicoll, K. A:, R.G. Harrison, H.G. Silva, **R. Salgado**, M. Melgao, D. Bortoli, 2018 , Electrical sensing of the dynamical structure of the planetary boundary layer. Atmos(2018), doi: 10.1016/j.atmosres.2017.1 1.009

8. Lopes, F.M, Silva, H.G., Salgado, R., Cavaco, A., Canhoto, P., Collares-Pereira, M., 2018: Short-term forecasts of GHI and DNI for solar energy systems operation: assessment of the ECMWF integrated forecasting system in southern Portugal; Solar Energy, 170, pp 14-30,

https://doi.org/10.1016/j.solener.2018.05.039.

9. Palma, P., C. Matos, P. Alvarenga, M. Köck-Schulmeyer, I. Simões, D. Barceló, M.J. López de Alda. 2018. Ecological and ecotoxicological responses in the assessment of the ecological status of freshwater systems: A case-study of the temporary stream Brejo of Cagarrão (South of Portugal). Science of the Total Environment. 634:394-406 DOI: 10.1016/j.scitotenv.2018.03.281

10. Iakunin, M., Salgado, R. and Potes, M., 2018. Breeze effects at a large artificial lake: summer case study. Hydrol. Earth Syst. Sci. Discuss., https://doi.org/10.5194/hess-2018-201.

11. Obregón, M. A. , Costa, M. J., Silva, A. M., Serrano, A., 2018: Impact of aerosol and water vapour on SW radiation at the surface: Sensitivity study and applications. Atmospheric Research, Vol. 213, pp 252–263. https://doi.org/10.1016/j..

12. Potes, M., Rodrigues, G., Penha, A. M., Novais, M. H., Costa, M. J., Salgado, R. and Morais, M. 2018. Use of Sentinel 2 – MSI for water quality monitoring at Alqueva reservoir, Portugal, PIAHS, 95, 1-7.

13. Obregón, M. Á., Rodrigues, G., Costa, M. J., Potes, M., & Silva, A. M. (2019). Validation of ESA sentinel-2 L2A aerosol optical thickness and columnar water vapour during 2017-2018. Remote Sensing, 11(14) doi:10.3390/rs11141649

14. Novais M.H., Almeida S.F.P., Blanco S. & C. Delgado (2019). Morphology and ecology of *Fragilaria misarelensis* sp. nov. (Bacillariophyta), a new diatom species from southwest of Europe. *Phycologia*. http://dx.doi.org/10.1080/00318884.2018.1524245

15. Novais, M. H., Morales, E. A., Penha, A. M., Potes, M., Bouchez, A., Barthès, A., Morais, M. (2020). Benthic diatom community dynamics in mediterranean intermittent streams: Effects of water availability and their potential as indicators of dry-phase ecological status. Science of the Total Environment, 719 doi:10.1016/j.scitotenv.2020.137462

16. Palma, P., Fialho, S., Lima, A., Catarino, A., Costa, M. J., Barbieri, M. V., . . . de Alda, M. L. (2021). Occurrence and risk assessment of pesticides in a mediterranean basin with strong agricultural pressure (guadiana basin: Southern of portugal). Science of the Total Environment, 794 doi:10.1016/j.scitotenv.2021.148703

17. Lopes, F. M., Conceição, R., Silva, H. G., Fasquelle, T., Salgado, R., Canhoto, P., & Collares-Pereira, M. (2019). Short-term forecasts of DNI from an integrated forecasting system (ECMWF) for optimized operational strategies of a central receiver system. Energies, 12(7) doi:10.3390/en12071368

18. Pereira, S., Canhoto, P., Salgado, R., & Costa, M. J. (2019). Development of an ANN based

corrective algorithm of the operational ECMWF global horizontal irradiation forecasts. Solar Energy, 185, 387-405. doi:10.1016/j.solener.2019.04.070

19. Morales, E. A., Wetzel, C. E., Novais, M. H., Buczkó, K., Morais, M. M., & Ector, L. (2019). Morphological reconsideration of the araphid genus pseudostaurosira (bacillariophyceae), a revision of gedaniella, popovskayella and serratifera, and a description of a new nanofrustulum species. Plant Ecology and Evolution, 152(2), 262-284. doi:10.5091/plecevo.2019.1604

20. Lopes, F. M., Conceição, R., Silva, H. G., Salgado, R., Canhoto, P., & Collares-Pereira, M. (2019). Predictive value of short-term forecasts of DNI for solar energy systems operation. Paper presented at the AIP Conference Proceedings, , 2126 doi:10.1063/1.5117707 Retrieved from www.scopus.com

21. Sicard, M., M.J. Granados-Muñoz, L. Alados-Arboledas, R. Barragán, A.E. Bedoya-Velásquez, J.A. Benavent-Oltra, D. Bortoli, A. Comerón, C. Córdoba-Jabonero, M.J. Costa, A. del Águila, A.J. Fernández, J.L. Guerrero-Rascado, O. Jorba, F. Molero, C. Muñoz-Porcar, P. Ortiz-Amezcua, N. Papagiannopoulos, M. Potes, M. Pujadas, F. Rocadenbosch, A. Rodríguez-Gómez, R. Román, R. Salgado, V. Salgueiro, Y. Sola, M. Yela, 2019: Ground/space, passive/active remote sensing observations coupled with particle dispersion modelling to understand the inter-continental transport of wildfire smoke plumes. *Remote Sensing of Environment*, 232, 111294, https://doi.org/10.1016/j.rse.2019.111294.

22. Pereira, S., Abreu, E., Iakunin, M., Canhoto, P., & Salgado, R. (2019). Prediction of solar resource and photovoltaic energy production through the generation of a typical meteorological year and meso-NH simulations: Application to the south of portugal. Paper presented at the 2019 IEEE 2nd International Conference on Renewable Energy and Power Engineering, REPE 2019, 182-186. doi:10.1109/REPE48501.2019.9025118 Retrieved from www.scopus.com

23. Fernández, A. J., Sicard, M., Costa, M. J., Guerrero-Rascado, J. L., Gómez-Amo, J. L., Molero, F., Barragán, R., Bortoli, D., Bedoya-Velásquez, A. E., Utrillas, M. P., Salvador, P., Granados-Muñoz, M. J., Potes, M., Ortiz-Amezcua, P., Martínez-Lozano, J. A., Artíñano, B., Muñoz-Porcar, C., **Salgado, R.**, Román, R., Rocadenbosch, F., Salgueiro, V., Benavent-Oltra, J. A., Rodríguez-Gómez, A., Alados-Arboledas, L., Comerón, A., and Pujadas, M., 2019: Extreme, wintertime Saharan dust intrusion in the Iberian Peninsula: Lidar monitoring and evaluation of dust forecast models during the February 2017 event. *Atmospheric Research*, 228, 223-241, https://doi.org/10.1016/j.atmosres.2019.06.007.

24. Morales, E. A., Wetzel, C. E., Novais, M. H., Morais, M. M., & Ector, L. (2020). Nitzschia transtagensis sp. nov. (bacillariophyceae) from a spring in southern portugal. Botany Letters, 167(1), 32-41. doi:10.1080/23818107.2019.1688676

25. Tomaz, A., Palma, P., Fialho, S., Lima, A., Alvarenga, P., Potes, M., & Salgado, R. (2020). Spatial and temporal dynamics of irrigation water quality under drought conditions in a

large reservoir in southern portugal. Environmental Monitoring and Assessment, 192(2) doi:10.1007/s10661-019-8048-1

26. Rodrigues, G., Potes, M., Penha, A. M., Costa, M. J., & Morais, M. M. (2022). The use of sentinel-3/OLCI for monitoring the water quality and optical water types in the largest portuguese reservoir. Remote Sensing, 14(9) doi:10.3390/rs14092172

27. Palma, P., Fialho, S., Lima, A., Novais, M. H., Costa, M. J., Montemurro, N., . . . de Alda, M. L. (2020). Pharmaceuticals in a mediterranean basin: The influence of temporal and hydrological patterns in environmental risk assessment. Science of the Total Environment, 709 doi:10.1016/j.scitotenv.2019.136205

28. Lopes, F. M., Conceição, R., Fasquelle, T., Silva, H. G., Salgado, R., Canhoto, P., & Collares-Pereira, M. (2020). Predicted direct solar radiation (ECMWF) for optimized operational strategies of linear focus parabolic-trough systems. Renewable Energy, 151, 378-391. doi:10.1016/j.renene.2019.11.020

29. Novais, M. H., Morales, E. A., Penha, A. M., Potes, M., Bouchez, A., Barthès, A., . . . Morais, M. (2020). Benthic diatom community dynamics in mediterranean intermittent streams: Effects of water availability and their potential as indicators of dry-phase ecological status. Science of the Total Environment, 719 doi:10.1016/j.scitotenv.2020.137462

30. Iakunin, M., Stepanenko, V., Salgado, R., Potes, M., Penha, A., Helena Novais, M., & Rodrigues, G. (2020). Numerical study of the seasonal thermal and gas regimes of the largest artificial reservoir in western europe using the LAKE 2.0 model. Geoscientific Model Development, 13(8), 3475-3488. doi:10.5194/gmd-13-3475-2020

31. Couto, F. T., Iakunin, M., Salgado, R., Pinto, P., Viegas, T., & Pinty, J. -. (2020). Lightning modelling for the research of forest fire ignition in portugal. Atmospheric Research, 242 doi:10.1016/j.atmosres.2020.104993

32. Palma, P., Fialho, S., Lima, A., Mourinha, C., Penha, A., Novais, M. H., . . . Alvarenga, P. (2020). Land-cover patterns and hydrogeomorphology of tributaries: Are these important stressors for the water quality of reservoirs in the mediterranean region? Water (Switzerland), 12(10), 1-20. doi:10.3390/w12102665

33. Várbíró, G., Borics, G., Novais, M. H., Morais, M. M., Rimet, F., Bouchez, A., . . . B-Béres, V. (2020). Environmental filtering and limiting similarity as main forces driving diatom community structure in mediterranean and continental temporary and perennial streams. Science of the Total Environment, 741 doi:10.1016/j.scitotenv.2020.140459

34. Tomaz, A., Palma, P., Fialho, S., Lima, A., Alvarenga, P., Potes, M., & Salgado, R. (2020). Spatial and temporal dynamics of irrigation water quality under drought conditions in a large reservoir in southern portugal. Environmental Monitoring and Assessment, 192(2)

doi:10.1007/s10661-019-8048-1

35. Miranda Rodrigues, C., Moreira, M., Guimarães, R. C., & Potes, M. (2020). Reservoir evaporation in a mediterranean climate: Comparing direct methods in alqueva reservoir, portugal. Hydrology and Earth System Sciences, 24(12), 5973-5984. doi:10.5194/hess-24-5973-2020

36. Lopes, F. M., Conceição, R., Silva, H. G., Salgado, R., & Collares-Pereira, M. (2021). Improved ECMWF forecasts of direct normal irradiance: A tool for better operational strategies in concentrating solar power plants. Renewable Energy, 163, 755-771. doi:10.1016/j.renene.2020.08.140

37. Palma, P., Penha, A. M., Novais, M. H., Fialho, S., Lima, A., Mourinha, C., . . . Salgado, R. (2021). Water-sediment physicochemical dynamics in a large reservoir in the mediterranean region under multiple stressors. Water (Switzerland), 13(5) doi:10.3390/w13050707

38. Purificação, C., Potes, M., Rodrigues, G., Salgado, R., & Costa, M. J. (2021). Lake and land breezes at a mediterranean artificial lake: Observations in alqueva reservoir, portugal. Atmosphere, 12(5) doi:10.3390/atmos12050535

39. Palma, P., Fialho, S., Lima, A., Catarino, A., Costa, M. J., Barbieri, M. V., . . . de Alda, M. L. (2021). Occurrence and risk assessment of pesticides in a mediterranean basin with strong agricultural pressure (guadiana basin: Southern of portugal). Science of the Total Environment, 794 doi:10.1016/j.scitotenv.2021.148703

40. Iakunin, M., Abreu, E. F. M., Canhoto, P., Pereira, S., & Salgado, R. (2022). Impact of a large artificial lake on regional climate: A typical meteorological year meso-NH simulation results. International Journal of Climatology, 42(2), 1231-1252. doi:10.1002/joc.7299

41. Pereira, S., Abreu, E. F. M., Iakunin, M., Cavaco, A., Salgado, R., & Canhoto, P. (2022). Method for solar resource assessment using numerical weather prediction and artificial neural network models based on typical meteorological data: Application to the south of portugal. Solar Energy, 236, 225-238. doi:10.1016/j.solener.2022.03.003

42. Rodrigues, G., Potes, M., Penha, A. M., Costa, M. J., & Morais, M. M. (2022). The use of sentinel-3/OLCI for monitoring the water quality and optical water types in the largest portuguese reservoir. Remote Sensing, 14(9) doi:10.3390/rs14092172

43. Shevnina, E., Potes, M., Vihma, T., Naakka, T., Dhote, P. R., and Thakur, P. K.: Evaporation over a glacial lake in Antarctica, The Cryosphere, 16, 3101–3121, https://doi.org/10.5194/tc-16-3101-2022, 2022.

44. Palma, P., Penha, A. M., Novais, M. H., Fialho, S., Lima, A., Catarino, A., . . . Salgado, R. (2023). Integrative toolbox to assess the quality of freshwater sediments contaminated with potentially toxic metals. Environmental Research, 217 doi:10.1016/j.envres.2022.114798

45. Novais, M.H., Penha, A.M., Catarino, A., Martins, I., Fialho, S., Morais, M., Palma, P., 2023: The usefulness of ecotoxicological tools to improve the assessment of water bodies in a climate change reality. Science of the Total Environment, 2023, 901, 166392

A versão integral de todos os artigos está contida no anexo A, seguindo a mesma ordem cronológica.

5.2 Dissertações

Rúben Duarte, 2018: Identificação de genes responsáveis pela Fitotoxicidade na Albufeira de Alqueva. Relatório de estágio da licenciatura em Bioquímica. Orientador: Maria Alexandra Penha

Sara Lopes, 2018: Determinação da quantidade de clorofila a em amostras de aerossóis através de fluorimetria. Relatório de estágio da licenciatura em Biotecnologia. Orientadores: Eduardo A. Morales, Maria Helena Novais e Ana Costa

Inês Martins, 2018: ”Avaliação do Impacto dos afluentes na qualidade da água da Albufeira do Alqueva: Caso estudo Rib. Amieira e Alamos Captação”, Trabalho de Projecto Final de Curso da Licenciatura em Engenharia do Ambiente de Escola Superior Agrária do Instituto Politécnico de Beja. Orientação: Patrícia Palma

João Luís Parreira Rocha Homem, 2018: “Avaliação da qualidade das previsões de radiação solar global e direta para a região de Évora, efetuadas operacionalmente pelos modelos numéricos de previsão do tempo”, Tese de Mestrado do Mestrado em Engenharia de Energia Solar. Orientador: Rui Salgado

Sónia Isabel Cardoso Assunção, 2017: “Impacto da introdução da Albufeira de Alqueva no modelo de previsão AROME”. Tese de Mestrado do Mestrado em Ciências da Terra, da Atmosfera e do Espaço. Orientação de Maria José Monteiro (IPMA) e Rui Salgado.

5.3 Patentes

- Pedido de Patente na Europa EP19 217 875 4. Título: Shutter for an ultraviolet visible spectrometer, operation method and uses thereof. Em nome da Universidade de Évora, tendo por inventor o Daniele Bortoli.
- Pedido de Patente na Europa EP 19 217 885.3. Título: A multiple-stage method for the processing of airborne cyanobacteria in air-water interface emissions. Em nome da Universidade de Évora. Inventores: Célia Antunes, Ana Costa, Maria Alexandra Penha. Maria Manuela Morais, Maria Helena Novais e Eduardo Morales,

6. Disseminação dos resultados

6.2 Desenvolvimento do sítio da Internet do ALOP e partilha de dados

Foi desenvolvida a página web do projecto, www.ict.uevora.pt (ver figura). Esta página inclui notícias, publicações bem como também o acesso aos dados recolhidos.

Durante o 2º ano foi elaborada uma base de dados em MySQL que com recurso a código python

acrescenta diária e automaticamente os registos medidos na plataforma Montante instalada a meio da albufeira, entre eles: Parâmetros meteorológicos (Intensidade do Vento, Rajadas, Temperatura do Ar, Pressão atmosférica, Vapor de água e Radiação Solar), temperatura da água a vários níveis, parâmetros de qualidade da água e ainda dos parâmetros representativos de fluxos na interface água-ar. Procedeu-se à mesma metodologia para acrescentar na base de dados os dados meteorológicos das duas estações instaladas nas duas margens da albufeira.

Procedeu-se ainda à automatização do processo de produção diária de gráficos apresentando-se online no site criado em 2017 (Link: http://www.alop.ict.uevora.pt/obs/), os gráficos do dia anterior, dos últimos 7 dias e mensais para os parâmetros referidos nas três estações meteorológicas referidas. Apresenta-se igualmente no site Web criado as fotografias dos principais locais de trabalho na albufeira de Alqueva e ainda da instrumentação utilizada no contexto do projeto ALOP.

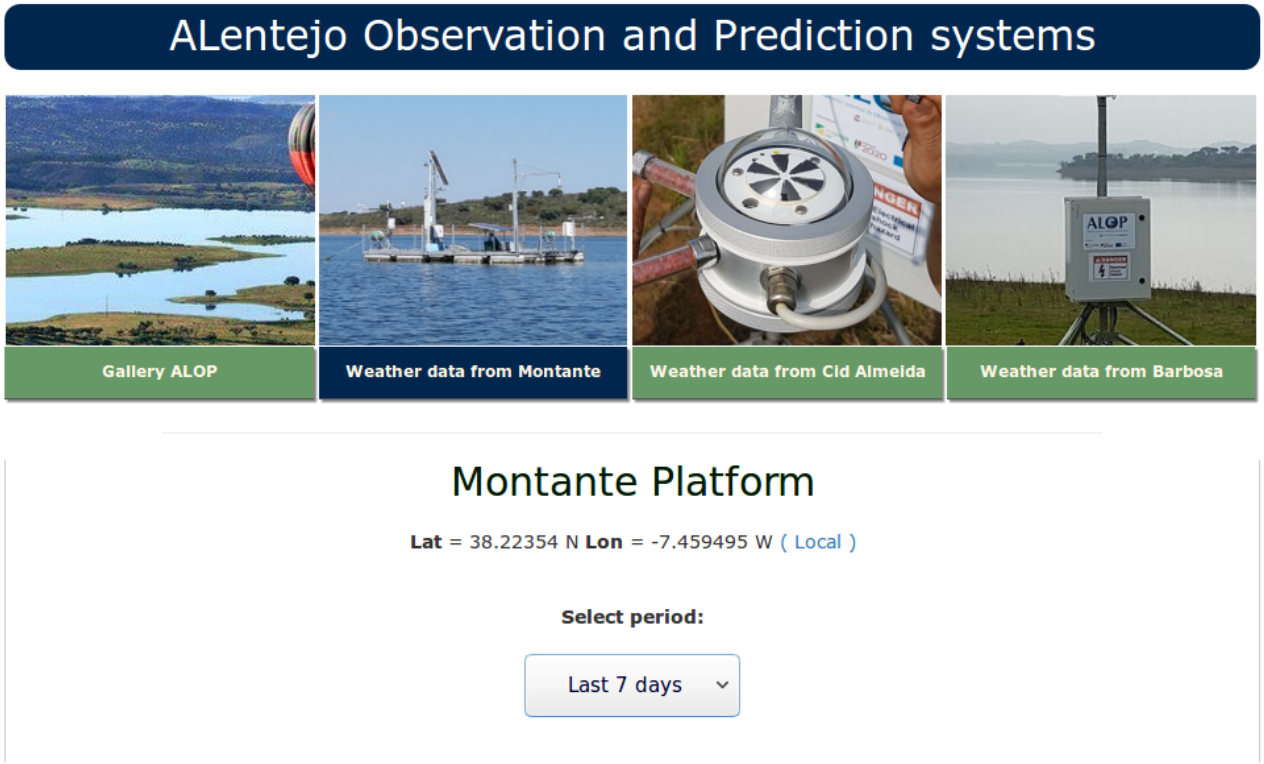

Imagem do separador Observações (http://www.alop.ict.uevora.pt/obs/) do site ALOP

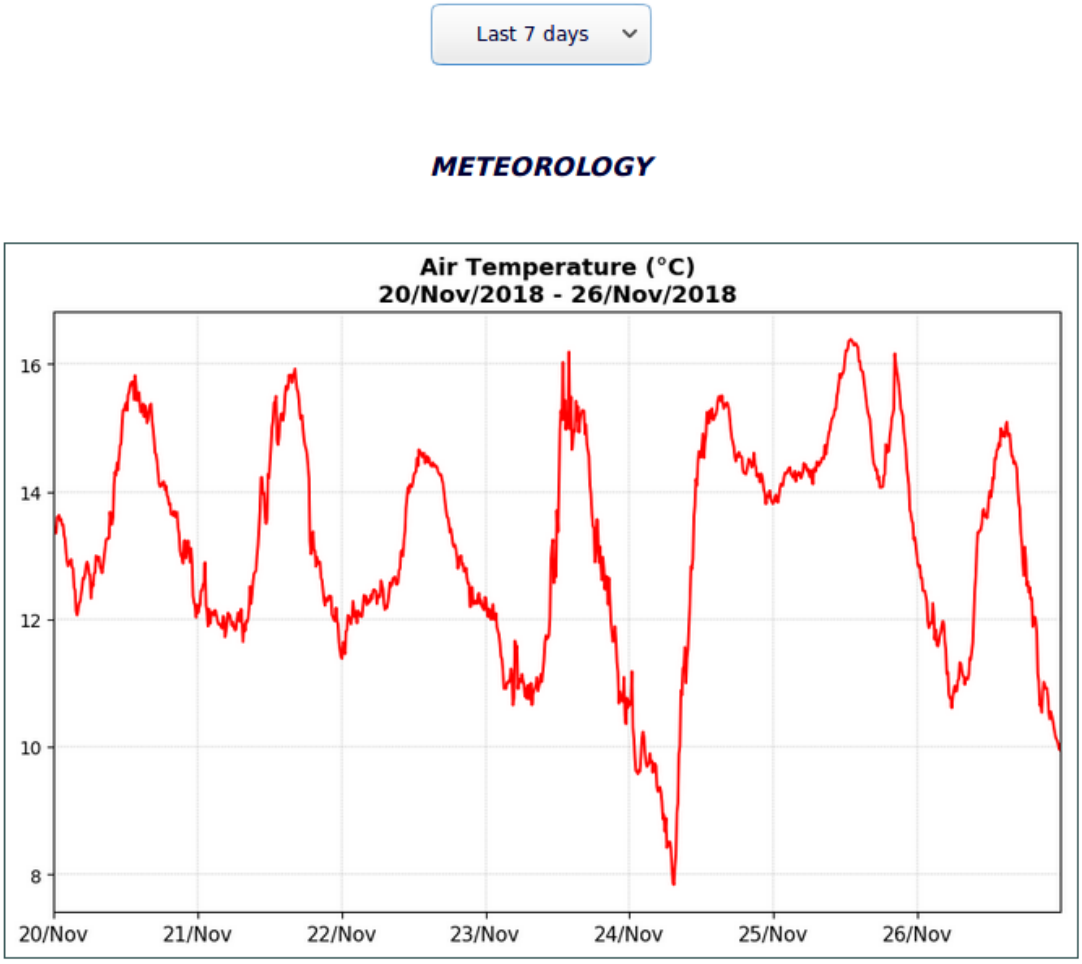

Exemplo de evolução da temperatura do ar para os últimos 7 dias na plataforma de Montante

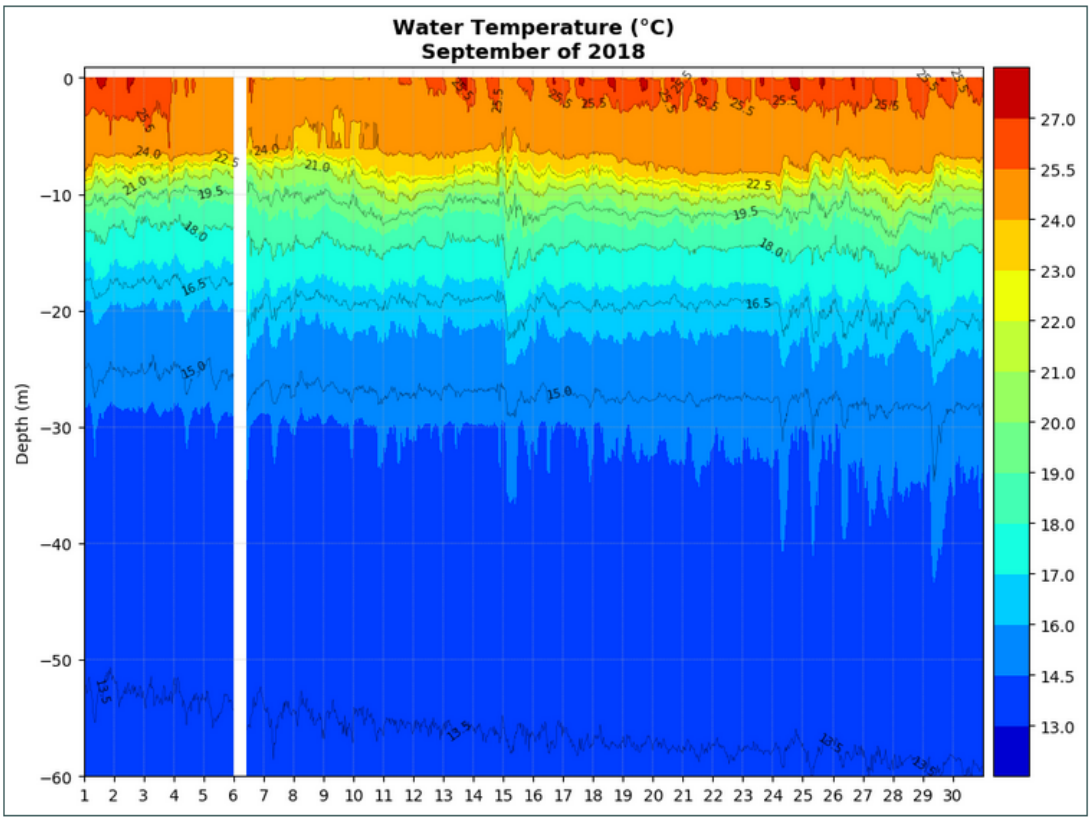

Exemplo da evolução do perfil da temperatura da água

Presentemente, o acesso aos dados numéricos é disponibilizado aos utilizadores que o requerem. A autenticação é efectuada através de uma password. Para além dos investigadores do projecto têm acedido aos dados outras instituições que o requereram.

6.2 Comunicações em encontros científicos nacionais

A equipa do projeto participou em muitos encontros técnico-científicos nacionais. Apresenta-se de seguida uma lista, não completa das comunicações efetuadas

- Assunção, S., Maria José Monteiro, Rui Salgado, 2017: Impacto da Introdução da Albufeira de Alqueva no Modelo de Previsão AROME.10º Simpósio de Meteorologia e Geofísica da APMG, 18º Encontro Luso-Espanhol de Meteorologia, Fundação C. Gulbenkian, Lisboa, 20 a 22 de Março de 2017.
- Costa, M. J., J. L. Guerrero Rascado, M. Potes, V. Salgueiro, R. Salgado, D. Bortoli, S. Pereira, M. A. Obregón, M. Melgão, A. Albino, P. Kulkarni, G. Rodrigues, V. Prior, A.M. Silva, L. Alados-Arboledas, 2017: Detecção Remota à Superfície de Perfis Verticais de Temperatura e Humidade. 10º Simpósio de Meteorologia e Geofísica da APMG, 18º Encontro Luso-Espanhol de Meteorologia, Fundação C. Gulbenkian, Lisboa, 20 a 22 de Março de 2017.

- Landim L., Fortes A., Silva V.S., Morales E.A., Novais M.H., Penha M.A. & Morais M.M., 2018: Caracterização físico-química e biológica de cinco albufeiras da ilha de Santiago, Cabo Verde [Physico-chemical and biological characterization of 5 reservoirs in Santiago Island, Green Cape]", p. 42. 14º Congresso da Água. Gestão dos Recursos Hídricos: Novos desafios. Évora, Portugal, 7-9 March 2018 (Oral Presentation)
- Morais M.M., Alves M.H., Novais M.H., Oliveira A. & Morales E.A., 2018: Estrutura, funcionamento e gestão de rios temporarios: Projecto SMIRES [Structure, functioning and management of temporary rivers: the SMIRES Project]", p.33. 14º Congresso da Água. Gestão dos Recursos Hídricos: Novos desafios. Évora, Portugal, 7-9 March 2018. (Oral Presentation)
- Morales E.A., Novais M.H., Bellém F., Penha A., Nunes S., Rosmarinho T. & Morais M.M., 2018: Blooms of cyanobacteria (Cyanoprokaryota) in southern Portugal and their impact on human health. VIII Sociedade Portuguesa de Bioquimica Clinical Biochemistry Workshop, Allergy and Environment, Évora, Portugal, 24 February 2018. (Oral Presentation)
- Obregón, M.A. , M.J. Costa, A. Serrano, A.M. Silva, 2018: Estimación del forzamiento radiativo de aerosoles durante un evento desértico sobre la Península Ibérica usando datos satelitales. II Congresso Luso-Extremadurense de Ciências e Tecnologia. Badajoz, Espanha, Outubro 2018.
- Obregón, M.A. , A. Serrano, M.J. Costa, M.L. Cancillo, J.A. García, A.M. Silva, 2018: Colaboración científica UEx/AIRE – UE/ICT para el estudio de los aerosoles atmosféricos. II Congresso Luso-Extremadurense de Ciências e Tecnologia. Badajoz, Espanha, Outubro 2018.
- Palma, P., S. Fialho, A. Penha, M.H. Novais, M. Potes, M. Yakunin, G. Rodrigues, M.A. Almeida, A. Durão, A. Tomaz, P. Alvarenga, M.J. Costa, M. Morais, R. Salgado: "ALOP: Sistemas de observação, previsão e alerta na atmosfera e em reservatórios de água do Alentejo". II Congresso Nacional das Escolas Superiores Agrárias, Elvas, Portugal, 16-18 November 2017.
- Penha M.A., Novais M.H., Morales E.A., Rodrigues G., Potes M., Morais M.M. & Salgado R., 2018: Aplicação de técnicas inovadoras para avaliação da produtividade primária em grandes reservatórios (Alqueva) [Application of innovative techniques for the evaluation of primary productivity in large reservoirs (Alqueva)]", p. 42. 14º Congresso da Água. Gestão dos Recursos Hídricos: Novos desafios. Évora, Portugal, 7-9 March 2018 (Oral Presentation)
- Penha, M.A., Maxim Yakunin , Helena Novais, Miguel Potes, Manuela Morais, Rui Salgado, 2017: Estudo da Evolução e Previsão da Temperatura da Água na Albufeira de Alqueva (Bacia do Guadiana) através do Modelo FLAKE. APMG2017: 10º Simpósio de Meteorologia e Geofísica da APMG, 18º Encontro Luso-Espanhol de Meteorologia, Fundação C. Gulbenkian, Lisboa, 20 a 22 de Março de 2017.
- Penha A., Saúde A., Rosado A., Zavattieri A., Morales E.A., Mavioso I., Figueira J., Morais

M., Cordeiro M., Novais M.H., Medalhas M., Mira M., Freira M., Lima M., Lopes O., Cabral S., Nunes S. & Rosmaninho T.: "Utilização de uma abordagem integrada para a avaliação de qualidade ecológica na região do Alentejo". ENEG 217 - Encontro Nacional de Entidades Gestoras de Água e Saneamento, Évora, Portugal, 21-24 November 2017. Poster

- Penha A., Saúde A., Rosado A., Zavattieri A., Morales E.A., Mavioso I., Figueira J., Morais M., Cordeiro M., Novais M.H., Medalhas M., Mira M., Freira M., Lima M., Lopes O., Cabral S., Nunes S. & Rosmaninho T.: "Avaliação da qualidade ecológica em rios do Sul de Portugal: diatomáceas e macroinvertebrados bentónicos".ENEG 217 - Encontro Nacional de Entidades Gestoras de Água e Saneamento, Évora, Portugal, 21-24 November 2017. Poster
- Penha A., Saúde A., Rosado A., Zavattieri A., Morales E.A., Mavioso I., Figueira J., Morais M., Cordeiro M., Novais M.H., Medalhas M., Mira M., Freira M., Lima M., Lopes O., Cabral S., Nunes S. & Rosmaninho T.: "Avaliação da qualidade ecológica em albufeiras no sul de Portugal". ENEG 217 - Encontro Nacional de Entidades Gestoras de Água e Saneamento, Évora, Portugal, 21-24 November 2017. Poster
- Penha A., Saúde A., Oliveira A., Rosado A., Zavattieri A., Morales E.A., Mavioso I., Figueira J., Morais M., Cordeiro M., Novais M.H., Medalhas M., Mira M., Freira M., Lima M., Lopes O., Cabral S., Nunes S. & Rosmaninho T.: "Rios temporários do Sul de Portugal: caracterização e importância para a avaliação da qualidade ecológica". ENEG 217 - Encontro Nacional de Entidades Gestoras de Água e Saneamento, Évora, Portugal, 21-24 November 2017. Poster.
- Potes, M.: Underwater radiance profiles on Alqueva Reservoir. Workshop on Earth Sciences 2016, Évora.
- Potes, M., Maria João Costa, Rui Salgado, Gonçalo Rodrigues, Daniele Bortoli, 2017: Cálculo de Coeficientes de Atenuação Espectral na Albufeira de Alqueva. 10º Simpósio de Meteorologia e Geofísica da APMG, 18º Encontro Luso-Espanhol de Meteorologia, Fundação C. Gulbenkian, Lisboa, 20 a 22 de Março de 2017. 10º Simpósio de Meteorologia e Geofísica da APMG, 18º Encontro Luso-Espanhol de Meteorologia, Fundação C. Gulbenkian, Lisboa, 20 a 22 de Março de 2017.
- Rodrigues G., Potes M., Costa M.J., Salgado R., Penha A. & Novais M.H., 2018: Qualidade da água no reservatório de Alqueva através de medições in situ e deteção remota de satélite. 14º Congresso da Água. Gestão dos Recursos Hídricos: Novos desafios. Évora, Portugal, 7-9 March 2018 (Oral Presentation)
- Rodrigues, G., M. Potes, M. J. Costa, R. Salgado, A. Penha, M. Morais, 2017: Qualidade da Água no Reservatório de Alqueva através de Medições *In Situ* e Deteção Remota de Satélite. 10º Simpósio de Meteorologia e Geofísica da APMG, 18º Encontro Luso-Espanhol de Meteorologia, Fundação C. Gulbenkian, Lisboa, 20 a 22 de Março de 2017.
- Salgado, R., F. M. Lopes, E. F. M. Abreu, A. Cavaco, M. R. Rashel, P. Canhoto, M. J. Costa, H. Silva, M. Tlemçani and C. Lac, 2017: Simulação da Radiação Solar Directa (DNI) no Alentejo com o Modelo Atmosférico MESO-NH. Alguns Casos de Estudo.10º Simpósio de

Meteorologia e Geofísica da APMG, 18º Encontro Luso-Espanhol de Meteorologia, Fundação C. Gulbenkian, Lisboa, 20 a 22 de Março de 2017.

- Salgado R., Almeida A., Alvarenga P., Aranha S., Bárias S., Bortoli D., Canhoto P., Costa M. J., Durão A., Fialho S., Figueira J., Iakunin M., Lima M., Lopes O., Morais M., Moreira. M., Novais M.H., Nunes, S., Palma P., Pavan K., Penha A., Potes M., Reis A.H., Rodrigues C.M., Rodrigues G., Silva A.M., Tomaz A.: "ALOP - Alentejo: Sistemas de Alerta e Previsão". ENEG 217 - Encontro Nacional de Entidades Gestoras de Água e Saneamento, Évora, Portugal, 21-24 November 2017. Poster
- Tomaz, A., Sara Fialho, Ana Lima, Paula Alvarenga, Miguel Potes, Rui Salgado, Patrícia Palma. 2018. Avaliação da Qualidade da Água de Rega e do Risco de Salinização do Solo em Condições de Seca: o Caso do Perímetro de Alqueva em 2017. Comunicação apresentada no âmbito do 4º Simpósio de Produção e Transformação de Alimentos em Ambiente Sustentável. 7 junho. Faculdade de Ciências e Tecnologia da Universidade NOVA de Lisboa (Portugal). pp102.
-

6.3 Comunicações em encontros científicos internacionais

A equipa do projeto participou em muitos encontros técnico-científicos nacionais. Apresenta-se de seguida uma lista, não completa das comunicações efetuadas.

- Costa, M.J., V. Salgueiro, D. Bortoli and A.M. Silva, 2018: Aerosol-cloud interactions and radiative effects estimated from surface remote sensing: a study for warm clouds in Southwestern Iberian Peninsula. RICTA 2018 - 6th Iberian Meeting on Aerosol Science and Technology. Bilbau, Espanha, Junho 2018. Comunicação poster
- Morais M.M., Silva Vitória S., Lobo de Pina A., Morales E.A., Nunes S., Novais M.H. & Penha A., 2018: Estudo preliminar do fitoplâncton em reservatórios na ilha de Santiago. Cabo Verde. XX Encontro da Rede de Estudos Ambientais de Países de Língua Portuguesa – REALP. Aveiro, Portugal, 8-12 May 2018. (Oral Presentation)
- Morales E.A., Trujillo I., Rodríguez I., Novais M.H., Barbosa L. & Morais M.M., 2018: The use of diatoms (Bacillariophyta) as indicators of water quality in an intermittent, urban and highly polluted river in Bolivia. XIX Conference of the Iberian Association of Limnology Inland waters and XXI century challenges: from scientific knowledge to environmental management. Coimbra, Portugal, 24-29 June 2018. (Oral Presentation)
- Morales E.A., Antunes C., Costa A., Costa M.J., Novais M.H., Penha A. & Morais M.M.: "Preliminary results on cyanobacterial aerosol emissions from the Alqueva reservoir, southern Portugal". RICTA2018 - 6th Iberian Meeting on Aerosol Science and Technology, Bilbao, Spain, 20-22 June 2018. (Poster)
- Novais M.H., Penha M.A., Morales E.A., Oliveira A., Bouchez A., Barthès A., Usseglio-Polatera P., Várbíró G. & Morais M.M, 2018: Effects of water intermittency on diatom (Bacillariophyta) and invertebrate (aquatic and terrestrial) communities in streams of

southern Portugal. XIX Conference of the Iberian Association of Limnology Inland waters and XXI century challenges: from scientific knowledge to environmental management. Coimbra, Portugal, 24-29 June 2018. (Oral Presentation)

- Novais, M.H., Alexandra Penha, Susana Nunes, Rui Salgado, Manuela Morais, 2017: Vertical dynamics in a large reservoir. 10th Symposium for European Freshwater Sciences, Olomouc, Czech Republic, 02-07 July 2017. Oral Presentation
- Obregón, M.A., M.J. Costa, A.M. Silva, A. Serrano, 2018: Estimation of aerosol radiative impacts at évora (portugal) during the period 2003-2015. RICTA 2018 - 6th Iberian Meeting on Aerosol Science and Technology. Bilbau, Espanha, Junho 2018. Comunicação oral
- Oliveira A., Novais M.H., Pinto P. & M. Morais: "Diatoms and ground beetles (Coleoptera) in intermittent and permanent rivers in Monchique mountains (Southern Portugal)".10 Symposium for European Sciences, Olomouc, Czech Republic, 02-07 July 2017. Oral Presentation
- Palma P., Fialho S., Lima A., Penha A., Novais M.H., Monllor-Alcaraz L.S., Guillem-Argiles N., Lopez de Alda M., Alvarenga P., Morais M. & Salgado R.: Ecotoxicological risk assessment of tributaries to the Alqueva Reservoir (Southern Portugal), Ecological and Environmental Engineering, Krakow, Poland, 26-29 June 2018. (Oral Presentation)
- Palma P., Fialho S., Lima A., Penha A., Novais M.H., Monllor-Alcaraz L.S., Guillem-Argiles N., Lopez de Alda M., Alvarenga P., Morais M. & Salgado R.: “Ecotoxicological tools to assess the impact pollution of tributaries to the Alqueva Reservoir (Southern Portugal)”. 28th Annual Meeting of the Society of Environmental Toxicology and Chemistry- Europe, Rome, Italy, 13-17 May 2018. Poster.
- Penha A., Novais M.H., Potes M., Morais M. & R. Salgado, 2017: “Biological and Physico-Chemical profiles of a large reservoir (Alqueva, Southern Portugal)”. 5th Workshop on Parameterization of Lakes in Numerical Weather Prediction and Climate Modelling, Berlin, Germany, 16-19 October 2017. (Oral Presentation)
- Penha, A. M.H. Novais, E.A. Morales, P. Palma, S. Fialho, A. Lima, S. Nunes, A. Rosado, A. Durão, R. Salgado, M. Morais. 2018. Factors affecting the development of algal assemblages in the Alqueva Reservoir, southern Portugal. Oral communication presented at Conference on Ecological and Environmental Engineering. 25-29 junho 2018. Cracóvia (Polónia). pp 156
- Potes, M., G. Rodrigues, A. Penha, M.H. Novais, M.J. Costa, R. Salgado, 2018: Use of Sentinel 2 – MSI for water quality monitoring at Alqueva reservoir, Portugal. RSHS’18, Remote Sensing & Hydrology Symposium ICRS-IAHS. Córdova, Espanha, Maio 2018. Comunicação oral.
- Potes, M., Maria João Costa, Rui Salgado, Gonçalo Rodrigues, Daniele Bortoli, 2017: Water column attenuation coefficient estimations in Alqueva reservoir. Geophysical Research Abstracts, Vol. **19**, EGU2017-14770, EGU General Assembly 2017.

- Potes, M., M. J. Costa, R. Salgado, M. Morais, D. Bortoli, I. Kostadinov. Measurements of solar spectral downwelling irradiance in the water column using a new apparatus coupled to a FieldSpec (ASD Inc.)". XXXIII Congress SIL, Torino, Italy, August 2016.
- Potes, M., M. J. Costa, R. Salgado, M. Morais, D. Bortoli, I. Kostadinov. Results from a new apparatus developed for measurements of solar spectral downwelling irradiance in the water column. 9ª Asamblea Hispano Portuguesa de Geodesia y Geofísica, Madrid, June 2016.
- Potes, M., M. J. Costa, R. Salgado, M. Morais, D. Bortoli, I. Kostadinov. Surface reflectance and underwater downwelling irradiance in Alqueva reservoir, southeast Portugal. I Jornada de usuarios ASD, Madrid, 29 de Junio de 2016.
- Potes, M., Rui Salgado, Maria Provenzale, and Ivan Mammarella, 2017: Eddy Covariance flux measurements over an ice/snow covered lake in Finland. Geophysical Research Abstracts, Vol. **19**, EGU2017-16201, EGU General Assembly 2017.
- Rodrigues, G., M. Potes, M.J. Costa, R. Salgado, A. Penha, M.H. Novais, M. Morais, 2018: Water Quality in Alqueva Reservoir Through In-Situ Measurements and Sentinel-2 MSI. EGU General Assembly. Viena, Áustria, Abril 2018. Comunicação poster
- Salgado, R., M. Potes, M. Yakunin, A. Penha, M. Morais and M.J. Costa, 2017: On the use of FLAKE in SURFEX coupled to Meso-NH. First SURFEX Users Workshop, Meteo France, Toulouse, February 27 to March 1, 2017.
- Tomaz A., Fialho S., Lima A., Penha A., Novais M.H., Potes M., Yakunin M., Rodrigues G., Alvarenga P., Costa M.J., Morais M., Salgado R. & Palma P.: "Contribution to the salinization risk assessment, under drought conditions, in the Alqueva irrigation area (South Portugal)". 28th Annual Meeting of the Society of Environmental Toxicology and Chemistry- Europe, Rome, Italy, 13-17 May 2018. Poster
- Tomaz, A., S. Fialho, A. Lima, P. Alvarenga, M. Potes, R. Salgado, P. Palma. 2018. Assessing water quality for irrigation and soil salinization risk under drought: the case of the Alqueva reservoir (Guadiana river basin). Oral communication presented at Conference on Ecological and Environmental Engineering. 25-29 junho 2018. Cracóvia (Polónia). pp 156-157.
- Várbíró G., Bouchez A., Rimet F., Tapolczai K., Novais M.H., Morais M.M., Usseglio-Polatera P. & Viktoria B.B: "Limiting similarity and environmental filtering under drought stress, a case study on diatoms". 25th International Diatom Symposium, Berlin, Germany, 25-30 June 2018. Oral Presentation

6.4 Sessão de Apresentação dos Resultados

No final do projeto foi realizada uma sessão para a qual foram convidados muitos agentes (stakeholders) da região, através do convite:

Estiveram presentes as seguintes entidades:

- Administração de Região Hidrográfica (ARH) Alentejo
- Administração de Região Hidrográfica (ARH) Tejo
- Comunidade Intermunicipal do Alto Alentejo - CIMAA
- Comunidade Intermunicipal do Baixo Alentejo CIMBAL
- Câmara Municipal de Mourão
- Câmara Municipal de Évora
- Câmara Municipal da Vidiueira
- Instituto de Ciências Agrárias e Ambientais Mediterrânicas - ICAAM
- Administração Regional de Saúde (ARS) do Alentejo
- Instituto Nacional de Investigação Agrária e Veterinária INIAV
- Associação Terras Dentro
- Instituto da Conservação da Natureza e das Florestas ICNF
- Agência de Desenvolvimento Regional do Alentejo ADRAL
- Agência Portuguesa do Ambiente (APA)
- Instituto Português do Mar e da Atmosfera (IPMA)
- Aquagri
- Empresa Municipal de Água e Saneamento de Beja – EMAS
-

O programa foi o seguinte:

Programa

9:30 -10:00	Receção dos participantes e entrega da documentação
10:00 – 10:15	**Sessão de Abertura** Presidente do Instituto Politécnico de Beja, Prof. João Paulo Trindade Diretor da Escola Superior Agrária de Beja, Prof. António Nunes Ribeiro Vice-Reitor para a Ciência da Universidade de Évora, Prof. António Candeias
10:15 – 10:45	Rui Salgado **ALentejo: sistemas de Observação e Previsão (ALOP): objectivos, resultados e desafios**
10:45 - 11:00	Pausa para Café
11:00 – 11:30	Miguel Potes e Gonçalo Rodrigues **A importância das observações atmosféricas no Alentejo**

11:30 – 12:00	Patrícia Palma e Maria Helena Novais **Avaliação ecológica de massas de água na região Alentejo: desafios e oportunidades**
12:00 – 13:00	Discussão
13:00 – 14:15	Pausa para almoço
14:15 – 14:35	Maksim Iakunin e Rui Salgado **O Impacto de Alqueva no Clima**
14:35 – 14:55	Maria João Costa **Avaliação de parâmetros da qualidade da água por deteção remota de satélite**
14:55 – 15:15	Manuela Morais **Sistema de alerta para prevenção de situações de risco associados a eventos de toxicidade**
15:15 – 15:30	Pausa para Café
15:30 – 16:45	Discussão
16:45 – 17:00	**Apresentação de conclusões e Encerramento**

Algumas fotografias da sessão

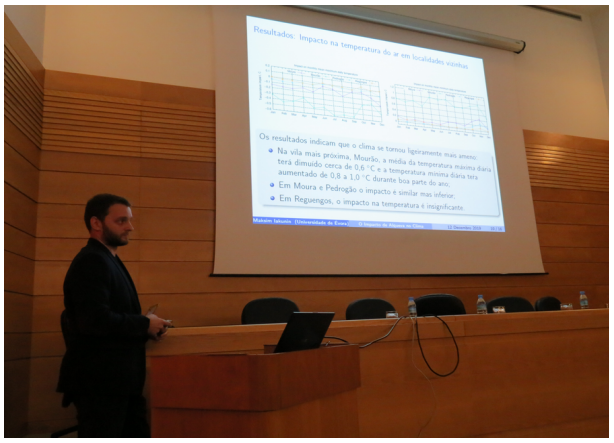

Relato do debate da parte da manhã

Questões para o debate:

• Quais os maiores desafios na avaliação ecológica das águas interiores?

• Quais as maiores dificuldades/desafios na avaliação e gestão de substâncias perigosas/compostos emergentes nas massas de água da região Alentejo?

• Quais os maiores constrangimentos para a monitorização/gestão das bacias hidrográficas?

• Fará sentido estruturar uma rede de monitorização meteorológica / climática para o Alentejo, Como poderia funcionar?

• Qual a importância de uma melhor avaliação da evaporação e das transferências de carbono entre as albufeiras e a atmosfera?

Alice Fialho (ARH Alentejo):

Importante disponibilizar não só os dados meteorológicos, como também dados de qualidade da água (Parte ecológica e química). Objetivo: Rede de transferência de conhecimento. Todas as entidades interessadas e participativas para um melhor controlo das massas de água;

Resposta Rui Salgado: Meteorologia é mais simples de fornecer, porque estão em contínuo. Qualidade da água depende das campanhas.

António Ramos (Aquagri):

Cada proprietário é responsável por cada uma das suas estações meteorológicas. Estações duram em média 10/15 anos. A localização costuma ser sempre a mesma. Em caso de alteração de local costuma ser de apenas alguns metros.

Ana Ilhéu (EDIA):

Interessados em disponibilizar dados para a rede de observação meteorológica no Alentejo.
Importante terem todos o mesmo tipo de informação. Essencial assegurar a qualidade dos dados. Têm dados das estações de Alqueva (ilha) e de Barrancos.
APA:
Importante desenvolver e partilhar de forma prática o conhecimento.
Importante a continuação em funcionamento da estação de Montante
Rui Salgado (ICT):
O ICT disponibiliza os dados obtidos na estação de qualidade em Montante, que tem interesse em manter e que possa ser actualizada.
Lucefecit – Muito fraca qualidade da água; Altas concentrações de azoto e fósforo. Metais como Cádmio também foram detectados, assim como pesticidas.
Ricardo Deus (IPMA):
IPMA tem dado alguns avanços na vigilância meteorológica, com a integração de dados de outras estações. Já têm 240 estações. Interessados em aproveitar os dados das estações no Alentejo. Muito importante a investigação na área da evaporação.
A melhorar: Dificuldade de controlo de dados. Uma melhor relação entre o IPMA e a investigação.
Susana Ramalho (Águas públicas do Alentejo):
Responsáveis pelo tratamento da água, para abastecimento público de 20 municípios no Alentejo. Os blooms algais representam um problema para o abastecimento, no entanto, o tempo necessário para detectar blooms de cianobactérias dificulta a capacidade para tomar medidas (demoram 8 dias em média a receber análises de cianobactérias). O problema da deteção de fármacos na água também dificulta o abastecimento, pelo que deve haver um reforço das análises a ser consideradas. A descarga das ETARs também é problemática. Importante ter maior rapidez, tais como, apresentar um sistema de alerta de forma a diminuir o tempo de resposta entre o evento e a informação.
Refere a importância da qualidade da água e da albufeira de Alqueva para o abastecimento público na região, considerando a ligação direta às albufeiras de Alvito, Roxo, Enxoé e Monte Novo. Existe uma preocupação com a qualidade da água da albufeira do Enxoé.

Pedro Costa (Câmara municipal de Évora):
O município de Évora já dispõe duma Estratégia de adaptação às alterações climáticas. Gestão dos recursos hídricos é muito importante. Precisam da informação científica de qualidade da água para atualizar documentos, como os planos municipais de ordenamento do território.
INIAV (Laboratório de Évora):
Não se deverá analisar a qualidade da água em locais mais próximo de Espanha?
Resposta Patrícia Palma – Lucefecit é representativo do que vem de Espanha.
Medidas para minimizar as cargas poluentes e identificar os problemas principais de qualidade da água na albufeira.
Alice Fialho (ARH Alentejo):
Acrescentou que a ETAR de Badajoz foi intervencionada recentemente.

Paulo Luz (INIAV Oeiras):
Interessado na qualidade e quantidade de água na aplicação para rega.
Importante ter relações entre evapotranspiração e evaporação. Impacto do Alqueva?
Integrar todo este conhecimento nas atividades, tais como na agricultura.

Relato do debate da sessão da tarde

Questões para o debate:

- *Quais os impactos de Alqueva no clima?*
- *Teria interesse dispor de um modelo tri-dimensional operacional de Alqueva que fornecesse a previsão de temperatura e de outras variáveis da albufeira?*
- *Qual o papel da detecção remota por satélite como ferramenta de apoio à monitorização da qualidade da água, e quais os parâmetros e periodicidade desejáveis para uma vigilância efectiva?*
- *Qual a importância da previsão a 3/10 dias da evolução na qualidade da água com informação de deteção remota de satélite e previsão meteorológica?*
- *Que tipos de toxicidade associada a situações de risco (ambiental e saúde pública) devem ser previstas na região Alentejo?*
- *Que variáveis monitorizar, de que forma? Com que periodicidade?*

Susana Ramalho – Águas Públicas do Alentejo
Abastecem 20 municípios do Alentejo, 40% da água usada no abastecimento é proveniente de albufeiras
Detectam cianobactérias em todas as albufeiras, especialmente no Enxoé, mas o tempo de espera para acionar processos é demasiado, apesar da importância para a tomada de decisões para afinar a ETA.
Perguntei se têm dados de outras albufeiras, e a Susana respondeu que sim.

Maria João Costa – ICT
Novos satélites permitem uma melhor resolução das imagens (até 2014 era só de 250m), assim actualmente podemos avançar para estudar albufeiras de menores dimensões, que são praticamente todas as albufeiras do Sul de Portugal.

Manuela Morais – ICT
Actualmente encontra-se em revisão os parâmetros (como a clorofila a) para avaliação da qualidade ecológica para as albufeiras do Sul. Existe a possibilidade desta informação ser complementada com pigmentos como as ficobiliproteínas.

Maria João Costa – ICT
É importante ter dados dos locais, análises feitas em laboratório, para se poder afinar os algoritmos para as albufeiras de menores dimensões.

Verónica – APA
A detecção remota é uma boa ferramenta. Perguntou qual a frequência? E quando não há satélite se se pode usar um modelo?
A APA tem dados que pode disponibilizar.
A Maria João respondeu: Que era uma pergunta que tínhamos pensado colocar para debate e que depois retirámos. É uma hipótese. Em relação à frequência, referiu que pode haver atraso de uma semana para se obter imagens de satélite.

Paulo Luz – INIAV
Para os agricultores faz falta um sistema como o "Risco de Incêndio". É preciso ideias para passar esta imagem para o público, é importante a ligação aos dados ambientais para passar a mensagem em níveis qualitativos e simples.
Perguntei se ele tinha interesse em que se realizassem medições directas de Evapotranspiração sobre as culturas novas na área de regadio de Alqueva? Ele respondeu que pode ter interesse para a EDIA (p.e.) para gerir o consumo de água para a agricultura.
Refere a necessidade de ter diferentes plataformas que integrem dados da atmosfera, sendo

importante a ligação com a energia.

Manuela Morais – ICT
Há guidelines para a qualidade da água, a caracterização da água para diferentes fins. Refere a importância da integração da agricultura e ambiente.

Rui Salgado – ICT
Não temos uma previsão hídrica em Portugal. Faz falta um modelo hídrico de quantidade para o Guadiana.
Devíamos ter um modelo 3D para o Alqueva. Mas não é propriamente um projecto científico que se enquadre num projecto FCT. Teria interesse para a EDIA ou APA?
O modelo suíço usa imagens de satélite para iniciar os resultados, as medições in situ para aferir as medições de satélite, e o modelo, quando não têm nenhum deles, para fazer a previsão.

Patrícia Palma – ICT
A transmissão do conhecimento é muito importante, criando plataformas com dados meteorológicos, de qualidade da água, etc.
Como criar estas plataformas, aferir e transmitir a quem precisa da informação?
Como transpôr os resultados para a região?
É importante incluir outras áreas como a agricultura nos projectos de investigação.
Temos de trabalhar o canal da comunicação. O IPBeja já tem alguma experiência no contacto com os agricultores.

Manuela Morais – ICT
Com o cenário das alterações climáticas temos que pensar e agir agora.

Susana Ramalho – Águas Públicas do Alentejo
Estão no grupo ADP.
Estamos no sexto ano consecutivo em seca no Baixo Alentejo.
Em 2019 já gastaram 1.2 Milhões de euros em abastecimento de populações (2000 pessoas) nas zonas mais afectadas, Serpa, Moura, Barrancos.
As reservas de águas precisam de 48h de descanso para deixar assentar a turvação da água.
Temos de sair daqui hoje com ideias concretas para o futuro.

Paulo Luz – INIAV
Temos de passar todas as vossas publicações científicas para publicações práticas! (referiu-se às 20 publicações do ALOP)

Manuela Morais – ICT
Temos de acionar os desafios societais.

Alexandra Tomaz – IPBeja
A rede meteorológica pode fornecer a evapotranspiração de referência. Há estações que já têm. O COTR já fornece aos associados a previsão da evapotranspiração do olival, amendoal, etc.

Verónica – APA
Se não tivermos as respostas hoje teremos de continuar a procurar amanhã.

Manuela Ruivo – EDIA
É importante testar os algoritmos e os modelos noutras albufeiras. A EDIA tem muitos dados de diferentes albufeiras e estão disponíveis para partilhar connosco e com outras identidades.

Manuela Morais – ICT
O Alqueva é uma albufeira que pertence à tipologia Albufeiras de Curso Principal, que é uma classificação diferente das pequenas albufeiras do SulEstas diferentes classificações têm diferentes limiares na Directiva-Quadro da Água.

Manuela Ruivo – EDIA
É importante articular os dados disponíveis com os planos de amostragem.
Também podem disponibilizar dados.

Susana Ramalho - Águas Públicas do Alentejo
Refere a necessidade de haver financiamento.

7. Indicadores

Como demonstrado anteriormente foram cumpridos os vários indicadores do projeto

Indicador	Propostos	Executados
Artigos em revistas de circulação internacional com arbitragem científica	18	45 (+ 100%)
Comunicações em eventos científicos	27	>27 (+100%)
Organização de cursos de verão para estudantes graduados	2	2 (100%)
Patentes	2	2 (100%)[1]
Seminários técnicos	3	3 (100%)
Estágios Científicos	3	>3 (100%)
Criação e manutenção de Website	1	1 (100%)[2]
Desenvolvimento de uma plataforma para partilha de dados	1	0 (50%)[3]
Bolseiros a tempo inteiro	5	>5 (+100%)
Sinergias com outros projectos de investigação	2	6 (+100%)

[1] Efectuados trabalhos de concepção e teste às invenções que se pretendem patentear; ainda não se iniciaram os trabalhos de submissão da patente
[2] A Website está criada e continua a ser mantida regularmente.
[3] Foram recolhidos dados e foram efectuadas reuniões. A Plataforma existe mas tem um conteúdo muito limitado

Anexo A Publicações científicas

Aerosol and Air Quality Research, 17: 2509–2521, 2017
Copyright © Taiwan Association for Aerosol Research
ISSN: 1680-8584 print / 2071-1409 online
doi: 10.4209/aaqr.2017.05.0159

Thirteen Years of Aerosol Radiative Forcing in Southwestern Iberian Peninsula

Maria A. Obregón[1*], Maria J. Costa[2], Ana M. Silva[2], Antonio Serrano[3]

[1] *Departamento de Física, Instituto de Ciências da Terra, Instituto de Investigação e Formação Avançada, Universidade de Évora, Évora, 7000-671, Portugal*
[2] *Departamento de Física, Instituto de Ciências da Terra, Escola de Ciências e Tecnologia, Universidade de Évora, Évora, 7000-671, Portugal*
[3] *Departamento de Física, Universidad de Extremadura, Badajoz, 06071, Spain*

ABSTRACT

Notable uncertainties in the aerosol impact on the Earth's radiative budget still remain, mainly at local scales. This study aims to accurately quantify the shortwave aerosol radiative forcing (ARF) and its efficiency (ARFE) at Évora (Portugal, Southwestern Europe). This is an interesting region affected by different aerosol types and sources. Towards this goal, ARF and ARFE are calculated for Évora during thirteen years (2003–2015), which is the longest period ever analyzed for this region. For this calculation, the most updated AERONET data have been used to simulate irradiance with the libRadtran code. Thus, 1676 daily values were analyzed, obtaining a mean ARF of –7.4 W m^{-2} at the Earth's surface (SURF) and –1.1 W m^{-2} at the top of the atmosphere (TOA), indicating a cooling of the Earth–atmosphere system. The difference in ARF between TOA and SURF indicates a mean net gain of 6.3 W m^{-2} for the atmosphere. While no ARF seasonal pattern is observed at the TOA, a clear seasonal cycle is detected at the SURF with the most negative values occurring in summer. On the other hand, ARFE shows mean values of –62.7 W m^{-2} τ^{-1} at the SURF and –14.3 W m^{-2} τ^{-1} at the TOA. Results show that ARFE highly depends on the aerosol single scattering albedo, showing opposite behavior at the SURF and at the TOA. The large temporal variability detected in the aerosol properties in the region of study confirms the general need for long time series of measurements to achieve an accurate estimation of the ARF and ARFE.

Keywords: Aerosol radiative effects; Long term analysis; Radiative transfer model; AERONET.

INTRODUCTION

Atmospheric aerosol particles, of natural or anthropogenic origin, interact directly with solar and terrestrial radiation through scattering and absorption as well as through emission processes, modifying the Earth's radiative balance. This effect is quantified by the aerosol radiative forcing (ARF) calculated as the change in the radiative balance due exclusively to the existence of aerosols. According to the Fifth Assessment Report delivered in 2013 by the Intergovernmental Panel on Climate Change, direct and indirect effects of aerosols in the atmosphere result in an overall radiative forcing of –0.9 (–1.9 to –0.1) W m^{-2} at the TOA (Boucher *et al.*, 2013). Although this global cooling effect due to aerosols is well established, significant uncertainties still remain, mainly referred to their spatial and temporal variability at regional and local scales. Thus, due to nearby point sources, the aerosol radiative forcing at the local scale can exceed the global values by an order of magnitude. Additionally, most climate models underestimate the negative radiative forcing caused by anthropogenic aerosols (Hansen *et al.*, 2011). Hence, this short-scale information is essential to achieve an accurate knowledge of the impact of aerosols on climate. It is, therefore, important to quantify the long-term aerosol radiative forcing in different areas worldwide, paying special attention to regions of climatic significance.

Within this framework, the Iberian Peninsula is a particularly interesting region affected by occasional intrusions coming from the largest source of dust worldwide: the Sahara Desert. The frequency of these intrusions is modulated by the annual latitudinal displacement of major semi-permanent pressure systems, showing a typical seasonal pattern (Cachorro *et al.*, 2005; Toledano, 2005; Salgueiro *et al.*, 2014) associated to specific synoptic situations (Rodriguez *et al.*, 2001; Querol *et al.*, 2002; Escudero *et al.*, 2005). In addition to the desert dust intrusions, the Iberian Peninsula is notably affected by other sources of aerosols. In particular, the southwestern interior part of the Iberian Peninsula is also exposed to local continental

* Corresponding author.
Tel.: +351 266740800 ext. 5472
E-mail address: nines@unex.es

aerosols and marine aerosols coming from the Atlantic Ocean (Pereira *et al.*, 2005; Elias *et al.*, 2006; Silva *et al.*, 2006; Pereira *et al.*, 2008; Pereira *et al.*, 2011; Obregón *et al.*, 2012). Additionally, wildfires are an occasional but intense source of aerosols for the area in summer. Due to its exposure to a diversity of local and remote aerosol sources, the Iberian Peninsula is a privileged location for studying the aerosol impact on the radiation balance.

A major research site for aerosols in this area is located in Évora (Portugal), deployed by the Institute of Earth Sciences at the University of Évora, where the AErosol Robotic NETwork (AERONET, http://aeronet.gsfc.nasa.gov) has a monitoring station. This station started to operate in 2003 and, since then, provides radiometric measurements of aerosol properties averaged in the atmospheric column according to AERONET standards and protocols. Notable research has been conducted based on these measurements focusing mainly on obtaining typical values for the physical and optical properties of the aerosols during long periods and specific interesting events (Silva *et al.*, 2003; Obregón *et al.*, 2012), identifying most frequent aerosol types in the area (Elias *et al.*, 2006), and studying their radiative effect (Santos *et al.*, 2008; Mateos *et al.* 2014; Obregón *et al.*, 2015a). However, these latter studies are based on a limited period of time (Santos *et al.*, 2008; Mateos *et al.*, 2014) or focus on specific short events (Obregón *et al.*, 2015a), failing to provide an accurate and complete estimation of the aerosol radiative forcing. Therefore, this study gathers the longest series of aerosol measurements ever used for this area in order to accurately estimate the direct aerosol radiative forcing and its efficiency in the shortwave spectral range. In order to thoroughly analyze the impact of aerosols in the total atmosphere, the aerosol radiative forcing and its efficiency will be calculated at the Earth's surface (SURF) and at the top of the atmosphere (TOA).

The paper is structured as follows: first, a brief description of the study region, instrumentation, measurements and methodology is provided (Section 2), followed by the description of the main results (Section 3), and, finally, the main conclusions (Section 4).

METHODOLOGY

Site Description

The current study is based on aerosol experimental measurements registered at the AERONET site located in the city of Évora (Portugal), in southwestern Iberian Peninsula. Fig. 1 shows the location of this station (38.6°N, 7.9°W, 293 m a.s.l), approximately 100 km eastwards from the Atlantic coast.

Évora shows a mainly continental climate attenuated by the maritime influence of the Atlantic Ocean. This climate is classified as Csa (Mediterranean climates with hot and dry summers) according to Köppen-Geiger types (Köppen, 1936). It features very hot and dry summers with prevailing cloud-free conditions. Very high irradiance values, among

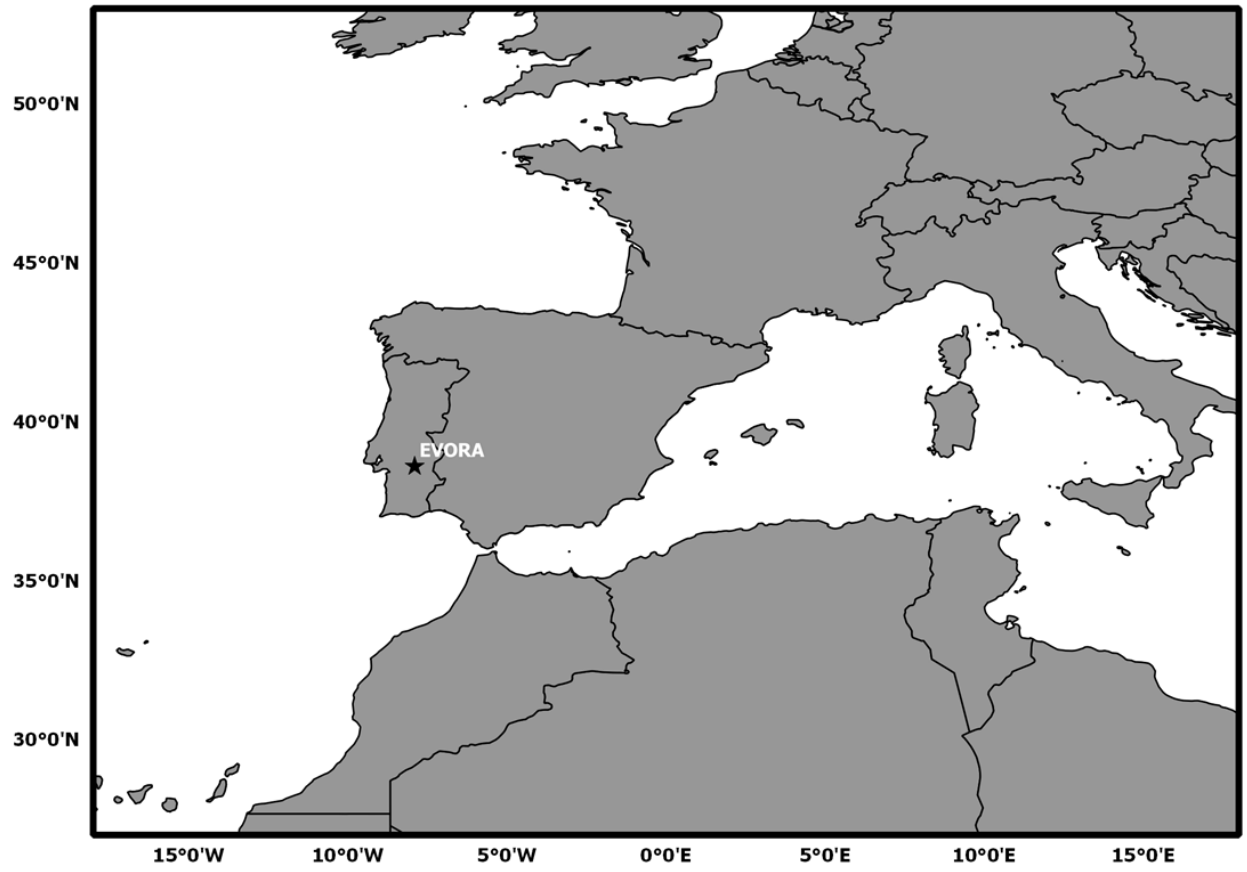

Fig. 1. Location of Évora in the Southwestern Iberian Peninsula.

the highest in Europe, are reached under clear conditions with values up to 1000 W m^{-2} near summer solstice at noon.

Instrumentation

This ground-based station is equipped with a CIMEL CE-318 sunphotometer integrated in the NASA AERONET (Aerosol Robotic NETwork) network (Holben *et al.*, 1998) since 2003. This network provides aerosol information with the aim to establish a ground-based climatology and to identify and characterize the most influential aerosols on the climatic system. The CIMEL CE-318 sunphotometer performs direct sun measurements at 340, 380, 440, 500, 675, 870, 940 and 1020 nm, and measurements of sky radiances in the almucantar and principal plane geometries at 440, 675, 870 and 1020 nm. These measurements are processed following AERONET protocols (Holben *et al.*, 1998) to obtain a variety of aerosol products at different quality levels (1.0, 1.5 and 2.0). The sunphotometer is calibrated annually following AERONET protocols by the AERONET-NASA, RIMA and PHOTONS networks (Holben *et al.*, 1998; Toledano *et al.*, 2006).

Method

It is important to note that the radiative forcing estimates obtained in this study differ from the IPCC definition of radiative forcing. While the IPCC calculates the radiative forcing as the difference between irradiances in the pre-industrial and present day atmosphere due to changes in the concentrations of a certain atmosphere component, in this study, radiative forcing stands for the instantaneous contribution of a particular component (in this case aerosols) to the radiation budget. Thus, it is calculated as the difference in the radiative energy at a given level between a situation where aerosols are present, F, and a situation where these atmospheric particles are absent (background/baseline conditions), F^0:

$$ARF = \left(F_{dn} - F_{up}\right) - \left(F_{dn}^0 - F_{up}^0\right) \quad (1)$$

where F is the flux (shortwave irradiance), the subscript "dn" indicates the downward direction and the subscript "up" the upward direction. In this study, the ARF values calculated at the SURF and at the TOA are analyzed. Thus, radiative forcing can be defined at these two levels as:

$$ARF_{TOA} = F_{up(TOA)}^0 - F_{up(TOA)} \quad (2)$$

$$ARF_{SURF} = \left(1 - A_s\right) \cdot \left(F_{dn(SURF)} - F_{dn(SURF)}^0\right) \quad (3)$$

where A_s is the surface albedo, assumed to be the same for both aerosol situations (background/baseline and presence of aerosols).

To estimate the amount of solar radiations trapped in the atmosphere due to aerosols, the difference in ARF between TOA and SURF is computed. Then, the heating rate (HR) due to aerosol absorption is calculated according to the first law of thermodynamics and assuming hydrostatic equilibrium, as suggested by Liou (2002):

$$\frac{\partial T}{\partial t} = \frac{g}{Cp}\frac{ARF_{ATM}}{\Delta P} \quad (4)$$

where $\partial T/\partial t$ is the HR in K day^{-1}, g is the acceleration due to gravity (9.8 m s^{-2}), Cp is the specific heat capacity of air at constant pressure (i.e., 1006 J kg^{-1} K^{-1}), and ΔP is the atmospheric pressure difference between surface and 3 km altitude, where most aerosols are present. According to several authors, in this study, ΔP was taken as equal to 300 hPa (Kaskaoutis *et al.*, 2013; Singh *et al.*, 2016).

From the ARF instantaneous data, the daily average value (DARF) can be calculated as follows:

$$DARF = \frac{\sum ARF_{hourly}}{24} \quad (5)$$

where ARF_{hourly} are hourly averaged values and the sum extends over the whole day (24 h).

ARF is very sensitive to the amount and type of aerosols existing in the atmosphere, increasing with the AOD. In order to quantify the rate at which the forcing varies per unit optical depth, the aerosol radiative forcing efficiency (ARFE) is defined. The mean ARFE was calculated as the slope of the regression line between ARF and AOD as suggested by Bush and Valero (2003). In this study AOD at 550 nm has been used. The conversion of AOD at 500 nm, which is the AERONET direct product, to AOD at 550 nm has been performed using the Ångstrom power law:

$$AOD550 = AOD500 \cdot \left(\frac{550}{500}\right)^{-\alpha} \quad (6)$$

where α is Ångstrom Exponent in the wavelength range of 440–870 nm (Alam *et al.*, 2011).

The dataset used in this study is composed of cloud-free shortwave irradiance simulated values integrated over the spectral interval 285–2800 nm. The simulations were performed during those days in the period 2003–2015 when level 2.0 AERONET data are available for this station. Thus, 1676 days were used, which is a much higher number than, for example, the 200 days used by Esteve *et al.* (2014). It is important to note that level 2.0 data correspond exclusively to cloud-free conditions.

The shortwave irradiances were simulated using the libRadtran version 1.7 radiative transfer code (Mayer and Kylling, 2005; Emde *et al.*, 2016). The uncertainties of libRadtran model were assessed by Emde *et al.* (2016), who showed that the estimated radiance and irradiance results agree very well with a reference validated model, presenting differences lower than 0.05%, with a few exceptions for cases that are not treated in this work (for example circum-solar radiation). References therein (Emde *et al.*, 2016) to a number of model intercomparison studies demonstrate the performance of libRadtran in comparison to a variety of other models. In addition, Obregón *et al.*

(2015b) analyzed the performance of libRadtran to simulate shortwave solar irradiances under different aerosol conditions, through comparison with corresponding calibrated pyranometer measurements. The authors obtained relative differences between irradiance simulations and measurements lower than 0.2%. Additionally, Román *et al.* (2014) analyzed the sensitivity of SW irradiances simulated with libRadtran model to the input uncertainties, obtaining a global sensitivity usually below 10%.

The main inputs for simulations were aerosol optical properties, precipitable water vapor column, surface albedo, and total ozone column. The inputs to describe the aerosols were provided by AERONET and consist of direct products as aerosol optical depth (AOD) and Ångström parameter, and inversion products as asymmetry parameter (ASY), and single scattering albedo (SSA). Ångström parameters were derived from level 2.0 AERONET aerosol optical depth (AOD) in the range 440–870 nm. Level 2.0 AERONET dataset also provided ASY values. Level 2.0 SSA data are very scarce, with only 226 values available in the period of study. The main reason is the requirement to only consider cases with AOD at 440 nm higher than 0.4. This AOD value is very unusual in Évora (the typical median value is 0.1) and corresponds almost exclusively to desert dust intrusions, which is a very specific situation. Therefore, in order to include different aerosol types and to have enough data available, level 1.5 SSA had to be used. Additionally, data were inspected to search for anomalous values. No negative AOD cases and only eight (0.06% of a total number of cases of 13920) negative Ångström exponent cases were found. The latter were filtered. SSA and ASY values for 675 nm have been used as suggested by some authors (Di Biagio *et al.*, 2010; Foyo-Moreno *et al.*, 2014). This wavelength has been chosen among the wavelengths available at AERONET data as it is close to the maximum of the solar irradiance per unit wavelength. Precipitable water vapor data were also obtained from level 2.0 AERONET products. Daily total ozone column was provided by the AURA Validation Data Center (AVDC) via its website (http://avdc.gsfc.nasa.gov/index.php?site=1593048672&id=28). Surface albedo was obtained from the Surface and Atmospheric Radiation Budget (SARB) working group, part of NASA Langley Research Center's Clouds and the Earth's Radiant Energy System (CERES) mission (http://ceres.larc.nasa.gov/). In order to take into account the time of the year, midlatitude summer/winter standard vertical profiles of thermodynamic variables, main gases and aerosols were considered depending on the season (Shettle *et al.*, 1989; Mayer and Kylling, 2005). The extraterrestrial irradiance was considered according to Gueymard (2004). The radiative transfer equation solver DISORT2, which is an improved version of the multi-stream discrete ordinate method of Stamnes *et al.* (2000), was used with 16 streams.

In order to more accurately model the instantaneous irradiance, 10-minute irradiances were simulated. For this, available AERONET values (α and β Ångström coefficients, ASY, SSA and PWC) were interpolated on a 10-minute basis. The dataset used was composed of 108843 10-minutes values of ARF corresponding to the 1676 days with available AERONET data. Fig. 2 shows the number of days analyzed in this study for each month during the period 2003-2015. Summer is the season with more days with available data (668 days, 40%), due to the prevailing cloud-free conditions during this period of the year. The relative frequency of days with available data for the other seasons was 21% (352 days) in spring, 20% (343 days) in autumn, and 19% (314 days) in winter.

To evaluate the aerosol radiative effects, simulations with and without aerosols were computed for the 108843 cases. Finally, ARF was calculated at the TOA and at the SURF levels, substituting the simulated irradiance in equations 2 and 3, respectively.

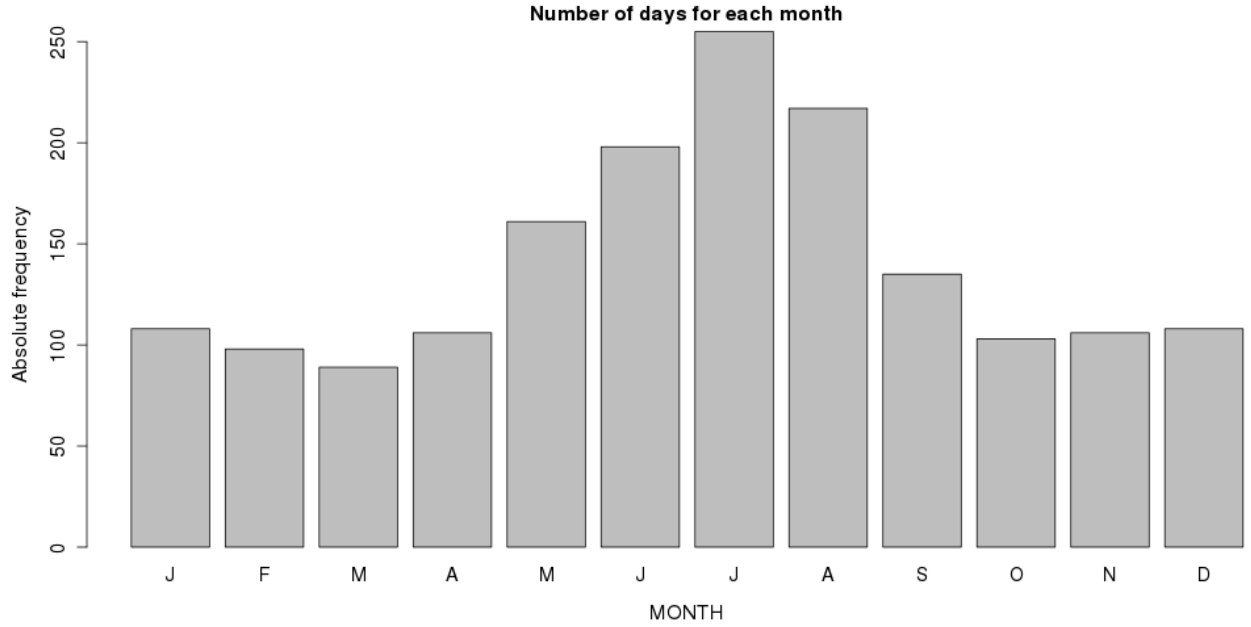

Fig. 2. Number of daily ARF values, DARF, for each month during the period 2003–2015.

The reliability of the libRadtran model for simulating SW irradiance in Évora was previously confirmed by comparing simulated values with irradiance measurements registered by an Eppley Black & White pyranometer (Obregón *et al.*, 2015a). This comparison included clean and turbid cases corresponding to periods before or after (clean), and during (turbid) two particular desert dust intrusion events occurred in summer 2012 (Obregón *et al.*, 2015a). Additionally, in this study the reliability of the libRadtran simulations will be tested by comparing our estimated instantaneous ARF with values provided by AERONET.

RESULTS AND DISCUSSION

Spectral Variation of AOD, SSA and ASY

As mentioned in the methodology, aerosol optical properties such as AOD, SSA and ASY along with their spectral variability are required for calculating ARF and ARFE. These properties have different spectral variations revealing information about the particle size and their absorptivity. Fig. 3 illustrates the AOD, SSA and ASY mean spectral variation for the different seasons.

The spectral variation of AOD provides information about the particle size distribution (Eck *et al.*, 1999). AOD seems to be more wavelength dependent during summer, when it decreases as wavelength increases, indicating the presence of fine particles. Conversely, the smaller spectral dependence is observed in winter, indicating the prevalence of coarser particles. Mean AOD in summer is 0.17 ± 0.12 at 440 nm wavelength and 0.07 ± 0.08 at 1020 nm, whereas, in winter, the mean value is 0.08 ± 0.05 at 440 nm and 0.03 ± 0.02 at 1020 nm.

In regard to SSA, Fig. 3 shows the mean values for each season of the year. As can be seen, mean SSA values for the four seasons decrease as wavelength increases. This SSA spectral behavior indicates the presence of absorbing aerosols (Dubovik *et al.*, 2002). This wavelength dependence is more intense in winter than during the other seasons of the year, with mean values of 0.88 ± 0.08 at 440 nm and 0.80 ± 0.14 at 1020 nm. This dependence is also reported for Lahore and Karachi by Alam *et al.* (2012), Delhi by Singh *et al.* (2010), and four locations in the Indo-Gangetic plains by Bibi *et al.* (2016), but only during winter, when dust is not a major contributor to the aerosol load.

Additionally, the mean value corresponding to AERONET level 2.0 SSA data has been added to Fig. 3(b). In contrast to the behavior found for the SSA data used in this work, level 2.0 SSA presents higher values and increases or is neutral with wavelength, which is a clear signature of the predominance of mineral dust (Dubovik *et al.*, 2002). This fact is due to the extremely restrictive threshold used for level 2.0 data, which requires AOD higher than 0.4. In the case of Évora, this threshold mostly retains those cases with desert dust aerosols originating from the Sahara region. Since this study attempts to analyze the mean aerosol radiative forcing in southwestern Iberian Peninsula during thirteen years, a variety of aerosol conditions needs to be sampled. Therefore, for this study, the level 2.0 AERONET data is too restrictive regarding the SSA.

Similarly to AOD and SSA, ASY shows spectral dependence (Fig. 3(c)). In general ASY decreases with increasing wavelength, except for high wavelengths, where a marginal increase can be observed for spring, summer and autumn seasons. Mean ASY (standard deviation) is 0.70 (0.03) at 440 nm and 0.66 (0.04) at 1020 nm in spring, 0.70 (0.03) at 440 nm and 0.65 (0.05) at 1020 nm in summer, 0.70 (0.03) at 440 nm and 0.64 (0.05) at 1020 nm in autumn, and 0.70 (0.03) at 440 nm and 0.62 (0.06) at 1020 nm in winter. The largest ASY decrease is thus observed in winter, in line with the results reported by Alam *et al.* (2012) in Lahore and Karachi.

Aerosol Radiative Forcing

In this section, the values of ARF at the SURF and at the TOA over Évora during the period 2003–2015 are analyzed. Fig. 4 shows the values of DARF at the SURF and at the TOA obtained in Évora during the period 2003–2015 in a box and whisker plot. As can be seen, the DARF at the SURF shows some variability during the year, with more negative values in warm months and less negative values in cold months. DARF ranged from –0.1 to –54.9 W m^{-2}, with a mean (and standard deviation) of –7.4 (5.5) W m^{-2},

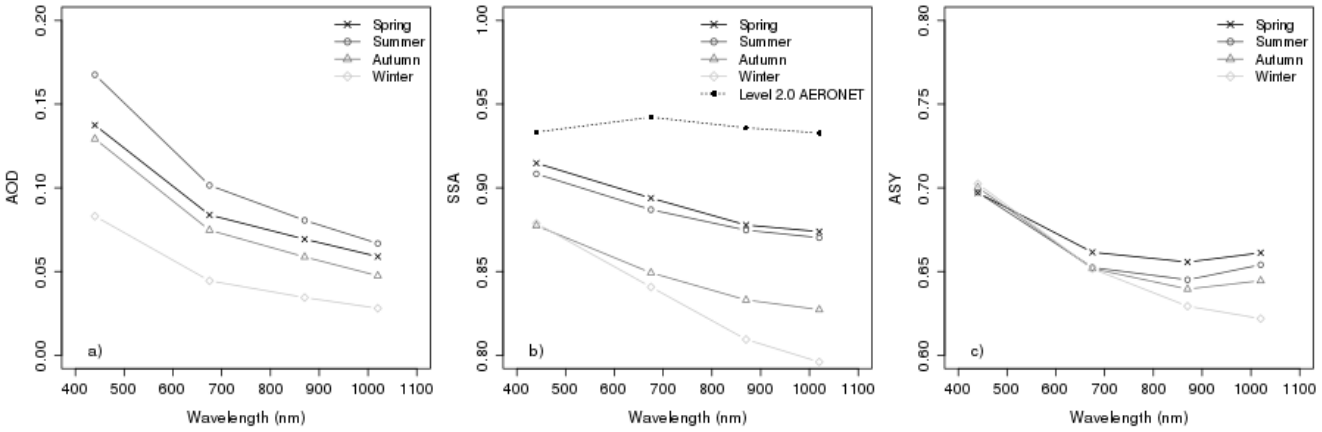

Fig. 3. (a), (b) and (c) show AOD, SSA and ASY mean values at wavelengths of 440 nm, 675 nm, 870 nm, and 1020 nm for different seasons. AERONET level 2.0 SSA has also been plotted in (b) for comparison purposes.

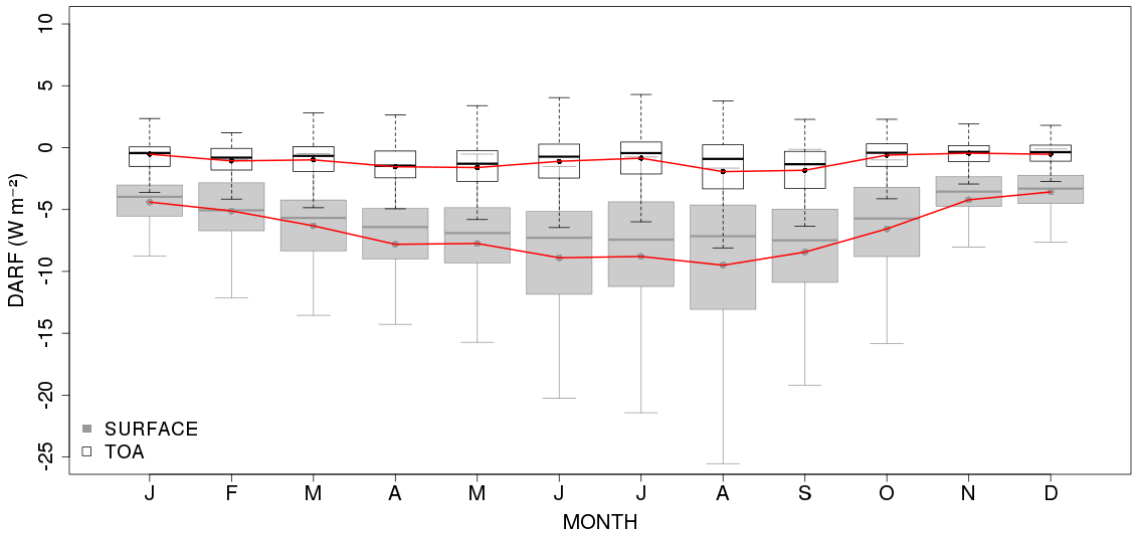

Fig. 4. Box and whisker plot of daily ARF values, DARF, at the surface and the top of the atmosphere for each calendar month over the 2003–2015 period. The mean (filled circles), median (horizontal segment within the box), 25th and 75th percentiles (top/bottom box limits) and data within 1.5 times the interquartile range (whiskers) are shown.

at the SURF, and from –15.6 to +18.9 W m^{-2}, with a mean value of –1.1 (2.5) W m^{-2}, at the TOA. The negative values indicate a decrease in the solar radiation reaching the SURF and an increase in the light scattered back to space at the TOA. This loss in net radiation at the TOA leads to cooling of the Earth–atmosphere system. It is worth mentioning that 491 DARF values are positive (29% of the total number of cases). These values are near zero, with 75% of cases below 1.3 W m^{-2}.

It is interesting to note that the absolute magnitude of the mean DARF at the SURF is higher than at the TOA, producing a mean net gain of energy by the atmosphere estimated in 6.3 (with a standard deviation of 4.8) W m^{-2}. This gain is due to the absorption of radiation by atmospheric components.

The monthly mean of this absorption by the atmosphere is represented by the difference between the two red lines in Fig. 4. These values ranged from 2.6 W m^{-2} in December to 7.1 W m^{-2} in August. These absorbing properties of aerosols are also particularly important for energy balance and cloud-aerosol interactions, as shown in the work of Su *et al.* (2008).

While no seasonal DARF pattern is observed at the TOA, a clear seasonal cycle is detected at the SURF (Fig. 4). This seasonality is not only due to the variation in the radiation along the year, but also to the seasonal pattern shown by AOD (Fig. 5(a)). This figure presents a box and whisker plot of daily AOD (at 550 nm) values over Évora for each calendar month, showing its annual variation. The lowest optical depths occur in November and December, contrasting with the highest optical depths found in August and September, when AOD is higher than 0.18 in more than 25% of the cases. These high AOD values during the summer months can be explained by a combination of several factors such as Saharan dust intrusions and forest fires, being the latter associated with high temperatures, very low atmospheric relative humidity and lack of precipitation. The arrival of air masses from the Saharan region transporting desert-dust aerosols constitutes a substantial source of aerosols, affecting the southwestern Iberian Peninsula generally in summer (Toledano *et al.*, 2007). This fact is confirmed by the low α values observed in August (Fig. 5(b)). Summer forest fires, particularly those extensive and long lasting that occurred in Portugal and Western Spain in 2003 and 2005 (Elias *et al.*, 2006), could mean also a substantial contribution to high optical depth values during these months. Both conditions (low AOD in winter months and high AOD values in summer months) are consistent with the ARF values shown in Fig. 4 (less negative in winter and more negative in summer). Also, a secondary maximum is observed in spring, being consistent with ARF values and observations reported for other stations of the Iberian Peninsula (Estellés *et al.*, 2007; Toledano *et al.*, 2007; Obregón *et al.*, 2012; Esteve *et al.*, 2014).

Fig. 5(b) depicts the annual variation of daily α, showing the highest mean values in January, December, February, and November. Conversely, α is low in April, May and August, being associated with large particles, typical of desert dust episodes or/and intrusions of marine aerosol in spring and summer (associated with sea breeze). In August, the low α values together with high AOD load, indicate the intrusion of dust from North Africa. Other studies have reported a similar seasonal pattern of AOD and α at other locations within the Iberian Peninsula, such as El Arenosillo (Cachorro *et al.*, 2005; Toledano *et al.*, 2007), Boecillo (Cachorro *et al.*, 2000), and Cáceres (Obregón *et al.*, 2015c). As it can be seen in Fig. 5(a), although AOD is high and similar in August and September, α differs between these two months. In August, α is lower than in September, indicating a stronger influence of desert dust aerosol in August than in September, and a higher cooling at the SURF. This tendency of cooling the Earth-atmosphere system due to the effect of desert dust aerosols agrees with results reported for other regions (e.g., Costa *et al.*, 2006; Derimian *et al.*, 2006;

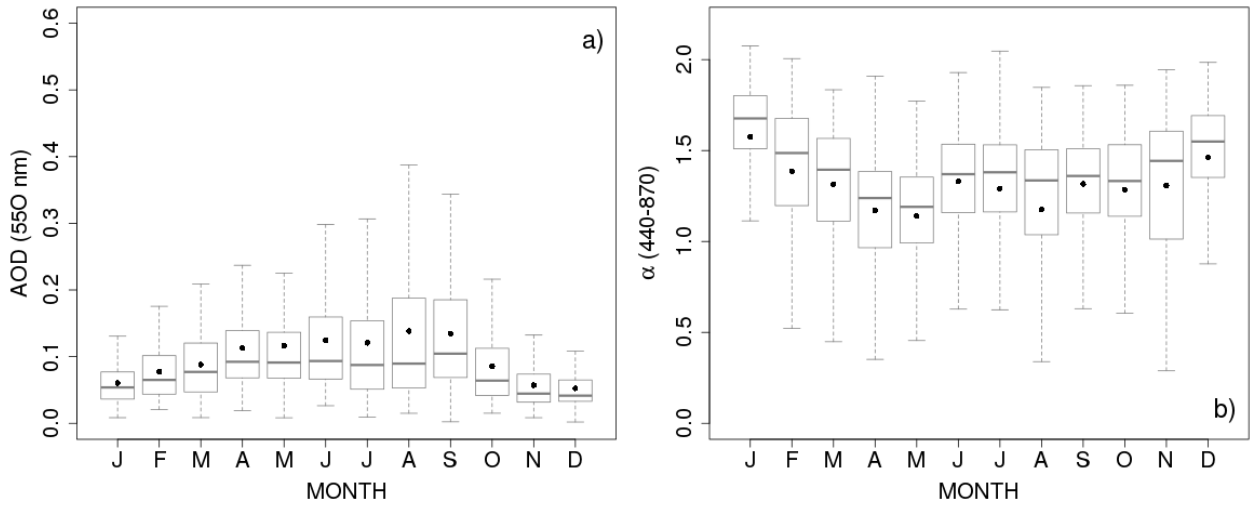

Fig. 5. Box and whisker plot of daily AOD (a) and α (b) values for each calendar month over the 2003–2015 period. The mean (filled circles), median (horizontal segment within the box), 25th and 75th percentiles (top/bottom box limits) and data within 1.5 times the interquartile range (whiskers) are shown.

Lyamani *et al.*, 2006; Cachorro *et al.*, 2008; Guerrero-Rascado *et al.*, 2009; Huang *et al.*, 2009; García *et al.*, 2012; Santos *et al.*, 2013; Valenzuela *et al.*, 2012; Obregón *et al.*, 2015a).

It is worth mentioning that our findings are not in line with results for the same station reported by Mateos *et al.* (2014) within a general study where several stations were analyzed. The monthly ARF values obtained here are generally more negative than theirs. In particular, the magnitude and the time of the year with the most negative ARF differ between both studies; while this study finds –9.5 W m^{-2} in August, they find around –8 W m^{-2} in April. One reason for this discrepancy could be related with the limited period of study considered by Mateos *et al.* (2014), which, for example, excluded the year 2003. During this year, as already mentioned above, there were numerous intense intrusions of desert dust and several forest fires all over Iberian Peninsula and south of France. The difference in ARF values emphasizes the need for relying on long term representative series of measurements in order to achieve an accurate estimation of the average regional aerosol radiative effect, mainly in areas with high variability such as the Iberian Peninsula.

An example of the spatial variability is the difference in ARF values reported for the Atlantic and the Mediterranean coastal areas within the Iberian Peninsula. Thus, the magnitude of the ARF obtained in this study at an Atlantic-influenced station such as Évora is around half the values measured at a Mediterranean station such as Burjassot (Valencia, Spain) (Esteve *et al.*, 2014). This difference is due to several factors such as the influence of the oceans, the prevailing circulation patterns and local aerosol sources. The results obtained in this study also show great differences with respect to those obtained in large polluted cities such as Lahore and Karachi in Pakistan. At these stations the ARF values are around –70 and –19 W m^{-2} at the SURF and at the TOA, respectively (Alam *et al.*, 2011; Alam *et al.*, 2014).

Fig. 6 shows comparisons between ARF at both levels SURF (a) and TOA (b), as provided by AERONET vs values estimated in this study using libRadtran. The comparisons are performed for the period of study. Values at the SURF show a good general agreement, with a high correlation coefficient of 0.97. This value is similar to those obtained by Alam *et al.* (2012) for Lahore and Karachi using SBDART model (0.99 and 0.98, respectively), and notably higher than those obtained by Bibi *et al.* (2017) over Karachi (0.51), Lahore (0.81), Jaipur (0.66) and Kanpur (0.69). This good correlation between AERONET and libRadtran surface forcing demonstrates that the input parameters, particularly the atmospheric profiles, constitute an appropriate representation of the prevailing atmospheric conditions in our location of study. On the other hand, the comparison between ARF at the TOA presents also a very high correlation coefficient (0.91) at the TOA (Fig. 6(b)). This value is notably higher than the values obtained by Bibi *et al.* (2017) over Karachi (0.46), Lahore (0.73), Jaipur (0.57) and Kanpur (0.55).

The libRadtran code allows to select two standard aerosol profiles, one typical of spring–summer and another of autumn–winter conditions. These profiles (Shettle, 1989) describe the change in the aerosol profile throughout the year. In order to analyze the sensitivity of the radiative forcing estimates to the vertical distribution of aerosols, these two profiles have been used. Thus, all the calculations have been repeated for both profiles separately regardless of the true season of the year and the daily aerosol radiative forcing has been obtained at the SURF and at the TOA. For the comparison analysis, the whole year 2012 has been used in order to account for the annual variability of the frequency of the aerosol conditions. The DARF estimated using both profiles show a very good agreement with a correlation coefficient near one. Differences in the DARF are very low at both levels, with mean differences of –0.001 Wm^{-2} (standard deviation of 0.009 Wm^{-2}) at the SURF, and of 0.012 Wm^{-2} (standard deviation of 0.050 Wm^{-2}) at the TOA. These results are in line with the sensitivity study

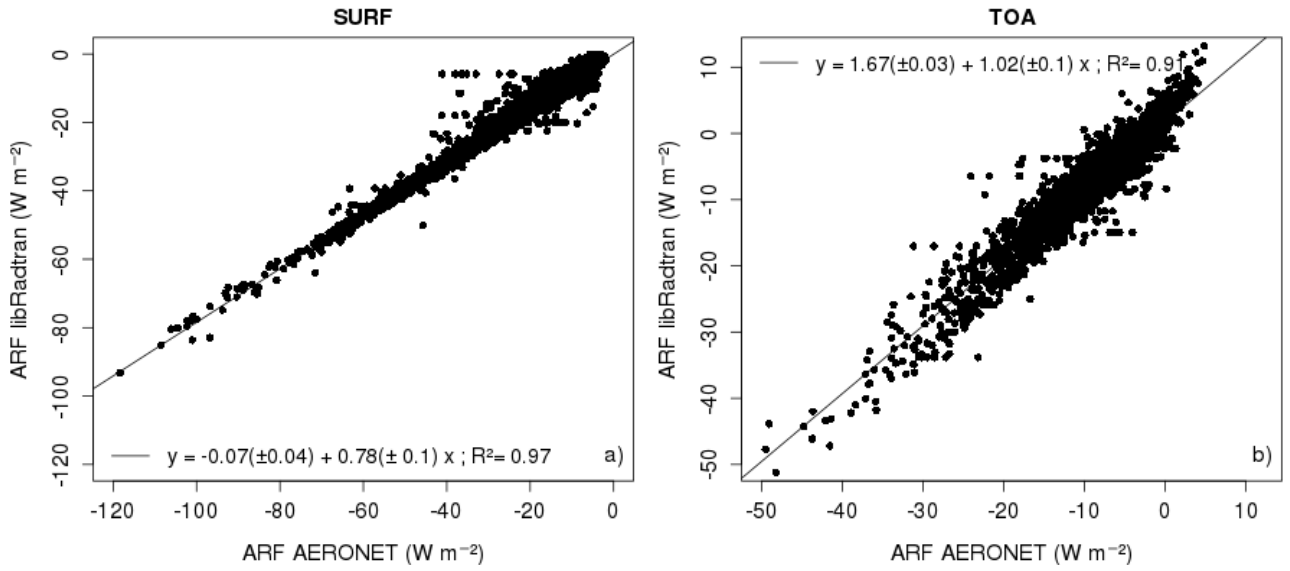

Fig. 6. Comparisons between ARF provided by AERONET and ARF estimated in this study using libRadtran, (a) for surface level and (b) for the top of the atmosphere level.

performed by Mishra *et al.* (2015), who concluded that aerosol forcing in the visible-near infrared range is less sensitive to changes in the aerosol layer height as compared to thermal-infrared and ultraviolet ranges.

As mentioned before, since the ARF depends on the particle load in the atmosphere, the forcing efficiency ARFE was calculated and analyzed at the SURF and at the TOA levels. The mean ARFE has been calculated as the slope of the regression line between ARF and AOD values. Since the ARF is expected to be zero when AOD is zero, a zero-intercept linear regression has been used to estimate the ARFE. Fig. 7 shows DARF at the SURF and at the TOA versus daily mean AOD (550 nm). The uncertainty in ARFE is quantified by the error associated to the regression slope. The ARFE obtained were –62.7 ± 0.4 W m^{-2} τ^{-1} and –14.3 ± 0.3 W m^{-2} τ^{-1} (per unit AOD or τ at 550 nm) for SURF and TOA datasets, respectively. In order to analyze the effect of SSA, in Fig. 7 the points have been colored according to their SSA value. As can be seen, for a given AOD, the most negative ARF values at the SURF correspond to low SSA values, i.e., to the most absorbing aerosols. Conversely, the opposite behavior is found at the TOA (Fig. 7(b)). Thus, the increase in the absorption by aerosols reduces the scattered radiation also towards TOA, thereby contributing to less negative (or even positive) ARF values at the TOA. These results are in line with those found during the CLEARCOLUMN/ACE2 campaign conducted at Sagres, Portugal (Silva *et al.*, 2002). They are also confirmed by the ARFE values calculated for different SSA intervals. Thus, the ARFE obtained for SURF were –140.2, –104.3, –81.4 and –55.48 W m^{-2} τ^{-1} for the SSA ranges [< 0.7], [0.7–0.8], [0.8–0.9], [>0 .9], respectively. Similarly, the following ARFE values: +44.5, +15.2, –3.4, –19.1 W m^{-2} $\tau^{-1,}$ were obtained for the TOA for the same SSA intervals mentioned above. While the aerosols at the SURF with low SSA result in highly negative ARFE values, at the TOA those aerosols are associated with less negative, or even positive, ARFE values.

The ARFE was also calculated at 500 nm in order to compare with the study performed by Esteve *et al.* (2014) for a Mediterranean station during the period 2003–2011. As mentioned before, notable differences exist between the Atlantic and the Mediterranean areas. Thus, while Évora shows –55.1 W m^{-2} τ^{-1} at the SURF and –15.1 W m^{-2} τ^{-1} at the TOA, Burjassot shows more negative values (–139 W m^{-2} τ^{-1} at the SURF and –19.2 W m^{-2} τ^{-1} at the TOA).

Fig. 8 shows the mean ARFE calculated for each season of the year at the SURF and at the TOA. Points have been colored according to their SSA value. No seasonal effect can be perceived at any level, with ARFE around –62 W m^{-2} τ^{-1} and –14 W m^{-2} τ^{-1} at the SURF and at the TOA, respectively. However, the aerosol tends to have a slightly stronger impact at the TOA in spring (–16.1 ± 0.7 W m^{-2} τ^{-1}) than in the remaining seasons: winter (–14.2 ± 0.9 W m^{-2} τ^{-1}), autumn (–13.9 ± 0.6 W m^{-2} τ^{-1}) and summer (–13.8 ± 0.4 W m^{-2} τ^{-1}).

Heating Rate

The amount of solar radiations trapped in the atmosphere by the aerosols as quantified by the atmospheric heating rate has been analyzed. The average heating rate (K day^{-1}) estimated from DARF during the study period was 0.18 (with a standard deviation of 0.15). Percentiles 10 and 90 indicate that in 80% of the days, HR falls between 0.04 and 0.35 K day^{-1}. These values are in line with the value of 0.11 K day^{-1} obtained by Valenzuela *et al.* (2017) for the same location (Évora) during one specific day. The heating rate in Évora is generally lower than values reported for stations with high atmospheric absorption such as, for example, two polluted mega-cities in Pakistan, with values higher than 1 K day^{-1} (Alam *et al.*, 2012). It is also lower than the values obtained for two desert dust events analyzed by Gharibzadeh *et al.* (2017), which showed mean values of 2.16 and 0.89 K day^{-1}.

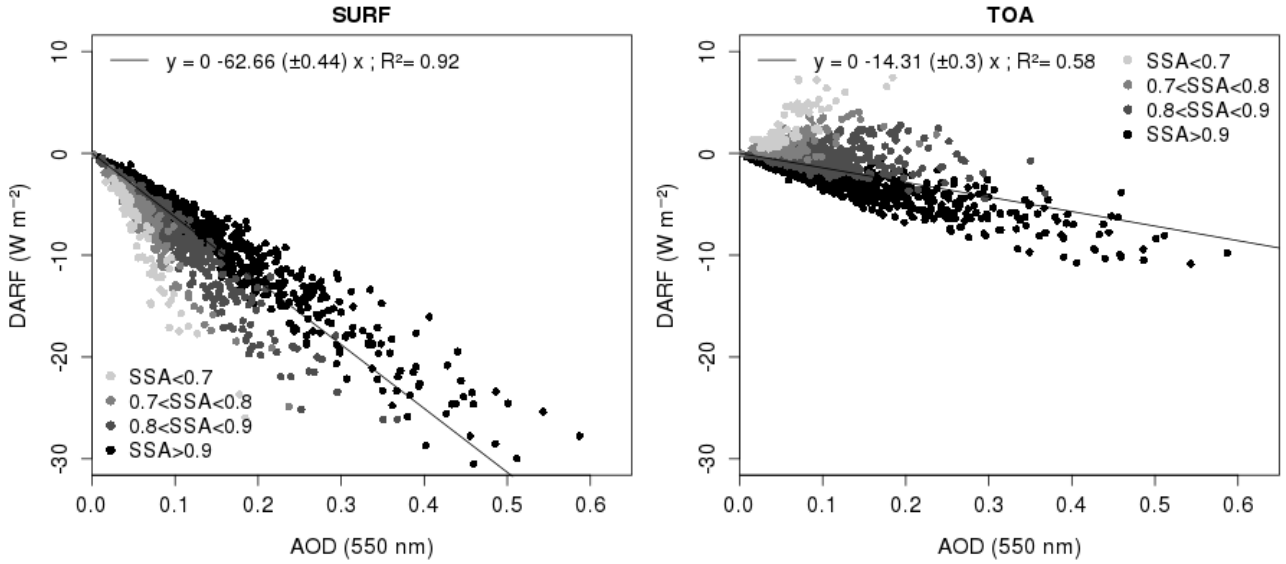

Fig. 7. Aerosol radiative forcing as a function of the AOD at 550 nm during the study period. (a) for surface level and (b) for the top of the atmosphere level. The regression equations are included and the points have been colored according to their SSA value.

In order to analyze the annual variation of the HR in Évora, the mean HR value was calculated for each calendar month (Fig. 9). The higher HR values occur mainly during summer (mean of 0.22 and standard deviation of 0.15), when ARF is also high. It is followed by spring (mean of 0.18 and standard deviation of 0.18), autumn (mean of 0.15 and standard deviation of 0.12) and winter (mean of 0.10 and standard deviation of 0.10). Spring is the season that shows the higher variability, with many high HR values during April. The annual variation in the amount of solar energy trapped by the atmosphere has strong implications for temperature changes and thermal structure of the atmosphere as well as important consequences for many processes, like cloud formation, precipitation, and synoptic circulation.

CONCLUSIONS

The aerosol radiative forcing (ARF) at Évora station has been studied with the goal of reducing the uncertainty of the aerosol impact at local scales. This station provides information about Southwestern Iberian Peninsula, a region of climatic significance largely affected by different aerosol types such as local continental particles, Atlantic marine aerosols, and desert dust coming from the largest source of dust worldwide: the Sahara Desert. Towards this aim, the aerosol radiative forcing and its efficiency (ARFE) in the shortwave solar spectrum have been calculated and analyzed. The study period extends from 2003 to 2015, being the longest period ever used in studies of aerosol radiative forcing in this region.

ARF and ARFE have been calculated at both the Earth's surface (SURF) and top of the atmosphere (TOA) levels. For this purpose, a high temporal resolution dataset, composed of 10-minute irradiance values simulated using the libRadtran code and previously validated, has been used. The ARF values calculated on a 10 minute basis have been integrated over 24 h to obtain daily mean values, DARF, for 1676 days. While no seasonal DARF pattern is observed at the TOA, a clear seasonal pattern can be distinguished at the SURF, with more negative values in summer, likely associated not only to the variation in the radiation along the year but also to the annual variability of AOD. The DARF values obtained for SURF ranged from –0.1 to –54.9 W m^{-2}, with a mean (and standard deviation) of –7.4 (5.5) W m^{-2}, and from –15.6 to +18.9 W m^{-2} at the TOA with a mean value of –1.1 (2.5) W m^{-2}. The negative values indicate a decrease in the solar radiation that reaches the Earth's surface and an increase in the light that is scattered back to space, cooling the Earth–atmosphere system. The difference in DARF magnitude between SURF and TOA indicates a mean net gain of energy by the atmosphere estimated in 6.3 (with a standard deviation of 4.8) W m^{-2}, due to absorption of radiation by atmospheric components.

The values of ARF at the SURF calculated in this study were compared with those reported by other authors for different regions, showing significant differences and indicating the importance to perform accurate local studies to achieve a thorough description of the impact of aerosols. The comparison with the study of Mateos *et al.* (2014) for the same station revealed notable differences, mainly in the ARF seasonal pattern. This discrepancy is likely associated to the use of a limited period of measurements in that study, emphasizing the need to use long high quality time series of data in order to guarantee an accurate description of the aerosol radiative forcing.

Instantaneous ARF values simulated with libRadtran have been compared with values provided by AERONET. The comparison showed a very good agreement at both levels: SURF and TOA, confirming the reliability of the calculations performed in this study with the libRadtran model.

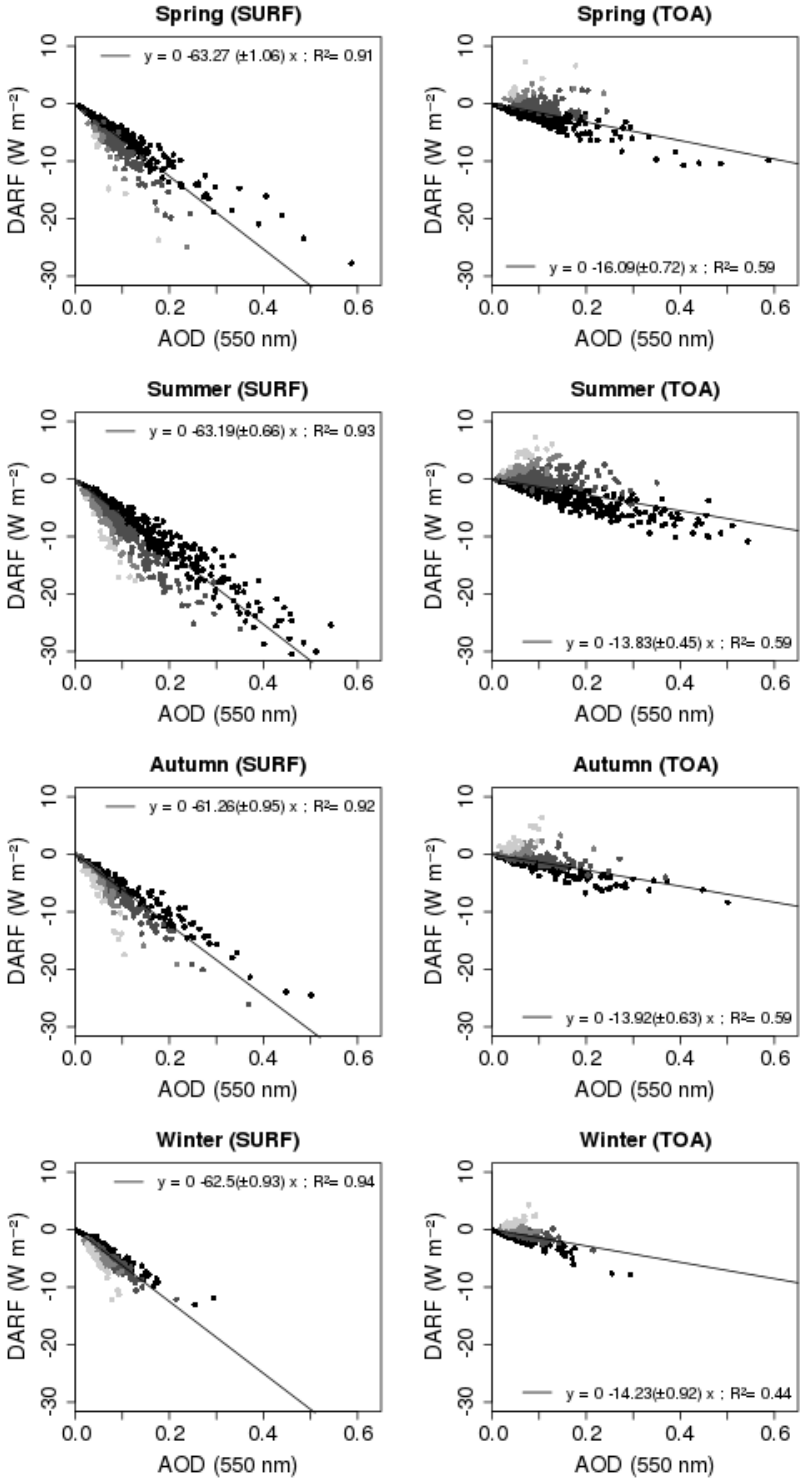

Fig. 8. Aerosol radiative forcing as a function of the AOD at 550 nm for each season of the year. The regression equations are included and the points have been colored according to their SSA value.

The ARFE (ARF per unit optical depth) was also calculated, and found to be –62.7 ± 0.4 W m^{-2} τ^{-1} and –14.3 ± 0.3 W m^{-2} τ^{-1} (per unit AOD or τ at 550 nm), at the SURF and at the TOA, respectively, showing no seasonality. These ARFE values are directly related to the SSA, with opposite behavior at the SURF and at the TOA. Thus, while at the SURF the aerosols with low SSA result in highly negative ARFE values, at the TOA those aerosols are associated with less negative or even positive ARFE values. This fact is due to the higher absorption by these aerosols, which results in less scattered radiation also towards the TOA and, therefore, in less negative ARFE at the TOA.

The values of ARF and ARFE reported for the region of study positively contributes to improve the understanding

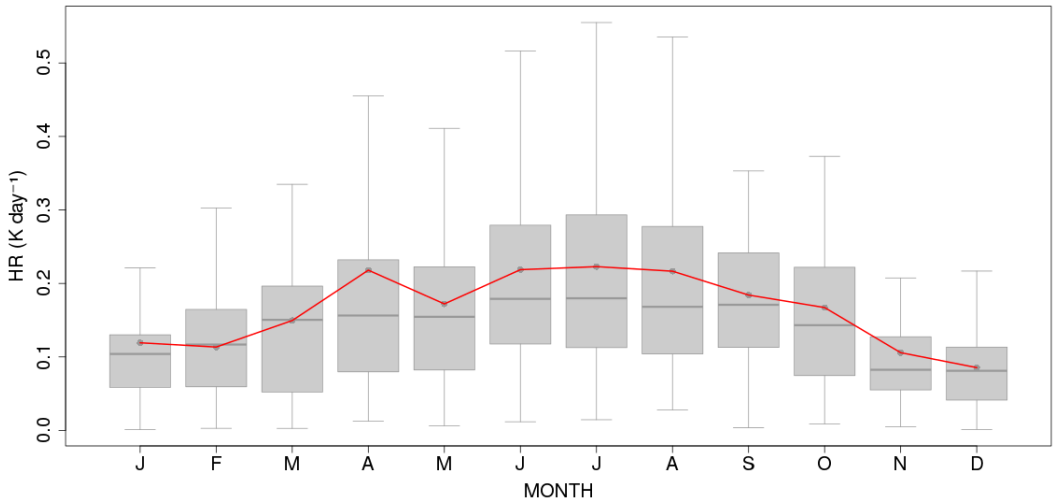

Fig. 9. Box and whisker plot of daily HR values for each calendar month over the 2003–2015 period. The mean (filled circles), median (horizontal segment within the box), 25th and 75th percentiles (top/bottom box limits) and data within 1.5 times the interquartile range (whiskers) are shown.

of the impact of aerosols in this area, mainly referred to its magnitude and temporal variability. In particular, the high temporal variability found in ARF and ARFE suggests the need to use long time series to guarantee the temporal representativeness in this interesting region.

ACKNOWLEDGMENTS

This work was partially supported by FCT (Fundação para a Ciência e a Tecnologia) through the grant SFRH/BPD/86498/2012. The work is co-funded by the European Union through the European Regional Development Fund, included in the COMPETE 2020 (Operational Program Competitiveness and Internationalization) through the ICT project (UID/GEO/04683/2013) with the reference POCI-01-0145-FEDER-007690 and also through the ALOP (ALT20-03-0145-FEDER-000004) and DNI-A (ALT20-03-0145-FEDER-000011) projects. The research is also co-funded by the research projects CGL2011-29921-C02-01/CLI and CGL2014-56255-C2-1-R granted by the "Ministerio de Economía y Competitividad" of Spain. The authors would like to acknowledge Samuel Bárias for maintaining instrumentation used in this work. Thanks are due to AERONET/PHOTONS and RIMA networks for the scientific and technical support. CIMEL calibration was performed at the AERONET-EUROPE GOA calibration center, supported by ACTRIS under agreement no. 654109 granted by European Union (H2020-INFRAIA-2014-2015). The data analyzed in this study are available from authors upon request (nines@unex.es).

REFERENCES

Alam, K., Trautmann, T. and Blaschke, T. (2011). Aerosol optical properties and radiative forcing over mega city Karachi. *Atmos. Res.* 101: 773–782.

Alam, K., Trautmann, T., Blaschke, T. and Majid, S. (2012). Aerosol optical and radiative properties during summer and winter seasons over Lahore and Karachi. *Atmos. Environ.* 50: 234–245.

Alam, K., Sahar, N. and Iqbal, Y. (2014). Aerosol characteristics and radiative forcing during pre-monsoon and post-monsoon in an urban environment. *Aerosol Air Qual. Res.* 14: 99–107.

Bibi, H., Alam, K., Blaschke, T., Bibi, S. and Iqbal, M.J. (2016). Long-term (2007-2013) analysis of aerosol optical properties over four locations in the Indo-Gangetic plains. *Appl. Opt.* 55: 6199–6211.

Bibi, H., Alam, K. and Bibi, S. (2017). Estimation of shortwave direct aerosol radiative forcing at four locations on the Indo-Gangetic Plains: Model results and ground measurement. *Atmos. Environ*. 163: 166–181.

Boucher, O. and Coauthors (2013). Clouds and aerosols in climate change 2013. In *Contribution of Working Group I to the Fifth Assessment Report of the Intergovernmental Panel on Climate Change*. Stocker, T.F., Qin, D., Plattner, G.K., Tignor, M., Allen, S.K., Boschung, J., Nauels, A., Xia, Y., Bex, V. and Midgley, P.M. (Eds.). The Physical Science Basis. Cambridge University Press, Cambridge, United Kingdom and New York, NY, USA.

Bush, B.C. and Valero, F.P.J. (2003). Surface aerosol radiative forcing at Gosan during the ACE-Asia campaign. *J. Geophys. Res.* 108: 1–8.

Cachorro, V.E., Durán, P., Vergaz, R. and Frutos, M.A. (2000). Measurement of the atmospheric turbidity of the North Centre continental area in Spain: Spectral aerosol optical depth and Ångström turbidity parameters. *J. Aerosol Sci*. 31: 687–702.

Cachorro, V.E., Toledano, C., de Frutos, A.M., Sorribas, M., Vilaplana, J.M. and de la Morena, B. (2005). Aerosol characterization at El Arenosillo (Huelva, Spain) with an AERONET/PHOTONS CIMEL sunphotometer. *Geophys. Res. Abstr.* 7: 08559.

Cachorro, V.E., Toledano, C., Prats, N., Sorribas, M., Mogo, S., Berjón, A., Torres, B., Rodrigo, R., de la Rosa, J. and De Frutos, A.M. (2008). The strongest desert dust intrusion

mixed with smoke over the Iberian Peninsula registered with Sun photometry. *J. Geophys. Res*. 113: D14S04.

Costa, M.J., Sohn, B.J., Levizzani, V. and Silva, A.M. (2006). Radiative forcing of Asian dust determined from the synergized GOME and GMS satellite data – A case study. *J. Meteorol. Soc. Jpn*. 84: 85–95.

Derimian, Y., Karnieli, A., Kaufman, Y.J., Andreae, M.O., Andreae, T.W., Dubovik, O., Maenhaut, W., Koren, I. and Holben, B.N. (2006). Dust and pollution aerosols over the Negev desert, Israel: Properties, transport, and radiative effect. *J. Geophys. Res*. 111: D05205.

Di Biagio, C., di Sarra, A. and Meloni, D. (2010). Large atmospheric shortwave radiative forcing by Mediterranean aerosols derived from simultaneous ground-based and spaceborne observations and dependence on the aerosol type and single scattering albedo. *J. Geophys. Res*. 115: D10209.

Dubovik, O., Holben, B., Eck, T.F., Smirnov, A., Kaufman, Y.J., King, M.D., Tanré, D. and Slutsker, I. (2002). Variability of absorption and optical properties of key aerosol types observed in worldwide locations. *J. Atmos. Sci.* 59: 590–608.

Eck, T.F., Holben, B.N., Reid, J.S., Dubovik, A., Smirnov, N.T.O'Neill,, Slutsker, I. and Kinne, S. (1999). Wavelength dependence of the optical depth of biomass burning, urban, and desert dust aerosols. *J. Geophys. Res.* 104: 00093–00095.

Elias, T., Silva, A.M., Belo, N., Pereira, S., Formenti, P., Helas, G. and Wagner, F. (2006). Aerosol extinction in a remote continental region of the Iberian Peninsula during summer. *J. Geophys. Res*. 111: 1–20.

Emde, C., Buras-Schnell, R., Kylling, A., Mayer, B., Gasteiger, J., Hamann, U., Kylling, J., Richter, B., Pause, C., Dowling, T., Bugliaro, L. (2016). The libRadtran software package for radiative transfer calculations (version 2.0.1). *Geosci. Model Dev.* 9: 1647–1672.

Escudero, M., Castillo, S., Querol, X., Avila, A., Alarcón, M., Viana, M.M., Alastuey, A., Cuevas, E. and Rodríguez, S. (2005). Wet and dry African dust events over eastern Spain. *J. Geophys. Res*. 110: D18S08.

Estellés, V., Martínez-Lozano, J.A., Utrillas, M.P. and Campanelli, M. (2007). Columnar aerosol properties in Valencia (Spain) by ground based sun photometry. *J. Geophys. Res*. 112: D11201.

Esteve, A.R., Estellés, V., Utrillas, M.P. and Martínez-Lozano, J.A. (2014). Analysis of the aerosol radiative forcing over a Mediterranean urban coastal site. *Atmos. Res*. 137: 195–204.

Foyo-Moreno, I., Alados, I., Antón, M., Fernández-Gálvez, J., Cazorla, A. and Alados-Arboledas, L. (2014). Estimating aerosol characteristics from solar irradiance measurements at an urban location in southeastern Spain. *J. Geophys. Res.* 119: 1845–1859.

García, O.E., Díaz, J.P., Expósito, F.J., Díaz, A.M., Dubovik, O., Derimian, Y., Dubuisson, P. and Roger, J.C. (2012). Shortwave radiative forcing and efficiency of key aerosol types using AERONET data. *Atmos. Chem. Phys*. 12: 5129–5145.

Gharibzadeh, M., Alam, K., Bidokhti, A.A., Abedini, Y. and Masoumi, A. (2017). Radiative effects and optical properties of aerosol during two dust events in 2013 over Zanjan, Iran. *Aerosol Air Qual. Res.* 17: 888–898.

Guerrero-Rascado, J.L., Olmo, F.J., Avilés-Rodríguez, I., Navas-Guzmán, F., Pérez-Ramírez, D., Lyamani, H. and Alados Arboledas, L. (2009). Extreme Saharan dust event over the southern Iberian Peninsula in september 2007: Active and passive remote sensing from surface and satellite. *Atmos. Chem. Phys*. 9: 8453–8469.

Gueymard, C. (2004). The sun's total and spectral irradiance for solar energy applications and solar radiation models. *Sol. Energy* 76: 423–453.

Hansen, J., Sato, M., Kharecha, P. and von Schuckmann, K. (2011). Earth's energy imbalance and implications. *Atmos. Chem. Phys*. 11: 13421–13449.

Holben, B., Eck, T.F., Slutsker, I., Tanre, D., Buis, J., Setzer, K., Vermote, E., Reagan, J., Kaufman, Y., Nakajima, T., Lavenu, F., Jankowiak, I. and Smirnov, A. (1998). AERONET—A federated instrument network and data archive for aerosol characterization. *Remote Sens. Environ*. 66: 1–16.

Holben, B.N., Eck, T.F., Slutsker, I., Smirnov, A., Sinyuk, A., Schafer, J., Giles, D. and Dubovik, O. (2006). Aeronet's Version 2.0 quality assurance criteria, Proc. SPIE 6408, *Remote Sensing of the Atmosphere and Clouds*, 64080Q (8 December 2006).

Huang, J., Fu, Q., Su, J., Tang, Q., Minis, P., Hu, Y., Yi, Y. and Zhao, Q. (2009). Taklimakan dust aerosol radiative heating derived from CALIPSO observations using the Fu–Liou radiation model with CERES constraints. *Atmos. Chem. Phys*. 9: 4011–4021.

Kaskaoutis, D., Sinha, P., Vinoj, V., Kosmopoulos, P., Tripathi, S., Misra, A., Sharma, M. and Singh, R. (2013). Aerosol properties and radiative forcing over Kanpur during severe aerosol loading conditions. *Atmos. Environ.* 79: 7–19.

Koppen, W. (1936). Das geographisca System der Klimate, In *Handbuch der Klimatologie*, Koppen, W. and Geiger, G. (Eds.), 1. C. Gebr, Borntraeger, pp. 1–44.

Liou, K.N. (2002). *An Introduction to Atmospheric Radiation*. Academic press.

Lyamani, H., Olmo, F.J., Alcántara, A and Alados-Arboledas, L. (2006). Atmospheric aerosols during the 2003 heat wave in southeastern Spain II: Microphysical columnar properties and radiative forcing. *Atmos. Environ*. 40: 6465–6476.

Mateos, D., Antón, M., Toledano, C., Cachorro, V.E., Alados-Arboledas, L., Sorribas, M., Costa, M.J. and Baldasano, J.M. (2014). Aerosol radiative effects in the ultraviolet, visible, and near-infrared spectral ranges using long-term aerosol data series over the Iberian Peninsula. *Atmos. Chem. Phys*. 14: 13497–13514.

Mayer, B. and Kylling, A. (2005). Technical note: The libRadtran software package for radiative transfer calculations — description and examples of use. *Atmos. Chem. Phys*. 5: 1855–1877.

Mishra, A.K., Koren, I. and Rudich, Y. (2015). Effect of aerosol vertical distribution on aerosol-radiation interaction: A theoretical prospect. *Heliyon* 1: e00036.

Obregón, M.A., Pereira, S., Wagner, F., Serrano, A., Cancillo, M.L. and Silva, A.M. (2012). Regional differences of column aerosol parameters in western Iberian Peninsula. *Atmos. Environ*. 12: 1–10.

Obregón, M.A., Pereira, S., Salgueiro, V., Costa, M.J., Silva, A.M., Serrano, A. and Bortoli, D. (2015a). Aerosol radiative effects during two desert dust events in August 2012 over the Southwestern Iberian Peninsula. *Atmos. Res*. 153: 404–415.

Obregón, M.A., Serrano, A., Costa, M.J. and Silva, A.M. (2015b). Validation of libRadtran and SBDART models under different aerosol conditions. *IOP Conf. Series: Earth and Environmental Science.* 28: 012010.

Obregón, M.A., Serrano, A., Cancillo, M.L., Cachorro, V.E. and Toledano, C. (2015c). Aerosol radiometric properties at Western Spain (Cáceres station). *Int. J. Climatol*. 35: 981–990.

Pereira, S., Silva, A.M., Elias, T. and Wagner, F. (2005). Aerosol monitoring at Cabo da Roca site. Paper presented at *4° Simpósio de Meteorologia e Geofísica da APMG/6° Encontro Luso-Espanhol de Meteorologia*, Sesimbra, Portugal.

Pereira, S., Wagner, F. and Silva, A.M. (2008). Scattering properties and mass concentration of local and long-range transported aerosols over the South Western Iberia Peninsula. *Atmos. Environ*. 42: 7623–7631.

Pereira, S.N., Wagner, F. and Silva, A.M. (2011). Seven years of measurements of aerosol scattering properties, near the surface, in the south-western Iberia Peninsula. *Atmos. Chem. Phys*. 11: 17–29.

Querol, X., Rodriguez, S., Cuevas, E., Viana, M.M. and Alastuey, A. (2002). Intrusiones de masas de aire africano sobre la Península Ibérica y Canarias: Mecanismos de transporte y variación estacional. *3rd Asamblea Hispano portuguesa de Geodesia y Geofísica*. Inst. Nac. de Meteorol. Esp., Valencia.

Rodriguez, S., Querol, X., Alastuey, A., Kallos, G. and Kakaliagou, O. (2001). Saharan dust contributions to PM_{10} and TSP levels in Southern and Eastern Spain. *Atmos. Environ.* 35: 2433–2447.

Román, R., Bilbao, J. and de Miguel, A. (2014). Solar radiation simulations in the Iberian Peninsula: Accuracy and sensitivity to uncertainties in inputs of a radiative transfer model. *J. Quant. Spectrosc. Radiat.* 145: 95–109.

Salgueiro, V., Costa, M.J., Silva, A.M. and Bortoli., D. (2014). Variability of the daily-mean shortwave cloud radiative forcing at the surface at a midlatitude site in Southwestern Europe. *J. Clim.* 27: 7769–7780.

Santos, D., Costa, M.J. and Silva, A.M. (2008). Direct SW aerosol radiative forcing over Portugal. *Atmos. Chem. Phys*. 8: 5771–5786.

Santos, D., Costa, M.J., Silva, A.M. and Salgado, R. (2013). Modeling Saharan desert dust radiative effects on clouds. *Atmos. Res*. 127: 178–194.

Shettle, E. (1989). Models of aerosols, clouds and precipitation for atmospheric propagation studies, atmospheric propagation in the UV, visible, IR and mm-region and related system aspects. In 454 *in AGARD Conference Proceedings*.

Silva, A.M., Von Hoyningen-Huene, W., Bugalho, L., Schmidt, T., Costa, M.J. and Heintzenberg, J. (2002). Aerosol optical properties from columnar data during the second Aerosol Characterization Experiment on the south coast of Portugal. *J. Geophys. Res.* 107: 4642.

Silva, A.M., Costa, M.J., Elias, T., Formenti, P., Belo, N. And Pereira, S. (2003). Ground-based aerosol monitoring at Évora, Portugal. *Global Change News Lett*. 56: 6–10.

Silva, A.M., Wagner, F., Pereira, S. and Elias, T. (2006). Aerosol properties at the most western point of continental Europe. *Paper presented at International Aerosol Conference*, Minnesota, USA.

Singh, A., Tiwari, S., Sharma, D., Singh, D., Tiwari, S., Srivastava, A.K., Rastogi, N. and Singh, A. (2016). Characterization and radiative impact of dust aerosols over northwestern part of India: A case study during a severe dust storm. *Meteorol. Atmos. Phys*. 128: 779–792.

Singh, S., Soni, K., Bano, T., Tanwar, R., Nath, S. and Arya, B. (2010). Clear-sky direct aerosol radiative forcing variations over mega-city Delhi. *Ann. Geophys*. 28: 1157–1166.

Stamnes, K., Tsay, S.C., Wiscombe, W. and Laszlo, I. (2000). DISORT, a general purpose Fortran program for discrete-ordinate-method radiative transfer in scattering and emitting layered media: Documentation of methodology. *Goddard Space Flight Center*, NASA.

Su, J., Huang, J., Fu, Q., Minnis, P., Ge, J. and Bi, J. (2008). Estimation of Asian dust aerosol effect on cloud radiation forcing using Fu-Liou radiative model and CERES measurements. *Atmos. Chem. Phys.* 8: 2763–2771.

Toledano, C. (2005). Climatología de los aerosoles mediante la caracterización de propiedades ópticas y masas de aire en la estación El Arenosillo de la red AERONET (PhD thesis) *Universidad de Valladolid*, Spain.

Toledano, C. (2006). Field calibration methods for aerosol optical depth determination with sun photometers. *Opt. Pura Apl*. 39: 303–311.

Toledano, C., Cachorro, V.E., de Frutos, A.M., Sorribas, M., Prats, N. and de la Morena, B. (2007). Inventory of African desert dust events over the southwestern Iberian Peninsula in 2000–2005 with an AERONET CIMEL Sun photometer. *J. Geophys. Res*. 112: D21201.

Valenzuela, A., Olmo, F.J., Lyamani, H., Antón, M., Quirantes, A and Alados-Arboledas, L. (2012). Aerosol radiative forcing during African desert dust events (2005–2010) over Southeastern Spain. *Atmos. Chem. Phys*. 12: 10331–10351.

Valenzuela, A., Costa, M.J., Guerrero-Rascado, J.L., Bortoli, D. and Olmo, F.J. (2017). Solar and thermal radiative effects during the 2011 extreme desert dust episode over Portugal. *Atmos. Environ*. 148: 16–29.

Received for review, May 3, 2017
Revised, September 5, 2017
Accepted, September 8, 2017

Hydrol. Earth Syst. Sci., 22, 5191–5210, 2018
https://doi.org/10.5194/hess-22-5191-2018
© Author(s) 2018. This work is distributed under
the Creative Commons Attribution 4.0 License.

Hydrology and Earth System Sciences
Open Access
EGU

Breeze effects at a large artificial lake: summer case study

Maksim Iakunin, Rui Salgado, and Miguel Potes

Department of Physics, ICT, Institute of Earth Sciences, University of Évora, 7000 Évora, Portugal

Correspondence: Maksim Iakunin (miakunin@uevora.pt)

Received: 12 April 2018 – Discussion started: 18 April 2018
Revised: 14 August 2018 – Accepted: 6 September 2018 – Published: 5 October 2018

Abstract. Natural lakes and big artificial reservoirs can affect the weather regime of surrounding areas but, usually, consideration of all aspects of this impact and their quantification is a difficult task. The Alqueva reservoir, the largest artificial lake in western Europe, located on the south-east of Portugal, was filled in 2004. It is a large natural laboratory that allows the study of changes in surface and in landscape and how they affect the weather in the region. This paper is focused on a 3-day case study, 22–24 July 2014, during which an intensive observation campaign was carried out. In order to quantify the breeze effects induced by the Alqueva reservoir, two simulations with the mesoscale atmospheric model Meso-NH coupled to the FLake freshwater lake model has been performed. The difference between the two simulations lies in the presence or absence of the reservoir on the model surface. Comparing the two simulation datasets, with and without the reservoir, net results of the lake impact were obtained. Magnitude of the impact on air temperature, relative humidity, and other atmospheric variables are shown. The clear effect of a lake breeze (5–7 m s^{-1}) can be observed during daytime on distances up to 6 km away from the shores and up to 300 m above the surface. The lake breeze system starts to form at 09:00 UTC and dissipates at 18:00–19:00 UTC with the arrival of a larger-scale Atlantic breeze. The descending branch of the lake breeze circulation brings dry air from higher atmospheric layers (2–2.5 km) and redistributes it over the lake. It is also shown that despite its significant intensity the effect is limited to a couple of kilometres away from the lake borders.

1 Introduction

Human activities, such as urbanization, deforestation, or water reservoir building, change the properties of the surface (vegetation cover, emissivity, albedo) that rule the surface energy fluxes (Cotton and Pielke, 2007). As a consequence, changes in surface energy fluxes affect local weather and climate. Lakes and reservoirs contain about 0.35 % of global freshwater storage (Hartmann, 1994) and cover only 2 % of the continental surface area (Segal et al., 1997). Thermal circulations triggered by lake–land thermal contrast have an impact on dispersion of air pollution and lake catchment transport (Lee et al., 2014). Big lakes, being a significant source of atmospheric moisture, can intensify storm formation (Samuelsson et al., 2006; Lin et al., 2012). Lakes and reservoirs, compared to land surfaces, have higher thermal inertia and heat capacity, and lower albedo and roughness length (Bonan, 1995). They can affect meteorological conditions and atmospheric processes at mesoscales and synoptic scales (Pielke, 1974; Bates et al., 1993; Pielke, 2013).

Normally, near-surface relative humidity is increased while daily air temperature is decreased above lake and shore areas. During the warm summer periods the relatively colder lake surface interacts with the atmosphere above, which leads to a reduction in clouds and precipitation. Formation of the local high-pressure areas over the lake surface in the summer season supports atmospheric circulation, which can be observed as a lake breeze (Bates et al., 1993). In autumn and winter it has the opposite effect: due to the fact that water is warmer than the air above, increases in evaporation and cloud formation can be observed (Ekhtiari et al., 2017). These regional lake effects have been seen in previous studies, e.g. Elqui Valley reservoir in Chile (Bischoff-Gauß et al., 2006) and the great African lakes (Thiery et al., 2014).

The theoretical aspects of lake breeze formations are well known; however, this phenomenon remains unexplored. Difficulties in studies of lake breeze are due to the diversity and complexity of lake shapes and surrounding landscapes, and the lack of observational data at sufficiently fine spatial resolution (Segal et al., 1997).

Lake breezes are mainly determined by the landscape and weather conditions. Formation and intensity of the breeze depend on the set of parameters such as large-scale winds, sensible heat flux, geometry of the lake, and terrain types of the surrounding area (Segal et al., 1997; Drobinski and Dubos, 2009; Crosman and Horel, 2012).

The focus of this work is on the study of the lake breeze at the Alqueva reservoir and its impact on atmospheric parameters of the surrounding area. This large artificial reservoir was filled in 2004, which makes it a big natural laboratory for studying physical, chemical, and biological effects. Few studies about the influence of Alqueva on atmosphere and climate were published. The first report, in Portuguese, was published even before the construction of the dam by Miranda et al. (1995), as a part of the environmental impact study of the reservoir on the basis of numerical simulations performed with the NH3D (non-hydrostatic three-dimensional) mesoscale model from Miranda and James (1992). It was concluded that the climate impact of the multipurpose Alqueva project should be mainly due to the irrigation of surrounding area. The influence of the reservoir itself was unclear as at that time it was not possible to perform high-resolution simulations. The studies were continued and improved by Salgado (2006) who made the first attempt to quantify the direct effect of the reservoir on the local climate, in particular on winter fog. Using the Meso-NH (non-hydrostatic mesoscale atmospheric model) model, the author concluded that the introduction of the reservoir should increase the winter fog slightly in the surrounding area, but decrease it over the filled area. Later on, Policarpo et al. (2017) used observations from two periods of 10 years (before and after the Alqueva reservoir) combined with Meso-NH simulations and showed a slight increase in the average number of days with fog during the winter (about 4 days per winter after 2003 in a downwind site).

Mesoscale atmospheric models, such as Meso-NH, allow obtainment of results with adequate horizontal resolution (250 m in present study) for studying the local effects of air temperature changes and the generation of small-scale circulations under different large-scale atmospheric situations. In this work simulations have been run for the Intensive Observation Period (IOP) of the ALEX project (ALqueva hydro-meteorological EXperiment, http://www.alex2014.cge.uevora.pt/, 28 September 2018). Data collected during this experiment were used to validate the numerical simulations.

The article outline is as follows. Section 2 provides a brief description of the Alqueva reservoir. Section 3 introduces information about the ALEX experiment and the measurements used in this paper. Section 4 contains a brief description of the numerical models used in this work: Meso-NH and FLake. Sections 5 and 6 are dedicated to the case study on 22–24 July 2014: validation of simulation results using in situ measurements and the studies of the lake effects respectively, with an illustration and discussion of the magnitude of the impact and intensity of a lake breeze. Section 7 summarizes the results and conclusions.

2 Object of study

The Alqueva reservoir, established in 2002, is an artificial lake located in the south-east part of Portugal. It spreads along 83 km over the Guadiana river valley covering, when completely filled, an area of 250 km^2 with a capacity of 4.15 km^3, which makes it the largest artificial lake in western Europe (Fig. 1a). The maximum and average depths of the reservoir are 92 and 16.6 m respectively. The dam is located in the southern part of the reservoir (Fig. 1c).

The Alqueva reservoir is mainly used to provide water supply, irrigation, and hydroelectric power. The region where it is located is known for the irregularity of its hydrological resources, with long periods of drought that could last for more than one consecutive year (Silva et al., 2014). The region has a Mediterranean climate with dry and hot summers (Csa according to the Köppen climate classification), with a small area within of the mid-latitude steppe (BSk) category. During summer, the maximum air temperature ranges between 31 and 35 °C on average (July and August), often reaching values close to 40 °C, or even higher. The incident solar radiation at the surface is one of the highest in Europe, with mean daily values (integrated over 24 h) of about 300 W m^{-2} and the daily maximum in July often reaching 1000 W m^{-2}. Rainfall periods are seasonal, normally from October to April. The annual average of accumulated precipitation in the climatological station of Beja, located 40 km away from the Alqueva reservoir, is 558 mm (1981–2010 normals from http://www.ipma.pt/pt/index.html, 28 September 2018).

Two major factors determine synoptic circulations over the region during the summer period: the shape and location of the Azores anticyclone, and the frequent establishment of a low-pressure system over the Iberian Peninsula, induced by the land–ocean thermal contrasts. The later phenomenon is known as the Iberian thermal low (Hoinka and Castro, 2003), which organizes the sea breezes generated at the Iberian coasts on a peninsular scale. At the west coast, the sea breeze controls the transport of the maritime air masses from the Atlantic to Iberian Peninsula, on distances more than 100 km reaching the Alqueva region in the late afternoon. This effect is observed in the local increase in wind intensity and in its rotation (Salgado et al., 2015).

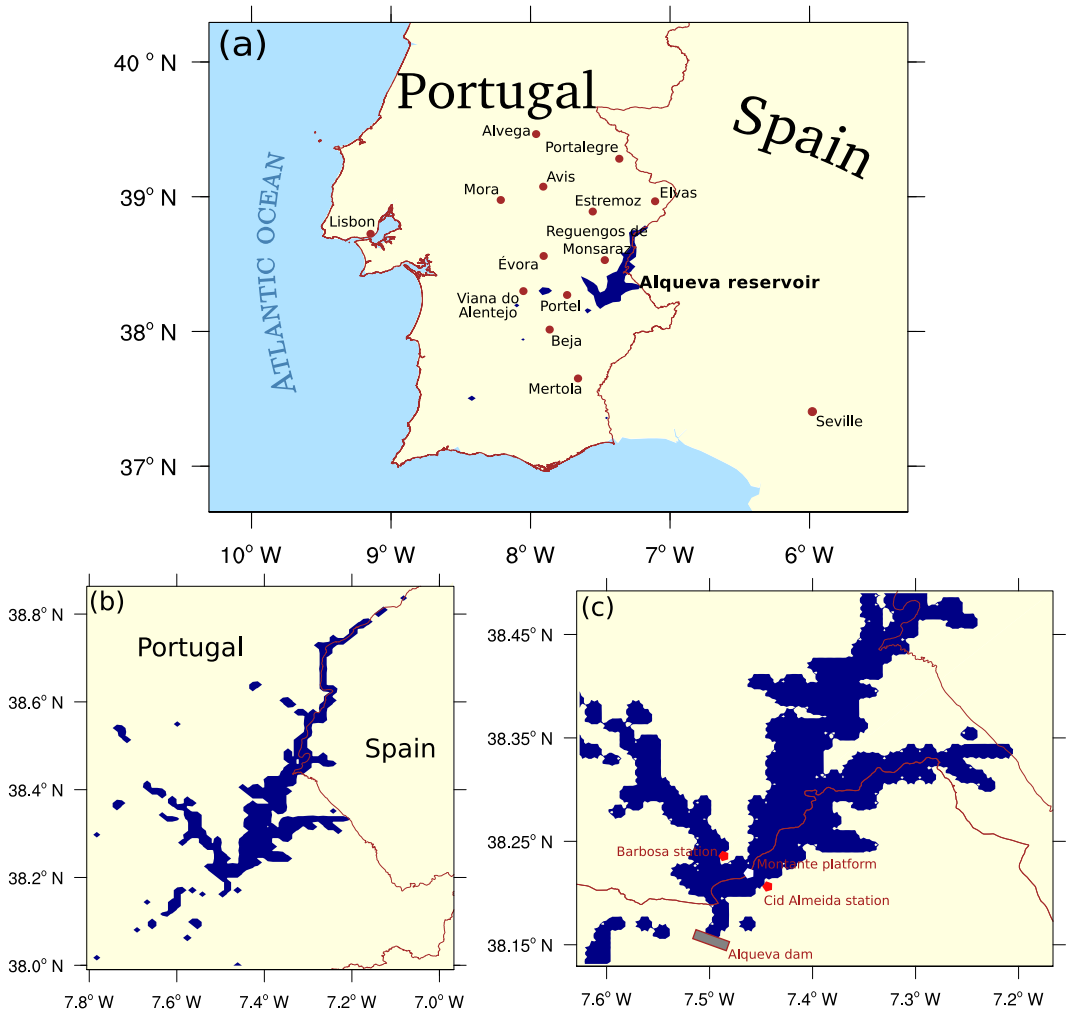

Figure 1. Nested domains used in the simulations: **(a)** the "father" domain at 4 km horizontal resolution with 100 × 108 grid points, with location of the 12 IPMA synoptic stations used for validation; **(b)** intermediate 1 km horizontal resolution domain, 96 × 72 grid points; **(c)** finer 250 m resolution domain comprising 160 × 160 grid points, together with the location of the ALEX land stations, the Montante floating platform and the dam.

3 Measurement data

The measured data used in this work were obtained during the ALEX campaign – a multidisciplinary observational experiment at the Alqueva reservoir that lasted from June to October 2014. One of the aims of this project was to perform a wide set of measurements of chemical, physical, and biological parameters in the water, air columns, and over the water-atmosphere interface. To reach this goal the project operated the following facilities:

- seven sites with meteorological measurements: two platforms (Montante and Mourão); one permanent weather station located in a small island nearby the dam (Alquilha), two dedicated weather stations (Barbosa and Cid Almeida), two compact weather stations in Solar Park and Amieira;
- four floating platforms where water quality and biological sampling was carried out: Montante, Mourão, Captação, and Alcarrache;
- three weather stations of the Institute of Earth Sciences (ICT), located in Mitra, Portel, and at the University of Évora;
- two air quality mobile units: Amieira and Solar Park;
- three atmospheric electricity stations: Amieira, Solar Park, and Beja.

Also, data from 42 IPMA (Portuguese Institute of Sea and Atmosphere) meteorological stations located in the region were integrated into the ALEX database. They provided typical sets of meteorological variables, e.g. air temperature, relative humidity, pressure, horizontal wind speed.

Two land weather stations (Barbosa and Cid Almeida) were installed on opposite shores (38.2235° N, 7.4595° W and 38.2164° N, 7.4545° W, correspondingly) while the floating platform Montante is situated in the middle (38.2276° N, 7.4708° W, Fig. 1c). These locations allowed the characterization of the lake effects on a fine scale. Land stations stored data at 1 min resolution including horizontal wind speed, relative humidity, air temperature, and downwelling short-wave radiation. Montante floating platform was the principal experimental site inside the reservoir. The following equipment was installed there on 2 June 2014 and data have been collected until the end of the campaign:

- an eddy-covariance system that provides data for pressure, temperature, water vapour and carbon dioxide concentrations, 3-D wind components, momentum flux, sensible and latent heat fluxes (with 30 min time step), carbon dioxide flux, and evaporation;
- one albedometer and one pirradiometer in order to measure upwelling and downwelling shortwave and total radiative fluxes;
- nine thermistors to measure water temperature profile.

The intensive observation period of the ALEX project from 22 to 24 July and included the launch of meteorological balloons every 3 h. In total, 18 radiosondes were launched: 2 from the boat over the lake and 16 from the land. Atmospheric profiles of air temperature, relative humidity, wind, and pressure were obtained. This period was chosen for a case study as it was well documented with typical anticyclonic conditions: hot, dry, and with low near-surface wind speed.

Data collected during the ALEX field campaign have already been used to study lake–atmosphere interactions, including the heat and mass (H_2O and CO_2) fluxes in the water–air interface (Potes et al., 2017); the effects of inland water bodies on the atmospheric electrical field (Lopes et al., 2016); and the evolution of the vertical electrical charge profiles and its relation with the boundary layer transport of moisture, momentum, and particulate matter (Nicoll et al., 2018).

4 Simulation setup

4.1 Meso-NH atmospheric model

To study the lake breeze effects in the Alqueva reservoir, the Meso-NH model (Lac et al., 2018) was used. Meso-NH is a non-hydrostatic mesoscale atmospheric research model. It can simulate the evolution of the atmosphere on scales ranging from large (synoptic) to small (large eddy) and has a complete set of physical parametrizations. Meso-NH is coupled with the SURFEX (Surface Externalisée, Masson et al., 2013) platform of models for the representation of surface–atmosphere interactions by considering different surface types (vegetation, city, ocean, inland waters).

Meso-NH allows a multi-scale approach through a grid-nesting technique (Stein et al., 2000). In this work, three nesting domains were used: a $400 \times 432\,km^2$ domain with 4 km horizontal resolution to take into account the large-scale circulations, namely the influence of the sea breeze (Fig. 1a); an intermediate $96 \times 72\,km^2$ domain with 1 km horizontal resolution centred at the Alqueva reservoir (Fig. 1b); and a finer $40 \times 40\,km^2$ domain with 250 m spatial resolution to track the small-scale effects of the lake (Fig. 1c). Hereinafter we denote these three domains A–C correspondingly. The two-way nesting technique used in Meso-NH allows to conduct simulations on different horizontal resolutions at the same time. Domain A is the "father" domain for B, which means that simulation results in domain A are interpolated and used as initial and boundary conditions for domain B. The same scheme applies for domains B and C. European Centre for Medium-Range Weather Forecast (ECMWF) operational analyses, updated every 6 h, were used for Meso-NH initialization and domain A boundary forcing.

For surface and orography, ECOCLIMAP II (Faroux et al., 2013) and SRTM (Shuttle Radar Topography Mission, Jarvis et al., 2008) databases were used, respectively, both updated with the inclusion of the Alqueva reservoir by Policarpo et al. (2017). All model domains had 68 vertical levels starting with 20 m up to 22 km, including 36 levels for the lower atmospheric level (2 km). The model configuration included a turbulent scheme based on a one-dimensional 1.5 closure (Bougeault and Lacarrere, 1989), and a mixed-phase microphysical scheme for stratiform clouds and explicit precipitation (Cohard and Pinty, 2000; Cuxart et al., 2000), which distinguishes six classes of hydrometeors (water vapour, cloud water droplets, liquid water, ice, snow, and graupel), was used. Longwave and shortwave radiative transfer equations are solved for independent air columns (Fouquart and Bonnel, 1980; Morcrette, 1991). Atmosphere–surface exchanges are taken into account through physical parametrizations: the surface soil and vegetation are described by the Interface Soil Biosphere Atmosphere (ISBA) model (Noilhan and Mahfouf, 1996); the town energy balance was handled according to Masson (2000). Basic parameters for each model domain are shown in the Table 1. Deep and shallow convection parametrization schemes were activated in the coarser domain A. The 1 km and 250 m resolutions of domains B and C are fine enough for the deep and shallow convection to be represented explicitly. The following schemes were used (see Table 1): KAFR (Kain and Fritsch, 1990; Bechtold et al., 2001), EDKF (Pergaud et al., 2009), WENO (Lunet et al., 2017), and ICE3 (Pinty and Jabouille, 1998).

To track the impact of the reservoir on the weather conditions, two numerical simulation were performed: one with the surface input files updated to include the Alqueva reservoir (ECOCLIMAP database version updated by Policarpo et al., 2017) and another with the previous version of this

Table 1. Summary of the Meso-NH physical schemes used in the simulations.

Schemes and parameters	Domains		
	A	B	C
Deep convection	KAFR	NONE	NONE
Shallow convection	EDKF	EDKF	NONE
Turbulence	BL89 1 dimension	DEAR 3 dimensions	DEAR 3 dimensions
Radiation transfer	ECMW	ECMW	ECMW
Advection	WENO	WENO	WENO
Clouds	ICE3	ICE3	ICE3
Time step	20 s	5 s	1 s

database where the reservoir is absent. In order to distinguish these simulations hereinafter we denote them LAKE1 and LAKE0, correspondingly. Both simulations covered the case study period, 22–24 July 2014, with 1 h output. To reproduce the atmospheric conditions more realistically the simulations included the previous 24 h (21 July), so the model was integrated for 96 h. The differences between these two simulations were then computed, with the aim of evaluating the direct influence of the lake on the atmosphere.

4.2 FLake model

In order to better represent the evolution of the lake surface temperature and therefore the water–air heat fluxes, the FLake (Freshwater Lake) model (Mironov, 2008) was used. FLake is a bulk-type model capable of predicting the evolution of the lake water temperature at different depth on timescales from a few hours to many years. For an unfrozen lake it uses a two-layer approach: upper mixing layer, with a constant water temperature, and the thermocline beneath it where the temperature decreases with depth. Parametrization of the thermocline profile is based on the concept of self-similarity, assuming that such an approach could be applied to all natural and artificial freshwater lakes.

The FLake model requires at least the following sets of variables and parameters to run: four initial parameters to describe the lake temperature structure, six atmospheric input variables for each time step, and two parameters – lake depth and the attenuation coefficient of light in the water. This coefficient is used to compute the penetration of the solar radiation in the water body. In this work, the attenuation coefficient was set to 0.85 based on in situ measurements carried out in Alqueva by Potes et al. (2017).

The FLake prognostic variables that need to be initialized are water temperature at the bottom, temperature and depth of the mixing layer, and shape factor C_f – a parameter that describes the shape of the thermocline curve. In the parametrization proposed by Mironov (2008) for the normalized temperature profile it varies from 0.5 to 0.8. The initial values of the shape factor C_f, a water mixing layer temperature, and depth were determined using a fitting technique applied to the observed water temperature profile at a given time in Montante platform (Fig. 2a). Short-term FLake model runs are very sensitive to initial parameters. The fitting technique is based on the assumption that the bottom temperature is fixed and given by the value of the lowermost sensor. Thereby, the other three parameters could vary within some range until the best set is found. The initial conditions for our simulations were obtained following this technique: $C_f = 0.8$, mixed layer temperature is 23.8 °C, and depth is 3.4 m. Test simulation with these set of inputs was carried out using a stand-alone version of the FLake model (not coupled to Meso-NH). The results of the comparison of water mixing layer temperature is shown in Fig. 2b. The maximum difference does not exceed 0.8 °C, which is a very good result for such a short-term simulation.

The observed daytime temperature profiles showed strong skin effects (higher temperatures in the first 10 cm) and could not be well fitted by a FLake type temperature profile, which assumes a constant temperature in the mixed layer. Thus, the midnight profile was used initially and the simulation started at midnight, 21 July 2014.

The required atmospheric variables were taken interactively from the Meso-NH simulation since FLake was implemented in the SURFEX model by Salgado and Le Moigne (2010).

The depth of artificial lakes decreases rapidly from the centre to the shore, because the bottom of the reservoirs used to be valleys. In case of Alqueva, when completely filled, the mean depth is of about 17 m (http://www.edia.pt/pt/, 28 September 2018). However, the local depth at Montante platform can reach 70 m. As a 1-D bulk model, FLake has only one depth value, which should be seen as an effective depth and is not easy to assess. Moreover, the FLake model is not capable of representing deep lakes; it works well for depths from 20 to 50 m with the sediments routine switched off. After a series of sensitivity tests of short-term (2–4 days) and long-term (2–4 months) simulation it was found that the best simulations results can be obtained with the bottom depth value of 20–30 m. Thus, since the deepest temperature probe was installed at the depth of 27 m, this value was chosen for the effective lake depth in this work. The comparison between measurements of water temperature near the surface (at 1 m depth) and FLake-simulated values of mixed layer temperature is shown in Fig. 2b. The sensor at 1 m depth was chosen because it always stays in the mixed layer and is not affected by surface "skin" effects. Modelled values are close to measurements, which indicates that the initial conditions were realistically imposed.

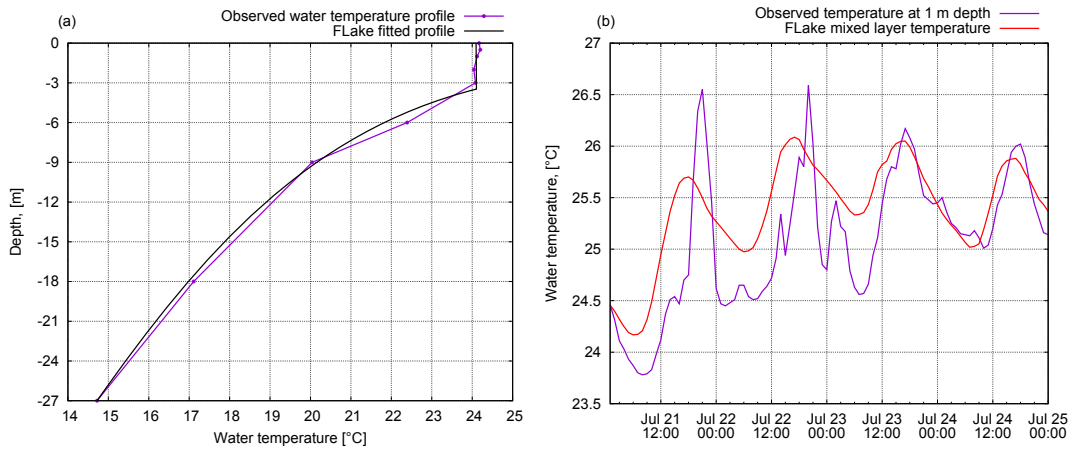

Figure 2. Water temperature observed and fitted profiles on 21 July, 00:00 UTC at the Montante platform **(a)** and comparison of upper level water temperature between measurements and FLake results **(b)**.

5 Validation

The simulation LAKE1 results were validated against radiosonde data (vertical profiles) and meteorological data from ALEX and IPMA stations located on land and in the floating platforms. All three domains were considered in the validation. The size of the domain A was enough to consider 12 synoptic stations located in the region, domain B was used to track the radiosondes trajectory, and domain C results were validated against stations installed on the lake shores and on the Montante floating platform. The variables under analysis were air temperature, relative humidity, wind speed, and sensible and latent heat fluxes.

5.1 Comparison with radiosonde data

The ALEX IOP took place between 22 and 24 July 2014 at the Alqueva reservoir. It included the launch of 18 meteorological balloons every 3 h. The radiosondes took measurements of air temperature, humidity, pressure, and wind speed. As the balloons did not ascend vertically and flew several kilometres away from the launching point, a trajectory profile comparison was performed. Each balloon had a GPS tracker to register its coordinates every 2 s, which was used to build a corresponding numerical trajectory on the simulation domain. Radiosondes reached the altitude of the top of the model (about 22 km in about 2.5 h). Therefore in order to build the simulated profile, three consecutive hourly outputs from the model were used.

Figure 3a–c represent examples of the daytime profiles of air temperature, relative humidity, and horizontal wind speed. Examples of night profiles can be found in Fig. 3d–f. In general, the night-simulated profiles show slightly better accordance with model results.

Figure 4 shows the same profiles, but for the lower troposphere level (3000 m altitude). Simulations are in good accordance with observations. The simulation results are within the confidence interval of the measurements as given by the radiosonde accuracy – $\pm 0.5\,^{\circ}\mathrm{C}$, $\pm 5\,\%$ relative humidity, and $\pm 0.15\,\mathrm{m\,s^{-1}}$ wind speed with 2σ confidence level (95.5 %).

The principal features of the profiles are well represented by the model. During daytime, air temperature and relative humidity curves indicate that the model tends to represent the height of the boundary layer at 2–2.5 km altitude well (around 2 km in Fig. 4a and b). Overall, Meso-NH reproduces the air temperature above the surface layer (over 500 m) very well. Near the surface, the Meso-NH tends to anticipate the development of the unstable boundary layer in the morning (09:00 and 12:00 UTC), simulating higher temperatures in the lower levels. In the late afternoon (18:00 and 21:00 UTC) the model also tends to anticipate the decrease in the temperature in the surface layer (see the Supplement, Fig. S1).

The vertical patterns of relative humidity and wind speed are good, as observed and modelled curves look similar; nevertheless simulations tend to be more conservative and their values do not represent all changes in altitude recorded by the radiosonde. Nocturnal low-level jets at the edge of the boundary layer are represented by the model, but their magnitude is slightly weaker than that observed. The complete set of observed versus simulated profiles can be found in the Supplement (Fig. S2). The moisture vertical profile in the boundary layer is well reproduced by the model, as can be seen in the graphs of the relative humidity (Figs. 4b, e, and S3). Above the boundary layer, the radiosondes show a dry layer, which is also well simulated. From 23 July the observations show the appearance of a moist layer close to the troposphere, the magnitude of which is overestimated by the model. At dawn on 24 July the radiosondes and the model indicate the existence of a very moist layer close to the surface, with the formation of low clouds that were not formed in the simulations.

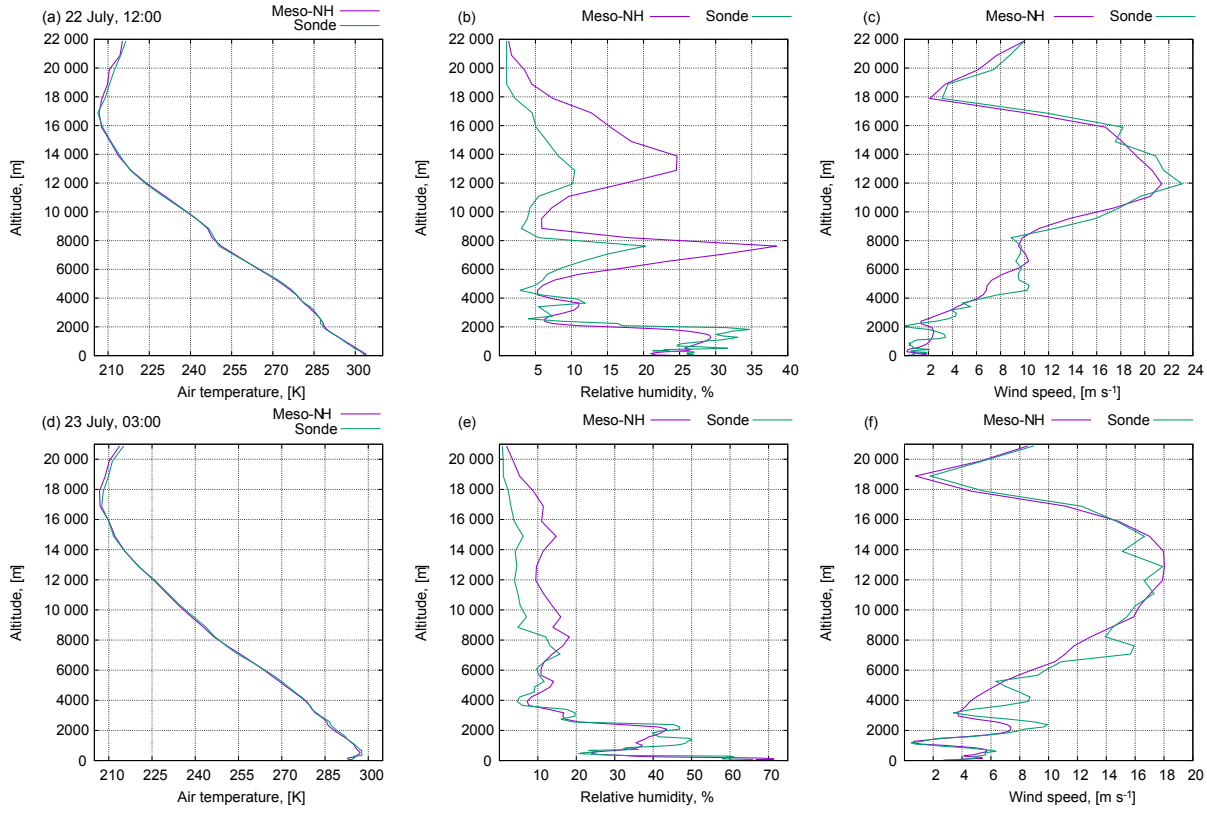

Figure 3. Examples of observed and simulated vertical profiles for 22 July at 12:00 UTC and 23 July at 03:00 UTC of air temperature **(a, d)**, relative humidity **(b, e)**, and wind speed **(c, f)**.

Statistical results for them are the following: temperature average bias is −0.13 °C, RMSE is 1.49 °C, and the correlation coefficient is 0.99; relative humidity average bias is 0.59 %, RMSE is 11.26 %, and the correlation coefficient is 0.87; and for the wind speed average bias is 0.05 m s^{-1}, RMSE is 2.07 m s^{-1}, and the correlation coefficient is 0.90. These values testify that the simulation is in a good accordance with the observations, in line with similar studies of Meso-NH validation against radiosonde data (e.g. Masciadri et al., 2013).

5.2 Comparison with IPMA stations data

The model was also validated against 12 IPMA automatic meteorological stations. For this comparison the output of the bigger domain A was used. Geographical positions of the stations can be found in Fig. 1a. Scatter plots of air temperature, relative humidity, and wind speed are shown in Fig. 5. It should be mentioned that not all stations provided the same set of variables. The scatter plots show the intercomparison of the model data (x axis) and the measured values (y axis) over all stations in the simulated period. The model tends to overestimate lower values of air temperature (14–24 °C) and slightly underestimate higher values (> 30 °C), as can be seen from Fig. 5a.

In some stations and for several times, the model simulates lower values of relative humidity within the range from 40 to 100 % (Fig. 5b). Figure 5c indicates that the wind speed is slightly underestimated by the model.

Statistical parameters (bias, mean absolute error, root mean square, and the correlation coefficient) for each station are shown in Table 2.

Simulated and observed air temperature are highly correlated (the correlation coefficient is higher that 0.91) with bias always less than 1°. The worst results are observed in Portalegre (square points in relative humidity plot in Fig. 5b), and a possible reason for this relies on the location of the station, which is installed in a complex mountain area, possible not well represented in the model orography. Regarding wind speed, Meso-NH provides values for 10 m height while the measurements were made at 2 m. For proper comparison modelled values were interpolated to the height of the sensors using a known logarithmic approach and a roughness length (which was also obtained from the model). Table 2 shows small biases, in general lower than 1 m s^{-1}, and relatively high correlation coefficients for wind simulations (0.68–0.92). The lowest correlation coefficient is also obtained for Portalegre data. Overall, simulation results are in good agreement with synoptic station data, and the statis-

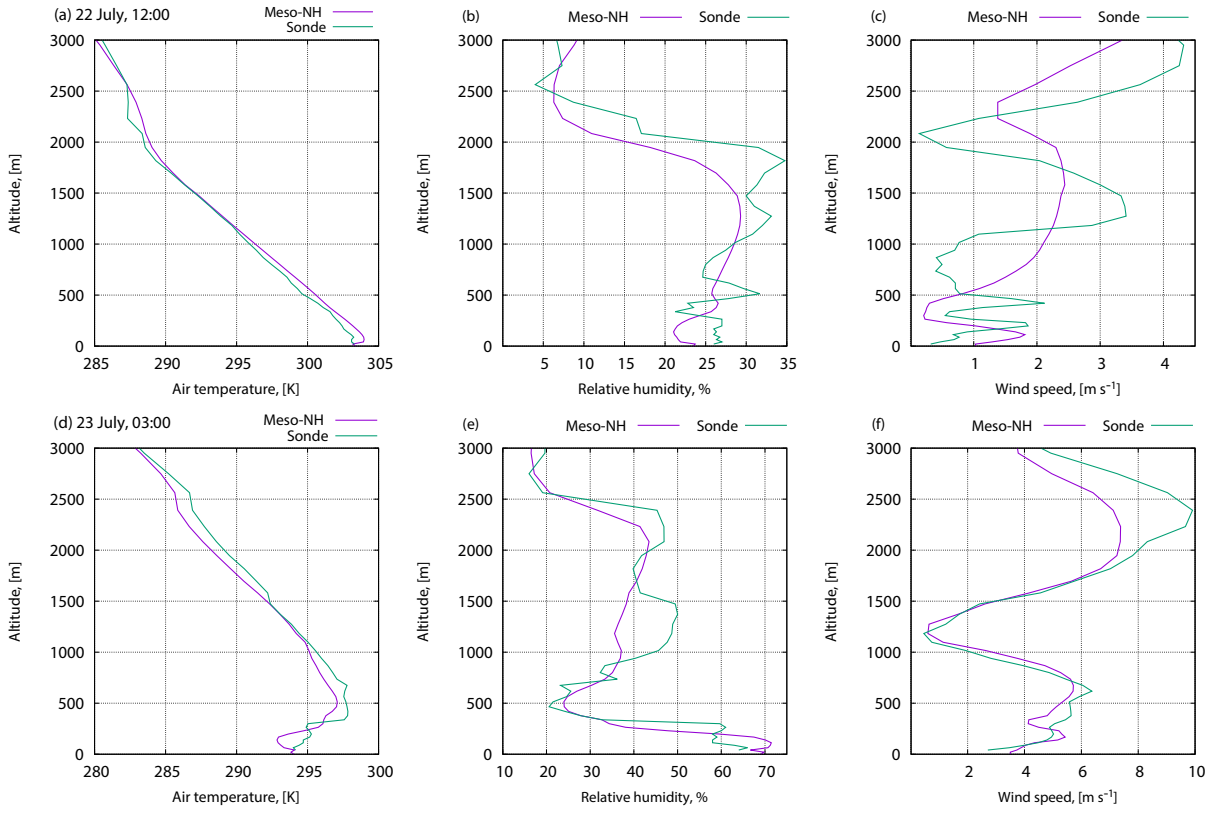

Figure 4. Profiles of air temperature, relative humidity, and wind speed in low atmosphere on 22 July at 12:00 UTC and 23 July at 03:00 UTC.

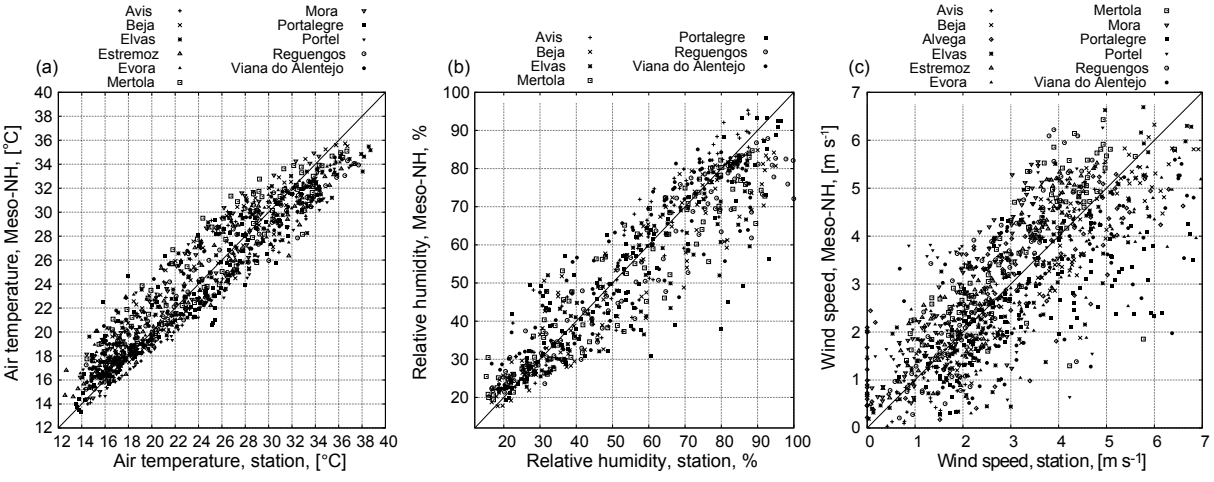

Figure 5. Scatter plots of the comparison between Meso-NH simulation LAKE1 and measured values at synoptic stations. Air temperature **(a)**, relative humidity **(b)**, and horizontal wind speed **(c)**.

tical parameters are similar to other published works that use Meso-NH (e.g. Lascaux et al., 2013, 2015).

5.3 Comparison with data from the ALEX database

In addition to the validation against the IPMA synoptic stations, comparisons were made with data obtained at ALEX meteorological stations (Barbosa, Cid Almeida, and Montante platform). Their coordinates were used to locate corresponding grid points on the C domain output. For land stations with grid points associated with water fraction, the nearest land grid point was chosen.

Figure 6 shows the time evolution of simulated and observed air temperature and wind speed at Cid Almeida, Bar-

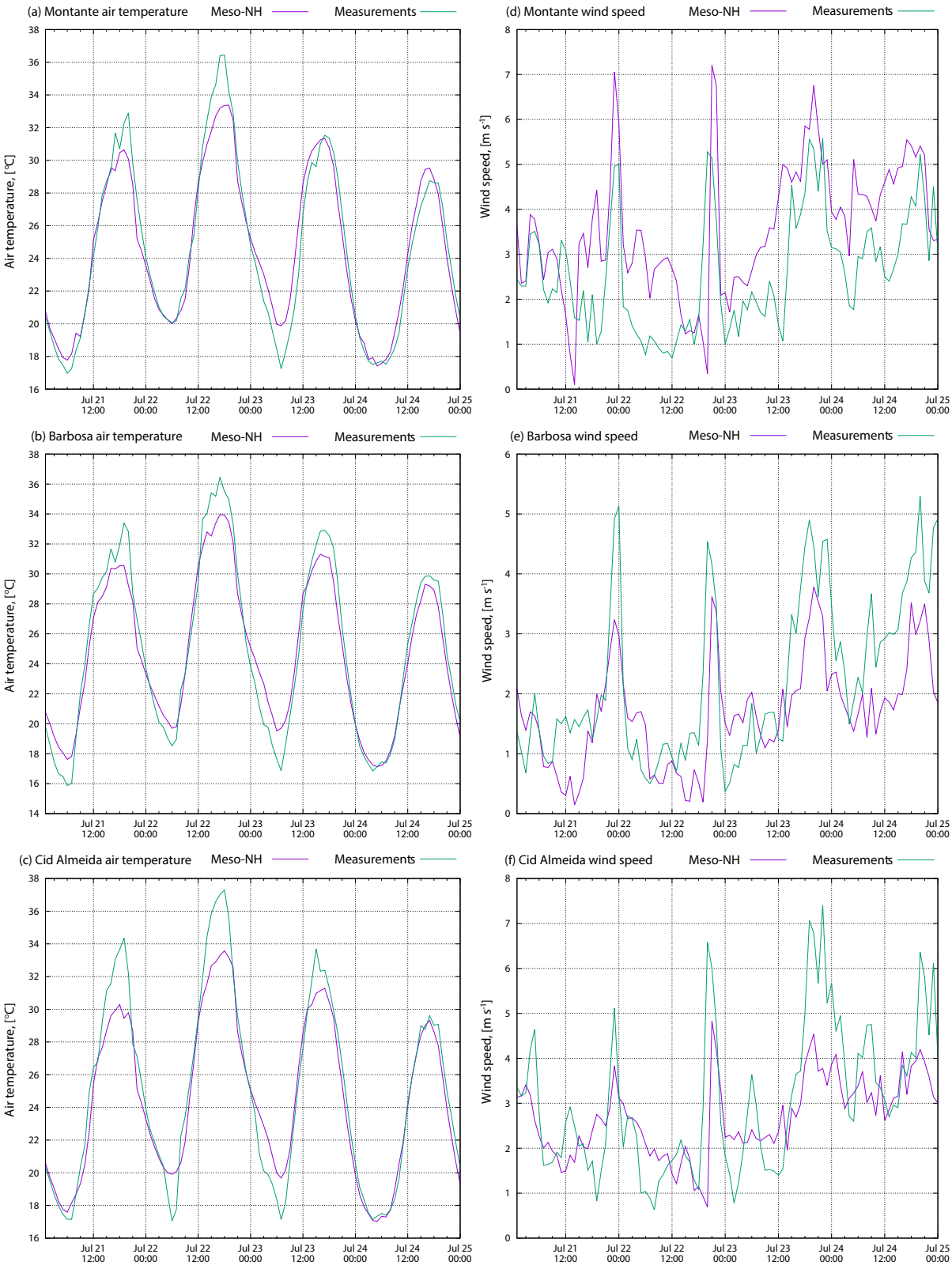

Figure 6. Observed and simulated air temperature and wind speed at 2 m for ALEX stations: Montante platform **(a, d)**, Barbosa **(b, e)**, and Cid Almeida **(c, f)** sites.

Table 2. Statistics for the hourly values of the station validation.

Stations:		Alvega	Avis	Beja	Elvas	Estrem.	Évora	Mert.	Mora	Portal.	Portel	Reguen.	V. Alen.
Temp., °C	Bias:	–	−0.08	0.68	−0.39	0.00	0.56	0.85	0.9	−0.08	−0.30	−0.33	0.52
	MAE:	–	1.49	1.60	1.76	1.65	1.60	1.71	1.54	1.82	1.91	1.44	1.82
	RMS:	–	1.84	1.96	2.18	2.02	1.96	2.20	1.93	2.38	2.27	1.82	2.13
	Corr:	–	0.95	0.96	0.96	0.96	0.96	0.95	0.96	0.91	0.94	0.97	0.96
Rel. hum., %	Bias:	–	0.53	−2.98	−3.42	–	–	−1.29	−4.19	−2.79	–	−4.10	1.80
	MAE:	–	5.80	7.48	5.87	–	–	6.61	6.88	7.83	–	6.94	8.08
	RMS:	–	7.41	9.49	8.61	–	–	8.49	8.43	11.91	–	9.11	9.80
	Corr:	–	0.93	0.93	0.93	–	–	0.94	0.94	0.86	–	0.95	0.90
Wind speed, $m\,s^{-1}$	Bias:	−0.46	−0.34	−0.16	−0.09	−0.91	0.27	−1.11	−1.09	0.53	−0.78	−0.86	0.18
	MAE:	2.33	0.26	0.22	0.88	1.28	0.44	0.74	1.19	0.68	1.02	0.32	0.43
	RMS:	1.01	0.73	0.74	1.01	0.69	0.94	0.93	0.93	1.12	1.16	1.03	1.19
	Corr:	0.85	0.92	0.91	0.86	0.92	0.82	0.81	0.85	0.68	0.69	0.86	0.71

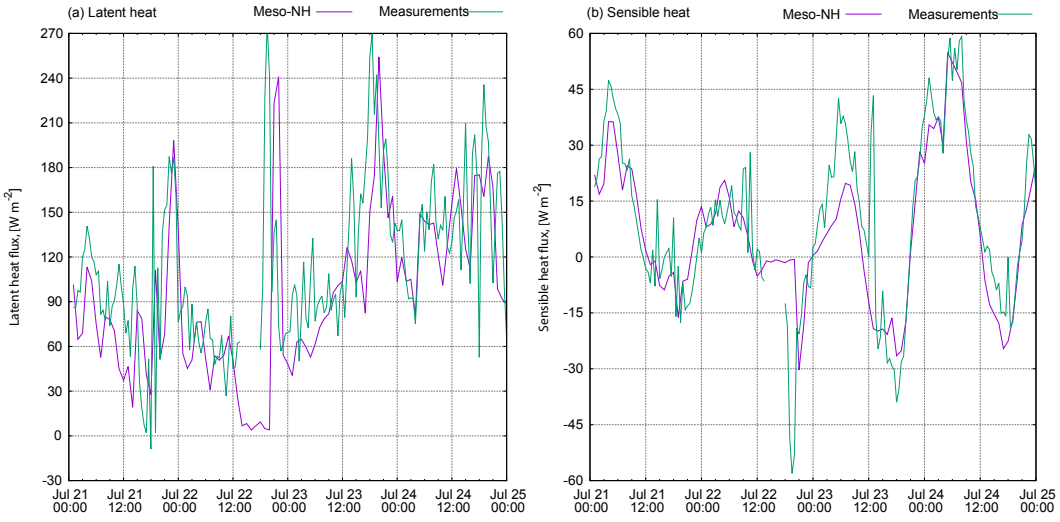

Figure 7. Observed and simulated latent **(a)** and sensible **(b)** heat fluxes at Montante floating platform.

bosa, and Montante sites. Overall, the simulation results are slightly more conservative (except wind speed over the Montante platform), but in general, the patterns are well represented. The model could not represent the maximum and minimum temperatures well, especially in land stations where the temperature range is larger. Regarding wind speed, the model underestimates the maximum values at land stations (Fig. 6e and f) and, on the contrary, overestimates the values at Montante platform (Fig. 6d), but the principal features of the curves are represented. Statistical values for this validation are as follows. For Barbosa, air temperature average bias is 0.23 °C, RMSE is 1.37 °C and the correlation coefficient is 0.98; for wind speed these values are as follows: average bias is 0.55 $m\,s^{-1}$, RMSE is 1.08 $m\,s^{-1}$, and the correlation coefficient is 0.73. For Cid Almeida, temperature average bias is 0.5 °C, RMSE is 1.57 °C, and the correlation coefficient is 0.98, wind speed average bias is −0.36 $m\,s^{-1}$, RMSE is 1.24 $m\,s^{-1}$, and the correlation coefficient is 0.69. For the Montante platform, air temperature average bias is −0.1 °C, RMSE is 1.22 °C, correlation is 0.98, wind speed average bias is −0.97 $m\,s^{-1}$, RMSE is 1.55 $m\,s^{-1}$, and the correlation coefficient is 0.61.

The temporal evolution of simulated and observed latent and sensible heat fluxes at Montante platform is shown in Fig. 7a and b. Overall patterns of the curves are similar but the simulated one is more smooth. Comparison demonstrates that for latent heat the RMSE is 57.34 $W\,m^{-2}$ with correlation coefficient of 0.47, and for sensible heat the RMSE is 13.39 $W\,m^{-2}$ with the correlation of 0.82.

Both observed and simulated curves of Fig. 7a reveal that sensible heat flux has two different periods during the day, positive when air-water temperature difference is negative, and vice versa, showing that during daytime the water receives energy from the air and during nighttime the water warms the nearby air. The transition between the two regimes is well captured by the model. Figure 7b also shows that

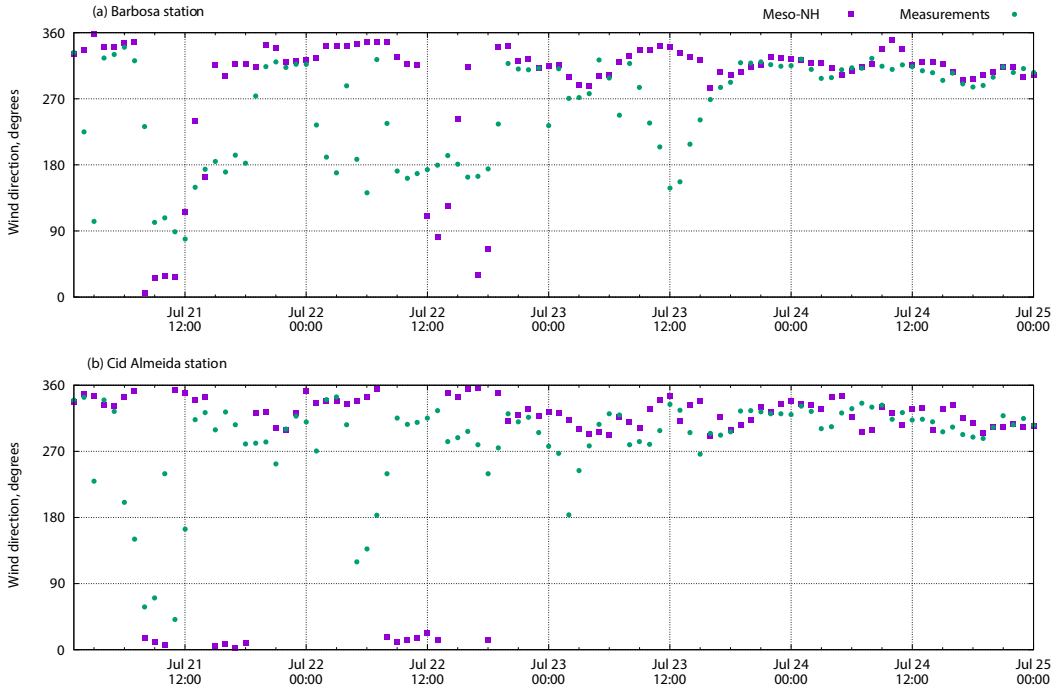

Figure 8. Observed and simulated wind direction at Barbosa and Cid Almeida stations.

the magnitude of the sensible heat flux is relatively small when compared with the other terms of the energy balance. Daily maximum positive (negative) fluxes between 30 and 60 W m^{-2} (-15 and -30 W m^{-2}) are well reproduced by the model. An apparently strange behaviour appears on the afternoon of 22 July, with the sensible heat flux being almost zero. This effect, unfortunately not documented due to the lack of data, will be discussed later and is linked to the fact that the wind is very weak during this period (see Fig. 6d).

More detailed analysis of Fig. 7a shows that the lowest heat flux values usually occur during the afternoon (12:00–18:00 UTC), under windless conditions, and high peaks in the early evening (20:00–21:00 UTC). The simulation reproduces these peaks with 1–2 h delays that are related to the delay on the simulated wind speed. The magnitude of the latent heat flux daily maximum (order of 200–250 W m^{-2}) is well captured by the model. The delay in the simulation of the peaks reduces the value of the correlation coefficient and is a manifestation of the so-called double-penalty that penalize high-resolution model scores. As seen in Fig. 7b the simulated latent heat flux is almost zero between 14:00 and 16:00 UTC of 22 July. As pointed out before, there is a gap in the flux measurements during this period, but data from the day before indicate that the results are realistic. This effect of almost zero evaporation from water on a very hot day is contrary to common sense and will be discussed later.

Wind direction at ALEX stations is represented in Fig. 8. Different behaviour in wind direction between the two stations from 21 to 23 July is clearly seen from measurement data (green dots). In Barbosa station the wind changes from a north-west to a south regime during daytime while in Cid Almeida this effect is not observed. In the simulations this difference is not so clear, but is still visible during the afternoon on 22 July. Barbosa station, located on the north-west shore of the lake, indicates the presence of the lake breeze because its direction is the opposite to the dominant wind. At Cid Almeida station, on the south-east shore, the lake breeze is co-directed with the dominant wind.

6 Lake impact

To analyse the impact of the Alqueva reservoir on the local area the changes in the following atmospheric variables were considered: air temperature and potential temperature, relative humidity and water mixing ratio, and vertical and horizontal wind speed. In this section only B and C domain datasets were used.

6.1 Impact on air temperature and relative humidity

The lower layers of air are the first to be affected by the presence of the water surface. Differences in air temperature at 2 m during 22 July are shown in Fig. 9, the warmest day of the IOP and thus with a stronger lake breeze. The positive anomaly (up to 3–4 °C) can be traced during the period from 1 h after the sunset (21:00 UTC) to 1 h after the sunrise (07:00 UTC). By positive and negative anomalies here we mean differences between LAKE1 and LAKE0 simula-

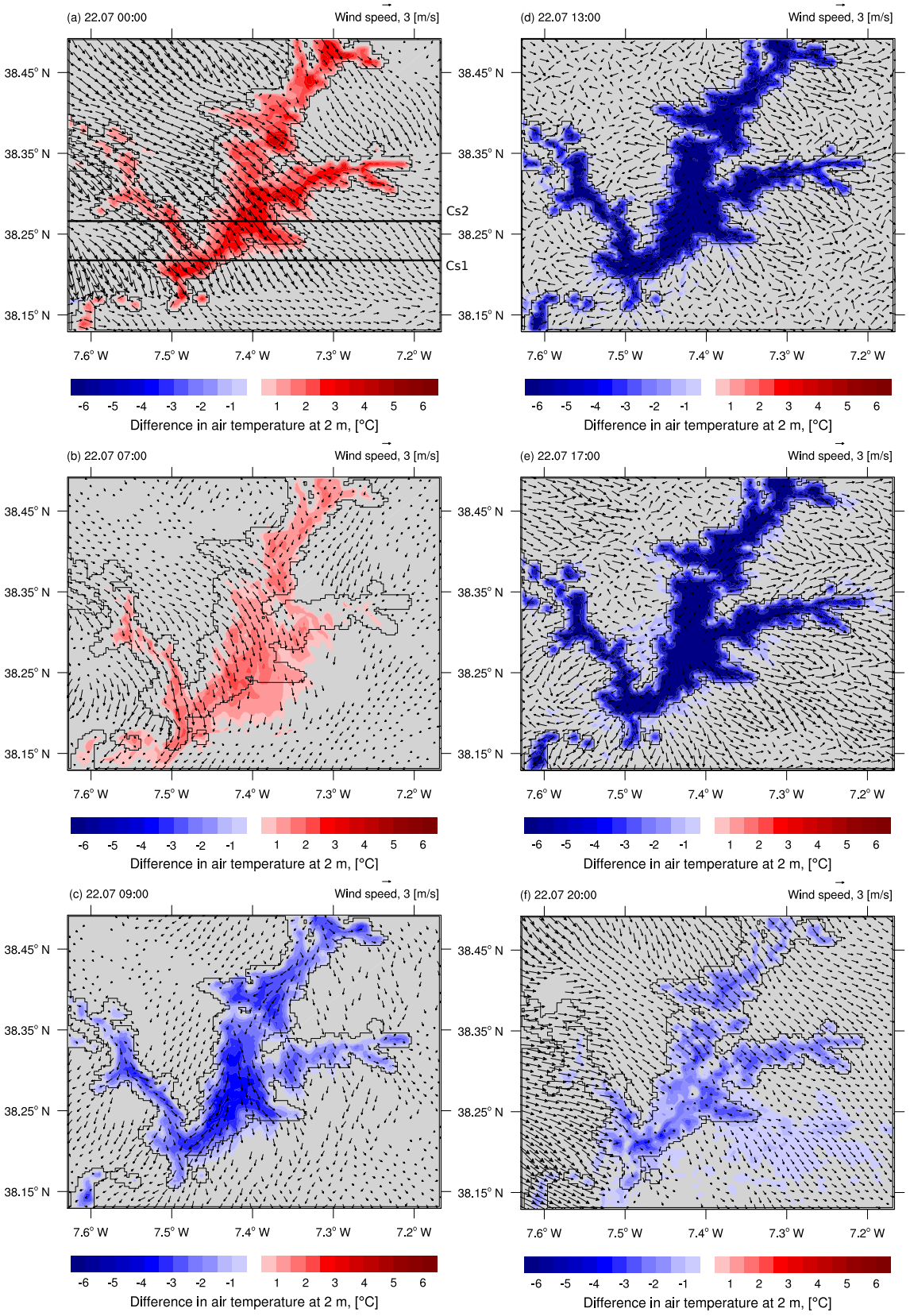

Figure 9. Anomalies in air temperature at 2 m (in filled contours) and horizontal wind in LAKE1 experiment (arrays, the scale is indicated in the upper right corner of each figure) of the reservoir on 22 July 2014 in domain C. Horizontal lines in **(a)** indicate the location of cross sections Cs1 (southern) and Cs2 (northern).

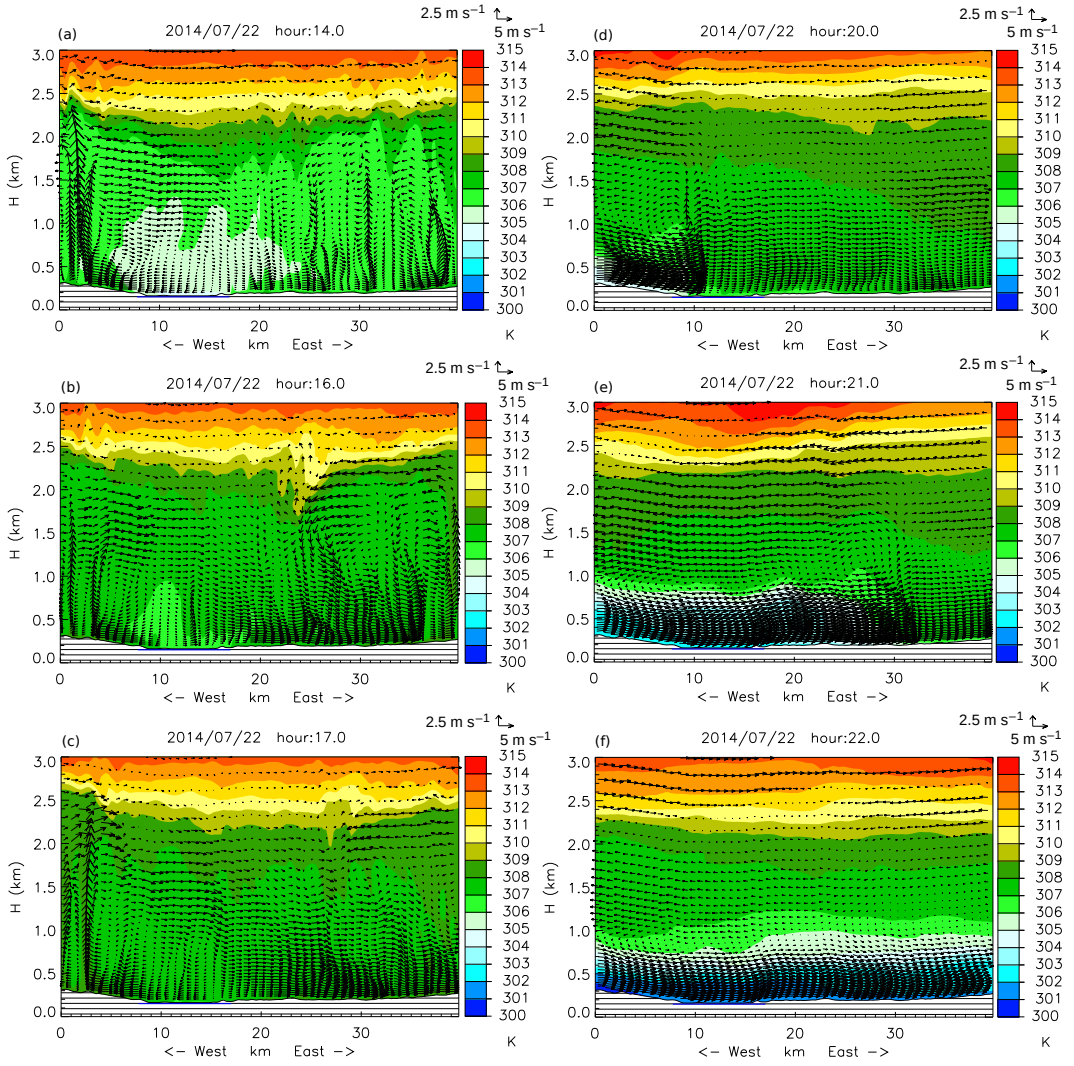

Figure 10. East–west direction cross sections along 38.215° N (Cs1, crosses the lake near Montante platform, Fig. 9a) of potential temperature (filled contours) and wind vectors in the plane of the cross section (arrows), at different hours (indicated in the top of each figure) in the LAKE1 experiment at 250 m horizontal resolution. The wind vertical and horizontal scales are indicated in the upper right corner of each figure. The blue line on the surface level indicates the location of the reservoir.

tions. Examples of positive night anomalies are illustrated in Fig. 9a and b. Night north-west wind transports warm air from the lake to the south-east part of the reservoir for up to 2 km away from the shore. The daytime period is characterized by negative temperature anomalies up to 7 °C (Fig. 9c–f). Initially, the effect is essentially limited by the lake borders. When the large-scale sea breeze system arrives, temperature trace of the lake impact is advected by the wind and can be found in 10–12 km away from the south-east part of the reservoir (Fig. 9f).

Vertical cross sections help to illustrate the processes at different altitudes. Two different cross sections Cs1 and Cs2 are shown to provide a better visualization of the three-dimensional structure of air circulation above the lake. The first one crosses the lake near Montante platform and the second in the middle, exact locations are indicated in Fig. 9a. Cross sections Cs1 along 38.215° N (Fig. 10) show the evolution of wind and potential temperature during 22 July in the experiment with Alqueva (simulation LAKE1). The highest impact on the air temperature can be observed in the early afternoon (12:00–14:00 UTC). The boundary layer is cooling down and its height decreases from more than 2 km above the land outside to values close to 1 km over the lake surface (Fig. 10a). The thermal anomaly induced by the presence of the reservoir seems to affect an area greater than what was identified at the surface, especially in the middle of the boundary layer. Later on, at 19:00–20:00 UTC the powerful ocean breeze system reaches the area and cools the lower (1 km) layer of air by 6–7 K. The progression of the sea breeze front is impressively well shown in Fig. 10d

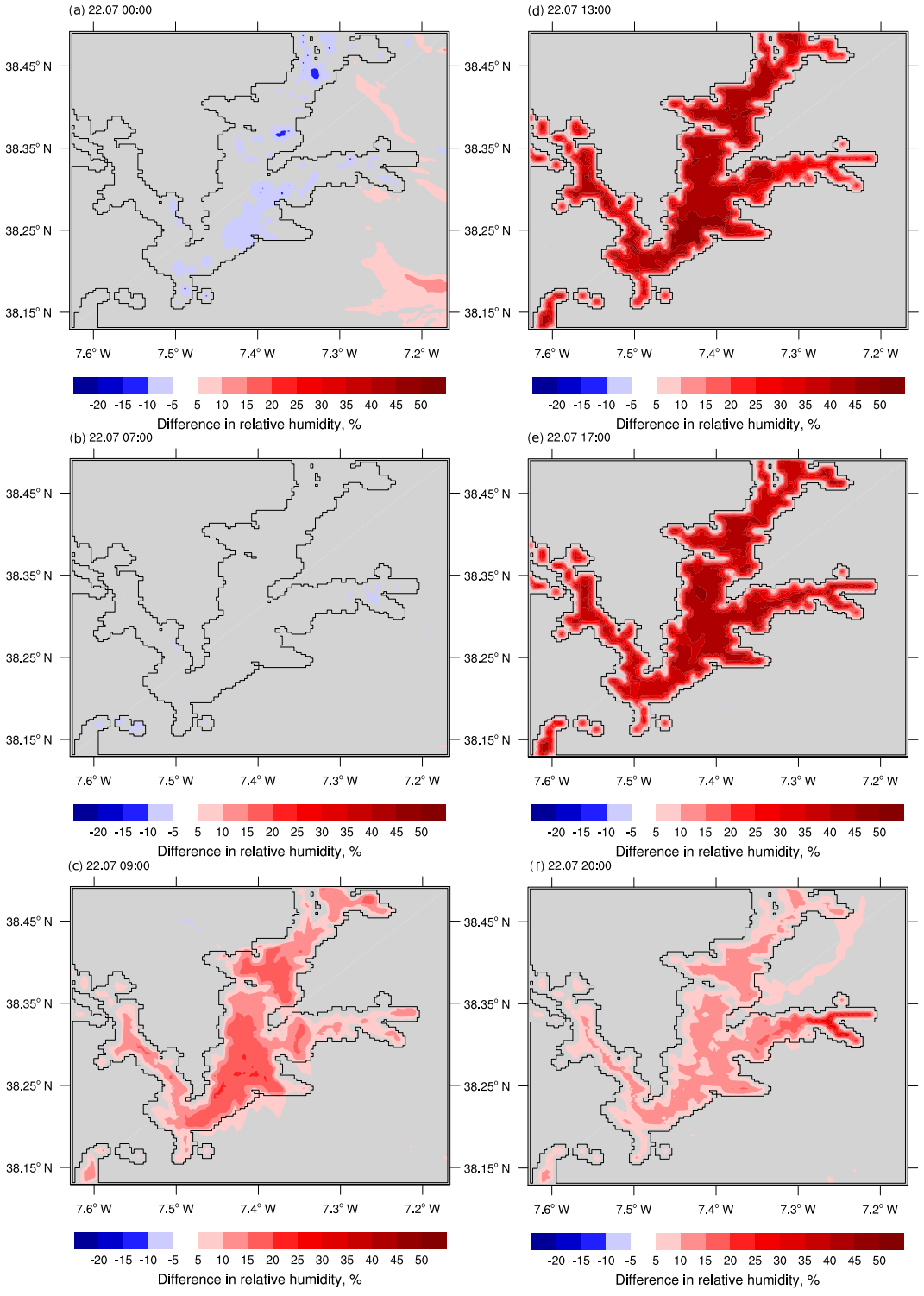

Figure 11. 2 m relative humidity anomalies (in filled contours) on 22 July 2014 in domain C.

(20:00 UTC), when it reaches the border of the reservoir, and in Fig. 10e and f (21:00–22:00 UTC), when it is already beyond the east bank of the Alqueva reservoir. More cross sections of 22 July 2014 with potential temperature can be found in Fig. S4.

Alqueva causes a similar anomaly on 2 m relative humidity, which is shown in Fig. 11.

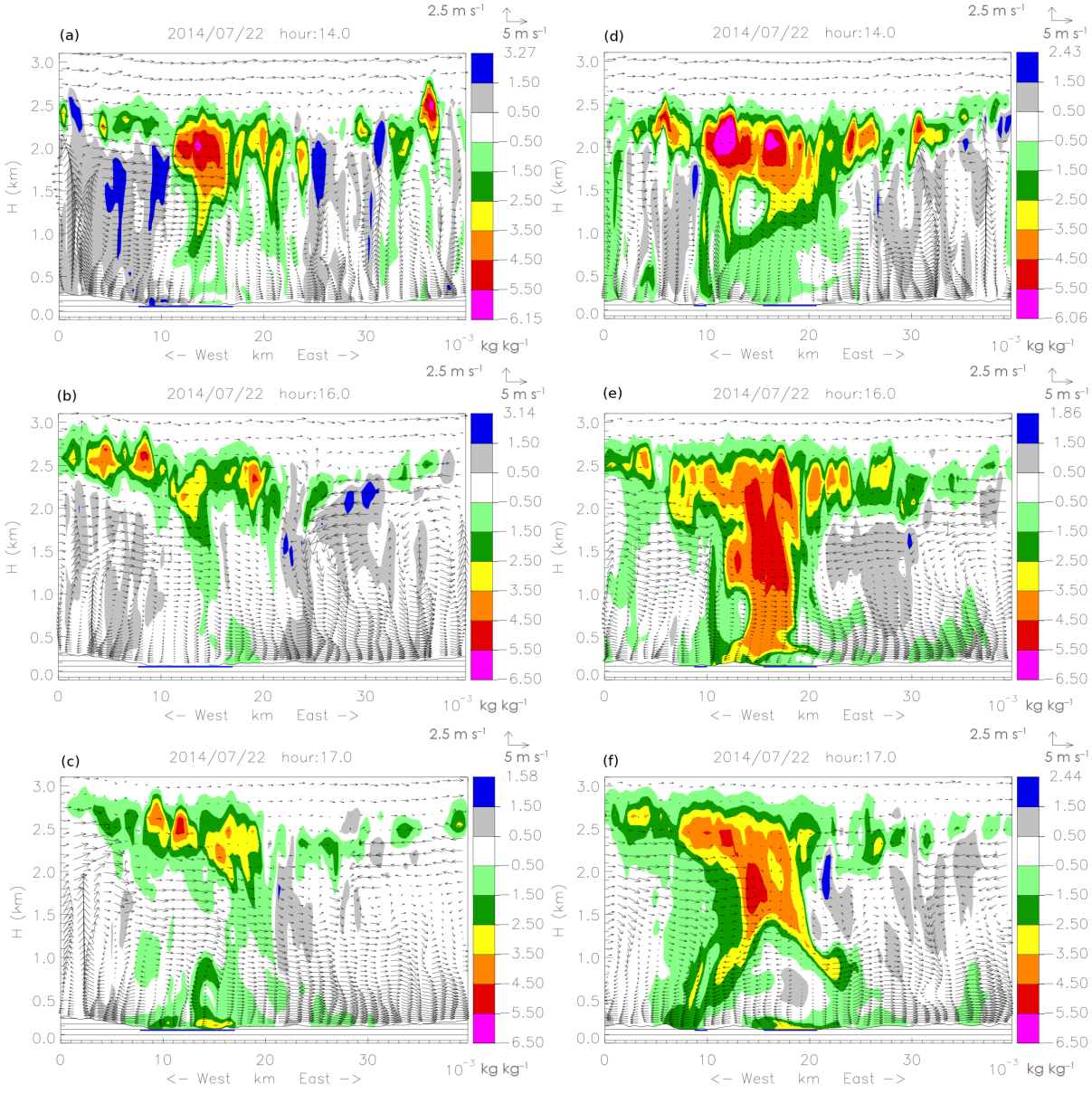

Figure 12. East–west direction cross sections Cs1 along 38.215° N **(a–c)** and Cs2 along 38.274° N **(d–f)** with the difference (LAKE1 minus LAKE0 simulations) of water mixing ratio (filled contours), and wind vectors in the plane of the cross section (arrows) in the LAKE1 experiment at 250 m horizontal resolution at different times (indicated in the top of each figure). The blue line on the surface level indicates the location of the reservoir.

At night when the temperature impact is negative some small negative differences in relative humidity can be seen over the lake surface (Fig. 11a). There are also traces of daytime positive impact, essentially due to the decrease in air temperature, advected by the sea breeze in the south-east direction. In the morning, however, the difference of relative humidity cannot be detected because the thermal impact is not strong enough (Fig. 11b). Figure 11c–e show how relative humidity increases during the daytime over the water surface. The peak of the difference can reach 50 % in the afternoon (Fig. 11f). In general, lake impact on relative humidity is limited by the area of the reservoir and does not spread over the surrounding land.

6.2 Breeze effects

Differences in near-surface sensible heat fluxes and contrast of the air temperature over the land and water surfaces during the daytime induce the formation of the lake breeze system. The development of the lake breeze is illustrated in Fig. 9 (arrows that correspond to the wind speed lesser than 0.5 m s^{-1}

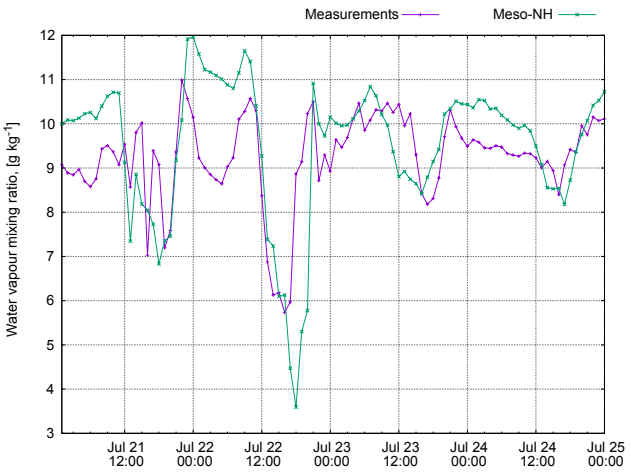

Figure 13. Observed and simulated water vapour mixing ratio at the Montante platform.

are not plotted). During the night, the large-scale circulation (Fig. 9a and b) is dominant in the area. After the sunrise (07:00–08:00 UTC) the air temperature over the water surface becomes lower than the air temperature over the surrounding areas, which induce a thermal circulation directed from the centre of the lake to its shores. The breeze intensifies during the afternoon reaching 6 m s^{-1} in some areas (Fig. 9d and e).

Daytime cross sections Cs1 in Fig. 10a–c indicate that the direct lake breeze can be found on altitudes up to 300 m above the lake, with a divergent flow over the water surface. The lake breeze intensity and pattern depends on the local orography, but usually the traces can be found 4–6 km away from the lake shores (Fig. 10c). In altitude, a return flow is visible in the eastward wind component over the west shore and a westward component in the east of the reservoir, which causes an upper-level convergence that can be seen in Fig. 10a–c. This will be discuss together with the effects of the reservoir on the moisture field, in which the structure of the lake breeze system is more visible.

In the late afternoon (18:00 UTC) the negative temperature anomaly due to the presence of the lake is getting weaker, and the breeze system starts to wane and dissipate. At 19:00–20:00 UTC the ocean breeze arrives to the area and overlaps the local circulations (Fig. 10d–f).

Cross sections Cs1 and Cs2 presented in Fig. 12 show that the lake breeze system includes a descending branch over the reservoir that carries dry air from a height of about 2–2.5 km and redistributes it over the lake surface. Additional cross sections illustrating this process can be found in the Supplement (Figs. S5 and S6).

This dry downstream is confirmed by the measurements of water vapour mixing ratio at the Montante platform. As can be seen in Fig. 13 the observed and the simulated mixing ratio of water vapour have a daily minimum with average values of about 8–8.5 g kg^{-1} around 14:00–16:00 UTC. During the afternoon of 22 July, the day with a strong lake breeze, the minimum reached a value lower than 6 g kg^{-1}. Out of the period in which the air over the lake subsides, the water vapour mixing ratio returns back to 9–10.5 g kg^{-1}. The presence of this dry downstream was proposed as a hypothesis by Potes et al. (2017) and is proved through the performed simulations. In the same figure it is clearly seen that the model tends to overestimate the mixing ratio, except during the afternoon of 22 July.

However, Fig. 12 also shows that outside the reservoir there are zones of low-level convergence and upward motion that increase the moisture of the boundary layer and form some kind of lake breeze fronts. The complex shape of the reservoir implies also an complex 3-D structure of the breeze system. Towards the southernmost part, near the dam, the low-level divergent breeze circulation is very clear, but the convergence upper-level return current is weaker (Fig. 12a–c). In contrast, near the middle of the reservoir (cross section Cs2 in Fig. 12d–f) where two water branches exist, the circulation near the surface is more complex due to the presence of a land area in between, but the subsidence motion is more prominent, inducing a decrease in mixing ratio through the boundary layer, which reaches a magnitude of about 4 g kg^{-1} at 16:00 UTC (Fig. 12f).

Figure 14 illustrates this process in a horizontal plane. At midnight (Fig. 14b) the reservoir does not directly affect vapour mixing ratio in the air. In the morning hours, when the sun rises, but the breeze system is not yet formed, a positive impact on the moisture over the lake can be seen due to the increase in the evaporation. This anomaly affects the air above the central and southern parts of the reservoir and is advected to nearby areas (Fig. 14c). Later in the afternoon, with the formation of the lake breeze, a negative impact can be traced over the water surface due to the descending branches of the local circulation (Fig. 14d and e). This explains the afternoon decrease in the water vapour mixing ratio observed at the Montante platform, as seen in Fig. 13. The localization of the area of this negative anomaly changes in time, but predominantly it is over the larger southern part of the reservoir. With the dissipation of the local lake breeze system and the arrival of the stronger large-scale north-western wind, the negative moisture anomaly over the reservoir disappears and a positive effect is visible in the downwind region (Fig. 14a and f), due to the increase in evaporation (note that Fig. 14a corresponds to the night of 21 to 22 July, when the effect was more noticeable).

During daytime, water temperature is lower than air temperature, which is associated with a very weak air circulation over the water surface, which leads to very low evaporation from the lake (refer to low latent heat flux values in Fig. 7a). This period of day is characterized by higher evaporation over the land than over water. By late afternoon when the dominant sea breeze system reaches the region, the north-western wind accelerates significantly when passing over the

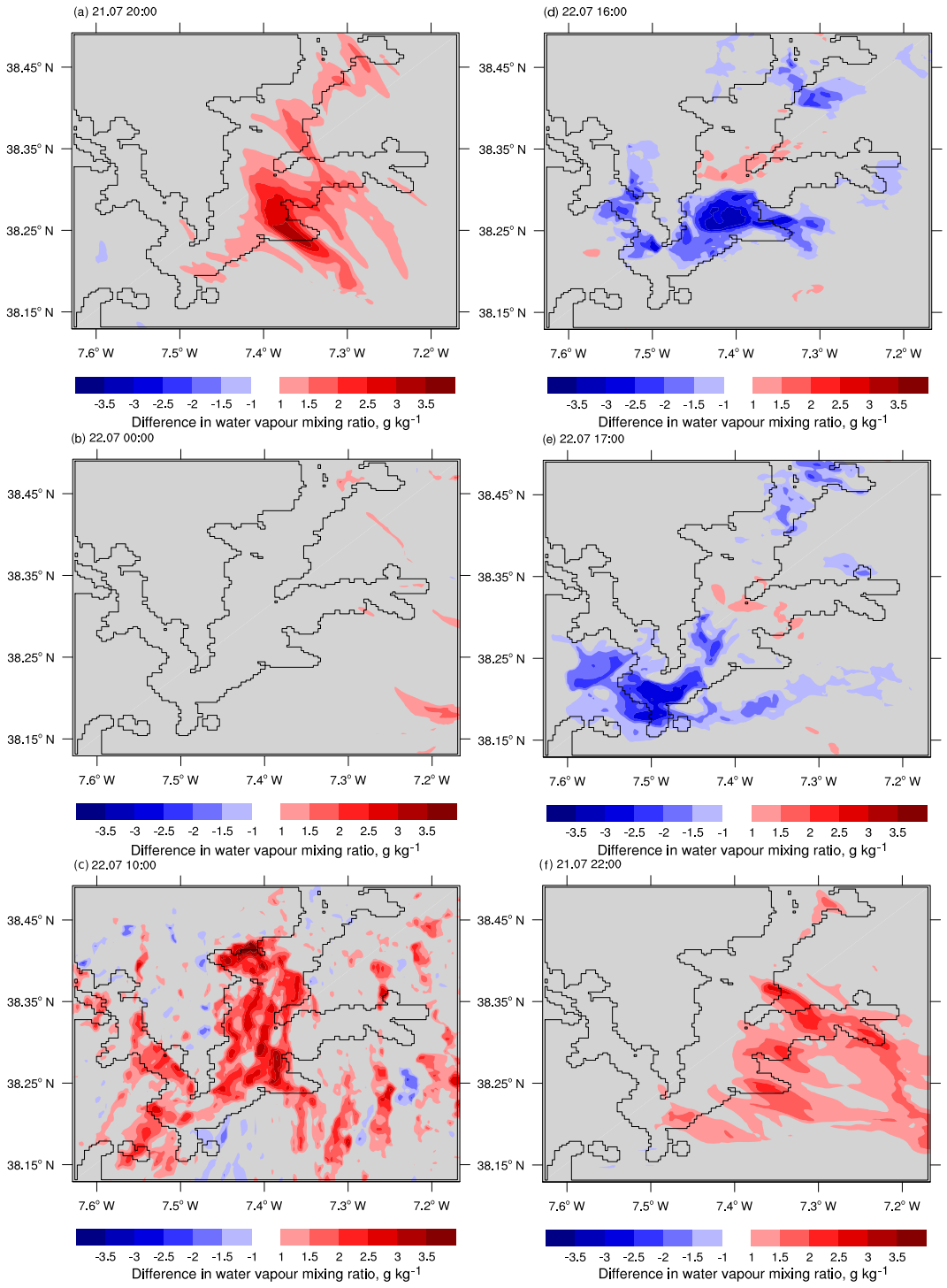

Figure 14. Observed and simulated water vapour mixing ratio anomalies in filled contours on 22 July 2014 in domain C for selected hours.

smooth surface of the lake. As result, evaporation from the lake becomes very intense.

7 Conclusions

In this work the authors studied the formation and magnitude of the summer lake breeze in the Alqueva reservoir, southern Portugal, and its impacts on local weather. The study was based on Meso-NH simulations of a well documented case

study of 22–24 July 2014. This period was used for several reasons. First, a large volume of meteorological data was collected during these days, which allowed for a validation of the simulation results. Secondly, this period was hot and dry, which is typical for most summer days in the region.

The model allowed simulations with horizontal resolution of 250 m, which is fine enough to resolve such relatively small-scale lake breeze and to spot the impact of the reservoir on the detailed local boundary layer structure. Due to the "youth" of the Alqueva reservoir it is possible to run an atmospheric model with the surface conditions prevailing before the filling of the reservoir. Two simulations, one with Alqueva and another one without it, allow the raw impact of the lake on the local weather regime to be evaluated.

Formation and dissipation of the daytime breeze system induced by the reservoir are described in the work. On hot summer mornings the difference between air temperatures above water and neighbouring land surfaces induces the radial movement of air from the lake. The breeze system starts to form in the morning and the peak of the wind speed reaches 6 m s^{-1} during the afternoon. Simulation results show that the lake breeze could be detected at a distance of more than 6 km away from the shores and on altitudes up to 300 m above the water surface. In late afternoon the dissipation stage of the lake breeze system is anticipated with the arrival of the larger-scale sea breeze from the Portuguese west Atlantic coast. In early evening (19:00–20:00 UTC) the local lake breeze system cannot be detected anymore. No reverse land breeze is detected during the night.

Lake breeze system brings dry air from upper atmospheric layers (2–2.5 km) to near-surface levels above the reservoir. This effect leads to the fact that the air above the surface of the lake becomes more dry in terms of water vapour mixing ratio, in spite of the fact that its relative humidity can increase up to 50 % due to the decrease in air temperature.

The simulations testify to the observed very low evaporation from water surface during the daytime (0–120 W m^{-2} in terms of latent heat flux), due to weak winds and the stable stratification of the internal atmospheric surface layer. At nighttime, the strong wind associated with the peninsular larger-scale circulation induced by the sea–land contrasts, originates a very high evaporation rate (200–250 W m^{-2}).

The cooling effect of the reservoir can decrease the air temperature by up to 7 °C; nevertheless it is limited by the lake borders and normally cannot be seen farther than few kilometres away from the shore, mostly in the south-east direction. The cooling can be found up to 1200 m above the lake surface.

Further work suggests two options: first, tuning the lake model and its initialization in order to obtain more accurate results and reduce validation biases; second, carry out a longer experiment, which would cover a 12-month period. Such a simulation could reveal seasonal aspects of the impact of Alqueva on local weather.

Data availability. Data obtained during the ALEX 2014 observational experiment and used here are available via http://www.alex2014.cge.uevora.pt/data/ (Salgado, 2018).

Supplement. The supplement related to this article is available online at: https://doi.org/10.5194/hess-22-5191-2018-supplement.

Author contributions. The three authors conceptualized the study. MI and RS performed the Meso-NH simulations and the exploitation of its results. MP prepared the measured data and assisted in its use. MI wrote the first draft manuscript. All the three authors contributed to the analysis, interpretation and writing.

Competing interests. The authors declare that they have no conflict of interest.

Special issue statement. This article is part of the special issue "Modelling lakes in the climate system (GMD/HESS interjournal SI)". It is a result of the 5th workshop on "Parameterization of Lakes in Numerical Weather Prediction and Climate Modelling", Berlin, Germany, 16–19 October 2017.

Acknowledgements. The work is co-funded by the European Union through the European Regional Development Fund, included in COMPETE 2020 (Operational Program Competitiveness and Internationalization) through the ICT project (UID/GEO/04683/2013) with the reference POCI-01-0145-FEDER-007690 and also through the ALOP project (ALT20-03-0145-FEDER-000004). Experiments were accomplished during the field campaign funded by FCT and FEDER-COMPETE: ALEX (EXPL/GEO-MET/1422/2013) FCOMP-01-0124-FEDER-041840.

Edited by: Wim Thiery
Reviewed by: two anonymous referees

References

Bates, G. T., Giorgi, F., and Hostetler, S. W.: Toward the Simulation of the Effects of the Great Lakes on Regional Climate, Mon. Weather Rev., 121, 1373–1387, https://doi.org/10.1175/1520-0493(1993)121<1373:TTSOTE>2.0.CO;2, 1993.

Bechtold, P., Bazile, E., Guichard, F., Mascart, P., and Richard, E.: A mass-flux convection scheme for regional and global models, Q. J. Roy. Meteorol. Soc., 127, 869–886, https://doi.org/10.1002/qj.49712757309, 2001.

Bischoff-Gauß, I., Kalthoff, N., and Fiebig-Wittmaack, M.: The influence of a storage lake in the Arid Elqui Valley in Chile on local climate, Theor. Appl. Climatol., 85, 227–241, https://doi.org/10.1007/s00704-005-0190-8, 2006.

Bonan, G. B.: Sensitivity of a GCM Simulation to Inclusion of Inland Water Surfaces, J. Cli-

mate, 8, 2691–2704, https://doi.org/10.1175/1520-0442(1995)008<2691:SOAGST>2.0.CO;2, 1995.

Bougeault, P. and Lacarrere, P.: Parameterization of Orography-Induced Turbulence in a Mesobeta–Scale Model, Mon. Weather Rev., 117, 1872–1890, https://doi.org/10.1175/1520-0493(1989)117<1872:POOITI>2.0.CO;2, 1989.

Cohard, J. M. and Pinty, J. P.: A comprehensive two-moment warm microphysical bulk scheme. I: Description and tests, Q. J. Roy. Meteorol. Soc., 126, 1815–1842, https://doi.org/10.1002/qj.49712656613, 2000.

Cotton, W. R. and Pielke, R. A. S.: Human Impacts on Weather and Climate, 2nd Edn., Cambridge University Press, Cambridge, 2007.

Crosman, E. T. and Horel, J. D.: Idealized Large-Eddy Simulations of Sea and Lake Breezes: Sensitivity to Lake Diameter, Heat Flux and Stability, Bound.-Lay. Meteorol., 144, 309–328, https://doi.org/10.1007/s10546-012-9721-x, 2012.

Cuxart, J., Bougeault, P., and Redelsperger, J.-L.: A turbulence scheme allowing for mesoscale and large-eddy simulations, Q. J. Roy. Meteorol. Soc., 126, 1–30, https://doi.org/10.1002/qj.49712656202, 2000.

Drobinski, P. and Dubos, T.: Linear breeze scaling: from large-scale land/sea breezes to mesoscale inland breezes, Q. J. Roy. Meteorol. Soc., 135, 1766–1775, https://doi.org/10.1002/qj.496, 2009.

Ekhtiari, N., Grossman-Clarke, S., Koch, H., Meira de Souza, W., Donner, R. V., and Volkholz, J.: Effects of the Lake Sobradinho Reservoir (Northeastern Brazil) on the Regional Climate, Climate, 5, 50, https://doi.org/10.3390/cli5030050, 2017.

Faroux, S., Kaptué Tchuenté, A. T., Roujean, J. L., Masson, V., Martin, E., and Le Moigne, P.: ECOCLIMAP-II/Europe: a twofold database of ecosystems and surface parameters at 1 km resolution based on satellite information for use in land surface, meteorological and climate models, Geosci. Model Dev., 6, 563–582, https://doi.org/10.5194/gmd-6-563-2013, 2013.

Fouquart, Y. and Bonnel, B.: Computations of Solar Heating of the Earth's Atmosphere – A New Parameterization, Beitr. Phys. Atmos., 53, 35–62, 1980.

Hartmann, D. L.: Global physical climatology, Int. Geophys., Elsevier Science, 498 pp., 1994.

Hoinka, K. P. and Castro, M. D.: The Iberian Peninsula thermal low, Q. J. Roy. Meteorol. Soc., 129, 1491–1511, 2003.

Jarvis, A., Guevara, E., Reuter, H. I., and Nelson, A. D.: Hole – filled SRTM for the globe: version 4: data grid, CGIAR-CSI, Washington, USA, 19 August 2008.

Kain, J. S. and Fritsch, M. J.: A One-Dimensional Entraining/Detraining Plume Model and Its Application in Convective Parameterization, J. Atmos. Sci., 47, 2784–2802, https://doi.org/10.1175/1520-0469(1990)047<2784:AODEPM>2.0.CO;2, 1990.

Lac, C., Chaboureau, J.-P., Masson, V., Pinty, J.-P., Tulet, P., Escobar, J., Leriche, M., Barthe, C., Aouizerats, B., Augros, C., Aumond, P., Auguste, F., Bechtold, P., Berthet, S., Bielli, S., Bosseur, F., Caumont, O., Cohard, J.-M., Colin, J., Couvreux, F., Cuxart, J., Delautier, G., Dauhut, T., Ducrocq, V., Filippi, J.-B., Gazen, D., Geoffroy, O., Gheusi, F., Honnert, R., Lafore, J.-P., Lebeaupin Brossier, C., Libois, Q., Lunet, T., Mari, C., Maric, T., Mascart, P., Mogé, M., Molinié, G., Nuissier, O., Pantillon, F., Peyrillé, P., Pergaud, J., Perraud, E., Pianezze, J., Redelsperger, J.-L., Ricard, D., Richard, E., Riette, S., Rodier, Q., Schoetter, R., Seyfried, L., Stein, J., Suhre, K., Taufour, M., Thouron, O., Turner, S., Verrelle, A., Vié, B., Visentin, F., Vionnet, V., and Wautelet, P.: Overview of the Meso-NH model version 5.4 and its applications, Geosci. Model Dev., 11, 1929–1969, https://doi.org/10.5194/gmd-11-1929-2018, 2018.

Lascaux, F., Masciadri, E., and Fini, L.: MOSE: operational forecast of the optical turbulence and atmospheric parameters at European Southern Observatory ground-based sites – II. Atmospheric parameters in the surface layer 0–30 m, Mon. Notic. Roy. Astron. Soc., 436, 3147–3166, https://doi.org/10.1093/mnras/stt1803, 2013.

Lascaux, F., Masciadri, E., and Fini, L.: Forecast of surface layer meteorological parameters at Cerro Paranal with a mesoscale atmospherical model, Mon. Notic. Roy. Astron. Soc., 449, 1664–1678, https://doi.org/10.1093/mnras/stv332, 2015.

Lee, X., Liu, S., Xiao, W., Wang, W., Gao, Z., Cao, C., Hu, C., Hu, Z., Shen, S., Wang, Y., Wen, X., Xiao, Q., Xu, J., Yang, J., and Zhang, M.: The Taihu Eddy Flux Network: An Observational Program on Energy, Water, and Greenhouse Gas Fluxes of a Large Freshwater Lake, B. Am. Meteorol. Soc., 95, 1583–1594, https://doi.org/10.1175/BAMS-D-13-00136.1, 2014.

Lin, Z., Jiming, J., Shih-Yu, W., and Ek, M. B.: Integration of remote-sensing data with WRF to improve lake-effect precipitation simulations over the Great Lakes region, J. Geophys. Res.-Atmos., 117, d09102, https://doi.org/10.1029/2011JD016979, 2012.

Lopes, F., Silva, H. G., Salgado, R., Potes, M., Nicoll, K. A., and Harrison, R. G.: Atmospheric electrical field measurements near a fresh water reservoir and the formation of the lake breeze, Tellus A, 68, 31592, https://doi.org/10.3402/tellusa.v68.31592, 2016.

Lunet, L., Lac, C., Auguste, F., Visentin, F., Masson, V., and Escobar, J.: Combination of WENO and Explicit Runge–Kutta Methods for Wind Transport in the Meso-NH Model, Mon. Weather Rev., 145, 3817–3838, https://doi.org/10.1175/MWR-D-16-0343.1, 2017.

Masciadri, E., Lascaux, F., and Fini, L.: MOSE: operational forecast of the optical turbulence and atmospheric parameters at European Southern Observatory ground-based sites – I. Overview and vertical stratification of atmospheric parameters at 0–20 km, Mon. Notic. Roy. Astron. Soc., 436, 1968–1985, https://doi.org/10.1093/mnras/stt1708, 2013.

Masson, V.: A Physically-Based Scheme For The Urban Energy Budget In Atmospheric Models, Bound.-Lay. Meteorol., 94, 357–397, https://doi.org/10.1023/A:1002463829265, 2000.

Masson, V., Le Moigne, P., Martin, E., Faroux, S., Alias, A., Alkama, R., Belamari, S., Barbu, A., Boone, A., Bouyssel, F., Brousseau, P., Brun, E., Calvet, J.-C., Carrer, D., Decharme, B., Delire, C., Donier, S., Essaouini, K., Gibelin, A.-L., Giordani, H., Habets, F., Jidane, M., Kerdraon, G., Kourzeneva, E., Lafaysse, M., Lafont, S., Lebeaupin Brossier, C., Lemonsu, A., Mahfouf, J.-F., Marguinaud, P., Mokhtari, M., Morin, S., Pigeon, G., Salgado, R., Seity, Y., Taillefer, F., Tanguy, G., Tulet, P., Vincendon, B., Vionnet, V., and Voldoire, A.: The SURFEXv7.2 land and ocean surface platform for coupled or offline simulation of earth surface variables and fluxes, Geosci. Model Dev., 6, 929–960, https://doi.org/10.5194/gmd-6-929-2013, 2013.

Miranda, P. M. A., Abreu, F., and Salgado, R.: Estudo de Impacte Ambiental do Alqueva, Tech. rep., Instituto de ciencia aplicada e

tecnologia, Faculdade de Ciências, Universidade de Lisboa, Lisboa, 1995.

Miranda, P. M. and James, I. N.: Non-linear three-dimensional effects on gravity-wave drag: Splitting flow and breaking waves, Q. J. Roy. Meteorol. Soc., 118, 1057–1081, 1992.

Mironov, D.: Parameterization of lakes in numerical weather prediction, Description of a lake model, COSMO Technical Report, Deutscher Wetterdienst, Offenbach am Main, 41 pp., 2008.

Morcrette, J. J.: Radiation and cloud radiative properties in the European Centre for Medium Range Weather Forecasts forecasting system, J. Geophys. Res.-Atmos., 96, 9121–9132, https://doi.org/10.1029/89JD01597, 1991.

Nicoll, K. A., Harrison, R. G., Silva, H. G., Salgado, R., Melgâo, M., and Bortoli, D.: Electrical sensing of the dynamical structure of the planetary boundary layer, Atmos. Res., 202, 81–95, https://doi.org/10.1016/j.atmosres.2017.11.009, 2018.

Noilhan, J. and Mahfouf, J. F.: The ISBA land surface parameterisation scheme, Global Planet. Change, 13, 145–159, https://doi.org/10.1016/0921-8181(95)00043-7, 1996.

Pergaud, J., Masson, V., Malardel, S., and Couvreux, F.: A Parameterization of Dry Thermals and Shallow Cumuli for Mesoscale Numerical Weather Prediction, Bound.-Lay. Meteorol., 132, 83–106, https://doi.org/10.1007/s10546-009-9388-0, 2009.

Pielke Sr., R. A.: A Three-Dimensional Numerical Model of the Sea Breezes Over South Florida, Mon. Weather Rev., 102, 115–139, https://doi.org/10.1175/1520-0493(1974)102<0115:ATDNMO>2.0.CO;2, 1974.

Pielke Sr., R. A.: Mesoscale Meteorological Modeling, 3rd Edn., Academic Press, 760, 2013.

Pinty, J. P. and Jabouille, P.: A mixed-phase cloud parameterization for use in mesoscale non-hydrostatic model: simulations of a squall line and of orographic precipitations, in: Proc. Conf. of Cloud Physics, Everett, WA, USA, 217–220, 1998.

Policarpo, C., Salgado, R., and Costa, M. J.: Numerical Simulations of Fog Events in Southern Portugal, Adv. Meteorol., 2017, 16 pp., 2017.

Potes, M., Salgado, R., Costa, M. J., Morais, M., Bortoli, D., Kostadinov, I., and Mammarella, I.: Lake–atmosphere interactions at Alqueva reservoir: a case study in the summer of 2014, Tellus A, 69, 1272787, https://doi.org/10.1080/16000870.2016.1272787, 2017.

Salgado, R.: Interacção solo-atmosfera em clima semi-àrido, PhD thesis, Universidade de Èvora, Èvora, 2006.

Salgado, R. and Le Moigne, P.: Coupling of the FLake model to the Surfex externalized surface model, Boreal Environ. Res., 15, 231–244, 2010.

Salgado, R., Miranda, P. M. A., Lacarrère, P., and Noilhan, J.: Boundary layer development and summer circulation in Southern Portugal, Tethys, 12, 33–44, https://doi.org/10.3369/tethys.2015.12.03, 2015.

Salgado, R., Potes, M., Albino, A., Apolinário, J., Barbosa, S., Bárias, S., Beliche, P., Bortoli, D., Canhoto, P., Costa, M. J., Fernandes, R. M., Harrison, G., Ilhéu, A., Le Moigne, P., Lima, R., Lopes, F., Lopes, T., Marques, J., Melgão, M., Miranda, P. M., Morais, M., Murteira, M., Nicoll, K., Novais, M. H., Parrondo, M. C., Pereira, S., Policarpo, C., Prior, V., Rodrigues, C. M., Rosado, J., Sá, A., Serafim, A., Silva, H., Soares, P. M. M., Tlemçani, M., and Zavattieri, A.: The ALEX2014 Alqueva hydro-meteorological database, available at: http://www.alex2014.cge.uevora.pt/data/, last access: 3 October 2018.

Samuelsson, P., Kourzeneva, E., and Mironov, D.: The impact of lakes on the European climate as simulated by a regional climate model, Boreal Environ. Res., 15, 113–129, 2006.

Segal, M., Leuthold, M., Arritt, R. W., Anderson, C., and Shen, J.: Small Lake Daytime Breezes: Some Observational and Conceptual Evaluations, B. Am. Meteorol. Soc., 78, 1135–1147, https://doi.org/10.1175/1520-0477(1997)078<1135:SLDBSO>2.0.CO;2, 1997.

Silva, A., De Lima, I., Santo, F. E., and Pires, V.: Assessing changes in drought and wetness episodes in drainage basins using the Standardized Precipitation Index, Bodenkultur, 65, 31–37, 2014.

Stein, J., Richard, E., Lafore, J. P., Pinty, J. P., Asencio, N., and Cosma, S.: High-Resolution Non-Hydrostatic Simulations of Flash-Flood Episodes with Grid-Nesting and Ice-Phase Parameterization, Meteorol. Atmos. Phys., 72, 203–221, https://doi.org/10.1007/s007030050016, 2000.

Thiery, W., Martynov, A., Darchambeau, F., Descy, J.-P., Plisnier, P.-D., Sushama, L., and van Lipzig, N. P. M.: Understanding the performance of the FLake model over two African Great Lakes, Geosci. Model Dev., 7, 317–337, https://doi.org/10.5194/gmd-7-317-2014, 2014.

Atmospheric Research 213 (2018) 252–263

Contents lists available at ScienceDirect

Atmospheric Research

journal homepage: www.elsevier.com/locate/atmosres

Impact of aerosol and water vapour on SW radiation at the surface: Sensitivity study and applications

M.A. Obregón[a,*], M.J. Costa[b], A.M. Silva[b], A. Serrano[c]

[a] Departamento de Física, Instituto de Ciências da Terra, Instituto de Investigação e Formação Avançada, Universidade de Évora, Évora, Portugal
[b] Departamento de Física, Instituto de Ciências da Terra, Escola de Ciências e Tecnologia, Universidade de Évora, Évora, Portugal
[c] Departamento de Física, Facultad de Ciencias, Universidad de Extremadura, Badajoz, Spain

ARTICLE INFO

Keywords:
Sensitivity analysis
Aerosol radiative effects
Water vapour radiative effects
Radiative transfer model
AERONET

ABSTRACT

This study provides a sensitivity analysis of the downwelling shortwave (SW) irradiance at the Earth's surface with respect to the aerosols and the water vapour. Aerosols are characterized by optical thickness (AOD) and single scattering albedo (SSA), while water vapour is quantified by precipitable water vapour (PWV). For this purpose, downwelling SW irradiances under cloud-free conditions and a wide range of AOD, SSA and PWV values are simulated using libRadtran radiative transfer code. Results show SW irradiance decreases as AOD or PWV increases or as SSA decreases. The general analysis also shows that the combined effect of these quantities is not just the sum of the individual effects. Based on the results, two models are proposed to estimate the effect of aerosols and water vapour on SW irradiance. The two models are validated through comparing their results with radiation measurements registered at nine stations around the world. Models using two and three quantities show differences lower than 3% in 84% and 88% of cases, respectively. This good performance indicates the reliability of the models to estimate the effect of aerosols and water vapour on SW irradiance when no radiation measurements exist, provided that aerosol and water vapour information is available.

1. Introduction

Solar radiation is the main energy source for the Earth–atmosphere system. It is well known that changes in the atmospheric composition could significantly affect the radiative budget and, as a result, the global temperature of the Earth (Forster et al., 2007). Two of the most important components of this system affecting the atmospheric transfer of solar radiation toward the Earth's surface are, for cloud-free conditions, aerosols and water vapour. Aerosols are atmospheric particles, of natural and anthropogenic origin, playing an important role in the climate system due to their (direct and indirect) effects on the Earth's radiative balance (Boucher et al., 2013). On the other hand, water vapour is an important gas, since it induces a surface warming through the trapping of longwave radiation (greenhouse effect) and a surface cooling by the absorption of shortwave radiation. Water vapour strongly absorbs in the spectral region beyond 0.5 μm of the solar spectrum, in the visible and the infrared solar wavelengths (Liou, 1980).

Aerosol direct effects have been thoroughly studied in the shortwave (SW) spectral range, which is the portion of the solar spectrum that extends from approximately 280 to 2800 nm. Many studies performed to analyse the effect of aerosols on downwelling SW irradiance at the surface are based on the calculation of the aerosol radiative forcing (ARF) (e.g., Costa et al., 2006; Di Sarra et al., 2008; Santos et al., 2008; Tzanis and Varotsos, 2008; Di Biagio et al., 2009; García et al., 2012; Santos et al., 2013; Esteve et al., 2014; Mateos et al., 2014; Che et al., 2015; Obregón et al., 2015a; Dhar et al., 2017; Fernández et al., 2017; Obregón et al., 2017; Mai, B.R., and Coauthors, 2018; Péré et al., 2018). However, the effect of water vapour on the downwelling SW radiation is scarcely studied (e.g., Mateos et al., 2013; Obregón et al., 2015b; Vaquero-Martínez et al., 2018). It should also be mentioned that in most radiative forcing studies, usually the effect of the whole set of aerosols or water vapour is analysed but not their individual effects. Only some of them analyse the effect of individual aerosol quantities on the ARF. For example, Di Biagio et al. (2009) and Mateos et al. (2014) have investigated the effects of the single scattering albedo (SSA) on ARF, concluding that absorbing aerosols lead to more negative ARF values.

The effect of water vapour and aerosols on downwelling SW irradiance is scarcely analysed (e.g., Bilbao et al., 2014; Trabelsi et al., 2015). In addition, these studies are based on measurements and, therefore, limited to specific periods, events or experimental

* Corresponding author at: Departamento de Física, Instituto de Ciências da Terra, Instituto de Investigação e Formação Avançada, Universidade de Évora, Évora, Portugal.
E-mail address: nines@unex.es (M.A. Obregón).

https://doi.org/10.1016/j.atmosres.2018.06.001
Received 2 February 2018; Received in revised form 23 May 2018; Accepted 4 June 2018
Available online 15 June 2018
0169-8095/ © 2018 Elsevier B.V. All rights reserved.

campaigns, and restricted to the specific aerosol and water vapour values of the study areas. Thus, for example, Bilbao et al. (2014) analysed the effects of individual aerosol and water vapour quantities on the SW irradiance. Specifically, this study addresses the quantification of the relative change of SW irradiance measured in Marsaxlokk, Malta, for different aerosol optical depth (AOD) and precipitable water vapour (PWV) values registered in that station during a measurement campaign between May and October 2012. Only 47 days were used. During this campaign, the AOD values at 550 nm does not exceed 0.6, with the majority of the cases in the range 0–0.3, and the majority of the PWV values in the range 20–40 mm. The validity of the results is limited to the campaign and, as a result, not of general use at other sites. This is the main limitation of this type of studies, especially when the sensitivity of a given quantity to different variables is the aim of the analysis. Therefore, modelling appears as a good alternative to analyse a variety of atmospheric situations (such as different aerosol and water vapour conditions), which may not be registered during an intensive campaign or at a specific location, and provided that the model results can be trusted. A good example of using modelling for this purpose is the work performed by Di Biagio et al. (2012) for the Arctic. In this work, we propose a similar approach but generalizing for different latitudes, water vapour and aerosols conditions.

To our knowledge, there are no studies that quantify in a general way the effect of aerosols and water vapour on the solar radiation at the surface. The main objective of this study is twofold: 1) analyse and quantify the sensitivity of the downwelling SW irradiance at the Earth's surface with respect to AOD, SSA and PWV, and 2) from the results of the sensitivity analysis, propose two models to estimate the effect of aerosols and water vapour on SW irradiance and validate through comparing with radiation measurements. Among the factors involved in the sensitivity analysis, AOD and SSA are used to describe the aerosol conditions and PWV quantifies the water vapour amount. This validation will allow proposing an empirical relationship to estimate the aerosol and water vapour effects on SW radiation based on AOD, SSA and PWV data, when no radiation measurements are available. This can be important for climate, air quality or energy applications. Most studies proposing empirical or semi-empirical models or equations are focused on estimating surface radiation from satellite data or models (e.g., Janjai et al., 2013; Lefèvre et al., 2013; Laaroussi et al., 2016), but few propose these models or equations to calculate effects on SW radiation (e.g. Xia et al., 2007; Stone et al., 2011). So, for example, Xia et al. (2007) developed empirical equations to describe AOD effects on surface irradiance and Stone et al. (2011) proposed empirical determinations of the longwave and shortwave radiative forcing efficiencies of wildfire smoke.

For this purpose, downwelling SW irradiance values in cloud-free conditions have been simulated with a radiative transfer model for a wide range of values of each quantity. The use of simulations also allows analysing the direct effect of each quantity on the downwelling SW irradiance, as well as their combined effect, which according to Bhatia et al. (2015) is not usually analysed therefore worth to be investigated. Also this combined effect upon the SW irradiance would not be possible if SW measurements were used instead of simulated SW irradiance, since those already incorporate the joint effect of the above mentioned quantities. Moreover, the quantification of the effects of these atmospheric constituents on the SW irradiance is not limited to the period with available measurements, and it is neither limited to the availability of radiation measurements under clear sky conditions, less frequent at certain times of the year. For these reasons, this study has a greater potential of generalization compared with other studies (e.g., Di Biagio et al., 2012) and contributes to improve the understanding and quantification of the influence of these atmospheric constituents on the downwelling SW irradiance at the Earth's surface.

The paper is structured as follows: the materials and methods are presented in Section 2. Section 3 shows the principal results. In Subsection 3.1 are shown the results regarding the effects of aerosols and water vapour on the SW irradiance, both the individual effect of each quantity as well as the combined effects of the three quantities. In Subsection 3.2, the validation of the models proposed is presented. Finally, the main conclusions are summarized in Section 4.

2. Materials and methods

As mentioned in the introduction, the main objective is twofold, the first one aiming to analyse and quantify the sensitivity of the downwelling SW irradiance at the Earth's surface with respect to aerosols and water vapour quantities and the second one aiming to propose two models to estimate the effect of aerosols and water vapour on SW irradiance and validate through comparing with radiation measurements. The following subsections describe how downwelling SW irradiance values have been simulated (2.1), how the sensitivity study and its uncertainties have been performed (2.2), and how the models have been validated (2.3).

2.1. Model simulation

Downwelling SW irradiance values in cloud-free conditions have been simulated using libRadtran radiative transfer code (version 1.7) (Mayer and Kylling, 2005). The uncertainties of libRadtran model were appraised by Emde et al. (2016), who demonstrated that the simulated SW irradiances agree with a reference model, obtaining, in general, differences lower than 0.05%. Additionally, Obregón et al. (2015c) analysed the performance of libRadtran model to simulate SW irradiance under different aerosol conditions. From this comparison with calibrated pyranometer measurements, relative differences lower than 0.2% were obtained.

The aerosol quantities selected for this study are the AOD and the SSA. These quantities are usually used to characterize the interaction of aerosols with radiation (Yu et al., 2006). AOD is representative of the aerosol load in the atmospheric column, and SSA is defined as the fraction of the aerosol light scattering over the extinction, being related with the absorption properties of aerosols. Specifically, the AOD at 550 nm has been used here since this is an input of libRadtran code and a reference wavelength widely used (e.g. Bilbao et al., 2014; Goto et al., 2011), therefore convenient for comparison purposes. The other aerosol quantity considered was the SSA at 675 nm. This wavelength has been chosen because it is close to the maximum of the solar irradiance per unit wavelength and has been suggested by some authors (Di Biagio et al., 2010; Foyo-Moreno et al., 2014; Obregón et al., 2017). The quantity used to characterize the water vapour content in the atmospheric column is the PWV.

The ranges of values of AOD, SSA and PWV selected for the sensitivity analysis are summarized in Table 1. As it can be seen, the range of AOD values is between 0 and 1.0, and of SSA between 0.78 and 0.99. These ranges were selected based on the occurrences in the available databases. The SSA range is due to the different aerosol composition, size, origin, and aging in the atmosphere. In the case of PWV, the selection of the range (0–60 mm) was based on the work of Trenberth et al. (2005). For each range of values, equidistant steps have been considered. Specifically, the number of steps for AOD is 7, for PWV is 10, and for SSA is 4, which leads to a total of 280 possible combinations of the effects of the three quantities on the SW irradiance, therefore

Table 1
Values of aerosol optical depth (AOD), single scattering albedo (SSA) and precipitable water vapour (PWV) selected for sensitivity analysis.

Quantity	Selected values
AOD	0, 0.16, 0.33, 0.50, 0.66, 0.83, 1.00
SSA	0.78, 0.85, 0.92, 0.99
PWV	0, 6.66, 13.33, 20.00, 26.66, 33.33, 40.00, 46.66, 53.33, 60

covering a wide range of aerosol and water vapour situations.

Downwelling SW irradiances at the Earth's surface have been simulated using the libRadtran radiative transfer model for each of the 280 combinations obtained from the values of AOD, SSA and PWV presented in Table 1. Version 1.7 of this model has been employed. The extraterrestrial irradiance was considered according to Gueymard (2004). The radiative transfer equation solver DISORT2, which is an improved version of the multi-stream discrete ordinate method of Stamnes et al. (2000), was used with 16 streams. This is the default number of computational angles in libRadtran model (Mayer and Kylling, 2005). In order to take into account the time of the year, midlatitude summer/winter standard vertical profiles of the thermodynamic variables, main gases and aerosols were considered depending of the season (Shettle, 1989).

Irradiance values have been simulated under cloud-free conditions for the 15th day of each month, to have representative values for each month of any year. In order to more accurately model the instantaneous irradiance, 10-min irradiances were simulated for these days. In addition, only solar zenith angles lower than 70° have been considered since, in this range, the differences obtained between simulations of downwelling SW irradiances and SW measurements are within the uncertainty of measurements (García et al., 2013). This is due to the cosine error of pyranometers that increases with the solar zenith angle and, on the other hand, to the limitations of the plane parallel assumption used in the radiative transfer calculations, which is not valid for high solar zenith angles. Monthly values, calculated as the average value of all 10-min irradiance values simulated for the 15th day of each month, have been used to calculate annual values. So that only a single value (annual) of each combination of values of the three quantities will be available to carry out the sensitivity analysis.

2.2. Sensitivity analysis

Subsequently, the individual effects of each of these quantities on the downwelling SW irradiance have been analysed. The individual analyses consist on the quantification of the impact of changing one quantity while the other two remain fixed. The quantification of this impact is done by calculating the variation caused in the SW irradiance due to a change in the value of the quantity. This variation has been expressed as relative difference values (in percentages) and calculated with respect to the value of the SW irradiance corresponding to the smallest value considered in this study for each quantity. To calculate the percentage variation with respect to each quantity, for example AOD, Eq. (1) is applied:

$$Rel.\ Dif\,(AOD),\ \% = \frac{I - I_{ref}}{I_{ref}} \cdot 100 = \frac{I_{(AOD,SSA,PWV)} - I_{(0,SSA,PWV)}}{I_{(0,SSA,PWV)}} \times 100 \quad (1)$$

where I is the simulated SW irradiance value for each AOD value and I_{ref} is the simulated SW irradiance value for the smallest value of AOD, which in our study is equal to 0, while SSA and PWV values remain fixed. This calculation is done for every possible combination of SSA and PWV values.

Since aerosols and water vapour are always present in the atmosphere, the individual analysis performed according to Eq. (1) can mask possible interactions between the three quantities. In order to quantify possible interactions between the three quantities and their combined effect on the downwelling SW irradiance, the relative differences have been calculated by varying the values of the three quantities simultaneously according to Eq. (2).

$$Rel.\ Dif,\ \% = \frac{I - I_{ref}}{I_{ref}} \cdot 100 = \frac{I_{(AOD,SSA,PWV)} - I_{(0,0,0)}}{I_{(0,0,0)}} \times 100 \quad (2)$$

where I is the simulated SW irradiance values for any combination of the three quantities, and I_{ref} is the simulated SW irradiance value for the smallest values considered in this study for the three quantities, i.e. no aerosols and no water vapour. This analysis allows calculating the effects that these constituents really produce on SW irradiance, which as far as the author's' know has never been performed yet.

Another objective of this study was to verify if relative difference values obtained from combined analysis could be applied to any aerosol and water vapour situation anywhere from any combination of AOD, SSA and PWV values, in order to propose a simple empirical model of surface SW downward radiation forecast. This model would consist of estimating the SW relative difference values, $Rel.Dif_{model}$, for any combination of diurnal average values of AOD, SSA and PWV, without using radiometric measurements, only relative difference values obtained from combined analysis. As already mentioned, the sensitivity analysis was performed for specific values of the above mentioned three quantities within a wide range (Table 1). Therefore it was necessary to interpolate between the different quantities values to estimate $Rel.Dif_{model}$. Since the above three quantities have been used, it has been decided to do trilinear interpolation, which is a method of multivariate interpolation on a 3-dimensional regular grid.

Considering that the uncertainty of SSA decreases with increasing AOD (Hu et al., 2007), a reduction of the lower limit of AOD is suggested to minimize this uncertainty. For example Dubovik et al. (2000) do not consider those cases with AOD at 440 nm lower than 0.4. This can greatly limit the existence of quality SSA data in some sites, since these values of SSA correspond to very hazy events. For this reason, a two-quantity model, based on diurnal average values of AOD and PWV, has also been proposed in this study to estimate $Rel.Dif_{model}$. As in the three-quantity model was necessary to interpolate. Since only two quantities have been considered, a bilinear interpolation has been performed. Finally, effects on downwelling SW irradiance estimated with the two models have been compared.

In this study, the sensitivity of $Rel.Dif_{model}$ to different input variables of the model, as the asymmetry parameter (g), the atmospheric and aerosol vertical profiles and the surface albedo, has also been calculated. Although the asymmetry parameter was not considered as an aerosol characterizing quantity in this study, its uncertainty must be taken into account here because it is an important parameter that represents the fraction of the SW radiation that is scattered toward the forward direction. In order to estimate the sensitivity of $Rel.Dif_{model}$ to g, $Rel.Dif_{model}$ values have been calculated for extreme values of g (0.4 and 0.8), considering the highest values of the three quantities used in this study (AOD = 1.0, SSA = 0.99, PWV = 60 mm). A maximum relative difference of 9.86% was obtained due to the variation of g considered (0.4 and 0.8). In the case of the aerosol vertical profile, $Rel.Dif_{model}$ values have been calculated for different aerosol vertical profiles defined by the season and the aerosol type (Shettle, 1989). Spring-summer and fall-winter are the seasons considered; and rural, maritime, urban and tropospheric, the aerosol types. $Rel.Dif_{model}$ values present low variability with respect to the season, obtaining maximum relative differences lower than 0.15%. When the aerosol type is considered these relative differences are higher but they do not exceed the value of 4.5%. This maximum relative difference was obtained due to the difference between urban and maritime aerosol types. To calculate the sensitivity of $Rel.Dif_{model}$ to the atmospheric profile, $Rel.Dif_{model}$ values have also been calculated for different profiles. In this case, midlatitude summer/winter standard vertical profiles were considered depending of the season (Shettle, 1989), obtaining a maximum relative difference between them of 0.24%.

The surface albedo also plays an important role, in particular for surfaces with high albedo conditions, as it can be found in mountain or polar/subpolar areas. For this purpose, the impact of surface albedo on $Rel.Dif_{model}$ has also been calculated. A maximum relative difference of 8.31% was obtained due to the variation of surface albedo between 0.05 and 0.8. In this study, a constant albedo equal to 0.2 has been considered. It should be noted that the aerosol, water vapour, or albedo effects on SW radiation are modulated by the solar zenith angle.

Fig. 1. World map showing the location of Barcelona, Bondville, Cáceres, Évora, Fukuoka, Granada, Hohenpeissenberg, Thessaloniki and Valladolid sites with red dots. (For interpretation of the references to colour in this figure legend, the reader is referred to the web version of this article.)

2.3. Validation

2.3.1. Validation methodology

In order to validate the two models proposed, $Rel.Dif_{model}$ values estimated using the models have been compared with those values calculated from the pyrometer measurements ($Rel.Dif_{pyra}$). $Rel.Dif_{model}$ values have been estimated from diurnal average values of AOD, SSA (only for the two-quantity model) and PWV, corresponding to different days under cloud-free conditions and to different sites. $Rel.Dif_{pyra}$ values have been calculated applying Eq. (2) at the same sites, where I corresponds to the diurnal average of SW irradiance hourly measurements obtained at the Earth's surface, and I_{ref} to the simulated downwelling SW irradiance diurnal average values under no aerosols and no water vapour conditions, for the same days and sites as the measurements. The comparison of $Rel.Dif_{pyra}$ and $Rel.Dif_{model}$ has been made by calculating the difference between both, Dif, according to Eq. (3):

$$Dif = Rel.\ Dif_{model} - Rel.\ Dif_{pyra} \quad (3)$$

2.3.2. Sites and data

Data registered at nine sites around the world have been used for validation: Évora (Portugal; 38.6° N, 7.9° W, 293 m a.s.l.), Barcelona (Spain; 41.3° N, 2.1° E, 125 m a.s.l.), Cáceres (Spain; 39.4° N, 6.3° W, 397 m a.s.l.), Granada (Spain; 37.1° N, 3.6° W, 680 m a.s.l.), Valladolid (Spain; 41.7° N, 4.7° W, 705 m a.s.l.), Hohenpeissenberg (Germany; 47.8° N, 11.0° E, 980 m a.s.l.), Thessaloniki (Greece; 40.6° N, 22.9° E, 60 m a.s.l.), Bondville (Illinois, USA; 40.0° N, 88.4° W, 213 m a.s.l.), and Fukuoka (Japan; 33.6° N, 130.4° E, 2.5 m a.s.l.). Fig. 1 shows the location of the selected sites.

The sites were selected according to different criteria. The main reason was the availability of enough simultaneous measurements of downwelling SW irradiance and aerosol properties during cloud-free days. Another important reason was the climatological diversity of the selected sites, aimed at covering a wide range of diurnal average values of the three main quantities analysed (AOD, SSA and PVW) as well as different aerosol "types" and hygrometric conditions.

In Évora, Portugal, an Eppley Black & White pyranometer was used to provide global shortwave irradiance (285–2800 nm) values. This instrument is not ventilated nor installed on a sun tracker. It is installed at the atmospheric sciences observatory of the Institute of Earth Sciences of the University of Évora and is daily maintained. It measures global irradiance every 10 s and records 10-min averages. The uncertainty associated with this instrument is estimated to be about 5% encompassing calibration, temperature and cosine characteristics of the instrument.

Regarding the four Spanish stations, hourly-averaged global shortwave irradiance data were provided by the Spanish Weather Service (Agencia Estatal de Meteorología, AEMET). Its radiometric network is certified to ISO 9001 and uses Kipp & Zonen CM-11 pyranometers. This instrument is classified as a "first class" by the World Meteorological Organization (WMO). The pyranometers belonging to this network are ventilated, installed on a sun tracker and maintained daily. Since 2004, they are calibrated approximately every two years against a pattern instrument which is, in turn, calibrated at PMOD/Word Radiation Center in Davos.

On the other hand, Hohenpeissenberg station is a rural meteorological observatory of the German Weather Service (Deutscher Wetterdienst, DWD). It belongs to the Global Atmosphere Watch (GAW) programme, a worldwide system established by the WMO. This programme has calibration and data quality centres aimed at ensuring all data produced by the system measure up to international standards. Thus, the station follows standard measurement and operating methods and procedures.

At Thessaloniki (Greece), global solar irradiance is monitored since January 1993 using a CM-21 pyranometer manufactured by Kipp & Zonen. The instrument is installed on the roof of the Physics Department building at the Aristotle University of Thessaloniki. Data are sampled every 1 or 2 s and averaged on a 1 min basis. The high stability of the CM-21 pyranometer was confirmed by two calibrations performed in 2005 and 2011 at the Deutscher Wetterdienst, Meteorologisches Observatorium Lindenberg (Germany), showing changes in sensitivity lower than 0.1% in 19 years of operation (Lindfors et al., 2013). This instrument, along with the Kipp & Zonen CM-11 used in the four Spanish stations and in Fukuoka, are fully

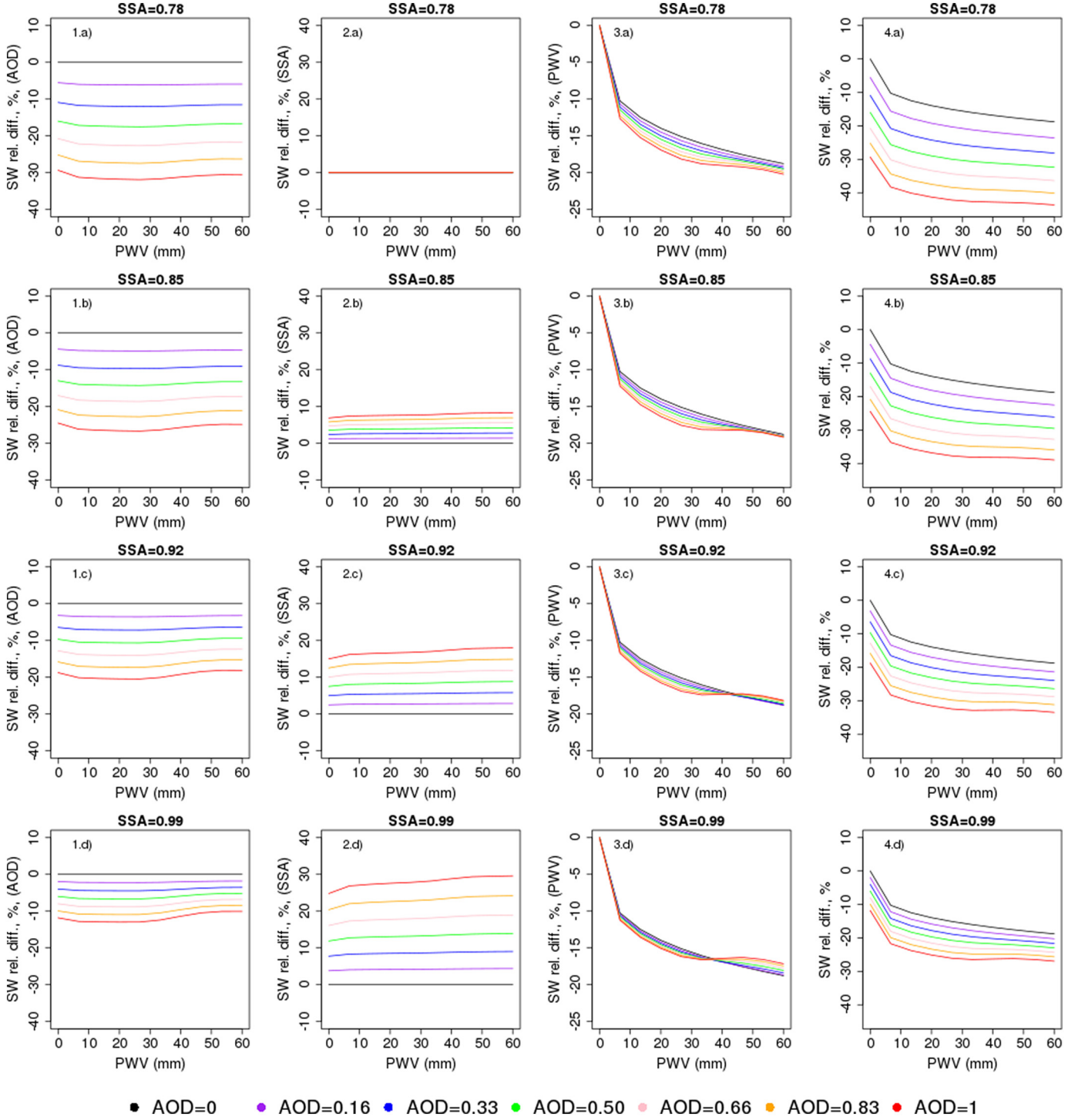

Fig. 2. SW global irradiance relative differences due to AOD as function of the PWV for different AOD and SSA values (1.a, 1.b,1.c, 1.d graphs), SW global irradiance relative differences due to SSA as a function of the PWV for different AOD and SSA values (2.a, 2.b, 2.c, 2.d graphs), SW global irradiance relative differences due to PWV as a function of PWV for different AOD and SSA values (3.a, 3.b, 3.c, 3.d graphs), and SW global irradiance relative differences due to AOD, α and PWV simultaneously (4.a, 4.b, 4.c, 4.d graphs).

compliant with all ISO 9060:1990 Secondary Standard Instrument performance criteria, which is the highest possible ISO pyranometer performance category.

Finally, Bondville (USA) and Fukuoka (Japan) stations belong to the Baseline Surface Radiation Network (BSRN), which is a joint project of the World Climate Research Programme (WCRP) and the Global Energy and Water Cycle Experiment (GEWEX). An Spectrolab SR-75 pyranometer is installed in Bondville, and a Kipp & Zonen CM-11 pyranometer in Fukuoka. Since the BSRN network aims to produce observational data to be used for validating theoretical models and satellite measurements, it pays particular attention to the quality of the measurements. For achieving the best possible quality it establishes high standards of measurement procedures, calibration and accuracy (McArthur, 2005). The pyranometers belonging to this network are

ventilated, its body temperature is monitored, and they comply with strict requirements regarding QA/QC protocols; all this with the objective of achieving an uncertainty lower than 2% or 5 W m^{-2}. In this context, pyranometers are maintained daily and calibrated every six months and, additionally, data acquisition system are calibrated regularly (annually).

The hourly-averaged global shortwave irradiance data of Bondville, Fukuoka, Hohenpeissenberg and Thessaloniki were provided by the World Radiation Data Centre (WRDC). The WRDC is one of the recognised World Data Centres sponsored by the WMO.

Regarding the aerosol data, it is to mention that the nine selected sites are equipped with CIMEL CE-318 sunphotometers integrated in the NASA AERONET (AErosol RObotic NETwork) network. This network provides aerosol information with the aim to establish a ground-based climatology and to identify and characterize the most influential aerosols on the climatic system (Holben et al., 1998). Data of AOD, SSA and PWV provided by AERONET, have been used in this study. In order to estimate these quantities, the CIMEL CE-318 sunphotometer performs direct sun measurements at 340, 380, 440, 500, 675, 870, 940 and 1020 nm, and measurements of sky radiances in the almucantar and principal plane geometries, at 440, 675, 870 and 1020 nm. Direct sun measurements at 940 nm obtained with the CIMEL photometer are used by AERONET to retrieve PWV since there is a strong wavelength-dependence absorption by water vapour. All AERONET sunphotometers and periodically calibrated according to AERONET protocols. A more detailed description about the CIMEL sunphotometer is given by Holben et al. (1998). All radiance measurements, as well as a variety of aerosol quantities at different quality levels (1.0, 1.5 and 2.0) are processed following the AERONET protocol as described by Holben et al. (1998). AOD and PWC data used in this study belong to quality level 2.0. Specifically, in this study AOD at 550 nm was employed because it is a reference wavelength widely used and it is within the wavelength range considered (285–2800 nm). The conversion of AOD at 500 nm, which is the AERONET direct product, to AOD at 550 nm has been performed using the Angstrom power law (Eq. (4)):

$$AOD550 = AOD500\left(\frac{550}{500}\right)^{-\alpha} \quad (4)$$

where α is Angstrom Exponent in the wavelength range of 440–870 nm (Alam et al., 2011).

In the case of SSA, level 1.5 has been used in order to have enough data available for the study. Level 2.0 SSA data are very scarce, because only cases with AOD at 440 nm higher than 0.4 and solar zenith angle above to 50° are considered (Dubovik et al., 2000). The uncertainty in AOD is 0.01–0.02 for wavelengths larger than 380 nm (Holben et al., 1998; Smirnov et al., 2000), and less than 12% in PWV (Holben et al., 1998). According to Dubovik et al. (2000) and Dubovik and King (2000) the uncertainty in the retrieved SSA varies between 0.03 and 0.07 depending on the aerosol type and loading.

It should be noted that the installation of the CIMEL sunphotometer at the Valladolid station was in 2012. Since the period with available radiation data is prior to 2012, data corresponding to the nearby Palencia station have been used. This station has been considered because, despite having a distance of 50 km from Valladolid, their altitude is similar altitude (around 700 m a.s.l.) and they show similar average values of aerosol and water vapour quantities over the common period of measurement 2012- current date. The average values of the three quantities for Palencia (Valladolid), corresponding to this period, are the following: AOD equal to 0.8 (0.8), SSA equal to 0.87 (0.88) and PWV equal to 12.6 (12.9). Therefore, it can be considered that both locations have close aerosol and water vapour characteristics.

Thus, all days under cloud-free conditions, and with data of AOD, SSA, PWV and SW irradiance, were considered for the validation. The number of days used for each site fulfilling the aforementioned conditions, is: 119 (Barcelona), 45 (Bondville), 179 (Cáceres), 179 (Évora), 47 (Fukuoka), 184 (Granada), 30 (Hohenpeissenberg), 147 (Thessaloniki) and 152 (Valladolid). It should be noted that the number of days used greatly fluctuates from one site to another due to variations in the period with available data. The longest periods and, therefore, highest number of days, correspond to the stations located in the Iberian Peninsula (2003 − 2010) and to Thessaloniki (2004–2016). The other stations have shorter periods with available data: Bondville (2012–2017), Fukuoka (2014–2017) and Hohenpeissenberg (2013–2017).

3. Results

3.1. Sensitivity analysis

In this section, individual and combined effects of AOD, SSA and PWV on the downwelling SW irradiance have been analysed. As explained in the previous section these analyses have been based on the irradiance relative differences (expressed in percentage) calculated according to Eqs. (1) and (2), respectively. Fig. 2 shows these values of the irradiance relative differences, both for the individually effects (from Fig. 1.a to 3.d) and for the combined ones (from 4.a to 4.d). As can be seen in the graphs of the first column of Fig. 2 (1.a, 1.b, 1.c, 1.d), which shows the effect of AOD on the SW irradiance, there is a decrease of the SW irradiance reaching the Earth's surface when the values of this quantity increases, as expected. This decrease becomes 32% for AOD values equal to 1.0 and SSA values equal to 0.78 (1.a). This effect is not so pronounced (less negative relative difference values for the same AOD values) when SSA values are higher, i.e. when aerosols are less absorbent. For example, when SSA is equal to 0.99 (1.d) the decrease of the SW irradiance does not exceed 15%. Relative difference values of SW irradiance with respect to AOD slightly depend on PWV values, as can be observed in 1.a, 1.b, 1.c and 1.d graphs. In this graph it is observed that relative difference values are more negative as PWV increases, up to approximately 30 mm, although these differences are very small, between 0 and 2%. When PWV values are greater than 30 mm the effect produced depends on the aerosol quantities values. For highly absorbing aerosols (smaller SSA values), the decrease of radiation reaching the surface remains constant. However, when aerosols are less absorbent, the decrease of radiation is not so high since there is an increase of the multiple scattering radiation enhancing the downwelling diffuse component of the radiation. This is also observed in the graphs of the third column (3.a, 3.b, 3.c, 3.d graphs), where the PWV effects on SW radiation are represented. In these graphs it is observed that relative difference values are more negative as PWV and AOD increase, provided that aerosols are absorbent, reaching a reduction of 20%. However, when aerosols are less absorbent (higher SSA values), relative difference values are less negative due to an increase in the downwelling diffuse component. In addition, with high PWV values it is observed a change in the trend of relative difference values, beginning to decrease, i.e. are less negative due to an increase in the diffuse radiation reaching the surface by the presence of water vapour. The PWV value for which the trend of the relative difference values changes depends on the SSA value, being lower for higher SSA values. As discussed above with higher SSA values (less absorbent and more scattering aerosols), there is an increase in the dispersion and hence in the diffuse component of the global radiation, which overcompensates the amount of direct radiation that is extinguished by the atmospheric constituents. Hence, once the trend changes, the less negative relative difference values correspond to situations in which there are large amount of dispersing aerosols, i.e. situations with both higher AOD and SSA values.

With regard to the effect of SSA on the SW irradiance (2.a, 2.b, 2.c, 2.d graphs), an inverse behaviour to that produced by AOD and PWV upon SW irradiance is observed. There is an increase in the downwelling SW irradiances at the Earth's surface when SSA values increase. This is due to the fact that high SSA values indicate the presence of highly scattering aerosols; therefore there is an increase of the multiple

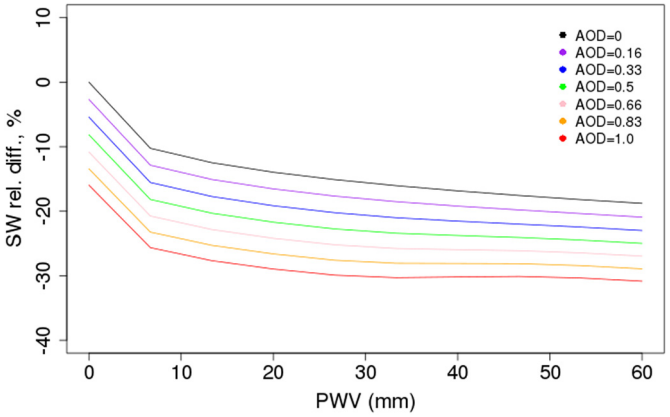

Fig. 3. SW global irradiance relative differences due to AOD and PWV simultaneously.

scattering radiation enhancing the downwelling diffuse component of the radiation. This increase is also directly related to the aerosol load in the atmosphere, (AOD), leading to the highest increases in SW irradiance for the highest AOD values. For example, the increase of SW irradiance of 30% is obtained for AOD = 1.0 and SSA = 0.99, while for AOD = 0.5 and SSA = 0.99 the increase is 12%. Relative difference values of SW irradiance with respect to SSA slightly dependent on PWV. The amount of SW radiation reaching the Earth's surface increases slightly as PWV increases. This increase in surface radiation also depends on SSA, being higher for high SSA values due to an increase in the diffuse component of the radiation by multiple scattering.

The individual analysis (shown in the first three columns of Fig. 2) highlights the great influence of the three quantities on the SW irradiance reaching the surface. However, when the combined effect of the three quantities (the last column of the Fig. 2) is analysed, its combined influence of the three quantities upon the SW irradiance is different from the sum of the individual effects on the SW irradiance. For example, if the individual effects were added, for the cases with SSA = 0.92 (1.c, 2.c, 3.c graphs), the sum of these three effects would be similar to that produced only by PWV, since the effect of AOD and SSA would be annulled for having similar values but of opposite sign. Also when the 4.a–4.d graphs are analysed one can notice that the SW relative difference values are always negative whereas in the individual effects due to the AOD and PWV they are also but not in the individual effect due to the SSA (2.a–2.d) where they are always positive for SSA above the reference SSA value = 0.78. SW relative difference values shown in the 4.a, 4.b, 4.c and 4.d graphs are also presented in Appendix A.

As mentioned in the previous section, due to the limitations to have quality SSA data with low AOD values, the sensitivity analysis was also performed for diurnal average values of AOD and PWV. SW relative difference values for each combination of AOD and PWV values have been calculated using the Eq. (2). These values are shown in Fig. 3 and in Appendix B. As can be observed in this figure, the combined effect of the two quantities on SW irradiance is similar to that produced when the three quantities are considered. Specifically, it is observed that the values of SW relative difference are in the middle of the range obtained considering the quantity SSA varying from 0.92 up to 0.99. When a SSA value is not specified, the libRadtran model uses values of this quantity close to 0.95, which is automatically included in the midlatitude models of Shettle (1989).

3.2. Validation

From SW relative difference values obtained from combined analyses, shown in Appendix A and Appendix B, two models to estimate SW relative difference values have been proposed. These models, as already described above in section 2, are based on a trilinear interpolation between diurnal average values of AOD, SSA and PWV (three-quantity model) and on a bilinear interpolation between diurnal average values of AOD and PWV (two-quantity model).

In order to validate them, $Rel.Dif_{model}$ values have been compared with $Rel.Dif_{pyra}$ values, corresponding to different days under cloud-free conditions and to different sites during the available periods, using Eq. (3). Data from these nine sites have been used: Barcelona, Bondville, Cáceres, Évora, Fukuoka, Granada, Hohenpeissenberg, Thessaloniki and Valladolid. The selected sites cover a wide geographic/climatological diversity, with a wide range of AOD, SSA, PWV and SW irradiance diurnal average values, very convenient for validating the proposed models. The number of days considered in each site is different, as commented, due to the different availability of simultaneous AOD, SSA, PWV and SW irradiance data, under cloud-free conditions, at the selected sites. Fig. 4 shows the distribution of the selected days throughout the year. As can be seen, this distribution also varies from one site to another, but in all of them the highest number of days that are going to be considered in this study are concentrated in the summer months or, in some cases, also in the spring months, where the cloud-free conditions are more frequent. Moreover, since only zenith angles less than 70° are considered, it is difficult to have cloud-free days in the winter months with a significant number of data to calculate the diurnal average values of the AOD, SSA, PWV and SW irradiance values.

Fig. 5 shows the values of AOD, SSA and PWV, for each site over the days considered in this study in a box and a whisker plot. As can be seen, the highest average AOD values correspond to Fukuoka, Thessaloniki, Barcelona and Granada, followed by Bondville, Valladolid, Évora, Cáceres and Hohenpeissenberg, with the following values: 0.20, 0.18, 0.16, 0.12, 0.11, 0.10, 0.08, 0.07 and 0.05, respectively. In the same order are the values of the other statistics describing this quantity, such as the median. A wide range of AOD values is available, between 0 and 0.70, as can be seen in the histogram of frequency shown in the Fig. 6. For the case of SSA, a wide range of values is also available, the majority being between 0.78 and 0.99. With respect to this quantity, differences are also observed, obtaining the smallest average values in Évora and Granada (0.85, 0.86), followed by Cáceres, Valladolid, Hohenpeissenberg, Barcelona, Fukuoka and Thessaloniki (0.87, 0.88, 0.88, 0.89, 0.90, 0.91). The highest average value is obtained in Bondville (0.92). The range of PWV values used to validate the proposed model is also broad, since the values registered during the days selected in each site range between 1.5 and 45. As for the other two quantities, average PWV values also vary between the different sites. The highest average values are obtained in Thessaloniki and Barcelona (23.36 and 19.64), due its proximity to the coast, while in the rest of the stations the PWV average values are lower (16.90, 16.49, 14.24, 13.82, 13.33, 13.21 and 11.7, in Bondville, Fukuoka, Évora, Granada, Cáceres, Hohenpeissenberg and Valladolid, respectively).

The comparison of SW $Rel.Dif_{model}$ values and SW $Rel.Dif_{pyra}$ values has been made by calculating the difference, Dif, (expressed in percentage) of both values using Eq.(3) and their subsequent analysis. Dif values for each site and which each model are shown in Fig. 7 in a box and whisker plot. As can be observed in this figure Dif values are close to zero. If three-quantity model is considered, it is obtained that only 24% of the cases show differences greater than 2%, exceeding differences of 5% only in 4 days. Analysing each site independently, one can notice that the smallest average Dif values are obtained in Cáceres (0.01%) and Évora (0.29%). This indicates that $Rel.Dif_{pyra}$ values differ very little from $Rel.Dif_{model}$ values, estimated by trilinear interpolation from the daily average values of AOD, SSA and PWV observed at these two sites. In both sites Dif values are positive or negative as can be expected if no systematic error occurs. Average Dif values in the other sites are slightly higher: 0.45% (Bondville), −0.88% (Granda), −1.02% (Barcelona), −1.04% (Valladolid), −1.31% (Hohenpeissenberg), −1.68% (Fukuoka) and −2.37% (Thessaloniki), although they

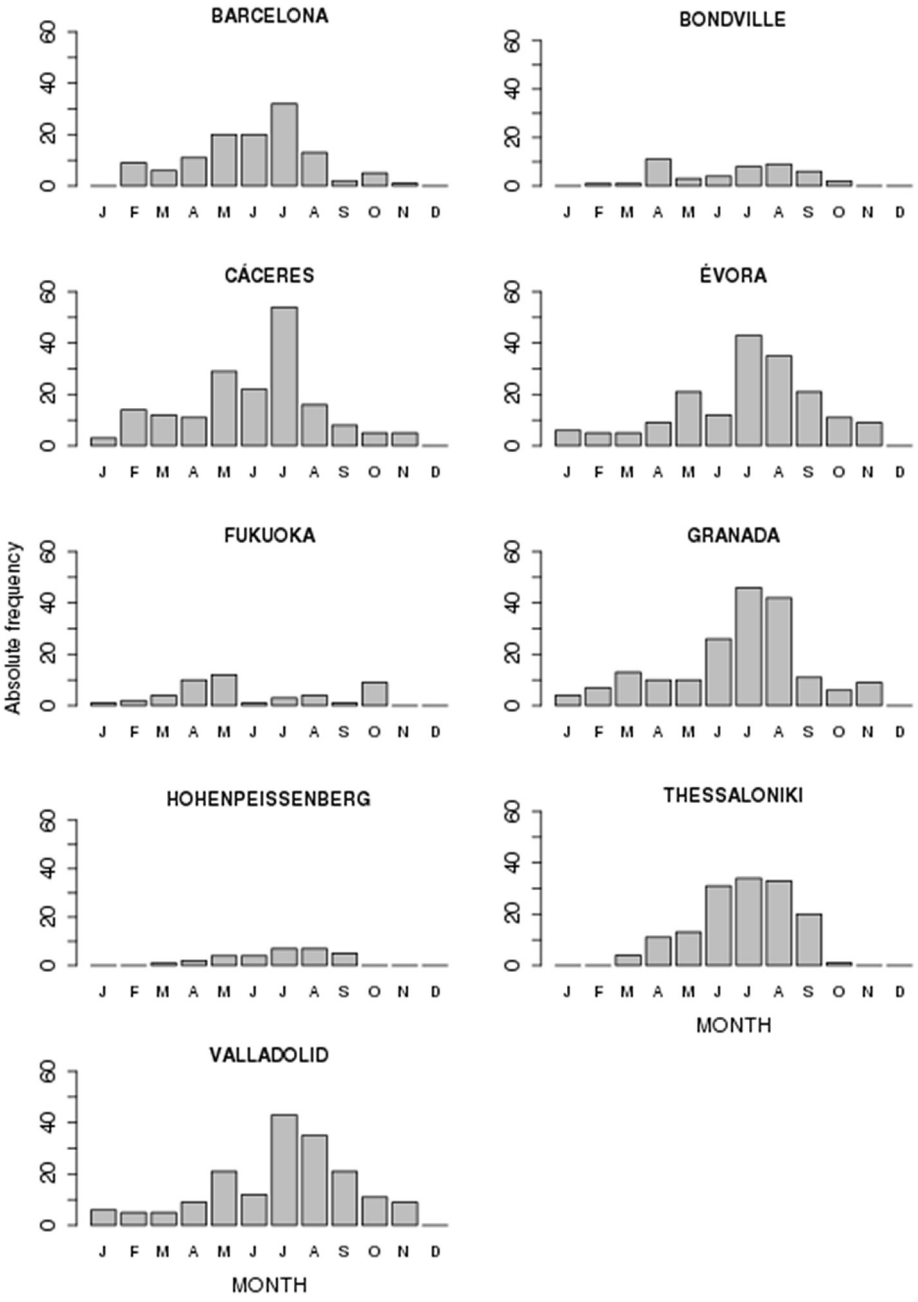

Fig. 4. Number of days, for each month and site, considered for the validation of the models proposed.

are also very low. From the small Dif values obtained for the different sites one may infer that the proposed three-quantities model can be applied to estimate, in a simple way, the combined effect of aerosols and water vapour on the downwelling SW irradiance at the Earth's surface, without needing the use of radiometers.

If the two-quantity model is considered, $Rel.Dif_{model}$ also differs very little from $Rel.Dif_{pyra}$. But as observed in Fig. 7, Dif values obtained with two quantities are, in general, higher and more negative than those obtained with three quantities. For example, average Dif values for each site with two (three) quantities are the following: Cáceres −0.55% (0.01%), Évora −0.18% (0.29%), Bondville 0.15% (0.45%), Granada −1.88% (−0.88%), Barcelona −1.73% (−1.02%), Valladolid −1.93% (−1.04%), Hohenpeissenberg −1.53% (−1.31%), Fukuoka −2.57% (−1.68%) and Thessaloniki −2.92% (−2.37%). With this model, the percentage of cases with Dif higher than 2% is 33%, while with three quantities this percentage is equal to 24%. But even so, almost 84% of the cases have Dif values lower than 3% (slightly smaller than in the three quantities case, 88%), which allows estimating the combined effect of only the two quantities on the downwelling SW irradiance, avoiding the need of installing radiometers, as in the previous three quantities case. Therefore, the two physical quantities AOD and PWV can be considered to estimate with high confidence the effect of aerosols and water vapour on the downwelling SW irradiance at the Earth's surface under cloud-free conditions.

The seasonal variation of the impact of aerosol and water vapour on SW radiation has also been analysed for each season. It must be noted that the data number differs from one season to another, being smaller in winter: 583 (summer), 277 (spring), 171 (autumn) and 61 (winter). Therefore, mean $Rel.Dif_{model}$ values for each season were calculated for the comparison. The higher $Rel.Dif_{model}$ values occur mainly during

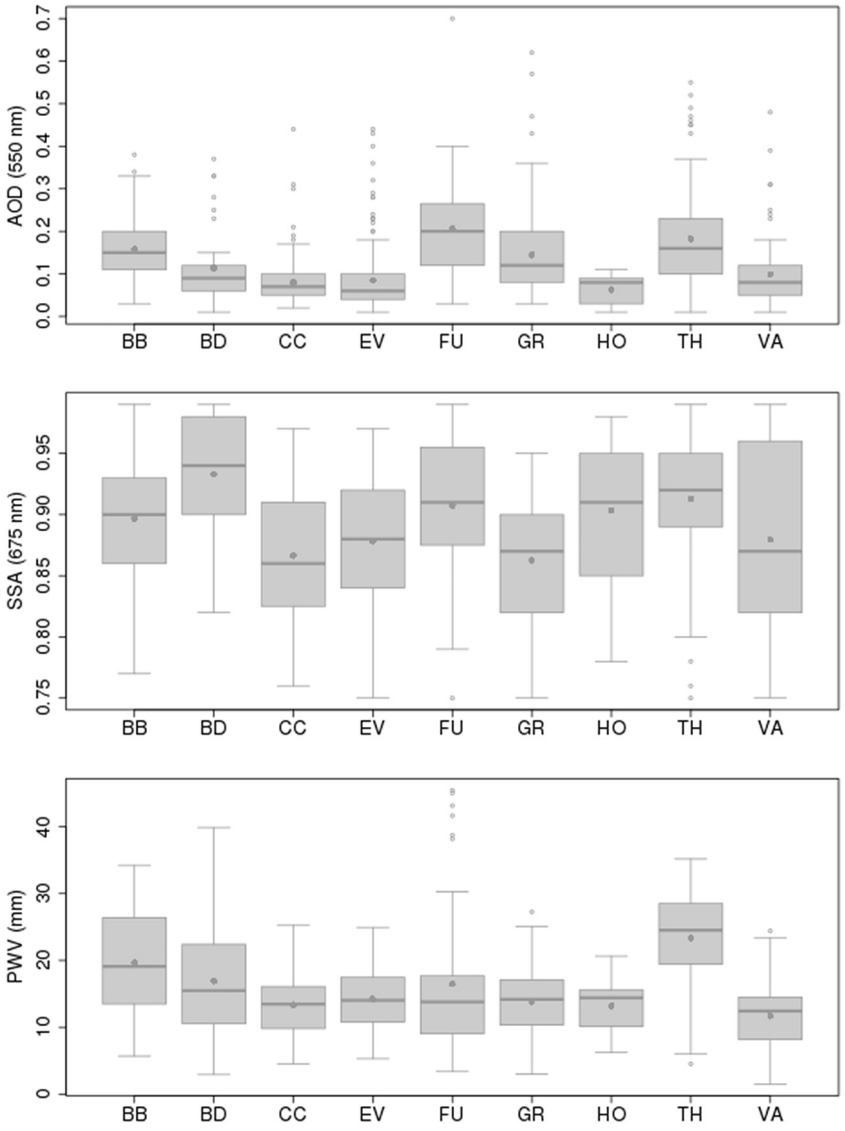

Fig. 5. Box and whisker plot of diurnal average values of AOD, SSA and PWV, for each site (BB: Barcelona; BO: Bondville; CC: Cáceres; EV: Évora; FU: Fukuoka; GR: Granada; HO: Hohenpeissenberg; TH: Thessaloniki, VA: Valladolid) over the days considered in this study. The mean (filled circles), median (horizontal segment within the box), 25 th and 75 th percentiles (top/bottom box limits) and data within 1.5 times the interquartile range (whiskers) are shown.

summer (mean of −16.17% and standard deviation of 1.98), when AOD and PWV mean values are also high, 0.14 and 19.34, respectively. It is followed by autumn (mean of −14.63% and standard deviation of 1.87), spring (mean of −14.04 and standard deviation of 2.39) and winter (mean of −12.68 and standard deviation of 2.35). The mean values of AOD (and PWV) for this seasons are the following: 0.09 (15.05), 0.12 (11.59) and 0.10 (8.29).

4. Conclusions

Atmospheric constituents attenuate the radiation (both solar and terrestrial radiation) while it propagates through the atmosphere, being their accurate quantification highly important for the quantification of radiative effects. In this work the effect of two of the most important atmospheric constituents, as aerosols and water vapour, on the downwelling SW irradiance reaching the Earth's surface, has been quantified. For that purpose, the downwelling SW irradiance under clear sky conditions has been simulated by applying the libRadtran radiative transfer code (version 1.7) to a wide range of values of the quantities characterizing these atmospheric constituents. These quantities are the aerosol optical depth (AOD), the single scattering albedo (SSA) and the precipitable water vapour (PWV).

The individual and combined effects of these constituents on the downwelling SW irradiance values have been analysed. For this aim, relative differences of irradiance with respect to the pristine atmospheric conditions have been calculated ($Rel.Dif_{model}$, %). Individual analyses show how the SW irradiance reaching the Earth's surface decreases as AOD or PWV increase and as SSA decreases. The magnitude of the decrease depends on the quantity to be analysed, with values as high as 32% for AOD equal to 1.0 (highest value considered in this study) and SSA equal to 0.78 (the lowest value considered in this study, which corresponds to highly absorbent aerosols). This effect is reduced for less absorbent aerosols (higher SSA values), since there is an increase of the multiple scattering radiation, which dominates over the absorption of radiation, enhancing the downwelling diffuse component of the radiation. The decrease of the SW irradiance is enhanced when PWV increases, although there is a change in the trend with high PWV values, due to an increase in diffuse radiation by the presence of high values of water vapour concentration. The combined effects of the three quantities and of two of them (AOD and PWV) have also been analysed. However, when the combined effects of the two or of the three quantities are analysed, it can be observed that, in both situations, they are

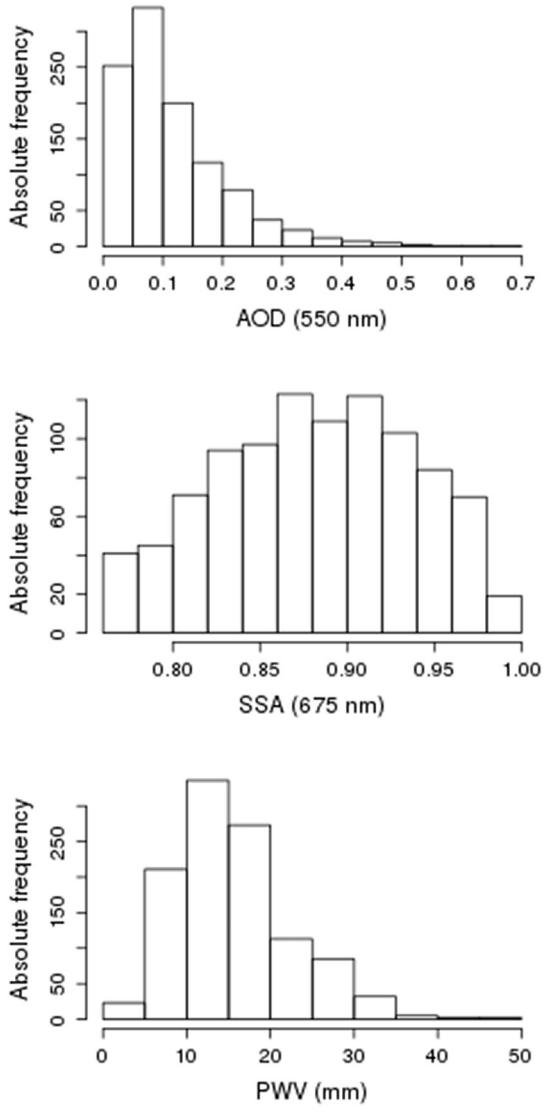

Fig. 6. Frequency histogram of diurnal average values of AOD, SSA and PWV for all the sites over the days considered in the study.

not the sum of the individual effects of each quantity on the downwelling SW irradiance reaching the Earth's surface. Therefore, the combined effect of these quantities should preferably be considered for modelling and forecasting their effect on solar radiation reaching Earth's surface, since it must be closed to the actual role of these atmospheric constituents upon the solar radiation propagating through the atmosphere. The sensitivity of $Rel.Dif_{model}$ to different input variables of the model as g, surface albedo and aerosol and atmospheric vertical profiles has also been calculated for extreme values. The maximum relative differences obtained are 9.86%, 8.31%, 4.5% and 0.24%, respectively.

Additionally, this study has proposed two models to estimate the effects of AOD, SSA and PWV on the SW radiation at ground level, based on the results obtained in the previous sensitivity analyses. In order to validate them, both models have been applied to several days in different stations around the world and the results have been compared to real measurements registered at those stations. The comparison showed the good performance achieved by both models, being the three-quantity model slightly better. Thus, the two- and three-quantities model estimations show differences with real measurements lower than 3% in 84% and 88% of cases, respectively. Therefore, it is acceptable to conclude that these models constitute a reliable approach to estimate the effect of aerosols and water vapour on SW radiation, when no radiation measurements are available. To note that these models have been validated for the ranges of AOD (up to 0.7) and PWV (up to 50 mm) existing in the stations used, and for specific low albedo conditions.

Acknowledgments

This work was partially supported by FCT (Fundação para a Ciência e a Tecnologia) through the grant SFRH/BPD/86498/2012. The work is co-funded by the European Union through the European Regional Development Fund, included in the COMPETE 2020 (Operational Program Competitiveness and Internationalization) through the ICT project (UID/GEO/04683/2013) with the reference POCI-01-0145-FEDER-007690 and also through ALOP (ALT20-03-0145-FEDER-000004) and DNI-A (ALT20-03-0145-FEDER-000011) projects. The research is also co-funded by the research projects CGL2011-29921-C02-01/CLI and CGL2014-56255-C2-1-R granted by the "Ministerio de Economía y Competitividad" of Spain. Thanks are due to AERONET/PHOTONS and RIMA networks for the scientific and technical support. CIMEL calibration was performed at the AERONET-EUROPE GOA calibration center, supported by ACTRIS under agreement no. 654109 granted by European Union (H2020-INFRAIA-2014-2015). The authors also thank AEMET and WRDC for the data provided to carry out this work.

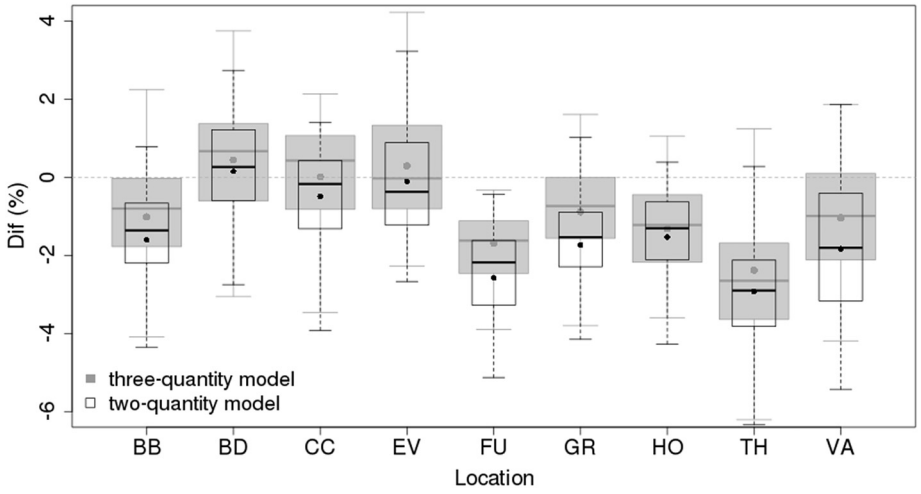

Fig. 7. Box and whisker plot of diurnal average values of difference, Dif, for each site (BB: Barcelona; BO: Bondville; CC: Cáceres; EV: Évora; FU: Fukuoka; GR: Granada; HO: Hohenpeissenberg; TH: Thessaloniki, VA: Valladolid), obtained from the two- and three-quantity models. The mean (filled circles), median (horizontal segment within the box), 25 th and 75 th percentiles (top/bottom box limits) and data within 1.5 times the interquartile range (whiskers) are shown.

Appendix A. SW relative difference values estimated for the combined effect of each combination of AOD, SSA and PWV values considered in this study

AOD	SSA	PWV (mm)									
		0	6.66	13.33	20	26.66	33.33	40	46.66	53.33	60
0	0.78	0	−10.25	−12.48	−13.96	−15.10	−16.04	−16.85	−17.56	−18.20	−18.78
	0.85	0	−10.25	−12.48	−13.96	−15.10	−16.04	−16.85	−17.56	−18.20	−18.78
	0.92	0	−10.25	−12.48	−13.96	−15.10	−16.04	−16.85	−17.56	−18.20	−18.78
	0.99	0	−10.25	−12.48	−13.96	−15.10	−16.04	−16.85	−17.56	−18.20	−18.78
0.16	0.78	−5.54	−15.62	−17.79	−19.23	−20.33	−21.19	−21.89	−22.49	−23.06	−23.60
	0.85	−4.39	−14.52	−16.70	−18.15	−19.25	−20.12	−20.81	−21.41	−21.97	−22.52
	0.92	−3.19	−13.38	−15.58	−17.03	−18.14	−19.01	−19.70	−20.30	−20.86	−21.41
	0.99	−1.95	−12.19	−14.41	−15.87	−16.99	−17.86	−18.54	−19.14	−19.70	−20.25
0.33	0.78	−10.91	−20.77	−22.88	−24.26	−25.31	−26.09	−26.66	−27.15	−27.63	−28.14
	0.85	−8.75	−18.72	−20.86	−22.26	−23.32	−24.10	−24.65	−25.13	−25.60	−26.11
	0.92	−6.45	−16.53	−18.69	−20.11	−21.19	−21.97	−22.51	−22.97	−23.44	−23.96
	0.99	−3.99	−14.18	−16.37	−17.81	−18.90	−19.68	−20.20	−20.65	−21.12	−21.65
0.50	0.78	−15.99	−25.62	−27.65	−28.98	−29.99	−30.67	−31.10	−31.48	−31.89	−32.38
	0.85	−12.98	−22.76	−24.84	−26.19	−27.21	−27.89	−28.28	−28.62	−29.03	−29.53
	0.92	−9.67	−19.62	−21.74	−23.12	−24.16	−24.83	−25.19	−25.50	−25.90	−26.42
	0.99	−6.01	−16.13	−18.29	−19.70	−20.76	−21.42	−21.76	−22.05	−22.46	−22.98
0.66	0.78	−20.75	−30.15	−32.12	−33.39	−34.35	−34.95	−35.26	−35.55	−35.90	−36.37
	0.85	−17.01	−26.61	−28.63	−29.94	−30.92	−31.50	−31.75	−31.98	−32.33	−32.81
	0.92	−12.80	−22.63	−24.69	−26.04	−27.04	−27.61	−27.81	−27.99	−28.33	−28.83
	0.99	−8.00	−18.05	−20.18	−21.56	−22.59	−23.15	−23.30	−23.45	−23.80	−24.32
0.83	0.78	−25.21	−34.37	−36.27	−37.49	−38.41	−38.93	−39.15	−39.36	−39.66	−40.12
	0.85	−20.85	−30.26	−32.22	−33.48	−34.42	−34.92	−35.06	−35.19	−35.48	−35.96
	0.92	−15.84	−25.52	−27.54	−28.85	−29.82	−30.30	−30.35	−30.41	−30.70	−31.20
	0.99	−9.94	−19.92	−22.01	−23.37	−24.37	−24.83	−24.82	−24.83	−25.13	−25.64
1	0.78	−29.36	−38.29	−40.12	−41.30	−42.18	−42.64	−42.79	−42.93	−43.19	−43.63
	0.85	−24.48	−33.71	−35.61	−36.84	−37.74	−38.16	−38.20	−38.25	−38.49	−38.96
	0.92	−18.76	−28.30	−30.28	−31.55	−32.49	−32.88	−32.82	−32.77	−33.01	−33.50
	0.99	−11.83	−21.73	−23.79	−25.12	−26.09	−26.46	−26.31	−26.19	−26.44	−26.95

Appendix B. SW relative difference values estimated for the combined effect of each combination of AOD and PWV values considered in this study

AOD	PWV (mm)									
	0	6.66	13.33	20	26.66	33.33	40	46.66	53.33	60
0	0	−10.25	−12.48	−13.96	−15.10	−16.04	−16.85	−17.56	−18.20	−18.78
0.16	−2.67	−12.87	−15.08	−16.54	−17.66	−18.52	−19.21	−19.80	−20.36	−20.92
0.33	−5.42	−15.55	−17.72	−19.15	−20.23	−21.01	−21.54	−22.00	−22.46	−22.99
0.50	−8.15	−18.18	−20.31	−21.70	−22.75	−23.41	−23.76	−24.07	−24.47	−24.99
0.66	−10.83	−20.75	−22.84	−24.20	−25.21	−25.78	−25.96	−26.12	−26.46	−26.97
0.83	−13.43	−23.24	−25.29	−26.62	−27.60	−28.07	−28.10	−28.13	−28.43	−28.93
1	−15.96	−25.65	−27.67	−28.96	−29.91	−30.30	−30.19	−30.11	−30.35	−30.85

References

Alam, K., Trautmann, T., Blaschke, T., 2011. Aerosol optical properties and radiative forcing over mega city Karachi. Atmos. Res. 101, 773–782.

Bhatia, N., Tolpekin, V.A., Reusen, I., Sterckx, S., Biesemans, J., Stein, A., 2015. Sensitivity of reflectance to water vapor and aerosol optical thickness. IEEE J. Sel. Top. Appl. Earth Obs. Remote Sens. 8 (6), 3199–3208. http://dx.doi.org/10.1109/JSTARS.2015.2425954.

Bilbao, J., Roman, R., Yousif, C., Mateos, D., de Miguel, A., 2014. Total ozone column, water vapour and aerosol effects on erythemal and global solar irradiance in Marsaxlokk, Malta. Atmos. Environ. 99, 508–518.

Boucher, O., Randall, D., Artaxo, P., Bretherton, C., Feingold, G., Forster, P., Kerminen, V.M., Kondo, Y., Liao, H., Lohmann, U., Rasch, P., Satheesh, S.K., Sherwood, S., Stevens, B., Zhang, Z.Y., 2013. Clouds and aerosols in climate change 2013. In: Stocker, T.F., Qin, D., Plattner, G.-K., Tignor, M., Allen, S.K., Boschung, J., Nauels, A., Xia, Y., Bex, V., Midgley, P.M. (Eds.), The Physical Science Basis. Contribution of Working Group I to the Fifth Assessment Report of the Intergovernmental Panel on Climate Change. Cambridge University Press, Cambridge, United Kingdom and New York, NY, USA.

Che, H., Zhao, H., Wu, Y., Xia, X., Zhu, J., Wang, H., Wang, Y., Sun, J., Yu, J., Zhang, X., Shi, G., 2015. Analyses of aerosol optical properties and direct radiative forcing over urban and industrial regions in Northeast China. Meteorol Atmos Phys. 127, 345–354. http://dx.doi.org/10.1007/s00703-015-0367-3.

Costa, M.J., Sohn, B.J., Levizzani, V., Silva, A.M., 2006. Radiative forcing of Asian dust determined from the synergized GOME and GMS satellite data – a case study. J. Meteorol. Soc. Jpn. 84, 85–95. http://dx.doi.org/10.2151/jmsj.84.85.

Dhar, P., Kumar, B., Banik, T., Gogoi, M.M., Suresh Babu, S., Guha, A., 2017. Atmospheric aerosol radiative forcing over a semi-continental location Tripura in North-East India:

Model results and ground observations. Sci. Total Environ. 580, 499–508. https://doi.org/10.1016/j.scitotenv.2016.11.200.
Di Biagio, C., di Sarra, A., Meloni, D., Monteleone, F., Piacentino, S., Sferlazzo, D., 2009. Measurements of Mediterranean aerosol radiative forcing and influence of the single scattering albedo. J. Geophys. Res. Atmos. 114, D06211. http://dx.doi.org/10.1029/2008JD011037.
Di Biagio, C., di Sarra, A., Meloni, D., 2010. Large atmospheric shortwave radiative forcing by Mediterranean aerosols derived from simultaneous ground-based and spaceborne observations and dependence on the aerosol type and single scattering albedo. J. Geophys. Res. 115, D10209.
Di Biagio, C., di Sarra, A., Eriksen, P., Ascanius, S.E., Muscari, G., Holben, B., 2012. Effect of surface albedo, water vapour, and atmospheric aerosols on the cloud-free shortwave radiative budget in the Arctic. Clim. Dyn. 39, 953–969. http://dx.doi.org/10.1007/s00382-011-1280-1.
Di Sarra, A., Pace, G., Meloni, D., De Silvestri, L., Piacentino, S., Monteleone, F., 2008. Surface shortwave radiative forcing of different aerosol types in the Mediterranean. Geophys. Res. Lett. 35, L02714. http://dx.doi.org/10.1029/2007GL032395.
Dubovik, O., King, M.D., 2000. A flexible inversion algorithm for retrieval of aerosol optical properties from sun and sky radiance measurements. J. Geophys. Res. 105 (D16), 20673–20696.
Dubovik, O., Smirnov, A., Holben, B.N., King, M.D., Kaufman, Y.J., Eck, T.F., Slutsker, I., 2000. Accuracy assessments of aerosol optical properties retrieved from aerosol robotic network (AERONET) Sun and sky radiance measurements. J. Geophys. Res. 105 (D8), 9791–9806.
Emde, C., Buras-Schnell, R., Kylling, A., Mayer, B., Gasteiger, J., Hamann, U., Kylling, J., Richter, B., Pause, C., Dowling, T., Bugliaro, L., 2016. The libRadtran software package for radiative transfer calculations (version 2.0.1). Geosci. Model Dev. 9, 1647–1672.
Esteve, A.R., Estellés, V., Utrillas, M.P., Martínez-Lozano, J.A., 2014. Analysis of the aerosol radiative forcing over a Mediterranean urban coastal site. Atmos. Res. 137, 195–204. http://dx.doi.org/10.1016/j.atmosres.2013.10.009.
Fernández, A.J., Molero, F., Salvador, P., Revuelta, A., Becerril-Valle, M., Gómez-Moreno, F.J., Artíñano, B., Pujadas, M., 2017. Aerosol optical, microphysical and radiative forcing properties during variable intensity African dust events in the Iberian Peninsula. Atmos. Res. 196, 129–141. https://doi.org/10.1016/j.atmosres.2017.06.019.
Forster, P., Ramaswamy, V., Artaxo, P., Berntsen, T., Betts, R., Fahey, D.W., Haywood, J., Lean, J., Lowe, D.C., Myhre, G., Nganga, J., Prinn, R., Raga, G., Schulz, M., Van Dorland, R., 2007. Changes in atmospheric constituents and in radiative forcing. In: Solomon, S., Qin, D., Manning, M., Chen, Z., Marquis, M., Averyt, K.B., Tignor, M., Miller, H.L. (Eds.), Climate Change 2007: The Physical Science Basis. Contribution of Working Group I to the Fourth Assessment Report of the Intergovernmental Panel on Climate Change. Cambridge University Press, Cambridge, United Kingdom and New York, NY, USA.
Foyo-Moreno, I., Alados, I., Antón, M., Fernández-Gálvez, J., Cazorla, A., Alados-Arboledas, L., 2014. Estimating aerosol characteristics from solar irradiance measurements at an urban location in Southeastern Spain. J. Geophys. Res. Atmos. 119, 1845–1859. http://dx.doi.org/10.1002/2013JD020599.
García, O.E., Díaz, J.P., Expósito, F.J., Díaz, A.M., Dubovik, O., Derimian, Y., Dubuisson, P., Roger, J.C., 2012. Shortwave radiative forcing and efficiency of key aerosol types using AERONET data. Atmos. Chem. Phys. 12, 5129–5145. https://doi.org/10.5194/acp-12-5129-2012.
García, R.D., Cuevas, E., Cachorro, V.E., Ramos, R., de Frutos, A., 2013. Comparison between measurements and model simulations of solar radiation at a high altitude site: case studies for the Izana BSRN station. AIP Conf. Proc. 1531, 864. (2013). https://doi.org/10.1063/1.4804907.
Goto, D., Schutgens, N.A.J., Nakajima, T., Takemura, T., 2011. Sensitivity of aerosol to assumed optical properties over Asia using a global aerosol model and AERONET. Geophys. Res. Lett. 38, L17810. http://dx.doi.org/10.1029/2011GL048675.
Gueymard, C., 2004. The sun's total and spectral irradiance for solar energy applications and solar radiation models. Sol. Energy 76, 423–453.
Holben, B., Eck, T.F., Slutsker, I., Tanre, D., Buis, J., Setzer, K., Vermote, E., Reagan, J., Kaufman, Y., Nakajima, T., Lavenu, F., Jankowiak, I., Smirnov, A., 1998. AERONET—a federated instrument network and data archive for aerosol characterization. Remote Sens. Environ. 66, 1–16.
Hu, R.M., Martin, R.V., Fairlie, T.D., 2007. Global retrieval of columnar aerosol single scattering albedo from space-based observations. J. Geophys. Res. D02204. http://dx.doi.org/10.1029/2005JD006832.
Janjai, S., Pattarapanitchai, S., Wattan, R., Masiri, I., Buntoung, S., Promsen, W., Tohsing, K., 2013. A semi-empirical model for estimating surface solar radiation from satellite data. AIP Conf. Proc. 1531, 324. http://dx.doi.org/10.1063/1.4804772.
Laaroussi, N., El Azhary, K., Garoum, M., Raefat, S., Feiz, A., 2016. Semi-Empirical Models for the Estimation of Global Solar Irradiance measurements in Morocco. 3rd International Conference on Renewable Energies for Developing Countries (REDEC).
Lefèvre, M., Oumbe, A., Blanc, P., Espinar, B., Gschwind, B., Qu, Z., Wald, L., Schroedter-Homscheidt, M., Hoyer-Klick, C., Arola, A., Benedetti, A., Kaiser, J.W., Morcrette, J.-J., 2013. Mc-Clear: a new model estimating downwelling solar radiation at ground level in clear-sky conditions. Atmos. Meas. Tech. 6, 2403–2418. http://dx.doi.org/10.5194/amt-6-2403-2013.
Lindfors, A.V., Kouremeti, N., Arola, A., Kazadzis, S., Bais, A.F., Laaksonen, A., 2013. Effective aerosol optical depth from pyranometer measurements of surface solar radiation (global radiation) at Thessaloniki, Greece. Atmos. Chem. Phys. 13 (7), 3733–3741.
Liou, K.N., 1980. An Introduction to Atmospheric Radiation. Academic Press (ISBN: 0124514502, 9780124514508).
Mai, B.R., and Coauthors, 2018. Aerosol optical properties and radiative impacts in the Pearl River Delta region of China during the dry season. Adv. Atmos. Sci. 35 (2), 195–208(https://doi.org/10.1007/s00376-017-7092-4).
Mateos, D., Antón, M., Sánchez-Lorenzo, A., Calbó, J., Wild, M., 2013. Long-term changes in the radiative effects of aerosols and clouds in a mid-latitude region (1985–2010). Glob. Planet. Chang. 111, 288–295. http://dx.doi.org/10.1016/j.gloplacha.2013.10.004. (2013).
Mateos, D., Antón, M., Toledano, C., Cachorro, V.E., Alados-Arboledas, L., Sorribas, M., Costa, M.J., Baldasano, J.M., 2014. Aerosol radiative effects in the ultraviolet, visible, and near-infrared spectral ranges using long-term aerosol data series over the Iberian Peninsula. Atmos. Chem. Phys. 14, 13497–13514. http://dx.doi.org/10.5194/acp-14-13497-2014.
Mayer, B., Kylling, A., 2005. Technical note: the libRadtran software package for radiative transfer calculations — description and examples of use. Atmos. Chem. Phys. 5, 1855–1877.
McArthur, L.J.B., 2005. Baseline Surface Radiation Network (BSRN)-Operation Manual Version 2.1.
Obregón, M.A., Pereira, S., Salgueiro, V., Costa, M.J., Silva, A.M., Serrano, A., Bortoli, D., 2015a. Aerosol radiative effects during two desert dust events in August 2012 over the Southwestern Iberian Peninsula. Atmos. Res. 153, 404–415. https://doi.org/10.1016/j.atmosres.2014.10.007.
Obregón, M.A., Costa, M.J., Serrano, A., Silva, A.M., 2015b. Effect of water vapor in the SW and LW downward irradiance at the surface during a day with low aerosol load. IOP Conf. Ser. 28, 012009. http://dx.doi.org/10.1088/1755-1315/28/1/012009.
Obregón, M.A., Serrano, A., Costa, M.J., Silva, A.M., 2015c. Validation of libRadtran and SBDART models under different aerosol conditions. IOP Conf. Ser. 28, 012010.
Obregón, M.A., Costa, M.J., Silva, A.M., Serrano, A., 2017. Thirteen years of aerosol radiative forcing in Southwestern Iberian Peninsula. Aerosol Air Qual. Res. 17, 2509–2521. http://dx.doi.org/10.4209/aaqr.2017.05.0159.
Péré, J.-C., Rivellini, L., Crumeyrolle, S., Chiapello, I., Minvielle, F., Thieuleux, F., Choëlc, M., Popovici, I., 2018. Simulation of African dust properties and radiative effects during the 2015 SHADOW campaign in Senegal. Atmos. Res. 199, 14–28. https://doi.org/10.1016/j.atmosres.2017.07.027.
Santos, D., Costa, M.J., Silva, A.M., 2008. Direct SW aerosol radiative forcing over Portugal. Atmos. Chem. Phys. 8, 5771–5786.
Santos, D., Costa, M.J., Silva, A.M., Salgado, R., 2013. Modeling Saharan desert dust radiative effects on clouds. Atmos. Res. 127, 178–194. https://doi.org/10.1016/j.atmosres.2012.09.024.
Shettle, E., 1989. Models of aerosols, clouds and precipitation for atmospheric propagation studies, atmospheric propagation in the UV, visible, IR and mm-region and related system aspects. In: 454 in AGARD Conference Proceedings.
Smirnov, A., Holben, B.N., Eck, T.F., Dubovik, O., Slutsker, I., 2000. Cloud screening and 495 quality control algorithms for the AERONET data base. Remote Sens. Environ. 73, 337–349.
Stamnes, K., Tsay, S.C., Wiscombe, W., Laszlo, I., 2000. DISORT, a General Purpose Fortran Program for Discrete-Ordinate-Method Radiative Transfer in Scattering and Emitting Layered Media: Documentation of Methodology. Goddard Space Flight Center, NASA.
Stone, R., Augustine, J., Dutton, E., O'Neill, N., Saha, A., 2011. Empirical determinations of the longwave and shortwave radiative forcing efficiencies of wildfire smoke. J. Geophys. Res. Atmos. 116, 1984–2012.
Trabelsi, A., Saad, M., Masmoudi, M., Alfaro, S.C., 2015. Atmospheric aerosols and their impact on surface solar irradiation in Kerkennah Islands (eastern Tunisia). Atmos. Res. 161 (162), 102–107. https://doi.org/10.1016/j.atmosres.2015.04.006.
Trenberth, K.E., Fasullo, J., Smith, L., 2005. Trends and variability in column-integrated atmospheric water vapor. Clim. Dyn. 24, 741–758.
Tzanis, C., Varotsos, C.A., 2008. Tropospheric aerosol forcing of climate: a case study for the greater area of Greece. Int. J. Remote Sens. 29 (9), 2507–2517. http://dx.doi.org/10.1080/01431160701767575.
Vaquero-Martínez, J., Antón, M., Ortiz de Galisteo, J.P., Román, R., Cachorro, V.E., 2018. Water vapor radiative effects on short-wave radiation in Spain. Atmos. Res. 205, 18–25. https://doi.org/10.1016/j.atmosres.2018.02.001.
Xia, X., Li, Z., Wang, P., Chen, H., Cribb, M., 2007. Estimation of aerosol effects on surface irradiance based on measurements and radiative transfer model simulations in northern China. J. Geophys. Res. 112, D22S10. http://dx.doi.org/10.1029/2006JD008337.
Yu, H., Kaufman, Y.J., Chin, M., Feingold, G., Remer, L.A., Anderson, T.L., Balkanski, Y., Bellouin, N., Boucher, O., Christopher, S., DeCola, P., Kahn, R., Koch, D., Loeb, N., Reddy, M.S., Schulz, M., Takemura, T., Zhou, M., 2006. A review of measurement-based assessments of the aerosol direct radiative effect and forcing. Atmos. Chem. Phys. 6, 613–666.

Proc. IAHS, 380, 73–79, 2018
https://doi.org/10.5194/piahs-380-73-2018
© Author(s) 2018. This work is distributed under
the Creative Commons Attribution 4.0 License.

Use of Sentinel 2 – MSI for water quality monitoring at Alqueva reservoir, Portugal

Miguel Potes[1], Gonçalo Rodrigues[1], Alexandra Marchã Penha[1], Maria Helena Novais[1], Maria João Costa[1,2], Rui Salgado[1,2], and Maria Manuela Morais[1,3]

[1]Institute of Earth Sciences – ICT, IIFA, University of Évora, Évora, 7000-671, Portugal
[2]Department of Physics, ECT, University of Évora, Évora, 7000-671, Portugal
[3]Department of Biology, ECT, University of Évora, Évora, 7000-671, Portugal

Correspondence: Miguel Potes (mpotes@uevora.pt)

Received: 18 April 2018 – Revised: 10 July 2018 – Accepted: 27 July 2018 – Published: 18 December 2018

Abstract. Alqueva reservoir located in southeast of Portugal has a surface area of 250 km^2 and total capacity of 4150 hm^3. Since 2006 the water quality of this reservoir is explored by the authors using remote sensing techniques. First using MERIS multi-spectral radiometer on-board of ENVISAT-1 and presently with MSI multi-spectral radiometer on-board SENTINEL-2. The existence of two satellites (A and B) equipped with MSI enable the area to be revisited, under the same viewing conditions, every 2–3 days. Since 2017 the multidisciplinary project ALOP (ALentejo Observation and Prediction systems) expands the team knowledge about the physical and bio-chemical properties of the reservoir. This project includes an integrated field campaign at different experimental sites in the reservoir and its shores, at least until September 2018. Previous algorithms developed by the team for MERIS are tested with the new MSI instrument for water turbidity, chlorophyll *a* concentration and density of cyanobacteria. Results from micro-algae bloom occurred in late summer/early autumn 2017 on the reservoir are presented, showing the capabilities of MSI sensor for detection and high resolution mapping over the reservoir. The results are compared with in situ sampling and laboratorial analysis of chlorophyll *a* associated with the bloom.

1 Introduction

The water quality monitoring of inland reservoirs is essential to ensure that it remains within acceptable boundaries or otherwise, to trigger actions that may revert the water quality degradation. The set-up of early warning systems is important for reservoirs, which may be affected by pollution events, alerting the authorities to water quality degradation episodes. The Alqueva reservoir, located in southwestern Iberian Peninsula (south of Portugal), has a total capacity of 4.150 hm^3 and a surface area of 250 km^2, constituting the largest reservoir in the Iberian Peninsula. It is a multipurpose structure used for water supply, irrigation, hydroelectric power generation and recreation, thus water quality management is critical. Since 2017 the multidisciplinary project ALOP (ALentejo Observation and Prediction systems) expands the knowledge about the physical and bio-chemical properties of Alqueva reservoir. This project includes an integrated field campaign at different experimental sites in the reservoir and its shores, at least until September 2018. It aims to develop a multi-functional activity in the field of atmosphere-water-ecosystem interaction, which embraces observation, prediction and risk alert. It intends to develop tools of observation, forecasting and alert in the domains of meteorology and water (quantity and quality), at regional scale. Satellite remote sensing constitutes a useful tool to complement in situ data sampling and laboratorial analysis of water quality parameters, which is laborious and expensive and thus spatially and temporally limited. Unless a water body is adequately instrumented with in situ sensors, remote-sensing is the only suitable method to monitor the quality of remote and large inland waters (WMO, 2013) and can undoubtedly contribute to early warning systems. Several satellite remote sensing studies have been proposed using a variety of sensors over a number of worldwide reservoirs (Gholizadeh et al., 2016). Remote sensing of water bodies

rely on the varying colour of natural waters that correspond to different spectral reflectances, assuming that these variations depend on the water constituents. Water remote sensing was used to monitor ocean colour already since the 1960s, and in the last three decades there has been a growing interest to apply these remote sensing techniques also to inland water quality. For this purpose, remote sensing measurements, mainly using visible and near-infrared wavelengths, are used to develop bio-optical models that aim to relate radiometric (optical) and biological quantities. Inland waters are optically complex due to the presence of several constituents that may interact, creating uncertainties in the remote sensing retrievals (Toming et al., 2016; Ogashawara et al., 2017). Thus there is a need to study inland waters at a local and regional scale and to quantify the performance of remote sensing methods to monitor inland water quality. The first remote sensing studies over Portuguese reservoirs were carried out by the authors, proposing semi-empirical bio-optical models to estimate concentrations of chlorophyll *a* and cyanobacteria (Potes et al., 2011), as well as turbidity (Potes et al., 2012) over Alqueva from MERIS sensor onboard ENVISAT satellite.

The launch of ESA Sentinel-2 (MSI) mission (S-2A launched in June 2015 and S-2B launched in March 2017), carrying as single payload the Multi-Spectral Instrument (MSI), brought a great opportunity to study inland reservoirs. It presents a systematic global coverage of two to three days at mid-latitudes, which supports monitoring of changes in reservoirs, with relatively high spatial resolution. MERIS sensor, on board ENVISAT, presented maximum spatial resolution of 300 m, whereas MSI presents a spatial resolution of 10, 20 or 60 m, depending on the spectral band. Potes et al. (2011, 2012) proposed a method to monitor chlorophyll *a*, cyanobacteria and turbidity over inland reservoirs using MERIS data. The objective of this work is to show the potential of MSI used with the set of algorithms developed for MERIS, to study the water quality of inland waters. Specifically, a micro-algae bloom that occurred in early autumn 2017 is analysed and its evolution related to the influence of a hurricane progressing over the Eastern North Atlantic region.

Section 2 presents the data used and methodology. Results are presented and discussed in Sect. 3 and finally Sect. 4 summarizes the main conclusions.

2 Data and methods

Data from Sentinel 2 is used in this work, namely level 2A from MSI instrument, which corresponds to images with atmospheric correction, providing information of surface reflectance in 12 spectral channels from 443 to 2190 nm (central wavelength). The product Maximum Chlorophyll Index (MCI) was also extracted from the level 2 images which is an indicator of the amount of chlorophyll present in water mass (Gower et al., 2008) and thus a useful tool in the monitoring of algae blooms of inland waters. The bands selected for MCI index were the 665, 705 and 740 nm.

Table 1. MERIS bands wavelengths and equivalent MSI bands used in the algorithms.

MERIS		MSI	
Wavelength (nm)	Bandwidth (nm)	Wavelength (nm)	Bandwidth (nm)
412.5	10	443	20
442.5	10	443	20
490	10	490	65
560	10	560	35
620	10	665	30

The algorithms from Potes et al. (2011, 2012) developed for MERIS are:

$$\text{Chl } a = 4.23\left(\frac{560\,\text{nm}}{442.5\,\text{nm}}\right)^{3.94}\left[\text{mg m}^{-3}\right] \quad (1)$$

$$\text{Cya} = 115\,530.31\left(\frac{560\,\text{nm}\cdot 620\,\text{nm}}{490\,\text{nm}}\right)^{2.38}\left[10^3\,\text{cells mL}^{-1}\right] \quad (2)$$

$$\text{Turb} = 8.93\left(\frac{560\,\text{nm}}{412.5\,\text{nm}}\right) - 6.39\ [\text{NTU}] \quad (3)$$

Table 1 presents the information about MERIS bands used in the algorithms to estimate the concentration of chlorophyll *a* (Chl *a* in Eq. 1), density of cyanobacteria (Cya in Eq. 2) and water turbidity (Turb in Eq. 3). In the same table the equivalent MSI wavelengths applied in this work is presented.

The algorithms represented by Eqs. (1) to (3) were applied now to the same water body as in Potes et al. (2011, 2012). The chlorophyll *a* concentration was also obtained on a bimensal basis from in situ sampling and laboratory analysis in the framework of ALOP project, in order to validate the results. The method used was the molecular absorption spectroscopy and the equations developed by Lorenzen (1967).

3 Study site and case study

Alqueva reservoir project was concluded in 2002 and the reservoir reached the capacity of 80 % in March 2004. Figure 1 shows the surface area of the reservoir at its full capacity as well as the sites considered in this work.

The algorithms developed by Potes et al. (2011, 2012) for MERIS have been applied to MSI imagery in Alqueva reservoir. ALOP field campaign is ongoing since January 2017 and a case study of October 2017 was chosen, because this was a particular month in Portugal with the influence of Ophelia hurricane amidst a very dry period. Ophelia started as a tropical storm but it reached category 3 hurricane in Saffir–Simpson hurricane wind scale, South of Azores islands being the strongest hurricane ever recorded so far East

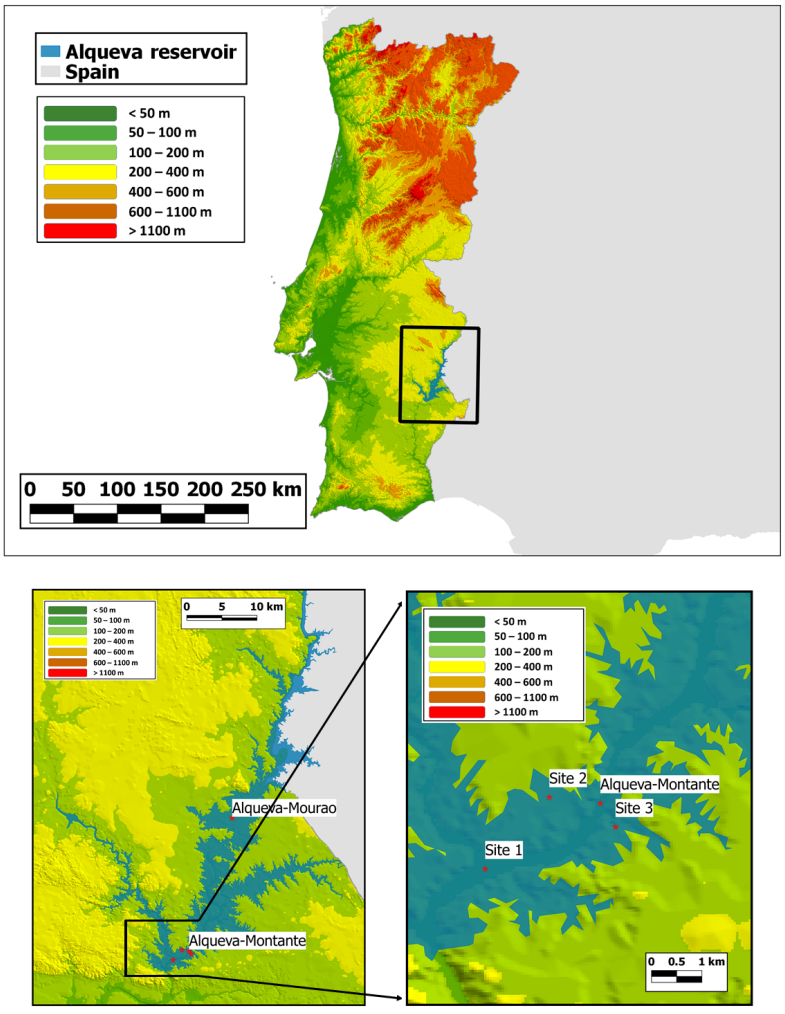

Figure 1. Map of Alqueva reservoir located in Southeast Portugal. The sites used in this work are also represented.

in the Atlantic (Fig. 2). In its trajectory towards Ireland it started to lose strength as is entered in cold waters being very close to Iberian Peninsula, about 360 km from Cape Finisterre (Spain).

This hurricane brought a meteorological breakup window in the unprecedented drought scenario that the country was facing by October (which is normally the beginning of the rainy season). In particular, this event led to the increase of wind speed and relative humidity and a decrease in the air temperature. Precipitation was concentrated in two days (17 and 18 October) with an accumulated value of 32.0 mm. Figure 3 shows the evolution of air temperature for October 2017 recorded in CidAlmeida meteorological station installed in the area of Alqueva (ALOP project) where the influence of the hurricane can be detected between 16 and 22 October.

Figure 4 presents a wind rose from the same inland station for the period 15 to 22 October, where the stronger winds from the South and West quadrants are clearly visible, as a consequence of hurricane Ophelia passing by Portugal.

According to this scenario, three Sentinel-2 images from October 2017 were selected on clear sky days (12, 22 and 29) to use the MSI instrument in Alqueva reservoir. Table 2 shows acquisitions date and time for both satellite data and in situ water collection.

4 Results

On 12 October the reservoir was under a micro-algae bloom especially on the northern part as can be seen in Fig. 5 (row a) in terms of concentration of chlorophyll *a*, density of cyanobacteria and water turbidity. Values greater than 50 mg m^{-3} of chlorophyll *a* were estimated for the northern part, as well as greater than 75 000 cells mL^{-1} cyanobacteria with turbidity values reaching 30 NTU.

On 22 October (Fig. 5 – row b), six days after, all the three parameters decreased sharply in the northern part probably due to very different weather conditions in the six days under the influence of the hurricane Ophelia passage along

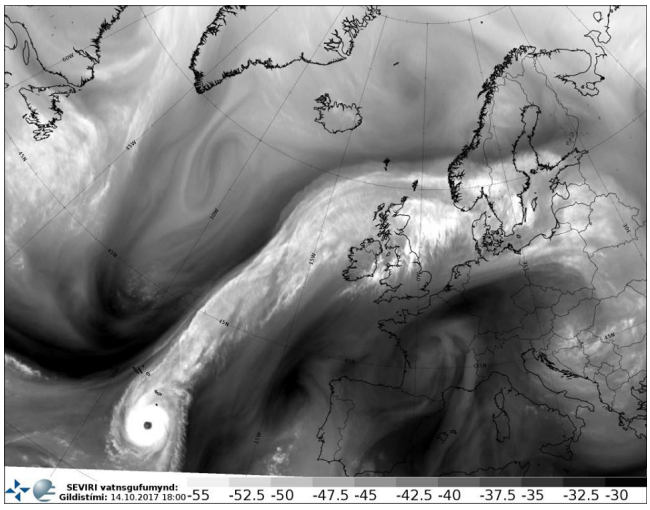

Figure 2. Spinning Enhanced Visible and Infrared Imager (SEVIRI) image of hurricane Ophelia located South of Azores islands on 14 October 2017, at 18:00 UTC (https://irishweatheronline.wordpress.com/, last access: 15 April 2018).

Table 2. MSI acquisition dates and in situ date for water collection.

Date	Time (UTC)	Type
12 Oct 2017	11:21	Satellite
22 Oct 2017	11:21	Satellite
27 Oct 2017	11:00–14:00	Laboratory
29 Oct 2017	11:12	Satellite

the Portuguese coast. It is well known that lower temperatures inhibit the phytoplankton growth (Wu et al., 2015) the same occurs with increasing wind speed and precipitation, which leads to increasing in water mixing (Fleming-Lehtinen and Laamanen, 2012). For these reasons a regress of the bloom due to the changes in meteorological conditions was expected.

In the central part of the reservoir the values are above the eutrophic threshold for chlorophyll *a* presented by Bukata et al. (1995), of 6 mg m^{-3}. In addition, most of the branches of reservoir present values are above the ecological potential and eutrophic threshold for chlorophyll *a* for reservoirs in the South of Portugal, which according with the Water Frame Directive is 9.5 and 8 mg m^{-3}, respectively (INAG, 2009). Nine days after 22 October, on the images of 29 October presented in Fig. 5 (row c) the reservoir is clear from the presence of the micro-algae bloom. All the three parameters present low values indicating good water quality on that day. Nevertheless, some thinner branches of the reservoir still present some occasional high values. A summary table with minimum, maximum and mean values is presented for the three parameters in the three days (Table 3).

Figure 6 presents a scatter plot between the MCI and concentration of chlorophyll *a* obtained from satellite. All

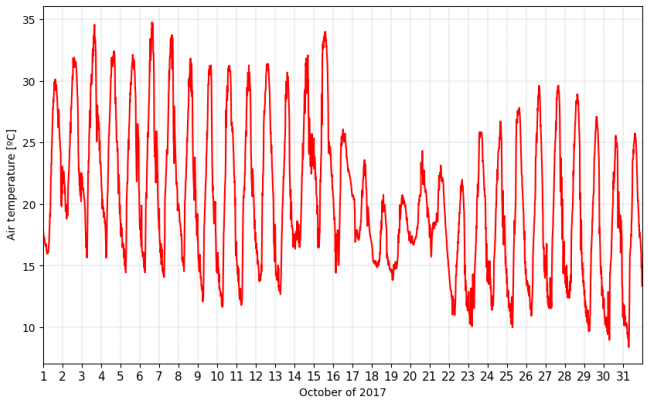

Figure 3. One-minute averages of air temperature recorded in CidAlmeida meteorological station located inland nearby Alqueva-Montante site (Fig. 1) for October 2017.

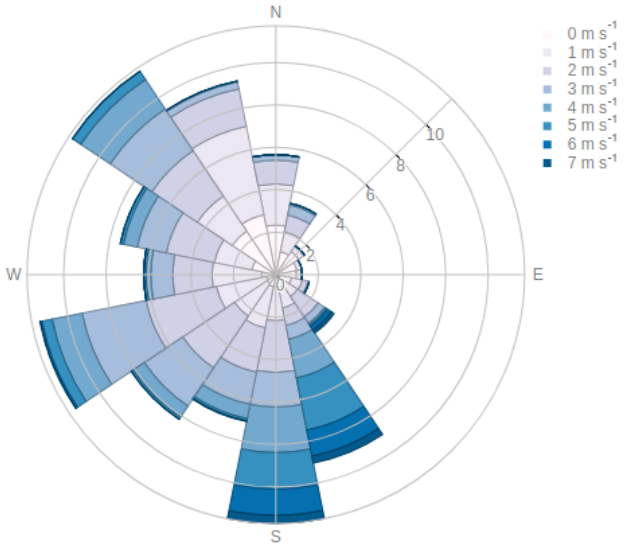

Figure 4. Wind rose recorded in a meteorological station located inland nearby Alqueva-Montante site (Fig. 1) for the period 15 to 22 October 2017.

pixels from 22 October are used in the plot, in a total of 28 251 points. These two parameters are well correlated (correlation coefficient of 0.70) with a RMSE (Root Mean Square Error) of 21.5 mg m^{-3}. Future work foresees the use of longer data series to quantify MCI as chlorophyll concentration.

Satellite derived results were compared with data obtained from laboratory analysis. Unfortunately, there are no water laboratory analyses for the same days as MSI acquired images, rather five days before (22 October) and two days after (29 October). From the analysis of MSI retrieved data, it was concluded that the water quality has improved from 22 to 29 October and thus it is expected that the water analysis should be more or less similar or in-between the values of MSI. This is shown in Fig. 7 where the chlorophyll *a*

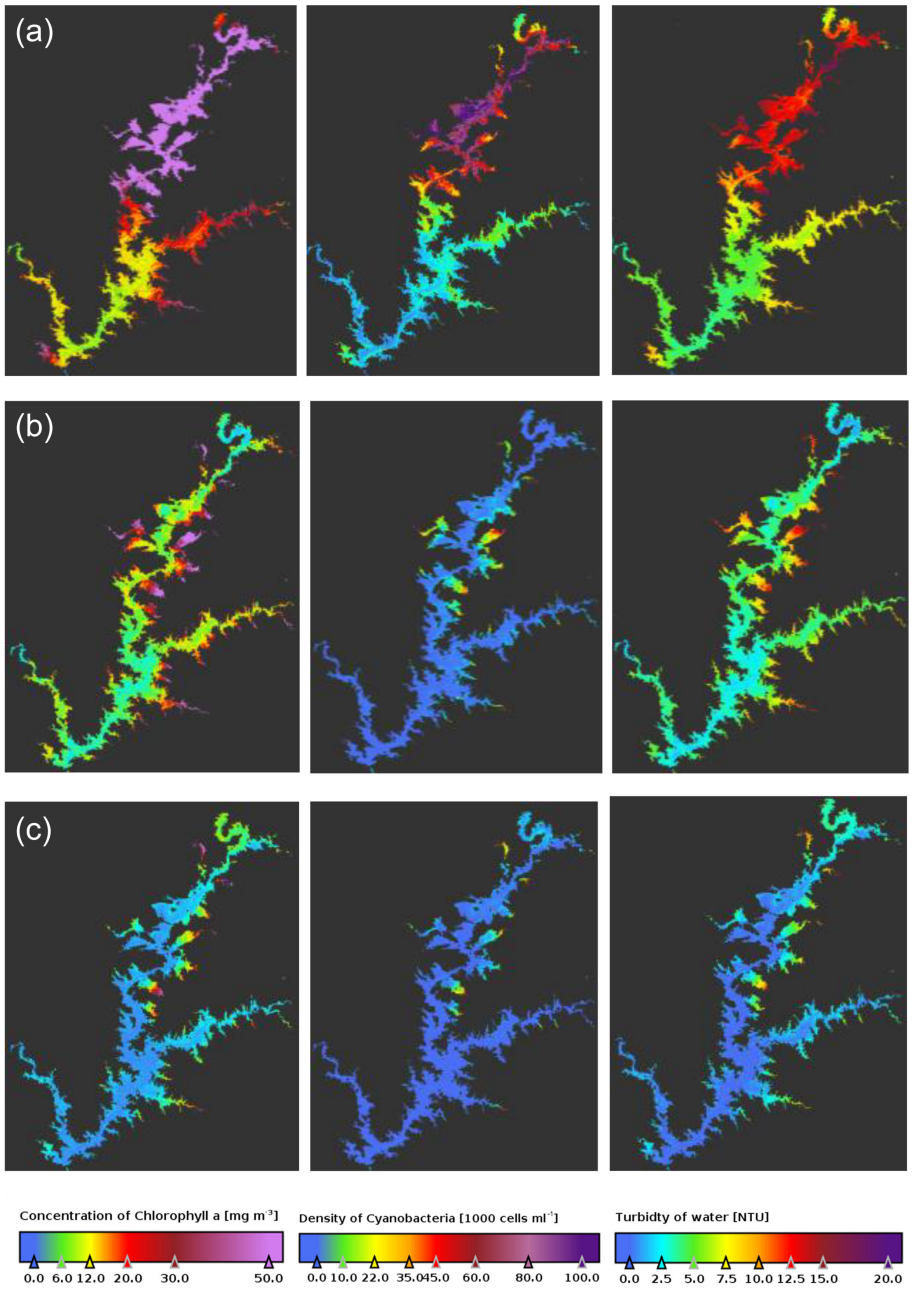

Figure 5. Concentration of chlorophyll *a*, density of cyanobacteria and water turbidity estimated from the Eqs. (1) to (3) for 12 October (row **a**), 22 October (row **b**) and 29 October (row **c**).

concentration estimated from MSI (22 and 29 October) and obtained in laboratory (27 October) for five sites (Fig. 1) is plotted. The results are generally in agreement. From 22 to 29 October, MSI reports a decrease in chlorophyll *a* concentration and the laboratory analysis (middle day) confirms this decrease presenting a middle value in all sites, except for Alqueva-Montante and Site 1, which presents a very similar value nevertheless slightly greater than the MSI value for 22 October. In these two sites the MSI values, nearby the in situ measurement place, were more heterogeneous than in the other sites probably due to their central location where the water is under more currents than in the other sites, in this part of the year. The results also suggest that the decrease of chlorophyll *a* was not linear in time, but more pronounced near the end of the five day period.

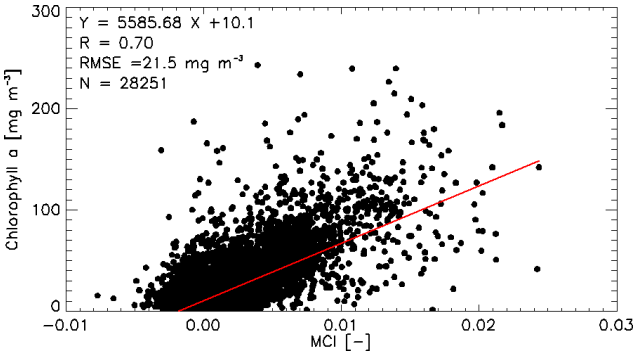

Figure 6. Scatter plot between MCI and concentration of chlorophyll *a* estimated by Eq. (1) for day 22 October all pixels.

Table 3. Range and mean values of the maps presented in Fig. 5.

Date		Chlorophyll *a* [mg m^{-3}]	Cyanobacteria [10^3 cells mL^{-1}]	Turbidity [NTU]
12 Oct	Range	[2.6; 600.1]	[0.1; 228.1]	[1.5; 25.0]
	Mean	46.1	33.3	8.6
22 Oct	Range	[0.5; 263.7]	[0.2; 283.0]	[0.1; 19.1]
	Mean	14.1	4.0	4.5
29 Oct	Range	[0.1; 140.1]	[0.1; 179.7]	[0.3; 15.3]
	Mean	4.6	3.8	1.2

5 Conclusions

In this work the potential of Sentinel-2 MSI instrument for monitoring the water quality of inland waters is shown. In the case study reported, different conditions of Alqueva reservoir are analysed for one month. Systems like Alqueva reservoir are highly dynamic and respond rapidly to changes in atmospheric conditions, thus is very importance to have these kinds of tools for monitoring the water surface as a whole. In this work, a set of algorithms developed for another space borne spectroradiometer (MERIS) were applied with good results. The team is now working to tune the algorithms in order to make use of the full potential of MSI instrument. Specific algorithms were already developed successfully by Toming et al. (2016) using the same MSI instrument over Estonian lakes, regarding chlorophyll *a* concentration as well as colored dissolved organic matter (CDOM) and dissolved organic carbon (DOC).

Data availability. Data used in this work is available on request to the first author.

Author contributions. MP conceptualized and led the team on this research. He also wrote great part of the manuscript and carried out the corrections during the write-up. GR gathered, processed and prepared the spatial data and maps used for this article. AMP and

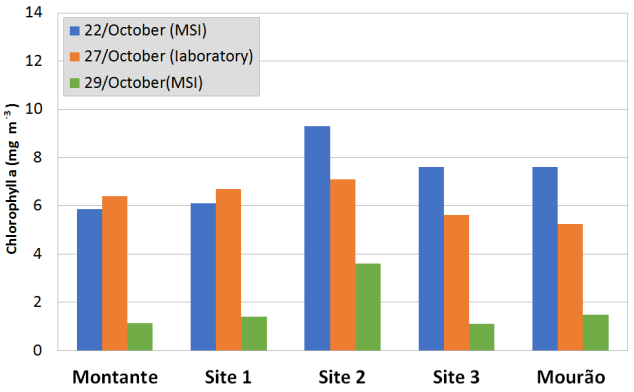

Figure 7. Bar plot of concentration of chlorophyll *a* estimated by Eq. (1) for 22 and 29 October and obtained in laboratory for 27 October for 5 sites shown on Fig. 1.

MHN were responsible for the in situ and laboratory data analysis used in the work. MJC participated in the data processing and discussion and wrote the first part of the manuscript. RS and MMM participated in the discussion of results and reviewed the manuscript for necessary corrections.

Competing interests. The authors declare that they have no conflict of interest.

Special issue statement. This article is part of the special issue "Earth Observation for Integrated Water and Basin Management: New possibilities and challenges for adaptation to a changing environment". It is a result of The Remote Sensing & Hydrology Symposium, Cordoba, Spain, 8–10 May 2018.

Acknowledgements. The work was funded by the ALOP project (ALT20-03-0145-FEDER-000004) and also through the European Union through the European Regional Development Fund, included in the COMPETE 2020 (Operational Program Competitiveness and Internationalization) through the ICT project (UID/GEO/04683/2013) with the reference POCI-01-0145-FEDER 007690.

Edited by: María José Polo
Reviewed by: two anonymous referees

References

Bukata, R. P., Jerome, J. H., Kondratyev, K. Y., and Pozdnyakov, D. V.: Optical Properties and Remote Sensing of Inland and Coastal Waters, 135–250, CRS Press, Boca Raton, Florida 33431, USA, 1995.

Fleming-Lehtinen, V. and Laamanen, M.: Long-term changes in Secchi depth and the role of phytoplankton in explaning light attenuation in the Baltic Sea, Estuar. Coast. Shelf S., 102–103, 1–10, 2012.

Gholizadeh, M. H., Melesse, A. M., and Reddi, L.: A Comprehensive Review on Water Quality Parameters Estimation Using Remote Sensing Techniques, Sensors, 16, 1298, https://doi.org/10.3390/s16081298, 2016.

Gower, J. F., King, R. S., and Goncalves, P.: Global monitoring of plankton blooms using MERIS MCI, Int. J. Remote Sens., 29, 6209–6216, https://doi.org/10.1080/01431160802178110, 2008.

INAG (Instituto da Água Instituto Público): Critérios para a Classificação do Estado das Massas de Água Superficiais – Rios e Albufeiras, Ministério do Ambiente, do Ordenamento do Território e do Desenvolvimento Regional, Lisboa, Portugal, 2009.

Lorenzen, C. J.: Determination of chlorophyll and phaeopigments: Spectrophotometric equations, Limnol. Oceanogr., 12, 348–356, 1967.

Ogashawara, I., Mishra, D. R., and Gitelson, A. A.: Chapter 1 – Remote Sensing of Inland Waters: Background and Current State-of-the-Art, in: Bio-optical Modeling and Remote Sensing of Inland Waters, edited by: Mishra, D. R., Ogashawara, I., and Gitelson, A. A., Elsevier, 1–24, https://doi.org/10.1016/B978-0-12-804644-9.00001-X, 2017.

Potes, M., Costa, M. J., Silva, J. C. B., Silva, A. M., and Morais, M.: Remote sensing of water quality parameters over Alqueva reservoir in the south of Portugal, Int. J. Remote Sens., 32, 3373–3388, https://doi.org/10.1080/01431161003747513, 2011.

Potes, M., Costa, M. J., and Salgado, R.: Satellite remote sensing of water turbidity in Alqueva reservoir and implications on lake modelling, Hydrol. Earth Syst. Sci., 16, 1623–1633, https://doi.org/10.5194/hess-16-1623-2012, 2012.

Toming, K., Kutser, T., Laas, A., Sepp, M., Paavel, B., and Nõges, T.: First Experiences in Mapping Lake Qater Quality Parameters with Sentinel-2 MSI Imagery, Remote Sens., 8, 640, https://doi.org/10.3390/rs8080640, 2016.

WMO: Planning of water-quality monitoring systems, WMO-No. 1113, Geneva, Switzerland, 2013.

Wu, Z., Zhang, Y., Zhou, Y., Liu, M., Shi, K., Yu, Z., and Lin, Y.-P.: Seasonal-Spatial Distribution and Long-Term Variation of Transparency in Xin'anjiang Reservoir: Implications for Reservoir Management, Int. J. Environ. Res. Pu., 12, 9492–9507, 2015.

remote sensing

MDPI

Article

Validation of ESA Sentinel-2 L2A Aerosol Optical Thickness and Columnar Water Vapour during 2017–2018

María Ángeles Obregón [1,*], Gonçalo Rodrigues [1], Maria Joao Costa [2], Miguel Potes [1] and Ana Maria Silva [1]

[1] Department of Physics, Institute of Earth Sciences, Institute for Advanced Studies and Research, University of Évora, 7000-671 Évora, Portugal

[2] Department of Physics, Institute of Earth Sciences, School of Science and Technology, University of Évora, 7000-671 Évora, Portugal

* Correspondence: nines@unex.es

Received: 23 May 2019; Accepted: 9 July 2019; Published: 11 July 2019

Abstract: This study presents a validation of aerosol optical thickness (AOT) and integrated water vapour (IWV) products provided by the European Space Agency (ESA) from multi-spectral imager (MSI) measurements on board the Sentinel-2 satellite (ESA-L2A). For that purpose, data from 94 Aerosol Robotic Network (AERONET) stations over Europe and adjacent regions, covering a wide geographical region with a variety of climate and environmental conditions and during the period between March 2017 and December 2018 have been used. The comparison between ESA-L2A and AERONET shows a better agreement for IWV than the AOT, with normalized root mean square errors (NRMSE) of 5.33% and 9.04%, respectively. This conclusion is also reflected in the values of R^2, which are 0.99 and 0.65 for IWV and AOT, respectively. The study period was divided into two sub-periods, before and after 15 January 2018, when the Sentinel-2A spectral response functions of bands 1 and 2 (centered at 443 and 492 nm) were updated by ESA, in order to investigate if the lack of agreement in the AOT values was connected to the use of incorrect spectral response functions. The comparison of ESA-L2A AOT with AERONET measurements showed a better agreement for the second sub-period, with root mean square error (RMSE) values of 0.08 in comparison with 0.14 in the first sub-period. This same conclusion was attained considering mean bias error (MBE) values that decreased from 0.09 to 0.01. The ESA-L2A AOT values estimated with the new spectral response functions were closer to the correspondent reference AERONET values than the ones obtained using the previous spectral response functions. IWV was not affected by this change since the retrieval algorithm does not use bands 1 and 2 of Sentinel-2. Additionally, an analysis of potential uncertainty sources to several factors affecting the AOT comparison is presented and recommendations regarding the use of ESA-L2A AOT dataset are given.

Keywords: validation; aerosol optical depth; integrated water vapour; Sentinel-2; AERONET

1. Introduction

Aerosols and water vapour are two of the most important atmospheric constituents of the Earth-atmosphere system because they attenuate solar radiation through scattering and absorption processes, and also modulate terrestrial radiation mainly by absorption and emission. The effect of aerosols and water vapour on short wave (SW) irradiance was analysed by Obregón et al. [1], who showed that the combined effect of those quantities was not simply the sum of their individual effects. The effect of each constituent has been also studied by Alexandri et al. [2]. Atmospheric aerosols also

indirectly affect the radiation balance by influencing cloud formation. Changes in the atmospheric composition due to these constituents can modify the radiative budget and, as a result, the global temperature of the Earth [3]. Moreover the aerosol load in the atmospheric column (AOT) and the total water vapour integrated over an atmospheric column (IWV) are key quantities for atmospheric correction of satellite radiation measurements, and their reliability greatly influence the accuracy of the surface reflectance satellite derived products [4].

AOT and IWV data can be obtained from sunphotometer measurements. However, these are representative of point measurements at the surface, providing local information corresponding to the specific locations where the measurement stations are located and, therefore, cannot provide the spatial coverage required for global monitoring. Consequently, if the objective is to perform studies on a regional or global scale, it is better to use data with global coverage, such as those provided by instruments on board satellite platforms. Some of the instruments used to retrieve aerosol related quantities and/or water vapour on board satellite platforms as Terra, Aqua, Aura, Calipso, Meteosat or Sentinel-2, among others, are moderate resolution imaging spectroradiometer (MODIS), multi-angle imaging spectro-radiometer (MISR), ozone monitoring instrument (OMI), spinning enhanced visible and infrared imager (SEVIRI), cloud-aerosol LIdar with orthogonal polarization (CALIOP), multi-spectral imager (MSI), etc. Most AOT and IWV data derived from observations with these instruments have already been validated with data obtained from the Aerosol Robotic Network (AERONET) sunphotometer measurements [4–12]. These last three studies have validated AOT and IWV data obtained from the implementation of the offline version of an atmospheric correction algorithm to data from MSI measurements on board the Sentinel-2 satellite, termed Sen2Cor [13]. However, there are more recent AOT and IWV data, such as those obtained from MSI measurements on board the Sentinel-2 satellite and processed by the European Space Agency (ESA) for Europe, concretely level 2A (ESA-L2A) data, and its validation has not yet been performed in a general way. Djamai et al. [14] validated ESA-L2A AOT and IWV but only used five data points belonging to three AERONET stations, one in Spain and two in France, during the period April - October 2017. Due to the reduced number of data points and the very short time period, this validation is very limited, both spatially and temporally. Therefore, the objective of this work is to validate ESA-L2A AOT and IWV over Europe and adjacent regions (western Asia and northern Africa), under cloud-free conditions, using as many reference data as possible. Satellite AOT products that present high spatial resolution are of great interest since they can be used to study local sources of aerosols in urban areas [15] and monitor local air pollution [16]. In these areas, aerosol distributions can present important spatial variations due to the means of transportation, construction infrastructure, industrial activity or variations in the density of the human population. The use of high spatial resolution satellite AOT data support the identification of local peak concentrations and allow defining concentration gradients between surface monitoring stations. In addition, Sentinel-2 satellite is of great interest to study surface features and processes taking advantage of its high spatial resolution. This requires an accurate atmospheric correction of the images, therefore the need for assessing and improving Sentinel-2 atmospheric products. The reference data used, as in other similar validation studies, are AOT and IWV data derived from AERONET sunphotometer measurements. Specifically, data from 94 AERONET stations Supplementary Materials during the period between March 2017 and December 2018 have been used for this study. This time period covers four seasons, which may be of some interest at particular regions.

This paper is organized as follows. The data used in this study are described in Section 2. In Section 3, the methodology is presented. The main results are shown and discussed in Section 4. An analysis of potential uncertainty sources is provided in Section 5 and conclusions are given in Section 6.

2. Data

2.1. SENTINEL-2

Sentinel-2 is an Earth observation mission from the Copernicus Programme, developed and operated by the ESA that acquires high spatial resolution images over land and coastal waters. The mission consists of a constellation of two twin satellites operating in the same sun-synchronous orbit (180° apart; descending node at 10:30 am), Sentinel-2A and Sentinel-2B, launched on 23 June 2015 and 7 March 2017, respectively. The swath width is 290 km, with a repeat cycle of five days under the same viewing conditions. In some regions the revisit time is lower under different viewing conditions, due to overlap between swaths from adjacent orbits. A MSI is installed on both satellites. The MSI measures the Earth's reflected radiance in 13 spectral bands (Table 1) from visible/near infrared (VNIR) to short wave infrared spectral range (SWIR), with four bands at 10 m, six bands at 20 m, and three bands at 60 m of spatial resolution. The bands at 60 m are used to perform atmospheric correction and cloud screening [17].

Table 1. Wavelengths, bandwidths and spatial resolutions of the 13 bands of the multi-spectral imager (MSI) instruments.

Band Number	S2A		S2B		Spatial Resolution (m)
	Central Wavelength (mm)	Bandwidth (mm)	Central Wavelength (mm)	Bandwidth (mm)	
1	442.7	27	442.2	45	60
2	492.4	98	492.1	98	10
3	559.8	45	559.0	46	10
4	664.6	38	664.9	39	10
5	704.1	19	703.8	20	20
6	740.5	18	739.1	18	20
7	782.8	28	779.7	28	20
8	832.8	145	832.9	133	10
8a	864.7	33	864.0	32	20
9	945.1	26	943.2	27	60
10	1373.5	75	1376.9	76	60
11	1613.7	143	1610.4	141	20
12	2202.4	242	2185.7	238	20

Sentinel-2 MSI Level-1C products are atmospherically corrected through the implementation of Sen2Cor method [18], obtaining Level-2A bottom of the atmosphere (BOA) reflectance products (L2A). The method was developed for application over land surfaces but it can be also applied over water surfaces. However, it should be noted that the processor does not consider water surface effects such as sunglint. L2A products include BOA reflectance images, maps of AOT at 550 nm, IWV and scene classification (SCL), among others. Sen2Cor estimates AOT at 550 nm on the basis of the dense dark vegetation (DDV) pixel method introduced by Kaufman and Sendra [19]. AOT is derived from a correlation of short wave infra-red (SWIR) reflectance (band 12, see Table 1) with the blue (band 2, see Table 1) and red (band 4, see Table 1) reflectances. If there are no DDV pixels in the image, the AOT cannot be estimated and Sen2Cor uses a fallback solution. This solution is to perform the atmospheric correction with a constant AOT, which is specified by the start (default) visibility of 40 km, corresponding to an AOT of approximately 0.2 at sea level. IWV is retrieved from a Level-1C image by means of a Sentinel-2 adapted atmospheric pre-corrected differential absorption (APDA) algorithm [20], which uses spectral bands 8A and 9 (see Table 1). Band 8a is the reference

channel in an atmospheric window region, whereas band 9 is the measurement channel in the water vapour absorption region. The total Sun-ground-sensor and path radiances are calculated for both bands, assuming that the surface reflectance is the same in both. The radiance ratio obtained between the measurement channel (water vapour absorption) and the reference channel (not influenced by water vapour) is then a measure of the water vapour column content (IWV). The scene classification is separated into the 11 classes presented in Table 2. The objective of this product is not to classify the land cover in a strict sense, but to distinguish between cloudy, clear and water pixels, to be used internally in Sen2Cor for atmospheric correction purposes. The accuracy requirement limits defined by ESA [21] for AOT and IWV equal 10% of the reference AOT value plus 0.03, and 10% of the reference IWV value plus 0.2, respectively.

Table 2. Sen2Cor Scene classification classes for Sentinel-2.

	Sen2Cor Class
0	No data
1	Saturated_or_defective
2	Dark_Area_PIXELS
3	Cloud_Shadows
4	Vegetation
5	Bare_soils
6	WATER
7	Cloud_LOW_PROBABILITY
8	Cloud_MEDIUM_PROBABILITY
9	Cloud_HIGH_PROBABILITY
10	Thin_CIRRUS
11	Snow

ESA provides L2A products based on an implementation of the Sen2Cor algorithm [13], but also provides an offline version of the Sen2Cor to produce L2A products [22]. In this study, the data used belong to the first option, and more specifically to the ESA-L2A products that are systematically generated at the ground segment over Europe and adjacent areas since March 2017. The Copernicus Open Access Hub provides complete, free and open access to Sentinel-2 data that are available to users in SENTINEL-SAFE format (https://scihub.copernicus.eu/dhus/#/home). The Sentinel-2 tiles (granules of 100 km × 100 km) were downloaded with cloud cover conditions lower than 90%. AOT and IWV products are provided with a spatial resolution of 20 m. Only pixels with SCL of dark area, vegetation or bare soils were considered.

2.2. AERONET

The aerosol robotic network (AERONET) products (https://aeronet.gsfc.nasa.gov/) were used here as ground-based reference values to validate Sentinel-2 ESA-L2A AOT at 550 nm and IWV. It is very common to use this reference data because: (a) The sunphotometer provides a near-direct measurement of the extinction, which is therefore much more reliable than the satellite measurements; (b) AERONET provides a globally distributed long-term and accessible public database of these products; (c) AERONET has a high level of standardization of instruments, calibration, processing and distribution [23]. Specifically, data from 94 AERONET stations distributed throughout Europe, western Asia and northern Africa have been used. Figure 1 displays the geographical location of the AERONET sites considered, located in various regions, coastal and inland, at different altitudes, latitudes and longitudes, representing a great variety of climate and environmental conditions.

This constitutes a valuable set of reference data to assess the accuracy of Sentinel-2 level 2A AOT and IWV atmospheric products.

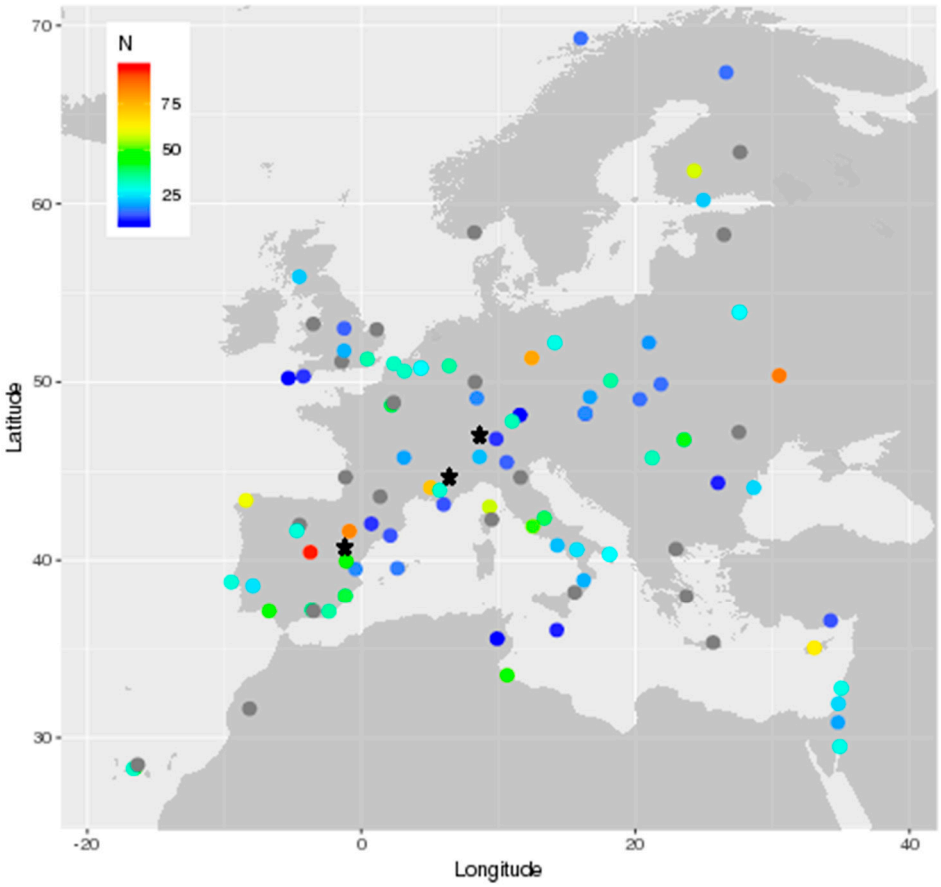

Figure 1. Geographical distribution of the 94 selected AERONET test sites and number of data N available at each site, for the ESA-L2A AOT at 550 nm and integrated water vapour (IWV) validation. The sites with less than 10 data points are represented by the grey dots. The location of the three stations used by Djamai et al. [14] are shown with a black star.

All ground-based stations are equipped with CIMEL CE-318 sunphotometers, the standard instrument of the AERONET network. This instrument performs direct sun measurements in 9 channels covering the spectral range between 340 and 1020 nm. In particular, the 940 nm channel is used to retrieve IWV, since water vapour has a strong absorption at this wavelength. The estimated uncertainty in AOT under cloud-free conditions is 0.01 for wavelengths higher than 440 nm and 0.02 for shorter wavelengths [23,24]. For IWV, the uncertainty is less than 12% [23]. A more detailed description about the CIMEL sunphotometer, as well as the protocol applied by AERONET to process all radiance measurements and provide AOT, IWV and inversion products have been documented by Holben et al. [23]. AERONET version 3 algorithm processing includes three different quality levels (1.0, 1.5 and 2.0). Levels 1.0 and 1.5 (cloud-screened and quality controlled) are provided in near real-time, whereas level 2.0 (quality-assured) may present a delay of more than 12-months due to final calibration and manual inspection, ensuring the highest data quality. In this study, AOT and IWV from version 3 level 2.0 have been used. This means that the data at this level are not available until the sunphotometers are subjected to calibration which is usually done once a year. Hence, the period of data used in this study is from March 2017 (beginning of the ESA-L2A database) until December 2018, when most stations used already had Level 2.0 data available when the study began.

The ESA-L2A AOT product is provided at the reference wavelength of 550 nm, however this is not a direct product of AERONET. Therefore, it is necessary to convert AERONET AOT at λ wavelength to AOT at 550 nm. The conversion has been performed using the Ångström power law (Equation (1)):

$$\mathrm{AOT}_{550} = \mathrm{AOT}_{\lambda}\left(\frac{550}{\lambda}\right)^{-\alpha} \quad (1)$$

where α is the Ångström exponent in the wavelength range of 440–870 nm and λ is the wavelength.

3. Methodology

The ESA-L2A retrieved AOT and IWV products were compared with independent space–time-collocated AERONET AOT and IWV quantities retrieved from the sunphotometer measurements. For this purpose, subsets of 9 km × 9 km, around the coordinates of each AERONET site were extracted from the MSI tiles, following the procedures of other validation studies (e.g., [12,14]). The procedure was limited at each site by the existence of AERONET level 2.0 data with a temporal difference of less than ±1 h from the satellite time overpass. The next step was to identify the valid pixels within the subsets for the validation process. Each of the subset pixels, with a spatial resolution of 20 m, is assigned a value of AOT, IWV and scene classification, among other products. In this study, only those pixels with scene classifications of a dark area (codified as 2), vegetation (codified as 4) or bare soils (codified as 5) were considered. Once these pixels were identified, their percentage was calculated, finally selecting those subsets with percentages greater than 50%. It is noted that pixels classified as water (scene classification 6), have not been taken into account in the calculation of this percentage. Subsequently, the AOT and IWV averages were computed for each subset with the pixels that met the defined criteria. The closest AOT and IWV AERONET data to the satellite overpass were selected for each station, considering a maximum difference of ±1 h from the satellite overpass, as mentioned before. AERONET data fulfilling this condition were then selected and linearly interpolated to estimate the value of these products at the exact time of the satellite overpass. The existence of AERONET AOT and IWV products, both in the previous and subsequent hour, is a necessary condition to perform such an interpolation.

After these collocation steps, the two initial databases (ESA-L2A and AERONET Level 2.0) are reduced to two composed of spatial and temporal coincident cases in a total of 2398 pairs of data. AOT and IWV of both databases have been compared in order to evaluate the accuracy of AOT and IWV ESA-L2A products. Common statistical indicators have been used in this study to obtain an appropriate comparative assessment of both datasets. The mean bias error (MBE), which is a measure of the overall error or systematic error, was calculated as follows:

$$\mathrm{MBE} = \frac{1}{\mathrm{N}}\sum(\mathrm{X} - \mathrm{X}_{\mathrm{ref}}) \quad (2)$$

where N is the size of the sample corresponding to the total number of data, X are ESA-L2A products data and Xref are the ground-based reference values, i.e., AERONET Level 2.0 data.

The root mean square error (RMSE) gives a measure of the error existing between ESA-L2A products data and AERONET Level 2.0 products data. Small values of the RMSE indicate that the regression fit is acceptable. This parameter is expressed as:

$$\mathrm{RMSE} = \sqrt{\frac{1}{\mathrm{N}}\sum(\mathrm{X} - \mathrm{X}_{\mathrm{ref}})^2} \quad (3)$$

Also, normalized values of the previous statistic indicators (NMBE and NRMSE) have been calculated to compare AOT and IWV.

$$\mathrm{NMBE} = \frac{\mathrm{MBE}}{\max(\mathrm{X}_{\mathrm{ref}}) - \min(\mathrm{X}_{\mathrm{ref}})} \times 100 \quad (4)$$

$$\mathrm{NRMSE} = \frac{\mathrm{RMSE}}{\max(X_{\mathrm{ref}}) - \min(X_{\mathrm{ref}})} \times 100 \quad (5)$$

Another statistical indicator is the determination coefficient (R2), which indicates the accuracy of the obtained regression fit from the comparison. This parameter, which shows how much the model is able to describe the data, should be close to 1.

4. Results

Figure 2 presents the scatter plots of the 2398 ESA-L2A retrievals of AOT (a) and IWV (b) versus the coincident reference AERONET Level 2.0 quantities retrieved from the ground-based measurements. This figure also shows the regression line, MBE, NMBE, RMSE, NRMSE and R2 values obtained for each quantity. The intercomparison of ESA-L2A and AERONET derived quantities showed a better agreement for IWV than for the AOT, with NRMSE of 5.33 and 9.04%, respectively. This conclusion was also reflected in the values of R^2, which are 0.99 and 0.65 for IWV and AOT, respectively. From this figure, it was extracted that the NMBE corresponding to AOT was 3.75%, while for IWV, it presented a negative value of −3.24%. These results indicated that ESA-L2A AOT data overestimated the reference values, while the opposite occurred with IWV. The value of MBE for AOT (0.05) was lower than the value of MBE reported in Djamai et al. [14] (0.07). However, the value of MBE for IWV (−0.14 cm), although with the same sign, presented a higher absolute value than that reported by Djamai et al. [14] (−0.02 cm). It should be taken into account that these authors only used five data points belonging to three AERONET stations from the south of Europe (see Figure 1) during the period April 2017–October 2017. This was a reduced dataset compared with the 94 AERONET sites covering a wide geographical region with a variety of climate and environmental conditions considered in the present study.

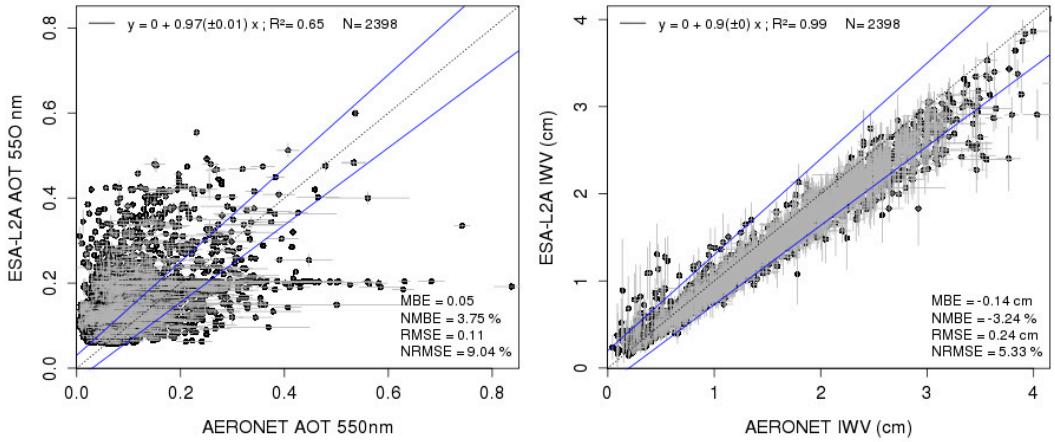

Figure 2. Scatter plots of aerosol optical thickness (AOT) (**a**) and IWV (**b**) from ESA-L2A retrievals versus coincident AERONET Level 2.0 data. The dashed grey line indicates the x = y line and the solid blue lines show the accuracy requirement limits (a) $|\Delta\mathrm{AOT}\ 550| \leq 0.1 \times \mathrm{AOT}\ 550\ \mathrm{ref} + 0.03$, and (b) $|\Delta\mathrm{IWV}| \leq 0.1 \times \mathrm{IWV\ ref} + 0.2$ [21].

Figure 2 also shows the accuracy requirement limits for AOT and IWV defined by ESA [21], represented with solid blue lines. As it can be observed, IWV meets the accuracy requirements better than AOT. Specifically, from the 2398 data points used in this study, 2167 IWV data points (90.4%) were within the limits defined by ESA, while, in the case of AOT, only 875 (36.5%) met the requirement. Another aspect to be highlighted in this figure was that the minimum value of ESA-L2A AOT was 0.06. This value is greater than the minimum value of AERONET AOT, which is close to zero. In fact, 26.9% of AERONET AOT data were lower than 0.06. With respect to IWV, it was also observed that the minimum value of ESA-L2A IWV, 0.15, was higher than the minimum value of AERONET IWV, which was 0.04. However, in this case only sixteen AERONET IWV data were lower than 0.15.

According to information from ESA (https://earth.esa.int/web/sentinel/missions/sentinel-2/news/; last accessed 21/05/2019), a new version of the Sentinel-2A spectral response functions is used from 15 January 2018 onwards, mainly correcting the responses for bands 1 and 2 due to inaccurate spectral responses provided previously and used in the above retrievals before 15 January 2018. Band 2, centered at 492 nm, is used to estimate AOT, thus one of the reasons for the poor agreement between ESA-L2A AOT estimates and AERONET AOT data could be the use of incorrect spectral response functions to estimate ESA-L2A AOT. This is investigated by dividing the data into two sub-periods, before and after the spectral response function update, and inter-comparing ESA-L2A AOT and AERONET AOT in the two sub-periods. The first sub-period includes the data obtained with the old spectral response functions, i.e., from the beginning of the study period (March 2017) until 14 January, 2018 and the second sub-period includes the data obtained with the new spectral response functions, from 15 January to December 2018.

Figure 3 presents the scatter plots of AOT from ESA-L2A retrievals versus coincident AERONET Level 2.0 data for the two sub-periods. As it can be seen in this figure, the inter-comparison of ESA-L2A AOT and AERONET showed a better agreement for the second sub-period than for the first one, with RMSE values of 0.14 and 0.08, respectively for the first and second sub-periods. Therefore, ESA-L2A AOT values estimated with the new spectral response functions are closer to the reference values than the ones obtained with the previous spectral response functions. This conclusion was also verified through the calculation of the MBE values, obtaining 0.01 for the period after 15 January, 2018 compared with the 0.09 value obtained for the period before 15 January, 2018. The values of RMSE and MBE for the two sub-periods have also been compared with the values obtained for the whole period, displayed in Table 3. This indicated that the two statistical indicators have been drastically reduced for the sub-period with the new spectral response functions, compared with the entire period, being even smaller than the ones reported by Djamai et al. [14] of 0.07 (MBE) and 0.09 (RMSE). It can be concluded that with the use of these new spectral response functions, the quality of the ESA-L2A AOT estimates has significantly improved. The results of this study are compared to those reported by Bilal et al. [25], regarding the evaluation of AOT retrievals from MODIS using AERONET, in the same region. Despite the different spatial resolutions considered in both studies, the results obtained were very similar in terms of RMSE and MBE values.

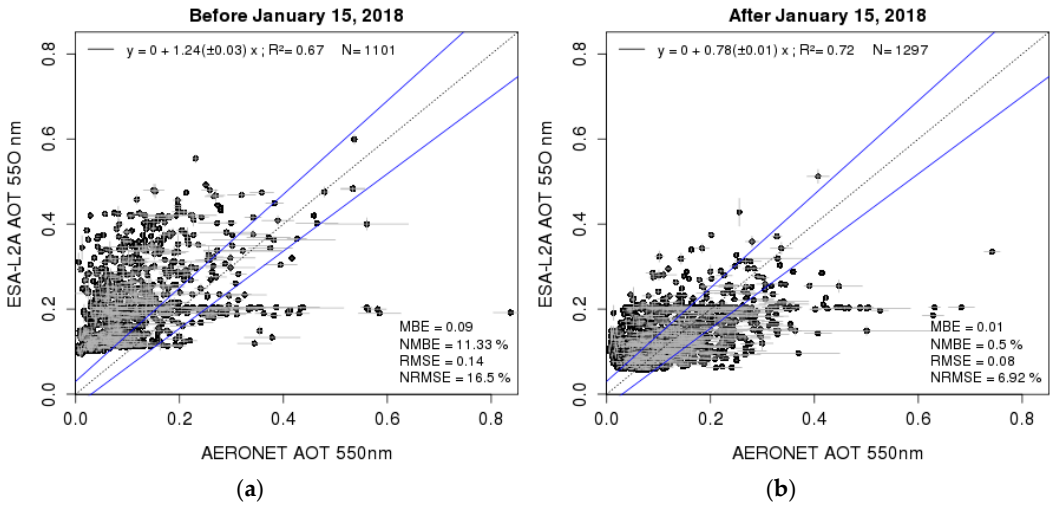

Figure 3. Scatter plots of AOT from ESA-L2A retrievals versus coincident AERONET Level 2.0 data for (**a**) before 15 January, 2018 and (**b**) after 15 January, 2018. The dashed grey line indicates the x = y line and the solid blue lines show the accuracy requirement limits (a) $|\Delta AOT\ 550| \leq 0.1 \times AOT\ 550\ ref + 0.03$, and (b) $|\Delta IWV| \leq 0.1 \times IWV\ ref + 0.2$ [21].

The differences between the two AOT datasets (ESA-L2A and AERONET) calculated for the entire study period (March 2017–December 2018), for the first (March 2017–January 2018) and the second

sub-periods (January 2018 onwards) are also discernible when a seasonal analysis is carried out as presented in Figure 4. This figure presents the box and whisker plots for each period of analysis (complete, first and second sub-periods) of ESA-L2A AOT and AERONET AOT databases for the entire time period and for each season (spring- M,A,M-, summer-J,J,A-, autumn- S,O,N- and winter- D, J, F). When the entire study period was considered (Figure 4a), no seasonality was observed, and the statistical values for each season were very similar. It was also observed that ESA-L2A AOT values were higher than AERONET AOT values in all seasons. However, when the sub-periods were analysed separately, the behaviors were moderately different. For example, in Figure 4b, corresponding to the sub-period before 15 January, 2018, seasonality was observed in the AOT values of the two databases, obtaining the highest values in summer, and the lowest in winter. The small overlap between the two databases in winter was due to the minimum value of ESA-L2A AOT, which was 0.06, while the minimum value of AERONET was lower. However, the differences between the values of ESA-L2A and AERONET estimates were greater in this sub-period (for each season and the entire time) than when the entire study period was considered (Figure 4a). It should be noticed that in Figure 4b the boxes characterizing the inter-quartile ranges only overlap in autumn, whereas in Figure 4a, they overlap in all seasons and for the whole time period. On the other hand, if the second sub-period is used (Figure 4c) a greater overlap of both databases is obtained, which means that ESA-L2A AOT and AERONET AOT values show a better agreement when using the new spectral response functions in the ESA AOT retrievals. Moreover, the AOT values also showed seasonality, with the highest values in summer and the lowest in winter. The high AOT values in summer are due to a combination of factors that occur in this period of the year. One of them is the lack of precipitation, favoring the presence of aerosols in the atmosphere. Another factor is the arrival of desert-dust aerosols from the Saharan region and the summer forest fires, which are important sources of aerosols in the stations of the Mediterranean region [26,27] (South Europe and North Africa/Middle East). In this study, stations of the Mediterranean region predominate with respect to those of northern Europe, hence, these aerosol sources have a great influence on summer AOT values. This seasonal variation of AOT was also observed by other authors [28–30].

Table 3. Mean bias error (MBE) and root mean square error (RMSE) AOT values for the whole period, the period before 15 January, 2018 and the period after 15 January, 2018.

	Whole Period (March 2017–December 2018)	Before 15 January 2018	After 15 January 2018
MBE AOT	0.05	0.09	0.01
RMSE AOT	0.11	0.14	0.08

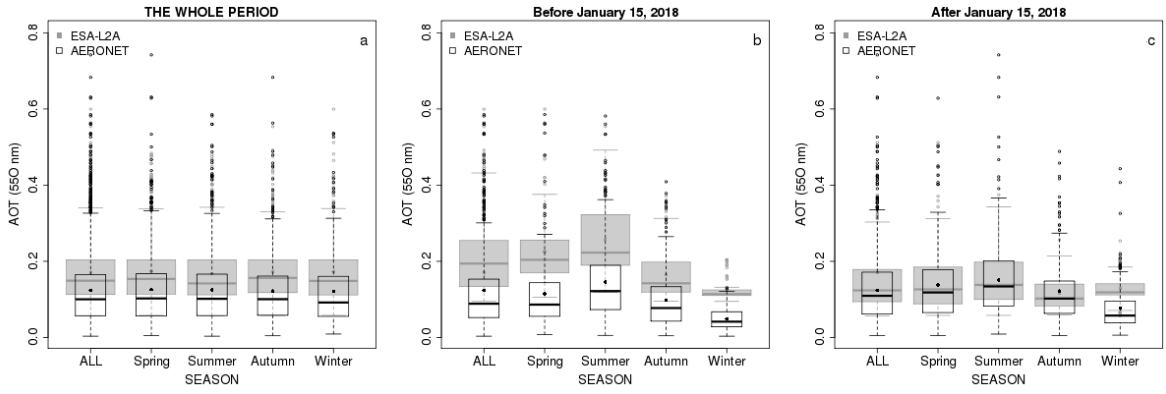

Figure 4. Box and whisker plots of AOT ESA-L2A and AERONET databases for the entire time period and for each season of that time period, considering the entire study period (**a**), the first sub-period (**b**) and the second sub-period (**c**). The mean (filled circles), median (horizontal segment within the box), 25 th and 75 th percentiles (top/bottom box limits) and the data within 1.5 times the interquartile range (whiskers) are shown.

5. Analysis of Potential Uncertainty Sources

Since the correlation between ESA-L2A AOT estimates and AERONET AOT data is not very good, it improves when the correct spectral response functions are applied. Hence, a sensitivity analysis to key factors, as the scene classification class, the region and the aerosol type, has also been performed.

As mentioned, in this study only pixels with scene classifications classes 2 (Dark_Area_PIXELS), 4 (Vegetation) and 5 (Bare_soils) were considered. In order to estimate the sensitivity of the intercomparison to scene classification, the study was performed individually for each scene classifications class. The results obtained are shown in Table 4, both for the whole period and for the sub-period after 15 January, 2018. From this table, the best agreement between the two AOT datasets was obtained for the scene class 4 (Vegetation), with RMSE of 0.08 and 0.10, respectively. This conclusion was also reflected in the values of R^2, which were 0.74 and 0.81 for the whole period and for the sub-period after 15 January, respectively.

Table 4. MBE, RMSE and R^2 AOT values for each scene classification class, both for the whole period and for the sub-period after January 15 2018.

	WHOLE PERIOD			After January 15 2018		
	Scene 2	**Scene 4**	**Scene 5**	**Scene 2**	**Scene 4**	**Scene 5**
N	27	687	720	19	401	328
MBE	0.04	0.03	0.07	0.01	−0.01	0.02
RMSE	0.13	0.08	0.14	0.12	0.10	0.12
R^2	0.61	0.74	0.56	0.70	0.81	0.62

Regional variation is also an important factor to take into account in the assessment of Sentinel-2 AOT values, since each region presents different environmental conditions and is typically influenced by different aerosol types. For this reason, the stations have been grouped into three regions (North Europe, South Europe, and North Africa/Middle East) in order to investigate the effect of regional variations on the ESA-L2A AOT product accuracy. The results obtained are presented in Table 5 and show that there are regional differences, with the best agreement obtained for the North Europe region and the worst agreement in North Africa/Middle East region, both for the whole period and for the sub-period after 15 January, 2018. The reason for the poor correlation between the two AOT datasets in the North Africa and Middle East regions is due to the assignment of AOT values of 0.2 (corresponding to the initial visibility assumed by the algorithm), as illustrated in Figure 5, which occurs when the scene does not contain reference pixels for the calculation. The sensitivity of the comparison to different aerosol types was analysed using the classification proposed by Elias et al. [31], who presented a criterion to classify the aerosol turbidity situations based on both the values of AOT and the Ångström exponent. The aerosol types proposed are clean (CL), continental (CO), maritime (MA), forest fires emissions (FF) and desert dust (DD). Table 6 shows the values of MBE, RMSE and R2 for each aerosol type, both for the whole period and for the sub-period after 15 January, 2018. From this table, CO type presented the best agreement between ESA-L2A AOT estimates and AERONET AOT data, with the lowest MBE and RMSE values. However, DD type presented the worst correlation due to the existence of a large number of cases with ESA-L2A AOT value equal to 0.2, showing the relationship between this aerosol type and the North Africa region. The most negative value of MBE corresponded to FF aerosol type. This means that there is an underestimation of ESA-L2A AOT in relation to AERONET AOT during these episodes, characterized by very high AOT values. Followed by these values of MBE were those corresponding to CL and MA types, although with positive values which indicated an overestimation of ESA-L2A AOT. This was because the minimum value of ESA-L2A AOT was 0.06, which was much higher than most of the lowest values of AERONET AOT, characterizing CL and MA aerosol types. Also the highest values of AOT were not well represented by ESA-L2A AOT product, as illustrated in Figure 5.

Table 5. MBE, RMSE and R^2 AOT values for different regions (North Europe, South Europe, and North Africa/Middle East) corresponding to the whole period and to the period after 15 January, 2018.

	WHOLE PERIOD			After January 15 2018		
	North Europe	**South Europe**	**North Africa**	**North Europe**	**South Europe**	**North Africa**
N	823	1251	324	532	614	151
MBE	0.01	0.07	0.05	−0.02	0.02	0.03
RMSE	0.07	0.12	0.15	0.07	0.08	0.16
R^2	0.78	0.67	0.54	0.846	0.75	0.53

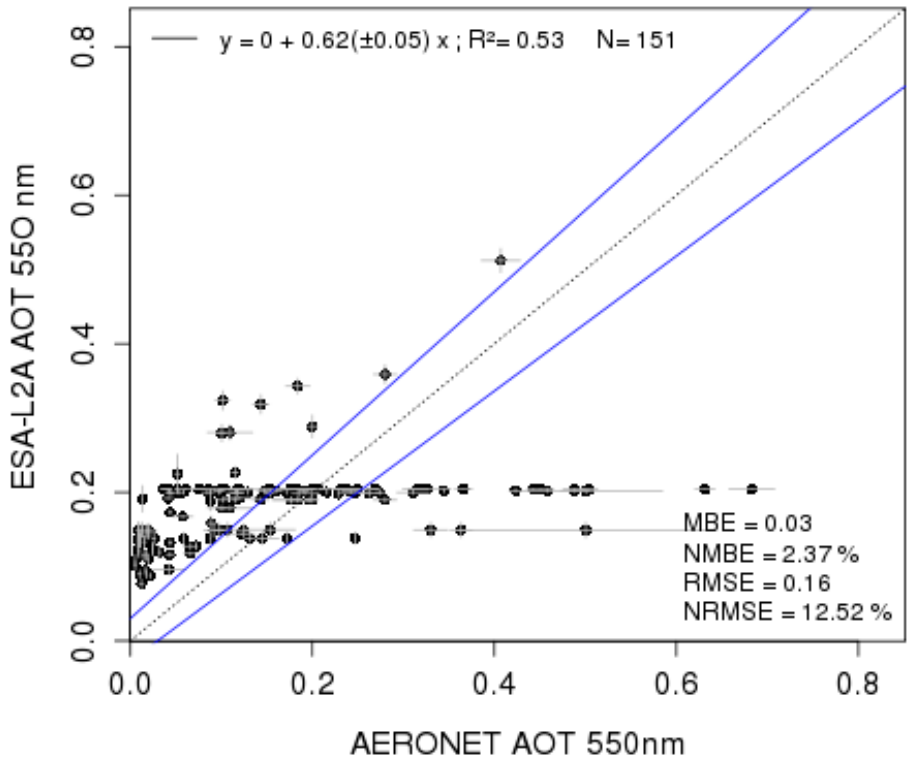

Figure 5. Scatter plot of AOT from ESA-L2A retrievals versus coincident AERONET Level 2.0 data for the sub-period after 15 January, 2018 in North Africa/Middle East region. The dashed grey line indicates the x = y line and the solid blue lines show the accuracy requirement limits (a) $|\Delta AOT\ 550| \leq 0.1 \times AOT\ 550\ ref + 0.03$, and (b) $|\Delta IWV| \leq 0.1 \times IWV\ ref + 0.2$ [21].

Table 6. MBE, RMSE and R^2 AOT values for different aerosol types (clean (CL), continental (CO), maritime (MA), forest fires emissions (FF) and desert dust (DD)) corresponding to the whole period and to the period after 15 January, 2018.

	WHOLE PERIOD					After 15 January 2018				
	CL	**CO**	**MA**	**FF**	**DD**	**CL**	**CO**	**MA**	**FF**	**DD**
N	223	598	305	65	392	89	370	164	36	212
MBE	0.11	0.01	0.09	−0.10	0	0.09	−0.03	0.07	−0.13	−0.05
RMSE	0.13	0.09	0.11	0.13	0.14	0.10	0.07	0.09	0.15	0.13
R^2	0.75	0.81	0.72	0.92	0.67	0.78	0.87	0.75	0.94	0.76

The previous sensitivity analyses allows the conclusion that ESA-L2A AOT estimates equal to 0.2 and AERONET AOT values lower than 0.06 and higher than 0.4 worsen the correlations between ESA-L2A AOT estimates and AERONET AOT data. Therefore, in the following analysis, AERONET

AOT values lower than 0.06, higher than 0.4 and data corresponding to stations that present more than 20% of the ESA-L2A AOT values equal to 0.2 have not been considered. This analysis has been performed only for the sub-period after 15 January, 2018. The results obtained are presented in Figure 6 and constitute the recommended dataset to use for quantitative purposes. This figure shows that the correlation between ESA-L2A AOT estimates and AERONET AOT data is better (R^2 equal to 0.84) than that obtained without the exclusions described and shown in Figure 3 (R^2 equal to 0.72). The value of RMSE also decreased, from 0.08 to 0.07. This new AOT dataset meets the ESA accuracy requirements better than the complete AOT dataset presented in Figure 3 (without the exclusions described). Specifically, from the 838 data points used, 526 AOT data points (62.8%) were within the error limits defined by ESA, whereas previously only 36.5% of the AOT data met this requirement.

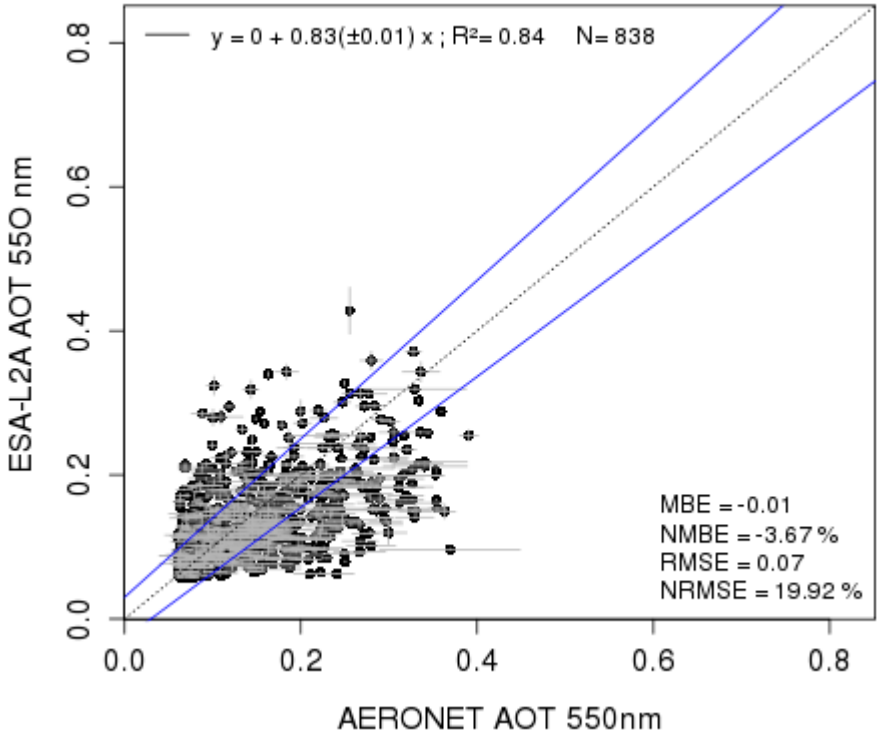

Figure 6. Scatter plot of AOT from ESA-L2A retrievals versus coincident AERONET Level 2.0 data for the sub-period after 15 January, 2018 excluding data corresponding to AERONET AOT lower than 0.06 and to stations with a percentage of cases of AOT = 0.2 higher than 20%. The dashed grey line indicates the x = y line and the solid blue lines show the accuracy requirement limits (a) $|\Delta AOT\ 550| \leq 0.1 \times AOT\ 550\ ref + 0.03$, and (b) $|\Delta IWV| \leq 0.1 \times IWV\ ref + 0.2$ [21].

Therefore, it can be concluded that ESA-L2A AOT product should be used with caution in two cases: (a) Regions where the appropriate AOT value is often not estimated (due to the lack of DDV regions) and the value of 0.2 is assigned, and (b) regions with extreme visibility values (high or low), that is, sites that normally have very low or high AOT values. It would be advisable to use more than one default value (start visibility), according to the geographic area and season. These reference values could be obtained from a climatological analysis of ground-based or satellite reference data (AERONET for example). This would be important because in the cases with no DDV pixels available to obtain ESA-L2A AOT estimates, the AOT corresponding to the start visibility is used, which causes important errors as demonstrated here.

6. Conclusions

This study contributes to the validation of AOT and IWV products provided by ESA from MSI measurements on board the Sentinel-2 satellite, respectively AOT ESA-L2A and IWV ESA-L2A. These

products have been validated by comparison with data from 94 AERONET stations over Europe and adjacent regions and during the period between March 2017 and December 2018. The results indicated that ESA-L2A AOT data overestimated the reference values with NMBE of 3.75%, while the opposite occurred with IWV presenting a NMBE of −3.24%. The results showed a good agreement for IWV with NRMSE of 5.33% and R^2 above 0.99. However, a larger disagreement was obtained for AOT, with NRMSE of 9.04% and R^2 equal to 0.65. One possible cause for this lack of agreement in the AOT values could be due to the use of inaccurate spectral response functions, which impacted the retrieval of AOT ESA-L2A product from MSI measurements (the most affected were bands 1 and 2 and AOT retrieval uses band 2, among others). A new version of the Sentinel-2A spectral response functions is used from 15 January, 2018 onwards. Therefore, the study period was divided into two sub-periods, before and after 15 January, 2018. The inter-comparison of ESA-L2A AOT with AERONET AOT showed a better agreement for the second sub-period than for the first one, with RMSE (and MBE) values of 0.08 (0.01) for the second sub-period and 0.14 (0.09), for the first one. These values of RMSE and MBE were also smaller than the ones reported by Djamai et al. [14], of 0.09 and 0.07, respectively. The seasonal differences between AOT ESA-L2A and AOT AERONET data for the entire study period, the first sub-period and the second sub-period have also been analysed. The results showed no seasonality for the entire period. However, when the sub-periods were analysed separately, seasonality was observed, obtaining the highest AOT values in summer and the lowest in winter. For the first sub-period, the differences between the ESA-L2A and AERONET AOT estimates were greater in this sub-period than for the entire study period for all seasons. On the other hand, if the second sub-period is considered, a greater overlap of both databases is obtained for all seasons. Therefore, it can be concluded that with the use of these new spectral response functions the quality of the ESA-L2A AOT estimates has significantly improved. An analysis of potential uncertainty sources showed that the algorithm accuracy highly depended on the AOT first guess and that this was a critical issue over bright surfaces. It is recommended to update the algorithm in order to consider different initial visibility values, based for example, on reference climatologies.

Supplementary Materials: The following are available online at http://www.mdpi.com/2072-4292/11/14/1649/s1, Table S1: List of the 94 AERONET stations used in the validation. Columns indicate the designation, longitude, latitude, altitude and number of data.

Author Contributions: Conceptualization, M.Á.O., G.R., M.J.C., M.P. and A.M.S.; Methodology, M.Á.O., G.R. and M.J.C.; Software, M.Á.O., G.R.; Validation, M.Á.O., G.R., M.J.C., M.P. and A.M.S.; Formal Analysis, M.Á.O., G.R., M.J.C., and A.M.S.; Investigation, M.Á.O., G.R., M.J.C., M.P. and A.M.S.; Resources, M.Á.O., G.R., and M.J.C.Data Curation, M.Á.O., G.R., and M.J.C.; Writing—original draft preparation, M.Á.O.; Writing—Review and Editing, M.Á.O., G.R., M.J.C., M.P. and A.M.S.; Visualization, M.Á.O.; Supervision, M.J.C. and A.M.S.; Project Administration, M.J.C., and A.M.S.; Funding Acquisition, M.J.C., M.P. and A.M.S.

Funding: This work was partially supported by FCT (Fundação para a Ciência e a Tecnologia) through the grants SFRH/BPD/86498/2012 and SFRH/BSAB/143164/2019 with national funding. The work is co-funded by the European Union through the European Regional Development Fund, included in the COMPETE 2020 (Operational Program Competitiveness and Internationalization) through the ICT project (UID/GEO/04683/2013) with the reference POCI-01-0145- FEDER-007690 and also through ALOP (ALT20-03-0145-FEDER- 000004), DNI-A (ALT20-03-0145-FEDER-000011), TOMAQAPA (PTDC/CTAMET/29678/2017) projects, and in the framework of the Interreg V A Spain - Portugal program (POCTEP) through the CILIFO project (Ref: 0753_CILIFO_5_E).

Acknowledgments: The authors thank Copernicus and ESA for the data Sentinel-2 provided to carry out this work and to Olivier Hagolle for providing open source codes to massive Sentinel-2 data download. Thanks are due to AERONET/PHOTONS for the scientific and technical support. We thank the (PI(s) and Co-I(s)) and their staff for establishing and maintaining the 94 sites used in this investigation. CIMEL calibration was performed at the AERONET-EUROPE GOA calibration center, supported by ACTRIS under agreement no. 654109 granted by European Union (H2020-INFRAIA-2014-2015).

Conflicts of Interest: The authors declare no conflicts of interest.

References

1. Obregón, M.A.; Costa, M.J.; Silva, A.M.; Serrano, A. Impact of aerosol and water vapour on SW radiation at the surface: Sensitivity study and applications. *Atmos. Res.* **2018**, *213*, 252–263. [CrossRef]

2. Alexandri, G.; Georgoulias, A.K.; Zanis, P.; Katragkou, E.; Tsikerdekis, A.; Kourtidis, K.; Meleti, C. On the ability of RegCM4 regional climate model to simulate surface solar radiation patterns over Europe: An assessment using satellite-based observations. *Atmos. Chem. Phys.* **2015**, *15*, 13195–13216. [CrossRef]
3. Forster, P.; Ramaswamy, V.; Artaxo, P.; Berntsen, T.; Betts, R.; Fahey, D.W.; Haywood, J.; Lean, J.; Lowe, D.C.; Myhre, G.; et al. Changes in atmospheric constituents and in radiative forcing. In *Climate Change 2007: The Physical Science Basis. Contribution of Working Group I to the Fourth Assessment Report of the Intergovernmental Panel on Climate Change*; Solomon, S., Qin, D., Manning, M., Chen, Z., Marquis, M., Averyt, K.B., Tignor, M., Miller, H.L., Eds.; Cambridge University Press: Cambridge, UK; New York, NY, USA, 2007.
4. Gascon, F.; Bouzinac, C.; Thépaut, O.; Jung, M.; Francesconi, B.; Louis, J.; Lonjou, V.; Lafrance, B.; Massera, S.; Gaudel-Vacaresse, A.; et al. Copernicus sentinel-2 calibration and products validation status. *Remote Sens.* **2017**, *9*, 584. [CrossRef]
5. Chu, D.A.; Kaufman, Y.J.; Ichoku, C.; Remer, L.A.; Tanre, D.; Holben, B.N. Validation of MODIS aerosol optical depth retrieval over land. *Geophys. Res. Lett.* **2002**, *29*, 1617. [CrossRef]
6. Kahn, R.A.; Gaitley, B.J.; Martonchik, J.V.; Diner, D.J.; Crean, K.A.; Holben, B. Multiangle Imaging Spectroradiometer (MISR) global aerosol optical depth validation based on 2 years of coincident Aerosol Robotic Network (AERONET) observations. *J. Geophys. Res.* **2005**, *110*, D10S04. [CrossRef]
7. Levy, R.C.; Mattoo, S.; Munchak, L.A.; Remer, L.A.; Sayer, A.M.; Patadia, F.; Hsu, N.C. The Collection 6 MODIS aerosol products over land and ocean. *Atmos. Meas. Tech.* **2013**, *6*, 2989–3034. [CrossRef]
8. Prasad, A.K.; Singh, R.P. Validation of MODIS Terra, AIRS, NCEP/DOE AMIP-II Reanalysis-2, and AERONET Sun photometer derived integrated precipitable water vapor using ground-based GPS receivers over India. *J. Geophys. Res.* **2009**, *114*, D05107. [CrossRef]
9. Bibi, H.; Alam, K.; Chishtie, F.; Bibi, S.; Shahid, I.; Blaschke, T. Intercomparison of MODIS, MISR, OMI, and CALIPSO aerosol optical depth retrievals for four locations on the Indo-Gangetic plains and validation against AERONET data. *Atmos. Environ.* **2015**, *111*, 113–126. [CrossRef]
10. Sayer, A.M.; Munchak, L.A.; Hsu, N.C.; Levy, R.C.; Bettenhausen, C.; Jeong, M.J. MODIS Collection 6 aerosol products: Comparison between Aqua's e-Deep Blue, Dark Target, and merged data sets, and usage recommendations. *J. Geophys. Res. Atmos.* **2014**, *119*, 13–965. [CrossRef]
11. Pflug, B.; Main-Knorn, M.; Bieniarz, J.; Debaecker, V.; Louis, J. Early Validation of Sentinel-2 L2A Processor and Products. In Proceedings of the Living Planet Symposium 2016, Prague, Czech Republic, 9–13 May 2016. ESA SP-740.
12. Doxani, G.; Vermote, E.; Roger, J.C.; Gascon, F.; Adriaensen, S.; Frantz, D.; Hagolle, O.; Hollstein, A.; Kirches, G.; Li, F.; et al. Atmospheric Correction Inter-Comparison Exercise. *Remote Sens.* **2018**, *10*, 352. [CrossRef]
13. Mueller-Wilm, U.; Devignot, O.; Pessiot, L. Sen2Cor Configuration and User Manual. S2-PDGS-MPC-L2A-SUM-V2.4. 2017. Available online: http://step.esa.int/thirdparties/sen2cor/2.4.0/Sen2Cor_240_Documenation_PDF/S2-PDGS-MPC-L2A-SUM-V2.4.0.pdf (accessed on 1 December 2017).
14. Djamai, N.; Fernandes, R. Comparison of SNAP-Derived Sentinel-2A L2A Product to ESA Product over Europe. *Remote Sens.* **2018**, *10*, 926. [CrossRef]
15. Thomas, C.; Briottet, X.; Santer, R. Remote sensing of aerosols in urban areas from very high spatial resolution images: Application of the OSIS code to multispectral PELICAN airborne data. *Int. J. Remote Sens.* **2013**, *34*, 919–937. [CrossRef]
16. Engel-Cox, J.A.; Hoff, R.M.; Haymet, A.D.J. Recommendations on the Use of Satellite Remote-Sensing Data for Urban Air Quality. *J. Air Waste Manag. Assoc.* **2004**, *54*, 1360–1371. [CrossRef] [PubMed]
17. Drusch, M.; Del Bello, U.; Carlier, S.; Colin, O.; Fernandez, V.; Gascon, F.; Hoersch, B.; Isola, C.; Laberinti, P.; Martimort, P.; et al. Sentinel-2: ESA's Optical High-Resolution Mission for GMES Operational Services. *Remote Sens. Environ.* **2012**, *20*, 25–36. [CrossRef]
18. Richter, R.; Louis, J.; Müller-Wilm, U. *Sentinel-2 MSI—Level 2A Products Algorithm Theoretical Basis Document*; S2PAD-ATBD-0001, Issue 2.0; Telespazio VEGA Deutschland GmbH: Darmstadt, Germany, 2012.
19. Kaufman, Y.J.; Sendra, C. Algorithm for automatic atmospheric corrections to visible and near-IR satellite imagery. *Int. J. Remote Sens.* **1988**, *9*, 1357–1381. [CrossRef]
20. Schläpfer, D.; Borel, C.C.; Keller, J.; Itten, K.I. Atmospheric precorrected differential absorption technique to retrieve columnar water vapour. *Remote Sens. Environ.* **1998**, *65*, 353–366. [CrossRef]

21. Clerc, S.; MPC Team. *Level 2A Data Quality Report (Ref. S2-PDGS-MPC-L2ADQR)*; European Space Agency: Paris, France, 2018.
22. Louis, J.; Debaecker, V.; Pflug, B.; Main-Knorn, M.; Bieniarz, J.; Mueller-Wilm, U.; Cadau, E.; Gascon, F. Sentinel-2 Sen2Cor: L2A processor for users. In Proceedings of the Living Planet Symposium 2016, Prague, Czech Republic, 9–13 May 2016. ESA SP-740.
23. Holben, B.; Eck, T.F.; Slutsker, I.; Tanre, D.; Buis, J.; Setzer, K.; Vermote, E.; Reagan, J.; Kaufman, Y.; Nakajima, T.; et al. AERONET—A federated instrument network and data archive for aerosol characterization. *Remote Sens. Environ.* **1998**, *66*, 1–16. [CrossRef]
24. Smirnov, A.; Holben, B.N.; Eck, T.F.; Dubovik, O.; Slutsker, I. Cloud screening and quality control algorithms for the AERONET data base. *Remote Sens. Environ.* **2000**, *73*, 337–349. [CrossRef]
25. Bilal, M.; Qiu, Z.; Shen, X.; Nazeer, M. A New MODIS C6 Dark Target and Deep Blue Merged Aerosol Product on a 3 km Spatial Grid. *Remote Sens.* **2018**, *10*, 463. [CrossRef]
26. Pace, G.; Meloni, D.; di Sarra, A. Forest fire aerosol over the Mediterranean basin during summer 2003. *J. Geophys. Res.* **2005**, *110*, D21202. [CrossRef]
27. Obregón, M.A.; Costa, M.J.; Silva, A.M.; Serrano, A. Thirteen years of aerosol radiative forcing in Southwestern Iberian Peninsula. *Aerosol Air Qual. Res.* **2017**, *17*, 2509–2521. [CrossRef]
28. Barnaba, F.; Gobbi, G.P. Aerosol seasonal variability over the Mediterranean region and relative impact of maritime, continental and Saharan dust particles over the basin from MODIS data in the year 2001. *Atmos. Chem. Phys.* **2004**, *4*, 2367–2391. [CrossRef]
29. Kaskaoutis, D.G.; Kosmopoulos, P.; Kambezidis, H.D.; Nastos, P.T. Aerosol climatology and discrimination of different types over Athens, Greece, based on MODIS data. *Atmos. Environ.* **2007**, *41*, 7315–7329. [CrossRef]
30. Obregón, M.A.; Pereira, S.; Wagner, F.; Serrano, A.; Cancillo, M.L.; Silva, A.M. Regional differences of column aerosol parameters in western Iberian Peninsula. *Atmos. Environ.* **2012**, *12*, 1–10. [CrossRef]
31. Elias, T.; Silva, A.M.; Belo, N.; Pereira, S.; Formenti, P.; Helas, G.; Wagner, F. Aerosol extinction in a remote continental region of the Iberian Peninsula during summer. *J. Geophys. Res.* **2006**, *111*, 1–20. [CrossRef]

© 2019 by the authors. Licensee MDPI, Basel, Switzerland. This article is an open access article distributed under the terms and conditions of the Creative Commons Attribution (CC BY) license (http://creativecommons.org/licenses/by/4.0/).

Phycologia

Phycologia

ISSN: 0031-8884 (Print) 2330-2968 (Online) Journal homepage: https://www.tandfonline.com/loi/uphy20

Morphology and ecology of *Fragilaria misarelensis sp. nov.* (Bacillariophyta), a new diatom species from southwest of Europe

Maria Helena Novais, Salomé F.P. Almeida, Saúl Blanco & Cristina Delgado

To cite this article: Maria Helena Novais, Salomé F.P. Almeida, Saúl Blanco & Cristina Delgado (2019) Morphology and ecology of *Fragilaria misarelensis sp. nov.* (Bacillariophyta), a new diatom species from southwest of Europe, Phycologia, 58:2, 128-144, DOI: 10.1080/00318884.2018.1524245

To link to this article: https://doi.org/10.1080/00318884.2018.1524245

View supplementary material

Published online: 29 Jan 2019.

Submit your article to this journal

Article views: 320

View related articles

View Crossmark data

Citing articles: 4 View citing articles

Full Terms & Conditions of access and use can be found at
https://www.tandfonline.com/action/journalInformation?journalCode=uphy20

PHYCOLOGIA
2019, VOL. 58, NO. 2, 128–144
https://doi.org/10.1080/00318884.2018.1524245

International Phycological Society
Taylor & Francis
Taylor & Francis Group
Check for updates

Morphology and ecology of *Fragilaria misarelensis sp. nov.* (Bacillariophyta), a new diatom species from southwest of Europe

Maria Helena Novais [1], Salomé F.P. Almeida [2], Saúl Blanco [3], and Cristina Delgado [2,4]

[1]*Water Laboratory, University of Évora, P.I.T.E. Rua da Barba Rala No. 1, 7005-345 Évora, Portugal Institute of Earth Sciences - ICT, University of Évora, Rua Romão Ramalho n° 59, 7000-671 Évora, Portugal*
[2]*Departamento de Biodiversidad y Gestión Ambiental, Facultad de Ciencias Biológicas y Ambientales, Universidad de León, Campus de Vegazana s/n, 24071 León, España*
[3]*The Institute of the Environment, La Serna, 58, Leon 24007, Spain*
[4]*Department of Ecology and Animal Biology, University of Vigo, Campus As Lagoas Marcosende, Vigo 36330, Spain*

ABSTRACT

A new freshwater diatom species was described from southwest Europe (Portugal), based on morphological and ultrastructural characteristics. *Fragilaria misarelensis* Almeida, C.Delgado, Novais & S.Blanco is characterised by lanceolate valves, with slightly capitate ends, alternate striae and lacking spines joining adjacent cells, which are solitary. The valve shape of *Fragilaria misarelensis*, when compared to similar forms, is unique, as revealed by a thorough literature survey of *Fragilaria* species, geometric morphometry and discriminant analysis. *Fragilaria misarelensis sp. nov*. was frequent and abundant in central Portugal, in poorly mineralized watercourses under low anthropogenic influence, characterised by neutral pH, low conductivity and high dissolved oxygen concentration. The analysis of type material belonging to similar species, *Fragilaria capucina* fo. *sublanceolata-baikali*, *F. capucina* fo. *lanceolata-baikali* and *F. nevadensis*, contributed to improving their characterisation and illustration, also supporting the delimitation of the new Portuguese species. *Fragilaria capucina* fo. *sublanceolata-baikali* and *F. capucina* fo. *lanceolata-baikali* were considered to differ substantially from *F. capucina* and raised to species level as *Fragilaria sublanceolata-baikali* (Flower & D.M.Williams) Novais, C. Delgado & S.Blanco, *comb. et stat. nov*. and *Fragilaria lanceolata-baikali* (Flower & D.M.Williams) Novais, C. Delgado & S.Blanco, *comb. et stat. nov.*

ARTICLE HISTORY
Received 8 May 2018
Accepted 12 September 2018
Published online 29 January 2019

KEYWORDS
Diatoms; Freshwater; Geometric morphometry; Taxonomy; Type material

INTRODUCTION

The genus *Fragilaria* Lyngbye has been a primary target of diatom studies during the last decades (e.g. Tuji 2004; Tuji & Williams 2006a, 2006b, 2008, 2013; Williams & Round 1987). The *Fragilaria capucina/vaucheriae* species complex *sensu* Lange-Bertalot in Krammer & Lange-Bertalot (1991) is one of the most frequent and abundant, and widely illustrated in the literature. It includes several recently described new species (e.g. Delgado *et al.* 2015, 2016; Linares-Cuesta & Sánchez-Castillo 2007; Van de Vijver *et al.* 2012; Wetzel & Ector 2015). However, the diagnostic features allowing the discrimination of *Fragilaria* Lyngbye are difficult to solve. Ribbon-like colony formation due to interlocking spines, present on the surface, was usually attributed to *Fragilaria* Lyngbye; whereas, *Synedra* Ehrenberg was attached to the surface of rocks or plants by means of mucilage pads or aggregated into radiate colonies not forming long, linear filamentous structures (Patrick & Reimer 1966; Poulin *et al.* 1986; Round *et al.* 1990; Williams 1986). With the development and progress of microscopy techniques, researchers gradually updated previous morphological observations and definitions, expanding our knowledge by detailed microstructural observations. Though colony formation in itself was not considered by Williams & Round (1987) sufficient to justify the separation between *Fragilaria* and *Synedra* (this feature is difficult to observe on treated material and on isolated valves), their investigations reveal differences in other characters to support their subdivision. In their revision of the genus, species of *Fragilaria* Lyngbye form linear colonies, with frustules attached by adjacent interdigitating spines, but the genus definition was restricted to those species with simple striae, a few open girdle bands and a simple type of ocellulimbus at each pole. Later, the scanning electron microscopy (SEM) features that characterise the genus were compiled by Morales (2001), which consist of mostly uniseriate striae, composed of round or slightly elongated areolae, discoid closing plates, a well-developed central sternum, apical pore fields of a weakly developed ocellulimbus type, and the presence of rimoportulae and spines (of variable shape and located on or between the striae). *Synedra* Ehrenberg was characterised by Williams (1986) by having closed bands in the cingulum, a basal siliceous layer, modification of the ocellulimbus, with a denser inset plate of 12–14 porelli per row and 20–25 rows per plate, biseriate striae, and ornamentation of the pars exterior on all band components. The recent view of Williams (2011) simplifies the *Fragilaria/Synedra* issue, based on open girdle

CONTACT Maria Helena Novais hnovais@uevora.pt
Colour versions of one or more of the figures in the article can be found online at www.tandfonline.com/uphy.
Supplemental data for this article can be accessed on the publisher's website.
© 2019 International Phycological Society

bands in *Fragilaria* and closed girdle bands in *Ulnaria*, one of the defining features of the *Synedra ulna* (Nitzsch) Ehrenberg group and hypothesised as a synapomorphy for this group (Williams 2011). This author, based on nomenclatural reasons, suggested the use of the generic name *Ulnaria* for the group previously typified by the freshwater species *Synedra ulna*, and the use of *Synedra* for the group of diatoms typified by the marine species *S. gaillonii* (Bory) Ehrenberg.

A literature survey of diatom studies in Portugal (Novais *et al.* 2015) revealed that more than 40 taxa belonging to the genus *Fragilaria* have been recorded (Table S1). *Fragilaria rhabdosoma* Ehrenberg 1832 was the first *Fragilaria* species cited in the earliest study of diatoms from Portugal (Ehrenberg 1845). *Fragilaria capucina* Desmazières 1825 (Colmeiro 1889), *F. danica* (Kützing) Lange-Bertalot in Lange-Bertalot & Metzeltin 1996 (Colmeiro 1889), *F. mutabilis* (W.Smith) Grunow 1862 (Trelease 1897) and *F. radians* (Kützing) D.M.Williams & Round 1987 (Trelease 1897) were also recorded in the first diatom studies carried out in the country during the 19th century. Amongst these, we find *Fragilaria capucina*, which continues to be recorded and is one of the most commonly cited and widespread *Fragilaria* species in the country (Table S1). *Fragilaria vaucheriae* (Kützing) J.B.Petersen 1938 is also widely distributed in Portugal and cited in several studies (Table S1). Given the importance of the species complex around *Fragilaria capucina/vaucheriae* in the country, the present work was carried out in order to thoroughly study a *Fragilaria* species belonging to this complex, present in several samples and reaching considerable abundances. An extensive literature survey on *Fragilaria* species was carried out, allowing a thorough comparison of the Portuguese species morphological with comparable taxa. In this study, specimens from the type materials of the similar *Fragilaria capucina* fo. *sublanceolata-baikali* Flower & D.M.Williams 2004, *Fragilaria capucina* fo. *lanceolata-baikali* Flower & D.M.Williams 2004 and *Fragilaria nevadensis* Linares-Cuesta & Sanchez-Castillo 2007, which are poorly illustrated in the literature, were also examined.

MATERIAL AND METHODS

Portuguese samples

A total of 53 samples, collected in 28 watercourses from three adjacent river catchments (total area of 11,215 km^2) in central Portugal (Mondego, Vouga, and Lis river basins; Fig. 1) were analysed in this study. Epilithic diatoms were sampled in spring, autumn and winter in 2007, 2011 and 2012, in streams and rivers, following standard methodology (Association Française de Normalisation 2003; European Committee for Standardization 2003; Inag 2008) and preserved with formaldehyde solution (4% v/v) immediately after sampling. Details of the samples thoroughly analysed are listed in Table S2.

At each sampling site, current velocity was measured (m s^{-1}), water samples for chemical analysis were collected from lotic zones, and environmental variables such as water temperature (° C), pH, dissolved oxygen (mg l^{-1}), oxygen saturation (% O_2) and conductivity (µS cm^{-1}) were determined *in situ* with portable metres calibrated in the field. Temperature and oxygen were measured with a WTW Oxi 197 oxymeter, conductivity with an Orion Model 115 at 25°C, and pH with a Thermo Orion 290+. Water samples were collected in polypropylene bottles, stored at 4 °C in the darkness and transported to the laboratory for analysis. The parameters alkalinity (mg $CaCO_3$ l^{-1}), total hardness (mg $CaCO_3$ l^{-1}), chlorides (mg Cl^- l^{-1}), ammonium (µg N-NH_4^+ l^{-1}), nitrates (µg N-NO_3^- l^{-1}), nitrites (µg N-NO_2^- l^{-1}), phosphates (µg P-PO_4^{3-} l^{-1}), total phosphorus (µg P l^{-1}), sulphates (mg SO_4^{2-} l^{-1}), chemical oxygen demand (mg l^{-1}), silica (mg SiO_2 l^{-1}) and total dissolved solids (mg l^{-1}) were analysed according to standard methods (American Public Health Association 1995).

An aliquot of each Portuguese and type material samples (*ca.* 3 ml) was oxidised with 4–6 ml of nitric acid (65% v/v) and potassium dichromate ($K_2Cr_2O_7$) at room temperature for 24 hours. Afterwards, samples were repeatedly centrifuged (1500 rpm) and rinsed with distilled water at least three times to remove oxidation by-products. Permanent slides were mounted with Naphrax® (Brunel Microscopes Ltd, Chippenham, UK) for light microscopy (LM) analysis. For SEM analysis, metal stubs were prepared with organic free samples air-dried on a thin pellicle of graphite (EMITECH K 950X) and coated with gold–palladium (Polaron equipment limited SEM coating unit E5000).

The distribution map showing the Portuguese species (Fig. 1) was created using Quantum GIS 1.8.0 (QGIS Development Team 2018).

Type material analysis

Type material of *Fragilaria capucina* fo. *sublanceolata-baikali, F. capucina* fo. *lanceolata-baikali* and *F. nevadensis* was observed and analysed (Table S3).

The type materials of *Fragilaria capucina* fo. *sublanceolata-baikali* Flower & D.M.Williams (slide BM 100321, illustrated in Fig. 2) and *F. capucina* fo. *lanceolata-baikali* Flower & D.M. Williams (slide BM 100321, Fig. 2) from Lake Baikal, station number 3.10 (BK 8), coll number 3.1 (26 June 1997), are housed in the Natural History Museum of London (BM). *Fragilaria nevadensis* Linares-Cuesta & Sánchez-Castillo (slide 3013) is housed in the Diatom Phycoteca of Granada (Spain), University Herbarium (GDA; Table S3).

The permanent slide loaned by the Natural History Museum of London (BM 100321) was used for the LM analysis of the type material of *Fragilaria capucina* fo. *sublanceolata-baikali* and *F. capucina* fo. *lanceolata-baikali*. An aliquot with the type material of *Fragilaria nevadensis* was oxidised, and a permanent slide (for LM observations) and a metal stub (for SEM analysis) were prepared following the same procedure as for the Portuguese samples.

Microscopy observations (LM and SEM)

LM observations of both the Portuguese samples and type material were carried out using a Leitz® Biomed 20 EB bright-field microscope equipped with a 100× oil immersion objective (NA 1.32). Light micrographs were obtained using an Olympus DP70 camera attached to a Zeiss® Axioplan 2 imaging microscope with differential interference contrast and the same magnification (NA 1.40). Morphometric measurements (length, width and number of striae, counted along the axial area) were registered for each species, using the micrographs. A Hitachi SU-70 scanning

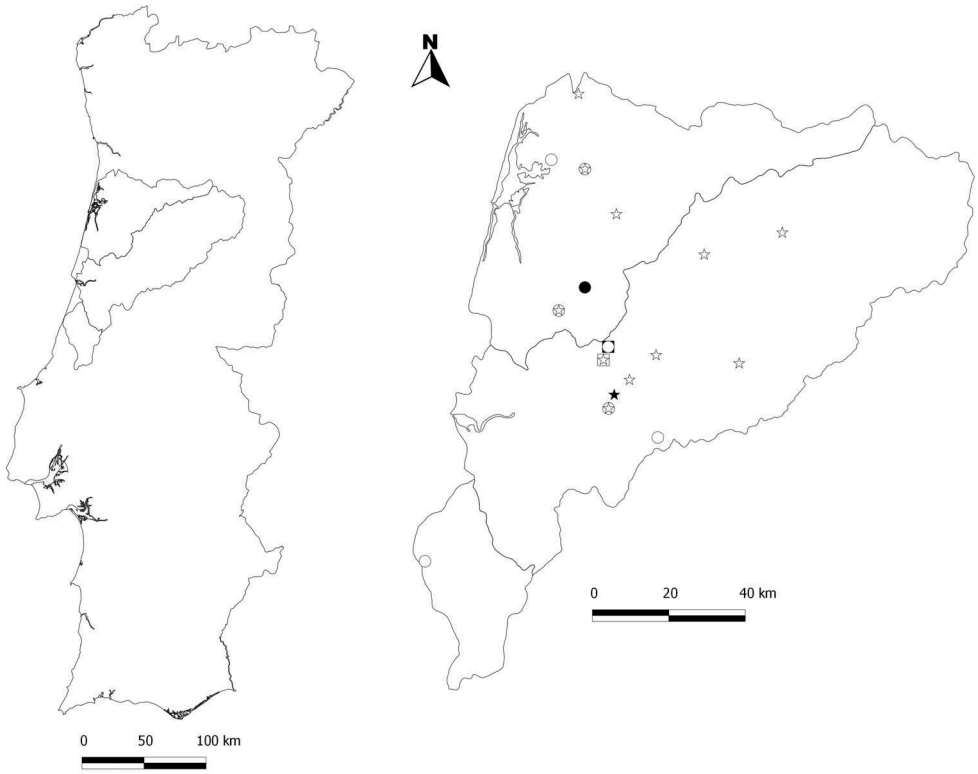

Fig. 1. Distribution map with sampling sites where the Portuguese *Fragilaria* species were identified in central Portugal. Star: *Fragilaria misarelensis sp. nov.*; square: *F. candidagilae*; circle: *F. rinoi*. Black represents type localities.

electron microscope operated at 7 kV and 10-mm working distance was used for image acquisition of the Portuguese samples and the type material of *Fragilaria nevadensis*. Ultrastructural analysis of areolae types, number and placement of rimoportulae, girdle bands, volae and apical pore fields were observed in SEM micrographs. Micrographs were digitally manipulated and plates containing LM and SEM pictures were mounted using Corel Draw X5® (Corel, Mountain View, CA, USA).

Comparison with morphologically similar species

In addition to the type material analysis, a thorough literature survey was carried out, allowing a detailed comparison of the Portuguese species with similar *Fragilaria* species commonly found in freshwater or recently described from European watercourses.

Information about *Fragilaria recapitellata* Lange-Bertalot & Metzeltin and *F. perminuta* (Grunow) Lange-Bertalot was retrieved from Tuji & Williams (2008) and Delgado *et al.* (2015); for *F. pectinalis* (O.F.Müller) Lyngbye we used the manuscript by Tuji & Williams (2008); for *F. microvaucheriae* Wetzel & Ector, information was obtained from Wetzel & Ector (2015); for *F. rhabdosoma* Ehrenberg from Tuji (2004); for *F. capucina* Desmazières and *F. rumpens* (Kützing) G.W.F.Carlson from Tuji & Williams (2006b); *F. vaucheriae* (Kützing) J.B.Petersen was checked in Krammer & Lange-Bertalot (1991), Tuji & Williams (2006a), Delgado *et al.* (2015) and Wetzel & Ector (2015); *F. sandellii* Van de Vijver & Jarlman from Van de Vijver *et al.* (2012); *F. candidagilae* Almeida, C.Delgado, Novais & S.Blanco and *F. rinoi* Almeida & C.Delgado were recently described by Delgado *et al.* (2015, 2016).

Valve shape analysis

Valve shape analysis and morphometric comparisons were carried out to compare *F. misarelensis sp. nov.* with morphologically and morphometrically similar *Fragilaria* species whose type material is well illustrated in the literature, including the type materials photographed in this study.

Valve shape analysis and morphometric comparison were based on measurements of 10–30 valves. More than 100 individuals of each taxon were observed under LM and SEM for morphological characterisation.

Morphological terminology follows Round *et al.* (1990), Ross *et al.* (1979), Barber & Haworth (1981) and Williams & Round (1987; used for terminology on areolae, girdle band features and apical pore field characteristics).

Valve shape differences between the studied taxa were analysed using geometric morphometry. To perform this analysis, valve outline was captured as a geometric configuration of ~100 non-homologous pseudolandmarks per valve using CLIC software (Dujardin *et al.* 2010), directly digitised from the LM micrographs taken in this study and from illustrations of the type material of comparable taxa available in the literature. In total, 200 images were processed. The Cartesian coordinates of the pseudolandmarks were aligned (translated, rotated and scaled) by the Procrustes generalised orthogonal least-squares superimposition procedure (Rohlf & Slice 1990). A principal components analysis

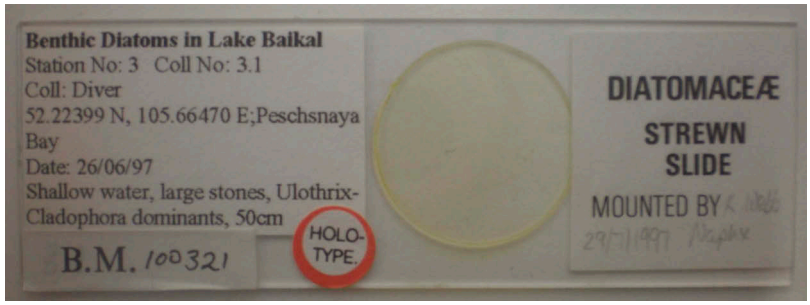

Fig. 2. Original glass slide (holotype) with type material of *Fragilaria capucina* fo. *sublanceolata-baikali* Flower & D.M.Williams and *Fragilaria capucina* fo. *lanceolata-baikali* Flower & D.M.Williams, BM 100321.

(PCA) was carried out on the resulting normalised co-ordinates by means of the software PAST v3.14 (Hammer *et al.* 2001). To visualise the size and shape of the scatterplot for each predefined group, the resulting groups were fitted to 95% confidence ellipses. Finally, a one-way nonparametric multivariate analysis of variance test (NPMANOVA; Anderson 2001) using Euclidean distances was performed between the transformed co-ordinates in order to test for significant differences between the *a priori* defined groups. Main morphometric parameters (valve length and width, density of striae and areolae) were measured directly on LM/SEM micrographs. The type material of taxa illustrated in the literature was also measured and compared to the parameters obtained in the populations here described by means of a NPMANOVA (Euclidean distance metric), in order to test the null hypothesis of no differences between the morphometry of the populations under study and that of the types of similar species.

Measurements of the type material of *Fragilaria capucina* fo. *sublanceolata-baikali, F. capucina* fo. *lanceolata-baikali* and *F. nevadensis* were taken in this study. For the type material illustrations of the other species, the following manuscripts were consulted: Delgado *et al.* (2015) for *Fragilaria recapitellata, F. perminuta* and *F. vaucheriae*; Tuji & Williams (2008) for *Fragilaria pectinalis* and Wetzel & Ector (2015) for *F. microvaucheriae*.

RESULTS

Portuguese species

Fragilaria misarelensis Almeida, C.Delgado, Novais & S. Blanco, *sp. nov.*

Figs 3–34, S1–S55 (LM); Figs 35–43 (SEM)

HOLOTYPE: BM 101 857 (Natural History Museum, London, UK), microscopic slide and preserved sample.

ISOTYPES: ZU10/77 (Hustedt Collection, Bremerhaven, Germany), microscopic slides.

TYPE LOCALITY: Mondego River, Mondego basin, Casal da Misarela, Coimbra Municipality, district: Coimbra, region: Centre, Portugal; coordinates 40°11′54.233″N, 08°21′59.582″W; coll. Carmen Elias and Cristina Delgado; coll date 20 March 2012.

ETYMOLOGY: The specific epithet *misarelensis* refers to Casal da Misarela, the type locality.

DESCRIPTION: Valves lanceolate with capitate apices, sometimes with a slight central swelling (Figs 13, 15). Frustules rectangular in girdle view with interruption of striation in the middle portion (Figs 16–18). Valve dimensions (Casal da Misarela, holotype population, n = 29; Foz do Caneiro, n = 36; Côja, n = 19): Length 13.6–29.2 µm (Casal da Misarela), 10.5–32.0 µm (Foz do Caneiro), 15.4–26.7 µm (Côja); width 3.6–4.7 µm (Casal da Misarela), 3.1–5.2 µm (Foz do Caneiro), 3.3–5.2 µm (Côja); stria density 15–18 in 10 µm (Casal da Misarela), 15–18 in 10 µm (Foz do Caneiro), 16–18 in 10 µm (Côja). Striae alternate, subparallel throughout the valve or slightly radiant towards the valve apices (Figs 3–15, 19–34, 35–37). Striae uniseriate, composed of slightly elongated areolae that become more rounded along the apical axis (six to seven areolae in 1 µm) in both valves (Figs 35–37, 40, 41). Central area bilaterally expanded in the majority of the valves (e.g. Figs 3, 5, 6, S1–S19), sometimes central area unilaterally expanded, especially in smaller valves (Figs 24–27). Siliceous plaques present along the valve mantle edge (Figs 39, 43). Axial area narrow, slightly expanded towards the valve centre (Figs 3, 5, 36, 40). Each valve has two apical pore fields of the ocellulimbus type made up of four to five rows, each composed of 10 to 13 poroids (Figs 35, 36, 38–40, 43). Isolated cells without spines (Figs 35, 36, 39, 40, 43). Girdle bands open, with small, unoccluded perforations (Fig. 43). One rimoportula per valve present near the apex and might have different orientations (Figs 35–38).

Comparison with similar species

Morphological features of *Fragilaria misarelensis sp. nov.* are described in Table 1 and a comparison of the valve shape of the three populations of *Fragilaria misarelensis sp. nov.* illustrated in LM is presented in Fig. 92. Here the overlapping is visible, revealing that the three populations represented belong to the same species.

Type materials of Baikal endemics *Fragilaria capucina* fo. *sublanceolata-baikali, F. capucina* fo. *lanceolata-baikali* and *F. nevadensis* were analysed and summarised in Table 1, in Figs 44–91 (LM) and S56–S60 (SEM). In addition, Figs 93-96 provide comparisons with species similar to *F. misarelensis sp. nov.* that are poorly illustrated in the original descriptions. From these, only *Fragilaria nevadensis* and *F. capucina* fo. *sublanceolata-baikali* overlap in valve dimensions (Tables 1, 2, Figs 94, 95). Comparing the central area of *Fragilaria nevadensis*, it is also bilaterally expanded as in *F. misarelensis*. Nevertheless, it is well delimited in the latter; whereas, it is more undefined in *F. nevadensis*, where ghost striae are also visible. *Fragilaria misarelensis* shares several ultrastructural characters with *F. nevadensis*, namely, the shape of the areolae (linear along the valve edge and round along the apical axis), type of apical pore fields (ocellulimbus type, composed of three to five rows including 8 to 14 poroids) and presence

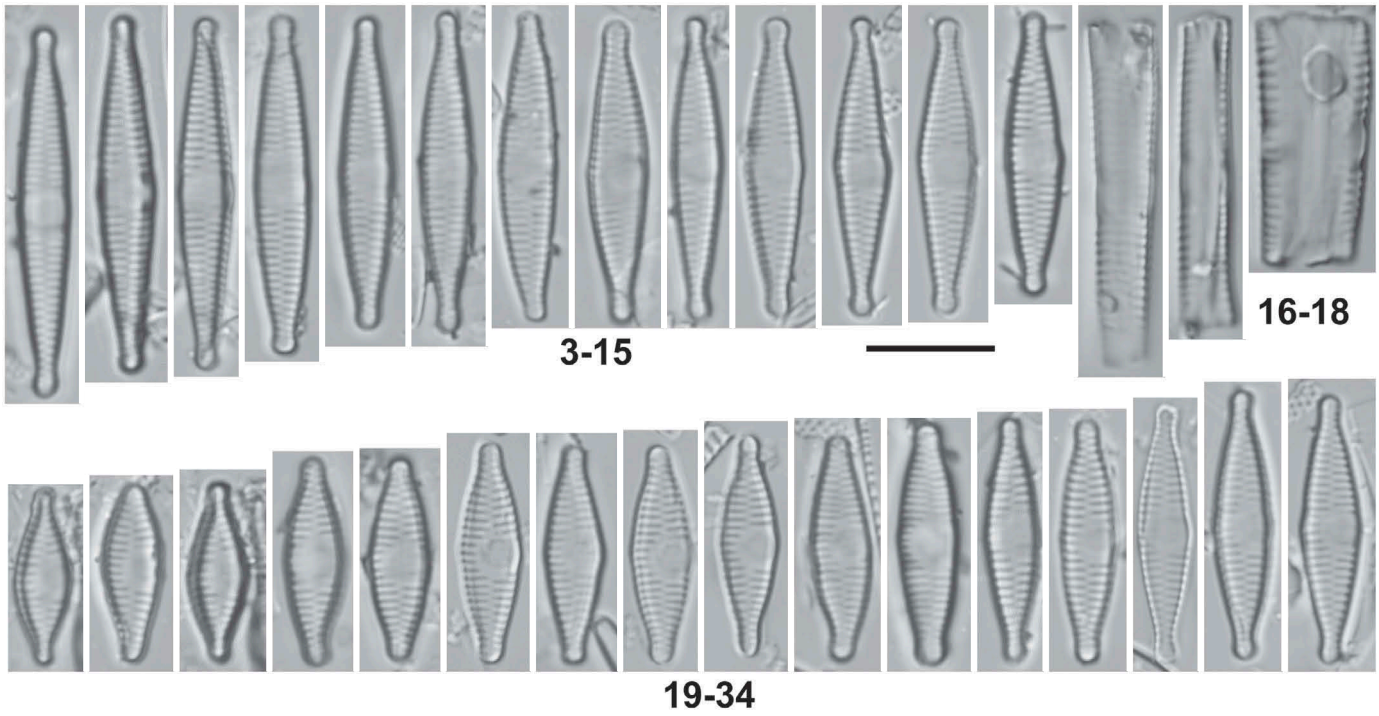

Figs 3–34. Light micrographs of *Fragilaria misarelensis sp. nov*. from Casal da Misarela, Mondego River, Mondego basin, 20 March 2012 (holotype population).
Figs 3–15. Valve view.
Figs 16–18. Complete frustules in girdle view.
Figs 19–34. Valve view.
Scale bar = 10 µm.

of one single rimoportula. However, *Fragilaria misarelensis* lacks spines, which are present in *F. nevadensis*, being conical close to the apex to spatulate in the middle of the valve (Figs S57, S58 and SEM illustrations in Linares-Cuesta & Sánchez-Castillo 2007). *Fragilaria capucina* f. *sublanceolata-baikali* has lanceolate-elliptical valves with convex margins between the central area and the rostrate apices; whereas, the valve is lanceolate with capitate apices in *F. misarelensis sp. nov*. The ultrastructure of *Fragilaria capucina* f. *sublanceolata-baikali* is similar to that of *F. misarelensis* in the features that characterise the genus, such as the presence of two apical pore fields, one rimoportula and uniseriate striae. Furthermore, both species present copulae with a single row of puncta; however, they differ in the shape of the areolae (elongated in *Fragilaria capucina* f. *sublanceolata-baikali* and with variable shape in *F. misarelensis*) and in the small spines sometimes present in *F. capucina* fo. *sublanceolata-baikali* (Flower *et al*. 2004).

The PCA plot with the results from the geometric morphometric analysis shows that the valve outline of the individuals from the holotype population of *Fragilaria misarelensis sp. nov*. partially overlaps with species such as *F. perminuta, F. capucina* fo. *sublanceolata-baikali, F. capucina* f. *lanceolata-baikali, F. microvaucheriae* and *F. vaucheriae* (Fig. 93); however, the NPMANOVA analysis revealed statistically significant ($P < 0.05$) differences from all of these species in more than one character analysed except *F. vaucheriae* which only differed significantly from *F. misarelensis* in stria density (Table 2). With respect to length, it partially overlaps with *Fragilaria perminuta, F. capucina* fo. *sublanceolata-baikali* and *F. vaucheriae*, and the width overlaps with *F. vaucheriae, F. capucina* fo. *sublanceolata-baikali* and *F. capucina* f. *lanceolata-baikali*; whereas, there is no overlapping in stria density (Fig. 96, Table 2). Nevertheless, *Fragilaria perminuta* forms colonies, *F. capucina* fo. *sublanceolata-baikali* has lanceolate-elliptical valves with margins between central area and convex and rostrate apices, and *F. vaucheriae* has coarser striation. *F. microvaucheriae* has generally narrower valves, sometimes presents small conic spines and has a wide unilateral central area, with a rectangular aspect; whereas, it is bilaterally expanded in most specimens of *F. misarelensis sp. nov*. (Table 3).

Fragilaria species recently described from Portugal (*F. candidagilae* and *F. rinoi*) differ morphologically and morphometrically from *F. misarelensis sp. nov*., because the valve shape of *F. candidagilae* is very distinctive, with the strongly capitate apices, coarser striation, usually wider valves and central area unilaterally expanded; whereas, *F. misarelensis sp. nov*. does not present strongly capitate apices, has denser striation, and a central area mostly bilaterally expanded. *Fragilaria rinoi* is characterised by slightly rostrate apices, has generally wider valves and a central area unilaterally expanded; whereas, the apices are capitate in *F. misarelensis*, the central area is bilaterally expanded (sometimes with a slight central swelling) and valves are generally narrower (Tables 1, 3). The ultrastructure of *Fragilaria misarelensis* is similar to that of *F. rinoi* and *F. candidagilae*, differing only in the shape of the areolae, variable in *F. misarelensis* and round in *F. candidagilae* and *F. rinoi* (also presenting a higher dentity of areolae, with 13–14 areolae in 1 µm vs 6–7 areolae in 1 µm in *F. misarelensis*). From an ecological point of view,

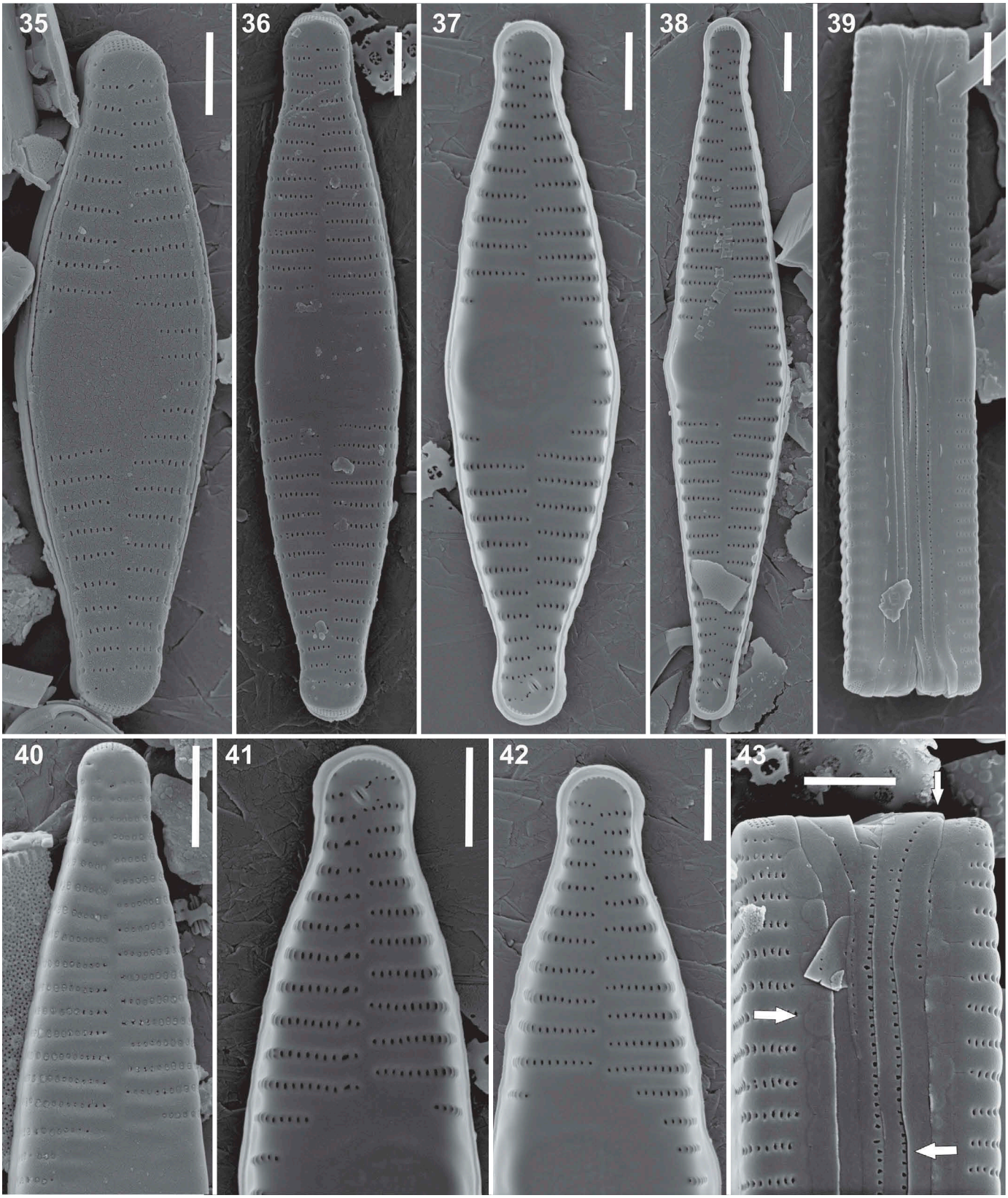

Figs 35–43. Scanning electron micrographs of *Fragilaria misarelensis sp. nov.* from Casal da Misarela, Mondego River, Mondego basin, 20 March 2012 (holotype population).
Figs 35, **36**. Valves in external view.
Figs 37, **38**. Valves in internal view.
Fig. 39. Frustule in girdle view.
Fig. 40. Detail of an apex in external view, with the apical pore field and rimoportula.
Figs 41, **42**. Details of the apices of Fig. 37 in internal view, with the single rimoportula and the apical pore fields.
Fig. 43. Detail of the apex in girdle view, with the open girdle bands with small, unoccluded perforations and siliceous plaques visible (indicated by the arrows). Scale bar = 2 µm.

Table 1. Morphological features of the new Portuguese species and the type material analysed in detail.

	Fragilaria misarelensis Almeida, C.Delgado, Novais & S.Blanco	*Fragilaria capucina* fo. *sublanceolata-baikali* Flower & D.M.Williams	*Fragilaria capucina* fo. *lanceolata-baikali* Flower & D.M.Williams	*Fragilaria nevadensis* Linares-Cuesta & Sánchez-Castillo
References	This study	Flower *et al.* (2004); this study	Flower *et al.* (2004); this study	Linares-Cuesta & Sánchez-Castillo (2007); this study
Valve morphometry: length (µm); width (µm)	13.6–29.2; 3.6–4.7 (Casal da Misarela, type population)	12–35; 3.5–4.5 (Flower *et al.* 2004); 11.6–23.8; 3.8–4.7 (this study)	35–57; 3.5–4.5 (Flower *et al.* 2004); 33.9–39.3; 3.5–4.3 (this study)	30–50; 3.5–5.0 (Linares-Cuesta & Sánchez-Castillo 2007); 23.9–47.7; 3.2–4.1 (this study)
Striation	Alternate, subparallel throughout the valve to slightly radiant towards the ends; 15–18 in 10 µm	Alternate, subparallel in the middle of the valve to slightly radiant towards the ends, 19–20 in 10 µm (Flower *et al.* 2004); 17–21 in 10 µm (this study)	Alternate, subparallel in the middle of the valve to slightly radiant towards the ends, 19–20 in 10 µm (Flower *et al.* 2004); 17–18 in 10 µm (this study)	Alternate, parallel, not punctate, 14–18 in 10 µm
Valve outline	Lanceolate	Lanceolate–elliptical, with valve margins convex between the central area and the apices	Lanceolate	Lanceolate
Apices	Capitate	Rostrate	Slightly developed, subrostrate	Subcapitate
Central area	Bilaterally expanded in the majority of the valves	Unilaterally expanded from the axial area to the valve margin, small inflation to one side of the central area margin	Asymmetric and sometimes extending to the margins of the valve, small inflation to one side of the central area margin	Elliptic, usually extending to the valve margins; swollen central part
Colonies	No	–	–	Yes
Number of rimoportula	1	1	1	1
Apical pore fields	Ocellulimbus type, made up of four to five rows, each composed of 10 to 13 poroids	Ocellulimbus type	Ocellulimbus type	Ocellulimbus type, made up of three to five rows, each composed of 8 to 14 poroids
Girdle bands	Open, with small, unoccluded perforations	Open, each with a single row of puncta	Open, each with a single row of puncta	–
Spines	Absent	Small spines sometimes present	Small spines sometimes present	Spines are conical near the apex and spatulate in the middle of the valve

Fragilaria misaralensis sp. nov. and *F. candidagilae* are present in poorly mineralized waters with low conductivity and low nitrate, nitrite and phosphate concentrations; whereas, *F. rinoi* is present in watercourses with medium to high conductivity and high nutrient concentrations, with mean values of nitrate–nitrogen of 3.7 mg l^{-1} (Delgado *et al.* 2015, 2016).

The literature analysis (compiled in Table 3) also revealed that smaller specimens of *Fragilaria capucina* Desmazières, *F. pectinalis* (O.F.Müller) Lyngbye and *F. rumpens* (Kützing) G.W.F.Carlson may overlap in valve length; nevertheless, larger specimens of these species exceed the length of *F. misarelensis sp. nov.* (Table 3). Other noticeable differences amongst the aforementioned taxa are the following: *F. capucina* possesses two rimoportula, one at each end, and forms ribbon-like colonies (Tuji & Williams 2006b); *F. rumpens* has a lanceolate to fusiform valve outline with rostrate ends and denser striation and presents irregular spines located on the costae (at mantle–face junction). These are rectangular at the central area and very small and triangular at the valve poles (Tuji & Williams 2006a). *F. pectinalis* has coarser striation, linear–lanceolate valves with a central area unilaterally expanded and linking spines (Tuji & Williams 2008). *Fragilaria sandellii* Van de Vijver & Jarlman, a species recently described from a small oligotrophic Swedish stream, has similar length but is characterised by wider valves with a central area forming a large asymmetrical fascia, small rounded areolae and the occasional presence of very small marginal spines (Van de Vijver *et al.* 2012).

Additionally, *Fragilaria neointermedia* Tuji & D.M. Williams presents a central area slightly bilaterally expanded in some specimens; however, this species has coarser striation (8–10 in 10 µm), rostrate ends and spatulate linking spines (Delgado *et al.* 2015).While this paper was in press, it came to our attention the publication of the similar *F. drouotiana* Heudre, Wetzel, Moreau & Ector. However, it can be easily differentiated from *F. misarelensis* by the narrower valves (*F. drouotiana*: width 2.4 - 3.2 mm and *F. misarelensis*: width 3.6 - 4.7 mm) with central area unilateral, whilst it is bilaterally expanded in the majority of *F. misarelensis* valves. *Fragilaria* drouotiana also has denser striation than *F. misarelensis* (17 - 22 vs 15 - 18 striae in 10 µm). With respect to the ecology, *F. drouotiana* was found in epiphyton in lakes while F. misarelensis was identified from sediments and hard substrate in rivers and can tolerate higher concentrations of nitrates, nitrites and ammonium than *F. drouotiana*.

Distribution, ecology and associated diatom flora

From 53 samples belonging to the river basins of Mondego, Vouga and Lis, *Fragilaria misarelensis sp. nov.* was found in the

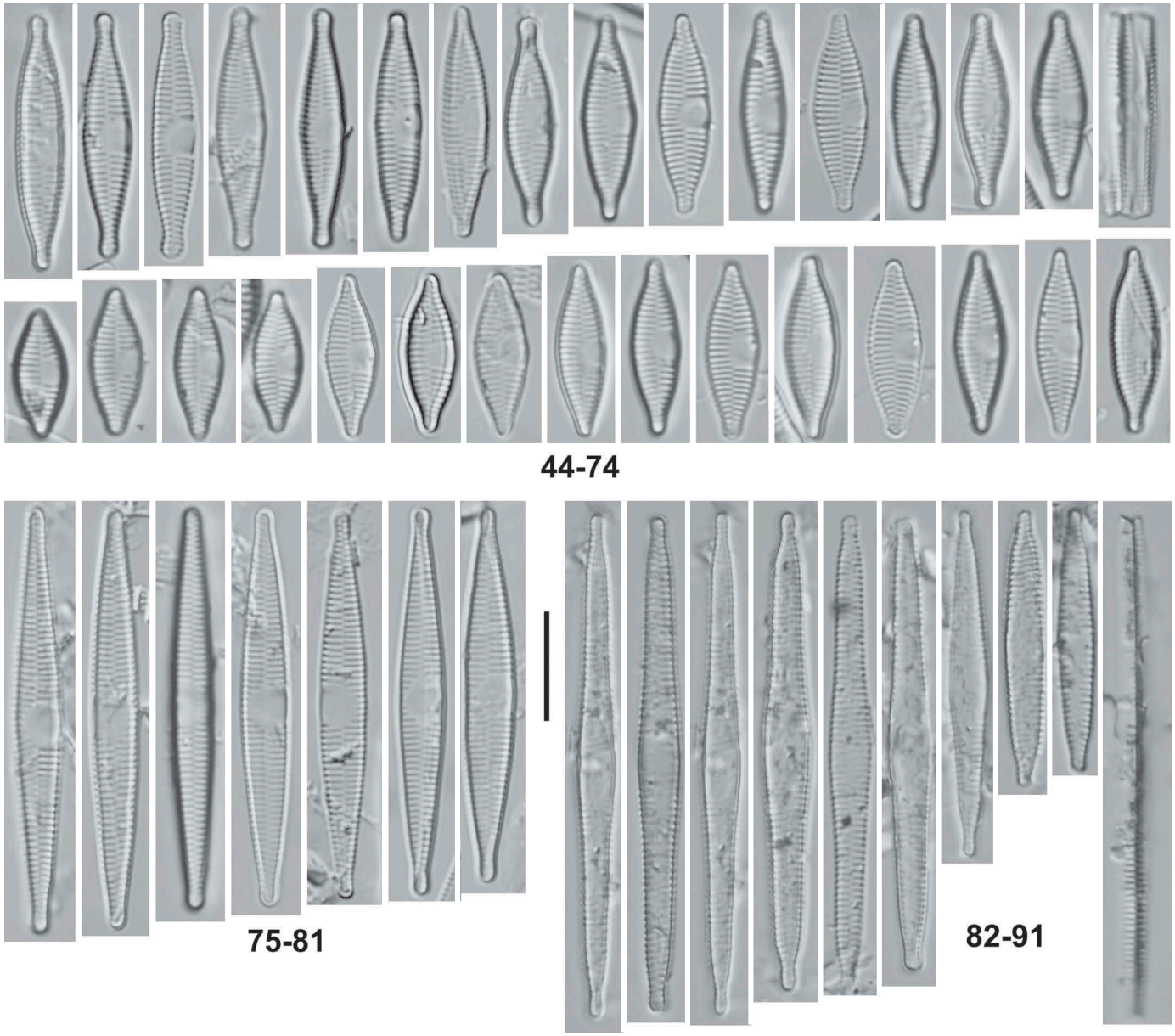

Figs 44–91. Light micrographs of type material.
Figs 44–74. *Fragilaria capucina* fo. *sublanceolata-baikali* Flower & D.M.Williams (BM 100321).
Figs 75–81. *Fragilaria capucina* fo. *lanceolata-baikali* Flower & D.M.Williams (BM 100321).
Figs 82–91. *Fragilaria nevadensis* Linares-Cuesta & Sanchez-Castillo (GDA 3013). Scale bar = 10 µm.

epilithon and sediment of 15 samples collected in 12 sites (of which 9 were located in the Mondego and 3 in the Vouga river basin; Fig. 1, Table S2). The relative abundance of this species ranged from 0.48% in the sample collected in sediment from Cunha Baixa (19 March 2012) to 13.66% sampled on hard substrate from Foz do Caneiro (12 June 2007). It was present with relative abundance above 1% at 10 sites. Three samples were from the type locality, Casal da Misarela, May and October 2011 and March 2012. *Fragilaria misarelensis* was present in poor to mineralized rivers with low to high conductivity (16–1060 µS cm^{-1}), neutral–alkaline pH (6.83–7.75) and low nitrates (0.34 - 3.29 mg NO_3- l^{-1}), nitrites (0.002 -0.09 mg NO_2- l^{-1}) and ammonium (0.002 - 2.31 mg NH_4+ l^{-1}) concentrations (Table S4). This diatom species occurred at a high range of dissolved oxygen (between 45.6% and 114.8%) and silica (between 1.34 and 8.7 mg SiO_2 l^{-1}) (Table S4). However, abundance-weighted averages for several environmental parameters revealed that it occurs preferentially in watercourses with low mineralization (conductivity = 111 µS cm^{-1}; alkalinity = 21.5 mg $CaCO_3$ l^{-1}; total hardness = 35.3 mg $CaCO_3$ l^{-1}), neutral pH (pH = 7.1), low nutrient concentrations (nitrates = 1632 µg NO_3^- l^{-1}; nitrites = 20 µg NO_2^- l^{-1}; phosphates = 132 µg PO_4^{3-} l^{-1}; total P = 290 µg P l^{-1}) and high dissolved oxygen (DO = 93.2% sat.) (Table S4).

In the type locality (Casal da Misarela, 20 March 2012), the relative abundance of *Fragilaria misarelensis sp. nov.* was 1.23% and the associated diatoms co-occurring with this new taxon were *Achnanthidium minutissimum* (Kützing) Czarnecki

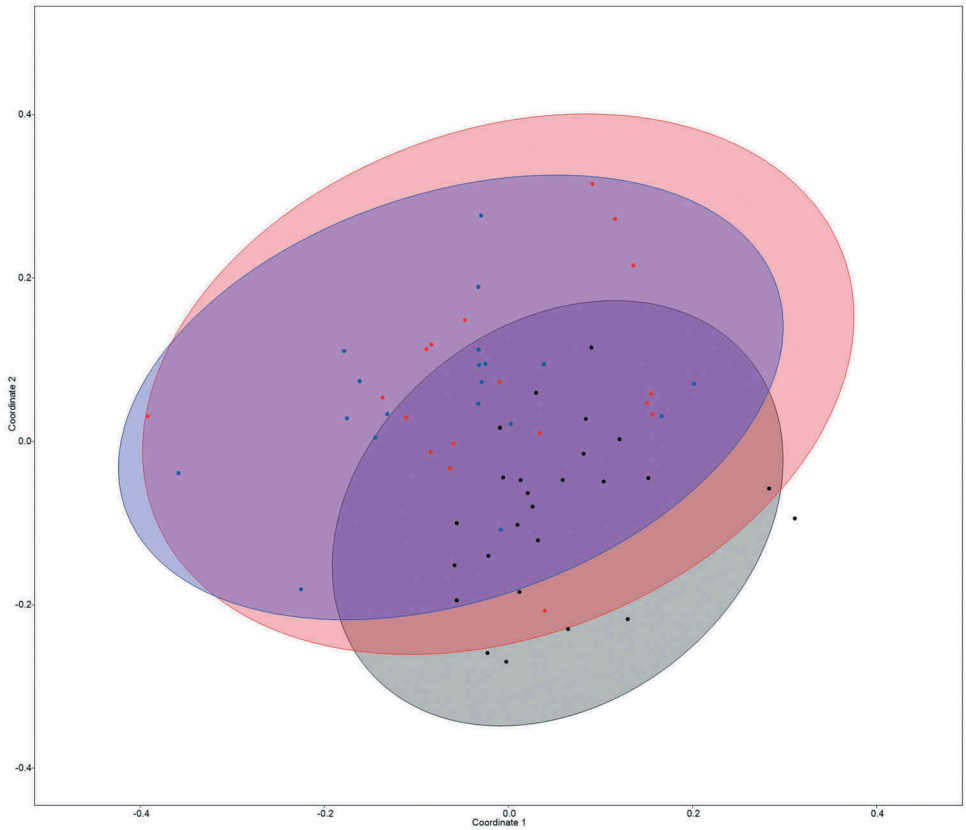

Fig. 92. Comparison of the three populations of *Fragilaria misarelensis sp. nov*. illustrated in LM. Black: Casal da Misarela, Mondego River, Mondego basin, 20 March 2012 (holotype population). Red: Foz do Caneiro, Mondego River, Mondego basin, 12 June 2007. Blue: Côja, Alva River, Mondego basin, 11 June 2007.

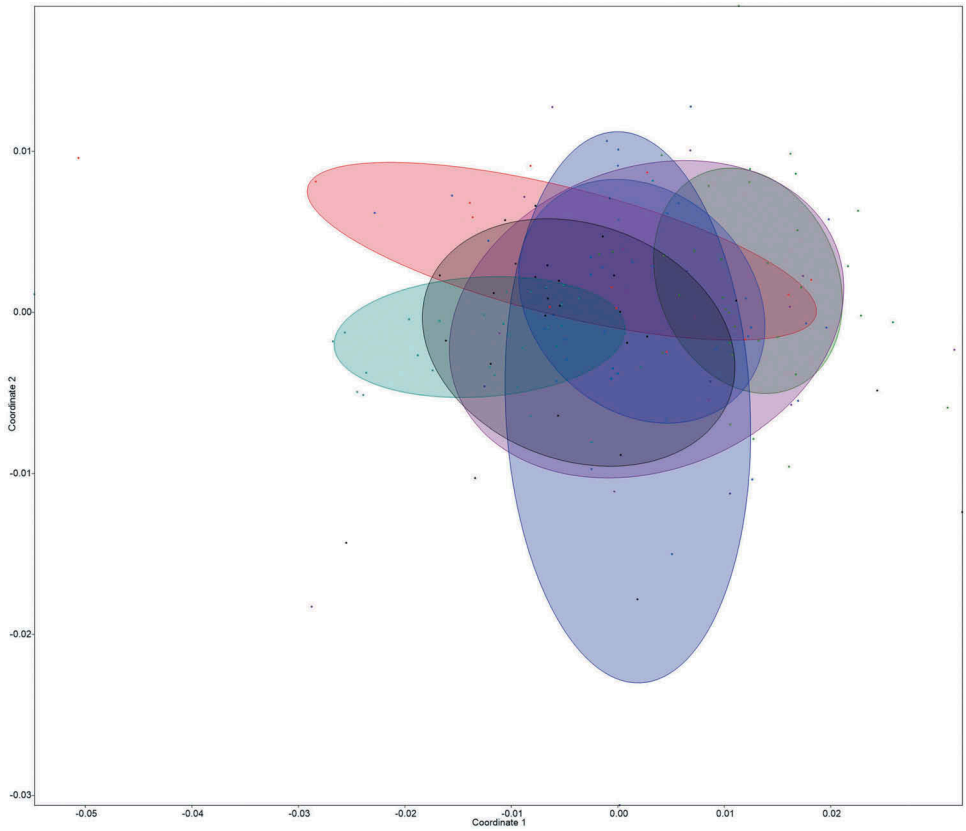

Fig. 93. Comparison of the holotype of *Fragilaria misarelensis sp. nov*. with the type material of other related taxa. Data fitted to 95% confidence ellipses. NMDS plot of Bookstein-transformed valve outline pseudolandmark ordinates. Red: *Fragilaria microvaucheriae*. Dark blue: *F. lanceolata-baikali*. Light blue: *F. perminuta*. Olive green: *F. recapitellata*. Dark green: *F. sublanceolata-baikali*. Violet: *F. vaucheriae*. Grey: *F. misarelensis*.

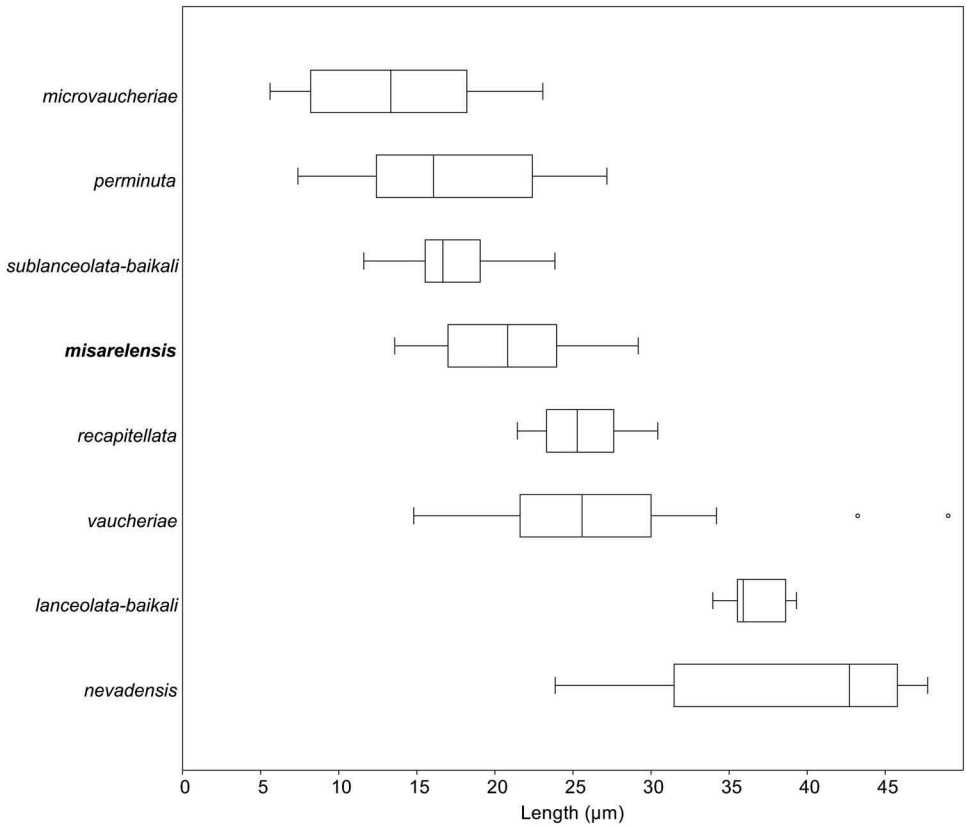

Fig. 94. Box plot of length measurements of different *Fragilaria* species (type populations). The boxes represent the 25%–75% quartiles, the median is shown with vertical line inside the box, and minimum and maximum values are shown with short vertical lines (whiskers). Outliers are plotted as individual points.

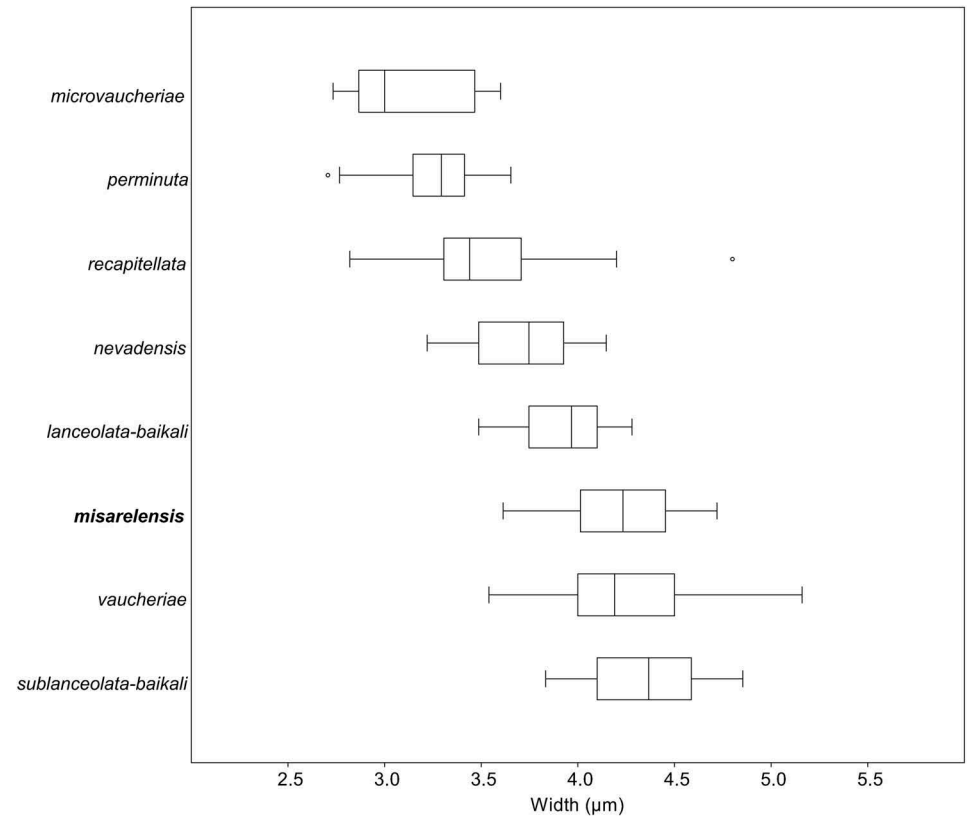

Fig. 95. Box plot of width measurements of different *Fragilaria* species (type populations). The boxes represent the 25%–75% quartiles, the median is shown with vertical line inside the box, and minimum and maximum values are shown with short vertical lines (whiskers). Outliers are plotted as individual points.

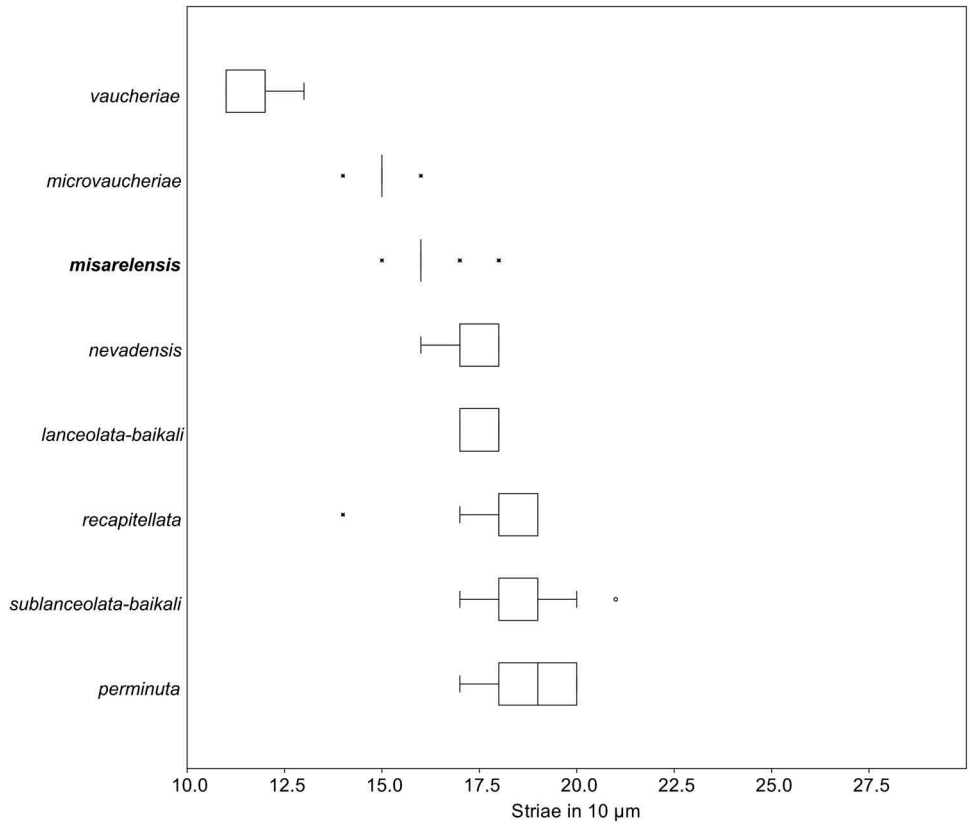

Fig. 96. Box plot of measurements of different *Fragilaria* species. Variation in the number of striae in 10 µm measured in the type populations. The boxes represent the 25%–75% quartiles, the median is shown with vertical line inside the box, and minimum and maximum values are shown with short vertical lines (whiskers). Outliers are plotted as individual points.

(43.97%), *Fragilaria* aff. *rumpens* (Kützing) G.W.F.Carlson (3.27%), *Reimeria sinuata* (W.Gregory) Kociolek & Stoermer (2.86%), *Achnanthidium atomoides* Monnier, Lange-Bertalot & Ector (4.70%), *A. lineare* W.Smith (1.02%), *A. rivulare* Potapova & Ponader (16.97%), *Aulacoseira granulata* (Ehrenberg) Simonsen (3.48%), *Cocconeis euglypta* Ehrenberg (1.02%), *Encyonema minutum* (Hilse) D.G.Mann (9.00%), *Eunotia pectinalis* (Kützing) Rabenhorst (1.63%), *Fragilaria* sp. (2.04%), *Gomphonema minutum* (C.Agardh) C.Agardh (1.23%) and *Navicula cryptotenella* Lange-Bertalot (1.84%). From these, the most abundant taxa are circumneutral, oligo to β-mesosaprobous, freshwater (<100 mg Cl^{-} l^{-1}) or freshwater to brackish (<500 mg Cl^{-} l^{-1}), nitrogen autotrophic tolerating very small to elevated concentrations of organically bound nitrogen and requiring continuously high dissolved oxygen concentrations (Van Dam *et al.* 1994; retrieved from the 2013 OMNIDIA v5.5 database [Lecointe *et al.* 1993]).

Type material analysis

The type material of *Fragilaria capucina* fo. *sublanceolata-baikali* Flower & D.M.Williams, *F. capucina* fo. *lanceolata-baikali* Flower & D.M.Williams and *F. nevadensis* Linares-Cuesta & Sánchez-Castillo were analysed in detail for comparison with the Portuguese species. Detailed information about the type material is presented in Table S3, LM and SEM illustrations of the type populations are provided in Figs 44–91 (LM) and S56–S60 (SEM) and morphological features are summarised in Table 1.

Fragilaria capucina fo. *sublanceolata-baikali* Flower & D. M.Williams in Flower *et al.* (2004) Figs 13, 15 (SEM) Figs 44–74 (LM)

MORPHOLOGY: Valve dimensions (n = 30): Length 11.6–23.8 µm, width 3.8–4.7 µm, striae 18–21 in 10 µm in the type material analysed in this study; and length 12–35 µm, width 3.5–4.5 µm, striae 19–20 in 10 µm described in Flower *et al.* (2004). The valves are lanceolate–elliptical with valve margins between the central area and apices convex, apices rostrate, single rimoportula at the valve apex (Fig. 13; SEM illustration in Flower *et al.* 2004). Small conical spines are present in the costae (Fig. 15; SEM illustration in Flower *et al.* 2004).

Fragilaria capucina fo. *lanceolata-baikali* Flower & D.M. Williams in Flower *et al.* (2004) Figs 14, 16 (SEM) Figs 75–81 (LM)

MORPHOLOGY: Valve dimensions (n = 7): Length 33.9–39.3 µm, width 3.5–4.3 µm, striae 17–18 in 10 µm in the type material analysed in this study; and length 35–57 µm, width 3.5–4.5 µm, striae 19–20 in 10 µm described

Table 2. Morphometric and morphological comparison between the type material of *Fragilaria misarelensis sp. nov.* and related taxa. NPMANOVA results, Fischer's statistic and Bonferroni-corrected *P* values are presented (significant values highlighted in bold). *n* = sample size; GM = geometric morphometry; M = morphometry. *F. misarelensis* n (GM = 26; M = 29); *F. lanceolata-baikali* n (GM = 7; M = 7); *F. microvaucheriae* n (GM = 13; M = 12); *F. nevadensis* n (GM = –; M = 11); *F. perminuta* n (GM = 35; M = 31); *F. recapitellata* n (GM = 35; M = 38); *F. sublanceolata-baikali* n (GM = 30; M = 30); *F. vaucheriae* n (GM = 15; M = 26). L/W = length/width.

		Fragilaria lanceolata-baikali	*Fragilaria microvaucheriae*	*Fragilaria nevadensis*	*Fragilaria perminuta*	*Fragilaria recapitellata*	*Fragilaria sublanceolata-baikali*	*Fragilaria vaucheriae*
Length	*R*	0.9303	0.3086	0.7533	0.04877	0.2965	0.1027	0.1185
	P	**0.0021**	**0.0144**	**0.0021**	1	**0.0021**	0.1176	0.1188
Width	*R*	0.09099	0.8686	0.3977	0.8686	0.5538	−0.0041	−0.007907
	P	1	**0.0021**	**0.0042**	**0.0021**	**0.0021**	1	1
Stria density	*R*	0.5679	0.4847	0.3981	694	0.7246	721	0.9979
	P	**0.0063**	**0.0021**	**0.0084**	**0.0021**	**0.0021**	**0.0021**	**0.0021**
L/W	*R*	0.9022	0.1364	0.8784	0.05551	0.4289	0.08798	0.08798
	P	**0.0021**	0.9576	**0.0021**	0.9639	**0.0021**	0.2268	0.3416
Outline	*R*	0.2126	0.1668	–	0.2019	0.4128	0.1619	0.1243
	P	**0.0126**	**0.0462**	–	**0.0021**	**0.0021**	**0.0042**	0.1617

in the type material (Flower *et al.* 2004). The valves were lanceolate with valve margins essentially straight between the central area and apices. Apices slightly developed, subrostrate. Small conical spines present in the costae (Fig. 16; SEM illustration in Flower *et al.* 2004).

According to Flower *et al.* (2004), both forms were identified from shallow-water sampling stations in Lake Baikal, but the number of valves of *Fragilaria capucina* fo. *sublanceolata-baikali* (referred to as Morphotype 1 throughout the text in Flower *et al.* 2004) exceeded those of *F. capucina* fo. *lanceolata-baikali* (referred to as Morphotype 2). The shallow-water epilithic communities were dominated by forms of *Fragilaria capucina* Desmazières (including the two morphotypes above mentioned), *Hannaea arcus* (Ehrenberg) Patrick & Reimer, *Encyonema minutum* (Hilse) D.G.Mann, *Cocconeis placentula* Ehrenberg, *Nitzschia dissipata* (Kützing) Rabenhorst and gomphonemoid taxa (Flower *et al.* 2004).

Fragilaria capucina fo. *sublanceolata-baikali* and *F. capucina* fo. *lanceolata-baikali* were described as two forms of *F. capucina* from Lake Baikal by Flower *et al.* (2004). These two morphotypes were described as 'forms' pending revision of the entire species group. Recently, several studies on the *Fragilaria capucina/vaucheri*ae complex were published, including the revision of the type material of *Fragilaria capucina* Desmazières (Tuji & Williams 2006b). According to Tuji & Williams (2006b), valves with alternate striae, linking spines, allowing the formation of ribbon-like colonies, open girdle bands and one rimoportula at each apex, characterise *Fragilaria capucina*. Alternate striae, open girdle bands, sometimes the presence of small spines and only one rimoportula per valve characterise both Baikal 'forms'. Given the above-mentioned differences, we propose to raise these forms to species level.

Fragilaria sublanceolata-baikali (Flower & D.M.Williams) Novais, C.Delgado & S.Blanco, *comb. et stat. nov.*

BASIONYM: *Fragilaria capucina* fo. *sublanceolata-baikali* Flower & D.M. Williams in Flower *et al.* 2004, Proceedings of the Seventeenth International Diatom Symposium, p. 92, figs 13, 15.

Fragilaria lanceolata-baikali (Flower & D.M.Williams) Novais, C.Delgado & S.Blanco, *comb. et stat. nov.*

BASIONYM: *Fragilaria capucina* fo. *sublanceolata-baikali* Flower & D.M. Williams in Flower *et al.* 2004, Proceedings of the Seventeenth International Diatom Symposium, p. 92, figs 14, 16.

Fragilaria nevadensis Linares-Cuesta & Sánchez-Castillo in Linares-Cuesta & Sanchez-Castillo (2007) Figs 1–3 (LM) Figs 4–9 (SEM) Figs 82–91 (LM) Figs S56–S60 (SEM)

MORPHOLOGY: Valve dimensions (*n* = 11): Length 23.9–47.7 µm, width 3.2–4.1 µm, striae 16–18 in 10 µm in the type material analysed in this study; and length 30–50 µm, width 3.5–5.0 µm, striae 14–18 in 10 µm in the original description by Linares-Cuesta & Sánchez-Castillo (2007). The valves were lanceolate with subcapitate ends and axial sternum narrow (Figs 83, 86). The central parts were swollen with an elliptical central area usually extending to the margins of the valve (Figs 83, 86). The striation was alternate, parallel and not punctate (Fig. 83). Spines present, being conical near the apex to spatulate in the middle of the valve (Figs S57, S58).

Table 3. Morphological features of selected *Fragilaria* taxa similar to *F. misarelensis sp. nov.*

	Fragilaria candidagilae Almeida, C. Delgado, Novais & S. Blanco	*Fragilaria capucina* Desmazières	*Fragilaria recapitellata* Lange-Bertalot & Metzeltin	*Fragilaria microvaucheriae* C.E.Wetzel & Ector	*Fragilaria pectinalis* (O. F.Müller) Lyngbye	*Fragilaria perminuta* (Grunow) Lange-Bertalot	*Fragilaria rhabdosoma* Ehrenberg	*Fragilaria rinoi* Almeida & C.Delgado	*Fragilaria rumpens* (Kützing) G.W.F.Carlson	*Fragilaria sandellii* Van de Vijver & Jarlman	*Fragilaria vaucheriae* (Kützing) J.B. Petersen
Basionym	–	–	*Synedra capitellata* Grunow in Van Heurck	–	*Conferva pectinalis* O. F.Müller	*Synedra* (*vaucheriae* var.?) *perminuta* Grunow in Van Heurck	–	–	*Synedra rumpens* Kützing	–	*Exilaria vaucheriae* Kützing 1833
References	Delgado *et al.* (2015)	Tuji & Williams (2006a)	Van Heurck (1881); Tuji & Williams (2008); Delgado *et al.* (2015)	Wetzel & Ector (2015)	Tuji & Williams (2008)	Van Heurck 1881; Tuji & Williams (2008); Delgado *et al.* (2015)	Tuji (2004)	Delgado *et al.* (2016)	Tuji & Williams (2006b)	Van de Vijver *et al.* (2012)	Krammer & Lange-Bertalot (1991); Tuji & Williams (2006b, 2013)
Valve morphometry: length (µm); width (µm)	13.0–25.8; 4.5–5.0	25.6–67.5; 3.1–3.8	20–39; 3–4 (Tuji & Williams 2008); 21.4–30.4; 3–4 (Delgado *et al.* 2015)	5.7–23.4; 2.5–3.8	28–37; 3.5–4.0	9–24; 3.0–3.5 (Tuji & Williams 2008); 7.5–32.6; 3.0–3.5 (Delgado *et al.* 2015)	15.6–28.3 (20.8 in Ehrenberg's original description 1832); 3.3–3.9	8.8–24.1; 4.2–5.6	25–63; 3.0–4.0	11.5–22.0; 4.5–6.0	22–42.7; *ca.* 4.0 (Krammer & Lange-Bertalot 1991)
Striation	Alternate, punctuate and parallel to slightly radiate towards the ends; 12–14 in 10 µm	Alternate, parallel to slightly radiate towards ends; *ca.* 15–16 striae/ 10 µm	Alternate, parallel to slightly radiate towards ends; 17–19 in 10 µm (both Tuji & Williams [2008] and Delgado *et al.* [2015])	Coarse, uniseriate, radiate throughout, 15–16 in 10 µm	Alternate, parallel to slightly radiate towards ends; 14–15 in 10 µm	Alternate, parallel to slightly radiate towards ends; 18–19 in 10 µm	Alternate, parallel to slightly radiate towards ends; *ca.* 18–20 in 10 µm	Parallel, becoming slightly radiate at the ends; 14–16 in 10 µm	Parallel throughout; 18–20 in 10 µm	Very slightly radiate to almost parallel throughout, alternating although not always very clearly, 16–18 in 10 µm	Alternate, parallel to slightly radiate towards ends; 12–14/10 µm (Krammer & Lange-Bertalot 1991); 9–14/ 10 µm (Tuji & Williams 2006)
Valve outline	Linear–lanceolate to elliptical in smaller specimens	Linear	Lanceolate	Lanceolate in larger specimens to rhombic–lanceolate in smaller specimens	Linear–lanceolate	Lanceolate	Linear–lanceolate	Lanceolate to rhombic lanceolate in smaller specimens	Lanceolate, fusiform, sometimes irregularly curved	Lanceolate to elliptic–lanceolate in smaller specimens	Linear–lanceolate
Apices	Strongly capitate	Weakly rostrate	Strongly apiculate	Slightly rostrate to cuneate (in smaller specimens)	Weakly rostrate to capitate	Slightly rostrate	Weakly rostrate	Slightly rostrate	Rostrate	Protracted, rostrate	Capitate

(*Continued*)

Table 3. (Continued).

	Fragilaria candidagilae Almeida, C. Delgado, Novais & S. Blanco	*Fragilaria capucina* Desmazières	*Fragilaria recapitellata* Lange-Bertalot & Metzeltin	*Fragilaria microvaucheriae* C.E.Wetzel & Ector	*Fragilaria pectinalis* (O. F.Müller) Lyngbye	*Fragilaria perminuta* (Grunow) Lange-Bertalot	*Fragilaria rhabdosoma* Ehrenberg	*Fragilaria rinoi* Almeida & C.Delgado	*Fragilaria rumpens* (Kützing) G.W.F.Carlson	*Fragilaria sandellii* Van de Vijver & Jarlman	*Fragilaria vaucheriae* (Kützing) J.B. Petersen
Central area	Unilaterally expanded from the axial area to the valve face margin	Rectangular to rhombic	Unilateral, often expanded just until the sternum	Wide and unilateral (bilateral in large specimens)	Unilateral, often expanded just until the sternum	Strongly unilateral	Characteristic swellings, slightly unilateral in small individuals, bilateral in larger	Unilateral	A wide transverse fascia, sometimes unilaterally or bilaterally gibbous	Asymmetrical fascia, on one side bordered by shortened striae; ghost striae sometimes present in the fascia	Unilateral in small and bilateral in larger individuals
Colonies	No	Ribbon-like	No	No	–	Yes	Yes	No	Ribbon-like, adhering by their valve faces	No	–
Number of rimoportula	1	2	1	1	1	–	1	1	One, eccentric, adjacent to sternum	One, very difficult to resolve in LM	1
Apical pore fields	Ocellulimbus type, made up of six to seven rows, each composed of 8 to 14 poroids	Rectangular, bearing neatly arranged rows of poroids	Rectangular	Composed of fine porelli arranged in regular rows parallel to the apical axis	Rectangular, bearing neatly arranged rows of poroids	–	Rectangular, bearing neatly arranged rows of poroids	Ocellulimbus type, made up of four rows, each composed of 10 to 11 poroids	Rectangular	Present	Rectangular
Girdle bands	Open with perforations	Open bands, each with a single row of small punctae	–	Open, with small unoccluded perforations	Open	–	–	Open	Open bands with puncta	–	–
Spines	Absent	Present	Absent	Small conical spines (spinules) sometimes present	–	–	Present	Absent	Spines irregular, located on the costae, at mantle–face junction, often deformed and rectangular at central area, very small and triangular at valve poles	Very small marginal spines occasionally present	Either do not exist or are very small, and they do not link with sibling cells

DISCUSSION

Fragilaria misarelensis sp. nov. was compared with several similar species, from which it differs morphologically, morphometrically or ecologically. Optimal conditions for *Fragilaria misaralensis sp. nov*. are watercourses under low anthropogenic impacts, characterised by low mineralization, neutral pH, low nutrient concentrations and high dissolved oxygen. It is probable that *F. misarelensis sp. nov*. is common in European rivers with the same characteristics, because a population was found in Italy (E. Falasco, pers. comm. by e-mail).

From the type material analysed in this study, only *Fragilaria nevadensis* was identified in Portugal. It was present, in low abundance, at 10-m depth in the pelagic zone of Alqueva reservoir near Mourão, southern Portugal (0.25%), in July 2014 and in Coura River (Minho basin) in June 2017 (0.49%; Novais M.H., pers. comm.). According to Linares-Cuesta & Sánchez-Castillo (2007), the ecological preferences of this species are similar to *Fragilaria capucina* var. *austriaca*, which lives in oligotrophic to mesotrophic and circumneutral to alkaline waters, and is frequent in the Alps and Pyrenees (Krammer & Lange-Bertalot 1991). The sample collected in the Alqueva reservoir was slightly alkaline (pH = 7.8), with medium conductivity (420 µS cm^{-1}), low dissolved oxygen (41.5%), high temperature (21.25°C) and low nitrates, nitrites, total nitrogen, total phosphorus and phosphates concentrations. Regardless, the low occurrence of the species does not allow further comments on its optimal growth conditions.

Fragilaria misarelensis sp. nov. is placed in *Fragilaria*, even though its cells are not joined to form ribbon-like colonies, and occur as single cells, lacking spines located on or between the striae. This was one of the main features that originally characterised the genus (Williams & Round 1987). Nevertheless, Williams & Round (1987) noted that some *Fragilaria* species have been reported as growing singly, and the presence of spines characterises a much larger group, being present in other genera, i.e. *Staurosirella* D.M. Williams & Round, *Staurosira* (Ehrenberg) D.M.Williams & Round, *Stauroforma* Flower, Jones & Round or *Punctastriata* D.M.Williams & Round (Morales 2001). This species presents other SEM features that corroborate placement in genus *Fragilaria*, such as uniseriate striae, composed of round or slightly elongated areolae, a well-developed central area, apical pore fields of ocellulimbus type, the presence of one rimoportula (Morales 2001), and open girdle bands (Williams & Round 1987). The presence of spines is a dubious character in the characterisation of the genus, because it is absent in *Fragilaria rinoi* (Delgado *et al.* 2016), *F. candidagilae* (Delgado *et al.* 2015) and *F. pectinalis* (Wetzel & Ector 2015; Table 3). Furthermore, according to Wetzel & Ector (2015), spines are usually absent in *F. microvaucheriae* but can also be present (being small, conic and irregularly located on the costae). The variability of this character (presence/absence of spines) within the same species leads us to propose the exclusion of this character in the description of the genus *Fragilaria*.

Fragilaria species are abundant in European river basins, but it remains difficult to determine their ecological preferences, because they are often present in low abundances and only recently are several species belonging to the *Fragilaria capucina/vaucherie* complex being described and characterised in detail. Once these new species are described and well illustrated, it is expected to find them in other European regions or elsewhere, as is the case of *Fragilaria candidagilae*, described from central Portugal, that was illustrated by Lange-Bertalot *et al.* (2017) from central Europe and by Bishop *et al.* (2017) from southeast rivers in the United States (identified in Figs 45–48 as *Fragilaria* sp.35).

The comparison between *Fragilaria misarelensis sp. nov*. and similar taxa revealed that it presents a unique combination of characters: the valve shape (lanceolate valves and slightly capitate ends); density of striae; absence of linking spines; and the type of areolae, not found in the literature.

ACKNOWLEDGEMENTS

We are grateful to David Williams, Jovita Yesilyurt and Pat Sims of the Natural History Museum of London (BM), for receiving us so well on our visit to the museum and for the facilities to work with samples of the collections and bibliography search.

FUNDING

This work was cofunded by the European Union through the European Regional Development Fund, framed in COMPETE 2020 (Operational Programme Competitiveness and Internationalization), through the ICT project (UID/GEO/04683/2013) with reference POCI-01-0145-FEDER-007690 and the Alentejo Observation and Prediction Systems–ALOP project (ALT20-03-0145-FEDER-000004), which awarded a postdoc grant to the first author. The Foundation for Science and Technology (FCT, Portugal) granted financial support to GeoBioTec through the UID/GEO/04035/2013 project. The government of Xunta de Galicia (I2C Posdoctoral Fellow–2014) awarded a postdoc grant to the last author. This research received support from the SYNTHESYS Project (http://www.synthesys.info/) titled, "Study and Revision of the Different Type Materials of *Fragilaria*/*Synedra* Genera (Bacillariophyceae) and Comparison with Portuguese Taxa" (GB-TAF-3736), financed by European Community Research Infrastructure Action under the FP7 "Capacities" Program.

ORCID

Maria Helena Novais http://orcid.org/0000-0002-0870-2221
Salomé F.P. Almeida http://orcid.org/0000-0001-7240-7967
Saúl Blanco http://orcid.org/0000-0002-9015-2512
Cristina Delgado http://orcid.org/0000-0003-3954-0146

REFERENCES

American Public Health Association. 1995. *Standard methods for the examination of water and wastewater*, ed. 19. American Public Health Association, American Water Works Association, and Water Pollution Control Federation, Washington, DC. 541 pp.

Anderson M.J. 2001. A new method for non-parametric multivariate analysis of variance. *Austral Ecology* 26: 32–46.

Association Française de Normalisation. 2003. *Norme française NF EN 13946. Qualité de l'eau – Guide pour l'échantillonnage en routine et le prétraitement des diatomées benthiques de rivières*. Association Française de Normalisation, La Plaine Daint-Denis, France. 18 pp.

Barber H.G. & Haworth E.Y. 1981. A guide to the morphology of the diatom frustule with a key to the British freshwater genera. *Freshwater Biological Association Scientific Publication* 44: 1–112.

Bishop I.W., Esposito R.M., Tyree M. & Spaulding S.A. 2017. A diatom voucher flora from selected southeast rivers (USA). *Phytotaxa* 332: 101–140. DOI: 10.11646/phytotaxa.332.2.

Colmeiro M. 1889. *Enumeración y revisión de las plantas de la Península Hispano-Lusitana e Islas Baleares. Tomo V (Monocotiledóneas y criptógamas)*. Fuentenebro, Madrid. 1087 pp.

Delgado C., Novais M.H., Blanco S. & Almeida S.F.P. 2015. Examination and comparison of *Fragilaria candidagilae sp. nov*. with type material of *Fragilaria recapitellata, F. capucina, F. perminuta, F. intermedia* and *F. neointermedia* (Fragilariales, Bacillariophyceae). *Phytotaxa* 231: 1–18. DOI: 10.11646/phytotaxa.231.1.

Delgado C., Novais M.H., Blanco S. & Almeida S.F.P. 2016. *Fragilaria rinoi sp. nov*. (Fragilariales, Fragilariophyceae) from periphytic river samples in central Portugal. *European Journal of Taxonomy* 248: 1–16.

Desmazières J.B.H.T. 1825. *Plantes cryptogames de la France*, ed. 1. Lille. Leleux.

Dujardin J.P., Kaba D. & Henry A.B. 2010. The exchangeability of shape. *BioMed Central Research Notes* 3: 1–7.

Ehrenberg C.G. 1832. Beiträge zur Kenntnis der Organisation der Infusorien und ihrer geographischen Verbreitung, besonders in Sibirien. *Abhandlungen der Königlichen Akademie der Wissenschaften zu Berlin* 1830: 1–88.

Ehrenberg C.G. 1845. Novorum generum et specierum brevis definitio. Zusätze zu seinen letzten Mittheilung über die mikroskopischen Lebensformen von Portugal und Spanien, Süd-Afrika, Hinter-Indien, Japan und Kurdistan, und legte die folgenden Diagnosen u. s. w. Bericht über die zur Bekanntmachung geeigneten. *Verhandlungen der Königlich-Preussischen Akademie der Wissenschaften zu Berlin* 1845: 357–377.

European Committee for Standardization. 2003. *Water quality: guidance for routine sampling of benthic algae in shallow swift running waters*. Comité Europeén de Normalisationn, Brussels. 14 pp.

Flower R.J., Pomazkina G.V., Rodionova E. & Williams D.M. 2004. Local and meso-scale diversity patterns of benthic diatoms in Lake Baikal. In: *Proceedings of the seventeenth international Diatom symposium* (Ed. by M. Poulin), pp. 69–92. Biopress Limited, Bristol, UK.

Grunow A. 1862. Die Österreichischen Diatomaceen nebst Anschluss einiger neuen Arten von andern Lokalitäten und einer kritischen Uebersicht der bisher bekannten Gattungen und Arten. *Verhandlungen der kaiserlich-königlichen zoologisch-botanischen Gesellschaft in Wien* 12: 315–472, 545–588.

Hammer Ø., Harper D.A.T. & Ryan P.D. 2001. PAST: paleontological statistics software package for education and data analysis. *Palaeontologia Electronica* 4: 1–9.

Heudre D., Wetzel C.E., Moreau L. & Ector L. 2018. Fragilaria drouotiana sp. nov.: a new epiphytic freshwater diatom species (Fragilariaceae, Bacillariophyta) in lakes of Northeastern France. Algological Studies. DOI: 10.1127/algol_stud/2018/0310.

Inag I.P. 2008. *Manual para a Avaliação Biológica da Qualidade da Agua em Sistemas Fluviais Segundo a Directiva-Quadro da Água – protocolo de Amostragem e Análise para o Fitobentos – diatomáceas*. Ministério do Ambiente, do Ordenamento do Território e do Desenvolvimento Regional, Instituto da Água, I. P., Lisboa. 35 pp.

Krammer K. & Lange-Bertalot H. 1991. Bacillariophyceae 3. Teil: centrales, Fragilariaceae, Eunotiaceae. In: *Süsswasserflora von Mitteleuropa*, vol. 3/1 (Ed. by H. Ettl, J. Gerloff, H. Heynig & D. Mollenhauer), pp. 576. G. Fischer, Stuttgart & New York.

Lange-Bertalot H. & Metzeltin D. 1996. Indicators of oligotrophy – 800 taxa representative of three ecologically distinct lake types, carbonate buffered – Oligodystrophic – weakly buffered soft water. In: *Iconographia diatomologica. annotated diatom micrographs. ecology, diversity, taxonomy* (Ed. by H. Lange-Bertalot), pp. 1-390. Koeltz Scientific Books, Königstein, Germany.

Lange-Bertalot H., Hofmann G., Werum M.,. & Cantonati M. 2017. Freshwater benthic diatoms of central Europe: over 800 common species used in ecological assessment. (Ed. by. M. Cantonati, M.G. Kelly & H. Lange-Bertalot), pp. 1-942. Koeltz Botanical Books, Schmitten-Oberreifenberg, Germany.

Lecointe C., Coste M. & Prygiel J. 1993. "Omnidia": software for taxonomy, calculation of diatom indices and inventories management. *Hydrobiologia* 269–270: 509–513. DOI: 10.1007/BF00028048.

Linares-Cuesta J.E. & Sánchez-Castillo P.M. 2007. *Fragilaria nevadensis sp. nov*., a new diatom taxon from a high mountain lake in the Sierra Nevada (Granada, Spain). *Diatom Research* 22: 127–134. DOI: 10.1080/0269249X.2007.9705700.

Morales E.A. 2001. Morphological studies in selected fragilarioid diatoms (Bacillariophyceae) from Connecticut waters (U.S.A.). *Proceedings of the Academy of Natural Sciences of Philadelphia* 151: 105–120. DOI: 10.1635/0097-3157(2001)151[0105:MSISFD]2.0.CO;2.

Novais M.H., Blanco S., Morais M., Hoffmann L. & Ector L. 2015. Catalogue of continental diatoms from Portugal, including the Archipelagos of Azores and Madeira: updated nomenclature, distribution and bibliography. *Diatom Monographs* 17: 1–2245.

Patrick R.M. & Reimer C.W. 1966. The Diatoms of the United States exclusive of Alaska and Hawaii. Volume 1. Fragilariaceae, Eunotoniaceae, Achnanthaceae, Naviculaceae. *Monographs of the Academy of Natural Sciences of Philadelphia* 13: 1–688.

Petersen J.B. 1938. *Fragilaria intermedia – Synedra vaucheriae*? *Botaniska Notiser* 1938: 164–170.

Poulin M., Bérard-Therriault L. & Cardinal A. 1986. *Fragilaria* and *Synedra* (Bacillariophyceae): a morphological and ultrastructural approach. *Diatom Research* 1: 99–112. DOI: 10.1080/0269249X.1986.9704961.

QGIS Development Team, 2018. QGIS Geographic Information System. Open Source Geospatial Foundation. http://qgis.osgeo.org

Rohlf F.J. & Slice D.E. 1990. Extensions of the Procrustes method for the optimal superimposition of landmarks. *Systematic Zoology* 39: 40–59. DOI: 10.2307/2992207.

Ross R., Cox E.J., Karayeva N.I., Mann D.G., Paddock T.B.B., Simonsen R. & Sims P.A. 1979. An amended terminology for the siliceous components of the diatom cell. *Nova Hedwigia, Beiheft* 64: 513–533.

Round F.E., Crawford R.M. & Mann D.G. 1990. *The diatoms. Biology and morphology of the genera*. Cambridge University Press, Cambridge, UK.

Trelease W. 1897. Botanical observations on the Azores. *Annual Report of the Missouri Botanical Garden* 8: 77–220. DOI: 10.2307/2992160.

Tuji A. 2004. Type examination of the ribbon-forming *Fragilaria capucina* complex described by Christian Gottfried Ehrenberg. In: *Proceedings of the seventeenth international diatom symposium* (Ed. by M. Poulin), pp. 411–422. Biopress Limited, Bristol, UK.

Tuji A. & Williams D.M. 2006a. Examination of the type material of *Synedra rumpens = Fragilaria rumpens*, Bacillariophyceae. *Phycological Research* 54: 99–103. DOI: 10.1111/pre.2006.54.issue-2.

Tuji A. & Williams D.M. 2006b. Typification of *Conferva pectinalis* O.F. Müll. (Bacillariophyceae) and the identity of the type of an alleged synonym, *Fragilaria capucina* Desm. *Taxon* 55: 193–199. DOI: 10.2307/25065541.

Tuji A. & Williams D.M. 2008. Examination of types in the *Fragilaria pectinalis-capitellata* species complex. In: *Proceedings of the nineteenth international diatom symposium* (Ed. by Y. Likhoshway), pp. 125–139. Biopress Limited, Bristol, UK.

Tuji A. & Williams D.M. 2013. Examination of types in the *Fragilaria vaucheriae-intermedia* species complex. *Bulletin of the National Museum of Natural Sciences Series B* 39: 1–9.

Van Dam H., Mertens A. & Sinkeldam J. 1994. A coded checklist and ecological indicator values of freshwater diatoms from The Netherlands. *Netherlands Journal of Aquatic Ecology* 28: 117–133. DOI: 10.1007/BF02334251.

Van de Vijver B., Jarlman A., de Haan M. & Ector L. 2012. New and interesting diatom species (Bacillariophyceae) from Swedish rivers. *Nova Hedwigia, Beiheft* 141: 237–254.

Van Heurck H. 1881. *Synopsis des Diatomées de Belgique*. Atlas. Ducaju & Cie., Anvers, pls 31-77.

Wetzel C.E. & Ector L. 2015. Taxonomy and ecology of *Fragilaria microvaucheriae sp. nov*. and comparison with the type materials of *F. uliginosa* and *F. vaucheriae*. *Cryptogamie, Algologie* 36: 271–289. DOI: 10.7872/crya/v36.iss3.2015.271.

Williams D.M. 1986. Comparative morphology of some species of *Synedra* Ehrenb. with a new definition of the genus. *Diatom Research* 1: 131–152. DOI: 10.1080/0269249X.1986.9704963.

Williams D.M. 2011. *Synedra, Ulnaria*: definitions and descriptions – a partial resolution. *Diatom Research* 26: 149–153. DOI: 10.1080/0269249X.2011.587646.

Williams D.M. & Round F.E. 1987. Revision of the genus *Fragilaria*. *Diatom Research* 2: 267–288. DOI: 10.1080/0269249X.1987.9705004.

Science of the Total Environment 659 (2019) 1242–1255

Contents lists available at ScienceDirect

Science of the Total Environment

journal homepage: www.elsevier.com/locate/scitotenv

Vertical distribution of benthic diatoms in a large reservoir (Alqueva, Southern Portugal) during thermal stratification

Maria Helena Novais [a,b,*], Alexandra Marchã Penha [a,b], Eduardo A. Morales [a,b], Miguel Potes [a], Rui Salgado [a,c], Manuela Morais [a,b]

[a] Institute of Earth Sciences - ICT, University of Évora, Rua Romão Ramalho n°. 59, 7000-671 Évora, Portugal
[b] Water Laboratory, University of Évora, P.I.T.E. Rua da Barba Rala No. 1, 7005-345 Évora, Portugal
[c] Department of Physics, ECT, University of Évora, Rua Romão Ramalho n° 59, 7000-671 Évora, Portugal

HIGHLIGHTS

- Diatoms in lentic systems are poorly studied and their vertical dynamics is often neglected.
- Meteorological, water physico-chemical and biological characterizations were carried out.
- Diatom assemblages attached to artificial substrates were studied in the ALEX campaign.
- Vertical gradient of diatom assemblages, diatom guilds, diversity and SPI indices was detected.
- Living diatoms were observed at 30 m, far below the photic zone.

GRAPHICAL ABSTRACT

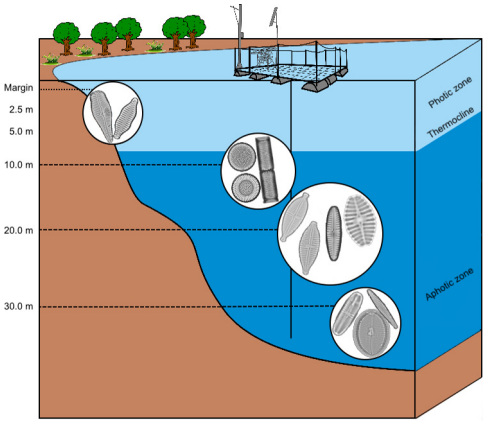

ARTICLE INFO

Article history:
Received 11 October 2018
Received in revised form 15 December 2018
Accepted 16 December 2018
Available online 24 December 2018

Editor: Sergi Sabater

Keywords:
Benthic diatoms
Depth-gradient
Ecological guilds
Physico-chemical characterization

ABSTRACT

Freshwater diatom communities are known to respond to a wide range of environmental factors, however, the depth gradient is usually neglected and few studies are available, especially in large reservoirs. During the ALqueva hydro-meteorological EXperiment (ALEX) field campaign, diatom communities were studied in the margins and in three platforms (from the surface to the bottom of the reservoir) located in the limnetic zone of the Alqueva reservoir, one of the largest artificial lakes in western Europe. A detailed meteorological and physico-chemical characterization of the reservoir was carried out from June to September in Summer 2014, when the reservoir was stratified, to relate these variables with diatom assemblages. Despite the large dimensions of the reservoir, no differences in the water physico-chemical characteristics and diatom descriptors were detected among platforms. Small changes in diatom assemblages, ecological guilds, taxa richness and Shannon diversity index were observed between sampling campaigns. Nevertheless, differences in diatoms were detected along a depth gradient, both in terms of diatom assemblages and ecological guilds. Taxa richness, Shannon diversity index, Pielou's evenness and Specific Pollution sensitivity Index (SPI) also differed with depth, with the lowest values of all indices detected at surface samples, increasing with depth, reaching the highest values at 20 m for taxa richness, Shannon diversity and Pielou's evenness indices.

© 2018 Elsevier B.V. All rights reserved.

* Corresponding author.
E-mail address: hnovais@uevora.pt (M.H. Novais).

https://doi.org/10.1016/j.scitotenv.2018.12.251
0048-9697/© 2018 Elsevier B.V. All rights reserved.

1. Introduction

Water resources in the Mediterranean Region are limited, fragile and threatened, and there is an urgent need for their sustainable management, which can only be achieved by understanding and predicting the complex interactions between climate, hydrology, ecosystem processes, water quality and biodiversity (Ferragina, 2010; Hamdy, 2001).

Lakes and reservoirs, due to their vulnerability, have been considered sentinels of environmental changes caused by anthropogenic effects such as intensive agriculture, livestock raising, dam construction, global warming and eutrophication (Hsieh et al., 2011), considered by Sutton et al. (2013) as one major threat to the ecological integrity of lentic systems. The determination of the trophic condition is therefore an important step in the ecological assessment of a reservoir because of the powerful predictive statements that can be made describing abiotic and biotic relationships for a given trophic state (Karadžić et al., 2010). The assessment of the trophic status of lentic systems is commonly based on water chemistry and phytoplankton attributes such as biomass. But fish and macrophytes are also often monitored because of the importance of fish as suppliers of significant ecosystem services and macrophytes as providers of habitat for invertebrates and fish (DeNicola and Kelly, 2014). Despite their important role in primary productivity, nutrient cycling and food web interactions (Vadeboncoeur and Steinman, 2002), there are only a few published studies incorporating benthic diatoms as a means to assess lake ecological status (e.g. Rimet et al., 2015). However, some countries are already incorporating littoral diatoms for the assessment of lake ecological status within a European regulatory context related to the application of the Water Framework Directive (WFD; The European Parliament & European Council, 2000), as described by Kelly et al. (2014). Until now, research on lake primary production has focused much more on planktic than on benthic algae, with phytoplankton studies outnumbering periphyton studies by an order of magnitude (Cantonati and Lowe, 2014; Poikane et al., 2016). In turn, more attention has been given to stream than to lentic systems phytobenthos, with twice the number of papers focusing on the former, which has implications for monitoring and the application of the European Union (EU) Water Framework Directive (WFD; The European Parliament & European Council, 2000; Poikane et al., 2016). In 2014, only 1/3 of EU member states had phytobenthos assessment methods for lentic systems, whereas almost all (22 of 27, including Portugal) had methods for streams (DeNicola and Kelly, 2014; Poikane et al., 2016). DeNicola and Kelly (2014) questioned whether a dedicated periphyton assessment of lentic systems was justified and if the decision not to include periphyton could lead to instances where important information is overlooked. The conceptual model presented in their review consists on an attempt to provide a guide for developing quantitative periphyton-based approaches for the assessment of the biological condition of lentic systems.

The few existing lacustrine periphyton studies focus on littoral zones (e.g. Vadeboncoeur et al., 2014; Rimet et al., 2015; Faria et al., 2017), probably due to the physical heterogeneity that increases the spatial variation in periphyton biomass and productivity, especially where macrophytes provide a temporally variable and structurally complex substratum (Vadeboncoeur et al., 2014). However, studies including periphyton from the limnetic lacustrine zones are rare (e.g. Stevenson and Stoermer, 1981; Hoagland and Peterson, 1990; Flower et al., 2004; Cantonati et al., 2009), even though the importance of a thorough knowledge of the biological depth-distribution patterns and their environmental controls is well-recognized as a valuable tool for an ecologically sensible management of reservoirs and natural lakes (Cantonati et al., 2009).

Light and nutrients are considered the most frequently reported environmental controls of phytobenthos in lakes (Cantonati et al., 2009). Yang and Flower (2012) suggested that light influences benthic diatom abundance, whereas substrate type has a higher influence on species composition in the case of oligotrophic lakes. Also, the results presented by Vadeboncoeur et al. (2014) indicate that light is the primary structuring mechanism for epipelon in lakes of all sizes, whilst productivity patterns point to an added role of wave disturbance in limiting biomass. In the case of epiphyton, wind disturbance acts as a structuring force in its dynamics (Faria et al., 2017). These findings concur with the previous work of Stevenson and Stoermer (1981) that distinguished three zones (shallow, mid-depth and deep) in Lake Michigan, based on diatom community composition, structure and abundance. These attributes were shaped by substrate disturbance, wave action in the shallow zone, and by low light levels in the deep zone. Also, Cantonati et al. (2009) identified the same three zones in Lake Tovel, defined for diatoms and total epilithic phytobenthos (using physiological, functional and community organization parameters) and having water-level fluctuations, photosynthetically active radiation (PAR), silica and nitrates as the main environmental controls. Among biotic regulating factors, zooplankton grazing plays an important role in epiphyton dynamics in a large shallow lake (Faria et al., 2017); also Higgins et al. (2014) identified the important effect of large-bodied zooplankton and dreissenid mussels (grazers of phytoplankton) on total ecosystem production (TEP) and autotrophic structure (the partioning of TEP between phytoplankton and periphyton) across gradients in lake size and total phosphorus concentration.

As a contribution to the knowledge of benthic diatoms in large reservoirs, the present work explores the influence of water physicochemistry on diatoms in the margins and in a stratified depth gradient in the limnetic zone of the Alqueva reservoir, southern Portugal. Data were collected within the framework of the ALqueva hydro meteorological Experiment (ALEX 2014), an integrated field campaign with measurements of chemical, physical and biological parameters at different experimental sites in the reservoir and in its surrounding area, from June to September 2014, with the main purpose of studying lake-atmosphere interactions. Data obtained during the ALEX 2014 are available via http://www.alex2014.cge.uevora.pt/data/ (Salgado et al., 2018). These data have already been used in different studies, including the heat, vapour and CO_2 fluxes in the water–air interface (Potes et al., 2017), the formation and development of a lake breeze system at a large reservoir (Iakunin et al., 2018), and the effects of an inland water body on the atmospheric electrical field (Lopes et al., 2016; Nicoll et al., 2018).

Given the vertical zonation of diatoms observed in European and US natural lakes, we hypothesize that similar dynamics can occur in Alqueva reservoir, a deep and relatively young system. To do so, spatial and temporal variations are explored for biotic and abiotic variables, and benthic diatoms are analysed in terms of assemblages, ecological guilds, and the Specific Pollution Sensitivity (SPI) and diversity indices.

2. Methodology

2.1. Study area

The ALEX field campaign took place in the Alqueva Reservoir, Guadiana basin (SW Iberian Peninsula) from June to September 2014. The construction of the dam started in 1995 and the dam floodgates were closed in 2002. The reservoir, an 83 km section along the main course of the Guadiana River, is one of the largest western European reservoirs, with a surface of 25,000 ha when completely filled, a capacity to store 4500 million m^3 of water, a catchment area of 55,000 km^2 and maximum depth of >70 m.

The Guadiana basin is characterized by a Mediterranean climate (Csa according to the Köppen climate classification). Summer periods are dry and hot, with high solar radiation at the surface and high potential evapotranspiration, whilst winter periods are colder and relatively harsh.

Three fixed platforms located in the limnetic zone of the reservoir were selected to carry out this study: Montante, Mourão and Alcarrache (Fig. 1). Montante and Mourão platforms are located in clear cut

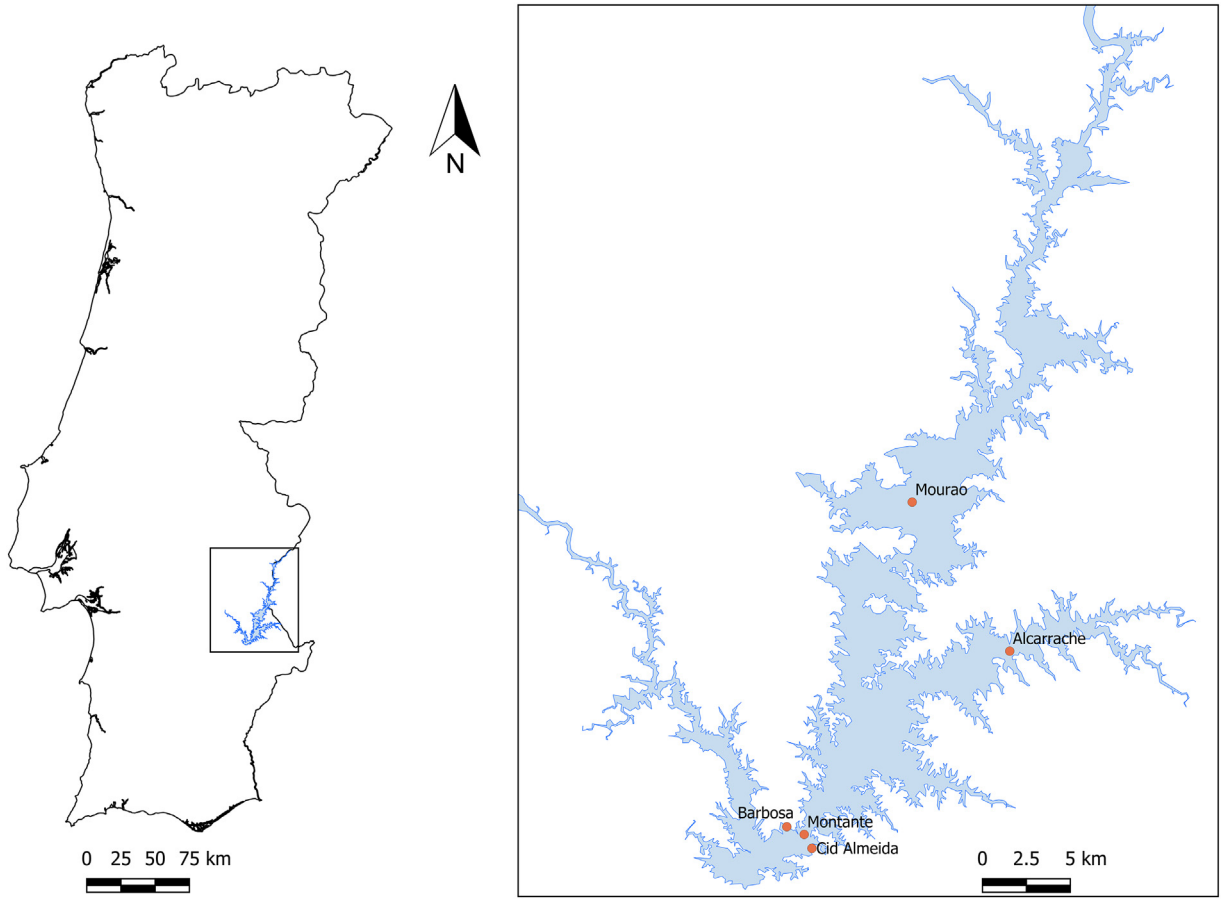

Fig. 1. Map of Portugal with the Alqueva reservoir and a detail with the location of the three sampling platforms, including the meteorological stations Barbosa and Cid Almeida.

surroundings and deep areas of the reservoir, with >60 m and 50 m depth, respectively; whilst Alcarrache platform is located in a forested surrounding and a ca. 20 m deep area.

Along this period, meteorological measurements were carried out in Montante platform and in Cid Almeida and Barbosa, two meteorological stations located on the shore nearby Montante platform (Fig. 1). The water physico-chemical characterization was based in in situ measurements and in laboratory analysis of water samples monthly collected from the three fixed platforms (Fig. 1). Biological characterization started in July 2014 and comprised monthly sampling of littoral benthic diatoms collected from the margins (in the nearest sites, accessible by car, of the platforms) and in diatoms collected from artificial substrates placed along a depth gradient from the surface to the bottom of the reservoir in Alcarrache platform and to 30 m in the Montante and Mourão platforms.

2.2. Meteorological, physico-chemical and biological characterization

The Montante platform was the main ALEX meteorological experimental site, equipped with an eddy-covariance system (IRGASON from Campbell Scientific), which directly measures atmospheric pressure, air temperature, water vapour and carbon dioxide concentrations, 3D wind components, and computes, among other quantities related to turbulence, the momentum flux, sensible and latent heat fluxes, carbon dioxide flux. The platform also had an albedometer (CM7B from Kipp & Zonen) and a pyrradiometer (8111 from Philipp Schenk) to assess downwelling and upwelling short and longwave radiative fluxes. On the lake shore, nearby the Montante platform, two standard meteorological stations were installed, known as Barbosa and Cid Almeida. It includes wind speed and direction (Wind Sonic from Gill Instruments), air temperature and relative humidity (CS 215 from Campbell Scientific) and precipitation (ARG 100 STD from Institute of Hydrology). Data were acquired at 1 s sampling rate and values for 1-minute intervals were recorded.

To characterize the water column, vertical profiles of temperature (T, °C), dissolved oxygen (DO, mg L^{-1} and % of O_2 saturation), pH, oxidation-reduction potential (ORP, V) and Electrical Conductivity (EC, μS cm^{-1}) were taken in situ using a TROLL 9500 PROFILER XP multi parametric probe. Simultaneously, an integrated sample was collected for phytoplanktic chlorophyll *a* (Chl *a*) determination and water samples for physico-chemical analyses were collected at three depths (surface, metalimnion and bottom) using a Van Dorn bottle (3 L capacity) and kept cool, in the dark until laboratory processing. Water transparency was measured using a 20 cm black and white Secchi disk. Profiles of downwelling spectral irradiance were made in the water column, until 3 m depth, using the device developed by Potes et al. (2017). With these profiles the water spectral extinction coefficients were obtained using the formulation from Preisendorfer (1959). In the laboratory, standard methods for water chemical analyses were applied according to Apha (1995) and comprised the following parameters: alkalinity (Alk, mg HCO_3^- L^{-1}), ammonium (NH_4, μg NH_4-N L^{-1}), biochemical oxygen demand after 5 days (BOD_5, mg O_2 L^{-1}), chemical oxygen demand (COD, mg O_2 L^{-1}), Kjeldahl nitrogen (KN, μg N L^{-1}), nitrates (NO_3, μg NO_3-N L^{-1}), nitrites (NO_2, μg NO_2-N L^{-1}), phosphates (PO_4, μg PO_4-P L^{-1}), silica (Si, mg Si L^{-1}), total hardness (TH, mg $CaCO_3$ L^{-1}), total nitrogen (TN, μg N L^{-1}), total phosphorus (TP, μg P L^{-1}), total suspended solids (TSS, mg L^{-1}) and turbidity (TU, NTU). Additionally, in the bottom samples, iron (Fe, μg Fe L^{-1}) and manganese

(Mn, μg Mn L^{-1}) were also analysed. Samples for Chl *a* analysis were filtered using Whatman GF:C glass fiber filters, chlorophyll *a* was extracted for 24 h in 8 mL acetone (90%) at 4 °C in the dark, measured spectrophotometrically and corrected for degradation products using the equations by Lorenzen (1967).

Littoral diatoms were sampled from stones in the margins following the European norms for sampling in lakes (King et al., 2006), which consisted in brushing the upper surface of 5 stones collected at ~40 cm depth. In each platform, 3 untreated ceramic tiles (dimension 7.5 cm × 5 cm) were attached at discrete depths (surface ca. 20 cm, 2.5 m, 5 m, 10 m, 20 m in the three platforms, and also at 30 m in Montante and Mourão) to a rope tied to the platform (this procedure is more cost-effective than the sampling by scuba divers, commonly used in this kind of studies). Artificial substrates were selected to include live diatoms in the analysis (dead frustules commonly deposited on hard substrates in lentic system are washed from these tiles) and intends also to eliminate differences in diatom assemblages caused by the substrate type, considered by Yang and Flower (2012) as one of the main factors influencing benthic diatom composition in oligotrophic lakes. Diatoms were collected by brushing the tiles with a toothbrush, washing them with distilled water (to avoid contamination with planktic diatoms present in the reservoir water) and preserving them with a formaldehyde solution (4% v/v) immediately after sampling. At lab arrival an aliquot of fresh sample (not preserved) was checked to verify if diatoms were alive. All diatom samples were treated by oxidation using hot hydrogen peroxide (35%) and dilute HCl (37%), in order to obtain a suspension of clean frustules. Permanent slides were mounted with Naphrax®. Diatoms were identified to specific or subspecific level using light microscopy (LM) (Leica DMLB with 100× oil immersion objective, N.A. 1.40). At least 400 valves were identified and counted from each slide to estimate the relative abundance of each taxon (Inag, 2008). The identification was based on reference floras (e.g. Krammer and Lange-Bertalot, 1986, 1988, 1991a, 1991b; Hofmann et al., 2011), as well as on recent bibliographic sources, including the series 'Diatoms of Europe', 'Iconographia Diatomologica', 'Bibliotheca Diatomologica' and relevant taxonomic papers, such as Reichardt (1997), Van de Vijver et al. (2011) and Novais et al. (2011, 2015). Furthermore, the samples were identified and counted by a single analyst, in order to decrease possible identification error effects, which can be the main source of variability according to Prygiel et al. (2002) and Kahlert et al. (2009).

2.3. Statistical analysis

2.3.1. Environmental parameters

The water physico-chemical parameters were log-transformed prior to the analysis and appropriate tests for normality were conducted (Shapiro–Wilk normality test, $p < 0.05$). These data were first tested for correlations among 19 parameters, by means of Pearson correlations using STATISTICA 8.0 (StatSoft Inc, 2001), to avoid multicollinearity in the selection of the variables to include in the following multivariate analysis. Afterwards, a Principal Component Analysis (PCA) (Goodall, 1954) was conducted in order to detect patterns and explore the relationships between environmental variables among the sites, depths and campaigns using CANOCO v. 4.5 (ter Braak and Šmilauer, 2002). Later, a one-way Analysis of Variance (one-way ANOVA) or a Kruskal-Wallis One Way Analysis of Variance on Ranks (Kruskal-Wallis test) were carried out, depending on whether the data followed the normality assumption. As post hoc and Pairwise Multiple Comparison analysis, both Dunn's and Holm-Sidak methods (Dunn, 1961; Holm, 1979) were performed, to test the preliminary results obtained with the PCA, i.e., to verify which physico-chemical parameters vary with depth and whether there are differences between platforms and sampling dates, using SigmaPlot 12.0 (Systat Software Inc., Chicago, IL).

2.3.2. Diatoms

Only diatom taxa reaching an abundance of >1% in at least one sample were included in the statistical analyses (123 diatom taxa in total).

A non-metric multidimensional scaling (nMDS) ordination technique was applied to the species data, based on a matrix with 123 diatom taxa x 56 samples, log-transformed (nMDS; Bray-Curtis distance; minimum stress 0.01; Kruskal fit scheme). In nMDS, site points are arranged in the best possible way so that closer points correspond to sites similar in their species composition, and points far apart are more dissimilar. Afterwards, statistical differences in diatom assemblages between platforms, sampling dates and depths (taking into account the preliminary nMDS results) were tested by the non-parametric Analysis of Similarity (ANOSIM; Bray-Curtis distance measure, 999 permutations) based on species abundances. ANOSIM is a randomization-based method of multivariate analysis and it is mainly used to test significant differences between two or more groups (defined a priori), based on any distance measure (Clarke and Ainsworth, 1993). R is scaled to lie between −1 and +l, a value of zero (or small negative or positive values near to zero) representing the null hypothesis of no differences among a set of samples, and its magnitude depends on the amount by which samples differ (Clarke 1993). The percentage breakdown of average dissimilarity between the platforms, sampling campaigns and depths was determined by means of SIMPER analysis, using the Bray-Curtis dissimilarity index (Clarke and Gorley, 2001). Both nMDS, SIMPER and ANOSIM analyses were performed using PRIMER Version 5.2.0 (Clarke and Gorley, 2001).

The indicator value (IndVal) method was used to identify the key species at each depth (Dufrêne and Legendre, 1997) using PC-Ord 6.0 (MjM Software Ltd., 217–219 Hamstel Road, Southend on Sea Essex SS2 4LB). This method provides IndVals for each species, based on the combination of information on the specificity and fidelity of occurrence of a taxon in a group. The statistical significance of the species IndVal was evaluated using Monte Carlo random permutation tests.

Ecological guilds were assigned to all taxa identified following the classification of Passy (2007), Berthon et al. (2011) and Rimet and Bouchez (2012): low-profile, high-profile, motile and planktic guilds. For each sample, taxa richness (S), Shannon diversity index (H′) and the Pielou's evenness index (J′) were determined. The Specific Pollution Sensitivity Index (SPI) was calculated from diatom abundances (Coste in CEMAGREF, 1982), using the OMNIDIA v. 5.5 software (Lecointe et al., 1993). This index is based on the Zelinka and Marvan (1961) formula, i.e., assigning each taxon a pair of individual values, pollution tolerance (S) and stenoecy degree (V), and the initial results ranging from 1 to 5 are transformed on a note to 20, in which higher values correspond to lower pollution. SPI was selected because it is the only diatom index based on the autecological parameters of virtually all known taxa, it has been developed for assessing the quality of running waters and has been recommended as a reference index for several Iberian basins (Gomà et al., 2005; Blanco et al., 2008). One-way ANOVA or a Kruskal-Wallis test were carried out, depending on whether the data met the normality and the equal variance requirements, followed by post hoc analysis, to test the abovementioned descriptors for differences between sampling sites, campaigns and depth gradient, using SigmaPlot 12.0 (Systat Software Inc., Chicago, IL).

Spearman rank order correlations were calculated to explore possible correlations between diatoms (expressed as taxa richness, Shannon diversity and Pielou's evenness indices, number of genera, SPI and ecological guilds) and water physico-chemical parameters (selected among those that varied with depth), using STATISTICA 8.0 (StatSoft Inc, 2001).

3. Results

3.1. Meteorological characterization

Table 1 shows the average air temperature, accumulated precipitation and wind speed recorded at Barbosa weather station (Fig. 1).

Table 1
Temperature, wind speed and precipitation values recorded at Barbosa weather station during the ALEX field campaign. Monthly and eight days before the field campaigns averages, maximum and minimum of air temperature at two meters height (ºC) and wind speed at three meters height (ms^{-1}); and accumulated precipitation (mm) for the same time periods.

Campaigns	Average temp. (°C)	Average temp. 8 days (°C)	Minimum temp. (°C)	Minimum temp. 8 days (°C)	Maximum temp. (°C)	Maximum temp. 8 days (°C)	Average wind speed (m s^{-1})	Average wind speed 8 days (m s^{-1})	Maximum wind speed (m s^{-1})	Maximum wind speed 8 days (m s^{-1})	Accumulated precipitation (mm)	Accumulated precipitation 8 days (mm)
25 June	20.71	20.36	15.62	17.51	29.22	28.30	2.42	2.53	8.28	9.56	13.33	13.33
24 July	24.27	24.09	16.83	17.00	32.67	31.99	2.34	2.44	8.51	8.49	3.98	0.00
27 August	24.64	24.80	16.77	16.29	33.78	34.31	2.83	2.38	9.41	8.78	0.00	0.00
25 September	21.44	20.33	17.57	16.37	28.58	26.24	2.11	1.90	8.45	8.13	56.32	13.93

Data are shown only for Barbosa, since similar values were measured in the Montante platform and the Cid Almeida weather station. The mentioned table presents monthly values as well as values from eight days prior to the field campaigns. In July and August, average temperatures were higher, with lower or no precipitation. In the eight days before the field campaigns of June and September record, lower temperatures occurred and a similar amount of rain (around 13 mm) fell on both months. Comparing these values with the temperature and precipitation Normals (1981–2010 normals – www.ipma.pt), we found that temperature and precipitation values agreed with the averages, with exception of the accumulated precipitation in September, which was 90% higher (average value was 29.5 mm in 1981–2010 period for Beja climatological station). The wind speed was low in average, with the highest values recorded in August (monthly average 2.83 m s^{-1}; maximum 9.41 m s^{-1}). However, wind speed varies throughout the day, with low values during the night and morning (<2.5 m s^{-1}) increasing at the end of the afternoon, with the maritime breeze influence (reaching values above 4 m s^{-1}) (Fig. 2).

3.2. Water physico-chemical characterization

Descriptive statistics of the environmental parameters recorded from the three platforms and depths are presented in Table 2.

From the in situ parameters, strong positive correlations were only detected among T and pH; whilst negative strong correlations between in situ parameters and nutrients were only found for ORP and NH_4. Strong negative correlations were not detected among the nutrients, but strong positive correlations were found for NH_4 with KN and TN; and PO_4 strongly correlated with TP. Among the other descriptors strong negative correlations were detected between Si and T, pH and DO, and TU was highly correlated with TSS (Table A.1 with the correlations is presented as Appendix).

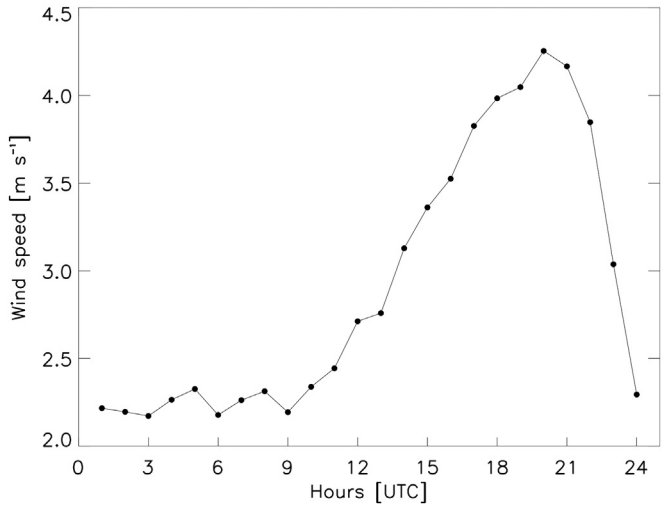

Fig. 2. Hourly averages of the wind speed (m s^{-1}) during the ALEX experiment at the Montante platform.

The strong correlations detected between TSS and TU; NH_4, KN and TN; PO_4 and TP, allowed the identification of the parameters that could be excluded from the PCA analysis, given their possible multicollinearity. Therefore, from the above-mentioned parameters, only TSS, TN and TP were part of the 15 parameters included in the PCA.

The PCA conducted to explore the variation of physico-chemical variables (Fig. 3) showed that the first PCA axis accounted for 36.7% variance and corresponded to the nutrient gradient (mainly TP and TN), revealing a depth gradient. Surface and metalimnion samples were separated from bottom samples, with higher concentrations of TP in the latter, especially in Mourão and Alcarrache platforms during August and September (in the positive side of the axis). By opposition to higher ORP and DO values in surface and metalimnion samples, collected in June and July (in the negative side of the axis). Complementarly, a Kruskal-Wallis test proved: 1) no differences between sampling campaigns ($H = 1.814$ with 3 degrees of freedom, $p = 0.612$); 2) the differences in depth ($H = 31.369$ with 2 degrees of freedom, $p < 0.001$), with Dunn's Method separating surface and metalimnion from bottom samples, but no distinction between the former two ($p > 0.05$). A One-way ANOVA or a Kruskal-Wallis test were further used to verify which parameters differed between surface, metalimnion and bottom samples. Differences with depth were detected for: T ($F = 230.818$, $p < 0.001$), EC ($F = 5.340$, $p = 0.009$) and Si ($F = 95.710$, $p < 0.001$), with Holm-Sidak method separating surface, metalimnion and bottom samples for T and Si ($p < 0.001$) and surface from bottom samples for EC ($p = 0.008$); pH ($H = 31.282$ with 2 degrees of freedom, $p = 0.001$), DO ($H = 22.294$ with 2 degrees of freedom, $p < 0.001$), PO_4 ($H = 9.332$ with 2 degrees of freedom, $p = 0.009$), TP ($H = 8.747$ with 2 degrees of freedom, $p = 0.013$), NO_3 ($H = 9.505$ with 2 degrees of freedom, $p = 0.009$) and TSS ($H = 8.429$ with 2 degrees of freedom, $p = 0.015$) with, Dunn's Method distinguishing surface and metalimnion from bottom samples ($p < 0.05$) for pH and DO; surface from bottom samples for PO_4, TP and TSS; bottom and metalimnion from surface samples ($p < 0.05$) for NO_3.

The second axis explained 28.9% variance, reflecting a temporal gradient, correlated with NO_3, EC, TSS and TH. Higher values of TSS and EC were detected in surface and metalimnion samples collected in August and September (negative side of the axis), whilst in the positive side of the axis higher concentrations of NO_3 were detected in the beginning of the Summer (June and July) in bottom samples.

In the PCA ordination plot no clear separation of samples collected in different platforms was detected, neither in the further Kruskal-Wallis test. ($H = 1.584$ with 2 degrees of freedom, $p = 0.453$).

The previous results show no differences between sites but reveal a depth gradient for the parameters measured in situ, such as T, pH, EC and DO; therefore, vertical profiles for these parameters (additionally, ORP was also included) are presented for Mourão platform (Fig. 4), as representative of the three platforms. The vertical profiles show the stratification of the reservoir during the whole period of the campaign (from June to September), thus allowing its classification as warm monomictic, with the thermocline depth around 10 m in Mourão in

Table 2
Physical-chemical characterization of the water column in Montante, Mourão and Alcarrache platforms, median (interquartile range) values are presented.

Variable	Alqueva-Montante			Alqueva-Mourão			Alcarrache	
	Surface	Metalimnion	Bottom	Surface	Metalimnion	Bottom	Surface	Bottom
T (°C)	24.65 (23.51–25.71)	20.02 (19.24–20.54)	13.64 (13.32–13.96)	24.40 (23.62–25.62)	23.12 (22.99–23.42)	14.19 (13.88–14.57)	25.68 (24.78–26.88)	14.75 (14.35–15.31)
pH	9.19 (8.99–9.44)	8.03 (7.85–8.27)	7.50 (7.41–7.55)	8.97 (8.90–9,09)	8.85 (8,75-8,93)	7.32 (7,17-7,51)	9.03 (8.92–9.12)	7.25 (7.17–7.34)
DO (% O_2 sat)	101.18 (98.64–124.75)	89.54 (69.47–107.41)	22.91 (18.05–43.40)	101.84 (98.20–107.90)	98.12 (89.21–104.92)	15.44 (7.58–29.19)	90.26 (83.41–100.44)	10.72 (8.55–19.63)
EC (μS cm^{-1})	387.5 (375.8–399.7)	385.8 (375.5–394.0)	369.4 (357.7–382.3)	422.1 (404.2–445.2)	390.6 (371.6–413.8)	377.7 (351.3–493.0)	387.0 (375.2–399.0)	368.8 (355.2–383.1)
ORP (V)	0.090 (−0.003–0.090)	0.110 (−0.015–0.113)	0.110 (−0.128–0.123)	0.110 (0.045–0.115)	0.100 (0.020–0.110)	0.065 (−0.150–0.098)	0.125 (0.025–0.140)	−0.080 (−0.373–0.088)
Alk (mg L^{-1})	98.50 (95.50–100.75)	100.50 (93.25–101.00)	98.00 (89.25–111.25)	98.50 (95.00–101.50)	100.00 (97.00–107.25)	100.00 (96.25–110.50)	100.50 (97.75–105.75)	104.50 (102.00–109.00)
NH_4 (μg N L^{-1})	23 (10–37)	31 (14–43)	47 (16–153)	43 (29–99)	35 (17–116)	353 (203–519)	39 (29–97)	395 (192–620)
BOD_5 (mg L^{-1})	1.00 (0.25–1.75)	2.00 (1.25–3.50)	1.00 (0–2.00)	0 (0–0.25)	0 (0–0.25)	0 (0–0.25)	0 (0–0.25)	1.00 (1.00–1.25)
COD (mg L^{-1})	12.00 (6.00–15.00)	10.50 (7–16.25)	9.00 (3.00–14.25)	15.00 (8.50–21.25)	10.00 (4.50–15.50)	6.50 (0.75–12.75)	12.5 (7.5–17.5)	15.5 (11.25–19.5)
KN (μg L^{-1})	0 (0–450)	0 (0–450)	600 (150–600)	0 (0–150)	0 (0–150)	0 (0–700)	0	0 (0–1125)
NO_3 (μg N L^{-1})	50 (20–60)	150 (140–180)	280 (120–350)	4.5 (0–14.1)	60 (22–95)	109 (55–282)	65 (30–168)	130 (30–443)
NO_2 (μg N L^{-1})	0.5 (0.1–11.6)	2 (1–5)	0.5 (0.3–1.1)	1 (0–2)	2 (1–3)	3 (2–3)	0 (0–0.2)	5 (1–9)
PO_4 (μg P L^{-1})	2 (0—11)	8 (2–42)	20 (8–26)	0 (0–9)	0 (0–15)	101 (52–146)	0 (0–9)	13 (9–72)
Si (μg L^{-1})	150 (100—200)	400 (250–550)	1150 (1025–1200)	250 (175–325)	300 (300–400)	1450 (1225–1600)	100	1050 (950–1175)
TH (mg L^{-1})	162.5 (151.8–169.5)	157.5 (150.3–176.0)	174.5 (153.5–186.5)	155.0 (148.8–163.5)	160.0 (146.8–173.8)	142.5 (125.5–154.5)	166.5 (148.8–189.0)	156.5 (149.8–164.8)
TP (μg P L^{-1})	25 (13—30)	50 (18–60)	50 (43–125)	15 (10–43)	20 (10–73)	180 (133—203)	30 (8–68)	80 (68–143)
TN (μg N L^{-1})	84 (57–477)	244 (157–630)	765 (440–1055)	21 (7–174)	74 (23–261)	416 (132—1213)	15 (7–38)	135 (9–1333)
TSS (mg L^{-1})	3.25 (2.25–4.63)	1.85 (1.55–2.00)	1.00 (1.00–2.50)	4.50 (3.50–5.00)	2.25 (2.00–3.00)	1.75 (1.13–2.20)	3.25 (2.93–3.75)	1.85 (1.03–7.88)
TU (NTU)	2.91 (2.26–3.64)	2.09 (1.87–2.27)	2.43 (2.14–12.02)	3.45 (2.75–4.14)	1.81 (1.58–2.03)	1.95 (1.87–2.02)	3.57 (2.965–4.175)	17.16 (9.84–24.48)
Fe (μg L^{-1})	–	–	70 (70–350)	–	–	215 (80–333)	–	275 (245–365)
Mn (μg L^{-1})	–	–	0 (0—210)	–	–	220 (125–305)	–	510 (398–610)
Chl *a* (μg L^{-1})		7.45 (5.80–9.48)			13.10 (8.23–17.63)		7.85 (5.40–11.03)	

June, decreasing to ca. 8.5 m in July and August, and increasing again in September to ca. 14 m. The T of epilimnetic mixed waters reached 27.3 °C in the 2014 summer hottest periods (August), in contrast with the hypolimnetic waters that maintained the T between 13 and 14 °C. Therefore, there was a difference of >10 °C between the two layers, which remained constant over the monitoring period, despite the slight warming of the hypolimnion through time. Water pH values are higher in the epilimnion (8.8–9.3) than in the hypolimnion (7.0–7.8) due to photosynthesis, which is also shown in the oxygen oversaturation of surface waters (particularly evident in July, with 121.8% O_2 sat). However, the hypolimnion does not present anoxia in June (49.1% O_2 sat at the bottom) neither in September (22.5% O_2 sat at the bottom), most probably due to the precipitation events in the days prior to the sampling (Table 1). Anoxia (0–10% O_2 sat) occurs at 43 m in July and higher in the water column (35 m depth) in August (Fig. 4). The analysis of the ORP shows positive values from June to August.

During the study period, Secchi disk water transparency decreased in Montante, from 3 m in July to 1.6 m in September, whilst the light extinction coefficient (k) increased from 0.495 m^{-1} to 0.905 m^{-1}. The mean lower depth limit of the euphotic zone (1% of surface PAR) was 6.7 m in Montante. Whilst in Alcarrache and Mourão, lowest transparency values were detected in August, the peak of the Summer (1.0 m and 1.2 m, respectively), with high k values (0.695 m^{-1} in Alcarrache and 1.21 m^{-1} in Mourão).

3.3. Diatoms

A total of 237 specific and infraspecific diatom taxa were identified in the dataset (56 samples), from which only 123 were present with a relative abundance above 1% in at least one sample (presented as Appendix in Table A.2). These taxa were comprised in 37 genera, from which *Nitzschia* (20 taxa), *Navicula* (12 taxa), *Gomphonema* (11 taxa) and *Achnanthidium* (10 taxa) were the most specious. The most abundant species (relative abundance >20%) occurring in >50% of all samples were: *Cyclotella ocellata* Pantocsek (96.4% of samples), *Navicula cryptotenelloides* Lange-Bertalot (94.6%), *Achnanthidium minutissimum* (Kützing) Czarnecki (92.9%), *Navicula cryptotenella* Lange-Bertalot (80.4%), *Achnanthidium caravelense* Novais & Ector (76.8%), *Amphora pediculus* (Kützing) Grunow (69.6%), *Fragilaria recapitellata* Lange-Bertalot & Metzeltin (69.6%) and *Fragilaria radians* (Kützing) D.M. Williams & Round (64.3%). Other taxa, such as *Achnanthidium lineare* W. Smith (66.1% of samples), *Puncticulata radiosa* (Lemmermann) Håkansson (64.3%), *Navicula capitatoradiata* Germain (62.5%), *Nitzschia inconspicua* Grunow (60.7%), *Fragilaria tenera* (W.Smith) Lange-Bertalot

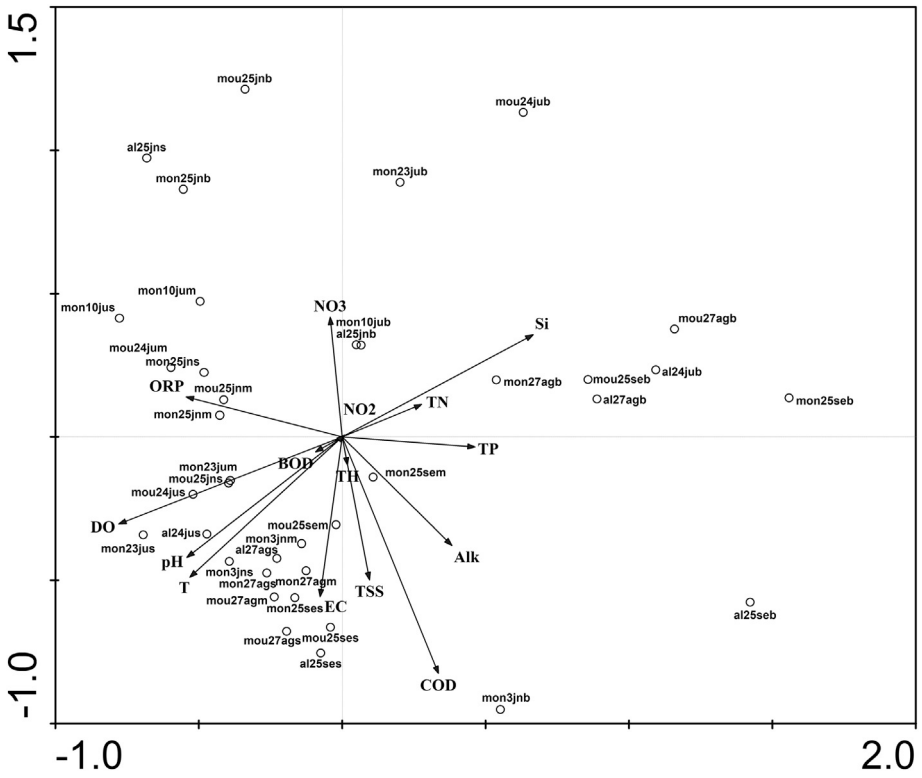

Fig. 3. PCA plot for the first two components, showing the distribution of sites according to the water physico-chemical gradients.

(57.1%), *Nitzschia dissipata* (Kützing) Grunow (51.8%), *Actinocyclus normanii* (Gregory ex Greville) Hustedt (50%), *Cyclostephanos dubius* (Fricke) Round (50%) and *Encyonopsis minuta* Krammer & E. Reichardt (50%) were present in >50% of the samples, but in low abundance (relative abundance always <20%). On the other hand, there are taxa such as *Cocconeis lineata* Ehrenberg (42.1% of relative abundance), *Achnanthidium nanum* (F. Meister) Novais & Jüttner (25%), *Eolimna minima* (Grunow) Lange-Bertalot (24.9%) and *Achnanthidium* aff. *kranzii* (Lange-Bertalot) Round & Bukhtiyarova (21.2%) that are abundant (>20% relative abundance in at least one sample), but not widely distributed in the dataset.

The nMDS analysis (2D ordination plots presented in Figs. 5, 6 and 7) presented a stress level (indicator of the adequacy of the representation) of 0.18, which is below the limit for a potentially useful 2-D representation (0.2). This analysis revealed that the samples are not grouped by platform, despite the large dimensions of the reservoir (ordination plot in Fig. 5). These results were further confirmed by the ANOSIM analysis, with no differences detected between the three platforms

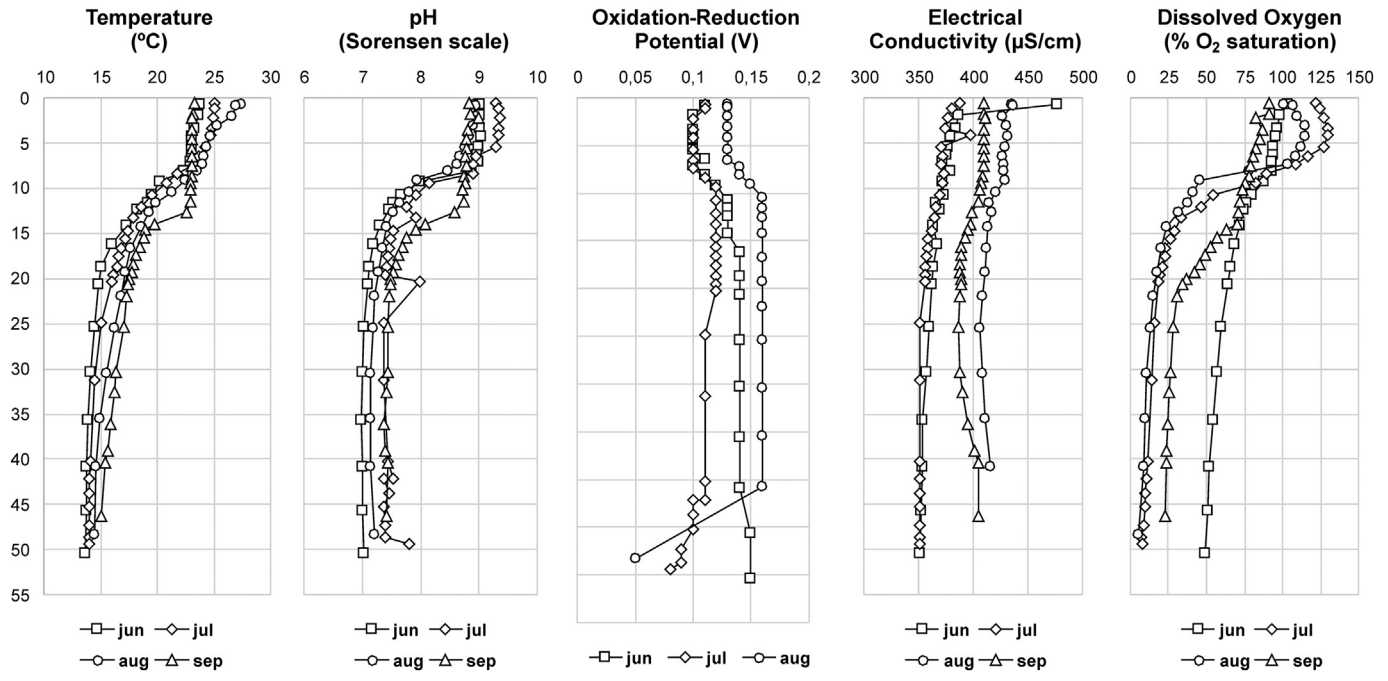

Fig. 4. Vertical profiles of in situ physical-chemical parameters in Mourão platform.

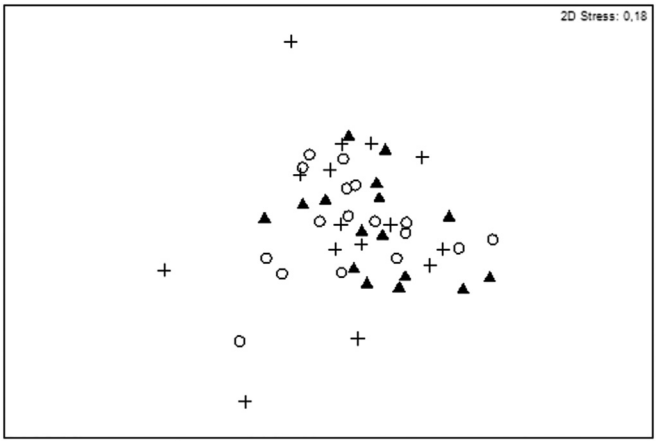

Fig. 5. 2D Non-Metric Multidimensional Scaling (nMDS) ordination plot of sites based on diatom assemblages. Black triangle: Montante; white circle: Mourão; cross: Alcarrache.

(Global $R = 0.123$, $p < 0.001$). Nevertheless, diatom assemblages in Montante and Mourão are more similar ($R = 0.09$, $p < 0.05$) than in Montante/Alcarrache ($R = 0.131$, $p < 0.05$) and in Mourão/Alcarrache ($R = 0.147$, $p < 0.05$) (Table 3). Also, the SIMPER analysis revealed a lower average dissimilarity between Montante and Mourão platforms (61.25%), presented in Table 3. The nMDS analysis revealed that the samples are also not grouped by month, with the three samplings randomly represented (ordination plot in Fig. 6). The ANOSIM analysis did not detect differences between the sampling dates (Global $R = 0.158$, $p < 0.001$), either; even though there is some evidence of small shifts in diatom assemblages, given that the campaigns in July/August ($R = 0.073$, $p < 0.05$; 60.69% average dissimilarity) are more similar than in August/September ($R = 0.123$, $p < 0.001$; 64.46% average dissimilarity) and July/September ($R = 0.279$, $p < 0.001$; 65.31% average dissimilarity) (Table 3). On the other hand, samples are grouped according to the depth (Fig. 7). These results were further confirmed by the ANOSIM analysis (presented in Table 3), revealing differences among diatom assemblages collected at different depths (Global $R = 0.336$, $p < 0.001$). Littoral samples collected from the margin were significantly different from the platform samples, independently of the depth (Table 3). There was a gradual shift in diatom assemblages with depth, revealed by the low R values between adjacent depths, and complemented by the lower average dissimilarity percentages. Diatom assemblages were more different with higher distances in depths, revealed by the higher R values and average dissimilarities (Table 3), except for the comparisons with the 30 m depth, probably because of the lower number of samples that were possible to collect (some tiles detached from the rope and were impossible to recover).

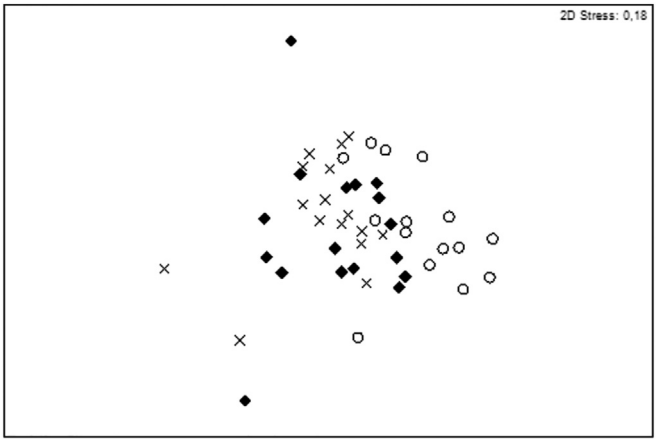

Fig. 6. 2D Non-Metric Multidimensional Scaling (nMDS) ordination plot of sampling months based on diatom assemblages. x: July; black diamond: August; white circle: September.

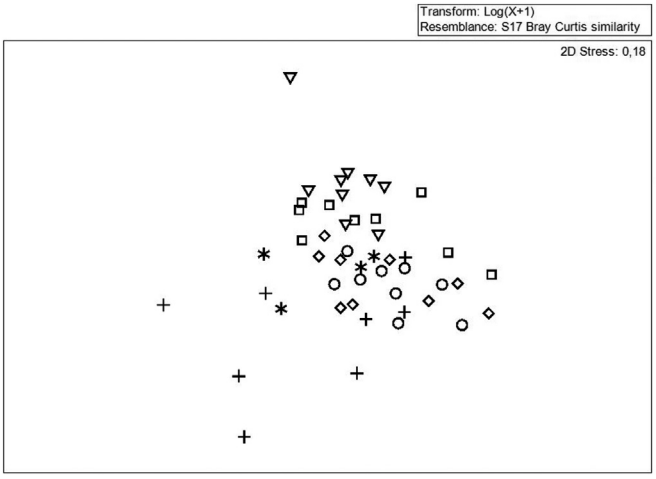

Fig. 7. 2D Non-Metric Multidimensional Scaling ordination plot of sampling depths based on diatom assemblages. Inverted triangle: Surface; square: 2.5 m; diamond: 5 m; circle: 10 m; cross: 20 m; asterisk: 30 m.

Indicator value analysis undertaken to identify characteristic taxa for the margin and different depths of the reservoir revealed that *Gomphonema italicum* Kützing, *Navicula antonii* Lange-Bertalot and *Staurosira binodis* Lange-Bertalot were indicators of the littoral areas of the reservoir, whilst *Actinocyclus normanii*, *Aulacoseira ambigua* (Grunow) Simonsen, *Cyclostephanos dubius* and *Nitzschia subacicularis* Hustedt were indicators of 10 m depth; *Chamaepinnularia* sp., *Discostella pseudostelligera* (Hustedt) Houk & Klee, *Gomphonema lagenula* Kützing, *G. parvulum* (Kützing) Kützing, *G. pumilum* var. *rigidum* E. Reichardt & Lange-Bertalot, *Mayamaea permitis* (Hustedt) Bruder & Medlin and *Planothidium frequentissimum* (Lange-Bertalot) Lange-Bertalot were indicators of 20 m depth; and *Achnanthidium nanum*, *Cocconeis pseudolineata* (Geitler) Lange-Bertalot and *Gomphonema rhombicum* M. Schmidt were indicators of 30 m; and no indicator taxa were identified for the surface, 2.5 m and 5 m (Table 4). From these, there is no information available on the autecology of *Gomphonema italicum*, *G. lagenula*, *G. pumilum* var. *rigidum*, *G. rhombicum*, *Chamaepinnularia* sp. and *Achnanthidium nanum* (Van Dam et al., 1994, retrieved from the OMNIDIA v.5.5). For the other taxa, most are classified as alkaliphilous (*Staurosira binodis*, *Navicula antonii*, *Actinocyclus normanii*, *Aulacoseira ambigua*, *Nitzschia subacicularis*, *Mayamaea permitis*, *Planothidium frequentissimum* and *Cocconeis pseudolineata*), only *Cyclostephanos dubius* is alkalibiontic, and *Discostella pseudostelligera* and *Gomphonema parvulum* are circumneutral. The majority of the indicator taxa is nitrogen autotrophic, tolerating elevated concentrations of organically bound nitrogen, but *Nitzschia subacicularis* only tolerates very small concentrations of organically bound nitrogen, and *Gomphonema parvulum* and *Mayamaea permitis* are facultatively nitrogen-heterotrophic taxa, needing periodically elevated concentrations of organically bound nitrogen. The oxygen requirements of these taxa are more variable, since *Staurosira binodis* and *Nitzschia subacicularis* require continuously high oxygen levels (aprox. 100% O_2 sat), *Cyclostephanos dubius* fairly high (<75% O_2 sat), *Actinocyclus normanii*, *Aulacoseira ambigua*, *Discostella pseudostelligera* and *Planothidium frequentissimum* moderate (<50% O_2 sat.) and *Gomphonema parvulum* and *Mayamaea permitis* low (>30% O_2 sat.). Only *Staurosira binodis* is oligosaprobous, *Aulacoseira ambigua* and *Nitzschia subacicularis* are β-*meso*saprobous, *Actinocyclus normanii*, *Cyclostephanos dubius*, *Discostella pseudostelligera* are α-mesosaprobous and *Gomphonema parvulum*, *Mayamaea permitis* and *Planothidium frequentissimum* are α-meso/polysaprobous. The great majority of these taxa are eutraphentic, except for the meso-eutraphentic *Staurosira binodis* and for *Nitzschia*

Table 3
Percentage breakdown of average dissimilarity between the platforms, sampling campaigns and depths, using SIMPER analysis. Statistical and global R values for the pairwise analysis of similarity (ANOSIM) tests are presented, $^{***}p < 0.001$ and $^{*}p < 0.05$ were regarded as significant, n.s. = not significant.

Factors	Groups	Average similarity (%)	Average dissimilarity (%)	ANOSIM (statistical R)	ANOSIM (Global R)
Platform	Montante	40.83%	Mont/Alc = 64.25	R = 0.131*	Global R = 0.123***
	Alcarrache	35.74%	Mont/Mou = 61.25	R = 0.09*	
	Mourão	40.89%	Alc/Mou = 64.50	R = 0.147*	
Month	July	43.34%	Jul/Aug = 60.69	R = 0.073*	Global R = 0.158***
	August	38.32%	Jul/Sep = 65.31	R = 0.279***	
	September	37.77%	Aug/Sep = 64.46	R = 0.123*	
Depth	Littoral	45.11%	Mar/Surf = 65.17	*R* = 0.599***	Global R = 0.336***
			Mar/2.5 m = 65.88	*R* = 0.477***	
			Mar/5 m = 64.83	*R* = 0.454***	
			Mar/10 m = 66.85	*R* = 0.81***	
			Mar/20 m = 69.75	*R* = 0.393***	
			Mar/30 m = 62.22	*R* = 0.467*	
	Surface	49.06%	Surf/2.5 m = 56.46	*R* = 0.085 n.s.	
			Surf/5 m = 63.75	*R* = 0.48***	
			Surf/10 m = 63.29	*R* = 0.647***	
			Surf/20 m = 72.31	*R* = 0.499***	
			Surf/30 m = 59.35	*R* = 0.374*	
	2.5 m	41.28%	2.5 m/5 m = 59.07	*R* = 0.089 n.s.	
			2.5 m/10 m = 59.97	*R* = 0.36*	
			2.5 m/20 m = 71.09	*R* = 0.333*	
			2.5 m/30 m = 59.23	*R* = 0.062 n.s.	
	5 m	43.55%	5 m/10 m = 53.51	*R* = 0.027 n.s.	
			5 m/20 m = 66.99	*R* = 0.194*	
			5 m/30 m = 58.79	*R* = 0.163 n.s.	
	10 m	49.91%	10 m/20 m = 64.11	*R* = 0.237*	
			10 m/30 m = 56.16	*R* = 0.29*	
	20 m	30.04%	20 m/30 m = 63.61	*R* = −0.222 n.s.	
	30 m	42.23%			

subacicularis and *Planothidium frequentissimum* that can range from oligo to eutraphentic (Van Dam et al., 1994, retrieved from the OMNIDIA v.5.5). All the characteristic species of the 10 m depth are aquatic and euplanktonic, except *Nitzschia subacicularis*, for which this information is not available (Denys, 1991, retrieved from the OMNIDIA v.5.5).

Other community descriptors such as taxa richness, Shannon diversity and Pielou's evenness indices did not reveal differences between the three sampling sites, confirming our nMDS results for diatom assemblages (One-way ANOVA, with F = 2.919, $p = 0.063$ for taxa richness; Kruskal-Wallis test with H = 3.134 with 2 degrees of freedom, $p = 0.209$ for Shannon diversity index and H = 2.183 with 2 degrees of

Table 4
Indicator values for the characteristic taxa of littoral areas and different depths of the reservoir. Monte Carlo tests were used to assess the significance of each taxon as a group-specific indicator ($p < 0.05$). Fidelity (F) and Specificity (S) values are also presented. Highlighted in bold are species with high fidelity and specificity values identified as group-specific indicator by Monte Carlo tests.

		Littoral			Surface			2.5 m			5 m			10 m			20 m			30 m		
Code	Taxon name	F	S	IndVal	F	S	IndVal	F	S	IndVal	F	S	IndVal	F	S	IndVal	F	S	IndVal	F	S	IndVal
	Achnanthidium nanum (F.Meister) Novais & Jüttner	0	0	0	0	0	0	2	11	0	0	0	0	4	22	1	14	63	9	**80**	**75**	**60**
ANMN	*Actinocyclus normanii* (Gregory ex Greville) Hustedt	3	25	1	2	22	0	4	44	2	10	78	8	**43**	**89**	**38**	31	50	15	7	25	2
AAMB	*Aulacoseira ambigua* (Grunow) Simonsen	3	13	0	0	0	0	3	22	1	12	44	5	**49**	**78**	**38**	25	63	16	7	25	2
CHSP	*Chamaepinnularia* sp.	0	0	0	0	0	0	0	0	0	0	0	0	0	0	0	**100**	**25**	**25**	0	0	0
COPL	*Cocconeis pseudolineata* (Geitler) Lange-Bertalot	16	38	6	0	0	0	4	11	0	4	11	0	0	0	0	8	13	1	**69**	**50**	**35**
CDUB	*Cyclostephanos dubius* (Fricke) Round	2	25	0	2	11	0	2	22	0	12	56	7	**48**	**100**	**48**	14	75	10	21	75	15
DPST	*Discostella pseudostelligera* (Hustedt) Houk & Klee	0	0	0	0	0	0	6	11	1	3	11	0	6	11	1	**86**	**50**	**43**	0	0	0
GITA	*Gomphonema italicum* Kützing	**100**	**25**	**25**	0	0	0	0	0	0	0	0	0	0	0	0	0	0	0	0	0	0
GLGN	*Gomphonema lagenula* Kützing	0	0	0	0	0	0	0	0	0	0	0	0	0	0	0	**100**	**25**	**25**	0	0	0
GPAR	*Gomphonema parvulum* (Kützing) Kützing	0	0	0	0	0	0	28	22	6	1	11	0	3	11	0	**69**	**50**	**34**	0	0	0
GPRI	*Gomphonema pumilum* var. *rigidum* E. Reichardt & Lange-Bertalot	0	0	0	0	0	0	0	0	0	12	22	3	0	0	0	**88**	**50**	**44**	0	0	0
GRHB	*Gomphonema rhombicum* M. Schmidt	13	25	3	0	0	0	24	11	3	0	0	0	5	22	1	0	0	0	**58**	**50**	**29**
MPMI	*Mayamaea permitis* (Hustedt) Bruder & Medlin	4	13	0	0	0	0	0	0	0	1	11	0	0	0	0	**95**	**50**	**48**	0	0	0
NANT	*Navicula antonii* Lange-Bertalot	**78**	**50**	**39**	0	0	0	0	0	0	9	11	1	5	22	1	8	13	1	0	0	0
NSUA	*Nitzschia subacicularis* Hustedt	2	13	0	0	0	0	7	22	1	24	22	5	**61**	**78**	**48**	6	13	1	0	0	0
PLFR	*Planothidium frequentissimum* (Lange-Bertalot) Lange-Bertalot	4	50	2	1	11	0	0	11	0	6	67	4	12	56	7	**67**	**88**	**58**	10	75	8
SBND	*Staurosira binodis* Lange-Bertalot	**55**	**63**	**34**	9	33	3	4	11	0	21	22	5	11	22	2	0	0	0	0	0	0

freedom, $p = 0.336$ for Pielou's evenness index). The shift in diatom communities during the sampling campaign was also verified for these biological parameters (One-way ANOVA, $F = 4.243$, $p < 0.05$ for taxa richness and $F = 7.123$, $p < 0.05$ for Shannon diversity index; Kruskal-Wallis test, $H = 7.081$ with 2 degrees of freedom, $p = 0.029$ for Pielou's evenness index). Taxa richness and Shannon diversity index differ between July/September and August/September (Holm-Sidak method, $p < 0.05$), confirming the small shifts in diatom taxonomic composition detected by the ANOSIM results, and present the lowest values in September. Pielou's evenness index differs only between July/September (Dunn's Method, $p < 0.05$) and the lowest values were also detected in September (Table 5). Taxa richness changed with the depth gradient, according to the One-way ANOVA results ($F = 5.269$, $p < 0.001$), since surface samples differ from 5, 10 and 20 m samples (Holm-Sidak method, $p < 0.05$). Additionally, surface and littoral samples are also different (Holm-Sidak method, $p < 0.05$). Even though significant differences were obtained for the globality of Shannon diversity index data (littoral, surface and different depths) $F = 2.742$, and $p = 0.022$; further tests only detected significant differences between littoral and surface samples (Holm-Sidak method, $p < 0.05$). Lowest values of all parameters were detected at surface samples, increasing with depth, reaching the highest values at 20 m for taxa richness, Shannon diversity and Pielou's evenness indices. Comparable values with deeper samples were detected for littoral samples (Table 5).

Comparison of SPI index revealed that littoral samples SPI was lower than in upper layers of the limnetic zone of the reservoir, surface samples presented the highest SPI values and samples in the mid depth of the reservoir are more similar with each other (10 m and 20 m) (Table 5). These results were further validated by One-way ANOVA ($F = 9.532$, $p < 0.001$), with surface samples differing from littoral and samples collected at 5 m, 10 m and 20 m; samples collected at 2.5 m are also different from those at 10 m and 20 m (Holm-Sidak method, $p < 0.05$). SPI index varied during the campaign, with highest values in July, decreasing throughout the campaign (Table 5). These differences were further confirmed by the Kruskal-Wallis test ($H = 8.855$ with 2 degrees of freedom, $p = 0.012$, with July significantly different from September (Dunn's Method, $p < 0.05$). As expected no differences were detected between SPI index from different sites (Kruskal-Wallis test, $H = 0.133$ with 2 degrees of freedom, $p = 0.936$).

Diatom guilds showed a shift with depth, with surface and 2.5 m depth samples dominated by the low-profile guild (except for Montante surface and 2.5 m in August and September, respectively); whilst deeper samples were dominated by the planktic guild (Fig. 8), except for bottom samples in Alcarrache (20 m), that were dominated by the motile guild, especially in September (Fig. 8).

The high profile and motile guilds presented the lowest abundances in all sites and throughout the study, except for high profile in littoral samples collected in Montante in August. There was a shift in diatom guilds dominance in littoral samples, in July the low-profile dominated, but the relative abundance of the high-profile guild increased throughout the campaign. An increase of the low-profile guild was revealed in Montante at 30 m and Mourão at 20 m and 30 m (Fig. 8). Despite data transformation, only the high-profile and motile guilds data passed the normality and equal variance tests. Therefore, differences on diatom guilds between platforms, sampling date and depth were tested by One-way ANOVA only for the motile and high-profile guilds, whilst for the remaining data a Kruskal-Wallis test was carried out. This analysis proved the results visible in Fig. 8, with the relative abundance of low-profile ($H = 23.436$ with 6 degrees of freedom, $p < 0.001$) and planktic ($H = 25.252$ with 6 degrees of freedom, $p < 0.001$) guilds differing with depth. Dunn's Method revealed that the low-profile guild at the surface of the reservoir differs from 5 m and 10 m samples ($p < 0.05$); and the planktic guild from littoral and surface samples differ from the 10 m depth ($p < 0.05$). The motile guild relative abundance from littoral samples showed differences from that of the surface samples ($H = 13.922$ with 6 degrees of freedom, $p = 0.031$), according to the Dunn's Method ($p < 0.05$). Differences between platforms were only detected for high-profile guild ($p = 0.031$), with Holm-Sidak method detecting changes between Montante and Mourão ($p < 0.05$). Throughout the summer, there was a shift in low-profile ($H = 13.923$ with 2 degrees of freedom, $p < 0.001$) and planktic diatom guilds ($H = 9.337$ with 2 degrees of freedom, $p = 0.009$), with the Dunn's Method separating July from September samples ($p < 0.05$).

Positive Spearman rank order correlations were detected between: 1) taxa richness (S) and depth, TP and Si; 2) H′ index, TP and Si; 3) J′ index and Si; 4) number of genera, depth and Si; 5) SPI, DO and T; and 6) the motile guild and Si. Whilst negative correlations were detected between: 1) S and T; 2) number of genera, pH and T; 3) SPI, depth, PO_4-P, NO_3-N and Si (Table 6).

4. Discussion

During this study, vertical profiles of T, pH and DO showed the stratification of the reservoir, starting in June and lasting until the end of the campaign, at the end of September. However, the depth of the thermocline changed throughout the experiment, from ca. 10 m in June, decreasing in July and August to ca. 8.5 m and deepening again in September to ca. 14 m (see Fig. 4). These changes in thermocline depth and thickness of epilimnetic waters can be related to the meteorological conditions during the experiment, such as the monthly average temperature, the average, minimum and maximum temperature 8 days before the sampling campaign and the maximum temperature, that increased in July and August and decreased again in September. Furthermore, this decrease in atmospheric temperature was associated with the precipitation events before the campaign in September, contributing to the decrease of the water T.

An interesting finding, observed in all vertical profiles, is the absence of any inflexion in the vertical pattern. This demonstrated the low

Table 5
Mean values ± standard deviation for the taxa richness (S), Shannon index of diversity (H′), Pielou's evenness index (J′) and Specific Pollution Sensitivity Index (SPI) for the depth gradient, sampling campaign and site.

		S	H′	J'	SPI
Depth gradient	Littoral	36.75 ± 10.22	3.76 ± 0.60	0.73 ± 0.06	14.04 ± 1.11
	Surface	18.78 ± 8.94	2.24 ± 0.83	0.53 ± 0.14	16.60 ± 1.81
	2.5 m	26.44 ± 8.50	2.64 ± 0.99	0.55 ± 0.17	14.38 ± 2.19
	5 m	34.00 ± 11.52	2.72 ± 1.41	0.52 ± 0.24	12.33 ± 1.56
	10 m	38.89 ± 10.68	2.77 ± 0.89	0.52 ± 0.14	11.90 ± 1.30
	20 m	40.75 ± 11.57	3.62 ± 0.93	0.68 ± 0.13	11.83 ± 1.67
	30 m	36.75 ± 4.27	3.18 ± 0.47	0.62 ± 0.11	13.83 ± 1.42
Sampling campaign	July	36.26 ± 10.75	3.34 ± 0.80	0.65 ± 0.11	14.70 ± 2.03
	August	35.21 ± 11.61	3.21 ± 0.90	0.63 ± 0.13	13.34 ± 1.97
	September	26.22 ± 12.04	2.26 ± 1.13	0.48 ± 0.20	12.58 ± 2.41
Sampling site	Montante	30.11 ± 10.09	2.77 ± 1.01	0.56 ± 0.17	13.41 ± 2.22
	Alcarrache	29.59 ± 13.04	2.75 ± 1.01	0.57 ± 0.16	13.76 ± 2.74
	Mourão	37.75 ± 11.99	3.29 ± 1.09	0.63 ± 0.17	13.52 ± 2.61

Fig. 8. Depth gradient of relative abundance of diatom guilds for the three platforms and sampling campaigns. Mont: Montante; Alc: Alcarrache; Mour: Mourão; Jul: July; Aug: August; Sep: September.

influence of a riverine inflow. Therefore, the Alqueva reservoir seems to present the typical characteristics of a lake system throughout the campaign.

The surface oxygen concentration is constantly regulated by the air-water fluxes, which tend to bring the surface concentration towards the saturation value (Capet et al., 2013). However, in July the surface waters

Table 6
Spearman rank order correlation coefficients between diatoms, expressed as taxa richness (S), Shannon diversity (H′) and Pielou's evenness (J′) indexes, number of genera, SPI and ecological guilds, depth and water physical-chemical parameters depth dependent $^{*}p < 0.05$, in bold.

	pH	T	%OD	EC	Depth	PO_4	TP	NO_3	Si	TSS
S	**−0.34***	**−0.40***	−0.28	−0.28	**0.59***	0.34	**0.44***	0.20	**0.55***	−0.21
H′	−0.21	−0.22	−0.13	−0.28	**0.37***	0.40	0.42*	0.13	**0.59***	−0.10
J′	−0.12	−0.14	−0.05	−0.23	0.22	0.32	0.28	0.09	**0.50***	0.00
Number of genera	**−0.45***	**−0.49***	**−0.34***	−0.21	**0.64***	0.26	0.38	0.30	**0.58***	−0.41
SPI	**0.39***	**0.49***	**0.45***	−0.09	**−0.54***	**−0.47***	−0.37	**−0.48***	**−0.52***	0.37
Low-profile	0.25	**0.32***	**0.31***	−0.20	**−0.36***	−0.32	−0.17	−0.37	−0.32	0.18
High-profile	−0.04	0.16	−0.06	0.18	−0.10	0.39	0.27	−0.20	0.03	0.22
Motile	−0.13	−0.14	−0.14	−0.19	0.26	0.39	0.39	−0.10	**0.57***	−0.08
Planktic	−0.10	−0.26	−0.15	0.12	0.26	0.01	−0.09	0.52	0.04	−0.14

in the three sites were oversaturated with oxygen due to enhanced photosynthesis, revealed also by the higher pH in the epilimnion. Stratification should allow the settlement of bottom anoxic conditions by preventing the bottom oxygen-depleted waters from mixing with the surface ventilated waters (Boulton and Brock, 1999). However, the hypolimnion does not present anoxia in June and September, most probably due to the precipitation events in the days prior to the sampling, and in July and August, anoxia occurs deep in the water column (Fig. 4). Hence, the consumption of oxygen by respiration is not sufficiently high to deplete oxygen in the whole hypolimnion, contrary to what occurs in highly eutrophic reservoirs (Wetzel, 1993). The analysis of ORP (Fig. 4) shows positive values from June to August. This oxidized environment during the stratified period contrasts with other Mediterranean eutrophic reservoirs, where ORP is highly negative due to respiration (i.e. degradation of organic matter).

Horizontal gradients in physical, chemical and biological factors in reservoirs result from the combined influence of hydrodynamics and basin morphology (Kennedy and Walker, 1990), separating the nearshore (the littoral zone) from the offshore environment (Lewis, 2009). No significant differences were detected between sampling platforms for water physico-chemical variables and neither for diatoms (in terms of diatom communities, diversity indices and SPI). This spatial homogenization can be related with the absence of a riverine effect, detected on the smooth vertical profiles for T, pH, DO and EC, with no visible inflexions (Fig. 4). This absence of a riverine effect during summer can reflect the lower discharge from the Guadiana River (regulated upstream), and the null discharge from the other intermittent tributaries.This means that other factors, like the light extinction coefficient (k), nutrient and dissolved oxygen availability, and sedimentation are shaping the system organization, along the vertical axis. Kahlert et al. (2002), obtained opposite results for Lake Erken (Sweden), with horizontal variation accounting for 60–80% and 7–70% of the total variation in biomass and in nutrient status, respectively. Among the physico-chemical variables, nutrients are one of the most important factors controlling reservoir water quality and productivity, and nutrient distribution and concentrations are affected by several processes, such as nutrient loading, sedimentation, flow, mixing and discharge (Kennedy and Walker, 1990; Zhenyao et al., 2013). No differences were detected in nutrient concentration between platforms. A depth gradient was observed, with higher values of PO_4 and TP detected in bottom samples than at the surface; and bottom and metalimnion presented higher NO_3 concentrations than surface samples. This can be related to the low contribution of external loads to the system, during summer.

The fact that there is no information about the autecology of several indicator species in Van Dam et al. (1994, retrieved from the OMNIDIA v.5.5) reveals the need to study more in detail these systems, combining a fine-grained taxonomy with a good environmental characterization. From these, *Achnanthidium nanum* was first described from high altitude lakes in the Swiss Alps and was later found in streams in the Centre and North of Portugal by Novais et al. (2015), characterized by soft waters, but with concentrations of nutrients within the same range as in the present study, and also associated with *A. caravelense* and *Gomphonema rhombicum*. These taxa found at 30 m depth should be studied in more detail, since there is also not enough data to assess the Red List status (Lange-Bertalot and Steindorf, 1996, retrieved from the the OMNIDIA v.5.5) for *A. nanum* and *C. pseudolineata*, whilst *Gomphonema rhombicum* is evaluated as "in risk" for German watercourses by Hofmann et al. (2011).

The indicator species identified in this study are mostly alkaliphilous or alkalibiontic, reflecting the alkaline characteristic of the reservoir, revealed in the vertical profile of pH, with values >7 during the whole campaign and in all depths (Fig. 4). Interestingly, all indicator species of the 20 m depth have moderate (<50% O_2 sat.) or low (>30% O_2 sat.) oxygen requirements, reflecting the low oxygen availability at these depths (<50% O_2 sat.) from July to September, as seen in Fig. 4.

Littoral benthic diatoms differ from the limnetic zone in terms of diatom communities, diversity indices and SPI, with highest values for diversity indices detected in littoral zones. A depth gradient was detected for diatoms (diatom assemblages and ecological guilds) and diversity indices, as can be seen in the nMDS plot (Fig. 7) validated by the ANOSIM results in Table 3. This gradient is part of a continuum, but no zonation was detected, unlike the results obtained by Cantonati et al. (2009) and Stevenson and Stoermer (1981) who detected three zones in their studies in the oligotrophic lakes Tovel and Michigan. This zonation was characterized by disturbance due to wave and water fluctuation in the shallow zone, high stability with favourable growth conditions in terms of nutrients and light in the mid-depth zone and severe light limitation in the deep zone (Stevenson and Stoermer, 1981; Cantonati et al., 2009). Water level fluctuations were negligible, due to the large dimension of the reservoir and to the sampling carried out during stable weather conditions in summer. However, wave disturbance could be detected due to the increase of the wind speed at the end of the day (as seen in Fig. 2), playing an important role in shaping diatom communities of the upper layers and contributing to the differences between them and the communities present in the deeper layers of the reservoir. During the campaign the mean lower limit of the euphotic zone was 6.7 m in Montante, with the lowest value detected in Mourão in August (3.3 m), but this limit didn't have an apparent effect on diatom assemblages, given that living diatoms were present at 30 m depth. Richardson et al. (1983) stated that the adaptation of microalgae to very low photon flux densities may be related to a combination of structural, behavioural, physiological and biochemical factors, such as the lower amount of non-photosynthetic tissue when compared with macroalgae and vascular plants. Other possible adaptation to these harsh conditions may be the photosynthetic pigments composition related to light harvesting and photoprotection: chlorophylls and carotenoids. Diatoms are characterized by the presence of Chl *a* and Chl *c*, being Chl *c*1 and *c*2 the most abundant. The Chl *c* has a distinctive structure that allows changes in the absorption spectrum to produce a strong blue absorption band and a weak band in the red region (Kuczynska et al., 2015). This fact together with the higher penetration of blue/green/yellow light in waters of Alqueva reservoir than red light (Potes et al., 2017), allows diatoms to use light more efficiently, and can

contribute to explain their presence in deeper layers. Species present at low light depths can be supplementing their photosynthetic carbon assimilation with heterotrophic or photoheterotrophic use of organic carbon sources (Richardson et al., 1983). Stevenson and Stoermer (1981) also suggested that mobile taxa capable of heterotrophic nutrition could have gained competitive advantage in deeper habitats characterized by greater sediment accumulation.

In the Alqueva reservoir, diversity indices increased with depth (reaching a maximum at 20 m), similarly to the results obtained by Hostetter and Stoermer (1968), in a Summer campaign in Lake West Okoboji (Iowa, USA), who observed a consistent increase in diatom diversity. Cantonati et al. (2009) also stated that diversity increased with depth in the oligotrophic Lake Tovel (characterized by relevant seasonal water-level fluctuations) and Flower et al. (2004) found that diatom communities were more diverse and taxonomically complex in deeper water (ca. 20 m) samples from Lake Baikal. Whilst Stevenson and Stoermer (1981) present contrasting results, with a decrease in species diversity with depth. In the Alqueva reservoir, S and H′ were positively correlated with TP and Si, in agreement with the results of Cantonati et al. (2009), who also identified these environmental controls, together with water level fluctuations and PAR.

A depth-gradient was also observed for diatom guilds, with low-profile dominating the upper layers (surface and 2.5 m), and gradually being replaced by the planktic guild at 5 m and especially at 20 m. Exceptionally, the motile guild dominated the assemblages at the bottom of the Alcarrache platform (20 m), in accordance with the observations of Hoagland and Peterson (1990), who stated that the dominance of motile diatoms on substrata in deeper waters undoubtedly relates to the need of motility in a habitat subject to a constant rain of sediments. Furthermore, Admiraal and Peletier (1979) stated that heterotrophic diatoms are mainly found among pennate benthic forms, and proved that the growth rate in the dark of several motile *Nitzschia* and *Navicula* species was enhanced by organic substrates in the medium. The dominance at upper layers of low-profile guild, characterized by species adapted to high current velocities and low nutrient concentrations (Rimet and Bouchez, 2012), reflects the lower nutrient content at the surface of the reservoir (Table 2) and the wave disturbance due to the wind, especially at the end of the afternoon with the effect of the maritime breeze, as can be seen in Fig. 2. The 5 m and 10 m depths were dominated by the planktic guild, which includes taxa adapted to lentic conditions (Rimet and Bouchez, 2012), as is the case at these depths.

This is one of the few studies analysing the vertical variation of benthic diatoms in deeper layers in a large reservoir in the Mediterranean region. Our findings reveal a vertical succession of diatom assemblages (but no clear zonation was detected), with living diatoms present at 30 m in the Montante and Mourão platforms, and at the bottom in the Alcarrache platform. These preliminary results can lead to further studies, where physiological adaptations of diatoms to these conditions can be explored in detail, such as differences/changes in the photosynthetic apparatus. Furthermore, it would be interesting to verify if living diatoms are present in deeper areas of the reservoir, since it can reach >70 m, and if there are seasonal variations of deep diatom assemblages.

Acknowledgements

The work was funded by the ALEX 2014 (EXPL/GEOMET/1422/2013) and ALOP (ALT20-03-0145-FEDER-000004) projects and also the European Union through the European Regional Development Fund, included in the COMPETE 2020 (Operational Program Competitiveness and Internationalization) through the ICT project (UID/GEO/04683/2013) with the reference POCI-01-0145-FEDER 007690.

The ceramic tiles used for diatom sampling were kindly supplied by Eng. Patricia Cardoso from Gres Panaria Portugal, S.A.

Appendix A. Supplementary data

Supplementary data to this article can be found online at https://doi.org/10.1016/j.scitotenv.2018.12.251.

References

Admiraal, W., Peletier, H., 1979. Influence of organic compounds and light limitation on the growth rate of estuarine benthic diatoms. Br. Phycol. J. 14, 197–206. https://doi.org/10.1080/00071617900650211.

APHA, 1995. Standard Methods for the Examination of Water and Wastewater. 19th ed. American Public Health Association, American Water Works Association, and Water Pollution Control Federation, Washington, D.C.

Berthon, V., Bouchez, A., Rimet, F., 2011. Using diatom life-forms and ecological guilds to assess organic pollution and trophic level in rivers: a case study of rivers in south-eastern France. Hydrobiologia 673, 259–271. https://doi.org/10.1007/s10750-011-0786-1.

Blanco, S., Ector, L., Huck, V., Monnier, O., Cauchie, H.M., Hoffmann, L., Bécares, E., 2008. Diatom assemblages and water quality assessment in the Duero basin (NW Spain). Belg. J. Bot. 141 (39–50), S1–S6. https://doi.org/10.1007/s10661-012-2607-z.

Boulton, A., Brock, M., 1999. Australian Freshwater Ecology – Processes and Management. Gleneagles Publishing, Glen Osmosnd.

Cantonati, M., Lowe, R.L., 2014. Lake benthic algae: toward an understanding of their ecology. Fresh. Sci. 33, 475–486. https://doi.org/10.1086/676140.

Cantonati, M., Scola, S., Angeli, N., Guella, G., Frassanito, R., 2009. Environmental controls of epilithic diatom depth-distribution in an oligotrophic lake characterized by marked water-level fluctuations. Eur. J. Phycol. 44, 15–29. https://doi.org/10.1080/09670260802079335.

Capet, A., Beckers, J., Gregoire, M., 2013. Drivers, mechanisms and long-term variability of seasonal hypoxia on the Black Sea northwestern shelf – is there any recovery after eutrophication? Biogeosciences 10, 3943–3962. https://doi.org/10.5194/bg-10-3943-2013.

Clarke, K.R., Ainsworth, M.A, 1993. Method of linking multivariate community structure to environmental variables. Mar Ecol Prog Ser 92, 205–219.

Clarke, K.R., Gorley, R.N., 2001. PRIMER. PRIMER-E Ltd., Plymouth, UK.

Coste in CEMAGREF, 1982. Etude des Méthodes Biologiques Quantitatives d'Appréciation de la Qualité des Eaux. Rapport Q. E. Lyon – Agence de l'Eau Rhône-Méditerranée-Corse, Pierre-Bénite.

DeNicola, D.M., Kelly, M., 2014. Role of periphyton in ecological assessment of lakes. Fresh. Sci. 33, 619–638. https://doi.org/10.1086/676117.

Denys, L., 1991. A check-list of the diatoms in the Holocene deposits of the western Belgian coastal plain with a survey of their apparent ecological requirements. I. Introduction, ecological code and complete list. Geol. Surv. Belgium 1991/02, 246.

Dufrêne, M., Legendre, P., 1997. Species assemblages and indicator species: the need for a flexible asymmetrical approach. Ecol. Monogr. 67, 345–366. https://doi.org/10.1890/0012-9615(1997)067[0345:SAAIST]2.0.CO;2.

Dunn, O.J., 1961. Multiple comparisons among means. J. Am. Stat. Assoc. 56, 54–64. https://doi.org/10.2307/2282330.

Faria, D.M., Cardoso, L.S., Marques, D.M., 2017. Epiphyton dynamics during an induced succession in a large shallow lake: wind disturbance and zooplankton grazing act as main structuring forces. Hydrobiologia 788, 267–280. https://doi.org/10.1007/s1075.

Ferragina, E., 2010. The water issue in the Mediterranean. In: Scoullos, M., Ferragina, E. (Eds.), Environmental and Sustainable Development in the Mediterranean. European Institute of the Mediterranean, Girona, Spain, pp. 53–79.

Flower, R.J., Pomazkina, G.V., Rodionova, E., Williams, D.M., 2004. Local and meso-scale patterns of benthic diatoms in Lake Baikal. In: Poulin, M. (Ed.), Proceedings of the Seventeenth International Diatom Symposium, Ottawa, Canada, 25th–31st August 2002. Biopress Limited, Bristol, pp. 69–92.

Gomà, J., Rimet, F., Cambra, J., Hoffmann, L., Ector, L., 2005. Diatom communities and water quality assessment in Mountain Rivers of the upper Segre basin (La Cerdanya, Oriental Pyrenees). Hydrobiologia 551, 219–225. https://doi.org/10.1007/s10750-005-4462-1.

Goodall, D.W., 1954. Objective methods for the classification of vegetation. III. An essay in the use of factor analysis. Aust. J. Bot. 2, 304–324.

Hamdy, A., 2001. Water resources management in the Mediterranean countries: priority actions. MEDIT 2, 24–29.

Higgins, S.N., Althouse, B., Devlin, S.P., Vadeboncoeur, Y., Vander Zanden, M.J., 2014. Potential for large-bodied zooplankton and dreissenids to alter the productivity and autotrophic structure of lakes. Ecology 95, 2257–2267.

Hoagland, K.D., Peterson, C.G., 1990. Effects of light and wave disturbance on vertical zonation of attached microalgae in a large reservoir. J. Phycol. 26, 450–457. https://doi.org/10.1111/j.0022-3646.1990.00450.x.

Hofmann, G., Werum, M., Lange-Bertalot, H., 2011. Diatomeen im Süßwasser-Benthos von Mitteleuropa. Bestimmungsflora Kieselalgen für die ökologische Praxis. Über 700 der häufigsten Arten und ihre Ökologie. A.R.G. Gantner Verlag.

Holm, S., 1979. A simple sequentially rejective multiple test procedure. Scand. J. Stat. 6, 65–70.

Hostetter, H.P., Stoermer, E.F., 1968. A study of the vertical distribution of periphyton diatoms in Lake West Okoboji, Iowa. Proc. Iowa Acad. Sci. 75, 42–47.

Hsieh, C., Sakai, Y., Ban, S., Ishikawa, K., Ishikawa, T., Ichise, S., Yamamura, N., Kumagai, M., 2011. Eutrophication and warming effects on long-term variation of zooplankton in Lake Biwa. Biogeosciences 8, 1383–1399. https://doi.org/10.5194/bg-8-1383-2011.

Iakunin, M., Salgado, R., Potes, M., 2018. Breeze effects at a large artificial lake: summer case study. Hydrol. Earth Syst. Sci. 22, 5191–5210. https://doi.org/10.5194/hess-22-5191-2018 (2018).

Inag, I.P., 2008. Manual para a Avaliação Biológica da Qualidade da Agua em Sistemas Fluviais Segundo a Directiva-Quadro da Água – Protocolo de Amostragem e Análise para o Fitobentos – Diatomáceas. Ministério do Ambiente, do Ordenamento do Território e do Desenvolvimento Regional. Instituto da Água, I. P., Lisboa.

Kahlert, M., Hasselrot, A.T., Hillebrand, H., Pettersson, K., 2002. Spatial and temporal variation in the biomass and nutrient status of epilithic algae in Lake Erken, Sweden. Freshw. Biol. 47, 1191–1215. https://doi.org/10.1046/j.1365-2427.2002.00844.x.

Kahlert, M., Albert, R.-L., Anttila, E.-L., Bengtsson, R., Bigler, C., Eskola, T., Gälman, V., Gottschalk, S., Herlitz, E., Jarlman, A., Kasperoviciene, J., Kokociński, M., Luup, H., Miettinen, J., Paunksnyte, I., Piirsoo, K., Quintana, I., Raunio, J., Sandell, B., Simola, H., Sundberg, I., Vilbaste, S., Weckström, J., 2009. Harmonization is more important than experience – results of the first Nordic-Baltic diatom intercalibration exercise 2007 (stream monitoring). J. Appl. Phycol. 21, 471–482. https://doi.org/10.1007/s10811-008-9394-5.

Karadžić, V., Subakov-Simić, G., Krizmanić, J., Natić, D., 2010. Phytoplankton and eutrophication development in the water supply reservoirs Garaši and Bukulja (Serbia). Desalination 255, 91–96. https://doi.org/10.1016/j.desal.2010.01.009.

Kelly, M., Urbanic, G., Acs, E., Bennion, H., Bertrin, V., Burgess, A., Denys, L., Gottschalk, S., Kahlert, M., Karjalainen, S.M., Kennedy, B., Kosi, G., Marchetto, A., Morin, S., Picinska-Faltynowics, J., Poikane, S., Rosebery, J., Schoenfelder, I., Schoenfelder, J., Varbiro, G., 2014. Comparing aspirations: intercalibration of ecological status concepts across European lakes for littoral diatoms. Hydrobiologia 734, 125–141. https://doi.org/10.1007/s10750-014-1874-9.

Kennedy, R.H., Walker, W.W., 1990. Reservoir nutrient dynamics. In: Thornton, K.W., Kimmel, B.L., Payne, F.E. (Eds.), Perspectives in Reservoir Limnology. John Wiley and Sons, New York, pp. 109–121.

King, L., Clarke, G., Bennion, H., Kelly, M., Yallop, M., 2006. Recommendations for sampling littoral diatoms in lakes for ecological status assessments. J. Appl. Phycol. 18, 15–25. https://doi.org/10.1007/s10811-005-9009-3.

Krammer, K., Lange-Bertalot, H., 1986. Bacillariophyceae 1. Teil: Naviculaceae. In: Ettl, H., Gerloff, J., Heynig, H., Mollenhauer, D. (Eds.), Süsswasserflora von Mitteleuropa. Gustav Fischer Verlag, Stuttgart 2/1, pp. 1–876.

Krammer, K., Lange-Bertalot, H., 1988. Bacillariophyceae 2. Teil: Bacillariaceae, Epithemiaceae, Surirellaceae. In: Ettl, H., Gerloff, J., Heynig, H., Mollenhauer, D. (Eds.), Süsswasserflora von Mitteleuropa. Gustav Fischer Verlag, Stuttgart 2/2, pp. 1–596.

Krammer, K., Lange-Bertalot, H., 1991a. Bacillariophyceae 3. Teil: Centrales, Fragilariaceae, Eunotiaceae. In: Ettl, H., Gerloff, J., Heynig, H., Mollenhauer, D. (Eds.), Süsswasserflora von Mitteleuropa. Gustav Fischer Verlag, Stuttgart 2/3, pp. 1–576.

Krammer, K., Lange-Bertalot, H., 1991b. Bacillariophyceae 4. Teil: Achnanthaceae. Kritische Ergänzungen zu *Navicula* (Lineolatae) und *Gomphonema*. Gesamtliteraturverzeichnis Teil 1–4. In: Ettl, H., Gerloff, J., Heynig, H., Mollenhauer, D. (Eds.), Süsswasserflora von Mitteleuropa. 2/4. Gustav Fischer Verlag, Stuttgart, pp. 1–437.

Kuczynska, P., Jemiola-Rzeminska, M., Strzalka, K., 2015. Photosynthetic pigments in diatoms. Mar. Drugs 13, 5847–5881. https://doi.org/10.3390/md13095847.

Lange-Bertalot, H., Steindorf, A., 1996. Rote Liste der limnischen Kieselalgen (Bacillariophyceae) Deutschlands. Schr. -R. f. Vegetationskde. 28 pp. 633–677.

Lecointe, C., Coste, M., Prygiel, J., 1993. "Omnidia": software for taxonomy, calculation of diatom indices and inventories management. Hydrobiologia 269–270, 509–513. https://doi.org/10.1007/BF00028048.

Lewis, V.M., 2009. Ecological zonation in lakes. In: Likens, G. (Ed.), Encyclopedia of Inland Waters. 1. Elsevier, Oxford, pp. 416–422.

Lopes, F., Silva, H.G., Salgado, R., Potes, M., Nicoll, K.A., Harrison, R.G., 2016. Atmospheric electrical field measurements near a fresh water reservoir and the formation of the lake breeze. Tellus A 68, 31592. https://doi.org/10.3402/tellusa.v68.31592 (2016).

Lorenzen, C.J., 1967. Determination of chlorophyll and phaeopigments: spectrophotometric equations. Limnol. Oceanogr. 12, 342–346. https://doi.org/10.4319/lo.1967.12.2.0343.

Nicoll, K.A., Harrison, R.G., Silva, H.G., Salgado, R., Melgão, M., Bortoli, D., 2018. Electrical sensing of the dynamical structure of the planetary boundary layer. Atmos. Res. 202, 81–95. https://doi.org/10.1016/j.atmosres.2017.11.009 (2018).

Novais, M.H., Hlúbiková, D., Morais, M., Hoffmann, L., Ector, L., 2011. Morphology and ecology of *Achnanthidium caravelense* (Bacillariophyceae), a new species from Portuguese rivers. Algol. Stud. 136, 131–150. https://doi.org/10.1127/1864-1318/2011/0136-0131.

Novais, M.H., Jüttner, I., Van de Vijver, B., Morais, M.M., Hoffmann, L., Ector, L., 2015. Morphological variability within the *Achnanthidium minutissimum* species complex (Bacillariophyta): comparison between the type material of *Achnanthes minutissima* and related taxa, and new freshwater *Achnanthidium* species from Portugal. Phytotaxa 224, 101–139. https://doi.org/10.11646/phytotaxa.224.2.1.

Passy, S.I., 2007. Diatom ecological guilds display distinct and predictable behavior along nutrient and disturbance gradients in running waters. Aquat. Bot. 86, 171–178. https://doi.org/10.1016/j.aquabot.2006.09.018.

Poikane, S., Kelly, M., Cantonati, M., 2016. Benthic algal assessment of ecological status in European lakes and rivers: challenges and opportunities. Sci. Total Environ. 568, 603–613. https://doi.org/10.1016/j.scitotenv.2016.02.027.

Potes, M., Salgado, R., Costa, M.J., Morais, M., Bortoli, D., Kostadinov, I., Mammarella, I., 2017. Lake–atmosphere interactions at Alqueva reservoir: a case study in the summer of 2014. Tellus A 69 (1), 1272787. https://doi.org/10.1080/16000870.2016.1272787.

Preisendorfer, R.W., 1959. Theoretical proof of the existence of characteristic diffuse light in natural waters. J. Mar. Res. 18, 1–9.

Prygiel, J., Carpentier, P., Almeida, S., Coste, M., Druart, J.-C., Ector, L., Guillard, D., Honoré, M.-A., Iserentant, R., Ledeganck, P., Lalanne-Cassou, C., Lesniak, C., Mercier, I., Moncaut, P., Nazart, M., Nouchet, N., Peres, F., Peeters, V., Rimet, F., Rumeau, A., Sabater, S., Straub, F., Torrisi, M., Tudesque, L., Van de Vijver, B., Vidal, H., Vizinet, J., Zydek, N., 2002. Determination of the biological diatom index (IBD NF T 90-354): results of an intercomparison exercise. J. Appl. Phycol. 14, 27–39. https://doi.org/10.1023/A:1015277207328.

Reichardt, E., 1997. Taxonomische revision des Artenkomplexes um *Gomphonema pumilum* (Bacillariophyceae). Nova Hedwigia 65, 99–130.

Richardson, K., Beardall, J., Raven, J.A., 1983. Adaptation of unicellular algae to irradiance: an analysis of strategies. New Phytol. 93, 157–191. https://doi.org/10.1111/j.1469-8137.1983.tb03422.x.

Rimet, F., Bouchez, A., 2012. Life-forms, cell-sizes and ecological guilds of diatoms in European rivers. Knowl. Manag. Aquat. Ecosyst. (406), 01 https://doi.org/10.1051/kmae/2012018.

Rimet, F., Bouchez, A., Montuelle, B., 2015. Benthic diatoms and phytoplankton to assess nutrients in a large lake: complementarity of their use in Lake Geneva (France–Switzerland). Ecol. Indic. 53, 231–239. https://doi.org/10.1016/j.ecolind.2015.02.008.

Salgado, R., Potes, M., Albino, A., Apolinário, J., Barbosa, S., Bárias, S., Beliche, P., Bortoli, D., Canhoto, P., Costa, M.J., Fernandes, R.M., Harrison, G., Ilhéu, A., Le Moigne, P., Lima, R., Lopes, F., Lopes, T., Marques, J., Melgão, M., Miranda, P.M., Morais, M., Murteira, M., Nicoll, K., Novais, M.H., Parrondo, M.C., Pereira, S., Policarpo, C., Prior, V., Rodrigues, C.M., Rosado, J., Sá, A., Serafim, A., Silva, H., Soares, P.M.M., Tlemçani, M., Zavattieri, A., 2018. The ALEX2014 Alqueva hydro-meteorological database. available at:. http://www.alex2014.cge.uevora.pt/data/ (last access: 3 October 2018).

StatSoft Inc, 2001. STATISTICA for Windows (Computer Program Manual). Tulsa.

Stevenson, R.J., Stoermer, E.F., 1981. Quantitative differences between benthic algal communities along a depth gradient in Lake Michigan. J. Phycol. 17, 29–36. https://doi.org/10.1111/j.1529-8817.1981.tb00815.x.

Sutton, M.A., Howard, C.M., Bleeker, A., Datta, A., 2013. The global nutrient challenge: from science to public engagement. Environ. Dev. Sustain. 6, 80–85. https://doi.org/10.1016/j.envdev.2013.03.003.

ter Braak, C.J.F., Šmilauer, P., 2002. CANOCO reference manual and CanoDraw for Windows user's guide. Software for Canonical Community Ordination (Version 4.5). Biometris, Wageningen.

The European Parliament & European Council, 2000. Directive 2000/60/EC of the European Parliament and of the Council establishing a framework for the community action in the field of water policy. Off. J. Eur. Communities L327, 1–73.

Vadeboncoeur, Y., Steinman, A.D., 2002. Periphyton function in lake ecosystems. Sci. World J. 2, 1449–1468. https://doi.org/10.1100/tsw.2002.294.

Vadeboncoeur, Y., Devlin, S.P., McIntyre, P.B., Zanden, M.J.V., 2014. Is there light after depth? Distribution of periphyton chlorophyll and productivity in lake littoral zones. Fresh. Sci. 33, 524–536. https://doi.org/10.1086/676315.

Van Dam, H., Mertens, A., Sinkeldam, J., 1994. A coded checklist and ecological indicator values of freshwater diatoms from The Netherlands. Neth. J. Aquat. Ecol. 28, 117–133. https://doi.org/10.1007/BF02334251.

Van de Vijver, B., Ector, L., Beltrami, M.E., de Haan, M., Falasco, E., Hlúbiková, D., Jarlman, A., Kelly, M., Novais, M.H., Wojtal, A.Z., 2011. A critical analysis of the type material of *Achnanthidium lineare* W. Sm. (Bacillariophyceae). Algol. Stud. 136/137, 167–192. https://doi.org/10.1127/1864-1318/2011/0136-0167.

Wetzel, R.G., 1993. Limnologia. Fundação Calouste Gulbenkian, Lisboa.

Yang, H., Flower, R., 2012. Effects of light and substrate on the benthic diatoms in an oligotrophic lake: a comparison between natural and artificial substrates. J. Phycol. 48, 1166–1177. https://doi.org/10.1111/j.1529-8817.2012.01201.x.

Zelinka, M., Marvan, P., 1961. Zur Präzisierung der biologischen Klassifikation der Reinheit fliessender Gewässer. Arch. Hydrobiol. 57, 389–407.

Zhenyao, S., Junfeng, N., Ying, W., Hongyuan, W., Xin, Z., 2013. Distribution and transformation of nutrients in large-scale lakes and reservoirs. In: Zhenyao, S. (Ed.), Distribution and Transformation of Nutrients in Large-Scale Lakes and Reservoirs: The Three Gorges Reservoir. Zhejiang University Press, Hangzhou, pp. 1–15 (Springer-Verlag Berlin Heidelberg).

Science of the Total Environment 659 (2019) 84–94

Contents lists available at ScienceDirect

Science of the Total Environment

journal homepage: www.elsevier.com/locate/scitotenv

Assessment of the environmental impact of an abandoned mine using an integrative approach: A case-study of the "Las Musas" mine (Extremadura, Spain)

Patrícia Palma [a,b,*,1], Rocío López-Orozco [a], Clarisse Mourinha [a], Ana Lourdes Oropesa [c,d], Maria Helena Novais [b], Paula Alvarenga [e]

[a] Department of Technologies and Applied Sciences, Polytechnic Institute of Beja, 7801-295, Portugal
[b] ICT, Institute of Earth Sciences, University of Évora, Rua Romão Ramalho 59, Évora, Portugal
[c] Unidad de Toxicología, Departamento de Sanidad Animal, Facultad de Ciencias, Universidad de Extremadura, Badajoz 06071, Spain
[d] INBIO G+C - Instituto Universitario de Investigación en Biotecnología Ganadera y Cinegética, Universidad de Extremadura, Cáceres 10003, Spain
[e] Linking Landscape, Environment, Agriculture, and Food Research Unit (LEAF), Instituto Superior de Agronomia, Universidade de Lisboa, Tapada da Ajuda, 1349-017 Lisboa, Portugal

HIGHLIGHTS

- Environmental impact of an old abandoned Pb-Zn mine on soil and water was assessed.
- Soils still have high Pb levels and restricted habitat function to soil organisms.
- Water pollution with metals is low and mixed with other anthropogenic pollutants.
- Environmental risk is limited in the area of the study.
- Risk assessment of non-acid mining areas should integrate toxicological behavior responses.

GRAPHICAL ABSTRACT

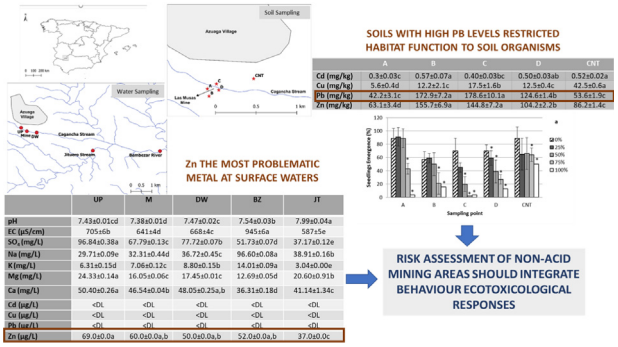

ARTICLE INFO

Article history:
Received 15 October 2018
Received in revised form 12 December 2018
Accepted 21 December 2018
Available online 22 December 2018

Keywords:
Abandoned mine
Potentially toxic metals
Soil pollution assessment
Water pollution assessment
Ecotoxicity

ABSTRACT

The mine abandonment is generally associated with the release of potentially toxic metals into the environment, which may depend on metals speciation, soil properties and climate conditions. The goal of the present work was to assess the environmental impact of the abandoned Pb-Zn mine "Las Musas" (Spain) using an integrative approach. The impact on soils and surface waters was performed using: chemical parameters, quantification of potentially toxic metals (Cd, Cu, Pb and Zn), and ecotoxicological responses using lethal and sub-lethal bioassays with organisms' representative of different trophic level ((soil: *Eisenia fetida* (mortality and reproduction test); *Latuca sativa* and *Lollium perenne* (seedling emergence); and water: *Vibrio fischeri* (luminescence inhibition), *Daphnia magna* (immobility and reproduction test), *Thamnocephalus platyurus* (mortality), *Pseudokirchneriella subcapitata* (growth inhibition)). The results showed soils with neutral to slight alkaline pH (7.64–8.18), low electric conductivity (125–953 μS/cm) and low organic matter levels (0.20–1.85%). For most of the soil samples, Pb was the only metal which surpassed the limit proposed by the Canadian soil quality guidelines, with values ranging from 42.2 to 181.4 mg/kg. The ecotoxicological results showed that the soils with the highest levels of Pb induced a decrease on *E. fetida* reproduction and on L. *sativa* germination, indicating negative impacts on

* Corresponding author at: Department of Applied Sciences and Technologies, Escola Superior Agrária - Instituto Politécnico de Beja, Rua Pedro Soares S/N, Apartado 6155, 7800-295 Beja, Portugal.
E-mail address: ppalma@ipbeja.pt (P. Palma).
[1] Present/permanent address: Department of Applied Sciences and Technologies, Escola Superior Agrária - Instituto Politécnico de Beja, Rua Pedro Soares S/N, Apartado 6155, 7800-295 Beja, Portugal.

https://doi.org/10.1016/j.scitotenv.2018.12.321
0048-9697/© 2018 Elsevier B.V. All rights reserved.

the habitat function. The analysis of the surface waters showed levels of Zn surpassing the legal limit adopted from the Water Framework Directive (37.0 to 69.0 μg/L). The ecotoxicological results highlight the importance of bioassays that evaluate the behavior of species, when assessing the risk of mining areas with non-acid soils and waters with high nutrients/organic matter concentrations and low concentrations of potentially toxic metals. The results indicated a moderate environmental risk from potentially toxic metals, at the areas analyzed around the Azuaga mine.

© 2018 Elsevier B.V. All rights reserved.

1. Introduction

One of the main deleterious effects of a mine abandonment is usually associated with the rejection of large volumes of wastes, which can have a negative impact on the environment, mainly as a consequence of the spread and accumulation of potentially toxic metals (Moreno-Jimenez et al., 2011; Romero-Baena et al., 2018). Soils may represent the main reservoir for these hazardous elements, which will usually affect their retention function and can contribute to the contamination of surface and groundwater, compromising their quality and the balance of the ecosystem's communities (Pereira et al., 2008; Mighanetara et al., 2009; Beane et al., 2016;). Indeed, studies have reported deleterious effect of toxic metals on the environment, aquatic organisms, and plants in many parts of the world (Alvarenga et al., 2013; Liu et al., 2013; Yanqun et al., 2004). Furthermore, the dispersion of these wastes can reach agricultural or urban soils and expose humans to toxic metals, either directly, by suspended dust particles in the air, or indirectly, by transfer into the food chain (Alvarenga et al., 2014; Mighanetara et al., 2009; Ngole-Jeme and Fantke, 2017).

The environmental risks posed by metal-contaminated sites were traditionally assessed through chemical analysis (Bori et al., 2017). Nevertheless, it was concluded that this approach do not provide enough information about: (i) the toxicity of hazardous substances in soil; (ii) the synergic and antagonist effects between contaminants; (iii) the interactions among harmful substances, soil matrix and terrestrial/aquatic organisms; and sometimes, (iv) may overestimate the risk (Alvarenga et al., 2012; Bes et al., 2014).

Recent researches highlighted the importance of using a tool-box comprising multiple lines of evidence for soil risk assessment framework (Antunes et al., 2013). In fact, the TRIAD approach, first proposed by Chapman (1990) for the sediment compartment, was adopted for the risk assessment of contaminated soils (Weeks and Comber, 2005; Jensen and Mesman, 2006). The ecotoxicological LoE must integrate terrestrial bioassays, which assess the habitat function of the soil, being a complementary tool to report the interactions among ecosystem communities and the soil compartment (Alvarenga et al., 2012; Bori et al., 2016). At the same time, the use of aquatic bioassays will allow to assess the impact of soil composition on runoff and receiving waters (Rocha et al., 2011). This approach includes information from three Lines of Evidence (LoE): (i) chemical (support parameters, quantification of hazardous substances); (ii) ecological (communities' diversity); and (iii) ecotoxicological (Antunes et al., 2013).

The Mediterranean region presents a historical mining activity since pre-Roman times, but most of the mines are presently abandoned (Doumas et al., 2018). Abandoned mines represent "hot spots" for local populations, because they are usually adjacent to villages and are surrounded by farmland. The local population is subjected to exposure to potential toxic metals through the air, water, soil, and the food chain. Furthermore, Spain had an intensive mining activity, particularly in the eastern Pyrenees, the Beatic Cordillera, and in the regions of Andalucia and Extremadura (Doumas et al., 2018).

Bearing this in mind, the aim of this study was to characterize the environmental risk of the abandoned mine "Las Musas", located at the Azuaga district (Extremadura, Spain), one of the most important mining areas of Zn/Pb exploitation in Spain. To do so, physicochemical parameters, metal quantification and a set of ecotoxicological responses were assessed in soils and waters from the area. The bioassays were selected taking into consideration: (i) the group of organisms commonly used/sensitive to assess the environmental impact of abandoned mines; (ii) different times of exposure, to assess acute and chronic responses during the entire life-cycle of the organism; and (iii) previous studies have already used the same bioassays, which may be an easier way for comparing results (Alvarenga et al., 2012; García-Gómez et al., 2014; Oberholster et al., 2013; Bori et al., 2017).

Further, this study is integrated in a research line about the quality of soils, rivers/streams in the Mediterranean areas, with a strong mining influence, that intends to deliver a tool-box, which can be used to respond to the main alterations that influence their ecological status and may compromise public health.

2. Material and methods

2.1. Characterization of the study area and sampling sites

"Las Musas" mining area (331,000 m^2), is located near the village of Azuaga (Badajoz province, SW Spain) (38°15′30″ N and 1°59′20″ W) (see Fig. 1). This mine belongs to the Azuaga mining district, which was one of the most important mining areas of Zn/Pb exploitation in Spain. The mineralization in this site is associated to Early-Middle Cambrian. The mineral association is mainly composed of blende (ZnS), pyrite (FeS_2), galena (PbS), and chalcopyrite ($CuFeS_2$), with quartz and carbonate gangues. Furthermore, the materials of interlocking of the fault filling extension of the mineralization are mainly secondary Pb carbonates (Zalduegui et al., 2007). "Las Musas" mine was active since the end of the XIX century until about the middle of the XX century. This mine exploitation generated a volume of wastes of about 100,000 t (Gumiel, 2001). "Las Musas" mine is abandoned, and its environmental restoration has been neglected, due to financial limitations, despite its proximity to the village. It is integrated in a protected area, named "Parque Periurbano of Conservación y Ocio da Serra de Azuaga" (Decree Law of 113/2002 of 10 September), constituting a special zone of conservation, due to its biodiversity. Previous reports indicated high bioaccumulation of Pb in wildlife animals (hunting animals) (Garcia-Fernandez and Soler, 2006), and in native plants of the area (Gala, 2014).

Azuaga is integrated in the Guadalquivir basin (Fig. 1) that presents a Mediterranean climate, characterized by dry and hot summers, as well as mild and wet winters. With an annual precipitation between 500 and 800 mm, the scarce rainfalls are concentrated during the October–April period.

Bémbezar river and its tributaries, Cagancha and Jituero streams, are located near the mine and the Azuaga village and belong to the Guadalquivir hydrographic basin. The Bembézar basin is dominated by Mediterranean vegetation and subjected to extensive livestock breeding (e.g., sheep, goat, pig), with some agricultural and forest areas (Gala, 2014; Novo et al., 1994). The Bembézar spring is near Azuaga, it crosses the Hornachuelos village (Córdoba, SW Spain) and receives waters from other tributary streams, forming the Bembézar reservoir. This river runs along the Natural Park of "Sierra de Hornachuelos", a zone of special conservation, declared as Site of Community Importance (Real Decreto 136, 2004).

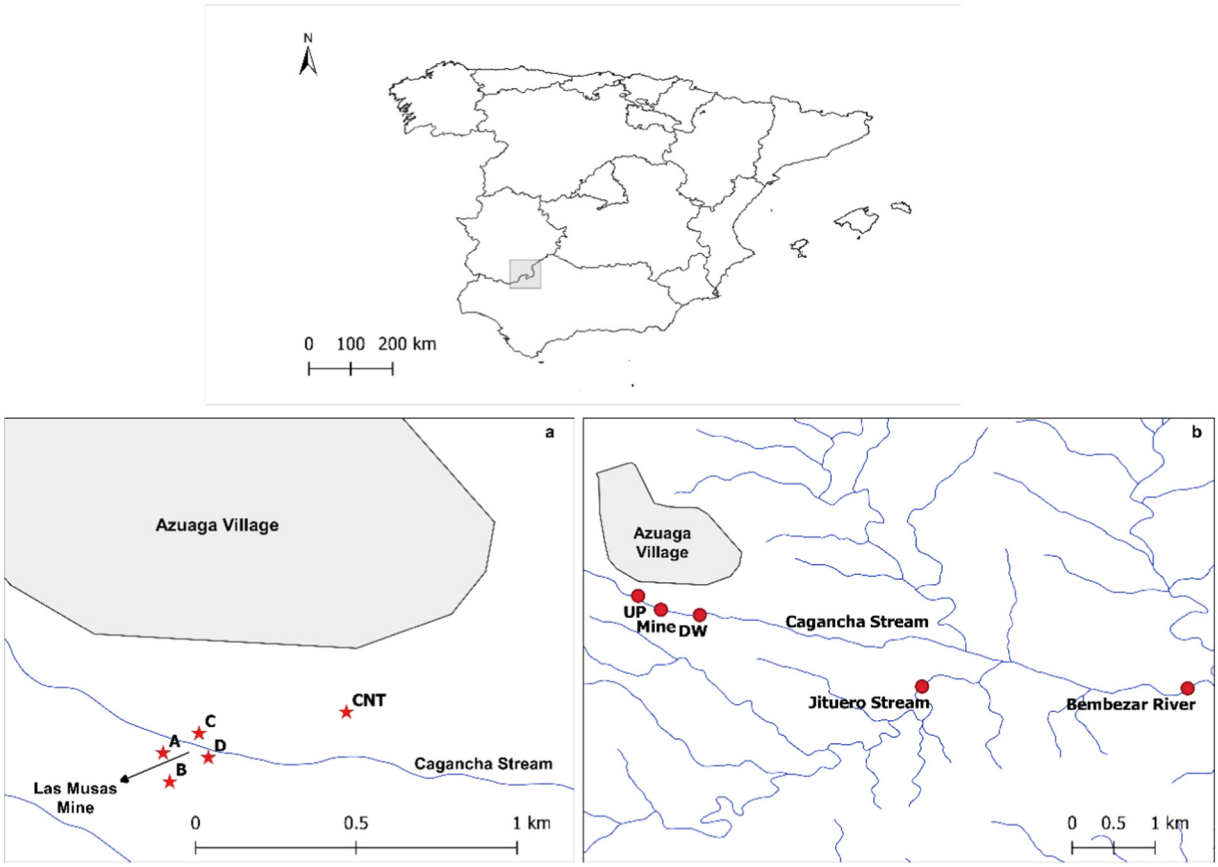

Fig. 1. Location of soils sampling points (a): A (38°15′4.13″ N and 5°40′43.39″ W), B (38°14′58.47″ N and 5°40′41.95″ W), C (38°15′4.68″ N and 5°40′38.20″ W) and D (38°15′2.48″ N and 5°40′37.24″ W), and CNT (38°15′7.40″ N and 5°40′19.33″ W); and water sampling points (b): Upstream mine (UP: 38°15′10.2″N and 5°40′51.7″W), Mine (38°15′03.3″N and 5°40′40.4″ W), Downstream mine (DW: 38°15′01.4″N and 5°40′20.7″W) at Cagancha stream, Bembézar river (38°14′21.8″N and 5°36′22.6″W) and Jituero stream (38°14′25.1″N and 5°38′30.9″W).

Soils were collected at five sampling sites, during May of 2015: (i) four sampling sites around the mine, collected at a distance between 3 and 292 m of the mine tailings, in the four cardinal directions, North, South, East, and West (A (38°15′4.13″ N and 5°40′43.39″ W), B (38°14′58.47″ N and 5°40′41.95″ W), C (38°15′4.68″ N and 5°40′ 38.20″ W) and D (38°15′2.48″ N and 5°40′37.24″ W)); and (ii) one sampling site near the village, considered the control soil, CNT (38°15′7.40″ N and 5°40′19.33″ W) (Fig. 1a). The distance between soil sampling points was chosen taking into consideration the results from Gala (2014), that delimited an area of 100–200 m from the mine tailing, as that with higher concentrations of Pb.

Water samples were collected at five locations (at the same period that soils) belonging to the Guadalquivir basin, to have a representative characterization of the aquatic systems in this area: (i) three sampling locations at Cagancha stream (watercourse that crosses the "Las Musas" mine, and it is a tributary to the Bembézar river): Upstream mine (UP; 38°15′10.2″ N and 5°40′51.7″ W), Mine (M; 38°15′03.3″ N and 5°40′40.4″ W), and Downstream mine (DW; 38°15′01.4″ N and 5°40′20.7″ W); one location at the Jituero stream (another tributary to the Bembézar river: JT; 38°14′25.1″ N and 5°38′30.9″ W); and one location at Bembézar river (BZ; 38°14′21.8″ N and 5°36′22.6″W) (Fig. 1b).

2.2. Soils collection and analysis

Soil samples were collected from the 20-cm topsoil, air-dried and sieved through a 2-mm non-metallic sieve. Soil physicochemical analysis were performed using well described methodologies (Alvarenga et al., 2008): particle-size distribution was determined by the pipet method (Gee and Bauder, 1986); soil pH (H_2O) was determined in a soil to deionized water suspension of 1:2.5 (w/v); electrical conductivity (EC; μS/cm) was determined in a soil to deionized water suspension of 1:5 (w/v); total nitrogen was analyzed by the Kjeldahl method ($N_{Kjeldahl}$; % w/w); total oxidizable organic carbon was determined according to Walkley and Black (1934), and converted to organic matter content (OM; % w/w) multiplying by a factor of 1.72; and extractable P and K (mg/kg) were determined using the Egner-Riehm method (Riehm, 1958). All results were reported in a dry weight basis (dw).

Total metal concentrations (Cd, Cr, Cu, Ni, Pb and Zn) were determined by flame atomic absorption spectrometry after digestion of the samples with aqua regia according to ISO 11466 (1995), using a Varian apparatus (SpectrAA 220FS). Three independent replicates were performed for each sample and blanks were measured in parallel. The choice of these elements was based on the type of mineral that was explored (Zn/Pb) and on the geological characteristics of the minerals, obtained in previous results from our group (not published), and in some works developed near the mining area (Garcia-Fernandez and Soler, 2006; Gala, 2014).

2.3. Water samples collection and analysis

Water samples were collected at a 50 cm depth (when possible) and transported to the laboratory in coolers at 4 °C, to be preserved and stored, following the requisites for water conservation for each parameter, until the analysis was performed (maximum storage time: 1 week) (APHA, 1998).

In the laboratory, the water chemical parameters were determined using officially recommended methods of analysis (APHA, 1998), which were reported by Palma et al. (2010). The parameters analyzed in the water samples were: pH, electrical conductivity (EC; μS/cm),

biochemical oxygen demand (BOD_5; mg/L), chemical oxygen demand (COD; mg/L), total phosphorus (TP; mg/L), total nitrogen (TN; mg/L), nitrate (NO_3-N; mg/L), nitrite (NO_2-N; mg/L), ammonium (NH_4-N; mg/L), chlorides (Cl; mg/L), sulphate (SO_4; mg/L), potassium (K; mg/L), magnesium (Mg; mg/L) and calcium (Ca; mg/L).

For the quantification of metallic elements, the water samples were digested with aqua regia, and Cd, Cu, Pb and Zn were assessed by flame atomic absorption spectrometry according to ISO 11466 (1995).

2.4. Ecotoxicological assessment

Table 1 summarizes the description of the ecotoxicological assays performed, in both matrices.

2.4.1. Terrestrial bioassays

Soil ecotoxicity evaluation was performed using three different tests: *E. fetida* mortality (OECD 207, 1984), *E. fetida* reproduction (OECD 222, 2004) and seedling emergence of L. *sativa* and L. *perenne* (ISO 17126, 2005), using the whole soil and its dilutions with an artificial soil. The artificial soil was prepared according to OECD 207 (1984) (10% sphagnum peat, 20% kaolin clay, 70% industrial sand, w/w dw, pH adjusted to 6.0 ± 0.5 with calcium carbonate). This artificial soil was also used as the control in these tests.

2.4.2. E. fetida bioassays

The mortality toxicity tests using earthworm *E. fetida* were conducted according to the standard protocol OECD 207 (1984), with some modifications (Conder et al., 2001). For each soil and its dilutions, 100 g of sample were moistened to approximately 70% water holding capacity (WHC), in perforated plastic boxes, 24 h prior to the addition of five earthworms (three replicates per concentration). Mature earthworms (clitellate worms), weighing approximately 0.2 to 0.4 g, were obtained from in-house cultures. The test was conducted in environmental chambers maintained at 20 ± 2 °C, with a photoperiod of 16 h light and 8 h darkness. Earthworm mortality and biomass were monitored daily. Mean percent cumulative mortality (%) was outputted.

The reproduction test was performed according to the OECD guideline "Earthworm Reproduction Test" (OECD 222, 2004). For each test, 500 ± 5 g dw of soils, and if its dilutions (25, 50, 75 and 100% w/w), were placed in each container (four replicates per concentration). Mixtures were moistened to reach 60% of the WHC, which was monitored during the test period. Ten earthworms, which have been conditioned for 24 h in the artificial soil and then washed quickly before use, were placed on the soil surface. The containers were kept at 20 ± 2 °C and a photoperiod of 16:8-h light/dark. After 4 weeks of exposure, the adults were removed from the soil and effects on reproduction assessed after a further 4 weeks, by counting the number of offspring present in the soil. The reproductive output of the worms exposed to the soil was compared with that of artificial soil to determine the no observed effect concentration (NOEC) and/or the EC_{50} value (concentration, % w/w, which promoted a reduction on 50% of the observed endpoint).

2.4.2.1. Seedling emergence bioassays. Seedling emergence of L. *sativa* L. and *L. perenne L.* were performed according to ISO 17126 (2005). For each test, 400 ± 5 g dw of the soil, or dilutions of it with artificial soil (25, 50, 75% w/w), was placed in each container (plastic, 10 cm length × 10 cm width). Mixtures were moistened to reach 60% of the WHC. Artificial soil was used as the control, and four replicates per concentration were prepared. Forty seeds of each plant were homogeneously spread on the surface of the soil and covered with a thin layer of dry sand. Containers were incubated for 48 h in the dark, at 20 ± 2 °C, and then subjected to a photoperiod of 16:8-h light/dark, at the same temperature, for a further 72 h. At the end of the test (5 d), the number of germinated seeds was counted and compared with that of the artificial soil, to determine the percentage of seedling emergence and, if possible, the EC_{50} value.

2.4.3. Aquatic toxicity tests

The toxicity of the water samples was tested through aquatic bioassays. When required, dilutions were prepared mixing water samples with the corresponding test medium. Toxicity results were expressed as the percentage of water sample in test medium (%; v/v) which promoted a reduction in 50% of the endpoint measured (EC_{50}). Organisms from the species *P. subcapitata* and *D. magna* were cultured and maintained, at Laboratory of Ecotoxicology of the Polytechnic Institute of Beja, (Portugal), according to the recommended protocols (ISO/DIS 8692, 2002; OECD 201, 2002; ASTM, 1998). Temperature, pH, dissolved oxygen and electrical conductivity (EC) of the samples were measured and were in accordance with the standard protocols used. A reference test with potassium dichromate ($K_2Cr_2O_7$) was conducted as a positive control.

2.4.3.1. Luminescent bacteria bioassay. Luminotox® was used to evaluate the inhibition on the luminescence of the marine bacteria *V. fischeri* (NRRL B-11177), according to the protocol "DR LANGE luminescent bacteria test" following ISO 11348-2 (1998). Tests were carried out using the following dilutions (100, 50, 25, 12.5, 6.25 and 3.125% v/v). Two replicates per treatment were used. The inhibition of the bacteria natural light emission was measured against a non-toxic control (2% w/v NaCl solution), at a temperature of 15 ± 0.5 °C. Tests were carried out with a LUMIStox 300 equipment. For each sample, luminescence decrease was measured before and after the desired incubation period (30 min) and EC_{50} (% v/v; the concentration of each sample that reduced 50% of the bacterial luminescence) was determined.

2.4.3.2. Algal bioassay. The potential inhibitory effect of the water samples on the growth of the unicellular algae *P. subcapitata* was assessed based on the protocol of OECD 201 (2002). The assay was initiated with 5×10^4 cells/mL of *P. subcapitata*, in the log exponential growth phase, and was carried out using six replicates per water sample concentration, and eight replicates for the control group (MBL medium without vitamins). Twenty-four-well plates containing 900 μL of sterilized MBL medium with the tested solutions (100, 75, 50 and 25% v/v) of the water samples diluted with MBL medium) and 100 μL of the

Table 1
Summary of bioassays used at ecotoxicological assessment of both matrices (soil and water) of the study.

	Specie	Control medium	Temperature (°C)	pH	Photoperiod ((light/dark (h)))	Exposure time	Endpoint
Soil samples	*Eisenia fetida*	Artificial soil[a]	20 ± 2.0	6.0 ± 0.5	16 h/8 h	7 days	Mortality
	Eisenia fetida	Artificial soil	20 ± 2.0	6.0 ± 0.5	16 h/8 h	56 days	Number of offspring
	Latuca sativa	Artificial soil	20 ± 2.0	5.0–7.0	16 h/8 h	5 days	Seedling emergence
	Lollium perenne	Artificial soil	20 ± 2.0	5.0–7.0	16 h/8 h	5 days	Seedling emergence
Water samples	*Vibrio fischeri*	NaCl (2%)	15 ± 0.5	7.0 ± 0.2	–	30 min.	Luminescent inhibition
	Daphnia magna	ASTM	20 ± 2.0	6.0–9.0	16 h/8 h	48 h	Immobility
	Daphnia magna	ASTM	20 ± 2.0	6.0–9.0	16 h/8 h	21 days	Number of offspring
	Thamnocephalus platyurus	Synthetic freshwater	25 ± 0.5	7.0–8.0	Continuous dark	24 h	Mortality
	Pseudokirchneriella subcapitata	MBL	24 ± 2.0	8.1 ± 0.2	Continuous light	72 h	Growth inhibition

[a] Artificial soil: 10% sphagnum peat, 20% kaolin clay, 70% industrial sand, w/w dw, pH adjusted to 6.0 ± 0.5 with calcium carbonate.

inoculum were incubated in an orbital shaker (100 rpm) under the conditions previously referred. After 72 h, the average specific growth rate was calculated as the logarithmic increase in cell concentration from the equation:

$$\mu_{i-j} = (\ln B_j - \ln B_i)/(t_j - t_i)$$

where: μ_{i-j} is the average specific growth rate from time i to j (per day); B_i is the cell concentration at time i (initial time of the exposure), and B_j is the cell concentration at time j (final time of the exposure).

The percent inhibition of the growth rate for each sample replicate was calculated from equation:

$$\%I = (\mu_c - \mu_T)/(\mu c) \times 100$$

where: %I, is the percent inhibition in average specific growth rate; μ_C is the mean value for average specific growth rate (μ) in the control group; μ_T is the average specific growth rate for the treatment replicate.

2.4.3.3. T. platyurus bioassay. The effect of the water samples on the mortality of *T. platyurus* was evaluated in accordance with the standard operational procedure provided from the THAMNOTOXKIT FTM kit (Persoone, 1999). The solutions to be tested were obtained by dilution of the samples with synthetic freshwater included in the test kit (100, 75, 50 and 25% v/v), also used as a nontoxic control. Larvae of shrimp *T. platyurus* (<24 h), obtained by the hatching of the cysts, were incubated in 24-well plates, ten animals per well (1 mL test dilution), three replicates for each of the five concentrations and the control group, at 25 °C for 24 h, in the dark. The number of dead shrimps after 24 h contact for each test solution was used as the selected endpoint.

2.4.3.4. D. magna bioassays. The *D. magna* acute bioassay was performed according to the ISO 6341 (1996) guideline. Five neonates (<24 h old) were exposed to 25 mL of the water samples and their dilutions with ASTM medium (100, 75, 50 and 25% v/v; ASTM, 1998), for a period of 48 h. Tests were conducted in environmental chambers at 20 ± 2 °C. A 16 h light and 8 h dark cycle was used. The endpoint used for the toxicological evaluation was the immobility of the daphnids.

Chronic toxicity tests were performed according to the Guideline for Testing of Chemicals N° 211: *Daphnia magna* reproduction test (OECD, 2012), to evaluate the potential effects of the water samples on the reproduction of this species. The chronic assay was initiated with the 3rd brood of offspring (<24 h old), from a single clone derived from a healthy parent stock culture. Daphnids were exposed to water samples diluted with ASTM solution (12.5, 25, 50, 75 and 100% v/v) (10 replicates per concentration containing one *D. magna* neonate). All assays had a negative control with ASTM. Test solutions were renewed three times a week and, at the same time, the organisms were fed with *Pseudokircheneriella subcapitata* (3.0×10^5 cells/ml/daphnia) and Marinure extract®. All experiments were conducted for 21 d, in a chamber with a constant temperature, 20 ± 1 °C, and a photoperiod of 16 h light and 8 h dark. During the assay the number of living offspring produced per female was recorded for each broad. After the exposure period, the total number of viable offspring produced by each female was used to estimate the reproduction rate.

2.5. Statistical analysis

All physicochemical data were checked for homogeneity of variance and normality (Kolmogorov–Smirnov test) and, when possible, subjected to one-way ANOVA. Whenever significant differences were found ($P \leq 0.05$) a post hoc Tukey's HSD test was used to further elucidate differences among sampling locations ($P \leq 0.05$).

The EC_{50} values for *T. platyurus* and *D. magna* mortality/immobility were calculated using the Probit analysis (Finney, 1971). In the *V. fischeri* bioluminescence inhibition test, the EC_{50} values were determined using LUMISsoft 4 Software™. Data on *P. subcapitata* growth and on *D. magna* reproduction, were checked for normality by the Kolmogorov–Smirnov test and variance homogeneity (Levene's tests). As the ANOVA assumptions were not met, data were analyzed non-parametrically using Kruskal–Wallis ANOVA by ranks test. When significant differences were found ($P \leq 0.05$), a post-hoc Dunnet's test was used to compare sampling stations with the control with a *P*-value of 0.05 as the minimum significant level (Zar, 1996). All statistical analyses were performed with the STATISTICA 7.0 (Software™ Inc., PA, USA, 2004).

3. Results and discussion

3.1. Soil general physicochemical characteristics and potentially toxic metals assessment

The studied soils presented marked variability in the physicochemical parameters obtained at different sites, with statistically significant differences among them ($P \leq 0.05$; Tukey's HSD test; Table 2). The pH ranged from neutral, in CNT, to slightly alkaline, in the soils around the mine (7.64–8.18). This gradient of pH had already been reported by Gala (2014), which identified values of pH around 6.5 to 8, in a total of 60 soil samples analyzed around the "Las Musas" mine, and reported a positive correlation with the percentage of carbonates, identifying the higher concentration of carbonates near the mine tailings, and the lower ones near the Azuaga village. Electrical conductivity is low, in all the studied points, with values from 12.7 μS/cm (CNT) to 690 μS/cm (3B), which indicated that the soils present low salinity. Comparing with the EC values obtained by Gala (2014), ranging from 125 to 953 μS/cm, a decrease of soils salinity was observed. The high pH values and the overall low EC were essentially due to the limestone environment (Azharia et al., 2017). In general, soils are poor in OM (<1.8% w/w; USEPA, 2004), classified as mineral soils. Similar physicochemical proprieties of mining soils, in the Mediterranean region, were observed by Azharia et al. (2017) in a study developed in an abandoned Pb/Zn-mining area at the Zeïda mining district (Maroccos) and by Bori et al. (2017) at the abandoned F–Ba–Pb–Zn Osor mining area (Catalonia, Spain).

Relatively to the nutrients, the results highlighted soils poor in $N_{Kjeldahl}$, being the higher values quantified in the locations with higher organic matter (CNT; C). Concerning to the other macronutrients, the soils presented medium (50 to 100 mg/kg) to high (100 to 200 mg/kg) amounts of the Egner-Rhiem extractable of P and K.

Total concentrations of potentially toxic metals presented a significant variability among sampling locations (Table 2). Among the metals assessed, Pb was the metal found with higher concentrations, followed by Zn, mainly at the B, C and D soils.

The concentrations observed for Pb were lower than the results generally reported in abandoned mines of Pb-Zn (940 up to >5000 mg/kg; Bori et al., 2017; Azharia et al., 2017). Furthermore, Gala (2014) reported concentrations of Pb higher than those found in the present study (82 to 3275 mg/kg), at similar distances from the mine tailings (3–292 m), directions (A, B, C, D) and depths (0–20 cm). Despite these facts, and taking into consideration, the possible migration of the metal to other abiotic and biotic compartments, the soils heterogeneity may be the main responsible for the differences found among concentrations, which are very pronounced in samples collected in the same area. Further, the pattern of the area of higher concentrations of Pb (area B) was like the results of Gala (2014). Nevertheless, the levels detected are still higher than the limit proposed by the Canadian soil quality guidelines for agricultural (70 mg/kg) and residential use (140 mg/kg) (CCME, 2018).

On the contrary, the concentrations of Zn are much more variable among the study sites, with levels 10,000 times lower than those found on the Osor mine district (Bori et al., 2017), and similar to those found at Zeïda district (Morocco) (Azharia et al., 2017). Copper contents

Table 2
Soils physicochemical characteristics and potentially toxic metals (mean ± SD; $n = 3$), determined in the four sampling locations (around of the Las Musas mine: A; B; D; C) and at the control location (CNT) near the village of Azuaga (Extremadura; Spain).

	A	B	C	D	CNT	Canadian soil quality guidelines for agriculture/residential use (*)
pH (1:2.5)	8.18 ± 0.07a	7.64 ± 0.03c	7.87 ± 0.02a	8.11 ± 0.03b	6.67 ± 0.09d	
EC (μS/cm)	65.50 ± 4.76c	690.00 ± 13.23a	147.97 ± 4.46c	75.87 ± 3.06b	12.70 ± 0.24d	
OM (%; w/w dw)	0.2 ± 0.02d	0.4 ± 0.00b	1.9 ± 0.02b	0.4 ± 0.01a	0.7 ± 0.02c	
$N_{Kjeldahl}$ (%; w/w dw)	0.01 ± 0.00d	0.02 ± 0.00c	0.08 ± 0.00c	0.02 ± 0.00b	0.10 ± 0.01a	
Extractable P (mg P_2O_5/kg dw)	81 ± 2d	111 ± 5c	127 ± 4b	242 ± 6a	48 ± 5e	
Extractable K (mg K_2O/kg dw)	68 ± 6c	79 ± 6c	104 ± 4b	96 ± 4b	124 ± 3a	
Texture (*)	Loamy clay	Loamy sand	Loamy clay	Loamy clay	Loamy clay	
Cd (mg/kg)	0.3 ± 0.03c	0.57 ± 0.07a	0.40 ± 0.03bc	0.50 ± 0.03ab	0.52 ± 0.02a	1.4/10
Cu (mg/kg)	5.6 ± 0.4d	12.2 ± 2.1c	17.5 ± 1.6b	12.5 ± 0.4c	42.5 ± 0.6a	63/63
Pb (mg/kg)	42.2 ± 3.1c	172.9 ± 7.2a	178.6 ± 10.1a	124.6 ± 1.4b	53.6 ± 1.9c	70/140
Zn (mg/kg)	63.1 ± 3.4d	155.7 ± 6.9a	144.8 ± 7.2a	104.2 ± 2.2b	86.2 ± 1.4c	250/250

Values in a row marked with the same letter are not significantly different (Tukey's HSD test, $P > 0.05$).
(*) Information from Gala, 2014.
DL(Pb) = 15.2 mg/kg; DL(Cd) = 0.3 mg/kg; DL(Zn) = 1.5 mg/kg; DL(Cu) = 1.5 mg/kg.
Values in a row marked with the same letter are not significantly different (Tukey's HSD test, $P > 0.05$).
(*) CCME (2018): https://www.ccme.ca/en/resources/canadian_environmental_quality_guidelines/.

were higher at C and CNT soils, presenting values in the same range to those obtained by Azharia et al. (2017) with mean values of about 26 mg/kg ($n = 20$), and by Bori et al. (2017), with values ranging from 11 to 47 mg/kg. Cadmium presented higher concentrations at B and CNT soils, lower than the stipulated limit by the Canadian soil quality guidelines for agricultural uses (1.4 mg/kg).

3.2. Water general physicochemical characteristics and potentially toxic metals assessment

The physicochemical properties of water samples of the Azuaga mining area are shown in Table 3. As for soils, the water samples presented statistically significant differences among locations for the analyzed parameters ($P < 0.05$; Tukey's HSD test).

The pH results showed values close to neutrality (UP, M and DW) and slightly alkaline (BZ and JT). The values of pH obtained at BZ are like those previously reported by Novo et al. (1994). In line with our results, Bori et al. (2017) have also reported neutral to slightly alkaline waters close to a Pb/Zn mining area at Catalonia region (Spain). This gradient of pH values is characteristic of non-acidic mines, which principal drainage problems are not associated with pyrite oxidation (Tiwary, 2001).

Regarding the conductivity of the water samples, the highest value was determined at BZ (954 μS/cm), followed by the samples from the Cagancha stream (UP, M and DW) that are probably suffering the influence of salts from the mine wastes, mainly of sulphate salts (Jiménez et al., 2009). These values of conductivity are in the same range of those observed by Allert et al. (2009), Ramani et al. (2014) and Bori et al. (2017) in rivers near to Pb/Zn mines.

In general, nutrient parameters, mainly NH_4-N, NO_3-N, TN and TP concentrations in surface waters around mining sites (Cagancha stream) were significantly higher than at Jituero stream. Some authors reported high concentrations of different nitrogen forms at surface waters near mining areas, considering nitrate as one of the major anions that constitute drainage waters, which might be, together with the sulphates, representative of the extension of the mine impact (Allert et al., 2009; Tiwary, 2001). Bembézar showed the highest amount of nutrients, mainly TP = 1.20 mg/L and NH_4-N = 4.20 mg/L, probably due to the influence of the drainage waters from "Las Musas", together with the contamination from domestic wastewater discharges and agriculture activities located along the river. In fact, when we analyzed the results obtained by Novo et al. (1994), which quantified values of TP below 0.06 μg/L and NH_4-N below 0.1 μg/L, we verified that the amounts of these parameters have been increasing since 1994. These

Table 3
Water physicochemical supporting parameters (mean ± SD; $n = 3$) and potentially toxic metals, determined in the five sampling locations (Bembézar river and its tributaries; Azuaga, Extremadura).

	UP	M	DW	BZ	JT	Max.
pH	7.43 ± 0.01 cd	7.38 ± 0.01d	7.47 ± 0.02c	7.54 ± 0.03b	7.99 ± 0.04a	6.5–8.7(i)
EC (μS/cm)	705 ± 6b	641 ± 4d	668 ± 4c	945 ± 6a	587 ± 5e	–
TN (mg/L)	1.80 ± 0.78c	20.71 ± 0.78a	1.35 ± 0.00d	5.40 ± 1.35b	3.60 ± 0.78b,c	–
NO_3-N (mg/L)	9.7 ± 0.3a,b	9.8 ± 0.7a,b	4.9 ± 0.3c	12.3 ± 2.4a	0.96 ± 0.0d	≤20 mg NO_3-N/L(i)
NH_4-N (mg/L)	0.19 ± 0.03c	1.39 ± 0.10b	0.16 ± 0.04c	4.20 ± 0.00a	0.03 ± 0.01c	≤0.3 mg NH_4-N/L(i)
TP (mg/L)	0.78 ± 0.00a	0.23 ± 0.11a	0.55 ± 0.33a	1.20 ± 0.39a	<DL	≤0.2 mg TP/L (i)
BOD_5 (mg/L O_2)	11	49	21	10	35	–
COD (mg/L O_2)	44.86 ± 0.00d	56.82 ± 2.59c	68.79 ± 2.59b	101.68 ± 2.59a	38.88 ± 2.59d	–
SO_4 (mg/L)	96.84 ± 0.38a	67.79 ± 0.13c	77.72 ± 0.07b	51.73 ± 0.07d	37.17 ± 0.12e	–
Na (mg/L)	29.71 ± 0.09e	32.31 ± 0.44d	36.72 ± 0.45c	96.60 ± 0.08a	38.91 ± 0.16b	–
K (mg/L)	6.31 ± 0.15d	7.06 ± 0.12c	8.80 ± 0.15b	14.01 ± 0.09a	3.04 ± 0.00e	–
Mg (mg/L)	24.33 ± 0.14a	16.05 ± 0.06c	17.45 ± 0.01c	12.69 ± 0.05d	20.60 ± 0.91b	–
Ca (mg/L)	50.40 ± 0.26a	46.54 ± 0.04b	48.05 ± 0.25a,b	36.31 ± 0.18d	41.14 ± 1.34c	–
Cd (μg/L)	<DL	<DL	<DL	<DL	<DL	0.45(ii)
Cu (μg/L)	<DL	<DL	<DL	<DL	<DL	5(iii)
Pb (μg/L)	<DL	<DL	<DL	<DL	<DL	14 (ii)
Zn (μg/L)	69.0 ± 0.0a	60.0 ± 0.0a,b	50.0 ± 0.0a,b	52.0 ± 0.0a,b	37.0 ± 0.0c	30(iii)

UP: (upstream); M: (mine); DW: (downstream); BZ: (Bembézar river); JT: (Jituero stream).
DL: detection limit: DL(TP) = 0.003 mg/L; DL(Cd) = 8 μg/L; DL(Cu) = 17 μg/L; DL(Pb) = 170 μg/L.
Values in a row marked with the same letter are not significantly different (Tukey's HSD test, $P > 0.05$).
(i) maximum concentration for the support parameters for good ecological status (Real Decreto 817/2015 adapted from ECC, 2000); (ii) maximum allowable concentration of hazardous substances in inland surface waters (ECC, 2013); (iii) maximum concentration for the annual average of preferential substances in surface waters (Real Decreto 817/2015).

concentrations lead to the decrease of ecological status of Bembézar river and Cagancha stream, classifying it as "less than good", being another factor that can be compromising the balance of the ecosystem communities.

The organic descriptor BOD_5 reached the highest concentrations in the Mine (49 mg/L) that, together with the concentrations of COD, highlighted a possible organic contamination with untreated wastewaters to the Cagancha stream.

Mining activities can lead to an increase in the concentrations of major ions (SO_4^{2-}, Na^+, K^+, Mg^{2+} and Ca^{2+}) in freshwaters, which can be toxic to aquatic organisms (Ingersoll et al., 1992; USEPA, 2009), making important the assessment of these ions. The concentrations of SO_4^{2-}, Ca^{2+}, Mg^{2+} were significantly higher in the samples around the mine, relatively to Bembézar and Jituero water samples, highlighting the impact of the mine wastes on these streams. In fact, sulphate is considered a useful indicator of mine drainage contamination, because it remains elevated even at neutral pH values, since sulphate ions are not easily adsorbed and thus migrate further than metals; its migration can represent the largest range of mine-tailing impact (Gray, 1996). Sodium, Mg^{2+} and Ca^{2+} concentrations did not exceed the freshwater-screening benchmarks defined by the USEPA (2016).

Among the metals assessed, only Zn was detectable, achieving the highest concentrations in the surface waters near the mine. Generally, metal concentrations detected on the water samples are in same range of those found in waters near non-acidic mines (Allert et al., 2009), but much lower than those found in mines affected by acid mine drainage. The speciation and solubility of metals in water depends, among other physicochemical parameters, on pH and on dissolved organic matter. Thus, Bird et al. (2010), indicated that a pH value above 6, as measured in the sampling points of this study, promotes the sorption of metals onto the particulate (including organic material) and sediment phases. This might be a possible explanation for the lowest concentrations of metals observed in the water samples collected in the mining area. Furthermore, the low salinity of the soils may be another factor to increment the adsorption of the metals, once when the concentrations of the major cations are low, like Na^+ and K^+, they may be replaced by trace metals in the adsorption sites (Bori et al., 2017).

Despite Pb being the metal with the higher concentrations in the soil samples, it was always found below the analytical detection limit on the surface waters. The contamination of the surface waters with Zn was much more pronounced than with Pb, even though Zn and Pb are present in similar amounts in Pb/Zn mines (Barnes, 1979). This could be explained by the greater solubility of Zn salts compared with Pb salts (Barnes, 1979), as well as, by the fact that Pb is readily adsorbed by Al and Fe oxides in sediment (Lee et al., 2002), thus resulting in a much quicker decrease of dissolved Pb than Zn concentration (Zhang et al., 2004). Therefore, Pb is present to a lesser degree in the dissolved phase in water, which is why Zn is a better indicator of the effects of mining works on receiving waters (Alderton et al., 2005). Further, previous studies on bioavailability assessment of metals in sediments, by sequential extraction procedures like BCR, indicated that the predominant fraction where metals were found was correlated with the textural and geological characteristics of the matrix, as well as with time of the collection (Palma et al., 2015). Therefore, results showed that, at the dry period, which corresponds to the period when our samples were collected, the major amounts of Pb were found in the reducible fraction (55 to 88%), indicating its reaction with Fe-Mn-oxyhydroxides, the main chemical form controlling its mobility in the environment. Consequently, metal concentrations were very low in the water column. Other studies reported that Pb, together with Cu and Cd, are up to 5 times enriched in the sediments than in the water column (Ciazela et al., 2018).

Zinc surpassed the legal limit for annual average to continental waters, for preferential substances, stipulated by the Real Decreto 817/2015, adapted from the Water Framework Directive (ECC, 2000). Despite, Zn did not surpass the limit value recommended for the aquatic life criteria for freshwater chronic exposure (Zn = 120 μg/L; USEPA, 2016). This apparent ambiguity in the results is concerning, since Zn presents a higher bioconcentration ability, with a high bioconcentration factor (BCF; Zn_{BCF} = 74,200; Liu et al., 2018), which increases the ecological and public health risk, due to the possibility of its transference throughout the trophic chain.

3.3. Ecotoxicological assessment

Terrestrial and aquatic ecotoxicological bioassays were successfully applied to soil and water samples. All ecotoxicological tests reported fulfilled the validity requirements established by their respective guidelines. Marked differences in sensitivity were observed depending on test endpoints and organisms.

3.3.1. Terrestrial bioassays

For the terrestrial bioassays with earthworms, lethality test was not sensitive enough to detect toxicity for the studied soils, which may be correlated with the avoidance strategy adopted by the earthworms: they arrange themselves in a cluster, near the wall of the box, avoiding contact with the soil (Alvarenga et al., 2012), as well as, with the low acute toxicity of the soil samples. The low sensitivity of this terrestrial bioassay was already reported, in other ecotoxicological studies with mine contaminated soils (Alvarenga et al., 2013; Bori et al., 2017). On the contrary, reproduction test was sensitive enough to detect toxicity in some of the studied soils (Fig. 2). Soil B was the only identified as toxic, in the chronic exposure of earthworms, being the NOEC (no observable effect concentration) lower than 25% (w/w) of soil. Despite the similarity of the metal concentrations of the soils collected at the sites B, C and D, the soil B presented low concentrations of organic matter and is mostly constituted by sand (particles >0.063 mm), factors that may influence the low adsorption of the metals to the soil, turning them more available. This increment in metal availability, together with the highest EC value, may be the reasons for the toxicity observed. Results from terrestrial bioassays with earthworms agreed with previous studies, that highlighted the higher sensitivity of sublethal endpoints in the ecotoxicological evaluation of metal contaminated soils (Alvarenga et al., 2012; Bori et al., 2016).

Percentages of seedling germination on the tested soils (Fig. 3), highlighted that L. *sativa* was more sensitive to these soils than L. *perenne*. In fact, the germination of L. *perenne* was not inhibited in any of the tested soils. The resistance of this specie to toxicity of non-acid mine soils, was already observed by Bori et al. (2017), leading to the conclusion that it is a not good specie/bioassay to be integrated in a tool-box for the risk assessment of soils contaminated with wastes from non-acid mines. On the other hand, all soils induced a decrease of the percentage of seedling germination of L. *sativa*, being soil C

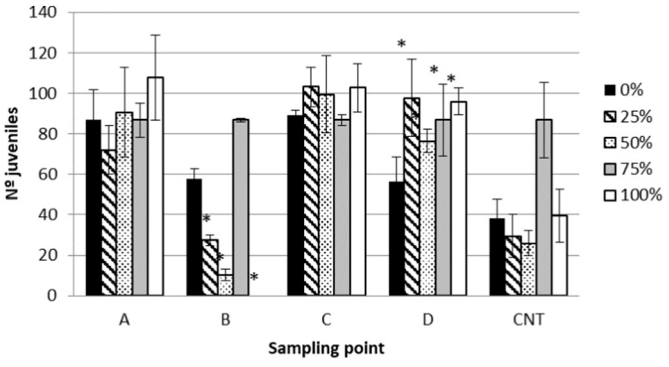

Fig. 2. *E. fetida* reproduction bioassay, total juvenile produced at each concentration (0, 25, 50, 75, 100% w/w) during the 21 days of exposure (mean ± standard deviation, $n = 4$). Bars marked with an asterisk represent values significantly different from control group in artificial soil (*$P < 0.05$, Dunnett's test with a control).

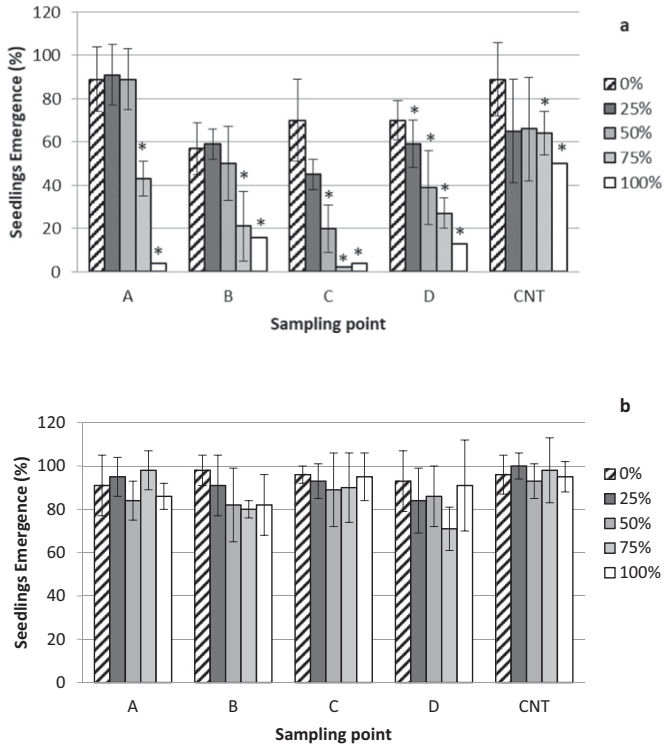

Fig. 3. *Latuca sativa* (a) and L. *perenne* (b) percentage of seedling emergence (%) at each concentration (0, 25, 50, 75, 100% w/w), after 5 d of exposure. Mean ± standard deviation ($n = 4$), $^{*}P < 0.05$, Dunnett's post-hoc comparison test with the control.

(NOEC = 25% (w/w) and D (NOEC <25% (w/w)) the most toxic, and CNT the least toxic, with a NOEC of 75% (w/w)). The CNT soil presented the lowest concentrations for Pb and Zn, and, for the nutritional conditions, presented the higher concentrations for $N_{Kjeldahl}$ and extractable K, justifying, in this way the results observed. Once again, the results showed that the contamination with metals contributed to the toxic responses of the specie, but, in the case of plant species, the nutritional status of the soil seemed to exert a preponderant effect on the response observed, as be already reported by Alvarenga et al. (2013).

Despite the differences observed in the toxicity responses, the habitat function of the soils may be compromised, once at least one specie was sensitive to all of them.

3.3.2. Aquatic bioassays

The toxicity of water samples towards aquatic organisms, obtained for the acute exposure bioassays, evidenced that *V. fischeri* was the most sensitive species, detecting toxicity in all the samples from Cagancha stream ((30 min-EC_{50} (% v/v; $n = 2$; mean ± standard deviation): UP (46.30 ± 0.16); M (67.66 ± 0.32); DW (88.15 ± 0.27))); and Bembézar river (54.84 ± 0.33). Upstream induced the greatest luminescence inhibition of the species, site that presented the highest concentrations of Zn. These results are contrary to those from studies that reported the less sensitivity of this species to waters from acid-mine areas (Alvarenga et al., 2008; Bori et al., 2016, 2017). Thus, in cases that, due to the low pH of the waters, is necessary to do its correction for values near neutrality, this species maybe not be a good choice, once the pH correction may mask the toxic effects induced by the metals, especially when their concentrations are not very high.

The toxic effects towards *V. fischeri* were probably correlated with Zn concentrations, as was reported by Baran et al. (2014), in water extracts of soils from a Pb/Zn mine in Poland. Nevertheless, the concentration of Zn presented by the samples was not enough, by itself, to explain the toxicity observed, once the Zn-EC_{50} to *V. fischerie* is between 4.64 and 13.40 mg/L (Teodorovic et al., 2009), concentrations several orders of magnitude greater than those found in our study area. Consequently, the results highlighted that the luminescence inhibition probably occurred due to the mixture of Zn and other parameters, such as NO_3-N. In fact, the concentrations of NO_3-N surpassed the maximum level recommended for protecting the most sensitive species in freshwater systems (2.0 mg/L; Kincheloe et al., 1979).

Results from the acute bioassays showed that, none of the water samples caused mortality or immobilization towards *T. platyurus* and *D. magna*, respectively. Lari et al. (2017), showed that Zn is the metal, among Zn, Cd, Cu and Ni, less toxic towards *D. magna*. Moreover, its lethal bioassay is less sensitive than the sub-lethal tests, such as the feeding bioassay. Further, Zn concentrations detected in the water samples were several times lower than those that promote acute toxicity to this crustacean (EC_{50}: 0.18–0.56 mg/L; Teodorovic et al., 2009; De Schamphelaere et al., 2014).

Relatively to the results obtained with *T. platyurus*, they are in contrast with previous results that highlighted the sensitivity of this crustacean to low levels of potentially toxic metals in surface waters and sediment pore-water samples, being considered as a good alternative to *D. magna*, when integrating primary consumers in toolboxes for environmental risk assessment (Palma et al., 2014; Palma et al., 2016).

Considering the results of chronic exposure, in general, the samples induced an increase on the growth of *P. subcapitata* (Fig. 4), as well as an increase on the reproduction rate of *D. magna* (Fig. 5).

Relatively to *P. subcapitata*, the only sample that induced a slight decrease of its growth rate (20%) was Jituero. Comparing with the other sampling sites, Jituero showed a concentration of TP lower than the detection limit (<0.003 mg/L) which could be a limiting factor for algal growth. According to Reynolds (1984), a concentration <0.005 mg/L of TP may limit the algal biomass. Studies reported the increment of toxic effect (algae growth inhibition) induced by potentially toxic metals in the presence of low concentrations of TP, probably due to the reduction of metal detoxification processes (Chia et al., 2017). Furthermore, Gao et al. (2016), in a study that assessed the effects of the correlation Zn-TP in *P. subcapitata* growth, reported that the first stress factor for the growth of the algae is the TP concentration, and the second one is the Zn concentration, which means that, if TP concentration in the water is not limiting, the possible toxic effect induced by Zn may be masked. This fact justifies the observed results in the rest of the samples, with high amount of Zn and TP.

The observed significant increase on the number of offspring per female, relatively to the control (Dunnet post-hoc test, $P \leq 0.05$), might be explained by the high concentrations of nutrients (especially TN and TP) and organic matter content in the samples, which might have improved the metabolism and, consequently, the reproduction of daphnids. This kind of pattern was already reported by Alexander et al. (2013), Ieromina et al. (2014) and Palma et al. (2016), who observed a better performance in the reproduction parameters of the *D. magna* when the organisms were exposed to surface waters with higher levels of nutrients and organic matter, and if the concentrations of the hazardous substances are low.

4. Conclusions

"Las Musas" mine exhibits non-acid wastes with non-acid drainage waters, which limits metals mobility, being an important factor to the lower environmental risk observed at the site. The application of chemical and ecotoxicological LoE to soils and waters from the "Las Musas" mining area, allowed the determination of the real impact of the mine wastes in this region and the selection of the best bioassays to use in the risk assessment of abandoned mines with the same geological characteristics.

Hence, the soils from this mining area still have concentrations of Pb above those allowed for agricultural use, supporting the results obtained for the bioassays with L. *sativa* and the earthworm reproduction. These ecotoxicological results may, at medium-long term, affect the balance of the ecosystem, once these species integrate a trophic chain and

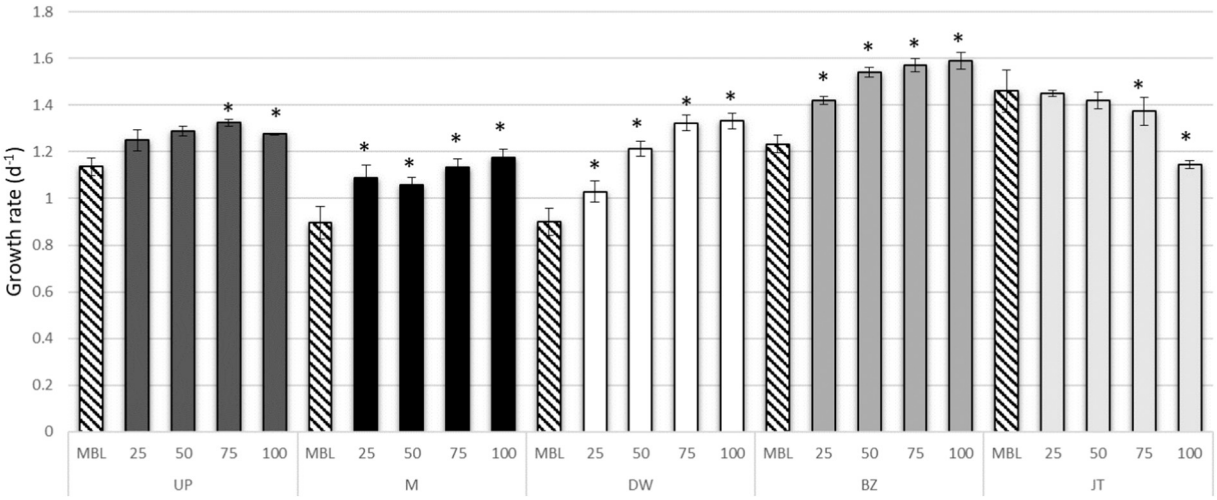

Fig. 4. Growth rate (d-1) of algae *P. subcapitata* after 72-h exposed to the different water samples tested ((Upstream mine (UP), Mine (M), Downstream mine (DW), Bembézar (BZ) and Jituero (JT))) (100% undiluted sample, 75%, 50% and 25% v/v dilutions with MBL medium). Mean ± standard deviation ($n = 6$), $^*P < 0.05$, Dunnett's post hoc comparison test with the control MBL.

the negative effect in one of them, a producer or a decomposer, will induce changes in all the chain.

Further, the results highlighted that the assessment of the terrestrial habitat function of these soils must integrate species that respond to soil contamination, as well as to the nutritional status of the soil.

As for the surface waters, the impact is not so clear and is apparently mixed with the responses to pollutants coming from other anthropogenic sources, e.g., the discharge of untreated wastewaters. Zinc was quantified in the waters at levels that deserve some attention, when considering the ecosystem balance. Despite that fact, the bioassays applied, except *V. fischerie* luminescence inhibition, did not reveal toxic responses. Indeed, *V. fischeri* bioassay showed good sensitiveness to metal contamination, as well as, to the ecological classification, highlighting the usefulness of its inclusion in a tool-box to test mining sites with non-acid wastes.

Therefore, in mining areas where the contamination by metals have decreased over time, with high concentrations of organic matter, and pH near the neutrality, the best ecotoxicological option is to choose species with responses less influenced by nutrients and organic matter, integrating behavioral endpoints, as feeding inhibition and avoidance habitat.

The results highlighted the linearity of the responses among the two groups of biological methodologies. Nevertheless, further studies including more sampling campaigns, the assessment of sediment matrices at the dry phase, and the use of a higher number of bioindicators would be needed, to generalize our findings and to establish thresholds easy to apply and understand in programs of management and restoration of this type of ecosystem.

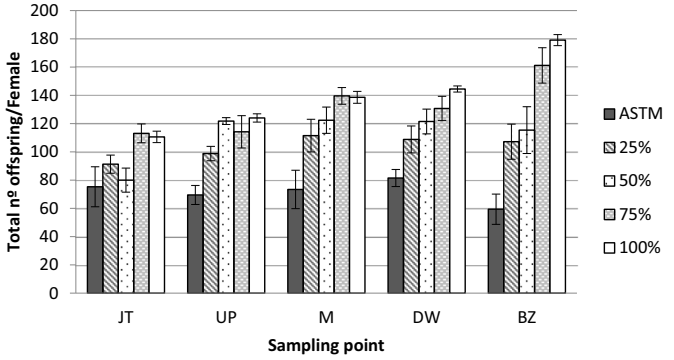

Fig. 5. Total number of offspring produced per female, after 21 d of exposure to the different water samples tested ((Upstream mine (UP), Mine (M), Downstream mine (DW), Bembézar (BZ) and Jituero (JT))) (100% undiluted sample, 75%, 50% and 25% v/v dilutions with ASTM medium). Mean ± standard deviation ($n = 10$), $^*P < 0.05$, Dunnett's post-hoc comparison test with the control ASTM.

In view of the results from our study, the abandoned mining area of "Las Musas" is considered to have, nowadays, a moderate environmental threat. Nevertheless, as the results obtained were from a confined zone, further studies are needed, to determine the real environmental and health risk impacts in a larger area surrounding the mine tailings, through studies of distribution and mobilization of the potentially toxic trace metals, complemented with ecotoxicological studies.

Conflicts of interest statement

The authors declare that there are no conflicts of interest.

Acknowledgments

Authors wish to thank the financial support given to R. López-Orozco by "V Convocatoria de Becas Internacionales Fórmula Santander (2014/2015)" under the framework of Extremadura University (Spain).

The present research is co-funded by the European Union through the European Regional Development Fund, included in the COMPETE 2020 (Operational Program Competitiveness and Internationalization) through the ICT project (UID/GEO/04683/2013) with the reference POCI-01-0145-FEDER-007690, the ALOP project (ALT20-03-0145-FEDER-000004), and through the Engage SKA (POCI-01-0145-FEDER-022217) and by the European Union through the EU FP7 project SOLUTIONS (603437).

References

Alderton, D.H.M., Serafimovski, T., Mullen, B., Fairall, K., James, S., 2005. The chemistry of waters associated with metal mining in Macedonia. Mine Water Environ. 24, 139–149.

Alexander, A.C., Luis, A.T., Joseph, M.C., Donald, J.B., Cessna, A.J., 2013. Can nutrients mask community responses to insecticide mixtures? Ecotoxicology 22, 1085–1100.

Allert, A.L., Fairchild, J.F., DiStefano, R.J., Schmitt, C.J., Brumbaugh, W.G., Besser, J.M., 2009. Ecological effects of lead mining on Ozark streams: in-situ toxicity to woodland crayfish (*Orconectes hylas*). Ecotoxicol. Environ. Saf. 72 (4), 1207–1219.

Alvarenga, P., Palma, P., Gonçalves, A.P., Baião, N., Fernandes, R.M., de Varennes, A., Vallini, G., Duarte, E., Cunha-Queda, A.C., 2008. Assessment of chemical, biochemical and ecotoxicological aspects in a mine soil amended with sludge of either urban or industrial origin. Chemosphere 72, 1774–1781.

Alvarenga, P., Palma, P., de Varennes, A., Cunha-Queda, A.C., 2012. A contribution towards the risk assessment of soils from the São Domingos Mine (Portugal): chemical, microbial and ecotoxicological indicators. Environ. Pollut. 161, 50–56.

Alvarenga, P., Laneiro, C., Palma, P., Varennes, A., Cunha-Queda, C., 2013. A study on As, Cu, Pb and Zn (bio)availability in an abandoned mine area (São Domingos,

Portugal) using chemical and ecotoxicological tools. Environ. Sci. Pollut. Res. 20, 6539–6550.
Alvarenga, P., Simões, I., Palma, P., Amaral, O., Matos, J.X., 2014. Field study on the accumulation of trace elements by vegetables produced in the vicinity of abandoned pyrite mines. Sci. Total Environ. 470–471, 1233–1242.
Antunes, S.C., Castro, B., Moreira, C., Gonçalves, F., Pereira, R., 2013. Community-level effects in edaphic fauna from an abandoned mining area: integration with chemical and toxicological lines of evidence. Ecotoxicol. Environ. Saf. 88, 65–71.
APHA (America Public Health Association), 1998. Standard Methods for the Examination of Water and Wastewater. 20th ed. America Public Health Association, New York.
ASTM (American Society of Testing Materials), 1998. Standard Practice for Conducting Toxicity Tests With Fishes, Microinvertebrates and Amphibians. (E729-90). Annual Book of ASTM Standards. American Society of Testing Materials, Philadelphia, pp. 271–296.
Azharia, A.E., Rhoujjatia, A., Hachimib, M.L., Ambrosic, J.P., 2017. Pollution and ecological risk assessment of heavy metals in the soil-plant system and the sediment-water column around a former Pb/Zn-mining area in NE Morocco. Ecotoxicol. Environ. Saf. 144, 464–474.
Baran, A., Czech, T., Wieczorek, J., 2014. Chemical properties and toxicity of soils contaminated by mining activity. Ecotoxicology 23, 1234–1244.
Barnes, H.L., 1979. The solubilities of ore minerals. In: Barnes, H.L. (Ed.), The Geochemistry of Hydrothermal Ore Deposits, 2nd ed Wiley, New York, pp. 404–460.
Beane, S.J., Comber, S.D.W., Rieuwerts, J., Long, P., 2016. Abandoned metal mines and their impact on receiving waters: a case study from Southwest England. Chemosphere 153, 294–306.
Bes, C.M., Pardo, T., Bernal, M.P., Clemente, R., 2014. Assessment of the environmental risks associated with two mine tailing soils from the La Union-Cartagena (Spain) mining district. J. Geochem. Explor. 147, 98–106.
Bird, G., Brewer, P.A., Macklin, M.G., Nikolova, M., Kotsev, T., Mollov, M., Swain, C., 2010. Dispersal of contaminant metals in the mining affected Danube and Maritsa drainage basins, Bulgaria, Eastern Europe. Water Air Soil Pollut. 206, 105–127.
Bori, J., Vallès, B., Navarro, A., Riva, M.C., 2016. Geochemistry and environmental threats of soils surrounding an abandoned mercury mine. Environ. Sci. Pollut. Res. 23, 12941–12953.
Bori, J., Vallès, B., Navarro, A., Riva, M.C., 2017. Ecotoxicological risks of the abandoned F–Ba–Pb–Zn mining area of Osor (Spain). Geochem. Health. 39, 665–679.
CCME (Canadian Environmental Quality Guidelines), 2018. Canadian Soil Quality Guidelines for the Protection of Environmental and Human Health. Canadian Council of Ministers of the Environment Available from. https://www.ccme.ca/en/resources/canadian_environmental_quality_guidelines/.
Chapman, P.M., 1990. The sediment quality TRIAD approach to determining pollution-induced degradation. Sci. Total Environ. 978, 815–825.
Chia, M.A., Lombardi, A.T., Melão, M.G., Parrish, G.C.C., 2017. Phosphorus levels determine changes in growth and biochemical composition of *Chlorella vulgaris* during cadmium stress. J. Appl. Phycol. 29 (4), 1883–1891.
Ciazela, J., Siepak, M., Wojtowicz, P., 2018. Tracking heavy metal contamination in a complex river-oxbow lake system: middle Odra Valley, Germany/Poland. Sci. Total Environ. 616–617, 996–1006.
Conder, J.M., Lanno, R.P., Basta, N.T., 2001. Assessment of metal availability in smelter soil using earthworms and chemical extractions. J. Environ. Qual. 30, 1231–1237.
De Schamphelaere, K.A.C., Nys, C., Janssen, C.R., 2014. Toxicity of lead (Pb) to freshwater green algae: development and validation of a bioavailability model and inter-species sensitivity comparison. Aquat. Toxicol. 155, 348–359.
Decree-Law 113/2002, of 10 September. Por el que se declara Parque Periurbano de Conservación y Ocio a la finca La Sierra en el término municipal de Azuaga. Consejería de Agricultura y Medio Ambiente (in Spanish).
Doumas, P., Munoz, M., Banni, M., Becerra, S., Bruneel, O., Casiot, C., Cleyet-Marel, J.C., Gardon, J., Noack, Y., Sappin-Didier, V., 2018. Polymetallic pollution from abandoned mines in Mediterranean regions: a multidisciplinary approach to environmental risks. Reg. Environ. Chang. 18, 677–692.
ECC (European Community Commission), 2000. Commission Directive 2000/60/EC of the European Parliament and the Council establishing the framework for community action in the field of water policy. Off. J. Eur. Commun. L 327.
ECC (European Community Commission), 2013. Decision 2013/39/EC on environmental quality standards in the field of water policy. Off. J. Eur. Commun. L 226/1.
Finney, D.J., 1971. Probit Analysis. Cambridge University Press, Cambridge, UK.
Gala, J.A., 2014. Estado Del Suelo y Vegetación en el Entorno de la Mina "las Musas" en Azuaga (Badajoz). (Doctoral Thesis presented at). Extremadure University Badajoz, Spain.
Gao, C., De Schamphelaere, K.A.C., Smoldersa, E., 2016. Zinc toxicity to the alga *Pseudokirchneriella subcapitata* decreases under phosphate limiting growth conditions. Aquat. Toxicol. 173, 74–82.
Garcia-Fernandez, A.J., Soler, F., 2006. Riesgos tóxicos por consumo de animales de caza. In: Cameán, A.M., Repettto, M. (Eds.), Toxicología Alimentaria. Díaz de Santos Madrid, Spain, pp. 413–436.
García-Gómez, C., Esteban, E., Sánchez-Pardo, B., Fernández, M.D., 2014. Assessing the ecotoxicological effects of long-term contaminated mine soils on plants and earthworms: relevance of soil (total and available) and body concentrations. Ecotoxicology 23, 1195–1209.
Gee, G.W., Bauder, J.W., 1986. Particle-size analysis. In: Klute, A. (Ed.), Methods of Soil Analysis, Part 1, Physical and Mineralogical Methods. Soil Science Society of America, Madison, pp. 383–412.
Gray, N.F., 1996. Field assessment of acid mine drainage contamination in surface and groundwater. Environ. Geol. 27, 358–361.
Gumiel, P., 2001. Recursos Minerales de Extremadura: La Importancia del Distrito Minero de Azuaga Conferencia en la Universidad Popular de Azuaga, Badajoz, Spain.
Ieromina, O., Peijnenburg, W.J.G.M., de Snoo, G.R., Vijver, M.G., 2014. Population responses of *Daphnia magna*, *Chydorus sphaericus* and *Asellus aquaticus* in pesticide contaminated ditches around bulb fields. Environ. Pollut. 192, 196–203.
Ingersoll, C.G., Dwyer, F.J., Burch, S.A., Nelson, M.K., Buckler, D.R., Hunn, J.B., 1992. The use of freshwater and saltwater animals to distinguish between the toxic effects of salinity and contaminants in irrigation drain water. Environ. Toxicol. Chem. 11 (4), 503–511.
ISO 11348-2, 1998. Determination of Inhibitory Effect of Water Samples on the Light Emission of *Vibrio fischeri* (Luminescent Bacteria Test). Part 2: Method Using Liquid-Dried Bacteria. International Organization for Standardisation, Geneve, Switzerland.
ISO 11466, 1995. Soil Quality—Extraction of Trace Elements Soluble in Aqua Regia. International Organization for Standardization, Geneva.
ISO 17126, 2005. Soil Quality—Determination of the Effects of Pollutants on Soil Flora—Screening Test for Emergence of Lettuce Seedlings (*Lactuca sativa* L.). International Organization for Standardization, Geneva.
ISO 6341, 1996. Water Quality – Determination of the Inhibition of the Mobility of *Daphnia magna* Straus (Cladocera, Crustacea) - Acute Toxicity Test. International Organization for Standardisation, Geneve, Switzerland.
ISO/DIS 8692, 2002. International Standard for Water Quality: Fresh Water Algal Growth Inhibition Test With Unicellular Green Algae. International Organization for Standardisation, Geneve, Switzerland.
Jensen, J., Mesman, M., 2006. Ecological Risk Assessment of Contaminated Land—Decision Support for Site Specific Investigations. (ISBN 90-6960-138-9/978-90-6960-138-0. Pdf Document). p. 138.
Jiménez, A., Aroba, J., de la Torre, M.L., Andujar, J.M., Grande, J.A., 2009. Model of behaviour of conductivity versus pH in acid mine drainage water, based on fuzzy logic and data mining techniques. J. Hydroinf. 11, 147–153.
Kincheloe, J.W., Wedemeyer, G.A., Koch, D.L., 1979. Tolerance of developing salmonid eggs and fry to nitrate exposure. Bull. Environ. Contam. Toxicol. 23, 575–578.
Lari, E., Gauthier, P., Mohaddes, E., Pyle, G.G., 2017. Interactive toxicity of Ni, Zn, Cu, and Cd on *Daphnia magna* at lethal and sub-lethal concentrations. J. Hazard. Mater. 15 (334), 21–28.
Lee, G., Bigham, J.M., Faure, G., 2002. Removal of trace elements with Fe, Al and Mn from natural waters contaminated with acid mine drainage in the Ducktown mining district, Tennessee. Appl. Geochem. 17, 569–581.
Liu, X., Song, Q., Tang, Y., Li, W., Xu, J., Wu, J., Wang, F., Brookes, P.C., 2013. Human health risk assessment of heavy metals in soil-vegetable system: a multi-medium analysis. Sci. Total Environ. 463–464, 530–540.
Liu, X., Jiang, J., Yan, Y., Dai, Y.Y., Deng, B., Ding, S., Su, S., Sun, W., Li, Z., Gan, Z., 2018. Distribution and risk assessment of metals in water, sediments, and wild fish from Jinjiang River in Chengdu, China. Chemosphere 196, 45–52.
Mighanetara, K., Braungardt, C.B., Rieuwerts, J.S., Azizi, F., 2009. Contaminant fluxes from point and diffuse sources from abandoned mines in the river Tamar catchment, UK. J. Geochem. Explor. 100, 116–124.
Moreno-Jimenez, E., Garcia-Gomez, C., Oropesa, A.L., Esteban, E., Haro, A., Carpena-Ruiz, R., Tarazona, J.V., Peñalosa, J.M., Fernandez, M.D., 2011. Screening risk assessment tools for assessing the environmental impact in an abandoned pyritic mine in Spain. Sci. Total Environ. 409, 692–703.
Ngole-Jeme, V.M., Fantke, P., 2017. Ecological and human health risks associated with abandoned gold mine tailings contaminated soil. PLoS One 12 (2), e0172517. https://doi.org/10.1371/journal.pone.0172517.
Novo, F.G., Gallego, J.B., Muñoz, C.E., Alvarez, E.M., Ruiz, A.R., Encina, L., Marín, J.P., Guervos, P.D., 1994. Ecologia dos Sistemas Aquáticos en Entorno de el Cabril Departamento de Ecologia Universidad de Sevilla, Spain.
Oberholster, P.J., Genthe, B., Hobbs, P., Cheng, P.H., de Klerk, A.R., Botha, A.M., 2013. An ecotoxicological screening tool to prioritise acid mine drainage impacted streams for future restoration. Environ. Pollut. 176, 244–253.
OECD 201, 2002. Freshwater alga and cyanobacteria, growth inhibition test. OECD Guidelines for Testing of Chemicals No. 201. Organization for Economic Cooperation and Development, Paris.
OECD 207, 1984. OECD guidelines for the testing of chemicals/section 2: effects on biotic systems. Test No. 207: Earthworm, Acute Toxicity Tests. The Organization for Economic Co-operation and Development (OECD), Paris.
OECD 211, 2012. *Daphnia magna*, reproduction test. OECD Guidelines for Testing of Chemicals No. 211. Organization for Economic Cooperation and Development, Paris.
OECD 222 (2004) OECD guidelines for the testing of chemicals/section 2: effects on biotic systems. Test No. 222: Earthworm Reproduction Test (*Eisenia fetida*/*Eisenia andrei*). The Organization for Economic Co-operation and Development (OECD), Paris.
Palma, P., Alvarenga, P., Palma, V., Matos, C., Fernandes, R.M., Soares, A., Barbosa, I.R., 2010. Evaluation of surface water quality using an ecotoxicological approach: a case study of the Alqueva Reservoir (Portugal). Environ. Sci. Pollut. Res. 17 (3), 703–716.
Palma, P., Ledo, L., Soares, S., Barbosa, I.R., Alvarenga, P., 2014. Spatial and temporal variability of the water and sediments quality in the Alqueva reservoir (Guadiana Basin; southern Portugal). Sci. Total Environ. 470–471, 780–790.
Palma, P., Ledo, L., Alvarenga, P., 2015. Assessment of trace element pollution and its environmental risk to freshwater sediments influenced by anthropogenic contributions: the case study of Alqueva reservoir (Guadiana Basin). Catena 128, 174–184.
Palma, P., Ledo, L., Alvarenga, P., 2016. Ecotoxicological endpoints, are they useful tools to support ecological status assessment in strongly modified water bodies? Sci. Total Environ. 541, 119–129.
Pereira, R., Antunes, S.C., Marques, S.M., Gonçalves, F., 2008. Contribution for tier 1 of the ecological risk assessment of Cunha Baixa uranium mine (Central Portugal): I soil chemical characterization. Sci. Total Environ. 390, 377–386.

Persoone, G., 1999. THAMNOTOXKIT FTM—Crustacean Toxicity Screening Test for Freshwater Standard Operational Procedure. Kluwer Academic / Plenum Publishers, Belgium, pp. 3–21.
Ramani, S., Dragun, Z., Kapetanović, D., Kostov, V., Jordanova, M., Erk, M., Hajrulai-Musliu, Z., 2014. Surface water characterization of three rivers in the lead/zinc mining region of northeastern Macedonia. Arch. Environ. Contam. Toxicol. 66 (4), 514–528.
Real Decreto 136/2004, de 2 de septiembre, por el que se declara el Corredor Ecológico y de Biodiversidad del Río Bembézar.
Real Decreto 817/2015, de 11 de Septiembre, por el que se establecen los criterios de seguimiento y evaluación del estado de las aguas superficiales y las normas de calidad ambiental (RD 817/2015).
Reynolds, C.S., 1984. The Ecology of Freshwater Phytoplankton. Cambridge University Press, Cambridge.
Riehm, H., 1958. Die ammoniumlaktatessigsaure-methode zur bestimmung der leichtloeslichen phosphosaure in karbonathaltigen boden. Agrochimica 3, 49–65 (in German).
Rocha, L., Rodrigues, S.M., Lopes, I., Soares, A.M.V.M., Duarte, A.C., Pereira, E., 2011. The water-soluble fraction of potentially toxic elements in contaminated soils: relationships between ecotoxicity, solubility and geochemical reactivity. Chemosphere 84, 1495–1505.
Romero-Baena, A.J., González, I., Galán, E., 2018. Soil pollution by mining activities in Andalusia (South Spain)—the role of mineralogy and geochemistry in three case studies. J. Soils Sediments 18, 2231–2247.
Teodorovic, I., Planojevic, I., Knezevic, P., Radak, S., Nemet, I., 2009. Sensitivity of bacterial vs acute *Daphnia magna* toxicity tests to metals. Open Life Sci. 4 (4), 482–492.
Tiwary, R.K., 2001. Environmental impact of coal mining on water regime and its management. Water Air Soil Pollut. 132, 185–199.
USEPA, 2004. Framework for Inorganic Metals Risk Assessment. U.S. Environmental Protection Agency, Washington, DC (Draft EPA/630/P-04/068B, 20460).
USEPA, 2009. The Effects of Mountain Top Mines and Valley Fills on Aquatic Ecosystems of the Central Appalachian Coalfields EPA/600/R-09/138A. National Center for Environmental Assessment, Washington, DC.
USEPA, 2016. Water quality criteria. http://www.epa.gov/wqc/national-recommendedwater-quality-criteria-aquatic-life-criteria-table, Accessed date: September 2018.
Walkley, A., Black, J.A., 1934. An examination of the Degtjareff method for determining soil organic matter and a proposed modification of the chromic acid titration method. Soil Sci. 37, 29–38.
Weeks, J.M., Comber, S.D.W., 2005. Ecological risk assessment of contaminated soil. Mineral. Mag. 69, 601–613.
Yanqun, Z., Yuan, L., Schvartz, C., Langlade, L., Fan, L., 2004. Accumulation of Pb, Cd, Cu and Zn in plants and hyperaccumulator choice in Lanping leadezinc mine area, China. Environ. Int. 30, 567–576.
Zalduegui, J., Guinea, A., Abalos y Ibarguchi, J., 2007. Composición isotópica del Pb en galenas de la región de la Falla de Azuaga Aportaciones al modelo plumbotectónico de la Zona de Ossa-Morena. Geogaceta 43, 7–10.
Zar, J.H., 1996. Biostatistical Analysis. Prentice Hall International Editions, New Jersey.
Zhang, G., Liu, C.-Q., Yang, Y., Wu, P., 2004. Characterization of heavy metals and sulphur isotope in water and sediments of a mine tailing area rich in carbonate. Water Air Soil Pollut. 155, 51–62.

energies

MDPI

Article

Short-Term Forecasts of DNI from an Integrated Forecasting System (ECMWF) for Optimized Operational Strategies of a Central Receiver System

Francis M. Lopes [1,2,*], Ricardo Conceição [1,2], Hugo G. Silva [1,2], Thomas Fasquelle [1], Rui Salgado [2,3], Paulo Canhoto [2,3] and Manuel Collares-Pereira [1,2,3,4]

1 Renewable Energy Chair, University of Évora, IIFA, Palácio do Vimioso, Largo Marquês de Marialva, Apart. 94, 7002-554 Évora, Portugal; rfc@uevora.pt (R.C.); hgsilva@uevora.pt (H.G.S.); thomasf@uevora.pt (T.F.); collarespereira@uevora.pt (M.C.-P.)
2 Institute of Earth Sciences, University of Évora, Rua Romão Ramalho 59, 7000-671 Évora, Portugal; rsal@uevora.pt (R.S.); canhoto@uevora.pt (P.C.)
3 Department of Physics, School of Sciences and Technology, University of Évora, Rua Romão Ramalho 59, 7000-671 Évora, Portugal
4 Portuguese Solar Energy Institute, IIFA, Palácio do Vimioso, Largo Marquês de Marialva, Apart. 94, 7002-554 Évora, Portugal
* Correspondence: fmlopes@uevora.pt

Received: 11 March 2019; Accepted: 4 April 2019; Published: 9 April 2019

Abstract: Short-term forecasts of direct normal irradiance (DNI) from the Integrated Forecasting System (IFS) and the global numerical weather prediction model of the European Centre for Medium-Range Weather Forecasts (ECMWF) were used in the simulation of a solar power tower, through the System Advisor Model (SAM). Recent results demonstrated that DNI forecasts have been enhanced, having the potential to be a suitable tool for plant operators that allows achieving higher energy efficiency in the management of concentrating solar power (CSP) plants, particularly during periods of direct solar radiation intermittency. The main objective of this work was to assert the predictive value of the IFS forecasts, regarding operation outputs from a simulated central receiver system. Considering a 365-day period, the present results showed an hourly correlation of ≈0.78 between the electric energy injected into the grid based on forecasted and measured data, while a higher correlation was found for the daily values (≈0.89). Operational strategies based on the forecasted results were proposed for plant operators regarding the three different weather scenarios. Although there were still deviations due to the cloud and aerosol representation, the IFS forecasts showed a high potential to be used for supporting informed energy dispatch decisions in the operation of central receiver units.

Keywords: short-term forecasts; direct normal irradiance; concentrating solar power; system advisor model; operational strategies; central solar receiver

1. Introduction

With the simultaneous increase of solar energy conversion units installed worldwide and computational technology, interest has been growing in using direct normal irradiance (DNI) forecasts in the field of solar power, at a regional or global scale, particularly for an efficient production of energy from concentrating solar power (CSP) plants. A strong reason for such an effort is the fact that CSP systems are able to provide high-quality dispatchable power at affordable prices, when compared to photovoltaic storage capacity, using molten salt as heat storage, a cheap, safe, and easily accessible material [1,2]. For a CSP plant operator, information concerning the day-ahead (up to 48 h) DNI values is required for an efficient energy planning and scheduling [3], allowing higher-penetration of

commercial solar power, into the electricity market. In particular, it is during periods of direct solar radiation intermittency that CSP technologies demand accurate forecasts of DNI [4], since these periods are characterized by scattered clouds (which can differ in type and dynamic coverage [5]) and aerosols species [6], which are two primary factors that affect the direct solar resource at the ground level.

To accurately characterize DNI, a combination of the state-of-the-art monitoring and assessment techniques, with advanced numerical weather prediction (NWP) modeling is recommended. NWP models are based on the numerical computation of dynamic flow equations that allow solving the state of the atmosphere and its evolution, up to several days-ahead [7]. However, despite being able to provide satisfactory results [8], current models still demand developments towards DNI forecasting, particularly the parameterization of cloud cover [9] and the use of real-time aerosol information, considering that nowadays an aerosol climatology is still used, despite recent advances [10]. Moreover, an accurate conversion of predicted DNI to predicted energy output values from simulated power plant models is also necessary. In this context, user-friendly software such as the System Advisor Model (SAM) can be used to simulate a CSP plant. This method has been carried out by the authors in a previous work [11], where forecasted data from the IFS was used in the simulation of a linear-focus parabolic trough (PT) system, with a configuration similar to the Andasol 3, a 50 MW_e power plant [12] located in Granada (Spain). Although the PT technology has dominated the solar thermal power industry in the last decades, central receiver (CR) units have been emerging, due to the potential that these have for higher efficiency and lower cost. This is possible because apart from having higher concentration ratios (300–800 suns versus only 25–30 in conventional linear concentration), modern CR technology uses molten salt as a heat transfer fluid (HTF) and, directly, as heat storage fluid. Most commercial PT solutions operate with thermal oils as HTF and even when heat storage is also performed with molten salts, the overall operating temperature is much lower (≈400 °C contrasting with 540 °C in the CR systems). In CR systems the higher temperatures place more stringent requirements on energy management and control of power block efficiency, than on lower temperature PT system [13].

Taking into account the aforementioned aspects, the present work uses day-ahead (24-h) forecasts of DNI from the Integrated Forecasting System (IFS), the global NWP model of the European Centre for Medium-Range Weather Forecasts (ECMWF) that possesses the highest scores regarding medium-range global weather forecast [14], together with a set of meteorological variables, in the simulation of a CR power plant. Moreover, an advantage in using the IFS, instead of higher resolution models, is that it allows the implementation of the present analysis and proposed method in any region of the world, with high prospects in the installment of CSP units. In this work, in order to convert DNI values to energy output forecasts of the modeled CSP system, the simulation of a CR power plant similarly configured as the 19.9 MW_e Gemasolar thermosolar power plant [15] (located in the province of Sevilla (Spain)), was carried out. The obtained energy outputs based on DNI predictions and local measurements of the simulated CR power plant were assessed and then compared with the results obtained for a PT system [11]. This simulation used the same dataset, i.e., input variables (DNI and meteorological data), as for the PT simulation, being related to the same period and location in Southern Portugal, in which it showed substantial improvements towards the prediction of DNI, due to the new operational radiative scheme of the IFS.

The proposed work has been structured as follows. In Section 2, a description is provided regarding the measured and forecasted data, the CSP plant model, and the adopted methodology; results and respective discussions are given in Section 3; operational strategies for the three different weather scenarios are given in Section 4; and in Section 5, conclusions and future work perspectives are summarized.

2. Data and Methodology

2.1. Measurements

Measurements of DNI were used from a ground-based station located in Évora city (38.567686°N, 7.911722°W), from the Institute of Earth Sciences (ICT—Instituto de Ciências da Terra) in Southern

Portugal, a semi-arid region [16] with a high frequency of clear sky day occurrences and annual energy maximums around 2100 kWh/m^2 [17].

Pyrheliometers (model CHP1) from Kipp and Zonen instruments were used, being calibrated every 2 years. With an estimated daily uncertainty of <1%, these instruments follow the international organization for standardization, the 9059:1990 standard [18], as first-class instruments. To compare with NWP values, hourly mean values were obtained by averaging the sixty 1-min records. The Évora station (denominated EVO station) had a strict and regular code for the maintenance of the instruments, being subjected to quality control tests, prior to the analysis. The DNI at the EVO station showed only 0.003% of missing data for the considered year of continuous measurements. This showed how well-maintained the EVO station is, and why it was used in this work as a reference station. This station allowed us to provide high-quality data, showing only very small gaps that could have resulted from sudden power shut downs. To fill gaps, adopted filters for the location of study were used, including standard data quality filters, the Baseline Surface Radiation Network (BSRN) for Global Network quality check tests V2.0 [19] and gap-filling procedures. The latter, consisted in the use of hourly values from the nearest ground-based measuring station located at Mitra, MIT (38.530522°N, 8.011221°W), installed approximately 9.6 km from EVO, to fill gaps that have more than two hours of missing records. For the gaps with less than two hours of missing records, a linear interpolation between the previous and the next hours was then used to fill the missing periods.

Similarly, as performed in [11], continuous measurements of local atmospheric variables, such as air temperature, relative humidity, wind speed, and atmospheric pressure at ground level, were also acquired by nearby standard meteorological measuring equipment. Since atmospheric pressure was not measured at the EVO station and the local wind was disturbed by existing neighboring buildings, not being representative of the measuring location, hourly data from a nearby station (≈4 km apart)—maintained by the Portuguese Meteorology Service (IPMA—Instituto Português do Mar e da Atmosfera)—was used for the considered period of study.

2.2. Forecasts

The IFS is the atmospheric model and data assimilation system from the ECMWF (which is currently operational) that was used to perform global medium-range weather forecasts. The model is able to provide deterministic predictions of a large set of meteorology-related variables, including DNI. The radiative variables, in both short and longwave spectral bands, were computed using the Rapid Radiative Transfer Model [20]. Operational high-resolution (HRES) deterministic forecasts were set to have an issue time to start at 00:00 or 12:00 UTC (the latter option is used in this work). The current IFS cycle uses a triangular-cubic-octahedral global grid, with a horizontal resolution of 0.125° × 0.125° (≈9 km), 137 terrain-following vertical levels from the surface up to 1 Pa (≈80 km height), and a 7.5-min time step. The radiation scheme is updated every hour, on a grid with 10.24 times fewer columns than the rest of the model [21]. Contrary to the previous versions of the IFS, in which the DNI was not a direct output of the model, the current version was able to directly calculate hourly accumulated direct irradiation values (J/m^2), which were then converted to mean power values (W/m^2), in order to enable a straight comparison with measurements. The output of the IFS used here as representative of DNI is the *dsrp* parameter, i.e., the direct solar radiation, incident on a plane perpendicular to the Sun's beams.

To perform accurate forecasts of DNI, NWP models have to take into account several parameters that can affect such forecasts, for instance the local weather (e.g., air temperature, relative humidity, wind speed and direction, and surface pressure). Along with weather conditions, the forecast horizon can also affect the prediction of DNI, since it has an associated uncertainty that tends to be smaller with the use of shorter time horizons. However, these are closely linked to a high computational cost [22]. Forecast horizons can range from: (i) the intra-hour scale, where persistence models [23] and all-sky imagers [24] are used; to (ii) the intra-day scale, where artificial neural networks [25], and satellite-based and NWP models [26] are used; and (iii) up to several days (i.e., day or week-ahead

forecasts) in which NWP models are able to perform [27]. Apart from the weather conditions and forecast horizons, initial conditions implemented in NWP models also play an important role [28]. These include the atmosphere, oceans, and ground surfaces physics, which are composed by a series of complex dynamical processes that comprise the spatial distribution of a large number of atmospheric parameters. Moreover, aside from these aspects that can hinder the prediction of DNI, particular attention has been given towards cloud microphysics and aerosol representation. The former is closely related to the complex parameterization of cloud cover and type [9], mainly during overcast periods, while the latter is usually based on monthly mean aerosol climatologies, which increases the errors of predicted DNI, especially during clear sky conditions. In particular, it is during very clean atmosphere periods that the implemented aerosol climatology affects the prediction of DNI more. This has been previously observed with day-ahead forecasts of DNI from the IFS [11,29], where the radiative effects of clouds and aerosols were, respectively, under- or over-estimated by the model, compared to local measurements. For instance, at the EVO station it was found that the predicted mean annual DNI had an overestimation of ≈7%, compared to local measurements [29], being essentially related to an underestimation of the cloud cover.

To improve DNI forecasts, the radiative schemes of NWP models have been constantly upgraded to new versions. One example is the current ecRad scheme that was recently implemented in the IFS [10], becoming operational in July 2017 (cycle 43R3). A detailed description of the ecRad and its use in the IFS can be found in [21]. Presently, the ecRad is composed of the following IFS atmospheric variables—pressure, temperature, cloud fraction, and the mixing ratios of water vapor, liquid water, ice, and snow. The cloud effective radius was computed diagnostically, using the parameterization stated in [30], for liquid clouds, and that stated in [31], for ice clouds. The optical properties for ice were computed using the scheme stated in [32] and that for liquid water were expressed in terms of a Padé approximation [33]. The mixing ratios for ozone, carbon dioxide, and an arbitrary number of aerosol species were computed from a climatology obtained from the Copernicus Atmospheric Monitoring Service (CAMS), being more realistic than the previous versions, in which the Tegen aerosol climatology [34] was implemented. The optical properties of aerosols were added to those of gases, with the assumption that aerosols were horizontally well-mixed, within each model grid box. Aerosol optical properties were computed off-line, using an assumed size distribution and the Mie theory, for 14 shortwave and 16 longwave bands. Moreover, in addition to an improved code that allowed us to reduce computational costs, ecRad was able to reduce numerical noise in cloudy periods, which enabled better DNI predictions than the previous radiative scheme [21]. A recent analysis [11] has shown that improvements of day-ahead forecasts of DNI from the ecRad were attained, in comparison to the previous version (McRad, cycle 41R2). Hourly and daily correlations of 0.87 and 0.91 between predicted and measured data in EVO were found for the same dataset used in the present work. Although the IFS still overestimated measurements, a relative difference of ≈1.2% was found regarding the annual mean values of DNI in EVO, which was much lower than the previous value obtained with the McRad (≈10.6%).

In this work, day-ahead forecasts produced by the ecRad were used to estimate the energy output from a CR power plant simulated through the SAM. Results were assessed by comparison with those obtained using the local measurements.

2.3. CSP Plant Model

The SAM software [35], version 2017.9.5, developed by the U.S. Department of Energy and National Renewable Energy Laboratory (NREL), was used here to assess the usefulness of DNI forecasts from the IFS, for the energy management of a CR power plant. Regarding the simulation of CSP systems, the SAM uses the transient system simulation (TRNSYS), comprising three components—(i) an interface where the setup of each simulation is performed in detail by the user; (ii) a calculation engine that implements discretization procedures in each simulation, and (iii) a programming interface. The power plant model calculates hourly performance values corresponding to a wide range of output parameters,

providing an annual performance and financial metrics summary at the end of each run. DNI and other atmospheric variables (air temperature, relative humidity, wind speed, and surface pressure) were the necessary input parameters for the power plant model to generate local hourly performance data. The resulting hourly outputs represent a full year of annual electricity production of the considered CR power plant.

To simulate a CR power plant, it is important to know all the design and control parameters that are characteristic of such a system. A CR system, also known as a solar power tower, uses sun-tracking mirrors (heliostats) to focus the Sun's direct beam onto a receiver installed at the top of the tower. Within the receiver, a HTF was then heated, reaching temperatures up to 565 °C, allowing the generation of water steam, through a heat exchanger. The latter was then used by conventional turbine-generators, to produce electricity (Rankine cycle). Due to the higher temperatures of use and superior heat transfer and energy storage capabilities than other CSP systems, such as PT systems, current CR plants used molten salt, such as HTF. One example of this kind of power system is the 19.9 MW_e Gemasolar thermosolar plant located in the Sevilla province (Spain), which has been operational since April 2011. This type of CR power plant possesses a 15-h storage capacity and is surrounded by 2650 heliostats (Figure 1), within an area less than 200 hectares. The Gemasolar was intended to produce 110,000 MW_eh/year [15], however, probably due to technical issues created by the new challenges that were addressed during the operation of the power plant, an annual generation of 80,000 MW_eh/year was reached [36]. In this work, in order to study the behavior of a CR solar power plant, a simulation with a similar configuration, such as the Gemasolar, was carried out. The criterion for selecting this power plant resulted from the fact that Gemasolar is considered to be a typical CR system, with the advantage of having considerable information available regarding the power plant operation input parameters, thus allowing to establish a case study for the CR power plants. Under Évora's conditions, this study used the same weather dataset as the SAM input parameters from the EVO station that were previously used for the simulation of a 50 MW_e PT system [11], with configurations similar to the Andasol 3 located in Granada (Spain). Due to privacy reasons, full access to the complete configuration of the Gemasolar was not possible. Consequently, several design and control input parameters needed for the simulation were not provided by NREL, creating a limitation to the present analysis. However, in order to obtain the best performance results that corresponded close to the actual performance outputs of the Gemasolar power plant, some input parameters were needed for the simulation result from research-based assumptions made by the authors, regarding the operation of the CR systems. For more detailed information concerning the configuration input parameters used in the SAM simulation, see Appendix A.

Figure 1. Gemasolar thermosolar power plant located in the province of Sevilla, Spain (37.560613°N, 5.331508°W). All rights reserved (© Google Earth 2019).

3. Results and Discussion

In this analysis, electrical and thermal output parameters generated by the SAM simulations using forecasted and measured hourly values of DNI and meteorological variables. The outputs were selected according to their importance for the power generation and management of a CR power plant since the plant operator should analyze these parameters on a daily basis. In that sense, the total electric energy to the grid, E_P ($MW_e h$), and the stored thermal energy, TES ($MW_t h$), charge and discharge energies were analyzed for a 365 day-period (from 1st July 2017 to 30th June 2018) with the study location centered at the EVO station.

In Table 1, a statistical summary for the E_P and the respective TES charge and discharge energies, based on forecasts and measurements of DNI and meteorological variables, is shown. As expected, due to the IFS underestimation of cloud cover [29], the obtained results using the simulated hourly values showed a general overestimation of the IFS forecasts towards measurements. A total of ≈115,992 $MW_e h$/year and ≈121,668 $MW_e h$/year was obtained, respectively, for the E_P based in DNI measurements and forecasts, with a correlation coefficient (r) of ≈0.78, between both outputs. The representation of clouds performed by the IFS, significantly influenced the forecasted DNI values at the Earth's surface and, consequently, the respective E_P output from the CR power plant. Taking into account the parasitic power consumption during non-production hours and a constant derating (i.e., a decrease of the power plant output due to unusual environmental conditions, for instance, higher ambient temperature than design set point, or excess power within the electrical grid) value of 4%, for the simulated plant, the SAM results showed an annual energy generation of ≈111,353 $MW_e h$/year and ≈116,801 $MW_e h$/year, regarding measurements and predictions, respectively, i.e., a relative difference of ≈4.9%. Despite the fact that the objective of the present work was not a direct comparison with the Gemasolar's actual production values, the obtained annual values through the SAM simulations could differ from the values that would be obtained if an actual Gemasolar was operating in Évora, due to several reasons: (i) DNI and meteorological data from Évora was being used for a different period, comprising different inter-annual variations; (ii) lack of data regarding design and control parameters for the simulation of Gemasolar; (iii) start-up time (0.5 h) and stop operations of the simulated plant together with the internal temporal discretization, considered by the SAM; and (iv) daily operational strategies adopted for the plant power management.

Table 1. Statistical and descriptive analyses for the hourly values of electric energies into the grid, E_P ($MW_e h$), and stored thermal energy, TES ($MW_t h$), charge and discharge energies based on measurements (obs) and forecasts (ecmwf). The sum of the hourly values (Total) of E_P and TES corresponded to one year of data (from 1st July 2017 to 30th June 2018), produced by a central receiver power plant with configuration similar to the Gemasolar thermal power plant (Sevilla province, Spain), simulated through the System Advisor Model (SAM). Hourly statistical error metrics for the correlation coefficient (r), root mean square error (RMSE), and mean absolute error (MAE) are presented.

Energy	Total $_{obs}$ ($MW_{e,t}h$)	Total $_{ecmwf}$ ($MW_{e,t}h$)	r	RMSE ($MW_{e,t}h$)	MAE ($MW_{e,t}h$)
E_P	115,992	121,668	0.78	6.30	2.31
TES $_{charge}$	151,104	153,187	0.88	16.46	5.97
TES $_{discharge}$	148,399	150,465	0.83	12.32	4.09

The charge and discharge powers also showed an overestimation when using the forecasted inputs, in comparison with those obtained when using measurements, although with higher correlations. Simulation results showed annual charge and discharge energies of ≈151,104 $MW_t h$/year and ≈148,399 $MW_t h$/year, based on measurements, while ≈153,187 $MW_t h$/year and ≈150,465 $MW_t h$/year were obtained for the forecast-based outputs. Although the discharge energy had a lower r than the charge-hourly values (≈0.83), it was shown to possess less deviations between the measured and forecasted outputs.

A closer look at the hourly outputs generated by the SAM, based on the forecasted and measured DNI values, was presented in the scatter plots of Figure 2a, and Figure 3a,b, respectively, for the E_P and TES charge and discharge energies. In these plots, the red dashed line represents the identity line

(y = x), in which the dots that are closer to the line depict higher correlations than the ones that deviate from it. Two green dashed–dotted lines (Figure 2a) bound an interval in which the predicted and measured E_P values had an absolute error (AE) less than the obtained mean absolute error (MAE) of ≈2.31 MW_eh. The total number of hourly values of E_P, within the established high and low thresholds corresponded to ≈85.94%.

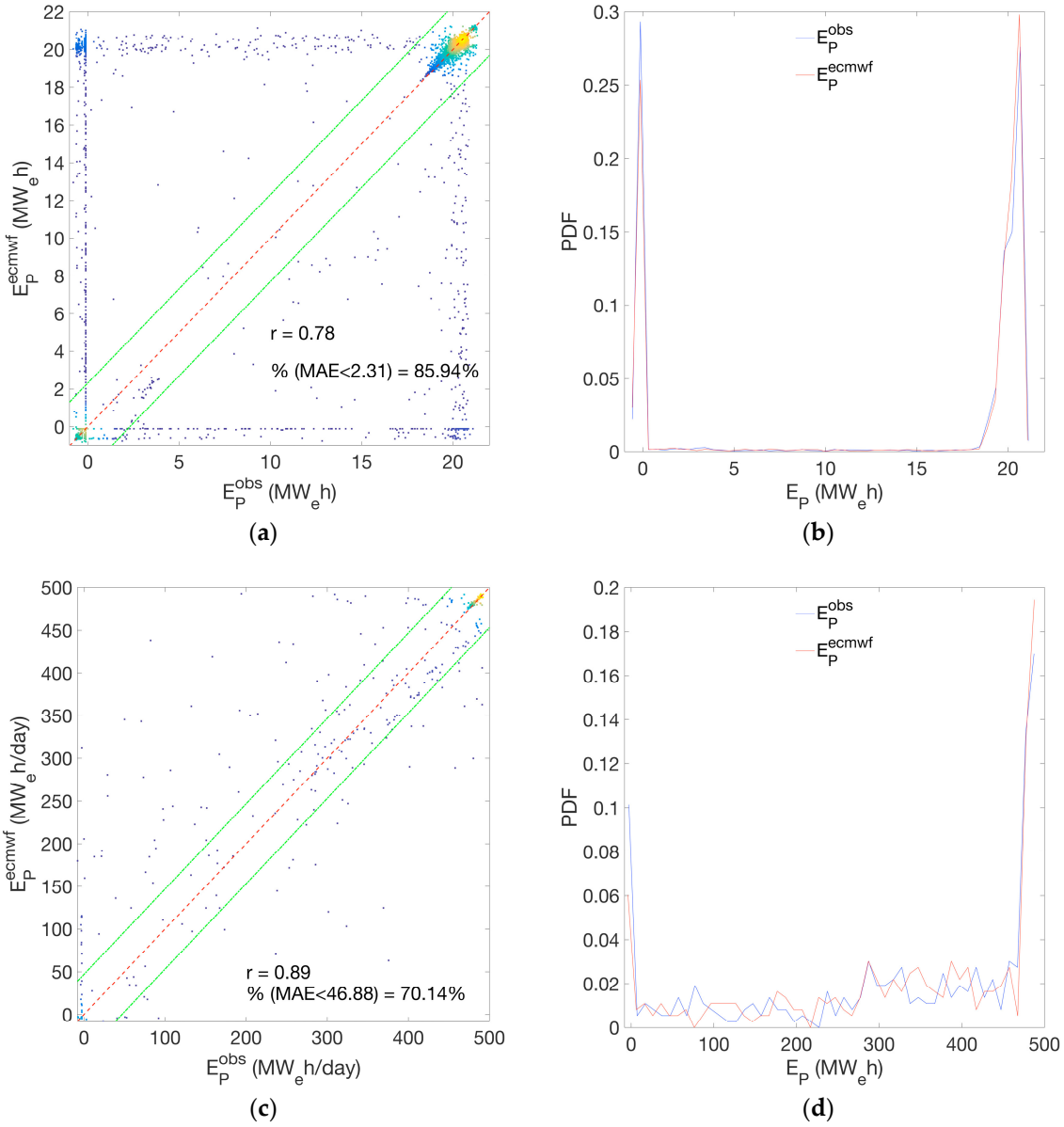

Figure 2. Estimated hourly (**a**, **b**) and daily (**c**, **d**) values of electric energies into the grid, E_P (MW_eh), and respective probability density functions (PDF), computed from forecasted (ecmwf) and measured (obs) data at Évora. Hourly values of direct normal irradiance (DNI) were used in the SAM to simulate the E_P from a central receiver (CR) power plant with configuration similar to the Gemasolar plant (Sevilla, Spain). In the scatter plots, identity lines (red dashed lines), corresponding correlation coefficients, r, and an interval defined by the calculated MAE (≈2.31 MW_eh), given by two green dashed–dotted lines, are shown. The period of study corresponds to one year, from 1 July, 2017 to 30 June, 2018.

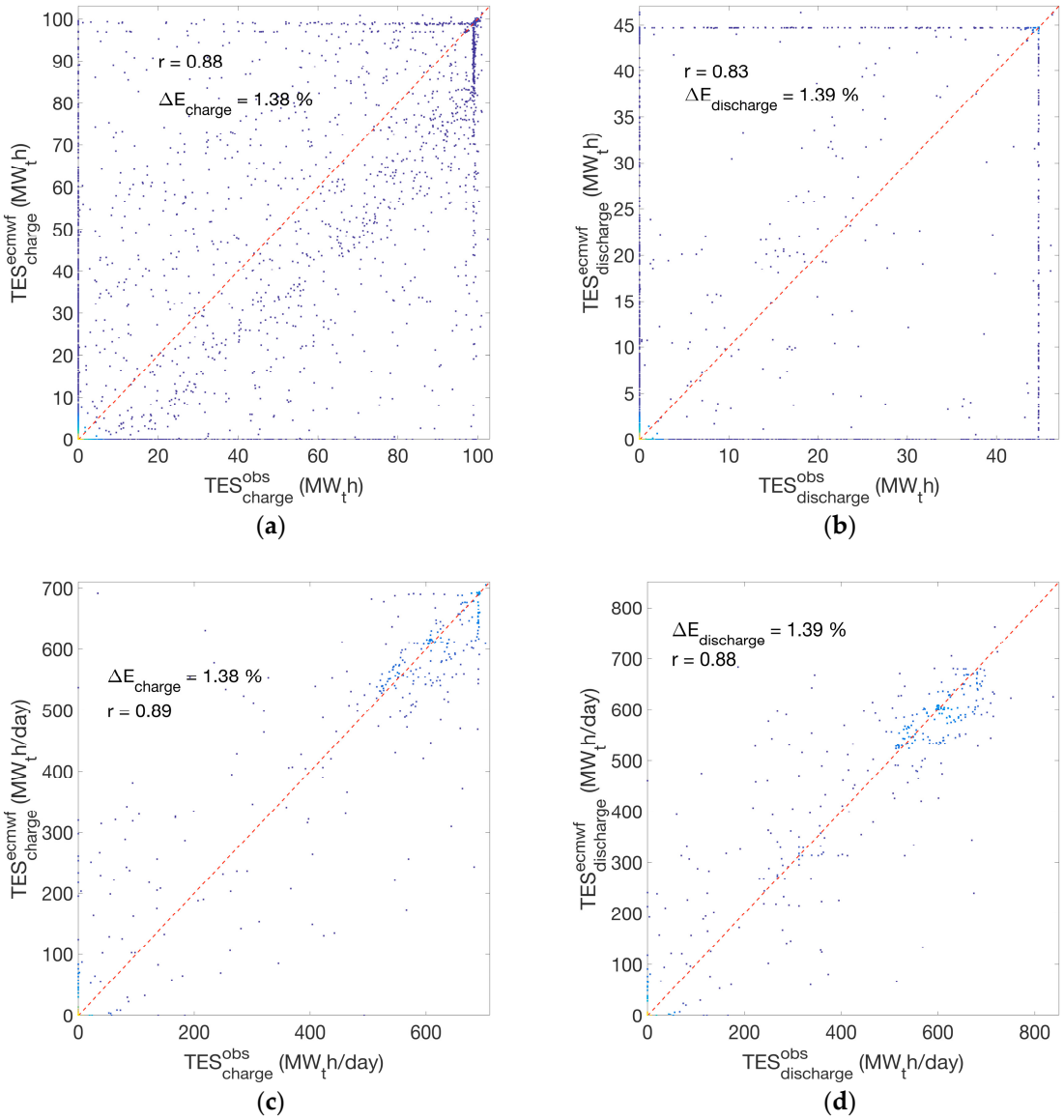

Figure 3. Estimated hourly values of stored thermal energy into the grid, TES (MW_th)—(**a**) charge and (**b**) discharge energies, computed from forecasted (ecmwf) and measured (obs) data at Évora, while corresponding daily values are presented in (**c**) and (**d**). Hourly values of DNI were used in the SAM to simulate the TES from a CR power plant, with a configuration similar to the Gemasolar plant (Sevilla, Spain). Identity lines (red dashed lines), the corresponding correlation coefficients, r, and relative differences, ΔE, are shown. The period of study corresponded to one year, from 1 July, 2017 to 30 June, 2018.

A few features that were characteristic of CSP systems were observed. Most of the values were centered on the high values of E_P, between 18 and 21 MW_eh, which took place during periods of clear sky conditions. Outside these limits were the E_P values (including negative ones) that corresponded to the non-production hours in which electricity for parasitic power consumption needed to be purchased from the grid. During these periods, deviations between the forecasted and measured E_P values occurred, in particular for—E_P (obs) > 0 and E_P (ecmwf) = 0; E_P (obs) = 0 and E_P (ecmwf) > 0. During cloudy days with short periods of unobstructed solar beam radiation, predicted and measured E_P values also had deviations. If only non-negative hourly values of E_P were considered, the correlation between the forecasted and measured values would drop significantly to 0.37, showing the importance that non-production hours have in the correlations, since these periods correspond to shut-down

and start-up operations carried out by the power plant. This meant that the predictions have a good correspondence with the measurements, during such periods. The respective probability density function (PDF) in Figure 2b clearly depicted the two observed features, as highlighted by the two peaks—the higher frequency of occurrence around the non-production hours (zero values), particularly by the E_P based in measurements; and the high frequency of occurrence for the higher values of E_P. Moreover, the hourly TES charge and discharge energies (Figure 3a,b) showed a slight improvement in correlation, for the charge periods (≈0.88), in comparison to the discharge ones (≈0.83), as these correlations were closely linked to the non-production (close to zero) and the high production periods (≈100 MW_th). Relative differences of ≈1.38% and ≈1.39% were found for the charge and discharge outputs, respectively. The hourly TES charge values depicted a tendency line (below the identity line), demonstrating that, less storage was gained with the forecasted based output, in comparison to the measured one. This was a consequence of the IFS underestimation towards measurements during days with very clean atmospheric conditions, in which the aerosol concentration was less than that in the prescribed climatology.

Daily values (i.e., calculated through the 24-h sum of each day) yielded higher correlations, as shown by the results in Table 2, despite overestimations from the forecasts, as depicted by the negative mean bias error (MBE) values. An r ≈0.89 was obtained for the daily E_P values (Figure 2c), with ≈70.14% of the total number of daily values having an AE below an MAE of ≈46.88 MW_eh. The respective daily PDF (Figure 2d) showed the same pattern as that for the hourly results, but with less frequency of occurrence, with two peaks, one for the non-production hours and another for the high values of E_P. Correlations of ≈0.89 and ≈0.88 were found between the daily TES charge and discharge energies, based on the measurements and forecasts (Figure 3c,d), respectively.

Table 2. Statistical analysis of the daily values (i.e., the sum of each 24-h values) of the estimated electric energy to the grid, E_P (MW_eh), and stored thermal energy, TES (MW_th) charge and discharge energies computed from measurements (obs) and forecasts (ecmwf). Hourly values of E_P and TES correspond to one year of data (from 1 July, 2017 to 30 June, 2018) produced by a CR power plant with a configuration similar to the Gemasolar plant (Sevilla, Spain) simulated through the SAM. Daily statistical error metrics such as the correlation coefficient (r), root mean square error (RMSE), mean absolute error (MAE), and mean bias error (MBE) are presented.

Energy	r	RMSE ($MW_{e,t}$h)	MAE ($MW_{e,t}$h)	MBE ($MW_{e,t}$h)
E_P	0.89	79.43	46.88	−15.55
TES $_{charge}$	0.89	119.96	74.25	−5.70
TES $_{discharge}$	0.88	111.66	71.37	−5.66

Since the same dataset (DNI and meteorological variables) from EVO station were used in both, the CR and the PT simulations, the performance of the 24-h predictions from the IFS in the operation of different CSP systems has been depicted in Table 3. The coefficient of variation regarding the RMSE and MAE, i.e., the normalized RMSE and MAE (nRMSE and nMAE, respectively), were obtained for the electric energy to grid outputs, from both Gemasolar and Andasol 3 simulations (E_P and E_G, respectively). The calculation of both nRMSE and nMAE are given in Equations (A1) and (A2) in Appendix A. The obtained hourly values of E_P and E_G show that forecasted data in the simulation of the Gemasolar power plant generates higher deviations than the ones obtained from the Andasol 3, with an increase of ≈7.3% for the nRMSE and ≈2.8% for the nMAE. Deviations were lower from the hourly to daily values, showing an increase of ≈2.9% for the nRMSE and ≈0.7% for the nMAE. These results indicated that the PT power plant considered (based on Andasol 3) was less sensitive to the DNI prediction than the CR one (based on Gemasolar). However, it must be taken into account that the considered PT system had less storage than the CR system, resulting in a larger number of non-production hours (i.e., zero values) for both forecasted and measured simulations, contributing to an apparent reduction of differences between them.

Table 3. Hourly and daily values of normalized root mean square error (nRMSE) and mean absolute error (nMAE) for the estimated total electric energy to the grid outputs, obtained from the 19.9 MW_e Gemasolar and the 50 MW_e Andasol 3 SAM simulations (E_P and E_G, respectively). The E_P and E_G simulated values are based on the same hourly dataset (DNI and meteorological data) of forecasted and measured input parameters acquired for Évora, for the same period of study (from 1 July 2017 to 30 June 2018).

Power Plant	nRMSE (%)		nMAE (%)	
	Hourly	Daily	Hourly	Daily
Gemasolar	28.48	15.88	10.43	9.37
Andasol 3	21.18	13.02	7.65	8.68

4. Operational Strategies for Typical Days

In order to maximize the energy efficiency of CSP plants, it is essential to adopt appropriated operational strategies, in accordance to the different weather scenarios (i.e., clear sky, partly cloudy, and overcast days), which could differently affect the CR power plant performance. For instance, for the CR systems, the advantage of knowing the energy availability for the day-ahead, allowed the operator to estimate the electricity generation in advance and sell it at the premium tariff [37], as an alternative to the fixed tariff option, thus, allowing the operator to have a direct role on the electricity market instead of being subjected to flat-rate prices.

As demonstrated in the previous study regarding solar assessment influence on a linear focus PT power plant operational strategies and production [11], the forecast model was able to generate satisfactory results for the days with clear sky conditions. However, results showed that such forecasts were hindered due to aerosol representation, particularly under very clean atmosphere conditions, in which the forecasts underestimated the DNI, or during overcast conditions, in which the IFS overestimated the DNI. The latter behavior can also be a result of extreme dust events, as shown by [38] and [39]. For cloudy days, the IFS was also reliable in predicting clouds, although temporal and spatial phase errors exist in the current cloud forecasting. For the case of the conventional 50 MW_e PT power plant, results have led to three different operational strategies related to specific meteorological scenarios: a clear sky, a partly-cloudy, and an overcast period. An example of the implemented global strategy is to avoid power block start-up and shutdown, allowing to maintain the plant at a nominal power and a maximum efficiency. Another aspect is the possible full state of charge of the storage tank, during the day. In this scenario, the operator is advised to perform a partial charge in the early morning to handle a possible cloud passing over, except for predicted clear sky days, in which production is to be started as soon as possible. For the present case study, the high storage capacity of the CR power plant allows the easing of the operator decision algorithm.

4.1. Clear Sky Days

Full charge for a 15-h storage system can only be encountered during days that have very high solar irradiation levels. For such days, the best strategy is to maximize electricity production by starting the power block at the earliest moment. An example of this scenario is shown in Figure 4, where a constant power production is observed, due to the huge storage capacity and higher availability. Here, defocusing of the solar field is also shown, leading to a lower receiver output power after 14 h (production with predicted DNI) or 15 h (production with measured DNI).

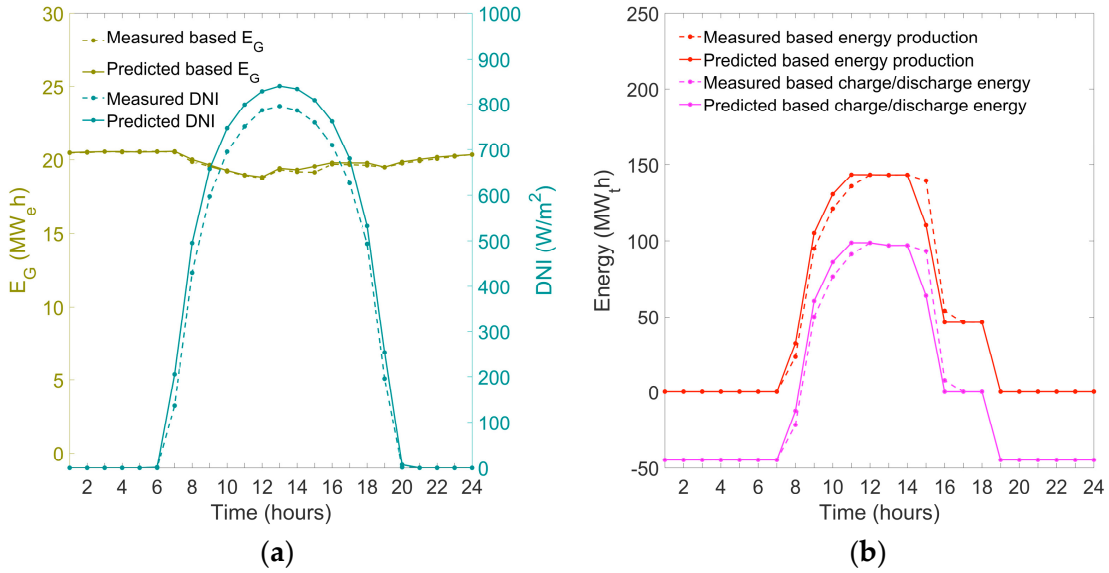

Figure 4. Comparison between the results of the SAM simulation for 21 August 2017 (prediction of high energy without clouds), with predicted and measured (**a**) hourly mean DNI (W/m^2) values (blue) and produced electrical energy E_G (MW$_e$h) values (green); and (**b**) thermal energy (MW$_t$h) of charge/discharge values (purple) and produced solar energy (red).

4.2. Cloudy Days

On cloudy days, different types of strategies can be applied—full shifting of the solar production to the evening, constant power generation during the entire day, among others. Since a solar power generation is easily higher than what the power block requires, this leads to a high amount of energy surplus in the system, even during the early morning periods. Under such conditions, in order to increase the safety of the power block continuous production, a small partial charge can be performed in the early morning. This partial charge does not lead to potential defocusing because the available energy is not sufficient to reach a 100% state of charge, during the day. Figure 5 shows an example of such an operation scenario, for a day, with low irradiation levels, because of passing clouds. Since the power block production can be started with a DNI higher than 300 W/m^2, a high amount of energy is charged during the morning hours. For the case of observed DNI, it drops to 300 W/m^2 after 12 h, due to the presence of clouds, leading to a stop of the charging process. After 16 h, DNI drops below 300 W/m^2 because of a second cloud and discharge is performed to maintain electricity production to a constant value.

In this example, the forecast model predicted only one long period of cloud obstruction, during the afternoon, with both forecasted and measured systems responding well, in terms of power production. It should be noted that this type of scenario tends to degrade the correlation between the forecasted and measured E_P, particularly under the hourly time scale, although for larger time scales, the differences between both outputs estimates are not so significant.

Other particular strategies can be given for the receiver protection of a CR system regarding thermal stress. For instance, avoiding periodic or sudden strong increases and decreases of the receiver temperature, due to a passing cloud. In such cases, the forecast model is by itself sufficient to warn the power plant operator that variations will take place but with a lower accuracy in the time of occurrence. Nonetheless, the available predicted information is already useful to apply thermal protection strategies on the receiver, or to strategize the energy management of the power plant for one day.

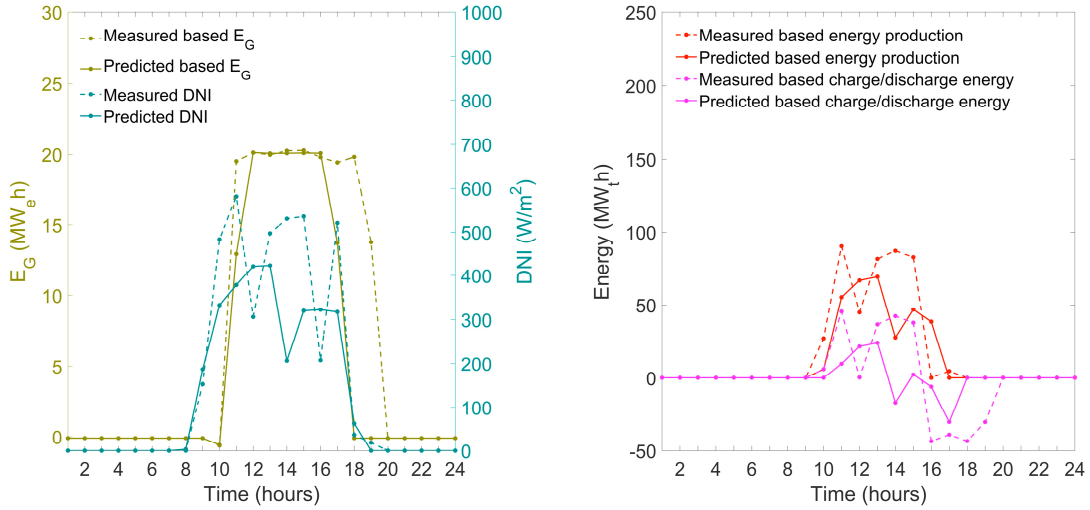

Figure 5. Comparison between results of the SAM simulation results for 11 January (prediction of low energy with clouds), with predicted and measured (**a**) hourly mean DNI (W/m^2) values (blue) and produced electrical energy E_G (MW_eh) values (green); and (**b**) thermal energy (MW_th) of charge/discharge values (purple) and produced solar energy (red).

4.3. Overcast Days

For operational purposes, the analysis of a specific day without any, or near null, DNI income is also relevant, simply because when there is no DNI to be collected, then there is no production, consequently the power plant should be running at the lowest power generation possible (or in stand-by mode to keep the equipment warm and the salt in liquid state), depending on the available storage. In that sense, it is important to anticipate such long periods of no production, and the impact that these have on the energy management, and to accordingly implement the necessary strategies. During such periods, and in the case of no available storage, the power plant has negative production values, since the system needs to consume energy, in order to maintain the continuous function of basic equipment. For that reason, in this last section, the success that the IFS has in predicting periods of negative production, using the simulated values, is analyzed. In such a scenario, a dichotomous analysis is performed with the use of a contingency table (Table 4) created to evaluate the forecasts of E_P values. Moreover, as described in [40], an equitable threat score (ETS) skill score is calculated through Equations (A3) and (A4) (Appendix A) to measure the fraction of the forecasted and observed E_P events that were accurately predicted. The ETS is usually used in the NWP models to evaluate other meteorological variables, such as rainfall [41], since it allows us to equitably compare the obtained scores across different regimes.

Table 4. Dichotomous analysis for the total number of forecasted (ecmwf) and measured (obs) occurrences and non-occurrences of daily negative electrical production values (E_P) for the Gemasolar power plant simulation through the SAM. The obtained E_P simulated values were based on hourly DNI and meteorological data (forecasted and measured) input parameters acquired for Évora for the same period of study (from 1 July, 2017 to 30 June, 2018). Four different events of negative E_P values occurrences and non-occurrences have been depicted—'Hits' (E_P (ecmwf) < 0 and E_P (obs) < 0), 'False alarms' (E_P (ecmwf) < 0 and E_P (obs) > 0), 'Misses' (E_P (ecmwf) > 0 and E_P (obs) < 0) and the 'correct rejections' (E_P (ecmwf) > 0 and E_P (obs) > 0).

Electrical Production	E_P (obs) < 0	E_P (obs) > 0
E_P (ecmwf) < 0	16	6
E_P (ecmwf) > 0	19	324

Considering together, the daily values of the forecasted or measured production values, it was found that there were 41 days (in a total of 365 days) with partial or complete cloudy (overcast) conditions, i.e., depicting negative production values (consumption). Results showed that the forecast model predicts a total of 16 days of negative production, which coincided with the measurements, following the condition E_P (ecmwf) < 0 and E_P (obs) < 0, which denominated the 'Hits'. For cloudy days with short periods of no production, where the model predicted overcast, but that was not observed, i.e., when E_P (ecmwf) < 0 and E_P (obs) > 0 (which denominated 'False alarms'), a number of 6 days were found. The opposite occurred when the IFS did not predict overcast which was observed, i.e., when E_P (ecmwf) > 0 and E_P (obs) < 0 (which denominated 'Misses'), with a number of 19 days being found in such conditions. The latter was a clear result of the IFS general overestimation, due to cloud representation, as previously discussed in detail [29]. Moreover, the number of days in which the IFS and measurements did not show the occurrence of negative production values was 324, denominated here as the 'correct rejections'. Thus, the obtained ETS (Equation (A3)) for the occurrence of negative production forecasted by the IFS was ≈36%. Considering such a rate, the power plant operator was advised to not proceed with the electrical energy generation, when the forecast model predicted negative production (E_P (ecmwf) <0). In the case of a wrong prediction, if solar energy was available for collection during the day, then production was to be started but without spending any storage. If a success rate of ≈90% was to be found, then the operator would simply be advised not to produce during that day.

5. Conclusions

In this work, it was confirmed that the use of DNI forecasts and the implementation of control strategies could contribute to a more efficient energy management of a CSP plant, improving the local energy distribution from a solar tower system. Hourly and daily correlations of ≈0.78 and ≈0.89, respectively, were found for the SAM predictions of the total electric energy injected into the grid, based on forecasted and measured DNI and meteorological conditions, an important variable for the power plant operator to handle on a daily basis. In the case of the power plant stored thermal energy, charge correlations of ≈0.88 and ≈0.89 were found for the hourly and daily values, respectively, while ≈0.83 and ≈0.88 were found for the hourly and daily discharge values, respectively. Regarding the performance of the forecast model in the simulations of the two different types of CSP plants enforced with the same datasets, results showed higher deviations in the case of a CR system than in the previous simulated PT. Increases of ≈7.3% and ≈2.8% were found, respectively, for the hourly and daily normalized RMSE values of the generated electric energy. To improve the energy efficiency of CR plants, operational strategies have been proposed for the three different scenarios. Although there were still deviations due to the cloud and aerosol representation, the present analysis has shown that the IFS predictions are a valuable tool to be used in the daily energy dispatch operations of a CR power plant, potentially the main type of CSP systems to be used in the future, due to its advantages. With the continuous improvements that the NWP models have demonstrated in recent years, for the prediction of DNI, future versions of the IFS should also demonstrate an enhancement of the predicted production values from a power plant and, consequently, the energy management during solar intermittency periods.

Author Contributions: The concept of this work was made by F.M.L. and H.G.S. The applied methodology was implemented by F.M.L, H.G.S., R.C., R.S., and P.C. The use of the SAM software was carried out by F.M.L. and T.F. Analysis, validation, investigation, resources, data curation, writing, and editing procedures were done by F.M.L. All authors have reviewed the article prior to submission. H.G.S., R.S., and M.C.-P. have supervised this work.

Funding: F.M.L. and R.C. are thankful to the FCT scholarships SFRH/BD/129580/2017 and SRFH/BD/116344/2016, respectively. T.F. acknowledges the New StOrage Latent and sensible Concept for high efficient CSP Plants, the NewSOL (H2020, GA: 720985) project, and H.G.S. at the Integrating National Research Agendas on Solar Heat for Industrial Processes, INSHIP (H2020, GA: 731287) project. Co-funding from the European Union through the European Regional Development Fund was also provided, being included in the COMPETE 2020 (Operational Program

Competitiveness and Internationalization), through the ICT (UID/GEO/04683/2013, POCI-01-0145-FEDER-007690), DNI-A (ALT20-03-0145-FEDER-000011), ALOP (ALT20-03-0145-FEDER-000004) projects.

Acknowledgments: Available measured data provided by Afonso Cavaco (Instituto Português de Energia Solar, IPES) and Jorge Neto (Instituto Português do Mar e da Atmosfera, IPMA), as well as the forecasts from the ECMWF, is acknowledged.

Conflicts of Interest: The authors declare no conflict of interest. The funders had no role in the design of the study; in the collection, analyses, or interpretation of data; in the writing of the manuscript, or in the decision to publish the results.

Appendix A

To calculate the normalized error metrics (i.e., the *n*RMSE and *n*MAE) of E_P (%), the following equations were used:

$$\text{nRMSE} = \text{RMSE}/(E_{Pmax} - E_{Pmin}), \quad \text{(A1)}$$

$$\text{nMAE} = \text{MAE}/(E_{Pmax} - E_{Pmin}), \quad \text{(A2)}$$

where the RMSE and MAE between measured and forecasted E_P was divided by the difference between the maximum and minimum values of the measured E_P.

To evaluate the performance of the forecast model in predicting negative production values, the equitable threat score (ETS) could be calculate through:

$$\text{ETS} = (\text{Hits} - \text{Hits}_{\text{random}})/(\text{Hits} + \text{Misses} + \text{False alarms} - \text{Hits}_{\text{random}}), \quad \text{(A3)}$$

with

$$\text{Hits}_{\text{random}} = [(\text{Hits} + \text{False alarms}) \times (\text{Hits} + \text{Misses})]/\text{Total}, \quad \text{(A4)}$$

where 'Hits' represents the number of occurrences (i.e., number of days) with forecasted and observed negative E_P values, 'Misses' represents the number of days in which the forecast model did not predict the E_P values when these were actually observed, 'False alarms' corresponds to the predicted occurrences of E_P values that were not observed. 'Total' is the total number of occurrences, which also took into account the number of days of 'correct rejections' (i.e., when the forecast model did not predict the E_P values that were not actually observed). A perfect forecast (i.e., a perfect score of 1) would be characterized only by 'Hits' and 'correct rejections', without 'Misses' and 'False alarms'.

A detailed description regarding the input parameters for the SAM software for the simulation of a CSP power plant designed to run a CR system has been given in this section. For the Gemasolar thermosolar plant (Figure A1) case study, the available online information from NREL [36], was complemented with the default SAM inputs characteristic from this type of tower power plant, together with the research carried out by the authors, towards a few parameters that were taken into account, as presented in Table A1.

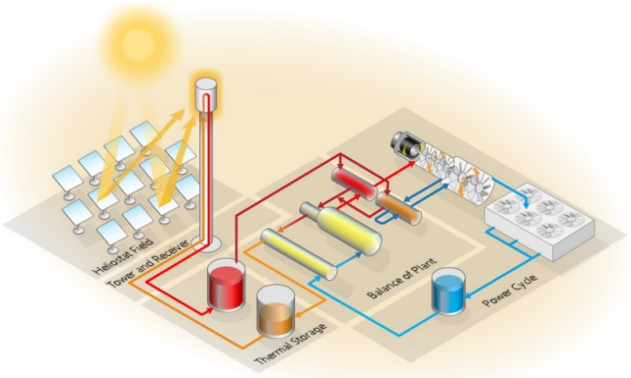

Figure A1. Schematic of the simulated Gemasolar thermosolar power plant in the SAM. The different components of a central receiver system are depicted. (© System Advisor Model Version 2017.9.5, SAM 2017.9.5).

Table A1. Input parameters for the SAM simulation of the Gemasolar thermosolar power plant during one year (from 1 July, 2017 to 30 June, 2018).

General		
Name	Value	Reference
Single heliostat net area	115.7 m^2	[42]
Ratio of reflective area	0.9642	[42]
Field gross collecting area	315,000 m^2	2625 heliostats generated by SAM, 2650 according to [42]
Irradiation at design	700 W/m^2	Chosen by authors
HTF	Solar Salt	[36]
Design loop inlet temperature	290 °C	[36]
Design loop outlet temperature	565 °C	[36]
Full load hours of TES	15 h	[36]
Storage HTF fluid	Solar Salt (direct storage)	[36]
Receiver		
Name	Value	Reference
Tower height	140 m	[36]
Receiver height	10 m	[42]
Receiver diameter	9 m	[42]
Number of panels	14	Chosen by authors
Tube outer diameter	4×10^{-2} m	SAM standard value
Minimum receiver turndown fraction	0.25	SAM standard value
Maximum receiver operation fraction	1.2	SAM standard value
Receiver startup delay time	0.25 h	Chosen by authors
Estimated receiver heat loss	30 kW/m^2	Calculated by authors (Equation (A5))
Piping length	360 m	Estimated by authors
Piping heat loss coefficient	1000 W_t/m	Calculated by authors (Equation (A7))
Power block		
Name	Value	Reference
Design gross output	19.9 MW_e	[36]
Gross to net conversion factor	1	[36]
Rated cycle conversion efficiency	0.445	Calculated from storage and receiver capacities
Fraction of thermal power needed for standby	0.2	SAM Standard value
Power block start-up time	0.5 h	SAM Standard value
Fraction of thermal power for start-up	0.5	SAM Standard value
Maximum turbine over design operation (ratio)	1.05	SAM Standard value
Minimum turbine operation (ratio)	0.2	SAM Standard value
Boiler operating pressure	105 bars	[43]
Turbine inlet pressure control	Fixed-pressure	SAM Standard value

Heat losses from the receiver are due to radiation to the environment and convection. The equation of heat losses per square meter of a receiver is, therefore, given by the following equation:

$$P_{rec} = \epsilon_{rec} \cdot \sigma \cdot \left(T_{rec}^4 - T_{ext}^4\right) + h_{conv,ext} \cdot (T_{rec} - T_{ext}) \quad \text{(A5)}$$

Using a receiver temperature (T_{rec}) of 565 °C (or 838.15 K), an external temperature (T_{ext}) of 20 °C (or 293.15 K), a receiver emittance (ϵ_{rec}) of 0.88 (input for the SAM), and a convection coefficient ($h_{conv,ext}$) of 10 $W.m^{-2}.K^{-1}$, Equation A5 can be solved as:

$$P_{rec} = 0.88 \times 5.67 \times 10^{-8} \cdot \left(838.15^4 - 293.15^4\right) + 10 \times (838.15 - 293.15), \quad \text{(A6)}$$

where the Stefan–Boltzman constant ($\sigma = 5.67 \times 10^{-8}$) is used. The obtained result can be approximated to 30 kW/m^2.

To calculate the heat loss from the pipes, the pipe loss coefficient is written as follows:

$$P_{loss,pipe}\left(W.m^{-1}\right) = \frac{T_f - T_{ext}}{\frac{\ln\left(\frac{r_{ext,p}+e_{ins}}{r_{ext,p}}\right)}{2\times\pi\cdot k_{ins}} + \frac{1}{h_{ext}\times 2\times\pi\cdot r_{ext,p}}} \quad \text{(A7)}$$

Assuming a pipe with an internal diameter of 800 mm and an external diameter of 812.8 mm, an external convection coefficient of 15 $W/m^2{\cdot}K$ and 15 cm of insulation (k_{ins} = 0.08 $W{\cdot}m^{-1}{\cdot}K^{-1}$), Equation (A7) can be solved as:

$$P_{loss,pipe}\left(W.m^{-1}\right) = \frac{565 - 20}{\frac{\ln\left(\frac{0.4064+0.15}{0.4064}\right)}{2\times\pi\times 0.08} + \frac{1}{15\times 2\times\pi\times 0.4064}} = 837\ W.m^{-1} \quad \text{(A8)}$$

Since pipe losses should take into account all heat bridges due to sensors, valves, etc., it has been decided to approximate the value to 1000 $W{\cdot}m^{-1}$.

References

1. Mendelshon, M.; Lowder, T.; Canavan, B. *Utility-Scale Concentrating Solar Power and Photovoltaics Projects: A Technology Market Overview*; Technical report NREL/TP-6A20-51137; NREL U.S. Department of Energy: Washington, DC, USA, 2012.
2. Kearney, D.; Kelly, B.; Herrmann, U.; Cable, R.; Pacheco, J.; Mahoney, R.; Price, H.; Blake, D.; Nava, B.; Potrovitza, N. Engineering aspects of a molten salt heat transfer fluid in a trough solar field. *Energy* **2004**, *29*, 861–870. [CrossRef]
3. Coimbra, C.; Kleissl, J.; Marquez, R. Overview of solar forecasting methods and a metric for accuracy evaluation. In *Solar Resource Assessment and Forecasting*; Elsevier: Waltham, MA, USA, 2013; ISBN 9780123971777.
4. Schroedter-Homscheidt, M.; Benedetti, A.; Killius, N. Verification of ECMWF and ECMWF/MACC's global and direct irradiance forecasts with respect to solar electricity production forecasts. *Meteor. Zeitschrift* **2017**, *26*, 1–19. [CrossRef]
5. Stull, R.B. *An Introduction to Boundary Layer Meteorology, Chapter 13*; Atmospheric Science Programme: Dordrecht, The Netherlands, 1999; ISBN 9027727686.
6. Conceição, R.; Silva, H.G.; Collares-Pereira, M. CSP mirror soiling characterization and modelling. *Sol. Energy Mater. Sol. Cells* **2018**, *185*, 233–239. [CrossRef]
7. Tyagi, H.; Agarwal, A.K.; Chakraborty, P.R.; Powar, S. Advances in solar energy research. *Energy Environ. Sustain.* **2019**, *1*, 48–50.
8. Troccoli, A.; Morcrette, J.-J. Skill of direct solar radiation predicted by the ECMWF global atmospheric model over Australia. *Am. Meteor. Soc.* **2014**, *53*, 2571–2587. [CrossRef]
9. Tompkins, A.M. *The Parametrization of Cloud Cover*; European Centre for Medium-Range Weather Forecasts (ECMWF): Reading, UK, 2005.
10. Bozzo, A.; Remy, S.; Benedetti, A.; Flemming, J.; Bechtold, P.; Rodwell, M.J.; Morcrette, J.-J. *Implementation of a CAMS-Based Aerosol Climatology in the IFS*; European Centre for Medium-Range Weather Forecasts (ECMWF): Reading, UK, 2017; Volume 801.
11. Lopes, F.M.; ConceiÇÃo, R.; Fasquelle, T.; Silva, H.G.; Salgado, R.; Canhoto, P.; Collares-Pereira, M. ECMWF forecasts of DNI for optimized operation strategies of linear focus parabolic-trough systems. *Appl. Energy* **2019**. In revision.

12. The Parabolic Trough Power Plants Andasol 1 to 3. The Largest Solar Power Plants in the World—Technology Premier in Europe. Solar Millenium AG. 2008. Available online: http://large.stanford.edu/publications/power/references/docs/Andasol1-3engl.pdf (accessed on 28 March 2019).
13. Rinaldi, F.; Binotti, M.; Giostri, A.; Manzolini, G. Comparison of linear and point focus collectors in solar power plants. *Energy Proc.* **2014**, *49*, 1491–1500. [CrossRef]
14. Haiden, T.; Janousek, M.; Bidlot, J.; Ferranti, L.; Prates, F.; Vitart, F.; Bauer, P.; Richardson, D.S. *Evaluation of ECMWF Forecasts, Including the 2016 Resolution Upgrade*; European Centre for Medium-Range Weather Forecasts (ECMWF): Reading, UK, 2016; Volume 792.
15. Burgaleta, J.; Arias, S.; Ramirez, D. Gemasolar, the first tower thermosolar commercial plant with molten salt storage. In Proceedings of the 17th SolarPACES Conference, Granada, Spain, 20–23 September 2011.
16. Salgado, R.; Miranda, P.M.A.; Lacarrère, P.; Noilhan, J. Boundary layer development and summer circulation in Southern Portugal. *Tethys* **2015**, *12*, 33–44. [CrossRef]
17. Cavaco, A.; Silva, H.G.; Canhoto, P.; Osório, T.; Collares-Pereira, M. Progresses in DNI measurements in Southern Portugal. *AIP Conf. Proc.* **2018**, *2033*, 1–7. [CrossRef]
18. International Organization for Standardization. *Solar Energy. Calibration of Field Pyrheliometers by Comparison to a Reference Pyrheliometer*; ISO 9059:1990(E.); International Organization for Standardization: Genève, Switzerland, 1990.
19. Long, C.N.; Dutton, E.G. BSRN Global Network Recommended QC Tests 2002, V2.0. Available online: 10013/epic.38770 (accessed on 20 February 2019).
20. Mlawer, E.; Clough, S. Shortwave and longwave radiation enhancements in the rapid radiative transfer model. In Proceedings of the 7th Atmospheric Radiation Measurement (ARM) Science team Meeting. U.S. Department of Energy ARM-CONF-970365, San Antonio, TX, USA, 3 March 1997; pp. 409–413.
21. Hogan, R.J.; Bozzo, A. A flexible and efficient radiation scheme for the ECMWF model. *J. Adv. Modell. Earth Syst.* **2018**, *10*, 1990–2008. [CrossRef]
22. Lara-Fanego, V.; Ruiz-Arias, J.A.; Pozo-Vázquez, A.D.; Gueymard, C.A.; Tovar-Pescador, J. Evaluation of DNI forecast based on the WRF mesoscale atmospheric model for CPV applications. *AIP Conf. Proc.* **2012**, *1477*, 317–322.
23. Voyant, C.; Notton, G. Solar irradiation nowcasting by stochastic persistence: A new parsimonious, simple and efficient forecasting tool. *Renew. Sustain. Energy Rev.* **2018**, *92*, 343–352. [CrossRef]
24. Richardson, W.; Krishnaswami, H.; Vega, R.; Cervantes, M. A low cost, edge computing, all-sky imager for cloud tracking and intra-hour irradiance forecasting. *Sustainability* **2017**, *9*, 482. [CrossRef]
25. Lauret, P.; Voyant, C.; Soubdhan, T.; David, M.; Poggi, P. A benchmarking of machine learning techniques for solar radiation forecasting in an insular context. *Sol. Energy* **2015**, *112*, 446–457. [CrossRef]
26. Aguiar, L.M.; Pereira, B.; Lauret, P.; Díaz, F.; David, M. Combining solar irradiance measurements, satellite-derived data and a numerical weather prediction model to improve intraday solar forecasting. *Renew. Energy* **2016**, *97*, 599–610. [CrossRef]
27. Larson, D.P.; Nonnenmacher, L.; Coimbra, C.F.M. Day-ahead forecasting of solar power output from photovoltaic plants in the American Southwest. *Renew. Energy* **2016**, *91*, 11–20. [CrossRef]
28. Smagorinsky, J.; Miyakoda, K.; Stickler, R.F. The relative importance of variables in initial conditions for dynamical weather prediction. *Tellus* **1970**, *22*, 141–157. [CrossRef]
29. Lopes, F.M.; Silva, H.G.; Salgado, R.; Cavaco, A.; Canhoto, P.; Collares-Pereira, M. Short-term forecasts of GHI and DNI for solar energy systems operation: Assessment of the ECMWF integrated forecasting system in Southern Portugal. *Sol. Energy* **2018**, *170*, 14–30. [CrossRef]
30. Martin, G.M.D.; Johnson, D.W.; Spice, A. The measurement and parameterization of effective radius of droplets in warm stratocumulus. *J. Atmos. Sci.* **1994**, *51*, 1823–1842. [CrossRef]
31. Sun, Z.; Rikus, L. Parameterization of effective sizes of cirrus-clouds particles and its verification against observations. *Q. J. R. Meteorol. Soc.* **1999**, *125*, 3037–3055. [CrossRef]
32. Fu, Q.; Yang, P.; Sun, W.B. An accurate parameterization of the infrared radiative properties of cirrus clouds of climate models. *J. Climate Atmos. Sci.* **1994**, *11*, 2223–2237. [CrossRef]
33. Edwards, J.M.; Slingo, A. Studies with a flexible new radiative code: 1. Choosing a configuration for a large-scale model. *Q. J. R. Meteorol. Soc.* **1996**, *122*, 689–719. [CrossRef]

34. Tegen, I.; Hollrig, P.; Chin, M.; Fung, I.; Jacob, D.; Penner, J. Contribution of different aerosol species to the global aerosol extinction optical thickness: Estimates from model results. *J. Geophys. Res.* **1997**, *102*, 895–915. [CrossRef]
35. Blair, N.; Dobos, A.; Freeman, J.; Neises, T.; Wagner, M.; Ferguson, T.; Gilman, P.; Janzou, S. *System Advisor Model, SAM 2014.1.14: General Description*; National Renewable Energy Laboratory: Golden, CO, USA, 2014. [CrossRef]
36. NREL, Concentrating Solar Power Projects-Gemasolar Thermosolar Plant. Available online: https://solarpaces.nrel.gov/gemasolar-thermosolar-plant (accessed on 27 March 2019).
37. Wittmann, M.; Breitkreuz, H.; Schroedter-Homscheidt, M.; Eck, M. Case studies on the use of solar irradiance forecast for optimized operation strategies of solar thermal power plants. *IEEE J. Sel. Top. Appl. Earth Obs. Remote Sens.* **2008**, *1*, 18–27. [CrossRef]
38. Kosmopoulos, P.G.; Kazadzis, S.; Taylor, M.; Athanasopoulou, E.; Speyer, O.; Raptis, P.I.; Amiridis, V. Dust impact on surface solar irradiance assessed with model simulations, satellite observations and ground-based measurements. *Atmos. Meas. Tech.* **2017**, *10*, 2435–2453. [CrossRef]
39. Mukkavilli, S.K.; Prasad, A.A.; Taylor, R.A.; Troccoli, A.; Kay, M. Mesoscale simulations of Australian direct normal irradiance, featuring an extreme dust event. *Am. Meteorol. Soc.* **2018**, *57*, 493–515. [CrossRef]
40. WWRP/WGNE Joint Group on Forecast Verification Research Website on Forecast Verification. Issues, Methods and FAQ. Available online: http://www.cawcr.gov.au/projects/verification (accessed on 28 March 2019).
41. Salgado, R. Interacção Solo—Atmosfera em Clima Semi-Árido. Ph.D. Thesis, University of Évora, Évora, Portugal, 2005.
42. Collado, F.; Guallar, J. A review of optimized design layouts for solar power tower plants with campo code. *Renew. Sustain. Energy Rev.* **2013**, *20*, 142–154. [CrossRef]
43. SIEMENS. Steam Turbines for CSP Plants. 2011. Available online: http://m.energy.siemens.com (accessed on 28 March 2019).

© 2019 by the authors. Licensee MDPI, Basel, Switzerland. This article is an open access article distributed under the terms and conditions of the Creative Commons Attribution (CC BY) license (http://creativecommons.org/licenses/by/4.0/).

Solar Energy 185 (2019) 387–405

Contents lists available at ScienceDirect

Solar Energy

journal homepage: www.elsevier.com/locate/solener

Development of an ANN based corrective algorithm of the operational ECMWF global horizontal irradiation forecasts

Sara Pereira[a,*], Paulo Canhoto[a,b], Rui Salgado[a,b], Maria João Costa[a,b]

[a] Instituto de Ciências da Terra, Universidade de Évora, Rua Romão Ramalho 59, 7000-671 Évora, Portugal
[b] Departamento de Física, Universidade de Évora, Rua Romão Ramalho 59, 7000-671 Évora, Portugal

ARTICLE INFO

Keywords:
Solar radiation
Solar energy
Artificial neural network
ECMWF
Forecast

ABSTRACT

This paper proposes a corrective algorithm for improving the accuracy of global horizontal irradiation (GHI) forecasts obtained from the numerical weather prediction (NWP) model of the European Centre for Medium-range Weather Forecast (ECMWF). Firstly, GHI forecasts were compared with experimental values from two ground-based stations located at the south of Portugal (Évora and Sines), and the influence of Sun-Earth geometry and atmospheric variables on the differences between predictions and measurements was analysed in order to identify the most relevant parameters. These differences are shown to be correlated mainly with the clearness index, solar zenith angle, mean air temperature, relative air humidity and total water column. Since the ECMWF model directly or indirectly provides all these variables, it is possible to estimate the bias of the predicted GHI as a function of forecast data taking as reference the measurements, which means that an algorithm based on correlations of such parameters can be used to correct forecasts in an operational time horizon. With that goal, an artificial neural network (ANN) based algorithm was developed in this work to improve GHI predictions, including also as input the global solar irradiation predicted by a reference clear sky model. The internal structure of the ANN was optimised, and a spatial and temporal downscaling procedure was also developed to obtain half-hour irradiation values. This algorithm was tested against the original ECMWF forecasts and a persistence model for four locations with different orography and climate as well as for various sky conditions (overcast, partly cloudy and clear sky), showing that it successfully improves the model predictions. Higher values of a Global Performance Index (GPI) based on seven statistical indicators and Forecast Score (FS) were found for the algorithm simulations, e.g. respectively 1.066 and 0.348 when considering all the locations and cloud cover conditions, while for the original ECMWF predictions the GPI is −1.874 and the FS is 0.282. This algorithm is useful if integrated into energy management tools of solar energy systems, namely low/medium temperature solar thermal and photovoltaic systems.

1. Introduction

Weather forecasts are a set of complex procedures that aims to predict the meteorological conditions based on global observations, physical laws and mathematical and numerical models executed in high-performance computers. The prognostic data are used in many applications and can help people plan their days and prevent damage in case of extreme atmospheric conditions. Weather forecasts are essential for businesses related to agriculture, transportations and energy, among others. Renewable energy resources like solar and wind energy are mainly dependent on the meteorological conditions and thus accurate weather forecasts are a powerful tool that can be used to predict the energy output of systems using these resources.

There are many techniques that can be used for solar radiation forecasting in different time scales. The models used for medium or long-term forecasts (generally a time horizon of hours or days in the case of mid-term and days or months for long-term) can be divided into two main categories: time series statistical models and physical models. In the statistical models, the relations between past values of meteorological parameters and solar radiation are established and then used in the prediction procedure. These include numerical techniques such as artificial neural networks (ANN), support vector machines (SVM), Markov chains, autoregressive models or regression models. The physical models are based on a set of equations that describe the transport phenomena and thermodynamic processes that occur in the atmosphere and on the Earth's surface, like numerical weather prediction (NWP) models. In the case of short-term forecasts (time horizons of minutes or hours), sky imagery or satellite imaging based models are widely used.

* Corresponding author.
E-mail address: spereira@uevora.pt (S. Pereira).

https://doi.org/10.1016/j.solener.2019.04.070
Received 22 November 2018; Received in revised form 18 April 2019; Accepted 22 April 2019
Available online 01 May 2019
0038-092X/ © 2019 International Solar Energy Society. Published by Elsevier Ltd. All rights reserved.

Nomenclature

b	bias of a neuron
E_p	prediction error
E_s	simulation error
f	activation function of a neuron
FS	forecast score
GPI	global performance index
I	hourly solar global irradiation
I_0	extraterrestrial irradiation on a horizontal surface
J	half-hourly solar global irradiation
K_t	clearness index
K_t'	clearness index of the day to simulate
MAE	mean absolute error
MAPE	mean absolute percentage error
MBE	mean bias error
MSE	mean squared error
N	number of simulated days
P	hourly GHI predictions by the IFS
Pe	hourly GHI estimates from the persistence model
R	coefficient of correlation
R^2	coefficient of determination
RMSE	root mean squared error
r_{Kt}	clearness index range
S	hourly GHI simulations by the ANN model
SS	skill score
TS	T-statistics
U95	uncertainty at 95%
w_i	weight of an input i in a neuron
x_i	input value i in a neuron
Y	output of a neuron
$\widetilde{y_j}$	median of the normalized value of the indicator j
y_{ij}	normalized value of the indicator j for model i

Greek Letters

α	GPI factor
Φ	solar zenith angle

Acronyms

ANN	artificial neural network
ECMWF	European Centre for Medium-range Weather Forecasts
GFS	global forecasting system
GHI	global horizontal irradiation
IFS	integrated forecasting system
MOS	model output statistics
NWP	numerical weather prediction model
RRTM	rapid radiation transfer model
SVM	support vector machines

There are also ensemble models that combine different approaches to enhance forecast accuracy (Wang et al., 2012). Ghimire et al. (2019) compared ANN, SVM, Gaussian process machine learning and genetic programming performances in the prediction of daily solar radiation at five different cities of Australia using reanalysis data from ECMWF as inputs and the ARIMA, temperature and time series with Fourier transform models as benchmarks. The developed ANN model outperformed all other machine learning models.

The integrated forecasting system (IFS) developed by the European Centre for Medium-range Weather Forecasts (ECMWF) is one of the most accurate global NWP models (Persson and Andersson, 2015) producing hourly forecasts of many different atmospheric variables. The forecasts are generated for discrete points in a grid with a spatial resolution that might not be enough for specific applications. A higher resolution with an improved description of orography and its effect on atmospheric processes results in more accurate forecasts but also requires a higher computation time. Thus, methods of spatial and temporal downscaling can be useful as post-processing of forecasts without such computational cost.

Recent studies reported the assessment of solar radiation forecasts by different NWP models. For example, Landelius et al. (2018), compares IFS and HARMONIE-AROME ensemble predictions (both using the same radiation code) global horizontal irradiance and direct normal irradiance, with measurements from three stations in Sweden, showing underestimations of direct normal irradiance in clear-sky conditions and a better performance of the HARMONIE-AROME ensemble when compared to the IFS. Mathiesen and Kleissl (2011) assessed and validated global horizontal irradiance forecasts for the continental US made by the North American Model (NAM), Global Forecast System (GFS) and ECMWF using the SURFRAD ground-based measurement data. The metrics used were the root mean squared error (RMSE) and mean bias error (MBE). Model output statistics (MOS) based on multivariate regressions were applied to decrease the MBE. GFS proved to be the most accurate model for clear sky conditions (classified according to observations) with a maximum bias of 50 W/m^2 for all NWP models, while for cloudy conditions the bias can exceed 200 W/m^2, being the ECMWF the most accurate model. In the study by Perez et al. (2013), measurements obtained from different locations in the US, Canada and Europe were used for three independent validations of several global horizontal irradiance forecast models that include global, multiscale and mesoscale NWP models and different post-processing techniques to derive hourly site-specific forecasts. The results show that the ECMWF forecasts perform better than the GFS-based WRF (Weather Research and Forecasting) mesoscale model, independently of the site and climatic conditions. They concluded that the simple averaging of the model outputs tend to perform better than the output of each model separately. Huang et al. (2018) evaluated solar irradiance forecasts for Australia produced by the GFS, the Australian Community Climate and Earth-System Simulator and ERA5 reanalysis by the ECMWF being the later the one with higher forecast skill score (FS) when compared to 1-day persistence model. Linearly blending the three NWP models a FS of 0.44 was achieved.

A persistence model is a method in which the forecast value is equal to the previous observation or an observation during a similar instant of the recent past. These are often used as benchmarks for forecast model evaluation (Alessandrini et al., 2015; Do et al., 2016; Silva Fonseca et al., 2011; Vaz et al., 2016). Lopes et al. (2018) analysed one year of direct normal and global horizontal irradiance forecasts produced by IFS against data from four measuring stations located in southern Portugal showing relative differences of annual availabilities between approximately 0.16% and 2.12% for global horizontal irradiance and between 7% and 12% for direct normal irradiance.

Machine learning techniques are tools with increasing popularity for solar radiation forecasting. ANNs is one of the most used machine learning techniques, which comprises input and output layers, as well as one or more hidden layers consisting of units defined as neurons. Such computing systems progressively improve task performance by considering examples, generally without task-specific programming. Many authors have used ANN in the field of renewable energy, e.g. for correction of wind speed or daily solar irradiance forecasts (Malik and Arora, 2014; Marzo et al., 2017; Voyant et al., 2017) and for simulation of photovoltaic power (Anderson and Yakimenko, 2018; Chu et al., 2015; Dimopoulou et al., 2016; Fleetwood and Galarza, 2018; Gigoni et al., 2018; Hachicha et al., 2013; Liu et al., 2018; Rosiek et al., 2018; Scolari et al., 2017; Son et al., 2018). The ANN inputs used are usually historical data, but some authors also use a combination of forecasting

models such as satellite imagery or the output of NWP models.

An example of the usage of historical measured data is presented in the work of Renno et al. (2016). Two models based on ANN combined with measured data were developed in order to forecast daily GHI and hourly direct normal irradiance. A mean absolute percentage error (MAPE) of 4.57% and RMSE of 160.3 W/m^2 for daily GHI and a MAPE of 5.57% and a RMSE of 17.7 W/m^2 for hourly direct normal irradiance was obtained. Sharifi et al. (2016) compared ANN with gene expression programming, wavelet regression and five temperature-based empirical models for estimation of daily GHI using a Global Performance Index (GPI) for model assessment, being the ANN model the one with the best performance. Rosiek et al. (2018) combined satellite images with ANN to predict the power output of a building integrated photovoltaic system up to three hours ahead using the minimum number of input variables as possible. Khosravi et al. (2018) developed forecasting models based on two different types of input data, one that uses local time, temperature, pressure, wind speed, and relative humidity measurements and the other only a time series of solar irradiance predictions. The authors developed and tested different model configurations finding best results (correlation coefficients above 0.95) when using multilayer feed-forward ANN and support vector regression to predict solar irradiance, for any of the two input datasets. Blaga et al. (2019) shows that generally, hybrid models that combine physical or statistical models with machine learning methodologies perform better than models belonging to only one category. Amrouche and Le Pivert (2014) presented a combination of NWP model outputs and ANN, where a spatial modelling was developed to produce daily global horizontal irradiance forecasts based on the weather forecasts provided by the US National Oceanic and Atmospheric Administration (NOAA), achieving satisfactory accuracy when tested for two locations in France.

Although forecasts of daily global horizontal irradiation are useful, intra-day GHI forecasts of solar radiation are also of utmost importance for solar energy systems operation. Larson et al. (2016) developed a method to generate the hourly average of day-ahead power output forecasts of two photovoltaic (PV) power plants using NAM and the regional deterministic prediction system models. They obtained an annual RMSE range of 11.7–14.0% and 10.2–12.4% and annual FS of 15–23% and 13–20% relative to the rated energy generation of each PV plant, respectively. Lima et al. (2016) developed a methodology based on the WRF model and several statistical post-processing procedures, namely ANN, to produce global horizontal solar irradiance forecasts for the north-eastern region of Brazil using data from rainy and dry seasons between 2009 and 2011. The results show a significant improvement of the WRF model forecasts when adjusted by the ANN, yielding lower bias and RMSE, and an increase in the correlation coefficient. Cornaro et al. (2015) described two models based on ANN that produce hourly global horizontal irradiance forecasts with a day in advance. One of these algorithms relies on a statistical (ST) analysis that uses only locally measured data, and the other is a MOS that corrects NWP data from ERA-Interim, which is a reanalysis of the ECMWF atmospheric global forecasts. These models were trained and validated using one year of data measured in Rome, Italy. The ST model results are similar to the NWP model output being the MOS the one with the best performance. This work also shows the benefit of using ANN methodologies for NWP output correction, although using a reanalysis database as input instead of operational forecasts. On the contrary, a methodology using the output of an operational model will allow actual short and mid-term forecasts.

The present work aims at the development of an ANN post-processing methodology for the correction of the predicted hourly global solar irradiation from the operational IFS forecasts from the ECMWF, including also the spatial and temporal downscaling for a time-step of half an hour and time horizon of 72 h. The output of half-hourly forecasts of GHI was one of the requirements of the research and development project in which this work was integrated.

This paper reports:

(i) An analysis of the influence of atmospheric and Sun-Earth geometry related variables on the differences between forecasted and measured GHI in southern Portugal;
(ii) The development of an ANN that uses IFS forecasts and a clear sky model of reference as inputs and incorporates methods of spatial and temporal downscaling to produce half-hourly GHI forecasts at a given site;
(iii) The optimisation of the ANN structure including the definition of different configurations (sub-models) according to the predicted cloud cover;
(iv) The comparison of the developed post-processing algorithm with the original ECMWF model and a persistence model using different metrics for performance assessment that include a Global Performance Index (GPI) and the Forecast Skill score (FS), for different locations that vary in orography and climate as well as for various sky conditions (overcast, partly cloudy and clear sky).

According to the knowledge of the authors, the main novelties of the present work are the use of the operational ECMWF forecasts together with a reference clear sky model to feed an ANN for the correction of the original forecasts, the analysis of the most relevant parameters and the optimisation of the ANN structure for different forecasted cloud cover conditions (sub-models). These innovating features of the developed methodology combined with the spatial and temporal downscaling of predicted GHI values contribute to developing an improved corrective algorithm. The predictions resulting from this post-processing can be used as inputs in energy management tools of solar thermal or photovoltaic systems as well as for other applications that require accurate forecasts of irradiation at a specific location.

The paper comprises five sections: after the introduction, a presentation of the data used is given in Section 2, followed by the development of the corrective algorithm (Section 3), which includes spatial and temporal downscaling methods, a preliminary analysis on the quality of the ECMWF forecasts and the development of the ANN based methodology; Section 4 presents the results and its analysis and finally, conclusions are drawn in Section 5.

2. Forecast and experimental data

2.1. Forecast data from the ECMWF

The IFS from the ECMWF produces hourly forecasts of different variables in a grid with a spatial resolution of 0.125° × 0.125° and comprises various components: an atmospheric general circulation model; an ocean wave model; an ocean general circulation model; a land surface model; a data assimilation system and perturbation models used for data assimilation (ensemble of data assimilation) and forecast ensemble. The radiative scheme of the IFS solves the short and longwave radiative fluxes using as inputs the predicted values of temperature, humidity, water species (water vapour, cloud liquid water, rain, cloud ice and snow), cloud cover, the monthly-mean climatologies for aerosols and the main trace gases concentrations (CO_2, O_3, CH_4, N_2O, $CFCl_3$ e CF_2Cl_2) (Keeley, 2013). The code is based on the Rapid Radiation Transfer Model, RRTM (Iacono et al., 2008; Mlawer et al., 1997), that uses values of cloud fraction and liquid, ice and snow water contents from the cloud model using the McICA (Monte Carlo Independent Column Approximation) method, McRad (Morcrette et al., 2008), which allows for a detailed representation of cloud-radiation interactions. ECMWF's version of RRTM for longwave radiation is composed of 16 spectral bands while for shortwave 14 spectral bands are used. The computational cost of solving the radiative transfer equations is very high, so full radiation calculations are performed on a reduced (coarser) grid or on a higher time step being the results then interpolated back to the original grid. More information on the radiative scheme of IFS can be found in (ECMWF, 2016). Since the computational cost is so high an alternative for improving forecasts is the

Table 1
Variables retrieved from ECMWF model output.

Name	Short name	Units	Range/observations
Longitude	longitude	° East	0°–360°
Latitude	latitude	° North	−90° to 90°
Time step	step	h	1–125
Date	date	Days	Days since 1900-01-01 00:00:00
Visibility	p3020	m	–
Cloud base height	cbh	m	Cloud fraction > 1% and condensate content > 1×10^{-6}
Total column water	tcw	kg/m^2	Includes vapour, cloud water and cloud ice
Total cloud cover	tcc	0–1	–
10 m U wind component	u10	m/s	–
10 m V wind component	v10	m/s	–
2 m temperature	t2m	K	Air temperature at 2 m
2 m dew point temperature	d2m	K	Dew point temperature at 2 m
Surface solar radiation downwards	ssrd	J/m^2	Accumulated values throughout the forecast
Total column ozone	tco3	kg/m^2	–

usage of post-processing techniques like the one developed and presented in this paper.

In this work, hourly global solar irradiation predictions were obtained as accumulated values in J/m^2 from the ECMWF archive (surface solar radiation downwards), from which other variables (see Table 1) were also downloaded.

These variables are provided with a time step of 1 h until the 90th hour, changing to a time step of 3 h until the 144th and to a time step of 6 h from the 144th to the 240th hour. The data were obtained for the period from May 13th 2015 to November 15th 2016 in GRIB files, which were converted to netCDF format.

2.2. Experimental data

Global solar irradiance measurements were made through pyranometers, in W/m^2, located in the observatories of the Institute of Earth Sciences (ICT) of the University of Évora in Évora (38.567687N 7.91704W) and in Sines (37.9540833N 8.8654722W) for the periods from May 13th 2015 to November 15th 2016 and from June 24th 2015 to November 15th 2016, respectively.

The pyranometer installed in Évora is a CM6B model from Kipp& Zonnen, classified as first class by the norm ISO 9060:1990 (International Organization for Standardization [ISO], 1990). The pyranometer installed in Sines is a Li-200R model from Li-COR, which has lower precision according to (International Organization for Standardization [ISO], 1990) than the one in Évora. The later also shows signs of shading during the first hour after sunrise due to local effects of the near orography. The sampling rate of the sensors output is 5 s and average, minimum, maximum and standard deviation values are registered every minute.

Hourly values of global solar irradiance from June 24th 2015 to November 15th 2016, measured with CM11 Kipp&Zonnen pyranometers belonging to IPMA (Portuguese Institute for Sea and Atmosphere) in Cabo da Roca (38.781633N 9.497539W) and Penhas Douradas (40.411396N 7.558630W) were also used to develop and test the corrective algorithm.

All instruments are subject to maintenance and cleaning procedures according to the recommendations of the World Meteorological Organization (Radiation Commission of IAMAP, 1986) and the four locations selected are representative of different climate and orography, with Évora (relatively flat terrain) and Penhas Douradas (mountainous terrain) in the interior of Portugal, while Cabo da Roca and Sines are both in the littoral of Portugal. Data from the four sites for the period from June 24th, 2015 to November 15th, 2016 were used for the development and validation of the correction algorithm. The data was subject to BSRN filters (Long and Dutton, 2010) based on physically possible and extremely rare values in the case of Évora and Sines. Days with measurement gaps longer than 20 min were discarded while linear interpolation was used to fill gaps up to 20 min. For Penhas Douradas and Cabo da Roca, since only hourly values are available, if gaps of one or more hours exist then the respective day is discarded. After applying the filters, 98.33%, 91.47%, 96.46% and 95.84% of the data were valid for Évora, Sines, Penhas Douradas and Cabo da Roca, respectively. For the development of the ANN only valid data simultaneously available at all four stations were used, thus meaning that 83.36% of the total data from the four stations were used, with 0.0023% being generated by interpolation due to gaps of Évora or Sines data series.

3. Development of a corrective algorithm based on ANN with spatial and temporal downscaling

3.1. Spatial and temporal downscaling of IFS predictions

Spatial downscaling is needed to obtain prediction values for specific locations other than the model grid points. Different methods were analysed in previous studies (Pereira, 2017; Pereira et al., 2016) using the four nearest grid points: each grid point separately; their average; a bi-linear interpolation; and a distance-weighted average. The results showed that the bi-linear interpolation of the nearest four points is the best solution, also following the recommendation of the ECMWF (Anderson, 2015).

A method for the temporal downscaling of GHI values from a hourly (I) to a half-hourly (J) basis was developed and tested by Pereira (2017), Pereira et al. (2016) based on energy conservation (irradiation) and assuming a linear variation of solar irradiance during each hour. The half-hourly values for the first and second half hour of the hour i are computed using Eq. (1) while for the hours of sunrise and sunset slightly different equations are employed (Appendix A) since the instant of sunrise and sunset must be taken into consideration. The half-hour irradiation values respect the total energy received per unit area during that hour, i.e., the irradiance integrated over a given period, also known as irradiation (Kalogirou, 2009) or insolation (Liou, 2002).

$$\begin{cases} J_{i-1/2} = \frac{1}{2} I_i \left[1 - \frac{1}{4} \left(\frac{I_{i+1} - I_i}{I_{i+1} + I_i} + \frac{I_i - I_{i-1}}{I_i + I_{i-1}} \right) \right] \\ J_i = \frac{1}{2} I_i \left[1 + \frac{1}{4} \left(\frac{I_{i+1} - I_i}{I_{i+1} + I_i} + \frac{I_i - I_{i-1}}{I_i + I_{i-1}} \right) \right] \end{cases} \quad (1)$$

Further explanations on the spatial and temporal downscaling methods can be found in Appendix A.

3.2. Direct comparison between predicted and measured values

As a first step, hourly measurements and forecast data were directly compared. The comparisons for Évora are presented in the following. The predicted hourly values of global solar irradiation for the first 72 h of forecast were spatially downscaled as described in Section 3.1. All

Table 2
Classification of hourly data according to clearness index.

Class	Clearness index range [%]
Clear sky	[65;100]
Partly cloudy sky	[40;65[
Overcast sky	[0;40[

data were divided into classes as shown in Table 2, according to the clearness index (K_t) calculated through Eq. (2) using the measured values of GHI and the irradiation on a horizontal surface at the top of the atmosphere (I_0) (Kalogirou, 2009).

$$K_t = \frac{GHI}{I_0} \tag{2}$$

Fig. 1 shows scatter plots with density distribution (in %) of irradiance corresponding to the hourly irradiation forecasts versus measurements for Évora under clear sky conditions for three different forecast lead-times: one, two and three days ahead. Values of MBE and RMSE were also computed and shown in Table 3 along with the number of points and the maximum value of density distribution obtained. Fig. 1 shows a high density distribution for lower values of GHI due to

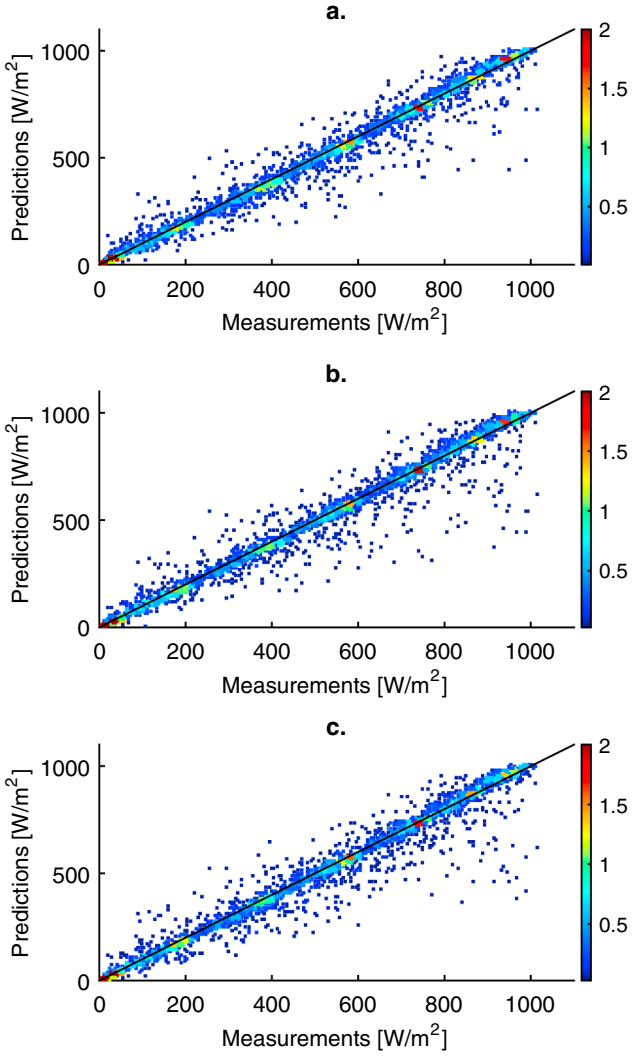

Fig. 1. Scatter density distribution of hourly predictions vs. measurements of global horizontal irradiance [%] for clear sky days in Évora: (a) 1-day ahead, (b) 2-day ahead, (c) 3-day ahead.

the initial and final hours of each day, every day. Good GHI predictions under clear sky conditions are observed, as there is a concentration of points around the line y = x. However, there is some dispersion of points below that line, which indicates some underestimation of GHI by the model also shown by the negative values of MBE (Table 3). A slight increase in the dispersion is observed for the second and third day of forecasts, thus showing a slight degradation of the predictions farther away in time, as expected.

The same comparison was carried out for the other classes of the clearness index (following Table 2) to understand the impact of cloud cover conditions on the quality of GHI predictions. Fig. 2 shows that comparison for Évora. It can be concluded that the scatter tends to be higher for lower clearness indexes and that a slight deviation from the $y = x$ line exists for partly cloudy skies and overcast conditions resulting in a positive value of MBE as is shown in Table 3. It means that the IFS model tends to overestimate GHI values under cloudy sky conditions, which can be due to an underestimation of the cloud fraction or of the cloud effects on the attenuation of the solar radiation that reaches the surface.

A sensitivity study of GHI forecasts to some atmospheric and Sun-Earth geometry related variables was carried out in Pereira et al. (2018, 2017). Hourly GHI data from Évora and Sines were used to calculate the prediction error E_p between the IFS predictions, P, and measurements, M, through Eq. (B.1). The different error metrics used throughout this work are presented in Appendix B.

The prediction errors were correlated with several variables: clearness index calculated using predictions, solar zenith angle (SZA, Φ) and ECMWF predictions of 2 m air temperature and relative humidity, cloud fraction, cloud base height, total water column, total ozone column, visibility and 10 m wind intensity. The relative humidity was computed using dew point and air temperature and the wind intensity using 10 m u and v wind components. The clearness index is calculated using the GHI predictions since the goal is the correction of forecasts for a future instant.

Pereira et al. (2018) showed that the prediction of energy output is highly sensitive to the clearness index and to the SZA, especially when the clearness index is between 40% and 70% and for lower SZA values.

Instead of the SZA the fraction of day can be used for this analysis. The fraction of day is the ratio of the time elapsed since sunrise to the total time between sunrise and sunset (duration of the day). Figs. 3 and 4 show the mean (MBE) and standard deviation of the prediction error, E_p, as a function of the clearness index and of the fraction of day, respectively. These show higher values of mean and standard deviation for intermediate values of clearness index and hours near the solar noon. The explanation for this is the presence of clouds that are difficult to predict by the model and the fact that near solar noon the values of irradiation are higher than in the rest of the hours of a day which in turn may result in higher differences between predictions and measurements (prediction error).

Other variables that showed high influence on the differences between predicted and measured GHI were mean air temperature, relative air humidity and total water column as shown in Fig. 5.

While temperature, for example, which is one of the most accurate IFS output variables (it is one of the focus of the model of ECMWF), it is strongly correlated with solar radiation, it is verified that the mean bias error of GHI predictions is not independent of air temperature forecasts (Fig. 5). This means that the predicted temperature can be used to correct the GHI predictions, which is the goal of the proposed ANN. The same occurs with other meteorological variables and, instead of correcting the GHI predictions with correlations, it was opted to use various atmospheric variables available from the IFS for the development of the ANN, and not only those showing higher influences in GHI differences. This will be explained further in the next section, also mentioning a pre-processing algorithm used to select the most relevant variables.

Table 3
Number of points, maximum density, MBE and RMSE for each analysis presented in Figs. 1 and 2.

Parameter	Clear sky			Partly cloudy sky (1-day ahead)	Overcast sky (1-day ahead)
	1-day ahead	2-day ahead	3-day ahead		
Number of points	4136	3909	3699	1958	1015
Maximum density [%]	7.01	7.09	7.03	9.55	13.30
MBE [W/m^2]	−6.46	−7.05	−9.14	7.93	40.82
RMSE [W/m^2]	44.60	51.84	54.24	109.35	124.80

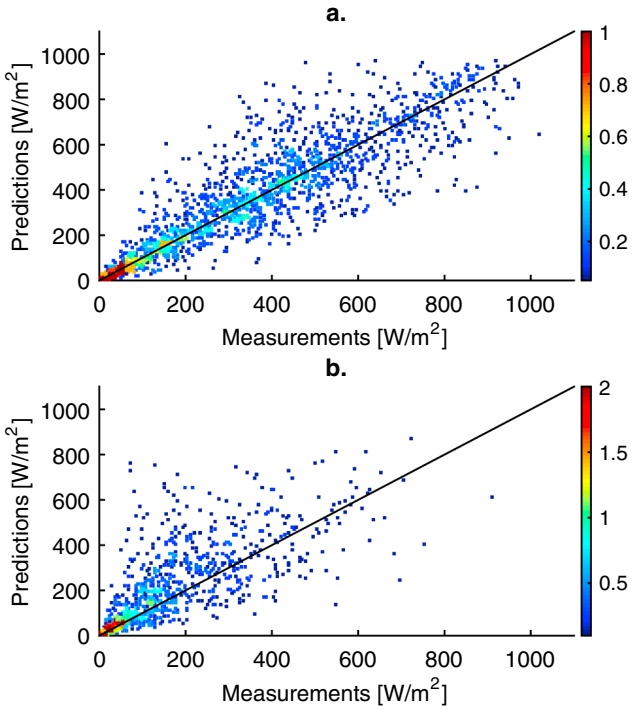

Fig. 2. Scatter density distribution of 1-day ahead hourly predictions vs. measurements of global horizontal irradiance [%]: (a) partly cloudy sky days and (b) overcast days in Évora.

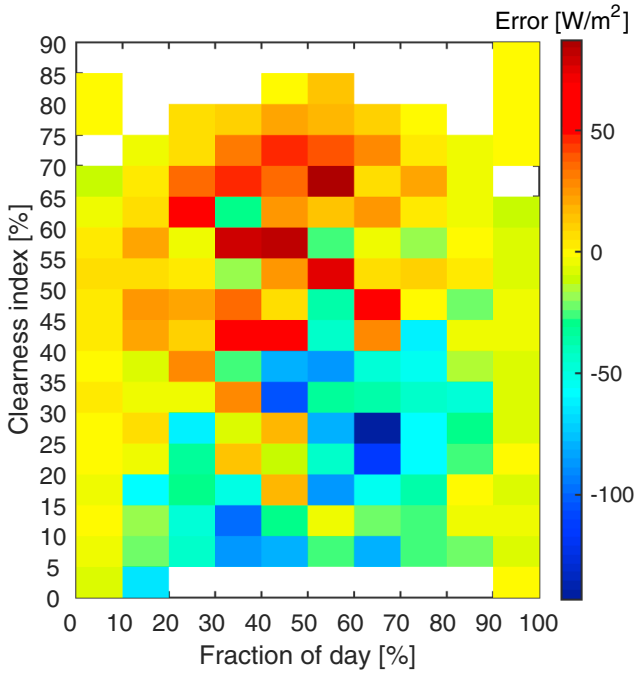

Fig. 3. Mean bias error (MBE) of predictions as a function of the clearness index and fraction of day for Évora.

3.3. Development of an ANN based corrective algorithm

An ANN based methodology was developed for the correction of the GHI forecasts. An ANN is a machine learning technique that possesses units (neurons) arranged in layers. The implementation of an ANN can be summarized in a few simple steps that occur in each neuron:

- All the input variables are multiplied by a predetermined weight and summed;
- A bias is added to the result;
- The activation function processes the sum which is altered accordingly;
- The signal becomes an input to the next neuron.

All these steps are shown in Fig. 6. Eq. (3) defines the output (Y) of a neuron where b is the bias for the neuron, w_i is the weight for the specific input, x_i is the actual value that is passed to the neuron for the summation and f is the activation function.

$$Y = f\left(b + \sum_i w_i x_i\right) \tag{3}$$

In the present work, the neural network toolbox of MATLAB® was used, and a feed-forward type ANN with supervised learning, more specifically a regression type of learning was developed. This type of ANN works by presenting examples of pairs of predictions and measurements (the estimation and its solution respectively) of GHI. Through training and validation, the ANN learns how to adjust future predictions of GHI in order to return a corrected value that is closer to reality.

The available data was divided using circa a year as a dataset for training and validation in order to simulate global solar radiation values of the next day. After the simulation, this day is added to the dataset and the day after is simulated and so on, until there is no more data, existing 103 days simulated for each location in the period from 1st of July 2016 to 15th November of 2016. Since the performance of the ANN is proportional to the amount of data available for training and validation and since the four measurement sites can be representative of different orography and climate, the data for all locations were used for training and validation. Testing different parameters of the ANN and finding the values that result in a better performance independently of the location, results in a more robust and performant algorithm that can be used in any site under different orography and climate conditions.

In order to select the best parameters of the ANN, the MBE (Eq. (B.3)), MSE (Eq. (B.6)) and the percentage of cases in which the ANN simulations resulted in GHI values closer to measurements than IFS predictions were used as indicators. The variation of these three indicators was concordant regarding the ANN performance for the tested combinations of parameters. Some configuration parameters were predefined such as the functions used for pre-processing data, the

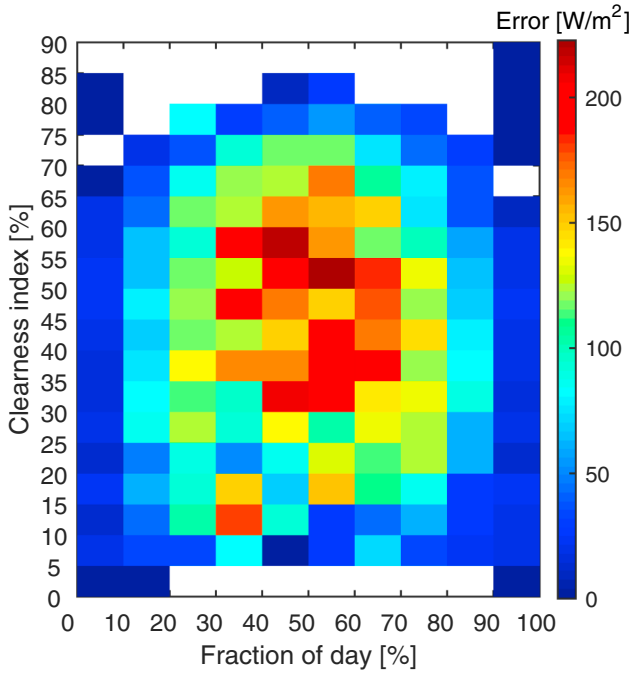

Fig. 4. Standard deviation of prediction error as a function of the clearness index and fraction of day for Évora.

performance function and the number of layers defined as shown in Table 4. For more information on ANN and the functions mentioned please refer to MATLAB®'s documentation. An improved approach to assess both the IFS predictions and ANN simulations is presented in Section 4, by including other statistical indicators and a persistence model, and by defining a Forecast Skill Score (FS), a Global Performance Index (GPI) based on seven statistical indicators and a Skill Score (SS) as a function of the FS and coefficient of correlation for model comparison.

The random number generator was fixed in order to create a predictable sequence of weights, so different runs of the ANN with different parameters could be compared. Different architectures, training and transfer functions and types of data division were tested, using the metrics previously mentioned. In accordance to these tests, the ANN type was configured as a fitting network, which comprises a feedforward neural network used to fit an input-output relationship with three layers. It has a hyperbolic tangent sigmoid function as the transfer function and Bayesian regulation backpropagation as a training function. This updates the weight and bias values according to the Lanvenberg-Marquardt optimisation, minimising a combination of squared errors and weights and then determining the correct combination to create a network that generalises well. For training termination, a value of 20 validation checks was applied, which represent the number of successive iterations that the validation performance fails to decrease using 80% of the data available for training and 20% for validation.

As shown in Table 5, the basic set of inputs was comprised of some of the variables retrieved from IFS (for each of the four grid points surrounding the measuring station) as well as the calculated values of solar radiation at the top of the atmosphere. Some of these variables are correlated to GHI and thus by using the principal component analysis as a pre-processing function, the size of the input matrix can be reduced and optimized (less computation time) and only uncorrelated and significant information in used in the ANN. Since this is a data driven approach, it has the ability to determine which model inputs are critical (Lachtermacher and David Fuller, 1994), nevertheless a more detailed analysis of the ANN performance with different sets of inputs could show better results.

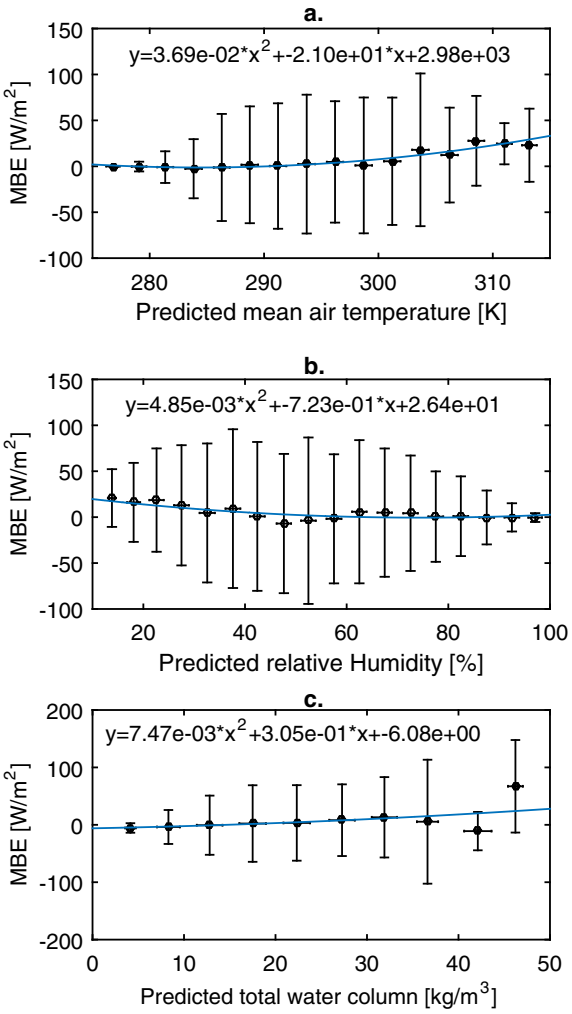

Fig. 5. Mean bias error (MBE) and standard deviation of hourly global horizontal irradiance predictions as a function of (a) predicted mean air temperature, (b) predicted relative air humidity and (c) predicted total water column in Évora.

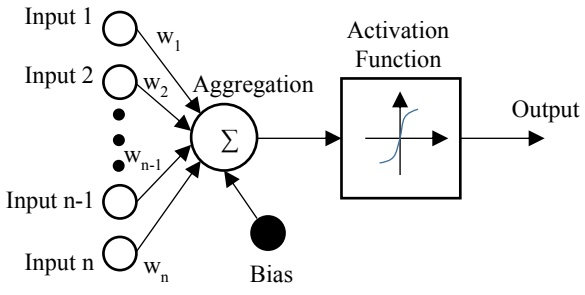

Fig. 6. Schematic representation of an artificial neuron.

Three different ANN configurations depending on the sky conditions (1 – Clear; 2 – Partly cloudy; 3 – Overcast) were developed and tested according to the daily clearness index (ratio of the daily irradiation at the surface and at the top of the atmosphere) of the day to simulate, to achieve a better simulation accuracy. All configurations have the same parameters described above but vary in the input, number of neurons and clearness index range. The clearness index range was a parameter created in order to train and validate the ANN with data from days with similar clearness indexes to that of the day to simulate. The clearness index range, r_{Kt}, is a deviation from the daily clearness index of the day to simulate, K_t'. The algorithm selects the days from the dataset defined

Table 4
Base parameters of the ANN configurations.

Parameter	Value	Description
Pre-processing data functions	processpca	Principal component analysis
	fixunknowns	Marks rows with unknown values
	mapminmax	Mapping row minimum and maximum values to [−1 1] respectively
Performance function	mse	Mean squared error function
Number of layers	3	Input, hidden and output layer
Validation checks	20	Number of successive iterations that the validation performance fails to decrease
Training-validation data ratio	80% training, 20% validation	Percentage of available data used for training and validation of the ANN
Architecture	fitnet	Fitting neural network
Training function	trainbr	Bayesian regulation backpropagation
Transfer function	tansig	Hyperbolic tangent sigmoid
Data division	divideind	Divide data by defined index
Common/Base inputs	Calculated values of solar radiation on the top of the atmosphere	Inputs used in every ANN configuration
	Predictions of GHI (4 grid points)	
	Predictions of 2 m temperature (4 grid points)	
	Predictions of relative humidity (4 grid points)	
	Predictions of 10 m wind velocity (4 grid points)	
	Predictions of cloud fraction (4 grid points)	
	Predictions of cloud base height (4 grid points)	
	Predictions of total ozone column (4 grid points)	
	Predictions of visibility (4 grid points)	
	Predictions of total water column (4 grid points)	

Table 5
MSE for different values of clearness index range.

Configuration/Sky condition	1 – Clear			2 – Partly cloudy			3 – Overcast		
Clearness index range	0.025	0.055	0.145	0.015	0.03	0.15	0.09	0.145	0.15
MSE [W^2/m^4]	1094.7	1134.0	1084.4	27,089	20,825	12,485	9171.8	7859.3	7959.7

Table 6
MSE for different values of number of neurons.

Configuration/Sky condition	1 – Clear			2 – Partly cloudy			3 – Overcast		
Number of neurons	2	17	58	30	57	69	27	30	39
MSE [W^2/m^4]	1125.0	1095.6	1084.5	12,485	12,731	12,546	7859.3	8066.6	8351.4

Table 7
Unique characteristics of each ANN configuration (defined by the clearness index calculated with predictions of GHI of the day to simulate).

Configuration/Sky condition	Additional inputs	Number of neurons in the hidden layer	Clearness index range
1 – Clear	Global solar radiation in clear sky conditions, hour, day and month	58	± 0.145
2 – Partly cloudy	–	30	± 0.150
3 – Overcast	Global solar radiation in clear sky conditions	27	± 0.145

for training and validation with daily clearness indexes ranging from $K_t^{'} - r_{Kt}$ to $K_t^{'} + r_{Kt}$ to train and validate the ANN that will simulate the day that has a clearness index K_t'. To define the appropriate clearness index range, this parameter was varied between 0.005 and 0.15 with a step of 0.005 for each simulated day and its sky condition class. The mean and most common (modes) range values that resulted in better performance for each sky condition class were retrieved and further tested obtaining the results shown in Table 5.

In the same manner, the number of neurons in the hidden layer was varied from 0 to 100 with a step of 1 and Table 6 shows the MSE results for the mean and most common values of number of neurons in the hidden layer (modes) that results in better performance for each sky condition.

The addition of the global solar radiation for clear sky conditions, hour, day and month in the inputs was tested resulting in the selection of the parameters defined in Table 7.

To validate the importance of the data selection for training and validation, 103 days were simulated using all data available or the data selected according to the clearness index range for training and validation. While the simulations of 103 days using all available data resulted in a MBE of 2.6 W/m^2 and MSE of 3366.3 W^2/m^4, when data for training and validation was restricted to days with similar clearness indexes to the day being simulated according to the clearness index range defined for these sky conditions, the MBE and MSE reduce to −0.1 W/m^2 and 3340.84 W^2/m^4, respectively.

The values of global solar irradiance in clear sky conditions were calculated using the ASHRAE model (ASHRAE Inc., 2005) for use as input to the ANN. This model was selected after a preliminary analysis

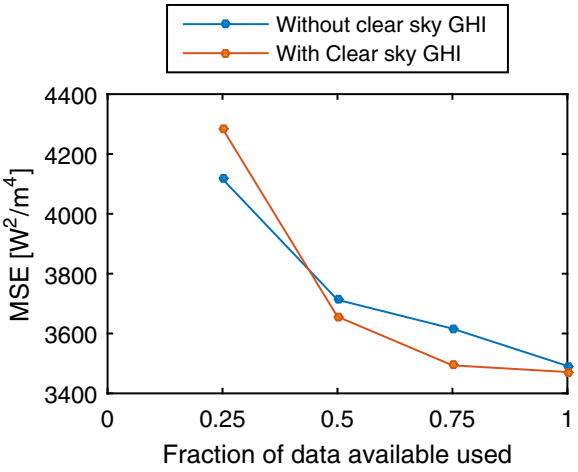

Fig. 7. MSE of the GHI simulations for 103 simulated days in Évora as a function of the data series length used for training and validation with and without the usage of clear sky GHI as input to the ANN.

of four different clear sky models that is presented in Appendix C. The usage of this variable as input according to Table 7 allowed to reduce MBE and MSE of the 103 simulated days from 1.7 W/m^2 and 3491.7 W^2/m^4 to −0.1 W/m^2 and 3340.84 W^2/m^4, respectively.

The corrective algorithm is executed every day and selects the ANN configuration according to the predicted daily clearness index calculated for the day to simulate, simulating the next three days. The selected ANN configuration (defined by the parameters referred in Tables 4 and 7) is executed resulting in corrected hourly values of GHI. These values are then downscaled as described in Section 3.1 to obtain half-hourly data. The forecasted and measured data in the first simulated day is stored in the dataset used for training and validation of the ANN so it can be used in the future.

It is expected that the continuous use and adding of data for training and validation will improve the performance of the developed ANN as shown in Fig. 7. There were 103 days simulated for Évora with different lengths of data series for training and validation and MSE for each percentage of data used was computed. Fig. 7 shows the MSE of the simulations for the cases of using and not using the predicted GHI as an ANN input according to Table 7. The input of the clear sky GHI improves the performance of the model except for when the percentage of data used for training and validation is only 25%. The figure also shows the improvement with the increment of data used for training and validation.

4. Results and analysis

The hourly simulations of GHI for each sunshine hour during the 103 days (from July to November 2016), were obtained using the methodology described in Section 3.4 for each location (Évora, Sines, Cabo da Roca and Penhas Douradas). The period from 24th June 2015 up to the eve of the day being simulated was used as the dataset for training and validation of the ANN.

The hourly results of the algorithm, S, were compared with the measurements, M, original predictions, P, and a persistence model, Pe, which assumes the value of measured GHI for the same hour of the eve. The comparison was made by computing 6 different metrics (Mean Bias Error - MBE, Mean Absolute Error - MAE, Root Mean Squared Error - RMSE, Uncertainty at 95% - U95, coefficient of determination - R^2 and T-statistics - TS, as presented in Appendix B) that were then combined into a global performance index (GPI) for each of the estimations of GHI (predicted, simulated and persistence) against measurements.

The GPI is a statistical tool that combines the individual metrics to allow for the comparison of the performance of different models and has been used in various works (e.g. Despotovic et al., 2015; Jamil and Akhtar, 2017; Sharifi et al., 2016). To compute this global metric, the n statistical indicators need to be normalized into values ranging from 0 to 1 and then Eq. (4) is applied, where the GPI value for the i^{th} model is determined using the median of the normalized values, $\tilde{y}_j$, of the indicator j, the normalized value of indicator j for model i, y_{ij}, and a factor α_j that has a value of 1 for all indicators except for the coefficient of determination for which is −1. A higher value of GPI represents better accuracy of the model.

$$GPI_i = \sum_{j=1}^{n} \alpha_j (\tilde{y}_j - y_{ij}) \tag{4}$$

The forecasting skill scores (FS) of the original predictions and of the algorithm simulations against the persistence model were also computed using the obtained RMSE values as shows Eq. (5) where the subscripts j and pe represent the model being evaluated and the persistence model, respectively.

$$FS_j = 1 - \frac{RMSE_j}{RMSE_{pe}} \tag{5}$$

This is a relative metric that evaluates the performance improvement of a model (regarding only the RMSE) when compared to a persistence model. Positive values of FS show an improvement of the analysed model over the persistence model where higher FS means a higher skill of the forecast model (Coimbra et al., 2013).

The performances of each ANN configuration for clear, partly cloudy and overcast sky were analysed for each measuring station.

Table 8 shows the number of simulated days, N, values of each metric used for the calculus of the GPI, the GPI for each model and the FS for ECMWF's model and the developed model for each sky condition. It should be taken into consideration that the sampling of overcast days is much lower than the sampling of partly cloudy and clear sky days, resulting in stronger conclusions for the latter.

Table 8 shows in general higher values of GPI and FS for the simulations in all cases except for Cabo da Roca under overcast conditions, where original predictions perform better (only 9 days). This indicates that the algorithm improves predictions in almost all cases with the value of GPI for all stations and conditions of 1.066 and a FS of 0.348 for simulations while for predictions is −1.874 and 0.282 respectively.

As expected the persistence is less performant, except for Sines, where the value of FS for the ECMWF's predictions shows that its RMSE is slightly better than the one of the persistence model but GPI (which considers all six metrics) is higher for persistence than for the original predictions. The low GPI of the original predictions is primarily due to a high bias which is probably caused by the fact that the Sines station is located very close to the seashore, where surface heterogeneity may induce local effects, namely mist and fog, not resolvable at the IFS resolution.

Regarding the GPI results it can also be concluded that the simulations have a higher accuracy when compared to the original predictions and persistence model for the station located in Sines followed by Penhas Douradas, Évora and finally Cabo da Roca. Concerning sky conditions, higher values of GPI were found for partly cloudy conditions followed by clear sky conditions and finally overcast conditions. This means that the ANN algorithm is better at improving GHI predictions in partly cloudy conditions. These conditions are characterised by scattered clouds in the sky, which are particularly difficult to predict by the NWP model.

Thus, the application of the ANN based algorithm to the IFS model output can improve the accuracy of GHI predictions, especially when the performance of the model is worse, namely under partly cloudy sky conditions.

Figs. 8 and 9 show modified Taylor diagrams adapted from the diagrams described in (Taylor, 2001). These are polar graphics in which the FS is the radial coordinate and the coefficient of correlation (R) is the azimuthal coordinate. In the figures, a variable SS is also shown

Table 8
Values of statistical metrics of predictions by the IFS (*P*), simulations made by the ANN (*S*) and modelled by the persistence model (*Pe*) for 103 days for each measuring site and sky condition. MBE, MAE, RMSE and U95 in W/m^2, N is the number of days simulated.

Conditions and metrics		Évora			Sines			Penhas Douradas			Cabo da Roca			All stations		
		P	*S*	*Pe*	*P*	*S*	Pe	*P*	*S*	*Pe*	*P*	*S*	Pe	*P*	*S*	*Pe*
Overcast	MBE	0.6	−6.7	89.6	11.6	17.3	130.1	17.5	10.8	69.4	−16.1	−30.2	87.9	3.5	−4.3	85.1
	MAE	61.0	57.5	117.3	62.0	62.1	137.4	70.4	60.3	110.8	59.2	57.5	132.2	64.3	59.0	121.0
	RMSE	92.4	91.7	171.3	103.8	83.1	207.2	116.1	102.1	187.0	93.3	94.1	205.8	103.6	95.8	191.3
	U95	256.7	254.4	442.3	288.6	229.4	516.9	320.4	282.5	500.8	257.1	254.6	544.9	287.2	265.6	503.5
	R^2	0.636	0.635	0.511	0.354	0.516	0.524	0.329	0.383	0.301	0.658	0.673	0.417	0.503	0.536	0.405
	TS	0.060	0.715	5.979	0.713	1.342	5.106	1.965	1.377	5.150	1.925	3.729	5.193	0.698	0.916	10.240
	GPI	0.115	0.154	−5.731	−0.759	0.372	−4.386	0.000	1.474	−4.526	0.560	0.208	−5.233	0.023	0.598	−5.379
	FS	0.461	0.465		0.499	0.599		0.379	0.454		0.547	0.543		0.458	0.499	
	N	7			3			12			9			31		
Partly cloudy	MBE	13.8	6.0	24.5	40.0	16.6	23.2	−20.5	−9.4	6.2	20.2	10.0	16.2	14.3	6.2	17.3
	MAE	55.6	58.8	83.0	84.4	74.2	94.2	95.2	82.7	110.1	74.6	73.6	109.3	78.3	73.0	100.2
	RMSE	108.4	108.3	142.5	146.8	124.5	156.2	144.3	132.3	195.7	114.1	111.2	187.3	129.9	119.6	173.4
	U95	299.6	300.3	392.5	399.6	343.8	430.9	398.4	366.6	542.7	314.1	307.8	518.4	359.1	331.3	479.6
	R^2	0.810	0.799	0.735	0.690	0.744	0.648	0.797	0.822	0.672	0.805	0.806	0.562	0.762	0.794	0.648
	TS	2.119	0.919	2.883	5.332	2.531	2.832	2.591	1.288	0.576	3.606	1.813	1.738	4.077	1.929	3.697
	GPI	0.271	1.034	−4.696	−1.609	2.814	−1.577	−0.232	0.995	−3.237	−1.356	0.708	−3.856	−0.177	2.344	−3.479
	FS	0.239	0.240		0.060	0.203		0.262	0.324		0.390	0.406		0.251	0.310	
	N	19			25			22			28			94		
Clear	MBE	5.4	−0.9	−8.3	43.0	8.0	−8.1	−22.8	7.0	−7.1	9.2	−8.3	−13.3	9.3	1.6	−9.2
	MAE	17.5	17.8	34.5	49.4	35.3	40.3	68.7	49.0	35.7	52.6	60.9	69.9	46.3	39.9	44.6
	RMSE	33.4	32.6	83.4	82.0	63.3	97.7	92.1	79.4	94.0	99.1	98.4	149.2	79.8	71.4	108.0
	U95	91.9	90.4	230.8	211.0	174.8	270.4	251.4	219.7	260.3	274.1	272.4	412.9	220.5	197.9	298.8
	R^2	0.991	0.990	0.938	0.958	0.962	0.911	0.958	0.958	0.941	0.920	0.922	0.826	0.948	0.958	0.906
	TS	5.709	1.003	3.521	21.321	4.403	2.890	8.495	2.949	2.504	3.068	2.761	2.945	7.972	1.506	5.773
	GPI	−0.896	0.561	−3.405	−2.251	1.364	−1.591	−0.994	1.191	−0.859	−0.699	0.641	−3.255	−1.024	2.039	−1.774
	FS	0.600	0.609		0.161	0.352		0.021	0.156		0.336	0.340		0.261	0.339	
	N	77			75			69			66			287		
All conditions	MBE	6.5	−0.1	3.2	41.5	10.1	2.4	−18.1	4.1	3.6	10.1	−5.3	1.8	10.0	2.2	2.8
	MAE	26.6	27.2	47.8	57.6	44.7	54.8	74.3	57.1	58.8	58.6	63.8	84.6	54.3	48.2	61.5
	RMSE	58.2	57.8	103.0	100.6	81.5	117.1	107.4	95.0	132.7	102.7	101.5	164.4	94.3	85.6	131.3
	U95	160.8	160.2	285.4	266.9	225.1	324.6	295.6	263.3	367.8	283.9	281.1	455.7	260.7	237.3	363.9
	R^2	0.968	0.967	0.899	0.920	0.933	0.863	0.926	0.934	0.875	0.903	0.905	0.765	0.920	0.934	0.851
	TS	4.510	0.060	1.232	18.083	5.008	0.822	6.845	1.706	1.098	3.939	2.107	0.435	8.508	2.044	1.678
	GPI	−1.202	0.771	−3.943	−1.776	1.921	−1.422	−0.813	0.843	−2.133	−0.861	0.508	−3.278	−1.874	1.066	−2.953
	FS	0.435	0.439		0.141	0.304		0.191	0.284		0.375	0.383		0.282	0.348	
	N	103			103			103			103			412		

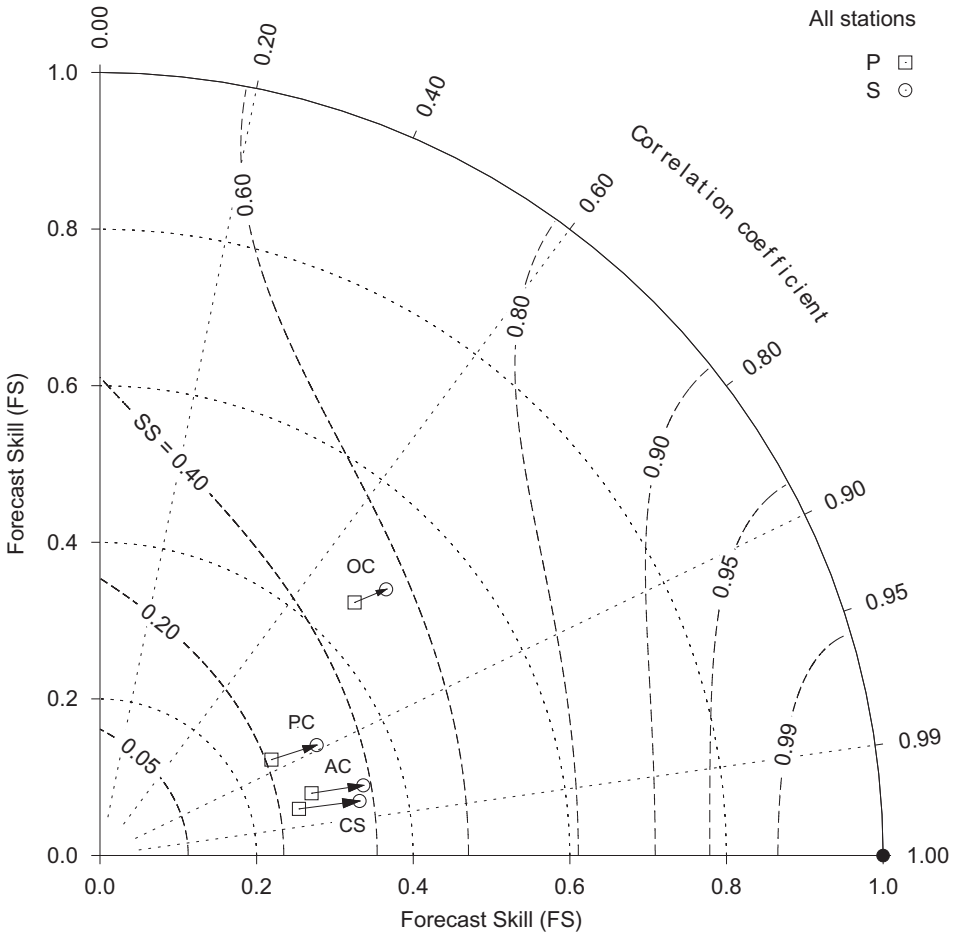

Fig. 8. Modified Taylor diagram with the results for the predictions, *P*, and simulations, *S*, for all stations and each sky condition: AC – all sky conditions; CS – clear sky; PC – partially cloudy; OC – overcast.

which represents a skill score determined as a function of FS and R (Taylor, 2001) through Eq. (6).

$$SS = \frac{4(1+R)}{(FS + 1/FS)^2(1 + max[R])} \quad (6)$$

This skill score is a measure of the closeness of the represented models to the observations using also the persistence model as a reference through the forecast score. The closer the SS value is to unity the better is the forecast, and so, better results show closer to the black dot with coordinates (FS = 1, R = 1). Since model closeness to observation is the distance to this point, the proposed definition of SS weights the FS and R in a way that the skill score still increases when FS increases even for lower values of R.

Fig. 8 shows the modified Taylor diagram for the results obtained for all stations and for each class of sky conditions. It can be clearly seen the increase in FS and SS resulting from the usage of the ANN and a small increase in R. The predictions and simulations are shown to be worse for partially cloudy conditions since these are the conditions which are more difficult to predict by the NWP model followed by all conditions, clear sky conditions and, finally, overcast conditions show higher SS (for which the data available for training and validation was limited).

Fig. 9 shows the results for all conditions and each station. It is verified that the usage of the ANN has higher impact for the stations of Sines and Penhas Douradas that result in simulations with a SS and FS closer to the values for Évora and Cabo da Roca, which already had higher SS and FS for the predictions. It can also be observed that predictions and simulations are better for the station of Évora followed by Cabo da Roca, Penhas Douradas and finally Sines.

Examples of the correction of hourly GHI forecasts for all stations and different sky conditions are shown in Fig. 10 and the respective statistical indicators in Table 9.

By comparing the errors, it can be seen if the simulations are better (E_s closer to zero than E_{pe} and E_p) than the original predictions and the persistence model.

The algorithm does not always result in values of GHI closer to measurements than the predictions made by the IFS, partly because the ANNs performance depends on the amount of data available for training and validation and this testing procedure had few data to work with.

Fig. 10a.1 presents a clear sky day for Évora. All models show values consistent with the measurements, but it can be observed (Fig. 10a.2) that the ANN simulation is closer to the measurements. Fig. 10b.1 shows a clear sky day for Sines. The large errors (Fig. 10b.2) given by the persistence model indicate that the previous day was not a clear sky day. The differences in the early morning are due to the horizon line near the radiometer. In this case the simulations are once again the closest to the observations, showing a successful correction of the predictions of GHI made by the IFS.

Fig. 10c.1 shows a partly cloudy day at Cabo da Roca. As mentioned before, precise GHI predictions in cloudy conditions are rather difficult to produce due to the variability of the atmospheric conditions. In these shifting conditions, hourly forecasts produced by NWP models are affected by the so-called double-penalty, due to the impact of small phase errors in time and space. The simulation results tend to follow the original predictions but with values closer to the observations.

Fig. 10d.1 presents an example of an overcast day at Penhas Douradas. The persistence model for this day shows a high bias with

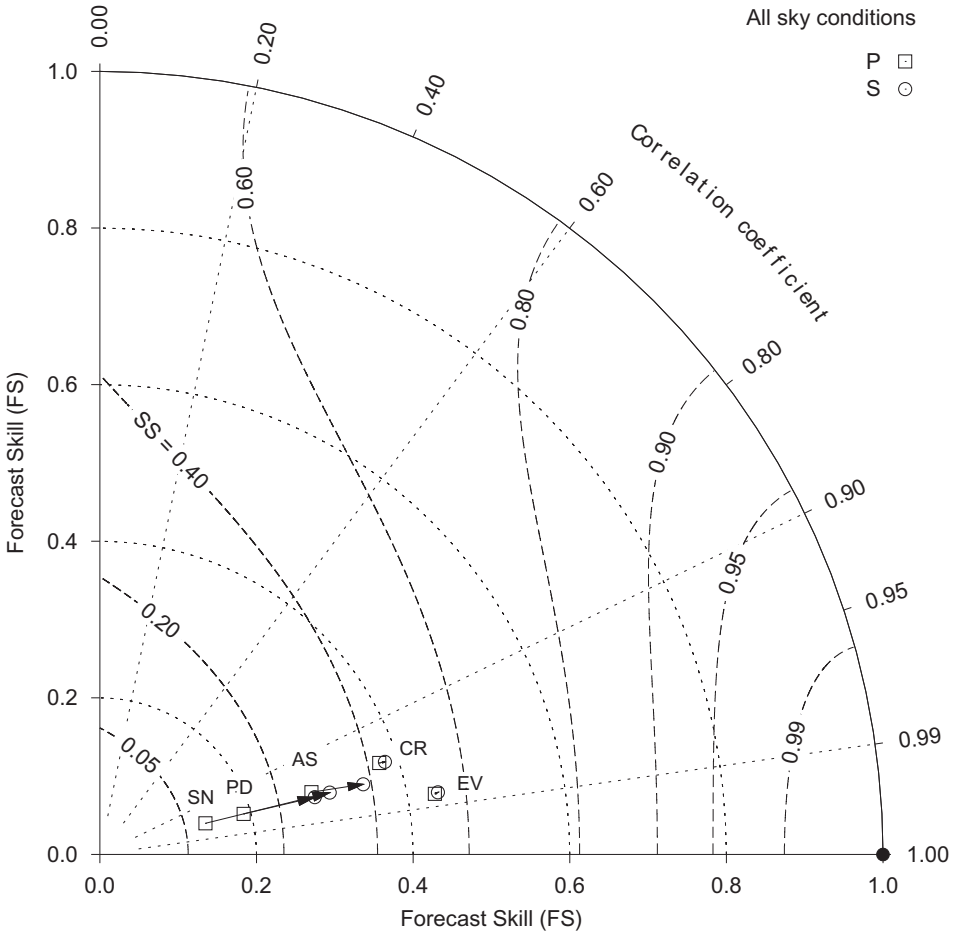

Fig. 9. Modified Taylor diagram with the results for the predictions, *P*, and simulations, *S*, for all sky conditions and each station: AS – all stations; EV – Évora; SN – Sines; PD – Penhas Douradas; CR – Cabo da Roca.

respect to the measurements since the previous day was not overcast. The simulation curve follows the measurement curve and is closer to the observations than the original predictions, a fact supported by the metrics shown in Table 9.

5. Conclusions

An algorithm developed for the correction of ECMWF's model predictions of GHI is presented. The algorithm was developed and validated using data from four Portuguese radiometric stations.

First, a direct comparison between a year and a half of predictions and measurements of GHI was performed for two measuring stations (Évora and Sines). GHI forecasts obtained from the IFS showed to be more accurate for clear sky conditions, slightly underestimating the value of GHI with MBE ranging from -6.46 to $-9.14\,W/m^2$. The model also tends to perform slightly better for the first day of forecasts followed by the second and third days, with absolute MBE and RMSE values increasing with forecasting time horizon. The IFS performance decreases for partly cloudy and overcast skies because the model presents limitations with respect to the representation of cloud type and fraction that strongly affect the solar radiation reaching the surface.

In order to develop a corrective algorithm, the influence of atmospheric and Sun-Earth geometry related variables in the prediction errors relative to the measurements was analysed. It is shown that the errors are higher, thus have a greater impact on the harvesting and conversion of energy, when the clearness index is between 40% and 70% and near solar noon. The errors of predicted GHI showed a relation with the predicted values of mean air temperature (higher errors for higher values of mean air temperature), relative air humidity (higher errors for lower relative air humidity) and total water column (higher errors for higher values of total water column).

A corrective algorithm based on ANN was developed consisting of three ANN configurations that run according to the predicted clearness index. 103 days were simulated for the four locations (Évora, Sines, Penhas Douradas and Cabo da Roca). It was shown that, by using clear sky GHI as input and applying different ANN configurations according to the sky conditions, improvemets in MBE and MSE were obtained. For the validation of the developed algorithm a global performance index (GPI) that considers various metrics and shows the improvement that the ANN brings over the original predictions, the Forecast Score (FS) that shows the improvement regarding RMSE over the persistence model and a Skill Score (SS) that shows which sky conditions and stations have better results regarding FS and R metrics, were used. GPI, FS and SS values showed that the corrective algorithm can improve GHI predictions made by the IFS. Higher values of GPI are found when the accuracy of the IFS model is lower, namely under partly cloudy sky conditions and for locations at the land-sea boundary. The GPI of the corrective algorithm was higher (the improvement that the ANN brought over the IFS predictions was higher) for the station of Sines followed by Penhas Douradas, Évora and finally Cabo da Roca, and for partly cloudy sky conditions followed by clear sky conditions and finally overcast conditions. As for the SS it showed that better predictions and simulations are found for the station of Évora followed by Cabo da Roca, Penhas Douradas and Sines and for overcast sky conditions followed by clear sky conditions and partially cloudy conditions.

This algorithm can be included in energy conversion and management models of medium/low temperature solar thermal and photovoltaic systems, which will allow for better management of the renewable energy and a better design and usage of conventional auxiliary systems. As the developed methodology is based on machine learning it

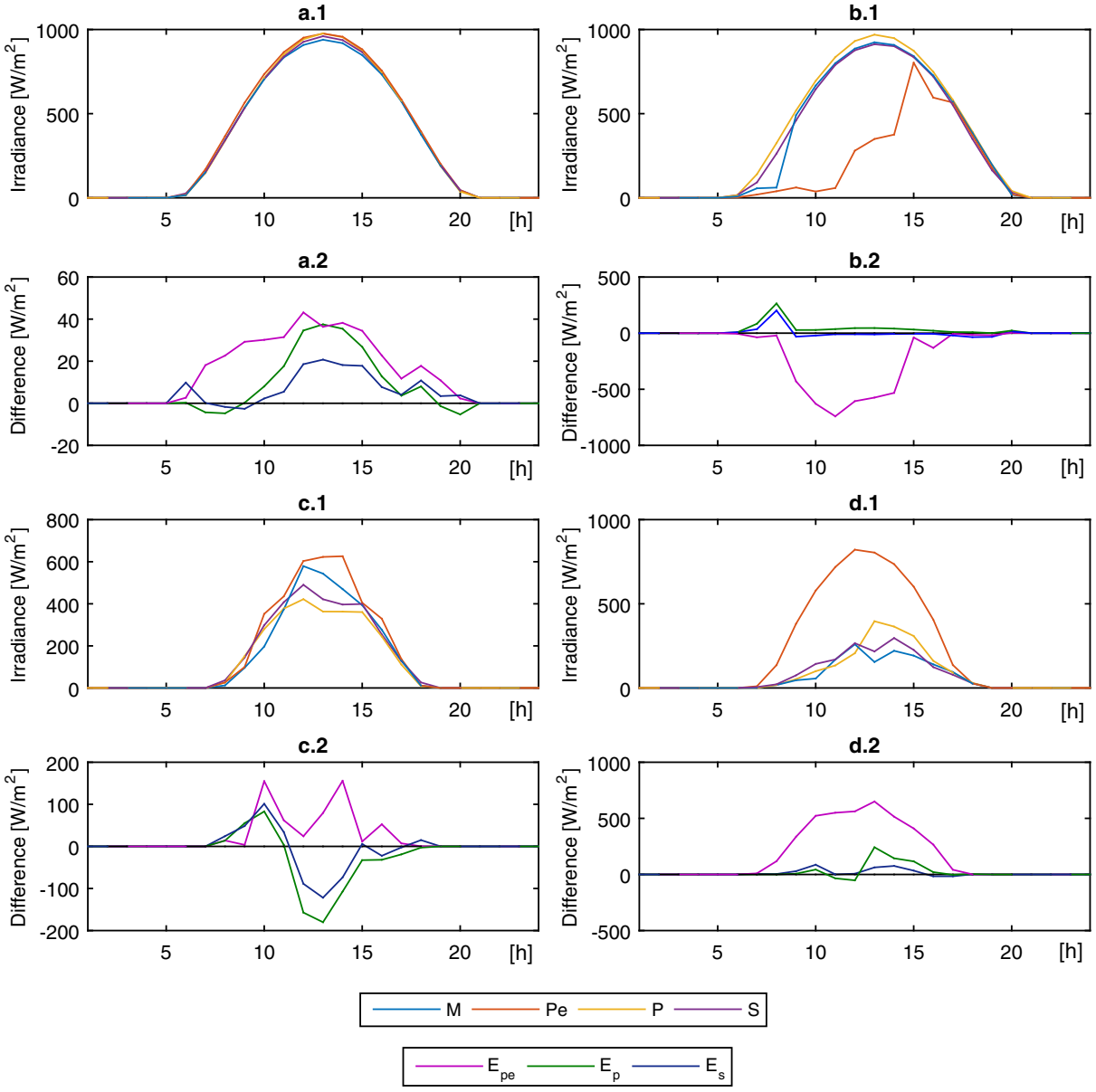

Fig. 10. Example of correction of the predicted hourly mean global horizontal irradiance: (a) Évora, 15th July 2016, clear sky day; (b) Sines, 8th July 2016, clear sky day; (c) Cabo da Roca, 8th November 2016, partly cloudy day; (d) Penhas Douradas, 12th October 2016, overcast day; (1) hourly mean global horizontal irradiance measured (M), from the persistence model (Pe), predicted (P), and simulated by the ANN (S); (2) hourly E_{pe} (difference between modelled by the persistence and measured global horizontal irradiance), E_p and E_s.

Table 9
Values of the statistical metrics computed for predictions by the IFS (P), simulations made by the ANN (S) and modelled by the persistence model (Pe) for the examples of Fig. 10.

Site and model		MBE [W/m^2]	MAE [W/m^2]	RMSE [W/m^2]	U95 [W/m^2]	R^2	TS	GPI	FS	Date and skycondition
Évora	*P*	10.0	11.8	17.6	45.3	1.000	2.745	−0.479	0.293	15/07/2016 Clear sky
	S	7.0	7.5	10.2	25.2	1.000	3.715	1.694	0.588	
	Pe	20.7	20.7	24.9	56.2	1.000	5.993	−2.784		
Sines	*P*	39.7	39.7	71.8	185.6	0.972	2.650	−0.136	0.797	08/07/2016 Clear sky
	S	4.0	26.6	52.5	147.5	0.980	0.305	0.997	0.852	
	Pe	−222.6	222.9	354.1	889.5	0.415	3.233	−3.139		
Cabo da Roca	*P*	−28.9	52.8	79.1	215.8	0.910	1.360	−2.285	−0.143	08/11/2016 Partly cloudy sky
	S	−6.2	41.4	57.7	162.7	0.938	0.374	1.354	0.166	
	Pe	43.5	43.5	69.2	174.4	0.961	2.803	−0.827		
Penhas Douradas	*P*	34.8	47.7	84.2	227.0	0.700	1.637	−0.126	0.774	12/10/2016 Overcast sky
	S	19.5	24.2	37.6	98.5	0.904	2.186	1.115	0.899	
	Pe	284.4	284.4	372.9	880.2	0.769	4.251	−4.338		

is expected that its continued use and adding of data will increasingly improve its performance. Also, if measurements become available in a nearby location of interest and are incorporated in the ANN, then the corrective algorithm will further improve the GHI predictions.

Acknowledgments

This work was carried out under the contract with the company Warmhole, lda for the development of a solar radiation forecast algorithm. The authors wish to acknowledge ECMWF and IPMA for providing the data. This work was also funded by the European Regional Development Fund, included in the COMPETE 2020 (Operational Program Competitiveness and Internationalization) through the ICT project (UID/GEO/04683/2013) with the reference POCI-01-0145-FEDER-007690, and the projects DNI-ALENTEJO (ALT20-03-0145-FEDER-000011) and ALOP (ALT20-03-0145-FEDER-000004).

Appendix A. Spatial and temporal downscaling methods

The bi-linear interpolation downscaling method was used in this paper. To obtain a downscaled value of a variable, V, two interpolations in latitude, L, were done using Eq. (A.1), which produces the values of the variable to the west (V_{west}) and east (V_{east}) and these results are then interpolated in longitude, Lon, using Eq. (A.2).

$$V_{west;east} = V_{north} - (V_{north} - V_{south})\frac{L_{north} - L_{site}}{L_{north} - L_{south}} \tag{A.1}$$

$$V = V_{east} - \frac{Lon_{east} - Lon_{site}}{Lon_{east} - Lon_{west}}(V_{east} - V_{west}) \tag{A.2}$$

The temporal downscaling method developed preserves the hourly solar irradiation value, I_i, for the hour i. A schematic representation of the downscaling can be seen in Fig. A1, where $J_{i-1/2}$ and J_i are the half-hourly irradiation values for the first and second half-hours of the hour i, respectively, thus $I_i = J_{i-1/2} + J_i$.

For any hour of the day, except the hours during which the sunrise and sunset occur, (represented in Fig. A1.b)) the half-hourly values of irradiation, J, for an hour with irradiation I_i, are estimated using two linear interpolations with the values of irradiation from the previous (I_{i-1}) and next (I_{i+1}) hours as given by the systems of Eqs. (A.3) and (A.4), respectively.

$$\begin{cases} J_{i-1/2}^{-} = \frac{1}{2}I_i\left(1 + \frac{1}{2}\frac{I_{i-1} - I_i}{I_{i-1} + I_i}\right) \\ J_i^{-} = I_i - J_{i-1/2}^{-} \end{cases} \tag{A.3}$$

$$\begin{cases} J_i^{+} = \frac{1}{2}I_i\left(1 + \frac{1}{2}\frac{I_{i+1} - I_i}{I_{i+1} + I_i}\right) \\ J_{i-1/2}^{+} = I_i - J_i^{+} \end{cases} \tag{A.4}$$

Then, by averaging these estimations (Eq. (A.5)), the system of Eq. (A.6) is obtained for the irradiation in each half-hour of the hour i.

$$\begin{cases} J_{i-1/2} = \frac{1}{2}(J_{i-1/2}^{+} + J_{i-1/2}^{-}) \\ J_i = \frac{1}{2}(J_i^{+} + J_i^{-}) \end{cases} \tag{A.5}$$

$$\begin{cases} J_{i-1/2} = \frac{1}{2}I_i\left[1 - \frac{1}{4}\left(\frac{I_{i+1} - I_i}{I_{i+1} + I_i} + \frac{I_i - I_{i-1}}{I_i + I_{i-1}}\right)\right] \\ J_i = \frac{1}{2}I_i\left[1 + \frac{1}{4}\left(\frac{I_{i+1} - I_i}{I_{i+1} + I_i} + \frac{I_i - I_{i-1}}{I_i + I_{i-1}}\right)\right] \end{cases} \tag{A.6}$$

When the sunrise and sunset occur, a different approach is needed. In the case of sunrise, if it occurs in the second half-hour of the hour of sunrise, then the value of irradiation for the first half-hour is zero and the value of irradiation for the second half hour is equal to the hourly irradiation. In order to compute the half hourly irradiation when the sunrise occurs in the first half hour as shown in Fig. A1a), a linear variation of the solar irradiance was assumed and thus the irradiation is given by Eq. (A.7). The irradiance value a (Eq. (A.8)) is determined through a linear interpolation between the sunrise (irradiance is assumed to be zero) and the hour i while b' (irradiance at hour i) is determined through energy conservation (Eq. (A.9)), in which x is the fraction of the hour from the hour $i - 1$ and the sunrise. The irradiation before the sunrise (twilight) is assumed to be zero. By combining Eqs. (A.7), (A.8) and (A.9), the half-hour irradiation is determined through Eq. (A.10), with x calculated for the day of the year and location of interest.

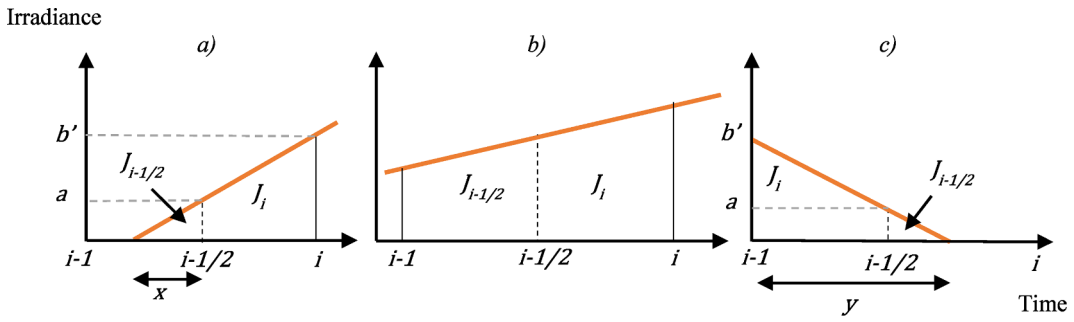

Fig. A1. Schematic representation of temporal downscaling of irradiation from hourly to half-hourly values: (a) sunrise occurs in the first half-hour; (b) hours during the day; (c) sunset occurs in the second half-hour.

$$\begin{cases} J_{i-1/2} = \frac{a(1/2-x)}{2} \\ J_i = \frac{1}{2}a + \frac{1/2(b'-a)}{2} \end{cases} \quad (A.7)$$

$$a = \frac{2I_i}{(1-x)^2}(1/2-x) \quad (A.8)$$

$$b^{'} = \frac{2I_i}{1-x} \quad (A.9)$$

$$\begin{cases} J_{i-1/2} = \frac{(1/2-x)^2}{(1-x)^2} I_i \\ J_i = \frac{3/4-x}{(1-x)^2} I_i \end{cases} \quad (A.10)$$

A similar approach was used for the hours during which sunset occurs. If the sunset is in the first half hour, then the irradiation of that half hour is equal to the hourly irradiation and the irradiation in the second half-hour is zero. When sunset occurs in the second half hour as shown in Fig. A1c), similar equations were developed, taking into account the energy conservation and assuming a linear variation of the irradiance. Considering the area under the curve (irradiation), the system of Eq. (A.11) can be obtained, resulting in the system of Eq. (A.12), with y the fraction of the hour from the instant $i-1$ to the sunset, assuming a value between 0.5 and 1, and where the irradiance a(Eq. (A.13)) is determined through linear interpolation between the hour i and sunset (irradiance is assumed to be zero) while b' (irradiance at hour i) is determined through energy conservation (Eq. (A.14)). Again, the half-hour values respect the hourly irradiation.

$$\begin{cases} J_{i-1/2} = \frac{1}{2}a + \frac{1/2(b'-a)}{2} \\ J_i = \frac{a(y-1/2)}{2} \end{cases} \quad (A.11)$$

$$\begin{cases} J_{i-1/2} = \frac{y-1/4}{y^2} I_i \\ J_i = \frac{(y-1/2)^2}{y^2} I_i \end{cases} \quad (A.12)$$

$$a = \frac{2y-1}{y^2} I_i \quad (A.13)$$

$$b^{'} = \frac{2I_i}{y} \quad (A.14)$$

Appendix B. Error metrics

For the development of this work different error metrics were taken into account.

For a first evaluation of the predictions made by the IFS and simulations made by the ANN model the obtained values were directly compared with observed data using the prediction error (Eq. (B.1)), which represents the difference between predictions, P, and measurements, M, and the simulation error (Eq. (B.2)), which represents the difference between simulations made by the ANN model, S, and measurements.

$$E_p = P - M \quad (B.1)$$

$$E_s = S - M \quad (B.2)$$

These errors lead to the usage of the mean bias error as well as 5 other error metrics to be used for the evaluation of the final ANN algorithm.

The mean bias errors (MBE) of predictions or simulations are computed by averaging the hourly prediction or simulation errors respectively (Eq. (B.3)), where γ represents a variable that can either be the predictions P or simulations S.

$$MBE_\gamma = \gamma - \bar{M} = \bar{E_\gamma} \quad (B.3)$$

The mean absolute error (MAE) is obtained by averaging the absolute hourly prediction or simulation errors (B.4).

$$MAE_\gamma = |\bar{E_\gamma}| \quad (B.4)$$

The root mean squared error (RMSE, Eq. (B.5)) is the squared root of the mean squared error (MSE, Eq. (B.6)), which is computed by performing the mean of the squares of the prediction or simulation errors obtained for each hour i. The MSE is the indicator used as performance function for the training and validation of the ANN. In the case of the developed ANN, its training and validation stops after 20 validation checks for which the MSE has failed to decrease.

$$RMSE_\gamma = \sqrt{MSE_\gamma} \quad (B.5)$$

$$MSE_\gamma = \bar{E_\gamma^2} \quad (B.6)$$

The Uncertainty at 95% (U95) is computed through Eq. (B.7) using the standard deviation (SD) and RMSE and represents the uncertainty with a 95% confidence level, which means that the lower its value the better the performance of the evaluated model.

$$U95_\gamma = 1.96\sqrt{SD_\gamma^2 + RMSE_\gamma^2} \quad (B.7)$$

The coefficient of determination, R^2, is the square of the coefficient of correlation, R, and is computed through Eq. (B.8). This coefficient

represents the fraction of the predicted or simulated values that are closest to the line of measurement data. For this metric, higher values (closer to 1) indicate higher performance of the model being evaluated.

$$R_\gamma^2 = \left(\frac{n\sum \gamma M - \sum \gamma \sum M}{\sqrt{n(\sum \gamma^2) - (\sum \gamma)^2}\sqrt{n(\sum M^2) - (\sum M)^2}} \right)^2 \tag{B.8}$$

Finally, the T-statistics (TS) is a metric whose higher value shows higher performance of the evaluated model just like any other metric presented in this section with the exception of the coefficient of determination. This metric uses the MBE and RMSE values and is computed through Eq. (B.9) where n is the number of elements.

$$TS_\gamma = \sqrt{\frac{(n-1)MBE_\gamma^2}{RMSE_\gamma^2 - MBE_\gamma^2}} \tag{B.9}$$

As explained in Section 4, these error metrics were combined into a Global Performance Indicator GPI, a forecasting skill score (FS) was also computed which is based on RMSE values, and a skill score (SS) that combines the FS and R metrics for the final evaluation of the developed model.

Appendix C. Clear sky model

The usage of clear sky irradiation as an input to the ANN was considered. A clear sky model produces an estimate of the solar irradiance that reaches the surface of the Earth in clear sky conditions (Engerer and Mills, 2015). These models are characterized for allowing the estimation of global solar irradiation using only readily available and/or offline calculated variables as inputs without the need for measurements. Four different clear sky models were analysed: Fu and Rich (Fu and Rich, 1999), HLJ (Hottel, 1976; Liu and Jordan, 1960), ASHRAE (ASHRAE Inc., 2005) and SMARTS (Gueymard, 2005).

The Fu and Rich model (Fu and Rich, 1999) is the simplest of the models analysed, using only as input the day of the year, *ND,* the solar zenith angle, Φ, and the altitude. This model computes direct normal irradiance, I_{bn}, in W/m^2 through Eq. (C.1) where T_b represents the atmospheric transmissivity (with a recommended value of 0.5), m_f is the corrected air mass with altitude, Z, in meters, obtained from Eq. (C.2) and I_{0n} is the irradiance on the top of the atmosphere in a plane normal to the sun's rays as given by Eq. (C.3), and in which I_{sc} = 1367 W/m^2 is the solar constant and ND is the day of the year.

$$I_{bn} = I_{0n} T_b^{m_f} \tag{C.1}$$

$$m_f = \frac{e^{-0{,}000118Z - 1{,}638\times10^{-9}Z^2}}{\cos(\Phi)} \tag{C.2}$$

$$I_{0n} = I_{sc}\left[1 + 0{,}033\cos\left(\frac{360ND}{365}\right)\right] \tag{C.3}$$

The diffuse irradiance, I_d, in W/m^2, is computed through Eq. (C.4), where R has a recommended value of 0.3. The global irradiance, I_g, is then obtained from Eq. (C.5).

$$I_d = I_{bn}\cos(\Phi)\left(\frac{R}{1-R}\right) \tag{C.4}$$

$$I_g = \left(1 + \frac{R}{1-R}\right) I_{0n} T_b^{m_f}\cos(\Phi) \tag{C.5}$$

The HLJ model was developed by Hottel (1976) and Liu and Jordan (1960) and has as inputs the solar zenith angle, the altitude of the location (in km) and the type of climate defined as one of four types shown in Table C.1. The atmospheric transmissivity is computed through Eq. (C.6) where a_0, $a_1$and k are parameters calculated using the variables a_0^*, a_1^* and k^* determined through Eq. (C.7), (C.8) and (C.9), respectively, which are corrected using the factors shown in Table C.1 by applying the relations $r_0 = a_0/a_0^*$, $r_1 = a_1/a_1^*$ and $r_k = k/k^*$. Direct normal irradiance is then calculated through Eq. (C.10).

$$T_b = a_0 + a_1 e^{\frac{-k}{\cos(\phi)}} \tag{C.6}$$

$$a_0^* = 0{,}4237 - 0{,}00821(6 - Z)^2 \tag{C.7}$$

$$a_1^* = 0{,}5055 + 0{,}00595([6{,}5 - Z)]^{\ 2} \tag{C.8}$$

$$k^* = 0{,}2711 + 0{,}01858(2{,}5 - Z)^2 \tag{C.9}$$

$$I_{bn} = I_{on} T_b \tag{C.10}$$

Table C1
Correction factors for different climate types for HLJ model (Hottel, 1976; Liu and Jordan, 1960).

Climate type	r_0	r_1	r_k
Tropical	0.95	0.98	1.02
Mid-latitude summer	0.97	0.99	1.02
Mid-latitude winter	1.03	1.01	1.00
Subarctic summer	0.99	0.99	1.01

Table C2
Coefficients of the ASHRAE model for the 21st day of each month. (ASHRAE, 1972).

Month	A_m [W/m^2]	B_m	C_m
January	1229.475	0.142	0.058
February	1213.713	0.144	0.060
March	1185.340	0.156	0.071
April	1134.900	0.180	0.097
May	1103.375	0.196	0.121
June	1087.613	0.205	0.134
July	1084.460	0.207	0.136
August	1106.528	0.201	0.122
September	1150.663	0.177	0.092
October	1191.645	0.160	0.073
November	1220.018	0.149	0.063
December	1232.628	0.142	0.057

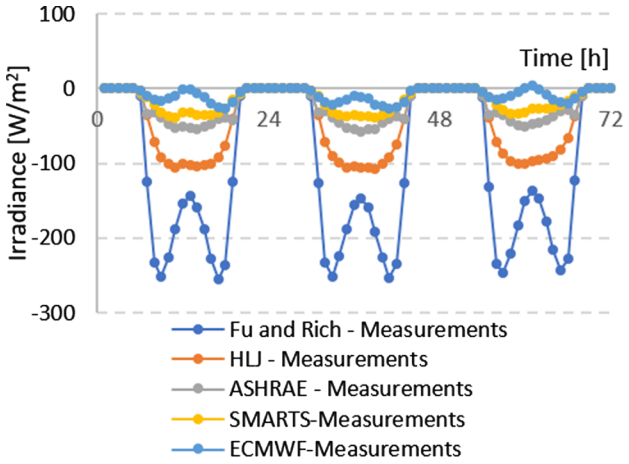

Fig. C1. Hourly errors for each clear sky model in W/m^2 for the days 1, 2 and 3 of May 2016 in Évora.

For the determination of the diffuse irradiance on a horizontal surface an empiric expression, Eq. (C.11), that correlates the transmission coefficient of the direct beam radiation with the transmission coefficient for the diffuse radiation T_{df} in clear sky conditions, thus allowing the calculus of the diffuse irradiance through Eq. (C.12) and consequently the determination of global solar irradiance through Eq. (C.13).

$$T_{df} = 0,271 - 0,294T_b \tag{C.11}$$

$$I_d = I_{on} T_{df} \cos(\phi) \tag{C.12}$$

$$I_g = (T_b + T_{df}) I_{on} \cos(\phi) \tag{C.13}$$

The ASHRAE model (ASHRAE Inc., 2005) is commonly used in engineering, energy analysis in buildings and for calculations of solar irradiation in simple solar systems (Gueymard, 2012). This model is based on empirical studies (ASHRAE, 1972) and the direct normal irradiance is computed through Eq. (C.14), where A_m e B_m are monthly coefficients presented in Table C.2. The diffuse irradiance is obtained from Eq. (C.15) using another monthly coefficient, C_m, and the direct normal irradiance, while the global solar irradiance is obtained through Eq. (C.16).

$$I_{bn} = A_m e^{-B_m/\cos(\Phi)} \tag{C.14}$$

$$I_d = C_m I_{bn} \tag{C.15}$$

$$I_g = [\cos(\phi) + C_m] A_m e^{-B_m/\cos(\Phi)} \tag{C.16}$$

The SMARTS model is a FORTRAN code developed for different clear sky solar energy applications (Gueymard, 2005). It is a spectral model that amongst other variables can estimate spectral and broadband values of irradiance. The formulae used for determining the atmosphere transmissivity and a detailed description of the model can be found in (Myers and Gueymard, 2004). For this study the main inputs used were the variables relative to time and location, a reference atmosphere according to the season, volumetric concentration of CO_2, the aerosol model (rural for Évora and maritime for Sines), the aerosol optical thickness and the albedo. The model output comprises variables related to the sun position, optical thickness, gas concentrations like carbon dioxide, methane, oxygen or ozone and extra-terrestrial, direct normal, direct horizontal, diffuse and global horizontal irradiances.

All these clear sky models were run for the period of 3 days of clear sky conditions (1, 2 and 3 of May 2016) for Évora and Sines and compared to measurements of global solar irradiation in these locations as well as with bi-linear interpolated values of forecasts made by the IFS, as shown in Fig. C1. For this specific period the less accurate predictions are made by Fu and Rich model followed by HLJ model. As expected, the model developed by ECMWF is the most accurate followed by the radiative transfer model SMARTS and ASHRAE model.

In this work a clear sky model was used as input of ANNs for the correction of GHI forecasts made by the IFS. Since the algorithm using this type of model must be rather accessible and fast to run, the chosen clear sky model was ASHRAE due to its simplicity and relatively good accuracy in typical clear sky conditions.

References

Alessandrini, S., Delle Monache, L., Sperati, S., Cervone, G., 2015. An analog ensemble for short-term probabilistic solar power forecast. Appl. Energy 157, 95–110. https://doi.org/10.1016/J.APENERGY.2015.08.011.

Amrouche, B., Le Pivert, X., 2014. Artificial neural network based daily local forecasting for global solar radiation. Appl. Energy 130, 333–341. https://doi.org/10.1016/j.apenergy.2014.05.055.

Anderson, E., 2015. User Guide for ECMWF forecast products. ECMWF.

Anderson, W.W., Yakimenko, O.A., 2018. Using neural networks to model and forecast solar PV power generation at Isle of Eigg. In: 2018 IEEE 12th International Conference on Compatibility, Power Electronics and Power Engineering (CPE-POWERENG 2018). IEEE, pp. 1–8. https://doi.org/10.1109/CPE.2018.8372522.

ASHRAE, 1972. Handbook of Fundamentals, pp. 1–602.

ASHRAE, 2005. ASHRAE Handbook of fundamentals, pp. 1–845.

Blaga, R., Sabadus, A., Stefu, N., Dughir, C., Paulescu, M., Badescu, V., 2019. A current perspective on the accuracy of incoming solar energy forecasting. Prog. Energy Combust. Sci. https://doi.org/10.1016/j.pecs.2018.10.003.

Chu, Y., Urquhart, B., Gohari, S.M.I., Pedro, H.T.C., Kleissl, J., Coimbra, C.F.M., 2015. Short-term reforecasting of power output from a 48 MWe solar PV plant. Sol. Energy 112, 68–77. https://doi.org/10.1016/j.solener.2014.11.017.

Coimbra, C.F.M., Kleissl, J., Marquez, R., 2013. Overview of solar-forecasting methods and a metric for accuracy evaluation. Sol. Energy Forecasting Resource Assess. 171–194. https://doi.org/10.1016/B978-0-12-397177-7.00008-5.

Cornaro, C., Pierro, M., Bucci, F., 2015. Master optimization process based on neural networks ensemble for 24-h solar irradiance forecast. Sol. Energy 111, 297–312. https://doi.org/10.1016/j.solener.2014.10.036.

Despotovic, M., Nedic, V., Despotovic, D., Cvetanovic, S., 2015. Review and statistical analysis of different global solar radiation sunshine models. Renew. Sustain. Energy Rev. 52, 1869–1880. https://doi.org/10.1016/j.rser.2015.08.035.

Dimopoulou, S., Oppermann, A., Boggasch, E., Rausch, A., 2016. Forecasting of photovoltaic power at hourly intervals with artificial neural networks under fluctuating. Energies 1–13.

Do, M.-T., Soubdhan, T., Robyns, Benoît, 2016. A study on the minimum duration of training data to provide a high accuracy forecast for PV generation between two different climatic zones. Renew. Energy 85, 959–964. https://doi.org/10.1016/J.RENENE.2015.07.057.

ECMWF, 2016. Part IV: Physical Processes. IFS Doc. – Cy38r1 3–213.

Engerer, N.A., Mills, F.P., 2015. Validating nine clear sky radiation models in Australia. Sol. Energy 120, 9–24. https://doi.org/10.1016/j.solener.2015.06.044.

Fleetwood, A., Galarza, A., 2018. Predicting solar energy generation through arti fi cial neural networks using weather forecasts for microgrid control. 126, pp. 855–864. https://doi.org/10.1016/j.renene.2018.03.070.

Fu, P., Rich, P., 1999. Design and implementation of the Solar Analyst: an ArcView extension for modeling solar radiation at landscape scales. In: 19th Annual ESRI User Conference.

Ghimire, S., Deo, R.C., Downs, N.J., Raj, N., 2019. Global solar radiation prediction by ANN integrated with European Centre for medium range weather forecast fields in solar rich cities of Queensland Australia. J. Clean. Prod. 216, 288–310. https://doi.org/10.1016/J.JCLEPRO.2019.01.158.

Gigoni, L., Betti, A., Crisostomi, E., Franco, A., Tucci, M., Bizzarri, F., Mucci, D., 2018. Day-ahead hourly forecasting of power generation from photovoltaic plants. IEEE Trans. Sustain. Energy 9, 831–842. https://doi.org/10.1109/TSTE.2017.2762435.

Gueymard, C.A., 2012. Clear-sky irradiance predictions for solar resource mapping and large-scale applications: Improved validation methodology and detailed performance analysis of 18 broadband radiative models. Sol. Energy 86, 2145–2169. https://doi.org/10.1016/j.solener.2011.11.011.

Gueymard, C.A., 2005. USER' S MANUAL SMARTS.

Hachicha, A.A., Rodríguez, I., Capdevila, R., Oliva, A., 2013. Heat transfer analysis and numerical simulation of a parabolic trough solar collector. Appl. Energy 111, 581–592. https://doi.org/10.1016/j.apenergy.2013.04.067.

Hottel, H.C., 1976. A simple model for estimating the transmittance of direct solar radiation through clear atmospheres. Sol. Energy 129–134.

Huang, J., Rikus, L.J., Qin, Y., Katzfey, J., 2018. Assessing model performance of daily solar irradiance forecasts over Australia. In: Solar Energy. Elsevier, pp. 615–626. https://doi.org/10.1016/j.solener.2018.10.080.

Iacono, M.J., Delamere, J.S., Mlawer, E.J., Shephard, M.W., Clough, S.A., Collins, W.D., 2008. Radiative forcing by long-lived greenhouse gases: Calculations with the AER radiative transfer models. J. Geophys. Res. 113, D13103. https://doi.org/10.1029/2008JD009944.

International Organization for Standardization [ISO], 1990. ISO 9060:1990. Solar energy – Specification and classification of instruments for measuring hemispherical solar and direct solar radiation.

Jamil, B., Akhtar, N., 2017. Comparative analysis of diffuse solar radiation models based on sky-clearness index and sunshine period for humid-subtropical climatic region of India: A case study. Renew. Sustain. Energy Rev. 78, 329–355. https://doi.org/10.1016/j.rser.2017.04.073.

Kalogirou, S., 2009. Solar Energy Engineering, pp. 1–701.

Keeley, S., 2013. Atmospheric Physics [WWW Document]. URL http://www.ecmwf.int/en/research/modelling-and-prediction/atmospheric-physics.

Khosravi, A., Koury, R.N.N., Machado, L., Pabon, J.J.G., 2018. Prediction of hourly solar radiation in Abu Musa Island using machine learning algorithms. J. Clean. Prod. 176, 63–75. https://doi.org/10.1016/j.jclepro.2017.12.065.

Lachtermacher, G., David Fuller, J., 1994. Backpropagation in hydrological time series forecasting. pp. 229–242. https://doi.org/10.1007/978-94-017-3083-9_18.

Landelius, T., Lindskog, M., Körnich, H., Andersson, S., 2018. Short-range solar radiation forecasts over Sweden. Adv. Sci. Res. 15, 39–44. https://doi.org/10.5194/asr-15-39-2018.

Larson, D.P., Nonnenmacher, L., Coimbra, C.F.M., 2016. Day-ahead forecasting of solar power output from photovoltaic plants in the American Southwest. Renew. Energy 91, 11–20. https://doi.org/10.1016/j.renene.2016.01.039.

Lima, F.J.L.L., Martins, F.R., Pereira, E.B., Lorenz, E., Heinemann, D., 2016. Forecast for surface solar irradiance at the Brazilian Northeastern region using NWP model and artificial neural networks. Renew. Energy 87, 807–818. https://doi.org/10.1016/j.renene.2015.11.005.

Liou, K.N., 2002. An Introduction to Atmospheric Radiation, International Geophysics. Elsevier Science.

Liu, B.Y.H., Jordan, R.C., 1960. The interrelationship and characteristic distribution of direct, diffuse and total solar radiation. Sol. Energy 4, 1–19. https://doi.org/10.1016/0038-092X(60)90062-1.

Liu, L., Zhao, Y., Chang, D., Xie, J., Ma, Z., Sun, Q., Yin, H., Wennersten, R., 2018. Prediction of short-term PV power output and uncertainty analysis. Appl. Energy 228, 700–711. https://doi.org/10.1016/j.apenergy.2018.06.112.

Long, C.N., Dutton, E.G., 2010. BSRN Global Network recommended QC tests, V2. J. Clim. 25, 8542–8567. https://doi.org/10.1175/JCLI-D-11-00618.1.

Lopes, F.M., Silva, H.G., Salgado, R., Cavaco, A., Canhoto, P., Collares-Pereira, M., 2018. Short-term forecasts of GHI and DNI for solar energy systems operation: assessment of the ECMWF integrated forecasting system in southern Portugal. Sol. Energy 170, 14–30. https://doi.org/10.1016/J.SOLENER.2018.05.039.

Malik, P., Arora, B., 2014. An effective weather forecasting using neural network. Int. J. Emerg. Eng. Res. Technol. 2, 209–212.

Marzo, A., Trigo, M., Alonso-Montesinos, J., Martínez-Durbán, M., López, G., Ferrada, P., Fuentealba, E., Cortés, M., Batlles, F.J., 2017. Daily global solar radiation estimation in desert areas using daily extreme temperatures and extraterrestrial radiation. Renew. Energy 113, 303–311. https://doi.org/10.1016/j.renene.2017.01.061.

Mathiesen, P., Kleissl, J., 2011. Evaluation of numerical weather prediction for intra-day solar forecasting in the continental United States. Sol. Energy 85, 967–977. https://doi.org/10.1016/j.solener.2011.02.013.

Mlawer, E.J., Taubman, S.J., Brown, P.D., Iacono, M.J., Clough, S.A., 1997. Radiative transfer for inhomogeneous atmospheres: RRTM, a validated correlated-k model for the longwave. J. Geophys. Res. Atmos. 102, 16663–16682. https://doi.org/10.1029/97JD00237.

Morcrette, J.-J., Barker, H.W., Cole, J.N.S., Iacono, M.J., Pincus, R., 2008. Impact of a new radiation package, McRad, in the ECMWF integrated forecasting system. Mon. Weather Rev. 136, 4773–4798. https://doi.org/10.1175/2008MWR2363.1.

Myers, D.R., Gueymard, C.A., 2004. Description and availability of the SMARTS spectral model for photovoltaic applications. In: Proceedings of SPIE -The International Society for Optical Engineering. https://doi.org/10.1117/12.555943.

Pereira, S., 2017. Desenvolvimento de um algoritmo de previsão de radiação solar através do refinamento espacial e temporal de dados de previsão meteorológica (Master's Thesis). Universidade de Évora, Évora, Portugal.

Pereira, S., Canhoto, P., Salgado, R., 2016. Spatial and temporal downscaling of solar global radiation and mean air temperature from weather forecast data - an introductory numerical study and validation. In: Workshop On Earth Sciences 2016, pp. 8–11.

Pereira, S., Canhoto, P., Salgado, R., Costa, M.J., 2018. Study and development of a solar radiation predicting algorithm based on Ecmwf ' S for Ecasts and Anns. In: Grand Renewable Energy 2018. Yokohama, pp. 2–3.

Perez, R., Lorenz, E., Pelland, S., Beauharnois, M., Van Knowe, G., Hemker, K., Heinemann, D., Remund, J., Müller, S.C., Traunmüller, W., Steinmauer, G., Pozo, D., Ruiz-Arias, J.A., Lara-Fanego, V., Ramirez-Santigosa, L., Gaston-Romero, M., Pomares, L.M., 2013. Comparison of numerical weather prediction solar irradiance forecasts in the US, Canada and Europe. Sol. Energy 94, 305–326. https://doi.org/10.1016/j.solener.2013.05.005.

Persson, A., Andersson, E., 2015. User guide to ECMWF forecast products.

Radiation Commission of IAMAP, 1986. Revised instruction manual on radiation instruments and measurements, WCRP Publications Series 7.

Renno, C., Petito, F., Gatto, A., 2016. ANN model for predicting the direct normal irradiance and the global radiation for a solar application to a residential building. J. Clean. Prod. 135, 1298–1316. https://doi.org/10.1016/j.jclepro.2016.07.049.

Rosiek, S., Alonso-Montesinos, J., Batlles, F.J., 2018. Online 3-h forecasting of the power output from a BIPV system using satellite observations and ANN. Int. J. Electr. Power Energy Syst. 99, 261–272. https://doi.org/10.1016/j.ijepes.2018.01.025.

Scolari, E., Sossan, F., Paolone, M., 2017. Photovoltaic model-based solar irradiance estimators: performance comparison and application to maximum power forecasting. IEEE Trans. Sustain. Energy 1–10. https://doi.org/10.1109/TSTE.2017.2714690.

Sharifi, S.S., Rezaverdinejad, V., Nourani, V., 2016. Estimation of daily global solar

radiation using wavelet regression, ANN, GEP and empirical models: a comparative study of selected temperature-based approaches. J. Atmos. Solar-Terrestrial Phys. 149, 131–145. https://doi.org/10.1016/j.jastp.2016.10.008.

Silva Fonseca, J.G., Oozeki, T., Takashima, T., Koshimizu, G., Uchida, Y., Ogimoto, K., 2011. Use of support vector regression and numerically predicted cloudiness to forecast power output of a photovoltaic power plant in Kitakyushu, Japan. Prog. Photovolt. Res. Appl. 20, 874–882. https://doi.org/10.1002/pip.1152.

Son, J., Park, Y., Lee, J., Kim, H., 2018. Sensorless PV power forecasting in grid-connected buildings through deep learning. Sensors 18. https://doi.org/10.3390/s18082529.

Taylor, K.E., 2001. Summarizing multiple aspects of model performance in a single diagram. J. Geophys. Res. Atmos. 106, 7183–7192. https://doi.org/10.1029/2000JD900719.

Vaz, A.G.R., Elsinga, B., van Sark, W.G.J.H.M., Brito, M.C., 2016. An artificial neural network to assess the impact of neighbouring photovoltaic systems in power forecasting in Utrecht, the Netherlands. Renew. Energy 85, 631–641. https://doi.org/10.1016/J.RENENE.2015.06.061.

Voyant, C., Notton, G., Kalogirou, S., Nivet, M., Paoli, C., Motte, F., Fouilloy, A., 2017. Machine learning methods for solar radiation forecasting: a review. Renew. Energy 105, 569–582. https://doi.org/10.1016/j.renene.2016.12.095.

Wang, F., Mi, Z., Su, S., Zhao, H., 2012. Short-term solar irradiance forecasting model based on artificial neural network using statistical feature parameters. Energies 5, 1355–1370. https://doi.org/10.3390/en5051355.

Plant Ecology and Evolution 152 (2): 262–284, 2019
https://doi.org/10.5091/plecevo.2019.1604

REGULAR PAPER

Morphological reconsideration of the araphid genus *Pseudostaurosira* (Bacillariophyceae), a revision of *Gedaniella*, *Popovskayella* and *Serratifera*, and a description of a new *Nanofrustulum* species

Eduardo A. Morales[1,2,3,*], Carlos E. Wetzel[3], Maria Helena Novais[1,2], Krisztina Buczkó[4], M. Manuela Morais[1,2] & Luc Ector[3]

[1]Water Laboratory, University of Évora, Rua da Barba Rala No. 1, Parque Industrial e Tecnológico, Évora 7005-345, Portugal
[2]Institute of Earth Sciences - ICT, University of Évora, Rua Romão Ramalho nº59, Évora 7000-671, Portugal
[3]Environmental Research and Innovation Department (ERIN), Luxembourg Institute of Science and Technology (LIST), 41 rue du Brill, 4422 Belvaux, Luxembourg
[4]Department of Botany, Hungarian Natural History Museum, Könyves Kálmán krt. 40, 1087, Budapest and MTA Centre for Ecological Research, Danube Research Institute, Karolina St 29, 1113 Budapest, Hungary
*Author for correspondence: edu_mora123@outlook.com

Background and aims – As a result of the description of many new species, reanalyses of type material, and information becoming available on valve morphogenesis in small araphid diatoms lacking a rimoportulae, the existing classification scheme at the genus level needs revision. Because morphological information has increased manyfold since the system provided by Williams & Round (1987), it may now be possible to find distinguishing characters in order to produce a more stable and useful framework, encompassing a morphogenetic perspective, which could then guide the placement of newly discovered taxa. This new framework could also be used to help assess the molecular information generated for the group, based on which many new genera are being erected, but perhaps without proper pondering of morphological data.
Methods – A thorough review was made of available published information on the ultrastructure of small-celled araphid diatoms lacking rimoportulae. In addition, image databases were searched, and new light and scanning electron microscopical observations made of some hitherto undescribed species.
Key results and conclusions – We provide a table of putative distinguishing features for nine genera (*Nanofrustulum*, *Opephora*, *Pseudostaurosira*, *Pseudostaurosiropsis*, *Punctastriata*, *Sarcophagodes*, *Stauroforma*, *Staurosira* and *Staurosirella*), together with a discussion on their value for discriminating these small diatoms using a morphogenetic perspective. Based on our findings, we amend the genus *Pseudostaurosira*, establishing wide and short vimines as its most characteristic feature. We use our system in describing a new species from Bolivia, which we place in *Nanofrustulum* based on its quasifract copulae, the distinguishing trait of the genus. The new species is distinguished from its congeners by its heteropolar valves, apical pore field features, and the multiseriate areolae. We also examine the three genera *Popovskayella*, *Gedaniella*, and *Serratifera*, the latter two recently erected based on molecular information. Since none of these latter genera pass the morphogenetic evaluation we think is essential, we place them in synonymy with other genera and provide the consequent nomenclatural changes. Finally, we make several new combinations in *Nanofrustulum*, *Pseudostaurosira*, *Sarcophagodes* and *Staurosirella*.

Key words – Araphids, Bolivian Altiplano, Fragilariaceae, molecular phylogenies, Pantocsek, systematics, type material**.**

© 2019 The Authors. This article is published and distributed in Open Access under the terms of the Creative Commons Attribution License (CC BY 4.0), which permits use, distribution, and reproduction in any medium, provided the original work (author and source) is properly cited.

Plant Ecology and Evolution is published by Meise Botanic Garden and Royal Botanical Society of Belgium
ISSN: 2032-3913 (print) – 2032-3921 (online)

INTRODUCTION

While the many features currently used for small araphids lacking rimoportulae might be appropriate for species level delimitation, synapomorphies at the genus level are more complicated to single out (see Williams 2011, 2013 and Kociolek & Williams 2015). This difficulty has generated an alternate view to the taxonomy proposed by Williams & Round (1987), which is expressed, for example, in Lange-Bertalot (1989, 1993), Krammer & Lange-Bertalot (1991) and Ognjanova-Rumenova et al. (1994). This alternative has gained partial support from molecular analyses (Medlin et al. 2012). Nevertheless, the Williams & Round (1987) proposal, based completely on morphology and later complemented with additional genera (*Stauroforma* Flower, V.J.Jones & Round, *Pseudostaurosiropsis* E.Morales and *Sarcophagodes* E.Morales), has become widely used. Perhaps, one of the reasons for acceptance comes from the fact that the morphological diversity found in samples can be relatively easily ascribed to these genera. This, of course, is helpful when diatoms are used in applied fields such as bioindication. While molecular analyses strive to seek the best way to express evolutionary relationships among existing genera (e.g. Medlin et al. 1993, 2008, 2012, Medlin & Desdevises 2016), morphological data continue to be the most trusted basis for identifying taxa and indeed for classifying them, as shown through the plethora of new taxa described in recent decades using a combination of light (LM) and scanning electron microscopy (SEM) (e.g. Witkowski et al. 2010, Morales et al. 2012, Grana et al. 2018).

In the last 30 years, the number of araphid species has increased significantly (Guiry & Guiry 2018). Newly described features have broadened the range of morphological characters used for genera and species delimitation. Therefore, there is now a need to start modifying the definitions of taxa in order to reflect what is known about their morphology (Morales & Manoylov 2006b, Morales et al. 2012, García et al. 2017). One of the genera in need of such reconsideration is *Pseudostaurosira* D.M.Williams & Round in which at least 40 species, some new, others transferred from *Fragilaria* Lyngb., *Opephora* P.Petit and *Staurosira* D.M.Williams & Round have been included (e.g. Morales & Edlund 2003, Cejudo-Figueiras et al. 2011, Kociolek et al. 2014, Kulikovskiy et al. 2015, García et al. 2017). Taking as a basis the SEM analysis of type material of the generitype, *Pseudostaurosira brevistriata* (Grunow) D.M.Williams & Round (Morales et al. 2015), and published SEM information for the majority of species currently ascribed to this genus, it is now possible to reassess the original protologue and delimit the genus in a more concise manner. Among the features that have been better revealed by studies published after Williams & Round (1987) are, for example, the spines, which are now known to be absent in some species (e.g. *Pseudostaurosira parasitica* (W.Sm.) E.Morales; Morales et al. 2015: figs 95–98), growing on the virgae in others (e.g. *Pseudostaurosira pseudoconstruens* (Marciniak) D.M.Williams & Round; Marciniak 1986: pl. 6, figs 229–232), or even occurring along the striae in some others (e.g. *Pseudostaurosira microstriata* (Marciniak) Flower; Marciniak 1986: pl. 6, figs 233, 234). Among the totally new features are the flaps covering the areolae externally (Morales et al. 2012: figs 45, 52, 53) and the stipulae at the base of spines (Morales et al. 2012: figs 46, 50).

But even with all this new information on *Pseudostaurosira*, it remains difficult to find derived characters that would unify all the species within the genus and at the same time separate them from other araphids without rimoportulae. Certainly, the characters mentioned before (spines and their associated structures) or even the areolae and their substructures (volae, rotae and flaps), the apical pore fields, and the girdle bands, which are traditionally used to separate small araphid genera, are not helpful in this task. Herein, we attempt to establish distinguishing traits through an analysis of features that are less frequently mentioned in araphid taxonomy and systematics, and also try to incorporate a morphogenetic perspective following the recommendations of Cox (2004, 2012) and Mann (1984, 2006).

During our search for SEM information to build a comparative table of distingushing features, we reviewed several new genera that were erected in recent years, such as *Popovskayella* Kulikovskiy & Lange-Bertalot, *Serratifera* Chunlian Li, Witkowski & Ashworth and *Gedaniella* Chunlian Li, Witkowski & Ashworth, and revise them together with some other araphid species, based on the discriminating characters we propose, making all the required nomenclatural rearrangements.

We also describe a new species in *Nanofrustulum* Round, Hallsteinsen & Paasche from the Andes of Bolivia. This is a small-valved diatom that has unusual features and that we use to test our morphological feature analysis.

MATERIALS AND METHODS

The search for characters for all currently described genera of small fragilarioids lacking rimoportulae was done on the basis of published information (cited throughout the manuscript) and through examination of image databases at the Luxembourg Institute of Science and Technology (LIST) and the Water Laboratory, University of Évora, Portugal.

In addition, two samples were analysed specifically for the present work. The material used for the description of the new *Nanofrustulum* was an epipsammic sample collected from the Desaguadero River, Bolivia, described in Morales et al. (2012). The second sample was diatomite material from Lutila (Hungarian Natural History Museum, HNHM-ALG-DC-0092), Slovakia, described in Morales et al. (2014b).

For LM analyses, an aliquot of the Bolivian material was boiled for 45 min in 70% nitric acid (1:1 by volume with the sample). The mixture was then rinsed with distilled water until neutrality. Permanent slides were mounted using Naphrax (Brunel Microscopes, Chippenham, UK) and analysed using a Zeiss Universal microscope (Zeiss, Jena) fitted with DIC (Differential Interference Contrast) and a Spot Insight 2 model 18.2 colour digital camera (Diagnostic Instruments Inc., Michigan). Microphotographs were taken at 2000× using a Zeiss PLAN 100×, 1.25 N.A., immersion objective and SpotSoftware version 4.6 (Diagnostic Instruments, Michigan). For the Lutila material, a rehydrated raw sample was dried, mounted in Zrax (product no longer available) and an-

alysed with a LEICA DM LB2 microscope (Leica Microsystems, Wetzlar), equipped with a FinePix S2 Pro digital camera (Fuji Photo Film, Tokyo), at 1000× using a Leica DMLB 100×, 1.40 N.A., oil immersion objective.

For SEM analysis, a 2 ml subsample of the Bolivian clean material was heated with 100 ml of hydrogen peroxide (35%) for 36 h in a sand bath at 210°C. The supernatant was then removed and 1 ml of hydrochloric acid (37%) added, the material allowed to rest for 2 h, and subsequently rinsed with distilled water until neutrality. The Lutila diatomite was used untreated. All materials were then rinsed with deionized water over 3-µm glass fibre filters. Specimens were coated with platinum using a BAL-TEC MED 020 Modular High Vacuum Coating System (Leica Microsystems, Wetzlar) for 30 s at 100 mA and observed with a Hitachi SU-70 electron microscope (Hitachi, Chiyoda), operated at 5 kV and 10 mm working distance. All micrographs were digitally manipulated and plates containing LM and SEM pictures were mounted using CorelDraw X6®.

Morphological terminology follows Barber & Haworth (1981) for valve shape and stria pattern; Cox & Ross (1981) and Cox (2012) for lateral extensions from the sternum (or annulus) (virgae) and cross bars developing later (vimines and viminules) that delimit the areolae; and Williams & Round (1987) and Round et al. (1990) for areolar substructures, spine features, apical pore fields and girdle bands.

RESULTS AND DISCUSSION

Finding distinguishing characters at the genus level

The analysis of several hundred SEM images of various described and potentially new taxa from all continents yielded the list of potential traits displayed in table 1. This table was constructed with difficulty due to the large volume of information available, but also because current genus descriptions in the literature are ambiguous and do not present clear-cut boundaries. The existence of a range of opinions regarding the features to be used for identification and classification of known species is also confusing (for example, see discussion in García et al. 2017, for *Staurosira* Ehrenb.). Also, many of the species names that are currently used refer to several entities that are morphologically similar (i.e. they belong to complexes) but that are clearly differentiated when SEM information is used (Morales et al. 2013, 2014a). In addition, some widely used reference works (e.g. Metzeltin & Lange-Bertalot 1998) do not include a thorough argumentation, a necessary step in building a strong taxonomic basis (Silva in Hegewald & Silva 1988).

The analysed information shows that the characters traditionally used to distinguish genera of small araphids lacking rimoportula (Williams & Round 1987) are in fact problematic, since they are too variable within each genus and often overlapping among different genera. In the case of *Pseudostaurosira*; for example, Lange-Bertalot et al. (2017) stated that the "most characteristic feature" is the short striae. While this may be true for the small and rather heterogeneous (regarding spines, apical pore fields, etc.) group of species included by these authors, consideration of characters in other species reveals that stria length is in fact one of the most variable characters in this genus and that there are overlaps with species in *Nanofrustulum*, *Pseudostaurosiropsis* and *Sarcophagodes*. It is therefore not surprising that the same authors consider *Pseudostaurosira* as "weakly circumscribed" and that its generitype, *P. brevistriata*, is "a heterogeneous group of species".

More robust and natural classifications can be achieved by using features that are shared only among the members of a genus and that do not appear in any other groups (Kociolek & Williams 2015). Such characters, synapomorphic for the species of the genus and autapomorphic for the genus, are difficult to recognize when limited morphological information is available. Fortunately, as many new species have been erected in recent years (e.g. Witkowski et al. 2010, Morales et al. 2012, Kulikovskiy et al. 2015) and type material has been reanalysed with both high resolution LM and SEM (e.g. Edlund et al. 2006, Cejudo-Figueiras et al. 2011, Morales et al. 2015), the ranges of variation of many features have become clearer and the status of particular characters – whether or not they are synapomorphies – can be assessed. Herein, we present only a first step in the recognition of these unique characters that separate genera. Later on we will present tests to evaluate their status as synapomorphies.

It must be added that having a well-delimited generitype gives an idea of the Bauplan (body plan) of that species and its evolutionary associates within the genus. However, as stated by Cox (2010), analysing characters that are fully formed can lead to a misappreciation of evolutionary relationship, since the morphogenetic basis for character variation remains hidden when only the end products of valve morphogenesis are considered. Therefore, pondering developmental pathways underlying character formation may be useful to establish the nature of these characters, why they vary, and whether they are homologous.

Unfortunately, there are not very many studies of valve morphogenesis in araphid diatoms, certainly not sufficient to represent the great diversity within the group. But some information available for diatoms in general lays a foundation for understanding the group of araphid diatoms treated here. For example, Cox & Kennaway (2004) and Cox (2010) analysed the origin of the sternum, virgae, vimines, viminules, areolae and associated structures, and the work of Kaluzhnaya & Likhoshway (2007) and Sato et al. (2008, 2009, 2011) showed how these features arise in the specific case of araphid diatoms.

Justification of the newly defined distinguishing characters

The characters contained in table 1 help to explain differences among the nine genera described to date, excluding *Gedaniella*, *Popovskayella* and *Serratifera*. These characters are arranged roughly in the order in which they develop during valve morphogenesis. For example, areolar substructures (volae, rotae and flaps) are the last to form when the valve is being constructed and girdle bands form synchronously with, or towards completion of, valve formation, depending on the species; growth of areolar substructures begins when the areolae are already well defined (e.g. Sato et al. 2011). At least part of the variation in the process of valve construction

Table 1 – Comparison of genera of small-celled fragilarioid diatoms lacking rimoportulae.
Bold indicates important distinguishing features.

Feature	*Nanofrustulum*	*Opephora*	*Pseudostaurosira*	*Pseudostaurosiropsis*	*Punctastriata*	*Sarcophagodes*	*Stauroforma*	*Staurosira*	*Staurosirella*
Virgae shape	doubly flared	doubly flared	doubly flared	doubly flared	doubly flared	doubly flared	**rectangular**	**singly flared towards mantle**	doubly flared
Vimen shape	slender and short	without vimines	**wide and short**	slender and short	slender and short	**wide and long**	slender and short	slender and short	**slender and long**
Viminule production	present in parts of the striae	without viminules	without viminules	without viminules	**present in the entire striae**	without viminules	without viminules	present in parts of the striae	present in parts of the striae
Areolae shape	round to transapically elliptical	**transapically elliptical**	round to transapically elliptical	**round**	round to apically elliptical	**apically reniform**	round to apically elliptical	round to apically elliptical	**apically oriented lineolae**
Areolae number	always more than two	**one**	two to many	two to many	always more than two	two to many	always more than two	always more than two	always more than two
Striae type	uniseriate to multiseriate	uniseriate	uniseriate	uniseriate	**multiseriate**	uniseriate	uniseriate	uniseriate to multiseriate	uniseriate to multiseriate
Volae origin	inner perimeter of the areola	**virgae**	inner perimeter of the areola	without volae	inner perimeter of the areola	inner perimeter of the areola	inner perimeter of the areola	inner perimeter of the areola	inner perimeter of the areola
Rotae production	without rotae	without rotae	without rotae	**present, originating from a single point within the areola**	without rotae	without rotae	without rotae	without rotae	without rotae
Girdle element structure	**valvocopula: open, without fimbriae. copula: quasifract, open. ligulae in valvocopulae and copulae morphologically different**	valvocopula: open, without fimbriae. copula: entire, open	valvocopula: open, without fimbriae. copula: entire, open	valvocopula: open, without fimbriae. copula: entire, open	valvocopula: open, with fimbriae. copula: entire, open	valvocopula: open, without fimbriae. copula: entire, open	valvocopula: open, without fimbriae. copula: entire, open	**valvocopulae: closed, with fimbriae. copula: entire, open**	valvocopula: open or closed, with fimbriae. copula: entire, open or closed
SEM references	Lee et al. 1980, Round et al. 1990, Witkowski et al. 2010, Li et al. 2018	Round et al. 1990, Sabbe & Vyverman 1995, Li et al. 2018	Williams & Round 1987, Cejudo-Figueiras et al. 2011, Morales et al. 2015	Morales 2001, Morales 2002	Williams & Round 1987, Hamilton & Siver 2008	Morales 2002	Flower et al. 1996, Talgatti et al. 2014	Williams & Round 1987, Morales 2006	Williams & Round 1987, Morales, 2006, Morales & Manoylov 2006a, 2006b

could arise from interactions with the environment through selection and adaptation, generating reproducible, inheritable patterns of valve formation (see discussions by Mann 1999, 2010); at least some of these variations could represent features expressing evolutionary relationship among the different genera.

We hypothesize that the formation of striae begins soon after the formation of the virgae (in *Opephora*), vimines (in *Pseudostaurosira*, *Pseudostaurosiropsis*, *Sarcophagodes* and *Stauroforma*) and viminules (in *Punctastriata* D.M.Williams & Round). We are herein using a restricted concept of *Opephora*, following Round et al. (1990) and Morales (2002). In exceptional cases, species of *Nanofrustulum*, *Staurosirella*, and *Staurosira* produce striae that are partially or completely multiseriate (Morales 2005), but in these genera the striae appear with the formation of the vimines, the production of viminules being rather sporadic and insufficient to characterize these genera as multiseriate as a whole. Only in the case of *Punctastriata* are all the striae always and entirely multiseriate invariably in all species.

During stria development, the areolae near the axial area form first and the ones near the valve margin form last (Cox 1999, 2010, Sato et al. 2011). In all the genera considered here, the areolar size increases toward the valve face-mantle junction and from there to the margin the size decreases in size again. In the case of *Opephora* with a single areola running uninterrupted from the valve face to the mantle, the ends on both valve face and mantle taper so that a transapical elliptical shape is formed (Round et al. 1990: 382, 383, figs d–j). In genera having a multiseriate areolar pattern, there are fewer areolae towards the extremes of the striae, so more or less elliptical striae shapes are produced (see illustrations for *Punctastriata* in Round et al. 1990; the case of the new species placed in *Nanofrustulum* is discussed below).

Because of this difference in the diameter or number of the areolae within the striae, the virgae in the genera considered should tend to be flared (i.e. they should become wider) at both ends; however, this is not always the case and genera tend to differ in specific patterns. We define the "shape of virgae" to be the geometrical pattern that the virgae assume in relation to neighbouring striae. Some taxa, such as *Stauroforma*, always have rectangular virgae and this is because these structures are thickened and raised in internal and external views, and remain somewhat independent from stria shape (Van de Vijver et al. 2002: pl. 15, figs 24–26, Genkal et al. 2011: pl. 19, figs 11, 12). *Staurosira* also has a unique virga shape. Here there is an enlargement of the valve face areolae as the striae proceed towards the valve margin, but the influence of smaller areolae on the shape of the virgae is compensated by the elevation of the latter. On the valve mantle, the virgae are less raised and therefore the smaller areolae found at the end of the striae make these virgae appear subtly flared (Lange-Bertalot 1989: pl. 5, figs 1, 2).

As stated before, there is an underlying mechanism for virga and areola formation, where the timing of areola production is the result of how the virgae and their associated structures (vimines and viminules) develop. The thickening of the virgae, as the striae and associated features develop, also has an influence on stria formation, especially on their internal structure (Sato et al. 2011). The majority of genera possess a conspicuous depression along each stria, the end result of virgae and sternum reinforcing in a trans and pervalvar direction. The thickened structures grow up above the striae often giving the impression of a semi-chambered internal structure like an alveolus (see for example Morales et al. 2015: fig. 141, for *Pseudostaurosira*; Round et al. 1990: 359, fig. E, for *Punctastriata*; Grana et al. 2018: figs 47, 48, 51 for *Staurosira*; and Morales et al. 2010c: fig. 47, for *Staurosirella*).

The features of the vimines and viminules determine the characteristics of the areolae they delimit, except in *Opephora* where the single areolar aperture runs from valve face to mantle. Here, therefore, the extension and shape of this single opening is determined solely by the degree of development of the virgae and sternum (Round et al. 1990: 382, 383, figs d–j). In the case of *Staurosirella*, the virgae are well separated from each other and the vimines are long (length expressed as the apical distance between virgae) and narrow, delimiting closely spaced, elongated openings or lineolae. The length and reduced width of the vimines in *Staurosirella* are unique, while in the case of *Pseudostaurosira* and *Sarcophagodes* the vimines are also long and wide, but they are thicker (thickness expressed as the transapical distance between areolae) in the former. The remaining genera either lack vimines or have them slender and short.

As stated previously, the production of viminules is constant in all species of *Punctastriata*, therefore this is a defining characteristic for this genus. Although *Nanofrustulum*, *Staurosira* and *Staurosirella* also produce viminules, in this case the biseriate nature of the striae is expressed only on portions along the same striae or on an entire stria within the same valve (Lange-Bertalot 1989, Morales 2005). Again, since there is an underlying ontogenetic mechanism and the end products are different, areolar shape and the varying features of vimines and viminules can be used as distinguishing features.

The stated differences in the formation of the virgae also determine the sites of production of structures within the areolae (Sato et al. 2011, Cox 2012). The volae arise from the virgae in *Opephora* and define and delimit the areolar openings (Round et al. 1990: 382, 383, figs e, f), while in the rest of the genera volae are either absent (e.g. *Pseudostaurosiropsis*: Morales 2001: figs i, j) or they are born from the inner perimeter of the areola, either on vimines or viminules (e.g. *Pseudostaurosira*: Morales et al. 2012: fig. 48). Rotae are produced only by *Pseudostaurosiropsis* (Morales 2002: pl. 2, figs 5, 6) and originate from a single point, usually near the base of a spine. In areolae that are not in close proximity to a spine, the rotae arise from a point on the side closest to where the spine is located (Morales 2001: figs 7a–d, g). The points of origin of the rotae are especially clear when the rotae are beginning to be formed or when they are somewhat eroded (Morales 2001: figs 7e, i, j). Rotae can be confused with 'flaps', but flaps originate from the base of spines or from other regions around the areolar perimeter, and a single areola can have several flaps (Morales et al. 2012: fig. 45). Flaps also differ from rotae in that they are produced on top of volae (Morales et al. 2012: figs 51–53), whereas rotae de-

velop in isolation within the areolar opening (Morales 2001: figs 7i, j).

Volae are very similar in the eight genera included in table 1 (excluding *Pseudostaurosiropsis*). The only difference is in the degree of thickening and development. In general, these are highly (dichotomously) branched structures that originate from the inner areolar opening, at different points in *Pseudostaurosira* (Morales 2003: figs 60–65). Smaller, thinner and less branched volae are produced in *Punctastriata* (Lilitskaya 2016: pl. 4, fig. 2), while larger, thicker, and profusely branched are produced in the large-valved species of *Pseudostaurosira* (Morales & Edlund 2003: figs 45–50).

Although there is not sufficient information on girdle band formation to permit any generalization, as shown by Tiffany (2015), these structures begin their formation early in valve development, but the end of the process terminates after the margin of the valve has formed. The latter begins its solidification as the last mantle areolae complete their definition, once the distal ends of the virgae fuse (Sato et al. 2011). Though there are no specific studies for these rimoportula-lacking araphids showing the formation of individual girdle elements, it is known that for diatoms, in general, each of these elements forms within its own silica deposition vesicle and that there are differential interactions with previously formed parts of the valve, i.e. the mantle as a whole, composed of virgae and striae (Mann 1984, Round et al. 1990). Therefore, there is a morphogenetic basis for the structural difference between those girdle elements. The valvocopula, for example, has a pars interior that is recessed to accommodate the valve mantle and to attach internally to it, sometimes directly (as in, for example, *Nanofrustulum*, *Opephora*, *Pseudostaurosira*; e.g. Morales et al. 2012: fig. 49), otherwise by means of delicate, narrow extensions called fimbriae, that attach to the internal faces of the virgae (as in, for example, *Staurosira* and *Staurosirella*; Morales 2005: fig. 103). The rest of the girdle elements in small araphids lacking a rimoportula tend to be plainer, but they can be open or closed. Sometimes, the same girdle is composed of open and closed bands as in the case of *Staurosira* (Morales 2006), or the girdle may contain all closed or all open elements, as in *Staurosirella* (Morales 2006). In other cases, the morphological difference in the copulae is even more extreme, as in *Nanofrustulum*, in which the copulae are much smaller than the valvocopulae, arranged around the girdle and attached to other copulae by well developed ligulae (Round et al. 1999, Morales 2001, Witkowski et al. 2010, Wetzel et al. 2013). Such differences among elements of the same girdle are not exclusive to small araphids. For example, the large araphid *Glyphodesmis* Grev. (Round et al. 1990: 240, 241, figs c, i, j) and the raphid *Tursiocola* R.W.Holmes, S.Nagas. & Takano (Frankovich et al. 2015) also have these differences between valvocopulae and copulae.

This view (that the nature of the girdle bands is variable among closely related taxa) conflicts with the current consideration of the open and closed nature of girdle bands as a distinguishing feature in *Fragilaria* and *Ulnaria* (Nitzsch) Compère (Compère 2001) (closed in the latter) (Williams 2011). Molecular phylogenies using four genes show a weak difference between the two genera (2.5%), insufficient to justify a morphological separation based on known characteristics, as stated by Medlin et al. (2012). The latter authors also stated that looking to other sources of information such as reproduction might reveal further differences. Until such studies are done, the open or closed feature of girdle bands remains a practical way of separating species in the two genera even though the synapomorphic nature of this feature is challenged from a morphogenetic standpoint. Besides, a wider analysis of other morphological features, in the light of the numerous new species that are being published for both genera, it could be possible to find synapomorphies; we reserve this task for later.

Are there any other distinguishing characters?

There are perhaps other sources of distinguishing features among the nine genera delimited in table 1. For example, morphogenesis of apical pore fields and spines might hold useful information. We have detected several variations in the structure of apical pore fields such as presence/absence, external and internal depressions, internal and external troughs, rims surrounding the pores, etc. It is known that apical pore fields appear earlier in the formation of the valve of araphids possessing a rimoportula, and they complete their formation before the completion of silicification of the valve (Tiffany 2002, Kaluzhnaya & Likhoshway 2007, Sato et al. 2011). However, the process of formation of associated structures such as the troughs seen in *Pseudostaurosira parasitica* (Morales 2003), the "volcano" shaped domes seen in individual poroids of *Stauroforma inermis* Flower, V.J.Jones & Round (Morales 2001), or the whitish rims frequently seen in species of *Staurosira* and *Staurosirella*, remain unknown.

Likewise, there are several character states for spines in araphids, which seem to be interesting from the ontogenetic standpoint. For example, certain taxa are reported as having hollow or solid spines (see discussion in Morales & Manoylov 2006b), some even have spines with a soft core (Morales et al. 2015: fig. 45). Yet it is difficult to determine whether spine features can be regarded as distinguishing at some level, simply because we do not know the mechanism of their formation and the actual processes determining whether spines are solid or lack a "filling" material altogether. It is possible that at least some of the reports of hollow or solid spines may be more related to stages of development than to actual character states (e.g. Morales et al. 2010b: figs 45, 47). Whether spines are formed in a fashion similar to centric diatoms, in which there is an active deposition of siliceous material guided from within the cell (Pickett-Heaps 1998), merits study. What is known thus far about cell wall formation in araphids, however, suggests that a centric-like mechanism might be more likely when spines are produced along striae, since holes would be readily available for cytoplasmic expansion from within the cell. In the case of spines growing on the virgae, it is surprising that one never finds openings within virgae in internal views of the valve face–mantle junction under SEM. Since sites of production of features such as areolae and apical pore fields are fixed within the organic apparatus that originates the new valves, it is logical to assume that there are also sites for spine production. The suppression of such sites would be a relatively simple evolutionary step, perhaps triggered by genetic, environmen-

tally-induced, or even mechanical influences. Explaining the change of location of sites for spine production from striae to virgae or *vice versa* appears more complex. Yet, there are genera that contain spiny and spineless species (e.g. *Staurosira* and *Staurosirella*; Morales & Manoylov 2006a, 2006b, Morales et al. 2010a) and species that have spines along the stria or growing from the virgae as in *Pseudostaurosira*. Studying the mechanism of spine production-suppression, therefore, could elucidate evolutionary relatedness at different taxonomic levels.

We disregarded the features of the sternum as a source of distinguishing traits because the formation of the new valves begins with the formation of the sternum and the process seems to be common not only to all araphids, but to all pennates (Cox 2012).

Redefinition of the genus *Pseudostaurosira*

Pseudostaurosira D.M.Williams & Round emend. E.Morales

Generitype – *Pseudostaurosira brevistriata* (Grunow) D.M.Williams & Round.

Microscopical study of generitype material – Morales et al. (2015: figs 107–127 (LM), 128–143 (SEM)).

Description – Frustules symmetrical in side view, forming chains in taxa that possess spines. Taxa with incipient or no spines, presumably attached by mucilage stalks. Valves cruciform, bigibbous, lanceolate, rhombic or elliptic. Sternum of variable width and shape. Transition from valve face to mantle varies from abrupt to more gradual, with formation of a transition zone. Striae composed of one to (rarely) a few rows of wide, round, transapically elliptical, or irregularly polygonal areolae running from valve face to mantle. Internally, areolae open into a single depression running from valve face to mantle, which may become chamber-like. Volae highly branched, usually dichotomously, arising from the inner perimeter of the areolae and at different depths. Virgae rectangular or flared at their proximal and distal ends. Vimines short and wide, the one at the valve face-mantle transition usually being wider, giving the impression of a single apical rib running along the valve face margin. Viminules seldom produced and, when formed, occupying only a part of a stria. Flaps or flat siliceous growths originate from several points around the external perimeter of the areolae, close to their external surface. Concentric discs sometimes present, partially occluding the depression into which the areolae open internally. Solid spines can grow from the enlarged vimen that connects the virgae along the valve-face edge or from the virgae themselves, or they can be absent. Spines of varying shape, but usually spatulate, with or without terminal branching, with a cylindrical base, and often bearing stipulae. Stipules produced near the base of spines and projecting downward. Apical pore fields absent, reduced or more fully developed, of the ocellulimbus type; in many cases they are sunken into the apical portion of the valve. They are composed of round poroids, which are sometimes arranged along external troughs parallel to the apical axis of the valve. Mantle plaques present in many species and situated along the abvalvar edge of the valve mantle. Cingulum composed of a larger valvocopula and few to many ligulate copulae, always open, lacking fimbriae and perforations.

Distinguishing character – Wide and short vimines. Though these vimines are also found in other genera having round areolae, such as *Nanofrustulum* (Li et al. 2018: figs 286–289), *Pseudostaurosiropsis* (Morales 2001: figs 7a–d, g, i, j, l) and *Sarcophagodes* (Morales 2002: pl. 5, figs 1–3), in *Pseudostaurosira* they are wider due to transapical expansion during valve ontogeny, and shorter due to the areolae being transapically expanded, thus having their shortest axis parallel to the longitudinal axis of the vimines (Morales & Edlund 2003: figs 39, 45, Cejudo-Figueiras et al. 2011: figs 108–111, Morales et al. 2012: figs 42, 48).

Other salient, but not unique features – Rectangular or doubly flared virgae. The degree of flaring varies depending on the size reduction of terminal vimines (those located towards the axial area of the valve and towards the abvalvar edge of the mantle) and the shape of terminal areolae along a stria (Morales et al. 2015: figs 128, 129, 137, 141, 142).

The striae lie within an internal depression. This depression varies among species from shallow (Witkowski et al. 2010: figs 50–55) to deep, the striae appearing semi-chambered (Morales 2002: pl. 4, fig. 2).

There is a high variability in spine presence, position and associated structures. Spines can be absent (Morales et al. 2015: figs 95, 96, 99, 100, 103, 104), or produced on virgae (Round et al. 1990: 356, 357, figs d, e) or on vimines (Cejudo-Figueiras et al. 2011: figs 100, 101, Morales et al. 2015: figs 130, 132, 135). Spines are always solid, although the presence of a soft core in some species gives the impression of spines being hollow after breakage and erosion (Edlund et al. 2006: figs 18, 20).

Stipules and flaps are produced. The stipules, originating at the base of the spines and projecting at an angle, away from the valve mantle, are a rather common feature among spiny species of *Pseudostaurosira* (Morales et al. 2012: fig. 50). The shape of these structures varies among species (Morales 2002: pl. 4, fig. 6). Stipules are also present in other genera such as *Nanofrustulum* (Li et al. 2018: fig. 288, as "lateral projections") and *Punctastriata* (Williams & Round 1987: fig. 43; Flower 2005, fig. 6). Stipules are frequently helpful in the SEM identification of chains in valve view, which can easily be confused with chains of *Staurosira*, but where stipulae are always lacking.

Flaps originate from different points along the inner perimeter of the areolae and sometimes resemble disks lying atop the volae. Morales et al. (2012: fig. 45) show a valve in which some mantle flaps are broken, while others (that originated very close to the basis of the spines on the valve face) are still attached. Figure 50 of the same publication (Morales et al. 2012) is helpful in the distinction of stipules and flaps; stipules can be seen projecting downward along the mantle and originate from the body of the spine.

At least two species (*Pseudostaurosira decipiens* E.Morales, G.Chávez & Ector and *Pseudostaurosira laucensis* var. *vulpina* Lange-Bert. & Rumrich) have been found to produce internal accumulations of siliceous material on the volae, depositions that appear as two concentric disks (Morales et al. 2012: figs 40, 44; E. Morales, unpublished obs.).

The functions of these are unknown, but they can be used to help identify the two species. However, in *P. laucensis* var. *vulpina*, eroded valves lack depositions (e.g. Rumrich et al. 2000: pl. 10, fig. 9).

Apical pore fields are variable among different *Pseudostaurosira*. In this genus they invariably occupy the mantle portion of the apex and never subtend striae, unlike in e.g. *Staurosira* (Morales et al. 2012: figs 57, 58, 62). Their development ranges from absent or present even in the same species (e.g. *Pseudostaurosira sajamaensis* E.Morales & Ector: Morales et al. 2012 and may be slightly developed (e.g. *P. brevistriata*: Morales et al. 2015) or fully developed (*P. parasitica*: Morales 2003). Internally, poroids open into a single, circular depression, as seen in the type of *P. brevistriata* (Morales et al. 2015: figs 140–142), but this feature might also be present in species of *Staurosirella* (e.g. Kulikovskiy et al. 2015: pl. 10, fig. 22). In some cases there are external transapical troughs along which there are lines of pores (Morales 2003: figs 54–58, 64).

Lange-Bertalot et al. (2017) considered that the width of the sternum is a diagnostic feature of *Pseudostaurosira* (see also the dichotomous key presented in Li et al. 2018). They even placed species such as *Pseudostaurosira subsalina* (Hust.) E.Morales in *Staurosira* due to their narrower axial area. There is no support for this, however, and such an area should be regarded as a variable character that can be diagnostic, but at the species level, e.g. to distinguish *Pseudostaurosira elliptica* (Schum.) Edlund, E.Morales & S.A.Spauld. (Edlund et al. 2006) from *Pseudostaurosira americana* E.Morales (Cejudo-Figueiras et al. 2011) (see discussion in Grana et al. 2018). *Pseudostaurosira* and *Staurosira* each have their distinguishing features and are well delimited genera (table 1, and compare our emended description herein with the discussion in García et al. 2017). Moreover, the sternum width is also variable in genera such as *Staurosirella* (Morales et al. 2010c) and *Staurosira* (Grana et al. 2018).

The placement of a newly discovered diatom in the nine genera scheme

Nanofrustulum rarissimum E.Morales, Novais, C.E.Wetzel & Ector, **sp. nov.**

Figs 1 & 2

Type material – Bolivia, Desaguadero River, Department of Oruro (17°23′51″S, 68º14′33″W, 3701 m a.s.l.), 5 Jul. 2009, *G. Chávez* s.n. (holo-: ANSP, slide ANSP GC 26815 partially illustrated here in figs 1A–F (LM), 1G–K, 2A–D (SEM); iso-: Diatomotheca Boliviensis, Cochabamba, Bolivia, slide DBOL-0246)

Description – Frustules rectangular in girdle view. Valves ovoid with broadly rounded head poles and narrower, almost cuneate foot poles (figs 1A–H, 2B & 2D). Length 7.3–9.5 µm, width 2.5–3.3 µm, stria density 13–14 in 10 µm. Sternum narrowly lanceolate (figs 1A, 2B & D). Virgae doubly flared raised externally and internally (figs 1G, 2A, 2D). Transition between valve face and valve mantle abrupt (figs 1G–K & 2A–C). Valve mantle edge parallel to valve face–mantle junction (fig. 2A). Siliceous plaques along valve mantle edge present (fig. 2A). One to several rows of areolae present on the same stria, progressing uninterruptedly towards valve mantle (figs 1G–K & 2A–C). Areolae square, trapezoid or elliptical, apically or transapically elongated, all opening internally into a single depression (figs 1G–K & 2A–D). Volae robust relative to areolar opening and arising from the inner periphery of each areola (figs 1G, I–K, 2B & 2D). Spines located on vimines, arising from at least two points along the width of striae (figs 1G–K, 2A & B). A wide, laminar, skirt-like stipula is present near the base of each spine (fig. 1G–K). Wart-like, whitish depositions sometimes present on the valve face, more numerous at the valve head pole (figs 1H, J & 2B). Apical pore fields composed of variable rows of poroids, present at both apices, but more developed at the foot pole (figs 1G–I, 1K & 2B–D). Pore field at head pole located closer to the mantle abvalvar edge (fig. 1G, I & J), while foot pole pore field lies at the transition between valve face and mantle (figs 1G, H, K, 2B & D). Poroids of latter pore field sit within cavernous troughs carved deep into the valve (figs 1G, K & 2C). Girdle composed of an open, ligulated valcocopula lacking perforations, and quasifract, ligulated copulae, also lacking perforations (fig. 2A).

Etymology – "*Rarissimum*" refers to the fact that the features of the new taxon are rather infrequent within the genus.

Taxonomic remarks – Using traditional morphological characters, the new taxon shows several features that link it to *Pseudostaurosira*. The individual areolae bearing well developed volae, the well developed apical pore fields composed of round poroids, and even the position of these poroids within troughs have all been described in other species of the genus. Regarding the areola structure, the new taxon resembles *P. brevistriata*. Observing figs 128–130 and 132 in Morales et al. (2015) and comparing with figures presented herein, the resemblance in areolar openings and the manner in which the volae are born and developing to the valve interior can be seen. Likewise, figs 140–142 in the same publication show how volae project into the valve interior and even collect extra siliceous material, similarly as what happens in the new *Nanofrustulum* species. Other features of the new taxon, similar to those in taxa currently ascribed to *Pseudostaurosira*, are the uneven development of the apical pore fields and the development of troughs at the foot pole, which have also been seen in *Pseudostaurosira clavatum* E.Morales (compare Morales 2002: pl. 4, figs 1, 4, with our figs 1G, K & 2C) and *Pseudostaurosira perminuta* (Grunow) Sabbe & Vyverman (Sabbe & Vyverman 1995: figs 54, 57, 58), though not as developed as in the new taxon.

However, as shown in table 1, *N. rarissimum* has a feature not present in *Pseudostaurosira* as defined here, namely quasifract valvocopulae ("segmented copulae" in Li et al. 2018), only present in representatives of *Nanofrustulum*. Quasifract copulae are present in the type of the genus *N. shiloi* (J.J.Lee, Reimer & McEnery) Round, Hallsteinsen & Paasche (Round et al. 1999: fig. 8). Quasifract copulae are also reported for *Pseudostaurosira cataractarum* (Hust.) C.E.Wetzel, E.Morales & Ector (Wetzel et al. 2013: figs 2F, G), but this species needs to be transferred to *Nanofrustulum* (see below). Viminules are lacking in *Pseudostaurosira* and *Nanofrustulum*, as currently circumscribed, but the new taxon produces them regularly. Due to the complexity of girdle band morphogenesis, the nature of this structure can be con-

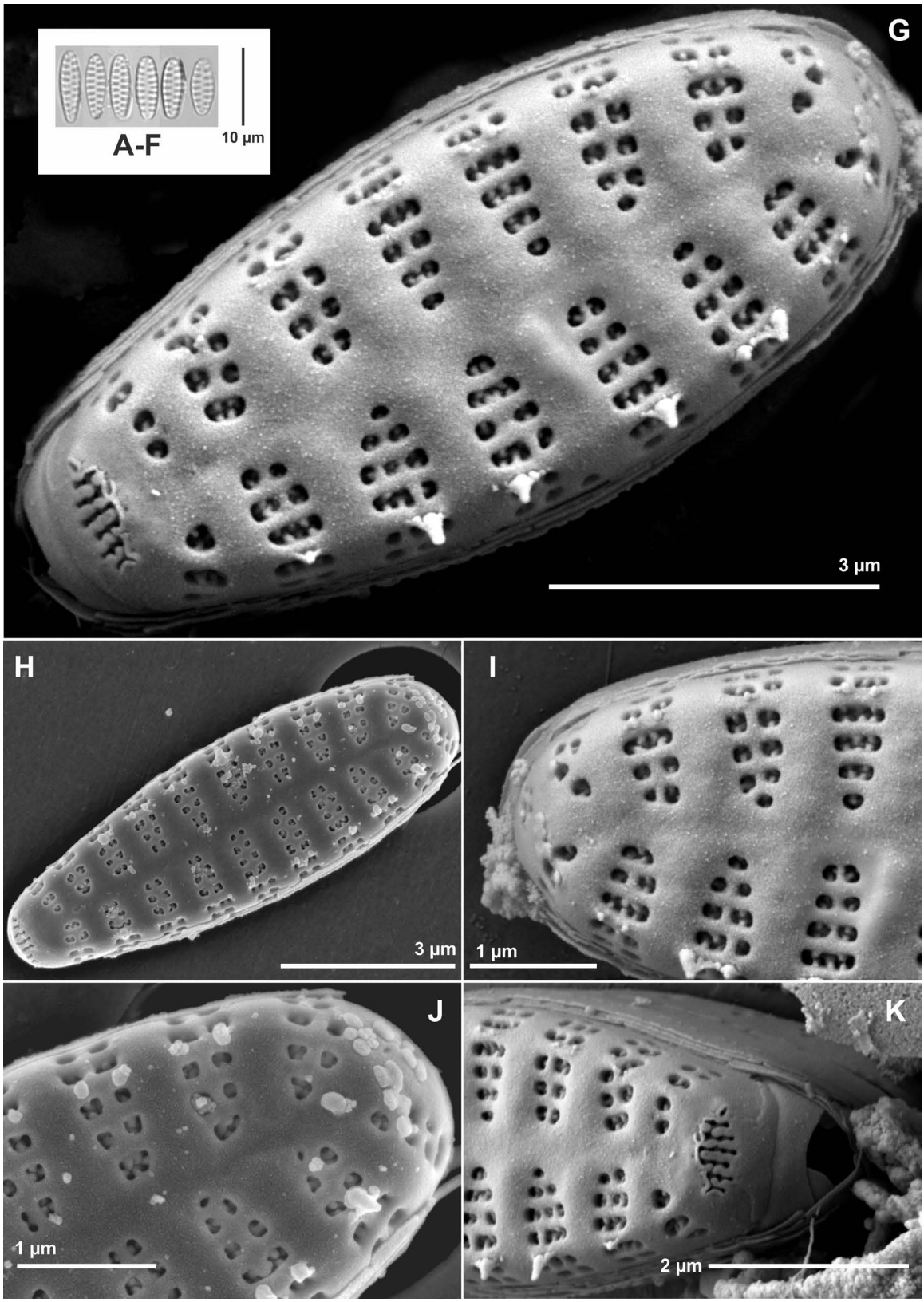

Figure 1 – *Nanofrustulum rarissimum*, LM and SEM images taken from type material (ANSP GC 26815): A–F, size diminution series in LM; G–K, SEM images of external details; G & H, view of entire outer surface showing details of sternum, virgae, striae, spines and apical pore fields. Notice heterovalvarity, also expressed in the apical pore fields, and the skirt-like appearance of the stipulae; I & J, detail of head pole. Notice small apical pore fields near the abvalvar edge of the mantle, and the volae; K, detail of foot pole showing the apical pore field with deep throughs, the closed extreme of the valvocopula and ends of some copulae.

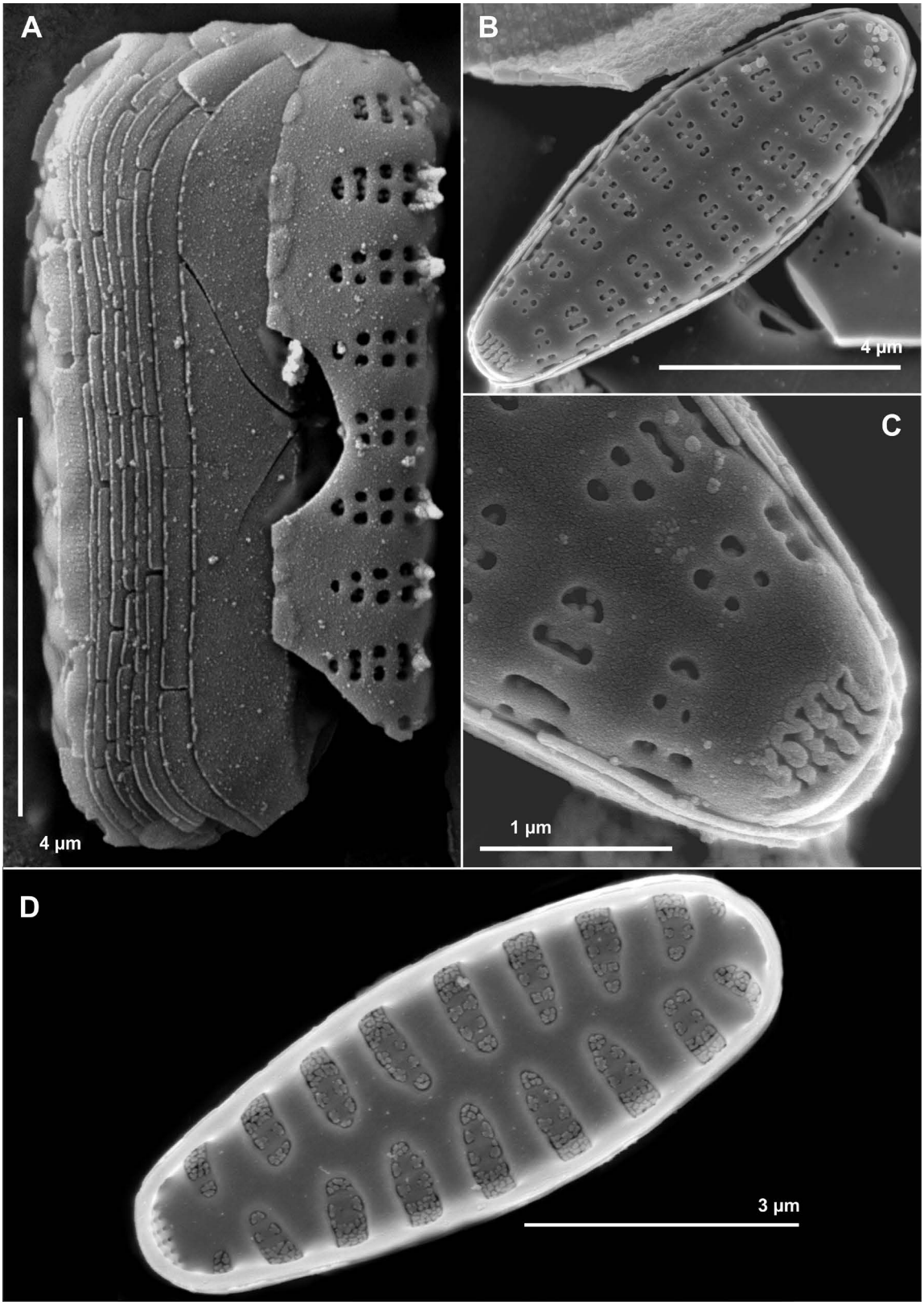

Figure 2 – *Nanofrustulum rarissimum*, SEM images taken from type material (ANSP GC 26815): A, detail of a broken frustule showing girdle structure. Notice entire valvocopula and quasifract copulae, as well as siliceous depositions or plaques on the abvalvar edge of the mantle; B & D, contrast of surfaces. Notice deposition of material on the volae in internal view, and the depressions in which the internal openings of the areolae are contained; C, detail of foot pole showing variability of areolar shape and infrequency of viminule formation.

sidered to have more weight as that of viminules, especially considering that viminule formation may simply require a mechanical reason , i.e. a wider spacing between virgae (Cox 2012). Therefore, *N. rarissimum* can be ascribed to *Nanofrustulum* as the only taxon that produces viminules, thus far.

Another genus that produces viminules is *Punctastriata*. However, the species of this genus have entirely multiseriate striae, with no partial production of viminules as in *N. rarissimum*. Additionally, *Punctastriata* lacks quasifract bands and its valvocopula have fimbriae.

The following combined features differentiating *N. rarissimum* from other taxa currently assigned to *Nanofrustulum* are: heteropolarity of the valves, production of developed apical pore fields and multiseriate areolae, the latter being the most prominent feature characterizing the new taxon. Another salient feature is the heteropolarity of the apical pore fields and the cavernous structure of the one at the foot pole.

The epipsammic sample from Bolivia in which *N. rarissimum* was found contains several new araphid taxa (Morales et al. 2012). It is characterized by a high taxon richness (228 species and varieties), with a high proportion of unknowns. *Nanofrustulum rarissimum* was rare in the material, and does not appear in a 500 valve count made by Morales et al. (2012: table 1). Analysis of nearby localities, other than the Desaguadero River (Morales, unpublished data) did not yield additional valves of the new taxon, suggesting that it is restricted to the river. One reason could be that the river is dominated by high sediment in the water and the entire river bed at the site of collection is dominated by sand and finer sediments, with no development of aquatic vegetation. The characteristics of sites nearby are quite different, varying from small streams with high flow of clear water (with beds covered by rock, moss and other High Andean vegetation), to shallow lentic systems that are ephemeral or permanent and fed by ice melting or ground water (with emergent vegetation and with much lower deposition of fine sediments and sand). These latter waterbodies are strongly affected by metamorphic rock due to their proximity to the Sajama volcano, while although the Desaguadero has the same rock bottom, it is isolated under several metres of fine sediments on top.

The richness of diatom taxa in the Desaguadero River sample is not uncommon for samples collected in the pristine area of the Titicaca-Sajama Volcano region, far from human-related activities (Morales et al. 2012, 2014c) and contrasting with the European view of the Andean diatom flora (Metzeltin & Lange-Bertalot 1998, Rumrich et al. 2000). The contrast could be explained by the areas that have been commonly collected by foreign scientists, which tend to be located more along roads and close to populated areas, where human activities affect ecosystems and tend to make habitats more uniform and similar in the assemblages they contain (Morales et al. 2012, Goldenberg Vilar et al. 2014).

Assessing the validity of *Popovskayella*

SEM images of *Popovskayella* from Lake Baikal are reminiscent of *Pseudostaurosira*. In fact, Kulikovskiy et al. (2015) state that the latter is the most closely related genus. The distinguishing features of *Popovskayella* are the presence of "one apical row of very small areolae" (which we interpret as one row on the valve face and one on the valve mantle on each stria, based on the fact that none of its species has a single areola composing the striae), the lack of branched volae, the presence of three areolae on the transapical striae, and the presence of a single internal groove running from valve face to mantle, through which, the external openings of individual areolae can be observed. The protologue also mentions the presence of sponge-like silica membranes. Let us consider each of these features.

Because striae are formed independently from each other during valve ontogeny, it is difficult to conceive the existence of "apical striae". That is, in araphid diatoms striae are morphogenetically transapical structures. Therefore, it does not seem useful, at least for small araphids, to consider that areolae are arranged in apical rows and use this as a taxonomic criterion. What is more, the single apical alignments of areolae (one on valve face and one on valve mantle) are also present in several representatives of *Pseudostaurosira*, such as *Pseudostaurosira tenuis* E.Morales & Edlund (Morales & Edlund 2003), *Pseudostaurosira elliptica* (Schumann) Edlund, E.Morales & S.A.Spauld., *Pseudostaurosira microstriata* (Marciniak) Flower, and the generitype *Pseudostaurosira brevistriata* (Grunow) D.M.Williams & Round (Morales et al. 2015). The areolar opening in the latter taxon is much wider than in any of the *Popovskayella* taxa, but areolar diameter is not a distinguishing character since all the genera in table 1 vary widely in the size of the areola opening. Regarding volae, it is difficult to make out why Kulikovskiy et al. (2015) stated that there are no closing plates since these structures occur in the generitype *Popovskayella nanobaculum* Kulikovskiy & Lange-Bert. (Kulikovskiy et al. 2015: pl. 11, fig. 15), *Popovskayella simplex* Kulikovskiy & Lange-Bert. (Kulikovskiy et al. 2015: pl. 12, fig. 8), *Popovskayella minutula* Kulikovskiy & Lange-Bert. (Kulikovskiy et al. 2015: pl. 13, fig. 8) and *Popovskayella tenerrima* Kulikovskiy & Lange-Bert. (Kulikovskiy et al. 2015: pl. 14, fig. 8). These volae can obviously not be highly branched since the areolar aperture is narrow in all these taxa, impeding the profuse development of volae, but it is evident that they are in fact dichotomously branched (e.g. see Kulikovskiy et al. 2015: pl. 13, fig. 8).

What Kulikovskyi et al. (2015) regarded as a single areola in internal view is in fact the extreme expression of the depressed striae that are present in all nine genera in table 1. What they term an areola in internal view does not correspond to such a structure from a morphogenetic perspective. Areolae are formed by production of vimines, which in conjunction with the virgae delimit the areolar openings. A single internal opening, therefore, corresponds to a depression where individual areolae open to the valve interior, in this case much deeper due to heavy silicification of sternum and virgae. Because of the small size of the valves in all the *Popovskayella* species, it is expected that the stria depression becomes deeply marked as the sternum and the virgae thicken in a transapical and pervalvar direction. In small-valved taxa of *Pseudostaurosira* such deep depressions can be seen, as in, for example, *Pseudostaurosira microstriata* (Marciniak 1982: pl. 2, fig. 6) and *Pseudostaurosira tenuis* (Morales & Edlund 2003: fig. 41).

The sponge-like silica membranes seem to be a misinterpretation of the structure shown in Kulikovskiy et al. (2015: pl. 12, fig. 5). This figure shows small volae projecting inward from the inner periphery of the areolae. The apical portions of the valve in this figure are covered by material which could correspond to excess amounts of the coating applied for SEM analysis or to an organic layer impregnated with mineral depositions, frequent in material that is only partially clean.

Using the information for *Pseudostaurosira* in table 1, we conclude that *Popovskayella* species are in fact members of the former genus and should be transferred to this genus (see section New combinations). They have as distinguishing features wide and short vimines, they lack viminules, their areolae are round to transapically ellipsoid and arranged in a single series along the striae. The volae originate from the inner perimeter of the areolae, and there is no evidence of rotae. Unfortunately, there is no information on girdle band structure for any of the species.

Evaluation of genera based on molecular information

The molecular phylogenies presented to date for small araphids lacking rimoportulae are based on very limited taxon sampling. Genera such as *Pseudostaurosira*, *Staurosira* and *Staurosirella* now contain dozens of taxa (Guiry & Guiry 2018) and including even ten species per genus in any phylogeny (many are currently represented by only one in most trees) might still be unrepresentative of the larger groupings. Thus far, the separation of small araphids from the larger fragilarioids having a rimoportula seems to be convincingly resolved; this seems to hold regardless of the genes used (Medlin et al. 2008). A more recent tree, used for many important taxonomic decisions (Li et al. 2018), does not offer better resolution than that of older phylogenies.

Ninety-nine strains were used by Li et al. (2018: table 3), representing 33 taxa (six of which are unknown) in eight known and one unknown genera. Eight of the nine genera included in our table 1 appear in that phylogeny (Li et al. 2018, S1), where they are represented by ten known species (with several strains) and nine undetermined strains. Of the strains used, 119 belong to eightteen genera, but twelve of them are represented by three strains or less. Although the phylogeny presented by Li et al. (2018) is informative, taxon sampling can be a serious shortcoming in any phylogenetic analysis (Theriot 2008, Theriot et al. 2010) and perceptions of relationships may change drastically as more taxa and genes are added (Sato et al. 2008, Theriot 2008). Additionally, the approach adopted by Medlin et al. (2012), Medlin & Desdevises (2016), and Li et al. (2016), which all have tried to fit morphological data into inferred molecular phylogenies *a posteriori* is risky (Theriot 2008, Williams 2013), because phylogenies and morphology are not treated using a common methodology, or because morphological data are not analysed at all before they are incorporated into phylogenetic reconstructions. This may explain why the morphogenetic approach we follow here, yielding a clear-cut pattern among the nine genera presented in table 1, appears to be in conflict with the conclusions of previous authors (Medlin et al. 2012, Medlin & Desdevises 2016, Li et al. 2018).

Superimposing ecological information *a posteriori* onto phylogenies also requires further and careful consideration. For example, Medlin & Desdevises (2016) stated that the members of their new family Staurosiraceae (comprising *Nanofrustulum*, *Opephora*, *Plagiostriata* and *Staurosira*) are bottom-dwelling or planktonic, never epiphytic. However, Frenguelli (1945) reported that, for example, *Opephora schwartzii* (Grunow) P.Petit ex Pelletan grows on marine littoral algae, and Sullivan (1978) listed the same species and two additional ones in the same genus from salt marsh spermatophytes. We add that ecological information should also be analysed using a common methodology, before being added to phylogenetic interpretations.

Williams (2013) took the phylogeny-morphology discussion a step further and expressed that the phylogenies for araphid diatoms presented in the literature do not provide evidence for the nodes formed during tree construction. For us, this deficiency is hard to justify given the amount of available morphological information on fossil and extant araphid diatoms. Indeed, the simultaneous treatment of morphological and molecular data is possible as demonstrated by Frankovich et al. (2018), and this approach might produce a more parsimonious consideration of species and their relationships.

Perhaps, one of the most conspicuous shortcomings in the *a posteriori* attempt to merge morphological and molecular data is that the morphological characterization of taxa used in phylogenies is poorly done. In Li et al. (2018), for example, the size diminution series for taxa presented in figs 39–129 contains a mixture of morphological variants that do not seem to fit with each other. Since the authors stated that all microscope analyses were performed using old and new cultures, as well as field collected material, their arrangement of LM photographs and SEM plates seems rather haphazard. This of course, is counterproductive for users of plates and figures at the bench, with the risk of producing misidentifications and ecological misinterpretations. This is precisely one of the implications of Theriot's (2008) and Williams' (2013) reasoning: the degree of attention given to the molecular part of these studies is not the same as that given to the morphological data, to the point that it seems rather impractical (and risky) to join them together.

As stated before, the large amount of work done on analyses of type material of many araphid species has greatly clarified the boundaries of taxa widely cited in the literature and used for applied purposes (e.g. Morales et al. 2015). Therefore, the rather hasty use of names for identification of strains used for phylogenetic reconstruction (e.g. Medlin et al. 2008) is completely unjustified (see also argumentation by Williams 2013). Thus, it seems that investing more effort in the so called "total evidence approach", combining molecular, physiological and ecological information, together with data from nomenclatural types, would add value to current phylogenies.

Clearly then, the elucidation of molecular phylogenies and the search of robust trees that would indicate stable, trustable and statistically plausible relationships among taxa is work in progress. Meanwhile, it is possible to turn our eyes to alternative, equally trustable and testable hypotheses that

find support from expressed features, which in the end are the targets of natural selection (Mann 1999). Besides, there is now evidence pointing to the evolutionary functionality of valve features for nutrient acquisition, control of diatom sinking rate and turbulence, as antipredator mechanisms, etc. (Aitken et al. 2016), features that undoubtedly have an underlying genetic mechanism for their generation.

Also using table 1, we can analyze the validity of *Serratifera* (Li et al. 2016) and *Gedaniella* (Li et al. 2018), two genera erected based on molecular information. Using the distinguishing feature approach, there is no one feature that would separate *Serratifera* from the rest of the nine genera included in table 1. The general Bauplan of this genus is reminiscent of *Pseudostaurosira*. Li et al. (2016) stated that their new genus can be characterized by lack of rimoportulae (all genera considered in table 1 do), possession of a "short, single round-to-elliptical areolae per stria" and lack of mantle areolae. Since in their ontogenetic explanation the authors refer to the striae as a single structure running continuously from the axial area to the mantle, considering striae as composed of single areola and then mentioning a lack mantle areola is an unnecessary redundancy. Their figs 2a–f show valve formation in *Serratifera varisterna* Chunlian Li, Ashworth & Witkowski, the generitype, which mirrors the process we described above: the areolae that appear in a mantle in related diatoms are simply covered with a further growth of the virgae – a slit between virgae is produced initially and then gradually reduces in length until only one areola is left on the valve face. During this process, a short and wide vimen (the distinguishing character of *Pseudostaurosira*) is formed at the future valve face-mantle transition (fig. 2c) and then the open virgae ends fuse and fill all the space on the mantle (fig. 2d). In fact, filling of the areolae is a common process in some species of *Pseudostaurosira*. In *P. subsalina*, for example, some of the areolae are filled in on the valve face (Cejudo-Figueiras et al. 2011: figs 94, 97), and this also happens in *Pseudostaurosira alvareziae* Cejudo-Figueiras, E.Morales & Ector (Cejudo-Figueiras et al. 2011: figs 103, 104). This latter species also presents filled-in areolae on the mantle (Cejudo-Figueiras et al. 2011: figs 101, 103), a process also occurring in *P. sajamaensis* (Morales et al. 2012: fig. 55).

Therefore, the valves produced in *S. varisterna* are congruent with those in *Pseudostaurosira*, except for the production of mantle areolae; we propose to consider the latter as a feature at the species level, not as a discriminating character for the genus. That is, the shape of the areolae, features of the volae, the entire, open, ligulate, non-areolate girdle bands, and even the way colonies are formed (Li et al. 2016: fig. 1l) in species of *Serratifera*, are all shared by species currently placed in *Pseudostaurosira*.

In 2018, Li et al. amended their protologue of *Serratifera* to include species having two areolae per striae (sometimes even three), one located on the valve mantle. They added (Li et al. 2018: 63) "…we have been unable to find a synapomorphic character to define this genus". Then, they stated that several combinations of characters can be used to distinguish the species they describe in the genus, which (we add) could be used to perfectly distinguish them once they are transferred into *Pseudostaurosira* instead. The fact that three *S. varisterna* clones (*S. varisterna* is the generitype of *Serratifera*) cluster together with clones of *Nanofrustulum* and *Pseudostaurosira* in a subgrouping within their "Clade "A" Fragilariaceae" is partial molecular support for our conclusion (Li et al. 2016: fig. 10).

The genus *Gedaniella* (Li et al. 2018) contains at least two forms that can be easily separated from each other: those with entire, open, unperforated girdle bands and those with quasifract copulae. Unfortunately, the type species *G. boltonii* Chunlian Li, Krawczyk, Dąbek & Witkowski is in itself a mixture of these two forms, which we separate in the new combinations section below. The larger valves shown by Li et al. (2018: figs 191–198) belong in *Sarcophagodes*, since they have wide and long vimines delimiting apically elongated areolae. They also have the entire, unperforated, open girdle bands characteristic of this latter genus (Li et al. 2018: fig. 198). At least some of the small forms presented as *G. boltonii*, such as the one depicted by Li et al. (2018: fig. 204), have quasifract copulae and they belong in *Nanofrustulum*, but we do not transfer these small forms until more precise information regarding their structure is available.

Gedaniella flavovirens (Takano) Chunlian Li, Witkowski & Ashworth, is also an undefined mixture of morphologically different small and large valves that do not seem to belong to the same diminution series. Takano (1986), when describing *Fragilaria flavovirens* Takano, the basionym of *G. flavovirens*, stated that the change from the small to the large forms he included in his taxon was never observed in culture, but the reasons were never stated. Therefore, the type material should be reanalysed and a diligent study using SEM and morphometrics (if needed) should clarify the relationship between small and large valves and the identity of this taxon as a whole. As for the material presented in Li et al. (2018), larger forms surely belong in *Pseudostaurosira* since they have short and wide vimines and entire and open bands (Li et al. 2018: figs 235–240), while smaller forms belong in *Nanofrustulum* since they have slender and short vimines and quasifract bands (Li et al. 2018: figs 249, 250).

Once redefined, *Fragilaria flavovirens* should be compared with *Pseudostaurosira americana*, *P. trainori* E.Morales, *Pseudostaurosira sopotensis* (Witkowski & Lange-Bert.) E.Morales, C.E.Wetzel & Ector (the latter two being transferred to *Nanofrustulum* below) and *P. ovalis* Lilitskaya to confirm conspecificity. Thus far, there are no solid grounds to merge some of these species as suggested by Li et al. (2018, see comment for *Nanofrustulum sopotensis* comb. nov. and *N. trainori* comb. nov. below). Regarding *Pseudostaurosira americana*, there also seem to be differences with *Fragilaria flavovirens* in valve outline among larger forms, those of *P. americana* being cuneate to subrostrate and having the valve width rather stable (4.5–5 μm).

Other species currently under *Gedaniella*, such as *G. alfred-wegeneri* Chunlian Li, Shin.Sato & Witkowski, and *G. arenaria* Chunlian Li, Witkowski & Shin.Sato belong in *Sarcophagodes* (see below) since they have wide, long vimines and apically elongate areolae. Other species such as *G. paucistriata* Chunlian Li & Witkowski should be transferred to *Pseudostaurosira* based principally on its wide and short vimines. In the case of *G. panicellus* Chunlian Li, S.X.Yu

& Witkowski it is hard to decide in which genus to allocate it, given the mixed information presented in Li et al. (2018). Some of the forms seem to belong in *Sarcophagodes* due to their apically elongated areolae separated by wide and long vimines (e.g. Li et al. 2018: figs 269–274), while others seem to belong to *Staurosira* (e.g. Li et al. 2018: fig. 263). Their transfer is deferred until more information is available.

NOMENCLATURAL CHANGES

Some of the combinations demonstrated to be needed are given here, while others are pending until more SEM information is gathered (e.g. *Fragilaria gedanensis* Witkowski, for which there is no information on girdle band structure and confirmation of hymens in the areolae is required: see Witkowski 1993). Comments are provided for taxa requiring some clarification.

Li et al. (2018) stated that *Serratifera opephoroides* (Takano) Chunlian Li & Witkowski, based on *Fragilaria opephoroides* Takano (Takano 1988) is conspecific with *Pseudostaurosira naveana* (Le Cohu) E.Morales & Edlund. Until this is proven through analysis of type material of both species, we defer the transfer of *S. opephoroides* to the genus *Pseudostaurosira*.

Nanofrustulum cataractarum (Hust.) C.E.Wetzel, E.Morales & Ector, **comb. nov.**

Basionym – *Melosira cataractarum* Hust., Archiv für Hydrobiologie, Supplement 15: 142, pl. 9, figs 6, 7. 1938 (Hustedt 1938). – Type: Java, Tjibeureum Wasserfall, TJ2.III.c., BRM material AS1524 (holo-: BRM, slide no. A2/27).

Synonym – *Pseudostaurosira cataractarum* (Hust.) C.E.Wetzel, E.Morales & Ector in Wetzel et al. (2013).

Comment – This species, as shown by Wetzel et al. (2013: fig. 2F & G), has quasifract copulae, the distingushing feature of the genus *Nanofrustulum*. All the morphological features of this taxon and its distinction from closely related taxa are presented by these authors.

Nanofrustulum krumbeinii (Witkowski, Witak & Stachura) E.Morales, **comb. nov.**

Basionym – *Opephora krumbeinii* Witkowski, Witak & Stachura in Lange-Bert. & Genkal, Iconographia Diatomologica 6: 80, pl. 3, figs 1–17, pl. 4, figs 1–3. 1999 (Lange-Bertalot & Genkal 1999). – Type: Poland, Baltic Sea, Puck Bay, coastal shallows, Oct. 1993, *A. Witkowski* s.n. (holo-: SZCZ, slide Chalupy X.1993A). Not seen.

Comment – This taxon also possesses quasifract copulae (Lange-Bertalot & Genkal 1999: pl. 3, fig. 12). Other features such as areolae, volae, spines and apical pore fields are similar to those in *N. shiloi* (Round et al. 1999).

Nanofrustulum sopotensis (Witkowski & Lange-Bert.) E.Morales, C.E.Wetzel & Ector, **comb. nov.**

Basionym – *Fragilaria sopotensis* Witkowski & Lange-Bert., Limnologica 23: 67, figs 6a–p. 1993 (Witkowski & Lange-Bertalot 1993). – Type: Poland, Puck Bay, salt meadow in Wladyslawowo, 1991, *A. Witkowski* s.n. (holo-: Institute of Oceanography, University of Gdansk, Gdynia, Poland, slide no. WL (A, IV. 91)).

Comment – The species has quasifract copulae (Witkowski & Lange-Bertalot 1993: figs 6m, o). All the rest of the features of this small species are reminiscent of other species ascribed to the genus. It is very similar to *P. trainori*, also transferred to *Nanofrustulum* below. Analysis of type material of both species is needed to establish further differences than those highlighted in Morales (2001) and Morales et al. (2010a). At the LM level, both species can be distinguished based on stria density (13–17 in *N. sopotensis* comb. nov. and 20–25 in *N. trainori* comb. nov.).

Nanofrustulum sourniae (Chunlian Li, Riaux-Gob. & Witkowski) E.Morales, Novais & M.Morais, **comb. nov.**

Basionym – *Serratifera sourniae* Chunlian Li, Riaux-Gob. & Witkowski in Li et al. 2018, Phytotaxa 355: 83, figs 36, 172–175, 437–448. 2018 (Li et al. 2018). – Type: Madagascar, Nosy Be coastal zone, 13°29′4.8″S, 48°14′13.2″E, rock surface, Jul. 2014, *A. Witkowsky & C. Riaux-Gobin* s.n. (holo-: BM, slide BM 101907; iso-: SZCZ, slide SZCZE517). Not seen.

Comment – This species clearly belongs to *Nanofrustulum* since it has quasifract copulae. Unfortunately, Li et al. (2018) in their amended description of the genus *Serratifera* did not discuss the girdle bands, so it is difficult to find what their complete interpretation of this structure is, beyond what is written in their protologue on page 63. It is advisable to reanalyse type material of this taxon since the range of valve size and features seem too broad, with larger, clavate forms (Li et al. 2018, figs 439, 443–446, 448) being different from smaller, round to elliptical individuals, especially regarding the shape of the areolae and apical pore fields.

Nanofrustulum trainori (E.Morales) E.Morales, **comb. nov**.

Basionym – *Pseudostaurosira trainori* E.Morales, Proceedings of the Academy of Natural Sciences of Philadelphia 151: 113, 114, figs 6a–l. 2001 (Morales 2001). – Type: Connecticut, Avery Pond, surface sediment, *P.A. Siver* s.n. (holo-: ANSP, material no. 4198).

Comment – This taxon also has quasifract copulae, a feature that had not been mentioned in the original publication, but it was illustrated (Morales 2001: fig. k) and confirmed upon our re-analysis of material from the type locality. The remaining features of the taxon are similar to those of other species in the genus. It was originally though that one of the main features of this species at the SEM level was the serrate spines, however, *N. shiloi* (Li et al. 2018: fig. 282) and *N. sopotensis* also have this feature (C.E. Wetzel, unpublished).

Pseudostaurosira andersonii (Chunlian Li, Dąbek & Wachn.) E.Morales, C.E.Wetzel & Ector, **comb. nov.**

Basionym – *Serratifera andersonii* Chunlian Li, Dąbek & Wachn. in Li et al., Phytotaxa 355: 63, figs 29, 120–129, 360–373. 2018 (Li et al. 2018). – Type: South Africa, Kraalbaai, 33°08′16.4″S, 18°01′34.6″E, muddy rock pools, May 2015, *P. Dąbek* s.n. (holo-: BM, slide BM 101898; iso-: SZCZ, slide SZCZCH1126). Not seen.

Pseudostaurosira brevis (Chunlian Li & Ashworth) E.Morales, C.E.Wetzel & Ector, **comb. nov.**

Basionym – *Serratifera brevis* Chunlian Li & Ashworth in Li et al., Phytotaxa 355: 66, figs 31, 138–142, 385–392. 2018 (Li et al. 2018). – Type: Hawaii, unspecified benthic environment, Jan. 2012, *N. Leclear* s.n. (holo-: BM, slide BM 101900; iso-: Theriot Lab Collection, University of Texas, Austin, slide HK446). Not seen.

Pseudostaurosira bronkei (Witkowski, Lange-Bert. & Metzeltin) C.E.Wetzel & E.Morales, **comb. nov.**

Basionym – *Fragilaria bronkei* Witkowski, Lange-Bert. & Metzeltin, Iconographia Diatomologica 7: 48 (English), 427 (Latin), pl. 12, figs 1–12. 2000 (Witkowski et al. 2000). – Type: Poland, Gulf of Gdansk, Mar. 1992, *A. Witkowski* s.n. (holo-: SZCZ Collection Cholnoky, slide SO5/III.93/BB). Not seen.

Pseudostaurosira coralina (Chunlian Li, Górecka & C.J.Kwon) E.Morales, C.E.Wetzel & Ector, **comb. nov.**

Basionym – *Serratifera corallina* Chunlian Li, Górecka & C.J.Kwon in Li et al. 2018, Phytotaxa 355: 71, figs 148–151, 399–404. 2018 (Li et al. 2018). – Type: Philippines, Cebu Island, Moal Boal, 09°56′57.7″N, 123°21′55.4″E, submarine rock cliff, water depth of 50 m, *Dr. Kwon* s.n. (holo-: BM, slide BM 101897; iso-: SZCZ, slide SZCZE1544). Not seen.

Pseudostaurosira frugalis (Kulikovskiy & Lange-Bert.) E.Morales, C.E.Wetzel & Ector, **comb. nov.**

Basionym – *Popovskayella frugalis* Kulikovskiy & Lange-Bert. in Kulikovskiy et al., Iconographia Diatomologica 26: 21, 22, pl. 13, figs 9–11. 2015 (Kulikovskiy et al. 2015). – Type: Lake Baikal, Bolshoi Ushkaniy Island, Jul. 1965, *A.P. Skabitschewsky* (holo-: Collection Maxim Kulikovskiy, I.D. Papanin Institute for Biology of Inland Waters, Russian Academy of Sciences (IBIW), slide no. 15650m; iso-: SZCZ, slide SZCZ15650a). Not seen.

Pseudostaurosira liae E.Morales, **nom. nov.**

Replaced synonym – *Serratifera clavata* Chunlian Li, Tomczak & Witkowski in Li et al., Phytotaxa 355: 68, figs 32, 143–147, 393–398. 2018 (Li et al. 2018). – Type: Abu Dhabi, Persian Gulf, 24°28′53.4″N, 54°20′43.2″E, sand in shallow water, Oct. 2014, *M. Tomczak* s.n. (holo-: BM, slide BM 101901; iso-: SZCZ, slide SZCZCH752). Not seen.

Comment – A new name is required for this taxon in order to transfer it to *Pseudostaurosira* since the epithet *clavatum* is already taken by *P. clavatum* E.Morales (Morales 2002).

Etymology – This diatom is named after Dr. Chunlian Li for her contributions to diatom systematics.

Pseudostaurosira linearis (Pant.) E.Morales, Buczkó & Ector, **comb. & stat. nov.**

Lectotype (here designated): permanent slide HNHM-ALG-D002264, Algological Collection of Hungarian Natural History Museum Budapest (HNHM). English Finder Q32; Figs 3A–AC & 4A–L.

Basionym – *Fragilaria pinnata* var. *linearis* Pant., A pozsonyi Orvos-Természettudományi Egyesület közleményei 23: 30, pl. 2, figs 65, 68 (as *F. mutabilis* var. *linearis* in figure legend). 1913 (Pantocsek 1913).

Synonym – *Fragilaria pinnata* var. *ovalis* Pant., A pozsonyi Orvos-Természettudományi Egyesület közleményei 23: 30, pl. 2, figs 66, 67 (as *F. mutabilis* var. *ovalis* in figure legend). 1913 (Pantocsek 1913).

Comment – We synonymize these two taxa described by Pantocsek (1913: figs 16–43) since no differences were observed between them under SEM (fig. 4). Outer and inner valve features of sterna, areolae, spines (T-shaped, bearing M- or inverted V-shaped stipulae), and apical pore fields are the same for all valves of all sizes found in the sample from Lutila (compare smaller and larger forms in fig. 3B–X). Both varieties have equal priority, but we choose "*linearis*" since it describes well the valve outline of the larger valves of this taxon, which can vary in the width of its apices, from more broadly rounded to almost cuneate. Based on new measurements, we expand the valve dimension ranges for this taxon to length: 2–34 µm, width: 2.5–4.8 µm. The stria density is 12–14 in 10 µm.

Pseudostaurosira linearis resembles *Pseudostaurosira polonica* (Witak & Lange-Bert.) E.Morales & Edlund (Witkowski et al. 1995); their valve dimensions intergrade to a large extent (length: 10–30 µm, width: 3.5–5 µm in *P. polonica*). We have found that the median for stria density in *P. linearis* is 13 and that for *P. polonica* is 16. Also, the areolae in *P. polonica* are more transapically elongated, while they are round in *P. linearis.* On the other hand, smaller forms of *P. linearis* could be confused with *P. elliptica*, but they can be distinguished mainly by the stria density, which is 14–16 per 10 µm in the latter.

One salient feature of *P. linearis* is the transitional zone between valve face and mantle. This is a feature also found in the generitype *P. brevistriata* (Morales et al. 2015) and in *P. polonica* (Witkowski et al. 1995). Thus far, *P. linearis* has only been reported from fossil material.

Pseudostaurosira marciniakae Ector, E.Morales, C.E.Wetzel, **nom. & stat. nov.**

Replaced synonym – *Fragilaria pseudoconstruens* var. *rhombica* Marciniak, Acta Geologica Academiae Scientiarum Hungaricae 25: 164–165, pl. 2, fig. 5. 1982 (Marciniak 1982). – Type: Poland, Tatra Mountains, Przedni Staw Lake, *B. Marciniak* core no. 2. (holo-: Collection of Institute of Geological Sciences, Polish Academy of Sciences, Warsaw, slide no. 3024).

Etymology – This species is named in honour of Dr. Barbara Marciniak for her contributions in paleoecology and the study of fossil diatoms.

Comment – An alternative name is necessary because the epithet *rhombica* is in use at species level in the genus (see below).

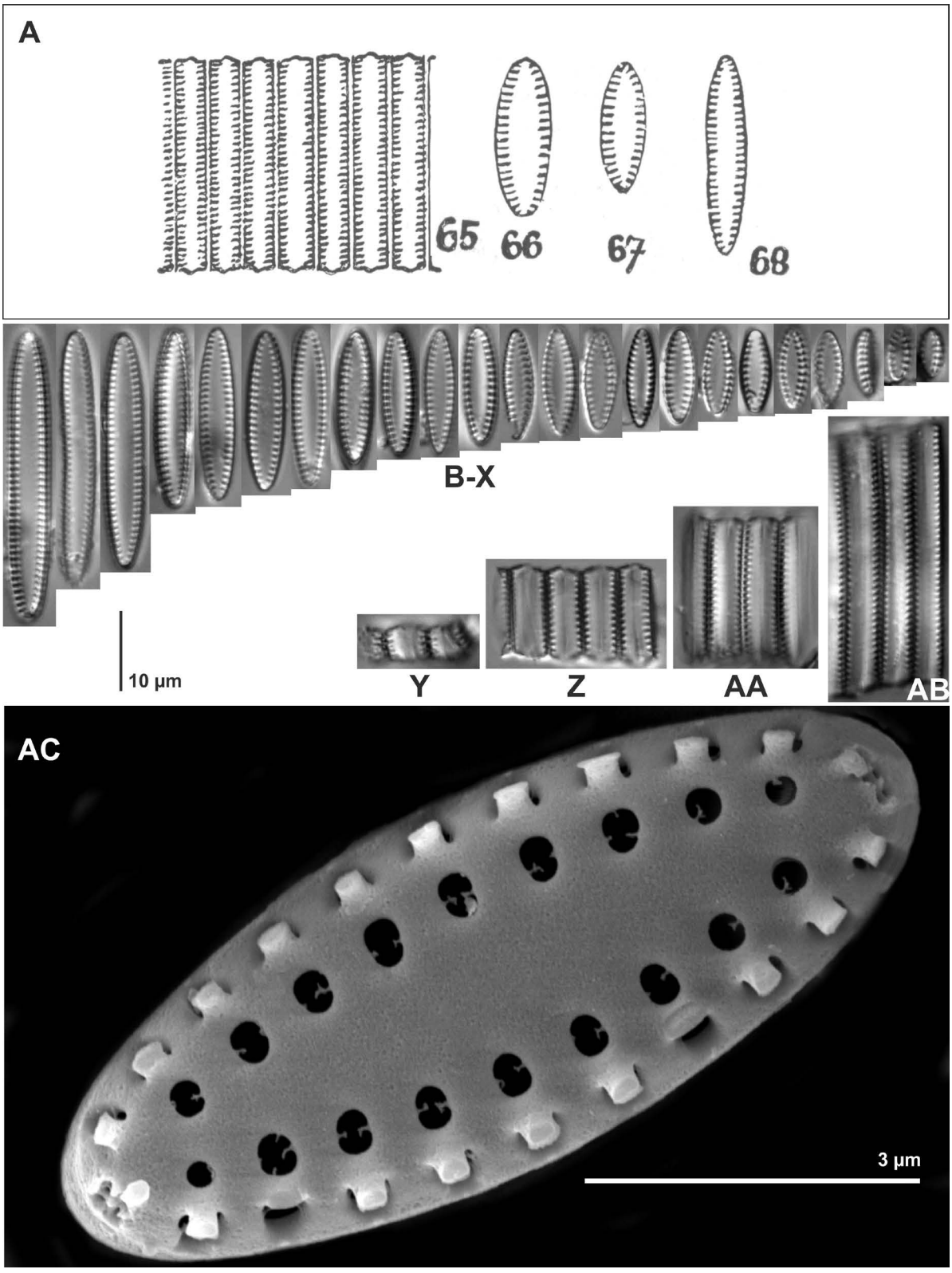

Figure 3 – *Pseudostaurosira linearis*, drawings, LM and SEM depictions from the fossil Lutila material, Slovakia: A, reproduction of Pantocsek's original drawings (1913: p. 14, pl. 2, figs 65–68). His figs 65 and 68 were orignally labelled as *Fragilaria mutabilis* var. *ovalis*, while 66 and 67 were labelled as *Fragilaria mutabilis* var. *linearis*; B–AB, size diminution series and girdle views of colonies in LM. Notice that wider and slender valves have all other features (sternum, striae, frustule shape and valve outline) similar to each other; AC, external features of a valve (SEM) showing details of areolae, spine position, apical pore fields and the characteristic transition zone between valve face and abvalvar portion of mantle. Also note point of insertion within the areolae of eroded volae.

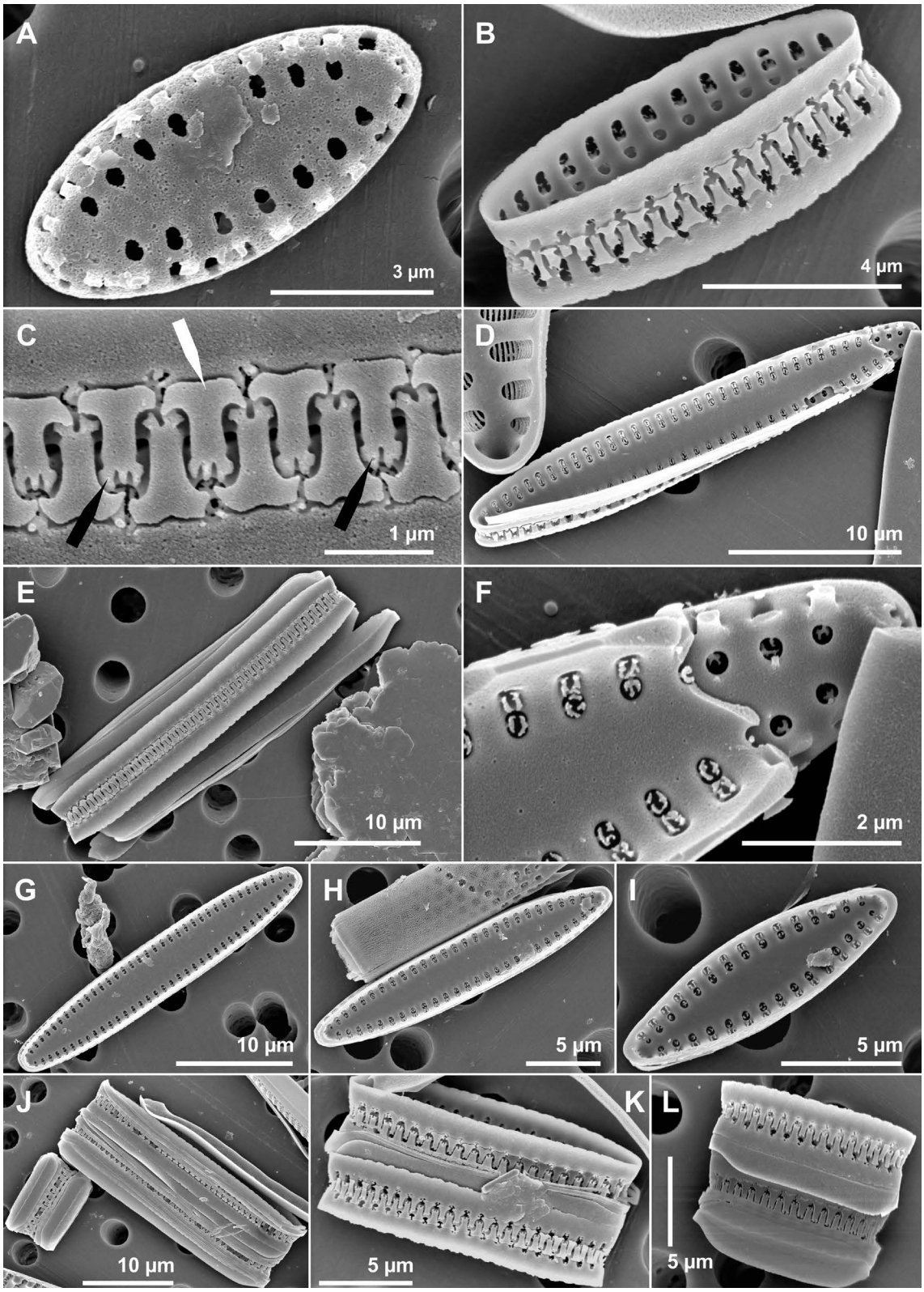

Figure 4 – SEM images of *Pseudostaurosira linearis*, from the fossil Lutila material, Slovakia: A, external view; B & C, side view of attached neighbouring valves and detail of spine connection. Notice "T" shape of spines (white arrow) and "M" or inverted "V" shaped stipulae (black arrows); D & F, broken valve in inner view on top of a complete valve in outer view. Notice that in the zoomed image of this large specimen the characteristic transitional zone of the valve mantle is also present; E & J–L, side views of connected valves showing details of open, unperforated girdle bands and the resemblance among large and small connected valves; G–I, diminution series of internal views also showing similarities among larger and smaller representatives.

Pseudostaurosira minutula (Kulikovskiy & Lange-Bert.) E.Morales, C.E.Wetzel & Ector, **comb. nov.**

Basionym – *Popovskayella minutula* Kulikovskiy & Lange-Bert. in Kulikovskiy et al., Iconographia Diatomologica 26: 22, pl. 13, figs 1–8. 2015 (Kulikovskiy et al. 2015). – Type: Lake Baikal, Bolshoi Ushkaniy Island, Jul. 1965, *A.P. Skabitschewsky* s.n. (holo-: Collection Maxim Kulikovskiy, I.D. Papanin Institute for Biology of Inland Waters, Russian Academy of Sciences (IBIW), slide no. 15646m; iso-: SZCZ, slide SZCZ15646a). Not seen.

Pseudostaurosira namibica (Chunlian Li & Witkowski) E.Morales, C.E.Wetzel & Ector, **comb. nov.**

Basionym – *Serratifera namibica* Chunlian Li & Witkowski in Li et al., Phytotaxa 355: 71, 72, figs 152–156, 405–412. 2018 (Li et al. 2018). – Type: Namibia, Sandwich Harbor lagoon, sediment core, Apr. 2013, *A. Witkowski & P. Dąbek* s.n. (holo-: BM, slide BM 101902; iso-: SZCZ, slide SZCZP88). Not seen.

Pseudostaurosira nanobaculum (Kulikovskiy & Lange-Bert.) E.Morales, C.E.Wetzel & Ector, **comb. nov.**

Basionym – *Popovskayella nanobaculum* Kulikovskiy & Lange-Bert. in Kulikovskiy et al., Iconographia Diatomologica 26: 22, 23, pl. 11, figs 1–18. 2015 (Kulikovskiy et al. 2015). – Type: Lake Baikal, Bolshoi Ushkaniy Island, Jul. 1965, *A.P. Skabitschewsky* s.n. (holo-: Collection Maxim Kulikovskiy, I.D. Papanin Institute for Biology of Inland Waters, Russian Academy of Sciences (IBIW), slide no. 15646m; iso-: SZCZ, slide SZCZ15646a). Not seen.

Pseudostaurosira nosybeana (Chunlian Li, Witkowski & Riaux-Gob.) E.Morales, C.E.Wetzel & Ector, **comb. nov.**

Basionym – *Serratifera nosybeana* Chunlian Li, Witkowski & Riaux-Gob. in Li et al., Phytotaxa 355: 74, figs 157–160, 413–419. 2018 (Li et al. 2018). – Type: Madagascar, Nosy Be Island, 13°29′4.8″S, 48°14′13.2″E, rock surface, Jul. 2014, *A. Witkowski & C. Riaux-Gobin* s.n. (holo-: BM, slide BM 101903; iso-: SZCZ, slide SZCZCH992). Not seen.

Pseudostaurosira parkii (Chunlian Li & Ashworth) E.Morales, Novais & M.Morais, **comb. nov.**

Basionym – *Serratifera parkii* Chunlian Li & Ashworth in Li et al., Phytotaxa 355: 79, figs 33, 161–165, 420–424. 2018 (Li et al. 2018). – Type: South Korea, Tongyeong, vicinity of the LNG Terminal, 34°56′46.2″N, 128°25′46.2″E, mud from sand, Oct. 2014, *J. Park* s.n. (holo-: BM, slide BM 101904; iso-: Theriot Lab Collection, University of Texas, Austin, slide HK507). Not seen.

Pseudostaurosira paucistriata (Chunlian Li & Witkowski) E.Morales, C.E.Wetzel & Ector, **comb. nov.**

Basionym – *Gedaniella paucistriata* Chunlian Li & Witkowski in Li et al., Phytotaxa 355: 42, 46, 47, figs 15, 90–94, 275–281. 2018 (Li et al. 2018). – Type: Qingdao, China, 36°05′32″ N, 120°28′10″E, sand at low tide, Jun. 2015, *A. Witkowski & S.X. Yu* s.n. (holo-: BM, slide BM 101893; iso-: SZCZ, slide SZCZCH1281). Not seen.

Pseudostaurosira punctata (Shin.Sato & Chunlian Li) E.Morales, Novais & M.Morais, **comb. nov.**

Basionym – *Serratifera punctata* Shin.Sato & Chunlian Li in Li et al., Phytotaxa 355: 79, figs 34, 166–168, 425–430. 2018 (Li et al. 2018). – Type: Senegal, Dakar, Goree Island, sand in port, Sep. 2006, *S. Matsumoto* s.n. (holo-: BM, slide BM 101905; iso-: Sato Collection, Faculty of Marine Bioscience, Fukui Prefectural University, Fukui, Japan, slide s0386). Not seen.

Pseudostaurosira pusilla (Kulikovskiy & Lange-Bert.) E.Morales, Novais & M.Morais, **comb. nov.**

Basionym – *Popovskayella pusilla* Kulikovskiy & Lange-Bert. in Kulikovskiy et al., Iconographia Diatomologica 26: 23, pl. 13, figs 12–35. 2015 (Kulikovskiy et al. 2015). – Type: Lake Baikal, Bolshoi Ushkaniy Island, Jul. 1965, *A.P. Skabitschewsky* s.n. (holo-: Collection Maxim Kulikovskiy, I.D. Papanin Institute for Biology of Inland Waters, Russian Academy of Sciences (IBIW), slide no. 15646m; iso-: SZCZ, slide SZCZ15646a). Not seen.

Pseudostaurosira rhombica (Shin.Sato, Chunlian Li & Witkowski) E.Morales, Novais & C.E.Wetzel, **comb. nov.**

Basionym – *Serratifera rhombica* Shin.Sato, Chunlian Li & Witkowski in Li et al., Phytotaxa 355: 81–83, figs 35, 169–171, 431–436. 2018 (Li et al. 2018). – Type: Okinawa, Iriomote Island, Japan, 24°12′36″N, 123°25′48″E, Oct. 2005, *T. Watanabe* s.n. (holo-: BM, slide BM 101906; iso-: Sato Collection, Faculty of Marine Bioscience, Fukui Prefectural University, Fukui, Japan, slide s0357). Not seen.

Pseudostaurosira simplex (Kulikovskiy & Lange-Bert.) E.Morales, Novais & M.Morais, **comb. nov.**

Basionym – *Popovskayella simplex* Kulikovskiy & Lange-Bert. in Kulikovskiy et al., Iconographia Diatomologica 26: 24, pl. 12, figs 1–8. 2015 (Kulikovskiy et al. 2015). – Type: Lake Baikal, Bolshoi Ushkaniy Island, Jul. 1965, *A.P. Skabitschewsky* s.n. (holo-: Collection Maxim Kulikovskiy, I.D. Papanin Institute for Biology of Inland Waters, Russian Academy of Sciences (IBIW), slide no. 15645m; iso-: SZCZ, slide SZCZ15645a). Not seen.

Pseudostaurosira takanoi (Shin.Sato & Chunlian Li) E.Morales, Novais & M.Morais, **comb. nov.**

Basionym – *Serratifera takanoi* Shin.Sato & Chunlian Li in Li et al., Phytotaxa 355: 86, 87, figs 37, 176, 449–454. 2018 (Li et al. 2018). – Type: Okinawa, Iriomote Island, Japan, 24°12′36″N, 123°25′48″E, Oct. 2005, *T. Watanabe*, s.n. (holo-: BM, slide BM 101908; iso-: Sato Collection in Faculty of Marine Bioscience, Fukui Prefectural University, Fukui, Japan, slide s0308). Not seen.

Pseudostaurosira tenerrima (Kulikovskiy & Lange-Bert.) E.Morales, Novais & M.Morais, **comb. nov.**

Basionym – *Popovskayella tenerrima* Kulikovskiy & Lange-Bert. in Kulikovskiy et al., Iconographia Diatomologica 26: 24, pl. 14, figs 1–8. 2015 (Kulikovskiy et al. 2015). – Type: Lake Baikal, Bolshoi Ushkaniy Island, Jul. 1965, *A.P. Skabitschewsky* s.n. (holo-: Collection Maxim Kulikovskiy, I.D. Papanin Institute for Biology of Inland Waters, Russian Academy of Sciences (IBIW), slide no. 15646m; iso-: SZCZ, slide SZCZ15646a). Not seen.

Pseudostaurosira varisterna (Chunlian Li, Ashworth & Witkowski) E.Morales, **comb. nov.**

Basionym – *Serratifera varisterna* Chunlian Li, Ashworth & Witkowski in Li et al., Journal of Phycology 52: 1021–1022, figs 1a–l, 2a–f. 2016 (Li et al. 2016). – Type: Texas, Mustang Island, Packary Channel, 27°37.070′N, 97°12.70′W, plankton net, Dec. 2013, *M. Ashworth, C.H. Li, A. Witkowski & E. Theriot* s.n. (holo-: BM, slide BM 101829; iso-: SZCZ, slide SZCZCH168). Not seen.

Comments – Wide and short vimines, the distinguishing feature of *Pseudostaurosira*, characterize the striae of this taxon, which are also composed of transapically elongated areolae. The spines located on the vimines, the reduced apical pore fields present at both valve apices and the entire, open, unperforated girdle bands, are features that also appear in other species included in the genus.

Pseudostaurosira wachnickiana (Chunlian Li, Witkowski & Ashworth) E.Morales, Novais & M.Morais, **comb. nov.**

Basionym – *Nanofrustulum wachnickianum* Chunlian Li, Witkowski & Ashworth in Li et al., Phytotaxa 355: 50, figs 18, 19, 97, 98, 300–311. 2018 (Li et al. 2018). – Type: Florida, Marquesas, sediment in shallow water, Aug. 2013, *A. Wachnicka* s.n. (holo-: BM, slide BM 101896; iso-: SZCZ, slide SZCZCH285). Not seen.

Comments – This taxon has entire, open, unperforated girdle bands. The distinguishing trait of *Pseudostaurosira*, wide and short vimines, is also present in this taxon. All the remaining features such as transapically elongated areolae, spines bearing stipulae and presence of flaps and plaques on the abvalvar edge of the mantle are characteristic of other species in *Pseudostaurosira*.

Sarcophagodes alfred-wegeneri (Chunlian Li, Shin.Sato & Witkowski) E.Morales, Novais & M.Morais, **comb. nov.**

Basionym – *Gedaniella alfred-wegeneri* Chunlian Li, Shin. Sato & Witkowski in Li et al., Phytotaxa 355: 30, 32–34, figs 8, 60–62, 217–221. 2018 (Li et al. 2018). – Type: Bremerhaven, River Weser, mud, Jul. 2005, *S. Sato* s.n. (holo-: BM, slide BM 101894; iso-: SZCZ, slide SZCZs0263). Not seen.

Comment – This taxon has wide and long vimines and the areolae are apically elongated, some of them having a reniform shape, the unique traits of the genus (table 1). Though the striae are longer since they are composed of a larger number of areolae, the general features of this taxon are similar to *S. delicatula* E.Morales, the generitype of *Sarcophagodes* (Morales 2002). As it happens in the latter species, the vimines situated at the valve face–mantle transition are thicker and bear rudimentary spines or a ridge (Li et al. 2018: fig. 220). All the other features (heteropolarity of valves, volae, and apical pore fields) are similar in both taxa.

Sarcophagodes arenaria (Chunlian Li, Witkowski & Shin. Sato) E.Morales, C.E.Wetzel & Ector, **comb. nov.**

Basionym – *Gedaniella arenaria* Chunlian Li, Witkowski & Shin.Sato in Li et al., Phytotaxa 355: 34, figs 9, 63–67, 222–234. 2018 (Li et al. 2018). – Type: Międzyzdroje, Amber Baltic Hotel sand beach, Baltic Sea, Nov. 2006, *S. Sato & A. Witkowski* s.n. (holo-: BM, slide BM 101895; iso-: SZCZ, slide SZCZCH1765 (originally labeled as "s0393"). Not seen.

Comment – Although this taxon lacks the rudimentary spines or a ridge at the valve face-mantle junction, it does possess wide and long vimines and the apically elongated areolae, the features defining *Sarcophagodes* (table 1). In this taxon, the large valvocopula and the slender, open, unperforated copulae are also similar to those in *S. delicatula*, the generitype.

Sarcophagodes boltonii (Chunlian Li, Krawczyk, Dąbek & Witkowski) C.E.Wetzel, E.Morales & Ector, **comb. nov.**

Basionym – *Gedaniella boltonii* Chunlian Li, Krawczyk, Dąbek & Witkowski in Li et al., Phytotaxa 355: 24, 27, *pro parte*, figs 191–198. 2018 (Li et al. 2018). – Type: South Africa, Kraalbaai, 33°08′16.4″S 18° 01′34.6″E, muddy rock pool, May 2015, *P. Dąbek* s.n. (holo-: BM, slide BM 101891; iso-: SZCZ, slide SZCZCH1528). Not seen.

Comments – Since *G. boltonii* is a mixture of at least two morphological variants, we transfer here the larger form presented by Li et al. (2018) to the genus *Sarcophagodes*. This taxon has wide and long vimines and the areolae are apically reniform, the two distinguishing characters of the genus. We choose the SEM images of Li et al. (2018) as examples showing the features of this taxon, since the LM information presented by these authors is difficult to discern. *Sarcophagodes boltonii* has fully developed spines, located on a vimen situated at the junction of the valve face and mantle.

Sarcophagodes mutabilis (Grunow) E.Morales, **comb. nov.**

Basionym – *Sceptroneis mutabilis* Grunow (*marina* var.?) in Cleve & Möller, Diatoms (1877–1882), Part 5: no. 255. 1879 (Cleve & Möller 1877–1882). – Type: Pointe du Hourdel, Cayeux-sur-Mer, Hauts-de-France, mouth of the Somme river, *P. Petit* s.n. Not seen.

Comments – This taxon has the wide and long vimines and the areolae are apically reniform, the two discriminating features of the genus. The combination *Opephora mutabilis* (Grunow) Sabbe & Vyverman (Sabbe & Vyverman 1995) is untenable following the concept proposed by Round et al. (1990).

Sarcophagodes poulinii (Witkowski, Riaux-Gob. & Daniszewska-Kowalczyk) E.Morales, **comb. nov.**

Basionym – *Staurosirella poulinii* Witkowski, Riaux-Gob. & Daniszewska-Kowalczyk, Vie et milieu 60: 277, figs 68–78. 2010 (Witkowski et al. 2010). – Type: Kerguelen, Île Haute, intertidal sediments, Dec. 1991, *C. Riaux-Gobin* s.n. (holo-: SZCZ, slide SZCZ7350_8; iso-: Collection C. Riaux-Gobin, U SR 3278 CNRS-EPHE, CRIOBE-Université de Perpignan, slide No. KER16; BRM, slide BRM ZU7/84). Not seen.

Comments – This species has wide and long vimines delimiting transapically elongated areolae, the distinguishing character of the genus *Sarcophagodes*. Additionally, the species has spines located on vimines, that is, they are situated along the striae at the valve face–mantle junction. *Staurosirella* has slender, long vimines, lineolae (unique features for the genus), and the spines are located on the virgae.

Staurosira viereckiana (Gerd Moser) C.E.Wetzel & E.Morales, **comb. nov.**

Basionym – *Fragilaria viereckiana* Gerd Moser, Bibliotheca Diatomologica 43: 127–129, pl. 2, figs 1–17, pl. 3, fig. 2. 1999 (Moser 1999). – Type: Nouvelle-Calédonie, Houaïlou, upstream, 10 km past village, Mar. 1994, *Moser et al.* PN 83 (holo-: Collection Lange-Bertalot, Botanisches Institut, Universität Frankfurt/Main, slide Neukaledonien OTL 70). Not seen.

Staurosirella guenter-grassii (Witkowski & Lange-Bert.) E.Morales, C.E.Wetzel & Ector, **comb. nov.**

Basionym – *Fragilaria guenter-grassii* Witkowski & Lange-Bert., Limnologica 23: 65, 66, figs 5a–l. 1993 (Witkowski & Lange-Bertalot 1993). – Type: Poland, Puck Bay, 1992, *A. Witkowski* s.n. (holo-: Institute of Oceanography, University of Gdansk, Gdynia, Poland, slide no. P3 (A, V. 92)). Not seen.

Comments – This species has the distinguishing trait for the genus, i.e., long and slender vimines. Thus the areolae are apically elongated. The volae are branched (Witkowski 1994: pl. 8, fig. 3). Apical pore fields are developed at the foot pole and are composed of round poroids in the manner of, for example, *S. minuta* E.Morales & Edlund (Morales & Edlund 2003: figs 33–38). For all this, the combination *Gedaniella guenter-grassii* (Witkowski & Lange-Bert.) Chunlian Li, Shin.Sato & Witkowski presented in Li et al. (2018) is untenable. Likewise, since we are following the concept of *Opephora* suggested by Round et al. (1990), the combination *O. guenter-grassii* (Witkowski & Lange-Bert.) Sabbe & Vyverman (Sabbe & Vyverman 1995) is unsupported.

ACKNOWLEDGMENTS

We thank Drs. M. Guiry and Saúl Blanco for guidance regarding nomenclature. Dr. D.G. Mann and two anonymous reviewers greatly contributed to improving the text. Funding for this research was partly provided in the framework of the DIATOMS project (LIST - Luxembourg Institute of Science and Technology). This work was also co-funded by the European Union through the European Regional Development Fund, framed in COMPETE 2020 (Operational Programme Competitiveness and Internationalization), through the ICT project (UID/GEO/04683/2013) with reference POCI-01-0145-FEDER-007690 and the Alentejo Observation and Prediction Systems - ALOP project (ALT20-03-0145-FEDER-000004) and the Agencia Portuguesa do Ambiente, APA-000004DFIN.AALP/2017 integrated within the Operational Program for Sustainability and Efficiency in the Use of Resources 2014-20, POSEUR-03-2013-FC-000001. We dedicate this manuscript to Eileen J. Cox for her contribution to the knowledge of diatoms and the advancements she made in the fields of taxonomy and systematics. We learned so much through her work, and we are greatful for that.

REFERENCES

Aitken Z.H., Luo S., Reynolds S.N., Thaulow C., Greer J.R. (2016) Microstructure provides insights into evolutionary design and resilience of Coscinodiscus sp. frustule. Proceedings of the National Academy of Sciences of the United States of America 113: 2017–2022. https://doi.org/10.1073/pnas.1519790113

Barber H.G., Haworth E.Y. (1981) A guide to the morphology of the diatom frustule. With a key to the British Freshwater genera. Freshwater Biological Association, Ambleside. Scientific Publication No. 44: 1–112.

Cejudo-Figueiras C., Morales E.A., Wetzel C.E., Blanco S., Hoffmann L., Ector L. (2011) Analysis of the type of Fragilaria construens var. subsalina (Bacillariophyceae) and description of two morphologically related taxa from Europe and the United States. Phycologia 50: 67–77. https://doi.org/10.2216/09-40.1

Cleve P.T., Möller J.D. (1879) Diatoms. Part V, No. 217–276. Upsala, Esatas Edquists Boktryckeri.

Compère P. (2001) Ulnaria (Kützing) Compère, a new genus name for Fragilaria subgen. Alterasynedra Lange-Bertalot with comments on the typification of Synedra Ehrenberg. In: Jahn R., Kociolek J.P., Witkowski A., Compère P. (eds) Lange-Bertalot-Festschrift. Studies on diatoms dedicated to Prof. Dr. Dr. h.c. Horst Lange-Bertalot on the occasion of his 65th birthday: 97–101. Ruggell, A.R.G. Gantner Verlag K.G.

Cox E.J. (1999) Variation in patterns of valve morphogenesis between representatives of six biraphid diatom genera (Bacillariophyceae). Journal of Phycology 35: 1297–1312. https://doi.org/10.1046/j.1529-8817.1999.3561297.x

Cox E.J. (2004) Pore occlusions in raphid diatoms - a reassessment of their structure and terminology, with particular reference to members of the Cymbellales. Diatom 20: 33–46. https://doi.org/10.11464/diatom1985.20.0_33

Cox E.J. (2010) Morphogenetic information and the selection of taxonomic characters for raphid diatom systematics. Plant Ecology and Evolution 143: 271–277. https://doi.org/10.5091/plecevo.2010.403

Cox E.J. (2012) Ontogeny, homology, and terminology-wall morphogenesis as an aid to character recognition and character state definition for pennate diatom systematics. Journal of Phycology 48: 1–31. https://doi.org/10.1111/j.1529-8817.2011.01081.x

Cox E.J., Kennaway G.M. (2004) Studies of valve morphogenesis in pennate diatoms: investigating aspects of cell biology in a systematic context. In: Poulin M. (ed.) Proceedings of the Seventeenth International Diatom Symposium. Ottawa, Canada, 25th–31st August 2002: 35–48. Bristol, Biopress Limited.

Cox E.J., Ross R. (1981) The striae of pennate diatoms. In: Ross R. (ed.) Proceedings of the Sixth Symposium on Recent and Fossil

Diatoms, Budapest, September 1–5, 1980: 267–278. Koenigstein, Otto Koeltz - Science Publishers.

Edlund M.B., Morales E.A., Spaulding S.A. (2006) The type and taxonomy of Fragilaria elliptica Schumann, a widely misconstrued taxon. In: Witkowski A. (ed.) Proceedings of the Eighteenth International Diatom Symposium. Międzydroje, Poland, 2nd–7th September 2004: 53–59. Bristol, Biopress Limited.

Flower R.J. (2005) A taxonomic and ecological study of diatoms from freshwater habitats in the Falkland Islands, South Atlantic. Diatom Research 20: 23–96. https://doi.org/10.1080/02692 49X.2005.9705620

Flower R.J., Jones V.J., Round F.E. (1996) The distribution and classification of the problematic Fragilaria (virescens v.) exigua Grun. / Fragilaria exiguiformis (Grun.) Lange-Bertalot: a new species or a new genus? Diatom Research 11: 41–57. https:// doi.org/10.1080/0269249X.1996.9705363

Frankovich T.A., Sullivan M.J., Stacy N.I. (2015) Three new species of Tursiocola (Bacillariophyta) from the skin of the West Indian manatee (Trichechus manatus). Phytotaxa 204: 33–48. https:// doi.org/10.11646/phytotaxa.204.1.3

Frankovich T.A., Ashworth M.P., Sullivan M.J., Theriot E.C., Stacy N.I. (2018) Epizoic and apochlorotic Tursiocola species (Bacillariophyta) from the skin of Florida manatees (Trichechus manatus latirostris). Protist 169: 539–568. https://doi.org/10.1016/j.protis.2018.04.002

Frenguelli J. (1945) XIX contribución al conocimiento de las diatomeas argentinas. Las diatomeas del Platense. Revista del Museo de La Plata, Nueva Serie, Sección Paleontología 3(16): 77–221, pls 1–15.

García M.L., Maidana N.I., Ector L., Morales E.A. (2017) Staurosira patagonica sp. nov., a new diatom (Bacillariophyta) from southern Argentina, with a discussion on the genus Staurosira Ehrenberg. Nova Hedwigia, Beiheft 146: 103–123. https://doi.org/10.1127/1438-9134/2017/123

Genkal S.I., Bondarenko N.A., Shchur L.A. (2011) Diatoms of lakes in south and north of the Eastern Siberia. Rybinsk, Rybinsky Dom Pechati. (In Russian).

Goldenberg Vilar A., van Dam H., van Loon E.E., Vonk J.A., van der Geest H., Admiraal W. (2014) Eutrophication decreases distance decay of similarity in diatom communities. Freshwater Biology 59: 1522–1531. https:// doi.org/10.1111/fwb.1236

Grana L., Morales E.A., Maidana N.I., Ector L. (2018) Two new species of Staurosira and Pseudostaurosira (Bacillariophyta) from the highlands of Argentina (south-central Andes) and two new nomenclatural combinations. Phytotaxa 365: 60–72. https://doi.org/10.11646/phytotaxa.365.1.2

Guiry M.D., Guiry G.M. (2018) AlgaeBase. World-wide electronic publication, National University of Ireland, Galway. Available from http://www.algaebase.org [accessed 25 Jul. 2018].

Hamilton P.B., Siver P.A. (2008) The type for Fragilaria lancettula Schumann 1867 and transfer to the genus Punctastriata as P. lancettula (Schum.) Hamilton & Siver comb. nov. Diatom Research 23: 355–365. https://doi.org/10.1080/026924 9X.2008.9705762

Hegewald E., Silva P.C. (1988) Annotated catalogue of Scenedesmus and nomenclaturally related genera, including original descriptions and figures. Bibliotheca Phycologica 80: 1–587.

Hustedt F. (1938) Systematische und ökologische Untersuchungen über die Diatomeen-Flora von Java, Bali und Sumatra nach dem Material der Deutschen Limnologischen Sunda-Expedition. Systematischer Teil I. Archiv für Hydrobiologie, Supplement-Band 15: 131–177.

Kaluzhnaya Ol.V., Likhoshway Ye.V. (2007) Valve morphogenesis in an araphid diatom Synedra acus subsp. radians. Diatom Research 22: 81–87. https://doi.org/10.1080/026924 9X.2007.9705696

Kociolek J.P., Williams D.M. (2015) How to define a diatom genus? Notes on the creation and recognition of taxa, and a call for revisionary studies of diatoms. Acta Botanica Croatica 74: 195–210. https://doi.org/10.1515/botcro-2015-0018

Kociolek J.P., Laslandes B., Benett D., Thomas E., Brady M., Graeff C. (2014) Diatoms of the United States 1. Taxonomy, ultrastructure and descriptions of new species and other rarely reported taxa from lake sediments in the western U.S.A. Bibliotheca Diatomologica 61: 1–188.

Krammer K., Lange-Bertalot H. (1991) Bacillariophyceae 3. Teil: Centrales, Fragilariaceae, Eunotiaceae. In: Ettl H., Gerloff J., Heynig H., Mollenhauer D. (eds) Süßwasserflora von Mitteleuropa 2/4: 1–576. Stuttgart, Gustav Fischer Verlag.

Kulikovskiy M.S., Lange-Bertalot H., Kuznetsova I.V. (2015) Lake Baikal: Hotspot of endemic diatoms II. Iconographia Diatomologica 26: 1–656.

Lange-Bertalot H. (1989) Können Staurosirella, Punctastriata und weitere Taxa sensu Williams & Round als Gattungen der Fragilariaceae kritischer Prüfung standhalten? Generic rank for Punctastriata, Staurosirella and other taxa sensu Williams & Round? Nova Hedwigia 49: 79–106.

Lange-Bertalot H. (1993) Once more: Staurosirella, Punctastriata etc. A reply to Round & Williams (1992). Nova Hedwigia 56: 179–182.

Lange-Bertalot H., Genkal S.I. (1999) Diatomeen aus Sibirien I. Inseln im Arktischen Ozean (Yugorsky-Shar Strait) [Diatoms from Siberia I. Islands in the Arctic Ocean (Yugorsky-Shar Strait)]. Iconographia Diatomologica 6: 1–271.

Lange-Bertalot H., Hofmann G., Werum M., Cantonati M. (2017) Freshwater benthic diatoms of Central Europe: Over 800 common species used in ecological assessment. English edition with updated taxonomy and added species. Edited by Cantonati M., Kelly M.G., Lange-Bertalot H. Schmitten-Oberreifenberg, Koeltz Botanical Books.

Lee J.J., Reimer Ch.W., McEnery, M.E. (1980) The identification of diatoms isolated as endosymbionts from larger foraminifera from the Gulf of Eilat (Red Sea) and the description of 2 new species, Fragilaria shiloi sp. nov. and Navicula reissii sp. nov. Botanica Marina 23: 41–48. https://doi.org/10.1515/botm.1980.23.1.41

Li C.L., Ashworth M.P., Witkowski A., Lobban C.S., Zgłobicka I., Kurzydłowski K.J., Qin S. (2016) Ultrastructural and molecular characterization of diversity among small araphid diatoms all lacking rimoportulae. I. Five new genera, eight new species. Journal of Phycology 52: 1018–1036. https://doi.org/10.1111/jpy.12460

Li C.L., Witkowski A., Ashworth M.P., Dąbek P., Sato S., Zgłobicka I., Witak M., Khim J.S., Kwon C.-J. (2018) The morphology and molecular phylogenetics of some marine diatom taxa within the Fragilariaceae, including twenty undescribed species and their relationship to Nanofrustulum, Opephora and Pseudostaurosira. Phytotaxa 355: 1–104. https://doi.org/10.11646/phytotaxa.355.1.1

Lilitskaya G.G. (2016) Bacillariophyta of small water bodies of Kiev (Ukraine). 2. Araphid diatoms: Fragilariaceae, Diatomaceae, and Tabellariaceae. International Journal on Algae 18: 225–246. https://doi.org/10.1615/InterJAlgae.v18.i3.30

Mann D.G. (1984) An ontogenetic approach to diatom systematics. In: Mann D.G. (ed.) Proceedings of the Seventh International

Diatom Symposium Philadelphia, August 22–27, 1982: 113–144. Koenigstein, Otto Koeltz.

Mann D.G. (1999) The species concept in diatoms. Phycologia 38: 437–495. https://doi.org/10.2216/i0031-8884-38-6-437.1

Mann D.G. (2006) Specifying a morphogenetic model for diatoms: an analysis of pattern faults in the Voigt zone. Nova Hedwigia, Beiheft 130: 97–118.

Mann D.G. (2010) Discovering diatom species: is a long history of disagreements about species-level taxonomy now at an end? Plant Ecology and Evolution 143: 251–264. https://doi.org/10.5091/plecevo.2010.405

Marciniak B. (1982) Late Glacial and Holocene new diatoms from a glacial Lake Przedni Staw in the Pięć Stawów Polskich Valley, Polish Tatra Mts. Acta Geologica Academiae Scientiarum Hungaricae 25: 161–171.

Marciniak B. (1986) Late Glacial Fragilaria flora from lake sediments of the Tatra Mts. and the Alps. In: Round F.E. (ed.) Proceedings of the Ninth International Diatom Symposium. Bristol, August 24–30, 1986: 233–243. Bristol, Biopress Ltd. and Koenigstein, Koeltz Scientific Books.

Medlin L., Desdevises, Y. (2016) Phylogeny of 'araphid' diatoms inferred from SSU and LSU rDNA, RBCL and PSBA sequences. Vie et Milieu 66: 129–154.

Medlin L., Williams D.M., Sims P.A. (1993) The evolution of the diatoms (Bacillariophyta). I. Origin of the group and assessment of the monophyly of its major divisions. European Journal of Phycology 28: 261–275. https://doi.org/10.1080/09670269300650381

Medlin L., Jung I., Bahulikar R., Mendgen K., Kroth P., Kooistra W.H.C.F. (2008) Evolution of the diatoms. VI. Assessment of the new genera in the araphids using molecular data. Nova Hedwigia, Beiheft 133: 81–100.

Medlin L., Yang I., Sato S. (2012) Evolution of the diatoms. VII. Four gene phylogeny assesses the validity of selected araphid genera. Nova Hedwigia, Beiheft 141: 505–514.

Metzeltin D., Lange-Bertalot H. (1998) Tropische Diatomeen in Südamerika I. 700 überwiegend wenig bekannte oder neue Taxa repräsentativ als Elemente der neotropischen Flora [Tropical diatoms of South America I. About 700 predominantly rarely known or new taxa representative of the neotropical flora]. Iconographia Diatomologica 5: 1–695.

Morales E.A. (2001) Morphological studies in selected fragilarioid diatoms (Bacillariophyceae) from Connecticut waters (U.S.A.). Proceedings of the Academy of Natural Sciences of Philadelphia 151: 105–120.

Morales E.A. (2002) Studies in selected fragilarioid diatoms of potential indicator value from Florida (USA) with notes on the genus Opephora Petit (Bacillariophyceae). Limnologica 32: 102–113. https://doi.org/10.1016/S0075-9511(02)80002-0

Morales E.A. (2003) On the taxonomic status of the genera Belonastrum and Synedrella proposed by Round and Maidana (2001). Cryptogamie Algologie 24: 277–288.

Morales E.A. (2005) Observations of the morphology of some known and new fragilarioid diatoms (Bacillariophyceae) from rivers in the USA. Phycological Research 53: 113–133. https://doi.org/10.1111/j.1440-183.2005.00378.x

Morales E.A. (2006) Staurosira incerta (Bacillariophyceae) a new fragilarioid taxon from freshwater systems in the United States with comments on the structure of girdle bands in Staurosira Ehrenberg and Staurosirella Williams et Round. In: Ognjanova-Rumenova N., Manoylov K. (eds) Advances in Phycological Studies. Festschrift in Honour of Prof. Dobrina Temniskova-Topalova: 133–145. Sofia-Moscow, Pensoft Publishers & University Publishing House.

Morales E.A., Edlund M.B. (2003) Studies in selected fragilarioid diatoms (Bacillariophyceae) from Lake Hovsgol, Mongolia. Phycological Research 51: 225–239.

Morales E.A., Manoylov K.M. (2006a) Morphological studies on selected taxa in the genus Staurosirella Williams et Round (Bacillariophyceae) from rivers in North America. Diatom Research 21: 343–364. https://doi.org/10.1080/026929X.2006.9705674

Morales E.A., Manoylov K.M. (2006b) Staurosirella incognita Morales et Manoylov sp. nov., a non-spiny species from North America, with an emended description of Staurosirella Williams et Round (Bacillariophyceae). In: Witkowski A. (ed.) Proceedings of the Eighteenth International Diatom Symposium. Międzyzdroje, Poland, 2nd–7th September 2004: 325–336. Bristol, Biopress Limited.

Morales E.A., Edlund M.B., Spaulding S.A. (2010a) Description and ultrastructure of araphid diatom species (Bacillariophyceae) morphologically similar to Pseudostaurosira elliptica (Schumann) Edlund et al. Phycological Research 58: 97–107. https://doi.org/10.1111/j.1440-1835.2010.00567.x

Morales E.A., Manoylov K.M., Bahls L.L. (2010b) Three new araphid diatoms (Bacillariophyta) from rivers in North America. Proceedings of the Academy of Natural Sciences of Philadelphia 160: 29–46. https://doi.org/10.1635/053.160.0105

Morales E.A., Wetzel C.E., Ector L. (2010c) Two short-striated species of Staurosirella (Bacillariophyceae) from Indonesia and the United States. Polish Botanical Journal 55: 107–117.

Morales E.A., Novais M.H., Chávez G., Hoffmann L., Ector L. (2012) Diatoms (Bacillariophyceae) from the Bolivian Altiplano: three new araphid species from the Desaguadero River draining Lake Titicaca. Fottea 12: 41–58. https://doi.org/10.5507/fot.2012.004

Morales E.A., Guerrero J.M., Wetzel C.E., Sala S., Ector L. (2013) Unraveling the identity of Fragilaria pinnata Ehrenberg and Staurosira pinnata Ehrenberg: research in progress on a convoluted story. Cryptogamie Algologie 34: 89–102. https://doi.org/10.7872/crya.v34.iss2.2013.89

Morales E.A., Buczkó K., Wetzel C.E., Novais M.H., Ognjanova-Rumenova N., Hoffmann L., Ector L. (2014a) Transfer of Staurosira grunowii to Staurosirella. Diatom Research 29: 105–110. https://doi.org/10.1080/0269249X.2013.804446

Morales E.A., Rivera S.F., Wetzel C.E., Novais M.H., Hamilton P.B., Hoffmann L., Ector L. (2014b) New epiphytic araphid diatoms in the genus Ulnaria (Bacillariophyta) from Lake Titicaca, Bolivia. Diatom Research 29: 41–54. https://doi.org/10.1080/0269249X.2013.860399

Morales E.A., Wetzel C.E., Rivera S.F., Van de Vijver B., Ector L. (2014c) Current taxonomic studies on the diatom flora (Bacillariophyceae) of the Bolivian Altiplano, South America, with possible consequences for palaeoecological assessments. Journal of Micropalaeontology 33: 121–129. https://doi.org/10.1144/jmpaleo2014-007

Morales E.A., Wetzel C.E., Van de Vijver B., Ector L. (2015) Morphological studies on type material of widely cited araphid diatoms (Bacillariophyta). Phycologia 54: 455–470. https://doi.org/10.2216/15-21.1

Moser G. (1999) Die Diatomeenflora von Neukaledonien. Bibliotheca Diatomologica 43: 1–205.

Ognjanova-Rumenova N., Temniskova-Topalova D., Valeva M. (1994) Ultrastructure of Fragilaria Lyngbye species (Bacillariophyta) from Neogene sediments in Bulgaria. In: Kociolek

J.P. (ed.) Proceedings of the 11th International Diatom Symposium. San Francisco, California 12–17 August 1990: 291–300. San Francisco, California Academy of Science.

Pantocsek J. (1913) A lutillai ragpalában elöforduló Bacillariák vagy Kovamoszatok leírása [Bacillarien des Klebschiefers von Lutilla]. A pozsonyi Orvos-Természettudományi Egyesület közleményei [Verhandlungen des Vereins für Natur-und Heilkunde zu Pozsony, Neue Folge] 23: 19–35, 2 pls. Pozsonyban, Wigand K.F. könyvnyomdája.

Pickett-Heaps J.D. (1998) Cell division and morphogenesis of the centric diatom Chaetoceros decipiens (Bacillariophyceae) II. Electron microscopy and a new paradigm for tip growth. Journal of Phycology 34: 995–1004. https://doi.org/10.1046/j.1529-8817.1998.340995.x

Round F.E., Crawford R.M., Mann D.G. (1990) Diatoms: biology and morphology of the genera. Cambridge, Cambridge University Press.

Round F.E., Hallsteinsen H., Paasche E. (1999) On a previously controversial "fragilarioid" diatom now placed in a new genus Nanofrustulum. Diatom Research 14: 343–356. https://doi.org/10.1080/0269249X.1999.9705476

Rumrich U., Lange-Bertalot H., Rumrich M. (2000) Diatomeen der Anden. Von Venezuela bis Patagonien/Feuerland [Diatom from the Andes. From Venezuela to Patagonia/Tierra del Fuego]. Iconographia Diatomologica 9: 1–649.

Sabbe K., Vyverman W. (1995) Taxonomy, morphology and ecology of some widespread representatives of the diatom genus Opephora. European Journal of Phycology 30: 235–249. https://doi.org/10.1080/09670269500651011

Sato S., Mann D.G., Matsumoto S., Medlin L.K. (2008) Pseudostriatella (Bacillariophyta): a description of a new araphid diatom genus based on observations of frustule and auxospore structure and 18S rDNA phylogeny. Phycologia 47: 371–391. https://doi.org/10.2216/PH08-02.1

Sato S., Matsumoto S., Medlin L.K. (2009) Fine structure and 18S rDNA phylogeny of a marine araphid pennate diatom Plagiostriata goreensis gen. et sp. nov. (Bacillariophyta). Phycological Research 57: 25–35. https://doi.org/10.1111/j.1440-1835.2008.00518.x

Sato S., Watanabe T., Nagumo T., Tanaka J. (2011) Valve morphogenesis in an araphid diatom Rhaphoneis amphiceros (Rhaphoneidaceae, Bacillariophyta). Phycological Research 59: 236–243. https://doi.org/10.1111/j.1440-1835.2011.00621.x

Sullivan M.J. (1978) Diatom community structure: taxonomic and statistical analyses of a Mississippi salt marsh. Journal of Phycology 14: 468–475. https://doi.org/10.1111/j.1529-8817.1978.tb02471.x

Takano H. (1986) A new diatom in the genus Fragilaria from shallow waters in Mikawa Bay, Japan. Bulletin of the Tokai Regional Fisheries Research Laboratory 120: 27–37.

Takano H. (1988) Two new diatoms found in marine waters of Japan. Bulletin of the Tokai Regional Fisheries Research Laboratory 125: 33–44.

Talgatti D., Wetzel C.E., Morales E.A., Ector L., Torgan L.C. (2014) Transfer of Fragilaria atomus Hust. to the genus Stauroforma (Bacillariophyta) based on observation of type and newly collected material. Phytotaxa 158: 43–56. https://doi.org/10.11646/phytotaxa.158.1.3

Theriot E.C. (2008) Application of phylogenetic principles to testing evolutionary scenarios: a comment on Kaczmarska et al. "Molecular phylogeny of selected members of the order Thalassiosirales (Bacillariophyta) and evolution of the fultoportula". Journal of Phycology 44: 821–833. https://doi.org/10.1111/j.1529-8817.2008.00522.x

Theriot E.C., Ashworth M., Ruck E., Nakov T., Jansen R.K. (2010) A preliminary multigene phylogeny of the diatoms (Bacillariophyta): challenges for future research. Plant Ecology and Evolution 143: 278–296. https://doi.org/10.5091/plecevo.2010.418

Tiffany M.A. (2002) Valve morphogenesis in the marine araphid diatom Gephyria media (Bacillariophyceae). Diatom Research 17: 391–400. https://doi.org/10.1080/0269249X.2002.9705556

Tiffany M.A. (2015) Valve and girdle band morphogenesis in the pseudocellate diatom species Biddulphia biddulphiana J.E. Smith (Boyer) and Isthmia nervosa Kütz. Nova Hedwigia, Beiheft 144: 61–95. https://doi.org/10.1127/nova_suppl/2015/0030

Van de Vijver B., Frenot Y., Beyens L. (2002) Freshwater diatoms from Ile de la Possession (Crozet Archipelago, Subantarctica). Bibliotheca Diatomologica 46: 1–412.

Wetzel C.E., Morales E.A., Blanco S., Ector L. (2013) Pseudostaurosira cataractarum comb. nov. (Bacillariophyta): type analysis, ecology and world distribution of a former "centric" diatom. Acta Nova 6: 53–63. https://doi.org/10.6084/m9.figshare.7654673

Williams D.M. (2011) Synedra, Ulnaria: definitions and descriptions – a partial resolution. Diatom Research 26: 149–153. https://doi.org/10.1080/0269249X.2011.587646

Williams D.M. (2013) Why is Synedra berolinensis so hard to classify? More on monotypic taxa. Phytotaxa 127: 113–127. https://doi.org/10.11646/phytotaxa.127.1.13

Williams D.M., Round F.E. (1987) Revision of the genus Fragilaria. Diatom Research 2: 267–288. https://doi.org/10.1080/0269249X.1987.9705004

Witkowski A. (1993) Fragilaria gedanensis sp. nov. (Bacillariophyceae), a new epipsammic diatom species from the Baltic Sea. Nova Hedwigia 56: 497–503.

Witkowski A. (1994) Recent and fossil diatom flora of the Gulf of Gdańsk, Southern Baltic Sea. Origin, composition and changes of diatom assemblages during the Holocene. Bibliotheca Diatomologica 28: 1–313.

Witkowski A., Lange-Bertalot H. (1993) Established and new diatom taxa related to Fragilaria schulzii Brockmann. Limnologica 23: 59–70.

Witkowski A., Lange-Bertalot H., Witak M. (1995) Diatom taxa of unusual frustule structure belonging to the genus Fragilaria. Fragmenta Floristica et Geobotanica 40: 729–741.

Witkowski A., Lange-Bertalot H., Metzeltin D. (2000) Diatom flora of marine coasts I. Iconographia Diatomologica 7: 1–925.

Witkowski A., Riaux-Gobin C., Daniszewska-Kowalczyk G. (2010) New marine littoral diatom species (Bacillariophyta) from Kerguelen Islands. II. Heteropolar species of Fragilariaceae. Vie et Milieu 60: 265–281.

Managing Editor: David G. Mann

Submission date: 27 Aug. 2018

Acceptance date: 22 Feb. 2019

Aerosol and Air Quality Research, 17: 2509–2521, 2017
Copyright © Taiwan Association for Aerosol Research
ISSN: 1680-8584 print / 2071-1409 online
doi: 10.4209/aaqr.2017.05.0159

Thirteen Years of Aerosol Radiative Forcing in Southwestern Iberian Peninsula

Maria A. Obregón[1*], Maria J. Costa[2], Ana M. Silva[2], Antonio Serrano[3]

[1] *Departamento de Física, Instituto de Ciências da Terra, Instituto de Investigação e Formação Avançada, Universidade de Évora, Évora, 7000-671, Portugal*
[2] *Departamento de Física, Instituto de Ciências da Terra, Escola de Ciências e Tecnologia, Universidade de Évora, Évora, 7000-671, Portugal*
[3] *Departamento de Física, Universidad de Extremadura, Badajoz, 06071, Spain*

ABSTRACT

Notable uncertainties in the aerosol impact on the Earth's radiative budget still remain, mainly at local scales. This study aims to accurately quantify the shortwave aerosol radiative forcing (ARF) and its efficiency (ARFE) at Évora (Portugal, Southwestern Europe). This is an interesting region affected by different aerosol types and sources. Towards this goal, ARF and ARFE are calculated for Évora during thirteen years (2003–2015), which is the longest period ever analyzed for this region. For this calculation, the most updated AERONET data have been used to simulate irradiance with the libRadtran code. Thus, 1676 daily values were analyzed, obtaining a mean ARF of –7.4 W m^{-2} at the Earth's surface (SURF) and –1.1 W m^{-2} at the top of the atmosphere (TOA), indicating a cooling of the Earth–atmosphere system. The difference in ARF between TOA and SURF indicates a mean net gain of 6.3 W m^{-2} for the atmosphere. While no ARF seasonal pattern is observed at the TOA, a clear seasonal cycle is detected at the SURF with the most negative values occurring in summer. On the other hand, ARFE shows mean values of –62.7 W m^{-2} τ^{-1} at the SURF and –14.3 W m^{-2} τ^{-1} at the TOA. Results show that ARFE highly depends on the aerosol single scattering albedo, showing opposite behavior at the SURF and at the TOA. The large temporal variability detected in the aerosol properties in the region of study confirms the general need for long time series of measurements to achieve an accurate estimation of the ARF and ARFE.

Keywords: Aerosol radiative effects; Long term analysis; Radiative transfer model; AERONET.

INTRODUCTION

Atmospheric aerosol particles, of natural or anthropogenic origin, interact directly with solar and terrestrial radiation through scattering and absorption as well as through emission processes, modifying the Earth's radiative balance. This effect is quantified by the aerosol radiative forcing (ARF) calculated as the change in the radiative balance due exclusively to the existence of aerosols. According to the Fifth Assessment Report delivered in 2013 by the Intergovernmental Panel on Climate Change, direct and indirect effects of aerosols in the atmosphere result in an overall radiative forcing of –0.9 (–1.9 to –0.1) W m^{-2} at the TOA (Boucher *et al.*, 2013). Although this global cooling effect due to aerosols is well established, significant uncertainties still remain, mainly referred to their spatial and temporal variability at regional and local scales. Thus, due to nearby point sources, the aerosol radiative forcing at the local scale can exceed the global values by an order of magnitude. Additionally, most climate models underestimate the negative radiative forcing caused by anthropogenic aerosols (Hansen *et al.*, 2011). Hence, this short-scale information is essential to achieve an accurate knowledge of the impact of aerosols on climate. It is, therefore, important to quantify the long-term aerosol radiative forcing in different areas worldwide, paying special attention to regions of climatic significance.

Within this framework, the Iberian Peninsula is a particularly interesting region affected by occasional intrusions coming from the largest source of dust worldwide: the Sahara Desert. The frequency of these intrusions is modulated by the annual latitudinal displacement of major semi-permanent pressure systems, showing a typical seasonal pattern (Cachorro *et al.*, 2005; Toledano, 2005; Salgueiro *et al.*, 2014) associated to specific synoptic situations (Rodriguez *et al.*, 2001; Querol *et al.*, 2002; Escudero *et al.*, 2005). In addition to the desert dust intrusions, the Iberian Peninsula is notably affected by other sources of aerosols. In particular, the southwestern interior part of the Iberian Peninsula is also exposed to local continental

* Corresponding author.
Tel.: +351 266740800 ext. 5472
E-mail address: nines@unex.es

aerosols and marine aerosols coming from the Atlantic Ocean (Pereira *et al.*, 2005; Elias *et al.*, 2006; Silva *et al.*, 2006; Pereira *et al.*, 2008; Pereira *et al.*, 2011; Obregón *et al.*, 2012). Additionally, wildfires are an occasional but intense source of aerosols for the area in summer. Due to its exposure to a diversity of local and remote aerosol sources, the Iberian Peninsula is a privileged location for studying the aerosol impact on the radiation balance.

A major research site for aerosols in this area is located in Évora (Portugal), deployed by the Institute of Earth Sciences at the University of Évora, where the AErosol Robotic NETwork (AERONET, http://aeronet.gsfc.nasa.gov) has a monitoring station. This station started to operate in 2003 and, since then, provides radiometric measurements of aerosol properties averaged in the atmospheric column according to AERONET standards and protocols. Notable research has been conducted based on these measurements focusing mainly on obtaining typical values for the physical and optical properties of the aerosols during long periods and specific interesting events (Silva *et al.*, 2003; Obregón *et al.*, 2012), identifying most frequent aerosol types in the area (Elias *et al.*, 2006), and studying their radiative effect (Santos *et al.*, 2008; Mateos *et al.* 2014; Obregón *et al.*, 2015a). However, these latter studies are based on a limited period of time (Santos *et al.*, 2008; Mateos *et al.*, 2014) or focus on specific short events (Obregón *et al.*, 2015a), failing to provide an accurate and complete estimation of the aerosol radiative forcing. Therefore, this study gathers the longest series of aerosol measurements ever used for this area in order to accurately estimate the direct aerosol radiative forcing and its efficiency in the shortwave spectral range. In order to thoroughly analyze the impact of aerosols in the total atmosphere, the aerosol radiative forcing and its efficiency will be calculated at the Earth's surface (SURF) and at the top of the atmosphere (TOA).

The paper is structured as follows: first, a brief description of the study region, instrumentation, measurements and methodology is provided (Section 2), followed by the description of the main results (Section 3), and, finally, the main conclusions (Section 4).

METHODOLOGY

Site Description

The current study is based on aerosol experimental measurements registered at the AERONET site located in the city of Évora (Portugal), in southwestern Iberian Peninsula. Fig. 1 shows the location of this station (38.6°N, 7.9°W, 293 m a.s.l), approximately 100 km eastwards from the Atlantic coast.

Évora shows a mainly continental climate attenuated by the maritime influence of the Atlantic Ocean. This climate is classified as Csa (Mediterranean climates with hot and dry summers) according to Köppen-Geiger types (Köppen, 1936). It features very hot and dry summers with prevailing cloud-free conditions. Very high irradiance values, among

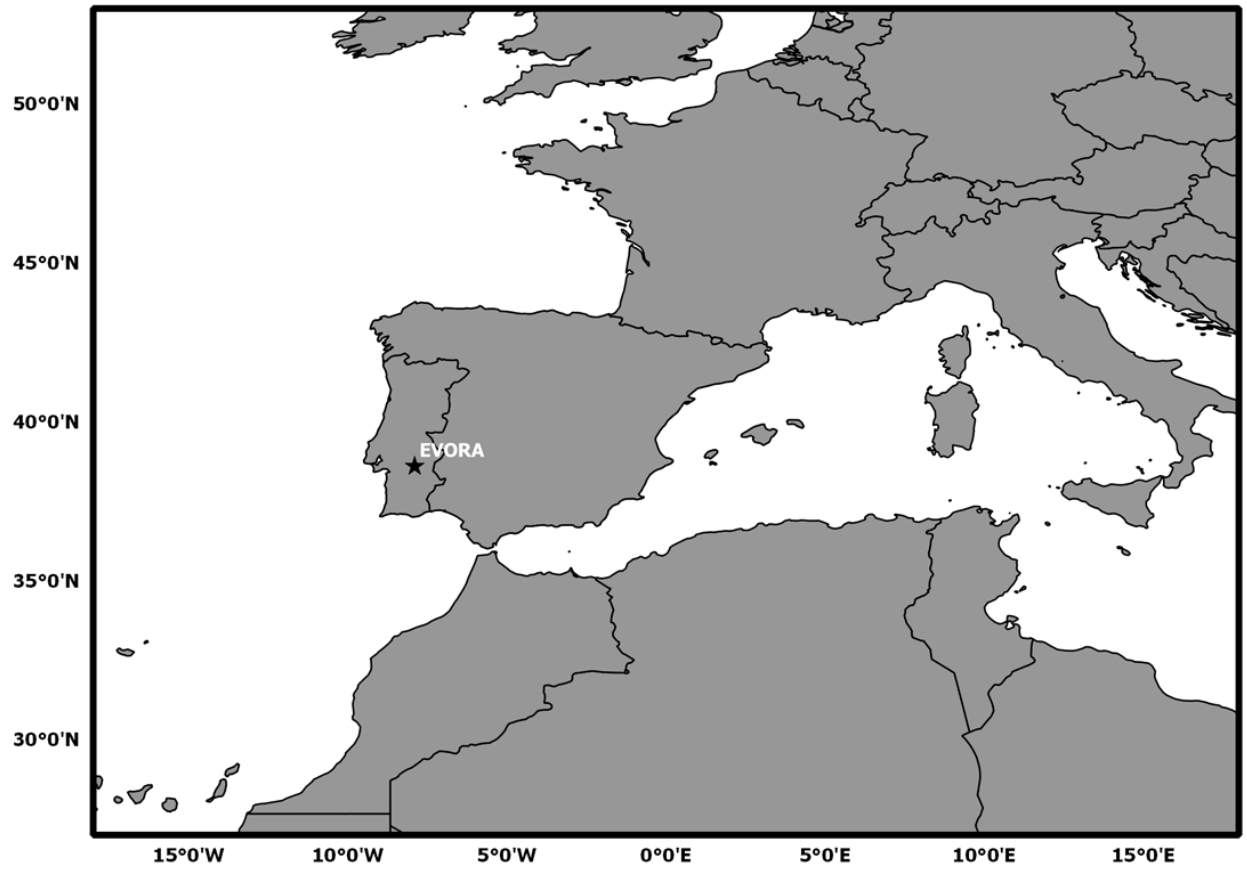

Fig. 1. Location of Évora in the Southwestern Iberian Peninsula.

the highest in Europe, are reached under clear conditions with values up to 1000 W m^{-2} near summer solstice at noon.

Instrumentation

This ground-based station is equipped with a CIMEL CE-318 sunphotometer integrated in the NASA AERONET (Aerosol Robotic NETwork) network (Holben *et al.*, 1998) since 2003. This network provides aerosol information with the aim to establish a ground-based climatology and to identify and characterize the most influential aerosols on the climatic system. The CIMEL CE-318 sunphotometer performs direct sun measurements at 340, 380, 440, 500, 675, 870, 940 and 1020 nm, and measurements of sky radiances in the almucantar and principal plane geometries at 440, 675, 870 and 1020 nm. These measurements are processed following AERONET protocols (Holben *et al.*, 1998) to obtain a variety of aerosol products at different quality levels (1.0, 1.5 and 2.0). The sunphotometer is calibrated annually following AERONET protocols by the AERONET-NASA, RIMA and PHOTONS networks (Holben *et al.*, 1998; Toledano *et al.*, 2006).

Method

It is important to note that the radiative forcing estimates obtained in this study differ from the IPCC definition of radiative forcing. While the IPCC calculates the radiative forcing as the difference between irradiances in the pre-industrial and present day atmosphere due to changes in the concentrations of a certain atmosphere component, in this study, radiative forcing stands for the instantaneous contribution of a particular component (in this case aerosols) to the radiation budget. Thus, it is calculated as the difference in the radiative energy at a given level between a situation where aerosols are present, F, and a situation where these atmospheric particles are absent (background/baseline conditions), F^0:

$$ARF = \left(F_{dn} - F_{up}\right) - \left(F_{dn}^0 - F_{up}^0\right) \quad (1)$$

where F is the flux (shortwave irradiance), the subscript "dn" indicates the downward direction and the subscript "up" the upward direction. In this study, the ARF values calculated at the SURF and at the TOA are analyzed. Thus, radiative forcing can be defined at these two levels as:

$$ARF_{TOA} = F_{up(TOA)}^0 - F_{up(TOA)} \quad (2)$$

$$ARF_{SURF} = \left(1 - A_s\right) \cdot \left(F_{dn(SURF)} - F_{dn(SURF)}^0\right) \quad (3)$$

where A_s is the surface albedo, assumed to be the same for both aerosol situations (background/baseline and presence of aerosols).

To estimate the amount of solar radiations trapped in the atmosphere due to aerosols, the difference in ARF between TOA and SURF is computed. Then, the heating rate (HR) due to aerosol absorption is calculated according to the first law of thermodynamics and assuming hydrostatic equilibrium, as suggested by Liou (2002):

$$\frac{\partial T}{\partial t} = \frac{g}{Cp}\frac{ARF_{ATM}}{\Delta P} \quad (4)$$

where $\partial T/\partial t$ is the HR in K day^{-1}, g is the acceleration due to gravity (9.8 m s^{-2}), Cp is the specific heat capacity of air at constant pressure (i.e., 1006 J kg^{-1} K^{-1}), and ΔP is the atmospheric pressure difference between surface and 3 km altitude, where most aerosols are present. According to several authors, in this study, ΔP was taken as equal to 300 hPa (Kaskaoutis *et al.*, 2013; Singh *et al.*, 2016).

From the ARF instantaneous data, the daily average value (DARF) can be calculated as follows:

$$DARF = \frac{\sum ARF_{hourly}}{24} \quad (5)$$

where ARF_{hourly} are hourly averaged values and the sum extends over the whole day (24 h).

ARF is very sensitive to the amount and type of aerosols existing in the atmosphere, increasing with the AOD. In order to quantify the rate at which the forcing varies per unit optical depth, the aerosol radiative forcing efficiency (ARFE) is defined. The mean ARFE was calculated as the slope of the regression line between ARF and AOD as suggested by Bush and Valero (2003). In this study AOD at 550 nm has been used. The conversion of AOD at 500 nm, which is the AERONET direct product, to AOD at 550 nm has been performed using the Ångstrom power law:

$$AOD550 = AOD500 \cdot \left(\frac{550}{500}\right)^{-\alpha} \quad (6)$$

where α is Ångstrom Exponent in the wavelength range of 440–870 nm (Alam *et al.*, 2011).

The dataset used in this study is composed of cloud-free shortwave irradiance simulated values integrated over the spectral interval 285–2800 nm. The simulations were performed during those days in the period 2003–2015 when level 2.0 AERONET data are available for this station. Thus, 1676 days were used, which is a much higher number than, for example, the 200 days used by Esteve *et al.* (2014). It is important to note that level 2.0 data correspond exclusively to cloud-free conditions.

The shortwave irradiances were simulated using the libRadtran version 1.7 radiative transfer code (Mayer and Kylling, 2005; Emde *et al.*, 2016). The uncertainties of libRadtran model were assessed by Emde *et al.* (2016), who showed that the estimated radiance and irradiance results agree very well with a reference validated model, presenting differences lower than 0.05%, with a few exceptions for cases that are not treated in this work (for example circum-solar radiation). References therein (Emde *et al.*, 2016) to a number of model intercomparison studies demonstrate the performance of libRadtran in comparison to a variety of other models. In addition, Obregón *et al.*

(2015b) analyzed the performance of libRadtran to simulate shortwave solar irradiances under different aerosol conditions, through comparison with corresponding calibrated pyranometer measurements. The authors obtained relative differences between irradiance simulations and measurements lower than 0.2%. Additionally, Román *et al.* (2014) analyzed the sensitivity of SW irradiances simulated with libRadtran model to the input uncertainties, obtaining a global sensitivity usually below 10%.

The main inputs for simulations were aerosol optical properties, precipitable water vapor column, surface albedo, and total ozone column. The inputs to describe the aerosols were provided by AERONET and consist of direct products as aerosol optical depth (AOD) and Ångström parameter, and inversion products as asymmetry parameter (ASY), and single scattering albedo (SSA). Ångström parameters were derived from level 2.0 AERONET aerosol optical depth (AOD) in the range 440–870 nm. Level 2.0 AERONET dataset also provided ASY values. Level 2.0 SSA data are very scarce, with only 226 values available in the period of study. The main reason is the requirement to only consider cases with AOD at 440 nm higher than 0.4. This AOD value is very unusual in Évora (the typical median value is 0.1) and corresponds almost exclusively to desert dust intrusions, which is a very specific situation. Therefore, in order to include different aerosol types and to have enough data available, level 1.5 SSA had to be used. Additionally, data were inspected to search for anomalous values. No negative AOD cases and only eight (0.06% of a total number of cases of 13920) negative Ångström exponent cases were found. The latter were filtered. SSA and ASY values for 675 nm have been used as suggested by some authors (Di Biagio *et al.*, 2010; Foyo-Moreno *et al.*, 2014). This wavelength has been chosen among the wavelengths available at AERONET data as it is close to the maximum of the solar irradiance per unit wavelength. Precipitable water vapor data were also obtained from level 2.0 AERONET products. Daily total ozone column was provided by the AURA Validation Data Center (AVDC) via its website (http://avdc.gsfc.nasa.gov/index.php?site=1593048672&id=28). Surface albedo was obtained from the Surface and Atmospheric Radiation Budget (SARB) working group, part of NASA Langley Research Center's Clouds and the Earth's Radiant Energy System (CERES) mission (http://ceres.larc.nasa.gov/). In order to take into account the time of the year, midlatitude summer/winter standard vertical profiles of thermodynamic variables, main gases and aerosols were considered depending on the season (Shettle *et al.*, 1989; Mayer and Kylling, 2005). The extraterrestrial irradiance was considered according to Gueymard (2004). The radiative transfer equation solver DISORT2, which is an improved version of the multi-stream discrete ordinate method of Stamnes *et al.* (2000), was used with 16 streams.

In order to more accurately model the instantaneous irradiance, 10-minute irradiances were simulated. For this, available AERONET values (α and β Ångström coefficients, ASY, SSA and PWC) were interpolated on a 10-minute basis. The dataset used was composed of 108843 10-minutes values of ARF corresponding to the 1676 days with available AERONET data. Fig. 2 shows the number of days analyzed in this study for each month during the period 2003-2015. Summer is the season with more days with available data (668 days, 40%), due to the prevailing cloud-free conditions during this period of the year. The relative frequency of days with available data for the other seasons was 21% (352 days) in spring, 20% (343 days) in autumn, and 19% (314 days) in winter.

To evaluate the aerosol radiative effects, simulations with and without aerosols were computed for the 108843 cases. Finally, ARF was calculated at the TOA and at the SURF levels, substituting the simulated irradiance in equations 2 and 3, respectively.

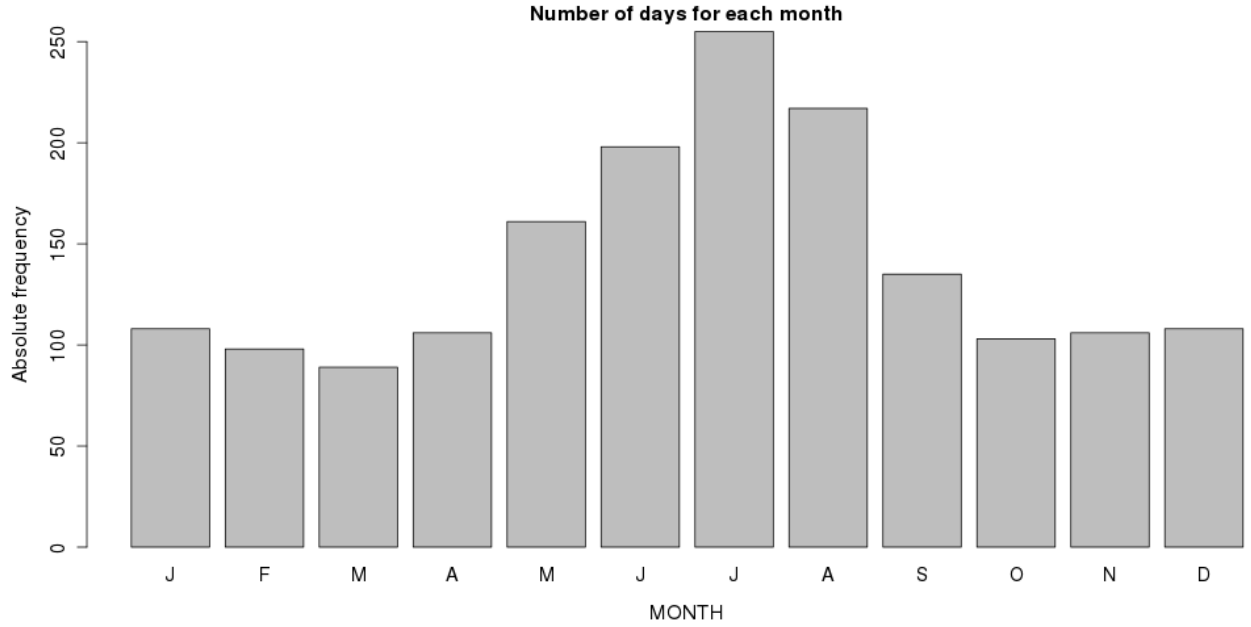

Fig. 2. Number of daily ARF values, DARF, for each month during the period 2003–2015.

The reliability of the libRadtran model for simulating SW irradiance in Évora was previously confirmed by comparing simulated values with irradiance measurements registered by an Eppley Black & White pyranometer (Obregón *et al.*, 2015a). This comparison included clean and turbid cases corresponding to periods before or after (clean), and during (turbid) two particular desert dust intrusion events occurred in summer 2012 (Obregón *et al.*, 2015a). Additionally, in this study the reliability of the libRadtran simulations will be tested by comparing our estimated instantaneous ARF with values provided by AERONET.

RESULTS AND DISCUSSION

Spectral Variation of AOD, SSA and ASY

As mentioned in the methodology, aerosol optical properties such as AOD, SSA and ASY along with their spectral variability are required for calculating ARF and ARFE. These properties have different spectral variations revealing information about the particle size and their absorptivity. Fig. 3 illustrates the AOD, SSA and ASY mean spectral variation for the different seasons.

The spectral variation of AOD provides information about the particle size distribution (Eck *et al.*, 1999). AOD seems to be more wavelength dependent during summer, when it decreases as wavelength increases, indicating the presence of fine particles. Conversely, the smaller spectral dependence is observed in winter, indicating the prevalence of coarser particles. Mean AOD in summer is 0.17 ± 0.12 at 440 nm wavelength and 0.07 ± 0.08 at 1020 nm, whereas, in winter, the mean value is 0.08 ± 0.05 at 440 nm and 0.03 ± 0.02 at 1020 nm.

In regard to SSA, Fig. 3 shows the mean values for each season of the year. As can be seen, mean SSA values for the four seasons decrease as wavelength increases. This SSA spectral behavior indicates the presence of absorbing aerosols (Dubovik *et al.*, 2002). This wavelength dependence is more intense in winter than during the other seasons of the year, with mean values of 0.88 ± 0.08 at 440 nm and 0.80 ± 0.14 at 1020 nm. This dependence is also reported for Lahore and Karachi by Alam *et al.* (2012), Delhi by Singh *et al.* (2010), and four locations in the Indo-Gangetic plains by Bibi *et al.* (2016), but only during winter, when dust is not a major contributor to the aerosol load.

Additionally, the mean value corresponding to AERONET level 2.0 SSA data has been added to Fig. 3(b). In contrast to the behavior found for the SSA data used in this work, level 2.0 SSA presents higher values and increases or is neutral with wavelength, which is a clear signature of the predominance of mineral dust (Dubovik *et al.*, 2002). This fact is due to the extremely restrictive threshold used for level 2.0 data, which requires AOD higher than 0.4. In the case of Évora, this threshold mostly retains those cases with desert dust aerosols originating from the Sahara region. Since this study attempts to analyze the mean aerosol radiative forcing in southwestern Iberian Peninsula during thirteen years, a variety of aerosol conditions needs to be sampled. Therefore, for this study, the level 2.0 AERONET data is too restrictive regarding the SSA.

Similarly to AOD and SSA, ASY shows spectral dependence (Fig. 3(c)). In general ASY decreases with increasing wavelength, except for high wavelengths, where a marginal increase can be observed for spring, summer and autumn seasons. Mean ASY (standard deviation) is 0.70 (0.03) at 440 nm and 0.66 (0.04) at 1020 nm in spring, 0.70 (0.03) at 440 nm and 0.65 (0.05) at 1020 nm in summer, 0.70 (0.03) at 440 nm and 0.64 (0.05) at 1020 nm in autumn, and 0.70 (0.03) at 440 nm and 0.62 (0.06) at 1020 nm in winter. The largest ASY decrease is thus observed in winter, in line with the results reported by Alam *et al.* (2012) in Lahore and Karachi.

Aerosol Radiative Forcing

In this section, the values of ARF at the SURF and at the TOA over Évora during the period 2003–2015 are analyzed. Fig. 4 shows the values of DARF at the SURF and at the TOA obtained in Évora during the period 2003–2015 in a box and whisker plot. As can be seen, the DARF at the SURF shows some variability during the year, with more negative values in warm months and less negative values in cold months. DARF ranged from –0.1 to –54.9 W m^{-2}, with a mean (and standard deviation) of –7.4 (5.5) W m^{-2},

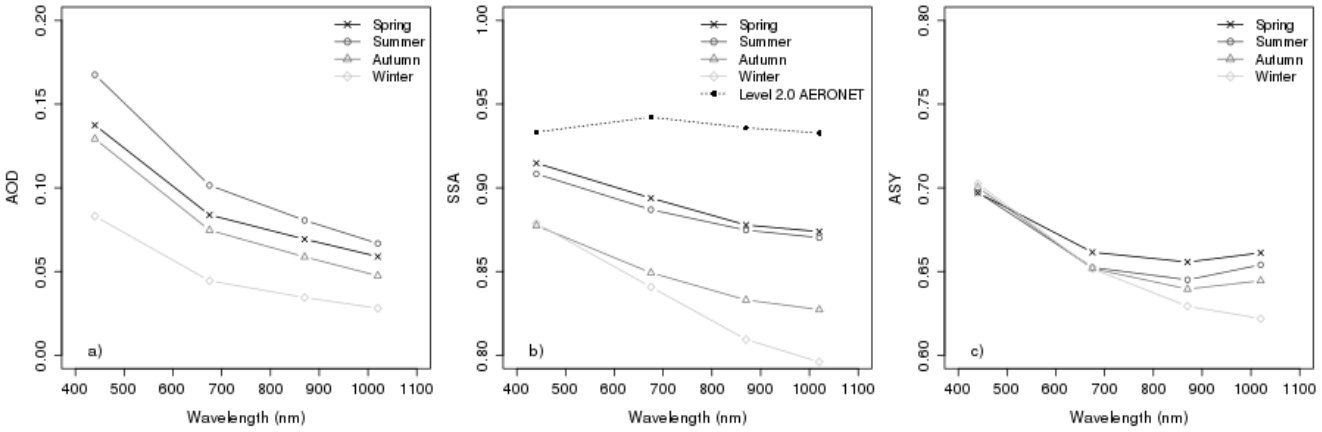

Fig. 3. (a), (b) and (c) show AOD, SSA and ASY mean values at wavelengths of 440 nm, 675 nm, 870 nm, and 1020 nm for different seasons. AERONET level 2.0 SSA has also been plotted in (b) for comparison purposes.

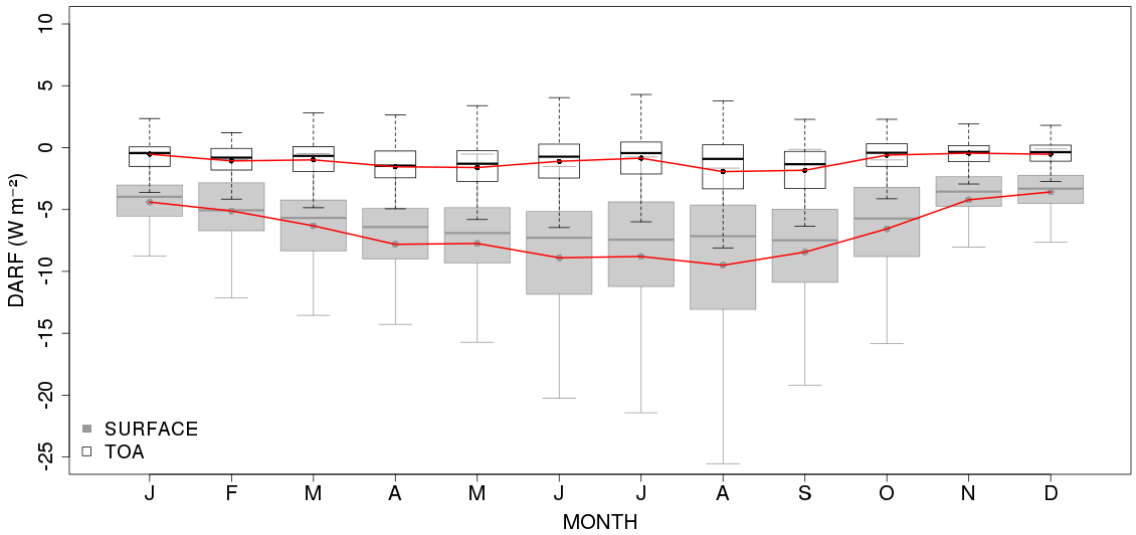

Fig. 4. Box and whisker plot of daily ARF values, DARF, at the surface and the top of the atmosphere for each calendar month over the 2003–2015 period. The mean (filled circles), median (horizontal segment within the box), 25th and 75th percentiles (top/bottom box limits) and data within 1.5 times the interquartile range (whiskers) are shown.

at the SURF, and from –15.6 to +18.9 W m^{-2}, with a mean value of –1.1 (2.5) W m^{-2}, at the TOA. The negative values indicate a decrease in the solar radiation reaching the SURF and an increase in the light scattered back to space at the TOA. This loss in net radiation at the TOA leads to cooling of the Earth–atmosphere system. It is worth mentioning that 491 DARF values are positive (29% of the total number of cases). These values are near zero, with 75% of cases below 1.3 W m^{-2}.

It is interesting to note that the absolute magnitude of the mean DARF at the SURF is higher than at the TOA, producing a mean net gain of energy by the atmosphere estimated in 6.3 (with a standard deviation of 4.8) W m^{-2}. This gain is due to the absorption of radiation by atmospheric components.

The monthly mean of this absorption by the atmosphere is represented by the difference between the two red lines in Fig. 4. These values ranged from 2.6 W m^{-2} in December to 7.1 W m^{-2} in August. These absorbing properties of aerosols are also particularly important for energy balance and cloud-aerosol interactions, as shown in the work of Su *et al.* (2008).

While no seasonal DARF pattern is observed at the TOA, a clear seasonal cycle is detected at the SURF (Fig. 4). This seasonality is not only due to the variation in the radiation along the year, but also to the seasonal pattern shown by AOD (Fig. 5(a)). This figure presents a box and whisker plot of daily AOD (at 550 nm) values over Évora for each calendar month, showing its annual variation. The lowest optical depths occur in November and December, contrasting with the highest optical depths found in August and September, when AOD is higher than 0.18 in more than 25% of the cases. These high AOD values during the summer months can be explained by a combination of several factors such as Saharan dust intrusions and forest fires, being the latter associated with high temperatures, very low atmospheric relative humidity and lack of precipitation. The arrival of air masses from the Saharan region transporting desert-dust aerosols constitutes a substantial source of aerosols, affecting the southwestern Iberian Peninsula generally in summer (Toledano *et al.*, 2007). This fact is confirmed by the low α values observed in August (Fig. 5(b)). Summer forest fires, particularly those extensive and long lasting that occurred in Portugal and Western Spain in 2003 and 2005 (Elias *et al.*, 2006), could mean also a substantial contribution to high optical depth values during these months. Both conditions (low AOD in winter months and high AOD values in summer months) are consistent with the ARF values shown in Fig. 4 (less negative in winter and more negative in summer). Also, a secondary maximum is observed in spring, being consistent with ARF values and observations reported for other stations of the Iberian Peninsula (Estellés *et al.*, 2007; Toledano *et al.*, 2007; Obregón *et al.*, 2012; Esteve *et al.*, 2014).

Fig. 5(b) depicts the annual variation of daily α, showing the highest mean values in January, December, February, and November. Conversely, α is low in April, May and August, being associated with large particles, typical of desert dust episodes or/and intrusions of marine aerosol in spring and summer (associated with sea breeze). In August, the low α values together with high AOD load, indicate the intrusion of dust from North Africa. Other studies have reported a similar seasonal pattern of AOD and α at other locations within the Iberian Peninsula, such as El Arenosillo (Cachorro *et al.*, 2005; Toledano *et al.*, 2007), Boecillo (Cachorro *et al.*, 2000), and Cáceres (Obregón *et al.*, 2015c). As it can be seen in Fig. 5(a), although AOD is high and similar in August and September, α differs between these two months. In August, α is lower than in September, indicating a stronger influence of desert dust aerosol in August than in September, and a higher cooling at the SURF. This tendency of cooling the Earth-atmosphere system due to the effect of desert dust aerosols agrees with results reported for other regions (e.g., Costa *et al.*, 2006; Derimian *et al.*, 2006;

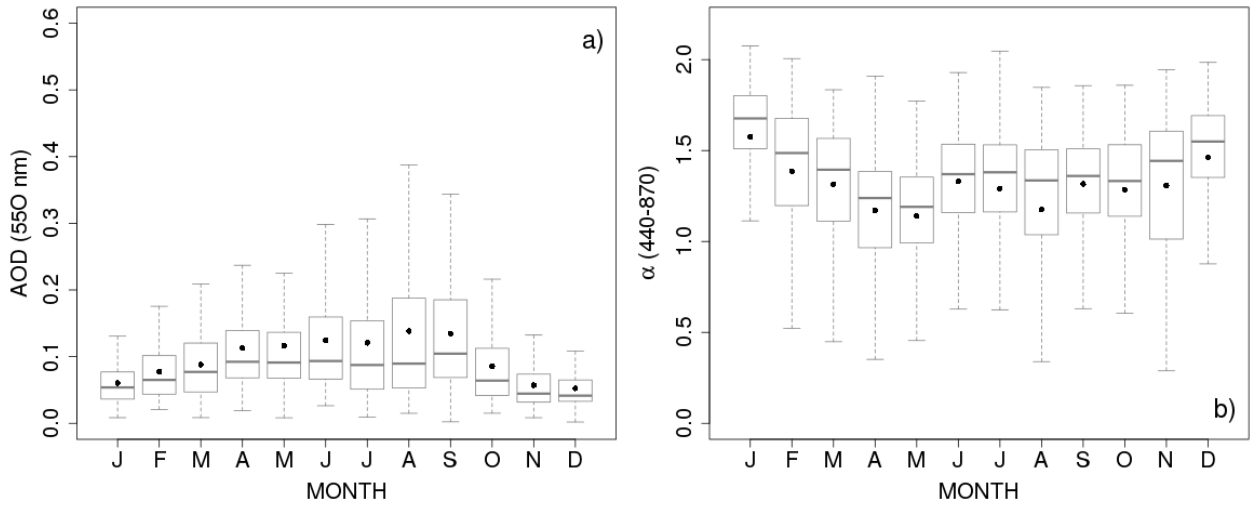

Fig. 5. Box and whisker plot of daily AOD (a) and α (b) values for each calendar month over the 2003–2015 period. The mean (filled circles), median (horizontal segment within the box), 25th and 75th percentiles (top/bottom box limits) and data within 1.5 times the interquartile range (whiskers) are shown.

Lyamani *et al.*, 2006; Cachorro *et al.*, 2008; Guerrero-Rascado *et al.*, 2009; Huang *et al.*, 2009; García *et al.*, 2012; Santos *et al.*, 2013; Valenzuela *et al.*, 2012; Obregón *et al.*, 2015a).

It is worth mentioning that our findings are not in line with results for the same station reported by Mateos *et al.* (2014) within a general study where several stations were analyzed. The monthly ARF values obtained here are generally more negative than theirs. In particular, the magnitude and the time of the year with the most negative ARF differ between both studies; while this study finds –9.5 W m^{-2} in August, they find around –8 W m^{-2} in April. One reason for this discrepancy could be related with the limited period of study considered by Mateos *et al.* (2014), which, for example, excluded the year 2003. During this year, as already mentioned above, there were numerous intense intrusions of desert dust and several forest fires all over Iberian Peninsula and south of France. The difference in ARF values emphasizes the need for relying on long term representative series of measurements in order to achieve an accurate estimation of the average regional aerosol radiative effect, mainly in areas with high variability such as the Iberian Peninsula.

An example of the spatial variability is the difference in ARF values reported for the Atlantic and the Mediterranean coastal areas within the Iberian Peninsula. Thus, the magnitude of the ARF obtained in this study at an Atlantic-influenced station such as Évora is around half the values measured at a Mediterranean station such as Burjassot (Valencia, Spain) (Esteve *et al.*, 2014). This difference is due to several factors such as the influence of the oceans, the prevailing circulation patterns and local aerosol sources. The results obtained in this study also show great differences with respect to those obtained in large polluted cities such as Lahore and Karachi in Pakistan. At these stations the ARF values are around –70 and –19 W m^{-2} at the SURF and at the TOA, respectively (Alam *et al.*, 2011; Alam *et al.*, 2014).

Fig. 6 shows comparisons between ARF at both levels SURF (a) and TOA (b), as provided by AERONET vs values estimated in this study using libRadtran. The comparisons are performed for the period of study. Values at the SURF show a good general agreement, with a high correlation coefficient of 0.97. This value is similar to those obtained by Alam *et al.* (2012) for Lahore and Karachi using SBDART model (0.99 and 0.98, respectively), and notably higher than those obtained by Bibi *et al.* (2017) over Karachi (0.51), Lahore (0.81), Jaipur (0.66) and Kanpur (0.69). This good correlation between AERONET and libRadtran surface forcing demonstrates that the input parameters, particularly the atmospheric profiles, constitute an appropriate representation of the prevailing atmospheric conditions in our location of study. On the other hand, the comparison between ARF at the TOA presents also a very high correlation coefficient (0.91) at the TOA (Fig. 6(b)). This value is notably higher than the values obtained by Bibi *et al.* (2017) over Karachi (0.46), Lahore (0.73), Jaipur (0.57) and Kanpur (0.55).

The libRadtran code allows to select two standard aerosol profiles, one typical of spring–summer and another of autumn–winter conditions. These profiles (Shettle, 1989) describe the change in the aerosol profile throughout the year. In order to analyze the sensitivity of the radiative forcing estimates to the vertical distribution of aerosols, these two profiles have been used. Thus, all the calculations have been repeated for both profiles separately regardless of the true season of the year and the daily aerosol radiative forcing has been obtained at the SURF and at the TOA. For the comparison analysis, the whole year 2012 has been used in order to account for the annual variability of the frequency of the aerosol conditions. The DARF estimated using both profiles show a very good agreement with a correlation coefficient near one. Differences in the DARF are very low at both levels, with mean differences of –0.001 Wm^{-2} (standard deviation of 0.009 Wm^{-2}) at the SURF, and of 0.012 Wm^{-2} (standard deviation of 0.050 Wm^{-2}) at the TOA. These results are in line with the sensitivity study

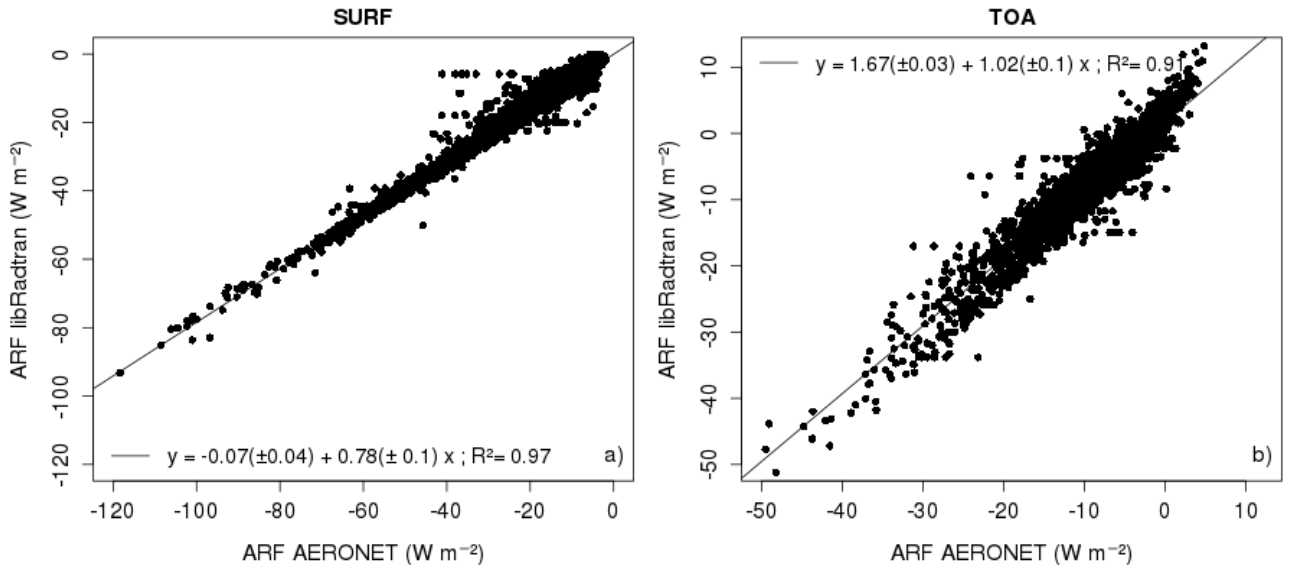

Fig. 6. Comparisons between ARF provided by AERONET and ARF estimated in this study using libRadtran, (a) for surface level and (b) for the top of the atmosphere level.

performed by Mishra *et al.* (2015), who concluded that aerosol forcing in the visible-near infrared range is less sensitive to changes in the aerosol layer height as compared to thermal-infrared and ultraviolet ranges.

As mentioned before, since the ARF depends on the particle load in the atmosphere, the forcing efficiency ARFE was calculated and analyzed at the SURF and at the TOA levels. The mean ARFE has been calculated as the slope of the regression line between ARF and AOD values. Since the ARF is expected to be zero when AOD is zero, a zero-intercept linear regression has been used to estimate the ARFE. Fig. 7 shows DARF at the SURF and at the TOA versus daily mean AOD (550 nm). The uncertainty in ARFE is quantified by the error associated to the regression slope. The ARFE obtained were –62.7 ± 0.4 W m^{-2} τ^{-1} and –14.3 ± 0.3 W m^{-2} τ^{-1} (per unit AOD or τ at 550 nm) for SURF and TOA datasets, respectively. In order to analyze the effect of SSA, in Fig. 7 the points have been colored according to their SSA value. As can be seen, for a given AOD, the most negative ARF values at the SURF correspond to low SSA values, i.e., to the most absorbing aerosols. Conversely, the opposite behavior is found at the TOA (Fig. 7(b)). Thus, the increase in the absorption by aerosols reduces the scattered radiation also towards TOA, thereby contributing to less negative (or even positive) ARF values at the TOA. These results are in line with those found during the CLEARCOLUMN/ACE2 campaign conducted at Sagres, Portugal (Silva *et al.*, 2002). They are also confirmed by the ARFE values calculated for different SSA intervals. Thus, the ARFE obtained for SURF were –140.2, –104.3, –81.4 and –55.48 W m^{-2} τ^{-1} for the SSA ranges [< 0.7], [0.7–0.8], [0.8–0.9], [>0 .9], respectively. Similarly, the following ARFE values: +44.5, +15.2, –3.4, –19.1 W m^{-2} $\tau^{-1,}$ were obtained for the TOA for the same SSA intervals mentioned above. While the aerosols at the SURF with low SSA result in highly negative ARFE values, at the TOA those aerosols are associated with less negative, or even positive, ARFE values.

The ARFE was also calculated at 500 nm in order to compare with the study performed by Esteve *et al.* (2014) for a Mediterranean station during the period 2003–2011. As mentioned before, notable differences exist between the Atlantic and the Mediterranean areas. Thus, while Évora shows –55.1 W m^{-2} τ^{-1} at the SURF and –15.1 W m^{-2} τ^{-1} at the TOA, Burjassot shows more negative values (–139 W m^{-2} τ^{-1} at the SURF and –19.2 W m^{-2} τ^{-1} at the TOA).

Fig. 8 shows the mean ARFE calculated for each season of the year at the SURF and at the TOA. Points have been colored according to their SSA value. No seasonal effect can be perceived at any level, with ARFE around –62 W m^{-2} τ^{-1} and –14 W m^{-2} τ^{-1} at the SURF and at the TOA, respectively. However, the aerosol tends to have a slightly stronger impact at the TOA in spring (–16.1 ± 0.7 W m^{-2} τ^{-1}) than in the remaining seasons: winter (–14.2 ± 0.9 W m^{-2} τ^{-1}), autumn (–13.9 ± 0.6 W m^{-2} τ^{-1}) and summer (–13.8 ± 0.4 W m^{-2} τ^{-1}).

Heating Rate

The amount of solar radiations trapped in the atmosphere by the aerosols as quantified by the atmospheric heating rate has been analyzed. The average heating rate (K day^{-1}) estimated from DARF during the study period was 0.18 (with a standard deviation of 0.15). Percentiles 10 and 90 indicate that in 80% of the days, HR falls between 0.04 and 0.35 K day^{-1}. These values are in line with the value of 0.11 K day^{-1} obtained by Valenzuela *et al.* (2017) for the same location (Évora) during one specific day. The heating rate in Évora is generally lower than values reported for stations with high atmospheric absorption such as, for example, two polluted mega-cities in Pakistan, with values higher than 1 K day^{-1} (Alam *et al.*, 2012). It is also lower than the values obtained for two desert dust events analyzed by Gharibzadeh *et al.* (2017), which showed mean values of 2.16 and 0.89 K day^{-1}.

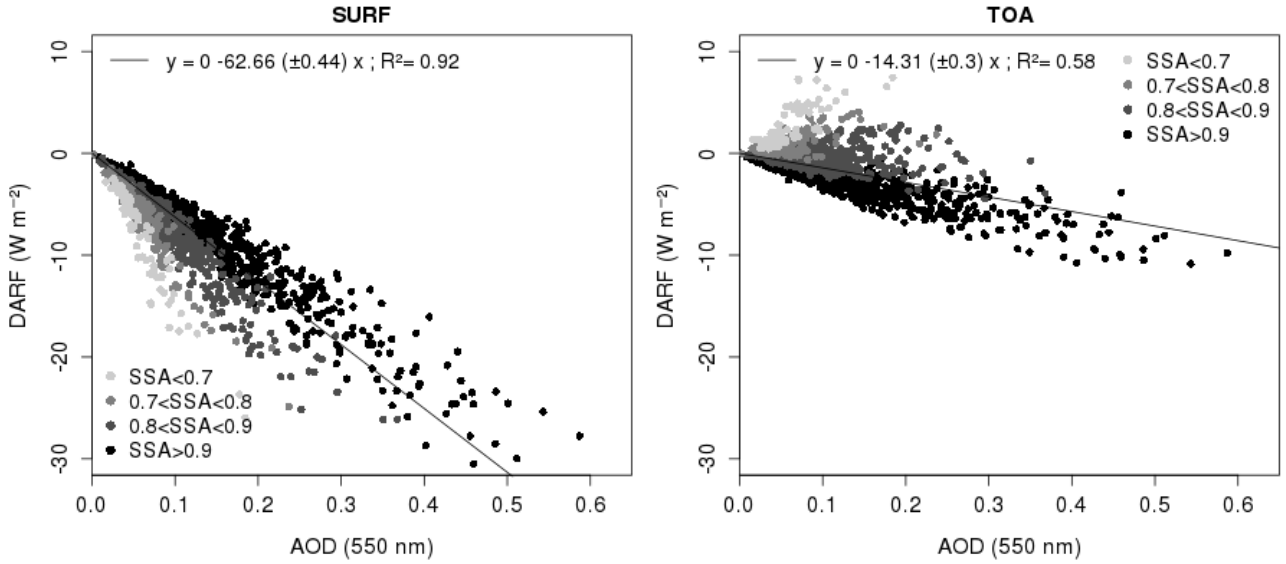

Fig. 7. Aerosol radiative forcing as a function of the AOD at 550 nm during the study period. (a) for surface level and (b) for the top of the atmosphere level. The regression equations are included and the points have been colored according to their SSA value.

In order to analyze the annual variation of the HR in Évora, the mean HR value was calculated for each calendar month (Fig. 9). The higher HR values occur mainly during summer (mean of 0.22 and standard deviation of 0.15), when ARF is also high. It is followed by spring (mean of 0.18 and standard deviation of 0.18), autumn (mean of 0.15 and standard deviation of 0.12) and winter (mean of 0.10 and standard deviation of 0.10). Spring is the season that shows the higher variability, with many high HR values during April. The annual variation in the amount of solar energy trapped by the atmosphere has strong implications for temperature changes and thermal structure of the atmosphere as well as important consequences for many processes, like cloud formation, precipitation, and synoptic circulation.

CONCLUSIONS

The aerosol radiative forcing (ARF) at Évora station has been studied with the goal of reducing the uncertainty of the aerosol impact at local scales. This station provides information about Southwestern Iberian Peninsula, a region of climatic significance largely affected by different aerosol types such as local continental particles, Atlantic marine aerosols, and desert dust coming from the largest source of dust worldwide: the Sahara Desert. Towards this aim, the aerosol radiative forcing and its efficiency (ARFE) in the shortwave solar spectrum have been calculated and analyzed. The study period extends from 2003 to 2015, being the longest period ever used in studies of aerosol radiative forcing in this region.

ARF and ARFE have been calculated at both the Earth's surface (SURF) and top of the atmosphere (TOA) levels. For this purpose, a high temporal resolution dataset, composed of 10-minute irradiance values simulated using the libRadtran code and previously validated, has been used. The ARF values calculated on a 10 minute basis have been integrated over 24 h to obtain daily mean values, DARF, for 1676 days. While no seasonal DARF pattern is observed at the TOA, a clear seasonal pattern can be distinguished at the SURF, with more negative values in summer, likely associated not only to the variation in the radiation along the year but also to the annual variability of AOD. The DARF values obtained for SURF ranged from –0.1 to –54.9 W m^{-2}, with a mean (and standard deviation) of –7.4 (5.5) W m^{-2}, and from –15.6 to +18.9 W m^{-2} at the TOA with a mean value of –1.1 (2.5) W m^{-2}. The negative values indicate a decrease in the solar radiation that reaches the Earth's surface and an increase in the light that is scattered back to space, cooling the Earth–atmosphere system. The difference in DARF magnitude between SURF and TOA indicates a mean net gain of energy by the atmosphere estimated in 6.3 (with a standard deviation of 4.8) W m^{-2}, due to absorption of radiation by atmospheric components.

The values of ARF at the SURF calculated in this study were compared with those reported by other authors for different regions, showing significant differences and indicating the importance to perform accurate local studies to achieve a thorough description of the impact of aerosols. The comparison with the study of Mateos *et al.* (2014) for the same station revealed notable differences, mainly in the ARF seasonal pattern. This discrepancy is likely associated to the use of a limited period of measurements in that study, emphasizing the need to use long high quality time series of data in order to guarantee an accurate description of the aerosol radiative forcing.

Instantaneous ARF values simulated with libRadtran have been compared with values provided by AERONET. The comparison showed a very good agreement at both levels: SURF and TOA, confirming the reliability of the calculations performed in this study with the libRadtran model.

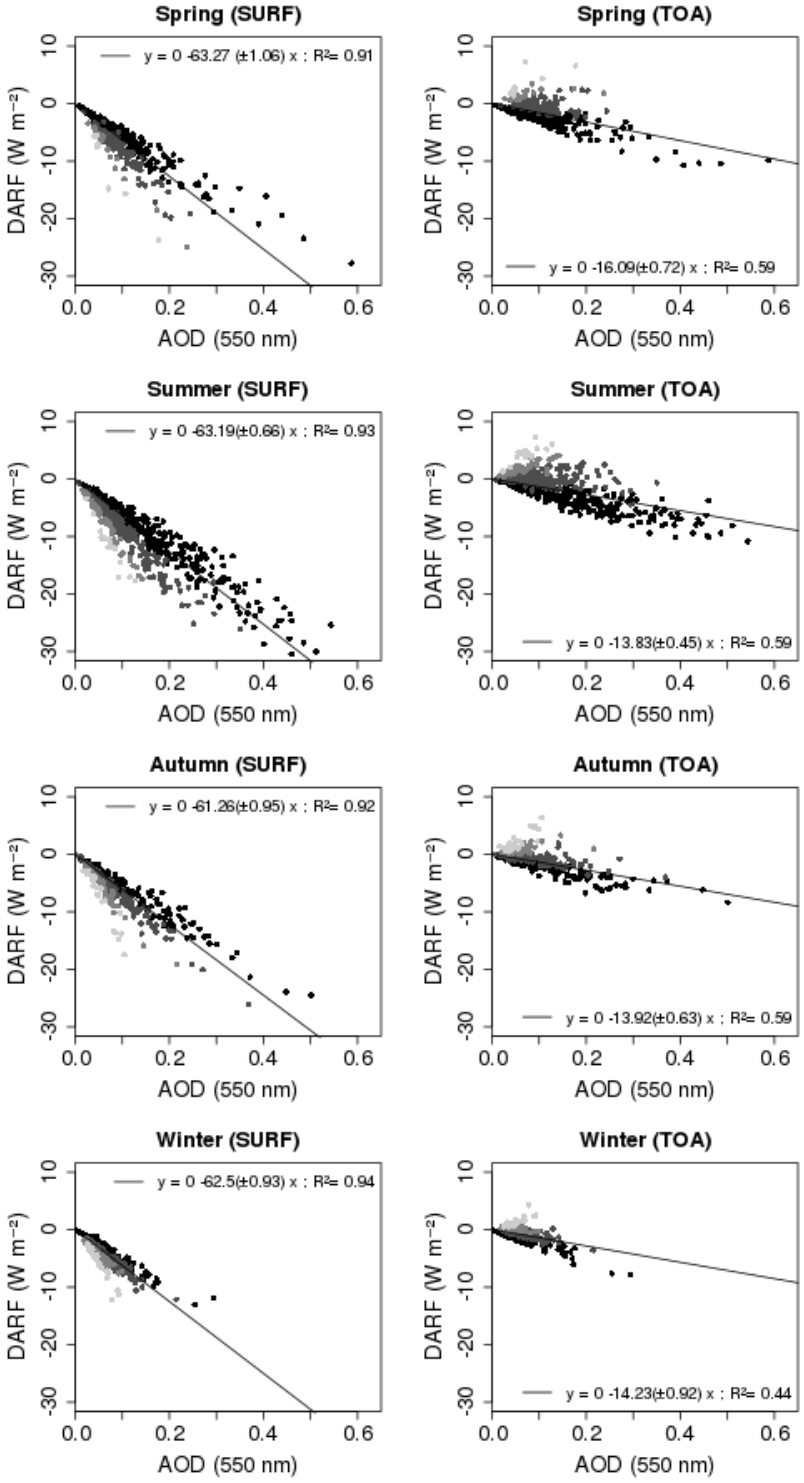

Fig. 8. Aerosol radiative forcing as a function of the AOD at 550 nm for each season of the year. The regression equations are included and the points have been colored according to their SSA value.

The ARFE (ARF per unit optical depth) was also calculated, and found to be –62.7 ± 0.4 W m^{-2} τ^{-1} and –14.3 ± 0.3 W m^{-2} τ^{-1} (per unit AOD or τ at 550 nm), at the SURF and at the TOA, respectively, showing no seasonality. These ARFE values are directly related to the SSA, with opposite behavior at the SURF and at the TOA. Thus, while at the SURF the aerosols with low SSA result in highly negative ARFE values, at the TOA those aerosols are associated with less negative or even positive ARFE values. This fact is due to the higher absorption by these aerosols, which results in less scattered radiation also towards the TOA and, therefore, in less negative ARFE at the TOA.

The values of ARF and ARFE reported for the region of study positively contributes to improve the understanding

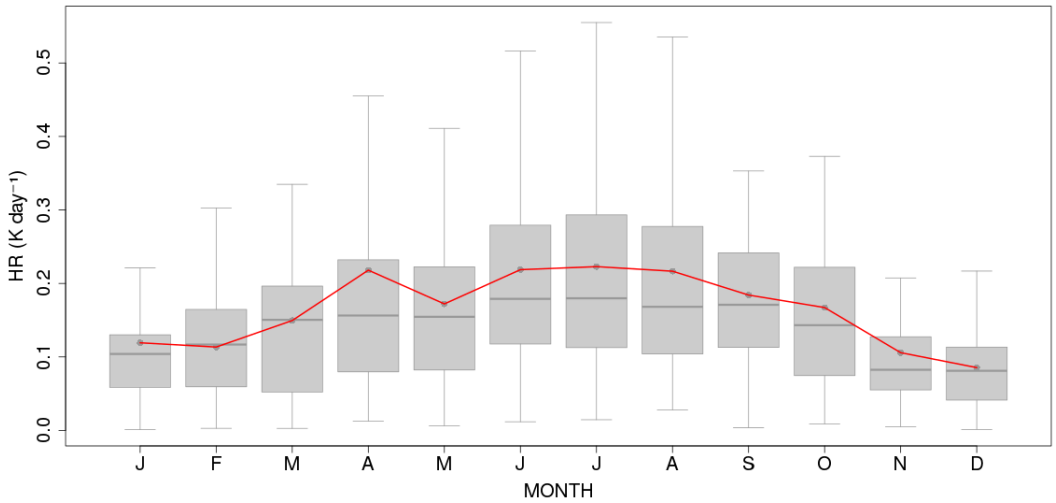

Fig. 9. Box and whisker plot of daily HR values for each calendar month over the 2003–2015 period. The mean (filled circles), median (horizontal segment within the box), 25th and 75th percentiles (top/bottom box limits) and data within 1.5 times the interquartile range (whiskers) are shown.

of the impact of aerosols in this area, mainly referred to its magnitude and temporal variability. In particular, the high temporal variability found in ARF and ARFE suggests the need to use long time series to guarantee the temporal representativeness in this interesting region.

ACKNOWLEDGMENTS

This work was partially supported by FCT (Fundação para a Ciência e a Tecnologia) through the grant SFRH/BPD/86498/2012. The work is co-funded by the European Union through the European Regional Development Fund, included in the COMPETE 2020 (Operational Program Competitiveness and Internationalization) through the ICT project (UID/GEO/04683/2013) with the reference POCI-01-0145-FEDER-007690 and also through the ALOP (ALT20-03-0145-FEDER-000004) and DNI-A (ALT20-03-0145-FEDER-000011) projects. The research is also co-funded by the research projects CGL2011-29921-C02-01/CLI and CGL2014-56255-C2-1-R granted by the "Ministerio de Economía y Competitividad" of Spain. The authors would like to acknowledge Samuel Bárias for maintaining instrumentation used in this work. Thanks are due to AERONET/PHOTONS and RIMA networks for the scientific and technical support. CIMEL calibration was performed at the AERONET-EUROPE GOA calibration center, supported by ACTRIS under agreement no. 654109 granted by European Union (H2020-INFRAIA-2014-2015). The data analyzed in this study are available from authors upon request (nines@unex.es).

REFERENCES

Alam, K., Trautmann, T. and Blaschke, T. (2011). Aerosol optical properties and radiative forcing over mega city Karachi. *Atmos. Res.* 101: 773–782.

Alam, K., Trautmann, T., Blaschke, T. and Majid, S. (2012). Aerosol optical and radiative properties during summer and winter seasons over Lahore and Karachi. *Atmos. Environ.* 50: 234–245.

Alam, K., Sahar, N. and Iqbal, Y. (2014). Aerosol characteristics and radiative forcing during pre-monsoon and post-monsoon in an urban environment. *Aerosol Air Qual. Res.* 14: 99–107.

Bibi, H., Alam, K., Blaschke, T., Bibi, S. and Iqbal, M.J. (2016). Long-term (2007-2013) analysis of aerosol optical properties over four locations in the Indo-Gangetic plains. *Appl. Opt.* 55: 6199–6211.

Bibi, H., Alam, K. and Bibi, S. (2017). Estimation of shortwave direct aerosol radiative forcing at four locations on the Indo-Gangetic Plains: Model results and ground measurement. *Atmos. Environ*. 163: 166–181.

Boucher, O. and Coauthors (2013). Clouds and aerosols in climate change 2013. In *Contribution of Working Group I to the Fifth Assessment Report of the Intergovernmental Panel on Climate Change*. Stocker, T.F., Qin, D., Plattner, G.K., Tignor, M., Allen, S.K., Boschung, J., Nauels, A., Xia, Y., Bex, V. and Midgley, P.M. (Eds.). The Physical Science Basis. Cambridge University Press, Cambridge, United Kingdom and New York, NY, USA.

Bush, B.C. and Valero, F.P.J. (2003). Surface aerosol radiative forcing at Gosan during the ACE-Asia campaign. *J. Geophys. Res.* 108: 1–8.

Cachorro, V.E., Durán, P., Vergaz, R. and Frutos, M.A. (2000). Measurement of the atmospheric turbidity of the North Centre continental area in Spain: Spectral aerosol optical depth and Ångström turbidity parameters. *J. Aerosol Sci*. 31: 687–702.

Cachorro, V.E., Toledano, C., de Frutos, A.M., Sorribas, M., Vilaplana, J.M. and de la Morena, B. (2005). Aerosol characterization at El Arenosillo (Huelva, Spain) with an AERONET/PHOTONS CIMEL sunphotometer. *Geophys. Res. Abstr.* 7: 08559.

Cachorro, V.E., Toledano, C., Prats, N., Sorribas, M., Mogo, S., Berjón, A., Torres, B., Rodrigo, R., de la Rosa, J. and De Frutos, A.M. (2008). The strongest desert dust intrusion

mixed with smoke over the Iberian Peninsula registered with Sun photometry. *J. Geophys. Res*. 113: D14S04.

Costa, M.J., Sohn, B.J., Levizzani, V. and Silva, A.M. (2006). Radiative forcing of Asian dust determined from the synergized GOME and GMS satellite data – A case study. *J. Meteorol. Soc. Jpn*. 84: 85–95.

Derimian, Y., Karnieli, A., Kaufman, Y.J., Andreae, M.O., Andreae, T.W., Dubovik, O., Maenhaut, W., Koren, I. and Holben, B.N. (2006). Dust and pollution aerosols over the Negev desert, Israel: Properties, transport, and radiative effect. *J. Geophys. Res*. 111: D05205.

Di Biagio, C., di Sarra, A. and Meloni, D. (2010). Large atmospheric shortwave radiative forcing by Mediterranean aerosols derived from simultaneous ground-based and spaceborne observations and dependence on the aerosol type and single scattering albedo. *J. Geophys. Res*. 115: D10209.

Dubovik, O., Holben, B., Eck, T.F., Smirnov, A., Kaufman, Y.J., King, M.D., Tanré, D. and Slutsker, I. (2002). Variability of absorption and optical properties of key aerosol types observed in worldwide locations. *J. Atmos. Sci.* 59: 590–608.

Eck, T.F., Holben, B.N., Reid, J.S., Dubovik, A., Smirnov, N.T.O'Neill,, Slutsker, I. and Kinne, S. (1999). Wavelength dependence of the optical depth of biomass burning, urban, and desert dust aerosols. *J. Geophys. Res.* 104: 00093–00095.

Elias, T., Silva, A.M., Belo, N., Pereira, S., Formenti, P., Helas, G. and Wagner, F. (2006). Aerosol extinction in a remote continental region of the Iberian Peninsula during summer. *J. Geophys. Res*. 111: 1–20.

Emde, C., Buras-Schnell, R., Kylling, A., Mayer, B., Gasteiger, J., Hamann, U., Kylling, J., Richter, B., Pause, C., Dowling, T., Bugliaro, L. (2016). The libRadtran software package for radiative transfer calculations (version 2.0.1). *Geosci. Model Dev.* 9: 1647–1672.

Escudero, M., Castillo, S., Querol, X., Avila, A., Alarcón, M., Viana, M.M., Alastuey, A., Cuevas, E. and Rodríguez, S. (2005). Wet and dry African dust events over eastern Spain. *J. Geophys. Res*. 110: D18S08.

Estellés, V., Martínez-Lozano, J.A., Utrillas, M.P. and Campanelli, M. (2007). Columnar aerosol properties in Valencia (Spain) by ground based sun photometry. *J. Geophys. Res*. 112: D11201.

Esteve, A.R., Estellés, V., Utrillas, M.P. and Martínez-Lozano, J.A. (2014). Analysis of the aerosol radiative forcing over a Mediterranean urban coastal site. *Atmos. Res*. 137: 195–204.

Foyo-Moreno, I., Alados, I., Antón, M., Fernández-Gálvez, J., Cazorla, A. and Alados-Arboledas, L. (2014). Estimating aerosol characteristics from solar irradiance measurements at an urban location in southeastern Spain. *J. Geophys. Res.* 119: 1845–1859.

García, O.E., Díaz, J.P., Expósito, F.J., Díaz, A.M., Dubovik, O., Derimian, Y., Dubuisson, P. and Roger, J.C. (2012). Shortwave radiative forcing and efficiency of key aerosol types using AERONET data. *Atmos. Chem. Phys*. 12: 5129–5145.

Gharibzadeh, M., Alam, K., Bidokhti, A.A., Abedini, Y. and Masoumi, A. (2017). Radiative effects and optical properties of aerosol during two dust events in 2013 over Zanjan, Iran. *Aerosol Air Qual. Res.* 17: 888–898.

Guerrero-Rascado, J.L., Olmo, F.J., Avilés-Rodríguez, I., Navas-Guzmán, F., Pérez-Ramírez, D., Lyamani, H. and Alados Arboledas, L. (2009). Extreme Saharan dust event over the southern Iberian Peninsula in september 2007: Active and passive remote sensing from surface and satellite. *Atmos. Chem. Phys*. 9: 8453–8469.

Gueymard, C. (2004). The sun's total and spectral irradiance for solar energy applications and solar radiation models. *Sol. Energy* 76: 423–453.

Hansen, J., Sato, M., Kharecha, P. and von Schuckmann, K. (2011). Earth's energy imbalance and implications. *Atmos. Chem. Phys*. 11: 13421–13449.

Holben, B., Eck, T.F., Slutsker, I., Tanre, D., Buis, J., Setzer, K., Vermote, E., Reagan, J., Kaufman, Y., Nakajima, T., Lavenu, F., Jankowiak, I. and Smirnov, A. (1998). AERONET—A federated instrument network and data archive for aerosol characterization. *Remote Sens. Environ*. 66: 1–16.

Holben, B.N., Eck, T.F., Slutsker, I., Smirnov, A., Sinyuk, A., Schafer, J., Giles, D. and Dubovik, O. (2006). Aeronet's Version 2.0 quality assurance criteria, Proc. SPIE 6408, *Remote Sensing of the Atmosphere and Clouds*, 64080Q (8 December 2006).

Huang, J., Fu, Q., Su, J., Tang, Q., Minis, P., Hu, Y., Yi, Y. and Zhao, Q. (2009). Taklimakan dust aerosol radiative heating derived from CALIPSO observations using the Fu–Liou radiation model with CERES constraints. *Atmos. Chem. Phys*. 9: 4011–4021.

Kaskaoutis, D., Sinha, P., Vinoj, V., Kosmopoulos, P., Tripathi, S., Misra, A., Sharma, M. and Singh, R. (2013). Aerosol properties and radiative forcing over Kanpur during severe aerosol loading conditions. *Atmos. Environ.* 79: 7–19.

Koppen, W. (1936). Das geographisca System der Klimate, In *Handbuch der Klimatologie*, Koppen, W. and Geiger, G. (Eds.), 1. C. Gebr, Borntraeger, pp. 1–44.

Liou, K.N. (2002). *An Introduction to Atmospheric Radiation*. Academic press.

Lyamani, H., Olmo, F.J., Alcántara, A and Alados-Arboledas, L. (2006). Atmospheric aerosols during the 2003 heat wave in southeastern Spain II: Microphysical columnar properties and radiative forcing. *Atmos. Environ*. 40: 6465–6476.

Mateos, D., Antón, M., Toledano, C., Cachorro, V.E., Alados-Arboledas, L., Sorribas, M., Costa, M.J. and Baldasano, J.M. (2014). Aerosol radiative effects in the ultraviolet, visible, and near-infrared spectral ranges using long-term aerosol data series over the Iberian Peninsula. *Atmos. Chem. Phys*. 14: 13497–13514.

Mayer, B. and Kylling, A. (2005). Technical note: The libRadtran software package for radiative transfer calculations — description and examples of use. *Atmos. Chem. Phys*. 5: 1855–1877.

Mishra, A.K., Koren, I. and Rudich, Y. (2015). Effect of aerosol vertical distribution on aerosol-radiation interaction: A theoretical prospect. *Heliyon* 1: e00036.

Obregón, M.A., Pereira, S., Wagner, F., Serrano, A., Cancillo, M.L. and Silva, A.M. (2012). Regional differences of column aerosol parameters in western Iberian Peninsula. *Atmos. Environ*. 12: 1–10.

Obregón, M.A., Pereira, S., Salgueiro, V., Costa, M.J., Silva, A.M., Serrano, A. and Bortoli, D. (2015a). Aerosol radiative effects during two desert dust events in August 2012 over the Southwestern Iberian Peninsula. *Atmos. Res*. 153: 404–415.

Obregón, M.A., Serrano, A., Costa, M.J. and Silva, A.M. (2015b). Validation of libRadtran and SBDART models under different aerosol conditions. *IOP Conf. Series: Earth and Environmental Science.* 28: 012010.

Obregón, M.A., Serrano, A., Cancillo, M.L., Cachorro, V.E. and Toledano, C. (2015c). Aerosol radiometric properties at Western Spain (Cáceres station). *Int. J. Climatol*. 35: 981–990.

Pereira, S., Silva, A.M., Elias, T. and Wagner, F. (2005). Aerosol monitoring at Cabo da Roca site. Paper presented at *4° Simpósio de Meteorologia e Geofísica da APMG/6° Encontro Luso-Espanhol de Meteorologia*, Sesimbra, Portugal.

Pereira, S., Wagner, F. and Silva, A.M. (2008). Scattering properties and mass concentration of local and long-range transported aerosols over the South Western Iberia Peninsula. *Atmos. Environ*. 42: 7623–7631.

Pereira, S.N., Wagner, F. and Silva, A.M. (2011). Seven years of measurements of aerosol scattering properties, near the surface, in the south-western Iberia Peninsula. *Atmos. Chem. Phys*. 11: 17–29.

Querol, X., Rodriguez, S., Cuevas, E., Viana, M.M. and Alastuey, A. (2002). Intrusiones de masas de aire africano sobre la Península Ibérica y Canarias: Mecanismos de transporte y variación estacional. *3rd Asamblea Hispano portuguesa de Geodesia y Geofísica*. Inst. Nac. de Meteorol. Esp., Valencia.

Rodriguez, S., Querol, X., Alastuey, A., Kallos, G. and Kakaliagou, O. (2001). Saharan dust contributions to PM_{10} and TSP levels in Southern and Eastern Spain. *Atmos. Environ.* 35: 2433–2447.

Román, R., Bilbao, J. and de Miguel, A. (2014). Solar radiation simulations in the Iberian Peninsula: Accuracy and sensitivity to uncertainties in inputs of a radiative transfer model. *J. Quant. Spectrosc. Radiat.* 145: 95–109.

Salgueiro, V., Costa, M.J., Silva, A.M. and Bortoli., D. (2014). Variability of the daily-mean shortwave cloud radiative forcing at the surface at a midlatitude site in Southwestern Europe. *J. Clim.* 27: 7769–7780.

Santos, D., Costa, M.J. and Silva, A.M. (2008). Direct SW aerosol radiative forcing over Portugal. *Atmos. Chem. Phys*. 8: 5771–5786.

Santos, D., Costa, M.J., Silva, A.M. and Salgado, R. (2013). Modeling Saharan desert dust radiative effects on clouds. *Atmos. Res*. 127: 178–194.

Shettle, E. (1989). Models of aerosols, clouds and precipitation for atmospheric propagation studies, atmospheric propagation in the UV, visible, IR and mm-region and related system aspects. In 454 *in AGARD Conference Proceedings*.

Silva, A.M., Von Hoyningen-Huene, W., Bugalho, L., Schmidt, T., Costa, M.J. and Heintzenberg, J. (2002). Aerosol optical properties from columnar data during the second Aerosol Characterization Experiment on the south coast of Portugal. *J. Geophys. Res.* 107: 4642.

Silva, A.M., Costa, M.J., Elias, T., Formenti, P., Belo, N. And Pereira, S. (2003). Ground-based aerosol monitoring at Évora, Portugal. *Global Change News Lett*. 56: 6–10.

Silva, A.M., Wagner, F., Pereira, S. and Elias, T. (2006). Aerosol properties at the most western point of continental Europe. *Paper presented at International Aerosol Conference*, Minnesota, USA.

Singh, A., Tiwari, S., Sharma, D., Singh, D., Tiwari, S., Srivastava, A.K., Rastogi, N. and Singh, A. (2016). Characterization and radiative impact of dust aerosols over northwestern part of India: A case study during a severe dust storm. *Meteorol. Atmos. Phys*. 128: 779–792.

Singh, S., Soni, K., Bano, T., Tanwar, R., Nath, S. and Arya, B. (2010). Clear-sky direct aerosol radiative forcing variations over mega-city Delhi. *Ann. Geophys*. 28: 1157–1166.

Stamnes, K., Tsay, S.C., Wiscombe, W. and Laszlo, I. (2000). DISORT, a general purpose Fortran program for discrete-ordinate-method radiative transfer in scattering and emitting layered media: Documentation of methodology. *Goddard Space Flight Center*, NASA.

Su, J., Huang, J., Fu, Q., Minnis, P., Ge, J. and Bi, J. (2008). Estimation of Asian dust aerosol effect on cloud radiation forcing using Fu-Liou radiative model and CERES measurements. *Atmos. Chem. Phys.* 8: 2763–2771.

Toledano, C. (2005). Climatología de los aerosoles mediante la caracterización de propiedades ópticas y masas de aire en la estación El Arenosillo de la red AERONET (PhD thesis) *Universidad de Valladolid*, Spain.

Toledano, C. (2006). Field calibration methods for aerosol optical depth determination with sun photometers. *Opt. Pura Apl*. 39: 303–311.

Toledano, C., Cachorro, V.E., de Frutos, A.M., Sorribas, M., Prats, N. and de la Morena, B. (2007). Inventory of African desert dust events over the southwestern Iberian Peninsula in 2000–2005 with an AERONET CIMEL Sun photometer. *J. Geophys. Res*. 112: D21201.

Valenzuela, A., Olmo, F.J., Lyamani, H., Antón, M., Quirantes, A and Alados-Arboledas, L. (2012). Aerosol radiative forcing during African desert dust events (2005–2010) over Southeastern Spain. *Atmos. Chem. Phys*. 12: 10331–10351.

Valenzuela, A., Costa, M.J., Guerrero-Rascado, J.L., Bortoli, D. and Olmo, F.J. (2017). Solar and thermal radiative effects during the 2011 extreme desert dust episode over Portugal. *Atmos. Environ*. 148: 16–29.

Received for review, May 3, 2017
Revised, September 5, 2017
Accepted, September 8, 2017

AIP Conference Proceedings

RESEARCH ARTICLE | JULY 25 2019

Predictive value of short-term forecasts of DNI for solar energy systems operation

Francis M. Lopes ✉; Ricardo Conceição; Hugo G. Silva; Rui Salgado; Paulo Canhoto; Manuel Collares-Pereira

Check for updates

AIP Conference Proceedings 2126, 190010 (2019)
https://doi.org/10.1063/1.5117707

View Online Export Citation CrossMark

06 July 2023 14:18:07

AIP Publishing

Predictive Value of Short-Term Forecasts of DNI for Solar Energy Systems Operation

Francis M. Lopes[1,2,a)], Ricardo Conceição[1,2,b)], Hugo G. Silva[1,2,c)], Rui Salgado[2,d)], Paulo Canhoto[2,e)], Manuel Collares-Pereira[1,2,f)]

[1]*Renewable Energies Chair, University of Évora, IIFA, Palácio do Vimioso, Largo Marquês de Marialva, 7002-554, Évora, Portugal.*
[2]*Institute of Earth Sciences, University of Évora, Rua Romão Ramalho, 7000-671, Évora, Portugal.*

[a)]Corresponding author: fmlopes@uevora.pt
[b)]rfc@uevora.pt
[c)]hgsilva@uevora.pt
[d)]rsal@uevora.pt
[e)]canhoto@uevora.pt
[f)]collarespereira@uevora.pt

06 July 2023 14:18:07

Abstract. Solar power forecasting plays a critical role in power-system management, scheduling, and dispatch operations. Accurate forecasts of direct normal irradiance (DNI) are essential for an optimized operation strategy of concentrating solar thermal (CST) systems, particularly during partly cloudy days, due to solar intermittency. In this work, short-term forecasts from the radiative scheme *McRad* (Cycle 41R2) included in the Integrated Forecasting System (IFS), the global numerical weather prediction model of the European Centre for Medium-Range Weather Forecasts (ECMWF), together with in-situ ground-based measurements, are used in a simulated linear focus parabolic-trough power system through the System Advisor Model (SAM). Results are part of a preliminary analysis concerning the value of DNI predictions from the IFS for operation improvement of a CST system with similar configurations as the Andasol 3 CST power plant. For a 365-day period, the present results show high correlations between predictions of energy to grid based on measurements and IFS forecasts mainly for daily values (≈0.94), while lower correlations are obtained for hourly values (≈0.88), due to cloud representation of the IFS during overcast periods, leading to small deviations with respect to those from measurements. Moreover, to measure the forecasting skill of the IFS, daily and hourly skill scores based on local measurements and a persistence model are obtained (≈0.66 and ≈0.51, respectively), demonstrating that the IFS has a good overall performance. These aspects show the value that forecasted DNI has in the operation management of CST power systems, and, consequently, in the electricity market.

INTRODUCTION

Accurate predictions of DNI, i.e. the solar direct irradiance that is received on a plane normal to the sun's rays over the total solar spectrum [1], are essential for CST power systems particularly during partly cloudy days [2, 3], allowing to reduce the uncertainty of a solar plant outputs due to solar irradiance intermittency [4]. Forecasts of DNI can contribute for an efficient CST operation and management, which convert solar energy into thermal energy and then into electric energy. Such information is important for the operators of CST power plants, since it allows to know, with a certain level of confidence, the energy output into the electrical grid for a given day and to anticipate the corresponding production price in the electricity market. Consequently, this allows the increase of the economic return during more demanding and valuable periods [5], reaching a higher level of profitability.

Current state-of-the-art numerical weather prediction (NWP) models have inaccuracies in the representation of clouds (cloud cover and type) and atmospheric aerosols. This modeling issue leads to deviations in DNI forecasts, since clouds and aerosols are the primary parameters that affect the variation of DNI in space and time due to the

SolarPACES 2018
AIP Conf. Proc. 2126, 190010-1–190010-9; https://doi.org/10.1063/1.5117707
Published by AIP Publishing. 978-0-7354-1866-0/$30.00

processes of scattering and absorption of irradiance, including those that result from the interaction with cloud microphysical and dynamical processes [6]. For instance, high altitude clouds, such as cirrus, can suppress DNI almost to zero [7], while in the case of aerosols, DNI reductions in the order of 80-90% can be observed, due to extreme desert dust events [8, 9]. However, such inaccuracies can be corrected through the use of post-processing bias-correction procedures, such as the one performed in [10], in which DNI predictions from the IFS are shown with satisfactory results. Moreover, accurate solar forecasts also have a dependency on the forecast horizon, since forecasting uncertainty tends to decrease with the reduction of the latter. For electrical grid operators, intra-day and day-ahead forecasts are essential to ensure stable grids and to enhance the power supply quality by reducing energy losses and energy fluctuations. This has been a recent standard practice in Europe (e.g. Spain and Germany), as one example being the 11 MW_e commercial solar thermal power plant in Sevilla, Spain [11].

Taking into account the aforementioned aspects, the DNI predictions from the IFS (ECMWF) are compared with in-situ measurements in a 24-hour forecast horizon, which are used to predict the energy output of a CST power plant modeled through the SAM software [12], developed by the U.S. Department of Energy and National Renewable Energy Laboratory (NREL). This exercise can enable the output of the respective annual performance and financial metrics from a CST power plant, which includes the effect that DNI and meteorological variables have in a CST power system efficiency. A case study concerning a linear focus parabolic-trough system with similar configurations as the Andasol 3 CST project power plant (Granada, Spain) is presented. As a first step, this validation method aims to be a contribution to understand how to improve the overall performance of a solar unit, having the potential to be adapted to any other type of power plant system and region in the world.

DATA

A 365-day period of in-situ ground-measured and forecasted data, based in a 24-hour prediction horizon from the IFS, are analyzed from April 1st, 2016 to March 31st, 2017. Both measured and forecasted time-series include irradiance and meteorological data, which are used as input parameters for the SAM power plant model in order to calculate the corresponding energy production.

Continuous measured data gathered from one of twelve radiometric stations of an existing national network in Portugal [13] is used. The network, designed and installed for DNI resource mapping, will also contribute for the operationalization of solar power plants, as part of the DNI-A project (reference ALT20-03-0145-FEDER-000011). The selected measuring station (EVO) is located in Évora city (N38.567686, W7.91172), installed on the top of a research building of the Institute of Earth Sciences (ICT - *Instituto de Ciências da Terra*), in the southern region of Portugal. The climate of this region is of the Mediterranean type (Csa, based on the Köppen classification) with maximum temperatures that generally fluctuate from 31˚C to 35˚C during the summer months, and occasionally reaching values above 40˚C [14]. The region is characterized in general by a clean atmosphere and has exceptional conditions for harvesting of solar energy, since it has one of the highest solar resource potentials in Europe, with a DNI annual availability over 2100 kWh/m^2/year [13]. DNI measurements were performed using a CHP1 pyrheliometer from Kipp & Zonen, being attached to a SOLYS2 Sun-Tracker. The pyrheliometer has been calibrated every 2 years, following the International Organization for Standardization (ISO) 9059:1990 [15], and is a First-Class instrument according to the ISO 9060:1990 [16], with an estimated uncertainty on a daily basis of < 1%. The EVO station is considered to be a reference in the entire national network, since it has been having a regular maintenance protocol with daily cleaning and standard data quality control since February 2015 [17]. Moreover, other relevant meteorological parameters were also measured near the Sun-Tracker with standard high-quality instruments. Measured DNI and local meteorological parameters, such as air temperature (˚C), relative humidity (%), atmospheric pressure (hPa) and wind speed (m/s), were acquired on a 1-minute sampling rate and then averaged. The hourly time-series for atmospheric pressure was obtained from the ground-based measuring station of the Portuguese Meteorological Service (IPMA - *Instituto Português do Mar e da Atmosfera*) near Évora (N38.536542, W7.887958), since no atmospheric pressure data was available for the considered period of study in the EVO station.

For the region of study, the quality of DNI 24-hour forecasts has been recently assessed in [18]. The IFS (cycle 41R2) results showed a mean annual overall overestimation against measurements for the same period of the present work. It was also demonstrated that DNI predictions are mainly hindered due to the representation of clouds and aerosols used in the IFS, since these two parameters strongly affect the predicted DNI. In the case of partly cloudy days, the IFS tends to overestimate the radiative effect of clouds, while during clear-sky days under very clean atmospheric conditions it shows an underestimation of the radiative effect of aerosols, due to the use of a mean monthly aerosol climatology. Nonetheless, taking these aspects into account, the forecasted DNI showed a general good

06 July 2023 14:18:07

agreement with ground-based measurements, with relative differences for DNI in various locations within the region raging between ≈7% and ≈12%. Higher deviations are probably due to local aerosols and small scale fogs or low clouds that formed nearby the selected measuring station. In this work, the first 24-hour predictions of the 0000 UTC IFS run were used with an average grid resolution of 9 km (0.125° x 0.125°). Since the DNI was not an available output parameter from the IFS, and in order to obtain hourly values of DNI, the predicted direct horizontal irradiance, i.e. the projection of direct solar radiation on a horizontal surface, represented by the *fdir* parameter of the IFS was used. The *fdir* parameter, which is an accumulated value (irradiation, in J/m^2), was converted to mean irradiance values (W/m^2) and then divided by the hourly averaged local cosine of the solar zenith angle (CZA) in order to compute the DNI (in power) to be used in the SAM.

SAM MODEL

The SAM, version 2017.9.5 [19], from NREL, is used here in a preliminary analysis to validate the predicted value of DNI forecasts from the IFS for CST power systems operation managing. The power plant model can generate hourly calculations through a physical (thermo-electric) and financial model, allowing to compute the respective annual efficiency and financial metrics of renewable energy systems, such as CST systems. Predictions of energy output and cost estimations are generated for a given power plant, parameterized through several input parameters for each run, e.g. type of installation and system design variables. DNI and meteorological parameters at the project location are also needed in order to generate the hourly outputs. These outputs include a wide range of metrics, such as the annual electricity production of a power plant, detailing the respective annual efficiency. It should be noted that the SAM calculates hourly outputs based on the CZA starting at January 1st. In the present work, to overcome this aspect, the period between January 1st and March 31st, 2017 was concatenated at the beginning of the input time-series for the SAM simulation. In this study, a CST physical linear focus parabolic-trough system of a 50 MW_e power plant with a similar configuration as the operational Spanish Andasol 3 CST project [20] is simulated. Real performance input parameters have been used in order to simulate the desired CST system. Additionally, and for reference in the present study, the Andasol 3 CST power plant has an estimated electricity generation of 175.000 MWh/year.

06 July 2023 14:18:07

METHODOLOGY

As common practice for data control quality check, adopted filters for the considered local measurements were applied prior to analysis. These include basic filters for solar irradiance records and gap-filling techniques, due to the presence of possible missing periods of data caused by any instrumentation malfunction. A list of data quality filters that were considered for the present analysis is indicated below:

1. $DNI \geq 0$.
2. $DNI > CZA^{+}$.
3. $DNI < DNI_{TOA}$.
4. DNI < BSRN-QFPPL [21].
5. Gap-filling with linear interpolation for missing periods less or equal than 2 hours.
6. Gap-filling with data from the nearest station for missing periods above 2 hours.

Considering a 365-day period, measurements showed a percentage of missing data of ≈0.01% and ≈0.05% for the local DNI and meteorological data, respectively. This highlights the high-quality data of EVO station, particularly for DNI measurements. The second filter has also been applied to the IFS data, considering the CZA of the nearest IFS grid point to the corresponding measuring location. In the third filter, the total solar irradiance, defined as the total power from the Sun at the mean Earth-Sun distance, 1361 W/m^2 accordingly to [22], is used to calculate the DNI at the top-of-atmosphere (TOA), as given by Eq. 2.77 in [23]. For the fourth filter, established physical possible limits were used. Regarding the six filter, the nearest measuring station used to fill possible data gaps of the EVO data series for the same period, is located at Mitra (N38.530522, W8.011221), in the outskirts of Évora city, about 13 km apart.

It is important to measure the forecasting skill of the IFS predictions in order to quantify their inaccuracies [24] towards measurements. In this context, the forecasting metric mean square error skill score (*SS*) is used in this analysis, being usually calculated using the root mean square error (*RMSE*). The *RMSE* is a recommended statistical metric for the application of electricity grid management issues [2], since only large errors are significant to the safety of the electrical grid system. Thus, the *SS* is computed as the decrease in the mean square error (*MSE*) of the forecast with

respect to a reference, i.e. a persistence model time-series that is obtained here by persisting previous observational values over the 24-hour forecast horizon, as shown by [25]:

$$SS = 1 - \frac{MSE_{for}}{MSE_{per}}, \quad (1)$$

$$MSE = RMSE^2 = \frac{1}{n} \times \sum_{j=1}^{n} [I(j) - \hat{I}(j)]^2, \quad (2)$$

where MSE_{for} and MSE_{per} are the corresponding error metrics for the forecast and the persistence, while $I(j)$ and $\hat{I}(j)$ are the measured and the forecasted value at time j, respectively, and n the number of assessed pairs. Skill values equal to one state that results are close to a perfect forecast, negative values are related to a lower performance of the IFS as compared to the persistence model, while zero values show that there is no improvement over the reference.

RESULTS AND DISCUSSION

The focus of this work concerns the value of 24-hour horizon forecasts of DNI for a 365-day period, as means to improve the management of operational CST power systems. To this end, an important quantity to know is the daily electric energy demand that an electrical grid operator has to handle on a daily basis. The electricity generated by a CST power plant with similar characteristics as those of the Andasol 3 power plant can be estimated by the software SAM through the output parameter energy injection to the grid E_G ($MW_e h$).

Hourly values of E_G based on measured and forecasted data are depicted in **Fig. 1**, together with the respective DNI. As expected, it is during the summer that more electricity is generated and stored due to: i) higher frequency of clear-sky days with high DNI availability; ii) an increase in the number of sun hours during the day (an important feature for the total energy production); and iii) smaller CZA and a thinner air mass. The opposite case occurs during the winter, where the E_G tends to be lower and, in some cases, almost zero due to a higher occurrence of overcast periods which can prevail during several consecutive days. It is during these periods that the IFS clearly shows difficulties in representing clouds which, consequently, leads to lower values of E_G than the ones obtained with measurements. In general, the total E_G based on forecasted data shows an overestimation of ≈20.000 $MW_e h$ against E_G based on measurements, i.e. a relative difference of ≈12.75%. This is a consequence of the annual DNI overestimation shown by the IFS, which is here transferred to the energy output of a CST power plant through a non-linear transfer function (thermo-electric model) including the effect of other meteorological variables, namely the air temperature and wind speed that affect the system efficiency. Taking in consideration parasitic power consumption during non-production hours, together with a constant derating value of 4% for the simulated plant, the annual energy values generated based in measurements and IFS are ≈153.655 MWh/year and ≈159.795 MWh/year, respectively. Although with small deviations in relation to the referenced annual energy generation of the Andasol 3 CST power plant (175.000 MWh/year), the IFS annual energy based E_G are closer than the ones obtained with measurements. Deviations from the real annual production value are mainly related to the capability of the IFS in representing clouds and aerosols, as well as the adopted energy management schedules that the real Andasol 3 implements daily accordingly to the energy demand in the electricity market. Moreover, a limit for the energy generated in the SAM is also considered, which is clearly seen during summer in both measured and forecasted E_G, meaning that more energy could be produced during this period instead.

06 July 2023 14:18:07

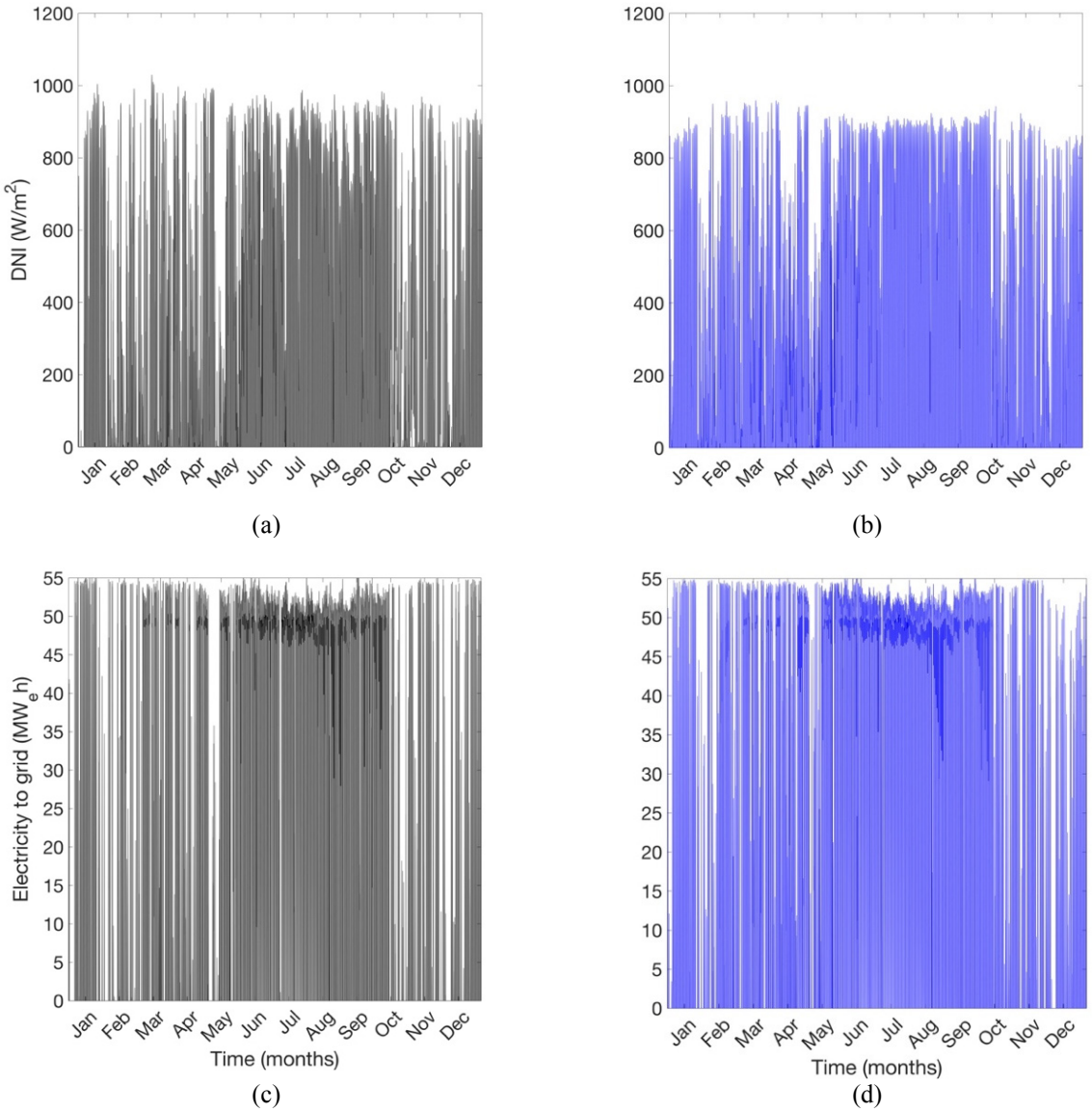

FIGURE 1. Direct Normal Irradiances, DNI (W/m^2), from measured (a) and IFS forecasted data (b) in EVO station (Évora, southern Portugal) together with the respective energy injection to the grid, E_G (MW$_e$h), (c) and (d), calculated through the SAM. Period of study relates April 1st, 2016 to March 31st, 2017.

A deeper comparison for the hourly and daily values of E_G obtained through measurements, IFS and the persistence model (**Fig. 2**), shows a significantly higher correlation coefficient (r) between E_G based on measured and forecasted data, mainly for daily values where an r of ≈0.94 (**Fig. 2c**) is found, while for the daily values of the persistence model, a lower r (≈0.77) is obtained (**Fig. 2d**). For the hourly values, r of ≈0.88 (**Fig. 2a**) and ≈0.75 (**Fig. 2b**) are obtained. The lower correlations result from the fact that hourly values can induce more errors, mainly during overcast periods, in which the IFS predictions still need to be improved regarding cloud representation. It is in the range of 40-50 MW$_e$h that there is a better correspondence (**Fig. 2a** and **b**) between the various E_G hourly values. This is shown by the high frequency of occurrences of E_G values, which are related to periods of clear-sky conditions, while a higher dispersion occurs for lower E_G values, corresponding to cloudy periods. It should be noted that the zero values found in the hourly results are due to shutdown periods (highlighted in E_G based on both measurements and IFS forecasts), being related to unusable stored energy.

06 July 2023 14:18:07

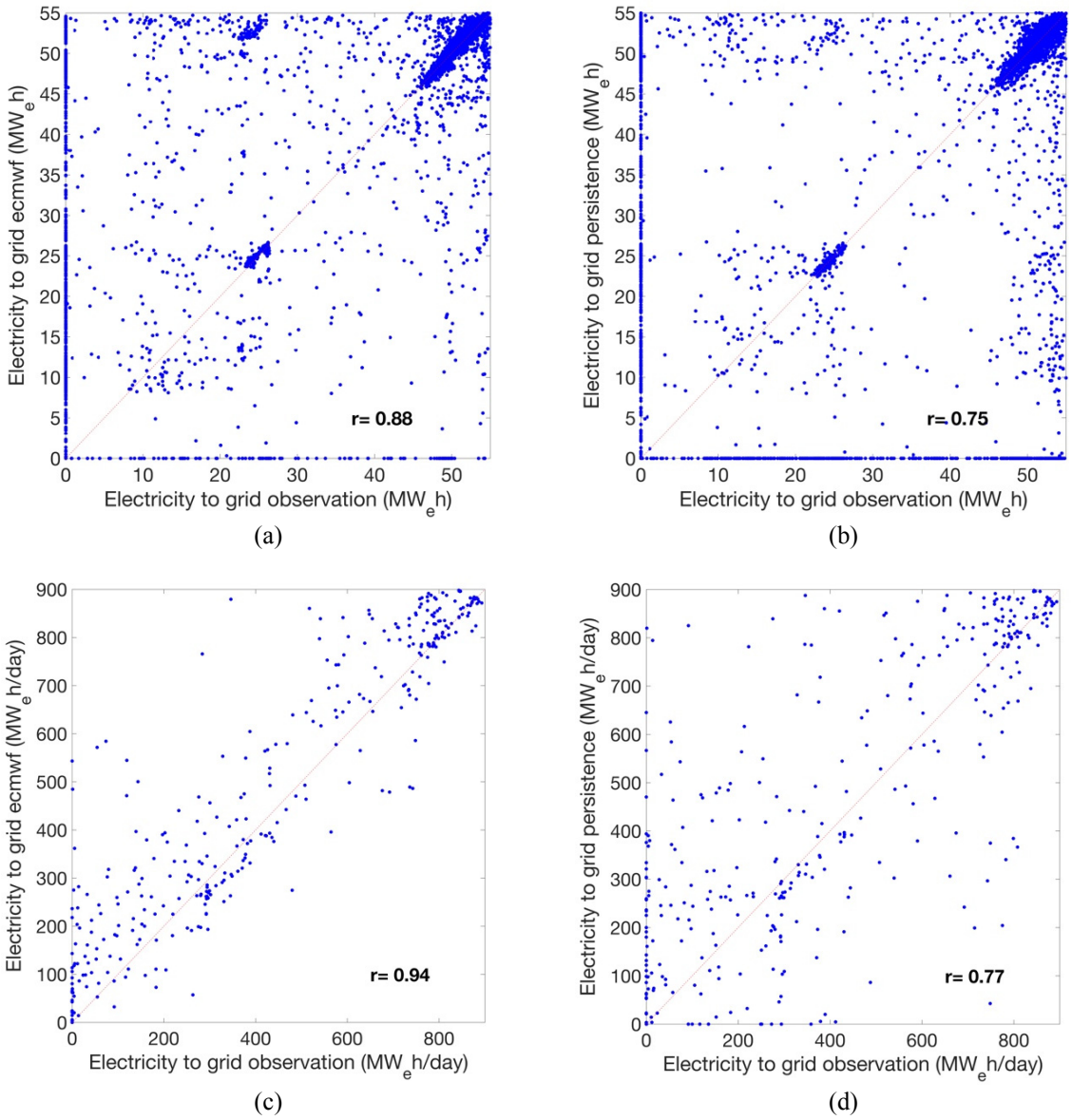

FIGURE 2. Energy injection to the grid, E_G ($MW_e h$), based on DNI measurements, persistence and IFS forecast models. Hourly (a, b) and daily (c, d) results are shown for EVO station (Évora, southern Portugal). Corresponding correlation coefficient, r, and a red-dashed identity line ($y=x$) are also depicted. Period of study relates April 1st, 2016 to March 31st 2017.

In **Table 1**, a statistical summary for both hourly and daily values of E_G is presented. In general, the IFS forecast model tends to overestimate the E_G, as shown by the negative values of mean bias error (*MBE*). However, the IFS also depicts a better performance than the persistence model, with lower *RMSE* values. The calculated *SS* (based on the *MSE*) are above 0.5, particularly for the daily values (≈0.66), which prove that the IFS forecast model performs better than the persistence model. This means that, with the appropriated post process techniques of forecasted DNI data, the use of NWP modeling in a CST power plant system is potentially a valuable tool for an efficient management of CST power systems operations.

06 July 2023 14:18:07

TABLE 1. Statistical summary of the energy injection to the grid, E_G ($MW_e h$), obtained through the SAM based on measurements (Obs), IFS forecasts (IFS) and persistence models (Per) for EVO station (Évora, southern Portugal). Correlation coefficient (*r*), root mean square error (*RMSE*), mean bias error (*MBE*), mean absolute error (*MAE*) and the (dimensionless) skill score (*SS*) of the hourly and daily results are shown. Period of study relates April 1st, 2016 to March 31st, 2017.

	Hourly		Daily	
	E_G (Obs) – E_G (IFS)	E_G (Obs) – E_G (Per)	E_G (Obs) – E_G (IFS)	E_G (Obs) – E_G (Per)
r	0.88	0.75	0.94	0.77
RMSE	11.58	16.54	124.21	212.34
MBE	-2.28	7.40×10^{-17}	-54.78	3.89×10^{-16}
MAE	4.16	6.77	82.70	142.53
SS	0.51		0.66	

CONCLUSIONS

Measured and IFS forecasted DNI were used to simulate the energy production of a real linear focus parabolic-trough power system with the purpose of contributing to improve the operation of CST power plant systems. Results of energy injection to the grid, E_G, an important quantity to know for the day-ahead energy management, have shown the high potential that the use of the forecasted DNI has such power systems, with correlations of ≈0.89 and ≈0.94 for the hourly and daily predicted energy generation, respectively. A good overall performance by the IFS has been shown despite the current difficulties that NWP models have in predicting DNI during overcast periods.

Future work includes: i) the use of an upgraded version of the radiative scheme, *McRad* (Cycle 41R2), named *ecRad* (Cycle 43R3) which has recently become operational in July 11th, 2017 [26]. This improvement contains a more efficient radiative code to perform deterministic predictions of DNI and also uses an aerosol data assimilation system through the Copernicus Atmosphere Monitoring Service (CAMS) instead of the previous aerosol monthly means; ii) unlike the previous analysis carried out by the authors, the incident radiation on a plane normal to the Sun's direction (*drsp*) will be used as a direct DNI output from the IFS, thus allowing to improve calculations; and iii) a more robust statistical analysis that includes the simulation of different types of CST power systems, e.g. central receiver systems, with higher number of input parameters from real power plants in the SAM software. These aspects will certainly allow for higher levels of confidence to be reached when using forecasted DNI in CST power systems.

06 July 2023 14:18:07

ACKNOWLEDGMENTS

This work was co-funded by the European Union through the European Regional Development Fund, framed in COMPETE 2020 (Operational Program Competitiveness and Internationalization), through the Institute of Earth Sciences (UID/GEO/04683/2013) with reference POCI-01-0145-FEDER-007690, and through the projects DNI-A (ALT20-03-0145-FEDER-000011), ALOP (ALT20-03-0145-FEDER-000004) and INSHIP (H2020, grant agreement 731287). F.M. Lopes and R. Conceição are thankful for the FCT scholarships SFRH/BD/129580/2017 and SFRH/BD/116344/2016, respectively, and H.G. Silva to DNI-A and INSHIP for his research contract. The initial recommendations of P. Gilman (SAM Support) and R. Hogan (ECMWF), is recognized and appreciated. The authors are also grateful to T. Fasquelle, for the provided SAM input parameters during the Andasol 3 simulation, to the ECMWF for the forecasts availability, and to the Portuguese Meteorological Service (IPMA) in providing data.

REFERENCES

1. P. Blanc, B. Espinar, N. Geuder, C. Gueymard, R. Meyer, R. Pitz-Paal, B. Reinhardt, D. Renné, M. Sengupta, L. Wald, S. Wilbert, "Direct Normal Irradiance Related Definitions and Applications: The Circumsolar Issue", Solar Energy, **110**, pp. 561-577, doi: 10.1016/j.solener.2014.10.001, 2014.
2. M. Schroedter-Homscheidt, A. Benedetti, and N. Killius. "Verification of ECMWF and ECMWF/MACC's Global and Direct Irradiance Forecasts with Respect to Solar Electricity Production Forecasts", Meteorologische Zeitschrift, PrePub Article, doi: 10.1127/metz/2016/0676, 2016.
3. M. Collares-Pereira, A. Rabl. "Simple Procedure for Predicting Long Term Average Performance of Nonconcentrating and Concentrating Solar Collectors", Solar Energy, **23**, pp. 235-253, 1979.

4. W. Law, Edward and Prasad, Abhnil and Kay, Merlinde and Taylor, Robert. "Direct Normal Irradiance Forecasting and Its Application to Concentrated Solar Thermal Output Forecasting – A Review", Solar Energy, **108**, pp. 287-307, doi: 10.1016/j.solener.2014.07.008, 2014.
5. L. Ramirez, J. M. Vindel, "Forecasting and Nowcasting of DNI for Concentrating Solar Thermal Systems", Advances in Concentrating Solar Thermal Research and Technology, Chapter 13, pp. 294-310, doi:10.1016/B978-0-08-100516-3.00013-7, 2017.
6. J. Fan, "Review of Aerosol-Cloud Interaction: Mechanisms, Significance, and Challenges. American meteorological Society, Vol. **73**, pp. 4221-4252. doi: 10.1175/JAS-D-16-0037.1, 2016.
7. S. Quesada-Ruiz, Y. Chu, J. Tovar-Pescador, H. T. C Pedro, C. F. M. Coimbra, "Cloud-Tracking Methodology for Intra-Hour DNI Forecasting", Solar Energy, **102**, pp. 267-275. doi: 10.1016/j.solener.2014.01.030, 2014.
8. R. Conceição, H. G. Silva, J. Mirão, M. Gostein, L. Fialho, L. Navarte, M. Collares-Pereira, "Saharan Dust Transport to Europe and its Impact on the Photovoltaic Performance: A Case Study of Soiling in Portugal", Solar Energy, **160**, pp. 94-102. doi: 10.1016/j.solener.2017.11.059, 2018.
9. P. G. Kosmopoulos, S. Kazadzis, M. Taylor, E. Athanasopoulou, O. Speyer, P. I. Raptis, E. Marinou, E. Proestakis, S. Solomos, E. Gerasopoulous, V. Amiridis, A. Bais, and C. Kontoes, "Dust Impact on Surface Solar Irradiance Assessed with Model Simulations, Satellite Observations and Ground-based Measurements", Atmos. Meas. Tech. Discuss, doi: 10.5194/amt-2017-79, 2017.
10. A. Troccoli, J.-J. Morcrette, "Skill of Direct Solar Radiation Predicted by the ECMWF Global Atmospheric Model over Australia. American Meteorology Society, pp. 2571-2587. doi: 10.1175/JAMC-D-14-0074.1, 2014.
11. M. Wittman, H. Breitkreuz, M. Schroedter-Homscheidt, and M. Eck, "Case Studies on the Use of Solar Irradiance Forecast for Optimized Operation Strategies of Solar Thermal Power Plants", IEEE J-STARS, **1**, No.1, doi: 10.1109/JSTARS.2008.2001152, 2008.
12. N. Blair, A. Dobos, J. Freeman, T. Neises, M. Wagner, T. Ferguson, P. Gilman, S. Janzou, "System Advisor Model, SAM 2014.1.14: General Description. NREL/TP-6A20-61019", National Renewable Energy Laboratory, Golden, CO, 2014. Accessed October 31, 2016.
13. A. Cavaco, H. G. Silva, P. Canhoto, T. Osório, M. Collares-Pereira, "Progresses in DNI Measurements in Southern Portugal", Solar Paces 2017, AIP Conf. Proc., 2017. Submitted for publication.
14. F. Lopes, H. G. Silva, R. Salgado, M. Potes, K. Nicoll, R. G. Harrison, "Atmospheric Electric Field Measurements Near a Fresh Water Reservoir and the Formation of the Lake Breeze", Tellus, 68:31592. doi: 10.3402/tellusa.v68.31592, 2016.
15. ISO 9059:1990, Solar energy – Calibration of field pyrheliometers by comparison to a reference pyrheliometer, International Organization for Standardization (www.iso.org/standard/16628.html), 2014.
16. ISO 9060:1990, Solar energy, Specification and classifications of instruments for measuring hemispherical solar and direct solar radiation, International Organization for Standardization (www.iso.org/standard/16629.html), 2003.
17. P. Canhoto, "Preliminary Analysis of Irradiance Data for the Generation of a Typical Solar Radiation year for Évora, Portugal", Technical Report, Institute of Earth Sciences, University of Évora, Évora, Portugal. doi: 10.13140/RG.2.2.12258.94401, March 2016.
18. F. M. Lopes, H. G. Silva, R. Salgado, A. Cavaco, P. Canhoto, M. Collares-Pereira, "Short-term Forecasts of GHI and DNI for Solar Energy Systems Operation: Assessment of the ECMWF Integrated Forecasting System in Southern Portugal", Solar Energy, **170**, pp. 14-30, doi: 10.1016/j.solener.2018.05.039, 2018.
19. The System Advisor Model (SAM), version 2017.9.5, www.sam.nrel.gov/content/downloads, NREL 2018.
20. The Andasol 3 CST project (Granada, Spain), www.nrel.gov/csp/solarpaces/project_detail.cfm/projectID=117, NREL 2018.
21. C. N. Long, and E. G. Dutton: BSRN Global Network recommended QC tests, V2.x, Bremerhaven, PANGAEA, 2010.
22. S. K. Solanki, N. A. Krivova, J. D. Haigh, "Solar Irradiance Variability and Climate", Annu. Rev. Astrono. Astrophys, **51**, pp. 311–351. doi: http://dx.doi.org/10.1146/annurev- astro-082812-141007, 2013.
23. Kalogirou, S.A., 2014. Solar Energy Engineering: Processes and Systems, second ed. Chapter 2, 51–63, Elsevier. ISBN: 978-0123972705.
24. C. Coimbra, J. Kleissl, and R. Marquez, "Overview of Solar Forecasting Methods and a Metric for Accuracy Evaluation", Solar Resource Assessment and Forecasting, Cp 8, 183-185, Elsevier, Waltham, Massachusetts.
25. R. Perez, E. Lorenz, S. Pelland, M. Beauharnois, G. V. Knowe, K. Hemker Jr., D. Heinemann, J. Remund, S. C. Müller, W. Traunmüller, G. Steinmauer, D. Pozo, J. A. Ruiz-Arias, V. Lara-Fanego, L. Ramirez-Santigosa, M.

06 July 2023 14:18:07

Gaston-Romero, L. M. Pomares, “Comparison of Numerical Weather Prediction Solar Irradiance Forecasts in the US, Canada and Europe”, Solar Energy, **94**, pp. 305–326, doi: 10.1016/j.solener.2013.05.005, 2013.
26. European Centre for Medium-Range Weather Forecasts (ECMWF) Newsletter 2017, Shinfield Park, Reading, RG2 9AX, England.

06 July 2023 14:18:07

Remote Sensing of Environment 232 (2019) 111294

Contents lists available at ScienceDirect

Remote Sensing of Environment

journal homepage: www.elsevier.com/locate/rse

Ground/space, passive/active remote sensing observations coupled with particle dispersion modelling to understand the inter-continental transport of wildfire smoke plumes

M. Sicard[a,b,*], M.J. Granados-Muñoz[a], L. Alados-Arboledas[c,d], R. Barragán[a,b], A.E. Bedoya-Velásquez[c,d], J.A. Benavent-Oltra[c,d], D. Bortoli[e], A. Comerón[a], C. Córdoba-Jabonero[f], M.J. Costa[e], A. del Águila[f], A.J. Fernández[g], J.L. Guerrero-Rascado[c,d], O. Jorba[h], F. Molero[g], C. Muñoz-Porcar[a], P. Ortiz-Amezcua[c,d], N. Papagiannopoulos[a,i], M. Potes[e], M. Pujadas[g], F. Rocadenbosch[a,b], A. Rodríguez-Gómez[a], R. Román[j], R. Salgado[e], V. Salgueiro[e], Y. Sola[k], M. Yela[f]

[a] Remote Sensing Laboratory/CommSensLab, Universitat Politècnica de Catalunya, Barcelona 08034, Spain
[b] Ciències i Tecnologies de l'Espai - Centre de Recerca de l'Aeronàutica i de l'Espai/Institut d'Estudis Espacials de Catalunya (CTE-CRAE/IEEC), Universitat Politècnica de Catalunya, Barcelona 08034, Spain
[c] Department of Applied Physics, University of Granada, Granada 18071, Spain
[d] Andalusian Institute for Earth System Research (IISTA-CEAMA), Granada 18006, Spain
[e] Institute of Earth Sciences and Dept. of Physics, Universidade de Évora, Évora 7000-671, Portugal
[f] Instituto Nacional de Técnica Aeroespacial (INTA), Atmospheric Research and Instrumentation Branch, Torrejón de Ardoz, Madrid 28850, Spain
[g] Dept. of Environment, Research Centre for Energy, Environment and Technology (CIEMAT), Madrid 28040, Spain
[h] Dept. of Earth Sciences, Barcelona Supercomputing Center (BSC), Barcelona 08034, Spain
[i] Consiglio Nazionale delle Ricerche, Istituto di Metodologie per l'Analisi Ambientale (CNR-IMAA), Tito Scalo 85050, Italy
[j] Atmospheric Optics Group (GOA), University of Valladolid, 47002, Spain
[k] Dept. of Astronomy and Meteorology, Universitat de Barcelona, Barcelona 08028, Spain

ARTICLE INFO

Edited by: Menghua Wang

Keywords:
Time-space monitoring
Ground-based and space-borne lidars
Long-range transport of smoke plume
Injection of particles up to the upper troposphere
Particle dispersion model
Smoke particle absorption and depolarization properties

ABSTRACT

During the 2017 record-breaking burning season in Canada/United States, intense wild fires raged during the first week of September in the Pacific northwestern region (British Columbia, Alberta, Washington, Oregon, Idaho, Montana and northern California) burning mostly temperate coniferous forests. The heavy loads of smoke particles emitted in the atmosphere reached the Iberian Peninsula (IP) a few days later on 7 and 8 September. Satellite imagery allows to identify two main smoke clouds emitted during two different periods that were injected and transported in the atmosphere at several altitude levels. Columnar properties on 7 and 8 September at two Aerosol Robotic Network (AERONET) mid-altitude, background sites in northern and southern Spain are: aerosol optical depth (AOD) at 440 nm up to 0.62, Ångström exponent of 1.6–1.7, large dominance of small particles (fine mode fraction > 0.88), low absorption AOD at 440 nm (< 0.008) and large single scattering albedo at 440 nm (> 0.98). Profiles from the Cloud-Aerosol Lidar with Orthogonal Polarization (CALIOP) show the presence of smoke particles in the stratosphere during the transport, whereas the smoke is only observed in the troposphere at its arrival over the IP. Portuguese and Spanish ground lidar stations from the European Aerosol Research Lidar Network/Aerosols, Clouds, and Trace gases Research InfraStructure Network (EARLINET/ACTRIS) and the Micro-Pulse Lidar NETwork (MPLNET) reveal smoke plumes with different properties: particle depolarization ratio and color ratio, respectively, of 0.05 and 2.5 in the mid troposphere (5–9 km) and of 0.10 and 3.0 in the upper troposphere (10–13 km). In the mid troposphere the particle depolarization ratio does not seem time-dependent during the transport whereas the color ratio seems to increase (larger particles sediment first). To analyze the horizontal and vertical transport of the smoke from its origin to the IP, particle dispersion modelling is performed with the Hybrid Single Particle Lagrangian Integrated Trajectory Model (HYSPLIT) parameterized with satellite-derived biomass burning emission estimates from the Global Fire Assimilation System (GFAS) of the Copernicus Atmosphere Monitoring Service (CAMS). Three compounds are simulated: carbon monoxide, black carbon and organic carbon. The results show that the first smoke plume

* Corresponding author at: Remote Sensing Laboratory/CommSensLab, Universitat Politècnica de Catalunya, Barcelona 08034, Spain.
E-mail address: msicard@tsc.upc.edu (M. Sicard).

https://doi.org/10.1016/j.rse.2019.111294
Received 28 August 2018; Received in revised form 17 June 2019; Accepted 1 July 2019
0034-4257/ © 2019 Elsevier Inc. All rights reserved.

which travels slowly reaches rapidly (~1 day) the upper troposphere and lower stratosphere (UTLS) but also shows evidence of large scale horizontal dispersion, while the second plume, entrained by strong subtropical jets, reaches the upper troposphere much slower (~2.5 days). Observations and dispersion modelling all together suggest that particle depolarization properties are enhanced during their vertical transport from the mid to the upper troposphere.

1. Introduction

It is well established that atmospheric biomass burning from either prescribed fires or natural wildfires have effects on air quality, atmospheric circulation and climate (Stocks et al., 2003). Wildfires have recently become a focus of growing interest and attention because of their capabilities to inject smoke particles at high altitude levels. The mechanisms leading to the vertical transport of smoke particles are either direct injection by pyroconvection (Fromm et al., 2000; Fromm and Servranckx, 2003), a combination of pyroconvection and radiatively driven uplift forces (de Laat et al., 2012) or a combination of pyroconvection and gravito-photophoresis (Rohatschek, 1996; Pueschel et al., 2000). The first mechanism, pyroconvection, materializes through the formation of pyrocumulus (pyroCu) and their most extreme form, namely pyrocumulonimbus (pyroCb; Fromm et al., 2005). The characteristic injection height of pyroCu and pyroCb emissions is the upper troposphere (UT) and less frequently the lower stratosphere (LS) (Fromm et al., 2010). The second mechanism, called self-lifting, is based on the absorption of incoming solar radiation by soot and smoke particles which may cause sufficient warming for air masses to provide buoyancy and subsequent lofting of the injected plume (Boers et al., 2010; de Laat et al., 2012). The third mechanism, gravito-photophoresis, is due to "a sunlight-induced force acting on particles which are geometrically asymmetric and which have uneven surface distribution of thermal accommodation coefficients" (Pueschel et al., 2000). It is strongly altitude-dependent because of the weak lifting forces involved and it is most effective above 10 km. Renard et al. (2008) suggested that soot from biomass burning could reach the stratosphere owing to the gravito-photophoresis effect. The last two mechanisms, self-lifting and gravito-photophoresis, can only act on particles which are already settled in the free troposphere or in the stratosphere, and thus require a prior injection of the particles usually produced by pyroconvection.

Once in the UT, the tropopause acts as a dynamic barrier to the upward transport of smoke particles from the troposphere because of the steep gradient in the temperature lapse rate, and in most cases the particles stay in the troposphere. The conditions (burnt matter, fire characteristics, latitude range, local meteorology, synoptic conditions, dynamics, etc.) allowing for the penetration of smoke particles through the tropopause are still not yet entirely clear, and many conclusions of the recent literature on the subject call for more investigation on the topic. The transport of particles in the upper troposphere and lower stratosphere (UTLS) has several effects: (i) in this altitude range, the particles can persist for long durations (Robock, 2000), allowing for gradual spread over hemispheric or global scales; (ii) the long-lived aerosol radiative effects, especially marked for smoke which is a warming agent, may cause differential regional heating patterns that affect regional circulation (Lau et al., 2008; Son et al., 2009); (iii) complex interactions with clouds due to their capability to serve as cloud condensation nuclei, producing in the end a reduction of precipitation (see details in Rosenfeld et al., 2007); (iv) effects on UTLS ozone chemistry (Crutzen and Andreae, 1990; Forster et al., 2001; Real et al., 2008). An increasing number of recent studies report on the observation of the presence of smoke particles in the UTLS: Nédélec et al. (2005), Damoah et al. (2006), Rosenfeld et al. (2007), Fromm et al. (2010) (and references therein), Siddaway and Petelina (2011), de Laat et al. (2012), Khaykin et al. (2018), Ansmann et al. (2018), Haarig et al. (2018), and Hu et al. (2019), among others. The number of modelling studies dealing with the injection of smoke into the UTLS is more reduced: Trentmann et al. (2006), Luderer et al. (2006), Cunningham and Reeder (2009), Cammas et al. (2009), and Peterson et al. (2017).

During summer 2017, North America lived one of its worst burning season on record. On 16 August an aerosol index (AI), a qualitative index indicating the presence of elevated layers of aerosols with significant absorption, of 55.4 was recorded over Canada by the Ozone Mapping and Profiling Suite (OMPS) on board Suomi National Polar-orbiting Partnership satellite (Seftor, 2017a). It breaks the record of AI values by far, the previous record being 31.2 registered by the Total Ozone Mapping Spectrometer (TOMS) on 29 May 2001 during the Canadian Chisholm fires (Fromm et al., 2008). The cluster of the most intense fires of August 2017 was located in Canada near the intersection border of Saskatchewan, Alberta and the Northern Territories at

Table 1
Instruments used in this study. The nomenclature 3β + 2α + 1δ stands for 3 elastic channels (here, 355, 532, 1064 nm), 2 Raman channels and one depolarization channel; 1β + 1δ stands for 1 elastic channel (here, 532 nm) and one depolarization channel; 3β stands for 3 elastic channels (here, 355, 532, 1064 nm). 8-λ refers to the number (8) of wavelengths of the photometers.

Ground-based			
	Station/network	Latitude, longitude, altitude	Instrument type
Active	EV/EARLINET	38.57 N, 7.91 W, 293 m asl	3β + 2α + 1δ lidar
	AR/MPLNET	37.10 N, 6.73 W, 59 m asl	1β + 1δ lidar
	GR/EARLINET	37.16 N, 3.61 W, 680 m asl	3β + 2α + 1δ lidar
	MA/EARLINET	40.45 N, 3.72 W, 669 m asl	3β lidar
	BA/MPLNET	41.39 N, 2.11E, 115 m asl	1β + 1δ lidar
Passive	Cerro Poyos/AERONET	37.11 N, 3.49 W, 1830 m asl	8-λ sun-sky photometer
	Montsec/AERONET	42.05 N, 0.73E, 1574 m asl	8-λ sun-sky photometer

Spaceborne			
	Instrument	Satellite	Instrument type
Active	CALIOP	CALIPSO	2β + 1δ lidar
Passive	MODIS	Aqua and Terra	Moderate resolution imaging radiometer
	AIRS	Aqua	High-spectral resolution, multispectral infrared sounder

latitude 60°N. These intense fires produced strong pyroCb which injected smoke particles in the LS which travelled eastward, entrained and dispersed zonally by polar jet streams (Khaykin et al., 2018). Smoke layers at 14–16 km with an aerosol optical depth (AOD) at 532 nm of 0.6 were observed in Germany (Ansmann et al., 2018) on 22 August. The event is already documented by a series of papers: Khaykin et al. (2018), Ansmann et al. (2018), Haarig et al. (2018), Hu et al. (2019) and Baars et al. (2019). Fifteen days later, on 30 August, AI from OMPS peaked again at 23 in a smoke plume detected over the southern parts of Alberta and Saskatchewan and the upper Great Plains of the United States (US) (Seftor, 2017b). Most of the fires of this new burning period were in the Pacific northwestern region (British Columbia, Alberta, Washington, Oregon, Idaho, Montana and northern California). In the US severe air quality issues were reported in Washington and Oregon at least until 6 September (NYT, 2018). Prevailing winds and the presence of a frontal boundary across the North American continent created the conditions for the formation of a long, wide, arching ribbon of smoke that stretched thousands of kilometers from the source region all the way to Newfoundland, location from where it was further transported towards Europe. The smoke hit the Iberian Peninsula (IP) in southwestern Europe on 7 and 8 September (Sicard et al., 2018). Although the smoke plume was detected in the LS at some points during its transport, it was only detected in the UT over the IP.

This paper investigates the time-space evolution of the smoke plume detected at its arrival over the IP on 7 and 8 September with ground-based multi-wavelength lidars and backward in time with the CALIOP (Cloud-Aerosol Lidar with Orthogonal Polarization) spaceborne lidar, in terms of optical properties and vertical distribution. Sun-sky photometers at mid-altitude, background sites with no local sources are used to monitor the smoke columnar properties over the IP. A dispersion model parameterized with satellite-derived fire products simulates the vertical and horizontal transport of 3 smoke-related compounds: carbon monoxide, black carbon and organic carbon. Simulations, and especially the injection heights computed by the dispersion model, are qualitatively evaluated against observations and used to understand the atmospheric causal mechanisms yielding to the differences observed in the optical properties over the IP in the mid and upper troposphere.

2. Instrumentation and tools

The tools used in our methodology include passive/active, ground-based and spaceborne observations, as well as a particle dispersion model. The observations, listed in Table 1, are used to follow the transport of the smoke plumes from the source to the IP. In addition, passive spaceborne observations are also used to parameterize the emission of the particle dispersion model.

2.1. Ground observations

The ground-based observations include lidars and sun-sky photometers in the IP. A total of five lidar systems are used: three from the EARLINET/ACTRIS (European Aerosol Research Lidar Network/Aerosols, Clouds, and Trace Gases Research Infrastructure Network; https://www.actris.eu/default.aspx; Pappalardo et al., 2014) network in Évora (EV), Granada (GR) and Madrid (MA), and two from MPLNET (Micro-Pulse Lidar Network; https://mplnet.gsfc.nasa.gov/; Welton et al., 2001) in El Arenosillo/Huelva (AR) and Barcelona (BA; see Table 1 for more details and Fig. 1 for the geographical position of the stations). The EARLINET lidars are multi-wavelength systems measuring at least at three elastic wavelengths. In addition, EV and GR have Raman and depolarization-sensitive channels. The MPLNET systems have one wavelength at 532 nm and an additional polarization-sensitive channel. A review of the lidar techniques using elastic, Raman and depolarization-sensitive channels, among others, for the remote sensing of aerosols can be found in Comerón et al. (2017). For the characterization of the smoke plume, we use the particle depolarization ratio, δ_p, in EV, AR, GR and BA and the pair (color ratio, depolarization ratio) in EV and GR. The particle depolarization ratio and the color ratio provide significant information on the particle shape and dominant size (Burton et al., 2012), respectively. The particle depolarization ratio is defined as (Freudenthaler et al., 2009):

$$\delta_p = \frac{\beta^{\parallel}}{\beta^{\perp}} \tag{1}$$

where $\beta^{\parallel}$ and $\beta^{\perp}$ are the particle parallel and perpendicular backscatter coefficients, respectively. The color ratio, CR, is defined as a function of

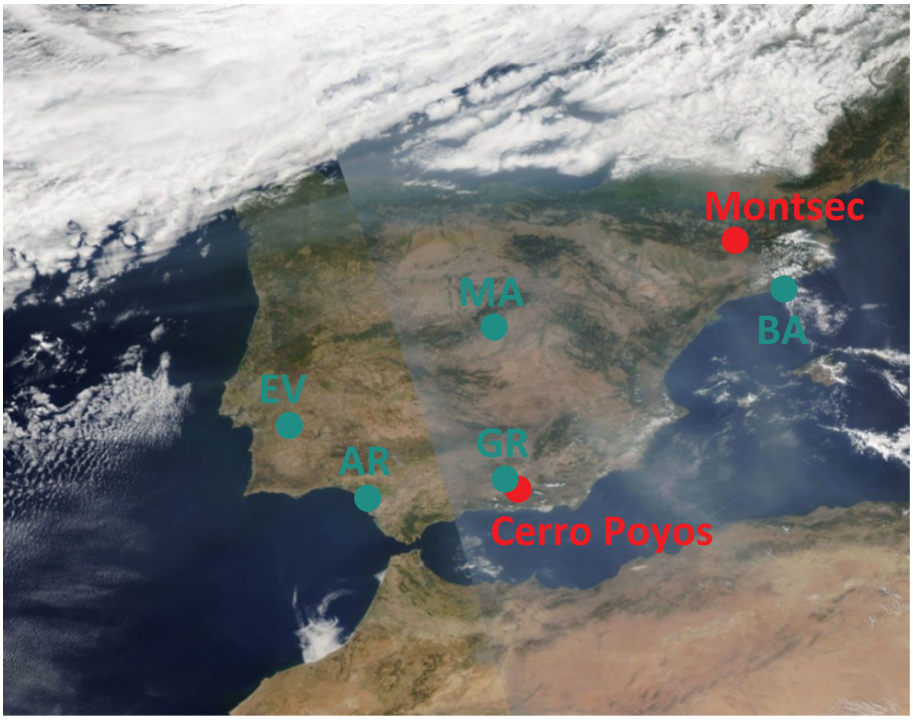

Fig. 1. MODIS/Aqua corrected reflectance (true color) map centered over Spain on 8 September. Green bullets indicate lidar stations (EV: Évora, AR: El Arenosillo/Huelva, GR: Granada, MA: Madrid, BA: Barcelona) and red bullets indicate AERONET sites. Map created from https://firms.modaps.eosdis.nasa.gov/map/. (For interpretation of the references to color in this figure legend, the reader is referred to the web version of this article.)

the particle backscatter coefficient at 532 nm, β_{532}, and at 1064 nm, β_{1064}, as:

$$CR = \frac{\beta_{532}}{\beta_{1064}} \quad (2)$$

The reason for using this definition of the color ratio between the wavelengths of 532 and 1064 nm is that it allows direct comparison with the space-borne lidar (see Section 2.2) and it is a common parameter used in aerosol classification (Burton et al., 2012; Groß et al., 2013). To understand the reasons of the differences and similarities found in the upcoming discussion, we also define the extinction-related Ångström exponent (AE) between the wavelengths of 355 and 532 nm:

$$\alpha - AE = -\ln\left(\frac{\alpha_{355}}{\alpha_{532}}\right)/\ln\left(\frac{355}{532}\right) \quad (3)$$

where α_{355} and α_{532} are the extinction coefficient at 355 and 532 nm, respectively. This quantity is calculated only at EV which is the only stations where Raman inversions were successfully performed. Similarly to the color ratio, $\alpha - AE$ provides information on the particle dominant size. The advantage of $\alpha - AE$ is that it can be directly compared to the Ångström exponent retrieved by AERONET and defined in the next paragraph. While the MPLNET and the EV systems work continuously 24/7, GR and MA measurements are discontinuous.

Due to the high vertical extension of the smoke plume (up to 14 km) and the high AOD values at 440 nm reached at peak (0.6), no Raman inversions could be performed satisfactorily in Granada. Raman inversions performed in Évora yielded a lidar ratio (the extinction-to-backscatter ratio), *LR*, at 532 nm, LR_{532}, in the mid troposphere smoke plume on the order of 55 sr (sr) (see Section 5.2). This value of 55 sr is used in the elastic inversions performed for the other systems at both 532 and 1064 nm. To maximize the signal-to-noise ratio and thus minimize the retrieval uncertainties, all ground-based lidar measurements presented in this work are nighttime measurements. For the EARLINET systems, the Raman-inverted extinction coefficient has an accuracy of 10–30%, the backscatter coefficient of 5–10% and the lidar ratio of 20–35% (Ansmann et al., 2002). As far as elastic inversions are concerned, the uncertainty of the backscatter coefficient is 10–20% according to Ansmann et al. (2002) and the one of the extinction coefficient is almost directly proportional to the uncertainty of the lidar ratio assumed. Thus, a 25% uncertainty in the lidar ratio input parameter (assuming variations of 14 sr around 55 sr, see Section 5.2) of the elastic inversion leads to a relative uncertainty of about 25% in the extinction coefficient. The particle depolarization ratio uncertainty can reach up to 50% in the UTLS (Rodríguez-Gómez et al., 2017). For the MPLNET systems, according to Córdoba-Jabonero et al. (2018) the backscactter coefficient and the particle depolarization ratio retrieved from MPL data have a relative uncertainty of 5 to 20% and of 10 to 60%, respectively.

In order to monitor the event over the IP from columnar optical properties we looked at mid-altitude AERONET (Aerosol Robotic Network; Holben et al., 1998) sites with no local sources so as to maximize the signature of the smoke long-range transport. Such sites are Montsec in northeastern Spain and Cerro Poyos in south Spain (see Table 1 for more details and Fig. 1 for the geographical position of the stations). We considered AERONET Version 3 products: AOD and SDA (Spectral Deconvolution Algorithm; O'Neill et al., 2001, 2003) inversions data level 1.5 in Montsec (level 2.0 is not available yet) and 2.0 in Cerro Poyos; and aerosol inversions data level 1.5 at both sites. The AERONET products used in our work are:

- The AOD at 440 nm, AOD_{440}, which has an estimated accuracy of ± 0.02 (Eck et al., 1999).
- The Ångström exponent calculated between the wavelengths of 440 and 870 nm, $AE_{440-870}$, which has an accuracy of ± 0.25 for $AOD_{440} \geq 0.1$ (Toledano et al., 2007).
- The fine mode fraction, *FMF*, which has an uncertainty of ~25% for an AOD at 500 nm > 0.3 (O'Neill et al., 2003). *FMF* represents the ratio of the fine-mode AOD to the total AOD.
- The absorption aerosol optical depth, *AAOD*, which has an accuracy of ± 0.01 for wavelengths > 440 nm (Sicard et al., 2016). *AAOD* represents the AOD due to absorption.
- The single scattering albedo, *SSA*, which has an accuracy of ± 0.03 for $AOD_{440} \geq 0.5$ for biomass burning (Sicard et al., 2016). *SSA* represents the fraction of the AOD due to scattering (i.e. $AOD - AAOD$) to the total AOD.
- The asymmetry factor, *g*, which has an accuracy in the range [± 0.03, ± 0.08] for biomass burning (Sicard et al., 2016). *g* represents a measure of the preferred scattering direction and varies between −1 (only backward-scattering, i.e., at 180° relative to the incident direction) and +1 (only forward-scattering at 0°).

2.2. Spaceborne observations

Several types of satellite sensors are used to fulfill the objectives of the study. The Atmospheric Infrared Sounder (AIRS; Chahine et al., 2006), on board the Aqua satellite, is a hyperspectral instrument with 2378 infrared channels and 4 visible/near-infrared channels. AIRS, together with the Advanced Microwave Sounding Unit (AMSU-A) and the Humidity Sounder for Brazil (HSB), form the AIRS instrument suite which is designed to measure the Earth's atmospheric water vapor and temperature profiles on a global scale. The physical product from AIRS used in our study is the Carbon Monoxide (CO) Total Column science parameter which is a parameter of the AIRS Level 2 standard retrieval product using AIRS only (AIRS2RET_NRT). It indicates the amount of CO in the vertical column of the atmosphere and is measured in parts per billion by volume (ppbv). The spatial resolution of the AIRS2RET_NRT product is 45 km at nadir. The temporal resolution is twice daily (day and night).

To track back the vertical distribution of the smoke plume before its arrival in the IP, we use the spaceborne lidar Cloud-Aerosol Lidar with Orthogonal Polarization (CALIOP; Winker et al., 2007), on board the Cloud-Aerosol *Lidar* and Infrared Pathfinder Satellite Observation (CALIPSO) satellite. CALIOP is a two-wavelength polarization-sensitive lidar that provides high-resolution vertical profiles of aerosols and clouds. It utilizes three receiver channels: one measuring the 1064 nm backscatter intensity and two channels measuring orthogonally polarized components of the 532 nm backscattered signal. The data used in our study are the CALIOP Aerosol Profile Lidar Level 2 data, version 4.10. Profiles of extinction and backscatter coefficients at 532 and 1064 nm, as well as particle depolarization ratio at 532 nm, are given at a horizontal resolution of 5 km and a vertical resolution of 60 m. The uncertainty in the aerosol extinction coefficient is 40% (assumed a 30-% lidar ratio uncertainty) and the one in the aerosol backscatter coefficient is 20–30% at 532 nm (Young and Vaughan, 2009). The CALIOP Level 2, version 4.10 data products used in this study contain substantial changes over the earlier releases, among which the most significant is the updated lidar ratio assignment (Young et al., 2018). Information on CALIOP aerosol sub-typing algorithm and assigned lidar ratios can be found in Omar et al. (2018) and Kim et al. (2018). CALIOP observations have been used for the study of long-range transport of fire smoke locally (Kar et al., 2018) and also globally (Mehta and Singh, 2018).

The Moderate Resolution Imaging Spectroradiometer (MODIS; Kaufman et al., 2003), on board Aqua and Terra satellites, is used for various purposes: 1) to quantify and monitor the smoke AOD at the global scale, 2) to confirm the fires position and active period, and 3) to parameterize the smoke emission in the dispersion model. For the AOD we use the near real-time value-added MODIS AOD level 3 gridded product (MCDAODHD) based on MODIS level 2 aerosol products combined from Aqua and Terra satellites. The sensor resolution is 0.5°, imagery resolution is 2 km, and the temporal resolution is daily. For the

fire information (position and active period), MODIS Fire and Thermal Anomalies products, either from Terra (MOD14), Aqua (MYD14) or a combination of them (MCD14), are used. Each MODIS active fire location represents the center of a 1-km pixel that is flagged by the algorithm as containing one or more fires within the pixel.

2.3. Particle dispersion modelling

2.3.1. Model overview

Back-trajectory and dispersion calculations are performed with the Hybrid Single Particle Lagrangian Integrated Trajectory Model (HYSPLIT; Stein et al., 2015; Rolph et al., 2017). HYSPLIT is developed at NOAA's Air Resources Laboratory and is one of the most widely used models for atmospheric trajectory and dispersion calculations. It is a complete system for computing simple air parcel trajectories as well as complex transport, dispersion, chemical transformation, and deposition simulations. The model calculation method is a hybrid between the Lagrangian approach and the Eulerian methodology. Apart from calculating back-trajectories, HYSPLIT is mostly used in this study to calculate the transport, dispersion, and deposition of emitted CO (used as a tracer of the transport) and particulate matter (black carbon, BC, and organic carbon, OC). The specificity of our HYSPLIT runs is that the heat release from the fires is used to estimate the smoke release height, i.e. no release heights were a priori set. The initial particle height is assumed equal to the final buoyant rise height as computed using the method of Briggs (1969) with the fire heat release given in input, implying that the final rise is a function of the estimated fire heat release rate, the atmospheric stability, and the wind speed. Stein et al. (2009) tested the sensitivity of HYSPLIT to fixed and variable release heights by comparing PM2.5 levels modelled and measured at the surface of northwestern US fires in September 2006. They found that the case when the heat release from the fire was used to estimate the release height showed the best performance, although they also concluded that the model is highly sensitive to variations in the smoke release height and to whether the smoke injection actually occurred below or above the planetary boundary layer. Rolph et al. (2009) also used HYSPLIT plume rise computation from the fire heat release.

For each fire simulated, a series of common parameters (in brackets we indicate HYSPLIT denomination) are necessary: location (Release location), start time (Release start time), duration (Release duration) and heat release (Heat release for plume rise). And for each chemical compound simulated (gas or particle), the emission rate (Emission rate) is necessary. Such information is extracted from the biomass burning emission estimates from GFAS (Global Fire Assimilation System; Kaiser et al., 2012) data from CAMS (Copernicus Atmosphere Monitoring Service). GFAS assimilates fire radiative power (FRP) observations from satellite-based sensors (Freeborn et al., 2014), namely MODIS/Aqua and Terra and SEVIRI (Spinning Enhanced Visible and InfraRed Imager), to produce daily estimates of biomass burning emissions. GFAS data (in brackets we indicate GFAS denomination) used in our work include daily information of the fire location and heat release (Wildfire radiative power), and for each chemical compound the emission rate (Wildfire flux). Data are available globally on a regular latitude-longitude grid with horizontal resolution of $0.125^\circ \times 0.125^\circ$. We used the current version of GFAS, i.e. GFAS v1.2. This work contains modified Copernicus Atmosphere Monitoring Service Information (CAMS, 2018).

The quantification of the HYSPLIT dispersion model uncertainties is not straightforward and it is usually performed through complex sensitivity studies (Mosca et al., 1998; Pielke and Uliasz, 1998; Straume, 2001; Warner et al., 2002). In general, the performance of dispersion models is largely attributed to uncertainty in the input fields (Challa et al., 2008). For our case, the GFAS data used for estimating the magnitude and timing of fire emissions have a typical uncertainty around 30% (Andela et al., 2013).

2.3.2. Model parametrization

The dispersion of CO, BC and OC is simulated in the forward direction, with a time resolution of 6 h and at 15 altitude levels: one between 0 and 2.5 km and then 14 adjacent 1-km thick layers up to 16.5 km. The meteorology is taken from GDAS (Global Data Assimilation System) data with a horizontal resolution of $0.5^\circ \times 0.5^\circ$. Noteworthy is the fact that the first simulations with GDAS $1^\circ \times 1^\circ$ meteorological data (not shown) simulated the dispersion of the smoke plume too far north reaching France and Germany, instead of the IP. The use of the finer resolution of $0.5^\circ \times 0.5^\circ$ improved significantly the arrival location of the plume, and put forward the importance of the horizontal resolution of the meteorological data upon the correct dispersion of the emitted plume studied. The vertical limit of the internal meteorological grid of HYSPLIT was set to 20 km, which, according to the following sections, is well above the maximum height at which the smoke particles were observed. The daily number of active fires, the FRP per fire and the emission rate per fire and chemical compound are from GFAS $0.125^\circ \times 0.125^\circ$ data. Since the time resolution of GFAS data is daily, the emission rate and FRP are assumed constant during the day the fires are active. In all simulations 2500 particles were released to calculate the transport.

In the case of CO, dry deposition is neglected and wet removal is parameterized with a Henry's law constant of 9.9×10^{-4} mol atm^{-1}.

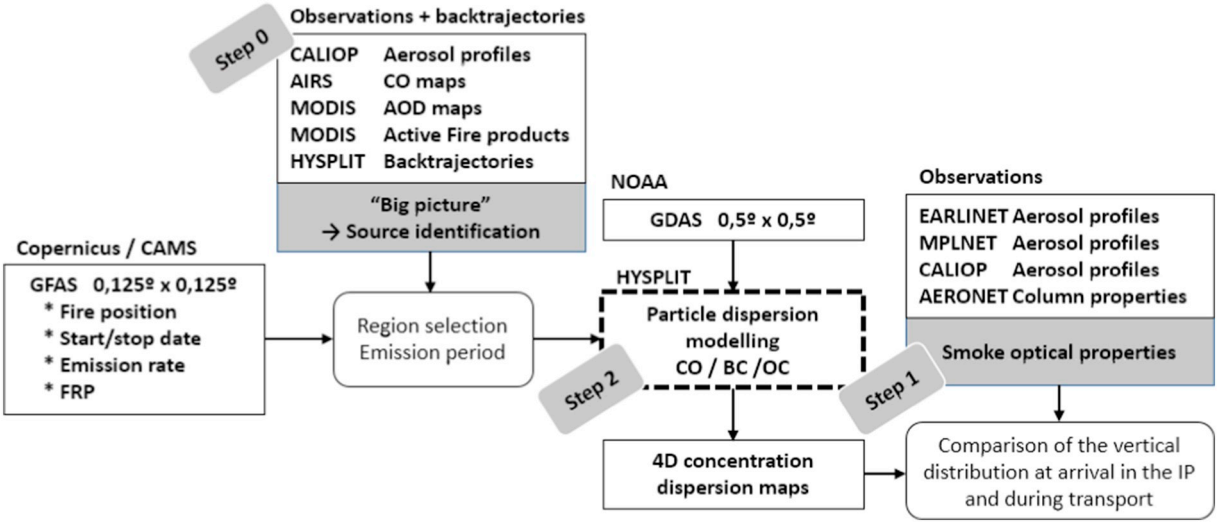

Fig. 2. Flowchart of the methodology.

BC (OC) is parameterized with the following values (Chin et al., 2002):

- Particle radius: 0.0118 (0.0212) μm.
- Particle density: 1.0 (1.8) g cm^{-3}.
- Gravitational settling velocity (for dry deposition): 0.5 cm s^{-1} for both types.
- Scavenging coefficient in- and below-cloud (for wet deposition): 8×10^{-5} s^{-1} for both types.

3. Methodology

The proposed methodology is a two-way process, posterior to an initial phase (step 0) consisting in visualizing the "big picture" of the event at global scale with satellite images and back-trajectories. A flowchart of the methodology is shown in Fig. 2. The first step of the methodology (step 1) consists in monitoring the smoke optical properties observed over the IP and their backward evolution back to the source with CALIOP retrievals. The second step (step 2) consists in parameterizing the smoke emission and run HYSPLIT forward simulations to obtain 4D (space and time) dispersion maps of the concentration of smoke-related compounds such as carbon monoxide, black carbon and organic carbon. The main contribution of the modelling in Section 6 is to support the possible hypothesis made along the discussion in Section 5.2.

4. Canadian/United States fires and general overview

The first hint of the arrival and the presence of the smoke plume over the IP is given by the temporal evolution of a combination of AERONET parameters in Montsec and Cerro Poyos, namely the AOD at 440 nm, $AE_{440-870}$, and *FMF* (Fig. 3). According to Sola Salvatierra et al. (2014) the mean AOD at 500 nm ($AE_{440-870}$) in Montsec during the month of September is ~0.1 (~1.5) which corresponds to an AOD at 440 nm of 0.12. In Montsec AOD_{440} starts to exceed this value on 4 September, day from which the AOD increases continuously until it reaches its peak value of 0.55 (0.54) on 7 (8) September. These peak values of AOD are associated with values of $AE_{440-870}$ of 1.7 (1.6) on 7 (8) September. On both days the fine mode fraction is higher than 0.98, leaving basically no room for the presence of coarse mode smoke particles (diameter > 1 μm). In Cerro Poyos, the background AOD at 440 nm is even lower than in Montsec, being smaller than 0.1 (AERONET, 2018). This value is exceeded from 5 September on, and the AOD increases until 7 September when it reaches its peak value of 0.62 with an associated $AE_{440-870}$ of 1.6. The fine mode fraction is higher than 0.88 on both 7 and 8 September. The main difference between Montsec and Cerro Poyos is their proximity to anthropogenic emissions: while Montsec is a remote site, far away from any industrial or large metropolitan area, Cerro Poyos, although higher in altitude, is only 12 km SE of the city of Granada (~600,000 inhabitants including metropolitan area). Due to its position with respect to Granada and the prevailing winds during the period under study, Cerro Poyos was downwind of the city. This has several implications: the AOD in Cerro Poyos shows a diurnal cycle related to the anthropogenic emissions of Granada, and the fine mode fraction is lower than in Montsec due to the same emissions. However one can appreciate from Fig. 3 that during the night of 7–8 September *FMF* in Cerro Poyos is nearly 1 like in Montsec. In terms of AOD, the biomass burning contribution at both sites is roughly five times higher than the background values, and the peak values (~0.6) are considered very large for biomass burning long-range transport. In comparison the North American biomass burning event detected 15 days earlier (~22 August 2017) in northern Europe produced AODs at 500 nm near 1, $AE_{440-870}$~1.1 and *FMF*~1 (Ansmann et al., 2018).

To track back the plume transport in the atmosphere from the source to the IP, we use maps of columnar CO (AIRS) and AOD (MODIS; Fig. 4) as well as CALIOP curtains and HYSPLIT back-trajectories (Fig. 5). The combined day/night columnar CO maps are reported for the period 30 August – 8 September and a threshold of 95 ppb was applied in order to highlight strong concentrations. The active fires are indicated by a red star (Fig. 4) centered in a region defined by the orange square visible in Fig. 5 (bottom plot). This square covers the provinces of British Columbia and Alberta (Canada) and the states of Washington, Oregon, Idaho, Montana and northern California (US) where > 90% of the active fires in North America are present during the period considered. The habitat type, a little more south than the Canadian boreal forests, corresponds to temperate coniferous forests (Ricketts et al., 1999). Some important forests in this region of North America are the National Forests of Wenatchee, Flathead, Nez Perce-Clearwater or Payette, among others, which, under the influence of both continental and maritime climates, produce a large variety of ecosystems ranging from wet, western redcedar bottoms to high alpine peaks, and forests of alpine larch and whitebark pine. So, from this region, a first plume (Plume 1) is released from the source region on 30 August, travels E-NE on 31 August and then eastwards on 1 and 2 September. On 3 September a second plume (Plume 2) is released from the same source region and starts travelling east, slightly SE. On 4, 5, and 6 September Plume 2 is carried by the jet stream and travels rapidly towards the east, while at the same time Plume 1 travels slowly eastwards above the Atlantic. The column concentration of Plume 2 is stronger than the one of Plume 1. On 7 September both plumes merge into one and reach the IP. The high MODIS AOD values on 8 September over the IP confirm that the high level of column CO is accompanied with high aerosol loads. These aerosols are also clearly visible especially in the eastern part of the IP as a gray/brownish smoke shroud on MODIS true color image of 8 September (Fig. 1).

The 10-day back-trajectories at selected heights are shown in Fig. 5.

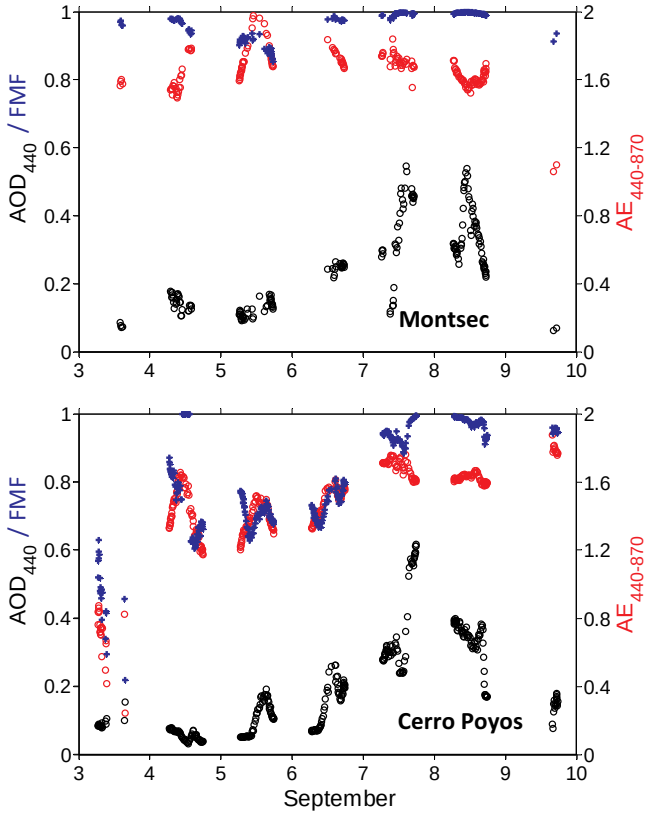

Fig. 3. AOD_{440} (black), FMF (blue) and $AE_{440–870}$ (red) in (top) Montsec, northeastern Spain, and (bottom) Cerro Poyos, south Spain. The gray areas in the bars on top of the figures indicate coincident lidar measurements. (For interpretation of the references to color in this figure legend, the reader is referred to the web version of this article.)

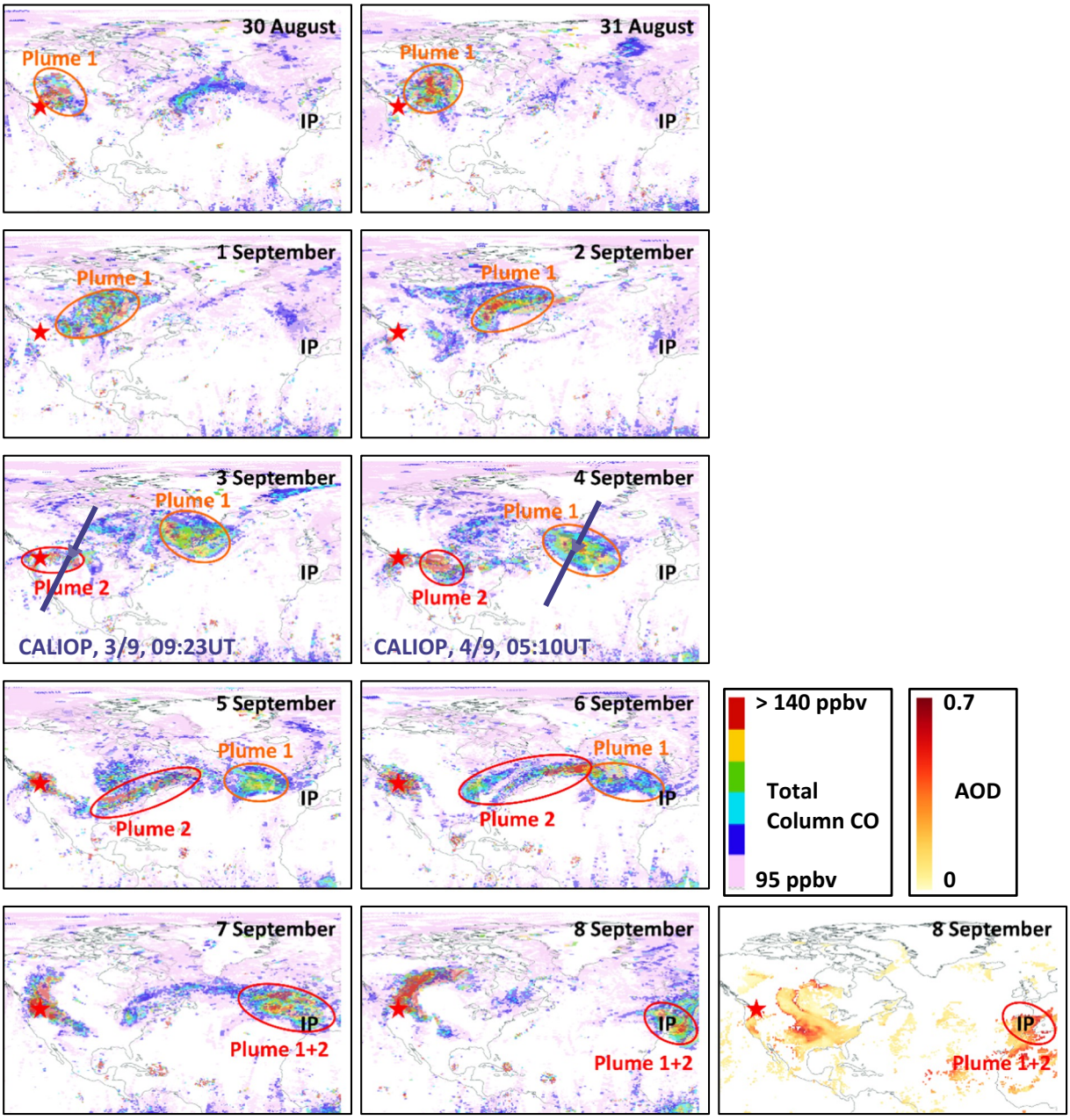

Fig. 4. Total column carbon monoxide (day/night) from AIRS/AQUA from 30 August until 8 September. The extra plot at the bottom to the right represents the MODIS combined (Aqua and Terra) value-added AOD at 550 nm on 8 September. The red star indicates the position of the active fires. On the plots of 3 and 4 September the descending, nighttime orbits of CALIPSO are reported. Maps created from https://worldview.earthdata.nasa.gov/. (For interpretation of the references to color in this figure legend, the reader is referred to the web version of this article.)

Although we computed back-trajectories at all lidar stations, only Madrid is shown as point of arrival for the sake of clarity of the figure and because Madrid is located in the center of the IP. The selected heights (3, 6 and 11 km asl) have been chosen by looking at the smoke vertical distribution from the lidar data (see next section). All three trajectories pass over the region containing most of the active fires (orange square): the trajectory arriving in Madrid at 3 km passes over this region on 31 August at 08UT (7–8 days of transport) and the trajectories arriving at 6 and 11 km, very similar in path and speed, pass over the region of the fires on 3 September between 17 and 22UT (4–5 days of transport). These results suggest that the airmasses arriving above the IP at 3 km on 8 September picked up smoke most likely from Plume 1, while those arriving at 6 and 11 km most likely from Plume 2. During the transport CALIPSO orbits intersect the back-trajectories in space and time in two occasions: once southeast of Greenland on 4 September at 05:10 UT (D-4, 4 days before arrival in Madrid, intersects with Plume 1 which is 5 days old) at 3 km height, and another time on 3 September at 09:23 UT (D-5, intersects with Plume 2 which is < 1 day old) at 6 and 11 km heights. On D-5 the shortest distance between CALIPSO curtain and the center of the region of the fires (orange square) is 700 km. On both occasions the cloud-free CALIOP curtains show clearly the large spatial extension of the smoke: 1700 km (below orbit) × 15 km (height) on D-4 and 1100 km (below orbit) × 8–9 km (height) on D-5. The attenuated backscatter of CALIOP on D-5 is clearly much stronger than on D-4 because of the proximity of the orbit to the source region. On D-5, in the southernmost part of the plume, most of the smoke between 4 and 7 km height is optically so thick that it attenuates the lidar signal below it.

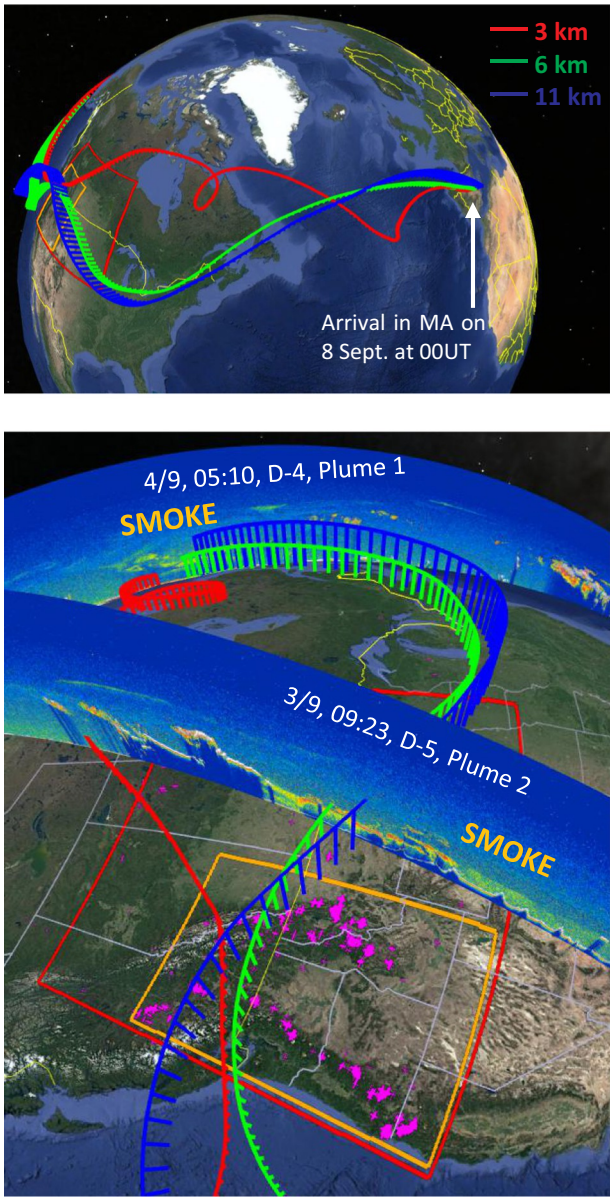

Fig. 5. (top) 10-day back-trajectories, 1-hour resolution, arriving in Madrid, in the center of Spain, on 8 September at 00UT at heights of 3 (red), 6 (green) and 11 (blue) km; (bottom) Same back-trajectories, different viewing angle and superposition of CALIOP curtains on 4 September at 05:10UT (D-4, day-4 before arrival) and on 3 September at 09:23UT (D-5) where the smoke plumes, clearly visible, match very well in space and time with the back-trajectories. Pink crosses indicate active fires in the period 30 August – 5 September. The red rectangle of corner coordinates (125 W, 40 N; 93 W, 58 N) is the area in which the fires were taken into account in the dispersion modelling analysis (see Section 6). The orange rectangle simply highlights the region containing most of the fires. Maps created with Google Earth.

5. Optical properties of the smoke particles

Many papers, most of them listed in the literature overview of Ortiz-Amezcua et al. (2017) or of Haarig et al. (2018), deal with the optical properties of long-range transport smoke particles derived from observations of photometers, lidars or a combination of them. More general aerosol-typing literature based on lidar remote sensing and including biomass burning are available in Burton et al. (2012), Groß et al. (2013), Illingworth et al. (2015) and Baars et al. (2016, 2017).

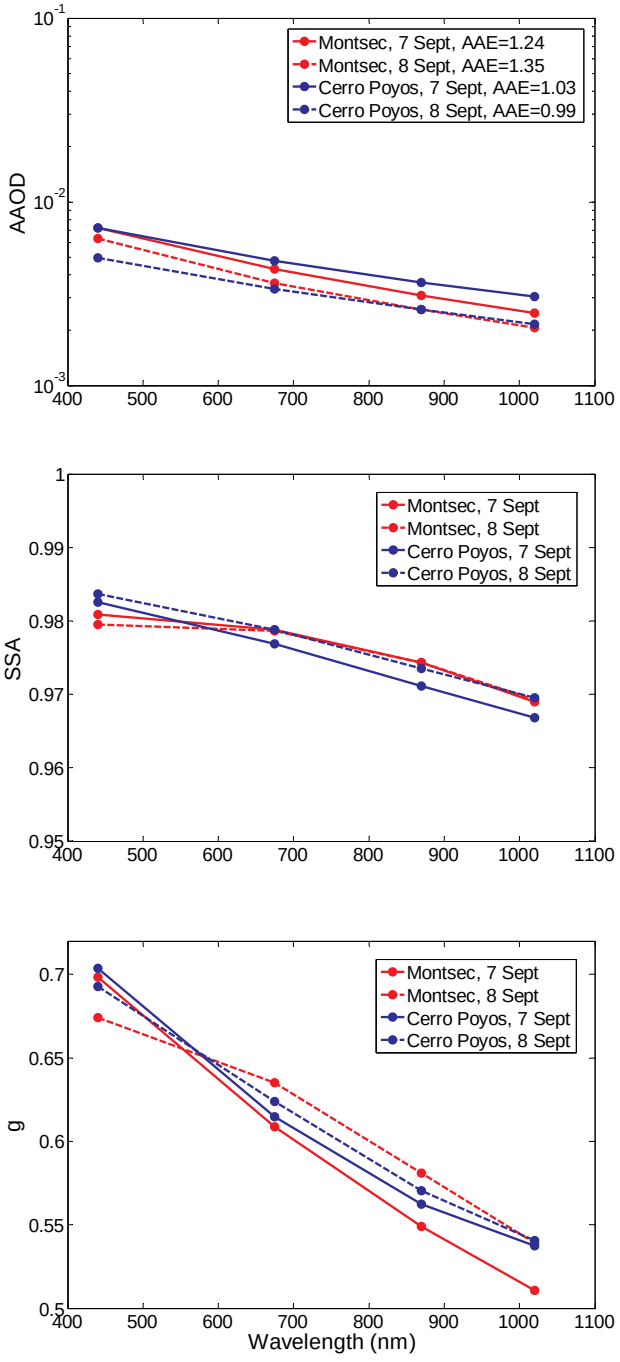

Fig. 6. AERONET daily mean spectral (top) AAOD, (center) SSA, and (bottom) asymmetry factor at Montsec and Cerro Poyos on 7 and 8 September.

5.1. Column-averaged properties

Fig. 6 shows the spectral AAOD, SSA and asymmetry factor retrieved from AERONET sun-sky photometer measurements at Montsec and Cerro Poyos on 7 and 8 September. Several aspects are noteworthy. AAOD, similar at both sites in absolute values, is surprisingly very low. Compared to the climatological AAOD representative of boreal forests from US and Canada (Russell et al., 2010), recalculated from Dubovik et al. (2002), our AAOD values are 2 to 3 times lower. As a consequence of the small AAOD observed in Montsec and Cerro Poyos, SSA is large (~0.98 at 440 nm) and indeed much larger than the climatological values for boreal forest biomass burning (0.94 at 440 nm) from Dubovik et al. (2002). However it is in the range of values of SSA at 355 nm

obtained in Europe by Markowicz et al. (2016), 0.91–0.99, and Ortiz-Amezcua et al. (2017), 0.965–0.991, in smoke plumes originating from North America in July 2013. In particular Markowicz et al. (2016) attribute these high SSA values to "a transformation of [biomass burning] during long-range transport […] and mixing of the [biomass burning] with non-absorbing aerosol species". The high transport altitude of the fire smoke observed over the IP in summer 2017 makes the second hypothesis (mixing with non-absorbing aerosol species) highly improbable. If these low AAOD and high SSA were due to low BC emission at the source, the following rationale can be made. According to Radke et al. (1991) and more recently to Russell et al. (2014) the absorption properties of biomass burning in its smoldering combustion phase are lower than during its flaming phase, the reason being a larger production of black carbon in the flaming phase relative to the smoldering phase (Radke et al., 1991). In addition, smoldering combustion occurs over a much longer period of time relative to the comparatively short lives flaming phase of tree-crown fires of, e.g., pines, cedar or cypress that commonly populate temperate coniferous forests. These results suggest that the smoke particles observed over the IP might be the product essentially of smoldering combustion at the source. We also recall that level 1.5 AERONET data are not totally quality assured and that the values of AAOD and SSA should be taken with certain caution. The values and spectral behavior of g in Montsec and Cerro Poyos are in good agreement with results for biomass burning aerosols from other studies (Dubovik et al., 2002; Sayer et al., 2014; Nikonovas et al., 2015), with g presenting a sharp decrease with increasing wavelength. Nikonovas et al. (2015) distinguished the behaviour of fresh (within the first 24 h) and aged (> 72 h) smoke and values reported therein for aged smoke agree quite well with the mean values obtained at Montsec and Cerros Poyos on 7 and 8 September 2017 (~0.70 at 440 nm and ~0.53 at 1020 nm). This spectral behavior is typical of the dominance of fine particles that are scatterers of solar radiation more efficient at lower wavelengths, with the forward scattering decreasing with increasing wavelength.

We analyze the wavelength dependence of AAOD by means of the absorption Ångström exponent, AAE, calculated between the wavelength of 440 and 870 nm. Although a clear difference is observed between both sites in terms of AAE: 1.24 < AAE < 1.35 in Montsec and 0.99 < AAE < 1.03 in Cerro Poyos, conclusions are not straightforward. We rely our discussion on the results of Lack and Cappa (2010). According to these authors, the AAE for pure BC cores varies in the range [−0.2, +1.3], for BC cores coated in non-absorbing matter (i.e. coated with a purely scattering shell) it can be as high as 1.6–1.7, and for BC cores coated in absorbing matter, namely brown carbon (mildly absorbing organic matter; Andreae and Gelencser, 2006), it is usually greater than unity even if for certain combinations of core/shell size pairs and values of the imaginary part of the refractive index, it can be close to unity. Thus the absolute attribution of BC or brown carbon is hampered when AAE < 1.6. However Lack and Cappa (2010) also showed that high SSA values (> 0.9) could only be achieved for BC cores coated in absorbing matter. The results allow us to conclude (i) that, without any doubt, the AAE values in Montsec (~1.3) are representative of brown carbon (or BC coated in brown carbon), likely contained in the long-range transport smoke plume detected, and (ii) that the AAE ~1 in Cerros Poyos is most probably caused by brown carbon from biomass burning origin and maybe pure BC from the anthropogenic fossil fuel emissions of the nearby city of Granada. Another possible reason for AAE ~1 in Cerros Poyos may be the presence of nearby persistent local fires in Sierra Morena, approximately 150 km northwest of Cerro Poyos. For comparison, Bergstrom et al. (2007) measured an AAE of 1.45 in the range 325–1000 nm in a plume of South Africa biomass burning with data from the SAFARI (Southern Africa Regional Science Initiative) campaign.

5.2. Vertically-resolved properties

To relate smoke optical properties and their vertical distribution, we use ground- and space-borne lidar profiles. The availability of lidar measurements in the period 3–9 September is indicated by the gray areas in the bars of Fig. 3. Because of the high aerosol load and the high vertical extension of the plumes (> 10 km) on the night of 7 to 8

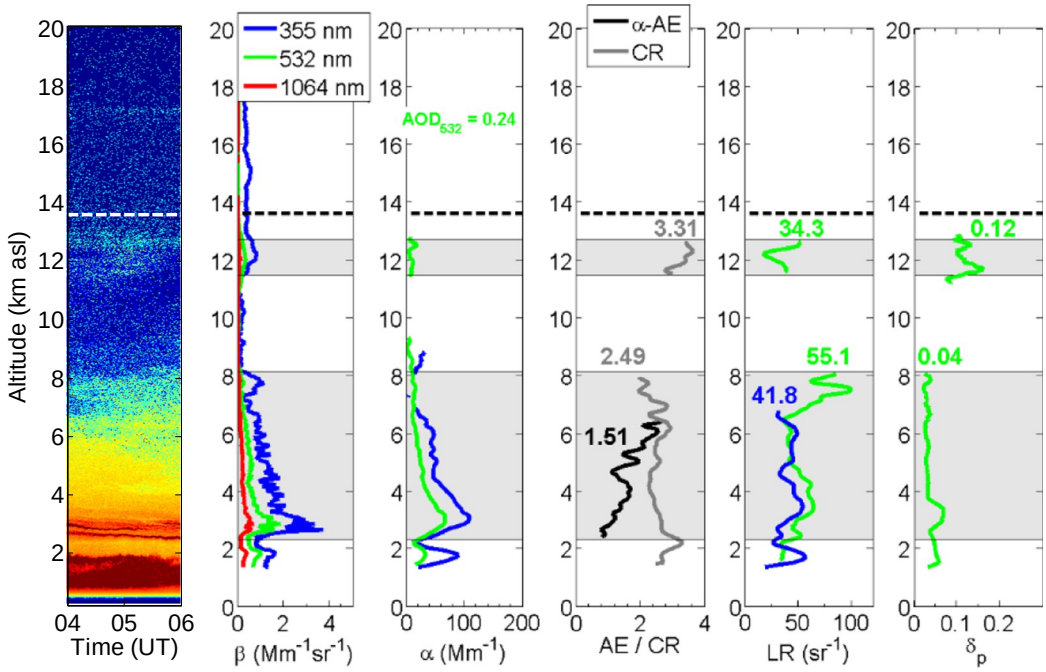

Fig. 7. Nighttime multi-wavelength lidar inversion in Évora on 7 September between 04 and 06UT. The first plot represents the quicklook of range-square corrected signal at 1064 nm in arbitrary units. β is the particle backscatter coefficient, α the particle extinction coefficient, $\alpha - AE$ the extinction-related AE, CR the color ratio, LR the lidar ratio and δ_p the particle depolarization ratio. Mean values in the mid troposphere and stratosphere (as depicted by the gray rectangles) for $\alpha - AE$, CR, LR and δ_p are reported in the plots. The horizontal dash lines at 13.6 km indicate the tropopause height calculated with 1° × 1° GDAS data.

September and their implication on the signal-to-noise ratio of the lidar signals and thus on the quality of the inversions, Raman inversions were performed only the night of 6 to 7 September. In Fig. 7 we show the result of a Raman inversion in Évora on 7 September between 04 and 06UT. Although this measurement time is a few hours before the arrival time fixed for the back-trajectory simulations (8 September at 00UT) our back-trajectory analysis (not shown) confirms that air mass paths were very similar during the 48 h of both days 7 and 8 September. A series of quality checks have been applied to Évora lidar profiles: negative optical properties are not considered and intensive properties ($\alpha - AE$, $\beta - AE$, CR, LR and δ^p, see caption of Fig. 7 for symbol definition) are calculated only for optical properties greater than a minimum threshold in order to guarantee the presence of aerosols and to avoid physically meaningless retrievals. In addition to the profiles, smoke layer-mean values are given in two altitude ranges corresponding to the mid and upper troposphere. These layer mean values are also reported in Table 2. We find smoke particles up to 12.7 km, below the tropopause height, with a clear plume extending from 2.3 to 8.1 km and a very shallow one from 11.5 to 12.7 km. The AOD at 532 nm is 0.24. The color ratio is significantly different in the two altitude levels considered (~2.49 in the mid troposphere and ~3.31 in the upper troposphere). For comparison Haarig et al. (2018) found color ratios of 1.8 and 2.3 in the troposphere and the stratosphere, respectively, for the North American biomass burning detected in northern Europe 15 days earlier (22 August). Our higher values indicate particles of smaller size. This finding is corroborated by the columnar effective fine mode radius measured by AERONET in Montsec and Cerro Poyos on 7 September which vary in the range 0.14–0.18 μm, while values larger than 0.23 μm were found during the 22 August event (Ansmann et al., 2018). $\alpha - AE$, only retrieved in the mid troposphere, is 1.51. For comparison Haarig et al. (2018) found a $\alpha - AE$ of 0.9 in the troposphere. The difference with our $\alpha - AE$ is probably due to different absorption properties: low in our case and rather large on 22 August (Ansmann et al., 2018). Low absorption properties yield to $\alpha - AE$ very similar to the scattering Ångström exponent. According to Valenzuela et al. (2015) scattering AE larger than 1.5 indicates that submicron particles dominate the aerosol size distribution, which is in agreement with our findings.

The lidar ratio at 532 nm is 55.1 ± 14.2 and 34.3 ± 10.5 sr in the mid and upper troposphere, respectively. Our LR_{532} values are slightly lower than those of Haarig et al. (2018), 65–80 sr, if we take into account the standard deviations associated to our retrievals, but are definitely in the range of literature values (26–80 sr) for North American biomass burning detected in Europe (Ortiz-Amezcua et al., 2017). A lower lidar ratio in the upper troposphere compared to the mid troposphere might indicate less absorbing particles in higher altitude (Ortiz-Amezcua et al., 2017), maybe related to a lesser amount of BC with respect to organic carbon, or to a lesser degree of coating on BC since coatings on BC enhance scattering and absorption properties (Cheng et al., 2014). These hypotheses are further investigated in the next section. At 355 nm we find in Évora $LR_{355} = 41.8 \pm 6.8$ sr in the mid troposphere, which is in good agreement with the range of 40–45 sr found by Haarig et al. (2018) and with the range of literature values (26–80 sr) from Ortiz-Amezcua et al. (2017).

Last but not least, the analysis of the profile of the particle depolarization ratio at 532 nm also reveals interesting results. The layer mean values of δ_p are 0.04 and 0.12 in the mid- and upper troposphere, respectively. While the mid troposphere value falls in the range of literature values (Ortiz-Amezcua et al., 2017) and indicate spherical or almost spherical smoke particles, the value of 0.12 in the upper troposphere is rather unusual. Some works investigating the inter-continental transport of North American fire smoke to Europe from August 2017 also report unusually high depolarization ratios (Khaykin et al., 2018; Haarig et al., 2018; Hu et al., 2019; Sicard et al., 2018) up to 0.20 at 532 nm in the stratosphere. The causes of such high depolarizing capabilities of smoke particles are still not well understood. Recently Burton et al. (2015) made a nice discussion based on literature to explain the high values of three-wavelength depolarization ratios and their spectral dependence that they observed for smoke particles from North American fires retrieved by high-spectral resolution lidar. They proposed two possible explanations of the depolarization by smoke: the "lifting and entrainment of surface soil into the smoke plume and asymmetry of smoke particles themselves". Haarig et al. (2018) hypothesized that high δ_p values may be the result of dried out smoke particles (relative humidity ~0%) with a non-spherical shape. This hypothesis, however, is probably unlikely in the range of altitude considered here (< 13 km over the IP) as radiosoundings in Barcelona (not available in Évora) on 8 September at 00 UT indicate a relative humidity in the range 20–30% in the upper troposphere. At this stage of the paper, our intention is not to give a single explanation of our high δ_p values, as we believe that the main features observed over the IP (injection in the upper troposphere, low absorption and high depolarization properties) are somehow connected, but to list some fire characteristics and physical/chemical mechanisms which could lead to such features: the burnt material at the source (BC and OC contents), flaming versus smoldering phases, fire power, BC aging processes (coagulation, condensation, and heterogeneous reactions) during transport resulting in changes in its morphology and mixing state, relative humidity. Literature on these issues can be found in Fromm and Servranckx (2003), Fromm et al. (2008), Zhang et al. (2008), Lack and Cappa (2010), Adachi et al. (2010), Cheng et al. (2014), China et al. (2015). Forrister et al. (2015), Burton et al. (2015), among many others, and will be used in the discussion of the next section.

To analyze the spatio-temporal evolution of the smoke transport, we compare the smoke CR and δ_p profiles from Évora (7 September at 04 UT) with CALIOP retrievals in Plume 1 (5 days old, D-4) and in Plume 2 (fresh < 1 day, D-5). CALIOP retrievals are shown in Fig. 8. CALIOP quicklooks of the total attenuated backscatter at 532 nm show a spatial extension clearly larger for Plume 1 than for Plume 2 both horizontally and vertically. Plume 1 extends up to ~15 km and into the stratosphere while Plume 2 stays in the troposphere below 9 km. This result suggests that the UTLS injection of smoke particles does not occur immediately a few hours after fire ignition but during the transport. Indeed Cammas et al. (2009) simulated with the anelastic non-hydrostatic mesoscale model Meso-NH the time needed for a boundary layer tracer to reach the tropopause to be about 7.5 h. Logically, the particle backscatter

Table 2
Layer mean values of the color ratio, the Ångström exponent, the lidar ratios at 355 and 532 nm and the particle depolarization ratio at 532 nm in Évora, and from CALIOP on D-4 and D-5.

	UTLS			Mid troposphere		
Parameter	Évora 7/9 at 04UT	CALIOP D-4 Plume 1	CALIOP D-5 Plume 2	Évora 7/9 at 04UT	CALIOP D-4 Plume 1	CALIOP D-5 Plume 2
Color ratio	3.31 ± 0.27	3.06 ± 1.19	–	2.49 ± 0.24	2.17 ± 0.28	1.86 ± 0.36
α-AE	–	NA	NA	1.51 ± 0.76	NA	NA
LR_{355} (sr)	–	NA	NA	41.8 ± 6.8	NA	NA
LR_{532} (sr)	34.3 ± 10.5	NA	NA	55.1 ± 14.2	NA	NA
δ_p	0.12 ± 0.02	0.12 ± 0.03	–	0.04 ± 0.01	0.05 ± 0.01	0.05 ± 0.02

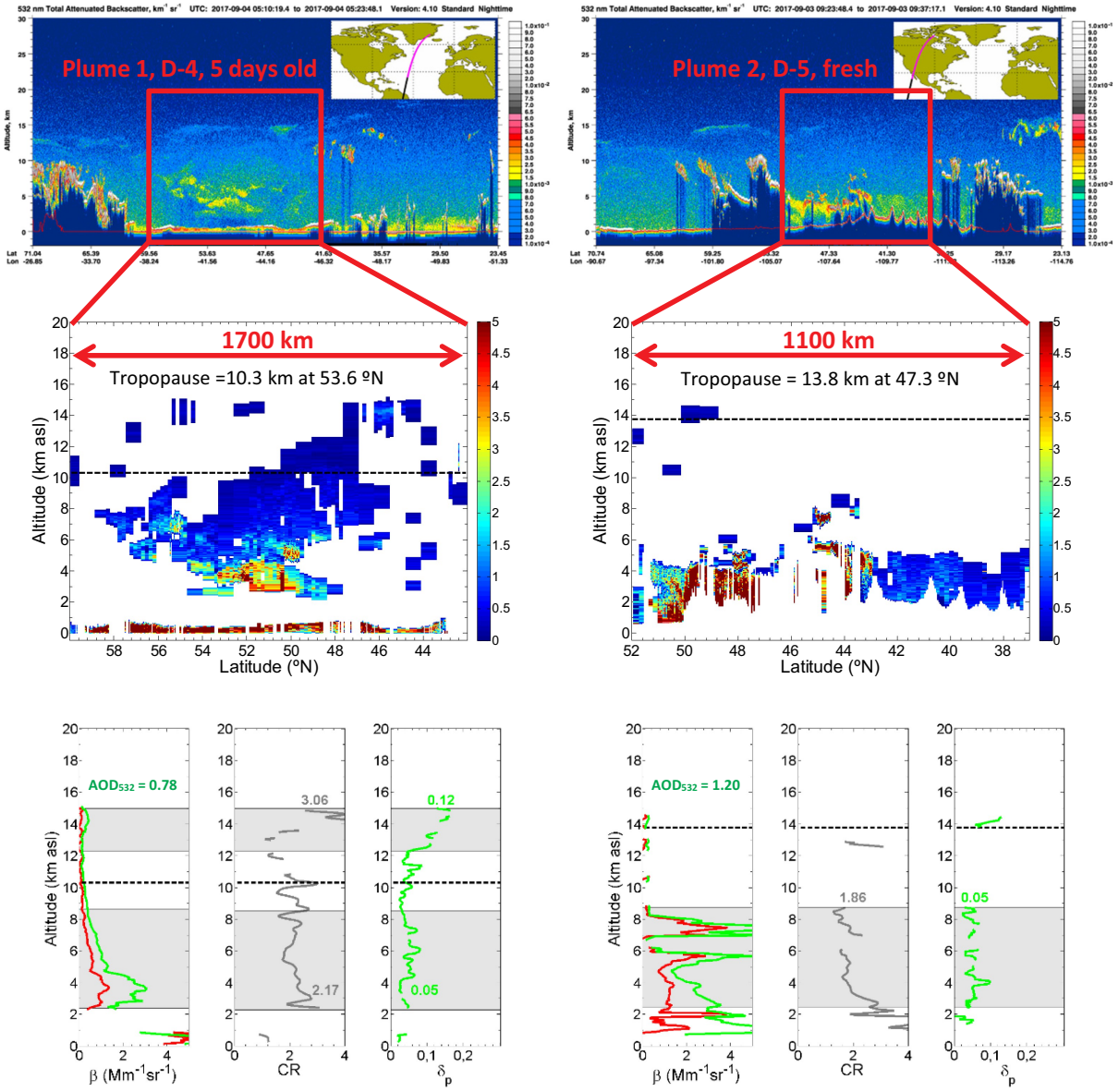

Fig. 8. CALIOP images and products on (left) 4 September at 05:10UT (D-4, Plume 1 released 5 days earlier) and (right) 3 September at 09:23UT (D-5, Plume 2, fresh < 1 day). (top) CALIOP quicklooks of the total attenuated backscatter signal at 532 nm; (center) CALIOP quicklooks of the retrieved backscatter coefficient at 532 nm restricted to the smoke plume (red squares); (bottom) CALIOP mean profiles of backscatter coefficient at 532 and 1064 nm, the color ratio and the particle depolarization ratio at 532 nm. The horizontal black dash lines indicate the tropopause height calculated with 1° × 1° GDAS data. (For interpretation of the references to color in this figure legend, the reader is referred to the web version of this article.)

coefficient at 532 nm is much stronger in Plume 2 ($> 5\,Mm^{-1}\,sr^{-1}$ below 4 km at latitudes of 48–50°N) resulting in a high AOD at 532 nm of 1.20 (versus 0.78 for Plume 1). The color ratios in the troposphere are 2.17 and 1.86 for Plume 1 (5 days old) and Plume 2 (< 1 day), respectively, indicating a decrease of the particle size as the plume gets older. In Évora *CR* is 2.49. In the stratosphere the color ratio of Plume 1 is 3.06, while it is 3.31 in the upper troposphere in Évora. Given the large standard deviation of CALIOP *CR* retrieval in the stratosphere (Table 2), the relatively small difference between both values (3.06 and 3.31) cannot be interpreted as a decrease of particle size. In fact, once in the UTLS the smallest particles (with radii < 0.5 µm), tend to maintain at their altitude level or to ascend. Rohatschek (1996) and Pueschel et al. (2000) explained the self-lofting of UTLS-level BC with the gravito-photophoresis mechanism consisting in sunlight-induced upward forcing. It is interesting to note a significant increase of *CR* (> 3) close to the ground in Plume 2 which probably reflects freshly emitted, small soot particles, before they undergo any of the various aging processes that lead to their size increase. The CALIOP particle depolarization ratio at 532 nm in the troposphere is 0.05 in both plumes, a value similar to $\delta_p = 0.04$ found in Évora in the mid troposphere. It is an indication that the smoke particle depolarizing capabilities, and subsequently also their shape, in the troposphere are stable during transport. In the stratosphere δ_p in Plume 1 increases from 0.04 to a peak value of 0.16, the mean value being 0.12. In Évora the same value of 0.12 is found in the upper troposphere between 11.5 and 12.7 km. As far as Plume 1 is concerned, the smoke particles reached the UTLS in < 5 days after their release in the atmosphere and it seems that the smoke particle depolarizing capabilities (and thus their shape) at UTLS level are also stable during transport. The quasi-linear increase of δ_p with height may be an indication of the height-dependence of the ongoing aging processes leading to the transformation of the smoke particle depolarization properties from low- (0.04 at 12.25 km) to moderately-depolarizing (0.16 at 14.95 km). In Évora δ_p in the upper troposphere does not seem height-dependent as the particles must have

already undergone these aging processes.

To close this section, we compare the time-height evolution of mid and upper tropospheric particle depolarization ratio at all Iberian lidar stations (capable of measuring particle depolarization) plus CALIOP, and the dependency of δ_p versus *CR* in Évora and Granada plus CALIOP. The results are shown in Fig. 9. The reason for choosing to plot δ_p versus *CR* is twofold: 1) they are the two intensive parameters provided by CALIOP, and 2) low-level aerosol typing is possible with these parameters (Groß et al., 2013), although the classification they propose also includes the lidar ratio. The profiles in the IP were selected during the night of 7 to 8 September, close to the back-trajectory arrival time (8 September at 00UT), according to measurement availability and clear-sky conditions. They all fall around the back-trajectory arrival time −3/+1 h. Contrarily to the observations of North American smoke in the stratosphere in France (Khaykin et al., 2018; Hu et al., 2019) and Germany (Ansmann et al., 2018; Haarig et al., 2018) earlier in August 2017, over the IP no aerosols are observed in the stratosphere in the period considered. At all stations of the IP, a continuum of aerosols is observed up to the upper troposphere: aerosols are present in the whole troposphere. In order to identify representative layers and give layer mean values, we selected in both the mid and upper troposphere the layers centered around the backscatter coefficient peak value in each altitude range. This methodology guarantees a higher representativeness of the smoke particle properties, but in certain cases the selected layer may be spatially thin which may bias the interpretation of the top plot of Fig. 9. Hence the layer height and its thickness represented in this plot has to be interpreted as the layer of maximum intensity, i.e. of maximum aerosol load. Before entering in the discussion, it is worth noting the important difference between the AOD at 532 nm in Barcelona (0.65) and the rest of the stations of the IP (0.27–0.34). This difference is indeed not that surprising if we look back at MODIS AOD on 8 September (Fig. 4) which clearly shows a decreasing AOD tendency along the axis NE-SW. In the mid troposphere, with the exception of Granada, all measurements including CALIOP give a particle depolarization ratio of 0.05–0.06. This result reflects again that in the mid troposphere the smoke particle depolarization ratio was neither time- nor plume-dependent. The particle depolarization in Granada at ~7 km is 0.01 and clearly indicates non-depolarizing particles, slightly different from what is observed over the other stations of the IP in the mid troposphere. The layers of maximum intensity are rather high (between 6 and 8.3 km) and are higher in Évora, Granada and El Arenosillo/Huelva than in Barcelona. The center of the youngest plumes (CALIOP) are slightly below the layers of maximum intensity detected over the IP. In the upper troposphere δ_p varies between 0.09 and 0.10 over the IP, while in the low stratosphere δ_p = 0.12 is found for Plume 1 (CALIOP, D-4). Given the large standard deviations associated to the retrieval of δ_p in the UTLS, these findings are here again not sufficient to point out a clear difference between the plume over the IP on D-0 and CALIOP on D-4. In case this difference is real, at this stage our findings only allow to give hypothetical explanations to be taken with care, listed in order of likelihood: 1) the stations over the IP are representative of Plume 1 + Plume 2 while CALIOP D-4 is representative of Plume 1; 2) on D-0 the plume is in the upper troposphere while on D-4 it is in the stratosphere; and 3) a transformation of the smoke depolarizing capabilities between D-4 and D-0.

The bottom plot of Fig. 9 represents pairs of (δ_p, *CR*) mean layer values in Évora and Granada (D-0) and in Plume 1 (D-4) and Plume 2 (D-5). The color-coded shaded areas, representative of different aerosol classes, are adapted from Groß et al. (2013). The results can be summarized as follows:

- UTLS-level smoke particles have large color ratios (~2.5–3) and moderate particle depolarization ratios (~0.10). Between D-4 and D-0 a small decrease of both parameters, within the statistical variability of one another, is noted.
- In the mid troposphere, δ_p = 0.05 is stable with time, except in Granada. CALIOP *CR* values are smaller than in Évora (and also Madrid (not shown) as *CR* ≃ 2.95 in the smoke layer centered around 6 km on 7 September at 21UT; in Madrid no smoke layer was observed in the UTLS), indicating that as the smoke gets closer to its arrival in the IP, the particles get smaller. The difference between CALIOP *CR* values cannot be evaluated since they correspond to two different smoke plumes which may initially have different morphology and thus different optical properties. The results obtained in Granada (δ_p = 0.01, *CR* = 4.30) are an indication of ultrafine, non-depolarizing particles and reveals a clear difference in the smoke properties with the rest of observations in the mid troposphere. The back-trajectories in all three southern stations (EV, AR and GR) are very similar and do not allow to give an explanation related with long-range transport. In turn, locally, Granada may have been exposed to nearby persistent fires in Sierra Morena, approximately 150 km northwest of the city. Fresh smoke produces low δ_p and large *CR*, but this is only an hypothesis at this stage.
- The pairs of (δ_p, *CR*) fall in the Canadian biomass burning type, but often on the edges. In the mid troposphere, except in Granada, the pairs of (δ_p, *CR*) actually overlap between the classes of Canadian and African biomass burning and marine aerosols. It is worth

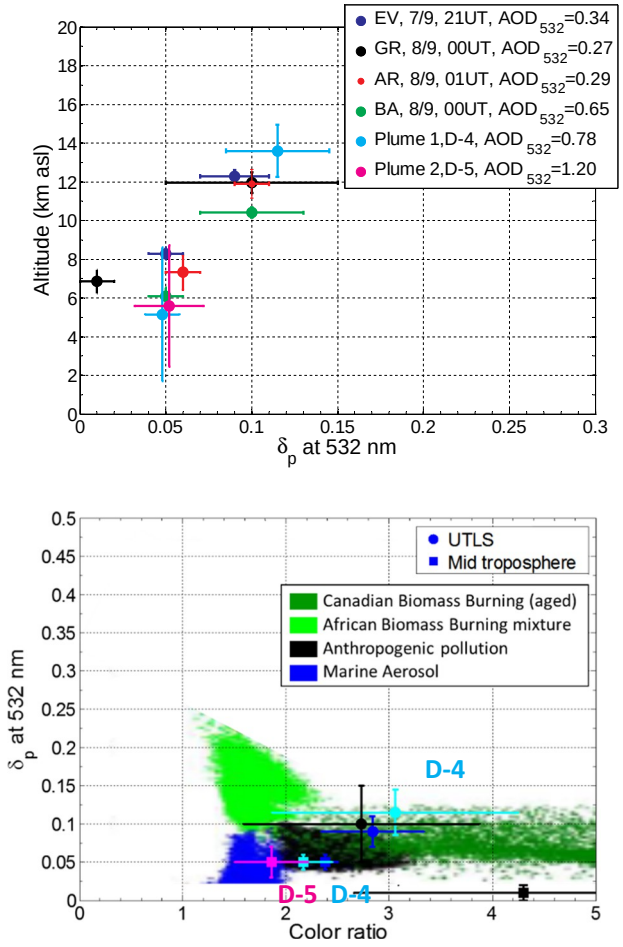

Fig. 9. (top) Mid and upper tropospheric layer mean particle depolarization ratios at 532 nm at all Iberian lidar stations on the night of 7 to 8 September. Cyan and Purple bullets represent CALIOP measurements. The vertical bars indicate the vertical extension of the smoke layers of maximum intensity (base to top height). The horizontal bars indicate the standard deviation associated to δ_p in these layers. (bottom) Layer mean particle depolarization ratios at 532 nm vs. layer mean color ratio. The bullet color code is the same as in the top plot. We have reported four aerosols classes adapted from Groß et al. (2013). The vertical and horizontal bars indicate the standard deviation associated to δ_p and *CR*, respectively.

recalling that the fires studied are not exactly "Canadian biomass burning", which stands for boreal forest fires in the literature, but fires from temperate coniferous forests. This result calls for further investigation on biomass burning properties in relation to their origin which goes beyond the usual Amazonian, African and North American classes.

Note *en passant* that the mid and upper tropospheric values of δ_p and *CR* in Évora on 7 September at 21UT (close in time to the back-trajectory arrival time of 8 September at 00UT, so called D-0) are not significantly different from the values found on 7 September at 04UT, for which the Raman inversion was performed (see Fig. 7 and associated text).

6. UTLS injection and inter-continental transport

In order to investigate the role of each of the plumes identified in Fig. 4, each plume is simulated separately and then together. The emission of Plume 1 is set to 30/8–1/9 (3 days) and the emission of Plume 2 to 2/9–5/9 (4 days). Only fires falling inside the red square defined in Fig. 4 are considered. For each chemical compound (CO, BC and OC), three simulations are run, corresponding to:

- Plume 1 (noted P1 from now on) from 30/8 until 8/9 with emissions limited to the period 30/8–1/9.
- Plume 2 (P2) from 2/9 until 8/9 with emissions limited to the period 2/9–5/9.
- Plume 1 + Plume 2 (P1 + 2) from 30/8 until 8/9 with emissions from 30/8 until 5/9.

From the results of Section 4, the hypothesis is implicitly made that the emitted matter before 30/8 and after 5/9 is not affecting the IP on 7 and 8 September. The fire characteristics are summarized in Table 3.

Before entering in the discussion, we recall the questions raised in Section 5.2 and left opened: 1) injection mechanisms responsible of the injection in the upper troposphere, 2) smoke particles with low-absorbing properties and decrease of the absorption properties with height, 3) high depolarization properties, and 4) differences observed between the smoke plume observed in the IP (D-0) and the younger plume (D-4) observed by CALIOP.

During the emission period 30 August – 5 September a total of 1073 fires were detected in the domain considered (red square, Fig. 5), which in terms of fires per day, defined as the sum of all fires multiplied by the number of days they were active, represents nearly 4000 emitting fires. From these numbers one can deduce that, on average, each fire had an emission duration of approximately 4 days. The mean FRP is 117.5 MW and it is approximately 50% higher during P2 than during P1. Maxima are also higher during P2 (7162.2 MW) than during P1 (5405.7 MW). Two hundred and seventy seven fires had a FRP larger than 50 MW. For comparison, Ansmann et al. (2018) reports a number of 10,000 fires with FRP larger than 50 MW in Canada for the month of August 2017.

Before presenting the results of the dispersion analysis, we will make a point about the geographic location of the fires of this study. A notable difference between the fires of August (Khaykin et al., 2018; Ansmann et al., 2018; Haarig et al., 2018; Hu et al., 2019) vs. September 2017 (this study) is the latitude at which they occurred. In August the most intense fires were located in Canada, 49 < latitudes < 67°N (see Ansmann et al., 2018), while the emission region considered in our study goes from British Columbia down to northern California, 40 < latitudes < 53°N. In this lower part of the mid-latitude region, air masses can be under the influence of either the polar or the subtropical jet streams, and therefore be entrained either north- or south-ward, respectively. The latitude difference, 49–67°N vs. 40–53°N, also results in a higher tropopause height in September than during the August event, and also a thicker troposphere-stratosphere transition layer due to the vicinity of the subtropical jet in September (Pan et al., 2004). It has also another important implication: the material burnt, and consequently the content of emitted CO, BC and OC, are different. While the fires in August were from boreal forests, in September the fires occurred in a region of temperate coniferous forests. According to Lavoué et al. (2000) the main difference between boreal and temperate forests does not rely on the canopy itself, but in the shrubland and the grassland which are more abundant in temperate forests. McMeeking et al. (2009) who made controlled laboratory burns of Alaskan spruce and forest floor (duff), among other fuels, found that the forest floor has a strong contribution from smoldering combustion, but a lower carbon monoxide emission factor than most of the other fuels because it contains less carbon per mass unit. This result supports low BC and OC contents at the source and thus low absorption properties as discussed in Section 5.1.

Results are shown in Fig. 10 and Supplements (S) 1–12. Fig. 10 shows the dispersion maps of CO, BC and OC over the IP at time of arrival on 8 September at 00UT in terms of column density, i.e. the concentration integrated along the vertical axis. S1-S4, S5-S8 and S9-S12 are 6-h time resolution animated gif images of the dispersion of, respectively, CO, BC and OC for the total column density, and the concentration at 3, 6 and 11 km. The heights of 6 and 11 km are representative of the mid- and upper troposphere, where smoke particles were detected in the IP. The images of the total column density (S1, S5 and S9) are the same as in Fig. 10, i.e. a dispersion map on top and a

Table 3
Characteristics of the fires at the origin of the emission of Plume 1 (emission: 30/8–1/9), Plume 2 (emission: 2/9–5/9) and for the whole period (emission: 30/8–5/9). The data are from GFAS daily estimates of biomass burning emissions.

		P1	P2	P1 + 2
Simulation period		30/8–8/9 (10 days)	2/9–8/9 (7 days)	30/8–8/9 (10 days)
Emission period		30/8–1/9 (3 days)	2/9–5/9 (4 days)	30/8–5/9 (7 days)
Number of active fires		836	772	1073
Number of active fires × day		1843	2123	3966
FRP per fire (MW)	Min	0.1	0.1	0.1
	Mean	95.1	137.0	117.5
	Max	5405.7	7162.2	7162.2
Number of fires with FRP > 50 MW		232	190	277

		P1			P2			P1 + 2		
		CO	BC	OC	CO	BC	OC	CO	BC	OC
Emission rate per fire ($T\,h^{-1}$)	Min	0	0	0	0	0	0	0	0	0
	Mean	26.63	0.15	2.23	32.39	0.17	2.79	29.71	0.16	2.53
	Max	2031.15	10.80	175.79	2561.98	13.63	221.73	2561.98	13.63	221.73

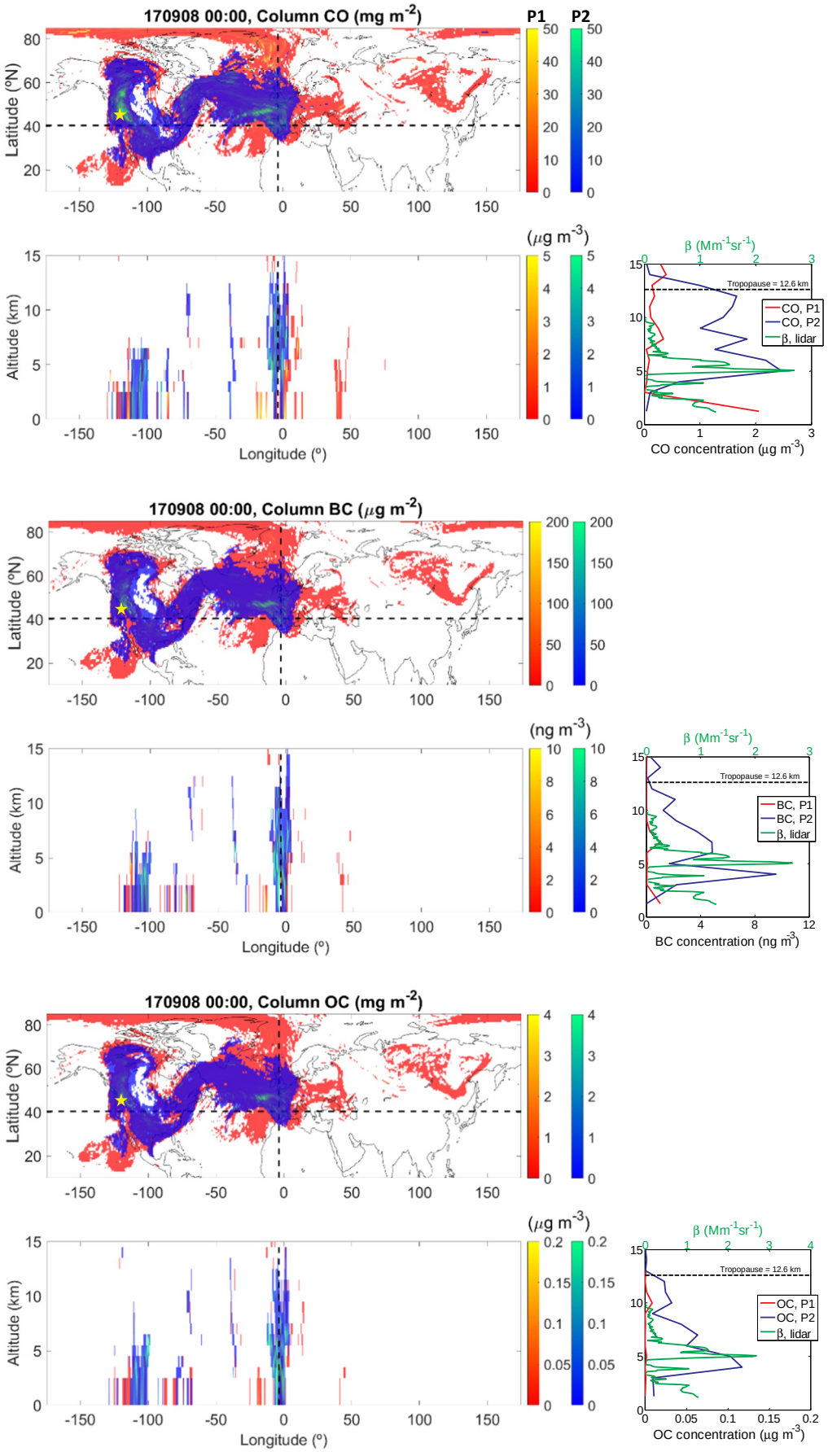

(caption on next page)

Fig. 10. (top) Dispersion map of CO column density and longitudinal cross-section of CO concentration at the latitude of Madrid on 8 September at 00UT; (center) the same for BC; (bottom) the same of OC. Note the different scales. The emission and dispersion of P1 (red-yellow color bar) and P2 (blue-green color bar) are separated. To the right of the longitudinal cross-sections we report the vertical profile of each chemical compound at the coordinates of Madrid for P1 and P2, as well as the backscatter coefficient at 532 nm retrieved in Madrid on 7 September at 21UT. The yellow star indicates the fire source region.

longitudinal cross-section below at the latitude of Madrid, taken as a central point in the IP. On all dispersion maps, the color bar for P1 goes from red (low) to yellow (high) and for P2 from blue (low) to green (high). On a horizontal scale all three compounds have similar dispersion patterns. For this reason, the interpretation of the dispersion maps is made independently of the compound. Partly because the simulation time of P1 is longer relative to P2, its dilution in the northern hemisphere is wider and circulations around the globe start to be visible, although in low concentration level, in the final dispersion maps of all compounds. On 8 September CO/BC/OC from P1 are present around the pole and also in eastern Russia. Interpretations of S1, S5 and S9 confirm that:

- P1 is transported northeast-ward the first four days of the simulation. On 3 September a large swath of the US is covered by P1. This feature is confirmed by OMPS images (Seftor, 2017c). Later, as a large smoke tongue travels slowly over the Atlantic towards the IP (this transport coincides with the interpretation of the satellite images in Fig. 4, see Section 4), large scale jets make the plume start meandering anti-clockwise around a point centered initially above Iceland which drifts slowly with time towards Ireland.
- P1 reaches the IP (Madrid) on 6 September at 12UT with column density levels of CO of 0.02 mg m^{-2}. For comparison on 8 September at 00UT the CO column density of P1 is on the order of 0.83 mg m^{-2}.
- P2 is travelling eastward since the first day of emission. On 4 September at 18UT one can already observe the beginning of the stretching of P2 located on the cyclonic-shear side of a strong jet, probably of subtropical origin since it ends up in northern Africa. Later a relatively thin smoke tongue travels rapidly along the large scale jet towards the IP. Residual smoke from P1 is also marginally carried with this flow.
- P2 reaches the IP (Madrid) on 7 September at 12UT with column density levels of CO below 1.20 mg m^{-2}. For comparison on 8 September at 00UT the CO column density of P2 is on the order of 18.60 mg m^{-2}. This result indicates that at the peak of the event the CO level observed over the IP and emitted by P2 is roughly 20 times larger than the one emitted by P1. For comparison, Yurganov et al. (2011) reports values of total column CO in Moscow, Russia, in the vicinity of strong wildfires ~50 times larger than the our values of ~20 mg m^{-2}.

As far as the vertical transport is concerned, we first analyze S3, S7 and S11 to identify where and when the injection at 6 km (mid troposphere) occurs, and then S4, S8 and S12 for the injection at 11 km (upper troposphere). CO/P1 (S3) appears for the first time at 6 km 18 h after the first emission of the fires and close to the source region. CO/P2 appears for the first time at 6 km much later, ~30 h after the emission, but also much farther, ~2000–3000 km from the source. In the upper troposphere, CO/P1 (S4) appears for the first time at 11 km 36 h after the first emission of the fires and at ~2000 km from the source region, while CO/P2 appears for the first time at 11 km 60 h after the emission and about 4000 km east of the source region. The time difference between injections from 6 to 11 km is 18 h for P1 and 30 h for P2, indicating a much faster ascending rate for P1 than for P2, despite higher FRPs during P2 relative to P1 (Table 3). It seems there is a tradeoff between vertical and horizontal transport: slow horizontal transport is favorable to vertical motion whereas strong horizontal transport reduces it. In the case of P2, it is highly probable that the strong jets leading to its fast transport towards the IP contributed at the same time to limit its vertical transport. In addition, we believe that the injection at higher altitudes of P1 is favored by its transport above the region of Lake Winnipeg (a large lake visible on the Supplements to the southwest of Hudson Bay) where wildfires are active, especially in the northern part of the lake. The hot region of the active fires is prone to increase the convection of upper air masses travelling above it. The analysis of S7 and S11 (BC and OC at 6 km) and S8 and S12 (same compounds at 11 km) indicates that the ascending rate of BC and OC is slower than for CO. BC and OC reach the altitude of 6 km approximately 6 h after CO does, and they reach the altitude of 11 km approximately 12 h later than CO. No significant difference is observed between the two types of particles in terms of ascending rate.

As far as the maximum injection height is concerned, interestingly none of the altitude levels is empty, indicating that the dispersion model injects smoke at all altitude levels considered, i.e. up to 16 km. However, above 10 km the number of pixels with non-zero concentration significantly decreases. We investigate the maximum injection height calculated by the model by defining a threshold of significant aerosol load at a given height when the probability of occurrence is > 2%, i.e. when > 2% of the pixels at a given height are filled with non-zero values. With such a criterion, we find that CO/P1 (CO/P2) generally stays below 13 (9) km, BC/P1 (BC/P2) below 12 (9) km and OC/P1 (OC/P2) below 12 (11) km. These approximations of the maximum injection heights are in good agreement with the profiles of both the ground-based lidar stations and CALIOP. One sees clearly that the injection at high levels is much less efficient for P2 than for P1. One singular feature is the small difference (1 km) between the maximum injection heights of OC/P1 and OC/P2. It may be related to the emission rate increase between P1 and P2 which is the strongest for OC compared to CO or BC.

To the right of the longitudinal cross-sections of Fig. 10 we plot the vertical distribution of both P1 and P2 above Madrid on 8 September at 00UT and superimpose the particle backscatter coefficient measured in Madrid on 7 September at 21 UT. In order not to rely on a single profile of the simulations, P1 and P2 profiles are averaged over a square of 9 pixels centered around the coordinates of Madrid. At time of arrival over the IP, HYSPLIT results for all compounds contribute to assign Plume 2 as the main source of smoke particles, representing > 90% of the column density. At arrival over the IP CO is present up to 13 km, BC up to 11 km and OC up to 12 km (Fig. 10, right plots). The concentration of all three compounds is low in the first height interval between 0 and 2.5 km, except for CO/P1. For CO and BC the concentration levels of P1 are higher than for P2 which supports a former suggestion (see Section 4) that the airmasses arriving above the IP at 3 km on 8 September picked up smoke most likely from Plume 1, while those arriving at 6 and 11 km most likely from Plume 2. The peak of CO near 5-km height is very well reproduced by the model: it matches exactly the peak of the backscatter coefficient. For BC and OC the concentration peak (at 4 km) is 1 km lower than the peak of the backscatter coefficient (at 5 km). For both types of particles the gradual decrease of the concentration with increasing height above the peak reflects well the behavior of the backscatter coefficient. Given the poor model vertical resolution and the long distance of the horizontal transport (~10,000 km), the particle transport is indeed very well simulated at its arrival in the IP. HYSPLIT simulates the presence of a layer of BC at ~11 km in the upper troposphere and a layer of OC at 10–12 km just below the tropopause, whereas the observation indicates that the smoke plume is not present above 10 km. Interestingly enough if the fact that a tiny layer of BC is simulated by HYSPLIT above the tropopause at 14 km. With respect to the literature, the concentrations simulated by

HYSPLIT correspond to relatively small amount of what is usually measured at ground level. In a city like Barcelona, where BC is abundantly produced, the background BC concentration is usually higher than 1000 ng m^{-3} (Pérez et al., 2010), i.e. much higher than the values simulated after long-range transport which peak at 10 ng m^{-3}.

Finally, we now come back to some of the hypotheses made in Section 5.2 and look for supporting arguments with the results of the dispersion modelling. With respect to the material burnt possibly containing low carbon content or the dominance of smoldering combustion, the dispersion modelling is of no help. The lower lidar ratio at 532 nm in the upper troposphere compared to the mid troposphere reflects less absorbing particles and possibly a lesser amount of BC with respect to OC. This tendency is actually confirmed by the vertical distributions of BC and OC at their arrival over the IP: BC and OC peak at 4 km and then gradually decrease up to 12 km, and the relative decrease of BC is stronger than for OC. About the increase of the depolarization ratio with height, the dispersion modelling is of little help, the result the most useful being that in the upper troposphere only P2 is present. Overall the observations and the dispersion modelling point out to the following: near the source the smoke particles slightly depolarize (δ_p = 0.05 at ~6 km height, CALIOP, D-5) and at the arrival over the IP after a 5-day transport the particles have gained altitude and δ_p has increased (δ_p = 0.10 at ~12 km, Évora, D-0). The particles arriving over the IP at ~6 km have unchanged.

depolarization properties (δ_p = 0.05) with respect to CALIOP, D-5. These findings enlighten the enhancement of the smoke depolarization properties with vertical transport. As smoke particles are relatively effective cloud condensation nuclei (Reid and Hobbs, 1998; Warner and Twomey, 1967), we finally hypothesize that smoke particles at non-dry altitude levels such as the upper troposphere (relative humidity ~ 20–30%, see Section 5.2) may suffer freezing which may accentuate their asymmetric form and thus their depolarization properties.

7. Conclusions

This paper documents the time-space evolution of a smoke plume detected at its arrival over the Iberian Peninsula on 7 and 8 September 2017. The smoke was emitted by strong and powerful wildfires in the Pacific northwestern region of North America, a region mostly composed of temperate coniferous forests. The column properties retrieved at two mid-altitude, background AERONET sites in northern and southern Spain reveal AOD_{440} as high as 0.62, exceeding the background AOD by a factor larger than 6, $AE_{440-870}$ of 1.6–1.7, a large dominance of small particles ($FMF > 0.88$), low $AAOD_{440}$ (< 0.008) and large SSA_{440} (> 0.98). The low absorption properties are attributed either (i) to the burning of low carbon content fuels such as forest floors, particularly abundant in temperate forests, (ii) the dominance of smoldering vs. flaming combustion, and/or (iii) a transformation (coating processes) of the smoke particles during transport. AAE ~1.3, together with large SSA_{440}, in northern Spain is representative of brown carbon, while AAE ~1.0, also associated with large SSA_{440}, in southern Spain is representative of brown carbon probably mixed with pure BC from the anthropogenic fossil fuel emissions of the nearby city of Granada, or from local fires approximately 150 km northwest of the site.

Satellite images of total column CO allows to identify two strong periods of emission that gave birth to two different plumes reaching the IP almost simultaneously: Plume 1 is emitted from 30 August until 1 September and Plume 2 from 2 to 5 September. The vertical distribution of the smoke plumes was monitored by ground-based lidars from both EARLINET and MPLNET networks, and from space by CALIOP. Over the IP a continuum of aerosols is observed up to the upper troposphere: aerosols are present in the whole troposphere. No particles are observed in the low stratosphere. Results are given for the mid (5–9 km) and upper (10–13 km) troposphere. The analysis of the ground-based lidars indicates a color ratio of 2.5 (3.0), LR_{532} of 55 (34) sr, and δ_p of 0.05 (0.10) in the mid (upper) troposphere, which points out to smaller, less absorbing and more depolarizing particles in the upper troposphere than in the mid troposphere. Rewinding in time with CALIOP, one observes that the older the smoke plume, the larger the color ratio, i.e. that the particle size gets smaller during transport. As far as the particle depolarization ratio is concerned, no changes related to the transport are observed in the mid troposphere. The unusual values of δ_p in the upper troposphere (0.10) are further analyzed with dispersion modelling.

To analyze the horizontal and vertical transport of the smoke from its origin to the IP, particle dispersion modelling is performed with HYSPLIT parameterized with satellite-derived biomass burning emission estimates from GFAS/CAMS. We simulated CO, BC and OC, for separately P1 and P2, with a time resolution of 6 h, at 15 altitude levels and using meteorology data from GDAS with a horizontal resolution of 0.5 × 0.5°. The smoke release height was not artificially fixed, but calculated internally by the model and assumed to be equal to the final buoyant plume rise height as computed using Briggs (1969), implying that the final rise is a function of the input fire radiative power and the meteorology. The results show that the dispersion of both plumes is quite different: P1 travels slowly and disperses over a large area of the northern hemisphere, while P2 is entrained by a strong subtropical jet and travels quickly towards the IP. The ascending rate of CO is nearly twice larger for P1 than for P2: CO/P1 reaches the height of 11 km in 36 h, while CO/P2 needs 60 h. There is undeniably a tradeoff between vertical and horizontal transport: slow horizontal transport is favorable to vertical motion whereas strong horizontal transport reduces it. At time of arrival over the IP, both BC and OC profiles over the IP are similar in shape to the lidar-derived backscatter coefficient profile: they both peak at 4 km and then gradually decrease up to 12 km, and the relative decrease of BC is stronger than for OC, which corroborates one of the former hypothesis, namely that particles in the upper troposphere are less absorbing than in the mid troposphere because of a smaller ratio of BC to OC. HYSPLIT results for all compounds contribute to assign P2 as the main source of smoke particles over the IP, representing > 90% of the column density. These findings, all together, show that δ_p increase from 0.05 to 0.10 occurs during the vertical transport from the mid to the upper troposphere, and stress the influence of the vertical transport on the smoke depolarization properties. As smoke particles are relatively effective cloud condensation nuclei, we finally hypothesize that smoke particles at non-dry altitude levels such as the upper troposphere may suffer freezing which may accentuate their asymmetric form and thus their depolarization properties.

Acknowledgments

This work was supported by the European Union through H2020 programme (ACTRIS-2, grant 654109, EUNADICS-AV, grant 723986; GRASP-ACE, grant 778349), and the European Fund for Regional Development (ref. POCI-01-0145-FEDER-007690, ALT20-03-0145-FEDER-000004, ALT20-03-0145-FEDER-000011 and 0753_CILIFO_5_E). Spanish groups acknowledge the Spanish Ministry of Economy and Competitivity (MINECO) (ref. CGL2013-45410-R, CGL2014-52877-R, CGL2014-55230-R, TEC2015-63832-P, CGL2015-73250-JIN, CGL2016-81092-R and CGL2017-85344-R), the Spanish Ministry of Sciences, Innovation and Universities (ref. CGL2017-90884-REDT), and the Unidad de Excelencia María de Maeztu (grant MDM-2016-0600) funded by the Spanish Agencia Estatal de Investigación, Spain. This work was also supported by the Juan de la Cierva-Formación program (grant FJCI-2015-23904), the MINECO Programa de Ayudas a la Promoción del Empleo Joven e Implantación de la Garantía Juvenil en i+D+i (grant PEJ-2014-A-52129), the Spanish Ministry of Education, Culture and Sport (MECD) (grant FPU14/03684), and the Portuguese Portuguese Foundation for Science and Technology and national funding and national funding (ref. SFRH/BSAB/143164/2019). Co-funding was also provided by the Andalusia

Regional Government (grant P12-RNM-2409), by the University of Granada through "Plan Propio. Programa 9 Convocatoria 2013", and by the Madrid Regional Government (projects TIGAS-CM, ref. Y2018/EMT-5177 and AIRTEC-CM, ref. P2018/EMT4329). The MPLNET project is funded by the NASA Radiation Sciences Program and Earth Observing System. The authors gratefully acknowledge the NOAA Air Resources Laboratory (ARL) for the provision of the HYSPLIT transport and dispersion model and/or READY website (http://www.ready.noaa.gov), and the CALIPSO mission scientists and associated NASA personnel for the production of the data used in this research.

Appendix A. Supplementary data

Supplementary data to this article can be found online at https://doi.org/10.1016/j.rse.2019.111294.

References

Adachi, K., Chung, S.H., Buseck, P.R., 2010. Shapes of soot aerosol particles and implications for their effects on climate. J. Geophys. Res. 115, D15206. https://doi.org/10.1029/2009JD012868.

AERONET (AErosol RObotic NETwork), 2018. https://aeronet.gsfc.nasa.gov/, Accessed date: 8 May 2018.

Andela, N., Kaiser, J.W., Heil, A., van Leeuwen, T.T., van der Werf, G.R., Wooster, M.J., Remy, S., Schultz, M.G., 2013. Assessment of the Global Fire Assimilation System (GFASv1). Technical Memorandum for the ECMWF. .

Andreae, M.O., Gelencser, A., 2006. Black carbon or Brown carbon? The nature of light absorbing carbonaceous aerosols. Atmos. Chem. Phys. 6, 3131–3148. https://doi.org/10.5194/acp-6-3131-2006.

Ansmann, A., Wagner, F., Müller, D., Althausen, D., Herber, A., von Hyoningen-Huene, W., Wandinger, U., 2002. European pollution outbreaks during ACE 2: optical particle properties inferred from multiwavelength lidar and star-Sun photometry. J. Geophys. Res. 107, 4259. https://doi.org/10.1029/2001JD001109.

Ansmann, A., Baars, H., Chudnovsky, A., Haarig, M., Veselovskii, I., Mattis, I., Seifert, P., Engelmann, R., Wandinger, U., 2018. Canadian wildfire smoke over Europe. Atmos. Chem. Phys. 18, 11831–11845. https://doi.org/10.5194/acp-18-11831-2018.

Baars, H., Kanitz, T., Engelmann, R., Althausen, D., Heese, B., Komppula, M., Preißler, J., Tesche, M., Ansmann, A., Wandinger, U., Lim, J.-H., Ahn, J.Y., Stachlewska, I.S., Amiridis, V., Marinou, E., Seifert, P., Hofer, J., Skupin, A., Schneider, F., Bohlmann, S., Foth, A., Bley, S., Pfüller, A., Giannakaki, E., Lihavainen, H., Viisanen, Y., Hooda, R.K., Pereira, S.N., Bortoli, D., Wagner, F., Mattis, I., Janicka, L., Markowicz, K.M., Achtert, P., Artaxo, P., Pauliquevis, T., Souza, R.A.F., Sharma, V.P., van Zyl, P.G., Beukes, J.P., Sun, J., Rohwer, E.G., Deng, R., Mamouri, R.-E., Zamorano, F., 2016. An overview of the first decade of PollyNET: an emerging network of automated Raman-polarization lidars for continuous aerosol profiling. Atmos. Chem. Phys. 16, 5111–5137. https://doi.org/10.5194/acp-16-5111-2016.

Baars, H., Seifert, P., Engelmann, R., Wandinger, U., 2017. Target categorization of aerosol and clouds by continuous multiwavelength-polarization lidar measurements. Atmos. Meas. Tech. 10, 3175–3201. https://doi.org/10.5194/amt-10-3175-2017.

Baars, H., Ansmann, A., Ohneiser, K., Haarig, M., Engelmann, R., Althausen, D., Hanssen, I., Gausa, M., Pietruczuk, A., Szkop A., Stachlewska, I., Wang D.,, Reichardt, J., Skupin, A., Mattis, I., Trickl, T., Vogelmann H., Navas-Guzmán, F., Haefele, A., Acheson, K., Ruth A. A., Tatarov, B., Müller, D., Hu, Q., Podvin T., Goloub, O., Vesselovski, I., Pietras, C., Haeffelin, M., Fréville, P., Sicard, M., Comerón, A., Fernández García, A.J., Molero Menéndez F., Córdoba Jabonero, C., Guerrero-Rascado, J.L., Alados Arboledas, L., Bortoli, D., Costa M.J., Dionisi, D., Liberti, G., Wang X., Sannino A.,, Papagiannopoulos, N., Boselli A., Mona, L., D'Amico, G., Romano, S., Perrone, M.R., Belegante, L., Nicolae, D., Grigorov, I., Gialitaki, A., Amiridis, V., Soupiona, O., Papayannis, A., Mamouri, R.-E., Nisantzi, A., Heese, B., Hofer, J., Schechner Y.Y., Wandinger, U., Pappalardo, G., 2019. The unprecedented 2017–2018 stratospheric smoke event: decay phase and aerosol properties observed with EARLINET. Atmos. Chem. Phys. Discuss submitted on 28 June, 2019.

Bergstrom, R.W., Pilewskie, P., Russell, P.B., Redemann, J., Bond, T.C., Quinn, P.K., Sierau, B., 2007. Spectral absorption properties of atmospheric aerosols. Atmos. Chem. Phys. 7, 5937–5943. https://doi.org/10.5194/acp-7-5937-2007.

Boers, R., de Laat, A.T., Stein Zweers, D.C., Dirksen, R.J., 2010. Lifting potential of solar-heated aerosol layers. Geophys. Res. Lett. 37, L24802. https://doi.org/10.1029/2010GL045171.

Briggs, G.A., 1969. Plume Rise. TID-25075, USAEC Critical Review Series. National Technical Information Service, Springfield, VA (81 pp).

Burton, S.P., Ferrare, R.A., Hostetler, C.A., Hair, J.W., Rogers, R.R., Obland, M.D., Butler, C.F., Cook, A.L., Harper, D.B., Froyd, K.D., 2012. Aerosol classification using airborne High Spectral Resolution Lidar measurements – methodology and examples. Atmos. Meas. Tech. 5, 73–98. https://doi.org/10.5194/amt-5-73-2012.

Burton, S.P., Hair, J.W., Kahnert, M., Ferrare, R.A., Hostetler, C.A., Cook, A.L., Harper, D.B., Berkoff, T.A., Seaman, S.T., Collins, J.E., Fenn, M.A., Rogers, R.R., 2015. Observations of the spectral dependence of linear particle depolarization ratio of aerosols using NASA Langley airborne High Spectral Resolution Lidar. Atmos. Chem. Phys. 15, 13453–13473. https://doi.org/10.5194/acp-15-13453-2015.

Cammas, J.-P., Brioude, J., Chaboureau, J.-P., Duron, J., Mari, C., Mascart, P., Nédélec, P., Smit, H., Pätz, H.-W., Volz-Thomas, A., Stohl, A., Fromm, M., 2009. Injection in the lower stratosphere of biomass fire emissions followed by long-range transport: a MOZAIC case study. Atmos. Chem. Phys. 9, 5829–5846. https://doi.org/10.5194/acp-9-5829-2009.

CAMS, 2018. Copernicus Atmosphere Monitoring Service Information. http://apps.ecmwf.int/datasets/data/cams-gfas/, Accessed date: 18 May 2018.

Chahine, M.T., Thomas, S.P., Hartmut, H.A., Robert, A., Christopher, B., John, B., Luke, C., Murty, D., Eric, J.F., Mitch, G., Catherine, G., Stephanie, G., Scott, H., Fredrick, W.I., Ramesh, K., Eugenia, K., Bjorn, H.L., Sung-Yung, L., John, L.M., Mcmillan, W.W., Larry, M., Edward, O.T., Henry, R., Philip, R., William, S.L., David, S., Strow, L.L., Joel, S., David, T., Walter, W., Lihang, Z., 2006. AIRS: improving weather forecasting and providing new data on greenhouse gases. Bull. Am. Meteorol. Soc. 87, 911–926. https://doi.org/10.1175/BAMS-87-7-911.

Challa, V.S., Indrcanti, J., Baham, J.M., Patrick, C., Rabarison, M.K., Young, J.H., Hughes, R., Swanier, S.J., Hardy, M.G., Yerramilli, A., 2008. Sensitivity of atmospheric dispersion simulations by HYSPLIT to the meteorological predictions from a meso-scale model. Environ. Fluid Mech. 8, 367–387. https://doi.org/10.1007/s10652-008-9098-z.

Cheng, T., Wu, Y., Chen, H., 2014. Effects of morphology on the radiative properties of internally mixed light absorbing carbon aerosols with different aging status. Opt. Express 22 (13), 15,904–15,917.

Chin, M., Ginoux, P., Kinne, S., Torres, O., Holben, B.N., Duncan, B.N., Martin, R.V., Logan, J.A., Higurashi, A., Nakajima, T., 2002. Tropospheric aerosol optical thickness from the GOCART model and comparisons with satellite and sun photometer measurements. J. Atmos. Sci. 59, 461–483. https://doi.org/10.1175/1520-0469(2002)059<0461:TAOTFT>2.0.CO;2.

China, S., Scarnato, B., Owen, R.C., Zhang, B., Ampadu, M.T., Kumar, S., Dzepina, K., Dziobak, M.P., Fialho, P., Perlinger, J.A., Hueber, J., Helmig, D., Mazzoleni, L.R., Mazzoleni, C., 2015. Morphology and mixing state of aged soot particles at a remote marine free troposphere site: implications for optical properties. Geophys. Res. Lett. 42, 1243–1250. https://doi.org/10.1002/2014GL062404.

Comerón, A., Muñoz-Porcar, C., Rocadenbosch, F., Rodríguez-Gómez, A., Sicard, M., 2017. Current research in Lidar technology used for the remote sensing of atmospheric aerosols. Sensors 17, 1450. https://doi.org/10.3390/s17061450.

Córdoba-Jabonero, C., Sicard, M., Ansmann, A., del Águila, A., Baars, H., 2018. Separation of the optical and mass features of particle components in different aerosol mixtures by using POLIPHON retrievals in synergy with continuous polarized Micro-Pulse Lidar (P-MPL) measurements. Atmos. Meas. Tech. 11, 4775–4795. https://doi.org/10.5194/amt-11-4775-2018.

Crutzen, P.J., Andreae, M.O., 1990. Biomass burning in the tropics: impact on atmospheric chemistry and biogeochemical cycles. Science 250, 1669–1678.

Cunningham, P., Reeder, M.J., 2009. Severe convective storms initiated by intense wildfires: numerical simulations of pyro-convection and pyro-tornadogenesis. Geophys. Res. Lett. 36, L12812. https://doi.org/10.1029/2009GL039262.

Damoah, R., Spichtinger, N., James, P., Servranckx, R., Fromm, M., Eloranta, E.W., Razenkov, I.A., James, P., Shulski, M., Forster, C., Stohl, A., 2006. A case study of pyro-convection using transport model and remote sensing data. Atmos. Chem. Phys. 6, 173–185. http://www.atmos-chem-phys.net/6/173/2006/.

de Laat, A.T.J., Stein Zweers, D.C., Boers, R., Tuinder, O.N.E., 2012. A solar escalator: observational evidence of the self-lifting of smoke and aerosols by absorption of solar radiation in the February 2009 Australian Black Saturday plume. J. Geophys. Res. 117, D04204. https://doi.org/10.1029/2011JD017016.

Dubovik, O., Holben, B.N., Eck, T.F., Smirnov, A., Kaufman, Y.J., King, M.D., Tanré, D., Slutsker, I., 2002. Variability of absorption and optical properties of key aerosol types observed in worldwide locations. J. Atmos. Sci. 59, 590–608.

Eck, T.F., Holben, B.N., Reid, J.S., Dubovik, O., Kinne, S., Smirnov, A., O'Neill, N.T., Slutsker, I., 1999. Wavelength dependence of the optical depth of biomass burning, urban and desert dust aerosols. J. Geophys. Res. 104, 31333–31349. https://doi.org/10.1029/1999JD900923.

Forrister, H., Liu, J., Scheuer, E., Dibb, J., Ziemba, L., Thornhill, K.L., Anderson, B., Diskin, G., Perring, A.E., Schwarz, J.P., Campuzano-Jost, P., Day, D.A., Palm, B.B., Jimenez, J.L., Nenes, A., Weber, R.J., 2015. Evolution of brown carbon in wildfire plumes. Geophys. Res. Lett. 42, 4623–4630. https://doi.org/10.1002/2015GL063897.

Forster, C., Wandinger, U., Wotawa, G., James, P., Mattis, I., Althausen, D., Simmonds, P., ODoherty, S., Jennings, S.G., Kleefeld, C., Schneider, J., Trickl, T., Kreipl, S., Jäger, H., Stohl, A., 2001. Transport of boreal forest fire emissions from Canada to Europe. J. Geophys. Res. 106 (D19), 22887–22906.

Freeborn, P.H., Wooster, M.J., Roy, D.P., Cochrane, M.A., 2014. Quantification of MODIS fire radiative power (FRP) measurement uncertainty for use in satellite-based active fire characterization and biomass burning estimation. Geophys. Res. Lett. 41, 1988–1994. https://doi.org/10.1002/2013GL059086.

Freudenthaler, V., Esselborn, M., Wiegner, M., Heese, B., Tesche, M., Ansmann, A., Muller, D., Althausen, D., Wirth, M., Fix, A., Ehret, G., Knippertz, P., Toledano, C., Gasteiger, J., Garhammar, M., Seefeldner, M., 2009. Depolarization ratio profiling at several wavelengths in pure Saharan dust during SAMUM 2006. Tellus B 61, 165–179. https://doi.org/10.1111/j.1600-0889.2008.00396.x.

Fromm, M.D., Servranckx, R., 2003. Transport of forest fire smoke above the tropopause by supercell convection. Geophys. Res. Lett. 30, 1542. https://doi.org/10.1029/2002GL016820.

Fromm, M.D., Alfred, J., Hoppel, K., Hornstein, J., Bevilacqua, R., Shettle, E., Servranckx, R., Li, Z., Stocks, B., 2000. Observations of boreal forest fire smoke in the stratosphere by POAM III, SAGE II, and lidar in 1998. Geophys. Res. Lett. 27, 1407–1410.

Fromm, M.D., Bevilacqua, R., Servranckx, R., Rosen, J., Thayer, J., Herman, J., Larko, D., 2005. Pyro-cumulonimbus injection of smoke to the stratosphere: observations and impact of a super blowup in northwestern Canada on 3-4 August 1998. J. Geophys.

Res. 110, D08205. https://doi.org/10.1029/2004JD005350.
Fromm, M., Shettle, E.P., Fricke, K.H., Ritter, C., Trickl, T., Giehl, H., Gerding, M., Barnes, J., O'Neill, M., Massie, S.T., Blum, U., McDermid, I.S., Leblanc, T., Deshler, T., 2008. The stratospheric impact of the Chisholm Pyrocumulonimbus eruption: 2. Vertical profile perspective. J. Geophys. Res. 113, D08203. https://doi.org/10.1029/2007JD009147.
Fromm, M., Lindsey, D.T., Servranckx, R., Yue, G., Trickl, T., Sica, R., Doucet, P., Godin-Beekmann, S.E., 2010. The untold story of pyrocumulonimbus. B. Am. Meteorol. Soc. 91, 1193–1209. https://doi.org/10.1175/2010bams3004.1.
Groß, S., Esselborn, M., Weinzierl, B., Wirth, M., Fix, A., Petzold, A., 2013. Aerosol classification by airborne high spectral resolution lidar observations. Atmos. Chem. Phys. 13, 2487–2505. https://doi.org/10.5194/acp-13-2487-2013.
Haarig, M., Ansmann, A., Baars, H., Jimenez, C., Veselovskii, I., Engelmann, R., Althausen, D., 2018. Depolarization and lidar ratios at 355, 532, and 1064 nm and microphysical properties of aged tropospheric and stratospheric Canadian wildfire smoke. Atmos. Chem. Phys. 18, 11847–11861. https://doi.org/10.5194/acp-18-11847-2018.
Holben, B., Eck, T.F., Slutsker, I., Tanré, D., Buis, J.P., Setzer, A., Vermote, E., Reagan, J.A., Kaufman, Y.J., Nakajima, T., Lavenu, F., Jankowiak, I., Smirnov, A., 1998. AERONET – a federated instrument network and data archive for aerosol characterization. Remote Sens. Env. 66, 1–16.
Hu, Q., Goloub, P., Veselovskii, I., Bravo Aranda, J.-A., Popovici, I., Povdin, T., Haeffelin, M., Lopatin, A., Dubovik, O., Pietras, C., Huang, X., Torres, B., Chen, C., 2019. Long-range-transported Canadian smoke plumes in the lower stratosphere over northern France. Atmos. Chem. Phys. 19, 1173–1193. https://doi.org/10.5194/acp-19-1173-2019.
Illingworth, A.J., Barker, H.W., Beljaars, A., Ceccaldi, M., Chepfer, H., Clerbaux, N., Cole, J., Delanoe, J., Domenech, C., Donovan, D.P., Fukuda, S., Hirakata, M., Hogan, R.J., Hünerbein, H., Kollias, P., Kubota, T., Nakajima, T., Nakajima, T.Y., Nishizawa, T., Ohno, Y., Okamoto, H., Oki, R., Sato, K., Satoh, M., Shephard, M., Velázquez-Blázquez, A., Wandinger, U., Wehr, T., Zadelhoff, G.-J., 2015. THE EARTHCARE SATELLITE: the next step forward in global measurements of clouds, aerosols, precipitation and radiation. B. Am. Meteorol. Soc. 96, 1311–1332. https://doi.org/10.1175/BAMS-D-12-00227.1.
Kaiser, J.W., Heil, A., Andreae, M.O., Benedetti, A., Chubarova, N., Jones, L., Morcrette, J.-J., Razinger, M., Schultz, M.G., Suttie, M., van der Werf, G.R., 2012. Biomass burning emissions estimated with a global fire assimilation system based on observed fire radiative power. Biogeosciences 9, 527–554. https://doi.org/10.5194/bg-9-527-2012.
Kar, J., Vaughan, M., Tackett, J., Liu, Z., Omar, A., Rodier, S., Trepte, C., Lucker, P., 2018. Swelling of transported smoke from savanna fires over the Southeast Atlantic Ocean. Remote Sens. Env. 211, 105–111. https://doi.org/10.1016/j.rse.2018.03.043.
Kaufman, Y., Ichoku, C., Giglio, L., Korontzi, S., Chu, D., Hao, W., Li, R.-R., Justice, C., 2003. Fire and smoke observed from the Earth Observing System MODIS instrument – products, validation, and operational use. Int. J. Remote Sens. 24, 1765–1781.
Khaykin, S.M., Godin-Beekmann, S., Hauchecorne, A., Pelon, J., Ravetta, F., Keckut, P., 2018. Stratospheric smoke with unprecedentedly 20 high backscatter observed by lidars above southern France. Geophys. Res. Lett. 45. https://doi.org/10.1002/2017GL076763.
Kim, M.-H., Omar, A.H., Tackett, J.L., Vaughan, M.A., Winker, D.M., Trepte, C.R., Hu, Y., Liu, Z., Poole, L.R., Pitts, M.C., Kar, J., Magill, B.E., 2018. The CALIPSO version 4 automated aerosol classification and lidar ratio selection algorithm. Atmos. Meas. Tech. 11, 6107–6135. https://doi.org/10.5194/amt-11-6107-2018.
Lack, D.A., Cappa, C.D., 2010. Impact of brown and clear carbon on light absorption enhancement, single scatter albedo and absorption wavelength dependence of black carbon. Atmos. Chem. Phys. 10, 4207–4220. https://doi.org/10.5194/acp-10-4207-2010.
Lau, K.-M., Ramanathan, V., Wu, G.-X., Li, Z., Tsay, S.C., Hsu, C., Sikka, R., Holben, B., Lu, D., Tartari, G., Chin, M., Koudelova, P., Chen, H., Ma, Y., Huang, J., Taniguchi, K., Zhang, R., 2008. The joint aerosol–monsoon experiment: a new challenge for monsoon climate research. Bull. Am. Meteorol. Soc. 89, 369–383. https://doi.org/10.1175/BAMS-89-3-369.
Lavoué, D., Liousse, C., Cachier, H., Stocks, B.J., Goldammer, J.G., 2000. Modeling of carbonaceous particles emitted by boreal and temperate wildfires at northern latitudes. J. Geophys. Res. 105, 26871–26890.
Luderer, G., Trentmann, J., Winterrath, T., Textor, C., Herzog, M., Graf, H.F., Andreae, M.O., 2006. Modeling of biomass smoke injection into the lower stratosphere by a large forest fire (PartII): sensitivity studies. Atmos. Chem. Phys. 6, 5261–5277. http://www.atmos-chem-phys.net/6/5261/2006/.
Markowicz, K., Chilinski, M.T., Lisok, J., Zawadzka, O., Stachlewska, I.S., Janicka, L., Rozwadowska, A., Makuch, P., Pakszys, P., Zielinski, T., Petelski, T., Posyniak, M., Pietruczuk, A., Szkop, A., Westphal, D.L., 2016. Study of aerosol optical properties during long-range transport of biomass burning from Canada to Central Europe in July 2013. J. Aerosol Sci. 101, 156–173.
McMeeking, G.R., Kreidenweis, S.M., Baker, S., Carrico, C.M., Chow, J.C., Collet Jr., J.L., Hao, W.M., Holden, A.S., Kirch-stetter, T.W., Malm, W.C., Moosmuller, H., Sullivan, A.P., Wold, C.E., 2009. Emissions of trace gases and aerosols during the open combustion of biomass in the laboratory. J. Geophys. Res. 114, D19210. https://doi.org/10.1029/2009JD011836.
Mehta, M., Singh, N., 2018. Global trends of columnar and vertically distributed properties of aerosols with emphasis on dust, polluted dust and smoke-inferences from 10-year long CALIOP observations. Remote Sens. Env. 208, 120–132. https://doi.org/10.1016/j.rse.2018.02.017.
Mosca, S., Graziani, G., Klug, W., Bellasio, R., Bianconi, R., 1998. A statistical methodology for the evaluation of long-range dispersion models: an application to the ETEX exercise. Atmos. Environ. 32, 4307–4324. https://doi.org/10.1016/S1352-2310(98)00179-4.
Nédélec, P., Thouret, V., Brioude, J., Sauvage, B., Cammas, J.-P., Stohl, A., 2005. Extreme CO concentrations in the upper troposphere over North-East Asia in June 2003 from the insitu MOZAIC aircraft data. Geophys. Res. Lett. 32, L14807. https://doi.org/10.1029/2005GL023141.
Nikonovas, T., North, P.R.J., Doerr, S.H., 2015. Smoke aerosol properties and ageing effects for northern temperate and boreal regions derived from AERONET source and age attribution. Atmos. Chem. Phys. 15, 7929–7943. https://doi.org/10.5194/acp-15-7929-2015.
NYT, 2018. https://www.nytimes.com/2017/09/06/us/wildfires-oregon-washington.html?_r=0, Accessed date: 25 June 2018.
Omar, A., Tackett, J., Kim, M.-H., Vaughan, M., Kar, J., Trepte, C., Winker, D., 2018. Enhancements to the caliop aerosol subtyping and lidar ratio selection algorithms for level II version 4. EPJ Web Conf 176, 02006. https://doi.org/10.1051/epjconf/201817602006.
O'Neill, N.T., Dubovik, O., Eck, T.F., 2001. Modified Ångström coefficient for the characterization of submicrometer aerosols. App. Opt. 40, 2368–2375. https://doi.org/10.1364/AO.40.002368.
O'Neill, N.T., Eck, T.F., Smirnov, A., Holben, B.N., Thulasiraman, S., 2003. Spectral discrimination of coarse and fine mode optical depth. J. Geophys. Res. 108, 4559–4573. https://doi.org/10.1029/2002JD002975.
Ortiz-Amezcua, P., Guerrero-Rascado, J.L., Granados-Muñoz, M.J., Benavent-Oltra, J.A., Böckmann, C., Samaras, S., Stachlewska, I.S., Janicka, Ł., Baars, H., Bohlmann, S., Alados-Arboledas, L., 2017. Microphysical characterization of long-range transported biomass burning particles from North America at three EARLINET stations. Atmos. Chem. Phys. 17, 5931–5946. https://doi.org/10.5194/acp-17-5931-2017.
Pan, L.L., Randel, W.J., Gary, B.L., Mahoney, M.J., Hintsa, E.J., 2004. Definitions and sharpness of the extratropical tropopause: a trace gas perspective. J. Geophys. Res. 109, D23103. https://doi.org/10.1029/2004JD004982.
Pappalardo, G., Amodeo, A., Apituley, A., Comeron, A., Freudenthaler, V., Linné, H., Ansmann, A., Bösenberg, J., D'Amico, G., Mattis, I., Mona, L., Wandinger, U., Amiridis, V., Alados-Arboledas, L., Nicolae, D., Wiegner, M., 2014. EARLINET: towards an advanced sustainable European aerosol lidar network. Atmos. Meas. Tech. 7, 2389–2409. https://doi.org/10.5194/amt-7-389-2014.
Pérez, P., Pey, J., Cusack, M., Reche, C., Querol, X., Alastuey, A., Viana, M., 2010. Variability of particle number, black carbon, and PM10, PM2.5, and PM1 levels and speciation: influence of road traffic emissions on urban air quality. Aerosol Sci. Technol. 44 (7), 487–499. https://doi.org/10.1080/02786821003758286.
Peterson, D.A., Hyer, E.J., Campbell, J.R., Solbrig, J.E., Fromm, M.D., 2017. A conceptual model for development of intense pyrocumulonimbus in western North America. Mon. Wea. Rev. 145, 2235–2255. https://doi.org/10.1175/MWR-D-16-0232.1.
Pielke, R.A., Uliasz, M., 1998. Use of meteorological models as input to regional and mesoscale air quality models—limitations and strengths. Atmos. Environ. 32, 1455–1466. https://doi.org/10.1016/S1352-2310(97)00140-4.
Pueschel, R.F., Verma, S., Rohatschek, H., Ferry, G.V., Boiadjieva, N., Howard, S.D., Strawa, A.W., 2000. Vertical transport of anthropogenic soot aerosol into the middle atmosphere. J. Geophys. Res. 105 (D3), 3727–3736. https://doi.org/10.1029/1999JD900505.
Radke, L.F., Hegg, D.A., Hobbs, P.V., Nance, J.D., Lyons, J.H., Laursen, K.K., Weiss, R.E., Riggan, P.J., Ward, D.E., 1991. Particulate and trace gas emissions from large biomass fires in North America. In: Levine, J.S. (Ed.), Global Biomass Burning: Atmospheric, Climatic, and Biopheric Implications. MIT Press, pp. 209–224.
Real, E., Law, K.S., Schlager, H., Roiger, A., Huntrieser, H., Methven, J., Cain, M., Holloway, J., Neuman, J.A., Ryerson, T., Flocke, F., de Gouw, J., Atlas, E., Donnelly, S., Parrish, D., 2008. Lagrangian analysis of low altitude anthropogenic plume processing across the North Atlantic. Atmos. Chem. Phys. 8, 7737–7754. http://www.atmos-chem-phys.net/8/7737/2008/.
Reid, J.S., Hobbs, P.V., 1998. Physical and optical properties of young smoke from individual biomass fires in Brazil. J. Geophys. Res. 103 (D24), 32013–32030.
Renard, J.-B., Brogniez, C., Berthet, G., Bourgeois, Q., Gaubicher, B., Chartier, M., Balois, J.-Y., Verwaerde, C., Auriol, F., Francois, P., Daugeron, D., Engrand, C., 2008. Vertical distribution of the different types of aerosols in the stratosphere: detection of solid particles and analysis of their spatial variability. J. Geophys. Res. 113, D21303. https://doi.org/10.1029/2008JD010150.
Ricketts, T.H., Dinerstein, E., Olson, D.M., Loucks, C.J., Eichbaum, W., DellaSala, D.A., Kavanagh, K., Hedao, P., Hurley, P., Carney, K., Abell, R., Walters, S., 1999. Terrestrial Ecoregions of North America: A Conservation Assessment. et al.. Island Press, Washington, D.C.9781559637220 485 p.
Robock, A., 2000. Volcanic eruptions and climate. Rev. Geophys. 38, 191–219. https://doi.org/10.1029/1998RG000054.
Rodríguez-Gómez, A., Sicard, M., Granados-Muñoz, M.-J., Ben Chahed, E., Muñoz-Porcar, C., Barragán, R., Comerón, A., Rocadenbosch, F., Vidal, E., 2017. An architecture providing depolarization ratio capability for a Multi-Wavelength Raman Lidar: implementation and first measurements. Sensors 17, 2957. https://doi.org/10.3390/s17122957.
Rohatschek, H., 1996. Levitation of stratospheric and mesospheric aerosols by gravito-photophoresis. J. Aerosol Sci. 27, 467–475.
Rolph, G.D., Draxler, R.R., Stein, A.F., Taylor, A., Ruminski, M.G., Kondragunta, S., Zeng, J., Huang, H., Manikin, G., McQueen, J.T., Davidson, P.M., 2009. Description and verification of the NOAA smoke forecasting system: the 2007 fire season. Wea. Forecasting 24, 361–378.
Rolph, G., Stein, A., Stunder, B., 2017. Real-time environmental applications and display sYstem: READY. Environ. Model Softw. 95, 210–228. https://doi.org/10.1016/j.envsoft.2017.06.025.
Rosenfeld, D., Fromm, M., Trentmann, J., Luderer, G., Andreae, M.O., Servranckx, R., 2007. The Chisholm firestorm: observed microstructure, precipitation and lightning

activity of a pyro-cumulonimbus. Atmos. Chem. Phys. 7, 645–659. https://doi.org/10.5194/acp-7-645-2007.
Russell, P.B., Bergstrom, R.W., Shinozuka, Y., Clarke, A.D., De-Carlo, P.F., Jimenez, J.L., Livingston, J.M., Redemann, J., Dubovik, O., Strawa, A., 2010. Absorption angstrom exponent in AERONET and related data as an indicator of aerosol composition. Atmos. Chem. Phys. 10, 1155–1169. https://doi.org/10.5194/acp-10-1155-2010.
Russell, P.B., Kacenelenbogen, M., Livingston, J.M., Hasekamp, O.P., Burton, S.P., Schuster, G.L., Johnson, M.S., Knobelspiesse, K.D., Redemann, J., Ramachandran, S., Holben, B., 2014. A multiparameter aerosol classification method and its application to retrievals from spaceborne polarimetry. J. Geophys. Res. Atmos. 119, 9838–9863. https://doi.org/10.1002/2013JD021411.
Sayer, A.M., Hsu, N.C., Eck, T.F., Smirnov, A., Holben, B.N., 2014. AERONET-based models of smoke-dominated aerosol near source regions and transported over oceans, and implications for satellite retrievals of aerosol optical depth. Atmos. Chem. Phys. 14, 11493–11523. https://doi.org/10.5194/acp-14-11493-2014.
Seftor, 2017a. Very Smoky Skies Persist over Canada and, Now. Goddard Space Flight Center, Ozone and Air Quality blog, New England. https://ozoneaq.gsfc.nasa.gov/omps/blog/2017/8/18/very-smoky-skies-persis-over-canada-and-now-new-en, Accessed date: 13 June 2018.
Seftor, 2017b. Oregon PyroCbs produce large, high altitude smoke cloud, Goddard Space Flight Center, ozone and air quality blog. https://ozoneaq.gsfc.nasa.gov/omps/blog/2017/8/31/oregon-pyrocbs-produce-large-high-altitude-smoke, Accessed date: 13 June 2018.
Seftor, 2017c. Fire (and Smoke) Situation Worsens over. Goddard Space Flight Center, Ozone and Air Quality blog, US. https://ozoneaq.gsfc.nasa.gov/omps/blog/2017/9/5/fire-and-smoke-situation-worsens-over-us, Accessed date: 6 July 2018.
Sicard, M., Barragan, R., Dulac, F., Alados-Arboledas, L., Mallet, M., 2016. Aerosol optical, microphysical and radiative properties at regional background insular sites in the western Mediterranean. Atmos. Chem. Phys. 16, 12177–12203. https://doi.org/10.5194/acp-16-12177-2016.
Sicard, M., Granados-Muñoz, M.J., Papagiannopoulos, N., Alados-Arboledas, L., Barragán, R., Bedoya-Velásquez, A.E., Benavent-Oltra, J.A., Bortoli, D., Comerón, A., Córdoba-Jabonero, C., Costa, M.J., del Águila, A., Fernández, A.J., Gómez Amo, J.L., Guerrero-Rascado, J.L., Jorba, O., Martínez-Lozano, J.A., Molero, F., Muñoz-Porcar, C., Ortiz-Amezcua, P., Potes, M., Pujadas, M., Rocadenbosch, F., Rodríguez-Gómez, A., Román, R., Salgado, R., Salgueiro, V., Utrillas, M.P., Yela, M., 2018. Tropospheric and stratospheric impact of Canadian smoke plumes over the Iberian Peninsula in August-September 2017. In: Proc. European Lidar Conference (ELC), (Thessaloniki, Greece, 3-5 July, 2018).
Siddaway, J.M., Petelina, S.V., 2011. Transport and evolution of the 2009 Australian Black Saturday bushfire smoke in the lower stratosphere observed by OSIRIS on Odin. J. Geophys. Res. 116, D06203. https://doi.org/10.1029/2010JD015162.
Sola Salvatierra, Y., Lorente, A., Lorente, J., 2014. Analysis of the aerosol optical properties at a continental background site in the southern Pyrenees (El Montsec, 1574 m a.s.l.). In: Proc. RICTA 2014. 978-84-695-9978-5, pp. 184.
Son, S.-W., Tandon, N.F., Polvani, L.M., Waugh, D.W., 2009. Ozone hole and Southern Hemisphere climate change. Geophys. Res. Lett. 36, L15705. https://doi.org/10.1029/2009GL038671.
Stein, A.F., Rolph, G.D., Draxler, R.R., Stunder, B.S., Ruminski, M.S., 2009. Verification of the NOAA smoke forecasting system: model sensitivity to the injection height. Wea. Forecasting 24, 379–394.
Stein, A.F., Draxler, R.R., Rolph, G.D., Stunder, B.J.B., Cohen, M.D., Ngan, F., 2015. NOAA's HYSPLIT atmospheric transport and dispersion modeling system. Bull. Amer. Meteor. Soc. 96, 2059–2077. https://doi.org/10.1175/BAMS-D-14-00110.
Stocks, B.J., Mason, J.A., Todd, J.B., Bosch, A.M., Wotton, B.M., Amiro, B.D., Flannigan, M.D., Hirsch, K.G., Logan, K.A., Martell, D.L., Skinner, W.R., 2003. Large forest fires in Canada, 1959–1997. J. Geophys. Res. 108 (D1), 8149. https://doi.org/10.1029/2001JD000484.
Straume, A.G., 2001. A more extensive investigation of the use of ensemble forecasts for dispersion model evaluation. J. Appl. Meteorol. 40, 425–445. https://doi.org/10.1175/1520-0450(2001)040.
Toledano, C., Cachorro, V.E., Berjon, A., de Frutos, A.M., Sorribas, M., de la Morena, B.A., Goloub, P., 2007. Aerosol optical depth and Ångström exponent climatology at El Arenosillo AERONET site (Huelva, Spain). Q. J. Roy. Meteor. Soc. 133, 795–807. https://doi.org/10.1002/qj.54.
Trentmann, J., Luderer, G., Winterrath, T., Fromm, M.D., Servranckx, R., Textor, C., Herzog, M., Graf, H.-F., Andreae, M.O., 2006. Modeling of biomass smoke injection into the lower stratosphere by a large forest fire (part I): reference simulation. Atmos. Chem. Phys. 6, 5247–5260. http://www.atmos-chem-phys.net/6/5247/2006/.
Valenzuela, A., Olmo, F.J., Antón, M., Lyamani, H., Titos, G., Cazorla, A., Alados-Arboledas, L., 2015. Aerosol scattering and absorption Angström exponent as indicators of dust and dust-free days over Granada (Spain). Atmos. Res. D–14-00217. https://doi.org/10.1016/j.atmosres.2014.10.015.
Warner, J., Twomey, S., 1967. The production of cloud nuclei by cane fires and the effect on cloud droplet concentration. J. Atmos. Sci. 4, 704–706.
Warner, T.T., Sheu, R., Bowers, J., Sykes, R.I., Dodd, G.C., Henn, D.S., 2002. Ensemble simulations with coupled atmospheric dynamic and dispersion models: illustrating uncertainties in dosage simulations. J. Appl. Meteorol. 41, 448–504. https://doi.org/10.1175/1520-0450(2002)041.
Welton, E.J., Campbell, J.R., Spinhirne, J.D., Scott, V.S., 2001. Global Monitoring of Clouds and Aerosols Using a Network of Micropulse Lidar Systems, Proc. SPIE 4153. Bellingham, WA, USA. pp. 151–159.
Winker, D.M., Hunt, W.H., McGill, M.J., 2007. Initial performance assessment of CALIOP. Geophys. Res. Lett. 34, L19803. https://doi.org/10.1029/2007GL030135.
Young, S.A., Vaughan, M.A., 2009. The retrieval of profiles of particulate extinction from Cloud Aerosol Lidar Infrared Pathfinder Satellite Observations (CALIPSO) data: algorithm description. J. Atmos. Ocean. Tech. 26, 1105–1119. https://doi.org/10.1175/2008JTECHA1221.1.
Young, S.A., Vaughan, M.A., Garnier, A., Tackett, J.L., Lambeth, J.D., Powell, K.A., 2018. Extinction and optical depth retrievals for CALIPSO's version 4 data release. Atmos. Meas. Tech. 11, 5701–5727. https://doi.org/10.5194/amt-11-5701-2018.
Yurganov, L.N., Rakitin, V., Dzhola, A., August, T., Fokeeva, E., George, M., Gorchakov, G., Grechko, E., Hannon, S., Karpov, A., Ott, L., Semutnikova, E., Shumsky, R., Strow, L., 2011. Satellite- and ground-based CO total column observations over 2010 Russian fires: accuracy of top-down estimates based on thermal IR satellite data. Atmos. Chem. Phys. 11, 7925–7942. https://doi.org/10.5194/acp-11-7925-2011.
Zhang, R., Khalizov, A.F., Pagels, J., Zhang, D., Xue, H., McMurry, P.H., 2008. Variability in morphology, hygroscopicity, and optical properties of soot aerosols during atmospheric processing. Proc. Natl. Acad. Sci. U. S. A. 105, 10291–10296. https://doi.org/10.1073/pnas.0804860105.

Prediction of Solar Resource and Photovoltaic Energy Production through the Generation of a Typical Meteorological Year and Meso-NH Simulations: Application to the South of Portugal

Sara Pereira, Edgar Abreu, Maksim Iakunin
Institute of Earth Sciences
University of Évora
Évora, Portugal
e-mail: spereira@uevora.pt, eabreu@uevora.pt, miakunin@uevora.pt

Paulo Canhoto, Rui Salgado
Physics Department and Institute of Earth Sciences
University of Évora
Évora, Portugal
e-mail: canhoto@uevora.pt, rsal@uevora.pt

***Abstract*—The goal of this work is the generation of solar resource and photovoltaic (PV) energy maps based on simulations of a Numerical Weather Prediction model (NWP) for a Typical Meteorological Year (TMY). This approach is applied to the South of Portugal. Sixteen years of observations were used to determine a TMY for the city of Évora, which is located near the center of the region, through the Sandia method and the Finkelstein-Schafer statistics. The NWP Meso-NH model, with the ecRad radiation scheme integrated, is used to simulate the TMY, allowing for the generation of solar resource and air temperature maps that are helpful in predicting PV potential, thus constituting a useful tool for planning and designing this type of solar systems.**

Keywords-Typical meteorological year; Solar energy; Photovoltaic systems; Meso-NH

I.ⁿ INTRODUCTION

Knowledge of the solar resource is crucial when designing or simulating solar energy systems. In the development of a solar energy project, it is necessary to consider several time scales in the solar resource assessment, varying from annual average values in a first approach, to the short-term characterization of solar radiation and other relevant meteorological variables which affect the performance of the solar system, such as air temperature and wind speed. Thus, temporal resolution of solar radiation data can have a significant impact on the viability analysis of a solar energy project [1]. Project planning, as well as its economic viability, are directly related to both the magnitude and variability of the local solar resource [2]–[5], making its characterization in different temporal resolutions imperative.

Typical Meteorological Years (TMY) are generated by concatenating typical months of real measurements and reproduce the long-term statistics. Thus, being useful for energy simulation of solar power plants and in buildings, either to determine their thermal response under different environmental conditions or to design and simulate integrated renewable energy systems.

The TMY comprises hourly values of solar radiation and other meteorological parameters during a period of one year [6] usually including mean and extreme values of temperature, wind and relative humidity.

The first version of TMY was developed using the Sandia method [7] proposed by Hall in 1978. The National Renewable Energy Laboratory (NREL) has developed a second (TMY2) [8] and third version (TMY3) [9] by adding some changes in the process of selecting the typical data. Regardless of the method used, the TMY has been recently used in applications related to solar energy as reported in the literature [10]–[13].

In this work, a TMY for Évora (Portugal) is determined with the goal of generating solar energy resource maps for the South of Portugal. These maps are obtained by simulating the weather conditions in the region of interest for the days of the TMY using a numerical weather prediction model (NWP). This type of model represents the evolution of atmospheric conditions by integrating the constitutive and state equations that describe the dynamics and the physical phenomena occurring in the atmosphere, subject to boundary and initial conditions.

Regarding the solar power plants, the usage of photovoltaic (PV) systems for energy generation has been growing not only due to the public concern with climate change but also due to its economic benefits. However, the energy generation of these systems is extremely dependent on weather conditions, not only irradiance but also temperature, and thus, knowing the conditions in a certain region can allow for the accurate estimation of energy generation.

In this work, the monthly PV potential in the South of Portugal is determined through the output of the Meso-NH NWP model [14] simulations for a typical year, using previously documented methods which are based on simplified models that correlate air temperature, PV cell temperature and PV energy generation [15]–[17].

II.ⁿ TMY GENERATION

A. Experimental Data, Quality Control and Gap Filling

Long and complete series of daily data is required to determine TMY. There are 16 years of observations made in Évora (from 2003 to 2018, inclusive) which, however, have gaps due to instrumentation failure and malfunction. Thus, it was necessary to carry out a careful quality control and gap filling of the observations so that the data series are correct and complete.

Daily data of global horizontal irradiation (GHI), minimum, mean and maximum air temperature, minimum, mean and maximum relative humidity, mean wind speed and

978-1-7281-4562-4/19/$31.00 ©2019 IEEE

Authorized licensed use limited to: b-on: Universidade de Evora. Downloaded on July 06,2023 at 17:20:11 UTC from IEEE Xplore. Restrictions apply.

maximum daily wind gust were used. Observations were filtered and values that were out of physical limits were removed [18]. Over time, measurements of relative humidity show a gradual decrease in their value (approximately linearly) until there is a new calibration. To take this into account, slopes were determined for each period of observations between calibrations in order to apply corrections.

Data gaps were filled using correlations between data from the Évora station (EVR: 38.567811, -7.911459) and two other stations: Mitra (MTR: 38.525389, -8.016611) and Portel (PRL: 38.306528, -7.689500), located 10 and 35 km from Évora, respectively. When the usage of correlations was not possible the gap filling was performed by linear interpolation. As for the wind components the software Windographer™ was used to filter data, fill gaps and extrapolate wind speed values from 6 to 10 m above the ground (standard height).

TABLE I. " STATISTICAL WEIGHTS OF VARIABLES

Air Temperature			Relative Humidity			Wind Speed		GHI
Mean	*Max*	*Min*	*Mean*	*Max*	*Min*	*Mean*	*Max*	
2/24	1/24	1/24	2/24	1/24	1/24	2/24	2/24	12/24

B. TMY Generation Method

The TMY was determined using the Sandia method [7], which consists of concatenating twelve typical meteorological months (TMMs). The first step on selecting the TMMs is to evaluate the Finkelstein-Schaffer (FS) statistics [19] of the daily values for all variables used. The Cumulative Distribution Function (CDF) of each month and variable is computed and a corresponding weighted sum (WS) of the FS statistics is determined, considering the statistical weights presented in Table I. This procedure is used to determine the relative importance of each variable on the selection of the TMMs, thus allowing some degree of freedom in the TMY generation regarding its final application. After the WS determination, the years of the data series are sorted in ascending order of its WS value and the five years with lowest WS are kept.

In the original Sandia method [7], the persistence of GHI and mean air temperature are evaluated determining the frequency and length of runs of consecutive days with values within a specific range of percentiles. However, in this work, the more simple procedure proposed by Pissimanis *et al*. [20] was adopted, in which the root mean square differences (RMSD) of the hourly GHI are determined. This procedure has been used in several works, e.g. Abreu *et al.* [21]. These values are used to select the year with lowest RMSD and the years with RMSD lower than min{RMSD} + 0.02 kWh/m^2. Then, the FS values of GHI of these years are analyzed and the years with lowest FS value and the years with FS lower than min{FS} + 0.03 are selected. If this is not enough to obtain only one year, the FS values for the mean air temperature are also analyzed and the year with the lowest FS value is selected.

To smooth the transition between the months selected for the TMY, an interpolation in the period between the six hours before and six hours after the end of each month is carried out, by using a centered moving average.

C. Generated TMY for Évora, Portugal

The years selected for each calendar month of the generated TMY for Évora, Portugal, are presented in Table II. To validate the selected months, the monthly mean values of GHI, mean air temperature, mean relative humidity and mean wind speed were compared against the long-term mean values of those variables. It was found that the TMY monthly mean values are close to the long-term mean values, which validates the selection of typical months. Fig. 1 shows the example for the case of GHI.

III." MESO-NH SIMULATIONS

The Meso-NH model is a non-hydrostatic mesoscale atmospheric model and aims to simulate the state of the atmosphere by incorporating a system of non-hydrostatic equations that computes balances over a wide range of scales, and having a set of physical parameterizations with high detail in the representation of clouds and precipitation [14], [22]. To represent the interactions between atmosphere and surface, the model uses the SURFEX surface scheme [23] and the ECOCLIMAP database, which contains surface parameters with 1km resolution [24].

TABLE II. " SELECTED MONTHS/YEARS FOR EACH CALENDAR MONTH FOR THE TMY IN ÉVORA

Jan.	Feb.	Mar.	Apr.	May	Jun.	Jul.	Aug.	Sep.	Oct.	Nov.	Dec.
2018	2006	2017	2008	2005	2010	2014	2007	2011	2008	2004	2018

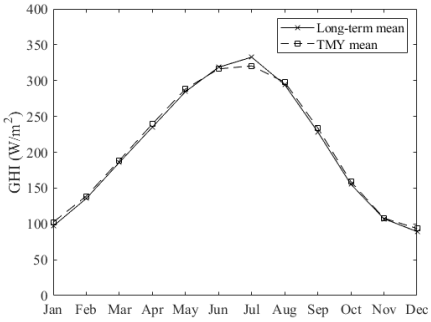

Figure 1. " Comparison between the TMY monthly mean values and the long-term monthly mean values of daily mean global horizontal irradiance.

The radiation transport in the atmosphere is modeled through the ecRad scheme developed by the European Centre for Medium range Weather Forecasts (ECMWF). This scheme is based on the Rapid Radiative Transfer Model (RRTM) [25], [26], which takes into account the cloud parameterization, liquid water content, ice and snow, using the Monte Carlo Independent Column Approximation

Authorized licensed use limited to: b-on: Universidade de Evora. Downloaded on July 06,2023 at 17:20:11 UTC from IEEE Xplore. Restrictions apply.

(McICA) method that allows a more accurate representation of the interaction between radiation and the clouds.

The Meso-NH model is used to simulate the days of the typical months previously selected. The simulations were initiated and forced with analysis data from ECMWF model, generating 1-minute data of global horizontal irradiance, direct normal irradiance (DNI), diffuse horizontal irradiance (DHI) and air temperature (10 m) with 1.25 km of horizontal resolution, which can then be converted to daily, monthly or yearly data by accumulation in the case of solar radiation variables, while for air temperature the minute values that occur during the day are averaged. The mean air temperature during the day period (sun above the horizon) is presented here instead of the daily mean temperature because that is the variable needed for estimating the photovoltaic (PV) energy production.

Fig. 2 shows how the 10-minute averaged values of simulated global horizontal irradiance compare to 10-minute observations for the first three days of June 2010, used here as an example for model validation. This comparison shows a good performance of the Meso-NH model for clear sky days and a lower accuracy in the prediction of clouds at this time scale. Nevertheless, if the daily irradiation is considered, differences of –0.53 %, –18.12 % and –2.33 % between predicted and measured values are obtained for the three days, respectively. A detailed analysis of the solar radiation outputs from ecRad while integrated in the NWP model by ECMWF can be found in [27].

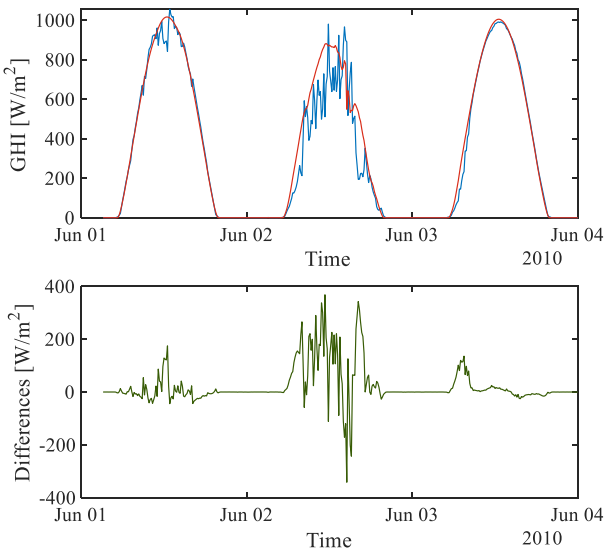

Figure 2. " Measured (blue) and simulated (red) values of global horizontal irradiance and respective difference (green) for three days of June 2010.

IV." Solar Resource and Photovoltaic Energy Production

Using the data generated through the Meso-NH simulations for days in the TMY the monthly GHI values for December (typically the month with lowest solar resource in this region) is shown in Fig. 3, while Fig. 4 shows the mean air temperature during the day for the same month.

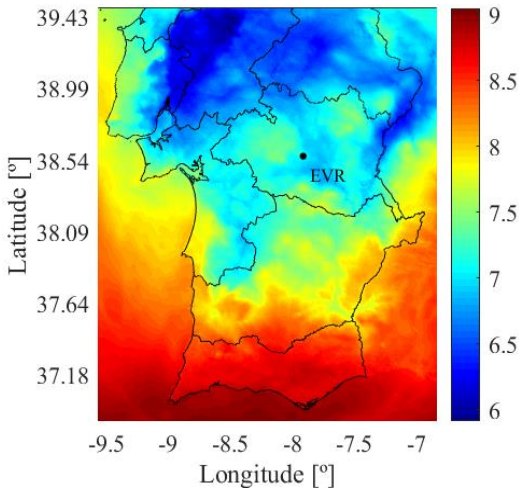

Figure 3. " Monthly GHI (x10^4 Wh/m^2) in the South of Portugal for the typical December from the Meso-NH simulations.

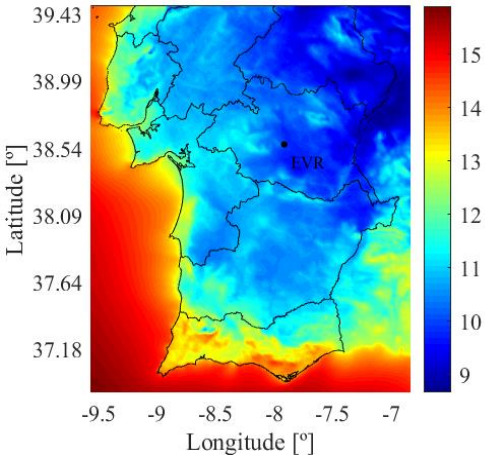

Figure 4. " Monthly mean air temperature (ºC) during the day in the South of Portugal for the typical December from the Meso-NH simulations.

With this data, the photovoltaic potential per nominal installed power can be computed through (1) [16], assuming a PV system of crystalline silicon modules (mono or poly-crystalline) operated without any kind of storage such as batteries.

$$Y = (K'/G_S)[1 + \alpha_{Pmax}(T_c - 25)]H_{Am} \quad (1)$$

Here, K' = 0.75 [16] accounts for all losses in the system except for the effect of temperature on the PV module, G_S = 1000 W/m^2 is the solar irradiance at standard test conditions, α_{Pmax} = –0.0041 °C^{-1} is the maximum power temperature coefficient for crystalline silicon PV modules [16], H_{Am} is the monthly total solar irradiation on the PV array and T_c is the mean temperature of the PV cells. This temperature is computed through (2), where T_{Am} is the mean air

Authorized licensed use limited to: b-on: Universidade de Evora. Downloaded on July 06,2023 at 17:20:11 UTC from IEEE Xplore. Restrictions apply.

temperature during the day, n is the number of hours with the sun above the horizon (290.036 h for the month of December) and the factor $\tau\alpha/U_L$ can be obtained through (3), in which $\tau\alpha$ is the optical efficiency and U_L is the overall heat transfer coefficient between the PV modules and the ambient air. Here, the factor $\tau\alpha/U_L$ is considered constant and calculated from the values of cell temperature ($T_{c,\ NOCT}$ = 46 °C), ambient temperature ($T_{a,\ NOCT}$ = 20 °C) and global solar irradiance (I_{NOCT} = 800 W/m^2) at nominal operating cell temperature (NOCT) conditions as reported in [17].

$$T_c = 0.9[(\tau\alpha/U_L)/n]H_{Am} + T_{Am} \quad (2)$$

$$\tau\alpha/U_L = (T_{c,\ NOCT} - T_{a,\ NOCT})/I_{NOCT} \quad (3)$$

The monthly global solar irradiation on the tilted surface of the PV system, H_{Am}, was computed from the 1-minute simulated values of DNI and DHI using the isotropic model by Hottel and Woertz [28] and Liu and Jordan [29], considering a PV system with a tilt angle of 38°, a surface azimuth of 0° and a ground albedo of 0.2.

Fig. 5 shows the PV potential per nominal power installed in the South of Portugal and for the typical December in this region. The effect of temperature and incidence angle of solar radiation can be observed when comparing the GHI (Fig. 3) and PV potential (Fig. 5) maps. It can be seen in Fig. 5 that the southernmost region of Portugal has higher PV potential in December. The same analysis is being carried out for the other calendar months as well as an annual assessment.

V.ⁿ Conclusions

In this work the TMY for Évora, Portugal, was determined based on 16-year experimental data, thus obtaining a complete year that can adequately represent the atmospheric conditions in this location having a focus on the solar resource. The days that constitute the TMY were simulated using the model Meso-NH coupled to the ecRad radiation scheme, obtaining 1-minute data for this region with 1.25 km of resolution.

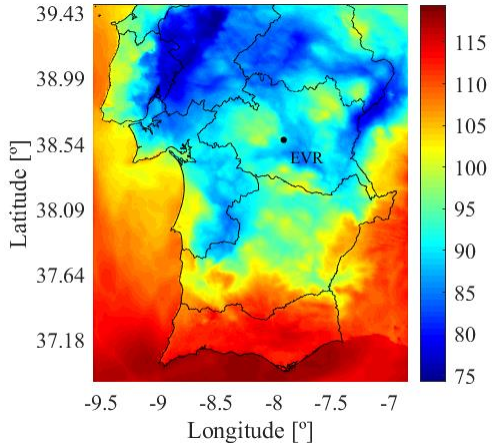

Figure 5. ⁿ Monthly PV potential per nominal power installed (kWh/kW-month) in the South of Portugal for typical December.

Solar resource maps were generated and the PV potential per nominal power installed was computed producing maps of this region that are extremely helpful for applications related to the solar resource and, ultimately, for planning and design of photovoltaic energy systems.

Acknowledgment

This work was funded by the European Regional Development Fund, included in the COMPETE 2020 (Operational Program Competitiveness and Internationalization) through the ICT project (UID/GEO/04683/2013) with the reference POCI-01-0145-FEDER - 007690, and the projects DNI-ALENTEJO (ALT20-03-0145-FEDER-000011) and ALOP (ALT20-03-0145-FEDER-000004). E.F.M. Abreu acknowledges FCT for the grant SFRH/BD/136433/2018. S. Pereira acknowledges FCT for the grant SFRH/BD/145378/2019.

References

[1] S. Moreno-Tejera, M. A. Silva-Pérez, I. Lillo-Bravo, and L. Ramírez-Santigosa, "Solar resource assessment in Seville, Spain. Statistical characterisation of solar radiation at different time resolutions," *Sol. Energy*, **132**, 2016, pp. 430–441.

[2] C. A. Gueymard and S. M. Wilcox, "Assessment of spatial and temporal variability in the US solar resource from radiometric measurements and predictions from models using ground-based or satellite data," *Sol. Energy*, **85**, 2011, pp. 1068–1084.

[3] M. Journée, R. Müller, and C. Bertrand, "Solar resource assessment in the Benelux by merging Meteosat-derived climate data and ground measurements," *Sol. Energy*, **86**, 2012, pp. 3561–3574.

[4] J. C. Perdigão, R. Salgado, M. J. Costa, H. P. Dasari, and A. Sanchez-Lorenzo, "Variability and trends of downward surface global solar radiation over the Iberian Peninsula based on ERA-40 reanalysis," *Int. J. Climatol.*, **36**, 2016, pp. 3917–3933.

[5] F. M. Lopes, H. G. Silva, R. Salgado, A. Cavaco, P. Canhoto, and M. Collares-Pereira, "Short-term forecasts of GHI and DNI for solar energy systems operation: assessment of the ECMWF integrated forecasting system in southern Portugal," *Sol. Energy*, **170**, 2018, pp. 14–30.

[6] T. Lhendup and S. Lhundup, "Comparison of methodologies for generating a typical meteorological year (TMY)," *Energy Sustain. Dev.*, **11**, 2007, pp. 5–10.

[7] I. J. Hall, R. Praire, H. Anderson, and E. Boes, *Generation of Typical Meteorological Years for 26* SOLMET *Stations*. Sandia Laboratories, 1978.

[8] W. Marion and K. Urban, *User's Manual for TMY2s - Typical Meteorological Years*. United States. Department of Energy. Office of Energy Efficiency and Renewable Energy, 1995.

[9] S. Wilcox and W. Marion, "Users Manual for TMY3 Data Sets," 2008.

[10] O. S. Ohunakin *et al.*, "Photovoltaic performance prediction in Northern Nigeria using generated typical meteorological year dataset," *African J. Sci. Technol. Innov. Dev.*, **10**, 2018, pp. 579–591.

[11] T. Huld, E. Paietta, P. Zangheri, and I. P. Pascua, "Assembling typical meteorological year data sets for building energy performance using reanalysis and satellite-based data," *Atmosphere (Basel).*, **9**, 2018.

Authorized licensed use limited to: b-on: Universidade de Evora. Downloaded on July 06,2023 at 17:20:11 UTC from IEEE Xplore. Restrictions apply.

[12] N. A. Al-Azri and S. Al-Saadi, "Variant developments of typical meteorological years (TMYs) for Seeb, Oman and their impact on energy simulation of residential buildings," *J. Eng. Res.*, **15**, 2018, pp. 29–41.

[13] M. Ernst and J. Gooday, "Methodology for generating high time resolution typical meteorological year data for accurate photovoltaic energy yield modelling," *Sol. Energy*, **189**, 2019, pp. 299–306.

[14] C. Lac *et al.*, "Overview of the Meso-NH model version 5.4 and its applications," *Geosci. Model Dev.*, **11**, 2018, pp. 1929–1969.

[15] S. Dubey, J. N. Sarvaiya, and B. Seshadri, "Temperature dependent photovoltaic (PV) efficiency and its effect on PV production in the world - A review," *Energy Procedia*, **33**, 2013, pp. 311–321.

[16] K. Kawajiri, T. Oozeki, and Y. Genchi, "Effect of temperature on PV potential in the world," *Environ. Sci. Technol.*, **45**, 2011, pp. 9030–9035.

[17] T. Hove, "A method for predicting long-term average performance of photovoltaic systems," *Renew. Energy*, **21**, 2000, pp. 207–229.

[18] World Meteorological Organization, "Guidelines on Quality Control Procedures for Data from Automatic Weather Stations," 2004.

[19] J. M. Finkelstein and R. E. Schafer, "Improved goodness-of-fit tests," *Biometrika*, **58**, 1971, pp. 641–645.

[20] D. Pissimanis, G. Karras, V. Notaridou, and K. Gavra, "The generation of a 'typical meteorological year' for the city of Athens," *Sol. Energy*, **40**, 1988, pp. 405–411.

[21] E. F. M. Abreu, P. Canhoto, V. Prior, and R. Melicio, "Solar resource assessment through long-term statistical analysis and typical data generation with different time resolutions using GHI measurements," *Renew. Energy*, **127**, 2018, pp. 398–411.

[22] Meso-NH, "The Mesonh User's Guide," 2016.

[23] V. Masson *et al.*, "The SURFEXv7.2 land and ocean surface platform for coupled or offline simulation of earth surface variables and fluxes," *Geosci. Model Dev.*, **6**, 2013, pp. 929–960.

[24] S. Faroux, A. T. Kaptué Tchuenté, J.-L. Roujean, V. Masson, E. Martin, and P. Le Moigne, "ECOCLIMAP-II/Europe: a twofold database of ecosystems and surface parameters at 1 km resolution based on satellite information for use in land surface, meteorological and climate models," *Geosci. Model Dev.*, **6**, 2013, pp. 563–582.

[25] R. J. Hogan and A. Bozzo, "ECRAD: A new radiation scheme for the IFS," *ECMWF Tech.*, **787**, 2016, pp. 1–33.

[26] R. J. Hogan and A. Bozzo, "A Flexible and Efficient Radiation Scheme for the ECMWF Model," *J. Adv. Model. Earth Syst.*, **10**, 2018, pp. 1990–2008.

[27] S. Pereira, P. Canhoto, R. Salgado, and M. J. Costa, "Development of an ANN based corrective algorithm of the operational ECMWF global horizontal irradiation forecasts," *Sol. Energy*, **185**, 2019, pp. 387–405.

[28] H. C. Hottel and B. B. Woertz, "The performance of flat-plate solar –heat collectors," *Am. Soc. Mech. Eng. Trans.*, 1942.

[29] B. Y. H. Liu and R. C. Jordan, "The interrelationship and characteristic distribution of direct, diffuse and total solar radiation," *Sol. Energy*, **4**, 1960, pp. 1–19.

Authorized licensed use limited to: b-on: Universidade de Evora. Downloaded on July 06,2023 at 17:20:11 UTC from IEEE Xplore. Restrictions apply.

Botany Letters

ISSN: 2381-8107 (Print) 2381-8115 (Online) Journal homepage: https://www.tandfonline.com/loi/tabg21

Nitzschia transtagensis sp. nov. (Bacillariophyceae) from a spring in Southern Portugal

Eduardo A. Morales, Carlos E. Wetzel, Maria Helena Novais, M. Manuela Morais & Luc Ector

To cite this article: Eduardo A. Morales, Carlos E. Wetzel, Maria Helena Novais, M. Manuela Morais & Luc Ector (2020) *Nitzschia transtagensis* sp. nov. (Bacillariophyceae) from a spring in Southern Portugal, Botany Letters, 167:1, 32-41, DOI: 10.1080/23818107.2019.1688676

To link to this article: https://doi.org/10.1080/23818107.2019.1688676

Published online: 14 Nov 2019.

Submit your article to this journal

Article views: 157

View related articles

View Crossmark data

Citing articles: 4 View citing articles

Full Terms & Conditions of access and use can be found at
https://www.tandfonline.com/action/journalInformation?journalCode=tabg21

BOTANY LETTERS
2020, VOL. 167, NO. 1, 32–41
https://doi.org/10.1080/23818107.2019.1688676

Taylor & Francis
Taylor & Francis Group

ARTICLE

Check for updates

Nitzschia transtagensis sp. nov. (Bacillariophyceae) from a spring in Southern Portugal

Eduardo A. Morales [a,b,c], Carlos E. Wetzel [c], Maria Helena Novais [a,b], M. Manuela Morais [a,b] and Luc Ector [c]

[a]Water Laboratory, University of Évora, Évora, Portugal; [b]Institute of Earth Sciences - ICT, University of Évora, Évora, Portugal; [c]Environmental Research and Innovation Department (ERIN), Luxembourg Institute of Science and Technology (LIST), Belvaux, Luxembourg

ABSTRACT

A new species of *Nitzschia* Hassall is described from a small spring in southern Portugal. *Nitzschia transtagensis* sp. nov. has a unique morphology in the *Lineares* section, resembling *Nitzschia hierosolymitana, N. vitrea* and its variety *salinarum*. The new species is unique in that it has a convex primary (raphe) side with a slightly undulated abvalvar edge of the mantle, and a clearly undulated secondary valve side. This taxon also has a dimorphic open, ligulate cingulum composed of an apically asymmetric valvocopula having one row of roundish pores on the pars interior and attached to the valve secondary side, and two rows of pores (one of roundish and one of elongate pores) attached to the primary side of the valve. All remaining girdle elements have a single row of approximately round pores. The new species is compared to morphologically similar taxa and its ecology is discussed based on available information and literature. Additionally, it was found that a variant of the new species had been reported previously from Sardinia as "*Nitzschia* aff. *ebroicensis*", but the Italian population has coarser stria and puncta densities.

ARTICLE HISTORY
Received 15 July 2019
Accepted 12 October 2019

KEYWORDS
Bacillariaceae; diatoms; Iberian Peninsula; Europe; taxonomy

Introduction

The genus *Nitzschia* Hassall comprises a large group of morphologically diverse species (Mann 1981). Although certain groups within the genus, such as the *Lanceolatae* section (*sensu* Krammer and Lange-Bertalot 1988), including the widely cited *Nitzschia palea* (Kützing) W. Smith and *Nitzschia inconspicua* Grunow, are regarded as lacking sufficient morphological differences to distinguish them reliably (Denys and Lange-Bertalot 1998; Trobajo et al. 2013; Rovira et al. 2015), the reality is that a taxonomy based on geographically and metapopulation wide surveys is still under development. Together with the study of type material, these metapopulation studies could serve in a better delimitation of taxonomic boundaries (Hlúbiková et al. 2009).

Though molecular studies prove to be useful in the distinction of taxa with similar appearance (e.g. Lobban et al. 2019), the analysis of morphological characters using a combination of light (LM) and scanning electron (SEM) microscopy continues to be a powerful tool to find distinguishing features and producing clear cut separations among populations regarded as single, broadly circumscribed species (e.g. Tudesque et al. 2008; Morales 2015).

The recent efforts in using molecular tools to ease the identification of *Nitzschia* species (e.g. Trobajo et al. 2010; Rimet et al. 2011, 2016) are impaired by a dearth of complete reference databases for diatoms and the difficulty to apply such incomplete information on a broad geographical and taxonomically spread bases (Zimmermann et al. 2014; Khan-Bureau et al. 2017). Therefore, traditional morphological identification, which is still largely used in applied ecological analyses, still represents a viable tool and utilizes considerably less and cheaper resources than molecular studies, even when SEM studies are included.

In fact, new species of *Nitzschia* are constantly being described based on morphology, however, very few of the new species can be considered as morphologically strikingly different (e.g. Xie and Li 1994; Lundholm and Moestrup 2000) and, therefore, the great majority often require a strong literature support and taxonomic argumentation (e.g., Hamilton and Laird 2001; Hamsher et al. 2016), and in some cases even the examination of type material is necessary (Hlúbiková et al. 2009).

While some regions of Europe, e.g. central Europe, have been largely explored for diatoms, but continue to yield new taxa, some other regions are seriously understudied and the reference bibliography is poor and insufficient to represent the local floras. This is a serious shortcoming for the implementation of the Water Framework Directive (Wallin et al. 2003), which, at this point, should already count with a rather strong taxonomic basis for water quality determination. The Iberian Peninsula is one of those regions in urgent need of updated taxonomical works since water quality issues are aggravated by dam construction and climate change

CONTACT Eduardo A. Morales edu_mora123@outlook.com Water Laboratory, University of Évora, Évora, Portugal
© 2019 Société botanique de France

Published online 14 Nov 2019

(Morais 2008; Cardoso et al. 2016; Soares et al. 2017). To date, there are only a few floristic works (e.g. Blanco et al. 2010), but the majority of information comes in the form of articles focusing on specific groups (none on *Nitzschia*), or specific habitats (e.g. Cantoral-Uriza and Aboal Sanjurjo 2008; Novais et al. 2015).

In this manuscript, we describe a new *Nitzschia* species in the *Lineares* section (*sensu* Krammer and Lange-Bertalot 1988) from southern Portugal, collected from a spring. The rather distinctive features of the new species are described based on combined LM and SEM data and contrasted to taxa from the literature.

Material and methods

Diatoms were collected in spring (May 26) and summer (Sept. 21) 2017, and winter (Jan. 16) and spring (June 7) 2018 from the João Dias spring and the stream of the same name formed by it (Guadiana basin, Figure 1, coordinates 37º 51 17.75" N, 7º 18 00.52" W).

Simultaneously with diatom sampling, water chemistry was determined *in situ* using a multi parametric probe TROLL 9500 PROFILER XP, measuring temperature (T, °C), pH, dissolved oxygen (DO, % of O_2 saturation), and electrical conductivity (EC, µS cm ^{1}). In the laboratory, the following parameters were determined following APHA (1995) standard methods, total nitrogen (TN, mg N L ^{1}), nitrates (NO_3, mg NO_3-N L ^{1}), nitrites (NO_2, mg NO_2-N L ^{1}), total phosphorus (TP, mg P L ^{1}) and phosphates (PO_4, mg PO_4-P L ^{1}).

Biological samples collected in the stream were obtained by brushing 5–7 hand-sized rocks with a toothbrush and washing them with ethyl alcohol (96%), while the spring samples were collected from moss. Aliquots from each sample were oxidized in the laboratory with hydrogen peroxide (35%) in a sand bath (210°C) for 36 h after which material was rinsed with distilled water until neutrality (INAG 2008). Permanent slides were mounted in Naphrax® and valves and frustules were identified to species level using a Leica DMLB light microscope equipped with a 100x HCX PL APO oil immersion objective (N.A. 1.40) and a Leica DC 500 camera. A minimum of 400 valves were identified and counted on each slide in order to assess the relative abundance of taxa composing the community (INAG I. P. 2008). The identification was based on reference floras (e.g., Krammer and Lange-Bertalot 1986, 1988, 1991a, 1991b; Hofmann et al. 2011; Lange-Bertalot et al. 2017) as well as recent bibliographic sources, including the series "Diatoms of Europe", "Iconographia Diatomologica", "Bibliotheca Diatomologica" and relevant taxonomic papers, such as Reichardt (1997), Van de Vijver et al. (2011) and Novais et al. (2011).

For SEM analysis, a portion of the oxidized material was rinsed with deionized water over a 3-µm pore glass fiber filter and coated with platinum using a BAL-TEC MED 020 Modular High Vacuum Coating System for 30 s at 100 mA. A Hitachi SU-70 electron microscope operated at 5 kV and 10 mm distance was used for the analysis. All micrographs were digitally manipulated

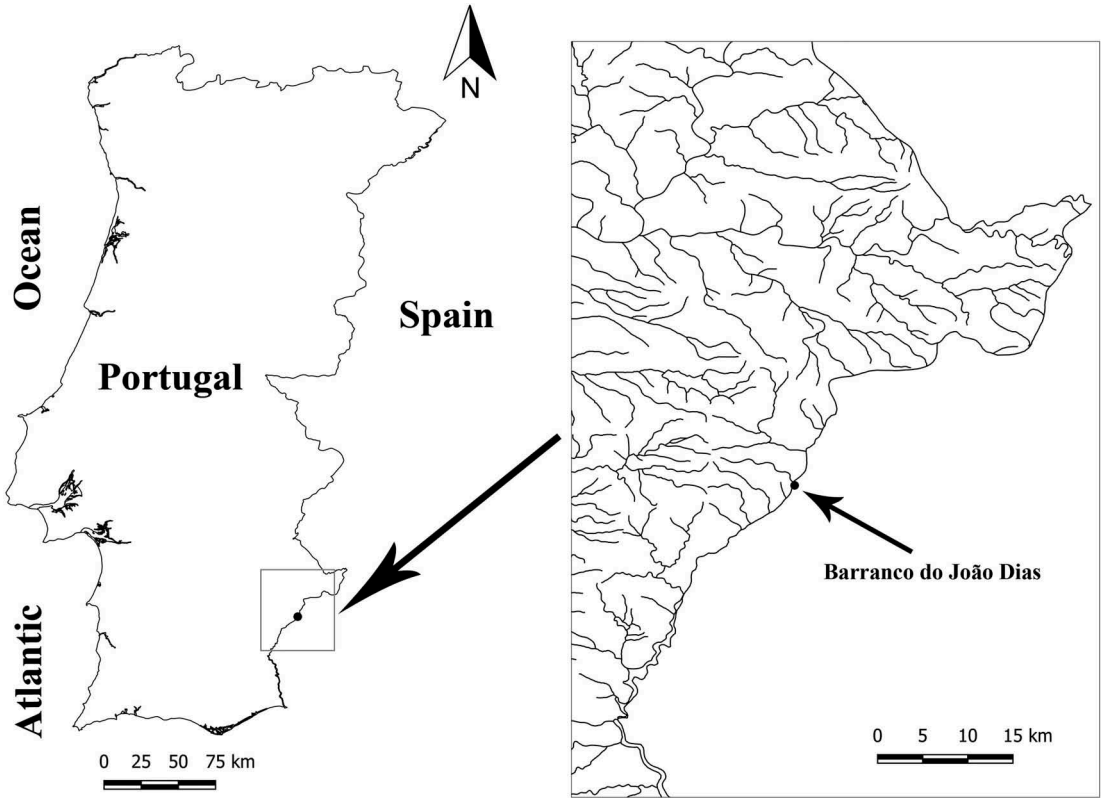

Figure 1. Localization of type locality in southern Portugal.

and plates containing LM and SEM pictures were mounted using CorelDraw X6®.

The Specific Pollution Sensitivity Index (SPI) was calculated from diatom abundances (Coste in Cemagref 1982), using the OMNIDIA v. 5.5 software (Lecointe et al. 1993).

Morphological terminology follows Barber and Haworth (1981) for valve shape and stria pattern, Cox and Ross (1981) and Cox (2012) for lateral extensions (virgae) and crossbars (vimines), and Round et al. (1990) for areolar substructures, raphe and girdle bands.

Results

Nitzschia transtagensis E.Morales, Novais, C.E.Wetzel, Morais & Ector sp. nov. (Figure 2–26)

Description

Frustules with nitzschioid symmetry, lanceolate with a convex raphe side and clearly undulated opposite side of the valve (Figure 2–12, 20). Valves with rostrate to capitate ends, apically asymmetrical (Figure 2–11), sometimes slightly heteropolar (Figure 3, 4, 10) with convex primary side, but sometimes with undulated abvalvar edge of mantle (Figure 12, 23), and conspicuously undulated secondary side (Figure 2–12, 20). Length 30.5–50.4 µm, width 4.5–6.0 µm, fibula density 6–10 in 10 µm, stria density 30–35 in 10 µm (n = 15). Raphe eccentric, situated along an unornamented hyaline area, distinctly elevated on a keel with respect to the valve face and mantle (Figure 12–16). Raphe slit continuous at central nodule (Figure 12, 14), curved toward mantle at both distal extremes (Figure 15, 16) and internally ending in raised helictoglossa (Figure 19, 20). Fibulae round to square, irregularly spaced at central nodule, with valve face base extending onto 2–4 virgae (Figure 2–11, 17–22). Fibula at central nodule wider. Striae barely visible in LM, composed of round to transapically elongated areolae (Figure 12–22), continuous from valve face to the secondary side of mantle, but interrupted by the hyaline area of the keel on the primary side. Areolae unevenly spaced due to variability in vimen length (Figure 12–16, 18–22), and internally occluded by hymens (Figure 18–22). Girdle bands open, ligulate and with a recessed pars interior to accommodate the valve mantle or the previous girdle element (Figure 23–26). Copula narrower, bearing a single row of poroids located on the transition between pars interior and exterior (Figure 23–26). Valvocopula with one row of ca. round poroids on pars interior located on the valve secondary side, and two rows, one of elongated and another of ca. round pores, positioned on both sides of the transition between pars interior and exterior on primary (raphe) side of the valve (Figure 24).

Holotype

Slide BR-4564, Botanic Garden Meise, Belgium (BR). The holotype is represented by Figure 2 herein.

Isotypes. ZU11/27 and ZU11/28, Hustedt Collection, Bremerhaven (ZU), not illustrated herein.

Type locality

The new species was found in a spring feeding the small creek Barranco do João Dias, Alentejo region, Portugal (Figure 1), coordinates 37º 51 17.75" N, 7º 18 00.52" W, Collected by E.A. Morales on 16 January 2018.

Etymology

The species epithet makes reference to the Portuguese southern region of Alentejo, which name etymologically translates as "beyond the Tagus River".

Associated diatom species

Nitzschia transtagensis was found growing on mosses in a spring feeding a small watercourse called Barranco de João Dias. The relative abundance of *N. transtagensis* was 0.6%, the taxa richness was 33, and the value of the Shannon diversity index was 3.45. The associated diatoms co–occurring with this taxon were *Achnanthidium minutissimum* (Kützing) Czarnecki (33.1%), unidentified *Gomphonema* (16.1%) and *Pinnularia* (10.6%) species, *Nitzschia* cf. *inconspicua* Grunow (6.8%), *Nitzschia paleacea* (Grunow) Grunow (6.1%), *Humidophila contenta* (Grunow) R.L.Lowe et al. (4.2%), *Nitzschia amphibia* Grunow (4.2%) and *Nitzschia inconspicua* Grunow (3.8%). From these, there is no information yet about the ecological requirements of the unidentified *Gomphonema* and *Pinnularia* species, *N.* cf. *inconspicua* and *Humidophila contenta*. From the remaining taxa, only *A. minutissimum* has high sensibility value (5.0), is circumneutral, nitrogen autotrophic tolerating elevated concentrations of organically bound nitrogen, -mesosaprobous and requires continuously high dissolved oxygen concentrations. Whilst *N. paleacea, N. amphibia* and *N. inconspicua* present lower sensibility values (2.5; 2.0, and 2.8, respectively), are considered alkaliphilous (pH>7), are facultatively or obligately nitrogen-heterotrophic taxa, needing periodically or continuously elevated concentrations of organically bound nitrogen, require moderate dissolved oxygen concentrations (>50% sat. O_2) and are -mesosaprobous (Van Dam et al. 1994) retrieved from the 2013 OMNIDIA v. 5.5 (Omnis Software, Inc.) database (Lecointe et al. 1993). The presence of these taxa more tolerant to organic contamination leads to an SPI index value of 14.2.

Nitzschia transtagensis was also identified from two other streams in southern Portugal: Lampreia stream (Guadiana basin), on 29 March 2017 and in Valverde stream (Sado basin) on 30 March 2017. However, in these sites, it was only identified in the qualitative survey and did not appear along counting transects.

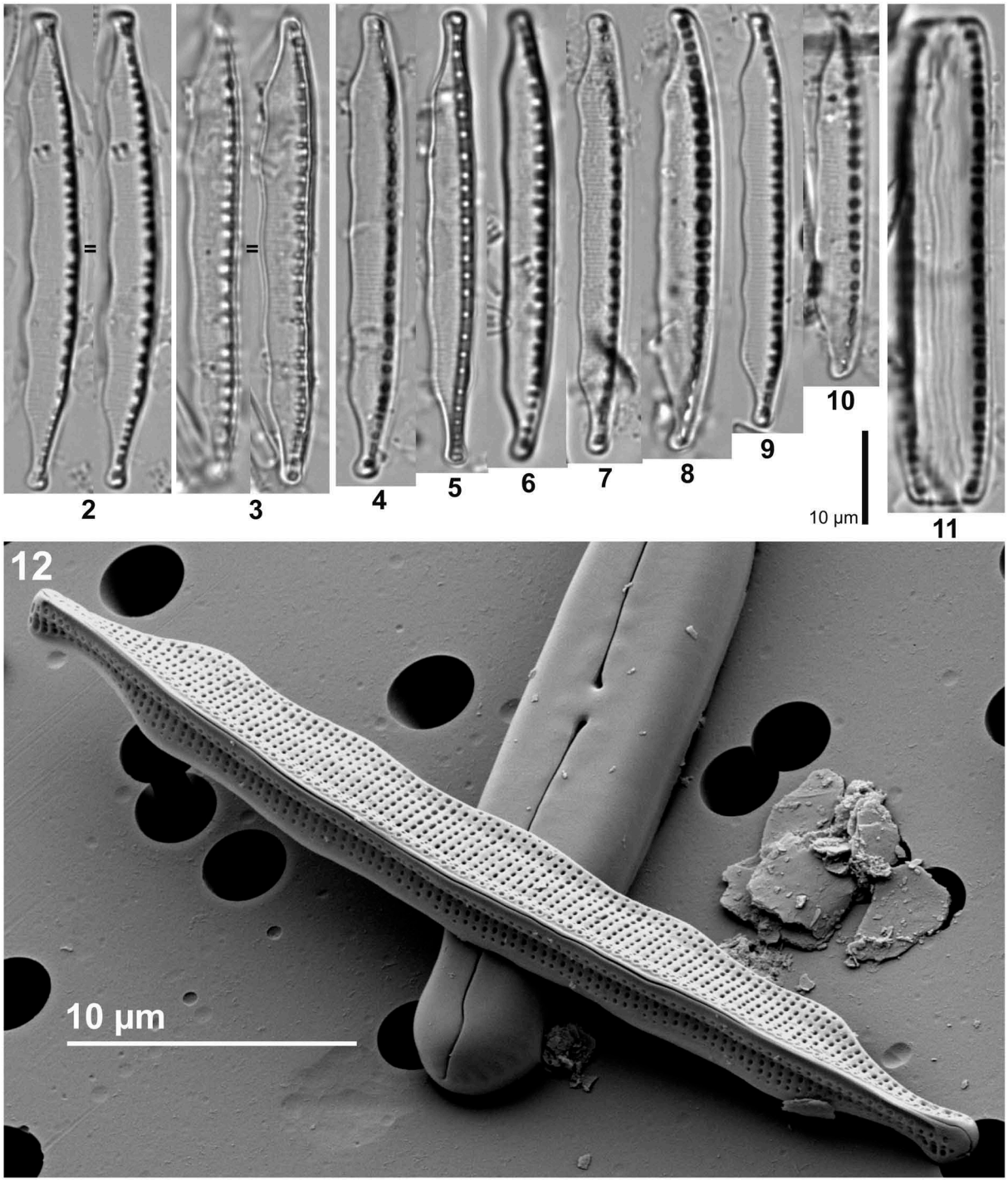

Figure 2-12. *Nitzschia transtagensis*. LM and SEM from type material. Figure 2–10. LM photographs from slide BR-4564. Valve views showing convex primary side and undulated secondary side. Figure 11. LM. Girdle view showing wavy girdle bands. Figure 12. SEM. Tilted and external view of a valve showing continuous raphe running along a suspended hyaline area, and pattern of areolation.

Physical and chemical characteristics of the spring water

The stream fed by the spring presented, at the time of collection of the type material, 21.3 ºC, pH moderately alkaline (8.4), high DO saturation (80.9%), low EC (237 S cm ^{1}), low TN (2.04 mg N L ^{1}), NO_3 (0.89 mg NO_3 L ^{1}) and NO_2 (0.003 mg NO_2 L ^{1}) concentrations; low PO_4 concentration (0.4 mg PO_4 L ^{1}). However, the TP concentration (1.44 mg P L ^{1}) is above the limit (0.13 mg P L ^{1}) for the "good" ecological status classification for small streams in southern Portugal (type S1 <100 km^2), according to the Water Framework Directive.

Additional sampling of the spring, carried out on 15 November 2018, yielded a neutral pH (7.2), medium DO saturation (58.7%), EC of 337 S cm ^{1}, low concentrations of TN (2.42 mg N L ^{1}), NO_3 (6.99 mg NO_3 L ^{1}) and NO_2 (0.003 mg NO_2 L ^{1}), low PO_4 concentration (0.1 mg PO_4 L ^{1}), but high TP concentration (0.92 mg P L ^{1}). These fall measurements

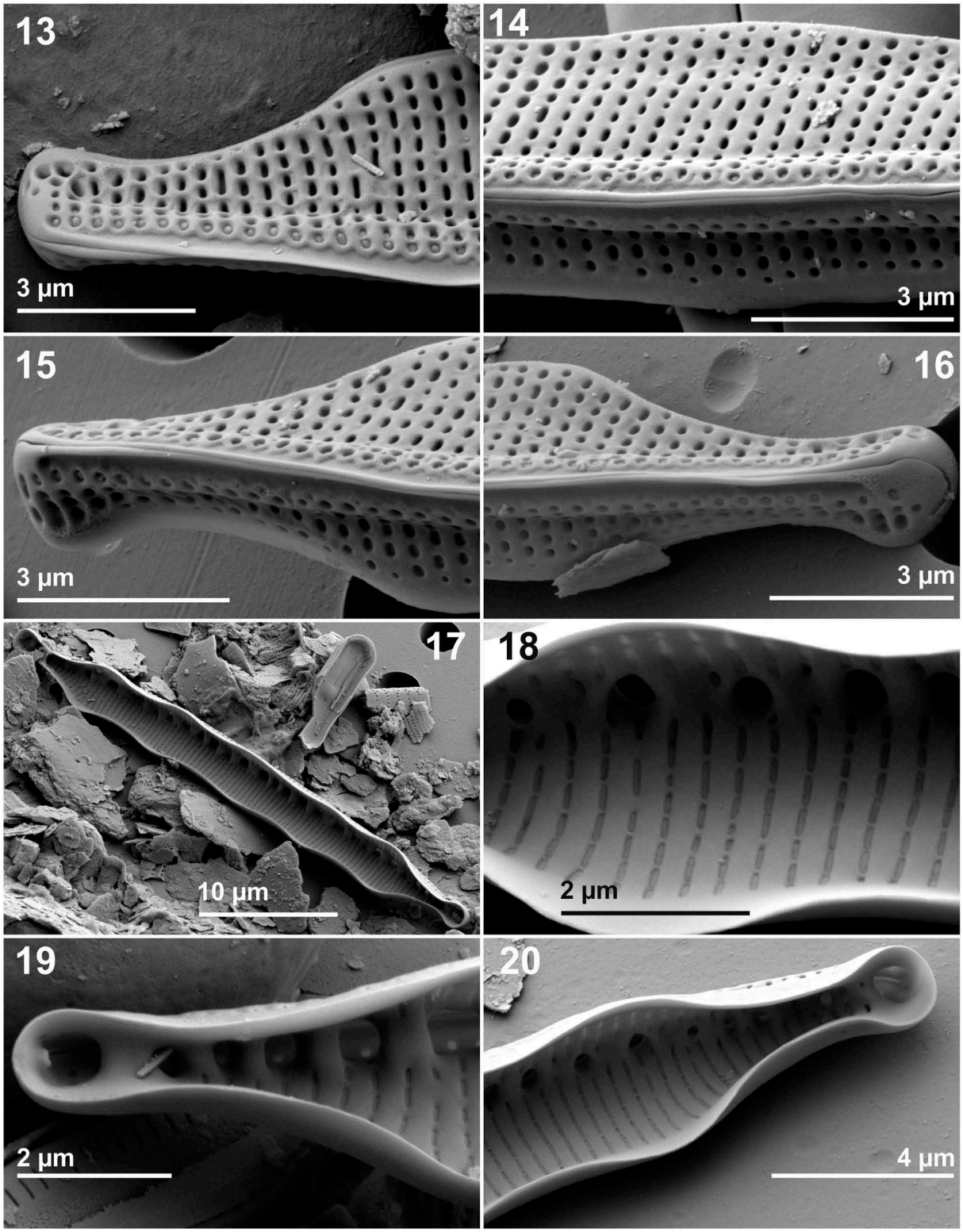

Figure 13-20. SEM images of *Nitzschia transtagensis* from type material. Figure 13, 15, 16. External views of distal ends showing features of the raphe, areolae, hyaline suspended area and valve face and mantle. Figure 14. External view of the central area showing continuous raphe. Internal views of whole (17) and distal ends of valves. Notice position of hymens occluding the areolae, fibulae, raphe canal and the helictoglossa.

indicate that water chemistry is variable at the type locality. Since the highest number of valves of the new taxon was found in January, winter conditions are probably closer to the optima it requires.

Discussion

Nitzschia transtagensis belongs to the *Lineares* section *sensu* Krammer and Lange-Bertalot (1988). The characteristics that the new taxon shares with members of

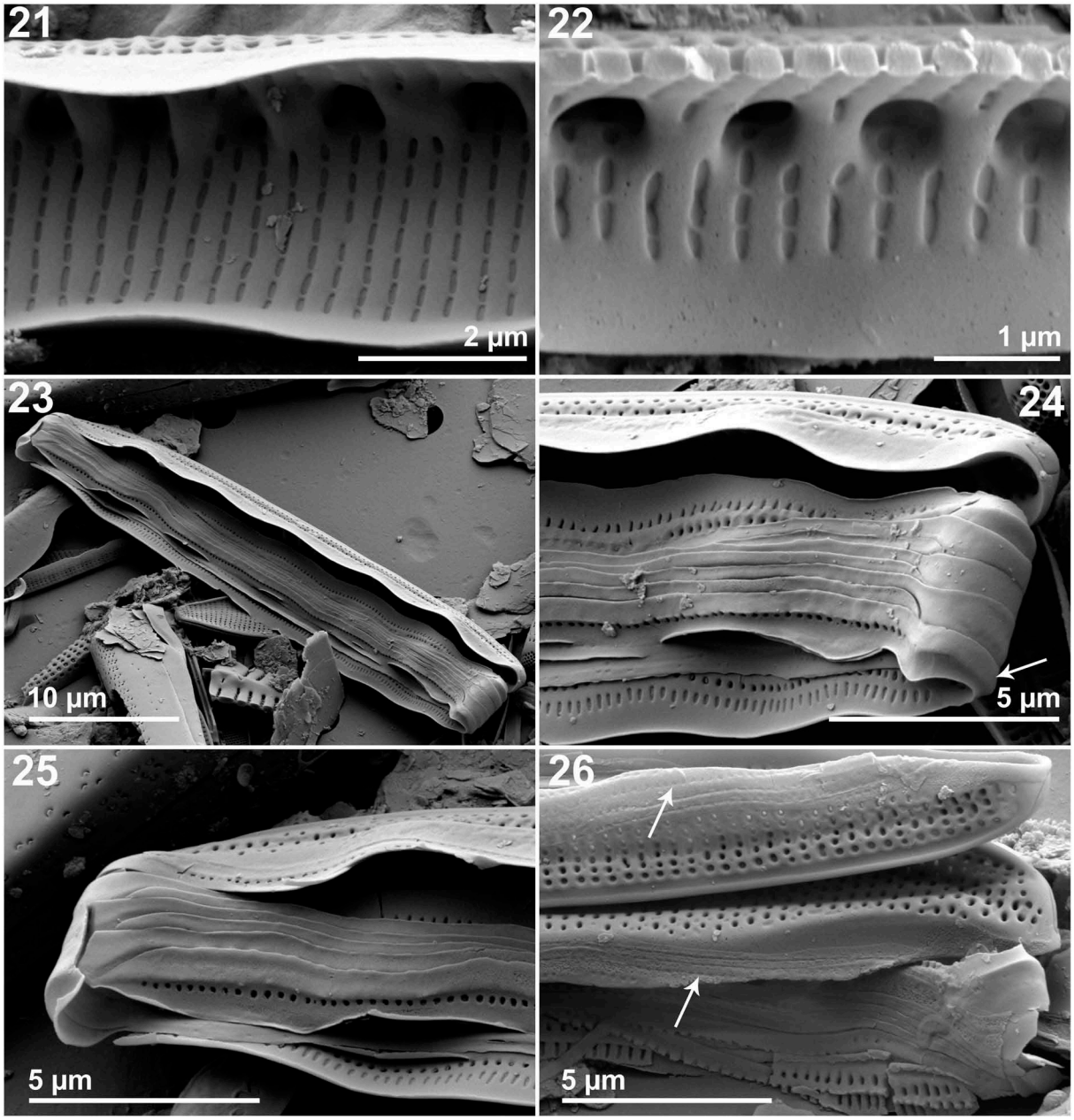

Figure 21–26. SEM images of *Nitzschia transtagensis* from type material. Figure 21, 22. Close internal views of hymens and fibulae. Notice thick structure of the valve in the broken portion of Figure 22. Figure 23–26. Views of the girdle (Figure 24 and 25 are close-ups of 23). Notice apically asymmetric copulae (arrow in Figure 24) and copulae bearing a single row or pores (arrows in Figure 26). Figure 24 also shows close contact of valves of two continuous cells.

that section are that valves are not sigmoid (Figure 10), no transapical costae are present (Figure 2–11) and thus the fibulae do not extend onto the valve face (Figure 17–22). The new species also lacks a conopeum (Figure 12–16) and the valve apices are rostrate to capitate with the keel fully eccentric. Although there could be a slightly wider separation of fibulae at the valve center in the new taxon (Figure 17, 21), denoting the central nodule, the raphe slit is continuous (Figure 14).

The apical asymmetry with an undulated pattern on the secondary side of *N. transtagensis* has not been reported for any other taxon. In the case of *Nitzschia sinuata* (Thwaites) Grunow both the primary and secondary sides are wavy and in *Nitzschia brevissima* Grunow there is a middle constriction that produces two swollen areas from the center of the valve to its apices on each side of the valves (Krammer and Lange-Bertalot 1997) (Table 1). However, the structure of both of these diatoms is very different from that in the new species. *Nitzschia sinuata* belongs to the *Grunowia* section (Krammer and Lange-Bertalot 1988), which is now recognized as a separate genus from *Nitzschia* (Kociolek 2018), though a type still needs to be chosen for it (Guiry and Guiry 2019). *Nitzschia transtagensis* has a central nodule only visible in internal view (Figures 17 and 21) and denoted by a wide fibula; a central nodule is absent in

N. sinuata. The extended fibulae over the valve face in inner view are absent in *N. transtagensis* and the striae are denser and composed of narrower areolae than in *N. sinuata*.

On the other hand, *Nitzschia brevissima* belongs to the *Obtusae* section (Krammer and Lange-Bertalot 1988). The valve ends are short, generally rostrate, with strong middle valve constriction that results in a wide concavity on the primary side of the valve and a slight to absent concavity on the secondary side. Valves are sigmoid and the central nodule is not only evident in the separation of the fibulae, but also in the discontinuity of the raphe (Krammer and Lange-Bertalot 1997). The multiple undulations on the secondary valve side and the convex primary side of *N. transtagensis* (Figure 2–9) are absent in *N. brevissima*, while the concavity of the primary side present in the latter is absent in *N. transtagensis*. The new species is not sigmoid and, as stated before, the central nodule only shows a wider spacing of the fibulae, but not a discontinuity of the raphe.

The new species (except for the apical asymmetry) resembles species such as *Nitzschia vitrea* G.Norman, *N. vitrea* var. *salinarum* Grunow, and *N. hierosolymitana* D. G.Mann, but none of them has a wavy secondary valve side and a primary abvalvar mantle edge (Mann 1980; Krammer and Lange-Bertalot 1988; Stenger-Kovács and Lengyel 2015) (Table 1). As in the three taxa mentioned above, *N. transtagensis* has square to rectangular fibulae, with square to round interfibular spaces. Also, the three taxa have round to elongated areolae delimited by vimines of varying lengths. Likewise, the three taxa have a raphe that is elevated along a hyaline keel. We have not been able to find high magnification SEM images of the valve interior and central areas of *N. vitrea*, its var. *salinarum* or *N. hierosolymitana*, thus we can not determine if there is also a resemblance with the new species regarding the inner position of hymens and the continuous character of the raphe. Mann (1980) presented two external SEM images of *N. vitrea* in girdle view, partially showing the cingulum. From these images, it can be noticed that the girdle elements are open, ligulated, and that the valvocopula is perforated and larger. Also, it is noticeable that none of the elements in *N. vitrea* are undulated, therefore, the wavy feature of the cingulum of *N. transtagensis* seems to be a unique feature within the group (Table 1).

Regarding the asymmetry in the structure of girdle elements, it is known that copulae and valvocopulae may have different structures in other nitzschioids, as it happens in *Nitzschia bizertensis* Smida, Lundholm, Hlaili & Mabrouk, in which the copulae bear one row of pores, while the valvocopula has two (Smida et al. 2014). Also, *Nitzschia navis-varingica* Lundholm & Moestrup has valvocopulae with 2–3 rows of pores, while the copulae may have 1–2 rows, possess scattered pores or lack them altogether (Lundholm and

Table 1. Comparison of *Nitzschia transtagensis* with close morphological relatives within the *Lineares* section.

Feature	*N. transtagensis*	*N. ebroicensis*	*N.* aff. *ebroicensis*	*N. hierosolymitana*	*N. vitrea*	*N. vitrea* var. *salinarum*
Length; width (µm)	L: 30.5–50.4; W: 4.5–6.0	L: 32–40; W: 4–5	L: 34–45; W: 4.5–4.8	L: 25–45; W: 5–6	L: 30–200; W: 9.5–14	L: 30–85; W: 5–9
Striae, fibulae and areolae in 10 µm	Str.: 30–35; Fib.: 8–10; Ar.: 35–45	Str.: 28–30; Fib.: 7–8; Ar.: 26	Str.: 26; Fib.: ca. 9; Ar.: 23–25	Str.: 33–35; Fib.: 2.5–5	Str.: 20–22; Fib.: 4–8	Str.: 25–30; Fib.: 5–7
Outline	Convex primary side with slightly undulated abvalvar edge of mantle, undulated secondary side	Convex primary side, convex to straight secondary side	Convex primary side, undulated secondary side	Convex primary side, convex to straight secondary side	Convex primary side, convex to straight secondary side	Convex primary side, convex to straight secondary side
Cingulum	Dimorphic with apically asymmetric valvocopula. All elements open	Unknown	Unknown	Dimorphic, valvocopula closed, not apically asymmetric, bearing a single row of pores and fringed abvalvar edge. All other elements open	Valvocopula larger, but can not be determined to be dimorphic based on available information. All elements open	Unknown
Reference	This study	Lange-Bertalot et al. (2003)	Lange-Bertalot et al. (2003)	Mann (1980, also as *Hantzschia fenestrata* Hustedt)	Krammer and Lange-Bertalot (1988); Lange-Bertalot et al. (2003)	Krammer and Lange-Bertalot (1988)

Moestrup 2000). Mann (1980) showed that *N. hierosolymitana* also has dimorphic girdle bands. The valvocopulae in this species are closed, have a single row of pores and are fringed along their abvalvar perimeter, while the open copulae bear a single row of pores and are not fringed. Mann (1980) also showed that the row of pores in all elements is located on the pars interior so when the girdle is intact they are unnoticed. *Nitzschia transtagensis* in turn, has girdle elements that are open all less silicified, but the pores in all are located in the pars interior as in *N. hierosolymitana* (Figure 23–25).

Nitzschia transtagensis, besides having dimorphic girdle elements, also exhibits an apical asymmetry in the valvocopula with one row of pores on the portion attached to the valve secondary side and two rows present on the portion attached to the primary valve side (Table 1, Figure 23, 24). As far as we know, this feature is also unique to this species and constitutes the first report of an apically asymmetric valvocopula within the Bacillariaceae. However, this uniqueness has to be confirmed by close inspection of the cingulum in the *Dubiae* and *Bilobatae* sections of *Nitzschia* species.

Lange-Bertalot et al. (2003) reported *Nitzschia* (aff.) *ebroicensis* R.Maillard from Sardinian pools. Their Figure 11–13 (pl. 97) coincide with what we are presenting here as *N. transtagensis*. Both populations have a convex primary side and an undulated secondary side. Length and width of the valves (34–45 µm and 4.5–4.8 µm in the aff. *ebroicensis* against 30.5–50.4 µm and 4.5–6.0 µm in *N. transtagensis*, respectively) overlap in both, and the features of the fibulae (9 in aff. *ebroicensis* against 8–10 in the Portuguese taxon) and interfibular spaces are also similar. Regarding the stria density, however, the aff. *ebroicensis* from Sardinia is coarser (26 in 10 µm against 30–35 in 10 µm in *N. transtagensis*). Additionally, the punctae are also coarser in the Sardinian population (23–25 in 10 µm against 35–45 in 10 µm in the Portuguese population) (Table 1).

We agree with Lange-Bertalot et al. (2003) that the Sardinian population is not *N. ebroicensis* for all the arguments they exposed (e.g. difference in valve outline and dimensions) and that what they called *N.* aff. *ebroicensis* should be considered as a new taxon. They did not erect a new species since they considered they lacked sufficient information, but with the information we collected from Portugal, we consider that it is now possible to include the Sardinian population within *N. transtagensis*. However, since there are differences in stria and puncta density, the Italian population could be kept as a separate variety. Since the locality and sample information in Lange-Bertalot et al. (2003) is not clear, the erection of the new variety is postponed until more information is available.

Acknowledgments

We thank Dr. Saúl Blanco for guidance regarding the name of the new species.

Disclosure statement

No potential conflict of interest was reported by the authors.

Funding

Funding for this research was partly provided the European Union through the European Regional Development Fund, framed in COMPETE 2020 (Operational Programme Competitiveness and Internationalization), through the ICT project (UID/GEO/04683/2013) with reference POCI-01-0145-FEDER-007690, the Alentejo Observation and Prediction Systems - ALOP project (ALT20-03-0145-FEDER-000004), and the Agência Portuguesa do Ambiente, APA-00004DFIN.AALP/2017 integrated within the Operational Program for Sustainability and Efficiency in the Use of Resources 2014-20, POSEUR-03-2013-FC -000001. Co-funding was provided by in the framework of the DIATOMS project (LIST - Luxembourg Institute of Science and Technology).

Notes on contributors

Eduardo A. Morales Contribution: Fieldwork, LM analysis, discovery of the new species, paper project designer and promoter, writing and development of the manuscript.

Carlos E. Wetzel Contribution: SEM analysis, plates, discussion of results and development of the manuscript.

Maria Helena Novais Contribution: fieldwork, sample processing and preparation, data analysis and development of the manuscript.

M. Manuela Morais Contribution: research project designer, paper promoter and development of the manuscript.

Luc Ector Contribution: Provision of literature, discussion of results and development of the manuscript.

ORCID

Eduardo A. Morales http://orcid.org/0000-0001-5998-4831
Carlos E. Wetzel http://orcid.org/0000-0001-5330-0494
Maria Helena Novais http://orcid.org/0000-0002-0870-2221
M. Manuela Morais http://orcid.org/0000-0003-0482-4309
Luc Ector http://orcid.org/0000-0002-4573-9445

References

APHA. 1995. Standard methods for the examination of water and wastewater. 19th. Washington (D.C): American Public Health Association, American Water Works Association, and Water Pollution Control Federation.

Barber, HG, EY Haworth. 1981. A guide to the morphology of the diatom frustule with a key to the British freshwater Genera. Freshw Biol Assoc Sci Pub. 44:1–112.

Blanco, S, C Cejudo-Figueiras, I Álvarez-Blanco, E Bécares, L Hoffmann, L Ector. 2010. Atlas de las diatomeas de la cuenca del Duero. Léon: Universidad de León, Área de Publicaciones; p. 382.

Cantoral-Uriza, EA, M Aboal Sanjurjo. 2008. Diatomeas (Bacillariophyceae) del marjal Oliva-Pego (Comunidad Valenciana, España). Anales del Jardín Botánico de Madrid. 65(1):111–128. doi:10.3989/ajbm.2008.v65.i1.249

Cardoso, RM, PMM Soares, DCA Lima, A Semedo. 2016. The impact of climate change on the Iberian low-level wind jet: EURO-CORDEX regional climate simulation. Tellus. 68(1):29005. doi:10.3402/tellusa.v68.29005

Cemagref. 1982. Etude des méthodes biologiques quantitatives d'appréciation de la qualité des eaux. Pierre-Bénite: Rapport Division Qualité des Eaux Lyon - Agence financière de Bassin Rhône-Méditerranée-Corse.

Cox, EJ. 2012. Ontogeny, homology, and terminology – wall morphogenesis as an aid to character recognition and character state definition for pennate diatom systematics. J Phycol. 48(1):1–31. doi:10.1111/j.1529-8817.2011.01081.x

Cox, EJ, R Ross. 1981. The striae of pennate diatoms. In R Ross, editor. *Proceedings of the sixth symposium on recent and fossil diatoms. Budapest, September 1-5, 1980*. Koenigstein: Otto Koeltz; p. 267–278.

Denys, L, H Lange-Bertalot. 1998. Observations on two taxa of the section Nitzschiae Lanceolatae (Bacillariophyceae): *Nitzschia blankaartensis* sp. nov. and *N. bulnheimiana*. Nova Hedwig. 67(1–2):247–258.

Guiry, MD, GM Guiry. 2019. "*AlgaeBase*". World-wide electronic publication, National University of Ireland, Galway. Accessed 2019 Jun 17. http://www.algaebase.org

Hamilton, PB, KR Laird. 2001. *Nitzschia pseudosinuata* sp. nov., a new Holocene diatom from the sediment of Moon Lake, North Dakota, U.S.A. Diatom Res. 16(2):317–324. doi:10.1080/0269249X.2001.9705523

Hamsher, S, K Kopalová, JP Kociolek, R Zidarova, B Van de Vijver. 2016. The genus *Nitzschia* on the South Shetland Islands and James Ross Island. Fottea. 16(1):79–102. doi:10.5507/fot.2015.023

Hlúbiková, D, S Blanco, E Falasco, J Gomà, L Hoffmann, L Ector. 2009. *Nitzschia alicae* sp. nov. and *N. puriformis* sp. nov., new diatoms from European rivers and comparison with the type material of *N. sublinearis* and *N. pura*. J Phycol. 45(3):742–760. doi:10.1111/j.1529-8817.2009.00692.x

Hofmann, G, M Werum, H Lange-Bertalot. 2011. Diatomeen im Süßwasser-Benthos von Mitteleuropa. Bestimmungsflora Kieselalgen für die ökologische Praxis. Über 700 der häufigsten Arten und ihre Ökologie. Rugell: A.R.G. Gantner Verlag K.G.

INAG, IP. 2008. Manual para a Avaliação Biológica da Qualidade da Agua em Sistemas Fluviais Segundo a Directiva-Quadro da Água – protocolo de Amostragem e Análise para o Fitobentos – diatomáceas. Lisboa: Ministério do Ambiente, do Ordenamento do Território e do Desenvolvimento Regional. Instituto da Água, I. P; p. 35.

Khan-Bureau, DA, L Ector, EA Morales, EJ Wade, LA Lewis. 2017. Contrasting morphological and DNA barcoding methods for diatom (Bacillariophyta) identification from environmental samples in the Eightmile River in Connecticut, USA. Nova Hedwig Beih. 146:279–302. doi:10.1127/1438-9134/2017/279

Kociolek, JP. 2018. A worldwide listing and biogeography of freshwater diatom genera: a phylogenetic perspective. Diatom Res. 33(4):509–534. doi:10.1080/0269249X.2019.1574243

Krammer, K, H Lange-Bertalot. 1986. "Bacillariophyceae 1. Teil: naviculaceae. In H Ettl, J Gerloff, H Heynig, D Mollenhauer, G F Verlag, editors. Süsswasserflora von Mitteleuropa 2/1. Stuttgart (Jena): Gustav Fischer Verlag; p. 876.

Krammer, K, H Lange-Bertalot. 1988. Bacillariophyceae 2. Teil: bacillariaceae, Epithemiaceae, Surirellaceae. In H Ettl, J Gerloff, H Heynig, D Mollenhauer, editors. Süsswasserflora von Mitteleuropa 2/2. Stuttgart (Jena): Gustav Fischer Verlag; p. 596.

Krammer, K, H Lange-Bertalot. 1991a. Bacillariophyceae 3. Teil: centrales, Fragilariaceae, Eunotiaceae. In H Ettl, J Gerloff, H Heynig, D Mollenhauer, editors. Süsswasserflora von Mitteleuropa 2/3. Stuttgart (Jena): Gustav Fischer Verlag; p. 576.

Krammer, K, H Lange-Bertalot. 1991b. Bacillariophyceae 4. Teil: achnanthaceae. Kritische Ergänzungen zu *Navicula* (Lineolatae) und *Gomphonema*. Gesamtliteraturverzeichnis Teil 1–4. In H Ettl, J Gerloff, H Heynig, D Mollenhauer, editors. *Süsswasserflora von Mitteleuropa* 2/4. Stuttgart (Jena): Gustav Fischer Verlag; p. 437.

Krammer, K, H Lange-Bertalot. 1997. Bacillariophyceae 2. Teil: bacillariaceae, Epithemiaceae, Surirellaceae. In H Ettl, J Gerloff, H Heynig, D Mollenhauer, editors. Süsswasserflora von Mitteleuropa 2/2. Stuttgart (Jena): Gustav Fischer; p. 611.

Lange-Bertalot, H, P Cavacini, N Tagliaventi, S Alfinito. 2003. Diatoms of Sardinia. Rare and 76 new species in rock pools and other ephemeral waters. Iconographia Diatomologica. 12:1–438.

Lange-Bertalot, H, G Hofmann, M Werum, M Cantonati. 2017. Freshwater benthic diatoms of central europe: over 800 common species used in ecological assessment. English edition with updated taxonomy and added species. edited by, M Cantonati, M G Kelly, H Lange-Bertalot. Schmitten-Oberreifenberg: Koeltz Botanical Books. p. 1–942.

Lecointe, C, M Coste, J Prygiel. 1993. "Omnidia": software for taxonomy, calculation of diatom indices and inventories management. Hydrobiologia. 269/270:509–513. doi:10.1007/BF00028048

Lobban, CS, MP Ashworth, JJM Calaor, EC Theriot. 2019. Extreme diversity in fine-grained morphology reveals fourteen new species of conopeate *Nitzschia* (Bacillariophyta: bacillariales). Phytotaxa. 401(4):199–238. doi:10.11646/phytotaxa.401.4.1

Lundholm, N, Ø Moestrup. 2000. Morphology of the marine diatom *Nitzschia navis-varingica*, sp. nov. (Bacillariophyceae), another producer of the neurotoxin domoic acid. J Phycol. 36(6):1162–1174. doi:10.1046/j.1529-8817.2000.99210.x

Mann, DG. 1980. *Hantzschia fenestrata* Hust. (Bacillariophyta) – *Hantzchia* or *Nitzschia*? Br Phycol J. 15(3):249–260. doi:10.1080/00071618000650241

Mann, DG. 1981. A new species of sigmoid *Nitzschia* (Bacillariophyta). Isr J Bot. 30(1):1–10.

Morais, P. 2008. Review on the major ecosystem impacts caused by damming and watershed development in an Iberian basin (SW-Europe): focus on the Guadiana estuary. Int J Limnol. 44(2):105–117. doi:10.1051/limn:2008012

Morales, EA. 2015. On the synonymy of *Nitzschia frustulum* var. *subsalina, N. inconspicua* and *N. boliviana sensu* Trobajo et al. 2013. Acta Nova. 7(2):112–119.

Novais, MH, D Hlúbiková, M Morais, L Hoffmann, L Ector. 2011. Morphology and ecology of *Achnanthidium caravelense* (Bacillariophyceae), a new species from Portuguese rivers. Arch Hydrobiol Suppl Algol Stud. 136/137:131–150. doi:10.1127/1864-1318/2011/0136-0131

Novais, MH, I Jüttner, B Van de Vijver, MM Morais, L Hoffmann, L Ector. 2015. Morphological variability within the *Achnanthidium minutissimum* species complex (Bacillariophyta): comparison between the type material of *Achnanthes minutissima* and related taxa, and new freshwater *Achnanthidium* species from Portugal. Phytotaxa. 224 (2):101–139. doi:10.11646/phytotaxa.224.2.1

Reichardt, E. 1997. Taxonomische Revision des Artenkomplexes um *Gomphonema pumilum* (Bacillariophyceae). Nova Hedwig. 65(1–4):99–129.

Rimet, F, P Chaumeil, F Keck, L Kermarrec, V Vasselon, M Kahlert, A Franc, A Bouchez. 2016. R-Syst::diatom:an open-access and curated barcode database for diatoms and freshwater monitoring. Database (Oxford). article ID baw016. doi:10.1093/database/baw016

Rimet, F, L Kermarrec, A Bouchez, L Hoffmann, L Ector, LK Medlin. 2011. Molecular phylogeny of the family Bacillariaceae based on 18s rDNA sequences: focus on freshwater *Nitzschia* of the section *Lanceolatae*. Diatom Res. 26(3):273–291. doi:10.1080/0269249X.2011.597988

Round, FE, RM Crawford, DG Mann. 1990. The diatoms: biology & morphology of the genera. Cambridge: Cambridge University Press.

Rovira, L, R Trobajo. 2023. S. Sato, C. Ibáñez, and D. G. Mann. 2015. "Genetic and physiological diversity in the diatom *Nitzschia inconspicua*.". J Eukaryot Microbiol. 62(6):815–832. doi:10.1111/jeu.12240

Smida, DB, N Lundholm, WHCF Kooistra, I Sahraoui, MV Ruggiero, Y Kotaki, M Ellegaard, C Lambert, HH Mabrouk, AS Hlaili. 2014. Morphology and molecular phylogeny of *Nitzschia bizertensis* sp. nov.–A new domoic acid-producer. Harmful Algae. 32:49–63. doi:10.1016/j.hal.2013.12.004

Soares, PMM, RM Cardoso, DCA Lima, PMA Miranda. 2017. Future precipitation in Portugal: high-resolution projections using WRF model and EURO-CORDEX multi-model ensembles. Clim Dyn. 49(7–8):2503–2530. doi:10.1007/s00382-016-3455-2

Stenger-Kovács, C, E Lengyel. 2015. Taxonomical and distribution guide of diatoms in soda pans of Central Europe. Stud Bot Hung. 46(Suppl.):3–203. doi:10.17110/StudBot.2015.46.Suppl.3

Trobajo, R, DG Mann, E Clavero, KM Evans, P Vanormelingen, RC McGregor. 2010. The use of partial *cox*1, *rbc*L and LSU rDNA sequences for phylogenetics and species identification within the *Nitzschia palea* species complex (Bacillariophyceae). Eur J Phycol. 45 (4):413–425. doi:10.1080/09670262.2010.498586

Trobajo, R, L Rovira, L Ector, CE Wetzel, M Kelly, DG Mann. 2013. Morphology and identity of some ecologically important small *Nitzschia* species. Diatom Res. 28(1):37–59. doi:10.1080/0269249X.2012.734531

Tudesque, L, F Rimet, L Ector. 2008. A new taxon of the section Nitzschiae Lanceolatae Grunow: *Nitzschia costei* sp. nov. compared to *N. fonticola* Grunow, *N. macedonica* Hustedt, *N. tropica* Hustedt and related species. Diatom Res. 23(2):483–501. doi:10.1080/0269249X.2008.9705771

Van Dam, H, A Mertens, J Sinkeldam. 1994. A coded checklist and ecological indicator values of freshwater diatoms from The Netherlands. Neth J Aquat Ecol. 28(1):117–133. doi:10.1007/BF02334251

Van de Vijver, B, L Ector, ME Beltrami, M de Haan, E Falasco, D Hlúbiková, A Jarlman, M Kelly, MH Novais, AZ Wojtal. 2011. A critical analysis of the type material of *Achnanthidium lineare* W. Sm. (Bacillariophyceae). Arch Hydrobiol Suppl Algol Stud. 136/137:167–191. doi:10.1127/1864-1318/2011/0136-0167

Wallin, M, T Wiederholm, RK Johnson. 2003. Guidance on establishing reference conditions and ecological status class boundaries for inland surface waters. Luxembourg: CIS (EU Common Implementation Strategy for the Water Framework Directive) Working Group 2.3.

Xie, S-Q, T Li. 1994. A new diatom species of salt lake from Shanxi Province. Acta Phytotaxonomica Sinica. 32 (3):273–274. in Chinese.

Zimmermann, J, N Abarca, N Enk, O Skibbe, W-H Kusber, R Jahn. 2014. Taxonomic reference libraries for environmental barcoding: a best practice example from diatom research. PLoS One. 9(9):e108793. doi:10.1371/journal.pone.0108793

Atmospheric Research 228 (2019) 223–241

Contents lists available at ScienceDirect

Atmospheric Research

journal homepage: www.elsevier.com/locate/atmosres

Extreme, wintertime Saharan dust intrusion in the Iberian Peninsula: Lidar monitoring and evaluation of dust forecast models during the February 2017 event

Alfonso J. Fernández[a], Michäel Sicard[b,c,*], Maria J. Costa[d], Juan L. Guerrero-Rascado[e,f], José L. Gómez-Amo[g], Francisco Molero[a], Rubén Barragán[b,c], Sara Basart[h], Daniele Bortoli[d], Andrés E. Bedoya-Velásquez[e,f], María P. Utrillas[g], Pedro Salvador[a], María J. Granados-Muñoz[b,1], Miguel Potes[d], Pablo Ortiz-Amezcua[e,f], José A. Martínez-Lozano[g], Begoña Artíñano[a], Constantino Muñoz-Porcar[b], Rui Salgado[d], Roberto Román[e,f,i], Francesc Rocadenbosch[b,c], Vanda Salgueiro[d], José A. Benavent-Oltra[e,f], Alejandro Rodríguez-Gómez[b], Lucas Alados-Arboledas[e,f], Adolfo Comerón[b], Manuel Pujadas[a]

[a] Department of Environment, Research Centre for Energy, Environment and Technology (CIEMAT), Madrid, Spain
[b] Department of Signal Theory and Communications, CommSensLab, Universitat Politècnica de Catalunya, Barcelona, Spain
[c] Ciències i Tecnologies de l'Espai - Centre de Recerca de l'Aeronàutica i de l'Espai/Institut d'Estudis Espacials de Catalunya (CTE-CRAE/IEEC), Universitat Politècnica de Catalunya, Barcelona, Spain
[d] Institute of Earth Sciences and Department of Physics, ECT and IIFA, Universidade de Évora, Évora, Portugal
[e] Department of Applied Physics, University of Granada, Granada, Spain
[f] Andalusian Institute for Earth System Research (IISTA-CEAMA), Granada, Spain
[g] Department of Physics of the Earth and Thermodynamics, University of Valencia, Valencia, Spain
[h] Earth Sciences Department, Barcelona Supercomputing Center (BSC), Barcelona, Spain
[i] Atmospheric Optic Group (GOA), University of Valladolid, Valladolid, USA

ARTICLE INFO

Keywords:
Extreme Saharan dust intrusion
Particle optical properties
Sun-photometer
Multi-wavelength lidar
Dust forecast model
Model evaluation
Vertical distribution

ABSTRACT

An unprecedented extreme Saharan dust event was registered in winter time from 20 to 23 February 2017 over the Iberian Peninsula (IP). We report on aerosol optical properties observed under this extreme dust intrusion through passive and active remote sensing techniques. For that, AERONET (AErosol RObotic NETwork) and EARLINET (European Aerosol Research LIdar NETwork) databases are used. The sites considered are: Barcelona (41.38°N, 2.17°E), Burjassot (39.51°N, 0.42°W), Cabo da Roca (38.78°N, 9.50°W), Évora (38.57°N, 7.91°W), Granada (37.16°N, 3.61°W) and Madrid (40.45°N, 3.72°W). Large aerosol optical depths (AOD) and low Ångström exponents (AE) are observed. An AOD of 2.0 at 675 nm is reached in several stations. A maximum peak of 2.5 is registered in Évora. During and around the peak of AOD, AEs close to 0 and even slightly negative are measured. With regard to vertically-resolved aerosol optical properties, particle backscatter coefficients as high as 15 Mm^{-1} sr^{-1} at 355 nm are recorded at the lidar stations. Layer-mean lidar ratios are found in the range 40–55 sr at 355 nm and 34–61 sr at 532 nm during the event. The particle depolarization ratios are found to be constant inside the dust layer, and consistent from one site to another. Layer-mean values vary in the range 0.19–0.31. Another remarkable aspect of the event is the limited vertical distribution of the dust plume which never exceeds 5 km. The extreme aspect of the event also presented a nice case for testing the ability of two dust forecast models, BSC-DREAM8b and NMMB/BSC-Dust, to reproduce the arrival, the vertical distribution and the intensity of the dust plume over a long-range transport region. In the particular case of the February 2017 dust event, we found a large underestimation in the forecast of the extinction coefficient provided by BSC-DREAM8b at all heights independently of the site. In contrast NMMB/BSC-Dust forecasts presented a better agreement with the observations, especially in southwestern part of the IP. With regard to the forecast skill as a function of lead time, no clear degradation of the prognostic is appreciated at 24, 48 and 72 h for Évora and Granada stations (South). However the prognostic does degrade (bias increases and/or correlation decreases) for Barcelona

* Corresponding author at: Department of Signal Theory and Communications, CommSensLab, Universitat Politècnica de Catalunya, Barcelona, Spain.
E-mail address: msicard@tsc.upc.edu (M. Sicard).
[1] Now at: Andalusian Institute for Earth System Research (IISTA-CEAMA), Granada, Spain

https://doi.org/10.1016/j.atmosres.2019.06.007
Received 13 March 2019; Received in revised form 7 June 2019
Available online 18 June 2019
0169-8095/ © 2019 The Authors. Published by Elsevier B.V. This is an open access article under the CC BY-NC-ND license (http://creativecommons.org/licenses/BY-NC-ND/4.0/).

(North), which is attributed to the fact that Barcelona is at a greater distance from the source region and to the singularity of the event.

1. Introduction

Mineral aerosols are usually originated over arid or semiarid regions as a consequence of continuous soil erosion produced by wind. The strong warming of desert areas during daytime produces vertical thermal turbulences that can reach altitudes of up to 5 km, followed by periods of nocturnal stability (Santos et al., 2013). Massive resuspension of huge amounts of mineral aerosols are thus produced and can be transported long distances by different mechanisms. Forty percent of the aerosol mass emitted into the troposphere is attributed to desert dust and it is considered as the second largest source of natural aerosols, after sea salt (Andreae, 1995; IPCC, 2001; Salvador et al., 2014). The main desert dust sources is the Sahara desert since it is responsible for more than half of the world atmospheric mineral dust (Prospero et al., 2002; Mahowald et al., 2005; Wagner et al., 2009; Salvador et al., 2016). Under specific synoptic meteorological situations, a large amount of Saharan dust is transported towards the Mediterranean basin over which the planetary boundary layer is usually relatively shallow (Lafontaine et al., 1990; Obregón et al., 2015; Khan et al., 2015; Cuevas et al., 2017).

In the last two decades the number of surveys addressing the study of atmospheric mineral aerosols, especially around the Mediterranean basin, has increased for several reasons. Firstly, from the climate change standpoint, mineral aerosols play an important role on the atmospheric radiative budget through scattering and absorption of the incoming solar and outgoing infrared radiation, and they act as cloud condensation nuclei (Klein et al., 2010; IPCC, 2013). Their large temporal and spatial variability is responsible for a high uncertainty degree in aerosol radiative forcing estimates (Forster et al., 2007; Boucher et al., 2013). Secondly, from the point of view of air quality, it has been demonstrated that African dust is the main particle source, contributing to the regional background levels of PM_{10} across the Mediterranean (35–50% of PM_{10}) with maximum contributions up to 80% of the total PM_{10} mass (Pey et al., 2013). The sporadic but intense natural contributions of PM have been responsible for a high number of exceedances of the PM_{10} daily limit value (50 $\mu g/m^3$, according to the 2008/50/EC European Directive) as registered in different rural and urban monitoring sites across the Mediterranean Basin (Querol et al., 2009; Salvador et al., 2013).

The large temporal and spatial variability of mineral dust in the atmosphere mentioned earlier makes its systematic monitoring a difficult task which, as of today, still represents a problematic issue that the scientific community, and especially the observation and modelling communities, are trying to address. Some works based on long-term databases have indicated that the Mediterranean basin is affected by African dust intrusions following a marked seasonal pattern (Mona et al., 2006; Salvador et al., 2013; Pey et al., 2013; Sicard et al., 2016): summer prevalence has been detected in the western part; no seasonal trend has been observed in the central region and higher contributions of desert dust have been commonly produced in spring-early summer in the eastern part of the basin. Very recently an increasing number of works have reported statistics and tendency of intense (i.e. strong and extreme) Saharan dust events in the Mediterranean Basin. At a given site and for a given aerosol optical depth (AOD) climatology (from either ground- or satellite-based sensors), Gkikas et al. (2013) suggested to define strong and extreme events with two threshold levels defined as a function of the mean (Mean) and standard deviation (Std) of the AOD: Mean + 2 x Std and Mean + 4 x Std. Strong events fulfil Mean + 2 x Std ≤ AOD < Mean + 4 x Std, and extreme events fulfil AOD ≥ Mean + 4 x Std. To get an idea of the low probability of occurrence of strong and extreme mineral dust events in winter, Gkikas et al. (2013) calculated the seasonal frequency of occurrence in the western Mediterranean Basin over land and for the period 2000–2007 of strong and extreme events to be 1 and 1.2%, respectively. In spite of this small percentage, two relevant strong and extreme mineral dust events (following the definition of Gkikas et al. (2013)) have been recorded in the last three years in the Iberian Peninsula (IP) during the winter season. In February 2016 a strong event (AOD ~ 0.4) affecting the whole IP has been documented with in situ/remote sensing instrumentation (Titos et al., 2017), ceilometers (Cazorla et al., 2017) and in-situ/AERONET/satellite instrumentation (Sorribas et al., 2017). In February 2017 an exceptionally extreme event (AOD > 2.0) affected again the whole IP, as examined with AERONET and MPLNET (Micro Pulse Lidar Network) lidars by Córdoba-Jabonero et al. (2019). The mineralogy of the event has been reported by Rodríguez-Navarro et al. (2018). The prediction of extreme dust intrusions by dust forecast models has only been treated seldomly in the literature (Huneeus et al., 2016, event with an AOD ~ 1.0; Ansmann et al., 2017, AOD ~ 0.6; Tsekeri et al., 2017, AOD ~ 0.4) as compared to single moderate events or long-term database of events independently of their intensity (Gobbi et al., 2013; Santos et al., 2013; Mona et al., 2014; Binietoglou et al., 2015; Sicard et al., 2015). However such predictions are essential to warn populations in advance and set plans to mitigate the severe effects that high levels of particulate matter may cause to lives and property.

In this article, we report on the extreme dust event that hit the Iberian Peninsula (IP) on 20–23 February 2017. The aim of the paper is twofold: 1) to provide an overview of the 4D spatio-temporal evolution of the dust optical properties observed by remote sensing instruments throughout the IP, and 2) to evaluate the capabilities of dust transport models to reproduce such extreme dust events. The paper is organized as follows: the instruments and methodology are briefly described in Section 2. Section 3 deals with the description of the synoptic situation and columnar aerosol optical properties from sun and sky photometers. In Section 4, vertically-resolved optical properties are discussed. Section 5 presents the performance of the dust models. Finally, conclusions can be found in Section 6.

2. Instruments and methodology

2.1. AERONET sun-photometers in the IP

The AErosol RObotic NETwork (AERONET) is a global ground-based network of sun/sky multi-wavelength CIMEL CE-318 sun-photometers that provides long-term records of atmospheric columnar aerosol optical properties (Holben et al., 1998). The CIMEL spectral sun-photometer measures the direct solar irradiances with a field of view of approximately 1.2° and the sky radiances (in the almucantar and principal plane scenarios), at several spectral channels (see Table 1). The direct-sun measurements are used to obtain the spectral AOD, Ångström exponent at several wavelength pairs and precipitable water vapor, approximately every 15 min. The AOD uncertainty, mainly due to the calibration, is estimated to vary between 0.01 and 0.02 (Holben et al., 1998).

The sky radiance measurements can be inverted to estimate aerosol optical properties such as the size distribution, the percentage of spherical particles in the aerosol mixture, several microphysical parameters describing the total, fine and coarse aerosol modes and numerous spectral quantities: complex refractive index, single scattering albedo, phase function, asymmetry parameter, extinction and absorption optical depths. The aerosol properties retrieved are also used for calculating the broad-band fluxes at the bottom and top of the

Table 1
Summary of the sites considered in the study: main characteristics of the AERONET sun-photometers and EARLINET lidars used.

Site	Long.	Lat.	Altitude	AERONET		EARLINET				
				Wavelengths		Elastic wavelengths	Raman wavelengths	Vertical resolution	Start time	Stop time
	(°)	(°)	(m a.s.l.)	(nm)		(nm)	(nm)	(m)	(UTC)	(UTC)
BA	2.11 E	41.39 N	115	440, 675, 870, 1020		355, 532 total, 532 cross, 1064	387, 407, 607	3.75	08:11 (23 Feb)	23:54 (23 Feb)
BU	0.42 W	39.51 N	60	340, 380, 440, 500, 675, 870, 1020, 1640		355 cross and parallel	387	15	No measurements available	
CR	9.50 W	38.78 N	140	340, 380, 440, 500, 675, 870, 1020		No lidar available				
EV	7.91 W	38.57 N	293	340, 380, 440, 500, 675, 870, 1020		355, 532, 532 cross, 1064	387, 607	30	00:00 (20 Feb)	23:59 (23 Feb)
GR	3.61 W	37.16 N	680	340, 380, 440, 500, 675, 870, 1020		355, 532 parallel, 532 cross, 1064	387, 407, 607	7.5	12:00 (20 Feb)	18:00 (20 Feb)
									19:00 (20 Feb)	21:00 (20 Feb)
									07:31 (21 Feb)	14:21 (21 Feb)
									07:31 (22 Feb)	20:00 (22 Feb)
MA	3.72 W	40.45 N	669	340, 380, 440, 500, 675, 870, 1020		355, 532, 1064	387, 407, 607	7.5 (elastic) 3.75 (Raman)	21:00 (22 Feb)	23:36 (22 Feb)
									05:00 (23 Feb)	08:00 h UTC (23 Feb)
									11:00 (23 Feb)	11:52 (23 Feb)

The site acronyms are: BA for Barcelona, BU for Burjassot, CR for Cabo da Roca, EV for Évora, GR for Granada and MA for Madrid.

atmosphere. An estimation of the aerosol radiative forcing and forcing efficiencies are also provided. A detailed description of the version 2 AERONET inversion products is given by Holben et al. (2001). Table 1 shows the six AERONET stations distributed in the IP that were considered in this study: Barcelona (BA), Burjassot (BU), Cabo de Roca (CR), Évora (EV), Granada (GR) and Madrid (MA).

2.2. EARLINET lidars in the IP

The European Aerosol Research Lidar Network, EARLINET, included in the European Research Infrastructure for the observation of Aerosol, Clouds and Trace Gases (ACTRIS), aims at creating a quantitative, comprehensive, and statistically significant database for the horizontal, vertical, and temporal distribution of aerosols on a continental scale, providing the most extensive collection of ground-based data for the aerosol vertical distribution over Europe (Pappalardo et al., 2014). In this work four Iberian EARLINET stations (BA, MA, EV and GR) provided lidar data, all of them equipped with multi-wavelength lidars and some of them with depolarization capabilities (see Table 1). Burjassot lidar station was not available at this moment.

The EARLINET protocol establishes that lidar measurements have to be carried out on a regular basis: on Monday (at 14 UTC and at sunset) and on Thursday (sunset). Under exceptional events, as the one described in this work, EARLINET stations are encouraged to perform additional measurements in order to monitor the event over the longest period of time possible. During the period of 20–23 February 2017, EARLINET lidar measurements over the IP were performed as reported in Table 1. A temporal averaging of the profiles of 30 to 60 min was performed depending on the measurement duration available in order to guarantee a proper signal-to-noise ratio throughout the vertical column. Vertically resolved particle coefficients were derived by means of the Klett-Fernald algorithm (Klett, 1981; Fernald, 1984). This algorithm requires an assumption of the lidar ratio (LR), defined as the ratio of the particle extinction (α) to the particle backscatter (β) coefficient. We have used a generic value of 50 sr which can be considered a typical value of mineral dust (Guerrero-Rascado et al., 2008, 2009; Müller et al., 2009, 2010; Preissler et al., 2011). Whenever possible during nighttime, α and β coefficient profiles were retrieved independently with the Raman algorithm (Ansmann et al., 1992), which in turn allows computing the vertically-resolved lidar ratios. The benefit of Raman, multi-wavelength lidar products is that they provide some intensive parameters, such as the lidar ratio and the Ångström exponent, useful for the analysis of aerosol optical properties. The Ångström exponent (Ångström, 1964) is inversely related to the size of the particles: the greater the exponent, the smaller the particles and vice versa (Amiridis et al., 2009). The Ångström exponent, $AE(\lambda_1, \lambda_2)$, of a quantity α is defined for the wavelength pair (λ_1, λ_2) as:

$$AE(\lambda_1, \lambda_2) = -\frac{\log\left(\frac{\alpha(\lambda_1)}{\alpha(\lambda_2)}\right)}{\log\left(\frac{\lambda_1}{\lambda_2}\right)} \quad (1)$$

The Ångström exponent can be calculated for both the extinction and the backscatter coefficients. Whenever Raman, multi-wavelength inversions were available, the extinction Ångström exponent, AE, was calculated. The backscatter Ångström exponent, $\beta - AE$, was calculated for all inversions. Lidar systems equipped with depolarization channels (BA, EV and GR) also provided the aerosol volume and particle depolarization ratio and thus relevant information about the aerosol shape.

With regard to the errors associated to the measurements, we made use of the Monte-Carlo technique to estimate the uncertainties of the vertically-resolved backscatter and extinction coefficients. This technique is based on the random extraction of new lidar signals, where each bin is considered a sample element of a given probability distribution with the experimentally observed mean value and standard deviation. The extracted lidar signals are then processed with the same algorithm to obtain a set of solutions from which the standard deviation

is inferred as a function of height (Pappalardo et al., 2004). These statistical errors appear as error bars in the lidar-derived profiles of the backscatter and extinction coefficients.

2.3. Description of the models evaluated and methodology

The present analysis utilizes the operational 72-h dust forecasts of the BSC-DREAM8b (Pérez et al., 2006; Basart et al., 2012) and the NMMB/BSC-Dust (Pérez et al., 2011) models (http://www.bsc.es/ess/information/bsc-dust-daily-forecast) for the period from 19 to 22 February 2017. Both models are developed and operated at the Barcelona Supercomputing Center (BSC) and they are the two models considered for the development of the near-real time (NRT) evaluation within the Sand and Dust Storm Warning Advisory and Assessment System (SDS-WAS) Regional Center (https://sds-was.aemet.es/projects-research/evaluation-of-model-derived-dust-vertical-profiles). The NRT evaluation consists in comparing the modeled dust optical thickness to the observed total AOD provided by AERONET Version 3 and 2, Level 1.5 data. The Ångström exponent calculated between the wavelength pair (440, 870 nm) is used to distinguish the situations in which mineral dust is the dominant aerosol type. Threshold discrimination is made by discarding observations with an Ångström exponent higher than 0.6. Table 2 summarizes the main parameters used in the configuration of the models.

The modeled dust extinction values at 550 nm are directly compared with the observed particle extinction values at 532 nm because of the wavelength proximity and the low spectral extinction dependence of mineral dust (see Section 4). In order to have continuous observations and to maximize their number, day and nighttime inversions of particle backscatter coefficients are used and converted to extinction using a constant lidar ratio of 50 sr, a value validated later in Section 4. The vertical resolution of both dust models is much coarser than the lidar vertical resolution. In order to evaluate the models' capability to reproduce the vertical distribution of the dust extinction coefficient, the original lidar vertical resolution is downgraded to the resolution of the modeled profiles.

Given that the extinction value at a given height, h_i, of the models is the average extinction of the layer comprised between $h_i - \frac{h_i - h_{i-1}}{2}$ and $h_i + \frac{h_{i+1} - h_i}{2}$, the extinction value of the lidar profile at height h_i is calculated as the mean value of the original lidar profile (at the lidar original vertical resolution) calculated in the exact same layer of each model. For the horizontal resolution, the lidar data can be considered as point observations, while the models represent uniform pixels of 0.33° resolution (~33 km). The temporal resolution is also different: while the models provide instantaneous profiles with time steps of 3 h, the lidar profiles are averaged over 30 or 60 min. Here we have compared each modeled profile at time t with a 30- (60-) min. Averaged lidar-derived profile included in the interval [t − 30, t + 29 min.] ([t − 60, t + 59 min.]). In case two consecutive measurements fulfil this criterion, the measurement which was running at time t is selected. The forecast skill analysis is performed in terms of two vertically integrated statistical indicators, namely the fractional bias (*FB*), and the correlation coefficient (r), as well as in terms of the center of mass (CoM). *FB* and r are both calculated for the extinction coefficient. The fractional bias is a normalized measure of the mean bias and indicates only systematic errors, which lead to an under/overestimation of the estimated values. The linear correlation coefficient is a measure of the models' capability to reproduce the shape of the aerosol profile. The vertical integration is made from the lowest pair of simultaneously available model and observed values up to 6 km. No lower limit was fixed because of the dust plume proximity to the ground surface. The upper limit was fixed to 6 km because nearly no dust was detected above that height. The CoM was approximated by the particle backscatter weighted altitude as defined in Mona et al. (2006) who noted that this approximation "exactly coincides with the true center of mass if both composition and size distribution of the particles are constant with the altitude".

In Section 5 we evaluate the model performances for forecasts of 24 h (Section 5.1) and then we compare these forecasts to longer ones of 48 and 72 h (Section 5.2) to see how the forecast skill behaves as the lead time increases. A forecast (or a lead time) of 24 h represents all forecasts in the range [0; 23 h] since the model initialization. 48 and 72 h forecasts represent all forecasts in the range [24; 47 h] and [48; 71 h] since the model initialization, respectively.

3. Synoptic situation, columnar properties and singularity of the event

3.1. Synoptic situation

During the period from 20 to 23 February 2017, the synoptic situation in the IP was dominated by the influence of an anticyclone centered northwest from the Western coast, extending in ridge to South Central Europe and by the existence of a low pressure system, initially centered over Morocco, as illustrated in the European Centre for Medium-Range Weather Forecasts (ECMWF) ERA5 reanalysis of the Geopotential height at 850 hPa at several hours (Fig. 1). This low is very likely to be associated to a Sharav cyclone (Alpert and Ziv, 1989). The plots presented in Fig. 1 also include the surface wind friction velocity (u_*), which is a good indicator of possible dust emissions from deserts (Alfaro and Gomes, 2001; Darmenova et al., 2009 and references therein). It is generally assumed that the dust flux from the surface involves a power law of the wind friction velocity, as well as some parameters that characterize the surface, as the fraction of vegetation, the surface roughness and the soil texture and water content. Significant dust emissions are likely to occur for high friction velocities (above 0.6 m s^{-1}), presenting lower sensitivity to land surface parameters (Darmenova et al., 2009).

The Geopotential field at 850 hPa (Fig. 1) indicates the persistence of an atmospheric flow advecting air from the central North Africa (Algeria) crossing the IP. On 20 February strong friction velocity values ($>$ 6 m s^{-1}) over Algerian Sahara (Fig. 1a), a major dust source region (Ginoux et al., 2012), are suitable to force dust aerosol emissions (Darmenova et al., 2009). The well-shaped deep low, centered over central Morocco transported air from Algeria to southern Spain. Over the Central and Northern parts of the Peninsula, the dominant wind brought air from central Europe under the anticyclonic circulation. Wind vectors at 850 hPa are not represented in Fig. 1 for the sake of clarity, though at this level it is reasonable to assume geostrophic wind. The situation maintains very similar in the next day and on the 22 February the low provokes high winds on the western side (central-northern Algeria), which may be seen by the proximity of the isopleths and by the strong values of the friction velocity (Fig. 1c), which indicates strong dust emissions. On 23 February the northward shift of the Moroccan low originated weak precipitation events in several locations

Table 2
Main parameters of the dust models used in this study.

	BSC-DREAM8b	NMMB/BSC-Dust
Meteorological driver	Eta/NCEP	NMMB/NCEP
Model domain	North Africa-Middle East-Europe (25° W – 60° E and 0° – 65° N)	
Initial and boundary conditions	NCEP/GFS data (at 0.5° × 0.5° horizontal resolution) at 12 UT are used as initial conditions and boundary conditions at intervals of 6 h	
Horizontal resolution	0.33° x 0.33°	
Vertical resolution	24 Eta-layers	40 σ-hybrid layers
Time step	3 h	
Dust size bins	8 (0.1–10 μm)	
Radiation interactions	Yes	
Dust initial condition	24 h forecast from the previous day's model run	

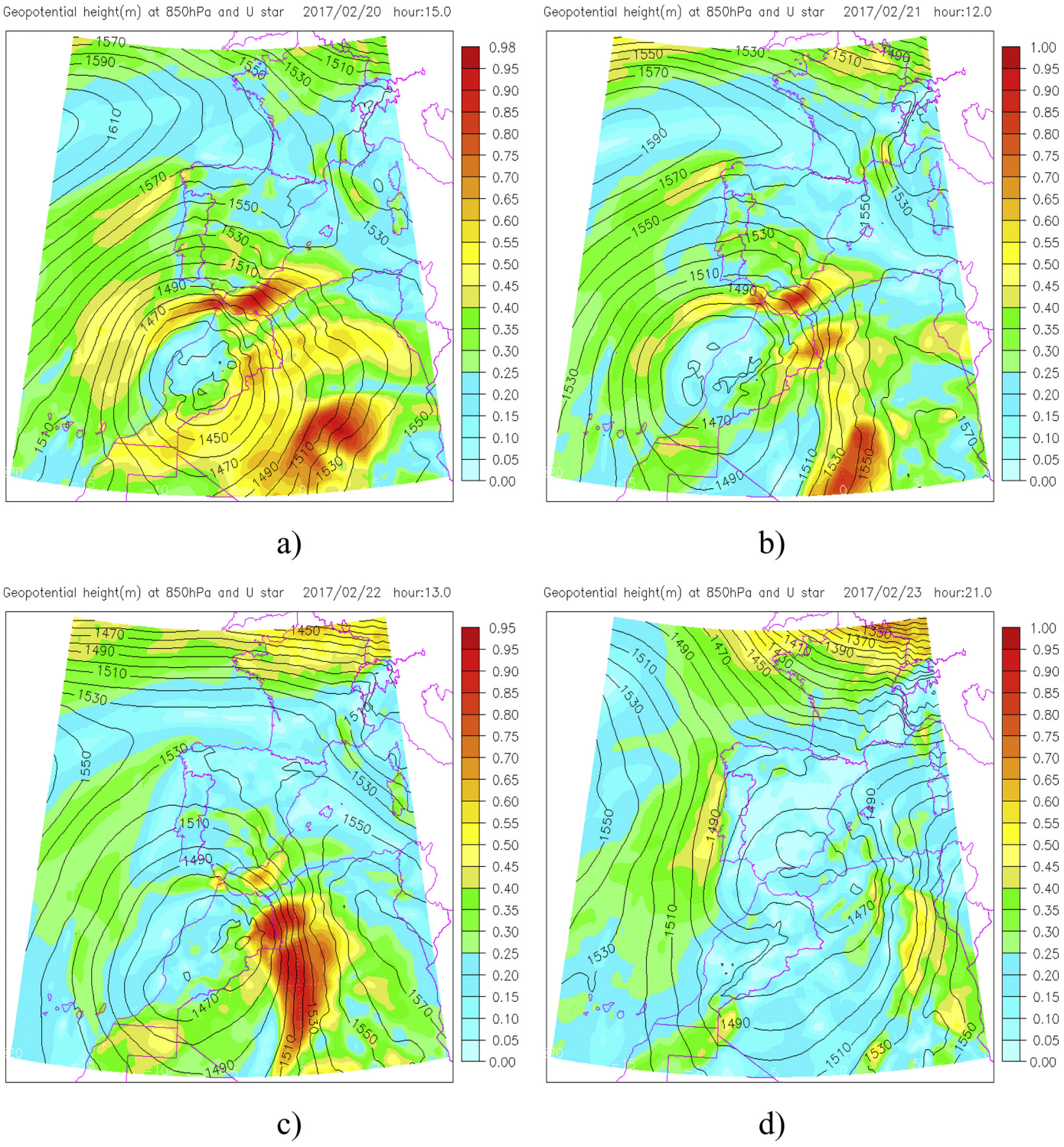

Fig. 1. ECMWF ERA5 reanalysis of the Geopotential height at 850 hPa (black height contours) and surface wind friction velocity (color bar in ms^{-1}) from 20 to 23 February 2017. Generated using Copernicus Atmosphere Monitoring Service information (CAMS, 2018). (For interpretation of the references to color in this figure legend, the reader is referred to the web version of this article.)

in the south of Portugal and Spain, but still transporting air from Algeria to Northeast Spain (Catalonia). The friction velocity over the desert regions dropped significantly, hinting at the end of the significant dust emissions. The synoptic conditions changed radically on 24 February with the passage of a frontal system that affected all the IP (not shown in Fig. 1).

Fig. 2 presents RGB composites based upon the combination of infrared channels (8.7, 10.8 and 12.0 μm) from the Spinning Enhanced Visible and InfraRed Imager (SEVIRI) on board Meteosat-10, showing the dust transport evolution (magenta) from 20 to 24 February 2017. The dust was transported across the Alboran Sea (western Mediterranean Sea) and infiltrated in southern Iberian atmosphere on 20 February (Fig. 2a), gradually transported towards west and north by the synoptic circulation, affecting the southern and western sites (CR, EV, GR) as illustrated by Fig. 2b and c. On the 22 February the dust intrusion was reinforced by a thick plume that progressively entered the

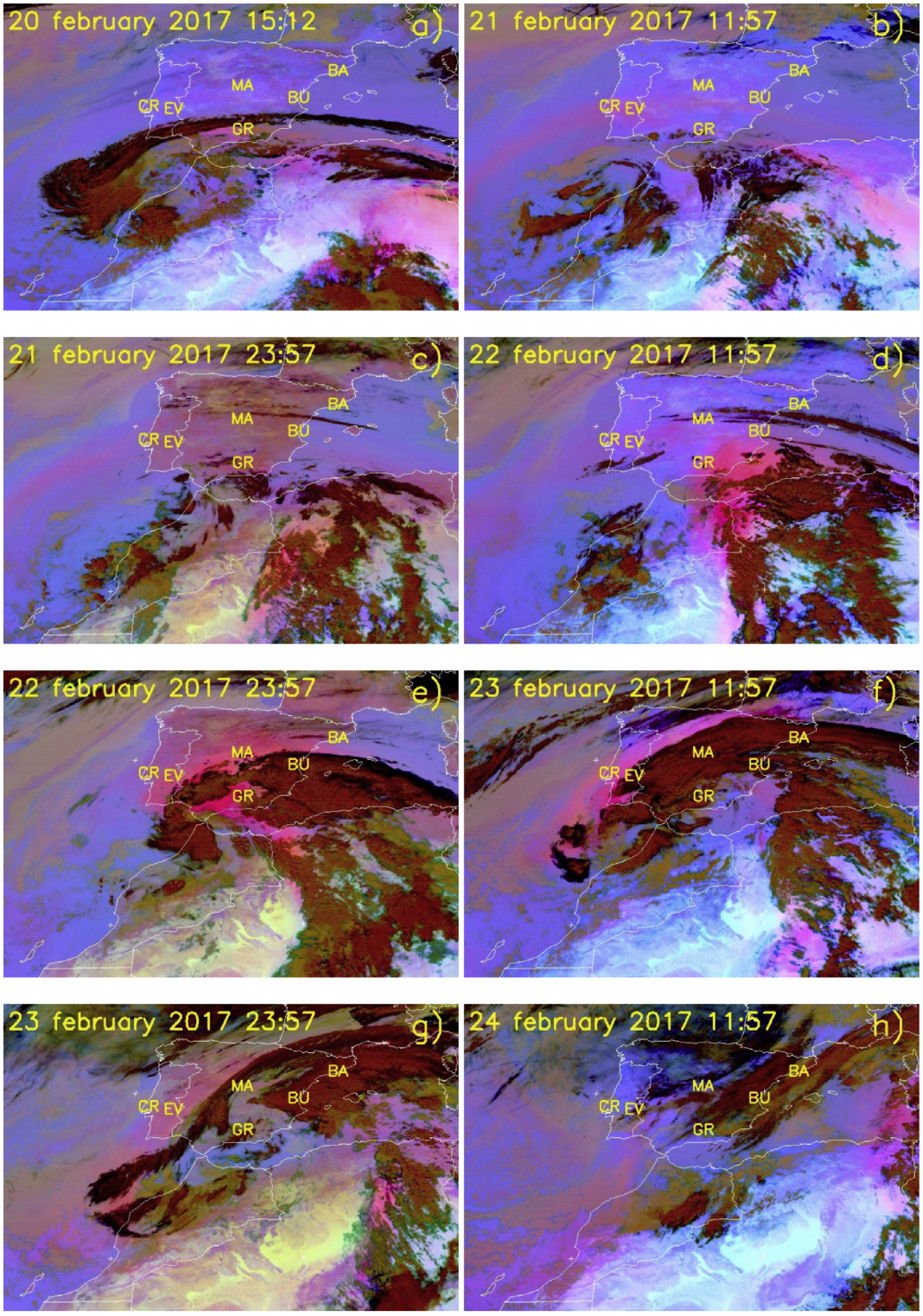

Fig. 2. Meteosat RGB composites showing the evolution of the dust plume from 20 to 24 February 2017. The Iberian sites considered in the study are also represented in the images: Barcelona (BA), Burjassot (BU), Cabo da Roca (CR), Évora (EV), Granada (GR) and Madrid (MA).

IP through the southeastern coast (Fig. 2d) extending north and westwards and affecting all sites represented in the images (Fig. 2e). This new intrusion was accompanied by the presence of high clouds that on the 23 February affected most of the IP, associated with the intensification and northward shift of the Moroccan low (Fig. 2f and g). The arrival of a frontal system from northwest on the 24 February interrupted the North African dust flow, pushing it towards the central Mediterranean regions (Fig. 2h).

The temporal evolution of the back-trajectories, from 20 to 24 February 2017, arriving over the six sites considered, at three atmospheric levels (2000, 3000 and 4000 m agl) is represented in the supplementary material in Fig. S1. The back-trajectories were calculated using the Hybrid Single-Particle Lagrangian Integrated Trajectory (HYSPLIT) model (Stein et al., 2015; Rolph et al., 2017), available

online at http://ready.arl.noaa.gov/HYSPLIT.php. The sequence shows that the first sites overpassed by air masses originating in northern Africa were: Granada (20 February; Fig. S1a), followed by Évora and Cabo da Roca (21 February; Fig. S1b and S1c). Burjassot and Madrid sites started to be influenced by North African air masses between the 21 and 22 February (Fig. S1d and S1e) and finally also Barcelona remained under the influence of the same air masses between the 23 and 24 February (Fig. S1f to S1h). Information from Meteosat RGB composites (Fig. 2) displaying the dust distribution over North African regions and back-trajectories (Fig. S1), hint at dust originating from central Algeria, where also strong values of wind friction velocities were found (Fig. 1).

3.2. Columnar properties

The desert dust plume entered the IP from the South on the 20 February, and then it gradually reached the northwest and later on the eastern part of the IP. Fig. 3 shows the time series data of AOD at 675 nm, Ångström exponent (440 and 870 nm) and SSA at 675 nm from 20 to 25 February 2017 in six sites distributed across the IP. An increase of the AOD was first noticed in Granada site on the 20 February, where the AOD values reach about 1.5, accompanied by very low values of AE, typical of desert dust intrusions, which is confirmed by the Meteosat composite in Fig. 2a. The dust plume maintains its influence over Granada and extends towards the western part of the IP, affecting in the next day also Évora and Cabo da Roca sites, with AOD values ranging between about 0.6 and 1.2, once again with very low AE (< 0.2). The dust transport continues and on the 22 February, during daytime, desert dust is detected in all stations except for Barcelona where it is measured on the next day. Still on the 22 February, extremely high AOD values are reached in Granada and Burjassot (> 2.0) and moderately high in Madrid, Évora and Cabo da Roca (0.5 < AOD < 1.0), with AE values lower than 0.2 for all these stations. The columnar size distribution (not shown) on 22 February shows a clear 3-mode distribution at Évora, Granada and Burjassot, with a coarse mode mean radius between 1.7 and 2.3 μm and a peak of the coarse mode volume concentration of

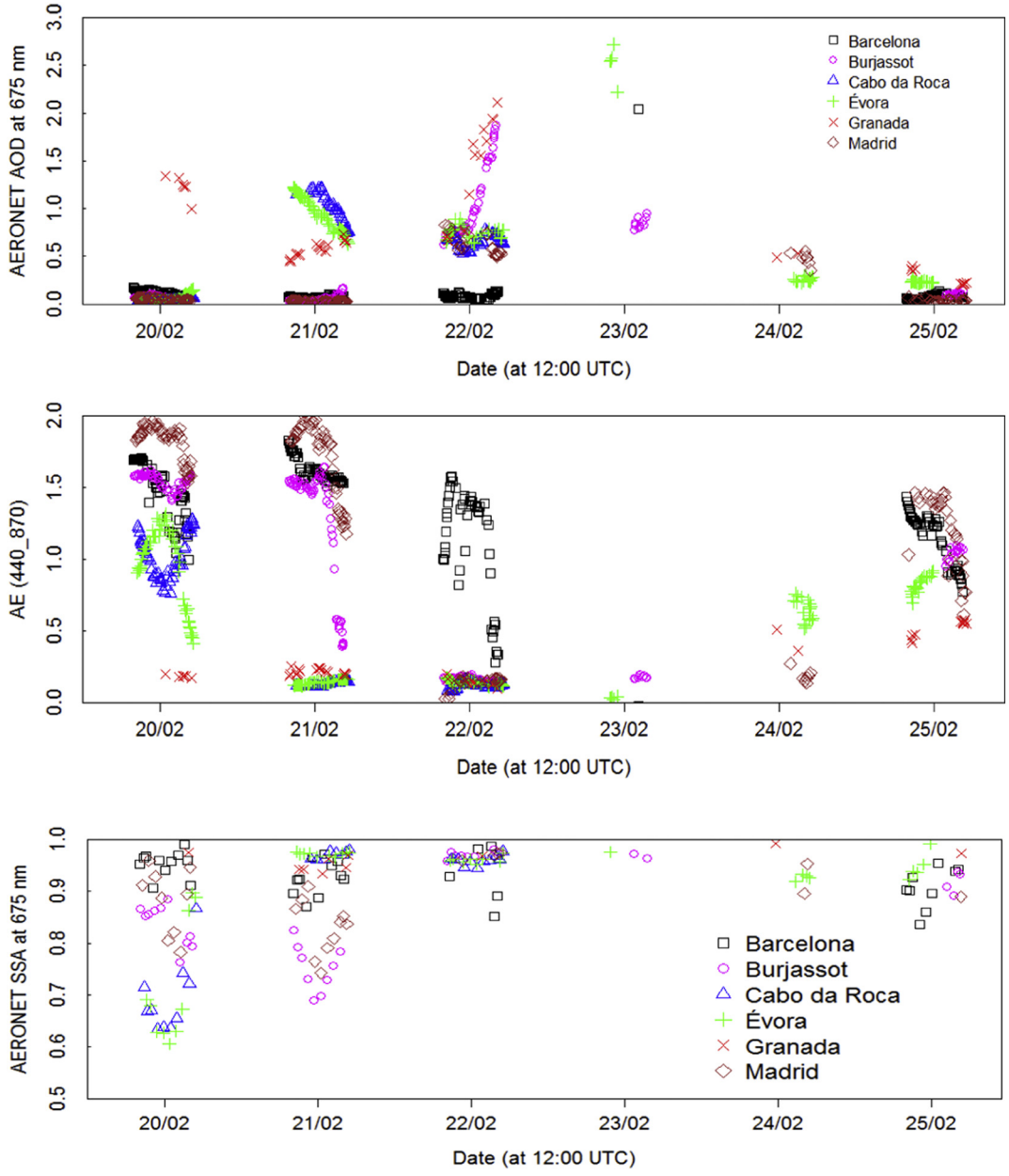

Fig. 3. AERONET AOD at 675 nm, AE (440 and 870 nm) and SSA at 675 nm from 20 to 25 February 2017 in six sites distributed across the IP.

$1\ \mu m^3\ \mu m^{-2}$ reached in the afternoon.

On the 23 February there are only a few AERONET measurements available due to the persistence of clouds over the region; nevertheless the AOD is still considerably high (> 2.0) at Évora and Barcelona with corresponding AE values around zero indicating the presence of air masses from desert dust source regions supported by the back-trajectories presented in the supplementary material (Fig. S1). As mentioned before, the frontal system on the 24 February interrupted the dust transport and the AOD values on the 24 and 25 February show a consistent decrease at all sites with a corresponding increase of the AE.

The single scattering albedo is characterized by relatively high values in all the stations during the dust event, showing the predominant dispersive nature of these particles. The lower SSA values (greater absorption) in the first two days in some of the sites (BU, CR, EV, MA) depicted in Fig. 3 are related with polluted air masses coming from northwestern Europe (not shown here).

3.3. Singularity of the dust event

The dust transport analyzed here regards a record-breaking episode that hit the Iberian Peninsula (IP) from 20 to 23 February 2017. According to AERONET (2019), this dust intrusion was the strongest over the IP since July 2012 and it is the strongest event (in terms of AOD) ever recorded over the IP during the month of February. It is noteworthy to mention that the AOD at 675 nm was > 2 in several AERONET stations and, during the most intense periods, some lidar and sun-photometer retrievals could not be performed due to high aerosol load, respectively, attenuating the lidar signal and blocking the sun. A

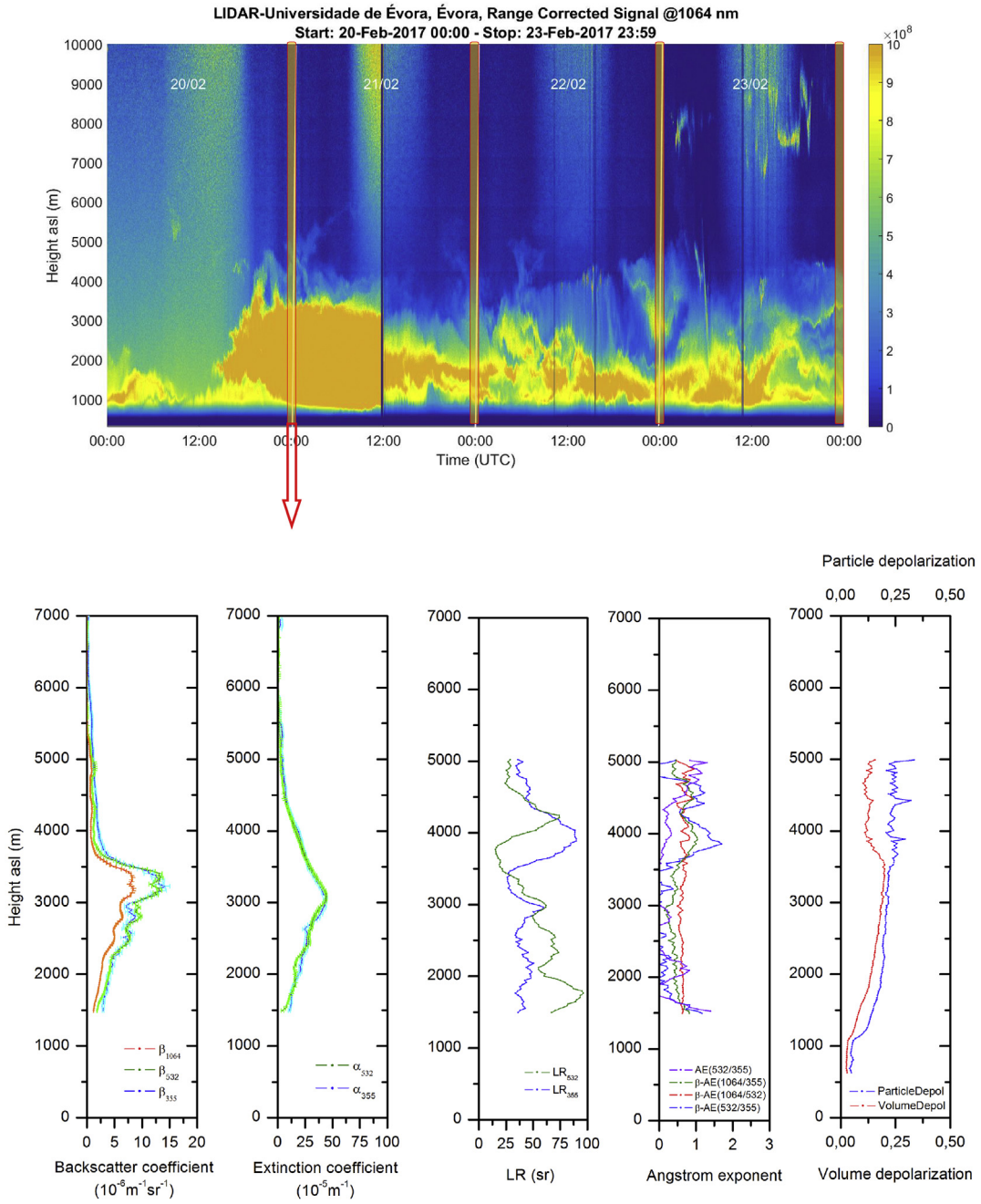

Fig. 4. (top) RCS at 1064 nm on 20–23 February 2017 at Évora (293 m asl); (bottom) Backscatter coefficient, extinction coefficient, Lidar ratio, Ångström exponents, and volume and particle depolarization ratio on 21 February 2017 at 00:00 UTC.

previous work concerning such events at the IP found AODs at 500 nm up to 1.5 in the south of Spain (Guerrero-Rascado et al., 2009), with maximum values of particle backscatter coefficients (15·Mm^{-1} sr^{-1} at 355 nm) similar to those registered during this event, however that event took place in September. Preissler et al. (2011) reported an aerosol optical thickness up to 2 in Portugal as a consequence of another extreme dust intrusion episode in April (Preissler et al., 2011).

Winter is the season when these phenomena are less likely to occur across the whole Mediterranean basin (Querol et al., 2009). However, extreme dust intrusions, as the one described in this paper or others that took place quite recently (Cazorla et al., 2017; Sorribas et al., 2017), occurred during the coldest season.

AERONET data presented in the supplementary material in Figs. S2 to S4 and Table S1 illustrate the exceptionality of this event in the region. Figs. S2 (and S3) show the density scatter plots of the AE (440–870) versus the AOT at 675 nm, using all available AERONET level 1.5 (level 2.0) data for each of the stations considered in the study. The black dots superimposed in these plots illustrate the values measured during the February 2017 desert dust intrusion. It can be noted that the event is positioned in a tail of the data group with very low AE accompanied by high AOT values. When quality-assured AERONET data is considered (Fig. S3), the event under study is characterized by the highest AOT values in almost all stations, except for Cabo da Roca and Madrid where these values are still very high and near the maxima.

Fig. S4 of the supplementary material shows percentile plots of AOT at 675 nm and AE (440–870) using all available Level 1.5 AERONET data, as well as the data corresponding to the event under study (black dots). Table S1 presents percentiles of AOT at 675 nm and AE (440–870), as well as a characterization of the desert dust based on the AOT at 550 nm following Gkikas et al. (2013). According to the fifth IPCC (2013) report, an extreme weather event can be defined as a rare phenomenon taking into account its historical statistical distribution for a particular place and/or time. Then 10th and 90th percentiles are usually considered as reference to define “rare”. As shown in Fig. S4, all AOT values measured during the February 2017 desert dust event are above the 90th percentile; simultaneously, all AE (440–870) values are below the 10th percentile, which in conformity with IPCC allows affirming that this was a rare event. Additionally, the methodology proposed by Gkikas et al. (2013) was applied and results are shown in the third table of Table S1. The mean AOT at 550 nm during the event, at each of the considered AERONET sites, was always greater than Mean + 4 x Std, which allows to define the episode as extreme. This is important to be highlighted as extreme weather events have been discussed and suggested to be connected to climate change. For instance some remaining questions concern whether or not such events take place earlier or later in the season or if their severity has been increased (WMO, 2011).

4. Vertically-resolved optical properties

4.1. Situation in Évora

Fig. 4 represents the temporal evolution of the Range Corrected Signal (RCS) during 4 days which provides a very detailed overview of the phenomenon, as well as a lidar inversion at a selected time. To note that on 21 February (12:00 UTC) a change of the neutral-density filters in front of the detection channel was necessary to be carried out in order to attenuate the received light. This obviously reduced the RCS at this point but did not affect the retrieval of aerosol optical properties. Four different periods have been selected so as to analyze aerosol optical properties from the African plume observed in Évora (highlighted in red in the top plot of Fig. 4). Nighttime measurements have been chosen for the analysis in order to estimate accurately such properties given the fact that independent extinction from Raman signals was available at this lidar station. The first period (21st Feb from 0:00–0:30 UTC) presents the highest backscatter coefficient values out of all periods evaluated, so a special attention has been paid to this period (bottom plot of Fig. 4). Notwithstanding the other 3 periods are also analyzed and results are shown in the supplementary material Figs. S5, S6 and S7. Mean aerosol optical properties are reported in Table 3 for specific atmospheric layers in which the dust plume is representative. During the first period analyzed (21st Feb from 0:00–0:30 UTC, bottom plot of Fig. 4) the African dust plume is detected up to 5 km height asl with a peak of the particle backscatter coefficient at 3.2 km asl. In the layer between 1.5 and 3.5 km asl, the layer-averaged values of the backscatter-related Ångström exponent at the wavelength pairs 532/355, 1064/532 and 1064/355 are 0.08 ± 0.33, 0.62 ± 0.04 and 0.42 ± 0.13, respectively. The extinction-related Ångström exponent at 532/355 nm is 0.16 ± 0.45. These small values are typical for dust as previously reported during extreme African dust intrusions (Guerrero-Rascado et al., 2009; Preissler et al., 2011; Mamouri et al., 2016). The other periods, except on 23 Feb. at 00:00 UTC, also show relatively low backscatter- and extinction-related Ångström exponent values. The relative high value on 23 Feb. at 00:00 UTC (β-AE between the pairs 1064/532–1.28) is probably due to artefacts from the optical inversions. On 23 Feb. around noon the highest aerosol load was recorded in Évora (AOD ~ 2.5). The signal attenuation on the lidar measurement was very strong and may have hampered the correct

Table 3
Summary of mean aerosol optical properties retrieved from Raman and elastic lidar measurements in Évora and in Granada for 4 selected periods.

Atmospheric layer	LR_{355} (sr)	LR_{532} (sr)	β-AE 1064-532	β-AE 532-355	β-AE 1064-355	AE 532-355	δ-vol.	δ-part.
ÉVORA								
00:00 UTC-21Feb 1.5–3. km asl	40 ± 8	61 ± 18	0.62 ± 0.04	0.08 ± 0.33	0.42 ± 0.13	0.16 ± 0.45	0.16 ± 0.03	0.19 ± 0.02
00:00 UTC-22Feb 1.5–4 km asl	45 ± 4	38 ± 8	0.76 ± 0.12	−0.12 ± 0.23	0.44 ± 0.08	0.16 ± 0.19	0.16 ± 0.01	0.21 ± 0.01
00:00 UTC-23Feb 1.5–5 km asl	52 ± 7	40 ± 9	1.28 ± 0.33	−0.62 ± 0.48	0.58 ± 0.19	0.01 ± 0.27	0.16 ± 0.02	0.19 ± 0.01
23:39 UTC-23Feb 1.5–4. km asl	55 ± 12	34 ± 8	1.00 ± 0.18	−0.96 ± 0.29	0.28 ± 0.17	0.18 ± 0.24	0.12 ± 0.01	0.15 ± 0.01
GRANADA								
13:30 UTC-20Feb 2.0–4.0 km asl			0.27 ± 0.12	0.19 ± 0.30	0.24 ± 0.04		0.19 ± 0.03	0.22 ± 0.04
20:00 UTC-20Feb 1.8–4.0 km asl	52 ± 7	53 ± 6	0.19 ± 0.08	0.54 ± 0.21	0.32 ± 0.07	0.51 ± 0.43	0.20 ± 0.02	0.25 ± 0.03
07:31 UTC-21Feb 1.5–3.4 km asl			0.86 ± 0.07	0.64 ± 0.13	0.77 ± 0.08		0.18 ± 0.03	0.28 ± 0.01
12:30 UTC-22Feb 1.5–4.0 km asl			0.39 ± 0.12	0.32 ± 0.17	0.36 ± 0.07		0.26 ± 0.01	0.31 ± 0.02

retrieval of the Rayleigh signal above the dust layer. The same phenomenon is observed at other stations.

Since Raman signals were available and extinction coefficients were obtained independently, particle lidar ratios were derived as well. The dust layer located between 1.5 and 3.5 km asl on 21Feb (00:00 UTC) presented a lidar ratio of 40 ± 8 sr and 61 ± 18 sr at 355 and 532 nm, respectively. Our estimates at 355 nm are in agreement with Mona et al. (2006) who found a mean lidar ratio at 355 nm of 38 ± 15 sr for three years of Raman lidar measurements of Saharan dust in southern Italy. Conversely, lidar ratio at 532 nm is found greater than the lidar ratio at 355 nm for the first period analyzed (21 Feb, 00:00 UTC), which is not usual for dust particles as it has been already pointed out by other authors (Müller et al., 2010). Nevertheless, this trend is only observed in the first period analyzed, the other three analyzed periods show a lidar ratio at 532 lower than the lidar ratio at 355 nm. The reason behind this observation (high unexpected lidar ratio values at 532 nm) can be attributed to non-accurate retrievals hampered by the high aerosol load which produces a great extinction and consequently a decrease of the signal-to-noise ratio. It is noteworthy to mention that the standard deviation of the mean lidar ratio at 532 nm on 21Feb (00:00 UTC) is significantly higher compared to the rest of the studied period. The lidar ratio at 355 nm on 23 Feb (at 00:00 and 23:39 UTC) seems a bit higher than values reported in the literature (Mona et al., 2006) and it could be due to a decrease of the African dust intrusion intensity and therefore a greater proportion of local aerosol might be present in the atmosphere. The lidar ratio at 532 nm in all cases (apart from the first period) are consistent with literature since typical values range 35–45 sr for typical desert dust (Mamouri et al., 2013; Nisantzi et al., 2015; Mamouri et al., 2016). In addition, the volume and particle depolarization ratio were 0.16 ± 0.03 and 0.19 ± 0.02 for the aforementioned atmospheric layer on 21Feb 00:00 UTC. These two latter parameters are constant with altitude, which indicates that no change in the aerosol type is observed within the atmospheric layer of interest. They are also very similar for the four periods studied,

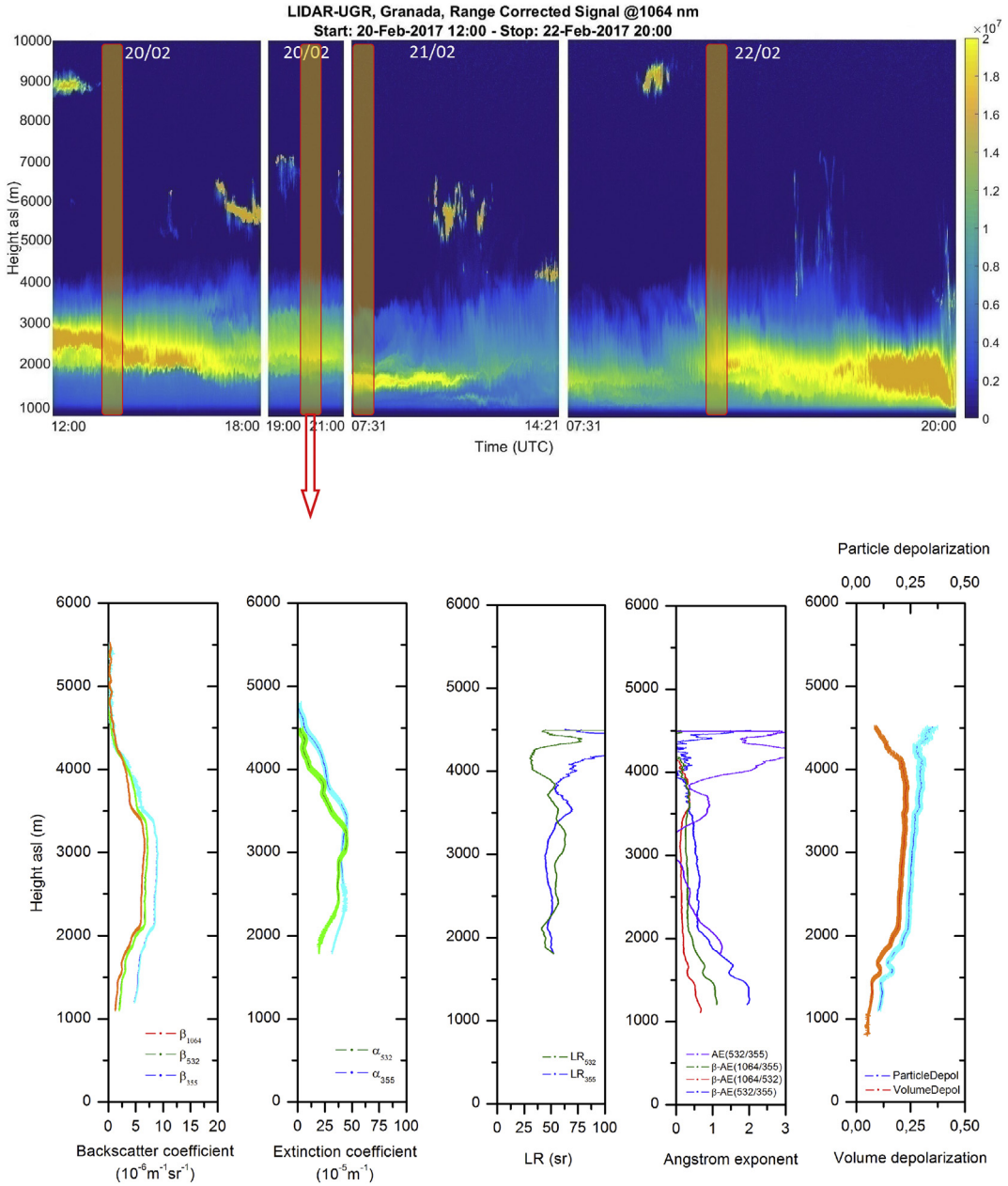

Fig. 5. (top) RCS at 1064 nm during four periods in the interval 20–23 February 2017 at Granada (680 m asl); (bottom) Backscatter coefficient, extinction coefficient, Lidar ratio, Ångström exponents, and volume and particle depolarization ratio on 20 February 2017 at 20:00 UTC.

however the last period indicates lower volume and particle depolarization values that is associated with the decrease of intensity of the Saharan dust intrusion and a greater contribution of local aerosols.

4.2. Situation in Granada

In Granada, lidar measurements were carried out during four periods of time during the extreme African dust intrusion: 12:00-18:00 and 19:00-21:00 UTC on 20 February, 07:31-14:21 UTC on 21 February, and 07:31-20:00 UTC on 22 February. Such measurements are represented in Fig. 5, as well as a lidar inversion at a selected night time. The red areas indicate the selected periods where vertically-resolved aerosol optical properties have been derived. Such vertical profiles can be seen in the bottom plot of Fig. 5 and in the supplementary material in Figs. S8, S9 and S10. For a better comprehension of these data, layer-averaged aerosol optical properties are also presented in Table 3. In general terms, the maximum altitude of the dust plume was registered at 4 km asl approximately and it maintained relatively constant throughout the four lidar measurements. For certain periods (13:30–14:21 UTC on 21st Feb) intensification of the RCS is observed at the top of the dust plume, which may indicate cloud formation processes related to mineral dust.

Concerning intensive aerosol optical properties, backscatter-related and extinction-related Ångström exponents were low, in accordance with previous lidar observations, which indicates a large aerosol size. The Raman retrieval could be performed only for the period 19:00-21:00 UTC on 20 February. On 22 February, the African dust intrusion was so intense that it produced large extinction and hampered proper retrieval. The lidar ratios obtained at Granada were 52 ± 7 and 53 ± 6 at 355 and 532 nm respectively. As far as volume and particle depolarization ratios are concerned, these parameters show similar and consistent values to data obtained in the Évora station. Nevertheless, it is noteworthy to mention that the last analyzed period (12:30 UTC on 22nd Feb) exhibits the greatest volume (0.26 ± 0.01) and particle

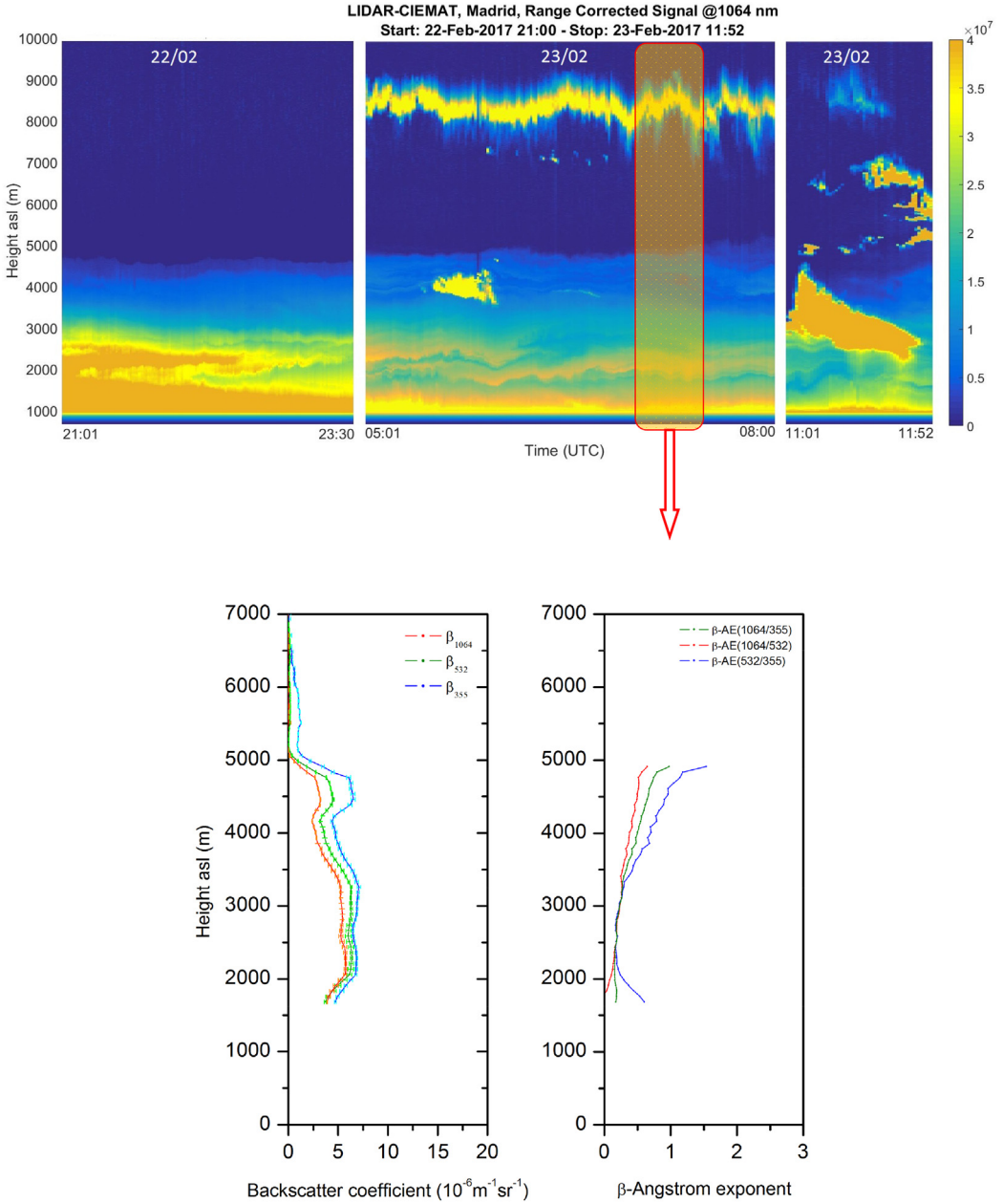

Fig. 6. (top) RCS at 1064 nm during three periods in the interval 22–23 February 2017 at Madrid (669 m asl); (bottom) Backscatter coefficient and backscatter-related Ångström exponents on 23 February 2017 at 06:59 UTC.

(0.31 ± 0.02) depolarization ratios observed in all lidar stations. This value of the particle depolarization ratio (0.31) is representative of pure mineral dust (fine and coarse mode) (Mamouri and Ansmann, 2014).

4.3. Situation in Madrid

In Madrid the African dust plume was only detected in the last stage of the African event (from 22 February on) when the dust intrusion was at its peak of intensity. Lidar measurements on 20 February (not shown) at Madrid still did not present any sign of this extraordinary plume. Three lidar measurement periods were available at this station: on 22 Feb (21:00-23:36 UTC) and 23 Feb (05:00-08:00 and 11:00-11:52 UTC). They are represented in Fig. 6. As it can be seen the thickness of the plume ranged from the ground to 5 km asl and in the last lidar measurement the plume was accompanied by thick clouds. Concerning the retrieval of vertically-resolved aerosol optical properties, only the period 05:00–08:00 UTC (23 Feb) was considered for this purpose. Such profiles are represented in the bottom plot of Fig. 6, which concerns the period 06:59–07:29 UTC. The signal attenuation observed on the first (due to dust) and third (due to dust and clouds) lidar measurement periods was again very strong, and in most cases the Rayleigh signal could not be reached with enough signal-to-noise ratio in order to properly retrieve the aerosol optical properties. This is a problem that needs to be highlighted in this study as it appeared in several lidar stations: the dust load was so strong that at the peak of the event it had the same effect on lidar signals than clouds have in terms of signal attenuation.

Finally, the bottom plot of Fig. 6 presents 3 backscatter coefficient

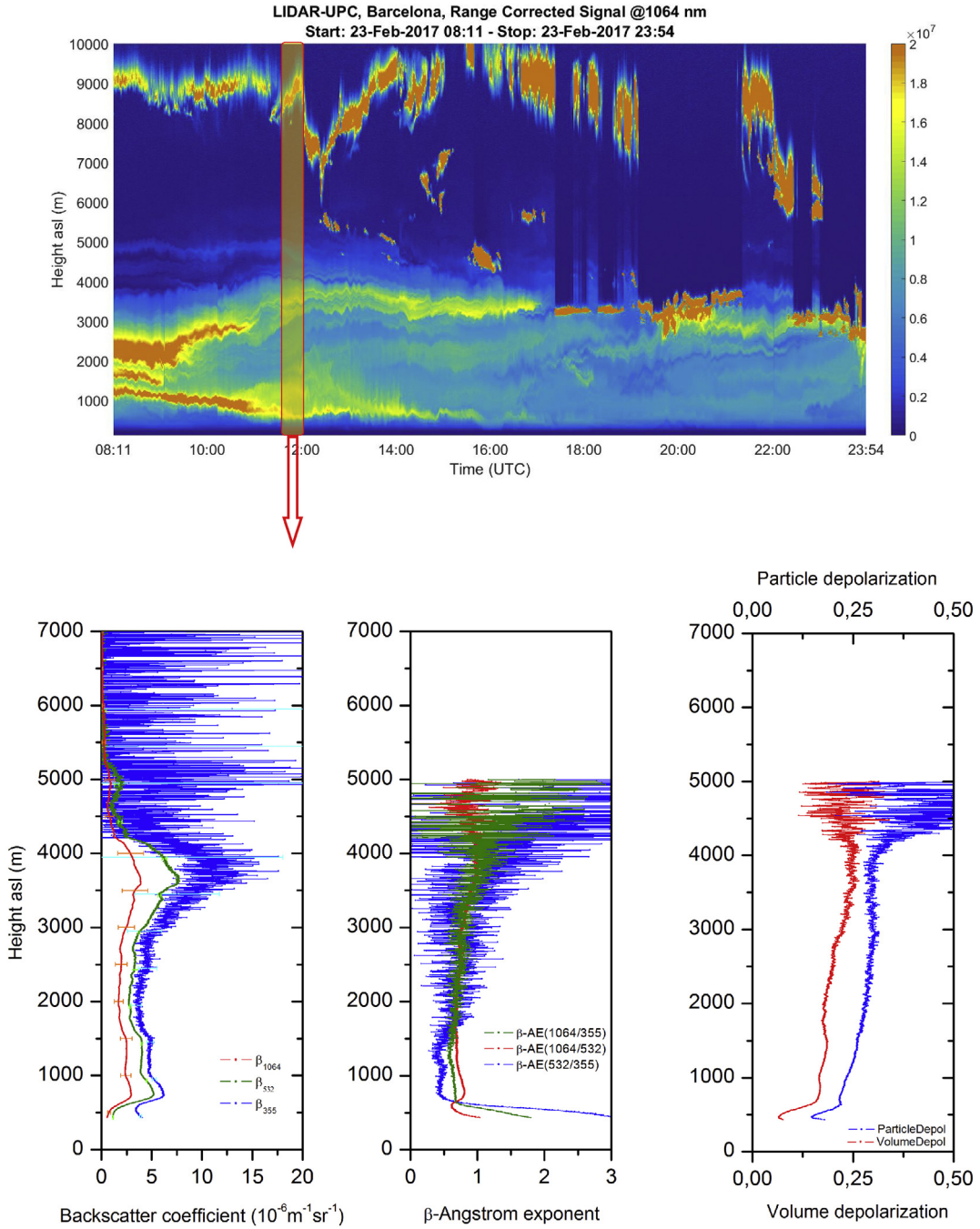

Fig. 7. (top) RCS at 1064 nm on 23 February 2017 at Barcelona (115 m asl); (bottom) Backscatter coefficient, backscatter-related Ångström exponents and volume and particle depolarization ratios on 23 February 2017 at 11:34 UTC.

profiles at 1064, 532 and 355 nm and their respective backscatter-related Ångström exponents. No particle extinction coefficients could be obtained independently as Raman signal were too noisy due to the aforementioned reasons. Maximum values of particle backscatter coefficient are reached at 2.2–2.3 km asl. At this altitude β_{355} is 6.85 ± 0.09, β_{532} is 6.35 ± 0.13 and β_{1064} is 5.75 ± 0.01 $Mm^{-1}\,sr^{-1}$. Mean backscatter-related Ångström exponents were found to be 0.52 ± 0.34, 0.28 ± 0.17, 0.37 ± 0.22 at the wavelength pairs: 532/355, 1064/532 and 1064/355 nm for the atmospheric layer established from lidar full overlap height to 4.9 km. These low backscatter-related Ångström exponents are in accordance with previous lidar observations, which partially indicate a large aerosol size.

4.4. Situation in Barcelona

According to the meteorological overview, the Barcelona site was the latest place from the time standpoint that was hit by the extreme African dust intrusion. As it can be seen in Fig. 7 the African dust plume was registered throughout almost the entire 23 February. At the beginning of the lidar measurement (from 08:11 to 12:00 UTC), the maximum altitude of the plume was detected at 5 km asl approximately and after that it decreased gradually until it reached the value of 3–3.5 km at 23:54 UTC. One period of 30 min has been selected at 11:34 UTC to show the retrieval of aerosol optical properties from the lidar measurement (bottom plot of Fig. 7). The reason to choose this period lies on the availability of a clear atmosphere to derive Rayleigh extinction. As indicated by the color code, the RCS was considerably high for the atmospheric layer between 1 and 3 km before 11:00 UTC. From 11:00 UTC onward the RCS intensity decreases and the dust layer structure is a bit different than in the morning. It must also be noted that from 12:00 UTC on the aerosol optical properties retrieval is quite complex since it is quite difficult to detect a clean atmospheric layer so as to derive the Rayleigh extinction, which is mandatory to infer the aforementioned aerosol optical properties. For the period 12:00–16:00 UTC dispersed clouds can be observed at 5–7 km and from 17:00 UTC

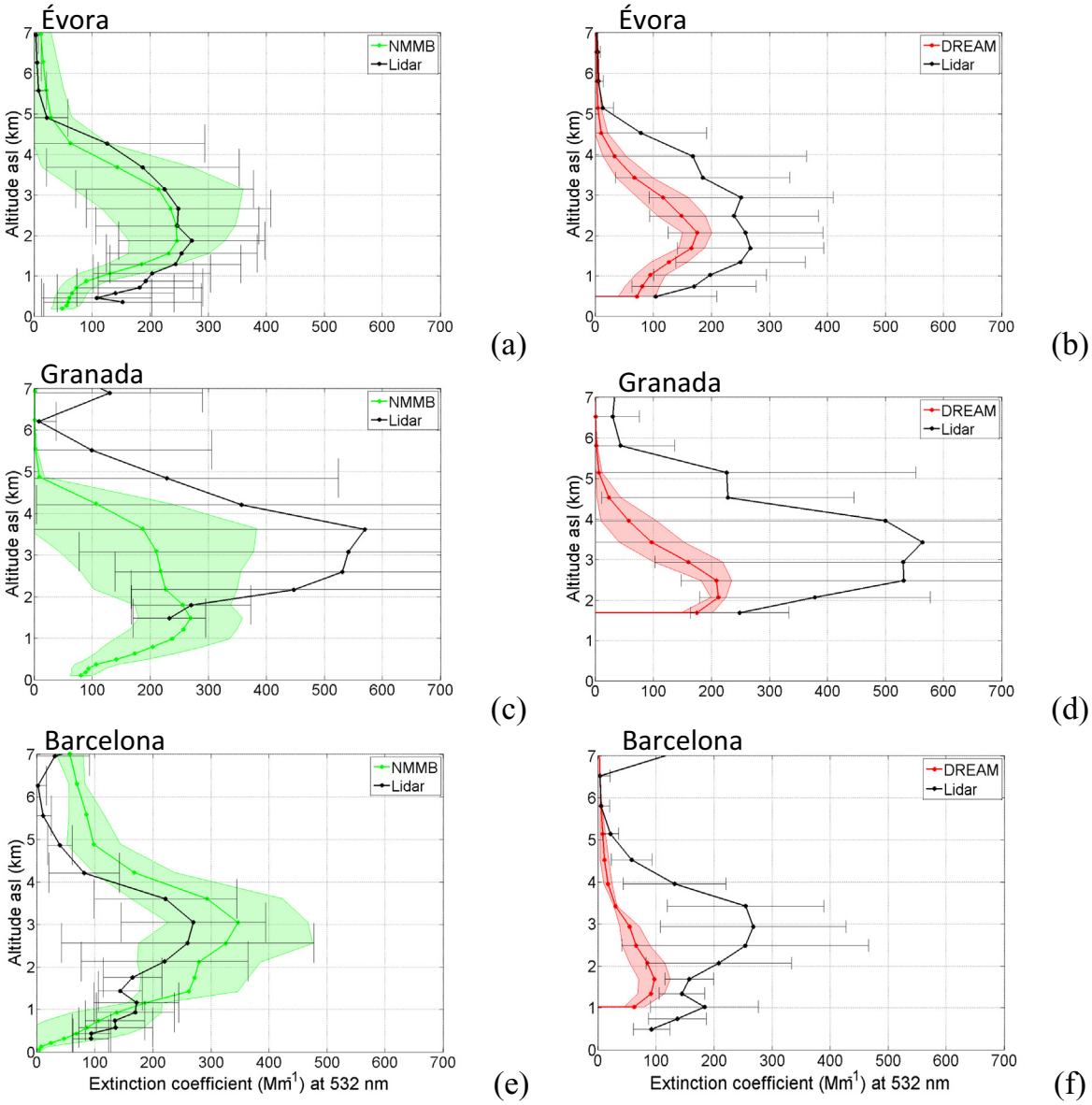

Fig. 8. Mean vertical distribution of mineral dust extinction coefficient estimated by NMMB/BSC-Dust in (a) Évora, (c) Granada and (e) Barcelona and by BSC-DREAM8b in (b) Évora, (d) Granada and (f) Barcelona. The period considered, not always continuous, are 21 Feb. 12UT – 23 Feb. 23UT, 21 Feb. 12UT – 22 Feb. 19UT and 23 Feb. 08UT – 23 Feb. 21UT for Évora, Granada and Barcelona, respectively. The model shaded areas and the error bars of the lidar represent the standard deviations. All model forecasts are for a lead time of 24 h.

onward clouds are registered at the top of the dust plume layer (at 3.5–4 km), which prevents the Rayleigh extinction computation. This latter observation is also interesting from the point of view of cloud formation processes. Considering the evolution of the plume throughout the entire lidar measurement at 4 km, it is plausible that African dust aerosol might act as cloud condensation nuclei (see how the RCS at 4 km from 18:00 to 23:54 UTC becomes more intense than earlier during the day).

The bottom plot of Fig. 7 shows aerosol optical properties obtained for the period 11:34-12:04 UTC. While the backscatter coefficient values are comparable to the ones observed in Madrid, the backscatter-related Ångström exponents seem to be higher in Barcelona. In Barcelona below 1.7 km asl the Ångström exponents are below 1 and have a non-negligible spectral dependence, and above 1.7 km asl they are very similar and nearly constant at 0.7–0.8. Volume and particle depolarization ratios for the atmospheric layer situated at 1–3 km asl are similar than in the previous period. The mean values are 0.19 ± 0.01 and 0.28 ± 0.02 respectively.

5. Performance of dust models during extreme events

This section aims at examining the performance of dust models to predict the 3D evolution of mineral dust during such intense intrusions. The literature available on the evaluation of modeled dust vertical profiles usually inspects the behavior of such models on long time series or for a single moderate intrusion (Gobbi et al., 2013; Santos et al., 2013; Mona et al., 2014; Binietoglou et al., 2015; Sicard et al., 2015), and only rarely for intense intrusions (Huneeus et al., 2016; Ansmann et al., 2017; Tsekeri et al., 2017).

The results are presented for the three sites of Évora, Granada and Barcelona. There are too few measured profiles in Madrid to allow for a statistical comparison. The lidar-derived profiles of extinction coefficient were retrieved as explained in Section 2.3. As it has been observed on the plots of the backscatter coefficients (Figs. 4–7) the error associated to the backscatter coefficient is rather small, so that the error on the extinction is driven by the variability of the lidar ratio which according to Table 3 is on the order of 25%. As a comparison, Córdoba-Jabonero et al. (2018) calculated the error on the extinction coefficient using the same methodology but applied to elastic MPL systems and found errors associated to the extinction on the order of 15–40%.

Before looking at the vertical distribution we briefly discuss the models horizontal transport by comparing Fig. S11 which shows BSC-DREAM8b and NMMB/BSC-Dust forecast of dust optical thickness to the maps of Meteosat (Fig. 2) on the same dates and times. The first result is that both models predict a similar horizontal distribution of the dust although BSC-DREAM8b predicts a much less intense event and seems to depict horizontal structures with less details than NMMB/BSC-Dust does. When comparing to Meteosat images, the agreement of NMMB/BSC-Dust is relatively good. On 23 Feb. at 00 and 12UT the shape and position of the dust cloud with respect to the IP is very well captured by NMMB/BSC-Dust although it may be displaced a little towards the northwest compared to the satellite observations. Towards the end of the event both models seem to predict the persistence of dust off the coast of Morocco while the observations show that the dust cloud has moved northeast.

5.1. Forecast skill for a lead time of 24 h

The comparison of the temporal mean profiles of extinction coefficient is made for NMMB/BSC-Dust and BSC-DREAM8b in Fig. 8. The temporal means are averaged over the whole period (see caption of Fig. 8). For each individual profile the correlation coefficient is plotted as a function of fractional bias (FB) in Fig. 9 and the temporal evolution of the latter two parameters is shown in Fig. 10. In the latter figure the time evolution of *FB* and *r* is also shown for lead times of 48 and 72 h and discussed in Section 5.2. The mean values of the fractional bias, the correlation coefficient and the center of mass for both models at each site are reported in Table 4. Table 4 also contains these mean values for lead times of 48 and 72 h, which are discussed in Section 5.2.

When looking at the temporal mean profiles of extinction coefficient (Fig. 8), the most striking feature is the general large underestimation of BSC-DREAM8b at all heights independently of the site. This underestimation is smaller in Évora (mean $FB = -57.3$ %, Table 4) than in Granada (mean $FB = -95.0$ %) and Barcelona (mean $FB = -93.8$ %), where the underestimation is larger. In Fig. 9 we observe a horizontal spread of the variability of *FB* larger in Évora ([−115; +65%]) than in Granada ([−150; −20%]) and Barcelona ([−130; −30%]) probably due to the smaller amount of vertical profiles available at both sites. The same tendency is observed on NMMB/

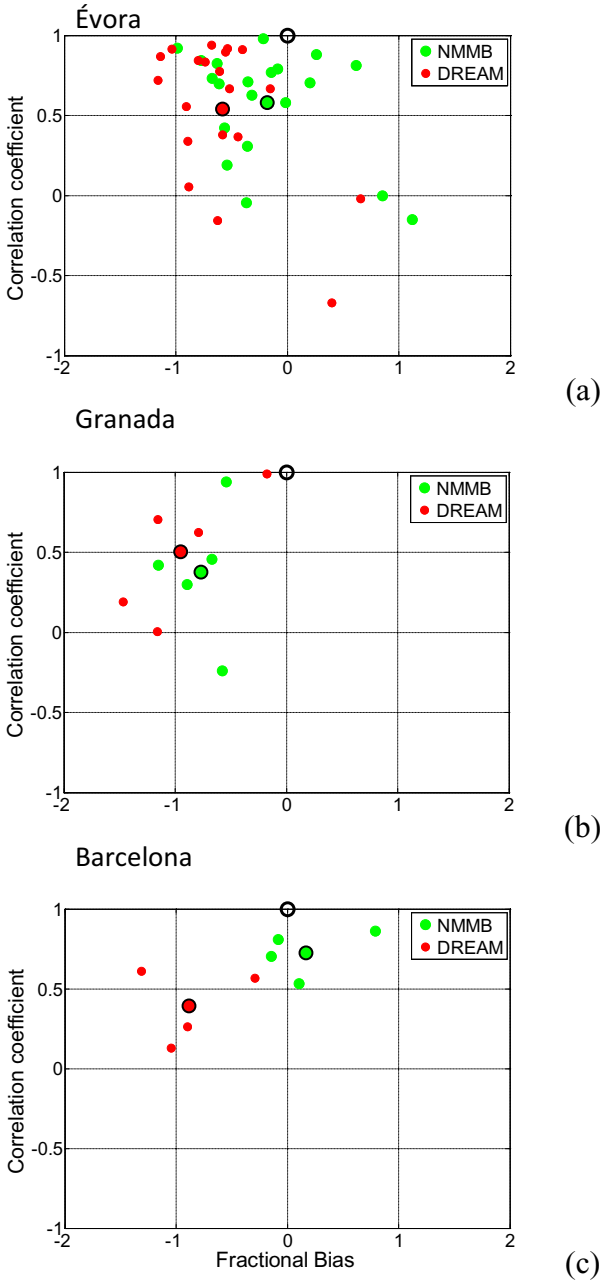

Fig. 9. Correlation coefficient vs. fractional bias, both calculated for the extinction coefficient, calculated for each individual profile in (a) Évora, (b) Granada and (c) Barcelona. All model forecasts are for a lead time of 24 h. The mean values are represented by larger dots edged by a black line. The ideal (*FB*/*r*) pair, (0/1), is indicated by a black circle.

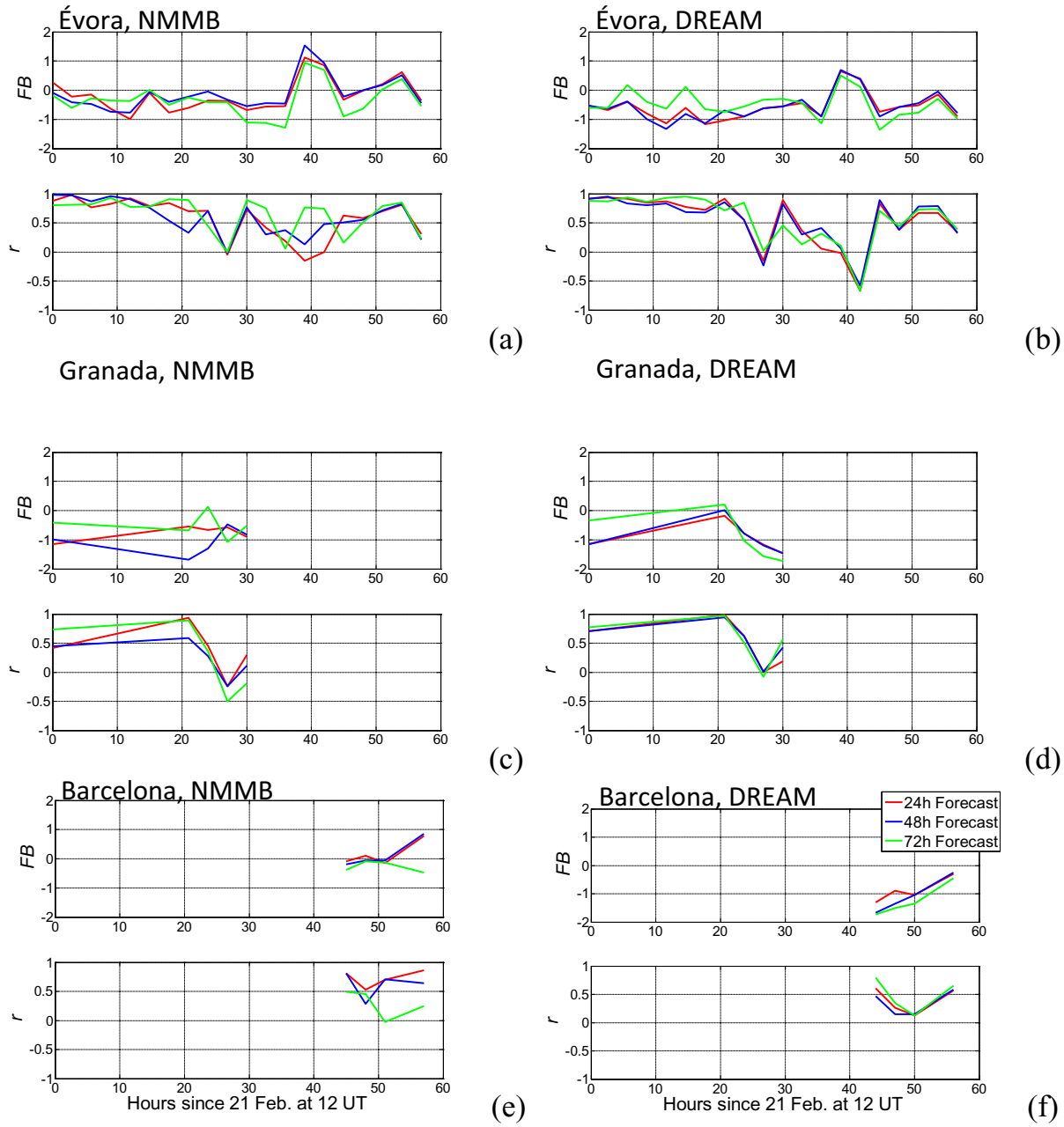

Fig. 10. Correlation coefficient and fractional bias, both calculated for the extinction coefficient, vs. time for forecast lead times of 24, 48 and 72 h for NMMB/BSC-Dust in (a) Évora, (c) Granada and (e) Barcelona and for BSC-DREAM8b in (b) Évora, (d) Granada and (f) Barcelona. The legend shown in the last plot applies to all plots.

BSC-Dust data. NMMB/BSC-Dust forecasts show a rather good agreement with the observations, especially in Évora and in Barcelona. While the model tends to underestimate the observations in Évora (especially below the CoM; the mean *FB* is −20.5%) and in Granada (especially near the CoM; the mean *FB* is −72.6%), it tends to overestimate the observations in Barcelona (especially above 1 km; the mean *FB* is +16.6%). The agreement between NMMB/BSC-Dust and the Évora lidar is remarkably good (Fig. 13a), taking into account the atmospheric variability represented by the lidar error bars and the rather long period considered (60 h). While the NMMB/BSC-Dust profiles reach zero at an approximate height of 5 km in Évora and Granada (similarly to the observations), the profiles in Barcelona start decreasing linearly from ~100 Mm^{-1} at 5 km height to ~50 Mm^{-1} at 7 km (when the observations indicate an extinction coefficient lower than 50 Mm^{-1} above 4.5 km and reaching zero at 6 km). The increase of the lidar profile at 7 km is due to the presence of a cloud above 7 km (see Fig. 7) taken into account in the computation of the layer-average lidar extinction coefficient at the model height. Possible explanations of the differences observed between NMMB/BSC-Dust and the observation in Barcelona in the upper part of the profile are given in the next paragraph. Also in Barcelona the lidar profiles show a layer connected to the surface below 1.5 km, which is not reproduced by either of the models. The main reason is probably the presence of non-dust type particles mixed with the dust detected in the observations but not taken into account in the models. It is also worth noting that BSC-DREAM8b reproduces less atmospheric variability than NMMB/BSC-Dust (in Fig. 8, the red shaded areas are smaller than the green ones), whereas the atmospheric variability denoted by the lidar error bars is large at all sites. This seems to indicate that BSC-DREAM8b has lower vertical variability in comparison to NMMB/BSC-Dust.

Table 4
Main results of the comparison between models and observations. *FB* and *r* are both calculated for the extinction coefficient.

	Évora (21 Feb. 12UT – 23 Feb. 23UT)					
	NMMB/BSC-Dust			BSC-DREAM8b		
Number of profiles	20					
Lead time (hours)	24	48	72	24	48	72
FB (%)	−20.5	−11.1	−35.7	−57.3	−57.0	−47.9
r	0.56	0.57	0.61	0.54	0.55	0.57
Model CoM (km)	2.70	2.82	3.04	2.21	2.26	2.38
Lidar CoM (km)	2.73			2.47		
	Granada (21 Feb. 12UT – 22 Feb. 19UT)					
	NMMB/BSC-Dust			BSC-DREAM8b		
Number of profiles	5					
Lead time (hours)	24	48	72	24	48	72
FB (%)	−72.6	−98.4	−46.9	−95.0	−91.5	−89.0
r	0.37	0.21	0.25	0.49	0.53	0.54
Model CoM (km)	2.26	2.38	2.14	2.70	2.79	2.95
Lidar CoM (km)	3.31			3.38		
	Barcelona (23 Feb. 08UT – 23 Feb. 21UT)					
	NMMB/BSC-Dust			BSC-DREAM8b		
Number of profiles	4					
Lead time (hours)	24	48	72	24	48	72
FB (%)	+16.6	+13.6	−27.0	−93.8	−112.8	−131.4
r	0.72	0.60	0.30	0.36	0.31	0.46
Model CoM (km)	3.61	3.72	4.37	2.51	2.53	2.69
Lidar CoM (km)	2.57			2.59		

The capacity of the models to reproduce the shape of the dust vertical distribution is estimated with the correlation coefficient calculated between individual modeled and observed profiles. NMMB/BSC-Dust seems to perform better in Barcelona (*r* values of 0.72) and in Évora (0.56) than in Granada (0.37). BSC-DREAM8b seems to perform better in Évora (*r* values of 0.54) and in Granada (0.49) than in Barcelona (0.36). The low *r* value obtained with BSC-DREAM8b in Barcelona (0.36) is apparently due to a vertical downward transport forecast by the model and not visible from the observations (the peak of BSC-DREAM8b profile is approximately 2 km lower than the peak of the lidar, see Fig. 8f). Huneeus et al. (2016) who compared NMMB/BSC-Dust and BSC-DREAM8b, among other models, to CALIOP (Cloud Aerosol Lidar with Orthogonal Polarization) profiles during an intense dust intrusion in April 2011 with an AOD ~ 0.8, found a general underestimation of the dust layer height, that was attributed to an overestimation of the dust deposition near the source. Wet scavenging is another source of uncertainty in dust forecast models. As mentioned in Section 3.1 this event was associated to a convective cell giving some precipitation over North Algeria and Southern Iberian Peninsula. These severe convective events have associated more uncertainty in the predicted weather fields (e.g. amount of precipitation) and consequently in the dust prediction. This is directly linked with the removal of dust from the atmosphere and to the aerosol lifetime in the upper layers. The fact that the cloud of points along the *r*-axis is more spread in Évora (Fig. 9a) than in Granada or Barcelona (Fig. 9b and c) is probably due to the longer time series available in Évora covering two and a half days of the event. Another indicator of the score of the models related to the vertical structure of the dust layer is the center of mass. In Évora both models retrieve well the center of mass of the dust layers (differences between modeled and observed CoM are < 0.21 km, see Table 4). In Granada, both models reproduce smaller CoM values with discrepancies vs. the observations of 1.05 km (NMMB/BSC-Dust) and 0.68 km (BSC-DREAM8b). At this site both models predict a center of mass of the dust plume closer to the ground than it is in reality. In Barcelona BSC-DREAM8b predicts well the CoM with a discrepancy of 0.06 km, The overall performance of BSC-DREAM8b at all three stations are in relatively good agreement with the difference of 0.3 ± 1.0 km found between the same model and the EARLINET station of Potenza, Italy, over a period of 12 years and for dust events with AOD < 0.9 (Mona et al., 2014). In Barcelona, the mean CoM forecasted by NMMB/BSC-Dust is 3.61 km while the lidar measured a mean value of 2.57 km. This large difference is due to the mean NMMB/BSC-Dust profile of extinction in Barcelona which does not reach zero at ~5 km, unlike at the other sites (Fig. 8e; see also the former paragraph). This finding suggests that one or several processes taken into account in NMMB/BSC-Dust and inducing vertical motion of the dust layers did actually not occur. In our case the vertical upward transport of the dust layers at high altitudes forecast in Barcelona but not in the southern sites is probably due to a too long aerosol lifetime in the upper layers and/or underestimated deposition processes (Mona et al., 2014). Interestingly this overestimation of NMMB/BSC-Dust in the upper layers was also observed by Binietoglou et al. (2015) who found a slight overestimation of NNMB/BSC-Dust above 4.5–5 km when comparing the model with LIRIC (Lidar/Radiometer Inversion Code) profiles of mass concentration at several sites in Europe and by Sicard et al. (2015) who compared the model with profiles from EARLINET stations during a moderate dust event affecting the western Mediterranean Basin in July 2012.

5.2. Forecast skill temporal evolution and comparison for different lead times

The temporal evolution of the score of the models (in terms of *FB* and *r*) for different lead times shown in Fig. 10 allows us to evaluate the forecast skill of each model as a function of time since the forecast initialization. The start of the time series is fixed on 21 February 2017, at 12 UTC, referred in the following as time T_0, when the first observations are available (in Évora and Granada). The observations available allow us to have 20 points of comparison (at a 3-h time step)

from the 21st at 12 UTC until the 23rd at 23 UTC in Évora; 5 points of comparison on the 22nd between 07 and 19 UTC in Granada; and 4 points of comparison on the 23rd between 08 and 21 UTC in Barcelona. In all plots we have represented the temporal evolution of *FB* and *r* for lead times of 24, 48 and 72 h. We first discuss the forecast skill temporal evolution for a lead time of 24 h, and then compare it to the evolution at 48 and 72 h.

In Évora during the first 20 h (Fig. 10a and b, red lines) both models have similar and more or less stable correlation coefficients with values larger than 0.5. The fractional bias is negative and varies in the range [−100; 0%]. It is larger (in absolute value) for BSC-DREAM8b than for NNMB/BSC-Dust. At T_0 + 20 hours (the 22nd at 08 UTC) the situation starts to degrade: *FB* variations are larger from one prognostic to the next, especially for NNMB/BSC-Dust, and *r* passes regularly below the value of 0.5. A few hours before T_0 + 40 hours (the 23rd at 04 UTC) and only for a period of 5–6 h both models overestimate the extinction coefficient ($+50 < FB < +150$ %). During the first hours of the 23rd the AOD in Évora reached its highest values (~2.5; see Fig. 3). In that sense, it seems that the peak of the event is well reproduced in time by the models but its intensity is overestimated. In Granada (Fig. 10c and d, red lines) the prognostic of NNMB/BSC-Dust is quantitatively better (smaller values of *FB*) but qualitatively worst (smaller correlation coefficients) than for BSC-DREAM8b. Our findings in Granada are in the same line as those found by Sicard et al. (2015) for a moderate dust event affecting the western Mediterranean Basin in July 2012 who also found that NNMB/BSC-Dust reproduced quantitatively better the profiles while BSC-DREAM8b reproduced better the shape of the profiles. The decrease of *FB* visible for both models in Granada and starting at T_0 + 20 (the 22nd at 08 UTC) coincides with the increase of AOD from ~0.5 to values above 2.0 (see Fig. 3). While on the peak day in Évora (the 23rd) both prognostics show an overestimation for a short period of time, on the peak day in Granada (the 22nd) the general underestimation of both prognostics is accentuated, especially for BSC-DREAM8b. In Barcelona (Fig. 10e and f, red lines) the comparison starts at T_0 + 44 (the 23rd at 08 UTC) at the peak of the event in Barcelona ($AOD > 2.0$, see Fig. 3). NNMB/BSC-Dust shows a very good quantitative agreement in the morning and an overestimation in the afternoon, while BSC-DREAM8b shows an underestimation, which decreases with time. The shape of the vertical profiles is better reproduced by NNMB/BSC-Dust ($r > 0.5$) than by BSC-DREAM8b ($r < 0.5$). In general the forecast skills of BSC-DREAM8b in Barcelona are not as good as those of the southernmost sites. This difference, also observed by Huneeus et al. (2016) for dust northward transport, might be explained by the difficulties of the models in simulating horizontal winds and vertical dust propagation.

If we now look at the forecast skill as a function of lead time, i.e. at the differences between the red, blue and green lines in Fig. 10, corresponding, respectively, to lead times of 24, 48 and 72 h, the most striking result is that, at first sight, no clear degradation of the prognostics is clearly visible. There is a difference in the temporal evolution of the prognostics: the prognostics at 24 and 48 h are usually quite similar and the one at 72 h is the one that differs the most from the prognostic at 24 h. Nevertheless, the overall mean values in Table 4 do not show any clear tendency neither in terms of *FB*, nor *r*, for Évora and Granada, the two stations closest to the source. In this sense these results are in agreement with those of Huneeus et al. (2016) who found that the forecast skill of both models for AOD was independent of the forecasting lead time in the domain they defined as southern Europe. In Barcelona a slight degradation of the model scores occurs with increasing lead times: the fractional bias increases (in absolute value; BSC-DREAM8b) and the correlation coefficient decreases (NMMB/BSC-Dust) between the prognostics at 24 and 72 h. This deterioration of the forecast skills is not observed in Huneeus et al. (2016) and may be due to the singularity and exceptionality of the event described in our study.

6. Conclusions

An extreme dust intrusion transported from Northern Africa to the western Mediterranean during 20–23 February 2017 has been reported and analyzed in the IP. By means of lidar and sun-photometer measurements, we have provided a representative picture of this extreme event by means of a detailed 4-D characterization of aerosol optical properties and their evolution during the dust intrusion. Furthermore, the combined use of active and passive remote sensing instruments along with dust models has provided useful information to better understand the complexity of dust long-range transport, its extreme character and also the capability of dust models to forecast such events.

The synoptic conditions that led to such an extreme event are the combination of a Moroccan low and the Atlantic anticyclonic system which were responsible for the tropospheric flow that advected mineral dust over the IP. According to AERONET sites over the IP, the aerosol optical depth at 675 nm peaked at values larger than 2.0 with associated Ångström Exponents (440–870 nm) close to 0 and single scattering albedos close to 1. On the most intense days of the event (22 and 23 February) the high load of atmospheric mineral dust blocked the sun and prevented quality-assured AERONET AOD inversions. Towards the end of the event (23 February) clouds started to form on top of the dust layer.

EARLINET/ACTRIS lidar measurements confirmed the presence of atmospheric dust in all stations (EV, GR, MA and BA). In general, the dust plume was observed between the ground until 4–5 km asl approximately. Maximum values of backscatter coefficients at 532 nm were registered in the range 10–15·Mm^{-1} sr^{-1}. Like for the AERONET sun-photometer, during the most intense period of the event the dust attenuation was such that the lidar signal-to-noise ratio in the molecular region above the dust layer was not high enough to perform reliable inversions. Backscatter-related Ångström exponents were monitored very close to 0. Lidar ratios were found in the range 40–55 sr at 355 nm and 34–61 sr at 532 nm during the event at Évora and Granada. Particle depolarization ratios, registered at those stations where depolarizing channels were available (EV, GR and BA), have revealed to be rather constant in the dust layer. Mean particle depolarization ratios in the dust layer of 0.19 were observed at the beginning of the event (20–21 February, Évora) and up to 0.31 at the peak of the event (22 February, Granada; 23 February, Barcelona).

The study also focused on the ability of the dust forecast models to reproduce the arrival, the vertical distribution and the intensity of the dust plume over a long-range transport region. The two dust models considered are the ones currently in development for the NRT evaluation within the SDS-WAS Regional Center: BSC-DREAM8b and NMMB/BSC-Dust. In general, the models' performances are highly dependent on the type of event and the region. Therefore, from a single event, we cannot conclude that one model is better than the other. However, and in the particular case of the February 2017 dust event, we found a large underestimation in the forecast of the extinction coefficient provided by BSC-DREAM8b at all heights independently of the site. In contrast NMMB/BSC-Dust forecasts presented a better agreement with the observations, especially in Évora. However NMMB/BSC-Dust reproduced a higher atmospheric variability than BSC-DREAM8b. Some discrepancies such as the forecast of dust by NMMB/BSC-Dust in layers well above 5 km are still not completely understood and further research is needed. Finally, with regard to the forecast skill as a function of lead time, no clear degradation of the prognostic is appreciated at 24, 48 and 72 h for Évora and Granada stations. However the prognostic does degrade (bias increases and/or correlation decreases) for Barcelona, which is attributed to the singularity of the event.

Acknowledgments

The research leading to these results has received funding from the H2020 program from the European Union (grant agreement no.

654109, 778349) and also from the Spanish Ministry of Industry, Economy and Competitiviness (MINECO, ref. CGL2013-45410-R, CGL2016-81092-R, CGL2017-85344-R, TEC2015-63832-P), the Spanish Ministry of Science, Innovation and Universities (ref. CGL2017-90884-REDT); the CommSensLab "Maria de Maeztu" Unity of Excellence (ref. MDM-2016-0600) financed by the Spanish Agencia Estatal de Investigación. Co-funding was also provided by the European Union through the European Regional Development Fund (ref. POCI-01-0145-FEDER-007690, ALT20-03-0145-FEDER-000004, ALT20-03-0145-FEDER-000011); by the Andalusia Regional Government (ref. P12-RNM-2409); by the Madrid Regional Government (projects TIGAS-CM, ref. Y2018/EMT-5177 and AIRTEC-CM, ref. P2018/EMT4329); by the University of Granada through “Plan Propio. Programa 9 Convocatoria 2013” and by the Portuguese Foundation for Science and Technology and national funding (ref. SFRH/BSAB/143164/2019). The BSC-DREAM8b and NNMB/BSC-Dust (now NMMB-MONARCH) model simulations were performed by the Mare Nostrum supercomputer hosted by the Barcelona Supercomputer Center (BSC). S. Basart acknowledges the AXA Research Fund for supporting aerosol research at the BSC through the AXA Chair on Sand and Dust Storms Fund, as well as the InDust project (COST Action CA16202). The authors gratefully acknowledge the NOAA Air Resources Laboratory (ARL) for the provision of the HYSPLIT transport and dispersion model and/or READY website (http://www.ready.noaa.gov) used in this publication.

Appendix A. Supplementary data

Supplementary data to this article can be found online at https://doi.org/10.1016/j.atmosres.2019.06.007.

References

AERONET (AErosol RObotic NETwork), https://aeronet.gsfc.nasa.gov/, last access: 13 March 2019.

Alfaro, S., Gomes, L., 2001. Modeling mineral aerosol production by wind erosion: Emission intensities and aerosol size distributions in source areas. J. Geophys. Res. 106 (D16), 18075–18078.

Alpert, P., Ziv, B., 1989. The Sharav Cyclone: Observations and some theoretical considerations. J. Geophys. Res. 94. https://doi.org/10.1029/88JD04228.

Amiridis, V., Balis, D., Giannakaki, E., Stohl, A., Kazadzis, S., Koukouli, M., Zanis, P., 2009. Optical characteristics of biomass burning aerosols over Southeastern Europe determined from UV-Raman lidar measurements. Atmos. Chem. Phys. 9 (7), 2431–2440.

Andreae, M., 1995. Climate effects of changing atmospheric aerosol levels. In: Henderson-Sellers, A. (Ed.), World Survey of Climatology, 16, Future Climate of the World. Elsevier, New York, pp. 341–392.

Ångström, A., 1964. The parameters of atmospheric turbidity. Tellus 16 (1), 64–75.

Ansmann, A., Wandinger, U., Riebesell, M., Weitkamp, C., Michaelis, W., 1992. Independent measurement of extinction and backscatter profiles in cirrus clouds by using a combined Raman elastic-backscatter lidar. Appl. Opt. 31 (33), 7113–7131.

Ansmann, A., Rittmeister, F., Engelmann, R., Basart, S., Jorba, O., Spyrou, C., Rémy, S., Skupin, A., Baars, H., Seifert, P., 2017. Profiling of Saharan dust from the Caribbean to western Africa–Part 2: Shipborne lidar measurements versus forecasts. Atmos. Chem. Phys. 17 (24), 14987–15006.

Basart, S., Perez, C., Nickovic, S., Cuevas, E., Baldasano, J., 2012. Development and evaluation of the BSC-DREAM8b dust regional model over Northern Africa, the Mediterranean and the Middle East. Tellus B 64.

Binietoglou, I., Basart, S., Alados-Arboledas, L., Amiridis, V., Argyrouli, A., Baars, H., Baldasano, J., Balis, D., Belegante, L., Bravo-Aranda, J., Burlizzi, P., Carrasco, V., Chaikovsky, A., Comeron, A., D'Amico, G., Filioglou, M., Granados-Munoz, M., Guerrero-Rascado, J., Ilic, L., Kokkalis, P., Maurizi, A., Mona, L., Monti, F., Munoz-Porcar, C., Nicolae, D., Papayannis, A., Pappalardo, G., Pejanovic, G., Pereira, S., Perrone, M., Pietruczuk, A., Posyniak, M., Rocadenbosch, F., Rodriguez-Gomez, A., Sicard, M., Siomos, N., Szkop, A., Terradellas, E., Tsekeri, A., Vukovic, A., Wandinger, U., Wagner, J., 2015. A methodology for investigating dust model performance using synergistic EARLINET/AERONET dust concentration retrievals. Atmos. Measure. Techniq. 8 (9), 3577–3600.

Boucher, O., Randall, D., Artaxo, P., Bretherton, C., Feingold, G., Forster, P., Kerminen, V.-M., Kondo, Y., Liao, H., Lohmann, U., Rasch, P., Satheesh, S.K., Sherwood, S., Stevens, B., Zhang, I.X.Y., Stocker, T.F., Qin, D., Plattner, G.-K., Tignor, A.M., Boschung, S.K., Nauels, J., Xia, A., Bex, Y., Midgley, P.M., 2013. Clouds and Aerosols. Climate Change 2013: The Physical Science Basis. Cambridge, United Kingdom and New York, NY, USA. pp. 571–657.

CAMS, Copernicus Atmosphere Monitoring Service Information, http://apps.ecmwf.int/datasets/data/cams-gfas/, last access: 18 May 2018.

Cazorla, A., Casquero-Vera, J.A., Román, R., Guerrero-Rascado, J.L., Toledano, C., Cachorro, V., Orza, J.A., Cancillo, M.L., Serrano, A., Titos, G., Pandolfi, M., Alastuey, A., Hanrieder, N., Alados-Arboledas, L., 2017. Near-real-time processing of a ceilometer network assisted with sun-photometer data: monitoring a dust outbreak over the Iberian Peninsula. Atmos. Chem. Phys. 17, 11861–11876.

Córdoba-Jabonero, C., Sicard, M., Ansmann, A., del Águila, A., Baars, H., 2018. Separation of the optical and mass features of particle components in different aerosol mixtures by using POLIPHON retrievals in synergy with continuous polarized Micro-Pulse Lidar (P-MPL) measurements. Atmos. Meas. Tech. 11, 4775–4795. https://doi.org/10.5194/amt-11-4775-2018.

Córdoba-Jabonero, C., Sicard, M., Basart, S., del Águila, A., Jiménez, M., Ramón Moreta, J., Zorzano, M.-P., 2019. An unusually extreme wintertime Saharan dust intrusion observed at two Spanish MPLNET sites: Performance of a dust model mass concentration profiles versus lidar observations. Atmos. Environ (in review).

Cuevas, E., Gómez-Peláez, A.J., Rodríguez, S., Terradellas, E., Basart, S., Garcia, R.D., Garcia, O.E., Alonso-Perez, S., 2017. The pulsating nature of large-scale Saharan dust transport as a result of interplays between mid-latitude Rossby waves and the North African Dipole Intensity. Atmos. Environ. 167, 586–602.

Darmenova, K., Sokolik, I.N., Shao, Y., Marticorena, B., Bergametti, G., 2009. Development of a physically-based dust emission module within the Weather Research and forecasting (WRF) model: Assessment of dust emission parameterizations and input parameters for source regions in Central and East Asia. J. Geophys. Res. 114, D14201.

Fernald, F.G., 1984. Analysis of Atmospheric Lidar Observations - some comments. Appl. Opt. 23 (5), 652–653.

Forster, P., Ramaswamy, V., Artaxo, P., Berntsen, T., Betts, R., Fahey, D., Haywood, J., Lean, J., Lowe, D., Myhre, G., Nganga, J., Prinn, G., Raga, G., Schulz, M., Van Dorland, R., 2007. Changes in Atmospheric Constituents and in Radiative Forcing. Climate Change 2007: The Physical Science Basis. Cambridge University Press, U.K, pp. 129–234.

Ginoux, P., Prospero, J.M., Gill, T.E., Hsu, N.C., Zhao, M., 2012. Global-scale attribution of anthropogenic and natural dust sources and their emission rates based on MODIS Deep Blue aerosol products. Rev. Geophys. 50.

Gkikas, A., Hatzianastassiou, N., Mihalopoulos, N., Katsoulis, V., Kazadzis, S., Pey, J., Querol, X., Torres, O., 2013. The regime of intense desert dust episodes in the Mediterranean based on contemporary satellite observations and ground measurements. Atmos. Chem. Phys. 13, 12135–12154. https://doi.org/10.5194/acp-13-12135-2013.

Gobbi, G., Angelini, F., Barnaba, F., Costabile, F., Baldasano, J., Basart, S., Sozzi, R., Bolignano, A., 2013. Changes in particulate matter physical properties during Saharan advections over Rome (Italy): a four-year study, 2001-2004. Atmos. Chem. Phys. 13 (15), 7395–7404.

Guerrero-Rascado, J., Ruiz, B., Alados-Arboledas, L., 2008. Multi-spectral Lidar characterization of the vertical structure of Saharan dust aerosol over southern Spain. Atmos. Environ. 42 (11), 2668–2681.

Guerrero-Rascado, J., Olmo, F., Aviles-Rodriguez, I., Navas-Guzman, F., Perez-Ramirez, D., Lyamani, H., Arboledas, L., 2009. Extreme Saharan dust event over the southern Iberian Peninsula in september 2007: active and passive remote sensing from surface and satellite. Atmos. Chem. Phys. 9 (21), 8453–8469.

Holben, B., Eck, T., Slutsker, I., Tanre, D., Buis, J., Setzer, A., Vermote, E., Reagan, J., Kaufman, Y., Nakajima, T., Lavenu, F., Jankowiak, I., Smirnov, A., 1998. AERONET - a federated instrument network and data archive for aerosol characterization. Remote Sens. Environ. 66 (1), 1–16.

Holben, B., Tanre, D., Smirnov, A., Eck, T., Slutsker, I., Abuhassan, N., Newcomb, W., Schafer, J., Chatenet, B., Lavenu, F., Kaufman, Y., Castle, J., Setzer, A., Markham, B., Clark, D., Frouin, R., Halthore, R., Karneli, A., O'Neill, N., Pietras, C., Pinker, R., Voss, K., Zibordi, G., 2001. An emerging ground-based aerosol climatology: aerosol optical depth from AERONET. J. Geophys. Res.-Atmos. 106 (D11), 12067–12097.

Huneeus, N., Basart, S., Fiedler, S., Morcrette, J.-J., Benedetti, A., Mulcahy, J., Terradellas, E., Garcia-Pando, C.P., Pejanovic, G., Nickovic, S., 2016. Forecasting the northern African dust outbreak towards Europe in April 2011: a model intercomparison. Atmos. Chem. Phys. 16 (8), 4967.

IPCC, 2001. In: McCarthy, J.J., Canziani, O.F., Leary, N.A., Dokken, D.J., White, K.S. (Eds.), Climate Change 2001: Impacts, Adaptation and Vulnerability, Contribution of Working Group II to the Third Assessment Report of the Intergovernmental Panel on Climate Change. Cambridge University Press, Cambridge, United Kingdom and New York, NY, USA, pp. 1032 (0-521-01500-6).

IPCC, 2013. Summary for Policymakers. In: Stocker, T.F., Qin, D., Plattner, G.-K., Tignor, M., Allen, S.K., Boschung, J. ... Midgley, P.M. (Eds.), Climate Change 2013: The Physical Science Basis. Contribution of Working Group I to the Fifth Assessment Report of the Intergovernmental Panel on Climate Change. Cambridge University Press, Cambridge, United Kingdom and New York, NY, USA.

Khan, B., Stenchikov, G., Weinzierl, B., Kalenderski, S., Osipov, S., 2015. Dust plume formation in the free troposphere and aerosol size distribution during the Saharan Mineral Dust Experiment in North Africa. Tellus B 67 (1). https://doi.org/10.3402/tellusb.v67.27170.

Klein, H., Nickovic, S., Haunold, W., Bundke, U., Nillius, B., Ebert, M., Weinbruch, S., Schuetz, L., Levin, Z., Barrie, L.A., 2010. Saharan dust and ice nuclei over Central Europe. Atmos. Chem. Phys. 10 (21), 10211–10221.

Klett, J.D., 1981. Stable analytical Inversion solution for Processing Lidar returns. Appl. Opt. 20 (2), 211–220.

Lafontaine, C., Bryson, R., Wendland, W., 1990. Airstream regions of North-Africa and the Mediterranean. J. Clim. 3 (3), 366–372.

Mahowald, N., Baker, A., Bergametti, G., Brooks, N., Duce, R., Jickells, T., Kubilay, N., Prospero, J., Tegen, I., 2005. Atmospheric global dust cycle and iron inputs to the ocean. Glob. Biogeochem. Cycles 19 (4).

Mamouri, R.E., Ansmann, A., 2014. Fine and coarse dust separation with polarization

lidar. Atmos. Meas. Tech. 7, 3717–3735. https://doi.org/10.5194/amt-7-3717-2014.
Mamouri, R., Ansmann, A., Nisantzi, A., Kokkalis, P., Schwarz, A., Hadjimitsis, D., 2013. Low Arabian dust extinction-to-backscatter ratio. Geophys. Res. Lett. 40 (17), 4762–4766.
Mamouri, R., Ansmann, A., Nisantzi, A., Solomos, S., Kallos, G., Hadjimitsis, D., 2016. Extreme dust storm over the eastern Mediterranean in September 2015: satellite, lidar, and surface observations in the Cyprus region. Atmos. Chem. Phys. 16 (21), 13711–13724.
Mona, L., Amodeo, A., Pandolfi, M., Pappalardo, G., 2006. Saharan dust intrusions in the Mediterranean area: three years of Raman lidar measurements. J. Geophys. Res.-Atmos. 111 (D16).
Mona, L., Papagiannopoulos, N., Basart, S., Baldasano, J., Binietoglou, I., Cornacchia, C., Pappalardo, G., 2014. EARLINET dust observations vs. BSC-DREAM8b modeled profiles: 12-year-long systematic comparison at Potenza, Italy. Atmos. Chem. Phys. 14 (16), 8781–8793.
Müller, D., Heinold, B., Tesche, M., Tegen, I., Althausen, D., Arboledas, L., Amiridis, V., Amodeo, A., Ansmann, A., Balis, D., 2009. EARLINET observations of the 14-22-May long-range dust transport event during SAMUM 2006: validation of results from dust transport modelling. Tellus B 61 (1), 325–339.
Müller, D., Ansmann, A., Freudenthaler, V., Kandler, K., Toledano, C., Hiebsch, A., Gasteiger, J., Esselborn, M., Tesche, M., Heese, B., Althausen, D., Weinzierl, B., Petzold, A., von Hoyningen-Huene, W., 2010. Mineral dust observed with AERONET Sun photometer, Raman lidar, and in situ instruments during SAMUM 2006: Shape-dependent particle properties. J. Geophys. Res.-Atmos. 115.
Nisantzi, A., Mamouri, R., Ansmann, A., Schuster, G., Hadjimitsis, D., 2015. Middle East versus Saharan dust extinction-to-backscatter ratios. Atmos. Chem. Phys. 15 (12), 7071–7084.
Obregón, M., Pereira, S., Salgueiro, V., Costa, M.J., Silva, A.M., Serrano, A., Bortoli, D., 2015. Aerosol radiative effects during two desert dust events in August 2012 over the Southwestern Iberian Peninsula. Atmos. Res. 153, 404–415.
Pappalardo, G., Amodeo, A., Pandolfi, M., Wandinger, U., Ansmann, A., Bosenberg, J., Matthias, V., Amirdis, V., De Tomasi, F., Frioud, M., Iarlori, M., Komguem, L., Papayannis, A., Rocadenbosch, F., Wang, X., 2004. Aerosol lidar intercomparison in the framework of the EARLINET project. 3. Raman lidar algorithm for aerosol extinction, backscatter, and lidar ratio. Appl. Opt. 43 (28), 5370–5385.
Pappalardo, G., Amodeo, A., Apituley, A., Comeron, A., Freudenthaler, V., Linne, H., Ansmann, A., Bosenberg, J., D'Amico, G., Mattis, I., Mona, L., Wandinger, U., Amiridis, V., Alados-Arboledas, L., Nicolae, D., Wiegner, M., 2014. EARLINET: towards an advanced sustainable European aerosol lidar network. Atmos. Meas. Techniq. 7 (8), 2389–2409.
Pérez, C., Nickovic, S., Pejanovic, G., Baldasano, J., Ozsoy, E., 2006. Interactive dust-radiation modeling: a step to improve weather forecasts. J. Geophys. Res.-Atmos. 111 (D16).
Pérez, C., Haustein, K., Janjic, Z., Jorba, O., Huneeus, N., Baldasano, J., Black, T., Basart, S., Nickovic, S., Miller, R., Perlwitz, J., Schulz, M., Thomson, M., 2011. Atmospheric dust modeling from meso to global scales with the online NMMB/BSC-Dust model - Part 1: model description, annual simulations and evaluation. Atmos. Chem. Phys. 11 (24), 13001–13027.
Pey, J., Querol, X., Alastuey, A., Forastiere, F., Stafoggia, M., 2013. African dust outbreaks over the Mediterranean Basin during 2001–2011: PM 10 concentrations, phenomenology and trends, and its relation with synoptic and mesoscale meteorology. Atmos. Chem. Phys. 13 (3), 1395–1410.
Preissler, J., Wagner, F., Pereira, S., Guerrero-Rascado, J., 2011. Multi-instrumental observation of an exceptionally strong Saharan dust outbreak over Portugal. J. Geophys. Res.-Atmos. 116.
Prospero, J., Ginoux, P., Torres, O., Nicholson, S., Gill, T., 2002. Environmental characterization of global sources of atmospheric soil dust identified with the Nimbus 7 Total Ozone Mapping Spectrometer (TOMS) absorbing aerosol product. Rev. Geophys. 40 (1).
Querol, X., Pey, J., Pandolfi, M., Alastuey, A., Cusack, M., Pérez, N., Moreno, T., Viana, M., Mihalopoulos, N., Kallos, G., 2009. African dust contributions to mean ambient PM10 mass-levels across the Mediterranean Basin. Atmos. Environ. 43 (28), 4266–4277.
Rodríguez-Navarro, C., di Lorenzo, F., Elert, K., 2018. Mineralogy and physicochemical features of Saharan dust wet deposited in the Iberian Peninsula during an extreme red rain event. Atmos. Chem. Phys. 18, 10089–10122. https://doi.org/10.5194/acp-18-10089-2018.
Rolph, G., Stein, A., Stunder, B., 2017. Real-time Environmental applications and Display sYstem: READY. Environ. Model Softw. 95, 210–228.
Salvador, P., Artíñano, B., Molero, F., Viana, M., Pey, J., Alastuey, A., Querol, X., 2013. African dust contribution to ambient aerosol levels across Central Spain: Characterization of long-range transport episodes of desert dust. Atmos. Res. 127, 117–129.
Salvador, P., Alonso-Perez, S., Pey, J., Artinano, B., de Bustos, J., Alastuey, A., Querol, X., 2014. African dust outbreaks over the western Mediterranean Basin: 11-year characterization of atmospheric circulation patterns and dust source areas. Atmos. Chem. Phys. 14 (13), 6759–6775.
Salvador, P., Almeida, S.M., Cardoso, J., Almeida-Silva, M., Nunes, T., Cerqueira, M., Alves, C., Reis, M.A., Chaves, P.C., Artinano, B., Pio, C., 2016. Composition and origin of PM_{10} in Cape Verde: Characterization of long-range transport episodes. Atmos. Environ. 127, 326–339.
Santos, D., Costa, M.J., Silva, A.M., Salgado, R., 2013. Modeling Saharan desert dust radiative effects on clouds. Atmos. Res. 127, 178–194.
Sicard, M., D'Amico, G., Comeron, A., Mona, L., Alados-Arboledas, L., Amodeo, A., Baars, H., Baldasano, J., Belegante, L., Binietoglou, I., Bravo-Aranda, J., Fernandez, A., Freville, P., Garcia-Vizcaino, D., Giunta, A., Granados-Munoz, M., Guerrero-Rascado, J., Hadjimitsis, D., Haefele, A., Hervo, M., Iarlori, M., Kokkalis, P., Lange, D., Mamouri, R., Mattis, I., Molero, F., Montoux, N., Munoz, A., Porcar, C., Navas-Guzman, F., Nicolae, D., Nisantzi, A., Papagiannopoulos, N., Papayannis, A., Pereira, S., Preissler, J., Pujadas, M., Rizi, V., Rocadenbosch, F., Sellegri, K., Simeonov, V., Tsaknakis, G., Wagner, F., Pappalardo, G., 2015. EARLINET: potential operationality of a research network. Atmos. Meas. Tech. 8 (11), 4587–4613.
Sicard, M., Barragan, R., Dulac, F., Alados-Arboledas, L., Mallet, M., 2016. Aerosol optical, microphysical and radiative properties at regional background insular sites in the western Mediterranean. Atmos. Chem. Phys. 16 (18), 12177–12203.
Sorribas, M., Adame, J., Andrews, E., Yela, M., 2017. An anomalous African dust event and its impact on aerosol radiative forcing on the Southwest Atlantic coast of Europe in February 2016. Sci. Total Environ. 583, 269–279.
Stein, A.F., Draxler, R.R., Rolph, G.D., Stunder, B.J.B., Cohen, M.D., Ngan, F., 2015. NOAA's HYSPLIT atmospheric transport and dispersion modeling system. Bull. Am. Meteorol. Soc. 96, 2059–2077.
Titos, G., Ealo, M., Pandolfi, M., Pérez, N., Sola, Y., Sicard, M., Comerón, A., Querol, X., Alastuey, A., 2017. Spatiotemporal evolution of a severe winter dust event in the western Mediterranean: Aerosol optical and physical properties. J. Geophys. Res. Atmos. 122. https://doi.org/10.1002/2016JD026252.
Tsekeri, A., Lopatin, A., Amiridis, V., Marinou, E., Igloffstein, J., Siomos, N., Solomos, S., Kokkalis, P., Engelmann, R., Baars, H., 2017. GARRLiC and LIRIC: strengths and limitations for the characterization of dust and marine particles along with their mixtures. Atmos. Meas. Tech. 10 (12), 4995.
Wagner, F., Bortoli, D., Pereira, S., Costa, M.J., SILVA, A., Weinzierl, B., Esselborn, M., Petzold, A., Rasp, K., Heinold, B., 2009. Properties of dust aerosol particles transported to Portugal from the Sahara desert. Tellus B 61 (1), 297–306.
WMO (World Meteorological Organization), 2011. Weather Extreme in a Changing Climate: Hindsight on Foresight. WMO-No. 1075. (ISBN: 978-92-63-11075-6).

Environ Monit Assess (2020) 192: 93
https://doi.org/10.1007/s10661-019-8048-1

Spatial and temporal dynamics of irrigation water quality under drought conditions in a large reservoir in Southern Portugal

Alexandra Tomaz · Patrícia Palma · Sofia Fialho · Ana Lima · Paula Alvarenga · Miguel Potes · Rui Salgado

Received: 26 July 2019 / Accepted: 19 December 2019 / Published online: 6 January 2020
© Springer Nature Switzerland AG 2020

Abstract Water is a scarce resource in the Mediterranean region where adverse climatic conditions promoting water shortages tend to increase with climate change. Under water scarcity conditions and high atmosphere evaporative demand, the risks of decreased water quality, and land salinization are major threats to the sustainability of irrigated agriculture in this region. The assessment of the quality of irrigation water is increasingly important to ensure the maintenance of long-term salt balance at a crop, farm, and regional scale. This study is focused on the spatial and temporal variability of water quality for irrigation in the Alqueva reservoir (Southern Portugal). The assessment was performed every 2 months during a distinctive drought year (2017) and included inorganic ions (Na^+, Ca^{2+}, Mg^{2+}, K^+, NH_4^+, Cl^-, F^-, SO_4^{2-}, NO_3^-, and NO_2^-), pH, and electric conductivity (EC_W) of water. Sodium adsorption ratio (SAR) was calculated, and potential soil permeability problems were estimated. The assessment showed significantly higher values of the physicochemical parameters in the most upstream sites, located near tributaries inflows, and an upward trend in ion concentrations throughout the year, with significantly higher concentrations of Na^+, Mg^{2+}, Cl^-, and SO_4^{2}, registered through May to November, reflecting the severe drought felt in the summer, autumn, and winter. The evaluation of water quality for irrigation indicated a slight to moderate risk of reduced infiltration rates, which should be considered whenever sprinkler irrigation is used, mainly in fine-textured soils, which are prevalent in the irrigated area. The multivariate statistical approach, using principal component analysis and factor analysis, identified two principal components related to salinity and nutrient concentrations. The cluster analysis revealed three groups of similarity between samples pointing to a more time- than space-controlled pattern. Overall, the temporal dynamics of the water physicochemical parameters could indicate that an abnormal annual distribution of precipitation and temperature may distort seasonal differences. To prevent water and soil degradation, a more frequent assessment of the water quality should be considered, allowing for the selection of appropriate soil and water management measures in irrigated areas.

Electronic supplementary material The online version of this article (https://doi.org/10.1007/s10661-019-8048-1) contains supplementary material, which is available to authorized users.

A. Tomaz · P. Palma · S. Fialho · A. Lima
Escola Superior Agrária, Instituto Politécnico de Beja, R. Pedro Soares S/N, 7800-295 Beja, Portugal

A. Tomaz (✉)
GeoBioTec, Universidade Nova de Lisboa. Campus da Caparica, 2829-516 Caparica, Portugal
e-mail: atomaz@ipbeja.pt

P. Palma · M. Potes · R. Salgado
Instituto de Ciências da Terra (ICT), Universidade de Évora, Évora, Portugal

P. Alvarenga
LEAF – Centro de Investigação em Agronomia, Alimentos, Ambiente e Paisagem, Instituto Superior de Agronomia, Universidade de Lisboa, Lisbon, Portugal

R. Salgado
Escola de Ciências e Tecnologia, Universidade de Évora, Évora, Portugal

Keywords Irrigation areas · Water salinity · SAR · Drought · Water quality assessment

Introduction

Pronounced seasonal and interannual variability in the distribution of precipitation is a trait of the Mediterranean climate. This variability can lead to long drought periods whose severity has increased in the past decades because of greater atmospheric evaporative demand resulting from temperature rise caused by climate change (EEA 2012; IPCC 2014; Vicente-Serrano et al. 2014). Increased climatic aridity is leading to higher crop water requirements, making agriculture in many Mediterranean regions more dependent on irrigation networks to counteract low water availability. However, the expansion of irrigation is usually accompanied by agricultural intensification and large-scale changes in land use, which are likely to increase soil degradation processes (EC 2000; Valverde et al. 2015). The reduction in water quantity and quality and the development of soil salinization induce deleterious and often irreparable impacts on crop production and soil quality, increasing the risk of desertification (Iglesias et al. 2018; Williams 1999; Zalidis et al. 2002). Scanlon et al. (2007) refer that we are far from understanding the full impact of land use changes in many areas, since there are long time lags between land use changes and system response. However, as stated by Hillel (2000), when referring to the processes of degradation that have threatened the sustainability of irrigated agriculture since its beginning in the Fertile Crescent, "the (salinization) problem is age-old" and "continue to plague irrigation districts today no less than in the past". Several recent studies focusing on the evaluation of drought impacts on the degradation of water quality in rivers, lakes, and reservoirs (e.g., Mosley et al. 2012; Mosley 2015; van Vliet and Zwolsman, 2008), or on water and soil salinity (e.g., Etteieb et al. 2017; Gkiougkis et al. 2015; Hu et al. 2019; Jones and van Vliet 2018; Merchán et al. 2013), have exposed a global growing trend in regions with water limitations and under climatic uncertainty conditions.

In semiarid or Mediterranean-type climate regions, as the Southern Portugal region of Alentejo, traditional rainfed agriculture, conditioned by water availability constraints, has been gradually replaced by irrigated agriculture, whenever private or public investments have been made in the establishment of irrigation projects. In recent years, with the irrigation network of the Alqueva Multi-Purpose Development Project (EFMA – Emprendimanto de Fins Múltiplos de Alqueva), farmers in Alentejo are more and more resorting to the irrigation of their crops, and the region is witnessing a profound transformation of the agricultural landscape and of the farming systems (Tomaz et al. 2018; Valverde et al. 2015). This large irrigation scheme started to operate in 2002 and presently covers nearly 120,000 ha (EDIA 2017). The growing demand for irrigation water in the region has been inevitably accompanied by an increase in the use of additional inputs, like mineral fertilizers and pesticides, which can be a cause of resource degradation when unsuitable agronomic practices are used, threatening the agroecosystems sustainability in the medium to long term (Paranychianakis and Chartzoulakis 2005; Valverde et al. 2015; Zalidis et al. 2002).

The EFMA is centered on the Alqueva reservoir, the largest artificial lake in the Iberian Peninsula, which provides water for public supply, irrigation, industry uses, energy production, and tourism. In fact, it constitutes the most important water supply source in Southern Portugal, so its sustainability is essential to meet the problems of water scarcity in this region. Studies carried out in this reservoir during its filling period, by Serafim et al. (2006), report a spatial and temporal heterogeneity of water quality, determined by stratification/mixture processes, inorganic (mineral) content, and oxygenation. Based on the total phosphorus and chlorophyll content in its early years, Morais et al. (2007) classified the Alqueva reservoir as an eutrophic system. Palma et al. (2010, 2014a, 2014b, 2015) found results that showed a heavily modified water body, with ecotoxicological risk to aquatic organisms induced mainly by pesticide and metal pollution. Furthermore, the results highlighted an increment over time of organic matter and nutrients in the water body and of trace elements in the sediments. The results from these studies, although very important as an alert for the need to a continuous assessment of the chemical and ecological status of the system, did not focus on the water quality for irrigation and did not account for the possible restrictions in its use when considering agricultural productivity and impacts on soil properties, namely, soil structure deterioration resulting from an excess of sodium (Na^+) in the soil. The knowledge of water chemical composition, and of its spatial and temporal trends, is required to (i) evaluate water suitability for irrigation;

(ii) define the appropriate criteria for water quality evaluation; (iii) outline tools for water and soils management; and (iv) implement appropriate irrigation and drainage practices (Beltrán 1999; Hillel 2000; Lutz et al. 2016; Machado and Serralheiro 2017; Paranychianakis and Chartzoulakis 2005; Zalidis et al. 2002). All these endpoints are useful to increase the environmental sustainability of agricultural soils and of surface and groundwater, in irrigated lands of the Mediterranean basin.

Taking the above into consideration, this study aimed to contribute to the implementation of sustainable resources management strategies in regions affected by water scarcity. For this purpose, the objectives of this study were (i) to assess the Alqueva reservoir water quality for irrigation; (ii) to understand spatial and/or temporal patterns in a drought year using multivariate statistical analyses; (iii) to support the design of strategies for an effective sampling and assessment of water quality for irrigation; and (iv) to indicate water resources and agricultural water management adaptations to cope with salinization processes in the Mediterranean region when intensive agricultural practices supported by irrigation are used.

Materials and methods

Study area

The study area is the Alqueva reservoir, located along the main course of the Guadiana River, in the Portuguese southern region of Alentejo (Fig. 1). The lithology of the Guadiana Basin is dominated by greywacke, schist, and a volcano–sedimentary complex with polymetallic sulfide complexes of Cu, Pb, and Fe–Mn and carbonate rocks (Mil-Homens et al. 2007). The reservoir, with a total storage capacity of 4150 hm^3, is the center of the EFMA, providing water for public supply, irrigation, industry uses, energy production, and tourism. The global irrigation plan benefits a total area of 120,000 ha, of which about 70,000 ha were in operation in 2017 with a total water supply of over 245 hm^3 per year (EDIA 2017). Predominant soils in the irrigation area are Luvisols (orthic, calcic, vertic, and gleyic), Vertisols (chromic and pelic), and Cambisols (calcic and chromic) where the main parent materials are intermediate or basic igneous rocks (diorite and gabbro), limestone, and schist (GPAa 2005; IUSS Working Group WRB 2014). According to EDIA (2017), the main crops grown in the area during 2017 were olive (*Olea europaea* L.), occupying more than half of the irrigated area (56% in 2017); maize (*Zea mays* L.), the second most important crop, occupying 10% of the area; grapevine (*Vitis vinifera* L.) in 7% of the area; almond (*Prunus dulcis* (Mill.) D. A. Webb), in 5% of the area; forage crops in 5% of the area; wheat (*Triticum aestivum* L. and *Triticum durum* Desf.), and barley (*Hordeum vulgare* L.), in 3% of the area. The remaining area is mainly occupied by open-field horticultural crops, like melon (*Cucumis melo* L.) and tomato (*Solanum lycopersicum* L.).

Climate conditions and meteorological data

The meteorological data used in this study were recorded in seven automatic weather stations, belonging to IPMA, the Portuguese Institute for Sea and Atmosphere (Beja and Évora); to SAGRA, the Agro-meteorological network support service to farmers in the Alentejo region (Beja) (COTR 2017); and to ICT, Earth Sciences Institute (Mitra, Portel, Barbosa and Cid Almeida) (ICT 2019). The latter two (Barbosa and Cid Almeida) are installed close to the Alqueva reservoir, in order to characterize the climate near the reservoir and the impact of the water mass on the atmosphere (some results using data from these stations can be found in Potes et al. 2017 and Iakunin et al. 2018). The locations of the stations are indicated in Fig. 1.

In the region, climate is predominantly Mediterranean, or temperate with hot and dry summer (Csa, in Köppen classification), with a small area of midlatitude steppe (Bsk, in Köppen classification). According to IPMA (2018), the 1981–2010 climatological normal for annual rainfall, in the two main towns in the area, Beja and Évora (stations No 562 and No 588 of the Portuguese synoptic network), is 558 and 585 mm, respectively (Table 1), and for average temperature is 16.9 °C in Beja and 16.5 °C in Évora. The year 2017, in Portugal, was classified as extremely hot and dry, being the third-driest and the second-warmest year since routine observations were established in 1931. The period from April to December, with persistently negative precipitation anomalies (except August, in the region under study), was the driest of the last 87 years IPMA

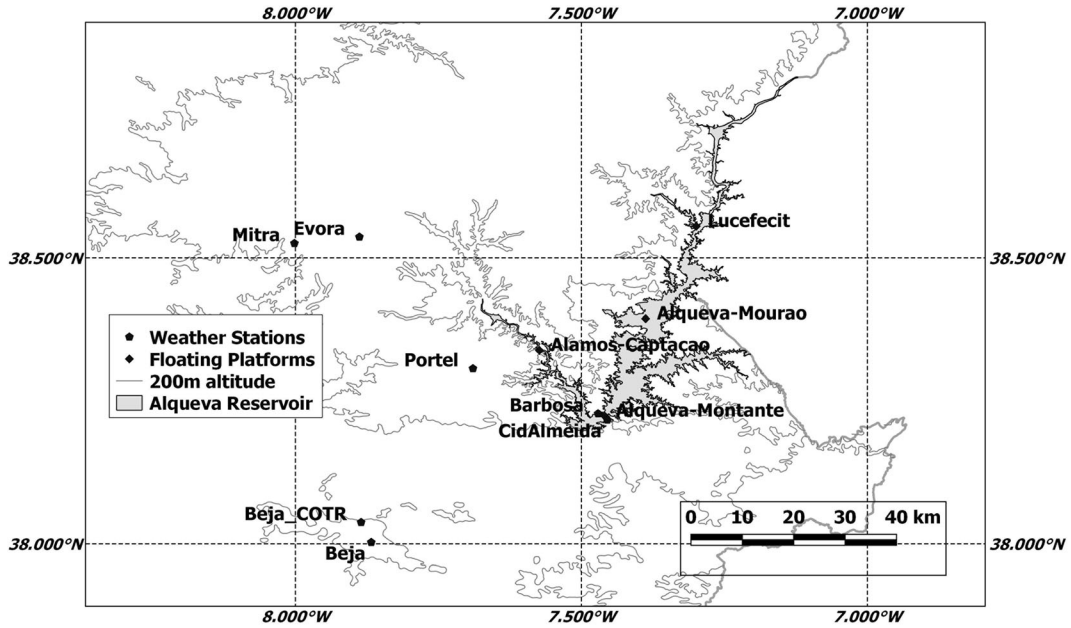

Fig. 1 Map showing the location of the Alqueva irrigation area, the sampling sites in floating platforms at the Alqueva reservoir (Alamos-Captação (Al), Alqueva-Montante (Mn), Alqueva-Mourão (Mr), and Lucefécit (Lf)), and the automatic weather stations (Beja, Beja-COTR, Évora, Mitra, Portel, Barbosa, and Cid Almeida)

(2017). Daily precipitation registered at the automatic weather station in Beja (COTR) is presented in Fig. S1.

On the basis of data, in Table 1, and on the information of the National Climatological Bulletin (IPMA 2017), the main characteristics of the weather in the EFMA area during 2017 were the: (i) from January to March, the values of precipitation and temperature were close to the climatological normal; (ii) from April to December, the precipitation was below the normal, particularly in April, June, July, September, and October; (iii) in April and May, temperatures were higher than the normal; and (iv) in June and October, temperatures were exceptionally high, with several heat waves and temperature records. These long periods of high temperatures and low precipitation gave rise to increased aridity, so that by the end of October the whole EFMA area was under extreme drought, the severest class according to the PDSI index (Palmer drought severity Index; Palmer 1965).

Sampling and water physicochemical analyses

Four sampling sites in floating platforms were established at the Alqueva reservoir (Fig. 1): Álamos-Captação (Al; 38°20′30.00″N, 7°34′40.00″W), Alqueva-Montante (Mn; 38°12′55”N, 7°29′28”W), Alqueva-Mourão (Mr; 38°23′60.00″N, 7°23′25.80″W), and Lucefécit (Lf; 38°33′6.32″N, 7°17′52.86″W). The Al site was chosen because it is near the Álamos pumping station, an inlet where water is elevated to the conveyance network of the Alqueva subsystem, one of the three irrigation subsystems in the plan. The Mn site was selected to ensure representativeness of the reservoir area. Mr and Lf sites were chosen considering previous results for the reservoir water quality assessment, which indicated these sites among those with worst water quality (Morais et al. 2007; Palma et al. 2010, 2014a; Serafim et al. 2006).

The study comprised six sampling campaigns during 2017, performed in January (Jan), March (Mar), May, July (Jul), September (Sept), and November (Nov) (Fig. S1). The months of Jan, Mar, and Nov are included in the wet season, and the dry season includes May, Jul, and Sept, according to the Portuguese Environment Agency (APA – Agência Portuguesa de Ambiente), for the Alentejo region. This hydrological permanence classification (permanent or intermittent streams) takes into account the importance of the variability of the tributary's hydrological regimes for water quality, especially in the southern regions of Portugal, reflecting the regional expression of the Mediterranean climate, which is

Table 1 1981–2010 Climatological normal for Beja and Évora synoptic stations (Portuguese network from IPMA) and meteorological data from 2017, registered in automatic weather stations located in the region

	1981–2010 Climatological normal		2017 Meteorological data						
	Beja	Évora	Beja (IPMA)	Beja (COTR)	Évora (IPMA)	Mitra	Portel	Barbosa	Cid Almeida
	a) Monthly and annual mean temperatures (°C)								
Jan	9.7	9.6	8.7	8.9	8.2	8.3	8.0	–	–
Feb	10.8	10.7	11.2	11.6	11.0	11.0	10.6	–	11.4
Mar	13.4	13.3	12.7	12.9	12.2	12.2	12.1	12.7	12.4
Apr	14.6	14.3	16.9	16.8	16.5	16.6	16.7	17.3	16.6
May	17.7	17.1	19.6	19.8	19.4	19.2	19.7	20.5	20.0
Jun	22.0	21.4	24.0	24.3	24.0	24.0	24.8	25.4	25.2
Jul	24.6	23.9	24.3	24.4	24.5	24.3	25.3	25.8	25.5
Aug	24.8	24.1	24.6	24.6	24.8	24.6	25.5	26.0	25.6
Sept	22.4	21.9	21.4	21.7	21.7	21.7	22.4	22.7	22.4
Oct	18.2	17.7	21.5	21.5	20.8	20.8	20.7	21.5	20.4
Nov	13.6	13.4	14.2	14.3	13.2	13.1	12.9	14.1	13.4
Dec	10.7	10.5	10.0	10.1	9.3	9.2	9.0	10.0	9.3
Year	16.9	16.5	17.5	17.6	17.2	17.1	17.4	–	–
	b) Monthly and annual accumulated precipitation (mm)								
Jan	66	61	65	62	39	33	58	–	–
Feb	55	52	58	45	50	43	64	–	–
Mar	41	44	84	79	78	71	89	–	51
Apr	59	55	5	7	1	5	3	–	8
May	43	47	17	20	44	44	23	–	23
Jun	13	17	3	5	8	5	4	–	2
Jul	2	4	0	0	0	0	0	–	0
Aug	4	8	22	9	17	8	5	–	0
Sep	30	32	0	0	0	0	0	–	0
Oct	72	84	18	22	21	19	14	–	33
Nov	77	88	64	63	45	32	43	–	30
Dec	98	95	40	52	45	54	60	–	48
Year	558	585	376	363	348	312	363		

– no record available. (a) Monthly and annual mean temperatures (°C); (b) monthly and annual accumulated precipitation (mm)

characterized by dry and hot summers and mild and wet winters with concentrated rains (ARH Alentejo 2011).

At each sampling location, 2 L of surface water were collected, at a depth of 50 cm, using a Van Dorn bottle. The water samples were stored in polyethylene bottles and transported to the laboratory, in a cooler at 4 °C, where they were conserved and stored, following the requisites for water conservation for each parameter (APHA 1998). The major inorganic ions, decisive in the evaluation of water quality for irrigation, were determined using the officially recommended methods of analysis (APHA 1998), namely, ionic chromatography: sodium (Na^+), calcium (Ca^{2+}), magnesium (Mg^{2+}), potassium (K^+), ammonium (NH_4^+), nitrate (NO_3^-), nitrite (NO_2^-), chloride (Cl^-), fluoride (F^-), and sulfate (SO_4^{2-}), all in mg L^{-1}. Water pH and water electrical conductivity (ECw; dS cm^{-1}) were measured in situ at a 50-cm depth using a multiparametric probe YSI 6820 MPS probe®.

To assess the potential impact of water on aggregates dispersion and soil structure due to an excess of sodium

present on the soil–exchange complex (US Salinity Laboratory Staff 1954), the sodium adsorption ratio (SAR) was calculated using Eq. (1) (ions concentrations in meq L^{-1}):

$$SAR = \frac{[Na^+]}{\sqrt{\frac{[Ca^{2+}] + [Mg^{2+}]}{2}}} \quad (1)$$

Assessment of water quality for irrigation

The evaluation of water quality for irrigation was performed using both the Portuguese legislation (Law-Decree No 236/1998 1998; which establishes quality standards, criteria and objectives with the purpose of protecting the aquatic environment and improving water quality according to its main uses) and the Food and Agriculture Organization of the United Nations (FAO) guidelines (Ayers and Westcot 1985) (Tables 2 and 3).

The FAO guidelines are based in the quality standards reported by Ayers and Westcot (1985), considering a "potential problem" approach assessed by three degrees of restriction on uses: none, slight to moderate, and severe (Table 3). The potential irrigation problems addressed are as follows: (i) salinity, assessed from ECw; (ii) infiltration rate of water into the soil, assessed using ECw and SAR, together; (iii) specific ion toxicity by Na^+, Cl^-, or boron (B) in sensitive crops; and (iv) miscellaneous effects on sensitive crops, regarding NO_3^- (an excess of nitrates can cause nutritional imbalances that influence yield or production quality) and bicarbonate (HCO_3^-) concentrations (an excess of bicarbonate can corrode irrigation equipment, increasing maintenance and repair costs) and pH.

Ayers and Westcot (1985) systematized and updated work previously developed by the US Salinity Laboratory Staff (1954), Wilcox (1955), Maas and Hoffman (1977), Rhoades (1977), or Oster and Schroer (1979). It establishes general standards for the assessment of the water quality for agricultural purposes to be used as a management tool, particularly at farm level, considering the specific local conditions of use. The proposed guidelines emphasize the long-term influence of water quality on crop production, soil conditions, and farm management and are intended for a wide range of conditions encountered in irrigated agriculture. Their range of usability is defined by the following basic assumptions: (i) a restriction on use does not indicate that the water is unsuitable for use, it indicates that there may be a limitation in choice of crop, or special management may be needed to achieve full productivity; (ii) the soil texture ranges from sandy loam to clay loam with good internal drainage; (iii) the climate is semiarid to arid and rainfall is low; (iv) the soil drainage is good, with no uncontrolled shallow water table present within 2 m of the surface; (v) surface or sprinkler irrigation methods (infrequent irrigation) are used, with at least 15% of percolation of the applied water below the root zone (the guidelines are too restrictive for drip irrigation, more frequent and efficient); (vi) the water uptake pattern by the crops in each quarter of the soil profile is 40%–30%–20%–10%, so salinity increases with depth and is greatest in the lower part of the root zone; and (vii) the division between the three degrees of restriction on use (none, slight to moderate, and severe) are gradual, and there is no clear-cut breaking point (Ayers and Westcot, 1985).

Table 2 Portuguese quality standards of water intended for irrigation (Decree-Law No 236/1998, 1998)

Parameter	Units	MRV [1)]	MPV [2)]
pH		6.5–8.4	4.5–9.0
Electric conductivity (ECw) [3)]	dS m^{-1}	1	–
Chloride (Cl^-)	mg L^{-1}	70	–
Fluoride (F^-)	mg L^{-1}	1	15
Nitrate (NO_3^-)	mg L^{-1}	50	–
Sulfate (SO_4^{2-})	mg L^{-1}	575	
Sodium adsorption Ratio (SAR) [4)]		8	

[1)] MRV, maximum recommended value (or interval)

[2)] MPV, maximum permissible value (or interval)

[3)] For ECw, there is a remark: "It depends heavily on the resistance of crops to salinity, as well as the irrigation method and soil texture"; however, no detailed criterion is established

[4)] In the case of SAR, the observation says: "It depends on the water salinity, the characteristics of the soil and the type of crop to be irrigated." Again, no detailed criterion is established

Statistical analyses

All statistical analyses were carried out with the software Statistica 7 (StatSoft, Inc. 2004). Mean and standard deviation of ion concentrations and SAR (three repetitions), and in situ measurements of ECw and pH, were plotted using graphical tools.

Table 3 FAO guidelines for interpretation of water quality for irrigation (adapted from Ayers and Westcot, 1985).

Potential irrigation problem	Units	Degree of restriction on use		
		None [1]	Slight to moderate [2]	Severe [3]
Salinity [4]				
ECw	dS m^{-1}	< 0.7	0.7 – 3.0	> 3.0
Infiltration [5] [6]				
SAR 0 – 3 and ECw	dS m^{-1}	> 0.7	0.7 – 0.2	< 0.2
SAR 3 – 6 and ECw		> 1.2	1.2 – 0.3	< 0.3
SAR 6 – 12and ECw		> 1.9	1.9 – 0.5	< 0.5
SAR 12 – 20 and ECw		> 2.9	2.9 – 1.3	< 1.3
SAR 20 – 40 and ECw		> 5.0	5.0 – 2.9	< 2.9
Specific ion toxicity [7]				
Sodium (Na^+)				
Surface irrigation	SAR	< 3	3 – 9	> 9
Sprinkler irrigation	mg L^{-1}	< 69	> 69	-
Chloride (Cl^-)				
Surface irrigation	mg L^{-1}	< 142	143 – 355	> 355
Sprinkler irrigation	mg L^{-1}	< 106	> 106	
Miscellaneous effects [8]				
Nitrate (NO_3^-)	mg L^{-1}	< 5	5 – 30	> 30
pH	-	Normal range: 6.5 – 8.4		

[1] None - no soil or cropping problems are experienced. [2] Slight to moderate - gradually increasing care in selection of crop and management alternatives is required if full yield potential is to be achieved. [3] Severe – there will be soil and cropping problems or reduced yields, but even with cropping management designed especially to cope with poor quality water, a high level of management skill is essential for acceptable production. [4] Affects crop water availability; [5] Affects infiltration rate of water into the soil. [6] Evaluated using ECw and SAR together; [7] Affects sensitive crops; [8] Affects susceptible crops.

Multivariate statistical analyses, namely, factor analysis (FA), including principal components analysis (PCA) for factor extraction, and cluster analysis (CA), were performed after methodologies described in Simeonov et al. (2003) and Palma et al. (2010, 2014a). Factor analysis tests latent factors causing observed variables; PCA extracts these factors by reducing correlated observed variables; CA assembles objects or cases into groups called clusters based on characteristics they possess (Shrestha and Kazama, 2007; Simeonov et al. 2003). The application of these multivariate statistical methods supports the interpretation of complex datasets, allowing the identification of possible factors or sources that influence the status of the water systems and offering valuable tools for the management of water resources (Muangthong and Shrestha 2015; Shrestha and Kazama, 2007; Simeonov et al. 2003; Li et al. 2018).

To sort the relative importance of time and site on the water physicochemical parameters, a preliminary analysis was performed using repeated measures ANOVA with two factors (month and site). One-way ANOVA was performed in the case of ECw and pH, given their single "in situ" measurements and the resulting degrees of freedom. Differences between means were compared using Tukey's test ($p < 0.05$).

FA and PCA were made on normalized data (log x; x = mean value) to avoid misclassification due to the wide differences in data dimensionality (Liu et al. 2003). The FA/PCA approach aimed to understand the data structure, to find the most meaningful parameters, and to reduce de number of variables into a small number of independent variables (principal components). The principal components were retained after applying the Scree test (Cattell 1966), considering principal components with eigenvalues > 1 that accounted for a proportion of variance > 10%. The factor loadings, representing the correlation between the factors and the variables, were classified as "strong," "moderate," and "weak,"

corresponding to absolute loading values of > 0.75, 0.75–0.50, and 0.50–0.30, respectively (Liu et al. 2003).

Hierarchical agglomerative CA was performed with the factor scores of the two-component model to detect similarity groups between sites and/or dates that could indicate spatial and/or temporal patterns in the data. The resulting clusters should exhibit high within-cluster homogeneity and high between-clusters heterogeneity (Shrestha and Kazama, 2007; Muangthong and Shrestha, 2015). The distance between clusters was evaluated using the Ward's method (Ward 1963) for the amalgamation (linkage) rule. The Euclidean distance for similarity measures was used as linkage distance (dlink), expressed as the percentage of the range from the maximum to the minimum distance (dmax) in the data, dlink/dmax*100 (Muangthong and Shrestha 2015; Shrestha and Kazama, 2007; Simeonov et al. 2003). Statistically significant clusters were first identified in a tree diagram considering a Euclidean distance of dlink/dmax*100 < or = to 60% (Muangthong and Shrestha 2015; Shrestha and Kazama, 2007) and then plotted in a two-dimensional plane defined by the two principle components model.

Results and discussion

Water physicochemical assessment

The temporal and spatial variability of the cation and anion concentrations was characterized by their mean and standard deviation, represented by columns and whiskers (Figs. 2 and 3). In general, the dominant ion in most samples was Cl^-, followed by SO_4^{2-} and Na^+. The order of cation abundance was $Na^+ > Ca^{2+} > Mg^{2+} > K^+ > NH_4^+$. Concerning the anion chemistry, the order of anion abundance was $Cl^- > SO_4^{2-} > NO_3^- > F^- > NO_2^-$.

The main water chemistry of the reservoir may reflect the geology of the area, and its weathering dynamics, as reported by Etteieb et al. (2017) that, in a study for the assessment of the suitability of surface water for irrigation in Northern Tunisia, found the main chemistry of the river system controlled by the dissolution of gypsum and halite. However, several studies have described the influence of farming, both in rainfed and irrigated agriculture, and its contribution for salt leaching through deep percolation and runoff, and of nutrient-rich discharges resulting from other human activities, e.g., in an 8-year study to evaluate the impact of the introduction of irrigation in a hydrological basin in Spain, Merchán et al. (2013) reported an increase in the annual loads of salts, mainly NO_3^-; Chotpantarat and Boonkaewwan (2018) observed a duplication in NO_3^- loads in a basin in Thailand affected by agriculture intensification and land use change; on a study to evaluate the effects of recent agricultural practices on drainage water quantity and quality in arid basins in Northwest China, Hu et al. (2019) found that the quality of drainage water deteriorated mainly due to expansion of new farmlands; Yang et al. (2019) reported that the fast development of agriculture and urbanization in the Hai He basin, in the North China plain, has resulted in discharging nutrient-rich wastewater into lakes and reservoirs, leading to eutrophication and water scarcity. Concentrations of Na^+, Mg^{2+}, NH_4^+, Cl^-, SO_4^{2}, NO_3^-, and F^- were significantly higher ($p < 0.05$) in Lf (Figs. 2 and 3; Table S1). Overall, and in accordance with Morais et al. (2007) and Palma et al. (2010, 2014a), ion concentrations were higher in Lf, followed by Mr, the most upstream sites, both located near tributary inflows, near the border, and more permeable to the influence of the input flux from Spain. There was an upward trend in ions concentrations throughout the year, with significantly higher concentrations of Na^+, Mg^{2+}, Cl^-, and SO_4^{2-}, registered through May to Nov (Figs. 2 and 3; Table S1). Except for SO_4^{2-}, NO_3^-, and NO_2^-, ion concentrations occurred in the samples collected in Nov were significantly higher, which may reflect the severe drought felt in the summer and begin of autumn months. Nitrate is present in nitrogen fertilizers, strongly applied in annual spring–summer and permanent irrigated crops, but also in annual autumn-winter rainfed crops. Thus, the higher concentrations found in the water for NO_3^-, during the wet period could be due to agricultural drainage and runoff. Although K^+ leaching losses are less frequent, due to its tendency to be retained in the structure of clay minerals, it is an important plant nutrient commonly present in mineral fertilizers (usually combined with phosphorus and nitrogen forms), which are applied during the sowing of autumn–winter crops or in post-harvest of olives and other fruit trees. An excessive fertilization or irrigation can explain the K^+ concentrations found in Al at Nov (Fig. 1).

While ECw is a measure of the total dissolved salts and their potential effect on the soil osmotic potential

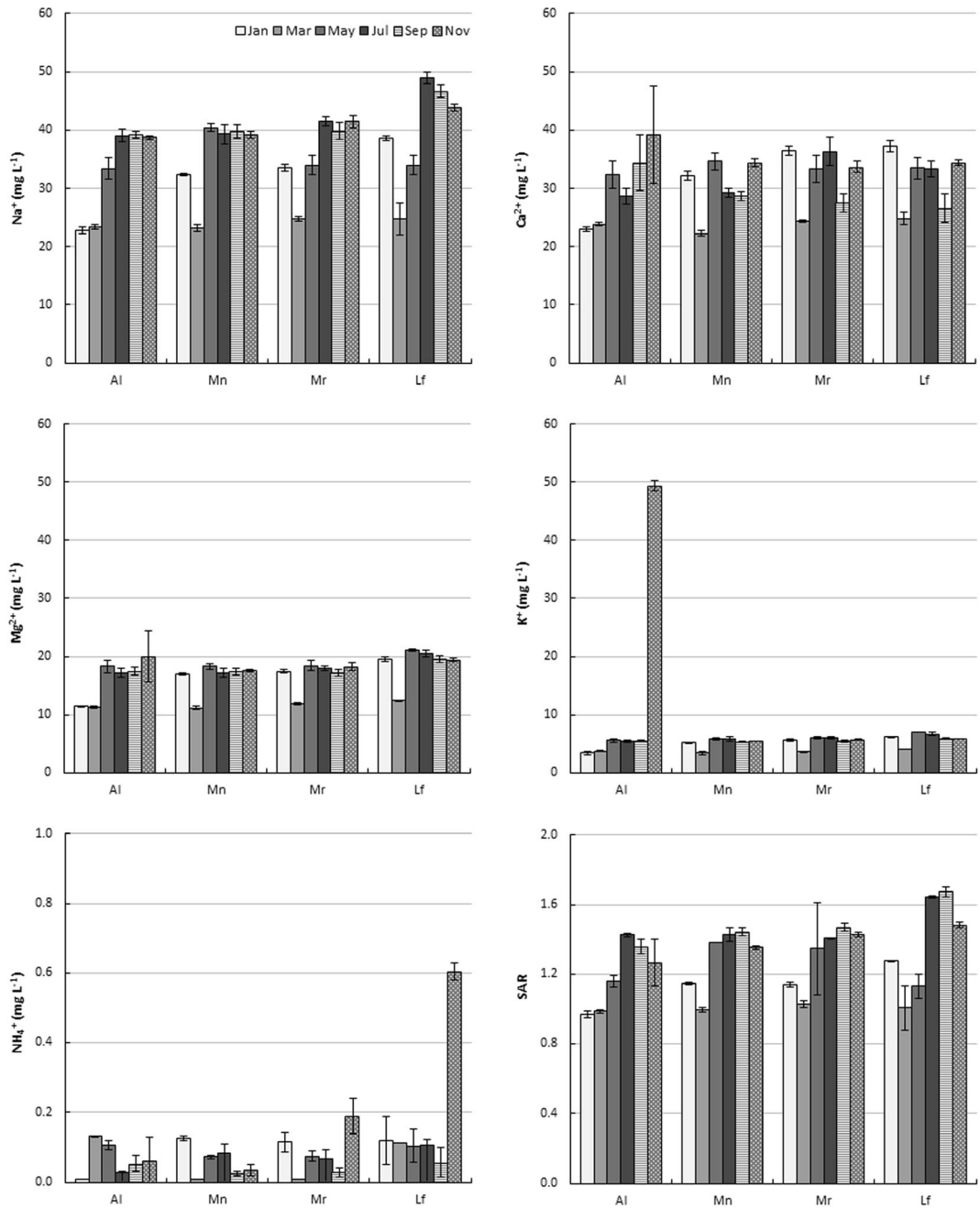

Fig. 2 Spatial and temporal variation of cations concentrations and SAR, during 2017, at the Alqueva reservoir. Bars represent the mean and whiskers represent the standard deviation for three repetitions. Al, Álamos; Mn, Montante; Mr, Mourão; Lf, Lucefécit. Jan, January; Mar, March; Jul, July; Sept, September; Nov, November

and on water stress in plants, SAR is related to the exchangeable sodium percentage, a soil property decisive in aggregate stability and soil permeability. Hence, SAR is considered an important indicator to predict the negative effects of Na^+ excess on soil physical properties (Ayers and Westcot 1985; Hanson 2006a; Rhoades et al. 1992; Tanji and Kielen 2002; U.S. Salinity Laboratory Staff 1954; Wilcox 1955). As expected, the patterns of temporal and spatial variation observed for Na^+ were also found for SAR (Fig. 2; Table S1). The same pattern can be observed for ECw (Fig. 4; Table S1), with spatial and temporal dynamics similar

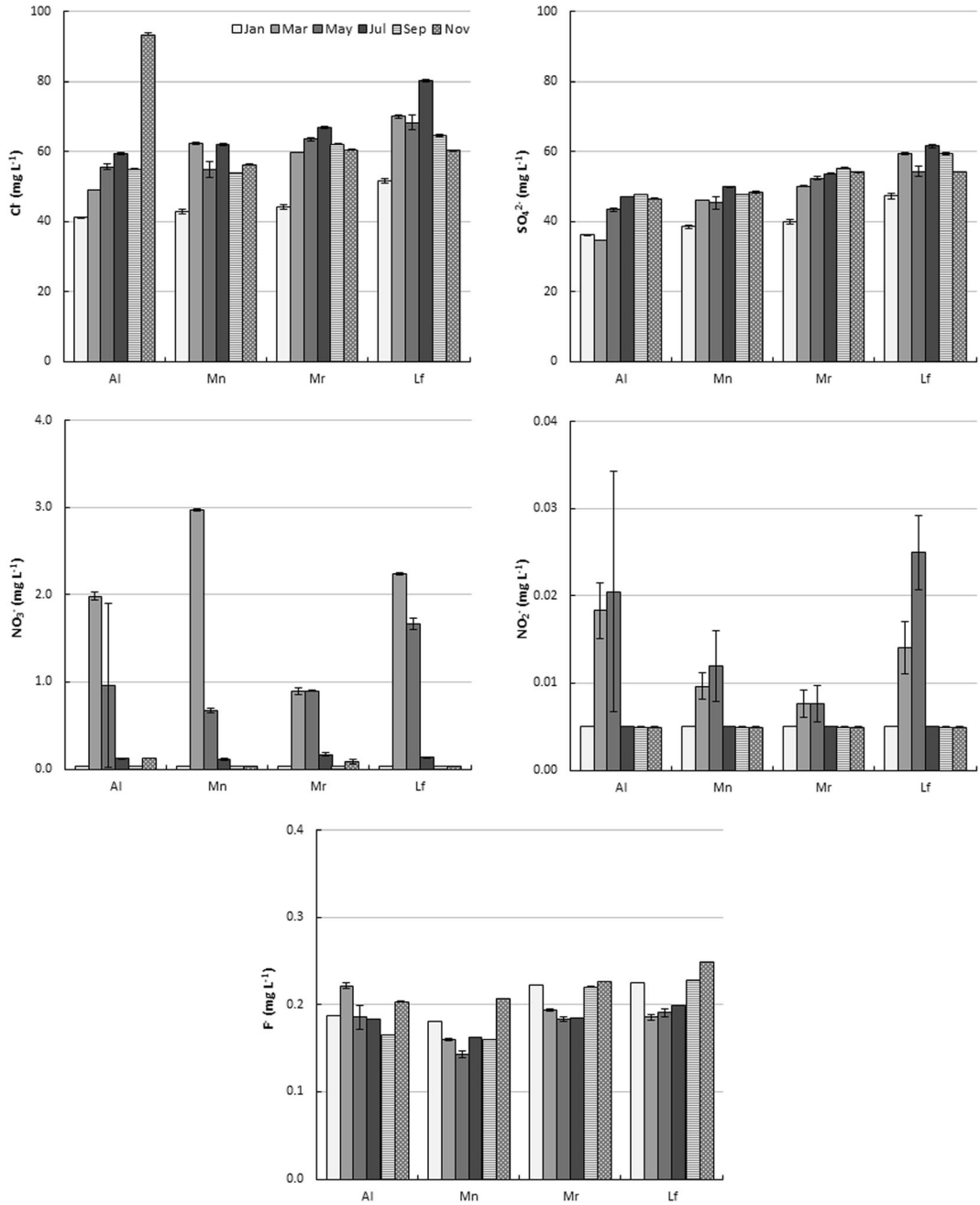

Fig. 3 Spatial and temporal variation of anions concentrations and SAR, during 2017, at the Alqueva reservoir. Bars represent the mean and whiskers represent the standard deviation for three repetitions. Al, Álamos; Mn, Montante; Mr, Mourão; Lf, Lucefécit. Jan, January; Mar, March; Jul, July; Sept, September; Nov, November

to Na^+ or Cl^-, two of the most abundant ions in the Alqueva reservoir. Considering the Portuguese or the FAO standards, the maximum recommended values for SAR and ECw were never surpassed. The pH values increased from March to September, reaching an average value outside the allowed range (6.5 to 8.4) in July. Although with no statistically significant differences, the highest pH values occurred in the most upstream sites (Mr and Lf) (Fig. 4; Table S1); the maximum value (9.1) was registered at September in Lf (Fig. 4).

Overall, the temporal dynamics of the water physicochemical parameters during the year 2017 could

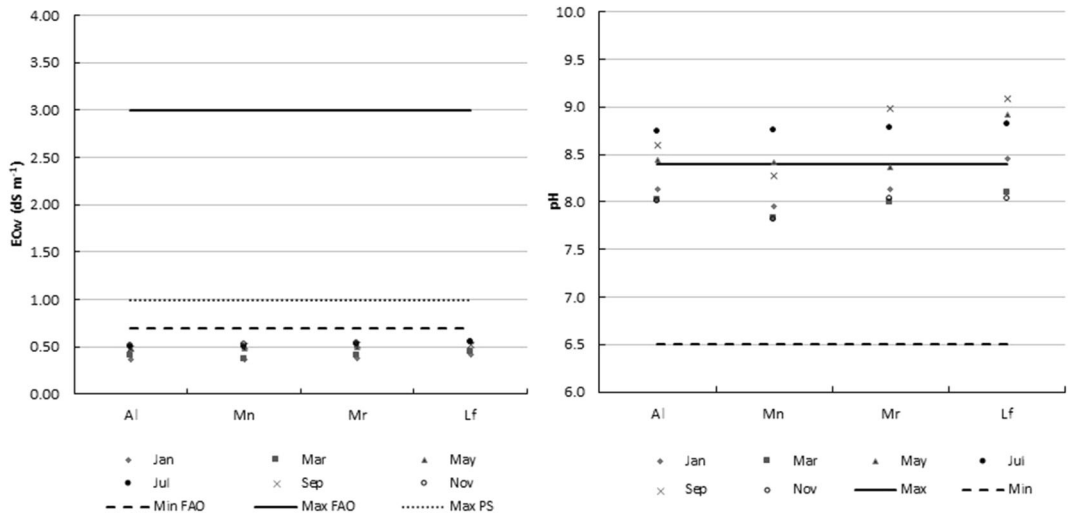

Fig. 4 Spatial and temporal variation of ECw and pH, during 2017, at the Alqueva reservoir. Dots correspond to single in situ measurements. Full lines correspond to maximum recommended values from water quality standards. Dashed lines correspond to minimum recommended values from water quality standards. Max FAO and Min FAO, maximum and minimum recommended values from the FAO guidelines, respectively; Max PS, maximum recommended value from the Portuguese standards; Min, minimum recommended value both from the FAO guidelines and from the Portuguese standards; Max, maximum recommended value both from the FAO guidelines and from the Portuguese standards. Al, Álamos; Mn, Montante; Mr, Mourão; Lf, Lucefécit. Jan, January; Mar, March; Jul, July; Sept, September; Nov, November

indicate that an abnormal annual distribution of precipitation and temperature may distort seasonal differences, and a more frequent assessment of the water quality should be considered.

Assessment of water quality for irrigation

Table 4 summarizes the potential risks obtained for the ions analyzed, identifying the parameters in noncompliance or

Table 4 Parameters and potential risks found in noncompliance or with some degree of restriction on use, at the four sites during the six campaigns of the study, according to the Portuguese legislation (Law-Decree No 236/1998, 1998) and the FAO guidelines (Ayers and Westcot, 1985)

Parameter/potential problem	Site	Portuguese legislation						FAO guidelines					
		Jan	Mar	May	Jul	Sep	Nov	Jan	Mar	May	Jul	Sep	Nov
Chloride	Al						NC						
	Mn												
	Mr												
	Lf		NC		NC	NC							
pH	Al			NC	NC	NC				NC	NC	NC	
	Mn			NC	NC					NC	NC		
	Mr				NC	NC					NC	NC	
	Lf	NC		NC	NC	NC		NC		NC	NC	NC	
Soil infiltration rate	Al	–	–	–	–	–	–	SM	SM	SM	SM	SM	SM
	Mn	–	–	–	–	–	–	SM	SM	SM	SM	SM	SM
	Mr	–	–	–	–	–	–	SM	SM	SM	SM	SM	SM
	Lf	–	–	–	–	–	–	SM	SM	SM	SM	SM	SM

Al, Álamos; Mn, Montante; Mr, Mourão; Lf, Lucefécit. NC, noncompliance; SM, slight to moderate degree of restriction

– not classified in these standards

with some degree of restriction on use, considering both the Portuguese legislation (Law-Decree No 236/1998 1998) and the FAO guidelines (Ayers and Westcot 1985). According to the Portuguese legislation, the only two parameters in noncompliance at some months and sites were Cl^- and pH. In the case of Cl^-, it exceeded the maximum recommended value of 70 mg L^{-1} in Al (Nov) and Lf (Mar, Jul and Sep). As for pH, in almost every site, from Jan to Sep, it exceeded 8.4, the upper limit of the allowed range. Considering the FAO standards, Cl^- concentrations would not constitute any degree of restriction, both for surface (with little relevance in the area) or sprinkler (most commonly used method in field crops) irrigation systems. When classified separately, in both the Portuguese and FAO recommended criteria, ECw and SAR values were not excessive. However, these parameters must be evaluated together to estimate possible soil infiltration rate decline and surface crust formation problems, because of the dispersing effect of an excess of sodium on the soil exchange complex (Hanson 2006a). This combined assessment showed a slight to moderate degree of restriction of use in all water samples analyzed. In fact, low-salt water can reduce infiltration even for a low SAR, that is, the effects of increasing sodium adsorption ratio grow as the salinity of the water decreases (Ayers and Westcot 1985; Compton 2011, Hanson 2006a; Rhoades et al. 1992). This outcome occurs when the salinity of the soil water or applied water is insufficient to counteract the negative effects of adsorbed sodium on soil structure.

Compton (2011) named it "the rainfall effect," referring that the leaching of salts from precipitation or excess irrigation water will reduce the salinity of the soil solution, while the reduction in SAR will be far smaller due to a buffer effect, performed by the exchangeable cations (Ca^{2+}, Mg^{2+}, Na^+, and K^+), adsorbed in the soil matrix, on the ions dissolved in the soil solution. Therefore, leaching, as a result of a rainfall event or an irrigation, can cause infiltration reduction in the surface soil because the stabilizing effects of salinity on aggregate stability is lost when the EC of the water is reduced.

Soils most likely to show reduced infiltration and crusting are fine-textured soils, like those containing more than 30% expansive clay (smectite) in the profile or in some argic or natric subsurface horizons, as is the case of Luvissols and Vertissols, prevalent in the Alqueva irrigation area (GPAa 2005). Tanji and Kielen (2002) stated that at lower SAR levels, when chemical bonding is weakened, but no spontaneous dispersion takes place, inputs of energy are required for actual dispersion, and the use of sprinkler irrigation can increase the probability of surface crusting due to the physical disruption caused by the water drops as they impact the soil surface aggregates.

It should be noted that the institution responsible for the EFMA management uses the Portuguese legislation, not the FAO guidelines, to provide to irrigators biannual water quality bulletins with the results of monitoring performed in superficial water samples collected in January and May, near two of the water conveyance systems inlets (Álamos and Pedrógão). Hence, these bulletins do not include the joint evaluation of water EC and SAR to predict potential soil infiltration and permeability problems. These results and considerations highlight the need of introducing an assessment of potential infiltration problems caused by Na^+ and salinity together in the water quality for irrigation monitoring programs of the Alqueva reservoir. The potential soil salinization or sodification caused by irrigation with low-quality water depends not only on the water characteristics but also on other factors, such as soil texture, climatic conditions, soil drainage, irrigation method, and irrigation schedule. Therefore, early warning systems can contribute to the adoption of control measures and management changes required for long-term productivity (Bauder et al. 2014; Hillel 2000; Lutz et al. 2016; Machado and Serralheiro 2017; Paranychianakis and Chartzoulakis 2005).

Multivariate statistical analysis

Three principal components (PC1, PC2, and PC3) explained about 73.9% of the total variance (Table 5).

Following Liu et al. (2003) classification, PC1, which explained 44.6% of total variance, was strongly correlated with Na^+, Mg^{2+}, SAR, and ECw and moderately correlated with Ca^{2+}, SO_4^{2-}, K^+, pH, and Cl^-; PC2 accounted for 17.0% of total variance and was mainly correlated with NO_3^- (strong correlation) but also NO_2^- and Cl^-; PC3 explained 12.3% of total variance and showed moderate participation of NH_4^+. Given the highest correlations obtained, PC1 was mainly a "salinity" component and PC2 a "nutrient" component. That is, PC1 denotes the influence of two of the most abundant cations in Alqueva water samples, Na^+ and Mg^{2+}, and of the water salinity parameters, ECw and SAR. PC2 represents influences from nonpoint sources such as agricultural runoff, given its primary correlation with

Table 5 Loadings of principal components (PC), eigenvalues, percentage of variance, and cumulative percentage of total variance for 13 water physicochemical parameters during 2017 at the Alqueva reservoir

	PC1	PC2	PC3
Na^+	**−0.960096**	−0.135086	−0.105107
NH_4^+	−0.467300	−0.020882	*0.669443*
K^+	*−0.575927*	0.072992	0.400283
Ca^{2+}	*−0.718910*	−0.194439	0.487443
Mg^{2+}	**−0.918220**	−0.045624	0.185715
F^-	−0.259387	−0.289497	0.346247
Cl^-	*−0.532594*	*0.673994*	−0.003300
NO_2^-	0.412487	*0.699674*	0.382078
NO_3^-	0.477753	**0.820020**	0.214723
SO_4^{2-}	*−0.636368*	0.487257	−0.302760
pH	*−0.543419*	0.265721	−0.442329
ECw	**−0.839021**	0.365434	−0.087922
SAR	**−0.899493**	−0.095039	−0.316255
Eigenvalue	5.794446	2.214555	1.598573
% total variance	0.445727	0.170350	0.122967
Cumulative % variance	5.794446	61.60770	73.90442

Classification after Liu et al. (2003): bold values, strong correlation (absolute values > 0.75); *italic values*, moderate correlation (absolute values in the range 0.75–0.50)

water-soluble nitrogen forms. Although in this assessment, NH_4^+ was independent from other nitrogen forms, Simeonov et al. (2003) and Palma et al. (2014a) found correlation between NO_3^-, NO_2^-, and NH_4^+ in their studies reporting, respectively, a monitoring program of surface waters in Northern Greece and the spatial and temporal variability of the water and sediments quality in the Alqueva reservoir. Contrary to the present study, where Cl^- is in PC2, Liu et al. (2003) found strong correlation between Cl^-, ECw, TDS (total dissolved salts), Na^+, K^+, Mg^+, and SO_4^{2-} in groundwater samples collected in a coastal area in Taiwan.

Cluster analysis gave three statistically significant groups from the 24 water samples collected during 2017 (Fig. S2; Fig. 5). The higher positive factor scores in PC1 were linked to season (Mar) and location (Al). Cluster 1 included all samples collected in Jan, except the ones from Lf. Cluster 2 grouped the largest number of samples, collected in Jul, Sept, and Nov, also including Lf samples collected in Jan (Lf/Jan). Due to the significantly higher concentrations found in Lf, when comparing with the other three sites, samples collected at this site during the wet season (Jan and Mar) were normally grouped with samples from other sites and driest months. Also, the drought levels felt during the autumn months are probably responsible for grouping the Nov samples along with samples collected during the typical dry season, in Jul and Sept. Cluster 3, with the higher positive scores in the "nutrient"-related principal component (PC2), groups water samples with higher NO_3^- and NO_2^- concentrations, collected in March (wet season) and May (dry season). Therefore, both clusters 2 and 3 grouped samples collected in all the sites but in different months, pointing to a homogeneity within clusters mainly due to the sampling date. This pattern indicates that the similarity between groups was more time-controlled than space-controlled, an important feature for the design of sampling strategies, especially in drought years.

Implications for monitoring programs and management adaptations

Taking the above into consideration, water quality monitoring and assessment programs in the Alqueva irrigation area should be long term and include not only sampling campaigns in January (winter) and May (spring) but also at the end of summer (September) and, when drought conditions set in, at the beginning of autumn (October), covering different periods in the wet and dry seasons. For an effective evaluation and mitigation of potential soil salinization processes (including soil sodicity), the combined evaluation of salinity and SAR in irrigation water should be introduced, following the FAO guidelines.

The effects of the reduction in osmotic and matric soil potential are additive, and soil salinity influences the range of available water for plants (Rengasamy 2010), thus influencing their water uptake and productivity. From a simple point of view, to achieve the salt balance in soil, the amount of salt coming in must be counterbalanced by the amount of salt being removed (Weil and Brady, 2016) in order to achieve a long-term "salt" sustainability of an irrigated field or an irrigation plan. Thereby, the monitoring and assessment of water quality for irrigation should be complemented with the recommendation of appropriate agricultural water management options for preventing those impacts, e.g., (i) leaching, the basic management tool for salinity control, refers to water that is purposely applied in excess to keep the salts in solution and transport them below the root zone; (ii) subsurface drainage systems to provide a

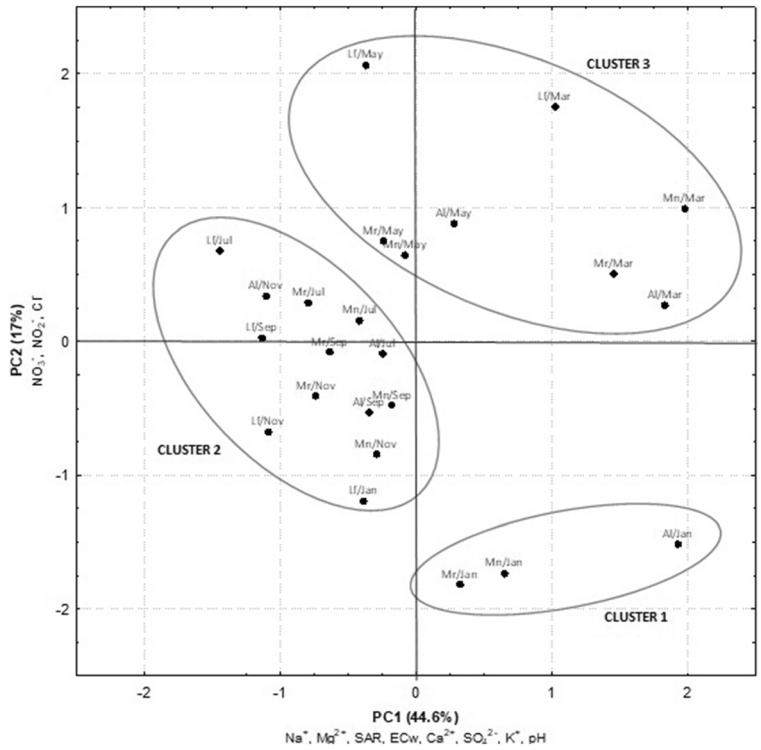

Fig. 5 Scores of the water samples on the two-dimensional plane defined by the two principle components model. Each point corresponds to a sample, represented by the combination site/month. The ellipses delimit statistically significant clusters defined by an Euclidean distance of dlink/dmax*100 < or = to 60%. Al, Álamos; Mn, Montante; Mr, Mourão; Lf, Lucefécit. Jan, January; Mar, March; Jul, July; Sept, September; Nov, November

desirable root zone environment, by lessening the root zone waterlogging and improving salinity control by leaching; (iii) improved irrigation timing to help maintain more favorable moisture content in the soil, aiding the leaching process and avoiding ascending capillary flow from saline water tables; (iv) fertilizer management in order to avoid excessive nutrient application rates, a source of many soluble salts; (v) the use of more salt tolerant crops; (vi) the use of precision agriculture technologies, like variable rate irrigation (VRI) with salt-sensing devices, to increase irrigation uniformity and efficiency; and (vii) the use of soil chemical amendments, like the application of gypsum ($CaSO_4.2H_2O$), for sodicity control, to remove Na^+ ions from the exchange complex, replacing them with Ca^{2+} (Ayers and Westcot 1985; Hanson 2006b; Lutz et al. 2016; Machado and Serralheiro 2017; Tanji and Kielen 2002).

Conclusions

Physicochemical parameters showed significantly higher values in the most upstream sites, Mr and, especially, Lf. Agricultural runoff or leaching losses through irrigation return flows may be the cause for anomalous concentrations of salts, commonly present in N or K fertilizers formulations. There was an upward trend in ion concentrations throughout the year, with significantly higher concentrations of Na^+, Mg^{2+}, Cl^-, and SO_4^{2-}, registered through May to Nov, which may reflect the severe drought felt in the summer and beginning of autumn months. Significantly higher NO_3^- concentrations were found in samples collected in March, a result that can be related to agricultural activities, namely, nitrogen fertilizations in the irrigation area.

The combined assessment of ECw and SAR showed a slight to moderate risk regarding soil infiltration rate decline and surface crust formation, in all water samples collected. These results should be considered whenever surface or sprinkler irrigation systems are used, particularly in fine-textured and poorly structured soils.

The multivariate approach with FA/PCA identified a "salinity"-related component, influencing Na^+, Mg^{2+}, ECw, and SAR, and a "nutrient"-related component, highly correlated with NO_3^- and NO_2^-. The CA methodology revealed three groups of similarity between samples, denoting a more time-controlled than space-controlled pattern, which can be an important feature for the design of water sampling and assessment strategies in irrigation areas located in regions conditioned by

seasonal and inter-annual climatic variability, especially under drought conditions.

Overall, these results could indicate that an abnormal annual distribution of precipitation and temperature may distort seasonal differences, and a more frequent assessment of the water quality should be considered.

The characteristics of the irrigation water can have a major role in the appearance or augmentation of soil secondary salinization and in the development of damaging effects of soil salinity on crops production, especially under climatic adverse conditions. In Mediterranean irrigation areas, water quality monitoring programs should be designed with sampling campaigns covering different wet and dry periods. In addition, the combined assessment of salinity and SAR should be introduced to evaluate potential infiltration problems, according to the FAO guidelines.

The assessment of water quality for irrigation should be complemented with guidance concerning the selection of appropriate management strategies for preventing those impacts. Further, it is also essential to conduct applied research, both in risk assessment studies and in ways to address the problems of soil and water degradation and resilience, especially under land use changes and climatic uncertainty.

Funding information This work was co-financed by the European Union through the European Regional Development Fund, under ALENTEJO 2020 (Alentejo Regional Operational Program) through the project "ALOP: Observation, forecasting and warning systems in the atmosphere and water reservoirs of the Alentejo" under the reference ALT20-03-0145-FEDER-000004.

This work is a contribution to the Projects UID/GEO/04035/2013 and UID/GEO/04683/2019, funded by FCT – Fundação para a Ciência e aTecnologia, Portugal.

Compliance with ethical standards

Conflict of interest On behalf of all authors, the corresponding author states that there is no conflict of interest.

References

ARH Alentejo (Administração da Região Hidrográfica do Alentejo - Administration of the Hydrographic Region of Alentejo). (2011). *Plano de gestão das bacias hidrográficas integradas nas regiões hidrográficas 6 e 7: Região Hidrográfica 7*. Lisboa: Administração da Região Hidrográfica do Alentejo I.P., Ministério do Ambiente e do Ordenamento do Território.

APHA (American Public Health Association). (1998). *Standard methods for the examination of water and wastewater* (twentieth ed.). Washington DC: American Public Health Association, American Water Works Association and Water Environmental Federation.

Ayers, R.S. & Westcot, D.W. (1985). *Water quality of agriculture*. FAO irrigation and drainage paper no. 29, revision 1. Rome: Food and agriculture Organization of the United Nations.

Bauder, T.A., Waskom, R.M., Sutherland, P.L.& Davis, J.G. (2014). Irrigation water quality criteria. Fact sheet no. 0.506, crop series – Irrigation, Colorado State University extension. https://extension.colostate.edu/docs/pubs/crops/00506.pdf. Accessed 7 September 2018.

Beltrán, J. M. (1999). Irrigation with saline water: Benefits and environmental impact. *Agricultural Water Management, 40*, 183–194.

Cattell, R. B. (1966). The Scree test for the number of factors. *Multivariate Behavioral Research, 1*(2), 245–276. https://doi.org/10.1207/s15327906mbr0102_10.

Chotpantarat, S., & Boonkaewwan, S. (2018). Impacts of land-use changes on watershed discharge and water quality in a large intensive agricultural area in Thailand. *Hydrological Sciences Journal, 63*(9), 1386–1407. https://doi.org/10.1080/02626667.2018.1506128.

Compton, A. (2011). A review of rationale for EC and SAR standards. Montana Dept. of Environmental Quality.

COTR (Centro Operativo e de Tecnologia de Regadio - Irrigation Technology and Operation Center) (2017) SAGRA – Sistema Agrometeorológico para a Gestão da Rega no Alentejo. http://www.cotr.pt/cotr/sagra.asp. Accessed 12 May 2018.

Decree-Law No 236/1998, 1 of August. *On water quality assessment*. Diário da República, 1ª SÉRIE-A N° 176 — 1-8-1998.

EC (European Commission) (2000). The environmental impacts of irrigation in the European Union. A report to the Environment Directorate of the European Commission, 147 pp http://ec.europa.eu/environment/agriculture/pdf/irrigation.pdf. .

EDIA (Empresa de Desenvolvimento e Infraestruturas de Alqueva – Alqueva Development and Infrastructures Company) (2017). Anuário Agrícola de Alqueva 2017. Empresa de Desenvolvimento e Infraestruturas de Alqueva, S.A. http://www.edia.pt/pt/o-que-fazemos/apoio-ao-agricultor/anuario-agricola/225. .

EEA (European Environment Agency) (2012). Climate change impacts and vulnerability in Europe 2012, 304 pp www.eea.europa.eu. Accessed 12 May 2018.

Etteieb, S., Cherif, S., & Tarhouni, J. (2017). Hydrochemical assessment of water quality for irrigation: A case study of, the Medjerda River in Tunisia. *Applied Water Sciences, 7*, 469–480. https://doi.org/10.1007/s13201-015-0265-3.

GPAa (Grupo de Projecto Alqueva Agrícola - Alqueva Agricultural Project Group) (2005). Atlas Rural Zona de Intervenção de Alqueva. Tomo 5 in Plano de intervenção para a zona de Alqueva http://sir.dgadr.gov.pt/conteudos/gpaa/ Accessed 2 May 2018.

Gkiougkis, I., Kallioras, A., Pliakas, F., Pechtelidis, A., Diamantis, V., Diamantis, I., Ziogas, A., & Dafnis, I. (2015). Assessment of soil salinization at the eastern Nestos River Delta, N.E. Greece. *Catena, 128*, 238–251. https://doi.org/10.1016/j.catena.2014.06.024.

Hanson, B.R. (2006a). How water quality affects infiltration. In: Hanson, B.R., Grattan, S.R. & Fulton, A. (Eds.), *Agricultural salinity and drainage* (pp 47-50). University of California,

Davis: Division of agriculture and natural resources publication 3375, University of California Irrigation Program.

Hanson, B.R. (2006b). Leaching fractions and irrigation uniformity. In: Hanson, B.R., Grattan, S.R. & Fulton, A. (Eds.), *Agricultural salinity and drainage* (pp 131-132). University of California, Davis: Division of agriculture and natural resources publication 3375, University of California Irrigation Program.

Hillel, D. (2000). *Salinity Management for Sustainable Irrigation. Integrating science, environment, and economics. Environmentally and socially sustainable development*. Washington DC: The World Bank.

Hu, Q., Yang, Y., Han, S., & Wang, J. (2019). Degradation of agricultural drainage water quantity and quality due to farmland expansion and water-saving operations in arid basins. *Agricultural Water Management, 213*, 185–192. https://doi.org/10.1016/j.agwat.2018.10.019.

Iakunin, M., Salgado, R., & Potes, M. (2018). Breeze effects at a large artificial lake: Summer case study. *Hydrology and Earth System Sciences, 22*, 5191–5210. https://doi.org/10.5194/hess-22-5191-2018.

ICT (Institute of Earth Sciences) (2019). Atmospheric sciences water and climate. http://www.i-c-t.pt/g1/index.php/observations-and-forecast/ Accessed 2 January 2019.

Iglesias, A., Santillán, D., & Garrote, L. (2018). On the barriers to adaption to less water under climate change: Policy choices in Mediterranean countries. *Water Resources Management, 2018*, 1–14. https://doi.org/10.1007/s11269-018-2043-0.

IPCC (Intergovernmental Panel on Climate Change) (2014). Climate change 2014 synthesis report, 133 pp. www.ipcc.ch/ Accessed 2 May 2018.

IPMA (Instituto Português do Mar e da Atmosfera - Portuguese Institute of the Sea and Atmosphere) (2017). Boletim Climatológico Anual de Portugal Continental 2017. Instituto Português do Mar e da Atmosfera, IP. http://www.ipma.pt/resources.www/docs/im.publicacoes/edicoes.online/20180323/cHAXzjMhUzLfdgCRJIKG/cli_20171201_20171231_pcl_aa_co_pt.pdf Accessed 12 May 2018.

IPMA (Instituto Português do Mar e da Atmosfera - Portuguese Institute for Sea and Atmosphere) (2018). Normais climatológicas 1981-2010 provisórias de Beja. Instituto Português do Mar e da Atmosfera, IP. https://www.ipma.pt/pt/oclima/normais.clima/1981-2010/002/ Accessed 12 May 2018.

IUSS Working Group WRB (2014). *World reference base for soil resources* 2014, *Update 2015*. Rome: World Soil Resources Report N° 106, FAO. http://www.fao.org/3/a-i3794e.pdf Accessed 12 May 2018.

Jones, E., & van Vliet, M. T. H. (2018). Drought impacts on river salinity in the southern US: Implications for water scarcity. *Science of the Total Environment, 644*, 844–853. https://doi.org/10.1016/j.scitotenv.2018.06.373.

Li, T., Li, S., Lian, C., Bush, R. T., & Xiong, L. (2018). A comparative assessment of Australia's lower lakes water quality under extreme drought and post-drought conditions using multivariate statistical techniques. *Journal of Cleaner Production, 190*, 1–11. https://doi.org/10.1016/j.jclepro.2018.04.121.

Liu, C.-W., Lin, K.-H., Kuo, Y.-M. (2003) Application of factor analysis in the assessment of groundwater quality in a blackfoot disease area in Taiwan. *Science of The Total Environment 313* (1-3):77-89

Lutz, S. R., Mallucci, S., Diamantini, E., Majone, B., Bellin, A., & Merz, R. (2016). Hydroclimatic and water quality trends across three Mediterranean river basins. *Science of the Total Environment, 571*, 1392–1406. https://doi.org/10.1016/j.scitotenv.2016.07.102.

Machado, R. M. A., & Serralheiro, R. P. (2017). Soil salinity: Effect on vegetable crop growth. Management practices to prevent and mitigate soil salinization. *Horticulturae, 3*(30), 1–13. https://doi.org/10.3390/horticulturae3020030.

Maas, E. V., & Hoffman, G. J. (1977). Crop Salt Tolerance-Current Assessment. *Journal of the Irrigation and Drainage Division, 103*(2), 115–134.

Merchán, D., Causapé, J., & Abrahão, R. (2013). Impact of irrigation implementation on hydrology and water quality in a small agricultural basin in Spain. *Hydrological Sciences Journal, 58*(7), 1400–1413. https://doi.org/10.1080/02626667.2013.829576.

Mil-Homens, M., Stevens, R. L., Cato, I., & Abrantes, F. (2007). Regional geochemical baselines for Portuguese shelf sediments. Environmental Pollution, 148(2), 418–427. https://doi.org/10.1016/j.envpol.2006.12.007

Mosley, L. M., Zammit, B., Leyden, E., Heneker, T. M., Hipsey, M. R., Skinner, D., & Aldridge, K. T. (2012). The impact of extreme low flows on the water quality of the lower Murray River and lakes (South Australia). *Water Resources Management, 26*, 3923–3946. https://doi.org/10.1007/s11269-012-0113-2.

Mosley, L. M. (2015). Drought impacts on the water quality of freshwater systems; review and integration. *Earth-Science Reviews, 140*, 203–214. https://doi.org/10.1016/j.earscirev.2014.11.010.

Morais, M. M., Serafim, A. M., Pinto, P., Ilhéu, A., & Ruivo, M. (2007). Monitoring the water quality in Alqueva reservoir, Guadiana River, southern Portugal. In G. Gunter & M. Carmo (Eds.), *The 12nd international specialized conference on watershed & river basin management* (pp. 96–112). Germany: Technical University of Berlin.

Muangthong, S., & Shrestha, S. (2015). Assessment of surface water quality using multivariate statistical techniques: Case study of the Nampong River and Songkhram River, Thailand. *Environmental Monitoring and Assessment, 187*, 548. https://doi.org/10.1007/s10661-015-4774-1.

Oster, J. D., & Schroer, F. W. (1979). Infiltration as influenced by irrigation water quality. *Soil Science Society of America Journal, 43*, 444–447.

Palma, P., Alvarenga, P., Palma, V., Fernandes, R. M., Soares, A. M. V. M., & Barbosa, I. R. (2010). Assessment of anthropogenic sources of water pollution using multivariate statistical techniques: A case study of the Alqueva's reservoir, Portugal. *Environmental Monitoring and Assessment, 165*, 539–552. https://doi.org/10.1007/s10661-009-0965-y.

Palma, P., Ledo, L., Soares, S., Barbosa, I. R., & Alvarenga, P. (2014a). Spatial and temporal variability of the water and sediments quality in the Alqueva reservoir (Guadiana Basin; southern Portugal). *Science of the Total Environment, 470–471*, 780–790. https://doi.org/10.1016/j.scitotenv.2013.10.035.

Palma, P., Köck-Schulmeyer, M., Alvarenga, P., Ledo, L., Barbosa, I. R., López de Alda, M., & Barceló, D. (2014b).

Risk assessment of pesticides detected in surface water of the Alqueva reservoir (Guadiana basin, southern of Portugal). *Science of the Total Environment, 488–489*, 208–219. https://doi.org/10.1016/j.scitotenv.2014.04.088.

Palma, P., Ledo, L., & Alvarenga, P. (2015). Assessment of trace element pollution and its environmental risk to freshwater sediments influenced by anthropogenic contributions: The case study of Alqueva reservoir (Guadiana Basin). *Catena, 128*, 174–184. https://doi.org/10.1016/j.catena.2015.02.002.

Palmer, W.C. (1965). Meteorological drought. Res. Paper no. 45, Washington, D.C.: Weather bureau.

Paranychianakis, N. V., & Chartzoulakis, K. S. (2005). Irrigation of Mediterranean crops with saline water: From physiology to management practices. *Agriculture, Ecosystems & Environment, 106*, 171–187. https://doi.org/10.1016/j.agee.2004.10.006.

Potes, M., Salgado, R., Costa, M. J., Morais, M., Bortoli, D., Kostadinov, I., & Mammarella, I. (2017). *Lake–atmosphere interactions at Alqueva reservoir: A case study in the summer of 2014* (p. 691). Tellus A: Dynamic Meteorology and Oceanography. https://doi.org/10.1080/16000870.2016.1272787.

Rengasamy, P. (2010). Soil processes affecting crop production in salt-affected soils. *Functional Plant Biology, 37*, 613–620. https://doi.org/10.1071/FP09249.

Rhoades, J.D. (1977). Potential for using saline agricultural drainage waters for irrigation. Free. Proc. water Management for Irrigation and Drainage. ASCE. Reno, Nevada. 20-22 July 1977, pp 85-116.

Rhoades, J. D., Kandiah, A., & Mashali, A. M. (1992). The use of saline waters for crop production. In *FAO irrigation and drainage paper 48*. Rome: Food and Agriculture Organization of the United Nations.

Scanlon, B., Jolly, I., Sophocleous, M., & Zhang, L. (2007). Global impacts of conversions from natural to agricultural ecosystems on water resources: Quantity versus quality. *Water Resources Research, 43*, 1–18. https://doi.org/10.1029/2006WR005486.

Serafim, A., Morais, M., Guilherme, P., Sarmento, P., Ruivo, M., & Magriço, A. (2006). Spatial and temporal heterogeneity in the Alqueva reservoir, Guadiana River, Portugal. *Limnetica, 25*(3), 161–176.

Shrestha, S., & Kazama, F. (2007). Assessment of surface water quality using multivariate statistical techniques: A case study of the Fuji river basin, Japan. *Environmental Modelling & Software, 22*, 464–475. https://doi.org/10.1016/j.envsoft.2006.02.001.

Simeonov, V., Stratis, J. A., Samara, C., Zachariadis, G., Voutsa, D., & Anthemidis, A. (2003). Assessment of surface water quality in northern Greece. *Water Research, 37*(17), 4119–4124.

StatSoft, Inc. (2004). STATISTICA (data analysis software system), version 7. https://www.tibco.com/products/tibco-statistica

Tanji, K. K., & Kielen, N. C. (2002). Agricultural drainage water management in arid and semi-arid areas. In *FAO irrigation and drainage paper 61*. Rome: Food and Agriculture Organization of the United Nations.

Tomaz, A., Patanita, M., Guerreiro, I., Dôres, J., Boteta, L., & Ferro Palma, J. (2018). Efficient use of water and nutrients in irrigated cropping systems in the Alqueva region. *Spanish Journal of Soil Science, 8*(1), 12–23. https://doi.org/10.3232/SJSS.2018.V8.N1.02 .

U.S. Salinity Laboratory Staff. (1954). *Diagnosis and improvement of saline and alkali soils. Handbook no. 60*. Washington, DC: US Department of Agriculture.

Valverde, P., Serralheiro, R., Carvalho, M., Maia, R., Oliveira, B., & Ramos, V. (2015). Climate change impacts on irrigated agriculture in the Guadiana river basin (Portugal). *Agricultural Water Management, 152*, 17–30. https://doi.org/10.1016/j.agwat.2014.12.012.

van Vliet, M. T. H., & Zwolsman, J. J. G. (2008). Impact of summer droughts on the water quality of the Meuse river. *Journal of Hydrology, 353*, 1–17. https://doi.org/10.1016/j.jhydrol.2008.01.001.

Vicente-Serrano, S. M., Lopez-Moreno, J., Beguería, S., Lorenzo-Lacruz, J., Sanchez-Lorenzo, A., García-Ruiz, J. M., Azorin-Molina, C., Morán-Tejeda, E., Revuelto, J., Trigo, R., Coelho, F., & Espejo, F. (2014). Evidence of increasing drought severity caused by temperature rise in southern Europe. *Environmental Research Letters, 9*, 44001, 9 pp. https://doi.org/10.1088/1748-9326/9/4/044001.

Ward Jr., J. H. (1963). Hierarchical grouping to optimize an objective function. *Journal of the American Statistical Association, 58*, 236–244.

Weil, R. R., & Brady, N. C. (2016). *The nature and properties of soils* (fifteenth ed.). Columbus: Pearson.

Wilcox, L. V. (1955). *Classification and use of irrigation waters, circular no. 969*. Washington, D.C.: United States Department of Agriculture.

Williams, W. D. (1999). Salinisation: A major threat to water resources in the arid and semi-arid regions of the world. *Lakes & Reservoirs: Research and Management, 4*, 85–91.

Yang, J., Strokal, M., Kroeze, C., Wang, M., Wang, J., Wu, Y., Bai, Z., & Ma, L. (2019). Nutrient losses to surface waters in Hai he basin: A case study of Guanting reservoir and Baiyangdian lake. *Agricultural Water Management, 213*, 62–75. https://doi.org/10.1016/j.agwat.2018.09.022.

Zalidis, G., Stamatiadis, S., Takavakoglou, V., Eskridge, K., & Misopolinos, N. (2002). Impacts of agricultural practices on soil and water quality in the Mediterranean region and proposed assessment methodology. *Agriculture, Ecosystems & Environment, 88*, 137–146.

Publisher's note Springer Nature remains neutral with regard to jurisdictional claims in published maps and institutional affiliations.

remote sensing

MDPI

Article

Temporal and Spatial Variations of Secchi Depth and Diffuse Attenuation Coefficient from Sentinel-2 MSI over a Large Reservoir

Gonçalo Rodrigues [1,*], Miguel Potes [1], Maria João Costa [1,2], Maria Helena Novais [1,3,4], Alexandra Marchã Penha [1,3], Rui Salgado [1,2] and Maria Manuela Morais [1,3,5]

1 Institute of Earth Sciences, Institute for Advanced Studies and Research, University of Évora, 7000-671 Évora, Portugal; mpotes@uevora.pt (M.P.); mjcosta@uevora.pt (M.J.C.); hnovais@uevora.pt (M.H.N.); mapenha@uevora.pt (A.M.P.); rsal@uevora.pt (R.S.); mmorais@uevora.pt (M.M.M.)
2 Department of Physics, School of Science and Technology, University of Évora, 7000-671 Évora, Portugal
3 Water Laboratory, University of Évora, P.I.T.E. Rua da Barba Rala No. 1, 7005-345 Évora, Portugal
4 Renewable Energies Chair, University of Évora, Casa Cordovil, Rua D. Augusto Eduardo Nunes, n.7, 7000-651 Évora, Portugal
5 Department of Biology, School of Science and Technology, University of Évora, 7000-671 Évora, Portugal
* Correspondence: grodrigues@uevora.pt

Received: 15 January 2020; Accepted: 26 February 2020; Published: 28 February 2020

Abstract: The Alqueva reservoir (South of Portugal) in the Guadiana river basin constitutes the most important water resource in southern Portugal for domestic and agricultural consumption. We present a methodology developed to characterize spatial and temporal variations of Secchi depth and diffuse attenuation coefficient (both related to dissolved/suspended particles and to water transparency), using high spatial resolution satellite images from Sentinel-2 Multi-Spectral Instrument (MSI). Empirical relations between satellite retrievals of surface reflectances and in situ measurements of water parameters were defined and applied to the entire reservoir for spatial and temporal analysis in the period July 2017–June 2019, useful in the identification of microalgae blooms and rapid variations in water characteristics, which allowed us to differentiate five zones. Water estimates with lower transparency and higher attenuation of radiation were found in the northern area of Alqueva reservoir during the months characterized by higher water temperatures, with Secchi depth monthly averages near 1.0 m and diffuse attenuation coefficient near or above 1.5 m^{-1}. Satellite retrievals of water with greater transparency in the reservoir were obtained in the southern area in months with low water temperature and atmospheric stability, presenting some monthly Secchi depth averages above 3 m, and diffuse attenuation coefficient below 0.8 m^{-1}. January 2018 presented great transparency of water with a Secchi depth of 7.5 m for pixels representing the 95th percentile and diffuse attenuation coefficient of 0.36 m for pixels representing the 5th percentile in the Southern region.

Keywords: 6SV; Alqueva reservoir; microalgae; water quality; Sen2Cor; turbidity

1. Introduction

Lake ecosystems are vital resources for aquatic wildlife and human needs, representing 98% of the liquid surface freshwater on the Earth's surface. Many organisms depend on freshwaters for survival, and humans frequently depend on lakes for many purposes such as drinking water, fisheries, agricultural irrigation, industrial services or recreation. In a warming climate associated with the increase of carbon dioxide concentration, changes are expected in precipitation patterns as the increase of extreme precipitation events, as well as the global increase in air temperature [1–5]. For southern

Portugal, Earth System models project a decrease in yearly mean precipitation (between -10% and -35 % for different scenarios) with an intensification of extreme precipitation, a significant increase of the maximum and minimum temperatures in all seasons and an increase in annual average number of heatwaves, much stronger and longer [6,7]. Lakes are sensitive to the impacts of climate change, and the impacts include a wide range of negative consequences, such as changes in thermal stratification, an acceleration of the eutrophication which favors periodic proliferation by cyanobacteria in many freshwaters, increased turbidity, and changes in salinity [8–10]. In this context, many studies have been carried out regarding the deterioration of water quality due to human influence, and its spatial and temporal variations in rivers or water reservoirs [11–14].

Alqueva reservoir is important for water supply and agricultural irrigation in the Alentejo (Southern Portugal), region with long periods of low precipitation associated with high values of air temperature, normally between May and September, and drought periods that can last more than 2 consecutive years [15]. Shifts in precipitation variability and seasonal runoff induce severe effects on water supply, water quality, and management of water resources in Southern Portugal. With warmer air temperatures expected for the Alentejo region, and consequently warmer surface waters in lakes, a favorable environment is created for the early growth of microalgae blooms, namely cyanobacteria, leading to an acceleration of the eutrophication [16,17].

The traditional field-based methods to monitor water quality in inland waters are usually costly and hardly allow adequate spatial and temporal analysis. Remote sensing could overcome these constraints, allowing to monitor water quality in large inland waters where conventional monitoring approaches tend to be limited [18]. From the launch of ERTS-1/Landsat-1 in August, 1972 up to and beyond the post-2000 launches of MODIS and MERIS, the mapping of water quality parameters using satellite images over inland lakes has exponentially increased [19–23]. Olmanson et al. [24] used the Landsat archive for mapping lake water clarity of over 10,000 Minnesota lakes, showing the great application to lakes of different dimensions and great agreement between satellite data and field measurements of Secchi depth (SD) within Landsat paths (range of R^2 between 0.71 and 0.96). In addition to the high spatial resolution, allowing the analysis of water quality in several reservoirs, remote satellite detection also allows for mapping water quality in lakes over the last 30 years [25]. The Sentinel-2 mission from the European Space Agency (ESA) is a land monitoring constellation of two satellites (S2A launched in June 2015 and S2B launched in March 2017) that provide high-resolution optical imagery (spatial resolution between 10 m and 60 m, depending on the spectral band) and presents a systematic global coverage of two to three days at mid-latitudes, which brought a great opportunity to study inland reservoirs. Several studies have been done in recent years in the analysis of water quality of inland waters using Sentinel-2 data, to measure water quality parameters of bodies of water [26–31].

Satellite data is used over lakes and reservoirs aiming to evaluate surface parameters, nevertheless, the satellite measures the signal of the surface plus the signal of atmosphere in-between. This unnecessary part of the signal is commonly removed using atmospheric correction codes that correct the top-of-atmosphere (TOA) signal, with respect to the atmospheric path, to obtain only the signal from the surface. In this study, the atmospheric correction is performed using two models: Sen2Cor and 6SV. Sen2Cor was developed by ESA for applications over land surfaces but it is also applied over water surfaces, with several studies presenting good estimates of surface reflectances used for monitoring water quality parameters in lakes and reservoirs, such as colored dissolved organic matter, chlorophyll *a*, turbidity, or SD [23,27,32]. The 6SV is an advanced radiative transfer code capable of accounting for radiation polarization in a mixed molecular–aerosol atmosphere being a vector version of the 6S [33]. The 6S atmospheric correction has already been successfully used in lakes and reservoirs [21,32,34–37].

Monitoring water quality using satellite remote sensing may involve relationships between surface reflectances in certain spectral bands (or band combinations) and water parameters analyzed in the laboratory or in situ. Potes et al. [21] developed a method to estimate concentrations of chlorophyll *a*

and cyanobacteria in the Alqueva reservoir, combining surface reflectances using the MERIS satellite and laboratory analyzes. In addition to these two parameters, the same author used MERIS satellite images to obtain estimates of turbidity in the same artificial lake [22]. In the past two years (2017 and 2018), microalgae blooms have been identified in the Alqueva reservoir through satellite images and in situ measurements, starting to develop in early summer in the northern region of Alqueva and gradually spreading through all reservoir. In October, these blooms tend to disappear with the normal decrease of air temperature and solar radiation, the beginning of precipitation and strong winds, associated with the arrival of the first Atlantic atmospheric fronts. Potes et al. [23] reported this situation, showing how an intense microalgae bloom vanished in early October of 2017 with the increase of water mixing due to the influence of hurricane Ophelia progressing along the Portuguese coast, causing significant precipitation, a decrease in the air temperature and inducing strong winds at Alqueva reservoir.

The main motivation of the present work is to explore reliable remote sensing methods for full spatial cover and continuous monitoring of key physical parameters, which affect the water quality of inland water bodies such as Alqueva reservoir. Within the multidisciplinary project ALOP (ALentejo Observation and Prediction systems), among other physical-chemical and biological variables, the Secchi depth and diffuse attenuation coefficient (KD) were measured, two parameters closely linked to the water transparency and the dissolved/suspended particles in the water. Nevertheless, this analysis is spatially and temporally limited. In order to derive reliable remote detection methods for continuous monitoring and adequate spatial coverage of physical parameters affecting the water quality of reservoirs such as Alqueva, data obtained from Sentinel-2 missions (Multi-Spectral Instrument (MSI)) was used. In addition to the high spatial resolution of 10-60 m, it presents a high re-visitation, with systematic global coverage in the Alqueva reservoir region of two to three days, considering the two twin satellites in operation. Landsat also has a high spatial resolution (30 m), but much shorter temporal resolution, with 16 days difference between each image, and this revisit time may be problematic for the detection of short events [38]. MODIS has high revisitation (every 1–2 days), but lower spatial resolution of 250–1000 m. Thus, Sentinel-2 represents the best choice for satellite monitoring of Alqueva reservoir compared with these two satellites.

SD and KD also control the vertical distribution of the absorption of solar radiation in the water column and thus play a relevant role in the air-water surface energy balance. For this reason, these parameters are used in numerical weather prediction, so their mapping from satellite remote sensing will contribute to improving the representation of lakes in operational forecasting systems, as shown in Potes et al. [22].

The main objective of this work is to develop a method based on satellite remote sensing to estimate SD and KD and subsequently analyze the spatial and temporal variations of these parameters in the period July 2017-June 2019 at Alqueva reservoir. These studies may also be relevant for the identification of areas with different patterns of water characteristics and their categorical relation with meteorological data.

2. Study Area and Data

2.1. Study Area

The study area presented in this paper is the Alqueva reservoir, located in the south of Portugal (Alentejo region) along 83 km of the main course of the Guadiana River. It constitutes the largest artificial lake in the Iberian Peninsula with a capacity of 4.150 hm^3 and a surface area of 250 km^2 at the full storage level of 152 m.

According to Köppen climate classification, this region is identified by type Csa—hot summer Mediterranean climate, featured by a temperate climate with dry and hot summers. The Alentejo region is characterized by relevant irregularity of inter-annual precipitation, with average accumulated precipitation of the order of 500 mm. It is normal that this region presents two summer months, July and

August, with nearly no precipitation and maximum temperatures above 30 °C in most of the days, and heat waves with temperatures near or greater than 40 °C, accompanied by very low relative humidity. The ALOP project aims to develop multifunctional activities in the field of interactions between the atmosphere, water and ecosystems, covering, among other tasks, meteorological observation. Three meteorological stations were installed in 2017, MontanteP station on a platform in the middle of the reservoir, and two stations on both margins, BarbosaM and Cid AlmeidaM (Figure 1). Figure 2 shows the great irregularity in accumulated monthly rainfall presenting periods of several consecutive months with very scarce precipitation (less than 25–50 mm). Data is obtained from a meteorological station, installed in March 2017 (Cid AlmeidaM station), in the East margin of the reservoir.

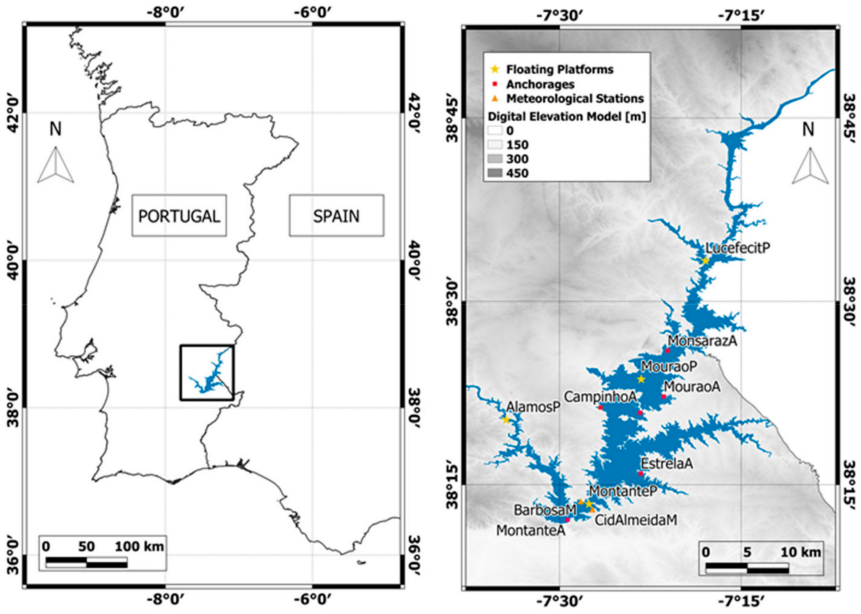

Figure 1. Alqueva reservoir and position of the sites used in this study.

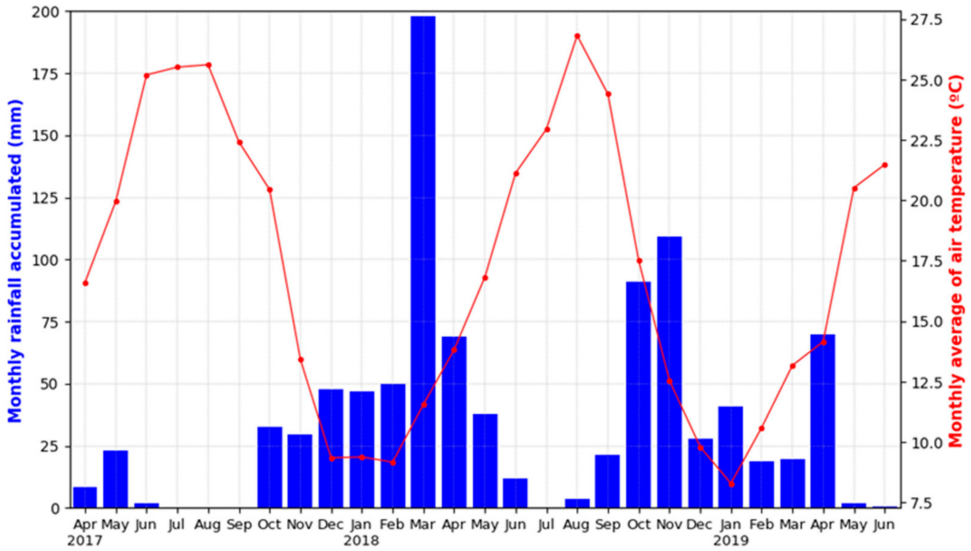

Figure 2. Monthly rainfall and air temperature in Alqueva for the period of April 2017–June 2019. Data from Cid Almeida meteorological station.

2.2. Data Collection

2.2.1. Diffuse Attenuation Coefficient and Secchi Depth Measurements

Since February 2016 periodic measurements of KD and SD have been made in the Alqueva reservoir. The measurements were carried out approximately every 1-2 months at various points in the Alqueva reservoir to monitor their temporal and spatial variations. Figure 1 shows the map with the location of the measurement sites. AlamosP, MontanteP, MouraoP and LucefecitP represent floating platforms installed in the deeper areas of the reservoir, and far from the margins. MontanteA, EstrelaA, LuzA, CampinhoA and MonsarazA represent anchorages, located in the margins of the reservoir.

In order to ensure adequate illumination, these measurements were limited to the daylight period between 10:00 a.m. and 4:00 p.m. UTC. In this study, the measurements of KD in water were made using the method described in Potes et al. [39]. According to this method, the measurements of underwater downwelling spectral irradiance were performed with the use of a portable FieldSpec (Analytical Spectral Devices; Boulder, CO, USA) together with an optical fiber linked to a hemispherical tip (180°). Then, an exponential fit was applied through the spectral profile and depth to obtain the spectral diffuse attenuation coefficient (KD). The spectral KD, with 1 nm resolution, is averaged for the spectral region 400–700 nm in order to obtain a value corresponding to the Photosynthetically Active Radiation (PAR) region, thus the KD used in this work is the KD (PAR). SD was measured only on clear days, at the shaded side of the anchorages or platforms to avoid direct sunlight reflections from the water surface. Two SD values were measured, each by a different person, to minimize deviations due to the observer, and the averaged SD value was used. A slight deviation between each SD measurement of approximately 0.14 m on average was observed.

The SD measures the transparency of the water and the values obtained in the study period ranged between 0.4 m and 7 m. KD measures the absorption and dispersion of the radiation by the particles present in the water, and the values ranged between 0.4 m^{-1} and 2.4 m^{-1}. The extreme values of low SD and high KD in the water coincide with a microalgae bloom in September 2017. Otherwise, the values of SD and KD related with the highest transparency were recorded in periods without rainfall, with a stable atmosphere and water temperature below 22 °C. The value of 7.0 m for SD was measured on 1 March 2019 and this measurement was by far the highest SD, with a previous maximum of 5.0 m. This impressive record for this reservoir should have been caused by a set of circumstances, such as the little precipitation in the previous month (February presented precipitation below average and no days of intense precipitation), mild temperatures (maximum between 15 °C and 20 °C), and very low wind speed both in the measurement day and in the previous days.

2.2.2. Sentinel-2 data

The Sentinel-2 mission consists of a constellation of two polar-orbiting satellites, Sentinel-2A and Sentinel-2B, each one equipped with an optical imaging sensor (MSI). Sentinel-2A was launched on 23 June 2015 and Sentinel-2B followed on 7 March 2017. These twin polar-orbiting satellites allow a high 2-3 days revisit time for Alqueva reservoir since July 2017. MSI data are acquired in 13 spectral bands in the visible and near-infrared and have very high spatial resolution, with three bands at 60 m, six bands at 20 m and four bands at 10 m (Table 1). The dataset used in this study is the Sentinel-2 Level-1C product, which is composed of 100 km × 100 km tiles in the UTM/WGS84 projection and provides the Top-Of-Atmosphere (TOA) reflectance. The Sentinel-2 tiles were downloaded from the Copernicus Open Access Hub, free and open access to Sentinel-2 data in SENTINEL-SAFE format (https://scihub.copernicus.eu/dhus/#/home).

Table 1. The central wavelength, bandwidth and spatial resolution of the 13 bands of the Multi-Spectral Instrument (MSI) instruments onboard Sentinel-2A and 2B.

Band Number	S2A		S2B		
	Central Wavelength (mm)	Bandwidth (mm)	Central Wavelength (mm)	Bandwidth (mm)	Spatial Resolution (m)
1	442.7	27	442.2	45	60
2	492.4	98	492.1	98	10
3	559.8	45	559.0	46	10
4	664.6	38	664.9	39	10
5	704.1	19	703.8	20	20
6	740.5	18	739.1	18	20
7	782.8	28	779.7	28	20
8	832.8	145	832.9	133	10
8a	864.7	33	864.0	32	20
9	945.1	26	943.2	27	60
10	1373.5	75	1376.9	76	60
11	1613.7	143	1610.4	141	20
12	2202.4	242	2185.7	238	20

3. Methodology

The process of developing an empirical remote sensing model for monitoring of spatial and temporal variations of SD and spectral KD during the period July 2017 - June 2019 was preceded by application of an atmospheric correction to images of the top of the atmosphere (TOA) in order to obtain surface spectral reflectance. Then the atmospherically corrected spectral reflectances obtained were validated (Section 3.1) and subsequently, regression techniques were used to develop relationships between field-measured parameters and water reflectance (Section 3.2).

3.1. Atmospheric Correction Validation

Satellite remote sensing of the surface in the visible and near-infrared is strongly affected by the presence of the atmosphere. Due to the low reflectance of water surfaces, the accurate removal of atmospheric effects is essential. Initial satellite data is provided at the top of the atmosphere (TOA), which is affected by atmospheric constituents through absorption and scattering processes. However, the analysis of water surface properties from remote sensing techniques requires the removal of the atmospheric effects, to obtain surface reflectances (or radiances). In the visible spectral region, in the absence of clouds, the main atmospheric effects that need to be corrected are aerosols, water vapor and ozone. In the solar spectrum, the atmospheric gaseous absorption is principally due to oxygen, carbon dioxide, methane, nitrous oxide, ozone and water vapor, but only the last two are not constant and depend on the time and location. The water vapor contribution affects mainly wavelengths greater than 700 nm and ozone presents a significant absorption between 550 and 650 nm. Therefore, the effect of ozone and water vapor can be accounted for since they have a great influence on the visible region, between 400 nm and 750 nm, the region of the spectrum used to estimate surface parameters at Alqueva reservoir.

In this paper, two atmospheric correction methods were assessed, applied to images acquired by the Multi-Spectral Instrument (MSI) on-board the European Space Agency's Sentinel-2A and Sentinel-2B:

i) 6SV which is a vector version of the 6S (Second Simulation of a Satellite Signal in the Solar Spectrum) radiative transfer code [40].

ii) Sen2cor, which is a processor provided by ESA for Sentinel-2 Level 2A product generation [41].

6SV is a new version of old 6S and is available at http://6s.ltdri.org and a summary of the code validation can be found in Kotchenova et al. [42] and in Kotchenova et al. [43]. The 6SV is an advanced radiative transfer code developed by the MODIS LSR SCF (Land Surface Reflectance Science Computing Facility).

The atmospheric correction processor Sen2Cor was developed by Telespazio VEGA Deutschland GmbH on behalf of ESA. Sen2Cor is a Level-2A processor to correct the Sentinel-2 Level-1C Top-Of-Atmosphere (TOA) products for the effects of the atmosphere in order to deliver a Level-2A Bottom-Of-Atmosphere (BOA) reflectance product. ESA not only provides the bottom of atmosphere reflectance based on the implementation of the Sen2Cor algorithm, but also additional products as Quality Indicators for cloud and snow probabilities, Aerosol Optical Thickness (AOT), Water Vapour (WV) and Scene Classification (SC). Obregón et al. [44] presented a validation of aerosol optical thickness (AOT) and integrated water vapor (IWV) products provided by ESA obtained from Sentinel MSI, and for this purpose used a significant number of stations over Europe and adjacent regions, between March 2017 and December 2018. The results showed the high reliability of the WV estimates, with normalized root mean square errors (NRMSE) of 5.33% and R^2 of 0.99. The comparison showed lower agreement, nonetheless reliable, for AOT with NRMSE of 9.04% and R^2 of 0.65. The AOT at 550 nm and WV provided by ESA Sen2Cor were used here as inputs for the 6SV radiative transfer code.

The TOA reflectances were all resampled to 60 m resolution, with downsampling of 10 m and 20 m data (Table 1) by block averaging and corrected using the 6SV considering the corresponding spectral response functions characterizing the Sentinel-MSI bands. A new version of the Sentinel-2A spectral functions, correcting the responses for bands 1 and 2 released after 15 January 2018 (https://earth.esa.int/web/sentinel/missions/sentinel-2/news/; last accessed 21/07/2019) was used. 6SV accounts for the adjacency effects due to reflection from contiguous pixels. However, in almost all its area, the reservoir is wide comparatively to MSI spatial resolution, and surrounded by soil or very low vegetation. We have assumed that the surface (all water pixels in the reservoir) behave as a homogeneous Lambertian reflector. 6SV accounts for a wide variety of sensor characteristics and atmospheric conditions. The 6SV used to correct the MSI images over Alqueva region, allows to account for the various effects of the atmosphere, namely the ozone and water vapor columns, aerosol optical thickness (AOT) at the reference wavelength of 550 nm, aerosol characterization (type and concentration), spectral/geometrical conditions, and in addition ground reflectance (type and spectral variation). The input parameters for the 6SV process to model the atmospheric effects are shown in Table 2.

Table 2. Input parameters of 6SV model applied to Sentinel-2 MSI.

	Source	**Parameters**
Input type	Sentinel-2 MSI	TOA reflectance
Geometrical Conditions	Sentinel-2 MSI	Solar Zenith angle, Solar Azimuth angle (°)
		View Zenith angle, View Azimuth angle (°)
		Month, Day
Atmospheric Conditions (User)	Product of SEN2COR	Water vapour (g/cm^2)
	Ozone Monitoring (OMI)	Ozone (cm-atm)
Aerosol Model (Type)	-	Continental
Aerosol Model (Concentration)	Product of SEN2COR	Aerosol Optical Thickness at 550 nm
Effect of the altitude	Water level	Target (km)
	-	Sensor aboard a Satellite
Spectral bands	Sentinel-2 MSI	Spectral function responses
Ground Reflectance	-	Homogeneous Lake Water

Satellite-derived water spectral reflectances were compared with surface spectral reflectance measurements at Alqueva selected sites, obtained with a portable spectroradiometer FieldSpec UV/VNIR (ASD, Inc), aiming at validating the results obtained with the atmospheric correction methods. In situ measurements were performed as close as possible to the satellite overpass (maximum difference of 1 day).

The spectroradiometer measures the intensity of the light field across a given point, so reflectance is calculated as the ratio between the energy leaving the sample by reflection and the energy incident on the sample (obtained from the measurement with the white reference panel). Since the calculation is a ratio, energy units cancel out. In fact, to calculate reflectance with the spectroradiometer, although it is calibrated, there is no need for radiometric calibration. The electrical current signals are converted into computer type digital numbers (DN). The reflectance is then calculated as the ratio between the raw DN of the energy reflected from the sample and the raw DN of the energy incident on the sample (obtained from white reference measurement) as described by ASD [45]. Measurements were made with the 10° field-of-view. In order to ensure correct reflectance measurement, the illumination should be practically the same for the lake and white reference measurements, so the measurement of the white plate was made immediately prior to the measurement of the lake, in order to avoid large variations of sun incidence in both measurements. In situ values were obtained by averaging 25 spectra selected to represent the Alqueva water reflectance. The mean satellite reflectance was calculated using a 2 × 2 pixel box close to each sampling station to perform a direct comparison with in-situ measurements. Statistical indicators have been used in this study to obtain an appropriate assessment of the atmospheric correction methods: The Bias error, which is a measure of the overall error or systematic error, check the average bias of the data, e.g., if positive indicates that the estimated values are overestimated compared to those observed and if negative are underestimated:

$$\text{Bias} = \frac{1}{N}\sum (X - X_{meas}), \tag{1}$$

where N corresponds to the total number of data, X are estimations of satellite data and X_{meas} corresponds to in situ measurements.

The mean absolute error (MAE) is an average of the absolute errors:

$$\text{MAE} = \frac{1}{N}\sum \left|(X - X_{meas})\right|. \tag{2}$$

The mean absolute percentage error (MAPE) is defined as the mean of absolute differences between estimates (satellite-derived) and observations and measures the size of the error in percentage terms:

$$\text{MAPE} = \frac{1}{N}\sum \left|\frac{X_{meas} - X}{X_{meas}}\right| \times 100. \tag{3}$$

The root mean square error (RMSE) gives a measure of the accuracy existing between estimated values (satellite retrievals) and the corresponding surface measurements:

$$\text{RMSE} = \sqrt{\frac{1}{N}\sum (X_{meas} - X)^2}. \tag{4}$$

The normalized value of the previous statistic indicator RMSE has been calculated to compare estimations of satellite and ground-based measurements, where a small value of NRMSE identifies a good agreement with the field observations:

$$\text{NRMSE}\ (\%) = \frac{RMSE}{mean(meas)} \times 100, \tag{5}$$

where mean (meas) corresponds to the average of observations.

The Nash–Sutcliffe efficiency (NSE) is a normalized statistic that determines the relative magnitude of the residual variance compared to the measured data variance:

$$\text{NSE} = 1 - \frac{\sum (X_{meas} - X)^2}{\sum (\ X_{meas} - mean(meas)\ )^2}. \tag{6}$$

Another statistical indicator used is the correlation coefficient which indicates the direction and strength of a linear relationship between two variables. This parameter, which shows how much the model can describe the data, should be close to 1 for an ideal situation of perfect match between both.

Figure 3 shows a comparison between the measured and satellite-derived water reflectance for the first five bands, with 6SV and Sen2Cor. Tables 3 and 4 shows the statistical indicators obtained for each of the two atmospheric correction methods considered.

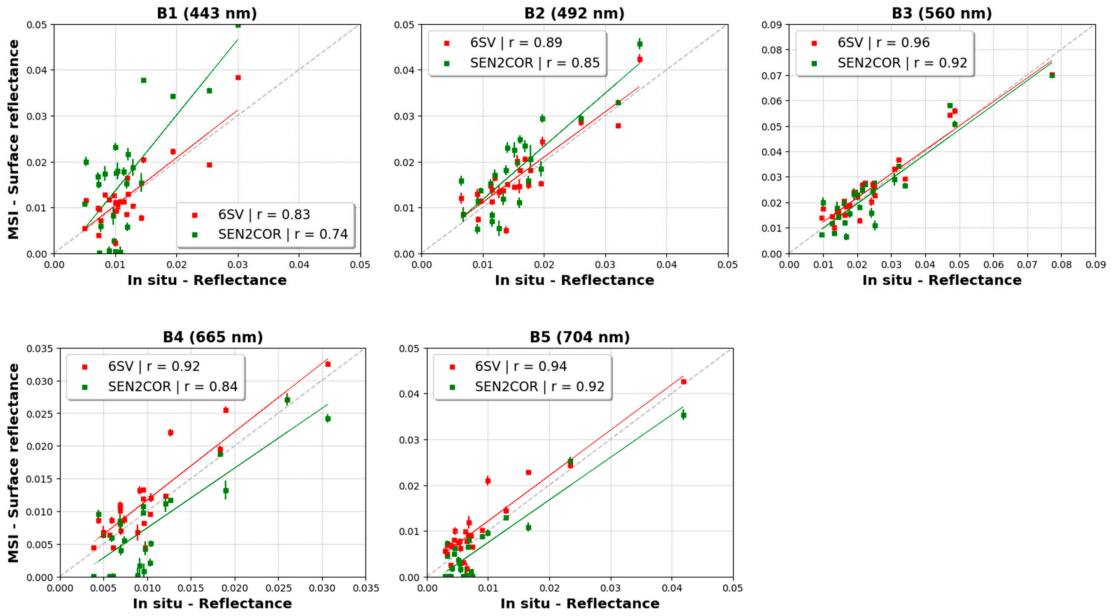

Figure 3. Comparison between in situ and MSI reflectances after atmospheric correction. The dashed line indicates the y = x, the solid lines (red and green) show the best-fits and the vertical error bars represent the standard deviations corresponding to the four selected pixels.

Table 3. Statistical indicators between the measured and satellite-derived water reflectance for the 6SV method.

N= 25	Bias	MAPE (%)	Correlation	RMSE	R^2	NSE
B1	0.0005	29	0.83	0.0039	0.69	0.51
B2	0.0010	22	0.89	0.0036	0.79	0.72
B3	0.0014	19	0.96	0.0044	0.92	0.91
B4	0.0017	30	0.92	0.0034	0.84	0.72
B5	0.0022	51	0.94	0.0037	0.88	0.79

Table 4. Same as in Table 3 but for the Sen2Cor method.

N= 25	Bias	MAPE (%)	Correlation	RMSE	R^2	NSE
B1	0.0046	85	0.74	0.0102	0.55	-2.29
B2	0.0026	36	0.85	0.0056	0.73	0.33
B3	-0.0007	23	0.92	0.0059	0.85	0.83
B4	-0.0026	44	0.84	0.0047	0.70	0.47
B5	-0.0024	54	0.92	0.0040	0.85	0.75

Sen2cor method presents several cases of null reflectances for band 1 (443 nm), band 4 (665 nm) and band 5 (704 nm), and generally worse statistical indicators than the radiative transfer code 6SV. The cases of null reflectances are often associated with situations of very clean waters causing the Sen2Cor to excessively correct the visible bands (Figure 3). Martins et al. [32] also reported this situation with MSI-corrected reflectances using Sen2Cor, obtaining a better match with in situ measurements over brighter lakes, rather than dark lakes.

With 6SV method, the bias is positive for all bands and the red solid line always above the dashed line y = x, denoting on average an overestimation of the calculated reflectances in relation to the measurements. In contrast, with Sen2Cor atmospheric correction process, there is overestimation in bands 1 and 2, and underestimation in the remaining bands of the visible region. Note the large error associated with the Sen2Cor process in band 1 of the MSI instrument, which despite having some null reflectances, has a positive bias, with several estimated values much higher than those observed, with a very high MAPE of 85% and worst correlation, RMSE and bias for this region of the spectrum. The very weak accuracy of the Sen2Cor method in band 1 is also proven by NSE = - 2.3, which, being lower than 0, indicates unreliable satellite estimations. Regarding the Sen2Cor atmospheric correction process only in band 3 (NSE = 0.83) and band 5 (NSE = 0.75) the satellite data fits with some accuracy the observations. As for the 6SV atmospheric correction, excluding band 1 from MSI (NSE = 0.51), this method features good accuracy, with NSE greater than 0.7 for all analyzed bands, indicating a good match between estimates and observed reflectances. The atmospheric correction performed using the 6SV method presents better statistical results compared to Sen2Cor for all analyzed bands, e.g., higher correlation and lower MAPE values, smaller deviations from the straight line to line y = x (also showing a lower bias) and even much lower RMSE values. With 6SV there are higher correlations, greater than 0.8 for all bands, and values lower than or equal to 30% of MAPE, except MSI band 5, with an associated MAPE of 51%. Excellent results are obtained for band 3 with a correlation coefficient of 0.96, MAPE below 20%, and NSE of 0.91, the nearest value to the perfect match of estimated vs observed data (NSE = 1). This excellent correction of the 6SV method to band 3 is essential, because high microalgae densities are present in the Alqueva reservoir for several months, which yield high reflectances in this region of the spectrum.

It is verified that the best atmospheric correction method for the Alqueva reservoir is achieved with the 6SV method using the WV and AOT 550 products from Sen2Cor. This method was then used to accurately estimate water parameters.

3.2. Empirical Algorithms

In situ measurements of SD and KD were related to the atmospherically corrected surface spectral reflectances obtained from MSI (using 6SV - Section 3.1), through regression algorithms. The average reflectance of the four closest pixels to the measurement site was calculated. The time gap between in-situ measurements and the satellite overpass affects the reflectance comparison and, in this context, several studies report between 3 to 8 days as the maximum time lag used between on-site measurements and satellite images for a correct comparison, with stable meteorological conditions and in the absence of algal blooms [24,27,46]. In the present study, due to the presence of algae in a large period of the year, and in order to reduce the error associated with rapid variations in water characteristics, only satellite images with maximum differences of 1 day were selected in relation to in situ measurements [47]. This time difference is considered a reasonable compromise for a reservoir of large dimensions as Alqueva, aiming at obtaining a dataset that ensures the robustness of the empirical algorithms. The data used to develop the regression algorithms refers to the period of April 2016–October 2017. The data used for the validation corresponds to a different period, between November 2017 and June 2019. The best algorithm of SD was found empirically by deriving a regression model for different combinations of bands in the visible region, selecting the best fit according to the first, with the greatest R^2 and second, with the lowest values of NRMSE. Only bands in the visible region were used, up to 704 nm (corresponding to band 5 of the MSI instrument), because the Alqueva reservoir has several days with very low reflectance for higher wavelengths, corresponding mainly to periods of the year and areas with low turbidity and biological activity. Several empirical algorithms available from the literature were tested for the Alqueva reservoir, with a poorer performance with respect to the algorithm proposed here as shown in Table 5. Rotta et al. [48] proposed an algorithm for KD retrieval applied to Nova Avanhandava Reservoir, using the 660 nm band. In this work the equivalent MSI band (band 4) is used, adjusting the linear regression coefficients to Alqueva reservoir, yielding Equation

(8). The results of R^2 and NRMSE obtained for the Alqueva reservoir with the algorithm proposed by Rotta et al. [48] are presented in Table 6.

Table 5. Statistical parameters obtained for the application of Secchi Depth algorithms from the literature and that proposed in this study, to the Alqueva reservoir.

Algorithms	Equation	R^2	NRMSE (%)
Verdin, J.P. [49]	$\frac{1}{(0.665+35.6\times B4)}$	0.69	28
Lavery et al. [50]	$2.5 - (0.56 \times B4) - (0.42 \times \frac{B2}{B4})$	0.60	53
Wu et al. [51]	EXP(1.3-(0.27×B2)-(0.65×B4))	0.69	71
Bonansea et al. [52]	$1.25 - 0.44\times B4 + 0.11\times \frac{B2}{B4}$	0.65	84
Rotta et al. [48]	$2.0709 \times \left(\frac{B3}{B4}\right)$ -1.2697	0.1	72
Jesús Delegido et al. [53]	$4.7134 \times (\frac{B2}{B3})^{2.5569}$	0.29	51
Page et al. [54]	$EXP(2.437\times\frac{B2}{B4} - 2717.82 \times (B4 \times B5) - 2.469)$	0.56	102
Proposed algorithm	$0.024 \times \frac{B2}{B3\times B4} + 0.72$	0.86	17

Table 6. Same as in Table 5 but for the diffuse attenuation coefficient.

Algorithms	Equation	R^2	NRMSE (%)
Rotta et al. [48]	67.4155 × B4 +0.3978	0.81	33
Proposed algorithm	54.3 × B4 + 0.32	0.82	21

The scatter plots, with the best fit for each algorithm, are shown in Figure 4. Both relations are of linear type, with high coefficients of determination: R^2 of 0.86 for the SD algorithm and R^2 of 0.82 for the KD algorithm. The NRMSE is equal to 17% and 21% for the SD and KD algorithms respectively.

$$SD = \left(0.024 \times \frac{B2}{B3 \times B4}\right) + 0.72 \quad (7)$$

$$KD = 54.3 \times B4 + 0.32. \quad (8)$$

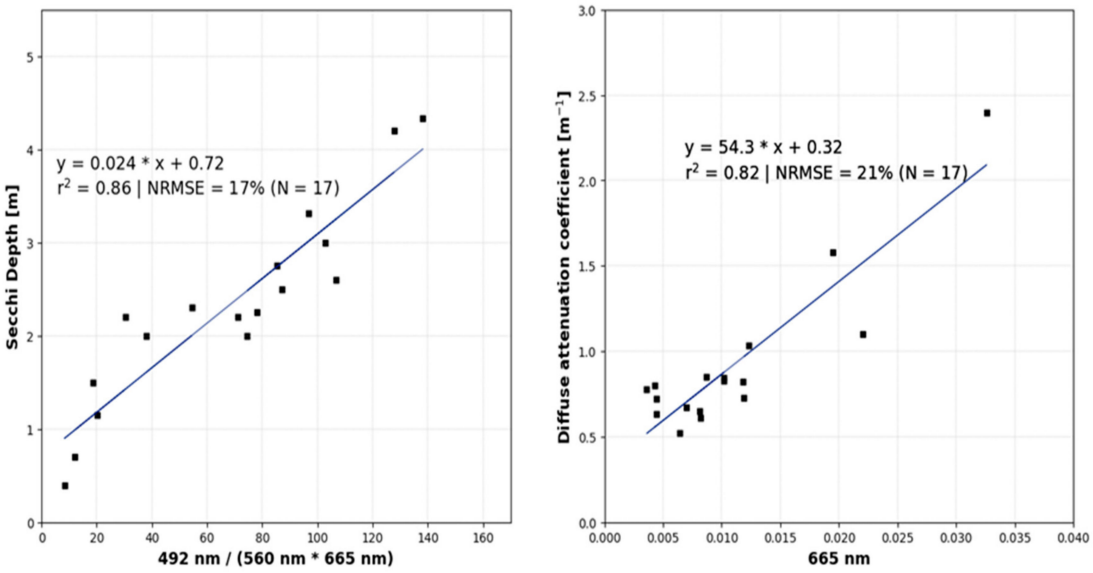

Figure 4. Scatter plot between parameters of water quality (SD on the left and KD on the right) and the bands of MSI. Shown also is the linear regression obtained.

4. Results and Discussion

4.1. Validation of Algorithms of Water Quality Parameters

The results obtained with the algorithms presented in Section 3.2 were validated for a different period, between November 2017 and June 2019, through the comparison of the satellite retrievals with the measurements obtained from in situ water sampling.

The algorithms presented in Section 3.2 were applied to the four nearest pixels with respect to the sites where the measurements were taken and the mean value was computed. In Figure 5 the relationships between estimated SD/KD and the corresponding data measurements, is shown.

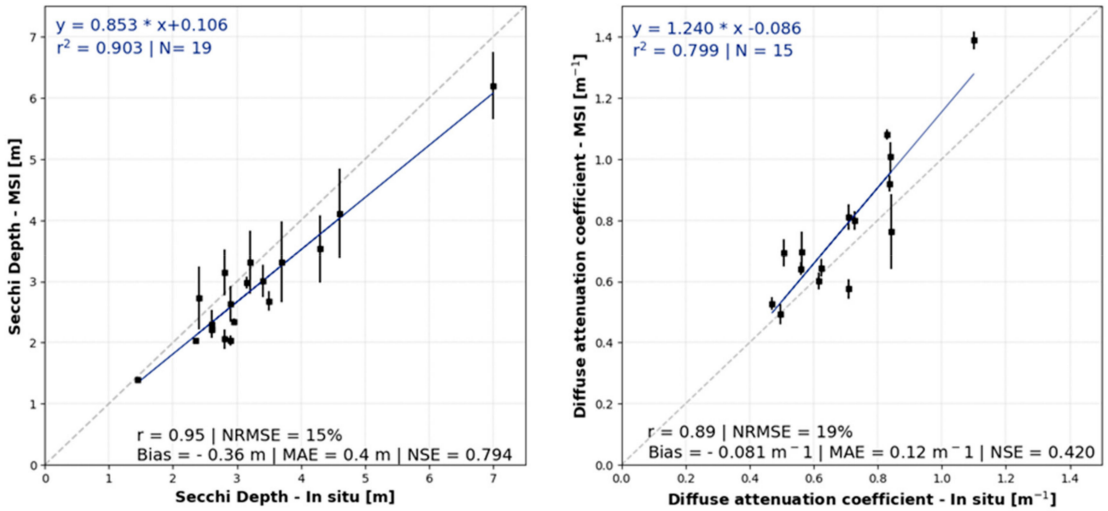

Figure 5. Scatter plot of predicted versus observed SD (left) and KD (right). The dashed line indicates the y=x, and solid line (blue) show the best-fit lines. The vertical error bars represent the standard deviations corresponding to the four selected pixels.

A good agreement is verified between estimations and measurements, presenting high correlation coefficient values, with r = 0.95 and r = 0.89 for SD and KD respectively. Data spread is also small, with NRMSE of 15% for SD algorithm and NRMSE of 19% for KD algorithm. The high NSE for the SD algorithm (NSE = 0.794) indicates a good fit between observations and estimations. The MAE shows good results, with 0.4 m for SD and 0.12 m^{-1} for KD. This means that on average there was a deviation of less than half a meter for SD, which is a small deviation value if considered that the validation values range between 1.5 m and 7.0 m. As for the KD, there is also a reduced MAE for the range of measured values. Most of the errors associated with the measurements are overestimated for the KD (Positive bias) and underestimated for SD, of 0.081 m^{-1} and - 0.36 m respectively. In the validation of the SD algorithm, it is verified that the absolute value of the Bias (0.36 m) is practically equal to the MAE (0.4 m), meaning that deviations to the observed data are practically all of underestimation satellite retrievals in relation to the observed data. The validation of the KD algorithm only presents 2 points below the y=x line, which demonstrates that for almost all cases analyzed, when there is a deviation from satellite estimates in relation to the observations, data are overestimated. Thus we can conclude that although the average associated errors are reduced, a lower transparency of water (Lower SD) is expected from the atmospheric correction method presented for Alqueva reservoir and a lower attenuation of radiation in water (Higher KD) compared to observation data.

4.2. Relation between Secchi Depth/Diffuse Attenuation Coefficient and Microalgae Bloom

In addition to validating the algorithms (comparing with independent data) it is also important to investigate how the SD and KD vary spatially in the entire reservoir. One of the useful and relevant applications of Sentinel-2 is the identification and monitoring of rapid variations of microalgae

blooms in the lakes through, for example, RGB image composites using three bands of MSI with 10 m of resolution: 492 nm (blue), 560 nm (green) and 665 nm (red). Figure 6 presents two examples of RGB images showing the beginning of a microalgae bloom development in July 2018 and the presence of microalgae in most of the reservoir in the end of September 2018 with measurements of chlorophyll *a* and turbidity of 10.19 µg/L and 2.22 NTU, respectively, on 6 September 2018 (nearest in situ measurement available). Chlorophyll *a* determination was based in molecular absorption spectroscopy and the equations developed by Lorenzen [55], according to the standard methods NP 4327:1996 [56] and EN ISO 10260:1992 [57]. Turbidity was determined using the nephelometric method [58].

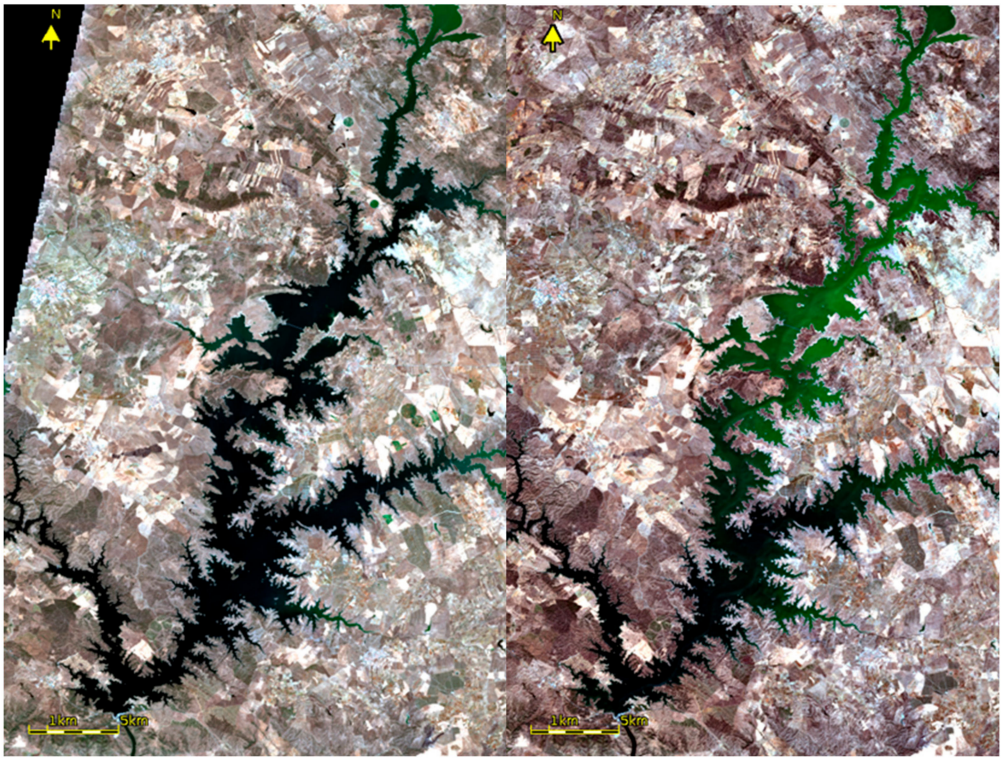

Figure 6. RGB Image showing the evolution of microalgae bloom for 16 July 2017 (left) and for 22 September 2017 (right) in the Alqueva reservoir.

Figure 7 represents the spatial distribution of SD and KD for 22 September 2017 obtained using the algorithms developed. The presence of algae in water tends to decrease the transparency of water. Therefore, under these conditions, a decrease in SD (associated with decreased water transparency) and an increase in the KD of water is expected due to an increase of solar radiation extinction in the water column (absorption plus scattering). This is precisely what is shown in Figure 7, with high KD and low SD values in the northernmost area of the reservoir, where the presence of algae in the RGB image (Figure 6) is evident, whilst there is no evidence of microalgae in the RGB image in the south and west of the reservoir. Figure 7 shows very high values of KD and low SD between Campinho and Monsaraz (see Figure 1), and on the right margins of the reservoir. The areas in the westernmost branch and south area of the reservoir, presented the highest SD and lowest KD values, with values of SDs greater than 2 m and KDs less than 1.0 m^{-1}. This will probably be associated with the non-propagation of the algae bloom to these locations, thus having smaller dissolved and suspended particles, more transparent water (greater SD) and less extinction of solar radiation in the water column.

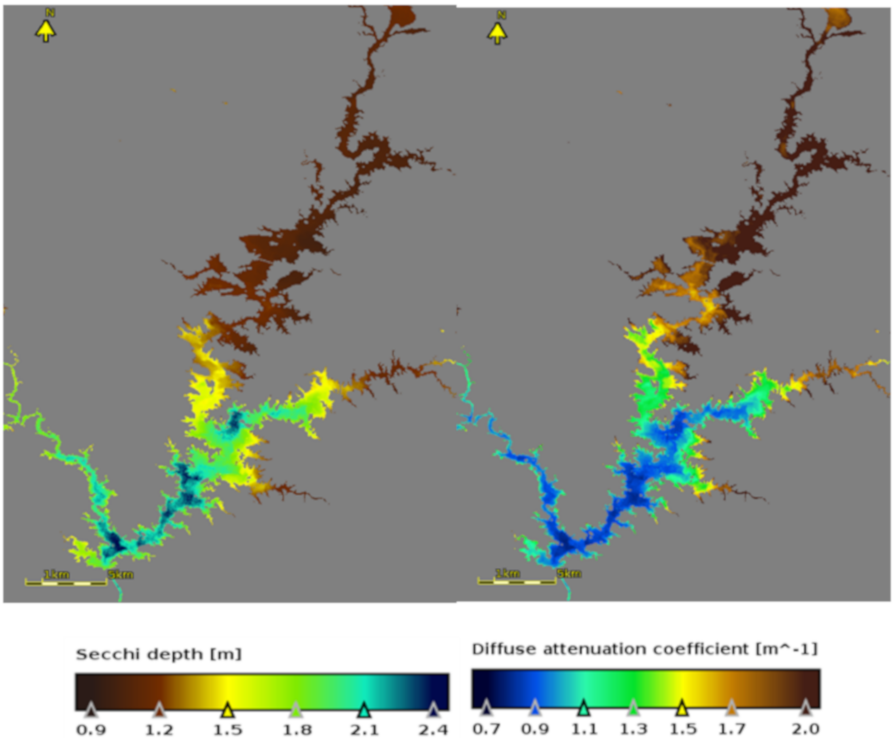

Figure 7. Secchi depth (left) and diffuse attenuation coefficient (right) maps for the Alqueva reservoir on 22 September 2017.

4.3. Seasonal and Spatial Distribution

The seasonal variation of the studied water parameters in Alqueva reservoir was evaluated using all Sentinel-2 MSI data available between July 2017 and June 2019. During this period and considering the use of the two satellite (S2A and S2B) overpasses in Alqueva region, it was possible to achieve at least 1 usable image per month. After atmospheric correction of the satellite images following the methodology described in Section 3.1, the empirical relations obtained (Equations (7) and (8)), were applied to the atmospherically corrected satellite measurements, obtaining full coverage of daily SD and KD in the reservoir during the period July 2017-June 2019.

In order to obtain a good distribution of the variables under study, an accurate identification of water pixels is essential. One of the advantages of the Sen2Cor output is the Scene classification (SC) product used to classify pixels, e.g., water, land, clouds. In this work, only water pixels were extracted from the images and used for atmospheric correction with 6SV. Occasional errors were found in the Sen2Cor classification, with water classification attributed to some pixels presenting effects of sunglint or cloudy shades. Various water body mapping approaches have been developed to identify water bodies in multispectral images. The Modified Normalized Difference Water Index (MNDWI) uses the green and Shortwave-Infrared (SWIR) bands and is one of the most popular methods [59]. In summary, to have a better mask of water pixels in the Alqueva reservoir, two conditions were imposed: Water scene Classification from Sen2Cor and positive values of MNDWI.

As for the seasonal analysis, the year was divided into 3 periods: July-October (JASO), November-February (NDJF), and March–June (MAMJ). JASO corresponds to the period of the highest air and water temperatures and with a great probability of microalgae blooms occurrence; NDJF is the coldest period and MAMJ is the period where the reservoir starts stratification.

For spatial characterization, the reservoir was divided into different areas with similar patterns of water characteristics. Only days with 100% of water pixels in the reservoir were considered, in order to calculate SD and KD averages counting the same sample of days for each pixel of the reservoir. In order to find patterns of water characteristics, not only the mean values are important, but also the

values corresponding to the days with extremes of SD and KD. Thus, the values corresponding to the 5th percentile and 95th percentile of SD and KD for each pixel were calculated.

It should be noted that the 5th percentile represents days with lower water transparency for SD and less attenuation of solar radiation in water for KD (for lower KD, more solar radiation penetrates in the water column, meaning more clear water). Figure 8 presents the 5th percentile (left panels), average (middle panels) and 95th percentile (right panels) of SD for the three different periods and Figure 9 presents the same parameters for the KD.

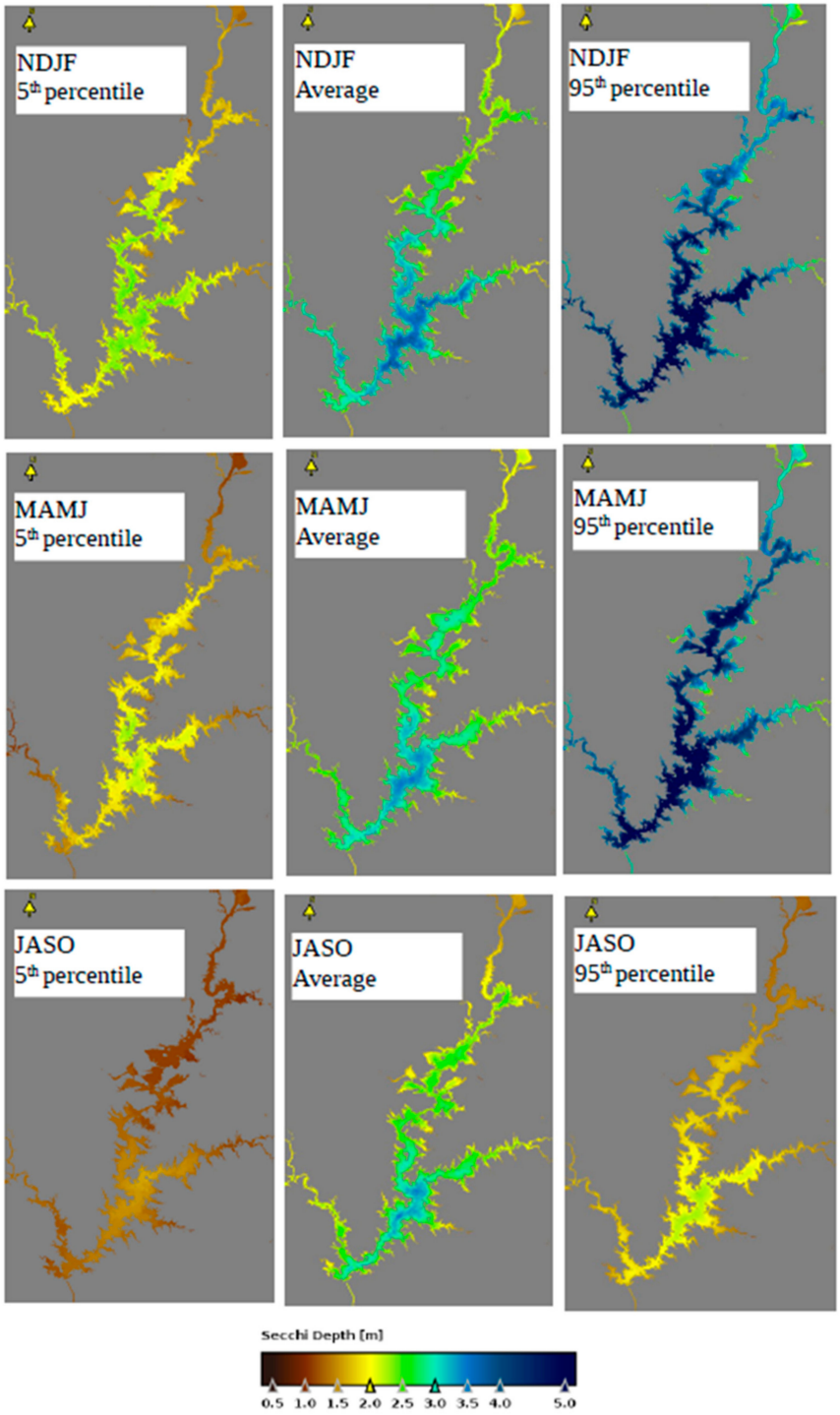

Figure 8. Spatial distribution of Secchi Depth shown from November to February (top), March to June (middle), and July to October (bottom) in Alqueva reservoir, for the period July 2017–June 2019.

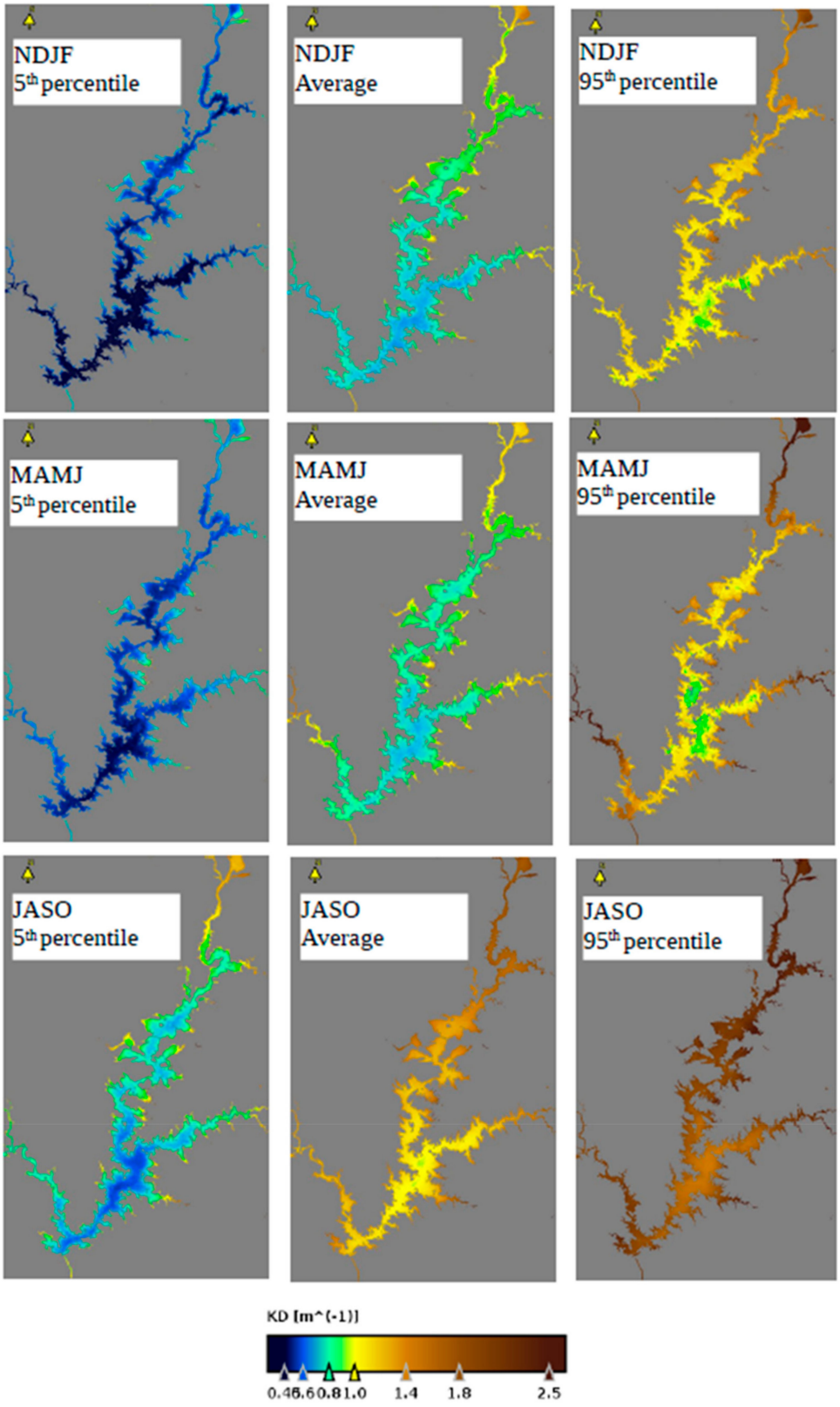

Figure 9. Same as in Figure 8 but for the diffuse attenuation coefficient.

As can be seen in Figure 8 and Figure 9, on the days representative of the 5th percentile for KD and 95th percentile for SD there is a greater spatial heterogeneity in the period July–October (JASO), comparatively to the other two analyzed periods. This fact is related to the beginning of the

development of microalgae blooms that usually occur in the northern region of the reservoir mainly by the Guadiana River (Figure 1), usually introducing organic and inorganic matter leading to an increase of biological activity. Only at the end of Summer, these microalgae blooms fill almost the entire reservoir. The southern area of the reservoir, further away from the origin of the microalgae blooms, has the lowest values of KD and the highest SD values. For the other two periods (MAMJ and NDJF), there are also higher SD and lower KD values in the southern region of the reservoir and in larger areas and away from the margins, that are shifting towards the north, with a decrease in SD and an increase in KD. As for the reservoir extensions, to the west and east, they have similar water characteristics to the southern region from November to February, but different patterns in the other periods analyzed. The differences between these regions in the period MAMJ are mainly related to several days of heavy precipitation in spring 2018, as shown in the following section. In the July–October period, more turbidity and lower/higher values of SD/KD respectively were detected in the east and west branches compared to the adjacent southern area, likely to be associated with the shorter distances between margins, with weaker winds in these locations due to less exposure, and thus higher biological activity was expected (Figures 8 and 9—JASO panels). It is observed that in the reservoir in these two years, lower/higher values of SD/KD, respectively, were detected in the July–October period compared to the other two periods, obtaining for almost all reservoir average values of SD lower than 2.5 m and KD over 1 m^{-1}. The maps representing the days with the lowest/highest values of SD/KD respectively (5th percentile to SD and 95th percentile to KD) in the MAMJ and NDJF periods are very similar to the average map in the JASO period, also showing the great deterioration in these months of formation and dissipation of these blooms. Thus, distinct areas in the Alqueva reservoir were selected considering: (1) spatial variation of SD and KD; (2) areas with different widths; (3) geometry, namely the orientation of the lake margins. The selection of the defined areas is presented in five different regions, presented in Figure 10.

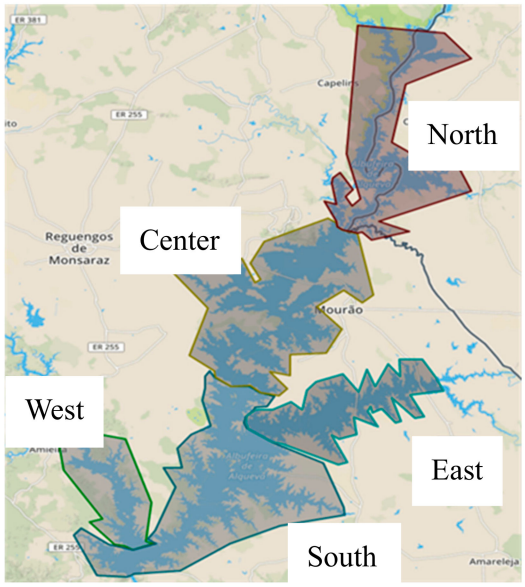

Figure 10. Selection of areas according to seasonal variation of water quality parameters, width and geometry of the reservoir.

4.4. Spatio-Temporal Variability for Period July 2017 – June 2019

The monthly evolution of SD and KD during the period of July 2017–June 2019, for each selected region of the Alqueva reservoir (Figure 11) was analyzed. When at least one of the regions defined in Section 4.3 less than 50% of water pixels (due to clouds, sunglint or smoke), the satellite image was rejected. To obtain a monthly estimation for each region, the average of all images for each month was

calculated for all water pixels within each area (Figure 11). Water pixels were considered according to the criteria explained in Section 4.3.

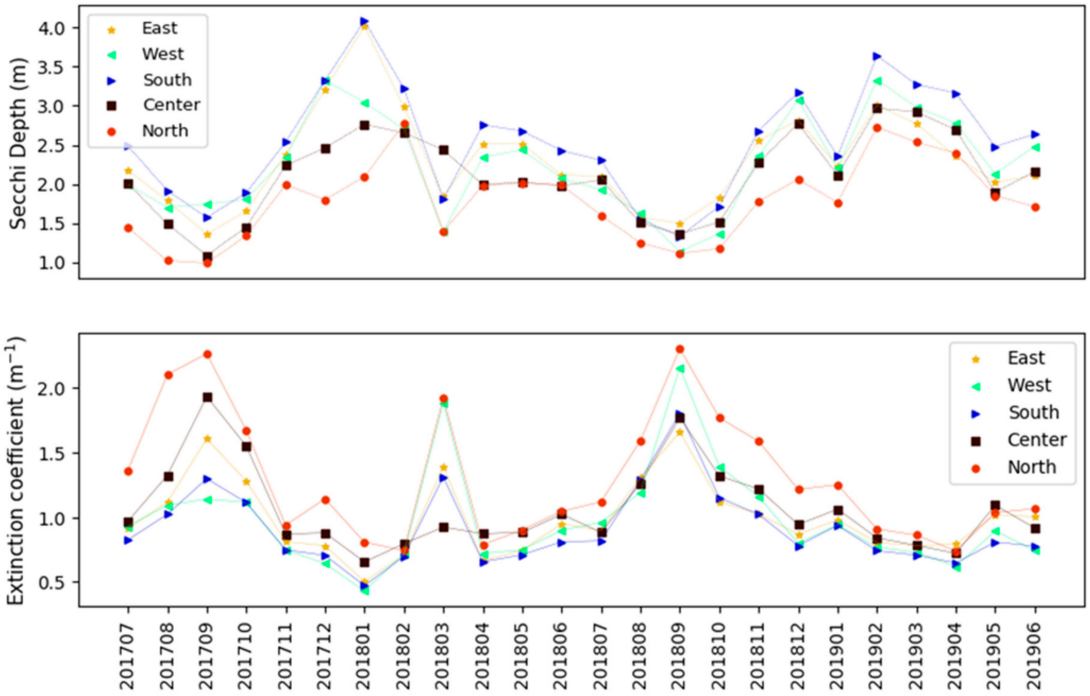

Figure 11. Monthly average of SD (top) and KD (bottom) for each reservoir region.

In order to examine conditions that may contribute to changes in water parameters in the reservoir, meteorological data from Cid Almeida station (at the east margin of MontanteP) were used, and compared with estimations of SD and KD, for the 24 months in the period July 2017–June 2019. The meteorological parameters used in this analysis were the monthly wind speed, monthly precipitation, and monthly water and air temperatures. The monthly mean evolution of wind speed, air temperature and water temperature are presented in Figure 12.

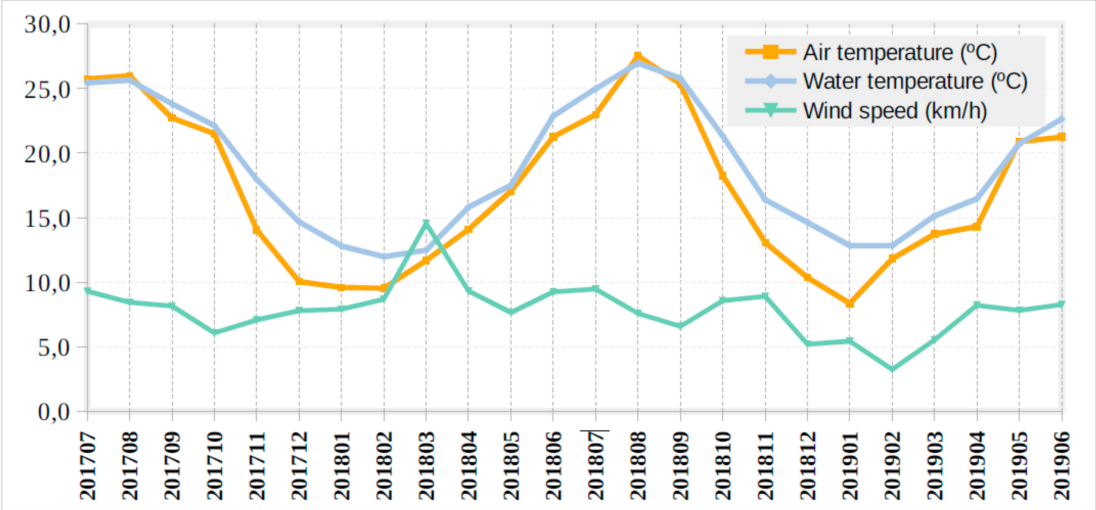

Figure 12. Monthly average of water temperature, air temperature and wind speed at the Alqueva reservoir.

In the period July 2017–June 2019, 3 critical periods are identified in terms of SD and KD: August–October (2017), March 2018 and August–October (2018). The variation in the monthly

estimates obtained for each region of SD and KD values is consistent with measurements. The values obtained show higher KD and lower SD values in these periods. Lower KD and higher SD values were estimated in colder months, with lower water temperature, and no significant rainfall events. An excellent relationship between the diffuse attenuation coefficient and turbidity has been identified in several studies (e.g., [60–63]) and also in the Alqueva reservoir with $r^2 = 0.95$ [39]. Since SD is directly related to turbidity, a strong indication of the quality of the estimations of SD and KD for the Alqueva reservoir is that the increase in one of the parameters is related to the decrease in the other.

Typically, in the Alqueva reservoir, critical water quality periods are associated with the usual long and dry summer months, with very high maximum temperatures, typically between 30 °C and 43 °C, inducing the formation of microalgae blooms in the reservoir [64,65]. It is identified that the northern area, between Lucefécit and Monsaraz (Figure 1), presents worse water quality in practically every month, which agrees with that reported by Palma et al. [66] and Palma et al. [67]. Algae blooms in recent years at the Alqueva reservoir developed in the north of Alqueva in July/August, as seen in the example in Figure 9. This is also observed by the estimates of KD and SD in July 2017 and July 2018 (Figure 11), with a significant difference between KD and SD between the northern area and the remaining reservoir regions. As summer progresses, algae expand to the south of the reservoir, with a maximum in September, with this month's SD averages estimations below 1.9 m for all areas, and KD of water over 1.2 m^{-1}. The western region of the reservoir, on the other hand, is the area furthest away from the region with the highest presence of algae in the warmer months (North area), however, locally in Summer cases, the development of these microalgae blooms is also possible. For instance, in September 2018, a month with weaker winds and a very hot previous month (August 2018 was the hottest month of the study period), led to the increase in microalgae densities also in this region of the reservoir, with estimations of SD and KD very close to the values of the northern region. This different behavior of the two September's in the evolution of algae on the reservoir and the different estimations of KD/SD can also be seen in the RGB images of the Figure 13, September 19 (2017) without evidence of algae, and September 19 (2018) with great presence of algae in the westernmost area of the reservoir. Except for the West area, the remaining regions of the reservoir behaved similarly in the July–October period for the two years analyzed. During March 2018, SD and KD estimations were like those obtained in the microalgae blooms (August–October), this was due to exceptional rain events. It was recorded nine days with precipitation exceeding 10 mm and almost 200 mm accumulated (Figure 2), a value much higher than average precipitation for March in the Alqueva region. The periods with the highest/lowest SD/KD respectively were December 2017–February 2018 and February–April 2019, periods with low air and water temperatures, associated with anticyclonic weather prevailing on most days, and monthly cumulative rainfall lower than 50 mm, except April 2019. Despite an accumulated rainfall of 70 mm in April 2019, this amount was scattered for 14 days, without heavy precipitation events, with daily precipitation lower than 15 mm. The month which presented the best SD/KD on average was January 2018, with very low KD estimations, of 0.4 m^{-1} for the West area and 0.5 m^{-1} for the South and East area. The best SD estimations were obtained, with average values of 4.0 m and 4.1 m for the East and South areas, respectively. Comparatively, for North and Central regions relevant differences are noticed, with modest SD values of 2.1 m and 2.8 m, respectively. This fact shows that the northern region, between Lucefécit and Monsaraz, presents degraded water quality and may even have large disparities compared with other areas for the same period.

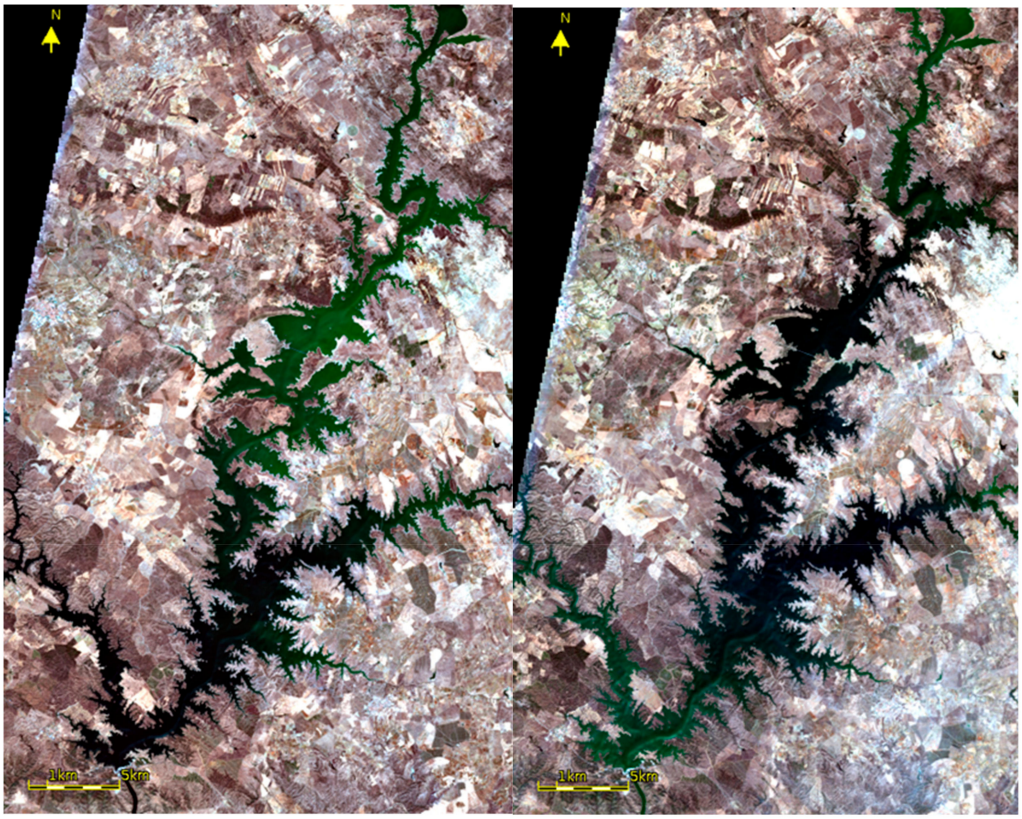

Figure 13. RGB Images showing a microalgae bloom for 19 September 2017 (left) and for 19 September 2018 (right) in the Alqueva reservoir.

Alqueva reservoir was classified as eutrophic based on mean total phosphorus (>35 µg P L^{-1}) and chlorophyll *a* (>8 µg L^{-1}) concentrations [64]. In this study, according to the monthly average of SD in the reservoir, the SD exceeds the limits for the eutrophic status in the northern and central regions of the reservoir for all analyzed months, considering the limit values of the trophic state of lakes and reservoirs [68]. In the Center, West and South regions, some months are already at or very close to the mesotrophic level (SD > 3.0 m), especially in the months with low rainfall and lower lake temperatures.

The southern area of the reservoir presents the best SD/KD values in practically every month analyzed, being expected that two of the main reasons are the widest area between margins (along with the central region) and the longest distance to the North area, where the worst values of the reservoir were found. The central area, between Campinho and Monsaraz, although also with a very large area, presents much highest KD/lowest SD, compared to the southern area for most of the months.

In addition to the monthly average, the 5th and 95th percentiles were calculated to get estimations for pixels representing water with greater and less transparency in each region. This is important to identify possible extreme values in each region and results are presented in Figures 14 and 15.

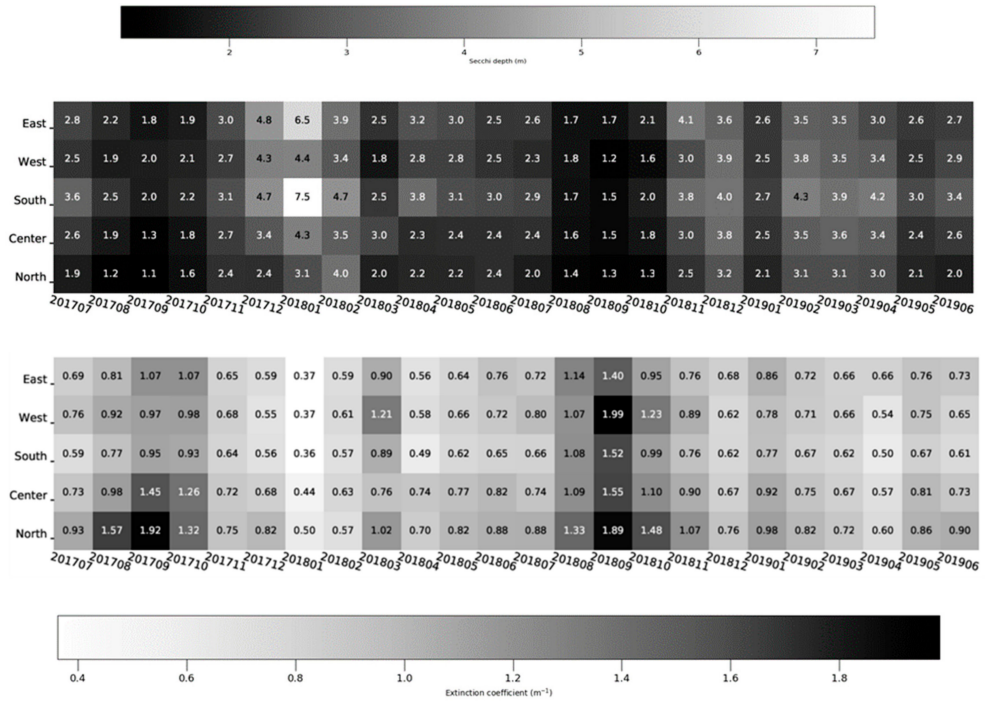

Figure 14. The 95th percentile and 5th percentile for SD (top) and for KD (bottom) respectively.

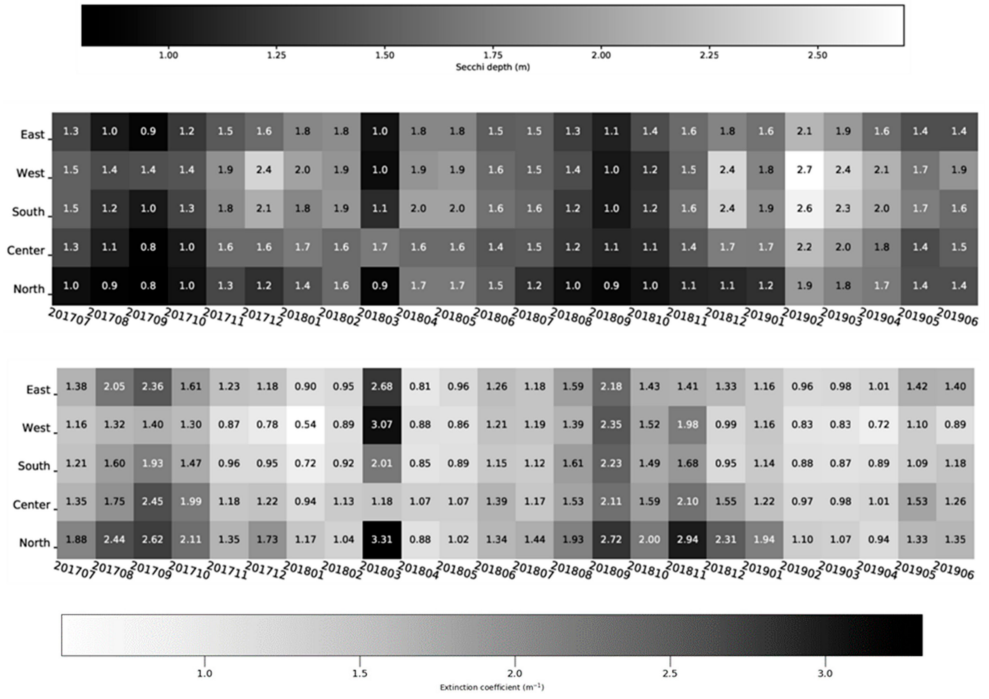

Figure 15. The 5th and 95th percentiles for SD (top) and KD (bottom), respectively.

Figure 14 shows the monthly average of pixels representing the highest SD and lowest KD values, and Figure 15 the opposite, that is, less transparent water (lower SD) and with greater radiation attenuation in the water (higher KD).

According to Figure 14, January 2018 features estimates of the highest SD and lowest KD values, with KD below 0.4 m^{-1} in the South, West and East areas, and very high SD values with 6.5 m to the east and 7.5 m to the south. These extreme values of SD and KD are very similar to the in situ extremes measured in the Alqueva reservoir. It should be noted that beyond January 2018 there are other months with a few days presenting SD (95th percentile) > 5.0 m, but which are very smooth on

average for months with large variations in water characteristics. February 2019 presents the smallest spatial variation of KD, that is, representing the smallest spatial variations of dissolved and suspended particles in water, with great uniformity. As an example, note the westernmost area of the reservoir in February 2019, with 90% of the KD values between 0.71 m^{-1} and 0.83 m^{-1}. The atmospheric stability in this month, with few precipitation days, and very light winds (Figure 12) should explain this very small spatial variation in the reservoir, characterizing this month as one of the greater transparency periods analyzed between July 2017 and June 2019. Distinctly, November 2018 was the second month in the period analyzed with the highest monthly accumulated precipitation, over 100 mm, and one of the months with the highest average wind, with the largest differences between the 5th percentile and 95th percentile, that is, a greater spatial variation. In the eastern region, SD has a value of 4.1 m (Figure 14) corresponding to 95th percentile (very high value) that is very far from the pixels corresponding to the 5th percentile with low values of only 1.6 m (Figure 15).

It can be seen from Figure 15 that September, in both years analyzed, and March 2018 are the months with the most extreme values of KD and SD. In March 2018, the most extreme KD values were obtained, with a value of 3.31 m^{-1} corresponding to the 95th percentile, e.g., 5% of the pixels in this area with estimated KD of 3.31 m^{-1} or higher. The largest areas (South and West), present for this month the lowest KD values corresponding to 95th percentile and the largest SD corresponding to the 5th percentile, not only on average (Figure 11), as well as for the extreme values. Still, for March 2018, the values for each area show a significant spatial variation in water physical parameters, much higher than for September in both years. This should be explained by the fact that in summer, the spatial variation of algae shows a smaller variation between shores and deeper areas of the reservoir, which is not the case for heavy rainfall, as in March 2018, with much higher values near the margins compared with deeper areas. The slightest differences between the values corresponding to the 5th percentile and 95th percentile, means that the area is homogeneous in water characteristics. For example, in relation to SD in the Northern region, if 90% of the pixels in March 2018 vary spatially between 0.9 m (5th percentile) and 2.0 m (95th percentile), in September 2018, they exhibit great spatial uniformity, with 90% of the pixels for this month presenting estimates between 0.8 m and 1.1 m.

5. Conclusions

The methodology developed in this work aimed to characterize spatial and temporal variations of water quality parameters in the Alqueva reservoir, using high spatial resolution images from Sentinel-2 MSI, which can be useful in other lakes with comparable trophic status. A reliable method of atmospheric correction was obtained with the radiative transfer code 6SV, using water vapor and AOT at the reference wavelength of 550 nm, obtained from Sen2Cor. Empirical relationships between satellite retrieved surface spectral reflectances and KD/SD measurements were obtained and subsequently validated, obtaining high correlation coefficients and low NRMSE values below 20% for the two analytically defined algorithms. In general, the southern area of the reservoir (between Montante e Campinho) features the highest SD and lowest KD values in the analyzed period. The western (Between Montante and Álamos) and eastern sections (Alcarrache) of the reservoir presented slightly lowest SD and highest KD values, compared to the southern part of the reservoir, especially during or immediately after extreme precipitation events, and in the August–October period. Every month, the northern region, between Lucefecit and Monsaraz, presents more turbid water and with greater attenuation of radiation in the water. As for the temporal variations, the Alqueva reservoir presented the lowest SD and highest KD values in August–October period and March 2018 compared to the other periods of the year. Between August and October, there is the usual formation of microalgae blooms in the reservoir, inducing average estimated SD between 1.9 m in Central area and 1.0 m to North area (September of 2017). The mean values of KD also denote more attenuation of radiation in water in this time of the year, with values between 1.02 m^{-1} in the southernmost area of the reservoir and 2.27 m^{-1} in the North area.

With exception of months with excessive precipitation and with the presence of microalgae, higher values of SD and low KD were obtained noting the SD of 7.5 m for pixels representing 95th percentile and 0.36 m of KD for pixels representing 5th percentile in South region to January 2018. These extremes obtained from the satellite are very close to the extremes measured in the field. A strong indicator of the correctness of the methodology presented is the good agreement between the evolution of SD estimations and KD with the evolution of meteorological parameters/water temperature. The highest KD/lowest SD was observed in the highest water temperature/March 2018 (very rainy month), with a smaller spatial variation of these parameters for months of low wind speed.

Highest KD and lowest SD were observed in the warmest months/highest water temperature, and in March 2018, they presented monthly accumulated precipitation of around 200 mm. On the other hand, estimations of the highest SD and lowest KD values were obtained in the months of lower monthly accumulated precipitation, coupled with lower air and water temperatures. A smaller spatial variation of these parameters is presented, for months of low wind speed, as is a clear example of February 2019, the month with lower monthly wind intensities. The months with the highest monthly rainfall, such as March 2018 and November 2018, show much greater spatial variations of SD and KD due to the large difference in values between margins compared to deeper zones.

The observations show high spatial and temporal heterogeneities in SD and KD. This means that the use of spatial and temporal constant values in NWP models (as at present) may lead to errors in the surface energy budget over water and subsequently in surface temperature forecasts. The methodology and the empirical relationships found in this work show that it will be possible to get global maps from satellite remote sensing for use in NWP models.

Author Contributions: Conceptualization, G.R., M.P., M.J.C.; methodology, G.R., M.P., M.J.C.; software, G.R.; validation, G.R., M.P., M.J.C., M.H.N., A.M.P., R.S., M.M.M.; formal analysis, G.R., M.P., M.J.C.; investigation, G.R., M.P., M.J.C.; resources, G.R., M.P., M.J.C.; data curation, G.R., M.P., M.J.C.; writing—original draft preparation, G.R.; writing—review and editing, G.R., M.P., M.J.C., M.H.N., A.M.P., R.S., M.M.M.; visualization, G.R.; supervision, M.P., M.J.C.; project administration, R.S. All authors have read and agreed to the published version of the manuscript.

Funding: The work was supported by COMPETE 2020 through the ICT project (UIDB/04683/2020) with the reference POCI-01-0145-FEDER-007690 and through the ALOP project (ALT20-03-0145-FEDER-000004).

Acknowledgments: The authors thank Copernicus and ESA for the data Sentinel-2 provided to carry out this work and to Olivier Hagolle for providing open-source codes to massive Sentinel-2 data download.

Conflicts of Interest: The authors declare no conflict of interest.

References

1. Coumou, D.; Rahmstorf, S. A decade of weather extremes. *Nature Clim. Chang.* **2012**, *2*, 491–496. [CrossRef]
2. Meehl, G.; Stocker, T.; Collins, W.; Friedlingstein, P.; Gaye, A.; Gregory, J.; Kitoh, A.; Knutti, R.; Murphy, J.; Noda, A.; et al. *Global Climate Projections, Climate Change 2007: The Physical Science Basis*; Cambridge University Press: Cambridge, UK, 2007; pp. 747–845.
3. Palmer, T.; Räisänen, J. Quantifying the risk of extreme seasonal precipitation events in a changing climate. *Nature* **2002**, *415*, 512–514. [CrossRef] [PubMed]
4. IPCC. Climate change 2013: The physical science basis. In *Contribution of Working Group I to the Fifth Assessment Report of the Intergovernmental. Panel on Climate Change*; Stocker, T.F., Qin, D., Plattner, G.-K., Tignor, M., Allen, S.K., Boschung, J., Nauels, A., Xia, Y., Bex, V., Midgley, P.M., Eds.; Cambridge University Press: Cambridge, UK; New York, NY, USA, 2013; p. 1535. [CrossRef]
5. Westra, S.; Fowler, H.; Evans, J.P.; Alexander, L.V.; Berg, P.; Johnson, F.; Kendon, E.J.; Lenderink, G.; Roberts, N.M. Future changes to the intensity and frequency of short-duration extreme rainfall. *Rev. Geophys.* **2014**, *52*, 522–555. [CrossRef]
6. Cardoso, R.M.; Soares, P.M.M.; Lima, D.C.A.; Miranda, P.M.A. Mean and extreme temperatures in a warming climate: EURO CORDEX and WRF regional climate high-resolution projections for Portugal. *Clim. Dyn.* **2018**, *52*, 129–157. [CrossRef]

7. Soares, P.M.M.; Cardoso, R.M.; Lima, D.C.A.; Miranda, P.M.A. Future precipitation in Portugal: High-resolution projections using WRF model and EURO-CORDEX multi-model ensembles. *Clim Dyn* **2017**, *49*, 2503–2530. [CrossRef]
8. Havens, K.; Jeppesen, E. Ecological Responses of Lakes to Climate Change. *Water* **2018**, *10*, 917. [CrossRef]
9. Jeppesen, E.; Brucet, S.; Naselli-Flores, L.; Papastergiadou, E.; Stefanidis, K.; Nõges, T.; Nõges, P.; Attayde, J.L.; Zohary, T.; Coppens, J.; et al. Ecological impacts of global warming and water abstraction on lakes and reservoirs due to changes in water level and salinity. *Hydrobiologia* **2015**, *750*, 201–227. [CrossRef]
10. Paerl, H.W.; Huisman, J. Climate change: A catalyst for global expansion of harmful blooms. *Environ. Microbiol* **2009**, *1*, 27–37. [CrossRef]
11. Duan, W.; He, B.; Nover, D.; Yang, G.; Chen, W.; Meng, H.; Zou, S.; Liu, C. Water Quality Assessment and Pollution Source Identification of the Eastern Poyang Lake Basin Using Multivariate Statistical Methods. *Sustainability* **2016**, *8*, 133. [CrossRef]
12. Duan, W.; Takara, K.; He, B.; Luo, P.; Nover, D.; Yamashiki, Y. Spatial and temporal trends in estimates of nutrient and suspended sediment loads in the Ishikari River, Japan, 1985 to 2010. *Sci. Total Environ.* **2013**, *461*, 499–508. [CrossRef]
13. Wu, Z.; Zhang, Y.; Zhou, Y.; Liu, M.; Shi, K.; Yu, Z. Seasonal-Spatial Distribution and Long-Term Variation of Transparency in Xin'anjiang Reservoir: Implications for Reservoir Management. *Int. J. Environ. Res. Public Health* **2015**, *12*, 9492–9507. [CrossRef]
14. Zou, S.; Jilili, A.; Duan, W.; Maeyer, P.D.; de Voorde, T.V. Human and Natural Impacts on the Water Resources in the Syr Darya River Basin, Central Asia. *Sustainability* **2019**, *11*, 3084. [CrossRef]
15. Silva, A.; De Lima, I.; Santo, F.; Pires, V. Assessing changes in drought and wetness episodes in drainage basins using the Standardized Precipitation Index. *Bodenkultur* **2014**, *65*, 31–37.
16. Donald, M.A.; Glibert, M.P.; Burkholder, M.J. Harmful algal blooms and eutrophication: Nutrient sources, composition, and consequences. *Estuar. Coasts* **2002**, *25*, 704–726.
17. Moss, B.; Kosten, S.; Meerhoff, M.; Battarbee, R.; Mazzeo, N.; Havens, K.; Lacerot, G.; Liu, Z.W.; Meester, D.L.; Paerl, H.; et al. Allied attack: Climate change and eutrophication. *Inland Waters* **2011**, *1*, 101–105. [CrossRef]
18. Palmer, S.C.; Kutser, T.; Hunter, P.D. Remote sensing of inland waters: Challenges, progress and future directions. *Remote Sens. Environ.* **2015**, *157*, 1–8. [CrossRef]
19. Chandrasekar, K.; Sesha Sai, M.V.R.; Roy, P.S.; Dwevedi, R.S. Land Surface Water Index (LSWI) response to rainfall and NDVI using the MODIS Vegetation Index product. *Int. J. Remote Sens.* **2010**, *31*, 3987–4005. [CrossRef]
20. Barrett, D.; Frazier, A. Automated Method for Monitoring Water Quality Using Landsat Imagery. *Water* **2016**, *8*, 257. [CrossRef]
21. Potes, M.; Costa, M.J.; Silva, J.C.B.; Silva, A.M.; Morais, M. Remote sensing of water quality parameters over Alqueva reservoir in the south of Portugal. *Int. J. Remote Sens.* **2011**, *32*, 3373–3388. [CrossRef]
22. Potes, M.; Costa, M.J.; Salgado, R. Satellite remote sensing of water turbidity in Alqueva reservoir and implications on lake modeling. *Hydrol. Earth Syst. Sci.* **2012**, *16*, 1623–1633. [CrossRef]
23. Potes, M.; Rodrigues, G.; Penha, A.; Novais, M.H.; Costa, M.J.; Salgado, R.; Morais, M. Use of Sentinel 2-MSI for water quality monitoring at Alqueva reservoir, Portugal. *Proc. Int. Assoc. Hydrol. Sci.* **2018**, *380*, 73–79. [CrossRef]
24. Olmanson, L.G.; Bauer, M.E.; Brezonik, P.L. A 20-year Landsat water clarity census of Minnesota's 10,000 lakes. *Remote Sens. Environ.* **2008**, *112*, 4086–4097. [CrossRef]
25. Kuster, T. The Possibility of Using the Landsat Image Archive for Monitoring Long Trend in Colored Dissolved Organic Matter Concentration in Lake Waters. *Remote Sens. Environ.* **2012**, *123*, 334–338.
26. Liu, H.; Li, Q.; Shi, T.; Hu, S.; Wu, G.; Zhou, Q. Application of Sentinel 2 MSI Images to Retrieve Suspended Particulate Matter Concentrations in Poyang Lake. *Remote Sens.* **2017**, *9*, 761. [CrossRef]
27. Toming, K.; Kutser, T.; Laas, A.; Sepp, M.; Paavel, B.; Nõges, T. First experiences in mapping lake water quality parameters with Sentinel-2 MSI imagery. *Remote Sens.* **2016**, *8*, 640. [CrossRef]
28. Pahlevan, N.; Sarkar, S.; Franz, B.A.; Balasubramanian, S.V.; He, J. Sentinel-2 MultiSpectral Instrument (MSI) data processing for aquatic science applications: Demonstrations and validations. *Remote Sens. Environ.* **2017**, *201*, 47–56. [CrossRef]
29. Ansper, A.; Alikas, K. Retrieval of Chlorophyll a from Sentinel-2 MSI Data for the European Union Water Framework Directive Reporting Purposes. *Remote Sens.* **2019**, *11*, 64. [CrossRef]

30. Molkov, A.A.; Fedorov, S.V.; Pelevin, V.V.; Korchemkina, E.N. Regional Models for High-Resolution Retrieval of Chlorophyll a and TSM Concentrations in the Gorky Reservoir by Sentinel-2 Imagery. *Remote Sens.* **2019**, *11*, 1215. [CrossRef]
31. Soomets, T.; Uudeberg, K.; Jakovels, D.; Brauns, A.; Zagars, M.; Kutser, T. Validation and Comparison of Water Quality Products in Baltic Lakes Using Sentinel-2 MSI and Sentinel-3 OLCI Data. *Sensors* **2020**, *20*, 742. [CrossRef]
32. Martins, V.S.; Barbosa, C.C.F.; De Carvalho, L.A.S.; Jorge, D.S.F.; Lobo, F.D.L.; Novo, E.M.L.M. Assessment of Atmospheric Correction Methods for Sentinel-2 MSI Images Applied to Amazon Floodplain Lakes. *Remote Sens.* **2017**, *9*, 322. [CrossRef]
33. Richter, R.; Louis, J.; Müller-Wilm, U. *Sentinel-2 MSI—Level 2A Products Algorithm Theoretical Basis Document*; S2PAD-ATBD-0001, Issue 2.0; Telespazio VEGA Deutschland GmbH: Darmstadt, Germany, 2012.
34. Markert, K.N.; Schmidt, C.M.; Griffin, R.E.; Flores, A.I.; Poortinga, A.; Saah, D.S.; Muench, R.E.; Clinton, N.E.; Chishtie, F.; Kityuttachai, K.; et al. Historical and operational monitoring of surface sediments in the lower mekong basin using landsat and Google earth engine cloud computing. *Remote Sens.* **2018**, *10*, 909. [CrossRef]
35. Shang, P.; Shen, F. Atmospheric correction of satellite GF-1/WFV imagery and quantitative estimation of suspended particulate matter in the yangtze estuary. *Sensors* **2016**, *16*, 1997. [CrossRef]
36. Wang, D.; Ma, R.; Xue, K.; Loiselle, S.A. The assessment of Landsat-8 OLI atmospheric correction algorithms for inland waters. *Remote Sens.* **2019**, *11*, 169. [CrossRef]
37. Flores-Anderson, A.I.; Griffin, R.; Dix, M.; Romero-Oliva, C.S.; Ochaeta, G.; Skinner-Alvarado, J.; Ramirez Moran, M.V.; Hernandez, B.; Cherrington, E.; Page, B.; et al. Hyperspectral Satellite Remote Sensing of Water Quality in Lake Atitlán, Guatemala. *Front. Environ. Sci.* **2020**, *8*, 7. [CrossRef]
38. Hansen, C.H.; Burian, S.J.; Dennison, P.E.; Williams, G.P. Spatiotemporal Variability of Lake Water Quality in the Context of Remote Sensing Models. *Remote Sens.* **2017**, *9*, 409. [CrossRef]
39. Potes, M.; Costa, M.J.; Salgado, R.; Bortoli, D.; Serafim, A.; Le Moigne, P. Spectral measurements of underwater downwelling radiance of inland water bodies. *Tellus A* **2013**, *65*, 20774. [CrossRef]
40. Kotchenova, S.Y.; Vermote, E.F. A vector version of the 6S radiative transfer code for atmospheric correction of satellitedata: An Overview. In Proceedings of the 29th Review of Atmospheric Transmission Models Meeting, Lexington, MA, USA, 13–14 June 2007.
41. Vermote, E.F.; Tanré, D.; Deuzé, J.L.; Herman, M.; Morcrette, J.J. Second Simulation of the Satellite Signal in the Solar Spectrum, 6S: An Overview. *IEEE Trans. Geosci. Remote Sens.* **1997**, *35*, 675–686. [CrossRef]
42. Kotchenova, S.Y.; Vermote, E.F.; Matarrese, R.; Klemm, F.J., Jr. Validation of a vector version of the 6S radiative transfer code for atmospheric correction of satellite data. Part I: Path radiance. *Appl. Opt.* **2006**, *45*, 6762–6774. [CrossRef]
43. Kotchenova, S.Y.; Vermote, E.F. Validation of a vector version of the 6S radiative transfer code for atmospheric correction of satellite data. Part II: Homogeneous Lambertian and anisotropic surfaces. *Appl. Opt.* **2007**, *46*, 4455–4464. [CrossRef]
44. Obregón, M.A.; Costa, M.J.; Silva, A.M. Validation of ESA Sentinel-2 L2A Aerosol Optical Thickness and Columnar Water Vapour during 2017–2018. *Remote Sens.* **2019**, *11*, 1649. [CrossRef]
45. ASD. *FieldSpec®HandHeld 2 Spectroradiometer User's Manual*; ASD Inc.: Boulder, CO, USA, 2010.
46. Kloiber, S.M.; Brezonik, P.L.; Olmanson, L.G.; Bauer, M.E. A procedure for regional lake water clarity assessment using Landsat multispectral data. *Remote Sens. Environ.* **2002**, *82*, 38–47. [CrossRef]
47. Kloiber, S.M.; Brezonik, P.L.; Bauer, M.E. Application of Landsat imagery to regional-scale assessments of lake clarity. *Water Res.* **2002**, *36*, 4330–4340. [CrossRef]
48. Rotta, L.H.S.; Alcântara, E.H.; Watanabe, F.S.Y.; Rodrigues, T.W.P.; Imai, N.N. Atmospheric correction assessment of SPOT-6 image and its influence on models to estimate water column transparency in tropical reservoir. *Remote Sens. Appl. Soc. Environ.* **2016**, *4*, 158–166. [CrossRef]
49. Verdin, J.P. 1985. Monitoring water quality conditions in a large western reservoir with Landsat Imagery. *Photogramm. Eng. Remote Sens.* **1985**, *51*, 343–353.
50. Lavery, P.; Pattiaratchi, C.; Wyllie, A.; Hick, P. Water quality monitoring in estuarine waters 511 using the Landsat Thematic Mapper. *Remote Sens. Environ.* **1993**, *46*, 268–280. [CrossRef]
51. Wu, G.; de Leeuw, J.; Skidmore, A.K.; Prins, H.H.T.; Liu, Y. Comparison of MODIS and 505 Landsat TM5 images for mapping tempo-spatial dynamics of Secchi disk depths in Poyang Lake 506 National Nature Reserve, China. *Int. J. Remote Sens.* **2008**, *29*, 2183–2198. [CrossRef]

52. Bonansea, M.; Ledesma, C.; Rodríguez, C.; Pinotti, L.; Antunes, M. Effects of atmospheric correction of Landsat imagery on lake water clarity assessment. *Adv. Space Res.* **2015**, *56*, 2345–2355. [CrossRef]
53. Delegido, J.; Urrego, E.P.; Vicente, E.; Perpinyà, X.S.; Soria, J.M.; Sandoval, M.P.; Ruiz-Verdú, A.; Peña, R.; Moreno, J. Turbidez y profundidad de disco de Secchi con Sentinel-2 en embalses con diferente estado trófico en la Comunidad Valenciana. *Revista de Teledetección* **2019**, 15–24. [CrossRef]
54. Page, B.P.; Olmanson, L.; Mishra, D.R. A harmonized image processing workflow using Sentinel-2/MSI and Landsat-8/OLI for mapping water clarity in optically variable lake systems. *Remote Sens. Environ.* **2019**, *231*, 111284. [CrossRef]
55. Lorenzen, C.J. Determination of chlorophyll and phaeopigments: Spectrophotometric equations. *Limnol. Oceanogr.* **1967**, *12*, 348–356. [CrossRef]
56. IPQ. *Qualidade da água. Doseamento da clorofila a e dos feopigmentos por espectrofotometria de absorção molecular. Método de extracção com acetona. NP 4327/1996*; Instituto Português da Qualidade: Monte de Caparica, Portugal, 1997.
57. ISO; EN ISO 10260:1992. *Water Quality—Measurement of Biochemical Parameters—Spectrometric Determination of the Chlorophyll-a Concentration*; International Organization for Standardization: Geneve, Switzerland, 1992.
58. APHA. *Standard Methods for the Examination of Water and Wastewater*, 19th ed.; American Public Health Association, American Water Works Association, and Water Pollution Control Federation: Washington, DC, USA, 1995.
59. Du, Y.; Zhang, Y.; Ling, F.; Wang, Q.; Li, W.; Li, X. Water bodies' mapping from Sentinel-2 imagery with modified normalized difference water index at 10-m spatial resolution produced by sharpening the SWIR band. *Remote Sens.* **2016**, *8*, 354. [CrossRef]
60. Grobler, D.C.; Toerien, D.F.; De Wet, J.S. Changes in turbidity as a result of mineralization in the lower Vaal River. *Water SA* **1983**, *9*, 110–116.
61. Roos, J.C.; Pieterse, J.H. Light, temperature and flow regimes of the Vaal River at Balkfontein, South Africa. *Hydrobiologia* **1994**, *277*, 1–15. [CrossRef]
62. Oliver, R.L.; Hart, B.T.; Olley, J.; Grace, M.; Rees, C.; Caitcheon, G. *The Darling River: Algal Growth and the Cycling and Sources of Nutrients*; Murray Darling Basin Commission Project M386; CRS for Freshwater Ecology, CSIRO Land and Water: Canberra, Australia, 1999.
63. Giblin, S.; Hoff, K.; Fischer, J.; Dukerschein, T. *Evaluation of Light Penetration on Navigation Pools 8 and 13 of the Upper Mississippi River. Long Term Resource Monitoring Program*; Technical Report 2010-T001; U.S. Geological Survey: Reston, VA, USA, 2010.
64. Morais, M.; Serafim, A.; Pinto, P.; Ilheu, A.; Ruivo, M. Monitoring the water quality in Alqueva reservoir, Guadiana River, southern Portugal. In *Reservoir and River Basin Management: Exchange of Experiences from Brazil Portugal and Germany*; Gunter, G., do Carmo Sobral, M., Eds.; Technical University of Berlin: Berlin, Germany, 2007; pp. 96–112.
65. Novais, M.H.; Penha, A.; Morales, E.; Potes, M.; Salgado, R.; Morais, M. Vertical distribution of benthic diatoms in a large reservoir (Alqueva, Southern Portugal) during thermal stratification. *Sci. Total Environ.* **2018**, 659. [CrossRef] [PubMed]
66. Palma, P.; Alvarenga, P.; Palma, V.; Fernandes, R.M.; Soares, A.M.V.M.; Barbosa, I.R. Assessment of anthropogenic sources of water pollution using multivariate statistical techniques: A case study of the Alqueva's reservoir, Portugal. *Environ. Monit. Assess.* **2010**, *165*, 539–552. [CrossRef]
67. Palma, P.; Alvarenga, P.; Palma, V.; Matos, C.; Fernandes, R.M.; Soares, A.; Barbosa, I.R. Evaluation of surface water quality using an ecotoxicological approach: A case study of the Alqueva Reservoir (Portugal). *Environ. Sci. Pollut. Res.* **2010**, *17*, 703–716. [CrossRef]
68. Bukata, R.P.; Jerome, J.H.; Kondratyev, K.Y.; Pozdnyakov, D.V. *Optical Properties and Remote Sensing of Inland and Coastal Waters*; CRS Press: Boca Raton, FL, USA, 1995.

© 2020 by the authors. Licensee MDPI, Basel, Switzerland. This article is an open access article distributed under the terms and conditions of the Creative Commons Attribution (CC BY) license (http://creativecommons.org/licenses/by/4.0/).

Science of the Total Environment 709 (2020) 136205

Contents lists available at ScienceDirect

Science of the Total Environment

journal homepage: www.elsevier.com/locate/scitotenv

Pharmaceuticals in a Mediterranean Basin: The influence of temporal and hydrological patterns in environmental risk assessment

Patrícia Palma [a,b,*], Sofia Fialho [a], Ana Lima [a], Maria Helena Novais [b], Maria João Costa [b,c], Nicola Montemurro [d], Sandra Pérez [d], Miren Lopez de Alda [d]

[a] Escola Superior Agrária, Instituto Politécnico de Beja, 7800-295 Beja, Portugal
[b] Instituto de Ciências da Terra (ICT), Universidade de Évora, Évora, Portugal
[c] Science and Technology School, University of Évora, Évora, Portugal
[d] Water, Environmental and Food Chemistry Unit (ENFOCHEM), Institute of Environmental Assessment and Water Research (IDAEA-CSIC), Barcelona, Spain

HIGHLIGHTS

- Streams of Guadiana Basin contaminated with pharmaceuticals;
- Intermittent regimes more sensitive to the pharmaceutical's contamination;
- Use of optimised risk quotient for obtaining a more real scenario of risk;
- Drought intensifies the risk of pharmaceuticals;
- Diclofenac, ibuprofen and carbamazepine with high risk, at intermittent streams;

GRAPHICAL ABSTRACT

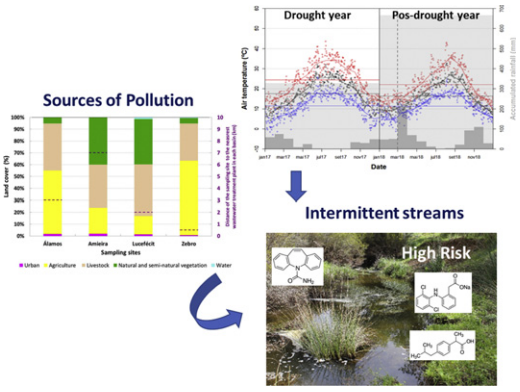

ARTICLE INFO

Article history:
Received 20 November 2019
Received in revised form 16 December 2019
Accepted 17 December 2019
Available online 18 December 2019

Editor: Daqiang Yin

Keywords:
Guadiana Basin
Water quality
Pharmaceuticals
Environmental risk assessment

ABSTRACT

Occurrence of pharmaceuticals in the aquatic environment is nowadays a well-established issue that has become a matter of both scientific and public concern. Tons of different classes of pharmaceuticals find their way to the environment at variable degrees, after their use and excretion through wastewater and sewage treatment systems.
The main goal of this study was to correlate the dynamics and the environmental risk of pharmaceuticals with different temporal and hydrological patterns, at the Guadiana Basin (South of Portugal). Water samples were collected bimonthly during 2017 (classified as a drought year) and 2018 (post-drought year) in: Zebro, Álamos and Amieira (intermittent hydrological streams), and Lucefécit (perennial hydrological stream). The pharmaceuticals quantified in higher concentrations, out of 27 investigated, were diclofenac (up to 4806 ng L^{-1}), ibuprofen (3161 ng L^{-1}), hydrochlorothiazide (2726 ng L^{-1}) and carbamazepine (3223 ng L^{-1}). Zebro and Álamos presented the highest contamination by this group of environmental hazardous substances, which may be correlated with the presence of wastewater treatment plants upstream the sampling point of each stream. Furthermore, the highest concentrations occurred mainly during the dry period (2017), when the flow was nearly inexistent in Zebro, and in Álamos after the first heavy rainfalls.

* Corresponding author at: Department of Applied Sciences and Technologies, Escola Superior Agrária - Instituto Politécnico de Beja, Rua Pedro Soares S/N, Apartado 6155, 7800-295 Beja, Portugal.
E-mail address: ppalma@ipbeja.pt (P. Palma).

https://doi.org/10.1016/j.scitotenv.2019.136205
0048-9697/© 2019 Elsevier B.V. All rights reserved.

In specific periods, the high concentrations of pharmaceuticals detected may induce risk for the organisms of lowest trophic levels, damaging the balance of the ecosystems at these streams. The risk quotient optimised approach (RQf) integrating exposure, toxicity and persistence factors, ranks the pharmaceuticals investigated in terms of risk for the aquatic ecosystems as follows: diclofenac, ibuprofen and carbamazepine (high risk), clarithromycin (moderate risk), acetaminophen, ofloxacin and bezafibrate (endurable risk), and hydrochlorothiazide (negligible risk).

© 2019 Elsevier B.V. All rights reserved.

1. Introduction

Aquatic emerging pollutants present a new global water quality challenge, with potential serious threats to human population, ecosystems balance and services (Ivanová et al., 2018). Among emerging pollutants, pharmaceuticals are the unique group structurally designed to maximize their intrinsic biological activity at low concentrations and developed to induce a continued action at biological systems. These properties highlight the risk associated with the unintentional presence of pharmaceuticals in the aquatic environments (Ebele et al., 2017; Ginebreda et al., 2010). Further, around 5000 different pharmaceutical forms are used in human and veterinary medicine in the European Union, covering a broad range of chemical structures and physic-chemical proprieties (Hughes et al., 2013). Complex mixtures of these compounds along with their metabolites are continuously introduced into the environment via distinct pathways, such as the disposal of unused, expired medicines or by untreated discharges and/or wastewater treatment plant (WWTP) effluents (e.g. from hospitals, veterinary practices and agriculture activities, namely, livestock) (Mandaric et al., 2019; Zhou et al., 2019). In water bodies, pharmaceuticals may be removed from the dissolved phase through adsorption to suspended particles and may accumulate in sediments, from which they can be remobilized by resuspension. The abiotic cycle and fate of these pollutants in the environment depend, not only on their physical-chemical proprieties, but also on other variables like seasonal changes as temperature variability, drought periods, and water hydrology (Nunes et al., 2019).

In the aquatic environment, pharmaceuticals may induce a variety of physiological changes, reversible or not, in non-target aquatic organisms (Godoy and Kummrow, 2017), such as macroalgae (Rosa et al., 2019), molluscs (Gonzalez-Rey and Bebianno, 2012; Joyce and Vogeler, 2018), crustaceans (Hossain et al., 2019; Oropesa et al., 2017, 2016) and fish (Mathias et al., 2018; Perussolo et al., 2019). Furthermore, chronic exposure to trace levels of pharmaceutical mixtures can also induce antibiotic resistances (Sabri et al., 2018) and endocrine disruption effects (Xu et al., 2019). Nevertheless, only recently, pharmaceuticals have emerged as one of the major concerns in Europe and worldwide (Ebele et al., 2017). Example of this is the fact that any of the 45 priority substances identified under the Directive 2013/39/EU (ECC, 2013) are pharmaceuticals, and only in 2007, diclofenac and carbamazepine were identified as future emerging priority candidates (Ebele et al., 2017). Following this, in 2015, six pharmaceutical compounds (17-α-ethynilestradiol, 17-β-estradiol, estrone, diclofenac, erythromycin, clarithromycin, and azithromycin) were included in the first European watch list of substances for Union-wide monitoring in the field of water policy (ECC, 2015). More recently, in 2018 (ECC, 2018), this list has been modified to include the antibiotics amoxicillin and ciprofloxacin and exclude diclofenac after the information gathered on it on the previous years. Thus, further studies are needed to identify, within this group of emerging substances, those that present a greater potential risk to the aquatic environment and introduce them in lists of priority substances for specific assessment and management at European member state's water bodies (Ribeiro et al., 2015). In this context, in order to increment the effectiveness of the rank systems, making them more realistic and useful at regional scale, it is essential: (i) to have high-quality methodologies with enough sensitivity to detect very low levels of these substances, allowing the chemical fingerprint characterization of the abiotic matrices (Brack et al., 2018; Sousa et al., 2019); (ii) to refine environmental risk assessment processes, integrating occurrence patterns, frequency of detection, chemical properties of pharmaceuticals, bioaccumulation, bioamplification and aquatic toxicity effects (Brack et al., 2018; Zhou et al., 2019); (iii) to develop risk assessment processes taking into consideration different temporal and spatial scenarios, mainly in regions where the impact of climate changes may be more stressed (Mandaric et al., 2019; Pereira et al., 2017); and (iv) to establish correlations among pharmaceuticals risk assessment and ecological status of water bodies (Brack et al., 2015).

Nowadays, occurrence, frequency of detection, and risk assessment studies have mostly been dealt with at a global scale, which is evident from the large number of research articles published (Fekadu et al., 2019; Gogoi et al., 2018; Li et al., 2019; Reis et al., 2019). In the Mediterranean region, one of the most affected by climate changes, some studies have already been developed at a local scale, assessing different temporal and spatial scenarios of pharmaceuticals risk for the aquatic environment (Barbosa et al., 2018; Desbiolles et al., 2018; Mandaric et al., 2019; Osorio et al., 2016; Sousa et al., 2019). All these studies focused on the importance of the work at local scale, namely at the level of basin, river and stream, to get answers about the influence of hydrologic patterns, attenuation processes, variability of temporal factors, and pollution pathways correlated with land cover and land uses, in the dynamics of emerging pollutants at the water systems. In fact, Mediterranean streams/rivers are characterized by inter-annual hydrological fluctuations encircling floods in spring and autumn and droughts in summer (Palma et al., 2018), which can cause streams intermittent regimes, processes that are becoming more frequent with the intensification of drought periods. Consequently, intermittent streams and rivers in the Mediterranean area, under climate-change conditions, are among the most frequent and dynamic freshwater systems (Acuña et al., 2017, 2014). Hence, the local studies are the midpoint to obtain specific results of different patterns allowing the outline of regional strategies that may be overlapped for global goals.

The main goals of this study were: (i) to analyze the presence and respective concentrations of pharmaceuticals belonging to different therapeutic classes in Mediterranean streams, with different flow regimes and affected by several land uses; (ii) to assess the joint effects of hydrological (river flow) and chemical stressors on the occurrence and distribution of pharmaceuticals, during drought and post-drought periods; and (iii) to estimate and analyze the environmental risk of pharmaceuticals, using an improved method. The results will add knowledge on the behavior of pharmaceuticals under a drought climate scenario, followed by a normal climate year, at streams with different flow regimes, contribution extremely significant for climate studies at the Mediterranean region. The results, integrated in European databases of pharmaceuticals risk assessment, will provide additional information on pharmaceuticals at regional and global scales and help identify those that deserve priority consideration in the European water policies.

2. Materials and methods

2.1. Site description and sampling procedures

The Guadiana basin integrates the international Hydrographic Region of Guadiana which has a total area of 66,800 km^2, of which 55,220 km^2 (83%) belong to Spain and 11,611 km^2 (17%; most of it at the Alentejo region) belong to Portugal. It is the fourth largest watershed in the Iberian Peninsula, after the Douro, Ebro and Tagus basins

(APA, 2016). The drainage basin of the Guadiana river section in Portugal and the corresponding land cover map are shown in Fig. 1. Land cover has been obtained from the 2018 CORINE Land Cover (CLC) inventory, produced with satellite imagery (Sentinel-2 and Landsat-8 for gap filling), available from Copernicus Land Monitoring Service (2018) (https://land.copernicus.eu/).

The Hydrographic Region of Guadiana basin is limited to the north by the Tagus river basin to the east by the Júcar region and to the south by the Guadalquivir region and the Tinto rivers, Odiel and Piedras (APA, 2016). The Guadiana River rises in the lagoons of Ruidera in Spain, at an altitude of 868 m, developing over 800 km to the mouth of the Atlantic Ocean, next to Vila Real de Santo António (Portugal). In Portugal,

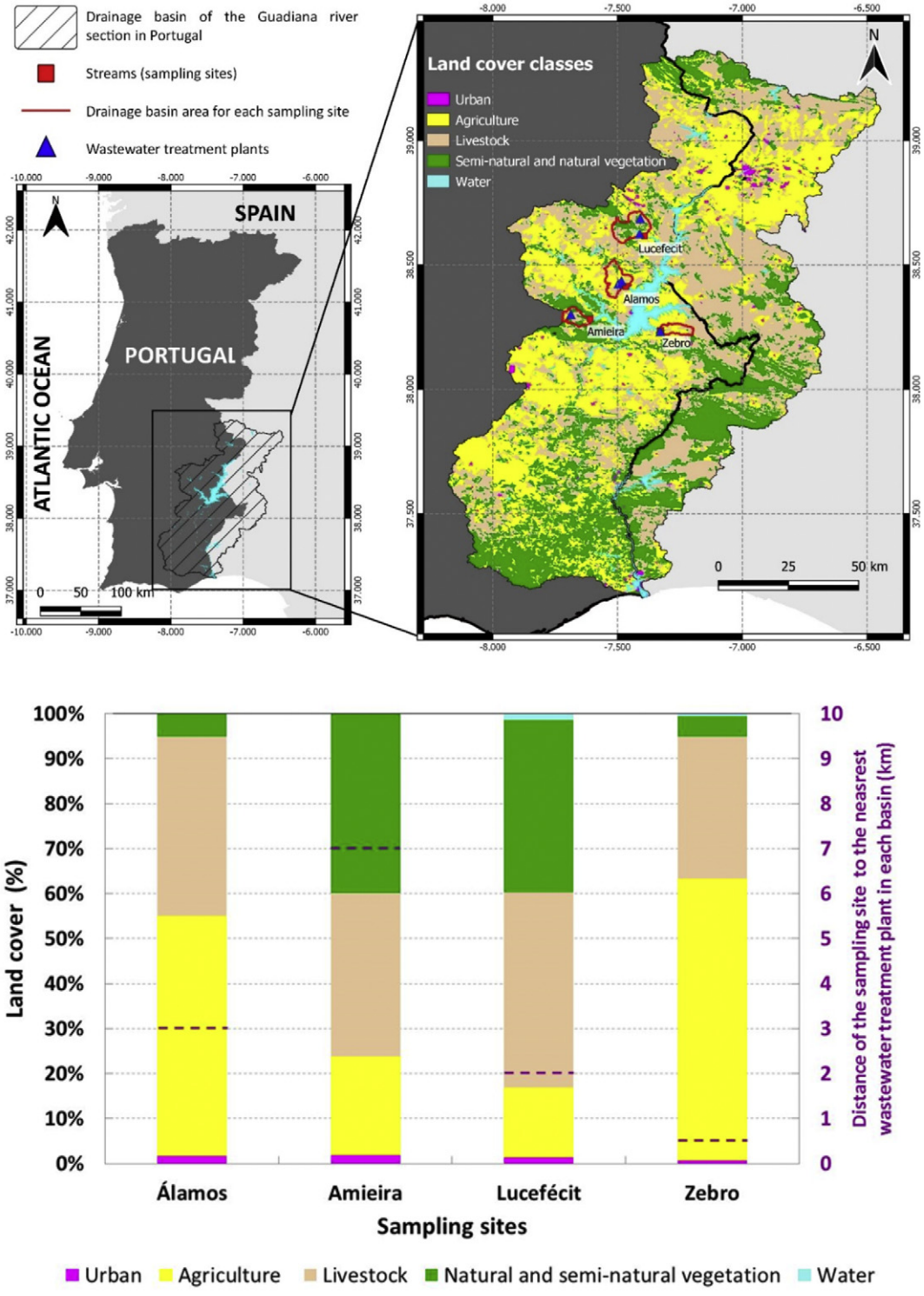

Fig. 1. a) Map of the study area and corresponding land cover map. The line pattern fill (left panel) delineates the drainage basin of the Guadiana river section in Portugal and the red lines (right panel) represent the drainage basin areas for each sampling site. The red squares represent the stream sampling sites (from North to South: Lucefécit - Lf; Álamos - Al; Amieira - Am; and Zebro – Zb) and the blue triangles indicate the location of the wastewater plants. b) The bars show the percentages of the land cover classes in the drainage basins of the stream sampling sites (left axis) and the dashed lines indicate the distance to the nearest wastewater treatment plant (right axis).

the river has a total length of 260 km, presenting nine sub-basins that integrate the main tributary waterlines to the rivers of Guadiana, Alcarrache, Ardila, Caia, Chança and Xévora (APA, 2016) (Fig. 1).

The soils are mostly heavy, essentially derived from schists and granite. This region is characterized by a very rich natural heritage, with a high conservative value, in terms of habitats and species of flora and fauna, such as Mediterranean oaks, cork oak (*Quercus suber* L.) and holm oak (*Quercus rotundifolia* Lam.) woodlands interspersed within the agricultural landscape. Few patches of forest plantations (eucalyptus and pines) are also found (APA, 2016). Fig. 1 also shows the distribution of land cover types, with agriculture and livestock activities widely disseminated in the Guadiana basin, and natural and semi-natural vegetation (including Montado landscape) more often found in the south-eastern regions. The lower panel of Fig. 1 presents the percentages of the land cover classes in each drainage basin, as well as the distances to the nearest wastewater treatment plant, as a way of identifying the main sources of pollution in the areas. Table 1 also presents information on the sources of pollution and wastewater treatment types and flow rates.

The climate at Guadiana basin is quite homogeneous, with dry Mediterranean characteristics, as hot summers, high levels of insolation and evapotranspiration and severe winters. The average annual temperature is in almost the whole basin near 16 °C, with values of 24 to 28 °C in the warmer months (July/August), and with average air temperature around 9 °C in the coldest month (January). The weighted average annual rainfall is 550 mm (561 mm in Portugal and 540 mm in Spain). The annual distribution of precipitation is extremely irregular, falling to 386 and 422 mm in dry years and rising to 722 and 766 mm in wet years, being the majority (±80%) concentrated in the period of October–April (APA, 2016).

From a climatological point of view, the years of 2017 and 2018 in Portugal were quite different, with 2017 classified as extremely warm and dry in comparison with the climatological normal of 1971–2000, whereas 2018 was considered normal with respect to the same reference (www.ipma.pt; last accessed on 25/09/2019). The year of 2017 was characterized by extremely hot weather especially in April, June and October, with temperature values much higher than normal from April to October, in particular the maximum temperature. This, combined with the anomalously low precipitation values, caused high evapotranspiration values and significant deficits of soil moisture, which also contributed to a very severe forest fire season in the country. From April 2017 on, great part of the country was gradually affected by severe and extreme drought conditions, according to the Portuguese Institute for the Sea and Atmosphere (IPMA), including the Guadiana basin. In 2017 this area presented a mean annual temperature that was 1.5 °C higher than the normal, accompanied by a decrease of precipitation of roughly 55% of the normal, taking as reference the 1971–2000 climatological normal for the region. Fig. 2 presents the temperature and precipitation data measured in 2017 and 2018 at a meteorological station installed in the lower part of Guadiana basin at Alqueva reservoir (Potes et al., 2017). The differences between both years can be clearly distinguished with the annual values of average temperatures (minimum, mean and maximum represented by the blue, black and red horizontal lines, respectively) showing higher values in 2017 than in 2018. In contrast, the annual accumulated precipitation (represented by the light grey bars) in 2017 is roughly half of that in 2018. The monthly temperature lines for 2017 show that high temperatures were registered for a longer period than in 2018 and the dark grey bars confirm that after March 2017 precipitation was scarce, which caused the severe drought conditions. The precipitation that occurred in March 2018 triggered a relief of the drought conditions, which is represented by the dashed grey vertical line in Fig. 2. The year of 2018 does not present significant deviations from the climatological normal, with the mean annual temperature showing a slight deviation of +0.2 °C and the precipitation presenting a slightly higher annual value (112% of the climatological normal).

Four sampling sites were selected in streams located at the lower part of the Guadiana basin and draining to the Alqueva reservoir: Zebro (Zb; 38°14′15.54″N, 7°19′40.32″W); Álamos (Al; 38°24′50.46″N, 7°28′2.16″W); Amieira (Am; 38°16′58.80″N, 7°36′35.20″W) and Lucefécit (Lf; 38°36′59.19″N, 7°23′31.65″W), represented in Fig. 1, along with the land cover classes. The selection of these streams took into consideration: (i) the differences in hydrological regimes: Amieira and Álamos are intermittent streams, which dry to a series of disconnected pools part of the year, during the study this happened in July and September; Zebro with an intermittent regime presents water all year long but without flow during some periods; Lucefécit presents a perennial regime, with flow during the whole year; (ii) the type of pollution correlated with the land cover patterns; and (iii) the lack of knowledge about their chemical status. The characterization of each stream is displayed in Table 1.

Table 1
General characteristics, chemical and potential ecological status classification, and principal sources of pollution identified during the cycle of assessment of 2009–2015 (APA, 2016), including wastewater treatment types and flow conditions (ARHAlentejo, 2011). The flow was characterized qualitatively during the present study (Jn: January; Mr.: March; M: May; Jl: July; Sp: September; Nv: November; 17:2017; 18:2018).

Site	Typology	Basin	Sub-basin	Length (km)	Flow conditions	Sediments Texture (%)	Ecological potential	Chemical status	Principal sources of pollution	Wastewater treatment plant: type and flow rate (m^3/day)
Álamos	Small rivers of Southern Portugal (S1 ≤ 100 km^2)	Guadiana	Guadiana	17.0731	Low flow (M17, Sp17, Nv17, Jn18, M18, Sp18) Very fast (Mr17, Mr18 Nv18) No flow (Jl17, Jl18)	Sand: 65 Silt: 25 Clay: 9	Less than good	Unknown	Agriculture Livestock Urban	Reguengos de Monsaraz: Activated Sludge with Aeration (927) S. Pedro do Corval: Activated Sludge with aeration (157)
Amieira	Small rivers of Southern Portugal (S1 ≤ 100 km^2)	Guadiana	Degebe	17.6246	Low flow (Nv17, Jn18, M18) Moderate (M17, Mr18), Very fast (Nv18) No flow (Jl17, Sp17, Jl18, Sp18)	Sand: 90 Silt: 3 Clay: 8	Unknown	Unknown	Livestock Agriculture Urban	Portel: Stabilization Ponds (Natural Lagooning) (239)
Zebro	Small rivers of Southern Portugal (S1 ≤ 100 km^2)	Guadiana	Guadiana	13.295	Low flow (Jn18, Mr18, Nv18) No flow (Mr17, M17, Jl17, Sp17, Nv17, M18, Jl18, Sp18)	Sand:89 Silt:4 Clay:9	Less than good	Unknown	Agriculture Urban Livestock	Póvoa de S. Miguel: Percolator Bed (96)
Lucefécit	Small rivers of Southern Portugal (S1 ≤ 100 km^2)	Guadiana	Guadiana	44.101	Low flow (M17, Jl17, Sp17, Nv17, Jn18, M18, Jl18, Sp18, Nv18) Very fast (Mr18)	Sand: 59 Silt: 31 Clay: 10	Less than good	Unknown	Livestock Agriculture Urban	Terena: septic tank and macrophyte trench (150) Alandroal: Activated Sludge with Nitrogen and Phosphorus Removal (483)

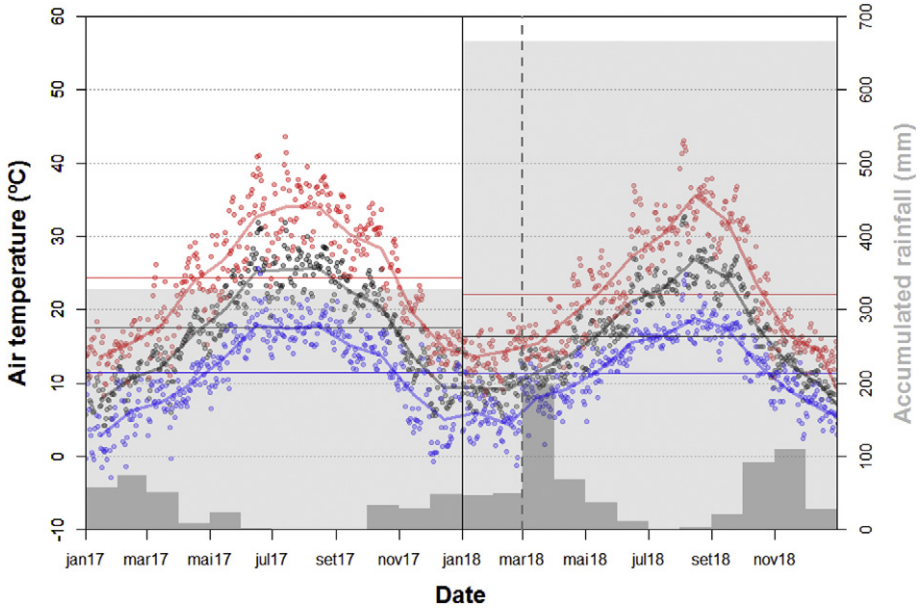

Fig. 2. Daily and monthly mean (black dots and line), maximum (red dots and line) and minimum (blue dots and line) air temperature and monthly rainfall (dark grey bars) from 2017 to 2018 in the Alqueva region (Guadiana Basin). The light grey bars represent the annual rainfall in this period and the black, red and blue horizontal lines, constant each year, denote the mean, maximum and minimum annual temperatures. The dashed grey vertical line indicates the end of the drought period.

Pharmaceuticals were evaluated during 12 sampling campaigns from January 2017 to November 2018 (in the months of January (Jn), March (Mr), May (M), July (Jl), September (Sp), November (Nv), for both years). The wet period included the months of November, January and March, and the dry period included the months of May, July and September, these periods were defined by APA, for the Alentejo region (ARHAlentejo, 2011). The water collection in the months of July and September for the intermittent streams was done at the existing pools. Due to technical problems with some laboratory facilities, it was not possible to collect the samples of January and March 2017 in Álamos and Lucefécit. During the study period, a total of 44 water samples (1 L) were collected at a depth of 30 cm and stored in amber PET bottles in the dark at −18 °C until analysis.

In situ measurements at each sampling site using a multiparametric YSI 6820 MPS probe® allowed to determine the water temperature (T; °C), pH, electrical conductivity (EC; μS cm^{-1}) and dissolved oxygen (DO; %).

The flow conditions of Guadiana river (sub-basin of the streams analysed) were obtained from the database of National Water Resources Information System (2019; https://snirh.apambiente.pt/). The existent data (until 2010) showed significant variations of river flow rates, between 0.8 m^3 s^{-1} (30/7/2009) and 552.0 m^3 s^{-1} (5/11/2006). This high flow variability, also observed in other Iberian rivers (Pereira et al., 2017), is justified by the climate-driven oscillations, which increment the water scarcity. Since no information about the specific hydrology of the studied streams was available at the national database, the flow conditions were qualitatively assessed, using the following scale: no flow, slow flow, flow, and very fast flow (results displayed in Table 1).

2.2. Chemicals

A total of 27 target pharmaceuticals representative of several therapeutic classes, and some of them included in the European Watch Lists, were selected for analysis (ECC, 2000, 2018). The list of analytical reference standards comprised the analgesics (ANALG) and no steroids anti-inflammatories drugs (NSAIDs) acetaminophen (ACET), diclofenac (DIC), ibuprofen (IBUP), indomethacin (IND), ketoprofen (KET), naproxen (NAP), and propyphenazone (PROPy), the antibiotics ofloxacin (OFLOX), sulfadiazine (SULFD), sulfamethazine (SULFM), trimetroprim (TRIM), sulfamethoxazole (SULFAMT), and clarithromycin (CLAR), the psychotropic drugs diazepam (DIAZ), lorazepam (LORAZ), paroxetine (PAR), and carbamazepine (CARB), the lipid regulators bezafibrate (BEZ), gemfibrozil (GEM), and fenofibrate (FEN), the β-blockers atenolol (ATEN), metoprolol (MET), propranolol (PROP), and sotalol (SOT), the diuretics furosemide (FUR) and hydrochlorothiazide (HYDR), and the opioid codeine (COD). All compounds were high purity (mostly 90%) and were bought from Sigma Aldrich (St. Luis, MO, U.S) or Cerilliant (Texas, USA). The CAS numbers, molecular formulas, molecular weights, and other relevant properties of all target compounds are reported in Electronic Supplementary Material (ESM, Table S1).

Isotope-labelled compounds (IS) acetaminophen-d_4, bezafibrate-d_4, carbamazepine-d_{10}, codeine-d_3, diazepam-d_5, diclofenac-d_4, furosemide-d_5, fenofibrate-d_6, gemfibrozil-d_6, ketoprofen-d_3, indomethacin-d_4, hydrochlorothiazide-d_2, lorazepam-d_4, metoprolol-d_7, naproxen-d_3, paroxetine-d_4, propranolol-d_7, sotalol-d_6, sulfamethoxazole-d_4, sulfadiazine-d_4, and sulfamethazine-d_4 were purchased from Sigma Aldrich (St. Luis, MO, U.S), Cerilliant (Texas, USA), Alsachim (Illkirch-Graffenstaden, France) or Santa Cruz Biotechnology (Dallas, TX, USA) (ESM, Table S2).

LC-MS grade acetonitrile (ACN) (≥99.9%), methanol (MeOH) (≥99.9%), ethyl acetate (EtAc) (≥99.9%), dimethyl sulfoxide (DMSO) (≥99.9%), and HPLC water were purchased from Merck (Darmstadt, Germany). Formic acid (≥96%, ACS reagent) and ammonium acetate were supplied by Sigma-Aldrich.

Individual stock standard solutions (concentration of 1000 μg mL^{-1}) were prepared in either 100% methanol or 100% DMSO, depending on the solubility of each compound. Working solutions mixtures containing all the aforementioned analytes and the isotopically labelled compounds (1 μg mL^{-1}), for analysis and calibration purposes, were prepared by diluting adequate volumes of the individual stock solutions with MeOH. All solutions were stored at −20 °C.

2.3. Chemical analysis

Pharmaceuticals were analysed in water following a method based on solid phase extraction (SPE) and analysis by liquid chromatography-tandem mass spectrometry (LC-MS/MS). The details of the method can be found in the Electronic Supplementary Material (ESM). In brief,

water samples (200 mL), previously filtered and spiked with a mixture of isotopically labelled compounds, were extracted with Oasis HLB (60 mg, 3 mL) cartridges (Waters Corporation, Milford, MA, US), using 2 × 4 mL of MeOH for elution. The extracts were then evaporated, reconstituted into 1 mL of water/MeOH (90:10 v/v), and filtered (through 0.45 μm PTFE syringe filters). LC-MS/MS analysis of the extracts (5 μL injection volume) was performed using a SCIEX ExionLC™ AD system (Sciex, Redwood City, CA, U.S.) and a Hibar® HR Purospher® STAR RP-C18 column (100 mm × 2.1 mm i.d., 2 μm particle size, Merck, Darmstadt, Germany) for chromatographic separation. MS detection was carried out in both positive and negative electrospray ionization modes (in separate runs) using a SCIEX X500R QTOF system (Sciex, Redwood City, CA, U.S.) with a Turbo V™ source. High resolution data were acquired using multiple reaction monitoring (MRMHR) following a workflow consisting of a TOF-MS survey (100–850 Da for 80 ms of Accumulation time (AT)). The MRMHR scanning mode was used for accurate quantification of product ion transitions (see Tables S3 and S4 in ESM), optimised with the Guided MRMHR tool from SCIEX. All relevant selected detection conditions (transitions, ion spray voltage, source temperature, declustering potential, collision energies, etc.) can be found in the ESM.

Qualitative and quantitative data analyses were performed using SCIEX OS™ Software version 1.5 (Sciex, Redwood City, CA, U.S.). Two high resolution product ions were used for each compound, the most abundant for quantification and the second most abundant for confirmation. Linearity of the method was evaluated using the internal standard calibration approach with a calibration curve constructed between 0.1 and 300 μg L^{-1} (equivalent to 0.5 and 1500 ng L^{-1} in surface water, taking into consideration a method concentration factor of 200 in the aqueous extract). Calibration curves were constructed using linear weighted least-squares regression (1/x as weighting factor) by plotting the ratio of the analyte signal to that of its corresponding IS (added at a fix concentration of 50 ng L^{-1}) as a function of the analyte and surrogate standard concentration ratio. The corresponding coefficient of determination together with the Method Detection Limits (MDLs) and Method Quantification Limits (MQLs) obtained for each compound can be found in Tables S3 and S4 of ESM. MDLs and MQLs, experimentally calculated using a signal-to-noise ratio of 3.3 and 10, respectively, from the mass spectrometry signal observed in the real samples, were between 0.05 and 1.3 ng L^{-1}.

2.4. Environmental risk assessment

To determine the pharmaceuticals that promoted a higher negative impact (higher risk) in the streams, and rank them accordingly as potentially harmful compounds specific for the Guadiana basin (Mediterranean region), a risk quotient optimised approach (RQf) was developed on the basis of the respective EU guidelines (ECC, 2003) and further improved to include the frequency of MECs (measured environmental concentrations) exceeding PNECs (predict no-effect concentrations) (Zhou et al., 2019). This approach allows highlighting the pollutants that repeatedly appear at potentially harmful concentrations at a given site and pinpoint them in the high risk compounds prioritization process (Desbiolles et al., 2018). To this end, the authors applied as a starting point the methodology previously used by them for evaluation of the risk assessment of pollutants (Palma et al., 2014), based on the calculation of the ratio between the MEC and the PNEC (RQ = MEC/(PNEC/AF)) in different scenarios: general (using the average of the quantified individual concentrations for each compound at each site) and worst (using the maximum concentrations), in each of the years 2017 (drought) and 2018 (pos-drought conditions). For the calculation of the PNEC, NOEC values were used and, in their absence, EC_{50} values for three trophic levels (algae, crustacean, fish), adjusted by an appropriate assessment factor (AF; 10, 50, 100 or 1000, depending on the toxicity values used) to overcome the uncertainty of this conservative approach. Ecotoxicological data was obtained from the United States EPA ECOTOX database (2019) (https://cfpub.epa.gov/ecotox/), and from Zhou et al. (2019). The toxicicity and PNEC data, as well as some chemical properties influencing the environmental persistence and bioaccumulation of compounds, are displayed in Table 2.

The optimised risk quotient value (RQf) is determined by multiplying the mean of the various RQ values obtained for a compound and site by the frequency (F) with which its MEC exceeds the corresponding PNEC in the considered period, that is, by the percentage of cases where the RQ is equal or higher than 1, according to the following equation:

$$RQf = RQ_{mean} \times F$$

According to Zhou et al. (2019), the RQf was classified into 5 groups: high environmental risk: RQf > 1; moderate environmental risk: 0.1 ≤ RQf < 1; endurable environmental risk (small scale adverse effect): 0.01 ≤ RQf < 0.1; negligible environmental risk: 0 < RQf < 0.01; no environmental risk: RQf = 0 (safe).

2.5. Statistical analysis

Water data were assessed by descriptive statistics (mean, range, standard deviation and frequency of detection) and the seasonal and annual variations of the pharmaceuticals were analysed. Since most of the data were not normally distributed, the Kruskal–Wallis ANOVA by

Table 2
Logarithm of the octanol-water partition coefficient ($LogK_{ow}$), degradation time in water (DT50), toxic value for the most sensitive species (ng L^{-1}) and PNEC value of the pharmaceuticals analysed in the Guadiana Basin.

Compound	$LogK_{ow}$ (25 °C)	Water DT50 (days)	Toxic value (mg L^{-1})	PNEC value (ng L^{-1})
Analgesics/NSAIDs				
Acetaminophen	0.46	3.10[a]	0.005 ($NOEC_{algae}$)	500
Diclofenac	4.51	5[b]	0.00001 ($NOEC_{crustaceans}$)	1
Ibuprofen	3.97	20[c]	0.0001 ($NOEC_{fish}$)	10
Indomethacin	4.27	17–18[d]	2.9 ($NOEC_{algae}$)	2900
Ketoprofen	3.12	–	1.24 ($EC50_{crustaceans}$)	1240
Naproxen	3.18	14[c]	36.7($EC50_{fish}$)	36,700
Propyphenazone	1.94	–	0.571($EC50_{algae}$)	571
Antibiotics				
Ofloxacin	−2.00	10.6[b]	0.005 ($NOEC_{algae}$)	100
Sulfadiazine	−0.09	9.8[e]	1.88 ($EC50_{crustaceans}$)	1880
Sulfamethazine	0.89	72–180[f]	1 ($NOEC_{algae}$)	20,000
Sulfamethoxazole	0.89	5.2[e]	0.12 ($NOEC_{crustaceans}$)	2400
Trimethoprim	0.91	6[e]	0.157($NOEC_{fish}$)	15,700
Clarithromycin	3.16	–	0.002 ($NOEC_{algae}$)	20
Psychotropic drugs				
Diazepam	2.82	34[a]	0.983 ($EC50_{crustaceans}$)	983
Lorazepam	3.98	–	1. 683 ($EC50_{algae}$)	1680
Paroxetine	2.57	–	0.22 ($NOEC_{crustaceans}$)	2200
Carbamazepine	2.45	63[c], 100[b]	0.0001 ($NOEC_{crustaceans}$)	100
Lipid regulators				
Bezafibrate	4.25	–	0.023 ($NOEC_{crustaceans}$)	230
Gemfibrozil	4.77	–	0.078 ($NOEC_{crustaceans}$)	1560
Fenofibrate	5.19	–	0.703 ($EC50_{fish}$)	7030
β-Blockers				
Atenolol	0.16	–	5 ($NOEC_{fish}$)	100,000
Metoprolol	1.88	–	7.3 ($NOEC_{algae}$)	73,000
Propranolol	3.48	16.8[b]	0.004 ($NOEC_{fish}$)	400
Sotalol	0.24	–	26.39 ($EC50_{algae}$)	26,390
Diuretics				
Furosemide	2.03	22[g]	19.78 ($NOEC_{algae}$)	197,800
Hydrochlorothiazide	−0.07	–	56.18 ($EC50_{algae}$)	56,180
Opioids				
Codeine	1.19	–	0.976 ($EC50_{crustaceans}$)	976

$LogK_{ow}$ (Log Octanol-Water Partition Coefficient) values were obtained from CHEMSpider (http://www.chemspider.com/); toxic values and PNEC where obtained from United States EPA ECOTOX database (https://cfpub.epa.gov/ecotox/) and (Zhou et al., 2019); the values of DT50 in water where obtained from: [a]Loffler et al., 2005; [b]Andreozzi et al., 2003; [c]Tixier et al., 2003; [d]Yamamoto et al., 2009; [e]Nguyen Dang Giang et al., 2015; [f]TOXNETdatabase: https://toxnet.nlm.nih.gov/; [g]Liu et al., 2019.

Ranks test was performed to assess statistical differences among pharmaceuticals and sampling locations, period and flow.

A correlation test was performed to evaluate possible associations among pharmaceuticals, hydrological and temporal patterns. Hence, considering the number of samples (<50), and that most data failed the Shapiro-Wilk normality test, correlations between parameters were assessed using the Spearman's rank coefficients, as a non-parametric measure computed over ranked data. The Spearman coefficient (R) was used to evaluate the statistical significance of the correlations, for a confidence level of $p < 0.05$.

All statistical analyses were performed with the STATISTICA 7.0 (Software™ Inc., PA, USA, 2004).

3. Results and discussion

3.1. In-situ physical-chemical parameters, meteorology and land cover

The results of the in-situ parameters are displayed in Fig. 3. In general, pH showed neutral to slightly alkaline values in all streams, with values between 7.01 (July 2017; Lucefécit) and 9.05 (July 2017, Zebro). The water temperature during 2017 ranged between 6.5 °C (January; Amieira) and 29 °C (July; Zebro) while in 2018 it varied between 10.5 °C (January, Lucefécit) and 34 °C (September; Amieira in the intermittent phase). These values are closely connected to air temperatures that in 2017 presented the highest monthly maximum in July (34 °C), with abnormally high values already from April, whereas in 2018 the highest monthly maxima were observed later, in August and September (36 °C and 32 °C, respectively) (Fig. 2). The higher water temperatures with long daylight periods may be important factors for the increment of biodegradation rates and phototransformation mechanisms of some pharmaceuticals (Barbosa et al., 2018). Furthermore, temperature and pH may influence the dynamics of pharmaceuticals among the water/sediment abiotic compartments, due to some variability of the logarithm of octanol-water partition coefficient ($LogK_{ow}$) (Mandaric et al., 2019; Nunes et al., 2019). Thus, the high solubility in water that occurs for compounds with a $LogK_{ow} < 2.5$ (25 °C), such as sulfamethoxazole, propyphenazone and trimethoprim (see Table 2), may increment the degradation processes and contribute to the low concentrations quantified in the streams. Zebro and Álamos were the streams that presented higher values of electrical conductivity, positively correlated with the urban ($R = 0.41$; $p < 0.05$) and livestock land cover classes ($R = 0.59$; $p < 0.05$), which was already reported by other authors (Bonansea et al., 2016; Rodrigues et al., 2018). To refer also that Álamos and Zebro drainage basins present very low percentages of natural and semi-natural vegetation areas (about 5%), in comparison with Amieira and Lucefécit basins that present almost 40% of this land cover type (Fig. 1b).

3.2. Pharmaceuticals occurrence

Relatively to pharmaceuticals, the study analysed 27 compounds, belonging to 7 different therapeutic classes, in 44 samples from four

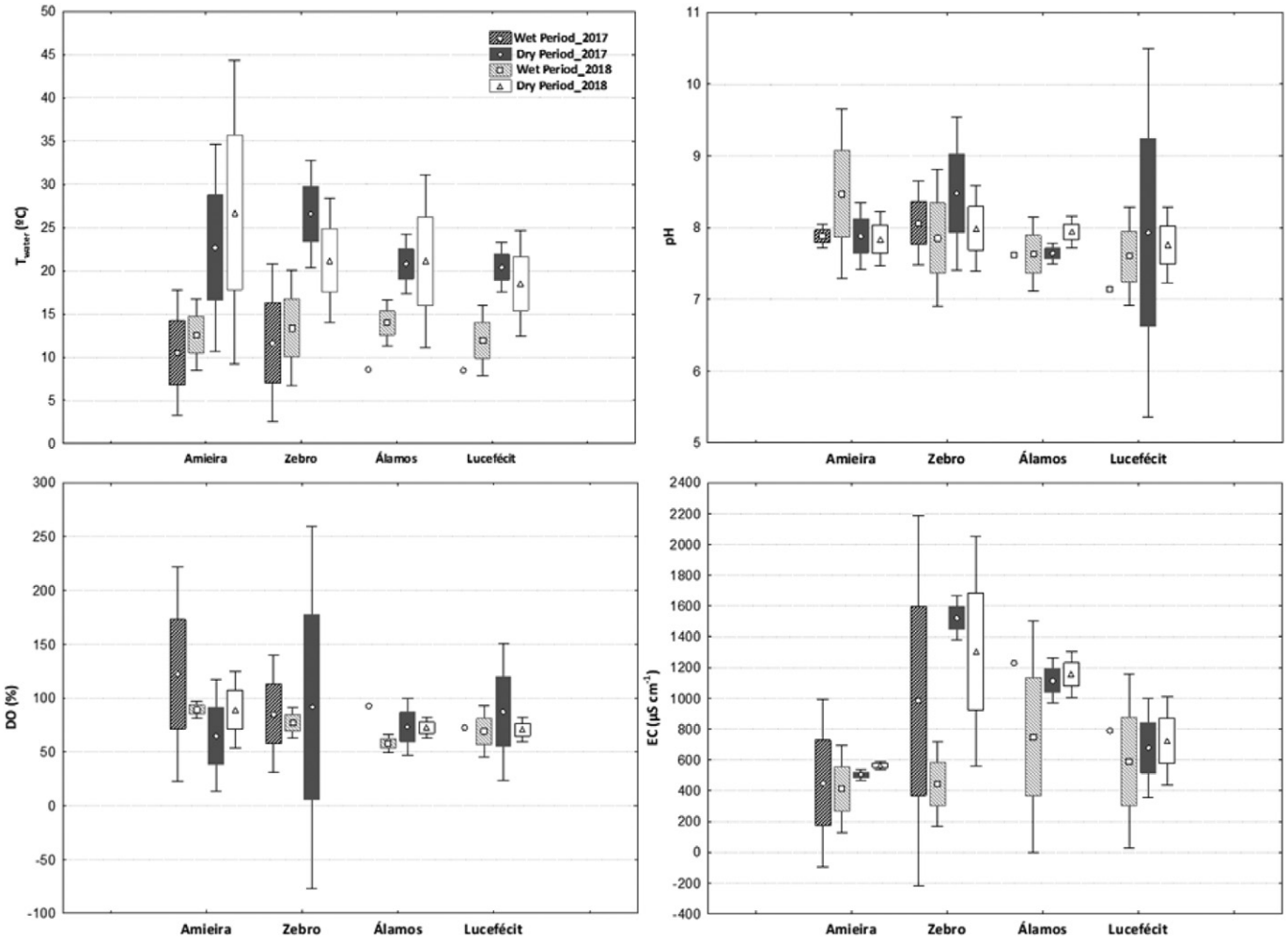

Fig. 3. Spatial and temporal (seasonal and yearly) variations of the in situ parameters measured in each stream. The mark across the box represents the mean, and the top and bottom of the box show the standard error, and the whiskers represent the standard deviation.

streams, distributed by two seasonal periods in two years, with distinct climate characteristics (2017 a drought year; 2018 a pos-drought year). The results of the principal therapeutic classes, detection frequencies, means, maximum concentrations and dynamics of the most representative pharmaceuticals, are displayed in Table 3, Figs. 4a, b and 5.

3.2.1. Pharmaceutical therapeutic groups

In general, the group of ANALG/NSAIDs was the most frequently detected (25–71%), followed by the class of diuretics (2–40%), and psychotropic drugs (1–38%), for both years (see Fig. 4a). Similar results were reported for other Mediterranean surface waters, such as waters from the Evotras River, at the Balkan Peninsula (Mandaric et al., 2019), Mondego and Tâmega rivers, in Portugal (Barbosa et al., 2018), and the natural Park of Pego-Oliva Marshlands in Valencia (Vazquez-Roig et al., 2012). In fact, Fekadu et al. (2019), in a study about pharmaceuticals in European and African freshwaters, reported that ANALG/NSAIDs were the most used and quantified drugs in European countries. An analysis of the consumption data in Portugal, obtained through the World Health Organization (WHO) Collaborating Centre for Drug Statistics Methodology (2019), shows that the averages of the defined daily doses (DDD) during the years of study (2017–2018) for NSAIDs, diuretics and psychotropic drugs were 70.8–71.7, 51–52 and 20–21 DDD per 1000 inhabitants per day, respectively (https://www.oecd.org/els/health-systems/pharmaceuticals.htm).

Among the analysed compounds of the ANALG/NSAIDs group, the most represented were diclofenac (total sum of concentrations 21,569 ng L^{-1}), ibuprofen (14,908 ng L^{-1}) and naproxen (12,709 ng L^{-1}). Hydrochlorothiazide (21,816 ng L^{-1}) was the most quantified drug within diuretics, while carbamazepine (7978 ng L^{-1}) predominated within the class of psychotropic drugs. The importance of these drugs (relatively to the detection frequency and concentrations), in each therapeutic class, has already been reported in other Mediterranean surface waters (Mandaric et al., 2019; Paíga et al., 2016; Pereira et al., 2017).

Fig. 4b shows that the year of 2017 (drought year) presented the highest concentrations of pharmaceuticals highlighting the correlation of extreme climate conditions with the increased presence of this group of emerging compounds in the waters ($R_{ibuprofen} = -0.47$, $p < 0.05$; $R_{ofloxacin} = -0.69$, $p < 0.05$; $R_{metoprolol} = -0.36$, $p < 0.05$).

3.2.2. Detection frequencies and concentrations of pharmaceuticals

All the 27 pharmaceuticals assessed were found in some or most of the samples analysed. In general, all the samples presented >15 compounds at levels higher than the corresponding MDLs. No pharmaceutical was detected in 100% of the samples. Propyphenazone and paroxetine were the least recurrent compounds, quantified occasionally, at Álamos (568 ng L^{-1}; January 2018) and Zebro (111 ng L^{-1}; Maio 2017), respectively (Table 3). Despite that, the concentrations detected were higher than in other Portuguese rivers, such as at Lis River (north Portugal), where paroxetine was detected at maximum concentrations of 25 ng L^{-1} (Paíga et al., 2016). Propranolol was only quantified at Álamos, with a FD of 70% and a mean concentration of

Table 3
Frequency of detection (FD) (%), and mean (ng L^{-1}) and maximum concentrations (Max) (ng L^{-1}) of individual pharmaceuticals in surface water samples, from 4 sampling stations in the Guadiana Basin, during the period of study (January 2017–November 2018).

	Amieira			Zebro			Álamos			Lucefécit		
	FD (%)	Mean (ng L^{-1})	Max. (ng L^{-1})	FD (%)	Mean (ng L^{-1})	Max. (ng L^{-1})	FD (%)	Mean (ng L^{-1})	Max. (ng L^{-1})	FD (%)	Mean (ng L^{-1})	Max. (ng L^{-1})
Analgesics/NSAIDs												
Acetominophen	45	173.91	699.60	42	77.41	176.48	30	30.00	62.50	44	5.23	7.87
Diclofenac	82	23.72	72.45	100	808.33	4208.00	100	1152.57	4806.00	89	18.09	80.25
Ibuprofen	91	72.14	255.80	83	1020.46	3082.00	100	364.02	3161.00	44	85.40	258.00
Indomethacin	27	5.38	11.18	83	32.15	121.44	100	42.32	124.00	22	43.21	80.25
Ketoprofen	45	27.47	112.64	92	68.92	321.40	100	14.72	38.49	56	12.88	43.91
Naproxen	55	50.61	90.05	83	978.77	2868.00	90	298.79	2293.50	44	9.09	18.49
Propyphenazone	nd			nd			10	568.00	568.00	nd		
Antibiotics												
Ofloxacin	45	31.70	75.72	75	31.28	106.00	60	27.87	115.18	33	31.38	80.94
Sulfadiazine	nd			8	75.24	75.24	nd			11	18.49	18.49
Sulfamethazine	9	24.94	24.94	8	3.61	3.61	10	1.62	1.62	33	59.58	156.20
Sulfamethoxazole	27	12.93	19.29	17	69.88	110.55	40	105.65	204.30	11	1.70	1.70
Trimethoprim	36	5.33	9.00	17	21.89	38.42	50	6.36	11.36	11	3.09	3.09
Clarithromycin	55	6.02	9.93	75	50.64	243.40	90	57.62	306.30	33	4.05	4.49
Psychotropic drugs												
Diazepam	9	1.13	1.13	25	4.70	9.32	70	4.50	7.12	11	0.78	0.78
Lorazepam	45	35.72	96.47	67	57.43	112.82	70	76.78	140.68	78	27.08	73.64
Paroxetine	nd			17	60.65	110.98	nd			nd		
Carbamazepine	100	49.37	91.32	67	63.61	425.20	100	689.65	3235.00	89	6.90	26.14
Lipid regulators												
Bezafibrate	nd			100	328.02	1672.40	70	20.81	120.30	11	0.48	0.48
Gemfibrozil	9	4.59	4.59	75	22.95	66.96	90	69.74	428.65	nd		
Fenofibrate	18	2.89	3.22	8	1.91	1.91	10	6.75	6.75	22	16.21	30.51
β-Blockers												
Atenolol	36	16.55	23.66	83	44.13	130.08	70	90.50	307.40	nd		
Metoprolol	27	12.13	22.46	58	115.08	333.20	80	48.64	147.80	33	1.65	2.06
Propranolol	nd			nd			70	46.71	188.00	nd		
Sotalol	9	3.36	3.36	25	10.84	12.57	90	240.03	656.80	nd		
Diuretics												
Furosemide	18	5.49	9.90	92	886.79	6894.00	100	288.87	1073.40	33	16.46	43.91
Hydrochlorothiazide	73	57.48	239.44	100	877.94	2678.00	100	1057.53	2726.00	100	49.96	156.20
Opioids												
Codeine	9	5.99	5.99	58	56.12	131.96	40	30.16	73.60	nd		

nd – not detected.

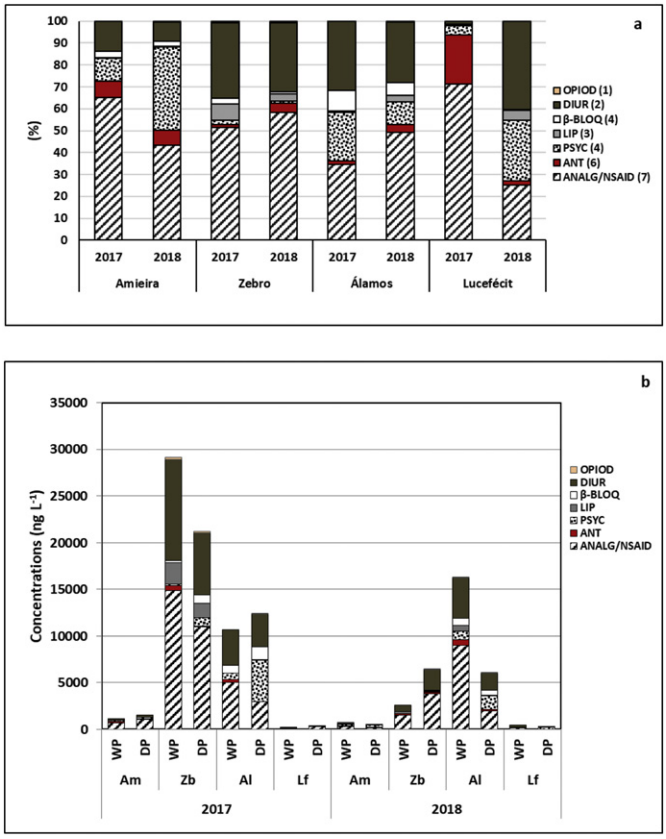

Fig. 4. Spatial and temporal variability of the therapeutic groups analysed: (a) Percentages of therapeutic groups in each stream, in both years. The total number of pharmaceuticals analysed per group are given in brackets. (b) Sum concentration of the therapeutic groups (ng L^{-1}) in each period (dry period: DP; wet period: WP) at the four streams (Amieira: Am; Zebro: Zb; Álamos: Al; Lucefécit: Lf). OPIOD: opioids; DIUR: diuretics; β-BLOQ: β-blockers; LIP: lipid regulators; PSYC: psychiatric drugs; ANT: antibiotics; ANALG/NSAID: analgesics and nonsteroidal anti-inflammatory drugs.

46.7 ng L^{-1} (Table 3), levels higher than those detected at the Douro river (North Portugal) (Madureira et al., 2010) and at freshwaters of the Pego-Oliva Marshlands (Valencia) (Vazquez-Roig et al., 2012). In general, the low levels detected, in spite this β-blocker be commonly used in Portugal (https://www.oecd.org/els/health-systems/pharmaceuticals.htm), are probably due to its low excretion rate in an unchanged form (<1%) (Ternes, 1998) and its high removal rates through WWTPs (96%) (Ternes, 1998). Accordingly, the concentrations detected may be correlated with low efficiency removal rates of the drug in the WWTPs located at Reguengos de Monsaraz and S. Pedro do Corval (both nearest at the sampling point; Fig. 1).

The most recurring and abundant pharmaceuticals were the anti-inflammatories diclofenac (FD: 82–100%; max. 4806 ng L^{-1} at Álamos-Nv2017) and ibuprofen (FD: 44–100%; max. 3161 ng L^{-1} at Álamos-Jn2018), the diuretic hydrochlorothiazide (FD:73–100%; max. 2726 ng L^{-1} at Álamos-Nv2017), and the antiepileptic drug carbamazepine (FD: 67–100%; max. 3235 ng L^{-1} at Álamos-Sp2017) (Table 3, Fig. 5). Most of the maximum individual concentrations occurred in 2017 (year of drought), in the temporary stream of Álamos, when the flows were very low or inexistent. Additionally, at Álamos the concentrations of diclofenac have always been above 9 ng L^{-1} (maximum acceptable detection limit proposed for this compound in the 2015 Watch List, which should be at least as low as the predicted no-effect concentration (PNEC)) (ECC, 2000). In fact, the concentrations found were much higher than those reported in other Portuguese rivers (Barbosa et al., 2018; Madureira et al., 2010; Paíga et al., 2016; Pereira et al., 2016) and also in other Mediterranean surface waters (Desbiolles et al., 2018; Mandaric et al., 2019; Stasinakis et al., 2012; Vazquez-Roig et al., 2012), indicating high contamination of the Guadiana basin streams by this drug. Up to now, only one study has assessed pharmaceuticals in the Guadiana River (near the estuarine area: Alcoutim; during the hydrological years of 2014/2015), at the time the researchers did not detect any of the 23 pharmaceuticals analysed (Pereira et al., 2017). Relatively to the anti-inflammatory drugs, the levels detected are probably more correlated with their high consumption rates, poor removal in the local WWTPs and hydrological regime of the streams (evident by the significant correlation among this drugs and flow: $R_{ibuprofen} = -0.47$, $p < 0.05$; $R_{diclofenac} = -0.32$, $p < 0.05$), than with their properties, provided that diclofenac and ibuprofen have $LogK_{ow} > 3.5$ (see Table 2), which would favor their adsorption to the sediments, and very short degradation times in water. In contrast, the concentrations of carbamazepine may be correlated with its properties ($LogK_{ow}$ of 2.45; large degradation time in water (up to 120 days)) and with the fact that it is one of the drugs least removed at WWTPs worldwide (<10%) (Paíga et al., 2016; Pereira et al., 2016; Ternes, 1998). These four pharmaceuticals presented significantly high variability among streams ($p < 0.005$; Kruskal-Wallis ANOVA by Ranks). Concerning the analgesic acetaminophen, the concentrations detected in Amieira (<MDL-670 ng L^{-1}) and Zebro (<MDL-177 ng L^{-1}) were similar or lower than those detected in the Lis River (up to 527 ng L^{-1}) and the Leça River (up to 925 ng L^{-1}) in the North of Portugal (Gonçalves et al., 2013; Paíga et al., 2016) and in other Mediterranean freshwaters (Vazquez-Roig et al., 2012). Detection frequency was always below 45% in all 4 streams, not supporting the pseudo-persistence of acetaminophen reported by other authors (Fairbairn et al., 2016; Paíga et al., 2016).

Regarding lipid regulators, bezafibrate occurred in all samples from Zebro with a mean concentration of 328 ng L^{-1} (Table 3). The concentrations at Zebro (0.3–1672 ng L^{-1} in Nv2017) and at Álamos (<MDL-120 ng L^{-1} in Jn2018) were higher than those reported at the Mondego (FD = 5%; 15.32 ng L^{-1}) and Tagus rivers (FD = 17%; 15.86 ng L^{-1}) (Pereira et al., 2016). Similar pattern was observed for gemfibrozil, with the highest FDs and concentrations observed at Álamos (90%; <MDL-429 ng L^{-1} in Jn2018) and Zebro (75%; <MDL-67 ng L^{-1} in Sp2017). These concentrations are higher than those detected at the Llobregat Basin (Spain) (Osorio et al., 2016). The present results may be justified by the inefficiency of the WWTPs located nearest the surface waters, since the removal rate for fenofibrate is 83% and for gemfibrozil is 69%, as reported by Ternes (1998).

The antibiotic group is one of the less detected at the streams. The less detected drugs belong to the classes of sulfonamides and penicillins. The macrolide clarithromycin was the most recurrent one, presenting FD > 55%, except at Lucefécit. The maximum concentrations detected at Álamos (306 ng L^{-1} in Jn2018) and Zebro (243 ng L^{-1} in Nv2017) were of the same range as those reported for the Ave river (North of Portugal) (Sousa et al., 2019). Clarithromycin surpassed the maximum acceptable method detection limit of 90 ng L^{-1} set in the 2015 Watch List (ECC, 2000) only occasionally, but with a considerably frequency (21%) in the case of the more strict limit of 19 ng L^{-1} established later in the 2018 Watch List (ECC, 2018). In spite that the presence of macrolide antibiotics may be related to the season, since these drugs are prescribed for infectious respiratory diseases more usually in winter and spring than in summer and fall, no significant statistical correlation was found between the drug and the period (wet or dry).

3.2.3. Spatial and temporal analysis

The spatial analysis showed that Zebro (with an intermittent regime having water all the year but without flow in some periods) was the most contaminated stream with a total pharmaceutical's concentration of 59,369 ng L^{-1} (Fig. 4b). The direct discharge of the domestic wastewaters from the wastewater treatment plant (WWTP) of Póvoa São Miguel (Municipality of Moura, Fig. 1) to the stream, located at a distance of only 500 m of the sampling point, may be one of the main reasons that justify these results, since this WWTP is undersized and

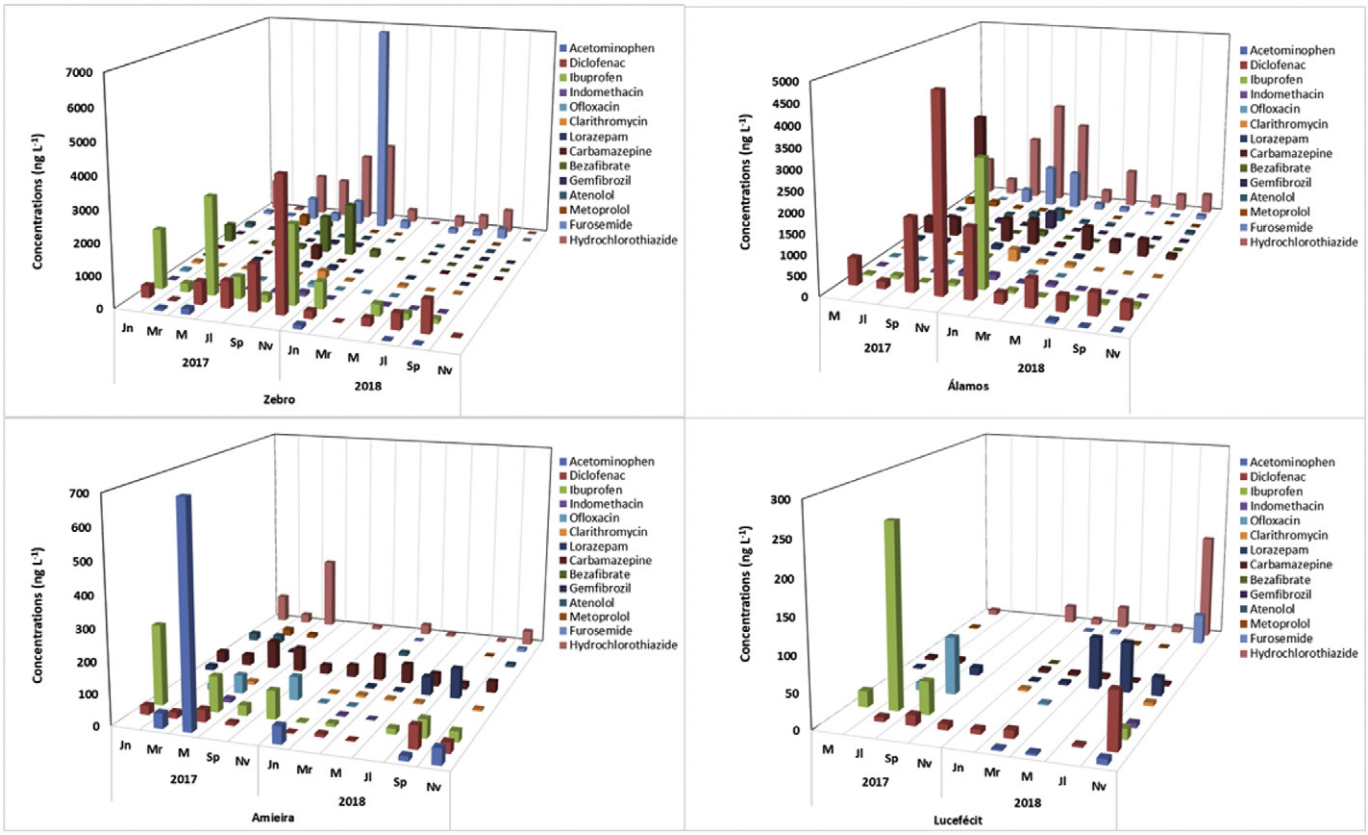

Fig. 5. Spatial (streams) and temporal (January: Jn; March: Mr; May: M; July: Jl; September: Sp; November: Nv) patterns observed for the pharmaceuticals quantified at higher concentrations (ng L^{-1}), during 2017 and 2018.

obsolete. Numerous authors have previously reported the importance of WWTPs in the pollution processes of pharmaceuticals (aus der Beek et al., 2016; Desbiolles et al., 2018; Vazquez-Roig et al., 2012), being this group of emerging contaminants considered markers of wastewater contamination (Čelić et al., 2019). The high concentrations observed could be also due to the absence of flow most of the time, which raises the accumulation processes, hypothesis supported by the significant negative correlations observed between flow and the concentrations of some therapeutics groups, such as ANALG/NSAIDs ($R = -0.42$; $p < 0.05$) and PSYC ($R = -0.31$; $p < 0.05$). Furthermore, in 2017, when Zebro did not present any flow (see Table 1) due to the drought conditions, the higher concentrations occurred during the wet period (31,738 ng L^{-1}; see Fig. 4b), when the temperatures and the photodegradation rates were lower. In contrast, during the post-drought year (2018), Zebro presented low flow in the wet months (Jn, Mr and Nv), and the higher concentrations of pharmaceuticals were observed in the dry period. Hence, the results highlighted that pharmaceuticals in surface waters were more dependent on flow than on temperature or daylight, as previously observed in other studies (Mandaric et al., 2019; Pereira et al., 2017). In fact, the highest individual concentrations at Zebro were achieved by furosemide (6894 ng L^{-1} at Nv2017), followed by diclofenac (4208 ng L^{-1} at Nv2017) and ibuprofen (3082 ng L^{-1} at M2017) (see Fig. 5). A different scenario occurred at Álamos, with an intermittent regime, having periods with the water concentrated only in isolated pools. In fact, in the drought year (2017), this stream presented a total concentration of pharmaceutics of 45,463 ng L^{-1}, mainly during the dry period, due to the accumulation at the pools (Fig. 4b). Results of the post-drought year showed higher levels of pharmaceuticals in the wet period, corresponding to the period when the stream presented moderate to very fast flow (due to heavy rainfall events). The high accumulation in the pools increments the adsorption to the sediment's particles for drugs with $LogK_{ow} > 2.5$, process more relevant in sediments that show higher percentages of fine particles, as occurs at Álamos (silt + clay = 33%). Consequently, when the heavy rainfall events take place (more frequently in the Mediterranean region; Reoyo-Prats et al., 2018), the intensification of flow (in the case of Álamos, in Mr and Nv 2018), and the increased resuspension of sediments, leads to a particularly high increase of concentration levels of pharmaceuticals. This process is more important in temporary rivers, where the accumulation rate is higher (Mandaric et al., 2019; Reoyo-Prats et al., 2018).

Amieira, also with an intermittent hydrologic regime, presented the highest concentrations of pharmaceuticals in 2017 (2697 ng L^{-1}) during the dry period, mostly corresponding to acetaminophen (670 ng L^{-1} in M2017) followed by hydrochlorothiazide (239 ng L^{-1}). This stream presented lower concentrations of pharmaceuticals than Álamos, which may be justified by textural characteristics of the sediments, constituted mostly by sand particles (90%), with low adsorption capacity. Additionally, Amieira is 40% covered by natural and semi-natural vegetation (Fig. 1b), which acts as a buffer to the input of contaminants (Shi et al., 2017). Further, these results also support those observed in Álamos, in the sense that in temporary rivers the low flow and the water scarcity are factors of upmost importance for the increase of pharmaceuticals` concentrations in surface waters.

Lucefécit was the less contaminated stream (1219 ng L^{-1}), probably due to its hydrology, perennial with a constant flow during the whole year, as well as to the characteristics of its sediments, constituted 41% by fine particles, which increment the dilution processes and the adsorption mechanisms, with the corresponding natural attenuation of the system (Mandaric et al., 2019). Although the livestock activity (one of the most important activities for pharmaceutical contamination; de Jesus Gaffney et al., 2015; Gogoi et al., 2018) represents >40% of the land cover, the area also presents a considerable percentage of natural and semi-natural vegetation (about 38%), which may act as a barrier

to the pollution inputs. At this stream, ibuprofen was the pharmaceutical that achieved the highest concentration (258 ng L^{-1} in Jl2017), followed by hydrochlorothiazide (156 ng L^{-1} in Nv2018).

3.3. Environmental risk assessment (ERA)

The prioritization lists of pharmaceuticals are based on the concept of environmental risk assessment (ERA), which conventionally takes into consideration the potential toxic effect of a specific pharmaceutical and its exposure level, determined by the risk quotient (RQ). Traditional pharmaceutical ranking usually assesses the risk of the substance under general (using the average of the quantified concentrations) and worst (maximum concentrations) scenarios. To refine the methodology, making it more realistic, we applied a risk quotient optimised approach (RQf), allowing highlighting the pharmaceuticals most frequently detected at concentrations eventually of concern. Fig. 6 shows the RQs corresponding to mean and maximum concentrations, and the RQf values corresponding to mean concentrations, of the compounds (8) showing risk in at least one of the sites investigated, for each stream and year. The pharmaceuticals hydrochlorothiazide, ofloxacin and acetaminophen showed moderate RQs and in general irrelevant RQf (Amieira: $RQf_{acetomiphen}$ – moderate risk, F = 20%; Zebro: $RQf_{ofloxacin}$ - endurable risk, F = 18%; Álamos: $RQf_{ofloxacin}$ – endurable risk, F = 17%) (Fig. 6). These results indicate that a potential moderate risk exists for these substances, but the possibility of the organisms to be exposed to unsafe levels of these compounds is lower than 20%. Pereira et al. (2017) also reported low risk of acetaminophen ($0.01 \leq RQ < 0.1$) in several Portuguese rivers (Tâmega, Mondego, Trancão, Tagus, Xarrama, Álamo). Vazquez-Roig et al. (2012) reported that acetominophen induced a moderate risk to crustaceans (RQ = 0.321) and ofloxacin a high risk to algae (RQ = 3.137) in surface waters of Pego-Oliva Marshlands (Valencia). Zhou et al. (2019) in a review about risk assessment of pharmaceuticals in European countries, using RQf, reported moderate risk for both substances ($RQf_{ofloxacin}$ = 0.74, F = 30%; $RQf_{acetaminophen}$ = 0.31, F = 30%). Bezofibrate showed RQf > 1 in Zebro, during the drought year (2017). Clarithromycin presented RQf > 1 in Zebro in 2017 (F = 50%) and Álamos in 2018 (F = 40%). In spite that high risk according to RQs was estimated in only a few occasions, the frequency of organisms' exposure to eventually dangerous levels is considerable. Furthermore, the high consumption of clarithromycin and its $LogK_{ow}$ of 3.16, contributing to its potential persistence and bioaccumulation (Palma et al., 2015), are important factors that justify the follow up of this substance. Clarithromycin presented moderate risk for algae ($0.1 < RQ < 0.1$) in the Portuguese rivers of Trancão, Tâmega and Xarrama (Pereira et al., 2017), and a moderate risk (RQf = 0.41) in the European context (Zhou et al., 2019). In fact, Zhou et al. (2019) has already proposed that substances with $LogK_{ow} > 3$ and those with high or moderate risk, should be both considered as priority, at the same risk level. Furthermore, clarithromycin was already included in the Watch List published in 2015 (ECC, 2015) and continues to be present in the one issued in 2018 after revision of the first one which means that it requires further monitoring for the purpose of supporting possible feature prioritization (ECC, 2018).

Carbamazepine presented RQf > 1 in Zebro 2017 (F = 50%), Álamos 2017 (F = 100%) and 2018 (F = 100%) and Amieira 2017 (F = 100%) and 2018 (F = 100%). These results highlight the danger that this drug represents to aquatic ecosystems. Studies in surface waters in the Mediterranean region reported lower risk values for this substance (Vazquez-Roig et al., 2012); however, the present results are in line with what was reported for Europe (RQf = 10.13) (Zhou et al., 2019).

Diclofenac, followed by ibuprofen, are the pharmaceuticals exhibiting the highest risk, with frequencies of organisms exposure to unsafe concentrations of these pollutants higher than 70% in Zebro, Álamos and Amieira. The fact that both compounds present $LogK_{ow} > 3$, and thus high capacity to bioaccumulate within the trophic chain, and high long-term toxicity, makes these substances a threat for the aquatic ecosystems. In the prioritization list of pharmaceuticals for European countries, diclofenac appeared with a RQf of 153.65 (F = 62%), and

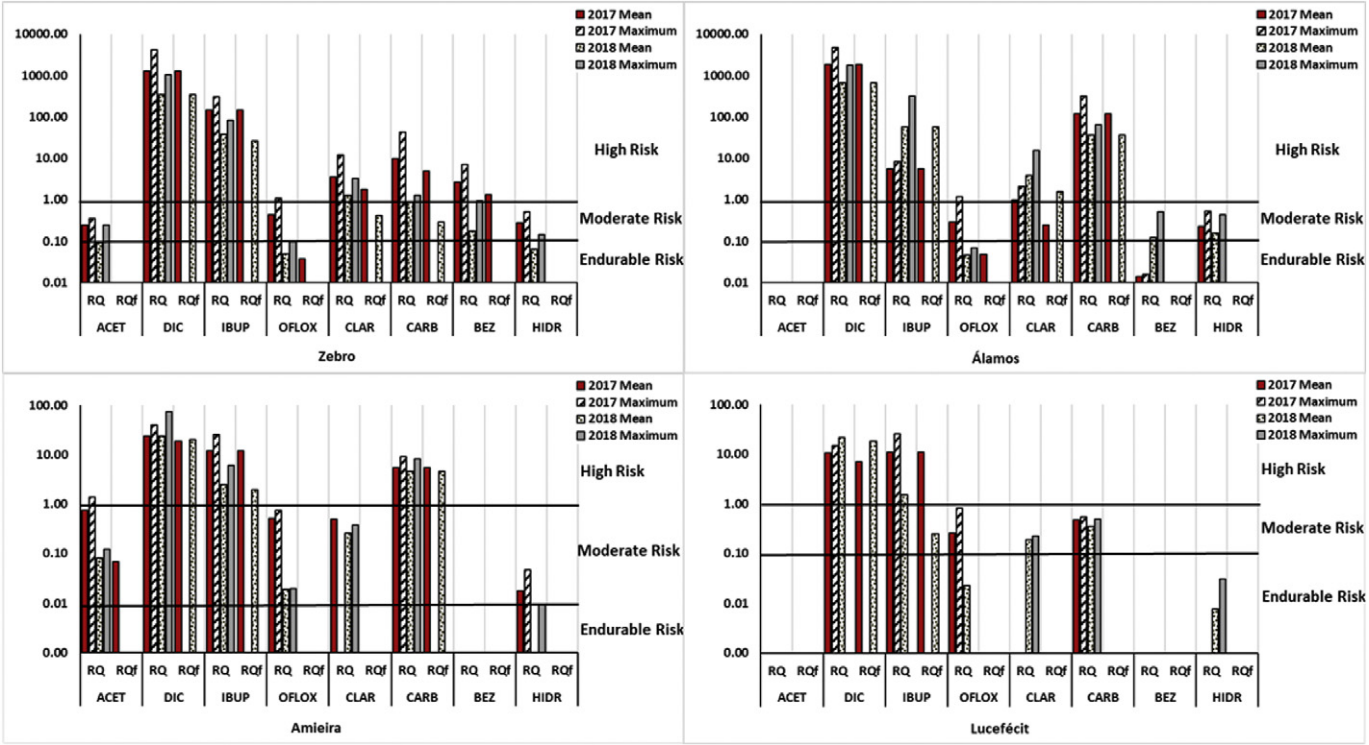

Fig. 6. The RQs calculated for mean and maximum concentrations, and the RQf values calculated for mean concentrations, retrieved from the analyses of the samples collected in 2017 and 2018, at each stream. ACET: acetaminophen; DIC: diclofenac; IBUP: ibuprofen; OFLOX: ofloxacin; CLAR: clarithromycin; CARB: carbamazepine; BEZ: bezafibrate; HIDR: hydrochlorothiazide.

ibuprofen with a RQf of 15.73 (47%) (Zhou et al., 2019). Moreover, in 2016 aus der Beek et al. (2016) reported that diclofenac is the most often detected pharmaceutical in the environment and that, due to its high ecotoxicological potential, it is becoming one of the most hazardous pharmaceuticals at global scale. Likewise, a European demonstration program for chemical identification and effect-based monitoring of organic pollutants in surface waters has recently included 8 pharmaceuticals in a list of 21 target compounds prioritized on the basis of their frequencies and extent of exceedance of PNECs (Tousova et al., 2017). Four of them are ranked in our work as having high or moderate risk (RQf), namely, diclofenac, ibuprofen, carbamazepine and clarithromycin. As clarithromycin, diclofenac was included in the first Watch List. However, unlike clarithromycin, diclofenac has been removed from the updated version of the Watch List published in 2018. The question now, after the most recently published studies and the present one, is whether diclofenac should be reconsidered as a potentially hazardous priority substance.

Finally, spatial and temporal analysis of the data showed that Zebro and Álamos were the streams under higher environmental risk by pharmaceuticals, mainly during dry periods. Therefore, the climatic conditions affected the hydrological regime, incrementing the stress factors to the aquatic ecosystems. Streams with temporary hydrological regimes (with no flow or without surface water in the whole channel during a period) became more vulnerable to the contamination by organic pollutants, in this case by pharmaceuticals, as highlighted by the results. In fact, Lucefécit, the only stream that always presented flow, showed lower risk scenarios. In this stream, diclofenac and ibuprofen were the compounds showing higher risk, mainly in the dry period (2017) with F higher than 70%.

4. Conclusions

This work put into evidence the presence and persistence of pharmaceuticals in streams of the Guadiana basin. Notwithstanding the high variability of concentrations observed among streams, periods and years, all 27 pharmaceuticals investigated were detected at quantifiable concentrations at least once. The most abundant pharmaceuticals were diclofenac, ibuprofen, carbamazepine and hydrochlorothiazide, all of them measured at levels that represent moderate to high risk for the aquatic ecosystems.

The streams investigated presented different hydrological regimes and sources of pollution. The presence of the pharmaceuticals found in the waters is attributed mainly to the continuous discharge of these substances from WWTPs, due to their incomplete removal at the facilities, as well as to intensive livestock.

The results obtained also showed the negative influence of drought periods, with the strengthening of no flow regimes, and the consequent increment of pharmaceuticals` concentrations. In the streams with temporary regimes, which are expected to increase in the Mediterranean region due to climate changes, the highest concentrations of pharmaceuticals were quantified in the dry period if the stream presented sediments with textures constituted mostly by sand as in the case of Amieira. On the contrary, in Álamos (with a higher percentage of fine particles), the highest concentrations of pharmaceuticals were detected after the rainfalls, due to the resuspension of the substances from the sediments.

The results showed that the use of the optimised risk assessment method, considering the frequency of concentrations above PNECs, is more realistic, and allows the prioritization of pharmaceuticals integrating the persistence as a key factor for the risk in the ecosystem. Consequently, the results support its application for screening-level risk assessment. The rank of the 8 pharmaceuticals that presented risk at the streams in the Guadiana basin is: (i) High Risk: diclofenac, ibuprofen, carbamazepine; (ii) Moderate Risk: clarithromycin; (iii) Endurable Risk: acetaminophen, ofloxacin, bezafibrate; (iv) Negligible risk: hydrochlorothiazide. This work displays that this group of 8 substances should be integrated in programs of water resource management, given priority to high-risk pollutants that are widely distributed and frequently detected.

Results highlighted that some surface waters from South Portugal are impacted with pharmaceuticals, particularly when looking up the increment of risk scenarios for the aquatic ecosystems in drought periods and after heavy rainfalls. Therefore, further research is needed to increment the knowledge about the influence of hydrological regimes, the effect of the intensification of dry periods, the response of different biological systems to the recovery, and the chronic toxic effects of the priority substances to improve water management programs in the Mediterranean region.

Declaration of competing interest

The authors declare that there are no conflicts of interest.

Acknowledgments

The present research is co-funded by the European Union through the European Regional Development Fund, included in the COMPETE 2020 (Operational Program Competitiveness and Internationalization) through the ICT project (UID/GEO/04683/2013) with the reference POCI-01-0145-FEDER-007690, the ALOP project (ALT20-03-0145-FEDER-000004), and through the Engage SKA (POCI-01-0145-FEDER-022217) and by the European Union through the EU FP7 project SOLUTIONS (603437).

Appendix A. Supplementary data

Supplementary data to this article can be found online at https://doi.org/10.1016/j.scitotenv.2019.136205.

References

Acuña, V., Datry, T., Marshall, J., Barceló, D., Dahm, C.N., Ginebreda, A., McGregor, G., Sabater, S., Tockner, K., Palmer, M.A., 2014. Why should we care about temporary waterways? Science (80-.) https://doi.org/10.1126/science.1246666.

Acuña, V., Hunter, M., Ruhí, A., 2017. Managing temporary streams and rivers as unique rather than second-class ecosystems. Biol. Conserv. 211, 12–19. https://doi.org/10.1016/j.biocon.2016.12.025.

Andreozzi, R., Raffaele, M., Nicklas, P., 2003. Pharmaceuticals in STP effluents and their solar photodegradation in aquatic environment. Chemosphere 50, 1319–1330.

APA (Agência Portuguesa do Ambiente), 2016. Plano de gestão de região hidrográfica 2016/2021. Parte 2. Caracterização e diagnóstico Anexo IV, 36 p. (in Portuguese).

ARHAlentejo (Administração da Região Hidrográfica do Alentejo I.P.), 2011. Plano de gestão das bacias hidrográficas integradas nas regiões hidrográficas 6 e 7: Região Hidrográfica 7. Ministério do Ambiente e do Ordenamento do Território, Lisboa (in Portuguese).

aus der Beek, T., Weber, F.-A., Bergmann, A., Grüttner, G., Carius, A., 2016. Pharmaceuticals in the environment: global occurrence and potential cooperative action under the Strategic Approach to International Chemicals Management (SAICM). Ger. Fed. Environ. Agency 94.

Barbosa, M.O., Ribeiro, A.R., Ratola, N., Hain, E., Homem, V., Pereira, M.F.R., Blaney, L., Silva, A.M.T., 2018. Spatial and seasonal occurrence of micropollutants in four Portuguese rivers and a case study for fluorescence excitation-emission matrices. Sci. Total Environ. 644, 1128–1140. https://doi.org/10.1016/J.SCITOTENV.2018.06.355.

Bonansea, M., Ledesma, C., Rodriguez, M.C., 2016. Assessing the impact of land use and land cover on water quality in the watershed of a reservoir. Appl. Ecol. Environ. Res. 14, 447–456. https://doi.org/10.15666/aeer/1402_447456.

Brack, W., Altenburger, R., Schüürmann, G., Krauss, M., López Herráez, D., van Gils, J., Slobodnik, J., Munthe, J., Gawlik, B.M., van Wezel, A., Schriks, M., Hollender, J., Tollefsen, K.E., Mekenyan, O., Dimitrov, S., Bunke, D., Cousins, I., Posthuma, L., van den Brink, P.J., López de Alda, M., Barceló, D., Faust, M., Kortenkamp, A., Scrimshaw, M., Ignatova, S., Engelen, G., Massmann, G., Lemkine, G., Teodorovic, I., Walz, K.H., Dulio, V., Jonker, M.T.O., Jäger, F., Chipman, K., Falciani, F., Liska, I., Rooke, D., Zhang, X., Hollert, H., Vrana, B., Hilscherova, K., Kramer, K., Neumann, S., Hammerbacher, R., Backhaus, T., Mack, J., Segner, H., Escher, B., de Aragão Umbuzeiro, G., 2015. The SOLUTIONS project: challenges and responses for present and future emerging pollutants in land and water resources management. Sci. Total Environ. https://doi.org/10.1016/j.scitotenv.2014.05.143.

Brack, W., Escher, B.I., Müller, E., Schmitt-Jansen, M., Schulze, T., Slobodnik, J., Hollert, H., 2018. Towards a holistic and solution-oriented monitoring of chemical status of European water bodies: how to support the EU strategy for a non-toxic environment? Environ. Sci. Eur. https://doi.org/10.1186/s12302-018-0161-1.

Čelić, M., Gros, M., Farré, M., Barceló, D., Petrović, M., 2019. Pharmaceuticals as chemical markers of wastewater contamination in the vulnerable area of the Ebro Delta (Spain). Sci. Total Environ. 652, 952–963. https://doi.org/10.1016/J.SCITOTENV.2018.10.290.

Copernicus Land Monitoring Service, 2018. . Avaliable at. https://land.copernicus.eu/.

Desbiolles, F., Malleret, L., Tiliacos, C., Wong-Wah-Chung, P., Laffont-Schwob, I., 2018. Occurrence and ecotoxicological assessment of pharmaceuticals: is there a risk for the Mediterranean aquatic environment? Sci. Total Environ. https://doi.org/10.1016/j.scitotenv.2018.04.351.

Ebele, A.J., Abou-Elwafa Abdallah, M., Harrad, S., 2017. Pharmaceuticals and personal care products (PPCPs) in the freshwater aquatic environment. Emerg. Contam. 3, 1–16. https://doi.org/10.1016/J.EMCON.2016.12.004.

ECC (European Community Commission), 2000. Commission Directive 2000/60/EC of the European Parliament and the Council establishing the framework for community action in the field of water policy. Off. J.Eur. Commun. L 327.

ECC (European Community Commission), 2003. Technical Guidance Document on Risk Assessment. Part II. JRC, Brussels. Belgium.

ECC (European Community Commission), 2013. Decision 2013/39/EC on environmental quality standards in the field of water policy. Off. J. Eur. Commun. L 226 (1).

ECC (European Community Commission), 2015. Decision 2015/495/EC establishing a watch list of substances for Union-wide monitoring in the field of water policy pursuant to Directive 2008/105/EC of the European Parliament and of the Council. Off. J. Eur. Commun. L 78.

ECC (European Community Commission), 2018. Decision 2018/840/EC establishing a watch list of substances for Union-wide monitoring in the field of water policy pursuant to Directive 2008/105/EC of the European Parliament and of the Council and repealing Commission Implementing Decision (EU) 2015/495. Off. J. Eur. Commun. L 141.

Fairbairn, D.J., Karpuzcu, M.E., Arnold, W.A., Barber, B.L., Kaufenberg, E.F., Koskinen, W.C., Novak, P.J., Rice, P.J., Swackhamer, D.L., 2016. Sources and transport of contaminants of emerging concern: a two-year study of occurrence and spatiotemporal variation in a mixed land use watershed. Sci. Total Environ. 551–552, 605–613. https://doi.org/10.1016/j.scitotenv.2016.02.056.

Fekadu, S., Alemayehu, E., Dewil, R., Van der Bruggen, B., 2019. Pharmaceuticals in freshwater aquatic environments: a comparison of the African and European challenge. Sci. Total Environ. 654, 324–337. https://doi.org/10.1016/J.SCITOTENV.2018.11.072.

Ginebreda, A., Muñoz, I., de Alda, M.L., Brix, R., López-Doval, J., Barceló, D., 2010. Environmental risk assessment of pharmaceuticals in rivers: relationships between hazard indexes and aquatic macroinvertebrate diversity indexes in the Llobregat River (NE Spain). Environ. Int. 36, 153–162. https://doi.org/10.1016/j.envint.2009.10.003.

Godoy, A.A., Kummrow, F., 2017. What do we know about the ecotoxicology of pharmaceutical and personal care product mixtures? A critical review. Crit. Rev. Environ. Sci. Technol. https://doi.org/10.1080/10643389.2017.1370991.

Gogoi, A., Mazumder, P., Tyagi, V.K., Tushara Chaminda, G.G., An, A.K., Kumar, M., 2018. Occurrence and fate of emerging contaminants in water environment: a review. Groundw. Sustain. Dev. https://doi.org/10.1016/j.gsd.2017.12.009.

Gonçalves, C.O.M., Augusta Sousa, M.D., de Fátima PSPM Alpendurada, M., 2013. Analysis of acidic, basic and neutral pharmaceuticals in river waters: clean-up by 1°, 2° amino anion exchange and enrichment using an hydrophilic adsorbent. Int. J. Environ. Anal. Chem. https://doi.org/10.1080/03067319.2012.702272.

Gonzalez-Rey, M., Bebianno, M.J., 2012. Does non-steroidal anti-inflammatory (NSAID) ibuprofen induce antioxidant stress and endocrine disruption in mussel Mytilus galloprovincialis? Environ. Toxicol. Pharmacol. 33, 361–371. https://doi.org/10.1016/j.etap.2011.12.017.

Hossain, M.S., Kubec, J., Grabicová, K., Grabic, R., Randák, T., Guo, W., Kouba, A., Buřič, M., 2019. Environmentally relevant concentrations of methamphetamine and sertraline modify the behavior and life history traits of an aquatic invertebrate. Aquat. Toxicol. https://doi.org/10.1016/j.aquatox.2019.105222.

Hughes, S.R., Kay, P., Brown, L.E., 2013. Global synthesis and critical evaluation of pharmaceutical data sets collected from river systems. Environ. Sci. Technol. 47, 661–677. https://doi.org/10.1021/es3030148.

Ivanová, L., Mackuľak, T., Grabic, R., Golovko, O., Koba, O., Staňová, A.V., Szabová, P., Grenčíková, A., Bodík, I., 2018. Pharmaceuticals and illicit drugs – a new threat to the application of sewage sludge in agriculture. Sci. Total Environ. https://doi.org/10.1016/j.scitotenv.2018.04.001.

de Jesus Gaffney, V., Almeida, C.M.M., Rodrigues, A., Ferreira, E., Benoliel, M.J., Cardoso, V.V., 2015. Occurrence of pharmaceuticals in a water supply system and related human health risk assessment. Water Res. 72, 199–208. https://doi.org/10.1016/J.WATRES.2014.10.027.

Joyce, A., Vogeler, S., 2018. Molluscan bivalve settlement and metamorphosis: neuroendocrine inducers and morphogenetic responses. Aquaculture https://doi.org/10.1016/j.aquaculture.2018.01.002.

Li, Y., Zhang, L., Liu, X., Ding, J., 2019. Ranking and prioritizing pharmaceuticals in the aquatic environment of China. Sci. Total Environ. https://doi.org/10.1016/j.scitotenv.2018.12.048.

Liu, F., Nielsen, A.H., Vollertsen, J., 2019. Sorption and degradation potential of pharmaceuticals in sediments from a stormwater retention pond. Water (Switzerland) 11. https://doi.org/10.3390/w11030526.

Loffler, Dirk, Rombke, Jorg, Meller Michael, T.T.A., 2005. Environmental Fate of Pharmaceuticals in Water/Sediment Systems. https://doi.org/10.1021/es0484146.

Madureira, T.V., Barreiro, J.C., Rocha, M.J., Rocha, E., Cass, Q.B., Tiritan, M.E., 2010. Spatiotemporal distribution of pharmaceuticals in the Douro River estuary (Portugal). Sci. Total Environ. 408, 5513–5520. https://doi.org/10.1016/j.scitotenv.2010.07.069.

Mandaric, L., Kalogianni, E., Skoulikidis, N., Petrovic, M., Sabater, S., 2019. Contamination patterns and attenuation of pharmaceuticals in a temporary Mediterranean river. Sci. Total Environ. 647, 561–569. https://doi.org/10.1016/J.SCITOTENV.2018.07.308.

Mathias, F.T., Fockink, D.H., Disner, G.R., Prodocimo, V., Ribas, J.L.C., Ramos, L.P., Cestari, M.M., Silva de Assis, H.C., 2018. Effects of low concentrations of ibuprofen on freshwater fish Rhamdia quelen. Environ. Toxicol. Pharmacol. https://doi.org/10.1016/j.etap.2018.03.008.

National Water Resources Information System, 2019. Hydrometrics. Available at. http://snirh.apambiente.pt/index.php?idMain=2&idItem=1.

Nguyen Dang Giang, C., Sebesvari, Z., Renaud, F., Rosendahl, I., Hoang Minh, Q., Amelung, W., 2015. Occurrence and dissipation of the antibiotics sulfamethoxazole, sulfadiazine, trimethoprim, and enrofloxacin in the Mekong Delta, Vietnam. PLoS One 10. https://doi.org/10.1371/journal.pone.0131855.

Nunes, C.N., dos Anjos, V.E., Quináia, S.P., 2019. Are there pharmaceutical compounds in sediments or in water? Determination of the distribution coefficient of benzodiazepine drugs in aquatic environment. Environ. Pollut. 251, 522–529. https://doi.org/10.1016/J.ENVPOL.2019.05.015.

Oropesa, A.L., Floro, A.M., Palma, P., 2016. Assessment of the effects of the carbamazepine on the endogenous endocrine system of Daphnia magna. Environ. Sci. Pollut. Res. 23. https://doi.org/10.1007/s11356-016-6907-7.

Oropesa, A.L., Floro, A.M., Palma, P., 2017. Toxic potential of the emerging contaminant nicotine to the aquatic ecosystem. Environ. Sci. Pollut. Res. 24. https://doi.org/10.1007/s11356-017-9084-4.

Osorio, V., Larrañaga, A., Aceña, J., Pérez, S., Barceló, D., 2016. Concentration and risk of pharmaceuticals in freshwater systems are related to the population density and the livestock units in Iberian Rivers. Sci. Total Environ. 540, 267–277. https://doi.org/10.1016/j.scitotenv.2015.06.143.

Paíga, P., Santos, L.H.M.L.M., Ramos, S., Jorge, S., Silva, J.G., Delerue-Matos, C., 2016. Presence of pharmaceuticals in the Lis river (Portugal): sources, fate and seasonal variation. Sci. Total Environ. 573, 164–177. https://doi.org/10.1016/j.scitotenv.2016.08.089.

Palma, P., Köck-Schulmeyer, M., Alvarenga, P., Ledo, L., Barbosa, I.R., López de Alda, M., Barceló, D., 2014. Risk assessment of pesticides detected in surface water of the Alqueva reservoir (Guadiana basin, southern of Portugal). Sci. Total Environ. 488–489. https://doi.org/10.1016/j.scitotenv.2014.04.088.

Palma, P., Köck-Schulmeyer, M., Alvarenga, P., Ledo, L., de Alda, López, Barceló, D., 2015. Occurrence and potential risk of currently used pesticides in sediments of the Alqueva reservoir (Guadiana Basin). Environ. Sci. Pollut. Res. 22, 7665–7675.

Palma, P., Matos, C., Alvarenga, P., Köck-Schulmeyer, M., Simões, I., Barceló, D., López de Alda, M.J., 2018. Ecological and ecotoxicological responses in the assessment of the ecological status of freshwater systems: a case-study of the temporary stream Brejo of Cagarrão (South of Portugal). Sci. Total Environ. 634. https://doi.org/10.1016/j.scitotenv.2018.03.281.

Pereira, A.M.P.T., Silva, L.J.G., Lino, C.M., Meisel, L.M., Pena, A., 2016. Assessing environmental risk of pharmaceuticals in Portugal: An approach for the selection of the Portuguese monitoring stations in line with Directive 2013/39/EU. Chemosphere 144, 2507–2515. https://doi.org/10.1016/j.chemosphere.2015.10.100.

Pereira, A.M.P.T., Silva, L.J.G., Laranjeiro, C.S.M., Meisel, L.M., Lino, C.M., Pena, A., 2017. Human pharmaceuticals in Portuguese rivers: the impact of water scarcity in the environmental risk. Sci. Total Environ. 609, 1182–1191. https://doi.org/10.1016/j.scitotenv.2017.07.200.

Perussolo, M.C., Guiloski, I.C., Lirola, J.R., Fockink, D.H., Corso, C.R., Bozza, D.C., Prodocimo, V., Mela, M., Ramos, L.P., Cestari, M.M., Acco, A., Silva de Assis, H.C., 2019. Integrated biomarker response index to assess toxic effects of environmentally relevant concentrations of paracetamol in a neotropical catfish (Rhamdia quelen). Ecotoxicol. Environ. Saf. https://doi.org/10.1016/j.ecoenv.2019.109438.

Portuguese Institute for the Sea and Atmosphere (IPMA), 2018. Climate report 2018. Avaliable at. http://www.ipma.pt/resources.www/docs/im.publicacoes/edicoes.online/20190131/ddliTNijyEWyfrhUMDTy/cli_20180901_20181231_pcl_aa_co_pt.pdf (in portuguese).

Potes, M., Salgado, R., Costa, M.J., Morais, M., Bortoli, D., Kostadinov, I., Mammarella, I., 2017. Lake–atmosphere interactions at Alqueva reservoir: a case study in the summer of 2014. Tellus A Dyn. Meteorol. Oceanogr. 69, 1272787. https://doi.org/10.1080/16000870.2016.1272787.

Reis, E.O., Foureaux, A.F.S., Rodrigues, J.S., Moreira, V.R., Lebron, Y.A.R., Santos, L.V.S., Amaral, M.C.S., Lange, L.C., 2019. Occurrence, removal and seasonal variation of pharmaceuticals in Brasilian drinking water treatment plants. Environ. Pollut. 250, 773–781. https://doi.org/10.1016/J.ENVPOL.2019.04.102.

Reoyo-Prats, B., Aubert, D., Sellier, A., Roig, B., Palacios, C., 2018. Dynamics and sources of pharmaceutically active compounds in a coastal Mediterranean river during heavy rains. Environ. Sci. Pollut. Res. 25, 6107–6121. https://doi.org/10.1007/s11356-017-0880-7.

Ribeiro, A.R., Nunes, O.C., Pereira, M.F.R., Silva, A.M.T., 2015. An overview on the advanced oxidation processes applied for the treatment of water pollutants defined in the recently launched Directive 2013/39/EU. Environ. Int. https://doi.org/10.1016/j.envint.2014.10.027.

Rodrigues, V., Estrany, J., Ranzini, M., de Cicco, V., Martín-Benito, J.M.T., Hedo, J., Lucas-Borja, M.E., 2018. Effects of land use and seasonality on stream water quality in a small tropical catchment: the headwater of Córrego Água Limpa, São Paulo (Brazil). Sci. Total Environ. 622–623, 1553–1561. https://doi.org/10.1016/j.scitotenv.2017.10.028.

Rosa, J., Leston, S., Freitas, A., Vila Pouca, A.S., Barbosa, J., Lemos, M.F.L., Pardal, M.A., Ramos, F., 2019. Oxytetracycline accumulation in the macroalgae Ulva: potential risks for IMTA systems. Chemosphere https://doi.org/10.1016/j.chemosphere.2019.03.112.

Sabri, N.A., Schmitt, H., Van der Zaan, B., Gerritsen, H.W., Zuidema, T., Rijnaarts, H.H.M., Langenhoff, A.A.M., 2018. Prevalence of antibiotics and antibiotic resistance genes in a wastewater effluent-receiving river in the Netherlands. J. Environ. Chem. Eng. https://doi.org/10.1016/j.jece.2018.03.004.

Shi, P., Zhang, Y., Li, Z., Li, P., Xu, G., 2017. Influence of land use and land cover patterns on seasonal water quality at multi-spatial scales. Catena 151, 182–190. https://doi.org/10.1016/j.catena.2016.12.017.

Sousa, J.C.G., Ribeiro, A.R., Barbosa, M.O., Ribeiro, C., Tiritan, M.E., Pereira, M.F.R., Silva, A.M.T., 2019. Monitoring of the 17 EU Watch List contaminants of emerging concern in the Ave and the Sousa Rivers. Sci. Total Environ. https://doi.org/10.1016/j.scitotenv.2018.08.309.

Stasinakis, A.S., Mermigka, S., Samaras, V.G., Farmaki, E., Thomaidis, N.S., 2012. Occurrence of Endocrine Disrupters and Selected Pharmaceuticals in Aisonas River (Greece) and Environmental Risk Assessment Using Hazard Indexes. https://doi.org/10.1007/s11356-011-0661-7.

Ternes, T.A., 1998. Occurrence of drugs in German sewage treatment plants and rivers. Water Res. 32, 3245–3260. https://doi.org/10.1016/S0043-1354(98)00099-2.

Tixier, C., Singer, H.P., Oellers, S., Müller, S.R., 2003. Occurrence and fate of carbamazepine, clofibric acid, diclofenac, ibuprofen, ketoprofen, and naproxen in surface waters. Environ. Sci. Technol. 37, 1061–1068. https://doi.org/10.1021/es025834r.

Tousova, Z., Oswald, P., Slobodnik, J., Blaha, L., Muz, M., Hu, M., Brack, W., Krauss, M., Di Paolo, C., Tarcai, Z., Seiler, T.B., Hollert, H., Koprivica, S., Ahel, M., Schollée, J.E., Hollender, J., Suter, M.J.F., Hidasi, A.O., Schirmer, K., Sonavane, M., Ait-Aissa, S., Creusot, N., Brion, F., Froment, J., Almeida, A.C., Thomas, K., Tollefsen, K.E., Tufi, S., Ouyang, X., Leonards, P., Lamoree, M., Torrens, V.O., Kolkman, A., Schriks, M., Spirhanzlova, P., Tindall, A., Schulze, T., 2017. European demonstration program on the effect-based and chemical identification and monitoring of organic pollutants in European surface waters. Sci. Total Environ. 601–602, 1849–1868. https://doi.org/10.1016/j.scitotenv.2017.06.032.

United States EPA ECOTOX database, 2019. Ecotoxicological data. Avaliable at. https://cfpub.epa.gov/ecotox/.

Vazquez-Roig, P., Andreu, V., Blasco, C., Picó, Y., 2012. Risk assessment on the presence of pharmaceuticals in sediments, soils and waters of the Pego-Oliva Marshlands (Valencia, eastern Spain). Sci. Total Environ. 440, 24–32. https://doi.org/10.1016/j.scitotenv.2012.08.036.

World Health Organization (WHO) Collaborating Centre for Drug Statistics Methodology, 2019. Consuption data in Portugal. Avaliable at. https://www.oecd.org/els/health-systems/pharmaceuticals.htm.

Xu, C., Niu, L., Guo, H., Sun, X., Chen, L., Tu, W., Dai, Q., Ye, J., Liu, W., Liu, J., 2019. Long-term exposure to the non-steroidal anti-inflammatory drug (NSAID)naproxen causes thyroid disruption in zebrafish at environmentally relevant concentrations. Sci. Total Environ. https://doi.org/10.1016/j.scitotenv.2019.04.323.

Yamamoto, H., Nakamura, Y., Moriguchi, S., Nakamura, Y., Honda, Y., Tamura, I., Hirata, Y., Hayashi, A., Sekizawa, J., 2009. Persistence and partitioning of eight selected pharmaceuticals in the aquatic environment: laboratory photolysis, biodegradation, and sorption experiments. Water Res. 43, 351–362. https://doi.org/10.1016/j.watres.2008.10.039.

Zhou, S., Di Paolo, C., Wu, X., Shao, Y., Seiler, T.-B., Hollert, H., 2019. Optimization of screening-level risk assessment and priority selection of emerging pollutants – the case of pharmaceuticals in European surface waters. Environ. Int. 128, 1–10. https://doi.org/10.1016/J.ENVINT.2019.04.034.

Renewable Energy 151 (2020) 378–391

Contents lists available at ScienceDirect

Renewable Energy

journal homepage: www.elsevier.com/locate/renene

Predicted direct solar radiation (ECMWF) for optimized operational strategies of linear focus parabolic-trough systems

Francis M. Lopes [a, b, *], Ricardo Conceição [a, b], Thomas Fasquelle [b], Hugo G. Silva [a, c], Rui Salgado [a, c], Paulo Canhoto [a, c], Manuel Collares-Pereira [a, b, c, d]

[a] Institute of Earth Sciences, University of Évora, Rua Romão Ramalho 59, 7000-671, Évora, Portugal
[b] Renewable Energies Chair, University of Évora, Casa Cordovil, Rua D. Augusto Eduardo Nunes 7, 7000-651, Évora, Portugal
[c] Physics Department, School of Sciences and Technology, University of Évora, Rua Romão Ramalho 59, 7000-671, Évora, Portugal
[d] Portuguese Solar Energy Institute, Palácio Do Vimioso, Largo Marquês de Marialva, Apart. 94, 7002-554, Évora, Portugal

ARTICLE INFO

Article history:
Received 29 July 2019
Received in revised form
31 October 2019
Accepted 8 November 2019
Available online 11 November 2019

Keywords:
Short-term forecasts
ECMWF
Direct normal irradiance
Concentrating solar power
System advisor model
Operational strategies

ABSTRACT

Day-ahead forecasts of direct normal irradiance (DNI) from the Integrated Forecasting System (IFS), the global model of the European Centre for Medium-Range Weather Forecasts (ECMWF), are used to simulate a concentrating solar power (CSP) plant through the System Advisor Model (SAM) to assess the potential value of the IFS in the electricity market. Although DNI forecasting from the IFS still demands advances towards cloud and aerosol representation, present results show substantial improvements with the new operational radiative scheme ecRad (cycle 43R3). A relative difference of approximately 0.12% for the total annual energy availability is found between forecasts and local measurements, while approximately 10.6% is obtained for the previous version. Results of electric energy injection to the grid from a simulated linear focus parabolic-trough system shows correlations coefficients of approximately 0.87 between hourly values of electric energy based on forecasted and measured DNI, while 0.92 are obtained for the daily values. In the context of control strategy, four operational strategies are given for different weather scenarios to handle the energy management of a CSP plant, including the effect of thermal energy storage capacity. Charge and discharge operational strategies are applied accordingly to the predicted energy availability.

© 2019 Elsevier Ltd. All rights reserved.

1. Introduction

In recent years, a remarkable increase has been observed regarding the number of solar energy conversion technologies installed worldwide, particularly photovoltaic (PV) and concentrating solar power (CSP) systems. The installation of PV systems has been growing exponentially over the last decades, with approximately 402.5 GW of cumulative worldwide installed capacity by the end of 2017 [1]. On the other hand, approximately 5.7 GW of cumulative worldwide installed capacity regarding CSP technology was available by the end of 2017 [2], as a consequence of a much smaller growth rate than PV. However, the fact that those CSP systems have the advantage of providing high-quality dispatchable power at lower prices when compared to PV electric storage, is one of the strongest reasons [3] for investing in such technology. Additionally, CSP storage materials, such as molten salts, are a more affordable, safer and locally available way of storing energy than conventional technologies such as Lithium batteries.

With the installed capacity increase for both PV and CSP systems, a growth in solar forecasting is also expected to occur, since information provided to a power plant operator, for instance, regarding day-ahead (i.e. up to 48 h) irradiance values, can have a key role not only in the production of energy but also in its distribution and management towards the electricity grid market. In particular, predictions of direct normal irradiance (DNI) are essential for CSP technologies [4,5], since these can provide the operator the capacity of improving the plant's energy management. For instance, during the most demanding and valuable periods [6], in which higher levels of profitability can be achieved [7]. In this context, accurate forecasts of DNI are demanded for clear-sky periods and, particularly, for partly cloudy skies [8,9], where a reduction of the uncertainty related to the solar power plant

* Corresponding author. Institute of Earth Sciences, University of Évora, Rua Romão Ramalho 59, 7000-671, Évora, Portugal.
E-mail addresses: fmlopes@uevora.pt (F.M. Lopes), rfc@uevora.pt (R. Conceição), thomasf@uevora.pt (T. Fasquelle), hgsilva@uevora.pt (H.G. Silva), rsal@uevora.pt (R. Salgado), canhoto@uevora.pt (P. Canhoto), collarespereira@uevora.pt (M. Collares-Pereira).

https://doi.org/10.1016/j.renene.2019.11.020
0960-1481/© 2019 Elsevier Ltd. All rights reserved.

outputs due to solar intermittency [10] is essential.

Solar intermittency is characterized by a very high variability over space and time, which partially depends on the local weather conditions. As a consequence, the spatial and temporal variability of solar radiation has an impact in the economic market, known as the "duck curve", named after the California Independent System Operator (CAISO). The "duck curve" simply shows a large portion of the electric energy demand during the day that is being modulated by solar power production. As described by Ref. [11], current challenges to mitigate the effect of CAISO's "duck curve" in the operation of power plants consist in the ability of: i) conventional power generation fleet to meet the downward and upward net load ramping needs that occur during sunrise and sunset hours, respectively; ii) conventional power plants to substantially decrease the generation levels or cease the energy output during a few hours at mid-day, i.e. during the period of lowest net demand in the day. To reduce the uncertainty of such challenges, and to reach a minimum generation (during mid-day) and ramping requirements (during sunrise and sunset), these authors give emphasis to the use of accurate solar power forecasts, a more stable and economic approach that embraces better unit commitment and financial choices.

DNI depends on many factors, which can influence the energy output of a solar power plant. Such dependency is predominantly related to atmospheric conditions, e.g. air temperature, air moisture, wind speed/direction and, more significantly, clouds (type and dynamic coverage) and aerosol concentration. An accurate characterization of these parameters can be obtained by combining the use of state-of-the-art monitoring and assessment techniques for solar radiation, together with advanced numerical weather prediction (NWP) modeling. Mainly, short-term forecasts, also known as day-ahead forecasting (<48 h), are known to be useful for energy resource planning and scheduling [12], allowing an increase of management effectiveness of CSP plants and higher-penetration of commercial solar power into the electricity grid market. The accuracy of DNI predictions depends on the forecast horizon, since forecasting uncertainty tends to be smaller with the reduction of the projection period. Smaller forecast horizons can be performed at higher resolutions with very expensive computational costs [13]. Currently, there is a wide range of DNI forecast horizons performed with different methods (see Table 1). As described by Ref. [12], very short-term forecasts (<30 min), also known as nowcasting, can be performed through the use of ground-based sky imagers and persistence models. Stochastic-learning techniques, such as autoregressive integrated moving averages (ARIMA) and artificial neural networks (ANN), can be suitable for short-term forecasts (<2 h). For a temporal horizon between 2 and 6 h, a combination of techniques is usually adopted through NWP models and satellite data. Ahead of the 6 h-horizon, forecasts are mainly carried out through physics-based models, which are able to produce week-ahead forecasts.

A key issue in NWP modeling is the generation of the initial state (i.e. initial conditions) of the atmosphere, the oceans and the surfaces. As described by Ref. [27], these conditions are composed by a spatial distribution from a set of variables (e.g. temperature, wind, pressure, moisture, among others) obtained through a very complex process, known as data assimilation. In the end, data assimilation provides estimations of the initial state of the system, considering available observations and previous model forecasts. Due to a shortage in the number of available observations, to fulfil the degrees of freedom of the system, uncertainties in the initial conditions of NWP models are always present.

NWP models represent and describe the dynamics of the atmosphere and the physical processes that take place (e.g. cloud-radiation interaction). However, despite the great developments attained in the last three decades, mainly due to the exponential growth of computational capabilities, the current state-of-the-art NWP models are still limited in certain aspects, since the atmosphere is a very complex and non-linear system. Thus, in one hand, the physical modeling of some phenomena can still be improved, particularly in the case of the radiation transfer in both solar and infrared spectral ranges. On the other hand, weather forecasts have always a certain degree of associated uncertainty. For instance, apart from uncertainties related to initial conditions, numerical representation of clouds and aerosols are usually hindered by the complexity of cloud microphysics [9] and aerosol [28] modeling, two key parameters that significantly affect the DNI, due to the radiation scattering and absorption phenomena and its interaction with cloud microphysical and dynamical processes [29]. Additionally, the generalized use of monthly climatology of aerosol types and concentrations in the NWP models, increases the errors of the predicted radiation [30]. The radiative effects of clouds tend to be underestimated by the models, while the radiative effects of the aerosols tend to be overestimated under very clear atmospheric conditions and underestimated under dusty conditions, namely desert dust events. Solutions for these problems have been pursued more intensely in the recent years with the development of advanced NWP methods. One example of such improvement is the radiative scheme used by the Integrated Forecasting System (IFS), the global NWP model of the European Centre for Medium-Range Weather Forecasts (ECMWF), which has been upgraded over the years to provide accurate forecasts of solar radiation, particularly DNI.

In this context, it is important to assess the quality of DNI predictions from NWP models, which can be made through forecasting skill. Appropriate forecasting metrics, such as mean square error skill score (SS), are suitable measures of forecasting performance that should be considered regarding forecast inaccuracies [12]. For instance, the comparison against DNI persistence models has shown to be a useful method to demonstrate how advantageous the NWP models are in terms of DNI forecasts [30].

It is also important that solar power plant models accurately convert predicted irradiation values to energy output forecasts. Most of the available software for the simulation of power plants, such as the System Advisor Model (SAM), use by default satellite-based data with the generation of a typical meteorological year (TMY), particularly for specific locations outside national territory in which the software is developed. An alternative approach to satellite data, is the use of local measurements for generating TMY, which should be considered together with *a priori* quality control of the data and an analysis of different typical periods [31]. Although using TMY data is suitable for solar power plants design, since it can provide an estimation of the amount and variability of energy generation in a specific location, it is still essential to know the predicted DNI availability for the day-ahead. The combined use of high-quality local measurements, NWP models and power plant modeling can generate useful information for the energy management and operation of a CSP power plant.

The present work is focused on the use of day-ahead (24 h) DNI forecasts and other relevant meteorological variables from the IFS, as the inputs of a power plant simulation model. The predicted energy output from the power plant is then assessed by comparing results with the ones obtained using local ground-based DNI measurements, for the same period and location in southern Portugal. In this context, the SAM software is used to simulate a CSP system (linear focus parabolic-trough) and assess the potential that accurate DNI forecasts can have in the electricity market. Following the introductory section, the remainder of the paper is structured as follows: in Section 2, a description of the measurements used in this study and respective data quality control is provided; in Section 3, an overview of the IFS radiative scheme used for this work is

Table 1
Summary of different methods used for DNI forecasting.

Time-scale	Methods	Scale
Intra-hour (1 min - 2 h)	Persistence models [14–16]; Sky imagers [17–19];	Microscale (about 0 m–1 km)
Intra-day (<2 h)	ARIMA models [20]; ANN [21–23];	Microscale (about 0 m–1.3 km)
Intra-day (2–6 h)	NWP models [24]; Satellite-based models [25];	Mesoscale (1–10 km)
Hour, day and week-ahead (>6 h to several days)	NWP models [26];	Mesoscale and synoptic (>10 km)

given; in Section 4, measurements and forecasted data are applied into the SAM software, with respective results and discussion regarding a simulated linear focus parabolic-trough power plant; considering the results obtained, operational strategies for typical days are given in Section 5; in Section 6, conclusions and future perspectives are provided.

2. Measurements

The southern region of Portugal has exceptional conditions for the development of CSP technologies, since it is characterized as a semi-arid region [32], with a clean atmosphere and one of the highest solar resource potentials in Europe, with mean annual energy availability values around 2100 kWh/m^2 [33]. For this reason, in southern Portugal, an operational network of 13 radiometric ground-based measuring stations was installed for mapping DNI, as well as, for defining strategies for an improved regional operation of CSP plants, as part of the DNI-ALENTEJO project. Amongst the current operational stations, the measuring station of the Institute of Earth Sciences (ICT- *Instituto de Ciências da Terra*), in Évora city, is used in this study as a reference station since a regular maintenance of the instruments has been performed to ensure the quality of the data used. For that matter, soiling effect [34], or any significant periods of missing data, is not present in the Évora station, EVO (N38.567686, W7.911722). All ground-based measurements of DNI were performed using pyrheliometers (model CHP1) from Kipp & Zonen instruments, a World Meteorological Organization First Class instrument with a daily associated estimated uncertainty of <1%, being calibrated every 2 years following the International Organization for Standardization (ISO) 9059:1990 standard [35]. The measured DNI data was acquired with a sampling rate of 5 s and then averaged and recorded every 1 min. In order to fill any data gaps, the following procedure was performed, prior to the analysis, for data quality control with the following adopted filters:

a. Positive DNI values.
b. BSRN Global Network quality check tests V2.0 [36].
c. Days that have more than 2 h of missing records, between sunrise and sunset, are filled with hourly values from the nearest ground-based measuring station located at Mitra, MIT (N38.530522, W8.011221), approximately 9.6 km from EVO station.
d. Days with less than 2 h of missing records, have the corresponding hourly value gaps subjected to a linear interpolation from the values of the neighboring hours.

Additionally, local meteorological parameters (air temperature, relative humidity, wind speed and atmospheric pressure at the ground level) were also considered, being acquired by standard meteorological measuring equipment. All measurements in EVO and MIT stations were obtained with the same sampling rate as DNI. It should be noted that the EVO station does not have wind and pressure data available. For that reason, hourly data from the Portuguese Meteorology Service (IPMA – *Instituto Português do Mar e da Atmosfera*) station, located at Évora aerodrome (N38.53654, W7.88795), approximately 4 km from EVO station, are used as representative of wind speed and atmospheric pressure in Évora. The geographic location of the measuring stations used is shown in Fig. 1, where all stations are within the same synoptic radius of approximately 10 km. Additionally, a summary of all measured parameters from each station is listed in Table 2.

3. The Integrated Forecasting System

As described by Ref. [38], the IFS radiative scheme has suffered major changes since the first implementation of the Morcrette scheme in 1991. Improvements have been made during the nineties [39], culminating with the introduction of the Rapid Radiative Transfer Model [40], which allows simulating clear-sky irradiances with higher accuracy. In 2007, the radiative scheme was upgraded to the McRad version, having experienced several improvements through the years (cycles 32R2, 35R3, 41R1, 41R2 and 43R1) until recently (July 2017) with the replacement of the McRad by the current operational ecRad radiative scheme (cycle 43R3). Until that time, the IFS had used Tegen aerosol climatology [41], which ended up being replaced by a more realistic monthly mean aerosol climatology from the Copernicus Atmosphere Monitoring Service (CAMS). The CAMS is able to predict aerosol concentrations, using a set of coupled modules for aerosol and chemistry, and an aerosol data assimilation system. A full coupled IFS-CAMS system is expected to be fully operational in future versions, with an increase of more than 50% towards the computational cost of the IFS [42]. The radiation transfer under cloudy periods is represented in the model through the Monte-Carlo Independent Column Approximation (McICA), which has been enhanced in the ecRad radiative scheme to reduce numerical noise.

In this work, operational forecast data for the next 24 h is provided by the IFS model with a forecast issue time set to start at 0 UTC using an average spatial resolution of approximately 9 km (0.125° x 0.125°). In the new version (ecRad), predicted hourly DNI is directly given by the parameter *dsrp*, the direct solar radiation incident on a plane perpendicular to the direct sun beam. This is not the case for the previous version (McRad), where the IFS only provides the total sky direct solar irradiance at surface, the *fdir* parameter, which is then divided by the determined hourly cosine of the solar zenith angle (in accordance to the selected location). This means that the predicted DNI from the McRad is subjected to additional source of errors. A more detailed description concerning the McRad and ecRad schemes is available in Ref. [43].

In order to compare the predicted DNI values with the measured ones, the IFS hourly accumulated irradiation values are divided by 3600 and then converted to mean energy flux values (W/m^2). Additionally, a comparison analysis between predicted and measured is carried out with the calculation of daily energy availabilities, E_b (kWh/m^2), through the integration of the hourly mean DNI values, while monthly availabilities are the sum of the corresponding daily availabilities. Relative differences, ΔE_b (%), for the total energy availability between observations and model for a given period of days are also calculated. To further evaluate the differences between measurements and model outputs, the overall performance of the IFS model is tested through forecasting skills. In this analysis, a forecasting skill was calculated through the use of the skill score (*SS*), computed as the decrease in the mean square error (*MSE*) obtained by the hourly clearness indexes of the model with respect to the persistence model (reference model), as

described in Ref. [44]:

$$SS = 1 - MSE_{for} \Big/ MSE_{per}, \quad (1)$$

where MSE_{for} and MSE_{per} are the error metrics respectively for the forecast model and the persistence with respect to the measurements (i.e. by persisting the observational values over a forecast range of 24 h). A similar method has been previously used in Ref. [30].

3.1. McRad and ecRad radiative schemes

A preliminary statistical analysis for the assessment of day-ahead DNI forecasts against measured data from EVO station showed a general improvement of DNI predictions from the previous radiative scheme McRad (cycle 41R2) to the upgraded scheme ecRad (cycle 43R3). In Table 3, a summary of the statistical analysis performed over each scheme in comparison with respective local measurements is presented. Since the McRad is no longer operational, the present analysis consists in using two consecutive periods of data, the first year (July 1st, 2016 to June 30th, 2017) comprising the McRad version and the second year (July 1st, 2017 to June 30th, 2018) the ecRad version. For each of the considered years, a total number of 4747 h of daylight, corresponding to the total number of daylight hours available, was used in the hourly analysis. Previous work [30] has shown that small data gaps can exist in the measurements time series, being related to sudden electric shutdowns. In EVO station, throughout an entire year of continuous measurements, 0.05% and 0.003% of missing data were found respectively for the McRad and ecRad periods. For the MIT station, which is solely used for the gap-filling procedure, 5.24% and 0.14% of gaps were also found for the McRad and ecRad periods, respectively. This demonstrates how-well maintained the EVO station is and why it is used as a reference for the assessment of DNI predictions.

Overall overestimations of approximately 1.2% and 10.6% were obtained regarding the predicted annual mean values of DNI towards the measured ones, respectively for the ecRad and McRad radiative schemes. Predicted values from the ecRad are shown to be much closer to the observations, and consequently with lower bias, as opposed to the previous version. This is also depicted by the hourly correlation coefficients (r_{hourly}) of approximately 0.86 and 0.87, and root mean square errors (*RMSE*) of approximately 188.60 W/m^2 and 180.44 W/m^2, obtained respectively for the McRad and ecRad. The corresponding mean absolute errors (*MAE*) were approximately 126.06 W/m^2 and 125.93 W/m^2, showing the tendency for lower errors from one version to the other.

Hourly and mean daily values of measured and predicted DNI are compared in Fig. 2, together with the identity line $y = x$ (depicted by a red dashed line). Higher correlations are observed for high DNI values (>800 W/m^2), which occur during clear sky periods. On the other hand, lower correlations are obtained for inferior values, being characterized by higher dispersion, corresponding to cloudy periods, as a consequence of the difficulties that the model still has in representing cloud microphysics. This is well shown by the model tendency to overestimate measurements for overcast and partly cloudy periods (depicted by a cluster of values for $x = 0$), and the model tendency to underestimate measurements during clear-sky periods, particularly under a very clean atmosphere (depicted by high DNI values), as previously observed in Ref. [30]. As expected, the daily values show higher correlations

Fig. 1. Geographic location of the ground-based station used in this study, Évora (EVO), and two other stations, Mitra (MIT) and Évora Aerodrome (IPMA), that were used for EVO data quality control. All rights reserved [37].

Table 2
Summary of the parameters used from the reference station in Évora (EVO), and the stations in Mitra (MIT) and in Évora Aerodrome (IPMA) used respectively for the gap-filling procedure and the inclusion of other meteorological parameters.

	DNI (W/m^2)	Air Temperature (℃)	Relative Humidity (%)	Surface Pressure (mbar)	Wind Speed (m/s)	Distance to EVO station (km)	Elevation (m)
EVO	✓	✓	✓	x	x	x	278
MIT	✓	✓	✓	x	x	9.6	220
IPMA	x	x	x	✓	✓	4.1	244

coefficients of approximately 0.88 and 0.91, respectively for the McRad and ecRad, in comparison with the hourly correlations. This increase is higher for the correlation between measurements and predictions provided by the ecRad, with a value of almost 4.6%, as opposed to 2.3% for the McRad correlations. The reduction of error from the hourly to the daily results is well represented in Fig. 3, where a decrease of the DNI absolute error (*AE*) is observed with the approximation of *AE* values towards zero, particularly in the case for the daily values. Additionally, the total annual energy availability obtained from the predicted DNI of the ecRad (E_b) is closer to the regional measured values, which can range from 1841 kWh/m^2/year to 2073 kWh/m^2/year [33]. The relative differences (ΔE_b) in Table 3, are approximately 0.19% and 10.6% for the ecRad and McRad schemes, respectively. The monthly energy availability, shown in Fig. 4 provide an overview of the performance of the model in predicting the DNI through the McRad and ecRad schemes. Relative differences of approximately 0.1% and 10.6% were found between monthly values of the IFS and measurements for the ecRad and McRad, respectively.

In the context of forecasting skill assessment for the IFS 24-h predictions of the IFS, the obtained *SS*, calculate with Eq. (1), shows a clear improvement of the model in performing DNI forecasting. From Table 3, hourly *SS* show an increase from approximately 0.60 to 0.67, and 0.70 to 0.77 for daily *SS*, respectively for McRad and ecRad schemes.

3.2. Summary

The previous analysis indicates that, for the 24-h horizon, DNI predictions from the IFS have been significantly improved with the new radiative scheme ecRad. This is a result of recent developments towards a better representation of cloud microphysics and the implementation of a more realistic aerosol climatology [38]. For the present analysis, it is therefore possible to conclude that the ecRad (cycle 43R3) is best suited to provide DNI forecasts to be used as an input parameter of a CSP plant model simulation, as it will be discussed in the next sections.

Table 3
Statistical and descriptive analysis of the McRad and ecRad radiative schemes from the IFS global model 24-h predictions. Several statistical parameters between measured and predicted hourly mean values of irradiance were calculated considering only the daylight period (i.e. a total of 4747 h) during an entire year of data: mean, median, standard deviation (*std. dev*), root mean square error (*RMSE*), mean absolute error (*MAE*), correlation coefficient (*r*), skewness, kurtosis, total energy availability (E_b), relative difference of E_b (ΔE_b) and the skill score (*SS*), with their respective units for power values (in W/m^2) and for energy values (kWh/m^2). In reference to the measuring station in Évora city, the periods used go from July 1st, 2016 to June 30th, 2017 (McRad, cycle 41R2) and from July 1st, 2017 to June 30th, 2018 (ecRad, cycle 43R3).

	McRad (41R2)		ecRad (43R3)	
	Measurements	IFS	Measurements	IFS
Mean (W/m^2)	463.61	512.76	444.24	444.76
Median (W/m^2)	501.74	563.31	452.32	457.80
Std. dev (W/m^2)	351.71	310.67	361.87	310.72
r_{hourly}	0.86		0.87	
r_{daily}	0.88		0.91	
RMSE (W/m^2)	188.60		180.44	
MAE (W/m^2)	126.06		125.93	
Skewness	−0.07	−0.31	0.03	−0.07
Kurtosis	1.44	1.66	1.40	1.50
E_b (kWh/m^2/year)	2192	2425	2097	2101
ΔE_b (%)	10.6		0.19	
r_{Eb}	0.90		0.91	
SS_{hourly}	0.60		0.67	
SS_{daily}	0.70		0.77	

4. Electric CSP production based on DNI measurements and forecasts

A CSP system consists in the harvesting of solar energy through the conversion of solar radiation into thermal energy and then into electric energy. The conversion from solar radiation into thermal energy can be achieved through four commercial types of concentrating solar systems: parabolic-trough (PT) collector, linear Fresnel reflector, central receiver and parabolic dish. These systems can be classified according to the focus type (line or point), the receiver type (fixed or movable) or the concentration level (medium or high), as described in Refs. [45,46]. Apart from the fact that these systems have different characteristics, they share the same operating principle, which consists in the concentration of solar radiation from reflector elements to receivers. Within these, a transfer medium, denominated as a heat transfer fluid (HTF), is heated, reaching temperatures up to 393 °C in PT commercial CSP systems. A thermodynamic power cycle equipped with a turbine is then used to convert thermal energy into electric energy, e.g. the Rankine cycle, while a fraction of the thermal energy generated during the day can be stored in a liquid or solid medium (e.g. molten salt), thus allowing the use of this energy at night and during cloudy periods in order to maintain the power plant operational.

4.1. The power plant model

The SAM [47], developed by the National Renewable Energy Laboratory (NREL) from the U.S. Department of Energy, is a free available modeling software [48] for renewable energy systems. The SAM (version 2017.9.5) is used here for the first time to validate the use of day-ahead DNI forecasts from the IFS (ecRad, cycle 43R3) for the operational management of CSP systems. The model has implemented the transient system (TRNSYS) simulation tool for the modeling of concentrating solar thermal power plant systems [49], being built around three components: a user-friendly interface, calculation engine and programming interface. All input and design variables, simulation controls, and a summary of the results in the form of data tables and graphs, are provided in the user interface. The calculation engine, the SAM simulation core (SSC), performs a step-by-step simulation of the power plant operation, calculating hourly values through a performance module, thus allowing to compute the respective annual performance metrics of, for instance, CSP systems. Since the source code for the SAM simulation and calculation modules is not available to the public, detailed information concerning the use of the SAM software is available online through the user's manual [50].

In order to run a SAM simulation, solar radiation resource and meteorological parameters are needed as input data. User data can be used to force the model, which can be based on observations or

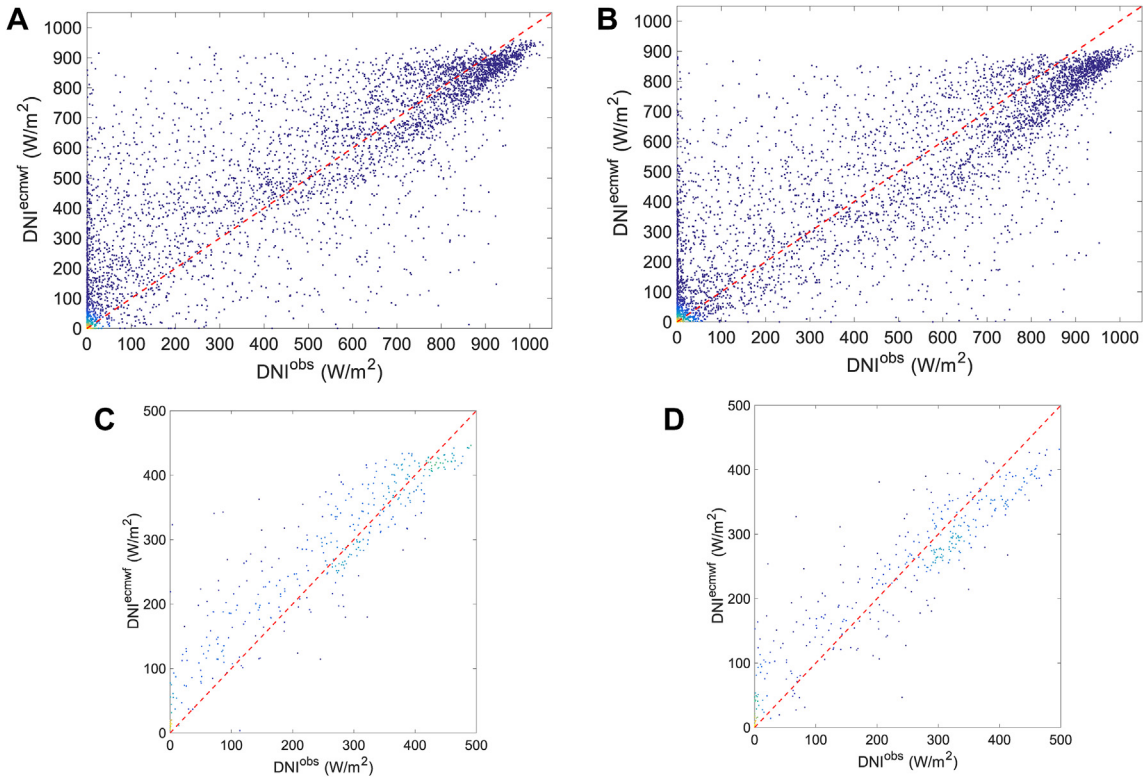

Fig. 2. Comparison of hourly (a, b) and daily (c, d) mean DNI values (W/m^2) between 24-h predictions (ecmwf) and measurements (obs), for the McRad (a, c) and ecRad (b, d) radiative schemes from the IFS, considering only daylight hours during an entire year of data. In reference to the measuring station in Évora city, the periods used go from July 1st, 2016 to June 30th, 2017 (McRad, cycle 41R2) and from July 1st, 2017 to June 30th, 2018 (ecRad, cycle 43R3). The red dashed line represents the identity line y = x between measurements and forecasts. (For interpretation of the references to colour in this figure legend, the reader is referred to the Web version of this article.)

predictions. It should be noted that intermittent generation technologies, such as CSP, depends on the weather conditions to produce electricity. Bad predictions related to underestimated and overestimated production values, and the consequently strategy for handling such cases, have an associated cost that can result in additional penalties per each kWh of deviation to the plant operator [51].

In this work, the case study of a CSP plant is considered for the simulation of current operational solar power systems. This simulation concerns a power plant with similar configurations as the Andasol 3 CSP (N37.228644, W3.051147), an upgraded installation of Andasol 1 and 2 (Fig. A1), located in the Spanish municipalities of Aldeire/La Calahorra (Granada, Spain). Being operational since August 2011, this 50 MW_e commercial power plant uses a linear focus PT system that runs with thermal oil (Downtherm A) as HTF, with a 7.5-h indirect molten salt storage capacity at full load. The system, which was designed to reach a net annual energy generation of 165,000 MW_eh/year at typical meteorological conditions [52], currently has an estimated annual energy generation of 175,000 MW_eh/year. Since the simulation is centered in Évora instead of Granada, a direct comparison between simulated outputs and real operational values is not the focus of this work. Moreover, details on the Andasol 3 CSP project can be consulted online [53] concerning the available information. Since full access to the actual information about the plant configuration is not possible, due to privacy reasons, the Andasol 3 plant simulation in the SAM uses a few design and control input parameters that are SAM's standard values for PT systems, while others are research-based assumptions made by the authors (see Table A1).

5. Results and discussion

The focus of this work is the assessment of the IFS 24-h temporal horizon DNI forecasts, given by the ecRad radiative scheme (cycle 43R3), as a mean to improve the energy management of operational CSP systems. In this context, an important output parameter is the daily power generation that a plant operator has to handle. Through the SAM simulations, hourly mean values of electricity generated by a CSP plant are represented by the parameter electricity injection to the grid, E_G (MW_eh), while the thermal energy into storage (charge and discharge periods) hourly values are given by the parameter *TES* (MW_th). In this exercise, a 365 day-period is considered and the study location is centered in EVO station, which is the current reference measuring station for DNI in southern Portugal, providing the necessary high-quality data for the following analysis, as previously shown.

For a CSP plant with similar configuration as the Andasol 3 CSP plant, the estimated hourly mean values of E_G and *TES* simulation based on measured and forecasted data are presented in Fig. 5.

As expected, results show that during the summer there is more electric energy being generated and higher thermal energy being stored, as represented by both measured and forecasted outputs. This is a consequence of i) the higher frequency of clear-sky days when DNI values are the highest, ii) the increase in the number of sunlight hours during the day (an important feature for the total energy production), and iii) the smaller solar zenith angle and thus a thinner air mass during more hours in a day, which leads to higher DNI values at ground-level. As opposed to these, during the winter, the E_G generation tends to be lower and, in some cases, zero due to a higher frequency of cloudy day occurrences (which can prevail during several consecutive days). It is during such periods

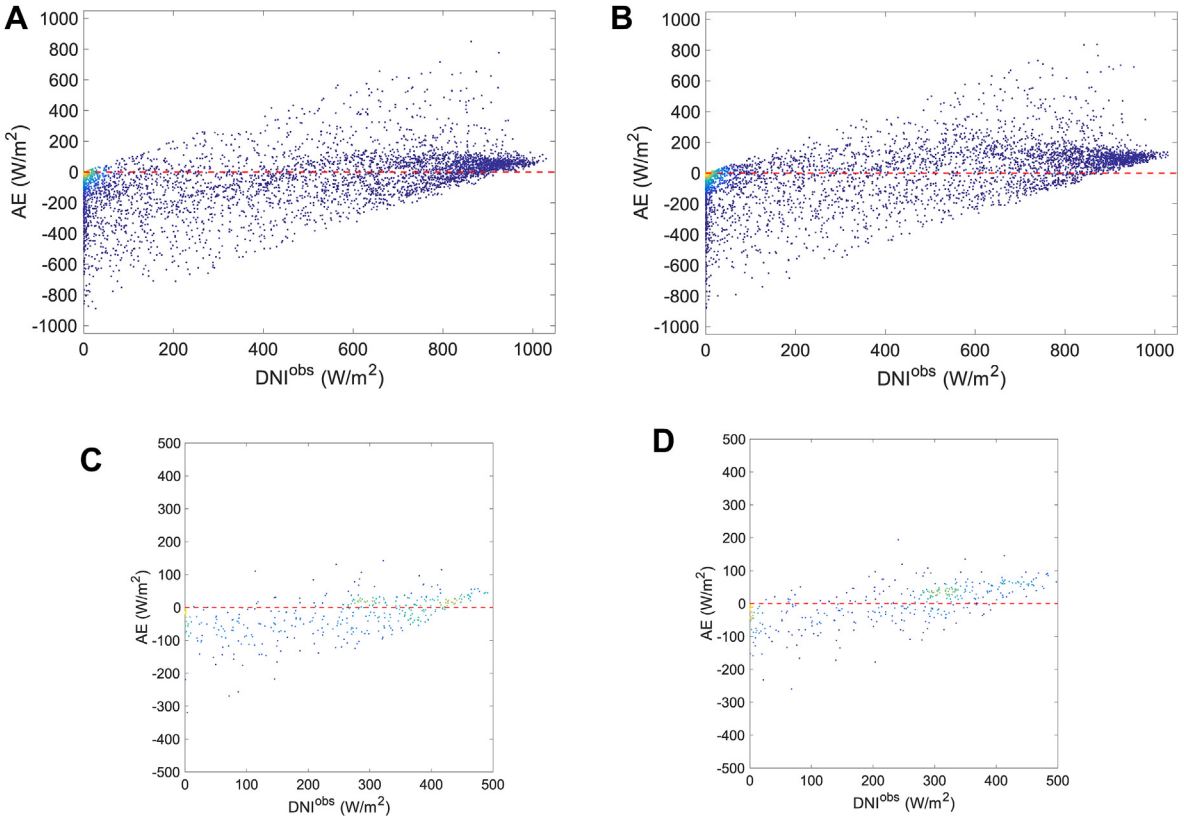

Fig. 3. Absolute error (AE) between hourly (a, b) and daily (c, d) mean DNI values (W/m^2), considering only daylight hours during an entire year of data. In reference to the measuring station in Évora city, the periods used go from July 1st· 2016 to June 30th· 2017 (McRad, cycle 41R2) (a, c) and from July 1st· 2017 to June 30th· 2018 (ecRad, cycle 43R3) (b, d). The horizontal line y = 0, represented by a red dashed line, establishes a threshold between positive and negative AE values. (For interpretation of the references to colour in this figure legend, the reader is referred to the Web version of this article.)

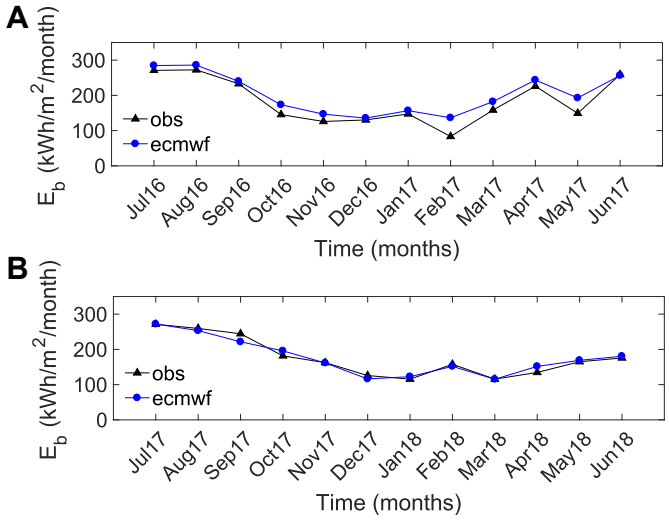

Fig. 4. Measured (*obs*) and predicted (*ecmwf*) monthly energy availability, E_b (kWh/m^2/month), considering only daylight hours during an entire year of data. In reference to the measuring station in Évora city, the periods used go from a) July 1st· 2016 to June 30th· 2017 (McRad, cycle 41R2) and b) from July 1st· 2017 to June 30th· 2018 (ecRad, cycle 43R3).

that the IFS forecasts are clearly hindered by the representation of clouds, leading to lower values of predicted E_G and *TES* than the ones obtained with measurements. This is evident during December, where a significant decrease of E_G is observed for the predicted data from the IFS, while CSP energy generation for measured data depicts a smaller decrease.

The total annual energy generated based on forecasted data (approximately 159,795 MW$_e$h/year) shows an overestimation of almost 6,140 MW$_e$h/year of the total annual energy against results based on DNI measurements (approximately 153,655 MW$_e$h/year), corresponding to a relative difference of nearly 3.99%. The obtained bias is a clear consequence of the annual DNI overestimation depicted by the IFS, which is transferred to the energy output of a CSP plant through a non-linear transfer function (thermo-electric model), including the effect of local meteorological variables that can affect the system efficiency. The annual energy based on measurements and predictions diverges from the one that would be obtained if the Andasol 3 power plant was operating in Évora. This is because the datasets (DNI and meteorological variables) from Évora are being used in the SAM during a different operational period than the one used for the obtained values from the actual Andasol 3 CSP plant in Granada, containing distinct inter-annual variations. Moreover, parasitic power consumption that occurs during non-production hours and a constant derating value of 4% also contribute to deviations. The latter is usually used to prevent decreases in the power plant output induced by unusual local weather conditions or excess power in the electric grid.

The total estimated E_G found for the forecasted and measured data is approximately 163,337 MW$_e$h/year and 158,836 MW$_e$h/year, respectively, with a correlation coefficient of approximately 0.87 between the hourly values and *RMSE* of 11.93 MW$_e$h and *MAE* of 4.31 MW$_e$h. This correlation increases up to 0.92 for the calculated daily values, having a *RMSE* of approximately 119.32 MW$_e$h and *MAE* of 79.59 MW$_e$h. For the *TES*, the amount of energy that is being

stored is higher for the simulations based on measurements than for the forecasted data, with a maximum that reaches 200,000 MW_th during the summer in comparison with 170,000 MW_th from the IFS. During the summer, particularly in days of very clean atmospheric conditions, the predicted DNI is lower than the measured since the IFS uses monthly mean aerosol climatology (i.e. the CAMS system), leading to lower predicted values of stored energy.

A closer comparison between measurements and IFS predictions regarding hourly mean values for E_G obtained through the SAM simulation is shown in Fig. 6. Higher correlations between measurements and predictions are given by values that are closer to the identity line $y = x$, where the predicted values meet the measured ones, while more values dispersed from this line lead to lower correlations. Considering the hourly values, a *MAE* of approximately 4.31 MW_eh was obtained and defined as an upper and lower limit for the establishment of a confidence interval (i.e. depicted by two green dashed dotted lines), with nearly 83.9% of the total number of hourly values that have an absolute error (*AE*) less than the obtained *MAE*. Moreover, two common features are observed here: i) a small cluster of E_G values around 25 MW_eh (half the nominal value), being related to the plant start-up time (0.5 h) and stop operations, as well as the temporal discretization implemented internally, considered by the SAM; ii) a better correspondence during clear-sky hours (leading to production values around 48–55 MW_eh), as shown by the large cluster of E_G values. Significant dispersions are found outside of this threshold, being linked to overcast and shutdown periods. The latter, corresponding to null E_G values, are also found in both *xx* and *yy* axis and are related to unusable stored energy. If all null E_G values are removed from the analysis, the correlation between measured and forecasted results decreases significantly to 0.58. This shows the dependency of shutdown periods in the overall performance of a power plant (having an important role in the daily energy management of a CSP plant), and how-well the IFS forecast such periods. Having into account these results, particular attention is given in the next section for the estimated *TES* outputs obtained by using measured and predicted data in the SAM, with proposed operational strategies regarding the use of forecast data in a linear focus PT CSP plant with similar configuration as the Andasol 3 CSP.

6. Operational strategies

An accurate solar resource prediction model has two advantages for a power plant operator: i) it allows the estimation of the electricity production of the power plant, helping the power grid management and enabling to sell electricity before production at a good price, i.e. the premium tariff option [50]; ii) it gives the opportunity to choose appropriate control strategies to maximize the power plant energy efficiency. The versatility of control strategies is deeply tight to TES capacity. Without a storage system, electricity production is constricted to solar resource availability. With a 7.5-h TES system, as in the Andasol 3 CSP plant, and considering no fossil-fuel backup, different strategies can be adopted [54,55]:

a. Constant load curve during the day with storage of surplus energy and discharge after sunset.
b. Delayed electricity generation for maximum profitability.
c. A growing number of industrial companies are currently considering using cost-effective PV systems to produce electricity during the day, while charging TES with CSP, i.e. hybridization. Thus, thermal energy should be discharged after sunset to produce electricity during night [56].

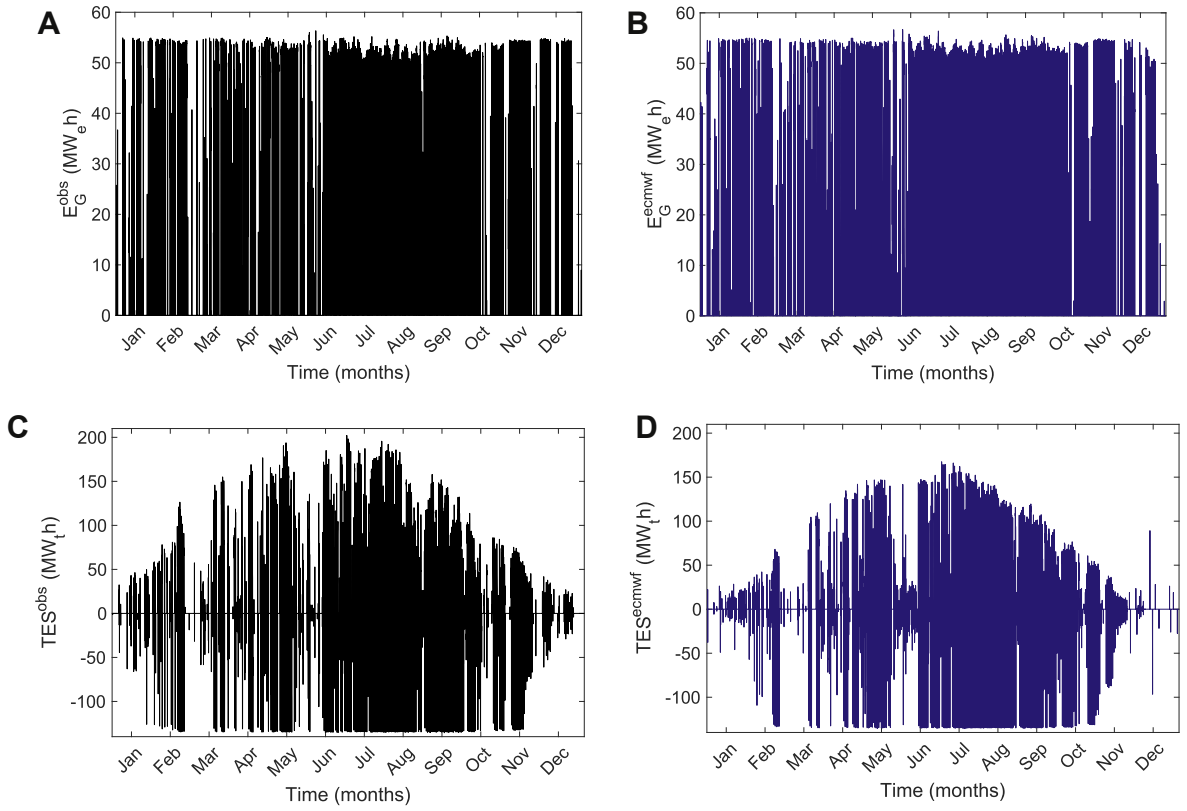

Fig. 5. Estimated hourly values of electricity to grid (E_G, MW_eh) based on: a) measured (*obs*); b) forecast (*ecmwf*) data through the simulation of the Andasol 3 CSP plant; Estimated hourly values of thermal energy into storage (*TES*, MW_th) based on: c) measured; d) forecast data. The period of study is related from July 1st, 2017 to June 30th, 2018 and considers data from the measuring reference station in Évora, southern Portugal.

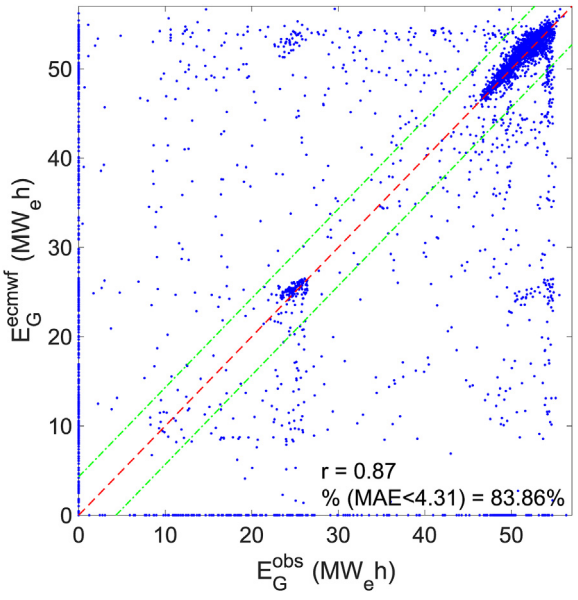

Fig. 6. Hourly values of energy injection into the grid, E_G (MW_eh), based on measurements (*obs*) and the IFS 24-h forecasts (*ecmwf*) for the Andasol 3 simulation in the SAM. The corresponding correlation coefficient, *r*, and a confidence interval based in the calculated *MAE* of approximately 4.31 MW_eh, given by two green dashed dotted lines, are also depicted. The period of study is related from July 1st, 2017 to June 30th, 2018 with the analysis being centered in the EVO station (Évora, southern Portugal). (For interpretation of the references to colour in this figure legend, the reader is referred to the Web version of this article.)

Other strategies exist when considering a fossil-fuel backup [57], such as minimizing fossil fuel consumption or maximizing profitability, however these scenarios are not included in the present study.

It should be noted that the SAM software does not incorporate high-level strategy algorithm. As a consequence, the power block is started when sufficient power is available, without considering neither the energy stored in the TES system or the evaluation of the DNI variability within previous instants. Since multiple starts and stops of the power block should be avoided (in order to increase its lifespan and efficiency), and nominal point operation should be targeted, the following proposed strategies are different from SAM's. The elaboration of appropriate strategies is accordingly to the DNI prediction model and was performed from two analyses: i) an annual comparison between storage behavior with predicted and measured irradiances; ii) a daily comparison between plant behavior with predicted and measured irradiances.

6.1. General observation and analysis

Discrepancies between estimated stored energy based on measured and predicted DNI for the simulation of the Andasol 3 CSP plant during one year is shown in Fig. 7, with the discharge energy being represented by a negative value. Hourly values of *TES* show an overall correlation coefficient of approximately 0.83 between simulated results with DNI predictions and measurements, with relative differences of approximately 8.62% for the charge and 8.29% for the discharge energies. Since DNI input values are hardly identical between prediction and measured, very few points will be located on the $y = x$ line, i.e. excess and lack of energy for a specific period is always different. However, a cluster of points can be observed below the $y = x$ line for charged energies ($TES^{ecmwf} > 0$ and $TES^{obs} > 0$). This is a result of the good DNI prediction performance, nonetheless with lower absolute values, leading to lower excess energy and therefore lower charged energy when compared with results based on measured DNI.

A "cross-like" pattern representing very strong discrepancies can also be observed. These points represent all the periods in which simulations predict any charge or discharge for forecasted DNI, while the contrary is obtained from measured DNI (i.e. $TES^{ecmwf} \neq 0$ and $TES^{obs} = 0$ or $TES^{ecmwf} = 0$ and $TES^{obs} \neq 0$). As previously stated, this is due to differences in the predicted and measured solar resource, leading to different states of charge and discharge of the TES system. Thus, one simulation might charge the TES for a longer duration than the other (top and right parts of the "cross"), or one simulation can show an earlier or longer discharge (left and bottom parts of the "cross"). These differences are also attributed to delays between predicted clouds and their actual occurrence, leading to out of sync charges and discharges between predicted and measured data. Lower prediction values are found when one simulation is performing a charge while the other is performing a discharge (top left corner and bottom right corner, i.e. $TES^{ecmwf} > 0$ and $TES^{obs} < 0$ or $TES^{ecmwf} < 0$ and $TES^{obs} > 0$). Fortunately, these situations are not frequent and only occur upon the use of DNI data that demonstrates a strong decrease during a part of the day for one simulation, while the other simulation shows a constant and higher DNI value, for instance, when a cloud is predicted but not observed. Moreover, a cluster of points is found when full nominal power discharge is performed in both cases (bottom left corner, i.e. $TES^{ecmwf} = TES^{obs} \approx -135$ MW_th). However, it is not uncommon that one simulation is performing discharge at full rate, while the other gives a partial discharge (due to residual power coming from the solar field), leading to the two "lines of points" (horizontal and vertical) that can be observed at the bottom left corner (i.e. $TES^{ecmwf} \approx -135$ MW_th and $TES^{obs} < 0$ or $TES^{ecmwf} < 0$ and $TES^{obs} \approx -135$ MW_th).

6.2. Recommended strategies for typical days

After analyzing the power plant response for an entire year with

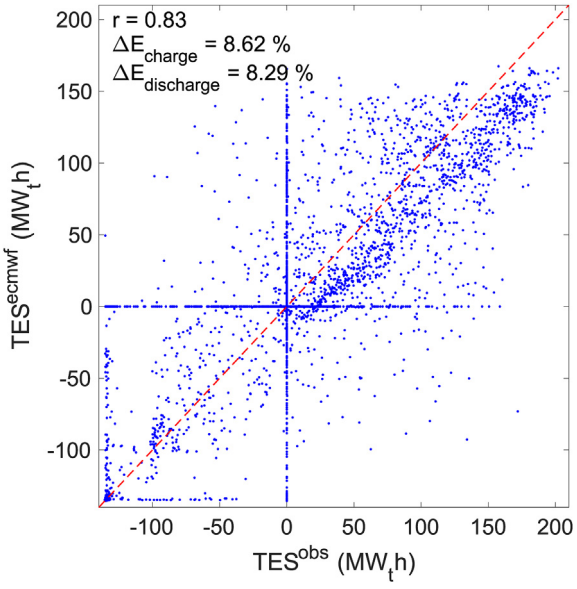

Fig. 7. Estimated hourly values of thermal energy into storage, *TES* (MW_th), obtained through the SAM simulation with the use of measurements (*obs*) and the IFS 24-h forecasts (*ecmwf*) for the Andasol 3 simulation in the SAM. The corresponding correlation coefficient, *r*, relative differences, ΔE (%), for charge and discharge powers, and the identity line $y = x$, given by a red dashed line, are also depicted. The period of study is related from July 1st, 2017 to June 30th, 2018 with the analysis being centered in the EVO station (Évora, southern Portugal). (For interpretation of the references to colour in this figure legend, the reader is referred to the Web version of this article.)

predicted and measured DNI data, a more thorough investigation is carried out considering a daily analysis, where four different strategy scenarios depending on four different predictions were defined. For every strategy, a typical day corresponding to a different weather condition has been used as an example.

6.2.1. Strategy I: high irradiance prediction, no clouds

The generated energy from solar, the stored energy and the electricity production during a day (August 2nd) with high irradiance and no clouds, for both simulations (use of predicted and measured DNI), are shown in Fig. 8. In the selected day, electricity production is maintained at a quasi-stationary value throughout the entire day and also after sunset due to discharge operations of the TES system. In both cases, during the afternoon, the energy value is subjected to a drop followed by a plateau, while DNI does not follow the same trend. This behavior is due to the fact that the TES system is full and is not able to absorb more energy surplus. As a consequence, a part of the solar field needs to be defocused to avoid overheating. It is possible to conclude that, if the prediction gives a sunny day with high irradiance (typical during the summer), then electricity production should be started as soon as possible, since the total amount of solar energy that can be collected is more important than the total needs of the power plant (50 MW_e production during the entire day, plus full charge of the TES system). This behavior will be emphasized since predicted DNI values are almost always lower than observations. For this reason, electricity production should start as soon as possible in order to maximize solar energy utilization. Moreover, a partial charge for safety at the beginning of the day is not required.

6.2.2. Strategy II: high irradiance prediction, with foreseen clouds

Like in the previous case, Fig. 9 shows the estimated solar produced power, stored power and electricity production, but for a day (May 12th) that has high irradiance and the passing of a cloud. During this day, the production of electricity is maintained at a quasi-stationary value during the entire day, since sufficient energy surplus has been stored in the TES system before the cloud occurrence. Although the prediction of a cloud passing by was accurate, its exact time of appearance and duration were not efficiently forecasted. Consequently, the charge and discharge power curves are different. This means that, if the global day prediction is good (i.e. high irradiance, typically in spring, summer or fall), but a cloud is foreseen, a partial charge should be performed at the beginning of the day. An early morning partial charge will ensure that a cloud will not stop electricity production, whenever it appears. After a partial charge, electricity production should be started as soon as possible to maximize solar production, while energy surplus (in case of existence) can be sent to the TES system.

6.2.3. Strategy III: medium irradiance prediction, with foreseen clouds

In Fig. 10, the solar produced power, the stored power and the electricity production are shown during a day (February 1st) with medium irradiance and the passing of clouds. In the present case, electricity production has a higher variation due to the clouds and an insufficient charged power before its occurrence. This means

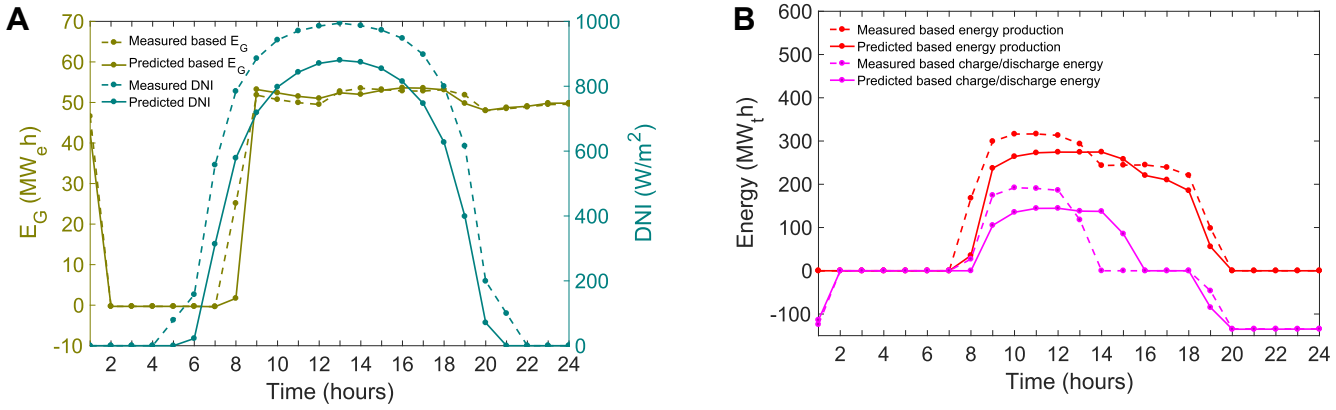

Fig. 8. a) Comparison between the SAM simulation results for August 2nd (prediction of high irradiance without clouds), with predicted and measured hourly mean DNI (W/m^2) and estimated electric energy, E_G ($MW_e h$), values; b) estimated thermal energy ($MW_t h$) and charge/discharge values.

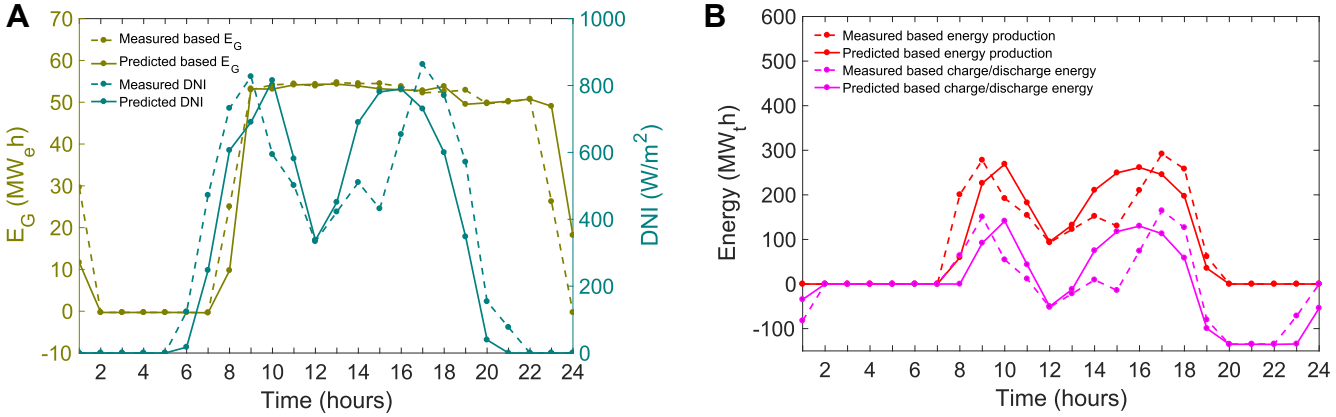

Fig. 9. a) Comparison between the SAM simulation results for May 12th (prediction of high irradiance with a foreseen cloud), with predicted and measured hourly mean DNI (W/m^2) and estimated electric energy, E_G ($MW_e h$), values; b) estimated thermal energy ($MW_t h$) and charge/discharge values.

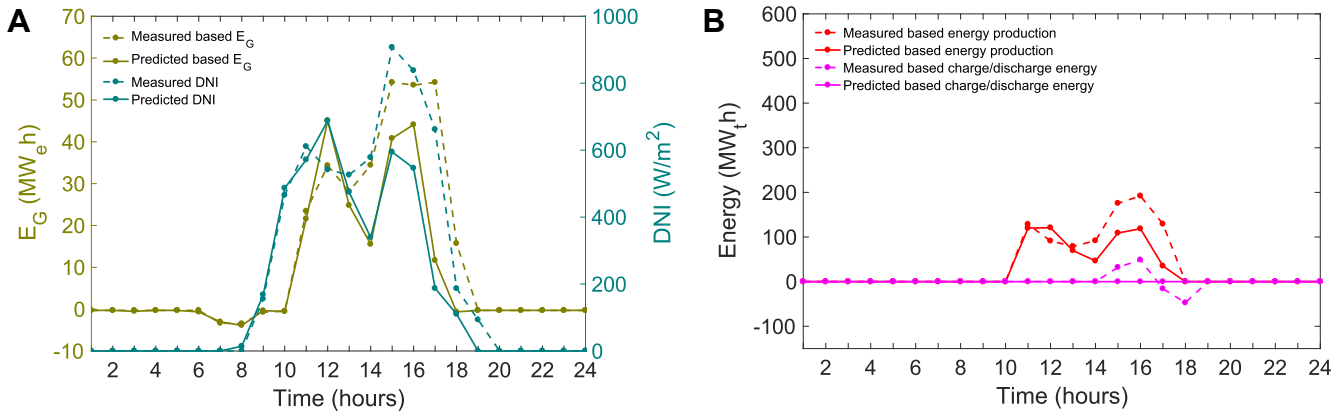

Fig. 10. a) Comparison between the SAM simulation results for February 1st (prediction of medium irradiance with a foreseen cloud), with predicted and measured hourly mean DNI (W/m^2) and estimated electric energy E_G (MW$_e$h) values; b) estimated thermal energy (MW$_t$h) and charge/discharge values.

that the adopted production strategy considered by the SAM is not the best choice. Moreover, as observed in the previous case, cloud prediction is not perfectly well represented by the model. Having into account these results, if the global day prediction is medium (i.e. medium irradiance, typically during winter, early spring or late fall) and a cloud is foreseen, then only a charge should be performed. In this case, the available power is not higher than the storage capacity of the TES system, and for that reason, it is relevant to produce electricity after sunset (discharge) and at a constant rate, without suffering from solar resource intermittency.

6.2.4. Strategy IV: prediction of low irradiance, with or without clouds

The last operational strategy example considers the solar produced power, the stored power and the electricity production during a day (January 13th) that has very low irradiance values (Fig. 11). For cloudy days, the SAM output gives a varying electricity production characterized by a very short duration. Knowing the storage capacity of the CSP plant, it should be reasonable to store all available energy. Thus, the subsequent applied strategy will depend on the TES state of charge and on the prediction for the following day:

a. If the model predicts high irradiance for the following day, then production should be started before sunrise thanks to the energy that has been previously stored.
b. If the model predicts high irradiance but with a foreseen cloud, then the previous day partial charge should serve as security margin to overcome poor solar inlet power. Therefore, the production should be started at sunrise.
c. If the model predicts medium irradiance with clouds, then produced energy should be entirely sent to the TES system until reaching a high state of charge (90%, for instance), and then electricity production should be started.
d. If the next day predicted DNI is very low, then all produced energy should be stored until reaching sufficient state of charge to produce electricity during a reasonable duration.

7. Conclusions

A synergistic DNI forecasting and control strategies can help integrating CSP into the electric grid and improve the local energy distribution performance. Results have shown that, despite an overall improvement of day-ahead DNI predictions through the use of the new operational ecRad radiative scheme of the IFS, there is still a demand for further developments towards the representation of clouds and aerosols, two fundamental parameters that still hinder DNI forecasting. For one location in southern Portugal, relative differences of approximately 0.12% for the total annual energy availabilities between forecasts and measurements during one year of data were obtained, as opposed to approximately 10.6% found for the previous radiative scheme McRad.

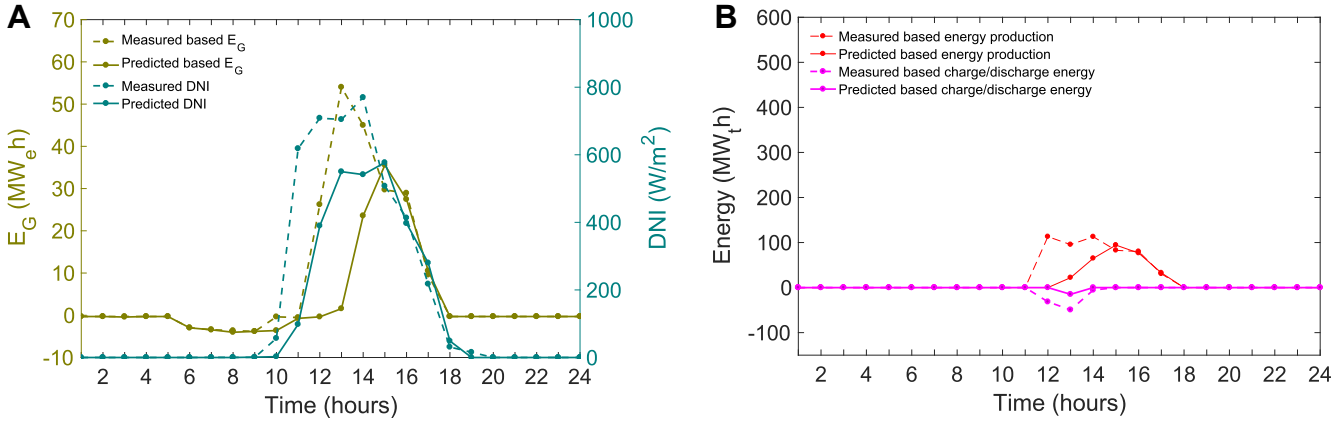

Fig. 11. a) Comparison between the SAM simulation results for January 13th (prediction of low irradiance with or without clouds), with predicted and measured hourly mean DNI (W/m^2) and estimated electric energy E_G (MW$_e$h) values; b) estimated thermal energy (MW$_t$h) and charge/discharge values.

In order to integrate forecasted data in the operations of a CSP system for the improvement of energy dispatch management during solar intermittency periods, a case study concerning the simulation of a linear focus PT power plant with similar configuration as the commercial Andasol 3 CSP was carried out through the use of the SAM. The estimated total annual energy values obtained for the Andasol 3 simulation showed a relative difference of nearly 2.8% between values based on forecasted data and the measured ones. Energy injection to the grid yield correlations of approximately 0.87 and 0.92 respectively between hourly and daily energy values based on forecasted and measured data. Since control strategy is deeply tight to the thermal energy storage capacity, four operational strategies were given for a set of typical days that had different weather conditions in order to handle the energy management of a CSP plant. Charge and discharge operations are applied accordingly to predicted energy availability, which is affected by the intermittency of cloud cover.

The present work demonstrates that day-ahead forecasts of DNI are suitable to predict the optimum injection of energy into the grid during a given hour period. It also shows that state-of-the-art NWP models can already be very useful tools for plant operators to apply appropriate strategies for the operational management of CSP systems.

Author contributions

The concept of this work was made by F.M.L. and H.G.S. The applied methodology was implemented by F.M.L, H.G.S., R.C., R.S., and P.C. The use of the SAM software was carried out by F.M.L. and T.F. Analysis, validation, investigation, resources, data curation, writing, and editing procedures were done by F.M.L. All authors have reviewed the article prior to submission. H.G.S., R.S., and M.C.-P. have supervised this work.

Declaration of competing interest

The authors declare that they have no known competing financial interests or personal relationships that could have appeared to influence the work reported in this paper.

Acknowledgements

F.M. Lopes and R. Conceição acknowledge the *Fundação para a Ciência e a Tecnologia* (FCT) scholarships, with the respective grant numbers SFRH/BD/129580/2017 and SRFH/BD/116344/2016, the Institute of Earth Sciences and the Renewable Energies Chair (both part of the University of Évora). R. Conceição, also acknowledges *Infraestrutura Nacional de Investigação de Energia Solar de Concentração* (INIESC). T. Fasquelle is thankful to the New StOrage Latent and sensible Concept for high efficient CSP Plants (NewSOL) project (H2020, GA: 720985). Co-funding was also provided by the European Union through the European Regional Development Fund, included in the Operational Program Competitiveness and Internationalization (COMPETE 2020) through the ICT (UID/GEO/04683/2013, POCI-01-0145-FEDER-007690), DNI-ALENTEJO (ALT20-03-0145-FEDER-000011) and ALOP (ALT20-03-0145-FEDER-000004) projects. The authors are also grateful to the European Centre for Medium-Range Weather Forecasts (ECMWF), to the Portuguese Institute for Sea and Atmosphere (IPMA), particularly Jorge Neto, and to the Portuguese Institute for Solar Energy (IPES), particularly Afonso Cavaco, for the data provided and care in data acquisition and quality control.

Appendix A

In this section, a detailed description is also given regarding the input parameters used within the SAM software for the simulation of a CSP power plant designed to run a PT system. For the Andasol 3 CSP (Fig. A1) case study, the available online information from NREL (2019) was complemented with the default SAM inputs characteristic from this type of power plant, together with the author's research towards a few parameters which were considered.

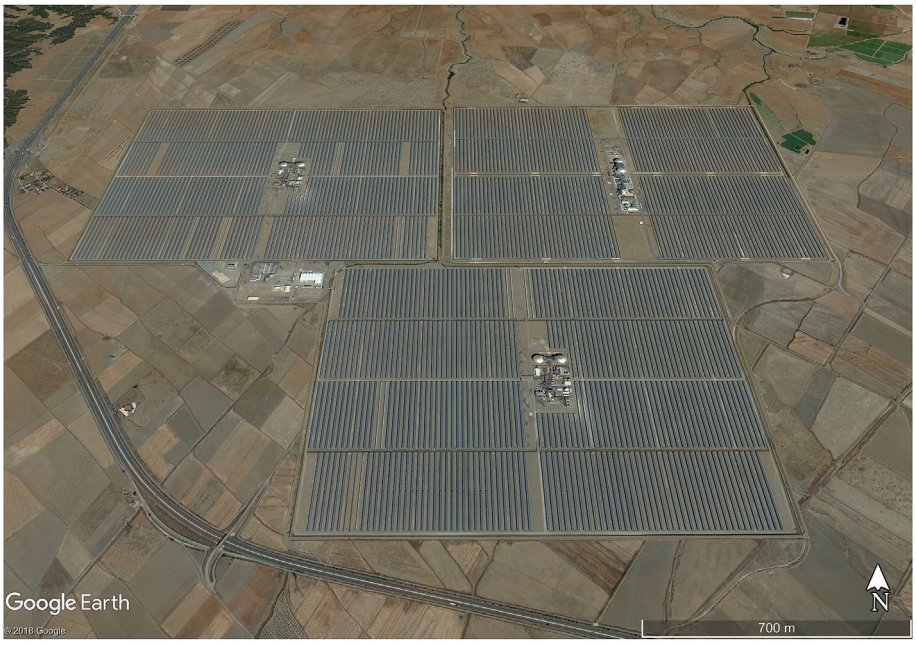

Fig. A.1. Andasol 1, 2 and 3 CSP project (NREL 2018) located in Aldeire (Granada, Spain). All rights reserved [58].

Table A.1
Input parameters for the SAM simulation of the Andasol 3 CSP station during one year (from July 1st, 2017 to June 30th, 2018).

General	
Name	Value
Field gross aperture	510120 m^2
Irradiance at design	700 W/m^2
Allow partial defocusing	Yes, simultaneous
HTF	Downtherm A
Design loop inlet temperature	293 °C
Design loop outlet temperature	393 °C
Full load hours of TES	7.5 h
Storage HTF fluid	Solar Salt
Solar field	
Min single-loop mass flow	1 kg/s
Max single-loop mass flow	11 kg/s
Aperture width	5.77 m
Length of one loop	600 m
Incidence angle modifier	$1-0.040107\cdot\theta/\cos(\theta)$ $-0.00206265\cdot\theta^2/\cos(\theta)$
Absorber tube inner diameter	0.066 m
Glass envelope inner diameter	0.119 m
Power block	
Design gross output	55 MW_e
Gross to net conversion factor	0.9
Rated cycle conversion efficiency	0.381
Fossil dispatch mode	Minimum backup
Auxiliary heater outlet set temperature	393 °C
Low resource standby period	2 h
Fraction of thermal power needed for standby	0.2
Power block start-up time	0.5 h
Fraction of thermal power for start-up	0.2
Minimum required start-up temperature	320 °C
Max turbine over design operation	1.05
Min turbine operation	0.2
Boiler operating pressure	100 bars
Turbine inlet pressure control	Fixed-pressure

References

[1] International Energy Agency (IEA, Photovoltaic Power Systems: Annual Report 2017, 2017, ISBN 978-3-906042-71-8.
[2] REN21, reportRenewable Energy Policy Network for the 21st Century. Renewables 2017 Global Status Report, 22-23. ISBN: 978-3-9818107-6-9.
[3] S.A. Kalogirou, Solar Energy Engineering: Processes and Systems, second ed., 2014, ISBN 978-0-12-397270-5, pp. 541–581 (Chapter 10).
[4] M. Schroedter-Homscheidt, A. Benedetti, N. Killius, Verification of ECMWF and ECMWF/MACC's Global and Direct Irradiance Forecasts with Respect to Solar Electricity Production Forecasts, Meteorologische Zeitschrift, 2016, https://doi.org/10.1127/metz/2016/0676. PrePub Article 2016.
[5] S.C. Müller, J. Remund, Shortest term forecasting of DNI for concentrated solar technologies, in: Meteotest, Fabrikstrasse 14, CH-3012 Bern, Switzerland. Conference Paper 2016, 2016, https://doi.org/10.4229/EUPVSEC20162016-5AO.8.5.
[6] L. Ramirez, J.M. Vindel, Forecasting and nowcasting of DNI for concentrating solar thermal systems, Chapter.13, in: Advances in Concentrating Solar Thermal Research and Technology, vol 2017, 2017, pp. 294–310, https://doi.org/10.1016/B978-0-08-100516-3.00013-7.
[7] L. Nonnenmacher, A. Kaur, C.F.M. Coimbra, Day-ahead resource forecasting for concentrated solar power, Renew. Energy 2016 (86) (2016) 866–876, https://doi.org/10.1016/j.renene.2015.08.068.
[8] M. Collares-Pereira, A. Rabl, Simple procedure for predicting long term average performance of nonconcentrating and concentrating solar collectors, Sol. Energy 23 (1979) (1979) 235–253, https://doi.org/10.1016/0038-092X(79)90163-4.
[9] M. Schroedter-Homscheidt, O. Oumbe, A. Benedetti, J.-J. Morcrette, Aerosols for concentrating solar electricity production forecasts: requirement quantification and ECMWF/MACC aerosol forecast assessment, Am. Meteorol. Soc. BAMS 2013 (2013) 903–914, https://doi.org/10.1175/BAMS-D-11-00259.1.
[10] E.W. Law, A.A. Prasad, M. Kay, R.A. Taylor, Direct normal irradiance forecasting and its application to concentrated solar thermal output forecasting – a review, Sol. Energy 2014 (108) (2014) 287–307, https://doi.org/10.1016/j.solener.2014.07.008.
[11] C. Brancucci Martinez-Anido, B. Botor, A.R. Florita, C. Draxl, S. Lu, H.F. Hamann, B.-M. Hodge, The value of day-ahead solar power forecasting improvement, Sol. Energy 2016 (129) (2016) 192–203, https://doi.org/10.1016/j.solener.2016.01.049.
[12] C. Coimbra, J. Kleissl, R. Marquez, Overview of Solar Forecasting Methods and a Metric for Accuracy Evaluation. Solar Resource Assessment and Forecasting 2013 (Chapter 8), Elsevier, Waltham, Massachusetts, 2013, ISBN 9780123971777, pp. 183–185.
[13] V. Lara-Fanego, J.A. Ruiz-Arias, A.D. Pozo-Vázquez, C.A. Gueymard, J. Tovar-Pescador, Evaluation of DNI forecast based on the WRF mesoscale atmospheric model for CPV applications, AIP Conf. Proc. 1477 (2012) (2012) 317–322. ISBN: 9780735410862.
[14] A. Martín, J. Trapero, Recursive estimation methods to forecast short-term solar irradiation. Environment, energy and climate change II: energies from new resources and the climate change 2014, Hdb Environ. Chem. 34 (2014) 17–32, https://doi.org/10.1007/698_2014_304.
[15] Y. Chu, C. Coimbra, Short-term probabilistic forecasts for direct normal irradiance, Renew. Energy 2017 (101) (2017) 526–536, https://doi.org/10.1016/j.renene.2016.09.012.
[16] C. Voyant, G. Notton, Solar irradiation nowcasting by stochastic persistence: a new parsimonious, simple and efficient forecasting tool, Renew. Sustain. Energy Rev. 2018 (92) (2018), https://doi.org/10.1016/j.rser.2018.04.116. In press. HAL Id: hal-01783937.
[17] R. Marquez, C. Coimbra, Intra-hour DNI forecasting based on cloud tracking image analysis, Sol. Energy 2012 (91) (2012) 327–336, https://doi.org/10.1016/j.solener.2012.09.018.
[18] S. Quesada-Ruiz, Y. Chu, J. Tovar-Pescador, H.T.C. Pedro, C.F.M. Coimbra, Cloud-tracking methodology for intra-hour DNI forecasting, Sol. Energy 2014 (102) (2014) 267–275, https://doi.org/10.1016/j.solener.2014.01.030.
[19] J. Nou, R. Chauvin, J. Eynard, S. Thil, S. Grieu, Towards the intrahour forecasting of direct normal irradiance using sky-imaging data, 2018, Heliyon 4 (4) (2018), https://doi.org/10.1016/j.heliyon.2018.e00598.
[20] G. Reikard, C. Hansen, Forecasting solar irradiance at short horizons: frequency and time domain models, Renew. Energy 2018 (135) (2018) 1270–1290, https://doi.org/10.1016/j.renene.2018.08.081. In press.
[21] R. Marquez, C. Coimbra, Forecasting of global and direct solar irradiance using stochastic learning methods, ground experiments and the NWS database, Sol. Energy 2011 (85) (2011) 746–756, https://doi.org/10.1016/j.solener.2011.01.007.
[22] C. Renno, F. Petito, A. Gatto, Artificial neural network models for predicting the solar radiation as input of a concentrating photovoltaic system, Energy Convers. Manag. 2015 (106) (2015) 999–1012, https://doi.org/10.1016/j.enconman.2015.10.033.
[23] I. Belhaj, O.E. Fatni, S. Barhmi, E.H. Saidi, A direct normal irradiation forecasting model based on artificial neural networks. Revue des Energies Renouvelables 2016, 19, N1, 21-28, Available from, http://www.cder.dz/download/Art19-1_3.pdf, 2016. accessed July 9th 2019.
[24] M. Gastón, L. Ramirez, I. Pagola, P.M. Fernandes, S. Lozano, X. Nicuesa, A system of direct radiation forecasting based on numerical weather predictions, satellite image and machine learning, in: 30th ISES Biennial Solar World Congress, vol 2011, 2011, https://doi.org/10.18086/swc.2011.16.03.
[25] T. Cebecauer, M. Suri, Site-adaptation of satellite-based DNI and GHI time series: overview and SolarGIS approach, in: AIP Conf. Proc, vol 2016, 2016, p. 150002, https://doi.org/10.1063/1.4949234, 1734.
[26] D.P. Larson, L. Nonnenmacher, C.F.M. Coimbra, Day-ahead forecasting of solar power output from photovoltaic plants in the American southwest, Renew. Energy 2016 (91) (2016) 11–20, https://doi.org/10.1016/j.renene.2016.01.039.
[27] C.M. Fernández-Peruchena, M. Gastón, M. Schroedter-Homscheidt, I.M. Marco, J.L. Casado-Rubio, J.A. Garcia-Moya, Increasing the temporal resolution of direct normal solar irradiance forecasted series, in: AIP Conf. Proc, vol 2017, 2017, p. 140007, https://doi.org/10.1063/1.4984515, 1850.
[28] J.P. Mulcahy, D.N. Walters, N. Bellouin, S.F. Milton, Impacts of increasing the aerosol complexity in the Met Office global numerical weather prediction model, Atmos. Chem. Phys. 2014 (14) (2014) 4749–4778, https://doi.org/10.5194/acp-14-4749-2014.
[29] J. Fan, Review of aerosol-cloud interaction: mechanisms, significance, and challenges, Am. Meteorol. Soc. 2016 (73) (2016) 4221–4252, https://doi.org/10.1175/JAS-D-16-0037.1.
[30] F.M. Lopes, H.G. Silva, R. Salgado, A. Cavaco, P. Canhoto, M. Collares-Pereira, Short-term forecasts of GHI and DNI for solar energy systems operation: assessment of the ECMWF integrated forecasting system in southern Portugal, Sol. Energy 2018 (170) (2018) 14–30, https://doi.org/10.1016/j.solener.2018.05.039.
[31] E.F.M. Abreu, P. Canhoto, V. Prior, R. Melicio, Solar resource assessment through long-term statistical analysis and typical data generation with different time resolutions using GHI measurements, Renew. Energy 2018 (127) (2018) 398–411, https://doi.org/10.1016/j.renene.2018.04.068.
[32] R. Salgado, P.M.A. Miranda, P. Lacarrère, J. Noilhan, Boundary layer development and summer circulation in Southern Portugal, Tethys 2015 (12) (2015), https://doi.org/10.3369/tethys.2015.12.03.
[33] A. Cavaco, H.G. Silva, P. Canhoto, T. Osório, M. Collares-Pereira, Progresses in DNI measurements in southern Portugal, in: AIP Conf. Proc, vol 2018, 2018, pp. 1–7, https://doi.org/10.1063/1.5067189, 2033, 190004.
[34] R. Conceição, H.G. Silva, J. Mirão, M. Gostein, L. Fialho, L. Navarte, et al., Saharan dust transport to Europe and its impact on the photovoltaic performance: a case study of soiling in Portugal, Sol. Energy 2018 (160) (2018)

94–102, https://doi.org/10.1016/j.solener.2017.11.059.
[35] International Organization for Standardization (ISO) 9059, Solar energy, Calibration of field pyrheliometers by comparison to a reference pyrheliometer, 2014. http://www.iso.org/standard/16628.html, 1990 accessed July 9th 2019.
[36] C.N. Long, E.G. Dutton, BSRN Global Network recommended QC tests 2002, V2.0, Available from, https://epic.awi.de/id/eprint/30083/1/BSRN_recommended_QC_tests_V2.pdf, 2002. accessed July 9th 2019.
[37] Google Earth V 7.3.2.5491, Évora city, southern Portugal. 3834'00.92"N, 754'41.68"W. Eye alt 10.32 km, Available from, https://earth.google.com/web/, 2019a. accessed July 9th 2019.
[38] R.J. Hogan, A. Bozzo, A flexible and efficient radiation scheme for the ECMWF model, Adv. Modell. Earth Syst. 2018 (10) (2018) 1990–2008, https://doi.org/10.1029/2018MS001364.
[39] J.-J. Morcrette, H.W. Baker, J.N.S. Cole, M.J. Iacono, R. Pincus, Impact of a new radiation package, McRad, in the ECMWF integrated forecasting system, Mon. Weather Rev. 136 (2008) 4773–4798, https://doi.org/10.1175/2008MWR2363.1, 2008.
[40] E. Mlawer, S. Clough, Shortwave and longwave enhancements in the Rapid radiative transfer model, in: Proc. Seventh Atmospheric Radiation Measurement (ARM) Science Team Meeting 1997, U.S. Department of Energy, San Antonio, TX, 1997, pp. 409–413. Available from, http://www.arm.gov/publications/proceedings/conf07/extended_abs/mlawer_ej.pdf. accessed July 9th 2019.
[41] I. Tegen, P. Hollrig, M. Chin, I. Fung, D. Jacob, J. Penner, Contribution of different aerosol species to the global aerosol extinction optical thickness: estimates from model results, 1997, Geophys. Res. 102 (23) (1997), https://doi.org/10.1029/97JD01864, 895-23, 915.
[42] A. Bozzo, S. Remy, A. Benedetti, J. Flemming, P. Bechtold, Rodwell, et al., Technical Memorandum, 801, Implementation of a CAMS-Based Aerosol Climatology in the IFS, vol 2017, European Centre for Medium-Range Weather Forecasts, 2017. Available from, http://www.ecmwf.int/sites/default/files/elibrary/2017/17219-implementation-cams-based-aerosol-climatology-ifs.pdf. accessed July 9th 2019.
[43] R.J. Hogan, M. Ahlgrimm, G. Balsamo, A. Beljaars, P. Berrisford, A. Bozzo, et al., Technical Memorandum, 816, Radiation in Numerical Weather Prediction, vol 2017, European Centre for Medium-Range Weather Forecasts, 2017. Available from, https://www.ecmwf.int/sites/default/files/elibrary/2017/17771-radiation-numerical-weather-prediction.pdf. accessed March 20th 2019.
[44] R. Perez, E. Lorenz, S. Pelland, M. Beauharnois, G.V. Knowe, K. Hemker Jr., et al., Comparison of numerical weather prediction solar irradiance forecasts in the US, Canada and Europe, Sol. Energy 94 (2013) 305–326, https://doi.org/10.1016/j.solener.2013.05.005, 2013.
[45] International Energy Agency (IEA, Technology roadmap: solar thermal electricity. https://www.iea.org/publications/freepublications/publication/technologyroadmapsolarthermalelectricity_2014edition.pdf, 2014 accessed July 9th 2019.
[46] M.I.R. Serrano, Concentrating solar thermal technologies, analysis and optimization by CFD modelling, 2017, Green Energy Technol. 1 (IX) (2017), https://doi.org/10.1007/978-3-319-45883-0 (Chapter 2).
[47] N. Blair, A. Dobos, J. Freeman, T. Neises, M. Wagner, T. Ferguson, et al., System Advisor Model, SAM 2014.1.14: General Description, vol 2014, National Renewable Energy Laboratory, Golden, CO, 2014. NREL/TP-6A20-61019.
[48] System Advisor Model (SAM) Software from NREL, U.S. Department of Energy, 2019a. Available from, https://sam.nrel.gov/download. accessed July 9th 2019.
[49] Transient System Simulation (TRNSYS) User's Manual, vol 18, 2019. http://www.trnsys.com/. Available from, accessed July 9th 2019.
[50] System Advisor Model (SAM) User's Manual from NREL, U.S. Department of Energy, 2019b. Available from, https://sam.nrel.gov/index.php. accessed July 9th 2019.
[51] M. Wittmann, H. Breitkreuz, M. Schroedter-Homscheidt, M. Eck, Case studies on the use of solar irradiance forecast for optimized operation strategies of solar thermal power plants, IEEE Select. Topics Appl. Earth Observ. Remote Sens. 1 (1) (2008), https://doi.org/10.1109/JSTARS.2008.2001152, 2008.
[52] F. Dinter, D.M. Gonzalez, Operability, reliability and economic benefits of CSP with thermal energy storage: first year of operation of ANDASOL 3, Energy Procedia 2014 (49) (2014) 2472–2481, https://doi.org/10.1016/j.egypro.2014.03.262.
[53] Andasol-3 CSP project, Available from, https://solarpaces.nrel.gov/andasol-3, 2019. accessed July 9th 2019.
[54] K.M. Powell, T.F. Edgar, Modeling and control of a solar thermal power plant with thermal energy storage, Chem. Eng. Sci. 2012 (71) (2012) 138–145, https://doi.org/10.1016/j.ces.2011.12.009.
[55] P. Wagner, M. Wittmann, Influence of different operation strategies on transient solar thermal power plant simulation models with molten salts as heat transfer fluid, Energy Procedia 2014 (49) (2014) 1652–1663, https://doi.org/10.1016/j.egypro.2014.03.174.
[56] X. Ju, C. Xu, X. Han, H. Zhang, G. Wei, L. Chen, Recent advances in the PV-CSP hybrid solar power technology, in: AIP Conf. Proc, vol 2017, 2017, p. 110006, https://doi.org/10.1063/1.4984480, 1850.
[57] J. Garcia-Barberena, P. Garcia, M. Sanchez, M.J. Blanco, C. Lasheras, A. Padros, et al., Analysis of the influence of operational strategies in plant performance using SimulCET, simulation software for parabolic trough power plants, Sol. Energy 2012 (86) (2012) 53–63, https://doi.org/10.1016/j.solener.2011.09.018.
[58] Google Earth V 7.3.2.5491, Andasol 1,2 and 3 in Aldeire, Granada (Spain). 3713'01.11"N, 303'22.02"W. Eye alt 3.42 km, Available from, https://earth.google.com/web/, 2019b. accessed July 9th 2019.

Atmospheric Research 202 (2018) 81–95

Contents lists available at ScienceDirect

Atmospheric Research

journal homepage: www.elsevier.com/locate/atmosres

Electrical sensing of the dynamical structure of the planetary boundary layer

K.A. Nicoll[a,b,*], R.G. Harrison[a], H.G. Silva[c], R. Salgado[d], M. Melgâo[d], D. Bortoli[d]

[a] Department of Meteorology, University of Reading, Earley Gate, Reading, Berkshire RG6 6BB, UK
[b] Department of Electronic and Electrical Engineering, University of Bath, Claverton Down, Bath BA2 7AY, UK
[c] Renewable Energies Chair, University of Évora, Palácio do Vimioso, Largo Marquês de Marialva, 7002-554 Évora, Portugal
[d] Departamento de Física, ICT, Instituto de Ciências da Terra, Universidade de Évora, Rua Romão Ramalho 59, 7002-554 Évora, Portugal

A B S T R A C T

Turbulent and convective processes within the planetary boundary layer are responsible for the transport of moisture, momentum and particulate matter, but are also important in determining the electrical charge transport of the lower atmosphere. This paper presents the first high resolution vertical charge profiles during fair weather conditions, obtained with instrumented radiosonde balloons over Alqueva, Portugal during the summer of 2014. The short intervals (4 h) between balloon flights enabled the diurnal variation in the vertical profile of charge within the boundary layer to be examined in detail, with much smaller charges (up to 20 pC m^{-3}) observed during stable night time periods than during the day. Following sunrise, the evolution of the charge profile was complex, demonstrating charged ultrafine aerosol, lofted upwards by daytime convection. This produced charge up to 92 pC m^{-3} up to 500 m above the surface. The diurnal variation in the integrated column of charge above the site tracked closely with the diurnal variation in near surface charge as derived from a nearby electric field sensor, confirming the importance of the link between surface charge generation processes and aloft. The local aerosol vertical profiles were estimated using backscatter measurements from a collocated ceilometer. These were utilised in a simple model to calculate the charge expected due to vertical conduction current flow in the global electric circuit through aerosol layers. The analysis presented here demonstrates that charge can provide detailed information about boundary layer transport, particularly in regard to the ultrafine aerosol structure, that conventional thermodynamic and ceilometer measurements do not.

1. Introduction

The effect of meteorological processes on the electrical state of the atmosphere has been known about for almost 250 years, even leading Lord Kelvin to suggest that weather forecasting would one day be achieved with an electrometer (e.g. Aplin and Harrison, 2013). The complexity, however, of relationships between atmospheric electrical variables and meteorological processes makes this difficult. What has become evident is that the same meteorological processes that act to transport heat, momentum, moisture and pollutants within the lower atmosphere also transport charge (see review by Hoppel et al., 1986). This has led to suggestions that so-called atmospheric electrical "convection currents" can be used as a method for determining turbulent transport processes in the lower atmosphere, e.g. Markson et al. (1981). The similarity between the convective flux of charge and turbulent transport processes is particularly strong near the surface, i.e. within the planetary boundary layer (PBL). The PBL is the lowest portion of the atmosphere which is directly influenced by the presence of the surface (often referred to historically in atmospheric electricity as the Exchange or Austausch layer), with a depth ranging from a few hundred meters to several km, varying with latitude and time of day (e.g. Stull, 2012). In the PBL, air-surface interactions take place in the form of mechanical and thermal forces, which drive turbulence and convection respectively. The PBL structure evolves considerably throughout the day (see e.g. Garratt, 1994 for example vertical profiles), and also varies between land and ocean surfaces (e.g. Kaimal and Finnigan, 1994). Processes within the PBL control transport of aerosol particles, moisture and momentum and the PBL top is typically characterised by a temperature inversion (known as a "capping inversion"), which traps these quantities beneath it. The height of the PBL is often used to characterise the vertical extent of mixing within the boundary layer and the level at which exchange with the free troposphere occurs.

Free charge is ubiquitous in the atmosphere and is released by ionisation from Galactic Cosmic Rays (GCRs) and radioactivity near the earth's surface (i.e. gamma and beta radiating directly from the surface, as well as radiation from radioactive gases). This ionisation gives rise to the electrical conductivity of air, σ, which is primarily due to the presence of small cluster ions (nm diameter) (e.g. Tammet, 1995).

* Corresponding author at: Department of Meteorology, University of Reading, Earley Gate, Reading, Berkshire RG6 6BB, UK.
E-mail address: k.a.nicoll@reading.ac.uk (K.A. Nicoll).

https://doi.org/10.1016/j.atmosres.2017.11.009
Received 2 June 2017; Received in revised form 2 November 2017; Accepted 6 November 2017
Available online 08 November 2017
0169-8095/ © 2017 The Authors. Published by Elsevier B.V. This is an open access article under the CC BY-NC-ND license (http://creativecommons.org/licenses/BY-NC-ND/4.0/).

Maintenance of charge within the atmosphere is a continual balance between ion generation and loss processes (Hoppel and Frick, 1986). As well as generation of ions by GCRs and radioactivity, ions are destroyed by ion-ion recombination (i.e. self-neutralisation), and lost by attachment to larger particles such as aerosol and cloud droplets. Ions are subject to the same turbulent eddies that transport momentum, moisture and pollutants throughout the PBL. Thus atmospheric electrical variables within the PBL depend on the local ionisation profile, aerosol size and number distribution as well as turbulent mixing of both ions and radioactive gases. Therefore they are heavily dependent on the combined influences of surface drag, heating, and evaporation from the underlying Earth's surface.

As well as being influenced by local meteorological variations, atmospheric electrical variables are also governed by global scale current flow in the global electric circuit, GEC, (e.g. Williams, 2009; Rycroft et al., 2008). This is most evident when studying the diurnal variation in atmospheric electric field, which is usually measured as the Potential Gradient, PG.[1] In clean air PG exhibits a minimum at ~0400 UT and a maximum at ~1900 UT, in accordance with the diurnal variation in global thunderstorm activity (Wilson, 1921; Whipple, 1929; Mach et al., 2011). The globally-invariant nature of this variation, at least on average, was first observed on the ocean cruises organised by the Carnegie Institution (Harrison, 2013), and hence is often referred to as the *Carnegie curve*. GEC effects on surface measurements of PG made within the PBL are often masked by dominant local meteorological effects such as convection or turbulent mixing, which can manifest themselves as additional fluctuations superimposed on the fair weather Carnegie curve (e.g. Israel, 1955). This is of particular importance during summer sunrise when convection causes mixing of the layer of positive charge which can form close to the nocturnal surface (known as the electrode layer[2]), thereby transiently disturbing the established local PG. Electrode layers only occur within a few meters of the surface most commonly over the calm ocean surface where there is no source of radioactive ionisation, but also over land during stable, low wind conditions (Crozier, 1963).

Although positive and negative ions are initially created in equal numbers, natural processes act to separate the different charge polarities, including the transfer of charge to aerosol and cloud droplets. This gives rise to the space charge density, ρ, which refers to the net difference between positive and negative charge per unit volume. ρ is not concerned with the nature of individual charge carriers, but only the total charge retained by all charge carriers. ρ is defined as

$$\rho = e\left[(n_+ - n_-) + \sum_{i=1}^{i=k}\sum_{j=-\infty}^{\infty} jN_{i,j}\right], \quad (1)$$

where the first term is the ionic space charge contribution and the second term is that due to particulate aerosol. e is the magnitude of the electronic charge, n_+ and n_- are the small ion number concentrations, and the aerosol size distribution is represented by k size categories, each of which spans j elementary charges. Charge separation can arise from flow of the air-Earth conduction current, J_c, which flows vertically between the ionosphere to Earth's surface through aerosol and cloud layers. The theory behind such phenomenon is described in detail in Zhou and Tinsley (2007), Harrison et al. (2015), and Nicoll and Harrison (2016).

Analytical studies of the influence of meteorological processes on atmospheric electric variables date back before the 1800s (e.g. Cavello, 1777), but since most measurements were performed near the surface, at low altitudes, these sites were almost always within the PBL. To study the effect of the PBL on atmospheric electricity, one must get above the inversion layer, thereby such as through mountaintop observatories, airborne measurements, or very tall towers (such as the Eiffel tower (e.g. Harrison and Aplin, 2003)). The pioneering aircraft measurements of Sagalyn and Faucher (1954, 1956) were amongst the first to demonstrate quantitatively that the electrical conductivity of air aloft was substantially reduced by the presence of aerosol particles trapped within the PBL, with a distinct change in behaviour in the free troposphere above. This was also found through mountaintop observations at the Zugspitze using an instrumented cable car (Reiter and Sládkovič, 1970). Moore et al. (1962) analysed hourly aircraft profiles of space charge (i.e. the net difference between positive and negative charge) throughout the day, demonstrating the similarity between this and the evolution of the PBL temperature profile, as well as the relation to fog and haze layers. More recently, Marshall et al. (1999) have studied the evolution of the electric field profile up to several hundred metres, demonstrating the existence of elevated layers of space charge close to the ground in the build up to sunrise.

In terms of quantifying the relationships between atmospheric electrical variables and turbulent diagnostic parameters, Markson et al. (1981), demonstrated good correlation between aircraft observations of the electrical eddy flux of space charge (found from PG measurements) and surface moisture flux over the ocean surface. In addition, several attempts at characterising the eddy diffusion coefficient (which represents the ability of turbulent eddies to transport atmospheric variables from a region of excess to a region of deficit) have been made both over land (e.g. Kawano, 1957; Kulkarni, 2010) and over the ocean (Hoppel and Gathman, 1971). The ocean situation is more straightforward to analyse due to the absence of radioactivity and low aerosol content, as well as reduced surface roughness.

Much of the modelling work studying atmospheric electricity in the PBL has focused on the electrode layer (Hoppel and Gathman, 1971; Willett, 1979; Willett, 1981; Kulkarni, 2010) as this is one of the main sources of local space charge in the atmosphere. Turbulent scenarios involving the electrode layer are complex, however, Hoppel and Gathman (1972) demonstrated reasonable agreement between a model of the turbulent electrode layer and observations over an ocean surface. More recent work over continental surfaces has demonstrated the existence of sub-mesoscale electrical structures superimposed on the mean wind flow in the PBL, which have been termed “Aero Electric Structures (AES)” (Anisimov et al., 1994) and are directly related to transport of turbulent eddies. These have typical dimensions of 500 to 1000 m and lifetimes of tens of minutes, detected experimentally from high frequency analysis of PG data. Anisimov et al. (1999, 2013) discuss the development of a detailed numerical model for AES formation which takes into account turbulent transport of space charge by convection and demonstrates that the dynamic and stability conditions of the PBL are key to controlling the evolution of the space charge profile.

This work presents new high resolution vertical profiles of space charge through and above the PBL in fair weather conditions. Measurements were made during the ALEX2014 field campaign in Portugal, during the summer of 2014, and consisted of surface measurement of Potential Gradient (PG), as well as a number of specially instrumented radiosonde balloon flights, carrying space charge sensors. Detailed analysis of the diurnal variation in the vertical profile of space charge is undertaken, as well as its relation to the surface PG and ceilometer measurements of aerosol backscatter. This is the first time that inexpensive, disposable electrical sensors have been demonstrated to provide indirect information about turbulent mixing processes in the lower atmosphere.

2. Methodology and instrumentation

The observations described here took place as part of the ALEX2014 field campaign (alex2014.cge.uevora.pt.) at the Alqueva reservoir,

[1] The Potential Gradient F is related to the vertical component of the electric field E_z by $F = -E_z$.

[2] The electrode layer results from the flow of ions under the atmospheric electric field (positive ions are driven downward, and negative ones upward) and the presence of the boundary of the surface. At this boundary positive ions flowing downward are forced to stop leading to a net accumulation of positive charge.

Portugal (38.27°N, 7.53°W) during July 2014. The main aim of the campaign was to study the impact of the reservoir on the local environment. Alqueva experiences a typical Mediterranean climate, with warm, dry summer periods, and sparse vegetation. The location of Alqueva is rural, with little anthropogenic pollution. The Alqueva reservoir is the largest inland lake in Portugal, of area 250 km^2 and 80 km from end to end. The size of the reservoir means that it is common for a lake breeze effect to develop during calm conditions when the lake/land temperature contrast is strong (e.g. see Potes et al., 2017). As this has been shown to affect local meteorological and electrical conditions close to the lake shore (Lopes et al., 2016), we also consider potential lake breeze effects here.

Surface PG measurements were made continuously throughout the campaign (see Lopes et al., 2016) using a JCI 131F electrostatic field mill at 2 m above the ground. The measurement site was located ~100 m from the shoreline at the southern end of the lake, on a small hill ~50 m above the water surface (Parque Solar). A map of the Alqueva reservoir and the location of the measurement at Parque Solar are provided in Appendix A. The field mill was set to a 0–2 kVm^{-1} range, with data sampled at 1 s and logged at 1 minute averages. Nearby meteorological measurements of temperature, relative humidity (RH), wind speed, wind direction and solar radiation were also made. Further instrumentation was used to provide information about the aerosol content at Alqueva in the form of a CL31 Ceilometer manufactured by Vaisala and a TSI Optical Particle Sizer (model OPS3330). The main features of these systems and the data processing and retrieval techniques are described in Appendices C and D.

Balloon-carried instruments were launched from a location ~100 m from the PG measurement site. Vaisala RS92 radiosondes were instrumented with the PANDORA system (Programmable ANalogue and Digital Radiosonde Accessory) developed by the University of Reading (Harrison et al., 2012), which provides a data acquisition system with which to interface additional science sensors to the standard meteorological radiosonde. Each sensor package carried a space charge sensor based on the design described in Nicoll (2013) (simplified to omit the self-calibrating mode). This charge sensor uses a spherical electrode connected to a sensitive electrometer circuit to measure the displacement current generated from a changing electric field, dominated by vertical electric field variations as the sonde ascends. The space charge is derived from the electrometer current and the ascent rate. Calibration details are given in Nicoll and Harrison, 2016. The typical 5 ms^{-1} ascent rate of the sonde, and 1 Hz sampling rate of the PANDORA system provides a measurement approximately every 5 m in altitude. An Intense Observation Period (IOP) during the ALEX2014 campaign took place on 22nd to 24th July 2014 when a total of 8 specially instrumented radiosonde packages were launched during the two days. Balloon flight details during the IOP are given in Table 1.

Sensor packages were flown beneath 600 g balloons, reaching, on average, altitudes of 31 km at burst. An example of a full height vertical profile from one of the specially instrumented radiosondes is shown in Fig. 1 which displays (a) temperature and RH data and (b) space charge density measured by the charge sensor. Considering the space charge profile, Fig. 1(b) clearly shows that the magnitude of the charge is large within the boundary layer but decreases markedly with altitude above this. The remainder of this paper is concerned with the vertical variation of space charge within the PBL.

3. Results

3.1. Diurnal variation of space charge with height in the PBL

During the most intensive period of the campaign, the specially instrumented radiosondes were launched approximately every 4 h which provides an opportunity to study the time evolution of the vertical profile in space charge as the PBL evolves throughout the day. The period of interest examined further is from 0200 UT 23rd July to 0200 UT 24th July (flights 3 to 8 in Table 1), with individual plots from each flight shown in Fig. 2. The weather during this period was characterised by anticyclonic conditions (surface pressure > 990 hPa for the entire IOP), with clear skies during the day and maximum air temperatures up to 38 °C. Overnight, the clear skies led to rapid cooling (minimum night time temperatures ~16 °C) and the formation of short lived cloud layers lasting only a few hours, which dissipated by 0700 UT most mornings. The 23rd July was dominated by a weak north westerly flow, which was sufficient enough to prevent any lake breeze effect from developing. This is in contrast to the previous day (22nd July), when the strongest lake breeze effect of the entire ALEX campaign was observed (see Potes et al., 2017 for more detail). The effect of the lake breeze on the meteorological conditions on 22nd is discussed in Section 3.2.

Fig. 2 shows thermodynamic quantities of temperature, potential temperature, relative humidity, (RH), horizontal wind speed and direction, as well as magnitude of space charge profiles for six ascents within a 24 hour period on 23rd July. The modulus of the space charge is used here due to the high degree of variability in the space charge measurement which makes the polarity difficult to interpret, which is partly a consequence of measuring at such high resolution. To make the space charge determination as robust as possible, we therefore use the absolute value of space charge. This is an alternative to providing an average profile which would remove the detailed vertical structure in the space charge, which is the main focus here.

Starting with the first ascent at 0208 UT on 23rd July (Fig. 2(a)), the temperature profile in the lower levels is characteristically stable, with a substantial inversion at ~300 m (associated with the formation of the nocturnal boundary layer), with a subsequent smaller near neutral residual layer up to ~2.5 km. The inversions at 2.5 and 3 km are likely to be associated with the remainder of the PBL top from the previous afternoon. The wind profile from the radiosonde demonstrates the presence of two jets between ~0.3–0.7 km and 2–3 km, with a maximum wind speed at 2.3 km. Substantial wind shear (confirmed by the vertical change in wind direction) is also evident at the top of the lower level jet at ~1 km. The space charge profile shows at least 3 distinct

Table 1
Summary of details of specially instrumented balloons launched during the IOP between 22nd and 24th July. Balloon launch times are given in UT which is 1 h behind local time. PBL height is derived according to the most significant inversion in the potential temperature profile. Max space charge is the maximum magnitude of space charge in the layer from the surface up to 3.5 km.

Flight number	Date	Launch time (UT)	PBL height (m)	Max space charge (pC m^{-3})
1	22/07/14	1134	1928	46.5
2	22/07/14	2030	2210	27.3
3	23/07/14	0208	317	23.2
4	23/07/14	0830	704	41.9
5	23/07/14	1130	811	44.5
6	23/07/14	1420	1733	91.7
7	23/07/14	1725	1774	73.6
8	24/07/14	0215	604	79.2

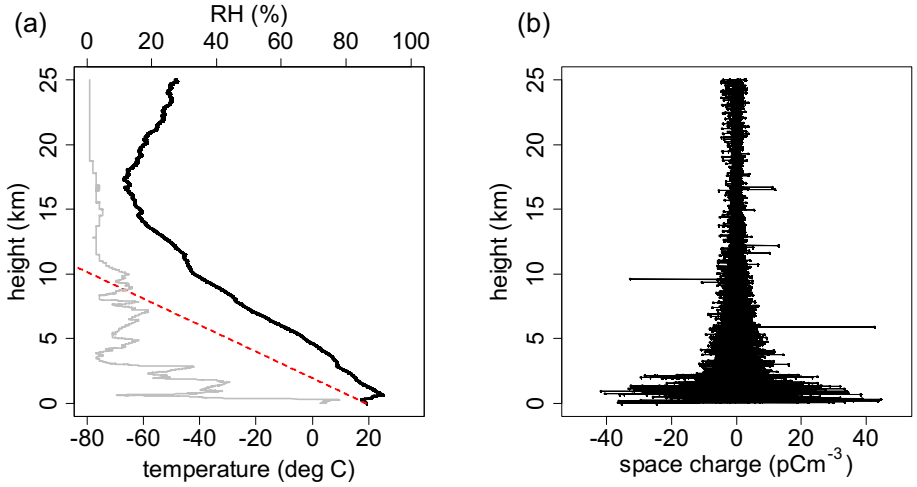

Fig. 1. (a) Vertical profile measured at Alqueva at 0830 UT on 23rd July 2014 (flight 4 in Table 1). Thermodynamic profiles of temperature (black) and RH (grey) as measured by the RS92 radiosonde's sensors (the red line shows the dry adiabatic lapse rate, DALR), (b) measured space charge. (For interpretation of the references to colour in this figure legend, the reader is referred to the web version of this article.)

thin layers of charge from the surface up to the inversion at 2.5 km, with a maximum value of ~23 pC m^{-3}. The charge layer at 2 km is suggested to result from trapping of charge underneath the main inversion of the residual layer, transported upwards from the surface from the earlier daytime convection. The layer at 1 km is not associated with a temperature inversion, but is coincident with a region of increased RH and wind shear.

Fig. 2(b) shows an ascent profile 6 h later at 0830 UT, by which time the surface layer has become convective; at 300 m the temperature inversion has strengthened, and the charge profile has become much more complex. During the 6 hour period between ascents a number of notable meteorological and solar changes occurred. Fig. 3 shows a time series of ceilometer backscatter during the IOP on 23rd and 24th July 2014. Deep blue areas indicate small backscatter signals demonstrating the absence of clouds, whereas colours from light blue through to red illustrate increasing backscatter values which represent an increase in the atmospheric optical depth. It is clear from the red backscatter between 0530 UT and 0800 UT on 23rd July that a shallow layer of cloud formed at ~600 m altitude during the early morning hours, between the balloon ascents. The remnants of this are also apparent from the RH data in Fig. 2(a) and (b) in which the maximum value of RH in the near surface layer increased from 60 to 76% between the 0200 UT and 0830 UT ascents. This occurred due to substantial cooling near the surface under clear skies. The lifetime of the cloud layer was very short, with dissipation by 0800 UT, due to the increase in surface heating (as well as warming from above the cloud) due to the sunrise at 0627 UT.

The space charge profile measured at 0830 UT is clearly very different from the night time profile at 0200 UT. The magnitude of the charge up to 2 km is ~twice as large as during the earlier ascent, with much deeper individual charge layers, extending from the surface up to 2 km. The most straightforward explanation is that the extra charge originated from horizontal advection, in the large scale synoptic flow. Fig. 4(a) and (b) shows modelled wind speed and direction plots for 1300 UT on 22nd and 23rd July at the surface over Alqueva dam using the non-hydrostatic Meso-NH (Lafore et al., 1998) atmospheric model at 1 km horizontal resolution. (The model and the setup of the simulation are described further in Appendix A.) Considerable differences in the wind conditions exist between the two days in that July 22nd is dominated by a local lake breeze (characterised by wind directions flowing from the centre of the lake to the shore), whilst July 23rd is dominated by a moderate north westerly flow. The increased space charge at 0830 UT on 23rd July is therefore likely to be linked to the advection of air which would have passed over more populated areas such as Lisbon and therefore contained a higher concentration of pollutants than would be present at Alqueva.

An additional contribution to the vertical charge profile at 0830 UT could arise from the earlier cloud layer at ~600 m, which would cause charge to accumulate on the horizontal cloud edges as a result of vertical conduction current flow in the GEC (see Section 3.3 for further discussion). Such charging has been observed to occur frequently due to the conductivity gradients present around stratiform cloud layers (e.g. Nicoll and Harrison, 2010, 2016) as well as aerosol layers (e.g. Moore et al., 1962), and leads to a net charging of droplets/particles in these areas. Although the droplets would evaporate as the cloud dissipates, the charge would be retained either in the form of small ions or on Cloud Condensation Nuclei (CCN) following ion-particle attachment; CCN typically have lifetimes of tens of minutes to hours.

Following the 0830 UT flight, Fig. 2(c) shows the subsequent measurements made at 1130 UT. The nocturnal inversion layer has almost been completely eroded by surface heating, being replaced by a convective boundary layer with a depth of ~900 m and the near surface RH reduced to below 50%. The elevated layers of charge observed in the previous flight are still observed, although the uppermost charge layer at 2 km contains a reduced charge density. There is also an enhancement of the charge at ~500 m, which is coincident with a substantial vertical change in wind direction, and therefore wind shear.

By 1420 UT (Fig. 2(d)) a substantial charge layer has formed from 100 m to 600 m and strengthened in magnitude to 100 pC m^{-3}. The fact that the temperature profile in the lowest 1.5 km follows the Dry Adiabatic Lapse Rate (DALR, or Γ_d, as shown by the red dashed line) almost exactly, suggests that by this time of day the boundary layer is effectively well mixed, however, this is certainly not the case for the charge profile. An explanation for the increased magnitude of charge in the lowest several hundred meters may be seen in Fig. 5(a), which shows the time series of aerosol concentration and Potential Gradient (PG) measured at Alqueva 2 m above the surface during the 23rd July. The aerosol measurements are 5 minute averages, made with a TSI3330 Optical Particle Sizer which counts and sizes particles from 0.3 to 10 μm diameter. Further information on the TSI3330 is given in Appendix D.

Fig. 5(a) demonstrates that around 1200 UT, the aerosol concentration starts to increase, reaching a max at 1330 UT. This is presumably due to the increase in daytime convection (supported by the relatively high vertical velocities in Fig. 4 at this time), which will easily loft particles upward. The extremely dry surface environment, characteristic of conditions which persist throughout the Mediterranean region in the summer months, means that particles are only very loosely bound to the surface. If charged, it follows that these lofted particles will contribute to the increased charge levels observed during the 1420 UT ascent. Fig. 5(a) also shows that most of the contribution to the total aerosol concentration is from small particles (< 1 μm), which are the most easy to be lofted. There will also be a further contribution

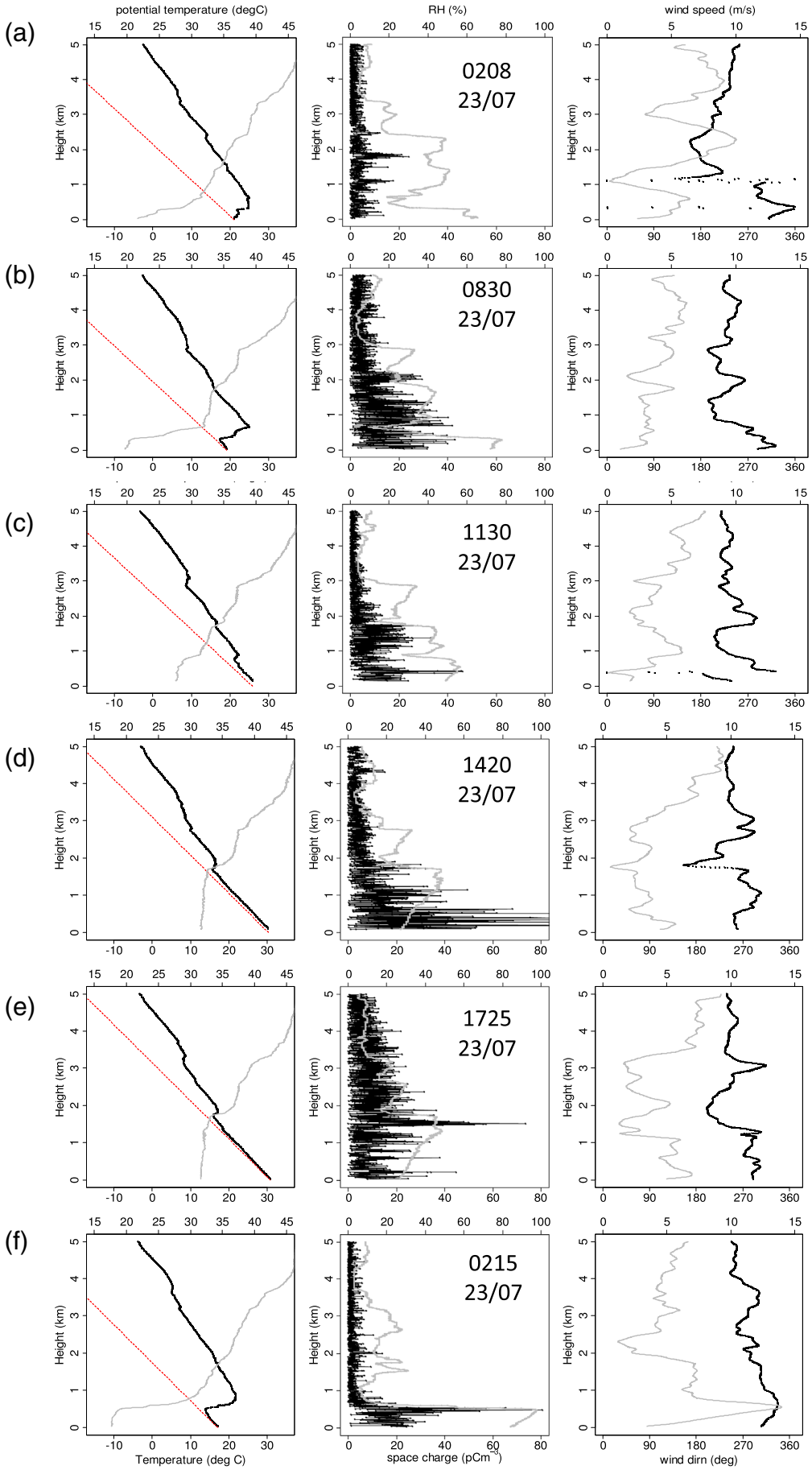

Fig. 2. Vertical profiles from specially instrumented radiosondes from (a) 0200 UT on 23rd to (f) 0200 UT on 24th July 2014. Each flight shows three plots. Left plot - temperature (black), potential temperature (grey) and Dry Adiabatic Lapse Rate (DALR) (red dashed); central plot - RH (grey), magnitude of space charge (black), Right plot - horizontal wind speed (grey) and wind direction (black). (For interpretation of the references to colour in this figure legend, the reader is referred to the web version of this article.)

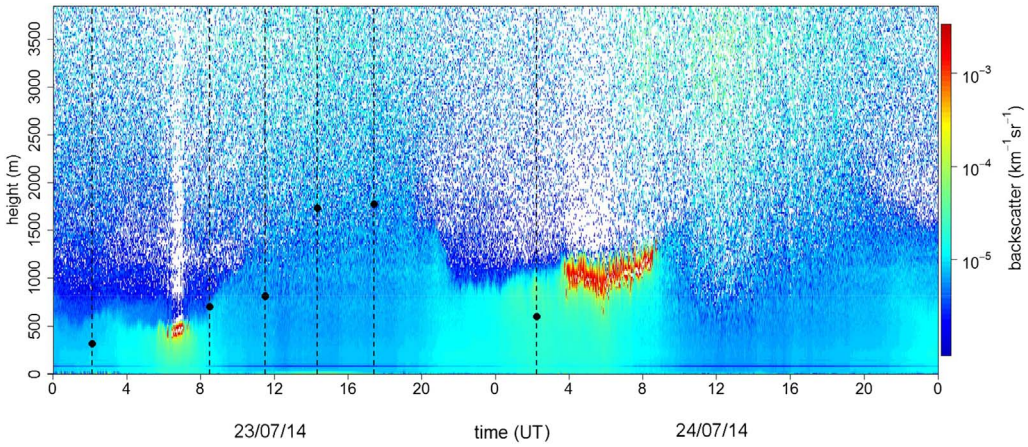

Fig. 3. Backscatter profile from the Vaisala CL31 ceilometer on 23rd and 24th July 2014 at Alqueva. Dashed vertical lines indicate the times of specially instrumented sonde ascents, and the black dots represent the height of the largest potential temperature inversion as determined from the sonde. The red and yellow points between 0500–0700 UT on 23rd and 0400–0900 UT on 24th denote periods when cloud was present. (For interpretation of the references to colour in this figure legend, the reader is referred to the web version of this article.)

from particles smaller than the 0.3 μm detection limit of the TSI3330 which were too small to be detected. Further evidence for the involvement of aerosol in the elevated charge levels is also given by the PG measurements shown in Fig. 5(a) (black line). During the period of enhanced aerosol concentration from 1200 UT to 1600 UT the PG is much greater, up to 350 V/m, and more variable than at other times. The reason for this may be twofold: 1) the aerosol concentration is sufficient to reduce the air conductivity, thereby increasing the PG in accordance with Ohm's law (for a constant vertical conduction current); 2) the aerosol particles are charged, and their separation into positive and negative charge regions causes a change in the net PG. A combination of both effects will occur, but the relatively small aerosol concentrations (which indicate that the lower tropospheric air in the Alqueva region is very clean) are very unlikely to lead to such large variability in the PG through the conductivity route alone. It is therefore suggested that space charge generation results mostly from movement of charge carried by ultrafine particles, as well as ionic space charge. The wind speed measurements shown in Fig. 5(b) show a gradual increase in near surface wind speed from 1200 UT onwards, supporting the lofting possibility. Dust particles are likely to charge through a variety of mechanisms including triboelectric charging (e.g. Lacks and Levandovsky, 2007) and investigators have previously observed substantial surface electric fields within desert dust storms (e.g. Esposito et al., 2016; Yair et al., 2016; Harrison et al., 2016; Silva et al., 2016). Although the particle concentration and wind speeds here are nowhere near as large as the values observed in storms, Fig. 7 (which shows modelled vertical velocities for 22nd July), does show a marked increase in vertical velocity (up to 1 ms^{-1} at the surface) around the period of the maxima in aerosol concentration from 1400 UT to 1800 UT which could certainly loft surface aerosol through convective updrafts (e.g. Adler and Kalthoff, 2014). The predicted vertical velocities of up to 1 m/s would enable particles at the surface to be transported upwards to the maximum observed altitude of charging at 500 m in around 8 min (assuming that the particles travel at the same speed as the updrafts). There may also be an additional contribution to aerosol above the surface from long range horizontal advection from the North

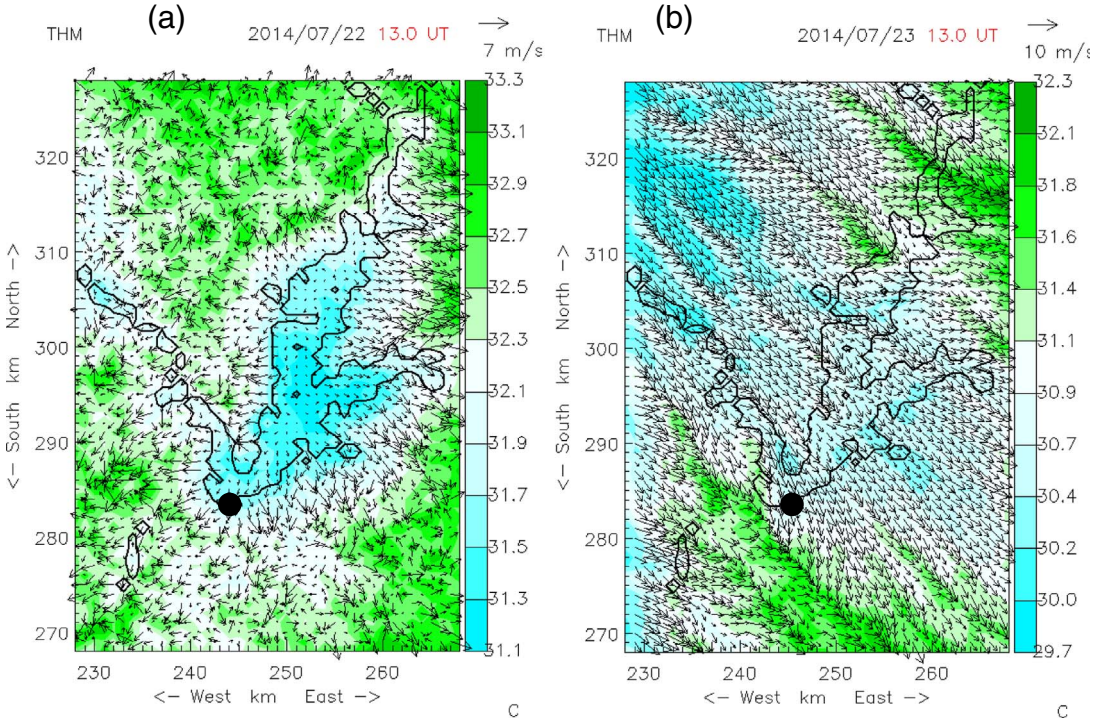

Fig. 4. Modelled horizontal wind (arrows) over potential temperature (coloured contours) in a model surface ~200 m above surface around Alqueva reservoir using the Meso-NH model with a resolution of 1 km at 1300 UT on (a) 22nd and (b) 23rd July. (For interpretation of the references to colour in this figure legend, the reader is referred to the web version of this article.)

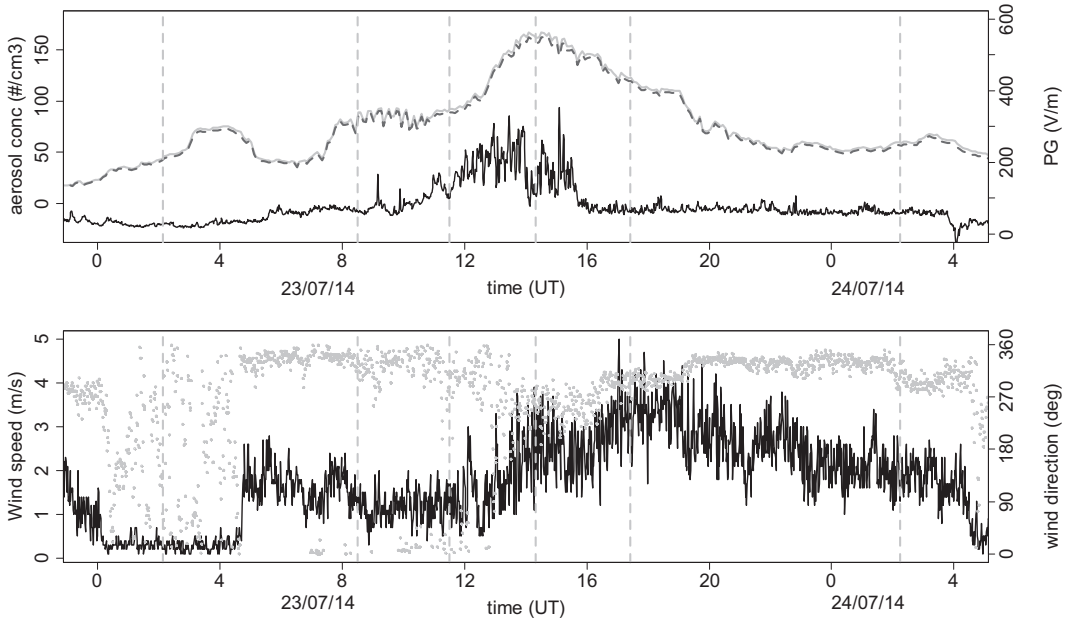

Fig. 5. (a) Aerosol number concentration (solid light grey = total concentration for all particles from 0.3–10 μm, dashed dark grey = concentration of particles < 1 μm), measured by a TSI3330 OPC. The black line shows measurements of Potential Gradient (PG) measured by a JCI 131F electric field mill. (b) 2 m wind speed (black solid line) and wind direction (grey points), all measured at Alqueva, Portugal on 23rd and 24th July 2014. Dashed grey lines denote the times of balloon ascents. Aerosol measurements are 5 minute averages, PG 1 minute averages and wind data 1 minute average.

Westerly flow which will have passed close to polluted cities such as Lisbon.

The movement of charged aerosol has been observed to cause rapid variations in PG (e.g. Matthews et al., 2012; Piper and Bennett, 2012; Conceição et al., 2017), very similar to those observed during 23rd July at Alqueva, therefore this is suggested as the cause of the unusually high variability in the PG during this period. The relationship between the surface PG and vertical charge profile will be discussed further in Section 3.2.

Returning to Fig. 2, Fig. 2(e) shows the vertical profile from the late afternoon ascent at 1725 UT. The temperature profile is almost identical to the 1420 UT ascent, suggesting a well-mixed atmosphere as before. The intense region of charge in the lower levels at 1420 UT is no longer present, instead a distinct charge layer exists between 1.5 and 2 km near the top of the boundary layer. This is suggested to result from the upward mixing of the surface lofted charge due to convection. By the time of the final vertical ascent at 0215 UT on 24th July (Fig. 2(f)), substantial surface cooling has led to an increase in the near surface RH up to 80% (this later led to the formation of a cloud layer, but not until 0330 UT). A well-defined charge layer is present in the region of high RH, related to hygroscopic growth of ions and aerosol, as in the previous night's ascent. The substantial temperature inversion at the top of this layer will lead to a sharp gradient between the moist air below and relatively dry air above, leading to charging of the particles as a result of flow of the vertical conduction current. This is likely to be the main source of charge for the flight shown in Fig. 2(f), which will be discussed further in Section 3.3.

To summarise the diurnal variation in the vertical charge profiles over Alqueva, it is observed that, as expected, the magnitude of the charge during night time profiles is much smaller (up to 20 pC m^{-3}) than during daylight hours (up to 92 pC m^{-3}). Considerable complexity in the charge profiles is observed once daytime convection begins, with lofting of ultrafine surface aerosol suggested to be the main contribution to the charge profile in the lowest 1 km. Early morning formation of thin cloud layers is also a source of charge separation through conduction current charging of droplets and aerosols at the upper and lower horizontal boundaries. Remnant effects of such charging can be seen several hours before and after the cloud becomes visible from ceilometer measurements, i.e. charge separation occurs during the cloud formation processes and remains after the droplets have evaporated.

3.2. Surface electrical measurements

This section examines more closely the effect of charges aloft on the surface PG by considering the integrated columnar charge. We define the columnar space charge, ρ_c, as the sum of all space charge layers above the measurement point. In practise we represent this as:

$$\rho_c = \sum_{m=0}^{m_\infty} \rho_m, \tag{2}$$

where ρ_m is the space charge associated with the mth layer measured above the surface, and m_∞ is the uppermost layer considered. Fig. 6 shows a PG time series (black line) for the entire duration of the two day IOP covering all eight balloon flights (from 22nd July to 24th). Also plotted (red dots) are the integrated space charge totals from the surface up to 5 km, for each of the 8 charge sensor flights, using Eq. (2). Further discussion of the choice of 5 km as the height of the upper boundary is given in Appendix B. Fig. 6 shows that although there is some variability, it is generally the case that the integrated space charge profiles follow the same trend as the near surface PG, particularly around the time of the increased aerosol concentration around 1200 UT on 23rd as discussed in Section 3.1. This demonstrates the importance of the link between the surface electrical environment and aloft. Also shown in Fig. 6 (grey dot-dashed line) is the average diurnal variation in PG at Alqueva on fair weather days for the entire duration of the Alex campaign (from 26th May to 27th September). The difference between the PG on 23rd (0900 UT to 1500 UT) and the average PG curve demonstrates the likelihood of enhanced space charge production on this day which is characterised by an increase in the magnitude (279 V/m compared to 93 V/m) and variability. This is in contrast to the similarity observed between the average curve and PG measured on 22nd, indicating a typical fair weather day. It is suggested that the differences result from a change in wind conditions at the site and thus aerosol concentration between the two days. The 22nd is dominated by a local lake breeze (as demonstrated in Fig. 4(a)), with wind flowing outwards

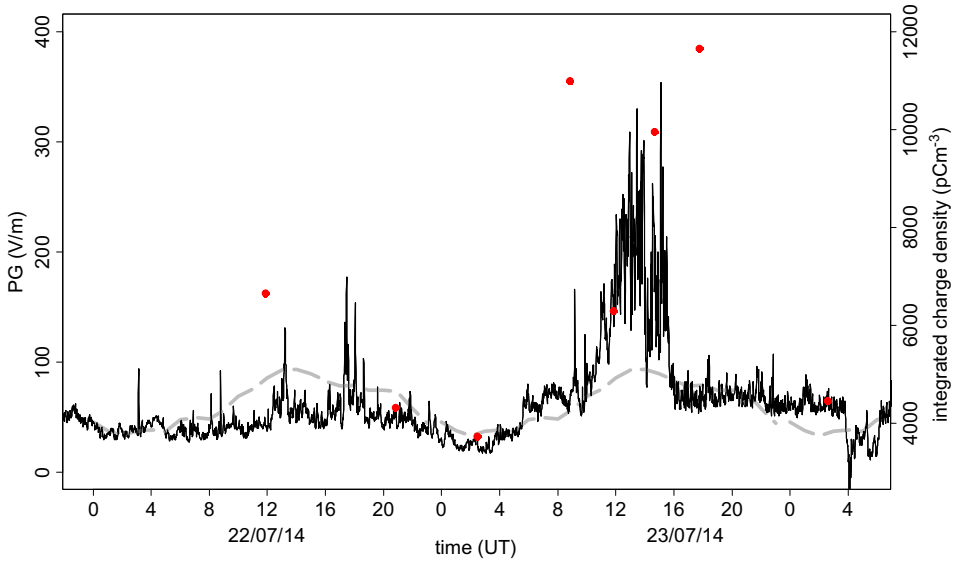

Fig. 6. Time series during the two days of the Alqueva IOP from 22nd to 24th July 2014. The black line denotes the PG, whilst the red dots show the calculated integrated space charge up to 5 km for each charge sensor balloon flight during the period (using Eq. (2)). The grey dash-dotted line show the averaged diurnal variation in PG for fair weather days at the Alqueva site during the entire ALEX campaign. (For interpretation of the references to colour in this figure legend, the reader is referred to the web version of this article.)

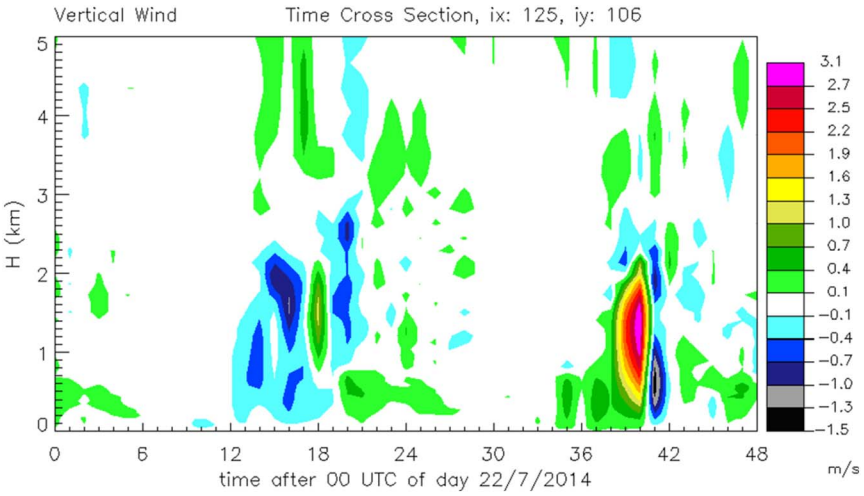

Fig. 7. Hovmöller plot of the vertical profile of Meso-NH modelled vertical velocity over the grid point nearest to the Parque Solar site at Alqueva, during 22nd and 23rd July.

from the lake towards the shore. This would contain relatively few aerosol particles (as supported by Fig. 5(a)), and the predominantly descending air over the lake body will inhibit vertical lofting of local aerosol at the PG measurement site. This is demonstrated in Fig. 7 which shows modelled time evolution of vertical velocity at Alqueva during 22nd and 23rd July, where it is evident that the vertical velocities on 22nd afternoon (12–18 UTC) are slightly negative (descending) in the boundary layer over the lake due to the development of the lake-breeze system. The fair weather conditions, low wind speeds and low aerosol content would lead to a predominately Carnegie like variation in PG as observed. This is contrasted with the predominantly north westerly wind flow on 23rd, which inhibits the formation of the lake breeze and therefore does not suppress the afternoon mesoscale convection. In addition, the circulation on 23rd is also likely to advect aerosol from more populated and industrialized coastal cities such as Lisbon The higher aerosol concentration on 23rd would increase the PG by both (a) reducing the conductivity and (b) causing an increased contribution to space charge by movement of charged aerosol. The presence of (b) is supported by the large variability in PG during peak convective hours.

Another factor that can cause variation in the PG and charge profiles is a change in the local ionisation. The vertical ionisation profile depends on both GCR ionisation generated from above and radioactivity from Earths' surface, mostly in the form of gamma radiation. Surface measurements of gamma radiation were made during the ALEX campaign at Alqueva and reported by Lopes et al. (2015). These measurements corroborated the initial assumption that the Alqueva region emits very little gamma radiation, with no diurnal cycle evident in the measurements. The low geomagnetic latitude of Alqueva suggests that the variability in the near surface ionisation profile from GCRs will also be small (e.g. Bazilevskaya et al., 2008), hence it is extremely unlikely that variations in ionisation rate contributed to the observed changes in PG and space charge during 23rd July at Alqueva.

3.3. Charge modelling

Particulate aerosol is known to have a profound effect on the electrical environment, both at the surface and aloft (e.g. Sagalyn and Faucher, 1954; Gringel and Muhleisen, 1978). It is therefore desirable to know the vertical aerosol profile in order to better understand the vertical charge profile. Although measurements of aerosol were made at the surface during the Alqueva IOP, none were made in-situ aloft. Backscatter profile measurements were, however, made from a nearby Vaisala CL31 ceilometer. Although ceilometers are normally used for cloud detection, they can also be used for aerosol profiling (Münkel et al., 2004; Tsaknakis et al., 2011), and their ability to measure close to the surface is a distinct advantage over lidars, despite the lower pulse energy of ceilometers. Previous investigators (e.g. Münkel et al., 2004)

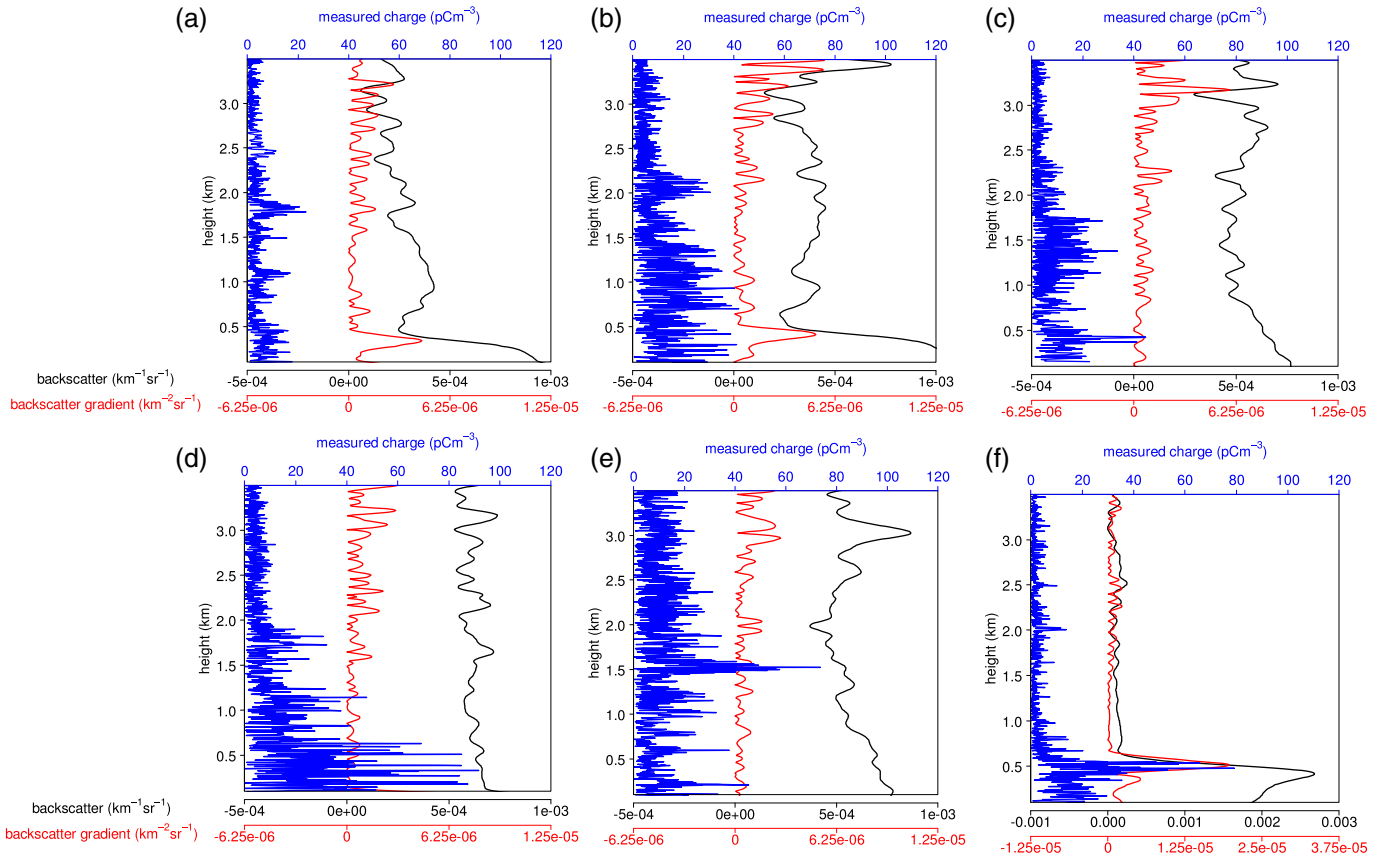

Fig. 8. Vertical profiles of the magnitude of space charge (blue) measured by the balloon charge sensor, processed backscatter from the surface ceilometer (black) (see Appendix C for details) and the magnitude of the vertical gradient in backscatter (red), which is indicative of the location of theoretically expected charge layers. Individual plots denote sonde flight times on 23rd and 24th July as follows: (a) 0208 UT, (b) 0830 UT, (c) 1130 UT, (d) 1420 UT, (e) 1725 UT, (f) 0215 UT. (For interpretation of the references to colour in this figure legend, the reader is referred to the web version of this article.)

have attempted to correlate ceilometer backscatter with surface aerosol measurements, however, artefacts in the backscatter profile have been demonstrated to occur in the ceilometer range gates providing information close to the surface, which reduces the usefulness of the comparison with ground based aerosol measurements. We therefore use the shape of the ceilometer backscatter profile as a qualitative indicator of the aerosol location, rather than attempt to infer anything quantitative about the aerosol concentration. Further discussion on the ceilometer instrument and the method used to process the ceilometer data is provided in Appendix C.

Fig. 8 shows the processed backscatter profiles (black line and detrended according to the methodology outlined in Appendix C) plotted alongside the measured charge profiles for each of the balloon flights in Fig. 2. In general, there is not much similarity observed between the charge and ceilometer backscatter profiles. Common features of the backscatter profiles are an increased layer of backscatter within approximately the lowest 800 m, particularly during night time and early morning hours (e.g. Fig. 8(a), (b) and (f)). This is related to the hygroscopic growth of aerosol (e.g. Silva et al., 2015), which results from the strong cooling overnight, eventually leading to cloud formation. As mentioned in Section 3.1, charge accumulation is expected to occur at the upper and lower horizontal boundaries of cloud and aerosol layers due to vertical flow of the GEC conduction current, J_c. The space charge is proportional to the vertical gradient in conductivity between the clear and aerosol laden air, which theoretically, produces positive charge at the top of the layer and negative charge at the base (see e.g. Nicoll and Harrison, 2016). If one assumes a mostly static situation, with no vertical mixing (which is only likely to occur here overnight when vertical ascent rates are low (e.g. Fig. 4)), a theoretical estimate of the charge generated by this phenomenon can be made by calculating the vertical gradient in conductivity (see e.g. Harrison and Carslaw, 2003, Nicoll and Harrison, 2016 for details). However, the extent to which the charge values are realistic is questionable due to the absence of a quantitative aerosol profile and the number of assumptions required to do this. Instead the approach taken here is simply to calculate the vertical gradient in backscatter, which avoids the need for the many assumptions but will indicate the location of any charge layers thought to be generated by gradients in conductivity. Accordingly, the red line in each of the plots in Fig. 8 shows the vertical gradient in backscatter, which is indicative of the theoretical profile of charge. The vertical gradient is found by applying a smoothing spline (smoothing parameter = 0.3) to the backscatter and differentiating. As was the case for the backscatter profile, for most of the flights there is little similarity between the backscatter gradient and the observed charge. The likely reason for this is low sensitivity and 910 nm IR operating wavelength of the ceilometer which will lead to an inability to detect small particles (< 1 μm) and low particle concentrations. This is particularly important if the space charge is mostly ultrafine (i.e. diameters < 0.1 μm) rather than particulate. Since the surface aerosol measurements at Alqueva showed a predominantly clean atmosphere, it is expected that the sensitivity of the ceilometer will not detect such small particle concentrations. It should also be noted that the application of the vertical gradient in conductivity approach to a non-static situation in which turbulent motion is present over-simplifies the charge mixing processes taking place. Although charge will be separated at the upper and lower horizontal edges of aerosol layers due to this process, in a turbulent situation (such as during Fig. 8(c), (d) and (e)), the charge will be mixed vertically, leading to less well defined charge layers, which is more similar to that observed in the profiles in Fig. 8.

The one flight in which the shape of the backscatter profile is very

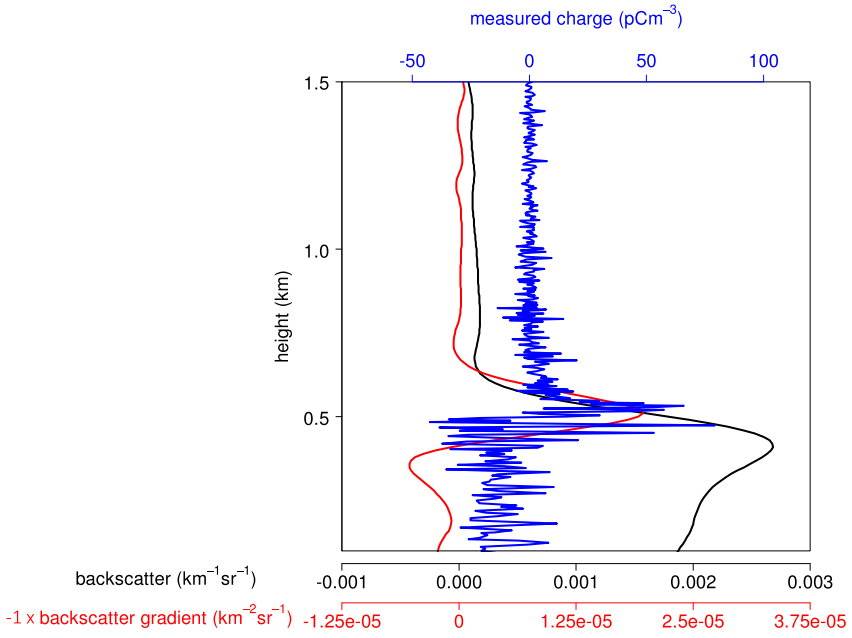

Fig. 9. Close up of Fig. 7(f), but showing bipolar charge and backscatter gradient instead of magnitude. Note that the backscatter gradient axis has been inverted in order to demonstrate the similarity in locations of the vertical backscatter gradient and the measured charge.

similar to the measured charge is Fig. 8(f). Fig. 9 shows a close up of the lowest 1.5 km of this flight, which demonstrates that a substantial gradient in backscatter occurs at 500 m altitude, which is coincident with the measured charge layer. The increased backscatter during this period is likely related to the later formation of a cloud layer which resulted from night time cooling under clear skies. The ceilometer algorithm did not classify this as a cloud until 0335 UT, more than an hour after the balloon measurements, therefore the profile shown in Fig. 9 was obtained before the cloud formed. The charge measurements and vertical gradient in backscatter in Fig. 9 are of both polarities (not simply magnitude as for the other plots), which demonstrates very close agreement between the location of the large backscatter gradients and the observed charge. Fig. 9 also shows the negative charge observed in the base of the layer and positive charge at the top, as expected by the theory of conduction current flow through aerosol and cloud layers (e.g. Zhou and Tinsley, 2007). Analysis of the data in Fig. 8 therefore suggests that this charging theory is valid for stratiform layers of aerosol and cloud, when the particle/droplet concentration is substantial and little vertical mixing is present, but not when substantial convective motion exists.

4. Discussion

From the results presented here it is apparent that the vertical profile of charge within the PBL can be complex, even in fair weather conditions. The analysis presented in Section 3 suggests a considerable influence for local charged aerosol on both the near surface PG measurements and vertical charge profile. Although the surface particle measurements and ceilometer backscatter profiles suggest relatively small aerosol particle number concentrations it is likely that larger concentrations of ultrafine (< 0.1 μm) particles and ionic space charge exist which will influence the charge distribution but will not be detected by either the ceilometer or surface particle counter. The ceilometer wavelength of 910 nm means that only particles greater than about 1 μm diameter will be detected, and only if the signal to noise is sufficiently large to permit a reliable signal to be measured. It is well documented that the day time signal-to-noise ratio in ceilometers in regions of low aerosol content is often poor (e.g. Heese et al., 2010), which is consistent with the findings reported here in that there is little structure in the ceilometer backscatter profile except during night time and periods of high humidity. Although there is no observational evidence for these ultrafine particles, we can infer their existence from the measurements of elevated space charge values, i.e. in order for charge to be maintained beyond the timescale for recombination effects, the charge must be carried on larger particles. This is most likely to result from attachment to ultrafine particles.

The measurements reported here also demonstrate the importance of daytime convection for the vertical space charge profile within the PBL. At Alqueva this is particularly evident in terms of the ability of turbulent updrafts to transport small aerosol particles from the surface, which occurs easily and mixed primarily due to the extreme dryness of soil. This leads to relatively large values of space charge (up to 100 pC m^{-3}), in comparison to those reported by other observers in less dry environments (e.g. $\sim$1 pC m^{-3} measured by Moore et al., 1962). In the absence of cloud layers, the largest values of space charge are observed during mid-afternoon when the vertical velocity is maximum and turbulent motion largest. Section 3.2 demonstrates clearly the difference in the electrical environment on days when convection is inhibited (such as on 22nd July when the lake breeze was present), and when it is not. This leaves little doubt that the main influence on the detailed structure of the vertical space charge profile at Alqueva is turbulent transport.

The relatively large values of space charge density reported here compared to other papers (e.g. of a few pC m^{-3} in Moore et al., 1962, Markson, 1975) may also result from differences in the measurement techniques as well as time resolution of the measurements. Markson (1975) and Markson et al. (1981) report measurements approximately every 200 m in the vertical, with no detail of any averaging or smoothing that has been applied. It may well be the case that this is an average value over 200 m rather than an instantaneous value. It is therefore likely that, in comparison to the approximately 5 m vertical resolution measurements reported here, the longer averaging periods reported in the literature resulted in smaller reported values of space charge. This therefore demonstrates the importance of high resolution measurements in understanding the detail of charge transfer within the boundary layer.

5. Conclusions

These results present rare high resolution vertical profiles of space charge within the planetary boundary layer, which are the first to be made over an inland Portuguese reservoir. The direct space charge determination reveals the complex structure of the vertical charge profiles, beyond that available indirectly from aerosol particle retrievals or thermodynamic inferences alone, which indicates the importance of charged ultrafine aerosol in the electrical environment of the boundary layer. Intensive balloon measurements over a 24 hour period of fair weather demonstrate variation of the charge profile within the planetary boundary layer and its dependence on convective mixing. The magnitude of observed charge is typically small during night time periods (up to 20 pC m^{-3}), with little vertical structure. Daytime convection leads to substantial vertical mixing, including lofting of aerosol particles upwards from the dry surface, which leads to substantial charge accumulations up to 92 pC m^{-3} within the lowest km. The diurnal variation in the integrated column of charge above the measurement site closely matches the diurnal variation in near surface charge as measured by an electric field mill at the same site. Vertical profiles of backscatter from an adjacent CL31 ceilometer were used to provide a proxy for the vertical aerosol profile, to which the measured charge profiles were compared. Little similarity between the two was observed, except during stable night time periods when reasonable aerosol layers accumulated. Most of the discrepancy is attributed to the likely existence of ultrafine aerosol (< 1 μm) which are too small to be detected by the ceilometer, but will contribute to the overall charge profile. Using such direct space charge measurements, the charge transfer processes can be identified and characterised, the variability in which is clearly apparent even in fair weather conditions. The simplicity with which these measurements can be obtained using conventional meteorological radiosondes therefore offers a new tool for improving boundary layer representations within radiative transfer models.

Acknowledgements

Data from the Alex campaign is available at http://www.alex2014.cge.uevora.pt/?page_id=27 (password access can be provided by contacting the corresponding author). NERC grant NE/H002081/1 and STFC grant ST/K001965/1 supported the radiosonde sensor development. KAN also acknowledges an Early Career Fellowship of the Leverhulme Trust (ECF-2011-225) and a NERC Independent Research Fellowship (NE/L011514/1). Field campaign funding was from FCT (Portuguese Science and Technology Foundation) and FEDER-COMPETE: ALEX 2014 (EXPL/GEO-MET/1422/2013): FCOMP-01-0124-FEDER-041840. MM acknowledges the support of the Portuguese Science and Technology Foundation (FCT) for the PhD grant (SFRH/BD/89218/2012). The Portuguese team was co-funded by FCT, in the frame of the European Regional Development Fund - COMPETE 2020, under the projects UID/GEO/04683/2013 (POCI-01-0145-FEDER-007690) and ALOP (ALT20-03-0145-FEDER-000004). Thanks are also given to the TOPROF (ES-1303) COST-Action. The authors express their gratitude to Maria Parrondo from Instituto Nacional de Técnica Aeroespacial for her assistance with the radiosonde launches, Maria João Costa for providing the ceilometer data, and Alec Bennet for discussions about the vertical profiles. HGS is grateful to Dr. John Chubb (1933–2015) for his insightful discussions into this topic, he shall be missed.

Appendix A. Meso-NH model

A map of southern Portugal with the orography, the Alqueva reservoir and the location of the Parque Solar measurement site during the ALEX 2014 campaign is provided in Fig. A1. Further maps of the Alqueva and the ALEX measurement stations may be found in Potes et al., 2017. In order to characterise the wind direction and evolution of the vertical profile of the vertical velocity at Alqueva, the results of a high resolution numerical simulation with Meso-NH model (Lafore et al., 1998) were used. The Meso-NH is a non-hydrostatic anelastic numerical model which includes several parametrization schemes to represent surface-atmosphere interactions, radiation, turbulence, clouds and precipitation, convection, atmospheric electricity, chemical reactions and aerosols. The model was run over two two-way nested domains, the farther (not shown) covering all the Iberian Peninsula and adjacent ocean at 4 km horizontal resolution (270 × 240 grid points). The finer domain is centred over the Alqueva reservoir and covers the Portuguese Alentejo region at a 1 km horizontal resolution (240 × 240 grid points) and is shown in Fig. A1 alongside with the location of Alqueva artificial lake. The simulation was started on July 21st at 1800 UT and the initial and boundary conditions were provided by the 6 hourly ECMWF analysis. For the surface, the SURFEX platform of schemes (Masson et al., 2013) were used, the water temperature at Alqueva reservoir was initialized by the temperatures obtained from MODIS satellite data, and an interactive lake model, the Flake, was activated as described in Salgado and Le Moigne (2010). To map the model surface, the ECOCLIMAP v2.0 (Masson et al., 2003) updated by Policarpo et al. (2017) was used. In the inner domain the convection is assumed to be explicitly resolved (no shallow or deep convection schemes were activated) and the turbulence was parametrized using the 1D scheme of Cuxart et al. (2000). The meso-NH results shown in this work came from the inner model (1 km resolution).

Appendix B. Integrated space charge profiles

This section provides further discussion of the integrated columnar charge discussed in Section 3.2. To calculate the integrated columnar charge it was decided to apply Eq. (2) up to a maximum height of 5 km as the majority of the space charge (90%) lies beneath this height. To demonstrate that the choice of this value is not important for the qualitative interpretation given, Fig. B1 shows the integrated space charge from the surface up to 2, 3, 4 and 5 km. It can be seen that the shape of the integrated charge time series is invariant of the value of maximum height chosen.

Appendix C. Ceilometer features and processing of the backscatter profiles

After a brief description of the ceilometer system, this section provides detail on the processing applied to the ceilometer backscatter data for Figs. 8 and 9, as a well as a discussion of the value of the shape of the profile.

The CL31 Vaisala ceilometer uses a single lens design, meaning that the centre of the lens is used for collimating the outgoing laser beam, whereas the outer part of the lens is used for focusing the backscattered light onto the receiver. The separation between transmitting and receiving areas is

provided by an inclined mirror with a hole in the centre. In this way very good performance is achieved, even at low altitudes. The ceilometer has a measurement range from 0 to 7.5 km, maximum reporting resolution of 5 m and programmable measurement cycle (from 2 to 120 s). It uses an eye-safe laser InGaAs diode emitting at 910 nm.

The backscatter signal obtained in clear sky conditions is mainly due to aerosols. Assuming that these particles are mostly concentrated in the mixing layer and that their concentrations above are much lower, it is then reasonable to expect an accentuated decrease of the backscatter signal at the top of the mixing layer. This is true for most situations, except in the case of intense aerosol events.

Although it is possible to use surface aerosol data to attempt to calibrate the ceilometer, for the Vaisala CL31 ceilometer at the Alqueva site, a distinct local minimum in the backscatter was evident at 40 m (4th range gate) in all backscatter profiles. This has also been detected by other investigators (e.g. Sokół et al., 2014) and is an artefact, potentially caused by incomplete optical overlap, or software corrections introduced by the ceilometer manufacturer (see e.g. Kotthaus et al., 2016). Although reasonable agreement between the surface OPC aerosol measurements and the backscatter from the lowest 2 ceilometer range gates (10 m and 20 m) was found at Alqueva, the artefact at 40 m makes it questionable to attempt any calibration between surface data and backscatter values beneath 70 m, which is typically the lowest altitude thought to be free from overlap issues.

In order to analyse the backscatter profile above 40 m, one must also take account of the errors inherent in the backscatter measurement and the processing already undertaken by the ceilometer manufacturer. The grey points in Fig. C1(b) show the vertical profile of backscatter during daylight conditions (0830 UT) on 23rd July (flight 4) at Alqueva, which appear reasonable in the lowest 1 km of the profile, but show an unphysical increase with height above this, as well as an increase in variability. This is apparent in all of the backscatter profiles coinciding with the radiosonde flights and is thought to be erroneous, due to noise from varying solar radiation as well as electronic and optical noise in the ceilometer. To extract a quantitative backscatter profile it is necessary to remove some of the noise by correcting the raw backscatter profile. This is achieved by producing an average background night time climatology profile (shown in black in Fig. C1(a)) from Alqueva, which should be devoid of any noise from solar radiation. This is calculated by finding the mean backscatter profile for all times from 0000 UT to 0300 UT from 22nd to 24th July 2016. Since the backscatter is typically highly variable within the PBL, this profile is therefore only calculated for altitudes above 800 m. The night time climatology profile is then scaled according to the maximum backscatter measured during any specific profile, and subtracted from the raw backscatter to produce a noise corrected version. A moving average (over 5 points) is then applied to the de-trended backscatter data to the processed backscatter, shown as the black line shown in Fig. C1(b). This process has been applied to the instantaneous backscatter profiles coincident with the six instrumented balloon flights shown in Fig. 2. It is also prudent to note the distinct decrease in the backscatter at 2.4 km observed for all Alqueva profiles (as seen in Fig. C1(a)), which is another artefact introduced in the processing by the manufacturer. This has been previously reported by Kotthaus et al. (2016) as likely due to a difference in averaging of data below and above this height. It is clear that removal of such artefacts (as is achieved by subtracting the scaled night time climatology profile) is vital to obtain reliable, quantitative backscatter measurements.

Appendix D. OPS 3330 features and particle concentration calculation

The Optical Particle Sizer (OPS) 3330, manufactured by TSI, is based on the principle of optical scattering from single particles. A laser beam shaped to a thin sheath focused below the inlet nozzle illuminates the particles entering the inlet nozzle. As particles pass through this light sheath, they scatter light in the form of pulses that are counted and sized simultaneously. Sheath flow keeps the particles well focused across the laser light and also prevents the optics from getting contaminated. Beam shaping optics focus the laser light and convert that to a fine sheath with maximum intensity across the particle beam. The viewing volume is created by the intersection of the laser sheath and the particle flow. Sophisticated electronics are used to perform the signal processing. Particle pulses are counted individually and binned in to the 16 channels of the detector, based on their pulse heights. The maximum particle size that can be counted is 10 μm, particles larger than this will be counted but not sized.

The OPS measures particle concentration counting individual pulses from the photodetector. When, pulses start to overlap each other, meaning high particle concentrations, the number of pulses underestimates the number of particles entering the viewing volume. When a particle is detected entering the optical viewing volume, no other particles can be counted until that particle leaves the viewing volume. As the particle concentrations increase, the amount of time blocked by the presence of particles becomes significant. If the particle concentration is computed using elapsed time, the value will be under reported. The actual sample time needs to be corrected for this blocked or dead-time. To adjust for this effect, the OPS measures the dead-time resulting from the presence of particles in the viewing volume and subtracts it from the sample time. This sample lifetime value is used in place of the sample time for the concentration calculations as in the following formula.

$$C_i = \frac{N_i}{Q \times (t_s - DTC \times t_d)}, \tag{D1}$$

where,

C_i = concentration at size channel i
N_i = number count in #/cm^3 at size channel i
Q = sample flow rate, 16.67 cm^3 s^{-1}
t_s = sample time in seconds
t_d = dead time in seconds
DTC = dead time correction factor

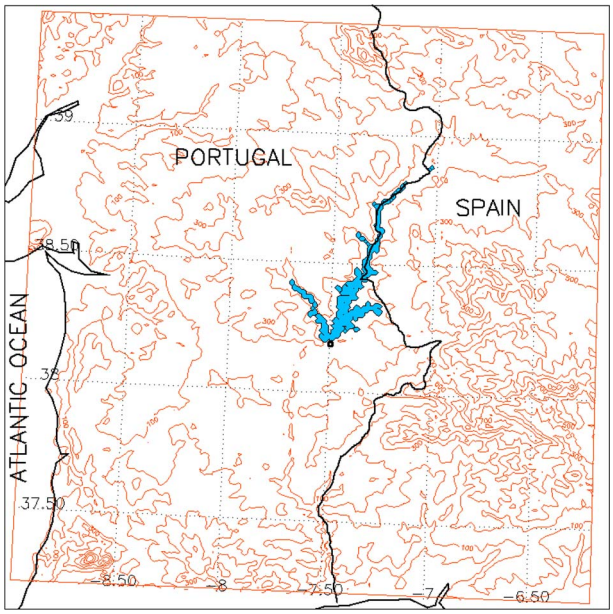

Fig. A1. Domain and orography at 1 km horizontal resolution used in the inner model of the Meso-NH simulation (contour intervals of 100 m). The Alqueva reservoir, as used in the simulations is shown in blue. The location of the Parque Solar (PS) site at which the PG and balloon measurements were made is represented by the black circle. (For interpretation of the references to colour in this figure legend, the reader is referred to the web version of this article.)

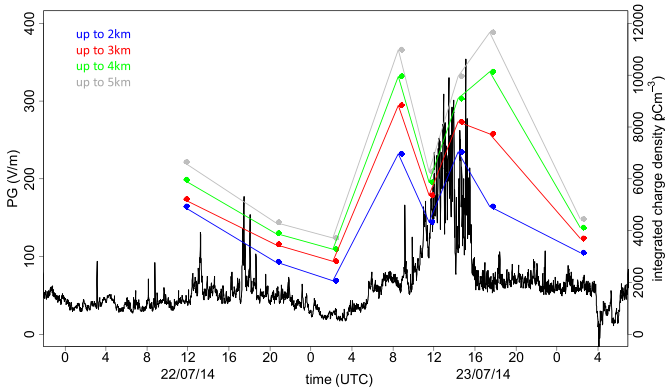

Fig. B1. Time series during the two days of the Alqueva IOP from 22nd to 24th July 2014. The black line denotes the PG, whilst the coloured red dots show the calculated integrated space charge up to 2 km (blue), 3 km (red), 4 km (green) and 5 km (grey) for each charge sensor balloon flight during the period (using Eq. (2)). (For interpretation of the references to colour in this figure legend, the reader is referred to the web version of this article.)

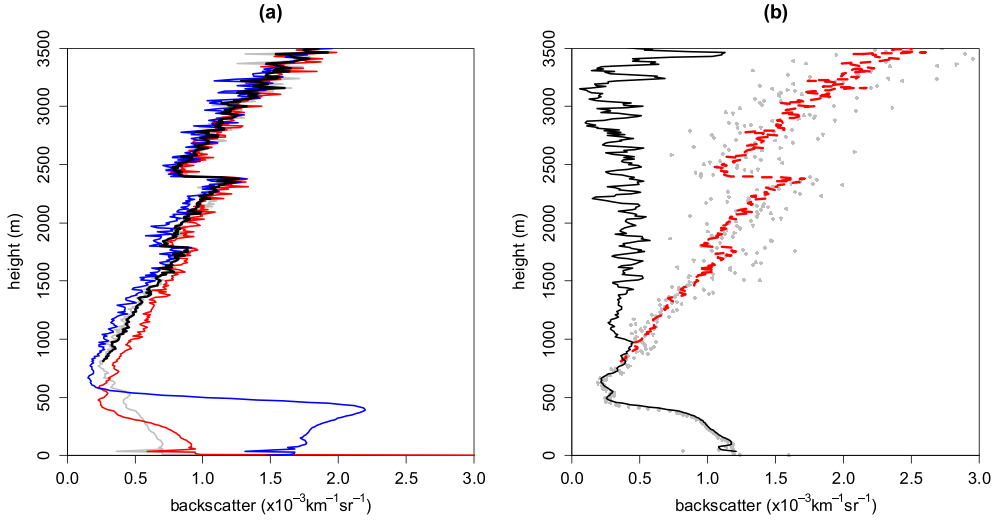

Fig. C1. (a) Average night time vertical profiles of backscatter from the CL31 ceilometer for nights of 22nd (grey), 23rd (red) and 24th (blue) July 2014 from 00 to 03 UT. The black line shows the mean of the three profiles, denoting the night time climatology. (b) Vertical profile of backscatter at 0830 UT on 23rd July (flight 4). The profile is the mean of a 30 minute window from the launch time. Grey points - raw backscatter, red – relative night time climatology profile, black – processed backscatter. (For interpretation of the references to colour in this figure legend, the reader is referred to the web version of this article.)

References

Adler, B., Kalthoff, N., 2014. Multiscale transport processes observed in the boundary layer over a mountainous island. Bound.-Layer Meteorol. 153, 515–537. http://dx.doi.org/10.1007/s10546-014-9957-8.

Anisimov, S.V., Bakastov, S.S., Mareev, E.A., 1994. Spatiotemporal structures of electric field and space charge in the surface atmospheric layer. J. Geophys. Res.-Atmos. 99 (D5), 10603–10610.

Anisimov, S.V., Mareev, E.A., Bakastov, S.S., 1999. On the generation and evolution of aeroelectric structures in the surface layer. J. Geophys. Res.-Atmos. 104 (D12), 14359–14367.

Anisimov, S.V., Mareev, E.A., Shikhova, N.M., Shatalina, M.V., Galichenko, S.V., Zilitinkevich, S.S., 2013. Aeroelectric structures and turbulence in the atmospheric boundary layer. Nonlinear Process. Geophys. 20 (5), 819–824.

Aplin, K.L., Harrison, R.G., 2013. Lord Kelvin's atmospheric electricity measurements. Hist. Geo Space Sci. 4, 83–95.

Bazilevskaya, G.A., Usoskin, I.G., Flückiger, E.O., Harrison, R.G., Desorgher, L., Bütikofer, R., Krainev, M.B., Makhmutov, V.S., Stozhkov, Y.I., Svirzhevskaya, A.K., Svirzhevsky, N.S., 2008. Cosmic ray induced ion production in the atmosphere. Space Sci. Rev. 137, 149–173.

Cavello, T., 1777. An account of some new electrical experiments. Philos. Trans. R. Soc. Lond. 67, 48–55.

Conceição, R., Silva, H.G., Bennett, A., Salgado, R., Bortoli, D., Costa, M.J., Collares Pereira, M., 2017. High frequency response of the atmospheric electric potential gradient under strong and dry boundary layer convection. Bound.-Layer Meteorol. http://dx.doi.org/10.1007/s10546-017-0298-2.

Crozier, W.D., 1963. Electrode effect during nighttime low-wind periods. J. Geophys. Res. 68 (11), 3451–3458.

Cuxart, J., Bougeault, P., Redelspergen, J., 2000. A turbulence scheme allowing for mesoscale and large-eddy simulations. Q. J. R. Meteorol. Soc. 126, 1–30.

Esposito, F., Molinaro, R., Popa, C.I., Molfese, C., Cozzolino, F., Marty, L., Taj-Eddine, K., Di Achille, G., Franzese, G., Silvestro, S., Ori, G.G., 2016. The role of the atmospheric electric field in the dust-lifting process. Geophys. Res. Lett. 43 (10), 5501–5508.

Garratt, J.R., 1994. The atmospheric boundary layer. Earth Sci. Rev. 37 (1–2), 89–134.

Gringel, W., Muhleisen, R., 1978. Saharan dust concentration in the troposphere over the North Atlantic derived from measurements of air conductivity. Beitr. Phys. Atmos. 51 (2), 121–128.

Harrison, R.G., 2013. The Carnegie curve. Surv. Geophys. 34 (2), 209–232.

Harrison, R.G., Aplin, K.L., 2003. Ninteenth century Parisian smoke variations inferred from Eiffel tower atmospheric electrical observations. Atmos. Environ. 37, 5319–5324.

Harrison, R.G., Carslaw, K.S., 2003. Ion–aerosol–cloud processes in the lower atmosphere. Rev. Geophys. 41 (3), 1012. http://dx.doi.org/10.1029/2002RG000114.

Harrison, R.G., Nicoll, K.A., Lomas, A.G., 2012. Programmable data acquisition system for research measurements from meteorological radiosondes. Rev. Sci. Instrum. 83, 036106. http://dx.doi.org/10.1063/1.3697717.

Harrison, R.G., Nicoll, K.A., Ambaum, M.H.P., 2015. On the microphysical effects of observed cloud edge charging. Q. J. R. Meteorol. Soc. 141, 2690–2699. http://dx.doi.org/10.1002/qj.2554.

Harrison, R.G., Barth, E., Esposito, F., Merrison, J., Montmessin, F., Aplin, K.L., Borlina, C., Berthelier, J.J., Déprez, G., Farrell, W.M., Houghton, I.M.P., Renno, N.O., Nicoll, K.A., Tripathi, S.N., Zimmerman, M., 2016. Applications of electrified dust and dust devil electrodynamics to Martian atmospheric electricity. Space Sci. Rev. http://dx.doi.org/10.1007/s11214-016-0241-8.

Heese, B., Flentje, H., Althausen, D., Ansmann, A., Frey, S., 2010. Ceilometer lidar comparison: backscatter coefficient retrieval and signal-to-noise ratio determination. Atmos. Meas. Tech. 3 (6), 1763–1770.

Hoppel, W.A., Frick, G.M., 1986. Ion—aerosol attachment coefficients and the steady-state charge distribution on aerosols in a bipolar ion environment. Aerosol Sci. Technol. 5 (1), 1–21. http://dx.doi.org/10.1080/02786828608959073.

Hoppel, W.A., Gathman, S.G., 1971. Determination of eddy diffusion coefficients from atmospheric electrical measurements. J. Geophys. Res. 76 (6), 1467–1477. http://dx.doi.org/10.1029/JC076i006p01467.

Hoppel, W.A., Gathman, S.G., 1972. Experimental determination of the eddy diffusion coefficient over the open ocean from atmospheric electric measurements. J. Phys. Oceanogr. 2 (3), 248–254.

Hoppel, W.A., Anderson, R.V., Willett, J.C., 1986. Atmospheric electricity in the planetary boundary layer. In: The Earth's Electrical Environment, pp. 149–165.

Israel, H., 1955. Synoptical researches on atmospheric electricity. In: Proc. Conference on Atmospheric Electricity, pp. 11–20.

Kaimal, J.C., Finnigan, J.J., 1994. Atmospheric Boundary Layer Flows: Their Structure and Measurement. Oxford University Press.

Kawano, M., 1957. The general expression of the diurnal variation of the atmospheric electric field considering the influence of the Eddy diffusion near the ground. J. Geomagn. Geoelectr. 9 (3), 123–132.

Kotthaus, S., O'Connor, E., Munkel, C., et al., 2016. Recommendations for processing atmospheric attenuated backscatter profiles from Vaisala CL31 ceilometers. Atmos. Meas. Tech. 9 (8), 3769.

Kulkarni, Madhuri N., 2010. On the modeling of electrical boundary layer (electrode layer) and derivation of atmospheric electrical profiles, eddy diffusion coefficient and scales of electrode layer. J. Earth Syst. Sci. 119 (1), 75–86.

Lacks, D.J., Levandovsky, A., 2007. Effect of particle size distribution on the polarity of triboelectric charging in granular insulator systems. J. Electrost. 65 (2), 107–112.

Lafore, J., Stein, J., Asencio, N., Bougeault, P., Ducrocq, V., Duron, J., Fischer, C., Hereil, P., Mascart, P., Pinty, J., Redelsperger, J., Richard, E., Arellano, J., 1998. The meso-nh atmospheric simulation system. Part 1: adiabatic formulation and control simulation. Ann. Geophys. 16, 90–109.

Lopes, F., Silva, H.G., Bárias, S., Barbosa, S.M., 2015. Preliminary results on soil-emitted gamma radiation and its relation with the local atmospheric electric field at Amieira (Portugal). J. Phys. Conf. Ser. 646, 012015. http://dx.doi.org/10.1088/1742-6596/646/1/012015.

Lopes, F., Silva, H.G., Salgado, R., Potes, M., Nicoll, K., Harrison, G., 2016. Atmospheric electrical field measurements near a fresh water reservoir and the formation of the lake breeze. Tellus A 68, 31592. http://dx.doi.org/10.3402/tellusa.v68.31592.

Mach, D.M., Blakeslee, R.J., Bateman, M.G., 2011. Global electric circuit implications of combined aircraft storm electric current measurements and satellite-based diurnal lightning statistics. J. Geophys. Res.-Atmos. 116 (D5).

Markson, R., 1975. Atmospheric electrical detection of organized convection. Science 188 (4194), 1171–1177.

Markson, R., Sedlacek, J., Fairall, C.W., 1981. Turbulent transport of electric charge in the marine atmospheric boundary layer. J. Geophys. Res. 86 (C12), 12–115.

Marshall, T.C., Rust, W.D., Stolzenburg, M., Roeder, W.P., Krehbiel, P.R., 1999. A study of enhanced fair-weather electric fields occurring soon after sunrise. J. Geophys. Res. 104 (D20), 24–455.

Masson, V., Champeaux, J., Chauvin, C., Meriguet, C., Lacaze, R., 2003. A global database of land surface parameters at 1 km resolution for use in meteorological and climate models. J. Clim. 16, 1261–1282.

Masson, V., Moigne, P., Martin, E., Faroux, S., Alias, A., Alkama, R., Belamari, S., Barbu, A., Boone, A., Bouyssel, F., Brousseau, P., Brun, E., Calvet, J., Carrer, D., Decharme, B., Delire, C., Donier, S., Essaouini, K., Gibelin, A., Giordani, H., Habets, F., Jidane, M., Kerdraon, G., Kourzeneva, E., Lafaysse, M., Lafont, S., Brossier, C., Lemonsu, A., Mahfouf, J., Marguinaud, P., Mokhtari, M., Morin, S., Pigeon, G., Salgado, R., Seity, Y., Taillefer, F., Tanguy, G., Tulet, P., Vincendon, B., Vionnet, V., Voldoire, A., 2013. The surfexv7.2 land and ocean surface platform for coupled or offline simulation of earth surface variables and fluxes. Geosci. Model Dev. 6, 929–960.

Matthews, J.C., Buckley, A.J., Wright, M.D., Henshaw, D.L., 2012. Comparisons of ground level measurements of ion concentration and potential gradient upwind and downwind of HV power lines in corona. J. Electrost. 70 (4), 407–417.

Moore, C.B., Vonnegut, B., Semonin, R.G., Bullock, J.W., Bradley, W., 1962. Fair-weather atmospheric electric potential gradient and space charge over central Illinois, summer 1960. J. Geophys. Res. 67 (3), 1061–1071.

Münkel, C., Emeis, S., Müller, W.J., Schaefer, K.P., 2004. Aerosol concentration measurements with a lidar ceilometer: results of a one year measuring campaign. In: Remote Sensing. International Society for Optics and Photonics, pp. 486–496.

Nicoll, K.A., 2013. A self-calibrating electrometer for atmospheric charge measurements from a balloon platform. Rev. Sci. Instrum. 84, 096107.

Nicoll, K.A., Harrison, R.G., 2010. Experimental determination of layer cloud edge charging from cosmic ray ionisation. Geophys. Res. Lett. 37 (13).

Nicoll, K.A., Harrison, R.G., 2016. Stratiform cloud electrification: comparison of theory with multiple in-cloud measurements. Q. J. R. Meteorol. Soc. 142, 2679–2691. http://dx.doi.org/10.1002/qj.2858.

Piper, I.M., Bennett, A.J., 2012. Observations of the atmospheric electric field during two case studies of boundary layer processes. Environ. Res. Lett. 7 (1), 014017.

Policarpo, C., Salgado, R., Costa, M.J., 2017. Numerical simulations of fog events in southern portugal. Adv. Meteorol. 2017. http://dx.doi.org/10.1155/2017/1276784.

Potes, M., Salgado, R., Costa, M.J., Morais, M., Bortoli, D., Kostadinov, I., Mammarella, I., 2017. Lake–atmosphere interactions at Alqueva reservoir: a case study in the summer of 2014. Tellus A 1 (1272787), 69.

Reiter, R., Sládkovič, R., 1970. Control of vertical transport of aerosols between 700 and 3000 meters by lapse rate and fine structure of temperature. J. Geophys. Res. 75 (15), 3065–3075. http://dx.doi.org/10.1029/JC075i015p03065.

Rycroft, M.J., Harrison, R.G., Nicoll, K.A., Mareev, E.A., 2008. An overview of Earth's global electric circuit and atmospheric conductivity. Space Sci. Rev. 137 (1–4), 83–105.

Sagalyn, R.C., Faucher, G.A., 1954. Aircraft investigation of the large ion content and conductivity of the atmosphere and their relation to meteorological factors. J. Atmos. Terr. Phys. 5 (1), 253–272.

Sagalyn, R.C., Faucher, G.A., 1956. Space and time variations of charged nuclei and electrical conductivity of the atmosphere. Q. J. R. Meteorol. Soc. 82 (354), 428–445.

Salgado, R., Le Moigne, P., 2010. Coupling of the flake model to the surfex externalized surface model. Boreal Environ. Res. 15, 231–244.

Silva, H.G., Conceição, R., Wright, M.D., Matthews, J.C., Pereira, S.N., Shallcross, D.E., 2015. Aerosol hygroscopic growth and the dependence of atmospheric electric field measurements with relative humidity. J. Aerosol Sci. 85, 42.

Silva, H.G., Lopes, F., Pereira, S., Nicoll, K., Barbosa, S.M., Conceição, R., Neves, S., Harrison, R.G., Collares Pereira, M., 2016. Saharan dust electrification perceived by a triangle of atmospheric electricity stations in Southern Portugal. J. Electrost. 84, 106–120.

Sokół, P., Stachlewska, I.S., Ungureanu, I., Stefan, S., 2014. Evaluation of the boundary layer morning transition using the CL-31 ceilometer signals. Acta Geophys. 62 (2), 367–380.

Stull, R.B., 2012. An Introduction to Boundary Layer Meteorology. vol. 13 Springer Science & Business Media.

Tammet, H., 1995. Size and mobility of nanometer particles, clusters and ions. J. Aerosol Sci. 26 (3), 459–475.

Tsaknakis, G., Papayannis, A., Kokkalis, P., Amiridis, V., Kambezidis, H.D., Mamouri, R.E., Georgoussis, G., Avdikos, G., 2011. Inter-comparison of lidar and ceilometer retrievals for aerosol and Planetary Boundary Layer profiling over Athens, Greece. Atmos. Meas. Tech. 4 (6), 1261–1273.

Whipple, F.J.W., 1929. On the association of the diurnal variation of the electric potential gradient in fine weather with the distribution of thunderstorms over the globe. Q. J. R. Meteorol. Soc. 55, 351–362. http://dx.doi.org/10.1002/qj.49705523206.

Willett, J.C., 1979. Fair weather electric charge transfer by convection in an unstable planetary boundary layer. J. Geophys. Res. 84 (C2), 703–718. http://dx.doi.org/10.1029/JC084iC02p00703.
Willett, J.C., 1981. Toward an Understanding of the Turbulent Electrode Effect Over Land. No. NRL-8519. Naval Research Lab, Washington D.C.
Williams, E.R., 2009. The global electrical circuit: a review. Atmos. Res. 91 (2–4), 140–152. http://dx.doi.org/10.1016/j.atmosres.2008.05.018.
Wilson, C.T.R., 1921. Investigations on lightning discharges and on the electric field of thunderstorms. Philos. Trans. R. Soc. London, Ser. A 221, 73–115. http://dx.doi.org/10.1098/rsta.1921.0003.
Yair, Y., Katz, S., Yaniv, R., Ziv, B., Price, C., 2016. An electrified dust storm over the Negev desert, Israel. Atmos. Res. 181, 63–71.
Zhou, L., Tinsley, B.A., 2007. Production of space charge at the boundaries of layer clouds. J. Geophys. Res. 112, D11203. http://dx.doi.org/10.1029/2006JD007998.

Geosci. Model Dev., 13, 3475–3488, 2020
https://doi.org/10.5194/gmd-13-3475-2020
© Author(s) 2020. This work is distributed under
the Creative Commons Attribution 4.0 License.

Geoscientific Model Development
Open Access
EGU

Numerical study of the seasonal thermal and gas regimes of the largest artificial reservoir in western Europe using the LAKE 2.0 model

Maksim Iakunin[1], Victor Stepanenko[2,3,4], Rui Salgado[1,5], Miguel Potes[1,5], Alexandra Penha[1,6], Maria Helena Novais[1,6], and Gonçalo Rodrigues[1]

[1]Institute of Earth Sciences – ICT, University of Évora, 7000-671 Évora, Portugal
[2]Lomonosov Moscow State University, Research Computing Center 119234 Moscow, Russia
[3]Lomonosov Moscow State University, Faculty of Geography, 119234 Moscow, Russia
[4]Moscow Center for Fundamental and Applied Mathematics, 119234 Moscow, Russia
[5]Department of Physics, ICT, University of Évora, 7000-671 Évora, Portugal
[6]Water Laboratory, University of Évora, P.I.T.E. Rua da Barba Rala Nº1, 7005-345 Évora, Portugal

Correspondence: Maksim Iakunin (miakunin@uevora.pt)

Received: 31 October 2019 – Discussion started: 17 January 2020
Revised: 26 June 2020 – Accepted: 5 July 2020 – Published: 5 August 2020

Abstract. The Alqueva reservoir (southeast of Portugal) is the largest artificial lake in western Europe and a strategic freshwater supply in the region. The reservoir is of scientific interest in terms of monitoring and maintaining the quality and quantity of water and its impact on the regional climate. To support these tasks, we conducted numerical studies of the thermal and gas regimes in the lake over the period from May 2017 to March 2019, supplemented by the data observed at the weather stations and floating platforms during the field campaign of the ALentejo Observation and Prediction (ALOP) system project. The 1D model, LAKE 2.0, was used for the numerical studies. Since it is highly versatile and can be adjusted to the specific features of the reservoir, this model is capable of simulating its thermodynamic and biogeochemical characteristics. Profiles and time series of water temperature, sensible and latent heat fluxes, and concentrations of CO_2 and O_2 reproduced by the LAKE 2.0 model were validated against the observed data and were compared to the thermodynamic simulation results obtained with the freshwater lake (FLake) model. The results demonstrated that both models captured the seasonal variations in water surface temperature and the internal thermal structure of the Alqueva reservoir well. The LAKE 2.0 model showed slightly better results and satisfactorily captured the seasonal gas regime.

1 Introduction

Inland water bodies are active and simultaneously sensitive regulators of the weather and climate processes of the Earth, and changing the temperature, wind, precipitation in the surrounding areas; their thermal and gas regimes, in turn, can serve as a response to the ecosystem status or climate change (Bonan, 1995; Adrian et al., 2009; Samuelsson et al., 2010). In modern climate and/or weather models, lakes and reservoirs are large-scale structures and are taken into account explicitly (Bonan, 1995); their parameterizations are intensively embedded in these models (Salgado and Le Moigne, 2010; Dutra et al., 2010; Subin et al., 2012). The 1D lake models, e.g. the freshwater lake (FLake) model (Mironov et al., 2010), the Dynamics Reservoir Simulation Model (DYRESM; Imberger and Patterson, 1981), and the generalized linear model (GLM; Hipsey et al., 2019), play a major role in this process. Their simplicity, computational efficiency, and reliability of the simulation results allow them to be used not only in studies of the dynamics of single lakes but also in the climate-related tasks of long-term numerical simulations, where vast territories with huge numbers of water bodies should be taken into account. As a result, the number of numerical studies connected with the vertical thermodynamics and biogeochemistry of lakes and their interaction with the atmosphere increases (Thiery et al., 2014;

Heiskanen et al., 2015; Le Moigne et al., 2016; Ekhtiari et al., 2017; Su et al., 2019).

A realistic representation of the thermal and gas regimes of lake models is important for solving current and prognostic tasks. For example, a high accuracy of the calculations of sensible and latent heat fluxes, momentum, and water surface temperature is required for atmospheric models in which these parameters are the boundary conditions (Bonan, 1995; Mironov et al., 2010; Dutra et al., 2010; Salgado and Le Moigne, 2010; Balsamo, 2013). On the other hand, an adequate simulation of the water temperature profiles would be a very interesting new output of weather prediction and earth system models because temperature is a key factor for lake ecosystem processes. This information might be useful for water quality management and for better representation of the gas emissions (CO_2, O_2, and CH_4) from lakes to the atmosphere, which are relevant to various atmospheric processes (Walter et al., 2007).

Fully filled only in 2004, the Alqueva reservoir is in the spotlight of many studies connected with its ecosystem services and ecology (Penha et al., 2016; Tomaz et al., 2017; Pereira et al., 2019), water quality (Potes et al., 2011, 2012, 2018; Novais et al., 2018), and lake–atmosphere interactions (Lopes et al., 2016; Policarpo et al., 2017; Potes et al., 2017; Iakunin et al., 2018). The aim of the present work is a numerical study of the seasonal variations in the thermal and gas regimes of the reservoir, which was held under the ALentejo Observation and Prediction (ALOP) system project in which an extensive field campaign and lake model simulations were combined. For the latter, we used the 1D model, LAKE 2.0 (Stepanenko et al., 2016), that features the biogeochemical block that simulates the concentrations of O_2, CO_2, and CH_4 in water. In addition, the FLake model, which is well established in weather and climate studies, was used as a reference to compare the results of the thermodynamic characteristics of the reservoir. Before starting the numerical simulations, the LAKE 2.0 model was adapted to the features of the Alqueva reservoir, including the introduction of the realistic values of the water pH and light extinction coefficients and adequate value of the coefficient of the hypolimnion turbulent mixing rate. Both models were forced with the observed meteorological data at the reservoir, which contributed to increasing the reliability of the results. The simulation covered the period from May 2017 to April 2019, and its results and the possibility of applying the LAKE 2.0 model in the operational mode might be used in future studies of weather and climate and biochemical-related tasks.

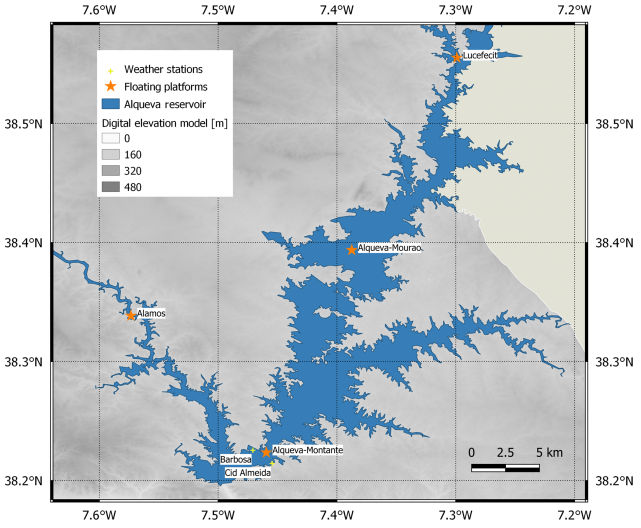

Figure 1. Location of the Alqueva reservoir and ALentejo Observation and Prediction (ALOP) stations. The map was built using the digital elevation model of the ASTER Global Digital Elevation Model (GDEM) version 2 (https://asterweb.jpl.nasa.gov/gdem.asp, last access: 1 August 2020).

2 Methods

2.1 Object of study

The Alqueva reservoir is located in the southeast of Portugal, spreading over 83 km in the former valley of the Guadiana River (Fig. 1).

Established in 2002 to meet the region's water and electricity needs, its surface covers an area of 250 km^2, the maximum depth is 92 m, the average depth is 16.6 m, and the storage capacity of water is estimated at 4.15 km^3, which makes it the largest reservoir in western Europe.

Long periods of drought that could last for more than 1 consecutive year (Silva et al., 2014) are typical in this part of the Iberian Peninsula. The Alqueva region is characterized by a hot Mediterranean summer climate (*Csa* type, according to the Köppen climate classification), with a small area that has a semi-arid climate (*BSk* type). In summer, the maximum daily air temperature ranges between 31 and 35 °C (July and August) while the record values may reach 44 °C. The winter period (December–February) in the region is relatively mild and wet, with an average air temperature of 10.3 °C. Nevertheless, even in January the air temperature can reach a maximum value of 24 °C during long periods of stable conditions when the Azores anticyclone settles into a favourable position. Seasonal rainfall normally occurs between October and May. The annual average values of the accumulated precipitation (1981–2010 normals from http://www.ipma.pt, last access: 1 August 2020) registered at the weather station in Beja, located 40 km away from the reservoir, is 558 mm. Mean daily values of the incident so-

lar radiation at the surface are about 300 $W m^{-2}$ (one of the highest in Europe) and the daily maximum in summer often may exceed 1000 $W m^{-2}$ (Iakunin et al., 2018).

2.2 Observed data

Geographical and climatological factors make the Alqueva reservoir a vital source of fresh water that is needed to support the population and economy in the region, while on the other hand, increasing anthropogenic and heat stress negatively affects the lake's ecosystem (Penha et al., 2016). Monitoring the quantity and quality of water in the reservoir has become an essential scientific task. This task is addressed in the framework of the ALOP project that is related to the observations and numerical experiments on the study of the processes of the atmosphere called the Alqueva reservoir system. Models of different spatial and timescales were used in the ALOP numerical experiments.

The ALOP field campaign was focused on measurements of physical, chemical, and biological parameters in the water and air columns at the water–atmosphere interface and on the shores of the reservoir. In the present work, the following facilities were used and equipped to obtain the required data for the numerical simulations during the field campaign: four floating platforms (namely, Montante, Mourão, Alamos, and Lucefécit) and two dedicated weather stations in the margins (namely, Barbosa and Cid Almeida); their locations are marked with circles in Fig. 1. The principal scientific site on the lake is the Montante floating platform, which is located in the southern and deeper part (74 m) of the reservoir (38.2276° N, 7.4708° W). The following equipment was deployed on the platform and continuously provided measurements during the whole field campaign:

- an eddy-covariance system (Campbell Scientific) provides data of atmospheric pressure, air temperature, water vapour and carbon dioxide concentrations, 3D wind components, linear momentum, sensible heat, latent heat, and carbon dioxide fluxes;

- an albedometer (model CM7B; Kipp & Zonen) and a pyrradiometer (type 8111; Philipp Schenk GmbH) was used in order to measure upwelling and downwelling shortwave and total radiative fluxes;

- a set of 14 probes (107 temperature probe; Campbell Scientific) measured the water temperature profile at the following depths, namely 5, 25, and 50 cm, and 1, 2, 4, 6, 8, 10, 12, 15, 20, 30, and 60 m.

Two probes were installed at the platform to assess water quality. A multiparametric probe (Aqua TROLL 600; In-Situ Inc.) that provided information about dissolved oxygen concentration and pH values, among other parameters, was mounted on the platform at a 25 cm depth on 3 July 2018 and worked until the end of the campaign. It was also used to make profiles during regular maintenance visits to the platform. A Pro-Oceanus Mini CO_2 analogue output probe was also mounted on the platform at a 25 cm depth to measure the dissolved CO_2 concentration continuously and was occasionally used to collect vertical profiles. Installed in the beginning of the campaign, the probe was working until the middle of June 2017 when it failed. It was repaired and reinstalled in October 2017, but another problem occurred in November and probe was removed for the remainder of the study.

Two land weather stations (namely, Barbosa and Cid Almeida) were installed on opposite shores with the floating platform in the middle, between them (38.2235° N, 7.4595° W and 38.2164° N, 7.4545° W, respectively; green circles in Fig. 1). The equipment of both weather stations is listed in Table 1. Data from the Montante floating platform, Barbosa, and Cid Almeida weather stations were automatically downloaded and transferred daily to the server in the Institute of Earth Sciences (ICT) at the University of Évora. An important part of the campaign were the regular field trips to the reservoir for the cleaning and maintenance of the instrumentation on the platforms and weather stations, conducting more detailed measurements, and collecting water samples at several depths and bottom sediments.

For further work, the data collected during the field campaign were treated before being used as a forcing for atmospheric- and/or lake-modelling-related tasks. Missed data (gaps in data smaller than 3 h) were carefully filled using linear interpolation. Longer gaps were substituted with values from the closest weather stations.

2.3 LAKE 2.0 model

For the simulation of the thermodynamic and biogeochemical processes in the Alqueva reservoir, the LAKE 2.0 (available at http://tesla.parallel.ru/Viktor/LAKE/wikis/LAKE-model, last access: 1 August 2020) model was chosen. A detailed description of the LAKE 2.0 model may be found in Stepanenko et al. (2016); briefly, the model equations are formulated in terms of water properties averaged over a lake's horizontal cross section, thus introducing into the model the fluxes of momentum, heat, and dissolved gases through a sloping bottom and water–atmosphere surfaces. The water temperature profile is simulated explicitly in LAKE 2.0, and a number of biogeochemical processes are represented, which makes it capable of reproducing the transfer of CO_2 and CH_4 from and to the atmosphere.

Governing equations for the basic processes of the lake dynamics in the model are obtained using the horizontally averaged Reynolds advection–diffusion equation for the quantity f which may be one of the velocity components, such as temperature, turbulent kinetic energy (TKE), TKE dissipation, or gas concentration as follows:

Table 1. Weather stations equipment. n/a – not applicable

Measured parameter	Station	
	Barbosa	Cid Almeida
Albedometer	n/a	Philipp Schenk (8104)
Air temperature and humidity	Campbell Scientific (CS 215)	Thies Clima (1.1005.51.512)
Wind speed	Gill Instruments WindSonic (1405-PK-021)	Vector Instruments (A100R)
Wind direction	Gill Instruments WindSonic (1405-PK-021)	Vector Instruments (W200P)

$$c\partial_t \bar{f} = \underbrace{A^{-1}\partial_z(Ak_f\partial_z\overline{f})}_{\text{I}} \underbrace{-A^{-1}\partial_z(A\overline{F_{nz}})}_{\text{II}} \underbrace{+R_\text{f}(\bar{f},\ldots)}_{\text{III}}, \qquad (1)$$

where term I describes the turbulent diffusion, thermal conductivity, or viscosity; term II is the divergence of non-turbulent flux of f; term III represents the horizontally averaged sum of sources and sinks; $\bar{F}_{nz}$ is the non-turbulent flux of f; and k_f is the turbulent diffusion coefficient (thermal conductivity coefficient for temperature, viscosity for momentum) for the f quantity. The LAKE 2.0 model successfully represents conditions in the well-mixed upper layer of lakes (epilimnion).

In water, the $k-\epsilon$ parameterization for computing turbulent fluxes is used. In ice and snow, a coupled transport of heat and liquid water is reproduced (Stepanenko et al., 2019). In bottom sediments, the vertical transport of heat is implemented in a number of sediment columns originating from different depths.

The water temperature profile in the model is driven by Eq. (1) with substitution $f \to T$, where $c = c_\text{w}\rho_\text{w0}$, c_w is water-specific heat, ρ_w0 is mean water density, $\overline{R_\text{f}} = 0$ represents heat flux from the sediments, and $\overline{F_{nz}}(z) = S_\text{rad}$ is the downward shortwave radiation flux attenuation according to the Beer–Lambert law in four wavebands (infrared, near-infrared, photosynthetically active, and ultraviolet) with corresponding extinction coefficients. The heat conductance is a sum of molecular and turbulent coefficients, $k_T = \lambda_\text{m} + \lambda_\text{t}$, where $\lambda_\text{t} = c_\text{w}\rho_\text{w0}\nu_\text{T}$ (ν_T is the turbulent coefficient of thermal diffusivity, and $\text{m}^2\,\text{s}^{-1}$ is derived from the $k-\varepsilon$ parameterization).

To solve the Eq. (1) for water temperature, the top and bottom boundary conditions should be defined. The top boundary conditions are represented by a heat balance equation, involving net radiation and a scheme for turbulent heat fluxes in the surface atmospheric layer based on the Monin–Obukhov similarity theory (Monin and Obukhov, 1954). The bottom boundary condition is set at the water–sediments interface and is based on the continuity of both heat flux and temperature at the interface. Bottom sediments are represented by the 1D multilayer model, which includes heat conductivity, liquid moisture transport (diffusion and gravitational percolation), ice content, and phase transitions of water.

Lake hydrodynamics described by Eq. (1) are applied to horizontal momentum components, with $F_{nz} = 0$, $c = 1$, and R_f representing the Coriolis force and bottom friction. The Coriolis force has to be included in the momentum equations for lakes with a horizontal size that exceeds the internal Rossby deformation radius (Patterson et al., 1984).

Wind stress, which is computed by the Monin–Obukhov similarity theory, is applied as a top boundary condition for momentum equations, bottom friction is set by logarithmic law with a prescribed roughness length. Friction at a sloping bottom (term R_f) is calculated with a quadratic law with a tunable drag coefficient.

The LAKE 2.0 model uses a $k-\varepsilon$ model (Canuto et al., 2001) to compute turbulent viscosity, temperature conductivity, and diffusivity. It takes both the shear and buoyancy production of turbulent kinetic energy into account; an equation for the dissipation rate is a highly parameterized one, with several constants calibrated in idealized flows.

Biochemical oxygen demand (BOD) is caused by the degradation of dissolved organic carbon (DOC) and dead particulate organic carbon (POCD). The dynamics of the latter two, together with living particulate organic carbon (POCL) are represented by the model from Hanson et al. (2004) adapted to the 1D framework. Photosynthesis is given by Haldane kinetics, where the chlorophyll a concentration in the mixed layer is computed from the photosynthetic radiation extinction coefficient (Stefan and Fang, 1994) and assumed to be zero below. The model does explicitly not take into account the nutrients concentrations. The fluxes of dissolved gases into the atmosphere are calculated using Henry's law and the surface-renewal model (Stepanenko et al., 2016) involving the subsurface turbulent kinetic energy dissipation rate below the mixed layer of the euphotic zone, as provided by the $k-\epsilon$ closure.

To calculate the dissolved carbon dioxide concentration in water, the same type of prognostic equation is used as for other gases. In LAKE 2.0, the sedimentary oxygen demand and BOD, respiration, and CH_4 oxidation act as CO_2 producers, while photosynthesis is the only sink of carbon dioxide in the water column. More detailed equations and comments on the biogeochemical processes in the model are given in the Supplement.

2.4 Model modifications and sensitivity tests

The given version of the LAKE 2.0 model used constant values for the light extinction coefficient in water for infrared (IR), near-infrared (NIR), photosynthetically active radiation (PAR), and ultraviolet (UV) bands. This could lead to significant errors, especially in long-term simulations, because these parameters control the vertical distribution of solar energy in different water layers. The light extinction coefficient for PAR (400–700 nm) undergoes a large annual variability in the Alqueva reservoir, as shown in Potes et al. (2012), and it was measured constantly during the ALOP field campaign. From April 2017 until March 2019 it varied from a minimum of $0.247\,m^{-1}$ (August 2017) to a maximum of $1.519\,m^{-1}$ (July 2018), with an average value of $0.643\,m^{-1}$ (12 measurements). Thus, prior to the simulation, the decision was made to upgrade the LAKE 2.0 model and introduce a new variable, namely the light extinction coefficient for PAR, to the model set-up. During the initialization, the model reads the available values of this coefficient and does a linear interpolation for every model time step. Although the model results are not very sensitive to it, the proposed modification led to improved results in some periods by about 1°, as exemplified in the Fig. S1 in the Supplement, for a selected period.

Water pH significantly affects the solubility of carbon dioxide (Fig. S4 in the Supplement), but its value is a model scalar constant. In reality, observations show that pH tends to decrease near the bottom and has a seasonal variation, changing from 7.8 to 8.8 during the years 2017–2019, in the mixed layer. After averaging the measurements, the pH constant inside the model code was altered from 6.0 to 8.48 for a better representation of real processes. Another modification has been done to the hypolimnetic diffusivity parameterization. According to Hondzo and Stefan (1993), for lakes of regional-scale hypolimnetic eddy diffusivity rate, K_z is related to stability frequency N^2 and the lake area A_s as follows:

$$K_z = c_1 (A_s)^{c_2} (N^2)^{c_3}, \tag{2}$$

where $c_1 = 8.17 \times 10^{-4}$, $c_2 = 0.56$, $c_3 = -0.43$ are empirical constants, $N^2 = -(\partial\rho/\partial z)(g/\rho)$, z is depth, g is acceleration of gravity, and ρ is the density of water. In the LAKE 2.0 model, Eq. (2) is presented as $K_{z,\mathrm{LAKE\,2.0}} = \alpha K_z$, where α is a calibration coefficient that allows one to adapt this parameterization to the specific features of a given lake. In a series of sensitivity experiments it was found out that, for a simulation of the thermal regime in the Alqueva reservoir, the value of $\alpha = 0.3$ provides the best representation of the heat diffusion from the surface to the depth of the lake (see the comparison in Fig. S5 of the Supplement).

2.5 FLake model

In addition to LAKE 2.0, the FLake model was used to simulate water temperatures for the chosen period. The FLake model (Mironov, 2008) is based on a two-layer representation of the lake's thermal structure. The upper layer is assumed to be well mixed, and the structure of the deep stratified layer is described using the concept of the self-similarity of the temperature–depth curve. The FLake model is widely used in climate and numerical weather prediction studies (Salgado and Le Moigne, 2010; Samuelsson et al., 2010; Le Moigne et al., 2016; Su et al., 2019) to simulate the feedback of freshwater lakes on the atmospheric boundary layer and in the intercomparison experiments with other parameterizations. In particular, FLake has been applied in studies of the Alqueva reservoir by Iakunin et al. (2018), Potes et al. (2012), and Salgado and Le Moigne (2010).

2.6 Simulation set-up

The simulation conducted in the present study covered 23 months from 1 May 2017 to 29 March 2019, with a 1 h time step for the input and output data. In the set-up stage, specific features of the Alqueva reservoir were prescribed, namely the series of the PAR extinction coefficients for the simulation period, the morphometry of the lake bottom expressed via the dependence of the horizontal cross section area on the depth and the initial profiles of the water temperature, namely CO_2, O_2, CH_4, and salinity (the last two profiles were set to zero due to the lack of observation data).

Both LAKE 2.0 and FLake models were initialized with ALOP data measured at Montante, on the reservoir's floating platform, and ran in the stand-alone version. Atmospheric forcing input data were taken from the Montante platform observations. A comparison between LAKE 2.0 and FLake models was made in terms of water temperature and heat fluxes over the water surface.

3 Results and discussion

3.1 Water temperature

Water temperature is a crucial factor for numerical weather prediction (NWP) applications and as a regulator of lake ecosystem activity. It is a key parameter of the lake–atmosphere interactions. Thus, a detailed representation of the evolution of the water temperature at various depths is an important task.

According to the definition given in Wetzel (1983), the summer stratification period is characterized by a stratum of thermal discontinuity (metalimnion) which separates an upper layer of warm, circulating water (epilimnion) and cold and relatively undisturbed water below (hypolimnion). The stratum of thermal discontinuity is usually defined as a change of $> 1\,°C\,m^{-1}$. The summer stratification periods are

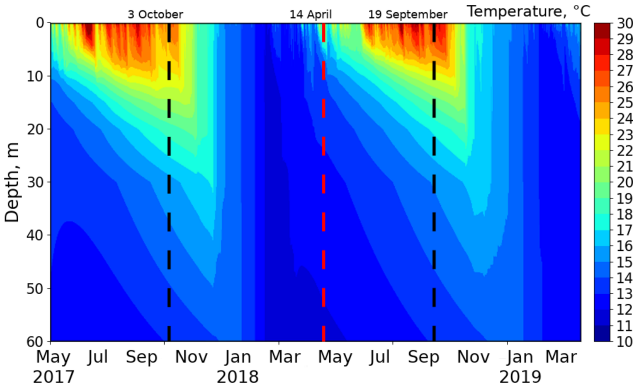

Figure 2. Time–depth Hovmöller diagram of the LAKE 2.0 simulated water temperature in the Alqueva reservoir based on hourly data. Dashed lines indicate the end (black) and the beginning (red) of stratification.

clearly seen in Fig. 2 (marked with dashed lines). The simulation began in a stratified condition which lasted until 3 October 2017, while in 2018 stratification lasted from 14 April to 19 September.

The water temperature in upper layers increases up to 30 °C in the warm period, and in the hottest months (July–September) it reaches 25 °C at a 10 m depth. In the winter turnover period, the water temperature becomes uniform at depths of up to 30 m. From December, when the lake shows no temperature stratification, it gradually cools from 19 to 12 °C (in late February).

The temperature of water in the mixed layer (ML) is of a particular interest in many studies. LAKE 2.0 provides the water temperature at different depths, as defined in the model set-up and ML thickness, assuming that the ML temperature is constant (not including the surface skin effect). Since the vertical gradient of the measured ML temperature is not exactly constant, measurements from the sensor at a 0.5 m depth were chosen to represent the mixed layer temperature in Fig. 3. During the whole simulation period, ML depth in the reservoir was never less than 70 cm. Figure 3a shows the LAKE 2.0 simulated results in comparison with the measured values and FLake results of ML temperature. To smooth hourly fluctuations in such long-term simulation, moving average was used with 6 h period.

Differences between the two model results and the measurements (errors) are shown in Fig. 3b. In the period from March to November in both years, when the lake is stratified, the LAKE 2.0 model demonstrates better results, while during the cold periods (November–March) both models show similar error rates. The statistics of the comparison are presented in Table 2. Overall, the mean absolute errors for the whole simulation period are 1.27 °C for FLake and 0.74 °C for LAKE 2.0. Mean errors of the LAKE 2.0 and FLake models for the simulation period are 0.56 and 1.18 °C, respectively (shown as dashed lines in Fig. 3b), which means that both models tend to slightly overestimate the ML temperature. The LAKE 2.0 model results are better for warm periods, while FLake results are better for cold. Both models demonstrate an almost identical correlation for the selected periods.

For a more detailed analysis of the surface water temperature evolution, we chose four months, namely July 2017–2018 and January 2018–2019, which represent the stratified and non-stratified lake states that show the daily cycles of the ML water temperature (Fig. 4).

It is seen that the LAKE 2.0 model shows exceptionally good results in summer months (Fig. 4a; average mean errors are −0.23 and −0.04 °C for 2017 and 2018, respectively), while FLake provides an overestimation of 1–2° and an underestimation of the daily amplitude. Correlation coefficients in this case are 0.94/0.88 (LAKE 2.0) and 0.90/0.89 (FLake), respectively. Diurnal ML temperature variations can reach 3° and are generally well represented by the LAKE 2.0 model. In January the water temperature profile in the reservoir is homogeneous, the daily amplitude is not so high (Fig. 4b), and so the FLake model shows a smaller overestimation (0.95 correlation for both months and mean errors of 0.45/0.78 °C). The LAKE 2.0 results show a positive offset; the average mean error for January 2018 was 0.78 °C and the correlation was 0.97. In January 2019, the LAKE 2.0 mean error was 1.22 °C but, in general, the shape of the curve was similar to the measured values, and the daily variations in temperature were represented quite well.

Temperature distribution with depth is another significant parameter for lake thermodynamics. The LAKE 2.0 model simulates water temperature at predefined depth levels. FLake outputs include ML depth temperature, shape factor for the thermocline curve, and temperature at the bottom. Using these values it is possible to retrieve a water temperature profile. Simulation results are shown in Fig. 5 for the following cases: 15 July 2017, 15 January 2018, 15 July 2018, and 15 January 2019, each at 12:00 UTC.

Summer water temperature profiles are well represented by both models, although FLake shows an overestimation in the ML. In winter, on the other hand, LAKE 2.0 overestimates the water temperature through whole water column. Although LAKE 2.0 reproduces the short-term (daily and weekly scales) thermal evolution of the ML very well, the simulated heat content of the entire water column seemed to be higher than in reality. The errors are higher in the second year of the simulation, with the results of winter 2018–2019 exceeding 1°. The modelled water column tends to heat slightly more than the actual water column (Fig. 5c–d). This behaviour may be due to a small misrepresentation of the energy balance at the lake surface or at the bottom and requires additional tests that could eliminate such systematic errors and improve the results, especially in cold periods.

The other important parameter, which is essentially connected with the lake's vertical thermal structure, is the depth of the mixed layer. To estimate it, we assumed that the ML

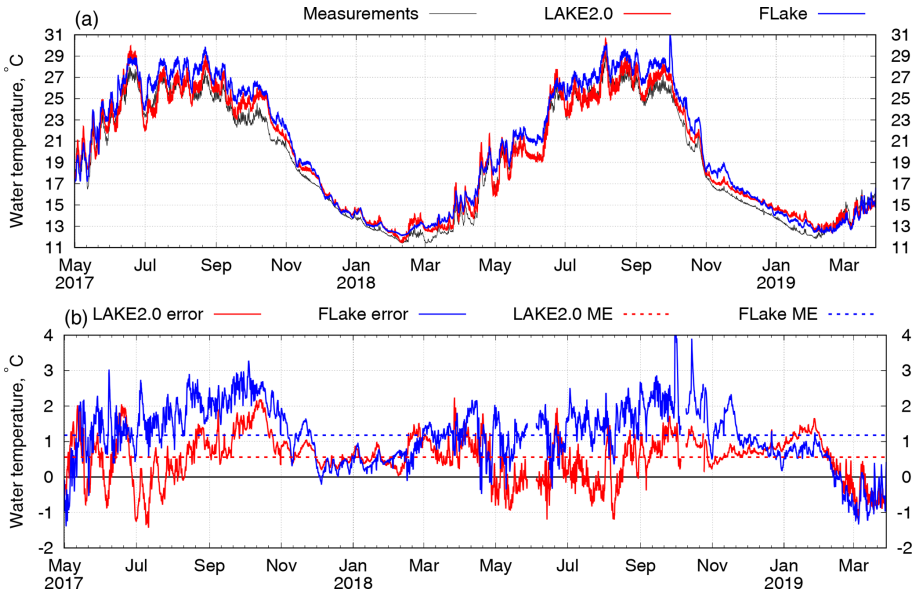

Figure 3. (a) Time series (6 h moving average) of the Alqueva water temperature in mixed layer showing measured (black curve) and modelled results from LAKE 2.0 (red curve) and FLake (blue curve). **(b)** Temperature differences (6 h moving average) between observations and LAKE 2.0 (red curve) and FLake (blue curve). Dashed lines show the corresponding mean errors for LAKE 2.0 and FLake.

Table 2. Statistical results of mixed layer (ML) water temperature intercomparison. MAE – mean absolute error.

	Correlation		Mean error, °C		MAE, °C	
Time periods	LAKE 2.0	FLake	LAKE 2.0	FLake	LAKE 2.0	FLake
May–Oct 2017	0.95	0.96	0.52	1.57	0.79	1.63
Nov 2017–Feb 2018	0.99	0.99	0.61	0.63	0.61	0.64
Mar–Oct 2018	0.99	0.99	0.48	1.50	0.69	1.51
Nov 2018–Feb 2019	0.98	0.98	0.83	0.92	0.83	0.92
All periods	0.99	0.99	0.56	1.18	0.74	1.27

ends at a point of half of the maximum temperature gradient (but not less than 0.5 °C). Such a criterion was used for observed data and LAKE 2.0 results. In FLake, the ML depth is a major diagnostic variable, updated at each time step using a sophisticated formulation, that treats both the convective and stable regimes (see Mironov et al., 2010). The time series of the ML depth for the 2017 and 2018 Alqueva reservoir's stratification periods are shown in Fig. 6.

The curves of the ML depth calculated from measurements and LAKE 2.0 results coincide quite well. However, since the simulated water temperature profiles are more smooth, the LAKE 2.0 ML depth has more "downward" peaks in the figure. Although FLake tends to underestimate the ML depth, the general pattern of it correlates with the measurements.

3.2 Heat fluxes

Sensible and latent heat fluxes play an important role in lake–atmosphere interaction, determining the rates of heat accumulation by water bodies or evaporation from the surface and consequently having effects on the local climate and on the establishment of thermal circulations (see for example Iakunin et al., 2018). The LAKE 2.0 model (and FLake) is capable of calculating heat fluxes, and Fig. 7 shows the daily averaged results of the simulation of these variables.

Sensible heat flux is well represented by both models (Fig. 7a–b), which is supported by low mean errors (see Table 3) and a high correlation coefficient. Latent heat flux, however, is overestimated by the LAKE 2.0 and FLake models (by 53–43 $W m^{-2}$), although both models demonstrate a high correlation (0.92) with the measurements.

In terms of latent heat fluxes the LAKE 2.0 model's results are worse than the FLake's when compared to the eddy-covariance (EC) measurements. However, it should be noted that several studies have indicated that the EC systems tend to underestimate the heat fluxes (e.g. Twine et al., 2000). Recent works showed comparable differences between the FLake and the LAKE 2.0 models and EC measurements over lakes (Stepanenko et al., 2014; Heiskanen et al., 2015) in

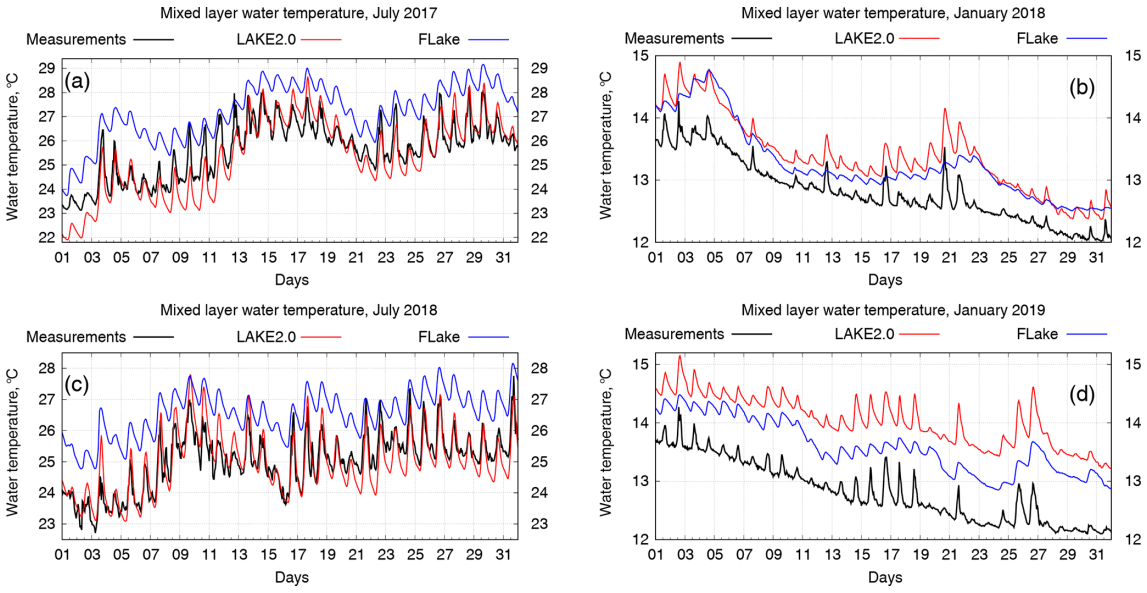

Figure 4. Time series of mixed layer water temperature for July 2017 and 2018 **(a** and **c)** and January 2018 and 2019 **(b** and **d)**.

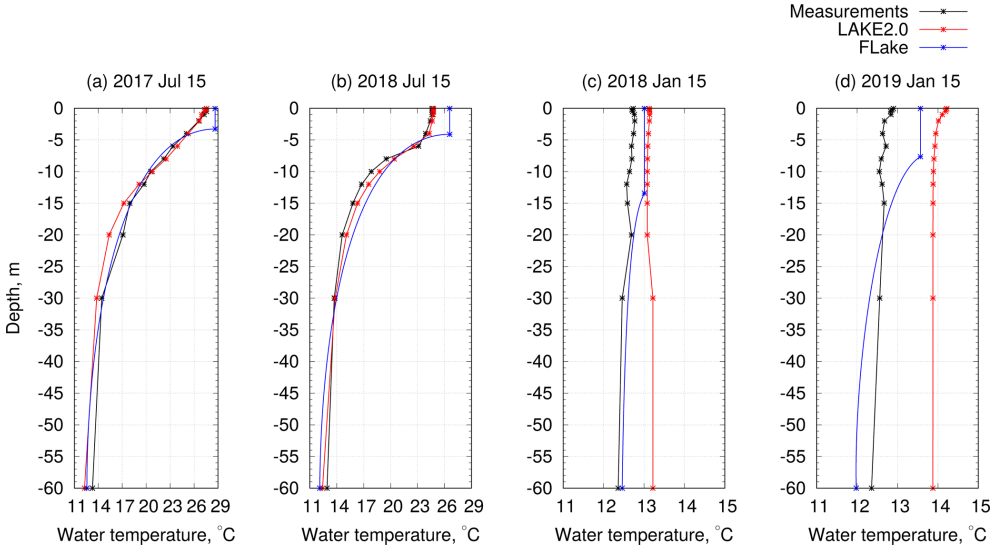

Figure 5. Water temperature profiles for 15 July 2017 **(a)**, 15 January 2018 **(b)**, 15 July 2018 **(c)**, and 15 January 2019 **(d)**, each at 12:00 UTC.

which the relative differences of about 35 % were noticed. The differences between model and EC observations can also come from model errors due to the fact that the Alqueva reservoir is an open lake with a continuous inflow and outflow of the Guadiana River. The horizontal flows, not represented in the 1D vertical models, can add or remove energy from the water body. Also, the water level in the Alqueva reservoir changes significantly during the year due to drought periods and discharges through the dam. It decreased to 7 m in 2018, which corresponds to the loss of 35 % of total volume of water. The models cannot take into an account those changes while they could be a major source of errors in heat flux computations.

Table 3. Sensible and latent heat flux errors and correlation coefficients.

	Sensible heat		Latent heat	
	LAKE 2.0	FLake	LAKE 2.0	FLake
Mean error, $W m^{-2}$	5.51	5.36	52.93	43.46
MAE, $W m^{-2}$	8.38	6.85	53.40	44.02
Correlation coefficient	0.88	0.87	0.92	0.92

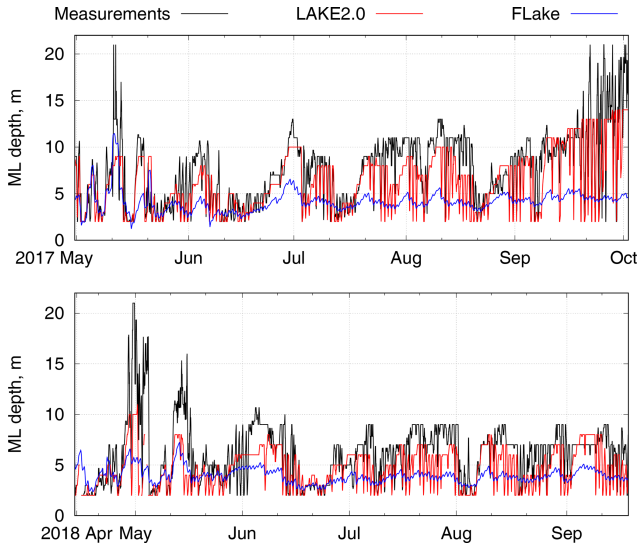

Figure 6. Evolution of mixed layer (ML) depth during stratification periods (with 6 h moving average).

3.3 Dissolved carbon dioxide

The diffusion of CO_2 from the atmosphere to water and its further dissociation are of major importance to photosynthetic organisms which depend on the availability of inorganic carbon (Wetzel, 1983). Dissolved inorganic carbon constituents also influence water quality properties such as acidity, hardness, and related characteristics.

The solubility of CO_2 in water depends on several factors such as pH, water temperature, etc. Observations indicate that pH may vary from 8.8 at the surface level to 7.4 at the bottom, while in the model it is a constant parameter value which was set to a value of 8.48, which corresponded to the mean pH value during the simulation period. Figure 8 reveals the dynamics of CO_2 concentrations in water in the first months of the ALOP field campaign in comparison with LAKE 2.0 simulated results.

In general, the LAKE 2.0 values are smoother than the observations as the model does not react to the changes in CO_2 as fast, but the mean values are well represented. On 20–26 May and at the beginning of June (subplots in Fig. 8a), daily cycles are represented quite well. In the second week of May, the CO_2 probe accidentally dismounted from the platform and floated in the water, attached to the connecting cord, until the next fieldwork trip (17 May). On 12 June the probe failed, and it was dismounted and removed from the Montante platform. Later, on 18 October, the probe was mounted on the platform again and it was working in a test mode for three weeks (Fig. 8b). In this period, LAKE 2.0 simulated values of CO_2 do not show much daily variation and have an increasing trend due to autumn water cooling. Small daily biases in simulated values coincide with peaks in measured data.

Thus, we can conclude that in long time simulations the LAKE 2.0 model represents CO_2 trends quite well. The model failed to reproduce the diurnal cycle of the surface carbon dioxide concentration, which calls for inquiry of parameterizations of photosynthesis and respiration in the model. However, the diurnal means are well captured which is enough with respect to using the model in climate applications.

3.4 Dissolved oxygen

Dissolved oxygen (DO) is essential to all aerobic organisms living in lakes or reservoirs. To understand the distribution, behaviour, and growth of these organisms, it is necessary to know the solubility and dynamics of oxygen distribution in water. The rates of supply of DO from the atmosphere and from photosynthetic inputs and the hydromechanical distribution of oxygen are counterbalanced by the consumptive metabolism. The rate of oxygen utilization in relation to synthesis permits an approximate evaluation of the metabolism of the lake as a whole (Wetzel, 1983).

The concentration of DO in the Alqueva reservoir was measured continuously on the Montante platform from 3 July 2018. A comparison of measured and model values is shown in Fig. 9. The model represents DO concentration in a realistic way during the first 2 months, until the middle of September, when a microalgal bloom occurred. It caused an intensive production of O_2 in the water that cannot be represented by the LAKE 2.0, which does not have an explicit representation of algae, and the bloom does not affect atmospheric forcing. Then, until the end of October, the model showed good results, but in November the observations demonstrated a decrease in oxygen concentration, which was not followed by the model; in fact, the model predicted an increase until the beginning of February. In November, following turnover, water temperature decreases and does not change significantly with depth; under these conditions the concentration of oxygen-producing organisms decreases, and so does the DO, which falls from 8–9 to 6 $mg\,L^{-1}$. The model does not reflect this decrease in photosynthesis but largely increases the DO concentration following the decrease in water temperature (oxygen is more soluble in colder water). When, in the middle of February, the temperature returns to a stratified regime, DO concentrations in the model and measurements coincide again.

The photosynthesis rate can be linked to chlorophyll *a* measurements (Table 4) which were done during the fieldwork at the Alqueva reservoir. In July 2018, when DO measurements began, the concentration of chlorophyll *a* ranged from 1.754 to 2.98 $mg\,m^{-3}$ in water ML (0–3 m). Furthermore, when the autumn bloom occurred in September, the chlorophyll concentration significantly increased and reached 14.036 $mg\,L^{-1}$ at the surface and came back to values of 2.309 $mg\,m^{-3}$ in November. The ALOP field campaign ended in December 2018, but the work on stations and

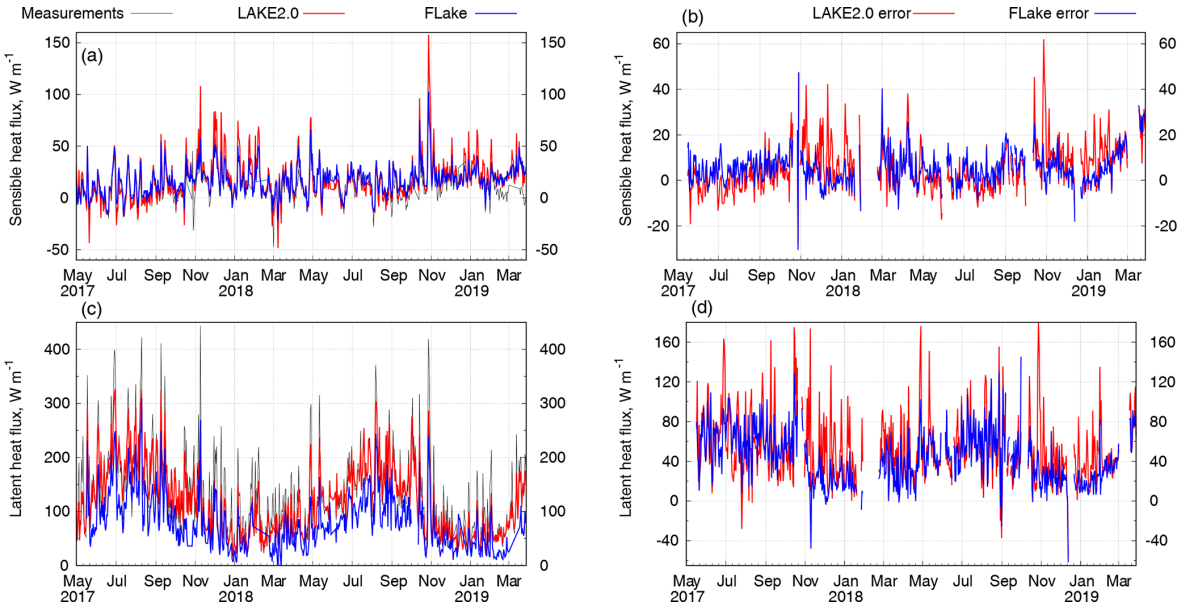

Figure 7. Daily averaged sensible **(a)** and latent **(c)** heat fluxes with corresponding errors **(b** and **d)**. Black curve represents the measured values, the red curve shows LAKE 2.0 results, and the blue curve shows FLAKE results.

Table 4. Chlorophyll *a* measurements at the Alqueva reservoir.

	Chlorophyll *a* concentration, mg m^{-3}										
Depth	2017 Jul	Sep	Nov	2018 Jan	Apr	Jun	Jul	Sep	Nov	2019 Jan	Feb
Surface	1.11	7.60	1.03	2.55	12.189	5.796	2.678	14.036	2.309	No pigments	1.2
1 m	0.00	6.33	0.78	2.33	12.695	4.344	1.754	6.279	1.385	–	–
2 m	1.11	6.65	1.03	2.44	11.573	3.989	2.124	7.849	1.847	–	–
3 m	2.77	6.65	0.96	1.99	9.973	3.022	2.980	9.603	1.385	–	–

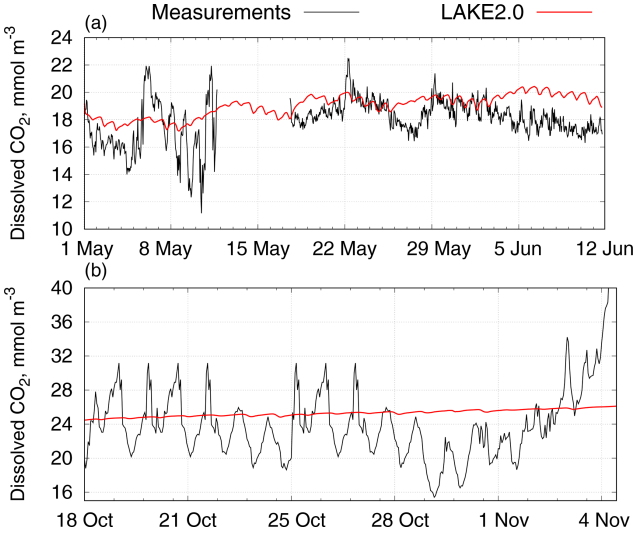

Figure 8. Time series of dissolved CO_2 in water at 25 cm depth.

the Montante platform maintenance continued, so, in January and February 2019, samples from water surface layer were taken. The sample from 15 January showed no traces of chlorophyll *a* in water, which is related to very low DO concentrations in this period (Fig. 9). The measurements of chlorophyll *a* in the water sample taken on 2 February showed the value of 1.3 mg m^{-3}. It corresponds to the relative increase in oxygen producers in water and, hence, DO concentration.

An analysis of DO profiles (Fig. 10) shows similar results. The distribution of oxygen with depth is well represented by the model for the July and September profiles, while in December and February, with no stratification in temperature and oxygen, the LAKE 2.0 model overestimates DO up to 2.5 mg L^{-1}. March profiles (1 and 29) show good similarities in the measured and simulated values.

4 Conclusions

Numerical studies of the seasonal variations in the thermal and gas regimes in the Alqueva reservoir using the LAKE 2.0

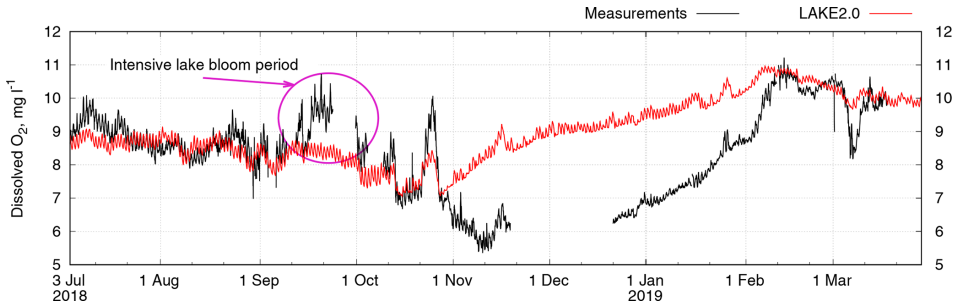

Figure 9. Time series of dissolved O_2 in water at 25 cm depth for the period 3 July 2018–29 March 2019 at the Alqueva reservoir.

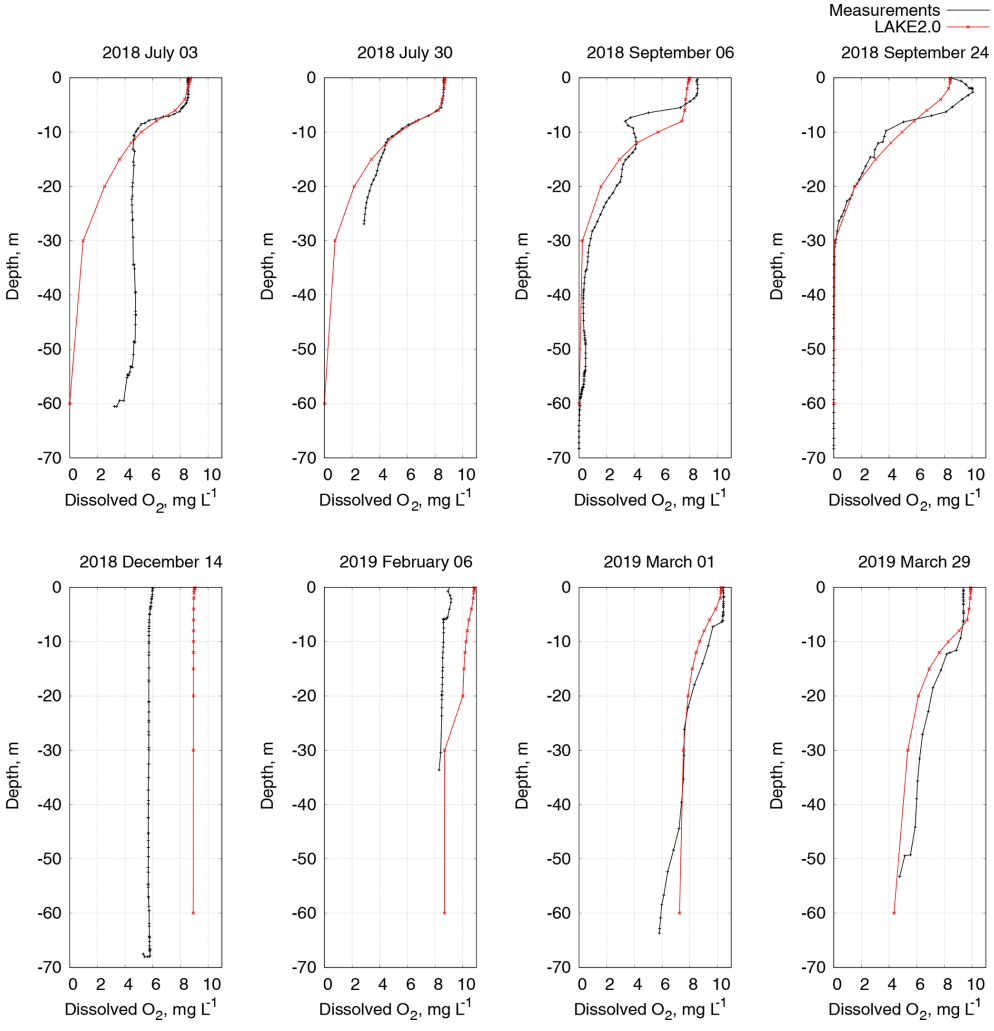

Figure 10. Profiles of dissolved O_2 in water measured during the field campaign (black) and model values (red).

and the FLake models are presented in this work. Simulated profiles and time series of water temperature, sensible and latent heat fluxes, and concentrations of dissolved CO_2 and O_2 were compared with observed data. The seasonal variations in the ML water temperature are well represented by both models. Mean absolute errors are 0.74 and 1.27 °C for LAKE 2.0 and FLake models, respectively, and the correlation coefficients for the relationship between simulated and measured temperatures are 0.99 for both. The LAKE 2.0 model overestimates ML water temperature only by 0.5 °C during the warm periods (March–October), while FLake shows an overestimation of about 1.5°. In the cold periods (November–February) both models show the same level of overestimation of ML temperatures (about 0.6–0.9 °C).

The model errors of the seasonal variations in sensible and latent heat fluxes are the following. Sensible heat mean absolute errors (MAEs) are 7.71 $W m^{-2}$ (LAKE 2.0) and 6.75 $W m^{-2}$ (FLake). Latent heat flux results of both models in terms of MAE are worse, namely 53.99 $W m^{-2}$ (LAKE 2.0) and 45.6 $W m^{-2}$ (FLake). Such errors occur mainly in periods when the wind increases suddenly. Strong single high hourly wind input data cause high latent heat simulated values, which are not always confirmed by the observations.

LAKE 2.0 simulated dissolved carbon CO_2 time series demonstrated a good correspondence with the observations in mean values; however, the model significantly underestimated the magnitude of the diurnal cycle. In the 18th month of the experiment (October 2018, when the probe was returned to the platform), the simulated CO_2 values did not show large residuals despite the fact that the pH value remained constant during the whole simulation.

Dissolved oxygen, reproduced by the model, reveals the need to include a more complete description of the processes that regulate photosynthesis and respiration in the LAKE 2.0 model before operational use. Although measured oxygen concentrations are well simulated over short time intervals, the annual Alqueva reservoir oxygen cycle cannot be reproduced because the model does not respond to changes in the algal concentration. The winter overestimation is probably due to relatively low water temperatures. Nevertheless, the high versatility and flexibility of the LAKE 2.0 model gives good opportunities for improving the model performance, with the aim of adequate modelling of seasonal variations in the gas regime of the lake.

Performed simulations showed that the LAKE 2.0 model accurately simulates the lake's thermal regime and the heat and gas fluxes from the ML. In terms of water temperature profile, LAKE 2.0 demonstrated a better performance than the FLake model. The results are encouraging regarding the ability of the LAKE 2.0 model to represent the evolution of physicochemical profiles of lakes, and it may be used operationally in the future, coupled with weather prediction models, to forecast variables that are useful in the management of water quality and aquatic ecosystems. Similarly, the results indicate that the LAKE 2.0 model could be used in climate modelling to estimate the impacts of the climate change in the thermal and gas regimes of the lake.

Code and data availability. The current versions of the models used in this work, and the atmospheric forcing data, can be found at https://doi.org/10.5281/zenodo.3608230 (Iakunin et al., 2020) or upon request from the corresponding author (miakunin@uevora.pt or m.yakunin89@gmail.com). The source code of the FLake model is available at (http://www.flake.igb-berlin.de/site/download, Mironov, 2008). The source code for the latest version of the LAKE 2.0 model is available at (http://tesla.parallel.ru/Viktor/LAKE/wikis/LAKE-model, Stepanenko et al., 2016).

Supplement. The supplement related to this article is available online at: https://doi.org/10.5194/gmd-13-3475-2020-supplement.

Author contributions. MI was responsible for the numerical simulation setup, run, processing and analysis of the results. VS assisted in LAKE model setup and upgrades. RS took part in the general experiment setup and analysis of the results. MP, AP, MHN, and GR provided and processed data of observations and took part in model result analysis. All the co-authors participated in writing and editing the article.

Competing interests. The authors declare that they have no conflict of interest.

Financial support. This work has been co-funded by the Portuguese Foundation for Science and Technology (FCT), through the project UIDB/04683/2020 of the Institute of Earth Sciences (ICT), and by the European Union through the European Regional Development Fund, included in the COMPETE 2020 (Operational Programme: "Competitiveness and Internationalization") programme, and through the ALOP project (grant no. ALT20-03-0145-FEDER-000004). Victor Stepanenko was supported by the Russian Science Foundation (grant no. 17-17-01210) and Russia's President Grant Council (grant no. MD-1850.2020.5).

Review statement. This paper was edited by Paul Ullrich and reviewed by two anonymous referees.

References

Adrian, R., O'Reilly, C. M., Zagarese, H., Baines, S. B., Hessen, D. O., Keller, W., Livingstone, D. M., Sommaruga, R., Straile, D., Van Donk, E., Weyhenmeyer, G. A., and Winder, M.: Lakes as sentinels of climate change, Limnol. Oceanogr., 54, 2283–2297, https://doi.org/10.4319/lo.2009.54.6_part_2.2283, 2009.

Balsamo, G.: Interactive lakes in the Integrated Forecasting System, ECMWF Newsletter, 137, 30–34, https://doi.org/10.21957/rffv1gir, 2013.

Bonan, G. B.: Sensitivity of a GCM Simulation to Inclusion of Inland Water Surfaces, J. Climate, 8, 2691–2704, https://doi.org/10.1175/1520-0442(1995)008<2691:SOAGST>2.0.CO;2, 1995.

Canuto, V. M., Howard, A., Cheng, Y., and Dubovikov, M. S.: Ocean Turbulence. Part I: One-Point Closure Model-Momentum and Heat Vertical Diffusivities, J. Phys. Oceanogr., 31, 1413–1426, https://doi.org/10.1175/1520-0485(2001)031<1413:OTPIOP>2.0.CO;2, 2001.

Dutra, E., Stepanenko, V., Balsamo, G., Viterbo, P., Miranda, P., Mironov, D., and Schaer, C.: An offline study of the impact of lakes on the performance of the ECMWF surface scheme, Boreal Environ. Res., 15, 100–112, 2010.

Ekhtiari, N., Grossman-Clarke, S., Koch, H., Souza, W. M., Donner, R. V., and Volkholz, J.: Effects of the Lake Sobradinho Reservoir

(Northeastern Brazil) on the Regional Climate, Climate, 5, 50, https://doi.org/10.3390/cli5030050, 2017.

Hanson, P. C., Pollard, A. I., Bade, D. L., Predick, K., Carpenter, S. R., and Foley, J. A.: A model of carbon evasion and sedimentation in temperate lakes, Glob. Change Biol., 10, 1285–1298, https://doi.org/10.1111/j.1529-8817.2003.00805.x, 2004.

Heiskanen, J. J., Mammarella, I., Ojala, A., Stepanenko, V., Erkkilä, K.-M., Miettinen, H., Sandström, H., Eugster, W., Leppäranta, M., Järvinen, H., Vesala, T., and Nordbo, A.: Effects of water clarity on lake stratification and lake-atmosphere heat exchange, J. Geophys. Res.-Atmos., 120, 7412–7428, https://doi.org/10.1002/2014JD022938, 2015.

Hipsey, M. R., Bruce, L. C., Boon, C., Busch, B., Carey, C. C., Hamilton, D. P., Hanson, P. C., Read, J. S., de Sousa, E., Weber, M., and Winslow, L. A.: A General Lake Model (GLM 3.0) for linking with high-frequency sensor data from the Global Lake Ecological Observatory Network (GLEON), Geosci. Model Dev., 12, 473–523, https://doi.org/10.5194/gmd-12-473-2019, 2019.

Hondzo, M. and Stefan, H. G.: Lake Water Temperature Simulation Model, J. Hydraul. Eng., 119, 1251–1273, https://doi.org/10.1061/(ASCE)0733-9429(1993)119:11(1251), 1993.

Iakunin, M., Salgado, R., and Potes, M.: Breeze effects at a large artificial lake: summer case study, Hydrol. Earth Syst. Sci., 22, 5191–5210, https://doi.org/10.5194/hess-22-5191-2018, 2018.

Iakunin, M., Stepanenko, V., Salgado, R., Potes, M., Rodrigues, G., Penha, A., and Novais, M. H.: Atmospheric forcing dataset for Numerical study of the seasonal thermal and gas regimes of the large artificial lake in Western Europe using LAKE2.0 [Data set], Zenodo, https://doi.org/10.5281/zenodo.3608230, 2020.

Imberger, J. and Patterson, J. C.: A dynamic reservoir simulation model-DYRESM: 5, in: Transport Models for Inland and Coastal Waters, edited by: Fischer, H. B., Academic Press, New York, 310–361, 1981.

Le Moigne, P., Colin, J., and Decharme, B.: Impact of lake surface temperatures simulated by the FLake scheme in the CNRM-CM5 climate model, Tellus A, 68, 31274, https://doi.org/10.3402/tellusa.v68.31274, 2016.

Lopes, F., Silva, H. G., Salgado, R., Potes, M., Nicoll, K. A., and Harrison, R. G.: Atmospheric electrical field measurements near a fresh water reservoir and the formation of the lake breeze, Tellus A, 68, 31592, https://doi.org/10.3402/tellusa.v68.31592, 2016.

Mironov, D.: Parameterization of lakes in numerical weather prediction. Description of a lake model, COSMO Technical Report, Deutscher Wetterdienst, 11, 41 pp., 2008.

Mironov, D., Rontu, L., Kourzeneva, E., and Terzhevik, A.: Towards improved representation of lakes in numerical weather prediction and climate models: Introduction to the special issue of Boreal Environment Research, Boreal Environ. Res., 15, 97–99, 2010.

Monin, A. S. and Obukhov, A. M.: Basic regularity in turbulent mixing in the surface layer of the atmosphere, U.S.S.R. Academy of Science, Works of the Geophysical Institute, 151, 163–187, 1954.

Novais, M. H., Penha, A., Morales, E., Potes, M., Salgado, R., and Morais, M.: Vertical distribution of benthic diatoms in a large reservoir (Alqueva, Southern Portugal) during thermal stratification, Sci. Total Environ., 659, 1242–1255, https://doi.org/10.1016/j.scitotenv.2018.12.251, 2018.

Patterson, J. C., Hamblin, P. F., and Imberger, J.: Classification and dynamic simulation of the vertical density structure of lakes, Limnol. Oceanogr., 29, 845–861, https://doi.org/10.4319/lo.1984.29.4.0845, 1984.

Penha, A. M., Chambel, A., Murteira, M., and Morais, M.: Influence of different land uses on groundwater quality in southern Portugal, Environ. Earth Sci., 75, 622, https://doi.org/10.1007/s12665-015-5038-7, 2016.

Pereira, H., Figueira, J. R., and Marques, R. C.: Multiobjective Irrigation Model: Alqueva River Basin Application, J. Irrig. Drain. E., 145, 05019006, https://doi.org/10.1061/(ASCE)IR.1943-4774.0001396, 2019.

Policarpo, C., Salgado, R., and Costa, M. J.: Numerical Simulations of Fog Events in Southern Portugal, Adv. Meteorol., 2017, 1276784, https://doi.org/10.1155/2017/1276784, 2017.

Potes, M., Costa, M. J., da Silva, J. C. B., Silva, A. M., and Morais, M.: Remote sensing of water quality parameters over Alqueva Reservoir in the south of Portugal, Int. J. Remote Sens., 32, 3373–3388, https://doi.org/10.1080/01431161003747513, 2011.

Potes, M., Costa, M. J., and Salgado, R.: Satellite remote sensing of water turbidity in Alqueva reservoir and implications on lake modelling, Hydrol. Earth Syst. Sci., 16, 1623–1633, https://doi.org/10.5194/hess-16-1623-2012, 2012.

Potes, M., Salgado, R., Costa, M. J., Morais, M., Bortoli, D., Kostadinov, I., and Mammarella, I.: Lake–atmosphere interactions at Alqueva reservoir: a case study in the summer of 2014, Tellus A, 69, 1272787, https://doi.org/10.1080/16000870.2016.1272787, 2017.

Potes, M., Rodrigues, G., Penha, A. M., Novais, M. H., Costa, M. J., Salgado, R., and Morais, M. M.: Use of Sentinel 2 – MSI for water quality monitoring at Alqueva reservoir, Portugal, Proc. IAHS, 380, 73–79, https://doi.org/10.5194/piahs-380-73-2018, 2018.

Salgado, R. and Le Moigne, P.: Coupling of the FLake model to the Surfex externalized surface model, Boreal Environ. Res., 15, 231–244, 2010.

Samuelsson, P., Kourzeneva, E., and Mironov, D.: The impact of lakes on the European climate as simulated by a regional climate model, Boreal Environ. Res., 15, 113–129, available at: http://www.borenv.net/BER/pdfs/ber15/ber15-113.pdf (last access: 1 August 2020), 2010.

Silva, A., De Lima, I., Santo, F., and Pires, V.: Assessing changes in drought and wetness episodes in drainage basins using the Standardized Precipitation Index, Bodenkultur, 65, 31–37, 2014.

Stefan, H. and Fang, X.: Dissolved Oxygen Model for Regional Lake Analysis, Ecol. Model., 71, 37–68, https://doi.org/10.1016/0304-3800(94)90075-2, 1994.

Stepanenko, V., Jöhnk, K. D., Machulskaya, E., Perroud, M., Subin, Z., Nordbo, A., Mammarella, I., and Mironov, D.: Simulation of surface energy fluxes and stratification of a small boreal lake by a set of one-dimensional models, Tellus A, 66, 21389, https://doi.org/10.3402/tellusa.v66.21389, 2014.

Stepanenko, V., Mammarella, I., Ojala, A., Miettinen, H., Lykosov, V., and Vesala, T.: LAKE 2.0: a model for temperature, methane, carbon dioxide and oxygen dynamics in lakes, Geosci. Model Dev., 9, 1977–2006, https://doi.org/10.5194/gmd-9-1977-2016, 2016.

Stepanenko, V. M., Repina, I. A., Ganbat, G., and Davaa, G.: Numerical Simulation of Ice Cover of Saline Lakes, Izvestiya, Atmos. Ocean. Phys., 55, 129–138, https://doi.org/10.1134/S0001433819010092, 2019.

Su, D., Hu, X., Wen, L., Lyu, S., Gao, X., Zhao, L., Li, Z., Du, J., and Kirillin, G.: Numerical study on the response of the largest lake in China to climate change, Hydrol. Earth Syst. Sci., 23, 2093–2109, https://doi.org/10.5194/hess-23-2093-2019, 2019.

Subin, Z. M., Riley, W. J., and Mironov, D.: An improved lake model for climate simulations: Model structure, evaluation, and sensitivity analyses in CESM1, J. Adv. Model. Earth Sy., 4, M02001, https://doi.org/10.1029/2011MS000072, 2012.

Thiery, W., Martynov, A., Darchambeau, F., Descy, J.-P., Plisnier, P.-D., Sushama, L., and van Lipzig, N. P. M.: Understanding the performance of the FLake model over two African Great Lakes, Geosci. Model Dev., 7, 317–337, https://doi.org/10.5194/gmd-7-317-2014, 2014.

Tomaz, A., Patanita, M., Guerreiro, I., Boteta, L., and Palma, J. F.: Water use and productivity of maize-based cropping systems in the Alqueva Region (Portugal), Cereal Res. Commun., 45, 1–11, https://doi.org/10.1556/0806.45.2017.036, 2017.

Twine, T., Kustas, W. P., Norman, J., Cook, D., Houser, P., Teyers, T. P., Prueger, J. H., Starks, P., and Wesely, M.: Correcting Eddy-Covariance Flux Underestimates over a Grassland, Agr. Forest Meteorol., 103, https://doi.org/10.1016/S0168-1923(00)00123-4, 2000.

Walter, K. M., Smith, L. C., and Chapin, F. S.: Methane bubbling from northern lakes: present and future contributions to the global methane budget, Philos. T. Roy. Soc. A, 365, 1657–1676, https://doi.org/10.1098/rsta.2007.2036, 2007.

Wetzel, R. G.: Limnology, Saunders College Publishing, 2nd Edn., 1983.

Tellus SERIES A DYNAMIC METEOROLOGY AND OCEANOGRAPHY
PUBLISHED BY THE INTERNATIONAL METEOROLOGICAL INSTITUTE IN STOCKHOLM

Lake–atmosphere interactions at Alqueva reservoir: a case study in the summer of 2014

By M. POTES[1]*, R. SALGADO[1], M. J. COSTA[1], M. MORAIS[1], D. BORTOLI[1], I. KOSTADINOV[2] and I. MAMMARELLA[3], [1]*Instituto de Ciências da Terra, Évora, Portugal;* [2]*Proambiente S.c.r.l., Emilia Romagna High Technology Network, c/o CNR Research Area, Bologna, Italy;* [3]*Department of Physics, University of Helsinki, Helsinki, Finland*

(Manuscript received 26 October 2016; in final form 12 December 2016)

ABSTRACT

The study of lake–atmosphere interactions was the main purpose of a 2014 summer experiment at Alqueva reservoir in Portugal. Near-surface fluxes of momentum, heat and mass [water vapour (H_2O) and carbon dioxide (CO_2)] were obtained with the new Campbell Scientific's IRGASON Integrated Open-Path CO_2/H_2O Gas Analyser and 3D Sonic Anemometer between 2 June and 2 October. On average, the reservoir was releasing energy in the form of sensible and latent heat flux during the study period. At the end of the 75 d, the total evaporation was estimated as 490.26 mm. A high correlation was found between the latent heat flux and the wind speed (R = 0.97). The temperature gradient between air and water was positive between 12 and 21 UTC, causing a negative sensible heat flux, and negative during the rest of the day, triggering a positive sensible heat flux. The reservoir acted as a sink of atmospheric CO_2 with an average rate of −0.026 mg m^{-2} s^{-1}. However, at a daily scale we found an unexpected uptake between 0 and 9 UTC and almost null flux between 13 and 19 UTC. Potential reasons for this result are further discussed. The net radiation was recorded for the same period and water column heat storage was estimated using water temperature profiles. The energy balance closure for the analysed period was 81%. In-water solar spectral downwelling irradiance profiles were measured with a new device allowing measurements independent of the solar zenith angle, which enabled the computation of the attenuation coefficient of light in the water column. The average attenuation coefficient for the photosynthetically active radiation spectral region varied from 0.849 ± 0.025 m^{-1} on 30 July to 1.459 ± 0.007 m^{-1} on 25 September.

Keywords: lake reservoir, eddy covariance, sensible and latent heat fluxes, energy balance closure, carbon fluxes, underwater spectral irradiance profiles, PAR attenuation coefficient

1. Introduction

Lakes and reservoirs affect the regional climate and are also affected by weather patterns. On the global scale, lakes cover an area of 4.2 million km^2, corresponding to more than 3% of the Earth's continental surface (Downing et al., 2006). Despite the small fraction of lakes, these freshwater reservoirs play an important role in mass, energy and momentum exchanges with the atmosphere. The variations in heat and moisture transfers between the inland waters and the atmosphere can influence regional patterns of atmospheric circulation, and thus an effort has been made in recent years to improve the coupling of lake models with weather prediction and climate models (e.g. Balsamo et al., 2012). Furthermore, inland waters can take up carbon dioxide (CO_2) from the atmosphere as well as release CO_2 and methane (CH_4) to the atmosphere, and thus these systems should be taken into account in the carbon cycle (Pacheco et al., 2013). Carbon exchanges between these media occur as a result of physical and biogeochemical processes (Wetzel, 1983). More accurate estimation of greenhouse gas exchanges between inland water bodies and the atmosphere has become of increasing concern in recent years (Cole et al., 2007). The eddy covariance (EC) method is the most common technique used to assess turbulent fluxes over all types of surfaces (Baldocchi, 2003). The EC method is a non-invasive technique, normally installed in a tower, with less impact on the environment compared to the use of chambers (Repo et al., 2007). These turbulent fluxes, obtained with direct and continuous measurements, are important to estimate the exchanges of energy, water and greenhouse gases between the surface and the atmosphere. This technique has also been used to estimate CO_2 and CH_4 fluxes over aquatic environments (e.g. Vesala et al., 2012; Podgrajsek et al., 2014;

*Corresponding author. e-mail: mpotes@uevora.pt

Tellus A 2017. © 2017 The Author(s). Published by Informa UK Limited, trading as Taylor & Francis Group
This is an Open Access article distributed under the terms of the Creative Commons Attribution License (http://creativecommons.org/licenses/by/4.0/), which permits unrestricted use, distribution, and reproduction in any medium, provided the original work is properly cited.

Citation: Tellus A 2017, **69**, 1272787, http://dx.doi.org/10.1080/16000870.2016.1272787

Mammarella et al., 2015). In 2014, a set of EC measurements was carried out at a Portuguese reservoir to estimate the CO_2, H_2O, heat and momentum fluxes over water, within the framework of the ALEX project (www.alex2014.cge.uevora.pt). During 4 months, continuous measurements were carried out on a floating platform in the Alqueva reservoir, located in the south-east of Portugal. This field campaign gave continuity to previous studies (e.g. Salgado and Le Moigne, 2010; Le Moigne et al., 2013) performed in Alqueva reservoir in the summer of 2007 and in Thau Lagoon in the summer of 2011, with the objectives of understanding mass, energy and momentum exchanges between the atmosphere and reservoirs.

The effect of climate variability on the reservoir thermal structure, water quality and aquatic ecosystems has long been known to be important (Nowlin et al., 2004; Lee and Biggs, 2014; McGloin et al., 2014). To understand the role of lakes on weather and climate, fully coupled models must be improved in which key lacustrine processes have to be represented. The aquatic photosynthesis processes occur in the euphotic zone, the layer between the surface and the depth of 1% of the subsurface irradiance, and this layer can be thicker in clear waters and thinner in turbid ones (Bukata et al., 1995; Wozniak et al., 2003). Some instrumentation has been developed to measure the underwater radiance field in lakes, fjords and oceans (Sasaki et al., 1958; Jerlov and Fukuda, 1960; Tyler, 1960; Lewis et al., 2011; Antoine et al., 2013; Potes et al., 2013). In particular, Potes et al. (2013) developed a new apparatus to be coupled with a portable spectroradiometer, allowing for spectral radiance measurements in underwater environments and to subsequently obtain estimates of the spectral and broadband light attenuation coefficients in water. The light attenuation coefficient is relevant in the water surface layer energy budget. In particular, it is an important parameter in lake models for computing the water surface temperature, which is used for estimating heat and moisture transfers between water bodies and the atmosphere (Mironov et al., 2010; Potes et al., 2012). Nevertheless, the use of measurements of hemispherical spectral radiance (irradiance) is preferable to obtain more reliable attenuation coefficients. Such irradiance measurements are scarce, but they have been performed in the Mediterranean Sea with moored radiometers at fixed levels below the surface (Gernez and Antoine, 2009), in field experiments in the Irish Sea and open ocean (Bowers and Mitchelson-Jacob, 1996; Darecki et al., 2011), and in lakes and reservoirs (Liu et al., 2010; Heiskanen et al., 2015). In this way, and within the framework of the above-mentioned ALEX project, sporadic measurements of underwater downwelling spectral irradiance were performed during the 4 month study with the new equipment.

In Sections 2 and 3, respectively, the study site and the instrumental set-up are introduced. The results obtained are discussed in Section 4, where a detailed analysis of the heat fluxes, energy balance and CO_2 flux is presented, followed by a detailed examination of the spectral underwater solar irradiance profiles and the resulting estimate of the spectral attenuation. A first study of observational evidence of lake breeze induction at Alqueva reservoir is presented at the end of this section. In Section 5, the main conclusions are summarized.

2. Study site

The Alqueva reservoir is located in the south-east of Portugal along 83 km of the main course of the Guadiana River, where the northern branch is shared with Spain (Fig. 1). The reservoir has maximum and average depths of 92.0 m and 16.6 m, respectively. It has a total capacity of 4150 km^3 and a surface area of 250 km^2, and constitutes the largest artificial lake in the Iberian Peninsula. The reservoir is used for water supply, irrigation and hydroelectric power generation. Water samples taken at the euphotic zone in Alqueva-Montante platform (Fig. 1) to evaluate the trophic status of the water indicate a mesotrophic status based on chlorophyll *a* as an indicator of phytoplankton productivity.

The reservoir was established in 2002 in a region long known for the irregularity of its hydrological resources, with periods of drought that may last for more than one consecutive year (Silva et al., 2014), and it is classified as a Csa region according to the Köppen climate classification. This class corresponds to temperate climates with dry and hot summers (Mediterranean climate). The rainfall period occurs seasonally between October and April, with an average annual precipitation of 558 mm, as recorded in Beja (about 40 km from the reservoir) for the period 1981–2010 (www.ipma.pt). The summer synoptic circulations over the region are strongly constrained by the location and shape of the Azores anticyclone and by the frequent establishment of a thermal low over the Iberian Peninsula, induced by the land–ocean thermal contrasts. Under the sea breeze system, organized at the peninsular scale by the thermal low, the maritime air mass penetrates towards the interior of the peninsula. The breeze originating on the west coast has been documented to reach more than 100 km inland, reaching the region in the late afternoon, as evident from the increase in wind intensity and its rotation (Salgado et al., 2015). The summer Local Time (LT) in Portugal has the following relation with UTC: LT = UTC + 1.

3. Instrumental set-up and methods

3.1. Eddy covariance system and other supporting measurements

This field campaign study was performed in the Alqueva reservoir area, implementing an appropriate experimental set-up, between 2 June and 2 October 2014 (Fig. 1). Three

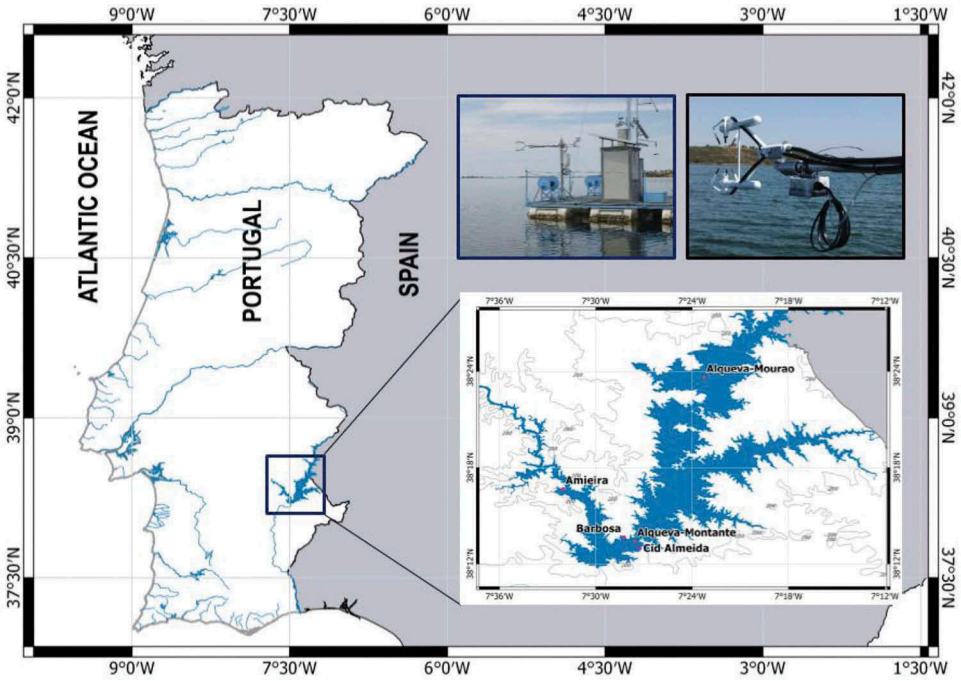

Fig. 1. Alqueva reservoir: geographic location, floating platforms and meteorological stations. A zoom from Alqueva-Montante platform equipped with the IRGASON instrument; details of the sonic anemometer, gas analyser and accelerometer.

meteorological stations were established over land near the reservoir shore: Amieira (38º 16′ 39.18″ N, 7º 32′ 2.10″ W), Barbosa (38º 13′ 39.18″ N, 7º 28′ 14.74″ W) and Cid Almeida (38º 12′ 59.00″ N, 7º 27′ 16.34″ W). Two floating platforms were equipped over water: Alqueva-Montante (38º 13′ 24.75″ N, 7º 27′ 34.18″ W) and Alqueva-Mourão (38° 23′ 37.08″ N, 7° 23′ 15.18″ W). The depths at Alqueva-Montante and Alqueva-Mourão are 65 m and 48 m, respectively.

The terrestrial stations measure air and soil temperature, relative humidity, wind speed and direction, and precipitation. Both floating platform stations measure water temperature profile, air temperature, and wind speed and direction. In addition, the instrumentation installed in Alqueva-Montante platform comprises: one EC system at 2 m above the water surface, the Integrated Open-Path CO_2/H_2O Gas Analyser and 3D Sonic Anemometer (IRGASON; Campbell Scientific); one albedometer (CM7B; Kipp&Zonen) for short-wave radiation measurements; one pyrradiometer (8111; Philipp Schenk) for long-wave radiative balances and nine temperature probes (107; Campbell Scientific) at several depths (0.05, 0.5, 1.0, 2.0, 3.0, 6.0, 9.0, 18.0 and 27.0 m).

Variables measured by IRGASON were *u, v* and *w* components of wind speed, sonic temperature, H_2O and CO_2 concentration, and sonic anemometer and gas analyser quality flags. Data were sampled at 20 Hz and the filter time delay was 200 ms.

In addition, occasional measurements of water temperature, turbidity, pH, dissolved oxygen and conductivity in the water column were taken with a multiparameter probe (In-Situ TROLL 9500 Profiler XP) nearly twice a month.

3.2. Eddy covariance flux calculation

Turbulent fluxes of momentum, heat and mass (H_2O and CO_2) were calculated as 30 min covariances between fluctuations of vertical wind component w and temperature, H_2O and CO_2 concentration, respectively. Before covariance calculation, the turbulent time series were linearly detrended (Rannik and Vesala, 1999) and double-axis rotation was applied to the wind speed components (Rebmann et al., 2012). Furthermore, two necessary corrections were applied to the flux calculations: the first one concerns the H_2O and CO_2 fluxes, and accounts for the air density fluctuations due to thermal expansion and water vapour dilution (Webb et al., 1980); the second is the humidity correction of sonic temperature according to Kaimal and Gaynor (1991). The corrected turbulent fluxes of momentum (τ, kg m^{-1} s^{-2}), sensible heat (H, W m^{-2}), latent heat (LE, W m^{-2}) and CO_2 (F_c, mg m^{-2} s^{-1}) were obtained as follows (positive when upward):

$$\tau = -\rho_a \sqrt{\left(\overline{u'w'}^2 + \overline{v'w'}^2\right)} \quad (1)$$

$$H_c = \rho_a C_p \overline{w'T_c'} \quad (2)$$

$$LE = L_v\overline{w'\rho_w'} + \left(\frac{M_{a,dry}}{M_w}\frac{\overline{\rho_w}}{\overline{\rho_{a,dry}}}\right)L_v\overline{w'\rho_w'} + \left(1 + \frac{M_a}{M_w}\frac{\overline{\rho_w}}{\overline{\rho_{a,dry}}}\right)L_v\frac{\overline{\rho_w}}{\overline{T_c}}\overline{w'T_c'} \quad (3)$$

$$F_C = \overline{w'\rho_c'} + \left(\frac{M_{a,dry}}{M_w}\frac{\overline{\rho_c}}{\overline{\rho_{a,dry}}}\right)\overline{w'\rho_w'} + \left(1 + \frac{M_{a,dry}}{M_w}\frac{\overline{\rho_w}}{\overline{\rho_{a,dry}}}\right)\frac{\overline{\rho_c}}{\overline{T}}\overline{w'T_c'} \quad (4)$$

where $\rho_a = \rho_{a,dry} + \rho_w$ is the air density (kg m^{-3}); ρ_w is the water vapour density (kg m^{-3}); $\rho_{a,dry} = \frac{P}{R_d T_c} - \left(\rho_w \frac{M_{a,dry}}{M_w}\right)$ is the density of dry air (kg m^{-3}); $R_d = \frac{R}{28.97}$ is the gas constant for dry air (kPa m^3 K^{-1} g^{-1}); R is the universal gas constant (8.3143×10^{-3} kPa m^3 K^{-1} mol^{-1}); P is the ambient pressure (kPa); $\frac{M_{a,dry}}{M_w}$ is the ratio of the molecular weight of dry air to water vapour; T_c is the temperature corrected for water vapour (K): $T_c = T_s / \left(\frac{1+0.32([\rho_w R T_s])}{P * 18.02}\right)$; T_s is the sonic temperature in air (K); $C_p = 1004.67\left(1 + 0.84\left[0.622 \times \rho_w R_v \left\{\frac{\overline{T_c}}{\overline{p}}\right\}\right]\right)$ is the specific heat of air (J kg^{-1} K^{-1}); $R_v = \frac{R}{18.02}$ is the gas constant for water vapour (kPa m^3 K^{-1} g^{-1}); $L_v = 2.501 \times 10^6 - \left(2.37 * \left[\overline{T_c} - 273.15\right]\right)$ is the latent heat of vaporization (J kg^{-1}); and ρ_c is CO_2 density (mg m^{-3}).

The footprint analysis was done according to Kljun et al. (2004), for 90% contribution (X_{90}, m) and peak contribution (X_{max}, m) distances:

$$X_{90} \approx X_{*,90} z \left(\frac{\sigma_w}{u_*}\right)^{-0.8} \quad (5)$$

$$X_{max} \approx X_{*,max} z \left(\frac{\sigma_w}{u_*}\right)^{-0.8} \quad (6)$$

where σ_w is the standard deviation of the vertical velocity fluctuation (m s^{-1}); $u_* = \left[\left(\overline{u'w'}\right)^2 + \left(\overline{v'w'}\right)^2\right]^{\frac{1}{4}}$ is the friction velocity (m s^{-1}); z is the sensor height (m); and $X_{*,90}$ and $X_{*,max}$ are parameters that depend on the roughness length (z_0, m). In this work, z_0 was computed according to Ferdorovich et al. (1991):

$$z_0 = \frac{0.135\vartheta_a}{u_*};\ u_* \leq 0.10856 \quad (7a)$$

$$z_0 = \frac{u_*^2}{69g};\ u_* > 0.10856 \quad (7b)$$

where $\vartheta_a = 1.48 \times 10^{-5}\left(\mathrm{m^2 s^{-1}}\right)$ is the air viscosity; and $g = 9.81\left(\mathrm{ms^{-2}}\right)$.

The atmospheric stability parameter ($\frac{z}{L}$) was calculated using the Obukhov length (L, m):

$$L = -\frac{\overline{T_s}u_*^3}{kg\overline{w'T_s'}} \quad (8)$$

where $k = 0.4$ is the von Karman constant.

3.2.1. Data quality criteria and filters applied. IRGASON provides diagnostic flags for the sonic anemometer and gas analyser. With these diagnostic flags, the data set was filtered for bad data or measurement problems of the sonic anemometer and gas analyser. The gas analyser provides the CO_2 and H_2O signal strength, which is an indicator of data quality, and ranges between 0.0 (not working or optical path obstructed) and 1.0 (working perfectly). Data with signal strength lower than 0.7 are discarded owing to poor quality. The fluxes are validated according the wind direction to avoid contamination of the measurements by the platform; thus, wind directions between the angles of 90º and 270º were discarded from the data set (see details in Section 4.1). Footprints (fetch) with values of X_{90} greater than 300 m were also discarded to ensure exclusively water body contributions to the measurements. In summary, about 37% of the data were discarded as a result of the criteria and applied filters described above.

3.3. Energy balance

The energy balance closure (*EBC*) and the energy residual (*Res*) of the lake can be obtained using the latent (*LE*) and the sensible (*H*) heat fluxes, the net radiation (*Rn*) and the water column heat storage (ΔQ), assuming horizontal homogeneity and neglecting the heat fluxes due to precipitation, runoff and bottom sediments, through eqs (9) and (10):

$$EBC = \frac{H + LE}{R_n - \Delta Q} \times 100\% \quad (9)$$

$$Res = R_n - \Delta Q - H - LE \quad (10)$$

The water column heat storage (ΔQ) is computed using eq. (11):

$$\Delta Q = \rho_{water} C_{pw} \sum_{i=1}^{n} \frac{\Delta T_{wi}}{\Delta t} \Delta z_i \quad (11)$$

where ρ_{water} is the water density, calculated as a function of depth-weighted average temperature according to Gill (1982); and C_{pw} is the specific heat of water (4192 J kg^{-1} K^{-1}). Since the continuous temperature profiles were available only to a depth of 27 m, the water temperature to the bottom was obtained through linear extrapolation using data from the multiparameter probe profiles (see Section 3.1). The error of these extrapolations should be small as the water temperature below 27 m has a small variation to the bottom, i.e. during this 4 months ΔT between 27 and 65 ms varied from 1.14 ºC in June to 3.42 ºC in September.

3.4. *Underwater spectral irradiance field*

In the study of Potes et al. (2013), the downwelling radiance measurements were carried out with an optical device fully described in this reference. Because of its small field of view (FOV = 22º), some problems were found under small solar zenith angles, e.g. when the water upper layers were exposed to the penetration of direct zenith sunlight due to the refraction on the surface and to light scattering (Potes et al., 2013). Thus, the need to have measurements that are independent of the solar zenith angle motivated the development of a new tip to measure the hemispherical radiance (180º), enabling the calculation of the attenuation coefficient from the subsurface level down to 3 m depth (see Fig. 2 for details). This new receiver, a Metcon GmbH brand, consists of an optical input system designed to collect incoming radiance from all directions of a hemisphere. The receiver is tuned by the manufacturer to achieve uniform transfer function on the 2π *sr*. The test measurements performed in the laboratory, with a collimated beam irradiating the device at ± 90° with respect to its longitudinal axis, confirmed the data provided by Metcon. This kind of device has already been used for the estimation of J values for atmospheric compounds and has been fully described previously (Kostadinov et al., 2003, 2009). This new receiver is attached to an apparatus similar to that described in the work of Potes et al. (2013) and is composed of a portable spectroradiometer, linked to an optical fibre bundle driven by a customized frame for protection and to keep the tip pointing to the zenith direction in the underwater environment. The portable FieldSpec UV/VNIR Spectroradiometer (Analytical Spectral Devices; Boulder, CO, USA) was used to record the spectral downwelling zenith irradiance measured across the spectral range 325–1075 nm with a spectral resolution ranging from 1 to 3 nm for the ultraviolet (UV) and near-infrared (NIR) spectral regions, respectively. The fibre bundle was chosen to meet the optical features of the spectroradiometer and the core is made of quartz, allowing measurements in the UV spectral region as well. To maximize the signal reaching the spectrometer, the packing factor of the bundle was optimized, using single fibres with the same numerical aperture but with different diameters: 0.11 and 0.22 mm. The frame was developed to guarantee the verticality and horizontality of the bare tip of the fibre bundle, which has to point upwards to the zenith to collect the downwelling zenith radiance at several levels below the water surface. Before every profile measurement, the integration time of the spectroradiometer was optimized to ensure the best illuminating conditions. Also, a dark current spectrum (which is an offset that varies with the temperature of the detector) was taken before every profile to correct the signal for temperature oscillations. A sample average of 10 spectra and three samples were taken per level. This choice was made to compromise between a preferentially high number of spectra per level and a relatively fast profiling under almost the same atmospheric conditions. This version was tested in a 5 m deep pool from the municipal swimming complex of Évora. After the test sessions, the apparatus was used to perform measurements in Alqueva reservoir in the summer of 2014, during the ALEX2014 field campaign. All underwater irradiance measurements during the campaigns were taken under clear sky conditions. The length of the fibre bundle allows for measurements to a maximum depth of 3 m and the levels chosen for the profiles were: above water surface, 0.01, 0.05, 0.25, 0.50, 0.75, 1.00, 1.50, 2.00, 2.50 and 3.00 m. These profiles allow for the calculation of the spectral attenuation coefficient ($K(Z', \theta, , \lambda)$) of the water column, using the equation presented by Preisendorfer (1959):

Fig. 2. Scheme of the apparatus developed for measurements of spectral underwater solar irradiance. Detail of the optical receiver and multilayer protecting frame of underwater device for measuring downwelling spectral irradiance.

$$E(Z,\theta,,\lambda) = E(0,\theta,,\lambda)exp\left\{-\int_{Z}^{0} K(Z',\theta,,\lambda)dZ'\right\} \quad (12)$$

where E is irradiance, Z is the depth, θ is the solar zenith angle, $\emptyset$ is the solar azimuth angle, and λ is the wavelength.

In the case of our measurements, the depth $Z = 0$ (in eq. 12) is replaced with depth $Z = \zeta$, which is the depth of the layer where the logarithmic slope of the underwater radiance becomes nearly constant with depth (eq. 5 in Potes et al., 2013).

4. Results and discussions

4.1. Flux data quality, footprint and atmospheric stability

Regarding the EC system installed in the floating platform (Fig. 1), some quality analysis need to be done for operational control of the system. Co-spectral analysis is normally used to evaluate the frequency response of the analyser (Kaimal et al., 1972; Nordbo et al., 2011; Mammarella et al., 2015). Comparison between actual co-spectra shapes and ideal ones obtained from models is generally a good method of evaluation. As an example, Fig. 3 shows the average normalized frequency-weighted co-spectra as a function of normalized frequency for temperature, CO_2 and water vapour for the period 23–26 July 2014. The three co-spectra are in accordance with the expected ideal curve; for higher frequencies, the slopes tend to the value of $n^{-4/3}$ (Kaimal et al., 1972), with peaks at frequencies around $n = 0.05$. Since no damping is present at high frequencies, there is no need for frequency response correction. In Fig. 4a, the X_{90} distribution is shown for the accepted wind sector. The average values of the footprint are 106.8 m and 53.2 m for X_{90} and X_{max}, respectively (the latter not shown here). With maximum values of around 300 m for X_{90}, it can be ensured that the footprint refers to the water surface and there is no contamination from the shores or land in the measurements. Figure 4b shows how the footprint (X_{90}) depends on the atmospheric stability. It is also clearly visible that unstable stratification ($z/L < 0$) corresponds frequently to calm wind conditions (low friction velocity) and lower footprints. In contrast, near-neutral stratification (z/L close to zero) corresponds to stronger wind (high friction velocities) and higher values of X_{90}. Under stable conditions, Fig. 4b shows some unusual cases of low X_{90}, probably due to the existence of local stability, during the afternoon, induced by the contact with colder water (high z/L and low σ_w) under a prevailing larger scale boundary layer circulation of unstable air (low friction velocity).

4.2. Heat fluxes and energy balance

The mean daily cycle of H and the difference between air temperature (2.0 m) and near-surface water temperature (0.05 m) are shown in Fig. 5. It is clear that when the temperature difference is negative, H is positive, with a maximum of 31.34 W m^{-2} at 7 UTC. During the afternoon, when the air temperature over the reservoir is higher than the water skin temperature, a slightly stable internal boundary layer

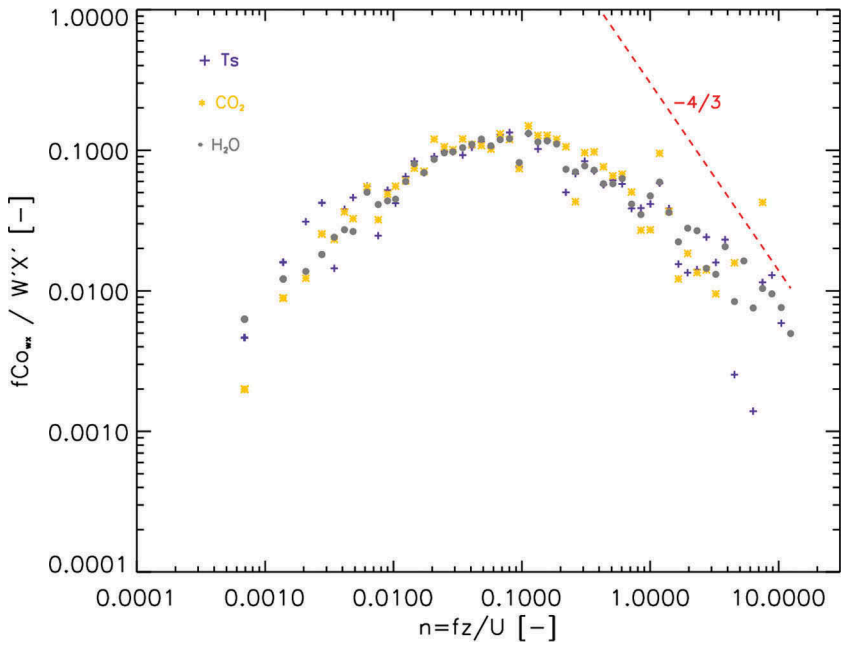

Fig. 3. Average normalized frequency-weighted co-spectra for CO_2, H_2O and sonic temperature (T_s) as a function of normalized frequency for the period 23–26 July 2014.

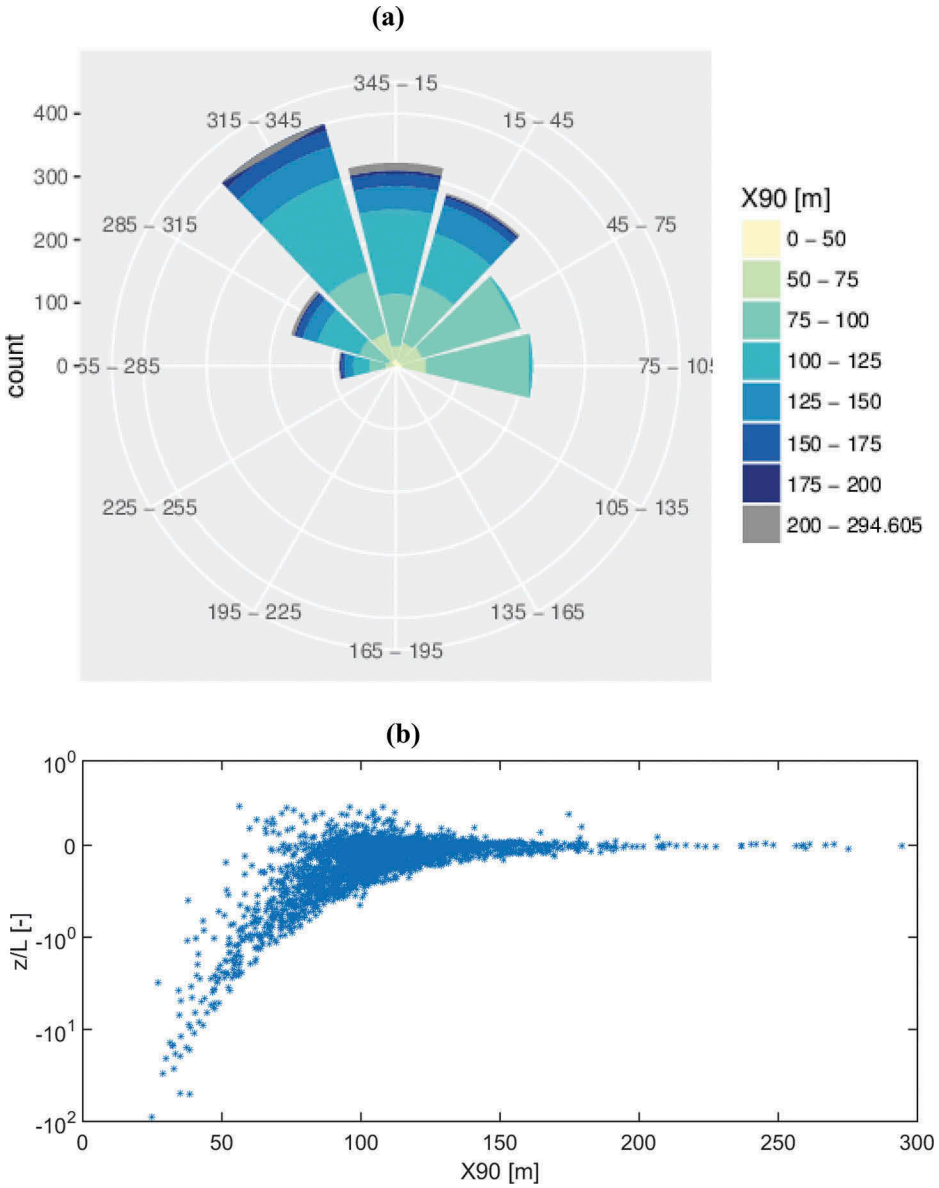

Fig. 4. (a) Footprint length (X_{90}) in the wind directions 270–90º; (b) scatterplot of footprint (X_{90}) and stability (z/L) during the period June–September 2014.

develops, leading to a negative H, with a minimum of −18.09 W m^{-2} at 18 UTC (Fig. 5). In the same period, the water vapour content minimum (9.78 g m^{-3} at 16 UTC) (Fig. 6a) occurs, partially related to the development of a lake breeze (discussed in Section 4.5). As seen in Fig. 6b, LE is highly correlated with the wind speed (R = 0.97). Wind speed strongly increases between 13 and 18 UTC, and reaches a maximum at 20 UTC (4.17 m s^{-1}), corresponding to the arrival of the sea breeze which originated on the west coast (Salgado et al., 2015). LE has a first and higher maximum of 148.83 W m^{-2} at 17 UTC and a second maximum at 21 UTC. These results are in agreement with a previous study by Salgado and Le Moigne (2010) for the same reservoir, showing an absolute maximum of LE at 21 UTC and also a change of sign in H according to the sign of the air–water temperature difference. Considering that the reservoir presents a homogeneous surface, it is estimated that 19.45 GJ of energy was released in the form of H and 490.26 mm of water was lost in the form of evaporation during the 4 month period of study. In contrast, the total precipitation in the same period was 74 mm, with 75% occurring in September.

The average diurnal cycle of LE and H, the net radiation (Rn) and the water column heat storage (ΔQ) over the entire period are plotted in Fig. 7a. In this case, the plotted ΔQ was

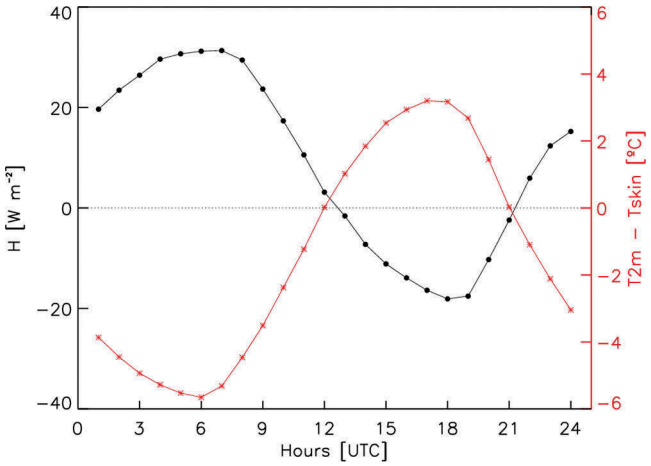

Fig. 5. Mean daily cycle of sensible heat flux (left *y*-axis; circles) and temperature difference between air (2 m) and near-surface water (right *y*-axis; stars) during the period June–September 2014.

computed considering only 4 m depth, which is the depth that best represents the daily cycle, because, at the daily scale, small errors in deep-layer temperature measurements rise to large errors on ΔQ estimation. *Rn* makes a major contribution, with an average value of 201.97 W m^{-2}, and part of this energy is used to heat up the first 4 m depth of the reservoir, resulting in an average value of 2.68 W m^{-2} to ΔQ. The sum of *H* and *LE* is, on average, 115.37 W m^{-2}. The energy balance closure (*EBC*) and the residual energy (*Res*) of the lake were estimated using eqs (9) and (10). ΔQ was estimated for different depths of the reservoir, e.g. 0.25, 4, 7, 14, 24, 38 and 65 m (Fig. 7b). For example, considering the 4 m depth discussed above, the *EBC* and *Res* values are 58% and 83.92 W m^{-2}. Better results are found with the depth of the reservoir in Alqueva-Montante platform (65 m), with values of 81% for *EBC* and 27.10 W m^{-2} for *Res*. This value of *EBC* is comparable to those found for two lakes in Finland by Nordbo et al. (2011), with average values of 82% and 73% for 2006 and 2007, and Mammarella et al. (2015), with average values of 83% and 79% for 2010 and 2011.

4.3. Carbon dioxide flux

The diurnal curves of atmospheric CO_2 concentration and flux, averaged over the 4 month period, are shown in Fig. 8. It can be noted that the CO_2 flux is negative during the day, more negative during the night and early morning, and nearly zero in the afternoon. The CO_2 concentration shows the opposite behaviour, with higher values during the night and early morning, and lower values in the afternoon, which is typically due to inland plant respiration throughout the night-time and plant photosynthesis during daytime. Higher CO_2 atmospheric concentrations may induce a gradient of CO_2 partial pressure between the near-surface atmosphere and the lake during the night and morning, which can explain a negative flux. During the afternoon, it seems that the gradient is smaller and an almost null CO_2 flux is observed.

There are no measurements of dissolved CO_2 concentrations in the water available for this study; nevertheless, it is well known that the solubility of CO_2 decreases with increasing temperature (Wetzel, 1983), whereby during the night, low water temperature favours CO_2 uptake. Applying Van't Hoff equations to Henry's solubility, it is possible to estimate the temperature dependence for Henry's constant (Sander, 2015): $\frac{\partial \ln K_H}{\partial\left(\frac{1}{T}\right)} = -\frac{\Delta_{sol}H}{R}$, where K_H is Henry's constant, $\Delta_{sol}H$ is the enthalpy of dissolution, and R is the universal gas constant. For example, for a 5 ºC decrease in water temperature (from 27 ºC to 22 ºC), Henry's constant will increase by 12.6%.

Furthermore, when absorbed CO_2 reacts with water molecules, it results in the production of carbonic acid ($CO_2 + H_2O \Leftrightarrow H_2CO_3$). Carbonic acid dissociates rapidly, relative to the hydration reaction (above mentioned), in bicarbonate (HCO_3^-) and carbonate ions (CO_3^{2-}), which in turn react with water, forming hydroxyl ions ($HCO_3^- + H_2O \Leftrightarrow OH^- + H_2CO_3$ and $CO_3^{2-} + H_2O \Leftrightarrow OH^- + HCO_3^-$), and consequently decrease the pH of water. The increase in water acidity is thus an indicator of CO_2 absorption by water. Unfortunately, there were no continuous pH measurements during the period under study. However, continuous measurements performed in previous years (data available at http://snirh.pt), at the same place, indicate the existence of a daily pH cycle (not shown here), with lower values during the night and morning, suggesting that during summer nights the reservoir acts as a sink of CO_2.

Sporadic measurements of water pH were performed during the field campaign and the values at the surface ranged between 8.9 in June and 9.6 in August. With these values of

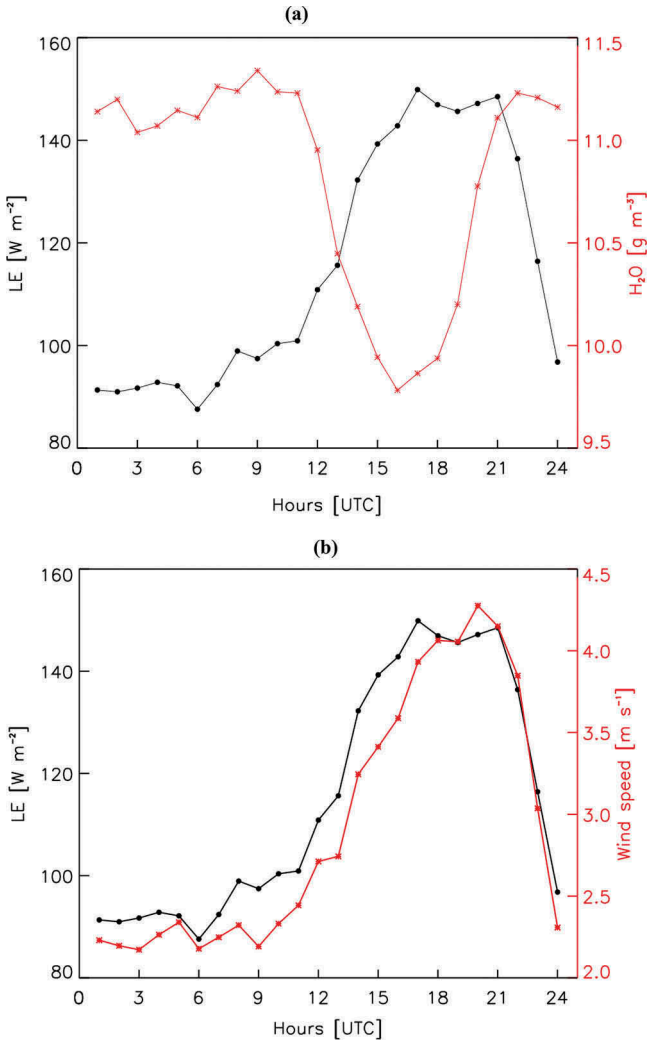

Fig. 6. (a) Mean daily cycle of latent heat flux (*LE*) (left *y*-axis; circles) and water vapour (right *y*-axis; stars); (b) mean daily cycle of latent heat flux (left *y*-axis; circles) and wind speed (right *y*-axis; stars), during the period June–September 2014.

pH, bicarbonate (HCO_3^-) is assumed to be the dominant species of the three major inorganic carbons (CO_2, HCO_3^- and CO_3^{2-}) present in water, with a relative percentage around 90%, while free CO_2 dominates with pH values of 5 (Emerson, 1975; Margalef, 1983; Wetzel, 1983). It was observed by Finlay et al. (2009) and Tranvik et al. (2009) that lakes with pH above 8.0 and 8.6, respectively, act as sinks of atmospheric carbon. Nevertheless, according to Helbig et al. (2016), a systematic bias was found in the CO_2 fluxes during a comparison study between two Campbell Scientific open-path sensors (Irgason and EC150) and two closed-path sensors (EC155 from Campbell Scientific and LI-7200 from LI-COR Biosciences). This bias is related to the so-called spectroscopic effect, and it is more evident when CO_2 fluxes are low and kinematic temperature fluxes are high (sensible heat flux). According to the same authors, the fast-response sonic temperature (instead of slow-response air temperature) should be used in the absorption-to-CO_2 density conversion, which cannot be done in our study since the raw absorption was not recorded during the field campaign. In our case, the period with low CO_2 flux and high sensible heat flux corresponds to night-time (see Figs 5 and 8) and thus the night-time CO_2 uptake by the reservoir may be, in reality, less pronounced than the one calculated in this study. Note that the mean values are always negative but very close to zero between 15 and 19 UTC, with values of the order of 10^{-3} and 10^{-4} mg m^{-2} s^{-1}. The minimum mean value is reached at 6 UTC, −0.071 mg m^{-2} s^{-1}, with an absolute minimum of −0.410 mg m^{-2} s^{-1} registered at the same time. During the night and morning, greater carbon uptake by the lake agrees with greater instability in the internal boundary layer

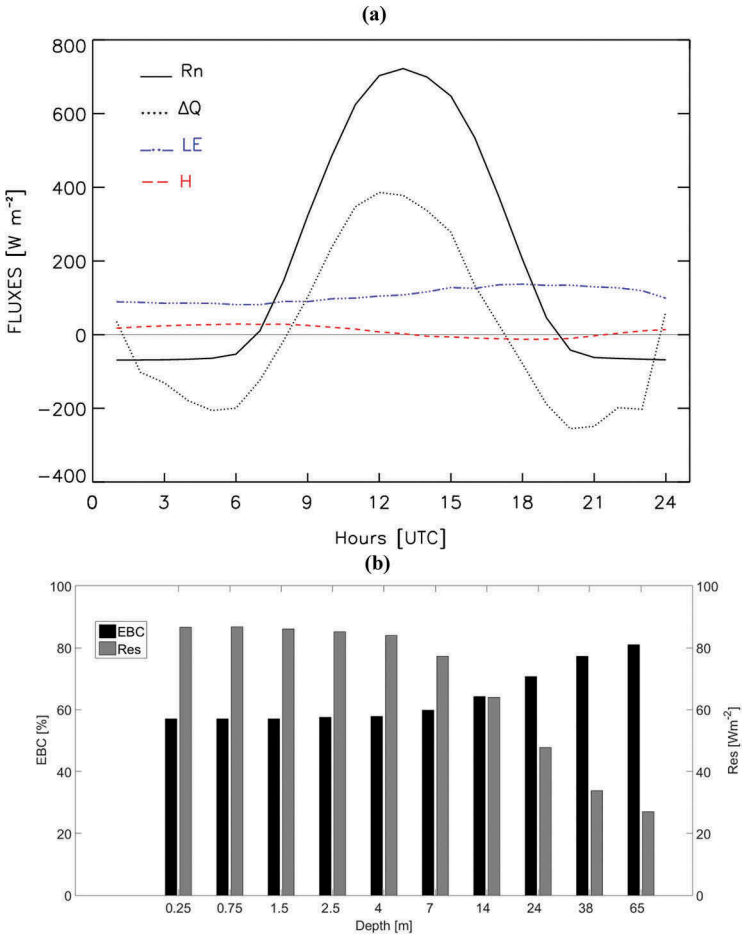

Fig. 7. (a) Mean daily cycle of net radiation (*Rn*), water column heat storage (ΔQ), latent heat flux (*LE*) and sensible heat flux (*H*) during the period June–September 2014. (b) Average energy residual (*Res*) measured with different depths for water column heat storage (ΔQ) calculations during the period June–September 2014. EBC = energy balance closure.

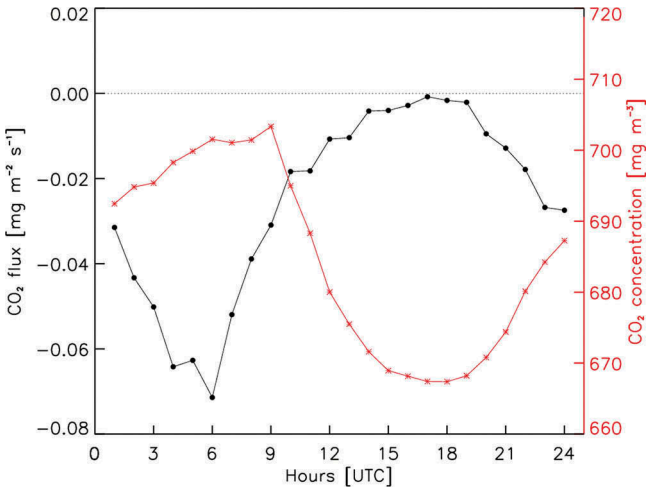

Fig. 8. Mean daily cycle of CO_2 flux (left *y*-axis; circles) and CO_2 concentration (right *y*-axis; stars) during the period June–September 2014.

(described in subsection 7.1 from Brutsaert, 1982), formed above water, since the water surface is warmer than the air (Fig. 5). It is also during the night that convective instability occurs in the water column, when the water surface temperature decreases and is slightly lower than that of the layers below (not shown), allowing unsaturated water to reach the surface. On the other hand, during the afternoon and under near-surface stability conditions (water being cooler than air), the mean values approach zero, indicating almost null transfer of carbon between the reservoir and the atmosphere. During this period, the water surface is much warmer than the layers below and thus no convection develops. The results discussed above were also found by Lee et al. (2014) at Lake Taihu in south-eastern China. This very large and eutrophic lake (2400 km^2) also presented a nocturnal uptake of CO_2 and during this period they found convective instability in the water column.

Considering the whole 4 month period, the average CO_2 flux was −0.026085 mg m^{-2} s^{-1}, with an average of −0.043683 mg m^{-2} s^{-1} between 0 and 12 UTC and −0.010700 mg m^{-2} s^{-1} between 12 and 24 UTC. Assuming this flux rate over 1 yr, the value of −13.71 g C m^{-2} yr^{-1} is comparable to the estimations obtained for other lakes and reservoirs described in Pacheco et al. (2013).

Nevertheless, this result represents only 4 months of the year (June to September) and uncertainties remain, especially because of the systematic bias of the IRGASON system, which at the moment is only partially understood (Helbig et al., 2016). Therefore, further long-term studies are necessary to fully characterize the annual carbon cycle in Alqueva reservoir.

4.4. *Underwater solar irradiation and spectral attenuation coefficient*

The vertical structure of the underwater radiative absorption plays an important role in the thermal dynamics of the water surface layer and consequently on the energy budget at the water–lake interface. So, a better estimation of the irradiance at different levels is relevant to understand the lake–air interactions. Figure 9 presents the profiles of the underwater downwelling irradiance measured with the new device, performed at 10:24 UTC (Fig. 9a), and the underwater downwelling radiance with the device from Potes et al. (2013), performed at 10:52 UTC. The profiles were obtained on 10 July 2014 in Alqueva-Montante (Fig. 1). It can be seen that the new device recorded a decrease in irradiance with depth (Fig. 9a), while the previous device recorded an increase in radiance from the surface to 1 m depth (Fig. 9b). This particular intensification of radiance is associated with the incidence of refracted direct and scattered solar radiation into the FOV cone (Potes et al., 2013). The average attenuation coefficient for the photosynthetically active radiation (PAR) spectral region was computed according to eq. (12) for both profiles. The attenuation coefficient with the new device was 0.709 ± 0.006 m^{-1} for the layer 0–3 m and with the previous device was 0.522 ± 0.017 m^{-1} for the layer 1–3 m, which is the layer where the logarithmic slope of the underwater radiance becomes nearly constant with depth (Potes et al., 2013). This comparison confirms that previous estimations of the attenuation coefficient obtained with the Potes et al. (2013) apparatus are comparable to those obtained with the new device; however, it tends to underestimate the coefficient and has a greater degree of uncertainty.

Figure 10 shows two profiles of the downwelling irradiance performed at the pool on 14 July 2014 at 10:32 UTC (Fig. 10a) and at Alqueva-Montante on 27 August 2014 at 10:25 UTC (Fig. 10b). These two profiles present similar spectral behaviour in the 700–900 nm spectral region, where both types of water absorb the radiation. Nevertheless, large differences are noticed in the PAR region. In the pool (Fig. 10a), the solar radiation penetrates more deeply in the range 400–500 nm, with a maximum of 70% of the subsurface irradiance at 3 m depth, while at Alqueva (Fig. 10b) only a maximum of 10% is recorded at 3 m depth, in the 500–600 nm spectral region. At 3 m depth in the pool, there is more than 50% of surface irradiance between 400 and 600 nm. At the same depth in the reservoir, there is only 1–10% between 500 and 700 nm. This indicates that in the reservoir the euphotic depth is reached (for almost all the wavelengths) within the 3 m profile. Figure 11 shows a plot of the spectral attenuation coefficient for the sporadic measurements performed during the field campaign (details are given in Table 1). The spectra from the municipal swimming complex are closer to pure water (Smith and Baker, 1981) from 600 to 800 nm and higher from 325 to 600 nm. The reservoir spectra are higher than pure water and swimming complex, and the minimum shifts from the blue region to the green region of the spectrum. This is due to different composition of the water masses in terms of organic and inorganic material, especially chlorophyll *a* and cyanobacteria concentration and water turbidity (Morais et al., 2007; Potes et al., 2011, 2012).

The average attenuation coefficient for the PAR region was computed according to eq. (12). The PAR attenuation coefficients of the most significant profiles obtained in the campaign are shown in Table 1. This spectral region concentrates about half of the solar radiation, and thus the radiation is able to penetrate more deeply in the PAR region than outside it (Fig. 10). Therefore, most of the water quality studies on lakes and lagoons focus on the PAR spectral region (Walmsley et al., 1980; Gallegos, 2001; Potes et al., 2012). Notice that the measurements performed on the same day and at different sites of the reservoir present considerable differences in the PAR attenuation coefficient (Table 1). For example, on 25 September 2014 the difference between the sites Alqueva-Mourão and Alqueva-Montante was about 0.404 m^{-1}, which is more than the double that with respect to the swimming complex water.

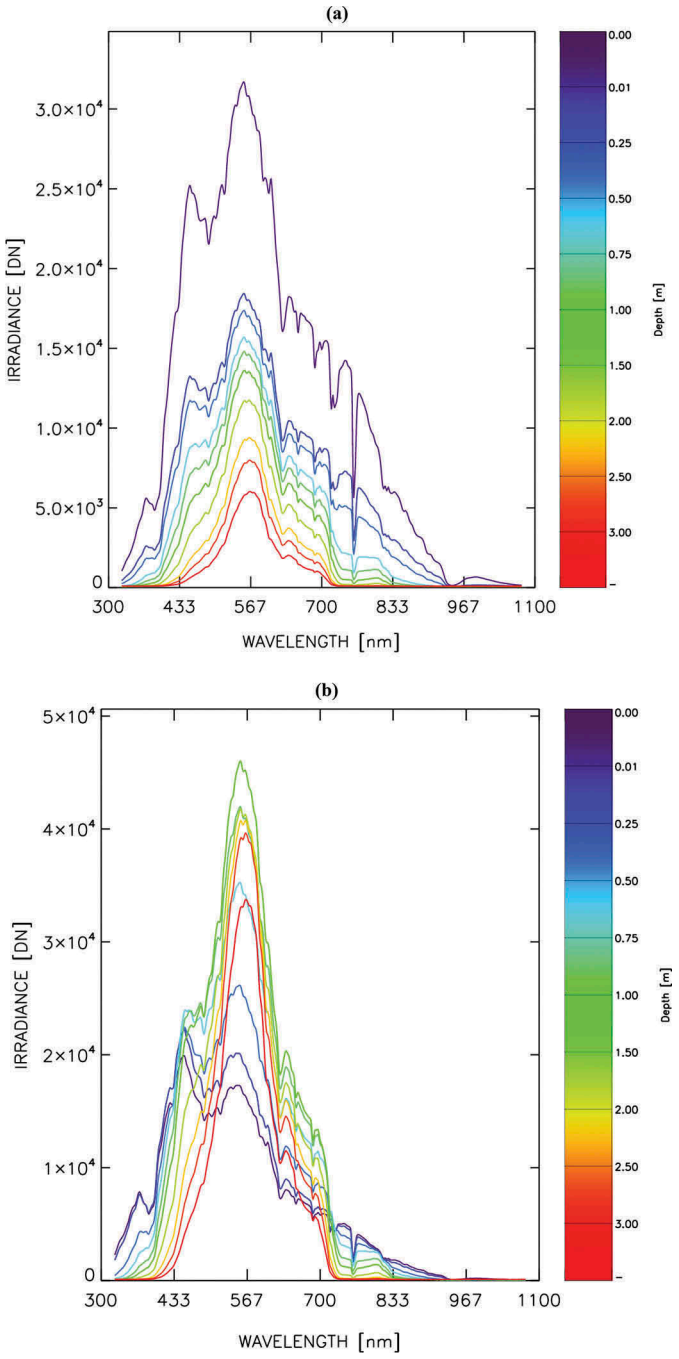

Fig. 9. Profiles in Alqueva-Montante on 10 July 2014: (a) underwater downwelling spectral irradiance measured with the new devices; (b) underwater downwelling spectral radiance with the device from Potes et al. (2013). Profiles are given in digital numbers (DN); output values without calibration.

4.5. Lake breeze on selected days

Differences in the surface energy budget between lake–atmosphere and land–atmosphere interfaces create heterogeneities in the air temperature and pressure fields that may induce the formation of local breezes. As the first study of observational evidence of breeze induction at Alqueva reservoir, it was decided to pay special attention to those days on which the effects of the lake on the atmosphere are expected to be more pronounced. The criteria for the selection were: the daily maximum of the temperature difference between air (in

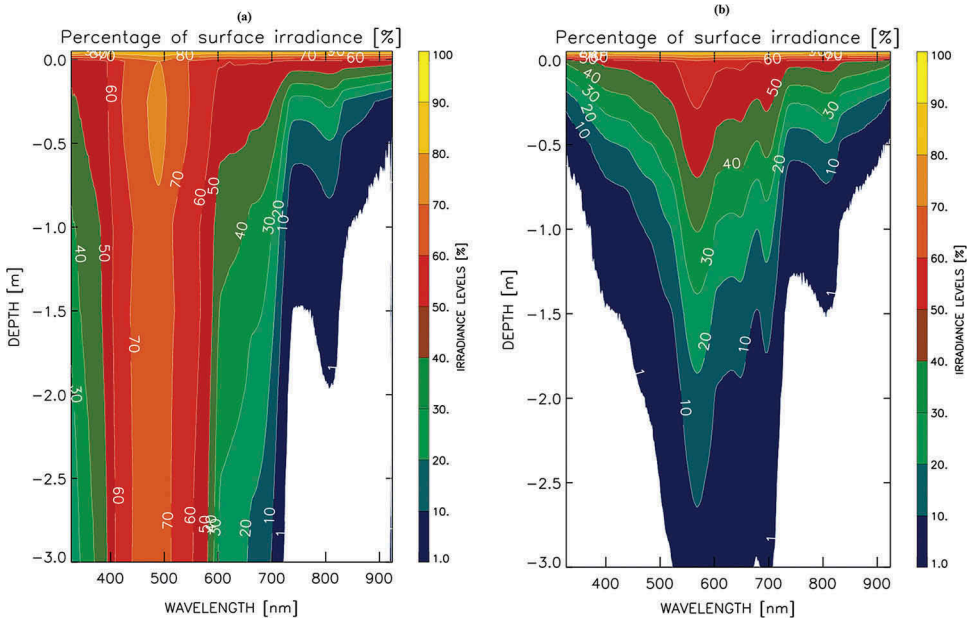

Fig. 10. Profiles of underwater downwelling spectral irradiance: (a) in the municipal swimming complex of Évora; (b) in Alqueva reservoir. Profiles are in percentage of surface irradiance.

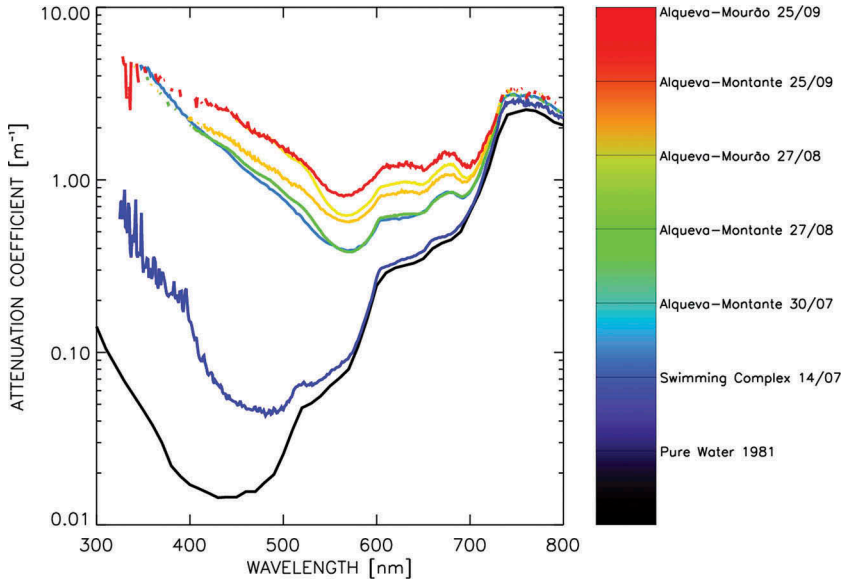

Fig. 11. Spectral attenuation coefficient for the field campaigns described in Table 1.

Barbosa station) and water (in Alqueva-Montante) was greater than 7 ºC (on average, this temperature difference was 8.17 ºC); and the daily average wind speed was lower than 3.5 m s^{-1} at Barbosa station. The application of these criteria resulted in the selection of 23 days. With these criteria, the selected days correspond to clear situations of lake breeze, avoiding the presence of a strong synoptic circulation or a strong sea breeze, which can mask the local effects. On these 23 selected days, a relatively strong lake breeze was found, comparing the measurements in three stations located on the lake shore: Amieira, Barbosa and Cid Almeida (see Fig. 1). Wind direction for the period 13–15 UTC is presented in Fig. 12 for Barbosa and Cid Almeida stations (1 min resolution), the first located on the north-western shore of the reservoir and the second on the south-eastern shore, at a distance of 1900 m from Barbosa station (see Fig. 1 for details). In the

Table 1. Measurement details

Date	Time (UTC)	Measurement location	PAR attenuation coefficient[a] (m^{-1})
Smith and Baker (1981)	–	Pure water	0.166
10 July 2014	10:24	Alqueva-Montante	0.709 ± 0.006
14 July 2014	10:32	Swimming complex	0.191 ± 0.002
30 July 2014	11:19	Alqueva-Montante	0.849 ± 0.025
27 August 2014	10:25	Alqueva-Montante	0.875 ± 0.023
27 August 2014	14:30	Alqueva-Mourão	1.112 ± 0.019
25 September 2014	15:31	Alqueva-Montante	1.055 ± 0.004
25 September 2014	10:39	Alqueva-Mourão	1.459 ± 0.007

[a]Photosynthetically active radiation attenuation coefficient for the layer 0–3 m.

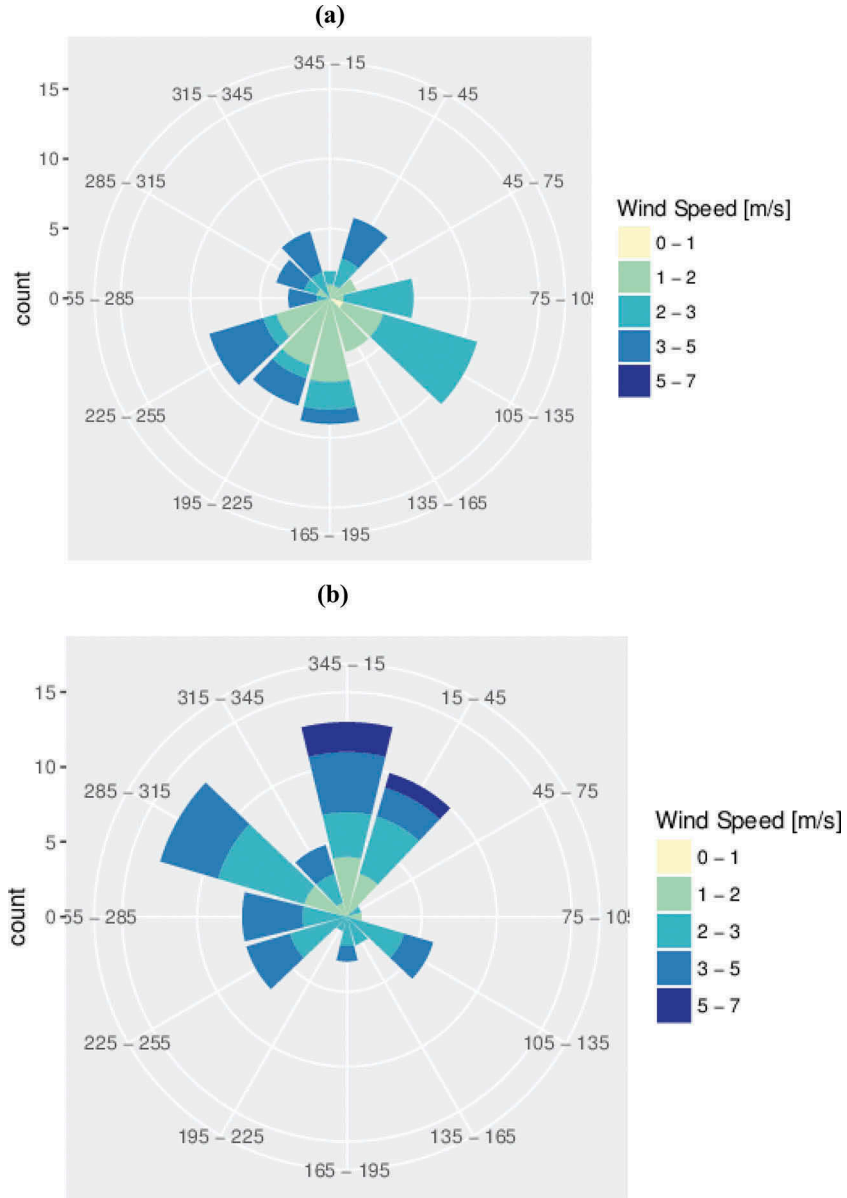

Fig. 12. Wind rose for 23 selected days in the period 13–15 UTC (units of m s^{-1}) for (a) Barbosa and (b) Cid Almeida stations (1 min resolution). The criteria for the selection were: daily maximum of the temperature difference between air (in Barbosa station) and water (in Alqueva-Montante) greater than 7 ºC, and daily average wind speed lower than 3.5 m s^{-1} at Barbosa station.

period considered (13–15 UTC, when the breeze is stronger), high percentages (65.15% and 79.54%) of wind blowing from the lake to the shore (from the south quadrant in this case) were found for the stations located on the northern shore, Amieira (not shown here) and Barbosa, respectively. For the same period, at Cid Almeida station, located on the south-eastern shore, 54.09% of the winds blew from the north quadrant, again from a lake-to-shore direction.

For the period 9–18 UTC, the wind changed from the north component to the south component at Barbosa station, which is located on the northern shore of the reservoir. In Cid Almeida station, located on the southern shore of the reservoir, the wind remained from the north quadrant during that period (not shown here). In terms of intensity and duration, 22 July 2014 was the day with the strongest lake breeze, recorded roughly from 9 to 18 UTC, with average wind velocities of 0.97 and 2.75 m s^{-1} in Barbosa and Cid Almeida, respectively. These values are slightly higher than the wind velocities before the lake breeze formation (values from 7–9 UTC: 0.72 and 2.40 m s^{-1} in Barbosa and Cid Almeida, respectively). The effect of the lake breeze, developed in Alqueva reservoir, on *LE* was explored. The daily cycle of *LE* flux averaged over the 23 lake breeze days is plotted in Fig. 13 together with the cycle for the 27 no lake breeze days. Those days without lake breeze were defined as days with a daily average temperature difference between air (in Barbosa station) and water (in Alqueva-Montante) lower than 2 ºC. On average, this temperature difference was −0.87 ºC. In the presence of a lake breeze, the latent heat flux was lower than in the cases when the breeze was absent, with average values of 93.45 and 133.58 W m^{-2}, respectively. In Fig. 13, a decrease in latent heat flux between 9 and 17 UTC is visible for the days with lake breeze overlapping the period of lake breeze. During lake breeze events, the maximum latent heat flux occurs at 22 UTC, with a much smaller value (145.20 W m^{-2}) than in the absence of lake breeze, 172.91 W m^{-2} at 17 UTC.

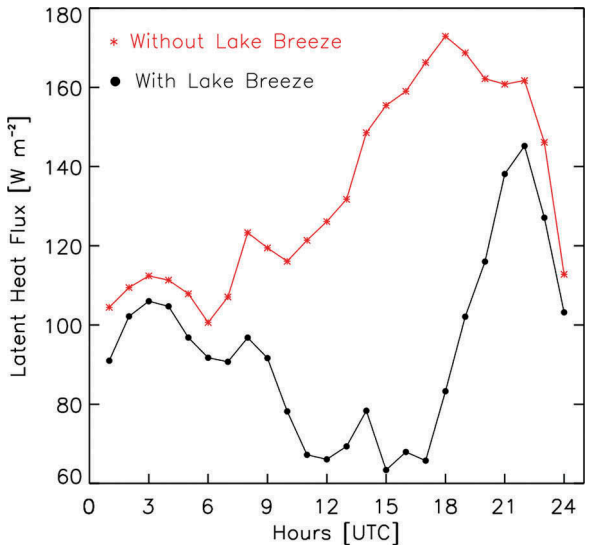

Fig. 13. Mean daily cycle of latent heat flux for 23 selected days with development of lake breeze and 27 selected days without lake breeze.

The days when a lake breeze develops are characterized by weak, large-scale winds in the low troposphere. On the other hand, in a lake breeze situation there is air subsidence over the centre of the lake (the descending branch of the thermal circulation) limiting the vertical fluxes. These two features, low near-surface winds (shown for all periods in Fig. 6b) and subsidence, contribute towards reducing the evaporation of the lake.

5. Conclusion

Measurements of energy and mass (H_2O and CO_2) fluxes were continuously performed from June to September 2014 at a floating platform in Alqueva reservoir, south-east of Portugal, with a Mediterranean climate (Csa according to the Köppen classification). During this period, the temperature gradient between the atmosphere and reservoir presents two opposite behaviours during the daily cycle. A positive gradient is observed during the afternoon; thus, a negative sensible heat flux is detected in the afternoon and, consequently, slightly stable atmospheric conditions near the water surface are noticed in this period. The wind speed presents a peak later in the afternoon owing to the arrival of the sea breeze from the west coast, leading to an increase in latent heat flux. During the night-time and morning, the temperature gradient is negative and thus a positive sensible heat flux is present, causing unstable conditions in the internal boundary layer established over the lake. Considering that the reservoir presents a homogeneous surface, the total evaporation for the 4 month period and the amount of energy released by the reservoir were estimated to be 490.26 mm and 19.45 GJ, respectively.

The energy balance of the reservoir was estimated for the four summer months and the results show consistency with other studies with values of *EBC* and *Res* of 81% and 27.10 W m^{-2}, respectively. These results indicate larger available energy (Rn-ΔQ) than the sum of turbulent fluxes ($LE + H$) for the study period. For some specific days, those with a positive gradient between the shore air temperature and the platform water temperature and also low wind speed, a lake breeze develops locally, being detected by the weather stations on the shore.

During the night and morning, higher CO_2 concentrations are found in the atmosphere, which may lead to a negative gradient in the CO_2 partial pressure between water and air, and may consequently be responsible for the maximum uptake of CO_2 by the reservoir. Nevertheless, the CO_2 concentration is lower in the afternoon, which can nullify the gradient,

allowing some small quantities of carbon to be released from the reservoir to the atmosphere on some days. On average, over the 4 month period, the reservoir is acting as a sink of atmospheric CO_2, with an average rate of −0.026085 mg m^{-2} s^{-1}. However, this result should be interpreted with caution, because of potentially important systematic bias related to CO_2 flux measured by the IRGASON system (Helbig et al., 2016). For this reason, further research is needed, especially in aquatic ecosystems, where the CO_2 fluxes are usually quite small (compared to forest systems).

A new apparatus was developed to be coupled with a portable spectroradiometer, allowing for spectral downwelling irradiance measurements in an underwater environment and estimation of the light attenuation coefficient in water. It ensures spectral downwelling irradiance measurements with an FOV of 180º, in the range 325–1075 nm, with a moderately high spectral resolution of 1–3 nm from the visible to the NIR regions. The spectral downwelling irradiance profiles allow for the calculation of the spectral attenuation coefficient through the exponential law. The attenuation coefficient retrieved in this work is assumed to be the diffuse attenuation coefficient, which is a property of the medium independent of the available irradiation field (inherent optical property). The comparison of the PAR attenuation coefficient from the different field campaigns confirms a spatial and temporal variation in the PAR attenuation coefficient. These results can constitute encouragement for the lake community to use in situ values of this coefficient instead of a constant value, since it is a key parameter for lake models coupled with weather forecast models.

Acknowledgements

The work is co-funded by the European Union through the European Regional Development Fund, included in COMPETE 2020 (Operational Program Competitiveness and Internationalization) through the ICT project (UID/GEO/04683/2013) with the reference POCI-01-0145-FEDER-007690 and also through the ALOP project (ALT20-03-0145-FEDER-000004). Experiments were accomplished during the field campaign funded by FCT and FEDER-COMPETE: ALEX 2014 (EXPL/GEO-MET/1422/2013) FCOMP-01-0124-FEDER-041840. The work was supported by FCT PostDoc grant SFRH/BPD/97408/2013. The authors want to acknowledge the useful discussions with and scientific clarification from Professor Luis Martins, University of Évora; the crucial technical support from Samuel Barias and Josué Figueira, both from the University of Évora; and the indispensable support from Ana Ilhéu, Martinho Murteira and Valter Rico from EDIA (Empresa de Desenvolvimento e Infraestruturas do Alqueva, S.A.).

Disclosure statement

No potential conflict of interest was reported by the authors.

Funding

This work was supported by the European Union through the European Regional Development Fund, [UID/GEO/04683/2013], ALOP, [ALT20-03-0145-FEDER-000004], Fundação para a Ciência e a Tecnologia (FCT), FEDER-COMPETE: ALEX 2014 [EXPL/GEO-MET/1422/2013], FCOMP-01-0124-FEDER-041840, FCT PostDoc, [SFRH/BPD/97408/2013], University of Évora and, EDIA (Empresa de Desenvolvimento e Infraestruturas do Alqueva, S.A.).

References

Antoine, D., Morel, A., Leymarie, E., Houyou, A., Gentili, B. and co-authors 2013. Underwater radiance distributions measured with miniaturized multispectral radiance cameras. *J. Atmos. Oceanic Technol.* **30**, 74–95. DOI:10.1175/JTECH-D-11-00215.1.

Baldocchi, D. D. 2003. Assessing the eddy covariance technique for evaluating carbon dioxide exchange rates of ecosystems: past, present and future. *Global Change Biol.* **9**, 479–492. DOI:10.1046/j.1365-2486.2003.00629.x.

Balsamo, G., Salgado, R., Dutra, E., Boussetta, S., Stockdale, T. and co-authors 2012. On the contribution of lakes in predicting near-surface temperature in a global weather forecasting model. *Tellus* **64A**, 15829.

Bowers, D. G. and Mitchelson-Jacob, E. G. 1996. Inherent optical properties of the Irish Sea determined from underwater irradiance measurements. *Estuarine, Estuar. Coast. Shelf S.* **43**, 433–447. DOI:10.1006/ecss.1996.0080.

Brutsaert, W. 1982. *Evaporation into the Atmosphere*. Kluwer Academic Publishers, Dordrecht, 299 p.

Bukata, R. P., Jerome, J. H., Kondratyev, K. Y. and Pozdnyakov, D. V. 1995. *Optical Properties and Remote Sensing of Inland and Coastal Waters*. CRC Press, Boca Raton, FL, 362 p.

Cole, J. J., Prairie, Y. T., Caraco, N. F., McDowell, W. H., Tranvik, L. J. and co-authors 2007. Plumbing the global carbon cycle: integrating inland waters into the terrestrial carbon budget. *Ecosystems* **10**, 171–184. DOI:10.1007/s10021-006-9013-8.

Darecki, M., Stramski, D. and Sokólski, M. 2011. Measurements of high-frequency light fluctuations induced by sea surface waves with an Underwater Porcupine Radiometer System. *J. Geophys. Res.* **116**, C00H09. DOI:10.1029/2011JC007338.

Downing, J. A., Prairie, Y. T., Cole, J. J., Duarte, C. M., Tranvik, L. J. and co-authors 2006. The global abundance and size distribution of lakes, ponds, and impoundments. *Limnol. Oceanogr.* **51**, 2388–2397. DOI:10.4319/lo.2006.51.5.2388.

Emerson, S. 1975. Chemically enhanced CO_2 gas exchange in a eutrophic lake: a general model. *Limnol. Oceanogr.* **20**, 743–753. DOI:10.4319/lo.1975.20.5.0743.

Ferdorovich, E. E., Golosov, S. D., Kreiman, K. D., Mironov, D. V., Shabalova, M. V. and co-authors 1991. Modeling air-lake

interaction. In *Physical Background* (ed. S. S. Zilitinkevich) Springer Verlag, Berlin, 130 p.

Finlay, K., Leavitt, P., Wissel, B. and Prairie, Y. T. 2009. Regulation of spatial and temporal variability of carbon flux in six hard-water lakes of the northern Great Plains. *Limnol. Oceanogr.* **54**, 2553–2564. DOI:10.4319/lo.2009.54.6_part_2.2553.

Gallegos, C. L. 2001. Calculating optical water quality targets to restore and protect submersed aquatic vegetation: overcoming problems in partitioning the diffuse attenuation coefficient for photosynthetically active radiation. *Estuaries* **24**(3), 381–397. DOI:10.2307/1353240.

Gernez, P. and Antoine, D. 2009. Field characterization of wave-induced underwater light field fluctuations. *J. Geophys. Res.* **114**, C06025. DOI:10.1029/2008JC005059.

Gill, A. 1982. *Atmosphere-Ocean Dynamics*. Academic, London, 662 p.

Heiskanen, J. J., Mammarella, I., Ojala, A., Stepanenko, V., Erkkilä, K.-M. and co-authors 2015. Effects of water clarity on lake stratification and lake-atmosphere heat exchange. *J. Geophys. Res. Atmos.* **120**(15), 7412–7428. DOI:10.1002/2014JD022938.

Helbig, M., Wischnewski, K., Gosselin, G. H., Biraud, S. C., Bogoev, I. and co-authors 2016. Addressing a systematic bias in carbon dioxide flux measurements with EC150 and the IRGASON open-path gas analysers. *Agric. For. Meteorol.* **228–229**, 349–359. DOI:10.1016/j.agrformet.2016.07.018.

Jerlov, N. G. and Fukuda, M. 1960. Radiance distribution in the upper layers of the sea. *Tellus XII* **12**, 348–355. DOI:10.1111/tus.1960.12.issue-3.

Kaimal, J. C. and Gaynor, J. E. 1991. Another look at sonic thermometry. *Boundary Layer Meteorol.* **56**, 401–410. DOI:10.1007/BF00119215.

Kaimal, J. C., Wyngaard, I. Y. and Coté, O. R. 1972. Spectral characteristics of surface-layer turbulence. *Q. J. R. Met. Soc.* **98**, 563–589. DOI:10.1002/qj.49709841707.

Kljun, N., Calanca, P., Rotach, M. W. and Schmid, H. P. 2004. A simple parameterisation for flux footprint predictions. *Boundary-Layer Meteorol.* **112**, 503–523. DOI:10.1023/B:BOUN.0000030653.71031.96.

Kostadinov, I., Bortoli, D., Giovanelli, G., Heland, J., Petritoli, A. and co-authors 2003. Aircraft measurements, modelled stratospheric [NO2]/[NO] ratio and photochemical steady-state approach within the frame of ENVISAT satellite data validation. ed. B. Warmbein In: *16th ESA Symposium on European Rocket and Balloon Programmes and Related Research, 2-5 June 2003, Sankt Gallen, Switzerland. Edition Barbara Warmbein. ESA SP-530*. ESA Publications Division, Noordwijk, ISBN 92-9092-840-9, pp. 509–514.

Kostadinov, I., Ravegnani, F., Petritoli, A., Bortoli, D., Masieri, S. and co-authors 2009. Airborne UV/Vis actinic measurements in the lower Antarctic stratosphere. eds. U. Michel and D. L. Civco In: *Remote Sensing for Environmental Monitoring, GIS Applications, and Geology IX, Edited by Ulrich Michel, Daniel L. Civco, Proceedings of SPIE VoL. 7478*. SPIE, Bellingham, WA, 74780P p.

Le Moigne, P., Legain, D., Lagarde, F., Potes, M., Tzanos, D. and co-authors 2013. Evaluation of the lake model FLake over a coastal lagoon during the THAUMEX field campaign. *Tellus A* **65**, 20951. DOI:10.3402/tellusa.v65i0.20951.

Lee, R. and Biggs, T. 2014. Impacts of land use, climate variability, and management on thermal structure, anoxia, and transparency in hypereutrophic urban water supply reservoirs. *Hydrobiologia*. DOI:10.1007/s10750-014-2112-1.

Lee, X., Liu, S., Xiao, W., Wang, W., Gao, Z. and co-authors 2014. The Taihu Eddy Flux Network: An observational program on energy, water, and greenhouse gas fluxes of a large freshwater lake. *Bull. Amer. Meteor. Soc.* **95**, 1583–1594. DOI:10.1175/BAMS-D-13-00136.1.

Lewis, M. R., Wei, J., Van Dommelen, R. and Voss, K. J. 2011. Quantitative estimation of the underwater radiance distribution. *J. Geophys. Res.* **116**, C00H06. DOI:10.1029/2011JC007275.

Liu, W.-C., Wu, R.-S., Wu, E. M.-Y., Chang, Y.-P. and Chen, W.-B. 2010. Using water quality variables to predict light attenuation coefficient: case study in Shihmen Reservoir. *Paddy Water Environ.* **8**(3), 267-275 (SCI). DOI:10.1007/s10333-010-0207-5.

Mammarella, I., Nordbo, A., Rannik, Ü., Haapanala, S., Levula, J. and co-authors 2015. Carbon dioxide and energy fluxes over a small boreal lake in Southern Finland. *J. Geophys. Res. Biogeosci.* **120**, 1296–1314. DOI:10.1002/2014JG002873.

Margalef, R. 1983. *Limnologia*. Editora Omega, Barcelona, 1100 p.

McGloin, R., McGowan, H. and McJannet, D. 2014. Effects of diurnal, intra-seasonal and seasonal climate variability on the energy balance of a small subtropical reservoir. *Int. J. Climatol.* DOI:10.10002/joc.4147.

Mironov, D. V., Heise, E., Kourzeneva, E., Ritter, B., Schneider, N. and co-authors 2010. Implementation of the lake parameterisation scheme FLake into the numerical weather prediction model COSMO. *Boreal Env. Res.* **15**, 218–230.

Morais, M., Serafim, A., Pinto, P., Ilhéu, A. and Ruivo, M. 2007. Monitoring the water quality in Alqueva Reservoir, Guadiana River, southern Portugal. In: *Reservoir and River Basin Management. Exchange of Experiences from Brazil, Portugal and Germany* (eds. G. Gunkel and M. Sobral). Universitätsverlag der TU Berlin Universitätsbibliothek Fasanenstr, Berlin, pp. 96–112.

Nordbo, A., Launiainen, S., Mammarella, I., Lepparanta, M., Huotari, J. and co-authors 2011. Long-term energy flux measurements and energy balance over a small boreal lake using eddy covariance technique. *J. Geophys. Res.* **116**, D02119. DOI:10.1029/2010JD014542.

Nowlin, W., Davies, J.-M., Nordin, R. and Mazumder, A. 2004. Effects of water level fluctuation and short-term climate variation on thermal and stratification regimes of a British Columbia reservoir and lake. *Lake Reservoir Manage* **20**(2), 91–109. DOI:10.1080/07438140409354354.

Pacheco, F. S., Roland, F. and Downing, J. A. 2013. Eutrophication reverses whole-lake carbon budgets. *Inland Waters* **4**, 41–48. DOI:10.5268/IW-4.1.614.

Podgrajsek, E., Sahlee, E. and Rutgersson, A. 2014. Diurnal cycle of lake methane flux. *J. Geophys. Res. Biogeosci.* **119**, 236–248. DOI:10.1002/2013JG002327.

Potes, M., Costa, M. J. and Salgado, R. 2012. Satellite remote sensing of water turbidity in Alqueva reservoir and implications on lake modeling. *Hydrol. Earth Syst. Sci.* **16**, 1623–1633. DOI:10.5194/hess-16-1623-2012.

Potes, M., Costa, M. J., Salgado, R., Bortoli, D., Serafim, A. and co-authors 2013. Spectral measurements of underwater downwelling radiance of inland water bodies. *Tellus-A* **65**, 20774. DOI:10.3402/tellusa.v65i0.20774.

Potes, M., Costa, M. J., Silva, J. C. B., Silva, A. M. and Morais, M. 2011. Remote sensing of water quality parameters over Alqueva reservoir in the south of Portugal. *Int. J. Remote Sens.* **32**(12), 3373–3388. DOI:10.1080/01431161003747513.

Preisendorfer, R. W. 1959. Theoretical proof of the existence of characteristic diffuse light in natural waters. *J. Mar. Res.* **18**, 1–9.

Rannik, Ü. and Vesala, T. 1999. Autoregressive filtering versus linear detrending in estimation of fluxes by the eddy covariance method. *Boundary-Layer Meteorol.* **91**, 259–280. DOI:10.1023/A:1001840416858.

Rebmann, C., Kolle, O., Heinesch, B., Queck, R., Ibrom, A. and co-authors 2012. Data acquisition and flux calculation. In: *Eddy Covariance: A Practical Guide to Measurement and Data Analysis* (ed. M. Aubinet, T. Vesala and D. Papale), Springer, Dordrecht, 439 p.

Repo, M. E., Huttunen, J. T., Naumov, A. V., Chichulin, A. V., Lapshina, E. D. and co-authors 2007. Release of CO_2 and CH_4 from small wetland lakes in western Siberia. *Tellus B* **59**, 788–796. DOI:10.1111/j.1600-0889.2007.00301.x.

Salgado, R. and Le Moigne, P. 2010. Coupling of the FLake model to the Surfex externalized surface model, Boreal Environ. *Res* **15**, 231–244.

Salgado, R., Miranda, P. M. A., Lacarrère, P. and Noilhan, J. 2015. Boundary layer development and summer circulation in Southern Portugal. *Tethys* **12**. DOI:10.3369/tethys.2015.12.03.

Sander, R. 2015. Compilation of Henry's law constants (version 4.0) for water as solvent. *Atmos. Chem. Phys.* **15**, 4399–4981. DOI:10.5194/acp-15-4399-2015.

Sasaki, T., Watanabe, S., Oshiba, G. and Okami, N. 1958. Measurements of angular distribution of submarine daylight by means of a new instrument. *J. Oceanographical Soc. Japan* **14**(2), 47–52.

Silva, A., De Lima, I., Santo, F. and Pires, V. 2014. Assessing changes in drought and wetness episodes in drainage basins using the Standardized Precipitation Index. *Bodenkultur* **65**(3–4), 31–37.

Smith, R. C. and Baker, K. S. 1981. Optical properties of the clearest natural waters (200-800 nm). *Appl. Opt.* **20**, 177–184.

Tranvik, L. J., Downing, J. A., Cotner, J. B., Loiselle, S. A., Striegl, R. G. and co-authors 2009. Lakes and reservoirs as regulators of carbon cycling and climate. *Limnol. Oceanogr.* **54**, 2298–2314. DOI:10.4319/lo.2009.54.6_part_2.2298.

Tyler, J. R. 1960. Radiance distribution as a function of depth in an underwater environment. *Bull. Scripps Inst. Oceanogr.* **7**, 363–411.

Vesala, T., Eugster, W. and Ojala, A. 2012. Eddy covariance measurements over lakes. In: *Eddy Covariance. A Practical Guide to Measurement and Data Analysis* (eds. M. Aubinet, T. Vesala and D. Papale). Springer, Dordrecht, The Netherlands, pp. 365–376.

Walmsley, R. D., Butty, M., Van Der Piepen, H. and Grobler, D. C. 1980. Light penetration and the interrelationships between optical parameters in a turbid subtropical impoundment. *Hydrobiologia* **70**, 145–157. DOI:10.1007/BF00015500.

Webb, E. K., Pearman, G. I. and Leuning, R. 1980. Correction of flux measurements for density effects due to heat and water vapour transfer. *Q. J. R. Meteorol. Soc.* **106**, 85–100. DOI:10.1002/qj.49710644707.

Wetzel, R. G. 1983. *Limnology.* 2nd. Complete Revision. Saunders College Publishing, Philadelphia, 858 p.

Wozniak, B., Dera, J., Ficek, D., Majchrowski, R., Ostrowska, M. and co-authors 2003. Modelling light and photosynthesis in the marine environment. *Oceanologia* **45**, 171–245.

Atmospheric Research 242 (2020) 104993

Contents lists available at ScienceDirect

Atmospheric Research

journal homepage: www.elsevier.com/locate/atmosres

Lightning modelling for the research of forest fire ignition in Portugal

Flavio Tiago Couto[a,*], Maksim Iakunin[a], Rui Salgado[b], Paulo Pinto[c], Tânia Viegas[c], Jean-Pierre Pinty[d]

[a] Instituto de Ciências da Terra – ICT (Polo de Évora), Universidade de Évora, Rua Romão Ramalho, 59, 7000-671 Évora, Portugal
[b] Instituto de Ciências da Terra – ICT (Polo de Évora), Universidade de Évora, Departamento de Física, Escola de Ciências e Tecnologia, Rua Romão Ramalho, 59, 7000-671 Évora, Portugal
[c] Instituto Português do Mar e da Atmosfera (IPMA), Rua C do Aeroporto, 1749-077 Lisbon, Portugal
[d] Laboratoire d'Aérologie, Université de Toulouse, CNRS, UPS, 14 avenue Edouard Belin, 31400 Toulouse, France

ARTICLE INFO

Keywords:
Fire ignition
Lightning modelling
Radar simulator
Meso-NH model
Fire weather

ABSTRACT

The study aims to assess the applicability of the current Meso-NH electrical scheme (CELLS) in the investigation of forest fire ignition. Therefore, the challenge is to diagnose cloud-to-ground (CG) lightning at 1 km spatial resolution and, subsequently, preferred regions where Forest Fire Events (FFE) could be naturally ignited. The afternoon of 17th June 2017 has been considered for the study, since the dry thunderstorm environment configured a perfect scenario for natural ignition and evolution of some fires. The Pedrógão Grande wildfire ignited in this period and was the deadliest single fire event in the Portuguese history, with at least 60 people killed. The available observational data are used to validate the numerical results and to provide a brief characterization of the meteorological environment when jointly analysed with the simulation. In addition, cloud microphysics and cloud electrical structure are explored from the model results. The spatial distribution of the simulated CG lightning showed a good agreement with the lightning strokes obtained from the national lightning detection network. Overall, this paper introduces a possible application of the Meso-NH electrical scheme, namely the study of forest fire ignition by lightning strokes.

1. Introduction

The natural ignition and the evolution of forest fires are influenced by several factors, such as the weather conditions, the orography and fuelling material. Their combination can greatly improve the assessment of the potential to trigger fires over large areas during days or weeks (Forest Fires Events – FFE). Among several origins of fire ignition, lightning are the main natural source of FFE and an important contributor to burned areas in many regions (e.g., Ganteaume and Syphard, 2018). For example, the extreme heat associated with a lightning strike is able to vaporize the water content of a tree and starting the fire process. In real situations, the thunderstorms produce lightning, but not all are accompanied by heavy precipitation, in particular those high-based and that occur over dry atmospheric layers. When such a situation is observed over large and dry forests, a CG lightning strike can easily start a fire, mainly in forests that have accumulated dead vegetation for several years. These dry lightning conditions, known as such due to the small amounts of accompanying rainfall involved, are recognized as one of the most important ignition sources for wildfires worldwide (Dowdy and Mills, 2012a).

The amount of burned area from 1940 to 2000 has significantly increased in some regions of the United States (US). In particular in western US, natural FFE are responsible for almost two-thirds of the burned areas. However, climate variability and the increase of fuel mass, rather than the number of lightning strokes, are suggested as the controlling factors of the amount of burned area by natural FFE (e.g., Stephens, 2005; Abatzoglou et al., 2016). Such reasons can explain the triggering of large fires, which have also shown a marked increase in the US, due to an increase in drought severity (Dennison et al., 2014; Barbero et al., 2014). Recently, Singleton et al. (2019) pointed out that during the last 3 decades, fires have been more frequent, larger, and more severe in the south-western US.

The estimated mean area of wildfires in Russia in the period of 1998–2010 is $8.2 \pm 0.8 \times 10^6$ ha yr^{-1}. Based on the prognostic scenarios of the Intergovernmental Panel on Climate Change (IPCC), the fire danger in Russian forests will keep increasing towards the end of the century. Current model estimations show the doubling of the number of wildfires, with an increase in severity and events ignited by

* Corresponding author.
E-mail addresses: couto.ft@gmail.com (F.T. Couto), miakunin@uevora.pt (M. Iakunin), rsal@uevora.pt (R. Salgado), paulo.pinto@ipma.pt (P. Pinto), tania.viegas@ipma.pt (T. Viegas), jean-pierre.pinty@aero.obs-mip.fr (J.-P. Pinty).

https://doi.org/10.1016/j.atmosres.2020.104993
Received 8 November 2019; Received in revised form 31 March 2020
Available online 11 April 2020
0169-8095/ © 2020 Elsevier B.V. All rights reserved.

lightning (Shvidenko and Schepaschenko, 2013).

In Canada, FFE triggered by lightning strokes are responsible for the largest burned areas. For example, they represent about 50% of the occurrences and account for 85% of the burned area (Ganteaume and Syphard, 2018). In Australia, where this type of ignition can also be the main source of wildfires, FFE from lightning may account for 90% of the total burned area and ~ 30% of the total number of fires (Dowdy and Mills, 2012b). Even with lower impact, lightning still plays an important role in the ignition of FFE in other regions worldwide. In Austria, FFE of natural origin are found from May to September and correspond to an amount of 15% of the total FFE, of which almost 40% occur between the months of June and August (Müller et al., 2013). Larjavaara et al. (2005a) verified that 13% of all analysed FFE were caused by lightning in Finland. Furthermore, Larjavaara et al. (2005b) showed that the polarity does not influence the probability of ignition in Finland. According to Vazquez and Moreno (1998), in the Iberian Peninsula, particularly in Spain, lightning does not play the same role for FFE ignition, with a small percentage (3.3%) and 7.5% of the total burned area affected.

In Portugal, every year, fires are spreading over forested areas, sometimes killing and injuring a number of people. After identifying the largest areas where fires occurred, Trigo et al. (2016) showed that higher temperatures and lower humidities during the summer months make the western half of Iberia more favourable to fire ignitions. For example, the 2003 fire season is memorable due to large forest fires during early August, some of them ignited by lightning flashes, such as the Santarém wildfire with 22,190 ha of burned area (Pugnet et al., 2010). The 2003 fire season was preceded by a wet winter followed by a dry May, which possibly aggravated the consequences of the synoptic heatwave that affected Europe during that period (Trigo et al., 2005, 2006). Pugnet et al. (2010) pointed out that 303 fires affecting 60,543,1 ha were caused by lightning between 1996 and 2008 in Portugal. The 2003 year maximum was marked by 67 lightning triggered fires, of which 9 burned an area above 1000 ha. On the other hand, Nunes et al. (2014) highlighted that fires of human origin are responsible for a large part of FFE in Portugal, whereas natural FFE represented < 1% of the total occurrences in the period 2001–2012. Nevertheless, such events cannot be neglected due to the large area that can be burned. In 2017, devastating forest fires brought a tragedy to Portugal, with fires burning repeatedly in late spring. The fires near Pedrógão Grande created a huge wall of pyrocumulus and flames, killing at least 60 people during a single event.

Evidently, one of the major questions regarding FFE is the diagnosis of their causes. Apart from arson, and as mentioned before, lightning flashes can plausibly be suspected as the main ignition factor in many wildfire cases. Therefore, to better explore the subject, this paper introduces an analysis based on atmospheric modelling with an explicit physical scheme for lightning.

In the last years, many efforts have been done in order to improve lightning forecast. They can be divided into three main groups: 1) Nowcasting based on observations or on a combination of observations and Numerical Weather Prediction (NWP) model outputs. For example, Blouin et al. (2016) used a supervised machine learning method, named random forests, to forecast lightning strikes relevant to wildfire occurrence for the province of Alberta, Canada. Meng et al. (2019) developed a system that combines a set of observational data with synoptic pattern forecasting products and an electrification and discharge model. Furthermore, Mostajabi et al. (2019) developed a four-parameter machine learning model based on only four commonly available surface weather variables, whereas Karagiannidis et al. (2019) proposed a scheme to estimate the lightning density of convective clouds using variables such as cloud top height, cloud top pressure and cold cloud depth. 2) Diagnostics computed from ice-phase hydrometeor fields in NWP global models and other convective parametrization outputs. For example, the ECMWF (European Centre for Medium-Range Weather Forecasts) introduced in IFS Cycle 45r1, released in June 2018, a relatively simple lightning parametrization scheme in order to estimate the lightning flash densities from diagnostic fields of the forecast model (Lopez, 2016). Using another global NWP model, Gijben et al. (2017) developed a lightning threat index (LTI) for South Africa, using six weather prognostic parameters from the NWP Unified Model (UM) as predictors to force a statistically based lightning prediction scheme. Even more simple, Tippett and Koshak (2018) successfully used the product of convective available potential energy (CAPE) and precipitation rate, forecasted by the NCEP Global Ensemble Forecast System (GEFS), as a proxy to predict cloud-to-ground (CG) lightning over the United States. 3) Prediction based on explicit electricity and lightning physics schemes coupled to cloud-resolving models. The current capability of the atmospheric models to integrate dynamic, microphysical and electrical processes has become possible to explore what happens inside the clouds during its evolution in time, although still computationally too expensive to be used operationally. Examples of such developments are found in Fierro et al. (2013), who implemented an explicit electrification and lightning forecast scheme within the Weather Research and Forecasting (WRF) model, and Barthe et al. (2012) that implemented the Cloud Electrification and Lightning Scheme (CELLS) in the Meso-NH model.

In the present study, the CELLS is used in the simulation of the "Pedrógão Grande" wildfire case to investigate the current representation of cloud-to-ground lightning flashes as a possible explanation of fire ignition. This study is motivated by the central question of assessing the likelihood of forest fire occurrence of natural origin, here triggered by lightning flashes.

A better understanding of FFE is necessary both from physical and operational points of view, which are the goals of the CILIFO (Centro Ibérico para la Investigacion y Lucha contra Incendios Forestales) project. The project concentrates on the efforts to evaluate forest fire risks and fire fighting strategy in the south-western Iberian Peninsula. The goal of this work is to check the possibility to correctly diagnose a high probability of cloud-to-ground flashes using high resolution simulations and also to locate where forest fires could be ignited. The paper is organized as follows: in Section 2 the FFE are considered, the dataset and numerical modelling features are presented, whereas the results from the model validation are found in Section 3. Section 4 brings a discussion followed by conclusions addressed in Section 5.

2. Forest fire events, data and numerical modelling features

2.1. Forest fires events on 17th June 2017

Data shown in Fig. 1 were taken from the MODIS Land Cover Type Product, International Geosphere-Biosphere programme – IGBP (Sulla-Menashe and Friedl, 2018). The figure indicates that the region where the FFE were reported is mainly covered by forests, also characterized by flammable trees, composed by Evergreen Needle-leaf forest (e.g., eucalyptus, oaks), with tree cover greater than 60%, and woody savanna (e.g., Cork oak tree, Holm oak) with tree cover of 30–60%.

The fires on 17th June 2017 occurred in an exceptional hot day and during a prolonged dry period marked by an anomalously dry and warm spring preceded by a dry winter. Such a period affected the low level of humidity of the local vegetation. In addition, large parts of the region had not been burnt for about 20 years, resulting in an accumulation of forest fuel and a high forest fire risk. This means that any ignition in places with complex orography and a favourable vegetation state could lead to an uncontrolled wildfire.

According to an official report of the Portuguese authorities (CTI Report, 2017), nine ignition points were reported during the afternoon of 17th June 2017. The "Pedrógão Grande" (28,914 ha) and the "Góis" (17,521 ha) fires, the second and eighth largest until that time, were caused by an electrical discharge from a power transmission line and from a lightning stroke, respectively. Besides that, 3 fires more were also probably caused by lightning strokes, other 3 fires have not a

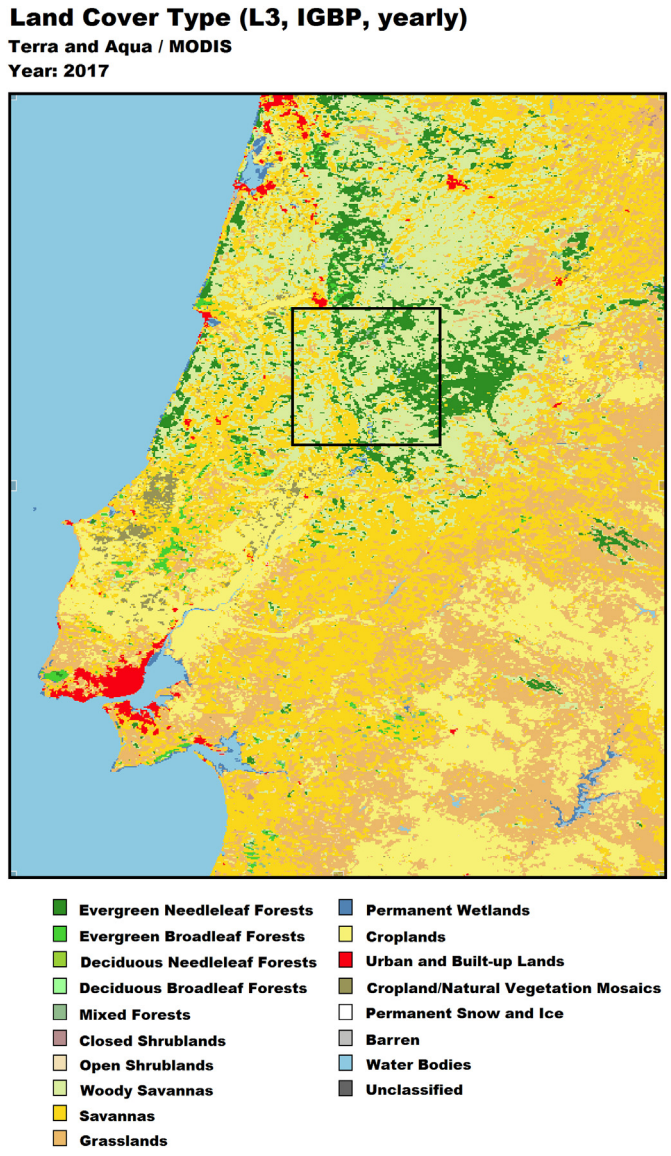

Fig. 1. MODIS Land Cover Type Product (MCD12Q1) with the International Geosphere-Biosphere Programme (IGBP) legend. The rectangle represents the region where the forest fires occurred.

clearly identified origin, while the last case was attributable to pyromaniac people. This study does not only account for the Pedrógão Grande episode, but also for all the smaller fires reported during the period, which are displayed in Fig. 2b.

2.2. Meteorological data

A set of meteorological data was used to validate the model results and to describe the prevailing atmospheric environment during the afternoon of 17th June 2017 over central Portugal (see Fig. 2). In order to investigate the atmospheric stability a few hours before the onset of the forest fires, upper-air data derived from the radiosonde of Lisbon, at 1200 UTC was analysed.

The Portuguese Institute for Sea and Atmosphere, I. P. (IPMA, IP) that maintains the national weather station network has provided the data for this study. The observations of 76 surface stations have been used, namely meteorological parameters such as temperature and relative humidity. The stations are located inside the inner domain of the grid-nesting model configuration (see sub-section 2.3.4 for the model set-up) showed in Fig. 2b. There were two C-band weather radars covering the region of interest (Fig. 2b): the Coruche/Cruz do Leão radar (latitude: 39°4′12”N; longitude: 8°23′24”W; altitude: 193 m) with a 14 elevation angle scanning strategy, and the Arouca/Pico do Gralheiro radar (latitude: 40°50′24”N; longitude: 8°16′12”W; altitude: 1097 m) with a 16 elevation angle scanning strategy. The radar reflectivity was obtained using the low to middle level angles of these Portuguese operational radars scans.

Finally, cloud-to-ground lightning data from the national lightning detection network of IPMA was analysed. According to IPMA Report (2017), the lightning detection network in Portugal consists of 4 sensors LS7002 (VAISALA). The positions of the sensors located within the region under study are displayed in Fig. 2b. The sensor network is able to detect the discharge location with a maximum accuracy of 250 m and an efficiency of 95% for CG lightning strokes and 50% for Intra-Cloud (IC) lightning. The system provides information about the discharges, such as location, date, hour with a millisecond resolution, lightning type (CG or IC), polarity, intensity, location error, among others. The coordinate of the location is related to the point of the impact at the ground.

The Alverca sensor was not available for the study, however, according to the IPMA report (2017), the detection system maintained a good detection efficiency coverage, so that the determination of the location of the lightning strokes was not highly influenced by the missing data.

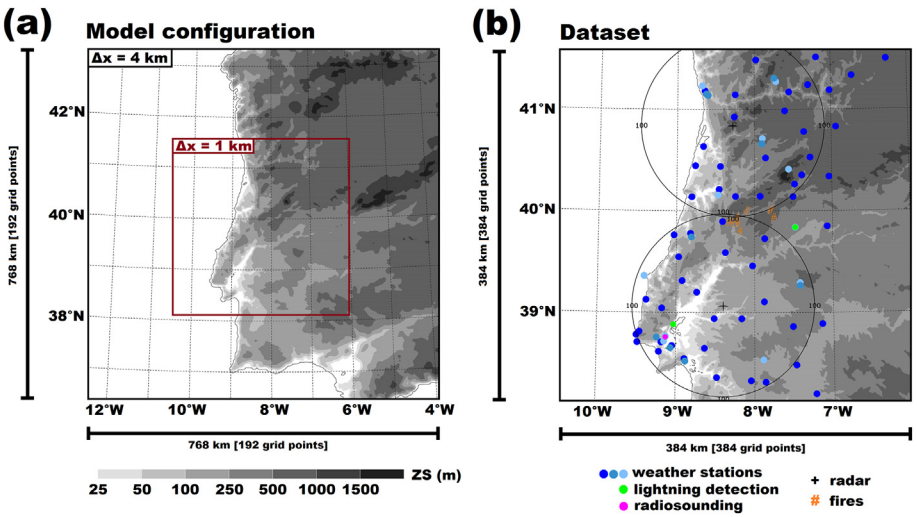

Fig. 2. Numerical configuration and dataset: a) model configuration with larger domain at 4 km horizontal resolution and the inner domain at 1 km horizontal resolution, b) Meteorological data network (surface, upper-air, weather radar, lightning sensors), as well as the location of fires reported on 17th June 2017. The orography is obtained from the SRTM database. The circles of 100 km radius represent the radar coverage.

2.3. Numerical modelling

Nowadays, current cloud-resolving models are able to provide an explicit representation of the clouds and the associated air motions that cannot be directly explored from standard observations (Guichard and Couvreux, 2017). The non-hydrostatic mesoscale atmospheric model Meso-NH of the French research community (Lafore et al., 1998; Lac et al., 2018) is one of these models. It is implemented with a rather complete parametrization package of sub-grid scale physical processes in the atmosphere, such as convection, cloud microphysics, cloud electricity, turbulence, surface processes, among others. In Portugal, Meso-NH has been successfully used in several research fields, related to precipitation over complex terrain (Couto et al., 2012, 2016), and fog events (Policarpo et al., 2017), for example. The near surface meteorological variables, such as air temperature and relative humidity at 2 m are both obtained from the externalised platform of surface models, SURFEX (Masson et al., 2013), which is coupled to Meso-NH.

2.3.1. Microphysical parametrization scheme

The microphysical scheme used in this study is known as ICE3 scheme (Pinty and Jabouille, 1998) and is based on several categories of hydrometeors, including a prognostic equation for each hydrometeor type. The one-moment bulk microphysical ICE3 predicts the mixing ratio of six atmospheric water categories. In addition to vapour, it considers two categories of liquid water (cloud droplets and rain drops), and three categories of ice particles (pristine ice crystals, snow-aggregates and graupel). Moreover, the multiple complex interactions between the different hydrometeor types are handled by the parametrization of several microphysical processes (e.g., condensation, evaporation, riming, melting, etc.). For example, the pristine ice crystals, a component of the electrification process, are generated by the nucleation processes. In ICE3 the heterogeneous nucleation is based on Meyers et al. (1992) while the homogeneous nucleation corresponds to the cloud droplet freezing when the air temperature drops below −35 °C approximately (Pruppacher, 1995). However most of the mass of the small ice crystals comes from the water vapour deposition (no supersaturation over ice is persisting) assuming the habit of hexagonal plates.

2.3.2. Radar Reflectivity

The Meso-NH system includes a grid point radar diagnostic given by the total equivalent radar reflectivity. It is calculated as a sum of radar reflectivities produced by each hydrometeor type illuminated by the radar wave. Here, it is assumed that the radar wavelength is large enough so that the radar waves are considered to propagate without attenuation and that the Rayleigh scattering approximation is valid (Richard et al., 2003).

Another radar diagnostic, the Plan Position Indicator (PPI), is an alternate simulator, which sweeping cones are projected on a horizontal plane determined by scanning the atmosphere at constant elevation. Such simulator adapted to conventional weather radar was developed inside the post processing Meso-NH procedure by Caumont et al. (2006). Currently, Augros et al. (2016) presented an upgraded version of this simulator allowing calculated polarimetric radar variables for S, C, and X band radars (e.g., radar reflectivity, specific differential phase and differential reflectivity). Backscattering and attenuation are considered in the calculation of the radar equivalent reflectivity, as well as the knowledge of each hydrometeor, in order to be completely consistent with the microphysical scheme of the Meso-NH.

2.3.3. Electrical scheme (CELLS: Cloud ELectrification and Lightning Scheme)

The description of the electrical state of a thunderstorm is based on the monitoring of the electrical charge densities, the computation of the electric field and the production of lightning flashes when the electrical breakdown is reached (Barthe et al., 2005, 2012). The electrical scheme CELLS is coupled to the standard 1-moment microphysics scheme of Meso-NH where the mixing ratios of the droplets, raindrops and 3 ice particle types are the state variables. The charges are carried out by each hydrometeor in clouds and precipitation, and also by positive and negative ions (not detailed here) to compute the total charge budget. The electrical scheme is a bulk scheme so that each hydrometeor type has a single polarity locally. The charge densities are state variables that follow the microphysical evolution of the hydrometeor mixing ratios (transport, sedimentation and internal mass transfers). Although the inductive charging mechanism is taken into account in the electrical scheme, using the parametrization of Ziegler et al. (1991), the cloud charging involves mostly the non-inductive mechanism, a charge separation process that occurs after rebounding collision between two ice particles of different categories (cloud ice, snow-aggregates and graupel) in the presence of supercooled water. The charging rate, as well as the polarity gained by the largest colliding particle (and the opposite gained by the smallest one), is a function of the temperature. The electric vector field is obtained by numerically inverting the Gauss equation that relates the electric field to the total charge density with appropriate boundary conditions (the ground level and the uppermost model level are equipotential surfaces). A flash is then triggered when the module of the electric field goes locally beyond a critical breakdown value, which is decreasing with height. The lightning flash propagates first vertically (bi-leader phase) and, then, horizontally, along two consecutive and opposite charged layers in the thunderstorm. The scheme is not detailed here but Intra-Cloud (IC) and Cloud-to-Ground (CG) flashes are considered. The purpose of the flash scheme is to reduce the electrical stress inside the clouds by neutralizing the same amount of positive and negative charges (IC) or an excess of positive/negative charges (CG) thus giving the flash polarity. It is worth to note that the impact coordinates of a CG are simply taken as the ground intersection to the vertical, passing through the flash triggering point. The electric field is recomputed after each flash and flashes are triggered as long as the electric field stays not disruptive in any part of the cloud.

The computation of the electric field as well as the lightning scheme leading to the partial and local neutralisation of the charges, complete the electrical scheme (see Barthe et al., 2012; Bovalo et al., 2019). Therefore, the charge structure of the thunderstorms is modified after lightning, allowing a temporal integration over the whole storm lifetime and providing a realistic representation of the electrical properties of precipitating cloud systems (Pinty et al., 2013).

A fully description of the lightning sub-scheme of CELLS can be found in Barthe et al. (2012). A complete description of the physical package of the Meso-NH model, including the CELLS and microphysical parametrization schemes is also found in the Meso-NH scientific documentation available on the Meso-NH website (http://mesonh.aero.obs-mip.fr/mesonh54/BooksAndGuides, last access 21 February 2020).

2.3.4. Numerical experiment

A single numerical experiment was performed with an adequate configuration to simulate the mesoscale environment of the Pedrógão fire event. However here, some fire effects (surface budget, aerosol emission, etc.) are not treated by Meso-NH, which is used in priority to retrieve the main characteristics of the deep convective developments in the atmosphere during the afternoon of 17th June 2017. At this time, as mentioned in Sub-section 2.1, several fires were reported in the surroundings of the Pedrógão Grande location, with an extreme FFE starting during the afternoon and lasting for the following days.

The simulation has been carried out with two nested domains of 4 km (Fig. 2a) and 1 km (Fig. 2b) horizontal resolution with 192 × 192 and 384 × 384 grid points, respectively. The innermost domain was centred over the area where forest fires occurred. The vertical grid was configured with 50 sigma levels not equally spaced, stretching gradually from 30 m, near the bottom, to 900 m, near the top. The simulation was initialized with the ECMWF analysis at 0600 UTC, and boundary

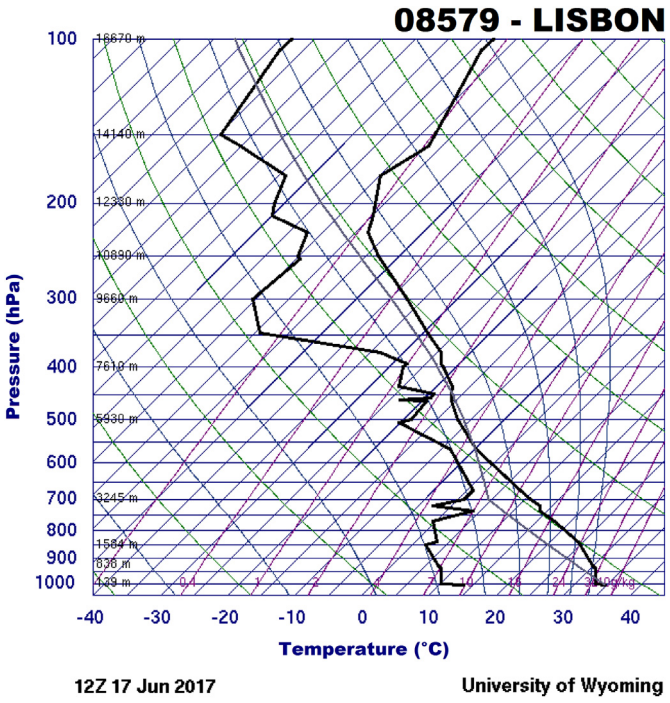

Fig. 3. Thermodynamic diagram of the radiosonde launched from Lisbon at 1200 UTC, 17th June 2017. Source: Wyoming University.

conditions of the coarser domain were updated every 6 h. Furthermore, at 1 km resolution, the experiment was performed with explicit resolved convection scheme (microphysics scheme). The electrical scheme was activated at 1400 UTC for a 6 h simulation with electrical variable outputs each 15 min. The non-inductive charging mechanism was parametrized according to Saunders et al. (1991).

3. Results

Model results are validated by comparing model outputs with available observations. This section is divided into two parts describing the main properties of the atmosphere during the afternoon of 17th June 2017.

3.1. Forest Fire atmospheric environment

The heating of the air originates unstable convective conditions that can be observed in the thermodynamic diagram of the radiosonde launched from Lisbon at 1200 UTC (Fig. 3). Temperatures around 30 °C are observed in the lowest few hundred meters (up to 900 hPa), and surface temperatures exceed 35 °C. As the air is heated enough to reach the level of free convection, high on this day, instability can be released and convective clouds start to develop with a high base, nearly close to the freezing level around 600 hPa. Clouds tops were around 12 km. The diagram shows the existence of a dry layer in the lower troposphere with an approximate depth of 3 km (up to 700 hPa). The Lisbon sounding was compared to the modelled sounding, showing a good representation of the vertical profile of temperature and dew-point temperature. Fig. 4 shows the comparison between the vertical profiles of temperature and water vapour mixing ratio (MRV), simulated at 4 km and 1 km horizontal resolution, and the observed one. In the first case, temperature is quite well represented (Fig. 4a), whereas the water vapour mixing ratio shows some deviation in the lowest levels (~500 m), with a slight overestimation by the model at 1 km resolution (Fig. 4b). Such overestimation is likely to be due to an imprecise positioning of the sounding and also due to the fact that the Meso-NH was initialised by the ECMWF analysis 6 h earlier. For other variables, such as the potential temperature, virtual potential temperature, and equivalent potential temperature, the comparison also showed a good agreement (Figures not shown) so the convective instability is likely to be well resolved.

The plots at a later instant (1430 UTC), in Fig. 5, illustrate a comparison between observations and simulation for the 2 m temperature and relative humidity maps. Here, the small squares represent the records of each weather station. Concerning the temperature (Fig. 5a), the comparison shows a remarkable agreement for the peak values well above 35 °C near Pedrógão Grande, and 40 °C over the south half of the simulation domain, with mesoscale features linked to the presence of orography (see Fig. 2b). Regarding the 2 m relative humidity and despite some occasional over or underestimation, the model has also captured well the horizontal distribution of the relative humidity, with values as low as 10% (Fig. 5b). All these features are, of course, leading to very favourable conditions to facilitate the fuelling and the propagation of wildfires.

3.2. Convective environment

The development of convective systems over the region of interest (Fig. 2b) is investigated now, paying attention to the microphysical properties and to the electrical structure of the clouds. The radar reflectivity was analysed and compared to the model generated reflectivity (Fig. 6), in order to evaluate the model representation of the cloud field.

The evolution of a mesoscale convective system (MCS) over central Portugal during the afternoon was identified through the radar survey. The radar simulator applied to Arouca radar site for the elevations of 2.8° and 3.7° shows that the model represents well the position and the structure of the anvil of the convective system (Fig. 6a-d). However, the reflectivity of the convective cores within the system seems to be slightly underestimated by the model, but better represented for the 3.7° elevation. In the case of the Coruche radar, located a little bit to the south with respect to the Arouca radar, the pattern of isolated convective cores in the southern half of the scan is well captured by the model, whereas the radar reflectivity associated with the convective cores within the MCS is underestimated by the model (Fig. 6e-f). It is noteworthy that the good location of the simulated MCS anvil is found over the Pedrógão region.

Fig. 7a-b shows a west-east cross-section of radar reflectivity at 1700 UTC, built from the radar scans and produced by the simulation at the same place (A-B vertical cross-section is indicated in Fig. 5a). The vertical structure of the simulated convective system over the region where FFE occurred is marked by an anvil of similar vertical and horizontal extensions of the observed one. The anvil is observed extending 50 km westward from the convective core with a depth of about 4 km. This pattern is qualitatively well captured by the model.

The vertical structure of the cloud condensate is presented in Fig. 8 (C-D vertical cross-section is indicated in Fig. 5b). The graupel mixing ratio (Fig. 8a) reaches values of around 3 g/kg between 0 °C and − 30 °C. The snow-aggregate lies above the graupel level with a large horizontal extension to compose the great part of the anvil in the −30 °C region (Fig. 8b). The maximum amount of pristine ice crystals (~1 g/kg) is found close to the top at 10 km with temperatures around −40 °C (Fig. 8c). The total condensate mixing ratio is peaking at middle levels (Fig. 8d), with values above 4 g/kg between 6 and 7 km altitude ($T = -15$ °C) and remains well above 0.1 g/kg at 12.5 km altitude. A large amount of the hydrometeors is found above the freezing level, showing a cloud cover essentially composed of ice particles. The amount of hydrometeors below the freezing level corresponds to cloud liquid water and essentially rain water. The rain only fills a small fraction of the cross-section, indicating that the precipitation events were highly localized. This was also confirmed by the radar observations (not shown).

In order to complement the characterization of the convective

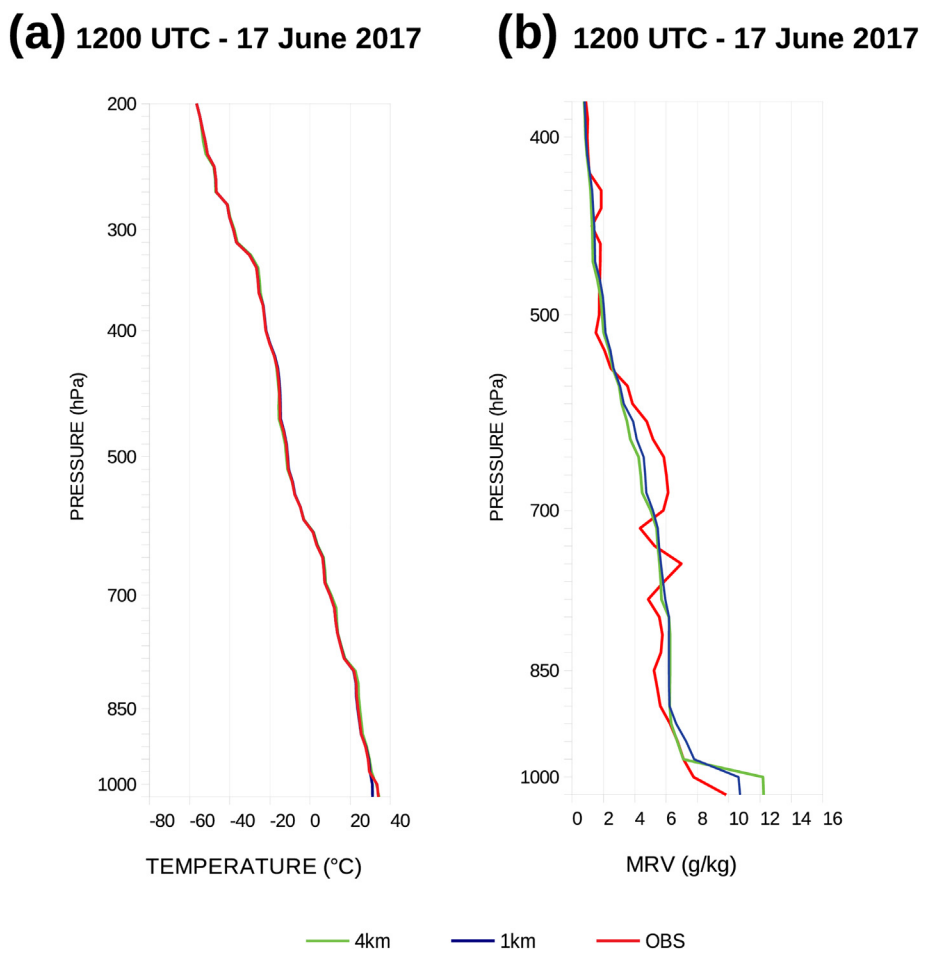

Fig. 4. Vertical profile comparison between radiosonde observation (red line), and simulation (4 km horizontal resolution, green line; 1 km horizontal resolution, blue line) for a) temperature, and b) water vapour mixing ratio (MRV), 1200 UTC, 17th June 2017. (For interpretation of the references to colour in this figure legend, the reader is referred to the web version of this article.)

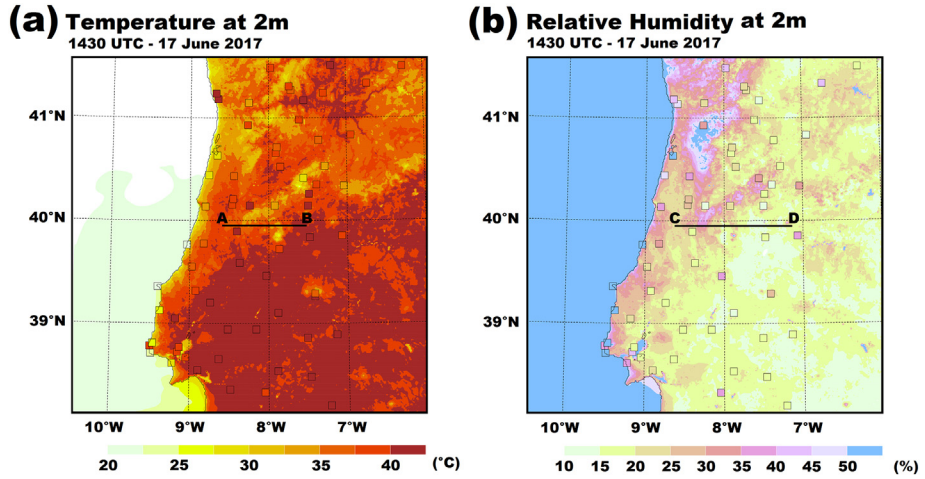

Fig. 5. Meteorological variables from the simulation at 1 km resolution (coloured areas) and observation of each weather station (squares) at 1430 UTC, 17th June 2017. a) temperature at 2 m, and b) relative humidity at 2 m. A-B and C-D lines represent the location of the vertical cross-sections considered in the study.

environment, Fig. 9 displays some Meso-NH fields associated to the convective system. The vertical motions are plotted in Fig. 9a, showing a region of a strong downdraught with maximum velocities around 7 m/s, between 1.5 km and 4 km altitude. The vertical cross-section is the same presented in Fig. 7. The high descending velocity values, as well as the overall streamlines pattern, are a fine model representation of a downburst. The wind gust field, computed as the sum of the module of the horizontal wind plus four times the square root of the turbulent kinetic energy (Fig. 9b), shows intense low level winds, with gusts well above 20 m/s and several divergent patterns consistent with convective outflows associated with downbursts. In particular, the divergent pattern visible in the south-southwest part of the area depicted in Fig. 9b is coherently associated with the downburst represented slightly earlier by the model, in the Fig. 9a representation. According to the IPMA

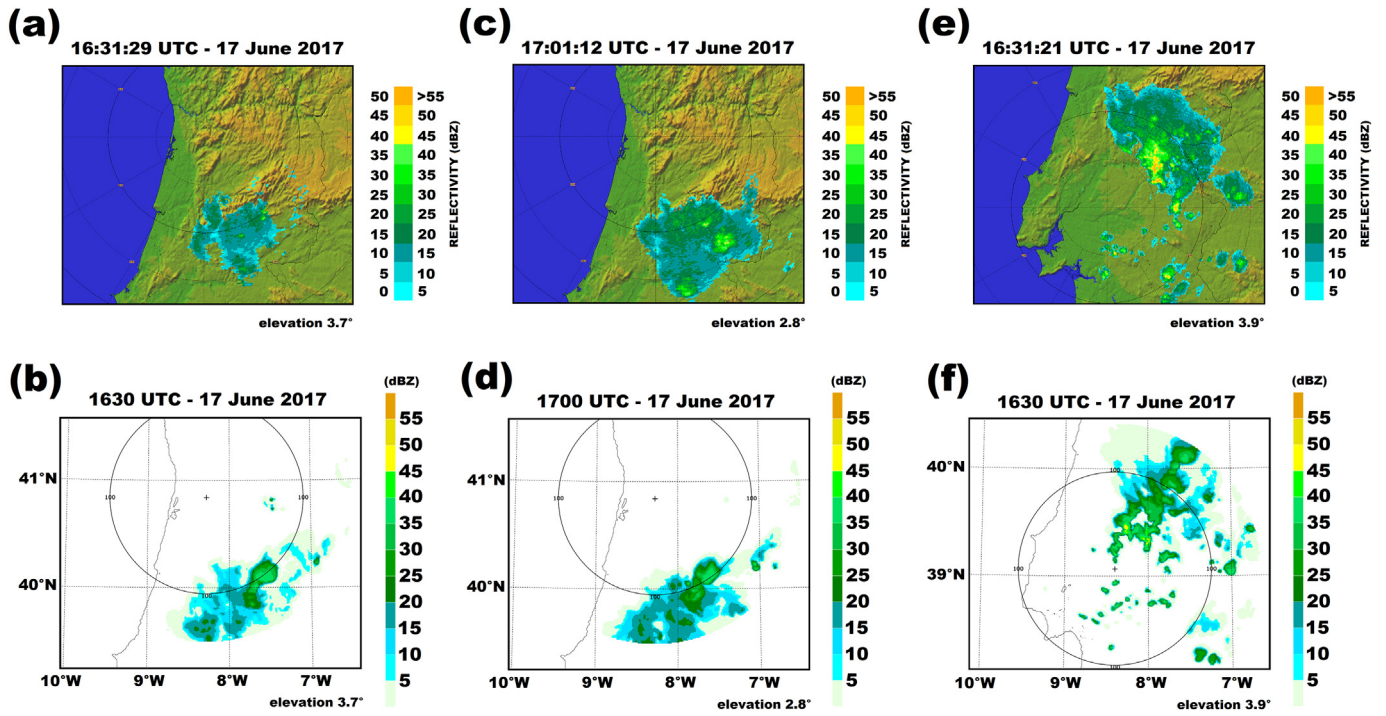

Fig. 6. Radar reflectivity for a) Arouca radar at 3.7° elevation, b) Arouca radar simulator at 3.7° elevation, c) Arouca radar at 2.8° elevation, d) Arouca radar simulator at 2.8° elevation, e) Coruche radar at 3.9° elevation, and f) Coruche radar simulator at 3.9° elevation.

report (2017), the strongest surface wind gusts were recorded on the meteorological stations of Alvega (21,7 m/s at 1650 UTC), Proença-a-Nova (23,6 m/s at 1710 UTC), Castelo Branco (20,3 m/s at 1720 UTC), and Pampilhosa da Serra (18,3 m/s at 1840 UTC), on the same order of magnitude of the model represented gusts. Concerning the total accumulated precipitation, Meso-NH simulates a low amount of spatially dispersed precipitation (< 10 mm) during the whole convective event (Fig. 9c). The low amount of precipitation due to an intense evaporation of the raindrops and the perturbation brought by the strong winds (forced by the convection) constitute favourable conditions for a high fire growth rate.

The cloud electrification has a microphysical origin, with non-inductive mechanism occurring in the mixed-phase regions of the storm (e.g., Barthe et al., 2016; Chmielewski et al., 2018). Therefore, the electrical structure of the cloud system is now analysed. The model is able to represent the charge density of each hydrometeor. Fig. 10 shows the vertical cross-section of the electrical structure of the thunderstorm at the same instant (1630 UTC) of Fig. 8. Regarding the polarity of individual hydrometeor ice categories, graupel is negatively charged with a maximum around -4 nC/m^3 (Fig. 10a). The snow carries most of the positive charges (max. is 4 nC/m^3), while the small ice crystals are responsible for the upper negatively charged zone peaking at -0.5 nC/m^3, as shown in Fig. 10b and c, respectively. In Fig. 10d, the hatched area corresponds to the mixing ratio of the condensate above 0.1 g/kg and where the total electrical charge density of the liquid and ice particles (i.e., cloud droplets, rain drops, graupel, snow-aggregate and pristine ice crystal) is superimposed. The electrical structure of the vertical cross-section reveals that the model simulates a tripole with an inverted polarity. A main positive charge region between 7 and 8 km height is surrounded by two negatively charged regions.

The module of the electric field (||E||) is shown in Fig. 11. It is recalled that the divergence of the electric field is proportional to the total charge density (Gauss law) so an inversion algorithm of a Laplacian is needed to solve the electric field with proper boundary conditions. The values of ||E|| are larger than 5,000 V/m throughout the convective area of the cloud in the troposphere. Moreover, values

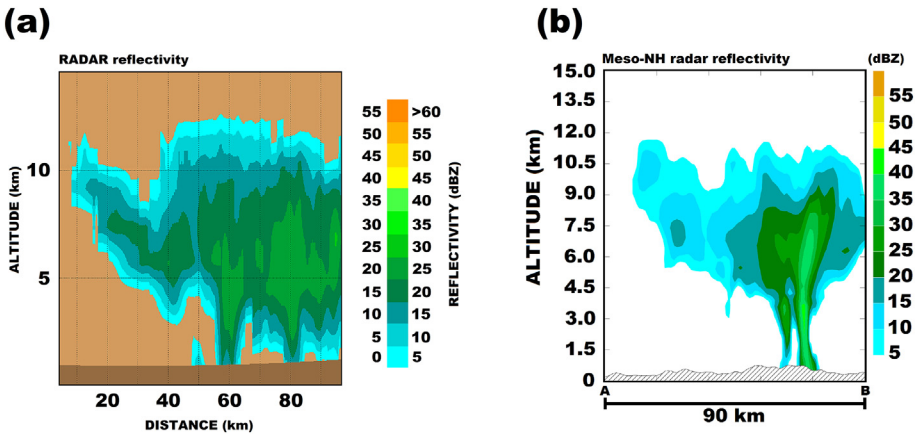

Fig. 7. Vertical cross-section at 1700 UTC for a) radar reflectivity (Coruche/CL radar) (horizontal distance markers are depicted every 10 km), and b) Meso-NH radar reflectivity at grid point, 17th June 2017. The A-B vertical cross-section is indicated in Fig. 5a.

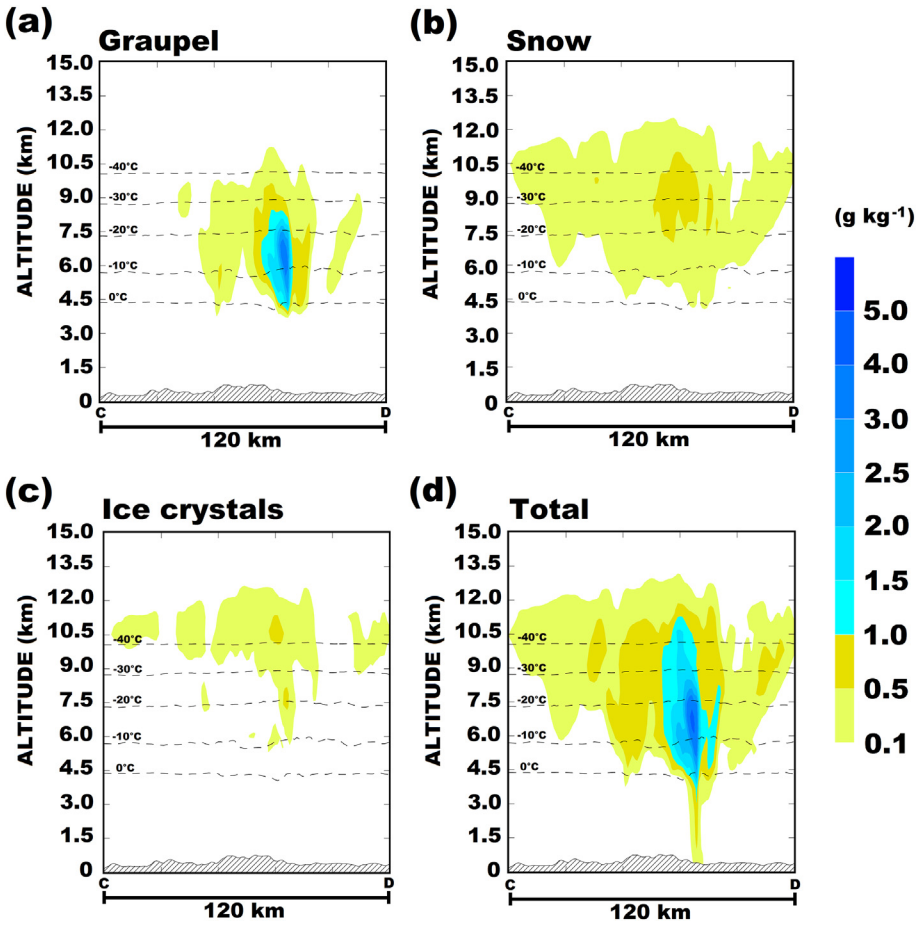

Fig. 8. Vertical cross-section at 1630 UTC of a) mixing ratio for graupel, b) mixing ratio for snow-aggregate, c) mixing ratio for ice crystals, and d) total of liquid and frozen water mixing ratios (cloud droplets, rain drops, graupel, snow-aggregate and ice crystals). The dashed lines indicate some isotherms above the freezing level. The C-D vertical cross-section is indicated in Fig. 5b.

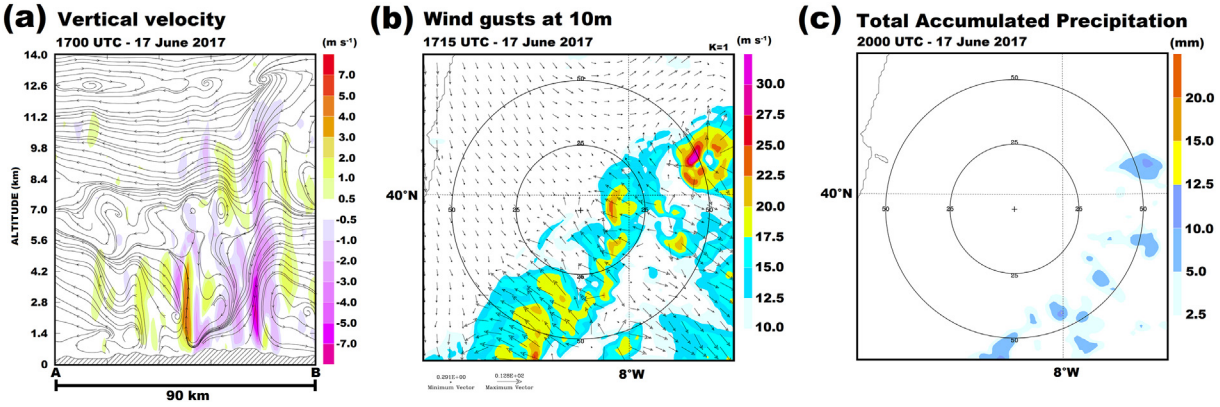

Fig. 9. a) Vertical velocity with streamlines at 1700 UTC, with A-B vertical cross-section indicated in Fig. 5a, b) wind gusts at 10 m at 1715 UTC, and c) total accumulated precipitation between 1430 UTC and 2000 UTC, 17th June 2017.

reaching about 100,000 V/m can be found in the interface of the charge densities of the graupel and the snow-aggregate around 7 km. A second maximum of about 30,000 V/m shows up at 10 km, in the region predominantly composed by ice crystals and snow.

As noted earlier, when the electric field goes beyond a critical breakdown value, the model produces lightning flashes in order to reduce the electrical stress. The amount of cloud-to-ground lightning strokes registered and produced by the CELLS scheme of the Meso-NH are now compared. The lightning strokes observed by the lightning detection system during the period between 1200 UTC and 2359 UTC is displayed in Fig. 12a with positive and negative CG values recorded east and south-east of Pedrógão Grande. According to the IPMA Report (2017), there were a total of 225 CG lightning strokes within a circle of 50 km radius from the Pedrógão Grande fire ignition point. From this record, 123 had a negative polarity and 102 a positive polarity. On the other hand, the maximum intensity was of 35.5 KA and the minimum of −87.2 KA.

The CG density strokes produced by the model, between 1400 UTC and 2000 UTC are plotted in Fig. 12b. This figure is the result of the vertical projection at the ground of all the grid points reached by the CG. The projected grid points count only "1" for each horizontal location, independently of the number of points of the CG, so that the final map (Fig. 12b) corresponds approximately to a density of CG stroke extensions (and not CG impact locations). The region of maximum density of CG is eastward of Pedrógão Grande. However, the area which could be affected at least by a strong CG flash, extends from south to

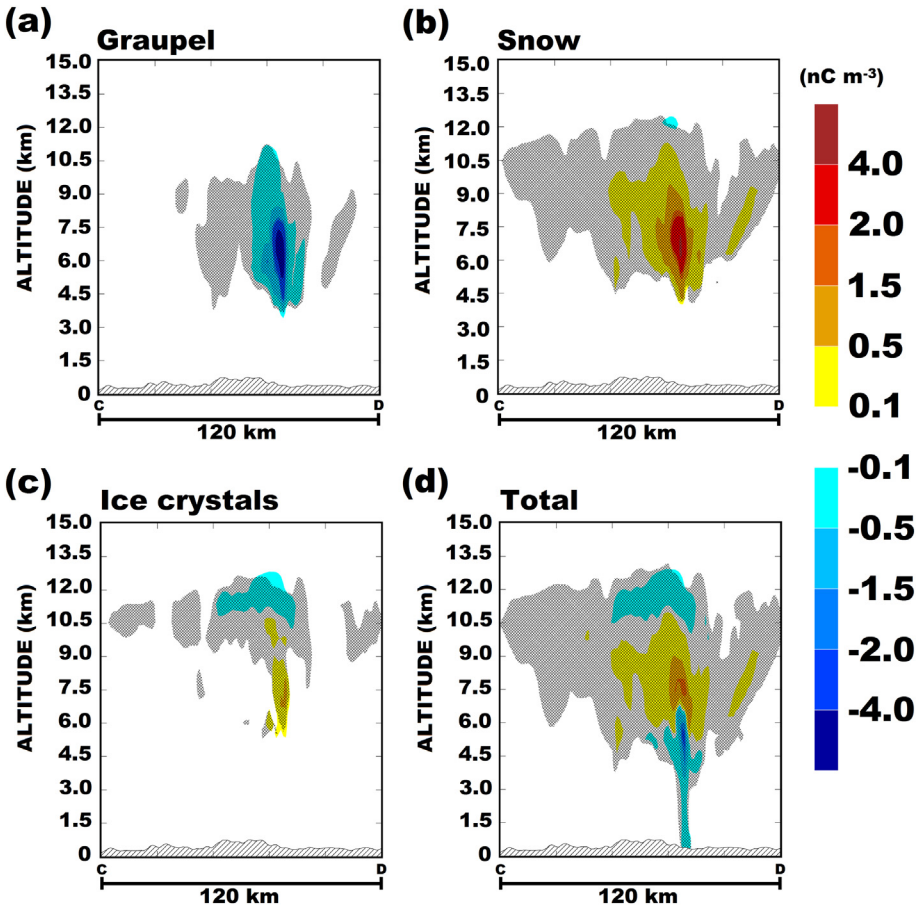

Fig. 10. Vertical cross-section at 1630 UTC for a) graupel charge density (coloured areas) and mixing ratio for graupel above 0.1 g/kg (hatched area), b) snow charge density (coloured areas) and mixing ratio for snow above 0.1 g/kg (hatched area), c) ice crystals charge density (coloured areas) and mixing ratio for ice crystals above 0.1 g/kg (hatched area), and d) total charge density (i.e., the sum of charge density for each hydrometeor category) through the cloud (coloured areas), and the total of liquid and frozen water mixing ratios above 0.1 g/kg (hatched area). The C-D vertical cross-section is indicated in Fig. 5b.

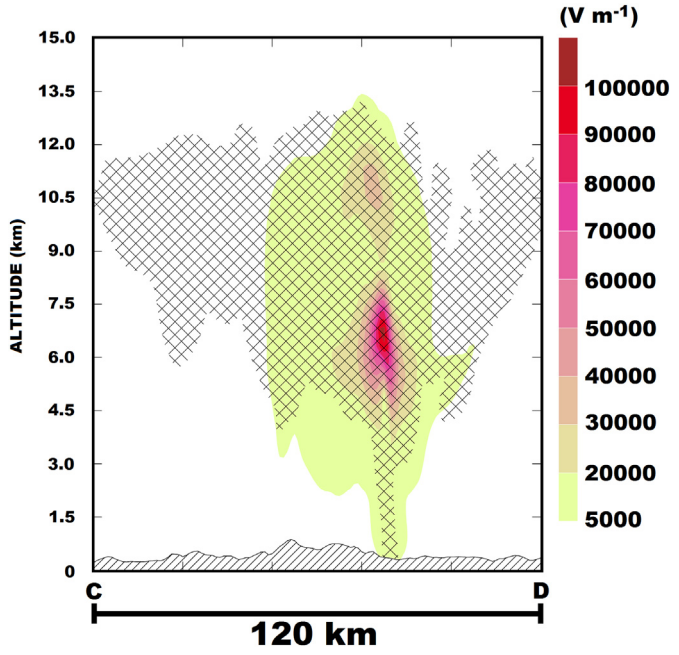

Fig. 11. The electric field modulus (V/m) at 1630 UTC (coloured areas) and the total of liquid and frozen water mixing ratios above 0.1 g/kg (hatched area). The C-D vertical cross-section is indicated in Fig. 5b.

northeast of Pedrógão, in agreement with the observations. Still in Fig. 12b, the symbols (#) indicate the triggering location of the fires during the period of study. The occurrences of CG lightning, in particular in the model grid points, in locations where fires were triggered is evident. Regarding the fires pointed out as "ignited by lightning strokes" by the CTI Report (2017), three out of the four events, namely the events in Oleiros County are found within the area where the model simulates CG lightning. For the Góis fire, however, and in contrast to the CTI report, the model suggests no fire ignition by lightning strokes. On the other hand, the Sertã fire with unassigned cause, could be plausibly considered as being ignited by a lightning flash, since the fire location and the model generated flashes are strikingly coincident.

4. Discussion

This paper proposes a novel approach to study forest fire ignition, which is based on coupled atmospheric – electrical model simulations, using the Meso-NH model linked to the CELLS electrical scheme. Besides the analysis of meteorological conditions that favoured the ignition of FFE, the meteorological dataset was used to check the ability of the model to represent the structure of the convective activity in the atmosphere during the fire period by comparing model outputs with observations.

The forest fires that ignited during the afternoon of 17th June 2017 occurred under a dry thunderstorm environment, marked by exceptionally hot and dry air at low levels. The air instability produced high-base thunderstorms with cloud bases around 4 km and cloud tops reaching 12 km. The analysis of the evolution of convective cells over the burnt area shows the possibility of downbursts with a strong outflow at lower levels (in the western boundary of the system), as well as low and dispersed precipitation. Such situation is well recognized as favourable for the natural ignition of forest fires by lightning strokes (e.g., Dowdy and Mills, 2012a) and for the fire propagation. All these features could have played a crucial role in the intensification and the evolution of the fire in Pedrógão Grande. On the other hand, it is

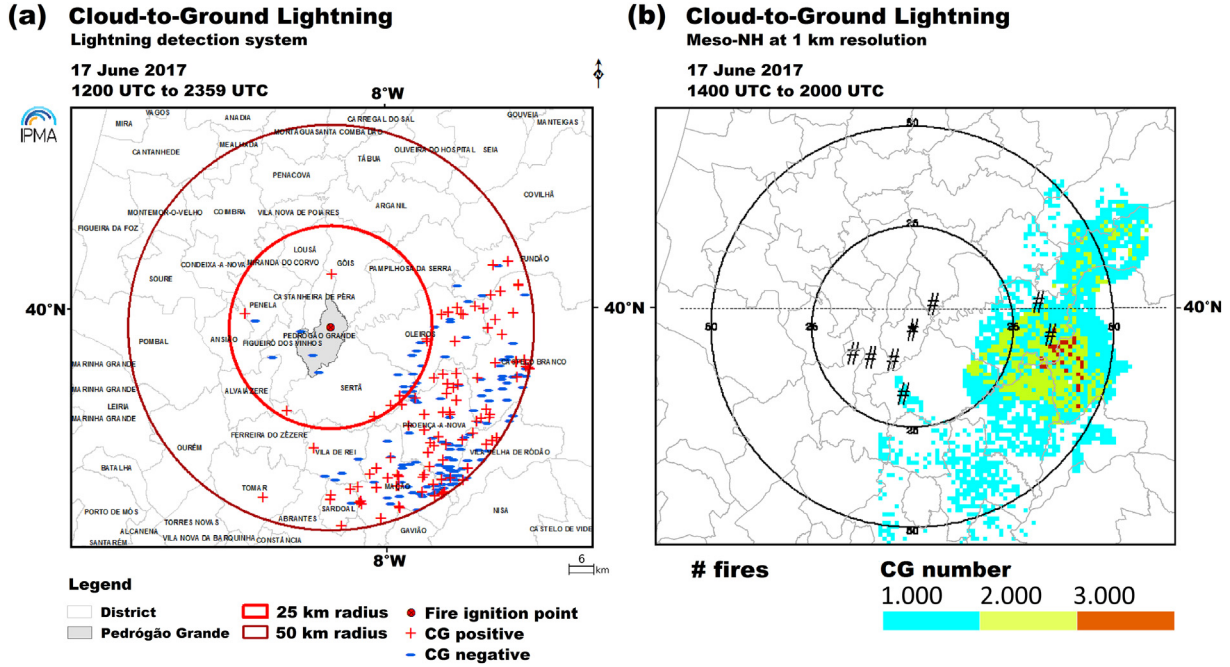

Fig. 12. Cloud-to-Groud lightning map as a) observed by the lightning detection system during the period between 1200 UTC and 2359 UTC, source: IPMA report (2017); b) simulated by the Meso-NH model. The symbols (#) indicate the location of fires that occurred during the afternoon of 17th June 2017.

noteworthy that the Arouca dual polarization radar observations (not presented) have clearly shown that smoke particles were, indeed, strongly ingested by the MCS. At first, they were observed to overshoot as high as 13,000 m, probably above the tropopause. Later on, signs of progressive glaciations were observed in the atmospheric volumes collocated with the smoke particles. However, a detailed discussion about the atmospheric conditions related with this tragic episode is beyond the goal of this paper.

Although the model captured well the timing and the spatial location of the MCS, it underestimates the radar reflectivity at the lowest elevations, while it is slightly better reproduced at middle elevations. Such discrepancy was found by other authors, who suggested that this may be due to the single moment characteristics of the bulk microphysical scheme employed (e.g., Varble et al., 2011; Augros et al., 2016; Taufour et al., 2018). It is worth also to stress that the acquisition of a full radar image needs several minutes during which microphysics can evolve at fine scale. Nevertheless, the model was able to represent the mesoscale system well enough, constituting an encouraging result for the combined hydrometeor and electrical structure analysis.

Several studies show that the vertical charge structure depends on environmental conditions and varies from storm to storm (e.g., Bruning et al., 2014; Fuchs et al., 2015; Chmielewski et al., 2018). Even so, two main patterns can still be considered by presenting a “normal” or “anomalous” charge structure. According to Fuchs et al. (2015), the first one is characterized by a negative charge density in the midlevels situated between regions of upper and lower positive charge (normal tripole case), also associated with -CG lightning. In the second pattern, an “anomalous” configuration is marked by a midlevel positive charge between layers of negative charges, as well as production of +CG lightning. Another noteworthy is that under colder and drier environments the storm polarity is reversed, with graupel gaining a net negative charge (e.g., Chmielewki et al., 2018).

The cloudy layer over central Portugal was characterized by a shallow layer of warm cloud microphysics, however, updraughts were still able to transport the small drops into the mixed-phase region thus increasing the supercooled liquid water content at high altitude where the non-inductive charge separation mechanism is very efficient. The atmospheric conditions favoured the formation of cold clouds composed in large extension by snow-aggregates particles. The pristine ice crystals and graupel co-existing inside the cloud produced propitious conditions for cloud electrification.

From the simulation, graupel starts to form at midlevels showing the early stages of the storm development. The collision between snow-aggregates and graupel produces opposite charge regions with graupel being negatively charged and snow-aggregates positively charged. Such condition is intensified in few ten minutes until the mature stage of the storm. During this stage, the collision of graupel with pristine ice crystals creates a region of ice crystals positively charged which is superimposed by ice crystals negatively charged, such as showed in the results. This negatively charged layer was identified during whole simulation in the upper levels of the system. According to Yair (2008), even though the amount of charge separated per collision is small at this cloud region (i.e., temperatures below −40 °C), it may still influence the charge distribution by carrying charges to the uppermost parts of the cloud. The maximum values of charge density occurs close to the convective core of the system. Below the freezing level, raindrops carries negative charges. The melting of graupel, which fall faster than the snow-aggregates produces precipitation negatively charged, as showed in the previous section. The net vertical charge structure is simulated as an “anomalous” tripole structure.

The modelling of cloud electrification depends on large number of physical processes and how they are parametrized. The cloud charge structure presented here is similar to the results presented by Pinty et al. (2013), but presented an inverted polarity which may be caused due the electrical parametrization scheme used. The idealized study of Tsenova et al. (2013) showed no regular tendency in the impact of the way in which the charge is determined in the cloud charge structure, i.e., by means of effective water content or rime accretion rate. However, an impact was observed in the determination of the separated charge. Then, it is possible to obtain a similar cloud charge structure if a different parametrization scheme is used, but with an inverted polarity.

The presence of ice particles and their interactions inside the cloud lead to the tripole charge structure simulated. The net vertical charge structure obtained from the simulation suggests that during the Pedrógão Grande event an “anomalous” configuration occurred, with a net positive charge, as well as negatively charged graupel. Such result is

consistent with those discussed in Fuchs et al. (2015) and Chmielewki et al. (2018), which have pointed out that high-based clouds are often associated to an anomalous vertical charge structure configuration. From the map of CG strokes, the Meso-NH results show the highest density of CG lightning south-east of Pedrógão, within a distance between 25 km and 50 km, which is consistent with the recorded lightning strokes. A good representation of the MCS location and structure was essential for a realistic prediction of CG strokes.

5. Conclusions

This paper introduces a new interest for the electrical scheme CELLS that is the study of fire ignition by cloud-to-ground lightning strokes. The advantage of such approach goes beyond the use of the electrical scheme of Meso-NH in the study of fire ignition. Thanks to computational advances, it is already further possible to represent complex fire-atmosphere interactions through the coupling between atmospheric models and fire propagation models (e.g., Filippi et al., 2009, 2011, 2013). In the future, the coupling of such numerical capabilities will allow a more complete knowledge of natural FFE, in order to assess the importance of several factors associated with the natural ignition and the evolution of fires in a single numerical simulation.

The Meso-NH model has successfully captured the atmospheric environment during the period preceding the Pedrógão Grande forest fire and the first hours of its spread. The efficiency and the accuracy of the electrical scheme representing the spatial distribution of CG lightning strokes in the region where fires were reported, encourages its use as a new approach to study naturally ignited forest fires. There is a complex interaction between weather, lightning, fires, forests, and so improving our understanding of these relationships is essential to better predict the possibility of the occurrence of natural ignitions and the evolution of FFE.

On the other hand, such approach may also have an impact on risk evaluation or be used under operational environment. The implementation of simplified electrical scheme (a proxy) in operational models is a big challenge. However, the Application of Research to Operations at Mesoscale (AROME; Seity et al., 2011) model is operational in many European countries, namely in Portugal at IPMA and share the physical package with the Meso-NH. So it could be technically feasible to implement in AROME the configurations and parametrizations tested in the Meso-NH research model. Therefore, from an operational point of view, and jointly with the knowledge of the forest fuel and the dryness state of the living and death vegetation, the CELLS scheme can be employed to quantify a degree of fire risk and the regions where FFE can be initiated by lightning strokes. The current computational power has shown the potential for such approach.

In summary, this paper was designed to better explore some of the Meso-NH capabilities and to apply them to the study of tragic forest fire events in Portugal. The encouraging results that have been obtained here motivate a future work towards a better comprehension and physical interpretation of some processes that strongly influence the evolution of forest fires events.

Declaration of Competing Interest

The authors declare that they have no known competing financial interests or personal relationships that could have appeared to influence the work reported in this paper.

Acknowledgements

The work is co-funded by the European Union through the European Regional Development Fund in the framework of the Interreg V A Spain – Portugal program (POCTEP) through the CILIFO project (Ref.: 0753_CILIFO_5_E), and also through the ICT (UIDB/04683/2020, Ref.: POCI-01-0145-FEDER-007690) and the ALOP (ALT20-03-0145-FEDER-000004) projects. The authors also express their appreciation to the colleague Álvaro Silva (IPMA) for his contribution.

References

CTI Report, 2017. Relatório: Análise e apuramento dos factos relativos aos incêndios que ocorreram em Pedrógão Grande, Castanheira de Pera, Ansião, Alvaiázere, Figueiró dos Vinhos, Arganil, Góis, Penela, Pampilhosa da Serra, Oleiros e Sertã, entre 17 e 24 de junho de 2017. Comissão Técnica Independente (CTI). Assembleia da República.

Abatzoglou, J.T., Kolden, C.A., Balch, J.K., Bradley, B.A., 2016. Controls on interannual variability in lightning-caused fire activity in the western US. Environ. Res. Lett. 11, 045005. https://doi.org/10.1088/1748-9326/11/4/045005.

Augros, C., Caumont, O., Ducrocq, V., Gaussiat, N., Tabary, P., 2016. Comparisons between S, C, and X band polarimetric radar observations and convective-scale simulations of HyMeX first special observing period. Q. J. R. Meteorol. Soc. 142, 347–362. https://doi.org/10.1002/qj.2572.

Barbero, R., Abatzoglou, J.T., Steel, E.A., Larkin, N.K., 2014. Modeling very large-fire occurrences over the continental United States from weather and climate forcing. Environ. Res. Lett. 9, 124009. https://doi.org/10.1088/1748-9326/9/12/124009.

Barthe, C., Molinié, G., Pinty, J.-P., 2005. Description and first results of an explicit electrical scheme in a 3D cloud resolving model. Atmos. Res. 76, 95–113. https://doi.org/10.1016/j.atmosres.2004.11.021.

Barthe, C., Chong, M., Pinty, J.-P., Bovalo, C., Escobar, J., 2012. CELLS v1.0: updated and parallelized version of an electrical scheme to simulate multiple electrified clouds and flashes over large domains. Geosci. Model Dev. 5, 167–184. https://doi.org/10.5194/gmd-5-167-2012.

Barthe, C., Hoarau, T., Bovalo, C., 2016. Cloud electrification and lightning activity in a tropical cyclone-like vortex. Atmos. Res. 180, 297–309. https://doi.org/10.1016/j.atmosres.2016.05.023.

Blouin, K.D., Flannigan, M.D., Wang, X., Kochtubajda, B., 2016. Ensemble lightning prediction models for the province of Alberta, Canada. Int. J. Wildland Fire 25, 421–432. https://doi.org/10.1071/WF15111.

Bovalo, C., Barthe, C., Pinty, J.-P., 2019. Examining relationships between cloud-resolving model parameters and total flash rates to generate lightning density maps. Q. J. R. Meteorol. Soc. 145, 1250–1266. https://doi.org/10.1002/qj.3494.

Bruning, E.C., Weiss, S.A., Calhoun, K.M., 2014. Continuous variability in thunderstorm primary electrification and an evaluation of inverted-polarity terminology. Atmos. Res. 135–136, 274–284. https://doi.org/10.1016/j.atmosres.2012.10.009.

Caumont, O., Ducrocq, V., Delrieu, G., Gosset, M., Pinty, J.-P., Parent du Châtelet, J., Andrieu, H., Lemaître, Y., Scialom, G., 2006. A radar simulator for high-resolution nonhydrostatic models. J. Atmos. Ocean. Technol. 23, 1049–1067. https://doi.org/10.1175/JTECH1905.1.

Chmielewski, V.C., Bruning, E.C., Ancell, B.C., 2018. Variations of thunderstorm charge structures in West Texas on 4 June 2012. Journal of Geophysical Research: Atmospheres. 123, 9502–9523. https://doi.org/10.1029/2018JD029006.

Couto, F.T., Salgado, R., Costa, M.J., 2012. Analysis of intense rainfall events on Madeira Island during the 2009/2010 winter. Nat. Hazards Earth Syst. Sci. 12, 2225–2240. https://doi.org/10.5194/nhess-12-2225-2012.

Couto, F.T., Ducrocq, V., Salgado, R., Costa, M.J., 2016. Numerical simulations of significant orographic precipitation in Madeira island. Atmos. Res. 169, 102–112. https://doi.org/10.1016/j.atmosres.2015.10.002.

Dennison, P.E., Brewer, S.C., Arnold, J.D., Moritz, M.A., 2014. Large wildfire trends in the western United States, 1984–2011. Geophys. Res. Lett. 41, 2928–2933. https://doi.org/10.1002/2014GL059576.

Dowdy, A.J., Mills, G.A., 2012a. Atmospheric and fuel moisture characteristics associated with lightning-attributed fires. J. Appl. Meteorol. Climatol. 51, 2025–2037. https://doi.org/10.1175/JAMC-D-11-0219.1.

Dowdy, A.J., Mills, G.A., 2012b. Characteristics of lightning-attributed wildland fires in south-East Australia. Int. J. Wildland Fire 21, 521–524. https://doi.org/10.1071/WF10145.

Fierro, A.O., Mansell, E.R., MacGorman, D.R., Ziegler, C.L., 2013. The implementation of an explicit charging and discharge lightning scheme within the WRF-ARW model: benchmark simulations of a continental squall line, a tropical cyclone, and a winter storm. Mon. Weather Rev. 141, 2390–2415. https://doi.org/10.1175/MWR-D-12-00278.1.

Filippi, J.-B., Bosseur, F., Mari, C., Lac, C., Le Moigne, P., Cuenot, B., Veynante, D., Cariolle, D., Balbi, J.H., 2009. Coupled atmosphere-wildland fire modelling. Journal of Advances in Modeling Earth Systems. 1, 11. https://doi.org/10.3894/JAMES.2009.1.11.

Filippi, J.-B., Bosseur, F., Pialat, X., Santoni, P.-A., Strada, S., Mari, C., 2011. Simulation of coupled fire/atmosphere interaction with the MesoNH-ForeFire models. Journal of Combustion. 540390. https://doi.org/10.1155/2011/540390.

Filippi, J.-B., Pialat, X., Clements, C.B., 2013. Assessment of ForeFire/Meso-NH for wildland fire/atmosphere coupled simulation of the FireFlux experiment. Proc. Combustion Inst. 34, 2633–2640. https://doi.org/10.1016/j.proci.2012.07.022.

Fuchs, B.R., Rutledge, S.A., Bruning, E.C., Pierce, J.R., Kodros, J.K., Lang, T.J., MacGorman, D.R., Krehbiel, P.R., Rison, W., 2015. Environmental controls on storm intensity and charge structure in multiple regions of the continental United States. Journal of Geophysical Research: Atmospheres. 120, 6575–6596. https://doi.org/10.1002/2015JD023271.

Ganteaume, A., Syphard, A.D., 2018. Ignition sources in: Manzello S. (eds) Encyclopedia of Wildfires and Wildland-Urban Interface (WUI) Fires. Springer, Cham. doi:https://doi.org/10.1007/978-3-319-51727-8_43-1.

Gijben, M., Dyson, L.I., Loots, M.T., 2017. A statistical scheme to forecast the daily lightning threat over southern Africa using the Unified Model. Atmos. Res. 194, 78–88. https://doi.org/10.1016/j.atmosres.2017.04.022.

Guichard, F., Couvreux, F., 2017. A short review of numerical cloud-resolving models. Tellus A: Dynamic Meteorology and Oceanography. 69 (1), 1373578. https://doi.org/10.1080/16000870.2017.1373578.

IPMA Report, 2017. Relatório: Condições meteorológicas associadas ao incêndio de Pedrógão Grande de 17 Junho 2017. Instituto Português do Mar e Atmosfera, I.P., Departamento de Meteorologia e Geofísica, Lisboa, Portugal.

Karagiannidis, A., Lagouvardos, K., Lykoudis, S., Kotroni, V., Giannaros, T., Betz, H., 2019. Modeling lightning density using cloud top parameters. Atmos. Res. 222, 163–171. https://doi.org/10.1016/j.atmosres.2019.02.013.

Lac, C., et al., 2018. Overview of the Meso-NH model version 5.4 and its applications. Geosci. Model Dev. 11, 1929–1969. https://doi.org/10.5194/gmd-11-1929-2018.

Lafore, J.-P., Stein, J., Asencio, N., Bougeault, P., Ducrocq, V., Duron, J., Fischer, C., Héreil, P., Mascart, P., Masson, V., Pinty, J.-P., Redelsperger, J.-L., Richard, E., Vilà-Guerau de Arellano, J., 1998. The meso-NH atmospheric simulation system. Part I: adiabatic formulation and control simulations. Annales Geophysicae 16, 90–109. https://doi.org/10.1007/s00585-997-0090-6.

Larjavaara, M., Kuuluvainen, T., Rita, H., 2005a. Spatial distribution of lightning-ignited forest fires in Finland. For. Ecol. Manag. 208, 177–188. https://doi.org/10.1016/j.foreco.2004.12.005.

Larjavaara, M., Pennanen, J., Tuomi, T.J., 2005b. Lightning that ignites forest fires in Finland. Agric. For. Meteorol. 132, 171–180. https://doi.org/10.1016/j.agrformet.2005.07.005.

Lopez, P., 2016. A lightning parametrization for the ecmwf integrated forecasting system. Mon. Weather Rev. 144 (9), 3057–3075. https://doi.org/10.1175/MWR-D-16-0026.1.

Masson, V., et al., 2013. The SURFEXv7.2 land and ocean surface platform for coupled or offline simulation of earth surface variables and fluxes. Geosci. Model Dev. 6, 929–960. https://doi.org/10.5194/gmd-6-929-2013.

Meng, Q., Yao, W., Xu, L., 2019. Development of lightning nowcasting and warning technique and its application. Adv. Meteorol. https://doi.org/10.1155/2019/2405936.

Meyers, M.P., DeMott, P.J., Cotton, W.R., 1992. New primary ice-nucleation parameterizations in an explicit cloud model. J. Appl. Meteorol. 31, 708–721.

Mostajabi, A., Finney, D.L., Rubinstein, M., Rachidi, F., 2019. Nowcasting lightning occurrence from commonly available meteorological parameters using machine learning techniques. NPJ Clim Atmos Sci, vol. 41https://doi.org/10.1038/s41612-019-0098-0. 2.

Müller, M.M., Vacik, H., Diendorfer, G., Arpaci, A., Formayer, H., Gossow, H., 2013. Analysis of lightning-induced forest fires in Austria. Theor. Appl. Climatol. 111, 183–193. https://doi.org/10.1007/s00704-012-0653-7.

Nunes, A., Lourenço, L., Fernandes, S., Castro, A.C.M., 2014. Principais causas dos incêndios florestais em Portugal: variação espacial no periodo 2001/12. Territorium 21, 135–146.

Pinty, J.-P., Jabouille, P., 1998. A mixed-phase cloud parameterization for use in mesoscale non-hydrostatic model: simulations of a squall line and of orographic precipitation. In: Proc. Conf. of Cloud Physics, Everett, WA, USA, Amer. Meteor. Soc, pp. 217–220.

Pinty, J.-P., Barthe, C., Defer, E., Richard, E., Chong, M., 2013. Explicit simulation of electrified clouds: from idealized to real case studies. Atmos. Res. 123, 82–92. https://doi.org/10.1016/j.atmosres.2012.04.008.

Policarpo, C., Salgado, R., Costa, M.J., 2017. Numerical simulations of fog events in Southern Portugal. Adv. Meteorol. 1276784. https://doi.org/10.1155/2017/1276784.

Pruppacher, H.R., 1995. A new look at homogeneous ice nucleation in supercooled water drops. J. Atmos. Sci. 52, 1924.

Pugnet, L., Lourenço, L., Rocha, J., 2010. L'ignition des feux de forêt par l'action de la foudre au Portugal de 1996 à 2008. Territorium. In: Revista Portuguesa de riscos, prevenção e segurança. 17. pp. 57–70. https://doi.org/10.14195/1647-7723_17_6.

Richard, E., Cosma, S., Tabary, P., Pinty, J.-P., Hagen, M., 2003. High-resolution numerical simulations of the convective system observed in the Lago Maggiore area on 17 September 1999 (MAP IOP 2a). Q. J. R. Meteorol. Soc. 129, 543–563. https://doi.org/10.1256/qj.02.50.

Saunders, C.P.R., Keith, W.D., Mitzeva, R.P., 1991. The effect of liquid water on thunderstorm charging. Journal Geophysical Research. 96, 11007–11017. https://doi.org/10.1029/91JD00970.

Seity, Y., Brousseau, P., Malardel, S., Hello, G., Benard, P., Bouttier, F., Lac, C., Masson, V., 2011. The AROME-France convective-scale operational model. Mon. Weather Rev. 139, 976–991. https://doi.org/10.1175/2010MWR3425.1.

Shvidenko, A.Z., Schepaschenko, D.G., 2013. Climate Change and Wildfires in Russia. Contemp. Probl. Ecol. 6, 683–692. https://doi.org/10.1134/S199542551307010X.

Singleton, M.P., Thode, A.E., Sánchez Meador, A.J., Iniguez, J.M., 2019. Increasing trends in high-severity fire in the southwestern USA from 1984 to 2015. For. Ecol. Manag. 433, 709–719. https://doi.org/10.1016/j.foreco.2018.11.039.

Stephens, S.L., 2005. Forest fire causes and extent on United States forest service lands. Int. J. Wildland Fire 14, 213–222. https://doi.org/10.1071/WF04006.

Sulla-Menashe, D., Friedl, M.A., 2018. User guide to collection 6 MODIS Land Cover (MCD12Q1 and MCD12C1) Products. pp. 1–18.

Taufour, M., Vié, B., Augros, C., Boudevillain, B., Delanoë, J., Delautier, G., Ducrocq, V., Lac, C., Pinty, J.-P., Schwarzenböck, A., 2018. Evaluation of the two-moment scheme LIMA based on microphysical observations from the HyMeX campaign. Q. J. R. Meteorol. Soc. 144, 1398–1414. https://doi.org/10.1002/qj.3283.

Tippett, M.K., Koshak, W.J., 2018. A baseline for the predictability of U.S. cloud-to ground lightning. Geophys. Res. Lett. 45, 10,719–10,728. https://doi.org/10.1029/2018GL079750.

Trigo, R.M., García-Herrera, R., Díaz, J., Trigo, I.F., Valente, M.A., 2005. How exceptional was the early August 2003 heatwave in France? Geophys. Res. Lett. 32, L10701. https://doi.org/10.1029/2005GL022410.

Trigo, R.M., Pereira, J.M.C., Pereira, M.G., Mota, B., Calado, T.J., DaCamara, C.C., Santo, F.E., 2006. Atmospheric conditions associated with the exceptional fire season of 2003 in Portugal. Int. J. Climatol. 26, 1741–1757. https://doi.org/10.1002/joc.1333.

Trigo, R.M., Sousa, P.M., Pereira, M.G., Rasilla, D., Gouveia, C.M., 2016. Modelling wildfire activity in Iberia with different atmospheric circulation weather types. Int. J. Climatol. 36, 2761–2778. https://doi.org/10.1002/joc.3749.

Tsenova, B., Barthe, C., Mitzeva, R., Pinty, J.-P., 2013. Impact of parameterization of ice particle charging based on rime accretion rate and effective water content on simulated with MésoNH thunderstorm charge distributions. Atmos. Res. 128, 85–97. https://doi.org/10.1016/j.atmosres.2013.03.011.

Varble, A., Fridlind, A.M., Zipser, E.J., Ackerman, A.S., Chaboureau, J.P., Fan, J., Hill, A., McFarlane, S.A., Pinty, J.-P., Shipway, B., 2011. Evaluation of cloud-resolving model intercomparison simulations using TWP-Ice observations: Precipitation and cloud structure. J. Geophys. Res. 116, D12206. https://doi.org/10.1029/2010JD015180.

Vazquez, A., Moreno, J.M., 1998. Patterns of lightning-, and people-caused fires in Peninsular Spain. Int. J. Wildland Fire 8, 103–115. https://doi.org/10.1071/WF9980103.

Yair, Y., 2008. Charge Generation and Separation Processes. Space Sci. Rev. 137, 119–131. https://doi.org/10.1007/s11214-008-9348-x.

Ziegler, C.L., MacGorman, D.R., Dye, J.E., Ray, P.S., 1991. A model evaluation of noninductive graupel-ice charging in the early electrification of a mountain thunderstorm. J. Geophys. Res. 96 (12). https://doi.org/10.1029/91JD01246. 833–12 855.

water

MDPI

Article

Land-Cover Patterns and Hydrogeomorphology of Tributaries: Are These Important Stressors for the Water Quality of Reservoirs in the Mediterranean Region?

Patrícia Palma [1,2,*], Sofia Fialho [1], Ana Lima [1], Clarisse Mourinha [1], Alexandra Penha [2], Maria Helena Novais [2,3], Anabela Rosado [2], Manuela Morais [2,4], Miguel Potes [2], Maria João Costa [2,4] and Paula Alvarenga [5]

1 Department of Technologies and Applied Sciences, Polytechnic Institute of Beja, 7801-295 Beja, Portugal; sofiafialho16@gmail.com (S.F.); ana.filipa.lima89@gmail.com (A.L.); clarisse.mourinha@ipbeja.pt (C.M.)
2 ICT, Institute of Earth Sciences, University of Évora, Rua Romão Ramalho 59, 7000-671 Évora, Portugal; mapenha@uevora.pt (A.P.); hnovais@uevora.pt (M.H.N.); arosado@uevora.pt (A.R.); mmorais@uevora.pt (M.M.); mpotes@uevora.pt (M.P.); mjcosta@uevora.pt (M.J.C.)
3 Renewable Energies, University of Évora, Casa Cordovil, Rua D. Augusto Eduardo Nunes n 7, Évora, 7000-651, Portugal
4 Science and Technology School, University of Évora, 7000-671 Évora, Portugal
5 Linking Landscape, Environment, Agriculture, and Food Research Unit (LEAF), Instituto Superior de Agronomia, Universidade de Lisboa, Tapada da Ajuda, 1349-017 Lisboa, Portugal; palvarenga@isa.ulisboa.pt
* Correspondence: ppalma@ipbeja.pt; Tel.: +35-12-8431-4300

Received: 10 September 2020; Accepted: 21 September 2020; Published: 23 September 2020

Abstract: Four streams in the Guadiana watershed were followed up to assess hydrogeomorphological and physicochemical characteristics, and to analyze its correlation with land use/land cover (LULC), analyzing their possible influence in reservoir water quality and possible influence in the reservoir water quality. The highest amounts of organic descriptors and nutrients were quantified in streams with the major percentage of olive groves and vineyards and urban land cover classes. Streams more influenced by agro-silvo-pastoral class presented better water quality, as this type of LULC acts as a buffer of the contamination runoff. The results highlighted that the hydrogeomorphology of the streams may influence the transfer of pollutants loads to reservoirs. Hence, in intermittent streams characterized by coarse particles in the sediment, high amounts of pollutants are accumulated when the flow ceases, and are further transported to the reservoirs when the flow retakes. On the contrary, streams with sediments characterized by a great percentage of fine particles and organic matter do not induce so much stress in reservoirs, since these allow the adsorption of nutrients and trace elements, without their transfer to reservoirs.

Keywords: flow regime; hydrogeomorphology; water quality assessment; land use/land cover (LULC); Guadiana watershed

1. Introduction

Degradation of ecosystems at different spatial and temporal scales occurs through multiple stressors, resulting in a loss of biodiversity and in an impoverishment of ecosystem services [1]. Aquatic systems are among the most sensitive, exposed, and degraded habitats, due to societal demands for food, drinking water, transport, power generation, and leisure activities [2,3]. Thus, water scarcity, along with water quality problems, have become two of the most important threats

for the sustainability of aquatic ecosystems in semi-arid areas [4]. This situation becomes much more worrying in regions where the water scarcity is a serious problem, with the Mediterranean being one of the most vulnerable regions to the increasing pressure on water resources [5,6].

To overcome water shortage problems, dams were constructed, and their water quality assessment became crucial, not only to establish management actions to preserve their quality but also to prioritize rehabilitation processes. This assessment should encompass the water spatial and temporal variability and the identification of the main limnological factors that regulate the system, as the most important stressors that induce the highest environmental and public health concerns [7–11]. For a more efficient and integrative catchment management, it is also crucial to have knowledge about the inputs to the water bodies, from point and non-point sources of pollution, including the contribution from their tributaries [12–14]. Hence, developing studies in tributaries of reservoirs with a great flow variability as in Mediterranean region, and significantly influenced by land use/land cover (LULC), may contribute to identify the streams that strongly influence the water quality of reservoirs along time, essential to implement and improve watershed management measures [15].

In fact, LULC patterns are one of the main factors affecting water quality and ecosystems balance in a watershed [16]. As in many other regions, where the construction of dams induced an increment of economic activities [17], LULC changes have occurred in Alentejo (Southern Portugal) after the construction of the Alqueva Dam, mainly in the agricultural sector with the intensification of olive groves and vineyards and modification of the agricultural practices [18].

Several studies have been developed at the Alqueva reservoir, to evaluate limnological factors, biodiversity, point and non-point sources of pollution, and atmospheric processes, such as: (i) water quality and spatial-temporal variability [8,19,20]; (ii) nutrients and eutrophication processes [21]; (iii) biological communities and biodiversity [22–27]; (iv) quantification and risk assessment of hazardous substances, such as pesticides and potential toxic metals [28–31]; (v) remote sensing-based prediction of water quality and atmospheric processes [32,33]; and (vi) ecotoxicological assessment [34,35].

Currently, it is important to understand the linkage among tributaries and the Alqueva reservoir, to understand the effect of temporary regimes and geomorphological characteristics in the water quality of the reservoir, as well as the effect of LULC changes in the catchment, an understudied aspect, since intermittent streams have only recently gained scientific attention.

Taking the above statements into consideration, the aims of this study were to: (1) characterize the hydrogeomorphology of streams in the Guadiana watershed and LULC in the respective drainage areas; (2) assess the spatial and temporal chemicals dynamics of water and sediment; (3) analyze the correlations between water/sediments characteristics and LULC patterns; and (4) analyze the possible influence of streams hydrogeomorphology, chemical characteristics and LULC at the drainage areas in the water quality of the reservoir. To understand the relationship between landscape, hydrogeomorphological characteristics, and water quality, further improving water contamination estimations in catchments and providing tools to establish guidelines for land use/land cover (LULC) planning.

2. Materials and Methods

2.1. Study Area

The Alqueva reservoir is located in the main course of Guadiana river, and is the most important source of water supply for the populations of the Alentejo region (Southern Portugal), which is one of the driest regions in Portugal, with a Mediterranean climate [32], and where the agriculture is one of the most important economic activities [18].

The study was developed in four streams of the Guadiana watershed: Zebro (Zb; 38°14′15.5″ N, 7°19′40.32″ W); Álamos (Al; 38°24′50.46″ N, 7°28′2.16″ W); Amieira (Am; 38°16′58.80″ N, 7°36′35.20″ W), and Lucefécit (Lf; 38°36′59.19″ N, 7°23′31.65″ W) (Figure 1). In the framework of the ALOP project

(observation, prediction, and alert systems in atmosphere and in water reservoirs of Alentejo), four platforms previously installed in diverse limnetic areas of the reservoir were used to assess four areas of the reservoir. These platforms consist in floating structures fixed to the bottom of the reservoir with cables, used for sampling, to characterize the water quality, and where meteorological devices were installed. These streams were chosen considering their flow into the Alqueva reservoir towards each platform: Zebro drains into the reservoir near the Montante platform; Álamos near Mourão platform; Amieira near Álamos platform; and Lucefécit near Lucefécit platform (see Figure 1).

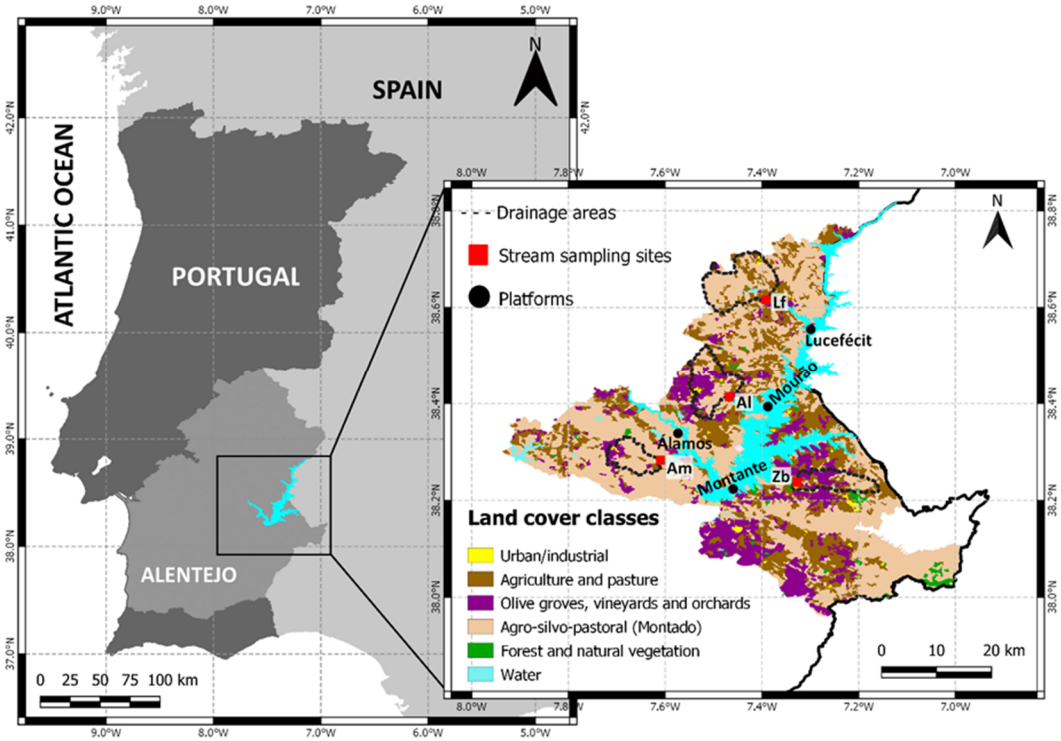

Figure 1. Map of the study area located in Alentejo region, with the municipalities that embrace Alqueva reservoir represented in the land cover zoomed map. The stream sampling sites from north to south are: Lucefécit—Lf; Álamos—Al; Amieira—Am; and Zebro—Zb).

With the increase and expansion of the irrigation system in the area, there has been a growth of intensive crops in a region traditionally occupied by agro-forestry systems (Montado), where urban areas have very little expression. The agricultural occupation in the irrigation perimeters of Alqueva has been diversifying, with olive groves as the predominant cultivation. Peanut is the second crop with the greatest expression in terms of farmers' bet. The production of almonds, corn, tomatoes, onions, garlic, melons, watermelons, and fruit trees (stone fruit, citrus fruits, table grapes, walnuts, among others), are also found in the irrigated areas of Alqueva, alongside the traditional cultivation of vines, cereals and fodder ((Empresa de Desenvolvimento e Infra-estruturas do Alqueva, S.A. (EDIA): https://www.edia.pt, last accessed on 3 September 2020)).

The studied streams are small and shallow watercourses, belong to the small drainage area rivers in Southern Portugal (S1 ≤ 100 km^2) according to the Water Framework Directive river typology [36], and are located in sites with siliceous lithology, with the studied reaches mainly characterized by: bank-full channel width ranging from 1–5 m in Álamos and Amieira to 5–10 m in Lucefécit and Zebro; the mean channel width from <1 m in Álamos to 1–5 m in the other sites, and channel depth ranging from <0.25 m to 0.5 m in Álamos, <0.25 m to 1 m in Amieira, 0.25 m to 1 m in Zebro, and only in Lucefécit the depth exceeded 1 m after a flooding in March 2018, whilst in the other sampling campaigns was between <0.25 m to 0.5 m. The riparian vegetation is continuous in Amieira stream,

semi-continuous in Lucefécit and Álamos and scattered in Zebro stream; furthermore, there is no shadow in the channel in Zebro and in Álamos, opposite to Lucefécit where more than 60% of the stretch is shadowed and in Amieira with a shadow between 30–60%. Amieira and Álamos are typical Mediterranean intermittent watercourses that dry or stop flowing during part of the year (only small isolated pools are present in summer, namely in July and September), whilst Zebro has no flow during summer and Lucefécit maintains flow during all the year, despite a substantial reduction during the summer. The main characteristics observed in each stream are summarized in Table S1. The four studied streams are subject to some anthropogenic impacts, both in the banks and in the channels, such as small bridges in Zebro and Álamos and upstream of Lucefécit sampling stretch, cattle raising in Amieira, Zebro, and Álamos, wastewater treatment plants upstream the sampling sites in Zebro and Álamos and intensive agriculture in the banks of Lucefécit sampling stretch. A detailed analysis of the LULC in each of the four tributaries is presented in Section 2.2.

The Mediterranean climate is characterized by dry and hot summers and temperate and wet winters, with concentrated rainfalls [37]. During the year of 2017, the onsite meteorological station [38] provided an annual average temperature of 17.8 °C, ranging from a minimum temperature of −1.8 °C in January to a maximum of 45.2 °C in August, with an annual precipitation of 327.8 mm. As for the year of 2018, the climate was characterized by an average temperature of 16.3 °C ranging from −1.8 °C in February to 44.7 °C in August, with an annual precipitation of 665.8 mm. Meteorological drought monitoring is performed by the Portuguese Institute for the Sea and Atmosphere (IPMA), using the Palmer Drought Severity Index (PDSI). The South of Portugal was considered in severe drought conditions, from April 2017 on, registering the highest temperatures observed in the last 80 years, and with the smallest precipitation values [39], whereas the year of 2018 was considered normal by IPMA regarding air temperature and rainfall, with the severe drought situation ending in March 2018. Furthermore, the precipitation was concentrated in storms, which may cause streams to flood.

2.2. LULC Characterization

The basis for the LULC analysis carried out for the area of study was the CORINE Land Cover (CLC) inventory produced in 2018 using satellite imagery (Sentinel-2 and Landsat-8 for gap filling), available from Copernicus Land Monitoring Service (https://land.copernicus.eu/pan-european/corine-land-cover/). The CLC inventory uses a minimum mapping unit of 25 ha for area phenomena and a minimum width of 100 m for linear phenomena and distinguishes 44 land cover classes (https://www.eea.europa.eu/publications/COR0-landcover). The analysis showed that 24 out of the 44 CLC classes are present in the area of study. These 24 classes were merged to yield six broader categories describing typical LULC in the region: urban/industrial; agriculture and pasture; olive groves, vineyards and orchards; agro-silvo-pastoral (Montado); forest and natural vegetation; water. Table S2 summarizes the integration of CLC classes into the adopted categories. The agro-silvo-pastoral class corresponds to a very typical landscape of southern Portugal termed Montado, characterized as a multifunctional agro-silvo-pastoral ecosystem, with varying densities of trees (mainly cork and/or holm oaks). The Montado system encompasses more than one CLC class due to its particularities [40], as indicated in Table S2.

The adopted classification considering the six classes was applied to the region comprising the five Portuguese municipalities surrounding Alqueva reservoir (Alandroal, Moura, Mourão, Portel, and Reguengos de Monsaraz). The resulting land cover map is presented in Figure 1, showing that Montado landscape dominates the region, with significant parts of the area also occupied by olive groves, vineyards and orchards, as well as, agriculture and pasture.

ASTER Global Digital Elevation Model (GDEM) V002 (ASTER GDEM is a product of NASA and METI) data were used to obtain the area of drainage basins associated to each of the sampling (outlet) points. The DEM data were obtained from the Land Processes Distributed Active Archive Center (LP DAAC: https://gdex.cr.usgs.gov/gdex/) in a grid of 1 arc-second (approximately 30–m at the

equator). The drainage basins of stream sampling points represent the appropriate areas to analyze and relate land cover to water quality, since these collect and drain off surface and ground water, as well as precipitation into the control point. The altitudes in the four drainage basins range between 141 and 416 m above mean sea level (a.m.s.l). The drainage basins delineated from DEM data are represented by the dotted black lines in Figure 1.

2.3. Sampling

Water and sediment samples were collected at the four selected streams (Lucefécit-Lf; Álamos-Al; Amieira-Am; and Zebro-Zb). The study comprised 12 sampling campaigns, from January 2017 to November 2018: in January (Jn), March (Mr), May (M), July (Jl), September (Sp), and November (Nv). The intermittency nature (with highly irregular flowing regime) of these streams in Mediterranean areas, justified the temporal evaluation proposal. In these regions, the stream discharges may range from zero (dry phase) to high discharge rates (flooding period). This river flow regime has implications in the water quality and makes the streams very sensitive to anthropogenic pressures [19].

In general, the sampling occurred in flowing conditions, except at Amieira in July and September 2017 and 2018 and at Álamos in July and September 2018 (dry phase), collected in an isolated pool upstream of the regular sampling sites. Sampling at each site included: (i) 2 L of surface water in polyethylene bottles, for the analysis of physicochemical parameters; and (ii) 5 L of surface sediments (<10 cm) on plastic bags. The samples were transported to the laboratory at 4 °C, conserved and stored until the analysis following the requisites for each parameter [41,42].

2.4. Water Characterization

Water temperature (T; °C), pH, electrical conductivity (EC; μS cm^{-1}), and dissolved oxygen (DO; %) were measured in situ using a multiparametric YSI 6820 MPS probe ® (Alemanha, Portugal).

The water parameters analyzed were the following: biochemical oxygen demand (BOD_5; mg L^{-1}; respirometric method), chemical oxygen demand (COD; mg L^{-1}; dichromate technique), total phosphorus (TP; mg L^{-1}; molecular absorption spectrometry), Kjeldahl nitrogen (KN; mg L^{-1}; molecular absorption spectrometry), nitrate (NO_3; mg L^{-1}; Ionic chromatography), nitrite (NO_2; mg L^{-1}; ionic chromatography), ammonium (NH_4; mg L^{-1}; molecular absorption spectrometry), chlorides (Cl; mg L^{-1}; ionic chromatography), and sulfates (SO_4; mg L^{-1}; Ionic chromatography) [41].

Total nitrogen (TN) was determined, using the following Equation (1) [41]:

$$TN\ (mg\ L^{-1}) = 0.226 \times [NO_3; mg\ L^{-1}] + 0.304 \times [NO_2; mg\ L^{-1}] + [KN; mg\ L^{-1}] \quad (1)$$

2.5. Sediment Characterization

As for the sediments, the pH ($pH_{pore\text{-}water}$) and the electrical conductivity ($EC_{pore\text{-}water}$; μS cm^{-1}) were analyzed in pore-water samples [42].

Sediment grain-size distribution was determined following the method E196 of the Portuguese Laboratory of Civil Engineering [43]. The chemical parameters determined were: organic matter content (OM; %; calcination at 500 °C; [42]); total nitrogen (TN; %; Kjeldahl method; [41]); total phosphorus (TP; %; molecular absorption spectrometry with molybdovanadate phosphoric acid; [41]).

Potentially hazardous trace elements contents (Cd, Cr, Cu, Ni, Pb, and Zn) were determined according to International Organization for Standardization (ISO) 11466 [44]. Flame atomic absorption spectrometry (FAAS) was used in the analysis, by a Varian equipment (SpectrAA 220FS, 220Z and 110Z, Palo Alto, CA, USA).

Quality Control

The quality of the analytical data was guaranteed through the implementation of laboratory quality assurance, as the use of standard operating procedures, calibration with standards, analysis of blanks and of replicates (three independent replicates per sample).

For the validation of the analytical procedures of the potentially hazardous trace elements quantification, a geological certified reference material, Buffalo Lake sediment (SRM 2704), was analyzed to validate the aqua regia extraction procedure. The assessment among reference material and the samples presented a mean relative error <10%, for all the elements analyzed (Cd, Cr, Cu, Ni, Pb, and Zn).

2.6. Statistical Treatment of Data

Water and sediments data were assessed by descriptive statistics (mean ± standard deviation) and multivariate statistical analysis (principal component analysis/factor analysis and cluster analysis), based on two matrixes, one for water (48 samples × 13 environmental parameters), and another for sediments (48 samples × 12 environmental parameters). Data were normalized (log x; x = mean value) prior to multivariate statistical analyses, avoiding misclassification due to differences in data dimensionality [45].

Spearman's rank coefficient correlations between variables were performed (since most of the data failed the Shapiro–Wilk normality test), and the Spearman coefficient (R) was used to evaluate the statistical strength of the correlations, obtained by the potential linear relationship between the classes of land cover and the environmental variables.

Principal component analysis/factor analysis (PCA/FA) and cluster analysis (CA) were applied to: (1) identify the main parameters that explain the variability of the stream water quality; (2) group the streams according to their water quality; (3) group the streams according to the land cover; and (4) identify the streams that may have the greatest influence on the Alqueva reservoir water quality.

The CA groups the most similar samples, using the Euclidean distance between samples as a measurement of similarity [46]. The linkage distance is obtained through the following Equation (2):

$$\text{Dlink/Dmax (Dlink: linkage distance for an individual case; Dmax: maximum linkage distance).} \quad (2)$$

All statistical analyses were performed with the STATISTICA 7.0 (Software ™ Inc., Palo Alto, CA, USA, 2004).

3. Results

3.1. LULC Description

The LULC patterns were analyzed in the drainage areas delimited for each of the stream sampling sites, corresponding to the following areas: Álamos—89.0 km^2; Amieira—50.8 km^2, Lucefécit—117.2 km^2, and Zebro—46.8 km^2, from which we calculated the percentages of LULC classes. Figure 2 shows the percentages obtained for each class within the considered catchments. Notice that the agro-silvo-pastoral class dominates in three of the four drainage areas (Álamos, Amieira, and Lucefécit with 43%, 73%, and 67%, respectively), which reflects the prevalence of this type of landscape in the region. In Lucefécit stream, agriculture and pasture class follows with 28%, whereas in Álamos and Amieira, the olive groves, vineyards, and orchards is the second class with 33% and 17%, respectively. Furthermore, while Álamos presents also a fairly significant amount of agriculture and pasture (22%), in Amieira this class is barely 8%. In Zebro drainage basin, the olive groves, vineyards, and orchards is the leading class (42%), followed by agriculture and pasture (31%). It is important to refer that Lucefécit drainage area is the only one including industrial activities (extractive and food processing, among others).

3.2. Stream Water Characterization

3.2.1. In Situ Parameters

Water quality varied markedly among streams, influenced by different LULC classes and by the temporal variability (Figures 3 and 4). Relatively to the results for the in situ parameters (Figure 3), the water pH presented low variability in all the streams with values always between the limits proposed for the good ecological status (GES) for small rivers of Southern Portugal ($6 \leq pH \leq 9$; [47]). The temperature changed markedly among seasons with values in the wet period from 6.5 to 15 °C and in the dry period from 17 to 34 °C, with the highest values registered at Amieira in 2018, when the stream was in its dry phase. The dissolved oxygen (DO), also showed a great temporal variability, with saturation percentages exceeding the limits for the good ecological status (60–120%; [47]) at Amieira, in January and July 2017 (DO = 181%), at Álamos in January 2017 (DO = 125%), and at Zebro in July 2017 (DO = 171%). In general, the DO variations are related with seasonal changes and rainfall patterns, being the higher values observed during the wet season [7,8,48], which may explain the high levels detected in January, characterized by low water temperature. The electric conductivity (EC) was the parameter that presented the major variability among streams, with the highest values (>1000 µS cm^{-1}) detected at Zebro and Álamos. In the present study, the EC was correlated with the LULC of olive groves, vineyards and orchards ($R = 0.42$; $p < 0.05$; Table S3), which dominates at Zebro stream (42%) and is the second one at Álamos (33%), followed in both drainage areas by the agriculture and pasture class, occupying 31% and 22%, respectively (see Figure 2).

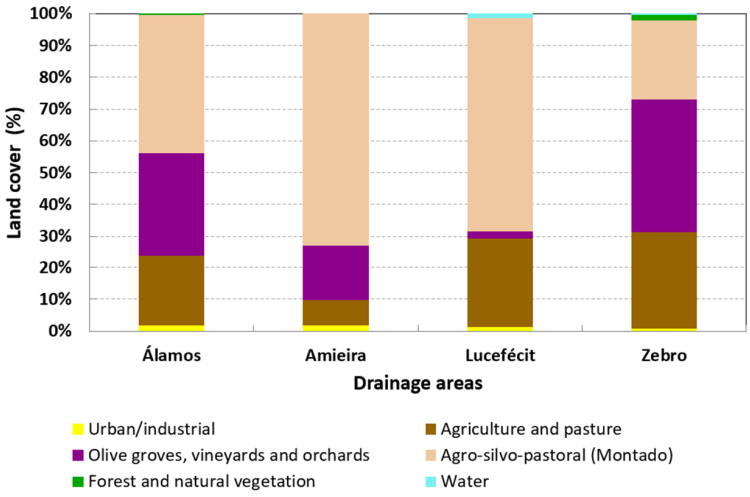

Figure 2. Percentages of the land use/land cover (LULC) classes in the selected drainage areas.

3.2.2. Nutrients and Organic Descriptors

Spearman rank coefficient (Table S3) showed positive correlations among T and EC, BOD_5, COD TP, NO_3 and NH_4, indicating that these parameters were the major source of temporal variability in the streams.

Regarding the organic descriptor BOD_5 (Figure 4), the concentrations were above the limit for the good ecological status ($BOD_5 \leq 6$ mg L^{-1}; [36]) at Zebro and Álamos, during most of the study. The results obtained seem to be linked with LULC, once the presence of BOD_5 at watercourses is correlated with the increment of olive groves, vineyards, and orchards area ($R = 0.40$; $p < 0.05$), impact more evident during the dry period. Further, the positive correlations between BOD_5 and TP ($R = 0.41$; $p < 0.05$), TN ($R = 0.48$; $p < 0.05$), and NH_4 ($R = 0.59$; $p < 0.05$) indicate similar sources of pollution, also supported by the linkage obtained between these parameters and the LULC class of olive groves, vineyards and orchards (Table S3). All streams presented concentrations of COD greater than 20 mg L^{-1}, limit value established for water bodies in risk [49]. In fact, concentrations of BOD_5 and COD,

above 5 mg L^{-1} and 20 mg L^{-1}, respectively, indicate a high organic load, which may be responsible for the degradation of ecological conditions.

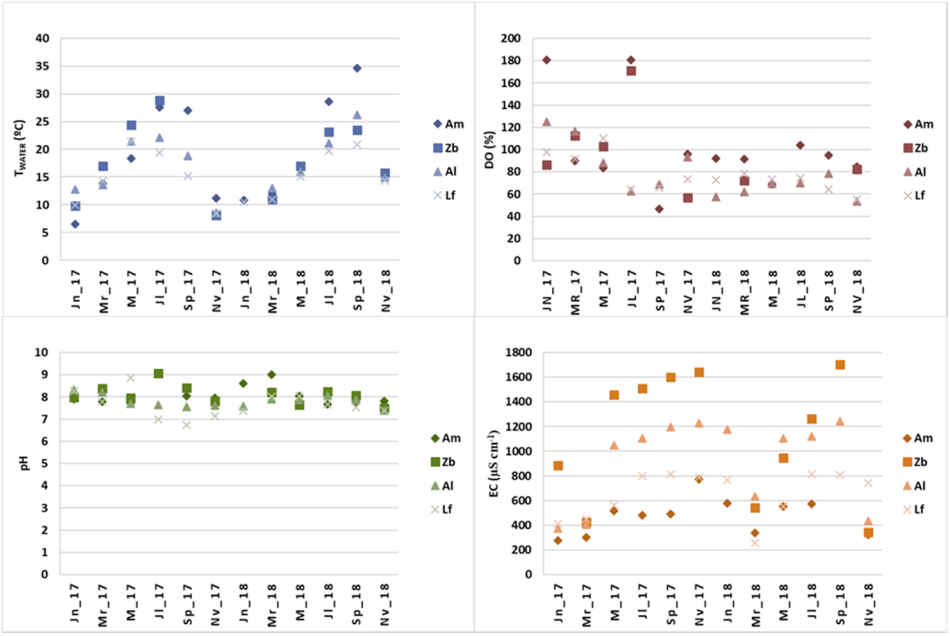

Figure 3. Parameters measured in situ, in each stream (Zb: Zebro; Am: Amieira; Al: Álamos: Lf: Lucefécit), during the 12 campaigns of the study (Jn_17: January 2017; Mr_2017: March 2017; M_2017: May 2017: Jl_2017: July 2017: Sp_2017: September 2017; Nv_2017: November 2017; Jn_18: January 2018; Mr_2018: March 2018; M_2018: May 2018: Jl_2018: July 2018: Sp_2018: September 2018; Nv_2018: November 2018).

The total nitrogen (TN) presented the highest concentrations at Zebro (0.69–29.89 mg L^{-1}) and Álamos (0.66–21.60 mg L^{-1}), without a pronounced temporal pattern, probably related with the hydrogeomorphology and LULC (Figures 2 and 4). Results highlighted by the positive correlation observed between TN and olive groves, vineyards and orchards class ($R = 0.32$; $p < 0.05$) and by the negative correlation with the class of agro-silvo-pastoral ($R = -0.43$; $p < 0.05$). Indeed, the Amieira stream, with a predominance of agro-silvo-pastoral class (73%), is the stream with the best water quality, during the flowing phase. Relative to NH_4, this parameter reached concentrations higher than 1 mg L^{-1} at Zebro (limit for the good ecological status; [36]). These results were influenced by the temporal factor (higher amounts in the dry period with low flow), and by the LULC (olive groves, vineyards and orchards class), and supported through the correlation between NH_4 and this class of LULC ($R = 0.46$; $p < 0.05$). Furthermore, the correlation between NH_4 and urban/industrial LULC ($R = 0.49$; $p < 0.05$), also indicates the influence of this class in the increment of nutrients in streams. Total phosphorus (TP) presented always values higher than 1 mg L^{-1}, being responsible for the failure to comply with the good ecological status of the streams, both in the wet and dry periods (0.13 mg L^{-1}; [47]). The results showed that the increase of TP at streams was correlated with olive groves, vineyards and orchards LULC ($R = 0.56$; $p < 0.05$).

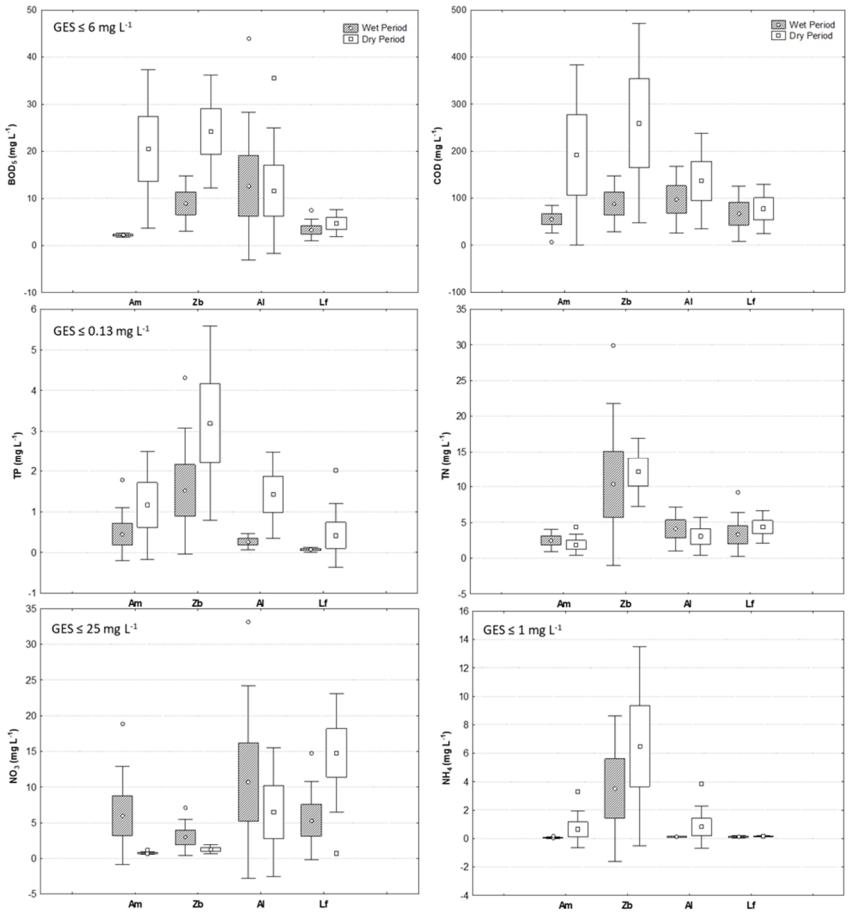

Figure 4. Spatial and temporal variation of the organic descriptors and nutrients in the water samples during the period of the study. The mark across the box represents the mean, and the bottom and top of the box show the standard deviation. Whenever possible, recommended guide levels for the good ecological status (GES) were represented [47].

3.2.3. The Effect of LULC and Hydrogeomorphology on the Water Quality

PCA was conducted using pooled data from the four streams, allowing the identification of two principal components (PCs) as important factors to explain 45% of the total variance of the water samples. Figure 5 shows the combined plot of scores and loadings on PC1 versus PC2. The PC1 represented the influence of LULC classes (urban/industrial; olive groves, vineyards and orchards, and agro-silvo-pastoral (Montado)) on the physico-chemical composition of water explaining 29% of the variance. This PC was highly associated with TN, NH_4, and Cl (negative participation) and moderately associated with NO_2 (negative participation). Hence, this PC is explained considering the nutrient discharges at streams under the influence of LULC classes of olive groves, vineyards, and orchards and urban/industrial (also negatively correlated with the PC). Further, the PC1 presented a positive correlation with flow characteristics ($R = 0.35$; $p < 0.05$), grouped in four classes (see Table S1: no flow, low flow, moderate flow, very fast flow). The LULC that explained PC2 was agriculture and pasture class, representing 16% of the variance with a strong negative participation of TP and a moderate participation of NO_3 (positive) and BOD_5 (negative). Moreover, this PC presented a positive correlation with flow characteristics ($R = 0.52$; $p < 0.001$). The positive correlation of both PC with the flow indicate the importance of this parameter in the transport of nutrients along the streams and downstream to reservoirs.

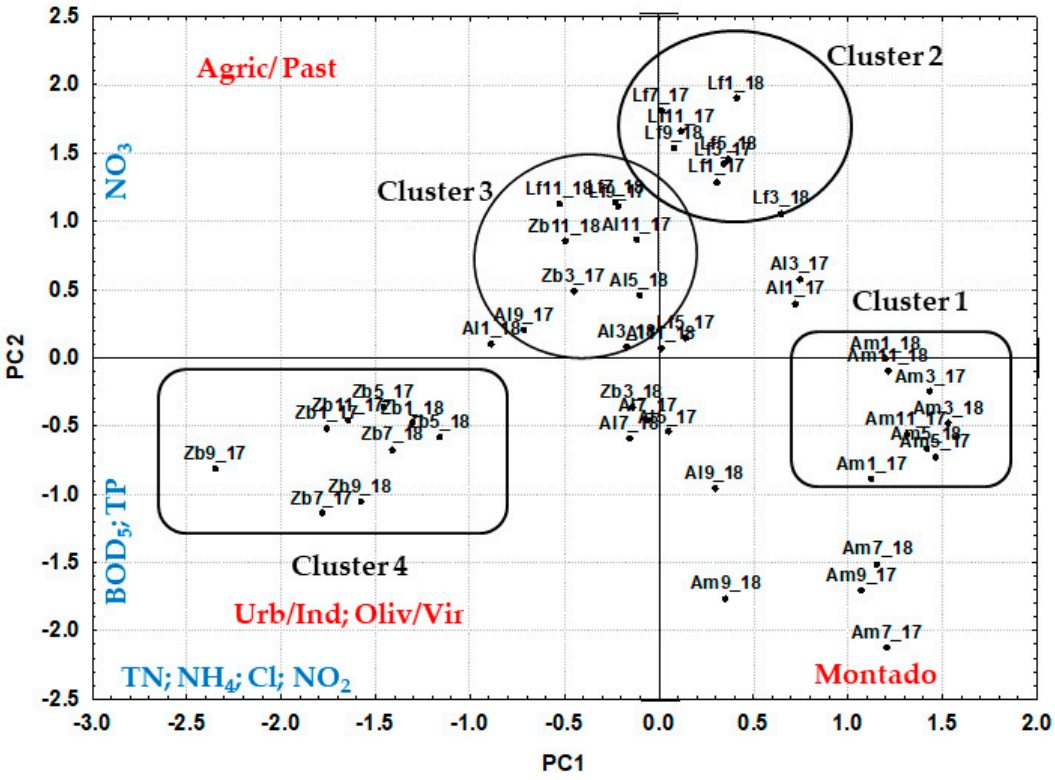

Figure 5. Scores of the water samples of streams, on the bidimensional plan defined by the first two principle components (PC) and parameters that most influence the explanation of each PC. In the figure are displayed the statistically significant clusters obtained with the Euclidean distance of (Dlink/Dmax) × 100 < 50.

Figure 5 also evidences the four statistically significant groups obtained through the cluster analysis (Dlink/Dmax) × 100 < 50. The samples that presented the best water quality were represented at the positive quadrant of PC1 and at the negative quadrant of PC2, integrating all samples from Amieira stream (Cluster 1), with high influence of the LULC Montado Class. Cluster 2 is represented in the positive quadrant of both PCs, integrating samples only from Lufecécit stream, with high concentrations of NO_3 from agriculture and pasture activities. Cluster 3 represents the samples more influenced by agriculture and pasture activities, integrating samples from Álamos and Lucefécit streams. The negative quadrant of both PCs, displayed the samples with the worst water quality, grouped at Cluster 4, and belonging to the Zebro stream. These samples presented high amounts of organic descriptors and nutrients, explained by the action of olive grove and vineyards and urban/industrial classes at the streams.

3.3. Sediment Characterization

3.3.1. Physico-Chemical Parameters

Relatively to sediment grain size, important characteristic that controls the natural and anthropogenic components in the water-sediment systems [50], the results showed that the streams are mostly constituted by coarse particles-sand (Table 1). In general, the predominance of this granulometric fraction induces higher levels of percolation with lower adsorption potential for nutrients and trace elements [51]. The $pH_{pore\text{-}water}$ values ranged from 6.5 to 7.9, being Zebro the stream with the highest $pH_{pore\text{-}water}$ values (Table 1). The $EC_{pore\text{-}water}$, presented high variability, ranging from 44 to 1820 µs cm^{-1}, with the highest values observed at Zebro (Table 1). The results evidence a positive correlation between $EC_{pore\text{-}water}$ and olive groves, vineyards and orchards class ($R = 0.46$; $p < 0.05$; Table S4), as already observed in the water column. The link between LULC and $EC_{pore\text{-}water}$ values is

consistent with other studies that reported positive correlations between this parameter and intensive agriculture activities and urban classes [7,52]. Further, streams surficial sediments were characterized as inorganic, with mean percentages of organic matter (OM) contents less than 6 [53].

Table 1. Sediments main physicochemical characteristics (mean (min–max); n = 12), in the studied streams: Lucefécit (Lf), Álamos (Al), Amieira (Am), and Zebro (Zb).

	Lf	Al	Am	Zb
$pH_{pore\text{-}water}$	7.5 (6.9–7.9)	7.5 (6.8–7.9)	7.3 (6.5–7.9)	7.6 (6.6–7.9)
$EC_{pore\text{-}water}$ (µs cm^{-1})	712 (429–929)	916 (115–1259)	532 (44–791)	1217 (233–1820)
OM (%)	5.7(1.6–39.0)	1.2 (0.6–3.6)	3.42 (1.4–12.1)	4.6 (1.4–5.9)
Granulometric Fractions				
Sand (%)	58.76	64.83	90.06	87.89
Silt (%)	31.01	25.27	2.77	4.27
Clay (%)	10.15	8.63	7.85	8.60

Relatively to the nutrients, the sediments presented TN concentrations always under the severe effect level (SEL) of 0.48% (Figure 6), according to the Ontario sediment quality guidelines [54]. In contrast, the concentrations of TP, despite its high variability, surpassed the SEL value, 0.2%, in most of the samples. This scenario is similar to what occurred in the water samples and in the reservoir [8], indicating that the load of TP is very high in the catchment.

3.3.2. Potentially Toxic Metals

The results displayed a high variability without a temporal and a spatial pattern (Figure 6), which together with the correlations observed among potentially toxic metals and LULC classes namely urban/industrial and olive groves, vineyards, and orchards (Table S4), support anthropogenic actions as the main sources of these elements into the streams sediments. The potentially toxic metals that surpassed the Canadian interim freshwater sediment quality guideline (ISQG) were Cu, Ni, and Cd, elements that may be able to induce continuously toxic effects to aquatic organisms. Copper is correlated with the urban/industrial class ($R = 0.37$; $p < 0.05$). Lucefécit stream presented the highest concentrations of Cu, generally higher than the ISQG (35.7 mg kg^{-1}; [55]). Nickel was the trace element that showed less variability over time, surpassing the sediment quality guideline (SQG; 15.9 mg kg^{-1}; [56]), except at Álamos. The highest concentrations for this element was observed at Lucefécit (10.1–96.4 mg kg^{-1}). Cadmium showed concentrations higher than the ISQG (0.6 mg kg^{-1}; [55]), in Amieira and Zebro during the dry-phase and in Lucefécit during the whole study.

3.3.3. The Effect of Textural Properties and LULC on the Sediments Quality

Principal component analysis/factor analysis of sediments samples allowed us to obtain two principal components explaining about 52% of the total variance of the data. Figure 7 shows the combined plot of scores and loadings on PC1 versus PC2, and the three statistically significant groups obtained through the cluster analysis (Dlink/Dmax) × 100 < 50. The PC1 (28%) represented the influence of physical proprieties namely grain size on the composition of sediments. The sediments parameters most influenced by this explanatory factor were Ni and Cu (with loadings ≥ 0.75), followed by the Pb and TN (with loadings among 0.75–0.50), all of these parameters with a positive participation in the PC1. PC2 was characterized by LULC classes explaining 23% of the variance and highly correlated with TP (positive participation). As for the three statistically significant clusters, the samples located in the positive quadrant of both PCs were grouped in Cluster 1, integrating samples from Zebro, most influenced by olive groves, vineyards and orchards and with high amounts of TP. The Cluster 2 grouped the samples from Amieira and Álamos, most constituted by sand particles, with low capacity of adsorption and higher rates of pollutant load transfer to the reservoir. The samples displayed in

the positive quadrant of PC1 and negative quadrant of PC2, represent the samples that presented higher percentages of fine particles (silt and clay) and higher concentrations of Ni, Cu, and Pb, and TN, integrating Lucefécit samples (Cluster 3).

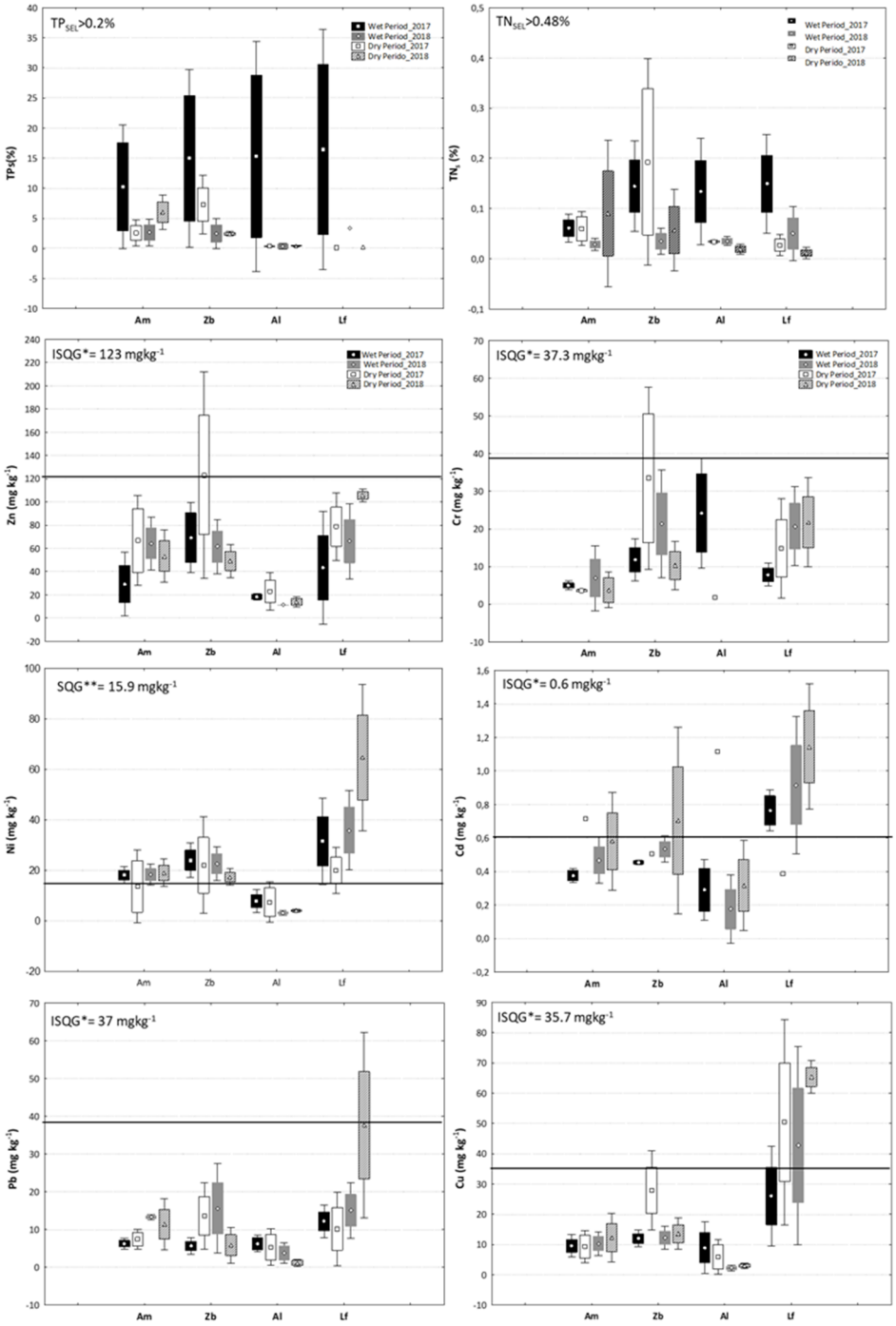

Figure 6. Variability of the nutrients and potential toxic trace elements at sediments. The mark across the box represents the mean, and the bottom and top of the box show the standard deviation. Guide levels were from: Severe Effect Level (SEL) Ontario Sediment Quality Guidelines [54]; Canadian Interim Freshwater Sediment Quality Guideline (ISQG) for the Protection of Aquatic Life [55]; Sediment Quality Guideline (SQG; [56]).

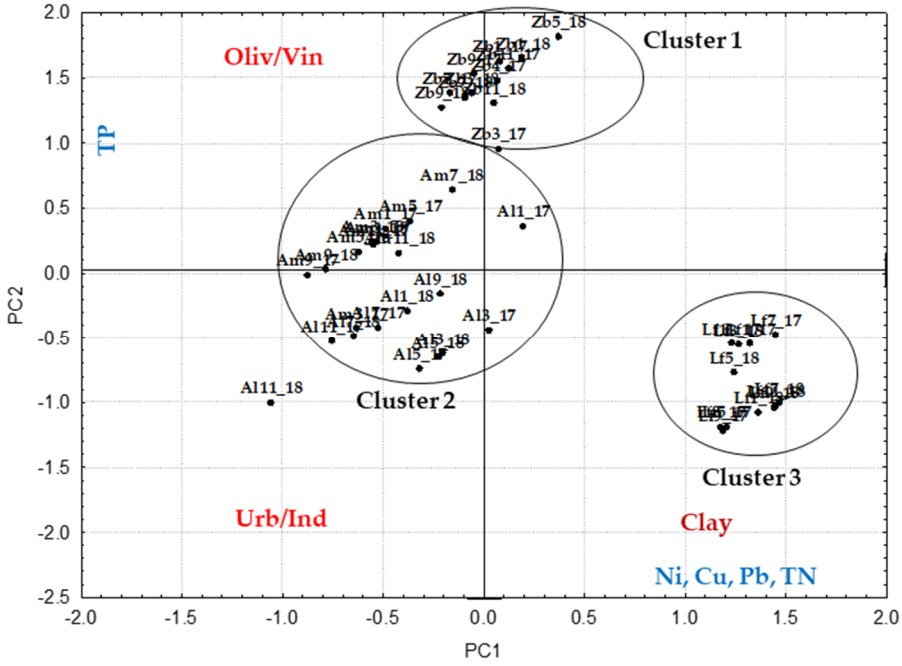

Figure 7. Scores of the sediments samples of streams, on the bidimensional plan defined by the first two principle components (PC) and parameters that most influence the explanation of each PC. At the figure are represented the statistically significant clusters obtained with the Euclidean distance of (Dlink/Dmax) × 100 < 50.

4. Discussion

4.1. LULC and Hydrogeomorphology Influence on the Physico-Chemical Characteristics of the Tributaries

Relatively to the in situ parameters, the results showed high seasonal variability of temperature with similar spatial patterns, indicating that this parameter is more influenced by climate conditions such as air temperature, than by other anthropogenic or natural stressors as reported elsewhere [57]. The other parameter that showed high fluctuation and, in this case, not only seasonal but also spatial was the EC, being Zebro the stream that presented the highest values, during the dry season. The results showed a high influence of LULC in this parameter, being in agreement with other studies that reported the agriculture and urban/industrial classes as the main LULC responsible for the increase of this parameter in the water of streams [7,12,58]. Further, the increase of ion concentrations, which results in the increase of EC during dry seasons, may be justified by low flows, decrease of runoff, and high evaporation rates, causing the water volume reduction in permanent hydrologic regimes, and water cessation in temporary [59].

The BOD_5, COD, and TP were the parameters that most negative influenced the water quality, being the responsible for Zebro and Álamos not achieving the good ecological status, mainly during the dry seasons. The results point to the great influence of LULC classes in the concentrations of nutrients and organic descriptors in water, the urban/industrial and olive groves, vineyards, and orchard classes being the most polluting. Several studies already reported this linkage in different climate and LULC scenarios, as in rural-urban regions with a humid-subtropical climate (rural-urban fringe, Georgia Piedmont, USA; [7]), or in bare land and natural forest areas with tropical climate and intensive rainfall (Natural Forest of Córdoba Province, Argentine; [12]). Furthermore, Shi et al. [60], already stated that the urban class of LULC is the one with a major influence on the raise of the nitrogen and phosphorus forms in streams, via runoff, during and after precipitations events. Furthermore, Du et al. [61], in a study about the correlation of nutrients concentrations and LULC, identified the increment of intensive agriculture and population density as the major factor responsible for the raise of nitrogen and phosphorus in streams. Additionally, Ongley et al. [62] reported that

intensive agriculture contributes with about 50% of the total contamination load to the streams, due to the inputs of inorganic fertilizers, organic manure, and pesticides. In addition to land uses, the hydrological regimes, very influenced by temporal conditions, also act in the concentrations of these parameters in water, being the temporary regimes (as occur in Zebro and Álamos) more sensitive to these anthropogenic conditions. Opposite, the results obtained in Amieira (stream with the best water quality) showed that, despite its temporary regime, the great percentage of agro-silvo-pastoral LULC may be a buffer to stop the runoff of contamination load. The results are in line with others that identified the forest and the riparian vegetation as the most important classes for the maintenance and improvement of the quality of water in streams, acting as a buffer to the pollution processes at the water body, and decreasing the soil erosion [63].

The assessment of sediment characteristics is essential for the whole analysis of the water quality, and for the evaluation of pollutant load transfer into a reservoir, being crucial in the establishment of management actions to preserve the aquatic environment. Hence, the sediments results reveled a great spatial and seasonal variability, being the granulometry and the LULC conditions, the great responsible for the concentrations of nutrients and potentially toxic metals observed. The streams sediments were mostly constituted by sand particles, as already observed in the upper part of Alqueva reservoir, near the border with Spain [8,28]. In general, the sediments presented low organic matter contents (OM; %) when compared with previous studies conducted in the Guadiana River Watershed [64,65]. The values detected in the present study were like those found at the upper part of Alqueva reservoir [8]. The presence of OM is one of the main factors responsible for the adsorption/accumulation of chemical elements to the sediments, which is corroborated by the positive correlations obtained with TP, TN, Ni, Cu, Pb, Cr, Zn, a fact that was also reported for sediments from the Alqueva reservoir [8]. In fact, Lucefécit presented the highest amounts of potentially toxic metals, which could be justified by the highest percentages of fine particles (silt = 31% and clay = 10%) and OM contents (3.6–39.3%). On the other hand, Lucefécit drainage area is distinguished from the others because the urban/industrial land cover class is not limited to urban pollution but includes also industrial activities that may be related with the higher trace elements contamination. On the contrary, and despite the fact that Zebro presented highest contamination levels in the water column, the characteristics of its sediments, with a high percentage of coarse materials (87.89% sand), and low organic matter percentages, do not facilitate the adsorption of nutrients and hazardous substances onto the sediments. Relatively to the potentially toxic metals the results showed that the sediments were contaminated with Cu, Ni, and Cd. Nickel surpassed its ISQG in at most of the streams, followed by Cd and Cu. At previous studies at the Guadiana Watershed, including at Alqueva reservoir, reported that Cd was the most widespread element in the sediments and Cu was the element responsible for the polluted status of the sediments collected in the reservoir areas of Lucefécit and Álamos. Both elements have as main pollution sources the wastewaters discharge, road traffic and agriculture activities. Furthermore, Ni was the trace element less influenced by anthropic actions, with less variability and its concentrations being justified mainly by the geological characteristics of the basin [31,66].

The importance of LULC, hydrological regimes, and granulometric proprieties was highlighted in the multivariate analysis, showing classes as urban/industrial and olive groves, vineyards, and orchards, fine particles of sediments, and flow (temporary regime) the main explicative factors of the presence of nutrients, organic descriptors, and potentially toxic metals in the Guadiana streams. Analysis and remarks already reported in different studies, such as at the Dan River Watershed, at China [61], at the Altamaha, and Savannah River watersheds, at State of Georgia [7], and at the Siriri River basin, Brazil [67].

4.2. Influence of the Tributaries on the Water Quality of Reservoirs

The influence of the transfer of nutrients, organic descriptors and potentially toxic metals from tributaries to the downstream reservoir was assessed. In general, results agree with what was previously observed in the Alqueva reservoir [8], evidencing a similar chemical pattern for some of the parameters

assessed, and supporting the possible influence of these tributaries on the water quality of the reservoir. Relatively to nutrients, previous studies in the Alqueva reservoir, reported TN concentrations lower than the observed in the tributaries, but also suggestive of the stand-up of the nitrogen content in the watershed [8,20]. Similar results were also observed for NO_3 and NH_4, which have been increasing over time [8,19,20]. TP is the nutrient that is causing the highest stress in the Guadiana catchment, and that may be transported into the reservoir from the tributaries. This statement is supported by: (1) the high amount of TP in the water and sediments of the streams; (2) the high variability of the observed TP concentrations; and (3) the opposite trend of the TP concentrations among tributaries and the respective Alqueva areas [8]; unpublished results. Furthermore, and regarding the speed up of the eutrophication process that was reported for the Alqueva reservoir [8,19], most of the tributaries presented high pollution rates with concentrations of TN > 1.5 mg L^{-1} and TP > 0.075 mg L^{-1}, values established by Dodds et al. [68] to characterize eutrophic waters.

Among the potentially toxic elements analyzed in the studied streams, Cd probably was the mostly transferred element to the Alqueva reservoir, due to its characteristics, namely the great bioavailability, being the most mobile metal, and its high anthropic enrichment factor (EF) at the Guadiana watershed [31].

Further, the results indicate that the contamination load at Zebro and Álamos may be a possible source of contamination for Montante and Mourão areas (extents of the Alqueva reservoir where those streams directly drain). In fact, the tributaries that may be exerting the greatest pressure in the reservoir were Zebro and Álamos, due to their LULC, with the increment of nutrients, organic descriptors and potentially toxic metals, which are concentrated during the dry phase and further transferred to the reservoir in the beginning of the rainfall period, with the flow resumption. This process was facilitated by the granulometric proprieties (mostly constituted by coarse materials) and by the low OM contents, important factors for the low capacity to adsorb the elements in the sediments of streams, stimulating the pollutants loads transfer.

Henceforth, in addition to temporal and LULC scales, it is important to assess the hydrogeomorphological characteristics of streams for a better understanding of the possible pollution loads that may be transferred to the watercourses or reservoirs downstream. In fact, streams with an intermittent flow regime (increasingly important in the Mediterranean region), influence the water quality downstream depending on their flow characteristics and on the textural characteristics of their sediments. The intermittent regime promotes the accumulation of organic matter and nutrients on the stream bed (in the dry-phase), with the transfer of higher amounts of pollutant loads downstream, during a specific temporal period (wet period). Additionally, for an integrative analysis, the sediments textural properties must be evaluated. In fact, when stream sediments are mostly constituted by sand, the pollutants are not easily adsorbed and, most of them are probably transferred. Contrariwise, streams presenting sediments mostly constituted by fine particles, with high organic matter contents, easily adsorb nutrients and potentially toxic trace elements, avoiding their transfer downstream.

5. Conclusions

Stream water characteristics in the Guadiana River catchment displayed significant spatial and temporal variability. The results showed temporal differences in the linkage among LULC and water quality, pointing to the importance of several spatial and temporal scales to understand the impacts of anthropic actions on catchment ecosystem services.

The water quality of the streams was significantly influenced by seasonality and LULC, which was more obvious during the wet period. The study highlighted that the agro-silvo-pastoral land cover (Montado), a class characteristic of the Mediterranean region, has an important positive effect on water quality, acting as a buffer to the contamination of the streams. Contrariwise, the intensive agricultural and urban LULC areas may contribute to the decline of water quality.

Results pointed to the sensitivity of intermittent regimes to loads of pollutants, being movers for its transfer to downstream reservoirs. So, it is urgent to stop the increase of agriculture intensification in

the Guadiana watershed, due to the impairment of these ecosystems and to the increment of pollution sources for the reservoirs.

The results highlight that the comprehension of the relationship between water quality, LULC, together with hydrogeomorphology conditions are essential tools for the improvement of the scientific knowledge about the main stressors at the Mediterranean region and the role of temporary regimes at its catchments. These results may be useful for a better and more specific management plan of the Guadiana watershed, which may be included in the next version of the River Basin Management Plan in 2021.

The increase, in the region, of temporary streams and its high sensitivity to pollution, makes urgent the development LULC policies to protect these ecosystems and improve its ecological status. Hence, policies that stop the intensification of agriculture activities, and encourage the creation of more areas of Montado, may be one of the best options for the preservation of this type of aquatic ecosystems.

Supplementary Materials: The following are available online at http://www.mdpi.com/2073-4441/12/10/2665/s1. Table S1. Main characteristics observed: flow conditions, dominant macrophytes, bank width, channel width, water depth. Legend for dates: the letters represent the month (Jn: January; Mr: March; M: May; Jl: July; Sp: September; Nv: November); the numbers indicate the year of observations and sampling (17:2017; 18:2018); Table S2. Adopted land cover categories and CORINE Land Cover (CLS) inventory classes present in the study area that integrates each broader category; Table S3. Spearman on ranks correlation coefficients between land cover classes and water physicochemical parameters in the four tributary studies (marked correlations in bold are significant at: $p < 0.05$; $n = 32$); Table S4. Spearman on ranks coefficients between land cover classes and sediments physicochemical parameters and potentially toxic metals in the four tributaries assessed (marked coefficients in bold are significant at: $p < 0.05$; $n = 34$).

Author Contributions: Conceptualization, P.P.; Investigation, S.F., A.L., C.M., A.P., M.H.N., A.R. and M.P.; Supervision, P.P.; Writing—original draft, P.P., M.H.N., M.M. and M.J.C.; Writing—review & editing, P.P., M.H.N., M.M., M.J.C. and P.A. All authors have read and agreed to the published version of the manuscript.

Funding: The present research is co-funded by the European Union through the European Regional Development Fund, included in the COMPETE 2020 (Operational Program Competitiveness and Internationalization) through the ICT project (UIDB/04683/2020) with the reference POCI-01-0145-FEDER-007690, the ALOP project (ALT20-03-0145-FEDER-000004), and through the Engage SKA (POCI-01-0145-FEDER-022217) and by the European Union through the EU FP7 project SOLUTIONS (603437).

Acknowledgments: The authors thank the European Commission Copernicus Program for Copernicus Land Monitoring Service products, as well as the Ministry of Economy, Trade, and Industry (METI) of Japan and the United States National Aeronautics and Space Administration (NASA) for ASTER GDEM data, both used in this study.

Conflicts of Interest: The authors declare no conflict of interest.

References

1. Ahtiainen, H.; Öhman, M.C. *Ecosystem Services in the Baltic Sea: Valuation of Marine and Coastal Ecosystem Services in the Baltic Sea*; Nordic Council of Ministers: Copenhagen, Denmark, 2014.
2. Costanza, R.; d'Arge, R.; de Groot, R.; Farber, S.; Grasso, M.; Hannon, B.; Limburg, K.; Naeem, S.; O'Neill, R.V.; Paruelo, J.; et al. The value of the world's ecosystem services and natural capital. *Nature* **1997**, *387*, 253–260. [CrossRef]
3. Tagliapietra, D.; Povilanskas, R.; Razinkovas-Baziukas, A.; Tamin, J. Emerald growth: A new framework concept for managing ecological quality and ecosystem services of transitional waters. *Water (Switzerland)* **2020**, *12*, 894. [CrossRef]
4. Arenas-Sánchez, A.; Rico, A.; Vighi, M. Effects of water scarcity and chemical pollution in aquatic ecosystems: State of the art. *Sci. Total Environ.* **2016**, *572*, 390–403. [CrossRef] [PubMed]
5. Field, C.B.; Barros, V.; Stocker, T.F.; Qin, D.; Dokken, D.J.; Ebi, K.L.; Mastrandrea, M.D.; Mach, K.J.; Plattner, G.-K.; Allen, S.K.; et al. *Managing the Risks of Extreme Events and Disasters to Advance Climate Change Adapt*; Cambridge University Press: Cambridge, UK, 2012.
6. IPCC. *Climate Change 2014: Synthesis Report. Contribution of Working Groups I, II and III to the Fifth Assessment Report of the Intergovernmental Panel on Climate Change*; Core Writing Team, Pachauri, R.K., Meyer, L.A., Eds.; IPCC: Geneva, Switzerland, 2014.

7. Ignatius, A.R.; Rasmussen, T.C. Small reservoir effects on headwater water quality in the rural-urban fringe, Georgia Piedmont, USA. *J. Hydrol. Reg. Stud.* **2016**, *8*, 145–161. [CrossRef]
8. Palma, P.; Ledo, L.; Soares, S.; Barbosa, I.R.; Alvarenga, P. Spatial and temporal variability of the water and sediments quality in the alqueva reservoir (Guadiana Basin; Southern Portugal). *Sci. Total Environ.* **2014**, *470*, 780–790. [CrossRef]
9. Tan, X.; Yu, X.; Cai, L.; Wang, J.; Peng, J. Microplastics and associated PAHs in surface water from the Feilaixia Reservoir in the Beijiang River, China. *Chemosphere* **2019**, *221*, 834–840. [CrossRef]
10. Terechovs, A.K.E.; Ansari, A.J.; McDonald, J.A.; Khan, S.J.; Hai, F.I.; Knott, N.A.; Zhou, J.; Nghiem, L.D. Occurrence and bioconcentration of micropollutants in Silver Perch (Bidyanus bidyanus) in a reclaimed water reservoir. *Sci. Total Environ.* **2019**, *650*, 585–593. [CrossRef]
11. Khan, M.B.; Dai, X.; Ni, Q.; Zhang, C.; Cui, X.; Lu, M.; Deng, M.; Yang, X.; He, Z. Toxic Metal Pollution and Ecological Risk Assessment in Sediments of Water Reservoirs in Southeast China. *Soil Sediment Contam.* **2019**, *28*, 695–715. [CrossRef]
12. Bonansea, M.; Ledesma, C.; Rodriguez, M.C. Assessing the impact of land use and land cover on water quality in the watershed of a reservoir. *Appl. Ecol. Environ. Res.* **2016**, *14*, 447–456. [CrossRef]
13. Han, C.; Zheng, B.; Qin, Y.; Ma, Y.; Yang, C.; Liu, Z.; Cao, W.; Chi, M. Impact of upstream river inputs and reservoir operation on phosphorus fractions in water-particulate phases in the Three Gorges Reservoir. *Sci. Total Environ.* **2018**, *610*, 1546–1556. [CrossRef]
14. Woldeab, B.; Ambelu, A.; Mereta, S.T.; Beyene, A. Effect of watershed land use on tributaries' water quality in the east African Highland. *Environ. Monit. Assess.* **2019**, *191*, 36. [CrossRef] [PubMed]
15. Pullanikkatil, D.; Palamuleni, L.; Ruhiiga, T. Impact of land use on water quality in the Likangala catchment, southern Malawi D Pullanikkatil, LG Palamuleni & TM Ruhiiga AFRICAN JOURNAL OF AQUATIC SCIENCE. *Afr. J. Aquat. Sci.* **2015**, *40*, 277–286. [CrossRef]
16. Mello, K.; Valente, R.A.; Randhir, T.O.; Santos, A.C.A.; Vettorazzia, C.A. Effects of land use and land cover on water quality of low-order streams in Southeastern Brazil: Watershed versus riparian zone. *Catena* **2018**, *167*, 130–138. [CrossRef]
17. Hering, D.; Carvalho, L.; Argillier, C.; Beklioglu, M.; Borja, A.; Cardoso, A.C.; Duel, H.; Ferreira, T.; Globevnik, L.; Hanganu, J.; et al. Managing aquatic ecosystems and water resources under multiple stress—An introduction to the MARS project. *Sci. Total Environ.* **2015**, *503*, 10–21. [CrossRef] [PubMed]
18. Canuto, N.; Ramos, T.B.; Oliveira, A.R.; Simionesei, L.; Basso, M.; Neves, R. Influence of reservoir management on Guadiana streamflow regime. *J. Hydrol. Reg. Stud.* **2019**, *25*, 100628. [CrossRef]
19. Morais, M.M.; Serafim, A.M.; Pinto, P.; Ilhéu, A.; Ruivo, M. *Reservoir and River Basin Management. Exchange of Experiences from Brazil, Portugal and Germany*; Univerlagtu: Berlin, Germany, 2007.
20. Palma, P.; Alvarenga, P.; Palma, V.L.; Fernandes, R.M.; Soares, A.M.V.M.; Barbosa, I.R. Assessment of anthropogenic sources of water pollution using multivariate statistical techniques: A case study of the Alqueva's reservoir, Portugal. *Environ. Monit. Assess.* **2010**, *165*, 539–552. [CrossRef] [PubMed]
21. Diogo, P.A.; Fonseca, M.; Coelho, P.S.; Mateus, N.S.; Almeida, M.C.; Rodrigues, A.C. Reservoir phosphorous sources evaluation and water quality modeling in a transboundary watershed. *Desalination* **2008**, *226*, 200–214. [CrossRef]
22. Chícharo, L.; Chícharo, M.A.; Ben-Hamadou, R. Use of a hydrotechnical infrastructure (Alqueva Dam) to regulate planktonic assemblages in the Guadiana estuary: Basis for sustainable water and ecosystem services management. *Estuar. Coast. Shelf Sci.* **2006**, *70*, 3–18. [CrossRef]
23. Collares-Pereira, M.J.; Cowx, I.G.; Ribeiro, F.; Rodrigues, J.A.; Rogado, L. Threats imposed by water resource development schemes on the conservation of endangered fish species in the Guadiana River Basin in Portugal. *Fish. Manag. Ecol.* **2000**, *7*, 167–178. [CrossRef]
24. Filipe, A.F.; Marques, T.A.; Tiago, P.; Ribeiro, F.; da Costa, L.M.; Cowx, I.G.; Collares-Pereira, M.J.; Collares-Pereira, M.J. Selection of Priority Areas for Fish Conservation in Guadiana River Basin, Iberian Peninsula. *Conserv. Biol.* **2004**, *18*, 189–200. [CrossRef]
25. Galvão, H.; Reis, M.; Valério, E.; Domingues, R.; Costa, C.; Lourenço, D.; Condinho, S.; Miguel, R.; Barbosa, A.; Gago, C.; et al. Cyanobacterial blooms in natural waters in southern Portugal: A water management perspective. *Aquat. Microb. Ecol.* **2008**, *53*, 129–140. [CrossRef]

26. Palma, P.; López-Orozco, R.; Lourinha, C.; Oropesa, A.L.; Novais, M.H.; Alvarenga, P. Assessment of the environmental impact of an abandoned mine using an integrative approach: A case-study of the "Las Musas" mine (Extremadura, Spain). *Sci. Total Environ.* **2019**, *659*, 84–94. [CrossRef] [PubMed]
27. Valério, E.; Faria, N.; Paulino, S.; Pereira, P. Seasonal variation of phytoplankton and cyanobacteria composition and associated microcystins in six Portuguese freshwater reservoirs. *Ann. Limnol. Int. J. Limnol.* **2008**, *44*, 189–196. [CrossRef]
28. Palma, P.; Köck-Schulmeyer, M.; Alvarenga, P.; Ledo, L.; de Alda, M.L.; Barceló, D. Occurrence and potential risk of currently used pesticides in sediments of the Alqueva reservoir (Guadiana Basin). *Environ. Sci. Pollut. Res.* **2015**, *22*, 7665–7675. [CrossRef]
29. Palma, P.; Köck-Schulmeyer, M.; Alvarenga, P.; Ledo, L.; Barbosa, I.R.; López de Alda, M.; Barceló, D. Risk assessment of pesticides detected in surface water of the Alqueva reservoir (Guadiana basin, southern of Portugal). *Sci. Total Environ.* **2014**, *488*, 208–219. [CrossRef]
30. Palma, P.; Kuster, M.; Alvarenga, P.; Palma, V.L.; Fernandes, R.M.; Soares, A.M.V.M.; López de Alda, M.J.; Barceló, D.; Barbosa, I.R. Risk assessment of representative and priority pesticides, in surface water of the Alqueva reservoir (South of Portugal) using on-line solid phase extraction-liquid chromatography-tandem mass spectrometry. *Environ. Int.* **2009**, *35*, 545–551. [CrossRef]
31. Palma, P.; Ledo, L.; Alvarenga, P. Assessment of trace element pollution and its environmental risk to freshwater sediments influenced by anthropogenic contributions: The case study of Alqueva reservoir (Guadiana Basin). *Catena* **2015**, *128*, 174–184. [CrossRef]
32. Iakunin, M.; Salgado, R.; Potes, M. Breeze effects at a large artificial lake: Summer case study. *Hydrol. Earth Syst. Sci.* **2018**, *22*, 5191–5210. [CrossRef]
33. Potes, M.; Costa, M.J.; da Silva, J.C.B.; Silva, A.M.; Morais, M. Remote sensing of water quality parameters over Alqueva Reservoir in the south of Portugal. *Int. J. Remote Sens.* **2011**, *32*, 3373–3388. [CrossRef]
34. Palma, P.; Ledo, L.; Alvarenga, P. Ecotoxicological endpoints, are they useful tools to support ecological status assessment in strongly modified water bodies? *Sci. Total Environ.* **2016**, *541*, 119–129. [CrossRef] [PubMed]
35. Palma, P.; Ledo, L.; Soares, S.; Barbosa, I.R.; Alvarenga, P. Integrated environmental assessment of freshwater sediments: A chemical and ecotoxicological approach at the Alqueva reservoir. *Environ. Geochem. Health* **2014**, *36*, 209–223. [CrossRef]
36. APA (Agência Portuguesa do Ambiente) Plano de gestão de região hidrográfica 2016/2021. Parte 2. Caracterização e diagnóstico, Anexo IV. 2016. Available online: https://apambiente.pt/_zdata/Politicas/Agua/PlaneamentoeGestao/PGRH/2016-021/PTRH7/PGRH7_Parte5_AnexoII_1.pdf (accessed on 10 July 2020).
37. Silva, Á.; de Lima, M.I.P.; Santo, F.E.; Pires, V. Assessing changes in drought and wetness episodes in drainage basins using the Standardized Precipitation Index. *Bodenkultur* **2014**, *65*, 31–37.
38. Potes, M.; Salgado, R.; Costa, M.J.; Morais, M.; Bortoli, D.; Kostadinov, I.; Mammarella, I. Lake–atmosphere interactions at Alqueva reservoir: A case study in the summer of 2014. *Tellus A Dyn. Meteorol. Oceanogr.* **2017**, *69*, 1272787. [CrossRef]
39. IPMA. Situação de Seca Meteorológica. Available online: https://www.ipma.pt/resources.www/docs/im.publicacoes/edicoes.online/20180406/pryhFYgszRoHXedniacN/cli_20180331_20180331_sec_mm_co_pt.pdf (accessed on 10 July 2020).
40. Godinho, S.; Guiomar, N.; Machado, R.; Santos, P.; Sá-Sousa, P.; Fernandes, J.P.; Neves, N.; Pinto-Correia, T. Assessment of environment, land management, and spatial variables on recent changes in montado land cover in southern Portugal. *Agrofor. Syst.* **2016**, *90*, 177–192. [CrossRef]
41. APHA (America Public Health Association). *Standard Methods for the Examination of Water and Wastewater*, 23rd ed.; America Public Health Association: New York, NY, USA, 2017.
42. USEPA. *Methods for Collection, Storage and Manipulation of Sediments for Chemical and Toxicological Analyses: Tech. Man*; EPA-823-B-01-002; EPA Region V.: Chicago, IL, USA, 2001.
43. LNEC (Laboratório Nacional de Engenharia Civil). *E 196—Solos. Análise Granulométrica*; LNEC: Lisboa, Portugal, 1966.
44. ISO (International Organization for Standardization). *ISO 11466: Soil Quality—Extraction of Trace Elements Soluble in Aqua Regia*; ISO: Geneve, Switzerland, 1995.
45. Simeonov, V.; Stratis, J.A.; Samara, C.; Zachariadis, G.; Voutsa, D.; Anthemidis, A.; Sofoniou, M.; Kouimtzis, T. Assessment of the surface water quality in Northern Greece. *Water Res.* **2003**, *37*, 4119–4124. [CrossRef]

46. Alberto, W.D.; Del Pilar, D.M.; Valeria, A.M.; Fabiana, P.S.; Cecilia, H.A.; De Los Angeles, B.M. Pattern recognition techniques for the evaluation of spatial and temporal variations in water quality. A case study: Suquía River Basin (Cordoba-Argentina). *Water Res.* **2001**, *35*, 2881–2894. [CrossRef]
47. Agencia Portuguesa Ambiente (APA). *Plano de Gestão de Região Hidrográfica 2016/2021: Região Hidrográfica do Guadiana (RH7)*; Agencia Portuguesa Ambiente (APA): Lisboa, Portugal, 2016.
48. Palma, P.; Matos, C.; Alvarenga, P.; Köck-Schulmeyer, M.; Simões, I.; Barceló, D.; López de Alda, M.J. Ecological and ecotoxicological responses in the assessment of the ecological status of freshwater systems: A case-study of the temporary stream Brejo of Cagarrão (South of Portugal). *Sci. Total Environ.* **2018**, *634*, 394–406. [CrossRef]
49. Instituto da Água. *Relatório Síntese Sobre a Caracterização das Regiões Hidrográficas Prevista na Directiva-Quadro da Água*; Instituto da Água: Lisboa, Portugal, 2005; p. 163. Available online: https://www.apambiente.pt/dqa/assets/relatorio_artigo_5_pt.pdf (accessed on 16 July 2020).
50. Rowlatt, S.M.; Lovell, D.R. Lead, zinc and chromium in sediments around England and Wales. *Mar. Pollut. Bull.* **1994**, *28*, 324–329. [CrossRef]
51. Oliveira, A.; Palma, C.; Valença, M. Heavy metal distribution in surface sediments from the continental shelf adjacent to Nazaré canyon. *Deep Sea Res. Part II Top. Stud. Oceanogr.* **2011**, *58*, 2420–2432. [CrossRef]
52. Petersen, J.C.; Justus, B.G.; Meredith, B.J. *Effects of Land Use, Stream Habitat, and Water Quality on Biological Communities of Wadeable Streams in the Illinois River Basin of Arkansas, 2011 and 2012*; US Geological Survey No.2014-5009: Reston, VA, USA, 2014.
53. Cardoso-Silva, S.; de Lima Ferreira, P.A.; Figueira, R.C.L.; da Silva, D.C.V.R.; Moschini-Carlos, V.; Pompêo, M.L.M. Factors that control the spatial and temporal distributions of phosphorus, nitrogen, and carbon in the sediments of a tropical reservoir. *Environ. Sci. Pollut. Res.* **2018**, *25*, 31776–31789. [CrossRef]
54. Fletcher, R.; Welsh, P.F.P. *Guidelines for Identify, Assessing and Managing Contaminated Sediments in Ontario: An Integrated Approach*; Water Resources Branch: Toronto, ON, Canada, 2008.
55. CCME—Canadian Council of Ministers for the Environment. *Canadian Sediment Quality Guidelines for the Protection of Aquatic life: Summary Tables*; CCME: Winnipeg, MB, Canada, 2002. Available online: http://st-ts.ccme.ca/ (accessed on 12 July 2020).
56. Long, E.R.; Macdonald, D.D.; Smith, S.L.; Calder, F.D. Incidence of adverse biological effects within ranges of chemical concentrations in marine and estuarine sediments. *Environ. Manag.* **1995**, *19*, 81–97. [CrossRef]
57. Nunes, J.P.; Jacinto, R.; Keizer, J.J. Combined impacts of climate and socio-economic scenarios on irrigation water availability for a dry Mediterranean reservoir. *Sci. Total Environ.* **2017**, *584*, 219–233. [CrossRef] [PubMed]
58. Rodrigues, V.; Estrany, J.; Ranzini, M.; de Cicco, V.; Martín-Benito, J.M.T.; Hedo, J.; Lucas-Borja, M.E. Effects of land use and seasonality on stream water quality in a small tropical catchment: The headwater of Córrego Água Limpa, São Paulo (Brazil). *Sci. Total Environ.* **2018**, *622*, 1553–1561. [CrossRef]
59. Stephan, K.; Kellner, E.; Freedman, Z.; Kutta, E.; Kelly, C.; Hubbart, J.; Morrissey, E. Characterization of sub-watershed-scale stream chemistry regimes in an Appalachian mixed-land-use watershed. *Environ. Monit. Assess.* **2018**, *190*, 586. [CrossRef]
60. Shi, P.; Zhang, Y.; Li, Z.; Li, P.; Xu, G. Influence of land use and land cover patterns on seasonal water quality at multi-spatial scales. *Catena* **2017**, *151*, 182–190. [CrossRef]
61. Du, L.F.; Liu, J.; Li, S.J.; Li, X.R.; Yang, J.F.; Zhao, T.K.; Ma, M.T. Dynamic characteristics of nitrogen and phosphorus in the representative input tributaries of Miyun Reservoir. *IOP Conf. Ser. Earth Environ. Sci.* **2017**, *82*, 012084. [CrossRef]
62. Ongley, E.D.; Xiaolan, Z.; Tao, Y. Current status of agricultural and rural non-point source Pollution assessment in China. *Environ. Pollut.* **2010**, *158*, 1159–1168. [CrossRef]
63. Zhou, Y.; Xu, J.F.; Yin, W.; Ai, L.; Fang, N.F.; Tan, W.F.; Yan, F.L.; Shi, Z.H. Hydrological and environmental controls of the stream nitrate concentration and flux in a small agricultural watershed. *J. Hydrol.* **2017**, *545*, 355–366. [CrossRef]
64. Batista, M.J.; Abreu, M.M.; Locutura, J.; De Oliveira, D.; Matos, J.X.; Silva, C.; Bel-Lan, A.; Martins, L. Evaluation of trace elements mobility from soils to sediments between the Iberian Pyrite Belt and the Atlantic Ocean. *J. Geochem. Explor.* **2012**, *123*, 61–68. [CrossRef]
65. Fonseca, R.; Barriga, F.J.A.S.; Fyfe, W.S. Reversing desertification by using dam reservoir sediments as agriculture soils. *Episodes* **1998**, *21*, 218–224. [CrossRef]

66. Mil-Homens, M.; Vale, C.; Raimundo, J.; Pereira, P.; Brito, P.; Caetano, M. Major factors influencing the elemental composition of surface estuarine sediments: The case of 15 estuaries in Portugal. *Mar. Pollut. Bull.* **2014**, *84*, 135–146. [CrossRef]
67. Cruz, M.A.S.; de Azevedo Gonçalves, A.; de Aragão, R.; de Amorim, J.R.A.; da Mota, P.V.M.; Srinivasan, V.S.; Garcia, C.A.B.; de Figueiredo, E.E. Spatial and seasonal variability of the water quality characteristics of a river in Northeast Brazil. *Environ. Earth Sci.* **2019**, *78*, 68. [CrossRef]
68. Dodds, W.K.; Jones, J.R.; Welch, E.B. Suggested classification of stream trophic state: Distributions of temperate stream types by chlorophyll, total nitrogen, and phosphorus. *Water Res.* **1998**, *32*, 1455–1462. [CrossRef]

© 2020 by the authors. Licensee MDPI, Basel, Switzerland. This article is an open access article distributed under the terms and conditions of the Creative Commons Attribution (CC BY) license (http://creativecommons.org/licenses/by/4.0/).

Science of the Total Environment 741 (2020) 140459

Contents lists available at ScienceDirect

Science of the Total Environment

journal homepage: www.elsevier.com/locate/scitotenv

Environmental filtering and limiting similarity as main forces driving diatom community structure in Mediterranean and continental temporary and perennial streams

Gábor Várbíró [a,b], Gábor Borics [a,b], Maria Helena Novais [c,d], Maria Manuela Morais [d,e], Frédéric Rimet [f], Agnès Bouchez [f], Kálmán Tapolczai [g,h], István Bácsi [i], Philippe Usseglio-Polatera [j], Viktória B-Béres [a,b,*]

[a] MTA Centre for Ecological Research, Danube Research Institute, Department of Tisza Research, 18/c. Bem square, 4026 Debrecen, Hungary
[b] MTA Centre for Ecological Research, GINOP Sustainable Ecosystems Group, 3. Klebelsberg Kuno str., H-8237 Tihany, Hungary
[c] Renewable Energies Chair, University of Évora, Casa Cordovil, Rua D. Augusto Eduardo Nunes n 7, Évora, 7000-651, Portugal
[d] Institute of Earth Sciences - ICT, University of Évora, Rua Romão Ramalho no. 59, 7000-671 Évora, Portugal
[e] Water Laboratory, Rua da Barba Rala, n.° 1, Parque Industrial e Tecnológico de Évora, 7005-345, Évora, Portugal
[f] UMR CARRTEL, INRAE, Université de Savoie Mont-Blanc, Thonon-les-Bains, France
[g] Department of Limnology, University of Pannonia, H-8200 Veszprém, Egyetem u. 10, Hungary
[h] Hungarian Academy of Sciences, Premium Postdoctoral Research Program, H-1051 Budapest, Nádor u. 7, Hungary
[i] University of Debrecen, Department of Hydrobiology, P.O. Box 57, H-4010 Debrecen, Hungary
[j] University of Lorraine, CNRS, LIEC, Metz, France

HIGHLIGHTS

- We studied trait composition of diatom assemblages in perennial and temporary streams.
- Trait differences in the two types of streams were greater in the continental region.
- Environmental filtering and limiting similarity shape community structure.
- Unpredictable drying up (continental) has more drastic effects than predictable one.
- The time-for-adaptation and in part the stress-dominance theories have been supported.

GRAPHICAL ABSTRACT

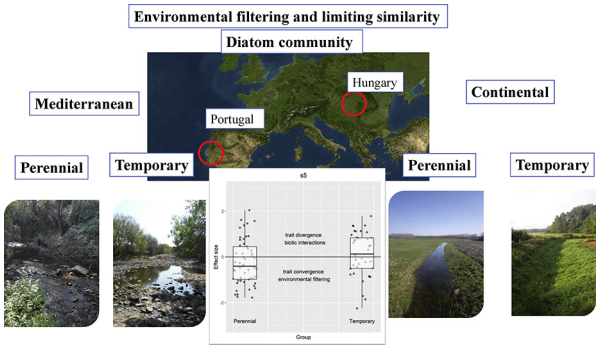

ARTICLE INFO

Article history:
Received 24 March 2020
Received in revised form 7 June 2020
Accepted 21 June 2020
Available online 23 June 2020

Editor: Sergi Sabater

ABSTRACT

Climatic extreme events such as droughts (unpredictable), dry periods (predictable) or even flush floods, threaten freshwater ecosystems worldwide. The filtering mechanisms of these events and their strength on communities, however, can be different among regions. While time-for-adaptation theory defines whether or not water scarcity can be considered as disturbance, the stress-dominance theory predicts an increase in importance of environmental filtering and a decrease in the role of biotic interactions in communities with increasing environmental stress. Here, we tested whether environmental filtering (leading to trait convergence) or limiting similarity (leading to trait divergence) is the main assembly rule shaping the structure and trait composition of benthic diatom assemblages in Mediterranean (Portuguese) and continental (Hungarian) temporary and

* Corresponding author at: MTA Centre for Ecological Research, Danube Research Institute, Department of Tisza Research, 18/c. Bem square, 4026 Debrecen, Hungary.
E-mail addresses: varbiro.gabor@okologia.mta.hu (G. Várbíró), borics.gabor@okologia.mta.hu (G. Borics), hnovais@uevora.pt (M.H. Novais), mmorais@uevora.pt (M.M. Morais), frederic.rimet@inrae.fr (F. Rimet), agnes.bouchez@inrae.fr (A. Bouchez), tapolczai.kalman@almos.uni-pannon.hu (K. Tapolczai), bacsi.istvan@science.unideb.hu (I. Bácsi), philippe.usseglio-polatera@univ-lorraine.fr (P. Usseglio-Polatera), beres.viktoria@okologia.mta.hu (V. B-Béres).

https://doi.org/10.1016/j.scitotenv.2020.140459
0048-9697/© 2020 The Authors. Published by Elsevier B.V. This is an open access article under the CC BY-NC-ND license (http://creativecommons.org/licenses/by-nc-nd/4.0/).

Keywords:
Temporary streams
Mediterranean and continental regions
Diatoms
Limiting similarity
Environmental filtering

perennial streams. We assumed that the trait composition of diatom assemblages in the two stream types would be less different in the Mediterranean than in the continental region (addressed to time-for-adaptation theory). We also hypothesized that trait composition would be shaped by environmental filtering in the Hungarian streams while by biotic interactions in Portuguese streams (addressed to stress-dominance theory). Our results supported our first hypothesis since traits, which associated primarily to temporary streams were found only in the continental region. Our findings, however, only partially proved the stress-dominance hypothesis. In the continental region, where drying up of streams were induced by unpredictable droughts, biotic interactions were the main assembly rules shaping community structure. In contrast, environmental filtering was nearly as important as limiting similarity in structuring trait composition in the Mediterranean region during the predictable dry phase with no superficial flow. These analyses also highlighted that drought events (both predictable and unpredictable ones) have a complex and strong influence on benthic diatom assemblages resulting even in irreversible changes in trait composition and thereby in ecosystem functioning.
© 2020 The Authors. Published by Elsevier B.V. This is an open access article under the CC BY-NC-ND license (http://creativecommons.org/licenses/by-nc-nd/4.0/).

1. Introduction

In the last century, freshwater became one of the most valuable goods in the world (Green et al., 2015). Freshwater in sufficient quantity and adequate quality is essential for healthy functioning of natural ecosystems and has a variety of ecosystem services to society (Francis, 2011; Jefferies et al., 2012). Freshwaters are fundamental resources for food production, drinking water services, industrial activities, transportation, human well-being services and also for nutrient cycling and maintenance of biodiversity, among others (Francis, 2011). Freshwater ecosystems, however, are under increasing pressures from anthropogenic activities and natural hazards (Dudgeon et al., 2006; Francis, 2011; Skoulikidis et al., 2017) and now, they are considered to be "the most endangered ecosystems worldwide" (Dudgeon et al., 2006).

In the last 50 years, the frequency and the intensity of extreme weather events including droughts and flash floods increased worldwide (IPBES, 2019). These extremities strongly threaten terrestrial, marine and freshwater ecosystems causing biodiversity loss and decrease in their functioning at local scale (IPBES, 2019). Drying up of freshwaters seems to be a typical example for disturbances, independently of their natural or anthropogenic origin. The time scale of dryness, however, is a key factor assessing whether this event is a disturbance or not (Poff et al., 1997; Acuña et al., 2017). In general, the naturally re-occurring predictable water shortage allows organisms to develop adaptations and strategies to overcome the critical environmental periods. In contrast the unpredictable human-induced drying up of waters and dry events with extraordinary magnitudes (even the natural ones) have strong influence on ecosystem structure and function (Acuña et al., 2017).

Drought-induced water scarcity is a direct driver causing reversible or even irreversible changes in freshwater ecosystems by changing the water flow conditions (e.g. Acuña et al., 2017; Stubbington et al., 2017). Depending on the surface flow conditions, lotic freshwaters can be classified as perennial (characterized by continuous flow) and temporary (characterized by drying up for a part of the year) (Skoulikidis et al., 2017). Temporary streams are widespread in arid, semi-arid and Mediterranean regions, but they are also common in oceanic climate regions (Stubbington et al., 2017). In the continental region, however, recurring drying up of formerly permanent streams began only in the last decades due to the effects of simultaneously acting human activities and climate change (B-Béres et al., 2019).

In the context of community assembly droughts can be considered as strong environmental filters. These filters operate on the traits or trait combinations of species rather than on the species themselves (McGill et al., 2006; Díaz et al., 2007; Zorger et al., 2019), and results in trait convergence within the assemblages. However, the decrease in trait diversity does not necessarily coincide with a decrease in species richness. There can be several species in the assemblages, which share almost identical traits, resulting in high functional redundancy. This functional redundancy gives stability to the systems, because species losses (caused by disturbances, competition or demographic stochasticity) do not bring losses in functioning. Species that successfully pass through the environmental filter have similar trait combinations, and due to this similarity they become exposed to strong biotic interactions. These interspecific interactions can be even more pronounced within the community if traits filtered are directly related to resources (including food and shelter). In these highly competitive environments, only those species, which differ remarkably in some relevant characteristics, can coexist (trait divergence within assemblages) (MacArthur and Levins, 1967; Pásztor et al., 2016). Thus, trait composition of the assemblages refers to the leading assembly rules (Götzenberger et al., 2012). To recognize these rules the most appropriate traits or trait combinations must be selected, which are responsive to disturbing effect (Zorger et al., 2019). Exclusion of responsive traits from analyses might lead to misunderstand the results and to draw incorrect findings. The strength of the environmental and biotic filters strongly depends on the abiotic characteristics of the habitats. This notion has been conceptualized in the stress dominance hypothesis, which states that composition is shaped by environmental filtering in harsh environmental conditions e.g. under extraordinary flow regimes, while biotic interaction plays pivotal role in formation of assemblages in benign environments (Grime, 1977; Weiher and Keddy, 1995; Coyle et al., 2014). However, harshness cannot be evaluated on an absolute scale. Extraordinary climatic events that caused drying up of streams can be assumed as harsh conditions in the continental region. Although, in Mediterranean region, the predictable dry periods cannot be considered as natural characteristics of the systems, at a longer historical timescale there is enough time for adaptation of the communities. This phenomenon was conceptualized in the time-for-adaptation theory by Acuña et al. (2017). Thus, while unpredictable droughts are strong filters in the continental region, periodically reoccurring dry periods have less severe impacts on the assemblages of Mediterranean streams, where biotic interactions can be supposed to be the major mechanisms structuring communities.

Benthic diatom assemblages as primary producers contribute significantly to the food webs in lotic ecosystems, especially in small streams (Kireta et al., 2012). Thus, changes in their structure induced by water shortage will finally influence the whole ecosystem (Stubbington et al., 2017). While studies on community structure or biodiversity dynamics of diatoms in temporary streams are considered as priority topics in Mediterranean regions (e.g. Novais et al., 2014; Falasco et al., 2016; Piano et al., 2017; Stubbington et al., 2019), only limited information is available on communities of benthic algae in drying waters in the continental region (B-Béres et al., 2019). It has been demonstrated that independently of ecoregions, aerophilous and/or terrestrial taxa can be characteristic in temporary streams (Falasco et al., 2016; B-Béres et al., 2019). However, considerable differences in trait composition can also be shown between Mediterranean and continental regions (Falasco et al., 2016; B-Béres et al., 2019). These differences may suggest that the strength of the water shortage-induced filtering mechanisms on benthic diatom communities differ among ecoregions.

Here, we tested whether environmental filtering or limiting similarity is the main assembly rule shaping trait composition of diatom

assemblages in Mediterranean and continental perennial and temporary streams.

According to the above-mentioned "time-for-adaptation" theory (Acuña et al., 2017) and "stress-dominance" theory (Coyle et al., 2014) we addressed the following research hypotheses:

(i) Benthic diatom assemblages of perennial and temporary streams in the continental region show larger compositional differences than those in the Mediterranean region.
(ii) Independently of the water regime, environmental filtering is the decisive assembly rule within diatom assemblages in continental streams, while trait composition is shaped by biotic interactions in the Mediterranean region.

2. Materials and methods

2.1. Sampling area

A total of 92 sites (39 temporary and 53 perennial) were sampled in southern and central Portugal belonging to the Ribeiras do Algarve (17), Guadiana (12), Mira and Sado (13), and Tejo (50) watersheds (Fig. 1). Sampling was carried out during spring 2006, under flowing conditions. The hydrological regime was determined by using a surface runoff model within a geographic information system (INAG, 2008). The studied streams belong to the R 17–20 river types (Solheim et al., 2019), and were subject to low anthropogenic pressure, based on REFCOND (2003) criteria and organized by the National Water Institute (INAG), such as land use in the watershed, urban area, presence and characteristics of the riparian vegetation, sediment loads, hydro-morphological alterations, changes in river connectivity caused by the presence of dams, toxicity, acidification and organic contamination.

In Hungary, the driest period shifted from winter to the growing season (summer) during the last decades (Bartholy et al., 2014), and the frequency of unpredictable droughts increased. Therefore, many formerly perennial streams were dried up recurrently in the last decade. These streams are referred as temporary and can be characterized by alternating dry and flowing phases within a year. However, there were several streams with irregular drying pattern, which made their characterization difficult. In some years, the flow conditions are permanent, while in others some stream reaches completely dry up during periods with no precipitation. Thus, here we defined the sampling events themselves "temporary" or "perennial" depending on the permanence of flow conditions. Accordingly, altogether 26 sites were sampled in the Eastern part of Hungary during spring from 2008 to 2015 in the course of the WFD-based national biomonitoring program (Fig. 1). In this period, a total of 96 samplings were conducted of which 71 have been considered as "temporary" and 25 have been considered as "perennial". The sampling was defined as temporary when only pools were present or no water was found in the streambed in the previous autumn. The studied lowland streams are calcareous with coarse or medium sized sediment, in small or medium sized catchments (R-05 Broad types, Solheim et al., 2019). In the region, the agricultural activity is intense, thus the ecological status of the streams was moderate (web 1, n.d.). Since in Hungary, continuous monitoring and collection of background data/information in some small temporary streams have begun very recently (van Dam et al., 2007), no information is available in the sampling period on topics such as pre-drought community composition, presence or absence of refugia during the drought, the duration of drying up, the velocity of water retreat, etc.

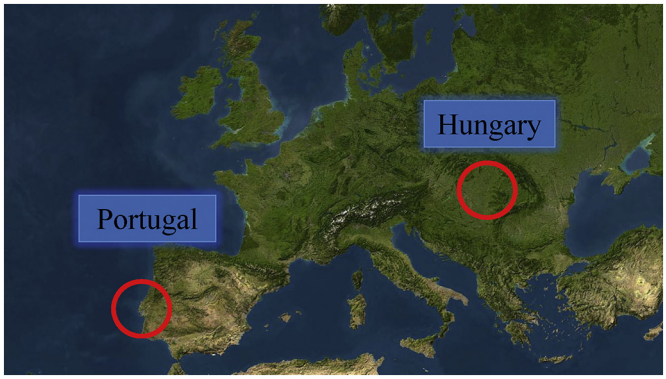

Fig. 1. The study area in Portugal and in Hungary.

2.2. Sample collection and preparation

All the samples were collected in the flowing phase of the streams. The sampling and preservation were performed according to the European standard (EN, 2003). In Portugal, the samples were collected from stones and cobbles while in Hungary, periphytic diatom samples were collected from emergent macrophytes (*Phragmites australis* (Cav.) Trin ex. Steud., or *Typha* spp.) as characteristic substrate types in the lowland area of the Carpathian Basin. Since some diatom species prefer certain substrate types (e.g. *Cocconeis placentula* ssp. favors plants as microhabitat; Soininen and Eloranta, 2004), we excluded problematic samples from the analyses in a pre-sorting process. According to the European standard (EN, 2003), hot hydrogen-peroxide method was used for the preparation of diatom valves and Naphrax resin was used for embedding. At least 400 diatom valves were counted and identified at least to species but also subspecies level using Leica DMRB (in Hungary) and Leica DMRX (for Portuguese samples) microscopes with 1000–1600-fold magnification. The identification of diatom taxa was carried out using references and also up-to-date literatures (Krammer and Lange-Bertalot, 1997a, 1997b; Krammer and Lange-Bertalot, 2004a, 2004b; Potapova and Hamilton, 2007; Bey and Ector, 2013 in PO and HU; Stenger-Kovács and Lengyel, 2015 in HU; the series 'Diatoms of Europe', 'Iconographia Diatomologica', 'Bibliotheca Diatomologica' and relevant taxonomic papers in PO).

2.3. Data processing and analyses

Altogether 168 and 299 taxa were found, respectively in the Portuguese and the Hungarian streams (Supplementary Table 1). According to Rimet and Bouchez (2012) diatom taxa were classified into 23 trait categories referring as traits in the paper (Table 1). Based on these traits species can be assigned one of to four guilds, to five cell size categories, to twelve life form groups, and mobility, spreading and colonization as binary categories.

The reliability of divergence/convergence analysis is based solely on the recorded traits, presence of non-recorded traits in assemblages might lead to unidentified relationships. Here, the most ecologically relevant 23 diatom traits were involved in the analyses that significantly indicate habitat diversity (see more in review Tapolczai et al., 2016). Other traits, such as formation of resting spores, or resting cysts, that enable taxa to endure disturbed environments are very rare in freshwater diatoms (Kaczmarska et al., 2013; Lange et al., 2016). Thus, these traits were excluded from analyses.

2.4. Statistical analyses

Two data matrix were prepared: one for taxonomic analysis with 188 samples and 378 taxa; another for traits analysis with 378 taxa and 23 traits. The calculation of convergence or divergence of traits follows the null model approach similarly to Lhotsky et al. (2016). We used Rao's quadratic entropy (RaoQ) (Botta-Dukát, 2005) as test statistic. RaoQ is the mean dissimilarity between two species weighted by the product of their relative abundances. First, we calculate the RAoQ test statistics, to 9999 random samples, created from the original species pool. Then, we repeated the same analysis for the real samples. Differences in trait distributions between the real and random communities were characterized

Table 1
Applied morphological and functional traits and their categories.

Type of traits	Trait categories
Guilds	Low profile
	High profile
	Motile
	Planktic
Cell size	S1: 5–99 μm^3
	S2: 100–299 μm^3
	S3: 300–599 μm^3
	S4: 600–1499 μm^3
	S5: ≥1500 μm^3
Life forms	Adnate
	Pedunculate
	Pad
	Stalk
	Non-colonial
	Colonial
	Mucous tubule colony
	Filament colony
	Zig-zag colony
	Rosette colony
	Ribbon colony
	Arbuscular colony
Mobility	Mobile
Spreading and colonization	Pioneers

by the *p*-values of the applied *t*-test. Probit transformed *p*-values were used as 'effect size values' (ES), which indicate the higher probability of trait divergence or convergence (Botta-Dukát, 2018). Positive ES values indicate that **competition** is the leading assembly rule, while negative ones refer to the leading role of **environmental filtering**. The positive values mean that the resident species in the assemblages have highly different values of the given trait than those in the random assemblages. In the case of negative ES values the resident species have more similar trait values than those in the randomised populations because species having highly different trait values are filtered out by the environment. This combination of test statistic and randomization algorithm allows detecting both trait convergence due to environmental filtering, and trait divergence due to limiting similarity (Botta-Dukát and Czúcz, 2016; Götzenberger et al., 2016).

We used the Student's *t*-test to show the significant differences in ES values from zero for the whole dataset. For visualizing the differences between perennial and temporary streams, we used box-plot approach with jitter plots and the significance of the differences between these two groups was tested with Mann-Whitney *U* test.

The entire procedure sketched out above was repeated for each trait independently.

Additional, two Principal Components Analyses (PCA) were performed to complement the interpretation of the ecological traits in perennial and temporary streams. For these analyses, we used the community weighted mean (CWM) approach, which expresses the mean trait value in the community weighted by the relative abundances of the species matrix of both, Hungarian and Portuguese datasets.

All statistical analyses and graphs were performed under R environment, with the relevant packages (vegan, tidyverse and ade4) (Dray and Dufour, 2007; Oksanen et al., 2019; R Core Team, 2019).

For the comparison of the taxonomic composition between the two regions, we used a Non-metric Multidimensional Scaling (NMDS) using the Jaccard coefficient of similarity. Since the Jaccard coefficient is based on binary distances and focuses on the similar taxa occurring in the two datasets. For the comparison of the trait compositions between the two regions, we used the community-weighted mean (CWM) matrix, in which the mean trait values in the community were weighted by the relative abundances of the species. An NMDS using the Bray-Curtis coefficient of dissimilarity was then produced. The multivariate statistical software Canoco 5 (ter Braak and Šmilauer, 2002) was used for the analysis.

3. Results

3.1. Traits–water regime relationships

3.1.1. General findings

Independently of the water regime, taxonomy-based NMDS analysis indicated clear separation between the diatom assemblages in the two ecoregions (Fig. 2), while the trait-based NMDS analysis showed a greater overlap among them (Fig. 3). Small size, pioneer and/or low profile guild taxa were characteristic of the Mediterranean region (no separation was observed according to water regime) and of the temporary streams in the continental region. Different types of colonial taxa seemed to prefer more likely the perennial streams independently of the ecoregion. Medium or large sized and/or motile taxa were, however, dominant in the continental streams independently of the water regime types (Fig. 3).

3.1.2. Ecoregional differences

Based on the trait composition of benthic diatoms, the N-PCA analysis performed for the first two components indicated only slight differences in the importance of water regime in explaining the functional composition of assemblages (63.38% in the continental region and 61.66% in the Mediterranean region). Characteristic traits of the two water regime types could be clearly identified in the continental region. However, occurrence of this kind of specific traits was not characteristic in the Mediterranean region. In the continental region, diatom communities in temporary streams were characterized by small size (S1) and/or pioneer taxa belonging mainly to low profile guild. Most of these taxa attached by stalk to the substrates. In contrast, different

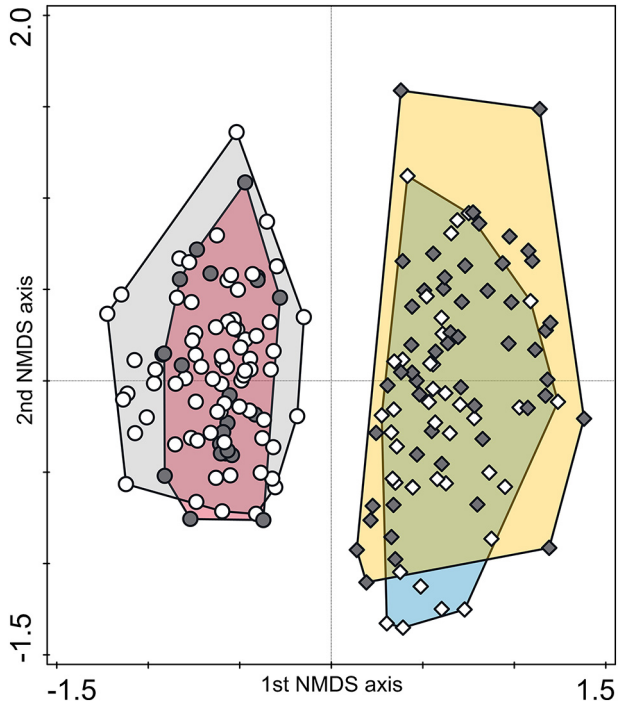

Fig. 2. Results of the species-based NMDS analysis of the diatom communities in streams of the continental and Mediterranean streams. The first and second axes explained 46.67% and 28.46% of the total variance, respectively. Temporary streams in the continental region are marked with white circles (their covered area is grey). Perennial watercourses in the continental region are marked with grey circles (their covered area is red). Temporary streams in the Mediterranean region are marked with white diamond (their covered area is blue). Perennial watercourses in the Mediterranean region are marked with grey diamond (their covered area is yellow).

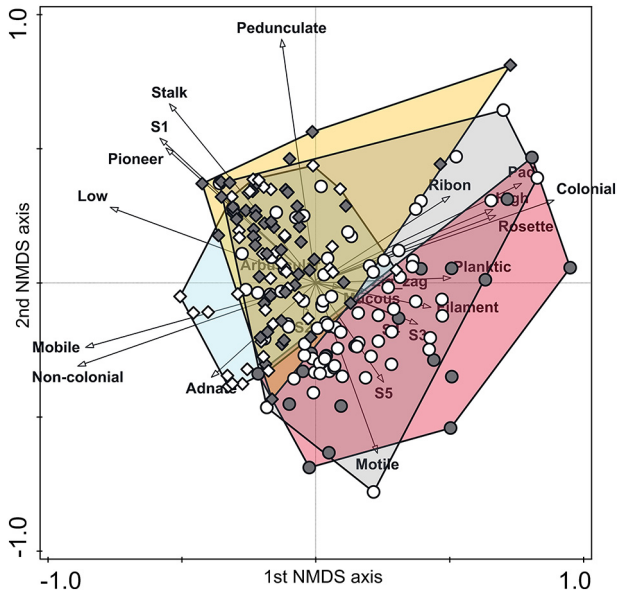

Fig. 3. Results of the trait-based NMDS analysis of the mean trait profiles of diatom assemblages in streams of the continental and Mediterranean regions for the first two axes. The first and second axes explained 52.94% and 30.15% of the total variance, respectively. Temporary streams in the continental region are marked with white circles (their covered area is grey). Perennial watercourses in the continental region are marked with grey circles (their covered area is red). Temporary streams in the Mediterranean region are marked with white diamond (their covered area is blue). Perennial watercourses in the Mediterranean region are marked with grey diamond (their covered area is yellow).

types of colonial, high profile taxa were characteristic for perennial streams (Fig. 4, Supplementary Table 2).

In the Mediterranean region, the perennial streams were mostly preferred by high profile, mostly colonial (in different types) taxa attached to substrate by pad, while there were no traits which could clearly indicate the temporary regime (Fig. 5).

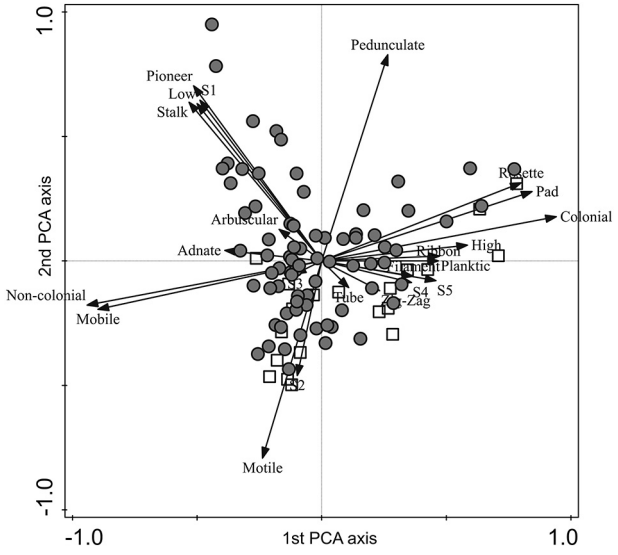

Fig. 4. Results of the PCA analyses of the mean trait profiles of diatom communities in Hungarian streams (continental region). The first and second axes explained 28.78% and 15.61% of the total variance, respectively. Temporary streams are marked with grey circles. Perennial watercourses are marked with squares.

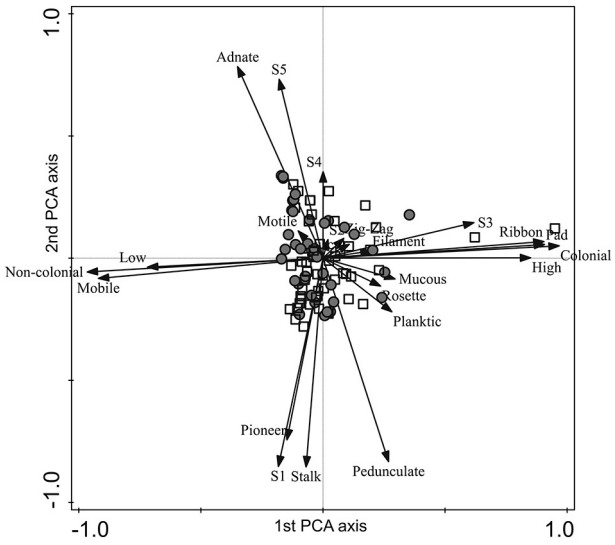

Fig. 5. Results of the PCA analyses of the mean trait profiles of diatom communities in Portuguese streams (Mediterranean region) for the first two components. The first and second axes explained 28.53% and 17.91% of the total variance, respectively. Temporary streams are marked with grey circles. Perennial watercourses are marked with squares.

3.2. Distribution of the effect size (ES) values in comparison with the null model in the continental region

In the continental region, the results of Mann-Whitney tests indicated that the ES values of adnate, low profile guild, pioneer, S1 and stalk traits were significantly higher in temporary streams than in perennial streams (Table 2). In contrast, significantly higher ES values were found in perennial streams than in temporary ones in the case of traits like S5 (Fig. 6, Table 2).

Regardless the water regimes, in the continental region nine traits were characterized by non-random distribution (low profile guild, S3, S4, adnate, pioneer and filament, zig-zag, rosette and arbuscular colonies;

Table 2
The significance of the difference in effect size values between perennial and temporary streams, based on Mann-Whitney *U* test. Significant differences are highlighted in bold (↑↓ indicates the increase or decrease in ES values of temporary streams compared to perennial ones).

Traits	*p* values	
	Continental region	Mediterranean region
Low profile	**0.000** ↑	0.950
High profile	0.184	0.204
Motile	0.431	0.637
Planktic	0.090	0.598
s1	**0.002** ↑	0.333
s2	0.228	0.185
s3	0.343	**0.0188** ↓
s4	0.298	0.106
s5	**0.013** ↓	0.051
Adnate	**0.003** ↑	0.765
Pedunculate	0.309	0.919
Pad	0.924	0.777
Stalk	**0.032** ↑	0.629
Non-colonial	0.706	**0.021** ↑
Colonial	0.512	**0.022** ↓
Mucous tubule colony	0.163	**0.002** ↓
Filament colony	0.170	0.431
Zig-zag colony	0.932	0.288
Rosette colony	0.798	0.783
Ribbon colony	0.809	0.427
Arbuscular colony	0.597	0.151
Mobile	0.664	0.055
Pioneer	**0.045** ↑	0.582

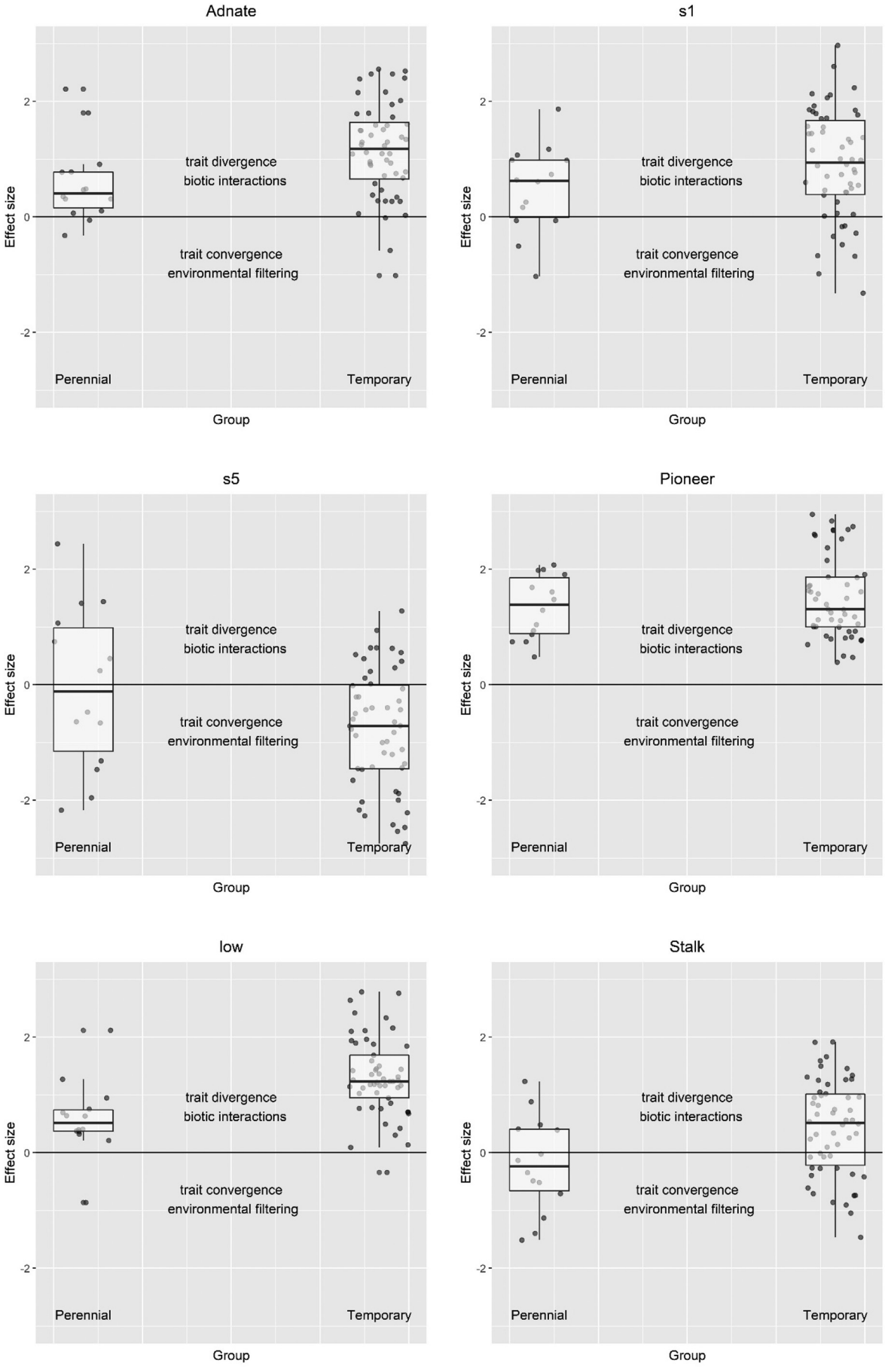
Adnate
s1
s5
Pioneer
low
Stalk
Effect size
2
0
-2
trait divergence
biotic interactions
trait convergence
environmental filtering
Perennial
Temporary
Group

Table 3
Results of the test on the effect size values from random distribution (0 value), the table includes the mean ES values and the *p*-value of the *t*-test; significant differences highlighted in red (in both water regimes), red and bold (exclusively in temporary streams), black and bold (exclusively in perennial streams).

	Continental region				Mediterranean region			
	ES values		p values		ES values		p values	
	perennial	*temporary*	*perennial*	*temporary*	*perennial*	*temporary*	*perennial*	*temporary*
Low profile	0.706	1.460	0.000	0.000	0.494	0.464	0.000	0.010
High profile	0.161	-0.150	0.523	0.138	-0.519	-0.666	0.000	0.000
Motile	-0.095	-0.345	0.746	**0.018**	-0.839	-0.861	0.000	0.000
Planktic	0.361	-0.043	**0.050**	0.702	-0.444	-0.393	0.000	0.001
s1	0.250	0.852	0.111	**0.000**	0.939	0.723	0.000	0.000
s2	0.283	-0.037	0.170	0.766	-0.003	-0.183	0.975	0.166
s3	0.454	0.642	0.015	0.000	0.014	-0.413	0.912	**0.002**
s4	-0.720	-0.473	0.002	0.000	-0.412	-0.165	**0.001**	0.229
s5	-0.190	-0.924	0.502	**0.000**	-0.215	0.157	0.210	0.354
Adnate	0.622	1.319	0.000	0.000	0.978	0.990	0.000	0.000
Pedunculate	0.241	0.481	0.313	**0.000**	-0.296	-0.226	0.082	0.303
Pad	0.174	0.144	0.536	0.303	-0.642	-0.687	0.000	0.000
Stalk	-0.013	0.456	0.946	**0.000**	0.384	0.411	**0.004**	0.071
Non-colonial	0.126	0.019	0.681	0.879	-0.583	-0.988	0.000	0.000
Colonial	0.207	0.016	0.531	0.894	-0.632	-1.173	0.000	0.000
Mucous tubule colony	0.170	-0.071	0.531	0.193	0.474	0.099	**0.000**	0.259
Filament colony	1.611	1.318	0.000	0.000	0.682	0.750	0.000	0.000
Zig-zag colony	0.217	0.210	0.023	0.000	0.819	0.734	0.000	0.000
Rosette colony	1.430	1.362	0.000	0.000	0.425	0.444	0.000	0.000
Ribbon colony	-0.220	-0.159	0.445	0.140	-0.466	-0.574	0.001	0.000
Arbuscular colony	4.753	4.753	0.000	0.000	0.301	0.365	0.001	0.000
Mobile	0.364	0.248	0.181	**0.039**	-0.539	-0.932	0.001	0.000
Pioneer	1.254	1.757	0.000	0.000	2.141	2.121	0.000	0.000

Table 3). Additionally, six traits showed also non-random distribution in temporary streams, while only the distribution of the planktic trait differed significantly from random in perennial streams (Table 3). In both stream water regime types, the means of ES values of traits like adnate, arbuscular, filamentous, low profile guild, pioneer, rosette colony, S3 and zig-zag colony were significantly higher than zero, indicating higher probability of trait divergence (biotic interactions). In contrast, the mean ES values of S4 trait were significantly lower than zero, related to a higher probability of convergence (environmental filtering). In the temporary streams of the continental region, traits like mobile, pedunculate, S1 and stalk were characterized by mean ES values >0, while mean ES values <0 are related to motile and S5 traits. In the case of planktic trait, the mean ES value >0 indicated higher probability of trait divergence in perennial streams (Table 3).

3.3. Distribution of the effect size (ES) values in comparison with the null model in the Mediterranean region

In the Mediterranean region, higher ES values of S3, colonial and mucous tube colony traits were more characteristic in perennial than in temporary streams (Fig. 7, Table 2). Only the ES values of non-colonial trait were significantly higher in temporary streams than in perennial ones (Table 2).

In the Mediterranean region, *t*-tests indicated non-random distribution of sixteen traits in both stream water regime types. There was only one trait (S3) which distribution differed from random exclusively in temporary streams, while non-random distribution characterized S4, stalk and mucous tube colony traits in perennial streams. In both stream water regime types, the mean ES values of traits like adnate, arbuscular, filamentous, low profile guild, pioneer, S1, rosette and zig-zag colony were significantly larger than 0, indicating higher probability of trait divergence. In contrast, significantly <0 mean values, characterized traits like colonial, high profile and motile guilds, mobile, non-colonial, pad, planktic and ribbon referring to higher probability of trait convergence. In the case of S3 trait, the mean ES values were significantly <0, indicating higher probability of environmental filtering in temporary streams. In perennial streams, significantly <0 mean ES values characterized the S4 trait, while the mean ES values of stalk and mucous tube colony traits were significantly >0. (Table 3).

4. Discussion

4.1. Ecoregional differences in trait composition - general findings

Traditionally, diatoms are considered as cosmopolitan taxa and might have a wide geographical distribution (Soininen and Niemela, 2002). Recent studies, however, emphasize that many species have rather limited distribution (Kociolek et al., 2017; Sakaeva et al., 2016). Furthermore, ecoregional differences in climate, soil or in geology can further modify the species responses to general water characteristics (e.g. nutrient supply, light conditions, etc.) (Besse-Lototskaya et al., 2011), highlighting strong microevolutionary pressure on taxa (Soininen et al., 2016). Thus, the clear separation of taxonomic composition between the ecoregions studied here was expected. The overlap in trait composition, however, was more pronounced due to the strong similarity among diatom assemblages in the continental temporary, in the Mediterranean temporary and in the Mediterranean perennial streams. Independently the water regime, Novais et al. (2014) also found high trait-based similarity in the Mediterranean region. However, they also highlighted the taxonomic differences between water regime

Fig. 6. The distribution of effect size values in perennial and temporary streams in the continental region (Hungary).

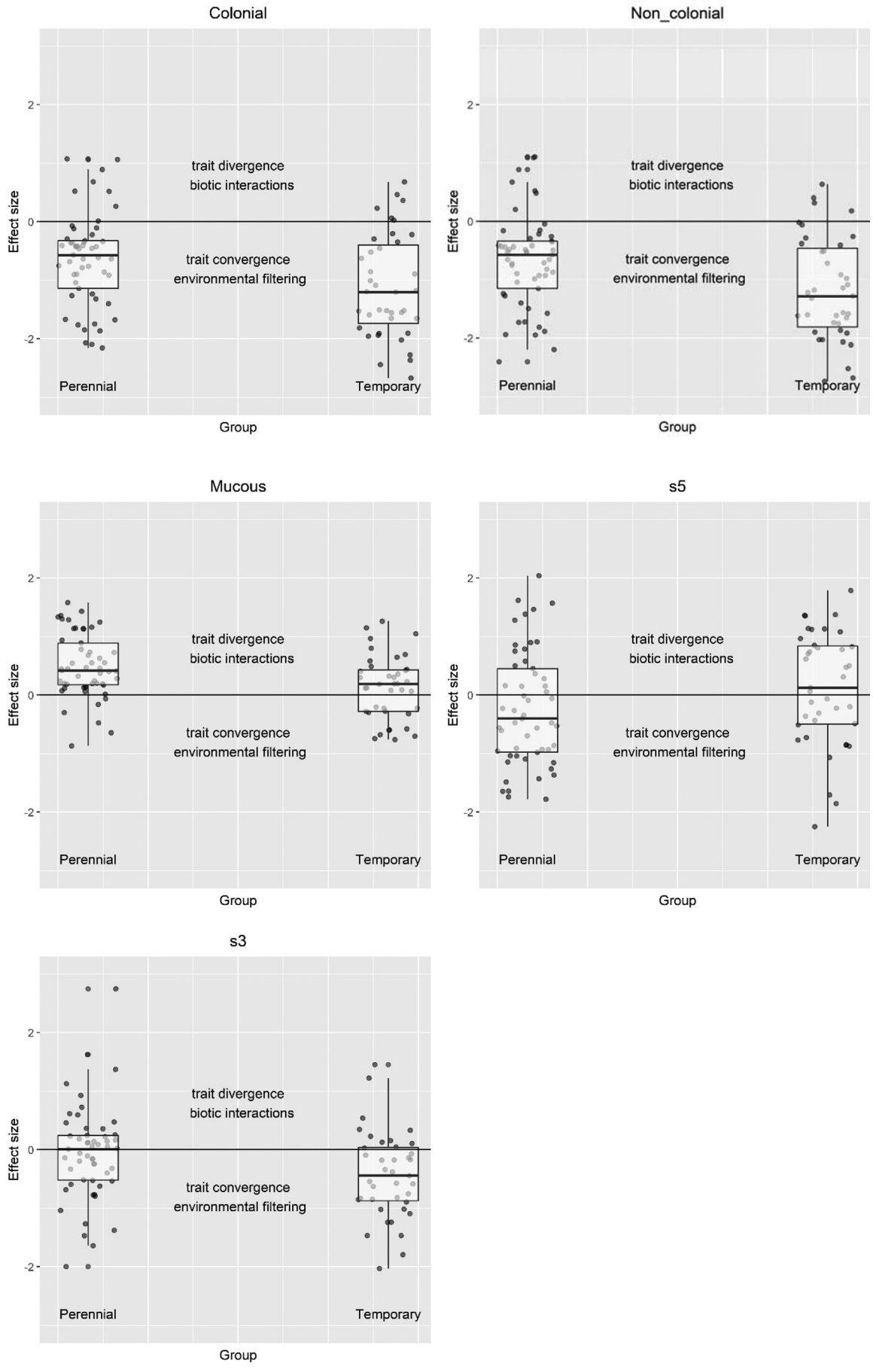
Colonial
Non_colonial
Mucous
s5
s3
Effect size
2
0
-2
trait divergence
biotic interactions
trait convergence
environmental filtering
Perennial
Temporary
Group

types, indicating the importance of temporary streams in biodiversity conservation. Traits, which were dominant in the Mediterranean region (small size, pioneer, low profile), were also characteristics in the continental temporary streams. Despite the fact, that taxa with different traits or trait combinations can cope with the same unpleasent circumstances (Le Bagousse-Pinguet et al., 2017; Pinho et al., 2019), our results clearly indicated the aprior benefits of the mentioned diatom traits in the continental and Mediterranean temporary and the Mediterranean perennial streams (detailed explanations of similarities of Mediterranean watercourses see in the next chapter).

Assessing the influence of water regime on colonial forms we found that depending on the complexity of the colonies, taxa are able to tolerate either stable, predictable conditions (simple colony) or unpredictable environments (complex colony) (Passy, 2002; Passy and Larson, 2011). Independently the ecoregions, colonial taxa preferred perennial streams to temporary ones in our study. Obviously, perennial water regime creates more stable conditions for assemblages comparing to temporary waters. Droughts and dry periods, however, can change the hydrological, physical and chemical conditions in these perennial streams. Even in the Mediterranean region, the strength and the duration of the dry period cannot be predicted from period to period.

Although nutrient enrichment can usually stimulate taxa in all guilds, high nutrient supply is especially favorable for members of the motile guild (Passy, 2007; Passy and Larson, 2011). Here we found, that independently of the water regime, richness and proportion of motile guild were higher in the continental than in the Mediterranean ecoregion. One reliable reason of this phenomenon is, that the studied lowland streams in the continental region were exposed to intense agricultural activity and their ecological status was moderate, while streams in the Mediterranean region were under low anthropogenic pressure. Furthermore, the decreasing water coupled with increasing nutrient concentrations in the dry period can significantly enhance the ratio of motile taxa, especially of the large ones, in the assemblages of the continental region (Kókai et al., 2015). Another possible reason of the above-mentioned phenomenon could be the use of different substrate types for sampling in the two ecoregions (stones vs emergent macrophytes). Although the substrate type can significantly influence the taxonomic and trait structure of communities, several studies have demonstrated the similarity between guild composition of diatom assemblages on epiphytic and epilithic substrates (Poulickova et al., 2004; Passy, 2007). Both of them are usually favored by high and low profile taxa.

4.2. Water regime influence on trait distribution – time-for-adaptation theory

Time scale of droughts and dry periods, i.e. the historical occurrence of these events, define the direction and strength of compositional changes in assemblages during these events. An intense influence of dryness on assemblages may be present in regions where these dry events with extraordinary magnitude do not fall within the annual average hydrological variations. In contrast, assemblages could adapt to the harsh circumstances of water scarcity in regions, where these conditions are expected (Acuña et al., 2017). Thus, more pronounced trait-based compositional differences in diatom assemblages were hypothesized between perennial and temporary streams in the continental than in the Mediterranean region. Although our results supported this hypothesis, they have encouraged us to rethink the adaptation theory in terms of diatoms. It was unexpected, that the importance of water regime in formation of functional composition was quite similar in the two ecoregions (61.66% in the Mediterranean vs. 63.38% in the continental region). In Hungary, however, the two hydrological regimes (perennial vs. temporary) clearly separated from each other and characteristic traits in these regimes have been recognized. In contrast, no traits clearly characterized the temporary streams in the Mediterranean region. Since nutrient supply and water quality were very similar in the studied Mediterranean streams, our results also reinforced that in such systems drying up in the dry period can be considered as an intense natural process influencing biodiversity and shaping community's structure (Novais et al., 2014; Piano et al., 2017; Tornes and Ruhi, 2013). Generally, it is hard to identify changes in adaptation strategies of microorganisms, especially in the field (Berthon et al., 2011; Tapolczai et al., 2016; B-Béres et al., 2017). The very similar trait composition in the Mediterranean streams, however, suggested that benthic diatoms have already adapted at community level to recurrent dry period by strong trait selection. Traits that have superior competitive abilities in marginally disturbed but nutrient rich environments (e.g. motile guild) were influenced by strong selective pressure here. In contrast, the resource poor habitats predictably disturbed by dry periods ensured the persistence of other traits (low profile, small size, pioneer) supporting survival during these conditions. Despite the community level adaptation of benthic diatoms to the recurrent dry periods in the Mediterranean region, annual changes in trait composition were obviously controlled by important factors such as the duration of the dry period, the pre-dry period community composition, the presence or absence of residual pools, the herbivorous pressure by macroinvertebrate grazers and even by the velocity of water retreat. Finally, our findings in the Mediterranean region (i.e. similar trait composition independently of the water regime) also reinforce the notion that disturbing effects increase the convergence of traits within assemblages highlighting the influence of environmental filtering on communities (Zorger et al., 2019).

Traits indicating permanent habitat, however, could be identified in both ecoregions. Colonial and high profile traits were characteristic of perennial stream communities independently of the region. Our findings denote the robustness of these traits as indicators of permanent habitat. Taxa having these characteristics prefer stable physical and chemical environments (Tapolczai et al., 2016; B-Béres et al., 2017) and also tolerate the grazing pressure (Passy, 2007). In addition, colonial and high profile taxa prefer stable substrates such as macrcophytes and stones, where they are less exposed to dislodgement (Passy, 2007).

As we mentioned above, small size generalists, including pioneers belonging to the low profile guild, dominated the temporary streams in Hungary. These mostly r-selected taxa are well-known as indicators of physically disturbed environments (Biggs et al., 1998; Passy, 2007). Their stress-tolerant character means that these taxa are capable of prevailing under extreme and even contrasted water regime conditions: either high current velocity or floods (Stenger-Kovács et al., 2006; Passy, 2007; B-Béres et al., 2014) or drying up of waters (Novais et al., 2014; B-Béres et al., 2019); either high light (Leira et al., 2015; Kókai et al., 2019) or low light conditions (Liess et al., 2009; Stenger-Kovács et al., 2013). In Hungary, the flow conditions of sampling in spring were followed by the drying up of temporary streams in summer. In addition, high light conditions were characteristic in dry periods, while low light availability was present during the flowing phase in spring. These circumstances were ideal for the colonization and fast reproduction of the small, r-strategist taxa.

4.3. Main assembly rules in the Mediterranean and continental region – stress-dominance theory

Independently of the geographical location, drying up in streams creates a very unique but also very constraining and selecting environment for populations. According to the stress-dominance theory

Fig. 7. The distribution of effect size values in perennial and temporary streams in the Mediterranean region (Portugal).

(Weiher and Keddy, 1995), environmental filtering could have a leading role in shaping community structure during dry periods and droughts compared to biotic interactions. It may be especially true in the continental region, where drying up of streams is mostly unpredictable. Here, the main factor leads to drying up, is the unpredictable annual distribution of the precipitation. In the last century, the annual precipitation decreased in the region parallel to an increase in the number of extreme precipitation days (Bartholy and Pongrácz, 2005), while the driest period shifted to the summer period (Bartholy et al., 2014). Additionally, agricultural activities as watering strengthen the negative effects of natural processes. In the Mediterranean region, however, effects of drying up may be less pronounced, since the assemblages are better adapted to these periodically reoccurring events (Acuña et al., 2017). Therefore, when formulating our hypothesis, we also considered the time-for-adaptation theory and we hypothesized a more pronounced environmental filtering effect in the continental than in the Mediterranean region. Furthermore, we also supposed that biotic interactions would play pivotal role in structuring of diatom assemblages in the Mediterranean region. Our results only partially supported this hypothesis: The main assembly rule was limiting similarity in the Hungarian streams resulting in strong biotic interaction within the assemblages and leading to trait divergence (rejecting stress-dominance hypothesis). But dryness influenced differently the diatom assemblages in the two water regime types because their trait composition significantly differed between temporary and perennial streams. In temporary streams, benthic algae had to regularly face dryness. Those taxa which were not able to tolerate these conditions, were filtered out rapidly from communities (e.g. large size and/or stalk or motile), while algae having the suitable traits (e.g. small size and/or pedunculated) were able to survive. Because in the continental region, the continuous monitoring of temporary streams and the collection of their background data have begun very recently, we have no information about important topics such as the community structure before, during and after drying up, the presence or absence of refugia during the drought, the duration of drying up. Therefore, the stability of the selected trait composition is unknown in these streams. The results, however, highlight a strong environmental filtering caused by drying up of streams. In contrast, taxa living in perennial streams were strongly affected by decreasing water supply and probably increasing nutrient supply. Although in this study, we did not examine the changes of physical and chemical parameters, our previous results have shown that droughts induce an increase in the concentration of nutrients in small lowland perennial streams (Kókai et al., 2015). In addition, the agricultural activity is basically intense in the region. The elevated nutrient concentrations are able to strengthen the negative impact of agriculture on communities. Thus, the dominance of colonial taxa, characterizing the perennial streams here, might also refer to elevated nutrient content, since most of those taxa prefer eutrophic conditions (van Dam et al., 1994 updated 2011). In addition, these circumstances also favor motile taxa, which have higher competitive abilities in nutrient-rich environments (Passy, 2007).

In the Mediterranean region, the ES values of most traits differed from 0. This highlights the importance of limiting similarity and environmental filtering in structuring the assemblages. Both temporary and perennial streams were mainly dominated by taxa with traits providing competitive advantage under physically disturbed and/or nutrient poor environments (ES values >0). The ES values of traits that characterized diatom assemblages of perennial streams (pad, high profile) were significantly lower than 0. Such values indicate the higher probability of trait convergence due to the major role of environmental filtering in trait selection. In contrast, ES values of some other traits characteristic of perennial streams (different colonial types) or usually characteristic of temporary streams were significantly higher than 0 indicating the higher importance of biotic interactions in structuring assemblages. Although these results supported only partially the stress dominance hypothesis, they clearly highlighted that the dry period is a very strong and complex environmental factor in the Mediterranean region that probably drives diatom community composition in combination with other factors (e.g. light, low nutrient supply, etc.).

5. Conclusion

Our findings have highlighted the ecoregional differences of drying up-induced filtering mechanisms on benthic diatom communities. While characteristic combinations of traits under both temporary and perennial aquatic regimes could be recognized in the diatom assemblages of the continental region, no traits were specifically associated to the diatom assemblages of temporary streams in the Mediterranean region. Our results, however, also pointed out the robustness of traits indicating perennial streams since almost the same combination of traits has characterized this aquatic regime in both ecoregions. Our results have also demonstrated that environmental filtering and limiting similarity play a pivotal role in structuring benthic diatom assemblages in both regions. Our findings, however, have only partially supported the stress-dominance hypothesis (importance of environmental filtering increases with increasing environmental stress; Grime, 1977; Weiher and Keddy, 1995). In Hungary, limiting similarity was the main force structuring communities denoting and resulting in a strong biotic interaction within assemblages, while both environmental filtering and limiting similarity controlled the trait composition of diatom assemblages in Portugal. These results have highlighted the complexity of drought-induced influences on benthic diatoms regardless of ecoregional differences.

Supplementary data to this article can be found online at https://doi.org/10.1016/j.scitotenv.2020.140459.

CRediT authorship contribution statement

Gábor Várbíró: Conceptualization, Methodology, Formal analysis, Writing - original draft, Visualization.**Gábor Borics:**Writing - original draft, Writing - review & editing, Investigation.**Maria Helena Novais:** Writing - original draft, Writing - review & editing, Investigation. **Maria Manuela Morais:**Conceptualization, Writing - original draft, Writing - review & editing, Investigation.**Frédéric Rimet:**Writing - original draft, Writing - review & editing.**Agnès Bouchez:**Conceptualization, Writing - original draft, Writing - review & editing.**Kálmán Tapolczai:** Writing - original draft, Writing - review & editing.**István Bácsi:**Writing - original draft, Writing - review & editing.**Philippe Usseglio-Polatera:** Writing - original draft, Writing - review & editing.**Viktória B-Béres:** Conceptualization, Methodology, Writing - original draft, Writing - review & editing, Investigation, Data curation.

Declaration of competing interest

The authors declare that there is no conflict of interest.

Acknowledgement

This paper supported from COST Action CA15113 (SMIRES, Science and Management of Intermittent rivers and Ephemeral streams; www.smires.eu) supported by COST (European Cooperation in Science and Technology) and by the Portuguese Foundation for Science and Technology (FCT) project UIDB/04683/2020 - ICT (Institute of Earth Sciences) and by the European Union through the European Regional Development Fund, included in the COMPETE 2020 (Operational Program Competitiveness and Internationalization) through the ALOP (ALT20-03-0145-FEDER-000004) project. Authors are financially supported by the GINOP 2.3.2-15-2016-00019 project and by NKFIH FK 132 142, FK 131 917 and K 132 150 grants. MHN was supported by Fundação para a Ciência e a Tecnologia – Portugal (PhD grant SFRH/BD/21625/2005), by the Fonds National de la Recherche du Luxembourg (grant AFR, PHD-09-120) and by the Public Research Centre - Gabriel Lippmann (Luxembourg). We

are grateful for the data provided by the Hungarian water quality monitoring network and by the National Water Institute (INAG), currently Portuguese Environment Agency (APA) for the Portuguese data on watershed characteristics and climatic data and for the assistance in statistical analysis by Zoltán Botta-Dukát.

References

Acuña, V., Hunter, M., Ruhi, A., 2017. Managing temporary streams and rivers as unique rather than second-class ecosystems. Biol. Conserv. 211, 12–19. https://doi.org/10.1016/j.biocon.2016.12.025.

B-Béres, V., Török, P., Kókai, Zs., T-Krasznai, E., Tóthmérész, B., Bácsi, I., 2014. Ecological diatom guilds are useful but not sensitive enough as indicators of extremely changing water regimes. Hydrobiologia 738, 191–204. https://doi.org/10.1007/s10750-014-1929-y.

B-Béres, V., Török, P., Kókai, Zs., Lukács, Á., T-Krasznai, E., Tóthmérész, B., Bácsi, I., 2017. Ecological background of diatom functional groups: comparability of classification systems. Ecol. Indic. 82, 183–188. https://doi.org/10.1016/j.ecolind.2017.07.007.

B-Béres, V., Tóthmérész, B., Bácsi, I., Borics, G., Abonyi, A., Tapolczai, K., Rimet, F., Bouchez, A., Várbíró, G., Török, P., 2019. Autumn drought drives functional diversity of benthic diatom assemblages of continental streams. Adv. Water Resour. 126, 129–136. https://doi.org/10.1016/j.advwatres.2019.02.010.

Bartholy, J., Pongrácz, R., 2005. Tendencies of extreme climate indices based on daily precipitation in the Carpathian Basin for the 20th century. Quarterly Journal of the Hungarian Meteorological Service 109, 1–20.

Bartholy, J., Pongrácz, R., Pieczka, I., 2014. How the climate will change in this century? Hungarian Geol. Bull. 63, 55–67. https://doi.org/10.15201/hungeobull.63.1.5.

Berthon, V., Bouchez, A., Rimet, F., 2011. Using diatom life-forms and ecological guilds to assess organic pollution and trophic level in rivers: a case study of rivers in south-eastern France. Hydrobiologia 673, 259–271. https://doi.org/10.1007/s10750-011-0786-1.

Besse-Lototskaya, A., Verdonschot, P.F.M., Coste, M., Van de Vijver, B., 2011. Evaluation of European diatom trophic indices. Ecol. Indic. 11, 456–467. https://doi.org/10.1016/j.ecolind.2010.06.017.

Bey, M.Y., Ector, L., 2013. Atlas des diatomées des cours d'eau de la région Rhône-Alpes. pp. 1182. http://www.auvergne-rhone-alpes.developpement-durable.gouv.fr/atlas-des-diatomees-a3480.html.

Biggs, B.J.F., Stevenson, R.J., Lowe, R.L., 1998. A habitat matrix conceptual model for stream periphyton. Arch. Hydrobiol. 143, 21–56. https://doi.org/10.1127/archiv-hydrobiol/143/1998/21.

Botta-Dukát, Z., 2005. Rao's quadratic entropy as a measure of functional diversity based on multiple traits. J. Veg. Sci. 16, 533–540. https://doi.org/10.1111/j.1654-1103.2005.tb02393.x.

Botta-Dukát, Z., 2018. Cautionary note on calculating standardized effect size (SES) in randomization test. Community Ecol 19, 77–83. https://doi.org/10.1556/168.2018.19.1.8.

Botta-Dukát, Z., Czúcz, B., 2016. Testing the ability of functional diversity indices to detect trait convergence and divergence using individual-based simulation. Methods Ecol. Evol. 7, 114–126. https://doi.org/10.1111/2041-210X.12450.

Coyle, J.R., Halliday, F.W., Lopez, B.E., Palmquist, K.A., Wilfahrt, P.A., Hurlbert, A.H., 2014. Using trait and phylogenetic diversity to evaluate the generality of the stress-dominance hypothesis in eastern North American tree communities. Ecography 37, 814–826. https://doi.org/10.1111/ecog.00473.

van Dam, H., Mertens, A., Sinkeldam, J., 1994. A coded checklist and ecological indicator values of freshwater diatoms from the Netherlands. Netherland J. Aquat. Ecol. 28, 117–133. https://doi.org/10.1007/BF02334251.

van Dam, H., Stenger-Kovács, C., Ács, É., Borics, G., Buczkó, K., Hajnal, É., Soróczki-Pinter, É., Várbíró, G., Tóthmérész, B., Padisák, J., 2007. Implementation of the European Water Framework Directive: development of a system for water quality assessment of Hungarian running waters with diatoms. Arch. Hydrobiol. Suppl. 161, 339–383.

Díaz, S., Lavorel, S., de Bello, F., Quétier, F., Grigulis, K., Robson, T.M., 2007. Incorporating plant functional diversity effects in ecosystem service assessments. P. Natl. Acad. Sci. USA 104, 20684–20689. https://doi.org/10.1073/pnas.0704716104.

Dray, S., Dufour, A., 2007. The ade4 package: implementing the duality diagram for ecologists. J. Stat. Soft. 22, 1–20. https://doi.org/10.18637/jss.v022.i04.

Dudgeon, D., Arthington, A.H., Gessner, M.O., Kawabata, Z., Knowler, D.J., Lévêque, C., 2006. Freshwater biodiversity: importance, threats, status and conservation challenges. Biol. Rev. 81, 163–182. https://doi.org/10.1017/S1464793105006950.

EN, 2003. EN:13946 Water Quality. Guidance Standard for the Routine Sampling and Pretreatment of Benthic Diatoms From Rivers.

Falasco, E., Piano, E., Bona, F., 2016. Diatom flora in Mediterranean streams: flow intermittency threatens endangered species. Biodivers. Conserv. 25, 2965–2986. https://doi.org/10.1007/s10531-016-1213-8.

Francis, R.A., 2011. The impact of modern warfare on freshwater ecosystems. Environ. Manag. 48, 985–999. https://doi.org/10.1007/s00267-011-9746-9.

Götzenberger, L., de Bello, F., Bråthen, K.A., Davison, J., Dubuis, A., Guisan, A., Leps, J., Lindborg, R., Moora, M., Pärtel, M., Pellissier, L., Pottier, J., Vittoz, P., Zobel, K., Zobel, M., 2012. Ecological assembly rules in plant communities—approaches, patterns and prospects. Biol. Rev. 87, 111–127. https://doi.org/10.1111/j.1469-185X.2011.00187.x.

Götzenberger, L., Botta-Dukát, Z., Leps, J., Partel, M., Zobel, M., de Bello, M., 2016. Which randomizations detect convergence and divergence in trait-based community assembly? A test of commonly used null models. J. Veg. Sci. 27, 1275–1287. https://doi.org/10.1111/jvs.12452.

Green, P.A., Vörösmarty, C.J., Harrison, I., Farrell, T., Sáenz, L., Fekete, B.M., 2015. Freshwater ecosystem services supporting humans: pivoting from water crisis to water solutions. Global Environ. Chang. 34, 108–118. https://doi.org/10.1016/j.gloenvcha.2015.06.007.

Grime, J.P., 1977. Evidence for the existence of three primary strategies in plants and its relevance to ecological and evolutionary theory. Am. Nat. 111, 1169–1194. https://www.jstor.org/stable/2460262.

INAG, I.P, 2008. Tipologia de rios em Portugal Continental no Âmbito da Implementação da Directiva Quadro da Água. I – Caracterização abiótica. Ministério do Ambiente, do Ordenamento do Território e do Desenvolvimento Regional. Instituto da Água, I. P, Lisboa (32 pp).

IPBES, 2019. Report of the plenary of the intergovernmental science-policy platform on biodiversity and ecosystem services on the work of its seventh session. https://ipbes.net/global-assessment-report-biodiversity-ecosystem-services.

Jefferies, D., Munoz, I., Hodges, J., King, V.J., Aldaya, M., Ercin, A.E., i Canals, L.M., Hoekstra, A.Y., 2012. Water footprint and life cycle assessment as approaches to assess potential impacts of products on water consumption. Key learning points from pilot studies on tea and margarine. J. Clean. Prod. 33, 155–166. https://doi.org/10.1016/j.jclepro.2012.04.015.

Kaczmarska, I., Poulickova, A., Sato, S., Edlund, M.B., Idei, M., Watanabe, T., Mann, D.G., 2013. Proposals for a terminology for diatom sexual reproduction, auxospores and resting stages. Diatom Res. 28, 263–294. https://doi.org/10.1080/0269249X.2013.791344.

Kireta, A.R., Reavie, E.D., Sgro, G.V., Angradi, T.R., Bolgrien, D.W., Hill, B.H., Jicha, T.M., 2012. Planktonic and periphytic diatoms as indicators of stress on great rivers of the United States: testing water quality and disturbance models. Ecol. Indic. 13, 222–231. https://doi.org/10.1016/j.ecolind.2011.06.006.

Kociolek, J.P., Kopalova, K., Hamsher, S.E., Kohler, T.J., Van der Vijver, B., Convey, P., MsKnight, D.M., 2017. Freshwater diatom biogeography and the genus Luticola: an extreme case of endemism in Antarctica. Polar Biol. 40, 1185–1196. https://doi.org/10.1007/s00300-017-2090-7.

Kókai, Zs., Bácsi, I., Török, P., Buczkó, K., T-Krasznai, E., Balogh, Cs., Tóthmérész, B., B-Béres, V., 2015. Halophilic diatom taxa are sensitively indicating even the short term changes in lowland lotic systems. Acta Bot. Croat. 74, 287–302. https://doi.org/10.1515/botcro-2015-0025.

Kókai, Zs., Borics, G., Bácsi, I., Lukács, Á., Tóthmérész, B., Csépes, E., Török, P., B-Béres, V., 2019. Water usage and seasonality as primary drivers of benthic diatom assemblages in a lowland reservoir. Ecol. Indic. 106, 105443. https://doi.org/10.1016/j.ecolind.2019.105443.

Krammer, K., Lange-Bertalot, H., 1997a. Bacillariophyceae 1. Naviculaceae. In: Gerloff, H., Heynig, J.H., Mollenhauer, D. (Eds.), Süsswasserflora Von Mitteleuropa. Elsevier, Heidelberg.

Krammer, K., Lange-Bertalot, H., 1997b. Bacillariophyceae 2. Bacillariaceae, Epithemiaceae, Surirellaceae. In: Gerloff, H., Heynig, J.H., Mollenhauer, D. (Eds.), Süsswasserflora Von Mitteleuropa. Elsevier Heidelberg.

Krammer, K., Lange-Bertalot, H., 2004a. Bacillariophyceae 3. Centrales, Fragilariaceae, Eunotiaceae. In: Gerloff, H., Heynig, J.H., Mollenhauer, D. (Eds.), Süsswasserflora Von Mitteleuropa. Spektrum Akademischer Verlag, Heidelberg.

Krammer, K., Lange-Bertalot, H., 2004b. Bacillariophyceae 4. Achnanthaceae. Kritische Ergänzungen zu Achnanthes s. l., Navicula s. str., Gomphonema. Gesamtliteraturverzeichnis teil 1–4. In: Gerloff, H., Heynig, J.H., Mollenhauer, D. (Eds.), Süsswasserflora Von Mitteleuropa. Spektrum Akademischer Verlag, Heidelberg.

Lange, K., Townsend, C.R., Matthaei, C.D., 2016. A trait based framework for stream algal communities. Ecol. Evol. 6, 23–36. https://doi.org/10.1002/ece3.1822.

Le Bagousse-Pinguet, Y., Gross, N., Maestre, F.T., Maire, V., de Bello, F., Fonseca, C.R., Fonseca, C.R., Kattage, J., Valencia, E., Leps, J., Liancourt, P., 2017. Testing the environmental filtering concept in global drylands. J. Ecol. 105, 1058–1069. https://doi.org/10.1111/1365-2745.12735.

Leira, M., Filippi, M.L., Cantonati, M., 2015. Diatom community response to extreme water-level fluctuations in two alpine lakes: a core case study. J. Paleolimnol. 53, 289–307. https://doi.org/10.1007/s10933-015-9825-7.

Lhotsky, B., Kovács, B., Ónodi, G., Csecserits, A., Rédei, T., Lengyel, A., Kertész, M., Botta-Dukát, Z., 2016. Changes in assembly rules along a stress gradient from open dry grasslands to wetlands. J. Ecol. 104 (2), 507–517. https://doi.org/10.1111/1365-2745.12532.

Liess, A., Lange, K., Schulz, F., Piggott, J.J., Matthaei, C.D., Townsend, C.R., 2009. Light, nutrients and grazing interact to determine diatom species richness via changes to productivity, nutrient state and grazer activity. J. Ecol. 97, 326–336. https://doi.org/10.1111/j.1365-2745.2008.01463.x.

MacArthur, R., Levins, R., 1967. The limiting similarity, convergence, and divergence of coexisting species. Am. Nat. 101, 377–385. www.jstor.org/stable/2459090.

McGill, B.J., Enquist, B.J., Weiher, E., Westoby, M., 2006. Rebuilding community ecology from functional traits. Trends Ecol. Evol. 21, 178–185. https://doi.org/10.1016/j.tree.2006.02.002.

Novais, M.H., Morais, M.M., Rosado, J., Dias, L.S., Hoffmann, L., Ector, L., 2014. Diatoms of temporary and permanent watercourses in southern Europe (Portugal). River Res. App. 30, 1216–1232. https://doi.org/10.1002/rra.2818.

Oksanen, J., Blanchet, F.G., Friendly, M., Kindt, R., Legendre, P., McGlinn, D., Minchin, P.R., O'Hara, R.B., Simpson, G.L., Solymos, P., Stevens, M.H.H., Szoecs, E., Wagner, H., 2019. Vegan: community ecology package. R package version 2.5-6. https://CRAN.R-project.org/package=vegan.

Passy, S.I., 2002. Environmental randomness underlies morphological complexity of colonial diatoms. Funct. Ecol. 16, 690–695. https://doi.org/10.1046/j.1365-2435.2002.00671.x.

Passy, S.I., 2007. Diatom ecological guilds display distinct and predictable behavior along nutrient and disturbance gradients in running waters. Aquat. Bot. 86, 171–178. https://doi.org/10.1016/j.aquabot.2006.09.018.

Passy, S.I., Larson, C.A., 2011. Succession in stream biofilms is an environmentally driven gradient of stress tolerance. Microb. Ecol. 62, 414. https://doi.org/10.1007/s00248-011-9879-7.

Pásztor, L., Botta-Dukát, Z., Magyar, G., Czárán, T., Meszéna, G., 2016. Theory-Based Ecology: A Darwinian Approach. Oxford University Press, Oxford.

Piano, E., Falasco, E., Bona, F., 2017. How does water scarcity affect spatial and temporal patterns of diatom community assemblages in Mediterranean streams? Freshw. Biol. 62, 1276–1287. https://doi.org/10.1111/fwb.12944.

Pinho, B.X., Tabarelli, M., Engelbrecht, B.M.J., Sfair, J., Melo, F.P.L., 2019. Plant functional assembly is mediated by rainfall and soil conditions in a seasonally dry tropical forest. Basic Appl. Ecol. 40, 1–11. https://doi.org/10.1016/j.baae.2019.08.002.

Poff, N.L., Allan, J.D., Bain, M.B., Karr, J.R., Prestegaard, K.L., Richter, B.D., Sparks, R.E., Stromberg, J.C., 1997. The natural flow regime. Bioscience 47, 769–784. https://doi.org/10.2307/1313099.

Potapova, M., Hamilton, P.B., 2007. Morphological and ecological variation within the Achnanthidium minutissimum (Bacillariophyceae) species complex. J. Phycol. 43, 561–575. https://doi.org/10.1111/j.1529-8817.2007.00332.x.

Poulickova, A., Dokulil, M., Duchoslav, M., 2004. Littoral diatom assemblages as bioindicators of lake trophic status, a case study from perialpine lakes in Austria. Eur. J. Phycol. 39, 143–152. https://doi.org/10.1080/0967026042000201876.

R Core Team, 2019. R: a language and environment for statistical computing. R Foundation for Statistical Computing, Vienna, Austria URL. www.R-project.org.

REFCOND, 2003. Guidance on Establishing Reference Conditions and Ecological Status Boundaries for Inland Surface Waters. Working Group 2.3. EU Common Implementation Strategy (CIS) for the Water Framework Directive (93 pp).

Rimet, F., Bouchez, Á., 2012. Life-forms, cell sizes and ecological guilds of diatoms in European rivers. Knowl. Manag. Aquat. Ec. 406, 1283–1299. https://doi.org/10.1051/kmae/2012018.

Sakaeva, A., Sokol, E.R., Kohler, T.J., Stanish, L.F., Spaulding, S.A., Howkins, A., Welch, K.A., Lyons, W.B., Barrett, J.E., McKnight, D.M., 2016. Evidence for dispersal and habitat controls on pond diatom communities from the McMurdo Sound Region of Antarctica. Polar Biol. 39, 2441–2456. https://doi.org/10.1007/s00300-016-1901-6.

Skoulikidis, N.T., Sabater, S., Datry, T., Morais, M.M., Buffagni, A., Dörflinger, G., Zogaris, S., Sánchez-Montoya, M.M., Bonada, N., Kalogianni, E., Rosado, J., Vardakas, L., de Girolamo, A.M., Tockner, K., 2017. Non-perennial Mediterranean rivers in Europe: status, pressures, and challenges for research and management. Sci. Total Environ. 577, 1–18. https://doi.org/10.1016/j.scitotenv.2016.10.147.

Soininen, J., Eloranta, P., 2004. Seasonal persistence and stability of diatom communities in rivers: are there habitat specific differences? Eur. J. Phycol. 39, 153–160. https://doi.org/10.1080/0967026042000201858.

Soininen, J., Niemela, P., 2002. Inferring the phosphorus levels of rivers from benthic diatoms using weighted averaging. Arch. Hydrobiol. 154, 1–18. https://doi.org/10.1127/archiv-hydrobiol/154/2002/1.

Soininen, J., Jamoneau, A., Rosebery, J., Passy, S.I., 2016. Global patterns and drivers of species and trait composition in diatoms. Glob. Ecol. Biogeogr. 25, 940–950. https://doi.org/10.1111/geb.12452.

Solheim, A.L., Globevnik, L., Austnes, K., Kristensen, P., Moe, S.J., Persson, J., Phillips, G., Poikane, S., van de Bund, W., Birk, S., 2019. A new broad typology for rivers and lakes in Europe: development and application for large-scale environmental assessments. Sci. Total Environ. 697, 134043. https://doi.org/10.1016/j.scitotenv.2019.134043.

Stenger-Kovács, Cs., Lengyel, E., 2015. Taxonomical and distribution guide of diatoms in soda pans of Central Europe. Stud. Bot. Hung. 46, 3–203. https://doi.org/10.17110/StudBot.2015.46.Suppl.3.

Stenger-Kovács, Cs., Padisák, J., Bíró, P., 2006. Temporal variability of *Achnanthidium minutissimum* (Kützing) Czarnecki and its relationship to chemical and hydrological features of the Torna-stream, Hungary. In: Ács, E., Kiss, K.T., Padisák, J., Szabó, K.É. (Eds.), Program, Abstracts & Extended Abstracts: 6th International Symposium on Use of Algae for Monitoring Rivers. Magyar Algológiai Társaság, Göd, pp. 139–145 (ISBN 963 06 0497 3).

Stenger-Kovács, Cs., Lengyel, E., Crossetti, L.O., Üveges, V., Padisák, J., 2013. Diatom ecological guilds as indicators of temporally changing stressors and disturbances in the small Torna-stream, Hungary. Ecol. Indic. 24, 138–147. https://doi.org/10.1016/j.ecolind.2012.06.003.

Stubbington, R., England, J., Sefton, C., Wood, P.J., 2017. Temporary streams in temperate zones: recognizing, monitoring and restoring transitional aquatic-terrestrial ecosystems. WIREs Water 4, e1223. https://doi.org/10.1002/wat2.1223.

Stubbington, R., Paillex, A., England, A., Barthès, A., Bouchez, A., Rimet, F., Sánchez-Montoya, M., Westwood, C.G., Datry, T.A., 2019. Comparison of biotic groups as dry-phase indicators of ecological quality in intermittent rivers and ephemeral streams. Ecol. Indic. 97, 165–174. https://doi.org/10.1016/j.ecolind.2018.09.0619.

Tapolczai, K., Bouchez, A., Stenger-Kovács, Cs, Padisák, J., Rimet, F., 2016. Trait-based ecological classifications for benthic algae: review and perspectives. Hydrobiologia 776, 1–17. https://doi.org/10.1007/s10750-016-2736-4.

ter Braak, C.J.F., Šmilauer, P., 2002. CANOCO Reference Manual and CanoDraw ForWindows User's Guide: Software for Canonical Community Ordination (Version 4 .5). Microcomputer Power, Ithaca, NY (Accessed. 2013). http://www.canoco.com.

Tornes, E., Ruhi, A., 2013. Flow intermittency decreases nestedness and specialisation of diatom communities in Mediterranean rivers. Freshw. Biol. 58, 2555–2566. https://doi.org/10.1111/fwb.12232.

web 1, d. http://ec.europa.eu/environment/water/participation/map_mc/countries/hungary_en.htm.

Weiher, E., Keddy, P.A., 1995. Assembly rules, null models, and trait dispersion: new questions from old patterns. Oikos 74, 159–164. http://www.jstor.org/stable/3545686.

Zorger, B.B., Tabarelli, M., de Queiroz, R.T., Rosado, B.H.P., Pinho, B.X., 2019. Functional organization of woody plant assemblages along precipitation and human disturbance gradients in a seasonally dry tropical forest. BioTropica 51, 838–850. https://doi.org/10.1111/btp.12721.

water

MDPI

Article

Risk Assessment of Irrigation-Related Soil Salinization and Sodification in Mediterranean Areas

Alexandra Tomaz [1,2,*], Patrícia Palma [1,3], Sofia Fialho [1], Ana Lima [1], Paula Alvarenga [4], Miguel Potes [3,6], Maria João Costa [3,5,6] and Rui Salgado [3,5,6]

1 Escola Superior Agrária, Instituto Politécnico de Beja, R. Pedro Soares S/N, 7800-295 Beja, Portugal; ppalma@ipbeja.pt (P.P.); sofiafialho16@gmail.com (S.F.); ana.filipa.lima89@gmail.com (A.L.)
2 GeoBioTec, Universidade Nova de Lisboa, Campus da Caparica, 2829-516 Caparica, Portugal
3 Instituto de Ciências da Terra (ICT), IIFA, Universidade de Évora, 7000-671 Évora, Portugal; mpotes@uevora.pt (M.P.); mjcosta@uevora.pt (M.J.C.); rsal@uevora.pt (R.S.)
4 LEAF—Centro de Investigação em Agronomia, Alimentos, Ambiente e Paisagem, Instituto Superior de Agronomia, Universidade de Lisboa, 1349-017 Lisboa, Portugal; palvarenga@isa.ulisboa.pt
5 Departamento de Física, Escola de Ciências e Tecnologia, Universidade de Évora, 7000-671 Évora, Portugal
6 Earth Remote Sensing Laboratory (EaRSLab), Universidade de Évora, 7000-671 Évora, Portugal
* Correspondence: atomaz@ipbeja.pt; Tel.: +351-284-314-300

Received: 27 November 2020; Accepted: 16 December 2020; Published: 19 December 2020

Abstract: Salinization and sodification are important processes of soil degradation affecting irrigated lands. A large proportion of the global irrigated area is affected by some degree of soil salinity or sodicity caused by the intensification of irrigation. The increase of the frequency of adverse climatic conditions, like high temperatures and variations in precipitation patterns caused by climate change, will potentially amplify these processes in arid, semi-arid, and Mediterranean areas. The use of integrated approaches for the spatial and temporal prediction of the risk of salinization and sodification in irrigated areas is of great value, helping in the decision-making regarding land uses and choice of more suitable agricultural practices. In this study, based on key criteria for the assessment of irrigation-related salinization processes (e.g., climate, topography, soil drainage, water quality for irrigation, and crop irrigation method), we developed a methodology for the prediction of soil salinity and sodicity risk in irrigated lands, using two composite indices, the Salinization Risk (RSA) index and the Sodification Risk (RSO) index. The application of these indices to a real scenario (a Mediterranean area in Southern Portugal) showed that 67% of the potentially irrigated area presented a low risk of salinity development, 68% had a moderate risk of sodification, and 16% was of high risk of sodicity development. Areas under moderate risk of salinization (26%) were mostly characterized by low slopes and fine-textured soils, like Luvisols and Vertisols, with limited drainage conditions. Areas with high risk of soil sodification presented a large incidence of low slope terrain, moderate-to-restricted soil drainage, in high clay content Luvisols, Vertisols and Cambisols, and land use dominated by annual crops irrigated with surface or sprinkler systems. These risk prediction tools have the potential to be used for resource use planning by policymakers and on-farm management decision by farmers, contributing to the sustainability of irrigated agriculture in Mediterranean regions.

Keywords: soil salinity; soil sodicity; water quality for irrigation; risk evaluation; Mediterranean regions

1. Introduction

Salinization and sodification are major processes of soil degradation threatening land productivity and global food security [1]. Salt-induced land degradation is common in arid and semi-arid regions,

where rainfall is insufficient to maintain percolation of rainwater through the soil and irrigation is practiced without adequate drainage [2]. The growing development of irrigated agriculture in arid and semi-arid lands has been essential for the food supply demanded by a growing world population. Over the last 50 years, the world's net cultivated area has grown 12%, and in the same period, the global irrigated area has doubled [3]. At present, about 20% of the world agricultural land is irrigated and this land produces 40% of the world food supply [4]. Although the undisputable contribution of irrigation for the increase in food production, in areas where precipitation is scarce or irregular, irrigated agriculture can cause a disharmony with the nature of dry regions' ecology, negatively affecting the quality of soils and water [3,5–7]. At present, it is estimated that more than 20% of the global irrigated area is affected by salinization caused by irrigation; in some countries, salt-affected soils occur in more than half of the irrigated land [2]. In the Mediterranean area, 25% of irrigated cropland is affected by moderate-to-high salinization, leading to moderate soil degradation [8], and adverse climatic conditions, like temperature increase and changes in the regional precipitation patterns, are likely to enhance the problem of salinization [9–12].

According to Rengasamy [13], there are three types of salinity, based on the processes of salt accumulation: (i) groundwater-associated salinity, occurring in discharge areas of the landscape, where water tables are close to the surface and evaporation leads to the upward movement of water and salts; (ii) non-groundwater-associated salinity, that occurs in landscapes with deep water table and poor drainage, when salts introduced by rain, weathering, and aeolian deposits are stored within the soil *solum*; and (iii) irrigation-associated salinity, when salts are introduced by irrigation water and accumulate within the root zone due to insufficient leaching. Certain factors lead to the acceleration of irrigation-induced salinity, like the poor-quality irrigation water, low hydraulic conductivity of soil layers, as found in heavy clay soils, and sodic soils, under high evaporative conditions.

Whether it is of natural genesis or induced by human activities, the progressive nature of salt-affected soils is a constraint for its early detection, and, although there are several reclamation techniques, the prevention of salt accumulation is more advisable than soil desalinization [14,15]. According to Eckelmann et al. [16], the risk of salinization is defined as a measure of the probability and severity of the salinization/sodification due to human activities which adversely affects one or more soil functions. In agricultural regions, soil salinization varies widely, vertically, horizontally, and temporally, depending on conditions, such as the variation in soil texture, plant growth, irrigation water quality, hydraulic conductivity, and the irrigation system. In this sense, any risk assessment methodology must be based in meaningful indicators of soil and water quality, in order to assess whether or not a soil is potentially salt-affected [17].

Risk assessment methodologies can be performed at different levels of scale and related levels of information detail, in each case using different types of approaches, namely, a qualitative, quantitative, or model approach [17,18]. Simulation models that deal with the dynamic and transient condition of soil salinity [19,20] can predict the effect of multiple scenarios (e.g., climatic variables, quality and quantity of irrigation water, fertilization rates, soil properties) on soil salinization, computing water and salt balances in the soil and leaching requirements, supporting the optimization of agricultural practices and land management [19–21]. The complexity of some of these models, and the usual lack of input data, is a constraint to its application on large areas, and simple approaches are welcome to be used at national or regional scales [18,22]. Monitoring and assessment of soil salinity is decisive for effective adaptation and mitigation through land reclamation measures. At field level and at larger scales, mapping of salinity is required to establish the most appropriate irrigation and soil management practices, to delineate crop management zones, and for regional land management [23].

The appropriate assessment methods are directly related to the spatial scale of interest [22,23]. In a continental scale, Tóth et al. [24] generated a map of saline and sodic soils from the European Soil Database [25], for the delineation of areas in the European Union that are threatened by salinization or sodification. For large spatial scales, the use of remote sensing (RS) or geographic information systems (GIS) techniques has been reported in several studies, frequently in combination with physically based

models, aiming to extend their prediction capabilities (for e.g., [15,26–28]). According to Zhou et al. [29], the use of risk indices or frameworks for soil salinity assessment may facilitate communication among scientists, policymakers, and practitioners by providing a basis for evaluating the environmental impact of agricultural practices and also government programs and policies. Frequently, these risk indices are GIS-based in order to ascertain priority areas, predict where it may occur in the future, and determine appropriate management options to mitigate salinity risk [30]. One of the earliest indices for the assessment of soil salinity risk was the Salinity Risk Index (SRI), proposed by Eilers et al. [31], later updated by Wiebe et al. [32] to evaluate the salinization risk trends on the Canadian Prairies. The SRI was composed of five risk factors: the current presence and extent of salinity, topography, soil drainage, aridity, and land use [31,32]. A four-component risk assessment framework for salinity prevention was proposed by Grundy et al. [33] for Queensland, Australia, where the components (current salinity stage, current land management, value of the assets under threat, and biophysical risk factors) interacted to give an overall salinity risk index. From this framework, Biggs et al. [30] developed a GIS-based system to assess the risk of salinity in the Condamine basin, Australia. Zhou et al. [29] presented a soil salinity risk assessment methodology by selecting a set of risk factors based on the conceptual Pressure–State–Response (PSR) sustainability framework of the Organisation for Economic Co-operation and Development (OECD) [34], where a set of fourteen risk factors were selected to develop a composite risk index for soil salinity in the Yinchuan Plain, China. Masoudi et al. [35] proposed a model for risk analysis of soil salinization for the Payab Basin, Iran, using GIS with the overlay of hazard maps of nine indicators as the causes of soil salinity (depth of water table, soil texture, slope, irrigation water quality, groundwater quality, efficacy of surface geology, climate, aridity index, status of soil salinity) to obtain a final risk map. Specifically for irrigated lands, similar salinization risk assessment methodologies were developed, using GIS, and considering irrigation water quality, soil properties, and climate indicators [15,24]. These methodologies have a dominant focus on the prediction of the development of saline soils, and the assessment of the risk of soil sodicity alone has generally received less attention [36]. Regardless of the modeling perspective or the soil deterioration problem to be predicted, the use of these integrated approaches evidenced its value for helping in decisionmaking regarding land resource management, allowing for the adoption of reclamation actions and the prediction of the spatial variation of irrigation-induced soil salinity and sodicity.

In this study, we aimed to: (i) present an overview of major criteria and respective indicators related with soil salinity and sodicity induced by irrigation; (ii) propose two composite risk indices, for soil salinization and soil sodification assessment in large areas, based on climate, irrigation water quality, soil information, and land-use data; (iii) present the risk indices when applied in a real scenario in a Mediterranean area in Southern Portugal.

2. Criteria and Indicators of Soil Salinization and Sodification

Indicators to predict soil salinization problems can be grouped following the common criteria for risk area identification according to soil threats [16] (Table 1), that considers a two-tiered approach, from a lower spatial resolution, less detailed and supported in available information, to a higher spatial resolution, requiring more detailed data and in situ measurements.

Table 1. Common criteria for risk area identification according to soil threats considering a two-tiered approach (Tier 1 for National/Continental level; Tier 2 for regional level) (adapted from [16]).

Criteria	Indicator	Data Source/Type of Information	
		Tier 1	Tier 2
Soil typological unit	European or National databases	Europe, National	Regional
Soil texture	Texture class; sand, silt and clay content	Texture class	Particle size distribution; Porosity

Table 1. *Cont.*

Criteria	Indicator	Data Source/Type of Information	
		Tier 1	**Tier 2**
Soil chemical properties	Salt content, expressed in Total Dissolved Salts (TDS) or electrical conductivity (EC), and profile distribution; ion composition; pH; Cation exchange capacity (CEC); Exchangeable sodium percentage (ESP)	Not required	National soil profile database; Soil inventory/mapping
Soil hydraulic properties	Infiltration rate; Hydraulic conductivity; Water retention curves; Drainage	Not required	National soil profile database; Soil inventory/mapping
Irrigation areas and chemical properties of irrigation water	Irrigated area; Irrigation intensity; Salt content, pH and Sodium Adsorption Ratio (SAR) of irrigation water	National registries	Regional registries
Groundwater information	Depth; Salt content, pH and SAR	European/National groundwater database	Regional database
Climate/Aridity	Annual rainfall; Annual potential evapotranspiration	National weather stations	Regional weather stations

The most common soil salinity indicator is the electrical conductivity, usually measured in a saturation paste extract (ECe; dS m^{-1}). Yield reduction of many crops can occur for ECe > 4 dS m^{-1}, a condition that defines a saline soil [37]. In saline soils, the large osmotic potential values on soil solution hinder plant transpiration, diminishing water availability to plants, which results in physiological deteriorations. Crop salt tolerance is the ability of plants to survive and produce profitable yields under the adverse conditions caused by soil salinity [38]. Data of tolerance to salinity were first reported by Maas and Hoffman [39] for numerous crops, by quantifying salt tolerance using the threshold (or breakpoint) model, that can be presented in terms of percentage of the maximum yield, known as the relative production function Equation (1):

$$Yr = \begin{cases} 100, if EC_e \le a \\ 100 + b \cdot (EC_e - a), if a < EC_e < c \\ 0, if EC_e \ge c \end{cases}, \quad (1)$$

where Yr is the relative crop yield, with 100 being the maximum yield, a is the threshold (breakpoint) salinity (dS m^{-1}), beyond which yield reduction will occur, ECe is the salinity of saturated soil extract, b is the slope, that represents the percentage of yield expected to be reduced for each unit of added salinity above the threshold salinity, and c is the level of soil salinity (dS m^{-1}), above which the yield is zero. Values of a and b, and relative tolerance ratings for several crops, can be found in Maas and Grattan [40], indicating, e.g., that while wheat (*Triticum aestivum* L.) or olive (*Olea europaea* L.) are classified as moderately tolerant, grapevine (*Vitis vinifera* L.), almond (*Prunus dulcis* (Mill.) D.A. Webb) and a majority of vegetable crops are moderately sensitive to salinity, which increases the restrictions for their cultivation [41] and the need for appropriate irrigation management measures for these crops [42].

For sodic conditions, in addition to salinity diagnosis based upon ECe, the Sodium Adsorption Ratio (SAR) of the soil solution or of the irrigation water Equation (2) can be calculated [38]:

$$SAR = \frac{\left[Na^+\right]}{\sqrt{\frac{\left[Ca^{2+}\right]+\left[Mg^{2+}\right]}{2}}}, \quad (2)$$

where $[Na^+]$, $[Ca^{2+}]$, and $[Mg^{2+}]$ are the concentrations (meq L^{-1}) in the saturated soil paste extract or in the irrigation water. A sodic soil presents a SAR value of 13 or higher. When ECe > 4 dS m^{-1} and SAR > 13, the soil is classified as saline-sodic [37]. In sodic soils, the high exchangeable sodium in the soil complex causes dispersion of its colloids, structural destruction, and aggregate failure, resulting in unfavorable physical properties, like low infiltration rate and low hydraulic conductivity [9,13]. When the salinity of the soil water is insufficient to counteract the negative effects of adsorbed Na^+ on soil structure, a "rainfall effect" [43] can occur. More specifically, the leaching of salts by precipitation or excess irrigation water reduces the salinity of the soil solution, while the reduction in exchangeable Na^+ will be far smaller due to a buffer effect, performed by the exchangeable cations adsorbed in the soil matrix, causing, therefore, a reduction in the stabilizing effects of salinity on aggregate stability [5,22,44]. When dry, sodic soils become denser and structureless since natural aggregation is destroyed. At the soil surface, dispersed clay particles can act as adhesive, forming relatively dense crusts that impede seedling rooting and emergence. The degree of crusting depends on soil texture, the mineralogy of the clay, the exchangeable sodium content, the energy of raindrop impact, and the rate of drying [22]. At lower SAR levels, when chemical bonding is weakened, but no spontaneous dispersion takes place, inputs of energy are required for actual dispersion. While in drip irrigated fields this is hardly a problem, given the low flow rates of the drippers, the use of surface or sprinkler irrigation can increase the probability of soil structure degradation and surface crusting due to the physical disruption caused by runoff or by the water drops as they impact the soil surface aggregates [45].

In addition to soils that are classified as saline or sodic due to their genesis conditions, like Solonchaks and Solonetz, there are other soils whose characteristics make them more susceptible to the development of secondary salinization. This is the case of poorly drained soils (soils with permanent or temporary water table close to the surface) or soils with unfavorable hydrophysical properties (low permeability, low porosity, fine-textured layers or horizons). A systematized list of saline or saline prone soils, according to the World Reference Base of Soil Resources [46], was presented by Daliakopoulos et al. [22] (Table 2).

Table 2. Saline soils and saline-prone soils, and their main characteristics, according to the World Reference Base [46] (adapted from [22]).

Saline or Saline-Prone Type	Soil Type	Code	Main Characteristics
Saline	Solonchak	SC	High concentration of soluble salts
	Solonetz	SN	High content of exchangeable Na
Saline-prone	Acrisol	AC	Low-activity clays and low base saturation
	Alisol	AL	High-activity clays and low base saturation
	Calcisol	CL	Accumulation of secondary calcium carbonates
	Durisols	DU	Accumulation of, and cementation by, secondary silica
	Fluvisol	FL	Stratified fluviatile, marine, and lacustrine sediments
	Gleysol	GL	Groundwater-affected, underwater and in tidal areas
	Gypsisols	GY	Accumulation of secondary gypsum
	Luvisol	LV	High-activity clays and high base saturation
	Vertisol	VR	Alternating wet–dry conditions, shrink–swell clays

Many of the laboratory and field methods used to determine soil hydraulic properties are time-consuming, laborious, and limited to the sampling quantity and location, which restricts their use due to soil heterogeneity [47,48]. In fact, texture variability is one of the determining factors of this heterogeneity, and several methods have been proposed to establish a relation between soil texture and soil hydraulic properties [47–49]. Following a methodology similar to de Paz et al. [15], a classification of soil drainage can be made considering its relationship with textural classes (Table 3). Drainage conditions are also affected by groundwater levels. Areas of low relief and particularly closed depressions encourage lateral translocation in surface and groundwater and salt accumulation [50].

Table 3. Drainage classes in relation with textural class and saturated hydraulic conductivity (systematized after [15] and [47–49]).

Textural Class [1)]	Saturated Hydraulic Conductivity (mm h^{-1}) [2)]	Drainage Class [2)]
S, LS	>50	Good
SL, SCL, L, CL, SiCL, SiL, Si	5–50	Moderate
SC, SiC, C	<5	Restricted

[1)] S—Sand; LS—Loamy Sand; SL—Sandy Loam; SCL—Sandy Clay Loam; L—Loam; CL—Clay Loam; SiCL—Silty Clay Loam; SiL—Silty Loam; Si—Silt; SC—Sandy Clay; SiC—Silty Clay; C—Clay; [2)] Classification after de Paz et al. [15].

For the risk assessment of irrigation-induced salinization and sodification, the evaluation of irrigation water quality is of primary importance since it often constitutes the main source of salts. Some of the parameters used to evaluate soil salinization problems are the same that are used to evaluate the irrigation water quality, namely, electrical conductivity, in this case, Water Electrical Conductivity (EC_W; dS m^{-1}), Total Dissolved Salts (TDS; %), SAR, and the concentration of some specific ions that might cause toxicity to crops.

Although the suitability of a saline water for irrigation depends on different conditions of use, like crop, climate, soil, irrigation method, and management practices, only very tolerant crops can have satisfactory yields if irrigated with waters with EC that exceeds 10 dS m^{-1}. In fact, few normally used irrigation waters exceed EC of about 2 dS m^{-1} [51]. It is consensual the use of the Food and Agriculture Organization of the United Nations (FAO) water quality guidelines for irrigation [52], which considers three levels of restriction for the use of an irrigation water: none, slight to moderate, and severe. In these guidelines, salinity is assessed from EC_W, and sodicity (more specifically, infiltration rate of water in the soil) is assessed using EC_W and SAR together (Table 4).

Table 4. Excerpt of the FAO guidelines for interpretation of water quality for irrigation (adapted from Ayers and Westcot [52]).

Potential Irrigation Problem	Units	Degree of Restriction on Use [1)]		
		None	Slight to Moderate	Severe
Salinity [2)]				
EC_W	dS m^{-1}	<0.7	0.7–3.0	>3.0
Infiltration [3)]				
SAR 0–3 and EC_W	dS m^{-1}	>0.7	0.7–0.2	<0.2
SAR 3–6 and EC_W		>1.2	1.2–0.3	<0.3
SAR 6–12 and EC_W		>1.9	1.9–0.5	<0.5
SAR 12–20 and EC_W		>2.9	2.9–1.3	<1.3
SAR 20–40 and EC_W		>5.0	5.0–2.9	<2.9

[1)] Based on [52]: None—no soil or cropping problems are experienced; Slight to moderate - gradually increasing care in selection of crop and management alternatives is required if full yield potential is to be achieved; Severe—there will be soil and cropping problems or reduced yields, but even with cropping management designed especially to cope with poor quality water, a high level of management skill is essential for acceptable production; [2)] Affects crop water availability; [3)] Affects infiltration rate of water into the soil.

Irrigated agriculture develops primarily in areas where the interannual and seasonal quantity and distribution of precipitation and evapotranspiration are irregular. This leads to permanent (aridity) or temporary (drought) imbalances in water availability consisting in low average annual rainfall, with high spatial and temporal variability resulting in overall low moisture [53]. These features contribute to unfavorable salt balances, which can be intensified by irrigation with poor-quality water [54]. Climate plays a key role in the process and, whenever data are available, should be considered when defining a set of indicators for salinization/sodification risk prediction. A well-known indicator used as a numerical expression of dryness for climate classification and for the identification of regional patterns of aridity is the United Nations Environmental Programme (UNEP) Aridity Index (AI) [55], a mean accumulated annual precipitation/potential evapotranspiration ratio (P/PET). Considering the AI scale, the classification of climate types is hyper-arid (<0.05), arid (0.05–0.2), semi-arid (0.2–0.5), dry sub-humid (0.5–0.65), and humid (≥0.65). For dryland climate subtypes, AI values are below 0.65, and, according to Schofield and Kirkby [50], values between 0.05 and 1 (arid to moist sub-humid) describe climatic conditions suitable for salinization to occur.

3. Materials and Methods

3.1. Study Area

The study region selected for this work, which we will refer to as Inland Alentejo, is part of a province in Southern Portugal, with a Mediterranean-type climate, named Alentejo (Figure 1). The region has a total area of 11,260 km^2, of which 10,114 km^2 are predominantly of agriculture and/or agroforestry use (excluding urban areas, artificial zones and rocky terrain). Large areas of traditional rainfed agriculture, conditioned by water availability constraints, have been gradually replaced by irrigated agriculture [56]. While there are some private irrigation systems, the main source of irrigation water is public. In this area, small public irrigation schemes with a total area of approximately 30,000 ha in operation in 2018 [57] were implemented in the last century. However, the largest public scheme, which started to operate in 2002, is the Alqueva irrigation plan, that presently covers nearly 120,000 ha and is expected to expand to 170,000 ha by 2022, totaling 15% of the study area. The irrigation plan is a part of the Alqueva Multi-Purpose Development Project (EFMA—*Emprendimento de Fins Múltiplos de Alqueva*). The EFMA is centered in the Alqueva reservoir (Guadiana River Basin), the largest artificial lake in the Iberian Peninsula, with a total storage capacity of 4150 hm^3, providing water for public supply, irrigation, industry uses, energy production, and tourism. Studies carried out in the water and sediments of this reservoir have reported ecotoxicological risk to aquatic organisms, induced mostly by pesticide and metal pollution, an increment over time of organic matter and nutrients in the water body, and of trace elements in the sediments [58–61]. More recently, a temporal trend of degradation in water quality for irrigation was reported [11,12], that could be attributed to the expansion of the irrigation area, with the concomitant intensification of agriculture, and to the increase of drier conditions resulting from climate change. These studies pointed to a potential increased risk of soil infiltration problems and of salinity-induced yield reductions in sensitive crops, especially in drought years, and during periods of high atmosphere evaporative demands.

The climate in the region is classified as temperate with hot and dry summer (Csa in Köppen Classification), with a small area of mid-latitude steppe (Bsk). The long-term means for the period 1981–2010 of annual precipitation and annual mean temperature are, respectively, 558 mm and 16.9 °C, for Beja, a main town located approximately in the center of the study area [62]. During 2018, the annual precipitation in Beja was 653 mm, mean temperature was 16.2 °C, and reference annual evapotranspiration totaled 1193 mm [63].

Predominant soils in the study area (approximately 81% of total area) are Luvisols, Leptosols, Regosols and Vertisols. For the purpose of this study, a map of Reference Soil Groups (RSG) was built for the study region, based on the World Reference Base for soil resources [46] and on previous studies [64,65] (Figure S1).

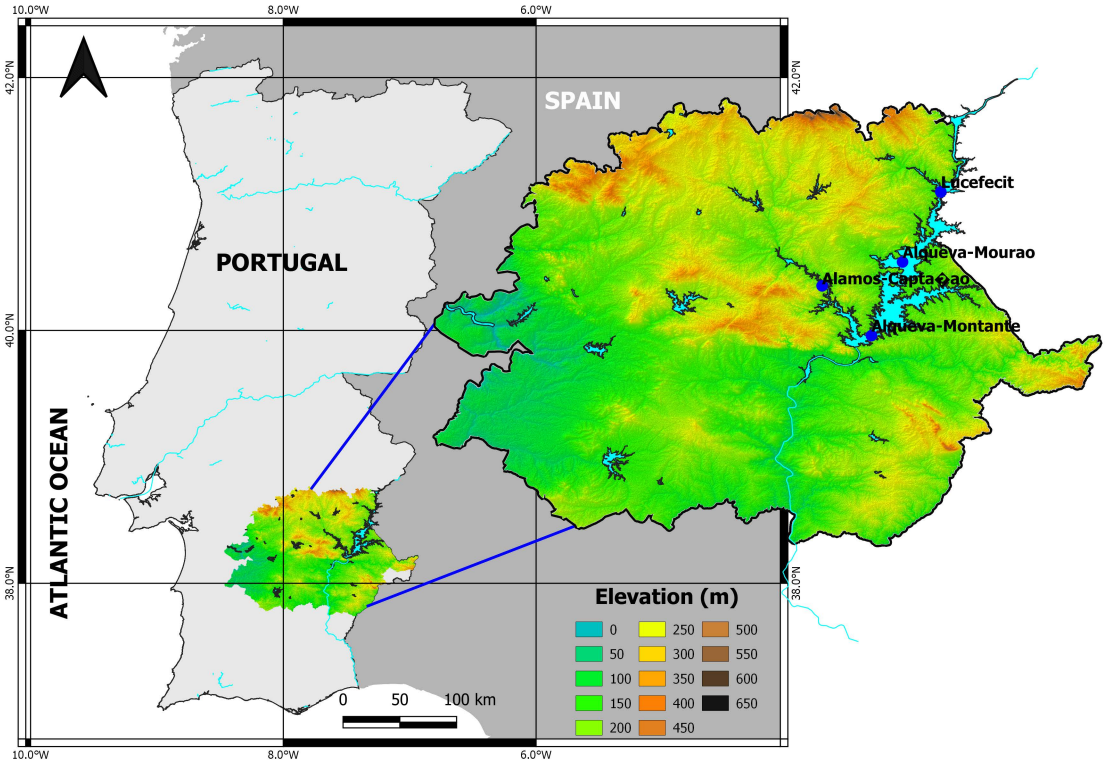

Figure 1. Map showing the location of Inland Alentejo, the Alqueva reservoir, and the sampling sites in floating platforms (Alamos-Captação, Alqueva-Montante, Alqueva-Mourão, and Lucefécit).

The chart of Land Use and Occupation (COS—*Carta de Uso e Ocupação do Solo*) produced in 2018 for Continental Portugal, made available from the Portuguese Directorate General for Territory (DGT—*Direcção-Geral do Território*) [66], was used to obtain the land occupation and use map of the study area (Figure S2). The minimum cartographic unit of COS is of 1 ha, with a minimum distance between lines of 20 m, and it comprises 83 classes, from which 11 distinguish different agricultural types. According to COS, the main agricultural land uses in the region in 2018 were temporary rainfed and irrigated crops, and olive groves, respectively 22% and 15% of the study area. When considering only the Alqueva irrigation area, the main irrigated crops grown in 2018 were (by descending order of importance): olive; fruit trees, mainly nuts like almond and walnut (*Juglans regia* L.), but also pear (*Pyrus communis* L.) or peach (*Prunus persica* (L.) Batsch); grapevine; maize (*Zea mays* L.); forage crops; oil crops; horticultural crops; cereals other than maize [67]. The non-irrigated land is occupied mostly by rainfed crops, pastures and agroforestry systems of holm oak and cork oak.

Given the importance of the EFMA irrigation area in the study region, the water quality data used for the study were collected in the Alqueva reservoir at four sampling sites in floating platforms, as shown in Figure 1: Álamos-Captação (Al; 38°20′30.00″ N, 7°34′40.00″ W), Alqueva-Montante (Mn; 38°12′55″ N, 7°29′28″ W), Alqueva-Mourão (Mr; 38°23′60.00″ N, 7°23′25.80″ W), and Lucefécit (Lf; 38°33′6.32″ N, 7°17′52.86″ W). The Al site was chosen because it was near the Álamos pumping station, an inlet where water is elevated to part of the EFMA conveyance network. The Mn site was selected to ensure representativeness of the reservoir area. Mr and Lf sites were chosen considering previous results for the reservoir water quality assessment [12,58].

3.2. Data Collection and Mapping Methodology

In order to compute a spatial distribution of the Aridity Index, ERA5 dataset of monthly mean averages values was used. ERA5 [68] is the fifth-generation reanalysis product provided by the European Centre for Medium-Range Weather Forecasts (ECMWF). Reanalysis combines observations and a numerical weather prediction model to produce complete atmospheric fields over a regular

3D atmospheric grid. In the present study, the monthly mean values of total precipitation, 2 m air temperature (T_{2m}; °C), and 2 m dew-point temperature (d_{2m}; °C) for the 30 year period 1990–2019 were downloaded from the ERA5-Land monthly averaged dataset with a horizontal resolution of 0.1° (~10 km) [69]. The monthly accumulated PET values were computed using Equation (3), the practical and well-known formulation of Romanenko [70]:

$$\mathrm{PET} = 0.0018(25 + T_a)^2(100 + RH), \quad (3)$$

where T_a (°C) is the monthly mean air temperature and RH (%) is the monthly mean relative humidity calculated from the ERA-5 T_{2m} and d_{2m} values. Finally, the 30 years (1990–2019) mean annual PET and P were computed for the study area to access the AI as defined by the UNEP [55].

The map with the Reference Soil Groups (RSG) in the study area is presented in Figure S1. Slope classes were obtained based on the slope of the predominant soil units [71].

From the textural classes of the surface horizons/layers of the predominant soil units [72], a map with drainage classes was built after the classification presented in Table 3, with the addition of a restricted drainage classification whenever soil use capacity was severely to very severely limited due to excess water.

Within the study area, a potentially irrigated area was established for the application of the risk indices. For this purpose, the following crops/type of crops from the COS classes were considered as possibly irrigated: a-temporary dry and irrigated crops; b-vineyards; c-orchards; d-olive groves; e-complex cultivation patterns. A most likely irrigation method was assigned to each crop/group of crops as follows: I—Drip irrigation, in the case of b, c, and d; II—Surface or Sprinkler irrigation, in the case of a and e.

The study covered six water sampling campaigns in 2018, performed in January (Jan), March (Mar), May, July (Jul), September (Sep), and November (Nov). At each sampling location, 2 L of surface water were collected, at a depth of 50 cm, using a Van Dorn bottle. The water samples were stored in polyethylene bottles and transported to the laboratory, in a cooler at 4 °C, where they were conserved and stored, following the requisites for water conservation for each parameter [73]. The concentrations of Ca^{2+}, Mg^{2+}, and Na^{+}, were determined by ionic chromatography methodology adapted from APHA [73]. Water EC_W was measured in situ on the same dates (except November due to a temporary equipment failure) at a 50 cm depth using a multiparametric probe YSI 6820 MPS probe®. Values of SAR were calculated using Equation (2). For the purpose of this work, ECW and SAR were evaluated after the FAO guidelines presented in Table 4.

3.3. Risk Indices

To obtain the composite risk indices of salinization and sodification, two sets of indicators were adopted, based on a tier 2 approach [16], previously presented in Table 1, and based on Masoudi et al. [35]. The Salinization Risk (RSA) index includes a set of four criteria and respective indicators, represented in classes (I to V or I to III, depending on the range of values or the classes considered), to which a rating score (1 to 5) was assigned (Table 5):

(i) Climate, quantified with the AI scale from [55];
(ii) Topography, represented by slope intervals obtained from the Portuguese soil and land-use capacity map [71];
(iii) Soil drainage, characterized by drainage classes according to Table 3;
(iv) Irrigation water quality, from in situ measurements, classified according to the degrees of restriction to its use with respect to salinity, as presented in Table 4.

Table 5. Criteria, indicators, class limits, and their rating score to evaluate the risk of soil salinization in irrigation areas in the Salinization Risk index (RSA).

Criteria	Indicator	Class and Respective Interval of Values				
		I	II	III	IV	V
Climate	(1) AI	≥0.65 (Humid)	0.50–0.65 (Dry sub-humid)	0.20–0.50 (Semi-arid)	0.05–0.20 (Arid)	<0.05 (Hyper-arid)
Rating score		1	2	3	4	5
Topography [1)]	(2) Slope (%)	>9		3–8		0–2
Rating score		1		3		5
Soil drainage [2)]	(3) Soil drainage class	Good		Moderate		Restricted
Rating score		1		3		5
Irrigation water quality (salinity) [3)]	(4) EC_W (dS m^{-1})	No restriction		Slight-to-moderate restriction		Severe restriction
Rating score		1		3		5

AI—Aridity Index; EC_W—Irrigation water electrical conductivity. [1)] According to the Portuguese soil and land-use capacity map [71]. [2)] According to Table 3. [3)] According to Table 4.

The Sodification Risk (RSO) index comprises a set of five criteria, and respective indicators, to which a rating score (1 to 5) was assigned (Table 6):

Table 6. Criteria, indicators, class limits and their rating score to evaluate the risk of soil sodification in irrigation areas in the Sodification Risk index (RSO).

Criteria	Indicator	Class and Respective Interval of Values				
		I	II	III	IV	V
Climate	(1) AI	≥0.65 (Humid)	0.50–0.65 (Dry sub-humid)	0.20–0.50 (Semi-arid)	0.05–0.20 (Arid)	<0.05 (Hyper-arid)
Rating score		1	2	3	4	5
Topography [1)]	(2) Slope (%)	>9		3–8		0–2
Rating score		1		3		5
Soil drainage [2)]	(3) Soil drainage class	Good		Moderate		Restricted
Rating score		1		3		5
Crop	(4) Irrigation method	Drip				Surface or Sprinkler
Rating score		1				5
Irrigation water quality (infiltration) [3)]	(5) SAR and EC_W (dS m^{-1})	No restriction		Slight-to-moderate restriction		Severe restriction
Rating score		1		3		5

AI—Aridity Index; EC_W—Irrigation water electrical conductivity; SAR—Sodium Adsorption Ratio. [1)] According to the Portuguese soil and land-use capacity map [71]. [2)] According to Table 3. [3)] According to Table 4.

(i) to (iii) equal to the ones considered in the RSA index;

(iv) crop, represented by a most likely irrigation method, considering two classes (I—drip irrigation and II—surface or sprinkler irrigation);

(v) Irrigation water quality, from in situ measurements and sample analyses, classified according to the degrees of restriction to its use with respect to infiltration, as presented in Table 4.

The RSA and RSO indices incorporated the effect of the indicators in each set, obtained by their score sum, using Equations (4) and (5):

$$\mathrm{RSA} = \sum_{i=1}^{4} S_i = S_{AI} + S_{Slope} + S_{Soildrainage} + S_{ECw}, \quad (4)$$

$$\mathrm{RSO} = \sum_{i=1}^{5} S_i = S_{AI} + S_{Slope} + S_{Soildrainage} + S_{Irrigationmethod} + S_{ECw \wedge SAR}, \quad (5)$$

where S_i is the rating score assigned to each of the indicators class.

From the RSA and RSO values, five risk classes were considered (Very Low, Low, Moderate, High and Very High), each corresponding to a level of management practice recommendation (Table 7),

an adaptation of the classification described in Wiebe et al. [32]. In the case of RSA, a condition was added to assign a Very High risk class (RSA > 18) whenever soils were Solonchaks, regardless of the remaining indicators scores. Likewise, in the case of RSO, a condition was added to assign a Very High risk class (RSA > 22) whenever soils were Solonetz, regardless of the remaining indicators scores.

Table 7. Risk classes of soil salinization (from RSA values) and soil sodification (from RSO values), classes description, and assessment of land-use practices (adapted from Wiebe et al. [32]).

RSA Value	RSO Value	Risk Class	Class Description	Assessment of Land-Use Practices
<7	<8	Very Low	Current land management practices are compatible with agri-environmental sustainability	Sustainable
7–10	8–12	Low	Management practices occasionally impact agri-environmental sustainability	Acceptable
11–14	13–17	Moderate	Management practices leave land exposed to agri-environmental degradation	Should be monitored carefully
15–18	18–22	High	Management practices conductive to agri-environmental degradation	Change should be considered
>18	>22	Very High	Management practices directly expose land to agri-environmental degradation	Changes are required

4. Results and Discussion

4.1. Climate, Topography, Drainage, and Irrigation Method

As observed in Figure 2, there was a clear positive gradient of aridity with continentality and from higher to lower latitudes, with a relative minimum over the Guadiana valley, where a large proportion of irrigated land is located. The AI calculated for the study area (period 1990–2019) varied between 0.26 and 0.44; hence, all the region is found within the same climate class, Semi-arid (III, with a rating score of 3). An Aridity Index of 0.415 was reported by Paulo et al. [74] for the period 1941–2006 in Beja.

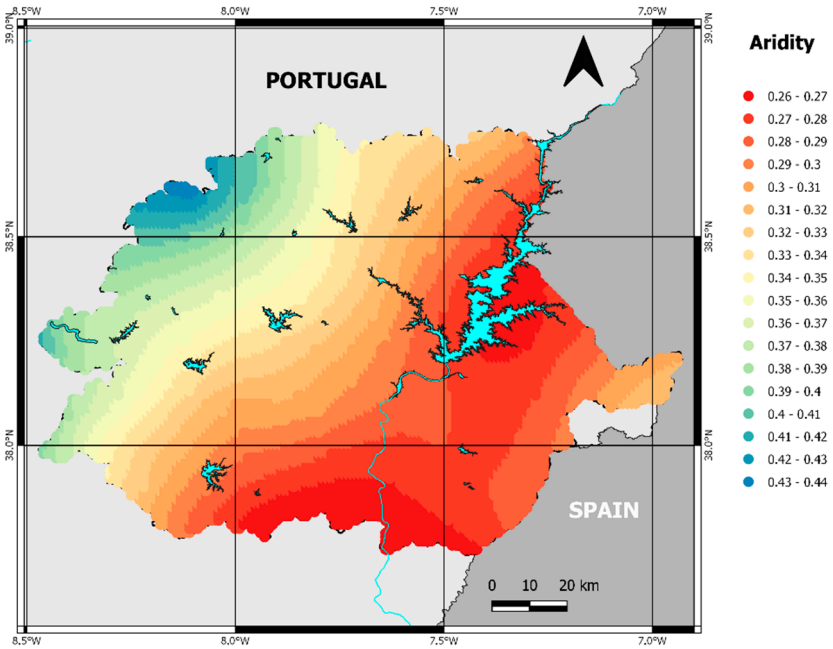

Figure 2. Aridity Index map of the study area, according to UNEP classification [55]: hyper-arid (<0.05); arid (0.05–0.2); semi-arid (0.2–0.5); dry sub-humid (0.5–0.65); humid (≥0.65).

A study by Valverde et al. [75], evaluating climate change potential impacts on irrigated agriculture in the Guadiana River Basin, projected a general increase in crop irrigation requirements, questioning the sustainability of irrigation area expansion in the region. Godinho et al. [76] reported the risk of increased aridity in the area resulting from changes in land surface albedo and land surface temperature caused by land cover transformations, such as deforestation to promote agricultural lands.

In relation to the topography criterion, more than half of the area (60%) presented slopes < 8%; thus, was grouped in slope classes II and III (Figure 3). Considering the drainage class, 73% of the area was in class II and 7% in class III, which related with the prevalence of medium-to-fine textured soils in the region (Figure 4). According to the assumptions of the model, the potentially irrigated area totaled 401,408 ha, corresponding to about 40% of the agricultural and forestry land. In this area, 43% is most likely irrigated with drip systems and the remaining with sprinkler or surface systems (Figure 5).

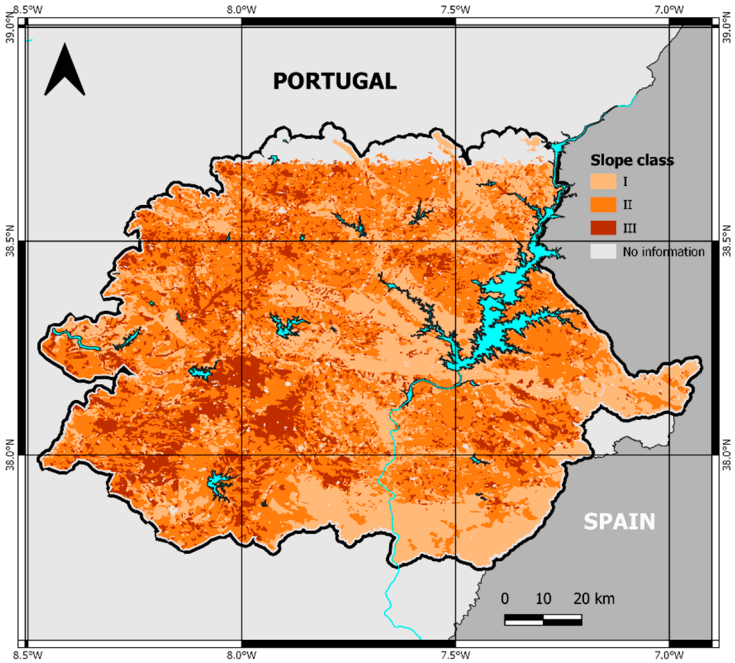

Figure 3. Slope classes of the study area. I—>9%; II—3% to 8%; III—0% to 2%.

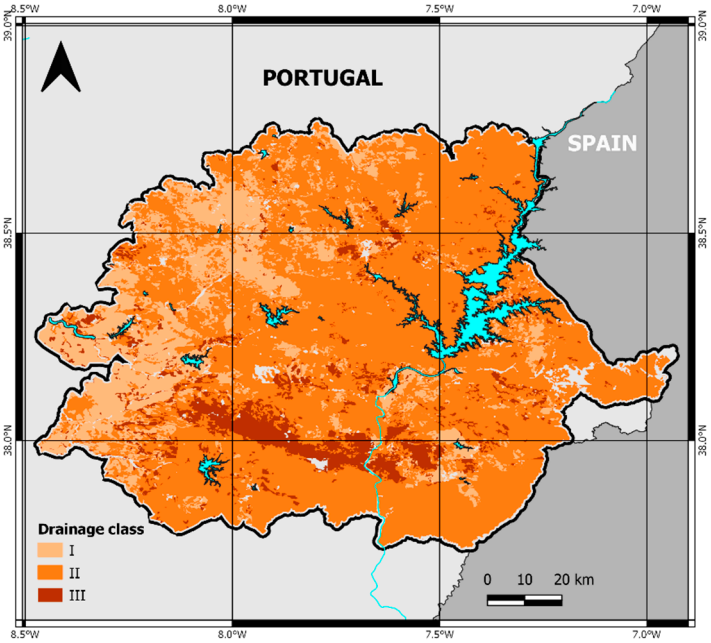

Figure 4. Drainage classes of the study area. I—Good; II—Moderate; III—Restricted.

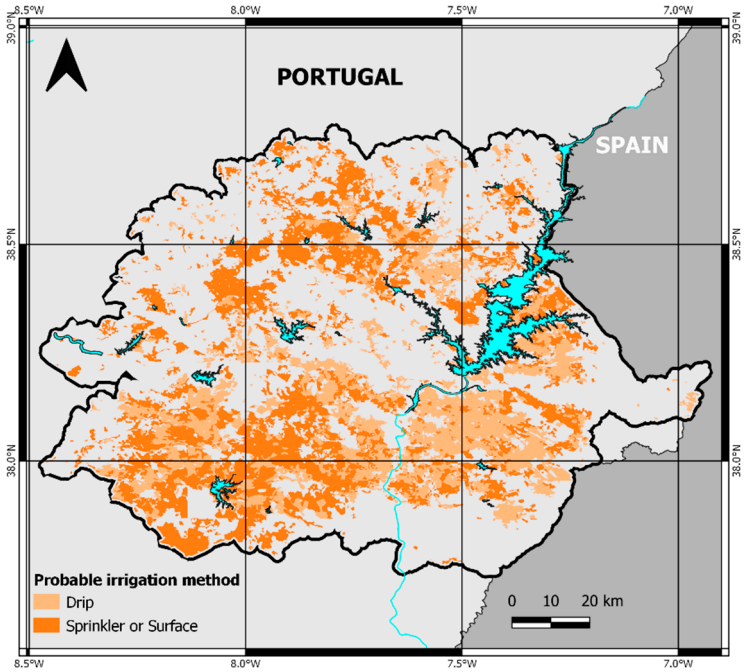

Figure 5. Most likely irrigation method in the potentially irrigated study area.

When considering only the potential irrigated area, some of the percentages previously presented had some significant variation: (i) the percentage of Leptosols varied from 17% in the total area to 3% in the potentially irrigated area, indicating a low agricultural, and accordingly, low irrigation aptitude of this reference soil group; (ii) slopes assigned to class II and III increased, respectively, from 46% to 49% and from 14% to 17%; (iii) the areas with restricted drainage (class III) increased from 7% to 12%; (iv) temporary crops and olive groves remained the predominant COS classes but with higher occupation within the potentially irrigated area of 57% and 37%, respectively. However, it may be that the percentage of temporary crops was overestimated since the COS class includes rainfed and irrigated crops and, from the information reported in EDIA (*Empresa de Desenvolvimento e Insfraestruturas do Alqueva*) [67], olive groves occupy a large proportion of the irrigated lands in the region.

4.2. Water Quality for Irrigation

The temporal variation observed for EC_W and SAR for the four sampling sites is presented in Figure 6a,b. In the case of EC_W, the highest average values were measured in September (0.56 ± 0.015 dS m^{-1}) and July (0.49 ± 0.020 dS m^{-1}), during the dry season. As for SAR, the highest values were registered at Álamos in January (1.64 ± 0.000), which was probably due to the 2017 and early 2018 drought that lead to low water storage and, possibly, reduced salt dissolution. The lowest SAR value occurred at the same site in July (1.12 ± 0.010). There were no relevant differences between sites.

According to the methodology of salinization and sodification risk prediction presented, the irrigation water quality indicators fall in the same classes for every date and site. EC_W values showed no degree of restriction of use, thus were grouped in class I (Table 5). The combined assessment of EC_W and SAR showed a slight-to-moderate degree of restriction of use in all water samples analyzed. Therefore, these sodification indicators fall within class II for every date and site (Table 6). In this case, low-salt water may reduce infiltration even for a low SAR, given that the salinity of the applied water is insufficient to counteract the negative effects of adsorbed sodium on soil structure [51,52,77].

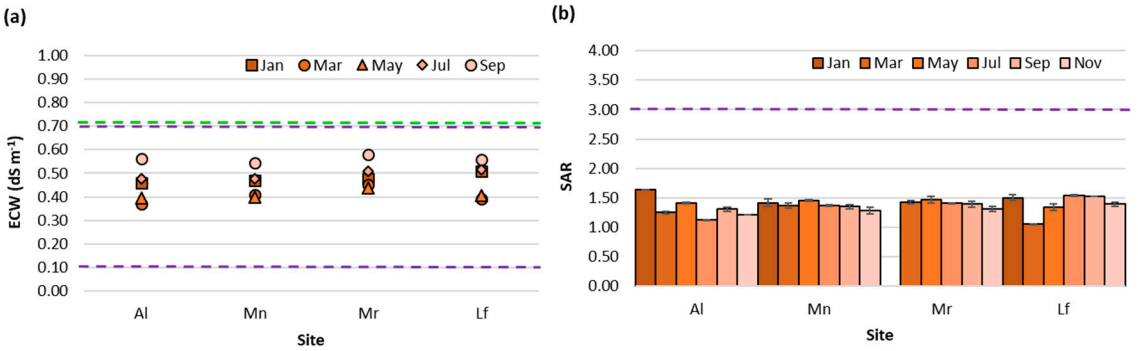

Figure 6. Spatial and temporal variation of EC_W (**a**) and SAR (**b**), during 2018, at the Alqueva reservoir. Dots represent single in situ measurements. Bars represent mean and whiskers represent the standard deviation for three repetitions Dashed lines correspond to the limit values from FAO water quality standards, as presented in Table 4 (green dashed line is the limit value for salinity problems and purple lines are the limit values for infiltration problems). Al—Álamos; Mn—Montante; Mr—Mourão; Lf—Lucefécit. Jan—January; Mar—March; Jul—July; Sep—September; Nov—November.

4.3. Salinization Risk Areas

The risk map of soil salinization in the potentially irrigated lands of Inland Alentejo shows that there was a predominance of low (67%) and moderate risk (26%) areas and that there were no areas within the higher risk classes (Figure 7).

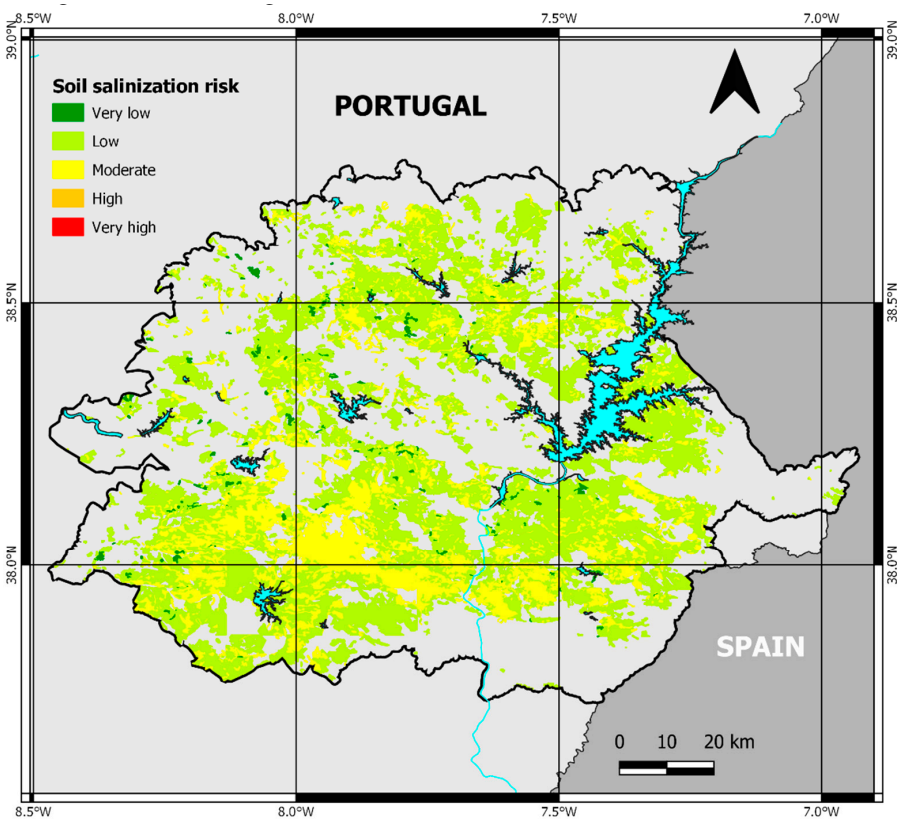

Figure 7. Salinization risk of the potentially irrigated area in the Inland Alentejo region based on the Salinization Risk index (RSA). Very Low risk: RSA < 7; Low risk: 7 ≤ RSA ≥ 10; Moderate risk: 11 ≤ RSA ≥ 14; High risk: 15 ≤ RSA ≥ 18; Very-High risk: RSA > 18.

Moderate risk of salinization was predominantly related to low slope areas (Figure 8a).

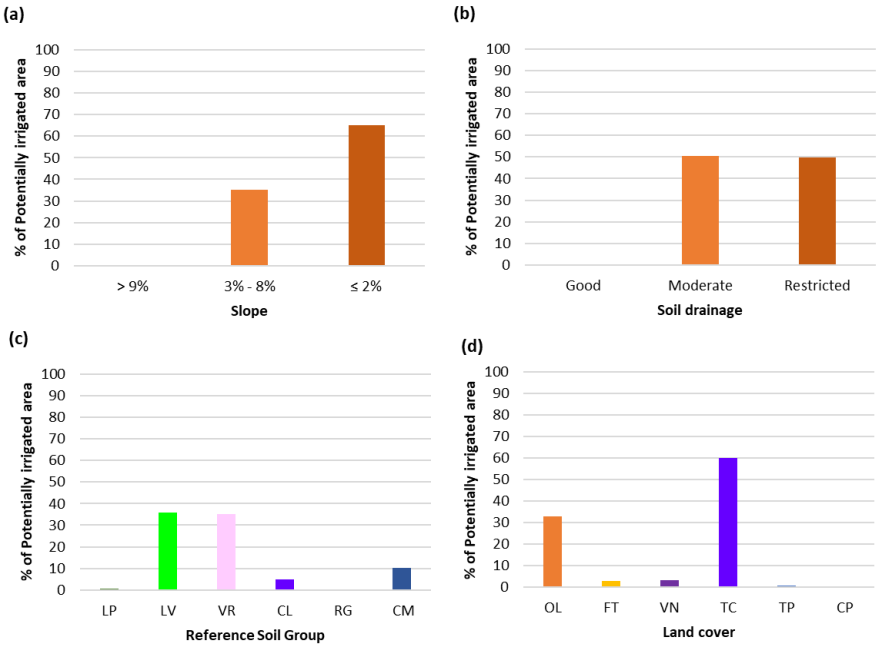

Figure 8. Percentages of Moderate Risk of Salinization areas per slope class (**a**), drainage class (**b**), soil reference group (**c**) and land cover (**d**). LP—Leptosols; LV—Luvisols; VR—Vertisols; CL—Calcisols; RG—Regosols; CM—Cambisols. OL—Olive groves; FT—Fruit trees; VN—Vineyards; TC—Temporary crops; TP—Temporary crops and/or improved pastures; CP—Complex crop patterns.

Also, moderate and restricted soil drainage, a characteristic of fine-textured soils, like Luvisols or Vertisols, (Figure 8b,c) lead to the augmentation of soil salinization risk. Similar relationships between slope and salinization-prone areas were obtained by other authors [78] when mapping the irrigation salinity risk in an arid region. Seydehmet et al. [78] found high salinization risk associated with flat and low terrain, high salt content in the subsoil, high salinity of groundwater and small depth of the water table. The development of soil salinity as a consequence of poor drainage conditions, fine texture and low saturated soil hydraulic conductivity was reported by de Paz et al. [15] and Bouksila et al. [79], in their works about salinization risk in semi-arid irrigated land. The influence of soil water storage capacity was referred to as the most important soil indicator affecting soil salinization by Kairis et al. [80], indicating that moderately fine and fine-textured soils were more likely to be affected by salinization.

As expected, the main types of land use where this level of risk appeared were olive groves and annual crops (Figure 8d), which was mainly a consequence of their extensive distribution in the area. In the case of irrigated high-density olive groves, largely grown in the region, Ramos et al. [81] found that the long-term (30 years) impact of current irrigation practices (including deficit irrigation, i.e., seasonal irrigation volumes corresponding to a fraction of the seasonal crop evapotranspiration) showed reduced risks of soil salinization, with simulated average root zone salinity values at the end of the irrigation seasons (normally, late summer or early autumn) remaining below the salinity threshold limit for olive groves. Additionally, these authors stated that the use of deficit irrigation practices in olive groves has the potential to improve soil salinity management by a better control of rising water tables and by a reduction in the import of salts by irrigation water, but it does not provide the same degree of leaching as full irrigation.

4.4. Sodification Risk Areas

The results obtained for the RSO index showed that most of the potentially irrigated area in Inland Alentejo is classified as moderate risk (68%), followed by high risk (16%) and low risk (10%) of sodification (Figure 9). Predictions were decidedly influenced by the indicators slope, drainage,

water quality, and irrigation method. Moderate risk areas comprised mainly medium slopes (Figure 10a), moderate drainage soils included in the Luvisols RSG (Figure 10b,c), annual crops irrigated by surface or sprinkler systems and, to a lesser extent, olive orchards irrigated by drip systems (Figure 10d,e).

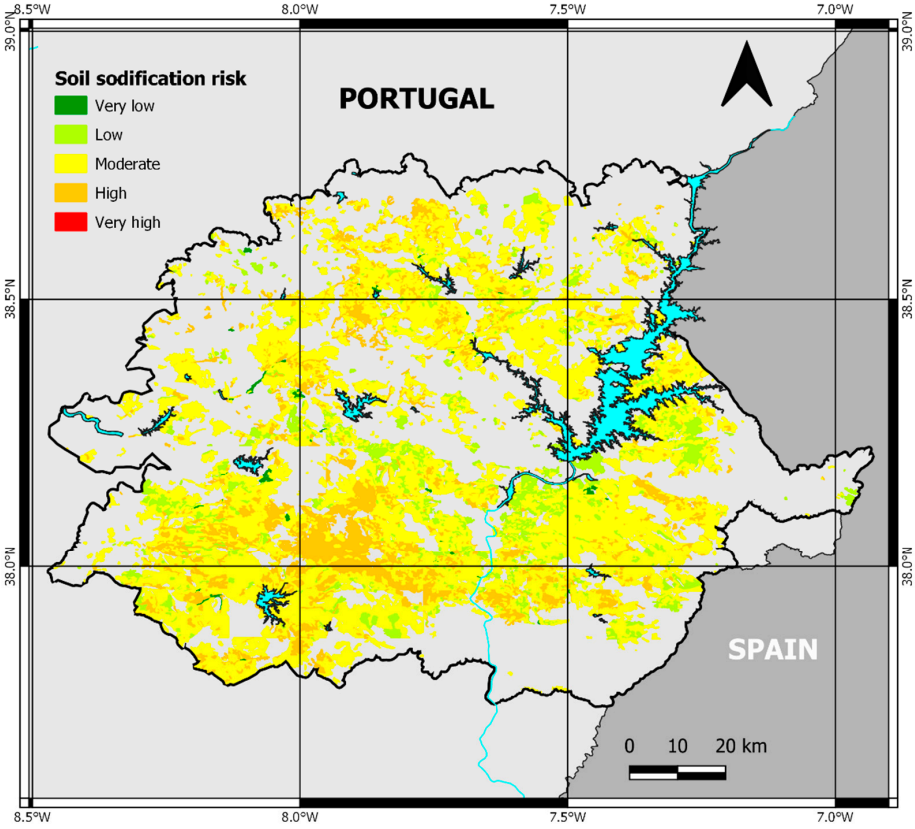

Figure 9. Sodification risk of the potentially irrigated area in the Inland Alentejo region based on the Sodification Risk index (RSO). Very Low risk: RSO < 8; Low risk: 8 ≤ RSO ≥ 12; Moderate risk: 13 ≤ RSO ≥ 17; High risk: 18 ≤ RSO ≥ 22; Very-High risk: RSO > 22.

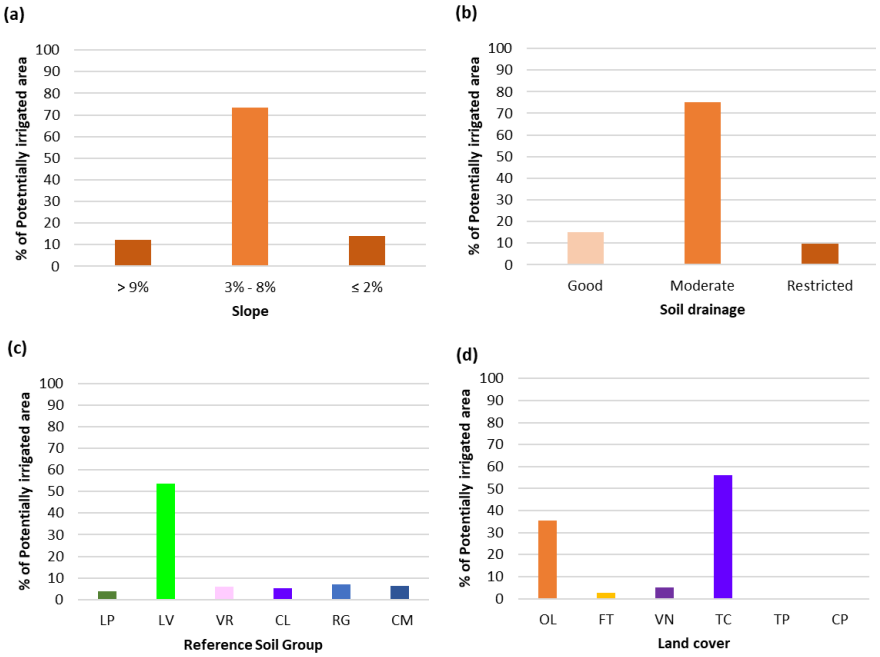

Figure 10. *Cont.*

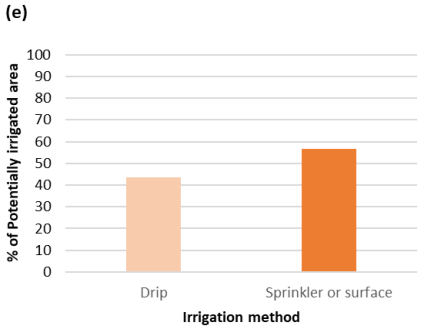

Figure 10. Percentages of Moderate Risk of Sodification areas per slope class (**a**), drainage class (**b**), soil reference group (**c**), land occupation (**d**) and irrigation method (**e**). LP—Leptosols; LV—Luvisols; VR—Vertisols; CL—Calcisols; RG—Regosols; CM—Cambisols. OL—Olive groves; FT—Fruit trees; VN—Vineyards; TC—Temporary crops; TP—Temporary crops and/or improved pastures; CP—Complex crop patterns.

The analysis of the relationships between the RSO index and its indicators in high-risk areas showed a strong prevalence of flat and low slope terrain (Figure 11a), moderate-to-restricted soil drainage in Luvisols, Vertisols and Cambisols (Figure 11b,c), and annual crops irrigated with surface or sprinkler systems (Figure 11d,e). The results were in accordance with Sentís [36], who, in their study to evaluate the development of secondary sodicity in the surface soil, found that it was strongly affected by inadequate drainage and inefficient irrigation. This risk prediction could indicate that even non-sodic soils with ESP (or SAR) < 3 can have a tendency for swelling, aggregate failure, and increase in dispersion rates, thus behaving like sodic soils at very low electrolyte concentration [82]. As a consequence, soil infiltration rates decline and surface crust formation problems can occur, conditions that may worsen due to the physical disruption of soils particles caused by the use of sprinkler irrigation systems. Although clay soils are more affected by sodicity, it should be considered that there are some soil properties, other than texture, that are significant in influencing the behavior of soils under sodification risk, namely, depth and thickness of the sodic horizons and clay mineralogy. For instance, the presence of high-activity clay minerals, like smectite, is likely to increase the soil susceptibility to sodification [83].

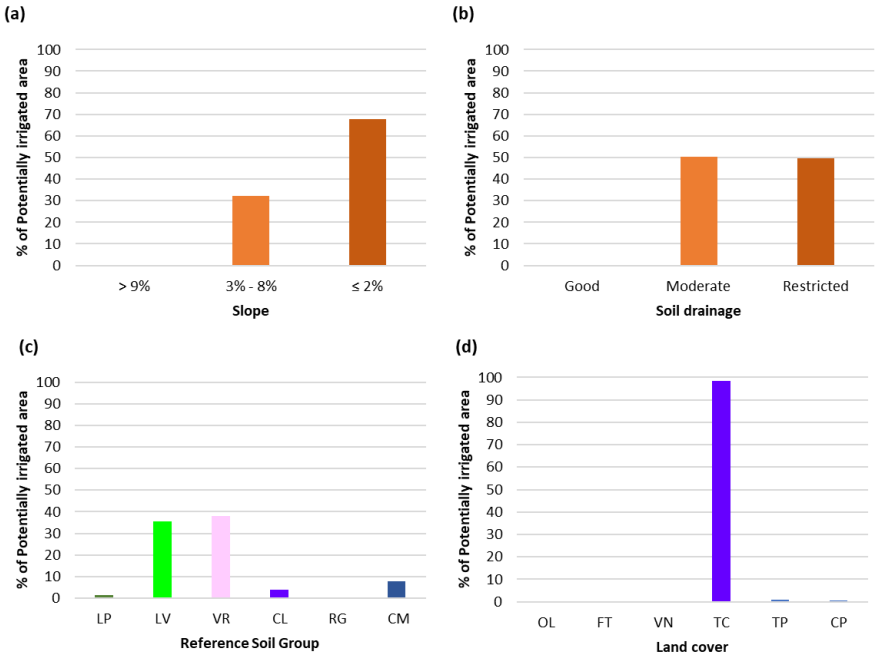

Figure 11. *Cont.*

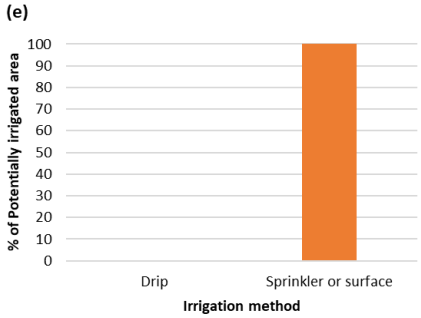

Figure 11. Percentages of High Risk of Sodification areas per slope class (**a**), drainage class (**b**), soil reference group (**c**), land occupation (**d**) and irrigation method (**e**). LP—Leptosols; LV—Luvisols; VR—Vertisols; CL—Calcisols; RG—Regosols; CM—Cambisols. OL—Olive groves; FT—Fruit trees; VN—Vineyards; TC—Temporary crops; TP—Temporary crops and/or improved pastures; CP—Complex crop patterns.

5. Conclusions

Negative impacts of soil salinity and sodicity in Mediterranean regions include decreased food production, deteriorating water quality in surface streams and groundwater, loss of biodiversity, and increased risk of flooding and desertification. The present study aimed to develop two risk indices for better prediction of soil salinity and sodicity in large areas, in order to provide farmers, rural planners, and resource managers with a tool to help identify susceptible areas, to apply appropriate agronomical strategies and management options and to avoid soil degradation in irrigated lands.

The application of the Salinization Risk (RSA) index to Inland Alentejo indicated that areas under moderate risk, where land-use practices should be monitored carefully, showed a prevalence of low slopes and fine-textured soils like Luvisols and Vertisols with limited drainage conditions.

The Sodification Risk (RSO) index calculations estimated a predominance of moderate- and high-risk potentially irrigated lands, corresponding to management practices which leave land exposed to agri-environmental degradation or are conductive to agri-environmental degradation. High-risk areas had a large incidence of low slope terrain, moderate-to-restricted soil drainage in high clay content Luvisols, Vertisols and Cambisols, and annual crops irrigated with surface or sprinkler systems.

Although the RSA and RSO indices have been proposed for a risk prediction purpose, and despite the fact that their validation with soil sampling or with in situ measurements with proximal sensors was outside the scope of this work, more precise knowledge is very important, especially in areas identified as of moderate and high risk. In this sense, it is our goal to develop work to validate the methodology presented in order to identify assumptions that must be adjusted or to integrate indicators of the current state of soil salinity and sodicity. Further possible developments of this methodology also include the application of these indices to different climate change scenarios, assessing the impact of expected increased aridity and decreased irrigation water quality on the risk of development of soil salinization and sodification processes in irrigated Mediterranean areas.

The proposed risk indices integrated climate, topography, soil, water quality, and crop indicators that are easily available for large scale assessments and territorial planning but can be applied at the farm level scale, encouraging farmers to get to know their land better, implement soil monitoring and adopt agronomic strategies that contribute to the sustainability of irrigated agriculture.

Supplementary Materials: The following are available online at http://www.mdpi.com/2073-4441/12/12/3569/s1, Figure S1: Predominant soils of the study area. Figure S2: Land occupation and use of the study area, in 2018.

Author Contributions: Conceptualization, A.T.; investigation, A.T., P.P., S.F., A.L., M.J.C., P.A., M.P., and R.S.; writing—original draft preparation, A.T.; writing—review and editing, A.T., P.P., M.J.C., P.A., M.P., and R.S; supervision, A.T. and P.P.; Visualization, A.T. and M.J.C. All authors have read and agreed to the published version of the manuscript.

Funding: This research is co-funded by the European Union through the European Regional Development Fund, included in the COMPETE 2020 (Operational Program Competitiveness and Internationalization) through the ICT project (UIDB/04683/2020) with the reference POCI-01-0145-FEDER-007690, the ALOP project (ALT20-03-0145-FEDER-000004), and through Geobiotec (UIDP/04035/2020), funded by FCT—Fundação para a Ciência e a Tecnologia, Portugal.

Acknowledgments: The authors thank the General Directorate of Agriculture and Rural Development of Portugal (DGADR—Direção Geral de Agricultura e Desenvolvimento Rural) for providing the Portuguese soil maps and soil capacity maps in digital form used in this study.

Conflicts of Interest: The authors declare no conflict of interest.

References

1. Butcher, K.; Wick, A.F.; DeSutter, T.; Chatterjee, A.; Harmon, J. Soil Salinity: A Threat to Global Food Security. *Agron. J.* **2016**, *108*, 2189–2200. [CrossRef]
2. Qadir, M.; Quillérou, E.; Nangia, V.; Murtaza, G.; Singh, M.; Thomas, R.J.; Drechsel, P.; Noble, A.D. Economics of salt-induced land degradation and restoration. *Nat. Resour. Forum* **2014**, *38*, 282–295. [CrossRef]
3. FAO. *The State of the World's Land and Water Resources for Food and Agriculture (SOLAW)—Managing Systems at Risk*; Food and Agriculture Organization of the United Nations: Rome and Earthscan: London, UK, 2011; ISBN 978-92-5-106614-0.
4. UNESCO. *WWDR2014 The United Nations World Water Development Report 2014: Water and Energy*; Facts and Figures; The United Nations World Water Development Report; UNESCO: Paris, France, 2014.
5. Weil, R.R.; Brady, N.C. *The Nature and Properties of Soils*, 15th ed.; Pearson: Columbus, OH, USA, 2016; ISBN 978-0-13-325448-8.
6. Zalidis, G.; Stamatiadis, S.; Takavakoglou, V.; Eskridge, K.; Misopolinos, N. Impacts of agricultural practices on soil and water quality in the Mediterranean region and proposed assessment methodology. *Agric. Ecosyst. Environ.* **2002**, *88*, 137–146. [CrossRef]
7. Aragüés, R.; Urdanoz, V.; Çetin, M.; Kirda, C.; Daghari, H.; Ltifi, W.; Lahlou, M.; Douaik, A. Soil salinity related to physical soil characteristics and irrigation management in four Mediterranean irrigation districts. *Agric. Water Manag.* **2011**, *98*, 959–966. [CrossRef]
8. Mateo-Sagasta, J.; Burke, J. *Agriculture and Water Quality Interactions: A Global Overview*; SOLAW Background Thematic Report-TR08; Food and Agriculture Organization of the United Nations: Rome, Italy, 2010.
9. Stolte, J.; Tesfai, M.; Øygarden, L.; Kværnø, S.; Keizer, J.; Verheijen, F.; Panagos, P.; Ballabio, C.; Hessel, R. *Soil Threats in Europe*; Publications Office: Luxembourg, 2015; ISBN 978-92-79-54018-9.
10. Yeo, A. Predicting the interaction between the effects of salinity and climate change on crop plants. *Sci. Hortic.* **1998**, *78*, 159–174. [CrossRef]
11. Tomaz, A.; Palma, P.; Alvarenga, P.; Gonçalves, M.C. Chapter 13—Soil salinity risk in a climate change scenario and its effect on crop yield. In *Climate Change and Soil Interactions*; Prasad, M.N.V., Pietrzykowski, M., Eds.; Elsevier: Amsterdam, The Netherlands, 2020; pp. 351–396, ISBN 978-0-12-818032-7.
12. Tomaz, A.; Palma, P.; Fialho, S.; Lima, A.; Alvarenga, P.; Potes, M.; Salgado, R. Spatial and temporal dynamics of irrigation water quality under drought conditions in a large reservoir in Southern Portugal. *Environ. Monit. Assess.* **2020**, *192*, 93. [CrossRef]
13. Rengasamy, P. Soil processes affecting crop production in salt-affected soils. *Funct. Plant Biol.* **2010**, *37*, 613. [CrossRef]
14. Hillel, D. *Salinity Management for Sustainable Irrigation: Integrating Science, Environment, and Economics*; The World Bank: Washington, DC, USA, 2000; ISBN 978-0-8213-4773-7.
15. de Paz, J.M.; Visconti, F.; Zapata, R.; Sánchez, J. Integration of two simple models in a geographical information system to evaluate salinization risk in irrigated land of the Valencian Community, Spain. *Soil Use Manag.* **2004**, *20*, 333–342. [CrossRef]
16. Eckelmann, W.; Baritz, R.; Bialousz, S.; Bielek, P.; Carre, F.; Houskova, B.; Jones, R.J.A.; Kibblewhite, M.; Kozak, J.; le Bas, C.; et al. *Common Criteria for Risk Area Identification According to Soil Threats*; Office for Official Publications of the European Communities: Luxembourg, 2006.
17. Bloem, E.; van der Zee, S.E.A.T.M.; Tóth, T.; Hagyo, A. *Risk Assessment methods of Salinity*; Publications Office of the European Union: Luxembourg, 2008.

18. Shahid, S. Developments in Soil Salinity Assessment, Modeling, Mapping, and Monitoring from Regional to Submicroscopic Scales. In *Developments in Soil Salinity Assessment and Reclamation*; Shahid, S., Abdelfattah, M., Taha, F., Eds.; Springer: Dordrecht, The Netherlands, 2013; pp. 3–43. ISBN 978-94-007-5683-0.
19. Corwin, D.L.; Rhoades, J.D.; Šimůnek, J. Leaching requirement for soil salinity control: Steady-state versus transient models. *Agric. Water Manag.* **2007**, *90*, 165–180. [CrossRef]
20. Letey, J.; Feng, G. Dynamic versus steady-state approaches to evaluate irrigation management of saline waters. *Agric. Water Manag.* **2007**, *91*, 1–10. [CrossRef]
21. Castanheira, N.; Paz, A.; Farzamian, M.; Paz, M.C.; Santos, F.; Fernandes, M.; Pires, F.; Gonçalves, M. Modelling of soil water and salt dynamics and prediction of salinity risks in Lezíria (Portugal) in response to different qualities of irrigation water. *Rev. Cienc. Agrarias* **2020**, *43*, 161–173. [CrossRef]
22. Daliakopoulos, I.N.; Tsanis, I.K.; Koutroulis, A.; Kourgialas, N.N.; Varouchakis, A.E.; Karatzas, G.P.; Ritsema, C.J. The threat of soil salinity: A European scale review. *Sci. Total Environ.* **2016**, *573*, 727–739. [CrossRef] [PubMed]
23. Thompson, R.; Amezketa, E.; Nuñez, M.; Falsone, G.; Toth, T.; Paz, A.; Gonçalves, M.; Castanheira, N.; Gould, I.; Tamvakidis, S. *EIP-AGRI Focus Group Soil salinisation: Final Report. MINIPAPER: Measuring, Mapping and Monitoring of Soil Salinity*; The European Innovation Partnership: Brussels, Belgium, 2020.
24. Toth, G.; Montananella, L.; Rusco, E. *Threats to Soil Quality in Europe*; EUR Scientific and Technical Research Series; Office for Official Publications of the European Communities: Luxembourg, 2008; ISBN 978-92-79-09529-0.
25. ESDB. *The European Soil Database Distribution Version 2.0*, European Commission and the European Soil Bureau Network, CD-ROM, EUR 19945 EN. 2004.
26. Odeh, I.O.A.; Onus, A. Spatial Analysis of Soil Salinity and Soil Structural Stability in a Semiarid Region of New South Wales, Australia. *Environ. Manag.* **2008**, *42*, 265–278. [CrossRef]
27. Echeverri-Sanchez, A.; Facundo-Péres, C.F.; Angulo-Rojas, P.; Urrutia-Cobo, N. A Methodological Approach for Assessing Soil Salinity Hazard in Irrigated Areas. Case Study: The Rut Irrigation District, Colombia. *Rev. Ing. Univ. Medellin* **2016**, *15*, 13–26. [CrossRef]
28. El Harti, A.; Lhissou, R.; Chokmani, K.; Ouzemou, J.E.; Hassouna, M.; Bachaoui, E.M.; El Ghmari, A. Spatiotemporal monitoring of soil salinization in irrigated Tadla Plain (Morocco) using satellite spectral indices. *Int. J. Appl. Earth Obs. Geoinf.* **2016**, *50*, 64–73. [CrossRef]
29. Zhou, D.; Lin, Z.; Liu, L.; Zimmermann, D. Assessing secondary soil salinization risk based on the PSR sustainability framework. *J. Environ. Manag.* **2013**, *128*, 642–654. [CrossRef] [PubMed]
30. Biggs, A.J.W.; Searle, R.D.; Watling, K.M.; Secombe, K.E.; Larkin, L.M. Implementation of an adaptive salinity risk framework in the Condamine catchment, Queensland Murray-Darling Basin, Australia. *Int. J. Geogr. Inf. Sci.* **2009**, *23*, 441–456. [CrossRef]
31. Eilers, R.G.; Eilers, W.D.; Fitzgerald, M.M. A Salinity Risk Index for Soils of the Canadian Prairies. *Hydrogeol. J.* **1997**, *5*, 68–79. [CrossRef]
32. Wiebe, B.H.; Eilers, R.G.; Eilers, W.D.; Brierley, J.A. Application of a risk indicator for assessing trends in dryland salinization risk on the Canadian Prairies. *Can. J. Soil Sci.* **2007**, *87*, 213–224. [CrossRef]
33. Grundy, M.; Silburn, D.; Chamberlain, T. A risk framework for preventing salinity. *Environ. Hazards* **2007**, *7*, 97–105. [CrossRef]
34. OECD. *OECD Environmental Indicators. Development, Measure and Use*; Organization for Economic Co-Operation and Development; OECD Environment Directorate; Environmental Performance and Information Division: Paris, France, 2003; p. 37.
35. Masoudi, M.; Patwardhan, A.M.; Gore, S.D. A new methodology for producing of risk maps of soil salinity, Case study: Payab Basin, Iran. *J. Appl. Sci. Environ. Mgt.* **2006**, *10*, 9–13. [CrossRef]
36. Sentís, I.P. Advances in the prognosis of soil sodicity under dryland irrigated conditions. *Int. Soil Water Conserv. Res.* **2014**, *2*, 50–63. [CrossRef]
37. Richards, L.A. *Diagnosis and Improvement of Saline and Alkali Soils*; Agriculture Handbook; USDA: Washington, DC, USA, 1954; Volume 60.
38. Bresler, E.; McNeal, B.L.; Carter, D.L. *Saline and Sodic Soils. Principles-Dynamics-Modeling*; Advanced Series in Agricultural Sciences; Springer: Berlin, Germany, 1982; Volume 10, ISBN 978-3-642-68326-8.
39. Maas, E.V.; Hoffman, G.J. Crop Salt Tolerance-Current Assessment. *J. Irrig. Drain. Div.* **1977**, *103*, 115–134.
40. Maas, E.V.; Grattan, S.R. Crop Yields as Affected by Salinity. In *Agricultural Drainage*; Agronomy Monograph; American Society of Agronomy, Crop Science Society of America, Soil Science Society of America: Madison, WI, USA, 1999; pp. 55–108, ISBN 978-0-89118-230-6.

41. Zörb, C.; Geilfus, C.-M.; Dietz, K.-J. Salinity and crop yield. *Plant Biol.* **2019**, *21*, 31–38. [CrossRef] [PubMed]
42. Machado, R.; Serralheiro, R. Soil Salinity: Effect on Vegetable Crop Growth. Management Practices to Prevent and Mitigate Soil Salinization. *Horticulturae* **2017**, *3*, 30. [CrossRef]
43. Compton, A. *A Review of Rationale for EC and SAR Standards*; Water Quality Planning Bureau, Water Quality Standards Section; Montana Department of Environmental Quality: Helena, MT, USA, 2011.
44. Pisinaras, V.; Tsihrintzis, V.A.; Petalas, C.; Ouzounis, K. Soil salinization in the agricultural lands of Rhodope District, northeastern Greece. *Environ. Monit. Assess.* **2010**, *166*, 79–94. [CrossRef]
45. Tanji, K.K.; Kielen, N.C. *Agricultural Drainage Water Management in Arid and Semi-Arid Areas*; FAO irrigation and drainage paper; Food and Agriculture Organization of the United Nations: Rome, Italy, 2002; ISBN 978-92-5-104839-9.
46. IUSS Working Group WRB. *World Reference Base for Soil Resources 2014: International Soil Classification System for Naming Soils and Creating Legends for Soil Maps. Update 2015*; World Soil Resources Report; Food and Agriculture Organization of the United Nations; FAO: Rome, Italy, 2015; ISBN 978-92-5-108369-7.
47. Ramos, T.; Gonçalves, M.C.; Martins, J.C.; Pires, F.; Pereira, L.S. Propriedades hidráulicas do solo para as diferentes classes texturais. *Rev. Ciências Agrárias* **2011**, *34*, 252–264.
48. Rawls, W.J.; Brakensiek, K.; Saxton, K.E. Estimation of soil water properties. *Trans. Am. Soc. Agric. Eng.* **1982**, *25*, 305–316. [CrossRef]
49. Freeze, R.A.; Cherry, J.A. *Groundwater*; Prentice-Hall, Inc.: Englewood Cliffs, NJ, USA, 1979; ISBN 0-13-365312-9.
50. Schofield, R.V.; Kirkby, M.J. Application of salinization indicators and initial development of potential global soil salinization scenario under climatic change. *Glob. Biogeochem. Cycles* **2003**, *17*. [CrossRef]
51. Rhoades, J.D.; Kandiah, A.; Mashali, A.M. *The Use of Saline Waters for Crop Production*; FAO irrigation and drainage paper; Food and Agriculture Organization of the United Nations: Rome, Italy, 1992; ISBN 978-92-5-103237-4.
52. Ayers, R.S.; Westcot, D.W. *Water Quality for Agriculture*; FAO irrigation and drainage paper; Food and Agriculture Organization of the United Nations: Rome, Italy, 1985; ISBN 978-92-5-102263-4.
53. Pereira, L.; Cordery, I.; Iacovides, I. *Coping with Water Scarcity: Addressing the Challenges*; Springer: Dordrecht, The Netherlands, 2009; ISBN 978-1-4020-9578-8.
54. Pla Sentis, I. Soil salinisation and land desertification. In *Soil Degradation and Desertification in Mediterranean Environments*; Rubio, J.L., Calvo, A., Eds.; Geoforma: Logroño, Spain, 1996; pp. 105–129.
55. UNEP. *World Atlas of Desertification*; The United Nations Environmental Programme: London, UK, 1993.
56. Tomaz, A.; Patanita, M.; Guerreiro, I.; Dôres, J.; Boteta, L.; Palma, J. Efficient use of water and nutrients in irrigated cropping systems in the Alqueva region. *Span. J. Soil Sci.* **2018**, *8*, 12–23. [CrossRef]
57. DGADR Sistema de Informação do Regadio. Available online: http://sir.dgadr.gov.pt/expl-alentejo (accessed on 6 September 2020).
58. Palma, P.; Alvarenga, P.; Palma, V.L.; Fernandes, R.M.; Soares, A.M.; Barbosa, I.R. Assessment of anthropogenic sources of water pollution using multivariate statistical techniques: A case study of the Alqueva's reservoir, Portugal. *Environ. Monit. Assess.* **2010**, *165*, 539–552. [CrossRef] [PubMed]
59. Palma, P.; Ledo, L.; Soares, S.; Barbosa, I.R.; Alvarenga, P. Spatial and temporal variability of the water and sediments quality in the Alqueva reservoir (Guadiana Basin; southern Portugal). *Sci. Total Environ.* **2014**, *470–471*, 780–790. [CrossRef] [PubMed]
60. Palma, P.; Köck-Schulmeyer, M.; Alvarenga, P.; Ledo, L.; Barbosa, I.R.; López de Alda, M.; Barceló, D. Risk assessment of pesticides detected in surface water of the Alqueva reservoir (Guadiana basin, southern of Portugal). *Sci. Total Environ.* **2014**, *488–489*, 208–219. [CrossRef] [PubMed]
61. Palma, P.; Ledo, L.; Alvarenga, P. Assessment of trace element pollution and its environmental risk to freshwater sediments influenced by anthropogenic contributions: The case study of Alqueva reservoir (Guadiana Basin). *CATENA* **2015**, *128*, 174–184. [CrossRef]
62. IPMA Climate Normals-1981–2010–Beja. Available online: https://www.ipma.pt/en/oclima/normais.clima/1981-2010/002/ (accessed on 6 July 2019).
63. COTR SAGRA—Sistema Agrometeorológico para a Gestão da Rega no Alentejo (Agrometeorological System for Irrigation Management in Alentejo). Available online: http://www.cotr.pt/servicos/sagranet.php (accessed on 30 September 2020).
64. Madeira, M.; Monteiro, F. A Base de Referência para os Solos do Mundo e a Classificação dos Solos de Portugal. *Rev. Cienc. Agrárias* **2004**, *27*, 13–23.

65. Lopes, R.; Madeira, M.; Arsénio, P. Mapping of land units and land capability classification in Portugal. The case of Lourinhã Municipality. *Finisterra* **2017**, *52*, 103–127. [CrossRef]
66. *DGT Carta de Uso e Ocupação do Solo (COS2018)*; Direção Geral do Território: Lisboa, Portugal, 2018.
67. EDIA. *Anuário Agrícola de Alqueva 2019*; Empresa de Desenvolvimento e Infraestruturas do Alqueva (Alqueva Development and Infrastructures Company): Beja, Portugal, 2019.
68. Hersbach, H.; Dee, D. ERA5 reanalysis is in production. In *ECMWF Newsletter 147*; European Centre for Medium-Range Weather Forecasts: Reading, UK, 2016.
69. ECMWF ERA5. Available online: https://cds.climate.copernicus.eu/cdsapp#!/dataset/reanalysis-era5-land-monthly-means?tab=overview (accessed on 3 November 2020).
70. Romanenko, V.A. Computation of the autumn soil moisture using a universal relationship for a large area. *Proc. Ukr. Hydrometeorol. Res. Inst.* **1961**, *3*, 12–25.
71. SROA/CNROA/IEADR Cartas de Solos e Capacidade de Uso. Available online: https://www.dgadr.gov.pt/cartografia/cartas-solos-cap-uso-digital (accessed on 15 May 2020).
72. DGADR Nota explicativa da Carta de Solos de Portugal e da Carta de Capacidade de Uso do Solo. Available online: https://www.dgadr.gov.pt/nota-explicativa (accessed on 22 April 2020).
73. APHA. *Standard Methods for the Examination of Water and Wastewater*, 12th ed.; American Public Health Association, American Water Works Association and Water Environmental Federation: Washington, DC, USA, 1998.
74. Paulo, A.A.; Rosa, R.D.; Pereira, L.S. Climate trends and behaviour of drought indices based on precipitation and evapotranspiration in Portugal. *Nat. Hazards Earth Syst. Sci.* **2012**, *12*, 1481–1491. [CrossRef]
75. Valverde, P.; Serralheiro, R.; de Carvalho, M.; Maia, R.; Oliveira, B.; Ramos, V. Climate change impacts on irrigated agriculture in the Guadiana river basin (Portugal). *Agric. Water Manag.* **2015**, *152*, 17–30. [CrossRef]
76. Godinho, S.; Gil, A.; Guiomar, N.; Costa, M.J.; Neves, N. Assessing the role of Mediterranean evergreen oaks canopy cover in land surface albedo and temperature using a remote sensing-based approach. *Appl. Geogr.* **2016**, *74*, 84–94. [CrossRef]
77. Hanson, B.R.; Grattan, S.R.; Fulton, A. *Agricultural Salinity and Drainage*; Division of Agriculture and Natural Resources Publication; University of California Irrigation Program: Davis, CA, USA, 2006; Volume 3375.
78. Seydehmet, J.; Lv, G.-H.; Abliz, A.; Shi, Q.-D.; Abliz, A.; Turup, A. Irrigation Salinity Risk Assessment and Mapping in Arid Oasis, Northwest China. *Water* **2018**, *10*, 966. [CrossRef]
79. Bouksila, F.; Bahri, A.; Berndtsson, R.; Persson, M.; Rozema, J.; Van der Zee, S.E. Assessment of soil salinization risks under irrigation with brackish water in semiarid Tunisia. *Environ. Exp. Bot.* **2013**, *92*, 176–185. [CrossRef]
80. Kairis, O.; Kosmas, C.; Karavitis, C.H.; Ritsema, C.; Salvati, L.; Acikalin, S.; Alcalá, M.; Alfama, P.; Atlhopheng, J.; Barrera, J.; et al. Evaluation and Selection of Indicators for Land Degradation and Desertification Monitoring: Types of Degradation, Causes, and Implications for Management. *Environ. Manag.* **2014**, *54*, 971–982. [CrossRef]
81. Ramos, T.B.; Darouich, H.; Šimůnek, J.; Gonçalves, M.C.; Martins, J.C. Soil salinization in very high-density olive orchards grown in southern Portugal: Current risks and possible trends. *Agric. Water Manag.* **2019**, *217*, 265–281. [CrossRef]
82. Minhas, P.S.; Qadir, M.; Yadav, R.K. Groundwater irrigation induced soil sodification and response options. *Agric. Water Manag.* **2019**, *215*, 74–85. [CrossRef]
83. Alexandre, C.; Borralho, T.; Durão, A. Evaluation of salinization and sodification in irrigated areas with limited soil data: Case study in southern Portugal. *Span. J. Soil Sci.* **2018**. [CrossRef]

Publisher's Note: MDPI stays neutral with regard to jurisdictional claims in published maps and institutional affiliations.

© 2020 by the authors. Licensee MDPI, Basel, Switzerland. This article is an open access article distributed under the terms and conditions of the Creative Commons Attribution (CC BY) license (http://creativecommons.org/licenses/by/4.0/).

Hydrol. Earth Syst. Sci., 24, 5973–5984, 2020
https://doi.org/10.5194/hess-24-5973-2020
© Author(s) 2020. This work is distributed under
the Creative Commons Attribution 4.0 License.

Hydrology and Earth System Sciences
Open Access
EGU

Reservoir evaporation in a Mediterranean climate: comparing direct methods in Alqueva Reservoir, Portugal

Carlos Miranda Rodrigues[1,2], **Madalena Moreira**[1,3], **Rita Cabral Guimarães**[1,2], **and Miguel Potes**[4]

[1]MED – Mediterranean Institute for Agriculture, Environment and Development,
Pólo da Mitra, Ap. 94, 7006-554 Évora, Portugal
[2]Department of Rural Engineering, University of Évora, Pólo da Mitra, Ap. 94, 7006-554 Évora, Portugal
[3]Department of Architecture, University of Évora, Escola dos Leões, Estrada dos Leões, 7000-208 Évora, Portugal
[4]Institute of Earth Sciences, Institute for Advanced Studies and Research, University of Évora, 7000-671 Évora, Portugal

Correspondence: Rita Cabral Guimarães (rcg@uevora.pt)

Received: 10 June 2020 – Discussion started: 15 July 2020
Revised: 6 November 2020 – Accepted: 6 November 2020 – Published: 17 December 2020

Abstract. Alqueva Reservoir is one of the largest artificial lakes in Europe and is a strategic water storage for public supply, irrigation, and energy generation. The reservoir is integrated within the Multipurpose Alqueva Project (MAP), which includes almost 70 reservoirs in a water-scarce region of Portugal. The MAP contributes to sustainability in southern Portugal and has an important impact on the entire country. Evaporation is the key component of water loss from the reservoirs included in the MAP. Evaporation from Alqueva Reservoir has been estimated by indirect methods or pan evaporation measurements; however, specific experimental parameters such as the pan coefficient were never evaluated. Eddy covariance measurements were performed at Alqueva Reservoir from June to September in 2014 as this time of the year provides the most representative evaporation volume losses in a Mediterranean climate. This period is also the most important period for irrigated agriculture and is, therefore, the most problematic period of the year in terms of managing the reservoir. The direct pan evaporation approach was first tested, and the results were compared to the eddy covariance evaporation measurements. The total eddy covariance (EC) evaporation measured from June to September 2014 was 450.1 mm. The mean daily EC evaporation in June, July, August, and September was 3.7, 4.0, 4.5, and 2.5 mm d^{-1}, respectively. A pan coefficient, K_{pan}, multivariable function was established on a daily scale using the identified governing factors: air temperature, relative humidity, wind speed, and incoming solar radiation. The correlation between the modelled evaporation and the measured EC evaporation had an R^2 value of 0.7. The estimated K_{pan} values were 0.59, 0.57, 0.57, and 0.64 in June, July, August, and September, respectively. Consequently, the daily mean reservoir evaporation (E_{Res}) was 3.9, 4.2, 4.5, and 2.7 mm d^{-1} for this 4-month period and the total modelled E_{Res} was 455.8 mm. The developed K_{pan} function was validated for the same period in 2017 and yielded an R^2 value of 0.68.

This study proposes an applicable method for calculating evaporation based on pan measurements in Alqueva Reservoir, and it can be used to support regional water management. Moreover, the methodology presented here could be applied to other reservoirs, and the developed equation could act as a first evaluation for the management of other Mediterranean reservoirs.

1 Introduction

Reservoirs and water storage are essential in the Mediterranean region for securing urban and industrial water supply, irrigation, and energy generation due to the huge challenges presented by water scarcity in this region (Hoekstra et al., 2012; Alcon et al., 2017; Tomas-Burguera et al., 2017; Rivas-Tabares et al., 2019). Reservoir evaporation is one of the most important components of the water balance, and thus it should be accurately evaluated (Liu et al., 2016). This is particularly important in southern Europe as large investments have been made in the irrigation sector here. For instance, in southern Portugal, the Multipurpose Alqueva Project (MAP)

with almost 70 reservoirs is the most important example of such an investment. The MAP contributes to sustainability in southern Portugal and has an important impact on the entire country. Alqueva Reservoir is the largest surface water reservoir in southern Europe, with a submerged area of 250 km^2 and a total storage volume of 4150×10^6 m^3 at full capacity. Each 10 mm of evaporation represents a water loss of 2.5×10^6 m^3, which is sufficient to irrigate almost 8.5 km^2 of land containing olive trees and, therefore, corresponds to an estimated annual return of EUR 1.1 million.

The methodology of Kohli and Frenken (2015), used to estimate evaporation for artificial reservoirs, is based on crop evapotranspiration; it assumes a crop coefficient equal to 1.0, which means that reservoir evaporation is equal to the reference evapotranspiration. Most reservoir managers in the MAP estimate evaporation based on the reference evapotranspiration. Some water system managers use 1000 mm as the reservoir annual evaporation for simplification. In the case of Alqueva Reservoir, with an average reference evapotranspiration of $\sim 1270\,mm\,yr^{-1}$ (calculated by the Penman–Montheith method), the evaporation can be 325×10^6 m^3, or 10 % of the total usage volume. This means that the local water budget balance has to be well studied to guarantee the sustainability of this important upstream reservoir. An increased accuracy in the evaporation estimation for Alqueva Reservoir is required because of the projected increase in the irrigation area of the MAP and the importance of regional socio-economic development. A previous study on evaporation from Alqueva Reservoir used indirect methods, including the energy budget approach, aerodynamic methods, a combination of approaches, and a lake model ("FLAKE") (Rodrigues, 2009). This work was based on measurements from a Class A evaporation pan, located on a floating platform in Alqueva Reservoir, between 2002 and 2006, and its comparison with evaporation values obtained by the energy budget approach to establish monthly pan coefficients. However, there has not been a systematic analysis of the governing factors relating to pan evaporation and reservoir evaporation in Alqueva Reservoir. Accordingly, the current study reports on direct evaporation measurements using eddy covariance (EC) equipment installed on the existing floating platform in Alqueva Reservoir, which is a part of the framework of the ALEX project (http://www.alex2014.cge.uevora.pt/, last access: 29 May 2020). Offshore measurements were conducted from June to September 2014, as this is the most representative period of the year for the evaporation volume in a Mediterranean climate, representing ~ 60 % of the total reference evapotranspiration. This period is also very important for irrigation and is, therefore, the most problematic period of the year for the management of Alqueva Reservoir.

The turbulent fluxes over the water surface, which can be obtained with direct and continuous measurements, evaluate the exchange of water and energy between the surface and the atmosphere (Arya, 2001; Potes et al., 2017). The EC method is usually applied in research because it is a non-invasive technique and provides the most accurate and reliable method for estimating evaporation (Stull, 2001; Allen and Tasumi, 2005; Tanny et al., 2008; Rimmer et al., 2009). The method is theoretically based on the correlation between the vertical wind speed and air moisture content fluctuation and is a reliable and accurate method to measure open-water evaporation in a location where it is installed (Blanken et al., 2000; Tanny et al., 2008; Nordbo et al., 2011; Richardson et al., 2012; Vesala et al., 2012; Liu et al., 2015; Ning et al., 2015; Ma et al., 2016). However, it requires sophisticated instrumentation that is capable of accurately recording the minimum variations in wind speed, air temperature, and humidity with a high sampling frequency. Furthermore, the equipment is quite expensive and requires continuous maintenance, which means that it is not possible to perform regular measurements. Several studies using EC measurements to evaluate reservoir evaporation have been conducted in various places worldwide (Blanken et al., 2000; Nordbo et al., 2011; Zhang and Liu, 2014; Metzger et al., 2018; Jansen and Teuling, 2020). Another technique to estimate the actual reservoir evaporation based on direct measurements is the pan evaporation method (Riley, 1966). The World Meteorological Organization suggests pan evaporation as the standard method for measuring open-water evaporation (Gangopadhyaya, 1966). However, the relationship between evaporation and meteorological parameters in the pan and in open-water bodies differs. Pan measurements generally overestimate evaporation from large water bodies because, in contrast to a lake, a pan receives large quantities of energy through its base and sides and thus becomes much hotter than a lake. Moreover, the surface area of the water in the pan is much smaller than that of a lake, thus allowing a greater air renewal over the free surface (Jacobs et al., 1998; Lim et al., 2013; Yu et al., 2017). The measured pan evaporation rates are generally 30 % higher than that of lake evaporation at the annual scale. The monthly pan coefficients can differ from the commonly used coefficient of 0.7 by more than 100 % (Kohler et al., 1955; Linsley et al., 1982; Ferguson et al., 1985). It is expected that the relationship between pan evaporation and lake evaporation should be a function of meteorological parameters through the modelled K_{pan}. The pan evaporation method remains the cheapest and simplest method; hence, this evaporimeter remains the most commonly used instrument to quantify reservoir evaporation. The application of a pan coefficient to convert measured pan evaporation to reservoir evaporation is a method frequently applied in reservoir studies, and this pan coefficient could be calculated as a function of meteorological parameters (Allen et al., 1998; Pereira et al., 1995; Pradhan et al., 2013).

The Portuguese public company (Empresa de Desenvolvimento e Infraestruturas do Alqueva – EDIA) that is responsible for the construction and operation of the MAP has a meteorological station with a Class A evaporation pan. The parameterisation of a pan coefficient to convert the measured

pan evaporation to reservoir evaporation would provide the MAP with an expeditious reservoir management tool.

Accordingly, the aims of this study were as follows: (i) to evaluate the actual evaporation rates from Alqueva Reservoir at the EC and Class A pan evaporation locations and to then analyse their variability with meteorological parameters (i.e. air temperature, relative humidity, wind speed, and radiation); (ii) to estimate the pan coefficient, K_{pan}, for the reservoir as an indirect multivariable function and assess the efficiency of pan evaporation in retrieving the evaporation component when EC measurements are unavailable. The study used daily data for the period from June to September 2014 and was validated using data from the same period in 2017.

The paper is organised as follows. Section 2 presents the measurement site, instrumentation, and data. The methodology used in this study is detailed in Sect. 3, and the results are presented and discussed in Sect. 4. Finally, Sect. 5 summarises the major conclusions.

2 Measurement site, instrumentation, and data

2.1 Alqueva Reservoir

Alqueva Reservoir is located within the Guadiana River in Alentejo, southern Portugal (Fig. 1). The reservoir is the largest artificial lake in southern Europe (EDIA, 2020), with an average depth of 16.6 m and a maximum depth of 92.0 m at full capacity. The reservoir has a total capacity of 4150×10^6 m^3 and a water surface area of 250 km^2. Alqueva Reservoir is the upstream reservoir of the MAP, which supplies water to approximately 200 000 inhabitants, irrigates 1200 km^2 (to be expanded to 1650 km^2 in the near future), and has an installed hydroelectric power capacity of 530 MW. The Alqueva River basin covers 55 289 km^2, and 85 % of the area is in Spain. The mean annual precipitation in the Alqueva River basin is less than 550 mm (in the Portuguese area) and the mean annual runoff at the border gauging station (Monte da Vinha station) is 23 mm. At the reservoir, the annual reference evapotranspiration is 1270 mm, as determined by the Food and Agriculture Organization (FAO) Penman–Monteith equation. More than 80 % of rainfall occurs between October and April, and during the summer the maximum air temperature ranges on average from 31 to 35 °C (July and August), often reaching values of > 40 °C. The region is classified as a Csa region according to the Köppen climate classification, which corresponds to a Mediterranean climate (i.e. a temperate climate with dry, hot summers). The summer local time (LT) in Portugal is coordinated universal time (UTC)+1.

2.2 Instrumentation, data sources, and quality

2.2.1 Class A pan evaporation

Alquilha meteorological station (38°13′22.80″ N, 07°30′03.60″ W; elevation of 162 m) is located on the first island upstream of the dam (Fig. 1). The station is part of the environmental monitoring network of Alqueva Reservoir and is monitored by EDIA, which manages the MAP. The hourly weather variables measured at the station include rainfall (rain gauge: YOUNG/52202), air temperature and relative humidity (combined sensor: HYDROCLIP), wind speed (3 m above ground) and direction (anemometer and direction sensor: CLIMA), incoming solar radiation (irradiance sensor: IMTSolar/Si-01TCext), and water-level readings in a Class A pan (level sensor: Druck/1830). Considering the fact that the station is located on a small island within the reservoir, a very large water fetch upwind of the pan was accounted for this study. The hourly Class A pan evaporation was equal to the hourly level depletion, accounted for the rainfall effect, and discarded the 3 h period after each refill of the pan. The daily pan evaporation was calculated by considering the starting time water level, the ending time water level, and the upward (water out of the pan) and downward (water into the pan) water-level changes during a day. The values obtained when the water level in the pan was below a threshold value (10 cm), according to Allen et al. (1998) and WMO (2018), were discarded. Anomalous values were also discarded. For the study period (June to September 2014), 18 % and 15 % of the data were discarded at hourly and daily scales, respectively, during the quality control process. Discarded and missing data were filled with the average value calculated for the study period (June–September).

2.2.2 Eddy covariance system

Alqueva-Montante (38°13′24.75″ N, 07°27′34.18″ W) meteorological and hydrologic station (Fig. 1) is part of the Portugal Network for Water Resource Monitoring (https://snirh.apambiente.pt, last access: 29 May 2020). The measuring equipment is installed on a floating platform to measure air temperature, relative humidity, wind speed/direction, downward radiation, pressure, and precipitation. These parameters (except for precipitation as this is accumulated during a given period) are measured at a frequency of one value per minute, while averages are calculated for 30 min. The weather station also measures the reservoir water temperature and water quality parameters, which are not used in the present study. The maximum water depth is ~ 65 m at the station site, and the shore distance is greater than 300 m; however, these values vary slightly with the type of platform anchorage (i.e. by ropes tied to three sunken blocks), thus allowing longitudinal displacements and rotation on itself.

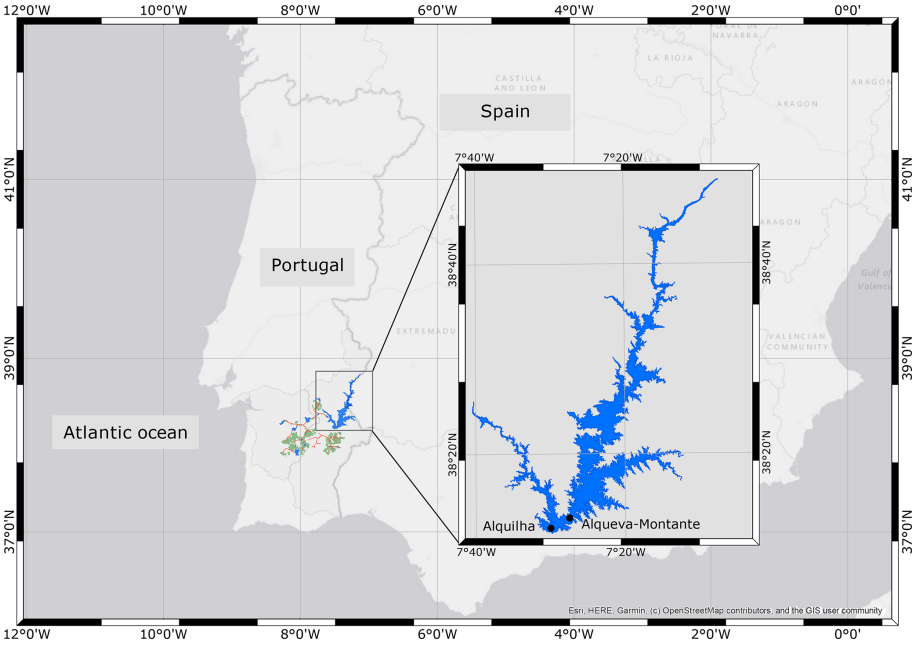

Figure 1. Multipurpose Alqueva Project (MAP) location. The expanded map is of Alqueva Reservoir, showing two meteorological stations: Alquilha and Alqueva-Montante.

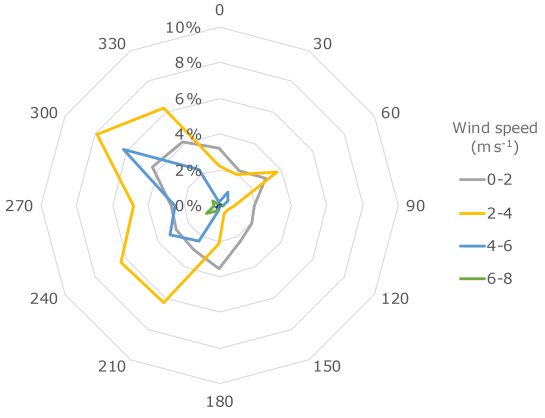

Figure 2. Wind rose for Alqueva-Montante meteorological station from June to September 2014.

Within the framework of the ALEX project (http://www.alex2014.cge.uevora.pt/, last access: 29 May 2020), this instrumented floating platform was equipped with one EC system – an integrated open path CO_2/H_2O gas analyser and a 3D sonic anemometer (IRGASON; Campbell Scientific) – at a height of 2 m above the reservoir surface. The variables measured by the IRGASON were u, v and w components of wind speed, sonic temperature (computed from the measured sound speed), H_2O and CO_2 concentration, and sonic anemometer and gas analyser quality flags. Data were sampled at 20 Hz and the filter time delay was 200 ms (Potes et al., 2017). Turbulent time series were linearly detrended and a double-axis rotation was applied to the wind speed components. The turbulent fluxes of momentum, heat, and mass (H_2O) were calculated as 30 min covariances between the fluctuations of the vertical wind component (w), temperature, and the H_2O concentration, respectively. The air density fluctuations were corrected for thermal expansion and water vapour dilution, and the sonic temperature was corrected for humidity. These corrections were, then, applied to the flux calculations (Potes et al., 2017). Furthermore, data quality criteria and filters were applied for the study period. Approximately 3 % of the original data were discarded based on (i) a signal strength (from the gas analyser) of < 0.7, (ii) footprints (fetch) with values of X_{90} of > 300 m, and iii) all data leading to negative values for the H_2O covariances resulting in negative latent heat (evaporation) fluxes. Discarded data were filled with the average value calculated for the study period (June–September). The predominant wind direction was between 210 and 360° (68 % with 30 min resolution), and 97 % of the mean speed wind measurements (with 30 min resolution) were $< 6\,\mathrm{m\,s^{-1}}$ (Fig. 2). In order to assess for the possible contamination for the floating platform on the EC evaporation measurement, two wind direction filters (having as reference the EC system orientation) were applied to flux data. The two filters considered (Evap_fill180 and Evap_fill100) were from wind directions between 90 and 270° and 130 and 230°, as they represent winds that pass through the platform before reaching the EC instrument. To understand the impact of applying a filter of wind direction on the EC evaporation dataset, a comparison was made between the daily cycle without any wind direction filter and with a wind direction filter of (i) 180° and (ii) 100° (Fig. 3a).

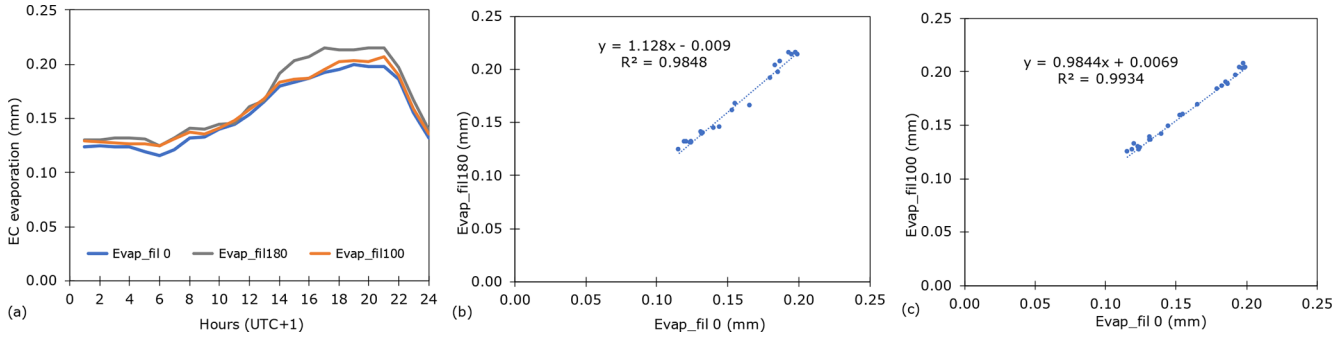

Figure 3. (a) Daily cycle of the eddy covariance (EC) evaporation (E_{EC}) with and without wind direction filters; **(b)** correlation between the EC evaporation with a 180° wind direction filter ("Evap_fil180") and without the filter ("Evap_fil 0"); **(c)** correlation between the EC evaporation with a 100° wind direction filter ("Evap_fil100") and without the filter ("Evap_fil 0"), for Alqueva-Montante station from June to September 2014.

The correlations between the daily cycle with a 180° filter and without a filter ($R^2 = 0.985$) and between the daily cycle with a 100° filter and without a filter ($R^2 = 0.993$) are presented in Fig. 3b and c. By analysing these figures, we can conclude that the platform does not affect the flux data, according to the wind direction.

3 Methodology

This section describes the methodology used to estimate evaporation from Alqueva Reservoir based on the measurements taken at Alquilha station. It is proposed that the actual evaporation from the reservoir could be estimated using the relationship between the Class A pan evaporation measurements (at Alquilha station) and a pan coefficient multivariable function, as determined by Allen et al. (1998), but for reference evapotranspiration. Although the conditions surrounding a site can influence the pan coefficient, this aspect is not considered here as the fetch in the wind direction was irrelevant, as mentioned in Sect. 2.2. Processed data of pan and EC evaporation (Sect. 2.2) were used to develop a multivariable pan function.

First, relationships between the EC measurements and meteorological parameters (air temperature, relative humidity, wind speed, and solar radiation) measured at Alqueva-Montante station were determined. These four meteorological parameters were selected primarily because they are the factors governing evaporation, as usually described in the literature (e.g. Allen et al., 1998), and are the parameters measured in Alquilha meteorological station. The daily cycle of evaporation and normalised meteorological parameters were analysed to assess their behaviours during the day. A sensitive analysis at the hourly scale was also performed for the factors governing evaporation from Alqueva Reservoir.

Second, the relationships between pan evaporation measurements and the same meteorological parameters, but as measured at Alquilha station (at hourly and daily scales), were determined.

Third, the correlation between EC evaporation and pan evaporation was determined and the daily cycles of the normalised pan evaporation and normalised EC evaporation were compared.

Fourth, a sensitivity analysis was performed, calculating the correlation of the daily pan evaporation and daily EC evaporation with air temperature, relative humidity, wind speed, and solar radiation.

Fifth, the daily multivariable pan coefficient series was calculated by dividing the daily values of EC evaporation by the corresponding daily values of pan evaporation.

Sixth, a function was fitted to this series based on the physical relationships among the different meteorological parameters measured at Alquilha station (at the daily scale). Several functions were attempted, and the one with the best determination coefficient (R^2) was chosen. To determine the optimal parameter estimates, the generalised reduced gradient (GRG) method (Lasdon et al., 1974) was used with the aid of the Excel solver tool. The best parameter estimates were those that minimised the residual sum of squares.

4 Results and discussion

4.1 Eddy covariance evaporation

The total EC evaporation measured from June to September 2014 was 450.1 mm. The mean daily EC evaporation in June, July, August, and September was 3.7, 4.0, 4.5, and 2.5 mm d^{-1}, respectively. The correlations between the hourly EC evaporation and wind speed, air temperature, relative humidity, and incoming solar radiation are presented in Fig. 4. At the hourly scale, a positive correlation was observed between the EC evaporation and (i) wind speed ($R^2 = 0.50$) and (ii) air temperature ($R^2 = 0.20$), whereas a negative correlation was observed between open evaporation

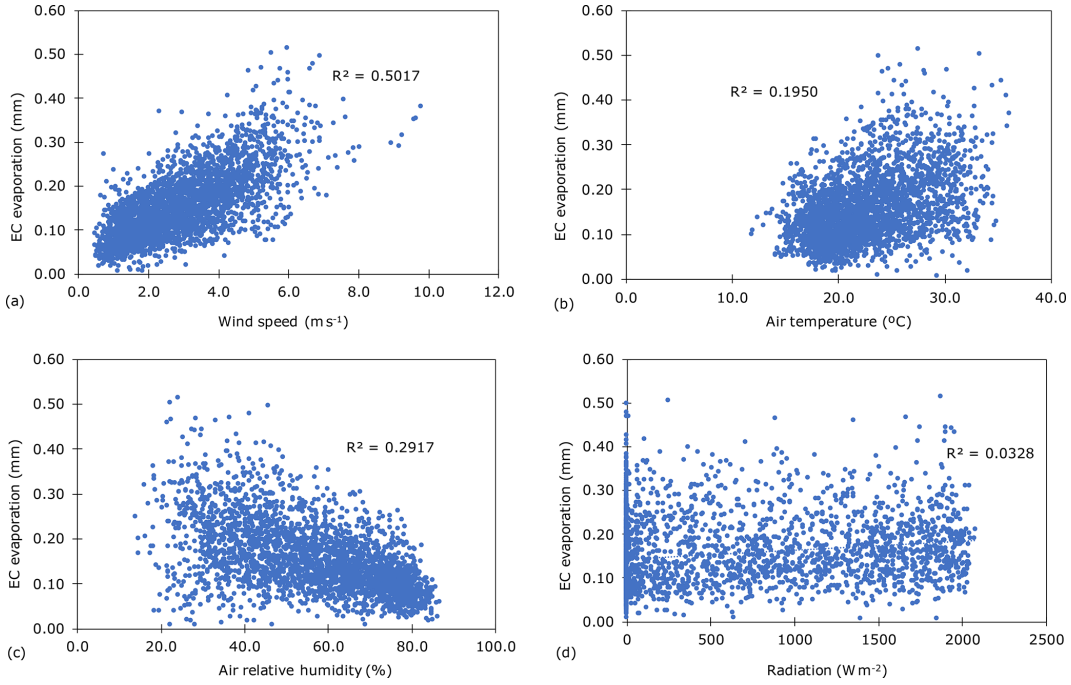

Figure 4. Hourly correlation between the EC evaporation (E_{EC}) and **(a)** wind speed (U), **(b)** air temperature (T_a), **(c)** relative humidity (RH) of air, and **(d)** solar radiation (Rad) at Alqueva-Montante station.

and relative humidity ($R^2 = 0.30$). There was no correlation between open-water evaporation and incoming solar radiation.

The daily cycles of evaporation and the meteorological parameters allow the variation during an average day to be analysed. The normalisation of the mean values of the meteorological parameters was performed to unify the scale of the parameters. The daily cycle of evaporation and the four normalised meteorological parameters measured at Alqueva-Montante station are presented in Fig. 5. As expected, the air temperature and relative humidity exhibited opposite trends. There was a slight variation in the wind speed during the morning and a considerable increase after 10:00 LT, which induced a variation in evaporation. After 06:00 LT, evaporation increased continuously until 21:00 LT, along with increases in radiation and wind speed but decreasing relative humidity. Incoming solar radiation contributed to evaporation with a delay that could be explained by the variation in the energy stored in the water column. The increase in solar radiation may lead to an increase in the stored energy in the water column (Potes et al., 2017; Nordbo et al., 2011). The air temperature subsequently decreased compared to the water temperature, and the energy was released into the air, thereby increasing evaporation. An evaporation inflexion point occurred at 14:00 LT, when the incoming solar radiation began to decrease. Accordingly, evaporation began to decrease at 21:00 LT, when there was no solar radiation.

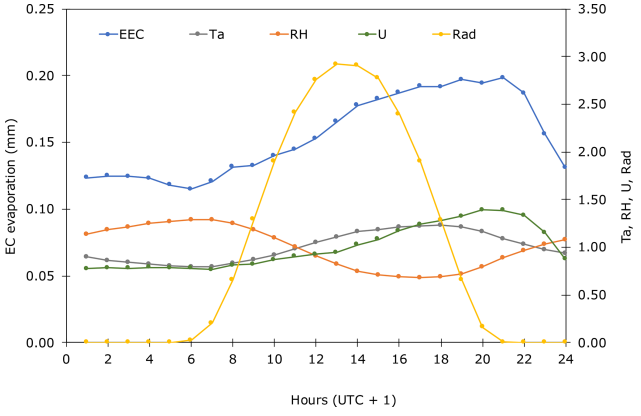

Figure 5. Mean daily cycle of the EC evaporation (E_{EC}) (left y axis) and normalised air temperature (T_a), relative humidity (RH) of air, wind speed (U), and solar radiation (Rad) (right y axis) from June to September 2014 at Alqueva-Montante station.

4.2 Class A pan evaporation

The total pan evaporation measured from June to September 2014 was 797.9 mm. The mean daily pan evaporation in June, July, August, and September was 6.9, 7.7, 7.3, and 4.3 mm d^{-1}, respectively.

Such as for the EC evaporation, a positive correlation was observed between the hourly pan evaporation and air temperature ($R^2 = 0.55$), whereas a negative correlation was found between the hourly pan evaporation and relative humidity

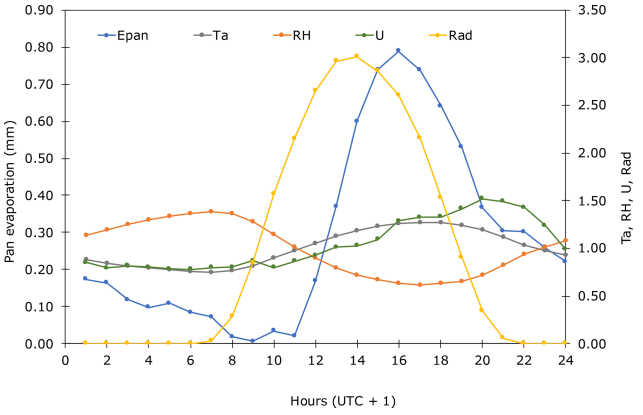

Figure 6. Mean daily cycle of pan evaporation (E_{pan}) (left y axis) and normalised air temperature (T_a), relative humidity (RH) of air, wind speed (U), and solar radiation (Rad) (right y axis) from June to September 2014 at Alquilha station.

($R^2 = 0.53$). In contrast, a positive correlation was observed between the hourly pan evaporation and incoming solar radiation ($R^2 = 0.35$), and a weak positive correlation was evident between the hourly pan evaporation and wind speed ($R^2 = 0.05$). The daily cycle of evaporation and the four normalised meteorological parameters (wind speed, air temperature, relative humidity, and solar radiation) measured at Alquilha station are presented in Fig. 6. In the morning period, the solar radiation begins at 08:00 LT and with that an increase in air temperature and a decrease in relative humidity. At 11:00 LT wind speed starts to increase, and around 12:00 LT occurs the trigger of the evaporation pan. The trend of the pan evaporation followed the trend of solar radiation but with a delay of about 3 h, whereby the maximum value was at 16:00 LT when the relative humidity was at the minimum. Pan evaporation reduced as the air relative humidity increased.

4.3 Correlation between EC evaporation and pan evaporation

The correlation between daily eddy covariance evaporation and daily pan evaporation was determined for the study period (June–September) and is shown in Fig. 7. Figure 7a shows a poor linear correlation between the EC evaporation and pan evaporation during the entire study period ($R^2 = 0.37$). This was also the case when observing the plots for each month: $R^2 = 0.1882$ in June (Fig. 7b), $R^2 = 0.0458$ in July (Fig. 7c), $R^2 = 0.3345$ in August (Fig. 7d), and $R^2 = 0.4693$ in September (Fig. 7e). These results show that the relationship between both evaporations could not be considered linear and reveal the importance of finding a non-linear function to correlate EC evaporation and pan evaporation. The daily cycles of the normalised pan evaporation and normalised EC evaporation are compared in Fig. 8. The two evaporations exhibited different behaviours: pan evaporation varied widely over the day, with zero evaporation at 09:00 LT and the maximum at 16:00 LT. The maximum mean daily pan evaporation was 2.75-fold that of the mean daily value. In contrast, the daily cycle of the EC evaporation fluctuated comparatively little over the day. During the night and early morning, EC evaporation was $\sim 80\,\%$ of the daily mean value, with the minimum at 06:00 LT. During the late afternoon, the EC evaporation increased due to the increased wind speed (Fig. 5). The maximum daily mean evaporation occurred at 21:00 LT, and it was 125 % of the daily mean value.

These results agree with a previous study by Salgado and Le Moigne (2010) for the same reservoir, wherein the authors observed an absolute minimum and maximum at 06:00 and 21:00 LT, respectively. Although both types of evaporation measurements used similar times for calculating the mean daily value (between 12:00 and 13:00 LT), the significant dissimilarities over the day resulted from the large difference between the size of the pan and the size of the reservoir as these may lead to different heat storage capacities. Owing to the reduced water height in the pan, the amount of energy it would have received through radiation and conduction through the walls of the pan is incomparably higher than that received by the reservoir water. Moreover, the reduced area of the pan would have tended to enhance the loss of water through evaporation because it facilitates the removal of air-saturated layers at the water–air interface.

4.4 Sensitivity analysis of pan evaporation and EC evaporation versus meteorological variables

A sensitivity analysis of the daily pan evaporation and daily EC evaporation with air temperature, relative humidity, wind speed, and solar radiation was carried out, and the results are presented in Fig. 9. Figure 9a shows a non-linear correlation between evaporation (EC and pan evaporation) and wind speed. It can be observed that both evaporations have a positive linear correlation with air temperature (Fig. 9b) and radiation (Fig. 9d). Figure 9c shows a negative correlation between evaporation and air relative humidity. The value of R^2 of pan evaporation with air temperature, air relative humidity, and radiation is greater than the R^2 of the EC evaporation with the same parameters. In contrast, the R^2 of EC evaporation with wind speed is greater than the pan evaporation with the wind speed parameter.

Based on this sensitivity analysis, it was inferred that the four parameters influence both EC evaporation and pan evaporation and strengthen the ability to establish a relationship between the open EC evaporation and pan evaporation on a daily scale as discussed in Sect. 4.5.

4.5 Pan evaporation coefficient model

The pan evaporation coefficient (K_{pan}) was calculated as a function of the four meteorological parameters measured at

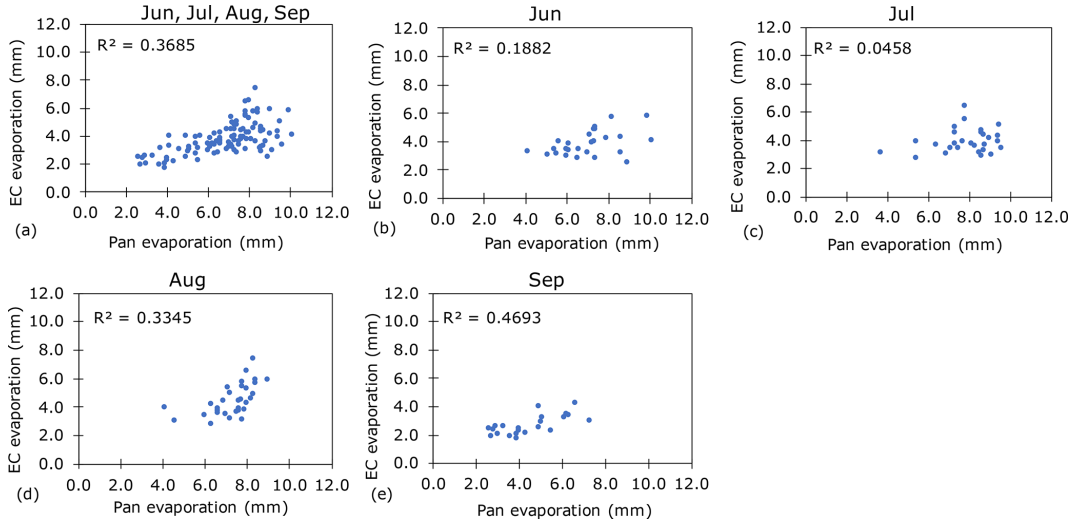

Figure 7. Correlation between the daily EC evaporation (E_{EC}) and the daily pan evaporation (E_{pan}): **(a)** June to September 2014; **(b)** June 2014; **(c)** July 2014; **(d)** August 2014; **(e)** September 2014.

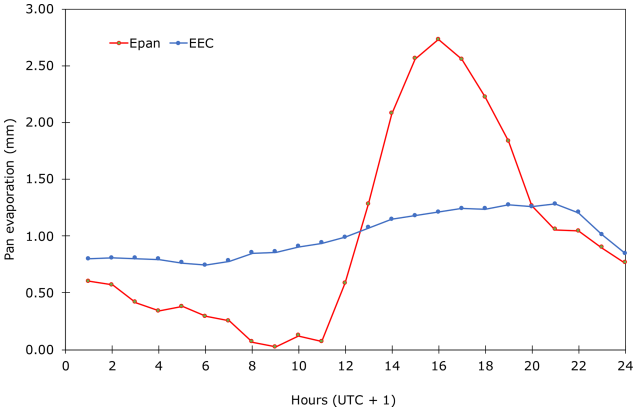

Figure 8. Mean daily cycle of the normalised pan evaporation (E_{pan}) and the EC evaporation (E_{EC}).

Alquilha station because this station will be used in the future to obtain data to support water management and decision-making. Consequently, the reservoir evaporation (E_{Res}) is estimated by multiplying the Alquilha Class A pan evaporation (E_{pan}) measurement (at Alquilha) by the modelled K_{pan}.

The pan evaporation coefficient model was expressed by a multivariable function as shown in Eq. (1):

$$K_{pan} = aU + bT_a + c\mathrm{LN(RH)} + d\mathrm{LN(Rad)} + eT_a\mathrm{LN(Rad)} + f, \quad (1)$$

where a–f are specific constants; U is the average daily wind speed at a height of 2 m at Alquilha station (m s^{-1}); T_a is the average daily temperature at Alquilha station (°C); RH is the average daily relative humidity at Alquilha station (%); and Rad is the total daily radiation at Alquilha station (W m^{-2}).

By using an objective function to minimise the residual sum of squares, the parameterisation of the specific constants was performed by optimisation using the GRG method; thus, Eq. (1) becomes

$$K_{pan} = 0.0925U + 0.1531T_a - 0.2558\mathrm{LN(RH)} + 0.2593\mathrm{LN(Rad)} - 0.0308T_a\mathrm{LN(Rad)} + 0.3489. \quad (2)$$

The daily mean modelled K_{pan} was 0.59, 0.57, 0.57, and 0.64 for June, July, August, and September, respectively. These values are slightly larger than those obtained directly by the ratio of the EC evaporation to pan evaporation (0.54). Rodrigues (2009) reported monthly K_{pan} values between 0.70 and 0.90 for the same summer period and reservoir but using a different approach; he estimated K_{pan} values by relating pan evaporation, measured from a floating pan at the Alqueba-Montante platform, and reservoir evaporation obtained by the energy budget approach.

Figure 10 presents E_{Res} determined from the pan evaporation coefficient model and the measured EC evaporation. The R^2 value of 0.74 indicates that this model can estimate the E_{Res} quite well. The total modelled E_{Res} for the period from June to September was 455.8 mm, which corresponds to 101.3 % of the EC evaporation and 76 % of the site reference evapotranspiration calculated by the Penman–Monteith equation (Allen et al., 1998). The modelled daily mean E_{Res} in June, July, August, and September was 3.9, 4.2, 4.5, and 2.7 mm d^{-1}, respectively.

The ability of the model was tested for the period from June to September 2017 (Fig. 11; $R^2 = 0.68$); thus, the model could estimate the E_{Res} despite high measured evaporation rates and a reduced number of available daily pan evaporation measurements.

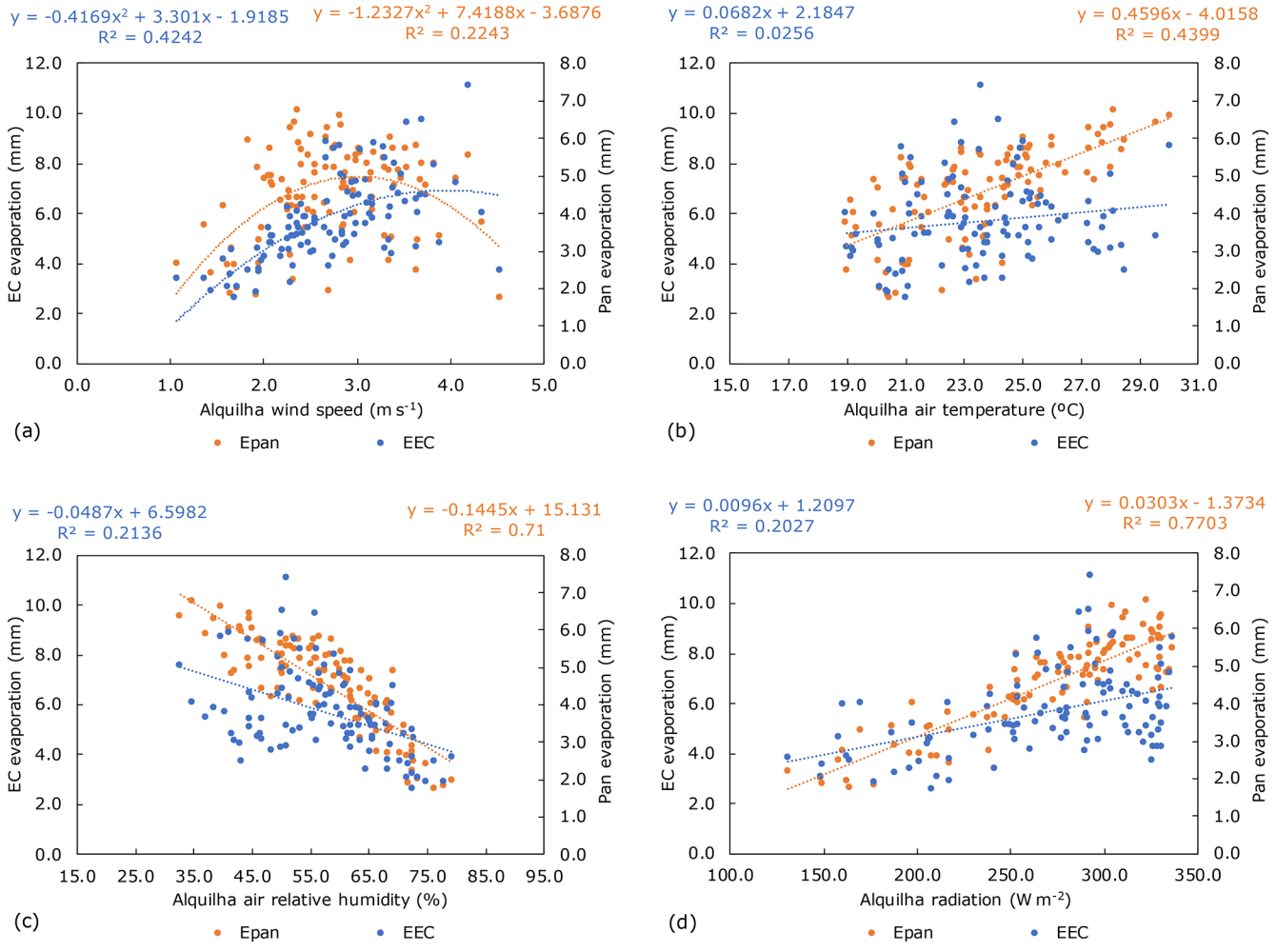

Figure 9. Sensitivity analysis of the daily EC evaporation (E_{EC}) and the daily pan evaporation (E_{pan}) from June to September 2014, with **(a)** wind speed, **(b)** air temperature, **(c)** relative humidity of air, and **(d)** solar radiation.

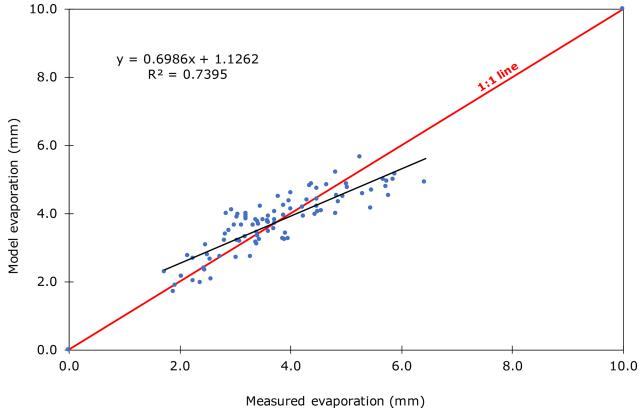

Figure 10. Modelled daily evaporation (E_{Res}) versus measured daily evaporation (E_{EC}) from June to September 2014.

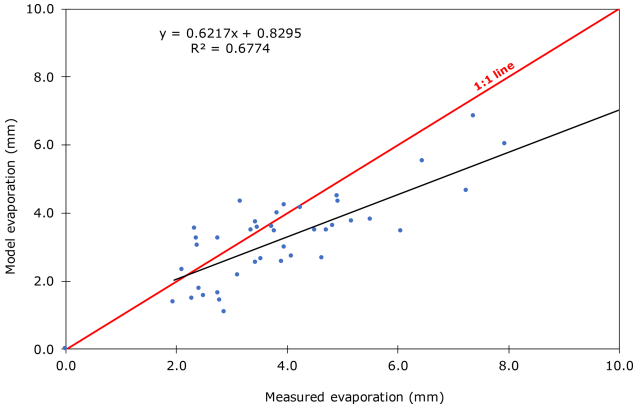

Figure 11. Modelled daily evaporation (E_{Res}) versus measured daily evaporation (E_{EC}) from June to September 2017.

5 Conclusions

The study aimed to develop a method to evaluate the evaporation from Alqueva Reservoir, located in south-eastern Portugal, based on Class A pan measurements, thus providing an evaluation tool for water management within the Multipurpose Alqueva Project (MAP) and for other reservoirs with a Mediterranean climate.

Water fluxes were continuously measured from June to September 2014 using the EC method at Alqueva-Montante station to obtain accurate reservoir evaporation measurements. The total EC reservoir evaporation from June to September 2014 was 450.1 mm, and the mean daily evaporation in June, July, August, and September was 3.7, 4.0, 4.5, and 2.5 mm d^{-1}, respectively. Considering the most important atmospheric factors controlling evaporation, a positive correlation between the EC evaporation, wind speed, and air temperature, a negative correlation for the relative humidity, and no correlation between EC evaporation and solar radiation were observed at an hourly scale.

The Class A pan installed at Alquilha station provided hourly and daily pan evaporation values. The total pan evaporation from June to September 2014 was 797.9 mm, and the mean daily evaporation in June, July, August, and September was 6.9, 7.7, 7.3, and 4.3 mm d^{-1}, respectively. Positive correlations were observed between the hourly pan evaporation and air temperature and solar radiation, whereas a negative correlation was found between the hourly pan evaporation and the relative humidity. A weak correlation existed between the hourly pan evaporation and wind speed.

A sensitivity analysis of the daily pan evaporation and daily EC evaporation with air temperature, relative humidity, wind speed, and solar radiation strengthens the ability to establish a relationship between the open EC evaporation and pan evaporation at the daily scale.

We found that the daily pan evaporation coefficient could be expressed by a multivariable function of wind speed, air temperature, relative humidity, and solar radiation measured at Alquilha station. Further, model validation was performed for the same four summer months in 2017. The modelled pan coefficients (K_{pan}) were 0.59, 0.57, 0.57, and 0.64 in June, July, August, and September, respectively; the modelled daily mean E_{Res} was 3.9, 4.2, 4.5, and 2.7 mm d^{-1} for June, July, August, and September, respectively. The total modelled evaporation was 455.8 mm, remarkably similar to the total output from EC measurements, and corresponds to 101.3 % of the measured EC evaporation from the reservoir.

The evaporation model proposed in this study can assist and improve water management in the MAP. Moreover, the methodology could also be applied to other reservoirs, and the equation developed for Alqueva Reservoir could act as a first evaluation for the management of other reservoirs in the region.

Data availability. Data obtained during the ALEX 2014 observational experiment and used in this study are available via http://www.alex2014.cge.uevora.pt/data/ (last access: 29 May 2020) (Salgado et al., 2020a). Data obtained during the ALOP and used here are available via http://www.alop.ict.uevora.pt/index.php/dados/?lang=en (last access: 29 May 2020) (Salgado et al., 2020b).

Author contributions. The four authors conceptualised the study. CMR and MP designed and carried out the experiments. RCG performed the model simulations. MM wrote the first draft manuscript. All four authors contributed to the analysis, interpretation and writing.

Competing interests. The authors declare that they have no conflict of interest.

Acknowledgements. The authors gratefully acknowledge the Foundation for Science and Technology (FCT), project ALEX 2014 (EXPL/GEO-MET/5 1422/2013) FCOMP-01-0124-FEDER-041840, project ALOP (ALT20-03-0145-FEDER-000004), and project AGIR (PDR2020-1.0.1-FEADER-031864). The authors would like to thank Martinho Murteira from EDIA (Empresa de Desenvolvimento e Infraestruturas do Alqueva S. A.) for providing direct access to Alquilha meteorological data. Special thanks to Rui Salgado, scientifically responsible for the ALEX 2014 and ALOP projects, for the indispensable support and encouragement.

Financial support. This research has been supported by the Foundation for Science and Technology (FCT) (grant no. UIDB/05183/2020), ALEX 2014 (grant no. EXPL/GEO-MET/1422/2013), ALOP (grant no. ALT20-03-0145-FEDER-000004), AGIR (grant no. PDR2020-1.0.1-FEADER-031864), and FCT PostDoc (grant no. SFRH/BPD/97408/2013).

Review statement. This paper was edited by Ryan Teuling and reviewed by Femke Jansen and one anonymous referee.

References

Alcon, F., García-Bastida, P. A., Soto-García, M., Martinez-Alvarez, V., Martin-Gorriz, B., and Baille, A.: Explaining the performance of irrigation communities in a water-scarce region, Irrig. Sci., 35, 193–203, https://doi.org/10.1007/s00271-016-0531-7, 2017.

Allen, R. G. and Tasumi, M.: Evaporation from American Falls Reservoir in Idaho via a combination of Bowen ratio and eddy covariance, in: Proceedings of the 2005 World Water & Environmental Resources Congress: Impacts of Global Climate Change, 15–19 May 2005, Anchorage, Alaska, https://doi.org/10.1061/40792(173)527, 2005.

Allen, R. G., Pereira, L. S., Raes, D., and Smith, M.: Crop evapotranspiration: Guidelines for computing crop water requirements, FAO Irrigation and Drainage Paper 56, FAO, Rome, p. 300, 1998.

Arya, S. P.: Introduction to Micrometeorology, 2nd edition, Academic Press, New York, p. 420, 2001.

Blanken, P. D., Rouse, W. R., Culf, A. D., Chris, S., Dale, B. L., Jasper, J. N., Bob, K., Schertzer, W. M., Philip, M., and Diana, V.: Eddy covariance measurements of evaporation from Great Slave Lake, Northwest Territories, Canada, Water Resour. Res., 36, 1069–1077, https://doi.org/10.1029/1999WR900338, 2000.

EDIA: Empresa de Desenvolvimento e Infraestruturas do Alqueva, abailable at: https://www.edia.pt/en/alqueva/the-territory, last access: 30 March 2020.

Ferguson, H. L., Hartog, G., and Louie, P. Y. T.: Estimation of shallow lake evaporation using Class A pan data, in: Casebook on Operational Assessment of Areal Evaporation, Operational Hydrology Reports 22, World Meteorological Organization, Geneva, 3–10, 1985.

Gangopadhyaya, M.: Measurement and estimation of evaporation and evapotranspiration, World Meteorological Organization, Report of a Working Group on evaporation Measurement of the Commission for Instruments and Methods of Observation, Geneva, Switzerland, p. 143, 1966.

Hoekstra, A. Y., Mekonnen, M. M., Chapagain, A. K., Mathews, R. E., and Richter, B. D.: Global monthly water scarcity: blue water footprints versus blue water availability, PLoS ONE, 7, e32688, https://doi.org/10.1371/journal.pone.0032688, 2012.

Jacobs, A., Heusinkveld, B., and Lucassen, D.: Temperature variation in a Class A evaporation pan, J. Hydrol., 206, 75–83, https://doi.org/10.1016/S0022-1694(98)00087-0, 1998.

Jansen, F. A. and Teuling, A. J.: Evaporation from a large lowland reservoir –(dis)agreement between evaporation models from hourly to decadal timescales, Hydrol. Earth Syst. Sci., 24, 1055–1072, https://doi.org/10.5194/hess-24-1055-2020, 2020.

Kohler, M. A., Nordenson, T. J., and Fox, W. E.: Evaporation from pans and lakes, Research Paper 38, US Weather Bureau, Washington, p. 21, 1955.

Kohli, A. and Frenken K.: Evaporation from artificial lakes and reservoirs, FAO – AQUASTAT Reports, FAO, Rome, p. 10, 2015.

Lasdon, L. S., Fox, R. L., and Ratner, M. W.: Nonlinear optimization using the generalized reduced gradient method, Revue Française d'Automatique, d'Informatique et de Recherche Opérationnelle, Recherche Opérationnelle, 8, 73–103, 1974.

Lim, W. H., Roderick, M. L., Hobbins, M. T., Wong, S. C., and Farquhar, G. D. The energy balance of a US Class A evaporation pan, Agr. Forest Meteorol., 182, 314–331, https://doi.org/10.1016/j.agrformet.2013.07.001, 2013.

Linsley, R. K., Kohler, M. A., and Paulhus, J. L. H.: Hydrology for engineers, 3rd Edn., McGraw-Hill, New York, p. 508, 1982.

Liu, H., Feng, J., Sun, J., Wang, L., and Xu, A.: Eddy covariance measurements of water vapor and CO_2 fluxes above the Erhai Lake, Sci. China Earth Sci., 58, 317–328, https://doi.org/10.1007/s11430-014-4828-1, 2015.

Liu, X., Yu, J., Wang, P., Zhang, Y., and Du, C.: Lake evaporation in a hyper-arid environment, Northwest of China – Measurement and estimation, Water 8, 527, https://doi.org/10.3390/w8110527, 2016.

Ma, N., Szilagyi, J., Niu, G. Y., Zhang, Y., Zhang, T., Wang, B., and Wu, Y.: Evaporation variability of Nam Co Lake in the Tibetan Plateau and its role in recent rapid lake expansion, J. Hydrol., 537, 27–35, https://doi.org/10.1016/j.jhydrol.2016.03.030, 2016.

Metzger, J., Nied, M., Corsmeier, U., Kleffmann, J., and Kottmeier, C.: Dead Sea evaporation by eddy covariance measurements vs. aerodynamic, energy budget, Priestley–Taylor, and Penman estimates, Hydrol. Earth Syst. Sci., 22, 1135–1155, https://doi.org/10.5194/hess-22-1135-2018, 2018.

Ning, M., Zhang, Y., Xu, C. Y., and Jozsef, S.: Modeling actual evapotranspiration with routine meteorological variables in the data-scarce region of the Tibetan Plateau: Comparisons and implications, J. Geophys. Res.-Biogeo., 120, 1638–1657, https://doi.org/10.1002/2015JG003006, 2015.

Nordbo, A., Launiainen, S., Mammarella, I., Lepparanta, M., Huotari, J., Ojala, A., and Vesala, T.: Long-term energy flux measurements and energy balance over a small boreal lake using eddy covariance technique, J. Geophys. Res.-Atmos., 116, 3–25, https://doi.org/10.1029/2010JD014542, 2011.

Pereira, R., Nova, N., Pereira, A., and Barbieri, V.: A model for the class A pan coefficient, Agr. Forest Meteorol., 76, 75–82, https://doi.org/10.1016/0168-1923(94)02224-8, 1995.

Potes, M., Salgado, R. Costa, M. J., Morais, M., Bortoli, D., Kostadinov, I., and Mammarella, I.: Lake–atmosphere interactions at Alqueva reservoir: a case study in the summer of 2014, Tellus A, 69, 1272787, https://doi.org/10.1080/16000870.2016.1272787, 2017.

Pradhan, S., Sehgal, B., Das, D., Bandyopadhyay, K. K., and Singh, R.: Evaluation of pan coefficient methods for estimating FAO-56 reference crop evapotranspiration in a semi-arid environment, J. Agrometeorol., 15, 90–93, 2013.

Richardson, A. D., Aubinet, M., Barr, A. G., Hollinger, D. Y., Ibrom, A., Lasslop, G., and Reichstein, M.: Uncertainty quantification, in: Eddy Covariance: A Practical Guide to Measurement and Data Analysis, edited by: Aubinet, M., Vesala, T., and Papale, D., Springer, Dordrecht, 173–210, 2012.

Riley, J. J.: The heat balance of Class A evaporation pan, Water Resour. Res., 2, 223–226, https://doi.org/10.1029/WR002i002p00223, 1966.

Rimmer, A., Samuels, R., and Lechinsky, Y.: A comprehensive study across methods and time scales to estimate surface fluxes from Lake Kinneret, Israel, J. Hydrol., 379, 181–192, https://doi.org/10.1016/j.jhydrol.2009.10.007, 2009.

Rivas-Tabares, D., Tarquis, A., Willaarts, B., and Miguel, A.: An accurate evaluation of water availability in sub-arid Mediterranean watersheds through SWAT: Cega-Eresma-Adaja, Agr. Water Manage., 212, 211–225, https://doi.org/10.1016/j.agwat.2018.09.012, 2019.

Rodrigues, C. M.: Cálculo da evaporação de albufeiras de grande regularização do sul de Portugal, PhD Thesis, Universidade de Évora, Évora, Portugal, available at: http://hdl.handle.net/10174/11108 (last access: 29 May 2020), 2009.

Salgado, R. and LeMoigne, P.: Coupling of the FLake model to the Surfex externalized surface model, Agr. Water Manage., 15, 231–244, 2010.

Salgado, R., Potes, M., Albino, A., Apolinário, J., Barbosa, S., Bárias, S., Beliche, P., Bortoli, D., Canhoto, P., Costa, M. J., Fernandes, R. M., Harrison, G., Ilhéu, A., Le Moigne, P., Lima, R., Lopes, F., Lopes, T., Marques, J., Melgão, M., Miranda, P. M., Morais, M., Murteira, M., Nicoll, K., Novais, M. H., Parrondo, M. C., Pereira, S., Policarpo, C., Prior, V., Ro-

drigues, C. M., Rosado, J., Sá, A., Serafim, A., Silva, H., Soares, P. M. M., Tlemçani, M., and Zavattieri, A.: The ALEX2014 Alqueva hydro-meteorological database, available at: http://www.alex2014.cge.uevora.pt/data/ (last access: 29 May 2020), 2020a.

Salgado, R., Morais, M., Palma, P., Potes, M., Penha, A., Novais, M. H., Antunes, C., Aranha, S., Bárias, S., Barrenho, J., Bortoli, D., Canhoto, P., Costa, A., Costa, M. J., Fialho, S., Figueira, J., Galveias, A., Lima, A. F., Lima, M., Lopes, O., Mavioso, I., Mira, M. I., Morales, E., Moreira, M., Nunes, S., Pereira, M., Purificação, C., Reis, A. H., Rodrigues, G., Rosado, A., Rodrigues, C. M., Saúde, A., Silva, A. M., Tomaz, A., and Yakunin, M.: The ALOP Alentejo Observation and Prediction system database, available at: http://www.alop.ict.uevora.pt/index.php/dados/?lang=en (last access: 29 May 2020), 2020b.

Stull, R. B.: An introduction to boundary layer meteorology, 3rd Edn., Kluwer Academic Publishers, Dordrecht, the Netherlands, p. 670, 2001.

Tanny, J., Cohen, S., Assouline, S., Lange, F., Grava, A., Berger, D., Teltch, B., and Parlange, M.: Evaporation from a small water reservoir: direct measurements and estimates, J. Hydrol., 351, 218–229, https://doi.org/10.1016/j.jhydrol.2007.12.012, 2008.

Tomas-Burguera, M., Vicente-Serrano, S. M., Grimalt, M., and Beguería, S.: Accuracy of reference evapotranspiration (ET_0) estimates under data scarcity scenarios in the Iberian Peninsula, Agr. Water Manage., 182, 103–116, https://doi.org/10.1016/j.agwat.2016.12.013, 2017.

Vesala, T., Eugster, W., and Ojala, A.: Eddy covariance measurements over lakes, in: Eddy Covariance. A Practical Guide to Measurement and Data Analysis, edited by: Aubinet, M., Vesala, T., and Papale, D., Springer, Dordrecht, 365–376, 2012.

WMO – World Meteorological Organization: Guide to Instruments and Methods of Observation, WMO No. 8, in: Volume I – Measurement of Meteorological Variables, WMO, Geneva, 2018.

Yu, T.-F., Si, J.-H., Feng, Q., Xi, H.-Y., Chu, Y.-W., and Li, K.: Simulation of Pan Evaporation and Application to Estimate the Evaporation of Juyan Lake, Northwest China under a Hyper-Arid Climate, Water, 9, 952, https://doi.org/10.3390/w9120952, 2017.

Zhang, Q. and Liu, H.: Seasonal changes in physical processes controlling evaporation over inland water, J. Geophys. Res.-Atmos., 119, 9779–9792, https://doi.org/10.1002/2014JD021797, 2014.

Renewable Energy 163 (2021) 755–771

Contents lists available at ScienceDirect

Renewable Energy

journal homepage: www.elsevier.com/locate/renene

Improved ECMWF forecasts of direct normal irradiance: A tool for better operational strategies in concentrating solar power plants

Francis M. Lopes [a, b, *], Ricardo Conceição [a, b, c], Hugo G. Silva [a, d], Rui Salgado [a, d], Manuel Collares-Pereira [a, b]

[a] Institute of Earth Sciences, University of Évora, Rua Romão Ramalho 59, 7000-671, Évora, Portugal
[b] Renewable Energies Chair, University of Évora, IIFA, Casa Cordovil, Rua D. Augusto Eduardo Nunes 7, 7002-651, Évora, Portugal
[c] High Temperature Processes Unit, IMDEA Energy, Avda. Ramón de la Sagra 3, 28935, Móstoles, Madrid, Spain
[d] Department of Physics, School of Sciences and Technology, University of Évora, Rua Romão Ramalho 59, 7000-671, Évora, Portugal

ARTICLE INFO

Article history:
Received 3 April 2020
Received in revised form
3 August 2020
Accepted 26 August 2020
Available online 4 September 2020

Keywords:
ECMWF
Direct normal irradiance
Short-term forecasting
Model output statistics
Concentrating solar power operation
Energy production simulations

ABSTRACT

To contribute for improved operational strategies of concentrating solar power plants with accurate forecasts of direct normal irradiance, this work describes the use of several post-processing methods on numerical weather prediction. Focus is given to a multivariate regression model that uses measured irradiance values from previous hours to improve next-hour predictions, which can be used to refine daily strategies based on day-ahead predictions. Short-term forecasts provided by the Integrated Forecasting System, the global model from the European Centre for Medium-Range Weather Forecasts (ECMWF), are used together with measurements in southern Portugal. As a nowcasting tool, the proposed regression model significantly improves hourly predictions with a skill score of ≈0.84 (i.e. an increase of ≈27.29% towards the original hourly forecasts). Using previous-day measured availability to improve next-day forecasts, the model shows a skill score of ≈0.78 (i.e. an increase of ≈6% towards the original forecasts), being further improved if larger sets of data are used. Through a power plant simulator (i.e. the System Advisor Model), a preliminary economic analysis shows that using improved hourly predictions of electrical energy allows to enhance a power plant's profit in ≈0.44 M€/year, as compared with the original forecasts. Operational strategies are proposed accordingly.

© 2020 Elsevier Ltd. All rights reserved.

1. Introduction

Numerical weather prediction (NWP) models have been improved continuously over the last decades due to advances in computational technology, meteorological analysis, physical parameterizations and numerical methods. Particularly, in the field of solar radiation forecasting, remarkable progress has been made in recent years with the constant upgrades regarding radiative and aerosol schemes implemented in NWP models. Such advances allowed NWP to provide the best possible forecasts for the two most important solar components used for solar energy harvesting, namely global horizontal and direct normal irradiances (GHI and DNI, respectively). These two solar resources are described in detail throughout literature, such as in Refs. [1].

A precise prediction of DNI is essential for the energy management of concentrating solar power (CSP) systems, particularly during partly cloudy conditions [2], in which CSP plants experience significant periods of solar intermittency. During such periods, clouds passing over the solar field lead to an energy reduction, since energy is suddenly not being collected and, at the same time, there is energy being consumed by the plant due to its operation, such as the production of electricity. Energy is mainly needed to feed the power block, but also for auxiliary consumption, such as maintaining the heat transfer fluid above a certain temperature (critical for molten salt systems). The duration of these energy deficiency periods can go from a few minutes to an entire day, depending on various atmospheric parameters such as size and depth of clouds, wind velocity and direction, and aerosols (concentration and type). The latter, while less frequent, can also significantly affect CSP energy production, as during desert dust storms [3] or severe air

* Corresponding author. Institute of Earth Sciences, University of Évora, Rua Romão Ramalho 59, 7000-671, Évora, Portugal.
E-mail addresses: fmlopes@uevora.pt (F.M. Lopes), rfc@uevora.pt (R. Conceição), rsal@uevora.pt (H.G. Silva), hgsilva@uevora.pt (R. Salgado), collarespereira@uevora.pt (M. Collares-Pereira).

https://doi.org/10.1016/j.renene.2020.08.140
0960-1481/© 2020 Elsevier Ltd. All rights reserved.

pollution events [4].

Although NWP models currently provide satisfactory solar radiation forecasts, depending on the forecast horizon, these have always an associated error (i.e. a forecast uncertainty). This uncertainty is a consequence of errors in the initial conditions and in the formulation of the models itself [5]. Since models provide deterministic values associated with systematic errors, the combined use of NWP data, statistical, and machine learning methods (e.g. Ref. [6]), allows the assessment of the uncertainty associated with the forecast results. The statistical post-processing of dynamical NWP outputs can be of practical use for weather forecasting [7], in which two main categories of classification for statistical downscaling methods exist [8]: perfect prognosis and model output statistics (MOS). Perfect prognosis [9] consists in the development of statistical relationships between large-scale free atmospheric and local surface variables (both sets of data are originated from historical or actual observations). Whereas in MOS [10], the free atmospheric variables are originated from numerical model outputs. Each method has its own advantages and disadvantages, but, essentially, MOS accounts for systematic model errors (e.g. dry bias) with the use of multiple predictors, allowing for a better fit to the predictand data and higher accuracy. Such accuracy, is generally better than pure statistical models, which have a high performance at very short time resolutions (<30 min) within the nowcasting range (i.e. from 0 to 6 h), or pure NWP models, which go beyond the 6-h range. After combining observations with NWP model outputs, statistical techniques, such as the use of statistical regression models (the most basic form of MOS), can be applied to derive forecast equations, allowing to improve the original forecasts [11]. To reduce NWP uncertainty and improve the systematic error correction of DNI forecasts, several statistical methods have been used. In Ref. [12], a simple post-processing correction was implemented over 3-h average values of predicted DNI, leading to satisfactory results with correlations in the order of 0.9. In their work, the authors concluded that clouds were the main source of numerical bias. In Ref. [13], a third-degree polynomial fit was performed over monthly mean hourly values, providing a high correlation coefficient of about 0.96 between the clearness index and historical DNI data. Depending on the forecast horizon, several other more complex approaches have been used to evaluate the systematic errors. For instance: Multi-Model [14]; Multi-Parameterization [15]; Stochastic Parameterization [16]; Multi-Parameter [17]; Stochastic Kinetic Energy Backscatter methods [18]; artificial neural networks [19]; autoregressive integrated moving average (ARIMA) models [20,21]; assemble MOS [22], among others. Besides statistical downscaling methods, the nesting of high-resolution limited-area models in global models (i.e. dynamic downscaling) can also be used to improve NWP outputs. As described by Ref. [23], the method has the advantage of not requiring local observations and the potential to provide better results than statistical methods, particularly the prediction of extreme events. However, the throwback lies in the fact that systematic errors present in the global models are propagated to the mesoscale ones. Moreover, higher computational cost is needed for implementing a high-resolution model.

In addition to NWP uncertainty, there are also particular difficulties in providing accurate forecasts of DNI due to the inaccurate prediction of clouds and aerosol concentrations. The misrepresentations of clouds and aerosols in the atmosphere significantly reduce the accuracy of the forecasted DNI, as these are the two main modulators of solar radiation at the surface [12]. For instance, extreme aerosol effects such as desert dusts, which are known to reduce the DNI up to 90% [24], are generally misrepresented in the models. Although aerosol implementation in NWP is commonly considered in several operational forecast models, the actual concentration levels are not predicted. Thus, its total effects in the radiative forcing mechanism (and therefore in solar radiation at the surface) are still not accurately represented [25]. Currently, the majority of NWP models consider monthly mean aerosol climatologies, not allowing to represent the actual aerosol content in the atmosphere, particularly on the hourly and daily resolutions. Moreover, despite the fact that cloud formation processes are quite well understood, the representation of clouds in NWP models is the most significant factor that contributes to the lack in DNI accuracy. This occurs not only during overcast periods, but also, and more severely, under partly cloudy days due to the complex nature and scale of cloud microphysical mechanisms. At such small scales, nonlinear and turbulent motions contribute to a chaotic and stochastic system, as oppose to deterministic [26]. For instance, during partly cloudy days, models are roughly able to predict that clouds will appear, however the exact location and timing of cloud formation and dissipation (i.e. cloud life cycle) are difficult to predict. This occurs especially for mesoscale clouds, i.e. below a horizontal resolution of several kilometres.

In this work, state-of-the-art statistical downscale methods are presented for the correction of the systematic error associated with hourly predictions of DNI to improve CSP plants operational strategies, an important information for the plant operator. In this context, day-ahead forecasts (i.e. next 24-h) of DNI from the Integrated Forecasting System (IFS), the global NWP model from the European Centre for Medium-Range Weather Forecasts (ECMWF), are used together with local measurements considering a period of two years in Évora (southern Portugal). The novelty of this work is based on the use of improved hourly and daily predictions from the ecRad (cycle 43R3) radiative scheme of the IFS to establish generic next-hour and next-day CSP operational strategies. To this end, several regression models are created, where a compound multivariate regression model (designated here by MRM2) that uses previous measured hour of irradiance values to forecast next-hour values (i.e. within the nowcasting range) is proposed. In order to define generic daily operational strategies, the proposed methodology combines improved daily availabilities of DNI (also important for day-ahead energy dispatchability operations) with improved hourly predictions to refine hour-by-hour operational procedures that occur throughout the day. Moreover, hourly predictions are used in the System Advisor Model (SAM), from the National Renewable Energy Laboratory (NREL), to simulated electrical energy values from a CSP plant with similar configurations to the Andasol 3, i.e. a conventional linear focus parabolic-trough system. The resulting electrical energy outputs of the simulated CSP plant based on measured, predicted and improved predicted data, are then analysed and compared as a rough verification of the implications of the DNI forecast improvement.

It should be noted that the present methodology is not limited to one region only, since it can be performed in other regions of high solar potential, such as in arid climates, ideally, far from major sources of pollution (e.g. southern Spain, northern and southern Africa, south and north America, northern Australia, and Saudi Arabia). Applying the proposed procedures of this work in other regions of interest, in which accurate DNI forecasts are demanded, will improve the regional management and, consequently, energy efficiency of solar electrical power plants.

After the introductory section, the remainder of the present paper is structured as follows: measurements, forecast model and power plant model are described in Section 2; the considered methodology is presented in Section 3, including evaluation metrics and applied statistical methods used; results are given in Section 4; the use of improved forecasts for CSP operations is discussed in Section 5; conclusions and future perspectives are briefly outlined in Section 6.

2. Data

2.1. Measurements

A ground measuring station (designated here by EVO station) located in southern Portugal, namely in Évora city (38.567686°N, 7.911722°W), was used to perform 1-min recordings of solar radiation. Measurements were carried out during a period of two consecutive years, i.e. from July 1st 2017 to June 30th 2018 and from July 1st 2018 to June 30th 2019. The selected location stands as a semi-arid region (cf. [27]), characterized by clean atmospheric conditions with high DNI annual availability values and low variability [28]. The optimal conditions for solar harvesting allowed the installation of several already operational solar power stations in the region, with more solar projects being foreseen to take place.

Continuous measurements were performed using state-of-the-art instrumentation. A pyranometer (model CMP11) was used to measure GHI, according to the International Organization for Standardization (ISO) 9060 Secondary Standard [29], with an associated estimated uncertainty (i.e. estimates of observation error) below 2% on a daily basis. In the case of measured DNI, a pyrheliometer (model CHP1) was used, according to the ISO 9059:1990 standard [30], with an associated estimated uncertainty below 1% on a daily basis. Both instruments were mounted on a SOLYS2 Sun-Tracker (Kipp & Zonen) installed at the Institute of Earth Sciences (ICT - *Instituto de Ciências da Terra*) observatory in the University of Évora. The solar measuring equipment has been operational since 2015, with a daily basis cleaning protocol in order to prevent any anomalous recordings due to equipment malfunction (e.g. sudden power shutdowns) or soiling deposition [31].

For the same period of study, standard meteorological equipment was used to measure EVO meteorological data, including air temperature and relative humidity through the use of a hygrothermo transmitter model 1.1005.50.512 (Thies Clima), installed near the SOLYS2 Sun-Tracker. Additionally, wind velocity and surface air pressure at 10 m height were also recorded using an anemometer model A100R (Vector Instruments) and a barometric pressure sensor model PTB101B-CS105 (Campbell Scientific), respectively. It should be noted that, in EVO station, surface pressure is not available, and the wind is not representative, since the flow is disturbed by nearby buildings. For these reasons, hourly data from the Portuguese meteorological service station (IPMA – *Instituto Português do Mar e da Atmosfera*), located at Évora aerodrome (38.53654N, 7.88795W), i.e. about 4 km apart from EVO station, was used as representative of the wind velocity and surface pressure in EVO.

Together with DNI measurements, this set of meteorological data is required as input for the simulation of a linear focus parabolic-trough system to assess the resulting CSP plant performance outputs, as shown in Section 5.

After acquiring all the measured data needed, prior to the analysis, data quality control procedures were carried out, as described in Section 1 (Appendix A). After the application of the proposed filters, and in order to compare with the predicted data, measured hourly values were calculated through hourly backward means, i.e. by considering the previous sixty 1-min records of measured data.

2.2. Forecast model

To simulate atmospheric processes, NWP models make use of equations based (as much as possible) in the fundamental principles of physics, requiring large computational effort. Among a wide range of current operational models, the IFS, the global model from the ECMWF, stands as one of the highest scored NWP models in terms of medium range global weather forecasting capacity [32]. The radiative scheme currently used in the IFS, the ecRad (cycle 43R3), provides hourly forecasts of DNI and GHI, among a wide range of available parameters. In order for the model to produce solar radiation outputs, several prognostic variables, such as temperature and cloud fraction, are interpolated horizontally into the radiation grid through cubic interpolation on an hourly basis [33]. Moreover, the IFS uses the Copernicus Atmosphere Monitoring Service (CAMS) system [34], an improvement towards the previous versions implemented in the model, for instance Ref. [35], providing the aerosol climatology.

In this work, day-ahead forecasts (i.e. next 24-h) from the IFS are used for a post-processing analysis considering local measurements over a grid of $0.125° \times 0.125°$. With its best horizontal resolution, and most accurate initial conditions, the model runs twice a day, after the conclusion of the data assimilation process. Specifically, the IFS issue time can be set to start at 0 UTC or 12 UTC for the day-ahead predictions, in which the former was used in this analysis. The acquisition procedure comprised several available atmospheric parameters due to their influence over DNI in the operational strategies of a CSP plant. These include GHI, DNI, air temperature, dew point temperature, wind velocity components, total precipitation and total cloud cover. The irradiation parameters given by the model were the surface solar radiation downwards (*ssrd*) and the total sky direct solar radiation (*dsrp*), respectively for GHI and DNI. To compare these predictions with actual observations, the hourly accumulated irradiation values (in J/m^2) from the IFS were divided by 3600 and converted to mean energy flux values (W/m^2). Air and dew point temperatures at 2 m height (*t2m* and *d2m*, respectively, in K) were used to calculate the relative humidity at 2 m height, as described in Eq. (A1) of Section 2 (Appendix A). Other predicted variables were also considered throughout the analysis: the horizontal components of wind velocity (*u* and *v*, in m/s) at 10 m height; the total accumulated precipitation (*tp*, in m), i.e. the sum of convective and large scale precipitation, being accumulated since the beginning of the forecast; surface pressure (*sp*, in Pa), which will be used only in the context of a CSP plant simulation; and the total cloud cover (*tcc*), i.e. the percentage of the sky hidden by all visible clouds.

2.3. Power plant model

The SAM software, version 2017.9.5 (NREL), enables the simulation of several types of CSP systems, in which local atmospheric variables that influence energy production values of a CSP plant are used as input parameters. These not only include DNI but also air temperature, relative humidity, wind speed and surface pressure.

Within the power plant model, a transient system (TRNSYS) is implemented to perform hourly simulations of performance output parameters, providing at the end of each run an annual performance metrics summary. The TRNSYS assembles three components: the first is given by a user-friendly interface, which allows the user to define in detail the setup for the selected CSP plant, including design and control procedures, as well as the input of measured or predicted parameters; the second is the calculation engine, which implements the hourly discretization procedures for the simulation; and the third is a programming interface, which allows the user to define the functions used within the SAM code to obtained performance outputs. A more detail description of the software is available online [36].

For this work, like in a previous study [37], the SAM was used to simulate a conventional linear focus parabolic-trough system installed at EVO location with similar configurations to the 50 MW_e Andasol 3 CSP plant, currently operational in Granada (Spain). The objective in using the Andasol 3 configuration for the simulations of

a CSP plant is not to compare the obtained results in EVO with the ones from the actual power plant installation. Instead, energy outputs based on different Andasol 3 simulations with EVO data are assessed considering measurements, predictions, and improved predictions as input parameters. Particular attention is given to production values outputs, namely to values of electricity generation, represented by the parameter electricity injection to the grid E_G (MW_eh). This parameter is important for the energy management of a power plant since information regarding the power plant's production values for the next hours will help to improve operational decisions performed by the plant's operator. Moreover, the use of improved predictions in these simulations will allow to reduce bad predictions of production values, which can be related to underestimation and overestimation of DNI. Although the inherent overestimation of DNI by the IFS is expected to be present in the estimated values of E_G (when compared with measured-based E_G values), previous results [37] have shown the potential that forecasted data has in the daily operational strategy of a CSP plant. It is also important to consider the subsequent strategies that result from the available E_G estimates from the simulations. In this context, generic operational strategies are also proposed accordingly, as discussed in the Section 5.

3. Methodology

3.1. Evaluation metrics

Due to forecasting inaccuracies in NWP, hourly predictions of DNI have a characteristic bias when compared with local measurements. Overestimation is expected under an overcast sky due to the known underestimation of the radiative effects of clouds. In global models, such as the IFS, this effect is augmented during partly cloudy days. Under very clean atmospheres, DNI predictions have the tendency to underestimate measurements due to the use of monthly mean aerosol values instead of actual values.

In order to quantify the forecast error and compare the performance of different forecasts, it is important to compute the forecasting accuracy. Although several conventional metrics exist, to determine the most appropriate ones depends on the user [38]. For instance, CSP plant operators can be sanctioned per kWh deviation from the expected production [39]. In such cases, error metrics, which allow operators to perform an accurate estimation of the costs related to forecasting errors, are crucial. Particularly, a very important evaluation metric recommended for the application of electrical grid management is the root mean square error (RMSE), due to the importance that large errors have for the safety of an electrical grid system [40]. Considering the mean square error (MSE) of both forecast and persistence (i.e. persistence of the previous measured 24-h values) models with respect to measurements (MSE_{for} and MSE_{per}, respectively), forecasting ability can be carried out using the MSE based skill score (SS). The SS allows to evaluate the global performance of the forecast model towards measurements, as described by Ref. [41] (Eq. (A2) in Section 2 of Appendix A). Other conventional metrics used to assess the forecast error are the mean bias error (MBE), mean absolute error (MAE), Pearson correlation coefficient (r) and coefficient of determination (R^2). More detailed information concerning the use of these and other error metrics for solar forecasting is available in Ref. [38].

3.2. Applied methods

Several methods have been used in this work to perform a comparative analysis between IFS predictions and local measurements at EVO station. In order to quantify the error metrics obtained, hourly and daily clearness indices of DNI (k_b and K_b, respectively) were considered. These dimensionless parameters are a fundamental tool in solar radiation analysis [12], allowing to define the type of irradiance that reaches the Earth's surface, and to further assess the forecasts towards measurements, e.g. Ref. [42]. Based on DNI, a clearness index close to zero is characteristic of overcast conditions, while a value close to 0.8 frequently occurs under clear sky conditions.

In the present analysis, measured, IFS predicted, and improved IFS predicted data were compared. The statistical results from the corresponding k_b and K_b were considered, similarly to Ref. [28], including the forecasting quality obtained for each method. Besides conventional metrics, probabilistic results from probability density functions (PDF's) were considered, allowing to determine the probability distribution (given by the frequency of occurrence) of k_b and K_b. Moreover, skewness and kurtosis analysis were also used, where the former measures the lack of symmetry in respect to the normal distribution and the latter relates with the presence of outliers in a distribution. Statistical models can also be used to correct the IFS predictions. For instance, regression models, in which a dependent variable, i.e. the predictand, is studied (in this case, measured DNI) considering a set of independent variables, i.e. the predictors (in this case, forecasted data), that influence and have impact over the predictand. Each regression coefficient obtained represents the effect that a predictor has in the predictand over time (at the same time that all other predictors remain constant). These basic regression models can be refined using complex multivariate and non-linear relationships between several predictors and the predictand, providing better estimations. In this work, three regression models are used to correct hourly predicted DNI. The first model consists in a simple regression model (SRM), based on a third-degree polynomial fit. The fitting method is based on the use of regression coefficients obtained between measured DNI (i.e. the predictand) and the predicted DNI (i.e. the predictor) from the first year as input to adjust the second year of predicted DNI. The second model is a linear multivariate regression model (MRM1), which uses an interactive *stepwise function* with an adjusted r-squared criterion. This function performs all possible combinations between predictors to find the best fitting option, in this case a second-degree polynomial is considered. The atmospheric predictors used in the MRM1 are: GHI^{IFS}, DNI^{IFS}, GHI^{TOA}, DNI^{TOA}, air temperature ($Temp^{IFS}$), relative humidity (Rh^{IFS}), wind velocity (W^{IFS}), total precipitation ($Prec^{IFS}$) and total cloud cover (Tcc^{IFS}). Then, by including the previous hour (i-1) of measured DNI and GHI as predictors to the MRM1 setup, a compound multivariate regression model (MRM2) is created to perform next-hour (i) predictions of DNI accordingly to the following relation:

$$DNI_i^{\mathrm{MRM2}} = F\left(\begin{array}{c} GHI_{i-1}^{OBS}, DNI_{i-1}^{OBS}, GHI_i^{IFS}, DNI_i^{IFS}, GHI_i^{TOA}, DNI_i^{TOA}, \\ Temp_i^{IFS}, Rh_i^{IFS} W_i^{IFS}, Prec_i^{IFS}, Tcc_i^{IFS} \end{array}\right) \quad (1)$$

where function F is adjusted so that the DNI prediction (DNI_i^{MRM2}) of the first year is closer to the predictand (DNI_i^{OBS}) for the same year, including the previous hour of measured GHI and DNI (GHI_{i-1}^{OBS} and DNI_{i-1}^{OBS}, respectively) as predictors. The function F is then applied to the second year of data for validation of the forecast improvement. Regarding the use of previous hour from measured data, only DNI and GHI were considered in the MRM2, since using other available measured variables would require a higher computational cost, with not significant improvement in the forecast. That is, increasing the number of predictors would lead to more complex polynomials, where the adjustments obtained would not improve significantly the hourly DNI, as compared with

the use of measured irradiances.

It should be noted that several polynomial terms, and respective metrics, were obtained after applying linear multivariate regression for hourly and daily adjustments of MRM1 (Table A1 and Table A2, respectively) and MRM2 (Table A3 and Table A4, respectively) using the *stepwise function*. More detail information regarding these can be seen in the Appendix A (section 3), including all possible iterations between predictors and predictand. After running the *stepwise function*, for the hourly adjustments of MRM1, nine predictors were considered, while for the daily adjustments, only five predictors were used. In the case of MRM2 adjustments, in which two more predictors were added (i.e. DNI_{i-1}^{OBS} and GHI_{i-1}^{OBS}) to the previous MRM1 setup, hourly adjustments considered ten predictors, while for the daily adjustments five predictors were used.

4. Results

4.1. IFS predictions

A first analysis was carried out between measured and predicted DNI over two consecutive years, i.e. from July 1st 2017 to June 30th 2018 and from July 1st 2018 to June 30th 2019. The respective statistical and descriptive results are presented and summarized in Table 1, showing how the IFS predictions behave in comparison with the EVO measured data. During these periods, the annual predicted DNI obtained was remarkably close to the observed one, with very slight overestimation (first year) and underestimation (second year) of the measured values. For instance, mean annual values of ≈480.38 and ≈ 502.04 W/m^2 predicted by the IFS corresponded to an overestimation of ≈0.09 W/m^2 and an underestimation of ≈0.01 W/m^2 for the first and second year, respectively. Moreover, these small differences were respectively attended with a MBE of ≈ -0.05 and ≈ 0.01 W/m^2. The overall good performed of the IFS is also shown by the annual availability obtained values, which were close to the expected regional ones (i.e. above 2100 kWh/m^2/year). This is clearly seen by very small relative differences obtained between annual measured and predicted availabilities (ΔE_b), particularly in the second year, where a value of ≈0.002% was found. Regarding the obtained annual standard deviation (STD), a smaller deviation was registered for the IFS in the second year (≈288.77 W/m^2), i.e. ≈8.01 W/m^2 less than the measured one. Despite the close approximation between the annual values, the RMSE found between hourly values shows the high variability that exists between hourly predicted and measured DNI, mainly due to cloud and aerosol misrepresentation. Nevertheless, such values are found to be consistent with the ones obtained in solar radiation forecasting, e.g. Ref. [40,41], reinforcing the need to improve DNI predictions, as this work aim at. A smaller RMSE of ≈186.20 W/m^2 was obtained in the second year, in comparison to the error associated with measurements. For the hourly r, values of ≈0.85 and ≈ 0.84 were found in the first and second year, respectively, corresponding to an R^2 of ≈0.72 and ≈ 0.71. Considering the daily correlations, values in the order of ≈0.91 and ≈ 0.83 were found respectively for r and R^2 in both years. Such high correlations on the daily scale are expected to be found, since the daily summations filter the hourly variability, in which cloud and aerosol misrepresentations are most noticed.

From the first to the second year of data, an overall decrease in the deviations was observed. This may be related to different intra-annual atmospheric variability. In fact, both measured and predicted data showed less variability in the second year. This can also be associated to the occurrence of less clouds, which resulted in a higher annual availability (2200 kWh/m^2/year), i.e. ≈95 W/m^2 more than in the first year.

In the context of assessing the error associated to the IFS original predictions towards local measurements of DNI, hourly clearness indices (k_b) and respective PDF's were also calculated for each year, as shown in Fig. 1. As expected, close to null-values of k_b, a cluster of values was obtained, as a consequence of the prediction overestimation (due to the misrepresentation of clouds) towards measurements during overcast periods. For instance, during a cloudy period, measurements yield k_b values close to zero while the IFS predictions consider values up to 0.6. As opposed to this, close to high values of k_b, another cluster of hourly values was found, corresponding to clear sky conditions (particularly, very clean atmospheric days), in which an underestimation of the predictions towards measurements occurs. This underestimation is most likely to result from a sub-estimation of the radiative effects towards subgrid clouds and, most importantly, to the use of an aerosol climatology, which overestimates the effect of the aerosols under such conditions. For instance, close to k_b values above 0.7, e.g. during a sunny day that occurs after a rainy day, the actual aerosol concentration in the atmosphere is very low, as opposed to the climatologic aerosol value implemented in the model. During very clean atmosphere conditions, the relation between predicted and measured data was depicted by a smaller dispersion of k_b values in comparison with the ones obtained under overcast and partly cloudy conditions. Particularly, between both extremities, i.e. during partly cloudy periods, there was a high distribution of hourly values that resulted from clouds passing over the measuring equipment, in which the forecast model had difficulties in representing these at the hourly scale. A similar behaviour was observed in both years, as previously discussed. Moreover, the PDF's allowed to observe the frequency of occurrence of k_b values, in which both of the previous discussed clusters (i.e. for low and high values of k_b) were clearly identified. A summary of the statistical results between IFS and measured based k_b values during the second year is presented in Table 2. During this preliminary analysis, an hourly SS of ≈0.66 was found for the second year, being similar to the value obtained for the previous year (not shown here).

When considering daily values, a general improvement of the deviation between predicted and measured values of K_b was found for both years, as shown in Fig. 2. The results, based on the daily availabilities of DNI, showed that the previous overestimation of

Table 1
Statistical and descriptive analysis summary between measured and IFS predicted DNI over two consecutive years in Évora (southern Portugal), from July 1st 2017 to June 30th 2018 and from July 1st 2018 to June 30th 2019. Several annual statistical and error metrics are presented. These include: standard deviation (STD); root mean square error (RMSE); mean absolute error (MAE); mean bias error (MBE); Skewness and Kurtosis; annual DNI availability (E_b) and respective relative differences (ΔE_b); hourly and daily correlation coefficients (r_{hourly}, r_{daily}); hourly and daily coefficient of determination (R^2_{hourly}, R^2_{daily}). Results are presented considering only the daylight period.

	Year 1		Year 2	
	Measurements	IFS	Measurements	IFS
Mean (W/m^2)	480.29	480.38	502.05	502.04
Median (W/m^2)	528.33	506.80	557.52	552.47
STD (W/m^2)	353.42	296.78	347.05	288.77
RMSE (W/m^2)	187.80		186.20	
MAE (W/m^2)	135.38		135.94	
MBE (W/m^2)	−0.05		0.01	
Skewness	−0.113	−0.198	−0.180	−0.311
Kurtosis	1.459	1.597	1.527	1.690
E_b (kWh/m^2/year)	2105	2105	2200	2199
ΔE_b (%)	0.019		0.002	
r_{hourly}	0.847		0.844	
R^2_{hourly}	0.718		0.712	
r_{daily}	0.910		0.912	
R^2_{daily}	0.829		0.832	

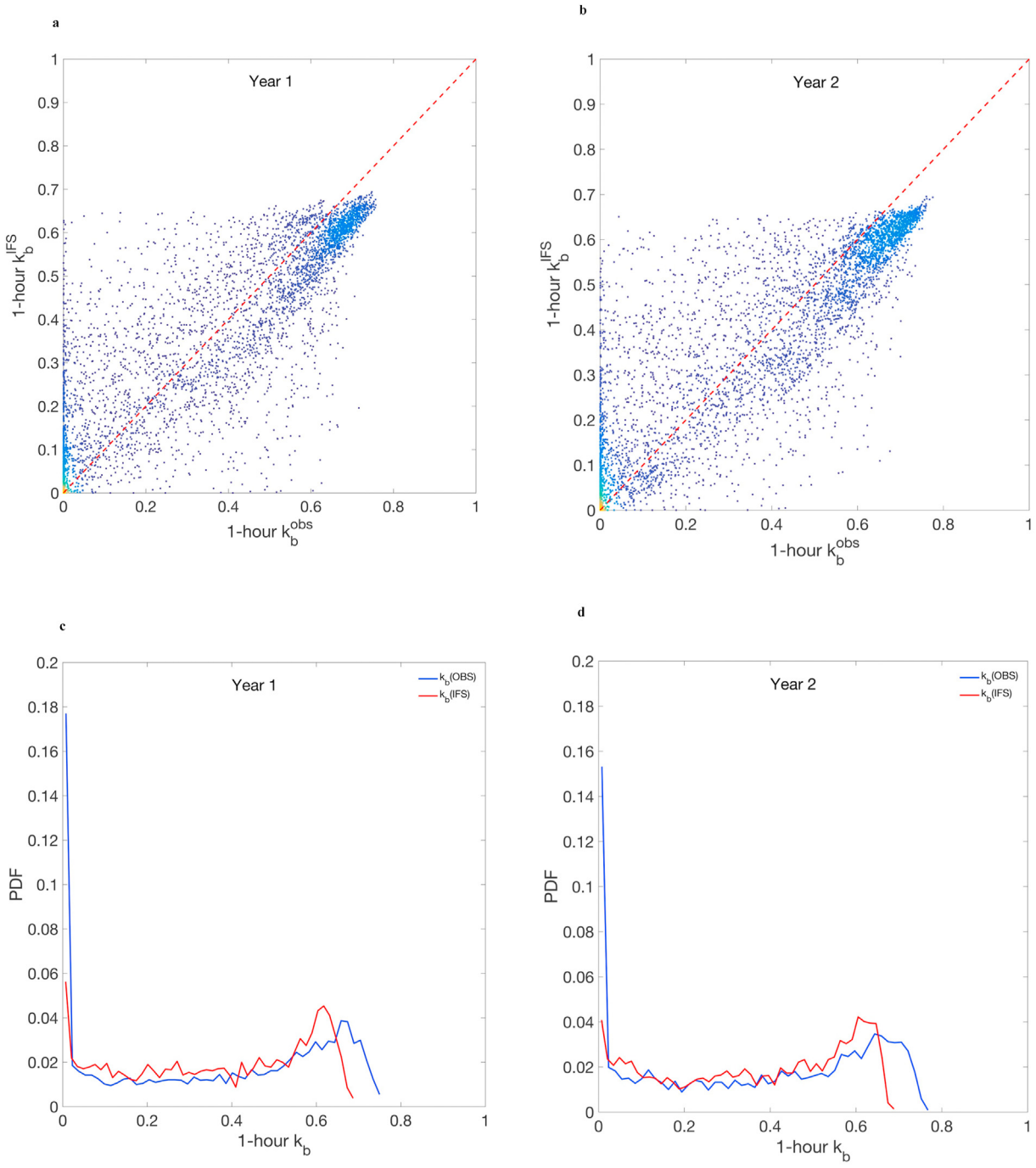

Fig. 1. Hourly (a, b) clearness indices for DNI (k_b) between measurements (OBS) and predictions (IFS) considering two consecutive years of data in Évora, from July 1st 2017 to June 30th 2018 (year 1) and from July 1st 2018 to June 30th 2019 (year 2), with the identity line $y=x$ being also represented (red-dashed line). The respective hourly probability density functions (PDF's) are also shown (c, d). (For interpretation of the references to colour in this figure legend, the reader is referred to the Web version of this article.)

the model close to null K_b values was significantly reduced, leading to higher correlations and lower errors. As previously discussed, at this scale, such effect is expected in NWP, since that the IFS, like most NWP models, has difficulties in predicting the precise location and moment when a variation of DNI occurs, particularly from 1 h to the next. For instance, cloud formation, advection and dissipation, result from complex microphysics process that can occur at sub-grid and sub-hourly scales, and therefore the model will not be able to represent them precisely. When considering daily values of DNI, temporal phase errors are filtered, allowing the IFS to provide satisfactory results when compared with local daily measured based values. This was showed by the narrowing of K_b values towards the identity line in Fig. 2, which depicted a closer behaviour between predicted and measured daily data, although the underestimation of the model during clear sky conditions still prevailed. The respective daily PDF's, besides showing a reduction of the error in comparison with the hourly results, showed a high inter-daily variability, corresponding to the different atmospheric conditions from one day to the other. Such effect is important, especially for the proposed adjusted models at the daily scale. The statistical

Table 2
Statistical summary of hourly clearness indices for DNI (k_b) between measurements and predictions (IFS, SRM, MRM1 and MRM2) for a one year (July 1st 2018 to June 30th 2019) in Évora (southern Portugal). Correlation coefficient (r), coefficient of determination (R^2), root mean square error (RMSE), mean bias error (MBE), mean absolute error (MAE) and skill score (SS) are presented. The SS is calculated towards a referenced persistence model (i.e. measurements time series displaced 24 h ahead).

	Year 2			
	IFS	SRM	MRM1	MRM2
R	0.846	0.849	0.866	0.929
R^2	0.716	0.720	0.750	0.864
RMSE	0.137	0.136	0.129	0.095
MAE	0.100	0.099	0.092	0.062
MBE	1.855×10^{-4}	5.091×10^{-4}	0.003	7.834×10^{-4}
SS	0.656	0.661	0.697	0.835

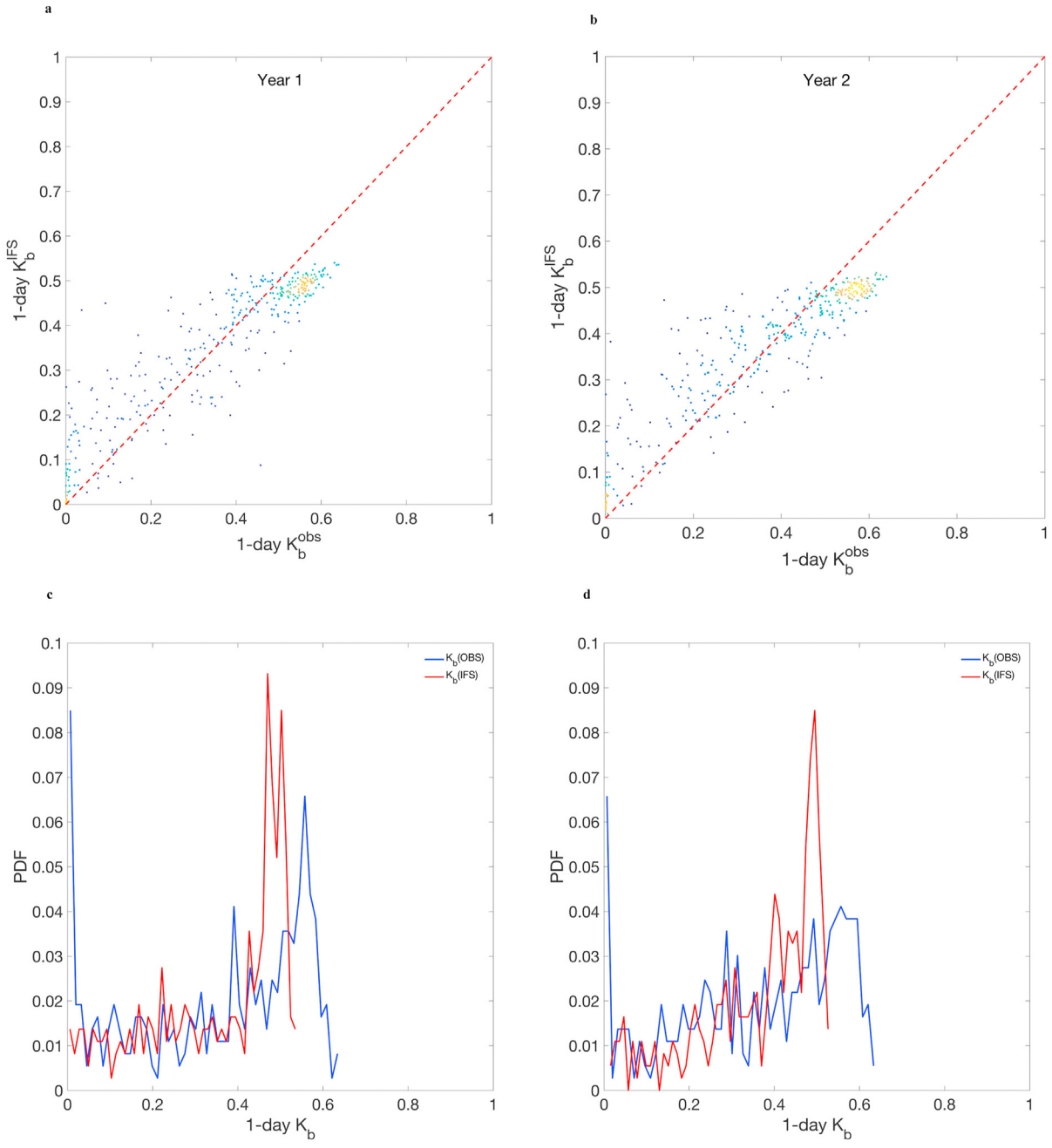

Fig. 2. Daily (a, b) clearness indices for DNI (K_b) between measurements (OBS) and predictions (IFS) for two consecutive years in Évora, from July 1st 2017 to June 30th 2018 (year 1) and from July 1st 2018 to June 30th 2019 (year 2), with the identity line $y=x$ being also represented (red-dashed line). Respective daily probability density functions (PDF's) are also shown (c, d). Daily values were calculated through DNI availabilities (kWh/m^2), i.e. the sum of each 24-h period. (For interpretation of the references to colour in this figure legend, the reader is referred to the Web version of this article.)

Table 3
Statistical summary of daily clearness indices for DNI (K_b) between measurements and predictions (IFS, SRM, MRM1 and MRM2, for one year of data in Évora (southern Portugal), from July 1st 2018 to June 30th 2019. Correlation coefficient (r), coefficient of determination (R^2), root mean square error (RMSE), mean bias error (MBE), mean absolute error (MAE) and skill score (SS) are presented. The SS is calculated towards a referenced persistence model (i.e. measurements time series displaced 24 h ahead).

	Year 2			
	IFS	SRM	MRM1	MRM2
R	0.892	0.897	0.911	0.899
R^2	0.795	0.804	0.831	0.809
RMSE	0.090	0.084	0.077	0.082
MAE	0.071	0.063	0.056	0.058
MBE	−0.002	−0.002	0.006	0.005
SS	0.734	0.772	0.805	0.779

results obtained are summarized in Table 3, where a daily SS of ≈0.73 was attained between measurements and predictions for the second year. The daily values, which consider predicted daily availabilities, also allowed to visualize the potential of the IFS regarding the definition of operational strategies of a CSP plant. Such information is particularly important to a plant operator concerning the expected DNI availability and the distribution of energy dispatchability for the next day.

To further improve hourly predictions of DNI, post-processing methods can be applied. Since the ecRad (cycle 43R3) was implemented in July 2017, this work only considers the period of two years. This can be seen as a limitation regarding statistical downscaling methods (e.g. the application of perfect prognosis) for the correction of DNI, particularly towards daily adjustments. However, MOS techniques are suitable for the present analysis, in which the previous results allowed to set up a statistical reference henceforth, using the first year to improve hourly predictions in the second year.

4.2. Spatial average

Prior to the application of regression analysis, a simple error correction was performed by implementing a spatial average that considers the closest grid points to the actual measuring location, instead of using the nearest global model grid point. The method has some benefits [43], in which small improvements can be attained when considering hourly predictions of DNI from the IFS. This was the case when performing an average from a 3 x 3 grid points (corresponding to an area of about 18 km × 18 km), centred in the nearest grid point to the EVO geographic coordinates. The spatial average, which was separately applied for both years, yield very similar results. Overall, when compared with the nearest point to the measuring location, results from the second year showed an hourly correlation increase of ≈0.51% and a decrease of ≈1.20% in the RMSE.

It should be noted that an increase in the number of available grid points used for averaging could be an option, however the resulting average DNI would be unrepresentative of the exact location of study. Moreover, performing the spatial average considering daily values did not provide any improvement, since intra-day variability is already reduced by the daily summation. For this matter, to further improve hourly DNI predictions, different techniques should be pursued to significantly reduce the associated error.

4.3. Simple regression model (SRM)

Regression coefficients obtained from a polynomial adjustment in first year, between measured and predicted values of DNI, can be used to correct the IFS predictions in the second year. To this end, several polynomials were tested, in which a third-degree polynomial was found to provide the best results with the IFS for the application of the SRM.

Results showed small improvements and the presence of a non-linear relation, as shown by the k_b obtained values (Fig. 3a). Comparing these results with the ones previously obtained between the IFS original predictions and measurements (Table 2), an increase of ≈0.35% and a decrease of ≈0.73% were found for the r and RMSE, respectively. An hourly SS of ≈0.66 was attained using the SRM, corresponding to an increase of ≈0.76%. When comparing the respective PDF's (Fig. 3b), the improvement is clear, particularly for higher values of k_b (i.e. in the absence of clouds) where hourly SRM values are closer to the observed behaviour than the ones obtained with the IFS (Fig. 1c).

A similar procedure but for the daily availabilities (Fig. 4a) revealed correlations of ≈0.90 and a SS of ≈0.77 (Table 3), i.e. an increase of ≈0.56% and ≈5.05% in comparison with the IFS daily K_b's, respectively.

These results, besides showing improvements using simple regression methods, evidence the need of using more complex approaches that can lead to a more substantial reduction of the error associated to hourly predicted DNI. One example is to include other variables related to DNI modulation for the polynomial adjustment, as discussed in the following sections.

4.4. Multivariate regression model (MRM1)

As it was shown in the previous section, adjusting only DNI forecast to the DNI observations, does not improve substantially the forecasts. This is a result of the complex nature of the DNI related physical processes. Thus, in this subsection, other forecasted meteorological variables along with predicted DNI are considered to match the observed DNI, using a multivariate regression technique. This technique uses the observed DNI as the objective function and determines the optimal combination of coefficients and input variables (in this case, the forecasted variables) to approximate the predictions to the observations. The method has the advantage of simulating some of the physical phenomena that actual occur, allowing to consider interaction terms between variables (e.g. predicted DNI with predicted temperature).

In this context, like in the previous section, regression coefficients, which resulted from the adjustment made between predictions and measurements for the first year, were used to correct the IFS predictions in the second year with the inclusion of eight new predictors. These include the same hour predicted variables, i.e. GHI, irradiances calculated at TOA (GHI^{TOA}, DNI^{TOA}), air temperature, relative humidity, wind velocity, total precipitation and total cloud cover. Due to the large number of predictors, the resulting model MRM1 was found to best perform through a second-degree polynomial fitting with the *stepwise function*. It

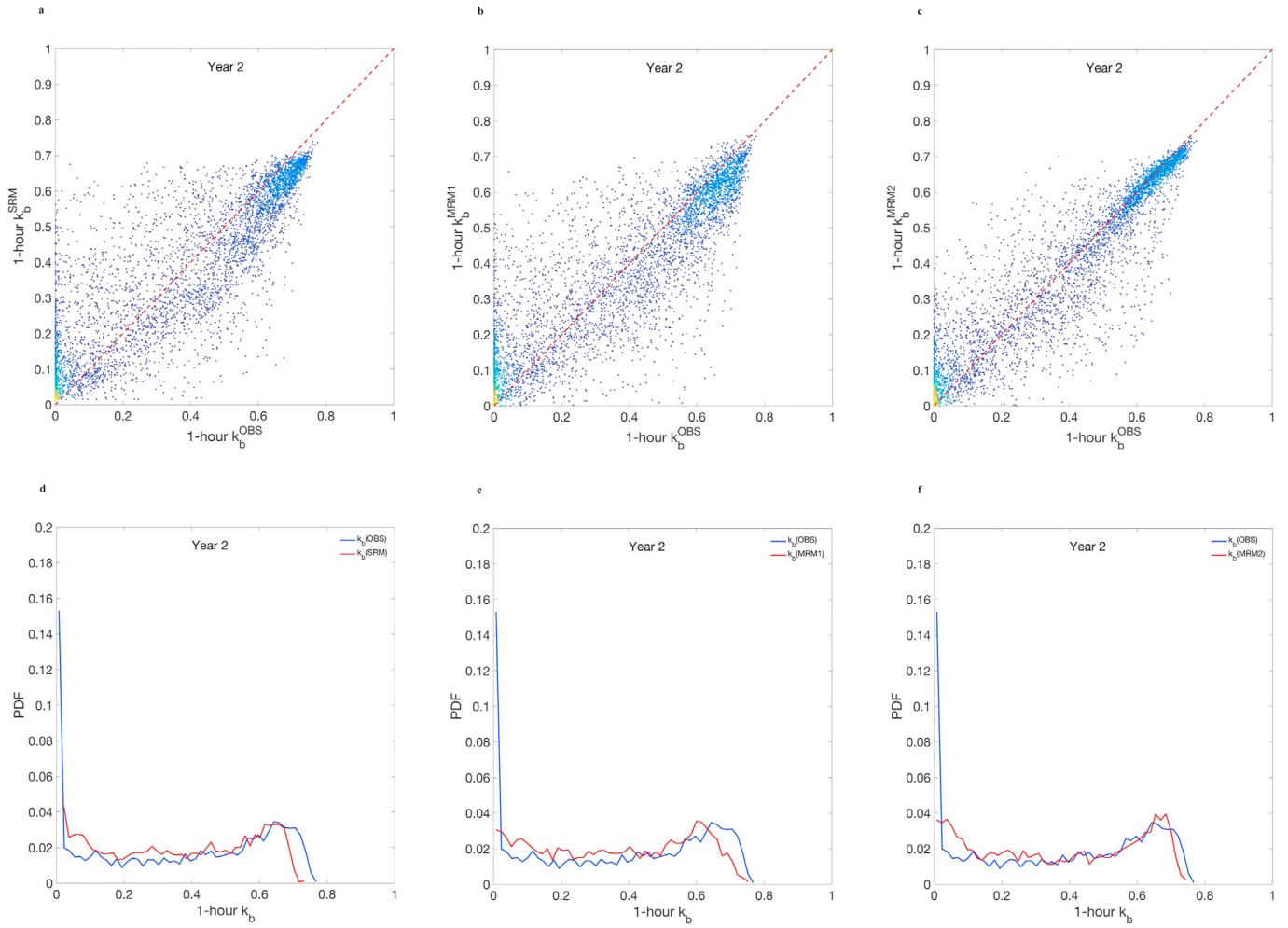

Fig. 3. Hourly clearness indices for DNI (k_b) between measurements (OBS) and improved DNI predictions with (a) SRM, (b) MRM1 and (c) MRM2, where the identity line $y=x$ is represented as a red-dashed line. Analysis is performed over one year of data in Évora (southern Portugal), from July 1st 2018 to June 30th 2019. The respective hourly probability density functions (PDF's) are also depicted (d, e and f). (For interpretation of the references to colour in this figure legend, the reader is referred to the Web version of this article.)

should be noted that when running the *stepwise function*, negative values can result from the multivariate correction of the original IFS data; especially for low observed and predicted DNI values. With this method, a total of 121 negative values were found to occur. In such cases, the original IFS predicted values of the second year of data were maintained. The application of the *stepwise function* for MRM1 was based on the best fitting found through an iterative process that tested 43 different formulations between predictand and all predictors (Table A1, Appendix A).

When performing an analogous method of multivariate regression but to daily DNI availabilities, daily mean values of air temperature, relative humidity, wind velocity, precipitation and cloud cover, were considered. In the case of solar radiation variables, availability values (i.e. the sum of each 24-h periods) were used. The resulting daily adjustment considered 11 different formulations between daily predictand and predictors (Table A2, Appendix A). After performing the correction to the originally predicted availabilities, 7 negative values were found, being the corresponding IFS daily predictions maintained instead.

Results showed that the hourly k_b values obtained, presented in Fig. 3b, and **3e**, illustrate further improvements attained through the MRM1, in comparison to simple linear regression methods. Particularly, during cloudy conditions, i.e. close to null-values of k_b, there is a reduction in the previous overestimation of the predictions towards measurements. It is also observed that for clear sky conditions, there is also a compensation in the underestimation of the predictions. From its original value (i.e. from the IFS) to the value obtained with MRM1, an increase of ≈2.36% in the correlation was attained, together with an overall decrease in the errors, such as ≈5.84% in the RMSE (Table 2). Regarding the hourly SS, a value of ≈0.70 was found, corresponding to an increase of ≈6.25% from the original value. Daily values (Fig. 4b and 4e), which resulted from the polynomial adjustment expressed in Table A2 (Appendix A), showed K_b values with correlations of ≈0.91 and RMSE of ≈0.08 (Table 3). Moreover, an increase of ≈9.55% in the daily SS was obtained in relation to the original value found when using the IFS daily predictions.

In the next section, a new addition to MRM1 is carried out by including the previous hour of measured GHI and DNI as predictors in the case of the hourly analysis. While for the daily analysis, the previous day of measured availability is used to improve the IFS day-ahead predictions.

4.5. Compound multivariate regression model (MRM2)

As means to optimize the MRM1 outputs, the proposed MRM2 was created using the same setup as MRM1, but with the inclusion of the previous hour measured GHI and DNI to the former MRM1

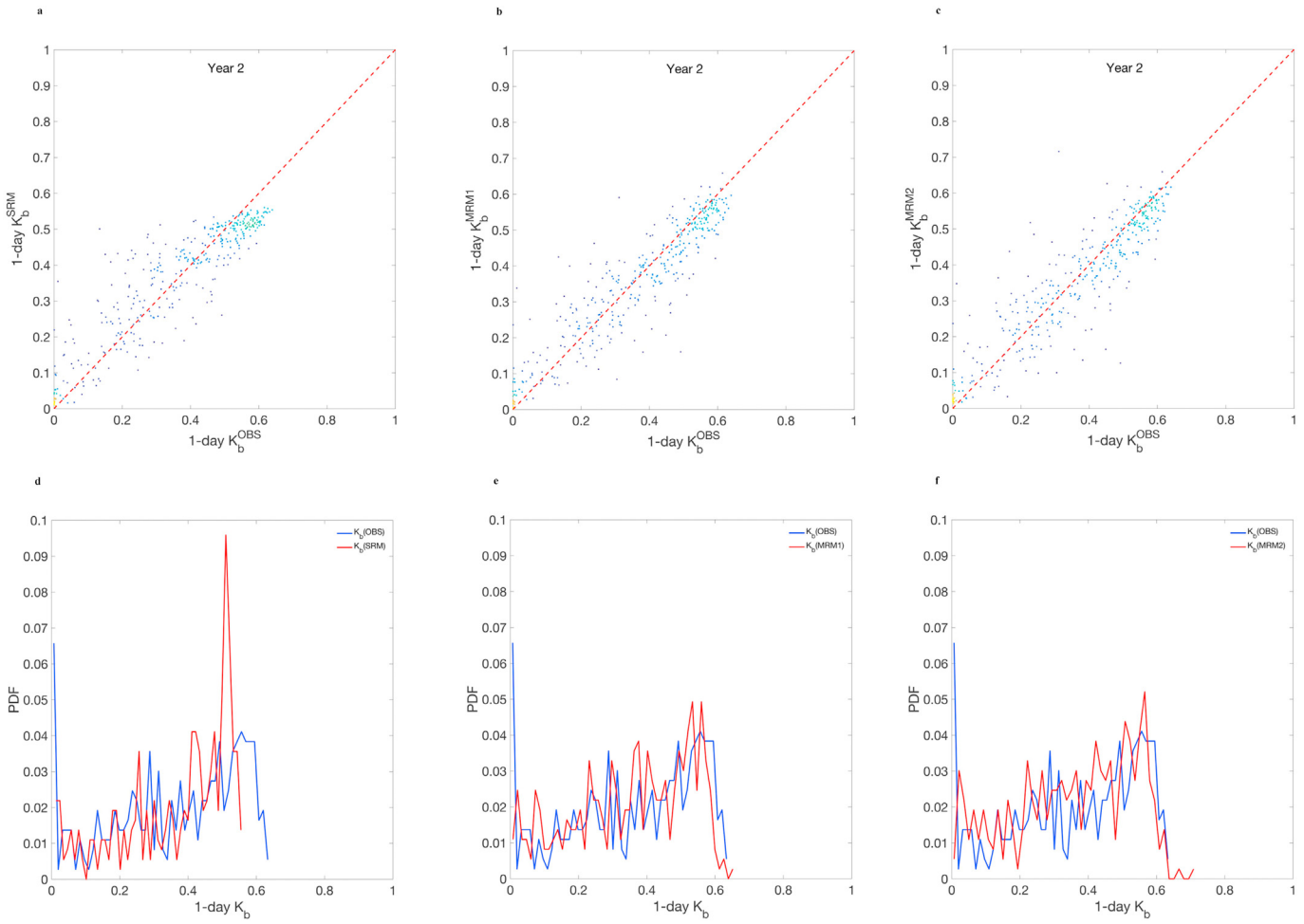

Fig. 4. Daily clearness indices for DNI (K_b) between measurements (OBS) and improved DNI predictions with (a) simple regression model (SRM), (b) multivariate regression model (MRM1) and (c) compound multivariate regression model (MRM2), with identity line $y=x$ represented as a red-dashed line. Analysis is performed over one year of data in Évora (southern Portugal), from July 1st 2018 to June 30th 2019. The respective hourly probability density functions (PDF's) are also being depicted (d, e and f). Daily values are calculated through DNI availabilities (kWh/m^2), i.e. the sum of each 24-h period. (For interpretation of the references to colour in this figure legend, the reader is referred to the Web version of this article.)

predictors. The resulting iterative process tested 50 different formulations between predictand and all predictors (i.e. a total of 11 predictors), as shown in Table A3 (Appendix A). As before with the MRM1, negative values (a total of 84) were obtained for the MRM2 during the regression procedure. Likewise, these values were maintained by the original IFS predicted values, as well as for the first forecast of the day (right after sunrise).

When compared with the IFS hourly values, the MRM2 significantly improves DNI predictions, as shown by the obtained k_b values (Fig. 3c and **d**). The results depict a narrowing towards the identity line $y=x$, i.e. closer to a linear relation than the previous results obtained. In addition to a lower occurrence of overestimated k_b values close to zero, a smaller dispersion of values was also attained for partly cloudy conditions, as well as less underestimated k_b values during clear sky conditions. As shown in the statistical summary (Table 2), an hourly correlation of $\approx$0.93 and a SS of $\approx$0.84 were found, corresponding to increases of $\approx$9.81 and $\approx$ 27.29%, together with a general decrease of the errors.

For the daily availability analysis, the IFS predicted availability of the first day was preserved. Moreover, daily DNI availabilities (Table 3), in which the previous day availability value was used to forecast the next day, resulted from the polynomial adjustment presented in Table A4 (Appendix A). After 23 different formulations, the best fitting found produced 8 negative values, in which the IFS forecasted values were maintained. The K_b values found with this method are showed in Fig. 4c, and **4f**, where high correlations and low errors between adjusted predictions and measurements were found. A daily correlation of $\approx$0.90 and an SS of $\approx$0.78 were obtained for the second year of data. In comparison with the original predicted value obtained with the IFS, these correspond to increases of $\approx$0.78 and $\approx$ 6.13%, respectively.

Despite a dependency on measurements taken in the previous hour or previous day (depending on the case of study), the MRM2 method presents itself as the best fitting found when using multivariate analysis. Through the use of the previous hour of measured DNI and GHI, the model allowed to achieve the best results with significant improvements for the hourly values in comparison with the other presented methods. Moreover, it is possible to observe that for daily availabilities, the improvements obtained are not as significant as the ones obtained on the hourly basis. This is due, in part, to the fact that the IFS daily predictions are already satisfactory, making it more difficult to achieve further

improvements. Another important reason is the fact that only one year of data is being used to correct DNI. This affects particularly the daily correction, in which the daily data can be nearly twelve times less than the data used for the hourly correction. For this matter, in the context of MRM2 daily predictions, more statistical information is required than the one used for this analysis. Thus, with more data (i.e. with an increased number of years) to perform the MRM2 daily adjustments, better predictions with less dispersion of values towards the measured ones from one day to the next should occur.

4.6. Application to CSP operation

After applying different methodologies to improved IFS forecasts, the following two-steps methodology is proposed for their implementation as a tool in CSP operations: i) the use of daily MRM1 improved DNI availabilities to define the generic operation strategy for each day, as suggested by the authors in Ref. [37]; and ii) the application of the improved hourly MRM2 improved DNI predictions to refine hour-by-hour the operation strategy throughout each day, similarly to nowcasting techniques [47]. In summary, using this information for the optimization of CSP plants is fundamental, since precise day-ahead forecasts of DNI allow to predict the day-ahead CSP plant's electricity generation. In addition to improved daily strategies based on different estimates of DNI availability, these can then be further refined with the use of hourly corrections, particularly from MRM2. Focus to these subjects will be given in the next section.

5. CSP operations with improved forecasts

5.1. Power plant daily strategies

Considering the previous results, improved forecasts can now be used for better operational strategies regarding CSP plant's energy management. Such strategies can be implemented on the hourly basis, to optimize energy use throughout the day (being related to short periods of solar intermittency), and, particularly, on the daily basis. This allows the plant operator to decide on how and when to sell the predicted electrical energy generated by the plant at a premium tariff in the electrical market. Information concerning the potential that day-ahead forecasts of DNI have in the operation of CSP systems is available in literature, see Ref. [37,44,45], where recommended strategies for typical days (i.e. days with different weather conditions) are proposed.

This section focuses the use of contingency tables with daily measured and predicted (IFS, SRM, MRM1 and MRM2) availabilities separated by different ranges, according to the previously defined strategies. Such tables aim to evidence the improved accuracy of daily availability range predictions with the use of the correction methods discussed previously. An improved prediction implies a better day-ahead planning regarding a plant operation strategy. This has the potential to lead, if properly articulated with the improved hourly predictions, to an overall enhancement of the solar to electricity conversion procedure. This will be reflected in an increase of the plant's efficiency (e.g. by enabling higher temperatures of the superheated steam in the power block), as well as its dispatchability (e.g. by smoothing temperature variations at the solar field outlet of the heat transfer fluid). The improved hourly predictions will be based on the MRM2 model, which was shown to be the best correction method. Thus, this analysis has the objective of combining improved daily availability predictions with improved hourly forecasts of DNI to increase a power plant operation reliability. Using such combined strategy would certainly improve the electrical energy production and its value, reducing the final levelized cost of electricity, i.e. the ratio between the sum of the discounted total cost during the lifetime of a plant and the sum of the discounted total amount of electrical energy delivered. Consequently, the client's electricity bill would also be reduced, (another strong reason to optimize CSP plants). Although such life cycle analysis is out of scope of the present analysis, it can certainly be carried out in future studies.

Results for the daily availabilities from the IFS, SRM, MRM1 and MRM2, respectively in Tables A5, A6, A7 and A8 (Appendix A), were obtained for a period of one year (from July 1st 2018 to June 30th 2019). In these tables, the number of occurrences when predictions coincide with measurements correspond to the 'Hits' (marked in green), whereas the corresponding success rate (%) was calculated considering the total number of measured availabilities values. The range by which this evaluation was carried out is divided in four intervals, which go from overcast to clear sky conditions, corresponding to different strategies defined for the corresponding atmospheric conditions that have distinct effects over a CSP plant electrical production [37]. As expected, all day-ahead correction models provide satisfactory results, with prediction accuracies generally above 50%, mainly due to the reduction of the intra-day variability, as a consequence of the daily summation. This includes the original IFS day-ahead predictions, which depict the highest daily success rates of 'Hits' between 3 and 9 kWh/m^2/day ($\approx$68.48 and 88.14%, respectively). The daily adjustments were able to significantly increase the day-ahead estimations accuracy during overcast and very clean atmospheric conditions. Success rates of 'Hits' between $\approx$70.89 and 73.42% were respectively found for the MRM2 and for both SRM and MRM1, corresponding to cloudy days (from 0 to 3 kWh/m^2/day). Considering clear sky days (from 9 to 13 kWh/m^2/day), success rates of $\approx$75 and 77.63% were respectively found for the MRM1 and for both SRM and MRM2. Overall, when planning CSP daily operational strategies, a plant operator can rely on the correction models, particularly the MRM2 if longer time-series are available, which can be complemented with the IFS daily predictions during partly cloudy periods. Then, during the day, the hour-ahead strategy could be improved by the hourly predicted DNI value based on the MRM2 (as discussed in the next section).

5.2. Power plant simulation

With the available data, i.e. measurements, IFS forecasts and corrected forecasts, during a one year period, hourly values of DNI and meteorological variables were used as input parameters for the simulation of a CSP plant with similar configurations to the Andasol 3 using the SAM. The corresponding electricity injected into the grid values (E_G, MW_eh), generated by each simulation, based on measured and predicted values (IFS, SRM, MRM1 and MRM2), were

Table 4
Hourly electrical energy injected into the grid (E_G, MW_eh) results through the SAM simulations based on measurements (OBS) and predictions (IFS, SRM, MRM1 and MRM2). One year of data was considered in each run for Évora (southern Portugal). The SAM simulations were performed with similar configurations to the Andasol 3 CSP plant. Correlation coefficient (r), coefficient of determination (R^2), root mean square error (RMSE), mean absolute error (MAE), mean bias error (MBE), total E_G, and relative differences (ΔE_G, %), are presented.

	OBS	IFS	SRM	MRM1	MRM2
R	–	0.89	0.89	0.90	0.97
R^2	–	0.79	0.79	0.82	0.93
RMSE (MW_eh)	–	11.38	11.25	10.40	6.29
MAE (MW_eh)	–	4.11	4.08	3.61	1.85
MBE (MW_eh)	–	−0.82	−0.62	−0.33	−0.11
E_G (MW_eh/year)	166,914	174,086	172,339	169,795	167,880
ΔE_G (%)	–	4.30	3.25	1.73	0.58

then compared and discussed accordingly. To perform this simulation in the SAM, input variables that influence the plant's annual performance (i.e. DNI, air temperature, relative humidity, surface pressure and wind velocity) are considered in each run based on measured or predicted data. Moreover, it is important to have in consideration that the results obtained assume all the plant's power consumption losses, including periods of non-production (i.e. nights and overcast periods) and a constant derating value of 4%.

The Andasol 3 annual performance results (Table 4) showed annual energies of ≈166,914 MW_eh/year for the measured data, while for the IFS predictions a value of ≈174,086 MW_eh/year was obtained. The predicted annual overestimation is a result of the IFS tendency to overestimate measured values during overcast periods, in which the plant efficiency is higher due to lower temperatures. Such conditions occur more frequently than very clean atmospheric periods, in which the IFS has the tendency to underestimate measured values (i.e. when the plant's efficiency is lower). Using the IFS improved DNI predictions, and the meteorological predicted data, an annual value of ≈172,339 MW_eh/year was found for the SRM, while for the MRM1 ≈169,795 MW_eh/year was reached. However, it is with the MRM2 that the best results based on hourly E_G values were attained, with ≈167,880 MW_eh/year and a relative difference of ≈0.58%, being the closest value to the one based on measurements. Moreover, a rough estimation of the economic value of the improved MRM2 predictions can also be performed, considering the average selling price of electricity of 7c€/kW_eh [46] for large industrial customers in Europe. In this context, considering the simulation that run the DNI observations for the considered year, the profit of the plant would be ≈ 11.68 M€, while the one expected with IFS original forecasted data would be higher, i.e. ≈12.19 M€, corresponding to a difference (Δ_{IFS}) of ≈0.51 M€. On the other hand, if the MRM2 predictions are used instead, such value would be ≈ 11.75 M€, i.e. an Δ_{MRM2} of ≈0.07 M€ would be attained. This allows to calculate the difference between the two predicted values obtained ($\delta = \Delta_{IFS} - \Delta_{MRM2}$), which can in some way quantify the increased profit with the use of the proposed improved predictions. Such value would be around 0.44 M€ (i.e. ≈3.80% of the total profit). A full range of possible economic improvements can only be accessed with a thorough CSP simulation that allows the implementation of hourly and daily operational strategies, which is out of the scope of this analysis. However, such implementations should be carried out in future studies.

6. Conclusions and future perspectives

In order to improve hourly and daily predictions of DNI from the ECMWF global model, statistical post-processing methods were applied to the provided 24-h forecasts of the IFS. Considering two consecutive years of predicted and measured data in Évora, the attained corrected predictions resulted from the use of simple techniques, suitable to be used from the operational point of view, including linear and multivariate regression analysis. It was observed that best results were achieved with the use of the MRM2 correction model. Through the use of hourly clearness indices, the MRM2 showed a high correlation (≈0.93), representing an increase of ≈9.81% in comparison with the IFS original value. Moreover, the MRM2 demonstrated a skill score (SS) of ≈0.84, i.e. ≈27.29% higher than the one obtained with the IFS. As expected, on the daily scale, the proposed correction models showed satisfactory results due to the reduction of the cloud overestimation characteristic of the hourly predictions, as a consequence to the daily summation. Lower daily errors and higher correlations were found using the daily correction models, where a daily SS of ≈0.78 was found for the MRM2. However, to further improve the MRM2 daily predictions, more than one year of data is required due to the high inter-daily variability of DNI. Nevertheless, daily contingency tables were created to provide generic strategies to a plant operator under different atmospheric conditions. On a daily basis, predictions can be used with the corrected values, particularly for overcast and clear sky days, while during partly cloudy periods the original daily availabilities from the IFS are maintained. Operational strategies based on day-ahead predictions can also be refined throughout the day using the MRM2, which was shown to be the most suitable model to be used on the hourly time scale. The application of measured and predicted data in the simulation of a conventional linear parabolic-trough power plant (similar to the Andasol 3 CSP) allowed to compare the electrical energy injected into the grid (E_G). The results showed that E_G hourly values were best predicted with the MRM2. Additionally, a preliminary economic analysis of the simulated plant showed that the MRM2 predicted hourly values of E_G allowed to enhance the plant's profit in ≈0.44 M€, as compared to the use of the original IFS forecasts.

To further improve this analysis, future studies should focus on the use of more robust post-processing techniques. At the same time, these should be of easy application to the plant operator in order to facilitate operational procedures, which sometimes can require fast decisions. Future corrections should give more emphasis in correcting hourly values during overcast and partly cloudy periods, i.e. periods of high energy demand, in which hourly overestimations towards measured values still remain one of the main challenge's in solar forecasting. For instance, the inclusion of other important parameters in the MRM2, such as the previous hour of measured aerosol optical depth values. Another method that can be beneficial for improvement of short-terms forecasts of DNI forecasts, is the integration of an all sky imager based nowcasting system, such as the one installed nearby Évora [47]. Since the SAM uses a single strategy, i.e. to produce electricity whenever there is DNI available, more emphasis should be given to a model that makes use of daily operational strategies [54], including the use of hourly values of the MRM2, as it was shown to be the best correction model found in this work.

CRediT authorship contribution statement

Francis M. Lopes: Conceptualization, Investigation, Resources, Methodology, Supervision, The concept of this work, investigation, resources, and the implemented methodology, were made by, ECMWF forecasts were obtained by, System Advisor Model simulations were carried out by, All authors have reviewed the article prior to the resubmission, ECMWF forecasts were obtained by, All authors have reviewed the article prior to the resubmission, Supervision, All authors have reviewed the article prior to the resubmission. have supervised this work. **Ricardo Conceição:** Writing - review & editing, Data curation, Funding acquisition, Data curation, Formal analysis, and post-processing analysis, writing and editing procedures, were done by. **Hugo G. Silva:** Writing - review & editing, Data curation, Funding acquisition, Data curation, Formal analysis, and post-processing analysis, writing and editing procedures, were done by. **Rui Salgado:** Supervision, All authors have reviewed the article prior to the resubmission. have supervised this work. **Manuel Collares-Pereira:** Supervision, All authors have reviewed the article prior to the resubmission. have supervised this work.

Declaration of competing interest

The authors declare that they have no known competing financial interests or personal relationships that could have appeared to influence the work reported in this paper.

Table A1
Hourly multivariate regression metrics obtained through the use of the stepwise function considering a second-degree polynomial adjustment of DNI (MRM1) during one year (from July 1st 2018 to June 30th 2019).

	MRM1			
Terms	Estimates	SE	tStat	pValue
'(Intercept)'	-3.59×10^{4}	1.27×10^{4}	−2.83	4.65×10^{-3}
'x_1'	8.18	2.10	3.90	9.84×10^{-5}
'x_2'	1.30	3.20	0.41	0.68
'x_3'	−3.56	1.40	−2.54	0.01
'x_4'	47.51	17.80	2.67	7.64×10^{-3}
'x_5'	174.09	65.97	2.64	8.35×10^{-3}
'x_6'	29.45	17.65	1.67	0.10
'x_7'	327.68	130.22	2.52	0.01
'x_8'	-1.35×10^{4}	4.18×10^{3}	−3.22	1.29×10^{-3}
'x_9'	3.54×10^{3}	850.58	4.16	3.25×10^{-5}
'$x_1 \bullet x_3$'	-8.65×10^{-4}	1.90×10^{-4}	−4.55	5.56×10^{-6}
'$x_1 \bullet x_4$'	-5.04×10^{-3}	1.45×10^{-3}	−3.48	5.07×10^{-4}
'$x_1 \bullet x_5$'	−0.03	7.20×10^{-3}	−3.90	9.68×10^{-5}
'$x_1 \bullet x_6$'	-4.43×10^{-3}	2.33×10^{-3}	−1.90	0.06
'$x_1 \bullet x_8$'	−16.42	10.71	−1.53	0.13
'$x_1 \bullet x_9$'	−0.06	0.11	−0.50	0.62
'$x_2 \bullet x_4$'	-1.88×10^{-3}	2.24×10^{-3}	−0.84	0.40
'$x_2 \bullet x_5$'	0.02	6.65×10^{-3}	2.26	0.02
'$x_2 \bullet x_6$'	2.70×10^{-3}	3.50×10^{-3}	0.77	0.44
'$x_2 \bullet x_7$'	−0.01	9.54×10^{-3}	−1.39	0.16
'$x_2 \bullet x_8$'	−5.94	18.78	−0.32	0.75
'$x_2 \bullet x_9$'	0.99	0.21	4.78	1.83×10^{-6}
'$x_3 \bullet x_4$'	3.57×10^{-3}	1.02×10^{-3}	3.52	4.44×10^{-4}
'$x_3 \bullet x_6$'	-4.27×10^{-3}	1.64×10^{-3}	−2.60	9.42×10^{-3}
'$x_3 \bullet x_8$'	15.35	7.20	2.13	0.03
'$x_3 \bullet x_9$'	−0.84	0.16	−5.13	3.02×10^{-7}
'$x_4 \bullet x_5$'	−0.11	0.04	−2.49	0.01
'$x_4 \bullet x_6$'	−0.02	0.01	−1.40	0.16
'$x_4 \bullet x_7$'	−0.22	0.09	−2.52	0.01
'$x_4 \bullet x_9$'	−2.50	0.59	−4.24	2.33×10^{-5}
'$x_5 \bullet x_6$'	−0.15	0.08	−1.97	0.05
'$x_5 \bullet x_7$'	−0.85	0.47	−1.80	0.07
'$x_5 \bullet x_9$'	−6.39	3.07	−2.08	0.04
'$x_6 \bullet x_7$'	0.20	0.15	1.39	0.16
'$x_6 \bullet x_9$'	−2.81	1.00	−2.80	5.06×10^{-3}
'$x_7 \bullet x_9$'	−23.55	5.83	−4.04	5.49×10^{-5}
'x_1^2'	7.81×10^{-4}	1.42×10^{-4}	5.51	3.83×10^{-8}
'x_2^2'	4.24×10^{-4}	1.49×10^{-4}	2.85	4.44×10^{-3}
'x_3^2'	-1.69×10^{-4}	5.91×10^{-5}	−2.85	4.35×10^{-3}
'x_4^2'	−0.02	6.30×10^{-3}	−2.51	0.01
'x_5^2'	−0.35	0.15	−2.38	0.02
'x_6^2'	−0.04	0.02	−2.52	0.01
'x_8^2'	4.68×10^{5}	1.20×10^{5}	2.34	0.02
'x_9^2'	246.04	52.12	4.72	2.42×10^{-6}

Table A2
Daily multivariate regression metrics obtained through the use of the stepwise function considering a second-degree polynomial adjustment of DNI (MRM1) during one year (from July 1st 2018 to June 30th 2019).

	MRM1			
Terms	Estimates	SE	tStat	pValue
'(Intercept)'	−5.98	4.06	−1.47	0.14
'x_1'	1.27	0.50	2.53	0.01
'x_2'	0.40	0.22	1.78	0.08
'x_5'	0.05	0.08	0.69	0.49
'x_6'	0.21	0.09	2.41	0.02
'x_9'	3.88	1.53	2.53	0.01
'$x_1 \bullet x_6$'	−0.02	6.16×10^{-3}	−2.97	3.16×10^{-3}
'$x_2 \bullet x_5$'	−0.01	0.01	−1.13	0.26
'$x_6 \bullet x_9$'	−0.11	0.03	−3.63	3.29×10^{-4}
'x_1^2'	0.05	0.02	2.46	0.01
'x_5^2'	-2.21×10^{-3}	2.88×10^{-3}	−0.77	0.44
'x_6^2'	-9.48×10^{-4}	4.81×10^{-4}	−1.97	0.05

Table A3
Hourly multivariate regression metrics obtained through the use of the stepwise function considering a second-degree polynomial adjustment of DNI that uses the previous measured irradiance (MRM2) values during one year (from July 1st 2018 to June 30th 2019).

	MRM2			
Terms	Estimates	SE	tStat	pValue
'(Intercept)'	-2.18×10^{4}	7.11×10^{3}	−3.06	2.21×10^{-3}
'x_1'	7.48	1.74	4.30	1.74×10^{-5}
'x_2'	−4.45	2.12	−2.10	0.04
'x_3'	0.39	0.18	2.21	0.03
'x_4'	33.55	10.60	3.16	1.57×10^{-3}
'x_5'	−10.92	2.74	−3.98	6.96×10^{-5}
'x_6'	−18.20	9.64	−1.89	0.06
'x_7'	103.16	72.98	1.41	0.16
'x_9'	−257.21	647.21	−0.40	0.69
'x_{10}'	−2.82	1.00	−2.81	4.96×10^{-3}
'x_{11}'	0.46	1.77	0.26	0.80
'$x_1 \bullet x_2$'	1.20×10^{-3}	3.48×10^{-4}	3.46	5.53×10^{-4}
'$x_1 \bullet x_3$'	-1.02×10^{-3}	2.56×10^{-4}	−3.97	7.25×10^{-5}
'$x_1 \bullet x_4$'	-4.25×10^{-3}	1.24×10^{-3}	−3.43	6.07×10^{-4}
'$x_1 \bullet x_5$'	−0.03	5.73×10^{-3}	−6.04	1.70×10^{-9}
'$x_1 \bullet x_6$'	-3.49×10^{-3}	1.81×10^{-3}	−1.93	0.05
'$x_1 \bullet x_9$'	−0.43	0.11	−3.95	7.90×10^{-5}
'$x_1 \bullet x_{10}$'	7.82×10^{-4}	1.58×10^{-4}	4.96	7.44×10^{-7}
'$x_1 \bullet x_{11}$'	-7.67×10^{-4}	3.00×10^{-4}	−2.55	0.01
'$x_2 \bullet x3'$	-5.72×10^{-4}	2.38×10^{-4}	−2.41	0.02
'$x_2 \bullet x_4$'	2.84×10^{-3}	1.47×10^{-3}	1.94	0.05
'$x_2 \bullet x_5$'	0.02	9.13×10^{-3}	2.53	0.01
'$x_2 \bullet x_6$'	1.26×10^{-3}	2.49×10^{-3}	0.50	0.61
'$x_2 \bullet x_9$'	0.66	0.22	2.98	2.93×10^{-3}
'$x_2 \bullet x_{10}$'	-1.57×10^{-3}	2.99×10^{-4}	−5.27	1.47×10^{-7}
'$x_2 \bullet x_{11}$'	1.34×10^{-3}	4.32×10^{-4}	3.10	1.96×10^{-3}
'$x_3 \bullet x_5$'	5.03×10^{-3}	4.73×10^{-3}	1.06	0.29
'$x_3 \bullet x_9$'	−0.30	0.15	−1.99	0.05
'$x_3 \bullet x_{10}$'	8.13×10^{-4}	1.70×10^{-4}	4.78	1.85×10^{-6}
'$x_3 \bullet x_{11}$'	5.20×10^{-4}	2.24×10^{-4}	2.33	0.02
'$x_4 \bullet x_6$'	0.01	6.87×10^{-3}	1.80	0.07
'$x_4 \bullet x_7$'	−0.07	0.05	−1.26	0.21
'$x_4 \bullet x_9$'	0.15	0.48	0.31	0.75
'$x_4 \bullet x_{10}$'	1.70×10^{-3}	6.91×10^{-4}	2.45	0.01
'$x_4 \bullet x_{11}$'	-3.11×10^{-4}	1.23×10^{-3}	−0.25	0.80
'$x_5 \bullet x_6$'	0.04	0.03	1.51	0.13
'$x_5 \bullet x_9$'	2.97	1.79	1.66	0.10
'$x_5 \bullet x_{10}$'	0.03	3.88×10^{-3}	7.06	1.96×10^{-12}
'$x_5 \bullet x_{11}$'	−0.01	6.50×10^{-3}	−1.97	0.05
'$x_6 \bullet x_{10}$'	4.06×10^{-3}	1.34×10^{-3}	3.03	2.44×10^{-3}
'$x_6 \bullet x_{11}$'	-1.97×10^{-3}	2.24×10^{-3}	−0.88	0.38
'$x_7 \bullet x_{10}$'	-6.48×10^{-3}	4.54×10^{-3}	−1.43	0.15
'$x_9 \bullet x_{10}$'	0.35	0.06	5.71	1.24×10^{-8}
'$x_9 \bullet x_{11}$'	−0.27	0.11	−2.40	0.02
'$x_{10} \bullet x_1$'	2.31×10^{-4}	1.30×10^{-4}	1.78	0.08
'x_1^2'	-2.48×10^{-4}	1.82×10^{-4}	−1.37	0.17
'x_3^2'	-1.37×10^{-4}	9.07×10^{-5}	−1.51	0.13
'x_4^2'	−0.01	3.97×10^{-3}	−3.23	1.27×10^{-3}
'x_7^2'	−0.64	0.61	−1.04	0.30
'x_9^2'	50.03	42.74	1.17	0.24
'x_{11}^2'	-6.98×10^{-4}	1.62×10^{-4}	−4.31	1.67×10^{-5}

Table A4
Daily multivariate regression metrics obtained through the use of the stepwise function considering a second-degree polynomial adjustment of DNI that uses the previous measured irradiance values (MRM2) during one year (from July 1st 2018 to June 30th 2019).

MRM2				
Terms	Estimates	SE	tStat	pValue
'(Intercept)'	−2.79	5.97	−0.47	0.64
'x_1'	0.61	1.13	0.54	0.59
'x_2'	−0.81	0.56	−1.44	0.15
'x_5'	0.31	0.15	2.07	0.04
'x_6'	0.25	0.09	2.68	7.81×10^{-3}
'x_9'	−4.84	5.57	−0.87	0.39
'x_{10}'	−0.47	0.18	−2.66	8.09×10^{-3}
'x_{11}'	1.18	0.75	1.59	0.11
'$x_1 \bullet x_2$'	0.08	0.05	1.50	0.13
'$x_1 \bullet x_5$'	−0.07	0.03	−2.62	9.24×10^{-3}
'$x_1 \bullet x_6$'	−0.03	8.80×10^{-3}	−3.14	1.82×10^{-3}
'$x_1 \bullet x_9$'	2.03	0.60	3.37	8.30×10^{-4}
'$x_1 \bullet x_{11}$'	−0.08	0.05	−1.77	0.08
'$x_2 \bullet x_5$'	0.07	0.03	2.06	0.04
'$x_5 \bullet x_9$'	−0.22	0.12	−1.83	0.07
'$x_5 \bullet x_{10}$'	0.04	9.72×10^{-3}	3.88	1.25×10^{-4}
'$x_5 \bullet x_{11}$'	−0.07	0.03	−2.48	0.01
'$x_6 \bullet x_9$'	−0.17	0.05	−3.46	6.06×10^{-4}
'$x_6 \bullet x_{11}$'	6.51×10^{-3}	5.43×10^{-3}	1.20	0.23
'$x_9 \bullet x_{11}$'	−0.74	0.31	−2.38	0.02
'x_1^2'	0.14	0.07	2.07	0.04
'x_5^2'	-3.53×10^{-3}	2.99×10^{-3}	−1.18	0.24
'x_6^2'	-9.45×10^{-4}	4.93×10^{-4}	−1.9	0.06
'x_9^2'	7.39	2.07	3.56	4.17×10^{-04}

Table A5
Contingency table for availability values of DNI (kWh/m^2/day) between observations (OBS) and IFS predictions. A range divided in four intervals defines different weather conditions during a one year period (from July 1st 2018 to June 30th 2019) in Évora (southern Portugal). The total number of measurements (Total OBS) is also presented.

IFS						
OBS		0–3	3–6	6–9	9–13	Total OBS
	0–3	47 (59.49%)	28 (35.44%)	4 (5.06%)	0	79
	3–6	2 (2.17%)	63 (68.48%)	27 (29.35%)	0	92
	6–9	0	12 (10.17%)	104 (88.14%)	2 (1.70%)	118
	9–13	0	1 (1.32%)	37 (48.68%)	38 (50.00%)	76

Table A6
Contingency table for availability values of DNI (kWh/m^2/day) between observations (OBS) and SRM predictions. A range divided in four intervals defines different weather conditions during a one year period (from July 1st 2018 to June 30th 2019) in Évora (southern Portugal). The total number of measurements (Total OBS) is also presented.

SRM						
OBS		0–3	3–6	6–9	9–13	Total OBS
	0–3	58 (73.42%)	17 (21.52%)	3 (3.80%)	1 (1.27%)	79
	3–6	10 (10.87%)	55 (59.78%)	26 (28.26%)	1 (1.09%)	92
	6–9	0	16 (13.56%)	97 (82.20%)	5 (4.24%)	118
	9–13	0	1 (1.32%)	16 (21.05%)	59 (77.63%)	76

Table A7
Contingency table for availability values of DNI (kWh/m^2/day) between observations (OBS) and MRM1 predictions. A range divided in four intervals defines different weather conditions during a one year period (from July 1st 2018 to June 30th 2019) in Évora (southern Portugal). The total number of measurements (Total OBS) is also presented.

MRM1						
OBS		0–3	3–6	6–9	9–13	Total OBS
	0–3	58 (73.42%)	19 (24.05%)	2 (2.53%)	0	79
	3–6	14 (15.22%)	57 (61.96%)	20 (21.74%)	1 (1.09%)	92
	6–9	1 (0.85%)	15 (12.71%)	98 (83.05%)	4 (3.39%)	118
	9–13	0	1 (1.32%)	18 (23.68%)	57 (75.00%)	76

Table A8
Contingency table for availability values of DNI (kWh/m^2/day) between observations (OBS) and MRM2 predictions. A range divided in four intervals defines different weather conditions during a one year period (from July 1st 2018 to June 30th 2019) in Évora (southern Portugal). The total number of measurements (Total OBS) is also presented.

MRM2						
OBS		0–3	3–6	6–9	9–13	Total OBS
	0–3	56 (70.89%)	21 (26.58%)	2 (2.53%)	0	79
	3–6	15 (16.30%)	62 (67.40%)	14 (15.22%)	1 (1.09%)	92
	6–9	1 (1.85%)	11 (9.32%)	97 (82.20%)	9 (7.63%)	118
	9–13	0	1 (1.32%)	16 (21.05%)	59 (77.63%)	76

Acknowledgements

F.M. Lopes and R. Conceição acknowledge the Portuguese Foundation for Science and Technology (FCT) PhD grant (SFRH/BD/129580/2017) and the National Research Infrastructure in Solar Energy Concentration (INIESC, ALT20-03-0145-FEDER-022113) post-doc research grant (BI_POS-DOC_INIESC_II), respectively. H.G. Silva wishes to acknowledge discussions hold with Dr. Klaus Hennecke from the German Aerospace Center (DLR) on related topics to this work that considerably inspired it. Co-funding was also provided by the European Union through the European Regional Development Fund included in the COMPETE 2020 (Operational Program Competitiveness and Internationalization) through the ICT (UID/GEO/04683/2020, POCI-01-0145-FEDER-007690), DNI-ALENTEJO (ALT20-03-0145-FEDER-000011) and ALOP (ALT20-03-0145-FEDER-000004) projects. The authors are grateful to: the Portuguese meteorological service (IPMA), particularly to Jorge Neto, for providing the necessary meteorological data; the European Centre for Medium-Range Weather Forecasts (ECMWF), for the provided forecasts; T. Fasquelle, whose collaboration in previous works that lead to this paper is highly appreciated; and P. Canhoto and E. Abreu, for the maintenance of solar radiation measurements in Évora.

Appendix A

1. Data quality-control

Although there is no definitive procedure for data processing [48], to perform a correct analysis of surface solar radiation, it is important to apply a *posteriori* proper filters to the measured data. Since the nature of the latter is site-dependent, several factors can affect the measured data, as described in Ref. [49]: geographical coordinates (latitude, longitude), astronomical factors (solar declination, daylight hours), geometric factors (solar azimuth angle), physical factors (scattering and absorption effects due to aerosol content present in the atmosphere), terrain topography, surface albedo, nearby structures (e.g. trees, buildings) and meteorological variables (e.g. clouds, air temperature, wind speed, air relative humidity, precipitation). Particularly, remote locations of difficult man-made access often show large missing periods of recorded data (from a few days to several weeks), whether due to equipment malfunction or to sudden power supply shutdowns, which can last up to several hours.

In this context, considering the study location (i.e. southern region of Portugal) and two years of continuous GHI and DNI measurements, the following filters were applied:

a. Only positive values, i.e. daylight hours, are considered.
b. Linear interpolation is performed for gaps greater than 15% of the total number of hours within each day.
c. BSRN Global Network maximum and minimum physically possible limits [50].
d. Deterministic variables, i.e. solar zenith angle, DNI and GHI at the top-of-the-atmosphere (TOA), respectively DNI^{TOA} and GHI^{TOA}, are calculated on an hourly basis, as described by Eq. 2.77 in Ref. [51], considering the geographical coordinates of EVO station and a total solar irradiance at TOA of 1361 W/m^2 [52].

Condition *a* allows to remove irradiance night values (i.e. negative values) from the analysis. In condition *b*, linear interpolation of GHI and DNI is performed for days that have ≈3.5 h (depending on the available number of daylight hours throughout the year) of missing data. In order to refine the analysis, condition *c* is used taking into consideration the physically possible limits for GHI and DNI (shortwave components), allowing to remove any irradiance value measured at surface that is higher than the respective value calculated at TOA (condition *d*). Such abnormal values can be recorded mainly due to equipment mal function.

The application of the proposed filters to the measured radiation data at EVO station resulted in the following percentage of missing data: ≈0.0011% (≈0.096 h) and ≈0.0015% (≈0.13 h) for the first and second years, respectively. Moreover, regarding the local meteorological parameters, ≈0.0076% (≈0.67 h) was found for the first year of measurements, whereas for the second only very few minutes of missing data occurred. These numbers show how well-maintained is the measuring equipment used. For consistency reasons, the same missing periods found in measurements are set equally in the IFS forecasts.

2. Relative humidity and skill score formulas

As described by Ref. [53], the following relation was used to calculate the relative humidity (Rh) considering both ECMWF predicted dew point and air temperatures (T_{dew} and T_{air}, respectively):

$$Rh = \left[6.11 \times 10^{\left(7.5 \times \frac{T_{dew}}{237.7+T_{dew}}\right)} \Big/ 6.11 \times 10^{\left(7.5 \times \frac{T_{air}}{237.7+T_{air}}\right)} \right] \times 100 \quad \text{(A1)}$$

The forecasting skill considered in the analysis made use of the skill score (SS) in regards to the mean square error obtained between measurements and forecast model (MSE_{for}) and measurements and persistence model (MSE_{per}), as described by Ref. [41]:

$$SS = 1 - MSE_{for} \Big/ MSE_{per} \quad \text{(A2)}$$

where an SS equal to one indicates a perfect forecast, negative values of SS mean that the forecast model performs worse than the persistence model, while a null result shows that the forecast model has no improvement towards the persistence model.

3. Multivariate regression tables

In the following tables (**A1**, **A2**, **A3** and **A4**) are all significant and possible relations between predictors and predictand (Terms), the weight (Estimates) that each relation has in the respective adjustment, the standard error (SE) obtained, the t-statistics (tStat), and the p-value (pValue), for both MRM1 and MRM2 hourly and daily adjustments. The following set of predictors were considered for the hourly adjustments: x_1 (DNI_i^{IFS}), x_2 (GHI_i^{IFS}), x_3 (GHI_i^{TOA}), x_4 (DNI_i^{TOA}), x_5 ($Temp_i^{IFS}$), x_6 (Rh_i^{IFS}), x_7 (W_i^{IFS}), x_8 ($Prec_i^{IFS}$), x_9 (Tcc_i^{IFS}), x_{10} (DNI_{i-1}^{OBS}) and x_{11} (GHI_{i-1}^{OBS}), with DNI_i^{OBS} as the predictand. In the case of the daily adjustments, predictors x_1, x_2, x_5, x_6 and x_9 were considered.

4. Daily contingency tables

For the evaluation of daily availability values regarding the operations of a CSP plant, contingency tables were used considering daily measured and predicted (IFS, SRM, MRM1 and MRM2) data for one year in EVO.

References

[1] P. Blanc, B. Espinar, N. Geuder, C. Gueymard, R. Meyer, R. Pitz-Paal, et al., Direct normal irradiance related definitions and applications: the circumsolar issue, Sol. Energy 110 (2014) 561–577, https://doi.org/10.1016/j.solener.2014.10.001.
[2] M. Schroedter-Homscheidt, O. Oumbe, A. Benedetti, J.-J. Morcrette, Aerosols for Concentrating Solar Electricity Production Forecasts: Requirement Quantification and ECMWF/MACC Aerosol Forecast Assessment, American Meteorological Society BAMS, 2013, pp. 903–914, https://doi.org/10.1175/BAMS-D-11-00259.1.
[3] R. Conceição, H.G. Silva, J. Mirão, M. Gostein, L. Fialho, L. Navarte, M. Collares-Pereira, Saharan dust transport to Europe and its impact on photovoltaic performance: a case study of soiling in Portugal, Sol. Energy 160 (2018) 94–102, https://doi.org/10.1016/j.solener.2017.11.059.
[4] R. Conceição, M. Melgão, H.G. Silva, K. Nicoll, R.G. Harrison, A.H. Reis, Transport of the smoke plume from Chiado's fire in Lisbon (Portugal) sensed by atmospheric electric field measurements, Air Qual.Atmosphere.Health 9 (2016) 275–283, https://doi.org/10.1007/s11869-015-0337-4.
[5] A. Callado, P. Escribà, J.A. García-Moya, J. Montero, C. Santos, D. Santos-Muñoz, J. Simarro, Ensemble forecasting, climate change and regional/local responses, in: Dr Pallav Ray (Ed.), In Tech, vol. 1, 2013, https://doi.org/10.5772/55699.
[6] S. Pereira, P. Canhoto, R. Salgado, M.J. Costa, Development of an ANN based corrective algorithm of the operational ECMWF global horizontal irradiation forecasts, Sol. Energy 185 (2019) 387–405, https://doi.org/10.1016/j.solener.2019.04.070.
[7] D. Wilks, Statistical Methods in the Atmospheric Sciences, second ed., vol. 100, 2005, ISBN 9780080456225 (Chapter 6).
[8] M. Rummukainen, Methods for Statistical Downscaling of GCM Simulations, Technical Report (80). ISSN: 0347-2116, Swedish Meteorological and Hydrological Institute, 1997. August 3rd 2020, http://www.smhi.se/polopoly_fs/1.1243221!/RMK_80.pdf. SMHI Reports Meteorology Climatology. Available from:.
[9] W.H. Klein, B.M. Lewis, I. Enger, Objective Prediction of Five-Day Mean Temperatures during Winter, vol. 16, American Meteorological Society, 1959, pp. 672–682, https://doi.org/10.1175/1520-0469(1959)016<0672:OPOFDM>2.0.CO;2.

[10] H.R. Glahn, D.A. Lowry, The use of model output statistics (MOS) in objective weather forecasting, Applied Meteorology 11 (1972) 1203–1211, https://doi.org/10.1175/1520-0450(1972)011<1203:TUOMOS>2.0.CO;2.
[11] W.Y.Y. Cheng, W.J. Steenburgh, Strengths and Weaknesses of MOS, Running-Mean Bias Removal, and Kalman Filter Techniques for Improving Model Forecasts over the Western United States, vol. 22, American Meteorological Society, 2007, pp. 1304–1318, https://doi.org/10.1175/2007WAF2006084.1.
[12] A. Troccoli, J.-J. Morcrette, Skill of direct solar radiation predicted by the ECMWF global atmospheric model over Australia, in: Applied Meteorology and Climatology, American Meteorological Society, 2014, pp. 2571–2587, https://doi.org/10.1175/JAMC-D-14-0074.1.
[13] A. Pérez-Burgos, J. Bilbao, A. de Miguel, R. Román, Analysis of solar direct irradiance in Spain, Energy Procedia (2014) 1070–1076, https://doi.org/10.1016/j.egypro.2014.10.070.
[14] T.N. Krishnamurti, C.M. Kishtawal, T.E. LaRow, D.R. Bachiochi, Z. Zhang, C.E. Williford, S. Gadgil, S. Surendran, Improved weather and seasonal climate forecast from multimodel superensemble, Science 285 (1999) 1548–1550, https://doi.org/10.1126/science.285.5433.1548.
[15] P.L. Houtekamer, H.L. Mitchell, Data Assimilation Using an Ensemble Kalman Filter Technique, vol. 126, American Meteorological Society, 1998, pp. 796–811, https://doi.org/10.1175/1520-0493(1998)126<0796:DAUAEK>2.0.CO;2.
[16] J.W. Lin, J.D. Neelin, Towards stochastic deep convective parameterization in general circulation models, Geophys. Res. Lett. 30 (N4) (2003) 1162, https://doi.org/10.1029/2002GL016203.
[17] J.M. Murphy, D.M.H. Sexton, D.N. Barnett, G.S. Jones, M.J. Webb, M. Collins, D.A. Stainforth, Quantification of modelling uncertainties in a large ensemble of climate change simulations, Nature 430 (7001) (2004) 768–772, https://doi.org/10.1038/nature02771.
[18] J. Berner, G.J. Shutts, M. Leutbecher, T.N. Palmer, A Spectral Stochastic Kinetic Energy Backscatter Scheme and its Impact on Flow-dependent Predictability in the ECMWF Ensemble Prediction System, vol. 66, American Meteorology Society, 2009, pp. 603–625, https://doi.org/10.1175/2008JAS2677.1.
[19] W.I. Hameed, B.A. Sawadi, S.J. Al-Kamil, M.S. Al-Radhi, Y.I.A. Al-Yasir, A.L. Saleh, R.A. Abd-Alhameed, Prediction of solar irradiance based on artificial neural networks, Inventions MDPI 4 (2019) 45, https://doi.org/10.3390/inventions4030045.
[20] G. Reikard, C. Hansen, Forecasting solar irradiance at short horizons: frequency and time domain models, Renew. Energy 135 (2019) 1270–1290, https://doi.org/10.1016/j.renene.2018.08.081.
[21] G. Reikard, S.E. Haupt, T. Jensen, Forecasting ground-level irradiance over short horizons: time series, meteorological, and time-varying parameter models, Renew. Energy 112 (2017) 474–485, https://doi.org/10.1016/j.renene.2017.05.019.
[22] D. Yang, Ensemble model output statistics as a probabilistic site-adaptation tool for satellite-derived and reanalysis solar irradiance, Renew. Sustain. Energy 12 (1) (2020), https://doi.org/10.1063/1.5134731, 016102.
[23] E. Díez, C. Primo, J.A. García-Moya, J.M. Gutiérrez, B. Orfila, Statistical and dynamical downscaling of precipitation over Spain from DEMETER seasonal forecasts, Tellus 57A 3 (2005) 409–423, https://doi.org/10.3402/tellusa.v57i3.14698.
[24] P.G. Kosmopoulos, S. Kazadzis, M. Taylor, E. Athanasopoulou, O. Speyer, P.I. Raptis, et al., Dust impact on surface solar irradiance assessed with model simulations, satellite observations and ground-based measurements, Atmos.-Meas. Tech. 10 (2017) 2435–2453, https://doi.org/10.5194/amt-2017-79.
[25] G. Myhre, D. Shindell, F.-M. Bréon, W. Collins, J. Fuglestvedt, J. Huang, et al., Anthropogenic and natural radiative forcing. Climate Change, in: Midgley (Ed.), The Physical Science Basis. Contribution of Working Group I to the Fifth Assessment Report of the Intergovernmental Panel on Climate Change, Cambridge University Press, 2013, pp. 659–740, https://doi.org/10.1017/CBO9781107415324.018.
[26] S.E. Haupt, P.A. Jiménez, J.A. Jared, B. Kosovic, Principles of meteorology and numerical weather prediction, in: Georges Kariniotakis (Ed.), Renewable Energy Forecasting: from Models to Applications vol. 1, 2017, pp. 3–28, https://doi.org/10.1016/B978-0-08-100504-0.00001-9.
[27] R. Salgado, P.M.A. Miranda, P. Lacarrére, J. Noilhan, Boundary layer development and summer circulation in Southern Portugal, Tethys 12 (2015) 33–34, https://doi.org/10.3369/tethys.2015.12.03.
[28] F.M. Lopes, H.G. Silva, R. Salgado, A. Cavaco, P. Canhoto, M. Collares-Pereira, Short-term forecasts of GHI and DNI for solar energy systems operation: assessment of the ECMWF integrated forecasting system in southern Portugal, Sol. Energy 170 (2018) 14–30, https://doi.org/10.1016/j.solener.2018.05.039.
[29] ISO 9060:1990, Solar Energy – Specification and Classifications of Instruments for Measuring Hemispherical Solar and Direct Solar Radiation, International Organization for Standardization, 2003. Available online from: www.iso.org/standard/16629.html. (Accessed 3 August 2020).
[30] ISO 9059:1990, Solar Energy – Calibration of Field Pyrheliometers by Comparison to a Reference Pyrheliometer, International Organization for Standardization, 2014. Available online from: www.iso.org/standard/16628.html. (Accessed 3 August 2020).
[31] R. Conceição, A.A. Merrouni, D. Lopes, A. Alae, H.G. Silva, E.G. Bennouna, et al., A comparative study of soiling on solar mirrors in Portugal and Morocco: preliminary results for the dry season, AIP Conference Proceedings 2126 (2019) 220001, https://doi.org/10.1063/1.5117760.
[32] T. Haiden, M. Janousek, F. Vitart, L. Ferranti, F. Prates, Evaluation of ECMWF forecasts, including the 2019 resolution upgrade, in: European Centre for Medium-Range Weather Forecasts, Technical Memorandum, vol. 853, 2019, https://doi.org/10.21957/mlvapkke10.21957/vltarm3ql.
[33] R.J. Hogan, A. Bozzo, A flexible and efficient radiation scheme for the ECMWF model, Adv. Model. Earth Syst. 10 (2018) 1990–2008, https://doi.org/10.1029/2018MS001364.
[34] A. Bozzo, S. Remy, A. Benedetti, J. Flemming, P. Bechtold, M.J. Rodwell, J.-J. Morcrette, Implementation of a CAMS-based aerosol climatology in the IFS, in: European Centre for Medium-Range Weather Forecasts, Technical Memorandum, vol. 801, 2017. Available from: https://www.ecmwf.int/sites/default/files/elibrary/2017/17219-implementation-cams-based-aerosol-climatology-ifs.pdf. (Accessed 3 August 2020).
[35] I. Tegen, P. Hollrig, M. Chin, I. Fung, D. Jacob, J. Penner, Contribution of different aerosol species to the global aerosol extinction optical thickness: estimates from model results, Geophysical Research, Atmospheres 102 (23) (1997) 895–915, https://doi.org/10.1029/97JD01864.
[36] N. Blair, A. Dobos, J. Freeman, T. Neises, M. Wagner, T. Ferguson, et al., System Advisor Model, SAM 2014.1.14: General Description, National Renewable Energy Laboratory, Golden, CO, 2014. NREL/TP-6A20-61019.
[37] F.M. Lopes, R. Conceição, H.G. Silva, T. Fasquelle, R. Salgado, P. Canhoto, M. Collares-Pereira, Predicted direct solar radiation (ECMWF) for optimized operational strategies of linear focus parabolic-trough systems, Renew. Energy 151 (2019) 378–391, https://doi.org/10.1016/j.renene.2019.11.020.
[38] C. Coimbra, J. Kleissl, R. Marquez, Overview of solar forecasting methods and a metric for accuracy evaluation, in: Solar Resource Assessment and Forecasting, vol. 8, Elsevier, Waltham, Massachusetts, 2013, ISBN 9780123971777, pp. 183–185.
[39] M. Wittmann, H. Breitkreuz, M. Schroedter-Homscheidt, M. Eck, Case studies on the use of solar irradiance forecast for optimized operation strategies of solar thermal power plants, IEEE.Sel. Top. Appl. Earth.Obs. Remote Sens. 1 (2008) 18–27, https://doi.org/10.1109/jstars.2008.2001152.
[40] M. Schroedter-Homscheidt, A. Benedetti, N. Killius, Verification of ECMWF and ECMWF/MACC's global and direct irradiance forecasts with respect to solar electricity production forecasts, Meteorologische Zeitschrift 26 (2016) 1–19, https://doi.org/10.1127/metz/2016/0676. PrePub Article.
[41] R. Perez, E. Lorenz, S. Pelland, M. Beauharnois, G.V. Knowe, K. Hemker Jr., et al., Comparison of numerical weather prediction solar irradiance forecasts in the US, Canada and Europe, Sol. Energy 94 (2013) 305–326, https://doi.org/10.1016/j.solener.2013.05.005.
[42] T.R. Ayodele, A.S.O. Ogunjuyigbe, Prediction of monthly average global solar radiation based on statistical distribution of clearness index, Energy 90 (2015) 1733–1742, https://doi.org/10.1016/j.energy.2015.06.137.
[43] I.T. Jolliffe, D.B. Stephenson, Forecast Verification: A Practitioner's Guide in Atmospheric Science, 5.4.4, Wiley, New York, 2003, ISBN 9780470660713, pp. 106–110.
[44] F.M. Lopes, R. Conceição, H.G. Silva, R. Salgado, P. Canhoto, M. Collares-Pereira, Predictive value of short-term forecasts of DNI for solar energy systems operation, AIP Conference Proceedings 2126 (2019) 190010, https://doi.org/10.1063/1.5117707.
[45] F.M. Lopes, R. Conceição, H.G. Silva, T. Fasquelle, R. Salgado, P. Canhoto, M. Collares-Pereira, Short-term forecasts of DNI from an integrated forecasting system (ECMWF) for optimized operational strategies of a central receiver system, Energies 12 (2019) 1368, https://doi.org/10.3390/en12071368.
[46] B.F. Towler, The Future of Energy, first ed., vol. 8, Academic Press, 2014, ISBN 9780128010273, pp. 183–184.
[47] N. Bijan, S. Wilbert, N. Blum, P. Kuhn, T. Schmidt, Z. Yasser, et al., Evaluation of an all sky imager based nowcasting system for distinct conditions and five sites, AIP Conference Proceedings (2020) (accepted for publication).
[48] C.A. Gueymard, J.A. Ruiz-Arias, Extensive worldwide validation and climate sensitivity analysis of direct irradiance predictions from 1-min global irradiance, Sol. Energy 128 (2016) 1–30, https://doi.org/10.1016/j.solener.2015.10.010, 2016.
[49] A.J. Gutiérrez-Trashorras, E. Villicaña-Ortiz, E. Álvarez-Álvarez, J.M. González-Caballín, J. Xiberta-Bernat, M.J. Suarez-López, Attenuation processes of solar radiation. Application to the quantification of direct and diffuse solar irradiances on horizontal surfaces in Mexico by means of an overall atmospheric transmittance, Renew. Sustain. Energy Rev. 81 (2018) 93–106, https://doi.org/10.1016/j.rser.2017.07.042.
[50] C.N. Long, E.G. Dutton, BSRN global network recommended QC tests, V2.0, Available online: https://bsrn.awi.de/fileadmin/user_upload/bsrn.awi.de/Publications/BSRN_recommended_QC_tests_V2.pdf. August 3rd 2020, , 2002.
[51] S.A. Kalogirou, Solar Energy Engineering: Processes and Systems, second ed., vol. 2, Elsevier, 2014, ISBN 978-0123972705, pp. 51–63.
[52] S.K. Solanki, N.A. Krivova, J.D. Haigh, Solar irradiance variability and climate, Annu. Rev. Astron. Astrophys. 51 (2013) 311–351, https://doi.org/10.1146/annurev-astro-082812-141007.
[53] M.G. Lawrence, The relationship between relative humidity and the dewpoint temperature in moist air, in: A Simple Conversion and Applications, American Meteorological Society, 2005, https://doi.org/10.1175/BAMS-86-2-225.
[54] T. Fasquelle, Q. Falcoz, P. Neveu, F. Lecat, G. Flamant, A termal model to predict the dynamic performances of parabolic trough lines, Energy 141 (2017) 1187–1203, https://doi.org/10.1016/j.energy.2017.09.063.

water

MDPI

Article

Water-Sediment Physicochemical Dynamics in a Large Reservoir in the Mediterranean Region under Multiple Stressors

Patrícia Palma [1,2,*], Alexandra Marchã Penha [2,3], Maria Helena Novais [2,4], Sofia Fialho [1], Ana Lima [1], Clarisse Mourinha [1], Paula Alvarenga [5], Anabela Rosado [3], Maksim Iakunin [2], Gonçalo Rodrigues [2,6], Miguel Potes [2,6], Maria João Costa [2,6,7], Manuela Morais [2,3,8] and Rui Salgado [2,6,7]

1 Department of Technologies and Applied Sciences, Polytechnic Institute of Beja, 7801-295 Beja, Portugal; sofiafialho16@gmail.com (S.F.); ana.filipa.lima89@gmail.com (A.L.); clarisse.mourinha@ipbeja.pt (C.M.)
2 ICT, Institute of Earth Sciences, University of Évora, Rua Romão Ramalho 59, 7000-671 Évora, Portugal; mapenha@uevora.pt (A.M.P.); hnovais@uevora.pt (M.H.N.); miakunin@uevora.pt (M.I.); grodrigues@uevora.pt (G.R.); mpotes@uevora.pt (M.P.); mjcosta@uevora.pt (M.J.C.); mmorais@uevora.pt (M.M.); rsal@uevora.pt (R.S.)
3 Water Laboratory, University of Évora, P.I.T.E. Rua da Barba Rala No. 1, 7005-345 Évora, Portugal; arosado@uevora.pt
4 Renewable Energies Chair, University of Évora, Herdade da Mitra–Valverde, 7000-083 Évora, Portugal
5 Linking Landscape, Environment, Agriculture, and Food Research Unit (LEAF), Instituto Superior de Agronomia, Universidade de Lisboa, Tapada da Ajuda, 1349-017 Lisboa, Portugal; palvarenga@isa.ulisboa.pt
6 Earth Remote Sensing Laboratory-EaRSLab, Science and Technology School, University of Évora, 7000-671 Évora, Portugal
7 Department of Physics, Science and Technology School, University of Évora, 7000-671 Évora, Portugal
8 Department of Biology, Science and Technology School, University of Évora, 7000-671 Évora, Portugal
* Correspondence: ppalma@ipbeja.pt; Tel.: +351-284314300

Abstract: Nowadays, the Mediterranean freshwater systems face the threat of water scarcity, along with multiple other stressors (e.g., organic and inorganic contamination, geomorphological alterations, invasive species), leading to the impairment of their ecosystem services. All these stressors have been speeding up, due to climate variability and land cover/land use changes, turning them into a big challenge for the water management plans. The present study analyses the physicochemical and phytoplankton biomass (chlorophyll-a) dynamics of a large reservoir, in the Mediterranean region (Alqueva reservoir, Southern Portugal), under diverse meteorological conditions and land cover/land use real scenarios (2017 and 2018). The most important stressors were identified and the necessary tools and information for a more effective management plan were provided. Changes in these parameters were further related to the observed variations in the meteorological conditions and in the land cover/land use. The increase in nutrients and ions in the water column, and of potentially toxic metals in the sediment, were more obvious in periods of severe drought. Further, the enhancement of nutrients concentrations, potentially caused by the intensification of agricultural activities, may indicate an increased risk of water eutrophication. The results highlight that a holistic approach is essential for a better water resources management strategy.

Keywords: Alqueva reservoir; climate variability; land cover/land uses; water-sediment dynamics

check for updates

Citation: Palma, P.; Penha, A.M.; Novais, M.H.; Fialho, S.; Lima, A.; Mourinha, C.; Alvarenga, P.; Rosado, A.; Iakunin, M.; Rodrigues, G.; et al. Water-Sediment Physicochemical Dynamics in a Large Reservoir in the Mediterranean Region under Multiple Stressors. *Water* **2021**, *13*, 707. https://doi.org/10.3390/w13050707

Academic Editor: Giovanni Libralato

Received: 23 December 2020
Accepted: 25 February 2021
Published: 5 March 2021

Publisher's Note: MDPI stays neutral with regard to jurisdictional claims in published maps and institutional affiliations.

Copyright: © 2021 by the authors. Licensee MDPI, Basel, Switzerland. This article is an open access article distributed under the terms and conditions of the Creative Commons Attribution (CC BY) license (https://creativecommons.org/licenses/by/4.0/).

1. Introduction

Currently, water scarcity and its quality are the main challenges concerning water resources [1]. In addition to being a stressor on its own, water scarcity can drive the actions of other stressors, the increment of chemical and ecological effects of water degradation and water abstraction. In fact, freshwater systems are constantly affected by multiple stressors, including urban and agricultural activities, growing population, hydropower

generation, and climate change. Understanding how stressors interfere in chemical and ecological status and in freshwater ecosystem services at a regional scale is essential for developing specific water management plans and shaping future environmental policies [2,3]. Currently, in Europe, the relevance of multiple stressors differs regionally [4]: in the north, the higher pressures are related to hydropower plants; in central Europe, the intensive agriculture and floods are the most important drivers of the hydromorphological pressures, whilst in the Mediterranean, the catchments are impaired mainly by water scarcity and intensive agriculture. Crosswise to all these pressures, the climate is changing globally, increasing the risk of floods and pollution in wet regions and droughts in water-scarce regions [5,6]. Current climate change models' projections indicate that the Mediterranean region will face a decrease in precipitation and an increase in temperatures, particularly in summer, leading to more severe extreme events, and promoting the decrease in the availability and quality of the water resources [6,7]. The Mediterranean is amongst the most vulnerable regions to climatic and anthropogenic changes and thus one of the world's water crisis hotspots [7]. Adding to these facts, the predictions for water demands indicate a global increase of about 20 to 30% by 2050 [8], inducing higher stress in arid and semi-arid regions already affected by water scarcity [5–7]. In Portugal, and despite being generally considered a low water stressor country, the southern region frequently suffers from water supply problems during summer [9]. In fact, the Alentejo region is already under hydrological stress with deficient water availability and is prone to meteorological extreme events, such as the severe droughts that occurred in 2003–2005, 2011–2012 and 2016–2017 [10]. The meteorological conditions impact the water quantity and quality, and may also lead to changes in Land use/ Land cover (LULC), such as the growth of irrigation crops and associated changes in management operations of reservoirs and water treatment plants.

In the south of Portugal, 10 to 30% of the freshwater systems are reservoirs, heavily modified water bodies (HMWB) [11], planned for water storage and mainly used for irrigation and water supply [12], with the largest one being the Alqueva Reservoir. These reservoirs are similar to natural lakes in some aspects, such as water storage and low flow [13]. Nevertheless, they differ in annual and inter-annual storage variability, management options and catchment areas, features that induce much larger fluctuations in the water level than in natural lakes [14]. For those reasons, they respond differently to climate change and to other stressors [15]. Several climate change scenarios foresee a decrease in water quality in reservoirs, mainly in semi-arid regions, due to the increase in pollutants concentration and sediments as a result of lower water levels [10,16]. This fact may be more evident in reservoirs located in intensive areas of agriculture and tourism, increasing abstraction and decreasing the ecological and chemical status. In this global change scenario, the sustainable management of reservoirs may be an important key issue, ensuring the water's quantity and quality, as well as the ecosystem's balance and services. To develop sustainable management strategies for a better balance between water abstraction and conservation, improving the ecological/ chemical status of reservoirs, it is essential to understand its dynamics and the main stressors of each system component. Although the impacts of multiple stressors on rivers and streams have been relatively well explored in the Mediterranean region [17–20], the specific consequences for reservoirs need further investigation. Most studies on reservoirs use modeling tools for the assessment of climate change impacts of on water quantity, in combination with socio-economic conditions, as well as changes in soils and water uses [15,16,21–23]. Few studies have linked the water-sediment dynamics with the ecosystem status in real conditions of climate change [24,25]. Studies developed in the Alqueva reservoir showed a nutrients increase and the presence of hazardous substances in water and sediments [26–28]. To help decision making about sustainable and specific management plans, considering the actual climate change scenario and intensive land use, it is important to link these results with those of the present study about the dynamics of the reservoir in different climate real conditions under several stressors.

Bearing in mind the above statements, the main aims of the present study were: (i) to assess the physicochemical and phytoplankton biomass dynamics in the water column and sediments of Alqueva reservoir, under diverse meteorological conditions and real land use scenarios; (ii) to correlate the changes of the analyzed parameters with variations in the meteorological conditions and in the land cover/land use; (iii) to identify the most important stressors, to improve the ecological and chemical status of the reservoir and its ecosystem services; (iv) to integrate the results obtained since 2006 in the Alqueva reservoir for a better understanding of the water body; (iv) to provide necessary tools and information to be used in a better and more specific management plan of the reservoir, which may be included in the upcoming River Basin Management Plans.

2. Materials and Methods

2.1. Study Area and Sampling Sites Characterization

The Alqueva reservoir is the largest artificial lake in Western Europe, with a surface area of 250 km^2, 85 km long, 4150 hm^3 maximum storage capacity with 3150 hm^3 useful capacity, and a catchment area of 55,000 km^2. Water stored in Alqueva reservoir allows multipurpose usages such as (i) public water supply, with the reinforcement of 5 dams that supply about 200,000 inhabitants; (ii) agriculture, with an irrigated area of about 120,000 ha and which will increase to 170,000 ha in the coming years; (iii) industry; (iv) clean energy production (520 MW); and (v) tourism [29]. It is located in the Guadiana basin in Alentejo, a semi-arid region in the south of Portugal, bordered by Spain in the east (see Figure 1). The Alqueva primary inflow is the river Guadiana, which flows north to south through the Portuguese territory. Guadiana flow has strong seasonal variations, typical wet season flows are of the order of 100 m^3/s, whereas dry season flows drop to values below 20 m^3/s. Smaller water input contributions come from other tributaries: Degebe, Álamo, Azevel, Lucefécit, and Asseca streams, along the reservoir west margin and the Zebro and Alcarrache streams, along the east margin [30]. The Guadiana catchment has a population of 1.9 million inhabitants, with a density of 28 inhabitants/km^2 in Spain and 114 inhabitants/km^2 in Portugal (https://ec.europa.eu/eurostat/home (accessed on 23 December 2020)).

The most representative types of soils are lithosols, litholic soils, Mediterranean brown soils, and podzols, primarily derived from shale, clay, and limestone [31]. Generally, the land was mainly used for olive trees growing, agroforestry of holm oaks ('*montado*'), and annual rainfed crops (wheat, oats, and sunflowers). Extensive livestock production is the most important animal-farming activity in the catchment [32].

Four sampling sites were selected in the Alqueva reservoir: Álamos (Al; 38°33′84.46″ N, 7°57′34.41″ W), Mourão (Mr; 38°39′36.33″ N, 7°38′75.51″ W), Montante (Mn; 38°22′35.42″ N, 7°45′94.95″ W) and Lucefécit (Lf; 38°55′52.83″ N, 7°29′91.37″ W). These sampling points, with lentic conditions, have fixed platforms installed by the Portuguese Environmental Agency (APA) to monitor the water quality of the reservoir. Montante and Mourão platforms are located in clear cut surroundings and deep areas of the reservoir, with 60 m and 50 m depth, respectively; whilst Álamos and Lucefécit platforms are located in a forested surrounding and a ca. 20 m deep area [33].

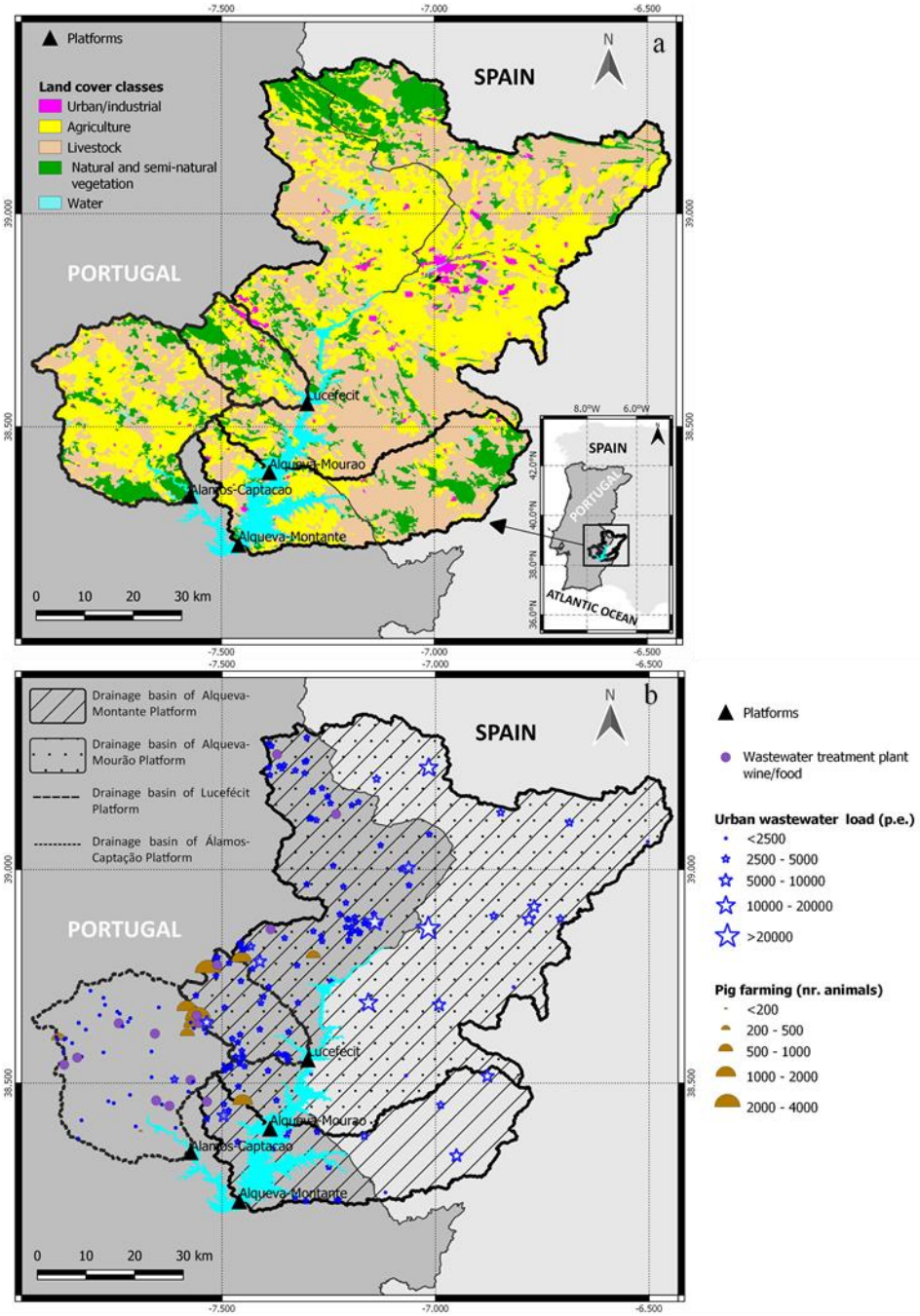

Figure 1. (**a**) Map of the study area located in Alentejo region. The black triangles indicate the platforms, from North to South: Lucefécit; Mourão; Álamos and Montante and the land cover classes are represented by the colors indicated in the legend. Bottom-right inset shows the study area location in the map of Portugal. (**b**) Map showing the location of the industrial wastewater treatment plants (wine and food related), the urban wastewater loads and the number of animals in pig farms distributed in the four drainage basins indicated in the legend.

2.2. Climatological and Land Use/Land Cover (LULC) Characterization

2.2.1. Climate Conditions

In general, the climate in the region is dry sub-humid to semi-arid, with Mediterranean characteristics (Csa in Köppen's classification), with hot summers, high level of insolation and evapotranspiration, and mild winters. The average annual temperature is about 16 °C, ranging from 9 °C to 23 °C. In the coldest month, January, the mean daily minimum temperature is lower than 6 °C, with frequent negative values, especially in the valleys.

In summer (July and August) the mean daily maximum temperature is above 30 °C, being frequent values close to 40 °C or higher. The precipitation regime is characterized by highly spatial and temporal irregular behavior, varying between abundant rainfall episodes (concentrated in only a few minutes or hours), and drought periods, that can last a few months. In the last Climatological normal, the average annual rainfall is less than 600 mm. The annual distribution of precipitation is extremely irregular, being less than 300 mm in dry years and rising to more than 900 mm in wet years [34]. Summer rainfall is very low and about 80% of annual precipitation occurs during the three winter months (December to February).

For the meteorological characterization of the study period (2017–2018), a weather station installed in the left margin of the reservoir, near the Montante platform, was used. This weather station measures and records the several meteorological variables, namely Air Temperature (Tair), Relative Humidity (RH), Precipitation (Prec), Wind Speed (Wins), and Shortwave Solar Radiation (Rad) [35].

2.2.2. Land Use/Land Cover (LULC) Patterns

Shuttle Radar Topography Mission (SRTM) elevation data at a resolution of 1 arc-second (30 m) were used to estimate the drainage basin areas associated with each platform (represented by the different black lines in Figure 1). The drainage basins of the platforms represent the appropriate areas to analyze and relate land cover to changes in the water column and sediments of the Alqueva reservoir since they collect and drain off the surface and groundwater, as well as precipitation into the control points. To note that Montante drainage basin encompasses Mourão and Lucefécit basins, Mourão includes the Lucefécit basin, and Álamos drainage basin does not overlap any of the other three basins.

Land Use/Land Cover (LULC) was obtained from the analysis of the 2018 CORINE Land Cover (CLC) inventory, retrieved from satellite imagery (Sentinel-2 and Landsat-8 for gap filling), available from Copernicus Land Monitoring Service (https://land.copernicus.eu/ (accessed on 23 December 2020)). Five main categories describing typical LULC types in the region were considered: urban/industrial (Urb/Ind); agriculture and pasture (Agr); livestock (Liv); natural and semi-natural vegetation (Nat); water (Wat). Figure 1 also shows the distribution of land cover types, with agriculture and livestock as the main activities around the Alqueva reservoir, followed by natural and semi-natural vegetation (including Montado landscape) more often found in the south-eastern regions. The pollution point sources information represented in Figure 1, such as the wastewater treatment plants (urban and industrial), and the pig farming, were courteously provided by the Administration of the Hydrographic Region of Alentejo (ARH Alentejo).

2.3. Sampling

Water and sediment samples were collected at the four selected platforms represented in Figure 1, Álamos (Al); Mourão (Mr), Montante (Mn); Lucefécit (Lf). The study comprised 12 sampling campaigns, from January 2017 to November 2018: in January (Jn), March (Mr), May (M), July (Jl), September (Sp), and November (Nv).

The wet period included the months of January, March, and November, and the dry period included the months of May, July, and September, as defined by the Portuguese Environmental Agency for the Alentejo region. This seasonal evaluation is justified by the importance of the variability of the tributaries' hydrologic regimes for the reservoir water quality, particularly in these semi-arid areas of Portugal, where the river discharges may range from zero in the dry period to high discharge rates during the wet period. These changes affect all the physical, chemical, and biologic parameters of the reservoir [32].

At each platform were collected: (i) surface water: 2 L for chlorophyll quantification and 2 L for chemical parameters analysis using a Van Dorn bottle; and (ii) 5 L of surface sediments (<10 cm), which were gathered using a stainless steel Van Veen grab of 0.05 m^2 with a maximum volume of 8 L. The water samples were stored in polyethylene bottles, and kept in the dark, and the sediment samples were packed in polyethylene bags. All samples

were transported in a cooler at 4 °C to the laboratory, where they were conserved and stored following the requisites for water and sediments conservation for each parameter until the analyses were performed (maximum storage time: 1 week) [36,37].

In situ, vertical profiles of water temperature (T; °C), pH, electrical conductivity (EC; µS/cm) and dissolved oxygen (DO; mg/L), were measured using a multiparametric probe YSI 6820 MPS probe®. The transparency (Secchi depth (SD); m) was measured with a Secchi disk and used as an indicator of the suspended particles and solutes presence, allowing the determination of the euphotic zone (EuphZ; 2.5 × SD).

In a reservoir, the water level is constantly changing, and thus the surface elevation, the water volume, and the surface area present constant fluctuations. These parameters were monitored in every campaign and considered for this study: surface elevation, surface fluctuation, volume, and surface area (Table S1).

2.4. Physical, Chemical and Phytoplankton Biomass Characterization

2.4.1. Water Parameters

The water chemical parameters analyzed were: biochemical oxygen demand (BOD_5; mg/L; Respirometric method), total phosphorus (TP; mg/L; Molecular absorption spectrometry), Kjeldahl nitrogen (KN; mg/L; Kjeldahl method), nitrate (NO_3; mg/L; Ionic chromatography), nitrite (NO_2; mg/L; Ionic chromatography), ammonium (NH_4; mg/L; Molecular absorption spectrometry), chlorides (Cl; mg/L; Ionic chromatography), sulphates (SO_4; mg/L; Ionic chromatography), calcium (Ca; mg/L; Ionic chromatography) and sodium (Na; mg/L; Ionic chromatography) [36].

Total nitrogen (TN was determined, using the following equation [36]):

$$TN\ (mg/L) = 0.226 \times [NO_3; mg/L] + 0.304 \times [NO_2; mg/L] + [KN; mg/L] \quad (1)$$

In general, chlorophyll-a (Chl-a) can be used to reflect the phytoplankton biomass and the trophic state of a reservoir, thus playing a key role in the eutrophication evaluation [38]. The determination of Chl-a was performed based on the Portuguese standard NP 4327 [39] and Standard Methods 10,200 H [36]. The pigment was extracted with 90% acetone after sample filtration in a glass fiber filter (GF/C Whatman).

2.4.2. Sediment Parameters

The sediments' pH ($pH_{pore\text{-}water}$) and the electrical conductivity ($EC_{pore\text{-}water}$; µS/cm) were analyzed in pore-water samples [37].

Sediment grain-size distribution was determined following the Portuguese Laboratory of Civil Engineering E196 method [40]. The chemical parameters determined were: organic matter content (OM; %; calcination at 500 °C; [37]); total nitrogen (TN; %; Kjeldahl method; [36]); total phosphorus (TP; %; molecular absorption spectrometry with molybdo-vanadate phosphoric acid; [36]).

2.5. Statistical Treatment of Data

The study assessed a total of 37 variables displayed by the following categories: (i) water and sediments physicochemical and biological parameters: (a) water: T_w; pH_w; EC_w; DO; BOD_5; TP; KN; TN; NO_2; NO_3; SO_4; NH_4; Cl; Na; Ca; Chl-a; (b) sediments: Sand; Silt; Clay; $pH_{pore\text{-}water}$; $EC_{pore\text{-}water}$; OM; TP_s; TN_s; (ii) drainage basin characteristics (LULC): Urb; Agr; Liv; Nat; Wat; (iii) climate conditions: T_{air}; RH; WinS; Prec; Rad; (iv) reservoir characteristics: EuphZ, surface elevation, surface fluctuation.

The variables were explored and described by descriptive statistics (mean ± standard deviation) and by multivariate statistical analysis (Principal component analysis and cluster analysis), based on two matrixes, one for water (48 samples × 19 physicochemical and biological parameters) and another for sediments (48 samples × 8 physicochemical parameters) integrating reservoir properties, LULC and climate conditions. Data were normalized (log x; x = mean value) prior to multivariate statistical analyses, avoiding misclassification due to differences in data dimensionality.

Spearman's rank correlation was used to analyze the strength of linear associations between water and sediments physicochemical parameters, drainage basin characteristics, reservoir properties, climate conditions, and years of the study (2017: drought and 2018: post-drought).

The multivariate statistical methodologies were used with the following aims: (i) principal component analysis (PCA): to assess the relationships and possible patterns between variables, determining the main climate and LULC parameters that account for the variability of the water body status,; (ii) cluster analysis (CA): to group the sampling locations according to their water characteristics. The CA groups were plot into clusters according to their similarities, using the Euclidean distance between samples. [41,42].

All statistical analyses were carried out using the STATISTICA 7.0 (Software™ Inc., Pottstown, PA, USA, 2007).

3. Results and Discussion

3.1. Meteorological and Land Use/Land Cover (LULC) Characterization

3.1.1. Meteorological Conditions

Figure 2 presents the temperature, precipitation, and wind speed data measured in 2017 and 2018. The temperature differences between years (1-minute temperature values represented by the grey dots) are clearly showing higher values in 2017 than in 2018, from April to November (Figure 2a). In contrast, the monthly accumulated precipitation (represented by the red bars) in 2017 is roughly half of the amount in 2018. The monthly mean temperature (blue line) shows that high temperatures were registered for a longer period in 2017 than in 2018, and the red bars confirm that after March 2017 the precipitation was scarce, which caused the severe drought conditions. The precipitation that occurred in March 2018 triggered a relief of the drought conditions, registered in 2017, a year that was classified as extremely warm and dry in comparison with the Climatological Normal of 1971–2000 (www.ipma.pt; last accessed on 25 September 2019). The year of 2018 did not present significant deviations from the climatological normal, with the mean annual temperature showing a slight deviation of +0.2 °C and the precipitation presenting a slightly higher annual value (112% of the climatological normal). Relative to solar radiation, 2017 was characterized by an accumulated global horizontal radiation of 6.84 × 106 kJ/m^2, higher than for the year 2018 (6.46 × 106 kJ/m^2). Regarding the wind speed (Figure 2b), grey dots present daily means and blue lines represent 15 days averages, the behavior along the year presents oscillations between calm and relative windy periods, frequently associated with the frontal precipitation events in the rainy period and to the summer Iberian thermal low and related sea breeze system [43].

3.1.2. LULC Characterization

The distribution of LULC was analyzed in terms of the percentages obtained for each class within the four drainage basins, corresponding to the following areas: Álamos: 1279 km^2; Montante: 7332 km^2; Mourão: 5912 km^2; Lucefécit: 425 km^2 (Figure 3). Notice that the agriculture class, as well as livestock, were the dominant classes in all the drainage basins, generally constituting 80% of the total LULC. Agriculture dominates in Álamos (46%) and livestock in Montante, Mourão and Lucefécit. Presently, the most representative crops in the Guadiana basin are olive and vineyard with an agriculture based in intensive cultural practices (irrigation, fertilization, and pesticides application). Pig farming is one of the most important livestock activities in the basin, which may constitute an important source of diffuse pollution, mainly by the transport of nutrients and organic matter to the reservoir (Figures 1 and 3). In the Portuguese territory of the Guadiana basin, the pig farms were mainly located at the drainage basins of Álamos (7028 animals) and Lucefécit (5300 animals), yielding 5.5 and 12.5 animals/km^2, respectively. In general, these effluents present high amounts of nutrients, particularly NH_4 from the animals urine, and metals such as Cu and Zn, used as supplements to increase animals´ growth and reproduction rates [44].

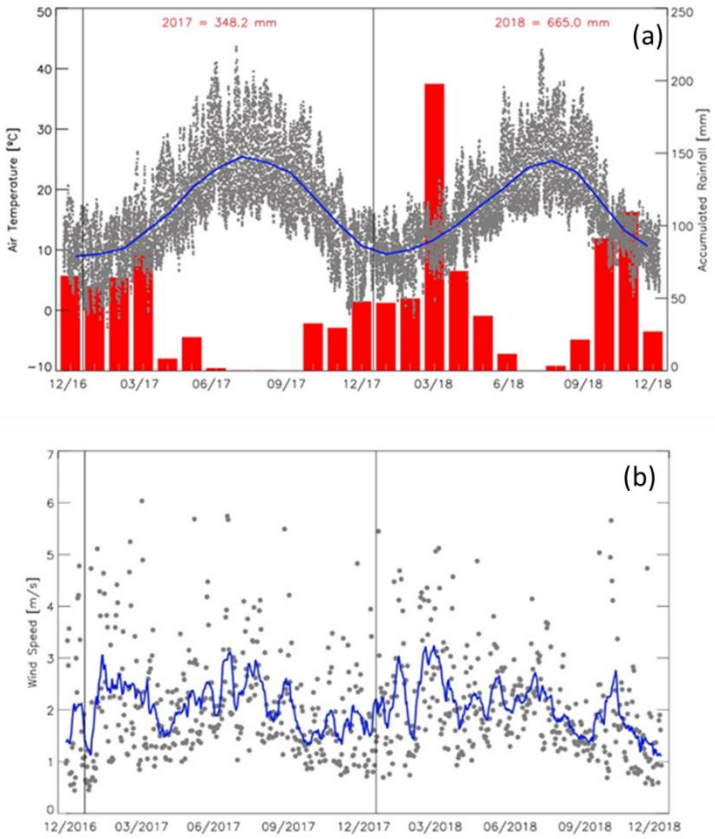

Figure 2. Meteorological charts from a station installed in the lower part of the Guadiana basin at the Alqueva reservoir shore in the period December 2016 to December 2018. (**a**) 1-min and monthly mean (grey dots and blue line) air temperature and monthly accumulated rainfall (red bars). The grey vertical line separates the years 2017 and 2018; (**b**) Daily and monthly mean wind speed (grey dots and blue line).

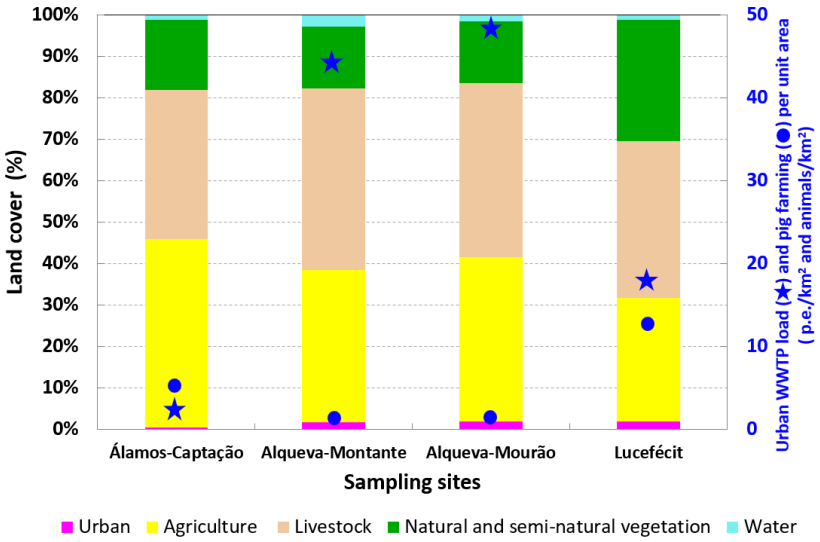

Figure 3. Percentages of the land use classes in the drainage basins of the sampling locations at Alqueva reservoir. Blue stars indicate the total urban wastewater treatment plants' (WWTP) load and blue circles illustrate the number of animals, both per unit area at each drainage basin.

Lucefécit had the highest percentage of natural and semi-natural vegetation (29%), mostly constituted by the Montado landscape (typical in the Mediterranean region), which

may act as a buffer to the pollution processes [45]. The urban class has small expressivity in the generality of the drainage basins, which is justified by the low population density corresponding to dispersed small villages. The drainage basins of Mourão and Montante are the most influenced by urban wastewater treatment plants' (WWTP) discharges, with the highest WWTP loads per unit area (49 p.e./km^2 and 44 p.e./km^2, respectively) (Figures 1 and 3). The remaining point sources of pollution in the region were winery wastewater treatment plants with seasonal effluents, mainly produced during autumn-winter and characterized by high concentrations of nutrients and low pH values [46] (Figures 1 and 3).

3.2. Water Column Seasonal and Spatial Dynamics

3.2.1. Temperature and Dissolved Oxygen Profiles

Understanding hydrodynamics and thermal stratification are of great importance for the mixing patterns knowledge, constituting useful tools for the management of reservoirs [47]. The physical characteristics of the reservoir are influenced by meteorological conditions and have an impact on its chemical and biological dynamics, as observed by the obtained Spearman "*on ranks*" correlations (Table S2). The vertical temperature profiles (Figure 4) indicate that the reservoir is stratified once per year, generally from May to September, presenting a monomictic regime as reported elsewhere [27,48]. Nevertheless, at Montante the reservoir presented a larger stratification beginning in March/ April with the maintenance of the differences among epilimnion and hypolimnion until September. Lucefécit was the location where the thermal stratification period was shorter as already observed in other works [27].

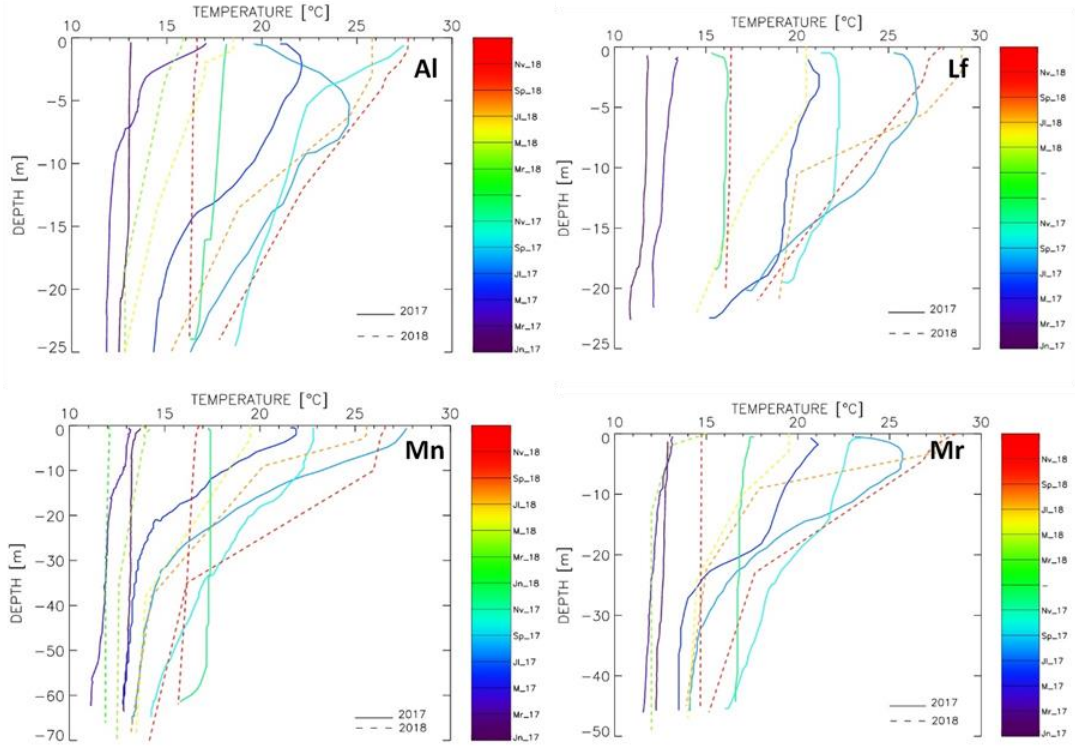

Figure 4. Temperature profiles, at the four sampling locations at Alqueva reservoir, in the months of January (Jn), March (Mr), May (M), July (Jl), September (Sp) and November (Nv), during 2017 (full lines) and 2018 (dashed lines). Al–Álamos, Lf–Lucefécit, Mn–Montante and Mr–Mourão.

These differences in the water mixing phases may be correlated with the wind regime, depth, and flow conditions (Table S1, Figure 2). Figure 5 shows the water temperature vertical profile for Montante (location with the highest depth of the reservoir (64–65 m)) where the development of the thermocline can be clearly seen on both years (black dots). In 2017, surface water temperatures ranged between 23 and 28 °C with bottom temperatures

of 13–16 °C. The maintenance of moderate temperatures (17–20 °C) was observed at up to 40 m of depth, during July to September. Meanwhile, in 2018 surface water temperatures were around 24–25 °C and bottom temperatures were 14–15 °C, with moderate temperatures observed up to 20 m of depth, indicating a warming of the water column during the drought year. The progress of temperature in the reservoir was influenced by meteorological conditions, highlighted by the correlations obtained with the mean air temperature ($R = 0.92$; $p < 0.01$), precipitation ($R = -0.79$; $p < 0.01$) and global radiation ($R = 0.80$; $p < 0.01$) (Table S2). The records of the thermal cycle of the reservoir showed a warming tendency, with the progress of water temperature values at the wet period, of 9–10 °C in 2006 [32], 10–12 °C in 2012 [46], and 11–13 °C currently. In the dry period, the warming tendency at the surface is not so clear, probably due to the high influence of air temperature in the epilimnion. These results may indicate that in years characterized by the intensification of drought conditions, with the increase in air temperatures and the decrease in rainfall events, accentuated changes in the physical regime of reservoirs may occur, even in those of large dimensions, like the Alqueva reservoir, as reported elsewhere [49–51].

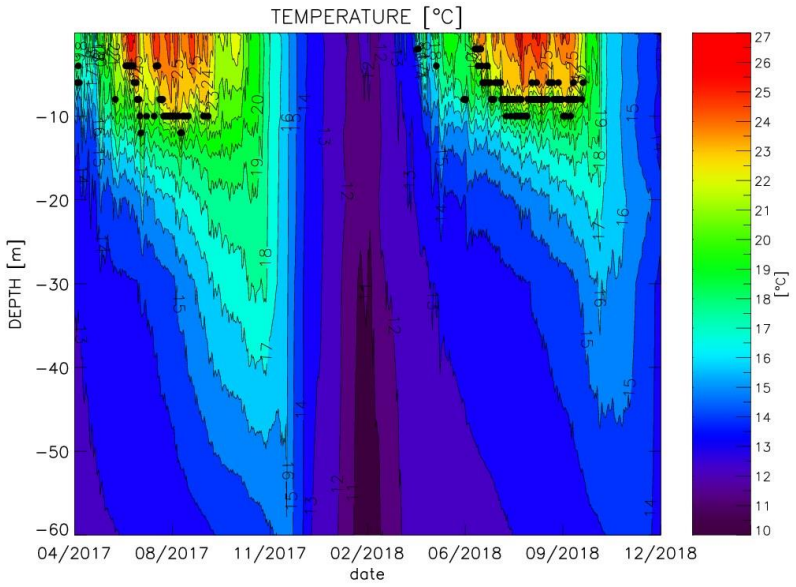

Figure 5. Vertical temperature profile and thermocline (black dots) over time in Montante during the period April 2017 to December 2018. The bottom of the graph (60 m) represents the bottom last thermistor depth and not the bottom of the reservoir.

The stratification period of the reservoir, in a large part of the year, is attended with a depletion of DO values in the hypolimnion as displayed in Figure 6, incrementing the differences in water chemical characteristics between the two layers. Dissolved oxygen values dropped sharply from the thermocline, leading to the development of anoxia during the dry period. This process was longer in 2017 (drought year) with DO values of 0–1% at the bottom, between May and September, correlated with the temperature water column stratification and with the settling and breakdown of organic material in the reservoir, as already reported by Naselli-Flores et al. [52]. During the wet period (November-January), the wind increase and the air temperature decrease ensure the complete mixing of the two phases, with DO values varying between 80 and 100%. The results highlight that DO percentages in surface water were positively correlated with the air temperature ($R = 0.39$; $p < 0.01$) and the water temperature ($R = 0.40$; $p < 0.01$), and negatively correlated with the rainfall ($R = -0.38$; $p < 0.01$) and the relative humidity ($R = -0.52$; $p < 0.01$), showing again the influence of the meteorological conditions on the physical status of the reservoir. Further, the increase in the DO levels was correlated with the increase in algae productivity (represented by the Chl-a in the present study) that occurred mainly during the dry period due to the atmospheric favorable conditions, ($R = 0.47$; $p < 0.01$)

(Table S2). The transparency, determined by the Secchi disk, showed small differences among the locations, generally with higher values in the wet period, as observed for other reservoirs [53,54]. Lucefécit was the location with the lowest transparency values, which may be explained by the proximity to the riparian zone, the lowest depth and the highest algae productivity (Table S1; Figure 1 and Figure 8) [53,54].

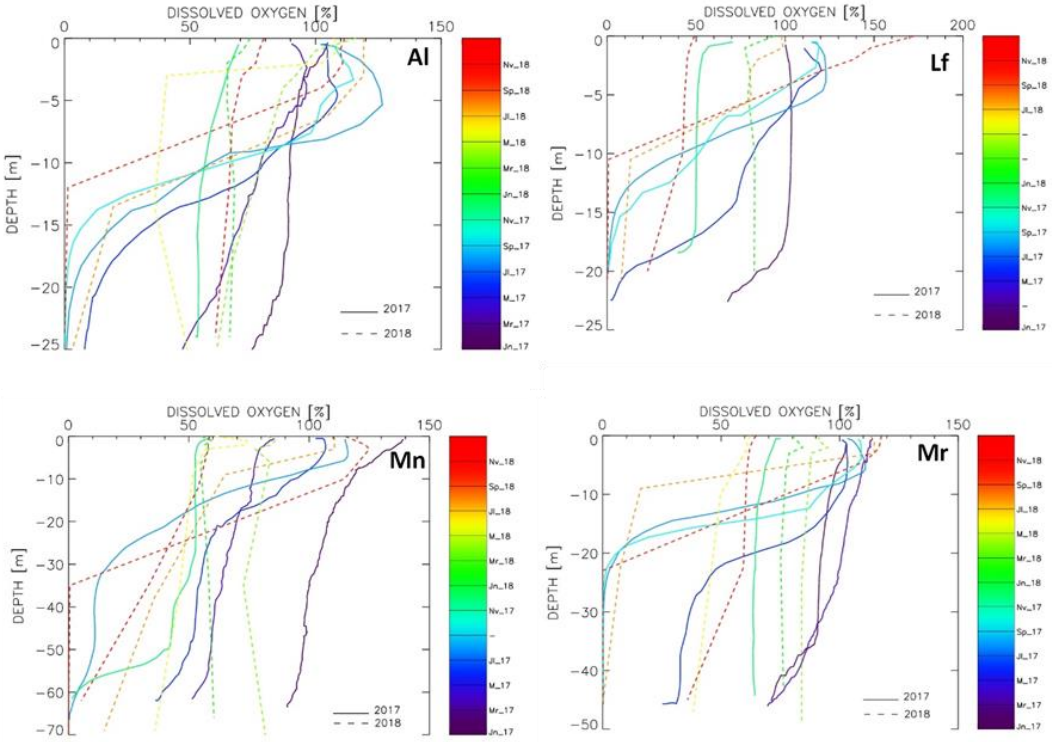

Figure 6. Dissolved oxygen profiles, at the four sampling locations at Alqueva reservoir, in the months of January (Jn), March (Mr), May (M); July (Jl); September (Sp) and November (Nv), during 2017 (full lines) and 2018 (dashed lines). Al: Álamos; Mn: Montante; Mr: Mourão; Lf: Lucefécit.

3.2.2. Chemical and Phytoplankton Biomass Patterns

Surface waters of the reservoir presented a slightly alkaline pH ranging from 7.51 to 9.44. Lucefécit showed the highest values of pH in the dry period 2018, surpassing sporadically the Water Framework Diretive (WFD) limit for the good ecological potential (pH < 9) [55] (Figure 7). Water EC ranged between 368 and 581 µS/cm, with the highest values observed at Mourão in September 2018 (581 µS/cm) (Figure 5). Both parameters were influenced by the meteorological conditions, increasing with T_{air} and dropping with precipitation (see Table S2). When the trends over the years were analyzed, a slight rise of the water pH and an obvious increase in the EC_w values (2006/2007 [28]; 2011/ 2012 [27]; and present), were observed. The trend of EC_w values was correlated with the rise of the concentrations of sodium, sulphate and chlorides over time, supported by the correlations observed among EC_w and these parameters (Table S2) [29,30]. Further, when we analyzed the concentrations of some cations (such as Na, Ca) with the conductivity values, and we verified similar patterns along the years [29,30]. These correlations have already been observed in other Mediterranean reservoirs [56].

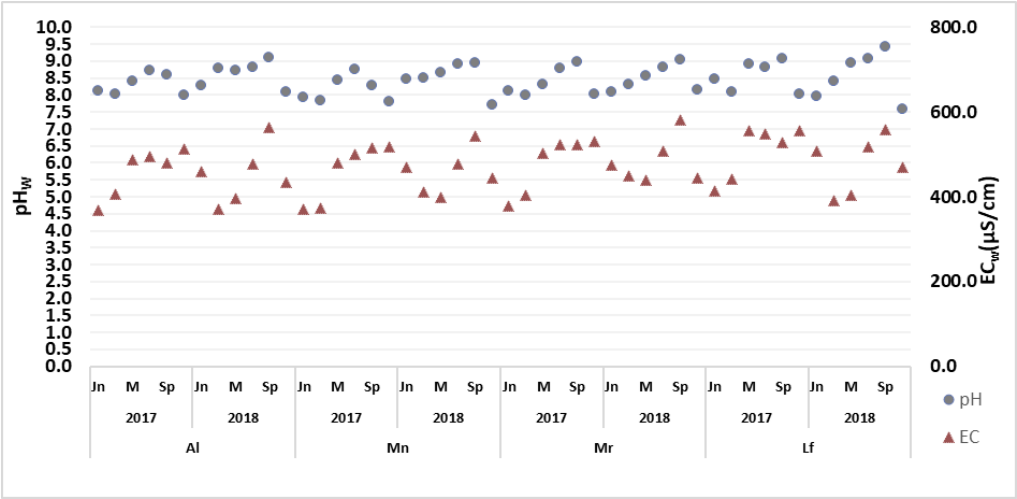

Figure 7. Values of pH_W and electric conductivity (EC_W; µS/cm) measured in situ of each location (Al: Álamos; Mn: Montante; Mr: Mourão; Lf: Lucefécit), during the study.

Concerning organic descriptors, the BOD_5 ranges from 2 to 10 mg/L, presenting, at dry period, values higher than the WFD limit proposed for the good ecological potential (5 mg/L). Lucefécit was the location that exhibited the maximum BOD_5 concentrations in both years (Figure 8). Concentrations of BOD_5 > 5 mg/L are considered significant pressures for the systems, putting them at risk of failing the environmental objectives related to the good potential [57]. Agriculture and livestock classes may have contributed to the levels of this parameter, at Álamos and Lucefécit. Currently, the results do not reveal a clear significant correlation among LULC and BOD_5, however this kind of linkage has already been observed in other studies [27,58–60].

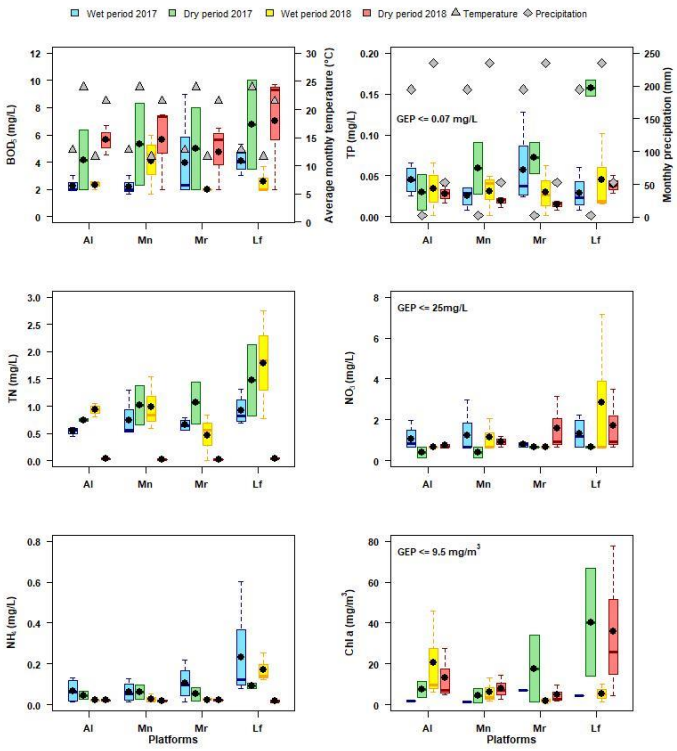

Figure 8. Spatial and temporal variation of the organic descriptors, nutrients, and Chl-a in the water samples during the period of the study. The black circles indicated the mean, the line across the box represents the median, and the bottom and top of the box show the standard error. Recommended guide levels for the good ecological potential (GEP) are indicated in the plot [55].

Nitrogen and phosphorus are the main factors leading to algae blooms, being important parameters for estimating reservoirs´ degrees of eutrophication, and ecological status [59]. Generally, algal blooms may occur when TP and TN concentrations in water reach 0.02 and 0.2 mg/L, respectively [55]. In the present work, TP and TN concentrations were above 0.02 and 0.2 mg/L, in most of the sampling campaigns (Figure 8), indicating the risk of algal blooms not only in the dry period but also in the wet one. The TN levels presented high spatial and temporal variability, ranging between 0.01 and 2.75 mg/L, Lucefécit being the location with the greater values detected. In fact, the highest values of TN, at the water column, occurred at Lucefécit in the wet period 2018, probably due to the runoff from agriculture practices and livestock activities, the LULC classes more representative in its drainage basin, as already observed in other Mediterranean reservoirs [60]. On the other hand, TP achieved the highest concentrations in the water column during the dry period 2017 at Lucefécit, surpassing the limit for the good ecological potential (TP $\leq$ 0.07 mg/L; [55]). This temporal pattern is not the most usual, once the greatest concentrations of TP generally occur during the wet period due to the increase in runoff, the decrease in algae productivity, and the overturn of the water. Nevertheless, it had already been observed in 2012 [29], a year also characterized by a severe drought [10]. This occurrence has been more evident in areas with low depth without external loading, making the internal loading an important driver for the increase in nutrient concentrations in the reservoir. A similar increase in nutrient concentrations due to higher internal loading had also been observed in other reservoirs during summer [61,62]. This internal source of nutrients results from the sediments under anoxic conditions during the stratification phase. In fact, Søndergaard et al. [62] suggested that during the mixed phase, the oxic conditions are maintained along the water column and phosphorus is adsorbed into iron (III) compounds, which partially inhibits the sediment´s phosphorus release. During the anoxic phase (stratification period), the iron (III) is reduced to iron (II) and subsequently both iron and phosphorus returned into the water solution. With the saturation of phosphorus in the lower phase of the water column, an upward transport occurred, from the deeper sediment to the oxic layers of the water. The observed decrease in TP concentrations in the Lucefécit sediment during the stratification period, achieving the lowest values in September 2017, supports the occurrence of this process (Figure 8).

The excess of organic matter and nutrients in water are a driving force for the increase in the algae productivity, supported by the positive correlations observed between Chl-a and BOD_5 (R = 0.46; $p < 0.001$), TP (R = 0.38; $p < 0.05$) and TN (R = 0.52; $p < 0.001$), as reported elsewhere [56]. Lucefécit presented the highest concentrations of Chl-a during the dry period, surpassing the limit for a good ecological potential (9.5 mg/m^3, for reservoirs of South Portugal [55]) in 56% of the total samples, and in 44% of the samples from Álamos. These locations, with the lowest depth and with considerable external sources of nutrients, as farming pigs and intensive agriculture activities, also showed the lowest euphotic zones. In fact, in a study carried out on 50 surface water bodies in Greece, the most impacted lakes by agricultural and urban classes had the lowest secchi depth [60]. The increase in phytoplankton also contributed to the lower levels of euphotic zone observed, supported by negative correlation between Chl-a and euphotic zone ($R = -0.814$; $p < 0.01$). Despite the similar patterns for the temporal and spatial variability of Chl-a observed, the concentrations in the Alqueva have been increasing over the years [63].

3.3. Sediments Seasonal and Spatial Dynamics

3.3.1. Granulometric Characteristics

The sediment particle size has a great influence on the distribution of natural and anthropogenic elements, as organic matter, nutrients and metals, showing usually high affinity to fine particles (<0.063 nm) [26,27,64]. These compounds may be released from the sediments to the bottom phase of the water column under specific limnological conditions. The granulometry analysis displayed spatial differences in the reservoir (Figure 9), with locations such as Álamos, Lucefécit and Montante mainly constituted by fine particles

(clay and silt), and others as Mourão with a sand particles fraction higher than 50%. The sediments' granulometric fractions of Álamos, Lucefécit and Mourão were consistent with the results obtained in 2012, a factor that may indicate a low sedimentation rate, at the reservoir [26,27]. Higher proportions of sand particles were recorded at Mourão and Montante, both areas with a sharp depth and steeper slopes, located in the middle of the reservoir. Lowest water flows, such as at Álamos and Lucefécit (locations in the tributaries of the reservoir), induce a greater accumulation of fine-grained sediments, according to the general pattern observed for reservoirs [65]. Further, the results pointed to the association between grain size and LULC, with the linkage between sand and urban class ($R = 0.63$; $p < 0.001$), and clay with agricultural uses ($R = 0.40$; $p < 0.001$) (Table S2).

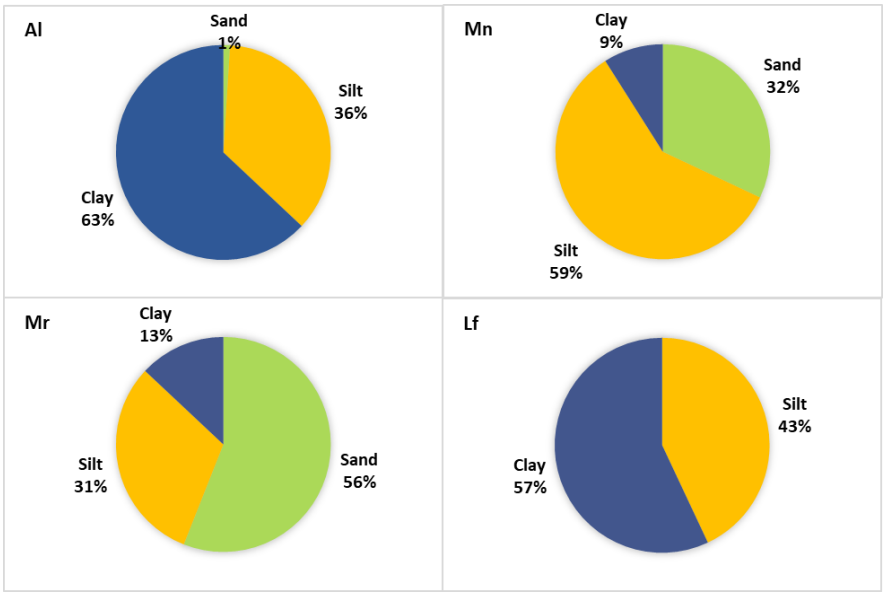

Figure 9. Sediments' granulometric fractions at each sampling location (Al: Álamos; Mn: Montante; Mr: Mourão; Lf: Lucefécit) in the Alqueva reservoir.

3.3.2. Chemical Patterns

The variability of the main chemical parameters of the Alqueva sediments is displayed in Figure 10a ($pH_{pore\text{-}water}$ and $EC_{pore\text{-}water}$) and Figure 10b (OM, TP, TN). The $pH_{pore\text{-}water}$ values ranged from slightly acid to slightly alkaline, with the sediments from Álamos having the lowest values during the dry period 2017. The $EC_{pore\text{-}water}$ values were greater than at surface water, ranging from 285 to 952 µS/cm (at Mourão_May 2018 and Montante_September 2018, respectively). The $EC_{pore\text{-}water}$ presented positive correlations with urban class ($R = 0.43$; $p < 0.001$) and livestock class ($R = 0.58$; $p < 0.001$), as already observed for the sediments of Alqueva tributaries at Guadiana Basin [66]. Generally, over the years, the sediments showed an acidification trend, with a slight decrease in $EC_{pore\text{-}water}$ [29]. The organic matter contents ranged from 5.1 to 13.1%, with the lowest values observed at Mourão (Figure 10b), a location mostly constituted by sand particles. Surface sediments of the Alqueva reservoir are mainly inorganic, with OM contents < 12% [67]. Despite the high variability of TPs concentrations, much influenced by oxic conditions, pH and iron forms [68], all the sediments presented concentrations of TPs higher than the severe effect level ($TP_{SEL} > 0.2\%$; [69]), classifying the sediments as heavily polluted, and likely to affect the health of sediment-dwelling organisms. Montante was the location with the highest concentrations of TP_s, achieving values of 17.5% in the wet period for both years. Notwithstanding the current TPs concentrations, an obvious decrease in TPs was observed since 2012, another fact that supports the hypothesis that the sediments of Alqueva constitute a significant internal sink and source of phosphorus of the reservoir. In general, the sediments presented TN_s concentrations higher than the SEL ($TN_{SEL} > 0.48\%$; [69]) during the wet period of 2017. Despite this scenario, the TNs concentrations have been presenting

a slight rising trend over time, which can be linked with the intensification of agriculture practices, as reported elsewhere [60].

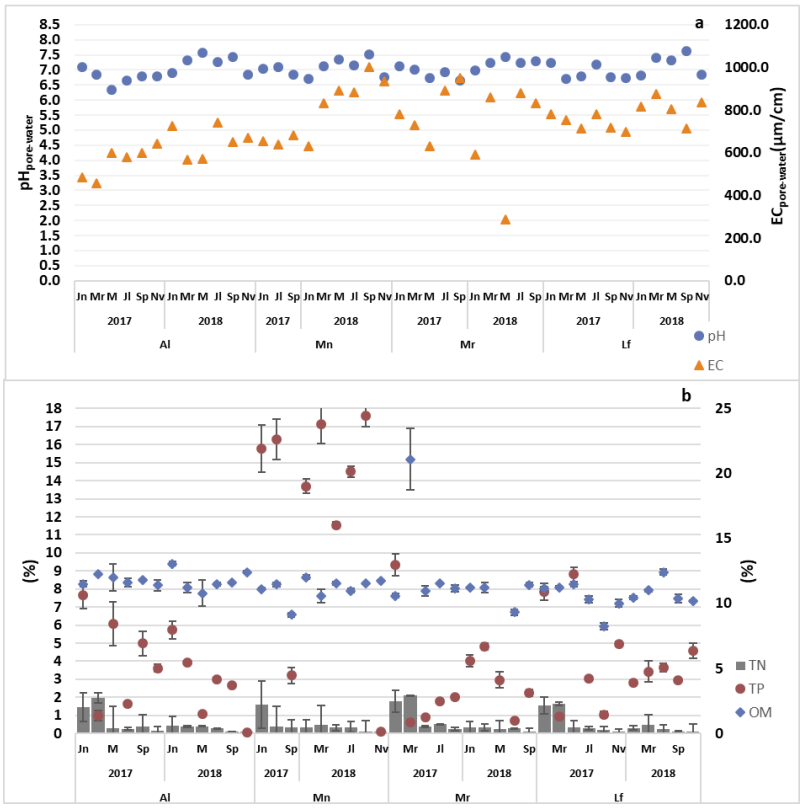

Figure 10. Dynamics of sediments' chemical characteristics: (**a**). $pH_{pore\text{-}water}$; electric conductivity ($EC_{pore\text{-}water}$) and (**b**). organic matter (OM); total phosphorus (TP_s); total nitrogen (TN_s), values represented by mean± standard deviation (n = 3), in the different sampling locations ((Álamos (Al), Montante (Mn), Mourão (Mr) and Lucefécit (Lf)).

3.4. Influence of Clime and LULC Patterns on Physic-Chemistry and Phytoplankton Biomass of the Reservoir

3.4.1. Drought and Post-Drought Periods

The annual dynamics of water chemistry showed that $pH_{pore\text{-}water}$, nutrients (TP, TN, NH_4, NO_3, TNs), and ions (Cl, Ca) were the parameters that presented the highest variability, being those that suffered a greater influence of the drought (2017) or the post-drought (2018) conditions (Table S2). Hence, TP, TN_s, Cl, Ca and NH_4 presented higher concentrations in the reservoir during 2017 (drought year). The opposite was observed for $pH_{pore\text{-}water}$, TN, and NO_3, that presented the highest values in the reservoir during 2018. The results showed that the effects of drought in the chemical parameters were not similar in the whole reservoir, revealing spatial differences that may be explained by variations in the hydro geomorphology and LULC of each drainage basin.

Several studies reported the effect of drought events on different water quality parameters, observing the increase in EC and ions concentrations (e.g., Cl, Na, Ca, SO_4), with the corresponding deterioration of water quality [50,51]. The increase in ions concentrations during the drought years may be justified by low flows, a decrease in runoff, and high evaporation rates, leading to a reduction in the reservoir water volume, as observed in the present study by the lower mean surface elevation (2017: 147.13m and 2018: 148.21m; Table S1) and the negative value of surface fluctuation mean (−0.72 m) during 2017. Contrarily, the results indicated that water EC was not related with the drought year. Some authors already reported that in agricultural and livestock areas, the drought effects on

EC are unclear, suggesting the influence of other variables, such as the inflow of ions from agriculture practices, in the values of EC_w [51].

Nutrients presented mixed responses during the drought period, with the concentrations of TP and NH_4 more influenced by drought, opposite to TN and NO_3 with higher concentrations more evident in the post-drought period. These results may indicate that the main sources of phosphorus and nitrogen pollution are not the same. In fact, TP showed an increase in the drought year with high significance at Lucefécit, probably resulting from a reduction in water volume and an intensification of loads from point sources of pollution, such as effluents from urban areas and pig farming, on its drainage basin (Figure 3). In the case of TN, a rise of the concentrations was not observed in the drought period, probably because the most important sources of pollution are the intensive agricultural practices, for which the loads to the reservoir are markedly influenced by precipitation, as reported by Barros et al. [70] in the Roxo reservoir. Nevertheless, in addition to the various sources of pollution (diffuse and/or point), other mechanisms/ processes in the reservoir can also influence the nutrient´s dynamics, such as the stratification and the algae productivity [51].

The results for Chl-a were similar to those reported by most of the studies, with significant elevated biomass during the droughts, which has been attributed to more favorable hydrodynamic conditions for algal growth and changed nutrient dynamics [51].

3.4.2. Meteorological Conditions and LULC Patterns

The application of a Principal Component Analysis (PCA) allowed the establishment of correlations among water and sediments physicochemical parameters and the LULC classes in the drainage basins, under different climate conditions. The results highlighted the importance of the climate conditions on the description of the water variability in the reservoir. In fact, the first component (PC1) represented the influence of meteorological conditions (T_{air}, Prec, Rad) on the characteristics of water (see Figure 11a), generating 35% of the total variance. Indeed, these climate factors were those that presented greater variances among the drought (2017) and post-drought (2018) years. The water parameters most influenced by these explanatory factors were the pH, Tw and EC_w (with loadings ≥ 0.75), followed by the DO and BOD_5 (with loadings between 0.75–0.50), all these parameters with a positive participation in PC1, indicating that their increase in the water reservoir is influenced by the air temperature increase and the precipitation decrease. The second component (PC2) represents the LULC classes as an explanatory factor, with 19% of the total variance, with agriculture and urban classes being the most important. The parameters most influenced by LULC were NH_4 and Cl, their increase being observed with the rise of urban activities and precipitation on the drainage basins. There was an obvious distribution of the water samples in the PCA according to the sampling period and the meteorological conditions, the samples from the dry period being located in the positive quadrant of the PC1 more influenced by T_{air} and Rad, and the samples from wet period, displayed at the negative quadrant of PC1, more influenced by precipitation. The positive quadrant of PC1 integrated 55% of samples belonging to the drought year (2017). Furthermore, Hierarchical Cluster Analysis (HCA) was used to classify the samples according to their similar characteristics. Hence, the water samples were grouped in three clusters, the first one (cluster 1) located at the positive quadrant of both PCs' integrated dry samples from Montante and Mourão, with high pH and EC and very influenced by urban activities. Cluster 2 grouped dry samples from Álamos, more influenced by agriculture activities. Cluster 3 grouped the wet samples, influenced by precipitation and urban activities.

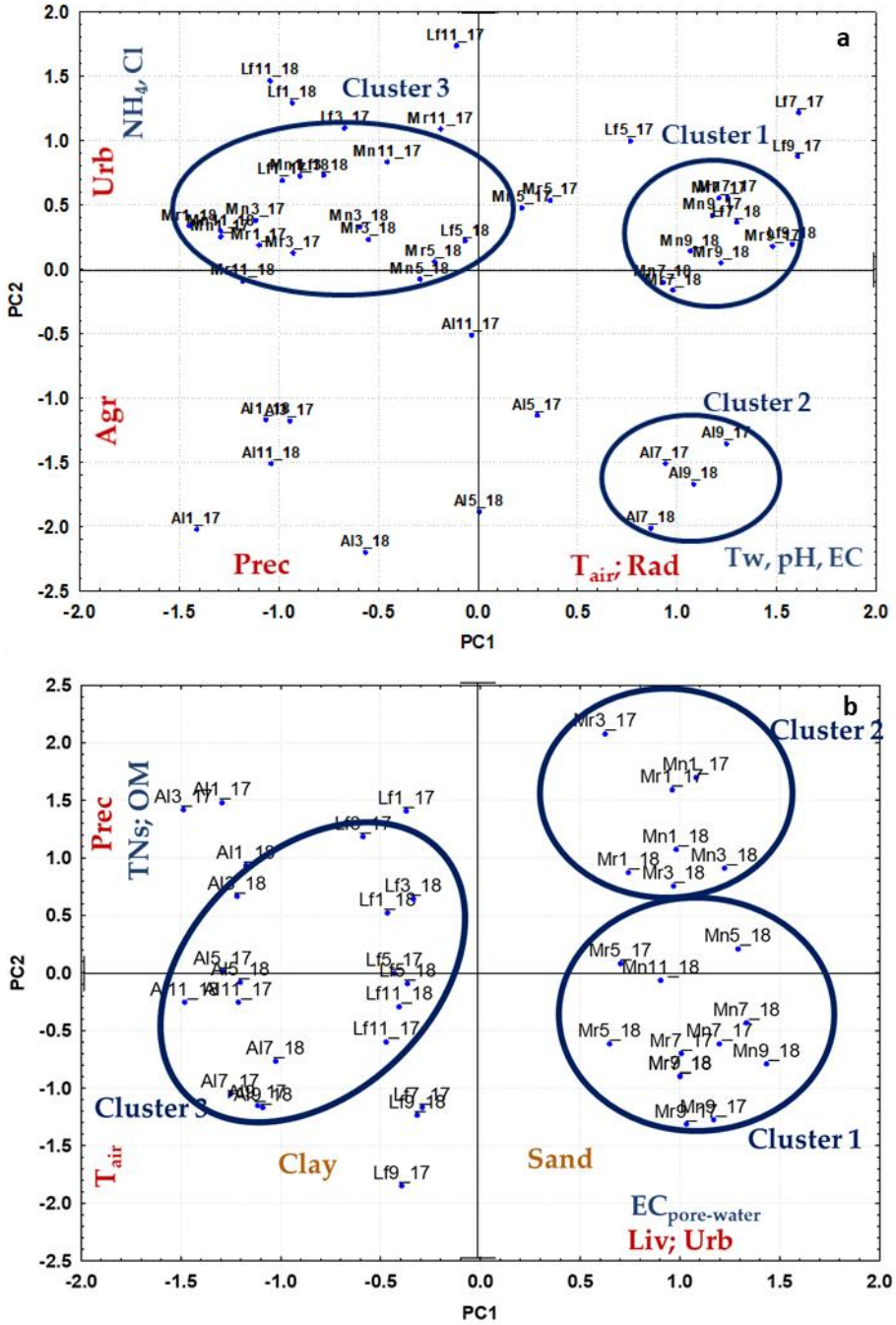

Figure 11. Principal Component Analysis (PCA) plot showing the distribution of the climate factors, Land use/ Land cover (LULC) factors and physicochemical parameters of the Alqueva reservoir water samples (**a**) and sediments samples (**b**) on the bidimensional plane defined by the first two principal components (PC). In the figure are displayed the samples' scores and the statistically significant clusters obtained through the Square Euclidean distance. Samples were collected at Al, Mn, Mr, Al, Lf, during the years of 2017 and 2018 in the months of January (1); March (3); May (5); July (7); September (9) and November (11).

Relatively to sediments, the PCA showed that the LULC classes (urban and livestock) and the sediments' granulometric fractions (clay and sand) presented higher importance on the distribution of the samples than meteorological conditions, explaining 33% of the total variance of the samples (Figure 10b). The $EC_{pore\text{-}water}$ was the parameter more influenced by LULC classes and occurred in higher values in samples constituted mostly by sand particles. The PC2 showed 22% of the total variance and was explained by meteorological

parameters such as precipitation (positive quadrant) and T_{air} (negative quadrant). The parameters with a major influence on PC2 were TNs and OM (positive participation). As for the water samples, a clear display of the sediment samples on the PC associated with the sampling period was observed. The cluster analysis allowed the construction of three clusters. Cluster 1 (positive quadrant of PC1) integrated dry samples from Mourão and Montante, very influenced by urban and livestock classes and granulometry constituted mostly by sand particles. Cluster 2 located at the positive quadrant of both PC gathered wet samples from Mourão and Montante more influenced by precipitation and with higher amount of TN and OM. Cluster 3 integrated the samples with higher amounts of fine particles, all from Lucefécit and Álamos.

4. Conclusions

Reservoirs play an important role in water management, especially in Mediterranean areas like Alentejo (Southern Portugal), where water is typically scarce and is projected to become even scarcer under climate and LULC changing scenarios.

In the present study, the aim was to understand the effects/ impact of climate and LULC changes in the physicochemical and biological dynamics of the Alqueva reservoir. In fact, climate change and overexploitation due to the intensification of agriculture practices could contribute to water scarcity and the impairment of water quality, significant issues nowadays. This type of forecast or projection requires the development of studies that disclose how the reservoirs will react to drought conditions and to the rise of certain LULC classes, such as the intensification of agricultural activities, likely to happen in the Alqueva's irrigated area.

Hence, the results indicated that during drought conditions, the reservoir undergoes physical and limnological changes with the increase in water temperature along the water column, an increase in stratification periods and anoxic conditions, as well as sediments acidification, with different patterns along the reservoir mainly influenced by depth, flow and geological properties. The LULC changes have influenced the concentrations of nutrients and organic descriptors in the reservoir, with their increase over time. In fact, the intensification of the agricultural activities (increasing the irrigation and the use of fertilizers and pesticides) has promoted the increment of nutrients loads transfer to the water system.

The impact of LULC changes becomes more evident during drought periods, mainly due to the increase in air temperature, inducing a high evaporation rate and a reduction in water volume. Among the nutrients, phosphorus is the most problematic, with sediments highly contaminated by it and becoming an important internal source of pollution for the reservoir, during drought conditions. This process could stimulate the algae productivity that the drought conditions already support by itself. The increase in water nutrients and algae productivity has been observed over the years, with the possible speed-up of eutrophication at the reservoir. Furthermore, higher TP concentrations and algae might compromise the compliance of the environmental objectives defined on Water Framework Directive, which is already happening at Lucefécit zone (north of the reservoir).

The multivariate analysis showed the importance of drought conditions in the impact of LULC changes to the reservoir, as well as in its entire physicochemical dynamics, which is much worrying, since the climate projections indicate that the number of drought periods will most probably increase in this region.

The results provide information to the decision-makers, to build strategies on how to avoid a higher deterioration of the water quality in the Alqueva reservoir, induced by interacting and synergistic effects of climate change and LULC management. It is essential to promote the sustainability of LULC, with the control of agriculture areas in the basin and the implementation of sustainable environmental management practices. In fact, the adaptation solutions based on LULC changes would seem the most effective to address reservoir water quality issues, and therefore territorial planning can play an important role in adaptation and mitigation in this region. Finally, this work shows that studies of the

vulnerability of reservoirs to climate and LULC changes should assess water/sediment dynamics and account for the reservoir's conditions (water volume stored; water demand; fluctuations of water levels). In that way, the water quality and its multiple uses within the watersheds can be preserved.

Further work is needed in this system during future drought scenarios, as in systems with similar LULC classes in the Mediterranean region, to derive scientific data for optimizing the water management sustainable policies in a climate changing World.

Supplementary Materials: The following are available online at https://www.mdpi.com/2073-4441/13/5/707/s1, **Table S1.** Sampling date, Secchi depth, and platform depth for each sampling location, together with details of surface elevation, surface fluctuation, volume, and surface area for the twelve field campaigns, considering the total study area of the Alqueva reservoir; **Table S2.** Spearman correlation coefficients between the climate conditions, LULC classes, water and sediments physicochemical parameters in the Alqueva reservoir: (*) significant at $p < 0.05$; (**) significant at: $p < 0.001$.

Author Contributions: Conceptualization: P.P.; Investigation: S.F., A.L., C.M., A.M.P., M.H.N., A.R., M.I., G.R., R.S., P.P.; Supervision: P.P.; Writing—original draft: P.P., M.J.C., A.M.P. and M.P.; Writing—review & editing: P.P., A.M.P., M.P., M.H.N., M.M., M.J.C., P.A., R.S. All authors have read and agreed to the published version of the manuscript.

Funding: The present research is co-funded by the European Union through the European Regional Development Fund, included in the COMPETE 2020 (Operational Program Competitiveness and Internationalization) through the ICT project (UIDB/04683/2020) with the reference POCI-01-0145-FEDER-007690, the ALOP project (ALT20-03-0145-FEDER-000004), and through the European Agricultural Fund for Rural Development through the FitoFarmGest Operational Group (PDR2020-101-030926).

Institutional Review Board Statement: Not applicable.

Informed Consent Statement: Not applicable.

Data Availability Statement: Not applicable.

Acknowledgments: The authors thank the European Commission Copernicus Program for Copernicus Land Monitoring Service products, as well as the Administration of the Hydrographic Region of Alentejo (ARH Alentejo) for the data provided. SRTM elevation data at 1 arc-second courtesy of the U.S. Geological Survey.

Conflicts of Interest: The authors declare no conflict of interest.

References

1. Smeti, E.; von Schiller, D.; Karaouzas, I.; Laschou, S.; Vardakas, L.; Sabater, S.; Tornés, E.; Monllor-Alcaraz, L.S.; Guillem-Argiles, N.; Martinez, E.; et al. Multiple stressor effects on biodiversity and ecosystem functioning in a Mediterranean temporary river. *Sci. Total Environ.* **2019**, *647*, 1179–1187. [CrossRef]
2. Sabater, S.; Bregoli, F.; Acuña, V.; Barceló, D.; Elosegi, A.; Ginebreda, A.; Marcé, R.; Muñoz, I.; Sabater-Liesa, L.; Ferreira, V. Effects of human-driven water stress on river ecosystems: A meta-analysis. *Sci. Rep.* **2018**, *8*, 1–11. [CrossRef] [PubMed]
3. Hering, D.; Carvalho, L.; Argillier, C.; Beklioglu, M.; Borja, A.; Cardoso, A.C.; Duel, H.; Ferreira, T.; Globevnik, L.; Hanganu, J.; et al. Managing aquatic ecosystems and water resources under multiple stress—An introduction to the MARS project. *Sci. Total Environ.* **2015**, *503–504*, 10–21. [CrossRef]
4. Capula-Rodríguez, R.; Valdez-Aguilar, L.A.; Cartmill, D.L.; Cartmill, A.D.; Alia-Tejacal, I. Supplementary Calcium and Potassium Improve the Response of Tomato (*Solanum lycopersicum* L.) to Simultaneous Alkalinity, Salinity, and Boron Stress. *Commun. Soil Sci. Plant Anal.* **2016**, 1–7. [CrossRef]
5. Füssel, H.-M.; Jol, A.; Kurnik, B.; Hemming, D. *Climate Change, Impacts and Vulnerability in Europe 2012: An Indicator-Based Report*; European Environment Agency: Copenhagen, Denmark, 2012; ISBN 9789292133467.
6. Castellari, S.; Kurnik, B. *Climate Change, Impacts and Vulnerability in Europe 2016*; European Environment Agency: Copenhagen, Denmark, 2017; ISBN 9789292138356.
7. Milano, M.; Ruelland, D.; Fernandez, S.; Dezetter, A.; Fabre, J.; Servat, E.; Fritsch, J.M.; Ardoin-Bardin, S.; Thivet, G. Current state of Mediterranean water resources and future trends under climatic and anthropogenic changes. *Hydrol. Sci. J.* **2013**, *58*, 498–518. [CrossRef]

8. UNESCO. *The United Nations World Water Development Report 2019: Leaving no One Behind*; UNESCO: Paris, France, 2019; ISBN 978-92-3-100309-7.
9. Mourato, S.; Moreira, M.; Corte-Real, J. Water Resources Impact Assessment Under Climate Change Scenarios in Mediterranean Watersheds. *Water Resour. Manag.* **2015**, *29*, 2377–2391. [CrossRef]
10. Rocha, J.; Carvalho-Santos, C.; Diogo, P.; Beça, P.; Keizer, J.J.; Nunes, J.P. Impacts of climate change on reservoir water availability, quality and irrigation needs in a water scarce Mediterranean region (southern Portugal). *Sci. Total Environ.* **2020**, *736*, 139477. [CrossRef]
11. Fehér, J.; Gáspár, J.; Veres, K.S.; Kiss, A.; Globevnik, L.; Kirn, T.; Peterlin, M.; Spiteri, C.; Prins, T.; Laukkonen, E.; et al. *Hydromorphological Alterations and Pressures in European Rivers, Lakes, Transitional and Coastal Waters*; ETC/ICM Technical Report 2/2012; European Topic Centre on Inland, Coastal and Marine Waters: Leipzig, Germany, 2012; ISBN 9788578110796.
12. Chamoglou, M.; Papadimitriou, T.; Kagalou, I. Key-Descriptors for the Functioning of a Mediterranean Reservoir: The Case of the New Lake Karla-Greece. *Environ. Process.* **2014**, *1*, 127–135. [CrossRef]
13. *Inag Critérios Para A Classificação do Estado das Massas de Água Superficiais—Rios e Albufeiras*; Ministério do Ambiente, do Ordenamento do Território e do Desenvolvimento: Lisbon, Portugal, 2009.
14. McCartney, M.; Sullivan, C.; Acreman, M.C. *Ecosystem Impacts of Large Dams*; International Union for Conservation of Nature and Natural Resources and the United National Enivronment Programme: Gland, Switzerland, 2001; p. 82.
15. Feldbauer, J.; Kneis, D.; Hegewald, T.; Berendonk, T.U.; Petzoldt, T. Managing climate change in drinking water reservoirs: Potentials and limitations of dynamic withdrawal strategies. *Environ. Sci. Eur.* **2020**, *32*. [CrossRef]
16. Azadi, F.; Ashofteh, P.S.; Loáiciga, H.A. Reservoir Water-Quality Projections under Climate-Change Conditions. *Water Resour. Manag.* **2019**, *33*, 401–421. [CrossRef]
17. Blasco, J.; Navarro-Ortega, A.; Barceló, D. Towards a better understanding of the links between stressors, hazard assessment and ecosystem services under water scarcity. *Sci. Total Environ.* **2015**, *503–504*, 1–2. [CrossRef] [PubMed]
18. Navarro-Ortega, A.; Acuña, V.; Batalla, R.J.; Blasco, J.; Conde, C.; Elorza, F.J.; Elosegi, A.; Francés, F.; La-Roca, F.; Muñoz, I.; et al. Assessing and forecasting the impacts of global change on Mediterranean rivers. The SCARCE Consolider project on Iberian basins. *Environ. Sci. Pollut. Res.* **2012**, *19*, 918–933. [CrossRef] [PubMed]
19. Crossman, J.; Elliott, J.A. Bridging the gap between terrestrial, riverine and limnological research: Application of a model chain to a mesotrophic lake in North America. *Sci. Total Environ.* **2018**, *622–623*, 1363–1378. [CrossRef] [PubMed]
20. Dupas, R.; Minaudo, C.; Abbott, B.W. Stability of spatial patterns in water chemistry across temperate ecoregions. *Environ. Res. Lett.* **2019**, *14*. [CrossRef]
21. Carvalho-Santos, C.; Monteiro, A.T.; Azevedo, J.C.; Honrado, J.P.; Nunes, J.P. Climate Change Impacts on Water Resources and Reservoir Management: Uncertainty and Adaptation for a Mountain Catchment in Northeast Portugal. *Water Resour. Manag.* **2017**, *31*, 3355–3370. [CrossRef]
22. Messina, N.J.; Couture, R.M.; Norton, S.A.; Birkel, S.D.; Amirbahman, A. Modeling response of water quality parameters to land-use and climate change in a temperate, mesotrophic lake. *Sci. Total Environ.* **2020**, *713*, 136549. [CrossRef]
23. Nunes, J.P.; Seixas, J.; Keizer, J.J. Modeling the response of within-storm runoff and erosion dynamics to climate change in two Mediterranean watersheds: A multi-model, multi-scale approach to scenario design and analysis. *Catena* **2013**, *102*, 27–39. [CrossRef]
24. Atique, U.; An, K.G. Reservoir water quality assessment based on chemical parameters and the chlorophyll dynamics in relation to nutrient regime. *Pol. J. Environ. Stud.* **2019**, *28*, 1043–1061. [CrossRef]
25. Liu, L.; Dong, Y.; Kong, M.; Zhou, J.; Zhao, H.; Wang, Y.; Zhang, M.; Wang, Z. Towards the comprehensive water quality control in Lake Taihu: Correlating chlorphyll a and water quality parameters with generalized additive model. *Sci. Total Environ.* **2020**, *705*, 135993. [CrossRef]
26. Palma, P.; Ledo, L.; Alvarenga, P. Assessment of trace element pollution and its environmental risk to freshwater sediments influenced by anthropogenic contributions: The case study of Alqueva reservoir (Guadiana Basin). *Catena* **2015**, *128*, 174–184. [CrossRef]
27. Palma, P.; Ledo, L.; Soares, S.; Barbosa, I.R.; Alvarenga, P. Spatial and temporal variability of the water and sediments quality in the alqueva reservoir (Guadiana Basin; Southern Portugal). *Sci. Total Environ.* **2014**, *470–471*. [CrossRef]
28. Palma, P.; Alvarenga, P.; Palma, V.L.; Fernandes, R.M.; Soares, A.M.V.M.; Barbosa, I.R. Assessment of anthropogenic sources of water pollution using multivariate statistical techniques: A case study of the Alqueva's reservoir, Portugal. *Environ. Monit. Assess.* **2010**, *165*. [CrossRef] [PubMed]
29. Agência Portuguesa do Ambiente. *Water Mirrors in Portugal—Emblematic Tangible and Intangible Projects in the Portuguese Water Sector*; Agência Portuguesa do Ambiente: Alfragide, Portugal, 2018.
30. Lindim, C.; Pinho, J.L.; Vieira, J.M.P. Analysis of spatial and temporal patterns in a large reservoir using water quality and hydrodynamic modeling. *Ecol. Modell.* **2011**, *222*, 2485–2494. [CrossRef]
31. Matono, P.; Batista, T.; Sampaio, E.; Ilhéu, M. Effects of Agricultural Land Use on the Ecohydrology of Small- Medium Mediterranean River Basins: Insights from a Case Study in the South of Portugal. In *Land Use—Assessing the Past, Envisioning the Future*; InTechOpen: London, UK, 2019. [CrossRef]
32. Agência Portuguesa do Ambiente. *Plano de Gestão de Região Hidrográfica 2016/2021. Parte 2. Caracterização e Diagnóstico, Anexo IV*; Agência Portuguesa do Ambiente: Alfragide, Portugal, 2016.

33. Novais, M.H.; Penha, A.M.; Morales, E.A.; Potes, M.; Salgado, R.; Morais, M. Vertical distribution of benthic diatoms in a large reservoir (Alqueva, Southern Portugal) during thermal stratification. *Sci. Total Environ.* **2019**, *659*, 1242–1255. [CrossRef] [PubMed]
34. Instituto Português do Mar e da Atmosfera. *Normais Climatológicas 1981–2010 Provisórias de Beja*; Instituto Português do Mar e da Atmosfera: Lisbon, Portugal; Available online: https://www.ipma.pt/pt/oclima/normais.clima/1981-2010/002/ (accessed on 25 September 2019).
35. Potes, M.; Salgado, R.; Costa, M.J.; Morais, M.; Bortoli, D.; Kostadinov, I.; Mammarella, I. Lake–atmosphere interactions at Alqueva reservoir: A case study in the summer of 2014. *Tellus A* **2017**, *69*. [CrossRef]
36. America Public Health Association. *Standard Methods for the Examination of Water and Wastewater*, 23th ed.; America Public Health Association: New York, NY, USA, 2017.
37. United States Environmental Protection Agency. *Methods for Collection, Storage and Manipulation of Sediments for Chemical and Toxicological Analyses: Technical Manual*; EPA-823-B-01-002.EPA Region V; United States Environmental Protection Agency: Chicago, IL, USA, 2001.
38. Vinçon-Leite, B.; Casenave, C. Modelling eutrophication in lake ecosystems: A review. *Sci. Total Environ.* **2019**, *651*, 2985–3001. [CrossRef]
39. Instituto Português da Qualidade. *NP 4327:Water Quality—Determination of Cholorophyll a and Pheopigments by Molecular Absorption Spectrometry. Extraction Method in Acetone*; Instituto Português da Qualidade: Monte de Caparica, Portugal, 1996.
40. Laboratório Nacional de Engenharia Civil. *E 196—Solos. Análise Granulométrica*; Laboratório Nacional de Engenharia Civil: Lisbon, Portugal, 1966.
41. Vega, M.; Pardo, R.; Barrado, E.D.L. Assessment of seasonal and polluting effects on the quality of river water by exploratory data analysis. *Water Res.* **1998**, *32*, 3581–3592. [CrossRef]
42. Wunderlin, D.A.; Díaz, M.P.; Amé, M.V.; Pesce, S.F.; Hued, A.C.B.M. Pattern recognition techniques for the evaluation of spatial and temporal variations in water quality. A case study: Suquía River Basin (Córdoba-Argentina). *Water Res.* **2001**, *35*, 2881–2894.
43. Salgado, R.; Miranda, P.M.A.; Lacarrère, P.; Noilhan, J. Boundary layer development and summer circulation in Southern Portugal. *Tethys* **2015**, *12*. [CrossRef]
44. Zhang, D.; Wang, X.; Zhou, Z. Impacts of small-scale industrialized swine farming on local soil, water and crop qualities in a hilly red soil region of subtropical China. *Int. J. Environ. Res. Public Health* **2017**, *14*, 1524. [CrossRef]
45. Zhou, Y.; Xu, J.F.; Yin, W.; Ai, L.; Fang, N.F.; Tan, W.F.; Yan, F.L.; Shi, Z.H. Hydrological and environmental controls of the stream nitrate concentration and flux in a small agricultural watershed. *J. Hydrol.* **2017**, *545*, 355–366. [CrossRef]
46. Saraiva, A.; Rodrigues, G.; Mamede, H.; Silvestre, J.; Dias, I.; Feliciano, M.; Oliveira, E.; Silva, P.; Oliveira, M. The impact of the winery's wastewater treatment system on the winery water footprint. *Water Sci. Technol.* **2020**, *80*, 1823–1831. [CrossRef] [PubMed]
47. Elçi, Ş. Effects of thermal stratification and mixing on reservoir water quality. *Limnology* **2008**, *9*, 135–142. [CrossRef]
48. Fontes, C.L. Modelling of Water Quality in the Alqueva Reservoir. Ph.D. Thesis, University of Minho, Braga, Portugal, 2010; p. 172.
49. Nunes, J.P.; Jacinto, R.; Keizer, J.J. Combined impacts of climate and socio-economic scenarios on irrigation water availability for a dry Mediterranean reservoir. *Sci. Total Environ.* **2017**, *584–585*, 219–233. [CrossRef] [PubMed]
50. Lisboa, M.S.; Schneider, R.L.; Sullivan, P.J.; Walter, M.T. Drought and post-drought rain effect on stream phosphorus and other nutrient losses in the Northeastern USA. *J. Hydrol. Reg. Stud.* **2020**, *28*, 100672. [CrossRef]
51. Mosley, L.M. Drought impacts on the water quality of freshwater systems; review and integration. *Earth Sci. Rev.* **2015**, *140*, 203–214. [CrossRef]
52. Gutiérrez-Cánovas, C.; Arribas, P.; Naselli-Flores, L.; Bennas, N.; Finocchiaro, M.; Millán, A.; Velasco, J. Evaluating anthropogenic impacts on naturally stressed ecosystems: Revisiting river classifications and biomonitoring metrics along salinity gradients. *Sci. Total Environ.* **2019**, *658*, 912–921. [CrossRef]
53. Krupa, E.; Barinova, S.; Amirgaliyev, N.A.; Issenova, G.; Kozhabayeva, G. Statistical approach to estimate the anthropogenic sources of potentially toxic elements on the shardara reservoir (Kazakhstan). *MOJ Ecol. Environ. Sci.* **2017**, *2*. [CrossRef]
54. Wu, Z.; Zhang, Y.; Zhou, Y.; Liu, M.; Shi, K.; Yu, Z. Seasonal-spatial distribution and long-term variation of transparency in Xin'anjiang Reservoir: Implications for reservoir management. *Int. J. Environ. Res. Public Health* **2015**, *12*, 9492–9507. [CrossRef]
55. Agencia Portuguesa do Ambiente. *Plano de Gestão de Região Hidrográfica 2016/2021: Região Hidrográfica do Guadiana (RH7)*; Agência Portuguesa do Ambiente: Alfragide, Portugal, 2016.
56. Zuccarello, P.; Manganelli, M.; Oliveri Conti, G.; Copat, C.; Grasso, A.; Cristaldi, A.; De Angelis, G.; Testai, E.; Stefanelli, M.; Vichi, S.; et al. Water quality and human health: A simple monitoring model of toxic cyanobacteria growth in highly variable Mediterranean hot dry environments. *Environ. Res.* **2021**, *192*, 110291. [CrossRef] [PubMed]
57. Instituto da Água Relatório. *Síntese Sobre a Caracterização das Regiões Hidrográficas prevista na Directiva-Quadro da Água*; Instituto da Água Relatório: Alfragide, Portugal, 2005; p. 163.
58. Al-Taani, A.A.; El-Radaideh, N.M.; Al Khateeb, W.M.; Al Bsoul, A. Reservoir water quality: A case from Jordan. *Environ. Monit. Assess.* **2018**, *190*. [CrossRef]
59. Naveedullah, N.; Hashmi, M.Z.; Yu, C.; Shen, C.; Muhammad, N.; Shen, H.; Chen, Y. Water Quality Characterization of the Siling Reservoir (Zhejiang, China) Using Water Quality Index. *Clean Soil Air Water* **2016**, *44*, 553–562. [CrossRef]

60. Mavromati, E.; Kagalou, I.; Kemitzoglou, D.; Apostolakis, A.; Seferlis, M.; Tsiaoussi, V. Relationships Among Land Use Patterns, Hydromorphological Features and Physicochemical Parameters of Surface Waters: WFD Lake Monitoring in Greece. *Environ. Process.* **2018**, *5*, 139–151. [CrossRef]
61. Coppens, J.; Özen, A.; Tavşanoğlu, T.N.; Erdoğan, Ş.; Levi, E.E.; Yozgatligil, C.; Jeppesen, E.; Beklioğlu, M. Impact of alternating wet and dry periods on long-term seasonal phosphorus and nitrogen budgets of two shallow Mediterranean lakes. *Sci. Total Environ.* **2016**, *563–564*, 456–467. [CrossRef]
62. Søndergaard, M.; Jensen, J.P.; Jeppesen, E. Role of sediment and internal loading of phosphorus in shallow lakes. *Hydrobiologia* **2003**, *506–509*, 135–145. [CrossRef]
63. Caetano, S. Toxicity Risks Linked to Cyanobacteria Blooms in Southern Portugal Reservoirs. Ph.D. Thesis, University of Algarve, Algarve, Portugal, 2015.
64. Rzetala, M.; Babicheva, V.A.; Rzetala, M.A. Composition and physico-chemical properties of bottom sediments in the southern part of the Bratsk Reservoir (Russia). *Sci. Rep.* **2019**, *9*, 1–9. [CrossRef]
65. Cardoso-Silva, S.; de Lima Ferreira, P.A.; Moschini-Carlos, V.; Figueira, R.C.L.; Pompêo, M. Temporal and spatial accumulation of heavy metals in the sediments at Paiva Castro Reservoir (São Paulo, Brazil). *Environ. Earth Sci.* **2016**, *75*, 1–16. [CrossRef]
66. Palma, P.; Fialho, S.; Lima, A.; Mourinha, C.; Penha, A.; Novais, M.H.; Rosado, A.; Morais, M.; Potes, M.; Costa, M.J.; et al. Land-cover patterns and hydrogeomorphology of tributaries: Are these important stressors for the water quality of reservoirs in the mediterranean region? *Water* **2020**, *12*, 2665. [CrossRef]
67. Cardoso-Silva, S.; Da Silva, D.C.V.R.; Lage, F.; de Paiva, T.C.B.; Moschini-Carlos, V.; Rosa, A.H.; Pompêo, M. Metals in sediments: Bioavailability and toxicity in a tropical reservoir used for public water supply. *Environ. Monit. Assess.* **2016**, *188*. [CrossRef]
68. Cardoso-Silva, S.; de Lima Ferreira, P.A.; Figueira, R.C.L.; da Silva, D.C.V.R.; Moschini-Carlos, V.; Pompêo, M.L.M. Factors that control the spatial and temporal distributions of phosphorus, nitrogen, and carbon in the sediments of a tropical reservoir. *Environ. Sci. Pollut. Res.* **2018**, *25*, 31776–31789. [CrossRef] [PubMed]
69. Fletcher, R.; Welsh, P.F.P. *Guidelines for Identify, Assessing and Managing Contaminated Sediments in Ontario: An Integrated Approach*; Water Resources Branch: Toronto, ON, Canada, 2008.
70. Barros, M.C.; Mendo, M.J.M.; Negrão, F.C.R. Surface water quality in Portugal during a drought period. *Sci. Total Environ.* **1995**, *171*, 69–76. [CrossRef]

atmosphere

MDPI

Article

Lake and Land Breezes at a Mediterranean Artificial Lake: Observations in Alqueva Reservoir, Portugal

Carolina Purificação [1,*], Miguel Potes [1,2], Gonçalo Rodrigues [1,2], Rui Salgado [1,2] and Maria João Costa [1,2]

[1] Science and Technology School, University of Évora, Rua Romão Ramalho 59, 7000-671 Évora, Portugal; mpotes@uevora.pt (M.P.); grodrigues@uevora.pt (G.R.); rsal@uevora.pt (R.S.); mjcosta@uevora.pt (M.J.C.)
[2] Institute of Earth Sciences—ICT, Pole of the University of Évora, Rua Romão Ramalho 59, 7000-671 Évora, Portugal
* Correspondence: m40949@alunos.uevora.pt or carolina.purificacao.20@gmail.com

Abstract: The Alqueva reservoir, in the Southeast of Portugal, has significantly changed the landscape of the region, with impacts also on the local climate, as documented in this manuscript, namely the thermal circulation in the form of lake and land breezes. Taking advantage of three strategic meteorological stations, two installed at the shores and another on a floating platform located near the center of the reservoir, a detailed analysis of lake and land breeze occurrences during two years is presented in this study. The thermal gradient between the reservoir and the surroundings is the main driver for the breeze development and the meteorological stations placed in opposite sides of the reservoir allow to establish the criteria in order to detect lake and land breezes. The results showed more land breeze than lake breeze occurrences, in line with the more negative thermal gradient between shores and reservoir in the annual cycle. Lake breezes are more frequent in summer months during daytime and land breezes in turn are more frequent in winter months during night-time.

Keywords: lake and land breezes; Alqueva reservoir; atmospheric observation; lake–atmosphere interaction

check for updates

Citation: Purificação, C.; Potes, M.; Rodrigues, G.; Salgado, R.; Costa, M.J. Lake and Land Breezes at a Mediterranean Artificial Lake: Observations in Alqueva Reservoir, Portugal. *Atmosphere* **2021**, *12*, 535. https://doi.org/10.3390/atmos12050535

Academic Editors: Sukanta Basu and Gunnar W. Schade

Received: 24 February 2021
Accepted: 20 April 2021
Published: 22 April 2021

Publisher's Note: MDPI stays neutral with regard to jurisdictional claims in published maps and institutional affiliations.

Copyright: © 2021 by the authors. Licensee MDPI, Basel, Switzerland. This article is an open access article distributed under the terms and conditions of the Creative Commons Attribution (CC BY) license (https://creativecommons.org/licenses/by/4.0/).

1. Introduction

Lake and land breezes are prominent events induced by the thermal contrasts between water and land surfaces, and its structure and magnitude depend on the topography [1,2], the surface area and the seasonality [3]. In particular, lake dimension is a very important point of the study, since the results from Wang et al. [4] indicate that the characteristics of lake and land breezes vary greatly with lake properties, such as lake size and depth. Particularly in regions such as Northern Europe, Asia and North America, the lake surface can be very large and the high density of lakes may affect the regional climate [5,6]. Generally, a larger frequency, longer duration, and stronger lake breezes occur more in large and deep lakes than in small or middle-sized lakes [7]. Keen and Lyons [8] found, more than 40 years ago, the existence of lake and land breezes on Lake Michigan that reached until 15 km away from the study site, while Schoenberger [9], a few years later, discussed land breeze development in wintertime at the same Lake Michigan.

In some regions, the abrupt variation of surface properties can generate organized atmospheric circulation in response to the existence of temperature differences between surfaces, commonly called breezes. The high-water heat capacity in relation to any type of terrestrial soil means that during the day, the solar radiation heats terrestrial surfaces much more intensely than the surface of the reservoir, with reduced variation of the surface water temperature over a daytime cycle [10]. Additionally, topography may contribute to the establishment of breeze circulations, with inversion of the circulation between daytime and night-time situations. During daytime, the surrounding land near a lake acts as a heating source inducing upward motions and allowing a cooler air circulation coming from the water, similar to what occurs in sea breezes. This phenomenon happens when the air

becomes less dense over land (lower pressure) than over the lake [11]. Consequently, warm air rises over land and cooler humid air descends over the lake creating a depression over land and high pressure over the reservoir, at the surface level. In altitude, the air moves to the lake (where the pressure is lower) and it circulates towards the Earth's surface, closing the circulation [12]. During the night, the opposite circulation can occur, with a current of fresh air taking place from the land to the lake along the slopes. This land breeze is triggered when the surrounding land cools down and the lake surface remains warmer causing the inversion of the circulation, with hot air rising upward in the lake and cooler air descending over the surroundings [13–16].

Observational studies have been used to characterize both the influence and the frequency of the lake and land breezes in several places around the world. Lemmin and Adamo [1] studied the importance of lake–land breezes from analysis of the summer wind components around Lake Geneva, Switzerland in terms of their spatial and temporal characteristics, in particular of lake–land breezes during the period May to September 1981–1987. The duration of individual events between May and October for wind speeds above 5 ms^{-1} was between 1 and 2 h, and during summer the wind events were shorter and of higher velocity. The authors evidenced that the local topography modifies the lake–land breeze pattern in some parts of the basin and leads in general to spatially variable distributions of wind stress around the lake. Giovannini et al. [17] described that the "Ora del Garda", which is a coupled lake–valley breeze, regularly blows during warm-season clear-sky days in Lake Garda, Italian Alps. The breeze develops on about 70% of the days in the warmest months, while it rarely occurs from October to February. Moreover, in the warmest months, the "Ora del Garda" reaches the inland weather station on about 80–90% of the days probably due to the combination of lake and valley effects. Le Moigne et al. [18] studied the Thau lagoon, located in Southern France, which is separated from Mediterranean Sea by a 1 km-wide strip of land. The authors have found sea-breeze events especially focusing on the boundary layer height over the lagoon that rise on average at around 11 UTC and drop in intensity from 18 UTC on, whilst the land breezes were observed on the lagoon from 07 UTC to 08:30 UTC. Nonetheless, sea breeze regimes are usually observed by the end of the afternoon during hot summertime and dry weather conditions [19]. Lake and land breezes may develop over lakes and lagoons located close to the sea, nevertheless these are difficult to distinguish from the sea breezes [20,21].

Tsujimoto and Koike [22] investigated the development mechanisms of lake and land breezes at low latitudes, in Tonle Sap Lake in Cambodia first using in situ observations and satellite images, and after exploring the circulation mechanism through numerical simulations using a mesoscale atmospheric model (Advanced Regional Prediction System, ARPS) that considered cloud formation. Results from the water surface temperature experiment suggest that warm water surface temperature (30.6 °C) served to initiate the updraft, whereas a lower water surface temperature (25.6 °C) could not. Tonle Sap Lake is a very shallow lake, with average and maximum depth of 2 and 10 m [23], thus easily warmed, hence, these lake characteristics enable the development of strong land breezes with updraft movements.

The Alentejo region, south of Portugal, is influenced by the continental and maritime climate depending on the distance to the coast. In the interior of the Alentejo region, the climate presents humid and cold winters and dry and hot summers [24]. Salgado et al. [25] showed that the low-level summer circulation in Alentejo is forced by land–sea thermal contrasts that give rise to a quasi-permanent thermal low frequently located over the central region of the Iberian Peninsula. In the region, the strong sea breeze can reach more than 100 km inland, influencing the interior areas of the country in the late afternoon, as shown by the increase in the wind intensity and its rotation [25].

The generation of lake breezes near the Alqueva reservoir has already been the subject of some studies. Lopes et al. [26] studied the effect of the lake breeze in Alqueva reservoir in the local atmospheric electric potential gradient. Potes et al. [27] studied lake–atmosphere interactions at the Alqueva reservoir and found observational evidence of lake breeze by

comparing the measurements in three stations located at the lake shores: Amieira, Barbosa and Cid Almeida. More recently, Iakunin et al. [16] quantified the lake breeze effects induced by the Alqueva reservoir from simulations with the mesoscale atmospheric model Meso-NH coupled to the FLake freshwater lake model. Two simulations with the presence and absence of the reservoir on the model surface were performed and compared with meteorological data collected during an intensive observational period in summer 2014. The authors stated that the breeze system starts to form in the morning and the peak of the wind speed reaches 6 ms^{-1} during the afternoon, while the dissipation stage of the lake breeze system is anticipated with the arrival of the larger-scale sea breeze from the Atlantic coast late in the afternoon. In addition, the simulations indicate that the lake breeze could be detected at a distance of more than 6 km away from the lake shores.

However, none of the previous studies dealt with land breezes. The present work intends to address thermal circulations in Alqueva reservoir in a global way, including lake and land breezes. Therefore, this is the first study of observational evidence of Land Breezes in the region. This study was performed in the framework of the ALOP (ALentejo: Observation and Forecasting systems, http://www.alop.ict.uevora.pt/?lang=en, accessed on 28 October 2020) project, and the lake and land breeze effects are investigated using data from automatic weather stations located at the shores and at the center of the reservoir during two years [28]. This work is organized as follows: Section 2 gives an overview of the Alqueva reservoir, Lake and Land breeze characterizations at Alqueva and details of the methodology adopted for detection of Breezes between onshore stations at opposite sides; In Section 3, results of two years of breezes are shown as well as stronger lake and land breeze cases during the period of study; conclusions are given in Section 4.

2. Data and Methodology

2.1. Site Description

The Alqueva reservoir is located along 83 km of the main course of Guadiana River, in the interior of Alentejo, as shown in Figure 1. Considered one of the largest artificial lakes in Europe, it represents a strategic water reserve for the south of Portugal covering the municipalities of Moura, Portel, Mourão, Reguengos de Monsaraz and Alandroal and occupying an area of 250 km^2 with a flood flow of 12,000 m^3/s [28–30] and maximum depth of 65 m. The reservoir is a large natural laboratory for the study of the interaction between inland water bodies and the atmosphere. This artificial lake, belonging to the Guadiana basin, has significantly modified the landscape of the region and has impacts on the local climate that are still poorly documented [31].

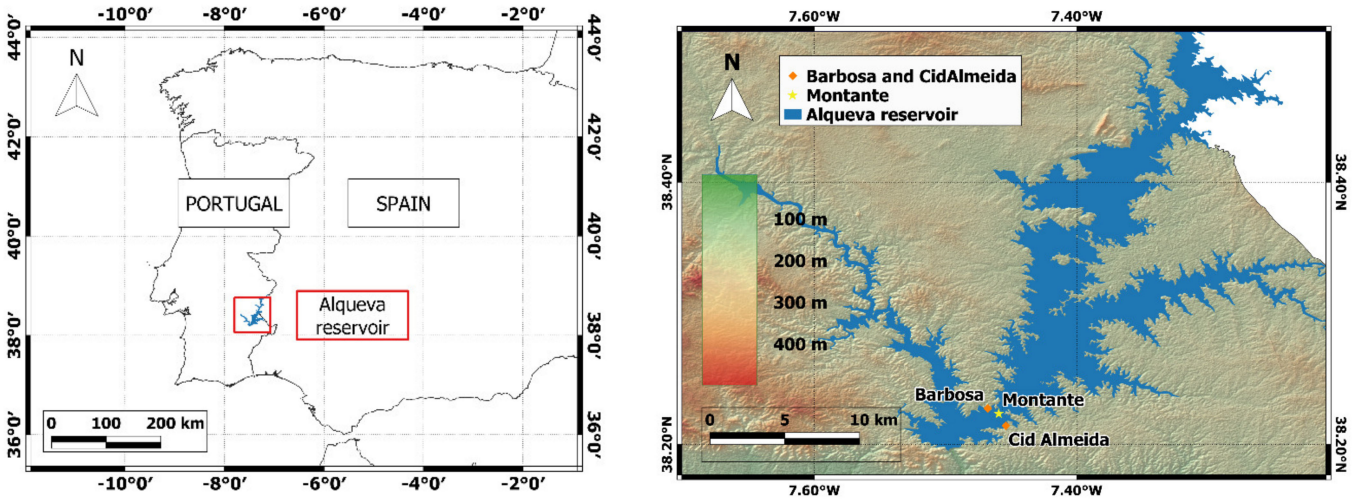

Figure 1. Localization of Alqueva reservoir (**left panel**) and location of meteorological stations used in this study (**right panel**). Source: QGIS.

Previously to the construction of the dam, a case study was carried out on the environmental impact that the influence area of the Alqueva Multipurpose Project (including an irrigation area of around 120,000 ha) would have on the climate. One of the conclusions of the study was that there could be a reduction in the 2 m air temperature during summer, with a substantial reduction in the maximum temperature (of the order of −7 °C) and also in the daily thermal amplitude (of the order of −5 °C) over densely irrigated areas [32]. However, since the filling phase of the reservoir until the present, only a few studies have been developed on the impact of the lake water body in the local climate.

2.2. Meteorological Stations at Alqueva Reservoir

In the framework of the ALOP project, the protocols for collection and storage of the data in the meteorological stations were harmonized in order to guarantee accurate comparison between the observations. This study is based on observations and analysis of meteorological parameters from a set of three automatic weather stations installed in the region in the period comprised between 1 May 2017 and 30 April 2019. The project ALOP takes advantage of the facilities already installed in the reservoir. The meteorological station on the floating platform Montante was installed during the filling phase (2002) by the Portuguese Environment Agency [29]. The onshore stations were installed in the vicinity of the Montante station on opposite shores to support the measurements of the platform and to study the effect of lake and land breeze. The three weather stations are separated by approximately 2 km (Figure 1): one at the north shore identified as Barbosa (38°13′39.18″ N, 7°28′14.74″ W), one at the south shore called Cid Almeida (38°12′59.00″ N, 7°27′16.34″ W) and another in the middle of these two, installed in a floating platform over the Alqueva reservoir named Montante (38°13′24.75″ N, 7°27′34.18″ W). Throughout the manuscript the time used is UTC. Local winter time is the same as UTC and local summer time is UTC + 1.

Barbosa and Cid Almeida stations include the following measuring instruments:

- Thermo-Hygrometer at 2 m height (air temperature and relative humidity);
- 2-axis Ultrasonic Anemometer at 3 m height (wind speed and direction);
- Udometer (precipitation);
- Albedometer (downwelling and upwelling solar irradiance).

In Montante the following equipment is installed:

- Temperature Array of 14 thermistors (water temperatures sensors measured at 0.05, 0.25, 0.50, 1, 2, 4, 6, 8, 10, 12, 15, 20, 30, and 60 m depth);
- Integrated open-path analyzer and sonic anemometer (IRGASON) measuring the following parameters at 1.75 m from the water surface:
    - Air temperature;
    - Atmospheric pressure;
    - Wind speed and direction;
    - Water vapor concentration;
    - Carbon dioxide concentration.
- Albedometer (downwelling and upwelling solar irradiance);

The meteorological variables of the three weather stations located in Alqueva (Figure 1) were measured every 5 s in the dataloggers and the averages/accumulation were recorded every minute.

2.3. Criteria for Breeze Detection between Onshore Stations at Opposite Sides

Lake and land breeze generation usually occurs under clear sky conditions, calm or light synoptic wind and considerable temperature differences between land and water surfaces. A few studies have proposed some criteria for breeze detection. Giovannini et al. [17] used a set of six objective criteria based on observations of solar radiation, wind speed and direction at two onshore stations, in order to identify lake-breeze days in lake Garda (Italy). Potes et al. [27] used the following criteria to select days with high probability

of lake breeze occurrence: daily maximum of the temperature difference between air (in Barbosa station) and water (in Montante) greater than 7 °C; and daily average wind speed lower than 3.5 m s^{-1} at Barbosa station. By applying these criteria, the authors ensure high temperature gradients between the lake and the surroundings and avoid the presence of a strong synoptic circulation or a strong sea breeze, which can mask the local effects. They noticed that the wind changed from the north component to the south component at Barbosa station, which is located on the northern shore of the reservoir, whereas at the same time in Cid Almeida station, located on the southern shore of the reservoir, the wind remained from the north quadrant during the period 9–18 UTC.

This study takes advantage of the position of the meteorological stations installed in the shores in relation to the reservoir. The wind directions that represent lake and land breezes should be divided according to the 225°–45° plane i.e., in the SW–NE axis (Figure 2). We based our criteria mainly on wind divergence and convergence over the lake, for lake and land breeze scenario, respectively, discarding some of the criteria presented above. Nevertheless, some of them will be examined in the results.

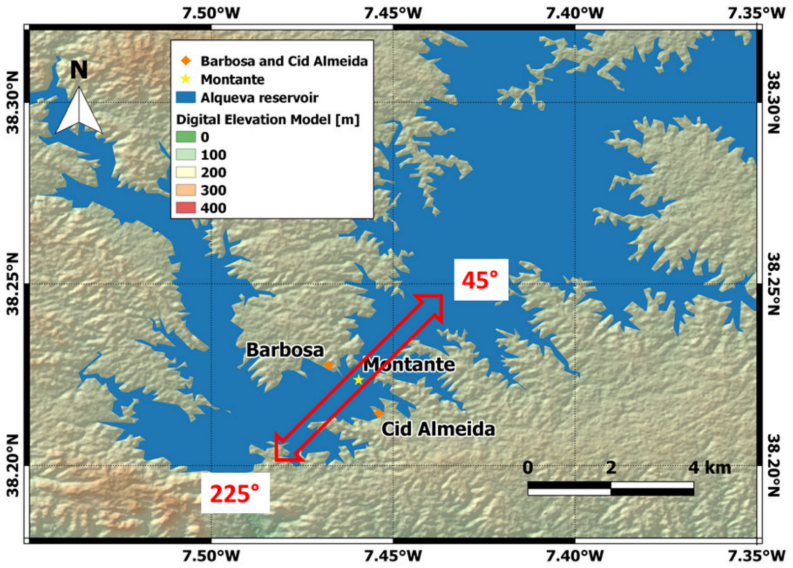

Figure 2. Location of the meteorological stations and the 225°–45° plane (in the SW–NE axis) used in this study to detect the lake and land breeze occurrences. Source: QGIS.

Thus, the following criteria were established:

- For lake breeze scenario, the wind direction on the north shore (Barbosa) had to be greater than 45° and lower than 225° (from the lower half—lake side) and at the same time on the south shore (Cid Almeida), the wind should have the opposite direction (from the upper half); we also tested other plans, namely the 240°–60° plane, which is roughly parallel to the southern shoreline of the reservoir, and the results showed only slight differences of the order of 1–3% of total breeze hours. We decided to apply the 225°–45° plane, which is closest to the reservoir's symmetry axis on this section.
- In case of land breeze circulation, the wind field should be reverse with respect to that of lake breeze case and wind should blow from the upper half (land side) in Barbosa and from the lower half in Cid Almeida;
- Additionally, for both cases the wind direction difference between the two onshore stations has to be greater than 90° to avoid close directions even in opposite quadrants, that do not represent breeze circulations;
- For both scenarios, daily precipitation events greater than 0.5 mm were discarded, following Román-Cascón et al. [33];
- Finally, in order to be considered a breeze event at a particular hour, the conditions should be fulfilled during at least twenty minutes.

With the criteria used in this work, eventual episodes of valley (mountain) breezes may be detected as lake (land) breezes. Given the low relief of the region and with water filling the valley, the anabatic and katabatic winds hardly generate an autonomous breeze system, rather reinforce the lake/land breeze. It is also possible that the flow channeling along the valley (now a reservoir) may generate difluence or confluence of the wind of purely mechanical origin. In this sense and in this work, it is considered that there is a lake breeze whenever the air blows from the lake to the land (simultaneously on both margins) and a land breeze whenever the air blows from land to the reservoir.

3. Results and Discussion

3.1. Thermal Gradient between Lake and Surroundings

Lake and land breeze events were detected during the two years of study period, between 1 May 2017 and 30 April 2019 at Alqueva reservoir. While lake breeze developed more often in summer and autumn months, land breeze developed along all the year with more occurrences in winter and autumn months. The thermal contrast between the reservoir and adjacent land is the crucial factor for the development of lake and land breezes. In Figure 3 the monthly temperature differences between the onshore stations (Cid Almeida and Barbosa) and the platform station (Montante) are shown. Figure 3a–c shows the monthly differences for average, maximum and minimum air temperatures, respectively, and Figure 3d illustrates the differences between air temperature in onshore stations and water temperature at 0.5 m depth obtained from the platform station. There are two gaps in the monthly data, in October 2018 and February 2019, due to lack of data in more than 10 days of these months.

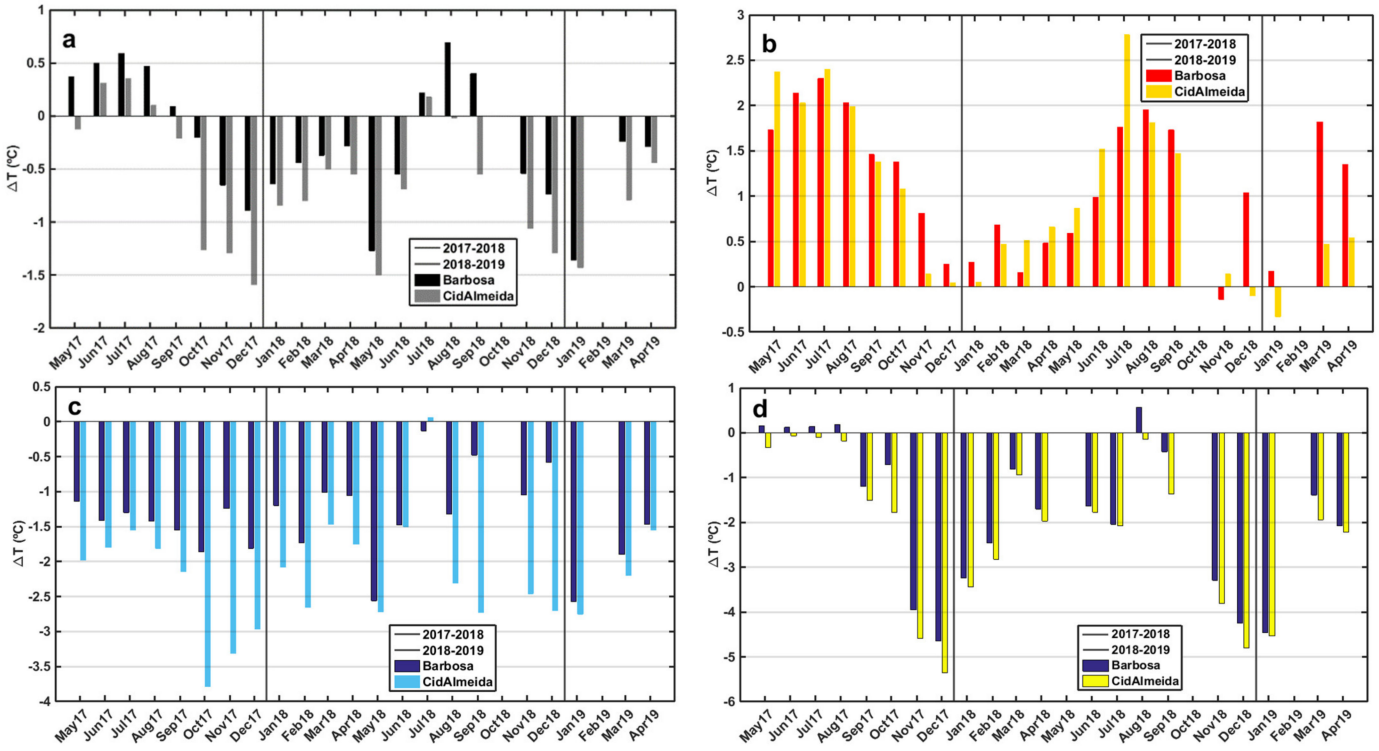

Figure 3. Monthly temperature differences between onshore stations (Barbosa and Cid Almeida) and platform station (Montante) for: (**a**) mean air temperature; (**b**) maximum air temperature; (**c**) minimum air temperature. (**d**) Monthly difference between air temperature in onshore stations and water temperature at 0.5 m depth (in Montante station). Grey vertical lines separate the years 2017, 2018 and 2019.

The temperature differences present seasonal dependence showing that in general during summer the average air temperature differences between shores and reservoir are

positive, while negative differences occur from autumn to spring with more pronounced values in Cid Almeida (Figure 3a). Positive differences mean that lake shores are warmer than the center of the lake, and vice-versa. Between autumn and spring, the air temperature over the lake is higher than at the shores due to higher water surface temperatures with respect to the surrounding land surface, and the opposite is noticed in the summer period. The average air temperature difference was maximum in Cid Almeida in July 2017 with a value of 0.4 °C and in Barbosa in August 2018 with 0.7 °C. The minimum differences were −1.6 °C in December 2017 in Cid Almeida and −1.4 °C in Barbosa in January 2019. We note that in May 2017 there was a positive difference in Barbosa and a slightly negative one in Cid Almeida, and in May 2018 both stations present a very negative difference, which can be due to very different meteorological conditions in the springs of these two years. April and May 2017 were drier and warmer than the equivalent months in 2018 that were very humid and colder (Figure 3a,c). For the same reason June 2017 had positive temperature difference and June 2018 had negative difference. Similarly, in September there are some differences between both years. In fact, spring and autumn months represent in the region transition seasons with highly variable conditions in terms of synoptic patterns conditioned by the movement of the polar front, determining the occurrence of Atlantic frontal systems over the area [34].

Regarding the monthly maximum temperature differences, shown in Figure 3b, the values are mostly positive throughout the study period with higher values in summer and lower (and slightly negative) during the winter. In Figure 3c the monthly minimum temperature difference is shown. An opposite behavior with respect to that of the maximum difference is noticed with almost all values being negative, presenting lower values in winter. These two plots illustrate the attenuation that the water mass can cause to the air temperature above its surface in relation to the air temperature at both shores, reducing the air temperature amplitude above the reservoir. Water is colder than air and land surface during summer and warmer during the winter.

Figure 3d shows the monthly difference between the average air temperature at the onshore stations and the water temperature at 0.5 m depth in Montante. This plot presents a similar behavior with respect to that shown in Figure 3a, nevertheless, the positive differences in summer are smaller and the negative differences in the rest of the seasons are higher. The different vertical structure of the thermal profile between the summer and the winter explains why, in summer, the lake surface temperature increases during daytime, reducing the thermal contrasts. Contrariwise, the nonstratified profile in winter nights, curbs the decrease of the surface temperature, reinforcing the contrast with the neighboring land. The wind roses for the whole period are presented in Figure 4 for Barbosa and CidAlmeida stations. It is evident the predominance of stronger Northwest winds, with almost 13% in Barbosa and 10% in CidAlmeida. In CidAlmeida we also note that more than 8% of the winds were from the Southeast quadrant.

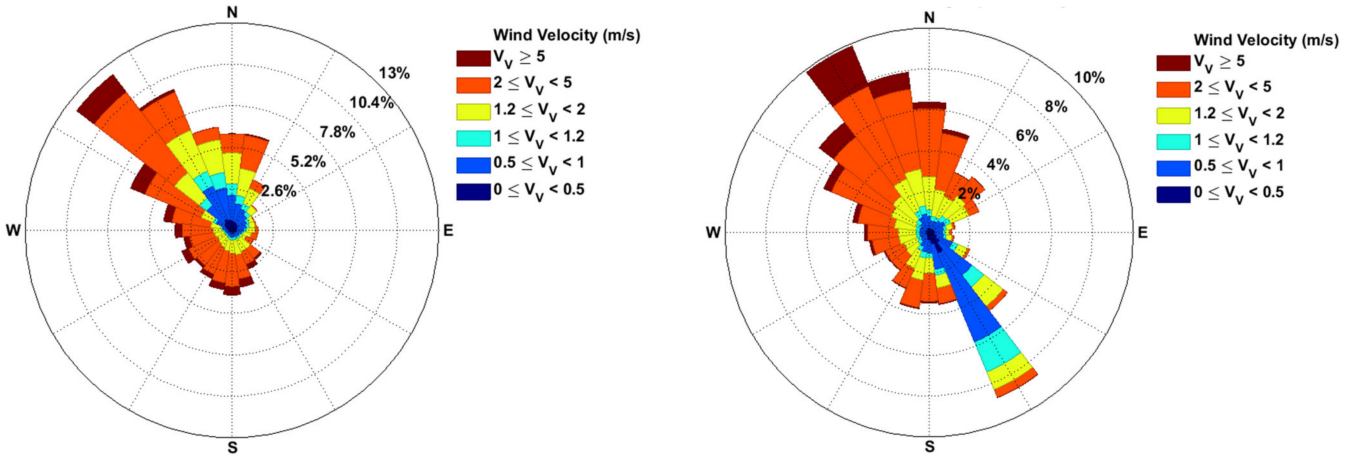

Figure 4. Wind roses for the full period in Barbosa station (**left panel**) and for CidAlmeida station (**right panel**).

3.2. Lake Breeze

The number of lake breeze occurrences in hours is shown in Figure 5 at the following scales: monthly (a), daily cycle per month (b) and daily cycle for all period (c). As expected, and according to the positive thermal gradient between the lake and the shores presented in the Section 3.1, the lake breezes are more frequent in summer, spring and autumn and less frequent in winter. There are only a few lake breeze events during night-time with prevalence of daytime events during the study period (Figure 5c). During the entire period (730 days) we found lake breeze in 386 days that more frequently starts at 07:00 and dissipates at 16:00. On average the lake breeze lasts 3.5 h with maximum duration of 10 h on 3 August 2018. It can be seen that the maximum number of occurrences happened in August 2018 with a total of 151 h, followed by June, July and August 2017. In August 2018, the highest positive difference between mean air temperature in Barbosa and Montante was registered (0.69 °C—Figure 3a), creating the conditions for lake breeze occurrences. The relationship between the temperature gradient and the strength of the lake breeze was studied. However, the slight tendency found is not statistically significant (not shown here). Most of the lake breeze velocities were between 1 and 2 m/s and occurred with temperature gradients between 1 and 3 °C. The breezes occurred in a larger period of the day with maximum incidence between 11:00 and 12:00 (Figure 5b). August 2018 contributes with 19 occurrences at 11:00, to a total of 220 h that were recorded at 12:00 during all of the study period (Figure 5c). June, July and August 2017 also present positive thermal gradient between onshore stations and platform (Figure 3a) allowing good conditions for lake breeze formation. A total of 112 occurrences were recorded both in June and July while 132 in August 2017.

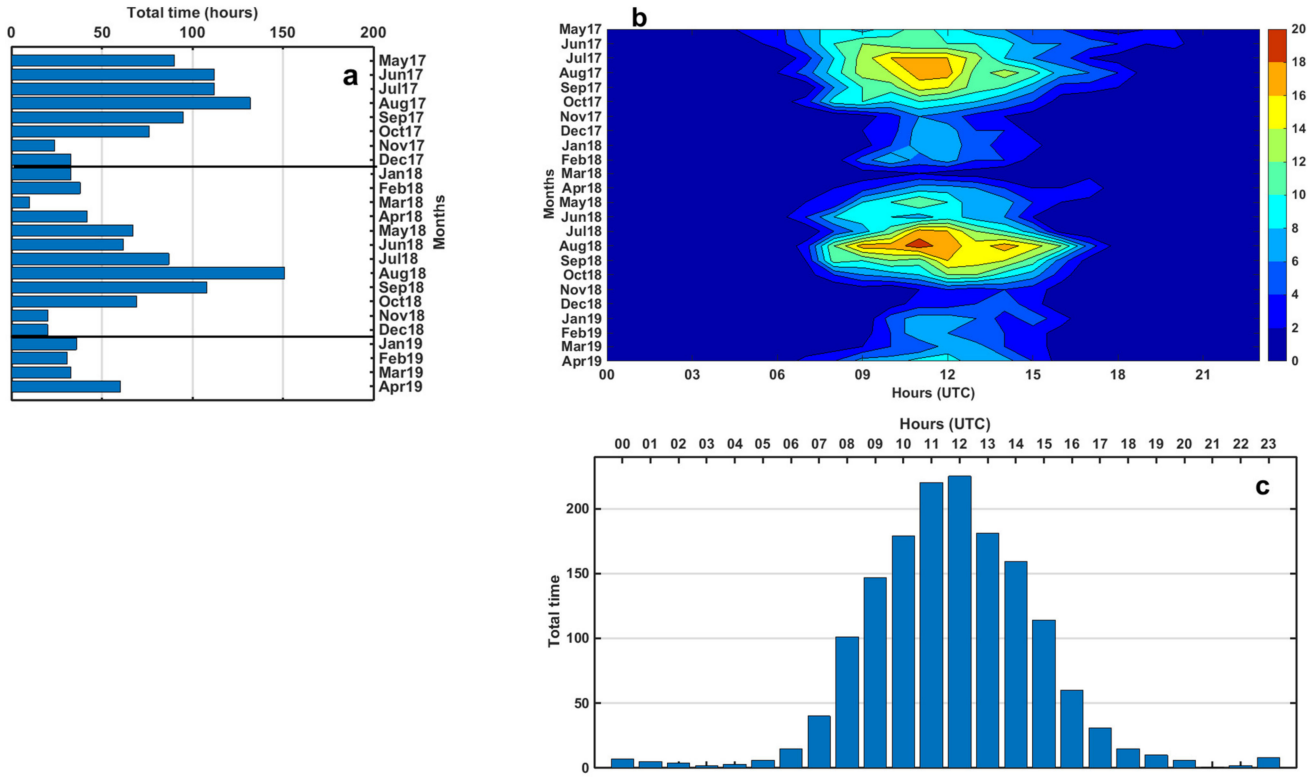

Figure 5. Lake breeze occurrences in hours representing monthly (**a**), daily cycle per month (**b**) and daily cycle for the whole period (**c**). Grey horizontal lines in panel (**a**) separate the years 2017, 2018 and 2019.

Still, according to Figure 5, the lake breeze occurred most frequently between 07:00 to 16:00. In June and July 2018, the average air temperature was lower than the water temperature at 0.5 m depth (Figure 3d) by around 2 °C. Thus, it was noticed that these months presented a lower number of lake breeze occurrences than the corresponding

months of 2017 (Figure 5a). This was due to a very rainy Spring in 2018 (and also February), with monthly accumulated values of precipitation above the climatological normal, e.g., March registered an accumulation of around 200 mm which is one third of the annual precipitation [35]. This period was very active regarding the passage of frontal systems in Portugal and this synoptic situation, with higher wind speed, inhibited the local thermal circulation. March 2018 presented the minimum number of occurrences, with only 10 h, nevertheless, it was in December 2017 and in January 2019 that the lowest average air temperature differences between Cid Almeida and Montante and Barbosa and Montante occur, respectively. In January 2019, 36 h of lake breeze were detected, mostly around 11:00 and 12:00. This is due to a period of around 15 days with clear sky, low wind speed and a high thermal amplitude allowing for both lake and land breeze occurrences in the same day.

August 2018 was the month with highest thermal gradient between Barbosa and the middle of the reservoir, as well as highest thermal gradient between air in the Barbosa and the lake water. While in Cid Almeida the highest thermal gradient occurred in July 2017, the second higher for Barbosa was in this month. The highest gradient in August 2018 led to the highest lake breeze occurrences of the whole period, as mentioned before. The daily cycle of the temperature difference between air at the shores and water in Montante for August 2018 is shown in Figure 6. The air temperature in the onshore stations is higher than the water temperature during daytime, coinciding with the period with the highest lake breezes occurrence. During night-time and early morning, the land surface cools and the difference becomes negative, inhibiting the formation of the lake breeze, but allowing the formation of land breezes (discussion in the next section).

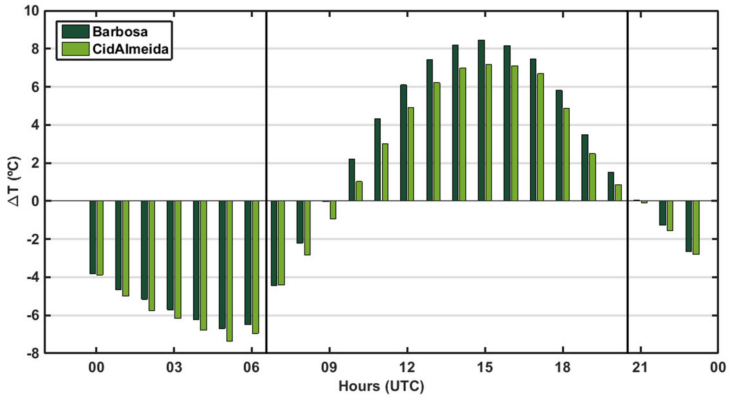

Figure 6. Daily cycle of the temperature difference between air and water at 0.5 m depth in Montante in August 2018. Grey vertical lines indicate the sunrise and sunset.

Stronger Lake Breeze Cases

A strong lake breeze case was considered when a day presented more than 6 h of lake occurrence. During the entire period (730 days) there were 102 days with 6 or more hours of lake breeze. On these days the average wind speed was 1.55 ms^{-1} with maximum wind speed of 3.65 ms^{-1} at onshore stations. The average air temperature difference between these stations and the center of the reservoir was 0.9 °C and between air on the shores and water in the reservoir was 3.55 °C. These particular days presented at the onshore stations an average solar radiation of 600.6 Wm^{-2}, relative humidity of 43% and air temperature of 27.4 °C.

Nonetheless, the day with more lake breeze occurrences was the 3 August 2018, with 10 h. The air temperature for the three stations (upper panel) as well as temperature difference of the onshore stations in relation to the platform (bottom panel) are shown in Figure 7. The air temperature on both shores presents a sharper increase with respect to that over the lake (Montante) and remains higher from 09:00 to 18:00. In the lower panel it is visible that in Barbosa the gradient is up to 8 °C and in Cid Almeida up to 6 °C, with a

point value of 7.6 °C around 13:00, with perfect conditions for lake breeze development. On this day, lake breezes occurred from 07:00 to 10:00, at 12:00, from 14:00 to 17:00 and at 23:00 when the air temperature on the shores suddenly increases and gets higher than that of air above the lake (lower panel of Figure 7).

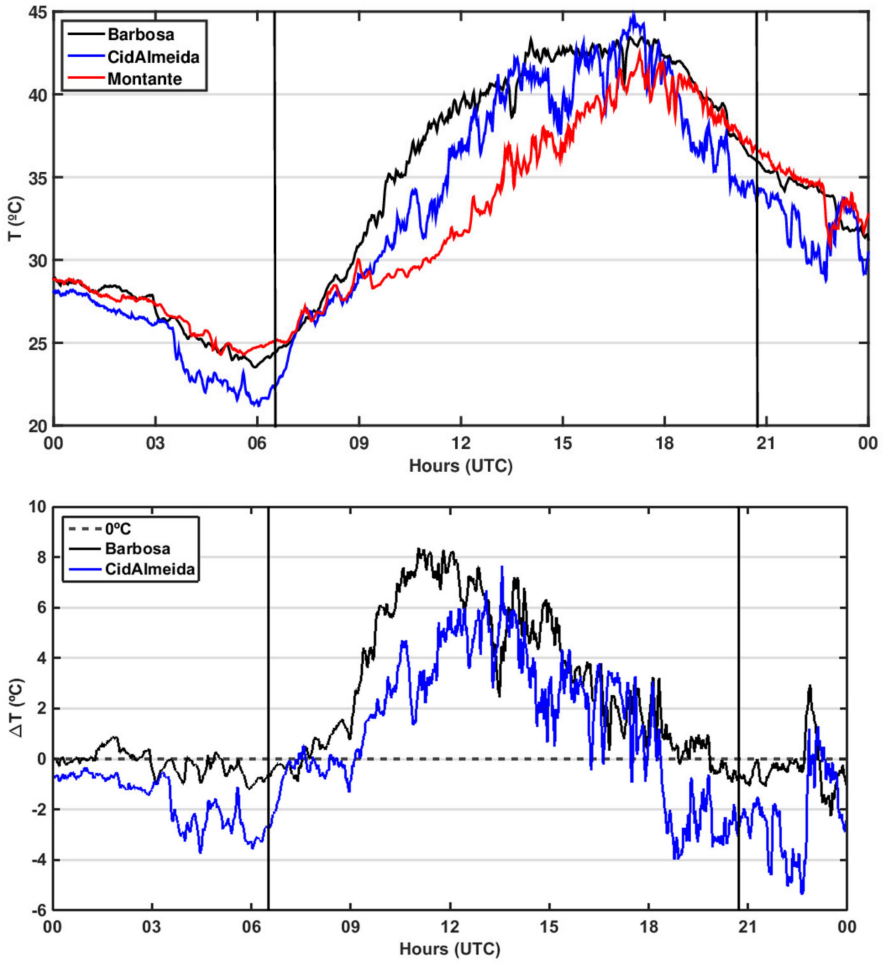

Figure 7. Air temperature in Alqueva (**upper panel**) and air temperature difference between shores and platform (**lower panel**) on 3 August 2018. Grey vertical lines indicate the sunrise and sunset.

During 3 August 2018 there was a gradual increase in water vapor concentration in Montante station, reaching 15 g/m^3, as can be seen in Figure 8. This situation lasted until around 11:00, followed by a decrease in water vapor concentration until 18:00 when it starts again to increase. The drop of water vapor in the early afternoon is a signature of the descending branch of the breeze circulation, which causes subsidence of dry air from the upper layers, as described in Iakunin et al. [16]. Finally, water vapor concentration increased again in the late afternoon, with the arrival of moist air associated to the Atlantic sea breeze. The establishment of this larger scale circulation is very common during summer (see Salgado et al. [25] and Iakunin et al. [16]) and overlaps the local wind systems caused by the thermal contrasts between reservoir and land surfaces.

In Figure 9, the wind variation is shown for 3 August 2018. The wind was synoptic from Southwest with maximum intensity between 2 and 3 m/s until 03:00, between 03:00 and 07:00 there were situations of land breezes, since there were low wind speeds and opposite quadrant of the wind in Barbosa and Cid Almeida. Lake breezes occurred when the wind blew from the Southernmost quadrant in Barbosa and from the Northernmost in Cid Almeida. As common in summer, the lake breezes tend to be interrupted by the arrival of the Atlantic sea breeze, stronger than the local circulation (see Figure S1 for August 2018

wind velocity). This phenomenon is visible in Figure 9 from 18:00 to 21:00 when the wind directions of both shores are the same and the wind speed increases. This day present the ideal conditions described by [27], for high probability of lake breeze occurrence: daily temperature difference between air and water greater than 7 °C and daily average wind speed lower than 3.5 m s^{-1}.

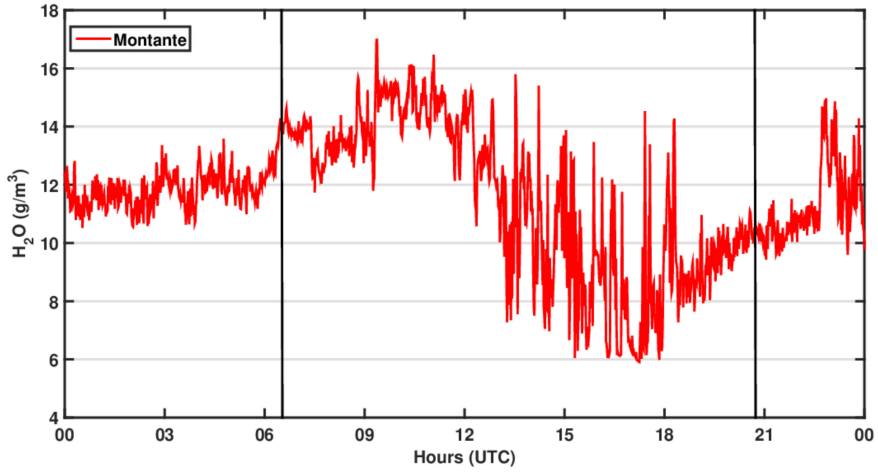

Figure 8. Water vapor in Alqueva (Montante station) on 3 August 2018. Grey vertical lines indicate the sunrise and sunset.

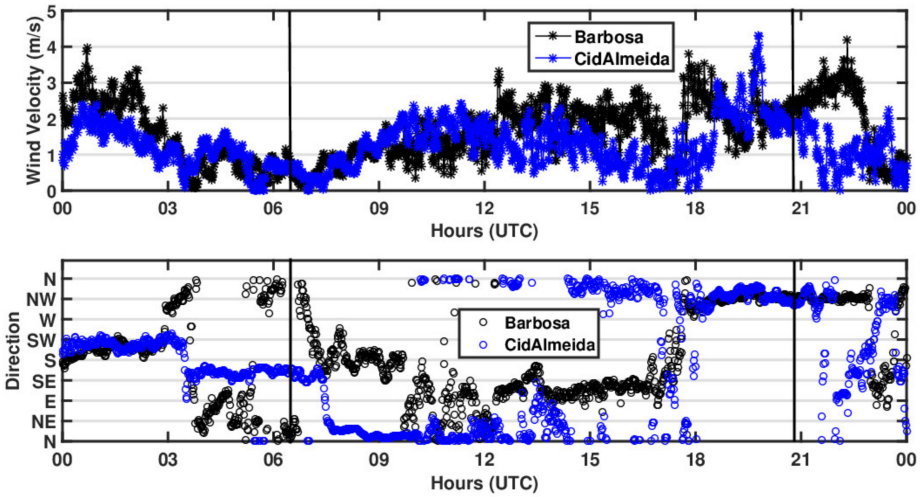

Figure 9. Wind speed (**Up panel**) and wind direction (**Down panel**) in Alqueva on 3 August 2018. Grey vertical lines indicate the sunrise and sunset.

To better illustrate the wind field on 3 August 2018, the day with more lake breeze hours (10 h), Figure 10 shows the wind roses, in the upper panel the full day and in the lower panel the lake breeze occurrences. The two upper wind roses show the great variety of directions with light and moderate intensities. However, there were lake breeze occurrence conditions for 10 h as can be seen in the lower wind roses. There was more variability in directions and speeds in Barbosa (reaching 3.5 m/s) than in Cid Almeida where the directions were more concentrated at just 45° and did not exceed 2.5 m/s (lower panels).

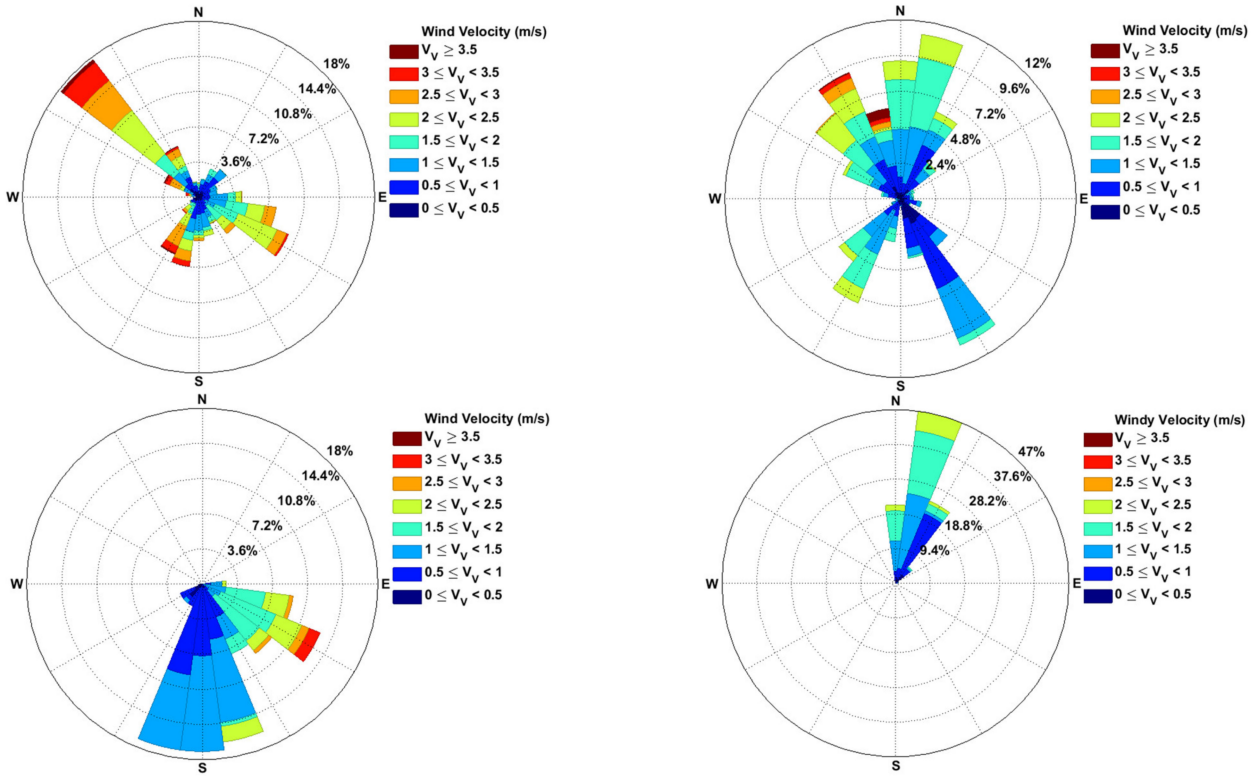

Figure 10. Wind roses for the full day (**upper panels**) and during land breeze occurrences (**lower panels**) for Barbosa station in the left panels and for Cid Almeida station in the right panels, on 3 August 2018.

3.3. Land Breeze

According to the thermal gradient between lake and shores, presented in Section 3.1, most of the study period presents a negative gradient, with exception for the summer period. Thus, more land breeze than lake breeze occurrences are expected. Figure 11 summarizes the monthly, daily by month and the daily variation of the whole period of land breeze occurrences during the study period. During the entire period (730 days) we found land breeze in 496 days (68% of the days) that normally starts at 17:00 and dissipates at 08:00. On average the land breeze lasts 8.1 h with a maximum of 17 h on 1 January 2019. According to Figure 11a, the number of land breeze occurrences per month vary from 28, in July 2018, and 292, in January 2019. Thus, land breeze conditions were twice as frequent as lake breeze conditions. There is also a huge interannual difference between January 2018 and the same month in 2019, which had less than 40% of land breeze events with respect to January 2019. The air temperature differences between onshore stations and Montante were more negative in 2019 than in 2018 (Figure 3a). The relationship between the temperature gradient and the strength of the land breeze was studied. As noticed for lake breeze case the slight tendency is not statistically significant. Most of the land breeze velocities were between 0.5 and 1.5 m/s and occurred with temperature gradients between -6 and -1 °C. This indicates that land breeze is weaker than lake breeze and develops under greater difference between the shores and the center of the reservoir. As expected, the land breezes occur essentially during night-time when the water temperature is higher than the air temperature. As shown in Figure 11c, the breezes were more frequent between 17:00 and 08:00 with focus in the period comprised between 00:00 and 05:00 (total occurrences greater than 230). The hourly period with more land breeze events was 01:00 with a total of 259 h, which indicates that in about two thirds of the days, a land breeze was identified in the first hour of the day. According to Figure 11b it is noticed that in October 2017 and January 2019, between 21:00 and 05:00 the total land breeze occurrences was maximum, with values greater than 20 occurrences.

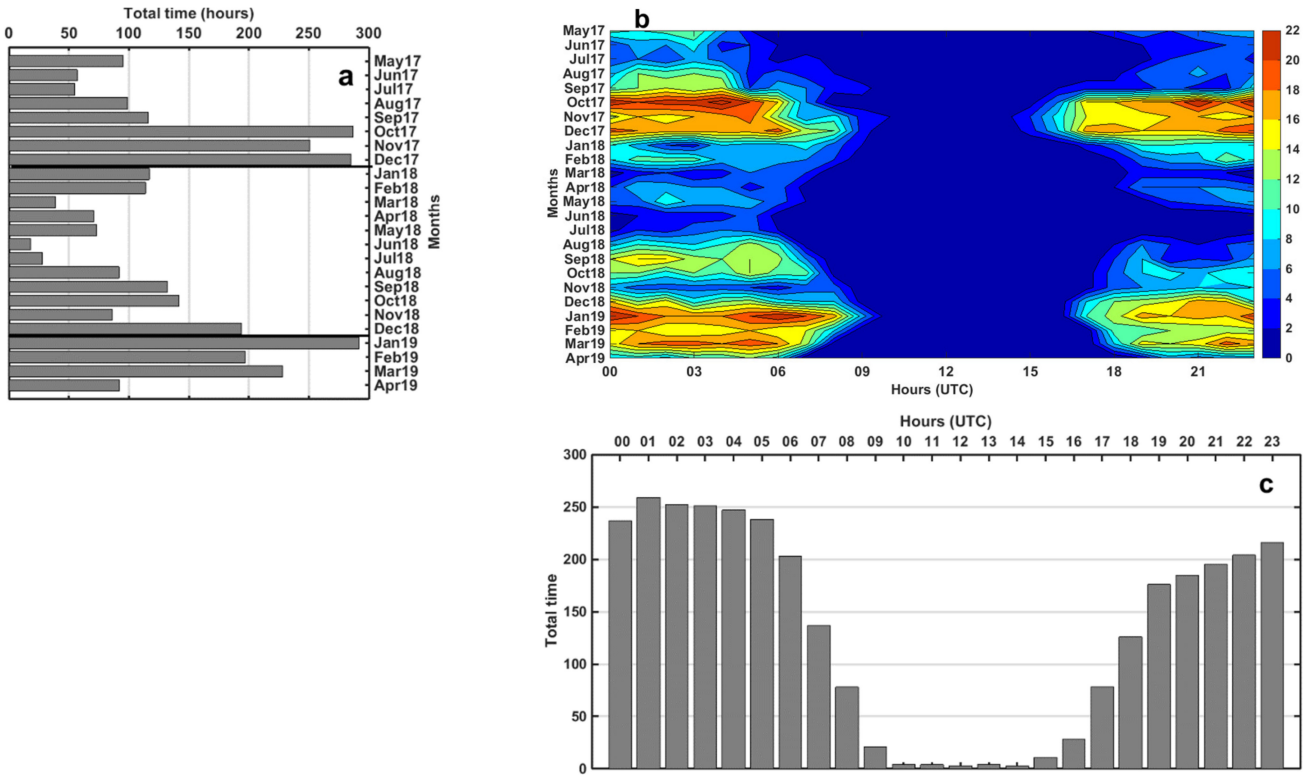

Figure 11. Land breeze occurrences in hours representing monthly (**a**), daily cycle per month (**b**) and daily cycle for all period (**c**). Grey horizontal lines in panel (**a**) separate the years 2017, 2018 and 2019.

On summer days, the air temperature can be very high, with maximum temperatures close to 40 °C, far above water temperature nevertheless, in the summer months of 2017 and in August 2018, the average temperature of the water is still slightly higher than air in Cid Almeida and slightly lower than air temperature in Barbosa (Figure 3d). This explains that, even in summer, there are frequent conditions for the development of land breezes, for example, land breeze episodes were detected in situations where the air temperature decreases rapidly and water temperature remains warm, causing a negative difference between shores and lake, resulting in a total of 92 h in August 2018 (151 h of lake breeze in the same month as shown in Figure 5a).

Figure 12 presents the daily cycle difference between the air temperature of the onshore stations and the water temperature in Montante, for January 2019, with 292 occurrences of land breeze. The more negative values occurred from 00:00 to 07:00, which coincides with the periods of more land breezes (Figure 11b), and also with the period with lower wind speeds (Figure S2). The mean difference in the afternoon is slightly positive, which inhibits land breeze formation until 16:00. From 17:00 onwards there are again conditions for land breeze formation.

Stronger Land Breeze Cases

In order to better describe the stronger land breeze events at Alqueva reservoir a detailed analysis of the days with more than 8 h was performed. In the entire period (730 days) there were 174 days with 8 or more hours of land breeze. On these days the average wind speed was 0.9 ms^{-1} with maximum wind speed of 2.5 ms^{-1} on shore stations. The average air temperature difference between these stations and the center of the reservoir was −1.9 °C and between air on the shores and water in the reservoir was −6.1 °C. These particular days presented at the shore stations an average solar radiation of 24.3 Wm^{-2} denoting mainly nocturnal breeze, relative humidity of 80% and air temperature of 11.5 °C.

The 1 January 2019, the day with the greatest land breeze duration (in hours) was chosen. Figure 13 shows the evolution of the air temperature in the three stations and the

temperature difference between shores and platform for that day. A total of 17 h of land breeze occurrence was registered divided in the periods 00:00 to 09:00 and from 17:00 until the end of the day.

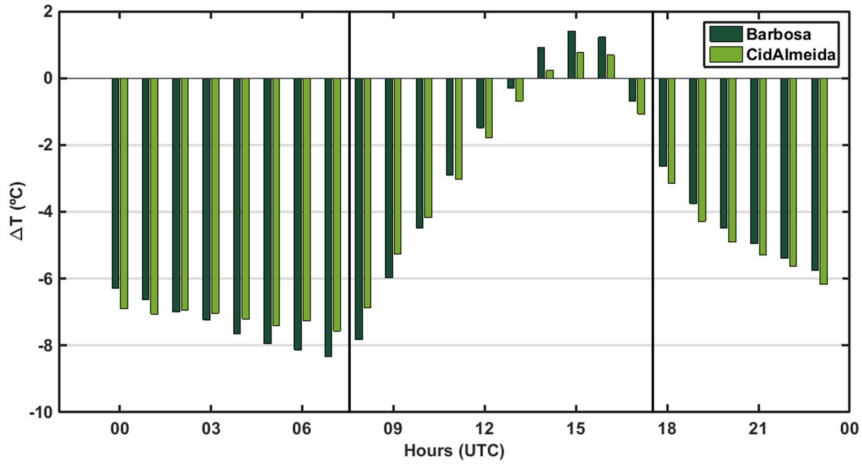

Figure 12. Daily cycle of the temperature difference between air temperature in the shore stations and water temperature at 0.5 m depth in Montante during January 2019. Grey vertical lines indicate the sunrise and sunset.

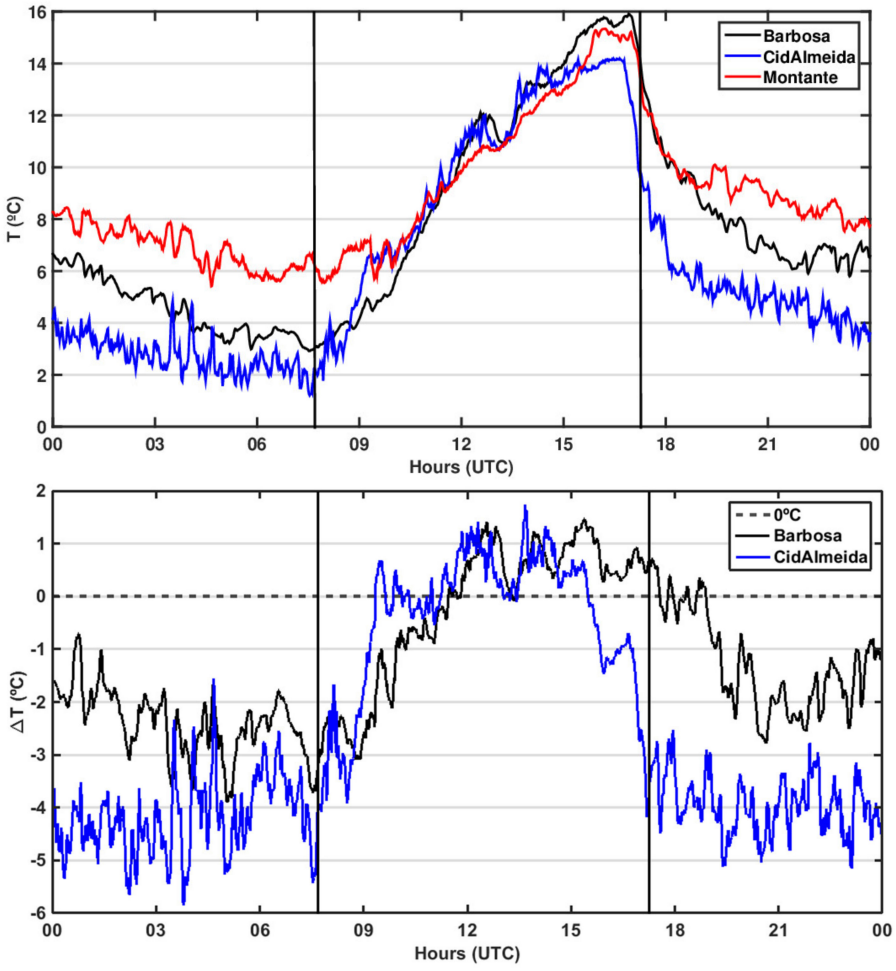

Figure 13. Air temperature in Alqueva (**upper panel**) and air temperature difference between shores and platform (**lower panel**) on 1 January 2019. Grey vertical lines indicate the sunrise and sunset.

During the night and early morning, air temperature in Montante (red line) is higher than the temperature in the onshore stations, with anomalies down to −5 °C, as can be seen in the lower panel, thus leading to the development of land breezes. During the morning and afternoon, the temperature was very close between the three stations, inhibiting the formation of breezes. From 16:00 onwards the difference became negative again in Cid Almeida while in Barbosa only at 19:00.

The evolution of the wind speed and direction are shown in Figure 14 for the same day. Wind speed does not exceed 3.0 m/s at both stations. From 00:00 to 09:00 it is visible in the lower panel of Figure 14 that wind blows from opposite directions on the reservoir shores, from Northern quadrant in Barbosa and from Southeast in Cid Almeida. However, during midday there were periods of coincident directions and a small period around 12:00 when the wind changes direction in the two stations, from Southernmost in Barbosa and Northernmost in Cid Almeida. From 17:00 on the wind direction in Cid Almeida maintains again in Southeast direction while in Barbosa some scatter is present, but mainly from Northern quadrant. In summary, the wind directions are opposite on the lake shores for a large part of the day at low wind speeds, resulting from the land breeze conditions.

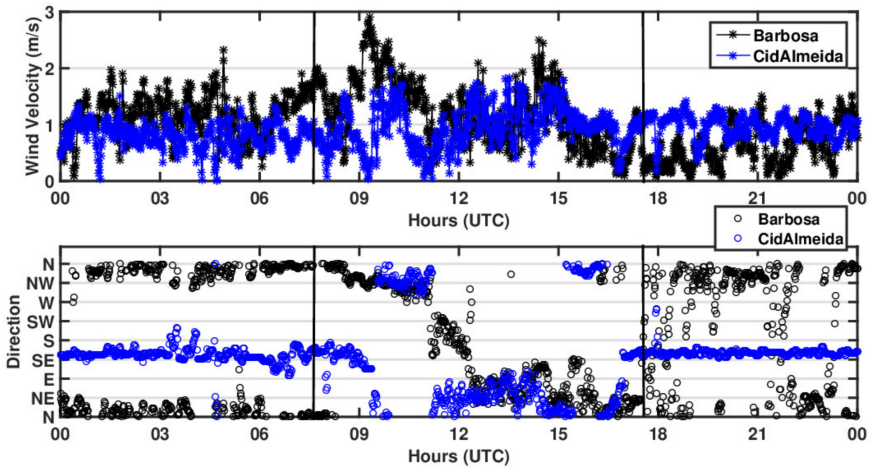

Figure 14. Wind speed (**Upper panel**) and wind direction (**lower panel**) in Alqueva on 1 January 2019. Grey vertical lines indicate the sunrise and sunset.

The same data represented in Figure 14 can be seen in Figure 15 for the same day, but in wind rose format. The first two wind roses (top panel) show the full day while the next two (bottom panel) only show the period of land breeze occurrences. The total 17 h, in the lower panel, are clearly marked with opposite wind directions, NNW in Barbosa and SSE in Cid Almeida station. In the upper panel a greater scatter of wind direction is visible in Barbosa, already mentioned above.

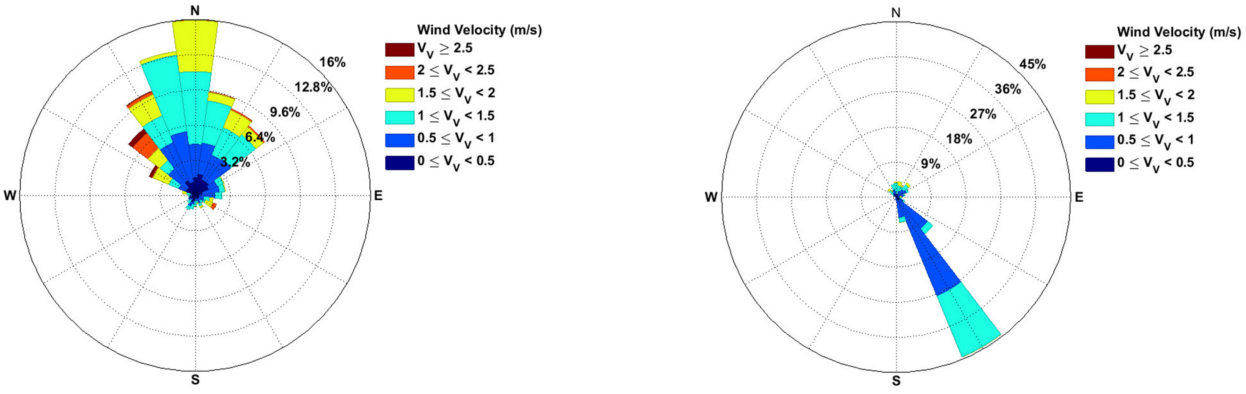

Figure 15. *Cont.*

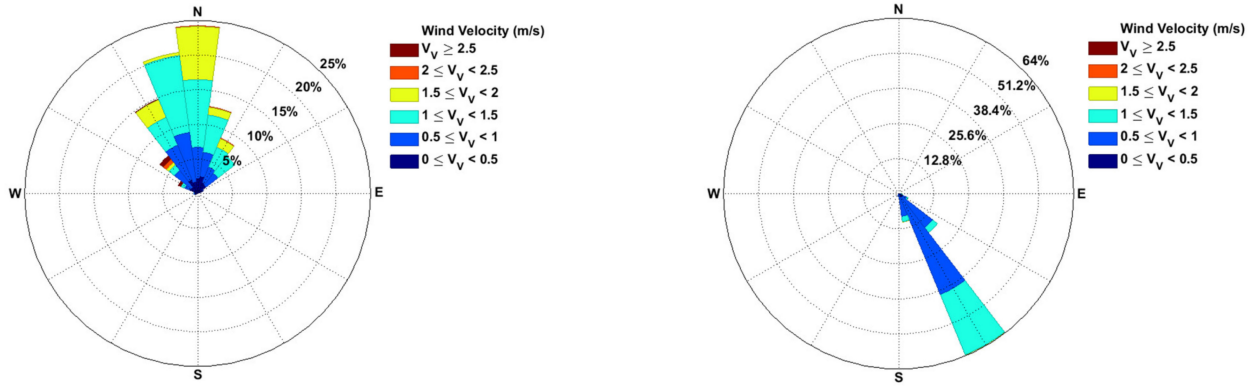

Figure 15. Wind rose for the full day and during land breeze occurrences for Barbosa station in the left panels and for Cid Almeida station in the right panels on 1 January 2019.

4. Conclusions

The objective of this study was to explore the lake and land breezes in a large Mediterranean reservoir: the Alqueva reservoir. The study was based on 2 years (May 2017 to April 2019) of in situ atmospheric measurements in three meteorological stations, in the framework of a regional Horizon 2020 project: the ALentejo Observation and Prediction system (ALOP project, [28]).

It was shown that the thermal gradient established between the shores and the center of the reservoir is the main trigger for the development of lake and land breezes, however, low wind speed is also a necessary condition to allow the development of the local circulation, thus excluding moderate and strong synoptic and convective circulation. The thermal gradient analysis was twofold: the air temperature difference between the shores and the center of the reservoir and difference between the air temperature in the shores and the water surface temperature (depth of 0.5 m) also in the center of the reservoir. Positive differences drive lake breezes while negative differences drive land breezes and the higher the difference, the greater is the probability to have local breeze development.

A couple of criteria based on wind direction in two meteorological stations installed at opposite shores of the reservoir, distanced about 2 km from each other, were proposed for lake and land breeze detection and quantification. Simultaneous wind should be from opposite directions in both onshore stations and from lake or land direction depending on the station. These criteria follow the studies of Giovannini et al. [17] and Potes et al. [27]. In this study the temperature difference between the air in Barbosa and the water in Montante in lake breeze scenario was on average 5.5 °C, whereas the threshold from Potes et al. [27] was greater than 7 °C. If these criteria are considered, only 31% of the occurrences will be detected, thus it can be concluded that the criteria from Potes et al. [27] underestimates the lake breeze. According to the same authors, the threshold for wind speed was lower than 3.5 ms^{-1} and for this study the average value for the same station is 1.46 ms^{-1}.

During the study period a higher frequency of land breezes was observed with respect to lake breezes, yielding a total of 3160 h versus 1541 h. This fact is due to the negative thermal gradient between the shores and the center of the reservoir, the lake surface in the middle is warmer than the ground surface in the shores, thus heating more of the air above the water than above the shores. This gradient is positive in summer when the lake breeze occurred more frequently. Lake breeze developed during daytime, more frequently between 07:00 and 16:00, and has no expression during night-time. Nevertheless, in summer the strong Atlantic sea breeze can often reach Alqueva region in the middle/late afternoon with stronger wind fields, suppressing the local circulations. On the contrary, the thermal gradient tends to be negative from autumn to spring and it is in this period that land breezes occur more frequently. The land breeze was also found during night-time when the air above the lake was warmer than the air in the shores, and almost insignificant

during the day due to radiative heating. Land breezes are more frequent between 17:00 and 08:00.

August 2018 was the month of the study period with the most lake breeze events, with a total of 151 h, and was the month with greater thermal gradient between the shores and the lake. In the case of land breeze, the month with more occurrences was January 2019 with a total of 292 h and was one of the months with lower negative thermal gradient. On the other hand, also in summer there are conditions for land breeze circulation, and examples of that are the 92 occurrences of land breezes detected in August 2018. Therefore, in some parts of the day, in this month, there were conditions for the development of both lake and land breezes.

Overall, this work documents the formation of thermal circulations, giving rise to lake and land breezes, due to thermal gradients between the shores and the center of an artificial lake. In line with other (few) studies, the results quantify the frequency of occurrence of breezes, showing their importance in the local wind regime. In particular, this study shows a very high frequency of occurrence of land breezes near the borders of a Mediterranean reservoir.

Supplementary Materials: The following are available online at https://www.mdpi.com/article/10.3390/atmos12050535/s1, Table S1: Number of hours of lake breeze occurrences, Table S2: Number of hours of land breeze occurrences, Figure S1: Daily cycle of the wind velocity in Alqueva in August 2018, Figure S2: Daily cycle of the wind velocity in Alqueva in January 2019.

Author Contributions: The five authors conceptualized the study. C.P., M.P. and G.R. installed the stations, carried out the maintenance and organized the database. R.S. and M.J.C. designed the methodology. C.P. wrote the first draft of the manuscript. All authors contributed to the analysis, interpretation and writing. All authors have read and agreed to the published version of the manuscript.

Funding: The work is cofunded by the European Union through the European Regional Development Fund, included in the COMPETE 2020 (Operational Program Competitiveness and Internationalization) through ALOP project (ALT20-03-0145-FEDER-000004) and by the national funds through FCT—Fundação para a Ciência e Tecnologia, I.P., in the framework of the ICT project with the references UIDB/04683/2020.

Data Availability Statement: Data used in this study are available at http://www.alop.ict.uevora.pt/index.php/dados/?lang=en, accessed on 28 October 2020.

Acknowledgments: The authors gratefully acknowledge the Foundation for Science and Technology (FCT), and the project ALOP (ALT20-03-0145-FEDER-000004).

Conflicts of Interest: The authors declare no conflict of interest.

References

1. Lemmin, U.; D'Adamo, N. Summertime Winds and Direct Cyclonic Circulation: Observations from Lake Geneva. *Ann. Geophys.* **1996**, *14*, 1207–1220. [CrossRef]
2. Gerken, T.; Biermann, T.; Babel, W.; Herzog, M.; Ma, Y.; Foken, T.; Graf, H.-F. A Modelling Investigation into Lake-Breeze Development and Convection Triggering in the Nam Co Lake Basin, Tibetan Plateau. *Theor. Appl. Climatol.* **2014**, *117*, 149–167. [CrossRef]
3. Crosman, E.T.; Horel, J.D. Sea and Lake Breezes: A Review of Numerical Studies. *Bound. Layer Meteorol.* **2010**, *137*, 1–29. [CrossRef]
4. Wang, Y.; Gao, Y.; Qin, H.; Huang, J.; Liu, C.; Hu, C.; Wang, W.; Liu, S.; Lee, X. Spatiotemporal Characteristics of Lake Breezes over Lake Taihu, China. *J. Appl. Meteorol. Climatol.* **2017**, *58*, 2053–2065. [CrossRef]
5. Balsamo, G.; Salgado, R.; Dutra, E.; Boussetta, S.; Stockdale, T.; Potes, M. On the Contribution of Lakes in Predicting Near-Surface Temperature in a Global Weather Forecasting Model. *Tellus A Dyn. Meteorol. Oceanogr.* **2012**, *64*, 15829. [CrossRef]
6. Kheyrollah Pour, H.; Duguay, C.; Martynov, A.; Brown, L.C. Simulation of Surface Temperature and Ice Cover of Large Northern Lakes with 1-D Models: A Comparison with MODIS Satellite Data and in Situ Measurements. *Tellus A Dyn. Meteorol. Oceanogr.* **2012**, *64*, 17614. [CrossRef]
7. Zhang, X.; Huang, J.; Li, G.; Wang, Y.; Liu, C.; Zhao, K.; Tao, X.; Hu, X.-M.; Lee, X. Improving Lake-Breeze Simulation with WRF Nested LES and Lake Model over a Large Shallow Lake. *J. Appl. Meteorol. Climatol.* **2019**, *58*, 1689. [CrossRef]

8. Keen, C.; Lyons, W. Lake/Land Breeze Circulations on the Western Shore of Lake Michigan. *J. Appl. Meteorol. Climatol.* **1978**, *17*, 1843. [CrossRef]
9. Schoenberger, L.M. Doppler Radar Observation of a Land-Breeze Cold Front. *Mon. Weather Rev.* **1984**, *112*, 2455–2464. [CrossRef]
10. Stull, R.B. *An Introduction to Boundary Layer Meteorology*, 2nd ed.; Kluwer Academic Publishers: Dordrecht, The Netherlands, 1988; pp. 587–595.
11. Mariani, Z.; Dehghan, A.; Joe, P.; Sills, D. Observations of Lake-Breeze Events during the Toronto 20155 Pan-American Games. *Bound. Layer Meteorol.* **2018**, *166*, 113–135. [CrossRef]
12. Sills, D.; Brook, J.; Levy, I.; Makar, P.; Zhang, J.; Taylor, P. Lake Breezes in the Southern Great Lakes Region and Their Influence during BAQS-Met 2007. *Atmos. Chem. Phys.* **2011**, *11*, 7955–7973. [CrossRef]
13. Miranda, P.B. *Meteorologia e Ambiente*; Universidade Aberta: Lisbon, Portugal, 2001; Volume 219.
14. Nogueira, M. Estudo de Brisas e Depressões Térmicas: Aplicação à Península Ibérica. Master's Thesis, University of Lisbon, Lisbon, Portugal, 2009.
15. Assunção, S. Impacto da Introdução da Albufeira de Alqueva no Modelo de Previsão AROME. Master's Thesis, University of Évora, Évora, Portugal, 2017.
16. Iakunin, M.; Salgado, R.; Potes, M. Breeze Effects at a Large Artificial Lake: Summer Case Study. *Hydrol. Earth Syst. Sci.* **2018**, *22*, 5191–5210. [CrossRef]
17. Giovannini, L.; Laiti, L.; Zardi, D.; Franceschi, M. Climatological Characteristics of the Ora del Garda Wind in the Alps. *Int. J. Climatol.* **2015**, *35*, 4103–4115. [CrossRef]
18. Le Moigne, P.; Legain, D.; Lagarde, F.; Potes, M.; Tzanos, D.; Moulin, E.; Barrié, J.; Salgado, R.; Messiaen, G.; Fiandrino, A.; et al. Evaluation of the Lake Model FLake over a Coastal Lagoon during the THAUMEX Field Campaign. *Tellus A Dyn. Meteorol. Oceanogr.* **2013**, *65*, 20951. [CrossRef]
19. Bouin, M.-N.; Caniaux, G.; Traullé, O.; Legain, D.; Le Moigne, P. Long-Term Heat Exchanges over a Mediterranean Lagoon. *J. Geophys. Res. Atmos.* **2012**, *117*, D23104. [CrossRef]
20. Crosman, E.T.; Horel, J.D. Idealized Large-Eddy Simulations of Sea and Lake Breezes: Sensitivity to Lake Diameter, Heat Flux and Stability. *Bound. Layer Meteorol.* **2012**, *144*, 309–328. [CrossRef]
21. Wang, C.-C.; Kirshbaum, D.; Sills, D. Convection Initiation Aided by Lake-Breeze Convergence over the Niagara Peninsula. *Mon. Weather Rev.* **2019**, *197*, 3955. [CrossRef]
22. Tsujimoto, K.; Koike, T. Land-lake Breezes at Low Latitudes: The Case of Tonle Sap Lake in Cambodia. *J. Geophys. Res. Atmos.* **2013**, *118*, 6970–6980. [CrossRef]
23. Kathleen, M.T.; Christopher, A.D.; Kenneth, P.C.; Kenneth, R.W.; John, W.L., III; Melody, L.H.; Joy, L.H.; Charles, D.S.; Scot, A.S. *Southeast Asia-A Climatological Study*; Air Force Combat Climatology Center (AFCCC), Scott Air Force Base: San Luis, IL, USA, 1997.
24. Purificação, A.C. Caracterização Meteorológica em Alqueva: Tratamento e Análise de dados. Master's Thesis, University of Évora, Évora, Portugal, 2020.
25. Salgado, R.; Miranda, P.M.A.; Lacarrère, P.; Noilhan, J. Boundary Layer Development and Summer Circulation in Southern Portugal. *Tethys* **2015**, *12*. [CrossRef]
26. Lopes, F.; Silva, H.G.; Salgado, R.; Potes, M.; Nicoll, K.A.; Harrison, R.G. Atmospheric Electrical Field Measurements Near a Fresh Water Reservoir and the Formation of the Lake Breeze. *Tellus A Dyn. Meteorol. Oceanogr.* **2016**, *68*, 31592. [CrossRef]
27. Potes, M.; Salgado, R.; Costa, M.J.; Morais, M.; Bortoli, D.; Kostadinov, I.; Mammarella, I. Lake–Atmosphere Interactions at Alqueva Reservoir: A Case Study in the Summer of 2014. *Tellus A Dyn. Meteorol. Oceanogr.* **2017**, *69*, 1272787. [CrossRef]
28. Salgado, R.; Morais, M.; Palma, P.; Potes, M.; Penha, A.; Novais, M.H.; Antunes, C.; Aranha, S.; Bárias, S.; Barrenho, J.; et al. The ALOP Alentejo Observation and Prediction System Database. Available online: http://www.alop.ict.uevora.pt/index.php/dados/?lang=en (accessed on 2 February 2019).
29. APA: Barragens de Portugal: Barragem de Alqueva. Available online: http://cnpgb.apambiente.pt/gr_barragens/gbportugal/FICHAS/Alquevaficha.htm (accessed on 28 October 2020).
30. EDIA, S. A Território: Empresa de Desenvolvimento e Infra-estruturas do Alqueva, S.A. Available online: https://www.edia.pt/pt/o-que-e-o-alqueva/oterritorio/103/ (accessed on 29 October 2020).
31. Purificação, A.C. (University of Évora); Potes, M. (University of Évora); Salgado, R. (University of Évora). Observação Termométrica em Alqueva entre 2017–2018. 2019. Available online: https://www.researchgate.net/publication/340830536_Observacao_Termometrica_em_Alqueva_entre_2017_e_2018 (accessed on 22 April 2021).
32. Miranda, P.; Abreu, F.; Salgado, R. (ICAT, Faculdade de Ciências, Universidade de Lisboa, Lisboa, Portugal). Estudo de Impacte Ambiental de Alqueva. 1995. Available online: https://core.ac.uk/download/pdf/62475212.pdf (accessed on 22 April 2021).
33. Román-Cascón, C.; Yagüe, C.; Steeneveld, G.J.; Morales, G.; Arrillaga, J.A.; Sastre, M.; Maqueda, G. Radiation and Cloud-Base Lowering Fog Events: Observational Analysis and Evaluation of Wrf and Harmonie. *Atmos. Res.* **2019**, *229*, 190–207. [CrossRef]
34. Salgueiro, V.; Costa, M.J.; Silva, A.M.; Bortoli, D. Variability of the Daily-Mean Shortwave Cloud Radiative Forcing at the Surface at a Midlatitude Site in Southwestern Europe. *J. Clim.* **2014**, *27*, 7769–7780. [CrossRef]
35. IPMA: Ficha Climatológica 1971–2000 da estação de Évora [557]. Available online: http://www.ipma.pt/bin/file.data/climate-normal/cn_71-00_EVORA.pdf (accessed on 11 February 2021).

Science of the Total Environment 794 (2021) 148703

Contents lists available at ScienceDirect

Science of the Total Environment

journal homepage: www.elsevier.com/locate/scitotenv

Occurrence and risk assessment of pesticides in a Mediterranean Basin with strong agricultural pressure (Guadiana Basin: Southern of Portugal)

P. Palma [a,b,*], S. Fialho [a], A. Lima [a], A. Catarino [a], M.J. Costa [b,c,d], M.V. Barbieri [e], L.S. Monllor-Alcaraz [e], C. Postigo [e], M. Lopez de Alda [e,**]

[a] Department of Technologies and Applied Sciences, Polytechnic Institute of Beja, Beja, Portugal
[b] ICT, Institute of Earth Sciences, University of Évora, Évora, Portugal
[c] Science and Technology School, University of Évora, Évora, Portugal
[d] Earth Remote Sensing Laboratory - EaRSLab, University of Évora, Évora, Portugal
[e] Water, Environmental and Food Chemistry Unit (ENFOCHEM), Institute of Environmental Assessment and Water Research (IDAEA-CSIC), Barcelona, Spain

HIGHLIGHTS

- Drought enhanced the impact of pesticides in the ecosystems of Guadiana Basin.
- Quantified 23 European banned pesticides in the Guadiana Basin.
- Of the 38 pesticides detected, 32 may have induced risk to aquatic species.
- Bentazone, Terbutryn, Terbuthylazine, Chlorfenvinphos, Diazinon with high risk
- Greater risk in the streams of the Guadiana Basin than in the Alqueva reservoir

GRAPHICAL ABSTRACT

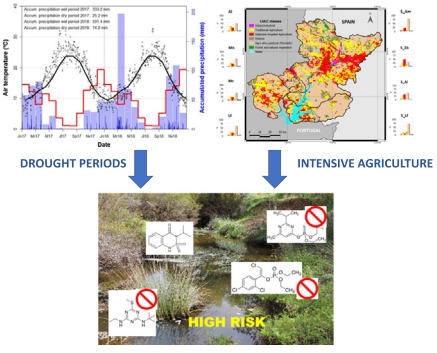

ARTICLE INFO

Article history:
Received 27 April 2021
Received in revised form 21 June 2021
Accepted 22 June 2021
Available online 28 June 2021

Editor: Dimitra A Lambropoulou

Keywords:
Plant protection products
Environmental risk assessment
Risk maps
Water pollution

ABSTRACT

The study aimed to assess the occurrence and the environmental risk of a group of 51 selected pesticides in the Guadiana Basin (a biodiversity hotspot, in the Mediterranean). The most abundant pesticides were bentazone and 2,4-D, while terbuthylazine together with terbutryn constituted the most ubiquitous pesticides. Eighteen out of the 38 pesticides detected are no longer approved in Europe, and 5 of them are included in the list of priority substances. The risk assessment showed that azinphos ethyl, diflufenican, irganol, imidacloprid, and oxadiazon occurred occasionally, but always in concentrations above their respective ecotoxicological threshold value. Contrary, bentazone, terbuthylazine, and terbutryn presented a high risk in most of the sampled locations and periods.

The site-specific risk assessment showed a spatial and temporal pattern, with a higher risk occurring mainly in intermittent streams, in the drought period. The presence of pesticides banned from the EU market since 2009 showed the importance of improving the monitoring process, to identify the main sources of pollution and the fate of these emerging compounds. The results showed the need of implementing actions to improve the sustainable use of pesticides in agricultural areas, working with farmers and management entities to reduce the contamination of aquatic ecosystems. Transboundary water governance is also required to solve potential transboundary contamination problems.

© 2021 Elsevier B.V. All rights reserved.

* Correspondence to: P. Palma, Department of Technologies and Applied Sciences, Polytechnic Institute of Beja, Beja, Portugal.
** Correspondence to: M. L. de Alda, Water, Environmental and Food Chemistry Unit, Institute of Environmental Assessment and Water Research (IDAEA-CSIC), Spain.
E-mail addresses: ppalma@ipbeja.pt (P. Palma), miren.lopezdealda@idaea.csic.es (M.L. de Alda).

https://doi.org/10.1016/j.scitotenv.2021.148703
0048-9697/© 2021 Elsevier B.V. All rights reserved.

1. Introduction

The "Green Revolution" changed the agriculture paradigm in the late 1960s. The introduction of selected seeds, the use of large quantities of fertilizers and pesticides, and the improvement of agriculture practices increased agricultural productivity and hence food production (Khush, 1999).

Cultivated land, with an extension of 15.3×10^6 km^2, has become the largest terrestrial biome in the world (Foley et al., 2011). Agriculture expansion resulted in a strong increase in pesticide production and use between 1955 and 2000 (Tilman et al., 2001). Pesticides still play a key role in the current agricultural model, as they generate substantial economic benefits. Their use reduces losses during the production process and promotes the corresponding decrease in product prices (Finizio and Villa, 2002).

Nowadays, there are almost 500 active substances approved in the European Union (EU), with sales of 360 million kg per year (Eurostat, 2018). Four countries, viz., France, Spain, Italy, and Germany, account for over two-thirds of the pesticide sales in the EU. While some European countries increased their pesticide sales during 2011–2018 ((Cyprus (+94%) and Austria (+53%)) other European countries made an effort to reduce them (−43% in Portugal and − 28% in Ireland) (Eurostat, 2018).

The massive use of pesticides becomes a serious threat as it may induce pest resistance (Heckel, 2012), leave pesticide traces in food commodities (levels above maximum residue limit (MRL) in 1.7% and 2.8% of the samples analyzed within the EU and Portugal, respectively, in 2015 (EFSA, 2017)), and unbalance the ecosystems (Llorens et al., 2020). To meet the world's future food security and sustainability needs, food production must grow substantially while, at the same time, agriculture's environmental footprint must shrink drastically (Foley et al., 2011). Actions such as the adoption of good agricultural practices that promote the decrease of pesticide use, the update of regulatory mechanisms, and the improved assessment of the occurrence and fate of pesticides in crops and watercourses can contribute to increment the environmental sustainability of agriculture.

The registration of new chemical substances in the European region is based on the REACH regulation (2006/1907/EC), while the protection of surface waters is based on the Water Framework Directive (2000/60/EC) and its daughter directives (Directives 2013/39/EC; 2008/105/EC; 2006/118/EC). Despite the current EU regulatory framework, studies continuously report pesticide contamination in the different environmental matrices worldwide (Barbieri et al., 2020a; Palma et al., 2015; Papadopoulou-Mourkidou et al., 2015; Ramírez-Morales et al., 2021; Silva et al., 2019). The levels found posed a potential risk for non-target organisms and overall, ecosystems (Čelić et al., 2021; Kandie et al., 2020; Llorens et al., 2020; Palma et al., 2009), which reveals the insufficiency of the regulatory and management procedures and the non-compliance of good agricultural practices (Köck-Schulmeyer et al., 2021; Ramírez-Morales et al., 2021).

Environmental monitoring is indeed an essential tool to increase the knowledge on pesticide pollution. It helps understand temporal and spatial pollution patterns at a regional scale, as well as the influence of stressors such as climate conditions and water scarcity on environmental concentrations (Ramírez-Morales et al., 2021; Sabater et al., 2018; Streissl et al., 2018). Furthermore, the combination of occurrence data with adverse effects allows the assessment of the potential impact of contamination in receiving aquatic ecosystems (Köck-Schulmeyer et al., 2021). Thus, the implementation of dynamic and integrative environmental risk assessment methodologies in post-registration real scenarios using advanced monitoring strategies (Altenburger et al., 2019) is a valuable tool to improve agricultural sustainability. This process can assist in the prioritization of pesticides in the environment, the adjustment of authorized doses, and the development of specific management actions.

In this context, the present study aimed at providing data on the occurrence of pesticides in the Guadiana River Basin (a Mediterranean Basin highly impacted by agriculture), and assessing the potential risk that the levels found may pose to freshwater organisms to obtain the ecotoxicological risk maps of the area. The study was conducted in hydrological years with accentuated meteorological differences, which allowed evaluating pesticide pollution patterns in drought and post-drought real scenarios, as well as the influence of climatic conditions in the associated environmental risk. The integration of the data obtained into maps of land use/land cover (LULC) also allowed identifying the crops that induce the greatest pressure in the basin. Moreover, the research also permitted to gain information about the Guadiana river basin specific pollutants (RBSP), a list of substances of concern that the water authorities must identify and control to ensure the good chemical and ecological status of the water bodies (Article 4 and Annex V; ECC, 2000). This set of results is very valuable to integrate the local farmers in the decision-making processes and raising concern on the adoption of good agricultural practice, allowing their integration and accountability in the decision-making processes.

Under such approach, the specific objectives addressed in the study were: (i) to identify the main pesticides occurring in the Guadiana River Basin; (ii) to analyze their spatial and temporal distribution; (iii) to assess the associated environmental risk; (iv) to obtain the pesticide risk areas and the major crops responsible for the risk observed, and (v) to prioritize pesticides for their eventual inclusion in the list of the Guadiana RBSP based on their occurrence and environmental risk.

2. Materials and methods

2.1. Study area and sampling sites characterization

The study was developed in the Portuguese territory of the Guadiana Basin, cataloged as one of the Portuguese areas most affected by water scarcity, reversed in part by the construction of the Alqueva Reservoir.

The Guadiana Basin is considered a biodiversity hotspot in the Mediterranean region. It is the most important national basin for the ichthyofauna conservation, with eleven species of freshwater fish, endemic to the Iberian Peninsula, four of them restricted to this basin, and among which are some endangered species, such as the Saramugo, the Boga, and the Shad of Guadiana. Further, it is the habitat to four native species of endangered bivalves, thirteen of the seventeen amphibian species existing in Portugal, and three species of turtles (www.icnf.pt). In addition, the Guadiana Basin is characterized by the presence of natural and semi-natural ecosystems included in the Habitat Directive (Directive 43/92/EU), such as *montado* (multifunctional agro-silvo-pastoral ecosystem, very typical at Southern Portugal, with varying densities of trees, mainly cork and/or holm oaks), temporary ponds, and intermittent rivers, to which high biodiversity is associated. The relief of the region is characterized by lowlands and smooth slopes, with dispersed mountains in the northwestern and southeastern areas that may reach up to 1000 m (see Fig. 1).

The Alqueva reservoir is a mover of Alentejo's economic development, as it allowed the intensification of agricultural activities and the implementation of large areas of irrigated crops. The reservoir, with a total storage capacity of 4150 hm^3, provides water for public supply, irrigation, industrial uses, energy production, and tourism. The global irrigation plan benefits a total area of 120,000 ha, of which about 70,000 ha were already in operation in 2017. The irrigation land increased to 93,000 ha during 2018 (www.edia.pt; Tomaz et al., 2020). This economic growth, based on the strengthening of the agricultural activity, may become a stress factor and an important diffuse source of pollution to the Guadiana Basin waters.

The study integrated the monitoring of eight freshwater sampling locations (coordinates provided in Table S1 as Supporting Information) at the Guadiana Basin during 2017 and 2018. Four of these sites were in the Alqueva reservoir: Álamos (Al), Mourão (Mr), Montante (Mn) and

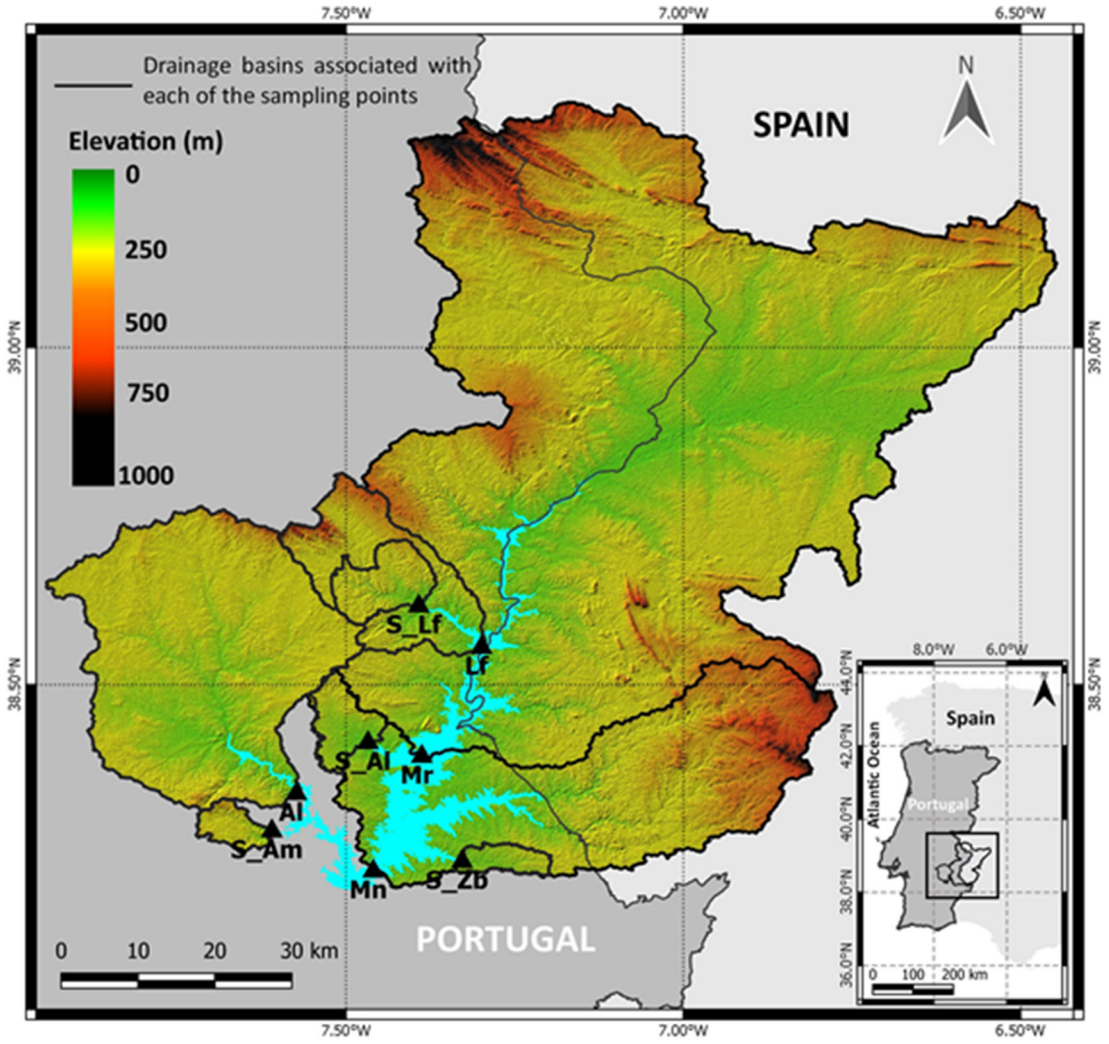

Fig. 1. Surface elevation map of the study region located in southwestern Iberia (bottom-right inset) illustrating the position of the sampling sites with the respective drainage basins.

Lucefécit (Lf). These sampling sites, with lentic conditions, have fixed platforms from where the samples were collected. These platforms also have meteorological devices installed to evaluate climate conditions. Montante and Mourão platforms are located in clear-cut surroundings and deep areas of the reservoir, with 60 m and 50 m depth, respectively; whilst Álamos and Lucefécit platforms are located in a forested surrounding and a 20 m depth area. The remaining four sampling points are located in Guadiana streams, tributaries to the Alqueva reservoir: Zebro drains into the reservoir near Montante platform (S_Zb); Álamos near Mourão platform (S_Al); Amieira near Álamos platform (S_Am); and Lucefécit near Lucefécit platform (S_Lf). The streams presented different hydrological regimes, characteristic of the Mediterranean region: (i) Amieira and Álamos are intermittent streams, drying to a series of disconnected pools part of the year (during the study this occurred in July and September in both years); (ii) Zebro presents an intermittent regime with water all year long but without flow during some periods (July, September, and November in 2017; and May, July, and September in 2018); and (iii) Lucefécit presents a perennial regime. A detailed description of the sampling locations can be found elsewhere (Palma et al., 2016; Palma et al., 2020a, 2020b; Palma et al., 2021). The region considered in this study matches the overlap of the drainage basins associated with each sampling site yielding an area of about 8660 km^2, and roughly corresponds to the northern half of the drainage basin of the Guadiana River section in Portugal (Palma et al., 2020a, 2020b). Fig. 1 displays the sampling locations with their respective drainage basins. Mn is the sampling location associated with the most extensive drainage basin. It drains an area of 7330.2 km^2, and includes Mr, Lf, S_Zb, S_Al, and S_Lf drainage basins. In turn, Mr comprises an area of 5910.3 km^2 and includes Lf and S_Lf drainage basins, whereas Lf (424.8 km^2) includes S_Lf (117.1 km^2). The drainage basins of Al (1279.0 km^2) and S_Am (50.8 km^2) are not overlapped by other basins.

Pesticides were analyzed during 12 sampling campaigns, performed bi-monthly from January 2017 to November 2018. The wet period included the months of November, January, and March, and the dry period included the months of May, July, and September. These periods were defined by the Environmental Portuguese Agency for the Alentejo region (ARHAlentejo, 2011). In general, when the streams were in the dry phase, the collection was performed in isolated pools upstream of the regular sampling sites. During the study period, a total of 96 water samples (300 mL) were collected at a depth of 50 cm, transported to the laboratory at 4 °C, and stored in amber polyethylene terephthalate (PET) bottles in the dark at −18 °C until analysis.

2.2. Meteorological conditions and land use/ land cover (LULC) analysis

The years under analysis in this study are 2017 and 2018, which from the meteorological point of view presented very different conditions in continental Portugal, as reported by the national authority - Portuguese Institute for Sea and Atmosphere (IPMA; www.ipma.pt; last accessed 19/03/2021). The year 2017 was warm and dry compared to the climatological normal for the period 1971–2000, with an average temperature 1 °C higher and about 40% less precipitation. This year was

indeed the second warmest and the third driest year in the country since 1931. In contrast, 2018 was very similar to the 1971–2000 climatological normal in terms of temperature and precipitation values. The meteorological drought that started in 2017 extended until the beginning of March 2018, which was the second rainiest March in the country since 1931.

As illustrated in Fig. 2, the year 2017 presented much lower monthly precipitation values (light blue bars) than the 1971–2000 climatological normal for the region (solid red line), and higher monthly air temperatures between April and October. The monthly temperature and precipitation values measured in 2018 were close to the monthly values of the climatological normal for this region. The monthly temperature was above the normal in August and September and while extremely high precipitation was recorded in March, December was drier compared to the normal monthly precipitation average. The accumulated precipitation values in the four periods considered in this study were also calculated (Fig. 2).

The LULC characterization was obtained from the 2018 CORINE Land Cover (CLC), a Pan-European inventory available from Copernicus Land Monitoring Service (https://land.copernicus.eu/). The CLC database uses high spatial resolution satellite imagery to classify LULC in 44 distinct classes, with a minimum width of 100 m for linear phenomena and an area of 25 ha for the smallest mapping unit (Kosztra et al., 2017). The inventory distinguishes 11 classes for agricultural areas, which were grouped into 4 classes for the study purposes as shown in Table S2: Traditional Agriculture, Intensive Irrigated Agriculture, Pasture, and Agro-silvopastoral system (Montado). The other classes considered in the study were: Urban/Industrial, which included all Artificial Surfaces in CLC, Forest and natural vegetation, and Water.

The drainage basins corresponding to each of the sampling points (represented in Fig. 1) were obtained from Shuttle Radar Topography Mission (SRTM) elevation data with 1 arcsecond (30 m) resolution, as described in Palma et al. (2021). The LULC map of the areas corresponding to each class inside each of the drainage basins (see Fig. 1) is presented in Section 3.1.

2.3. Analysis of pesticides

A total of 51 target pesticides, representative of different chemical classes and modes of action, were investigated (Table S3). Selected pesticides included EU priority substances, pesticides listed in the watch lists, pesticides commonly applied in Spain and Portugal, and some of their transformation products. Their analysis in the water samples collected was performed with a method based on online solid-phase extraction-liquid chromatography-tandem mass spectrometry (SPE-LC-MS/MS) as described in Barbieri et al. (2020a, 2020b). Briefly, samples are fortified with a mixture of 45 isotopically labeled pesticides for quantification purposes and centrifuged to remove suspended particles. Thereafter, the samples (5 mL), along with the aqueous calibration solutions, quality controls, and blanks, are SPE-extracted in a Prospekt-2 system (Spark Holland, Emmen, The Netherlands) using disposable CHROspe Polymer DVB (divinylbenzene polymer, 10 mm × 2 mm i.d., 25–35 μm particle size) cartridges (Axel Semrau GmbH & Co. KG, Srockhövel, Germany). The retained analytes are then released to the chromatographic column (a Purospher® STAR RP-18 end-capped column, 100 mm × 2 mm i.d., 5 μm particle size, Merck, Darmstadt, Germany) with a mobile phase consisting of acetonitrile and water delivered by a 1525 binary HPLC pump (Waters, Milford, MA, USA). Their MS/MS analysis is performed with a TQD triple-quadrupole mass spectrometer (Waters) equipped with an electrospray (ESI) interface. Acquisition of the 51 target pesticides is done in the selected reaction monitoring (SRM) mode, and alternating positive (43 analytes) and negative (8 analytes) ionization in a single analytical run. Further details on the method and its performance characteristics can be found in Barbieri et al. (2020a, 2020b). Method limits of detection (LODs) and determination (LODets) in surface water are in the range of 0.3–19 ng L^{-1} and 0.8–40 ng L^{-1}, respectively, for the majority of the target compounds (86%) (Table S3).

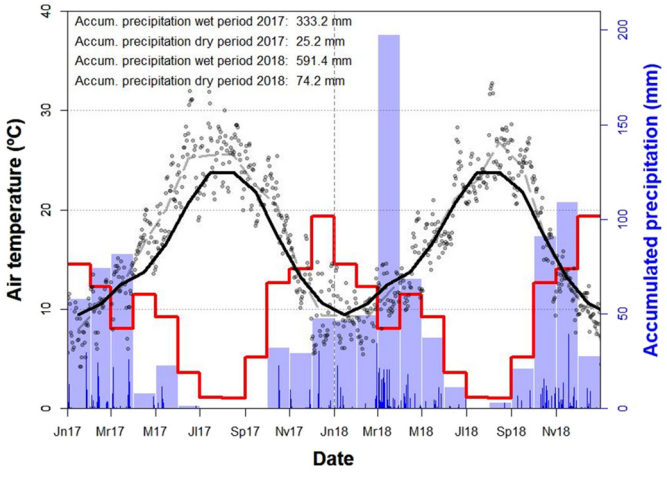

Fig. 2. Daily (grey circles) and monthly (grey dashed line) air temperature values and daily (dark blue bars) and monthly (light blue bars) accumulated precipitation measured in the region during 2017 and 2018. The solid black and red lines represent the 1971–2000 climatological normal for mean temperature and precipitation, respectively.

2.4. Environmental risk assessment

The risk quotient approach (RQ) was applied to identify the pesticides that may induce the major aquatic risk in the Guadiana Basin. The resulting information was used to elaborate the list of RBSP and the risk maps of the area. The risk quotient of a single pesticide (RQi) was calculated as the ratio between the pesticide measured environmental concentration (MEC) and its lowest predicted no-effect concentration (PNEC) (RQi = MEC/PNEC). The maximum concentration measured for each pesticide was used as MEC to assess the worst-case scenario (RQex) (Palma et al., 2014a). PNEC values were derived from: (i) the NORMAN Ecotoxicology Database (https://www.norman-network.com/nds/ecotox/; Dulio and Ohe, 2013); or (ii) ecotoxicological results reported for three freshwater trophic levels (algae, crustacean, fish) in the FOOTPRINT Pesticide Database (FOOTPRINT PPDB; AERU, 2013), adjusted by an assessment factor (AF), according to the Technical Guidance Document on Risk Assessment of the European Commission (ECC, 2003) (see Table S3).

According to Sanchez-Bayo and Baskaran (2002), the RQi was classified into four groups: No risk: RQ < 0.01; low risk: 0.01 ≤ RQ < 0.1; moderate risk: 0.1 ≤ RQ < 1; and high risk: RQ ≥ 1.

To obtain a broad analysis of water pollution by pesticides and the environmental risk associated with each sampling location of the Guadiana Basin, the site-specific risk (RQ*site*) was determined using an additive model (sum up of the RQi's of all compounds), which assumes an additive action (AA) of the contaminants, following the Eq. (1):

$$RQSite = \sum_{i=1}^{n} RQi \quad (1)$$

Even though not strictly applicable to many compounds with unknown behavior in a mixture, the AA model is generally accepted as a first-tier approach (Backhaus and Faust, 2012; Palma et al., 2014a).

The risk map of the area for each investigated year was obtained using the RQsite calculated at each sampling site (average of the six sampling campaigns). Spatial interpolation was done with the Inverse Distance Weighted interpolation method. This spatial analysis method assumes that the risks that are closer to each other are more similar than those that are more distant. Consequently, for a specific location, the risk values of the locations around will contribute with a greater

weight to the risk prediction than the risk values of more distant locations.

2.5. Prioritization of pesticides based on their potential risk

The pesticides that could be included in the Guadiana RBSPs list were identified and prioritized following the NORMAN network prioritization methodology (Dulio and Ohe, 2013). Target pesticides detected in each sampling site were ranked using two risk indicators: (i) Frequency of Exceedance (FoE) and ii) Extent of Exceedance. The FoE considers the temporal or spatial occurrence of a contaminant with an ecotoxicological effect associated (Eq. (2)); while EoE ponders the intensity of the ecotoxicological risk, following the equation (Eq. (3)).

$$FoE = \frac{\sum n}{N} \quad (2)$$

n: number of samples with concentrations exceeding the lowest PNECN: number of total samples

$$EoE = \frac{MEC95}{PNEC} \quad (3)$$

MEC_{95}: 95th percentile of the measured concentrations for each pesticidePNEC: lowest predicted no effect concentration

The FoE value (RS_{FoE}) is comprised between 0 and 1 and is directly applied in the final ranking score (RS) calculation. In the case of the EoE, the value obtained is ranked as follows prior to their use in the RS calculation: EoE < 1 - RS_{EoE} = 0; 10 ≥ EoE ≥ 1 - RS_{EoE} = 0.1; 100 ≥ EoE > 10 - RS_{EoE} = 0.2; 1000 ≥ EoE > 100 - RS_{EoE} = 0.5; EoE > 1000 - RS_{EoE} = 1.

The values of each of these two indicators are subsequently added to yield a final RS between 0 and 2 (Eq. (4)). For calculation purposes, "non detected" values and values "below the limit of determination" were treated as zeros.

$$RS = RS_{FoE} + RS_{EoE} \quad (4)$$

3. Results and discussion

3.1. Land use/ land cover (LULC) analysis

Fig. 3 shows the distribution in the study area of the seven LULC classes distinguished in this work.

The predominant class in most of the drainage basins is the Agro-silvo-pastoral (Montado), a particular ecosystem that only exists in the Mediterranean, especially in the southern Iberian Peninsula. Traditional Agriculture is the second most frequent class in five of the drainage basins (Al, Mn, Mr, Lf, and S_Lf), followed by the Intensive irrigated Agriculture class. Pasture class represents less than 10% of the area in all basins except for S_Lf (15%). The classes Urban/Industrial, Forest and natural vegetation, and Water hardly are expressed in all basins. Intensive Irrigated Agriculture, the class mostly correlated with the highest rates of pesticide application, covers an area of 1444.2 km^2, corresponding to 16.7% of the region. This was the predominant class in S_Zb (43%) and the second most frequent in S_Am (18.1%) and S_Al (33.1%).

Fig. S1 shows the map of the CLC Agricultural class distribution in the drainage basins, as well as the bar plots indicating the percentages of each CLC subclass included in the Intensive Irrigated Agriculture class used in this work (Table S2). In S_Zb basin, where Intensive Irrigated Agriculture is predominant, the main crop is olive groves (91.4%). This is also the major land cover within the Intensive Irrigated Agriculture class in S_Am (96.5%), and together with vineyards in S_Al (43.6% olive groves and 55% vineyards). In the remaining drainage basins (Al, Mn, Mr, Lf, and S_Lf), there is not a predominant CLC subclass, being most of their land cover shared by Permanently irrigated arable land, Vineyards, and Olive groves.

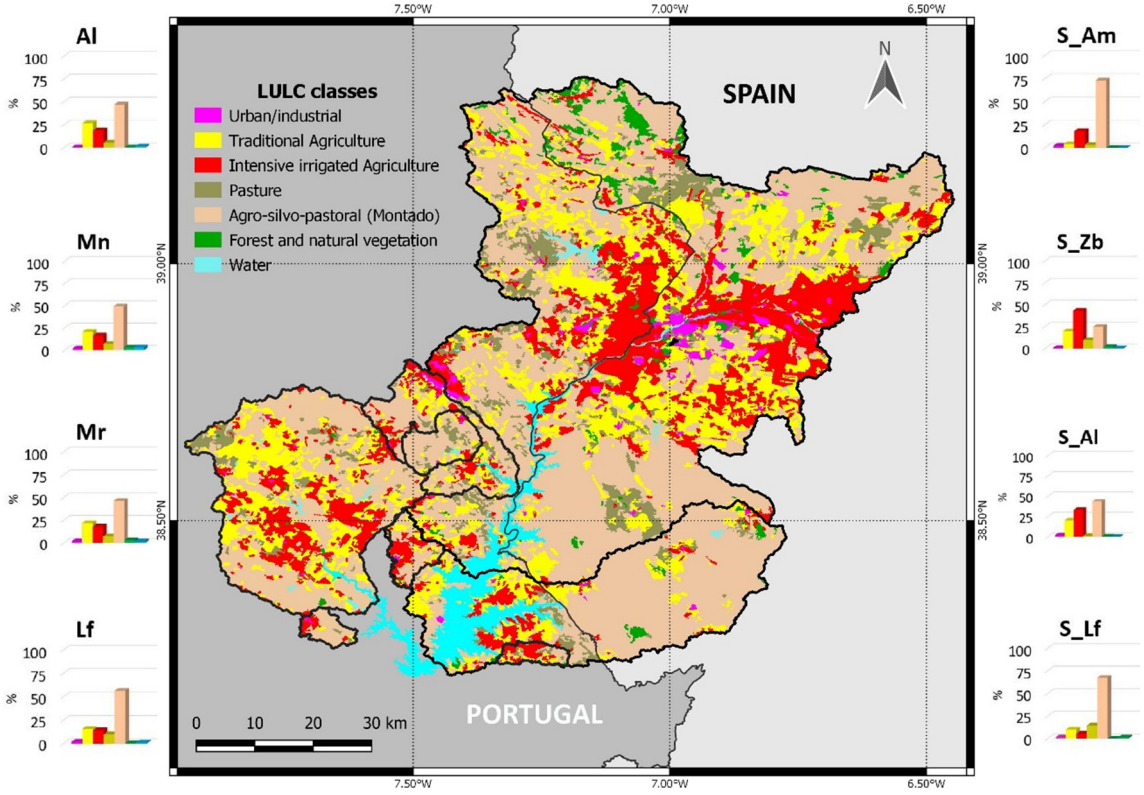

Fig. 3. Map of the LULC class distribution in the region of study and bar plots of the class percentages in each of the drainage basins. The seven classes are represented by the colors indicated in the legend. (For interpretation of the references to color in this figure legend, the reader is referred to the online version of this chapter.)

3.2. Occurrence of pesticides in the surface waters

Fig. 4 displays the total concentrations of pesticides quantified (a), with the corresponding distribution by classes (b), in each location and year (2017: drought year; 2018: pos-drought year). The results presented high spatial and temporal pesticide variability (Fig. 4a), showing no linkage among locations, and pointing out LULC and climate conditions as the most important factors for pesticide distribution. Spatial analysis showed overall higher concentrations of total pesticides in all Guadiana streams (4834 ng L^{-1} in S_Al, 5278 ng L^{-1} in S_Lf, and 6054 ng L^{-1} in S_Zb) except S_Am (158 ng L^{-1}), than in the reservoir. The low occurrence of pesticides in the Amieira (S_Am) may be justified by the low percentage of crops around the stream (22% of the land cover corresponding to traditional and intensive irrigated agriculture activities) and the high percentage of the agro-silvo-pastoral class (73%), which can also act as a buffer to the potential contamination generated in the crops (Palma et al., 2020a, 2020b).

The most contaminated area in the reservoir was Lucefécit (Lf) with a total pesticide concentration of 6931 ng L^{-1} in 2017. This location, however, has the lowest percentage of agricultural activities (traditional and intensive) in its drainage basin (30%), hence the occurrence of pesticides may be related to the steeper relief of the drainage basin that favors the runoff (Fig. 1). In contrast, Álamos (Al) was the location with the lowest occurrence of pesticides (total concentration: 630 ng L^{-1}), despite having 46% of its land covered by agricultural activities. This finding could be explained by the fact that this basin is extremely flat and thus, the runoff is hampered (Fig. 1). The results showed a spatial pesticide contamination pattern similar to that reported in previous studies, with the most contaminated areas occurring always in the northern part of the reservoir (Palma et al., 2009, 2014b).

Streams have been reported elsewhere as a source of nutrients and organic matter in the reservoir (Palma et al., 2020a, 2020b). However, the results obtained in this study did not support this hypothesis for pesticide contamination in the reservoir.

The temporal analysis revealed a marked difference between the two investigated years in terms of the pesticide contamination pattern, being 2017 considerably more contaminated than 2018 in all sites except S_Zb. As reported before, 2017 was classified as a drought year, extremely hot and dry. In general, in this year, the occurrence of pesticides in the waters was mainly observed between January and March, the period of rainy events (Tomaz et al., 2020).

Fig. 4b shows that the acidic class was dominant in the Guadiana Basin (44 to 88% contribution to the total pesticide concentrations), with bentazone as the most abundant herbicide in the group (63% of

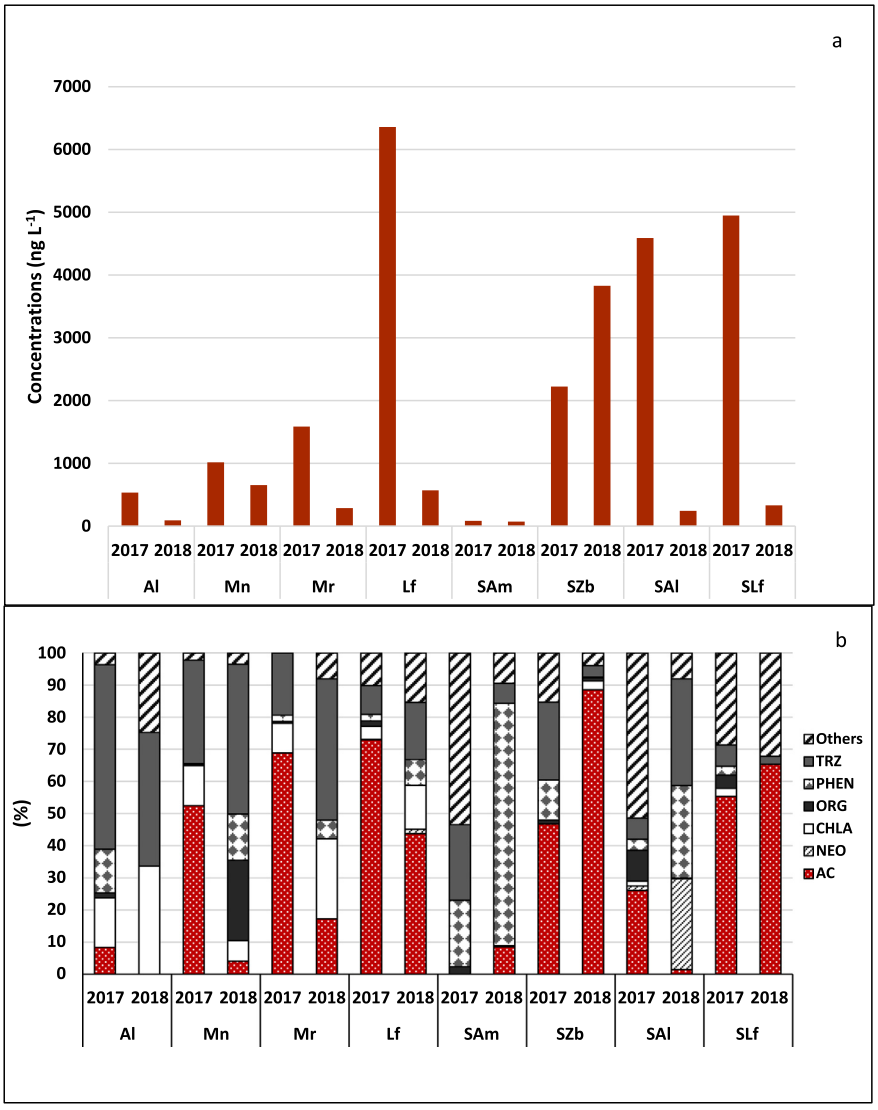

Fig. 4. a) Total concentration of pesticides in the analyzed water samples of the Guadiana Basin (Alqueva reservoir and Guadiana streams); b) Contribution of each class (TRZ: Triazines; PHEN: Phenylureas; ORG: Organophosphates; CHLA: Chloroacetanilides; NEO: Neocotinoids; AC: Acidics) to the total pesticide levels. The class "Others" includes Anilides, Pyridines, Carbamates, Thiocarbamates, Oxidiazoles, Quinolines, Sulfonylureas.

the total acidic pesticides detected in the area). Mecoprop, an acidic herbicide currently not approved for use in Portugal under the EC 1107/2009 (Table S3), was occasionally detected (S_Lf; May 2017: 23 ng L^{-1}). Mecoprop contamination could originate in the Spanish part of the Guadiana Basin, since this active substance was approved for use in Spain until January 2017 and it was detected in the northern part of the reservoir (near the border with Spain). The Acidic herbicides have also been reported to dominate the pesticide contamination profile in water samples from other Mediterranean areas. This is the case of the Ebro River Delta, an area of intensive rice cultivation (Barbieri et al., 2020b). The following most abundant pesticide class was triazines, represented mainly by terbuthylazine (64% of the class) and terbutryn (28% of the class), even though the latter is a substance no longer marketed in the European countries (Table S3). Atrazine, another triazine pesticide banned from the European market, was also occasionally detected in Lucefécit in 2017. Over the years, the acidic class, not detected in 2006/2007, has shown an increasing trend at the reservoir since 2011. In contrast, triazines have declined over time since 2006/2007, when they were the predominant class at the reservoir (Palma et al., 2009, 2014b).

In the temporary streams of Amieira (S_Am) and Álamos (S_Al), the pattern of pesticide contamination in 2017 was different than in 2018. The main contributing class to the total pesticide concentrations in 2017 was "others" in both cases, represented by sulfonylureas and pyridines in S_Am and S_Al, respectively. Phenylurea pesticides dominated the pesticide contamination profile in S_Am in 2018, while triazines, phenylureas, and neonicotinoids were the main classes in S_Al.

Thirty-eight out of the 51 pesticides analyzed were detected/quantified at least once in the basin. The compound with the highest total concentration (i.e., the sum of the concentrations measured in all samples) was bentazone. It globally reached 10,556 ng L^{-1}, occurring mainly at the reservoir in Lucefécit (Lf) (where it reached the maximum concentration of 2509 ng L^{-1}) and in the Lucefécit stream (S_Lf) (Fig. 5). High concentrations of bentazone have also been reported in other Mediterranean basins impacted by intensive agricultural activities (Barbieri et al., 2020b). The following most abundant pesticide was 2,4-D, with a total concentration of 3648 ng L^{-1}, mostly found in the Zebro stream (S_Zb). Despite the high maximum concentrations observed for these compounds, their occurrence was limited to certain areas of the basin (Table S4). Terbuthylazine, with a total concentration of 2202 ng L^{-1}, was the most frequently detected herbicide in the Guadiana Basin (streams and Alqueva reservoir), detected in all locations and also in all sampling campaigns in Mourão (Mr) and Montante (Mn). The high incidence of terbuthylazine could be attributed to its application in corn and sunflower fields, crops that occur all over the year. The ubiquitous presence of terbuthylazine in the reservoir is reported since 2006 (Palma et al., 2009, 2014b). Its concentration was reported to increase in this area from 2006 until 2011/2012, as expected due to the prohibition of atrazine and simazine use in Europe (ECC, 2004a, b). Ten years later, terbuthylazine concentrations are in the same order as those measured in 2006/2007 (39 ng L^{-1} to 85 ng L^{-1}).

Terbutryn also showed a ubiquitous pattern in the Guadiana Basin (Fig. 5). This is of concern because the use of this triazine was banned in Europe in 2002 (EC, 2002). Moreover, it occurred at concentrations above its environmental quality standards (AA (annual average): 65 ng L^{-1}; and MAC (maximum allowable concentration): 34 ng L^{-1} (ECC, 2013)) in the Zebro stream (S_Zb) in 2017.

The presence of banned pesticides in the Guadiana Basin is indeed a worrisome finding, since 23 out of the 38 substances detected are currently not approved for use in Europe (ECC 1107/2009; Table S2), and 5 of them are also priority substances (atrazine, chlorfenvinphos, diuron, simazine, and terbutryn; ECC, 2013). Six of the banned substances

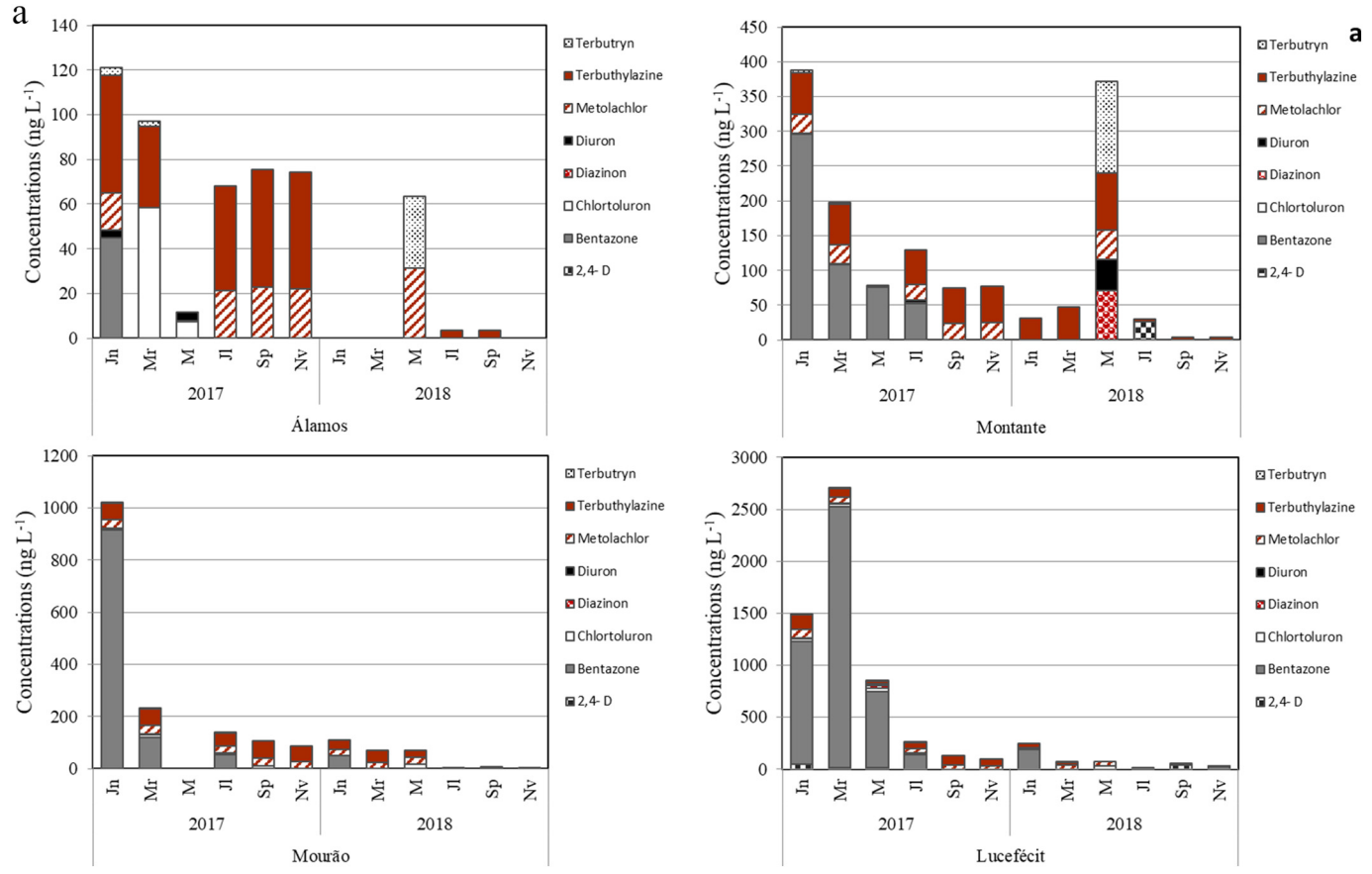

Fig. 5. Spatial (sampling stations) and temporal (2017: drought; and 2018: post-drought) variations observed for the pesticides measured at higher concentrations (ng L^{-1}), and with a detection frequency higher than 30% at least in one location of the Guadiana Basin (a: Alqueva Reservoir; b: Guadiana streams).

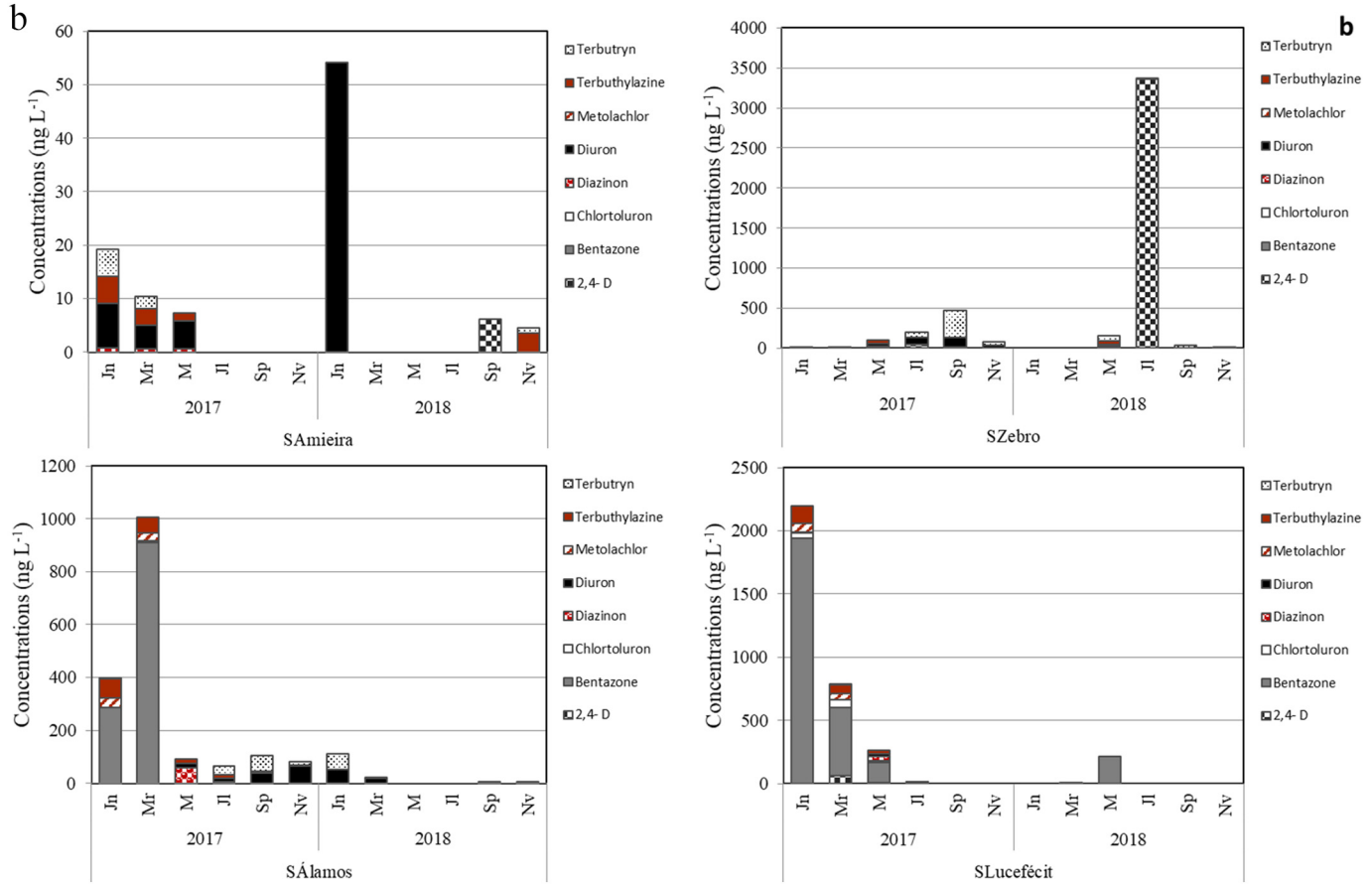

Fig. 5 (*continued*).

detected in the investigated samples, namely, chlorfenvinphos, diazinon, diuron, metolachlor, simazine, and terbutryn, were quantified more than once in several locations in the Guadiana Basin, indicating the existence of a continuous source of contamination. Thus, the presence of these substances could be attributed to their illegal use (metolachlor and terbutryn are not authorized in Portugal since 2003, simazine since 2005, chlorfenvinphos since 2007, and diazinon and diuron since 2009; https://sifito.dgav.pt/) or their release from soils and/or sediments where they could have adsorbed and accumulated during their application in the past due to their physical-chemical properties. The latter may be particularly the case of compounds such as chlorfenvinphos, diazinon, and terbutryn, which are characterized by low water solubility (< 50 mg/L), high octanol-water partition coefficient (log K_{ow} > 3), high organic carbon-water partition coefficient (K_{oc} = 500–4000 slightly mobile; K_{oc} ≥ 4000 non-mobile), and/or long soil half-life times (DT50 > 40 days) (Table S3). Similarly, these compounds are also likely to bioaccumulate in aquatic organisms. This points out the need for assessing the environmental risk that their occurrence may pose to aquatic organisms, and especially, to those species intended for human consumption.

Concerning the pesticides included in the various EU Watch Lists, imidacloprid, when quantified (only in Álamos stream), exceeded the maximum acceptable method LOD of 8.3 ng L^{-1} (EC, 2018), and consequently, its presence may pose undesired effects on aquatic organisms.

3.3. Environmental risk assessment

3.3.1. Environmental risk assessment of target pesticides

Fig. 6 displays the environmental risk of each pesticide in the worst-case scenario (RQex) for each sampling site and period (wet and dry) of each year (2017 and 2018). The corresponding RQex values are provided in Table S5. Thirty out of the 38 pesticides quantified at the basin may pose an environmental risk at least in one of the investigated periods and sites. The pesticide that showed the highest individual risk in the basin was Azinphos ethyl (RQi = 359; S_Lf: May of 2017) followed by 2,4-D (RQi = 168; S_Zb: July of 2018). Bentazone was the pesticide that presented a high risk for aquatic organisms in most sites of the Guadiana basin investigated and in most occasions (17%, 17%, 45%, 17%, and 33% of the samples collected at Mn, Mr, Lf, S_Al, S_Lf, respectively), mainly during the drought year (2017). The referred risk could be attributed to the high concentrations of bentazone found in the water, in line with its common use and moderate degradation (DT50 hydrolysis = 80 days; Table S3). Terbutryn presented a high risk in 42% of S_Zb samples, which may translate into persistent contamination with particularly harmful effects for the aquatic ecosystems of this watercourse. Terbuthylazine presented moderate to high environmental risk in all locations, except in the Amieira stream (S_Am) (with low risk throughout the study period) (Fig. 6). Irgarol showed high risk mainly in the streams in 2017. Chlorfenvinphos and diazinon although detected in relatively low concentrations (< 60 ng L^{-1} in the case of chlorfenvinphos and < 70 ng L^{-1} in the case of diazinon), presented a moderate to high risk (RQex) in streams and in some areas at the reservoir (Montante and Lucefécit), which is of concern, considering that these insecticides have been banned since 2007. The occurrence of dichlorvos, diflufenican, MCPA, metiocarb, and oxadiazon was always associated with a high risk for aquatic ecosystems. In contrast, low and moderate environmental risks were obtained for bromoxynil, chlortoluron, diuron, mecoprop metolachlor, propanil, quinoxyphen, thiacloprode, and methyl tifensulfuron under the worst contamination scenario.

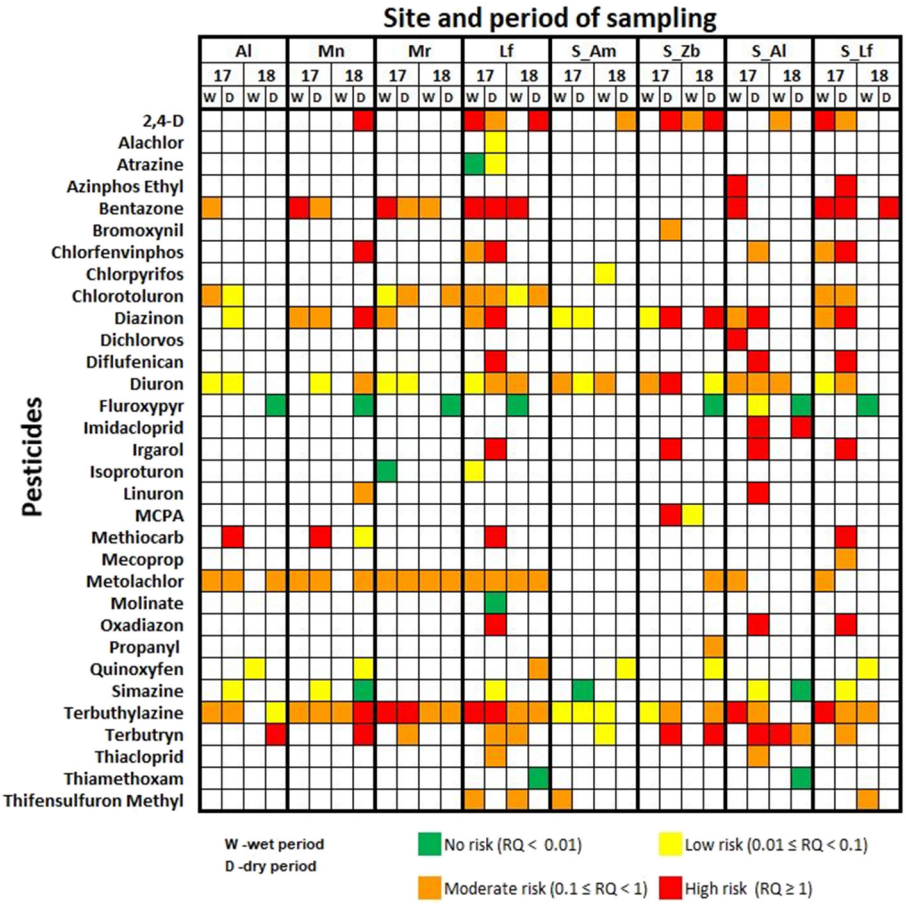

Fig. 6. Risk quotients calculated for each pesticide in the worst-case scenario (RQex), at the eight sampling sites and in the four periods analyzed (Wet and Dry in 2017 and 2018), according to the ranks proposed by Sanchez-Bayo and Baskaran (2002). The raw values are displayed in Table S5.

3.3.2. Guadiana River basin specific pollutants (RBSP)

The pesticides investigated were prioritized to be proposed as the Guadiana RBSPs following the NORMAN methodology. The pesticides having a non-zero ranking score (RS) were ranked and displayed in Table 1, showing the respective contributions of FoE and EoE. Among the 32 pesticides with risk in the basin, 17 showed an RS higher than 0, ranging between 0.26 and 0.01, and hence, proposed as candidates for priority pollutants of the Guadiana Basin. The FoE (number of sites where the concentration surpasses the PNEC) seems to be the dominating factor in the final RS. RS_{EoE} values higher than RS_{FoE}, which indicate high but occasional local ecotoxicological risk effects, were found only in the case of diazinon, imidacloprid, and thiacloprid. Top-ranked pesticides (RS > 0.10) included the herbicides bentazone (#1), terbutryn (#2), terbuthylazine (#4), and the insecticides diazinon (#3), imidacloprid (#5), and thiacloprid (#6). Two of them (terbutryn and diazinon) are no longer on the Portuguese market. Their use is also not authorized in Spain, and thus, transboundary contamination from application can be discarded. However, knowing their sources of contamination is essential to implement the correct mitigation actions. Due to their physical-chemical properties (low solubility <60 mg/L, an octanol-water partition coefficient of 3.7, high organic carbon-water partition coefficient, and relative persistence in soil, especially in the case of terbutryn; Table S3) previously contaminated agricultural soils and sediments can be plausible sources of terbutryn and diazinon contamination in the Alqueva reservoir and associated streams. Terbuthylazine and bentazone are systemic herbicides used in irrigated crops of corn and sunflower. These crops belong to the LULC subclass of annual crops associated with permanent crops (Fig. S1) that have been growing since the construction of the Alqueva reservoir. Regarding neonicotinoids, imidacloprid is used in irrigated vegetables such as tomatoes, and thiacloprid in olive and almond trees, crops very extended in the investigated area. Hence, it is important to work with the farmers and the environmental institutions to improve the environmental sustainability of the use of these pesticides and reduce their potential risk in the Guadiana Basin.

Table 1
Pesticides prioritization based on frequency and extent of exceedance scores (RS_{FoE}; RS_{EoE}), and total score priority ranking (RS).

	RS_{EoE}	RS_{FoE}	RS
Bentazone	0.1	0.16	0.26
Terbutryn	0.1	0.10	0.20
Diazinon	0.1	0.07	0.17
Terbuthylazine	0	0.14	0.14
Imidacloprid	0.1	0.02	0.12
Thiacloprid	0.1	0.00	0.10
2,4-D	0	0.06	0.06
Irgarol	0	0.05	0.05
Methiocarb	0	0.04	0.04
Oxadiazon	0	0.03	0.03
Diflufenican	0	0.03	0.03
Chlorfenvinphos	0	0.03	0.03
Diuron	0	0.02	0.02
Azinphos ethyl	0	0.02	0.02
MCPA	0	0.01	0.01
Linuron	0	0.01	0.01
Dichlorvos	0	0.01	0.01

3.3.3. Spatial and temporal risk in the study area (risk site)

The environmental risk associated with each area of the Guadiana Basin was investigated using an additive model based on the mixtures

of pesticides present in each sampling site and year, as reported elsewhere (Barbieri et al., 2020b; Köck-Schulmeyer et al., 2021; Palma et al., 2014a). Fig. 7 presents the environmental risk in each investigated location (RQ*site*: white filled circles) in the risk maps obtained from the spatial analysis, for both years. The Guadiana streams presented a greater risk than the reservoir (except the Amieira stream (S_Am)). These differences in risk were more obvious during the dry period of 2017. This result is relevant, as most streams are temporary and characterized by very sensitive ecosystems associated with high biodiversity. Álamos stream presented the highest quantified risk RQ*site* = 583, in March of 2017, followed by Lucefécit stream with an RQ*site* = 444 in May of 2017. Unlike other sites where the risk was higher in 2017 than in 2018, the Zebro stream presented the highest risk due to pesticide contamination in July 2018. Concerning the reservoir, the highest values of risk were observed in Lucefécit in May 2017. The results showed a temporal pattern, with the greatest risk for aquatic species during the drought year (2017), in line with previous studies in the Guadiana Basin (Palma et al., 2020b). Risk maps allow the spatial

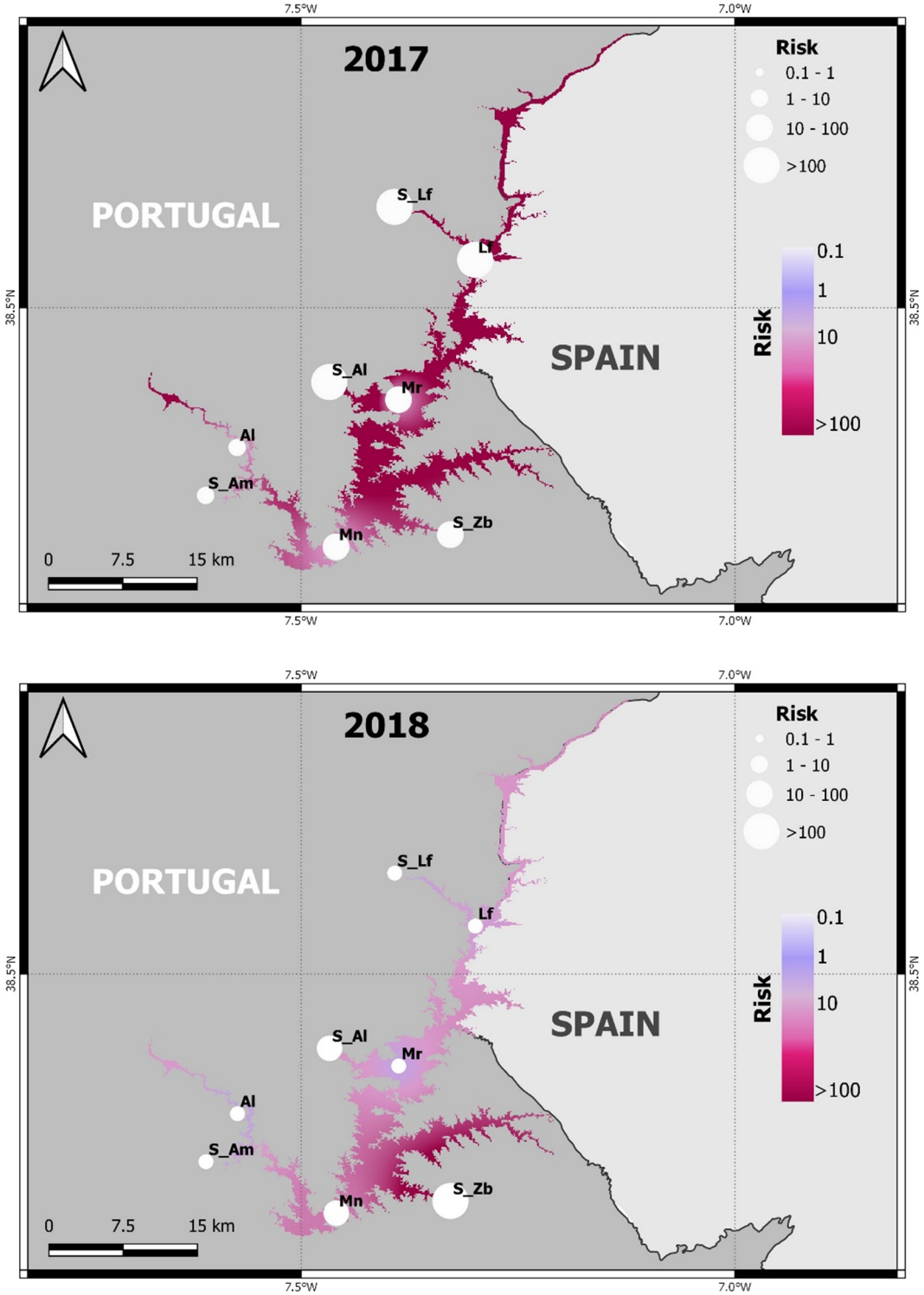

Fig. 7. Risk maps and the respective Risk Quotient (RQsite) calculated via the additive model for the mixture of the 32 pesticides detected within the Guadiana Basin, in 2017 and 2018.

visualization of the environmental risk posed by pesticides in the study area. These maps were obtained through the spatial interpolation of the environmental risk from each site of analysis (RQ*site*). As displayed in Fig. 7, the drought year (2017) presented a higher risk than the post-drought year (2018) in the whole study area. Further, the risk map of 2017 also highlighted the chemical stress of the pesticides in the streams. While the analysis of the risk map obtained for 2017 shows the highest impact on the aquatic ecosystems in the northern part of the study area, the risk map for the year 2018 reveals the highest risk in the southeast of the reservoir.

4. Conclusions

The results of the present study allowed understanding the influence of the land use/land cover and the meteorological conditions on the occurrence and the associated environmental risk of 51 pesticides in the Guadiana Basin. The highest total pesticide concentrations were detected in areas where intensive irrigation agriculture prevails, and olive groves and vineyards are the major crops. The strong drought that occurred during the year 2017 enhanced the impact of pesticides in the aquatic ecosystem of the Guadiana streams, most of them with intermittent regimes, and very sensitive to pollution.

The results showed that 61% of the 38 pesticides quantified in the Guadiana Basin were banned for use in Portugal between 2002 and 2009, and most of them also in Spain, which rules out their transboundary origin. Thus their source could be related to their persistence in sediments and soils during their application in the past. Their presence could also be attributed to the illegal use of the last stock reserves or after purchase of the formulations in other countries (as postulated in the case of mecoprop) countries), or legal application in Spain (as suggested for diuron).

The pesticide environmental risk study showed that 32 out of the 38 pesticides detected were in concentrations that may pose a risk to aquatic species. The greatest environmental risk was observed for azinphos ethyl, banned in Portugal in 2007. Bentazone, terbuthylazine, and 2,4-D were the pesticides whose concentrations could have induced ecological effects in most of the sampled locations and periods. The prioritization exercise allowed concluding that 17 pesticides should be considered in the Guadiana RBSP list, for strict control in the basin. Eight out of the 17 priority pesticides are currently banned for use in Portugal and all of them except diuron are also not allowed in Spain. Thus, understanding their sources is crucial to adopt the appropriate mitigation actions. For instance, in the case of terbutryn and diazinon, which were among the six top-ranked pesticides, their release from agricultural soils and sediments where they may have accumulated after application in the past is the most plausible source. Their potential to accumulate in these matrices is confirmed by their physical-chemical properties.

The environmental risk obtained for each location revealed a greater risk in the streams of the Guadiana Basin than in the reservoir, more evident in 2017 (drought year) than in 2018 (post-drought year). This is of concern due to the high biodiversity associated with this type of hydrological regime and the high sensitivity of these systems to pollution. Agriculture is an economic mover of the Alentejo region, but the results point to the negative effect that this activity may have on the waters of the Guadiana Basin. Consequently, it is crucial to group all the results of pesticides assessment in the region in a platform to support the environmental actions and policies that must be implemented in the basin. Further, the results highlighted the need to work with water management entities to outline actions to reverse the presence of pesticides and with farmers to implement best agricultural practices, to preserve and improve the ecosystem services provided by the Guadiana Basin.

It is important to highlight that due to the transboundary character of the Guadiana basin, pesticide contamination in the study area may be also ruled by extreme events in river runoff, climatological conditions, and pesticide use occurring upstream in the Spanish part. All these factors may have significant effects on the overall water quality in the lower river basin, in terms of sediment loading, total organic content, and chemical composition. The solution to transboundary contamination problems requires adopting transboundary water governance.

CRediT authorship contribution statement

P. Palma: Conceptualization, Investigation, Writing – original draft, Visualization, Writing – review & editing, Supervision, Funding acquisition, Project administration. **S. Fialho:** Investigation. **A. Lima:** Investigation. **A. Catarino:** Investigation. **M.J. Costa:** Writing – original draft, Visualization, Writing – review & editing. **M.V. Barbieri:** Investigation. **L.S. Monllor-Alcaraz:** Investigation. **C. Postigo:** Writing – review & editing. **M. Lopez de Alda:** Supervision, Writing – review & editing.

Declaration of competing interest

The authors declare that they have no known competing financial interests or personal relationships that could have appeared to influence the work reported in this paper.

Acknowledgment

The present research is co-funded by the European Union through the European Regional Development Fund, included in the COMPETE 2020 (Operational Program Competitiveness and Internationalization) through the ICT project (UIDB/04683/2020) with the reference POCI-01-0145-FEDER-007690, the ALOP project (ALT20-03-0145-FEDER-000004), and through the European Agricultural Fund for Rural Development through the FitoFarmGest Operational Group (PDR2020-101-030926). It has been partially funded also by the Spanish Ministry of Science and Innovation (Project CEX2018-000794-S) and the Government of Catalonia (2017 SGR 01404). LSMA acknowledges the support provided by the "National System of Youth Guarantee" contract within the National Operational programme on Youth Employment 2014-2020 (Youth Employment Initiative and the European Social Fund).

Appendix A. Supplementary data

Supplementary data to this article can be found online at https://doi.org/10.1016/j.scitotenv.2021.148703.

References

AERU (Agriculture and Environmental Research Unit), 2013. The PPDB Pesticides Properties Database. University of Herfordshire UK. http://sitem.herts.ac.uk/aeru/footprint/front_ppdb.htm;.

Altenburger, R., Brack, W., Burgess, R.M., Busch, W., Escher, B.I., Focks, A., Mark Hewitt, L., Jacobsen, B.N., de Alda, M.L., Ait-Aissa, S., Backhaus, T., Ginebreda, A., Hilscherová, K., Hollender, J., Hollert, H., Neale, P.A., Schulze, T., Schymanski, E.L., Teodorovic, I., Tindall, A.J., de Aragão Umbuzeiro, G., Vrana, B., Zonja, B., Krauss, M., 2019. Future water quality monitoring: improving the balance between exposure and toxicity assessments of real-world pollutant mixtures. Environ. Sci. Eur. 31, 1–17. https://doi.org/10.1186/s12302-019-0193-1.

ARHAlentejo (Administração da Região Hidrográfica do Alentejo I.P.), 2011. Plano de gestão das bacias hidrográficas integradas nas regiões hidrográficas 6 e 7: Região Hidrográfica 7. Ministério do Ambiente e do Ordenamento do Território, Lisboa (in Portuguese).

Backhaus, T., Faust, M., 2012. Predictive environmental risk assessment of chemical mixtures: a conceptual framework. Environ. Sci. Technol. 46, 2564–2573.

Barbieri, M.V., Monllor-Alcaraz, L.S., Postigo, C., López de Alda, M., 2020a. Improved fully automated method for the determination of medium to highly polar pesticides in surface and groundwater and application in two distinct agriculture-impacted areas. Sci. Total Environ. 745, 140650. https://doi.org/10.1016/j.scitotenv.2020.140650.

Barbieri, M.V., Peris, A., Postigo, C., Moya-Garcés, A., Monllor-Alcaraz, L.S., Rambla-Alegre, M., Eljarrat, E., López de Alda, M., 2020b. Evaluation of the occurrence and fate of pesticides in a typical Mediterranean delta ecosystem (Ebro River Delta) and risk assessment for aquatic organisms. Environ. Pollut., 115813 https://doi.org/10.1016/j.envpol.2020.115813.

Čelić, M., Jaén-Gil, A., Briceño-Guevara, S., Rodríguez-Mozaz, S., Gros, M., Petrović, M., 2021. Extended suspect screening to identify contaminants of emerging concern in

riverine and coastal ecosystems and assessment of environmental risks. J. Hazard. Mater. 404. https://doi.org/10.1016/j.jhazmat.2020.124102.
Dulio, V., Ohe, P.C. Von Der, 2013. Emerging Substances NORMAN Prioritisation Framework for Emerging Substances.
EC, 2002. Commission Regulation (EC) nº 2076/2002 of 20 November 2002 Extending the Time Period Referred to in Article 8(2) of Council Directive 91/414/EEC and Concerning the Non-inclusion of Certain Active Substances in Annex I to That Directive and the Withdrawal of Authorisations for Plant Protection Products Containing These Substances. Retrieved from. https://bit.ly/39iqNRc.
EC, 2018. Commission Implementing Decision (EU) 2018/840 of 5 June 2018 Establishing a Watch List of Substances for Union-wide Monitoring in the Field of Water Policy Pursuant to Directive 2008/105/EC of the European Parliament and of the Council and Repealing Commission Implementing Decision (EU) 2015/495.
ECC (European Community Commission), 2000. Commission Directive 2000/60/EC of the European Parliament and the Council establishing the framework for community action in the field of water policy. Off. J.Eur.Commun. L 327.
ECC (European Community Commission), 2003. Technical Guidance Document on Risk Assessment. Part II. JRC, Brussels. Belgium.
ECC (European Community Commission), 2004a. Decision 2004/247/EC Concerning the Non-inclusion of Simazine in Annex I to Council Directive 91/414/EEC and the Withdrawal of Authorizations for Plant Protection Products Containing This Active Substance.
ECC (European Community Commission), 2004b. Decision 2004/248/EC Concerning the Non-inclusion of Atrazine in Annex I to Council Directive 91/414/EEC and the Withdrawal of Authorizations for Plant Protection Products Containing this Active Substance.
ECC (European Community Commission), 2013. Decision 2013/39/EC on environmental quality standards in the field of water policy. Off. J. Eur. Commun. L 226/1.
EFSA (European Food Safety Autority), 2017. The 2015 European Union report on pesticide residues in food. EFSA J. 15. https://doi.org/10.2903/j.efsa.2017.4791.
Eurostat, 2018. Agriculture, Forestry and Fishery Statistics 2018 Edition. Eurostat.
Finizio, A., Villa, S., 2002. Environmental risk assessment for pesticides: a tool for decision making. Environ. Impact Assess. Rev. 22, 235–248. https://doi.org/10.1016/S0195-9255(02)00002-1.
Foley, J.A., Ramankutty, N., Brauman, K.A., Cassidy, E.S., Gerber, J.S., Johnston, M., Mueller, N.D., O'Connell, C., Ray, D.K., West, P.C., Balzer, C., Bennett, E.M., Carpenter, S.R., Hill, J., Monfreda, C., Polasky, S., Rockström, J., Sheehan, J., Siebert, S., Tilman, D., Zaks, D.P.M., 2011. Solutions for a cultivated planet. Nature 478, 337–342. https://doi.org/10.1038/nature10452.
Heckel, D.G., 2012. Insecticide resistance after silent spring. Science (80-.). 337, 1612–1614.
Kandie, F.J., Krauss, M., Beckers, L.M., Massei, R., Fillinger, U., Becker, J., Liess, M., Torto, B., Brack, W., 2020. Occurrence and risk assessment of organic micropollutants in freshwater systems within the Lake Victoria South Basin, Kenya. Sci. Total Environ. 714, 136748. https://doi.org/10.1016/j.scitotenv.2020.136748.
Khush, G.S., 1999. Green revolution: preparing for the 21st century. Genome 42, 646–655.
Köck-Schulmeyer, M., Ginebreda, A., Petrovic, M., Giulivo, M., Aznar-Alemany, Ò., Eljarrat, E., Valle-Sistac, J., Molins-Delgado, D., Diaz-Cruz, M.S., Monllor-Alcaraz, L.S., Guillem-Argiles, N., Martínez, E., Miren, L. de A., Llorca, M., Farré, M., Peña, J.M., Mandaric, L., Pérez, S., Majone, B., Bellin, A., Kalogianni, E., Skoulikidis, N.T., Milačič, R., Barceló, D., 2021. Priority and emerging organic microcontaminants in three Mediterranean river basins: occurrence, spatial distribution, and identification of river basin specific pollutants. Sci. Total Environ. 754. https://doi.org/10.1016/j.scitotenv.2020.142344.
Kosztra, B., Büttner, G., Hazeu, G., Arnold, S., 2017. Updated CLC illustrated nomenclature guidelines. Retrieved from. European Topic Centre on Urban, land and soil systems (ETC/ULS). Environment Agency Austria, Wien https://land.copernicus.eu/user-corner/technical-library/corine-land-cover-nomenclature-guidelines/docs/pdf/CLC2018_Nomenclature_illustrated_guide_20190510.pdf.
Llorens, E., Ginebreda, A., la Farré, M., Insa, S., González-Trujillo, J.D., Munné, A., Solà, C., Flò, M., Villagrasa, M., Barceló, D., Sabater, S., 2020. Occurrence of regulated pollutants in populated Mediterranean basins: ecotoxicological risk and effects on biological quality. Sci. Total Environ. 747, 141224. https://doi.org/10.1016/j.scitotenv.2020.141224.
Palma, P., Kuster, M., Alvarenga, P., Palma, V.L., Fernandes, R.M., Soares, A.M.V.M., López de Alda, M.J., Barceló, D., Barbosa, I.R., 2009. Risk assessment of representative and priority pesticides, in surface water of the Alqueva reservoir (south of Portugal) using on-line solid phase extraction-liquid chromatography-tandem mass spectrometry. Environ. Int. 35. https://doi.org/10.1016/j.envint.2008.09.015.
Palma, P., Köck-Schulmeyer, M., Alvarenga, P., Ledo, L., Barbosa, I.R., López de Alda, M., Barceló, D., 2014a. Risk assessment of pesticides detected in surface water of the Alqueva reservoir (Guadiana basin, southern of Portugal). Sci. Total Environ. 488–489. https://doi.org/10.1016/j.scitotenv.2014.04.088.
Palma, P., Ledo, L., Soares, S., Barbosa, I.R., Alvarenga, P., 2014b. Spatial and temporal variability of the water and sediments quality in the alqueva reservoir (Guadiana Basin; southern Portugal). Sci. Total Environ., 470–471 https://doi.org/10.1016/j.scitotenv.2013.10.035.
Palma, P., Köck-Schulmeyer, M., Alvarenga, P., Ledo, L., de Alda, M.L., Barceló, D., 2015. Occurrence and potential risk of currently used pesticides in sediments of the Alqueva reservoir (Guadiana Basin). Environ. Sci. Pollut. Res. 22. https://doi.org/10.1007/s11356-015-4390-1.
Palma, P., Ledo, L., Alvarenga, P., 2016. Ecotoxicological endpoints, are they useful tools to support ecological status assessment in strongly modified water bodies? Sci. Total Environ. 541, 119–129. https://doi.org/10.1016/j.scitotenv.2015.09.014.
Palma, P., Fialho, S., Lima, A., Mourinha, C., Penha, A., Novais, M.H., Rosado, A., Morais, M., Potes, M., Costa, M.J., Alvarenga, P., 2020a. Land-cover patterns and hydrogeomorphology of tributaries: are these important stressors for the water quality of reservoirs in the mediterranean region? Water (Switzerland) 12. https://doi.org/10.3390/w12102665.
Palma, P., Fialho, S., Lima, A., Novais, M.H., Costa, M.J., Montemurro, N., Pérez, S., de Alda, M.L., 2020b. Pharmaceuticals in a Mediterranean Basin: the influence of temporal and hydrological patterns in environmental risk assessment. Sci. Total Environ. 709. https://doi.org/10.1016/j.scitotenv.2019.136205.
Palma, P., Penha, A.M., Novais, M.H., Fialho, S., Lima, A., Mourinha, C., Alvarenga, P., Rosado, A., Iakunin, M., Rodrigues, G., Potes, M., Costa, M.J., Morais, M., Salgado, R., 2021. Water - Sediment Physicochemical Dynamics in a Large Reservoir in the Mediterranean Region under Multiple Stressors. pp. 1–23.
Papadopoulou-Mourkidou, E., Kotopoulou, A., Papadakis, E.N., Vryzas, Z., Kintzikoglou, K., Makris, K.C., 2015. A pesticide monitoring survey in rivers and lakes of northern Greece and its human and ecotoxicological risk assessment. Ecotoxicol. Environ. Saf. 116, 1–9. https://doi.org/10.1016/j.ecoenv.2015.02.033.
Ramírez-Morales, D., Pérez-Villanueva, M.E., Chin-Pampillo, J.S., Aguilar-Mora, P., Arias-Mora, V., Masís-Mora, M., 2021. Pesticide occurrence and water quality assessment from an agriculturally influenced Latin-American tropical region. Chemosphere 262. https://doi.org/10.1016/j.chemosphere.2020.127851.
Sabater, S., Bregoli, F., Acuña, V., Barceló, D., Elosegi, A., Ginebreda, A., Marcé, R., Muñoz, I., Sabater-Liesa, L., Ferreira, V., 2018. Effects of human-driven water stress on river ecosystems: a meta-analysis. Sci. Rep. 8, 1–11. https://doi.org/10.1038/s41598-018-29807-7.
Sanchez-Bayo, F., Baskaran, S.K.I.R., 2002. Ecological relative risk (EcoRR): another approach for risk assessment of pesticides in agriculture. Agric. Ecosyst. Environ. 91, 37–57.
Silva, V., Mol, H.G.J., Zomer, P., Tienstra, M., Ritsema, C.J., Geissen, V., 2019. Pesticide residues in European agricultural soils – a hidden reality unfolded. Sci. Total Environ. 653, 1532–1545. https://doi.org/10.1016/j.scitotenv.2018.10.441.
Streissl, F., Egsmose, M., Tarazona, J.V., 2018. Linking pesticide marketing authorisations with environmental impact assessments through realistic landscape risk assessment paradigms. Ecotoxicology 27, 980–991. https://doi.org/10.1007/s10646-018-1962-0.
Tilman, D., Fargione, J., Wolff, B., D'Antonio, C., Dobson, A., Howarth, R., Schindler, D., Schlesinger, W.H., Simberloff, D., S.D., 2001. Forecasting agriculturally driven global environmental change. Science (80-.) 292, 281–284.
Tomaz, A., Palma, P., Fialho, S., Lima, A., Alvarenga, P., Potes, M., Salgado, R., 2020. Spatial and temporal dynamics of irrigation water quality under drought conditions in a large reservoir in southern Portugal. Environ. Monit. Assess. 192. https://doi.org/10.1007/s10661-019-8048-1.

Received: 14 June 2020 | Revised: 7 July 2021 | Accepted: 9 July 2021 | Published on: 29 July 2021

DOI: 10.1002/joc.7299

RESEARCH ARTICLE

International Journal of Climatology RMetS

Impact of a large artificial lake on regional climate: A typical meteorological year Meso-NH simulation results

Maksim Iakunin[1,2] | **Edgar F.M. Abreu**[1] | **Paulo Canhoto**[1] | **Sara Pereira**[1] | **Rui Salgado**[1]

[1]Department of Physics, Institute of Earth Sciences—ICT, University of Évora, Évora, Portugal

[2]Institute of Bio- and Geosciences, Agrosphere (IBG-3) Research Centre Jülich (FZJ) Wilhelm-Johnen-Straße, Jülich, Germany

Correspondence
Maksim Iakunin, Department of Physics, Institute of Earth Sciences—ICT, University of Évora, Rua Romão Ramalho 59, Évora 7000-671, Portugal.
Email: m.iakunin@fz-juelich.de

Funding information
ALOP project, Grant/Award Number: ALT20-03-0145-FEDER-000004; COMPETE 2020 ICT project, Grant/Award Number: UID / GEO / 04683/2019 POCI-01-0145-FEDER-007690; Fundação para a Ciência e a Tecnologia, Grant/Award Number: SFRH/BD/136433/2018; TOMAQAPA, Grant/Award Number: FCT reference PTDC/CTA-MET/29678/2017

Abstract

Large artificial lakes and reservoirs affect the meteorological regime of the shore area and the local climate takes on a number of new features that were previously absent. This work focuses on the weather impact of the Alqueva reservoir, the largest artificial lake in Western Europe. An extensive set of numerical simulations using Meso-NH mesoscale atmospheric model coupled with FLake (Freshwater Lake) scheme was carried out. The simulations covered a 12-month period that was chosen to compose a so-called Typical Meteorological Year. This artificial time period is meant to represent the typical meteorological conditions in the region and the model results are used to assess the changes in the local climate. To evaluate the raw impact of the reservoir, two different scenarios of simulations were compared: (A) with the reservoir as it exists nowadays and (B) without the reservoir using the older surface dataset. The results show decrease of air temperature during daytime (10–9°C) and nighttime increase (up to 10°C). In nearest towns, daily maximum temperature decreased and daily minimum temperature increased, which refers to milder weather conditions. Alqueva mainly showed suppression in fog formation in the nearby area. Local breeze regime was studied and monthly lake/land breezes were described.

KEYWORDS

artificial reservoir, mesoscale atmospheric modelling, typical meteorological year, weather

1 | INTRODUCTION

Inland water bodies, in particular reservoirs, are peculiar living sensors in the weather/climate system of the Earth. Large and deep lakes have a significant impact on regional weather and climate (Samuelsson *et al.*, 2010; Eerola *et al.*, 2014), as shown in well-described examples, such as the Great American lakes (Bates *et al.*, 1993; Scott and Huff, 1996; Notaro *et al.*, 2013). Lakes have a higher heat capacity and thermal inertia and lower surface albedo and roughness length than land surface, which determine their impact on the atmosphere (Bonan, 1995). They interact with the atmospheric boundary layer through momentum, heat and moisture exchange, and their influence on local weather patterns is expressed in diurnal and seasonal variability at various spatial scales

This is an open access article under the terms of the Creative Commons Attribution-NonCommercial License, which permits use, distribution and reproduction in any medium, provided the original work is properly cited and is not used for commercial purposes.
© 2021 The Authors. *International Journal of Climatology* published by John Wiley & Sons Ltd on behalf of Royal Meteorological Society.

(Choulga *et al*., 2014; Le Moigne *et al*., 2016). Lakes' heat storage and emission cycles are responsible for summer/daytime cooling and winter/night warming effects (Bonan, 1995; Samuelsson *et al*., 2010) and the formation of characteristic features of local breeze patterns (Bates *et al*., 1993; Segal *et al*., 1997). Under certain atmospheric conditions such heat emissions may cause fog formation when cold moist air mass moves over a warmer lake surface. Recent numerical studies showed such effects in lakes and reservoirs, for example, in Chile (Bischoff-Gauß *et al*., 2006), African Great Lakes (Thiery *et al*., 2014), Lake Sobradinho in Brazil (Ekhtiari *et al*., 2017).

The Alqueva reservoir (south-east of Portugal) is the largest artificial lake in Western Europe (surface area of 250 km^2) and it was established in 2002 after the closing of the dam on the Guadiana river. An emergence of such a large water body significantly affected regional environment. The Alqueva reservoir was the object of various multidisciplinary studies, such as ecology and water quality monitoring (Potes *et al*., 2012, 2018; Iakunin *et al*., 2020; Rodrigues *et al*., 2020), biology (Novais *et al*., 2018), land use (Penha *et al*., 2016; Tomaz *et al*., 2017), and meteorology (Lopes *et al*., 2016; Policarpo *et al*., 2017; Potes *et al*., 2017). The aim of this study is to assess the impact of the reservoir on the local regional weather regime using an extensive set of atmospheric simulations. The Meso-NH atmospheric model (Lac *et al*., 2018) was used for that purpose. A previous case study experiment (Iakunin *et al*., 2018) showed that the Meso-NH model successfully represents the meteorological conditions and the local lake effects of the Alqueva reservoir. To capture the long-term meteorological effects of the lake the numerical simulation should cover 16 years (2004–2019) of the Alqueva lifetime, but such experiment would require enormous computing resources and data storage. A reasonable alternative is to make 1-year simulation over a period that is representative of the meteorological conditions of the region. One of the possible methodologies for creating such a period is to build a Typical Meteorological Year.

A Typical Meteorological Year (TMY) is a weather dataset, widely used for energy simulations in buildings and renewable energy systems (Chan, 2016; Abreu *et al*., 2018). This typical year comprises twelve concatenated typical months that are able to reproduce the long-term data statistics and, therefore, are useful to the scope of this work. Although several methodologies have been proposed in the literature to generate typical weather datasets (e.g., Festa and Ratto (1993); Gazela and Mathioulakis (2001)), the most used methodology was presented by Hall *et al*. (1978), known as Sandia method, and it was the methodology used here. Newer versions of this method were developed by the National Renewable Energy Laboratory (NREL), namely the TMY2 (Marion and Urban, 1995) and TMY3 (Wilcox and Marion, 2008). However, their implementation requires direct normal irradiance measurements, which were not readily available during all of the time period under analysis. The Sandia method allowed for TMYs to be reported in the literature for various locations, such as Athens (Pissimanis *et al*., 1988), different climates of Turkey (Pusat *et al*., 2015), distinct places in Madeira Island (Abreu *et al*., 2018) or the Argentine littoral region (Bre and Fachinotti, 2016), to mention a few. A TMY is widely used in renewable energy and building heat balance applications, but has also been used for other climate and environmental studies. In biometeorology, the TMY methodology was applied for greenhouses design (Fernández *et al*., 2015) or to optimize irrigation strategies and assess the atmospheric environmental impact of a combined district heating system (Domínguez *et al*., 2013; Haichao *et al*., 2013; Martínez-Romero *et al*., 2019).

The principal questions of the current study are: to what extent does a reservoir like Alqueva affect the air temperature under such climate conditions, does it increase (or decrease) the amount of fog days in the region, and what are the seasonal breeze patterns associated with the reservoir. The structure of the article is the following. The Introduction is followed by the Data and Methods section, which is dedicated to the specification of the study area, data, models, and the approach used in the work, case study that was made prior to the current work, design of the TMY, and the experiment setup. Section 3 summarizes the results obtained from the numerical simulations and the Discussion part concludes the results, the aim of the work, and possible perspectives.

2 | DATA AND METHODS

2.1 | Study area

The Alqueva reservoir was established in 2002 when the dam gates on the Guadiana river were closed (https://www.edia.pt). The reservoir fills the former river valley in the southeast of Portugal on the Portugal-Spain border and spreads along 83 km (Figure 1a). The lake surface area at the full storage level covers an area of 250 km^2 with a capacity of 4.15 km^3, 3.15 km^3 of which is usable volume under normal operation. This makes it the largest artificial reservoir in Western Europe. The main purpose of the Alqueva reservoir is to provide water supply for domestic use and irrigation and hydroelectric power in the region. The reservoir irrigates about 120,000 ha of agricultural land, ensures water for public supply to

10970088, 2022, 2, Downloaded from https://rmets.onlinelibrary.wiley.com/doi/10.1002/joc.7299 by Cochrane Portugal, Wiley Online Library on [06/07/2023]. See the Terms and Conditions (https://onlinelibrary.wiley.com/terms-and-conditions) on Wiley Online Library for rules of use; OA articles are governed by the applicable Creative Commons License

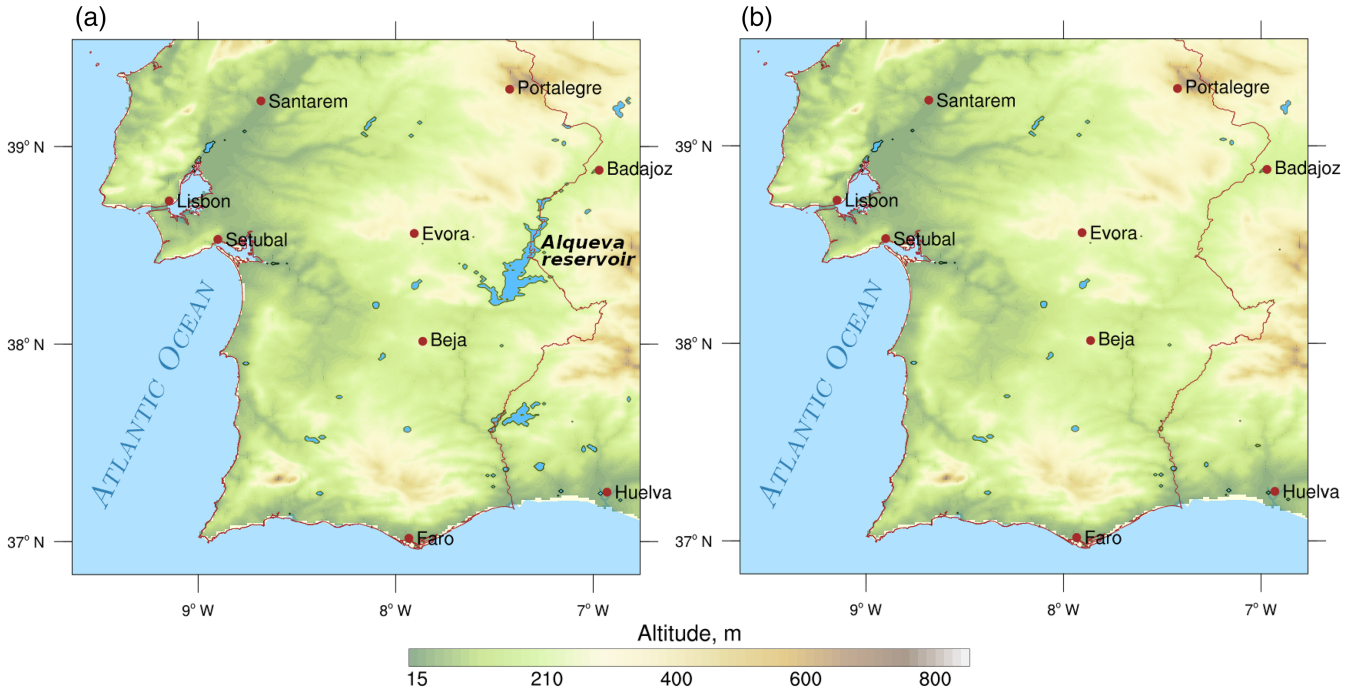

FIGURE 1 The map of working domains used in the simulations. Domain in figure (a) was build with updated surface databases where the Alqueva reservoir is presented and was used in A simulations. Figure (b) corresponds to the domain where the Alqueva was not existed yet B simulations) [Colour figure can be viewed at wileyonlinelibrary.com]

200,000 people and produces enough hydro-electricity to supply a city with more than 500,000 inhabitants.

The Alentejo region, where the Alqueva reservoir is located, is about 1/3 of mainland Portugal. It is known for the irregularity of hydrological resources and long periods of drought (more than 1 year; Silva *et al.*, 2014). According to the Köppen climate classification, the region is characterized by the Mediterranean type of climate, with a small area of the mid-latitude steppe climate.[1] The average daily temperature in summer period is 23°C (June–September), but extreme values may be higher than 45°C. Winter periods are mild and wet, average air temperature is 10.3°C (December–February), although, even in January air temperatures can reach 24°C during long periods of stable anticyclonic conditions. Rain periods are seasonal, normally from October to May. The annual average of accumulated precipitation registered at the climatological station of Beja is 558 mm (1981–2010 normals). Incident solar radiation at the surface is one of the highest in Europe: with mean daily values of about 300 Wm^{-2} and the daily maximum in summer period often reaches 1,000 Wm^{-2}.

2.2 | Models and data

The Meso-NH model (Lac *et al.*, 2018) version 5.4.2 was used for the atmospheric simulations in the present work. It is a non-hydrostatic mesoscale atmospheric model developed by the French research community and is widely used in various atmospheric simulations from synoptic to turbulent scales. Surface-atmosphere interaction is represented using SURFEX scheme version 8.1 (Surface Externalisée, Masson *et al.*, 2013) which is coupled with Meso-NH. The SURFEX scheme includes different surface types (cities, vegetation, etc.), lakes and reservoirs are considered as inland water surfaces and their interaction with atmosphere is simulated by the FLake model (Mironov, 2008; Salgado and Le Moigne, 2010). The FLakemodel is used in numerical weather prediction (NWP), climate modelling, and other numerical prediction systems for environmental applications (http://www.flake.igb-berlin.de/site/applications). It is capable to predict the evolution of the water temperature profile based on the atmospheric forcing data (e.g., air temperature, humidity, shortwave and longwave downwards radiation, wind speed, and pressure) and initial values of mixed layer temperature and depth, bottom temperature, and the thermocline shape factor.

Atmospheric simulations of the current work required the following databases: SRTM (Jarvis *et al.*, 2008) for the surface orography (250 m resolution), ECOCLIMAP II (Faroux *et al.*, 2013) for surface types, HWSD (Harmonized World Soil Database, Nachtergaele *et al.*, 2008) for soil surface textures. For initial conditions and boundary forcing the Meso-NH model used the

10970088, 2022, 2, Downloaded from https://rmets.onlinelibrary.wiley.com/doi/10.1002/joc.7299 by Cochrane Portugal, Wiley Online Library on [06/07/2023]. See the Terms and Conditions (https://onlinelibrary.wiley.com/terms-and-conditions) on Wiley Online Library for rules of use; OA articles are governed by the applicable Creative Commons License

European Centre for Medium-Range Weather Forecast (ECMWF) operational analyses.

Water temperature is required to initiate the FLake model (within the Meso-NH simulation or in stand-alone mode). Two past field campaigns held by the ICT (Institute of Earth Sciences), ALEX (ALqueva hydrometeorological EXperiment, 2014, http://www.alex2014.cge.uevora.pt/) and ALOP (ALentejo Observation and Prediction systems, 2017–2019, http://www.alop.ict.uevora.pt/) provide continuous data of water temperature profile measured at a floating platform on the Alqueva reservoir. In addition, water temperature data provided by the EDIA (Empresa de Desenvolvimento e Infraestruturas do Alqueva, a public company that operates the Alqueva Multipurpose Project) were used.

To produce a Typical Meteorological Year, data measured at the observatory of the Institute of Earth Sciences at University of Évora, Portugal (38.57°N, −7.91°E, 290 m a.s.l.) were used. The global horizontal irradiance is measured since 2002 using two Eppley 8–48 ('Black & White') pyranometers with a sample rate of 5 s and 10-min mean values are recorded. Since 2015, a new station was installed at the same location and global horizontal irradiance is measured using a Kipp&Zonnen CM6B pyranometer mounted on a suntracker system. The sample rate of the new data is 1 s and 1-min mean values are recorded.

2.3 | Method

To assess the raw impact of the Alqueva reservoir on local weather and climate an approach based on calculation of differences between two sets of numerical simulations was used. Within this approach two independent sets of simulations were done: the simulations A that correspond to the current surface and real case atmospheric conditions in the study domain, and the simulations B that share all the features with the set A except the surface database in which the Alqueva reservoir does not exist. This can be achieved by using the old versions of the databases that describe the surface (ECOCLIMAP, HSWD, and SRTM) and made before the reservoir was established. As shown in Figure 1, the big difference in the new ECOCLIMAP database is the presence of Alqueva, but other small reservoirs emerged in the south-west of Spain are also taken into account, the largest of which is the Andévalo reservoir. There are also other differences between the two ECOCLIMAP versions, for example, in vegetation related parameters (not shown), that lie within the area of emerged reservoirs. Thus, the differences between the simulations will show essentially the impact of the Alqueva reservoir on atmospheric parameters.

The simulation results are two- or three-dimensional datasets bounded to the chosen model domain. Considering the atmospheric parameter P, we denote P_A and P_B as sets of values of P from the A and B simulations, correspondingly. A derived dataset $P_Y = P_A - P_B$ is called the anomaly of P and corresponds to the 'raw' impact of the Alqueva reservoir. This approach was used for the evaluation of the lake impacts on air temperature and fog formation (low-level clouds). Depending on the result, either positive or negative anomaly on P may be observed (e.g., air temperature becomes higher or lower due to the presence of the Alqueva).

A case study experiment (Iakunin *et al*., 2018) that was conducted earlier used the aforementioned approach. It was aimed on the evaluation of the effects of the Alqueva reservoir under hot summer conditions and description of the breeze circulation induced. The case study covered the dates of 22–24 July, 2014, when intensive atmospheric observations including balloon radiosonde launches were fulfilled in the region in framework of the ALEX project. Validation of simulation results were done by comparison with values observed at the weather stations and floating platform (time series), and measured by radiosondes (vertical profiles). Time series included such atmospheric parameters as wind speed and direction, air temperature, relative humidity, and heat fluxes (latent and sensible). Parameters of vertical profiles were relative humidity, air temperature, and wind speed. Meso-NH showed good representation of the chosen atmospheric characteristics.

The simulation results revealed positive and negative impacts on air temperature and relative humidity due to lake influence and the existing lake breeze circulation. The formation, intensification, and dissipation stages of the lake breeze were documented during the case study. Lake breeze winds might reach 6 $m \cdot s^{-1}$. Daytime lake breeze at the Alqueva reservoir also includes a vertical branch that forces dry air from the altitudes up to 2,500 m to descend to the water surface level.

2.3.1 | Typical Meteorological Year

A TMY consists of 12 concatenated months representing the typical climatological conditions for a particular area. In this work, the TMY is determined using the code developed by Abreu *et al*. (2018) which applies the Sandia method (Hall *et al*., 1978) to find which months better describe the climatological phenomena of a given location. The typical meteorological months selected to be part of the TMY are chosen through the analysis of the following atmospheric parameters: hourly mean, maximum, and minimum values of air temperature and

10970088, 2022, 2, Downloaded from https://rmets.onlinelibrary.wiley.com/doi/10.1002/joc.7299 by Cochrane Portugal, Wiley Online Library on [06/07/2023]. See the Terms and Conditions (https://onlinelibrary.wiley.com/terms-and-conditions) on Wiley Online Library for rules of use; OA articles are governed by the applicable Creative Commons License

relative humidity, hourly mean and daily maximum wind speed, and hourly global horizontal irradiance (GHI, 305–2,800 nm) observed over a period of 16 years (2003–2018). The first step on implementing the Sandia method is to determine the cumulative distribution functions (CDF, Equation 1) for both long-term monthly data and each candidate month in each year, for all of the meteorological parameters, using the following equation:

$$CDF_n = \begin{cases} 0 \text{ if } x < x_{(1)} \\ (k-0.5)/n \text{ if } x_k \leq x \leq x_{k+1} \\ 1 \text{ if } x \geq x_n \end{cases} \quad (1)$$

where n is the number of days for the selected month, x is the value of the meteorological parameter, and k is the ranked order number (k = 1, 2, 3,..., n − 1). Then, the Finkelstein–Schafer (FS) statistics (Finkelstein and Schafer, 1971) are determined using Equation (2), given by:

$$FS = \frac{1}{N}\sum_{i=1}^{N}\delta_i \quad (2)$$

where N is the number of daily records for each month and δ_i is an absolute difference between the long-term and candidate month CDFs. The FS statistics enables comparison between each of the candidate months and the long-term data. To accommodate for different usages of the TMY, a weighted sum (WS) of the FS statistics is determined using specific statistical weights according to the meteorological parameter in question. The statistical weights used in this study, as stated in the Sandia method (Hall *et al.*, 1978), are the following: 1/24 for maximum and minimum air temperature and relative humidity, 2/24 for mean air temperature, mean relative humidity, and mean and maximum wind speed, and 12/24 for GHI. Therefore, the WS is given by:

$$WS = \sum_{j=1}^{9}\omega_j FS_j \quad (3)$$

where ω_j is the statistical weight of the meteorological parameter j. The years of the dataset are then sorted in ascending order according to its WS value, and the 5 years with lowest WS are selected as candidate years to be part of the TMY, for each one of the calendar months. The strict implementation of the Sandia method would require the evaluation of the persistence of the global solar irradiance and mean air temperature through the frequency and length of runs of consecutive days with values above and below fixed percentiles. However, a widely used simpler procedure proposed by Pissimanis *et al.* (1988) was followed here in which the GHI is analysed. The deviations of the monthly mean values of GHI with respect to the long-term values for the candidate years are determined using hourly GHI measurements and the root mean square difference statistical indicator given by:

$$RMSD_y = \sqrt{\sum_{g=1}^{Q}\left(GHI_{y,g} - \bar{GHI}_g\right)/Q} \quad (4)$$

where Q is the sunshine duration, $GHI_{y,g}$ is the hourly GHI average for year y and hour g and GHI_g is the long-term GHI mean at hour g. To get 1 year of the five candidate years selected using WS the years that have $RMSD_y > min(RMSD_y)$ + 0.02 kWh·m^{-2} were excluded. If more than one candidate year remained, the years that have $FS_{GHI} > min(FS_{GHI})$ + 0.03 were excluded. If there were still more than one candidate year, the year with lower FS mean temperature was selected. Applying this procedure for each one of the calendar months results in the TMY presented in Table 1). More information on the generation of TMY can be found in the work of Abreu *et al.* (2018).

The validation of the years selected to be part of the TMY is usually carried out by comparison between the monthly mean values of the long-term dataset and the year selected to be part of the TMY (e.g., [Abreu *et al.*, 2018; Pusat *et al.*, 2015]), as shown in Figure 2.

From Figure 2, it is possible to see how the statistical weights used in Equation (3) affect the comparison between the monthly means of the long-term and TMY data. Higher statistical weight results in higher proximity between the monthly means, as can be seen for the GHI comparison. Nonetheless, the monthly means of the TMY agree well with the long-term means for all meteorological parameters, which means that the TMY accurately characterizes the meteorological phenomena of the time period analysed here (2003–2018) in a single year of real measurements.

TABLE 1 Typical meteorological year used in present work

Month	Year	Month	Year
January	2018	July	2014
February	2006	August	2007
March	2017	September	2011
April	2008	October	2008
May	2005	November	2004
June	2010	December	2018

10970088, 2022, 2, Downloaded from https://rmets.onlinelibrary.wiley.com/doi/10.1002/joc.7299 by Cochrane Portugal, Wiley Online Library on [06/07/2023]. See the Terms and Conditions (https://onlinelibrary.wiley.com/terms-and-conditions) on Wiley Online Library for rules of use; OA articles are governed by the applicable Creative Commons License

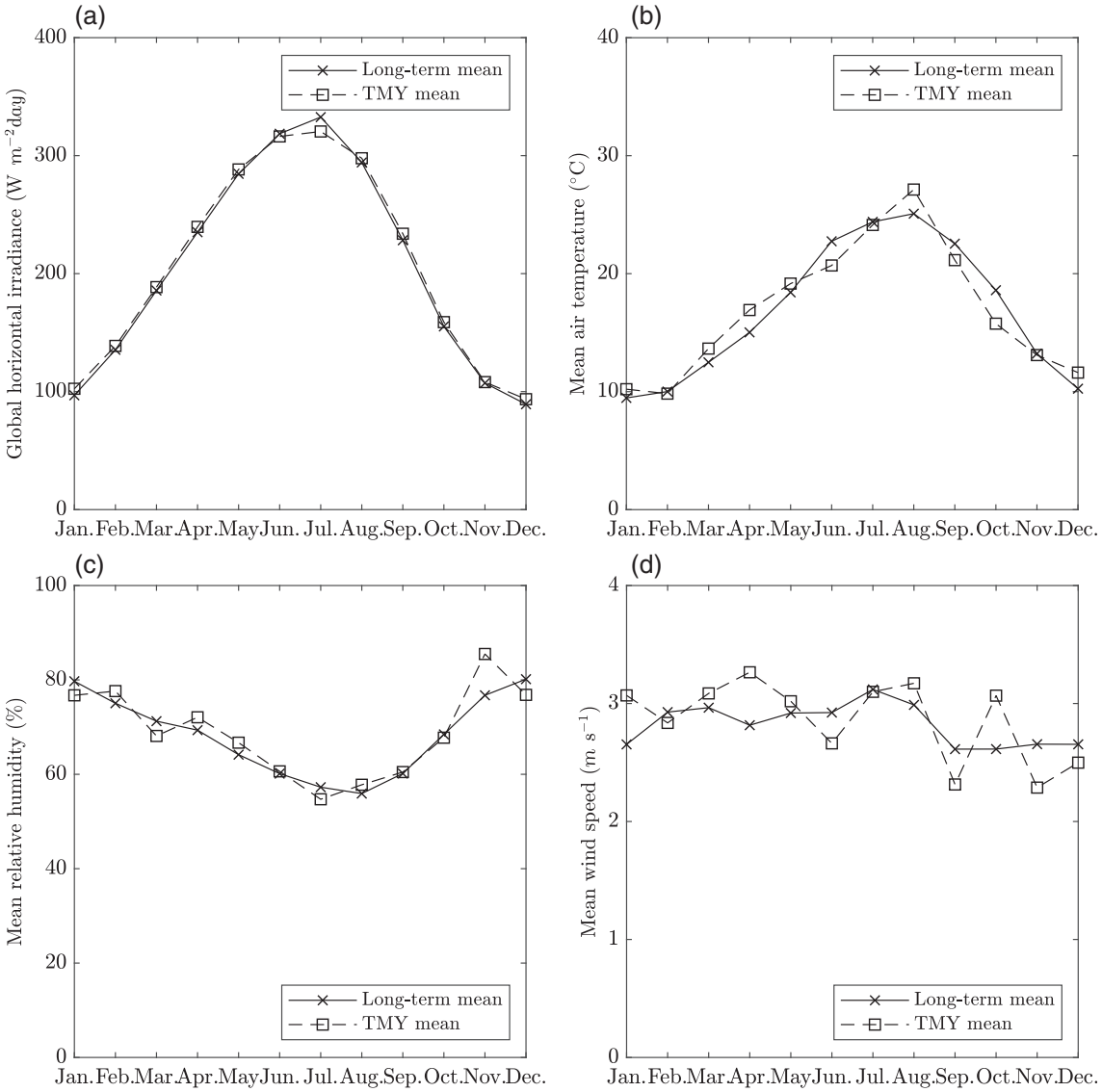

FIGURE 2 Monthly mean values comparison between TMY and long-term data for global horizontal irradiance, mean air temperature, relative humidity, and wind speed

2.3.2 | Experimental setup

The domain that was used for the present atmospheric simulation (Figure 1) is constrained within the rectangle between (36.8329; 39.5419°N) and (−9.63758; −6.76242°E). It consists of 200 × 240 grid pixels with horizontal resolution of 1.25 km, which allows Meso-NH to resolve convection explicitly. Such dimension covered southern part of Portugal, south-west of Spain, and coastal area of the Atlantic Ocean to ensure that the model would properly account for the large-scale maritime influence. There were 70 vertical levels in the domain (up to 23,886 m), 35 of which were below 2,000 m.

The simulations were performed on a single domain, dispensing the use of grid nesting, initialized and forced directly from the European Centre for Medium-Range Weather Forecast (ECMWF) operational analysis, updated every six hours. This practice has been used recently by other authors in studies with Meso-NH (e.g., Jiménez *et al.* (2019); Reinares Martínez *et al.* (2020). As argued by Capecchi and Buizza (2019), this is a pragmatic, low CPU cost, approach to take full advantage of increased resolution of large-scale models and to remove the need for any intermediate grid with the potential benefits outlined in Marsigli *et al.* (2014), namely, that of avoiding the gray zone, where the convection is partially resolved.

During the period covered by the TMY, the horizontal resolutions of the ECMWF operational high resolution analysis were the following: 9 km after March 16, 2016 km between January 2010 and March 2016, and

10970088, 2022, 2, Downloaded from https://rmets.onlinelibrary.wiley.com/doi/10.1002/joc.7299 by Cochrane Portugal, Wiley Online Library on [06/07/2023]. See the Terms and Conditions (https://onlinelibrary.wiley.com/terms-and-conditions) on Wiley Online Library for rules of use; OA articles are governed by the applicable Creative Commons License

25 km prior to 2010. Thus, it is likely that the simulations for months prior to 2010 will be affected by a higher error. However, it should be noted that the objective of this work is not to characterize the climate in an absolute way, but rather to assess the impact of a reservoir on local climate based on calculation of differences between two sets of numerical simulations. It was assumed that the errors and limitations introduced by the direct use of operational analyses to initialize and force simulations in a single domain will be approximately the same in both sets of experiments.

According to the chosen method described above, the Meso-NH model was set up for two (*A* and *B*) twelve months simulations. To keep the simulation close to the meteorological large-scale analysis, each month, in turn, was split into ten series of three days runs (except February, which was split into nine series). Three days model run was used earlier in the case study and showed good results in validation. With such an approach, model surface parameters are forced towards analysed values, creating a better conditions for a more accurate representation of the boundary layer. Thus, 238 model runs were made in total (for *A* and *B* experiments: 9 for February and 10 for each other month). Each simulation had a 6 hr spin-up period, so, every model run covered 6 + 72 hr.

The setup configuration included a turbulent scheme based on a 1D closure and the mixing length was computed according to Bougeault and Lacarrere (1989) (BL89). The BL89 is the recommended scheme for mesoscale kilometric scales (e.g., Verrelle *et al.*, 2015). For clouds and explicit precipitation, a mixed-phase microphysical scheme (Cohard and Pinty, 2000; Cuxart *et al.*, 2000) was used. Radiation transfer equations for longwave and shortwave are solved for independent vertical columns (Hogan and Bozzo, 2018). The following parametrizations were taken into account for atmosphere-surface exchanges: Interface Soil Biosphere Atmosphere (ISBA) model (Noilhan and Mahfouf, 1996) for the surface soil and vegetation; the city landscape energy balance was handled according to Masson (2000). The chosen horizontal resolution of 1.25 km allows the explicit resolving of deep convection while shallow convection should be parametrized. The following schemes were used (see Table 2): EDKF (Pergaud *et al.*, 2009), WENO (Lunet *et al.*, 2017), and ICE3 (Pinty and Jabouille, 1998). In the experiment *B* on lake locations ISBA model was running while in the experiment *A* FLake scheme was applied to the lake areas. Figure 3 shows land cover types according to ECOCLIMAP II database for the experiment *B* at the Alqueva area. Calculation time step was set to 30 s, radiation scheme was executed every 300 s in case of clear sky and every 60 s in cloudy conditions.

Initial values for the FLake scheme variables (surface and bottom water temperature, mixed layer depth, and shape function of the thermocline) were obtained from the observations that were made during the ALOP (2017–2019) and earlier ALEX (2014) field campaigns. These experiments included continuous measuring of water temperature profile at the floating platform which was enough for the simulations of three months (January 2018, July 2014, and December 2018) of the TMY. For the other TMY months, however, measurements of the water temperature profile were not available. To provide the Meso-NH—FLake with realistic initial water temperature profiles, series of preliminary FLake-standalone simulations were made. It was shown earlier that the FLake standalone model is capable of representing water temperature profile in Alqueva quite accurately (Iakunin *et al.*, 2020). The atmospheric data used to force FLake offline runs were obtained from the ECMWF analysis

TABLE 2 Meso-NH physical schemes used in the numerical experiment

Feature	Scheme name
Deep convection	—
Shallow convection	EDKF
Turbulance	BL89
Radiation transfer	EcRad
Advection	WENO
Clouds	ICE3

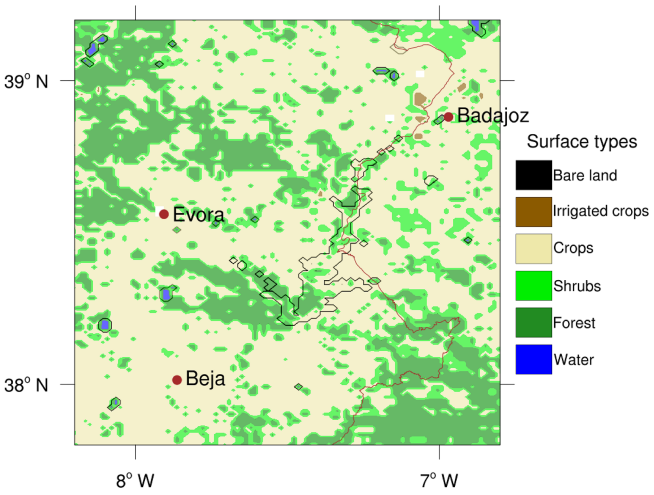

FIGURE 3 Land cover types in the area of interest prior to the emergence of the Alqueva according to ECOCLIMAP II database. Black contours correspond to the Alqueva and other small lakes borders [Colour figure can be viewed at wileyonlinelibrary.com]

10970088, 2022, 2, Downloaded from https://rmets.onlinelibrary.wiley.com/doi/10.1002/joc.7299 by Cochrane Portugal, Wiley Online Library on [06/07/2023]. See the Terms and Conditions (https://onlinelibrary.wiley.com/terms-and-conditions) on Wiley Online Library for rules of use; OA articles are governed by the applicable Creative Commons License

with satisfactory time resolution (3 hours), while data from the reservoir management company, EDIA, were used to initialize the water surface temperature. Taking into account the fact that bottom temperature does not vary much in a given month from year to year, the average monthly bottom temperature value from the ALOP observations was used. To minimize the traces of the initial uncertainties in the required data, each preliminary simulation included one-month spin-up period.

For example, to obtain the FLake input parameters for February 2006, a standalone FLake 2-months simulation starting in January was performed. The surface water temperature from the EDIA observations and mean January bottom temperature were used as initial conditions, and ECMWF data as atmospheric forcing. A month for a model spin-up highly reduces the uncertainties of the initial values, so the February data could be used as a realistic input for each Meso-NH further simulation.

2.4 | Validation

Before proceeding with analysis of the reservoir's impact on weather, it is important to assess the quality of Meso-NH simulation over the TMY by comparing the results against reference data from weather stations and ECMWF ERA5-Land reanalysis.

Three weather stations located in Évora, Mitra, and Portel provided hourly observations of air temperature, relative humidity, wind speed, and downwelling shortwave radiation to verify Meso-NH simulations through all months of the TMY. The choice of those stations is motivated by the following conditions: these are the closest weather stations to the Alqueva reservoir and they provide complete time series of observations that cover the whole simulation period. Figure 4 compares the hourly values of the selected variables at the weather station sites. A good comparison of the model values to the observations is presented, especially for air temperature and shortwave radiation, for which the linear fit of hourly values is close to the one-to-one line and the correlation coefficients are .97 and .94, respectively. Station and monthly averaged biases, mean absolute errors (MAE), and root mean square errors (RMSE) for data comparison against weather stations are presented in Table 3. Although a small constant overestimation of shortwave radiation (26 Wm^{-2}) and underestimation of relative humidity (10% during the TMY) is observed, the overall quality of reproduction of atmospheric parameters by Meso-NH is high.

Monthly averaged data of 10 m wind components, 2 m air temperature, surface level pressure and downwelling shortwave radiation obtained by Meso-NH for the TMY was compared against ECMWF ERA5-Land reanalysis. Combining model data with observations from all over the world, this reanalysis dataset provides a consistent view of the evolution of land variables over several decades at a resolution of $0.1 \times 0.1°$ (Muñoz, 2019). Monthly-mean averaged data used in the current work is a post-processed subset of the full ERA5-Land dataset. Meso-NH 1-hour outputs of 1.25 km horizontal resolution were monthly averaged and regridded to ERA5 9-km grid. Then, a sea mask was applied to both ERA5-Land and Meso-NH outputs. After this procedure it was possible to directly compare two datasets by subtracting ERA5 from Meso-NH field by field, results of which are presented in Table 4. A slight underestimation of Meso-NH data on air temperature (−1°C) and atmospheric pressure (−1.47 hPa) can be noticed. At the same time, the shortwave radiation is slightly overestimated by a value similar in magnitude (19 Wm^{-2}) to that which was obtained when comparing with the stations. It is worth noting the excellent comparison to the wind speed components of the reanalysis data with yearly MAE of 0.4 $m{\cdot}s^{-1}$.

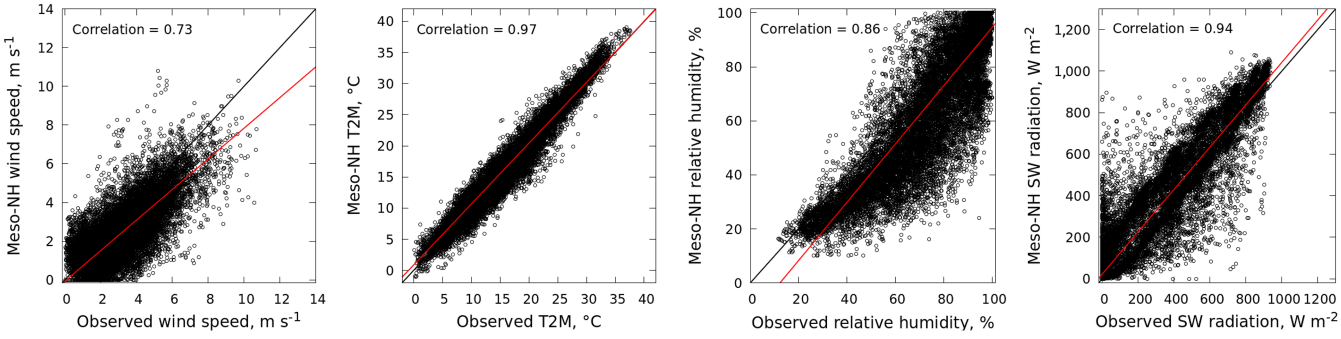

FIGURE 4 Scatterplots comparison of the TMY hourly 2 m air temperature, relative humidity, wind speed, and downwelling shortwave radiation between observations and Meso-NH simulation data at Evora (38.5679°N, −7.9115°E), Mitra (38.5292°N, −8.0169°E), and Portel (38.3092°N, −7.7030°E) sites. One-to-one lines and the least-squared fit through all data points are plotted with solid black and red lines, respectively [Colour figure can be viewed at wileyonlinelibrary.com]

10970088, 2022, 2, Downloaded from https://rmets.onlinelibrary.wiley.com/doi/10.1002/joc.7299 by Cochrane Portugal, Wiley Online Library on [06/07/2023]. See the Terms and Conditions (https://onlinelibrary.wiley.com/terms-and-conditions) on Wiley Online Library for rules of use; OA articles are governed by the applicable Creative Commons License

TABLE 3 Statistic results of the comparison of TMY monthly mean wind speed, 2 m air temperature, relative humidity, and shortwave radiation between observations at weather stations and Meso-NH simulation data

	Wind speed, $m \cdot s^{-1}$			T2M, K			Relative humidity, %			SWR, $W \cdot m^{-2}$		
	Bias	*MAE*	*RMSE*	*Bias*	*MAE*	*RMSE*	*Bias*	*MAE*	*RMSE*	*Bias*	*MAE*	*RMSE*
January	−0.7	1	1.2	0.7	1.3	1.6	−7	10	13	28	39	77
February	−0.4	1	1.3	0.8	1.2	1.5	−14	16	19	27	44	87
March	−0.6	1	1.3	0.7	1.4	1.7	−6	11	15	32	62	116
April	−0.8	1.1	1.5	−0.1	1.4	1.8	−16	17	20	35	62	118
May	−0.7	1	1.2	0.9	1.4	1.9	−24	24	25	12	79	132
June	−1	1.3	1.6	0	1.5	1.9	−6	10	12	35	65	111
July	−0.5	1.1	1.4	0.3	1.2	1.5	−4	8	9	36	67	106
August	−0.7	1.1	1.4	0.2	1.1	1.5	−7	9	11	19	51	86
September	−1	1.2	1.5	−0.6	1.5	1.9	−5	8	10	30	58	104
October	−0.7	1	1.3	0	1.4	1.8	−14	15	17	17	43	85
November	−0.4	0.9	1.1	1.1	1.4	1.7	−27	27	29	3	37	75
December	−0.2	1	1.2	0.8	1.4	1.8	−6	9	12	25	35	70
Year	−0.7	1.1	1.3	0.4	1.3	1.7	−10	12	15	26	53	97

3 | RESULTS

3.1 | Air temperature

To evaluate the impact of Alqueva on the 2 m air temperature (T2M), we calculated daily maximum and minimum of $T2M_Y$ (i.e., positive and negative anomalies), and then composed monthly average values. The results are shown in Figure 5. Positive $T2M_Y$ happens during the nighttime, when the water temperature is higher than the surrounded land. The highest values of positive anomalies occur over the reservoir normally close to sunrise. Negative anomalies, on the contrary, appear mostly during day time, frequently cole to the time of the maximum daily temperature. Over the land, lake impact on air temperature follows the dominant winds in the area. West winds prevail during the nights of the warm season (from March to September) due to the large-scale sea breeze circulation, and the negative temperature anomaly may stretch over 15–20 km to the east but their values rarely exceed 1°C. Cold season nights (October–February) are characterized by north and north-west dominant winds, so the corresponding positive anomalies (+1°C) spread to the south direction up to 20 km and the valley relief of that area contributes to this. Near the lake shores (within the area of less than 5 km), these anomalies usually reach +1.5°C.

Figure 6 shows extreme values of positive and negative T2M anomalies over the whole TMY and the 90th percentile of the daily minimum and maximum anomalies. Positive anomalies cover larger area and can be observed much farther from the reservoir in all directions, especially in the south and southwest. They might reach up to +5°C over land and up to +10°C over the water surface of the reservoir. Negative temperature anomalies are more local and usually rarely observed far from the lake shore, although, they might be equally strong, reaching −4°C over surrounding land and −9°C above the lake surface.

To assess how Alqueva affects daily temperature in nearby locations, four towns were chosen: Moura (7 km east of the reservoir), Mourão (1 km southeast of the reservoir), Pedrogão (15 km southwest of the reservoir), and Reguengos de Monsaraz (12.25 km northwest of the reservoir). Each town was represented by 9 grid points. Fraction of water in them was 0 and the fraction of urban land was 0.1 (Moura), 0.07 (Mourão), 0.006 (Pedrogão), and 0.136 (Reguengos de Monsaraz). Location of the chosen towns are shown in Figure 7. In this case, we examined how maximum and minimum daily temperatures have changed (Figure 8). Mourão, the closest town to the Alqueva, is more affected by the daily temperature impact, as the monthly mean maximum daily temperature decreased by 0.3–0.4°C in October–April, and up to 0.6°C in July–September. Monthly mean daily minimum temperature, on the contrary, increased by 0.5–1.0°C during the whole TMY (Figure 8 a, b). In Moura, which is located 7 km east of the Alqueva, the temperature impact is much weaker. During the TMY, the maximum daily T2M has not decreased more than 0.3°C (in December) and minimum daily T2M slightly increased by ∼0.4°C in October–November, while the anomalies during the rest

10970088, 2022, 2, Downloaded from https://rmets.onlinelibrary.wiley.com/doi/10.1002/joc.7299 by Cochrane Portugal, Wiley Online Library on [06/07/2023]. See the Terms and Conditions (https://onlinelibrary.wiley.com/terms-and-conditions) on Wiley Online Library for rules of use; OA articles are governed by the applicable Creative Commons License

TABLE 4 Statistic results of the comparison of the domain area averaged TMY monthly mean wind speed components, 2 m air temperature, surface level pressure, and shortwave radiation between ECMWF ERA5-Land reanalysis and Meso-NH simulation data

	U10, $m \cdot s^{-1}$			V10, $m \cdot s^{-1}$			T2M, K			Press, Pa			SWR, $W \cdot m^{-2}$		
	Bias	*MAE*	*RMSE*	*Bias*	*MAE*	*RMSE*	*Bias*	*MAE*	*RMSE*	*Bias*	*MAE*	*RMSE*	*Bias*	*MAE*	*RMSE*
January	0.0	0.3	0.4	0.2	0.5	0.6	−1.3	1.3	1.3	−143	357	522	5	6	6
February	0.1	0.3	0.4	0.1	0.4	0.5	−1.0	1.0	1.1	−108	351	509	13	13	14
March	0.1	0.3	0.3	0.1	0.3	0.4	−1.1	1.1	1.2	−150	353	516	20	20	21
April	0.3	0.5	0.6	0.2	0.3	0.4	−0.9	0.9	1.0	−194	357	525	29	29	29
May	0.1	0.3	0.4	−0.1	0.4	0.5	−1.1	1.2	1.3	−140	346	506	34	34	34
June	0.5	0.6	0.7	0.2	0.5	0.7	−1.0	1.0	1.1	−150	343	502	34	34	34
July	0.4	0.5	0.6	0.0	0.4	0.5	−0.5	0.6	0.8	−125	338	493	25	25	25
August	0.2	0.4	0.5	−0.2	0.5	0.6	−0.7	0.8	0.9	−155	341	500	22	22	23
September	0.2	0.4	0.4	0.2	0.4	0.5	−0.7	0.8	0.9	−148	341	500	18	18	19
October	0.0	0.3	0.4	−0.1	0.5	0.6	−0.8	0.8	0.9	−160	349	512	19	19	20
November	0.0	0.4	0.5	0.0	0.4	0.6	−1.4	1.4	1.5	−126	350	509	10	10	11
December	0.0	0.3	0.4	0.0	0.4	0.5	−1.4	1.4	1.5	−166	359	526	3	4	5
Year	0.2	0.4	0.5	0.0	0.4	0.5	−1.0	1.0	1.1	−147	349	510	19	20	20

10970088, 2022, 2, Downloaded from https://rmets.onlinelibrary.wiley.com/doi/10.1002/joc.7299 by Cochrane Portugal, Wiley Online Library on [06/07/2023]. See the Terms and Conditions (https://onlinelibrary.wiley.com/terms-and-conditions) on Wiley Online Library for rules of use; OA articles are governed by the applicable Creative Commons License

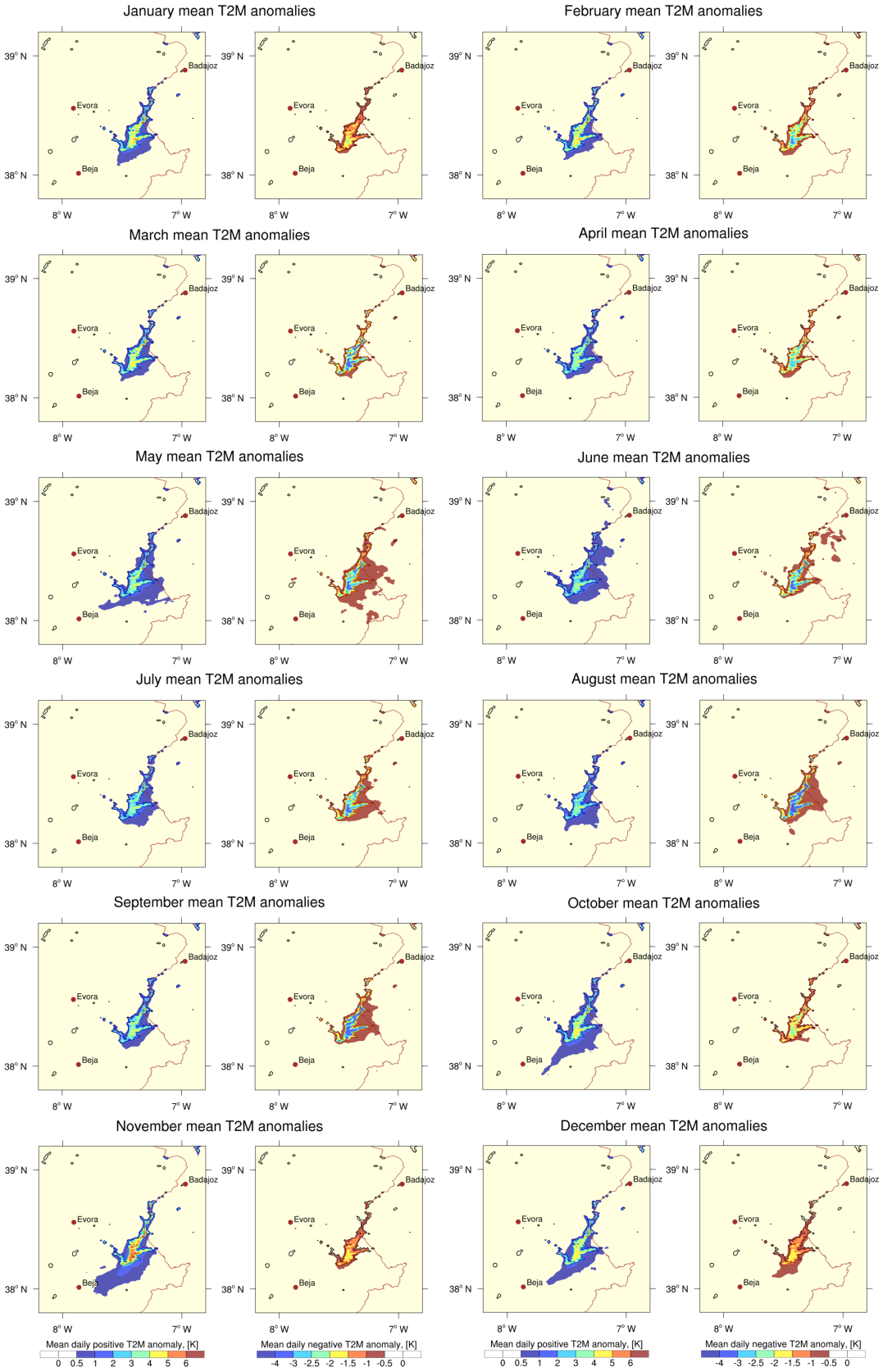

FIGURE 5 Alqueva impact on 2 m air temperature: seasonally averaged maximum positive and negative daily anomalies [Colour figure can be viewed at wileyonlinelibrary.com]

10970088, 2022, 2, Downloaded from https://rmets.onlinelibrary.wiley.com/doi/10.1002/joc.7299 by Cochrane Portugal, Wiley Online Library on [06/07/2023]. See the Terms and Conditions (https://onlinelibrary.wiley.com/terms-and-conditions) on Wiley Online Library for rules of use; OA articles are governed by the applicable Creative Commons License

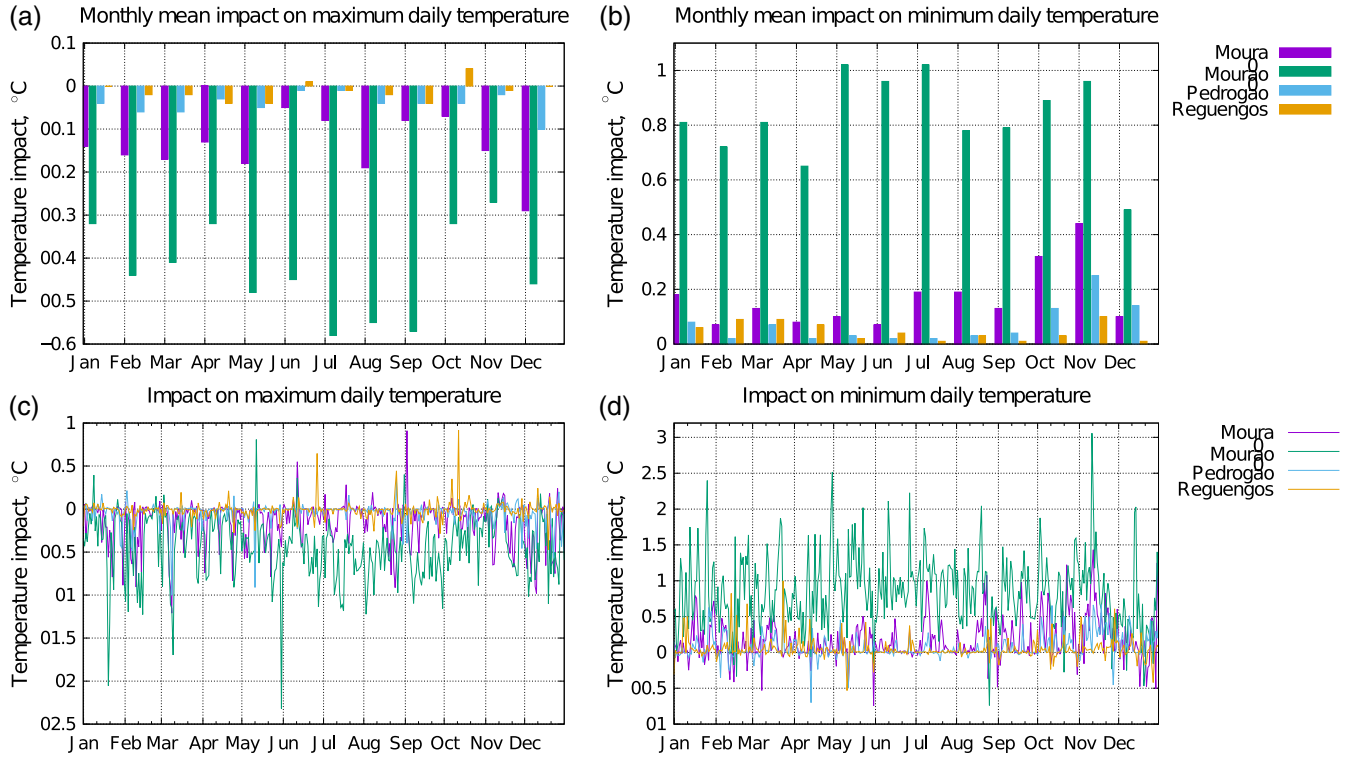

FIGURE 6 Minimum and maximum daily temperatures changes in chosen towns: monthly mean (a,b) and daily (c,d) values [Colour figure can be viewed at wileyonlinelibrary.com]

of the months were not higher than 0.2°C. In Reguengos de Monsaraz and Pedrogão the impact on daily temperature amplitude was quite insignificant due to the distance from the reservoir.

Daily lake impacts on maximum and minimum air temperature shown in Figure 8c,d (c, d), however, can be much higher. In Mourão, maximum daily temperature can increase by up to 0.8°C, and decrease by 2.2°C. In the town of Reguengos, which is the least affected among all, minimum and maximum daily temperatures can even increase by 0.9°C, although such cases are rare.

3.2 | Fog

The impact of the Alqueva reservoir on fogs occurrence was studied using the cloud fraction parameter (CLDFR) at the first atmospheric level. Figure 9 shows a seasonally accumulated values of the $CLDFR_Y$ anomalies. Negative values of this variable indicate the lack of fog due to the presence of the reservoir, while positive values indicate the fog that appeared because of the Alqueva. According to the Meso-NH simulation results, the dominant reservoir impact on fog is negative: the reservoir suppresses the formation of fog. This effect is more visible during winter months of the TMY, with more than 130 of 'fogless' hours registered in December. This number decreases when nights become warmer and during the summer (June–August) Alqueva's impact on fog formation is insignificant.

In annual terms, the simulation results indicate a negative impact on the number of hours of fog mainly over the reservoir, both at night and in the morning. As shown in Figure 10, the reservoir annually suppresses up to 240 hr of fog during nighttime and more than 120 hr in daytime. The suppression is almost over the water due to an increase of the surface and near-surface air temperature. On the other hand, the increase in water vapour due to lake evaporation causes some positive impacts on the neighbourhood. According to the model results shown in Figure 10, the presence of the reservoir contributes to an increase of up to 30 hr of fog per year during night in areas that can be a few tens of kilometres away from the water mirror. During morning, the model indicates the occurrence of positive anomalies of the same order of magnitude over the lake and in neighbouring areas.

Despite statements by local residents who say that there are much more foggy days since the reservoir was established, the simulations suggest only few hours of positive impact per month during the TMY. A detailed analysis shows, however, that under specific atmospheric conditions, there may be a significant positive impact on fog. Dates 19 and 20 of December are two extreme

10970088, 2022, 2, Downloaded from https://rmets.onlinelibrary.wiley.com/doi/10.1002/joc.7299 by Cochrane Portugal, Wiley Online Library on [06/07/2023]. See the Terms and Conditions (https://onlinelibrary.wiley.com/terms-and-conditions) on Wiley Online Library for rules of use; OA articles are governed by the applicable Creative Commons License

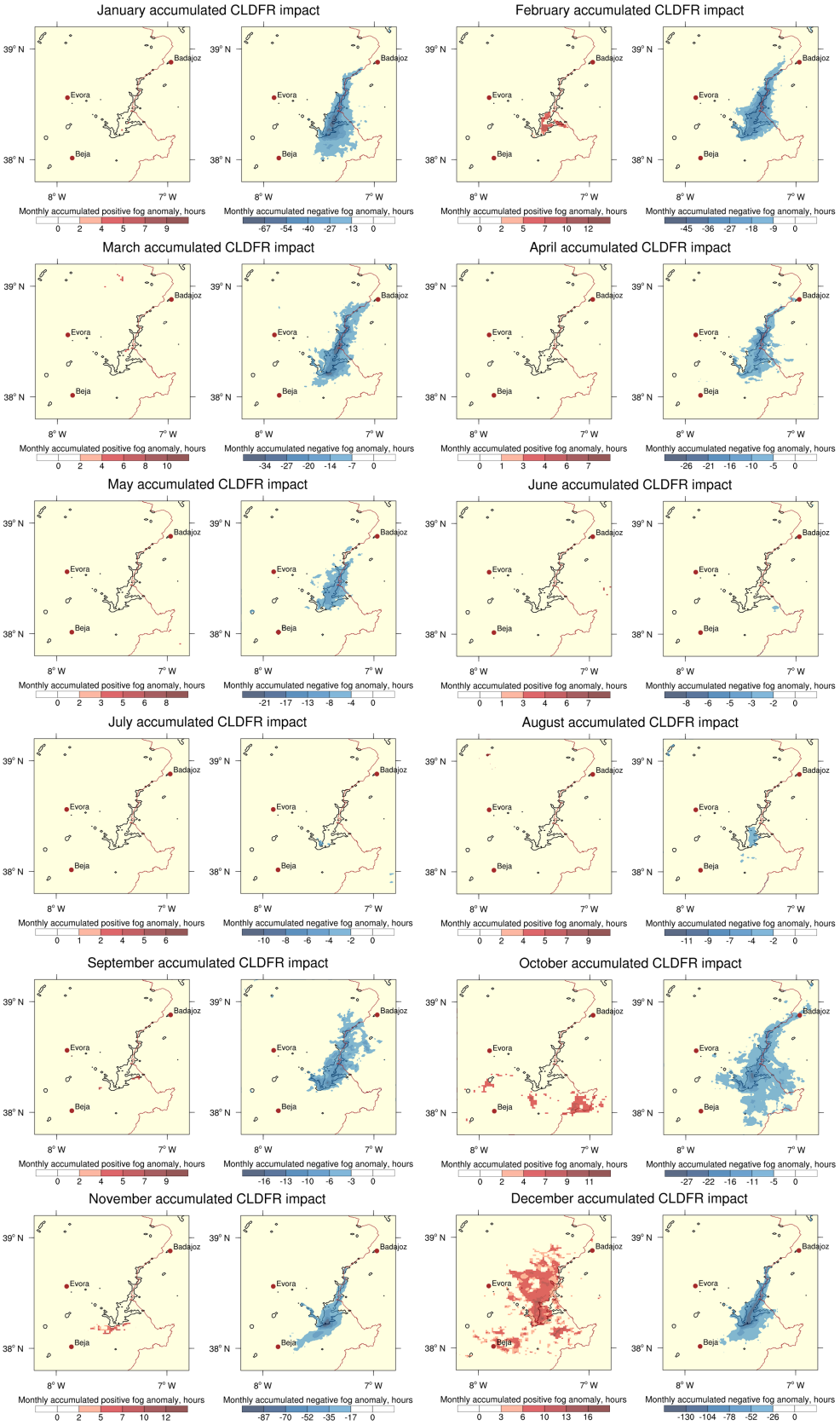

FIGURE 7 Alqueva impact on fog formation: monthly accumulated cloud fraction at 10 m anomalies [Colour figure can be viewed at wileyonlinelibrary.com]

examples of a very strong positive fog anomalies (Figure 11). The simulation showed that a day before these events a very cold weather was observed which led to a strong negative temperature anomaly. In the afternoon of 19 December warm air mass moved from the southeast and was cooled by the cold air above and near

10970088, 2022, 2, Downloaded from https://rmets.onlinelibrary.wiley.com/doi/10.1002/joc.7299 by Cochrane Portugal, Wiley Online Library on [06/07/2023]. See the Terms and Conditions (https://onlinelibrary.wiley.com/terms-and-conditions) on Wiley Online Library for rules of use; OA articles are governed by the applicable Creative Commons License

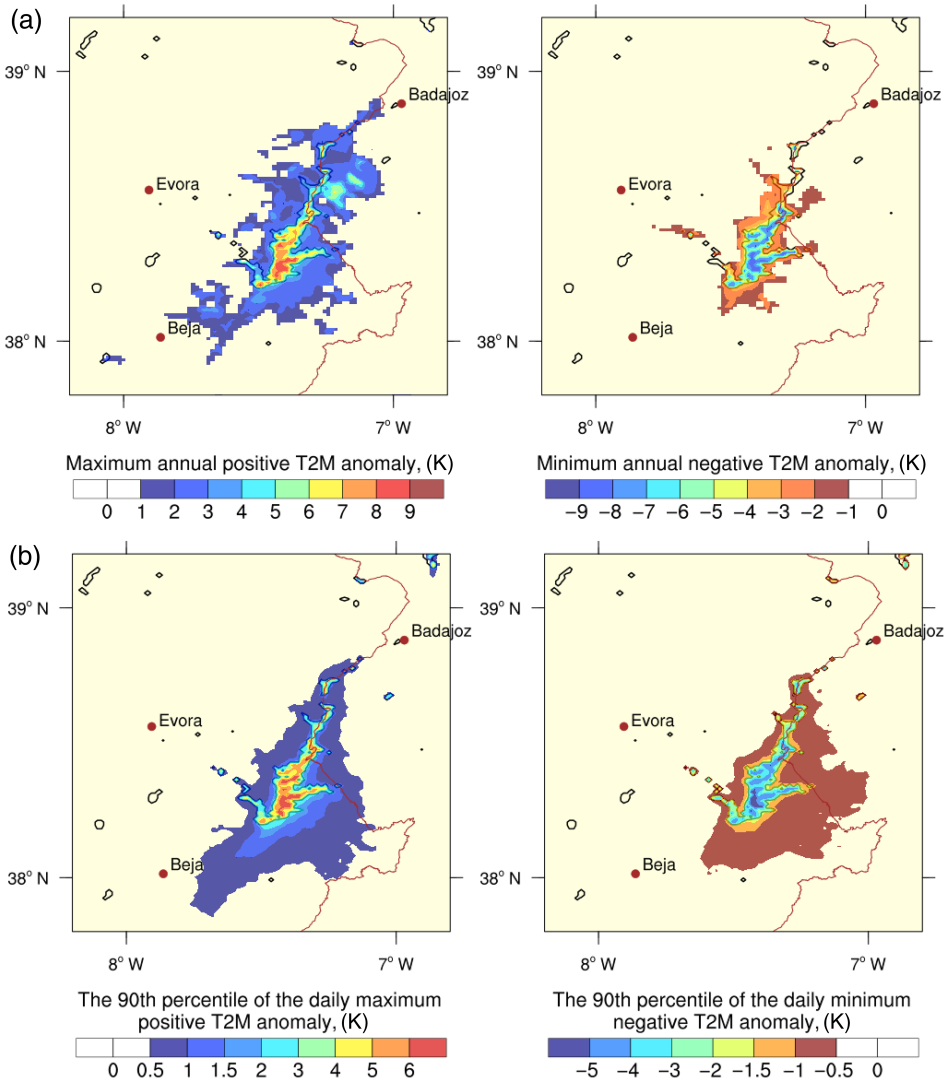

FIGURE 8 Extreme values of T2M anomalies over the TMY (a) and the 90th percentile of the daily minimum and maximum anomalies (b) [Colour figure can be viewed at wileyonlinelibrary.com]

the Alqueva resulting in fog formation. Clouds up to 300 m in altitude were forming over the water surface and shore area of the Alqueva in the afternoon during these days. They were growing and moving in north and northwest direction on the distance of 50–60 km and dissipated by midnight. Although such strong positive impact occurred during the TMY, it may happen in other months which are not typical, since the TMY is not suitable to represent rare/extreme conditions. As pointed out Bergot and Lestringant (2019), it should be noted that numerical prediction of fog remains a challenge due to a whole set of factors, including small-scale processes, complex mesoscale circulation or microphysical processes.

3.3 | Breeze

To study the lake breeze in the current work, three pairs of points on opposite shores of the reservoir were chosen (A/A', B/B', C/C', Figure 7). We assume the breeze system (lake breeze with wind blowing from the lake or land breeze with wind blowing from the land) overlaps the synoptic conditions when the wind directions are opposite in the pair of the chosen points. As an example, for the lake breeze in the A/A' pair of points, the following conditions were applied: wind direction at A point between 45° and 165° and at A' between 195° and 350°. Arithmetic conditions for each pair are listed in Table 5. As an additional condition an angle between two wind vectors should be higher than 60°. These conditions are graphically depicted as ring sectors around the chosen points in Figure 7. An annual regime of the lake and land breezes (average of three pairs of points) is illustrated in Figure 12.

Lake breeze occurs due to the thermal contrast when air above the water surface is colder than the air over the surrounding land. When such conditions are established, the wind starts to blow from the lake to the shores. Warm period of the TMY (June–October) can be considered as a daytime breeze season with 10–15 days of registered

10970088, 2022, 2, Downloaded from https://rmets.onlinelibrary.wiley.com/doi/10.1002/joc.7299 by Cochrane Portugal, Wiley Online Library on [06/07/2023]. See the Terms and Conditions (https://onlinelibrary.wiley.com/terms-and-conditions) on Wiley Online Library for rules of use; OA articles are governed by the applicable Creative Commons License

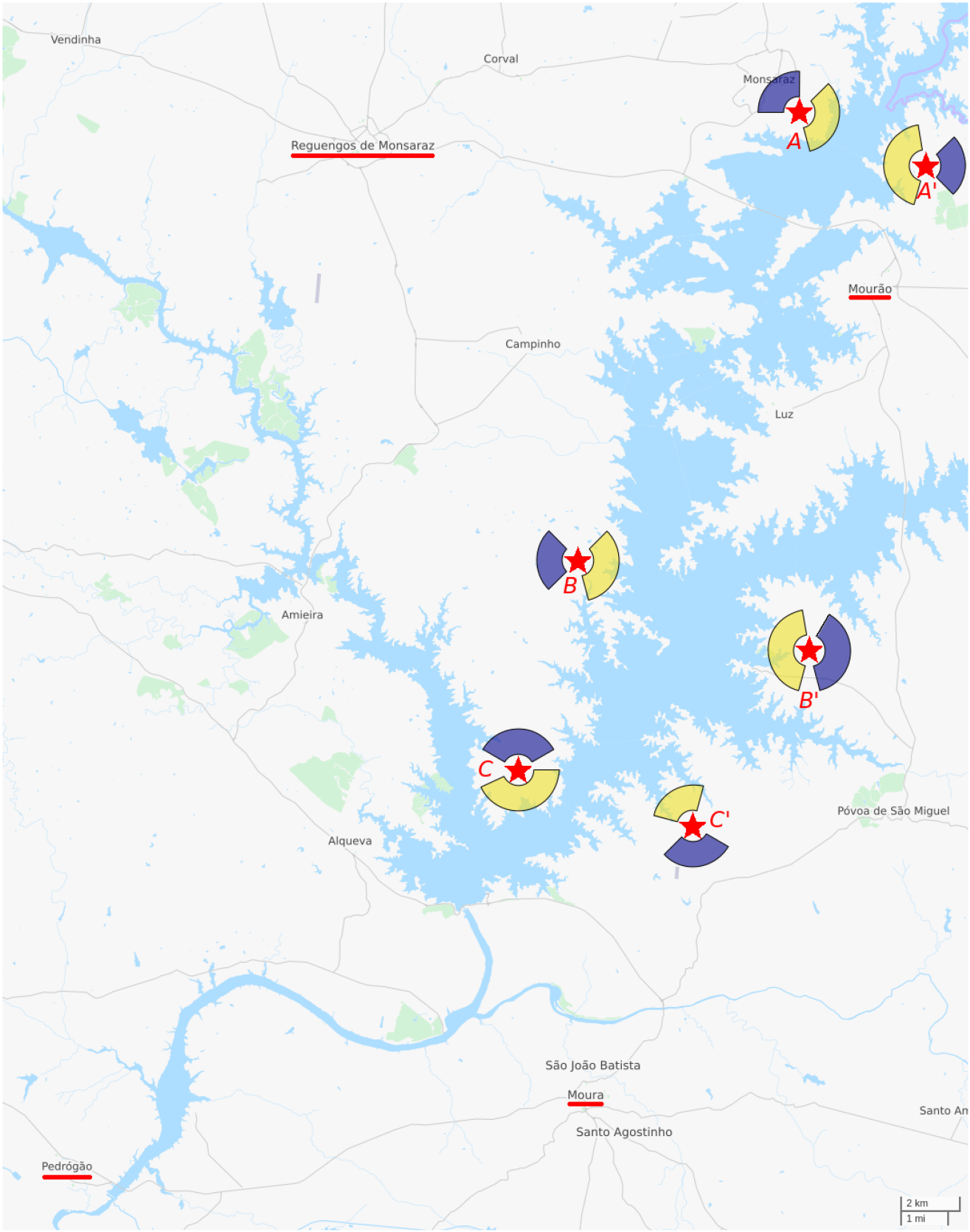

FIGURE 9 Location of the chosen towns (marked with red line) relative to the Alqueva reservoir. Stars mark the points of wind direction study. Yellow and blue ring sectors correspond to the conditions of the lake and land breeze, respectively (©OpenStreetMap contributors) [Colour figure can be viewed at wileyonlinelibrary.com]

10970088, 2022, 2, Downloaded from https://rmets.onlinelibrary.wiley.com/doi/10.1002/joc.7299 by Cochrane Portugal, Wiley Online Library on [06/07/2023]. See the Terms and Conditions (https://onlinelibrary.wiley.com/terms-and-conditions) on Wiley Online Library for rules of use; OA articles are governed by the applicable Creative Commons License

breeze (Figure 12a). Counting the amount of hours when the breeze was registered, June, July, and September hold the record, with more than 40 hr of breeze each month (Figure 12b). During the cold period of the TMY, favourable conditions for breeze occur less frequently: 8–10 days in February and March and only 6–7 days in

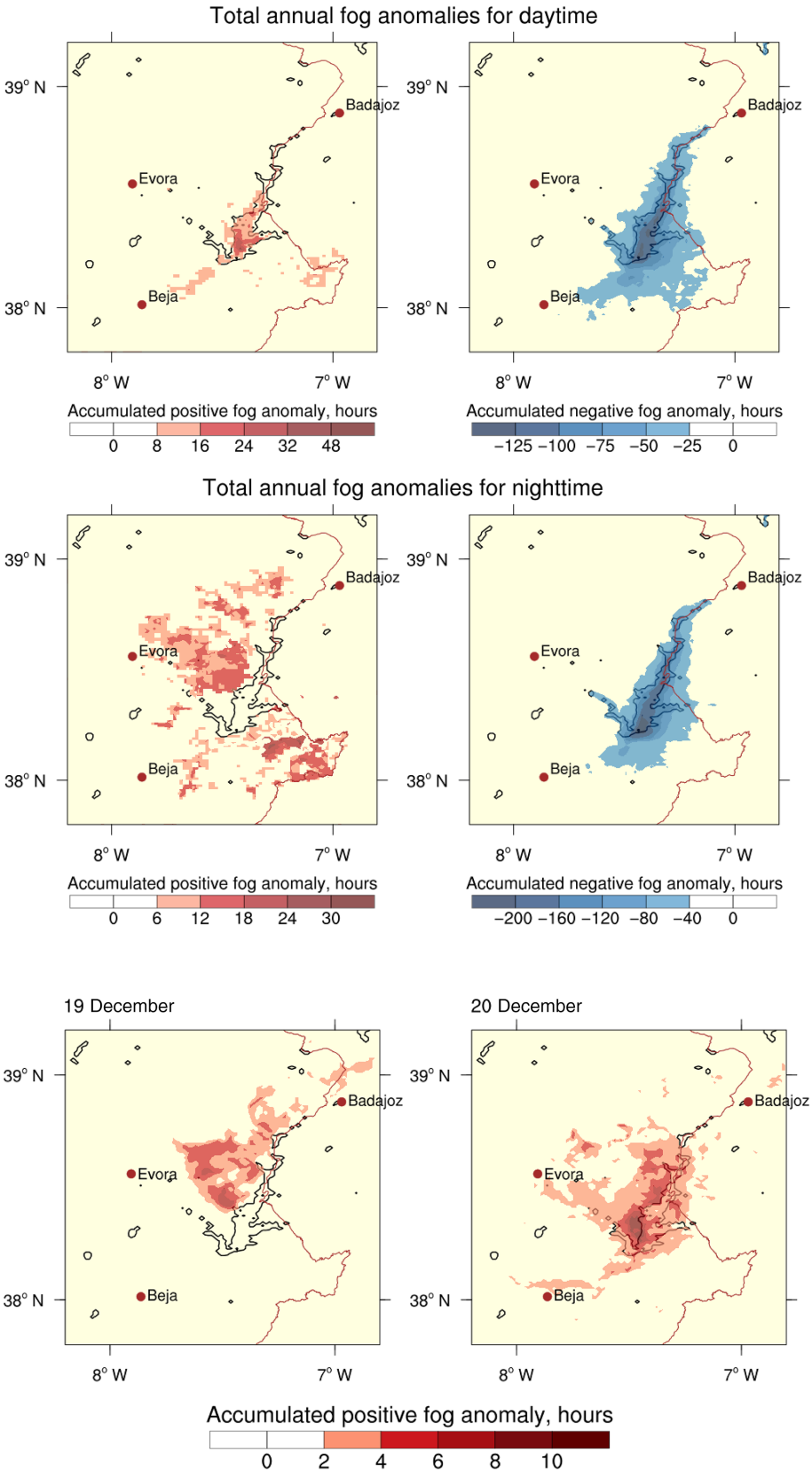

FIGURE 10 Alqueva impact on fog formation: TMY accumulated cloud fraction at 10 m anomalies for day (07–18 UTC) and night (19–06 UTC) time [Colour figure can be viewed at wileyonlinelibrary.com]

FIGURE 11 Cases of the strong positive fog anomalies registered in 19 and 20 of December [Colour figure can be viewed at wileyonlinelibrary.com]

10970088, 2022, 2, Downloaded from https://rmets.onlinelibrary.wiley.com/doi/10.1002/joc.7299 by Cochrane Portugal, Wiley Online Library on [06/07/2023]. See the Terms and Conditions (https://onlinelibrary.wiley.com/terms-and-conditions) on Wiley Online Library for rules of use; OA articles are governed by the applicable Creative Commons License

TABLE 5 Ranges of wind direction set to determine lake and land breeze at chosen pairs of points

	Lake breeze	Land breeze
A	[45°; 165°]	[270°; 360°]
A′	[195°; 350°]	[45°; 135°]
B	[45°; 165°]	[225°; 315°]
B′	[195°; 350°]	[30°; 165°]
C	[110°; 240°]	[300°; 60°]
C′	[290°; 10°]	[135°; 225°]

April, November, and December. Calculating an average time of when daytime breeze conditions have occurred, we see almost an annual cycle with maximum in August, when, on average, breezes lasted for 3.5 hr (Figure 12c). In this case, January is an exception: rare breeze days happened in this month revealing quite sustained winds. It is worth noting that in the pair of *B*/*B′* points (the most wide part of the Alqueva reservoir), 20 days of breeze were observed in September.

Land breeze, on the contrary, occurs when the air over the water is warmer than over the land. In this case, wind is blowing towards the lake surface. At the Alqueva reservoir, land breezes were registered more often during the cold months, in January and December (Figure 12a). The number of land breezes is minimal during the summer. At the *C*/*C′* point, for example, there was only one registered land breeze day in June and only one in August. Such pattern can be explained by the fact that during the summer nights the temperature difference between the water surface and the neighbouring land is not high enough to generate a thermal circulation that overlaps the dominant flow due to the major and much more stronger Ocean breeze system. In the cold period, however, the nocturnal temperature differences between the water surface and the neighbouring land tend to be greater and the ocean breeze system is absent, so that land breezes are easy to develop in the banks of Alqueva.

The simulation results for the lake breeze are consistent with data from 2 years observations at two sites on the opposite shores of the Alqueva, recently published by Purificação *et al.* (2021). However, this study suggests that simulations underestimate the occurrence of land breezes.

4 | DISCUSSION

Emergence of a large water reservoir in southwestern Iberia under Mediterranean climate has greatly transformed the local environment. Changes in the weather regime are only a small part of this transformation, however, they are significant for agriculture and people life. The simulation made in the present work revealed many aspects of the lake impact on the meteorological conditions. Although the strongest effects are obviously observed over the water surface, the traces of the impact can be found at distances up to 20 km away from the shores.

The analysis of the lake impact on air temperature showed that the warming effect dominates over the cooling. During the nights, the air warmed by the lake is frequently advected southeastwards following the large-scale circulation. This relatively warm air can reach distances of 20 km in the downwind direction. The air cooled by the reservoir during the daytime also spreads to the land with the dominant wind system. This kind of impact is most powerful during the summer and probably due to the frequent arrival of strong winds linked to the ocean breeze organized at the Iberia peninsular scale. In this case, lake cold air (1–1.2°C) can be found at 5–7 km in the east direction of the Alqueva. Over the water surface, air temperature anomalies varies from −9 to +10°C.

Since the lake impact on the air temperature is spread mainly to the south-east direction, towns to the north and west from the Alqueva are almost unaffected. In the close locations to the east of the reservoir (e.g., Mourão town), daily air temperature has changed significantly: the daily maximum temperature decreased by 0.3–0.6°C while the daily minimum temperature increased on average by 0.5–1.0°C. Hence, we can state that the weather in this location became milder due to the presence of the Alqueva reservoir. On certain days, however, lake impact on maximum and minimum temperature can be much higher, reaching 3°C.

Contrary to the common sense opinion and the feeling of many of the inhabitants, the impact of the reservoir on fog formation appeared to be mostly negative. Throughout the whole TMY, the simulation results suggest a reduction of fog in the nearby area around the reservoir. This is mainly due to a night-time increase of air temperature that suppresses the formation of radiative fogs. However, some cases of the strong Alqueva fogs can be found during the chosen time period. Low-level clouds formed at the reservoir's shore during the afternoon of 19 and 20 of December is an example. On both days, the clouds were developing during 8–10 hr, reached up to 300 m in altitude, and spread up to 60 km north-west. It is possible that such cases may occur more often in 'non-typical' meteorological conditions and could not be traced during the TMY.

The formation of the Alqueva local breeze system was demonstrated in the previous case study (Iakunin

10970088, 2022, 2, Downloaded from https://rmets.onlinelibrary.wiley.com/doi/10.1002/joc.7299 by Cochrane Portugal, Wiley Online Library on [06/07/2023]. See the Terms and Conditions (https://onlinelibrary.wiley.com/terms-and-conditions) on Wiley Online Library for rules of use; OA articles are governed by the applicable Creative Commons License

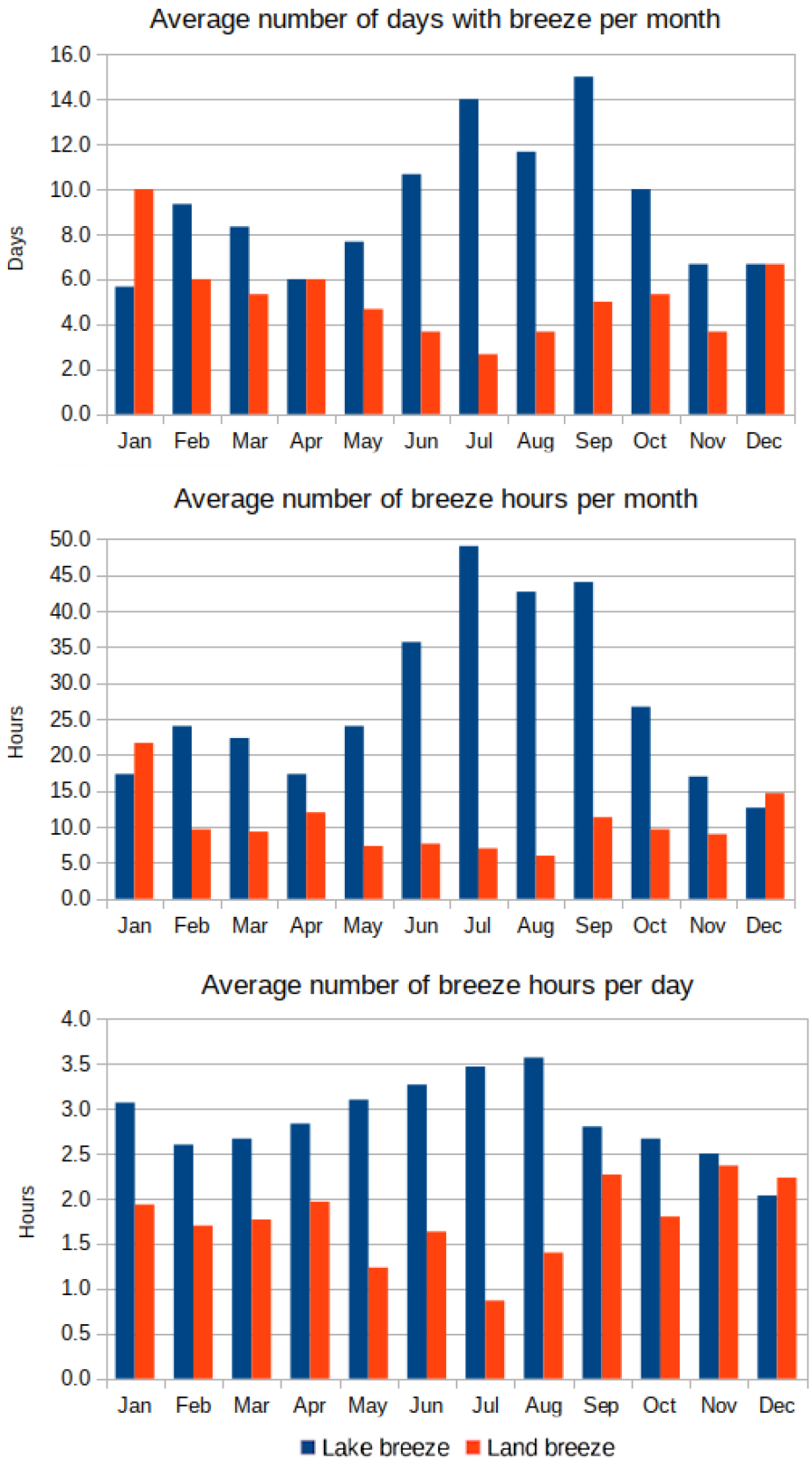

FIGURE 12 Lake and land breeze regime at the Alqueva over the TMY [Colour figure can be viewed at wileyonlinelibrary.com]

et al., 2018). The simulation over the TMY showed the presence of a 'lake breeze season' during June–October. However, even winter months can provide favourable conditions for the lake breeze formation. Land breezes at the Alqueva seem to be less frequent than lake breezes were simulated and observed mostly during the winter

10970088, 2022, 2, Downloaded from https://rmets.onlinelibrary.wiley.com/doi/10.1002/joc.7299 by Cochrane Portugal, Wiley Online Library on [06/07/2023]. See the Terms and Conditions (https://onlinelibrary.wiley.com/terms-and-conditions) on Wiley Online Library for rules of use; OA articles are governed by the applicable Creative Commons License

periods. Although the reservoir creates suitable atmospheric conditions (land/water surface thermal contrast) on some summer nights for the formation of land breezes, it cannot be traced due to the stronger large-scale Atlantic breeze system that invades the region in late afternoon and overlaps all local wind circulations.

The numerical experiment that were carried out in the current work demonstrated a success of the chosen approach and method, and, meanwhile, revealed several disadvantages of it. Thus, some atmospheric effects, probably, cannot be featured in the typical meteorological conditions (i.e., during the TMY) and may only appear in non-typical or extreme conditions. A numerical simulation covering the whole life period of the Alqueva reservoir could reveal more characteristic features of its impact, for example, some extreme events of fog or strong breezes. The present study did not investigate the impact of land use change or urbanization increase caused by the reservoir emergence, as the ECOCLIMAP II database used in the model runs does not reflect these changes in the region, which are source of additional effects.

Despite all the limitations, the proposed method for the assessment of the raw impact of the reservoir demonstrates general trends in the local weather changes due to the emergence of the Alqueva and allows to answer the questions posed in the work. The results of this study could be a starting point for a deeper research of the reservoir's impact on climate, or, on the opposite, become a reference for the study of the reservoir's ecosystem response to the climate change.

ACKNOWLEDGEMENTS

The work is co-funded by the European Union through the European Regional Development Fund, included in the COMPETE 2020 (Operational Program Competitiveness and Internationalization) through the ICT project (UID/GEO/04683/2019) with the reference POCI-01-0145-FEDER-007690, the ALOP project (ALT20-03-0145-FEDER-000004), and the TOMAQAPA project (FCT reference PTDC/CTA-MET/29678/2017). Edgar F. M. Abreu acknowledges the support of the FCT (the Portuguese Science and Technology Foundation) through the grant with reference SFRH/BD/136433/2018.

CONFLICT OF INTEREST

The authors declare that they have no conflict of interest.

AUTHOR CONTRIBUTIONS

Edgar Abreu: Data curation; methodology. **Paulo Canhoto:** Methodology; supervision. **Sara Pereira:** Methodology. **Rui Salgado:** Conceptualization; formal analysis; funding acquisition; project administration; resources; supervision; writing-review & editing.

ENDNOTE

[1] All climate data for this paragraph was taken from Portuguese Institute of the Sea and the Atmosphere, http://www.ipma.pt

DATA AVAILABILITY STATEMENT

Current version of the Meso-NH atmospheric model is available for download on the official website http://mesonh.aero.obs-mip.fr/mesonh54/Download.

ORCID

Maksim Iakunin https://orcid.org/0000-0002-8272-2626
Rui Salgado https://orcid.org/0000-0003-1311-6291

REFERENCES

Abreu, E.F.M., Canhoto, P., Prior, V. and Melicio, R. (2018) Solar resource assessment through long-term statistical analysis and typical data generation with different time resolutions using GHI measurements. *Renewable Energy*, 127, 398–411. https://doi.org/10.1016/j.renene.2018.04.068.

Bates, G.T., Giorgi, F. and Hostetler, S.W. (1993) Toward the Simulation of the Effects of the Great Lakes on Regional Climate. *Monthly Weather Review*, 121, 1373–1387. https://doi.org/10.1175/1520-0493(1993)121<1373:TTSOTE>2.0.CO;2.

Bergot T., Lestringant R. (2019) On the Predictability of Radiation Fog Formation in a Mesoscale Model: A Case Study in Heterogeneous Terrain. *Atmosphere*, 10(4), 165. http://dx.doi.org/10.3390/atmos10040165.

Bischoff-Gauß, I., Kalthoff, N. and Fiebig-Wittmaack, M. (2006) The influence of a storage lake in the Arid Elqui Valley in Chile on local climate. *Theoretical and Applied Climatology*, 85, 227–241. https://doi.org/10.1007/s00704-005-0190-8.

Bonan, G.B. (1995) Sensitivity of a GCM simulation to inclusion of inland water surfaces. *Journal of Climate*, 8, 2691–2704. https://doi.org/10.1175/1520-0442(1995)008<2691:SOAGST>2.0.CO;2.

Bougeault, P. and Lacarrere, P. (1989) Parameterization of orography-induced turbulence in a mesobeta–scale model. *Monthly Weather Review*, 117, 1872–1890. https://doi.org/10.1175/1520-0493(1989)117<1872:POOITI>2.0.CO;2.

Bre, F. and Fachinotti, V.D. (2016) Generation of typical meteorological years for the Argentine Littoral Region. *Energy and Buildings*, 129, 432–444. https://doi.org/10.1016/j.enbuild.2016.08.006.

Capecchi, V. and Buizza, R. (2019) Reforecasting the flooding of florence of 4 November 1966 With Global and Regional Ensembles. *Journal of Geophysical Research: Atmospheres*, 124, 3743–3764. https://doi.org/10.1029/2018JD030231.

Chan, A. (2016) Generation of typical meteorological years using genetic algorithm for different energy systems. *Renewable Energy*, 90, 144–151. https://doi.org/10.1016/j.renene.2015.12.052.

Choulga, M., Kourzeneva, E., Zakharova, E. and Doganovsky, A. (2014) Estimation of the mean depth of boreal lakes for use in numerical weather prediction and climate modelling. *Tellus A: Dynamic Meteorology and Oceanography*, 66, 295. https://doi.org/10.3402/tellusa.v66.21295.

Cohard, J.M. and Pinty, J.P. (2000) A comprehensive two-moment warm microphysical bulk scheme. I: Description and tests.

10970088, 2022, 2, Downloaded from https://rmets.onlinelibrary.wiley.com/doi/10.1002/joc.7299 by Cochrane Portugal, Wiley Online Library on [06/07/2023]. See the Terms and Conditions (https://onlinelibrary.wiley.com/terms-and-conditions) on Wiley Online Library for rules of use; OA articles are governed by the applicable Creative Commons License

Quarterly Journal of the Royal Meteorological Society, 126, 1815–1842. https://doi.org/10.1002/qj.49712656613.

Cuxart, J., Bougeault, P. and Redelsperger, J.-L. (2000) A turbulence scheme allowing for mesoscale and large-eddy simulations. *Quarterly Journal of the Royal Meteorological Society*, 126, 1–30. https://doi.org/10.1002/qj.49712656202.

Domínguez, A., Martínez-Romero, A., Leite, K.N., Tarjuelo, J.M., de Juan, J.A. and López-Urrea, R. (2013) Combination of typical meteorological year with regulated deficit irrigation to improve the profitability of garlic growing in central Spain. *Agricultural Water Management*, 130, 154–167. https://doi.org/10.1016/j.agwat.2013.08.024.

Eerola, K., Rontu, L., Kourzeneva, E., Homa, K.P. and Duguay, C. (2014) Impact of partly ice-free Lake Ladoga on temperature and cloudiness in an anticyclonic winter situation – a case study using a limited area model. *Tellus A: Dynamic Meteorology and Oceanography*, 66, 929. https://doi.org/10.3402/tellusa.v66.23929.

Ekhtiari N., Grossman-Clarke S., Koch H., Meira de Souza W., Donner R., Volkholz J. (2017) Effects of the Lake Sobradinho Reservoir (Northeastern Brazil) on the Regional Climate. *Climate*, 5(3), 50. http://dx.doi.org/10.3390/cli5030050.

Faroux, S., Kaptué Tchuenté, A.T., Roujean, J.L., Masson, V., Martin, E. and Le Moigne, P. (2013) ECOCLIMAP-II/Europe: a twofold database of ecosystems and surface parameters at 1 km resolution based on satellite information for use in land surface, meteorological and climate models. *Geoscientific Model Development*, 6, 563–582. https://doi.org/10.5194/gmd-6-563-2013.

Fernández, M.D., López, J.C., Baeza, E., Céspedes, A., Meca, D.E. and Bailey, B. (2015) Generation and evaluation of typical meteorological year datasets for greenhouse and external conditions on the Mediterranean coast. *International Journal of Biometeorology*, 59, 1067–1081. https://doi.org/10.1007/s00484-014-0920-7.

Festa, R. and Ratto, C. (1993) Proposal of a numerical procedure to select reference years. *Solar Energy*, 50, 9–17. https://doi.org/10.1016/0038-092X(93)90003-7.

Finkelstein, J. and Schafer, R. (1971) Improved goodness-of-fit tests. *Biometrika*, 58, 641–645. https://doi.org/10.1093/biomet/58.3.641.

Gazela, M. and Mathioulakis, E. (2001) A new method for typical weather data selection to evaluate long-term performance of solar energy systems. *Solar Energy*, 70, 339–348. https://doi.org/10.1016/S0038-092X(00)00151-1.

Haichao, W., Wenling, J., Lahdelma, R., Pinghua, Z. and Shuhui, Z. (2013) Atmospheric environmental impact assessment of a combined district heating system. *Building and Environment*, 64, 200–212. https://doi.org/10.1016/j.buildenv.2013.02.011.

Hall, I., Prairie, R.R., Anderson, H.E. and Boes, E.C. (1978) *Generation of Typical Meteorological Years for 26 SOLMET Stations*. Sandia Laboratories: Sandia Laboratories energy report.

Hogan, R.J. and Bozzo, A. (2018) A flexible and efficient radiation scheme for the ECMWF model. *Journal of Advances in Modeling Earth Systems*, 10, 1990–2008. https://doi.org/10.1029/2018MS001364.

Iakunin, M., Salgado, R. and Potes, M. (2018) Breeze effects at a large artificial lake: summer case study. *Hydrology and Earth System Sciences*, 22, 5191–5210. https://doi.org/10.5194/hess-22-5191-2018.

Iakunin, M., Stepanenko, V., Salgado, R., Potes, M., Penha, A., Novais, M.H. and Rodrigues, G. (2020) Numerical study of the seasonal thermal and gas regimes of the largest artificial reservoir in western Europe using the LAKE 2.0 model. *Geoscientific Model Development*, 13, 3475–3488. https://doi.org/10.5194/gmd-13-3475-2020.

Jarvis, A., Guevara, E., Reuter, H. I., and Nelson, A. D. (2008). Hole - filled SRTM for the globe: version 4: data grid, published by CGIAR-CSI on August 19, 2008.

Jiménez, M.A., Cuxart, J. and Martínez-Villagrasa, D. (2019) Influence of a valley exit jet on the nocturnal atmospheric boundary layer at the foothills of the Pyrenees. *Quarterly Journal of the Royal Meteorological Society*, 145, 356–375. https://doi.org/10.1002/qj.3437.

Lac, C., Chaboureau, J.-P., Masson, V., Pinty, J.P., Tulet, P., Escobar, J., Leriche, M., Barthe, C., Aouizerats, B., Augros, C., Aumond, P., Auguste, F., Bechtold, P., Berthet, S., Bieilli, S., Bosseur, F., Caumont, O., Cohard, J.-M., Colin, J., Couvreux, F., Cuxart, J., Delautier, G., Dauhut, T., Ducrocq, V., Filippi, J.-B., Gazen, D., Geoffroy, O., Gheusi, F., Honnert, R., Lafore, J.-P., Lebeaupin Brossier, C., Libois, Q., Lunet, T., Mari, C., Maric, T., Mascart, P., Mogé, M., Molinié, G., Nuissier, O., Pantillon, F., Peyrillé, P., Pergaud, J., Perraud, E., Pianezze, J., Redelsperger, J.-L., Ricard, D., Richard, E., Riette, S., Rodier, Q., Schoetter, R., Seyfried, L., Stein, J., Suhre, K., Thouron, O., Turner, S., Verrelle, A., Vié, B., Visentin, F., Vionnet, V. and Wautelet, P. (2018) Overview of the Meso-NH model version 5.4 and its applications. *Geoscientific Model Development Discussions*, 2018, 1–66. https://doi.org/10.5194/gmd-2017-297.

Le Moigne, P., Colin, J. and Decharme, B. (2016) Impact of lake surface temperatures simulated by the FLake scheme in the CNRM-CM5 climate model. *Tellus A: Dynamic Meteorology and Oceanography*, 68, 31274. https://doi.org/10.3402/tellusa.v68.31274.

Lopes, F., Silva, H.G., Salgado, R., Potes, M., Nicoll, K.A. and Harrison, R.G. (2016) Atmospheric electrical field measurements near a fresh water reservoir and the formation of the lake breeze. *Tellus A: Dynamic Meteorology and Oceanography*, 68, 31592. https://doi.org/10.3402/tellusa.v68.31592.

Lunet, L., Lac, C., Auguste, F., Visentin, F., Masson, V. and Escobar, J. (2017) Combination of WENO and Explicit Runge–Kutta Methods for Wind Transport in the Meso-NH Model. *Monthly Weather Review*, 145, 3817–3838. https://doi.org/10.1175/MWR-D-16-0343.1.

Marion, W. and Urban, K. (1995). *User's manual for TMY2s typical meteorological years: derived from the 1961–1990 national solar radiation data base*. Technical report., https://doi.org/10.2172/87130.

Marsigli, C., Montani, A. and Paccagnella, T. (2014) Provision of boundary conditions for a convection-permitting ensemble: comparison of two different approaches. *Nonlinear Processes in Geophysics*, 21, 393–403. https://doi.org/10.5194/npg-21-393-2014.

Martínez-Romero, A., Domínguez, A. and Landeras, G. (2019) Regulated deficit irrigation strategies for different potato cultivars under continental Mediterranean-Atlantic conditions. *Agricultural Water Management*, 216, 164–176. https://doi.org/10.1016/j.agwat.2019.01.030.

Masson, V. (2000) A physically-based scheme for the urban energy budget in atmospheric models. *Boundary-Layer Meteorology*, 94, 357–397. https://doi.org/10.1023/A:1002463829265.

10970088, 2022, 2, Downloaded from https://rmets.onlinelibrary.wiley.com/doi/10.1002/joc.7299 by Cochrane Portugal, Wiley Online Library on [06/07/2023]. See the Terms and Conditions (https://onlinelibrary.wiley.com/terms-and-conditions) on Wiley Online Library for rules of use; OA articles are governed by the applicable Creative Commons License

Masson, V., Le Moigne, P., Martin, E., Faroux, S., Alias, A., Alkama, R., Belamari, S., Barbu, A., Boone, A., Bouyssel, F., Brousseau, P., Brun, E., Calvet, J.-C., Carrer, D., Decharme, B., Delire, C., Donier, S., Essaouini, K., Gibelin, A.-L., Giordani, H., Habets, F., Jidane, M., Kerdraon, G., Kourzeneva, E., Lafaysse, M., Lafont, S., Lebeaupin Brossier, C., Lemonsu, A., Mahfouf, J.-F., Marguinaud, P., Mokhtari, M., Morin, S., Pigeon, G., Salgado, R., Seity, Y., Taillefer, F., Tanguy, G., Tulet, P., Vincendon, B., Vionnet, V. and Voldoire, A. (2013) The SURFEXv7.2 land and ocean surface platform for coupled or offline simulation of earth surface variables and fluxes. *Geoscientific Model Development*, 6, 929–960. https://doi.org/10.5194/gmd-6-929-2013.

Mironov, D. (2008). *Parameterization of lakes in numerical weather prediction. Description of a lake model. COSMO Technical Report*. Deutscher Wetterdienst, 11, pp. 41.

Muñoz, S.J. (2019). ERA5-Land monthly averaged data from 1981 to present. *Copernicus Climate Change Service (C3S) Climate Data Store (CDS)*. [Accessed 12th January 2020], https://doi.org/10.24381/cds.68d2bb3.

Nachtergaele, F., Van Velthuizen, H., Verelst, L., Batjes, N., Dijkshoorn, K., Van Engelen, V., Fischer, G., Jones, A., Montanarella, L., Petri, M. and Prieler, S. (2008) *Harmonized world soil database*. Rome: FAO.

Noilhan, J. and Mahfouf, J.F. (1996) The ISBA land surface parameterisation scheme. *Global and Planetary Change*, 13, 145–159. https://doi.org/10.1016/0921-8181(95)00043-7.

Notaro, M., Zarrin, A., Vavrus, S. and Bennington, V. (2013) Simulation of heavy lake-effect snowstorms across the Great Lakes Basin by RegCM4: synoptic climatology and variability. *Monthly Weather Review*, 141, 1990–2014. https://doi.org/10.1175/MWR-D-11-00369.1.

Novais M.H., Penha A.M., Morales E.A., Potes M., Salgado R., Morais M. (2019) Vertical distribution of benthic diatoms in a large reservoir (Alqueva, Southern Portugal) during thermal stratification. *Science of The Total Environment*, 659 1242–1255. http://dx.doi.org/10.1016/j.scitotenv.2018.12.251.

Penha, A.M., Chambel, A., Murteira, M. and Morais, M. (2016) Influence of different land uses on groundwater quality in southern Portugal. *Environmental Earth Sciences*, 75, 622. https://doi.org/10.1007/s12665-015-5038-7.

Pergaud, J., Masson, V., Malardel, S. and Couvreux, F. (2009) A parameterization of dry thermals and shallow cumuli for mesoscale numerical weather prediction. *Boundary-Layer Meteorology*, 132, 83. https://doi.org/10.1007/s10546-009-9388-0.

Pinty, J. P. and Jabouille, P. (1998) A mixed-phase cloud parameterization for use in mesoscale non-hydrostatic model: simulations of a squall line and of orographic precipitations. *Proceedings of the AMS Conference on Cloud Physics*. Everett, WA: American Meteorological Society, pp. 217–220.

Pissimanis, D., Karras, G., Notaridou, V. and Gavra, K. (1988) The generation of a "typical meteorological year" for the city of Athens. *Solar Energy*, 40, 405–411. https://doi.org/10.1016/0038-092X(88)90095-3.

Policarpo, C., Salgado, R. and Costa, M.J. (2017) Numerical Simulations of Fog Events in Southern Portugal. *Advances in Meteorology*, 16, 2017.

Potes, M., Costa, M.J. and Salgado, R. (2012) Satellite remote sensing of water turbidity in Alqueva reservoir and implications on lake modelling. *Hydrol. Earth Syst. Sci.*, 16, 1623–1633. https://doi.org/10.5194/hess-16-1623-2012.

Potes, M., Rodrigues, G., Penha, A., Novais, M.H., Costa, M.J., Salgado, R. and Morais, M. (2018) Use of Sentinel 2-MSI for water quality monitoring at Alqueva reservoir, Portugal. *Proceedings of the International Association of Hydrological Sciences*, 380, 73–79. https://doi.org/10.5194/piahs-380-73-2018.

Potes, M., Salgado, R., Costa, M.J., Morais, M., Bortoli, D., Kostadinov, I. and Mammarella, I. (2017) Lake–atmosphere interactions at Alqueva reservoir: a case study in the summer of 2014. *Tellus A: Dynamic Meteorology and Oceanography*, 69, 1272787. https://doi.org/10.1080/16000870.2016.1272787.

Purificação C., Potes M., Rodrigues G., Salgado R., Costa M.J. (2021) Lake and Land Breezes at a Mediterranean Artificial Lake: Observations in Alqueva Reservoir, Portugal. *Atmosphere*, 12(5), 535. http://dx.doi.org/10.3390/atmos12050535.

Pusat, S., Ekmekçi, M. and Akkoyunlu, M. (2015) Generation of a typical meteorological year for different climates of Turkey. *Renewable Energy*, 75, 144–151. https://doi.org/10.1016/j.renene.2014.09.039.

Reinares Martínez I., Chaboureau J.-P., Handwerker J. (2020) Warm Rain in Southern West Africa: A Case Study at Savè. *Atmosphere*, 11(3), 298. http://dx.doi.org/10.3390/atmos11030298.

Rodrigues G., Potes M., Costa M.J., Novais M.H., Penha A.M., Salgado R., Morais M.M. (2020) Temporal and Spatial Variations of Secchi Depth and Diffuse Attenuation Coefficient from Sentinel-2 MSI over a Large Reservoir. *Remote Sensing*, 12(5), 768. http://dx.doi.org/10.3390/rs12050768.

Salgado, R. and Le Moigne, P. (2010) Coupling of the FLake model to the Surfex externalized surface model. *Boreal Environment Research*, 15, 231–244.

Samuelsson, P., Kourzeneva, E. and Mironov, D. (2010) The impact of lakes on the European climate as simulated by a regional climate model. *Boreal Environment Research*, 15, 113–129, Available at: http://www.borenv.net/BER/pdfs/ber15/ber15-113.pdf.

Scott, R.W. and Huff, F.A. (1996) Impacts of the Great Lakes on regional climate conditions. *Journal of Great Lakes Research*, 22, 845–863. https://doi.org/10.1016/S0380-1330(96)71006-7.

Segal, M., Leuthold, M., Arritt, R.W., Anderson, C. and Shen, L. (1997) Small lake daytime breezes: some observational and conceptual evaluations. *Bulletin of the American Meteorological Society*, 78, 1135–1147. https://doi.org/10.1175/1520-0477(1997)078<1135:SLDBSO>2.0.CO;2.

Silva, A., De Lima, I., Santo, F. and Pires, V. (2014) Assessing changes in drought and wetness episodes in drainage basins using the Standardized Precipitation Index. *Bodenkultur*, 65(3–4), 31–37.

Thiery, W., Martynov, A., Darchambeau, F., Descy, J.-P., Plisnier, P.-D., Sushama, L. and van Lipzig, N.P.M. (2014) Understanding the performance of the FLake model over two African Great Lakes. *Geoscientific Model Development*, 7, 317–337. https://doi.org/10.5194/gmd-7-317-2014.

Tomaz, A., Patanita, M., Guerreiro, I., Boteta, L. and Palma, J.F. (2017) Water use and productivity of maize-based cropping

10970088, 2022, 2, Downloaded from https://rmets.onlinelibrary.wiley.com/doi/10.1002/joc.7299 by Cochrane Portugal, Wiley Online Library on [06/07/2023]. See the Terms and Conditions (https://onlinelibrary.wiley.com/terms-and-conditions) on Wiley Online Library for rules of use; OA articles are governed by the applicable Creative Commons License

systems in the Alqueva Region (Portugal). *Cereal Research Communications*, 45, 1–11. https://doi.org/10.1556/0806.45.2017.036.

Verrelle, A., Ricard, D. and Lac, C. (2015) Sensitivity of high-resolution idealized simulations of thunderstorms to horizontal resolution and turbulence parametrization. *Quarterly Journal of the Royal Meteorological Society*, 141, 433–448. https://doi.org/10.1002/qj.2363.

Wilcox, S. and Marion, W. (2008). *Users manual for TMY3 data sets*, https://doi.org/10.2172/928611.

How to cite this article: Iakunin, M., Abreu, E. F. M., Canhoto, P., Pereira, S., & Salgado, R. (2022). Impact of a large artificial lake on regional climate: A typical meteorological year Meso-NH simulation results. *International Journal of Climatology*, *42*(2), 1231–1252. https://doi.org/10.1002/joc.7299

10970088, 2022, 2, Downloaded from https://rmets.onlinelibrary.wiley.com/doi/10.1002/joc.7299 by Cochrane Portugal, Wiley Online Library on [06/07/2023]. See the Terms and Conditions (https://onlinelibrary.wiley.com/terms-and-conditions) on Wiley Online Library for rules of use; OA articles are governed by the applicable Creative Commons License

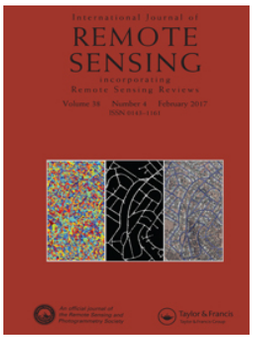

International Journal of Remote Sensing

ISSN: 0143-1161 (Print) 1366-5901 (Online) Journal homepage: https://www.tandfonline.com/loi/tres20

Cloud parameter retrievals from Meteosat and their effects on the shortwave radiation at the surface

Vanda Salgueiro, Maria João Costa, Ana Maria Silva, Christian Lanconelli & Daniele Bortoli

To cite this article: Vanda Salgueiro, Maria João Costa, Ana Maria Silva, Christian Lanconelli & Daniele Bortoli (2017) Cloud parameter retrievals from Meteosat and their effects on the shortwave radiation at the surface, International Journal of Remote Sensing, 38:4, 1137-1161, DOI: 10.1080/01431161.2017.1280630

To link to this article: https://doi.org/10.1080/01431161.2017.1280630

Published online: 23 Jan 2017.

Submit your article to this journal

Article views: 144

View related articles

View Crossmark data

Citing articles: 2 View citing articles

Full Terms & Conditions of access and use can be found at
https://www.tandfonline.com/action/journalInformation?journalCode=tres20

INTERNATIONAL JOURNAL OF REMOTE SENSING, 2017
VOL. 38, NO. 4, 1137–1161
http://dx.doi.org/10.1080/01431161.2017.1280630

Taylor & Francis
Taylor & Francis Group

ARTICLE

Cloud parameter retrievals from Meteosat and their effects on the shortwave radiation at the surface

Vanda Salgueiro [a], Maria João Costa [b], Ana Maria Silva [a], Christian Lanconelli [c*] and Daniele Bortoli [a,c]

[a]Departamento de Física, Instituto de Ciências da Terra, Instituto de Investigação e Formação Avançada, Universidade de Évora, Évora, Portugal; [b]Departamento de Física, Instituto de Ciências da Terra, Escola de Ciências e Tecnologia, Universidade de Évora, Évora, Portugal; [c]Institute of Atmospheric Sciences and Climate (ISAC-CNR), Bologna, Italy

ABSTRACT

A method based on Spinning Enhanced Visible and Infrared Imager (SEVIRI) measured reflectance at 0.6 and 3.9 μm is used to retrieve the cloud optical thickness (COT) and cloud effective radius (r_e) over the Iberian Peninsula. A sensitivity analysis of simulated retrievals to the input parameters demonstrates that the cloud top height is an important factor in satellite retrievals of COT and r_e with uncertainties around 10% for small values of COT and r_e; for water clouds these uncertainties can be greater than 10% for small values of r_e. The uncertainties found related with geometries are around 3%. The COT and r_e are assessed using well-known satellite cloud products, showing that the method used characterize the cloud field with more than 80% (82%) of the absolute differences between COT (r_e) mean values of all clouds (water plus ice clouds) centred in the range from ±10 (±10 μm), with absolute bias lower than 2 (2 μm) for COT (r_e) and root mean square error values lower than 10 (8 μm) for COT (r_e). The cloud water path (CWP), derived from satellite retrievals, and the shortwave cloud radiative effect at the surface (CRE_{SW}) are related for high fractional sky covers (F_{sc} >0.8), showing that water clouds produce more negative CRE_{SW} than ice clouds. The COT retrieved was also related to the cloud modification factor, which exhibits reductions and enhancements of the surface SW radiation of the order of 80% and 30%, respectively, for COT values lower than 10. A selected case study shows, using a ground-based sky camera that some situations classified by the satellite with high F_{sc} values correspond to situations of broken clouds where the enhancements actually occur. For this case study, a closure between the liquid water path (LWP) obtained from the satellite retrievals and the same cloud quantity obtained from ground-based microwave measurements was performed showing a good agreement between both LWP data set values.

ARTICLE HISTORY
Received 12 July 2016
Accepted 3 January 2017

CONTACT Vanda Salgueiro vsalgueiro@uevora.pt Instituto de Ciências da Terra, Rua Romão Ramalho nº 59, 7000-671 Évora, Portugal.

*Present address: European Commission, Joint Research Centre (JRC), Sustainable Resources, Knowledge for Sustainable Development and Food Security, Ispra, Italy.

© 2017 Informa UK Limited, trading as Taylor & Francis Group

1. Introduction

Clouds play a prominent role on the Earth's radiation budget through their interaction with solar and thermal radiation (Cess et al. 1989; Ramanathan et al. 1989; Harrison et al. 1990). The knowledge of the cloud physical properties, such as cloud optical thickness (COT) and particle effective radius, and its relationship with radiative fluxes is essential to understand the cloud radiation interactions. Clouds continuously vary in space and time as they are dynamic systems. Thus, methods to retrieve cloud properties with an adequate temporal frequency and large area coverage are crucial to monitor the cloud evolution and its radiative effects. Satellites are very instrumental for studying and monitoring cloud evolution at regional and global scales. In particular, operational geostationary meteorological satellites enable a near-real-time cloud monitoring on a large scale due to their unrivalled image space coverage and time repetition.

For several decades, remote-sensing techniques using selected spectral bands in the visible (VIS), near-infrared (NIR), and thermal infrared (IR) have been developed to determine cloud properties. Nakajima and King (1990) were among the first to use reflected solar radiation at VIS and NIR wavelengths to retrieve simultaneously the COT and the effective radius (r_e) of water clouds. Since then, different algorithms based on passive sensor measurements on board polar and geostationary satellites have been proposed to characterize the cloud field in terms of physical properties (e.g. COT, effective radius, thermodynamic phase, cloud top height, liquid, and ice water paths) (Nakajima and Nakajima 1995; King et al. 1997; Jolivet and Feijt 2003; Baum and Platnick 2006; Roebeling, Feijt, and Stammes 2006; Costa et al. 2007; Bugliaro et al. 2011). Examples of passive sensors used nowadays to obtain cloud properties from combined VIS/IR remote-sensing techniques are the Moderate Resolution Imaging Spectroradiometer (MODIS) flying on board the low Earth orbit Terra and Aqua Earth Observing System (EOS) platforms and the Spinning Enhanced Visible and Infrared Imager (SEVIRI) on board the Meteorological Satellite (Meteosat) satellites on a geostationary orbit. The Climate Monitoring Satellite Application Facility (CM-SAF) of the European Organization for the Exploitation of Meteorological Satellites (EUMETSAT) provides geophysical parameter datasets for climate monitoring (e.g. radiation budget and cloud parameters) derived from satellite measurements (Schulz et al. 2009). Among the data sets provided by the CM-SAF, the Cloud Property Data Set (CLAAS) (Stengel et al. 2014), obtained using hourly SEVIRI data, is based on a period of 8 year measurements (from 2004 until the end of 2011) and derived with the Cloud Physical Properties (CPP) algorithm (Roebeling, Feijt, and Stammes 2006; Meirink 2013). The National Aeronautics and Space Administration (NASA) Goddard Earth Sciences Distributed Active Archive Centre (GES DAAC) also provides cloud products (Baum and Platnick 2006) from MODIS low Earth orbit of the spacecraft (Terra and Aqua) twice a day over the same spot at mid-latitudes. MODIS Level 2 cloud property retrievals are assessed in the work of Painemal and Zuidema (2011), with the COT correlating well with aircraft-derived values, with MODIS presenting larger values (mean difference = 1.42) and the standard effective radius at 2.1 μm exceeding the *in situ* cloud top effective radius with a mean bias of 2.08 μm. MODIS is the reference used to compare cloud physical property retrievals from ground-based data (Min et al. 2012), as well as aircraft (Min et al. 2012) and space-born instruments. For example, Stengel et al. (2014) evaluate the CPP cloud

product of CM-SAF against MODIS retrievals at pixel level, reporting bias values of 1.8 for COT and of 0.1 g m ^{2} (6.7 g m ^{2}) for liquid water path (ice water path).

Cloud radiation interactions still represent a source of uncertainty (Boucher et al. 2013) because of the potential variations in cloud properties as the cloud droplet number concentration, which can be calculated by combining the COT and effective radius retrievals (Painemal and Zuidema 2011). The interaction between clouds and radiation can be estimated by using the cloud radiative forcing, which is a measure of the net total fluxes (all-sky fluxes minus clear-sky fluxes in shortwave plus longwave spectral ranges; in W m ^{2}) (Ramanathan et al. 1989). In general, the total radiative effect produced by clouds is negative causing a cooling effect in the earth-atmosphere system with negative and positive contributions of the shortwave and longwave components, respectively. Since the improvement of satellites, ground-based instrumentation and climate models, different studies of cloud radiative effects have been performed (Oreopoulos and Rossow 2011; Allan 2011; Calisto et al. 2014; Dong, Xi, and Minnis 2006; Berg et al. 2011). The International Satellite Cloud Climatology Project (ICCP; Schiffer and Rossow 1983) was the first project whose basic objective is to collect and analyse satellite radiance data to infer the global distribution of cloud radiative properties, in order to improve the modelling of cloud effects on climate. Oreopoulos and Rossow (2011) examined the cloud radiative effects of various cloud regimes using a 24-year long-term data set from the ICCP for three distinct geographical zones covering most of the Earth's surface area. Calisto et al. (2014) analysed and compared the radiative forcing for 10 years of the Clouds and the Earth's Radiant Energy System onboard Terra and Aqua satellites (CERES) measurements with 11 Coupled Model Intercomparison Project Phase 5 (CMIP5) models. A global mean SW cloud radiative forcing between 54.7 and 40.8 W m ^{2} for the CMIP5 models and 47.5 W m ^{2} for CERES was found. Allan (2011) used Geostationary Earth Radiation Budget (GERB) onboard Meteosat-9 satellite and CERES satellite data and numerical forecast model reanalysis data to compute an estimate of the cloud radiative effect on the global multi-annual mean radiative energy budget of the atmosphere and surface, and a net cooling of the climate system of 21 W m ^{2} was found. Using ground-based measurements, Berg et al. (2011) found a shortwave cloud radiative forcing average value of 45.5 W m ^{2} for shallow cumuli and Dong, Xi, and Minnis (2006) showed that the shortwave cloud radiative forcing for a mid-latitude site exhibits minimum values in spring for all sky conditions. This study aims at contributing to the understanding of the relation between cloud parameters and solar radiation received at the surface, taking advantage of the adequate temporal resolution of geostationary satellites to provide the cloud daily evolution. It is demonstrated here through a closure procedure that for certain cloud situations, it is indeed possible to relate satellite cloud retrievals (obtained from above the clouds) with ground-based observations (made below the clouds) of the same cloud quantity.

The Iberian Peninsula, located at mid latitudes in southwestern Europe, is usually affected by contrasting air masses (Raes et al. 2000), with marked differences in terms of cloud occurrences between the cold and warm seasons (Salgueiro et al. 2014), offering thus good opportunities not only for cloud studies but also for studies of cloud-aerosol interactions due to the different origin of the aerosols carried by the different air masses passing in the region (Silva et al. 2002; Santos, Costa, and Silva 2008). On the other hand,

the southern regions of the Iberian Peninsula typically present the highest values of annual surface solar radiation in Europe (Bojanowski, Vrieling, and Skidmore 2014), which highly depend on the COT (Mateos et al. 2014a; Salgueiro et al. 2014). For these reasons, the Iberian Peninsula presents suitable conditions to study the cloud properties and their influence on solar radiation at the surface, to deepen the understanding of cloud radiation interactions in the area.

This work aims to study the relation of two cloud quantities retrieved from satellite measurements (COT and effective radius) with shortwave cloud radiative effects obtained from ground-based global irradiance measurements taken in 2015 in Évora region, southwestern Iberian Peninsula. There are studies that analyse the relation between cloud properties and solar radiation at this region, using ground-based measurements of both (Antón et al. 2012; Mateos et al. 2014a, 2014b; Salgueiro et al. 2016). However, to our knowledge, no study has yet addressed the relation between cloud parameters obtained from geostationary satellite remote sensing and surface solar radiation measurements at the study region taking advantage of the adequate temporal resolution of Meteosat satellite to provide the cloud daily evolution while monitoring a suitable area.

The satellite and surface radiation data used as well as the description of the retrieval method can be found in Section 2. The results and discussion, including the comparison of the cloud properties retrievals with independent data, as well as the relation between the cloud properties and the shortwave radiative effects are presented in Section 3. Summary and conclusions are presented in Section 4.

2. Methods and data

2.1. Satellite data and cloud parameter retrievals

Satellite data of the SEVIRI radiometer on board Meteosat satellite were used in this work. SEVIRI is a passive imaging radiometer (Schmetz et al. 2002) that provides continuous observations (every 15 min), of the earth–atmosphere system covering a region that includes Europe. It measures radiation in 12 spectral channels in the VIS, NIR, and IR spectral regions. Eleven of these channels provide data of the Earth's full disc with an image sampling distance of 3 km at sub-satellite point, at wavelengths between 0.6 and 14 μm. A high-resolution visible (HRV) channel (broadband: 0.4–1.1 μm) is also included, with sampling distance of 1 km at nadir. The satellite data used in this work were obtained from EUMETSAT Earth Observation Portal, corresponding to SEVIRI level 1.5 image data.

The retrieval method used in this work is based on the well-known principle that cloud reflectances at non-absorbing wavelengths in the VIS spectral region are strongly related with COT, while at absorbing wavelengths, in the NIR region, they are primarily related to cloud particle size (Nakajima and King 1990; Nakajima and Nakajima 1995). In fact the sensitivity of the non-absorbing (absorbing) reflectances to the COT (cloud effective radius) are almost orthogonal functions (Nakajima and King 1990), Thus, the COT and effective droplet radius/ice particle size (r_e) can be determined from the comparison between pre-calculated reflectances and the corresponding measured quantities. The method uses two SEVIRI channels, VIS0.6 (centred at 0.635 μm) and

IR3.9 (centred at 3.90 μm), and is limited to daytime applications because it depends on solar radiation. In the VIS spectral region, the channel VIS0.6 was chosen due to the lower reflectivity of the surface and vegetation so that thin (or transparent) clouds are better detected. The channel IR3.9 was chosen due to its sensitivity to cloud top conditions (Rosenfeld et al. 2004), and it is used to obtain the effective droplet radius/ice particle size near the cloud tops. At 3.9 μm both solar reflection and thermal emission take place during daytime, since the emission by the surface, atmosphere and clouds provide a non-negligible contribution to the total IR3.9 radiance. Hence, the cloud reflectance at 3.9 μm is determined assuming the following assumptions (Charvát 2007; Kaufman and Nakajima 1992): the same type of cloud homogenously covers the whole pixel; clouds are partially opaque with respect to radiation, that is, there is no upward transmission of radiation through the cloud from the surface and from the atmosphere below the cloud therefore the cloud reflectance plus its emittance is unity. The relation between the total upward radiance ($I_{3.9}$) and the cloud reflectance ($r_{3.9}$) adopted is translated by Equation (1) from Kaufman and Nakajima (1992):

$$I_{3:9} \ldots \tau^{0}_{3:9} \frac{F_0 \mu_0}{\pi} r_{3:9} \text{ þ } \tau^{\uparrow}_{3:9} B_{3:9}\text{ðTÞð1} \quad r_{3:9}\text{Þ:} \tag{1}$$

In Equation (1), the first and second terms on the right side represent the solar and thermal components of the IR3.9 upward radiance at the satellite level (top of the atmosphere), respectively; τ° is the total downward and then upward transmission of sunlight above the cloud, τ is the upward transmission of thermal radiation above the cloud, F_0 is the extra-terrestrial solar flux at IR3.9 channel, μ_0 is the cosine of the solar zenith angle and $B_{3.9}(T)$ is the thermal radiance represented by the Planck function at temperature T and wavelength 3.9 μm. The temperature, T, is approximated by the brightness temperature of cloud top given by channel IR10.8, since at this wavelength the emissivity is close to one for all surfaces and the atmospheric absorption is low. The thermal component is then estimated following the relation between the SEVIRI radiances and the equivalent brightness temperature described in EUMETSAT (2012), and the transmittance follows the theory described in the work of Charvát (2007). The cloud reflectance at IR3.9 channel can be derived from Equation (1) as shown in Equation (2):

$$r_{3:9} \ldots \frac{I_{3:9} \quad \tau^{\uparrow}_{3:9} B_{3:9}\text{ðTÞ}}{\tau^{0}_{3:9} F_0 \mu_0 = \pi \quad \tau^{\uparrow}_{3:9} B_{3:9}\text{ðTÞ}}: \tag{2}$$

Look-up tables (LUTs) of calculated reflectances as seen by Meteosat were built using the one-dimensional (1D) radiative transfer code Library for Radiative transfer (LibRadtran) (Mayer and Kylling 2005). These reflectances were calculated for different values of COT, effective droplet radius/ice particle size, solar zenith angle (θ_0), satellite zenith angle (θ), and relative azimuth angle ($\Delta\varphi$) defined as the difference between solar and satellite azimuthal angles (see Table 1). The calculations were done using the different spectral response functions of the VIS0.6 and IR3.9 channels of the SEVIRI instrument. Solar and satellite zenith angles were chosen within the ranges of valid values over the Iberian Peninsula. The radiative transfer calculations were done considering a homogeneous and plane-parallel cloud layer constituted by liquid or ice

Table 1. Input parameters used in the LUT calculations: cloud effective droplet radius/ice particle size (r_e), cloud optical thickness (COT), solar zenith angle ($_0$), satellite zenith angle ( ), and relative azimuth angle ( ).

Input parameter	Values used	
r_e (μm)	Water clouds: 2, 4, 6, 9, 12, 15, **21**, 25	Ice clouds: 5, 7, 10, 15, 20, 30, **40**, 50
COT	0.5, 1, 2, 4, 7, 10, 14, 20, **30**, 50	
$_0$ (°)	From 5° to 70° with step of 1°	
(°)	From 35° to 55° with step of 1°	
(°)	From 0° to 180° with step of 1°	

The values considered for the sensitivity analysis are shown in bold.

particles with geometrical thickness of 1 km. The cloud top is located at 3 and 7 km for water and ice clouds, respectively. The main difference between water and ice clouds is that the latter usually are formed by non-spherical particles with no unique definition of their effective size. Thus, the conversion from microphysical to optical properties uses different parameterizations. For water clouds, hydrometeors are assumed spherical and the conversion is done using pre-calculated Mie tables. For the ice cloud properties, the conversion is done by using the parameterization from Baum et al. (2005a, 2005b) where the bulk scattering model is based on reanalysis of *in situ* data from a variety of midlatitude and tropical ice cloud field experiments. The atmosphere is characterized by default conditions for aerosols (Shettle 1989) and gases from a midlatitude profile comprising 50 levels between 0 and 120 km (Anderson et al. 1986). Gas absorption was parameterized using the LOWTRAN model (Pierluissi and Peng 1985), as adopted by the SBDART radiative transfer code (Ricchiazzi et al. 1998) that includes all radiatively active molecular species found in the Earth's atmosphere. The underlying surface albedo is selected from the LibRadtran database of the International Geosphere Biosphere Programme (IGBP) albedo libraries (Belward and Loveland 1996). The radiative transfer equation was numerically solved using the discrete ordinate method (Stamnes et al. 2000) with 16 quadrature angles.

Figure 1 shows a flowchart of the method followed to obtain COT and r_e for each SEVIRI pixel (approximately 3 × 3 km). As a first step, each pixel is classified in terms of thermodynamic phase as water or ice cloud following the cloud classification proposed by Costa et al. (2007). This cloud classification is based on the use of VIS and IR measurements assuming that clouds are made of either liquid water or ice particles, hence not considering mixed phase clouds. Afterwards, a pre-calculated LUT is selected according with the pixel content (water or ice cloud) and pixel viewing geometry (solar zenith angle, satellite zenith angle and relative azimuth angle). Subsequently, both quantities, COT and r_e, are retrieved evaluating the locations of the SEVIRI measured reflectances (VIS0.6 and IR3.9) on the selected LUT using linear interpolation.. The retrieved COT and r_e, hereinafter termed as Cloud Properties using SEVIRI (CPS), are compared with two sets of independent data: MODIS cloud product (MOD06_L2) collection 5.1 (Baum and Platnick 2006) and Cloud Physical Properties (CPP-Product) of CM-SAF (Stengel et al. 2014). The MOD06_L2 cloud product used includes thermodynamic phase, optical thickness and particle size derived at the spatial resolution of 1 km from the MODIS scanning radiometer flying on board Terra satellite platform. The CPP-Product is a pixel-based hourly product with spatial characteristics identical to the SEVIRI imaging projection and resolution

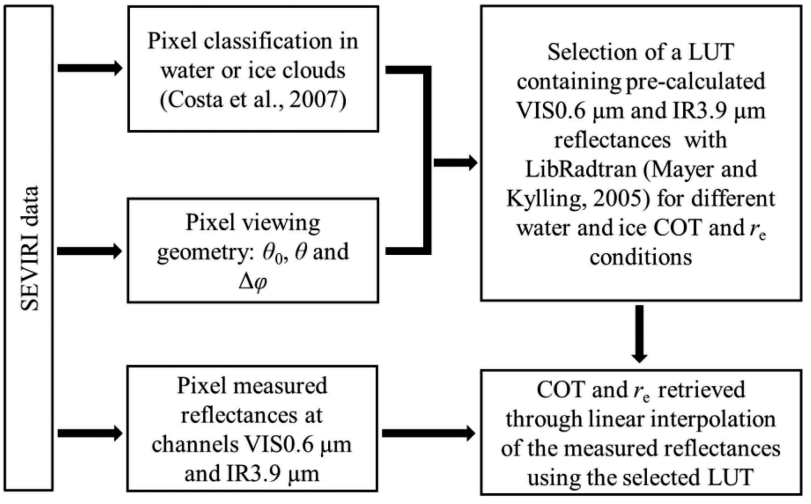

Figure 1. Flowchart of the method followed to obtain cloud optical thickness (COT) and r_e from Spinning Enhanced Visible and Infrared Imager (SEVIRI) measured reflectances.

(approximately 3 × 3 km at the sub-satellite point). The CPP-Product used here (COT, cloud effective radius and cloud thermodynamic phase) corresponds to SEVIRI/MSG2 level 1 (version 001).

2.2 Surface data and cloud radiative e□ects calculations

The shortwave cloud radiative effect at the surface (CRE_{SW}) can be defined as the difference between the net shortwave irradiance (downward minus upward shortwave irradiance) in cloudy and clear sky conditions, translating changes in the SW radiation that reaches the surface due to changes in clouds (type and/or cover). CRE_{SW} can be expressed by Equation (3) (Ramanathan et al. 1989), where α is the surface albedo and F represents the downward global SW irradiance at the surface under cloudy (cld) and clear sky (cs) conditions:

$$CRE_{SW} \ldots \eth 1 \quad a\text{þ} \quad F^{\#}_{cld} \quad F^{\#}_{cs} \quad : \tag{3}$$

The measured global and diffuse SW irradiance was recorded with a Kipp&Zonen CM 6B, which complies with the specifications for 'first class' pyranometer (broadband 305–2800 nm) during the period from January to December of 2015 with a temporal sampling of 1 min. The global SW clear sky irradiance corresponding to each measurement was calculated using the empirical clear sky method proposed by Long and Ackerman (2000), which identifies and produces continuous estimates of clear sky SW irradiance at the surface. A cloud screening algorithm based on independent tests of the SW components (global and diffuse), selects clear sky events on a 1 min basis comparing measured values and their temporal variability, with solar zenith angle corrected threshold limits. When enough points per day are flagged as clear (~100), a power law is fitted to represent the SW clear sky global irradiance, using the cosine of the solar zenith angle as the independent variable. The two regression parameters are interpolated in time for

days that do not satisfy the minimum requirement in terms of number of clear sky events.

Visual information using an all sky camera was also used to check the cloud cover conditions. Liquid water path measurements obtained using a RPG-HATPRO humidity and temperature profiling passive microwave radiometer (MWR), with an accuracy of ±20 g m ^{2} (Rose et al. 2005) were also used to perform a closure with the LWP obtained from the satellite retrievals. MWR has two bands 22–31 GHz (seven channel filter bank humidity profiler and LWP radiometer) and 51–59 GHz (seven channel filter bank temperature profiler) and presents zenith and azimuth scanning capabilities. Attached to the MWR there are also a meteorological station and an infrared radiometer providing cloud base detection. All ground-based instrumentation used in this work is installed at the atmospheric physics observatory of the Institute of Earth Sciences (ICT; 38° 34 N, 7° 54 W, 293 m above mean sea level) in Évora.

3. Results and discussion

3.1 COT and r_e retrievals

3.1.1 Sensitivity analysis of the LUTs to input parameters

A sensitivity analysis of the COT and r_e to LUT input parameters (cloud top height, surface albedo, aerosol optical thickness, and viewing geometries) was performed to quantify the uncertainties in COT and r_e retrievals using the method described in Section 2.1. Following the same methodology as in the LUT construction (Section 2.1), new reflectance calculations were done for each of the different input parameters keeping all the others as in Section 2.1. The COT and r_e, values considered in the sensitivity analysis are the same as in the LUTs, excluding the first and last values (see Table 1) in order to guarantee that the retrievals would fall inside the LUT domain. As for the analysed input parameters, they are varied one at a time while keeping the remaining ones fixed as done in the calculations of the LUTs: the cloud top height took the values 1, 1.5, 2, and 4 km for water clouds and 7.5, 8, 9, 10, and 11 km for ice clouds; the surface albedo (available from http://giovanni.gsfc.nasa.gov/giovanni/; last accessed 21 September 2016) took typical values of the different seasons (spatial averages over the Iberian Peninsula: winter = 0.14, autumn = 0.16, and summer = 0.17); the aerosol optical thickness was considered to take the values 0.05, 0.1, 0.2, 0.3, and 0.5. Since the viewing geometries vary in a large range of values (Table 1), fixed values of solar zenith angle (30°), satellite zenith angle (40°), and azimuthal angle (140°) were chosen for the sensitivity analysis of the cloud top height, surface albedo and aerosol optical thickness. For the sensitivity analysis of the LUT geometry, the new reflectances were calculated for several angles differing 0.5° from those indicated in Table 1, corresponding to the maximum possible geometric deviation of the LUT, since its geometric resolution is 1°. The retrieval method was then applied to these new reflectance values.

Figures 2(a–f) and 3(a–f) show the uncertainties in COT and r_e with the variations of cloud top height, surface albedo and aerosol optical thickness for water and ice clouds, respectively (the reference cases corresponding to the conditions considered in the LUTs are represented in each plot by the dotted line $y = 0$). The r_e (COT) variation in Figures 2 (a–f) and 3(a–f) are presented for fixed COT (r_e) values (intermediate values chosen from

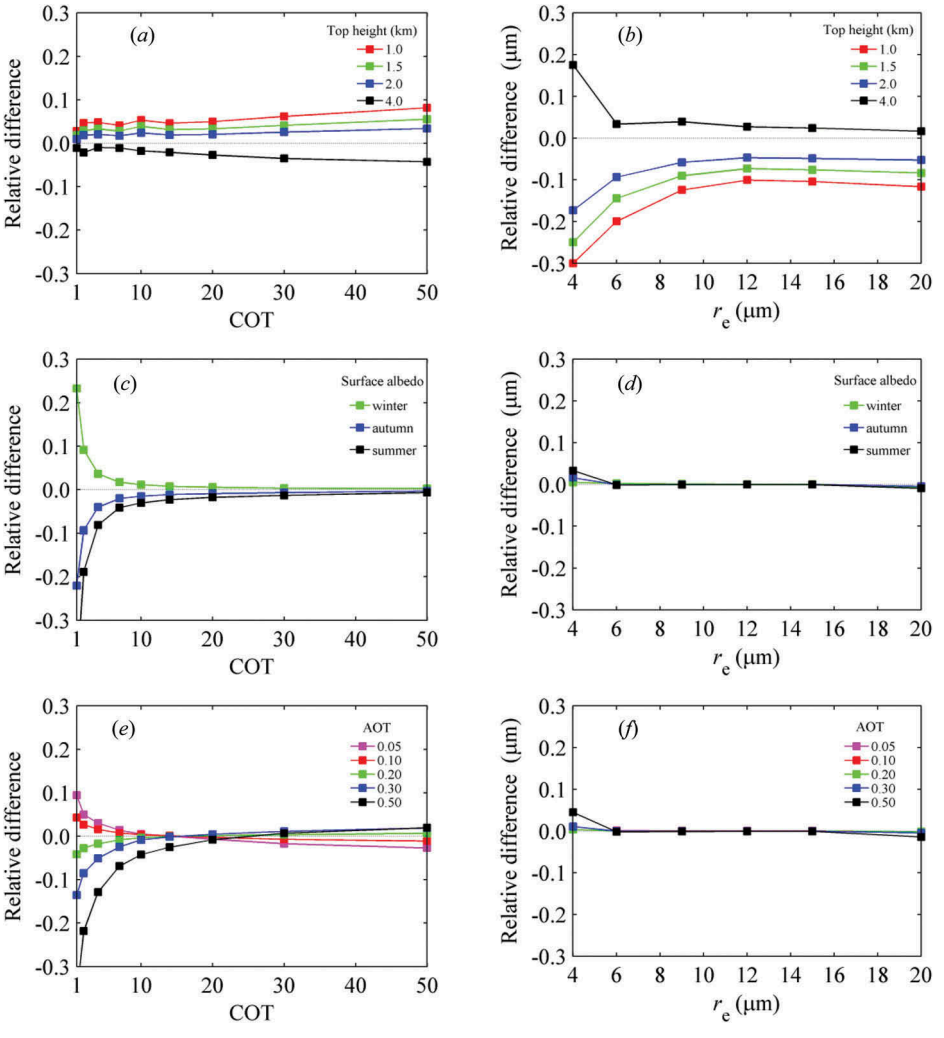

Figure 2. COT and r_e relative differences for water clouds (solar zenith angle of 30° satellite zenith angle of 40°, and relative azimuth angle of 140°) considering different values of cloud top height (a, b), surface albedo (c, d), and aerosol optical thickness (e, f). COT plots (a, c, and e) and r_e plots (b, d, and f) were done considering a fixed value of r_e = 12 μm and COT = 10, respectively.

the range considered in the sensitivity analysis) for intelligibility of the plots. A value of COT equal to 10 was chosen to present the results of r_e uncertainties for both water and ice clouds, whereas the results of COT refer to, r_e values of 12 and 10 μm were chosen for water and ice clouds, respectively. In general, for water and ice clouds, the uncertainties due to the cloud top height variation increase with the COT and decrease with r_e. The maximum values reach around 10% for the highest COT values and for the lowest ice cloud re considered. As for water clouds, the large uncertainties reaching around 30% for small r_e are connected with the fact that a lower initial r_e value is considered with respect to ice clouds; note that for r_e = 7 μm the uncertainties are of the same order both for water and ice clouds. Although the cloud height affects the TOA reflectance in

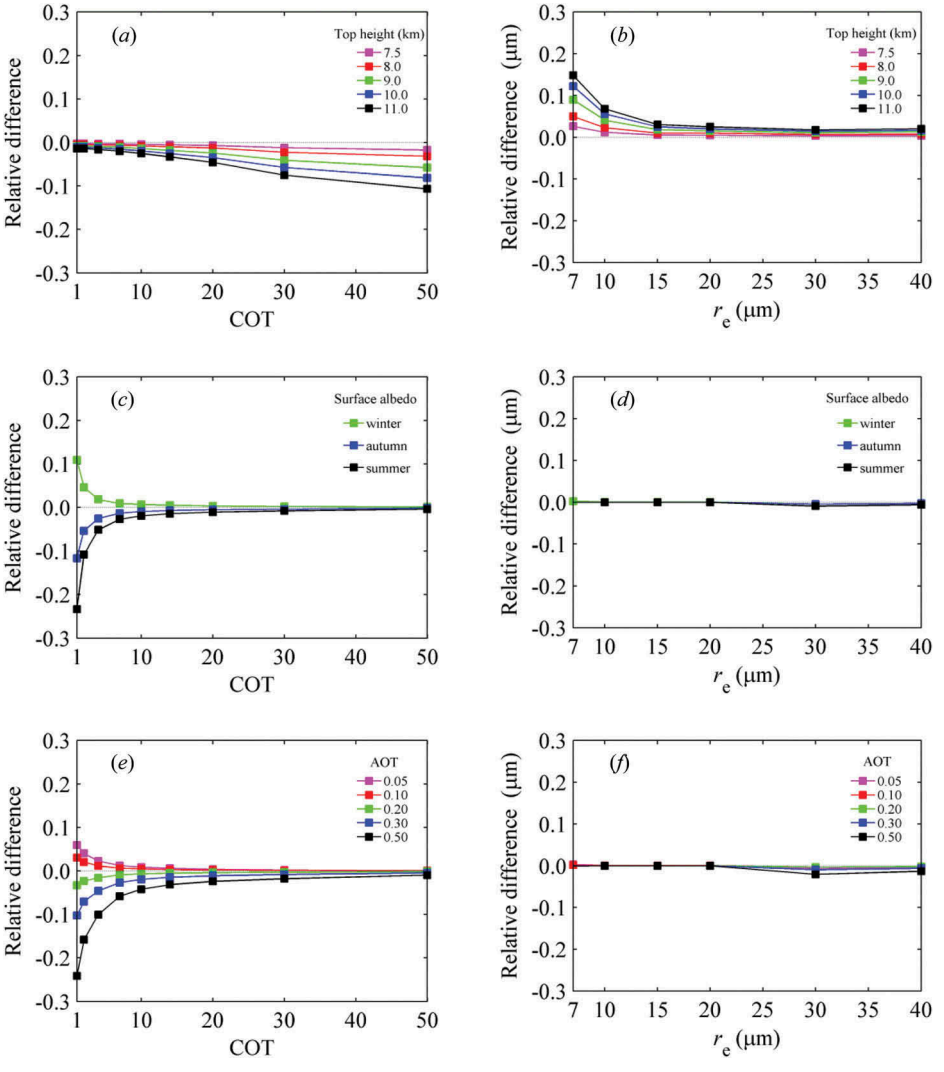

Figure 3. Same as in Figure 2 but for ice clouds. COT plots (a, c, and e) and r_e plots (b, d, and f) were done considering a fixed value of r_e = 10 μm and COT = 10, respectively.

both SW channels used (0.6 and 3.9 μm), the largest effect is on the NIR spectral region reflecting in the greater error of r_e with respect to COT retrievals. The seasonal albedo has little influence on r_e, but for small COT the uncertainties reach values larger than 10%. This happens because for small COT values the reflection from the surface becomes an important component of the reflectance that reaches the satellite, especially in the VIS spectral region; in the NIR, this contribution is less important, which is reflected in the minor effect obtained on r_e. A similar behaviour is found for the aerosol optical thickness, also with the largest uncertainties occurring for small COT values, as expected, since the aerosol role becomes increasingly important in these cases. For water clouds, the aerosol optical thickness has little influence in the r_e values similarly to the surface albedo. The sensitivity analysis of the solar and geometries gives maximum

uncertainties of the order of 3% both for COT and r_e, which may be attributed to the relatively high LUT geometric resolution considered (1°).

3.1.2 COT and r_e retrievals and comparison with independent data

A set of 22 SEVIRI images, covering the Iberian Peninsula (34° N to 44° N and 11° W to 4° E) during the period March–May 2011, were used to retrieve pixel-based COT and r_e values with the described methodology in Subsection 2.1. The values obtained are compared with the corresponding MODIS (MOD06_L2) and CM-SAF (CPP-product) cloud products. SEVIRI images were selected for cases of clouds over the Iberian Peninsula, once a day when the SEVIRI data acquisition time was closer to the acquisition time of MODIS data on board Terra satellite and CPP product, which was available with an hourly frequency. This yielded maximum time differences of 15 min between SEVIRI and MODIS images. Due to the differences in spatial resolution between MODIS and SEVIRI radiometers, the comparison is done by averaging the pixel-based COT and r_e values in a regular longitude–latitude grid of 0.05° × 0.05° considering all cloudy pixels in each grid cell. The averages for water and ice clouds in Table 2 were determined considering only the liquid or ice cloudy pixels in each cell, respectively. The distinction between water and ice clouds was done using the CPS cloud classification, as well as the MOD06_L2 and CPP cloud phase products.

Figure 4(a–f) show the spatial distribution of the COT and r_e mean values obtained with CPS (*a, b*) over the Iberian Peninsula at 11:00 UTC on 1 May 2011. The equivalent MODIS image at 11:05 UTC on the same day was chosen, and the MOD06_L2 COT and r_e mean values are also represented in Figure 4(c,d) as well as the CPP COT and r_e mean values (e,f). In general, the cloud patterns obtained with CPS are very similar to the results from MOD06_L2 and from CPP (Figure 4(a–f)). On the other hand, CPS seems to detect slightly fewer clouds than MOD06_L2 and CPP, which is more visible by the location of the grey areas in r_e figures. This detection of fewer clouds and the tendency to underestimate the r_e values by CPS are related to the inversely proportional relationship between the reflectance at 3.9 μm and r_e, that is, the reflectance at 3.9 μm decreases with increasing r_e, saturating for values higher than 30 μm (Rosenfeld et al. 2004). Therefore, because of this limitation, the method fails in certain ice cloud cases

Table 2. Statistical parameters bias and root mean square error(RMSE) of COT and r_e mean values.

	CPS vs CPP	CPS vs MOD06_L2	
Statistical parameter	All clouds		No. of grid points
Bias COT	1.26	1.74	672552
RMSE COT	7.94	9.58	
Bias r_e (μm)	0.92	1.61	
RMSE r_e (μm)	7.65	6.13	
	Water clouds		
Bias COT	0.47	1.08	204390
RMSE COT	7.62	8.93	
Bias r_e (μm)	2.24	1.32	
RMSE r_e (μm)	4.59	2.98	
	Ice clouds		
Bias COT	0.24	3.79	249841
RMSE COT	7.11	10.06	
Bias r_e (μm)	1.39	0.60	
RMSE r_e (μm)	9.37	7.28	

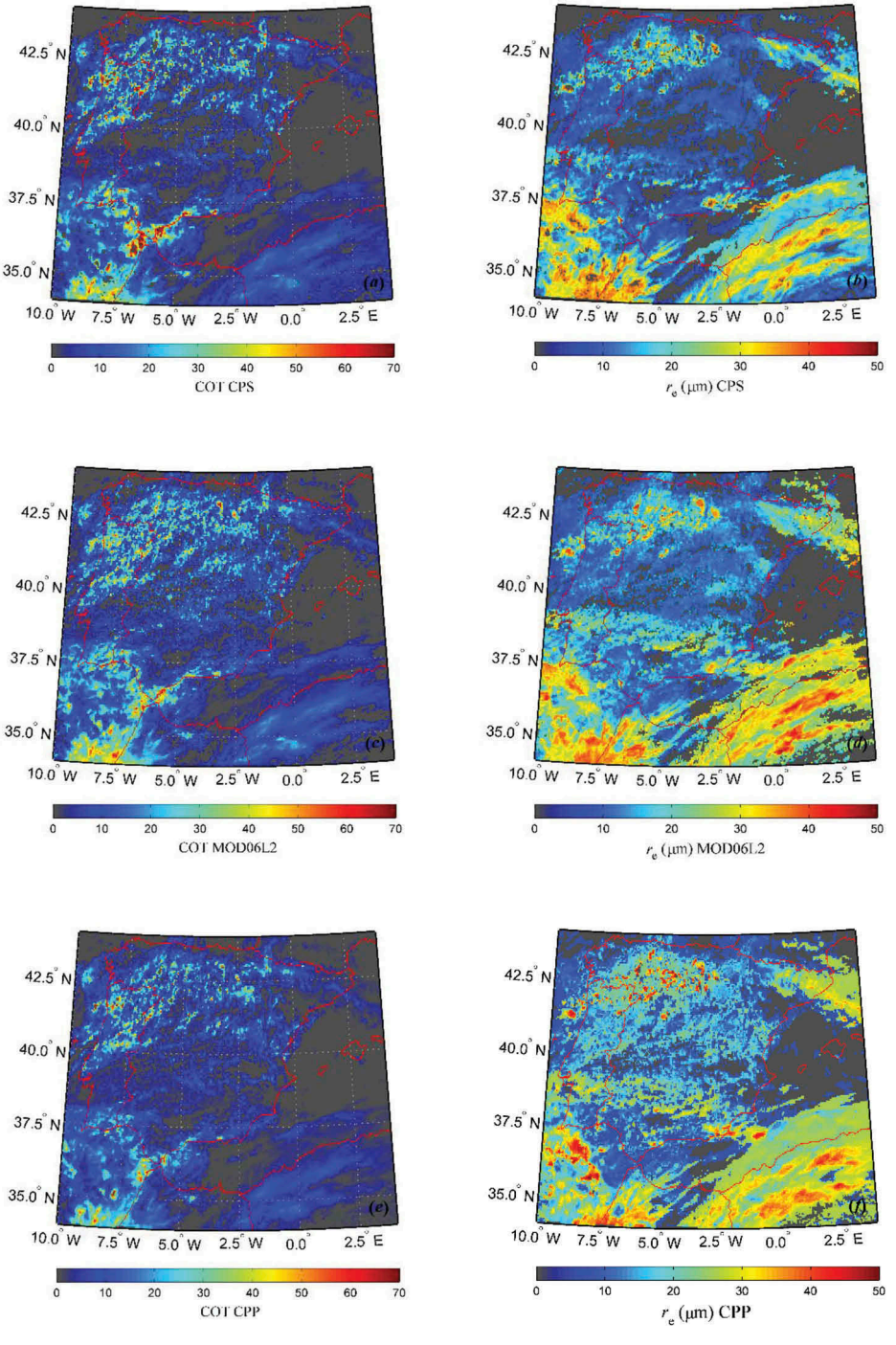

Figure 4. COT and r_e mean values in a regular grid of 0.05° × 0.05° on 1 May 2011 around 11:00 UTC. COT and r_e retrieved using CPS (a, b), MODIS (c, d), and CPP (e, f).

and the cloud properties are not retrieved explaining the detection of fewer clouds by CPS. For instance, in the north of the Iberian Peninsula there are areas in the cloud field where it is visible that the CPS presents some missing values of r_e, while for the same areas MOD06_L2 and CPP present r_e values higher than 40 μm. For all algorithms (CPS, CPP, and MOD06_L2), the COT presents maximum values around 60 in the south as well as in some cloud structures over the north of the Iberian Peninsula. The areas where CPS COT values are missing in the cloud field are the same as for r_e. Yet, it should be noted that the absolute peaks in COT and r_e might not be displayed in the maps due to the spatial average done on the 0.05° × 0.05° grid.

Density scatter plots showing the distribution of COT and r_e mean values between the different algorithms (CPS, CPP, and MOD06_L2) are represented in Figure 5(a–d). These mean values correspond to all clouds (water plus ice) in each grid cell (0.05° × 0.05°) considering the 22 SEVIRI images used. Most of the r_e values are between 0 and

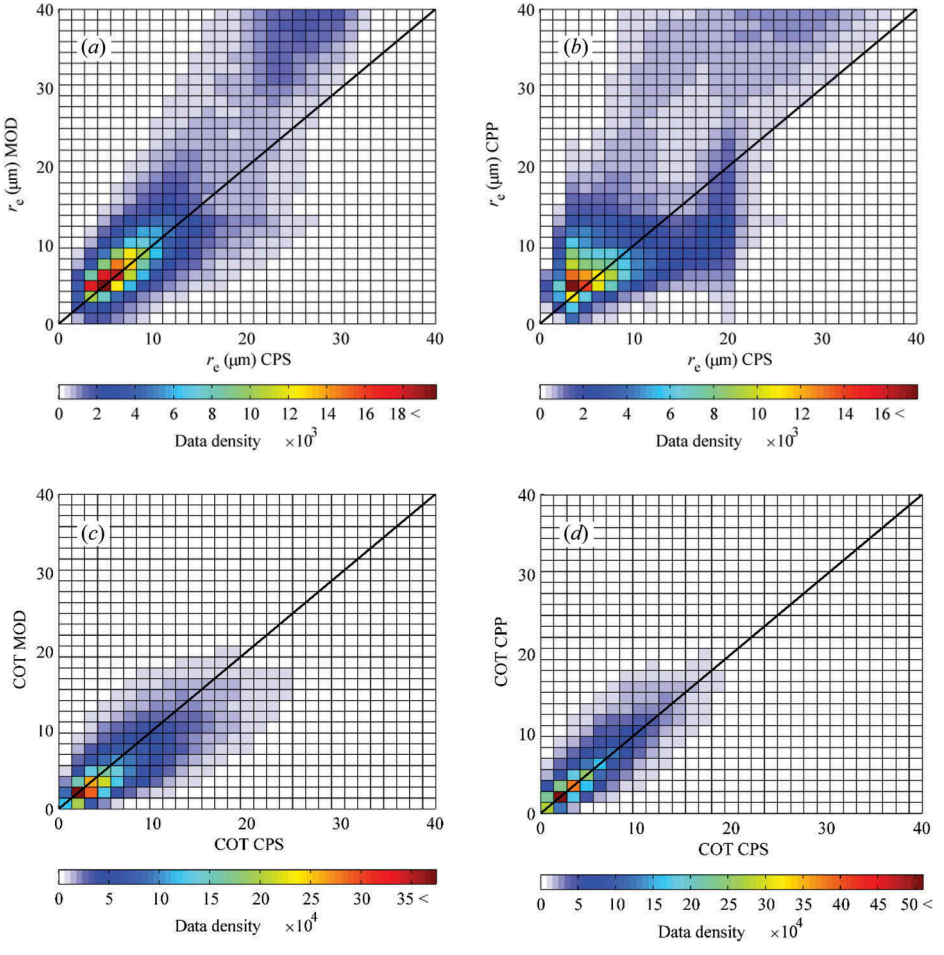

Figure 5. Density scatter plots of r_e (a, b) and COT (c, d) obtained from CPS, CPP, and MOD06_L2 for all data (22 SEVIRI images). These data correspond to averaged values in a regular grid of 0.05° × 0.05° considering all clouds (water plus ice clouds) in each grid cell. The black line represents the 1:1 relation.

15 µm, and the dispersion of the data seems to increase as r_e increases, being higher in the comparison with CPP than with MOD06_L2. The differences with respect to the r_e values are probably also due to differences in the algorithms, since the CPP algorithm weights the retrieved r_e with a climatological value of 8 µm for water clouds and 26 µm for ice clouds, respectively (Stengel et al. 2014). Both cases show the tendency of CPS to slightly underestimate the highest r_e values, which is in accordance with the bias values in Table 2 and related with the aforementioned limitation of the 3.9 µm reflectance that saturates for high r_e values. Still, the data density is low for higher r_e values. In general, the COT values are concentrated between 0 and 40. In both cases, the comparison of COT with the independent algorithms (CPP and MOD06_L2) shows a good agreement with low dispersion of the data. Considering the same data set, the frequency of occurrence of COT and r_e absolute differences between the different algorithms is presented in Figure 6(a,b). Most of the COT absolute differences are centred in the range from 10 to +10 (CPS- MOD06_L2: 80.3% and CPS–CPP: 86.8%). The r_e absolute differences found in the range 10 to +10 µm are 89.7% (CPS-MOD06_L2) and 81.9% (CPS–CPP). The results of bias and root mean square error (RMSE) are presented in Table 2 for all clouds in each grid cell and distinguished between water and ice clouds. These results show that CPS slightly overestimates the CPP COT and underestimates the MOD06_L2 COT in all cases (all clouds, water clouds and ice clouds). The behaviour of the effective radius is slightly different, since the CPS overestimates the CPP r_e for ice clouds and in the remaining cases it underestimates the CPP and MOD06_L2 r_e. The differences found between the different data sets are reasonable because the algorithms used in the comparisons are different. The main differences include the used spectral channel as non-absorbing and absorbing channels, as well as the slightly different image acquisition times and the different spatial resolutions of SEVIRI and MODIS. The CPP

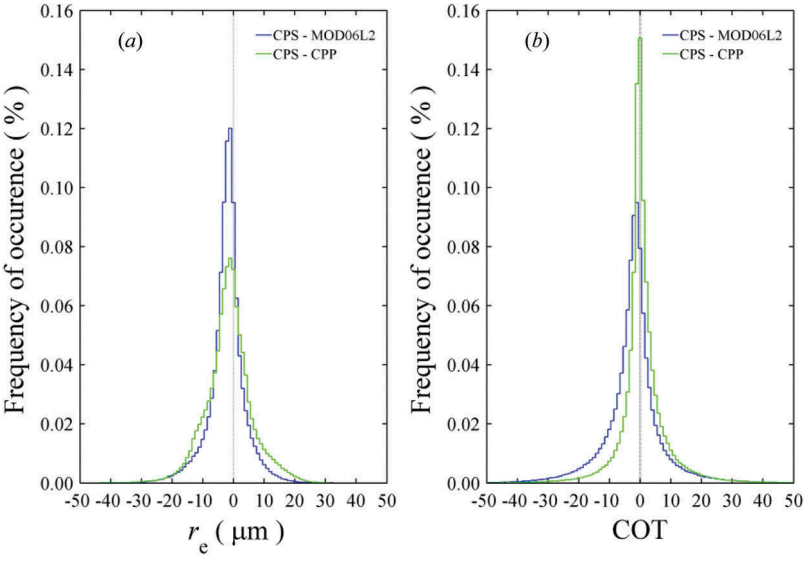

Figure 6. Histograms of the differences between CPS, CPP and MOD06L2 of r_e (a) and COT (b) mean values. These results are for all clouds (water plus ice clouds) in each grid cell of 0.05° × 0.05° using the data of the 22 SEVIRI images considered for the comparisons.

algorithm uses SEVIRI VIS0.6 and NIR1.6 as non-absorbing and absorbing channels, respectively (Stengel et al. 2014). As for MODIS cloud products, the retrieval scheme uses as non-absorbing band (0.65, 0.86, or 1.2 μm) combined with three longer wavelength bands where there is absorption (1.6, 2.1, and 3.7 μm). MOD06_L2 product provides three different effective sizes corresponding to each of the absorbing bands (Baum and Platnick 2006). The comparisons presented in this work were done for MODIS cloud effective radius retrieved at 3.7 μm. Zhang and Platnick (2011) performed a systematic assessment of the difference among effective radius retrieved at 1.6, 2.1, and 3.7 μm of marine water clouds and found that the r_e retrievals at 3.7 μm can be smaller than the ones at 1.6 and 2.1 μm. In addition, for convective clouds the radiation at 3.7 μm is more influenced by the uppermost part of the cloud, while at 1.6 μm the radiation originates from deep inside that same cloud and if the cloud droplets reach the precipitation potential, the r_e at 1.6 μm increases due to the precipitation droplets from the deeper portions of the cloud (Rosenfeld et al. 2004). In general, the retrieved r_e at 3.9 μm tends to be small than the MOD06_L2 r_e (at 3.7 μm) and CPP r_e (at 1.6 μm) as can be seen in Table 2 by the bias values lower than 0. MODIS with a higher spatial resolution is able to identify smaller cloudy or clear sky scenes, consequently for fractional cloud cover regions the TOA reflectances at different spatial resolutions may be considerably different resulting in COT differences between two sensors observing the same scene (Zeng et al. 2012). Cloud classification is another important factor to be considered when analysing the results. Pixel by pixel comparisons between the cloud classification used in CPS and in the CPP cloud phase product showed that both algorithms classify 86.3% of the pixels as clouds and in 72.5% of the cases they agree with the classification (water or ice). Overall results show a good agreement between the method applied and the well-established MOD06_L2 and CPP cloud product algorithms, with absolute bias lower than 2 (2 μm) for COT (r_e) and RMSE values lower than 10 (8 μm) for COT (r_e).

3.2 Cloud effects on the SW radiation at the surface

In this section, the cloud radiative effects at the surface are related with the cloud quantities retrieved with CPS method over Évora region for an area of 0.2° × 0.2° centred in the geographic coordinates of the ICT observatory. This area was chosen because is representative of the characteristics of the Évora site in terms of cloud extension and radiative properties of the surface (Salgueiro et al. 2016). For this purpose, daytime hourly images of SEVIRI covering the study site were collected from January to December 2015. Only cases of cloud contamination (all cloud situations in terms of type and fraction) and of solar zenith angles lower than 70° were selected, yielding a total of 603 images distributed by 124 days (30 days in winter, 34 in spring, 21 in summer, and 39 in autumn). The CPS method was applied to obtain the COT and the droplet effective radius/particle size at the cloud tops for the selected images. These retrieved quantities were then used to derive the cloud water path (CWP; g m ^{2}) using Equation (4) (Stephens 1978), where ρ is the water/ice density. CWP is referred as the vertical integral of cloud condensate, either for liquid clouds (LWP) or ice clouds (IWP). While COT is representative of the extinction of the whole cloud extension, the retrieved r_e is representative of the cloud tops. Thus, to relate the retrieved quantities with CRE_{SW}

at the surface, the CWP is used since it allows for relating simultaneously both quantities, r_e and COT, with the cloud radiative effects. Since the satellite takes approximately 12 min to scan the entire disc, the CRE_{SW} are calculated 10 min after each hour, which roughly corresponds to the scanning time in the study area:

$$CWP \ldots \frac{2}{3} r_e \eth COT \Þ \rho : \tag{4}$$

The SW radiative effects at the surface due to different types of clouds are presented for cases when water and ice clouds produce a surface cooling effect (CRE_{SW} <0) over the study area. These cases were filtered to situations of fractional sky covers (F_{sc}) higher than 0.8, which was considered the lower limit for overcast situations. The F_{sc} was calculated as the ratio between the number of cloudy pixels and the number of total pixels that constitute the study area. This resulted in 79 ice and 112 water cloud situations. The variation of the CRE_{SW} at the surface with the IWP and LWP (average over the study area) is represented in Figure 7(a,b) for different solar zenith angle ranges. In general, water clouds present lower values of LWP (less than 400 g m ^{2}) than ice clouds that present maximum values of IWP around 700 g m ^{2}. Since CWP is obtained from the retrieved cloud parameters (COT and r_e), cases classified as ice clouds may correspond to clouds of vertical development with high COT values that represent all cloud extent. In addition, in these cases if r_e, representing the value in cloud tops, is higher than the mean r_e of the cloud, the IWP can be overestimated justifying the high values showed in Figure 7(a,b). Nevertheless, the magnitude of the CRE_{SW} produced by water clouds is of the same order or higher than ice clouds. The different fittings of the data, although with dispersion, show the tendency of water clouds to produce more negative CRE_{SW} than ice clouds for a same value of CWP and this effect is more pronounced for higher solar zenith angles due to the longer atmospheric path made by radiation. The results shown in Figure 7(a,b) suggest that water clouds are

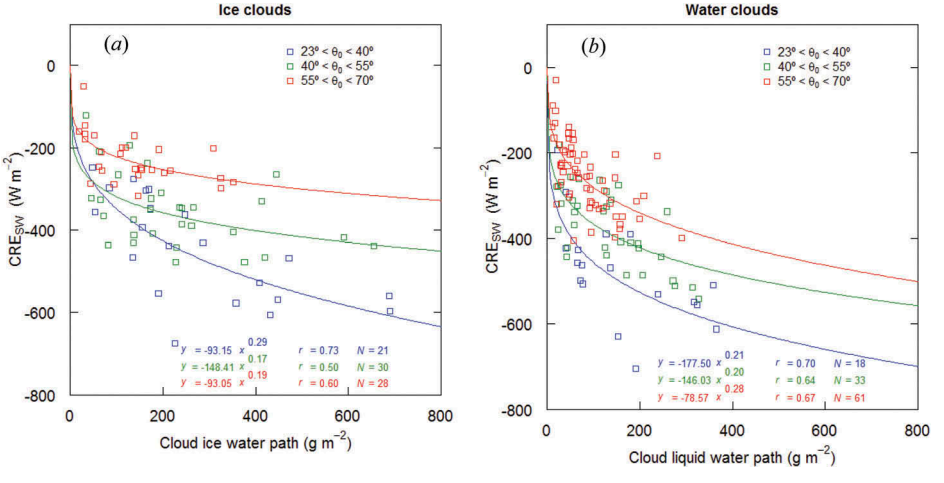

Figure 7. Variation of the CRE_{SW} at the surface with the IWP (a) and LWP (b) for cloud fractions greater than 0.8. The data take different colour according with the solar zenith angle range where they fall; N is the number of data and r is the correlation coefficient.

responsible for a higher CRE_{SW} efficiency than ice clouds. These results also show that the available sunlight is an important factor determining the CRE_{SW} (Boucher et al. 2013). Shupe et al. (2008) also demonstrate that for mixed-phase clouds, there is a strong radiative dominance of cloud liquid water over ice clouds.

The cloud radiative effects on solar radiation can be also expressed in terms of the cloud modification factor (CMF), which is used to characterize the attenuation of radiation by clouds. CMF is defined as the ratio between the measured SW irradiance under cloudy conditions and the estimated SW irradiance in clear-sky conditions, considering that all other atmospheric conditions are kept the same as in the actual measurement (Calbó, Pagès, and Gonzaléz 2005). In general, CMF assumes values lower than the unit. However, there are situations known as enhancement events in which the levels of SW radiation reaching the surface in cloudy conditions are higher than the levels in its corresponding clear sky conditions (Piedehierro et al. 2014). Figure 8 shows the variation of the CMF at the surface with the COT (average over the study area) for different fractional sky covers considering the complete set of data (603 images). It can be observed that the CMF decreases approximately exponentially as COT increases, which is more evident for F_{sc} values higher than 0.6, although with dispersion of the data. Similar results were found for solar ultraviolet radiation under overcast conditions by Antón et al. (2012). Most of the COT mean values are lower than 15, which is in agreement with the results obtained by Salgueiro et al. (2016) for Évora site using ground-based data. For small values of F_{sc}, corresponding to COT lower than 10, the CMF factor presents a large variation spanning from reductions in the SW radiation of the order of 80% (CMF = 0.2) to enhancements larger than 30% (CMF = 1.3), showing that the SW radiation at the surface is very sensitive to changes in clouds translated here by the COT variation. Yet, there are other cases in which CMF takes the value of approximately 1 meaning that clouds have an equivalent effect to clear sky conditions

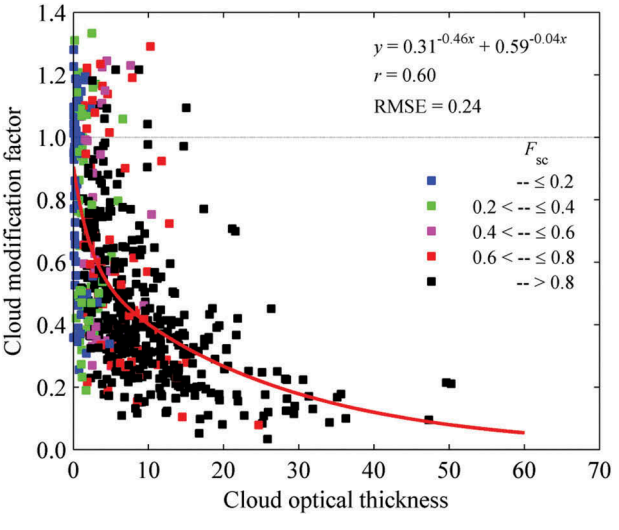

Figure 8. Variation of the experimental cloud modification factor with COT for several fractional sky cover (F_{sc}) values over Évora region.

in the SW radiation that reaches the surface due to multiple scattering by cloud particles.

Although the enhancement events generally occur for relatively low COT values, they are observed for all F_{sc} situations including F_{sc} higher than 0.8 (overcast). These events occurring for high F_{sc} situations are probably related to differences in the F_{sc} value derived from cloud classification by satellite and the true conditions at a sub-pixel scale. Since the enhancements events occur mostly when there is a broken cloud field in the sky without a concrete value of cloud cover (Piedehierro et al. 2014), the enhancement events corresponding to F_{sc} higher than 0.8 in Figure 8 may, therefore, correspond to broken cloud field conditions. These broken cloud fields appear as homogeneous fields of thin clouds at the SEVIRI resolutions (Roebeling, Feijt, and Stammes 2006), while using ground-based sky camera images these fields are shown either as cloud free or as broken clouds.

3.3 Analysis of a case study

To deepen the analysis of these enhancement situations corresponding to F_{sc} >0.8, a day case study (11 June 2015) was selected illustrating also the importance of taking advantage of the 15 min temporal frequency of Metetosat. Images from an all-sky-camera installed at the same site were used to check the cloud cover conditions and are shown for two different times (Figure 9(a,*b*). Figure 9(c) represents the daily series of the SW irradiances at the surface on 11 June 2015: global (tsw), direct (dir), and diffuse (dif) measurements, as well as clear-sky (csw) obtained from the empirical clear sky method proposed by Long and Ackerman (2000) (Subsection 2.2). The corresponding shortwave cloud radiative effects at the surface, CRE_{SW}, are represented simultaneously with the daily evolution of LWP (Figure 9(d)) and with the daily evolution of COT (Figure 9(e)). Both LWP (Figure 9(d)) and COT (Figure 9(e)) derived from satellite retrievals have SEVIRI time resolution (15 min). Note that the clouds presented over the Évora area on 11 June 2015 were classified as water clouds. It is observed that in the morning period the measured SW global irradiance, governed by its diffuse component, is always lower than the clear-sky irradiance and the corresponding CRE_{SW} is always negative. The sky camera image taken at 09:10 UTC shows overcast sky conditions Figure 9(a), which are in accordance with F_{sc} = 1 derived from the corresponding satellite image. In the afternoon, the oscillations of the SW global irradiance between high and low values is characteristic of a broken cloud field and in certain cases the global irradiance exceeds the clear-sky irradiance producing enhancement events with positive CRE_{SW} values and CMF higher than 1. In this situation, the sky camera image at 15:10 UTC (Figure 9(b)) shows that the true conditions are a broken cloud field with a cloud fraction lower than 0.85 responsible for the enhancement event observed at that time, while F_{sc} derived from the satellite image assumes values higher than 0.9.

Figure 9(d) shows the daily evolution of the LWP (left axis) and the corresponding CRE_{SW} (right axis). The red line represents the SEVIRI LWP obtained from the satellite COT and r_e retrievals and using Equation (4), while the blue line represents the LWP obtained from the microwave radiometer ground-based measurements (RPG LWP). The surface measurements of the LWP were averaged for the correspondent 15 min of the SEVIRI LWP. The error bars represent the spatial variability of the SEVIRI LWP calculations (red

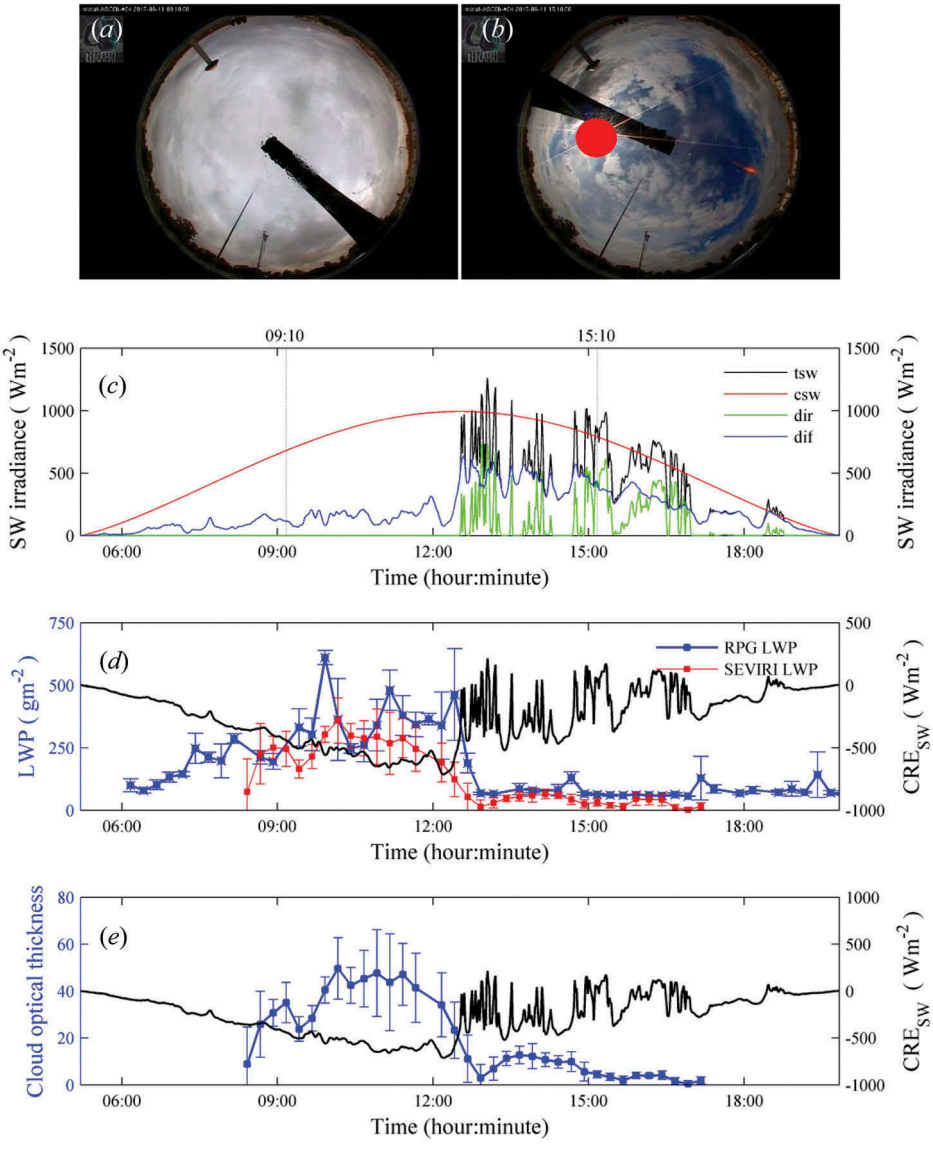

Figure 9. Sky camera images obtained on 11 June 2015 at 09:10 UTC (a) and at 15:10 UTC (b); (c) daily temporal series of SW irradiance, where tsw is the global irradiance, csw is the clear sky irradiance, dir is the direct irradiance and dif is the diffuse SW irradiance; (d) daily temporal series of CRE_{SW} and LWP obtained from surface microwave radiometer measurements (RPG LWP) and from SEVIRI derived data (SEVIRI LWP); (e) daily temporal series of CRE_{SW} and COT.

error bars) in the study area (0.2° × 0.2°) and the temporal variability over the 15 min for RPG LWP measurements (blue error bars). The results show that both LWP lines have a similar pattern and in some cases, they are almost coincident with maximum values in the morning and lower values in the afternoon. Although the two approaches (satellite retrievals and microwave radiometer measurements) refer to two distinct surfaces, the satellite is looking at the top of the clouds and the microwave radiometer is looking at

the bottom of the clouds, the matching of the LWP results is good, evidencing a remarkable LWP closure and showing that it is indeed possible to study clouds from the combined use of satellite and ground-based measurements. The retrieved COT (Figure 9(e)), with the error bars representing the spatial variability in the area considered, exhibits the same pattern as the LWP lines with maximum values during the morning period and lower values in the afternoon. The daily evolution of the cloud quantities, LWP and COT, agrees with the CRE_{SW} evolution as shown in the right axes of Figure 9(d,e). In the morning period, more negative values of CRE_{SW} are produced due to higher values of LWP and COT while in the afternoon the opposite situation is observed. In the afternoon, positive CRE_{SW} values are observed corresponding to the enhancement events, which occur when global irradiance exceeds the clear-sky irradiance, as shown in Figure 9(c). The observed enhancements are typical cases of positive cloud effects as discussed in the original paper of Long and Ackerman (2000). This enhancement effects occur because in the presence of a broken cloud cover (e.g. cumulus or broken stratus) the diffuse component enhances with respect to clear-sky situations due to the increase of scattering (compared to molecular scattering prevailing in clear-sky situations) by the cloud edges. Therefore, the total component results greater than in the clear-sky situations. This is recognized as a local effect in space and time, for example, when averaged in time, clouds are expected to reduce incoming radiation at the surface.

4. Summary and conclusions

The main purpose of this work was to use SEVIRI reflectance measurements to obtain cloud parameters and study the relation between these quantities and the cloud radiative effects at the surface in Évora region. The CPS method used to retrieve the cloud parameters, COT and r_e, is based in the principle of using reflectances in non-absorbing (0.6 μm) and in absorbing (3.9 μm) wavelengths. A sensibility analysis of simulated retrievals to input parameters (cloud top height, surface albedo and aerosol optical thickness) demonstrated that these parameters are important factors in COT and r_e retrievals with large uncertainties around 10% for small values of COT and r_e. It was also demonstrated that for water clouds the uncertainties related to cloud top height can be greater than 10% for small values of r_e. The uncertainties found related with geometry are around 3%. The CPS was tested for a set of 22 images and the obtained COT and r_e were compared with the corresponding MOD06_L2 (based on MODIS measurements) and CPP (based on SEVIRI measurements) cloud products. This comparison was done in terms of average values in a longitude–latitude grid of 0.05° × 0.05° showing that more than 80% (82%) of the absolute differences between COT (r_e) mean values are centred in the range from ±10 (±10 μm) considering all clouds (water plus ice clouds) in each grid cell. In general, the obtained COT (r_e) exhibit a tendency to slightly underestimate (underestimate) the MOD06_L2 COT (r_e) and to overestimate (underestimate) the CPP COT (r_e).

The CPS, able to characterize the cloud field in terms of COT and r_e evolution, was used to retrieve COT and r_e of the hourly images over Évora region during 2015. The CWP obtained from COT and r_e satellite retrievals and the COT were related with the CRE_{SW} and CMF. The relation between CWP and CRE_{SW} for F_{sc} greater than 0.8, considered as overcast conditions, revealed that the liquid water clouds exhibit a tendency to produce more negative CRE_{SW} than ice clouds. This behaviour was more pronounced for high solar zenith angles. The CMF,

translating the attenuation of radiation by clouds, exhibited approximately an exponential decrease with COT increasing for high fractional sky covers. It was found that for low fractional sky covers, the CMF presents a large variation with reductions of 80% and enhancements of 30% of the SW radiation for small COT values (<10). Yet, this relation between the CMF and the COT revealed that some enhancement events are included in situations classified as overcast (F_{sc} >0.8). Some enhancement events occurring for F_{sc} >0.8 were analysed in a case study using ground-based sky camera images. This allows to conclude that certain situations classified by satellite with high F_{sc} values (>0.9) are situations of broken clouds, ideal to produce radiation enhancements at the surface. Yet, the evolution of the cloud parameters (LWP and COT) obtained from satellite measurements is in good agreement with the CRE_{SW} evolution obtained from surface measurements and the SEVIRI LWP follows the same tendency as the LWP obtained from ground-based measurements. This also shows the very good LWP closure attained and shows the importance to combine satellite data with surface measurements to study clouds and their radiative effects.

Acknowledgements

This work was financed through FCT (the Portuguese Science and Technology Foundation) grant SFRH/BD/88669/2012. The work is co-funded by the European Union through the European Regional Development Fund, included in the COMPETE 2020 (Operational Program Competitiveness and Internationalization) through the ICT project (UID / GEO / 04683/2013) with the reference POCI-01-0145-FEDER-007690 and also through the ALOP project (ALT20-03-0145-FEDER-000004). METEOSAT imagery was kindly made available by EUMETSAT Data Centre Online Ordering (https://eoportal.eumetsat.int). The MODIS Cloud product was acquired from the Level-1 & Atmosphere Archive and Distribution System (LAADS) Distributed Active Archive Center (DAAC), located in the Goddard Space Flight Center in Greenbelt, Maryland (https://ladsweb.nascom.nasa.gov/). This work also made use of data from EUMETSAT Satellite Application Facility on Climate Monitoring (CM SAF) obtained from the web user interface (https://wui.cmsaf.eu). Thanks are due to Chuck Long (NOAA affiliated) that provided short wave clear identification and cloud cover analysis programmes.

Disclosure statement

No potential conflict of interest was reported by the authors.

Funding

This work was financed through FCT (the Portuguese Science and Technology Foundation) grant SFRH/BD/88669/2012. The work is co-funded by the European Union through the European Regional Development Fund, included in the COMPETE 2020 (Operational Program Competitiveness and Internationalization) through the ICT project (UID / GEO / 04683/2013) with the reference POCI-01-0145-FEDER-007690 and also through the ALOP project (ALT20-03-0145-FEDER-000004).

ORCID

Vanda Salgueiro http://orcid.org/0000-0003-0169-9231
Maria João Costa http://orcid.org/0000-0003-2981-2232

Ana Maria Silva http://orcid.org/0000-0003-2002-4774
Christian Lanconelli http://orcid.org/0000-0002-9545-1255
Daniele Bortoli http://orcid.org/0000-0002-2334-4055

References

Allan, R. P. 2011. "Combining Satellite Data and Models to Estimate Cloud Radiative Effect at the Surface and in the Atmosphere." *Meteorological Applications* 18: 324–333. doi:10.1002/met.285.

Anderson, G. P., S. A. Clough, F. X. Kneizys, J. H. Chetwynd, and E. P. Shettle, 1986, *AFGL Atmospheric Constituent Pro les (0-120 Km). AFGL-TR-86-0110, ADA175173, Air Force Geophysics Laboratory*, Hanscom Air Force Base, Bedford, MA.

Antón, M., L. Alados-Arboledas, J. L. Guerrero-Rascado, M. J. Costa, J. C. Chiu, and F. J. Olmo. 2012. "Experimental and Modeled UV Erythemal Irradiance under Overcast Conditions: The Role of Cloud Optical Depth." *Atmospheric Chemistry and Physics* 12: 11723–11732. doi:10.5194/acp-12-11723-2012.

Baum, B. A., A. J. Heymsfield, P. Yang, and S. T. Bedka. 2005a. "Bulk Scattering Properties for the Remote Sensing of Ice Clouds. Part I: Microphysical Data and Models." *Journal of Applied Meteorology* 44: 1885–1895. doi:10.1175/JAM2308.1.

Baum, B. A., and S. Platnick. 2006. "Introduction to MODIS Cloud Products." In *Earth Science Satellite Remote Sensing Vol. 1: Science and Instruments*, Edited by J. J. Qu, W. Gao, M. Kafatos, R. E. Murphy, and V. V. Salomonson. co-published by Tsinghua University Press (Beijing) and Springer-Verlag (Berlin, Heidelberg). doi:10.1007/978-3-540-37293-6_5.

Baum, B. A., P. Yang, A. J. Heymsfield, S. Platnick, M. D. King, Y.-X. Hu, and S. T. Bedka. 2005b. "Bulk Scattering Properties for the Remote Sensing of Ice Clouds. Part II: Narrowband Models." *Journal of Applied Meteorology* 44: 1896–1911. doi:10.1175/JAM2309.1.

Belward, A., and T. Loveland. 1996. "The DIS 1km Land Cover Data Set." *IGBP Global Change Newsletter* 27: 7–9.

Berg, L. K., E. I. Kassianov, C. N. Long, and D. L. Mills Jr. 2011. "Surface Summertime Radiative Forcing by Shallow Cumuli at the Atmospheric Measurement Southern Great Plains Site." *Journal of Geophysical Research* 116: 1–13. doi:10.1029/2010JD014593.

Bojanowski, S. J., A. Vrieling, and A. K. Skidmore. 2014. "A Comparison of Data Sources for Creating A Long-Term Time Series of Daily Gridded Solar Radiation for Europe." *Solar Energy* 99: 152–171. doi:10.1016/j.solener.2013.11.007.

Boucher, O., D. Randall, P. Artaxo, C. Bretherton, G. Feingold, P. Forster, and V.-M. Kerminen. 2013. "Clouds and Aerosols. Chap. 7 in Climate Change 2013: The Physical Science Basis." In *Contribution of Working Group I to the Fifth Assessment Report of the Intergovernmental Panel on Climate Change*, eds.)] T. F. Stocker, D. Qin, G.-K. Plattner, M. Tignor, S. K. Allen, J. Boschung, A. Nauels, et al. United Kingdom and New York, NY, USA: Cambridge University Press, Cambridge.

Bugliaro, L., T. Zinner, C. Keil, B. Mayer, R. Hollmann, M. Reuter, and W. Thomas. 2011. "Validation of Cloud Property Retrievals with Simulated Satellite Radiances: A Case Study for SEVIRI." *Atmospheric Chemistry and Physics* 11: 5603–5624. doi:10.5194/acp-11-5603-2011.

Calbó, J., D. Pagès, and J.-A. Gonzaléz. 2005. "Empirical Studies of Cloud Effects on UV Radiation: A Review." *Reviews of Geophysics* 43: RG2002. doi:10.1029/2004RG000155.

Calisto, M., D. Folini, M. Wild, and L. Bengtsson. 2014. "Cloud Radiative Forcing Intercomparison between Fully Coupled CMIP5 Models and CERES Data." *Annales Geophysicae* 32: 793–807. doi:10.5194/angeo-32-793-2014.

Cess, R. D., G. L. Potier, J. P. Blanchet, G. J. Boer, S. J. Ghan, J. T. Kiehl, H. Le Treut, et al. 1989. "Interpretation of Cloud-Climate Feedback as Produced by 14 Atmospheric General Circulation Models." *Science* 245: 513–516. doi:10.1126/science.245.4917.513.

Charvát, Z., 2007, Notes on Calculation of the SEVIRI Band IR3.9 Reflectivity. In *Joint* 2007 EUMETSAT Meteorological Satellite Conference and the 15th Satellite Meteorology and

Oceanography Conference of the American Meteorological Society, Amsterdam, Netherlands, EUMETSAT P.50. ISBN 92-9110-079-X.

Costa, M. J., E. Cattani, V. Levizzani, and A. M. Silva. 2007. "Cloud Microphysical Properties Retrieval during Intense Biomass Burning Events over Africa and Portugal". In *Measuring Precipitation from Space Advances in Global Change Research*, Ed. V. Levizzani, P. Bauer, and F. Joseph Turk, 97–111. Dordrecht, Netherlands: Springer. doi:10.1007/978-1-4020-5835-6_8.

Dong, X., B. Xi, and P. Minnis. 2006. "A Climatology of Midlatitude Continental Clouds from ARM SGP Central Facility. Part II: Cloud Fraction and Surface Radiative Forcing." *Journal of Climate* 19: 1765–1783. doi:10.1175/JCLI3710.1.

EUMETSAT, 2012, The Conversion from Effective Radiances to Equivalent Brightness Temperatures. Available online at: At https://www.eumetsat.int (accessed22 October 2016)

Harrison, E. F., P. Minnis, B. R. Barkstrom, V. Ramanathan, R. D. Cess, and G. G. Gibson. 1990. "Seasonal Variation of Cloud Radiative Forcing Derived from Earth Radiation Budget Experiment." *Journal of Geophysical Research* 95: 18703–186887. doi:10.1029/JD095iD11p18687.

Jolivet, D., and A. J. Feijt. 2003. "Cloud Thermodynamic Phase and Particle Size Estimation Using the 0.67 and 1.6 μm Channels from Meteorological Satellites." *Atmospheric Chemistry and Physics Discussion* 3: 4461–4488. doi:10.5194/acpd-3-4461-2003.

Kaufman, Y. J., and T. Nakajima. 1992. "Effect of Amazon Smoke on Cloud Microphysics and Albedo – Analysis from Satellite Imagery." *Journal of Applied Meteorology* 32: 729–744. doi:10.1175/1520-0450(1993)032<0729:EOASOC>2.0.CO;2.

King, M. D., S.-C. Tsay, S. E. Platnick, M. Wang, and K.-N. Liou, 1997, Cloud Retrieval Algorithms for MODIS: Optical Thickness, Effective Particle Radius and Thermodynamic Phase. MODIS Algorithm Theoretical Basis Document No. ATBD-MOD-05, MOD06 – Cloud product, version 5.

Long, C. N., and T. P. Ackerman. 2000. "Identification of Clear Skies from Broadband Pyranometer Measurements and Calculation of Downwelling Shortwave Cloud Effects." *Journal of Geophysical Research* 105: 15609–15626. doi:10.1029/2000JD900077.

Mateos, D., M. Antón, A. Valenzuela, A. Cazorla, F. J. Olmo, and L. Alados-Arboledas. 2014a. "Efficiency of Clouds on Shortwave Radiation Using Experimental Data." *Applied Energy* 113: 1216–1219. doi:10.1016/j.apenergy.2013.08.060.

Mateos, D., G. Pace, D. Meloni, J. Bilbao, A. di Sarra, A. de Miguel, G. Casasanta, and Q. Min. 2014b. "Observed Influence of Liquid Cloud Microphysical Properties on Ultraviolet Surface Radiation." *Journal of Geophysical Research Atmospheres* 119: 2429–2440. doi:10.1002/2013JD020309.

Mayer, B., and A. Kylling. 2005. "Technical Note: The Libradtran Software Package for Radiative Transfer Calculations – Description and Examples of Use." *Atmospheric Chemistry and Physics* 5: 1855–1873. doi:10.5194/acp-5-1855-2005.

Meirink, J. F., 2013, Algorithm Theoretical Basis Document Cloud Physical Products SEVIRI. EUMETSAT Satellite Application Facility on Climate Monitoring, Available online at: www.cmsaf.eu (accessed 10 November 2016) DOI: 10.5676/EUMETSAT_SAF_CM/CLAAS/V001.

Min, Q., E. Joseph, Y. Lin, L. Min, B. Yin, P. H. Daum, L. I. Kleinman, J. Wang, and Y.-N. Lee. 2012. "Comparison of MODIS Cloud Microphysical Properties with In-Situ Measurements over the Southeast Pacific." *Atmospheric Chemistry and Physics* 12: 11261–11273. doi:10.5194/acp-12-11261-2012.

Nakajima, T., and M. D. King. 1990. "Determination of the Optical Thickness and Effective Particle Radius of Clouds from Reflected Solar Radiation Measurements. Part I: Theory." *Journal of the Atmospheric Sciences* 47: 1878–1893. doi:10.1175/1520-0469(1990)047<1878:DOTOTA>2.0.CO;2.

Nakajima, T. Y., and T. Nakajima. 1995. "Wide-Area Determination of Cloud Microphysical Properties from NOAA AVHRR Measurements for FIRE and ASTEX Regions." *Journal of the Atmospheric Sciences* 52: 4043–4059. doi:10.1175/1520-0469(1995)052<4043:WADOCM>2.0.CO;2.

Oreopoulos, L., and W. B. Rossow. 2011. "The Cloud Radiative Effects of International Cloud Climatology Project Weather States." *Journal of Geophysical Research* 116: D12202. doi:10.1029/2010JD015472.

Painemal, D., and P. Zuidema. 2011. "Assessment of MODIS Cloud Effective Radius and Optical Thickness Retrievals over the Southeast Pacific with VOCALS-Rex in Situ Measurements." *Journal of Geophysical Research* 116: D24206. doi:10.1029/2011JD016155.

Piedehierro, A. A., M. Antón, A. Cazorla, L. Alados-Arboledas, and F. J. Olmo. 2014. "Evaluation of Enhancement Events of Total Solar Irradiance during Cloudy Conditions at Granada (Southeastern Spain)." *Atmospheric Research* 135-136: 1–7. doi:10.1016/j.atmosres.2013.08.008.

Pierluissi, J. H., and G.-S. Peng. 1985. "New Molecular Transmission Band Models for LOWTRAN." *Optical Engineering* 24: 541–547. doi:10.1117/12.7973523.

Raes, F., T. S. Bates, F. M. McGovern, and M. Van Liedekerke. 2000. "The 2nd Aerosol Characterization Experiment (ACE-2): General Overview and Main Results." *Tellus B* 52 (2): 111–125. doi:10.1034/j.1600-0889.2000.00124.x.

Ramanathan, V., R. D. Cess, E. F. Harrison, P. Minnis, B. R. Barkstrom, E. Ahmad, and D. Hartmann. 1989. "Cloud-Radiative Forcing and Climate: Results from the Earth Radiation Budget Experiment." *Science* 243: 57–63. doi:10.1126/science.243.4887.57.

Ricchiazzi, P., S. Yang, C. Gautier, and D. Sowle. 1998. "SBDART: A Research and Teaching Software Tool for Plane-Parallel Radiative Transfer in the Earth's Atmosphere." *Bulletin of the American Meteorological Society* 79: 2101–2114. doi:10.1175/1520-0477(1998)079<2101:SARATS>2.0.CO;2.

Roebeling, R. A., A. J. Feijt, and P. Stammes. 2006. "Cloud Property Retrievals for Climate Monitoring: Implications of Differences between Spinning Enhanced Visible and Infrared Imager (SEVIRI) on METEOSAT-8 and Advanced Very High Resolution Radiometer (AVHRR) on NOAA-17." *Journal of Geophysical Research* 111: D20210. doi:10.1029/2005JD006990.

Rose, T., S. Crewell, U. Lohnert, and C. Simmer. 2005. "A Network Suitable Microwave Radiometer for Operational Monitoring of the Cloudy Atmosphere." *Atmospheric Research* 75: 183–200. doi:10.1016/j.atmosres.2004.12.005.

Rosenfeld, D., E. Cattani, S. Melani, and V. Levizzani. 2004. "Considerations on Daylight Operation of 1.6 versus 3.7-μm Channel on NOAA and METOP Satellites." *Bulletim of the American Meteorological Society* 873–879. doi:10.1175/BAMS-85-6-873.

Salgueiro, V., M. J. Costa, A. M. Silva, and D. Bortoli. 2014. "Variability of the Daily-Mean Shortwave Cloud Radiative Forcing at the Surface at a Midlatitude Site in Southwestern Europe." *Journal of Climate* 27: 7769–7780. doi:10.1175/JCLI-D-13-00696.1.

Salgueiro, V., M. J. Costa, A. M. Silva, and D. Bortoli. 2016. "Effects of Clouds on the Surface Shortwave Radiation at a Rural Inland Mid-Latitude Site." *Atmospheric Research* 178-179: 95–101. doi:10.1016/j.atmosres.2016.03.020.

Santos, D., M. J. Costa, and A. M. Silva. 2008. "Direct SW Aerosol Radiative Forcing over Portugal." *Atmospheric Chemistry and Physics* 8: 5771–5786. doi:10.5194/acp-8-5771-2008.

Schiffer, R. A., and W. B. Rossow. 1983. "The International Satellite Cloud Climatology Project (ICCP): The First Project of the World Climate Research Programme." *Bulletin of American Meteorological Society* 64: 779–784.

Schmetz, J., P. Pili, S. Tjemkes, D. Just, J. KerkMann, S. Rota, and A. Ratier. 2002. "An Introduction to Meteosat Second Generation (MSG)." *Bulletin of the American Meteorological Society* 83: 977–992. doi:10.1175/1520-0477(2002)083<0977:AITMSG>2.3.CO;2.

Schulz, J., P. Albert, H.-D. Behr, D. Caprion, H. Deneke, S. Dewitte, B. Dürr, et al. 2009. "Operational Climate Monitoring from Space: The EUMETSAT Satellite Application Facility on Climate Monitoring (CM-SAF)". *Atmospheric Chemistry and Physics* 9: 1687–1709. 10.5194/acp-9-1687-2009.

Shettle, E. P. 1989. "Models of Aerosols, Clouds and Precipitation for Atmospheric Propagation Studies." In *AGARD Conference Proceedings CP No. 454, Atmospheric Propagation in the UV, Visible, IR and Mm-Region and Related System Aspects*, *Advisory Group for Aerospace Research and Development, NATO*. October 9–13. Denmark: Copenhagen.

Shupe, M. D., J. S. Daniel, G. De Boer, E. W. Eloranta, P. Kollias, C. N. Long, E. P. Luke, D. D. Turner, and J. Verlinde. 2008. "A Focus on Mixed-Phase Clouds: The Status of Ground-Based Observational Methods." *Bulletin of the American Meteorological Society* 1549–1562. doi:10.1175/2008BAMS2378.1.

Silva, A. M., M. L. Bugalho, M. J. Costa, W. von Hoyningen-Huene, T. Schmidt, J. Heintzenberg, and S. Henning. 2002. "Aerosol Optical Properties from Columnar Data during the Second Aerosol Characterization Experiment on the South Coats of Portugal." *Journal of Geophysical Research* 107: D22. doi:10.1029/2002JD002196.

Stamnes, K., S.-C. Tsay, W. Wiscombe, and I. Laszlo, 2000, DISORT a general-purpose Fortran program for discrete-ordinate method radiative transfer in scattering and emitting layered media: Documentation of methodology. NASA Tech. Rep., 112 pp.

Stengel, M. S., A. K. Kniffka, J. F. Meirink, M. L. Lockhoff, J. T. Tan, and R. H. Hollmann. 2014. "CLAAS: The CM SAF Cloud Property Data Set Using SEVIRI." *Atmospheric Chemistry and Physics* 14: 4297–4311. doi:10.5194/acp-14-4297-2014.

Stephens, G. L. 1978. "Radiation Profiles in Extended Water Clouds. II: Parameterization Schemes." *Journal of the Atmospheric Sciences* 35: 2123–2132. doi:10.1175/1520-0469(1978)035<2123:RPIEWC>2.0.CO;2.

Zeng, S., C. Cornet, F. Parol, J. Riedi, and F. Thieuleux. 2012. "A Better Understanding of Cloud Optical Thickness Derived from the Passive Sensors MODIS/AQUA and POLDER/PARASOL in the A-Train Constellation." *Atmospheric Chemistry and Physics* 12: 11245–11259. doi:10.5194/acp-12-11245-2012.

Zhang, Z., and S. Platnick. 2011. "An Assessment of Differences between Cloud Effective Particle Radius Retrievals for Marine Water Clouds from Three MODIS Spectral Bands." *Journal of Geophysical Research* 116: D20215. doi:10.1029/2011JD016216.

Solar Energy 236 (2022) 225–238

Contents lists available at ScienceDirect

Solar Energy

journal homepage: www.elsevier.com/locate/solener

Method for solar resource assessment using numerical weather prediction and artificial neural network models based on typical meteorological data: Application to the south of Portugal

Sara Pereira [a,*], Edgar F.M. Abreu [a], Maksim Iakunin [a], Afonso Cavaco [a,b], Rui Salgado [a,c], Paulo Canhoto [a,d]

[a] Institute of Earth Sciences, University of Évora, Évora, Portugal
[b] Renewable Energies Chair, University of Évora, Évora, Portugal
[c] Physics Department, University of Évora, Évora, Portugal
[d] Department of Mechatronics Engineering, University of Évora, Évora, Portugal

ARTICLE INFO

Keywords:
Solar radiation
Solar energy
Site adaptation
Typical meteorological year
Numerical weather prediction
Artificial neural network

ABSTRACT

In this work a method for regional solar resource assessment based on numerical weather prediction (NWP) and artificial neural network (ANN) models is presented. The method was developed using typical meteorological and solar radiation data and applied to the location of Évora, Portugal with the goal of assessing solar global horizontal (GHI) and direct normal (DNI) irradiations with 1.25 km of horizontal resolution in the south of Portugal. The NWP model used was the research model Meso-NH and a site adaptation model was developed based in ANNs and using as inputs the simulated meteorological variables from Meso-NH and aerosol data from Copernicus Atmospheric Monitoring Services (CAMS) for the observation site. The resulting annual relative mean bias errors for GHI and DNI at Évora and typical meteorological year are of 0.55 % and 0.98 %, respectively, while the values for the original Meso-NH simulations are of 8.24 % for GHI and 31.71 % for DNI. The developed site adaptation model is applied to the region for the purpose of solar radiation assessment and validated using data from a network of solar radiation measuring stations scattered throughout the south of Portugal, showing relative mean bias errors of 2.34 % for GHI and 3.41 % for DNI, while the original Meso-NH simulations presents relative mean bias errors of 8.50 % and 29.54 %, respectively. These results allowed the generation of improved solar resource availability maps which are a very useful tool in solar resource assessment, the study of shortwave radiative climate, as well as project planning and solar system design and operation.

1. Introduction

The solar energy industry has been growing since the 1990s mainly in response to environmental issues related to the use of fossil fuels. At the end of 2020, the total installed power worldwide was of 707 GW for photovoltaic technologies and 6.5 GW for solar concentration systems (International Renewable Energy Agency (IRENA), 2021). The number of new solar energy systems is expected to grow in the future as countries aim for low-carbon alternatives for electricity generation. Thus, a reliable assessment of the solar resource and solar radiation forecast tools are crucial as they are helpful not only for the understanding of the climate of the Earth but also for project planning and energy systems design and operation.

Solar radiation comprises two components, the direct normal irradiation (DNI), which is the direct beam on a plane perpendicular to the rays of the sun, and the diffuse irradiation, usually measured on a horizontal plane (DHI - diffuse horizontal irradiation). The total irradiation on a horizontal surface is known as Global Horizontal Irradiation (GHI). If the surface of interest is tilted, a photovoltaic panel or a solar thermal collector for instance, then a third component must be considered, which is the solar radiation reflected on the ground and surrounding objects. On the other hand, if the focus is solar concentration systems the component of interest is DNI, including circumsolar irradiance.

Ground-based measurements of solar irradiance are usually made by pyranometers for the global or diffuse components and by pyrheliometers for the direct normal component and can be used to assess the solar resource in a specific location or in a region using observations from

* Corresponding author.
E-mail address: spereira@uevora.pt (S. Pereira).

https://doi.org/10.1016/j.solener.2022.03.003
Received 15 November 2021; Received in revised form 29 January 2022; Accepted 2 March 2022
Available online 10 March 2022
0038-092X/© 2022 International Solar Energy Society. Published by Elsevier Ltd. All rights reserved.

Nomenclature

ALBD	Direct albedo (–)
ALBS	Scattered albedo (–)
AOD469	Aerosol optical depth at 469 nm (–)
AOD550	Aerosol optical depth at 550 nm (–)
AOD670	Aerosol optical depth at 670 nm (–)
AOD865	Aerosol optical depth at 865 nm (–)
AOD1240	Aerosol optical depth at 1240 nm (–)
avgCF	Vertical average cloud fraction (–)
DHI	Diffuse horizontal irradiation (Wh/m^2)
DNI	Direct normal irradiation (Wh/m^2)
DUAOD	Dust aerosol optical depth at 550 nm (–)
GHI	Global horizontal irradiation (Wh/m^2)
maxCF	Vertical maximum cloud fraction (–)
MSE_{rd}	Relative mean squared error difference (%)
OMAOD	Organic matter aerosol optical depth at 550 nm (–)
SSAOD	Sea salt aerosol optical depth at 550 nm (–)
T	Air temperature (°C)
WD	Wind direction (°)
WS	Wind speed (m/s)

Acronyms

ANN	Artificial Neural Network
CAMS	Copernicus Atmosphere Monitoring Service
CDF	Cumulative Distribution Function
ECMWF	European Centre for Medium-range Weather Forecasts
FS	Finkelstein-Schaffer
IFS	Integrated Forecasting System
NWP	Numerical Weather Prediction
MBE	Mean Bias Error
MSE	Mean Squared Error
RMSE	Root Mean Squared Error
RRTM	Rapid Radiation Transfer Model
TMM	Typical Meteorological Month
TMY	Typical Meteorological Year

different locations (Feng et al., 2021; Scharmer and Greif, 2000). For regional resource assessment, it would be ideal to have observations made throughout a long period of time in multiple sites and in a somewhat gridded layout. Such network, however, is difficult to install and maintain.

Once long-term data series are available for a given location, a way to assess solar resource is generating a Typical Meteorological Year (TMY) by concatenating typical meteorological months of real measurements that reproduce the long-term statistics. These are useful for energy simulation of solar power plants and buildings, either to determine their thermal response under different environmental conditions or to design and simulate integrated renewable energy systems. A TMY generated for solar resource assessment is composed of solar radiation and other meteorological variables during a period of one year (Lhendup and Lhundup, 2007) usually including mean and extreme values of temperature, wind and relative humidity.

The first version of TMY was developed using the Sandia method proposed by I. J. Hall et al. (1978). The National Renewable Energy Laboratory (NREL) has developed a second (TMY2) (Marion and Urban, 1995) and third version (TMY3) (Wilcox and Marion, 2008) by slightly modifying the process of selecting the typical months. Regardless of the method used, the TMY has been recently used in applications related to solar energy as reported in the literature (Al-Azri and Al-Saadi, 2018; Ernst and Gooday, 2019; Huld et al., 2018; Ohunakin et al., 2018).

In addition to observations, satellite data (Polo and Perez, 2019; Yang and Gueymard, 2019) and numerical weather prediction (NWP) models (Clifton et al., 2018; Jiménez et al., 2019; Perdigão et al., 2017) have been used to study the solar resource in more extensive regions instead of in discrete locations as is the case of TMY. NWP models solve the physical constitutive and state equations that describe atmospheric processes obtaining estimates of the evolution of atmospheric conditions over time. Usually, the main goal of these NWP models is weather forecast, so the detailed prediction of the different components of solar radiation is not essential for that purpose, namely the DNI and DHI, since only GHI is considered relevant for the computation of the energy balance of the surface and atmosphere. More recently, due to the need for solar energy system development, attention has been drawn to this aspect and to the improvement of the accuracy regarding solar radiation specific variables (Araujo, 2021). Soukissian et al. (2021) used the recently released ERA5 reanalysis dataset from the European Centre for Medium-Range Weather Forecasts (ECMWF) for the study of offshore wind and solar resource in the Mediterranean Sea.

The existence and location of clouds as well as the concentration and type of aerosols in the atmosphere strongly affect solar radiation at the surface, which is difficult to accurately describe in NWP models. In the case of aerosols, for example, monthly-mean aerosol climatologies are typically used to reduce the computational effort of the operational models. Modelling and prediction of aerosols has been recently studied (Bran et al., 2018; Obiso and Jorba, 2018; Zhang et al., 2018) and its application to NWP models tested. Breitkreuz et al. (2009) used aerosol predictions and experimental data to forecast solar irradiance, which was compared with the output of the ECMWF model. There was a decrease in the mean squared error (MSE) of hourly GHI for the second and third forecast days from 11.5 % to 7.2 % for clear sky conditions.

In another approach, site adaptation models are used to compare and correct modelled data against observations made at a specific site. This term is mainly used for the bias correction of satellite data but many other techniques can be used to correct modelled data (Polo et al., 2020), as is the case of machine learning models. Alfadda et al. (2018) compared hourly GHI, DNI and DHI forecasting ability of various machine learning models, including Artificial Neural Networks (ANN), using radiation and aerosol measurements as well as wind and aerosol forecasts in Saudi Arabia as inputs, showing that the ANN model performs better than the remaining tested models. Fonseca et al. (2020) developed a forecasting model for day-ahead solar irradiation using support vector machine learning algorithm that has as input NWP data from the mesoscale model of the Japan Meteorological Agency, achieving a reduction of 16 % of the root mean squared error (RMSE) on the regional scale taking measurements as reference.

ANN models consist of input and output layers, as well as one or more hidden layers containing units defined as neurons. Such computing systems progressively improve task performance by considering examples, generally without task-specific programming. Many authors have used ANN in the field of renewable energy, e.g., for correction of wind speed or solar irradiance forecasts (Marzo et al., 2017; Pereira et al., 2019; Voyant et al., 2017), and for simulation of photovoltaic power (Anderson and Yakimenko, 2018; Chu et al., 2015; Fleetwood and Galarza, 2018; Gigoni et al., 2018; Hachicha et al., 2013; Liu et al., 2018; Rosiek et al., 2018; Scolari et al., 2018; Son et al., 2018). Ghimire et al. (2019) assessed daily solar energy potential for five cities of Australia using different machine learning algorithms such as ANN, support vector machine, gaussian process machine learning and genetic programming using reanalysis data from ECMWF as inputs. The results show that the ANN model outperforms all other machine learning models as well as the deterministic models used for benchmarking.

In this work, a method is proposed to assess direct normal and global horizontal irradiations at a regional scale using an artificial neural network model for site adaptation of simulations from a numerical

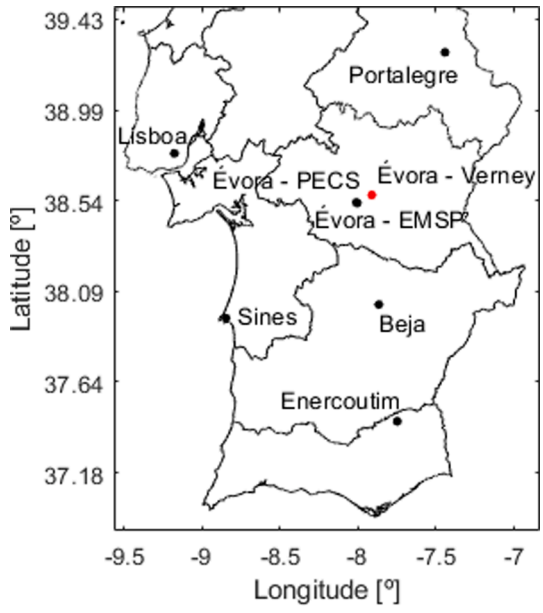

Fig. 1. Location of solar radiation measuring stations from the DNI-A network.

weather prediction model based on typical meteorological data and including aerosol information. This approach combines the advantage of TMY in identifying the typical periods that better represent the long-term climatology, the ability of NWP model to simulate solar radiation and meteorological variables in a regional scale and the capability of ANN models for data correction. Experimental meteorological and solar radiation data from Évora, Portugal, was used for model development while the validation of the developed method also used data from a network of solar radiation measuring stations dispersed throughout a region centered in Évora.

In Section 2, the experimental data and quality control tests are presented, and the generation of the typical meteorological year (TMY) is described. In Section 3 the typical months of the TMY are simulated using the NWP model Meso-NH and analysis data from ECMWF for initialization, generating atmospheric and solar radiation data for the desired region. The simulated variable of study (in this work there are two: GHI and DNI) for the selected location (Évora) is analyzed against observations and other simulated meteorological variables. In Section 4, a procedure for the development and optimization of a site adaptation model based on ANN is presented using not only the outputs from the Meso-NH simulations but also aerosol related variables from the Copernicus Atmosphere Monitoring Service (CAMS). After the ANN model is optimized for the selected location, it can be applied to the desired region allowing for a better assessment of the resource as shown in the results and discussion section of this work (Section 5). Finally, the conclusions are presented in Section 6.

2. Experimental data and typical meteorological year generation

To develop this work, long-term data series of observed meteorological and solar radiation variables are needed. In the following, a description of these data series and data processing procedure are presented as well as the generation of a typical meteorological year.

2.1. Experimental data

A long and complete series of daily meteorological data is required to determine a TMY. A long-term data series of 16 years (2003 to 2018) of observations made at Évora – Verney (Fig. 1) is available for the method development. However, these are subject to instrumentation failures, thus a careful analysis and processing of observations are necessary for the data series to be correct and complete. Hence, observations that are beyond the appropriate physical limits are identified and removed while data gaps are filled through linear interpolation or using adequate correlations with other observations made in nearby meteorological stations.

The first step is the identification and removal of data that are beyond the physical limits that can be admitted for each variable measured in Évora – Verney station (38.567811, −7.911459). The variables studied were GHI (obtained from global horizontal irradiance observations made with a Black & White Pyranometer from EPLAB model 8–48), average, maximum and minimum air temperature, and relative humidity (Hydro-Thermo Transmitter from Thies CLIMA, model 1.1005.50) and mean wind speed and wind gust (A100R contact closure anemometer from Vector Instruments until 2014 inclusive, and WindSonic ultrasonic wind sensor from Gill Instruments after 2014).

Adjustments were made for relative humidity and wind speed. Over time, values of daily relative humidity show a small linear drift (decreasing values) until a new calibration is made. To take this into account, slopes were determined for each period of observations between calibrations and corrections were applied. A restraint was applied limiting relative humidity to 100 %.

Adequate wind observations were only available in the Évora - Mitra meteorological station from ICT (38.525388, −8.016602, not shown in Fig. 1), approximately 10 km southwest of Évora-Verney (Fig. 1). However, these observations were not measured at the same height throughout time. From 2003 to 2014 they were obtained at 6 m height and from 2015 to 2018 at 10 m height. The measurements at 6 m were extrapolated through the power law of wind speed profile near the ground using the exponents determined for 12 wind direction sectors according to (Barreto and Canhoto, 2013) and a correction due to sensor degradation was applied using the software Windographer™, after which the daily values were computed.

Correlations were found between the observations of each variable (except wind) performed in Évora – Verney and two other meteorological stations nearby for data gap filling, namely the Évora – Mitra station and a station located in Portel (38.306528, −7.689500). If the use of correlations is not possible, then linear interpolation is performed. After this procedure, a complete data series of daily GHI, mean, maximum and minimum air temperature, mean, maximum and minimum relative humidity, mean wind speed and wind gust for the period since 01/01/2003 to 31/12/2018 were obtained.

DNI observations made at the Évora – Verney station were also needed for this work, being obtained from global horizontal irradiance and diffuse horizontal irradiance observations made with two Black & White Pyranometers from EPLAB (model 8–48) and a timestep of 10 min until 2016 (Canhoto, 2016). After 2016, direct normal irradiance and global horizontal irradiance data were obtained from 1-minute timestep observations from a Kipp & Zonen CHP1 pyrheliometer and a CM6B pyranometer, respectively.

The solar radiation data were subject to quality control procedures, namely those of the Baseline Surface Radiation Network (BSRN) (Long and Dutton, 2010) which account for physically impossible values, extremely rare values and values that are not reliable when considering the ratio between diffuse and global horizontal irradiance. To account for instrument and/or data acquisition system malfunctions, a procedure similar to that presented above was implemented to fill the missing global horizontal irradiance values using correlations with nearby meteorological stations, as presented in (Abreu et al., 2018).

For the validation of the method developed in this work, observation data of direct normal irradiance and global horizontal irradiance from stations of the DNI-A project network were used (Cavaco et al., 2021). The DNI-A network is a solar radiation measurement network which comprises 13 stations installed in the south of Portugal. These stations are equipped with Solys2 sun trackers with one CHP1 pyrheliometer, two CMP11 pyranometers to measure horizontal global and diffuse

Table 1
Statistical weights of the variables used on the determination of the TMY.

Variable	Air temperature			Relative humidity			Wind speed		GHI
	Mean	Max.	Min.	Mean	Max.	Min.	Mean	Max.	
Weight	2/24	1/24	1/24	2/24	1/24	1/24	2/24	2/24	12/24

Table 2
Selected months/years for each calendar month of the generated TMY for Évora.

Jan.	Feb.	Mar.	Apr.	May	Jun.	Jul.	Aug.	Sep.	Oct.	Nov.	Dec.
2018	2006	2017	2008	2005	2010	2014	2007	2011	2008	2004	2018

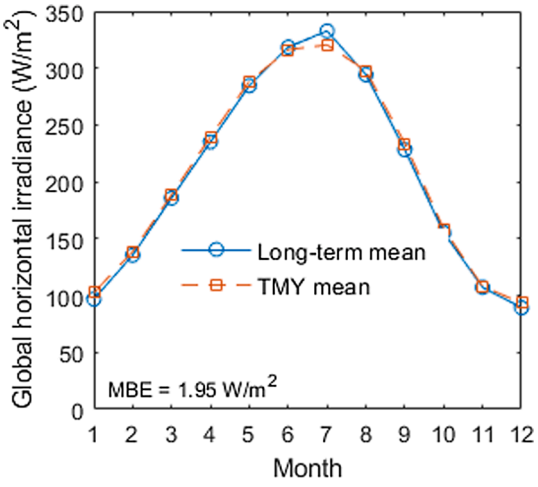

Fig. 2. Comparison between the TMY and long-term monthly mean values of daily mean global horizontal irradiance.

irradiance. The instruments were calibrated in accordance with ISO 9059:1990 and 9847:1992 and the observations are corrected regarding their zero offset, filtered according to the BSRN quality control procedure and gaps filled according to the method developed in (Cavaco et al., 2021).

The solar radiation observations used for the method validation were retrieved from the following stations of the DNI-A network: Évora – PECS (38.5306, −8.0112), Évora – EMSP (38.5289, −8.0053), Portalegre (39.2692, −7.4428), Beja (38.0249, −7.8672), Lisboa (38.7734, −9.1779), Sines (37.9576, −8.8473) and Enercoutim (37.4431, −7.7409). The location of these stations can be seen in Fig. 1 including the Évora – Verney station which data was used for the development of the method.

2.2. Generation of a typical meteorological year

Sixteen years (2003 to 2018 inclusive) of daily observations of GHI, average, maximum and minimum air temperature and relative humidity and average wind speed and wind gust in Évora – Verney (Fig. 1), in a total of nine variables, were used to determine a TMY. The TMY is obtained by concatenating twelve typical meteorological months (TMMs) which are selected through a sequence of steps starting with the determination of the Finkelstein-Schaffer (FS) statistics (Finkelstein and Schafer, 1971) of the daily values for all variables, according to the Sandia method (Hall et al., 1978). Next, the cumulative distribution function (CDF) for each variable in each month of the long-term series is computed and then a weighted sum of CDFs is determined for each month based on the weights shown in Table 1.

The five months (identified by their respective year, from here on termed month/year) for each calendar month which weighted CDFs are closest to the long-term CDF are selected as candidates for TMM. Next, the Sandia method with the slight alterations included by Pissimanis et al. (1988) and used in other studies (Abreu et al., 2018; Hall et al., 1978), is used. This procedure consists in the determination of the root mean square difference (RMSD) of the hourly global horizontal irradiation (GHI) and then the selection of the months/years that show a RMSD lower than min{RMSD} + 0.02 kWh/m^2 for each calendar month. Then, their FS values are computed and the month/year showing a FS lower than min{FS} + 0.03 is finally selected. If this procedure does not result in only one month/year for a given calendar month, the month/year that shows lowest FS values for mean air temperature is selected. The resulting months/years selected for each calendar month of the generated TMY are shown in Table 2. This TMY was validated by evaluating the monthly TMY means against long-term means (16 years) as shown for the example of global horizontal irradiance in Fig. 2.

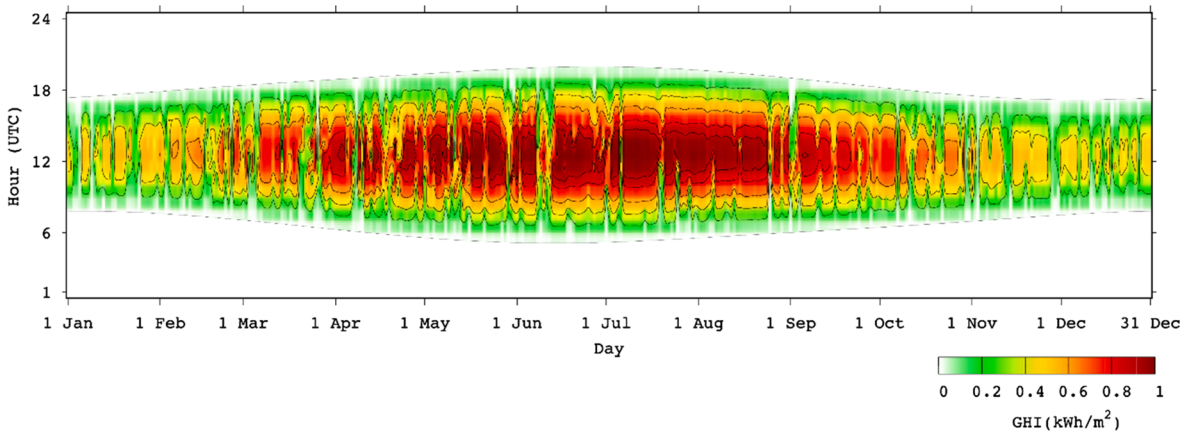

Fig. 3. GHI observed at Évora-Verney station for the generated TMY.

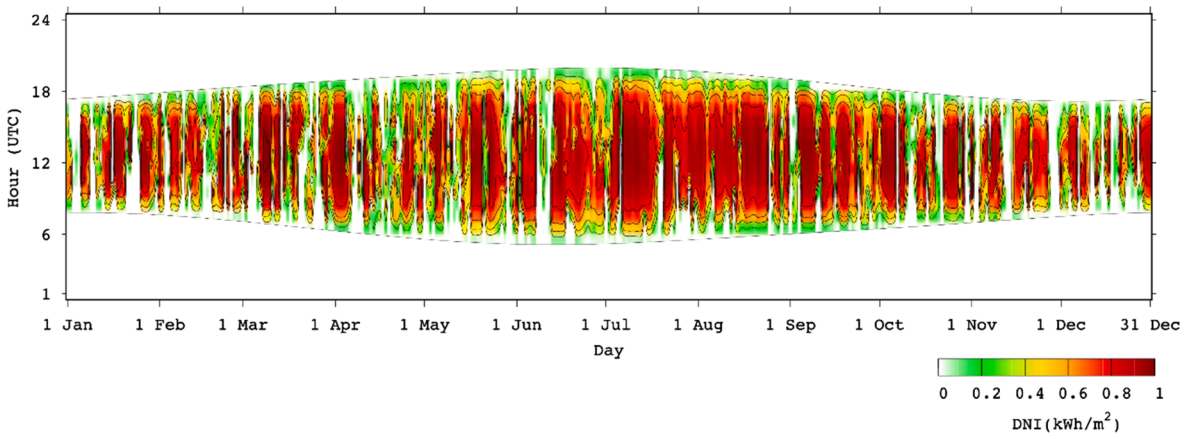

Fig. 4. DNI observed at Évora-Verney station for the generated TMY.

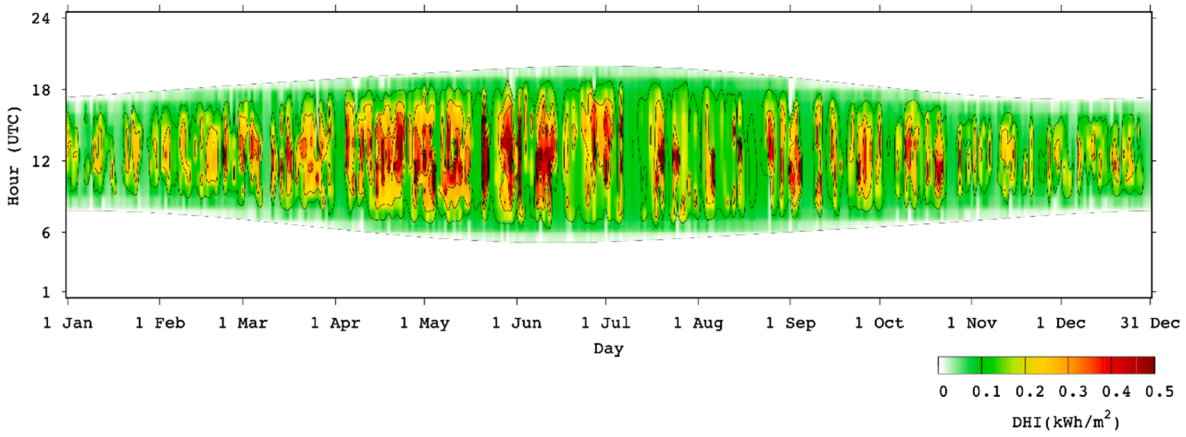

Fig. 5. DHI observed at Évora-Verney station for the generated TMY.

The GHI, DNI and DHI values of the generated TMY can be seen in Figs. 3–5, respectively.

3. Solar radiation results from the NWP model

The NWP model chosen to simulate the atmospheric conditions during the TMY was the research model Meso-NH (Lac et al., 2018). A brief description of the model and procedure for the simulation of the TMY is made in this section as well as an analysis of the model output data.

3.1. Meso-NH model simulations setup

The Meso-NH model is a mesoscale atmospheric model jointly developed by the Laboratoire d'Aérologie (CNRS/University of Toulouse) and by the Centre National de Recherches Météorologiques, CNRM (CNRS/Météo-France) that aims to simulate the state of the atmosphere by incorporating a system of non-hydrostatic momentum equations and computing balances over a wide range of scales. It has a set of physical parameterizations with high detail in the representation of clouds and precipitation (Lac et al., 2018; Meso-NH, 2016). Surface-atmosphere interactions are represented by the SURFEX surface platform of schemes (Masson et al., 2013) and the ECOCLIMAP database, which contains surface parameters with 1 km resolution (Faroux et al., 2013). The Meso-NH model is a cloud-resolving and large eddy simulation model that was extensively validated and inter-compared with other state-of-art models (see Lac et al., 2018, and the references herein or Capecchi, 2021). A detailed and comprehensive scientific and technical documentation is available on the Meso-NH web site (mesonh.aero.obs-mip.fr, last access: 11 January 2022), where a list of hundreds of publications can be accessed. The model has long been used successfully in Portugal for studies related to phenomena that are relevant to solar radiation forecast, namely convection, clouds and precipitation (e.g., Costa et al., 2010; Couto et al., 2020), fog (Policarpo et al., 2017) and dust atmospheric transport (e.g., Couto et al., 2021; Santos et al., 2013).

The radiation transport in the atmosphere is modelled through the most recent ecRad scheme developed by the ECMWF. This scheme is based on the Rapid Radiative Transfer Model (RRTM) (Hogan and Bozzo, 2018, 2016), which takes into account cloud parameterization, liquid water content, ice and snow, using the Monte Carlo Independent Column Approximation (McICA) method that allows for a more accurate representation of the interaction between radiation and the clouds.

The ECMWF developed the Integrated Forecasting System (IFS) which consists in several global operational models, namely an atmospheric general circulation model, an ocean wave model, a land surface model, an ocean general circulation model and perturbation models for the data assimilation and generation of forecast ensembles. This system generates forecasts that encompass different time ranges from the intermediate range (up to 15 days) to seasonal intervals (up to 7 months) with a horizontal resolution of 0.125° and temporal resolution of 1 h. Analyses are produced by combining short-range forecast data with observations to produce the best fit between them. These data are available twice per day and since this work falls under the scope of the development of an operational solar energy and photovoltaic power forecasting algorithm the operational forecasts of the ECMWF were

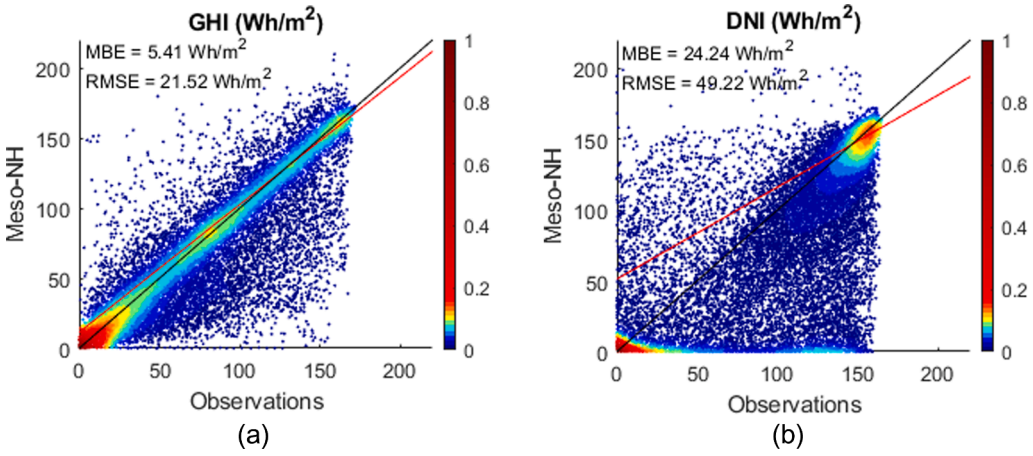

Fig. 6. Comparison between 10-minute simulated (using Meso-NH) and observed a) GHI and b) DNI at the station of Évora – Verney for the TMY (Wh/m^2).

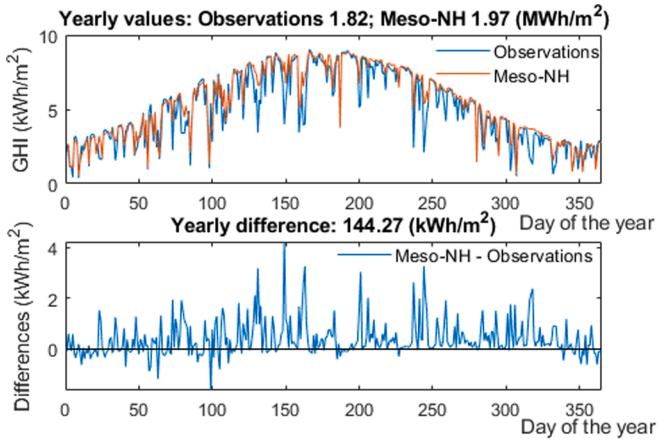

Fig. 7. Daily GHI values simulated using the Meso-NH model and observed at the station of Évora – Verney (top) and respective difference (bottom).

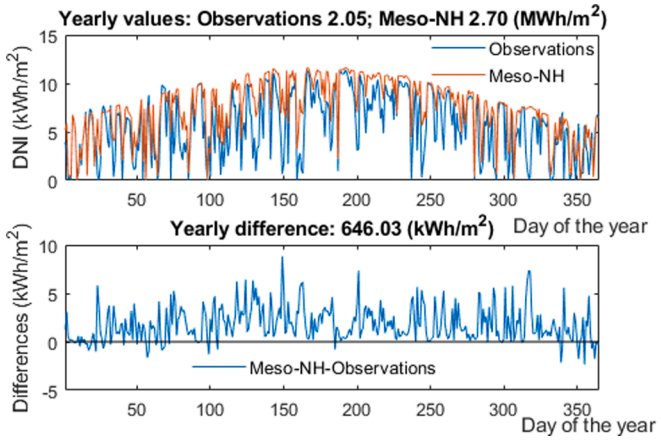

Fig. 8. Daily DNI values simulated using the Meso-NH model and observed at the station of Évora – Verney (top) and respective difference (bottom).

retrieved and used for initialization of the Meso-NH model.

The simulations of the TMY were performed in series of 3 days with a 6-hour spin-up period (every model run covered 6 + 72 h) for the region of the south of Portugal as in Fig. 1, with 1.25 km of horizontal resolution and generating several meteorologic near surface variables with the timestep of 1 min. This numerical experiment was also used for the evaluation of the impact of the Alqueva lake on the regional climate as described in detail in Iakunin et al. (2021) where the specific schemes and parameters used can be found as well as a validation of the simulations against several meteorological observations.

Table 3
Pearson's linear correlation coefficients of the simulated variables with respect to the GHI and DNI observations in Évora – Verney for the generated TMY.

Simulated Variables	Observed GHI	Observed DNI
GHI	0.91	0.62
DNI	0.74	0.73
DHI	0.34	0.00
Zen	−0.87	−0.48
T	0.49	0.37
WS	−0.04	−0.09
WD	0.02	−0.11
avgCF	−0.32	−0.43
maxCF	−0.35	−0.52
AOD469	−0.03	−0.23
AOD550	−0.04	−0.24
AOD670	−0.06	−0.26
AOD865	−0.08	−0.27
AOD1240	−0.12	−0.28
OMAOD	−0.06	−0.13
DUAOD	0.03	−0.08
SSAOD	−0.18	−0.29

Table 4
Configuration parameters of the ANN models for correction and site adaptation of GHI and DNI simulations from the NWP model.

Variable of interest	MSE_{rd} (%)	Function	Number of neurons	Inputs
GHI	67.60	*trainbr*	100	GHI, Zen, DNI, T, maxCF, DHI, avgCF, SSAOD, AOD1240, AOD865, AOD670, OMAOD, AOD550, WS, AOD469, DUAOD, WD
DNI	82.41	*trainbr*	97	DNI, GHI, maxCF, Zen, avgCF, T, SSAOD, AOD1240, AOD865, AOD670, AOD550, AOD469, OMAOD, WD, WS, DUAOD, DHI

3.2. Analysis of solar radiation data output from Meso-NH

After integrating the simulated 1 min global horizontal and direct normal irradiances into 10-minute values and interpolating these for the location of Évora – Verney station through a bi-linear interpolation of

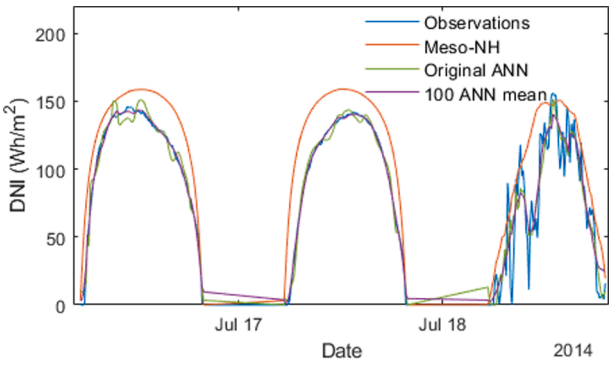

Fig. 9. 10-minute DNI observed, simulated through Meso-NH, corrected using the original ANN and computed through the mean of the results of the trained 100 ANNs for Évora-Verney from 16 to 18 of July 2014.

the values from the 4 neighboring grid-points, these were paired with the available observations for the whole TMY resulting in Fig. 6. The model tends to overestimate both variables, which is also visible when comparing the annual values of the modelled and observed variables for this site, which are approximately 1.97 MWh/m^2 and 1.82 MWh/m^2, respectively, for GHI and 2.70 MWh/m^2 and 2.05 MWh/m^2, respectively, for DNI. This results in a relative mean bias error (MBE) of 8.24 % for GHI and of 31.71 % for DNI.

As expected, the simulations of GHI tend to be better than DNI. This happens due to the increased uncertainty associated with DNI resulting from its higher variability and dependency of clouds and aerosols in the atmosphere which are particularly difficult to correctly simulate.

Figs. 7 and 8 show the daily values of simulated and observed GHI and DNI, respectively, in Évora – Verney as well as the daily differences between model and measurements, for the generated TMY. Once more, the overestimation of these two variables by the NWP model is visible. This overestimation happens not only on cloudy or partially cloudy days, when the model has difficulties in correctly simulating the effects of clouds on solar radiation, but also on clear sky days when the usage of monthly climatologies of aerosols by the NWP model affects the simulation accuracy, especially regarding DNI. This was the main motivation for the development of a correcting ANN model that could improve the simulation results.

4. ANN model development

Two ANN models, one for GHI and another for DNI, were developed using the neural network toolbox of MATLAB for site adaptation of the

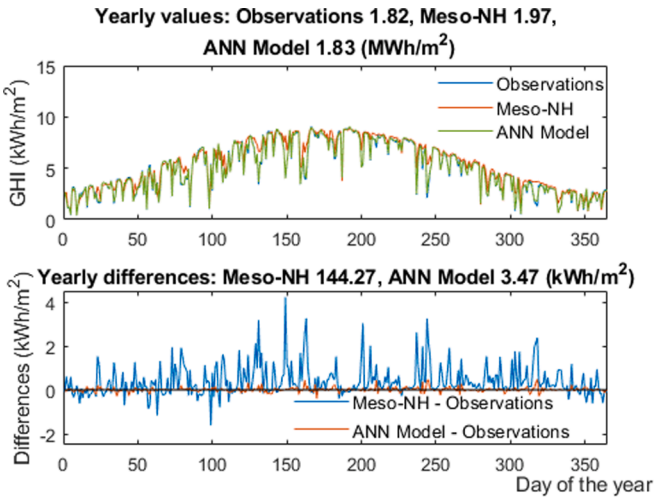

Fig. 11. Daily GHI observed and simulated with Meso-NH and the ANN model (top) and the differences between modelled and observed values (bottom) for the TMY and station of Évora – Verney.

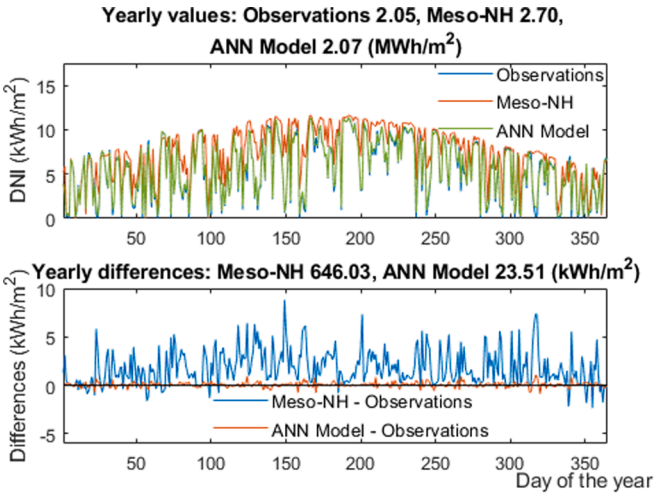

Fig. 12. Daily DNI observed and simulated with Meso-NH and the ANN model (top) and the differences between modelled and observed values (bottom) for the TMY and station of Évora – Verney.

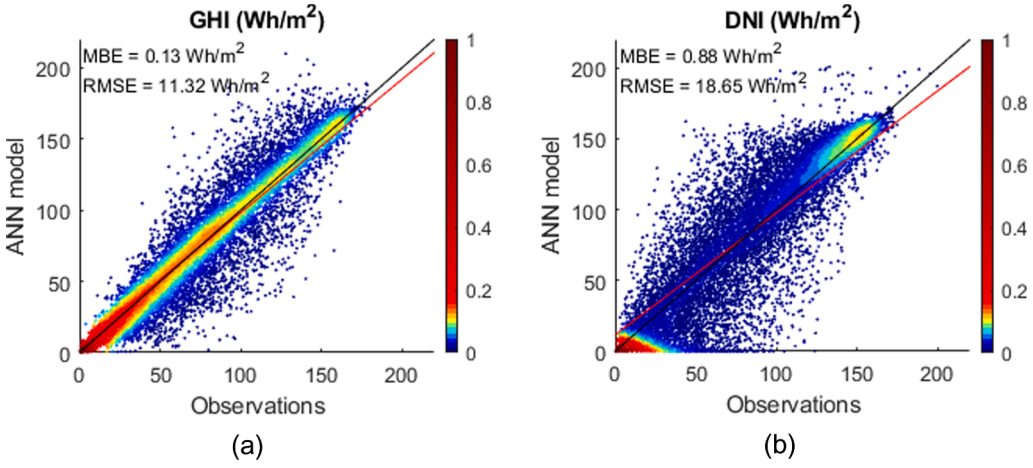

Fig. 10. Comparison between corrected 10-minute a) GHI and b) DNI simulations using the 100 ANNs and observations for TMY and the station of Évora – Verney (Wh/m^2).

Table 5
RMSE of 10-minute GHI and DNI simulated by the Meso-NH and ANN models for the generated TMY, in Wh/m^2.

Month	GHI		DNI	
	Meso-NH	ANN	Meso-NH	ANN
1	14.44	8.32	43.72	20.20
2	17.91	10.54	49.75	21.88
3	24.56	12.63	51.50	20.01
4	25.86	15.20	50.72	21.38
5	30.09	14.96	60.02	20.90
6	23.19	13.07	45.77	16.96
7	20.00	9.84	42.71	15.22
8	16.15	7.95	38.42	13.79
9	22.32	12.51	50.40	19.83
10	19.23	8.98	49.07	16.68
11	20.20	8.46	59.68	19.98
12	12.54	6.35	46.09	16.60
Year	21.52	12.33	49.22	18.65

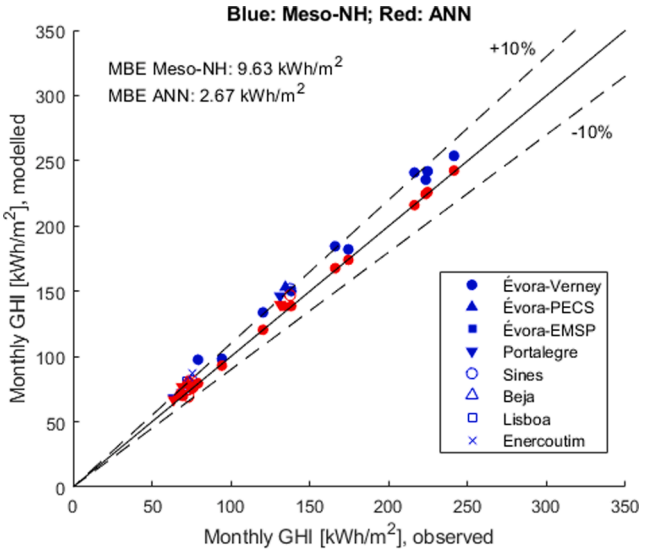

Fig. 13. Comparison between monthly modelled (Meso-NH in blue and ANN in red) and observed GHI values at different locations of the south of Portugal. (For interpretation of the references to color in this figure legend, the reader is referred to the web version of this article.)

Meso-NH simulations using various atmospheric related variables as inputs and 10-minute GHI and DNI observed at Évora – Verney station as targets. The developed ANNs are networks that were trained to map the inputs given to the desired targets. There are various parameters and specifications that can define an ANN thus, tests were performed to select the best configuration.

Some of the ANN parameters were pre-defined such as using a *fitnet* (which is a fitting network function), the initialization function *initnw* (which initializes the weights and biases of each layer according to the Nguyen-Widrow initialization algorithm), the hyperbolic tangent sigmoid transfer function *tansig* and the performance function *mse* (mean squared error). The input and output data were treated using *removeconstantrows*, which removes rows with constant values and *mapstd* that rescales the distribution of values so that the mean of each variable is 0 and the standard deviation is 1. The input data was randomly divided in 70% of data for training and 30% for validation, while the random seed was kept constant for comparison between different ANN configurations. The training functions tested were *trainlm* (uses Levenberg-Marquardt backpropagation) and *trainbr* (uses Bayesian regularization backpropagation).

As inputs, the meteorological variables obtained from the Meso-NH

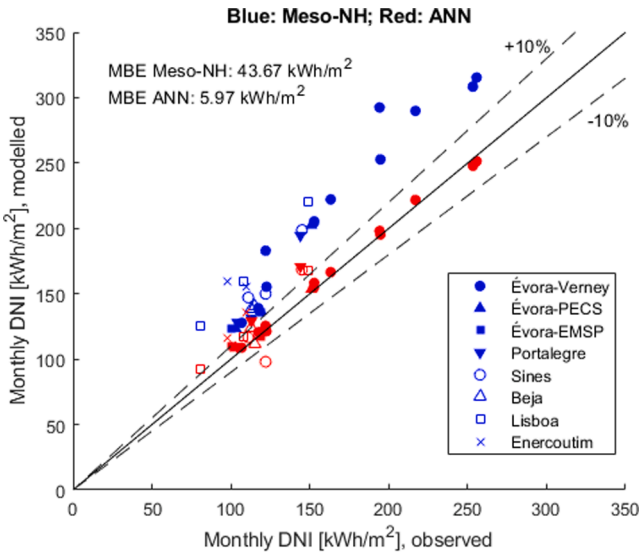

Fig. 14. Comparison between monthly modelled (Meso-NH in blue and ANN in red) and observed DNI values at different locations of the south of Portugal. (For interpretation of the references to color in this figure legend, the reader is referred to the web version of this article.)

simulations were considered, namely GHI, DNI, DHI, the solar zenith angle (Zen), mean air temperature (T), wind speed (WS) and direction (WD) and average (avgCF) and maximum (maxCF) cloud fraction.

To account for the effect of aerosols on solar radiation, aerosol variables obtained from the CAMS analysis data set were also considered to be used as inputs for the ANN models. The CAMS analysis data set is the most recent set of global reanalysis data for atmospheric composition produced by the ECMWF. It has atmospheric composition related variables, including aerosols, in a three-dimensional grid with approximately 80 km of horizontal resolution and 3 h of temporal resolution since 2003. The aerosol model of CAMS is a hybrid bulk-bin scheme with 12 prognostic tracers (three bins for sea salt, three for dust, hydrophilic and hydrophobic organic matter and black carbon, sulphate aerosol and a gas-phase sulfur dioxide precursor) (Morcrette et al., 2009). The total aerosol is corrected by the assimilation of total AOD observations which is done through a 4D-Var data assimilation system (Courtier et al., 1994).

The aerosol related variables retrieved from CAMS were aerosol optical depth at 469 nm (AOD469), 550 nm (AOD550), 670 nm (AOD670), 865 nm (AOD865) and 1240 nm (AOD1240), sea salt aerosol optical depth at 550 nm (SSAOD), organic matter aerosol optical depth at 550 nm (OMAOD) and dust aerosol optical depth at 550 nm (DUAOD). These variables were obtained in a grid with 0.125° of horizontal resolution and temporal resolution of 3 h.

The procedure for correction of simulations was the same for GHI and DNI resulting in the generation of an ANN model for each variable. After obtaining the 10-minute data by performing bi-linear interpolation of the 4 grid-points surrounding the site and matching the variables to the observed values (of GHI or DNI) for the observation site, in this case Évora – Verney, the correlations between the modelled variables and the observations (see Fig. A.1 in Appendix A) are determined. The Pearson's linear correlation coefficients are used to establish the order in which the different variables are added to the input matrix of the ANN for testing. The Pearson's linear correlation coefficients obtained in this work for each variable of study are presented in Table 3.

To find the optimal configuration in terms of training function, inputs, and number of neurons, these parameters are tested by computing the mean squared error (MSE) of the ANN and the original Meso-NH simulations for the variable of interest and applying a relative difference computed through Eq. (1). The parameters chosen are the ones that

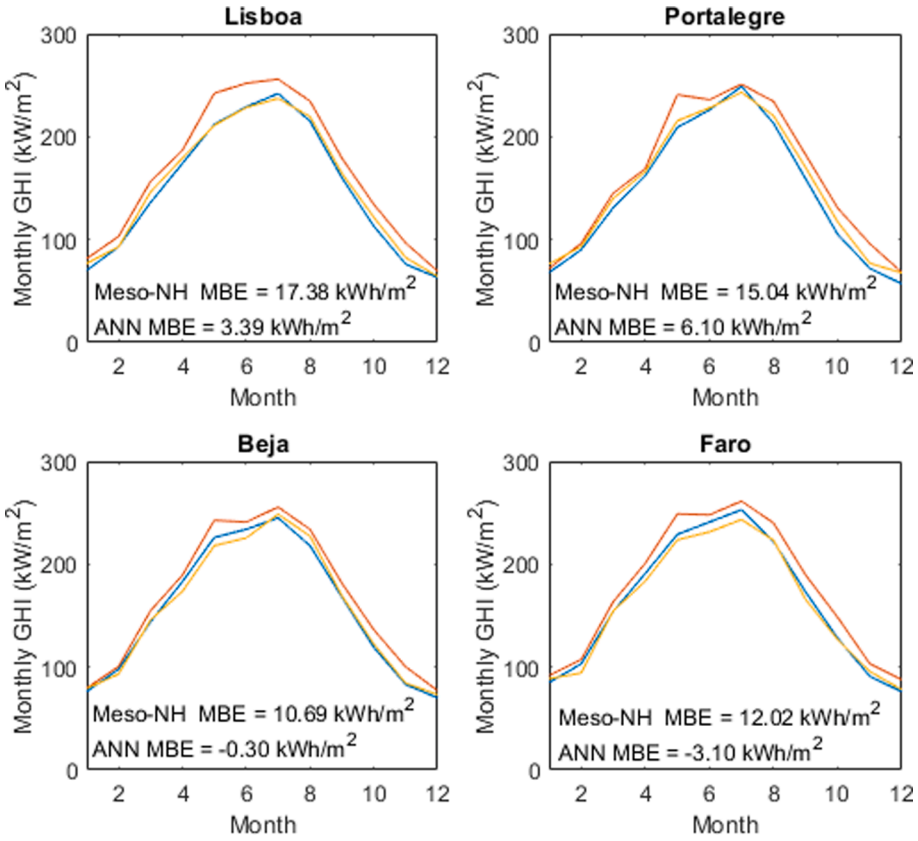

Fig. 15. Comparison between monthly GHI results of the Meso-NH and ANN models for four different locations in the south of Portugal obtained for the TMY of Évora with their long-term monthly means. Blue: Long-term GHI monthly means; Red: Meso-NH monthly GHI for the determined TMY; Yellow: ANN monthly GHI for the determined TMY. (For interpretation of the references to color in this figure legend, the reader is referred to the web version of this article.)

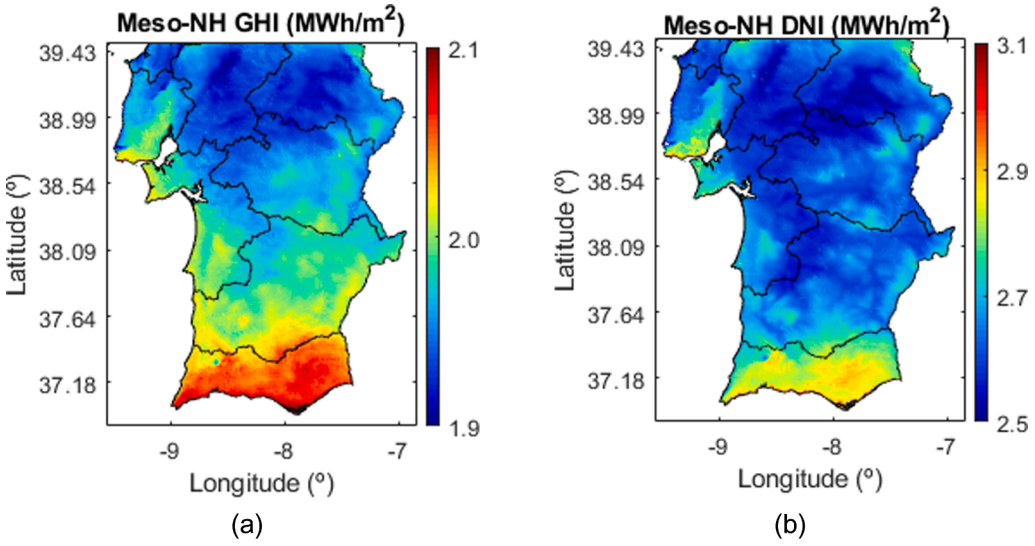

Fig. 16. Spatial distribution of a) GHI and b) DNI, for the south of Portugal and TMY obtained from Meso-NH simulations.

result in the highest value of relative MSE difference (MSE_{rd}), thus resulting in the best improvement (in terms of MSE) with respect to the original simulations.

$$MSE_{rd} = \frac{MSE_{Meso-NH} - MSE_{ANN}}{MSE_{Meso-NH}} \times 100\% \quad (1)$$

For each training function (*trainlm*, *trainbr*), the number of neurons in the hidden layer is made to vary between 1 and 100 and for each of these combinations, the variables used as inputs are changed by adding them to the input matrix of the ANN, one by one, in the order defined by the Pearson's linear correlation coefficients. After adding one variable to the inputs, the results of the ANN are evaluated and if the addition of this variable improves the MSE_{rd}, that variable is kept as input and the next is added, if not, the variable is removed from the input matrix and the next variable is added.

In Table 4, the ANN configurations that result in the highest values of

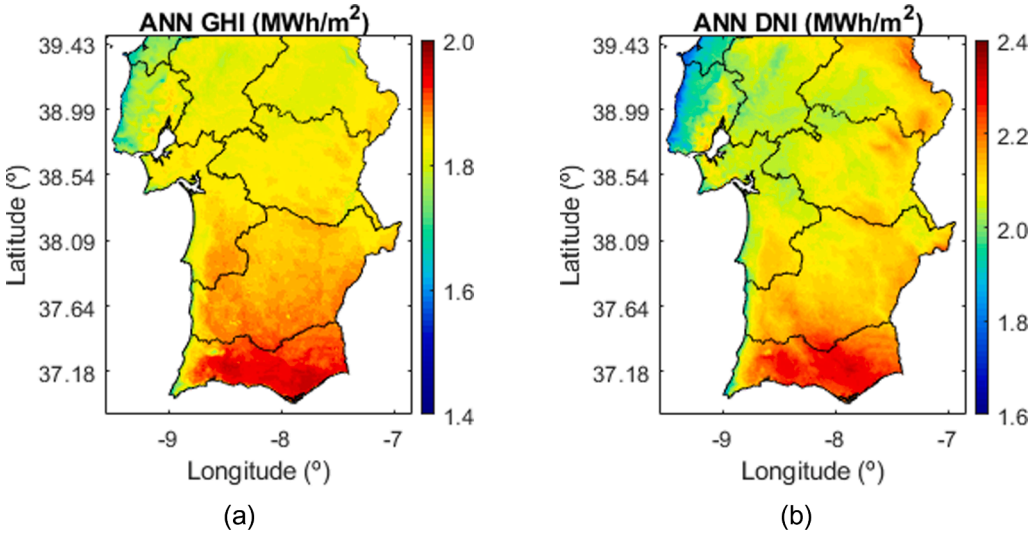

Fig. 17. Spatial distribution of a) GHI and b) DNI, for the south of Portugal and TMY obtained from the ANN model.

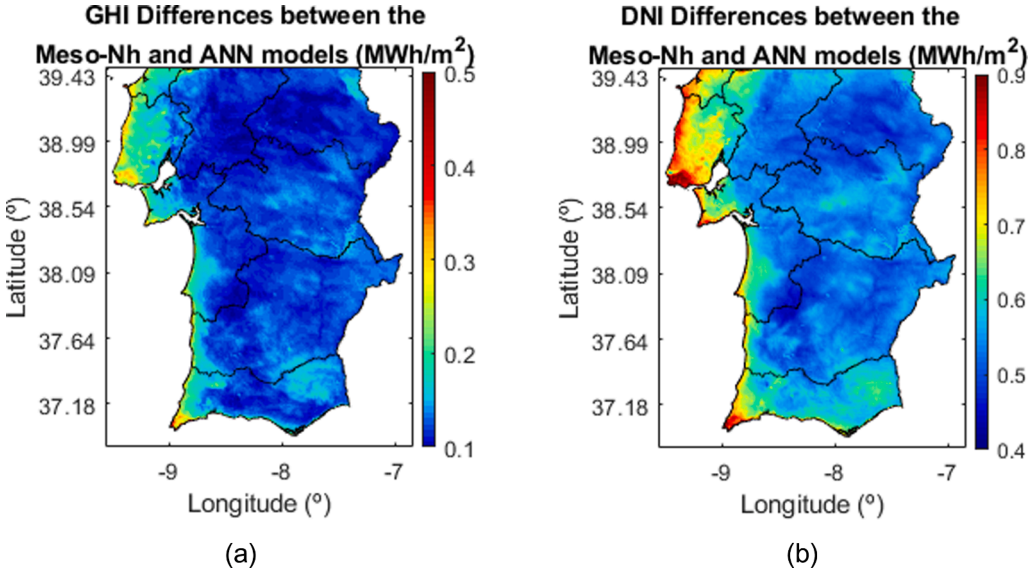

Fig. 18. Difference between the original Meso-NH GHI simulations of GHI and the corrected through the ANN model.

MSE_{rd} are presented, with two ANN models being produced, one for GHI and the other for DNI. The next best combinations and its results can be consulted in Table A.1 of Appendix A.

The results of the selected ANN models obtained a MSE_{rd} of 67.60% for GHI and 82.41% for DNI showing that they improve the Meso-NH simulations for the station of Évora – Verney. The higher improvement in DNI simulations when compared to the GHI model is explained by the fact that the NWP model is better at simulating GHI than DNI.

When comparing the 10-minute data obtained through these ANN models with the Meso-NH simulations and observations made in Évora-Verney, as is shown in Fig. 10 for the DNI as example, small oscillations in the ANN corrected values are detected which are not in accordance with observations. The solution found was to train 100 ANNs with the parameters defined above but without a fixed random seed (which means initialization values of each ANN model are different and randomized) and use as output of the model the mean of the results of those 100 ANNs (more details on this procedure can be found in Appendix A). Fig. 9 shows the improvement that results from this procedure for the DNI.

This procedure was adopted for the two variables being studied.

5. Results and discussion

After obtaining the output mean of the 100 ANNs based on the best combination of parameters for each variable (GHI and DNI) for the location of Évora, the developed models showed a MSE_{rd} of 72.36% for GHI and 85.65% for DNI for the TMY showing that the developed method can improve the Meso-NH simulations for the station of Évora – Verney. Moreover, using the mean of 100 ANNs with the same parameters but different initialization values, improves not only the results regarding the oscillation problem, as seen in Fig. 10, but also the MSE_{rd} when compared to the use of only one ANN.

Figs. 11 and 12 show a direct comparison between the obtained values of GHI and DNI, respectively, for the TMY and the station of Évora – Verney and the corresponding observations. The improvement of the ANN on the simulations can be seen when comparing these plots with Figs. 6 and 7, although some dispersion is still observed. The annual irradiation for the TMY in this location became 1.83 MWh/m^2 for GHI and 2.07 MWh/m^2 for DNI after applying the developed ANN models on the original Meso-NH simulations (1.97 MWh/m^2 for GHI and 2.70 MWh/m^2 for DNI), which is much closer to the observed values (1.82

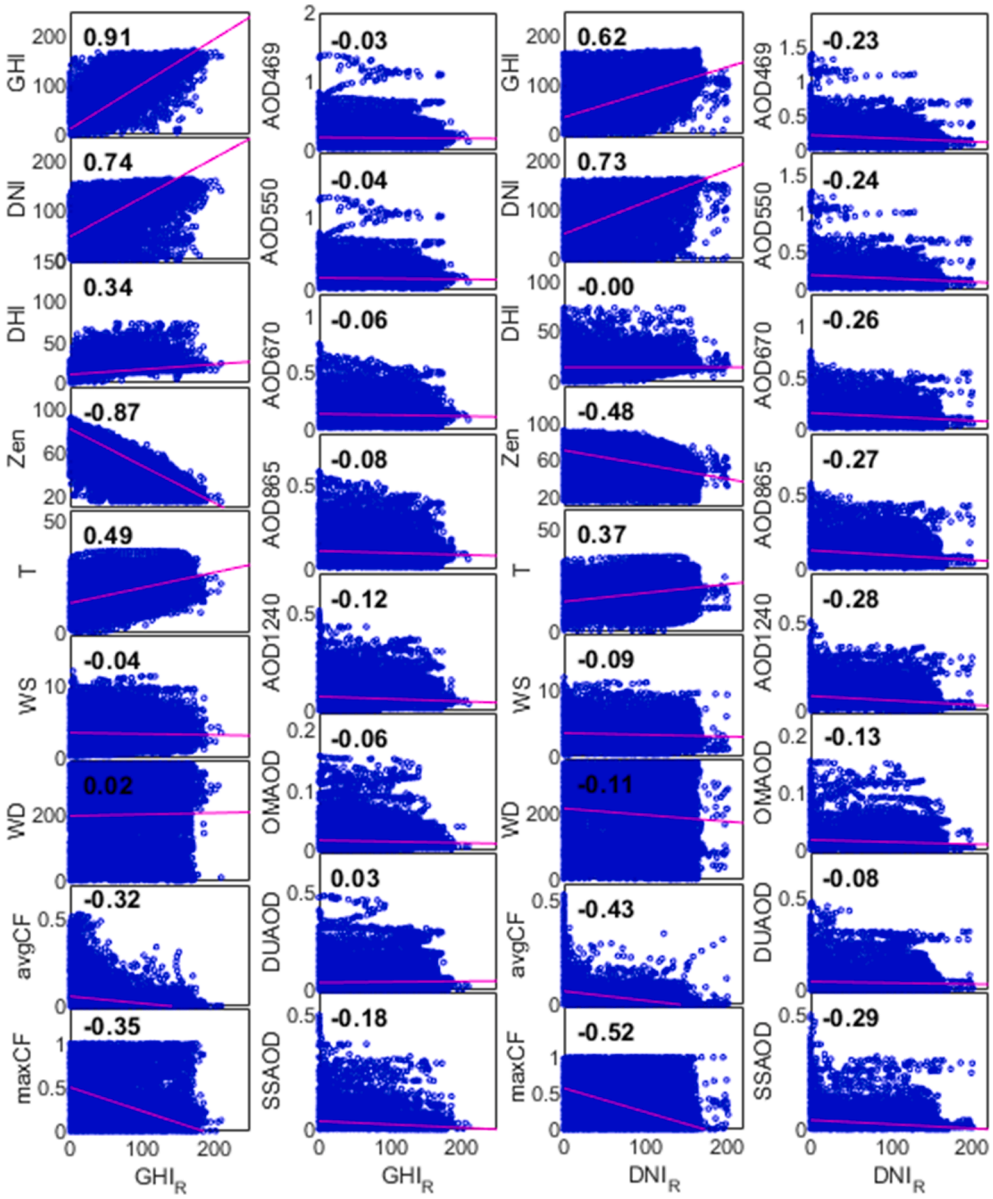

Fig. A1. Correlations and Pearson's linear correlation coefficients between modelled variables and observed global horizontal (GHI_R) and direct normal irradiation (DNI_R). Irradiation variables, GHI, DNI, DHI, GHI_R, DNI_R, in Wh/m^2, temperature, T, in °C, wind speed, WS, in m/s, zenith angle, Zen, and wind direction, WD, in degrees.

MWh/m^2 for GHI and 2.05 MWh/m^2 for DNI) than the NWP simulations. This represents a reduction in annual relative mean bias error from 8.24 % to 0.55 % for GHI and from 31.71 % to 0.98 % for DNI.

Table 5 shows the root mean squared error (RMSE) values for the modelled data for each calendar month and for the TMY. The developed method based on the ANN models showed a significant reduction of annual RMSE from 21.00 Wh/m^2 for GHI and 49.22 Wh/m^2 for DNI (obtained with the original Meso-NH simulations) to 12.33 Wh/m^2 for GHI and 18.65 Wh/m^2 for DNI.

Figs. 11 and 12 show the daily values of GHI and DNI, respectively, as simulated by the Meso-NH model, the ANN model and observed, as well as the daily differences between the modelled and observed data, showing the improvement of the simulated daily values when the developed method with the ANN models is applied.

The developed ANN models are then applied to the NWP simulations for the whole region of study and the generated TMY with two main purposes: i) validate the developed method; and ii) to evaluate the usage of the developed method for solar resource assessment and its accuracy.

For the validation of the developed method, Figs. 13 and 14 were generated where the monthly values of GHI and DNI from the Meso-NH and ANN models were compared against the available monthly values of observed data at other stations from the DNI-A network shown in Fig. 1.

The application of the method based on the ANN models resulted in monthly values much closer to observations than the original Meso-NH simulations for all stations. The monthly mean bias errors (MBE) resulting from the use of this method and including the available data from all measuring stations is of 2.67 kWh/m^2 for GHI and 5.97 kWh/m^2 for DNI, much lower than the MBEs for the Meso-NH simulations which are of 9.63 kWh/m^2 for GHI and 43.67 kWh/m^2 for DNI. This results in a decrease in relative mean bias error from 8.50 % to 2.34 % for GHI and from 29.54 % to 3.41 % for DNI.

The monthly RMSEs of the ANN are approximately 4.26 kWh/m^2 for GHI and 11.57 kWh/m^2 for DNI, which are also much lower than those of the Meso-NH (11.49 kWh/m^2 for GHI and 48.00 kWh/m^2 for DNI). This means that the use of an ANN model developed for a specific site centered in a limited region of interest, which was trained with typical

Table A.1
Five best combinations of ANN parameters for the improvement of GHI and DNI. For all models the best training function was shown to be trainbr.

Variable of interest		GHI					DNI				
ANN model rank		1	2	3	4	5	1	2	3	4	5
MSE_{rd} (%)		67.60	67.07	66.95	66.92	66.83	82.41	82.34	82.28	82.24	81.89
Number of neurons		100	99	95	97	98	97	99	100	98	96
Inputs	**GHI**	×	×	×	×	×	×	×	×	×	×
	DNI	×	×	×	×	×	×	×	×	×	×
	DHI	×	×	×	×	×	×	×	×	×	×
	Zen	×	×	×	×	×	×	×	×	×	×
	T	×	×	×	×	×	×	×	×	×	×
	WS	×	×	×	×	×	×	×	×	×	×
	WD	×	×	×	×	×	×	×	×	×	×
	avgCF	×	×	×	×	×	×	×	×	×	×
	maxCF	×	×	×	×	×	×	×	×	×	×
	AOD469	×	×	×			×	×			×
	AOD550	×	×	×	×	×	×	×	×	×	×
	AOD670	×	×	×	×	×	×	×	×	×	×
	AOD865	×	×	×	×	×	×	×	×	×	×
	AOD1240	×	×	×	×	×	×	×	×	×	×
	OMAOD	×	×	×	×	×	×	×	×	×	×
	DUAOD	×	×	×	×	×	×	×	×	×	×
	SSAOD	×	×	×	×	×	×	×	×	×	×

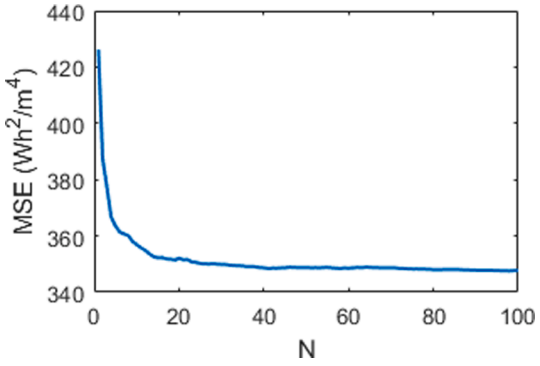

Fig. A2. MSE of the mean DNI of the first N trained ANNs, these being ordered from lowest to highest values of MSE.

meteorological data, can still improve NWP simulations for that region since an ANN model has the capability of capturing and learning the relations between the different input variables and the measured values.

Thus, besides approximating the solar irradiation simulated by the Meso-NH model to observations for these various locations and for typical meteorological months in Évora, it was also expected that the developed model would approximate these results to the typical values of each location. To verify that, the simulated GHI was compared with the monthly-mean values obtained from long-term observations, computed using 10 or more years (Cavaco et al, 2016), for two locations in the inland, Portalegre (37.0167, −7.9667) and Beja (38.0249, −7.8672), and other two in the coastal zone, Lisboa (38.7734, −9.1779) and Faro (39.2941, −7.4213), as shown in Fig. 15. A very good agreement is observed and, since the goal of a TMY is to reproduce the long-term climatology and the GHI is the meteorological variable with higher statistical weight in the typical meteorological month selection (Section 2.2), we may assume that the ANN model can reproduce the typical meteorological data in the entire region based on the NWP simulations.

Thus, the developed method successfully results in an accurate assessment of the solar resource by incorporating NWP models, allowing the physical simulation of the weather for a specified region, and ANN models, which work as a site adaptation model and incorporate aerosol data, thus improving the simulations previously done for the TMY data representative of the typical meteorological conditions. With the resulting data, one can generate solar resource maps where the spatial distribution of the resource is easily visible.

Fig. 16 shows the GHI and DNI resource maps for the south of Portugal from the original Meso-NH simulations for the generated TMY. Fig. 17 shows the GHI and DNI resource maps for the same region after applying the method described in this work.

The annual results of both the Meso-NH and the developed method show a positive difference when compared to observations as mentioned before, being the Meso-NH difference much higher than the one of the ANN models. Due to the difference in magnitude of the Meso-NH and ANN simulated variables and in order to be able to observe the distribution of the resource throughout the region, the color scales of these maps are not identical. For a better comparison between the original Meso-NH simulations and the solar resource modelled through the method based on ANNs, Fig. 18 was generated showing the differences between them.

The differences observed are more accentuated for the coastal region of Portugal (mainly the Atlantic one) but are also present at a smaller scale for regions with greater altitudes which can be interpreted as a greater overestimation by the Meso-NH model. The cause of this difference can be explained by the higher frequency of clouds in those regions, which are more difficult to accurately simulate, as well as the usage of monthly aerosol climatologies, more specifically at the coastal region where these climatologies don't adequately consider the effect of the Atlantic Ocean on the climate of Portugal.

According to the obtained spatial distribution of annual solar irradiation, the highest values of DNI are observed in the south coastal region of Portugal (coastal strip of Algarve) as well as in the Algarve region with highest altitudes. Higher values of DNI are also present close to the east border of Portugal.

6. Conclusion

This work presented a method for the assessment of the solar resource with 1.25 km of horizontal resolution obtained by developing a site adaptation model based on artificial neural networks and incorporating aerosol data from CAMS that is applied to simulations made by a numerical weather prediction model for typical meteorological data.

A typical meteorological year was generated for Évora, Portugal, using sixteen years of experimental data, which selected typical meteorological months can also be considered representative of the typical meteorological months of the surrounding region. The weather simulations for this TMY were done using the NWP model Meso-NH coupled with the ecRad radiation scheme which generates atmospheric data for the desired region (south of Portugal) with a resolution of 1.25 km.

The comparison between the NWP simulated and the observed GHI

and DNI showed an overestimation of these variables (higher for DNI) that can be caused due to difficulties in correctly simulating clouds and the usage of monthly-mean aerosol climatologies. It was shown that this overestimation is higher in the coastal strip region of Portugal, showing that the NWP model does not correctly account for the effect of maritime aerosols and clouds on the simulated solar radiation in this region.

The developed procedure for site adaptation using an optimized ANN model is based on the testing of different parameters, including the addition of analysis aerosol data from CAMS as inputs, and choosing the variables that result in higher improvements in terms of MSE.

The ANN models are obtained for the specific location used for the generation of the TMY, in this case Évora, and then applied to the whole region simulated by the Meso-NH model (south of Portugal). The monthly values obtained using the Meso-NH model and using the developed procedure were compared against observed values at stations located in this region, showing a reduction in relative mean bias error from 8.50 % to 2.34 % for GHI and from 29.54 % to 3.41 % for DNI. Thus, validating the method proposed by showing that even if the ANN models were designed to improve GHI or DNI simulations at Évora – Verney station, they can improve simulations for other locations in the same region.

This is a general method and can be applied to any region of the world, however, it should be noted that the area simulated in this work is of approximately 46 000 km^2 and the generation of larger maps and/or for locations with very different climates will probably decrease the improvement brought by the application of an ANN model developed for a specific site in that region. The understanding of these implications can be a topic for future research. In the future, this procedure can also be used for other meteorological variables, such as air temperature, which greatly affects the operating efficiency of photovoltaic systems and to generate solar energy potential maps for this specific technology that may consider photovoltaic cells temperature and other loss factors.

The high resolution GHI and DNI maps generated are extremely important for solar radiation related applications like planning and design of solar energy systems and while the usage of an atmospheric model allows for the assessment of the resource in a desired region, these tend to show large errors when solar radiation is concerned. Thus, the usage of post-processing tools like artificial neural networks incorporating aerosol data allows for a more accurate assessment of the solar resource.

Declaration of Competing Interest

The authors declare that they have no known competing financial interests or personal relationships that could have appeared to influence the work reported in this paper.

Acknowledgments

This work was funded by the European Regional Development Fund, included in the COMPETE 2020 (Operational Program Competitiveness and Internationalization) through the ICT project (UID/GEO/04683/2019) with the reference POCI-01-0145-FEDER-007690, and the projects DNI-ALENTEJO (ALT20-03-0145-FEDER-000011) and ALOP (ALT20-03-0145-FEDER-000004). E.F.M. Abreu acknowledges FCT for the grant SFRH/BD/136433/2018. S. Pereira acknowledges FCT for the grant SFRH/BD/145378/2019.

Appendix A. Details on the procedure for the development of the ANN model

For the development of the ANN models proposed in this work, firstly the 1-minute Meso-NH atmospheric variable simulations are processed obtaining 10-minute data for the location of Évora, Portugal through bilinear interpolation of the values of the 4 grid points surrounding the observation site. The data obtained from CAMS for the TMY is also processed in the same way and, additionally, is downscaled from 3-hour data to 10-minute data through piecewise cubic hermite interpolating polynomials which allows for the preservation of the shape of the data. The correlations of these variables with the GHI and DNI observations for the TMY are determined resulting in Fig. A1.

The simulated variables are ordered according to their Pearson's linear correlation coefficients with the observed variables so they can be added to the input matrix of each ANN model (GHI or DNI) according to what was described in Section 4.

Table A.1 shows not only the selected ANN models as shown in Table 4 but the five best combinations of parameters for the ANN models developed to improve GHI and DNI simulations for Évora – Verney station. All these models use the training function *trainbr* which is a training function that updates the weight and bias values according to Levenberg-Marquardt optimization and uses Bayesian regularization that minimizes a combination of squared errors and weights, determining the correct combination to produce a network that generalizes well. The best models tend to use higher number of inputs as well as neurons. Again, all models developed for GHI have lower MSE_{rd} than the ones developed for the correction of DNI since the NWP model is already better at simulating GHI.

To validate the use of 100 ANNs with the same parameters but random initializations as opposed to the use of the ANN trained and defined as the best combination, Fig. A2 was generated. This figure shows the MSE of the mean DNI obtained from the results of N trained ANNs, being these ordered from lowest to highest value of MSE, i.e., for $N = 1$, the MSE shown in the figure is the MSE resulting from the ANN with lowest MSE, for $N = 2$, the MSE shown in the figure is the MSE of the mean results of the two ANNs with lowest MSE, and so on. The MSE tends to decrease with the higher number of ANNs used in the average result.

References

Abreu, E.F.M., Canhoto, P., Prior, V., Melicio, R., 2018. Solar resource assessment through long-term statistical analysis and typical data generation with different time resolutions using GHI measurements. Renew. Energy 127, 398–411. https://doi.org/10.1016/J.RENENE.2018.04.068.

Al-Azri, N.A., Al-Saadi, S., 2018. Variant developments of typical meteorological years (TMYs) for Seeb, Oman and their impact on energy simulation of residential buildings. J. Eng. Res. 15, 29–41. https://doi.org/10.24200/tjer.vol15iss2p129-141.

Alfadda, A., Rahman, S., Pipattanasomporn, M., 2018. Solar irradiance forecast using aerosols measurements: A data driven approach. Sol. Energy 170, 924–939. https://doi.org/10.1016/J.SOLENER.2018.05.089.

Anderson, W.W., Yakimenko, O.A., 2018. Using neural networks to model and forecast solar PV power generation at Isle of Eigg, in: 2018 IEEE 12th International Conference on Compatibility, Power Electronics and Power Engineering (CPE-POWERENG 2018). IEEE, pp. 1–8. https://doi.org/10.1109/CPE.2018.8372522.

de Araujo, J.M.S., 2021. Improvement of Coding for Solar Radiation Forecasting in Dili Timor Leste—A WRF Case Study. J. Power Energy Eng. 09 (02), 7–20. https://doi.org/10.4236/jpee.2021.92002.

Barreto, G., Canhoto, P., 2013. Estudo e avaliação do recurso eólico na região de Évora a partir de dados de uma estação meteorológica, in: III Congresso Jovens Investigadores Em Geociências LEG 2013 & 6th Meeting of Post-Graduation in Physics and Earth Sciences of UÉ.

Bran, S.H., Jose, S., Srivastava, R., 2018. Investigation of optical and radiative properties of aerosols during an intense dust storm: A regional climate modeling approach. J. Atmos. Solar-Terrestrial Phys. 168, 21–31. https://doi.org/10.1016/J.JASTP.2018.01.003.

Breitkreuz, H., Schroedter-Homscheidt, M., Holzer-Popp, T., Dech, S., 2009. Short-Range Direct and Diffuse Irradiance Forecasts for Solar Energy Applications Based on Aerosol Chemical Transport and Numerical Weather Modeling. J. Appl. Meteorol. Climatol. 48, 1766–1779. https://doi.org/10.1175/2009JAMC2090.1.

Canhoto, P., 2016. Preliminary analysis of irradiance data for the Generation of a Typical Solar Radiation Year for Évora, Portugal. https://doi.org/10.13140/RG.2.2.12258.94401.

Capecchi, V., 2021. Reforecasting Two Heavy-Precipitation Events with Three Convection-Permitting Ensembles. Weather Forecast. 36, 769–790. https://doi.org/10.1175/WAF-D-20-0130.1.

Cavaco, A., Canhoto, P., Collares Pereira, M., 2021. Procedures for solar radiation data gathering and processing and their application to DNI assessment in southern Portugal. Renew. Energy 163, 2208–2219. https://doi.org/10.1016/J.RENENE.2020.10.075.

Chu, Y., Urquhart, B., Gohari, S.M.I., Pedro, H.T.C., Kleissl, J., Coimbra, C.F.M., 2015. Short-term reforecasting of power output from a 48 MWe solar PV plant. Sol. Energy 112, 68–77. https://doi.org/10.1016/j.solener.2014.11.017.

Clifton, A., Hodge, B.M., Draxl, C., Badger, J., Habte, A., 2018. Wind and solar resource data sets. Wiley Interdiscip. Rev. Energy Environ. 7. https://doi.org/10.1002/wene.276.

Costa, M.J., Salgado, R., Santos, D., Levizzani, V., Bortoli, D., Silva, A.M., Pinto, P., 2010. Modelling of orographic precipitation over Iberia: a springtime case study. Adv. Geosci. 25, 103–110. https://doi.org/10.5194/adgeo-25-103-2010.

Courtier, P., Thépaut, J.-N., Hollingsworth, A., 1994. A strategy for operational implementation of 4D-Var, using an incremental approach. Q. J. R. Meteorol. Soc. 120 (519), 1367–1387. https://doi.org/10.1002/qj.49712051912.

Couto, F.T., Cardoso, E.H.C., Costa, M.J., Salgado, R., Guerrero-Rascado, J.L., Salgueiro, V., 2021. How a mesoscale cyclonic vortex over Sahara leads to a dust outbreak in South-western Iberia. Atmos. Res. 249, 105302. https://doi.org/10.1016/j.atmosres.2020.105302.

Couto, F.T., Iakunin, M., Salgado, R., Pinto, P., Viegas, T., Pinty, J.-P., 2020. Lightning modelling for the research of forest fire ignition in Portugal. Atmos. Res. 242, 104993. https://doi.org/10.1016/j.atmosres.2020.104993.

Ernst, M., Gooday, J., 2019. Methodology for generating high time resolution typical meteorological year data for accurate photovoltaic energy yield modelling. Sol. Energy 189, 299–306. https://doi.org/10.1016/j.solener.2019.07.069.

Faroux, S., Kaptué Tchuenté, A.T., Roujean, J.-L., Masson, V., Martin, E., Le Moigne, P., 2013. ECOCLIMAP-II/Europe: a twofold database of ecosystems and surface parameters at 1 km resolution based on satellite information for use in land surface, meteorological and climate models. Geosci. Model Dev. 6, 563–582. https://doi.org/10.5194/gmd-6-563-2013.

Feng, Y.u., Zhang, X., Jia, Y., Cui, N., Hao, W., Li, H., Gong, D., 2021. High-resolution assessment of solar radiation and energy potential in China. Energy Convers. Manag. 240, 114265. https://doi.org/10.1016/j.enconman.2021.114265.

Finkelstein, J.M., Schafer, R.E., 1971. Improved goodness-of-fit tests. Biometrika 58, 641–645. https://doi.org/10.1093/biomet/58.3.641.

Fonseca, J.G.D.S., Uno, F., Ohtake, H., Oozeki, T., Ogimoto, K., 2020. Enhancements in day-ahead forecasts of solar irradiation with machine learning: A novel analysis with the Japanese mesoscale model. J. Appl. Meteorol. Climatol. 59, 1011–1028. https://doi.org/10.1175/JAMC-D-19-0240.1.

Ghimire, S., Deo, R.C., Downs, N.J., Raj, N., 2019. Global solar radiation prediction by ANN integrated with European Centre for medium range weather forecast fields in solar rich cities of Queensland Australia. J. Clean. Prod. 216, 288–310. https://doi.org/10.1016/J.JCLEPRO.2019.01.158.

Gigoni, L., Betti, A., Crisostomi, E., Franco, A., Tucci, M., Bizzarri, F., Mucci, D., 2018. Day-Ahead Hourly Forecasting of Power Generation from Photovoltaic Plants. IEEE Trans. Sustain. Energy 9 (2), 831–842. https://doi.org/10.1109/TSTE.2017.2762435.

Hachicha, A.A., Rodríguez, I., Capdevila, R., Oliva, A., 2013. Heat transfer analysis and numerical simulation of a parabolic trough solar collector. Appl. Energy 111, 581–592. https://doi.org/10.1016/j.apenergy.2013.04.067.

Hall, I.J., Praire, R., Anderson, H., Boes, E., 1978. Generation of Typical Meteorological Years for 26 SOLMET Stations, Sandia Laboratories energy report. Sandia Laboratories.

Hogan, R.J., Bozzo, A., 2018. A Flexible and Efficient Radiation Scheme for the ECMWF Model. J. Adv. Model. Earth Syst. 10 (8), 1990–2008. https://doi.org/10.1029/2018MS001364.

Hogan, R.J., Bozzo, A., 2016. ECRAD: A new radiation scheme for the IFS. ECMWF Tech. 787, 1–33.

Huld, T., Paietta, E., Zangheri, P., Pinedo Pascua, I., 2018. Assembling typical meteorological year data sets for building energy performance using reanalysis and satellite-based data. Atmosphere (Basel). 9 (2), 53. https://doi.org/10.3390/atmos9020053.

Iakunin, M., Abreu, E.F.M., Canhoto, P., Pereira, S., Salgado, R., 2021. Impact of a large artificial lake on regional climate: A typical meteorological year Meso-NH simulation results. Int. J. Climatol. 1–22 https://doi.org/10.1002/joc.7299.

International Renewable Energy Agency (IRENA), 2021. Renewable Energy Capacity Statistics 2021.

Jiménez, P.A., Lee, J.A., Kosovic, B., Haupt, S.E., 2019. Solar Resource Evaluation with Numerical Weather Prediction Models, in: Polo, J., Martín-Pomares, L., Sanfilippo, A. (Eds.), Solar Resources Mapping: Fundamentals and Applications. Springer International Publishing, Cham, pp. 199–219. https://doi.org/10.1007/978-3-319-97484-2_7.

Lac, C., Chaboureau, J.-P., Masson, V., Pinty, J.-P., Tulet, P., Escobar, J., Leriche, M., Barthe, C., Aouizerats, B., Augros, C., Aumond, P., Auguste, F., Bechtold, P., Berthet, S., Bielli, S., Bosseur, F., Caumont, O., Cohard, J.-M., Colin, J., Couvreux, F., Cuxart, J., Delautier, G., Dauhut, T., Ducrocq, V., Filippi, J.-B., Gazen, D., Geoffroy, O., Gheusi, F., Honnert, R., Lafore, J.-P., Lebeaupin Brossier, C., Libois, Q., Lunet, T., Mari, C., Maric, T., Mascart, P., Mogé, M., Molinié, G., Nuissier, O., Pantillon, F., Peyrillé, P., Pergaud, J., Perraud, E., Pianezze, J., Redelsperger, J.-L., Ricard, D., Richard, E., Riette, S., Rodier, Q., Schoetter, R., Seyfried, L., Stein, J., Suhre, K., Taufour, M., Thouron, O., Turner, S., Verrelle, A., Vié, B., Visentin, F., Vionnet, V., Wautelet, P., 2018. Overview of the Meso-NH model version 5.4 and its applications. Geosci. Model Dev. 11, 1929–1969. https://doi.org/10.5194/gmd-11-1929-2018.

Lhendup, T., Lhundup, S., 2007. Comparison of methodologies for generating a typical meteorological year (TMY). Energy Sustain. Dev. 11 (3), 5–10. https://doi.org/10.1016/S0973-0826(08)60571-2.

Liu, L., Zhao, Y., Chang, D., Xie, J., Ma, Z., Sun, Q., Yin, H., Wennersten, R., 2018. Prediction of short-term PV power output and uncertainty analysis. Appl. Energy 228, 700–711. https://doi.org/10.1016/j.apenergy.2018.06.112.

Long, C.N., Dutton, E.G., 2010. BSRN Global Network recommended QC tests, V2. J. Clim. 25, 8542–8567. https://doi.org/10.1175/JCLI-D-11-00618.1.

Marion, W., Urban, K., 1995. User's Manual for TMY2s - Typical Meteorological Years. United States. Department of Energy. Office of Energy Efficiency and Renewable Energy.

Marzo, A., Trigo, M., Alonso-Montesinos, J., Martínez-Durbán, M., López, G., Ferrada, P., Fuentealba, E., Cortés, M., Batlles, F.J., 2017. Daily global solar radiation estimation in desert areas using daily extreme temperatures and extraterrestrial radiation. Renew. Energy 113, 303–311. https://doi.org/10.1016/j.renene.2017.01.061.

Masson, V., Le Moigne, P., Martin, E., Faroux, S., Alias, A., Alkama, R., Belamari, S., Barbu, A., Boone, A., Bouyssel, F., Brousseau, P., Brun, E., Calvet, J.-C., Carrer, D., Decharme, B., Delire, C., Donier, S., Essaouini, K., Gibelin, A.-L., Giordani, H., Habets, F., Jidane, M., Kerdraon, G., Kourzeneva, E., Lafaysse, M., Lafont, S., Lebeaupin Brossier, C., Lemonsu, A., Mahfouf, J.-F., Marguinaud, P., Mokhtari, M., Morin, S., Pigeon, G., Salgado, R., Seity, Y., Taillefer, F., Tanguy, G., Tulet, P., Vincendon, B., Vionnet, V., Voldoire, A., 2013. The SURFEXv7.2 land and ocean surface platform for coupled or offline simulation of earth surface variables and fluxes. Geosci. Model Dev. 6, 929–960. https://doi.org/10.5194/gmd-6-929-2013.

Meso-NH, 2016. The Mesonh User's Guide.

Morcrette, J.-J., Boucher, O., Jones, L., Salmond, D., Bechtold, P., Beljaars, A., Benedetti, A., Bonet, A., Kaiser, J.W., Razinger, M., Schulz, M., Serrar, S., Simmons, A.J., Sofiev, M., Suttie, M., Tompkins, A.M., Untch, A., 2009. Aerosol analysis and forecast in the European Centre for Medium-Range Weather Forecasts Integrated Forecast System: Forward modeling. J. Geophys. Res. Atmos. 114 (D6) https://doi.org/10.1029/2008JD011235.

Obiso, V., Jorba, O., 2018. Aerosol-radiation interaction in atmospheric models: Idealized sensitivity study of simulated short-wave direct radiative effects to particle microphysical properties. J. Aerosol Sci. 115, 46–61. https://doi.org/10.1016/J.JAEROSCI.2017.10.004.

Ohunakin, O.S., Adaramola, M.S., Oyewola, O.M., Fagbenle, R.O., Adelekan, D.S., Gill, J., Abam, F.I., 2018. Photovoltaic performance prediction in Northern Nigeria using generated typical meteorological year dataset. African J. Sci. Technol. Innov. Dev. 10 (5), 579–591. https://doi.org/10.1080/20421338.2018.1511280.

Perdigão, J., Salgado, R., Magarreiro, C., Soares, P.M.M., Costa, M.J., Dasari, H.P., 2017. An Iberian climatology of solar radiation obtained from WRF regional climate simulations for 1950–2010 period. Atmos. Res. 198, 151–162. https://doi.org/10.1016/J.ATMOSRES.2017.08.016.

Pereira, S., Canhoto, P., Salgado, R., Costa, M.J., 2019. Development of an ANN based corrective algorithm of the operational ECMWF global horizontal irradiation forecasts. Sol. Energy 185, 387–405. https://doi.org/10.1016/j.solener.2019.04.070.

Pissimanis, D., Karras, G., Notaridou, V., Gavra, K., 1988. The generation of a "typical meteorological year" for the city of Athens. Sol. Energy 40 (5), 405–411. https://doi.org/10.1016/0038-092X(88)90095-3.

Policarpo, C., Salgado, R., Costa, M.J., 2017. Numerical Simulations of Fog Events in Southern Portugal. Adv. Meteorol. 2017, 1–16. https://doi.org/10.1155/2017/1276784.

Polo, J., Fernández-Peruchena, C., Salamalikis, V., Mazorra-Aguiar, L., Turpin, M., Martín-Pomares, L., Kazantzidis, A., Blanc, P., Remund, J., 2020. Benchmarking on improvement and site-adaptation techniques for modeled solar radiation datasets. Sol. Energy 201, 469–479. https://doi.org/10.1016/J.SOLENER.2020.03.040.

Polo, J., Perez, R., 2019. Solar Radiation Modeling from Satellite Imagery, in: Polo, J., Martín-Pomares, L., Sanfilippo, A. (Eds.), Solar Resources Mapping: Fundamentals and Applications. Springer International Publishing, Cham, pp. 183–197. https://doi.org/10.1007/978-3-319-97484-2_6.

Rosiek, S., Alonso-Montesinos, J., Batlles, F.J., 2018. Online 3-h forecasting of the power output from a BIPV system using satellite observations and ANN. Int. J. Electr. Power Energy Syst. 99, 261–272. https://doi.org/10.1016/j.ijepes.2018.01.025.

Santos, D., Costa, M.J., Silva, A.M., Salgado, R., 2013. Modeling Saharan desert dust radiative effects on clouds. Atmos. Res. 127, 178–194. https://doi.org/10.1016/j.atmosres.2012.09.024.

Scharmer, K., Greif, J., 2000. The European Solar Radiation Atlas: Fundamentals and maps. Les Presses de l'Ecole des Mines, The European Solar Radiation Atlas.

Scolari, E., Sossan, F., Paolone, M., 2018. Photovoltaic Model-Based Solar Irradiance Estimators: Performance Comparison and Application to Maximum Power Forecasting. IEEE Trans. Sustain. Energy 9 (1), 35–44. https://doi.org/10.1109/TSTE.2017.2714690.

Son, J., Park, Y., Lee, J., Kim, H., 2018. Sensorless PV Power Forecasting in Grid-Connected Buildings through Deep Learning. Sensors 18 (8), 2529. https://doi.org/10.3390/s18082529.

Soukissian, T.H., Karathanasi, F.E., Zaragkas, D.K., 2021. Exploiting offshore wind and solar resources in the Mediterranean using ERA5 reanalysis data. Energy Convers. Manag. 237, 114092. https://doi.org/10.1016/j.enconman.2021.114092.

Voyant, C., Notton, G., Kalogirou, S., Nivet, M., Paoli, C., Motte, F., Fouilloy, A., 2017. Machine learning methods for solar radiation forecasting : A review. Renew. Energy 105, 569–582. https://doi.org/10.1016/j.renene.2016.12.095.

Wilcox, S., Marion, W., 2008. Users Manual for TMY3 Data Sets, National Renewable Energy Laboratory Technical. Report.

Yang, D., Gueymard, C.A., 2019. Producing high-quality solar resource maps by integrating high- and low-accuracy measurements using Gaussian processes. Renew. Sustain. Energy Rev. 113, 109260. https://doi.org/10.1016/j.rser.2019.109260.

Zhang, M., Ma, Y., Gong, W., Liu, B., Shi, Y., Chen, Zhong Yong, 2018. Aerosol optical properties and radiative effects: Assessment of urban aerosols in central China using 10-year observations. Atmos. Environ. 182, 275–285.

remote sensing

MDPI

Article

The Use of Sentinel-3/OLCI for Monitoring the Water Quality and Optical Water Types in the Largest Portuguese Reservoir

Gonçalo Rodrigues [1,2,*], Miguel Potes [1,2,3], Alexandra Marchã Penha [1,4], Maria João Costa [1,2,3] and Maria Manuela Morais [1,4,5]

1 Institute of Earth Sciences, Institute for Advanced Studies and Research, University of Évora, 7000-671 Évora, Portugal; mpotes@uevora.pt (M.P.); mapenha@uevora.pt (A.M.P.); mjcosta@uevora.pt (M.J.C.); mmorais@uevora.pt (M.M.M.)
2 Earth Remote Sensing Laboratory-EaRSLab, Institute for Advanced Studies and Research, University of Évora, 7000-671 Évora, Portugal
3 Department of Physics, Science and Technology School, University of Évora, 7000-671 Évora, Portugal
4 Water Laboratory, University of Évora, Parque Industrial e Tecnológico de Évora, Rua da Barba Rala N1, 7005-345 Évora, Portugal
5 Department of Biology, Science and Technology School, University of Évora, 7000-671 Évora, Portugal
* Correspondence: grodrigues@uevora.pt

Abstract: The Alqueva reservoir is essential for water supply in the Alentejo region (south of Portugal). Satellite data are essential to overcome the temporal and spatial limitations of in situ measurements, ensuring continuous and global water quality monitoring. Data between 2017 and 2020, obtained from OLCI (Ocean and Land Color Instrument) aboard Sentinel-3, were explored. Two different methods were used to assess the water quality in the reservoir: K-means to group reflectance spectra into different optical water types (OWT), and empirical algorithms to estimate water quality parameters. Spatial (in five different areas in the reservoir) and temporal (monthly) variations of OWT and water quality parameters were analyzed, namely, Secchi depth, water turbidity, chlorophyll *a*, and phycocyanin concentrations. One cluster has been identified representing the typical spectra of the presence of microalgae in the reservoir, mainly between July and October and more intense in the northern region of the Alqueva reservoir. An OWT type representing the area of the reservoir with the highest transparency and lowest chlorophyll *a* concentration was defined. The methodology proposed is suitable to continuously monitor the water quality of Alqueva reservoir, constituting a useful contribution to a potential early warning system for identification of critical areas corresponding to cyanobacterial algae blooms.

Keywords: Alqueva reservoir; clustering; microalgae blooms; OWT; spatial variations; temporal variations

check for updates

Citation: Rodrigues, G.; Potes, M.; Penha, A.M.; Costa, M.J.; Morais, M.M. The Use of Sentinel-3/OLCI for Monitoring the Water Quality and Optical Water Types in the Largest Portuguese Reservoir. *Remote Sens.* **2022**, *14*, 2172. https://doi.org/10.3390/rs14092172

Academic Editors: Giuseppe Ruello and Donato Amitrano

Received: 28 February 2022
Accepted: 27 April 2022
Published: 30 April 2022

Publisher's Note: MDPI stays neutral with regard to jurisdictional claims in published maps and institutional affiliations.

Copyright: © 2022 by the authors. Licensee MDPI, Basel, Switzerland. This article is an open access article distributed under the terms and conditions of the Creative Commons Attribution (CC BY) license (https://creativecommons.org/licenses/by/4.0/).

1. Introduction

In the context of climate change, the monitoring of water quality in lakes and reservoirs is relevant to have an effective control of this resource due to an increasing scarcity in the Mediterranean region, with intermittent rainfall regimes, severe droughts, and an increase in evapotranspiration. Projections from climate models for the Alentejo region (southern Portugal) follow the global context and particularly indicate a decrease in wet days, increase in heat waves, a significant increase of the maximum/minimum temperatures in all seasons, and more frequent extreme temperatures [1–3]. High-resolution projections project relevant losses of precipitation in Portugal in spring, summer, and autumn, the simulations being more severe to the southern basins [3], where the Alqueva reservoir is located. Moreover, it is expected that by the end of the century, more than half of the heat waves will be stronger than the historic heat wave of 2003 in Portugal [2]. It is also anticipated that there will be longer heat waves that could, in the future, last for more than one month. All

these factors will lead to a higher evaporation rate throughout the year, and especially in the warmest months. Lakes respond directly to climate change, and some effects in water quality are expected, such as changes in salinity, water level, intensification of eutrophication which favors periodic proliferation by cyanobacteria, an increase of invasive species, increased turbidity, and enhanced vertical stratification, among other effects [4–10]. Water temperature, which is highly correlated with air temperature, exhibits a rapid and direct response to climatic forcing. With the expected warmer water and decreased water level (due to the expected increase in evaporation in the Mediterranean region), only with reductions in the inputs of nitrogen (N) and phosphorus (P) into the lakes and reservoirs will it be possible to control harmful algae blooms in the future [6].

An adequate monitoring of water bodies is essential, associated with an increasing of pressures as well as water need for human consumption, irrigation, and other purposes [11–14]. Satellite data can be very useful in this context, with a better temporal and spatial coverage compared with in situ methods. Estimates of water quality using satellite data are normally made using empirical algorithms established with satellite reflectances and in situ or laboratory measurements of water quality parameters. Several studies have proved that band ratio algorithms from remote sensing data are effective to estimate water quality parameters in lakes and reservoirs, such as chlorophyll a (Chl-a) concentrations, phycocyanin concentrations (PC), water turbidity (Turb), Secchi depth (SD), or suspended particulate matter [15–24]. Other authors [25–29] demonstrate how remote sensing sensors combined with machine learning allow for retrieval of water quality parameters, such as Chl-a concentrations, total suspended matter, or colored dissolved organic matter.

The phycocyanin pigment is more suitable for monitoring cyanobacterial blooms than Chl-a [19]. Cyanobacterial blooms are currently a great threat to the ecological integrity and sustainability for some of the lakes and reservoirs in the world. Episodes of microalgae bloom emergence in the Alqueva reservoir were identified through satellite data [30,31]. The present study analyzes the appearance of these microalgae blooms, also identifying and quantifying the presence of the pigment that signals the presence of cyanobacteria, the phycocyanin.

Spectral reflectances are grouped through clustering methods in order to be classified into different optical water types (OWT). This methodology allows for mapping a lake with a qualitative class, consenting to easily distinguish between areas with different spectral reflectance behavior and consequently different water quality. It can also be used to select which empirical water quality algorithm is used, that is, to use more than one empirical algorithm to estimate the same parameter for the same reservoir [32–35]. Hierarchical [33,36,37] or non-hierarchical approaches are normally used as clustering techniques to obtain OWT classifications. Non-hierarchical approaches consider the overall distribution of spectral pairs, the most popular of this techniques being the k-means [34,35,38,39] and fuzzy-c means [40–43]. These clustering techniques are commonly used for the classification of surface reflectances into groups based upon differences in magnitude and shape.

Empirical algorithms were already developed for the Alqueva reservoir to estimate the pigment Chl-a, cyanobacteria concentration, and water turbidity from the MERIS sensor onboard the ENVISAT satellite [44,45]. The same authors applied the semi-empirical bio-optical models from the MERIS sensor to the Sentinel-2 Multi-Spectral Instrument (MSI), estimating the turbidity and Chl-a/cyanobacteria concentrations during a microalgae bloom that occurred in late summer/early autumn of 2017 [31]. Empirical algorithms have recently been established for Secchi depth and diffuse attenuation coefficient using the instrument MSI [30].

The main motivation of the present work is to explore Sentinel-3 OLCI data for full spatial cover and continuous monitoring of water quality in the Alqueva reservoir. Although the instrument OLCI from Sentinel-3 has much lower spatial resolution (300 m) compared to Sentinel-2/MSI and Landsat data, it presents an adequate resolution to represent the spatial variations of water quality in the reservoir (the largest artificial lake

in Western Europe). The instrument OLCI has very high temporal resolution (better compared to MSI and much better than Landsat), with one overpass every day. OLCI is equipped with very adequate spectral bands (21 bands in the spectral range of 400–1020 nm) suitable for inland waters and for monitoring algae blooms. In this work is presented a qualitative analysis (OWT scheme) associated with estimations of water quality parameters (quantitative analyses) over a long period in the Alqueva reservoir, between 2017 and 2020. The added value of a qualitative analysis in lakes is the abridgment associated with the assignment of classes, allowing a faster and more effective analysis in the context of monitoring water quality. Associating the OWT classification with the estimates of water quality allow a robust analysis, which will ensure a very good degree of confidence in the estimations, also permitting to associate a degree of severity to each of the classes. The main contribution of the present study is the establishment of these two methods defined independently (OWT scheme and empirical algorithms), allowing to identify cases/pixels where the results have high or low reliability, without the need to confirm them in the field. With the traditional approach [32–35] there is a relationship between these two methods (empirical algorithm depending of the OWT assignment); therefore, it is not possible to directly assess the reliability of the retrievals using only satellite data.

The present work aims to improve estimates of bloom occurrence over inland waters for risk assessment, as well as to provide global spatiotemporal variations of water quality in the Alqueva reservoir, using remote sensing data. Section 2 gives a description of the area of study and data used. Section 3 summarizes the methodology used. Sections 4 and 5 present the results and their discussion. Section 6 summarizes the main conclusions of the work.

2. Materials

2.1. Area and Period of Study

The Alqueva reservoir (southeast of Portugal in Alentejo region) is the largest artificial lake in Western Europe, with a surface area of 250 km^2, 85 km length and a maximum depth of 65 m. Currently, the Alentejo region is an area with droughts that can persist for more than two years, and several months of low precipitation associated with very high maximum temperatures, between 25 °C and 45 °C (June to September). In this context, and with increasing water needs for human consumption, agriculture, and industries, the Alqueva reservoir constitutes a fundamental water resource in southern Portugal. The primary inflow to Alqueva is the river Guadiana (north of reservoir) bordered by Spain in the east. Temporal and spatial variations of water quality in the present study are analyzed in the Alqueva reservoir as a whole, and by five areas, the same used in the previous study [30] and shown in Figure 1. The period of study using OLCI data in this work comprises four years, between 2017 and 2020. However, the data used to define the empirical algorithms belong to different periods. Table 1 shows the periods of all data used in this paper.

Table 1. Periods considered for each dataset used.

Data	Objective	Period
Sentinel-3/OLCI (Satellite data)	Estimate water quality and OWTs	2017–2020 (Period of study)
Surface reflectances (Satellite data and measurements)	Validation of OLCI surface reflectances	May 2016–September 2020
SD (Measurements)	Empirical algorithm	May 2016–October 2021
Chl-a/Turb (Laboratory data)	Empirical algorithms	July 2017–October 2021
PC (Laboratory data)	Empirical algorithm	February 2018–October 2021

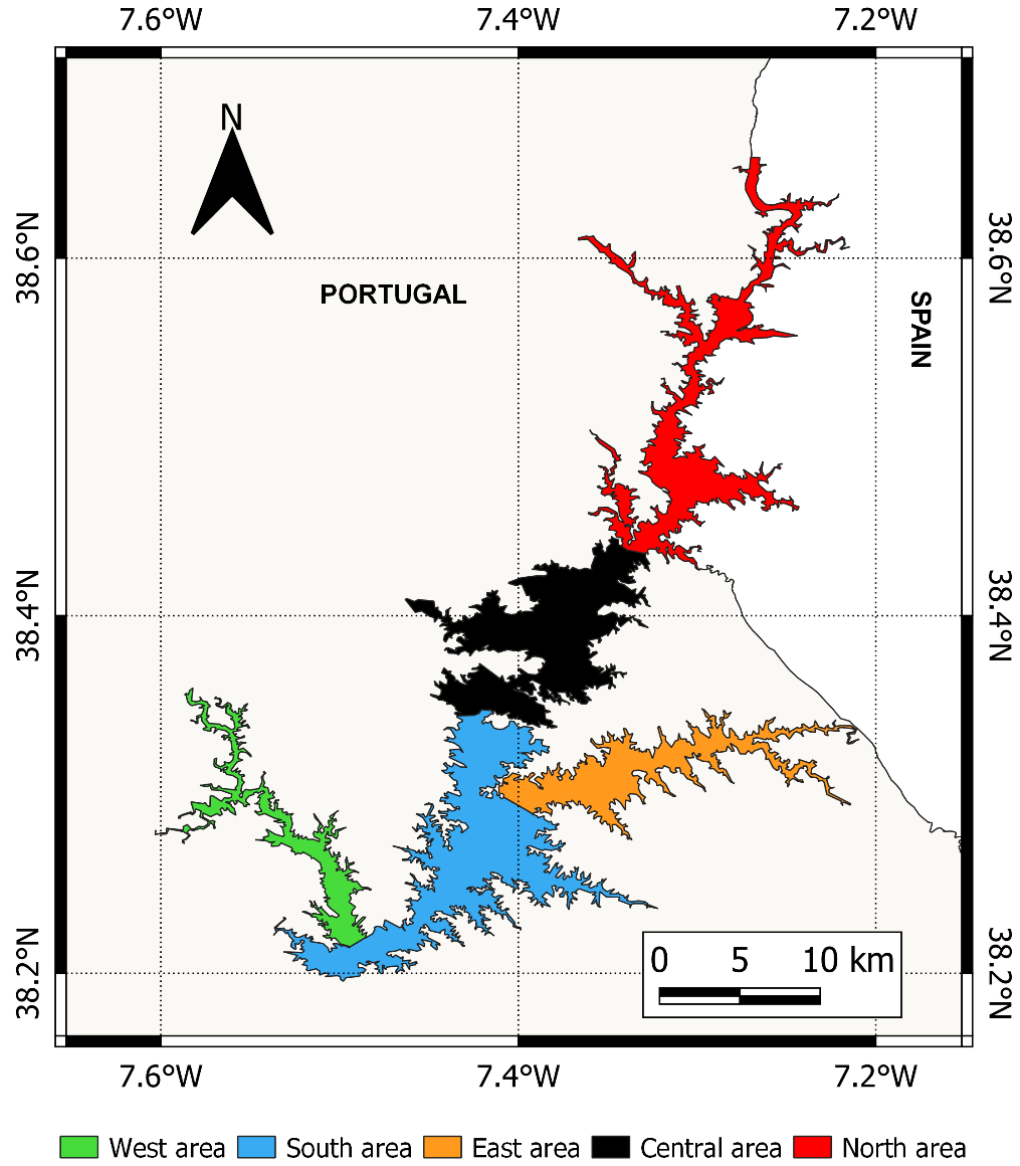

Figure 1. Alqueva reservoir divided into five areas for water quality analysis.

2.2. Sentinel-3/OLCI Data

The Ocean and Land Colour Instrument (OLCI) is a visible–near-infrared imaging spectrometer onboard the Sentinel-3 satellites launched by the European Space Agency (ESA). There is a constellation of two satellites: Sentinel-3A, launched in 2016, and Sentinel-3B, in 2018. OLCI will be widely used for studying the open ocean and inland/coastal waters since two more versions of the sensor are planned for launch over the next years (Sentinel-3C in the period 2023–2030 and Sentinel-3D in 2025–2032), thus allowing continuity. Since the launch of Sentinel-3B in April 2018, the Alqueva reservoir currently has a daily revisit. The instrument OLCI has a spatial resolution of 300 m (full resolution, FR) or 1200 m (reduced resolution, RR). Despite the spatial resolution of 300 m, it can be applied in large lakes, and due to its fairly high spectral resolution (21 bands in the range of 400–1020 nm), it is very useful for water and algae bloom monitoring. It also has a very relevant aspect in the study of lakes and oceans: sun-glint minimization [46]. With sun-glint minimization,

the OLCI allows to include in the study practically all cloud-free days between May and August, months when deterioration of water quality and the emergence/evolution of microalgae must be monitored. With the Sentinel-2/MSI instrument, despite its better spatial resolution, many days would be excluded due to sun-glint presence, as discussed in a previous work [30].

The dataset used in this study is the Sentinel-3 Level-1 (top of the atmosphere), with 300 m spatial resolution (full resolution product) and was downloaded from Copernicus Open Access Hub (https://scihub.copernicus.eu/dhus/#/home, accessed on 1 November 2021). The OLCI Level-2 Water Full (300 m) and Reduced (1200 m) resolution products are also available as Level-2 (with atmospheric correction). However, Level-1 reflectances were used here in order to apply the suitable atmospheric correction scheme (Section 3.1) to obtain the surface reflectances.

2.3. In Situ/Laboratory Data

Since 2016, measurements of SD have been carried out at various points in the Alqueva reservoir. The SD is a quick and simple way to assess the transparency of water. It consists of a disk divided into four, with black and white contrast, and it is used to measure the depth until is visible in the water column. Generally, the lower the SD, the higher the Turb. During the period 2016–2021, the highest SD value was obtained on 11 March 2019, with 7 m measured at two locations in the Alqueva reservoir (south region). This maximum is much higher than the previous maximum of 5.5 m on 24 May 2017. The average value of all measurements in the Alqueva reservoir from 2016 to 2021 is 2.94 m. A minimum value of just 0.4 m was measured in August 2017 in the northern region of the reservoir. The lowest values of SD were measured during periods with presence of microalgae in the reservoir.

Since 2017, water samples and laboratory analyses have been carried out to have concentrations of Chl-a, PC, and Turb (Table 1). Water samples were collected at 0.5 m depth. Chl-a determination was based in molecular absorption spectroscopy and the equations developed by Lorenzen [47], according to the standard methods NP 4327:1996 [48] and EN ISO 10260:1992 [49]. Turb was determined using the nephelometric method [50]. PC determination was performed following the procedure proposed by Horváth et al. (2013) [51], extracted with phosphate buffer with the modifications suggested by Lauceri et al. (2017) [52]. The highest values of Chl-a/PC concentrations and Turb were obtained in late summer or early autumn (August/September), coinciding with microalgae blooms.

2.4. Meteorological Data

Since 2017, three stations were installed in the Alqueva reservoir, recording meteorological data with a temporal resolution of one minute, namely, wind intensity and direction, air/water temperatures, relative humidity, solar radiation, and accumulated precipitation, among other parameters. One of the stations is installed in a floating platform (Montante station), and the other two meteorological stations (CidAlmeida and Barbosa stations) are installed on the margins of the reservoir. The water temperature was measured on the Montante station at various depths, namely, at 0.05, 0.25, 0.50, 0.75, 1, 2, 4, 6, 8, 10, 12, 15, 20, 30, and 60 m depth. In the Alentejo region, where the Alqueva reservoir is located, the summers are very hot and dry, with high solar radiation. Between May and September, the average rainfall is very low, and this rainfall is mainly convective. Almost all the accumulated precipitation is recorded in the period between October and May. Wind intensity is normally of weak (or weak to moderate) intensity in the Alqueva reservoir [53]. Over the entire analyzed period, only in March 2018 was the average wind intensity above 4 m/s. Figure 2 shows the monthly evolution of meteorological parameters in the period 2017–2020: air temperature, water temperature, and monthly accumulated precipitation.

The water temperature follows the variations of the air temperature but presents smaller differences between months due to its high heat capacity and thermal inertia.

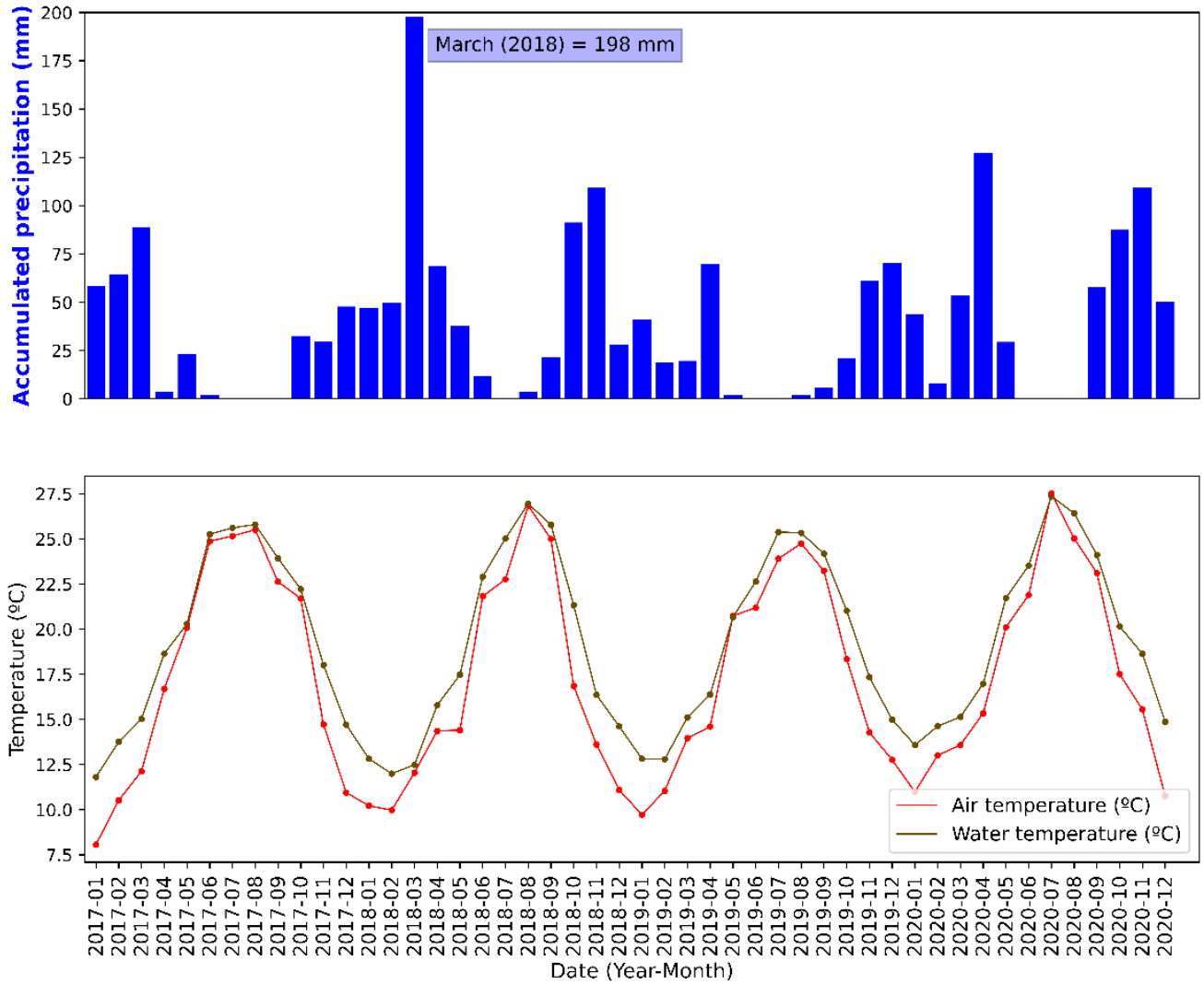

Figure 2. Monthly accumulated precipitation (above) and monthly average of air/water temperatures (below), in the Alqueva reservoir.

3. Methodology

Satellite remote sensing of water quality parameters relies on the use of surface spectral reflectances above water. However, Sentinel-3 OLCI measurements are taken at the top of the atmosphere (TOA). It is thus necessary to atmospherically correct the data in order to account for the absorption and scattering atmospheric effects and obtain the surface signal. In Section 3.1, the atmospheric correction method and the empirical algorithms are described. The k-means approach implemented to define different optical water types is presented in Section 3.2. Section 3.3 shows the methodology followed in the comparative analysis between quantitative and qualitative estimations of water quality. Figure 3 shows a flowchart summarizing the methodology and main results of this work. The grey boxes show the main results, and in parentheses the subchapter is shown.

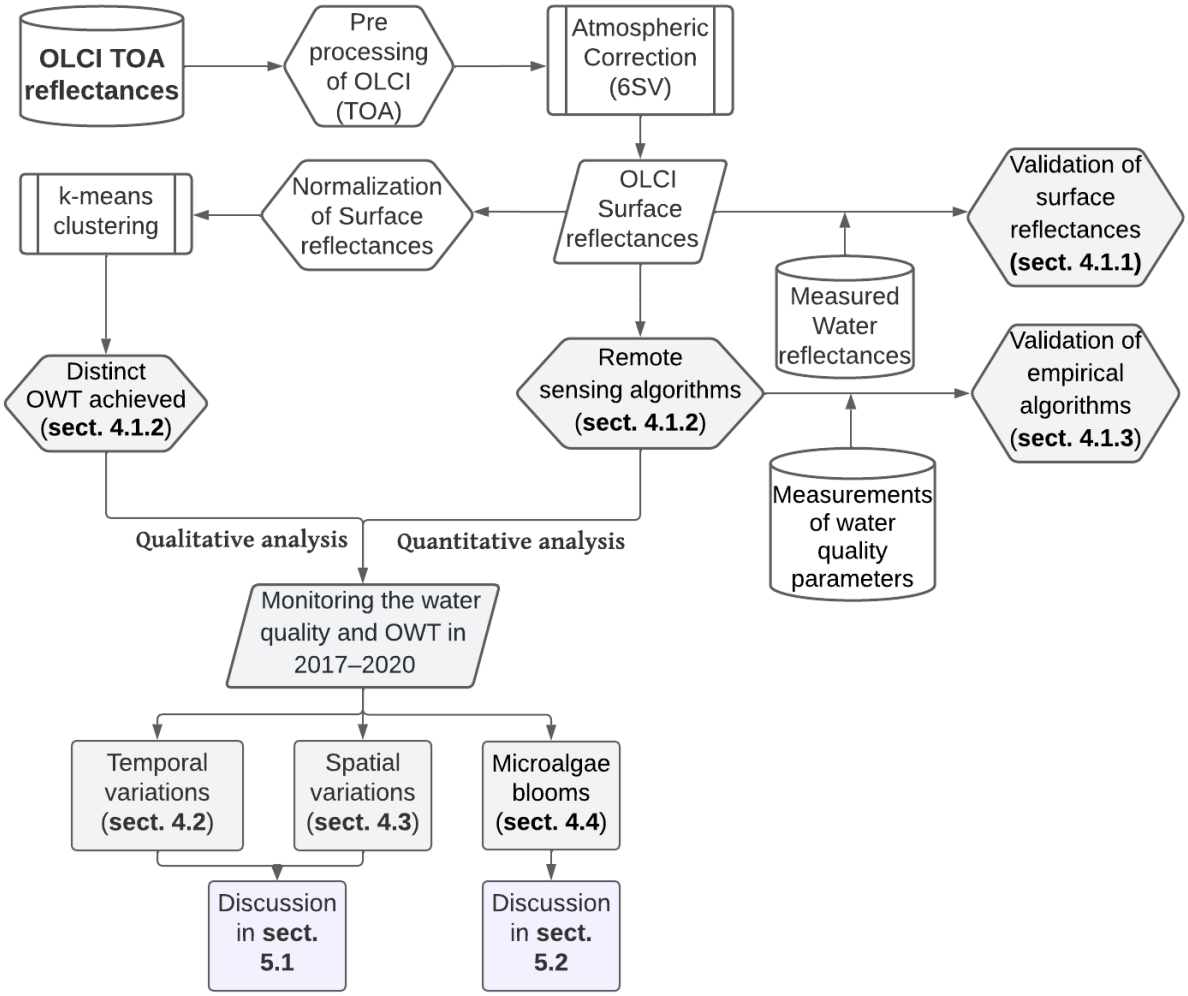

Figure 3. Flowchart showing the methodology using OLCI data and the main results (gray background) obtained in this work.

3.1. Atmospheric Correction and Empirical Algorithms

The satellite data of Sentinel-3/OLCI used are Level-1 (see Section 2.2) corresponding to TOA spectral measurements, which are subsequently corrected for the effects of the atmosphere in order to obtain the surface signal. Therefore, in order to obtain estimates of water parameters, the following procedures were carried out:

(i) The preprocessing of TOA Sentinel-3 imagery, including image reading, subset to Alqueva reservoir area, processing of radiances to reflectances, and extraction of the products. These four steps were performed using the toolbox SNAP (Sentinel Application Platform, http://step.esa.int/main/toolboxes/snap/, accessed on 1 November 2021), version 6.0. The top-of-atmosphere (TOA) reflectances were extracted from the OLCI images. The products SZA (solar zenith angle), SAA (solar azimuth angle), VZA (view zenith angle), and VAA (view azimuth angle) were also extracted, to be used in the atmospheric correction scheme as geometrical conditions.

(ii) The second step is the atmospheric correction of the various effects of the atmosphere, namely, ozone, water vapor, and aerosols. A reliable and adequate atmospheric correction process in the analysis of surface parameters in lakes or ocean is essential, as water usually has low reflectances, so small errors in the atmospheric correction can lead to large errors in surface reflectance estimates. In this work, the atmospheric correction method 6SV was assessed to obtain the surface reflectances, applied to cloud-free images acquired by the OLCI instrument. Python code was used to transform TOA to surface reflectances. Other atmospheric correction methods were verified in the

literature, such as the ACOLITE or C2RCC (Case 2 Regional CoastColour) processor. We selected the 6SV method mainly due to three factors: (a) There are high correlations between estimated and measured reflectances in the Alqueva reservoir considering previous studies [30,44,45]. These high correlations mean that when using the 6SV method, despite the associated errors (in absolute value), there is similarity between shape of estimated and measured reflectances, being a crucial factor for a correct definition of OWTs. (b) It is a method that normally does not have null or negative reflectances, in situations of high water transparency (low surface reflectances), while with C2RCC and ACOLITE processors this happens. We tested the C2RCC processor for days with clean water, i.e., low water reflectances, and we obtained negative reflectances, without necessarily having high AOTs. This result for the Alqueva reservoir is in agreement with other studies, where there is an underestimation of the reflectances compared to the surface reflectances measured using the C2RCC processor [20,54]. (c) It is a method of atmospheric correction that has been extensively used in several lakes and with good accuracy compared to measured surface reflectances [21–23,30,44,45,55,56].

The 6SV is a vector version of the 6S (Second Simulation of a Satellite Signal in the Solar Spectrum), being a robust radiative transfer code that is highly accurate, and was also used in the previous study in the Alqueva reservoir [30]. The 6SV method is used to correct the OLCI images over the Alqueva reservoir, allowing to account for the various effects of the atmosphere. We used input parameters for the 6SV process to model the atmospheric effects and spectral/geometrical conditions, as shown in Table 2.

Table 2. Input parameters of 6SV model applied to Sentinel-3/OLCI.

	Source	**Parameters**
Input type	Sentinel-3/OLCI	TOA reflectance
Geometrical conditions	Sentinel-3/OLCI	Solar zenith angle, solar azimuth angle (○)
		View zenith angle, view azimuth angle (○)
		Month, day
Atmospheric conditions (user)	Aeronet	Water vapor (g/cm^2)
	Ozone Monitoring (OMI)	Ozone (cm-atm)
Aerosol model (type)	-	Continental
Aerosol model (concentration)	Aeronet	Aerosol optical thickness at 550 nm
Spectral bands	Sentinel-3/OLCI	Spectral function responses

The validation dataset of surface spectral reflectances was obtained at the Alqueva reservoir with a portable spectroradiometer FieldSpec UV/VNIR (ASD, Inc., Bouler, Colorado USA). More details about the FieldSpec UV/VNIR (ASD, Inc.) can be found in [57,58]. In addition to the correlation coefficient between in situ reflectances and satellite data, the bias, the MAE (mean absolute error), and MAPE (mean absolute percentage error) were used. The bias error and the MAE measure of the overall errors are that the MAE correspond to absolute errors. MAPE is defined as the mean of absolute differences between estimates (satellite-derived) and observations and measures the error in percentage terms.

The remote sensing algorithms obtained for the Alqueva reservoir were based on empirical relationships between the water quality parameters and Sentinel-3/OLCI retrievals of surface reflectances. In situ measurements of SD and laboratory analysis of Chl *a*, PC, and Turb were related to the atmospherically corrected surface spectral reflectances obtained from OLCI, through regression algorithms. Maximum differences of 1 day were accepted between water quality parameters and OLCI surface reflectances. In order to relate satellite data with measured/laboratory data, the nearest water pixel was used. An additional filter

has been added to exclude pixels at the land/water boundary, the Modified Normalized Difference Water Index (MNDWI). This index evidences the open water features compared with NDWI (Normalized Difference Water Index) while efficiently suppressing land, vegetation, and soil noise [59]. Water pixel selection was performed considering an MNDWI index greater than 0.5. It was found that this index excludes not only many mixing spectra, but also pixels contaminated by cirrus and even light clouds visible by the RGB image and distinguishable in the reflectance spectrum (much less variation in the visible to NIR bands, comparatively to purely water pixels).

The defined regression algorithms were validated using different (independent) periods from those used to establish the algorithms. The period for the different water quality parameters is distinct due to different covering periods. Algorithms for PC and Turb were defined in the period 2018–2020 and 2017–2020, respectively. For these two water quality parameters, the validation period is 2021. For SD and Chl-a concentrations, the definition of the algorithms were in 2016–2018 and 2017–2018 respectively, and the validation period corresponds to 2019–2021.

3.2. Definition of Optical Water Types (OWT)

Distinct optical water types (OWT) were identified based in the surface reflectance spectra of Sentinel-3 data in the period 2017–2020. Each type of OWT represents a group of similar optical characteristics and similar reflectance spectra. Prior to clustering, preprocessing was performed. It was applied to each day with clear sky over the reservoir, excluding pixels or days in the following cases:

- Days with at least one pixel having null values of view azimuth angle. These images represent days when the reservoir is at the limit of the OLCI image, thus having degradation in image quality and reflectance spectra.
- Pixels with MNDWI less than 0.5.
- Days when there are less than 200 pixels with MNDWI greater than 0.5.
- Days with at least one pixel with negative reflectance in one band between 490 nm and 708.75 nm. Only five days were excluded with this filter, being days with high AOT values.

After applying these four filters, all the water pixels were used to divide the spectra with similar characteristics within each of the clusters. The wavelengths chosen were in the range of 490 nm to 709 nm, that is, between band B4 and band B11 of the instrument OLCI.

K-means and fuzzy-c means, being unsupervised clustering methods, aim to cluster all input samples within different classes but require a priori selection of the optimal number of clusters and a method for excluding data from the analysis. Some studies identify very similar results between these two clustering methods [30,38]. The k-means approach was used, being one of the most popular non-hierarchical clustering techniques [33,34], as a method with high efficiency in the classification of large datasets [60]. Python code was used to run the k-means method and assign each of the OLCI pixels to a different OWT. The k-means algorithm was applied to the normalized OLCI reflectances instead of using the raw surface reflectances, to reduce the influence of the magnitude on the clustering and give greater relevance to the spectral reflectance shape [32,34]. Giving greater relevance to the shape allows absorption characteristics to have more impact on clustering. It also allows to reduce the effects of errors in atmospheric correction because these uncertainties have a greater effect on the amplitude of the spectra rather than their shape [32]. The normalization of each reflectance was made using its integrated value between B4 and B11 bands. This method was used because it does not give a greater weight to a defined part of the reflectance spectra, contrarily to other normalization methods. Unsupervised methods such as the k-means approach do not allow to exclude spectra from the analysis. In this way, this method may include spectra in a given OWT of pixels that are on the border between two or more OWTs. However, after processing the clustering method, some spectra could be excluded, through the information provided from the "silhouette width" [61]. The silhouette width measures how well each spectrum is clustered, having ranges between

−1 to 1. A value of 0 of the silhouette width indicates that the spectra are on the boundary between two clusters and negative values indicate that those samples might have been assigned to the wrong cluster. In this work, only spectra with silhouette width above 0.05 were used. It was found that the silhouette index filter below 0.05 (pixel not assigned to any of the four clusters) excludes some spectra of doubtful quality (land/water mixture) that had not been excluded with the selection of MNDWI above 0.5. The silhouette width also allows to exclude spectra in areas that may have a mixture of two or more different OWTs. The silhouette width was also used to choose the statistically optimal number of clusters. The k-means method was run using two to ten clusters, and it was with four clusters that the highest mean silhouette value was obtained, that is, on average, the spectra are further apart spectrally compared to another selection of number of clusters.

3.3. Comparison between OWT and Water Quality Parameters

In order to have qualitative and quantitative estimations of water quality in the 2017–2020 period, the OWT classification was analyzed together with the estimations of water quality parameters. Aiming at full spatial cover and continuous monitoring of water quality parameters in the Alqueva reservoir, the atmospheric correction code 6SV was used to process all water pixels, for every cloud free day, obtained from Sentinel-3/OLCI (TOA) in the period. Filters were applied as explained in Section 3.2. The OWT classification allows assigning a cluster to each of the OLCI pixels, that is, an OWT spatialization map of the entire reservoir. The empirical algorithms provide, for every pixel, maps representing the estimates of water quality parameters. Then, the spatiotemporal variations of OWT and water quality parameters were analyzed, namely, Chl-a concentrations, PC concentrations, SD, and Turb. The silhouette index below 0.05 was used to exclude pixels, in addition to the MNDWI above 0.5. The water quality comparisons were performed based on boxplot representing the average conditions (average and median) and also the 10th, 25th (first quartile), 75th (third quartile), and 90th percentiles. The 10th and 90th percentiles were used to analyze the value corresponding to the 10% of highest and lowest severity for each water quality parameter. For the most correct comparison analysis between the OWT classification and water quality parameters, an intercomparison pixel-by-pixel (300 m of resolution) analysis was performed. The qualitative and quantitative comparisons were carried out by areas of the reservoir, dividing into the same five areas used in the previous study and presented in Section 2.1. The large differences in the number of OLCI pixels assigned to each Alqueva area would mean that analyzing the average characteristics of the entire reservoir would give greater relevance to the central and southern areas, possibly masking local variations in areas with much fewer pixels. In Table 3, the daily average of pixels per area and per year is presented. This average of pixels (by year and by area) was calculated, counting the number of pixels of all OLCI images used in this study.

Table 3. Daily average of pixels for each year and area.

	North	Center	South	West	East
2017	70	228	275	26	81
2018	70	227	282	27	85
2019	66	207	267	25	77
2020	47	172	237	20	62

4. Results

4.1. Definition of Optical Classification and Empirical Algorithms

4.1.1. Validation of OLCI Surface Spectral Reflectances

In order to estimate water quality parameters and the OWT classification, it is first necessary to obtain the surface reflectances applying the atmospheric correction process, as explained in Section 3.1. The validation of OLCI surface reflectances (after applying the 6SV method) is shown in Table 4 and corresponds to the period May 2016–September 2020.

In the present study, only the surface reflectances between B4 band (490 nm) and B11 band (709 nm) were used, where correlations are higher than 0.9 (close to 1) and MAPE lower than 40% (except B11 band). The estimated values are overestimated compared to those observed (positive bias).

Table 4. Statistical indicators between the measured and satellite-derived (OLCI) water reflectances using the 6SV method.

N = 27	Correl.	Bias	MAE	MAPE (%)
B4	0.92	0.006	0.006	39
B5	0.92	0.006	0.006	31
B6	0.96	0.004	0.005	18
B7	0.95	0.004	0.004	26
B8	0.94	0.003	0.003	31
B9	0.92	0.003	0.003	33
B10	0.92	0.003	0.003	29
B11	0.93	0.002	0.003	47

4.1.2. Definition of the Empirical Algorithms and the Four OWTs

Two independent methods were developed to estimate the water quality in the Alqueva reservoir: empirical algorithms for definition (Section 3.1), and using the k-means clustering method, four distinct OWTs were achieved (Section 3.2).

The best algorithm found for Chl-a, with the best results of R^2 and NRMSE, was adding the reflectance of the green band (560 nm) to the bands 709 nm and 665 nm. Normally, more than half of the year, Alqueva reservoir present low Chl-a concentrations. This fact helps to explain why the use of only red to NIR bands does not present good statistical results, widely used in the context of lakes [62]. The green band of 560 nm is a chlorophyll reference (chlorophyll minimum absorption), where the presence of greater reflectance represents greater Chl-a concentrations. The green band (560 nm in Sentinel-3 OLCI) is widely used in cases of lower Chl-a concentrations. The other two bands used in the algorithm (665 and 709 nm) are used in cases of high concentrations of Chl-a.

$$\text{Chl-a} = 7670.4 \times \left(\frac{B6 \times B11}{B8}\right)^2 - 260.23 \times \left(\frac{B6 \times B11}{B8}\right) + 4.61 \quad (1)$$

Although high concentrations of Chl-a are indicators for the appearance of cyanobacteria, they do not imply necessarily its presence. The pigment phycocyanin is a marker for cyanobacterial presence in eutrophic water and has an absorption peak at approximately 615–620 nm [18,19]. The PC algorithm determined with the best coefficient of determination uses this absorption peak (of OLCI), as well as a near-infrared (NIR) band, centered at 709 nm (very low PC absorption) and also the green band (of OLCI; medium absorption and high reflectance):

$$\text{PC} = 213,558.8 \times \left(\frac{B6 \times B11}{B7}\right)^3 - 6715.41 \times \left(\frac{B6 \times B11}{B7}\right)^2 + 52.11 \times \left(\frac{B6 \times B11}{B7}\right) + 0.11 \quad (2)$$

The SD algorithm developed by Rodrigues et al. [30] for Sentinel-2/MSI is adopted in the present study, using instead Sentinel-3/OLCI. The equivalents OLCI bands are used here, adjusting the linear regression coefficients:

$$\text{SD} = 0.036 \times \left(\frac{B4}{B6 \times B8}\right) + 0.79 \quad (3)$$

The Turb algorithm, determined with the best coefficient of determination, uses bands $B4$ and $B11$, presenting the following equation:

$$\text{Turb} = 5.10 \times \left(\frac{B11}{B4}\right)^2 - 0.92 \times \left(\frac{B11}{B4}\right) + 0.81 \quad (4)$$

The scatter plots, with the best fit for each algorithm between satellite-retrieved reflectances and water parameter data, are shown in Figure 4 (chlorophyll a, phycocyanin, SD, and Turb).

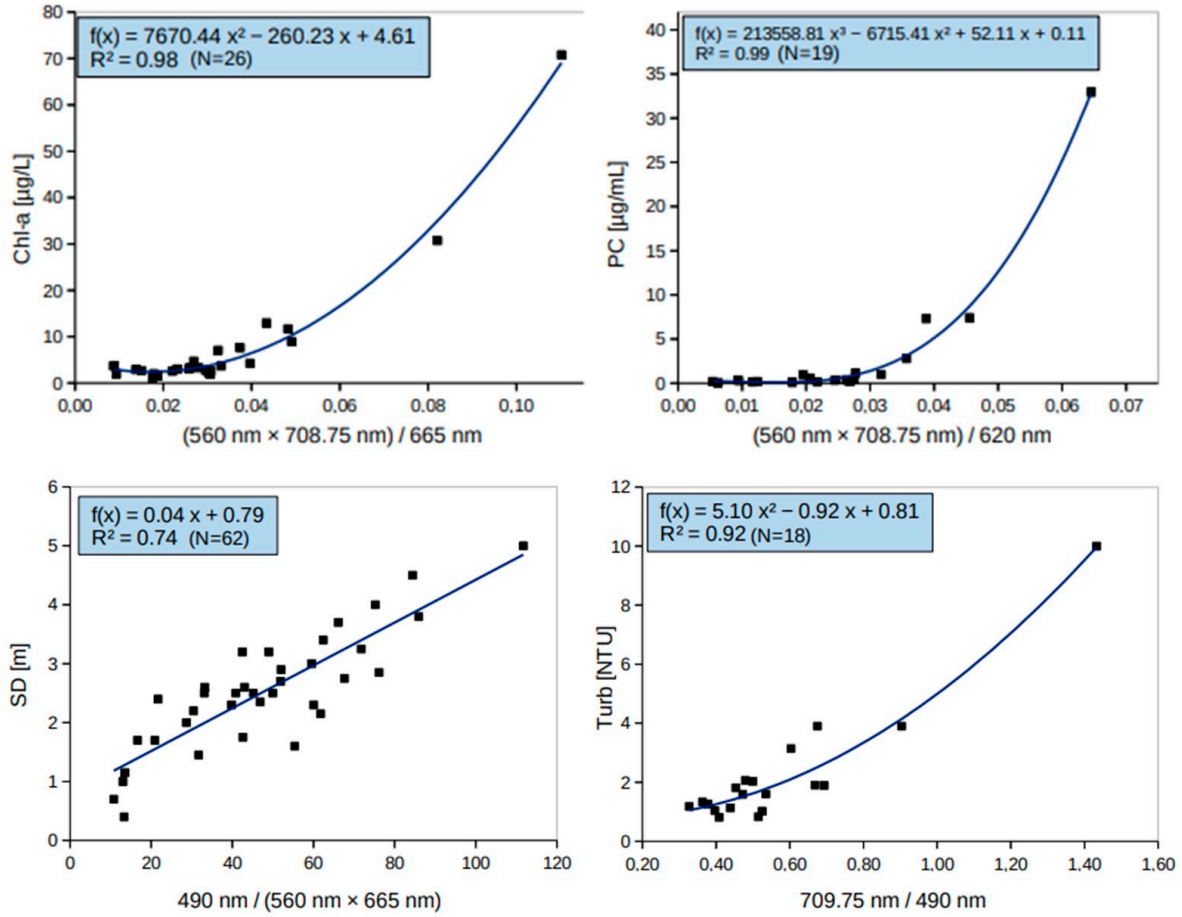

Figure 4. Scatter plot between the water quality parameters and the combination of OLCI band reflectances (Chl-a and PC on the top panel; SD and water turbidity on the bottom panel).

Four distinct sets of reflectance means were defined (Figure 5). These reflectance means form the OWT classification in the Alqueva reservoir, which are representative of the averaged conditions caused by the optical properties of the water column. In addition, the median for each of the clusters was also calculated and showed very identical spectra for the different selected clusters (not showed here). The OWTs were organized in ascending number (1 to 4) based on ascending water turbidity of the water.

4.1.3. Validation of Empirical Algorithms

The results obtained using the developed empirical algorithms were compared with in situ measurements (validation of the empirical algorithms) for a different period with respect to that used to derive the four equations (Section 4.1.2). These algorithms were applied to the nearest water pixel with respect to the sites where the water samples were collected (Turb, Chl-a, and PC) and to SD measurements. In Figure 6, the relationships between estimated water quality parameters and the corresponding data measurements are shown.

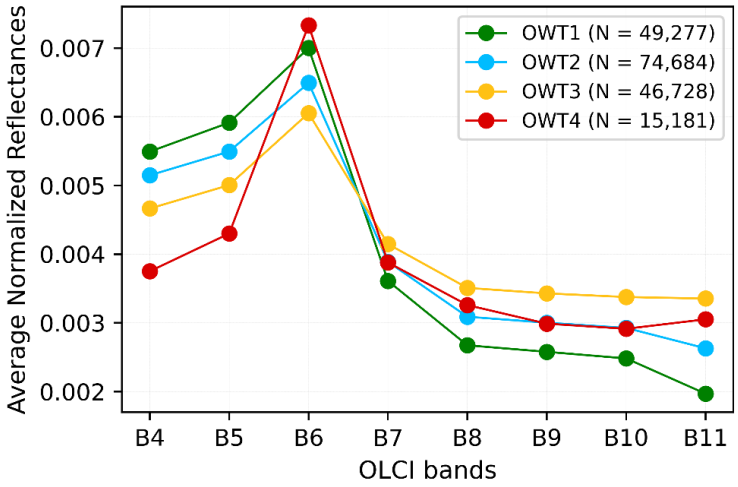

Figure 5. Average normalized reflectance spectra derived from the k-means classification by class (OWT1, OWT2, OWT3, and OWT4).

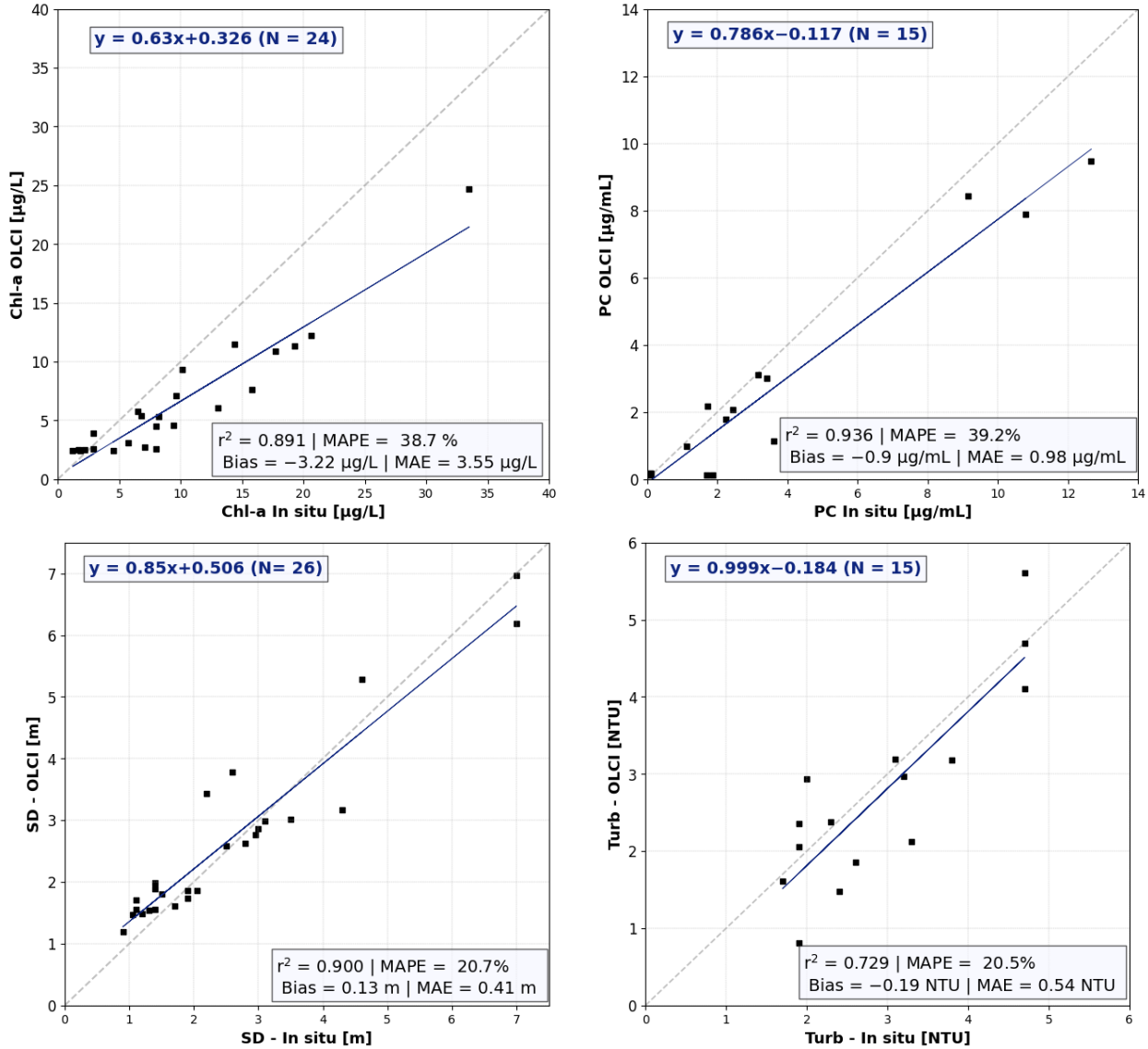

Figure 6. Scatter plot of predicted versus measurements/laboratory data (Chl-a and PC on the top panel; SD and Turb on the bottom panel).

In the validation of empirical algorithms (Figure 6), note the good agreement between observed and satellite estimates, with high coefficients of determination (above 0.9), except for Turb, with r^2 of 0.73. There are MAPEs close to 20% for SD and Turb, and 39% for Chl-a concentrations. Note that the MAPE near 40% in the validation of PC algorithm is also due to the fact that, in general, there are many low values of PC concentrations than higher values. Therefore, for very low PC concentrations, there can easily be obtained absolute mean errors in percentage above 100%. For SD and Turb, there is no relevant trend of overestimation or underestimation of the estimated data in relation to the measured data (bias close to 0). For Chl-a and PC, there is almost always an underestimation of the estimated data relative to the laboratory data, with negative bias (bias practically equal to the MAE), and almost all are points below the y = x line.

4.2. Qualitative and Quantitative Analysis of Water Quality

The clustering approach presented in this study (Section 3.2) has the advantage to differentiate subsets based mainly on the shape of surface reflectances. Four optical water types (OWT) were defined through a k-means approach applied to OLCI surface reflectances during the 2017–2020 period. The differences along the spectra of surface reflectances denote different optical characteristics and the predominance of one over another in water constituents (e.g., phytoplankton or non-phytoplankton particles). One of the essential features of spectral analysis is the verification of the variation between blue and green bands. Greater differences between band B5 (or other blue band) and band B6 represent greater presence of Chl-a (the greener the water is, the greater the reflectance of the green band in relation to the blue band). In the context of monitoring water turbidity, for minor ratios between reflectances in the blue and the red/NIR bands, greater water turbidity is expected.

Figure 7 shows the average raw reflectances (non-normalized) for each of the OWT groupings using the normalized reflectances. The typical spectrum of the OWT1 cluster (Figure 5 in Section 4.1.2 and Figure 7) represents conditions of low turbidity, that is, less dispersion and absorption by particles contained in the water. In the comparison between the typical conditions of the OWT1 and OWT2 cluster (Figure 5), a smaller difference was identified between the normalized reflectances (average) in the blue bands (B4 and B5 of OLCI); nevertheless, in the red and NIR bands (band B7) the cluster OWT2 overcomes the OWT1. Therefore, the areas assigned to the OWT2 cluster will normally have greater turbidity than areas assigned to the OWT1 cluster and weak or non-existent presence of microalgae. Analyzing the slope between the green (B6) and red (B7) band, it is identified that the OWT3 cluster represents the optical conditions with the highest absorption of the non-phytoplankton particles (sediments, for example). It is noted that the clusters OWT3 and OWT4 represent the most turbid optical waters, because in these clusters, on average, there are lower differences between the blue and red/NIR bands. The main source of turbidity in OWT3 is non-phytoplankton particles, while for cluster OWT4, it is the presence of microalgae, because this cluster represents areas with high concentrations of Chl-a. Another typical characteristic of the presence of microalgae in OWT4 is the peak at 708 nm, which is usually associated with high algae particle concentration [17,63].

The water quality algorithms and the OWT class through k-means clustering method (Section 4.1.2) were applied to all water pixels in the period 2017–2020. Therefore, a complete water quality characterization is obtained for all clear sky days, excluding pixels and days in the conditions defined in Section 3.2.

Figure 8 show the monthly evolution of Chl-a, PC concentrations, SD, and Turb obtained with the algorithms presented in Section 4.1.2 (Equations (1)–(4)). Each boxplot is composed of the mean, median, 25th percentile (1st quartile), 75th percentile (3rd quartile), and 10th/90th percentiles. In these graphs, the red bars represent the months (August to October) that normally have the highest presence of microalgae in the Alqueva reservoir. The frequency distribution of the four OWTs in the 4 years analyzed is shown in Figure 9.

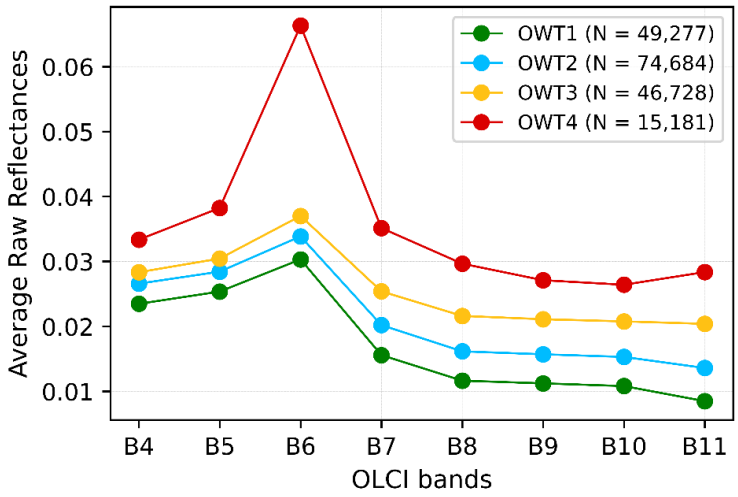

Figure 7. Average raw reflectance spectra derived for the k-means classification by class OWT.

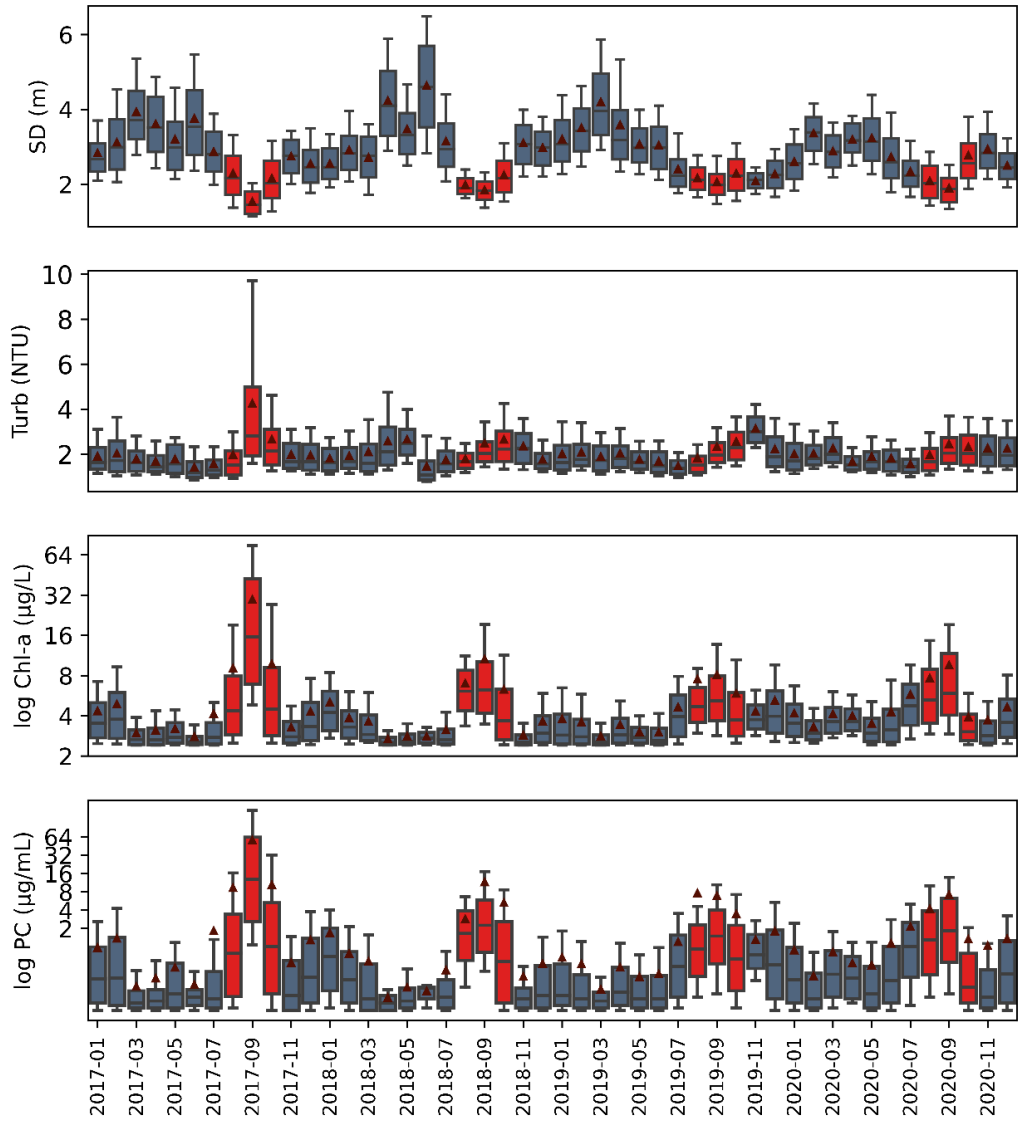

Figure 8. Boxplots with the monthly evolution of Chl-a, PC, SD, and Turb in the 2017–2020 period. The sample median is indicated by a horizontal line within the box while the triangle represents the monthly average.

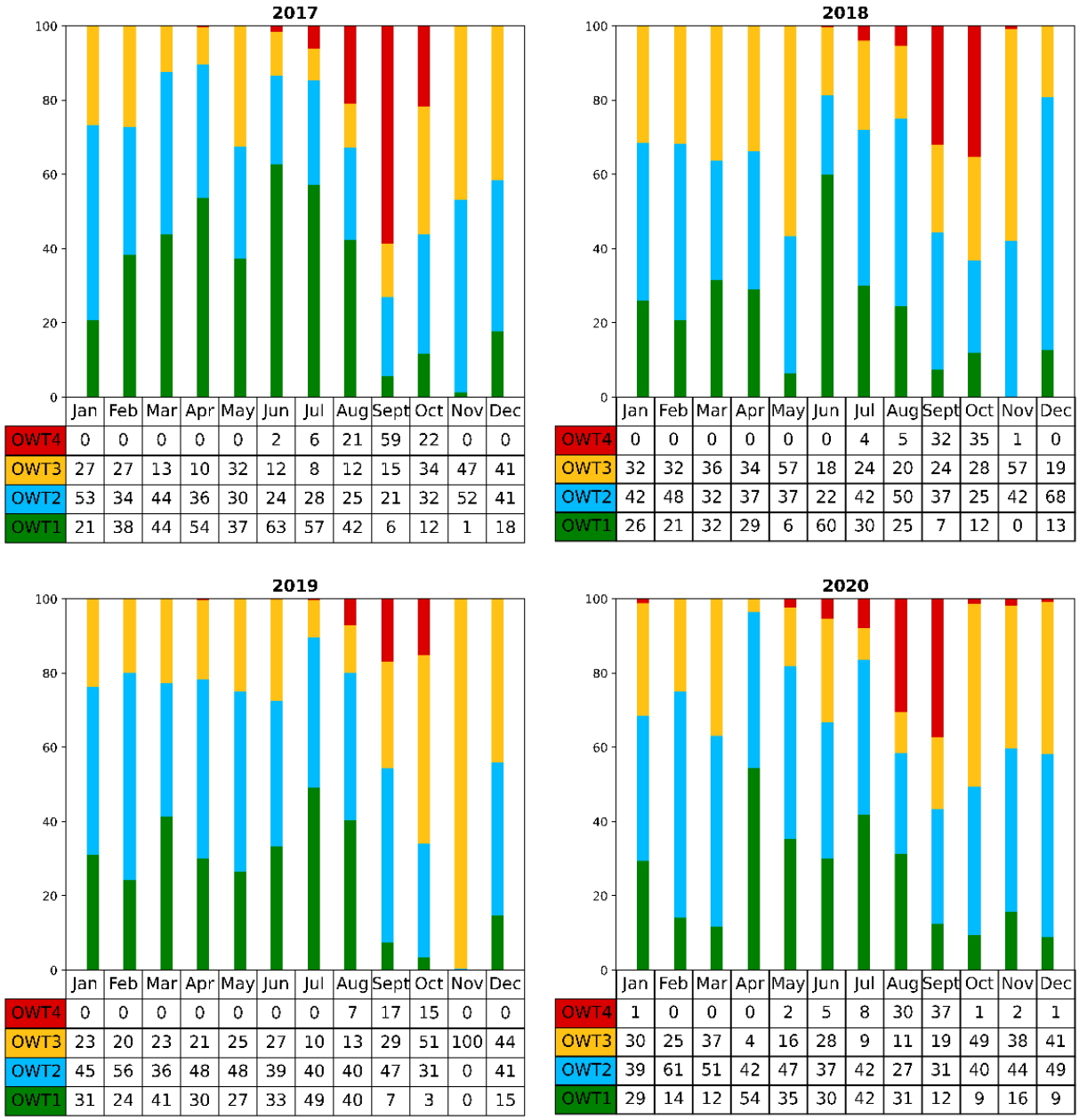

2017	Jan	Feb	Mar	Apr	May	Jun	Jul	Aug	Sept	Oct	Nov	Dec
OWT4	0	0	0	0	0	2	6	21	59	22	0	0
OWT3	27	27	13	10	32	12	8	12	15	34	47	41
OWT2	53	34	44	36	30	24	28	25	21	32	52	41
OWT1	21	38	44	54	37	63	57	42	6	12	1	18

2018	Jan	Feb	Mar	Apr	May	Jun	Jul	Aug	Sept	Oct	Nov	Dec
OWT4	0	0	0	0	0	0	4	5	32	35	1	0
OWT3	32	32	36	34	57	18	24	20	24	28	57	19
OWT2	42	48	32	37	37	22	42	50	37	25	42	68
OWT1	26	21	32	29	6	60	30	25	7	12	0	13

2019	Jan	Feb	Mar	Apr	May	Jun	Jul	Aug	Sept	Oct	Nov	Dec
OWT4	0	0	0	0	0	0	0	7	17	15	0	0
OWT3	23	20	23	21	25	27	10	13	29	51	100	44
OWT2	45	56	36	48	48	39	40	40	47	31	0	41
OWT1	31	24	41	30	27	33	49	40	7	3	0	15

2020	Jan	Feb	Mar	Apr	May	Jun	Jul	Aug	Sept	Oct	Nov	Dec
OWT4	1	0	0	0	2	5	8	30	37	1	2	1
OWT3	30	25	37	4	16	28	9	11	19	49	38	41
OWT2	39	61	51	42	47	37	42	27	31	40	44	49
OWT1	29	14	12	54	35	30	42	31	12	9	16	9

Figure 9. Frequency of the four OWTs by year and by month.

Three main characteristics are presented and described below. The first is related to the presence of microalgae blooms in the reservoir in late summer and early autumn. The second is the high turbidity resulting from the overturn period. These two periods of greater turbidity occurred sequentially in the 4 years analyzed, having generally occurred between August and November. Finally, there is verification that in the rest of the months there are low Chl-a/PC concentrations and high percentage of OWT1 or OWT2 attribution.

(1) There is worse water quality in the months between August and October, associated with the presence of microalgae in the Alqueva reservoir. This fact can be seen with the identification of OWT4 pixels (Figure 9) and even higher values of Chl-a/PC concentrations (Figure 8). It is identified that the OWT4 cluster is practically present only in this period, associated with the appearance of microalgae. In three of the four years analyzed, the worst month in terms of water quality was September, with the highest presence of OWT4 pixels (in frequency), greater turbidity, and highest Chl-a/PC concentrations (Figure 8).

In the four years analyzed, September of 2017 is by far the month with the highest presence of microalgae in the Alqueva reservoir:

- 58.3% of the pixels in the entire reservoir presented the OWT4 classification. September 2020 had the second highest attribution to OWT4 cluster with 37.1%.
- Water quality estimates in September present the highest values of biomass load (higher Chl-a concentrations), a greater presence of cyanobacteria (much higher PC concentrations than any other month) and Turb, and lower SD. A highlight is the value corresponding to the 90th percentile for an SD of less than 2 m, which denotes a very high turbidity in practically the entire reservoir and in all the days available for analysis.

Therefore, there is a clear sign of deterioration in water quality in September, with the results obtained from two distinct and independent methodologies (OWTs analysis and the use of empirical algorithms) giving the same indication. It is important to highlight the very relevant differences between the 75th and 90th percentile (as well as the difference between the mean and median) for Chl-a and PC concentrations in all the months of September of the 4 years, mainly in September 2017 (Figure 8). This fact denotes that the upper extremes of Chl-a and PC are very far from the median/average value of the entire sample. As will be explained in Section 4.3, this is related to the large spatial disparities in the reservoir.

(2) Every year, the phenomenon of the overturn occurs in the reservoir, associated with the cooling of the surface temperature, leading to the mixing between layers from surface to the bottom. In recent years, the overturn has mostly taken place in the end of November. Except for the year 2020 (when the overturn took place in December), it was in November that the highest turbidity values in the reservoir have been identified, caused by non-photosynthetic particles (not associated with the presence of microalgae). That is,

- Lower frequency (%) of spectra (OWT1) associated with the most transparent water.
- The month with the highest frequency (%) of pixels assigned to the OWT3 cluster, representative of pixels with high turbidity.

In November 2019, only one OLCI image was used for the monthly analysis of OWT and water quality parameters. In this month, the overturn was identified as happening between early and mid-November. The temperature profile was determined by measuring the water temperature at various depths (Section 2.4), from surface to the bottom (60 m depth). In mid-November the reservoir was fully mixed and the overturn was concluded, i.e., a homogeneous temperature profile was found throughout the water column (Figure 10). The only day (15) used in this month is precisely the day before the completion of the overturn. From the sample of 639 pixels used, 99.7% of these (Figure 9) were assigned to the OWT3 cluster.

In 2020, the overturn occurred in December, and it was the second month with the highest frequency of OWT3 pixels in this year.

(3) Most of the months present low to moderate values of Chl-a concentrations (range of 0–8 μg/L) and low turbidity. These months also present a frequency greater than 60% of all pixels assigned to clusters representing the best water quality, that is, with the attribution of OWT1 and OWT2 class. In the period between January and August, only in August 2020 was there an exception, with less 60% of the pixels assigned to the OWT1 and OWT2 cluster. There are a few months with the allocation of (OWT1 + OWT2) close to or greater than 90% of all pixels analyzed for each of those months. These are the months of March/April (2017), June/July (2017), July 2019, and April 2020. It can then be concluded that there are representative pixels of lower water turbidity and lower Chl-a concentrations in winter months (except December), spring, and early summer months. The influence of runoff in water turbidity is a fourth aspect that will only be analyzed in chapter 4.4, as it was only relevantly identified in narrower areas of the reservoir. This is also evidenced in the reflectance spectra, that is, in the OWT classification.

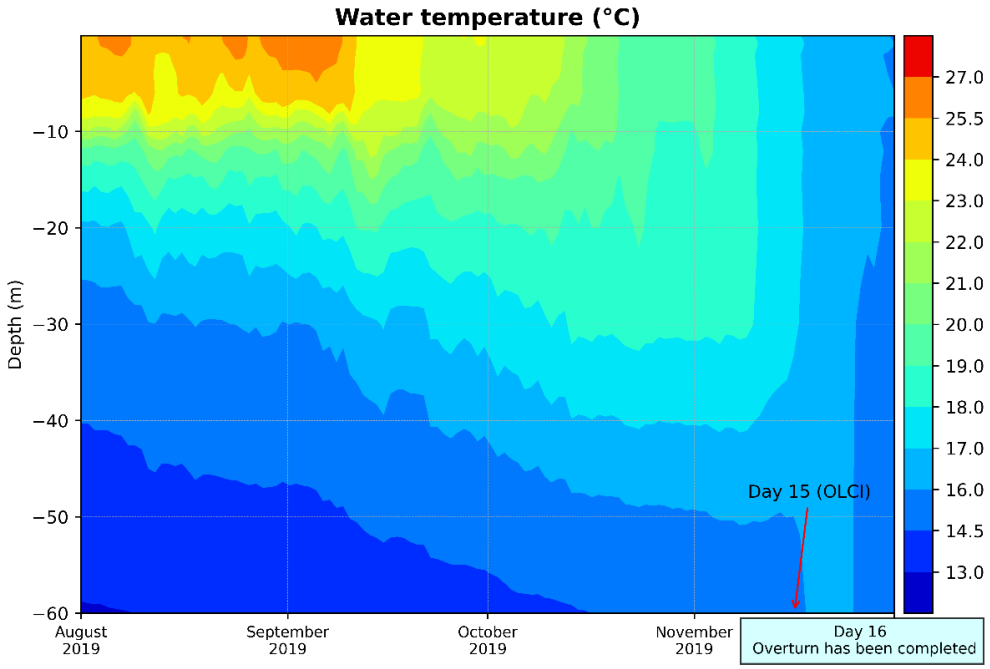

Figure 10. Temperature profile from August to November (2019).

A pixel-by-pixel intercomparison was also carried out in order to find relationships between the results of the water quality algorithms and the OWT attribution. To summarize the relationship between the four clusters and the parameters of water quality, four graphs are presented (Figure 11).

The water quality estimates from empirical algorithms generally present results in agreement with those expected for each of the clusters. That is, the typical values of Chl-a/PC concentration increased and SD decreased from OWT1 to OWT4. In the pixel-by-pixel intercomparison, a very significant number of points assigned to the OWT1 classification showed very low Chl-a/PC concentrations, and very low Turb. On the opposite side, almost all the pixels assigned to the OWT4 cluster presented estimates of very high Chl-a/PC concentrations and high Turb/low SD. Table 5 presents the main conclusions for each of the defined clusters.

Table 5. Summary of key findings from the four defined OWTs. Water turbidity and Chl-a concentrations increase from cluster OWT1 to OWT4.

OWT Type(s)	Summary
OWT1	Characteristic of more transparent water spectra with lower Chl-a concentrations, and no presence of PC
OWT1 + OWT2	Characteristic of high water transparency
OWT2	OWT2 typically with lower water transparency and higher Chl-a concentrations than OWT1
OWT3 + OWT4	Water with low/moderate water transparency
OWT3	Low to moderate water transparency, but not necessarily associated with microalgae blooms
OWT4	High or very high Chl-a concentrations; microalgae blooms and risk of cyanobacterial presence

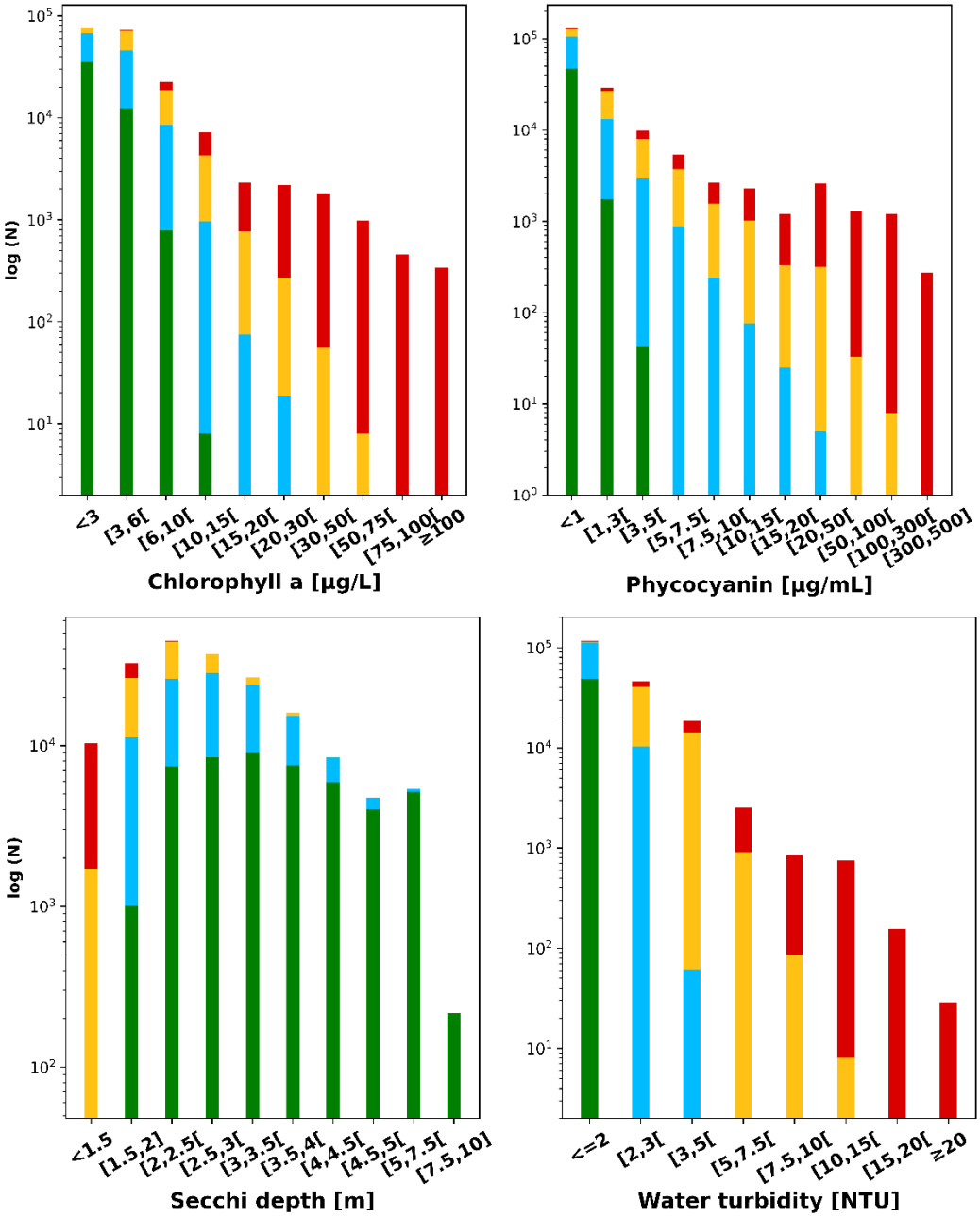

Figure 11. Number of pixels per OWT cluster and for each of the classes of water quality parameters. The figures above represent Chl-a concentrations (**left**) and PC concentrations (**right**). Below represent SD (**left**) and Turb (**right**). The green bars represent OWT1, in blue OWT2, in orange OWT3, and red is OWT4.

4.3. Spatial Variations of the Optical Water Types and Water Quality

In order to verify spatial variations, the reservoir was divided into five areas, calculating the OWT frequency for each month and area (Figure 12). Figure 13 shows the water quality mean by area and by month for the period 2017–2020. Spatial variations of OWT and parameters of water quality were analyzed, evidencing the following differences between the five areas of the reservoir:

- The northern area of the reservoir represents the area with the highest percentage of pixels assigned to OWT3 cluster or OWT4 during the four years analyzed. It is the area of the reservoir most affected by microalgae blooms (between July and October) and also by runoff phenomena after heavy rainfalls.

- The central area, being much wider than the northern area and further away from the Guadiana river inlet (in the north region), presents better water quality in all analyzed years compared to the north area. Precipitation and runoff affect this area less. However, microalgae blooms also disturb this area, mainly in the period between August and October, being the second area with greater deterioration of water quality in this period. This is verified not only by the analysis of OWT frequencies, but also by the estimates of Chl-a and PC concentrations.
- The southern area, one of the areas farthest from the area with the worst water quality (north area), presents, on average, the best conditions (lowest water turbidity and highest frequency of OWT1 + OWT2 pixels) of the entire reservoir. It also has the lowest impact of runoff effects or microalgae blooms.
- The western area (branch that starts in the south area towards the west/northwest) presented the most discrepant behavior in the 4 years analyzed, with respect to the July–October period, compared to the average of the entire reservoir. It was the area with the lowest frequency of pixels assigned to the OWT4 cluster in 2017, in the months with the presence of microalgae, being in 2018 the second worst (highest frequency of OWT3 + OWT4) area with high frequency identification of OWT3 pixels, in the month with highest rainfall (March 2018).
- The east area, despite being much narrower than the central and south areas, generally presents similarity to these two areas in relation to the frequency of OWT1 and OWT2. This area is also less representative of microalgae in 2018 and 2020, i.e., it presents lower frequency of pixels with OWT4 attribution and lower Chl-a/PC concentrations.

It is generally noted that in months without high rainfall and/or without the presence of microalgae (July to October mainly), a similar frequency of characteristic low turbidity spectra (OWT1 + OWT2) is observed between the four areas in the reservoir (except the north area). However, in these periods, the percentage of pixels assigned to the cluster featuring greater water transparency (OWT1) differs significantly between areas, being more significant in the south, center, and east areas. The north area is by far the one with the lowest frequency of OWT1 pixels. In this area, in 2020, there was no month with frequency higher than 20% attributed to the OWT1 cluster. In 2018, only June exceeded the 20% of pixels classified as OWT1, and in several months it did not even reach 0.1%. In 2018, the northern region of the reservoir presents 8 of 12 months with more than 85% of the pixels associated with either OWT3 or OWT4. Of these eight months, this area presents 4 months with practically 100% of the pixels attributed to the OWT3 cluster, representing turbid water. Of these four months, three coincide with high rainfall in the Alqueva reservoir and the other with the overturn phenomenon (November).

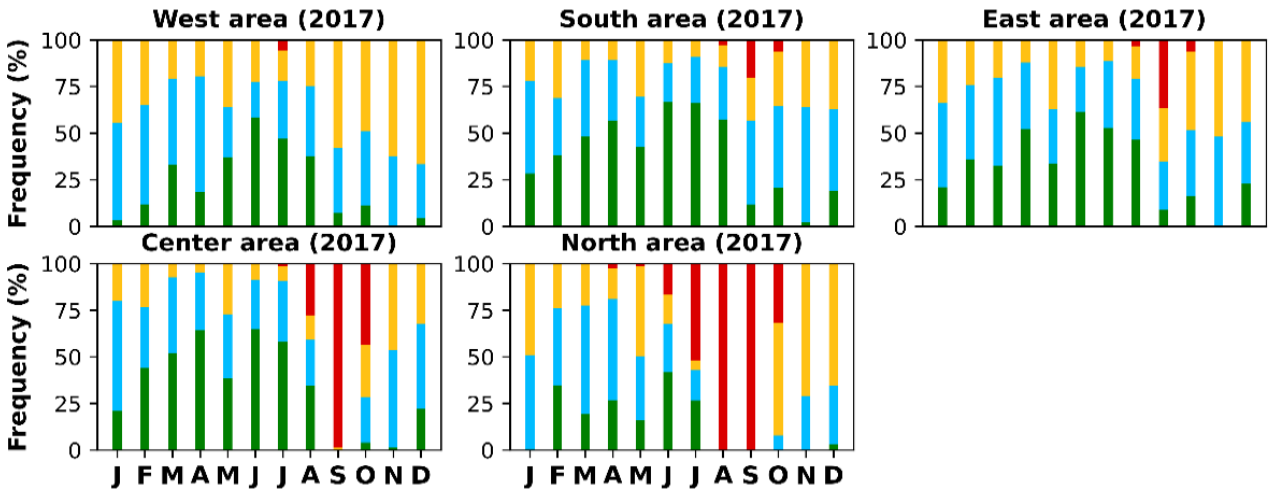

Figure 12. *Cont.*

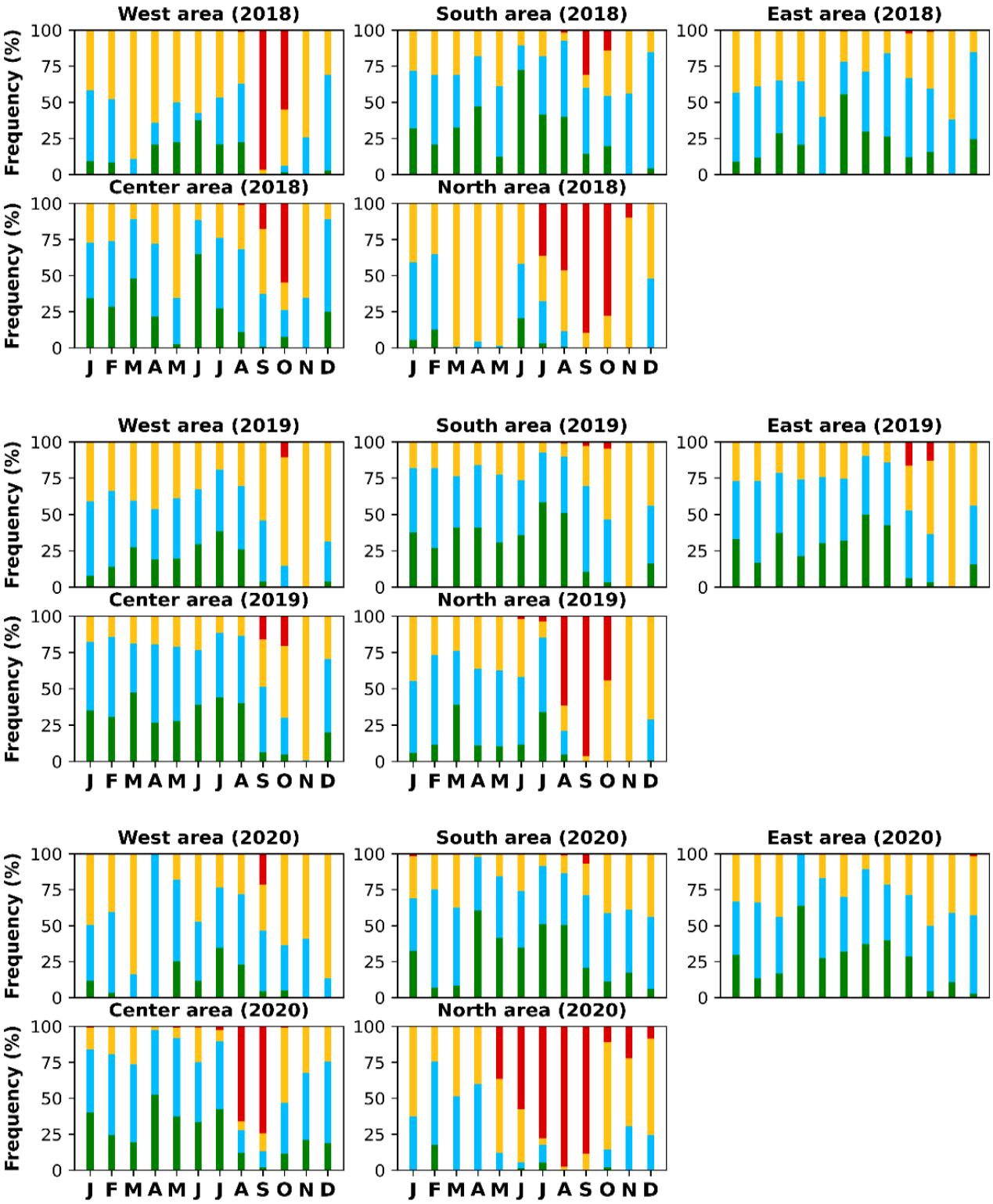

Figure 12. Monthly frequency (%) of each of the OWTs in the five areas of the reservoir, and for the 4 years analyzed. The green bars represent OWT1, in blue the OWT2, in orange the OWT3, and red is OWT4.

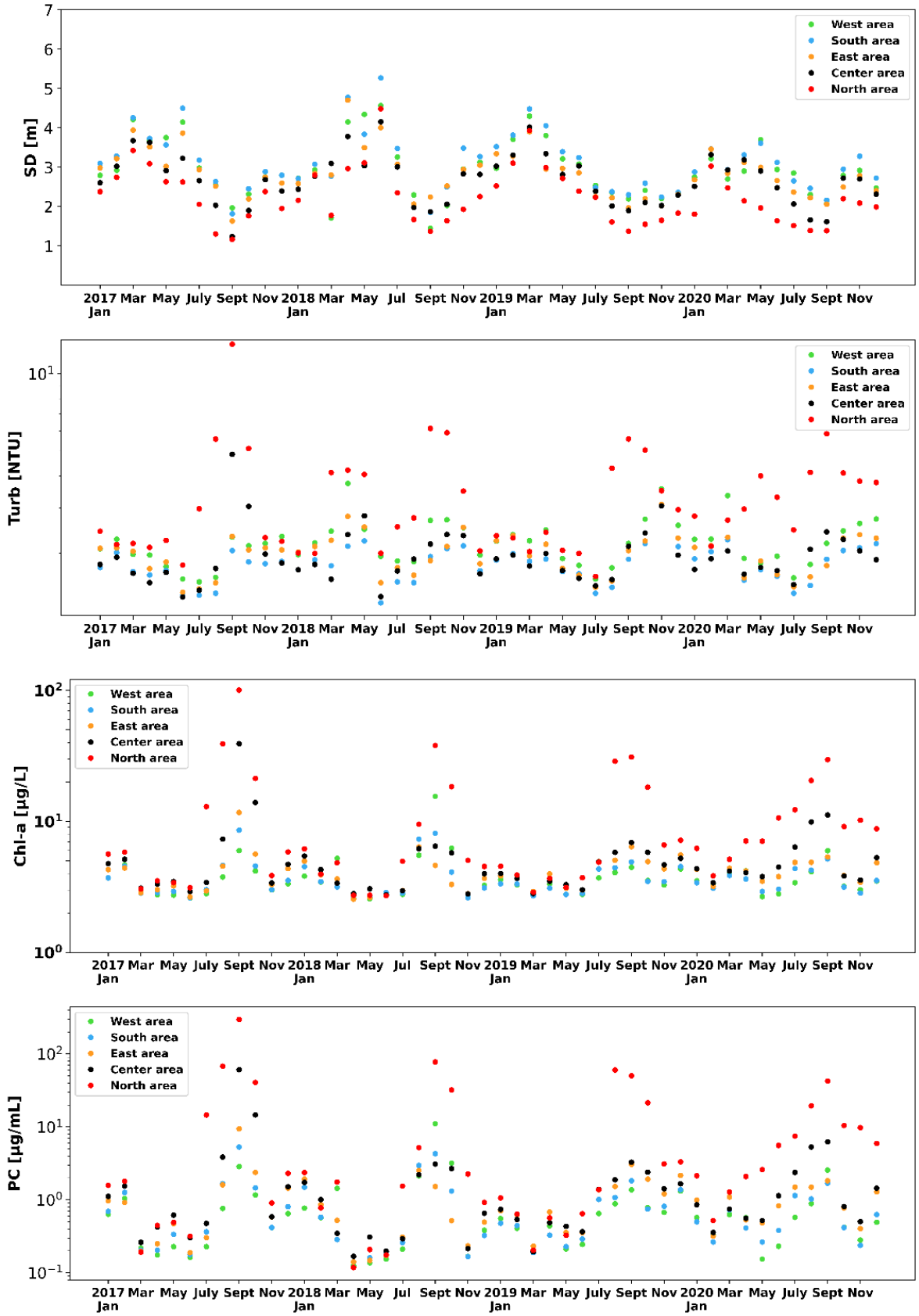

Figure 13. Monthly average for each of the areas and in the four water quality parameters analyzed in the period 2017–2020.

4.4. Extreme Events (Microalgae Blooms and Runoff after Heavy Rainfall)

The situations identified with the greatest spatial variations in the reservoir are related to intense precipitation events and microalgae blooms. In spring 2018 there was high rainfall, especially in March, with an accumulated value close to 200 mm at the CidAlmeida station (much higher than the average monthly precipitation). In a large reservoir, water quality varies more slowly than in a small reservoir. This can explain why March 2018 does not present high percentage of pixels associated with the OWT3 cluster in the entire reservoir (Figure 9). However, locally (in narrower areas) there is a significant increase in characteristic spectra of high turbidity, that is, associated with the OWT3 cluster. For the same month, the northern and western areas of the reservoir present 99% and 89% of the OWT3 class, respectively (Figure 12). These results are further corroborated by the RGB image obtained from the Sentinel-2 on 26 March 2018, identifying a brown color in north and west areas (Figure 14). This increase in water turbidity in the northern and western areas is identified by two methods of estimating water quality: OWT classification and water quality parameters. Figure 15 shows the maps of OWT and SD on 27 March 2018. The SD map is obtained by applying the algorithm (defined in Section 4.1.2) to all water pixels. In the central region, most pixels are assigned to the OWT1 cluster (blue pixels) with associated high water transparency (SD greater than 3 m). In the northern and western areas, practically all the pixels are assigned to OWT3 cluster, that is, representative of low to moderate water transparency. It is also in these two areas that the lowest values of SD are verified, with SDs normally below 2 m. On the frontier between the highest (OWT1) and lowest water transparency (OWT3) pixels, there are some intermediate water transparency (OWT2) pixels (blue pixels) with SDs around 2.5 m. There is a strong agreement between the brownish color in the RGB image (Figure 14) with the reduced SD and the OWT3 attribution (Figure 15).

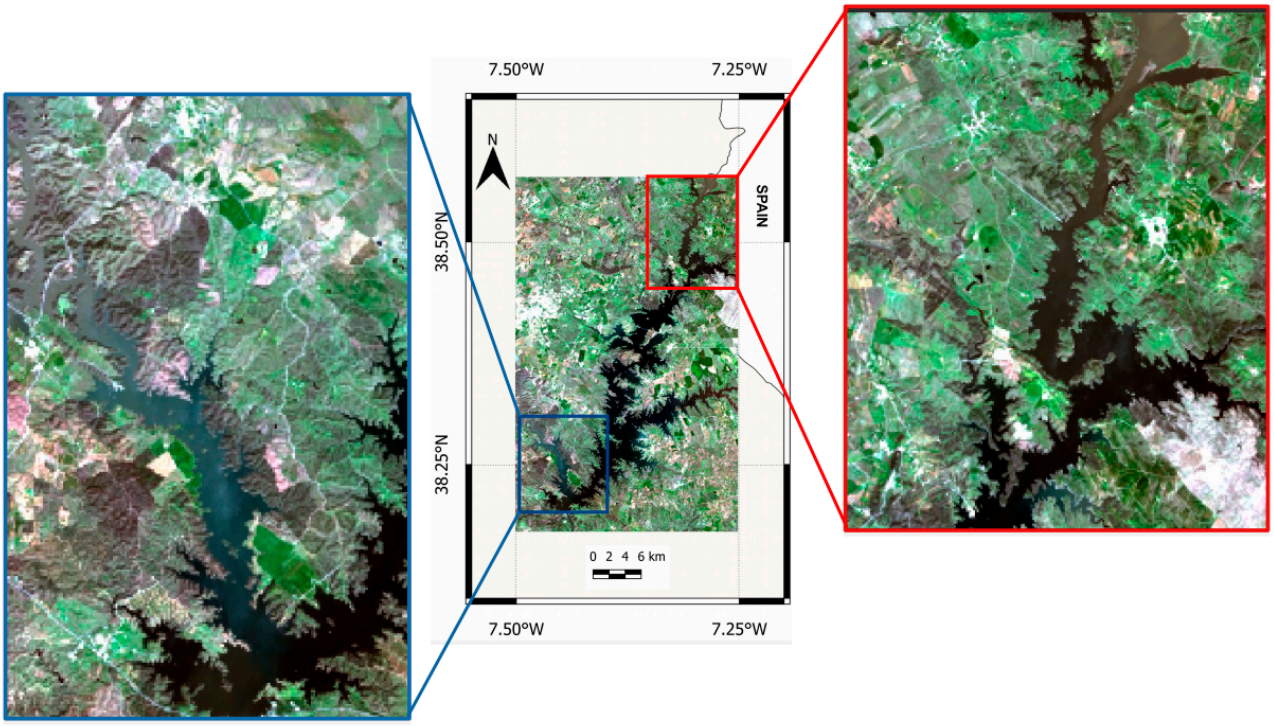

Figure 14. RGB image and more detailed images of the north and west areas on 26 March 2018 in the Alqueva reservoir.

During microalgae bloom events (July–October), there is also agreement between RGB images and water quality estimates (not shown here). Greenish colors in the RGB image (representing microalgae in water surface) correspond, in most cases, to the attribution of OWT4 cluster and high concentrations of Chl-a, PC, and low SDs. As in the intense precipitation events, there are high spatial variations. In July, the northern region of the reservoir normally presents microalgae, with high Chl-a concentrations and OWT4 classification. However, the other areas of the reservoir usually do not have a relevant frequency of OWT4 attribution. An example in Figure 16 for 23 July 2017 shows a map of Chl-a concentrations and the OWT classification. Very low Chl-a concentrations are associated with OWT1 assignment. Low to intermediate Chl-a concentrations are associated with the OWT2 or OWT3 cluster. High or very high Chl-a concentrations appear on this day in the northern region of the Alqueva reservoir and are already associated with the OWT4 cluster. At the end of summer, in September 2017, the microalgae evolve towards the south, also occupying the entire central area of the reservoir. The OWT classification and maps of Chl-a, PC, and SD for 26 September 2017 are presented in Figure 17. The areas without the presence of algae are assigned to the OWT1 or OWT2 clusters, and also have the lowest water turbidity in these areas (highest SD). On this day, several areas are identified with the presence of cyanobacteria blooms. There is agreement between the OWT classification (Cluster OWT4) with the estimates of Chl-a and PC (very high concentrations). These are therefore areas with a high probability of cyanobacteria presence.

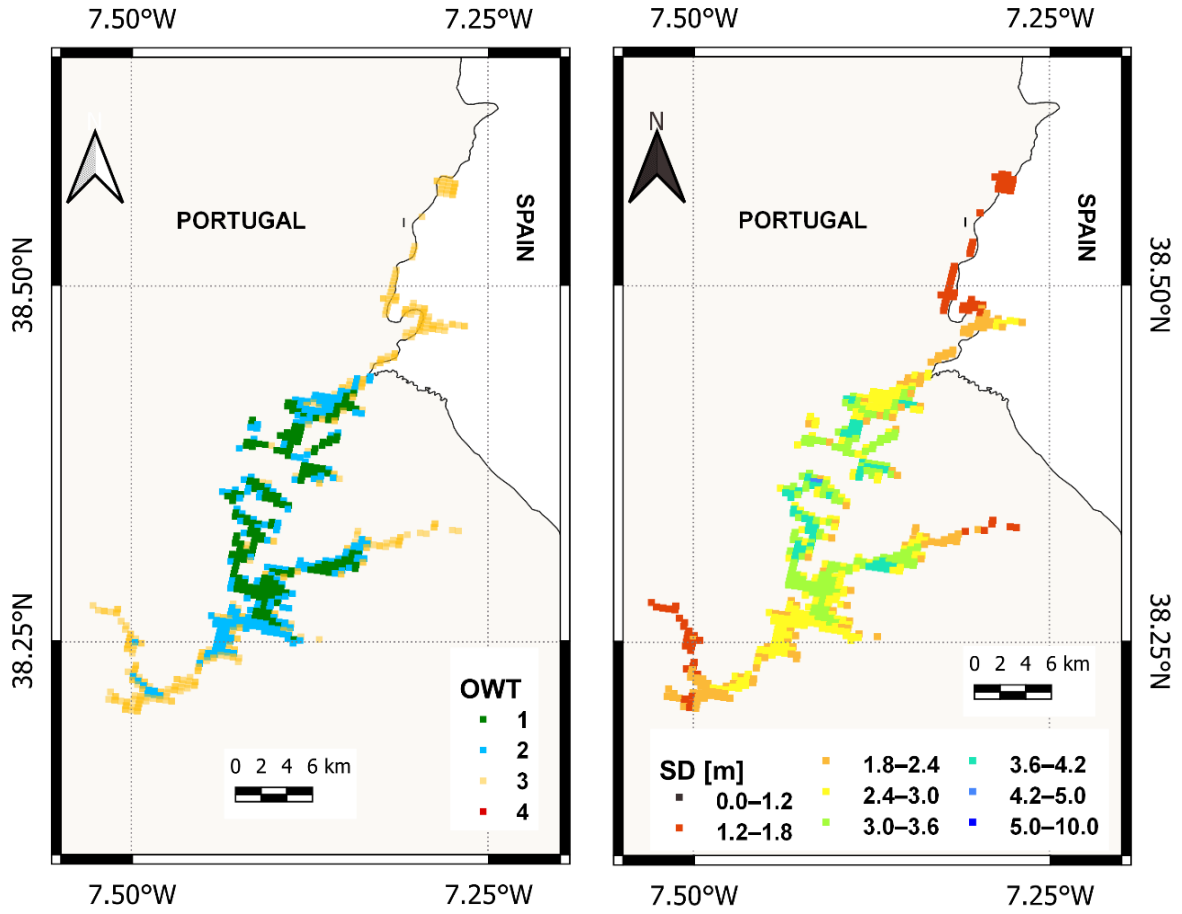

Figure 15. OWT (**left**) and Secchi depth (**right**) maps on 27 March 2018 in the Alqueva reservoir.

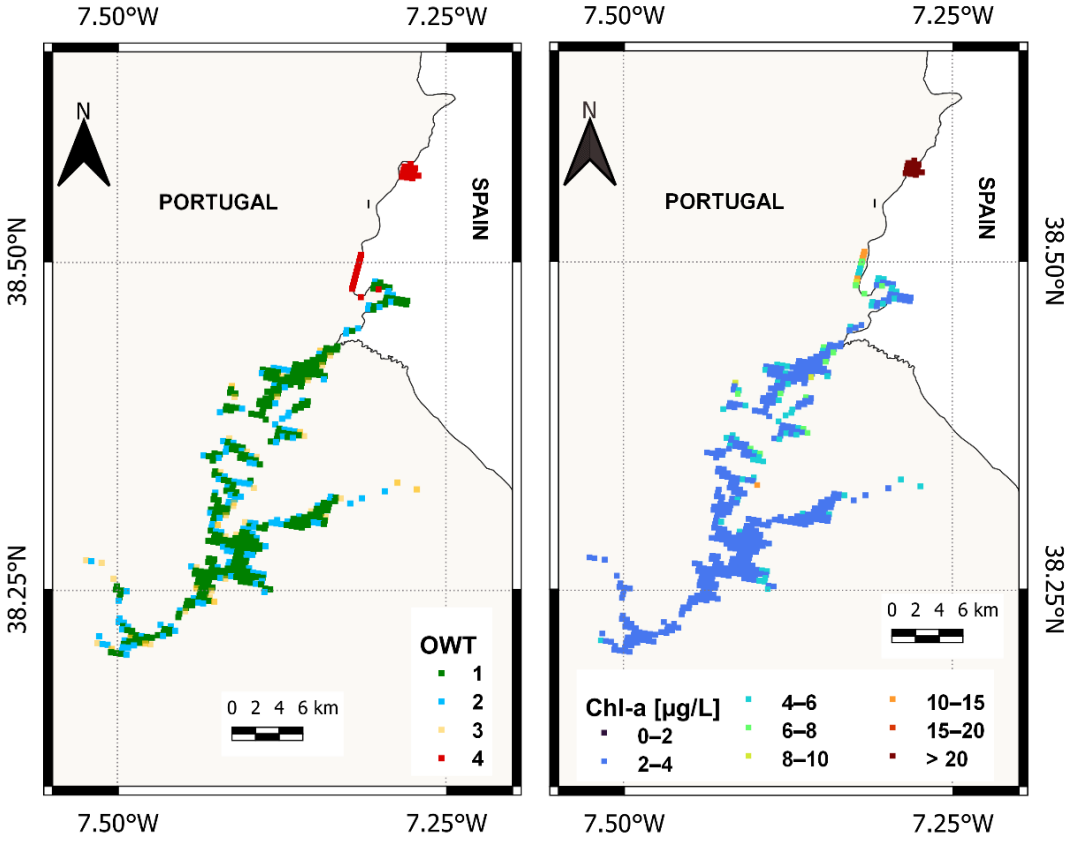

Figure 16. OWT (**left**) and Chl-a (**right**) maps on 23 July 2017 in the Alqueva reservoir.

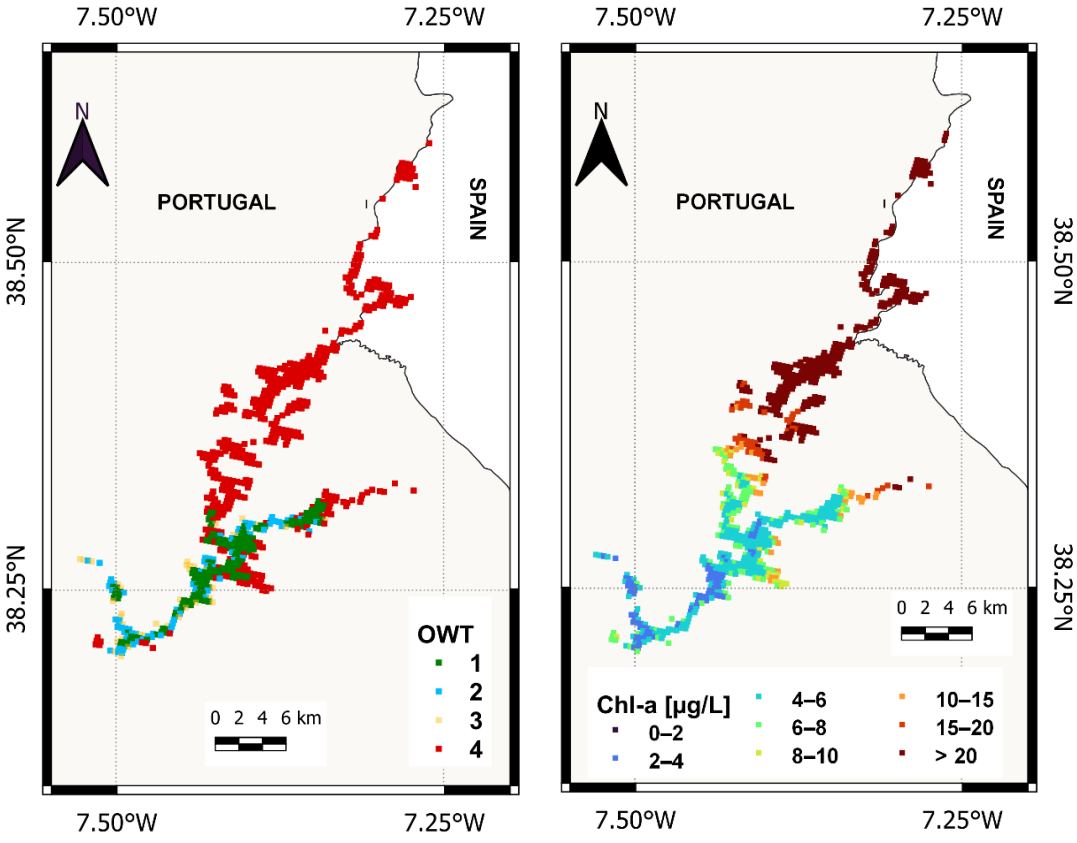

Figure 17. *Cont.*

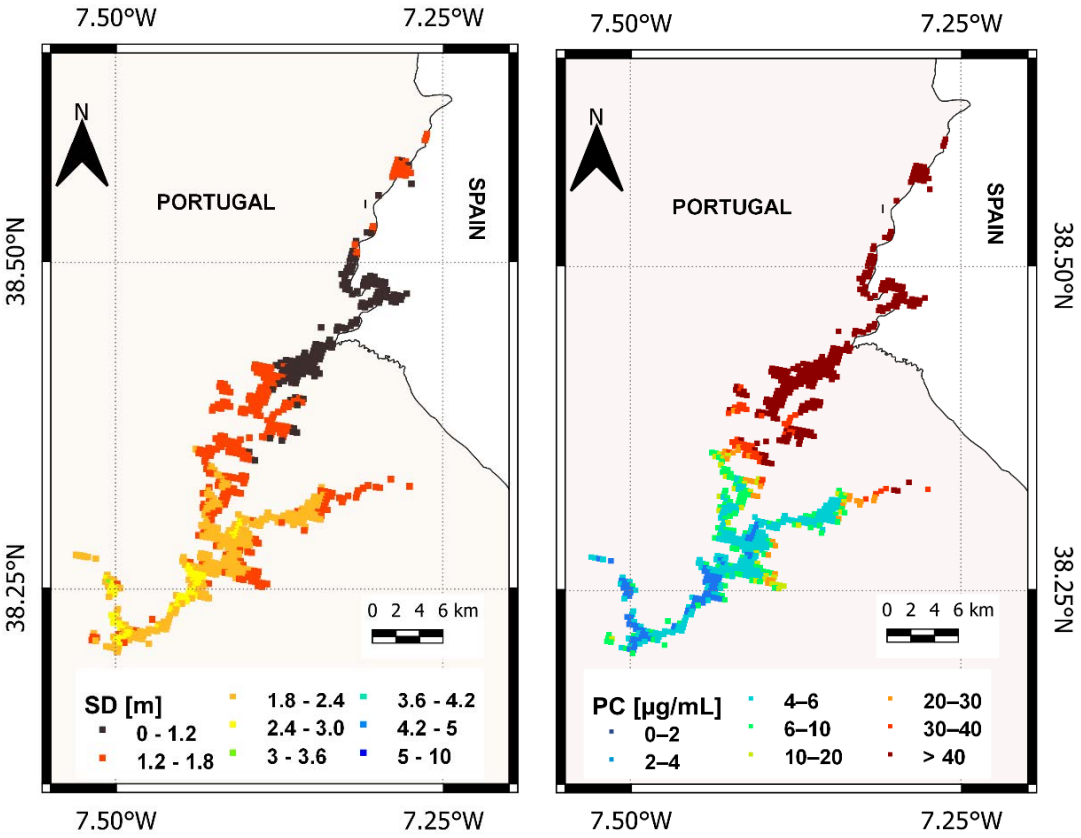

Figure 17. Above are the OWT (**left**) and Chl-a (**right**) maps on 26 September 2017 in the Alqueva reservoir. Below are the SD (**left**) and PC (**right**) maps for the same day.

5. Discussion

5.1. Monitoring Water Quality and Optical Water Types

We present two different methodologies to estimate the water quality in a large reservoir: the water quality parameters using a quantitative analysis (empirical algorithms), and the assignment of an optical water type (qualitative analysis). Water quality is expected to worsen from the OWT1 towards the OWT4 cluster, i.e., an increase in water turbidity and Chl-a concentration is likely. The OWT1 class represents the pixels with greater transparency and without the presence of microalgae. Cluster OWT4 is expected to be associated with microalgae blooms. The OWT4 pixels have a reflectance spectrum completely different from the other three clusters, mainly in relation to the peak in the green band (560 nm), and an increase from the B10 (681.3 nm) to B11 band of OLCI (708.75 nm). The OWT4 cluster typifies, then, an area of possible risk of presence or future appearance of cyanobacteria. As it is a cluster only representative of months of microalgae blooms (between July and October), it presents the lowest number of pixels assigned in the period 2017–2020 over the reservoir. This cluster only represents 8.2% of all pixels analyzed in the 4-year period. The OWT1, OWT2, and OWT3 represent 26.5%, 40.2%, and 25.1%, respectively. For the overall period, 66.7% of the pixels in the reservoir were attributed to the clusters OWT1 or OWT2, that are groups of spectra representative of slightly turbid water, and low concentrations of Chl-a. This means that the Alqueva reservoir, for most of the year and in most of the areas, has good water quality, considering these parameters, being little affected by runoff events and microalgae blooms. However, there are periods and areas of the reservoir (mainly the northern region of the reservoir, between Monsaraz and Lucefecit—see Figure 17) with the presence of high Chl-a and cyanobacteria concentrations. This conclusion is in line with results from previous works [30,64,65] identifying the northern area as the key area for the emergence of microalgae blooms, mainly in the period between August and October. Although the west area of the reservoir is far from the area with the worst water

quality (northern area), one microalgae bloom was also identified in the summer of 2018 in this area. As the summer progressed, there was an increase in the number of pixels assigned to the OWT4 cluster for areas further south in the reservoir. During autumn, with lower temperatures (air and water), the decrease in light intensity and even the increase in the wind events normally lead to the dissipation of these microalgae blooms, and to the improvement of the water quality. The episodes of extreme precipitation have been identified to mainly affect the narrowest areas, namely, the northern and western areas of the reservoir. This great distinction can be seen in March 2018, with practically 100% of the pixels being defined with OWT3 class in the north and west region (denoting the influence of runoff in the reflectance spectra), and with little variation in the other areas comparing with months without runoff.

In several studies, the empirical algorithms (to obtain estimates of water quality) are chosen depending on the OWT assignment. This methodology has great advantages, namely because there are empirical algorithms that work well in a given OWT, but present large errors in another. Thus, each algorithm is used for the OWT in which it works best. This means that for the same reservoir, two or more empirical algorithms are defined to represent the same water quality parameter. However, if the OWT assignment is wrong, the quantitative water quality estimate is also wrong. This methodology is also possible with a very significant number of data measured on site and can lead to relevant water quality discontinuities in nearby pixels with distinct OWT (and empirical algorithms) assigned. In the present study, the OWT and water quality parameters analysis was carried out independently, that is, without defining empirical algorithms dependent on the OWT assigned to each pixel. There are always some uncertainties when estimating water quality parameters using satellite remote sensing, but using two different and independent methodologies to represent the water quality in the same day/area provides greater reliability in the results.

5.2. Microalgae Blooms and Early Cyanobacteria Detection

Cyanobacterial blooms can emerge quickly in lakes with high nutrient levels, associated with calm weather and high water temperatures. The microalgae blooms already documented in the Alqueva reservoir using high-resolution satellite (Sentinel-2/MSI) [30,31] were also identified here. In summer and early autumn, until the arrival of the first rain episodes, the areas with low SD (high Turb) and high Chl-a concentrations are mainly due to microalgae and cyanobacteria presence. The existence of one OWT group associated with microalgae indicates that a pixel or an area in the lake will likely have high concentrations of Chl-a and presence of microalgae, but adding the quantification of Chl-a and/or PC concentrations will allow for quantifying the degree of severity. Moderate or high concentrations of Chl-a do not imply the presence of cyanobacteria in a lake. However, it increases the probability of cyanobacteria blooms' emergence. Therefore, two different risk levels were identified for the presence of cyanobacteria in the Alqueva reservoir using Sentinel-3/OLCI data:

Level (a) Moderate risk—area covered by OWT4 pixels, with high Chl-a concentrations, but low to moderate PC concentrations.

Level (b) High to very-high risk—area covered by OWT4 classification and simultaneously with high Chl-a and PC concentrations.

In order to predict an increase of the risk level for the presence of cyanobacteria in the following days or weeks, it is important to analyze the spatial/temporal predictions of meteorological parameters. For higher water temperature/solar radiation and lower wind intensities, there may be a risk of increase of PC concentrations. In the summer, the wind direction is mostly from the northwest, increasing in intensity in the late afternoon [53]. This fact may explain the shift of microalgae blooms, with increasing of frequency in the OWT4 cluster and high concentrations of Chl-a/PC during the summer towards to the south of Alqueva reservoir. On the other hand, if the weather forecast for the following days is of intense precipitation or a sudden decrease in air temperature, a decrease in the risk of the existence of cyanobacteria is expected.

The retrieval of the pigment phycocyanin coupled with information from OWTs can aid in the monitoring of cyanobacterial blooms. However, high presence of phycocyanin does not imply a public health risk, because most cyanobacteria do not produce toxins harmful to people. Areas simultaneously identified by OWT 4 and high Chl-a/PC concentrations (level **b**) may constitute relevant areas for water collection and subsequent laboratory analyses to confirm the presence of cyanobacteria and to check the toxicity to humans and wildlife.

6. Conclusions

In this work, we propose a methodology to combine the qualitative information from optical water type (OWT) classification with the estimations of water quality parameters (quantitative information) using Sentinel-3/OLCI data. Instead of using the OWT classification to determine which empirical algorithm is used, we propose to use this information independently. This allows to validate water quality estimates by verifying that the information from the OWT classification and from the empirical algorithms are in accordance.

The 2017–2020 satellite retrievals of atmospherically corrected spectral reflectance were separated into four distinct clusters using the k-means clustering method, with water turbidity and Chl-a concentrations increasing from cluster OWT1 to OWT4. The OWT4 group is representative of areas with microalgae presence, and with potential for emergence of cyanobacteria. These areas also show, in a pixel-by-pixel comparison, the highest Chl-a and PC concentrations, obtained from the empirical algorithms determined with OLCI band relationships and laboratory data. The presence of group OWT4 was identified mainly between July and October and more intensely in the northern region of the Alqueva reservoir. In three of the four years analyzed, the month in which the overturn took place was the month with the highest frequency (%) of OWT3 pixels. During the overturn process, the increase in turbidity and in OWT3 class occurs in the whole reservoir, whereas during the high precipitation and runoff events, this increase is more perceptible in some areas, mainly the west and north area of the reservoir. The period of greatest turbidity and worst water quality estimated in the four years analyzed was between August and November in the north area. On the other hand, between January and July, the conditions are generally of high water transparency and low Chl-a/PC concentrations, the southern area most of the time being the one with the best water quality in these indicators. In these months, at least 60% of the pixels were assigned to the OWT1/OWT2 clusters representing spectra with a large decrease in surface reflectance from green to red/NIR wavelengths. However, it is recommended to analyze specific areas of the reservoir, such as the northern area and the eastern/westernmost area of the reservoir, even if, on average, the results are of good water quality. This is because these three areas have much fewer OLCI pixels than the southern and central areas of the reservoir, thus masking local variations when the reservoir is analyzed as a whole.

This work proposes to increase the knowledge of the dynamics and evolution of the water quality in the Alqueva reservoir, as well as constitute a useful tool to be used in the future as part of an alert system to monitor sudden changes in water quality.

Author Contributions: Conceptualization, G.R., M.P. and M.J.C.; methodology, G.R., M.P. and M.J.C.; laboratory analyses, A.M.P. and M.M.M.; software, G.R.; validation, G.R. and M.P.; formal analysis, G.R., M.P. and M.J.C.; investigation, G.R., M.P. and M.J.C.; resources, G.R.; data curation, G.R.; writing—original draft preparation, G.R.; writing—review and editing, G.R., M.P. and M.J.C.; visualization, G.R. and M.P.; supervision, M.P. and M.J.C.; project administration, M.J.C.; funding acquisition, M.J.C. All authors have read and agreed to the published version of the manuscript.

Funding: G.R. thanks the Fundação para a Ciência e Tecnologia (FCT), Portugal for the Grant 2020.05752.BD. The work was co-funded by Portuguese funds through FCT—Fundação para a Ciência e Tecnologia, I.P. (projects UIDB/04683/2020 and UIDP/04683/2020) and also through projects TOMAQAPA (PTDC/CTAMET/29678/2017) and ALOP (ALT20-03-0145-FEDER-000004).

Data Availability Statement: Data used in this study are partially available at http://www.alop.ict.uevora.pt/index.php/dados/?lang=en, last accessed on 24 February 2022. Satellite data are made available by ESA at Copernicus Open Access Hub (https://scihub.copernicus.eu/dhus/#/home, accessed on 24 February 2022).

Acknowledgments: The authors gratefully acknowledge the Water Laboratory of the University of Évora for the water quality laboratory analyses used in this work, the Portuguese Environment Agency (APA) and "Empresa de Desenvolvimento e Infraestruturas do Alqueva S.A". (EDIA) for the collaboration in the water sample collections and facilities. The authors also thank the European Space Agency for providing Sentinel 3 OLCI data through the Copernicus Open Access Hub (https://scihub.copernicus.eu/dhus/#/home, accessed on 24 February 2022).

Conflicts of Interest: The authors declare no conflict of interest.

References

1. Giorgi, F.; Lionello, P. Climate Change Projections for the Mediterranean Region. *Glob. Planet. Chang.* **2008**, *63*, 90–104. [CrossRef]
2. Cardoso, R.M.; Soares, P.M.M.; Lima, D.C.A.; Miranda, P.M.A. Mean and Extreme Temperatures in a Warming Climate: EURO CORDEX and WRF Regional Climate High-Resolution Projections for Portugal. *Clim. Dyn.* **2019**, *52*, 129–157. [CrossRef]
3. Soares, P.M.M.; Cardoso, R.M.; Lima, D.C.A.; Miranda, P.M.A. Future Precipitation in Portugal: High-Resolution Projections Using WRF Model and EURO-CORDEX Multi-Model Ensembles. *Clim. Dyn.* **2017**, *49*, 2503–2530. [CrossRef]
4. Jeppesen, E.; Brucet, S.; Naselli-Flores, L.; Papastergiadou, E.; Stefanidis, K.; Nõges, T.; Nõges, P.; Attayde, J.L.; Zohary, T.; Coppens, J.; et al. Ecological Impacts of Global Warming and Water Abstraction on Lakes and Reservoirs Due to Changes in Water Level and Related Changes in Salinity. *Hydrobiologia* **2015**, *750*, 201–227. [CrossRef]
5. Jeppesen, E.; Meerhoff, M.; Davidson, T.A.; Trolle, D.; Søndergaard, M.; Lauridsen, T.L.; Beklioğlu, M.; Brucet, S.; Volta, P.; González-Bergonzoni, I.; et al. Climate Change Impacts on Lakes: An Integrated Ecological Perspective Based on a Multi-Faceted Approach, with Special Focus on Shallow Lakes. *J. Limnol.* **2014**, *73*, 88–111. [CrossRef]
6. Havens, K.E.; Paerl, H.W. Climate Change at a Crossroad for Control of Harmful Algal Blooms. *Environ. Sci. Technol.* **2015**, *49*, 12605–12606. [CrossRef]
7. Havens, K.; Jeppesen, E. Ecological Responses of Lakes to Climate Change. *Water* **2018**, *10*, 917. [CrossRef]
8. Moss, B. Allied Attack: Climate Change and Eutrophication. *Inland Waters* **2011**, *1*, 101–105. [CrossRef]
9. Erol, A.; Randhir, T.O. Climatic Change Impacts on the Ecohydrology of Mediterranean Watersheds. *Clim. Chang.* **2012**, *114*, 319–341. [CrossRef]
10. Paerl, H.W.; Huisman, J. Climate Change: A Catalyst for Global Expansion of Harmful Cyanobacterial Blooms. *Environ. Microbiol. Rep.* **2009**, *1*, 27–37. [CrossRef]
11. Palma, P.; Fialho, S.; Lima, A.; Catarino, A.; Costa, M.J.; Barbieri, M.V.; Monllor-Alcaraz, L.S.; Postigo, C.; Lopez de Alda, M. Occurrence and risk assessment of pesticides in a Mediterranean Basin with strong agricultural pressure (Guadiana Basin: Southern of Portugal). *Sci. Total Environ.* **2021**, *794*, 148703. [CrossRef] [PubMed]
12. Tomaz, A.; Palma, P.; Fialho, S.; Lima, A.; Alvarenga, P.; Potes, M.; Costa, M.J.; Salgado, R. Risk Assessment of Irrigation-Related Soil Salinization and Sodification in Mediterranean Areas. *Water* **2020**, *12*, 3569. [CrossRef]
13. Palma, P.; Fialho, S.; Lima, A.; Mourinha, C.; Penha, A.; Novais, M.H.; Rosado, A.; Morais, M.; Potes, M.; Costa, M.J.; et al. Land-Cover Patterns and Hydrogeomorphology of Tributaries: Are These Important Stressors for the Water Quality of Reservoirs in the Mediterranean Region? *Water* **2020**, *12*, 2665. [CrossRef]
14. Novais, M.H.; Morales, E.A.; Marchã Penha, A.; Potes, M.; Bouchez, A.; Barthès, A.; Costa, M.J.; Salgado, R.; Santos, J.; Morais, M. Benthic diatom community dynamics in Mediterranean intermittent streams: Effects of water availability and their potential as indicators of dry-phase ecological status. *Sci. Total Environ.* **2020**, *719*, 137462. [CrossRef] [PubMed]
15. Bukata, R.P.; Jerome, J.H.; Kondratyev, K.Y.; Pozdnyakov, D.V. *Optical Properties and Remote Sensing of Inland and Coastal Waters*; CRC Press: Boca Raton, FL, USA, 1995.
16. Dekker, A.G.; Vos, R.J.; Peters, S.W.M. Comparison of Remote Sensing Data, Model Results and in Situ Data for Total Suspended Matter (TSM) in the Southern Frisian Lakes. *Sci. Total Environ.* **2001**, *268*, 197–214. [CrossRef]
17. Gower, J.; King, S.; Borstad, G.; Brown, L. Detection of Intense Plankton Blooms Using the 709 nm Band of the MERIS Imaging Spectrometer. *Int. J. Remote Sens.* **2005**, *26*, 2005–2012. [CrossRef]
18. Simis, S.G.H.; Peters, S.W.M.; Gons, H.J. Remote Sensing of the Cyanobacterial Pigment Phycocyanin in Turbid Inland Water. *Limnol. Oceanogr.* **2005**, *50*, 237–245. [CrossRef]
19. Ruiz-Verdú, A.; Simis, S.G.H.; de Hoyos, C.; Gons, H.J.; Peña-Martínez, R. An Evaluation of Algorithms for the Remote Sensing of Cyanobacterial Biomass. *Remote Sens. Environ.* **2008**, *112*, 3996–4008. [CrossRef]
20. Ansper, A.; Alikas, K. Retrieval of Chlorophyll a from Sentinel-2 MSI Data for the European Union Water Framework Directive Reporting Purposes. *Remote Sens.* **2019**, *11*, 64. [CrossRef]
21. Cazzaniga, I.; Bresciani, M.; Colombo, R.; Della Bella, V.; Padula, R.; Giardino, C. A Comparison of Sentinel-3-OLCI and Sentinel-2-MSI-Derived Chlorophyll-a Maps for Two Large Italian Lakes. *Remote Sens. Lett.* **2019**, *10*, 978–987. [CrossRef]

22. Wang, D.; Ma, R.; Xue, K.; Loiselle, S. The Assessment of Landsat-8 OLI Atmospheric Correction Algorithms for Inland Waters. *Remote Sens.* **2019**, *11*, 169. [CrossRef]
23. Xue, K.; Ma, R.; Shen, M.; Li, Y.; Duan, H.; Cao, Z.; Wang, D.; Xiong, J. Variations of Suspended Particulate Concentration and Composition in Chinese Lakes Observed from Sentinel-3A OLCI Images. *Sci. Total Environ.* **2020**, *721*, 137774. [CrossRef] [PubMed]
24. Pahlevan, N.; Smith, B.; Schalles, J.; Binding, C.; Cao, Z.; Ma, R.; Alikas, K.; Kangro, K.; Gurlin, D.; Hà, N.; et al. Seamless Retrievals of Chlorophyll-a from Sentinel-2 (MSI) and Sentinel-3 (OLCI) in Inland and Coastal Waters: A Machine-Learning Approach. *Remote Sens. Environ.* **2020**, *240*, 111604. [CrossRef]
25. Canziani, G.; Ferrati, R.; Marinelli, C.; Dukatz, F. Artificial Neural Networks and Remote Sensing in the Analysis of the Highly Variable Pampean Shallow Lakes. *Math. Biosci. Eng.* **2008**, *5*, 691–711. [CrossRef]
26. Hafeez, S.; Wong, M.S.; Ho, H.C.; Nazeer, M.; Nichol, J.; Abbas, S.; Tang, D.; Lee, K.H.; Pun, L. Comparison of Machine Learning Algorithms for Retrieval of Water Quality Indicators in Case-Ii Waters: A Case Study of Hong Kong. *Remote Sens.* **2019**, *11*, 617. [CrossRef]
27. Niroumand-Jadidi, M.; Bovolo, F.; Bruzzone, L.; Gege, P. Inter-Comparison of Methods for Chlorophyll-a Retrieval: Sentinel-2 Time-Series Analysis in Italian Lakes. *Remote Sens.* **2021**, *13*, 2381. [CrossRef]
28. Pahlevan, N.; Smith, B.; Schalles, J.; Binding, C.; Cao, Z.; Ma, R.; Alikas, K.; Kangro, K.; Gurlin, D.; Hà, N.; et al. Re-Parameterization of a Quasi Analytical Algorithm and Phycocyanin Estimation in a Tropical Reservoir. Master's Thesis, Instituto Nacional de Pesquisas Espaciais, São José dos Campos, Brazil, 2014.
29. Ruescas, A.B.; Mateo-García, G.; Camps-Valls, G.; Hieronymi, M. Retrieval of Case 2 Water Quality Parameters with Machine Learning. In Proceedings of the IGARSS 2018—2018 IEEE International Geoscience and Remote Sensing Symposium, Valencia, Spain, 22–27 July 2018; pp. 124–127. [CrossRef]
30. Rodrigues, G.; Potes, M.; Costa, M.J.; Novais, M.H.; Penha, A.M.; Salgado, R.; Morais, M.M. Temporal and Spatial Variations of Secchi Depth and Diffuse Attenuation Coefficient from Sentinel-2 MSI over a Large Reservoir. *Remote Sens.* **2020**, *12*, 768. [CrossRef]
31. Potes, M.; Rodrigues, G.; Marchã Penha, A.; Helena Novais, M.; João Costa, M.; Salgado, R.; Manuela Morais, M. Use of Sentinel 2-MSI for Water Quality Monitoring at Alqueva Reservoir, Portugal. *Proc. Int. Assoc. Hydrol. Sci.* **2018**, *380*, 73–79. [CrossRef]
32. Vantrepotte, V.; Loisel, H.; Dessailly, D.; Mériaux, X. Optical Classification of Contrasted Coastal Waters. *Remote Sens. Environ.* **2012**, *123*, 306–323. [CrossRef]
33. Botha, E.J.; Anstee, J.M.; Sagar, S.; Lehmann, E.; Medeiros, T.A.G. Classification of Australian Waterbodies across a Wide Range of Optical Water Types. *Remote Sens.* **2020**, *12*, 3018. [CrossRef]
34. Spyrakos, E.; O'Donnell, R.; Hunter, P.D.; Miller, C.; Scott, M.; Simis, S.G.H.; Neil, C.; Barbosa, C.C.F.; Binding, C.E.; Bradt, S.; et al. Optical Types of Inland and Coastal Waters. *Limnol. Oceanogr.* **2018**, *63*, 846–870. [CrossRef]
35. Xue, K.; Ma, R.; Wang, D.; Shen, M. Optical Classification of the Remote Sensing Reflectance and Its Application in Deriving the Specific Phytoplankton Absorption in Optically Complex Lakes. *Remote Sens.* **2019**, *11*, 184. [CrossRef]
36. Ward, J.H. Hierarchical Grouping to Optimize an Objective Function. *J. Am. Stat. Assoc.* **1963**, *58*, 236–244. [CrossRef]
37. Shi, K.; Li, Y.; Zhang, Y.; Li, L.; Lv, H.; Song, K. Classification of Inland Waters Based on Bio-Optical Properties. *IEEE J. Sel. Top. Appl. Earth Obs. Remote Sens.* **2014**, *7*, 543–561. [CrossRef]
38. Palacios, S.L.; Peterson, T.D.; Kudela, R.M. Optical Characterization of Water Masses within the Columbia River Plume. *J. Geophys. Res. Ocean.* **2012**, *117*, C11020. [CrossRef]
39. Zhang, F.; Li, J.; Shen, Q.; Zhang, B.; Wu, C.; Wu, Y.; Wang, G.; Wang, S.; Lu, Z. Algorithms and Schemes for Chlorophyll a Estimation by Remote Sensing and Optical Classification for Turbid Lake Taihu, China. *IEEE J. Sel. Top. Appl. Earth Obs. Remote Sens.* **2015**, *8*, 350–364. [CrossRef]
40. Shen, Q.; Li, J.; Zhang, F.; Sun, X.; Li, J.; Li, W.; Zhang, B. Classification of Several Optically Complex Waters in China Using in Situ Remote Sensing Reflectance. *Remote Sens.* **2015**, *7*, 14731–14756. [CrossRef]
41. Bi, S.; Li, Y.; Xu, J.; Liu, G.; Song, K.; Mu, M.; Lyu, H.; Miao, S.; Xu, J. Optical Classification of Inland Waters Based on an Improved Fuzzy C-Means Method. *Opt. Express* **2019**, *27*, 34838. [CrossRef]
42. Eleveld, M.A.; Ruescas, A.B.; Hommersom, A.; Moore, T.S.; Peters, S.W.M.; Brockmann, C. An Optical Classification Tool for Global Lake Waters. *Remote Sens.* **2017**, *9*, 420. [CrossRef]
43. Moore, T.S.; Dowell, M.D.; Bradt, S.; Ruiz Verdu, A. An Optical Water Type Framework for Selecting and Blending Retrievals from Bio-Optical Algorithms in Lakes and Coastal Waters. *Remote Sens. Environ.* **2014**, *143*, 97–111. [CrossRef]
44. Potes, M.; Costa, M.J.; da Silva, J.C.B.; Silva, A.M.; Morais, M. Remote Sensing of Water Quality Parameters over Alqueva Reservoir in the South of Portugal. *Int. J. Remote Sens.* **2011**, *32*, 3373–3388. [CrossRef]
45. Potes, M.; Costa, M.J.; Salgado, R. Satellite Remote Sensing of Water Turbidity in Alqueva Reservoir and Implications on Lake Modelling. *Hydrol. Earth Syst. Sci.* **2012**, *16*, 1623–1633. [CrossRef]
46. Lamquin, N.; Clerc, S.; Bourg, L.; Donlon, C. OLCI A/B Tandem Phase Analysis, Part 1: Level 1 Homogenisation and Harmonisation. *Remote Sens.* **2020**, *12*, 1804. [CrossRef]
47. Lorenzen, C.J. Determination of Chlorophyll and Pheo-Pigments: Spectrophotometric Equations. *Limnol. Oceanogr.* **1967**, *12*, 343–346. [CrossRef]

48. *NP 4327/1996*; Qualidade da Água. Doseamento da Clorofila a e Dos Feopigmentos Por Espectrofotometria de Absorção Molecular. Instituto Português da Qualidade: Monte de Caparica, Portugal, 1997.
49. *ISO 10260:1992*; Water Quality: Measurement of Biochemical Parameters: Spectrometric Determination of the Chlorophyll-A Concentration. International Organization for Standardization: Geneva, Switzerland, 1992.
50. APHA. *Standard Methods for the Examination of Water and Wastewater*, 19th ed.; American Public Health Association: Washington, DC, USA, 1995.
51. Horváth, H.; Kovács, A.W.; Riddick, C.; Présing, M. Extraction Methods for Phycocyanin Determination in Freshwater Filamentous Cyanobacteria and Their Application in a Shallow Lake. *Eur. J. Phycol.* **2013**, *48*, 278–286. [CrossRef]
52. Lauceri, R.; Bresciani, M.; Lami, A.; Morabito, G. Chlorophyll A Interference in Phycocyanin and Allophycocyanin Spectrophotometric Quantification. *J. Limnol.* **2018**, *77*, 169–177. [CrossRef]
53. Purificação, C.; Potes, M.; Rodrigues, G.; Salgado, R.; Costa, M.J. Lake and Land Breezes at a Mediterranean Artificial Lake: Observations in Alqueva Reservoir, Portugal. *Atmosphere* **2021**, *12*, 535. [CrossRef]
54. Soomets, T.; Uudeberg, K.; Jakovels, D.; Brauns, A.; Zagars, M.; Kutser, T. Validation and Comparison of Water Quality Products in Baltic Lakes Using Sentinel-2 Msi and Sentinel-3 OLCI Data. *Sensors* **2020**, *20*, 742. [CrossRef]
55. Martins, V.S.; Barbosa, C.C.F.; de Carvalho, L.A.S.; Jorge, D.S.F.; Lobo, F.d.L.; de Moraes Novo, E.M.L. Assessment of Atmospheric Correction Methods for Sentinel-2 MSI Images Applied to Amazon Floodplain Lakes. *Remote Sens.* **2017**, *9*, 322. [CrossRef]
56. Shen, M.; Duan, H.; Cao, Z.; Xue, K.; Loiselle, S.; Yesou, H. Determination of the Downwelling Diffuse Attenuation Coefficient of Lakewater with the Sentinel-3A OLCI. *Remote Sens.* **2017**, *9*, 1246. [CrossRef]
57. ASD. *FieldSpec® HandHeld 2 Spectroradiometer User's Manual*; ASD Inc.: Boulder, CO, USA, 2010; Volume 1, pp. 1–93.
58. Potes, M.; Costa, M.J.; Salgado, R.; Bortoli, D.; Serafim, A.; Le Moigne, P. Spectral measurements of underwater downwelling radiance of inland water bodies. *Tellus A* **2013**, *65*, 20774. [CrossRef]
59. Xu, H. Modification of Normalised Difference Water Index (NDWI) to Enhance Open Water Features in Remotely Sensed Imagery. *Int. J. Remote Sens.* **2006**, *27*, 3025–3033. [CrossRef]
60. Huang, Z. Extensions to the K-Means Algorithm for Clustering Large Data Sets with Categorical Values. *Data Min. Knowl. Discov.* **1998**, *2*, 283–304. [CrossRef]
61. Rousseeuw, P.J. Silhouettes: A Graphical Aid to the Interpretation and Validation of Cluster Analysis. *J. Comput. Appl. Math.* **1987**, *20*, 53–65. [CrossRef]
62. Flores-Anderson, A.I.; Griffin, R.; Dix, M.; Romero-Oliva, C.S.; Ochaeta, G.; Skinner-Alvarado, J.; Ramirez Moran, M.V.; Hernandez, B.; Cherrington, E.; Page, B.; et al. Hyperspectral Satellite Remote Sensing of Water Quality in Lake Atitlán, Guatemala. *Front. Environ. Sci.* **2020**, *8*, 7. [CrossRef]
63. Craig, S.E.; Lohrenz, S.E.; Lee, Z.; Mahoney, K.L.; Kirkpatrick, G.J.; Schofield, O.M.; Steward, R.G. Use of Hyperspectral Remote Sensing Reflectance for Detection and Assessment of the Harmful Alga, *Karenia brevis*. *Appl. Opt.* **2006**, *45*, 5414–5425. [CrossRef]
64. Potes, M.; Salgado, R.; Costa, M.J.; Morais, M.; Bortoli, D.; Kostadinov, I.; Mammarella, I. Lake-Atmosphere Interactions at Alqueva Reservoir: A Case Study in the Summer of 2014. *Tellus Ser. A Dyn. Meteorol. Oceanogr.* **2017**, *69*, 1272787. [CrossRef]
65. Palma, P.; Penha, A.M.; Novais, M.H.; Fialho, S.; Lima, A.; Mourinha, C.; Alvarenga, P.; Rosado, A.; Iakunin, M.; Rodrigues, G.; et al. Water-Sediment Physicochemical Dynamics in a Large Reservoir in the Mediterranean Region under Multiple Stressors. *Water* **2021**, *13*, 707. [CrossRef]

Environmental Research 217 (2023) 114798

Contents lists available at ScienceDirect

Environmental Research

journal homepage: www.elsevier.com/locate/envres

Integrative toolbox to assess the quality of freshwater sediments contaminated with potentially toxic metals

Patrícia Palma [a,b,*], Alexandra Marchã Penha [b,c], Maria Helena Novais [b,c], Sofia Fialho [a], Ana Lima [a], Adriana Catarino [a], Clarisse Mourinha [a], Paula Alvarenga [d], Maksim Iakunin [b], Gonçalo Rodrigues [b], Miguel Potes [b], Manuela Morais [b,c,e], Maria João Costa [b,e], Rui Salgado [b,e]

[a] Department of Technologies and Applied Sciences, Polytechnic Institute of Beja, 7801-295, Portugal
[b] ICT, Institute of Earth Sciences, University of Évora, Rua Romão Ramalho 59, Évora, Portugal
[c] Water Laboratory, University of Évora, P.I.T.E, Rua da Barba Rala No. 1, 7005-345, Évora, Portugal
[d] Linking Landscape, Environment, Agriculture, and Food Research Unit (LEAF), Instituto Superior de Agronomia, Universidade de Lisboa, Tapada da Ajuda, 1349-017, Lisboa, Portugal
[e] Science and Technology School, University of Évora, Évora, Portugal

ARTICLE INFO

Keywords:
Sediments quality
Meteorological parameters
Land cover/land uses
Contamination indices
Ecotoxicological endpoints
Guadiana basin

ABSTRACT

The Guadiana Basin is a transnational basin, presenting historical contamination with potentially toxic metals (PTM), which origin can be both natural and anthropogenic. This study explores the use of a set of observational, chemical and ecotoxicological assays with *Heterocypris incongruens, Vibrio fischeri, Pseudokirchneriella subcapitata, Thamnocephalus platyurus,* identifying the most sensitive to be included in a toolbox to analyze the quality of freshwater sediments related to this type of contamination. The study included the analysis of a reservoir and streams sediments of Guadiana basin, in two consecutive years with different climate conditions 2017 (dry year) and 2018 (normal year). The results showed high chemical variability along the basin, with greater contamination with PTM in the reservoir sediments. The calculated Enrichment Factors (EF) indicated high anthropogenic contamination by Cd, followed by Pb (EF > 1.5). The geoaccumulation index (I*geo*) revealed that the sediments were severely polluted with Cd, and slightly polluted with Pb and Cu, inducing a higher sublethal toxicity to *Heterocypris incongruens*. Among the parameters evaluated, and after the use of multivariate statistical techniques, the toolbox for assessing sediments quality, in similar climate and geological conditions, should include the analysis of: meteorology, land use/cover in the area, granulometry, organic matter content, PTM concentrations, contamination indices (e.g., I*geo* and EF), and sublethal bioassays with *H. incongruens* (total sediment analysis) and *Vibrio fisheri* luminescence inhibition (pore water analysis).

1. Introduction

The importance of the sediments compartment in the aquatic ecosystem is unquestionable, and it is commonly accepted that the appropriate freshwater quality assessment is only possible if sediment analysis is also considered. Sediments are the habitat of several benthic species in lakes, reservoirs, and rivers, participating in their food webs (Burton, 2002). As a reservoir of hazardous substances, such as potentially toxic elements (PTM) and organic compounds, they act in the bioaccumulation and bioamplification in the food webs, as well as secondary sources of pollution to the aquatic ecosystems (Sahli et al., 2021).

Notwithstanding the above being accepted by the scientific community, in Europe, there is still a gap in guidelines for the protection of freshwater sediments. In fact, in several European countries such as Portugal, sediment quality assessment is not yet included in the river or reservoir management strategies.

Several authors have been working on proposing pollutants concentration limits, to ensure sediment health quality criteria (MacDonald et al., 2000; Macfarlane, 2003; USEPA, 2001). However, chemical concentrations are insufficient to demonstrate adverse environmental effects, to which toxic evidence is also needed. Indeed, in recent years, studies have been carried out and guidance manuals have been developed to identify the most promising bioassays to detect

* Corresponding author. Department of Technologies and Applied Sciences, Polytechnic Institute of Beja, 7801-295, Portugal.
E-mail address: ppalma@ipbeja.pt (P. Palma).

https://doi.org/10.1016/j.envres.2022.114798
Received 23 July 2022; Received in revised form 20 October 2022; Accepted 10 November 2022
Available online 24 November 2022
0013-9351/© 2022 Elsevier Inc. All rights reserved.

sediment-induced ecosystem disruption effects (Broccoli et al., 2021; Ingersoll and MacDonald, 2002; da Silva de Freitas et al., 2022). Researchers agree on the need to integrate tools from different areas of knowledge (physicochemical, biological/ecotoxicological) to improve the quality assessment of sediments, with a better response to different types of sediments, and to climate and land uses of each region/country (Broccoli et al., 2021; dos Santos Mendonça et al., 2021; Maradonna et al., 2020). The joint analysis of the results will allow a clearer interpretation of the most sensitive endpoints and the most important risk factors, considering the health of the sediments ecosystem.

One of the most important groups of contaminants that occur in sediments are PTMs, being their main accumulation compartment (Liu et al., 2021; Luo et al., 2021; Rani et al., 2021). Metals in freshwater sediments mainly derive from rock weathering, soil erosion, runoff from agricultural activities, wastewater, and atmospheric precipitation (Palma et al., 2015; Wang et al., 2021). Metals can be concentrated in sediments by adsorption to fine particles, organic matter, Fe/Mn oxides, and sulphides (Liu et al., 2021). However, sediments cannot fix metals permanently. In fact, under certain environmental conditions (such as, the decrease of pH, or the degradation of organic matter), the metals in sediments can be released, back into the overlying water column, and resulting in a secondary source of pollution (Boguta et al., 2022). In certain concentrations, metals are responsible for human diseases (Ehrlich et al., 2016; Huat et al., 2019; Soomro et al., 2019) and ecosystems unbalance (Rao et al., 2021; Varol et al., 2022), representing a real concern for health and environmental authorities.

The present study focused on the application of a set of observational and analytical parameters (chemical and ecotoxicological), to assess the impact of PTM on freshwater sediments during two consecutive years with marked climate differences, analyzing which parameters are the most effective to evaluate their quality and proposing an easy-to-use toolbox with the most sensitive ones. The study was carried out in the Guadiana Basin, a transnational Mediterranean basin, with a semi-arid climate. The set of parameters proposed initially included: (1) Land use/Land cover (LULC) analysis and meteorological indicators; (2) sediments characteristics: (a) physical parameters – granulometric parameters; (b) chemical parameters - quantification of PTM, as the Guadiana basin is part of a rich geological area, the Iberian Pyrite Belt (IPB), and within an intensive agriculture area; (3) degree of contamination using geochemical analysis through the Enrichment factor (EF) and the Geoaccumulation index (*Igeo*); and (4) Environmental risk analysis, using: (i) sediments quality guidelines (SQG), through the Interim Sediments Quality Guidelines (ISQG), for Cu, Cd, Cr, Pb and Zn (CCME, 2002), and ERL (effect range low) for Ni, as proposed by Long et al. (1995), once Ni was not considered in the ISQG; (ii) biological indicators – to assess the toxicity of the sediments by developing an ecotoxicological risk analysis using the whole sediment and the pore-water, with species from different trophic levels (*Heterocypris incongruens, Vibrio fischeri, Pseudokirchneriella subcapitata, Thamnocephalus platyurus*), and lethal and sub-lethal ecotoxicological endpoints.

2. Materials and methods

2.1. Study area and sampling sites characterization

The Guadiana is a transnational basin with a total area of 67 200 km^2, being 11 580 km^2 in the Portuguese territory. The hydrological regime is torrential, with a dominance of intermittent rivers/streams. From the morphological point of view, the basin is divided into three distinct zones: High, Medium and Lower Guadiana (APA, 2016). The Lower Guadiana zone corresponds essentially to the Portuguese area of the basin and includes part of the Iberian Pyrite Belt (IPB), one of the world's most important provinces for volcanogenic massive sulphide deposits (Gomes et al., 2014). In the IPB, more than 80 deposits have been referenced, with an estimated 1700 Mt total reserves (massive sulphides and stockworks) containing 14.6 Mt of Cu, 13.0 Mt of Pb, 34.9 Mt of Zn, 46 100 t of Ag, 880 t of Au and significant amounts of other metals, such as Sn (Leistel et al., 1997).

The study was performed in eight sites located in the Portuguese sector of Guadiana Basin: four at the Alqueva reservoir (Lucefécit – Lf; Mourão – Mr; Al – Álamos; Alqueva-Montante – Mn), and the remaining four in streams of Guadiana (S_Lf – Lucefécit Stream; S_Al – Álamos Stream; S_Am – Amieira Stream; S_Zb – Zebro Stream (Fig. 1). For each sampling site, a drainage basin was calculated as the region where precipitation, surface and groundwater are collected and drain off to the sampling point. The drainage basins are deemed proper areas to examine associations between LULC and meteorological conditions with chemical and ecotoxicological indicators obtained at the sampling points, since all water in the area converges to that point. The drainage basins for each of the sites were obtained from the 1 arcsecond (30 m) resolution Shuttle Radar Topography Mission (SRTM) elevation data (Palma et al., 2021a). Fig. 1 shows the region of study comprising a total area of 8660 km^2, including the delimitation of the drainage basins for each of the sites, and the respective LULC classes.

The general characterization of the sediments at each sampling location is displayed in Table S1, adapted from (Palma et al., 2020a, 2021b), with sediments of reservoir mostly constituted by fine particles, higher amounts of organic matter (OM) and nutrients, compared to the sediments of the streams.

2.2. Land use/land cover (LULC) and meteorological characterization

Land use, land cover (LULC) data used is available from the 2018 CORINE Land Cover Pan-European inventory obtainable at the Copernicus Land Monitoring Service (https://land.copernicus.eu/; last accessed on 9 May 2022). The CORINE LULC inventory distinguishes 44 classes, spanning into the following five categories: (i) Artificial surfaces, (ii) Agricultural areas, (iii) Forest and seminatural areas, (iv) Wetlands, and (v) Water bodies. The minimum mapping unit and width are 25 ha and 100 m, respectively. The geometric accuracy is lower than 10 m and thematic accuracy greater than 85% (Kosztra et al., 2017). Open data available from the Portuguese National Geographic Information and from the Directorate-General for Energy and Geology (DGEG) were also considered. These data consist of areas licensed by the DGEG, in force, for the exploration of mineral masses in mainland Portugal and of degraded mining areas, in mainland Portugal, which are under concession for environmental recovery (https://www.dgeg.gov.pt/; vector data are available through https://snig.dgterritorio.gov.pt/; last accessed 28 June 2022). The CORINE LULC classification was combined with the DGEG information and grouped considering that some of the classes may constitute potentially toxic metal sources, yielding 11 classes (Table S2). The class distribution in each of the drainage basins considered (Fig. 1) is shown and analyzed in section 3.1.2.

The meteorological data was obtained from the E-OBS dataset (Cornes et al., 2018) of the Copernicus Climate Change Service, based on observations from identified and recognized European ground-based networks of weather stations, most of them managed by the European national weather services (https://climate.copernicus.eu/; last accessed on 6 May) The E-OBS is provided with a daily resolution, over a regular horizontal grid of 0.1° × 0.1°, from 1 January 1950. The meteorological variables used were the daily minimum, maximum and mean air temperatures, as well as precipitation. The air temperatures were measured 2 m above the ground, in accordance with the World Meteorological Organization (WMO) standards. The daily accumulated precipitation corresponded to the height of the equivalent liquid water. Daily temperature and precipitation data, for the period 1 January 2017 to 31 December 2018, were averaged for the areas corresponding to each of the drainage basins considered (Fig. 1; results analyzed in section 3.1.1).

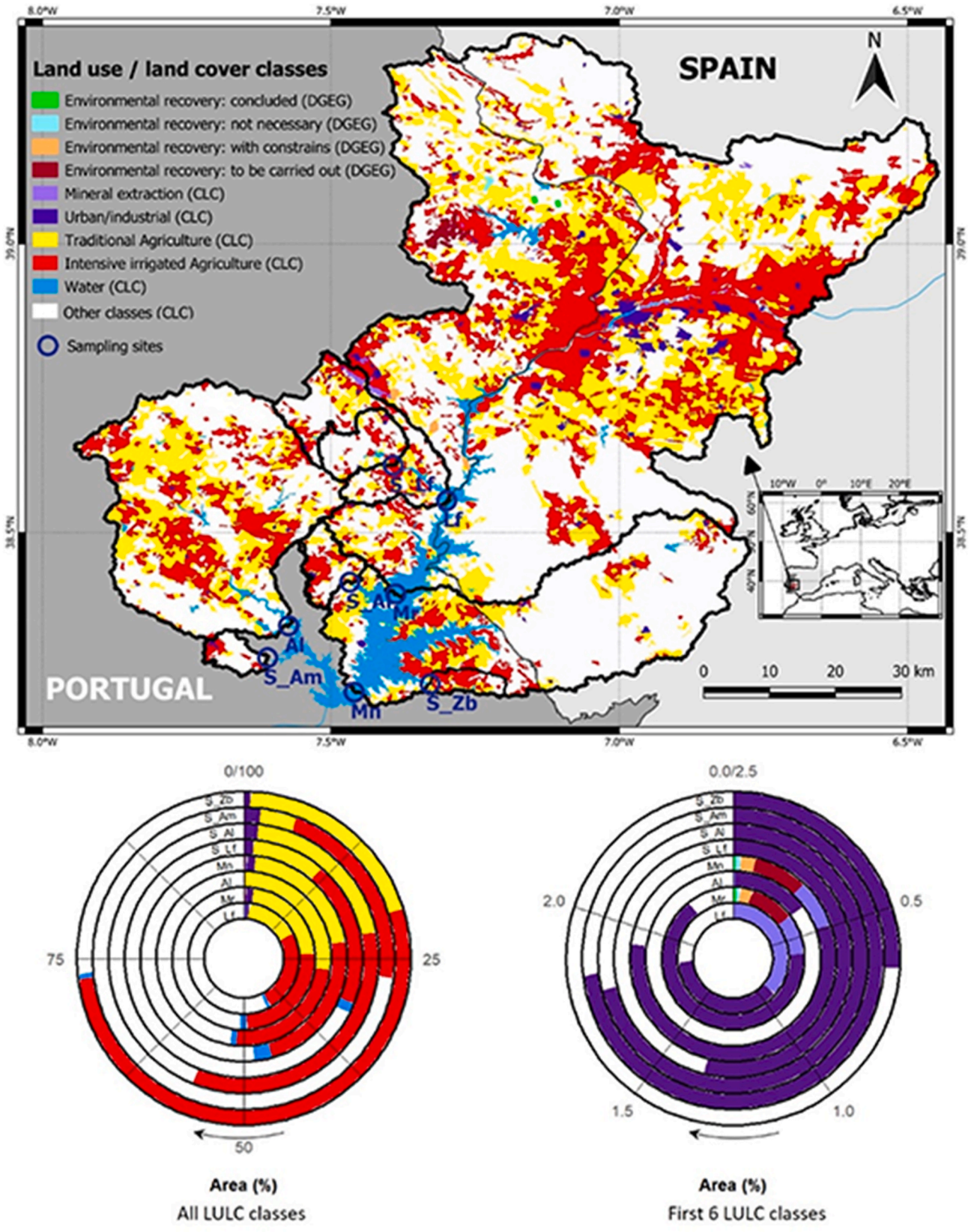

Fig. 1. Map illustrating the region considered for the study in the south of Portugal, encompassing Alqueva reservoir (in deep sky blue) and the respective LULC distribution. The blue circles indicate the sampling sites and the respective drainage basins are delimited by the black lines. Polar plots showing the percentage areas corresponding to each class (bottom left) and only to the first six classes indicated in the legend (bottom right). Each LULC class corresponds to a color, as illustrated in the legend. (For interpretation of the references to color in this figure legend, the reader is referred to the Web version of this article.)

2.3. Sampling campaigns

The study comprised 12 sampling campaigns, with bimonthly collections during 2017 (drought year) and 2018 (normal climate year). The temporal analysis was developed considering the seasonal classification for the Alentejo region: wet period comprising the months of January, March and November, and dry period that includes May, July and September (APA, 2016).

At each sampling point, five litters of surface sediments (collected to a depth <10 cm) were gathered using a stainless steel van Veen grab of 0.05 m^2. In Al, Mn, Mr and Lf (reservoir sampling points), sediments were collected in locations with different water columns depths (26, 65, 45 and 20 m, respectively), using platforms in the middle of the reservoir, while the sediments from the streams were collected along the banks. The sediment samples were packed in polyethylene bags and transported to the laboratory, refrigerated at 4 °C, after which they were preserved according to the standards recommendations (USEPA, 2001). The pore-water for the indirect ecotoxicological assays, was obtained until 72 h after the sampling, through centrifugation at 8000 rpm for 30 min, at 4 °C (USEPA, 2001). The whole-sediment and the pore-water to be used in the ecotoxicity tests were stored at −20 °C during a maximum period of one month before analysis.

2.4. Sediment analysis

2.4.1. Potentially toxic metals concentrations

Potentially toxic metals concentrations (Cd, Cr, Cu, Ni, Pb, Zn and Fe) were determined according to ISO 11466 (ISO, 1995), by atomic absorption spectrometry, with flame or electrothermal atomization, using a Varian equipment (SpectrAA 220FS and 220Z and 110Z), according to the methodology described in Palma et al. (2014). The quality control of the analysis was performed by evaluating blanks, triplicates, recovery rates, and relative deviations with standard reference materials (Palma et al., 2015).

2.4.2. Degree of contamination

The analysis of the degree of contamination by PTM in rich geological areas must be performed taking into consideration their background levels in the area, to distinguish the concentrations of metals of natural origin from those of anthropogenic sources. Background metal levels in the Guadiana Basin were obtained from previous studies (Delgado et al., 2008, 2010; Palma et al., 2015). In sediments, this kind of analysis is done by determining pollution indexes, such as the EF and the I*geo*. The EF is used to estimate the anthropogenic impact of each element, analyzed using a normalized element, which must be correlated with fine particles and have large concentrations in the area. In the present study, Fe was the element selected for the normalization (justified by *Spearman* correlation, Table S2). The EF was calculated by the equation (1) (Christophoridis et al., 2009; Liu et al., 2003).

$$EF = \frac{[X/N]\text{sample}}{[X/N]\ \text{background}} \quad (1)$$

Where, $[X/N]_{sample}$ and $[X/N]_{background}$ correspond to the ratios of mean concentrations (mg kg^{-1}, dry weight) of the target metal [X] and the normalizing element [N] in the sediment sample and in the regional background (Delgado et al., 2008, 2010), respectively. Enrichment Factors between 0.5 and 1.5 indicate that the PTM is mostly provided from natural origin; EF > 1.5 indicate that an important portion of the PTM is provided from biota or anthropogenic action (Zhang and Liu, 2002).

The I*geo* is used to assess the contamination by comparing the current and regional background concentrations of the metal in the sediments (Hanif et al., 2016). The I*geo* is calculated using the following equation (eq. (2); Loska et al., 1997):

$$I_{geo} = \log 2\left(\frac{Cn}{1.5\ Bn}\right) \quad (2)$$

where Cn is the measured concentrations of metal (n) and Bn is the geochemical background concentrations of the metal. The factor, 1.5, is the "background matrix correction value". I*geo* values are classified into seven levels (Duodu et al., 2016): I*geo*≤0, unpolluted; 0<I*geo*≤1, slightly polluted; 1<I*geo*≤2, moderately polluted; 2<I*geo*≤3, moderately severely polluted; 3<I*geo*≤4, severely polluted; 4<I*geo*≤5, severely extremely polluted; 5>I*geo*, extremely polluted.

2.4.3. Ecotoxicological analysis

Ecotoxicological analysis were performed in the whole-sediment and the extracted pore-water, using a set of representative bioindicator species from different trophic levels. The whole-sediment toxicity was assessed using *Heterocypris incongruens*, a cosmopolitan ostracod species, with a sensitivity quite like the amphipod crustacean *Hyalella azteca* and the midge larva *Chironomus riparius* (Belgis et al., 2003). The pore-water ecotoxicity was assessed using aquatic organisms, the bioluminescent bacterium *Vibrio fisheri*, the crustacean *Thamnocephalus platyurus* and the microalgae *Pseudokirchneriella subcapitata*. The results for the selected endpoints allowed the characterization of the levels of lethal and sublethal toxicity of the sediments for these species.

For all bioassays, a test with a reference substance was performed, as a positive control. The sensitivity of the organisms was in accordance with the followed protocols. The control groups had a survival rate above 90%.

2.4.3.1. Toxicity assessment of whole-sediment. The mortality and growth inhibition, of neonates of the ostracod crustacean *H. incongruens*, were performed according to the Ostracodtoxkit F standard operating procedure (Creasel, 2001). Test organisms were obtained from cysts, incubated for hatching at 25 °C under continuous illumination, 52-h before the test. After the first 48-h, neonates were pre-feed with *Spirulina* powder. The control and five replicates per sediment sample (without dilution), each with 10 neonates, were performed. After a 6-days exposure period, survival, and final length (in μm) were recorded. Toxicity was expressed in mortality, as acute endpoint, and growth inhibition as chronic criterion. Measurements of length were only performed when mortality was lower than 30%. The length increment was calculated based on equations (3) and (4) adapted from Creasel (2001):

$$\%\ \text{Growth inhibition} = 100 - (L_{\text{increment test sediment}} \ / \ L_{\text{increment control sediment}})\ x100 \quad (3)$$

where $L_{increment}$ is the mean length increment, calculated with the formula:

$$L_{increment} = L_{end} - L_{start} \quad (4)$$

where:

L_{end}: is the mean length at the end of the test (in μm)

L_{start}: is the mean length at the start of the test (in μm)

2.4.3.2. Toxicity assessment of pore-water

2.4.3.2.1. Luminescence inhibition of V. Fischeri. Luminotox® was used to evaluate the luminescence inhibition of the marine bacterium *V. fischeri* (NRRL B-11177), according to the protocol "DR LANGE luminescent bacteria test" following ISO 11348–2 (1998). Tests were carried out using the sediment pore-water samples and their dilutions with a 2% NaCl solution (50, 25, 12.5, 6.25 and 3.125%, v/v). Two replicates per treatment were used. The inhibition of the bacteria natural light emission was measured against a nontoxic control (2% NaCl solution), at a temperature of 15 ± 0.5 °C. For each sample, bioluminescence was measured before and after the desired incubation period (30 min). The EC_{50} (%), the concentration of each sample (%; v/v) that

reduced 50% of the bacterial luminescence, was determined.

2.4.3.2.2. Growth inhibition of the green microalgae P. subcapitata. Microalgae were exposed to pore-water samples for 72 h and algae growth was determined based on OECD 201 (2006). At the beginning of the test, *P. subcapitata* (100 μL of an inoculum with 3–5 × 10^4 cells mL^{-1}) was exposed to the respective diluted samples (12.5, 25, 50, 75, 100%; v/v; 900 μL of total volume) performed with MBL medium (negative control) in a 24-well microplate. Test vials were randomly incubated in an orbital shaker for 72 h at 21 ± 2 °C and with a constant luminous intensity (60–120 μE m^{-2} s^{-1}, equivalent to 6.000–10.000 lx). The concentration of the algal biomass at the beginning and after 72 h of exposure was calculated by counting the number of cells in a Neubauer chamber.

The average specific growth rate for a specific period was calculated from equation (5):

$$\mu_{i-j} = \left(\ln B_j – \ln B_i\right) / t_j - t_i \quad (5)$$

Where: μ_{i-j} is the average specific growth rate from time i to j; t_i is the time for the start of the exposure period; t_j is the time for the end of the exposure period, B_i is the biomass concentration at time i, and B_j is the biomass concentration at time j.

The inhibition of algal growth was estimated from equation (6):

$$\% I = [(\mu_c - \mu_t) / \mu_c] x\ 100 \quad (6)$$

Where: % I is the mean percentage of inhibition for specific growth rate; μ_c is the mean value for the growth rate in the control, and μ_t is the mean value for the growth rate in the water samples.

2.4.3.2.3. Mortality of the crustacean T. platyurus. The mortality assay with the crustacean *T. platyurus* was adapted from Persoone (1999). The test with *T. platyurus* was developed using the THAMNOTOXKIT F™ kit. Larvae of the shrimp *T. platyurus* (<24 h, obtained from the hatching of cysts) were exposed to different dilutions of sediment pore-water samples (12.5, 25, 50, 75 and 100%; v/v), during 24 h. Four replicates per dilution were performed. Organisms were not fed during the test. The number of dead organisms was used as endpoint and the EC_{50} (%), concentration (%; v/v) causing lethality on 50% of the exposed organisms, was calculated.

2.5. Statistical treatment of data

In the *V. fischeri* bioluminescence inhibition test, the EC_{50} (%) values were determined using LUMISsoft 4 Software™. The EC_{50} (%) values for the *T. platyurus* mortality were determined using the probit analysis (Finney, 1971). Data of sublethal bioassays were checked for homogeneity of variance by the Kolmogorov–Smirnov test (Sokal and Rohlf, 1995) and, when possible, subjected to one-way analysis of variance (ANOVA). Data that do not satisfy the assumption for ANOVA were analyzed non-parametrically using Kruskal–Wallis ANOVA by ranks test. Whenever significant differences were found ($p < 0.05$), a post hoc *Dunnett's* test was used to compare treatments with the control, for a p value of 0.05 as the significant level (Zar, 1996).

The *Spearman* rank correlation coefficients were used to evaluate the associations between the LULC, meteorological conditions, chemical indicators, ecotoxicological indicators (with the respective endpoints: EC_{50}, growth inhibition), with a level of significance $p < 0.05$.

All the variables were explored and described using descriptive statistics (mean ± standard deviation) and multivariate statistical analysis ((factor analysis (FA) and cluster analysis (CA)), using ((90 samples x 2 groups of observational parameters (LULC classes and climate conditions) x 9 chemical indicators (Clay, OM, pH, Cd, Cr, Cu, Ni, Pb, Zn) x 4 ecotoxicological indicators)). Multivariate analysis was used to identify the most important parameters that explain the variability of sediment quality, allowing their integration in an easy-to-use toolbox to assess the sediments quality. Furthermore, this statistical methodology can also be used to prove correlations previously established between the potentially toxic elements and the observed toxic effects. Data were normalized (log x; x = mean value) prior to multivariate statistical analyses, avoiding misclassification due to differences in data dimensionality (Simeonov et al., 2003).

All statistical analyses were performed with the STATISTICA 7.0 (Software™ Inc., PA, USA, 2007).

3. Results and discussion

3.1. Land use/land cover (LULC) and meteorological characterization

Fig. 1 characterizes the basin in terms of LULC classes, resulting from the information of the CORINE LULC classification and of the DGEG information in areas with environmental recovery or areas with exploration of mineral masses (Table S2), showing their distribution in each of the drainage basins. A relevant class that may be correlated with the existence of PTM in the area, because of the use of fertilizers and pesticides, is Intensive Irrigated Agriculture, which occupies at least 20% of each drainage basin, reaching more than 50% in the case of S_Zb (53%). Other important classes, that can be made accountable for an increase of PTM concentrations in the hydrographic basins, are Urban/Industrial and Mineral Extraction, both with low percentages in the area, but very significant as point sources of pollution. The distribution of classes as Urban/Industrial, or related with Mineral Extraction and environmental recovery, are presented in the lower right polar plot of Fig. 1 with a more appropriate scale to show their occupancy values (0–2.5%), evidencing that the drainage basin of the streams did not present mineral extraction class. Relatively to the locations in the Alqueva reservoir, Alamos present the lowest occupation for these classes, with a small area of Mineral Extraction and Urban/Industrial (0.11 km^2 and 4.67 km^2, respectively over a total area of 1279 km^2). Lucefécit is the location for which the drainage basin presents the highest percentage area of mineral extraction (3.80 km^2 in a total of 424.78 km^2), followed by Mr (0.23%), and Mn (0.19%), corresponding to an area of 13.70 km^2 over total areas of 5910.25 km^2 and 73 330.14 km^2, respectively. In addition, these sites have the highest occupancy of Environmental Recovery processes (with restrictions: 0.07% and to be carried out: 0.26%), which can be one of the major environmental problems in terms of PTM pollution. Traditional Agriculture generally occupies areas between 10 and 20%, except for S_Am (only 4%), which is dominated by natural vegetation, particularly the Agro-silvo-pastoral system (included in the class "Other"), the most important ecosystem in the western Mediterranean region (Godinho et al., 2016). The LULC class "Other" is also significative in the other drainage basins, with high percentage in S_Lf (67%), followed by Lf (57%) and Mn (52%), occupying less than 50% in the rest of the sites.

Fig. 2 displays the time series data of mean, maximum and minimum air temperatures, as well as accumulated precipitation, on a daily basis, for each of the eight drainage basins under study. The top panels of Fig. 2 illustrate the location of each drainage basin inside the study area and for each of these basins, air temperature (left plot) and precipitation (right plot) are represented for the two-year period considered ((y axis, from January 2017 (bottom) to December 2018 (top)). The mean temperature and accumulated precipitation are coded by the superior and inferior color scales, respectively, and represented by the colored bars in the plots. In the temperature plots, the left end of the horizontal bars indicates minimum air temperature, and the right end denotes the maximum values of air temperature. Conversely, the right end of the bars in the precipitation plots, conveys the daily accumulated precipitation values, with the left end of the bars in the origin (zero, corresponding to no precipitation).

During 2017, the south of Portugal (area of study included) suffered a severe meteorological drought with very low precipitation amounts (January 2017 to February 2018 as shown in the precipitation plots of Fig. 2) and high temperatures during a long period (April to November 2017 as illustrated in the temperature plots of Fig. 2). This drought lasted until March 2018, when heavy precipitation affected the area and

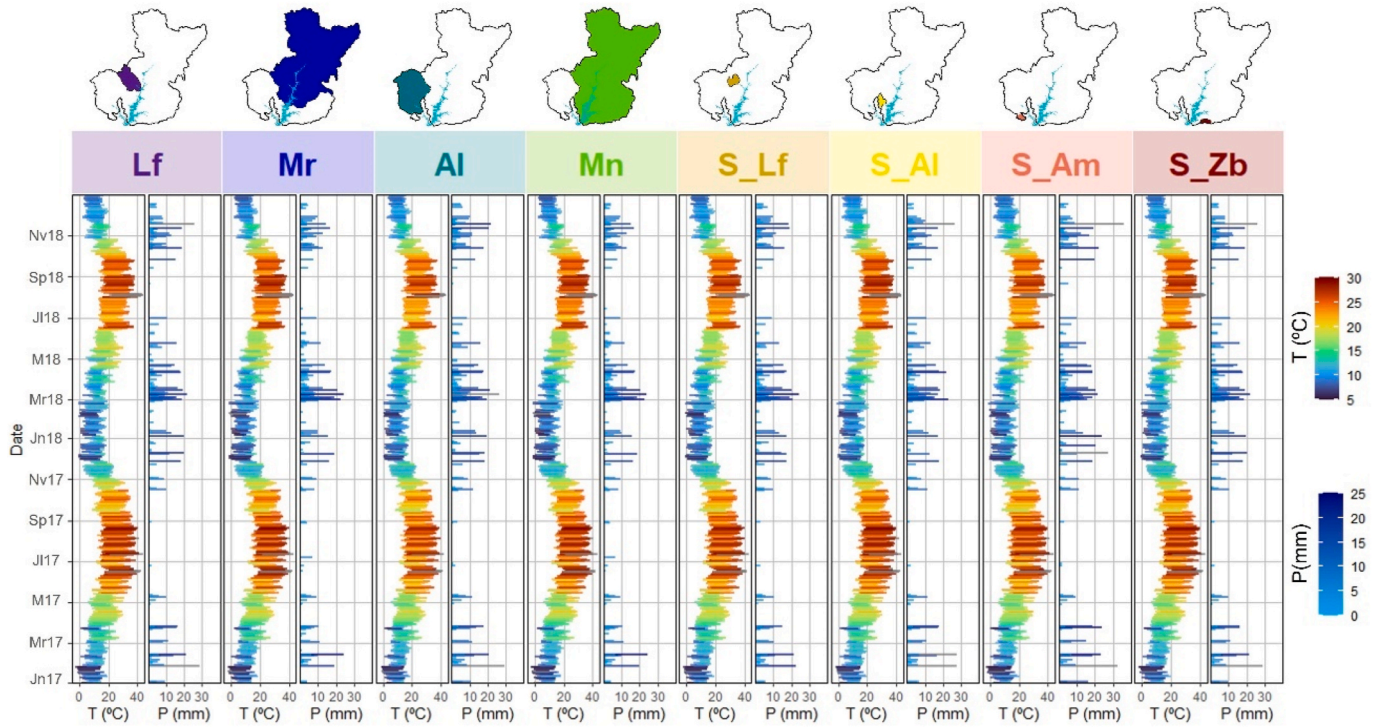

Fig. 2. Daily mean, maximum and minimum air temperatures, as well as precipitation values for each drainage basin considered (top representation), during the two-year period. Daily mean temperatures are indicated by the color scale. Daily minimum and maximum temperature values are represented by the beginning and end of each bar, respectively. Daily accumulated precipitation is indicated by the bar length, as well as, the color scale. The corresponding drainage basins are shown by the filled areas on top of each group of temperature plus precipitation plots.(For interpretation of the references to color in this figure legend, the reader is referred to the Web version of this article.).

ended the drought. The 2018, instead, was a normal year from a climatological point of view, with respect to temperature and precipitation values The longer extension of yellow to red colors during 2017 with respect to 2018, highlight the high temperatures that occurred over a long period during the year of 2017, roughly from April to November, along with very low precipitation during the whole year. Instead, the year of 2018 presents high temperatures between June and October and higher amounts of precipitation, especially from March on. Only very slight differences can be noted in the meteorological parameters, between the different drainage basins, which was expected given the proximity and overlap of some of these areas. Nevertheless, it can be noted that the highest air temperatures in both years were registered at the southernmost streams S_Am, S_Al and S_Zb, with the latter reaching a value of 44.7 °C on 4 August 2018. In general, mean air temperatures were higher in the southern streams. As for the precipitation, the highest amounts were obtained in the southwestern areas (S_Am, Al, S_Al and Lf), with highest values in S_Am of 32.7 and 36.1 mm in January 2017 and November 2018, respectively.

3.2. *Concentrations of potentially toxic metals and degree of contamination of the sediments*

The sediments along the Portuguese sector of Guadiana Basin showed physical and chemical differences (Table S1), being those from the streams most constituted by sand particles, with lower levels of OM and nutrients, comparing with the reservoir sediments, as discussed in previous studies (Palma et al., 2020a, 2021a). The pH of the Guadiana sediments was neutral to slight alkaline (Palma et al., 2021a), which can induce the immobilization of metallic elements in the sediment compartment, instead of their mobilization to the water column.

The concentrations of PTM followed similar spatial patterns, with the smallest amounts quantified in the streams (Fig. 3), which presented low levels of OM and coarse particles. In fact, the results evidence the high positive correlations among OM and all the PTM (Cu: $R = 0.68$, $p < 0.05$; Pb: $R = 0.64$, $p < 0.05$; Zn: $R = 0.58$, $p < 0.05$; Ni: $R = 0.50$, $p < 0.05$). The correlation among OM and PTM was already reported by other authors (Boguta et al., 2022; Varol et al., 2022). In the streams, S_Lf presented the highest concentrations of PTM, with Ni, Cu and Cd surpassing the guide levels for the Protection of Aquatic Life in most of 2018: Ni surpassed de ERL (effect range low), representing a range intended to estimate conditions in which an effect would be rarely observed (Long et al., 1995); while Cu and Cd surpassed the ISQG (Interim Freshwater Quality Guideline; CCME, 2002). At the reservoir, Al and Lf sediments presented the greatest concentrations of PTM, with levels of Cd, Pb above the ISQG (Interim Freshwater Quality Guideline; CCME, 2002) and Ni above the ERL guideline value (Long et al., 1995), in most of the study. Cadmium was the PTM that exceeded the guide value in all the sampling points of Guadiana Basin, at least once. Despite the great temporal variability, the results highlighted higher amounts of PTM in the sediments during 2018, with positive significant correlations for Ni and Cd (Table S3).

In regions of great geological richness, the origin of the PTM must be considered, since the quantities detected, even above the limit established for the protection of aquatic life, may be from natural origin. Thus, the determination of the enrichment factor (EF) for each metal, considering the background values, allows concluding the influence of anthropogenic actions on the observed PTM concentrations. The EF index of PTM in the Guadiana sediments, showed that the quantified concentrations of Ni and Cr were, in general, of natural origin ($EF_{Ni} < 1.48$; $EF_{Cr} < 1.45$), as was already observed on previous studies (Palma et al., 2015). Henceforth, Fig. 4 represents the EF for the PTM mainly influenced by anthropogenic actions ($EF > 1.5$; Cu, Pb, Cd and Zn). In the drainage basins of Lf, Mr and Mn, the LULC class that most contributed for the levels of PTM quantified was Mineral Extraction. In fact, despite the low percentage of this activity in all the drainage basins, its importance in the contamination/transport of metals is highlighted

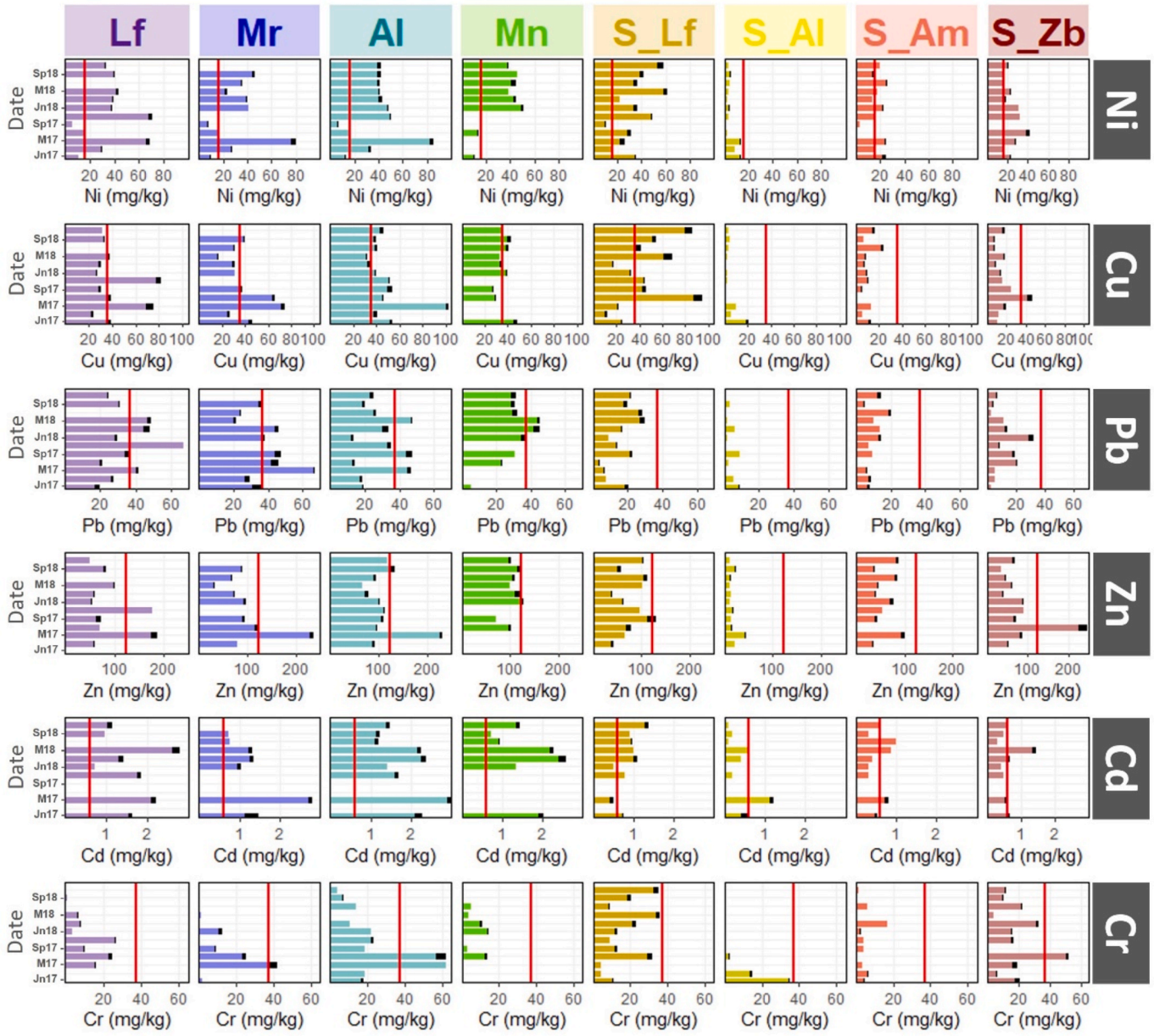

Fig. 3. Variability of potentially toxic metals on Guadiana sediments ((mean ± standard deviation (dark bar)). Red Line represents the Canadian Interim Freshwater (ISQG) for the Protection of Aquatic Life (CCME, 2002) for Cu, Pb, Cd, Cr and Zn; and ERL guideline value (effect range low) for Ni (ERL; Long et al., 1995). (For interpretation of the references to color in this figure legend, the reader is referred to the Web version of this article.)

by the *Spearman* correlation results, which indicate significant positive correlations between PTM (excepting Zn) and Mineral Extraction (Table S3). In addition, agricultural activity is another class of LULC that may have influenced the presence of some of the PTM, as Cd, in the sediments of the Guadiana Basin, due to the high use fertilizers in intensive agriculture (Smolders, 2013). Agricultural activities can also be a LULC class of diffuse pollution for concentrations of Cu (traditional agriculture $R = 0.32$; $p < 0.05$; irrigated agriculture $R = 0.58$; $p < 0.05$; Cu is used in fungicide formulations applied to vineyards), which have been increasing over the years in the Guadiana Basin (Gomes et al., 2014; Palma et al., 2015). In fact, previous studies in 2011_2012, in the Alqueva reservoir, Palma et al. (2015) reported that the presence of Cu in the sediments of the reservoir, was explained mainly by anthropogenic activities.

The I*geo* index (Fig. 4) provides information on the sediment pollution status for each PTM. For Cd, the Guadiana sediments were moderately polluted in the streams, to severely polluted in the reservoir. In fact, the temporal analysis over the years shows the increase in the state of pollution of the reservoir sediments with Cd (Palma et al., 2015), covering the entire Guadiana Basin. Further the mining activities, agriculture is another class of LULC that may have influenced the presence of Cd, in the sediments of the Guadiana Basin, due to the high use of phosphate fertilizers in intensive agriculture, formulations that naturally present Cd as an impurity in rock phosphate (Smolders, 2013; Roberts, 2014). The Alentejo region has a long history of cereals production, mainly wheat, which was produced before the water availability brought to the region by the Alqueva reservoir that allowed a diversification of crops, namely to irrigated crops. Phosphate fertilizers are a major source of trace metals to agricultural soils, especially Cd and, not only the rate of Cd:P in phosphate fertilizers used in Portugal were reported by Kabata-Pendias (2011) has the highest among the EU countries (3.1 g ha^{-1} $year^{-1}$) as, also, the application rates of P-fertilizers to cereals production in Portugal are, traditionally, very high (28 kg P_2O_5 ha^{-1} $year^{-1}$, values for 2010–2011; Smolders, 2013).

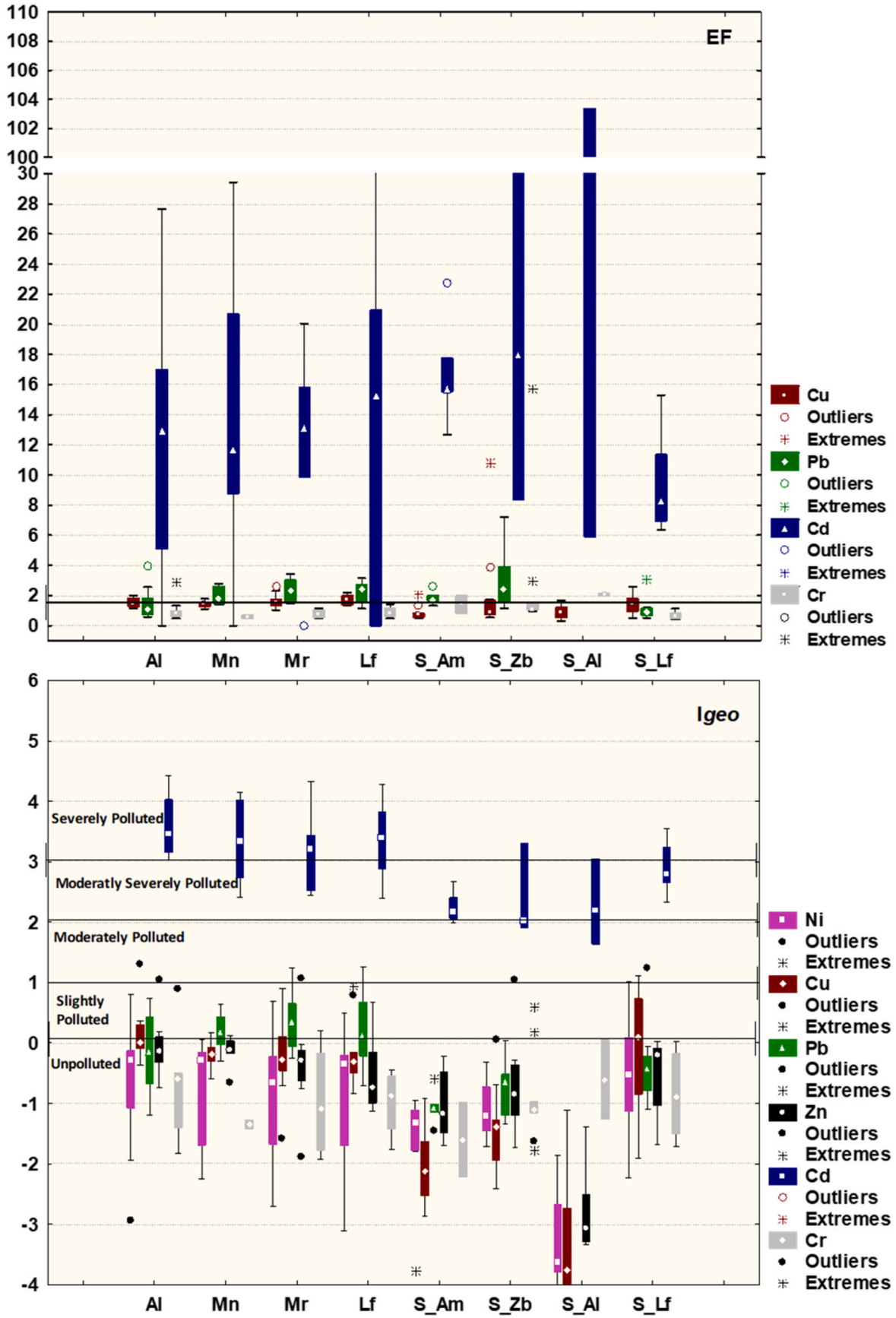

Fig. 4. Box-Whisker plots of the EF and I*geo* indexes calculated for the Guadiana sediments. The box shows the 25th and the 75th percentiles, and the whiskers represent the smallest and the largest indexes, while the line inside the box is the median. Sampling locations: Álamos (Al), Alqueva-Montante (Mn), Mourão (Mr), Lucefécit (Lf), Amieira Stream (S_Am), Zebro Stream (S_Zb), Álamos Stream (S_Al), Lucefécit Stream (S_Lf).

Relatively to the other PTM, the sediments were classified as unpolluted, except for Cu in Al and S_Lf, and for Pb in Al, Mn, Mr, and Lf, which were classified as "Slightly Polluted".

3.3. Ecotoxicological analysis

3.3.1. Toxicity of the whole-sediments

The lethal and sublethal toxicity of the sediments was evaluated with the bioindicator *H. incongruens*, using the mortality and the growth inhibition of the organisms, respectively.

Freshwater ostracods are reported as important bioindicators to assess anthropogenic stressors such as PTM, pesticides and hydrocarbons (Ruiz et al., 2013). Relatively to PTM, several studies in the literature reported its great sensitivity total Cr, Pb and Cd (Baran et al., 2015; Kudłak et al., 2011; Torokne and Toro, 2010). Further, several studies reported the sensitivity of the specie to some physical proprieties of the sediments, namely granulometry (Casado-Martinez et al., 2016). In fact, results evidenced the correlation between the presence of high percentages of clay and the inhibition of growth of the species (Table S3).

The mortality percentages in the assays with *H. incongrues* (control and samples sediments) were always less than 10%, indicating that the organisms were in good condition and also that the hazardous substances existing in the sediments were in concentrations that did not induce considerable levels of acute toxicity.

Regarding the growth inhibition endpoint, the results showed that the reservoir sediments were more toxic towards the ostracod (inhibition rate reaching 80% in Al_2018) than the stream sediments (inhibition rate reaching 60% in S_Al_2017) (Fig. 5). The sublethal toxicity results agreed with the degree of pollution determined, with Al being the site that induced the greatest growth inhibition to ostracod, mainly during 2018, followed by Mn sediments. In fact, the I*geo* index indicated that Al had the most polluted sediments, being classified as severely polluted with Cd and slightly polluted with Pb, Cu, and, sporadically, with Zn. In fact, the statistical results highlight the significant positive correlations between the observed toxic effects (rate of growth inhibition of the species) and the presence of these PTMs (Table S3). In addition, the observed effect may also be related to the granulometry of the sediments, since Al presented a high percentage of clay particles in its structure. The temporal analysis allowed to conclude that the sediments from the reservoir collected in 2018 induced a higher toxic response (higher growth inhibition rate) to the organisms than those of 2017.

3.3.2. Toxicity of the pore-water

The pore-water toxicity was evaluated with species from different trophic levels, using distinct toxicological endpoints, the results were displayed in Table S4 and Fig. 6, evidencing that *V. fisheri* was more sensitive than *T. platyurus* to the analyzed sediment samples (Table S4). Spatial analysis showed that the bacteria was more sensitive to stream sediments, with the highest number of toxic samples occurring during 2018. The toxicity detected by the bacteria is likely to be correlated with hazardous substances other than PTM, as pharmaceuticals or pesticides already detected in the basin (Palma et al., 2020b, 2021b), since the streams had the lowest concentrations of PTM, generally below the guiding limits for the protection of aquatic life (CCME, 2002). In fact, the results indicated no significant correlation among *V. fisheri* and the presence of PTM in the sediments (Table S3). Thus, despite the *V. fischeri* bioassay being known to be highly sensitive for detecting PTM toxicity (Codina et al., 2000), being generally a good choice to evaluate this type of risk, that was not the case in this study. Other authors have already observed this kind of result, justified by the low concentrations of PTM in the sediments (Hwang et al., 2021). *T. playturus* was more sensitive to samples from the wet period of 2017 (Jn, Mr and Nv). In fact, the mortality of *T. platyurus* showed a significant positive correlation with the concentrations of Zn in the sediments ($R = 0.80$; $p < 0.05$), suggesting that this species is sensitive to this metal, as reported by (Zhang et al., 2022) and explaining the results observed in the first months of 2017 (see Table S4). The results obtained for the growth rate of the green microalgae *P. subcapitata* revealed, in general, great sensitivity to the sediments of the Guadiana Basin (Fig. 6). Growth inhibition was more pronounced during the wet period of 2018, with S_Zb and Lf being the areas with the highest toxicity. The Guadiana sediments induced greater sublethal toxicity to this species than others from other countries (Broccoli et al., 2021), but this cannot be explained by the concentrations of PTM alone, fact highlighted by the *Spearman coefficients*, without significant correlations between PTM and the inhibition of microalgae growth. In fact, the observed result may be correlated with the presence of other hazardous substances such as herbicides (very toxic to green microalgae; Ma et al., 2002), from agricultural activities, which are one of the main activities in the basin. The results supported this hypothesis, since the highest growth inhibition rates occurred in wet period of 2018, when precipitation increased, enhancing the run-off of hazardous substances, previously applied to the crops.

3.4. Parameters to include in an easy-to-use toolbox to assess freshwater sediments quality

3.4.1. Correlation of LULC classes, geochemical parameters and ecotoxicological data

To analyze the most effective parameters to integrate in a toolbox for

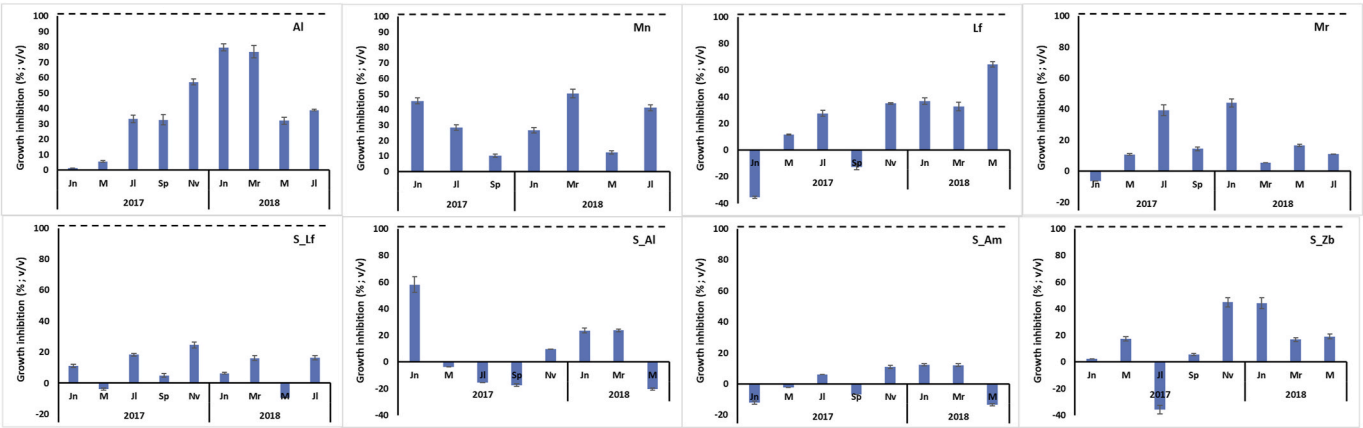

Fig. 5. Growth inhibition (%) of the ostracods *H. incongruens* neonates, after 6 days of exposure to sediments from the Guadiana Basin (mean ± standard deviation, n = 6). Sampling locations: Álamos (Al), Alqueva-Montante (Mn), Mourão (Mr), Lucefécit (Lf), Amieira Stream (S_Am), Zebro Stream (S_Zb), Álamos Stream (S_Al), Lucefécit Stream (S_Lf). Months of sampling: January (Jn), March (Mr), May (M), July (Jl), September (Sp), November (Nv).

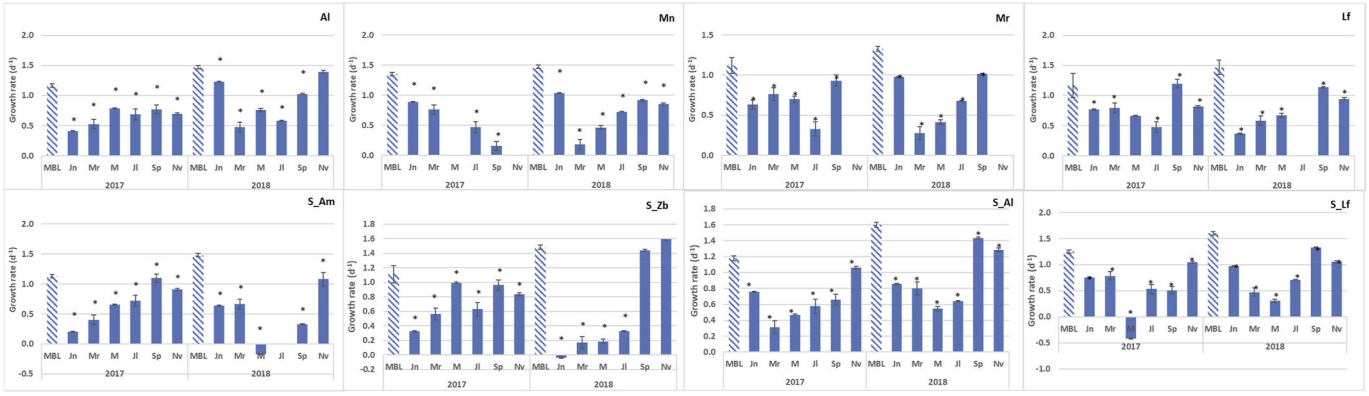

Fig. 6. Growth rate (d^{-1}) of the green microalgae *P. subcapitata* 72-h exposed to the different sediments samples tested (mean ± standard deviation; n = 6; *$p < 0.05$, *Dunnett's* post hoc comparison test with the control MBL (blue stripes). Sampling locations: Álamos (Al), Alqueva-Montante (Mn), Mourão (Mr), Lucefécit (Lf), Amieira Stream (S_Am), Zebro Stream (S_Zb), Álamos Stream (S_Al), Lucefécit Stream (S_Lf). Months of sampling: January (Jn), March (Mr), May (M), July (Jl), September (Sp), November (Nv). (For interpretation of the references to color in this figure legend, the reader is referred to the Web version of this article.)

sediment quality assessment, factor analysis (FA) and cluster analysis (CA) methods were used. The data were explored by year (2017: year of drought; 2018: year of normal climate), to understand if the climate conditions influenced the parameters that best explained the quality of sediments (Fig. 7).

The FA performed on the data from 2017 allowed the extraction of six factors with eigenvalue >1, accounting for 78% of the total variance. Factor 1 explained 30% of the total variance and presented factor loadings with positive absolute values > 0.50 for the variables: Mineral Extraction LULC class (0.54), clay content (0.68), OM content (0.58), PTM ((all of them with loadings between 0.63 (Cd) and 0.89 (Cu)), and growth inhibition of Ostrocod (0.53). Therefore, this factor reflects the link between the sediment properties and the metal pollution of the basin, identified by the bioassay with *H. incongruens*. All these parameters were projected in the positive quadrant of Factor 1. The Factor 2 with 15% of the total of variance was explained by Intensive Irrigated Agriculture (−0.88), Traditional Agriculture (−0.60) and mortality of *T. platyurus* (−0.57), which confirm that the mortality of the crustacean, induced by sediments from the Guadiana, was probably correlated with hazardous substances other than PTM, probably brought from agricultural activities. The CA applied to the 2017 samples (44 samples of the total), did not show similarities between those projected in the positive quadrant of Factor 1, and explained by metal pollution, which corresponded to 34% of the total samples. The two clusters formed (1 and 2), integrated samples from S_Am and Lf, influenced by Agriculture and Urban/Industrial classes.

The FA with the data from 2018 allowed the extraction of five factors with eigenvalue >1 that reported 77% of the total variance of the data. Factor 1 (34% of the variance) was positively correlated with Urban/Industrial LULC class (0.56) and luminescence inhibition of *V. fisheri* (0.52), and negatively explained by the same parameters correlated with metal pollution observed for 2017: clay (−0.62), OM (−0.80), PTM, excepting Cr, (−0.85 (Ni) to −0.77 (Cu)) and growth inhibition of ostracod (−0.52). Factor 2 was explained by intensive irrigated agriculture (−0.79) and traditional agriculture (−0.73) LULC classes, and by mortality of *T. platyurus* (−0.55), having as principal attribute the agriculture activities most identified by the *T. platyurus* bioassay responses. The 2018 samples (46 in the total), showed high similarities, allowing to project four clusters: cluster 1 (Al samples) and cluster 2 (Lf and Mr samples) mainly explained by metal pollution attribute; cluster 3, integrating samples from S_Am and S_ Lf, and cluster 4 (S_Al), were both mainly explained by the Urban/Industrial class, having high toxicity towards *V. fisheri*.

3.4.2. Toolbox proposal

The integrative analysis of all the results allowed to conclude that the toolbox for the assessment of freshwater sediments quality must include:

i Observational parameters: among the observational parameters used, those that showed greater importance in explaining the data related to the quality of the sediments were the CORINE LULC classification, allowing the correlation between the contamination indices and the sources of pollution.

ii Analytical parameters: (a) sediments granulometry and OM content are essential to understand the dynamics of hazardous substances in the sediments, the adsorption/desorption and leaching processes; (b) PTM quantification; (c) contamination degree indexes, both EF and I*geo*, must be used, to understand the type of contamination (natural or anthropic), given by the EF, and the degree of pollution, obtained by I*geo*. In both cases, we must have the PTM background of the area and the quantification of a normalized element, such as Fe or Al.

iii Biological parameters: The SQGs and the ISQG give us a general indication of the concentration of each PTM that can induce risk to the aquatic ecosystem, which is a limited information when an integrative assessment is needed. To understand the toxicological status and sediments, it is essential to include ecotoxicological parameters, that assess the impact of known and unknown substances. So, according to the data, among the tested bioassays, the toolbox should integrate the acute and chronic assay with *H. incongruens*, which was very sensitive and specific to detect PTM contamination in the whole sediment. Regarding the pore-water analysis, the data did not show clear evidence of which could be the best choice, although the *V. fisheri* bioassay was the one that detected the largest number of toxic samples. In fact, and despite *V. fisheri* being identified as a good bioindicator to detect toxic effect of PTM in sediments (Maradonna et al., 2020), the results showed some limitations of the assay, mainly when PTM concentrations were low, occurring a loss of bioindicator sensitivity.

4. Conclusions

The analyses of sediments are, nowadays, considered of crucial importance to understand the contamination processes in freshwater systems. Many of the studies carried out did not present an integrative approach, focusing mainly on chemical parameters. Presently, it is evident the need to include chemical and biological analysis to explain the action that sediments have in the water ecosystem. The question is, which parameters should be used to give the right answers? In the present study, a group of parameters were used to analyze the sediments, trying to identify the most sensitive ones to PTM's contamination. The study was carried out in a transnational basin (Iberian Peninsula), with Mediterranean climate conditions, which allow the

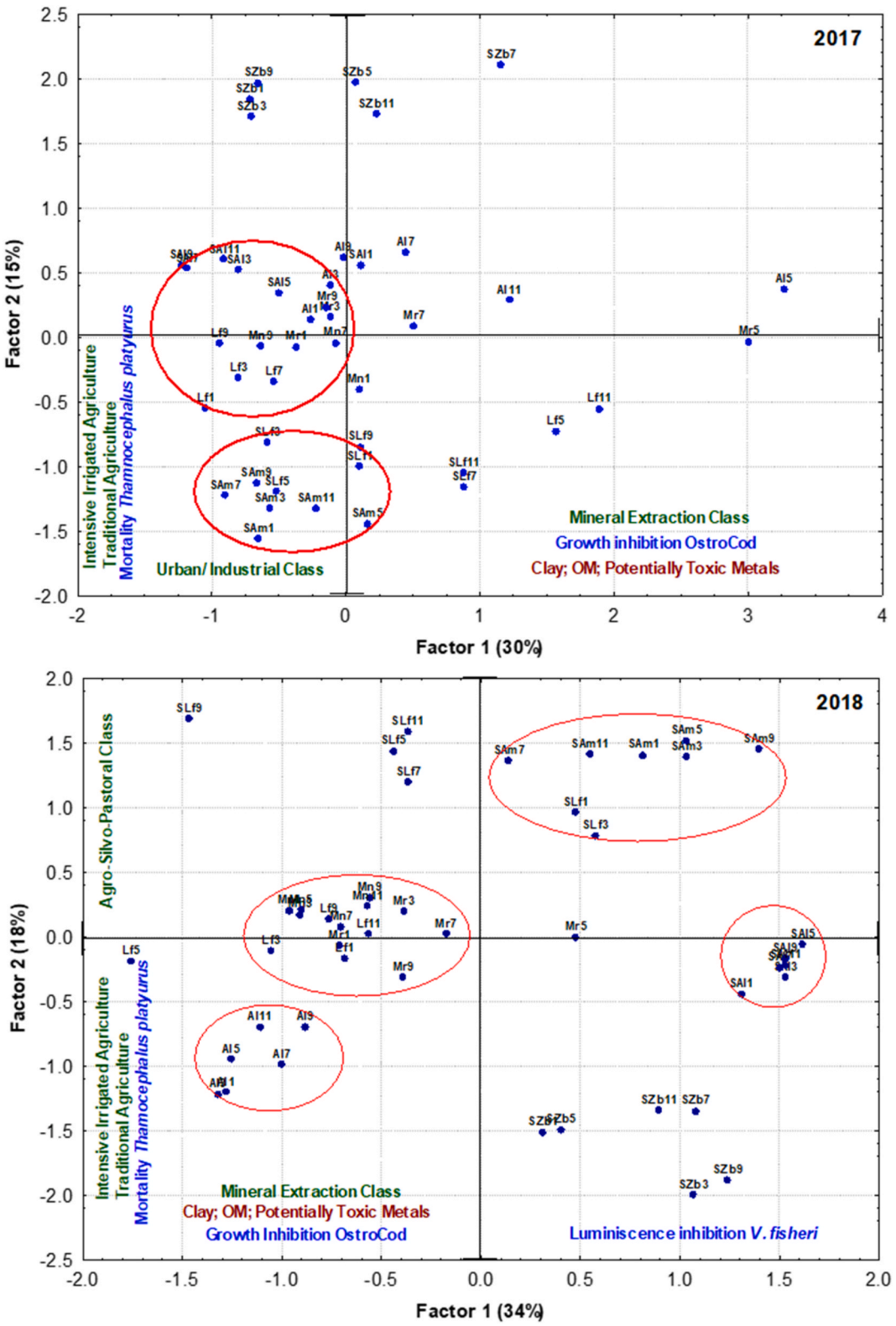

Fig. 7. Factor analysis plot showing the distributions of the LULC factors, physicochemical parameters and ecotoxicological indicators of Guadiana Basin sediments samples on the bidimensional plane defined by the first two principal components (PC). In the figure are displayed the samples scores and the statistically significant clusters obtained through the Square Euclidean distance. Samples were collected at Álamos (Al), Alqueva-Montante (Mn), Mourão (Mr), Lucefécit (Lf), Amieira Stream (SAm), Zebro Stream (SZb), Álamos Stream (SAl), Lucefécit Stream (SLf)., during the years of 2017 and 2018 in the months of January (1); March (3); May (5); July (7); September (9) and November (11).

transference of the conclusions to other basins with similar characteristics. Also, the results highlighted that the climate differences occurring in different years did not induce a pronounced variability in the organization of the data, allowing to assume that the proposal toolbox would be efficient in different climate conditions. Data analysis showed that, to be easier for the managing authorities to recognize existing problems in the basin area, and implement solutions, the toolbox must include three research fields: observational, analytical, and biological. The observational component should integrate the LULC class analysis; the analytical component the granulometry, OM, PTM quantification and degree of contamination indices; and the biological component the sub-lethal bioassay with *H. incongruens* and *V. fisheri*. Of course, this does not mean that the toolbox is closed to other parameters, it only means that they can be considered a basis for the quality assessment. Knowledge would increase with the inclusion of other chemical aspects, such as studies of metals bioavailability, or biological assays with benthic bioindicators, increasing the set of direct ecotoxicological studies.

Declaration of competing interest

The authors declare that they have no known competing financial interests or personal relationships that could have appeared to influence the work reported in this paper.

Data availability

Data will be made available on request.

Acknowledgements/Funding

The work is co-funded by National funds through FCT - Fundação para a Ciência e Tecnologia, I.P. (projects UIDB/04683/2020 and UIDP/04683/2020). The present research is also co-funded by the European Union through the European Regional Development Fund, included in the COMPETE 2020 (Operational Program Competitiveness and Internationalization) through the ALOP project (ALT20-03-0145-FEDER-000004), and through the European Agricultural Fund for Rural Development through the FitoFarmGest Operational Group (PDR 2020-101-030926).

The authors acknowledge the E-OBS dataset from the EU-FP6 project UERRA (https://www.uerra.eu), the Copernicus Climate Change Service, and the data providers in the ECA&D project (https://www.ecad.eu/). The authors also thank the European Commission Copernicus Program for Copernicus Land Monitoring Service, the Portuguese Directorate-General for Energy and Geology and the Portuguese Directorate General for Territory for providing data used in this work.

Appendix A. Supplementary data

Supplementary data to this article can be found online at https://doi.org/10.1016/j.envres.2022.114798.

References

APA (Agência Portuguesa do Ambiente), 2016. Plano de gestão de região hidrográfica 2016/2021. Parte 2. Caracterização e diagnóstico, Anexo IV.

Baran, A., Tarnawski, M., 2015. Assessment of heavy metals mobility and toxicity in contaminated sediments by sequential extraction and a battery of bioassays. Ecotoxicology 24, 1279–1293. https://doi.org/10.1007/s10646-015-1499-4.

Belgis, Z.C., Persoone, G., Blaise, C., 2003. Cyst-based toxicity tests XVI - sensitivity comparison of the solid phase *Heterocypris incongruens* microbiotest with the *Hyalella azteca* and *Chironomus riparius* contact assays on freshwater sediments from Peninsula Harbour (Ontario, Canada). Chemosphere 52, 95–101. https://doi.org/10.1016/S0045-6535(03)00186-3.

Boguta, P., Skic, K., Baran, A., Szara-Bąk, M., 2022. The influence of the physicochemical properties of sediment on the content and ecotoxicity of trace elements in bottom sediments. Chemosphere 287. https://doi.org/10.1016/j.chemosphere.2021.132366.

Broccoli, A., Morroni, L., Valentini, A., Vitiello, V., Renzi, M., Nuccio, C., Pellegrini, D., 2021. Comparison of different ecotoxicological batteries with WOE approach for the environmental quality evaluation of harbour sediments. Aquat. Toxicol. 237, 105905 https://doi.org/10.1016/j.aquatox.2021.105905.

Burton, G.A., 2002. Sediment quality criteria in use around the world. Limnology 3, 65–75. https://doi.org/10.1007/s102010200008.

CCME (Canadian Council of Ministers for the Environment), 2002. Canadian Sediment Quality Guidelines for the Protection of Aquatic Life: Summary Tables. http://st-ts.ccme.ca/.

Christophoridis, C., Dedepsidis, D., Fytianos, K., 2009. Occurrence and distribution of selected heavy metals in the surface sediments of Thermaikos Gulf, N. Greece. Assessment using pollution indicators. J. Hazard Mater. 168, 1082–1091. https://doi.org/10.1016/j.jhazmat.2009.02.154.

Codina, J.C., Cazorla, F.M., Pérez-García, A., De Vicente, A., 2000. Heavy metal toxicity and genotoxicity in water and sewage determined by microbiological methods. Environ. Toxicol. Chem. 19, 1552–1558. https://doi.org/10.1002/etc.5620190611.

Cornes, R., van der Schrier, G., van den Besselaar, E.J.M., Jones, P.D., 2018. An ensemble version of the E-OBS temperature and precipitation datasets. J. Geophys. Res. Atmos. 123 https://doi.org/10.1029/2017JD028200.

Creasel, 2001. Ostracodtoxkit F™. Chronic "Direct Contact" Toxicity Test for Freshwater Sediments. *Standard Operational Procedure*. Deinze, Belgium.

da Silva de Freitas, A., de Oliveira Santos, A.D., da Cruz Félix, L., dos Santos, R.F., Bila, D. M., de Carvalho Aguiar, V.M., da Fonseca, E.M., Neto, J.A.B., 2022. Multiproxy analysis in contaminated sediments from niterói harbour (guanabara bay), Brazil. Mar. Pollut. Bull. 175 https://doi.org/10.1016/j.marpolbul.2022.113348.

Delgado, J., Nieto, J.M., Boski, T., Albardeiro, L., 2008. Determination of the regional background in Holocene sediments of the Guadiana river estuary (SW Spain). Geogaceta 44, 235–238.

Delgado, J., Nieto, J.M., Boski, T., 2010. Analysis of the spatial variation of heavy metals in the Guadiana Estuary sediments (SW Iberian Peninsula) based on GIS-mapping techniques. Estuar. Coast Shelf Sci. 88, 71–83. https://doi.org/10.1016/j.ecss.2010.03.011.

Duodu, G.O., Goonetilleke, A., Ayoko, G.A., 2016. Comparison of pollution indices for the assessment of heavy metal in Brisbane River sediment. Environ. Pollut. 219, 1077–1091. https://doi.org/10.1016/j.envpol.2016.09.008.

Ehrlich, S., Lambers, D., Baccarelli, A., Khoury, J., Macaluso, M., Ho, S.-M., 2016. Endocrine disruptors: a potential risk factor for gestational diabetes mellitus. Am. J. Perinatol. 33, 1313–1318. https://doi.org/10.1055/s-0036-1586500.

Finney, D.J., 1971. Probit Analysis Cambridge. UK Cambridge University Press.

Godinho, S., Gil, A., Guiomar, N., Costa, M.J., Neves, N., 2016. Assessing the role of Mediterranean evergreen oaks canopy cover in land surface albedo and temperature using a remote sensing-based approach. Appl. Geogr. 74, 84–94. https://doi.org/10.1016/j.apgeog.2016.07.004.

Gomes, A., Connor, S., Boski, T., Moura, D., Camacho, S., 2014. Geochemical characteristics of sediments along the margins of an atlantic-mediterranean estuary (the Guadiana, Southeast Portugal): spatial and seasonal variations. Rev. Gestão Costeira Integr. 14, 129–148. https://doi.org/10.5894/rgci452.

Hanif, N., Eqani, S.A.M.A.S., Ali, S.M., Cincinelli, A., Ali, N., Katsoyiannis, I.A., Tanveer, Z.I., Bokhari, H., 2016. Geo-accumulation and enrichment of trace metals in sediments and their associated risks in the Chenab River, Pakistan. J. Geochem. Explor. 165, 62–70. https://doi.org/10.1016/j.gexplo.2016.02.006.

Huat, T.J., Camats-Perna, J., Newcombe, E.A., Valmas, N., Kitazawa, M., Medeiros, R., 2019. Metal toxicity links to alzheimer's disease and neuroinflammation. J. Mol. Biol. 1–26. https://doi.org/10.1016/j.jmb.2019.01.018.

Hwang, K., Lee, Junghyun, Kwon, I., Park, S.Y., Yoon, S.J., Lee, Jongmin, Kim, B., Kim, T., Kwon, B.O., Hong, S., Lee, M.J., Hu, W., Wang, T., Choi, K., Ryu, J., Khim, J. S., 2021. Large-scale sediment toxicity assessment over the 15,000 km of coastline in the Yellow and Bohai seas, East Asia. Sci. Total Environ. 792, 148371 https://doi.org/10.1016/j.scitotenv.2021.148371.

Ingersoll, Christopher G., MacDonald, Donald D., 2002. A Guidance Manual to Support the Assessment of Contaminated Sediments in Freshwater Ecosystems.

ISO (International Organization for Standardization), 1995. ISO 11466: Soil Quality—Extraction of Trace Elements Soluble in Aqua Regia. Geneve.

ISO (International Organization for Standardization), 1998. ISO 11348-2: Determination of Inhibitory Effect of Water Samples on the Light Emission of *Vibrio Fischeri* (Luminescent Bacteria Test). Part 2: Method Using Liquid-Dried Bacteria. International Organization for Standardisation, Geneve, Switzerland.

Kabata-Pendias, A., 2011. Trace Elements in Soils and in Plants, fourth ed. CRC Press, Boca Raton (USA), p. 505.

Kosztra, B., Büttner, G., Hazeu, G., Arnold, S., 2017. Updated CLC Illustrated Nomenclature Guidelines. Wien, p. 124.

Kudłak, B., Wolska, L., Namieśnik, J., 2011. Determination of EC_{50} toxicity data of selected heavy metals toward *Heterocypris incongruens* and their comparison to "direct- contact" and microbiotests. Environ. Monit. Assess. 174, 509–516. https://doi.org/10.1007/s10661-010-1474-8.

Leistel, J.M., Marcoux, E., Thiéblemont, D., Quesada, C., Sánchez, A., Almodóvar, G.R., Pascual, E., Sáez, R., 1997. The volcanic-hosted massive sulphide deposits of the iberian pyrite Belt: review and preface to the thematic issue. Miner. Depos. 33, 2–30. https://doi.org/10.1007/s001260050130.

Liu, W.X., Li, X.D., Shen, Z.G., Wang, D.C., Wai, O.W.H., Li, Y.S., 2003. Multivariate statistical study of heavy metal enrichment in sediments of the Pearl River Estuary. Environ. Pollut. 121, 377–388. https://doi.org/10.1016/S0269-7491(02)00234-8.

Liu, D., Wang, J., Yu, H., Gao, H., Xu, W., 2021. Evaluating ecological risks and tracking potential factors influencing heavy metals in sediments in an urban river. Environ. Sci. Eur. 33 https://doi.org/10.1186/s12302-021-00487-x.

Long, E.R., MacDonald, D.D., Smith, S.L., Calder, F.D., 1995. Incidence of adverse biological effects within ranges of chemical concentrations in marine and estuarine sediments. Environ. Manag. 19, 81–97.

Loska, Krzysztof, Jan, Cebula, Jacek Pelczar, D.W.J.K., 1997. Use of enrichment, and contamination factors together with geoaccumulation indexes to evaluate the content of Cd, Cu, and Ni in the rybnik water reservoir in Poland. Water. Air. Soil Pollut. 93, 347–365.

Luo, P., Xu, C., Kang, S., Huo, A., Lyu, J., Zhou, M., Nover, D., 2021. Heavy metals in water and surface sediments of the Fenghe River Basin, China: assessment and source analysis. Water Sci. Technol. 84, 3072–3090. https://doi.org/10.2166/wst.2021.335.

Ma, J., Xu, L., Wang, S., Zheng, R., Jin, S., Huang, S., Huang, Y., 2002. Toxicity of 40 herbicides to the green alga Chlorella vulgaris. Ecotoxicol. Environ. Saf. 51, 128–132. https://doi.org/10.1006/eesa.2001.2113.

MacDonald, D.D., Ingersoll, C.G., Berger, T.A., 2000. Development and evaluation of consensus-based sediment quality guidelines for freshwater ecosystems. Arch. Environ. Contam. Toxicol. 39, 20–31. https://doi.org/10.1007/s002440010075.

Macfarlane, M., 2003. A Guidance Manual to Support the Assessment of Contaminated Sediments in Freshwater, Estuarine, and Marine Ecosystems in British Columbia.

Maradonna, F., Ancillai, D., Notarstefano, V., Valenti, A., Leoni, T., Carnevali, O., 2020. An integrated approach to evaluate port sediment quality: from chemical characterization to multispecies bioassays. Sci. Total Environ. 746, 141204 https://doi.org/10.1016/j.scitotenv.2020.141204.

dos Santos Mendonça, J.M., de Souza, I.S., de Medeiros, G.F., Mina, I.M.C.A.P., 2021. Geochemical and ecotoxicological evaluation of sediments of a semiarid estuary on the northeast of Brazil (Natal/RN). Reg. Stud. Mar. Sci 43, 101676. https://doi.org/10.1016/j.rsma.2021.101676.

OECD (Organization for Economic Cooperation and Development), 2006. Freshwater alga and cyanobacteria, growth inhibition test. In: OECD Guidelines for Testing of Chemicals Nº 201. Organization for Economic Cooperation and Development, Paris.

Palma, P., Ledo, L., Soares, S., Barbosa, I.R., Alvarenga, P., 2014. Integrated environmental assessment of freshwater sediments: a chemical and ecotoxicological approach at the Alqueva reservoir, 2 Environ. Geochem. Health 36, 9559. https://doi.org/10.1007/s10653-013.

Palma, P., Ledo, L., Alvarenga, P., 2015. Assessment of trace element pollution and its environmental risk to freshwater sediments influenced by anthropogenic contributions: the case study of Alqueva reservoir (Guadiana Basin). Catena 128, 174–184. https://doi.org/10.1016/j.catena.2015.02.002.

Palma, P., Fialho, S., Lima, A., Mourinha, C., Penha, A., Novais, M.H., Rosado, A., Morais, M., Potes, M., Costa, M.J., Alvarenga, P., 2020a. Switzerland Land-cover patterns and hydrogeomorphology of tributaries: Are these important stressors for the water quality of reservoirs in the mediterranean region? Water 12. https://doi.org/10.3390/w12102665.

Palma, P., Lima, A., Helena, M., João, M., Montemurro, N., Pérez, S., Lopez, M., Alda, D., 2020b. Pharmaceuticals in a Mediterranean Basin: the influence of temporal and hydrological patterns in environmental risk assessment. Sci. Total Environ. 709 https://doi.org/10.1016/j.scitotenv.2019.136205.

Palma, P., Penha, A.M., Novais, M.H., Fialho, S., Lima, A., Mourinha, C., Alvarenga, P., Rosado, A., Iakunin, M., Rodrigues, G., Potes, M., Costa, M.J., Morais, M., Salgado, R., 2021a. Water - Sediment Physicochemical Dynamics in a Large Reservoir in the Mediterranean Region under Multiple Stressors, pp. 1–23.

Palma, P., Fialho, S., Lima, A., Catarino, A., Costa, M.J., Barbieri, M.V., Monllor-Alcaraz, L.S., Postigo, C., de Alda, M.L., 2021b. Occurrence and risk assessment of pesticides in a Mediterranean Basin with strong agricultural pressure (Guadiana Basin: southern of Portugal). Sci. Total Environ. 794, 148703 https://doi.org/10.1016/j.scitotenv.2021.148703.

Persoone, G., 1999. Thamnotoxkit F^{TM} - Crustacean toxicity screening test for Freshwater. Standard Operational Procedure 3–21 (Belgium).

Rani, S., Ahmed, M.K., Xiongzhi, X., Keliang, C., Islam, M.S., Habibullah-Al-Mamun, M., 2021. Occurrence, spatial distribution and ecological risk assessment of trace elements in surface sediments of rivers and coastal areas of the East Coast of Bangladesh, North-East Bay of Bengal. Sci. Total Environ. 801, 149782 https://doi.org/10.1016/j.scitotenv.2021.149782.

Rao, K., Tang, T., Zhang, X., Wang, M., Liu, J., Wu, B., Wang, P., Ma, Y., 2021. Spatial-temporal dynamics, ecological risk assessment, source identification and interactions with internal nutrients release of heavy metals in surface sediments from a large Chinese shallow lake. Chemosphere 282. https://doi.org/10.1016/j.chemosphere.2021.131041.

Roberts, T.L., 2014. Cadmium and phosphorous fertilizers: the issues and the science. Procedia Eng. 83, 52–59. https://doi.org/10.1016/j.proeng.2014.09.012.

Ruiz, F., Abad, M., Bodergat, A.M., Carbonel, P., Rodríguez-Lázaro, J., González-Regalado, M.L., Toscano, A., García, E.X., Prenda, J., 2013. Freshwater ostracods as environmental tracers. Int. J. Environ. Sci. Technol. 10, 1115–1128. https://doi.org/10.1007/s13762-013-0249-5.

Sahli, L., Belhiouani, H., Burga Pérez, K.F., El Hadef El Okki, M., Afri-Mehennaoui, F.Z., Férard, J.F., Mehennaoui, S., 2021. Assessment of freshwater sediment quality: potential ecological risk and ecotoxicity tests as complementary approaches. Chem. Ecol. 37, 219–233. https://doi.org/10.1080/02757540.2020.1853106.

Simeonov, V., Stratis, J.A., Samara, C., Zachariadis, G., Voutsa, D., Anthemidis, A., Sofoniou, M., Kouimtzis, T., 2003. Assessment of the surface water quality in Northern Greece. Water Res. 37, 4119–4124. https://doi.org/10.1016/S0043-1354(03)00398-1.

Smolders, E.L.L., 2013. Revisiting and Updating the Effect of Phosphate Fertilizers to Cadmium Accumulation in European Agricultural Soils. Final report KULeuven - DG Enterprise, Belgium.

Sokal, R.R., Rohlf, F.J., 1995. Biometry — the Principles and Practice of Statistics in Biological Research. Freeman, New York, DC.

Soomro, M.H., Baiz, N., Huel, G., Yazbeck, C., Botton, J., Heude, B., Bornehag, C.G., Annesi-Maesano, I., 2019. Exposure to heavy metals during pregnancy related to gestational diabetes mellitus in diabetes-free mothers. Sci. Total Environ. 656, 870–876. https://doi.org/10.1016/j.scitotenv.2018.11.422.

Torokne, A., Toro, K., 2010. Evaluation of the toxicity of river and creek sediments in Hungary with two different methods. Environ. Toxicol. 25, 504–509. https://doi.org/10.1002/tox.

USEPA, 2001. Methods for Collection, Storage and Manipulation of Sediments for Chemical and Toxicological Analyses: Technical Manual. EPA Region V, Chicago. EPA-823-B-01-002.

Varol, M., Ustaoğlu, F., Tokatlı, C., 2022. Ecological risks and controlling factors of trace elements in sediments of dam lakes in the Black Sea Region (Turkey). Environ. Res. 205 https://doi.org/10.1016/j.envres.2021.112478.

Wang, H., You, T., Gomez, M.A., Wang, Y., Li, S., Jia, Y., Shi, Z., 2021. Chemical speciation and ecological risk assessment of Cd, Pb and as in sediments: a case study in the Xijiang River basin, China. Environ. Earth Sci. 80, 1–14. https://doi.org/10.1007/s12665-021-09724-1.

Zar, J.H., 1996. Biostatistical Analysis. Prentice Hall International Editions, New Jersey.

Zhang, J., Liu, C.L., 2002. Riverine composition and estuarine geochemistry of particulate metals in China - weathering features, anthropogenic impact and chemical fluxes. Estuar. Coast Shelf Sci. 54, 1051–1070. https://doi.org/10.1006/ecss.2001.0879.

Zhang, Y., Zhang, M., Yu, W., Li, J., Kong, D., 2022. Ecotoxicological risk ranking of 19 metals in the lower Yangtze River of China based on their threats to aquatic wildlife. Sci. Total Environ. 812, 152370 https://doi.org/10.1016/j.scitotenv.2021.152370.

ResearchGate

See discussions, stats, and author profiles for this publication at: https://www.researchgate.net/publication/373222449

The usefulness of ecotoxicological tools to improve the assessment of water bodies in a climate change reality

Article *in* The Science of The Total Environment · August 2023

DOI: 10.1016/j.scitotenv.2023.166392

CITATIONS
0

READS
53

8 authors, including:

M.H. Novais
Universidade de Évora
71 PUBLICATIONS **1,074** CITATIONS
SEE PROFILE

Alexandra Penha
Universidade de Évora
29 PUBLICATIONS **225** CITATIONS
SEE PROFILE

Adriana Catarino
Polytechnic Institute of Beja
13 PUBLICATIONS **27** CITATIONS
SEE PROFILE

Patricia Palma
Polytechnic Institute of Beja
66 PUBLICATIONS **2,742** CITATIONS
SEE PROFILE

All content following this page was uploaded by M.H. Novais on 31 August 2023.

The user has requested enhancement of the downloaded file.

Science of the Total Environment 901 (2023) 166392

Contents lists available at ScienceDirect

Science of the Total Environment

journal homepage: www.elsevier.com/locate/scitotenv

The usefulness of ecotoxicological tools to improve the assessment of water bodies in a climate change reality

M.H. Novais [a,b,*], A. Marchã Penha [a,b], A. Catarino [a,c], I. Martins [c], S. Fialho [c], A. Lima [c], M. Morais [a,b], P. Palma [a,c,d]

[a] ICT, Institute of Earth Sciences, University of Évora, Rua Romão Ramalho 59, Évora, Portugal
[b] Water Laboratory, University of Évora, P.I.T.E. Rua da Barba Rala Nº 1, 7005-345 Évora, Portugal
[c] Department of Technologies and Applied Sciences, Polytechnic Institute of Beja, 7801-295, Portugal
[d] GeoBioTec, NOVA School of Science and Technology, Campus da Caparica, 2829-516 Caparica, Portugal

HIGHLIGHTS

- Development and testing of a classification system based on ecotoxicological endpoints
- Complementarity between ecotoxicological tools and WFD-based surface waters assessment
- Ecotoxicological tools for surface waters assessment under extreme conditions e.g., droughts and floods
- Ecotoxicological tools added value in the assessment of point-source pollution

GRAPHICAL ABSTRACT

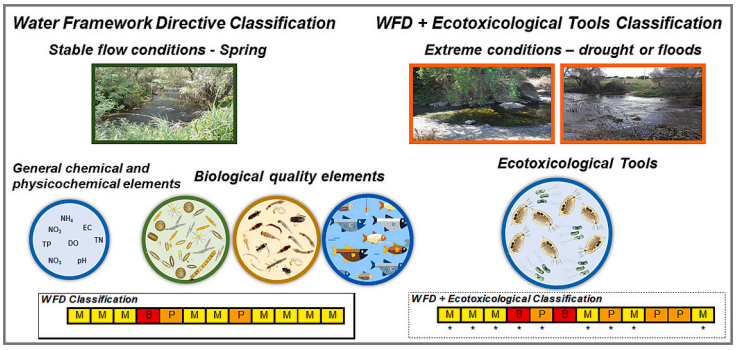

ARTICLE INFO

Editor: Sergi Sabater

Keywords:
Bioassays
Biotic indices
Diatoms
Ecotoxicological classification system
Specific pollution sensitivity index

ABSTRACT

This study aimed to analyse the added value of using ecotoxicological tools to complement and improve the assessment of natural water bodies status, in situations of climate change, with a higher frequency of extreme events as floods or droughts.

Four water bodies of streams in the Guadiana Basin (Álamos, Amieira, Lucefécit, Zebro) were studied in 2017 and 2018 and classified based on the Water Framework Directive (WFD) parameters: Biological Quality Element – Phytobenthos (diatoms), General chemical and physicochemical elements, Specific pollutants, and Priority Substances. Complementarily, bioassays (including lethal and sublethal parameters) were carried out with organisms of different trophic levels: (i) the bacteria *Aliivibrio fischeri;* (ii) the microalgae *Pseudokirchneriella subcapitata*; (iii) the crustaceans *Daphnia magna*, *Thamnocephalus platyurus* and *Heterocypris incongruens.* A classification system with 5 scores was developed, permitting to classify water bodies from non-toxic (EC_{50} > 100 %; growth and feeding rate > 80 %; blue) to highly toxic (EC_{50} < 10 %; growth and feeding rate < 10 %; red). The comparison between the classification based on the WFD parameters and on ecotoxicological endpoints showed similar results for 71 % of the samples, and significant positive Pearson correlations were detected between the diatom-based Specific Polluosensitivity Index (SPI) and $EC50_{V.fisheri}$, the algae growth rate and

* Corresponding author.
E-mail address: hnovais@uevora.pt (M.H. Novais).

https://doi.org/10.1016/j.scitotenv.2023.166392
Received 4 May 2023; Received in revised form 22 July 2023; Accepted 16 August 2023
Available online 18 August 2023
0048-9697/© 2023 The Authors. Published by Elsevier B.V. This is an open access article under the CC BY license (http://creativecommons.org/licenses/by/4.0/).

Shannon diversity index. These results indicate that when the biological quality elements cannot be used (namely under drought or flooding conditions) the application of ecotoxicological bioassays may be a good alternative. Further, when ecotoxicological parameters were included, an increase of worse classifications (Bad and Poor) was observed, revealing an improvement in the sensitivity of the classification, mainly in presence of specific and priority substances. So, the ecotoxicological analysis appears to provide useful information regarding the potential presence of both known and unknown contaminants at concentrations that cause biological effects (even within the WFD limits), in agreement with several authors that have already suggested its use in biomonitoring.

1. Introduction

Aware of the imperative need to stop, prevent and reverse the degradation of ecosystems, and to effectively restore aquatic ecosystems that have been degraded around the world, the United Nations (UN) has declared the period 2021 to 2030 as the Decade for Ecosystem Restoration (United Nations General Assembly, 2019). The European Green Deal is part of the European Commission's strategy to achieve the United Nations Sustainable Development Goals until 2030, providing an action plan to boost the efficient use of resources, restore biodiversity, reduce pollution, rebalance the aquatic ecosystems, and improve the well-being and health of citizens and future generations by providing clean water (European Commission, 2019).

The Water Framework Directive (WFD, Directive 2000/60/EC, 2000) is the central piece of water management legislation within Europe and its main aims are to prevent further deterioration of European water resources, to protect and enhance the status of the water bodies, in terms of their ecosystem structure and/or function (Martinez-Haro et al., 2022), and to contribute to mitigating the effects of floods and droughts (Directive 2000/60/EC, 2000). With the WFD, the water status assessment starts to include the concept of the 'Ecosystem Approach', reflecting the concern of European countries to preserve the ecological integrity of the aquatic ecosystems; as revealed in the Ecological status concept, defined in the WFD (Directive 2000/60/EC, 2000) as "an expression of the quality and functioning of aquatic ecosystems associated with surface waters, classified in accordance with Annex V". Hence, to follow the WFD strategy of inland surface, transition, coastal and groundwaters protection, it is necessary to implement monitoring programs and apply classification systems. These systems include the surface and groundwaters status classification, determined by the poorer of the ecological and chemical status for the surface and the quantitative and chemical status for the groundwaters. For surface waters (i.e., rivers, lakes, transitional waters, and coastal waters), according to the WFD Annex V, the ecological status classification is based on biological quality elements (BQEs), as well as hydromorphological, chemical and physicochemical elements supporting the BQEs.

To allow the comparability of the monitoring systems among Member States, the classification of the ecological status must be expressed as Ecological Quality Ratio (EQR, as a numerical value between 0 and 1), indicating the relationship between the values of the biological parameters for a given water body and those in reference conditions, with higher values representing higher ecological status (Directive 2000/60/EC, 2000). The ecological quality ratio scale is divided into five classes, to which a colour code is assigned: High (blue); Good (green); Moderate (yellow); Poor (orange); and Bad (red).

For rivers and lakes, the BQEs considered are: (i) the composition and abundance of aquatic flora (phytoplankton, macrophytes and phytobenthos); (ii) the composition and abundance of benthic invertebrate fauna; and (iii) the composition, abundance, and age structure of fish fauna (Directive 2000/60/EC, 2000). Most of the member states have considered the BQE "macrophytes and phytobenthos" as two separate sub-elements (Kelly, 2013), with diatoms already validated as proxies for phytobenthos in the ecological status assessment of standing waters (Kelly et al., 2008), and frequently representing phytobenthos in rivers (Kelly, 2013; Masouras et al., 2021). Therefore, diatoms have been used as ecological indicators during the last decades, with several studies supporting the use of diatom-based metrics in water quality monitoring, especially in lotic systems (Viso and Blanco, 2023). Several diatom indices have been developed, among which the weighted average-based Specific Polluosensitivity Index (SPI) stands out (Viso and Blanco, 2023).

The ecological and chemical assessment required by the WFD however, has some limitations as: (i) there is not an explicit requirement to establish cause-effect relationships in the assessment of quality status (Allan et al., 2006a, 2006b); (ii) overlooks ecosystem functioning and individual endpoints (Martinez-Haro et al., 2015; Palma et al., 2016); (iii) biotic indices lack preventive value, since they reflect the responses of the organisms after the ecosystem change/ damage (Rodrigues et al., 2021); (iv) isolated use of weighted average metrics risks overlooking other pressures than nutrient or organic pollution, e.g., acidification, as pointed out by Kelly (2013); (v) the SPI reflects the general water quality during the month before sampling (Viso and Blanco, 2023); (vi) diatom sampling for the ecological status assessment should be carried out in stable flow conditions (INAG I.P, 2008), avoiding zones of very slow current (European Committee For Standardization, 2003) and waiting four weeks before sampling after the occurrence of strong hydrological events as floods (AFNOR, 2007), which blocks the ecological status assessment during extreme flow conditions (dry periods and floods); (vii) furthermore, fish fauna are considered to be poor indicators in streams with temporary hydrological regimes (APA, 2021), as well as benthic invertebrates, that have high spatial (substrate-related) and temporal variability, related to insect hatching and water flow variation (European Commission. Directorate-General for the Environment, 2003).

All these limitations become more evident with climate change, which may be responsible for modulating the effects of stressors and playing a key role in defining the responses of aquatic ecosystems (Santos et al., 2021). Climate predictions include the increase in the frequency of extreme meteorological events such as floods, heat waves, severe droughts, and windstorms (Millennium Ecosystem Assessment, 2005). Changes in the hydrological cycle may also be expected (IPCC, 2018; Millennium Ecosystem Assessment, 2005), inducing a high variability of the level and flow of rivers, lakes, and oceans. Thus, it is essential to develop more comprehensive assessments, including new ecological perspectives, based on a holistic and multidisciplinary view, integrating multiple lines of evidence that allow an understanding of the exposure-response links between biological indicators, climatic factors, and anthropogenic stressors (Carvalho et al., 2019; Voulvoulis et al., 2017). So, with WFD as a driver, there is now an opportunity to start taking advantage of ecotoxicological research as rapid assessment tools, creating and integrating new cost-effective monitoring toolboxes, specifically in situations where biotic indices are not able to provide credible responses (Palma et al., 2016; Rodrigues et al., 2022). The ecotoxicological bioassays improve the ability to establish the reasons for a failing ecological status and whether pollutants are the cause for not reaching a 'good status', closing the gap between ecology and chemistry (Martinez-Haro et al., 2015; Santos et al., 2021).

Ecotoxicological bioassays aim to quantify the toxicity of individual chemicals or mixtures of known or unknown composition by exposing living organisms under standardised conditions, with the measurement of ecologically relevant responses (Rand, 1995), the so-called dose-response trials. Hence, to obtain pertinent outcomes at the ecosystem

level, the assessed responses should have consequences on the biological health of the individual (e.g., mortality, growth, reproduction, feeding rates) (Palma et al., 2016; Pinto et al., 2021; Rodrigues et al., 2021).

In this context, the present study aimed to assess whether the integration of ecotoxicological tools, reinforces (or not) the robustness of the assessment of the ecological status obtained through biotic indices, and can be an option when there are limitations in the use of biotic indices. This hypothesis was tested in streams of the Guadiana Basin (South of Portugal), some of them with intermittent hydrological regimes, including a period characterised by intense drought. The results can serve as a basis for the development of environmental management models that integrate biotic indices and ecotoxicological endpoints, especially in situations where biotic indices are insufficient for a relevant ecological analysis of the ecosystem.

2. Materials and methods

2.1. Site description and sampling procedures

In the framework of the project "Observation, prediction, and alert systems in atmosphere and water reservoirs of Alentejo" (ALOP, ALT20-03-0145-FEDER-000004), was carried out this study in four sampling sites in streams in the lower part of the Guadiana watershed, draining to the Alqueva reservoir: Zebro (Zb; 38°14,015.5" N, 7°19,040.32" W); Álamos (Al; 38°24,050.46" N, 7°2802.16" W); Amieira (Am; 38°16,058.80" N, 7°36,035.20" W), and Lucefécit (Lf; 38°36,059.19" N, 7°23,031.65" W) (Fig. 1). The sites were sampled bimonthly from January 2017 to November 2018 (in January (Jn), March (Mr), May (M), July (Jl), September (Sp), and November (Nv), for both years), in a total of 12 campaigns for the chemical and physicochemical elements supporting the biological elements and for the ecotoxicological assays. For Phytobenthos, sampling started in May 2017 and a total of 10 campaigns were carried out.

The year of 2017 was considered, according to IPMA (Instituto Português do Mar e Atmosfera), as in severe drought from April on, with the highest temperatures observed in the last 80 years, and with the lowest values of precipitation (IPMA, 2018), whereas the year of 2018 was classified as normal by IPMA regarding air temperature and rainfall, with the severe drought situation ending in March 2018. In addition, due to the marked difference in hydrological regimes throughout the year in the Alentejo region, a rainy season comprising the winter months, from October to April, and a dry season comprising the months of May to September were defined by the Agência Portuguesa do Ambiente (APA).

The sites have been thoroughly characterised by Palma et al. (2020a, 2020b). Briefly, they are small streams, classified as small rivers of Southern Portugal (S1 $\leq$ 100 km^2), according to the national WFD typology. Among the four streams, only Amieira integrates the Degebe sub-basin, whilst Álamos, Zebro and Lucefécit are located in the Guadiana sub-basin. Regarding the hydrological regimes, Amieira and Álamos are intermittent streams, forming a series of disconnected pools in summer campaigns (i.e., July and September); Zebro has an intermittent regime, with water all year long but without flow during some periods; Lucefécit is a perennial stream, with flowing water during the whole year.

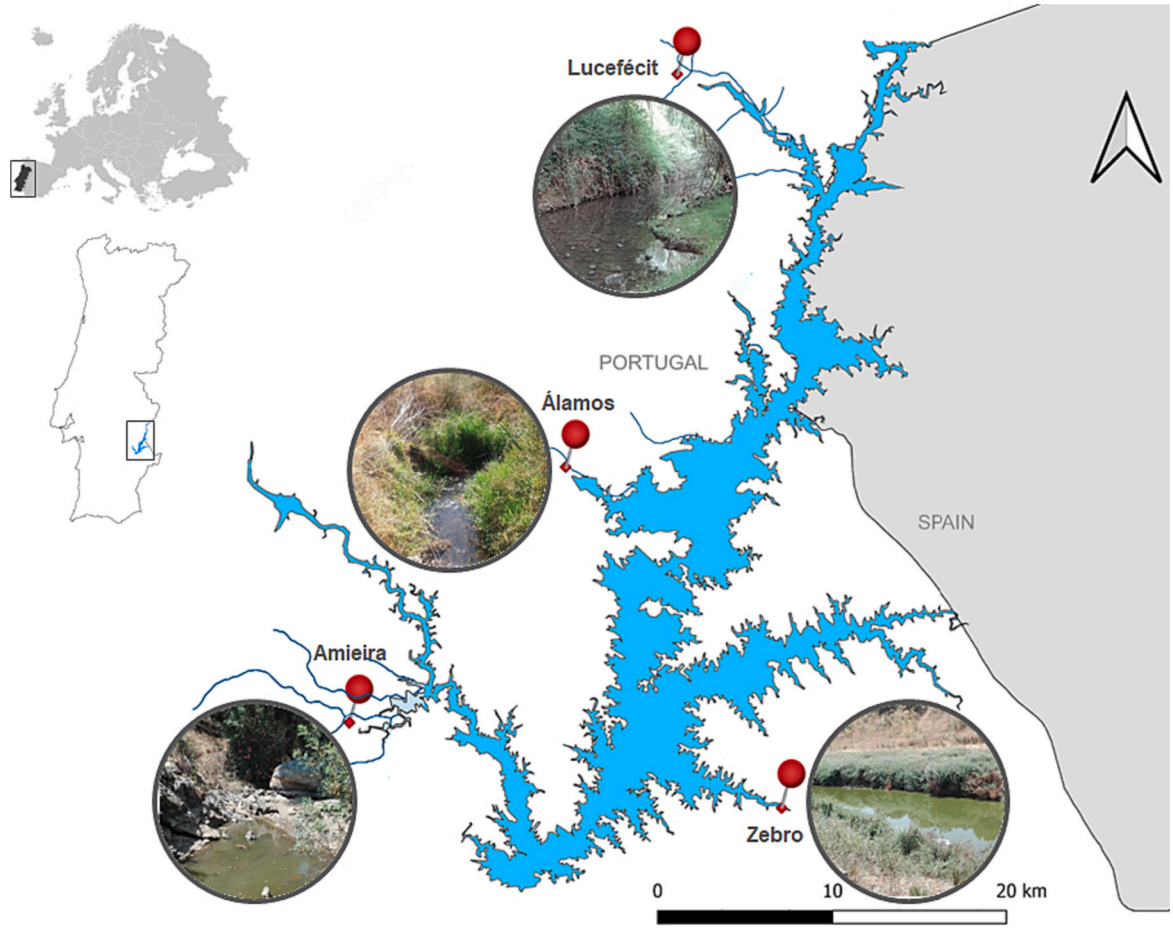

Fig. 1. Location of sampling sites in Alqueva reservoir.

2.2. Surface water status assessment – WFD-based

2.2.1. Ecological status assessment

The Biological Quality Element used for the ecological assessment was the Phytobenthos, with diatoms as representatives for the whole benthic algae, according to the standard national procedure (APA, 2016). Information on the other BQEs (macrophytes; the composition and abundance of benthic invertebrate fauna; and composition, abundance, and age structure of fish fauna) and the water bodies status classification was kindly provided by the Administration of the Hydrographic Region of Alentejo, a subdivision of the Portuguese Environment Agency, from the monitoring, carried out in Spring 2017. According to APA (2021), the sampling frequency, depicted in the 6-year planning cycle for biological quality elements, is 6 months for Phytoplankton, and every 3 years for the other aquatic flora (Phytobenthos and Macrophytes), benthic macroinvertebrates and fish.

2.2.1.1. Biological quality element - phytobenthos. Benthic diatoms were sampled following standard procedures during flowing conditions (INAG I.P., 2008; AFNOR, 2007; European Committee for Standardization, 2003), in brief, cobbles were collected in riffle areas not shaded, scrapped with a toothbrush, rinsed with stream water, and preserved with formaldehyde solution (4 %; *v*/v) immediately after sampling. However, the standards for sampling could not be applied in some situations, for instance, in the Amieira stream in July and September 2017 and 2018 and in the Álamos stream in July and September 2018 (dry phase), there were no flowing conditions and sampling was carried out in an isolated pool upstream of the regular sampling sites. In this case, the methodology presented by Novais et al. (2020) was applied. A minimum of 5 cobbles were collected at each pool and washed in the pool water to remove sand, sediment and dead diatoms that could have been deposited on the substrate, scraped with a toothbrush, rinsed with distilled water, and preserved with formaldehyde solution (4 %; v/v) immediately after sampling. In Lucefécit, sampling was not possible in the January 2018 campaign, due to flooding conditions.

A total of 39 diatom samples were oxidised with hot hydrogen peroxide (35 %) and diluted in hydrochloric acid (37 %), followed by rising and decantation (repeated at least 3 times) with distilled water to prepare a suspension of clean frustules (European Committee for Standardization, 2003; INAG I.P., 2008). Permanent slides were mounted using Naphrax, a high refractive index medium (Northern Biological Supplies, Ltd., UK, RI = 1.74). The identification was carried out to the possible lowest taxonomical level using light microscopy (LM) (Leica DMLB with 100× oil immersion objective, N.A. 1.40). The relative abundance of each taxon was determined, based on identifications, and counts of at least 400 valves per sample (INAG I.P., 2008). The identification was based on reference floras (e.g., Krammer and Lange-Bertalot, 1986, 1988, 1991a, 1991b; Blanco et al., 2010; Hofmann et al., 2011), as well as on recent bibliographic sources, including the series 'Diatoms of Europe', 'Iconographia Diatomologica', 'Bibliotheca Diatomologica' and relevant taxonomic papers, such as (Delgado et al., 2015, 2016; Novais et al., 2019, Novais et al., 2015; van de Vijver et al., 2011).

For each sample, taxa richness (S), Shannon diversity index (H′), and the Specific Pollution Sensitivity Index (SPI) (Coste, 1982) were determined using OMNIDIA v. 5.5 (Lecointe et al., 1993). SPI is a weighted average index based on the Zelinka and Marvan (1961) formula and consists in assigning pollution tolerance (S) and stenoecy degree (V) values to each taxon, with higher SPI values corresponding to lower pollution. The SPI was developed to assess the ecological quality of European rivers, is based on the autecology of almost all known taxa and has been recommended as a reference for Mainland Portugal (APA, 2016). The calculation formula is shown in Eq. (1).

$$SPI = \frac{\sum_{i=1}^{n} A_i s_i v_i}{\sum_{i=1}^{n} a_i v_i} \quad (1)$$

A_i = relative abundance of taxon *j* in the sample
si = pollution sensitivity of taxon *j*
vi = stenoecy degree /indicator value of taxon *j*

Specific Pollution Sensitivity Index values were then converted to EQR, considering the SPI reference value for the Small rivers of Southern Portugal (S1 ≤ 100 km^2) WFD type (16.35), and classified according to the thresholds defined for Mainland Portugal (APA, 2016): High ≥0.80; Good [0.60–0.80[; Moderate [0.40–0.60[; Poor [0.20–0.40[; Bad [0–0.20[.

2.2.1.2. General chemical and physicochemical elements (supporting biological elements). In Portugal the general chemical and physicochemical elements integrate seven parameters that allow the evaluation of the oxygenation, acidification and nutrient conditions (APA, 2016): dissolved oxygen (DO, $mgL^{-1}O_2$; oxygen saturation (O_2, %); Biochemical Oxygen Demand (BOD_5, mg O_2 L^{-1}); pH; ammoniacal nitrogen (NH_4, mg NH_4 L^{-1}); nitrate (NO_3, mg NO_3 L^{-1}); and total phosphorus (TP, mg P L^{-1}). The Boundary values for Good Status of these supporting elements, have been proposed for the Southern Grouping, which includes the Small rivers of Southern Portugal (S1 ≤ 100 km^2) type, to which the studied sites belong, and are as follows: DO ≥5 mg O_2 L^{-1}; O_2 saturation (%) between 60 % and 120 %; BOD_5 ≤ 6 mg O_2/L; pH between 6 and 9; NH_4 ≤ 1 mg NH_4 L^{-1}; NO_3 ≤ 25 mg NO_3 L^{-1}; and TP ≤ 0.13 mg P L^{-1} (APA, 2016).

A multiparametric YSI 6820 MPS probe® was used for the in situ measurements at each sampling site of the dissolved oxygen (DO; mg L^{-1} and %), and pH.

For the remaining general chemical and physicochemical elements, 2 L of surface water were collected in polyethylene (PET) bottles. The samples were transported to the laboratory at 4 °C, conserved and stored until the analysis following the requisites for each parameter (APHA, 2017). The BOD_5 was determined using the respirometric method, TP and NH_4 by molecular absorption spectrometry, and NO_3 by Ionic chromatography (APHA, 2017), as previously presented in Palma et al. (2020a).

2.2.1.3. Specific pollutants. Specific pollutants are chemical substances included in the Annex VII (Directive 2000/60/EC, 2000) that are not classified as Priority Substances. Among the 22 substances depicted in APA (2016), 2,4-Dichlorophenoxyacetic acid (2,4-D), bentazone, linuron, methylchlorophenoxypropionic acid (mecoprop or MCPP) and terbuthylazine were selected, taking into consideration that the most representative activity in the region is agriculture (Palma et al., 2020a).

For these specific pollutants analysis, water samples (250 mL) were collected in amber PET bottles, transported to the laboratory at 4 °C, and stored in the dark at −18 °C until analysis. The analysis was performed by online solid phase extraction-liquid chromatography-tandem mass spectrometry (SPE-LC-MS/MS) as described in Köck-Schulmeyer et al. (2012, 2013).

The classification of the water bodies based on the Specific Pollutants includes two statuses: Good (all pollutants are below the directive limits) or Insufficient (at least one of the pollutants was quantified in concentrations above its limits) (APA, 2016). The boundaries for these Specific Pollutants are as follows: 2,4-D (0.30 μg L^{-1}), bentazone (80 μg L^{-1}), linuron (0.15 μg L^{-1}), MCPP (5.5 μg L^{-1}) and terbuthylazine (0.22 μg L^{-1}).

2.2.2. Chemical status

The chemical status of surface waterbodies was analysed in

accordance with Directive 2013/39/EU of 12 August, which includes a group of 45 specific priority substances with their respective thresholds: Annual Average (AA) and Maximum Allowable Concentration (MAC); Annex I), classifying them as hazardous substances or priority hazardous substances. The chemical classification includes two statuses: Good (all pollutants are below the directive limits) or Insufficient (at least one of the pollutants was quantified in concentrations above its limits) (APA, 2016). For the Good status classification, the Annual Average (AA) of each pollutant or the Maximum Allowable Concentration (MAC) should be below the Environmental Quality Standard (APA, 2021). In the present study, were analysed 5 of those hazardous substances, namely: atrazine; alachlor; simazine; diuron; and chlorfenvinphos. The boundaries for these hazardous substances are as follows: atrazine (AA: 0.6 μg L^{-1}; MAC: 2.0 μg L^{-1}), alachlor (AA: 0.3 μg L^{-1}; MAC: 0.7 μg L^{-1}), simazine (AA: 1 μg L^{-1}; MAC: 4 μg L^{-1}), diuron (AA: 0.2 μg L^{-1}; MAC: 1.8 μg L^{-1}) and chlorfenvinphos (AA: 0.1 μg L^{-1}; MAC: 0.3 μg L^{-1}).

The water samples (250 mL), in a total of 48, were collected at 50 cm depth in amber PET bottles, transported to the laboratory at 4 °C, and stored in the dark at −18 °C until analysis. The analysis was performed by online solid phase extraction-liquid chromatography-tandem mass spectrometry (SPE-LC-MS/MS) as described in Köck-Schulmeyer et al. (2012, 2013).

2.3. Ecotoxicological analysis

Ecotoxicological assays were performed using 2 L of water samples with a set of representative bioindicators from different trophic levels, and sensitivity to detect surface waters ecosystems unbalances/disruption, which can be promoted by different known or unknown hazardous substances. In addition, a set of rapid and easy-to-use screening bioassays were selected, that can provide information about different life cycle stages of organisms, such as growth, feeding rate, light inhibition, in a short period of time, as a complement to the biotic indices. The methodology was developed with the ecotoxicological assessment of water and sediments. Hence, the aquatic organisms and the respective responses analysed in the water were: (i) light inhibition of the bacterial *Aliivibrio fischeri*; (ii) growth inhibition of the green microalgae *Pseudokirchneriella subcapitata*; (iii) mortality of the crustacean *Thamnocephalus platyurus;* and (iv) feeding rate of the crustacean *Daphnia magna*.

The *Daphnia magna* culture was from the clone K6 (originally from Antwerp, Belgium), successfully cultured in laboratory conditions for more than 10 years. The microalgae culture of *P. subcapitata* is obtained from agar solid medium, bacteria free, for better conservation of the culture (*P. subcapitata*, Bacteria-Free, Living acquired to the company Carolina Biological Supply®) resuspended when necessary to renew the culture, which occurs every two years. *Thamnocephalus platyurus* shrimp larvae were obtained from cysts incubated when exposed to an incubation medium provided in the THAMNOTOXKIT FTM kit (Persoone, 1999). This species is not cultivated in the laboratory; the hatching of the larvae is carried out when necessary for the development of the tests.

The integration of the sediment compartment in the proposed classification was carried out with the results of the growth inhibition bioassay of the benthic species *Heterocypris incongruens*. This bioassay methodology and the analysis of respective toxicological results have already been published in Palma et al. (2023). Therefore, in this manuscript we use the results only to complement the classification system proposal, making it more robust and comprehensive.

For all bioassays, a test with a reference substance was performed, as a positive control. The sensitivity of the organisms was in accordance with the followed protocols. The control groups had a survival rate above 90 %.

For an integrative interpretation of both classifications (ecological and ecotoxicological), a toxicological classification system (TCS) was developed, adapted from Roig et al. (2015), with 5 scores that classified the waters from: class 1: non-toxic (EC_{50} > 100 %; and growth and feeding rate > 80 %; blue) – score 0; class 2: slightly toxic (61 % < EC_{50} < 100 %; and 50 % < growth and feeding rate ≤ 80 %; green) - score 1; class 3: Marginally toxic (21 % < EC_{50} < 60 %; and 20 % < growth and feeding rate ≤ 50 %; yellow) - score 2; class 4: Moderately toxic (10 % < EC_{50} < 20 %; and 10 % ≤ growth and feeding rate ≤ 20 %; orange) - score 3; class 5 Highly toxic (EC_{50} < 10 %, and 10 % > growth and feeding rate; red) - score 4.

2.3.1. Aliivibrio fischeri luminescence inhibition assay

Luminotox® was used to evaluate the luminescence inhibition of *A. fischeri* (NRRL B-11177), according to the protocol "DR LANGE luminescent bacteria test" following ISO 11348-2 (1998). Tests were carried out using water samples and their dilutions with a 2 % NaCl solution (50, 25, 12.5, 6.25 and 3.125 %, *v*/v). Two replicates per dilution were used. The light inhibition was measured against a nontoxic control (2 % NaCl solution), at a temperature of 15 ± 0.5 °C. For each sample, bioluminescence was measured before and after the incubation period of 30 min. The concentration (%; *v*/v), which reduced 50 % of the bacterial luminescence, was determined (30 min - EC_{50}).

2.3.2. Pseudokirchneriella subcapitata growth inhibition assay

Microalgae were exposed to water samples for 72 h and algae growth was determined based on ISO 11348-2 (1998). At the beginning of the test, *P. subcapitata* (100 μL of inoculum with 3–5 × 10^4 cells mL^{-1}) was exposed to the respective diluted samples (12.5, 25, 50, 75, 100 %; v/v; 900 μL of total volume) performed with MBL medium (negative control). Test vials were incubated in an orbital shaker for 72 h at constant light (with an intensity of 60–120 μE m^{-2} s^{-1}, equivalent to 6000–10,000 lx) and a temperature of 21 ± 2 °C. The algal biomass was calculated by counting the number of cells using a Neubauer chamber.

The average growth rate for a specific period was determined from Eq. (2):

$$\mu_{i-j} = \left(ln\ B_j - ln\ B_i\right)/t_j - t_i \quad (2)$$

where: μ_{i-j} is the average specific growth rate from the time i to j; t_i is the time for the start of the exposure period; t_j is the time for the end of the exposure period, B_i is the biomass concentration at the time i, and B_j is the biomass concentration at time j.

The inhibition of algal growth was estimated from the Eq. (3):

$$\%I = [(\mu_c - \mu_t)/\mu_c] \text{ x } 100 \quad (3)$$

where: % I is the mean percentage of inhibition for specific growth rate; μ_c is the mean value for the growth rate in the control, and μ_t is the mean value for the growth rate in the water samples.

2.3.3. Thamnocephalus platyurus mortality assay

The mortality assay with the crustacean *T. platyurus* was adapted from Persoone (1999). Larvae of the shrimp *T. platyurus* (<24 h, obtained from the hatching of cysts) were exposed to different dilutions of water samples (12.5, 25, 50, 75 and 100 %; *v*/v), during 24 h. Four replicates per dilution were performed. Organisms were not fed during the test. The number of dead organisms was used as an endpoint to determine the 24 h-EC_{50} (%; v/v) concentration that causes mortality of 50 % of the exposed organisms.

2.3.4. Daphnia magna feeding rate assay

The feeding rate assay with *D. magna* was adapted from the methodology reported by Mcwilliam and Baird (2002). Groups of five neonates (4 or 5 days old born between the 3rd to 5th broods) were exposed to the different water samples (100 mL of total volume). To each sample, a volume of algae, corresponding to a density of 3.0 × 10^5 cell mL^{-1} $Daphnia^{-1}$ (equivalent to 2.65 mg C mL^{-1}), was added. In all experiments, a comparative control with sample and algae at the density of 3.0 × 10^5 cells mL^{-1} $Daphnia^{-1}$, without daphnids, was added to control the growth of algae under the test conditions. Five replicates per sample and

a negative control test (with ASTM) were carried out. At the start of the test, the number of algal cells was quantified using a Neubauer chamber, after which the organisms were added to each vessel. The test took place for 24 h at a temperature of 20 °C in the dark, to avoid algae growth. At the end of the test, the organisms were removed from each vessel, the solution was shaken to resuspend the algae in it, and the cells were counted. The Feeding rate was calculated according to Eq. (4), reported by Allen et al. (1995):

$$F = \mathrm{V} \times (\mathrm{C}_0 - \mathrm{C}_{24})/\mathrm{t} \quad (4)$$

where: F = feeding rate (cells*animal^{-1}*h^{-1}); V = volume of medium in the test vessel (mL); C_0 = the initial cell concentration (numbers*mL^{-1}); C_{24} = the final cell concentration (numbers*mL^{-1}); t = duration of the experiment (h).

2.4. Statistical analysis

General physicochemical elements (supporting biological elements), diatom indices (SPI, S, H′) and ecotoxicological essays endpoints were tested for normality (Shapiro-Wilk test), using SigmaPlot 12.0 (Systat Software Inc., Chicago, IL).

Relatively to the ecotoxicological endpoints, the *A. fischeri* bioluminescence inhibition test, the EC_{50} (%) values were determined using LUMISsoft 4 Software™. The EC_{50} (%) values for the *T. platyurus* mortality were determined using the probit analysis (Finney, 1971). Data of sublethal endpoints (growth inhibition and feeding rate) were checked for homogeneity of variance by the Kolmogorov–Smirnov test and, when possible, subjected to one-way analysis of variance (ANOVA). Data that do not satisfy the assumption for ANOVA were analysed non-parametrically using Kruskal–Wallis ANOVA by ranks test. Whenever significant differences were found ($p < 0.05$), a post hoc *Dunnett's* test was used to compare treatments with the control, for a p value of 0.05 as the significant level (Zar, 1996).

Further, *Spearman* Rank Order correlations were applied between the general physicochemical elements, specific pollutants, diatom indices (SPI, S, H′) and ecotoxicological endpoints, since the general physicochemical elements and specific pollutants did not follow a normal distribution (Table S1 in Supplementary material). The diatom indices followed a normal distribution, and from the ecotoxicological parameters, the EC_{50} of *T. platyurus* and *A. fischeri*, and the *P. subcapitata* algae growth inhibition passed the normality test (Shapiro-Wilk test). Therefore, Pearson correlations were carried out between diatom indices and EC_{50} of *T. platyurus* and *A. fischeri*, and the *P. subcapitata* algae growth inhibition (Table S2 in Supplementary material); and *Spearman* Rank Order correlation was applied between *D. magna* feeding rate and the biotic indices, since the *D. magna* feeding rate did not follow a normal distribution (Table S1 in Supplementary material).

Differences in SPI values between water bodies were statistically tested by the One-Way ANOVA, after being tested for normality (Shapiro-Wilk test) and Equal Variance, followed by the Pairwise Multiple Comparison Procedures (Holm-Sidak method, with 0.05 overall significance level) to test which water bodies differed, using SigmaPlot 12.0 (Systat Software Inc., Chicago, IL).

To test for differences between sampling years and periods (wet and dry), *t*-tests were applied, since data passed the normality test (Shapiro-Wilk) and the Equal Variance test, using SigmaPlot 12.0 (Systat Software Inc., Chicago, IL).

All statistical analyses applied to ecotoxicological results were performed with the STATISTICA 7.0 (Software™ Inc., PA, USA, 2007).

3. Results and discussion

3.1. Surface water status assessment – WFD-based

3.1.1. Ecological status assessment

3.1.1.1. Biological quality element - phytobenthos. Lucefécit presented the highest taxa richness (S), reaching 60 taxa in September 2018 and a wider Shannon diversity range (H′) (1.81–4.81), followed by Amieira with 21–46 taxa and H′ between 2.53 and 4.25. On the other hand, Zebro had the lowest S (10–39 taxa, mean 18.10), and the lowest H′ (1.24–3.79), as seen in Table 1.

Specific Pollution Sensitivity Index (SPI) values ranged between 1.5 in Zebro in July 2017 and 14.8 in Amieira in January 2018, as seen in Table 1. The lowest values were detected in Zebro, followed by Lucefécit, Álamos and Amieira, as visible in the plot depicted in Fig. 2.

This information is in agreement with the diatom communities analysis, dominated (relative abundance >10 %) in Zebro by species tolerant to organic contamination and high nutrient content. These taxa range from eutrophentic to hypereutraphentic and α–mesosaprobic to polysaprobic and include: *Planothidium frequentissimum* (Lange-Bertalot) Lange-Bertalot, *Nitzschia amphibia* Grunow, *Nitzschia inconspicua* Grunow and a similar but broader species, *Nitzschia* cf. *inconspicua* Grunow, *Nitzschia palea* (Kützing) W. Smith, *Cyclotella meneghiniana* Kützing, *Eolimna subminuscula* (Manguin) Moser, Lange-Bertalot & Metzeltin, *Gomphonema saprophilum* (Lange-Bertalot & E.Reichardt) Abarca, R. Jahn, J.Zimmermann & Enke, *Navicula veneta* Kützing, *Halamphora veneta* (Kützing) Levkov and *Gomphonema parvulum* (Kützing) Kützing. These dominant taxa differed in relative abundance between campaigns, and in the accompanying species. The sensibility (s) values for these species ranged between 1.0 (*Halamphora veneta* and *Nitzschia palea*) and 3.4 (*Planothidium frequentissimum*), thus explaining the low SPI values.

In Lucefécit diatom communities were dominated by *Eolimna minima* (Grunow) Lange-Bertalot, *Gomphosphenia holmquistii* (Foged) Lange-Bertalot, *Amphora pediculus* (Kützing) Grunow, *Navicula tripunctata* (O. F.Müller) Bory, *Nitzschia inconspicua* and *Thalassiosira pseudonana* Hasle & Heimdal. These species are also eutraphentic to hypereutraphentic, β-mesosaprobic to α-meso-polysaprobic, with S values between 2.0 (*Gomphosphenia holmquistii*) to the maximum of 4.0 (*Amphora pediculus*).

Diatom communities in Álamos were dominated (relative abundance >10 %) by *Planothidium frequentissimum*, *Cocconeis euglypta* Ehrenberg, *Nitzschia inconspicua*, *Navicula catalanogermanica* Lange-Bertalot & Hofmann, *Amphora pediculus*, *Navicula recens* (Lange-Bertalot) Lange-Bertalot, *Navicula gregaria* Donkin, *Eolimna minima* and *Sellaphora seminulum* (Grunow) D.G.Mann. Most of these species are tolerant to organic loads and high nutrient content and were also present in Zebro and Lucefécit, however, the presence of more sensitive species as *Navicula catalanogermanica* (with a higher S value, of 4.8, and indicator value of 2.0) contributes to the highest SPI value in July 2017 campaign (12.4).

The water body with the highest SPI values was Amieira, due to the community dominated by *Cocconeis euglypta*, *C. pseudolineata* (Geitler) Lange-Bertalot, *C. pediculus* Ehrenberg, *Eolimna minima*, *Amphora pediculus*, *Nitzschia inconspicua*, *Planothidium frequentissimum*, *Navicula gregaria* and *Eolimna subminuscula*. Most of these species were also present in the other three streams, however, in November 2017 the community was no longer dominated by tolerant species but was instead dominated by oligosaprobic to β-mesosaprobic, eutraphentic *Cocconeis* species, with S value between 3.6 (*C. euglypta*), 4.0 (*C. pediculus*) to 5.0 (*C. pseudolineata*), which contributed to the highest SPI value of 14.8.

In Fig. 2 it was possible to observe some differences between the four water bodies, further statistically validated by the One-Way ANOVA ($F = 9.787$, $p < 0.001$) since the data passed the normality Shapiro-Wilk test ($p = 0.235$) and the Equal Variance Test ($p = 0.253$). The Pairwise Multiple Comparison Procedures (Holm-Sidak method, with 0.05 overall significance level) revealed that Zebro was different from

Table 1
Range (minimum-maximum), mean and standard deviation (SD) values for SPI, S and H′ for the four water bodies (n=39).

Water body Index	Amieira (n = 10)		Zebro (n = 10)		Álamos (n = 10)		Lucefécit (n = 9)	
	Range	Mean ± SD	Range	Mean ± SD	Range	Mean ± SD	Range	Mean ± SD
SPI	8.20–14.80	11.08 ± 2.34	1.50–9.00	6.91 ± 2.35	8.40–12.40	10.69 ± 1.34	7.20–11.20	9.13 ± 1.25
S	21–46	32.20 ± 7.44	10–39	18.10–8.20	22–36	27.00 ± 4.81	17–60	37.22 ± 13.71
H′	2.53–4.25	3.44 ± 0.68	1.24–3.79	2.24–0.86	2.32–4.22	3.02 ± 0.54	1.81–4.81	3.43 ± 0.98

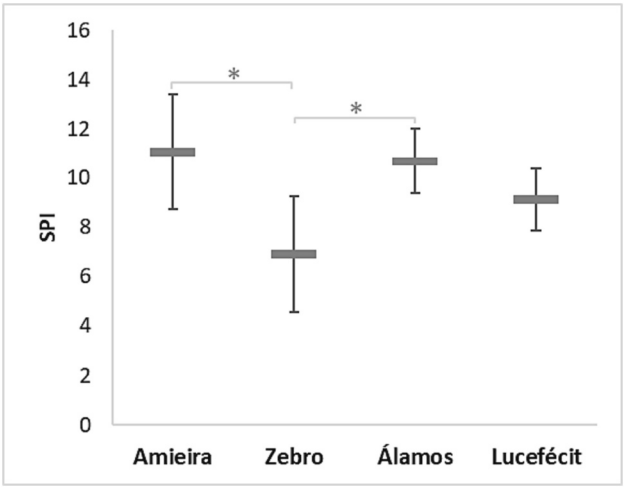

Fig. 2. Plot with the SPI mean values ± standard deviation, for the four water bodies. * Represents differences with $p < 0.05$.

Amieira and Álamos water bodies ($p < 0.05$), whilst no differences were detected between Lucefécit and Zebro, Amieira and Álamos, Lucefécit and Álamos nor Amieira.

The SPI temporal evolution (Fig. 3) revealed that Lucefécit presented the least variability, as seen in the lowest SD (1.25), whilst Zebro and Amieira presented the highest variability (SD in Zebro was 2.35 and in Amieira 2.34). However, this variability did not reflect the sampling year (2017 or 2018), as revealed in the *t*-test ($t = -0.766$ with 37 degrees of freedom, $p = 0.449$). Also, no differences were detected between the wet and the dry periods (t-test not significant, $t = -0.487$ with 37 degrees of freedom, $p = 0.629$).

Spearman Rank Order Correlations were further tested between SPI and General physicochemical elements, but no significant correlations were detected (Table S1). However, diatom richness (S) was negatively correlated ($p < 0.05$) with TP ($r = -0.41$) and NH_4^+ ($r = -0.63$). Also, Shannon diversity (H′) was negatively correlated ($p < 0.05$) with NH_4^+ ($r = -0.46$). When correlations between diatom indices and specific pollutants were tested, significant ($p < 0.05$) negative Spearman Rank Order correlations were obtained between S and 2.4-D ($r = -0.39$), between S and diuron ($r = -0.42$), between H′ and diuron ($r = -0.32$), and between SPI and 2.4-D ($r = -0.32$). This negative correlation between SPI and the 2.4-D is in accordance with Debenest et al. (2010), who also referred to an alteration in diatom communities when exposed to herbicides, with eutrophic species being more tolerant. These eutrophic species have lower pollution sensitivity values, therefore, their dominance in the community also decreases the SPI value. According to Debenest et al. (2010), the survival of species dominating the communities in the studied streams, such as *Planothidium frequentissimum*, *Gomphonema parvulum* or *Nitzschia palea* was favoured in streams with triazine herbicides (atrazine and irgarol) and *Eolimna minima* to isoproturon.

3.1.1.2. General physicochemical elements. The physicochemical results, considered for the WFD classification, are presented in Supplementary material (Table S3, Part 1 and 2), and were previously thoroughly analysed by Palma et al. (2020a, 2020b). In the present study, these results were further evaluated according to APA (2016) and with the WFD normative (Directive 2000/60/EC, 2000).

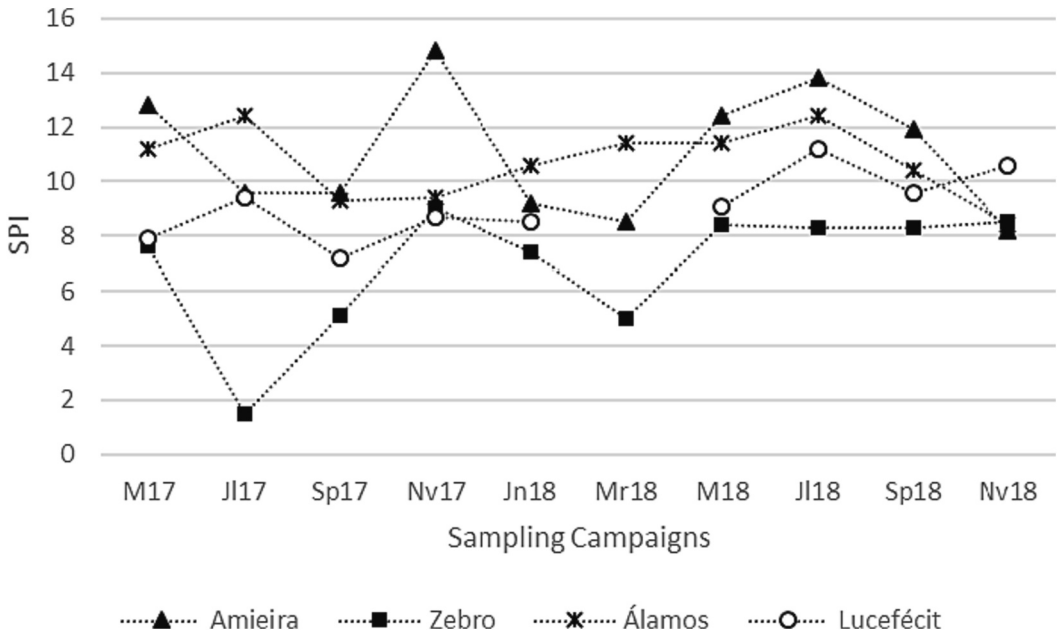

Fig. 3. SPI values over time for the studied water bodies. M17 = May 2017; Jl17 = July 2017; Nv17 = November 2017; Jn18 = January 2018; Mr18 = March 2018; M18 = May 2018; Jl18 = July 2018; Sp18 = September 2018; Nv18 = November 2018.

All the general physicochemical elements (DO, NO_3, NH_4, pH, TP and BOD_5) failed the normality test (Shapiro-Wilk), therefore, the results are presented as median and range (maximum-minimum) in Table 2.

Median DO levels were between the normal range (60 to 120 % of O_2 saturation), although in Amieira, Zebro and Álamos water bodies the maximum values were reached, and exceeded, in several campaigns. Lucefécit never surpassed the maximum value, nevertheless, in the last campaign (November 2018) the DO was below the low limit of 60 % of O_2 saturation. Minimum DO levels were registered in Zebro (Table 2). The median values of BOD_5 exceeded the limit of 6 mg O_2/L at Zebro and Álamos, as already reported by Palma et al. (2020a). In general, all the water bodies are slightly alkaline, with Amieira and Zebro presenting the highest pH values. Compared to the other water bodies, Zebro showed the highest median values of BOD_5, pH, NH_4 and NO_3, possibly mainly due to the Wastewater Treatment Plant (WTP) that discharges directly to this water body, as already reported in previous studies Palma et al. (2020a, 2020b).

Even though several physico-chemical parameters presented higher values during the dry phase in the intermittent streams, namely the BOD_5 in Zebro and Amieira; NH_4 in Amieira, Zebro and Álamos, as previously reported in Palma et al. (2020a), these differences were not visible in the classification, since TP exceeded the threshold for the Good status in most of the campaigns in Amieira, Zebro and Álamos, without a seasonal pattern.

3.1.1.3. Specific pollutants. The Specific pollutants results, considered for the WDF classification and analysed in the present study, are shown in Supplementary material (Table S3, Part 1 and 2).

Of the five substances analysed, three were detected (bentazone, terbuthylazine, 2,4-D). The concentrations of these specific pollutants were always below the limit reported in the WFD (Directive 2000/60/EC, 2000), generally allowing a classification of Good for this component of ecological status assessment. An exception was observed for 2,4-D in Zebro in July 2018, whose concentration of 3362 ng L^{-1} led the water body to be classified as insufficient in this specific month. Lucefécit was the water body with the highest concentration of the assessed specific pollutants.

3.1.2. Chemical status

Priority substances results, considered for the chemical status classification, are presented in Supplementary material (Table S3, Part 1 and 2). Among the five hazardous substances analysed, diuron and simazine were those quantified above the detection limit. In fact, the herbicide diuron was the substance that was most frequently detected in the four assessed water bodies, achieving the highest concentration in Zebro in September 2017. Despite that fact, the observed concentrations were always below the limits proposed in Directive 2013/39/EU of 12 August. According to these results, the water bodies presented a Good Chemical status.

3.2. Ecotoxicological analysis

The ecotoxicological results are displayed in Table S3 and Figs. 4 and 5. Relatively to the acute ecotoxicological bioassays, the most sensitive was the light inhibition of *A. fischeri*, detecting 33 % of the toxic samples, followed by the mortality test of the crustacean *T. platyurus*, with the identification of 23 % of the toxic samples (Table S3). The water bodies with the most toxic samples were Zebro and Álamos, in 2017. In the case of Zebro, of the 12 samples analysed, 6 presented a 30 min-EC_{50} lower than 61 % for *A. fischeri* and 5 of them with a 24 h-EC_{50} between 60 and 97 % for *T. platyurus*. Although the *A. fischeri* bioassay is mostly used to detect toxicity in effluents and samples contaminated with potentially toxic metals (Alvarenga et al., 2007; Bori et al., 2016, 2017), several studies have already reported its sensitivity in surface waters (Palma et al., 2016, 2018; Rodríguez Pérez et al., 2010). The results highlight the significant correlations observed between this bioassay and nutrients, mainly total phosphorus ($r = -0.78$), being a good option to detect eutrophic waters. Thus, it is currently considered a credible option to integrate Tier 1 of the Ecotoxicological Evidence Line (LoE), in alternative processes of ecological bioassessment, in relation to the current practice of compliance with the WFD (Santos et al., 2021).

The results with the green microalgae *P. subcapitata* showed a significant decrease in the growth of the algae for most samples ($p < 0.05$), being more pronounced in Zebro, during the drought year of 2017 (Fig. 4). Thus, the most toxic Zebro samples for the microalgae were those from March 2017, with a growth inhibition rate of 40 % (statistically validated by the One-Way ANOVA when comparing with the control MBL: $F_{4,24} = 209.47$; $p < 0.00005$), May 2017 (growth inhibition of 46 %; statistically validated by the One-Way ANOVA when comparing with the control MBL: $F_{4,21} = 87.87$; $p < 0.000001$), and July 2017 (growth inhibition of 50 %; statistically validated by the One-Way ANOVA when comparing with the control MBL: $F_{4,19} = 48.54$; $p < 0.00001$). The results of the feeding rate of the *D. magna* bioassay (Fig. 5) showed the high sensitivity of this test for assessing the quality of surface water. In fact, 62 % of the total samples analysed showed a reduction in the feeding rate greater than 80 %, with 12 % considered highly toxic, corresponding to the Zebro (November 2017) and Lucefécit (September 2017 and March 2018) samples. In this case, Lucefécit induced a high decrease in the feeding behaviour of *D. magna.* Contrary to the results observed for the other bioassays, Zebro was the water body that least disturbed the feeding behaviour of the crustacean, showing significant increases in relation to the control or slight decreases (<10 %) in 50 % of the analysed samples, mainly in spring-summer. Previous studies carried out in a Portuguese reservoir showed similar results, highlighting the loss of sensitivity of the bioassay with the increment of abiotic parameters such as light, temperature, nutrients and organic matter (Diogo

Table 2
Physicochemical parameters considered for the Ecological status assessment, with the APA (2016) limits for the Good status depicted. Median and range results, $n = 12$ per water body, are presented. Min – Minimum value; Max – Maximum value.

Parameter (Limits for the Good Status)	Amieira Median (Min - Max)	Zebro Median (Min - Max)	Álamos Median (Min - Max)	Lucefécit Median (Min - Max)
DO (% sat.)	91.65	84.36	69.46	73.09
(60 % - 120 % O_2 saturation)	(46.40–181.00)	(0.70–171.30)	(53.32–125.02)	(55.20–110.36)
BOD_5	2.33	15.00	6.83	3.00
($\leq$ 6 mg O_2 L^{-1})	(2.00–40.00)	(2.00–35.50)	(1.00–44.00)	(1.00–8.33)
pH (Sorensen scale)	7.93	8.07	7.79	7.60
(6–9)	(7.68–9.04)	(7.51–9.05)	(7.38–8.32)	(6.72–8.86)
Ammoniacal nitrogen	0.05	4.41	0.19	0.10
($\leq$ 1 mg NH_4 L^{-1})	(0.01–0.33)	(0.02–15.12)	(0.05–5.51)	(0.01–0.4)
Nitrate	0.67	1.51	0.85	9.70
($\leq$ 25 mg NO_3 L^{-1})	(0.32–18.86)	(0.67–7.12)	(0.67–33.19)	(0.67–23.46)
Total Phosphorus	0.24	1.75	0.45	0.07
($\leq$ 0.13 mg P L^{-1})	(0.10–3.29)	(0.10–6.10)	(0.02–3.07)	(0.01–2.00)

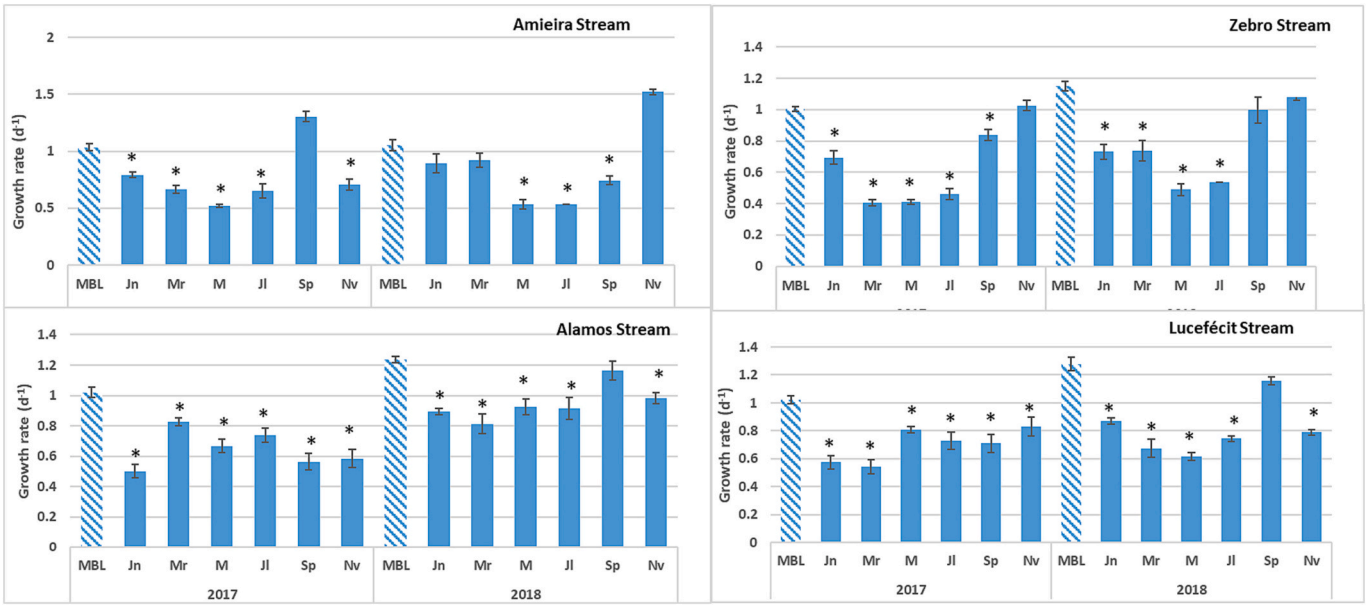

Fig. 4. Growth rate (d^{-1}) of algae *P. subcapitata* after 72-h exposure to water samples (undiluted sample), from Guadiana Basin streams, in January (Jn), March (Mr), May (M), July (Jl), September (Sp) and November (Nv) of 2017 and 2018. Mean ± standard deviation ($n = 6$), * $p < 0.05$, *Dunnett's* post hoc comparison test with the control MBL.

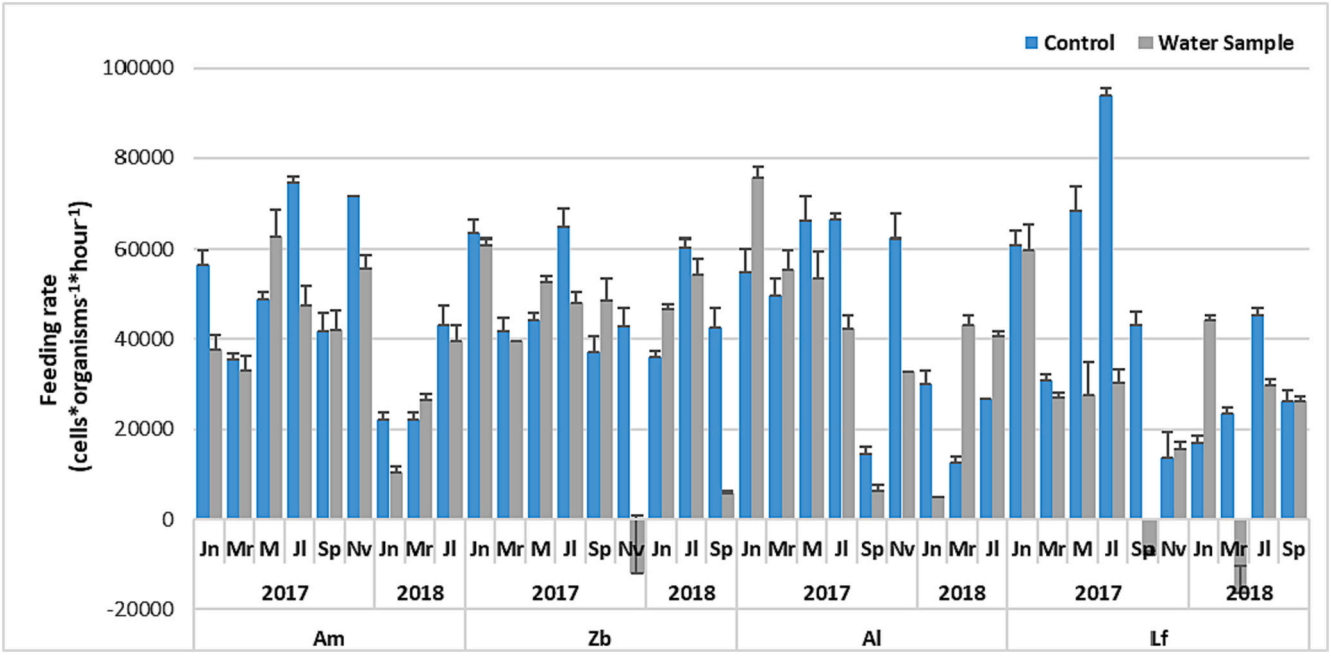

Fig. 5. Results of feeding rate of *D. magna,* after 24 h exposed to water samples from Guadiana Basin streams. Blue bars – control treatment; Grey bars: undiluted samples (100 %). January (Jn), March (Mr), May (M), July (Jl), September (Sp) and November (Nv) of 2017 and 2018. Am - Amieira, Zb - Zebro, Al - Álamos, Lf - Lucefécit. Mean ± standard deviation (n = 6), * $p < 0.05$, *Dunnett's* post hoc comparison test with the control MBL.

et al., 2022; Pinto et al., 2021). This behaviour can be correlated with the high concentrations of organic matter and total phosphorus, most of the time responsible for the moderate classification of the water body (Table 2 and Fig. 6).

Despite this, the results did not show significant correlations (Spearman rank order, since the general physicochemical elements, failed the normality test) between the feeding rate and the general physicochemical elements analysed (Table S1).

Only a significant correlation ($p < 0.05$) was obtained between algae growth inhibition and 2,4-D ($r = 0.31$), no other correlations were detected between the specific pollutants or hazardous substances and ecotoxicological assays.

3.3. *WFD surface water bodies status classification*

The result of the classification based on the BQE Phytobenthos-Diatoms varied between High (in November 2017 and in July 2018 in Amieira) and Bad (in July 2017 in Zebro). Álamos was classified as Good in six campaigns, followed by Amieira (with five campaigns as Good or above), whilst Lucefécit only had a Good status in two campaigns and

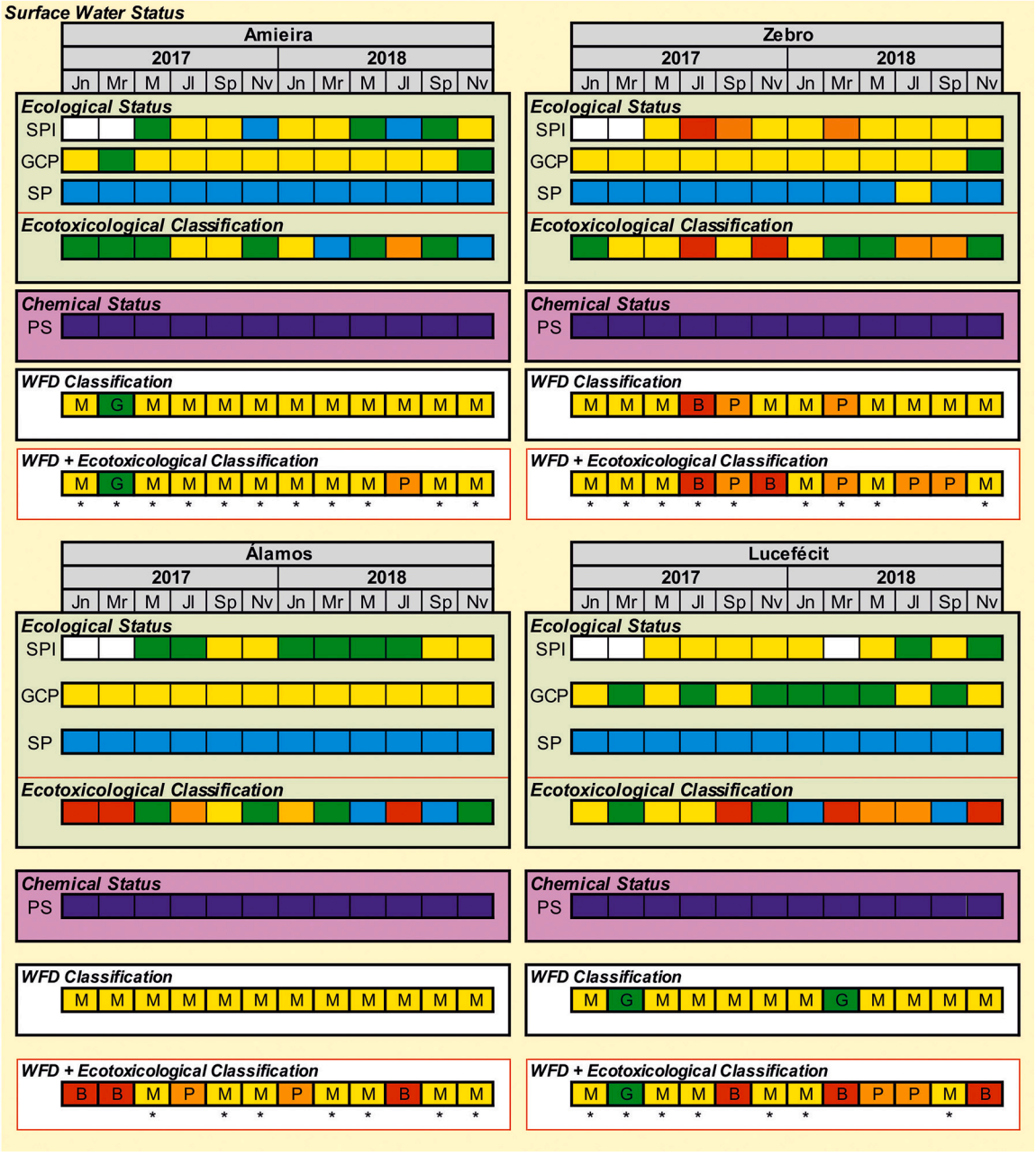

Fig. 6. Tables with the Surface water status classification based on the WFD parameters (including the Ecological and Chemical Status) and the Ecotoxicological Classification. SPI – Specific Polluosensitivity Index; GCP – General Chemical and physicochemical quality elements; SP – Specific pollutants; PS – Priority substances; WFD – Water Framework Directive; G – Good; M – Moderate; P – Poor; B – Bad. * - Cases where there is a correspondence between the WFD Classification and the WFD plus the Ecotoxicological assays.

Zebro was always classified below Good, with the classification ranging between Bad (July 2017), Poor (in September 2017 and March 2018) and Moderate in the remaining campaigns (as seen in Fig. 6). The High and Good classifications did not comply with the environmental standards for the supporting physicochemical conditions, especially the total phosphorus content, that exceeded the limit for the Good status in most of the analysed samples in Amieira, Zebro and Álamos. Amieira and Lucefécit are those water bodies where environmental standards for the general supporting physicochemical conditions were met during most of the studied period (see Table S3). In Álamos, the Phytobenthos-diatoms only slightly deviate from the reference condition values, however, the physicochemical conditions do not ensure the ecosystem functioning, exceeding the boundaries for the TP (except in January, March and September 2017, as previously reported), for NO_3 in November 2017, NH_4 in September 2017 and January, March and November 2018, and BOD_5 in January, March, May and September 2017 and January, March and September 2018. Almost all samples complied with the environmental standards for the selected specific pollutants, except for the 2,4-D, with a concentration of 3362 ng L^{-1} in the Zebro stream in July 2018, largely exceeding the 300 ng L^{-1} depicted in the environmental standards (APA, 2016).

Therefore, the Ecological status classification was mainly Moderate, with a few exceptions, such as the Bad and Poor classification of the Zebro in July 2017 (Bad) and in September 2017 and March 2018 (Poor). The Surface water status classification was only determined by the Ecological status, given that the analysed hazardous substances for the chemical status assessment were all within the thresholds depicted in Directive 2013/39/EU of 12 August (Annex I). In short, considering the

classification carried out by the WFD, Zebro presented the worst ecological status, and the remaining water bodies showed an ecological status mostly Moderate, occasionally reaching the Good status.

The results presented are in line with those provided by the Administration of the Hydrographic Region of Alentejo, from spring 2017 (sampled in April and May 2017), confirming that the four water bodies were classified below the Good ecological status. In Lucefécit this was due to the fact that the macroinvertebrates deviate from the reference condition, the physicochemical conditions do not ensure ecosystem functioning, namely the BOD_5, PO_4^{3-}, TP and TSS (total suspended solids), and the environmental standards were not met for 2,4-D and dissolved Zn (ARH Alentejo, pers. comm.). In the remaining water bodies, the physicochemical conditions do not ensure the ecosystem functioning, namely the TP in the Amieira stream; the NH_4^+, TN, PO_4^3, TP and NO_2^- in the Zebro stream; and the NH_4^+, TN, PO_4^{3-}, TP and NO_2^-, NO_3^- in the Álamos stream (ARH Alentejo, pers. comm.).

The Portuguese Environmental Agency has recently prepared a document on Water Bodies Classification Criteria (APA, 2021), which was under public consultation until December 2022. This document includes the classification for all general conditions represented in Annex V of the WFD Directive (Directive 2000/60/EC, 2000), and the boundaries for the classes High, Good and Moderate, for the following parameters (underlined are those recently included): Total Phosphorus, Phosphate (High: $\leq$ 0.20 mg PO_4/L; Good: $\leq$ 0.40 mg PO4/L), Total Nitrogen (High: $\leq$ 1 mg N L^{-1}; Good: $\leq$ 4.5 mg N L^{-1}), Ammoniacal Nitrogen, Ammonia (Good: $\leq$ 0.025 mg NH_3 L^{-1}), Nitrate, Nitrite (High: $\leq$ 0.03 mg NO_2 L^{-1}; Good: $\leq$ 0.20 mg NO_2 L^{-1}), Total Suspended Solids (High: $\leq$ 12.5 mg L^{-1}; Good: $\leq$ 25 mg L^{-1}), BOD_5, Dissolved Oxygen, Oxygen saturation, pH, Temperature (Good: 10.0–27.0 °C), and Conductivity (Good: $\leq$ 1000 µS/cm). Also, for some pre-existing parameters, stricter thresholds between the Good/Moderate classes were defined (APA, 2021), namely, for Ammoniacal Nitrogen (from 1 mg NH_4 L^{-1} to 0.5 mg NH_4 L^{-1}), for Nitrate (from 25 mg NO_3 L^{-1} to 10 mg NO_3 L^{-1}), for BOD_5 (from 6 mg O_2 L^{-1} to 5 mg O_2 L^{-1}). For oxygen saturation (%) the limits were slightly broadened (from 60 % - 120 % to 60 % - 125 %). Total Phosphorus was the only parameter with the boundary between the Good/Moderate status remaining unchanged. The results provided by the Administration of the Hydrographic Region of Alentejo for the Spring 2017, already used these last criteria of classification. The application of these stricter thresholds was further tested in the framework of this study, and five cases classified as Good according to APA (2016) are now classified below the Good status (APA, 2021), all in accordance with the Phytobenthos-Diatoms classification for these cases.

To increase the sensitivity of ecological status classification methodologies, the possible use of ecotoxicological parameters was assessed. Based on the toxicological classification system, Álamos and Lucefécit had 42 % of the samples classified as Moderately to Highly toxic (25 % highly toxic and 17 % classified as moderately toxic) (Table S3). Zebro was classified with 33 % of samples in a Moderately to Highly toxic status. Amieira was the least toxic stream, with 8 % of the samples classified as Moderately toxic. The comparison with the biotic indices showed similarities between the two approaches in 35 % of the samples (60 % in Amieira, 22 % in Lucefécit and 30 % in Álamos and Zebro). In fact, although bioassays do not replace the current methodologies (biotic indices) for the ecological status classification, it has been observed that the results of some assays are significantly correlated with those of biological indices, such as the positive Pearson correlations between SPI and $EC50_{A.fischeri}$ ($r = 0.80$, $p < 0.05$), and algae growth rate and Shannon diversity ($r = 0.34$, $p < 0.05$) (Table S2). This evidence may indicate that, in specific periods when some of the biotic indices cannot be used, the application of ecotoxicological bioassays may be a good alternative, as reported by other authors, using bioindicators and biomarkers in water and sediment compartments (Pinto et al., 2021; Rodrigues et al., 2021; Roig et al., 2015).

When we consider the ecotoxicological parameters, the results showed an increase in Bad and Poor classifications for the four streams (Fig. 6 – WFD + ecotoxicological endpoints). In Amieira, the use of ecotoxicological parameters maintained the 8 % of Good status (March 2017), decreasing the Moderate status from 92 % to 83 %, and in some periods of time from Moderate to Poor (8 %). The agreement between the two analysis strategies was 92 % (Fig. 6 – indicated with an asterisk *). In Zebro, the results of the integrative analysis pointed to a decrease in the Moderate classification (75 % to 50 %), with an increase in the Bad (8 % to 17 %) and Poor classification status (17 % to 33 %), and an accordance between the two methodologies of 75 %. In Álamos and Lucefécit, the addition of ecotoxicological status classification highlighted the increase in samples with Bad (0 % to 25 %) and Poor (0 % to 17 %) status. Lucefécit and Álamos were the sites where the combination of the ecotoxicological methodology for the classification of the ecological status showed more differences, with only 58 % of similarities between the two strategies. Overall, there was an agreement of 71 % in the classification based on the WFD parameters and on ecotoxicological endpoints. In fact, the addition of the ecotoxicological approach allows the increase in the sensitivity of the classification mainly in areas with greater number and quantity of specific and priority substances, as was observed in Lucefécit and Álamos, where the increase of Bad and Poor ecological conditions were of 42 %. Results consistent with those obtained in a previous study on the assessment of the environmental risk of pesticides in these streams, identifying Lucefécit and Álamos as the highest risk (Palma et al., 2021). Consequently, the ecotoxicological analysis appears to provide useful information regarding the potentially presence of both known and unknown contaminants at concentrations sufficient (even within the limit values proposed by the WFD) to cause biological effects, for which its use in biomonitoring has been suggested by several authors (Alvarenga et al., 2016; Martinez-Haro et al., 2015; Santos et al., 2021).

4. Conclusions

A classification system based on ecotoxicological endpoints was developed and tested with surface waters in Southern Portugal and can be further applied in regions with similar physicochemical conditions and pressures.

This study contributed to the validation of the hypothesis that the integration of ecotoxicological tools reinforces the robustness of the assessment of the water status based on the WFD elements. The integration of ecotoxicological endpoints increases the sensitivity of the assessment, allowing the detection of contaminants and their synergistic effects, even in conditions when these contaminants are not included in the legislation and therefore, are not included in the monitoring programs (e.g., most of the emerging contaminants, as newly synthesized molecules, or degradation products of existing ones). Further, these bioassays complement the information obtained using the WFD biological quality elements, since these do not detect the effects of punctual pollution events, which can be reflected only later in biological communities. Therefore, the integration of bioassays can fill in a temporal gap in the water status assessment, allowing the rapid detection of contamination and its effect on organisms of different trophic levels.

The integration of ecotoxicological endpoints in the water status assessment can also complement the current WFD elements when the legislated Biological Quality Elements are difficult to apply or give a mismatched result. This situation is particularly important under climate change, with the predictable increase in extreme events, such as floods and droughts, when the use of the current biological quality elements is difficult (visible in this study in the summer months in the temporary rivers, and in March 2018 in Lucefécit, when a flood occurred). In this case, the integration of sediments ecotoxicological analysis and biomarkers should be advised, to overcome the drawbacks that could arrive from the oversimplification of these methods. In this study, however, the integration of sediments in the proposed classification system did not change the results of the final classification, using

both types of biological tools, probably because this type of strategy is being tested in streams where the toxicity of sediments for benthic species was very low. The importance of analysing this abiotic compartment in the proposed classification system could probably be more evident in reservoirs or rivers with more toxic sediments.

CRediT authorship contribution statement

Maria Helena Novais: Writing- Original draft preparation; Writing- Reviewing and Editing; Investigation; Visualization; Formal Analysis.

Alexandra Marchã Penha: Writing- Reviewing and Editing; Investigation; Visualization.

Adriana Catarino: Investigation.

Inês Martins: Investigation.

Sofia Fialho: Investigation.

Ana Lima: Investigation.

Manuela Morais: Writing- Reviewing and Editing.

Patrícia Palma: Conceptualization; Writing- Original draft preparation; Writing- Reviewing and Editing; Investigation; Supervision; Visualization; Formal Analysis.

Declaration of competing interest

The authors declare the following financial interests/personal relationships which may be considered as potential competing interests: Novais M.H. reports financial support was provided by Foundation for Science and Technology. Novais M.H. reports was provided by Operational Program Competitiveness and Internationalization. Palma P. reports was provided by European Agricultural Fund for Rural Development. Alexandra Penha reports was provided by Foundation for Science and Technology. Morais M. reports financial support was provided by Foundation for Science and Technology. Palma P. reports was provided by Foundation for Science and Technology.

Data availability

Data will be made available on request.

Acknowledgements

The work is co-funded by National funds through FCT – Fundação para a Ciência e Tecnologia, I.P. (projects UIDB/04683/2020 and UIDP/04683/2020). The present research is also co-funded by the European Union through the European Regional Development Fund, included in the COMPETE 2020 (Operational Program Competitiveness and Internationalization) through the ALOP project (ALT20-03-0145-FEDER-000004), and through the European Agricultural Fund for Rural Development through the FitoFarmGest Operational Group (PDR 2020-101-030926).

We thank Josué Figueira for the valuable help with fieldwork. We also acknowledge the Agência Portuguesa do Ambiente I.P. / Administração da Região Hidrográfica do Alentejo (ARH Alentejo) for kindly providing the information with the surface water status classification.

Appendix A. Supplementary data

Supplementary data to this article can be found online at https://doi.org/10.1016/j.scitotenv.2023.166392.

References

AFNOR, 2007. pr NF T 90-354 - Qualité de l'eau - Détermination de l'Indice Biologique Diatomées (IBD).

Allan, I.J., Vrana, B., Greenwood, R., Mills, G.A., Knutsson, J., Holmberg, A., Guigues, N., Fouillac, A.M., Laschi, S., 2006a. Strategic monitoring for the European Water Framework Directive. TrAC Trends Anal. Chem. 25, 704–715. https://doi.org/10.1016/j.trac.2006.05.009.

Allan, I.J., Vrana, B., Greenwood, R., Mills, G.A., Knutsson, J., Holmberg, A., Guigues, N., Fouillac, A.M., Laschi, S., 2006b. Strategic monitoring for the European Water Framework Directive. TrAC Trends Anal. Chem. 25, 704–715. https://doi.org/10.1016/j.trac.2006.05.009.

Allen, Y., Calow, P., Baird, D.J., 1995. A mechanistic model of contaminant-induced feeding inhibition in *Daphnia magna*. Environ. Toxicol. Chem. 14, 1625–1630. https://doi.org/10.1002/etc.5620140923.

Alvarenga, P., Palma, P., Gonçalves, A.P., Fernandes, R.M., Cunha-Queda, A.C., Duarte, E., Vallini, G., 2007. Evaluation of chemical and ecotoxicological characteristics of biodegradable organic residues for application to agricultural land. Environ. Int. 33, 505–513. https://doi.org/10.1016/J.ENVINT.2006.11.006.

Alvarenga, P., Mourinha, C., Farto, M., Palma, P., Sengo, J., Morais, M.-C., Cunha-Queda, C., 2016. Ecotoxicological assessment of the potential impact on soil porewater, surface and groundwater from the use of organic wastes as soil amendments. Ecotox. Environ. Safe 126, 102–110. https://doi.org/10.1016/j.ecoenv.2015.12.019.

APA (Agência Portuguesa do Ambiente), 2016. Plano de gestão de região hidrográfica 2016–2021. Parte 2. Caracterização e diagnóstico, Anexo IV-Critérios de classificação do estado/potencial ecológico das massas de água superficial.

APA (Agência Portuguesa do Ambiente), 2021. Critérios para a Classificação das Massas de Água.

APHA (American Public Health Association), 2017. Standard Methods for the Examination of Water and Wastewater, 23rd ed. America Public Health Association, New York, NY, USA.

Blanco, S., Cejudo-Figueiras, C., Álvarez-Blanco, I., Bécare, E., Hoffmann, L., Ector, L., 2010. Atlas de las diatomeas de la cuenca del Duero/Diatom Atlas of the Duero Basin. Área de Publicaciones, Universidad de León, Spain (386 pp).

Bori, J., Vallès, B., Navarro, A., Riva, M.C., 2016. Geochemistry and environmental threats of soils surrounding an abandoned mercury mine. Environ. Sci. Pollut. Res. 23, 12941–12953. https://doi.org/10.1007/s11356-016-6463-1.

Bori, J., Vallè, B., Navarro, A., Riva, M.C., 2017. Ecotoxicological risks of the abandoned F-Ba-Pb-Zn mining area of Osor (Spain). Environ. Geochem. Health 39, 665–679. https://doi.org/10.1007/s10653-016-9840-2.

Carvalho, L., Mackay, E.B., Cardoso, A.C., Baattrup-Pedersen, A., Birk, S., Blackstock, K. L., Borics, G., Borja, A., Feld, C.K., Ferreira, M.T., Globevnik, L., Grizzetti, B., Hendry, S., Hering, D., Kelly, M., Langaas, S., Meissner, K., Panagopoulos, Y., Penning, E., Rouillard, J., Sabater, S., Schmedtje, U., Spears, B.M., Venohr, M., van de Bund, W., Solheim, A.L., 2019. Protecting and restoring Europe's waters: an analysis of the future development needs of the Water Framework Directive. Sci. Total Environ. 658, 1228–1238. https://doi.org/10.1016/j.scitotenv.2018.12.255.

Coste, M., 1982. Etude des Méthodes Biologiques Quantitatives d'Appréciation de la Qualité des Eaux. Cemagref. Agence de l'Eau Rhône-Méditerranée-Corse, Pierre-Bénite., Lyon, France.

Debenest, T., Silvestre, J., Coste, M., Pinelli, E., 2010. Effects of pesticides on freshwater diatoms. Rev. Environ. Contam. Toxicol. 203, 87–103. https://doi.org/10.1007/978-1-4419-1352-4_2.

Delgado, C., Novais, M.H., Blanco, S., Almeida, S.F.P., 2015. Examination and comparison of *Fragilaria candidagilae* sp. nov. with type material of *Fragilaria recapitellata*, *F. capucina*, *F. perminuta*, *F. intermedia* and *F. neointermedia* (Fragilariales, Bacillariophyceae). Phytotaxa 231, 1–18. https://doi.org/10.11646/phytotaxa.231.1.1.

Delgado, C., Novais, M.H., Blanco, S., Almeida, S.F.P., 2016. *Fragilaria rinoi* sp. nov. (Fragilariales, Fragilariophyceae) from periphytic river samples in central Portugal. Eur. J. Taxon. 248, 1–16. https://doi.org/10.5852/ejt.2016.248.

Diogo, P., Beça, P., Simoes, S., Fortes, P., Amorim, F., 2022. Simulated hydropower production under climate change scenarios at Torrão reservoir, in northern Portugal. In: Proceedings of the 39th IAHR World Congress, pp. 3477–3481. https://doi.org/10.3850/IAHR-39WC2521711920221138.

Directive 2013/39/EU. European Parliament and of the Council, 2013. Amending directives 2000/60/EC and 2008/105/EC as regards priority substances in the field of water policy. Off. J. Eur. Union L 226, 1–17.

ECC (European Community Commission), 2000. Commission Directive 2000/60/EC of the European Parliament and the Council establishing the framework for community action in the field of water policy. Off. J. Eur. Union 327.

European Commission, 2019. Commission Staff Working Document: European Overview - River Basin Management Plans 296.

European Commission. Directorate-General for the Environment, 2003. Monitoring Under the Water Framework Directive.

European Committee for Standardization, 2003. European Standard EN 13946:2003. Water Quality - Guidance Standard for the Routine Sampling and Pretreatment of Benthic Diatoms From Rivers.

Finney, D.J., 1971. Probit Analysis, Journal of Pharmaceutical Sciences. Cambridge University Press, New York.

Hofmann, G., Werum, M., Lange-Bertalot, H., 2011. Diatomeen im Süßwasser-Benthos von Mitteleuropa. Bestimmungsflora Kieselalgen für die ökologische Praxis. Über 700 der häufigsten Arten und ihre Ökologie. A.R.G. Gantner Verlag K.G., Rugell, Germany (908 pp).

INAG I.P, 2008. Manual para a avaliação biológica da qualidade da água em sistemas fluviais segundo a Directiva-Quadro da Água. Protocolo de amostragem e análise para o FITOBENTOS-DIATOMÁCEAS.

IPCC, 2018. Summary for policymakers. In: Masson-Delmotte, V., Zhai, P., Pörtner, H.-O., Roberts, D., Skea, J., Shukla, P.R., Pirani, A., Moufouma-Okia, W., Péan, C., Pidcock, R., Connors, S., Matthews, J.B.R., Chen, Y., Zhou, X., Gomis, M.I., Lonnoy, E., Maycock, T., Tignor, M., Waterfield, T. (Eds.), Global Warming of 1.5°C. an IPCC Special Report on the Impacts of Global Warming of 1.5 °C above Pre-Industrial Levels and Related Global Greenhouse Gas Emission Pathways, in the

Context of Strengthening the Global Response to the Threat of Climate Change, Sustainable Development, and Efforts to Eradicate Poverty. World Meteorological Organization, Geneva, Switzerland (32 pp).
IPMA, 2018. Situação de Seca Meteorológica. Available online: https://www.ipma.pt/resources.www/docs/im.publicacoes/edicoes.online/20180406/pryhFYgszRoHXednacN/cli_20180331_20180331_sec_mm_co_pt.pdf. (Accessed 10 July 2020).
ISO 11348-2, 1998. Determination of Inhibitory Effect of Water Samples on the Light Emission of *Vibrio fischeri* (Luminescent bacteria Test). Part 2: Method Using Liquid-Dried Bacteria. International Organization for Standardisation, Geneve, Switzerland.
Kelly, M., 2013. Data rich, information poor? Phytobenthos assessment and the Water Framework Directive. Eur. J. Phycol. 48, 437–450. https://doi.org/10.1080/09670262.2013.852694.
Kelly, M.G., King, L., Jones, R.I., Barker, P.A., Jamieson, B.J., 2008. Validation of diatoms as proxies for phytobenthos when assessing ecological status in lakes. Hydrobiologia 610, 125–129. https://doi.org/10.1007/s10750-008-9427-8.
Köck-Schulmeyer, M., Ginebreda, A., González, S., Cortina, J.L., de Alda, M.L., Barceló, D., 2012. Analysis of the occurrence and risk assessment of polar pesticides in the Llobregat River Basin (NE Spain). Chemosphere 86, 8–16. https://doi.org/10.1016/j.chemosphere.2011.08.034.
Köck-Schulmeyer, M., Villagrasa, M., López de Alda, M., Céspedes-Sánchez, R., Ventura, F., Barceló, D., 2013. Occurrence and behavior of pesticides in wastewater treatment plants and their environmental impact. Sci. Total Environ. 458–460, 466–476. https://doi.org/10.1016/j.scitotenv.2013.04.010.
Krammer, K., Lange-Bertalot, H., 1986. Bacillariophyceae 1. Teil: Naviculaceae. In: Ettl, H., Gerloff, J., Heynig, H., Mollenhauer, D. (Eds.), Süsswasserflora von Mitteleuropa. Gustav Fischer Verlag, Stuttgart, pp. 1–876 2/1.
Krammer, K., Lange-Bertalot, H., 1988. Bacillariophyceae 2. Teil: Bacillariaceae, Epithemiaceae, Surirellaceae. In: Ettl, H., Gerloff, J., Heynig, H., Mollenhauer, D. (Eds.), Süsswasserflora von Mitteleuropa. Gustav Fischer Verlag, Stuttgart, pp. 1–596 2/2.
Krammer, K., Lange-Bertalot, H., 1991a. Bacillariophyceae 3. Teil: Centrales, Fragilariaceae, Eunotiaceae. In: Ettl, H., Gerloff, J., Heynig, H., Mollenhauer, D. (Eds.), Süsswasserflora von Mitteleuropa. 2/3. Gustav Fischer Verlag, Stuttgart, pp. 1–576.
Krammer, K., Lange-Bertalot, H., 1991b. Bacillariophyceae 4. Teil: Achnanthaceae. Kritische Ergänzungen zu Navicula (Lineolatae) und Gomphonema. Gesamtliteraturverzeichnis Teil 1-4. In: Ettl, H., Gerloff, J., Heynig, H., Mollenhauer, D. (Eds.), Süsswasserflora von Mitteleuropa. 2/4. Gustav Fischer Verlag, Stuttgart, pp. 1–437.
Lecointe, C., Coste, M., Prygiel, J., 1993. "Omnidia": software for taxonomy, calculation of diatom indices and inventories management. Hydrobiologia 269–270, 509–513. https://doi.org/10.1007/BF00028048.
Martinez-Haro, M., Beiras, R., Bellas, J., Capela, R., Coelho, J.P., Lopes, I., Moreira-Santos, M., Reis-Henriques, A.M., Ribeiro, R., Santos, M.M., Marques, J.C., 2015. A review on the ecological quality status assessment in aquatic systems using community based indicators and ecotoxicological tools: what might be the added value of their combination? Ecol. Indic. 48, 8–16. https://doi.org/10.1016/j.ecolind.2014.07.024.
Martinez-Haro, M., Acevedo, P., Pais-Costa, A.J., Neto, J.M., Vieira, L.R., Ospina-Alvarez, N., Taggart, M.A., Guilhermino, L., Ribeiro, R., Marques, J.C., 2022. Ecotoxicological tools in support of the aims of the European Water Framework Directive: a step towards a more holistic ecosystem-based approach. Ecol. Indic. 145, 109645 https://doi.org/10.1016/j.ecolind.2022.109645.
Masouras, A., Karaouzas, I., Dimitriou, E., Tsirtsis, G., Smeti, E., 2021. Benthic diatoms in river biomonitoring-present and future perspectives within the water framework directive. Water 13, 478. https://doi.org/10.3390/w13040478.
McWilliam, R.A., Baird, D.J., 2002. Postexposure feeding depression: a new toxicity endpoint for use in laboratory studies with *Daphnia magna*. Environ. Toxicol. 21, 1198–1205. https://doi.org/10.1002/etc.5620210612.
Millennium Ecosystem Assessment, 2005. Ecosystems and Human Well-Being: Wetlands and Water Synthesis: A Report of the Millennium Ecosystem Assessment. World Resources Institute.
Novais, M.H., Jüttner, I., Van de Vijver, B., Morais, M.M., Hoffmann, L., Ector, L., 2015. Morphological variability within the *Achnanthidium minutissimum* species complex (Bacillariophyta): comparison between the type material of *Achnanthes minutissima* and related taxa, and new freshwater *Achnanthidium* species from Portugal. Phytotaxa 224, 101–139. https://doi.org/10.11646/phytotaxa.224.2.1.
Novais, M.H., Almeida, S.F.P., Blanco, S., Delgado, C., 2019. Morphology and ecology of *Fragilaria misarelensis* sp. nov. (Bacillariophyta), a new diatom species from southwestof Europe. Phycologia 58, 128–144. https://doi.org/10.1080/00318884.2018.1524245.
Novais, M.H., Morales, E.A., Marchã Penha, A., Potes, M., Bouchez, A., Barthès, A., João Costa, M., Salgado, R., Santos, J., Morais, M., Sabater, S., 2020. Benthic diatom community dynamics in Mediterranean intermittent streams: effects of water availability and their potential as indicators of dry-phase ecological status. Sci. Total Environ. 719, 137462 https://doi.org/10.1016/j.scitotenv.2020.137462.
Palma, P., Ledo, L., Alvarenga, P., 2016. Ecotoxicological endpoints, are they useful tools to support ecological status assessment in strongly modified water bodies? Sci. Total Environ. 541, 119–129. https://doi.org/10.1016/j.scitotenv.2015.09.014.
Palma, P., Matos, C., Alvarenga, P., Köck-Schulmeyer, M., Simões, I., Barceló, D., López de Alda, M.J., 2018. Ecological and ecotoxicological responses in the assessment of the ecological status of freshwater systems: a case-study of the temporary stream Brejo of Cagarrão (South of Portugal). Sci. Total Environ. 634, 394–406. https://doi.org/10.1016/J.SCITOTENV.2018.03.281.
Palma, P., Fialho, S., Lima, A., Mourinha, C., Penha, A., Novais, M.H., Rosado, A., Morais, M., Potes, M., Costa, M.J., Alvarenga, P., 2020a. Land-cover patterns and hydrogeomorphology of tributaries: are these important stressors for the water quality of reservoirs in the mediterranean region? Water 12, 2665. https://doi.org/10.3390/w12102665.
Palma, P., Fialho, S., Lima, A., Novais, M.H., Costa, M.J., Montemurro, N., Pérez, S., de Alda, M.L., 2020b. Pharmaceuticals in a Mediterranean Basin: the influence of temporal and hydrological patterns in environmental risk assessment. Sci. Total Environ. 709, 136205 https://doi.org/10.1016/j.scitotenv.2019.136205.
Palma, P., Penha, A.M., Novais, M.H., Fialho, S., Lima, A., Mourinha, C., Alvarenga, P., Rosado, A., Iakunin, M., Rodrigues, G., Potes, M., Costa, M.J., Morais, M., Salgado, R., 2021. Water-sediment physicochemical dynamics in a large reservoir in the Mediterranean region under multiple stressors. Water 13, 707. https://doi.org/10.3390/w13050707.
Palma, P., Penha, A.M., Novais, M.H., Fialho, S., Lima, A., Catarino, A., Mourinha, C., Alvarenga, P., Iakunin, M., Rodrigues, G., Potes, M., Morais, M., Costa, M.J., Salgado, R., 2023. Integrative toolbox to assess the quality of freshwater sediments contaminated with potentially toxic metals. Environ. Res. 217, 114798 https://doi.org/10.1016/j.envres.2022.114798.
Persoone, G., 1999. THAMNOTOXKIT FTM - Crustacean toxicity screening test for Freshwater. In: Standard Operational Procedure. Belgium.
Pinto, I., Rodrigues, S., Lage, O.M., Antunes, S.C., 2021. Assessment of water quality in Aguieira reservoir: Ecotoxicological tools in addition to the Water Framework Directive. Ecotoxicol. Environ. Safe 208, 111583. https://doi.org/10.1016/j.ecoenv.2020.111583.
Rand, G.M., 1995. Fundamentals of Aquatic Toxicology: Effects, Environmental Fate, and Risk Assessment, Edition: 2nd. Taylor and Francis, Bristol.
Rodrigues, S., Pinto, I., Martins, F., Formigo, N., Antunes, S.C., 2021. Can biochemical endpoints improve the sensitivity of the biomonitoring strategy using bioassays with standard species, for water quality evaluation? Ecotox. Environ. Safe 215, 112151. https://doi.org/10.1016/j.ecoenv.2021.112151.
Rodrigues, S., Pinto, I., Martins, F., Formigo, N., Antunes, S.C., 2022. An ecotoxicological approach can complement the assessment of natural waters from Portuguese reservoirs? Environ. Sci. Pollut. Res. 29, 52147–52161. https://doi.org/10.1007/s11356-022-19504-4.
Rodríguez Pérez, J., Loureiro, Susana, Menezes, Salomé, Palma, Patrícia, Fernandes, Rosa M., Barbosa, Isabel R., Soares, Amadeu M.V.M., Pérez, J.R., Loureiro, S., Menezes, S., Soares, A.M.V.M., Palma, P., Fernandes, R.M., Barbosa, I. R., 2010. Assessment of water quality in the Alqueva Reservoir (Portugal) using bioassays. Env. Sci. Pollut. Res. 17, 688–702. https://doi.org/10.1007/s11356-009-0174-9.
Roig, N., Sierra, J., Nadal, M., Moreno-Garrido, I., Nieto, E., Hampel, M., Gallego, E.P., Schuhmacher, M., Blasco, J., 2015. Assessment of sediment ecotoxicological status as a complementary tool for the evaluation of surface water quality: the Ebro river basin case study. Sci. Total Environ. 503–504, 269–278. https://doi.org/10.1016/j.scitotenv.2014.06.125.
Santos, J.I., Vidal, T., Gonçalves, F.J.M., Castro, B.B., Pereira, J.L., 2021. Challenges to water quality assessment in Europe – is there scope for improvement of the current water framework directive bioassessment scheme in rivers? Ecol. Indic. 121, 107030 https://doi.org/10.1016/j.ecolind.2020.107030.
United Nations General Assembly, UN, 2019. United Nations Decade on Ecosystem Restoration (2021−2030). available from. undocs.org/A/RES/73/284.
Van de Vijver, B., Ector, L., Beltrami, M.E., de Haan, M., Falasco, E., Hlúbiková, D., Jarlman, A., Kelly, M., Novais, M.H., Wojtal, A.Z., 2011. A critical analysis of the type material of *Achnanthidium lineare* W. Sm. (Bacillariophyceae). Arch. Hydrobiol. Suppl. Algol. Stud. 136–137, 167–191. https://doi.org/10.1127/1864-1318/2011/0136-0167.
Viso, R., Blanco, S., 2023. River diatoms reflect better past than current environmental conditions. Water 15, 333. https://doi.org/10.3390/w15020333.
Voulvoulis, N., Arpon, K.D., Giakoumis, T., 2017. The EU water framework directive: from great expectations to problems with implementation. Sci. Total Environ. 575, 358–366. https://doi.org/10.1016/j.scitotenv.2016.09.228.
Zar, J.H., 1996. Biostatistical Analysis. Prentice-Hall International, Englewood Cliff, USA, DC.
Zelinka, M., Marvan, P., 1961. Zur Präzisierung der biologischen Klassifikation der Reinheit fliessender Gewässer. Arch. Hydrobiol. 57, 389–407.

View publication stats

Hindawi
Advances in Meteorology
Volume 2017, Article ID 1276784, 16 pages
https://doi.org/10.1155/2017/1276784

Research Article

Numerical Simulations of Fog Events in Southern Portugal

Carlos Policarpo,[1] Rui Salgado,[2] and Maria João Costa[2]

[1]*Instituto de Ciências da Terra, Polo de Évora, Universidade de Évora, Évora, Portugal*
[2]*Instituto de Ciências da Terra, Polo de Évora, Departamento de Física, Escola de Ciências e Tecnologia, Universidade de Évora, Évora, Portugal*

Correspondence should be addressed to Carlos Policarpo; carlos.am.policarpo@gmail.com

Received 3 June 2016; Revised 30 August 2016; Accepted 5 October 2016; Published 5 January 2017

Academic Editor: Panagiotis Nastos

Copyright © 2017 Carlos Policarpo et al. This is an open access article distributed under the Creative Commons Attribution License, which permits unrestricted use, distribution, and reproduction in any medium, provided the original work is properly cited.

This work aims at improving the knowledge on fog formation and its evolution in the Alentejo region (Portugal). For this purpose, brief regional fog climatology, essentially based on information from the Beja Air Base meteorological station, was produced and several numerical high resolution simulations were performed using the Meso-NH. The ECOCLIMAP database used to generate the model physiography was improved to include the Alqueva reservoir (~250 km^2), filled in 2003. The model results were compared with surface and satellite observations, showing good agreement in terms of fog occurrence and persistence. Various forcing mechanisms for formation, development, and dissipation of fog were identified, confirming the influence of two small mountains that block the moist air from the Atlantic Ocean, preventing the fog from reaching innermost regions. The introduction of the Alqueva large reservoir induces changes in the landscape and environment. The effects of the water vapour addition and of the changes in mass and energy surface fluxes on fog formation and evolution were studied. It was found that the reservoir may have a direct impact on fog formation over the lake and its vicinity. Depending on the large scale meteorological conditions, their influence can be both positive and negative, in terms of spatial coverage and temporal persistence.

1. Introduction

Usually, a fog episode has a large impact on air, maritime, and land transportation, most particularly in aviation. Frequent delays, diversions, and cancellations have various impacts on society. Since visibility is one of the most difficult weather variables to predict, its understanding is crucial. There is the need to apply the latest techniques and approaches to improve the prediction of the formation and evolution of fog. Improved forecasts of fog in terms of location, duration, and variations in visibility have an enormous operational value in the transportation area under reduced visibility conditions, particularly for aviation. In the Alentejo region, in southern Portugal, there are an aeronautical infrastructure located near Beja Town (Portuguese Air Force) and a civilian airport terminal (Beja Airport) that are several times affected by fog events. The first motivation for the development of this work is to better understand this phenomenon in the region and how it forms and develops, in order to optimize techniques to analyse and predict the fog in that aerodrome. The effects on fog of a relatively recent man-made lake, the Alqueva large reservoir, localized in the region, are also discussed.

The fog formation involves several processes, such as cloud physics, aerosol chemistry, radiation, turbulence, the large and small scale dynamics, and surface conditions, including water bodies, topography, vegetation, and soil type. High moisture, condensation nuclei, and cooling processes are the conditions for its formation [1]. It often occurs under stable atmospheric situations during clear sky nights and with light to calm wind. Still, the local influence of these elements can play a vital role in the formation, duration, and intensity of fog events that can be enhanced if air pollutants are present [2].

As mentioned by Cotton and Anthes (1989) "*in the International Cloud Atlas from WMO (World Meteorological Organization)* [3] *Fog is not treated as a separate cloud genus. Instead it is defined in terms of its microstructure, visibility, and proximity to the earth's surface. Therefore, fog is composed by very small water droplets (sometimes ice crystals) in suspension in the atmosphere and reduces the visibility at the earth's surface*

to less than 1000 m" [4]. The vertical extent of fog ranges between a few meters and several hundred meters. However, the fog can be also considered as a cloud with the base in contact with the surface. Fog may be considered the less dynamic cloud type. The mean vertical velocity in fog is usually small. Typically the liquid water content in fog ranges from 0.05 to 0.2 g/m^3 with lifetimes of 2 to 6 h [4], but it can, in certain circumstances, lasts longer than 24 hours or even several days.

The improvement of fog forecasting in location, duration, and visibility restrictions has an enormous operational value. It is important to understand and diagnose thermodynamics, kinematics, and microphysics of the processes of formation and evolution of fog. The thermodynamic and kinematic components are easily quantified or inferred; however, the microphysical and atmospheric boundary layer processes are not [5]. Fog is a boundary layer phenomenon that typically develops in the surface stable nocturnal atmospheric boundary layer. Its development is strongly influenced by surface conditions, soil cover for fogs over land, and sea state for fogs at sea. Effects of the underlying surface on fogs can be direct when the surface influences the profiles of wind, temperature, humidity, and local circulations through horizontal heterogeneities or indirect through modification of radiative properties of the atmosphere by microphysical processes and varying aerosol spectra [1].

Turbulence and radiative processes play an important role in fog characteristics. They can contribute positively in its formation or negatively leading to its dissipation. For example, the turbulent mixing is an ambiguous but decisive factor in fog formation. If turbulent mixing is too low, dew deposition at the surface will inhibit condensation in the atmosphere and hence inhibit fog formation. If turbulence is strong enough, it may promote condensation in a supersaturated surface layer of sufficient depth and hence lead to fog formation and development [6].

Often, the numerical modeling does not provide a clear answer to the turbulence role, because the results depend on the parameterization used and radiative processes, both loaded with significant uncertainty. The complexity of turbulence and the surface parameterization, as well as the vertical and horizontal high resolutions required, represent a main obstacle to the fog forecasts success in time. Therefore, surface conditions and turbulent flux parameterizations will continue to be an important research topic in fog studies and modeling. One-dimensional models have been developed for operational and research purposes; for example, Teixeira and Miranda combined a suite of parameterizations based on finite element methods for the vertical discretization. The coupling of 1D and 3D models and their integration with observations also lead to promising results in fog prediction. Presently, detailed versions of fog microphysics from 1D models are incorporated into 3D models, allowing improving weather forecasts [7]. The success of numerical modeling and fog prediction depends heavily on the fog type. Some fog events are mainly stimulated by dynamic processes such as advection and orography. If the fog occurrence is dominated by other processes, for instance, radiation, turbulent, or direct interaction between the surface and the atmosphere, then the numerical modeling of the mist may become a very difficult task.

The fog forecasting using operational numerical weather models is usually a very difficult task due to their relatively coarse horizontal and vertical resolutions, causing that operational fog forecast to be usually performed based on empirical rules and statistical methods [7]. However, it is possible to obtain a deterministic three-dimensional fog model modifying existing numerical weather prediction models properly [8]. By increasing the horizontal and vertical resolutions of the grid near the surface and improving significantly the model physical parameterization such as turbulence, heat, and moisture fluxes at the surface, it is possible to represent fog events in realistic way. When using high resolution in the vertical, grid distances in the lowest layers of the atmosphere must be small enough to accurately solve the evolution of physical processes within the atmospheric boundary layer near the surface [9]. The observed fog structure is often irregular, mostly due to horizontal soil and vegetation heterogeneities. To perform realistic fog simulations it is important to have the geographical distribution of soil moisture, vegetation, and water bodies well represented.

The use of numerical weather prediction models in medium and short term fog forecasting for aviation purposes is still a problem that needs continued research. However, they are already implemented in certain airports, such as Charles de Gaulle, Paris [10], and San Francisco, California [11]. These models include precise parameterizations of radiative, turbulent, and surface processes and rely on detailed and continuous near surface observations of temperature, humidity, wind, radiation, and visibility. They produce accurate fog forecasts but their application remains local [12].

In this study, the atmospheric mesoscale Meso-NH is used [13]. The Meso-NH has been successfully used in simulation of fogs over different regions, for example, Cuxart and Jimenez [14] over the Ebro river basin, Spain [14], Bari et al. over Casablanca, Morocco [15], Bergot et al. over Paris, France [16], and Salgado over Alentejo, Portugal [17]. The Meso-NH mod was also used to improve the characterization of the atmospheric circulations in the south of Portugal (e.g., Costa et al., 2010, and Salgado et al., 2015) [18, 19]. In the present work, several Meso-NH simulations of real case studies are used in order to (i) reevaluate the ability of numerical prediction of fog in the region and (ii) characterize typical regional large fog events and discuss the impact of the Alqueva reservoir on fog.

This article is divided into four more sections, as follows. The study domain, the data, and the numerical experiments are described in Section 2, regional fog climatology is presented in Section 3, and the results around the case studies and the impact of the reservoir in fog are discussed in Section 4. The conclusions are presented in Section 5.

2. Materials and Methods

2.1. Study Area. The region under consideration is the Alentejo, located in southern Portugal (about a third of

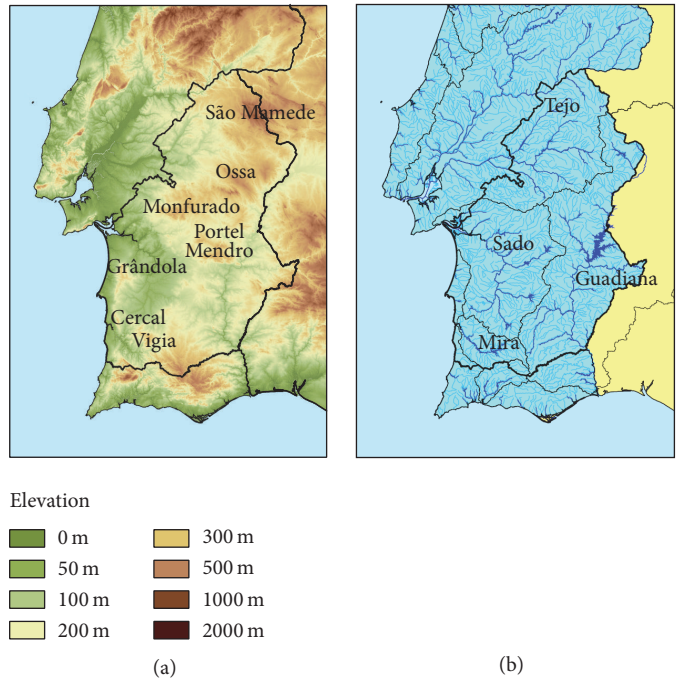

Figure 1: (a) Regional orography and main elevations; (b) main hydrographic basins.

the total country area), being limited to the north by the Central Region, to the east by Spain, to the south by the Algarve Region, and to the west by the Atlantic Ocean. The region is crossed by three large river basins (Tejo, Sado, and Guadiana), which greatly influence the fog formation and evolution in the area, especially its major courses and reservoirs. The relief of the region, shown in Figure 1, is characterized by great uniformity of plains, slightly uneven, whose average altitude is around 200 m, only with some mountainous outcrops, undervalued, with the exception of the São Mamede mountain chain (1025 m). However, focus should be given as well to mountains of Ossa, Monfurado, Portel, Mendro, Grândola, Cercal, and Vigia, which appear to have a significant impact on the fog development, particularly in their limits definition.

The Alentejo climate is characterized as Temperate Mediterranean type (Dry Subtropical), with hot, dry summers and rainy and mild winters. The eastward decrease of the maritime influence makes the inland areas particularly hot in summer and relatively cool in winter. The region is mainly influenced by the Atlantic Ocean in the west coastal regions, having a more continental influence in inland areas. Rainfall is weak, being predominant in the winter months. The Alqueva Multipurpose Project centered on the Alqueva dam and its strategic water reservoir at the Guadiana Basin (see Figure 1(b)), which extends for 83 km, covering an area of 250 km^2, with a total storage capacity of 4150 million m^3 located in the Alentejo [28]. The project aims to reinforce the water supply to around 200,000 inhabitants, to create an equipped irrigation area of around 120,000 hectares, to generate clean energy from a hydroelectric power plant (total installed capacity of 520 MW), and to develop regional tourism.

2.2. Observational Dataset. Data collected at the meteorological surface stations indicated and described in Table 1 and shown in Figure 2 were used. It should be noted that, among these stations, only Beja Air Base and Badajoz provide regular observations of horizontal visibility, as they are integrated in airports. However, only Beja Air Base provides aeronautical hourly meteorological observations continuously (24 hours a day) providing data from horizontal visibility, important to evaluate the occurrence of fog events.

Remote sensing data from geostationary orbit satellite (Meteosat: SEVIRI, Spinning Enhanced Visible and Infrared Imager) were used for a comparative event analysis. Data from polar orbiting satellites (TERRA and AQUA: sensor MODIS, Moderate Resolution Imaging Spectroradiometer) were used to obtain the water surface temperature of Alqueva reservoir for events with a lack of in situ observational data. Data from Meteosat-10 presents as main disadvantage the great distance to the Earth's surface, which restricts its spatial resolution (~3 km). The fog (or low clouds) is particularly difficult to detect using only one Infrared Band (IR) channel at night, because this is a very low altitude phenomena and the top of the fog and the surface, in areas without fog, present quite similar Brightness Temperatures (BT) [29].

In this work, two different IR channels, the IR3.9 and the IR10.8, were used. It was possible to detect fog using the BT difference between them. These channels are located in the atmospheric window regions, where the attenuation of the radiation due to absorption by atmospheric gases is not

Table 1: Weather stations used.

Type	Station	Latitude	Longitude	Altitude
I	Portalegre	39° 16′ 59″ N	7° 25′ 01″ W	597 m
I	Évora CC	38° 31′ 59″ N	7° 54′ 00″ W	245 m
I	Beja Town	38° 01′ 01″ N	7° 52′ 01″ W	246 m
I	Sines	37° 57′ 00″ N	8° 52′ 01″ W	98 m
II	Beja Air Base	38° 04′ 01″ N	7° 55′ 01″ W	194 m
II	Badajoz Talavera La Real	38° 52′ 59″ N	6° 49′ 59″ W	185 m

Type I: Synoptic Meteorological Station (Manual/Automated).
Type II: Synoptic Meteorological Station/Aeronautic (Manual/Automated).

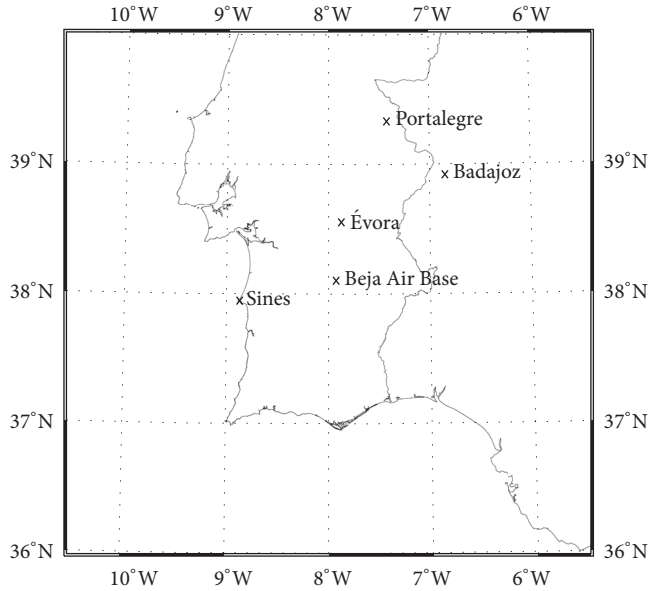

Figure 2: Meteorological stations in model domain 1.

significant. However, the emissivity of liquid water (case of fog) is smaller in the IR3.9 channel than in the IR10.8, and thus the fog BT will be lower in the IR3.9 overnight. Despite the fact that the emissivity of liquid water is lower in IR3.9, during the day, the reflected solar component is substantially greater in IR3.9, so the radiance in the IR3.9 channel is greater than in the IR10.8. These differences are very useful in fog identification, especially at night because during the day the VIS channels are available and allow better fog detection [30, 31]. RGB composites were also used in the fog detection, during both the night and day time. At night the RGB composite, Night Fog-RGB, uses channels 4 (3.9 μm), 9 (10.8 μm), and 10 (12.0 μm) of SEVIRI sensor. This product is only useful during the night; the main limitation is the fact that a thin layer of Cirrus can be enough to obstruct the fog or low stratus detection. During the day the Natural RGB was used, which is based on two channels of VIS, channel 1 (0.6 μm) and channel 2 (0.8 μm) of SEVIRI sensor, and one channel in the near infrared (NIR), channel 3 (1.6 μm).

2.3. Model Setup. The mesoscale atmospheric modeling system used was the Meso-NH [12] developed by CNRM (Météo *France*) and *Laboratoire d'Aérologie*. It is a nonhydrostatic anelastic numerical model, able to simulate the atmospheric motions, ranging from synoptic scale (hundreds of kilometers) to microscale (tens of meters), with a comprehensive physical package and an ensemble of facilities to prepare initial states, either idealized or interpolated from real meteorological analyses or forecasts. The version used in this work was the MNH-V4-9-3. The Meso-NH physical package includes several parameterization schemes to represent surface-atmosphere interactions, radiation, turbulence, clouds and precipitation, convection, atmospheric electricity, chemical reactions, and aerosols. For these processes, different parameterization options are available, which can be enabled or disabled depending on the study to make. The schemes activated in the present work are listed in Table 2. The microphysics scheme used in the simulations was the adopted scheme in the regional numerical weather prediction model of Météo France, the AROME, which is running operationally, two times per day, at the Portuguese Institute of Sea and Atmosphere to forecast the weather in Portugal.

This work was carried out launching simultaneous simulations on different scales using a two-way grid nesting technique [30, 31] in order to perform a further study in the

Table 2: Adopted features for the final Meso-NH simulations.

Domain	D1	D2
Discretization	Nx = Ny = 150 Dx = Dy = 3 km	Nx = Ny = 120 Dx = Dy = 1 km
	Nz = 55 (sigma coordinates) Dz (5 m) = 10 m; Dz (500 m) = 50 m; Dz (5 km) = 650 m; Dz (25 km) = 2000 m	
	Dt = 6 s	Dt = 2 s
Central point	Latitude: 38° 00′ N; longitude: 008° 00′ W	Latitude: 38° 22′ N; longitude: 007° 36′ W
Surface-atmosphere interactions.	ISBA [20] TEB [21] ECUME [22] Flake [23]	
Physics schemes	Radiation: ECMWF [24] Turbulence: Quasi-1D (on the vertical) [25] Clouds microphysics: ICE3 [26] No convection	
Horizontal visibility	Kunkel [27]	

areas of interest. Two domains were considered (see Table 2 for details). Surface schemes that improve the numerical simulations at the atmosphere lower levels are available in the Meso-NH, providing more realistic lower boundary conditions. These schemes are grouped on a surface model platform, called SURFEX (*Surface Externalisée)* [32]. The SURFEX platform includes the ISBA (Interaction Soil-Biosphere-Atmosphere), a land surface model [20] with 3 soil layers by default, the Flake (Freshwater Lake) 1D inland water model developed by Mironov et al. [23] and integrated in SURFEX by Salgado and Le Moigne [33], the TEB (Town Energy Balance) developed by Masson [21] in order to compute the fluxes over urban areas, and the ECUME (Exchange Coefficients from Unified Multicampaign Estimates) parametrization of sea surface fluxes [22]. Finally the Kunkel formulation provides the surface visibility parameter from the relationships between extinction coefficient and liquid water content [27].

In the present study, the simulations were performed using 6 hourly analyses from the ECMWF operational model (IFS, Integrated Forecasting System) with 0.125 degrees of horizontal resolution, as initial and boundary conditions. The model was configured with two nested horizontal domains by two-way interaction. The largest domain (D1) has a grid with 150 × 150 points, a spatial resolution of 3 km (450 × 450 km), and it is centered at the coordinates latitude, 38° 00′ N, and longitude, 008° 00′ W; the smallest area (D2) has a grid with 120 × 120 points, a spatial resolution of 1 km, and it is centered approximately at the following coordinates: latitude, 38° 22′ N, and longitude, 007° 36′ W. The latter are chosen in order to further study the region that includes the Alqueva reservoir and the Beja Air Base. The simulation domains can be seen in Figure 3, which depicts the orography used. Various vertical grids were tested, as several studies indicate its influence in fog modeling like PARISFOG Campaign [5]. After some tests, a vertical grid with 55 levels, with the lowest level at 5 m above the surface, was adopted. The temperature of the water surface at Alqueva reservoir was initialized by the temperatures obtained from MODIS satellite data, and the Flake model was activated.

Due to the complexity of the atmospheric system and its relations with the surface there is an increasing need to accurately represent the surface and the processes occurring therein and that significantly contribute to the interaction with the atmospheric boundary layer. Thus, there is a need to have a thorough and realistic description of the land surface characteristics in meteorological models, from mesoscale research and numerical weather prediction models to general circulation models [34]. The surface schemes need the right allocation of the land-water mask and of the soil-vegetation characteristics for the surface fluxes calculation of momentum, heat, and moisture. It is necessary to use some databases in order to provide the soil characteristics and vegetation cover [34]. In Meso-NH, the physiographic fields are created from specific data contained in the following global databases: ECOCLIMAP_v2.0 [34] for surface cover, GTOPO30 [35] for orography, and Clay and Sand databases derived from FAO [17].The databases have a horizontal resolution of 30 arc sec (~1 km).

The ECOCLIMAP database developed in the Météo France was created in order to provide the necessary surface parameters for soil-vegetation-atmosphere transfer models. This was produced from the combination of several other databases, such as the surface use, vegetation index, or soil texture maps. The GTOPO30 database is a global digital model representing the elevation of the terrain (Digital Elevation Model, DEM) and results from work led by the US Geological Survey's (USGS) EROS (Earth Resources Observation and Science) Data Center.

2.4. Landscape Changes. Despite its very recent review, the ECOCLIMAP v2.0 database lies with outdated data for the Alentejo region, including the area occupied by the Alqueva reservoir and other inland lakes created after the lake was filled up. To run the simulations with greater realism, it was necessary to make certain amendments in the existing surface parameters. The changes introduced in the inland water cover in the region can be seen in Figure 4. It was assumed that the reservoir is at its full storage level, corresponding to an elevation of 152 m above the mean sea level. This modification represents better the actual surface cover and is needed in order to study the possible impact of the Alqueva reservoir in relation to fog events [17].

Due to changes in the ECOCLIMAP database, it was also necessary to change the orography in GTOPO30 for Alqueva reservoir area due to its large dimension. The value of 152 m (full storage level) was imposed over the numerical flooded area.

2.5. Cases Studies Selection. The period considered for the case studies selection was between December 2012 and July 2013. In Beja Air Base, 47 fog events were registered during this period. Among these, five events were selected (see in Table 3) because they present different weather patterns,

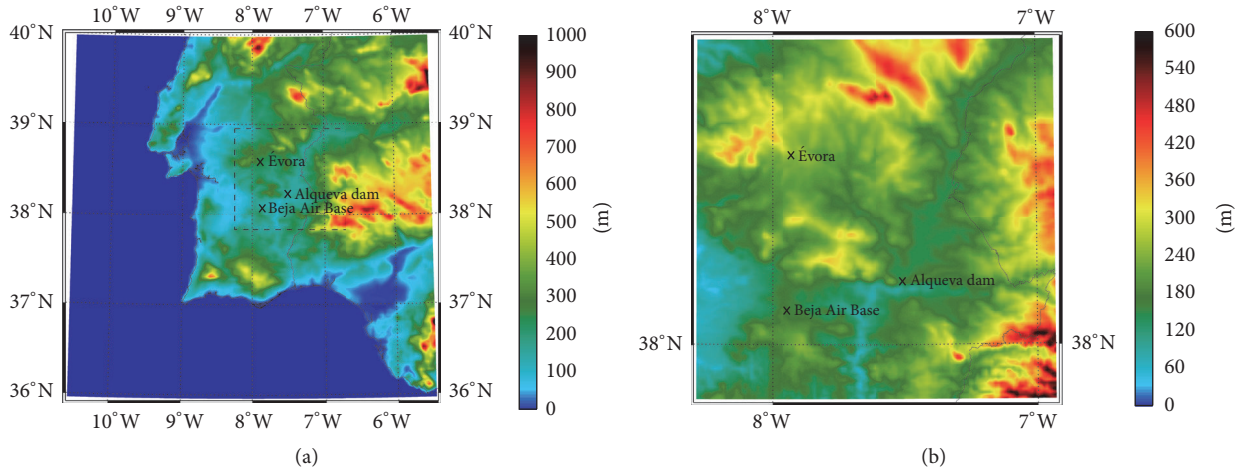

Figure 3: Orography of domains D1 and D2.

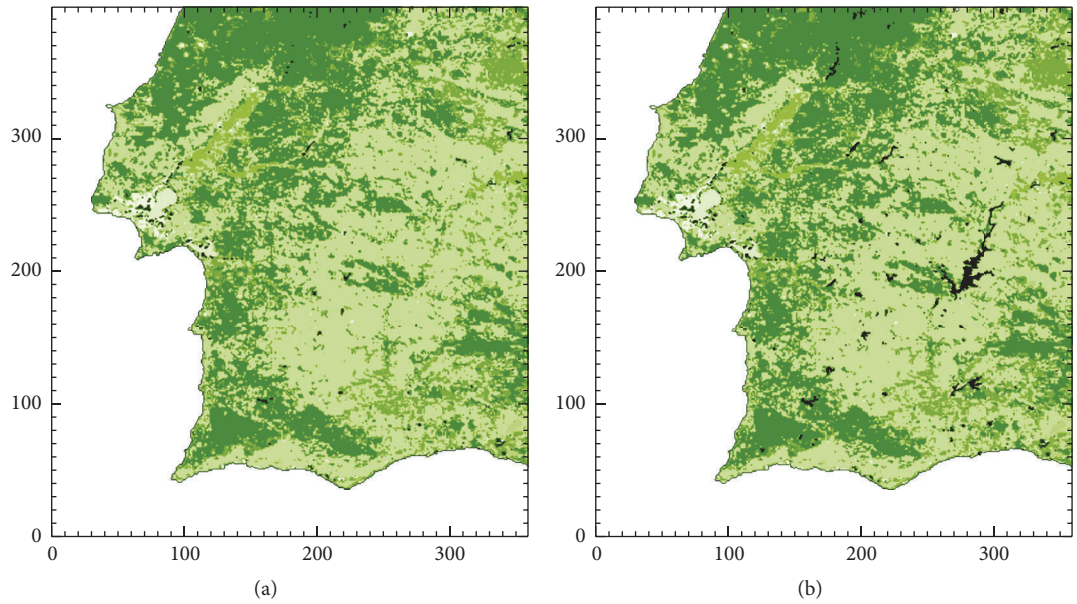

Figure 4: ECOCLIMAP v2.0 database: (a) original and (b) changed. Green colors (mean nature) and black colors (mean surface water bodies). Axis coordinates are in km.

considerable persistence, significant horizontal extension, and lack of high clouds, which allowed for using satellite observations. The first three cases occur in winter and are characterized as radiation fogs; the latter two occur in summer and are best characterized as advection and orographic fogs. Among the five simulated events, two will be discussed here in detail (Section 4): one winter case of radiative fog (23/12/2012) and one summer case of advection fog (18/07/2013). All the 5 simulations are used in Section 4.3 to access the impact of the Alqueva reservoir on fog.

3. Regional Fog Climatology

In the Alentejo region, the radiation fog occurs mainly in winter and the advection fog in the remaining seasons. Nevertheless, there are also frequent episodes of orographic fogs, particularly due to obstruction by the hills.

In winter, fogs in the Iberian Peninsula mainly occur during anticyclonic blocking situations that promote pronounced nocturnal cooling, especially in the inner regions. Fog is formed particularly in the vicinity of rivers, valleys, and lakes. In the remaining seasons, advection fogs mainly occur in coastal regions, under the influence of the Azores Anticyclone, especially when extending in ridge over the Iberian Peninsula. The dynamics associated with stable anticyclonic circulation also causes the fog occurrence in windward slopes, which sometimes blocks the transport and the fog evolution into the region, despite its small elevations.

Frontal fogs also occur occasionally in Alentejo region, especially in winter season, under sustained rainfall situations

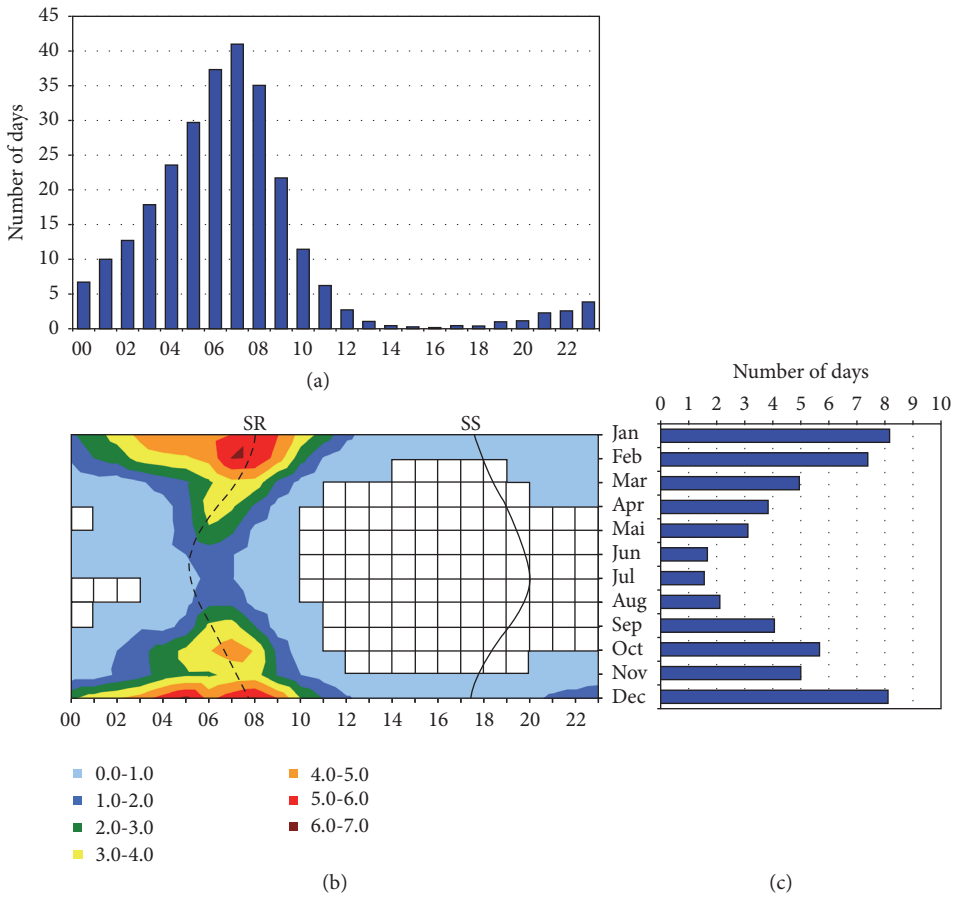

Figure 5: Mean number of days with fog over the entire year in Beja Air Base (2006–2012) by (a) hour, (b) hour and month, and (c) month. Hours in UTC. SR: sunrise; SS: sunset.

Table 3: Simulation periods for the selected case studies.

Date	Simulations	Study periods
2012-12-08	07 18:00–08 18:00 UTC	07 21:00–08 15:00 UTC
2012-12-23	22 18:00–23 18:00 UTC	22 21:00–23 15:00 UTC
2013-02-05	04 12:00–05 18:00 UTC	05 00:00–05 15:00 UTC
2013-07-16	15 18:00–16 12:00 UTC	15 21:00–16 12:00 UTC
2013-07-18	17 18:00–18 12:00 UTC	17 21:00–18 12:00 UTC

from warm fronts moving slowly, with southwest/westerly light wind and sometimes with drizzle. This type of fog occurs mainly during the night. Fog events in the warm sector of frontal systems during the night due to the lowering of low cloud bases are also reported. Fog may also develop in postfrontal cold air in winter, during dawn and early morning, due to noticeable nocturnal cooling, especially after large frontal precipitation and under light winds due to weakening of pressure gradient.

A more detailed description of fog occurrence in Beja is possible, based on information from Beja Air Base meteorological station. Figure 5 shows the distribution of the average number of foggy days per month and hour over the entire year between 2006 and 2012 (there is only a complete hourly series since 2006), with the distribution of average number of foggy days by hour (a) and the average monthly number of days with fog (c). From the analysis of Figure 5, it can be concluded that fogs in Beja Air Base occur more frequently in winter season (December, January, and February) and mostly between 04 and 10 UTC, with more than 20 days with fog at these times, and the maximum value is at 07-08 UTC (more than 40 days per year of fog). It should be noted that the number of days with fog is greater next to the indicator line of monthly average sunrise time. Figure 5 also suggests that the fog events, which occur during the winter months, are longer compared to those occurring in the rest of the year.

Figure 6 shows the distribution of the monthly average number of days with fog through the year for two periods 1994–2002 (before Alqueva dam concluded) and 2003–2012 (after Alqueva dam concluded). It can be seen in Figure 6 that the fog events occur most frequently during the months of winter (December, January, and February) at Beja aerodrome, with more than seven days on average during 2003–2012. When comparing the two periods, it seems that there is an increase in the average number of days with fog in the winter months (December and January, about 4 days in total) and an appreciable decrease in May, July, and August (about 4 days in total). As mentioned before, in winter the fogs in the region

Table 4: Mean absolute error (MAE) from the comparison between observed data and its simulations (Cases II and V).

Variable	23/12/2012		18/07/2013	
	Bias	MAE	Bias	MAE
Temperature (2 m) [°C]	0.1	1.6	2.9	2.9
Relative humidity (2 m) [%]	−0.3	3.2	−9.26	10.2
Wind speed (10 m) [m/s]	−1.0	0.7	0.2	0.8
Wind direction (10 m) [°]	−1.4	11.7	−19.2	28.0

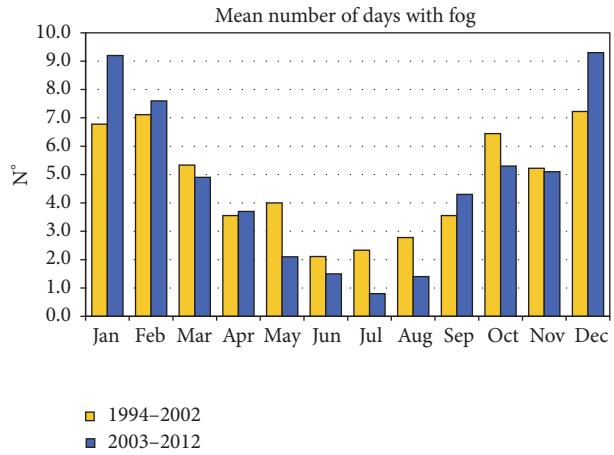

Figure 6: Monthly mean days of Fog in Beja Air Base in the periods 1994–2002 (yellow) and 2003–2012 (blue).

are frequently of radiative type, which highly depends on the local surface conditions. Thus, the data shown in Figure 6 suggest the existence of a slight impact caused by Alqueva in the increasing of the average number of foggy days in Beja aerodrome during winter. On the contrary, the decrease in the average number of foggy days in late spring and summer cannot be attributed to a specific regional effect, being mainly due to synoptic scale weather systems, unlike winter events that are often due to local effects.

4. Results and Discussion

4.1. Comparison between Observations and Simulations (Beja Air Base). The verification of simulated fog on a numerical grid (nearest neighbour grid point) against single point observations is not easy, especially in situations where the observations are made at locations in the fog limits. Anyway the results obtained from the Meso-NH simulations were compared with data taken at Beja Air Base meteorological station. The mean bias and the mean absolute error for the cases of 23/12/2012 and 18/07/2013 can be seen in Table 4.

From the comparison between the hourly data observed in the Beja Air Base and the simulated data, it can be concluded that the model satisfactorily simulated various parameters: wind speed and direction at 10 m; air temperature at 2 m; relative humidity at 2 m. The values found in Table 4 are comparable with other published state-of-the-art mesoscale simulations, as documented by Schlünzen et al. [36], based on the analysis of 80 journal articles published from 2000 in refereed journals that summarize evaluations of several models or of several model set-ups for one and the same case, focusing on surface measurements. The less good results concerning temperature and relative humidity in Case V are essentially due to the fact that model has anticipated, in about three hours, the fog dissipation over Beja. In a summer day this anticipation has a great impact in the daily mean bias on near surface air temperature and consequently on relative humidity.

With regard to fog, in the winter case there was a very good representation of fog, in its formation, evolution, and dissipation. There was a considerable similarity between the various parameters, emphasizing the horizontal visibility (see Figure 7(a)). In the summer case, the formation of fog was also well represented, but the model anticipated the dissipation in about 2 hours (see Figure 7(b)). The analysis of Figure 7 shows that the simulation of winter case had the best results. In general the remaining cases also showed reasonable results.

4.2. Results

4.2.1. Winter Case (23/12/2012). Regarding the winter case, using surface and satellite observations, it was found that around midnight an event of fog was established in the valleys of the Guadiana and Sado rivers, persisting for approximately 7 hours. After sunrise, with the increase of solar radiation, the areas of higher altitudes start to warm, and the fog remains only over the wetlands, especially in northern areas

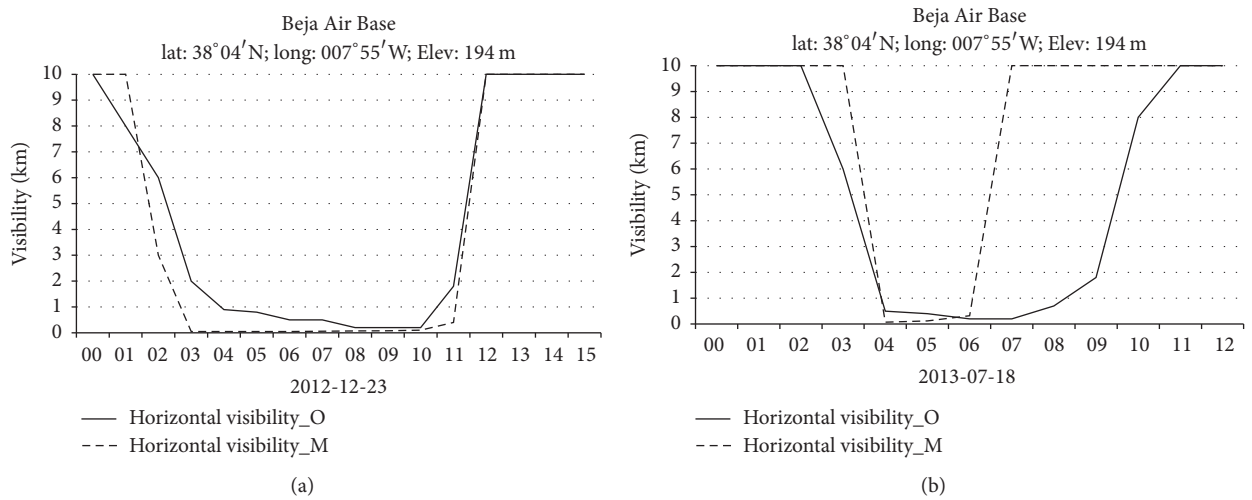

Figure 7: Comparison between the horizontal visibility observed and simulated data (D02) at Beja Air Base in (a) 23/12/2012 and (b) 18/07/2013. UTC hours.

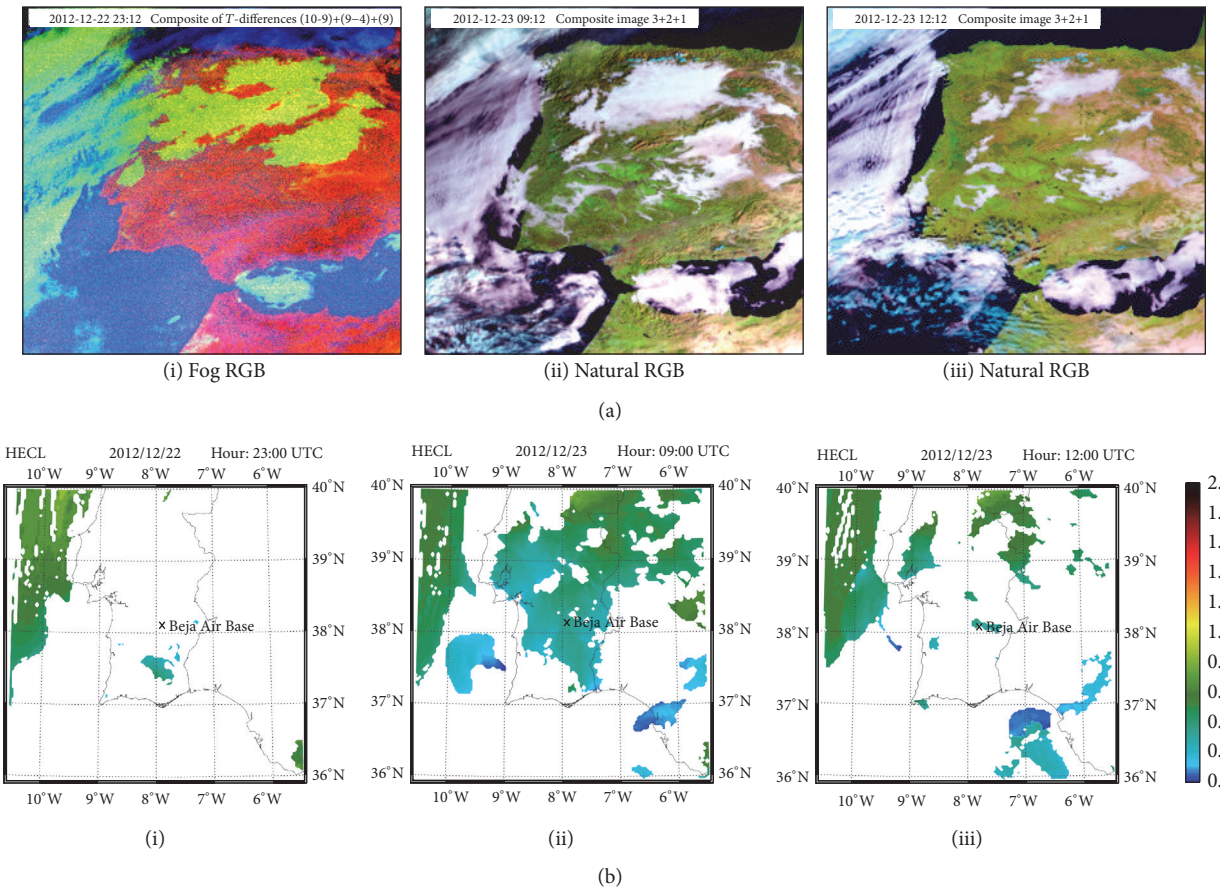

Figure 8: (a) Sequence of satellite images in 22/12/2012 at 23:12 UTC and in 23/12/2012 at 09:12 and 12:12 UTC of 23/12/2012; (b) simulation of explicit cloud top height from the surface in 22/12/2012 at 23:00 and in 23/12/2012 at 09:00 and 12:00 UTC in D1 domain.

of Alqueva reservoir, where there are still some places with fog or low clouds in the early afternoon (see Figure 8(a)). The cloud top height given by the Meso-NH simulations (see Figure 8(b)) indicates the development of low cloud cover around 23 UTC of 22/12/2012 in some areas of southern Alentejo, sprawling its occupation over the entire region before sunrise time, especially in the inland regions. After the sun rise and with the increased solar radiation, the clouds begin to dissipate, persisting, however, some low clouds during the early afternoon.

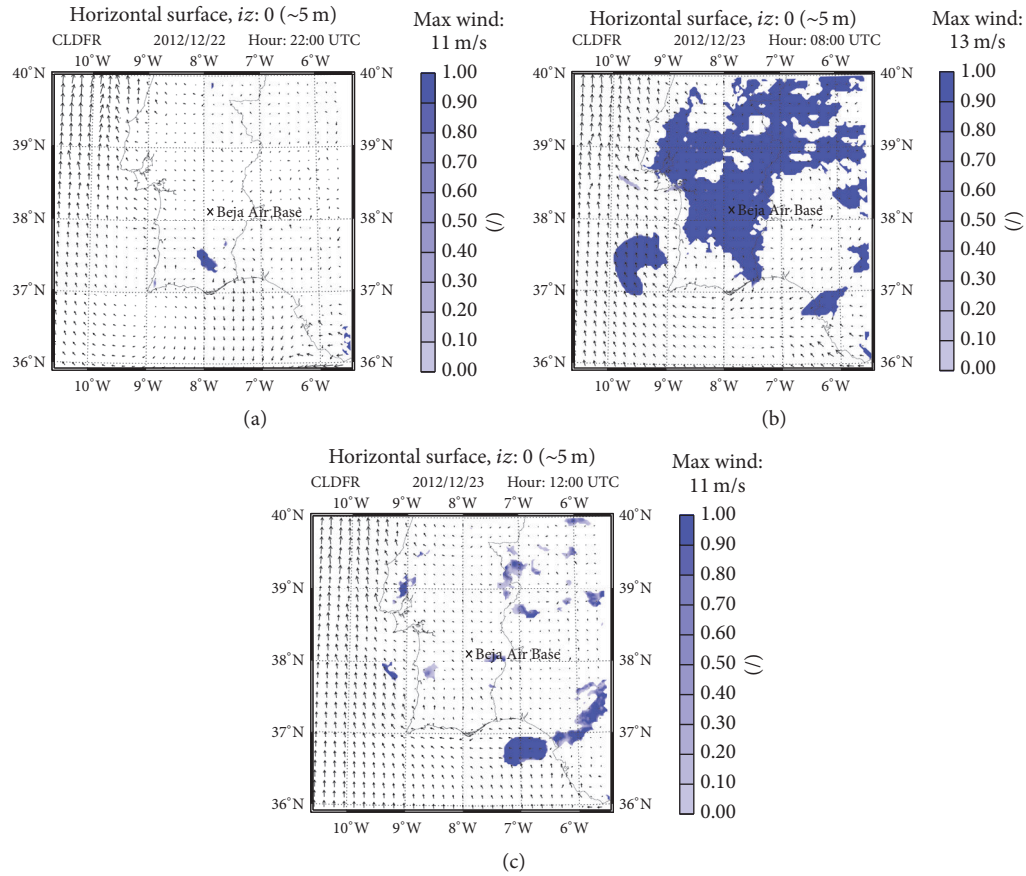

Figure 9: Simulation of cloud fraction (fog, blue scale) and flow (vectors) at 5 m height from the surface, at 22:00, 08:00, and 12:00 UTC in D1 domain.

In this case, the simulated fog occurs too early in southern regions (see Figure 9(a)). In late dawn, fog occupies almost the entire region of Alentejo, especially in the interior, except over the highs of São Mamede, Ossa, and Monfurado (see Figure 9(b)). With increased solar radiation after sunrise, the fog begins to dissipate, persisting in a few places around 12:00 UTC (see Figure 9(c)). Figure 9 also shows the horizontal flow at the lowest level of the model, showing that the flow from south-southeast regulates how the fog acquires its shape, being especially installed in the windward sides of the elevations. This is evident, especially in the initial phase of the formation of fog.

Figure 10 shows the number of hours with fog simulated in both domains. In the domain (D1) it may be seen that near the Cercal Hill and in the Guadiana Basin south of the Mendro Hill there were several areas where the fog rested for more than 12 hours. In the inner domain (D2) it is visible, with better details, the increase of fog in southern areas of Alqueva reservoir, with several locations with more than 14 hours of fog. In Beja Air Base the fog lasted about 9 hours.

In Beja Air Base, according to the Meso-NH simulation the fog formation occurs about 02:00 UTC (see Figure 11). The fog quickly acquires a thickness of 100 m, so that the base of the thermal inversion is high and reaches about 200 m at 11:00 UTC. After that, the dissipation of fog begins. After the dissipation of fog, low clouds do not appear to persist.

4.2.2. Summer Case (18/07/2013). There was a progressive cloudiness invasion formed over the Atlantic Ocean immediately following the sunset of July 17th as shown in Figure 12. There is a widespread occupation by low clouds (potentially fog), covering almost the entire region throughout the morning. Only at about 12:00 UTC, the entire region was free of cloud cover (see Figure 12(a)(iii)). The simulated cloud top height field (Figure 12(b)) shows the appearance of low cloudiness along the coast as early as 21:00 UTC and the occupation of much of the region, with advancing night and morning. After sunrise this cloudiness starts to dissipate, so that at 12:00 UTC the entire region is cloudless. In this case, the simulation of cloudiness compares quite well with satellite observations, even though the model underestimates the cloudiness in particular over the northern regions of Alentejo.

The simulations indicate the appearance of relatively small areas of fog in Alentejo around 02:00 UTC (see Figure 13(a)). With its progression after sunrise, fog occupies more inner areas, however not so generalized as suggested by the cloud cover simulations (see Figure 13(b)). After sunrise, fog dissipates quickly, covering at 08:00 UTC only a small

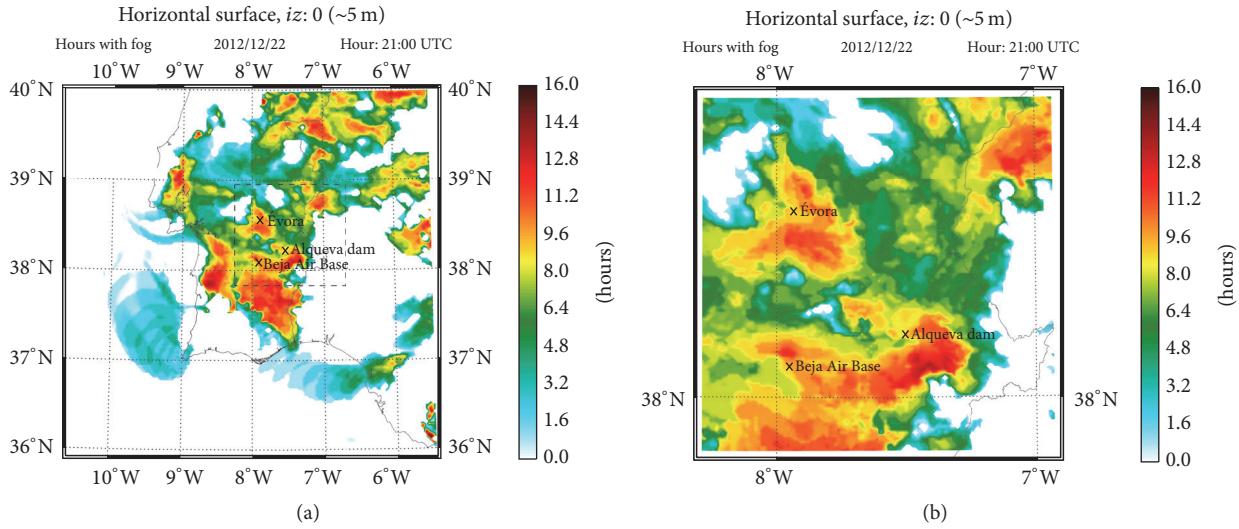

Figure 10: Simulation of the "number of hours with fog" in both domains, between 21:00 and 15:00 UTC.

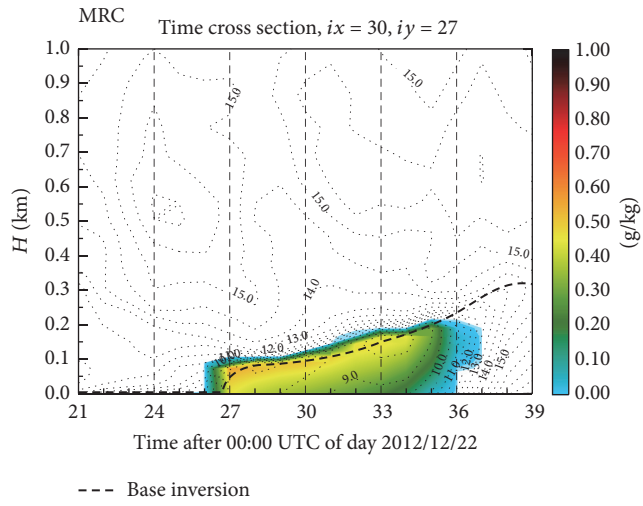

Figure 11: Temporal evolution (from 22/12/2012 at 21 UTC to 23/12/2012 at 15 UTC) of simulated air temperature (lines in °C) and liquid water mixing ratio (color scale in g/kg) over Beja Air Base nearest grid point of D2 domain. Fog > 0.05 g/kg liquid water mixing ratio (Introduction chapter).

area near the mouth of the Sado River (see Figure 13(c)). According to the model, at 09:00 UTC the whole region was free of fog. Figure 13 also shows the horizontal wind field at the lowest level of the model, which indicates that the predominant westerly flow drives the fog pattern that settles more in the windward sides of the elevations.

Figure 14 shows the number of hours with simulated fog in both domains. In the D1 domain it can be seen that, near Grândola Hill, fog remained in some places more than 8 hours, but in the rest of the domain the residence time of fog did not exceed three hours. In the D2 domain, with better details, an enhancement of fog in an area southwest of Beja Airbase can be seen, where fog lasted over 4 hours, as well as along Mendro, Monfurado, and Ossa Hills. According to the model, some places presented about three hours of fog. Once again, it appears that, beyond the effect of advection, the orography is also an important factor in the formation of fog. In Beja Airbase, the fog lasted nearly 3 hours (see Figure 14(b)).

In this case, simulations suggest that fog does not reach the region of the Alqueva reservoir due to orographic blocking, especially by the Mendro and Portel Hills.

According to the simulation, in the Beja Air Base, fog occurred between 03:00 and 07:00 UTC. With the fog development, the thickness of fog increased. After its dissipation, low clouds (stratus) persisted for several hours as seen in Figure 15.

4.3. Influence of Alqueva Reservoir. In order to investigate the influence of the Alqueva reservoir on fog, simulations were performed with (ALQ) and without Alqueva (PRE-ALQ), for

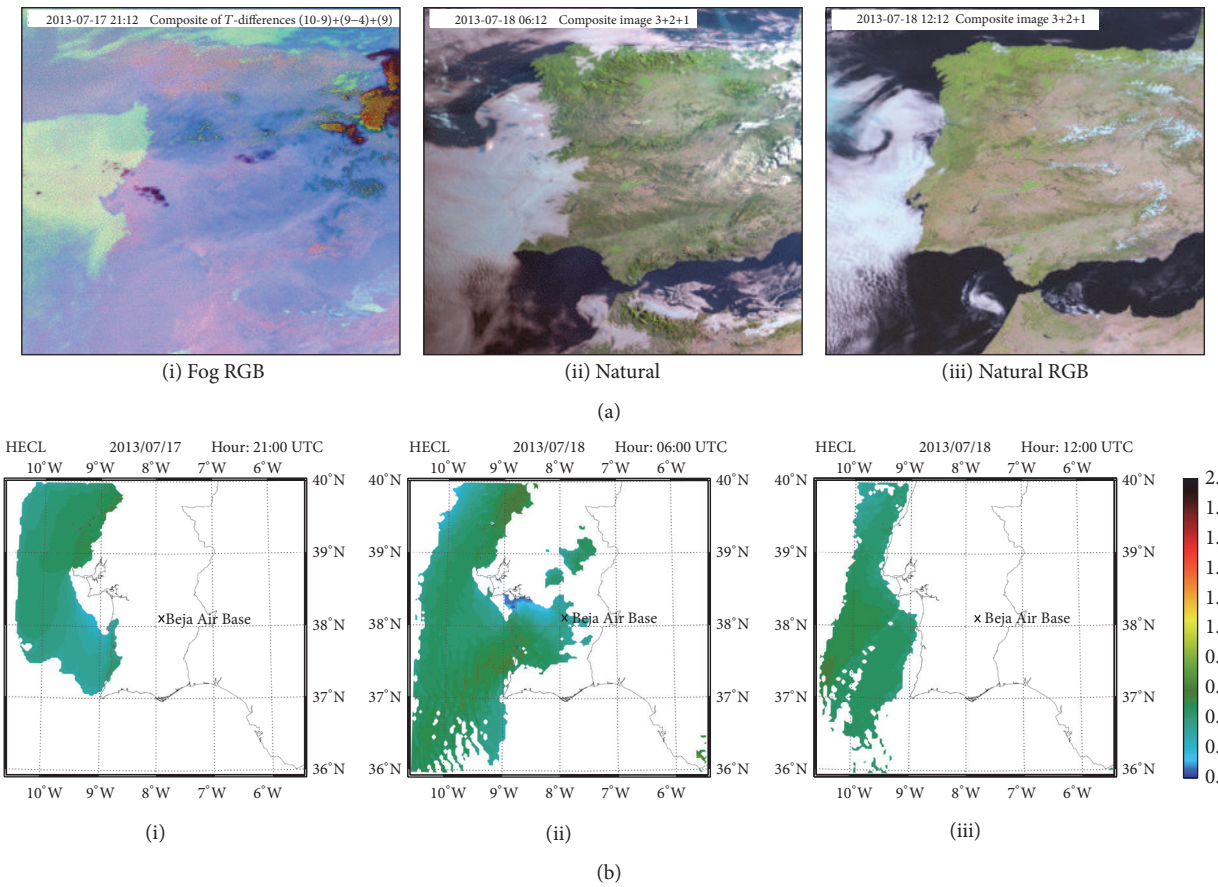

FIGURE 12: Sequence of satellite images in 17/07/2013 at 21:12 UTC and in 18/07/2013 at 06:12 and 12:12 UTC; (b) simulation of explicit cloud top height from the surface in 17/07/2013 at 21:00 UTC and in 18/07/2013 at 06:00 and 12:00 UTC in D1 domain.

the case studies considered in this work. The impact of the water body is assessed by the differences between the results of both simulations.

In Case I, referring to the 08/12/2012, there are no significant differences in fog occupation in the Alentejo region. However, the simulations indicate a negative difference over the Alqueva reservoir, suggesting that the presence of the water body inhibited the formation of fog over it, probably due to the higher water surface temperature. This is evident from the difference between the simulated number of hours with and without Alqueva (see Figure 16(a)). As shown, over the reservoir, there is a negative difference of 2 to 3 hours, reaching, locally, differences greater than 4 hours.

The results of Case II simulations also indicate that there are no major differences on fog distribution at the regional scale (not shown) and also show negative differences over and in the vicinity of the Alqueva reservoir, suggesting, as in Case I, that the presence of the lake inhibited the fog formation over the lake, probably due to higher temperatures of the water surface. This can be noticed especially in the northern part of the reservoir (see Figure 16(b)).

On the contrary, in Case III (05/02/2013) the results show that over the reservoir, particularly in the south, there are more places, with positive difference of 1 to 2 hours, suggesting that in this case the reservoir had a positive impact. The model shows also positive differences southwest (downstream) of the dam, suggesting that water vapour originated by the reservoir may have been advected to these zones and thus have increased the persistence of the phenomenon. These positive differences may be related to the fact that the flow was less intense when compared to the two previous cases, which favours water vapour availability for condensation (see Figure 16(c)).

For Cases IV and V (16 and 18/07/2013), summer cases, there were no significant differences between simulations with and without Alqueva, due to the fact that they correspond to events of advection fog, originated in the Atlantic Coast, and that the have not reached Alqueva reservoir.

5. Conclusion

A description of fog occurrence near the Alqueva dam was made, based on information from Beja Air Base meteorological station. It can be concluded that fogs in Beja Air Base occur more frequently in winter season (December, January, and February) and mostly between 04 and 10 UTC, with more

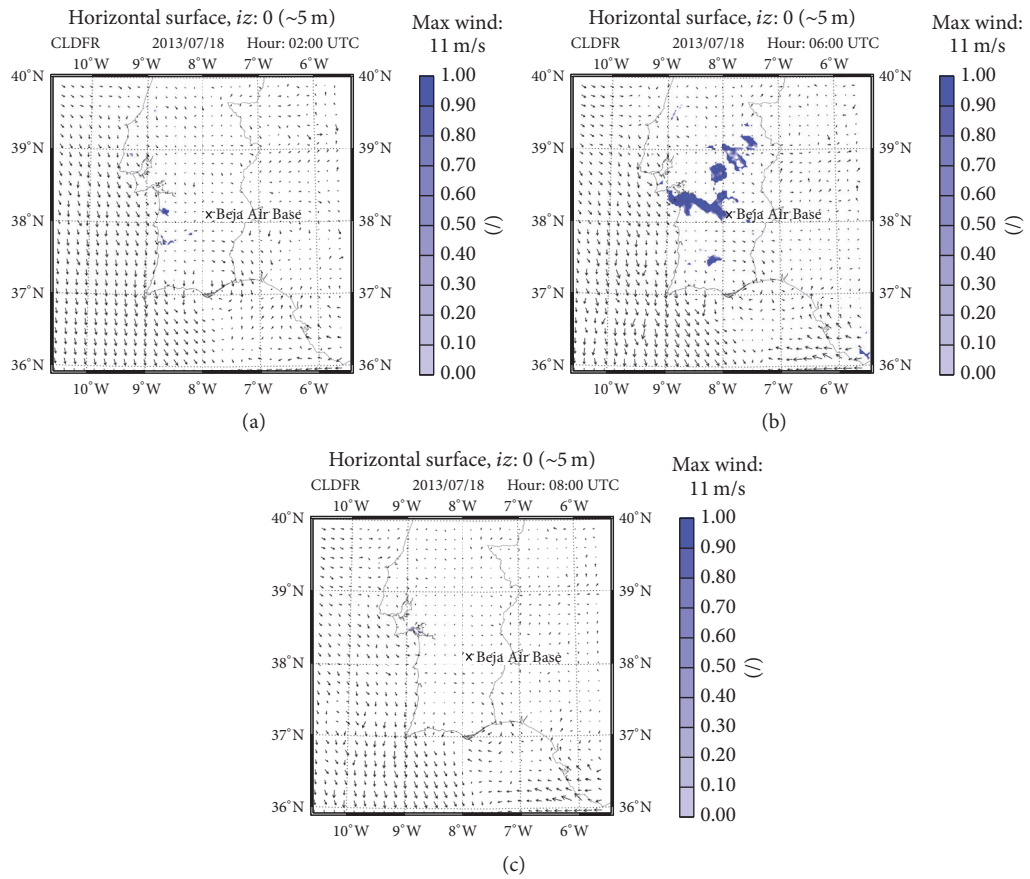

FIGURE 13: Simulation of cloud fraction (fog, blue scale) and flow (vectors) at 5 m height from the surface at 02:00, 06:00, and 08:00 UTC in D1 domain.

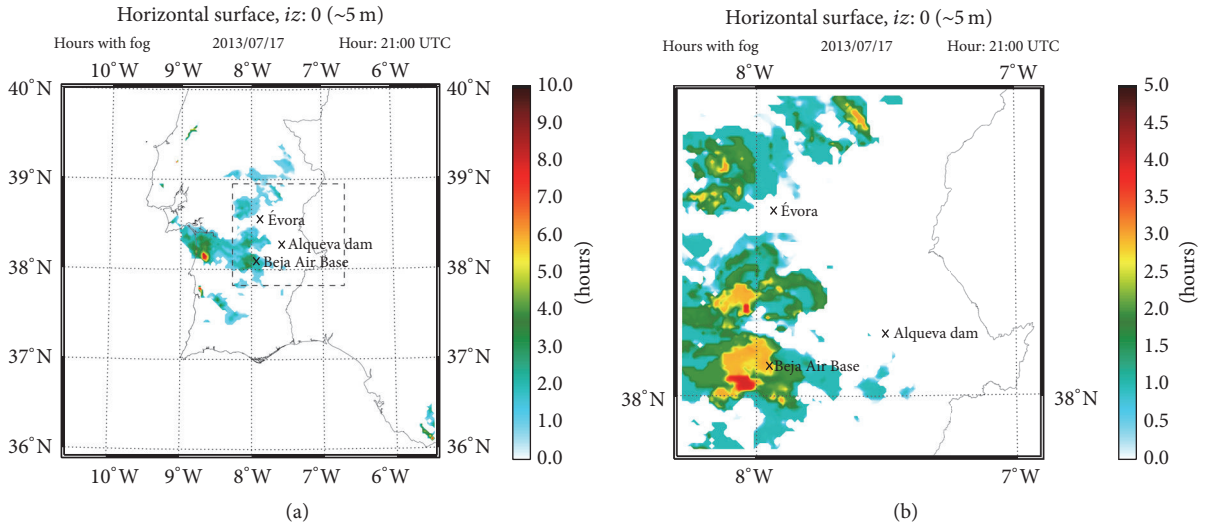

FIGURE 14: Simulation of the "number of hours with fog" in the two domains, between 21:00 and 12:00 UTC.

than 20 days with fog at these times and the maximum value at 07-08 UTC (more than 40 days per year of fog). It can also be stated that the fog events, which occur during the winter months, are longer compared to those occurring in the rest of the year.

To run the Meso-NH over the region it was necessary to update the ECOCLIMAP database, introducing the Alqueva and other smaller reservoirs, not present at the ECOCLIMAP v2.0. In the improved ECOCLIMAP database it was assumed that the reservoirs are at their full storage level.

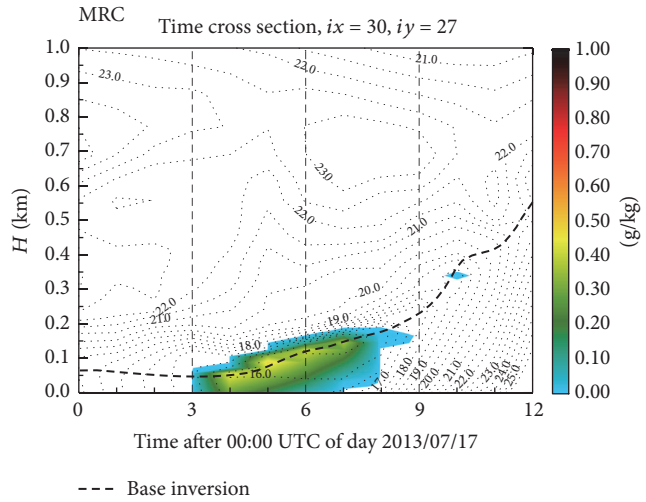

FIGURE 15: Temporal evolution (18/07/2013 from 00 to 12 UTC) of simulated air temperature (lines in °C) and liquid water mixing ratio (color scale in g/kg) over the Beja Air Base nearest grid point of D2 domain. Fog > 0.05 g/kg liquid water mixing ratio (Introduction chapter).

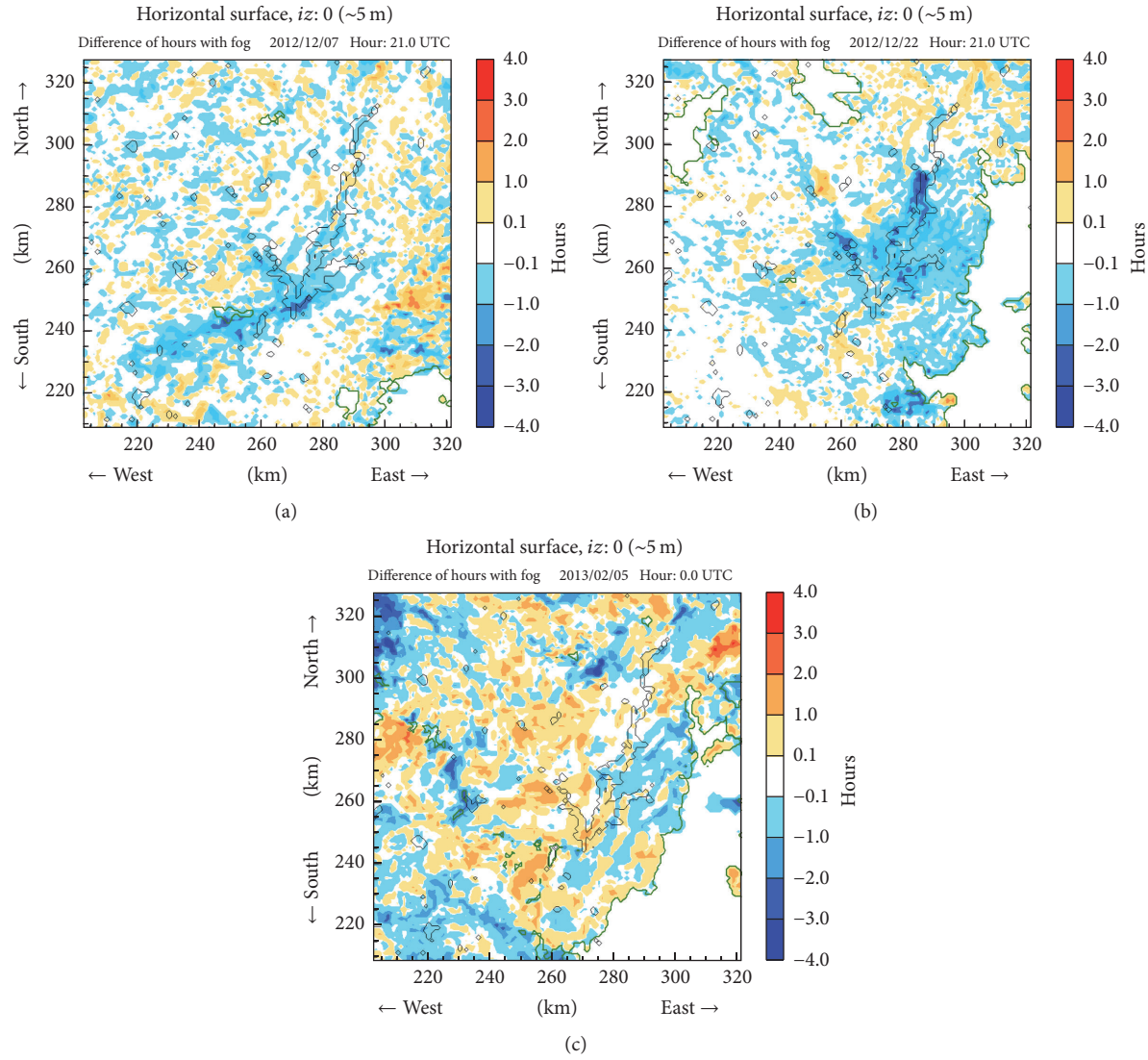

FIGURE 16: Difference between the "number of hours with fog" of simulations, with and without Alqueva from 21:00 to 15:00 UTC in D2 domain. Fog occupation boundaries with Alqueva (green line), color scale (Alqueva, original). (a) 2012/12/08, (b) 2012/12/23, and (c) 2013/02/05.

The numerical fog simulations done in this work show different results depending on the different influences exerted by several factors in the region. In winter cases, the fog occurred mainly due to night-time radiative cooling. In summer cases, fog is in general due to advection from ocean or caused by air elevation and adiabatic cooling. The examination of the simulations based on the ECMWF model analyses showed that there was a good similarity between the cloudiness patterns obtained and the corresponding satellite observations.

The horizontal flow near the surface determines how the fog progresses along the simulations, showing that the orographic influence is present in the cases shown, confirming the enormous influence of Mendro and Portel Mountains that block the moist air from the Atlantic Ocean, preventing the fog to reach innermost areas.

As a first observational evidence of the influence produced by the Alqueva reservoir, the distribution of the average monthly number of days with fog through the year for two periods 1994–2002 (before Alqueva) and 2003–2012 (after Alqueva) at Beja aerodrome was compared, showing a slight increase in the average number of days with fog during the winter (DJF), of about 4 days per winter after 2003. The numerical simulations for the case studies also show that only in winter cases the impact was visible, verifying a diversity of influences, confirming that, depending on the direction and wind speed, different effects may become dominant, causing different fog placement patterns. The fog duration over the reservoir had a shorter duration in the simulations with Alqueva during December, suggesting that its existence inhibited the fog formation and preservation. In the situation of February there has been a slight increase in the fog duration over the Alqueva reservoir, possibly due to the weak flow and also because of lower air temperatures. In the summer cases there were no appreciable differences between the simulations with and without Alqueva. The Meso-NH represented well the selected fog events, verifying a good approximation between the observed ones and their modeling for the five selected events. However, it was found that low clouds were slightly overestimated in winter cases and underestimated after the dissipation of fog in summer cases.

Based on this study, it can be concluded that the Alqueva reservoir may have a direct impact on fog formation in the lake region and its vicinity. Depending on the conditions, their influence can be both positive and negative, in the covered area and its duration. It is important to mention that, with the construction of the Alqueva dam, there was also a regional development that changed the land. It will be necessary to review all ECOCLIMAP database for the region, specifically water surfaces and vegetation cover, to improve the numerical modeling, where the soil-atmosphere interactions are fundamental.

The Meso-NH has proved to be extremely important, because it allowed for describing the selected events in a satisfactory manner, enabling the identification of surface coverage and orographic effects in the analysis and prediction of fog formation and its evolution in Alentejo region.

Competing Interests

The authors declare that there is no conflict of interests regarding the publication of this paper. The authors confirm that the received financial support mentioned in the "Acknowledgments" does not lead to any conflict of interests regarding the publication of this paper.

Acknowledgments

The authors would like to acknowledge the Beja Air Base of Portuguese Air Force, EDIA, and EUMETSAT, which are responsible for the several data used in this research. MODIS data used in this work were acquired as part of the NASA's Earth-Sun System Division and archived and distributed by the MODIS Adaptive Processing System (MODAPS) (https://ladsweb.nascom.nasa.gov). The work received financial support from the FCT through Project EXPL/GEO-MET/1422/2013 cofunded by FEDER (ref. COMPETE: FCOMP-01-0124-FEDER-041840) and from the European Union through the European Regional Development Fund, included in the COMPETE 2020 (Operational Program Competitiveness and Internationalization), through the ICT Project (UID/GEO/04683/2013) with the reference POCI-01-0145-FEDER-007690, and through the ALOP project (ALT20-03-0145-FEDER-000004).

References

[1] I. Gultepe, R. Tardif, S. C. Michaelides et al., "Fog research: a review of past achievements and future perspectives," *Pure and Applied Geophysics*, vol. 164, no. 6-7, pp. 1121–1159, 2007.

[2] W. T. Roach, "Back to basics: fog: part 1—definitions and basic physics," *Weather*, vol. 49, no. 12, pp. 411–415, 1994.

[3] WMO, *International Cloud Atlas, Volume I, Manual on the Observation of Clouds and Other Meteors*, WMO-no. 407, World Meteorological Organization, Geneva, Switzerland, 1975.

[4] W. Cotton and R. Anthes, *Storm and Cloud Dynamics*, Academic Press, San Diego, Calif, USA, 1989.

[5] P. J. Croft, R. L. Pfost, J. M. Medlin, and G. A. Johnson, "Fog forecasting for the southern region: a conceptual model approach," *Weather and Forecasting*, vol. 12, no. 3, pp. 545–556, 1997.

[6] T. Bergot, M. Haeffelin, L. Musson-Genon et al., "Paris-Fog: des chercheurs dans le brouillard," *La Météorologie*, vol. 62, pp. 1–10, 2008.

[7] J. Teixeira and P. M. A. Miranda, "Fog prediction at Lisbon airport using a one-dimensional boundary layer model," *Meteorological Applications*, vol. 8, no. 4, pp. 497–505, 2001.

[8] M. Müller, *Numerical simulation of fog and radiation in complex terrain Results from COST-722 / 1-DEFOP [Ph.D. thesis]*, University of Basel, Basel, Switzerland, 2006.

[9] R. Tardif, "The impact of vertical resolution in the explicit numerical forecasting of radiation fog: a case study," *Pure and Applied Geophysics*, vol. 164, no. 6-7, pp. 1221–1240, 2007.

[10] T. Bergot, "Quality assessment of the Cobel-Isba numerical forecast system of fog and low clouds," *Pure and Applied Geophysics*, vol. 164, no. 6-7, pp. 1265–1282, 2007.

[11] C. Ivaldi, D. Clark, and D. Reynolds, "Upgrade and technology transfer of the San Francisco Marine Stratus Forecast System to

the National Weather Service," in *Proceedings of the 12th Conference on Aviation Range and Aerospace Meteorology*, P1.16, American Meteorological Society, Atlanta, Ga, USA, January 2006.

[12] M. Haeffelin, T. Bergot, T. Elias et al., "PARISFOG: shedding new light on fog physical processes," *Bulletin of the American Meteorological Society*, vol. 91, no. 6, pp. 767–783, 2010.

[13] J. P. Lafore, J. Stein, N. Asencio et al., "The Meso-NH Atmospheric Simulation System—part I: adiabatic formulation and control simulations," *Annales Geophysicae*, vol. 16, no. 1, pp. 90–109, 1998.

[14] J. Cuxart and M. A. Jimenez, "Deep radiation fog in a wide closed valley: study by numerical modeling and remote sensing," *Pure and Applied Geophysics*, vol. 169, pp. 911–926, 2012.

[15] D. Bari, T. Bergot, and M. El Khlifi, "Numerical study of a coastal fog event over Casablanca, Morocco," *Quarterly Journal of the Royal Meteorological Society*, vol. 141, no. 690, pp. 1894–1905, 2015.

[16] T. Bergot, J. Escobar, and V. Masson, "Effect of small-scale surface heterogeneities and buildings on radiation fog: large-eddy simulation study at Paris-Charles de Gaulle airport," *Quarterly Journal of the Royal Meteorological Society*, vol. 141, no. 686, pp. 285–298, 2015.

[17] R. Salgado, *Interaccão solo—atmosfera em clima semi-árido [Ph.D. thesis]*, Universidade de Évora, 2006.

[18] M. J. Costa, R. Salgado, D. Santos et al., "Modelling of orographic precipitation over Iberia: a springtime case study," *Advances in Geosciences*, vol. 25, pp. 103–110, 2010.

[19] R. Salgado, P. M. A. Miranda, P. Lacarrère, and J. Noilhan, "Boundary layer development and summer circulation in Southern Portugal," *Tethys*, no. 12, pp. 33–44, 2015.

[20] J. Noilhan and S. Planton, "A simple parameterization of land surface processes for meteorological models," *Monthly Weather Review*, vol. 117, no. 3, pp. 536–549, 1989.

[21] V. Masson, "A physically-based scheme for the urban energy budget in atmospheric models," *Boundary-Layer Meteorology*, vol. 94, no. 3, pp. 357–397, 2000.

[22] S. Belamari and A. Pirani, "Validation of the optimal heat and momentum fluxes using the ORCA2-LIM global ocean-ice model," Marine EnviRonment and Security for the European Area—Integrated Project (MERSEA IP), Deliverable D4.1.3, 2007.

[23] D. Mironov, E. Heise, E. Kourzeneva, B. Ritter, N. Schneider, and A. Terzhevik, "Implementation of the lake parameterization scheme Flake into the numerical weather prediction model COSMO," *Boreal Environment Research*, vol. 15, pp. 218–230, 2010.

[24] J. Morcrette, "Description of the radiation scheme in the ECMWF model," ECMWF Tech. Memo 165, 1989.

[25] J. Cuxart, P. Bougeault, and J.-L. Redelsperger, "A turbulence scheme allowing for mesoscale and large-eddy simulations," *Quarterly Journal of the Royal Meteorological Society*, vol. 126, no. 562, pp. 1–30, 2000.

[26] J. Pinty and P. Jabouille, "A mixed-phase cloud parameterization for use in mesoscale non-hydrostatic model: simulations of a squall line and of orographic precipitations," in *Proceedings of the Conference on Cloud Physics*, pp. 217–220, American Meteorological Society, Everett, Wash, USA, 1998.

[27] B. A. Kunkel, "Parameterization of droplet terminal velocity and extinction coefficient in fog models," *Journal of Applied Meteorology*, vol. 23, pp. 34–41, 1984.

[28] EDIA, 2013, http://www.edia.pt/en/.

[29] M. Bader, G. S. Forbes, J. R. Grant, R. B. E. Lilley, and A. J. Waters, *Images in Weather Forecasting*, Cambridge University Press, Cambridge, UK, 1995.

[30] J. Cermak and J. Bendix, "A novel approach to fog/low stratus detection using Meteosat 8 data," *Atmospheric Research*, vol. 87, no. 3-4, pp. 279–292, 2008.

[31] J. Stein, E. Richard, J.-P. Lafore, J.-P. Pinty, N. Asencio, and S. Cosma, "High-resolution non-hydrostatic simulations of flash-flood episodes with grid-nesting and ice-phase parameterization," *Meteorology and Atmospheric Physics*, vol. 72, no. 2–4, pp. 203–221, 2000.

[32] V. Masson, P. Le Moigne, E. Martin et al., "The SURFEXv7.2 land and ocean surface platform for coupled or offline simulation of earth surface variables and fluxes," *Geoscientific Model Development*, vol. 6, no. 4, pp. 929–960, 2013.

[33] R. Salgado and P. Le Moigne, "Coupling of the flake model to the surfex externalized surface model," *Boreal Environment Research*, vol. 15, no. 2, pp. 231–244, 2010.

[34] V. Masson, J.-L. Champeaux, F. Chauvin, C. Meriguet, and R. Lacaze, "A global database of land surface parameters at 1-km resolution in meteorological and climate models," *Journal of Climate*, vol. 16, no. 9, pp. 1261–1282, 2003.

[35] USGS, 1997, https://lta.cr.usgs.gov/GTOPO30.

[36] K. H. Schlünzen, K. Conrady, and C. Purr, "Typical performances of mesoscale meteorology models," in *Air Pollution Modeling and Its Application XXIV*, D. G. Steyn and N. Chaumerliac, Eds., Springer Proceedings in Complexity, pp. 447–457, Springer, Berlin, Germany, 2016.

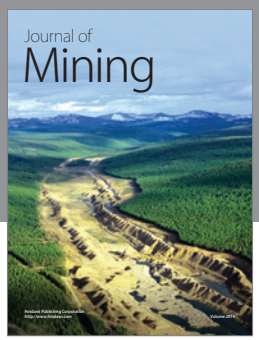

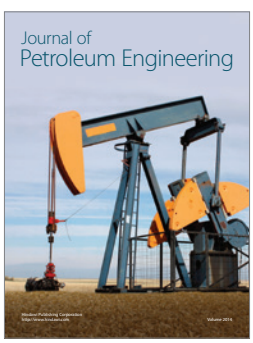

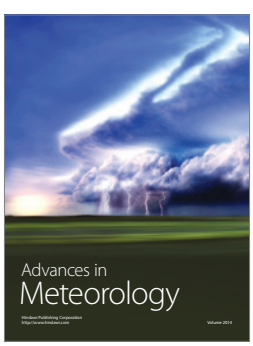

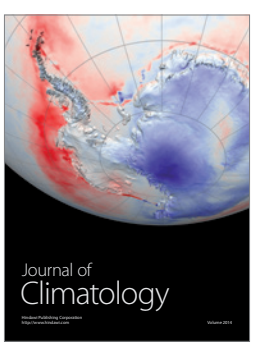

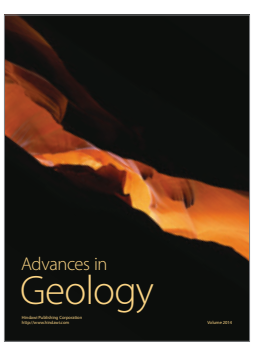

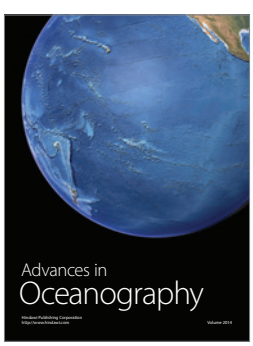

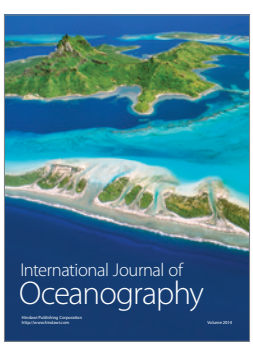

Hindawi
Submit your manuscripts at
https://www.hindawi.com

Atmospheric Research 198 (2017) 151–162

Contents lists available at ScienceDirect

Atmospheric Research

journal homepage: www.elsevier.com/locate/atmosres

An Iberian climatology of solar radiation obtained from WRF regional climate simulations for 1950–2010 period

João Perdigão[a,*], Rui Salgado[a], Clarisse Magarreiro[b,c], Pedro M.M. Soares[b,c], Maria João Costa[a], Hari Prasad Dasari[d]

[a] Departamento de Física, Instituto de Ciências da Terra, Instituto de Investigação e Formação Avançada, Universidade de Évora, Évora, Portugal
[b] Instituto Dom Luiz, Faculdade de Ciências da Universidade de Lisboa, Campo Grande, 1700-016 Lisboa, Portugal
[c] Departamento de Engenharia Geográfica, Geofísica e Energia, Faculdade de Ciências da Universidade de Lisboa, Campo Grande, 1700-016 Lisboa, Portugal
[d] Physical Sciences and Engineering Division, King Abdullah University of Science and Technology, Thuwal, Saudi Arabia

ARTICLE INFO

Keywords:
WRF model
Downscaling climatology
Downward solar radiation
Cloud fractions
Iberian peninsula

ABSTRACT

The mesoscale Weather Research and Forecasting (WRF) Model is used over the Iberian Peninsula to generate 60 years (1950–2010) of climate data, at 5 km resolution, in order to evaluate and characterize the incident shortwave downward radiation at the surface (SW↓), in present climate.

The simulated values of SW↓ in the period 2000–2009 were compared with data measured in Spanish and Portuguese meteorological stations before and a statistical BIAS correction was applied using data from Clouds and the Earth's Radiant Energy System (CERES), on board four different satellites. The spatial and temporal comparison between WRF results and observations show a good agreement for the analyzed period, although the model overestimates observations. This overestimation has a mean normalized bias of about 7% after BIAS correction (or 17% for original WRF output). Additionally, the present simulation was confronted against another previously validated WRF simulation performed with different resolution and set of parametrizations, showing comparable results. WRF adequately reproduces the observational features of SW↓ with correlation coefficients above 0.8 in annual and seasonal basis.

60 years of simulated SW↓ over the Iberian Peninsula were produced, which showed annual mean values that range from 130 W/m^2, in the northern regions, to a maximum of around 230 W/m^2 in the southeast of the Iberian Peninsula (IP). SW↓ over IP shows a positive gradient from north to south and from west to east, with local effects influenced by topography and distance to the coast.

The analysis of the simulated cloud fraction indicates that clear sky days are found in > 30% of the period at the southern area of IP, particularly in the Algarve (Portugal) and Andalusia (Spain), and this value increases significantly in the summer season for values above 80%.

1. Introduction

Incoming solar radiation is an important variable from meteorological, economic and social perspectives. In the last IPCC report it is stated that "CO_2 emissions from fossil fuel combustion and industrial processes contributed about 78 % of the total greenhouse gas emission increase from 1970 to 2010, with a similar percentage contribution for the period 2000–2010" (IPCC, 2014). To reduce CO_2 emissions it is necessary to decarbonize the electricity generation. Detailed knowledge of the solar resource in the present and in the near future is essential for assessing the viability of projects related to the harnessing of solar energy.

Solar radiation studies carried out in various regions have revealed that, in the past century, the Earth has undergone two opposite periods regarding the variability of solar radiation: Global Dimming (Stanhill and Cohen, 2001), with a reduction in solar radiation at the surface until the mid-1980s and later the global Brightening (Wild et al., 2005), with an increase of global radiation at the surface. Based on observations and ERA-40 reanalysis, Perdigão et al. (2016) confirmed the existence of these two distinct periods in Portugal, known as dimming and brightening, but with an earlier turning year than the one described in the literature, in particular over the south of Portugal. This latter study revealed an increasing trend of surface global radiation located in the south of Portugal, without a pronounced decrease before the 1980s, in the period 1964–1986.

Before reaching the Earth's surface, incoming solar radiation is

* Corresponding author at: Instituto de Ciências da Terra, Universidade de Évora, Colégio Luis António Verney, Rua Romão Ramalho nº 59, 7002-554 Évora
E-mail address: perdi.j@gmail.com (J. Perdigão).

http://dx.doi.org/10.1016/j.atmosres.2017.08.016
Received 29 January 2017; Received in revised form 31 July 2017; Accepted 14 August 2017
Available online 15 August 2017
0169-8095/ © 2017 Elsevier B.V. All rights reserved.

scattered, absorbed and reflected in the atmosphere. Clouds play a major role in spatiotemporal solar radiation variability. Hence, it is common that studies on solar radiation at Earth's surface include also an analysis of cloud cover. Sanchez-Lorenzo et al. (2009) analysed observational cloudiness series for Iberian Peninsula (IP) and found a decreasing trend in the IP between 1960 and mid 2000s. The authors report higher annual values over northern areas 4.5 (oktas) and smaller values in southern areas (3.5 oktas), reaching minimum values in July and August (< 3 oktas). According to the authors, the sunshine duration series show a decrease from 1950 to the mid-1980s that is not associated with total cloud cover. On the other hand, later on, Sanchez-Lorenzo et al. (2013) found, for the 1985–2010 period, a positive trend in the global radiation in line with the sunshine duration trends since the 1980s.

Many commercial systems have been installed in the IP intended for solar energy power generation, particularly in the southern regions. In the study of Ridao et al. (2007), present and future of renewable solar energy was analyzed for Andalusia, with an average solar radiation energy of 4.6 ± 0.3kWh/m^{2}day, which qualifies the southern IP as a strategic region in Europe regarding solar energy technology implementation. In the European Union, solar energy presents itself as the main source of renewable energy investment until 2030 (APREN, 2014). Spain is the fifth country of the European Union in the production of photovoltaic energy, with > 4GW of installed capacity (IDAE, 2016). In Portugal, the currently installed solar power capacity is > 450MW (almost 3% of the energy produced) and it is expected to double that capacity by 2030. Alentejo and Algarve are the Portuguese regions with the highest installed solar capacity (APREN, 2014).

Santabàrbara et al. (1996) built annual and seasonal maps of solar radiation in and around Catalonia province (Spain), for the period 1964–1993, from daily in situ global solar irradiation datasets and found maximum values over the inner part of Catalonia and at the south coast. According to Jerez et al. (2013), IP shows a strong potential in terms of complementarity between solar and wind power. The authors combined simulated data obtained from the MM5 numerical model with a new developed algorithm to identify optimum spatial distributions for solar and wind power plants in order to guarantee a certain energy generation provided by renewable resources. Results show Valencia, Murcia and Andalusia provinces (Spain), as well as Algarve (Portugal), as optimal locations for solar power plants. Šúri et al. (2007) used a solar radiation model (Šúri and Hofierka, 2004) and showed that Portugal and the Mediterranean regions have the greatest potential for solar electricity production with maximum values in summer months. Also, Ruiz-Arias et al. (2012) showed similar conclusions. The authors evaluated the potential of renewable energies in electricity production for the province of Jaén (southern of Spain) and proposed a scenario where PV could produce up to 21% of the electricity demand in that region.

Due to the increasing demand of solar energy systems, an accurate knowledge of the solar resource plays a key role from an economic perspective. There are several methodologies and models to obtain solar irradiation maps and to predict solar radiation. For instance, Ehnberg and Bollen (2005) proposed a model based on cloud observations. Alsamamra et al. (2009) used a statistical methodology for mapping global solar radiation at the surface. Martín et al. (2010), applied several statistical methods based on observational time series to predict half daily values of global solar irradiances. Martín et al. (2010), proposed an empirical model to estimate the solar energy as a function of other climatic variables. Ruiz-Arias et al. (2015) used an interpolation methodology to adjust global horizontal and direct normal irradiances obtained with WRF model with observational ground-based station data.

The application of Regional climate models (RCMs) in the evaluation of solar radiation features (trends, variability and climatology) in the past, present and future may overcome the problem of gaps in observational time series, the poor spatial coverage of ground-based stations and time series size. This approach allows for a detailed spatial characterization of any regions in order to select the one with best conditions to receive solar power plants, improving in that way the risk analysis of their implementations for political and economic decision-makers.

RCMs are used for downscaling of global climate simulations and have been extensively used in various regions (e.g. Feser et al., 2011; Soares et al., 2012). Reviews on RCMs can be seen in Dudhia (2014), Rummukainen (2010), Laprise (2008) or Giorgi and Mearns (1999). The mesoscale Weather Research and Forecasting (WRF) model (Skamarock et al., 2008) has been increasingly used as RCM. It is an open source tool, with considerable flexibility given the variety of parameterizations available, which makes it a very versatile tool for research in atmospheric physics. This model was used and evaluated over IP for different meteorological variables and by several authors such as Ruiz-Arias et al. (2015), Dasari et al. (2014), Rios-Entenza et al. (2014), Soares et al. (2014), Cardoso et al. (2013), Soares et al. (2012), Mercader et al. (2010), among others. For instance, Santos-Alamillos et al. (2012) proposed and evaluated a method to analyze the spatio-temporal balance between solar and wind resources over the southern part of IP, using the WRF model with a spatial resolution of 9 km. The results show the existence of complementarity between the solar and wind energy, but with a marked seasonality in strength and spatial coverage.

Lara-Fanego et al. (2012a) evaluated the reliability of WRF to predict global and direct irradiance over Andalusia (southern of Spain) and found that the model presents substantial quality. Nevertheless, their analysis showed that WRF tends to overestimate both irradiances with a relative seasonal bias of about 10% for global and twice higher for direct radiation.

The common practice in dynamical regional climate downscaling is to perform long continuous integrations with RCMs, starting from a single set of initial conditions, for a long period without re-initialization time slices. (e.g. Soares et al., 2012; Marteau et al., 2015). This technique allows the model to develop internal variability but it is computationally expensive. In this work, we used a WRF simulation of six decades with annual re-initializations to avoid such computation costs (Dasari et al., 2014). This approach allows to perform model simulations simultaneously, resulting in a gain of execution time of the complete numerical experiment. This procedure is in agreement with other authors, namely Raju et al. (2015) and Xue et al. (2014). Lo et al. (2008) discuss advantages and disadvantages of this technique. According to these authors, the re-initialization approach is widely accepted in weather forecasting to mitigate the problems of systematic error growth in long integrations but it is rarely used in regional climate simulations. This happens because: (i) it is not easily portable; (ii) long spin-up time of RCMs constrains the re-initialization process and (iii) possible occurrence of discontinuity points between consecutive simulations. However, Lo et al. (2008) compared long-term continuous integration with short-term reinitialized simulations showing that the re-initialization runs outperform the continuous simulation runs.

Many authors pointed out the difficulties RCMs have in the representation of the large-scale features as they are forced at their boundaries (e.g. Jones et al., 1995; Yhang and Hong, 2011). Waldron et al. (1996) and Von Storch et al., 2000firstly presented the nudging methodology. In the subsequent years nudging techniques were further developed and employed in many studies, but its use is not consensual (Alexandru et al., 2008; Miguez-Macho et al., 2004; Hong and Chang, 2012; Hong and Kanamitsu, 2014), due to disagreements regarding the advantage of reducing freedom from regional model's large scales and other potentially negative lateral consequences.

An important issue in NWP analysis is the evaluation of the model results. Usually, this evaluation is performed through the comparison between observational ground-based data with the nearest grid point of the model outputs. BIAS correction (eg, Ruiz-Arias et al., 2015; Acharya et al., 2013; Haddeland et al., 2012; Piani et al., 2010), in a post-

processing stage, is often performed. Ehret et al. (2012) present the state-of-the art of bias correction methods as well the assumptions and implications.

The main objectives of this paper are: firstly, to evaluate the quality of the 5 km resolution WRF simulations with annual re-initializations, to predict incident shortwave solar radiation at the surface (SW↓) through the comparison with observations and other WRF simulations (continuous and previously validated); secondly, to characterize the solar radiation at the surface with BIAS correction and the cloud fraction, in the 1950–2010 period over the IP, in order to assess the regions with major solar resource potential. The paper is structured as follows: section two describes the methodology used in this study, as well as the data, model setup and study area. The performance of the simulations and BIAS correction methodology is discussed in Section 3. A detailed climatology of SW↓ and cloud cover over IP is presented and discussed in Section 4. Finally, conclusions are presented in Section 5.

2. Datasets and methods

2.1. Model and numerical experiments

WRF mesoscale model V3.3.1. (Skamarock et al., 2008) was configured with two domains, using two-way nesting, with horizontal resolutions of 75 km and 25 km, and 30 vertical pressure levels. From the 25 km resolution simulation output, a dynamical downscaling to a 5 km resolution domain was carried out (Fig. 1), using one way nesting, with hourly output. The results of the 5 km resolution simulation (WRF5 hereinafter) are used in the characterization of the IP climatology.

In order to reduce the time required to simulate 60 years, the procedure adopted in this work consists in splitting the climate runs into several yearly simulations that are performed simultaneously. WRF5 was integrated continuously for 13 months starting from 00 UTC 1 May of each year for six decades (1950–2010). The first month of each simulation was used as model spin up time and was neglected in the analysis. The NCEP/NCAR (National Centers for Environmental Prediction/National Center for Atmospheric Research) reanalysis data at 2.5° latitude/longitude resolution (Kalnay et al., 1996), updated every 6 h, was used as initial and forcing boundary condition. The model setup for these simulations are described in detail in Dasari et al. (2014), where the results were validated for extreme events of heat and cold waves and showing a good agreement with E-OBS V7.0 dataset (Haylock et al., 2008).

Since the WRF5 simulation followed a less common simulation strategy based on multiple one year time-slices, its performance is also investigated through comparison with results obtained from a continuously integrated WRF simulation (WRF9). WRF9 simulation was previously validated for temperature and precipitation over Portugal (Soares et al., 2012), precipitation over Iberia (Cardoso et al., 2013) and offshore wind (Soares et al., 2014), with the results showing a good agreement with observations. In WRF9, the model simulation ran continuously from 00 UTC 1 January 1989 to the end of 2012 where the first month is used as model spin up. The WRF9 simulation was performed using two one-way nested grids (27 and 9 km horizontal resolution) and the results from the finer domain are used for comparison. The outermost domain was designed in a way to reduce spurious boundary effects in the inner region and both grids were centered in the Iberian Peninsula. Additionally, grid nudging (Stauffer and Seaman, 1990) was applied to the outermost grid, every 6 h at all levels above the planetary boundary layer. This WRF simulation was forced by ERA-Interim reanalysis (Berrisford et al., 2009). CAM3 was selected to parameterize radiation processes at sub-grid scales for both shortwave and longwave radiation (Collins et al., 2004). This scheme takes into account the interactions of the radiation with clouds and with several aerosol types and trace gases. A detailed description of WRF9 simulations can be found in Soares et al. (2012). Similarities and differences in physical parameterizations, for WRF5 and WRF9, can be seen in Table 1.

Table 1
Configurations of the physical parametrizations used in each model.

Model	NCEP/NCAR ARW WRF	
Acronym	WRF5	WRF9
Resolution	5 km	9 km
Vertical level	30σ	49σ
Microphysics	WSM3 – class simple ice scheme (Hong et al., 2004)	WSM6 – Class single moment (Hong and Lim, 2006)
SW	CAM3	
LW	(Collins et al., 2004)	
PBL	YSU (Hong et al., 2006)	Mellor-Yamada-Janjic (Janjic, 2001)
Convection scheme	Grell-Devenyi ensemble (Grell and Devenyi, 2002)	Betts-Miller-Janjic (Betts, 1986; Betts and Miller, 1986; Janjic, 1990, 1994, 2000)

2.2. Observational data

In order to assess the ability of WRF model to simulate the SW↓, these results were compared with daily observations obtained from 65 stations of IPMA (Portuguese Weather service) and AEMET (Spanish Weather service).

Global solar irradiance was measured using Kipp & Zonen pyranometers, model CM-11, with a spectral sensitivity in the wavelength range 305–2800 nm and with an uncertainty of ± 2% (according to the manufacturer). These instruments are classified, in accordance with International Standard ISO 9060/1990, as secondary standards. This classification was adopted by the World Meteorological Organization (WMO, 2008).

In the Spanish network, all radiometers are calibrated every two years. For more information see Ruiz-Arias et al. (2015) or García et al. (2014). Relatively to IPMA, calibration was performed only at the factory (Kipp & Zonen), and some of the pyranometers in the network

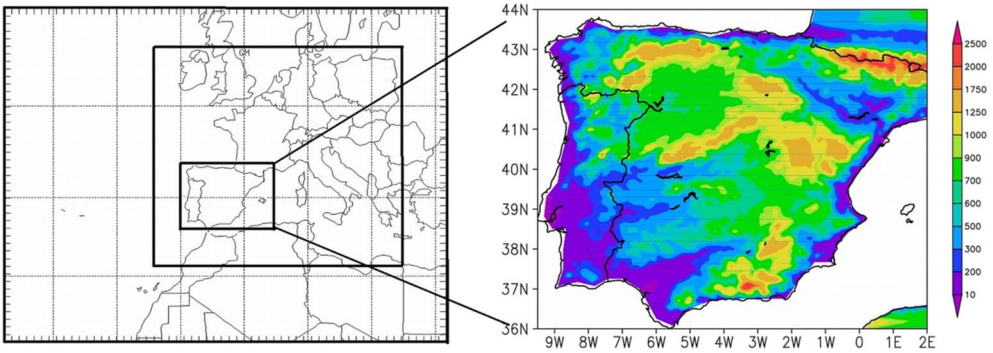

Fig. 1. 75 km, 25 km and 5 km WRF simulation domains (left) and orography (in meters) used by WRF simulations (right).

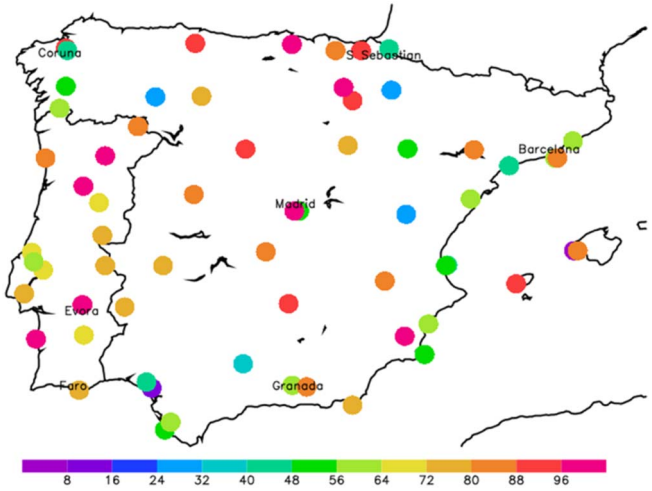

Fig. 2. Geographical location of the 65 observational stations used to evaluate the WRF simulations and length of the time series. The scale indicates the percentage of days available at each station for the period 2000–2009.

were replaced in the period used. The quality control is based mainly on the spatial distribution of records over all observational stations.

The comparison between simulations and observations was made using the nearest neighbour technique, i.e., the closest grid point model values were compared with the correspondent measured ones. The analysis was made for the time periods when observations and simulations were simultaneously available (2000–2009).

Fig. 2 presents the location of the SW↓ groundbased stations and the percentage of days with data within the mentioned period. Since the observations have different time periods, for seasonal analysis, it was decided not to compute monthly means for the stations with < 20 days for each month in the respective observation period, yielding a total of fifteen stations. In turn, a given yearly value is considered valid if at least 2/3 of valid monthly values are available in that year. IP average errors were computed considering all fifteen stations. Winter (DJF), Spring (MAM), Summer (JJA) and Autumn (SON) were defined according to standard procedures in meteorology.

2.3. Cloud fraction estimation

Clouds have a strong impact in the Earth's radiation budget by modifying the shortwave (SW) and longwave (LW) radiative fluxes. From RCMs it is possible to obtain radiation fluxes considering the presence (all sky) or absence (clear sky) of clouds. In this work, clear sky and all-sky shortwave downward radiation are used in order to estimate the cloud fraction simulated by the WRF model. In this sense, a shortwave radiative cloud fraction (SWRCLF) was defined as the ratio of the global solar radiation downward to clear-sky radiation as suggested by Deardorff, 1978; Crawford and Duchon (1999); Choi et al. (2008) and Gubler et al. (2012):

$$SWRCLF = 1 - \frac{SW_{all_{sky}}}{SW_{clear_{sky}}}$$

$SW_{all_{sky}}$ is the all-sky shortwave downward radiation at the surface, and $SW_{clear_{sky}}$ is the clear sky shortwave downward radiation that reaches the Earth's surface. The ratio $SW_{all_{sky}}/SW_{clear_{sky}}$ expresses the reduction of solar radiation mainly due to clouds, with values near one representing clear-sky conditions and near zero a total cloud cover. It should be noticed that the SWRCLF is not exactly a cloud fraction, in particular it never attains the value 1. Despite being different from the cloud cover estimated by the meteorological observers, this definition linked to the light attenuation by clouds, may be used as a proxy to cloud fraction, with the advantage of that it is directly applicable in the field of solar energy, as it is an indicator of the cloud effect on its availability at the surface. In this work, the term *clear sky days* means days without clouds or partially cloudy and refer to *SWRCLF* values lower than or equal to 0.10 (< 1 okta ~0.13).

2.4. Statistical error measures and methods

The results of global radiation for each station were compared with the ground-based measurements in order to assess the quality of the simulations. The mean bias (BIAS), mean absolute error (MAE), mean absolute percentage error (MAPE), root mean square error (RMSE) and correlation coefficient (r) were calculated and are defined as:

$$BIAS = \frac{1}{N}\sum_{i=1}^{N}(m_i - o_i)$$

$$MAE = \frac{1}{N}\sum_{i=1}^{N}|m_i - o_i|$$

$$MAPE = \frac{MAE}{\frac{1}{N}\sum_{i=1}^{N} o_i}$$

$$RMSE = \left[\frac{1}{N}\sum_{i=1}^{N}(m_i - o_i)^2\right]^{\frac{1}{2}}$$

$$r = \frac{\sum_{i=1}^{N}(o_i - \overline{o}) - (m_i - \overline{m})}{[\sum_{i=1}^{N}(o_i - \overline{o})^2 \sum_{i=1}^{N}(m_i - \overline{m})^2]^{\frac{1}{2}}}$$

where N is the number of data and m and o are respectively the model simulation and observed values. We defined normalized bias (NBIAS), and normalized root mean square error (NRMSE) as respectively BIAS and RMSE divided by the SW↓ mean.

2.5. Statistical BIAS correction methodology

In this study a BIAS correction was applied, based on the methodology proposed by Piani et al. (2010) where a detailed description may be found. The implementation described in Hagemann et al. (2011) was followed. The methodology is based on the adjustment of a transfer function that "transforms" the original simulated dataset in a corrected set with the same probability distribution function (PDF) as the observed set. In order to adjust the transfer function, the simulated and observed time series, of the same length and for the same period, are sorted in ascending order and plotted one versus another. The transfer function, with a few set of parameters is then the result of a fitting procedure. In general, different kinds of functions can be tested, but Hagemann et al. (2011) found that in the majority of the cases a two-parameter linear fit is sufficient.

In this study, data from the Clouds and the Earth's Radiant Energy System (CERES) were used as the observations, in order to correct the WRF5 model outputs. The CERES experiment is one of the scientific satellite instruments developed for NASA's Earth Observing System (EOS). The first CERES instrument was launched in December of 1997 aboard NASA's Tropical Rainfall Measurement Mission (TRMM) satellite. CERES instruments are now installed also on three separate satellite missions, including the EOS Terra and Aqua observatories more recently on the Suomi National Polar-orbiting Partnership (S-NPP) observatory. CERES is a set of three co-aligned broadband radiometer detectors whose spectral ranges are 8 to 12 μm for infrared, 0.3 to 5 μm for shortwave and 0.3 to 100 μm for global radiation. CERES products include both solar-reflected and Earth-emitted radiation from the top of the atmosphere to the Earth's surface. The Energy Balanced and Filled (EBAF) surface products (Kato et al., 2013) are used in this study corresponding to the Surface Downwelling Shortwave Radiation and Surface Downwelling Clear-Sky Shortwave Radiation, for the period March 2000 until December 2009. CERES data were obtained from NASA website (ceres.larc.nasa.gov) and are available on a monthly basis with

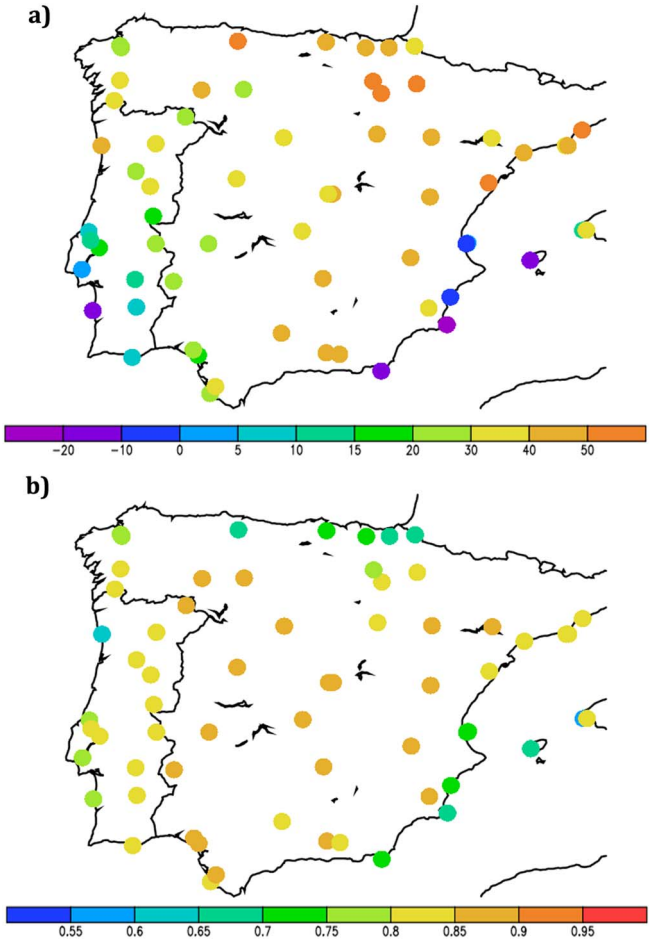

Fig. 3. Daily BIAS (a) and correlation coefficient (b) for the WRF5. BIAS in W/m^2. (In the computation of the correlation, the annual cycle was not suppressed).

a $1^{\circ} \times 1^{\circ}$ horizontal resolution. Detailed information about CERES origins, instrument calibrations, source of errors among other technical features, can be found in Wielicki et al. (1996).

3. Regional climate model simulations: assessment and BIAS correction

3.1. Comparison of daily and seasonal simulated SW↓ against observations

Fig. 3a shows the daily BIAS values of SW↓ and it is found that for the majority of the stations the model overestimates the SW↓ with values of approximately 30W/m^2. The highest BIAS values are mostly located in the north/northeastern part of IP (Asturias, Basque Country and Catalonia) with values between $30 - 50$W/m^2. In the central part of IP, WRF5 overestimates the SW↓ by 30 W/m^2. At southwest and southeast, WRF5 tends to underestimate observations exhibiting values in the range of -20W/m^2 to 0W/m^2.

The mean BIAS in WRF5 is consistent with the one obtained for Spain by Ruiz-Arias et al. (2016). These authors found a mean BIAS of approximately 29W/m^2 over the period 2003–2012, with highest values along the Cantabrian coast and mountains as in the case of present WRF5 analysis.

WRF5 daily simulation shows highest RMSE at the northern regions of IP (not shown here), especially over the Basque country (above 80W/m^2) and smallest values in central and south regions over IP (65W/m^2).

Daily correlation coefficients between ground-based observations and WRF5 (Fig. 3b) show that WRF5 performs better in the central part of IP, with high correlation coefficients, above 0.80. North/northwestern regions of IP present the smallest r values (above 0.6). It is important to notice that the correlation coefficient is insensitive to biases and thus it only explains the spatial similarities/differences between simulations and observations for the various stations over the figure. Table 2 summarizes the errors found for daily values.

Table 2
Performance of WRF model for both resolutions in a daily and seasonal basis (spatially averaged values over the IP).

	Resolution	DAILY	DJF	MAM	JJA	SON
BIAS (W/m^2)	WRF5	29.9	25.1	43.6	37.1	22.1
	WRF9	31.8	17.1	47.6	45.4	21.1
MAE (W/m^2)	WRF5	51.7	25.9	46.8	52.4	28.1
	WRF9	39.2	18.0	47.6	46.1	21.7
RMSE (W/m^2)	WRF5	71.6	29.7	53.9	61.7	33.0
	WRF9	55.5	21.6	51.6	52.5	25.5
r	WRF5	0.8	0.9	0.8	0.6	0.9
	WRF9	0.9	0.9	0.9	0.8	0.9

As detailed in Section 2.2, the seasonal analysis was done considering only fifteen ground-stations. The seasonal BIAS shows similar spatial patterns to the results obtained for the daily BIAS analysis. WRF5 is able to simulate the seasonal evolution of SW↓ (see Fig. 4), although an overall overestimation can be seen in the majority of the ground-based stations for all seasons, with only two exceptions: Sines (south-west coast of Portugal) and Ibiza (Spanish Mediterranean island).

WRF5 performance is better in winter and autumn in comparison with spring and summer (see Table 2). The smallest mean BIAS error is found in autumn (22W/m^2) and the highest value for spring (44W/m^2), which may be related to the larger variability of cloud conditions over the area in springtime (Salgueiro et al., 2014). According to Ramos et al. (2014), the cyclonic weather type over IP has a maximum in spring, imposing a considerably large cloud radiative effect as documented in Salgueiro et al., 2016. RMSE are relatively high in spring and summer, with values above 50W/m^2 (Table 2), and the smallest errors are found in the southwestern region and southeastern coast of Iberian Peninsula (not show here), in line with the spatial distribution obtained for BIAS analysis (Fig. 3a).

WRF5 seasonal errors are also consistent with the monthly errors found by Ruiz-Arias et al. (2016). The worst statistical results obtained in the mountainous regions of Cantabria and the Pyrenees suggest that the model, at this resolution, has limited skill in representing orographic clouds. However, this topic needs further investigation. Ruiz-Arias et al. (2016), suggest that the BIAS found in WRF could be a result of an underestimation of the actual cloud amount, and possibly, a misrepresentation of the radiative impact of low cumulus clouds.

Seasonal correlation coefficient varies between 0.6 in summer and ~0.9 in autumn, with large spatial dispersion in spring and especially in summer. The poor performance of the model in summer was also found by Dasari et al. (2014) for temperature, and it may be explained by an incorrect quantification of the aerosol effects, since the model uses a monthly mean distribution of aerosols (Collins et al., 2004) and not actual values. Cardoso et al. (2013) also found small correlation coefficients in summer precipitation as a result of a combination of strong surface heating, instability and the connected convection over some parts of IP. According to Alapaty et al. (2012), NWP models do not consider cumulus cloud feedbacks in radiation at a subgrid-scale, and these effects can cause a bias in shortwave and longwave radiation. This may also explain the relatively high RMSE found in our analysis.

3.2. Comparison with other validated WRF simulation

The WRF5 performance is additionally investigated by comparison with results obtained from the previously validated WRF9 experiment, where continuous model integration was performed.

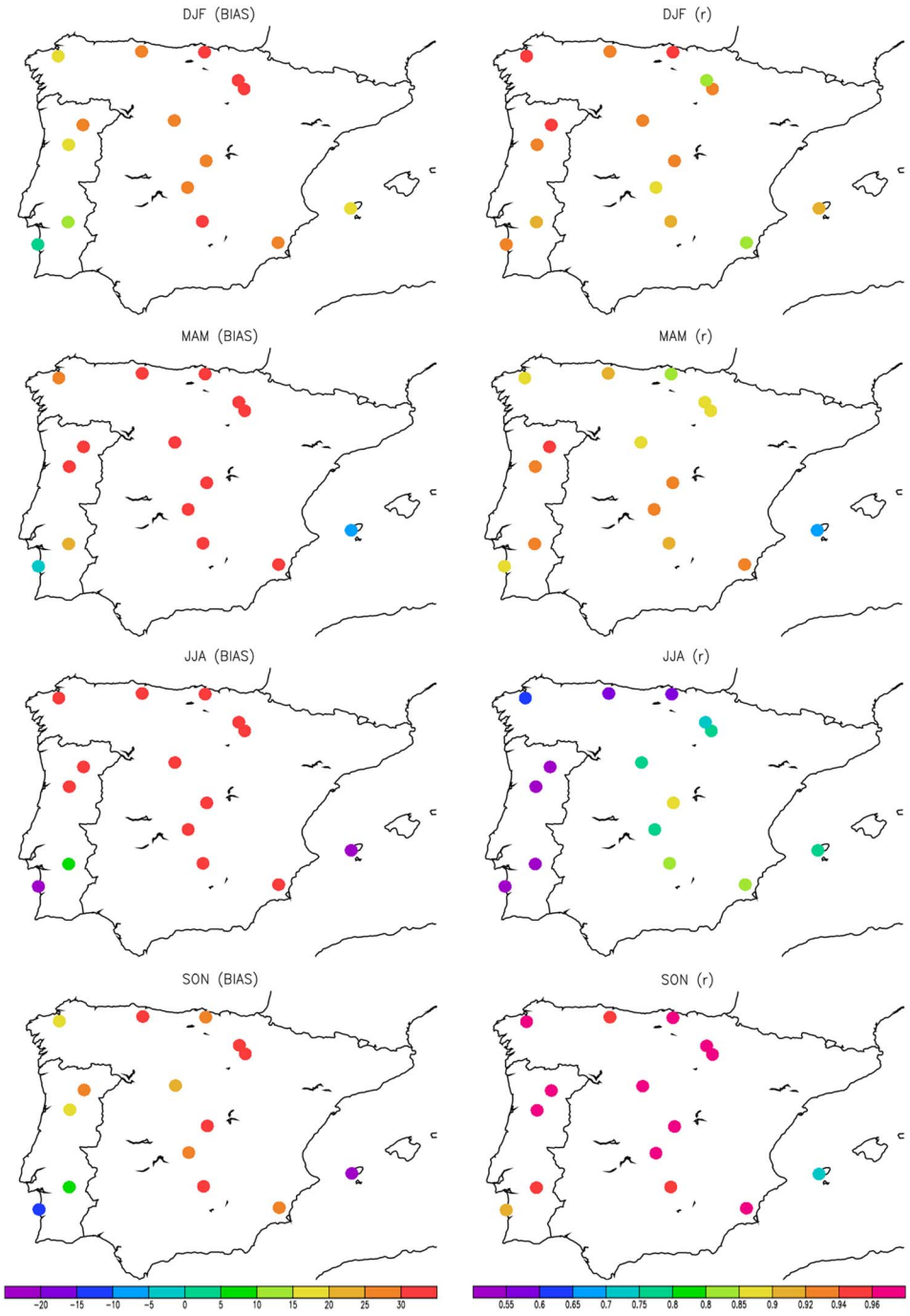

Fig. 4. Seasonal BIAS and correlation coefficient for SW↓ compared with ground-based observational data. BIAS in W/m^2.

Table 2 and Fig. 5 show the results of the comparison with the observation, for both models.

In general, WRF5 and WRF9 overestimate the observed SW↓, either on a daily or on a seasonal basis. Daily NBIAS of SW↓ in WRF5 is slightly smaller than in WRF9, whereas with respect to the MAPE, NRMSE and correlation coefficients, WRF9 shows a slightly better performance than WRF5. Daily NBIAS values show, for both configurations, errors below 17%. NRMSE for WRF5 are larger than for WRF9, with values of ~40% and ~30%, respectively. The correlation coefficients between daily simulated and observed SW↓, for both experiences during the whole period compared (2000–09) are > 0.8, revealing a good model behaviour

Seasonal NBIAS of SW↓ show that the WRF5 forecast has a slightly better performance than WRF9, with values varying between ~13% and ~28%. With respect to the NRMSE, WRF5 (WRF9) forecast shows values in the range of ~22% (~19%) in summer and ~33% (~24%) in winter (see Fig. 5). MAPE shows that WRF5 slightly outperforms WRF9 in spring with an error of ~22%, and in the summer season with an error of ~16%. Seasonal correlation coefficients produce very similar results with high correlations, for both experiences, especially in autumn ($r \geq 0.9$). It can be observed in Fig. 5, that for both experiences, the errors show a clear seasonal dependence.

Our errors present the same magnitude as those of other studies such as Lorenz et al. (2009) over the south of Spain, with NRMSE between irradiance forecasts and observations in the range of 20% to 35%.

The use of different parameterizations in numerical models inevitably leads to different results (Cossu and Hocke, 2014; Mercader et al., 2010) but, according to this analysis, statistical errors obtained in WRF5 and WRF9 are in agreement for SW↓ and presents comparable

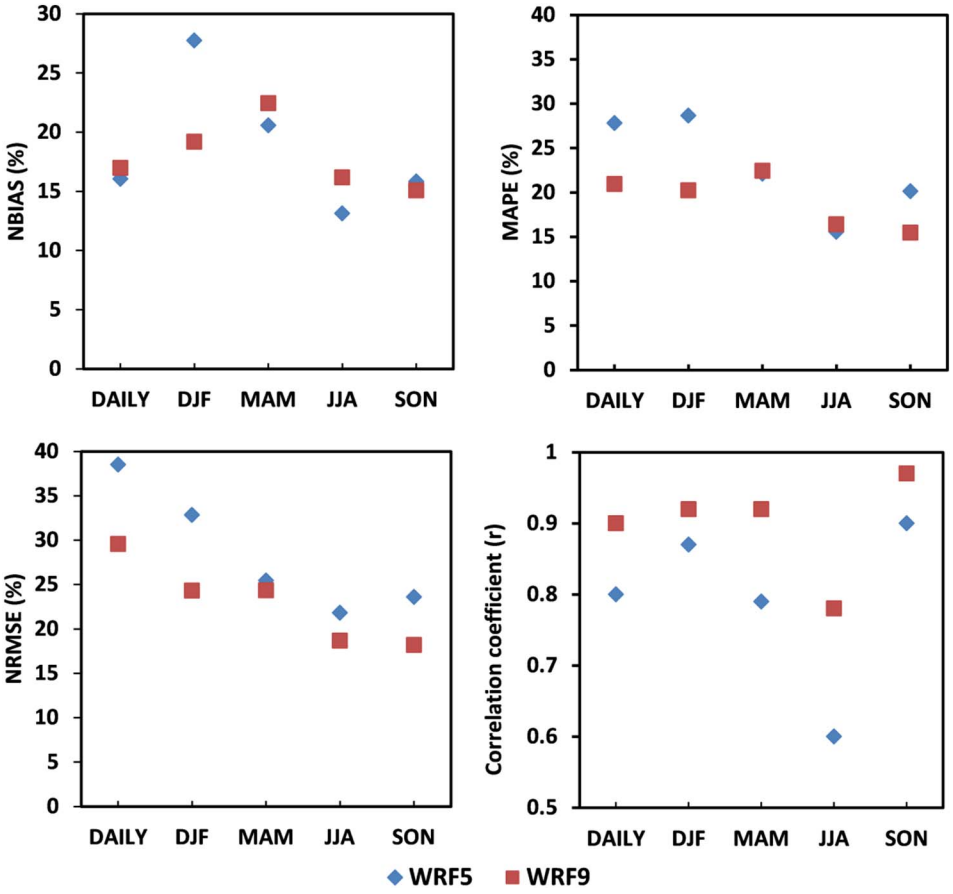

Fig. 5. Correlation coefficients and statistical errors (NBIAS, NMAE and NRMSE) over IP, in the 2000–2009 period for WRF5 and WRF9.

errors.

The comparisons of the simulations obtained in both experiments with the observations show that the quality of the prediction of solar radiation by the WRF5 simulation, which uses the less conventional technique of annual re-initializations, is not lower than the previously validated WRF9 simulation.

3.3. Statistical BIAS correction and comparison against observations

The BIAS between models and observations may be reduced by applying a BIAS correction. This methodology was applied to SW↓ radiation by Ruiz-Arias et al. (2015).

Following the methodology described in Hagemann et al. (2011), summarized in Section 2.5, the shortwave all sky and clear sky shortwave radiative fluxes at the surface were corrected using the CERES dataset. To obtain the transfer function, WRF and CERES data were spatially averaged over IP for the common period. The transfer function, shown in Fig. 6, was obtained using monthly average values.

Fig. 6b also reveals that the model produces higher clear sky shortwave radiation than estimated by CERES. The SWRCLF was determined from the BIAS corrected WRF5 clear sky radiation parameter.

The transfer function obtained was applied to all modelled values, at all grid points and time steps. The corrected values were then compared with ground-based observations for the same period. Note that these time series are independent from the CERES data used to compute the transfer function. Fig. 7 shows the correlation and the NBIAS between WRF5 and ground-based observed SW↓ fluxes, for the 2000–2009 period, after BIAS correction.

The analysis of Fig. 7 shows a strong correlation between WRF5 SW↓ and observations, with a mean correlation of the order of ~0.97, improving the scores obtained before the BIAS correction (see Section 3.1). The differences between model and observations were significantly reduced after the correction. The mean NBIAS fell from 17% to 7% (~11 W/m^2). The corrected NBIAS are close to those shown in Ruiz-Arias et al. (2015). NRMSE (Fig. 7c) and MAPE (Fig. 7d) dropped respectively from 39% to 18% and from 28% to 14%.

In general, WRF5 simulations show a very similar performance when compared with observational ground-based data, WRF9 and CERES data, which increases the confidence in the climatology that will be addressed in the next section.

4. SW↓ climatology over the Iberian Peninsula for 1950–2010 period

Fig. 8 illustrates the climatological 60 year mean SW↓ over IP, at a 5 km horizontal resolution, obtained from the WRF5 simulations after applying the post-processing BIAS correction methodology.

During this period, the mean SW↓ ranged from a minimum of ~140W/m^2 in the north of IP to a maximum value above ~230W/m^2 at the south corresponding to a spatial average value of ~190W/m^2. The spatial distribution clearly shows a gradient increasing from north to south and from west to east modelled by the effects of the coast and topography. Ruiz-Arias et al. (2015) also found this gradient, with lower irradiation values northward.

In Spain, Andalusia and Murcia are the regions with the highest SW↓. The greatest mean value of SW↓ (~230W/m^2) was found in Granada and Almeria. The lowest mean values are associated with the west and north Atlantic coastal zone and range between ~140W/m^2 and ~180W/m^2. The smallest values are found in Coruna (Galicia – Spain). For Portugal, the central and southern parts (Alentejo and Algarve) are those with the highest mean SW↓ values (above ~200W/m^2). This pattern is, in general, consistent with the study conducted by Sanchez-Lorenzo et al. (2009) for Spain, over the 1985–2010 period, which used observational sunshine duration data.

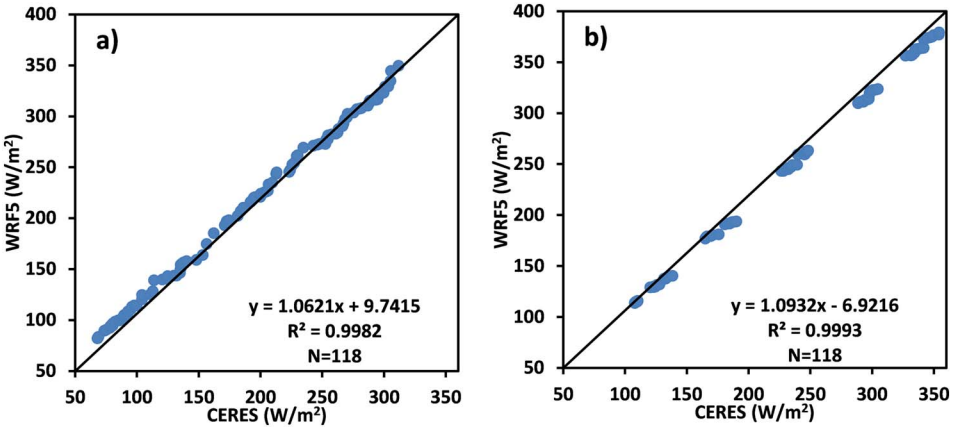

Fig. 6. Transfer functions obtained from WRF data and CERES data on a monthly basis for SW↓ (a) and clear Sky SW↓ (b). The functions were obtained from monthly spatial mean values over IP for 2000–2009 period.

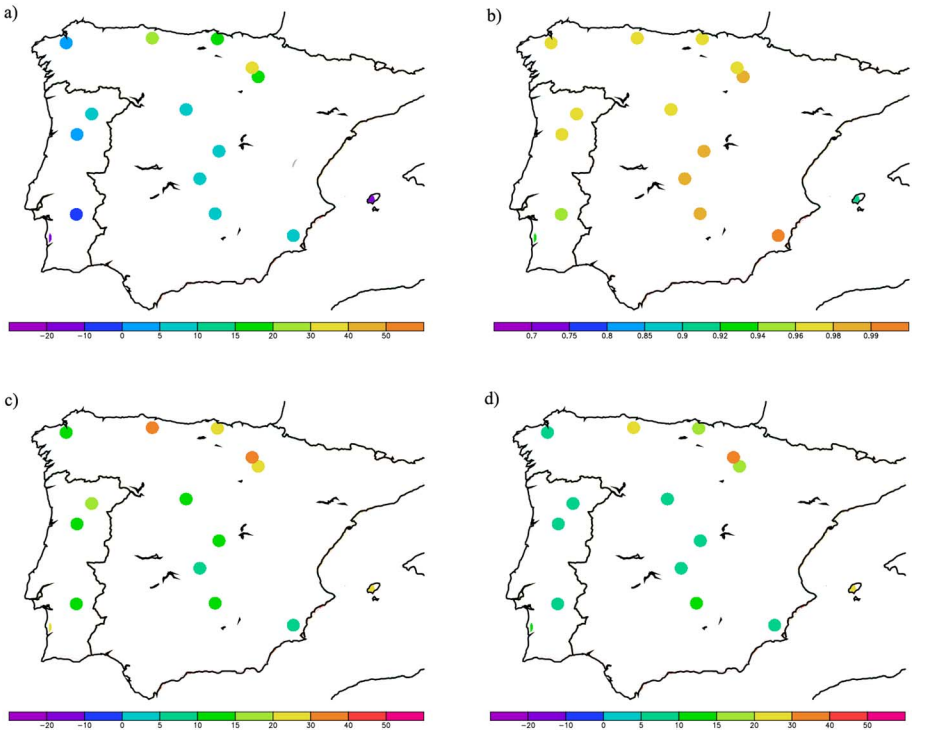

Fig. 7. (a) NBIAS (in percentage) and (b) correlation coefficient (c) NRMSE and (d) MAPE for SW↓ over 2000–2009 period between model and observations for several Iberian ground-based stations.

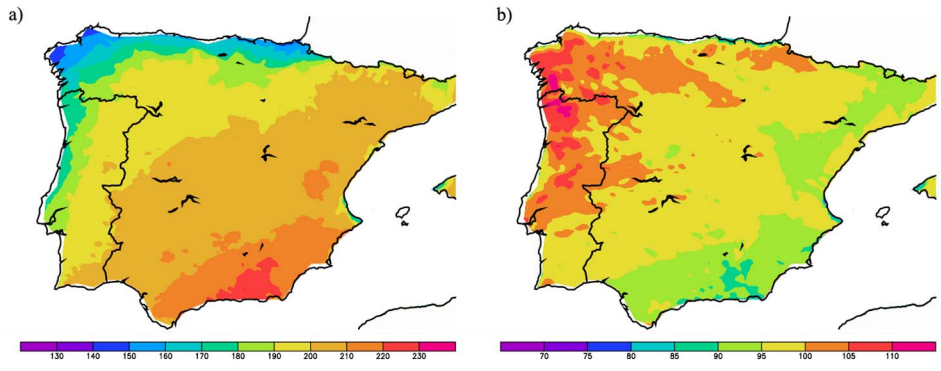

Fig. 8. Sixty-year annual mean for the 1950–2010 period of, (a) SW↓ and (b) standard deviation. Values are in W/m^2.

The SW variability (annual standard deviation) is relatively high in the northern part of IP, particularly in Galicia (Spain), with an average value of ~105W/m^2. For Portugal, Minho and Douro Litoral (at north) are the regions where the SW↓ variability is larger, with averages above 100W/m^2. The spatial distribution of SW↓ during the four seasons is depicted in Fig. 11 and reveals values that range from a minimum of 50W/m^2, in winter, to a maximum around 325W/m^2, in the summer season. Maximum SW↓ values are found over the south of Portugal and Spain. The lowest SW↓ values, independently of the season, are found over north/northeast regions of IP. High variability (standard deviation) is found in spring and summer seasons (Fig. 9), especially along the Atlantic coastal regions, with values above 80W/m^2. This same high

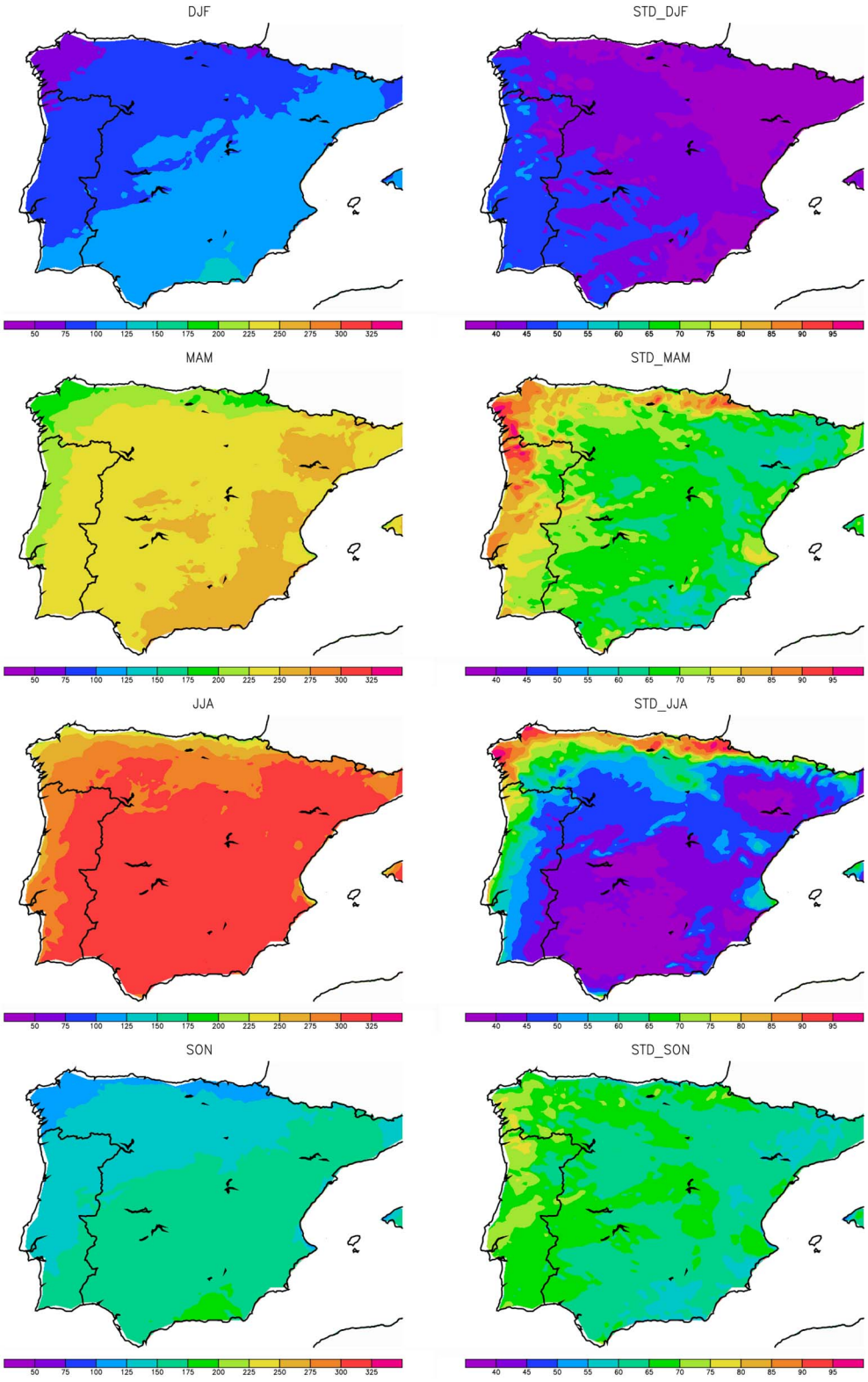

Fig. 9. Spatial seasonal average in the period 1950–2010 for SW↓, Winter (DJF), Spring (MAM), Summer (JJA), Autumn (SON), and standard deviation in Winter (STD_DJF), Spring (STD_MAM), Summer (STD_JJA) and Autumn (STD_SON). Values are in W/m^2.

variability was found by Ruiz-Arias et al. (2015), with the Cantabrian coast presenting lower values of radiation in comparison with the rest of Spain.

Annual cycles of SW↓ and SWRCLF, obtained from monthly means over land, are plotted in Fig. 10. These plots show, as expected, an annual pattern for SW with maximum values in summer, presenting a peak of 340W/m^2 (median value) in July and an inverse pattern for SWRCLF, with a minimum peak in June and July (0.04). It should be noted that SWRCLF is computed using SW↓, which reinforces their interdependence.

The shape of the boxplots show that the data distributions are generally symmetrical (see box and respective median). The inter-quartile ranges are relatively small in July and August for SW↓ and SWRCLF, which suggest a low inter-annual variability (long periods with no clouds) during summer. SW↓ variability is higher in March and September. For SWRCLF, larger spreads are obtained in the months of

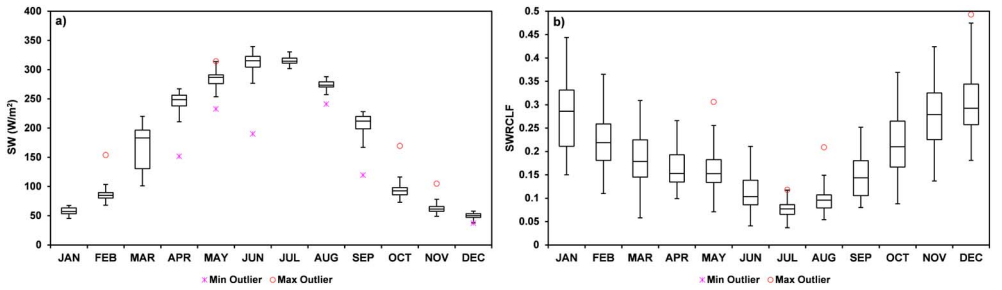

Fig. 10. Annual cycle of monthly mean area averaged SW↓ (a) and SWRCLF (b) over IP for the 1950–2010 period. The horizontal solid line within the box represents the median. The bottom and top of the boxes indicate the first and third quartiles, respectively. The circles and crosses represent outliers. The lower and upper ends of the whiskers are the minimum and maximum values of the datasets, respectively. SWRCLF varies between 0 (without clouds) and 1 (overcast).

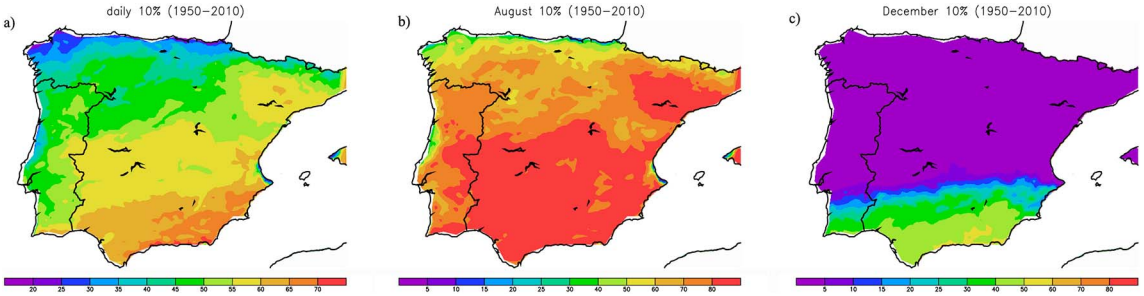

Fig. 11. Percentage of clear sky days of (a): daily, (b) August and (c) December. Values are in percentage.

autumn and winter (Fig. 10b). In those months, upper quartiles have values above 0.2 as expected and in accordance with the results obtained by Sanchez-Lorenzo et al. (2009), for total cloud cover in Spain. The boxplots of Fig. 10 allow for the identification of potential outliers. The existence of outliers may be partially explained by the interannual variability in the frontal system tracks affecting the region (Ramos et al., 2014; Trigo et al., 2002) and by the irregular occurrence of Saharan dust events (Obregón et al., 2015; Wagner et al., 2009; Alados-Arboledas et al., 2003). These events are not taken into account by the numerical model since the concentration and properties of the aerosols are fixed in the WRF simulations (Collins et al., 2004).

Fig. 11 shows maps of the percentage of clear sky days for the whole period and over two selected months: August and December. The maps show a high percentage of days without clouds, especially over central, south (Andalusia and Algarve) and northeast (Catalonia) parts of IP. Over these regions, > 30% of the days may be considered as clear sky (< 1 okta - SWRCLF less or equal to 0.1 for a conservative perspective, since the synoptic scale of WMO considers clear sky days until 2 oktas for the recording of the total cloud cover).

In December, for over 2/3 of the Iberian Peninsula (north coastal regions of Portugal until Tagus River, Galicia and Basque Country), the percentage of clear sky days is < 10% of the days in all period. However, areas along Spanish Mediterranean coast (Southeastern part of Andalusia, Murcia, Valencian community and Catalonia) present > 30% of clear sky days, even in December. On the other hand, in August, the percentage of clear sky days is above 70% in more than half of the Iberian Peninsula (central and south). This result is consistent with Ridao et al. (2007), which found that Andalusia (south of Spain) is the region with the greatest potential of all European regions for the implementation of solar energy systems.

5. Conclusions

A high resolution climatology of SW↓ solar radiation over IP, obtained from simulations performed using the WRF model at 5 km resolution (WRF5) is presented in this work. The comparison between WRF5 and observations for the downward shortwave radiation at the surface shows a good performance, although with a slight overestimation of radiation. The results indicate that the model simulations were significantly improved after applying a BIAS correction using CERES data. The daily BIAS over central IP was approximately 28W/m^2 (~17%) before BIAS correction and 7% after. In the northern coastal regions, namely in Galicia, Asturias, Cantabria and Basque Country, daily BIAS are above 40W/m^2 (before BIAS correction). Similar results were obtained for the seasonal analysis. Correlation coefficients obtained from the comparisons between the observations and the model results are high, above 0.8 for 70% of the ground-based stations. Seasonal correlation coefficients show a lower correlation in summer and higher values in autumn with values between 0.4 (summer) and 0.9 (autumn).

The WRF5 strategy, based on multiple one year time-slices, was found to be a valid alternative to the more computationally time demanding strategy based on continuous model integration, as its results exhibit a similar behaviour and comparable errors to those obtained in a previously validated WRF run simulation at 9 km (WRF9). NRMSE for SW↓ ranges from 22W/m^2 to 39W/m^2, for WRF5 and 18W/m^2 to 30W/m^2, for WRF9 configuration. Regardless of the season, WRF9 always presents smaller NRMSE than WRF5.

The errors found in the present work, although mitigated by the application of a BIAS correction, may be related with a misrepresentation of clouds at higher spatial resolution (see Lara-Fanego et al., 2012b), and first of all, by an incorrect quantification of the aerosol effects, since the run uses a monthly mean distribution of aerosols (Collins et al., 2004) and not actual values. In fact, the main limitation of this work is the failure to take into account the evolution of aerosol distribution over the Iberian Peninsula, which is known to have been very important during the last century (see for example Mateos et al., 2014; Antón et al., 2017). This misrepresentation of the aerosols may introduce large temporal and spatial deviations and prevents the utilization of the simulated series for trend analysis, as the uncertainties related to the non-aerosol inclusion are larger than those resulting from solar radiation changes. Future works should take into account the spatial and temporal evolution of aerosol loads.

The IP climatology of SW↓ produced for the 1950–2010 period confirms the existence of two gradients (latitudinal and longitudinal). Regions with higher SW↓ values are situated in the southeastern regions of IP (Andalusia and Murcia). The lowest values of mean SW↓ were found in the northwestern region of Galicia. The variability of SW↓ also increases from south to north and from east to west directions with higher values over Galicia.

The cloud cover was also evaluated following the definition proposed by Crawford and Duchon (1999) namely the shortwave radiative

cloud fraction (SWRCLF). Results show that the southern half of the Iberian Peninsula has a larger part of its territory with > 30% of clear sky days during the period under study, and these values are substantially higher in summer months (above 80% for almost all territory).

The SW↓ radiation climatology obtained from the WRF 5 km simulations is a solid base in the planning of renewable power plants on solar resources, providing estimates in areas where there are no measurements. It should however be taken into account that aerosols can attenuate on average 10 to 20% of the horizontal irradiance and even more when desert dust aerosols are present. Thus the simulation results presented should be used with some caution since a monthly mean distribution of aerosols was considered.

The presented climatology points out Andalusia (Spain), Murcia (Spain), Alentejo (Portugal) and Algarve (Portugal) as the regions with the greatest SW↓ potential to implement solar energy systems, allowing to identify, at a fine scale, the areas that have higher solar potential.

Based on these results, it can be stated that WRF simulations over Iberian Peninsula represent relatively well the downward solar radiation at the surface after a simple BIAS correction and can be used to study the future distribution of solar radiation over the region, according to different climate change scenarios.

Conflict of interests

The authors declare there is no conflict of interests with regard to this manuscript.

Acknowledgements

The work is co-funded by the European Union through the European Regional Development Fund, included in the COMPETE 2020 (Operational Program Competitiveness and Internationalization) through the ICT project (UID/GEO/04683/2013) with the reference POCI-01-0145-FEDER-007690 and also through the ALOP project (ALT20-03-0145-FEDER-000004).

Clarisse Magarreiro wishes to acknowledge the Portuguese Science Foundation (FCT) grant SFRH/BD/79544/2011.

Pedro M.M. Soares thanks the Portuguese Science Foundation (FCT) for funding under Project SOLAR - PTDC/GEOMET/7078/2014.

The authors are grateful to AEMET (Spanish Weather service) and IPMA (Portuguese Weather service) for providing surface data used in this work and NASA for providing CERES data.

References

Acharya, N., Chattopadhyay, S., Mohanty, U.C., Dash, S.K., Sahoo, L.N., 2013. On the bias correction of general circulation model output for Indian summer monsoon. Meteorol. Appl. 20 (3), 349–356. http://dx.doi.org/10.1002/met.1294.

Alados-Arboledas, L., Lyamani, H., Olmo, F.J., 2003. Aerosol size properties at Armilla, Granada (Spain). Q. J. R. Meteorol. Soc. 129, 1395–1413. http://dx.doi.org/10.1256/qj.01.207.

Alapaty, K., Herwehe, J.A., Otte, T.L., Nolte, C.G., Bullock, O.R., Mallard, M.S., Kain, J.S., Dudhia, J., 2012. Introducing subgrid-scale cloud feedbacks to radiation for regional meteorological and climate modelling. Geophys. Res. Lett. 39, L24809. http://dx.doi.org/10.1029/2012GL054031.

Alexandru, A., de Elia, R., Laprise, R., Separovic, L., Biner, S., 2008. Sensitivity study of regional climate model simulations to largescale nudging parameters. Mon. Weather Rev. 137, 1666–1686. http://dx.doi.org/10.1175/2008MWR2620.1.

Alsamamra, H., Ruiz-Arias, J.A., Pozo-Vázquez, D., Tovar-Pescador, J., 2009. A comparative study of ordinary and residual kriging techniques for mapping global solar radiation over southern Spain. Agric. For. Meteorol. 149 (8), 1343–1357. http://dx.doi.org/10.1016/j.agrformet.2009.03.005.

Antón, M., Román, R., Sanchez-Lorenzo, A., Calbó, J., Vaquero, J.M., 2017. Variability analysis of the reconstructed daily global solar radiation under all-sky and cloud-free conditions in Madrid during the period 1887–1950. Atmos. Res. 191, 94–100. http://dx.doi.org/10.1016/j.atmosres.2017.03.013.

APREN, 2014. Impacto macroeconómico do setor da eletricidade de origem renovável em Portugal. http://www.apren.pt/pt/projectos/nacionais/estudo-apren-deloitte/, (accessed: 15.09.2016).

Berrisford, P., Dee, D., Fielding, K., Fuentes, M., Kallberg, P., Kobayashi, S., Uppala, S., 2009. The ERA-Interim Archive. ERA Report Series. 1. Technical Report. European Centre for Medium-Range Weather Forecasts, Shinfield Park, Reading (pp16).

Betts, A.K., 1986. A new convective adjustment scheme. Part I: observational and theoretical basis. Q. J. R. Meteorol. Soc. 112, 677–691.

Betts, A.K., Miller, M.J., 1986. A new convective adjustment scheme. Part II: single column tests using GATE wave, BOMEX, and arctic air-mass data sets. Q. J. R. Meteorol. Soc. 112, 693–709.

Cardoso, R.M., Soares, P.M.M., Miranda, P.M.A., Belo-Pereira, M., 2013. WRF high resolution simulation of Iberian mean and extreme precipitation climate. Int. J. Climatol. 33 (11), 2591–2608. http://dx.doi.org/10.1002/joc.3616.

Choi, M., Jacobs, J.M., Kustas, W.P., 2008. Assessment of clear and cloudy sky parameterizations for daily downwelling longwave radiation over different land surfaces in Florida, USA. Geophys. Res. Lett. 35, L20402. http://dx.doi.org/10.1029/2008GL035731.

Collins, W.D., Rasch, P.J., Boville, B.A., Hack, J.J., McCaa, J.R., Williamson, D.L., Zhang, M., 2004. Description of the NCAR community atmosphere model (CAM 3.0). In: NCAR Tech. Note NCAR/TN-464 + STR, pp. 226.

Cossu, F., Hocke, K., 2014. Influence of microphysical schemes on atmospheric water in the weather research and forecasting model. Geosci. Model Dev. 7 (1), 147–160.

Crawford, T.M., Duchon, C.E., 1999. An improved parameterization for estimating effective atmospheric emissivity for use in calculating daytime downwelling longwave radiation. J. Appl. Meteorol. 38, 474–480.

Dasari, H.P., Salgado, R., Perdigao, J., Challa, V.S., 2014. A regional climate simulation study using WRF-ARW model over Europe and evaluation for extreme temperature weather events. Int. J. Atmos. Sci. 2014, 704079. http://dx.doi.org/10.1155/2014/704079. (22 p.).

Deardorff, J.W., 1978. Efficient prediction of ground surface temperature and moisture, with inclusion of a layer of vegetation. J. Geophys. Res. Oceans 83 (C4), 1889–1903.

Dudhia, J., 2014. A history of mesoscale model development. Asia-Pac. J. Atmos. Sci. 50 (1), 121–131. http://dx.doi.org/10.1007/s13143-014-0031-8.

Ehnberg, J.S., Bollen, M.H., 2005. Simulation of global solar radiation based on cloud observations. Sol. Energy 78 (2), 157–162. http://dx.doi.org/10.1016/j.solener.2004.08.016.

Ehret, U., Zehe, E., Wulfmeyer, V., Warrach-Sagi, K., Liebert, J., 2012. Should we apply bias correction to global and regional climate model data? Hydrol. Earth Syst. Sci. 16 (9), 3391–3404. http://dx.doi.org/10.5194/hess-16-3391-2012.

Feser, F., Rockel, B., Von Storch, H., Winterfeldt, J., Zahn, M., 2011. Regional climate models add value to global model data: a review and selected examples. Bull. Am. Meteorol. Soc. 92 (9), 1181. http://dx.doi.org/10.1175/2011BAMS3061.1.

García, R.D., Cuevas, E., García, O.E., Cachorro, V.E., Pallé, P., Bustos, J.J., Romero-Campos, P.M., de Frutos, A.M., 2014. Reconstruction of global solar radiation time series from 1933 to 2013 at the Izaña Atmospheric Observatory. Atmos. Meas. Tech. 7, 3139–3150. http://dx.doi.org/10.5194/amt-7-3139-2014.

Giorgi, F., Mearns, L.O., 1999. Introduction to special section: regional climate modeling revisited. J. Geophys. Res. 104 (D6), 6335–6352. http://dx.doi.org/10.1029/98JD02072.

Grell, G.A., Devenyi, D., 2002. A generalized approach to parameterizing convection combining ensemble and data assimilation techniques. Geophys. Res. Lett. 29 (14). http://dx.doi.org/10.1029/2002GL015311.

Gubler, S., Gruber, S., Purves, R.S., 2012. Uncertainties of parameterized surface downward clear-sky shortwave and all-sky longwave radiation. Atmos. Chem. Phys. 12 (11), 5077–5098.

Haddeland, I., Heinke, J., Voß, F., Eisner, S., Chen, C., Hagemann, S., Ludwig, F., 2012. Effects of climate model radiation, humidity and wind estimates on hydrological simulations. Hydrol. Earth Syst. Sci. 16 (2), 305–318. http://dx.doi.org/10.5194/hess-16-305-2012.

Hagemann, S., Chen, C., Haerter, J.O., Heinke, J., Gerten, D., Piani, C., 2011. Impact of a statistical bias correction on the projected hydrological changes obtained from three GCMs and two hydrology models. J. Hydrometeorol. 12 (4), 556–578. http://dx.doi.org/10.1175/2011JHM1336.1.

Haylock, M.R., Hofstra, N., Tank, A.M.G.K., Klok, E.J., Jones, P.D., New, M., 2008. A European daily high-resolution gridded dataset of surface temperature and precipitation. J. Geophys. Res. Atmos. 113, D20119. http://dx.doi.org/10.1029/2008JD10201.

Hong, S.-Y., Chang, E.-C., 2012. Asia-Pac. J. Atmos. Sci. 48, 345–355. http://dx.doi.org/10.1007/s13143-012-0033-3.

Hong, S.-Y., Kanamitsu, M., 2014. Asia-Pac. J. Atmos. Sci. 50, 83. http://dx.doi.org/10.1007/s13143-014-0029-2.

Hong, S.-Y., Lim, J.-O.J., 2006. The WRF single-moment 6-class microphysics scheme (WSM6). J. Korean Meteor. Soc. 42, 129–151.

Hong, S.-Y., Dudhia, J., Chen, S.H., 2004. A revised approach to ice microphysical processes for the bulk parameterization of clouds and precipitation. Mon. Weather Rev. 132, 103–120.

Hong, S.-Y., Noh, Y., Dudhia, J., 2006. A new vertical diffusion package with an explicit treatment of entrainment processes. Mon. Weather Rev. 134, 2318–2341. http://dx.doi.org/10.1175/MWR3199.1.

IDAE, 2016. Informe Estadistico Energias Renovables. http://informeestadistico.idae.es/t10.htm, (accessed: 15.01.2017).

IPCC, 2014. Summary for policymakers. In: Edenhofer, O., Pichs-Madruga, R., Sokona, Y., Farahani, E., Kadner, S., Seyboth, K., Adler, A., Baum, I., Brunner, S., Eickemeier, P., Kriemann, B., Savolainen, J., Schlömer, S., Von Stechow, C., Zwickel, T., Minx, J.C. (Eds.), Climate Change 2014: Mitigation of Climate Change. Contribution of Working Group III to the Fifth Assessment Report of the Intergovernmental Panel on Climate Change. Cambridge University Press, Cambridge, United Kingdom and New York, NY, USA.

Janjic, Z.I., 1990. The step-mountain coordinate: physical package. Mon. Weather Rev.

118, 1429–1443.
Janjic, Z.I., 1994. The step-mountain eta coordinate model: further developments of the convection, viscous sublayer and turbulence closure schemes. Mon. Weather Rev. 122, 927–945.
Janjic, Z.I., 2000. Comments on "development and evaluation of a convection scheme for use in climate models". J. Atmos. Sci. 57, 3686.
Janjic, Z.I., 2001. Nonsingular Implementation of the Mellor–Yamada Level 2.5 Scheme in the NCEP Meso Model. NCEP Office Note 437. (61 pp).
Jerez, S., Trigo, R.M., Sarsa, A., Lorente-Plazas, R., Pozo-Vázquez, D., Montávez, J.P., 2013. Spatio-temporal complementarity between solar and wind power in the Iberian Peninsula. Energy Procedia 40, 48–57.
Jones, R.G., Murphy, J.M., Noguer, M., 1995. Simulation of climate change over Europe using a nested regional-climate model. I: assessment of control climate, including sensitivity to location of lateral boundaries. Q. J. R. Meteorol. Soc. 121, 1413–1449.
Kalnay, E., Kanamitsu, M., Kistler, R., Collins, W., Deaven, D., Gandin, L., Zhu, Y., 1996. The NCEP/NCAR 40-year reanalysis project. Bull. Am. Meteorol. Soc. 77 (3), 437–471.
Kato, S., Loeb, N.G., Rose, F.G., Doelling, D.R., Rutan, D.A., Caldwell, T.E., Yu, L., Weller, R.A., 2013. Surface irradiances consistent with CERES-derived top-of-atmosphere shortwave and longwave irradiances. J. Clim. 26, 2719–2740.
Laprise, René, 2008. Regional climate modelling. J. Comput. Phys. 227 (7), 3641–3666.
Lara-Fanego, V., Ruiz-Arias, J.A., Pozo-Vázquez, A.D., Gueymard, C.A., Tovar-Pescador, J., 2012a. Evaluation of DNI forecast based on the WRF mesoscale atmospheric model for CPV applications. In: AIP Conference Proceedings-American Institute of Physics. vol. 1477. pp. 317. no. 1. http://dx.doi.org/10.1063/1.4753895.
Lara-Fanego, V., Ruiz-Arias, J.A., Pozo-Vázquez, D., Santos-Alamillos, F.J., Tovar-Pescador, J., 2012b. Evaluation of the WRF model solar irradiance forecasts in Andalusia (southern Spain). Sol. Energy 86 (8), 2200–2217. http://dx.doi.org/10.1016/j.solener.2011.02.014.
Lo, J.C.F., Yang, Z.L., Pielke Sr., R.A., 2008. Assessment of three dynamical climate downscaling methods using the Weather Research and Forecasting (WRF) model. J. Geophys. Res. 113, D09112. http://dx.doi.org/10.1029/2007JD009216.
Lorenz, E., Remund, J., Müller, S.C., Traunmüller, W., Steinmaurer, G., Pozo, D., Kurz, C., 2009. Benchmarking of different approaches to forecast solar irradiance. In: 24th European Photovoltaic Solar Energy Conference, Hamburg, Germany. Vol. 21. pp. 25.
Marteau, R., Richard, Y., Pohl, B., Smith, C.C., Castel, T., 2015. High-resolution rainfall variability simulated by the WRF RCM: application to eastern France. Clim. Dyn. 44 (3–4), 1093–1107.
Martín, L., Zarzalejo, L.F., Polo, J., Navarro, A., Marchante, R., Cony, M., 2010. Prediction of global solar irradiance based on time series analysis: application to solar thermal power plants energy production planning. Sol. Energy 84 (10), 1772–1781. http://dx.doi.org/10.1016/j.solener.2010.07.002.
Mateos, D., Antón, M., Toledano, C., Cachorro, V.E., Alados-Arboledas, L., Sorribas, M., Costa, M.J., Baldasano, J.M., 2014. Aerosol radiative effects in the ultraviolet, visible, and near-infrared spectral ranges using long-term aerosol data series over the Iberian Peninsula. Atmos. Chem. Phys. 14, 13497–13514. http://dx.doi.org/10.5194/acp-14-13497-2014.
Mercader, J., Codina, B., Sairouni, A., Cunillera, J., 2010. Results of the Meteorological Model WRF-ARW over Catalonia using different parameterizations of convection and cloud microphysics. Tethys 7, 75–86. http://dx.doi.org/10.3369/tethys.2010.7.07.
Miguez-Macho, G., Stenchikov, G.L., Robock, A., 2004. Spectral nudging to eliminate the effects of domain position and geometry in regional climate model simulations. J. Geophys. Res. 109, D13104. http://dx.doi.org/10.1029/2003JD004495.
Obregón, M.A., Pereira, S., Salguero, V., Costa, M.J., Silva, A.M., Serrano, A., Bortoli, D., 2015. Aerosol radiative effects during two desert dust events in August 2012 over the Southwestern Iberian Peninsula. Atmos. Res. 153, 404–415.
Perdigão, J.C., Salgado, R., Costa, M.J., Dasari, H.P., Sanchez-Lorenzo, A., 2016. Variability and trends of downward surface global solar radiation over the Iberian Peninsula based on ERA-40 reanalysis. Int. J. Climatol. 36, 3917–3933. http://dx.doi.org/10.1002/joc.4603.
Piani, C., Weedon, G.P., Best, M., Gomes, S.M., Viterbo, P., Hagemann, S., Haerter, J.O., 2010. Statistical bias correction of global simulated daily precipitation and temperature for the application of hydrological models. J. Hydrol. 395, 199–215. http://dx.doi.org/10.1016/j.jhydrol.2010.10.024.
Raju, A., Parekh, A., Chowdary, J.S., Gnanaseelan, C., 2015. Assessment of the Indian summer monsoon in the WRF regional climate model. Clim. Dyn. 44 (11 − 12), 3077–3100. http://dx.doi.org/10.1007/s00382-014-2295-1.
Ramos, A.M., Cortesi, N., Trigo, R.M., 2014. Circulation weather types and spatial variability of the daily precipitation in the Iberian Peninsula. Front. Earth Sci. 2, 1–17. http://dx.doi.org/10.3389/feart. 00025.
Ridao, A.R., Garca, E.H., Escobar, B.M., Toro, M.Z., 2007. Solar energy in Andalusia (Spain): present state and prospects for the future. Renew. Sust. Energ. Rev. 11 (1), 148–161.
Rios-Entenza, A., Soares, P.M., Trigo, R.M., Cardoso, R.M., Miguez-Macho, G., 2014. Moisture recycling in the Iberian Peninsula from a regional climate simulation: spatiotemporal analysis and impact on the precipitation regime. J. Geophys. Res. Atmos. 119 (10), 5895–5912. http://dx.doi.org/10.1002/2013JD021274.
Ruiz-Arias, J.A., Terrados, J., Pérez-Higueras, P., Pozo-Vázquez, D., Almonacid, G., 2012. Assessment of the renewable energies potential for intensive electricity production in the province of Jaén, southern Spain. Renew. Sust. Energ. Rev. 16 (5), 2994–3001. http://dx.doi.org/10.1016/j.rser.2012.02.006.
Ruiz-Arias, J.A., Quesada-Ruiz, S., Fernández, E.F., Gueymard, C.A., 2015. Optimal combination of gridded and ground-observed solar radiation data for regional solar resource assessment. Sol. Energy 112, 411–424. http://dx.doi.org/10.1016/j.solener.2014.12.011.
Ruiz-Arias, J.A., Arbizu-Barrena, C., Santos-Alamillos, F.J., Tovar-Pescador, J., Pozo-Vázquez, D., 2016. Assessing the surface solar radiation budget in the WRF Model: a spatiotemporal analysis of the bias and its causes. Mon. Weather Rev. 144 (2), 703–711. http://dx.doi.org/10.1175/MWR-D-15-0262.1.
Rummukainen, M., 2010. State of the art with regional climate models. Wiley Interdiscip. Rev. Clim. Chang. 1 (1), 82–96.
Salgueiro, V., Costa, M.J., Silva, A.M., Bortoli, D., 2014. Variability of the daily-mean shortwave cloud radiative forcing at the surface at a Midlatitude site in southwestern Europe. J. Clim. 27, 7769–7780. http://dx.doi.org/10.1175/JCLI-D-13-00696.1.
Salgueiro, V., Costa, M.J., Silva, A.M., Bortoli, D., 2016. Effects of Clouds on the Surface Shortwave Radiation at a Rural Inland mid-Latitude Site. Atmospheric Research. (in press).
Sanchez-Lorenzo, A., Calbó, J., Brunetti, M., Deser, C., 2009. Dimming/brightening over the Iberian Peninsula: Trends in sunshine duration and cloud cover and their relations with atmospheric circulation. J. Geophys. Res. 114, D00D09. http://dx.doi.org/10.1029/2008JD011394.
Sanchez-Lorenzo, A., Wild, M., Trentmann, J., 2013. Validation and stability assessment of the monthly mean CM SAF surface solar radiation dataset over Europe against a homogenized surface dataset (1983–2005). Remote Sens. Environ. 134, 355–366.
Santabàrbara, J.M., Calbó, J., Baldasano, J.M., Esteve, J., Mitjà, A., 1996. Month-to-month variation of global solar radiation in Catalonia (SPAIN). Int. J. Climatol. 16, 711–721. http://dx.doi.org/10.1002/(SICI)1097-0088(199606)16:6<711::AID-JOC42>3.0.CO;2-M.
Santos-Alamillos, F.J., Pozo-Vázquez, D., Ruiz-Arias, J.A., Lara-Fanego, V., Tovar-Pescador, J., 2012. Analysis of spatiotemporal balancing between wind and solar energy resources in the southern Iberian Peninsula. J. Appl. Meteorol. Climatol. 51 (11), 2005–2024. http://dx.doi.org/10.1175/JAMC-D-11-0189.1.
Skamarock, W.C., Klemp, J.B., Dudhia, J., Gill, D.O., Barker, D.M., Duda, M.G., Huang, X.-Y., Wang, W., Powers, J.G., 2008. A Description of the Advanced Research WRF Version 3. NCAR Technical Note, NCAR/TN-475 + STR. Mesoscale and Microscale Meteorology Division, National Center for Atmospheric Research, Boulder, CO, USA.
Soares, P.M., Cardoso, R.M., Miranda, P.M., de Medeiros, J., Belo-Pereira, M., Espirito-Santo, F., 2012. WRF high resolution dynamical downscaling of ERA-interim for Portugal. Clim. Dyn. 39 (9–10), 2497–2522. http://dx.doi.org/10.1007/s00382-012-1315-2.
Soares, P.M., Cardoso, R.M., Semedo, Á., Chinita, M.J., Ranjha, R., 2014. Climatology of the Iberia coastal low-level wind jet: weather research forecasting model high-resolution results. Tellus A 66. http://dx.doi.org/10.3402/tellusa.v66.223777.
Stanhill, G., Cohen, G., 2001. Global dimming: a review of the evidence for a widespread and significant reduction in global reduction with discussion of its probable causes on possible agriculture consequences. Agric. For. Meteorol. 107, 255–278. http://dx.doi.org/10.1016/S0168-1923(00)00241-0.
Stauffer, D.R., Seaman, N.L., 1990. Use of four-dimensional data assimilation in a limited-area mesoscale model. Part I: experiments with synoptic-scale data. Mon. Weather Rev. 118 (6), 1250–1277. http://dx.doi.org/10.1175/1520-0493(1990)118<1250:UOFDDA>2.0.CO;2.
Šúri, M., Hofierka, J., 2004. A new GIS-based solar radiation model and its application to photovoltaic assessments. Trans. GIS 8, 175–190. http://dx.doi.org/10.1111/j.1467-9671.2004.00174.x.
Šúri, M., Huld, T.A., Dunlop, E.D., Ossenbrink, H.A.., 2007. Potential of solar electricity generation in the European Union member states and candidate countries. Sol. Energy 81 (10), 1295–1305. http://dx.doi.org/10.1016/j.solener.2006.12.007.
Trigo, R.M., Osborn, T.J., Corte-Real, J.M., 2002. The North Atlantic Oscillation influence on Europe: climate impacts and associated physical mechanisms. Clim. Res. 20 (1), 9–17.
Von Storch, H., Langenberg, H., Feser, F., 2000. A spectral nudging technique for dynamical downscaling purposes. Mon. Weather Rev. 128, 3664–3673.
Wagner, F., Bortoli, D., Pereira, S., Costa, M.J., SILVA, A., Weinzierl, B., Tegen, I., 2009. Properties of dust aerosol particles transported to Portugal from the Sahara desert. Tellus B 61 (1), 297–306. http://dx.doi.org/10.1111/j.1600-0889.2008.00393.x.
Waldron, K.M., Peagle, J., Horel, J.D., 1996. Sensitivity of a spectrally filtered and nudged limited area model to outer model options. Mon. Weather Rev. 124, 529–547.
Wielicki, B.A., Barkstrom, B.R., Harrison, E.F., Lee III, R.B., Louis Smith, G., Cooper, J.E., 1996. Clouds and the Earth's Radiant Energy System (CERES): an earth observing system experiment. Bull. Am. Meteorol. Soc. 77 (5), 853–868. http://dx.doi.org/10.1175/1520-0477(1996)077<0853:CATERE>2.0.CO;2.
Wild, M., Gilgen, H., Roesch, A., Ohmura, A., Long, C.N., Dutton, E.G., Tsvetkov, A., 2005. From dimming to brightening: decadal changes in solar radiation at Earth's surface. Science 308 (5723), 847–850.
WMO, 2008. Guide to Meteorological Instruments and Methods of Observation. WMO-No. 8, Seventh edition. .
Xue, Y., Janjic, Z., Dudhia, J., Vasic, R., De Sales, F., 2014. A review on regional dynamical downscaling in intraseasonal to seasonal simulation/prediction and major factors that affect downscaling ability. Atmos. Res. 147, 68–85. http://dx.doi.org/10.1016/j.atmosres.2014.05.001.
Yhang, Y.B., Hong, S.Y., 2011. A study on large-scale nudging effects in regional climate model simulation. Asia-Pacific J. Atmos. Sci. 47 (235). http://dx.doi.org/10.1007/s13143-011-0012-0.

Boundary-Layer Meteorol (2018) 166:69–81
https://doi.org/10.1007/s10546-017-0298-2

RESEARCH ARTICLE

High-Frequency Response of the Atmospheric Electric Potential Gradient Under Strong and Dry Boundary-Layer Convection

Ricardo Conceição[1] · Hugo Gonçalves Silva[1] · Alec Bennett[2,3] · Rui Salgado[4] · Daniele Bortoli[4] · Maria João Costa[4] · Manuel Collares Pereira[1]

Received: 18 July 2016 / Accepted: 17 August 2017 / Published online: 8 September 2017
© Springer Science+Business Media B.V. 2017

Abstract The spectral response of atmospheric electric potential gradient gives important information about phenomena affecting this gradient at characteristic time scales ranging from years (e.g., solar modulation) to fractions of a second (e.g., turbulence). While long-term time scales have been exhaustively explored, short-term scales have received less attention. At such frequencies, space-charge transport inside the planetary boundary layer becomes a sizeable contribution to the potential gradient variability. For the first time, co-located (Évora, Portugal) measurements of boundary-layer backscatter profiles and the 100-Hz potential gradient are reported. Five campaign days are analyzed, providing evidence for a relation between high-frequency response of the potential gradient and strong dry convection.

Keywords Atmospheric electric potential gradient · Convection · Planetary boundary-layer backscatter · Space-charge dynamics

1 Introduction

Atmospheric electricity has been suggested as a promising tool for studying convection in the planetary boundary layer (PBL, e.g., Hoppel et al. 1986; Anisimov et al. 2002, 2014a; Yaniv et al. 2016). The key concept in this context is the turbulent transport of space charge (Anderson 1976), where space charge is defined as the difference between positive and negative charge carriers, usually divided into two categories: small ion clusters and charged

✉ Hugo Gonçalves Silva
hgsilva@uevora.pt

1 Renewable Energies Chair, IIFA, University of Évora, Palácio do Vimioso, Largo Marquês de Marialva, 7002-554 Évora, Portugal

2 Bristol Industrial and Research Associates Limited (Biral), Bristol, UK

3 Department of Electronic and Electrical Engineering, University of Bath, Bath, UK

4 Department of Physics, ICT, Institute of Earth Sciences, University of Évora, Rua Romão Ramalho 59, 7002-554 Évora, Portugal

aerosols. As the small ion clusters (with sizes around 10 nm) have higher electric mobilities, it is usual to consider them as the most important charge carriers in the atmosphere (Wright et al. 2014). Thus, space charge density (ρ) is normally simplified to

$$\rho = n_+ - n_-, \tag{1}$$

where n_+ and n_- are the concentrations of positive and negative small ion clusters, respectively. When an excess of negative ions occurs, ρ is negative, and negative values of the atmospheric electric potential gradient (PG[1]) are measured (Silva et al. 2016), while in the case of an excess of positive ions, positive values are observed. This makes potential gradient sensitive to the turbulent transport of space charges; these are, in fact, responsible for short-term potential gradient fluctuations (in the frequency range from ≈0.01 to ≈10 Hz), e.g., Anisimov et al. (2014a, b). It is important to mention that potential gradient is a result of the global electric circuit (GEC), being charged in shower clouds and thunderstorm active regions and discharged in poorly conductive fair-weather regions, (e.g., Rycroft et al. 2012; Conceição and Silva 2015). In this way, the GEC imposes a vertical electrical current between the ionosphere and the Earth's surface, generating the steady-state potential gradient through Ohm's Law. Therefore, GEC dynamics generates a global variation of the potential gradient that has its most recognised feature in the Carnegie curve (Harrison 2013). In contrast, processes occurring within the PBL tend to have a local influence on the potential gradient. An example of this is the effect of anthropogenic pollution, which tends to increase the potential gradient by ion scavenging of pollutant aerosols (Silva et al. 2014). Even so, scarce co-located observations of the PBL and electric parameters have been reported. One such account was made by Piper and Bennett (2012), where for the first time co-located measurements of clouds and aerosols (using a laser cloud-base recorder) and the potential gradient (using a field-mill) were performed. Nevertheless, potential-gradient measurements were taken at 1 Hz, which is insufficient to capture a complete signature of turbulent processes (occurring up to 100 Hz, Stull 1988). Another important reference can be found in Anisimov et al. (2014a), who combined a very well-instrumented campaign (an array of eight potential gradient sensors, a sodar and meteorological measurements) with numerical modelling to show that dynamic and stability conditions of the PBL influence turbulent space-charge flows and the formation of aeroelectric structures. In addition, they showed that generation of short-period aeroelectric pulsations (in the range 0.001–1 Hz) occurs during the transition from stable to convective conditions in the PBL. This observation is in line with previous work, which showed that the sunrise perturbation of the potential gradient (referred to as the sunrise effect) was due to upward convective transport of accumulated positive space charge (electrode layer) in the surface layer during the night (Marshall et al. 1999). Recently, Nicoll et al. (2017) went further by measuring high-resolution vertical charge profiles at Alqueva, southern Portugal, and concluded that, after sunrise, the evolution of the charge profiles was consistent with the fact that charged ultrafine aerosols were lifted upwards by convection.

In this context, the present study aims, for the first time, to combine PBL backscatter measurements with high-frequency potential gradient (HFPG) measurements taken at 100 Hz, to infer the effect of strong and dry convection on the high-frequency potential gradient response. In fact, measuring and analyzing potential gradient at frequencies above 1–10 Hz (historically used sample rates) entails various challenges, such as the difficulty of storing the large amount of data generated, and, most importantly, the contamination due to the

[1] Potential gradient is related to the vertical component of the atmospheric electric field, E_z, by the relation $PG = -E_z$ to guarantee positive values for potential gradient in fair-weather conditions as defined by Chalmers (1967). The fair-weather days are selected for cloudiness <0.2, wind speed <5 m s^{-1}, and the absence of fog or precipitation.

electric grid noise.[2] Records were made during a 5-day campaign during the summer of 2015 in southern Portugal (nearly 50 km from Alqueva reservoir, Nicoll et al. 2017) in an electromagnetic quiet region. Besides backscatter and HFPG measurements, meteorological and aerosol-optical-depth (AOD) measurements were made. The campaign coincided with dry and strongly convective days.

2 Methodology

The observation station is in the centre of Évora (38.567559°N, 7.911411°W) with approximately 50,000 inhabitants, located in southern Portugal. The major sources of pollutants are due to anthropogenic activity (mainly traffic). Background pollution levels at the site are low (discussed below) in comparison to levels observed in a large metropolis, which produce a significant signature on the potential gradient records, e.g. Silva et al. (2014). Measurements were made during a summer campaign from 17 to 21 June 2015. The field mill used, model JCI 131F developed by Chubb (2014) and manufactured by Chilworth UK, was installed at the University of Évora campus (at 2 m height) with a few trees and two buildings in its surroundings (approximately 50 m away). The instrument was calibrated in December 2013 and recent work reveals a flat spectral response up to frequencies of approximately 100 Hz (Chubb 2015). This fact makes the device suitable for the study of high-frequency electrical phenomena. The ceilometer used is a Vaisala CL31 instrument installed at the same site, which operates using a pulsed laser of 910 nm wavelength and monostatic optical configuration enabling accurate results at low altitudes (Costa et al. 2007). The ceilometer uses a lidar technique to determine the backscatter coefficients obtained from the signals returned by atmospheric scatter interacting with the collimated beam of near-infrared radiation emitted by the laser device equipping the instrument. The backscatter profile is determined with a vertical resolution of 10 m between the surface and roughly 7.5 km height, every 10 s. The CL31 instrument allows simultaneous detection of up to three layers of clouds. A Cimel CE-318 sun photometer, included in the AERONET network (Holben et al. 1998), was used for spectral AOD measurements, which represent the solar radiation extinction due to aerosol loading in the atmospheric column. Two wavelengths were used: 870 nm (A_{870}) and 440 nm (A_{440}). Air temperature was retrieved (every min) using a thermo-hygrometer (Thies Clima) and wind speed with a switching anemometer (Vector Instruments) both at 2-m height. Global horizontal irradiance (GHI) was measured using an Eppley pyranometer (model 8-48) and 10-min averages recorded. Finally, note that local summer time in the experimental location corresponds to UTC+1.

The observations are complemented by simulations of the non-hydrostatic Meso-NH (Lafore et al. 1998) atmospheric model v5.3 at 3-km horizontal resolution for the days of the campaign, over a domain of 102 × 130 grid points centred approximately at Évora. Initial and boundary conditions were obtained from the ECMWF operational analysis, updated every 6 h. The deep convection is assumed to be explicitly resolved, but an eddy-diffusivity Kain–Fritsch scheme for shallow convection (Pergaud et al. 2009) was used and turbulence parametrized using the one-dimensional scheme of Cuxart et al. (2000). The fluxes between the surface and the atmosphere are computed using the SURFEX (*Surface Externalisée*) platform of models (Masson et al. 2013) and the ECOCLIMAP v2.0 database (Masson et al. 2003) updated by Policarpo et al. (2017) for southern Portugal.

[2] Inspection of the signal spectra at least up to ≈50 Hz is recommended and to do that it is necessary to measure at least ≈100 Hz.

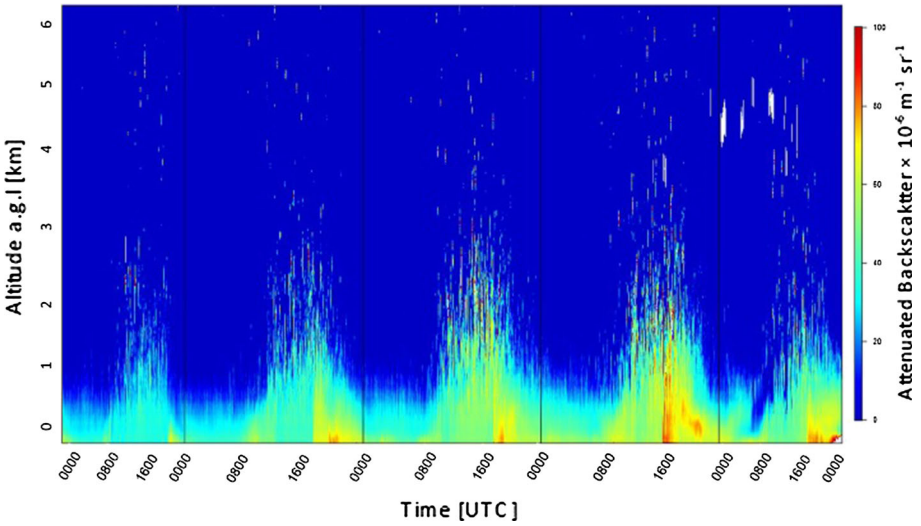

Fig. 1 Ceilometer backscatter as a function of height for the entire campaign, 17–21 June 2015

3 Results

The backscatter images retrieved by the ceilometer for the 5-day campaign, 17–21 June 2015, are presented in Fig. 1; apparently, days 17–19 June have almost no clouds or fog above the ceilometer. The wind speed <5 m s^{-1} (Fig. 2c) and global horizontal irradiance suggest almost clear skies (Fig. 2d); this confirms the fair-weather criterion on those days. In contrast, the 20 June, and more so 21 June, appear to be contaminated by clouds, as observed in both backscatter and global horizontal irradiance (Figs. 1, 2c respectively). Moreover, all days of the campaign presented strong and dry convection confirmed by the ceilometer data, corresponding to intense convection that led to high PBL tops, above approximately 2 km (Fig. 1). The low-level increased backscatter from aerosol (including those swelled by water moisture) present under the nocturnal inversion can be seen around 0000–0600 UTC and then 2100–0000 UTC. Sunrise initiates convection in the period of 0600–0800 UTC that develops during the following 2 h to form a strong and dry convective boundary layer, between 1000–2000 UTC. The PBL height reaches its maximum around 1500 UTC and starts to decrease around 1800 UTC; after 2000 UTC, the depth of the layer with high aerosol concentration is less than 1 km.

The measurements presented in Fig. 2 for all the campaign tend to behave in a remarkably similar way throughout this period. Coloured lines show raw data and the dots represent 1-h averages to highlight the daily behaviour of the five variables. In Fig. 2a the HFPG taken at 100 Hz is shown, and it can be inferred that this varies essentially between 0 and 100 V m^{-1}; which is the normal range in Portugal in the absence of thunderstorms and/or heavy pollution (Conceição et al. 2015). Significant fluctuations, both positive and negative, appear during the day, namely between 0800–2000 UTC, corresponding to the period when the mixed layer is most active (Fig. 1) and space-charge transport is more significant. As expected, the HFPG has its higher characteristic values around 1700–1800 UTC due to the well-known GEC planetary thunderstorm charging mechanism (Rycroft et al. 2012). Green dots show the Carnegie curve, which indicates that the potential gradient is in phase with this

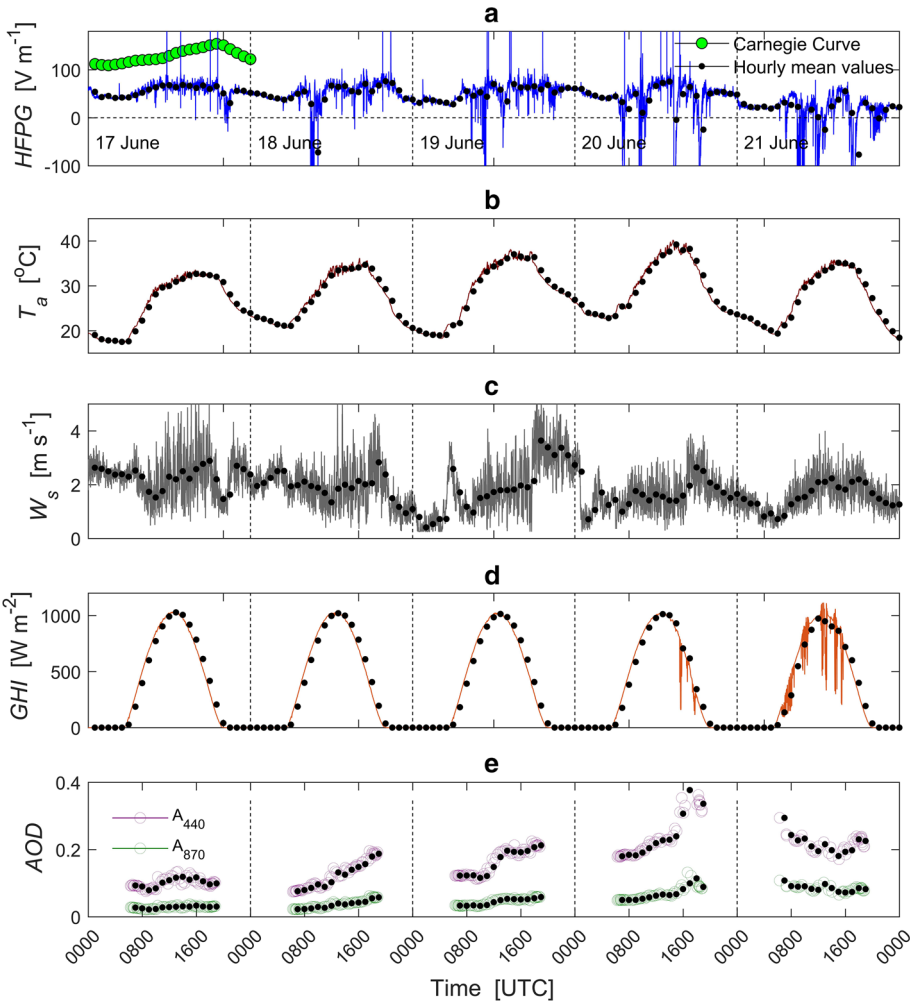

Fig. 2 Measurements made from 17 to 21 June 2015 campaign: **a** high-frequency potential gradient; **b** air temperature; **c** wind speed; **d** global horizontal irradiance; **e** aerosol optical depth. The black dots in the panels represent 1-h averaged values

reference curve when considering 1-h averages (black dots on Fig. 2a). Hourly variations of the potential gradient show a broad minimum between 0200–0600 UTC and a broad maximum between 1600–2000 UTC, suggesting that the GEC is the primary driver for the daily evolution of the potential gradient. Lower potential gradient values at Évora station as compared with the Carnegie curve are attributed to the ionization from natural radioactivity that increases the electric conductivity of the air and reduces the potential gradient. Such ground-generated ionization is present at land stations (as is the case of Évora) and absent over the sea. Discussion on potential gradient deviations from the Carnegie curve can be found in Tacza et al. (2014). The air temperature, T_a (Fig. 2b) at Évora has the expected behaviour for clear-sky summer days at Évora, an increasing trend is observed around sunrise after approximately 0600 UTC, reaching a plateau, with approximately 2 °C variability from

1500 until 1800 UTC, from which it starts to decrease coinciding with the PBL collapse. The air temperature, T_a, reaches a maximum of approximately 35–40 °C at low relative humidity (approximately 20%, not shown) at 1500 UTC. In terms of wind speed, W_s (Fig. 2c) reflects closely the PBL processes underway; a local W_s minimum is observed at approximately 0600 UTC, around sunrise, followed by a systematic increase through the day. In the late afternoon, approximately 1800 UTC, a sharp increase is found in the wind speed, probably associated with the arrival of the sea breeze from the west coast and the collapse of the convective PBL. After this maximum, W_s starts to decrease. The W_s remains below 5 m s^{-1} throughout the campaign. As mentioned above, global horizontal irradiance (Fig. 2d) indicates almost clear skies from the 17 to 20 June, while 21 June appears to be contaminated by clouds. The daily evolution of the AOD for the two reference wavelengths considered (440 and 870 nm) is shown in Fig. 2e, showing that AOD tends to increase in the morning, while remaining approximately stable during the rest of the day. As these measurements require sunlight, no records exist during the night (where a decrease in AOD is expected). It is also seen that AOD generally increases during the campaign, having an approximately constant value on the last day, 21 June. The increase in AOD values could relate to an increase in the surface aerosol load because of convection, in combination with other factors that transport aerosols aloft. These values are above the range of values for clean aerosol conditions, as defined by criteria in Elias et al. (2006): $A_{870} < 0.04$ and $A_{440} < 0.12$. Nevertheless, according to the same authors AOD values are consistent with a continental aerosol regime, characterized by $A_{440} < 0.3$ and represent typically 75% of summer days. This fact excludes the influence of any significant aerosol event, such as forest fires or Saharan dust storms (Silva et al. 2016).

Spectrograms in Fig. 3a were made using 10-s data bins (corresponding to 1000 potential-gradient values) of HFPG with an overlap of 2 s. On the one hand, persistent horizontal signals at approximately 50 Hz are due to the contamination from the electric grid and the constant narrowband signals around 20–30 Hz are likely to be aliased harmonics from the electric grid. No evidence of the typical frequencies corresponding to Schumann resonances can be seen, probably due to insufficient sensitivity resulting from the small aperture area of the field mill. On the other hand, similar vertical features (for example, the spikes around 0800 UTC) are observed in the 5 days of the campaign, but highlighted on some days more than others, which requires further inspection, see below. It is expected that certain high-frequency excitations derived from turbulent transport of space charge occur (Israël 1959), chiefly during PBL strong and dry convection, as in the present case. Generically, it can be seen at approximately 0800 UTC, 1500 UTC and 2000 UTC that there is an increase of frequencies being excited across the accessible bands (approximately 0.01–50 Hz). The 1500 UTC excitation appears to be the strongest, opening the possibility for the existence of a relation between HFPG excitations and turbulence due to strong and dry convection observed during the campaign. To clarify the nature of the spectral transient peaks just mentioned, an inset to the figure is included (Fig. 3b), in which the spectrogram is zoomed around the spectral peak for 19 June, starting around 1000 UTC. The zoom shows the particularly complex pattern of the peak with a duration of almost 1 h, and is incompatible with an impulsive source of noise, e.g., an electrical discharge, a rapid fluctuation on the electric grid, or even a fast bird passage. Moreover, the spikes in the spectrogram coincide with systematic negative excursions of the potential gradient, while positive ones tend not to contribute to those spectral transients. This coincidence can be confirmed in Fig. 3c, which presents the same HFPG raw data with which the zoomed spectra of Fig. 3b were produced. The coloured arrows mark the same moments in both the spectra and the data; very good agreement is found. The observed trend points to the fact that these spectral spikes arise from the HFPG response to environmental

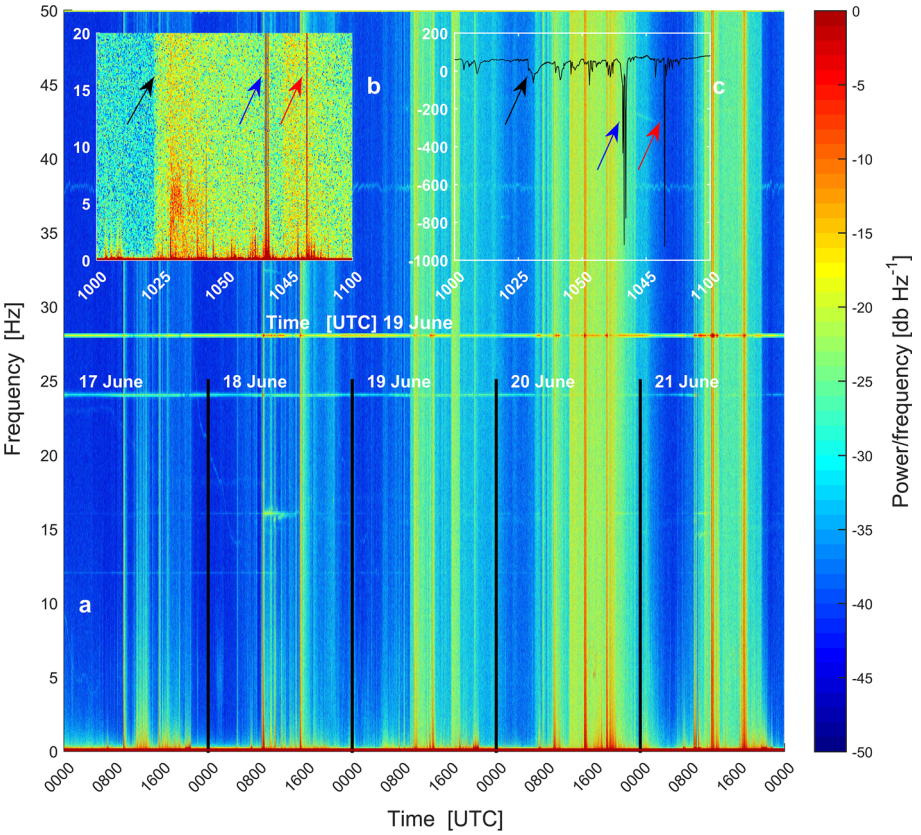

Fig. 3 **a** Spectrogram of the high-frequency potential gradient from 17 to 20 June 2015; **b** inset showing a 1-h zoom of the spectral peak for the 19 June, starting around 1000 UTC; this shows the particularly complex pattern of the peak. **c** inset showing the correspond HFPG values for the inset on (**b**). The coloured arrows in (**c**) and (**d**) mark the same moments in both the spectra and data

perturbations, rather than due to erroneous data points. A more detailed analysis of the HFPG variability is considered below.

In Fig. 4a the dashed black lines represent the standard deviation calculated for 30-min data bins (corresponding to approximately 180,000 values) of the 100-Hz potential gradient (σ_{PG}). The solid blue line represents data trends obtained through a locally weighted second-degree polynomial regression model, a robust loess smoothing at 5%, from 1-h averaged standard deviation of the potential gradient. All days of the campaign have high variability; in some cases, surpassing 150 V m^{-1}. Moreover, Fig. 4a shows the gross tendency seen in the spectrograms. There is an increase of the standard deviation of the potential gradient after approximately 0800 UTC, reaching a maximum at approximately 1000 UTC, and at approximately 1600 UTC a local minimum occurs, with the standard deviation decreasing after the 1800 UTC maximum. The 21 June 2015 is slightly different from this tendency. To further relate the observed standard deviation of the potential gradient with convection, three parameters have been considered from the Meso-NH model for the days of the campaign: Richardson number (Ri), surface sensible heat flux (H), and the near-surface turbulence kinetic energy (TKE). Ri was calculated using

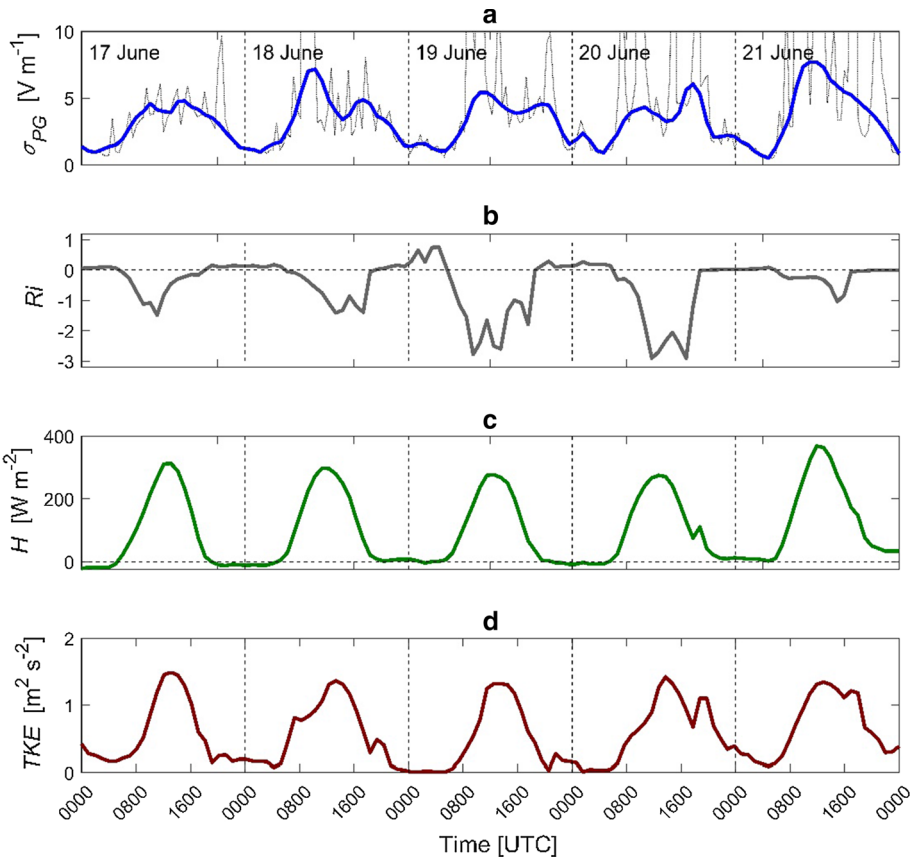

Fig. 4 **a** Standard deviation of high-frequency potential gradient (σ_{PG}); **b** Richardson number (Ri); **c** surface sensible heat flux (H); **d** turbulence kinetic energy (TKE). Parameters shown in (**b**), (**c**), and (**d**) were calculated from the Meso-NH model simulation described in the text

$$Ri = gz\frac{\theta_v\,(z) - \theta_v\,(0)}{0.5\,(\theta_v\,(z) + \theta_v\,(0))\,V^2\,(z)}, \tag{2}$$

where z is the height of the first atmospheric level, g is the acceleration due to gravity, $\theta_v(z)$ and $\theta_v(0)$ are the virtual potential temperature at z and at the surface, respectively; $V(z)$ is the wind speed at z. As expected, the simulated Ri becomes negative during the morning (see Fig. 4b), indicating an unstable surface layer around noon, more pronounced on 19th and 20th, corresponding to days with weaker winds. During the periods of very negative Ri, convective transport in the surface layer is buoyancy driven. The evolution of the simulated H is shown in Fig. 4c, where H can be interpreted as an indicator of the convective transport in the surface layer. At approximately 1500 UTC, H is at its maximum for all days of the campaign, implying that vertical velocity is a maximum too. As a matter of fact, H values show that convection commences at 0800 UTC, has a maximum at approximately 1500 UTC, and decreases until 2000 UTC; consistent with previous discussion on backscatter, see Fig. 1. H values are similar for 17–20 June, having higher values on the 21 June, probably due to the presence of stronger winds, even under a less thermal unstable environment (less negative Ri). The analyzed Meso-NH model TKE at the lowest atmospheric level (closest to the surface) is

Table 1 Daily correlation coefficients and the respective p-values in parentheses for the 5 days of the campaign relating standard deviation of the high-frequency potential gradient (σ_{PG}) with Richardson number (Ri), near-surface sensible heat flux (H), turbulence kinetic energy (TKE)

Correlation coefficients (p-value)	17 June	18 June	19 June	20 June	21 June
σ_{PG}-Ri	−0.6150	−0.5590	−0.7176	−0.6150	−0.5980
	(0.001)	(0.005)	(<0.0001)	(0.001)	(0.002)
σ_{PG}-H	0.7979	0.7637	0.7183	0.6094	0.9448
	(<0.0001)	(<0.0001)	(<0.0001)	(<0.0001)	(<0.0001)
σ_{PG}-TKE	0.7410	0.6848	0.7324	0.6422	0.9241
	(<0.0001)	(<0.0001)	(<0.0001)	(<0.0001)	(<0.0001)

shown represented in Fig. 4d. Its evolution follows that of H, showing that during the present case study the buoyant production of TKE predominates. However, Fig. 4d also shows an increase in TKE in the late afternoon due to an increase in wind speed and wind shear.

To quantify the relation between the HFPG excitations, the standard deviation of the potential gradient represented in Fig. 4a, and the simulated parameters related with convection, Fig. 4b–d, Pearson correlations were calculated for these parameters. The results are presented in Table 1, where the standard deviation of the potential gradient generally correlates better with H and TKE than with Ri. A tendency for lower correlation values on the 20 June and higher on the 21 June is found for the standard deviation of the potential gradient, and both H and TKE, while for the standard deviation of the potential gradient and Ri the lower absolute value is observed on 18 June and the higher absolute values on the 19 June (dominated by thermal convection). Moreover, the fact that both H and TKE have higher absolute correlation values with the standard deviation of the potential gradient than Ri implies that the HFPG variability is sensitive to convection independent of its origin. This is especially apparent on 21 June, characterized by turbulence from both thermal and dynamical mechanisms, but still with the higher correlation between the standard deviation of the potential gradient and H, see Table 1. In fact, from the evolution of the daily relation of these two parameters, it can be appreciated that there is an increase (decrease) in the Pearson correlation with increased (decreased) convection. Correlation is especially high on 21 June (the day with more intense convection) reaching approximately 0.94 (p-value <0.0001), confirming the association between HFPG and PBL convection. In line with these results, the same tendency is observed for the correlations of the standard deviation of the potential gradient and TKE, and on 21 June: it reaches 0.9241 (p-value <0.0001), which further demonstrates the close association between these two parameters.

4 Discussion

Low-level increased backscatter from aerosol present under the nocturnal inversion is seen on our observations around 0000–0600 UTC and at 2100–0000 UTC (Fig. 1) and the stable conditions prevent significant turbulence, giving low variability in HFPG (Fig. 4a), consistent with positive Ri (Fig. 4b). Sunrise initiates significant turbulence near to surface due to convection (Fig. 4c), leading to the formation of a convective boundary layer, which gradually grows into the residual layer of the previous day, breaking through it in the late morning, see (Fig. 1). At this stage, the near-surface space charge (atmospheric ions and charged

aerosols), increasing during the night, ascend from the surface and trigger the largest pulse of space charge of the day, with significant positive-to-negative HFPG spikes around 1000 UTC (Fig. 2a). Such spikes are also revealed by the broadband (up to 50 Hz) excitation of frequencies on HFPG spectrogram (Fig. 3) and a considerable increase in the standard deviation of the potential gradient (Fig. 4a). An increase in H values is observed at a similar time, reinforcing a link between the negative HFPG spikes and convection initiation. This process can be explained essentially by the elevation and erosion of the nocturnal electrode layer (Chalmers 1946) under the influence of convection, in which the rapid upward displacement of negative space charge within the convective plumes reduces the potential gradient considerably in relation to its typical value for this time of the day (approximately 50 V m^{-1}).

Space charge is then transported by numerous convective plumes throughout the day, producing an increased standard deviation of the potential gradient (Fig. 4a). Around 1500 UTC the convective process is at its maximum as can be seen by the backscatter data (Fig. 1) and confirmed by both H and TKE values (Fig. 4c, d respectively). At such time, all surface space charge should be aloft and being transported to higher altitudes (above 1 km); space charge would essentially be composed of easily transported small cluster ions. This implies that the space charge might form an elevated layer in which charge distribution changes rapidly from positive to negative, causing significant positive-to-negative fluctuations in the HFPG (Fig. 2a) associated with the initial development of convective plumes over the site. Such fluctuations would generate HFPG spectra excitations (Fig. 3) and increase the standard deviation of the potential gradient (Fig. 4a). The charge variability should then be associated with the translation of eddies containing different space-charge densities, but displacement of an elevated charge layer due to large eddies (thermal plumes) could also account for variability, although at longer periods of several seconds to minutes. After undergoing considerable mixing, the space-charge gradient will reduce, thereby reducing the relative intensity of charged eddies, and older space-charge parcels may recombine. Recombination, masking from space-charge parcels of different polarities and a weakening space-charge gradient, reduces the overall contribution of turbulent space charge to the potential gradient measured at the surface, weakening the HFPG fluctuations (Fig. 2a).

After this, around 1800 UTC, the decrease in solar radiation leads to a decrease in H (Fig. 4c), hence to a decrease in surface temperature (Fig. 4c), and initiates the collapse of the PBL (Fig. 1). During this process, which lasts approximately 2 h, vertical transport in the lower levels of the PBL increases and aerosols being transported increase the PBL backscatter of those levels (Fig. 1). The turbulent transfer of the near-surface space charge also increases, and consequently negative spikes appear again in the HFPG (Fig. 2a). This is reflected in excitations in the HFPG spectra (Fig. 3) and explain the observed local maximum of the standard deviation of the potential gradient around 1800 UTC (Fig. 4a). Stability increases after sunset, around 2000 UTC (Fig. 4b), and at the same time the convective boundary layer collapses reducing the convective space charge and aerosol transport, while increasing relative humidity, causing the aerosols to swell and become more confined to the surface. This can be seen by increased low altitude backscatter (Fig. 1). The extinction of convective transport at 2000–0000 UTC results in a reduction in the standard deviation of the potential gradient and TKE (Fig. 4a, d respectively).

To our knowledge, this is the first time it is proposed the occurrence of a quiet HFPG variability period between the disequilibrium in the turbulent eddy structure, early in the day as the boundary layer grows and, at the end of the day, as the sensible heat flux tends to zero. It should be emphasized that 17–19 June 2015 are working days (Wednesday to Friday, respectively), while 20 and 21 June 2015 are non-working days (Saturday and Sunday, respectively); similar results were observed for the non-working days in comparison to the

working ones. The fact that all days show similar behaviour implies that these observed phenomena were not significantly influenced by anthropogenic activities occurring mainly during the working days (e.g., space charge emitted by vehicle gas exhaustion). No lightning activity was detected in the region, and so excluding thunderstorms as a source of HFPG.

5 Conclusions

The influence of strong and dry convection within the PBL on high-frequency fluctuations of the potential gradient is assessed using co-located measurements of PBL backscatter, meteorological parameters, and 100-Hz recorded potential gradient, as well as the numerically simulated *Ri*, *H* and *TKE* quantities, using the Meso-NH atmospheric model v5.3. The results are consistent with the hypothesis that, under strong and dry convection, HFPG variability is closely associated with convective processes within the PBL. Fair correlations are found between the standard deviation of the potential gradient and *Ri*, and significant correlations are found between the standard deviation of the potential gradient, *H*, and *TKE* corroborating the proposed link. HFPG variability during this investigation was not expected to be strongly influenced by anthropogenic factors. Atmospheric convection plays a decisive role on particle deposition, which is a major problem for solar energy plants, as soiling of the panels produces a substantial reduction in the plant efficiency (Roth and Petit 1980; Sayyah 2014). Future work should focus on the understanding of particle rise and deposition due to convection, using HFPG variability as a convection proxy.

Acknowledgements RC and HGS acknowledge the Renewable Energy Chair for grants attributed by this research facility. RC also acknowledges the FCT Scholarship SFRH/BD/116344/2016. This work is co-funded by the European Union through the European Regional Development Fund, framed in COMPETE 2020 (Operational Programme Competitiveness and Internationalisation) through the ICT Project (UID/GEO/04683/2013) with Reference POCI-01-0145-FEDER-007690 and through the ALOP Project (ALT20-03-0145-FEDER-000004). Thanks are due to AERONET/PHOTONS and RIMA networks for the scientific and technical support. CIMEL calibration was performed at the AERONET-EUROPE GOA calibration centre, supported by ACTRIS under Agreement No. 654109 (H2020-INFRAIA-2014-2015). Gratitude are also given to the TOPROF (ES-1303) and ELECTRONET (CA15211) COST-Actions. Dr. John Chubb is honoured here for his overwhelming contribution to atmospheric electricity. More than a scientist, he was an exceptional person and friend, and he will be missed. A final acknowledgement is given to Giles Harrison and Keri Nicoll for discussions related to the present study.

References

Anderson RV (1976) Atmospheric electricity in the real world. In: Dolezalek H, Reiter R, Landsberg HE (eds) Electrical processes in atmospheres. Steinkopff, Darmstadt, pp 87–99. doi:10.1007/978-3-642-85294-7_13

Anisimov SV, Mareev EA, Shikhova NM, Dmitriev EM (2002) Universal spectra of electric field pulsations in the atmosphere. Geophys Res Lett 29(24):2217. doi:10.1029/2002GL015765

Anisimov SV, Galichenko SV, Shikhova NM (2014a) Space charge and aeroelectric flows in the exchange layer: an experimental and numerical study. Atmos Res 135–136:244–254. doi:10.1016/j.atmosres.2013.01.012

Anisimov SV, Afinogenov KV, Shikhova NM (2014b) Dynamics of undisturbed midlatitude atmospheric electricity: from observations to scaling. Radiophys Quantum Electron 56(11):709–722. doi:10.1007/s11141-014-9475-z

Chalmers JA (1946) The ionisation in the lower regions of the atmosphere. Q J R Meteorol Soc 72:199–205. doi:10.1002/qj.49707231217

Chalmers JA (1967) Atmospheric electricity, 2nd edn. Pergamon Press, New York

Chubb J (2014) The measurement of atmospheric electric fields using pole mounted electrostatic fieldmeters. J Electrostat 72:295–300. doi:10.1016/j.elstat.2014.05.002
Chubb J (2015) Limitations on the performance of 'field mill' fieldmeters with alternating electric fields. J Elesctrostat 78:1–3. doi:10.1016/j.elstat.2015.09.001
Conceição R, Silva HG (2015) Simulations of the global electrical circuit coupled to local Potential gradient measurements. J Phys Conf Ser 646:012017. doi:10.1088/1742-6596/646/1/012017
Conceição R, Melgão M, Silva HG, Nicoll K, Harrison RG, Reis AH (2015) Transport of the smoke plume from Chiado's fire in Lisbon (Portugal) sensed by atmospheric electric field measurements. Air Qual Atmos Health. doi:10.1007/s11869-015-0337-4
Costa MJ, Bortoli D, Pereira S, Silva AM, Wagner F, Belo N, Guerrero-Rascado JL, Navas-Guzman F, Alados-Arboledas L (2007) Analysis of the measurements taken by a ceilometer installed in the south of Portugal. In: Camerón A, Schäfer K, Slusser JR, Picard RH, Amodeo A (eds) Remote sensing of clouds and the atmosphere XII, Proceedings of SPIE (SPIE Bellingham, WA, 2007), pp 674523-1–674523-12
Cuxart J, Bougeault P, Redelsperger JL (2000) A turbulence scheme allowing for mesoscale and large-eddy simulations. Q J R Meteorol Soc 126(562):1–30. doi:10.1002/qj.49712656202
Elias T, Silva AM, Belo N, Pereira S, Formenti P, Helas G, Wagner F (2006) Aerosol extinction in a remote continental region of the Iberian Peninsula during summer. J Geophys Res 111(D14204):1–20. doi:10.1029/2005JD006610
Harrison RG (2013) The Carnegie curve. Surv Geophys 34:209–232. doi:10.1007/s10712-012-9210-2
Holben BN, Eck TF, Slutsker I, Tanre D, Buis JP, Setzer A, Vermote E, Reagan JA, Kaufman YJ, Nakajima T, Lavenu F, Jankowiak I, Smirnov A (1998) AERONET-A federated instrument network and data archive for aerosol characterization. Remote Sens Environ 66:1–16. doi:10.1016/S0034-4257(98)00031-5
Hoppel WA, Anderson RV, Willett JC (1986) Atmospheric electricity in the planetary boundary-layer. In: Krider EP, Roble RG (eds) The Earth's electrical environment. National Academy Press, Washington, pp 149–165
Isräel H (1959) Atmospheric electrical agitation. Q J R Meteorol Soc 85:91–104. doi:10.1002/qj.49708536403
Marshall TC, Rust WD, Stolzenburg M, Roeder WP, Krehbiel PR (1999) A study of enhanced fair-weather electric fields occurring soon after sunrise. J Geophys Res Atmos 104(D20):24455–24469. doi:10.1029/1999JD900418
Masson V, Champeaux JL, Chauvin F, Meriguet C, Lacaze R (2003) A global database of land surface parameters at 1-km resolution in meteorological and climate models. J Clim 16(9):1261–1282. doi:10.1175/1520-0442-16.9.1261
Masson V, Le Moigne P, Martin E et al (2013) The SURFEXv7.2 land and ocean surface platform for coupled or offline simulation of earth surface variables and fluxes. Geosci Model Dev 6(4):929–960. doi:10.5194/gmd-6-929-2013
Lafore J, Stein J, Asencio N, Bougeault P, Ducrocq V, Duron J, Fischer C, Hereil P, Mascart P, Pinty J, Redelsperger J, Richard E, Arellano J (1998) The Meso-NH atmospheric simulation system. Part 1: adiabatic formulation and control simulation. Ann Geophys 16:90–109. doi:10.1007/s00585-997-0090-6
Nicoll K, Harrison RG, Silva HG, Salgado R, Melgao M, Bortoli D (2017) Electrical sensing of the dynamical structure of the planetary boundary-layer. J Geophys Res **(submitted)**
Pergaud J, Masson V, Malardel S, Couvreux F (2009) A parameterization of dry thermals and shallow cumuli for mesoscale numerical weather prediction. Boundary-Layer Meteorol 132:83–106. doi:10.1007/s10546-009-9388-0
Piper IM, Bennett AJ (2012) Observations of the atmospheric electric field during two case studies of boundary-layer processes. Environ Res Lett 7:014017. doi:10.1088/1748-9326/7/1/014017
Policarpo C, Salgado R, Costa MJ (2017) Numerical simulations of fog events in southern Portugal. Adv Meteorol. doi:10.1155/2017/1276784
Roth EP, Petit RB (1980) Effect of soiling on solar mirrors and techniques used to maintain high reflectivity. In: Murr L (ed) Solar material science. Academic Press, New York, pp 199–227
Rycroft MJ, Nicoll KA, Aplin KL, Harrison RG (2012) Recent advances in global electric circuit coupling between the space environment and the troposphere. J Atmos Sol Terr Phys 90–91:198–211. doi:10.1016/j.jastp.2012.03.015
Sayyah A (2014) Yield loss of photovoltaic panels caused by depositions. Sol Energy 107:576–604. doi:10.1016/j.solener.2014.05.030
Silva HG, Conceição R, Melgão M, Nicoll K, Mendes PB, Tlemçani M, Reis AH, Harrison RG (2014) Atmospheric electric field measurements in urban environment and the pollutant aerosol weekly dependence. Environ Res Lett 9:114025. doi:10.1088/1748-9326/9/11/114025

Silva HG, Lopes FM, Pereira S, Nicoll K, Barbosa SM, Conceição R, Neves S, Harrison RG, Collares Pereira M (2016) Saharan dust electrification perceived by a triangle of atmospheric electricity stations in southern Portugal. J Electrostat 84:106–120. doi:10.1016/j.elstat.2016.10.002

Stull RB (1988) An introduction to boundary layer meteorology. Kluwer Academic Publishers, Dordrecht

Tacza J, Raulin JP, Macotela E, Norabuena E, Fernandez G, Correia E, Rycroft MJ, Harrison RG (2014) A new South American network to study the atmospheric electric field and its variations related to geophysical phenomena. J Atmos Sol Terr Phys 120:70–79. doi:10.1016/j.jastp.2014.09.001

Wright MD, Holden NK, Shallcross DE, Henshaw DL (2014) Indoor and outdoor atmospheric ion mobility spectra, diurnal variation, and relationship with meteorological parameters. J Geophys Res Atmos. doi:10.1002/2013JD020956

Yaniv Y, Yair Y, Price C, Katz S (2016) Local and global impacts on the fair-weather electric field in Israel. Atmos Res 172–173:119–125. doi:10.1016/j.atmosres.2015.12.025

Atmospheric Research 202 (2018) 81–95

Contents lists available at ScienceDirect

Atmospheric Research

journal homepage: www.elsevier.com/locate/atmosres

Electrical sensing of the dynamical structure of the planetary boundary layer

K.A. Nicoll[a,b,*], R.G. Harrison[a], H.G. Silva[c], R. Salgado[d], M. Melgâo[d], D. Bortoli[d]

[a] Department of Meteorology, University of Reading, Earley Gate, Reading, Berkshire RG6 6BB, UK
[b] Department of Electronic and Electrical Engineering, University of Bath, Claverton Down, Bath BA2 7AY, UK
[c] Renewable Energies Chair, University of Évora, Palácio do Vimioso, Largo Marquês de Marialva, 7002-554 Évora, Portugal
[d] Departamento de Física, ICT, Instituto de Ciências da Terra, Universidade de Évora, Rua Romão Ramalho 59, 7002-554 Évora, Portugal

A B S T R A C T

Turbulent and convective processes within the planetary boundary layer are responsible for the transport of moisture, momentum and particulate matter, but are also important in determining the electrical charge transport of the lower atmosphere. This paper presents the first high resolution vertical charge profiles during fair weather conditions, obtained with instrumented radiosonde balloons over Alqueva, Portugal during the summer of 2014. The short intervals (4 h) between balloon flights enabled the diurnal variation in the vertical profile of charge within the boundary layer to be examined in detail, with much smaller charges (up to 20 pC m^{-3}) observed during stable night time periods than during the day. Following sunrise, the evolution of the charge profile was complex, demonstrating charged ultrafine aerosol, lofted upwards by daytime convection. This produced charge up to 92 pC m^{-3} up to 500 m above the surface. The diurnal variation in the integrated column of charge above the site tracked closely with the diurnal variation in near surface charge as derived from a nearby electric field sensor, confirming the importance of the link between surface charge generation processes and aloft. The local aerosol vertical profiles were estimated using backscatter measurements from a collocated ceilometer. These were utilised in a simple model to calculate the charge expected due to vertical conduction current flow in the global electric circuit through aerosol layers. The analysis presented here demonstrates that charge can provide detailed information about boundary layer transport, particularly in regard to the ultrafine aerosol structure, that conventional thermodynamic and ceilometer measurements do not.

1. Introduction

The effect of meteorological processes on the electrical state of the atmosphere has been known about for almost 250 years, even leading Lord Kelvin to suggest that weather forecasting would one day be achieved with an electrometer (e.g. Aplin and Harrison, 2013). The complexity, however, of relationships between atmospheric electrical variables and meteorological processes makes this difficult. What has become evident is that the same meteorological processes that act to transport heat, momentum, moisture and pollutants within the lower atmosphere also transport charge (see review by Hoppel et al., 1986). This has led to suggestions that so-called atmospheric electrical "convection currents" can be used as a method for determining turbulent transport processes in the lower atmosphere, e.g. Markson et al. (1981). The similarity between the convective flux of charge and turbulent transport processes is particularly strong near the surface, i.e. within the planetary boundary layer (PBL). The PBL is the lowest portion of the atmosphere which is directly influenced by the presence of the surface (often referred to historically in atmospheric electricity as the Exchange or Austausch layer), with a depth ranging from a few hundred meters to several km, varying with latitude and time of day (e.g. Stull, 2012). In the PBL, air-surface interactions take place in the form of mechanical and thermal forces, which drive turbulence and convection respectively. The PBL structure evolves considerably throughout the day (see e.g. Garratt, 1994 for example vertical profiles), and also varies between land and ocean surfaces (e.g. Kaimal and Finnigan, 1994). Processes within the PBL control transport of aerosol particles, moisture and momentum and the PBL top is typically characterised by a temperature inversion (known as a "capping inversion"), which traps these quantities beneath it. The height of the PBL is often used to characterise the vertical extent of mixing within the boundary layer and the level at which exchange with the free troposphere occurs.

Free charge is ubiquitous in the atmosphere and is released by ionisation from Galactic Cosmic Rays (GCRs) and radioactivity near the earth's surface (i.e. gamma and beta radiating directly from the surface, as well as radiation from radioactive gases). This ionisation gives rise to the electrical conductivity of air, σ, which is primarily due to the presence of small cluster ions (nm diameter) (e.g. Tammet, 1995).

* Corresponding author at: Department of Meteorology, University of Reading, Earley Gate, Reading, Berkshire RG6 6BB, UK.
E-mail address: k.a.nicoll@reading.ac.uk (K.A. Nicoll).

https://doi.org/10.1016/j.atmosres.2017.11.009
Received 2 June 2017; Received in revised form 2 November 2017; Accepted 6 November 2017
Available online 08 November 2017
0169-8095/ © 2017 The Authors. Published by Elsevier B.V. This is an open access article under the CC BY-NC-ND license (http://creativecommons.org/licenses/BY-NC-ND/4.0/).

Maintenance of charge within the atmosphere is a continual balance between ion generation and loss processes (Hoppel and Frick, 1986). As well as generation of ions by GCRs and radioactivity, ions are destroyed by ion-ion recombination (i.e. self-neutralisation), and lost by attachment to larger particles such as aerosol and cloud droplets. Ions are subject to the same turbulent eddies that transport momentum, moisture and pollutants throughout the PBL. Thus atmospheric electrical variables within the PBL depend on the local ionisation profile, aerosol size and number distribution as well as turbulent mixing of both ions and radioactive gases. Therefore they are heavily dependent on the combined influences of surface drag, heating, and evaporation from the underlying Earth's surface.

As well as being influenced by local meteorological variations, atmospheric electrical variables are also governed by global scale current flow in the global electric circuit, GEC, (e.g. Williams, 2009; Rycroft et al., 2008). This is most evident when studying the diurnal variation in atmospheric electric field, which is usually measured as the Potential Gradient, PG.[1] In clean air PG exhibits a minimum at ~0400 UT and a maximum at ~1900 UT, in accordance with the diurnal variation in global thunderstorm activity (Wilson, 1921; Whipple, 1929; Mach et al., 2011). The globally-invariant nature of this variation, at least on average, was first observed on the ocean cruises organised by the Carnegie Institution (Harrison, 2013), and hence is often referred to as the *Carnegie curve*. GEC effects on surface measurements of PG made within the PBL are often masked by dominant local meteorological effects such as convection or turbulent mixing, which can manifest themselves as additional fluctuations superimposed on the fair weather Carnegie curve (e.g. Israel, 1955). This is of particular importance during summer sunrise when convection causes mixing of the layer of positive charge which can form close to the nocturnal surface (known as the electrode layer[2]), thereby transiently disturbing the established local PG. Electrode layers only occur within a few meters of the surface most commonly over the calm ocean surface where there is no source of radioactive ionisation, but also over land during stable, low wind conditions (Crozier, 1963).

Although positive and negative ions are initially created in equal numbers, natural processes act to separate the different charge polarities, including the transfer of charge to aerosol and cloud droplets. This gives rise to the space charge density, ρ, which refers to the net difference between positive and negative charge per unit volume. ρ is not concerned with the nature of individual charge carriers, but only the total charge retained by all charge carriers. ρ is defined as

$$\rho = e\left[(n_+ - n_-) + \sum_{i=1}^{i=k}\sum_{j=-\infty}^{\infty} jN_{i,j}\right], \quad (1)$$

where the first term is the ionic space charge contribution and the second term is that due to particulate aerosol. e is the magnitude of the electronic charge, n_+ and n_- are the small ion number concentrations, and the aerosol size distribution is represented by k size categories, each of which spans j elementary charges. Charge separation can arise from flow of the air-Earth conduction current, J_c, which flows vertically between the ionosphere to Earth's surface through aerosol and cloud layers. The theory behind such phenomenon is described in detail in Zhou and Tinsley (2007), Harrison et al. (2015), and Nicoll and Harrison (2016).

Analytical studies of the influence of meteorological processes on atmospheric electric variables date back before the 1800s (e.g. Cavello, 1777), but since most measurements were performed near the surface, at low altitudes, these sites were almost always within the PBL. To study the effect of the PBL on atmospheric electricity, one must get above the inversion layer, thereby such as through mountaintop observatories, airborne measurements, or very tall towers (such as the Eiffel tower (e.g. Harrison and Aplin, 2003)). The pioneering aircraft measurements of Sagalyn and Faucher (1954, 1956) were amongst the first to demonstrate quantitatively that the electrical conductivity of air aloft was substantially reduced by the presence of aerosol particles trapped within the PBL, with a distinct change in behaviour in the free troposphere above. This was also found through mountaintop observations at the Zugspitze using an instrumented cable car (Reiter and Sládkovič, 1970). Moore et al. (1962) analysed hourly aircraft profiles of space charge (i.e. the net difference between positive and negative charge) throughout the day, demonstrating the similarity between this and the evolution of the PBL temperature profile, as well as the relation to fog and haze layers. More recently, Marshall et al. (1999) have studied the evolution of the electric field profile up to several hundred metres, demonstrating the existence of elevated layers of space charge close to the ground in the build up to sunrise.

In terms of quantifying the relationships between atmospheric electrical variables and turbulent diagnostic parameters, Markson et al. (1981), demonstrated good correlation between aircraft observations of the electrical eddy flux of space charge (found from PG measurements) and surface moisture flux over the ocean surface. In addition, several attempts at characterising the eddy diffusion coefficient (which represents the ability of turbulent eddies to transport atmospheric variables from a region of excess to a region of deficit) have been made both over land (e.g. Kawano, 1957; Kulkarni, 2010) and over the ocean (Hoppel and Gathman, 1971). The ocean situation is more straightforward to analyse due to the absence of radioactivity and low aerosol content, as well as reduced surface roughness.

Much of the modelling work studying atmospheric electricity in the PBL has focused on the electrode layer (Hoppel and Gathman, 1971; Willett, 1979; Willett, 1981; Kulkarni, 2010) as this is one of the main sources of local space charge in the atmosphere. Turbulent scenarios involving the electrode layer are complex, however, Hoppel and Gathman (1972) demonstrated reasonable agreement between a model of the turbulent electrode layer and observations over an ocean surface. More recent work over continental surfaces has demonstrated the existence of sub-mesoscale electrical structures superimposed on the mean wind flow in the PBL, which have been termed “Aero Electric Structures (AES)” (Anisimov et al., 1994) and are directly related to transport of turbulent eddies. These have typical dimensions of 500 to 1000 m and lifetimes of tens of minutes, detected experimentally from high frequency analysis of PG data. Anisimov et al. (1999, 2013) discuss the development of a detailed numerical model for AES formation which takes into account turbulent transport of space charge by convection and demonstrates that the dynamic and stability conditions of the PBL are key to controlling the evolution of the space charge profile.

This work presents new high resolution vertical profiles of space charge through and above the PBL in fair weather conditions. Measurements were made during the ALEX2014 field campaign in Portugal, during the summer of 2014, and consisted of surface measurement of Potential Gradient (PG), as well as a number of specially instrumented radiosonde balloon flights, carrying space charge sensors. Detailed analysis of the diurnal variation in the vertical profile of space charge is undertaken, as well as its relation to the surface PG and ceilometer measurements of aerosol backscatter. This is the first time that inexpensive, disposable electrical sensors have been demonstrated to provide indirect information about turbulent mixing processes in the lower atmosphere.

2. Methodology and instrumentation

The observations described here took place as part of the ALEX2014 field campaign (alex2014.cge.uevora.pt.) at the Alqueva reservoir,

[1] The Potential Gradient F is related to the vertical component of the electric field E_z by $F = -E_z$.

[2] The electrode layer results from the flow of ions under the atmospheric electric field (positive ions are driven downward, and negative ones upward) and the presence of the boundary of the surface. At this boundary positive ions flowing downward are forced to stop leading to a net accumulation of positive charge.

Portugal (38.27°N, 7.53°W) during July 2014. The main aim of the campaign was to study the impact of the reservoir on the local environment. Alqueva experiences a typical Mediterranean climate, with warm, dry summer periods, and sparse vegetation. The location of Alqueva is rural, with little anthropogenic pollution. The Alqueva reservoir is the largest inland lake in Portugal, of area 250 km^2 and 80 km from end to end. The size of the reservoir means that it is common for a lake breeze effect to develop during calm conditions when the lake/land temperature contrast is strong (e.g. see Potes et al., 2017). As this has been shown to affect local meteorological and electrical conditions close to the lake shore (Lopes et al., 2016), we also consider potential lake breeze effects here.

Surface PG measurements were made continuously throughout the campaign (see Lopes et al., 2016) using a JCI 131F electrostatic field mill at 2 m above the ground. The measurement site was located ~100 m from the shoreline at the southern end of the lake, on a small hill ~50 m above the water surface (Parque Solar). A map of the Alqueva reservoir and the location of the measurement at Parque Solar are provided in Appendix A. The field mill was set to a 0–2 kVm^{-1} range, with data sampled at 1 s and logged at 1 minute averages. Nearby meteorological measurements of temperature, relative humidity (RH), wind speed, wind direction and solar radiation were also made. Further instrumentation was used to provide information about the aerosol content at Alqueva in the form of a CL31 Ceilometer manufactured by Vaisala and a TSI Optical Particle Sizer (model OPS3330). The main features of these systems and the data processing and retrieval techniques are described in Appendices C and D.

Balloon-carried instruments were launched from a location ~100 m from the PG measurement site. Vaisala RS92 radiosondes were instrumented with the PANDORA system (Programmable ANalogue and Digital Radiosonde Accessory) developed by the University of Reading (Harrison et al., 2012), which provides a data acquisition system with which to interface additional science sensors to the standard meteorological radiosonde. Each sensor package carried a space charge sensor based on the design described in Nicoll (2013) (simplified to omit the self-calibrating mode). This charge sensor uses a spherical electrode connected to a sensitive electrometer circuit to measure the displacement current generated from a changing electric field, dominated by vertical electric field variations as the sonde ascends. The space charge is derived from the electrometer current and the ascent rate. Calibration details are given in Nicoll and Harrison, 2016. The typical 5 ms^{-1} ascent rate of the sonde, and 1 Hz sampling rate of the PANDORA system provides a measurement approximately every 5 m in altitude. An Intense Observation Period (IOP) during the ALEX2014 campaign took place on 22nd to 24th July 2014 when a total of 8 specially instrumented radiosonde packages were launched during the two days. Balloon flight details during the IOP are given in Table 1.

Sensor packages were flown beneath 600 g balloons, reaching, on average, altitudes of 31 km at burst. An example of a full height vertical profile from one of the specially instrumented radiosondes is shown in Fig. 1 which displays (a) temperature and RH data and (b) space charge density measured by the charge sensor. Considering the space charge profile, Fig. 1(b) clearly shows that the magnitude of the charge is large within the boundary layer but decreases markedly with altitude above this. The remainder of this paper is concerned with the vertical variation of space charge within the PBL.

3. Results

3.1. Diurnal variation of space charge with height in the PBL

During the most intensive period of the campaign, the specially instrumented radiosondes were launched approximately every 4 h which provides an opportunity to study the time evolution of the vertical profile in space charge as the PBL evolves throughout the day. The period of interest examined further is from 0200 UT 23rd July to 0200 UT 24th July (flights 3 to 8 in Table 1), with individual plots from each flight shown in Fig. 2. The weather during this period was characterised by anticyclonic conditions (surface pressure > 990 hPa for the entire IOP), with clear skies during the day and maximum air temperatures up to 38 °C. Overnight, the clear skies led to rapid cooling (minimum night time temperatures ~16 °C) and the formation of short lived cloud layers lasting only a few hours, which dissipated by 0700 UT most mornings. The 23rd July was dominated by a weak north westerly flow, which was sufficient enough to prevent any lake breeze effect from developing. This is in contrast to the previous day (22nd July), when the strongest lake breeze effect of the entire ALEX campaign was observed (see Potes et al., 2017 for more detail). The effect of the lake breeze on the meteorological conditions on 22nd is discussed in Section 3.2.

Fig. 2 shows thermodynamic quantities of temperature, potential temperature, relative humidity, (RH), horizontal wind speed and direction, as well as magnitude of space charge profiles for six ascents within a 24 hour period on 23rd July. The modulus of the space charge is used here due to the high degree of variability in the space charge measurement which makes the polarity difficult to interpret, which is partly a consequence of measuring at such high resolution. To make the space charge determination as robust as possible, we therefore use the absolute value of space charge. This is an alternative to providing an average profile which would remove the detailed vertical structure in the space charge, which is the main focus here.

Starting with the first ascent at 0208 UT on 23rd July (Fig. 2(a)), the temperature profile in the lower levels is characteristically stable, with a substantial inversion at ~300 m (associated with the formation of the nocturnal boundary layer), with a subsequent smaller near neutral residual layer up to ~2.5 km. The inversions at 2.5 and 3 km are likely to be associated with the remainder of the PBL top from the previous afternoon. The wind profile from the radiosonde demonstrates the presence of two jets between ~0.3–0.7 km and 2–3 km, with a maximum wind speed at 2.3 km. Substantial wind shear (confirmed by the vertical change in wind direction) is also evident at the top of the lower level jet at ~1 km. The space charge profile shows at least 3 distinct

Table 1
Summary of details of specially instrumented balloons launched during the IOP between 22nd and 24th July. Balloon launch times are given in UT which is 1 h behind local time. PBL height is derived according to the most significant inversion in the potential temperature profile. Max space charge is the maximum magnitude of space charge in the layer from the surface up to 3.5 km.

Flight number	Date	Launch time (UT)	PBL height (m)	Max space charge (pC m^{-3})
1	22/07/14	1134	1928	46.5
2	22/07/14	2030	2210	27.3
3	23/07/14	0208	317	23.2
4	23/07/14	0830	704	41.9
5	23/07/14	1130	811	44.5
6	23/07/14	1420	1733	91.7
7	23/07/14	1725	1774	73.6
8	24/07/14	0215	604	79.2

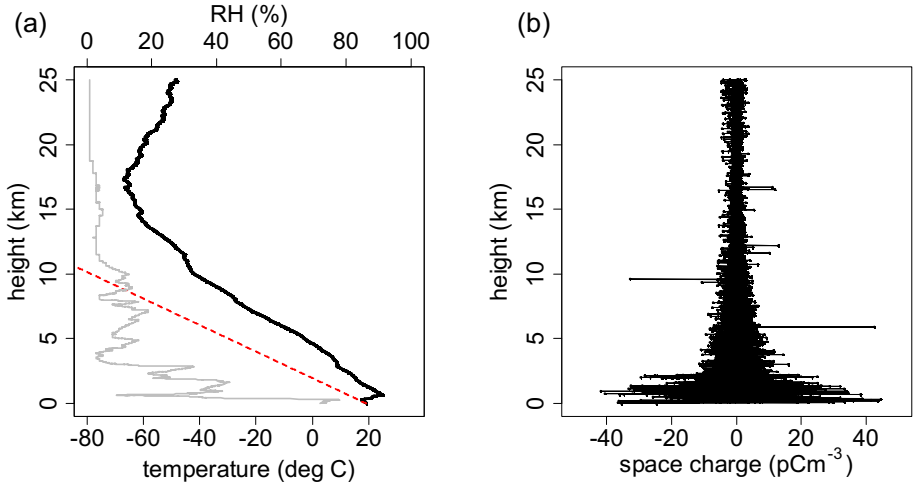

Fig. 1. (a) Vertical profile measured at Alqueva at 0830 UT on 23rd July 2014 (flight 4 in Table 1). Thermodynamic profiles of temperature (black) and RH (grey) as measured by the RS92 radiosonde's sensors (the red line shows the dry adiabatic lapse rate, DALR), (b) measured space charge. (For interpretation of the references to colour in this figure legend, the reader is referred to the web version of this article.)

thin layers of charge from the surface up to the inversion at 2.5 km, with a maximum value of ~23 pC m^{-3}. The charge layer at 2 km is suggested to result from trapping of charge underneath the main inversion of the residual layer, transported upwards from the surface from the earlier daytime convection. The layer at 1 km is not associated with a temperature inversion, but is coincident with a region of increased RH and wind shear.

Fig. 2(b) shows an ascent profile 6 h later at 0830 UT, by which time the surface layer has become convective; at 300 m the temperature inversion has strengthened, and the charge profile has become much more complex. During the 6 hour period between ascents a number of notable meteorological and solar changes occurred. Fig. 3 shows a time series of ceilometer backscatter during the IOP on 23rd and 24th July 2014. Deep blue areas indicate small backscatter signals demonstrating the absence of clouds, whereas colours from light blue through to red illustrate increasing backscatter values which represent an increase in the atmospheric optical depth. It is clear from the red backscatter between 0530 UT and 0800 UT on 23rd July that a shallow layer of cloud formed at ~600 m altitude during the early morning hours, between the balloon ascents. The remnants of this are also apparent from the RH data in Fig. 2(a) and (b) in which the maximum value of RH in the near surface layer increased from 60 to 76% between the 0200 UT and 0830 UT ascents. This occurred due to substantial cooling near the surface under clear skies. The lifetime of the cloud layer was very short, with dissipation by 0800 UT, due to the increase in surface heating (as well as warming from above the cloud) due to the sunrise at 0627 UT.

The space charge profile measured at 0830 UT is clearly very different from the night time profile at 0200 UT. The magnitude of the charge up to 2 km is ~twice as large as during the earlier ascent, with much deeper individual charge layers, extending from the surface up to 2 km. The most straightforward explanation is that the extra charge originated from horizontal advection, in the large scale synoptic flow. Fig. 4(a) and (b) shows modelled wind speed and direction plots for 1300 UT on 22nd and 23rd July at the surface over Alqueva dam using the non-hydrostatic Meso-NH (Lafore et al., 1998) atmospheric model at 1 km horizontal resolution. (The model and the setup of the simulation are described further in Appendix A.) Considerable differences in the wind conditions exist between the two days in that July 22nd is dominated by a local lake breeze (characterised by wind directions flowing from the centre of the lake to the shore), whilst July 23rd is dominated by a moderate north westerly flow. The increased space charge at 0830 UT on 23rd July is therefore likely to be linked to the advection of air which would have passed over more populated areas such as Lisbon and therefore contained a higher concentration of pollutants than would be present at Alqueva.

An additional contribution to the vertical charge profile at 0830 UT could arise from the earlier cloud layer at ~600 m, which would cause charge to accumulate on the horizontal cloud edges as a result of vertical conduction current flow in the GEC (see Section 3.3 for further discussion). Such charging has been observed to occur frequently due to the conductivity gradients present around stratiform cloud layers (e.g. Nicoll and Harrison, 2010, 2016) as well as aerosol layers (e.g. Moore et al., 1962), and leads to a net charging of droplets/particles in these areas. Although the droplets would evaporate as the cloud dissipates, the charge would be retained either in the form of small ions or on Cloud Condensation Nuclei (CCN) following ion-particle attachment; CCN typically have lifetimes of tens of minutes to hours.

Following the 0830 UT flight, Fig. 2(c) shows the subsequent measurements made at 1130 UT. The nocturnal inversion layer has almost been completely eroded by surface heating, being replaced by a convective boundary layer with a depth of ~900 m and the near surface RH reduced to below 50%. The elevated layers of charge observed in the previous flight are still observed, although the uppermost charge layer at 2 km contains a reduced charge density. There is also an enhancement of the charge at ~500 m, which is coincident with a substantial vertical change in wind direction, and therefore wind shear.

By 1420 UT (Fig. 2(d)) a substantial charge layer has formed from 100 m to 600 m and strengthened in magnitude to 100 pC m^{-3}. The fact that the temperature profile in the lowest 1.5 km follows the Dry Adiabatic Lapse Rate (DALR, or Γ_d, as shown by the red dashed line) almost exactly, suggests that by this time of day the boundary layer is effectively well mixed, however, this is certainly not the case for the charge profile. An explanation for the increased magnitude of charge in the lowest several hundred meters may be seen in Fig. 5(a), which shows the time series of aerosol concentration and Potential Gradient (PG) measured at Alqueva 2 m above the surface during the 23rd July. The aerosol measurements are 5 minute averages, made with a TSI3330 Optical Particle Sizer which counts and sizes particles from 0.3 to 10 μm diameter. Further information on the TSI3330 is given in Appendix D.

Fig. 5(a) demonstrates that around 1200 UT, the aerosol concentration starts to increase, reaching a max at 1330 UT. This is presumably due to the increase in daytime convection (supported by the relatively high vertical velocities in Fig. 4 at this time), which will easily loft particles upward. The extremely dry surface environment, characteristic of conditions which persist throughout the Mediterranean region in the summer months, means that particles are only very loosely bound to the surface. If charged, it follows that these lofted particles will contribute to the increased charge levels observed during the 1420 UT ascent. Fig. 5(a) also shows that most of the contribution to the total aerosol concentration is from small particles (< 1 μm), which are the most easy to be lofted. There will also be a further contribution

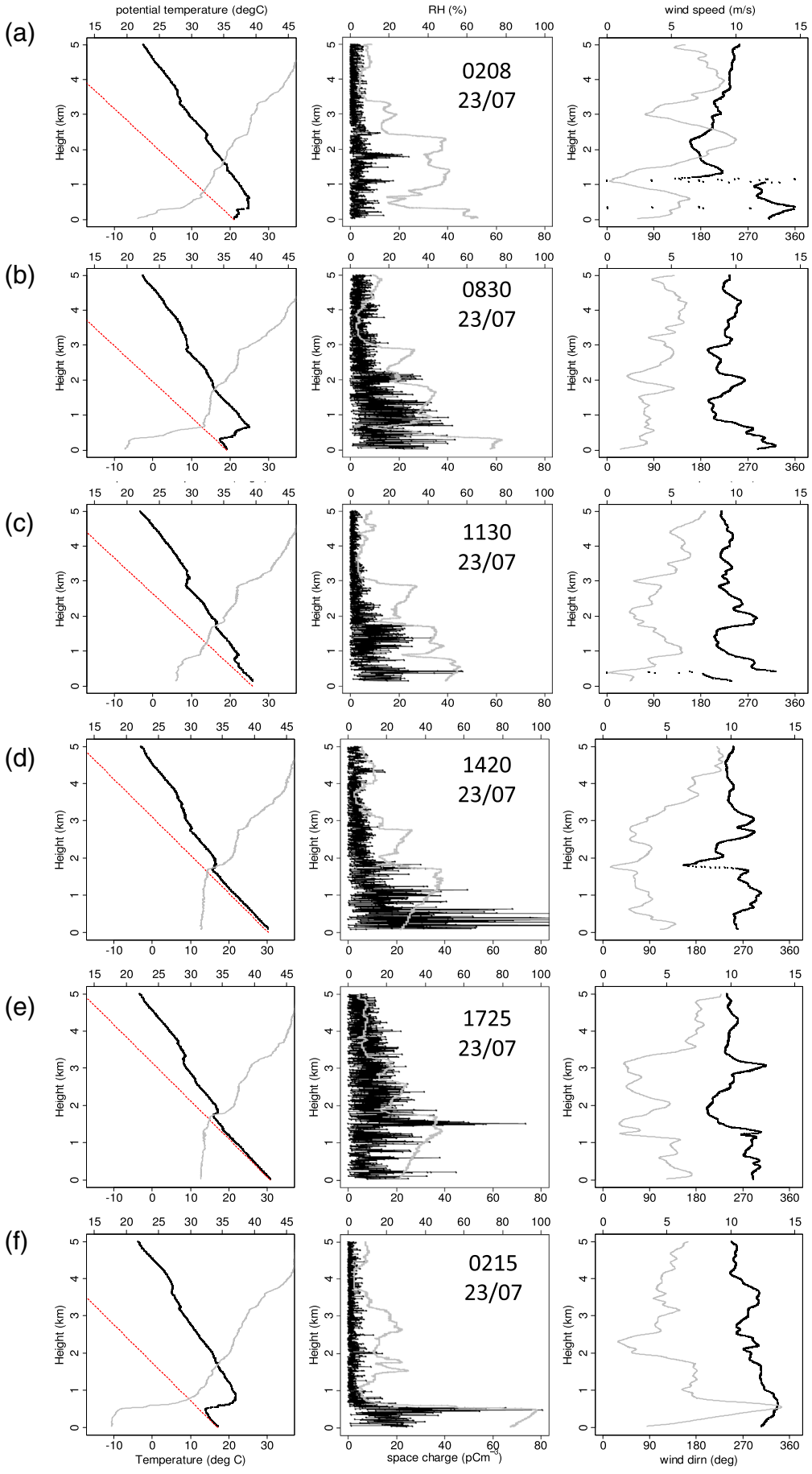

Fig. 2. Vertical profiles from specially instrumented radiosondes from (a) 0200 UT on 23rd to (f) 0200 UT on 24th July 2014. Each flight shows three plots. Left plot - temperature (black), potential temperature (grey) and Dry Adiabatic Lapse Rate (DALR) (red dashed); central plot - RH (grey), magnitude of space charge (black), Right plot - horizontal wind speed (grey) and wind direction (black). (For interpretation of the references to colour in this figure legend, the reader is referred to the web version of this article.)

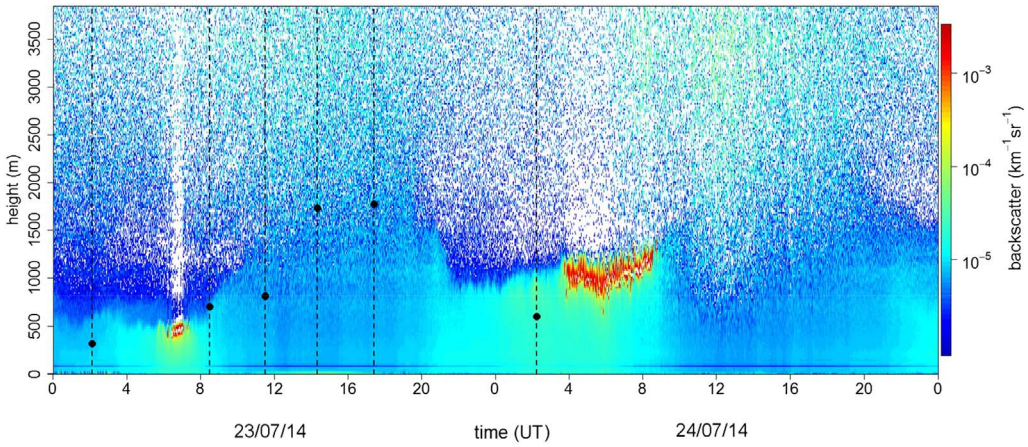

Fig. 3. Backscatter profile from the Vaisala CL31 ceilometer on 23rd and 24th July 2014 at Alqueva. Dashed vertical lines indicate the times of specially instrumented sonde ascents, and the black dots represent the height of the largest potential temperature inversion as determined from the sonde. The red and yellow points between 0500–0700 UT on 23rd and 0400–0900 UT on 24th denote periods when cloud was present. (For interpretation of the references to colour in this figure legend, the reader is referred to the web version of this article.)

from particles smaller than the 0.3 μm detection limit of the TSI3330 which were too small to be detected. Further evidence for the involvement of aerosol in the elevated charge levels is also given by the PG measurements shown in Fig. 5(a) (black line). During the period of enhanced aerosol concentration from 1200 UT to 1600 UT the PG is much greater, up to 350 V/m, and more variable than at other times. The reason for this may be twofold: 1) the aerosol concentration is sufficient to reduce the air conductivity, thereby increasing the PG in accordance with Ohm's law (for a constant vertical conduction current); 2) the aerosol particles are charged, and their separation into positive and negative charge regions causes a change in the net PG. A combination of both effects will occur, but the relatively small aerosol concentrations (which indicate that the lower tropospheric air in the Alqueva region is very clean) are very unlikely to lead to such large variability in the PG through the conductivity route alone. It is therefore suggested that space charge generation results mostly from movement of charge carried by ultrafine particles, as well as ionic space charge. The wind speed measurements shown in Fig. 5(b) show a gradual increase in near surface wind speed from 1200 UT onwards, supporting the lofting possibility. Dust particles are likely to charge through a variety of mechanisms including triboelectric charging (e.g. Lacks and Levandovsky, 2007) and investigators have previously observed substantial surface electric fields within desert dust storms (e.g. Esposito et al., 2016; Yair et al., 2016; Harrison et al., 2016; Silva et al., 2016). Although the particle concentration and wind speeds here are nowhere near as large as the values observed in storms, Fig. 7 (which shows modelled vertical velocities for 22nd July), does show a marked increase in vertical velocity (up to 1 ms^{-1} at the surface) around the period of the maxima in aerosol concentration from 1400 UT to 1800 UT which could certainly loft surface aerosol through convective updrafts (e.g. Adler and Kalthoff, 2014). The predicted vertical velocities of up to 1 m/s would enable particles at the surface to be transported upwards to the maximum observed altitude of charging at 500 m in around 8 min (assuming that the particles travel at the same speed as the updrafts). There may also be an additional contribution to aerosol above the surface from long range horizontal advection from the North

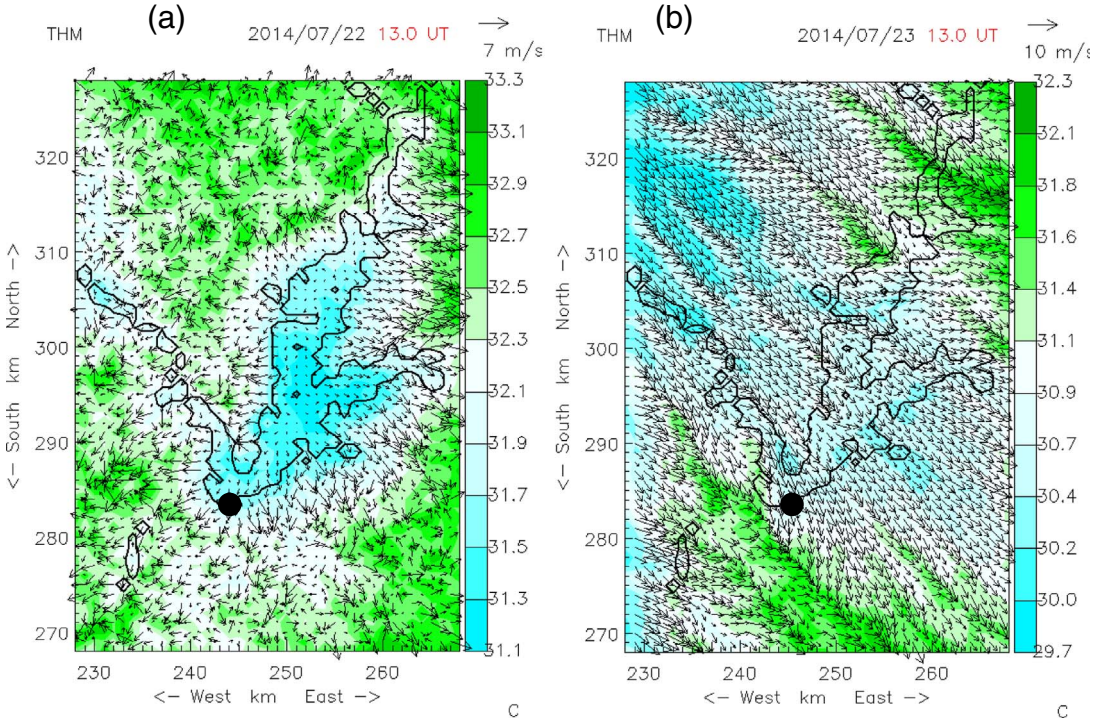

Fig. 4. Modelled horizontal wind (arrows) over potential temperature (coloured contours) in a model surface ~200 m above surface around Alqueva reservoir using the Meso-NH model with a resolution of 1 km at 1300 UT on (a) 22nd and (b) 23rd July. (For interpretation of the references to colour in this figure legend, the reader is referred to the web version of this article.)

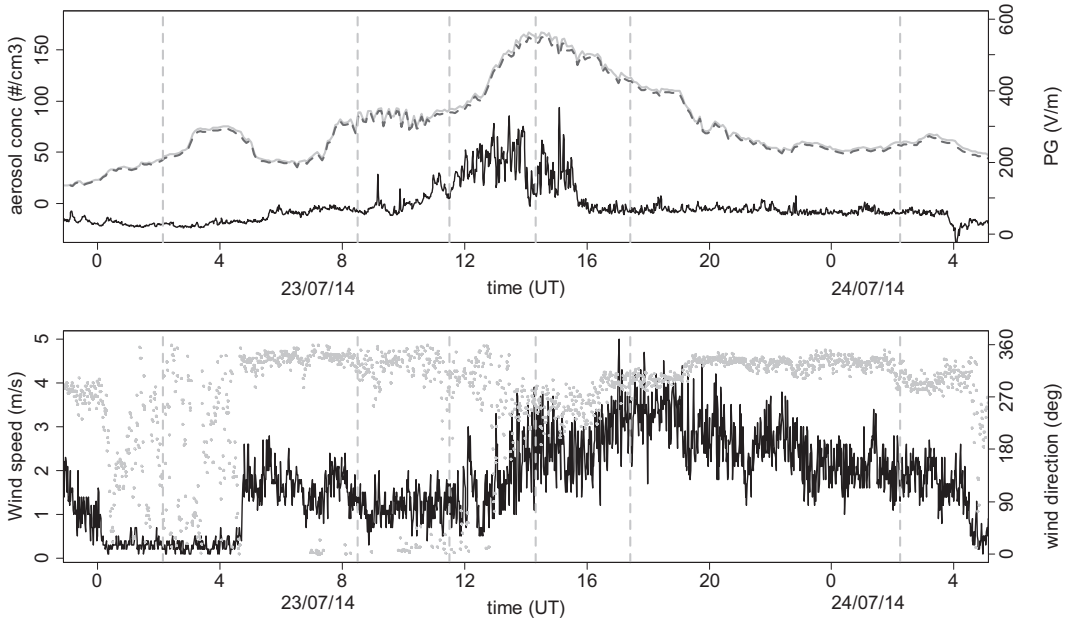

Fig. 5. (a) Aerosol number concentration (solid light grey = total concentration for all particles from 0.3–10 μm, dashed dark grey = concentration of particles < 1 μm), measured by a TSI3330 OPC. The black line shows measurements of Potential Gradient (PG) measured by a JCI 131F electric field mill. (b) 2 m wind speed (black solid line) and wind direction (grey points), all measured at Alqueva, Portugal on 23rd and 24th July 2014. Dashed grey lines denote the times of balloon ascents. Aerosol measurements are 5 minute averages, PG 1 minute averages and wind data 1 minute average.

Westerly flow which will have passed close to polluted cities such as Lisbon.

The movement of charged aerosol has been observed to cause rapid variations in PG (e.g. Matthews et al., 2012; Piper and Bennett, 2012; Conceição et al., 2017), very similar to those observed during 23rd July at Alqueva, therefore this is suggested as the cause of the unusually high variability in the PG during this period. The relationship between the surface PG and vertical charge profile will be discussed further in Section 3.2.

Returning to Fig. 2, Fig. 2(e) shows the vertical profile from the late afternoon ascent at 1725 UT. The temperature profile is almost identical to the 1420 UT ascent, suggesting a well-mixed atmosphere as before. The intense region of charge in the lower levels at 1420 UT is no longer present, instead a distinct charge layer exists between 1.5 and 2 km near the top of the boundary layer. This is suggested to result from the upward mixing of the surface lofted charge due to convection. By the time of the final vertical ascent at 0215 UT on 24th July (Fig. 2(f)), substantial surface cooling has led to an increase in the near surface RH up to 80% (this later led to the formation of a cloud layer, but not until 0330 UT). A well-defined charge layer is present in the region of high RH, related to hygroscopic growth of ions and aerosol, as in the previous night's ascent. The substantial temperature inversion at the top of this layer will lead to a sharp gradient between the moist air below and relatively dry air above, leading to charging of the particles as a result of flow of the vertical conduction current. This is likely to be the main source of charge for the flight shown in Fig. 2(f), which will be discussed further in Section 3.3.

To summarise the diurnal variation in the vertical charge profiles over Alqueva, it is observed that, as expected, the magnitude of the charge during night time profiles is much smaller (up to 20 pC m^{-3}) than during daylight hours (up to 92 pC m^{-3}). Considerable complexity in the charge profiles is observed once daytime convection begins, with lofting of ultrafine surface aerosol suggested to be the main contribution to the charge profile in the lowest 1 km. Early morning formation of thin cloud layers is also a source of charge separation through conduction current charging of droplets and aerosols at the upper and lower horizontal boundaries. Remnant effects of such charging can be seen several hours before and after the cloud becomes visible from ceilometer measurements, i.e. charge separation occurs during the cloud formation processes and remains after the droplets have evaporated.

3.2. Surface electrical measurements

This section examines more closely the effect of charges aloft on the surface PG by considering the integrated columnar charge. We define the columnar space charge, ρ_c, as the sum of all space charge layers above the measurement point. In practise we represent this as:

$$\rho_c = \sum_{m=0}^{m_\infty} \rho_m, \tag{2}$$

where ρ_m is the space charge associated with the mth layer measured above the surface, and m_∞ is the uppermost layer considered. Fig. 6 shows a PG time series (black line) for the entire duration of the two day IOP covering all eight balloon flights (from 22nd July to 24th). Also plotted (red dots) are the integrated space charge totals from the surface up to 5 km, for each of the 8 charge sensor flights, using Eq. (2). Further discussion of the choice of 5 km as the height of the upper boundary is given in Appendix B. Fig. 6 shows that although there is some variability, it is generally the case that the integrated space charge profiles follow the same trend as the near surface PG, particularly around the time of the increased aerosol concentration around 1200 UT on 23rd as discussed in Section 3.1. This demonstrates the importance of the link between the surface electrical environment and aloft. Also shown in Fig. 6 (grey dot-dashed line) is the average diurnal variation in PG at Alqueva on fair weather days for the entire duration of the Alex campaign (from 26th May to 27th September). The difference between the PG on 23rd (0900 UT to 1500 UT) and the average PG curve demonstrates the likelihood of enhanced space charge production on this day which is characterised by an increase in the magnitude (279 V/m compared to 93 V/m) and variability. This is in contrast to the similarity observed between the average curve and PG measured on 22nd, indicating a typical fair weather day. It is suggested that the differences result from a change in wind conditions at the site and thus aerosol concentration between the two days. The 22nd is dominated by a local lake breeze (as demonstrated in Fig. 4(a)), with wind flowing outwards

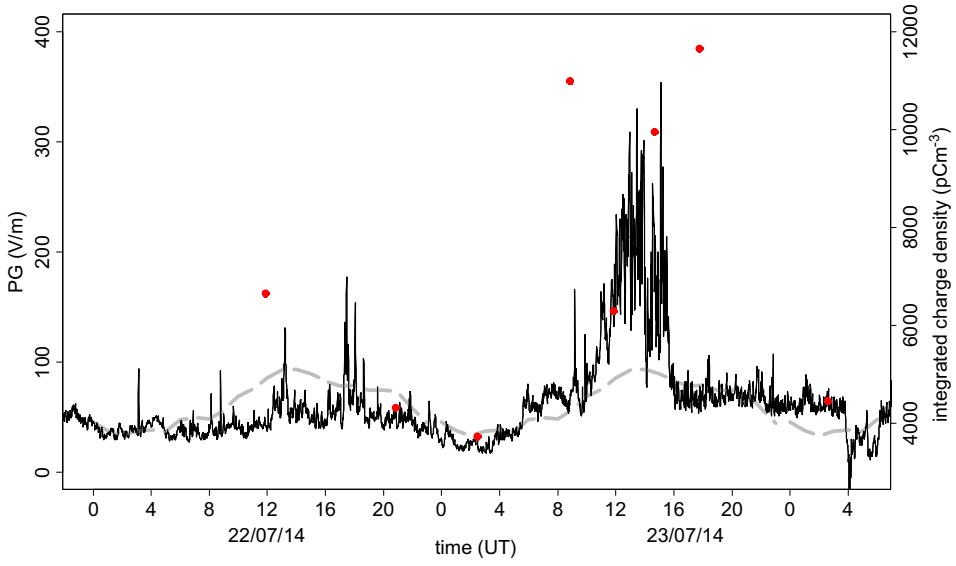

Fig. 6. Time series during the two days of the Alqueva IOP from 22nd to 24th July 2014. The black line denotes the PG, whilst the red dots show the calculated integrated space charge up to 5 km for each charge sensor balloon flight during the period (using Eq. (2)). The grey dash-dotted line show the averaged diurnal variation in PG for fair weather days at the Alqueva site during the entire ALEX campaign. (For interpretation of the references to colour in this figure legend, the reader is referred to the web version of this article.)

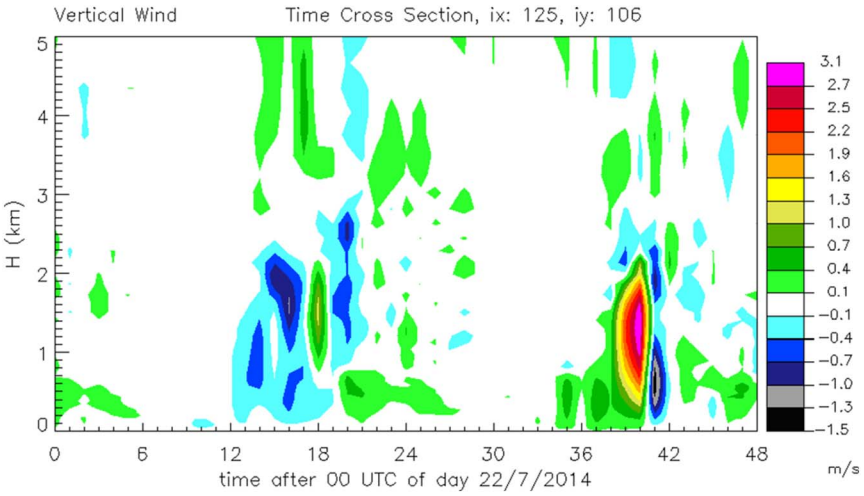

Fig. 7. Hovmöller plot of the vertical profile of Meso-NH modelled vertical velocity over the grid point nearest to the Parque Solar site at Alqueva, during 22nd and 23rd July.

from the lake towards the shore. This would contain relatively few aerosol particles (as supported by Fig. 5(a)), and the predominantly descending air over the lake body will inhibit vertical lofting of local aerosol at the PG measurement site. This is demonstrated in Fig. 7 which shows modelled time evolution of vertical velocity at Alqueva during 22nd and 23rd July, where it is evident that the vertical velocities on 22nd afternoon (12–18 UTC) are slightly negative (descending) in the boundary layer over the lake due to the development of the lake-breeze system. The fair weather conditions, low wind speeds and low aerosol content would lead to a predominately Carnegie like variation in PG as observed. This is contrasted with the predominantly north westerly wind flow on 23rd, which inhibits the formation of the lake breeze and therefore does not suppress the afternoon mesoscale convection. In addition, the circulation on 23rd is also likely to advect aerosol from more populated and industrialized coastal cities such as Lisbon The higher aerosol concentration on 23rd would increase the PG by both (a) reducing the conductivity and (b) causing an increased contribution to space charge by movement of charged aerosol. The presence of (b) is supported by the large variability in PG during peak convective hours.

Another factor that can cause variation in the PG and charge profiles is a change in the local ionisation. The vertical ionisation profile depends on both GCR ionisation generated from above and radioactivity from Earths' surface, mostly in the form of gamma radiation. Surface measurements of gamma radiation were made during the ALEX campaign at Alqueva and reported by Lopes et al. (2015). These measurements corroborated the initial assumption that the Alqueva region emits very little gamma radiation, with no diurnal cycle evident in the measurements. The low geomagnetic latitude of Alqueva suggests that the variability in the near surface ionisation profile from GCRs will also be small (e.g. Bazilevskaya et al., 2008), hence it is extremely unlikely that variations in ionisation rate contributed to the observed changes in PG and space charge during 23rd July at Alqueva.

3.3. Charge modelling

Particulate aerosol is known to have a profound effect on the electrical environment, both at the surface and aloft (e.g. Sagalyn and Faucher, 1954; Gringel and Muhleisen, 1978). It is therefore desirable to know the vertical aerosol profile in order to better understand the vertical charge profile. Although measurements of aerosol were made at the surface during the Alqueva IOP, none were made in-situ aloft. Backscatter profile measurements were, however, made from a nearby Vaisala CL31 ceilometer. Although ceilometers are normally used for cloud detection, they can also be used for aerosol profiling (Münkel et al., 2004; Tsaknakis et al., 2011), and their ability to measure close to the surface is a distinct advantage over lidars, despite the lower pulse energy of ceilometers. Previous investigators (e.g. Münkel et al., 2004)

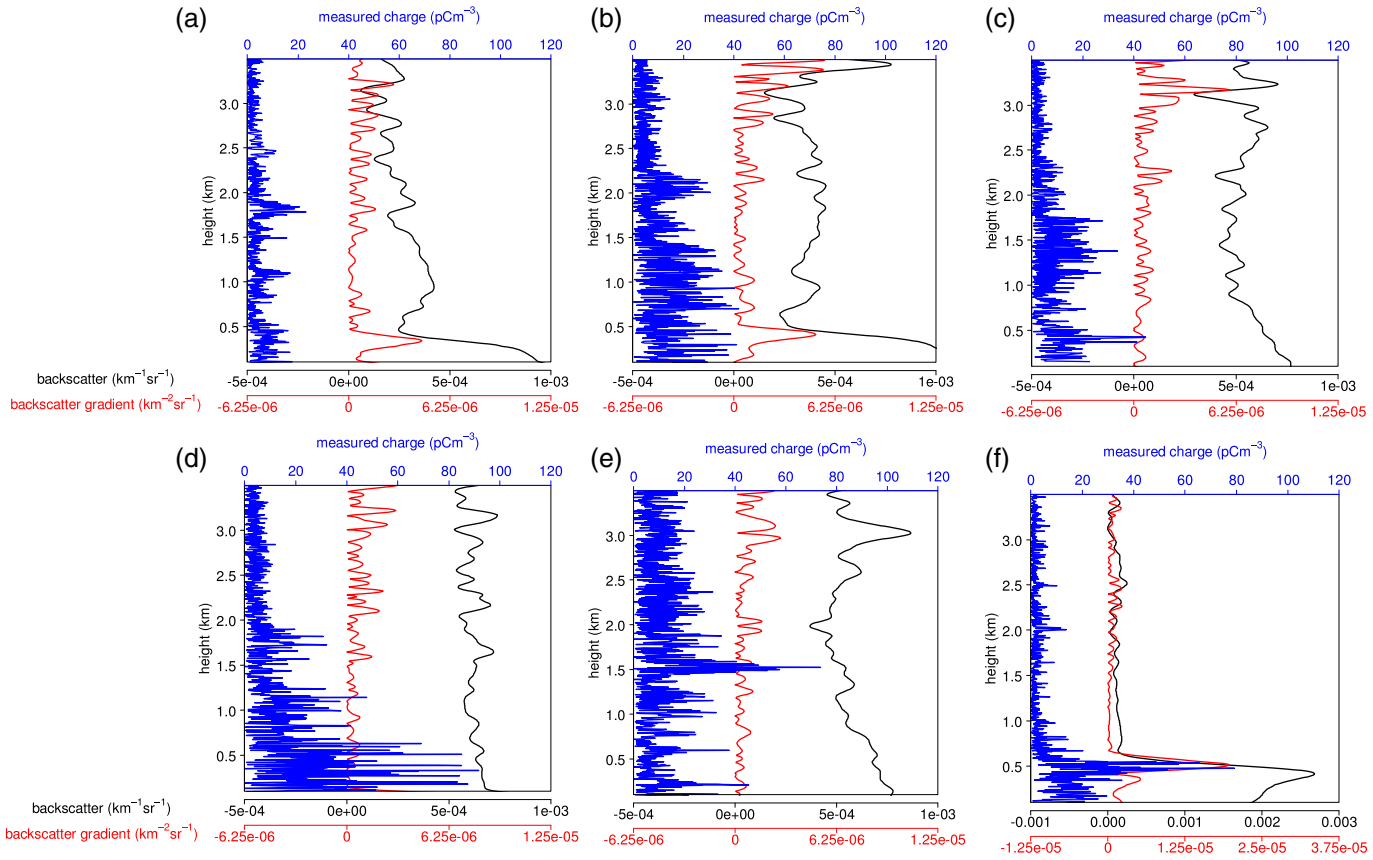

Fig. 8. Vertical profiles of the magnitude of space charge (blue) measured by the balloon charge sensor, processed backscatter from the surface ceilometer (black) (see Appendix C for details) and the magnitude of the vertical gradient in backscatter (red), which is indicative of the location of theoretically expected charge layers. Individual plots denote sonde flight times on 23rd and 24th July as follows: (a) 0208 UT, (b) 0830 UT, (c) 1130 UT, (d) 1420 UT, (e) 1725 UT, (f) 0215 UT. (For interpretation of the references to colour in this figure legend, the reader is referred to the web version of this article.)

have attempted to correlate ceilometer backscatter with surface aerosol measurements, however, artefacts in the backscatter profile have been demonstrated to occur in the ceilometer range gates providing information close to the surface, which reduces the usefulness of the comparison with ground based aerosol measurements. We therefore use the shape of the ceilometer backscatter profile as a qualitative indicator of the aerosol location, rather than attempt to infer anything quantitative about the aerosol concentration. Further discussion on the ceilometer instrument and the method used to process the ceilometer data is provided in Appendix C.

Fig. 8 shows the processed backscatter profiles (black line and detrended according to the methodology outlined in Appendix C) plotted alongside the measured charge profiles for each of the balloon flights in Fig. 2. In general, there is not much similarity observed between the charge and ceilometer backscatter profiles. Common features of the backscatter profiles are an increased layer of backscatter within approximately the lowest 800 m, particularly during night time and early morning hours (e.g. Fig. 8(a), (b) and (f)). This is related to the hygroscopic growth of aerosol (e.g. Silva et al., 2015), which results from the strong cooling overnight, eventually leading to cloud formation. As mentioned in Section 3.1, charge accumulation is expected to occur at the upper and lower horizontal boundaries of cloud and aerosol layers due to vertical flow of the GEC conduction current, J_c. The space charge is proportional to the vertical gradient in conductivity between the clear and aerosol laden air, which theoretically, produces positive charge at the top of the layer and negative charge at the base (see e.g. Nicoll and Harrison, 2016). If one assumes a mostly static situation, with no vertical mixing (which is only likely to occur here overnight when vertical ascent rates are low (e.g. Fig. 4)), a theoretical estimate of the charge generated by this phenomenon can be made by calculating the vertical gradient in conductivity (see e.g. Harrison and Carslaw, 2003, Nicoll and Harrison, 2016 for details). However, the extent to which the charge values are realistic is questionable due to the absence of a quantitative aerosol profile and the number of assumptions required to do this. Instead the approach taken here is simply to calculate the vertical gradient in backscatter, which avoids the need for the many assumptions but will indicate the location of any charge layers thought to be generated by gradients in conductivity. Accordingly, the red line in each of the plots in Fig. 8 shows the vertical gradient in backscatter, which is indicative of the theoretical profile of charge. The vertical gradient is found by applying a smoothing spline (smoothing parameter = 0.3) to the backscatter and differentiating. As was the case for the backscatter profile, for most of the flights there is little similarity between the backscatter gradient and the observed charge. The likely reason for this is low sensitivity and 910 nm IR operating wavelength of the ceilometer which will lead to an inability to detect small particles (< 1 μm) and low particle concentrations. This is particularly important if the space charge is mostly ultrafine (i.e. diameters < 0.1 μm) rather than particulate. Since the surface aerosol measurements at Alqueva showed a predominantly clean atmosphere, it is expected that the sensitivity of the ceilometer will not detect such small particle concentrations. It should also be noted that the application of the vertical gradient in conductivity approach to a non-static situation in which turbulent motion is present over-simplifies the charge mixing processes taking place. Although charge will be separated at the upper and lower horizontal edges of aerosol layers due to this process, in a turbulent situation (such as during Fig. 8(c), (d) and (e)), the charge will be mixed vertically, leading to less well defined charge layers, which is more similar to that observed in the profiles in Fig. 8.

The one flight in which the shape of the backscatter profile is very

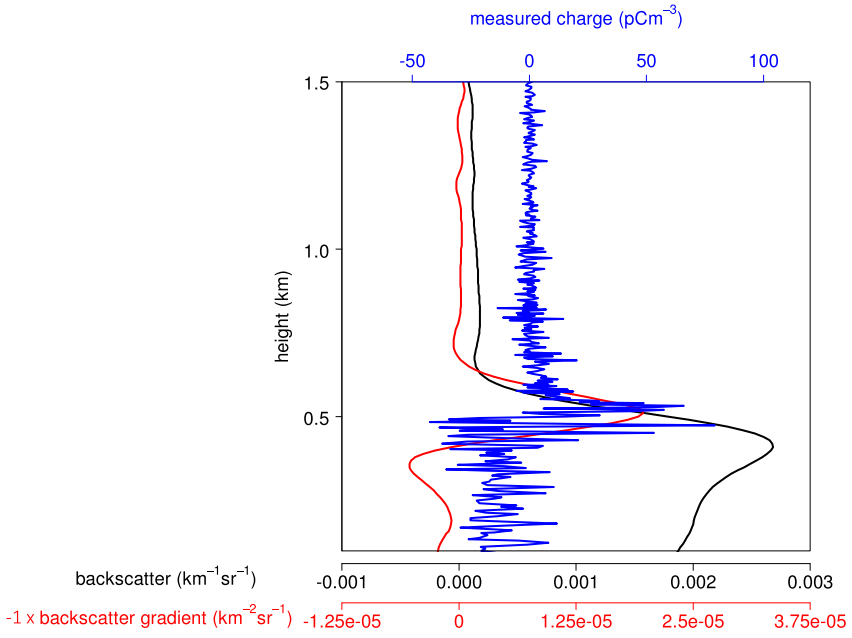

Fig. 9. Close up of Fig. 7(f), but showing bipolar charge and backscatter gradient instead of magnitude. Note that the backscatter gradient axis has been inverted in order to demonstrate the similarity in locations of the vertical backscatter gradient and the measured charge.

similar to the measured charge is Fig. 8(f). Fig. 9 shows a close up of the lowest 1.5 km of this flight, which demonstrates that a substantial gradient in backscatter occurs at 500 m altitude, which is coincident with the measured charge layer. The increased backscatter during this period is likely related to the later formation of a cloud layer which resulted from night time cooling under clear skies. The ceilometer algorithm did not classify this as a cloud until 0335 UT, more than an hour after the balloon measurements, therefore the profile shown in Fig. 9 was obtained before the cloud formed. The charge measurements and vertical gradient in backscatter in Fig. 9 are of both polarities (not simply magnitude as for the other plots), which demonstrates very close agreement between the location of the large backscatter gradients and the observed charge. Fig. 9 also shows the negative charge observed in the base of the layer and positive charge at the top, as expected by the theory of conduction current flow through aerosol and cloud layers (e.g. Zhou and Tinsley, 2007). Analysis of the data in Fig. 8 therefore suggests that this charging theory is valid for stratiform layers of aerosol and cloud, when the particle/droplet concentration is substantial and little vertical mixing is present, but not when substantial convective motion exists.

4. Discussion

From the results presented here it is apparent that the vertical profile of charge within the PBL can be complex, even in fair weather conditions. The analysis presented in Section 3 suggests a considerable influence for local charged aerosol on both the near surface PG measurements and vertical charge profile. Although the surface particle measurements and ceilometer backscatter profiles suggest relatively small aerosol particle number concentrations it is likely that larger concentrations of ultrafine (< 0.1 μm) particles and ionic space charge exist which will influence the charge distribution but will not be detected by either the ceilometer or surface particle counter. The ceilometer wavelength of 910 nm means that only particles greater than about 1 μm diameter will be detected, and only if the signal to noise is sufficiently large to permit a reliable signal to be measured. It is well documented that the day time signal-to-noise ratio in ceilometers in regions of low aerosol content is often poor (e.g. Heese et al., 2010), which is consistent with the findings reported here in that there is little structure in the ceilometer backscatter profile except during night time and periods of high humidity. Although there is no observational evidence for these ultrafine particles, we can infer their existence from the measurements of elevated space charge values, i.e. in order for charge to be maintained beyond the timescale for recombination effects, the charge must be carried on larger particles. This is most likely to result from attachment to ultrafine particles.

The measurements reported here also demonstrate the importance of daytime convection for the vertical space charge profile within the PBL. At Alqueva this is particularly evident in terms of the ability of turbulent updrafts to transport small aerosol particles from the surface, which occurs easily and mixed primarily due to the extreme dryness of soil. This leads to relatively large values of space charge (up to 100 pC m^{-3}), in comparison to those reported by other observers in less dry environments (e.g. $\sim$1 pC m^{-3} measured by Moore et al., 1962). In the absence of cloud layers, the largest values of space charge are observed during mid-afternoon when the vertical velocity is maximum and turbulent motion largest. Section 3.2 demonstrates clearly the difference in the electrical environment on days when convection is inhibited (such as on 22nd July when the lake breeze was present), and when it is not. This leaves little doubt that the main influence on the detailed structure of the vertical space charge profile at Alqueva is turbulent transport.

The relatively large values of space charge density reported here compared to other papers (e.g. of a few pC m^{-3} in Moore et al., 1962, Markson, 1975) may also result from differences in the measurement techniques as well as time resolution of the measurements. Markson (1975) and Markson et al. (1981) report measurements approximately every 200 m in the vertical, with no detail of any averaging or smoothing that has been applied. It may well be the case that this is an average value over 200 m rather than an instantaneous value. It is therefore likely that, in comparison to the approximately 5 m vertical resolution measurements reported here, the longer averaging periods reported in the literature resulted in smaller reported values of space charge. This therefore demonstrates the importance of high resolution measurements in understanding the detail of charge transfer within the boundary layer.

5. Conclusions

These results present rare high resolution vertical profiles of space charge within the planetary boundary layer, which are the first to be made over an inland Portuguese reservoir. The direct space charge determination reveals the complex structure of the vertical charge profiles, beyond that available indirectly from aerosol particle retrievals or thermodynamic inferences alone, which indicates the importance of charged ultrafine aerosol in the electrical environment of the boundary layer. Intensive balloon measurements over a 24 hour period of fair weather demonstrate variation of the charge profile within the planetary boundary layer and its dependence on convective mixing. The magnitude of observed charge is typically small during night time periods (up to 20 pC m^{-3}), with little vertical structure. Daytime convection leads to substantial vertical mixing, including lofting of aerosol particles upwards from the dry surface, which leads to substantial charge accumulations up to 92 pC m^{-3} within the lowest km. The diurnal variation in the integrated column of charge above the measurement site closely matches the diurnal variation in near surface charge as measured by an electric field mill at the same site. Vertical profiles of backscatter from an adjacent CL31 ceilometer were used to provide a proxy for the vertical aerosol profile, to which the measured charge profiles were compared. Little similarity between the two was observed, except during stable night time periods when reasonable aerosol layers accumulated. Most of the discrepancy is attributed to the likely existence of ultrafine aerosol (< 1 μm) which are too small to be detected by the ceilometer, but will contribute to the overall charge profile. Using such direct space charge measurements, the charge transfer processes can be identified and characterised, the variability in which is clearly apparent even in fair weather conditions. The simplicity with which these measurements can be obtained using conventional meteorological radiosondes therefore offers a new tool for improving boundary layer representations within radiative transfer models.

Acknowledgements

Data from the Alex campaign is available at http://www.alex2014.cge.uevora.pt/?page_id=27 (password access can be provided by contacting the corresponding author). NERC grant NE/H002081/1 and STFC grant ST/K001965/1 supported the radiosonde sensor development. KAN also acknowledges an Early Career Fellowship of the Leverhulme Trust (ECF-2011-225) and a NERC Independent Research Fellowship (NE/L011514/1). Field campaign funding was from FCT (Portuguese Science and Technology Foundation) and FEDER-COMPETE: ALEX 2014 (EXPL/GEO-MET/1422/2013): FCOMP-01-0124-FEDER-041840. MM acknowledges the support of the Portuguese Science and Technology Foundation (FCT) for the PhD grant (SFRH/BD/89218/2012). The Portuguese team was co-funded by FCT, in the frame of the European Regional Development Fund - COMPETE 2020, under the projects UID/GEO/04683/2013 (POCI-01-0145-FEDER-007690) and ALOP (ALT20-03-0145-FEDER-000004). Thanks are also given to the TOPROF (ES-1303) COST-Action. The authors express their gratitude to Maria Parrondo from Instituto Nacional de Técnica Aeroespacial for her assistance with the radiosonde launches, Maria João Costa for providing the ceilometer data, and Alec Bennet for discussions about the vertical profiles. HGS is grateful to Dr. John Chubb (1933–2015) for his insightful discussions into this topic, he shall be missed.

Appendix A. Meso-NH model

A map of southern Portugal with the orography, the Alqueva reservoir and the location of the Parque Solar measurement site during the ALEX 2014 campaign is provided in Fig. A1. Further maps of the Alqueva and the ALEX measurement stations may be found in Potes et al., 2017. In order to characterise the wind direction and evolution of the vertical profile of the vertical velocity at Alqueva, the results of a high resolution numerical simulation with Meso-NH model (Lafore et al., 1998) were used. The Meso-NH is a non-hydrostatic anelastic numerical model which includes several parametrization schemes to represent surface-atmosphere interactions, radiation, turbulence, clouds and precipitation, convection, atmospheric electricity, chemical reactions and aerosols. The model was run over two two-way nested domains, the farther (not shown) covering all the Iberian Peninsula and adjacent ocean at 4 km horizontal resolution (270 × 240 grid points). The finer domain is centred over the Alqueva reservoir and covers the Portuguese Alentejo region at a 1 km horizontal resolution (240 × 240 grid points) and is shown in Fig. A1 alongside with the location of Alqueva artificial lake. The simulation was started on July 21st at 1800 UT and the initial and boundary conditions were provided by the 6 hourly ECMWF analysis. For the surface, the SURFEX platform of schemes (Masson et al., 2013) were used, the water temperature at Alqueva reservoir was initialized by the temperatures obtained from MODIS satellite data, and an interactive lake model, the Flake, was activated as described in Salgado and Le Moigne (2010). To map the model surface, the ECOCLIMAP v2.0 (Masson et al., 2003) updated by Policarpo et al. (2017) was used. In the inner domain the convection is assumed to be explicitly resolved (no shallow or deep convection schemes were activated) and the turbulence was parametrized using the 1D scheme of Cuxart et al. (2000). The meso-NH results shown in this work came from the inner model (1 km resolution).

Appendix B. Integrated space charge profiles

This section provides further discussion of the integrated columnar charge discussed in Section 3.2. To calculate the integrated columnar charge it was decided to apply Eq. (2) up to a maximum height of 5 km as the majority of the space charge (90%) lies beneath this height. To demonstrate that the choice of this value is not important for the qualitative interpretation given, Fig. B1 shows the integrated space charge from the surface up to 2, 3, 4 and 5 km. It can be seen that the shape of the integrated charge time series is invariant of the value of maximum height chosen.

Appendix C. Ceilometer features and processing of the backscatter profiles

After a brief description of the ceilometer system, this section provides detail on the processing applied to the ceilometer backscatter data for Figs. 8 and 9, as a well as a discussion of the value of the shape of the profile.

The CL31 Vaisala ceilometer uses a single lens design, meaning that the centre of the lens is used for collimating the outgoing laser beam, whereas the outer part of the lens is used for focusing the backscattered light onto the receiver. The separation between transmitting and receiving areas is

provided by an inclined mirror with a hole in the centre. In this way very good performance is achieved, even at low altitudes. The ceilometer has a measurement range from 0 to 7.5 km, maximum reporting resolution of 5 m and programmable measurement cycle (from 2 to 120 s). It uses an eye-safe laser InGaAs diode emitting at 910 nm.

The backscatter signal obtained in clear sky conditions is mainly due to aerosols. Assuming that these particles are mostly concentrated in the mixing layer and that their concentrations above are much lower, it is then reasonable to expect an accentuated decrease of the backscatter signal at the top of the mixing layer. This is true for most situations, except in the case of intense aerosol events.

Although it is possible to use surface aerosol data to attempt to calibrate the ceilometer, for the Vaisala CL31 ceilometer at the Alqueva site, a distinct local minimum in the backscatter was evident at 40 m (4th range gate) in all backscatter profiles. This has also been detected by other investigators (e.g. Sokół et al., 2014) and is an artefact, potentially caused by incomplete optical overlap, or software corrections introduced by the ceilometer manufacturer (see e.g. Kotthaus et al., 2016). Although reasonable agreement between the surface OPC aerosol measurements and the backscatter from the lowest 2 ceilometer range gates (10 m and 20 m) was found at Alqueva, the artefact at 40 m makes it questionable to attempt any calibration between surface data and backscatter values beneath 70 m, which is typically the lowest altitude thought to be free from overlap issues.

In order to analyse the backscatter profile above 40 m, one must also take account of the errors inherent in the backscatter measurement and the processing already undertaken by the ceilometer manufacturer. The grey points in Fig. C1(b) show the vertical profile of backscatter during daylight conditions (0830 UT) on 23rd July (flight 4) at Alqueva, which appear reasonable in the lowest 1 km of the profile, but show an unphysical increase with height above this, as well as an increase in variability. This is apparent in all of the backscatter profiles coinciding with the radiosonde flights and is thought to be erroneous, due to noise from varying solar radiation as well as electronic and optical noise in the ceilometer. To extract a quantitative backscatter profile it is necessary to remove some of the noise by correcting the raw backscatter profile. This is achieved by producing an average background night time climatology profile (shown in black in Fig. C1(a)) from Alqueva, which should be devoid of any noise from solar radiation. This is calculated by finding the mean backscatter profile for all times from 0000 UT to 0300 UT from 22nd to 24th July 2016. Since the backscatter is typically highly variable within the PBL, this profile is therefore only calculated for altitudes above 800 m. The night time climatology profile is then scaled according to the maximum backscatter measured during any specific profile, and subtracted from the raw backscatter to produce a noise corrected version. A moving average (over 5 points) is then applied to the de-trended backscatter data to the processed backscatter, shown as the black line shown in Fig. C1(b). This process has been applied to the instantaneous backscatter profiles coincident with the six instrumented balloon flights shown in Fig. 2. It is also prudent to note the distinct decrease in the backscatter at 2.4 km observed for all Alqueva profiles (as seen in Fig. C1(a)), which is another artefact introduced in the processing by the manufacturer. This has been previously reported by Kotthaus et al. (2016) as likely due to a difference in averaging of data below and above this height. It is clear that removal of such artefacts (as is achieved by subtracting the scaled night time climatology profile) is vital to obtain reliable, quantitative backscatter measurements.

Appendix D. OPS 3330 features and particle concentration calculation

The Optical Particle Sizer (OPS) 3330, manufactured by TSI, is based on the principle of optical scattering from single particles. A laser beam shaped to a thin sheath focused below the inlet nozzle illuminates the particles entering the inlet nozzle. As particles pass through this light sheath, they scatter light in the form of pulses that are counted and sized simultaneously. Sheath flow keeps the particles well focused across the laser light and also prevents the optics from getting contaminated. Beam shaping optics focus the laser light and convert that to a fine sheath with maximum intensity across the particle beam. The viewing volume is created by the intersection of the laser sheath and the particle flow. Sophisticated electronics are used to perform the signal processing. Particle pulses are counted individually and binned in to the 16 channels of the detector, based on their pulse heights. The maximum particle size that can be counted is 10 μm, particles larger than this will be counted but not sized.

The OPS measures particle concentration counting individual pulses from the photodetector. When, pulses start to overlap each other, meaning high particle concentrations, the number of pulses underestimates the number of particles entering the viewing volume. When a particle is detected entering the optical viewing volume, no other particles can be counted until that particle leaves the viewing volume. As the particle concentrations increase, the amount of time blocked by the presence of particles becomes significant. If the particle concentration is computed using elapsed time, the value will be under reported. The actual sample time needs to be corrected for this blocked or dead-time. To adjust for this effect, the OPS measures the dead-time resulting from the presence of particles in the viewing volume and subtracts it from the sample time. This sample lifetime value is used in place of the sample time for the concentration calculations as in the following formula.

$$C_i = \frac{N_i}{Q \times (t_s - DTC \times t_d)}, \tag{D1}$$

where,

C_i = concentration at size channel i
N_i = number count in #/cm^3 at size channel i
Q = sample flow rate, 16.67 cm^3 s^{-1}
t_s = sample time in seconds
t_d = dead time in seconds
DTC = dead time correction factor

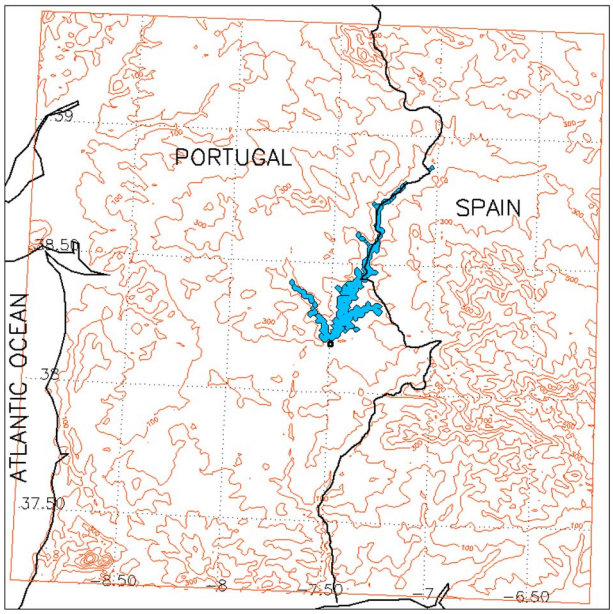

Fig. A1. Domain and orography at 1 km horizontal resolution used in the inner model of the Meso-NH simulation (contour intervals of 100 m). The Alqueva reservoir, as used in the simulations is shown in blue. The location of the Parque Solar (PS) site at which the PG and balloon measurements were made is represented by the black circle. (For interpretation of the references to colour in this figure legend, the reader is referred to the web version of this article.)

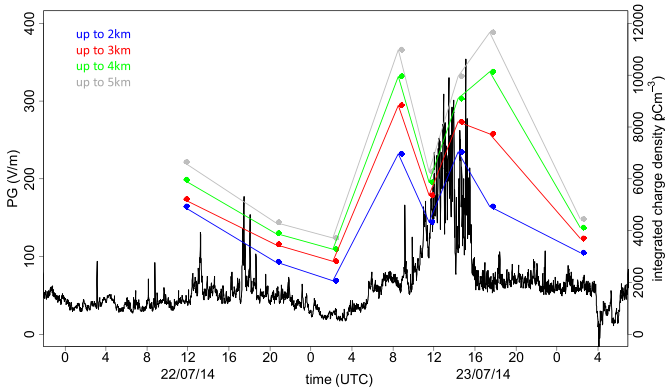

Fig. B1. Time series during the two days of the Alqueva IOP from 22nd to 24th July 2014. The black line denotes the PG, whilst the coloured red dots show the calculated integrated space charge up to 2 km (blue), 3 km (red), 4 km (green) and 5 km (grey) for each charge sensor balloon flight during the period (using Eq. (2)). (For interpretation of the references to colour in this figure legend, the reader is referred to the web version of this article.)

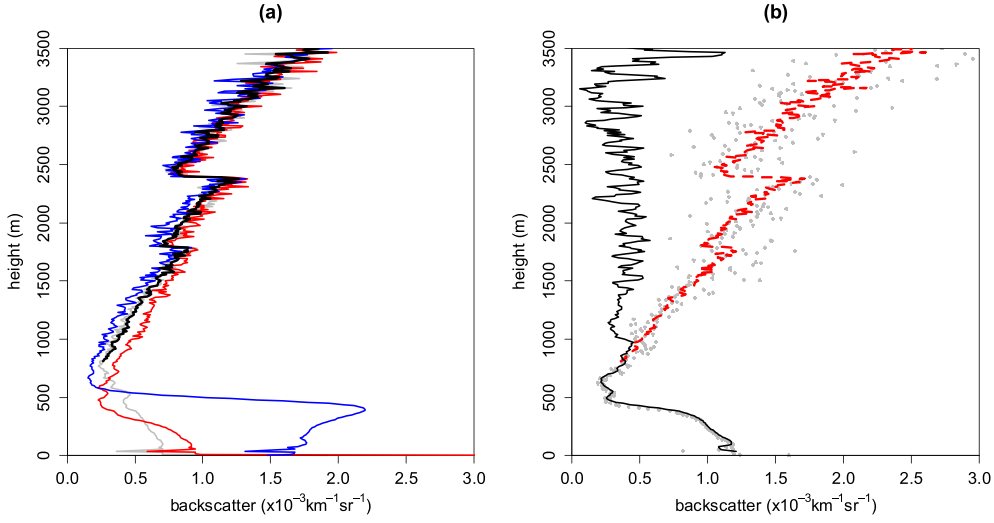

Fig. C1. (a) Average night time vertical profiles of backscatter from the CL31 ceilometer for nights of 22nd (grey), 23rd (red) and 24th (blue) July 2014 from 00 to 03 UT. The black line shows the mean of the three profiles, denoting the night time climatology. (b) Vertical profile of backscatter at 0830 UT on 23rd July (flight 4). The profile is the mean of a 30 minute window from the launch time. Grey points - raw backscatter, red – relative night time climatology profile, black – processed backscatter. (For interpretation of the references to colour in this figure legend, the reader is referred to the web version of this article.)

References

Adler, B., Kalthoff, N., 2014. Multiscale transport processes observed in the boundary layer over a mountainous island. Bound.-Layer Meteorol. 153, 515–537. http://dx.doi.org/10.1007/s10546-014-9957-8.

Anisimov, S.V., Bakastov, S.S., Mareev, E.A., 1994. Spatiotemporal structures of electric field and space charge in the surface atmospheric layer. J. Geophys. Res.-Atmos. 99 (D5), 10603–10610.

Anisimov, S.V., Mareev, E.A., Bakastov, S.S., 1999. On the generation and evolution of aeroelectric structures in the surface layer. J. Geophys. Res.-Atmos. 104 (D12), 14359–14367.

Anisimov, S.V., Mareev, E.A., Shikhova, N.M., Shatalina, M.V., Galichenko, S.V., Zilitinkevich, S.S., 2013. Aeroelectric structures and turbulence in the atmospheric boundary layer. Nonlinear Process. Geophys. 20 (5), 819–824.

Aplin, K.L., Harrison, R.G., 2013. Lord Kelvin's atmospheric electricity measurements. Hist. Geo Space Sci. 4, 83–95.

Bazilevskaya, G.A., Usoskin, I.G., Flückiger, E.O., Harrison, R.G., Desorgher, L., Bütikofer, R., Krainev, M.B., Makhmutov, V.S., Stozhkov, Y.I., Svirzhevskaya, A.K., Svirzhevsky, N.S., 2008. Cosmic ray induced ion production in the atmosphere. Space Sci. Rev. 137, 149–173.

Cavello, T., 1777. An account of some new electrical experiments. Philos. Trans. R. Soc. Lond. 67, 48–55.

Conceição, R., Silva, H.G., Bennett, A., Salgado, R., Bortoli, D., Costa, M.J., Collares Pereira, M., 2017. High frequency response of the atmospheric electric potential gradient under strong and dry boundary layer convection. Bound.-Layer Meteorol. http://dx.doi.org/10.1007/s10546-017-0298-2.

Crozier, W.D., 1963. Electrode effect during nighttime low-wind periods. J. Geophys. Res. 68 (11), 3451–3458.

Cuxart, J., Bougeault, P., Redelspergen, J., 2000. A turbulence scheme allowing for mesoscale and large-eddy simulations. Q. J. R. Meteorol. Soc. 126, 1–30.

Esposito, F., Molinaro, R., Popa, C.I., Molfese, C., Cozzolino, F., Marty, L., Taj-Eddine, K., Di Achille, G., Franzese, G., Silvestro, S., Ori, G.G., 2016. The role of the atmospheric electric field in the dust-lifting process. Geophys. Res. Lett. 43 (10), 5501–5508.

Garratt, J.R., 1994. The atmospheric boundary layer. Earth Sci. Rev. 37 (1–2), 89–134.

Gringel, W., Muhleisen, R., 1978. Saharan dust concentration in the troposphere over the North Atlantic derived from measurements of air conductivity. Beitr. Phys. Atmos. 51 (2), 121–128.

Harrison, R.G., 2013. The Carnegie curve. Surv. Geophys. 34 (2), 209–232.

Harrison, R.G., Aplin, K.L., 2003. Ninteenth century Parisian smoke variations inferred from Eiffel tower atmospheric electrical observations. Atmos. Environ. 37, 5319–5324.

Harrison, R.G., Carslaw, K.S., 2003. Ion–aerosol–cloud processes in the lower atmosphere. Rev. Geophys. 41 (3), 1012. http://dx.doi.org/10.1029/2002RG000114.

Harrison, R.G., Nicoll, K.A., Lomas, A.G., 2012. Programmable data acquisition system for research measurements from meteorological radiosondes. Rev. Sci. Instrum. 83, 036106. http://dx.doi.org/10.1063/1.3697717.

Harrison, R.G., Nicoll, K.A., Ambaum, M.H.P., 2015. On the microphysical effects of observed cloud edge charging. Q. J. R. Meteorol. Soc. 141, 2690–2699. http://dx.doi.org/10.1002/qj.2554.

Harrison, R.G., Barth, E., Esposito, F., Merrison, J., Montmessin, F., Aplin, K.L., Borlina, C., Berthelier, J.J., Déprez, G., Farrell, W.M., Houghton, I.M.P., Renno, N.O., Nicoll, K.A., Tripathi, S.N., Zimmerman, M., 2016. Applications of electrified dust and dust devil electrodynamics to Martian atmospheric electricity. Space Sci. Rev. http://dx.doi.org/10.1007/s11214-016-0241-8.

Heese, B., Flentje, H., Althausen, D., Ansmann, A., Frey, S., 2010. Ceilometer lidar comparison: backscatter coefficient retrieval and signal-to-noise ratio determination. Atmos. Meas. Tech. 3 (6), 1763–1770.

Hoppel, W.A., Frick, G.M., 1986. Ion—aerosol attachment coefficients and the steady-state charge distribution on aerosols in a bipolar ion environment. Aerosol Sci. Technol. 5 (1), 1–21. http://dx.doi.org/10.1080/02786828608959073.

Hoppel, W.A., Gathman, S.G., 1971. Determination of eddy diffusion coefficients from atmospheric electrical measurements. J. Geophys. Res. 76 (6), 1467–1477. http://dx.doi.org/10.1029/JC076i006p01467.

Hoppel, W.A., Gathman, S.G., 1972. Experimental determination of the eddy diffusion coefficient over the open ocean from atmospheric electric measurements. J. Phys. Oceanogr. 2 (3), 248–254.

Hoppel, W.A., Anderson, R.V., Willett, J.C., 1986. Atmospheric electricity in the planetary boundary layer. In: The Earth's Electrical Environment, pp. 149–165.

Israel, H., 1955. Synoptical researches on atmospheric electricity. In: Proc. Conference on Atmospheric Electricity, pp. 11–20.

Kaimal, J.C., Finnigan, J.J., 1994. Atmospheric Boundary Layer Flows: Their Structure and Measurement. Oxford University Press.

Kawano, M., 1957. The general expression of the diurnal variation of the atmospheric electric field considering the influence of the Eddy diffusion near the ground. J. Geomagn. Geoelectr. 9 (3), 123–132.

Kotthaus, S., O'Connor, E., Munkel, C., et al., 2016. Recommendations for processing atmospheric attenuated backscatter profiles from Vaisala CL31 ceilometers. Atmos. Meas. Tech. 9 (8), 3769.

Kulkarni, Madhuri N., 2010. On the modeling of electrical boundary layer (electrode layer) and derivation of atmospheric electrical profiles, eddy diffusion coefficient and scales of electrode layer. J. Earth Syst. Sci. 119 (1), 75–86.

Lacks, D.J., Levandovsky, A., 2007. Effect of particle size distribution on the polarity of triboelectric charging in granular insulator systems. J. Electrost. 65 (2), 107–112.

Lafore, J., Stein, J., Asencio, N., Bougeault, P., Ducrocq, V., Duron, J., Fischer, C., Hereil, P., Mascart, P., Pinty, J., Redelsperger, J., Richard, E., Arellano, J., 1998. The meso-nh atmospheric simulation system. Part 1: adiabatic formulation and control simulation. Ann. Geophys. 16, 90–109.

Lopes, F., Silva, H.G., Bárias, S., Barbosa, S.M., 2015. Preliminary results on soil-emitted gamma radiation and its relation with the local atmospheric electric field at Amieira (Portugal). J. Phys. Conf. Ser. 646, 012015. http://dx.doi.org/10.1088/1742-6596/646/1/012015.

Lopes, F., Silva, H.G., Salgado, R., Potes, M., Nicoll, K., Harrison, G., 2016. Atmospheric electrical field measurements near a fresh water reservoir and the formation of the lake breeze. Tellus A 68, 31592. http://dx.doi.org/10.3402/tellusa.v68.31592.

Mach, D.M., Blakeslee, R.J., Bateman, M.G., 2011. Global electric circuit implications of combined aircraft storm electric current measurements and satellite-based diurnal lightning statistics. J. Geophys. Res.-Atmos. 116 (D5).

Markson, R., 1975. Atmospheric electrical detection of organized convection. Science 188 (4194), 1171–1177.

Markson, R., Sedlacek, J., Fairall, C.W., 1981. Turbulent transport of electric charge in the marine atmospheric boundary layer. J. Geophys. Res. 86 (C12), 12–115.

Marshall, T.C., Rust, W.D., Stolzenburg, M., Roeder, W.P., Krehbiel, P.R., 1999. A study of enhanced fair-weather electric fields occurring soon after sunrise. J. Geophys. Res. 104 (D20), 24–455.

Masson, V., Champeaux, J., Chauvin, C., Meriguet, C., Lacaze, R., 2003. A global database of land surface parameters at 1 km resolution for use in meteorological and climate models. J. Clim. 16, 1261–1282.

Masson, V., Moigne, P., Martin, E., Faroux, S., Alias, A., Alkama, R., Belamari, S., Barbu, A., Boone, A., Bouyssel, F., Brousseau, P., Brun, E., Calvet, J., Carrer, D., Decharme, B., Delire, C., Donier, S., Essaouini, K., Gibelin, A., Giordani, H., Habets, F., Jidane, M., Kerdraon, G., Kourzeneva, E., Lafaysse, M., Lafont, S., Brossier, C., Lemonsu, A., Mahfouf, J., Marguinaud, P., Mokhtari, M., Morin, S., Pigeon, G., Salgado, R., Seity, Y., Taillefer, F., Tanguy, G., Tulet, P., Vincendon, B., Vionnet, V., Voldoire, A., 2013. The surfexv7.2 land and ocean surface platform for coupled or offline simulation of earth surface variables and fluxes. Geosci. Model Dev. 6, 929–960.

Matthews, J.C., Buckley, A.J., Wright, M.D., Henshaw, D.L., 2012. Comparisons of ground level measurements of ion concentration and potential gradient upwind and downwind of HV power lines in corona. J. Electrost. 70 (4), 407–417.

Moore, C.B., Vonnegut, B., Semonin, R.G., Bullock, J.W., Bradley, W., 1962. Fair-weather atmospheric electric potential gradient and space charge over central Illinois, summer 1960. J. Geophys. Res. 67 (3), 1061–1071.

Münkel, C., Emeis, S., Müller, W.J., Schaefer, K.P., 2004. Aerosol concentration measurements with a lidar ceilometer: results of a one year measuring campaign. In: Remote Sensing. International Society for Optics and Photonics, pp. 486–496.

Nicoll, K.A., 2013. A self-calibrating electrometer for atmospheric charge measurements from a balloon platform. Rev. Sci. Instrum. 84, 096107.

Nicoll, K.A., Harrison, R.G., 2010. Experimental determination of layer cloud edge charging from cosmic ray ionisation. Geophys. Res. Lett. 37 (13).

Nicoll, K.A., Harrison, R.G., 2016. Stratiform cloud electrification: comparison of theory with multiple in-cloud measurements. Q. J. R. Meteorol. Soc. 142, 2679–2691. http://dx.doi.org/10.1002/qj.2858.

Piper, I.M., Bennett, A.J., 2012. Observations of the atmospheric electric field during two case studies of boundary layer processes. Environ. Res. Lett. 7 (1), 014017.

Policarpo, C., Salgado, R., Costa, M.J., 2017. Numerical simulations of fog events in southern portugal. Adv. Meteorol. 2017. http://dx.doi.org/10.1155/2017/1276784.

Potes, M., Salgado, R., Costa, M.J., Morais, M., Bortoli, D., Kostadinov, I., Mammarella, I., 2017. Lake–atmosphere interactions at Alqueva reservoir: a case study in the summer of 2014. Tellus A 1 (1272787), 69.

Reiter, R., Sládkovič, R., 1970. Control of vertical transport of aerosols between 700 and 3000 meters by lapse rate and fine structure of temperature. J. Geophys. Res. 75 (15), 3065–3075. http://dx.doi.org/10.1029/JC075i015p03065.

Rycroft, M.J., Harrison, R.G., Nicoll, K.A., Mareev, E.A., 2008. An overview of Earth's global electric circuit and atmospheric conductivity. Space Sci. Rev. 137 (1–4), 83–105.

Sagalyn, R.C., Faucher, G.A., 1954. Aircraft investigation of the large ion content and conductivity of the atmosphere and their relation to meteorological factors. J. Atmos. Terr. Phys. 5 (1), 253–272.

Sagalyn, R.C., Faucher, G.A., 1956. Space and time variations of charged nuclei and electrical conductivity of the atmosphere. Q. J. R. Meteorol. Soc. 82 (354), 428–445.

Salgado, R., Le Moigne, P., 2010. Coupling of the flake model to the surfex externalized surface model. Boreal Environ. Res. 15, 231–244.

Silva, H.G., Conceição, R., Wright, M.D., Matthews, J.C., Pereira, S.N., Shallcross, D.E., 2015. Aerosol hygroscopic growth and the dependence of atmospheric electric field measurements with relative humidity. J. Aerosol Sci. 85, 42.

Silva, H.G., Lopes, F., Pereira, S., Nicoll, K., Barbosa, S.M., Conceição, R., Neves, S., Harrison, R.G., Collares Pereira, M., 2016. Saharan dust electrification perceived by a triangle of atmospheric electricity stations in Southern Portugal. J. Electrost. 84, 106–120.

Sokół, P., Stachlewska, I.S., Ungureanu, I., Stefan, S., 2014. Evaluation of the boundary layer morning transition using the CL-31 ceilometer signals. Acta Geophys. 62 (2), 367–380.

Stull, R.B., 2012. An Introduction to Boundary Layer Meteorology. vol. 13 Springer Science & Business Media.

Tammet, H., 1995. Size and mobility of nanometer particles, clusters and ions. J. Aerosol Sci. 26 (3), 459–475.

Tsaknakis, G., Papayannis, A., Kokkalis, P., Amiridis, V., Kambezidis, H.D., Mamouri, R.E., Georgoussis, G., Avdikos, G., 2011. Inter-comparison of lidar and ceilometer retrievals for aerosol and Planetary Boundary Layer profiling over Athens, Greece. Atmos. Meas. Tech. 4 (6), 1261–1273.

Whipple, F.J.W., 1929. On the association of the diurnal variation of the electric potential gradient in fine weather with the distribution of thunderstorms over the globe. Q. J. R. Meteorol. Soc. 55, 351–362. http://dx.doi.org/10.1002/qj.49705523206.

Willett, J.C., 1979. Fair weather electric charge transfer by convection in an unstable planetary boundary layer. J. Geophys. Res. 84 (C2), 703–718. http://dx.doi.org/10.1029/JC084iC02p00703.
Willett, J.C., 1981. Toward an Understanding of the Turbulent Electrode Effect Over Land. No. NRL-8519. Naval Research Lab, Washington D.C.
Williams, E.R., 2009. The global electrical circuit: a review. Atmos. Res. 91 (2–4), 140–152. http://dx.doi.org/10.1016/j.atmosres.2008.05.018.
Wilson, C.T.R., 1921. Investigations on lightning discharges and on the electric field of thunderstorms. Philos. Trans. R. Soc. London, Ser. A 221, 73–115. http://dx.doi.org/10.1098/rsta.1921.0003.
Yair, Y., Katz, S., Yaniv, R., Ziv, B., Price, C., 2016. An electrified dust storm over the Negev desert, Israel. Atmos. Res. 181, 63–71.
Zhou, L., Tinsley, B.A., 2007. Production of space charge at the boundaries of layer clouds. J. Geophys. Res. 112, D11203. http://dx.doi.org/10.1029/2006JD007998.

Solar Energy 170 (2018) 14–30

Contents lists available at ScienceDirect

Solar Energy

journal homepage: www.elsevier.com/locate/solener

Short-term forecasts of GHI and DNI for solar energy systems operation: assessment of the ECMWF integrated forecasting system in southern Portugal

Francis M. Lopes[a,b,*], Hugo G. Silva[a,b,c], Rui Salgado[b,c], Afonso Cavaco[d], Paulo Canhoto[b,c], Manuel Collares-Pereira[a,b,c,d]

[a] Renewable Energies Chair, University of Évora, IIFA, Palácio do Vimioso, Largo Marquês de Marialva, Apart. 94, 7002-554 Évora, Portugal
[b] Earth Sciences Institute, University of Évora, Rua Romão Ramalho, 59, 7000-671 Évora, Portugal
[c] Department of Physics, School of Sciences and Technology, University of Évora, Rua Romão Ramalho, 59, 7000-671 Évora, Portugal
[d] Portuguese Solar Energy Institute, IIFA, Palácio do Vimioso, Largo Marquês de Marialva, Apart. 94, 7002-554 Évora, Portugal

ARTICLE INFO

Keywords:
Solar irradiance
Short-term forecasting
ECMWF global model
Solar energy

ABSTRACT

Solar energy is key factor in the demand for clean energy development and management. In particular, global horizontal irradiance (GHI) and direct normal irradiance (DNI) are the foremost important solar resource components that need to be well characterized in order to seek an efficient operation of photovoltaic and concentrated solar power plants, respectively. The objective of the present work is to assess the quality of short-term (24 h) forecasts from a global Numerical Weather Prediction (NWP) model regarding the GHI and DNI components for solar energy applications. Forecast accuracy for the Integrated Forecasting System (IFS), the global model of the European Centre for Medium-Range Weather Forecasts (ECMWF), was verified through the comparison of the predicted hourly values with the corresponding ground-based measurements in southern Portugal. In this study, results from one year of IFS data are analysed, yielding a general good agreement between model and four ground-based measuring stations. High correlations occur particularly for GHI whilst DNI simulations are predominantly hindered by cloud and aerosol representation (i.e. the radiative effects of clouds tend to be underestimated by the model and the radiative effects of the aerosols are overestimated by the model under very clear atmospheric conditions), being closely linked to the parameterization of absorption and scattering phenomena as function of cloud and aerosol type and dimension. Relative differences of annual availabilities for GHI are found between ~0.16% to ~2.12% whilst for DNI values ranging from ~7% to ~12% are found. The respective correlations coefficients are around 0.95 for GHI and between 0.65 and 0.77 for DNI. Regional irradiation maps of GHI and DNI are presented, showing that NWP predictions are an important tool for the operation of electricity generation systems based on solar energy.

1. Introduction

Modern numerical weather forecasting can be separated into three categories: short-, medium- and long-term. Short-term forecasts are carried out to predict the weather over the next day or two. Medium-term are referred to predictions from three days to about two weeks ahead, while long-term forecasts can go up several months ahead in predicting the weather.

In order to perform forecasts, a combination of computer models and weather observations is used to simulate the atmospheric state and its evolution through the integration in the time domain of the constitutive and state equations that describe the physical phenomena in the atmosphere. During the last decades, there has been technological advances with continuous improvements in the quality of numerical models and solar radiation measuring equipment at ground-level, including the methods used for weather forecasting (Kalnay, 2003). In this context, forecasts of environmental energy fluxes, such as solar irradiance, for time-scales spanning from 1 to 2 days (hourly resolutions) are one fundamental approach for an efficient integration of renewable energy resources into existing energy supply structures. In particular, photovoltaic (PV) and non-concentrating solar thermal systems, which use both the direct and diffuse components, need global

* Corresponding author at: Renewable Energies Chair, University of Évora, IIFA, Palácio do Vimioso, Largo Marquês de Marialva, Apart. 94, 7002-554 Évora, Portugal.
E-mail addresses: fmlopes@uevora.pt (F.M. Lopes), hgsilva@uevora.pt (H.G. Silva), rsal@uevora.pt (R. Salgado), afonso.cavaco@ipes.pt (A. Cavaco), canhoto@uevora.pt (P. Canhoto), collarespereira@uevora.pt (M. Collares-Pereira).

https://doi.org/10.1016/j.solener.2018.05.039
Received 16 January 2018; Received in revised form 22 April 2018; Accepted 9 May 2018
Available online 17 May 2018
0038-092X/ © 2018 Elsevier Ltd. All rights reserved.

horizontal irradiance (GHI) forecasts while all concentrating solar photovoltaic (CPV) and thermal (CST) technologies require direct normal irradiance (DNI) forecasts (Schroedter-Homscheidt et al., 2016). PV, CPV and CST systems demand high GHI and DNI forecasting accuracy for an efficient management of solar energy harvesting, which occurs mainly under clear sky conditions (Ramirez and Vindel, 2017; Troccoli and Morcrette, 2014; Ruiz-Arias et al., 2014; Schroedter-Homscheidt et al., 2013; Collares-Pereira and Rabl, 1979).

The GHI consists in the direct and diffuse irradiances on a horizontal plane at the Earth surface (Quaschning, 2003). The diffuse component is commonly defined as diffuse horizontal irradiance (DHI) and can be directly calculated through DNI and GHI. The DNI component is defined as the solar direct irradiance that is received on a plane normal to the sun's rays over the total solar spectrum (Blanc et al., 2014), and is typically measured as the incoming beam from the Sun's disc and circumsolar irradiance within a 2.5° cone around the sun's center (WMO, 2008). For PV systems, the knowledge of GHI resource and prediction of solar energy generation allows to provide a higher power output under cloudy and clear sky conditions. Additionally, information about GHI availability is important to predict the energy output of PV systems and to help the mitigation of possible power fluctuations that can occur in electric grid injections (Pascual et al., 2015). In the case of CPV and CST systems, which have the advantage of having a higher energy storage capacity (Forrester, 2014), knowledge of DNI is fundamental if clear sky conditions occur. Forecasting DNI is important mainly for CST plants operation in order to reduce the uncertainty of solar power plant outputs due to solar irradiance intermittency (Law et al., 2014) and to optimize the necessary CST electrical energy generation (on time scales of few minutes to few hours) and maximize the energy output for a given day. In other words, there is the utility side where DNI predictions are important to project the impact of a possible sudden interruption in the grid and also to predict the total electricity needed in the grid. In fact, for medium and long-term periods such predictions are important for the power plant's operation and its energy dispatchability, i.e. the capability of a power plant to carry out energy outputs in the grid to increase economic return by delivering electricity during the more demanding and valuable periods (Ramirez and Vindel, 2017).

With the growth of the solar energy sector, in particular CST technologies, there has been a simultaneous increased interest and development in Numerical Weather Prediction (NWP) models in order to understand the spatio-temporal variation of solar irradiance and to perform short-term predictions of DNI (e.g. Ruiz-Arias et al., 2016; Schroedter-Homscheidt et al., 2009; Troccoli and Morcrette, 2014). For that matter, the forecast horizon, together with data quality control, is an important feature for an appropriated prediction. For instance, NWP models can provide accurate short-term forecasts above a forecast horizon of 6 h (in the upper limit of nowcasting, which is typically below 1-h) while artificial neural networks can perform accurate forecasts below the 6-h mark. However, current state-of-the-art NWP models have more difficulty in predicting DNI than GHI due to deviations mainly related to the representation of clouds (cloud cover and type) which are aggravated during overcast periods (Schroedter-Homscheidt et al., 2013). This generally affects the current NWP models, for example the European Centre for Medium-Range Weather Forecasts (ECMWF) global model, the Weather Research and Forecasting (WRF) model and the non-hydrostatic mesoscale (Méso-NH) model. Moreover, aerosol content is one key component that is not correctly taken into account, in detail, in operational NWP modelling (Mulcahy et al., 2014). However, it can induce substantial DNI variation as the result of scattering and absorption of radiation as well as the interaction with cloud microphysical and dynamical processes (Fan, 2016). For instance, these variations in DNI can reach a reduction of 80–90% in extreme events such as desert dusts (Kosmopoulos et al., 2017). Mukkavilli (2018) has recently shown that extreme dust events depicting large DNI mean bias overpredictions are found to be 4.6 times higher than background results. Under clear sky conditions, NWP models also reveal that aerosol component is essential to obtain accurate estimations of surface irradiance, with improvements found to be up to 58% and 76% in GHI and DNI, respectively, as described by Jimenez and Hacker (2016). Troccoli and Morcrette (2014) have used the ECMWF Integrated Forecasting System (IFS) model (Mozdzynski and Morcrette, 2014) to predict DNI with satisfactory results after a simple post processing bias-correction procedure which allowed to substantially enhance the model performance. An important improvement in the IFS would be is the use of coupled modules for aerosol and chemistry, as those developed within the Copernicus Atmosphere Monitoring Service (CAMS), allowing to use a prognostic aerosol scheme initiated by an aerosol data assimilation system. However, the use of such prognostic aerosol schemes has a high impact on the IFS efficiency, since the computational cost can increase more than 50% (Bozzo et al., 2017). For this reason, a monthly climatological description of the aerosol component is currently the most viable approach. Along with all the necessary corrections and improvements concerning cloud and aerosol representation within NWP, it is also important to quantify the forecast error of a model. To that end, the use of forecasting metrics, such as the mean square error skill score (as described in Section 2), reflect a suitable measure of forecasting skill that should be taken into account regarding forecast inaccuracies (Coimbra et al., 2013).

Another approach to improve forecasting precision should be by enhancing the ECMWF model through the use of a hybrid nowcasting system composed by a higher resolution NWP model and the use of an all-sky image (ASI) system (Seiz et al., 2002). The latter is comprised by a cloud tracking system as the one currently operational in Mitra (near Évora, Portugal) through the use of four ASI cameras, and soon to be implemented for further studies. Cloud shadow cameras have also been recently used for the prediction of GHI and DNI in Spain (Kuhn et al., 2018). Such methods can allow to generate more refined short-term forecasts of GHI and DNI for solar energy applications than the previous state-of-the-art (e.g. Cheng, 2016; Marquez and Coimbra, 2012; Chow et al., 2011).

This work is focused on the grid manager's point of view for the next 24-h horizon of available GHI and DNI by analysing model predictions with four ground-based measuring stations and, ultimately, by producing irradiance maps. This is of particular relevance for DNI due to the fact that there is still the need for development in the prediction of this solar resource as such tool can enhance the knowledge and investment in the energy and environmental sectors. Moreover, forecasts of hourly solar irradiance produced by the ECMWF global model for the next 24-h are here assessed with data from a network (DNI-A project, reference ALT20-03-0145-FEDER-000011), which was designed and installed for the operationalization of solar power plants, rather than Baseline Surface Radiation Network (BSRN) records (Roesch et al., 2011), which were typically installed for solar assessment only. As first step for the operationalization of existing and future solar energy applications in semi-arid and arid regions, this study aims to provide advice and optimization through the forecast of regional irradiation maps performed by the IFS model. The present study is not restricted to one region since it has the potential to contribute for a better management of solar electrical power plants demanding high accuracy forecasts in other regions with high solar potential such as near the equator and in arid climates away from major sources of pollution such as south of the Iberian Peninsula, northern and southern Africa, Australia, south and north America. The study is focused in southern Portugal, a semi-arid region (Chambel et al., 2007), where the climate is mostly of the Mediterranean type (Csa, according to the Köppen classification), with a small area within the mid-latitude steppe (Bsk) category (Lopes et al., 2016). Maximum temperatures can reach between 31 and 35 °C on average during July and August, often reaching values close to 40 °C, or even higher. The synoptic circulation in the region during the summer months is dominated by the frequent development of the shallow Iberian low-pressure system inside a larger scale high-pressure system,

the Azores anticyclone (e.g. Salgado et al., 2015). With clean atmosphere, the region has exceptional conditions for solar irradiance harvesting, holding one of the highest solar resource potentials measured in Europe with about 1900 kWh/m^2/year in GHI (Cavaco et al., 2017a) and over 2100 kWh/m^2/year in DNI (Cavaco et al., 2017b) annual availability. Usually, very low variabilities for solar irradiance are observed in the region with values going down to ~1.4% (Cavaco et al., 2017a). The results presented here are a first step towards the operationalization of ECMWF solar forecasting system, constituting a validation procedure in which the product can be of practice in similar regions. An assessment method for the IFS predictions against local measurement together with specific ideas on how to operationalize the model output is given here for the first time.

The remainder of this paper is structured as follows: Section 2 describes the methodology used; Section 3 presents the measurement locations in detail; Section 4 describes the ECMWF global model and respective setup; results and discussions are given in Section 5, while conclusions and future work perspectives are summarized in Section 6.

2. Methodology

In-situ measurements were used to assess hourly predictions of GHI and DNI in four different locations within southern Portugal: Évora (EVO), Mitra (MIT), Portalegre (PRT) and Alcoutim (ALC). The period of study comprises one year of measurements, from April 1st 2016 to March 31st 2017. All stations have maintenance protocols which consists typically in a daily cleaning (i.e. using a microfiber cleaning cloth and, if necessary, distilled water to clean each sensor) together with a calibration checkup of the instruments. Of all stations, EVO and MIT are the ones that are managed consistently nearby while the maintenance schedule of the other stations is subjected to local supervision which can result in missing periods of recording and/or abnormal behaviors (which are filtered or removed in that case). For the sake of comparison between ground-based observations and predictions, the same gaps of missing data found in measurements are set equally in the model output (i.e. in the nearest model grid point to the corresponding station). In order to check if all instruments measuring DNI, DHI and GHI are working properly, and to ensure a higher confidence level in the experimental data, data quality control is performed over these stations by applying filters adapted to the considered region of study. The following quality control data filters are taken into account for the model-observation analysis:

(1) Solar altitude threshold of 10°.
(2) Positive GHI and zero or positive DNI values.
(3) Irradiance values below the radiation on the top-of-atmosphere (TOA).
(4) The relative closure function: $|1-(DHI + DNI \times CZA)/GHI| \times 100\% < 10\%$, where CZA is the cosine of the solar zenith angle.
(5) Days that lack more than two hours of records, between sunrise and sunset, are rejected while days with less than two hours have the corresponding gaps interpolated from the values of the neighbouring hours.

A solar altitude threshold of 10° (condition 1) is found to be the proper value to be used here when horizon interferences exist, such as the case for orographic unevenness, being applied in all stations. Irradiance values during the night period and above radiation at TOA (conditions 2 and 3, respectively) are removed from analysis, while a relative closure function (condition 4) is considered to remove deviations related to calibration issues during the experimental period. Considering the characteristics of each station, a threshold of 10% was found to be the appropriated limit for the relative closure function, being applied in all stations with the exception of ALC station since no local DHI measurements were available, a requirement for the use of such filter. Additionally, linear interpolation for GHI and DNI irradiances is performed in days with 1 or 2 h of missing data while days with more than 2 h of gaps are rejected (condition 5). More details concerning the number of days used (N days) during this analysis, which correspond to the time period of usable data under the proposed filter criteria, are summarized in Table B.1 (in Appendix B) for each station. It should be taken into account, as described by Gueymard and Ruiz-Arias (2016), that there is currently no proper and definitive accepted procedure for an optimal quality control check of irradiance data and therefore different methods between Institutions are typically established.

Several models have been attaining an important role in the development of new forecast methods (Diagne et al., 2013) through linear models techniques that make usage of time series forecasting provide successful predictions such as the clearness index. In this context, for further assessment of the model against observations, 1-h clearness indices were calculated for both GHI (k_t) and DNI (k_b). The clearness index allows one to establish the type of irradiance that is received at ground-level (Troccoli and Morcrette, 2014), being fundamental in the context of solar radiation analysis. This parameter is defined as the ratio between terrestrial (observed at the Earth's surface) and extraterrestrial (calculated at TOA) irradiances on a horizontal and normal surface, respectively for GHI and DNI, as described by Kalogirou (2014):

$$k_t = GHI_{obs}/GHI_{TOA}, \quad (1)$$

$$k_b = DNI_{obs}/DNI_{TOA}. \quad (2)$$

The total solar irradiance at TOA (i.e. the total power from the Sun at the average Earth-Sun distance) is $I_0 = 1361\ W/m^2$, as recently described by Solanki et al. (2013), and is used in the analysis as reference value for GHI and DNI calculations on TOA[1]. The approach in using irradiance values at TOA has been documented in literature (Fernández-Peruchena and Bernardos, 2015; Lefévre et al., 2013) and was used in this analysis. Additionally, 1-day clearness indices for GHI (K_t) and DNI (K_b) were also calculated:

$$K_t = E_t^{obs}/E_t^{TOA}, \text{ with } E_t = \sum_1^{24} GHI, \quad (3)$$

$$K_b = E_b^{obs}/E_b^{TOA}, \text{ with } E_b = \sum_1^{24} DNI, \quad (4)$$

where GHI and DNI are the irradiation availabilities (kWh/m^2), Et and Eb, which were simply calculated by considering the integration of daily irradiances values for the entire period. Typical values of K_t and K_b can range from ~0.1 to 0.9 and from ~0 to 0.8, for overcast and for clear (and very clean aerosol) sky conditions, respectively. The relative differences (%) of the total energy availability (considering the daily values) between observations and model are given by:

$$\Delta E_t = (\sum E_t^{mod} / \sum E_t^{obs} - 1) \times 100\%, \quad (5)$$

$$\Delta E_b = (\sum E_b^{mod} / \sum E_b^{obs} - 1) \times 100\%, \quad (6)$$

where the summations are expressed by the sum of the daily availabilities obtained in Eqs. (3) and (4). Equivalent to the clearness index would be the use of the clear sky index (Bird and Hulstrom, 1981) which allows us to have a better compensation of the atmosphere impact on both GHI and DNI. Nevertheless, considering the available data and since it is not crucial for the present results, the clearness index is used in the analysis.

Probability density functions (PDF's) were used in this analysis as well as Pearson correlations (r) between the clearness indices. The PDF's allow to determine the probability distribution (i.e. the frequency

[1] As described by Kalogirou (2014), in Eq. 2.77: $GHI_{TOA} = I_0\left[1 + 0.033\cos\left(\frac{360N}{365}\right)\right] \times CZA$ and $DNI_{TOA} = I_0\left[1 + 0.033\cos\left(\frac{360N}{365}\right)\right]$, where N is the day number in the year.

of occurrence) of hourly clearness indices (k_t and k_b) obtained from the model and observations. A statistical test through the two sample Kolmogorov-Smirnov test was also used to analyse and compare the hourly clearness indices from the observations with the model, where the result H_0 is 1 if the test rejects the null hypothesis at the 5% significance level and 0 otherwise. The test statistic (D^*) between the two samples is also calculated.

Additionally, to assess the overall level of agreement between the EMCWF global model and observations, forecasting skill is taken into account through the use of a Skill Score (SS). The SS is computed as the decrease in the mean square error (MSE) obtained by the model with respect to the reference (i.e. persistence) and is given as described by Perez et al. (2013):

$$SS = 1 - MSE_{for}/MSE_{per}, \quad (7)$$

where MSEfor and MSEper are the error metrics respectively for the forecast model and the persistence calculated through Eq. (A.1) (in Appendix A). The latter is a simple forecast method obtained by persisting the previous observational values over the forecast range (1-day for the present study). If the obtained skill is equal to one, then a perfect forecast is achieved while negative skill values correspond to worse performances by the model than the persistence. Zero values indicate no improvement over the reference.

3. Measurements

As part of an existing national network of radiometric stations scattered across the country (12 currently in operation), the four measuring stations used in this work are designed and implemented for the study of direct, global and diffuse irradiances and their relation with meteorological variables (see DNI-A project, Cavaco et al., 2017b). Besides providing coverage of the country, some of these stations are relatively close from each other (Fig. 1). Further statistical details concerning the four used stations can be viewed in Table B.1.

In this analysis, one year of ground-based observations (from April 1st 2016 to March 31st 2017) is used from four stations, corresponding to the IFS model operational cycles 41R2 and 43R1. The EVO station (N38.567686, W7.91172) is located in Évora city, on the top of a research facility, and in the countryside at ~13 km of the city is the MIT station (N38.530522, W8.011221) where the measurements of solar irradiance are influenced by local shadows due to the orographic unevenness of the terrain as MIT is situated in a small valley. Consequently, in this analysis, a solar altitude threshold is set to 10°, corresponding to nearly 1-h after sunrise and 1-h before sunset. This allows one to avoid shadow and horizon interferences near to the morning and evening in all stations. In the north, the PRT station (N39.269221, W7.442716) is located in Portalegre city (~340 m) while more into the south is located the ALC station (N37.441844, W7.744901) in an open area in the outskirts of Alcoutim city which is ~30 km from the seashore. The two last stations are located in regions where the orography is characterized by mountains, allowing the frequent occurrence of small scale fogs.

The measured data was acquired with a sampling rate of 5 s and then averaged and recorded every 1 min, with the exception for the ALC station which was recorded every 15 min. In this study, all solar radiation measurements are performed through the use of Kipp & Zonen instruments (retrieved from http://www.kippzonen.com). DNI is measured with pyrheliometers (model CHP1), World Meteorological Organization (WMO) First Class instrument with an associated estimated uncertainty on a daily basis of < 1%. The pyrheliometers are calibrated every 2 years following the International Organization for Standardization (ISO) 9059:1990 standard. GHI and DNI are measured with pyranometers (model CMP11), ISO 9060 Secondary Standard with an associated estimated uncertainty at daily basis of < 2%. The pyranometers are also calibrated every 2 year following the ISO 9847:1992 standard. The continuous measurements of GHI, DHI and DNI were

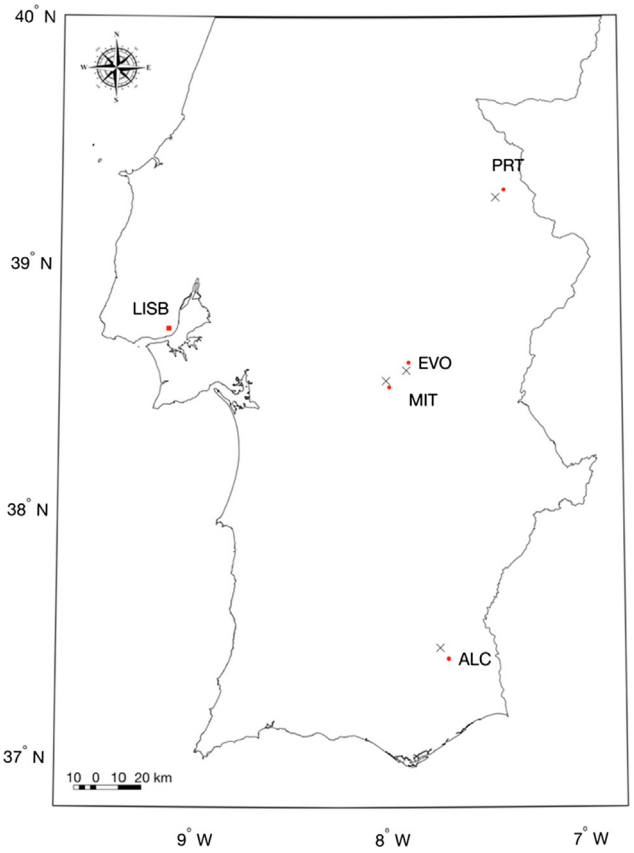

Fig. 1. Geographic locations of the measuring sites at Évora (EVO), Mitra (MIT), Portalegre (PRT) and Alcoutim (ALC) in southern Portugal. A depiction is shown of the nearest model grid points (red dots) to the measuring stations (black crosses). The geographical reference of Lisbon (LISB) is also shown (red square). (For interpretation of the references to colour in this figure legend, the reader is referred to the web version of this article.)

carried out with SOLYS2 Sun-Trackers, taking into consideration a total of 365 days for analysis (starting on April 1st 2016). Measurements should not be affected by soiling (Conceição et al., 2018) since regular maintenance of the instruments, particularly in EVO and MIT stations, is maintained.

Since the number of measurement days in each station is not the same, instead of an inter-comparison between stations, a systematic and robust statistical assessment of the model 24-h predictions against ground-based observations in each site is carried out. To that end, hourly data is calculated through hourly backward means, i.e. by considering the previous sixty 1-min records of observational data, with the exception for the ALC station where hourly means were calculated based on 15-min records. The measured hourly data is presented in Fig. 2, depicting the general tendency that solar irradiance values should have during the period of analysis. As expected, higher values of GHI take place in spring and summer months while lower values occur in winter months. In the same sense, the daily maximum DNI has a more constant trend throughout the year with higher values occurring under clear sky conditions, which are more frequent to occur in the summer period that is characterized by more sunshine hours and lower solar zenith angles (i.e. lower air masses around the solar noon). As it was previously mentioned in Section 2, and considering the applied filters, the same missing periods of measuring data have been placed in the model in order to allow a fair comparison between data sets and to correctly assess the model performance. The time period (in days) found outside the proposed filters for GHI are of ~185 for EVO, MIT and ALC stations and ~186 for PRT station; while on the other hand, for DNI there are ~183, ~197, ~210 and ~184 for EVO, MIT, PRT

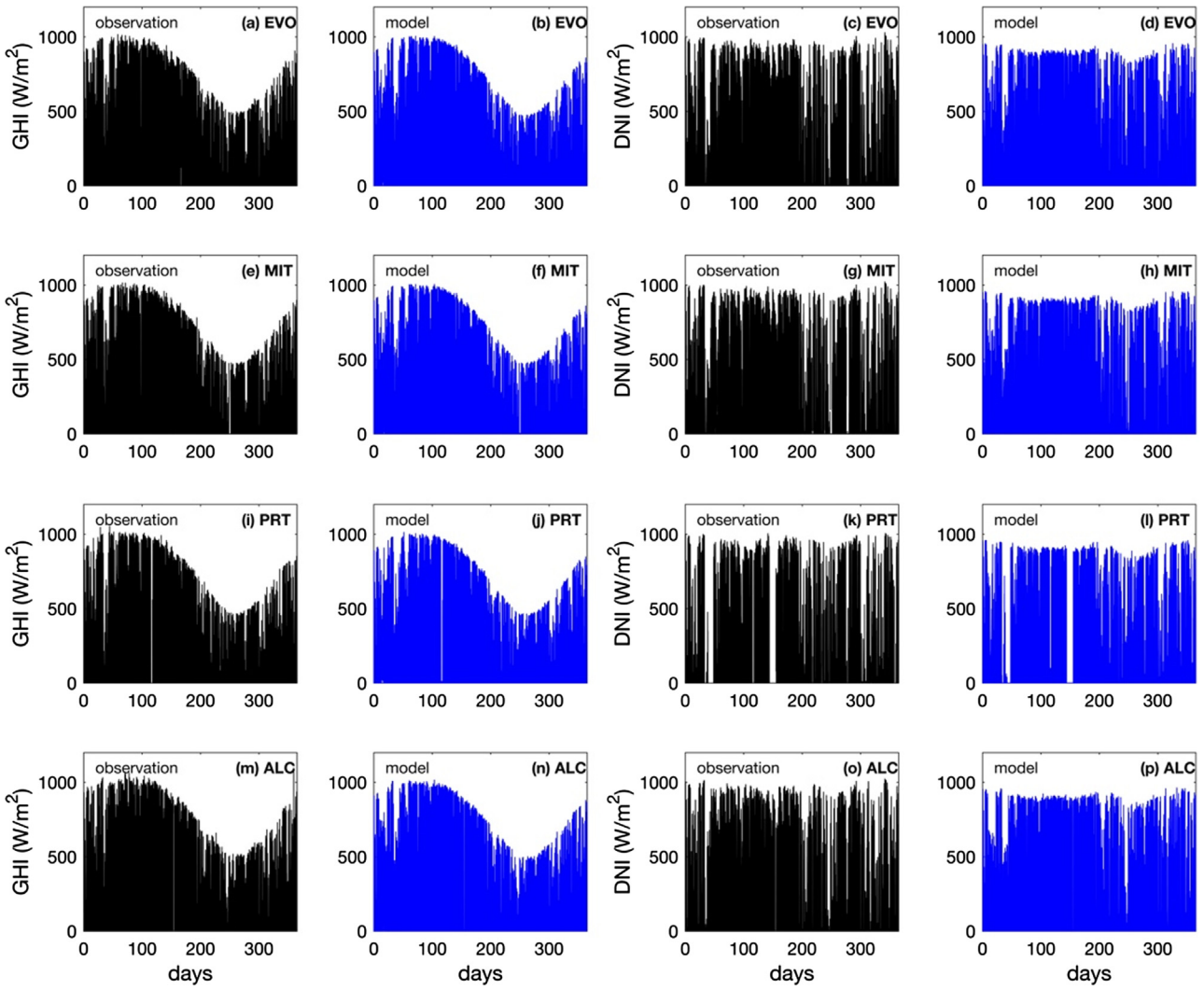

Fig. 2. Hourly means for ground-observations and model predictions of solar irradiance (W/m^2) in EVO (a–d), MIT (e–h), PRT (i–l) and ALC (m–p). Global horizontal irradiance (GHI) and direct normal irradiance (DNI) are analysed for the period of 365 days (from April 1st 2016 to March 31st 2017).

and ALC stations, respectively. Overall, the observational results yield higher mean values and standard deviations of DNI when comparing with the GHI in all stations, as expected. A statistical summary for each station is presented in Table B.1.

4. The ECMWF global model and the radiative scheme

The IFS model is currently the NWP model with the highest scores in terms of medium range global weather forecast (see for example, Haiden et al., 2016), with several radiative schemes being used throughout the past years (Hogan et al., 2017). The number of output parameters has increased over time and recently it has been improved with predictions of DNI (Troccoli and Morcrette, 2014). The IFS atmospheric model and data assimilation system makes use of the McRad radiative scheme (cycle 41R2) to perform deterministic predictions of GHI and DNI. The McRad provides a flexible radiation grid which is more suitable for more coarse applications, using several modules, including an improved description of the land-surface albedo from observations carried out by Moderate Resolution Imaging Spectroradiometer (MODIS), and is based on the Rapid Radiative Transfer Model (Mlawer and Clough, 1997), which allows one to calculate radiation fluxes (longwave and shortwave). The model also uses the Monte-Carlo Independent Column Approximation (McICA) which takes into account the radiation transfer in cloudy atmospheres (Morcrette et al., 2008).

The IFS provides an operational forecast data, where the forecast issue time can be set to start at 0 or 12 UTC (in this analysis, 0 UTC was chosen as the issue time) and uses an average spatial resolution of 9 km. The variables given by the model and which are used here for comparison analysis of GHI and DNI were *ssrd* and *fdir*, respectively. The former corresponds to the downward surface solar irradiance while the latter is defined as the total sky direct solar irradiance at surface. Both variables are assembled as integrated values (irradiation in J/m^2) from the start of the forecast. In order to directly compare model results with ground-based observations, the hourly accumulated irradiation values from the IFS were divided by 3600 and then converted to mean power values (W/m^2). Further ahead, and in the context of the energy sector, units for GHI and DNI are presented in the form of irradiation (energy by square meter), in kWh/m^2. More model specifications can be seen in Morcrette et al. (2008).

Previous studies have shown that NWP models have an inferior performance when forecasting DNI as compared to GHI under clear and cloudy conditions (Perez et al., 2013). This is highlighted by the fact that nowadays the main difficulties and challenges in weather forecasting is the representation of clouds and aerosols which are two of the most important subjects when predicting solar irradiance, along with its partition between direct and diffuse irradiances. It should be noted that a correct representation of clouds is critically dependent on the

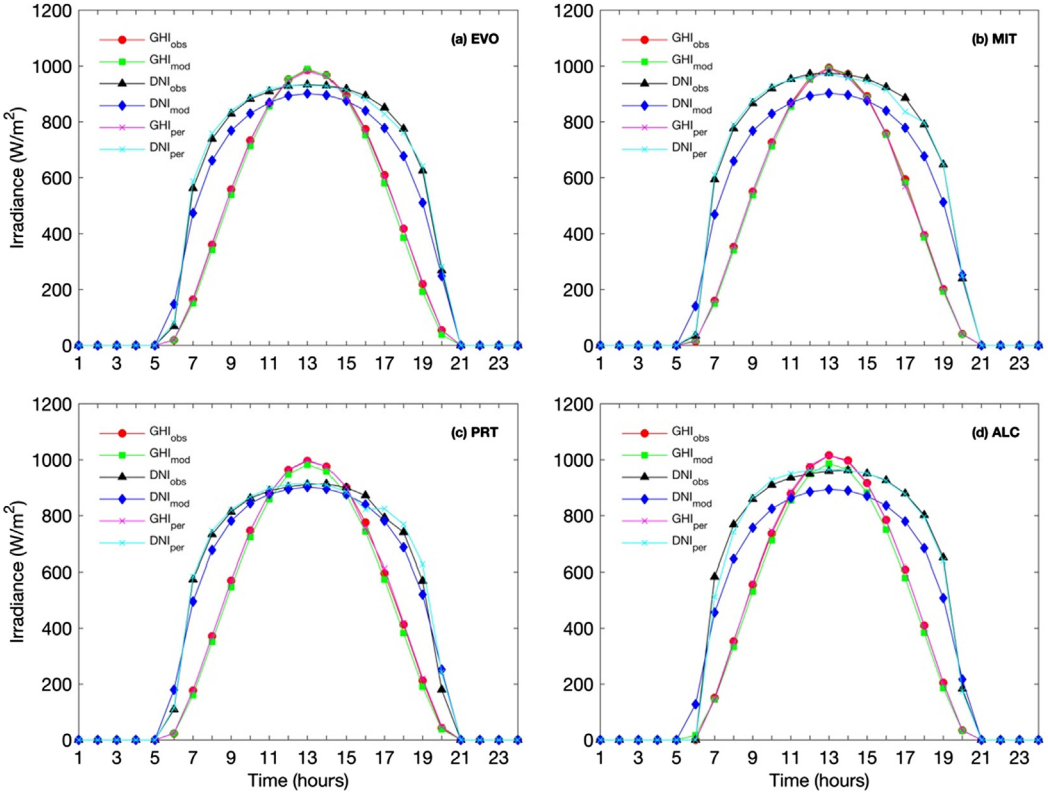

Fig. 3. Observed (*obs*) and IFS predicted (*mod*) solar irradiance (W/m^2) hourly means of global horizontal and direct normal irradiance (GHI and DNI, respectively) for EVO (a), MIT (b), PRT (c) and ALC (d). Persistence (*per*) forecast hourly means are also depicted. An example of one day with very clear sky conditions was selected (July 14th 2016).

accuracy of several environmental variables, namely temperature, moisture, wind and respective vertical profiles, which in turn are highly dependent on data assimilation quality and on the representation of surface processes. Also, the impact of an incorrect estimation of the aerosols distribution is higher in DNI than in GHI, as the decrease in direct radiation due to aerosols is partially compensated by the increase in diffuse radiation.

Since the output of the ECMWF model are hourly accumulated values (i.e. time step values integrated in an hourly basis), the direct irradiance in a horizontal surface given by the model was divided by the previously averaged CZA (Kalogirou, 2014), taking also into account the nearest model grid point to the corresponding station.

In order to perform data quality control between both time series, an assessment of the temporal alignment between model (GHI_{mod}, DNI_{mod}) and measurements (GHI_{obs}, DNI_{obs}) was firstly carried out for two case studies. To illustrate this exercise, one day with clear sky conditions (July 14th 2016) recorded in all stations is depicted in Fig. 3 while in Fig. 4 a cloudy day (July 8th 2016) is presented. During clear sky, results show good agreement between model and observation which is well represented by very similar daily amplitudes in all stations, particularly for GHI. DNI deviations that take place in the early hours of the day between 6 and 7 UTC (Fig. 3b–d) and in the early evening between 20 and 21 UTC (Fig. 3c) may be a consequence of local horizon interferences (e.g. orographic unevenness of the terrain and nearby trees), justifying the use of a proper value for such type of obstacles. The value found in this analysis was the 10° threshold for the solar altitude (as described in Section 2). Moreover, during this particular day, all stations show different amplitudes of DNI between observation and model. This is probably related to the representation of aerosols in the model which currently only considers a mean monthly aerosol climatology instead of an actual representation of the aerosol content in the atmosphere. In this context, under very clean atmosphere (such as the one depicted during this day), the aerosol concentration used in the model is higher than in reality, consequently the aerosol radiative effects (i.e. absorption and scattering of radiation as function of aerosol type and dimension) are overestimated by the model, as the predicted DNI values tend to be lower than the observed. Based on these results, average differences between model and observations of ~31 W/m^2, ~47 W/m^2, ~11 W/m^2 and ~45 W/m^2 are respectively found for this day in EVO, MIT, PRT and ALC stations, being related to the effects of an aerosol climatology instead of actual values. Moreover, during aerosol events, which are common in the region in this period, namely due to the atmospheric transport of Saharan dusts and wildfires, the effects of the aerosols are underestimated by the model leading to an overestimation in DNI and to a lesser extent in GHI, even under cloudless sky conditions. During cloudy days (Fig. 4) the model shows a general underestimation of cloud radiative effects. During these periods, there are low measured values as opposed to those produced by model which tend to be higher. This is evident in all plots of Fig. 4, particularly during the early hours of the day. The underestimation (overestimation) of the radiative effects of clouds (aerosols under very clean atmosphere) carried out by the model will be further discussed in the analysis. Additionally, a persistence test for the model GHI_{per} and DNI_{per} is also depicted, showing that the persistence forecast performs a better prediction than the IFS during the summer, as discussed further ahead (in Section 5).

5. Results and discussion

5.1. Statistical analysis

In all measuring stations the mean annual values between measurements and model results show very similar behavior for both GHI and DNI. With the adjustment of the same missing periods as the experimental data, the hourly values for the 24-h predictions (Fig. 2) show good agreement with measurements. However, small differences

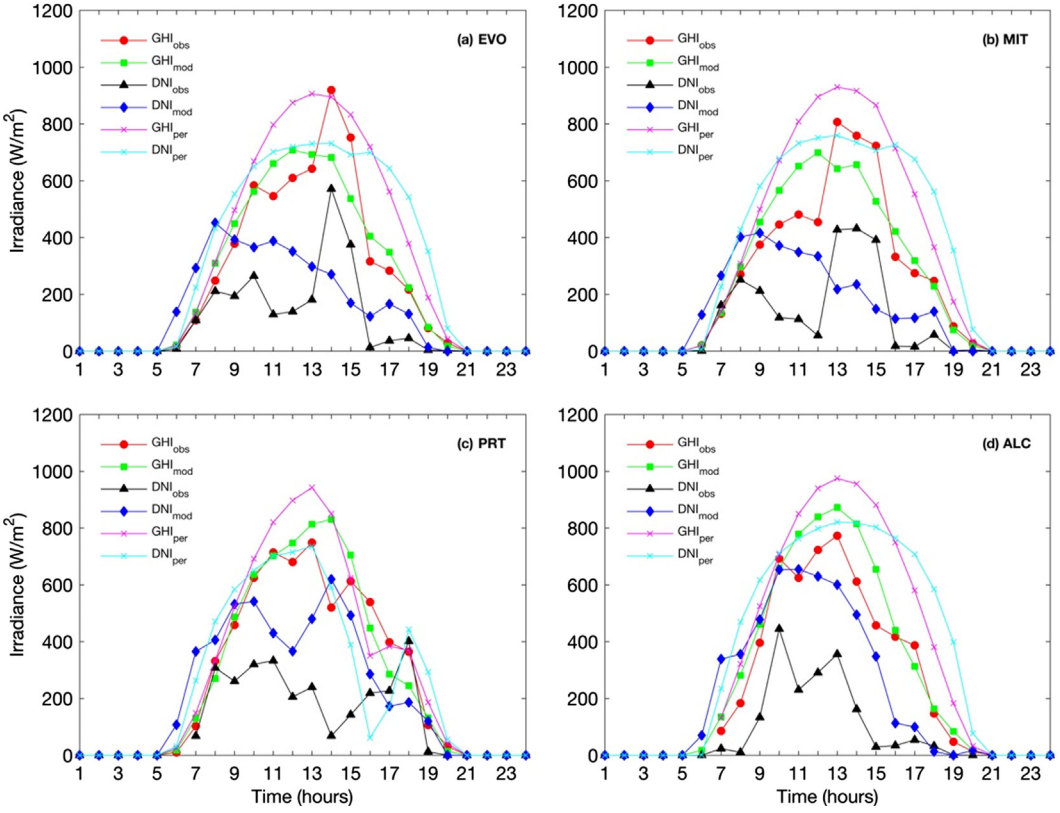

Fig. 4. Observed (*obs*) and IFS predicted (*mod*) solar irradiance (W/m^2) hourly means of global horizontal and direct normal irradiance (GHI and DNI, respectively) for EVO (a), MIT (b), PRT (c) and ALC (d). Persistence (*per*) forecast hourly means are also depicted. An example of one day with cloudy conditions was selected (July 8th 2016).

exist in all stations with the model depicting a general overestimation towards measurements, particularly for DNI (Table B.1). For instance, considering the mean values, a GHI maximum overestimation of 9.9 W/m^2 (~2.1%) in MIT station is obtained while ALC station shows the highest DNI model overestimation with 63.5 W/m^2 (~11.6%). As opposed to these, the lowest deviations occur in the same stations with small overestimations of 0.5 W/m^2 (~0.1%) in ALC station for GHI and 38.3 W/m^2 (~7%) in EVO station for DNI. This shows how the GHI seems to be better predicted by the model than DNI. The general difference in DNI predictions is mainly related to the presence of unpredicted clouds and fogs and to their respective intrinsic spatio-temporal inhomogeneity (Sirch et al., 2017), as they are key parameters that strongly impact on DNI variation. For instance, while GHI can be reduced to only 10%, DNI can be suppressed to almost zero as result of thin high-altitude clouds composed by ice crystals such as cirrus (Quesada-Ruiz et al., 2014). This happens because GHI is balanced both in the observations and model by the diffuse irradiance that results from light scattering in the clouds. The use of global and diffuse irradiances as a mean to measure cloud thickness and discriminate different cloud types has also been determined (e.g. Harrison et al., 2008).

Hourly clearness indices (Fig. 5), k_t for GHI and k_b for DNI (Eqs. (4) and (5), respectively), generally yield good correlations between model and observations in each station, in particular for GHI. A high density of k_t values occurs around 0.75 (as expected) while for k_b, values are more likely to be in the range between 0.60 and 0.75. The root mean square error (RMSE), as calculate in Eq. (A.1), demonstrates that GHI is being better predicted as compared with DNI, where minimum values of RMSE in k_t are observed in MIT (0.11) and the highest in PRT (0.13). In the case of DNI, the RMSE in k_b is higher in PRT station (0.17) while the lowest error is found in MIT station (0.15). Moreover, the mean bias error (MBE), as calculated in Eq. (A.2), for the hourly clearness indices is generally negative, corresponding to the model overestimation, with the exception for k_t values in EVO. Additionally, a few common features are observed amongst all stations: There is a tendency for the existence of higher dispersion of k_b towards lower values of the index, while close to zero there are clusters of k_b values, probably depicting the model overestimation of DNI under cloudy conditions, i.e. non-zero modelled values instead of the null observations; and the model seems to underestimate the measurements for high values of both k_t and k_b (i.e. for clear sky conditions). This underestimation of the model should be related to the use of the previously mentioned mean monthly aerosol climatology instead of a continuous updated aerosol content based on aerosol analysis (and eventually on the integration of a prognostic equation) inside the atmospheric model. One example that justifies such application would be the case of a very clear sky day during the summer and after a rainy day, in which the aerosol content should be significantly lower than the climatological value and where, consequently, the DNI should be substantially higher than the predicted.

The stated differences between k_t and k_b tend to agree with the fact that the hourly clearness indices are shaped by the sub-daily variability of GHI and DNI which are led by clouds and fogs, which in turn depend on sub-scale features (from the point of view of global NWP models) that can affect irradiances within a short time-frame. This is particularly depicted in the obtained k_b values in Fig. 5 which show lower correlations than k_t, with RMSE's of 0.16, 0.15, 0.17 and 0.16 respectively in MIT, EVO, PRT and ALC stations as opposed to higher correlations found the for k_t values and the obtained lower RMSE's of 0.12, 0.11, 0.13 and 0.12 respectively in MIT, EVO, PRT and ALC stations. These sub-scale features are difficult to be simulated by global NWP models, showing the need of dynamical downscaling through high-resolution models, such as the Méso-NH (Lafore et al., 1998). These results confirm that the IFS model has difficulties in simulating accurately the DNI irradiance under partly cloudy conditions. This is not so evident in the k_t values since in cloudy periods the decrease in GHI is partially

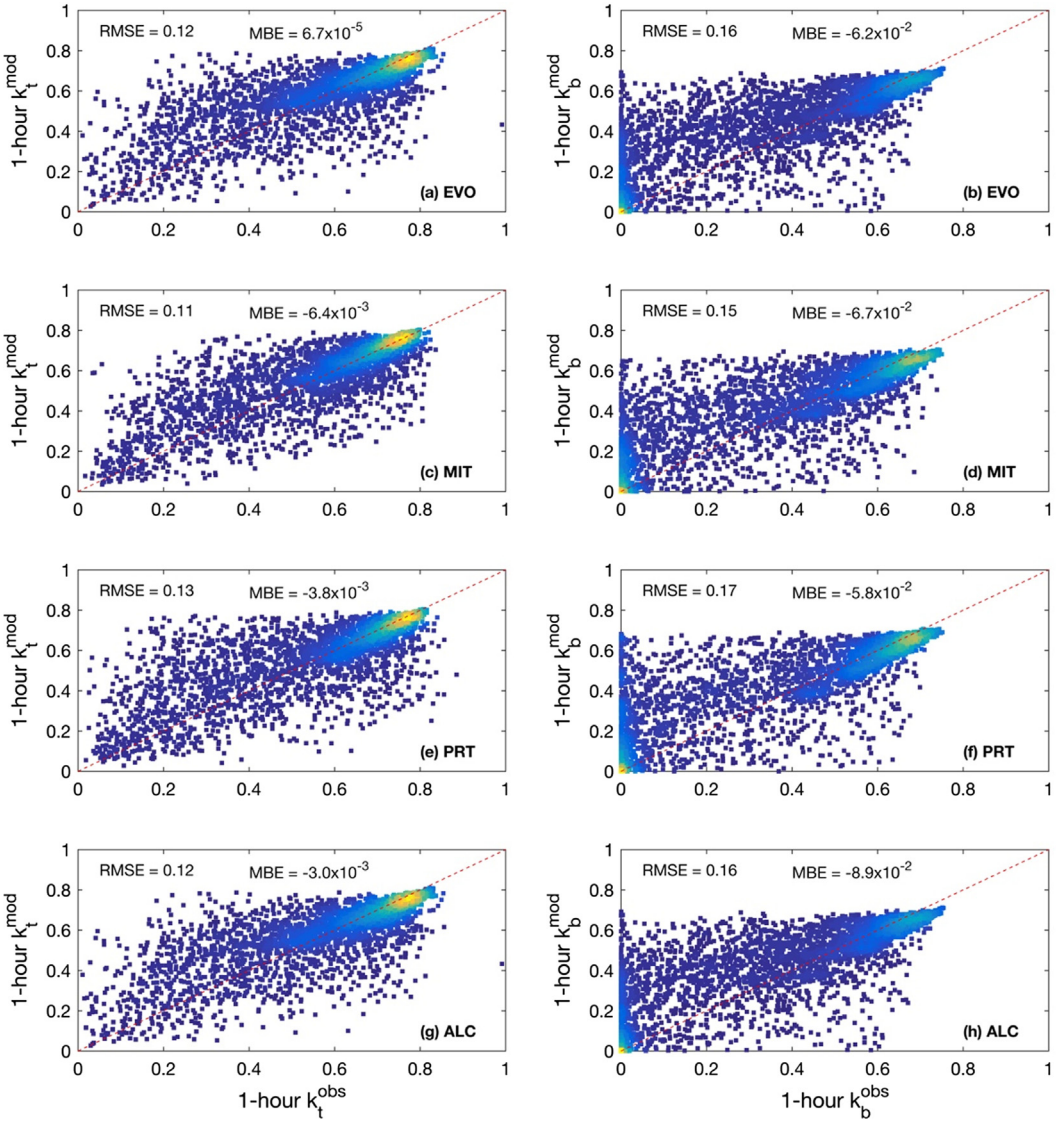

Fig. 5. Hourly clearness indices for GHI (k_t) and DNI (k_b) in EVO (a, b), MIT (c, d), PRT (e, f) and ALC (g, h) during one year of measurements (from April 1st 2016 to March 31st 2017). Root mean square error (RMSE) and mean bias error (MBE) are depicted together with a normal regression (dashed red line) between observation and model. (For interpretation of the references to colour in this figure legend, the reader is referred to the web version of this article.)

compensated by the increase in DHI.

The PDF for each k_t and k_b index is depicted in Fig. 6, as well as the respective correlations coefficients (*r* and *p-value*). As previously stated, good correlations values between measurements and model occur for the k_t indices. Correlations yield higher values in MIT with ~0.82 for k_t and ~0.79 for k_b, while PRT depicts the lowest correlation of k_t (~0.79) and k_b (~0.76) values. Although some of the difference between the stations may be related to the quality of the measurements (e.g. the PRT station has more days of missing periods), the most plausible reason should have to do with local surface heterogeneities, being PRT and ALC located in regions of more complex orography, close to mountains. The result of a global model, like the IFS, are representative, at best, for a grid of $9 \times 9\,km^2$. Thus, the greater the heterogeneity in the interior of a grid box, the greater will be the deviation between local values and mean grid box values. Regarding GHI, for both observation and model, the curve peaks are very close around k_t values of 0.75. For DNI, there is more substantial differences for low and high values of k_b, where for lower values, observations depict always a very high peak of probability density (related to cloud representation during overcast periods) while for higher values (~0.65), the model always overestimates observations (related to aerosol representation during very clear sky days). Additionally, the two sample Kolmogorov-Smirnov statistical test D^* (Table 1) indicates that in all stations k_b has higher values as compared to the ones found for k_t. It is clear that the null hypothesis H_0 is rejected in all cases, revealing a certain degree of relation between k_t and k_b from observations and model, respectively.

Daily clearness indices (Fig. 7), calculated from the hourly values of GHI and DNI during each day, i.e. K_t and K_b as given respectively by Eqs. (6) and (7), show lower values of absolute error (AE) for GHI, as expected. In this context, higher frequencies of K_t values occur around 0.75 in all stations, with EVO and MIT having correspondingly ~20% and ~30% of the total number of days with the RMSE below the threshold error of 0.01. A similar distribution is observed in the remaining stations for the same criteria, where K_t values are observed to occur ~21% and ~17% in PRT and ALC, respectively. The daily clearness indices based on DNI, show high frequency around 0.60 in all stations. Larger dispersion of errors between K_b values of each day occur during overcast and partly cloudy periods. Values of RMSE lower than 0.01 are ~10% of the total number of days in EVO while ~12%, ~9% and 11% are observed in the case of MIT, PRT and ALC stations, respectively. In the case of K_b values, as previously observed for the

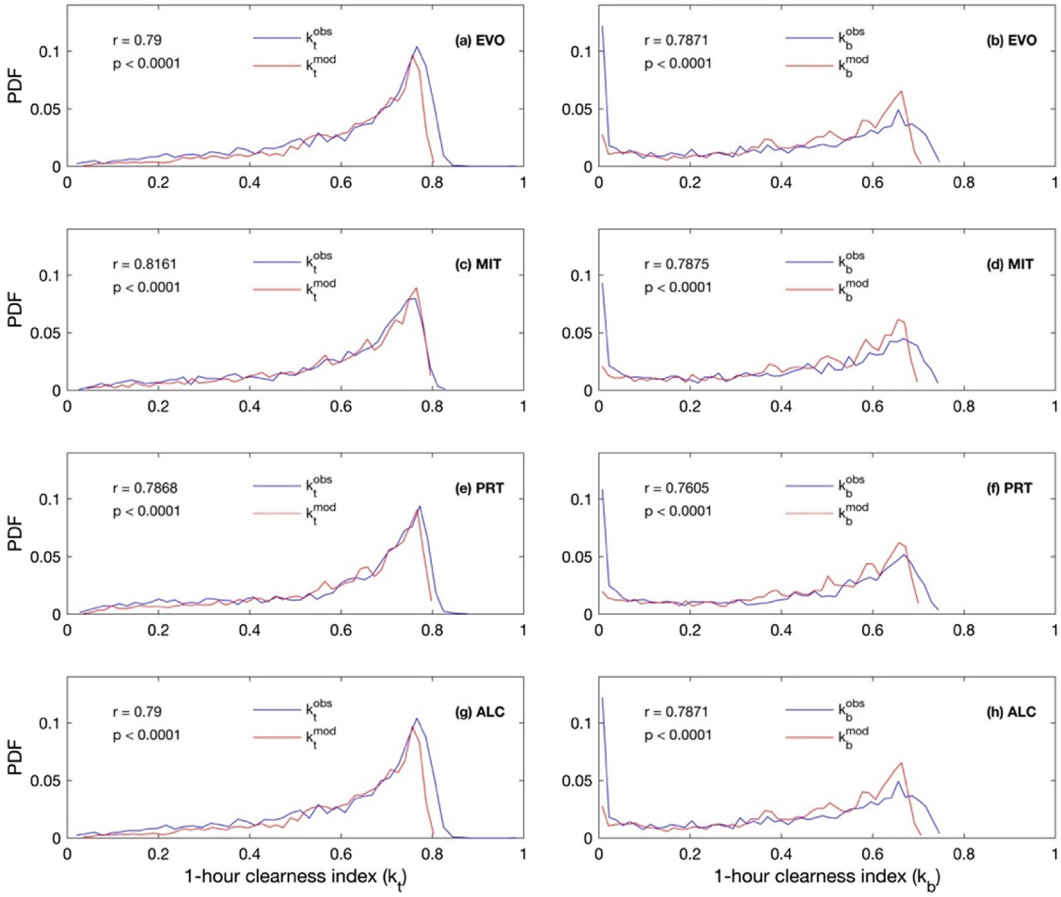

Fig. 6. Probability density functions (PDFs) and respective correlations coefficients (*r* and *p-value*) for the 1-h clearness indices for GHI (k_t) and DNI (k_b) in EVO (a, b), MIT (c, d), PRT (e, f) and ALC (g, h) during one year of measurements (from April 1st 2016 to March 31st 2017).

Table 1
Kolmogorov-Smirnov statistical test between two samples (observation, model) for GHI (k_t) and DNI (k_b) hourly indices in Évora (EVO), Mitra (MIT), Portalegre (PRT) and Alcoutim (ALC) stations. One year of measurements is considered in the study (from April 1st 2016 to March 31st 2017). Results are obtained taking in consideration a solar altitude angle above 10° in all stations.

	Kolmogorov-Smirnov test	EVO	MIT	PRT	ALC
k_t	H_0	1	1	1	1
	D^*	0.06	0.05	0.07	0.11
k_b	H_0	1	1	1	1
	D^*	0.09	0.10	0.11	0.12

hourly values in Fig. 5, there is a higher dispersion close to zero, with deviations related to the model difficulties in cloud representation (i.e. the model tendency to overestimate observations during cloudy periods). The AE, given by the difference between the measured and the predicted value, depicts higher occurrences of negative values close to zero which represent the non-zero values of modelled DNI when in fact the observation considers null values due to clouds. Moreover, a small increase of AE for $K_b > 0.6$ is observed, where these values correspond to very clean sky days, as this error should be related to the aerosol representation (no clouds are present).

Under very clean atmosphere, the model tends to overestimate the effect of aerosols, predicting lower DNI values. As previously mentioned, this is probably related to the use of mean monthly aerosols climatology instead of actual aerosol forecasts as proposed by Casado-Rubio et al. (2017), but also due to an incomplete representation of the radiative effects of aerosols. Recent efforts have been developed towards the improvement of the aerosol representation with the inclusion of aerosol indirect effects in high-resolution global NWP models in order to improve the accuracy of short-range weather forecasts (Mulcahy et al., 2014). As described in Bozzo et al. (2017), it is still possible and advantageous to improve aerosol climatology and reduce its induced errors, as these have a strong dependence on surface observations, through the improvement of transport models and the observations. Aerosol observations can be assimilated, enabling the filling of gaps that exist in sparse network of measurement sites (Kinne et al., 2013) and by the use of empirical methods (e.g. Liu et al., 2005), merging model fields, satellite and surface observational data.

Daily irradiations (i.e. daily accumulated values) of GHI and DNI for both observations and the hourly predictions have also been calculated for the considered 1-year period (Fig. 8). Restriction of solar altitudes above 10° is maintained here. As previously stated, the model performs well in simulating GHI, having higher correlations (R^2) than DNI. These high correlations take place under clear sky conditions in the summer period, where daily irradiations of GHI (E_t) and DNI (E_b) reach ~9 kWh/m^2 and more than 11 kWh/m^2, respectively. For instance, there is clear correspondence with the E_t fitting curve (dashed line) than for E_b values where for high values the model tends to significantly underestimate DNI. As previously discussed, this should be related to climatological values of aerosol concentration used by the IFS which appear to be higher than the real ones for the case of high DNI in all stations, which correspond to periods of no clouds and a very clean atmosphere. In EVO, the relative difference between model and observation shows deviations of ~0.20% and ~7.02%, correspondingly for GHI and DNI, while for MIT these are of ~2.12% and ~7.15%. In PRT the relative difference found is of ~0.85% for E_t and ~9.78% for E_b. The ALC station shows differences of ~0.16% for E_t and the highest for E_b of ~11.65%. These results confirm that in this analysis, in

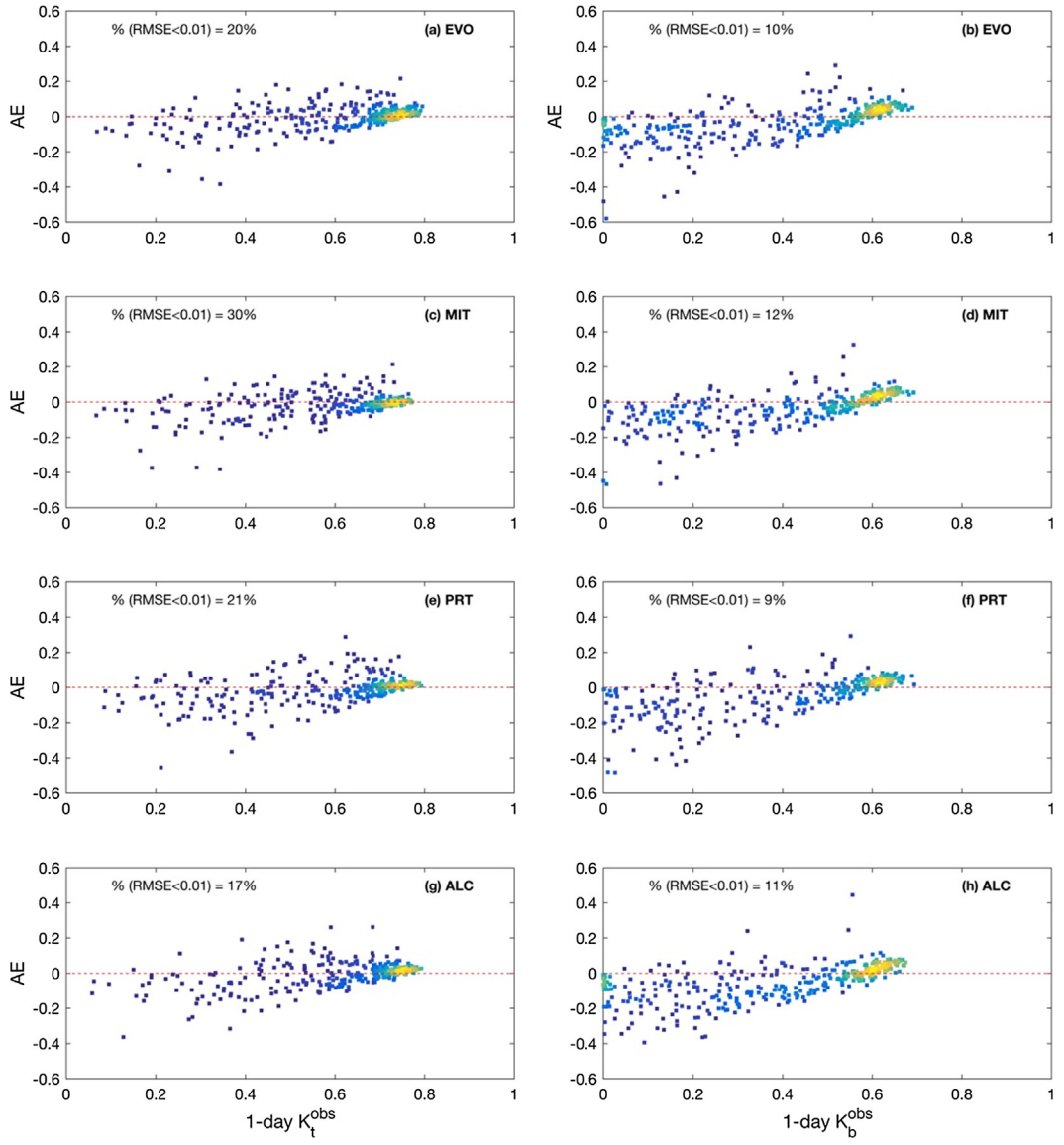

Fig. 7. Absolute error (AE) between 1-day clearness indices from measurements and model for GHI (K_t) and DNI (K_b) in EVO (a, b), MIT (c, d), PRT (e, f) and ALC (g, h) during one year of measurements (from April 1st 2016 to March 31st 2017). The red dashed line represents the threshold between positive and negative AE values. (For interpretation of the references to colour in this figure legend, the reader is referred to the web version of this article.)

comparison with the obtained results in EVO and MIT, the predictions are less valuable in PRT and ALC, partially due to the location in regions with a more pronounced relief, which enhance the formation of near surface sub-scale clouds.

Nevertheless, taking in consideration the assumptions described earlier in Section 2, these results show that the total energy irradiation availability obtained from the observations and predictions (for both GHI and DNI) are found to be close to the reference annual values in the region, with 1900 kWh/m^2/year for GHI (Cavaco et al., 2017a) and more than 2100 kWh/m^2/year for DNI (Cavaco et al., 2017b), respectively. The differences that are stated between reference and predicted values are mainly a consequence of (i) missing periods of data; (ii) the 10° threshold for solar altitude; (iii) the closure function; and (iv) the model tendency to overestimate daily irradiation availabilities under cloudy sky conditions, partially due to small sub-scale fogs and clouds unresolved by a global model at 9 km^2 horizontal resolution.

5.2. Forecast skill

Since solar forecast accuracy depends on a number of factors such as region, weather conditions and forecast horizon, it is important here to compare quantitatively the IFS hourly predictions with a reference forecast. To that end, an exercise of forecasting skill is taken into consideration by calculating the Skill Score, SS (Eq. (7)), between values of the daily clearness indices k_t and k_b of the model and the persistence forecast, i.e. a 24-h shift ahead of the local observed time series, for the entire period of analysis. Tables 2 and 3 summarize the statistical results between the IFS predictions and observations and the persistence with observations, respectively, while in Table 4 the obtained SS between model and persistence are shown. There is a clear forecast improvement taken by the IFS in comparison with the persistence for both GHI and DNI. Tables 2 and 3 show that, in all stations, there are higher correlations and lower errors between k_t and k_b for the model than the ones found for the persistence in relation to the observations. The obtained SS results (Table 4) are generally above 0.5 with higher values found to be in both EVO and MIT stations with ~0.70 for k_t and ~0.61 for k_b as they are relatively close to each other. On the other hand, lower scores occur in PRT and ALC stations with ~0.58 and ~0.64 for k_t and ~0.57 and ~0.56 for k_b, respectively. Such contrast indicates well how the model is better in predicting GHI

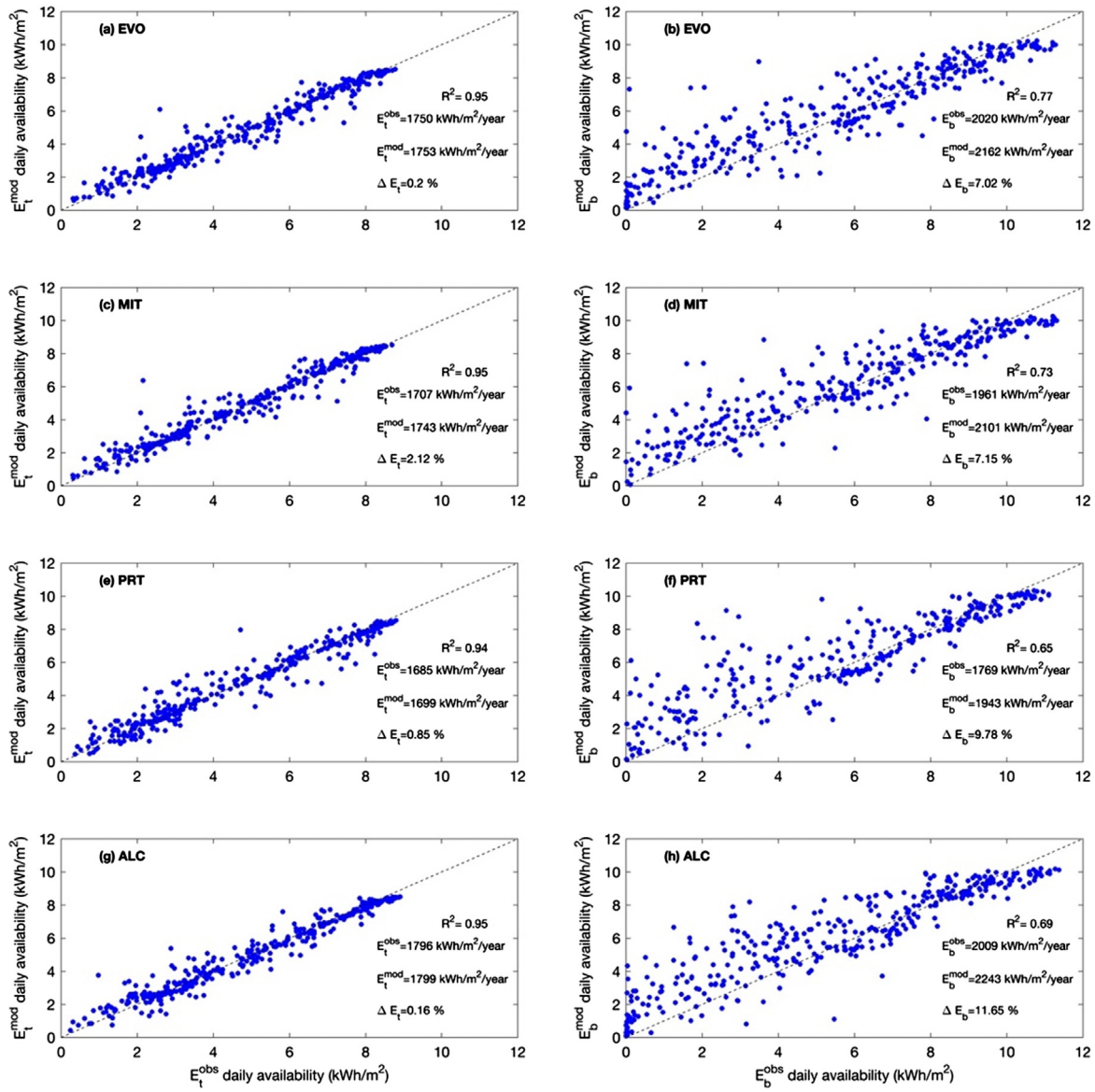

Fig. 8. Daily availabilities (kWh/m^2) for GHI (E_t) and DNI (E_b) in EVO (a, b), MIT (c, d), PRT (e, f) and ALC (g, h) during one year of measurements (from April 1st 2016 to March 31st 2017). Reference annual values ($E_{t,b}$), relative differences ($\Delta_{Et,b}$) and correlation coefficients (R^2) between model and observations are also presented. Equal values for observations and model is depicted by the dashed line.

Table 2
Statistical results between the hourly clearness indices for GHI (k_t) and DNI (k_b) obtained from the ECMWF global model and measurements for the period of one year. Pearson correlation (r), root mean square error (RMSE), mean bias error (MBE) and mean absolute error (MAE) are shown.

k_t	EVO	MIT	PRT	ALC
r	0.81	0.82	0.79	0.79
RMSE	0.11	0.11	0.13	0.12
MBE	1.2×10^{-03}	−0.01	-7.9×10^{-03}	-4.8×10^{-03}
MAE	0.07	0.07	0.08	0.08
k_b	EVO	MIT	PRT	ALC
r	0.81	0.79	0.76	0.79
RMSE	0.15	0.15	0.17	0.16
MBE	-2.8×10^{-02}	−0.03	−0.04	−0.05
MAE	0.10	0.11	0.11	0.11

Table 3
Statistical results between the hourly clearness indices for GHI (k_t) and DNI (k_b) obtained from the persistence forecast and measurements for the period of one year. Pearson correlation (r), root mean square error (RMSE), mean bias error (MBE) and mean absolute error (MAE) are shown.

k_t	EVO	MIT	PRT	ALC
r	0.43	0.45	0.51	0.48
RMSE	0.20	0.20	0.20	0.20
MBE	-8.12×10^{-04}	-3.43×10^{-04}	-8.57×10^{-04}	-4.23×10^{-05}
MAE	0.13	0.13	0.13	0.13
k_b	EVO	MIT	PRT	ALC
r	0.52	0.50	0.46	0.54
RMSE	0.24	0.24	0.26	0.24
MBE	-2.24×10^{-04}	-1.81×10^{-04}	4.00×10^{-03}	3.06×10^{-04}
MAE	0.17	0.17	0.17	0.16

Table 4
Skill score (SS) based in the mean square error (MSE) of hourly clearness indices for GHI (k_t) and DNI (k_b) between the ECMWF global model and persistence forecast considering the period of one year.

k_t	EVO	MIT	PRT	ALC
SS	0.6975	0.6975	0.5775	0.6400
k_b	EVO	MIT	PRT	ALC
SS	0.6094	0.6094	0.5725	0.5556

than DNI, being EVO the station where the highest performance is achieved by the IFS, especially for GHI. Ultimately, these results indicate that, for the 24-h horizon, the predictions of the ECMWF global model have significant predictive value.

5.3. Monthly analysis

Annual cycles of GHI and DNI are depicted in Fig. 9 for EVO, MIT, PRT and ALC stations. As expected, annual variations are characterized by high availabilities (both for GHI and DNI) in the summer period (from June to August), having maximum values that reach ~250 kWh/m^2/month for GHI and between 280 and 300 kWh/m^2/month for DNI. On the other hand, in the winter period (from December to February), low availabilities occur with minimum values of ~70 kWh/m^2/month for GHI and 80–150 kWh/m^2/month in the case of DNI. The higher values in the summer are mainly related to a higher irradiance at the Earth's surface due to lower solar zenith angles at noon and to longer periods of day light while the low values in the winter are the result of overcast periods, which are more frequent during this period of the year, and also to higher solar zenith angles and the shorter duration of day light. Higher correlations throughout the year are shown for GHI with very similar curve trends between model and observations. The annual cycle of the forecasted DNI depicts larger deviations of the model towards the observations when comparing with the predicted GHI. These deviations are expected, as they are smaller during the summer months since the main source of uncertainty of DNI predictions, i.e. clouds, are much less frequent in this period of the year. Nevertheless, spring and summer can be affected by aerosol events which can diminish the measured DNI while the model does not take them into account. These events are common features in the region, which may be made of pollens from nearby trees, ashes casted by forest fires or dusts from Saharan desert (e.g. Silva et al., 2016) transported by the synoptic circulation which, in summer, is dominated by the frequent development of the shallow Iberian low-pressure system. On the other hand, during the winter period the DNI deviations are much larger mainly due to cloud representation together with the assimilation of strong wind and its direct effect in clouds as these are more frequent to occur during these months. Particularly, significant deviations are found in February in all stations as this month was characterized by strong winds and heavy rain.

It should be noted that between June and September, in PRT station, there were missing periods of data, particularly a group of eleven consecutive days, which clearly suppressed the monthly availabilities for GHI and DNI.

5.4. GHI and DNI availability maps

Accurate forecasts of GHI and DNI are required in order to provide

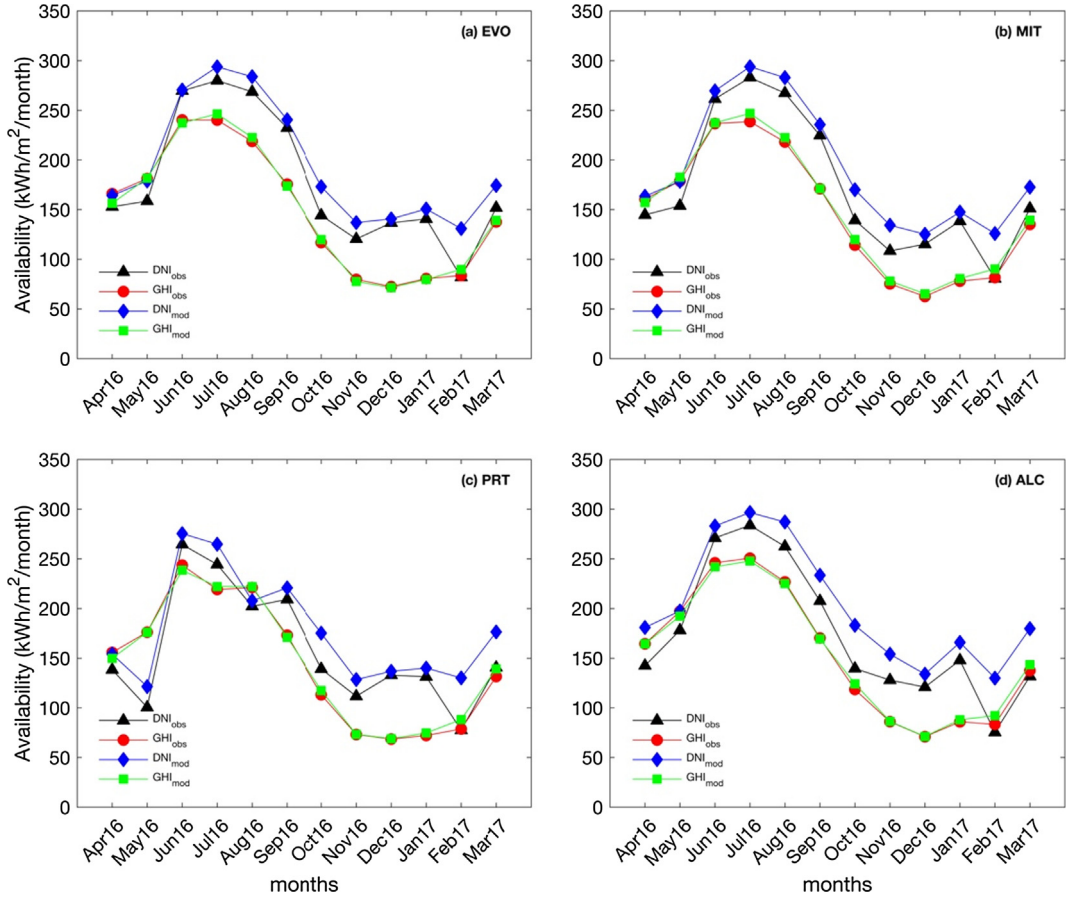

Fig. 9. Monthly values for GHI and DNI availability (kWh/m^2/month) in EVO (a), MIT (b), PRT (c) and ALC (d) during one year of measurements (from April 1st 2016 to March 31st 2017).

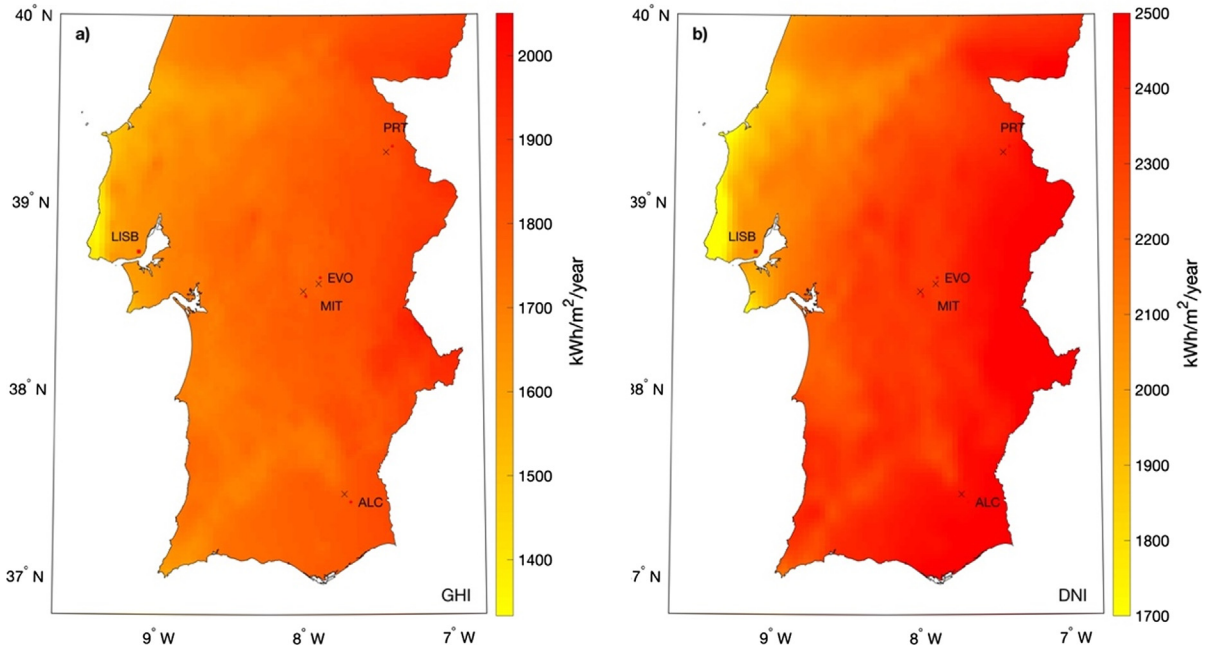

Fig. 10. Spatial distribution of predicted annual GHI (a) and DNI (b) availability (kWh/m^2/year) in the southern Portugal comprising the four measurements locations: Évora (EVO), Mitra (MIT), Portalegre (PRT) and Alcoutim (ALC) for the one year of measurements (April 1st 2016 to March 31st 2017).

information for an efficient operation of solar energy applications such as PV and non-concentrating solar thermal systems, as well as all the concentrating solar technologies (CPV and CST). In particular, CST systems, which are known to have a higher energy storage capacity than other systems, are in a current need for precise predictions of DNI (mainly for clear sky conditions). Such predictions will allow to reduce the uncertainty concerning solar power plants outputs and to optimize the necessary electrical energy generation and consequently to maximize the energy output for a given day. In this context, Fig. 10 depicts the annual GHI and DNI availability maps obtained with the IFS data considering the full period of study (i.e. a complete set of 365 days). For this purpose, without the application of previous filters, solar assessment was made for solar altitude angles above 0° and solar irradiation time series were built from the 24-h predictions. In the southern region of Portugal, predicted values of GHI (Fig. 10a) are found to be between 1700 and 2000 kWh/m^2/year while the predicted DNI availability (Fig. 10b) is higher, between 2000 and 2500 kWh/m^2/year. It should be mentioned that higher irradiation availability values of DNI can be found outside the unmasked area, corresponding to southern Spain and Atlantic Ocean. Taking in consideration the model overestimation, particularly for DNI, the values found for southern Portugal are in good agreement with the regional reference values established in the past for GHI (1900 kWh/m^2/year) and DNI (over 2100 kWh/m^2/year) as documented in literature (Cavaco et al., 2017a,b, respectively). Both GHI and DNI annual availabilities increase from northwest to southeast as consequence of the latitude effect and a lower average of cloudiness occurrences in the central and southern region of Portugal, as previously observed (Cavaco et al., 2017a). Despite the available different time periods considered for analysis, the DNI annual availability values obtained between 2015–2017 (EVO, MIT and PRT) and 2014–2017 (ALC) from the DNI national network (Cavaco et al., 2017b) allow to give a sense of comparison with the global model results (Table 5). Results show a general overestimation by the model with a significant difference for PRT (~19.3% more than the observed). This is likely to be attributed to the frequent occurrence of small scale fogs in the area, but overall differences are mainly related to the use of larger sets of observational data than that of the model output since annual means of more than one year are being referenced here.

Table 5
Comparison of annual DNI availability (kWh/m^2/year) between observations (Cavaco et al., 2017b) and ECMWF model predictions. Only one year (from April 1st 2016 to March 31st 2017) of simulations is considered while observations comprise longer periods: 2015–2017 for Évora (EVO), Mitra (MIT), Portalegre (PRT) and 2014–2017 for Alcoutim (ALC).

	EVO	MIT	PRT	ALC
Observations	2073	1989	1841	2015
Model	2155	2142	2197	2235

5.5. Prediction maps for GHI and DNI

Fig. 11 depicts an example on how GHI and DNI simulations can be used for an efficient operation of solar power plants, by considering two case studies with daily predictions for solar irradiation availability. During one day with clear sky conditions (July 12th 2016) over all stations, predictions show higher values occurring uniformly in the southern part of the country (Fig. 11a and b). For the prediction of GHI, only PRT station seems to show higher values (~8.4 kWh/m^2/day) as compared with the remaining stations which have ~8.32, ~8.33 and ~8.35 kWh/m^2/day for EVO, MIT and ALC, respectively. For DNI prediction, a general increase of irradiation is expected with ~10.12, ~10.16, ~10.63 and ~10.35 kWh/m^2/day respectively for EVO, MIT, PRT and ALC stations. It is also observed during this day the formation of fog in the northern part of the considered domain, near PRT, which is a common feature due to the orography of the terrain. During one day with cloudy conditions (May 8th 2016), predictions depict a more uneven spatial distribution of irradiation in the region (Fig. 11c and d). Here, GHI daily values are higher (~5.23 kWh/m^2/day) in the area that covers PRT station. Likewise, high values of DNI (~4.68 kWh/m^2/day) are foreseen to occur more in the north part of the region, above PRT station. More to the southeast the presence of clouds affect the daily irradiation at surface with lower values that range between 1 and 4 kWh/m^2/day.

In the context of an efficient management of the solar power plants, this means that during one clear day all hypothetical power plants in southern Portugal would be able to operate at high power outputs and thus optimizing the local harvesting of incoming DNI and GHI

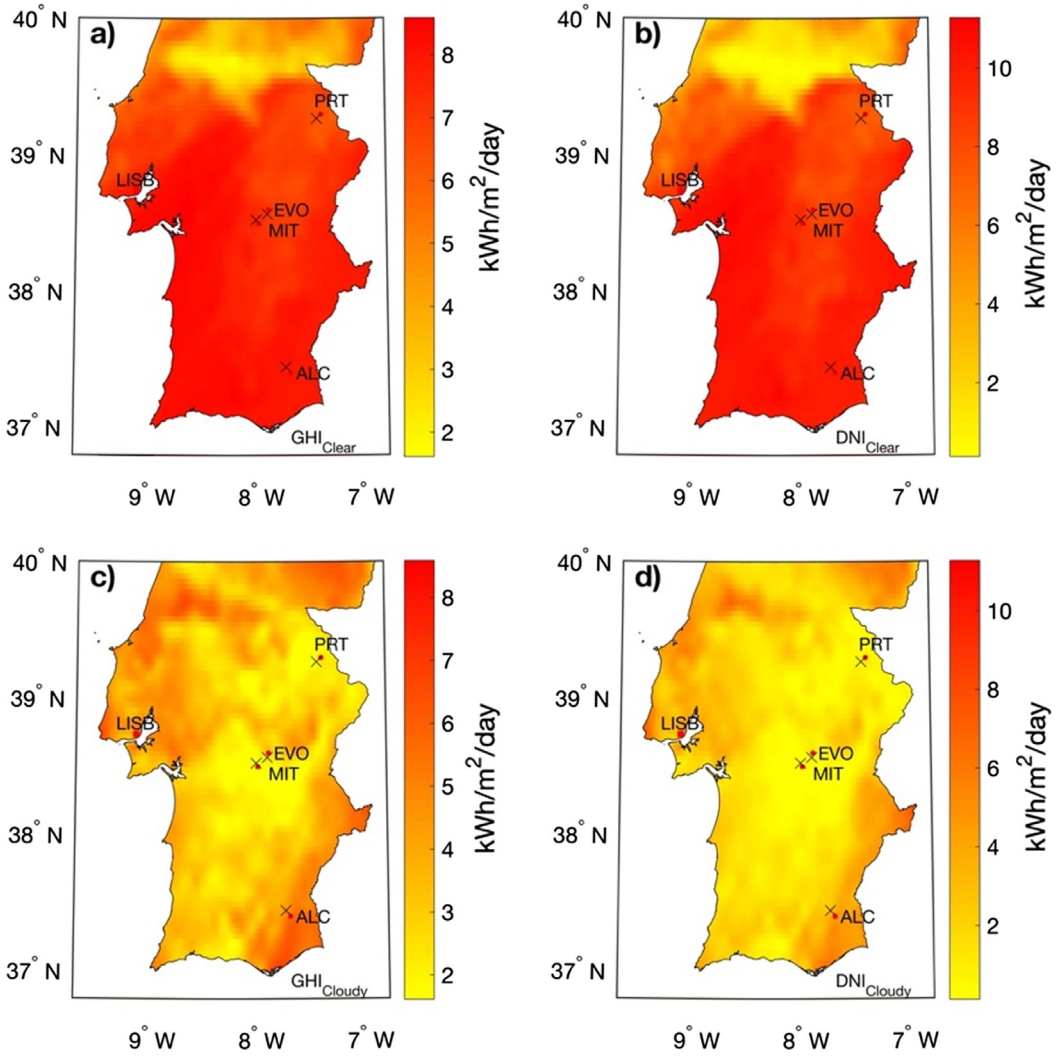

Fig. 11. Spatial distribution of predicted daily irradiation availability (kWh/m^2/day) from the ECMWF model for two test cases in southern Portugal: one clear sky day (July 12th 2016) and one cloudy day (May 8th 2016). Irradiation maps are portrayed as: (a) GHI_{clear}, (b) DNI_{clear}, (c) GHI_{cloudy} and (d) DNI_{cloudy}. The depicted measuring stations are Évora (EVO), Mitra (MIT), Portalegre (PRT) and Alcoutim (ALC).

irradiances. In the case of one cloudy day, all southeast stations should be at medium power output level while at north, in particular for DNI, the CST power plants should be more focused for a higher power output level. These results show that for a given day this information can be economically valuable from an electric grid operation management point of view and further efforts for the implementation of such practice for a regional (or even at a national level in the future) should be carried out.

6. Conclusions and future perspectives

The IFS global model from the ECMWF has been used to assess 24-h predictions of GHI and DNI for the first time for solar energy applications in southern Portugal during the period of 365 days (from April 1st 2016 to March 31st 2017). Results show that the model performs well in predicting GHI whilst DNI simulations are particularly hindered by cloud and aerosol representation. During overcast periods, the measured DNI is overestimated by the model mainly due to cloud representation as cloud 3D distribution and cloud microphysics are still difficult to be predicted in NWP. Under overcast conditions, this effect is not so important in GHI predictions due to a compensation through an increase in DHI. On the other hand, for clear sky conditions and a very clean atmosphere, the model tends to underestimate measurements of DNI and GHI as consequence of using climatological aerosol monthly means. This is of particular relevance since, during these periods, accurate forecasts of DNI are essential for an efficient operation of a CST power plant. Ultimately, cloud and aerosol representation can affect both GHI and DNI, although with more emphasis in the latter as shown throughout the entire analysis. Nevertheless, taking into account the aforementioned aspects of the model and the assumptions considered in this analysis for one year of data, results yield satisfactory values between model and measurements. Amongst the four study locations, relative differences of annual availabilities for GHI are found between ~0.16% to ~2.12% whilst for DNI values ranging from ~7% to ~12% are found. The respective obtained correlations are around 0.95 for GHI and between 0.65 and 0.77 for DNI. Additionally, solar irradiation availability maps of predicted GHI and DNI have been created. Predicted values are shown to be consistent with the references for the region. Differences stated between predictions and existing references result, first of all, from the fact that reference values comprise a larger set of data than the one year of simulations. However, these results are a good indication that GHI and DNI forecasting through this type of approach can be of valuable use to the efficiency of PV, CPV and CST systems management.

These results also encourage the use of other solar stations which are part of a national network in Portugal (Cavaco et al., 2017b) for

further analysis. Moreover, in order to produce Iberian irradiation maps of GHI and DNI, the co-joint effort involving Spanish radiometric stations should take place in the future, as well as the use of a prognostic aerosol scheme coupled to an aerosol data assimilation system through the CAMS instead of just climatological aerosol monthly means.

Acknowledgements

This work was co-funded by the European Union through the European Regional Development Fund, framed in COMPETE 2020 (Operational Program Competitiveness and Internationalization), through the ICT project (UID/GEO/04683/2013) with reference POCI-01-0145-FEDER-007690 and through the DNI-A project with the reference ALT20-03-0145-FEDER-000011 and the ALOP project (ALT20-03-0145-FEDER-000004). H.G. Silva acknowledges the Integrating National Research Agendas on Solar Heat for Industrial Processes (INSHIP) project (H2020, GA: 731287). The initial support of Robin Hogan for recommendations in this work is recognized and appreciated. The authors are also thankful for the availability of the ECMWF in providing the needed data. Francis M. Lopes is thankful for the FCT scholarship (SFRH/BD/129580/2017) and to Ricardo Conceição for the modelling support provided. Finally, the authors would also like to thank the two anonymous reviewers, and Jan Kleissl, for their helpful suggestions and comments.

Appendix A

In order to compare observations and the model time series, statistical analysis was performed through the use of conventional metrics for the model assessment with the root mean square error (RMSE), the mean bias error (MBE) and the mean absolute error (MAE) in Eqs. (A.1)(A.3) respectively, as follows:

$$RMSE = \sqrt{MSE} = \sqrt{1/n \times \sum_{j=1}^{n} [I(j) - \hat{I}(j)]^2}, \quad (A.1)$$

$$MBE = 1/n \times \sum_{j=1}^{n} [I(j) - \hat{I}(j)], \quad (A.2)$$

$$MAE = 1/n \times um_{j=1}^{n} |I(j) - \hat{I}(j)|, \quad (A.3)$$

where I(j) and Î(j) are the measured and the predicted value at time j, respectively, either for GHI or DNI, while n is the number of assessed pairs. The RMSE is the statistical metric that has been recommended for the application of electricity grid management issues since only large errors are significant to the safety of an electricity grid system (Schroedter-Homscheidt et al., 2016). Perfect predictions yield a RMSE equal to zero. The MBE allows one to characterize the performance of the model towards observations by establishing a balance between over- and underprediction (Coimbra et al., 2013). MBE equal to zero corresponds to an unbiased prediction, while negative and positive values of this metric depict an over- and underestimation by the model, respectively. The MAE metric is a global error measure metric that allows us to average the magnitude of the error without the account for extreme forecast events as opposed to the RMSE which gives more weight to large errors (Pelland et al., 2011).

Appendix B

See Table B1.

Table B1
Statistical and descriptive analysis summary for measurements and ECMWF model 24-h predictions of global horizontal and direct normal irradiances (GHI and DNI, respectively) in Évora (EVO), Mitra (MIT), Portalegre (PRT) and Alcoutim (ALC) stations. One year of measurements is considered in the study (from April 1st 2016 to March 31st 2017). Results have the consideration of a solar altitude threshold of 10° in all sites.

	EVO		MIT		PRT		ALC	
	Observation	Model	Observation	Model	Observation	Model	Observation	Model
Longitude (°)	W7.91172	W7.9	W8.011221	W8.0	W7.442716	W7.4	W7.744901	W7.7
Latitude (°)	N38.567686	N38.6	N38.530522	N38.5	N39.269221	N39.3	N37.441844	N37.4
Distance (km)	3.73		3.53		5.02		6.11	
Mean DNI (W/m^2)	548.85	587.15	566.19	611.19	559.27	617.79	547.80	611.29
Mean GHI (W/m^2)	474.53	475.41	467.52	477.40	462.40	466.23	489.21	489.72
Median DNI (W/m^2)	651.37	668.12	652.41	682.91	668.18	697.20	629.84	684.84
Median GHI (W/m^2)	452.55	448.96	441.71	453.25	421.34	439.33	468.26	469.83
Std DNI (W/m^2)	335.05	283.75	325.80	267.66	336.35	272.23	333.04	269.71
Std GHI (W/m^2)	258.31	255.53	261.91	255.85	268.63	255.62	270.28	255.50
Skewness DNI	−0.46	−0.69	−0.50	−0.78	−0.49	−0.81	−0.43	−0.82
Skewness GHI	0.22	0.29	0.27	0.28	0.31	0.30	0.23	0.25
Kurtosis DNI	1.73	2.22	1.82	2.44	1.73	2.44	1.74	2.51
Kurtosis GHI	1.98	2.03	1.97	2.02	1.97	2.03	1.96	2.01
N days DNI	181.58	181.58	168.46	168.46	154.63	154.63	181.46	181.46
N days GHI	180.21	180.21	179.71	179.71	179.13	179.13	179.83	179.83
E_b (kWh/m^2/year)	2020	2162	1961	2102	1770	1943	2010	2244
E_t (kWh/m^2/year)	1750	1754	1708	1744	1685	1699	1797	1800
ΔE_b (%)	7.02		7.15		9.78		11.65	
ΔE_t (%)	0.20		2.12		0.85		0.16	
R_b^2	0.77		0.73		0.65		0.69	
R_t^2	0.95		0.95		0.94		0.95	

References

Bird, R.E., Hulstrom, R.L., 1981. A simplified clear sky model for direct and diffuse insolation on horizontal surfaces. Solar Energy Research Institute (SERI). SERI/TR-642–761.

Blanc, P., et al., 2014. Direct normal irradiance related definitions and applications: the circumsolar issue. Sol. Energy 110, 561–577. http://dx.doi.org/10.1016/j.solener.2014.10.001.

Bozzo, A., Remy, S., Benedetti, A., Flemming, J., Bechtold, P., Rodwell, M.J., Morcrette, J.-J., 2017. Implementation of a CAMS-based aerosol climatology in the IFS. Technical Memorandum, 801. European Centre for Medium-Range Weather Forecasts.

Casado-Rubio, J.L., Revuelta, M.A., Postigo, M., Martínez-Marco, I., 2017. A post-processing methodology for direct normal irradiance forecasting using cloud information and aerossol load forecasts. Am. Meteorol. Soc. 1595–1602, http://dx.doi.org/10.1175/JAMC-D-16-0297.1.

Cavaco, A., Silva, H.G., Neves, S., Neto, J., Canhoto, P., Collares-Pereira, M., 2017a. Assessment of annual availability and variability of Global Solar Irradiation in continental Portugal. Solar Energy (submitted for publication).

Cavaco, A., Silva, H.G., Canhoto, P., Osório, T., Collares-Pereira, M., 2017b. Progresses in DNI measurements in Southern Portugal. Solar Paces, AIP Conf. Proc. (submitted for publication).

Chambel, A., Duque, J., Nascimento, J., 2007. Regional study of hard rock aquifers in Alentejo, South Portugal: methodology and results. In: Jirí Krásný, John M. Sharp (eds.), IAH-SP Series, Taylor & Francis, pp. 73–93.

Cheng, H.-Y., 2016. Cloud tracking using clusters of feature points for accurate solar irradiance nowcasting. Renewable Energy 104, 281–289. http://dx.doi.org/10.1016/j.renene.2016.12.023.

Chow, C.W., Urquhart, B., Lave, M., Dominquez, A., Kleissl, J., Shields, J., Washom, B., 2011. Intra-hour forecasting with a total sky imager at the UC San Diego solar energy testbed. Sol. Energy 85, 2881–2893. http://dx.doi.org/10.1016/j.solener.2011.08.025.

Coimbra, C., Kleissl, J., Marquez, R., 2013. Overview of solar forecasting methods and a metric for accuracy evaluation. Solar Resource Assessment and Forecasting, Chapter 8, 183–185. Elsevier, Waltham, Massachusetts.

Conceição, R., Silva, H.G., Mirão, J., Gostein, M., Fialho, L., Navarte, L., Collares-Pereira, M., 2018. Saharan dust transport to Europe and its impact on the photovoltaic performance: a case study of soiling in Portugal. Sol. Energy 160, 94–102. http://dx.doi.org/10.1016/j.solener.2017.11.059.

Collares-Pereira, M., Rabl, A., 1979. Simple procedure for predicting long term average performance of nonconcentrating and concentrating solar collectors. Sol. Energy 23, 235–253.

Diagne, H.M., David, M., Lauret, P., Boland, J., Schmutz, N., 2013. Review of solar irradiance forecasting methods and a proposition for small-scale insular grids. Renew. Sustain. Energy Rev., Elsevier 27, 65–76.

Fan, J., 2016. Review of aerosol-cloud interaction: mechanisms, significance, and challenges. Am. Meteorol. Soc. 73, 4221–4252. http://dx.doi.org/10.1175/JAS-D-16-0037.1.

Forrester, J., 2014. The value of CSP with thermal energy storage in providing grid stability. Energy Proc. 49, 1632–1641. http://dx.doi.org/10.1016/j.egypro.2014.03.172.

Fernández-Peruchena, C.M., Bernardos, A., 2015. A comparison of one-minute probability density distributions of global horizontal solar irradiance conditioned to the optical air mass and hourly averages in different climate zones. Sol. Energy 112, 425–436. http://dx.doi.org/10.1016/j.solener.2014.11.030.

Gueymard, C.A., Ruiz-Arias, J.A., 2016. Extensive worldwide validation and climate sensitivity analysis of direct irradiance predictions from 1-min global irradiance. Sol. Energy 128, 1–30. http://dx.doi.org/10.1016/j.solener.2015.10.010.

Haiden, T., Janousek, M., Bidlot, J., Ferranti, L., Prates, F., Vitart, F., Bauer, P., Richardson, D.S., 2016. Evaluation of ECMWF forecasts, including the 2016 resolution upgrade. ECMWF Technical Memorandum n° 792.

Harrison, R.G., Chalmers, N., Hogan, R.J., 2008. Retrospective cloud determinations from surface solar radiation measurements. Atmos. Res. 90, 54–62. http://dx.doi.org/10.1016/j.atmosres.2008.04.001.

Hogan, R.J., Ahlgrimm, M., Balsamo, G., Beljaars, A., Berrisford, P., Bozzo, A., Di Giuseppe, F., Forbes, R.M., Haiden, T., Lang, S., Mayer, M., Polichtchouk, I., Sandu, I., Vitart, F., Wedi, N., 2017. Radiation in numerical weather prediction. Technical Memorandum, 816. European Centre for Medium-Range Weather Forecasts.

ISO 9060:1990, 2003. Solar energy – specification and classifications of instruments for measuring hemispherical solar and direct solar radiation. International Organization for Standardization (www.iso.org/standard/16629.html).

ISO 9059:1990, 2014. Solar energy – calibration of field pyrheliometers by comparison to a reference pyrheliometer. International Organization for Standardization (www.iso.org/standard/16628.html).

ISO 9847:1992, 2013. Solar energy – calibration of field pyranometers by comparison to a reference pyranometer. International Organization for Standardization (www.iso.org/standard/17725.html).

Jimenez, P.A., Hacker, J.P., 2016. WRF-solar: description and clear-sky assessment of an augmented NWP model for solar power prediction. Am. Meteorol. Soc., BAMS, pp. 1249–1264, http://dx.doi.org/10.1175/BAMS-D-14-00279.1.

Kalnay, E., 2003. Atmospheric Modeling, Data Assimilation and Predictability. Chapter 1, 25–27. Published in the United States of America by Cambridge University Press.

Kalogirou, S.A., 2014. Solar Energy Engineering: Processes and Systems, second ed. Chapter 2, 51–63, Elsevier. ISBN: 978-0123972705.

Kinne, S., O'Donnel, D., Stier, P., Kloster, S., Zhang, K., Schmidt, H., Rast, S., Giorgetta, M., Eck, T.F., Stevens, B., 2013. MAC-v1: a new global aerosol climatology for climate studies. J. Adv. Model. Earth Syst. 5, 704740. http://dx.doi.org/10.1002/jame.20035.

Kosmopoulos et al., 2017. Dust impact on surface solar irradiance assessed with model simulations, satellite observations and ground-based measurements. Atmos. Meas. Tech. Discuss. http://dx.doi.org/10.5194/amt-2017-79.

Kuhn, P., Wilbert, S., Prahl, C., Garsche, D., Schüler, D., Haase, T., Ramirez, L., Zarzalejo, L., Meyer, A., Blanc, P., Pitz-Paal, R., 2018. Applications of a shadow camera system for energy meteorology. Adv. Sci. Res. 15, 11–14. http://dx.doi.org/10.5194/asr-15-11-2018.

Lafore, J.P., Stein, J., Asencio, N., Bougeault, P., Ducrocq, V., Duron, J., Fischer, C., Héreil, P., Mascart, P., Masson, P., 1998. The Meso-NH atmospheric simulation system. Part I: Adiabatic formulation and control simulations. Annales Geophysicae, European Geosciences Union, vol. 16 (1), 90–109. hal-00329074.

Law, Edward W., Prasad, Abhnil, Kay, Merlinde, Taylor, Robert, et al., 2014. Direct normal irradiance forecasting and its application to concentrated solar thermal output forecasting – a review. Sol. Energy 108, 287–307. http://dx.doi.org/10.1016/j.solener.2014.07.008.

Lefévre, M., Oumbe, A., Blanc, P., Espinar, B., Gschwind, B., Qu, Z., Wald, L., Schroedter-Homscheidt, M., Hoyer-Klick, C., Arola, A., Benedetti, A., Kaiser, J.W., Morcrette, J.-J., 2013. McClear: a new model estimating downwelling solar radiation at ground level in clear-sky conditions. Atmos. Meas. Tech. 6, 2403–2418. http://dx.doi.org/10.5194/amt-6-2403-2013.

Liu, H., Pinker, R.T., Holben, B.N., 2005. A global view of aerosols from merged transport models, satellite, and ground observations. J. Geophys. Res. 110, D10S15, http://dx.doi.org/10.1029/2004JD004695.

Lopes, F., Silva, H.G., Salgado, R., Potes, M., Nicoll, K., Harrison, R.G., 2016. Atmospheric Electric Field measurements near a Fresh Water Reservoir and the formation of the Lake Breeze. Tellus 68, 31592. http://dx.doi.org/10.3402/tellusa.v68.31592.

Marquez, R., Coimbra, C.F.M., 2012. Intra-hour DNI forecasting based on cloud tracking image analysis. Sol. Energy 91, 327–336. http://dx.doi.org/10.1016/j.solener.2012.09.018.

Mlawer, E., Clough, S., 1997. Shortwave and longwave en- hancements in the Rapid Radiative Transfer Model. Proc. Seventh Atmospheric Radiation Measurement (ARM) Science Team Meeting, San Antonio, TX, U.S. Department of Energy, pp. 409–413. Available online at < https://www.arm.gov/publications/proceedings/conf07/extended_abs/mlawer_ej.pdf > .

Morcrette, J., Barker, H.W., Cole, J.N., Iacono, M.J., Pincus, R., 2008. Impact of a new radiation package, McRad, in the ECMWF integrated forecasting system. Mon. Wea. Rev. 136, 4773–4798. http://dx.doi.org/10.1175/2008MWR2363.1.

Mozdzynski, G., Morcrette, J.-J., 2014. Reorganization of the Radiation Transfer Calculations in the ECMWF IFS. Technical Memorandum, European Centre for Medium-Range Weather Forecasts, Technical Report (721).

Mozdzynski, G., Morcrette, J.-J., 2014. Reorganization of the radiation transfer calculations in the ECMWF IFS. Technical Memorandum, European Centre for Medium-Range Weather Forecasts, Technical Report (721).

Mulcahy, J.P., Walters, D.N., Bellouin, N., Milton, S.F., 2014. Impacts of increasing the aerosol complexity in the Met Office global numerical weather prediction model. Atmos. Chem. Phys. 14, 4749–4778. http://dx.doi.org/10.5194/acp-14-4749-2014.

Pascual, J., Barricarte, J., Sanchis, P., Marroyo, L., 2015. Energy management strategy for a renewable-based residential microgrid with generation and demand forecasting. Appl. Energy 158, 12–25. http://dx.doi.org/10.1016/j.apenergy.2015.08.040.

Pelland, S., Galanis, G., Kallos, G., 2011. Solar and photovoltaic forecasting through post-processing of the Global Environmental Multiscale numerical weather prediction model. Prog. Photovoltaics Res. Appl. 21, 284–296. http://dx.doi.org/10.1002/pip.1180.

Perez, R., et al., 2013. Comparison of numerical weather prediction solar irradiance forecasts in the US, Canada and Europe. Sol. Energy 94, 305–326. http://dx.doi.org/10.1016/j.solener.2013.05.005.

Quaschning, Volker, 2003. Technology fundamentals – the sun as an energy resource. Renew. Energy World 6 (5), 90–93.

Quesada-Ruiz, S., Chu, Y., Tovar-Pescador, J., Pedro, H.T.C., Coimbra, C., 2014. Cloud-tracking methodology for intra-hour DNI forecasting. Sol. Energy 102 (267–275), 2014. http://dx.doi.org/10.1016/j.solener.2014.01.030.

Ramirez, L., Vindel, J.M., 2017. Forecasting and nowcasting of DNI for concentrating solar thermal systems. Adv. Concentrating Sol. Therm. Res. Technol. 294–310. http://dx.doi.org/10.1016/B978-0-08-100516-3.00013-7. (chapter 13).

Roesch, A., Wild, M., Ohmura, A., Dutton, E.G., Long, C.N., Zhang, T., 2011. Assessment of BSRN radiation records for the computation of monthly means. Atmos. Meas. Tech. 4, 339–354. http://dx.doi.org/10.5194/amt-4-339-2011.

Ruiz-Arias, J.A., Gueymard, C.A., Santos-Alamillos, F.J., Pozo-Vásquez, D., 2016. Worldwide impacto f aerossol's time scale on the predicted long-term concentrating solar power potential. Scientific Reports, 6, article number (30546). http://dx.doi.org/10.1038/srep30549.

Ruiz-Arias, J.A., Dudhia, J., Gueymard, C.A., 2014. A simple parameterization of the short-wave aerossol optical properties for surface direct and diffuse irradiances assessment in a numerical weather model. Geosci. Model Dev. 7, 1159–1174. http://dx.doi.org/10.5194/gmd-7-1159-2014.

Salgado, R., Miranda, P.M.A., Lacarrère, P., Noilhan, J., 2015. Boundary layer development and summer circulation in Southern Portugal. Tethys 12. http://dx.doi.org/10.3369/tethys.2015.12.03.

Schroedter-Homscheidt, M., Benedetti, A., Killius, N., 2016. Verification of ECMWF and ECMWF/MACC's global and direct irradiance forecasts with respect to solar electricity production forecasts. Meteorol. Z., PrePub Article. http://dx.doi.org/10.1127/

metz/2016/0676.
Schroedter-Homscheidt, M., Oumbe, O., Benedetti, A., Morcrette, J.-J., 2013. Aerosols for concentrating solar electricity production forecasts: requirement quantification and ECMWF/MACC aerosol forecast assessment. Am. Meteorol. Soc., BAMS 903–914. http://dx.doi.org/10.1175/BAMS-D-11-00259.1.
Schroedter-Homscheidt, M., Hoyer-Klick, C., Rikos, E., Tselepsis, S., Pulvermüller, B., 2009. Nowcasting and forecasting of solar irradiance for energy electricity generation. Solar PACES Conf., Berlin, Germany.
Seiz, G., Baltsavias, E.P., Gruen, A., 2002. Cloud mapping from the ground: use of photogrammetric methods. Photogrammic Eng. Rem. Sens. 68 (9), 941–951 0099-1112/02/6809-941$3.00/0.
Silva, H.G., Lopes, F., Barbosa, S.M., Nicoll, K., Pereira, S.N., Harrison, R.G., Collares-Pereira, M., 2016. Saharan dust electrification perceived by a triangle of atmospheric electricity stations in Southern Portugal. J. Electrostat. 84 (106–120), 2016. http://dx.doi.org/10.1016/j.elstat.2016.10.002.
Sirch, T., Bugliaro, L., Zinner, T., Möhrlein, M., Vazquez-Navarro, M., 2017. Cloud and DNI nowcasting with MSG/SEVIRI for the optimized operation of concentrating solar power plants. Atmos. Meas. Tech. 10, 409–429. http://dx.doi.org/10.5194/amt-10-409-2017.
Solanki, S.K., Krivova, N.A., Haigh, J.D., 2013. Solar irradiance variability and climate. Annu. Rev. Astrono. Astrophys. 51, 311–351. http://dx.doi.org/10.1146/annurev-astro-082812-141007.
Troccoli, A., Morcrette, J.-J., 2014. Skill of direct solar radiation predicted by the ECMWF global atmospheric model over Australia. Am. Meteorol. Soc. 2014, 2571–2587. http://dx.doi.org/10.1175/JAMC-D-14-0074.1.
World Meteorological Organization (WMO), 2008. Guide to Meteorological instruments and Methods of Observation: Measurement of Radiation. WMO (8), Chapter 7, 1.7-5.

Science of the Total Environment 634 (2018) 394–406

Contents lists available at ScienceDirect

Science of the Total Environment

journal homepage: www.elsevier.com/locate/scitotenv

Ecological and ecotoxicological responses in the assessment of the ecological status of freshwater systems: A case-study of the temporary stream Brejo of Cagarrão (South of Portugal)

P. Palma [a,b,*], C. Matos [a], P. Alvarenga [c], M. Köck-Schulmeyer [d], I. Simões [a], D. Barceló [d,e], M.J. López de Alda [d]

[a] Departamento de Tecnologias e Ciências Aplicadas; Escola Superior Agrária, Instituto Politécnico de Beja, 7800-295 Beja, Portugal
[b] ICT, Institute of Earth Sciences, University of Évora, Rua Romão Ramalho 59, Évora, Portugal
[c] LEAF, Centro de Investigação em Agronomia, Alimentos, Ambiente e Paisagem, Instituto Superior de Agronomia, Universidade de Lisboa, Tapada da Ajuda, 1349-017 Lisboa, Portugal
[d] Institute of Environmental Assessment and Water Research (IDAEA), Spanish Council for Scientific Research (CSIC), Jordi Girona 18-26, 08034 Barcelona, Spain
[e] Catalan Institute for Water Research (ICRA), H2O Building, Scientific and Technological Park of the University of Girona, Emili Grahit 101, 17003 Girona, Spain

HIGHLIGHTS

- Multi-metric indices classify the ecological status as reasonable to mediocre.
- Sublethal ecotoxicological endpoints complement the biotic indices.
- Dry phase of the stream occurred very early comparing with previous years.
- Stream with risk to the ecosystem and to public health
- Temporal periods with toxic effects for crustaceans' species and biodiversity compromised.

GRAPHICAL ABSTRACT

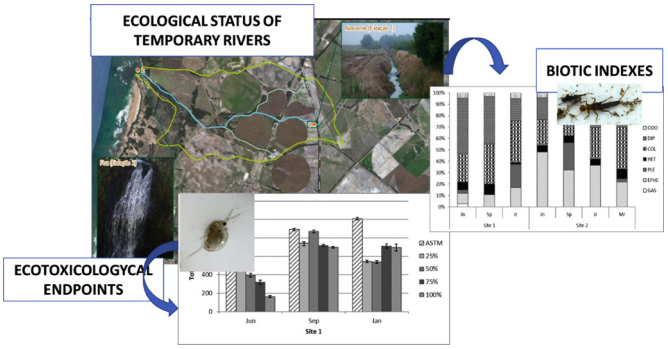

ARTICLE INFO

Article history:
Received 19 January 2018
Received in revised form 22 March 2018
Accepted 23 March 2018
Available online 6 April 2018

Editor: Henner Hollert

Keywords:
Temporary stream
Benthic macroinvertebrates
Ecotoxicological endpoints
Pesticides

ABSTRACT

The objective of the study was to assess the integrated use of macroinvertebrate indexes and ecotoxicological parameters in the evaluation of the ecological status of a temporary stream with a strong agricultural influence. Water quality was analysed at two sampling sites along the stream, considering: chemical supporting parameters; hazardous substances (pesticides); benthic macroinvertebrate communities, through quality (Iberian Biological Monitoring Working Party and Iberian Average Score Per Taxon) and multi-metric indices (Southern Portuguese Index of Invertebrates and Ecological Quality Ratio); and ecotoxicological responses using lethal and sub-lethal bioassays. The water chemical characterization showed high levels of organic matter and nutrients, mainly in the dry period ((biochemical oxygen demand (BOD_5): 18.5–25.5 mg L^{-1}, chemical oxygen demand (COD): 60.8–193.7 mg L^{-1}; total phosphorus (TP): 0.17–0.33 mg L^{-1})), which may compromise the support of biological life. In accordance with the physicochemical results, the stream had an ecological status less than good. Of the 25 pesticides analysed, only five, namely terbuthylazine, 2-methyl-chlorophenoxyacetic acid, bentazone, mecoprop and metolachlor were quantified. In general, the concentrations of pesticides detected were low, except at the source of the stream in January 2012 (sum of pesticides 2.29 μg L^{-1}), mainly due to the concentration of bentazone (1.77 μg L^{-1}), both values surpassing the European Commission threshold values. The analysis of benthic macroinvertebrates showed low levels of abundance and family diversity, with communities dominated by resistant groups to organic pollution and pesticides, such as the Chironomidae family. In

* Corresponding author at: Department of Applied Sciences and Technologies, Escola Superior Agrária - Instituto Politécnico de Beja, Rua Pedro Soares S/N, Apartado 6155, 7800-295 Beja, Portugal.
E-mail address: ppalma@ipbeja.pt. (P. Palma).

https://doi.org/10.1016/j.scitotenv.2018.03.281
0048-9697/© 2018 Elsevier B.V. All rights reserved.

general, the reproduction ecotoxicological results showed a very marked decrease in the number of juveniles per female. The Spearman correlation identified pesticides, namely MCPA ($R = -0.89$; $p < 0.05$), as the main responsible for the observed effect. The results showed the linearity and complementarity of the two groups of biological responses, allowing to cover the interactions between the ecosystem's species and the different types of pollutants.

© 2018 Elsevier B.V. All rights reserved.

1. Introduction

Nowadays, the preservation of the structure and function of freshwater ecosystems is essential to ensure economic, cultural, and recreational benefits for human population (Turner and Daily, 2008), and to guarantee the maintenance of ecological balance with the protection of biodiversity (Poff et al., 1997; Naiman et al., 2008). Nowadays, the global change scenario, which entails with the appearance of new stressors, namely changes of climatic patterns (including drought and temperature increase) or of economic, social, and demographic stressors, may influence negatively the quality of freshwater systems incrementing its scarcity and degradability (Stevenson and Sabater, 2010). All these new stressors and deviations impose new challenges for water management, which remain one of the keys for the next decades (Schinegger et al., 2012). Consequently, the implementation of appropriate management actions for each type of freshwater ecosystem ((wetlands, permanent rivers, temporary rivers and streams, and heavily modified waters bodies (HMWB)) requires periodic reviews of water policies and of monitoring programs (Araújo et al., 2014). Moreover, at present, some of these groups of freshwater ecosystems, namely, temporary waters, remain among the least studied freshwater systems worldwide (Acuña et al., 2014), with no parameters and standard values for the good chemical and ecological status. In fact, the Water Framework Directive (WFD) does not integrate assessment parameters for European Mediterranean (EU-Med) temporary waters (systems that are normally dry, at least during a part of the year; Gallart et al., 2016), since many of them are very small (lower than the stated threshold size of 50 ha; Van den Broeck et al., 2015; Nikolaidis et al., 2013). Despite this reality, temporary freshwater systems represent an important role in the Mediterranean region, once they constitute the most dynamic, complex and diverse systems concerning: (a) the hydrological regime (perennial, intermittent, which dry to a series of disconnected pools, or ephemeral, which dry completely; Bonada et al., 2007; Gallart et al., 2012); (b) the chemical characteristics, with great variability in the structural parameters and hazardous substances concentrations (Arenas-Sánchez et al., 2016; Petrovic et al., 2011); and (c) the biodiversity, housing both general opportunistic species, as well as temporary ponds species, which are extremely rare, with unknown mechanisms of resistance to extreme conditions (Cottarelli et al., 2010; Acuña et al., 2014; Van den Broeck et al., 2015). Moreover, under climate-change conditions, temporary freshwater systems probably may represent, the most dominant surface-water bodies of the Mediterranean region (Skoulikidis et al., 2017), giving them a major importance as source of water for local people and their livestock and agricultural activities, and, because of that, providing valuable ecosystem services including wildlife habitat, nutrient flux to adjacent ecosystems, flood control, water filtration, and cultural services (Calhoun et al., 2017).

To manage this kind of water body appropriately, incrementing its quality and avoiding the strong decrease of biodiversity observed, it is essential to understand its one dynamic, and determine, if possible, whose parameters (chemical and/or biological) are most sensitive to the pollutants detected in this type of scenario.

Presently, the ecological status of rivers/streams is determined by the assessment of ecological indices, which translate the biodiversity of the system. Relatively to temporary rivers, the structure and composition of the biological communities are adapted to the temporariness of hydrological regime, which induces a high heterogeneity at the system, hindering the definition of reference conditions, as well as the use of indicator species for defining the ecological status (Sánchez-Montoya et al., 2009). These facts highlight that the current classification, based in multi-metric indices, may not be sufficient to interpret the hydrological and biological variability present in the temporary rivers (Munné and Prat, 2009). In addition to this scenario, we cannot forget that, despite the biotic indices are relatively easy to apply, they do not identify causes of impairment, neither subtle effects at the individual level (Damásio et al., 2007; Muñoz et al., 2012), and, hence, when the detection of detrimental effects occur at the community level, it may be too late to recover the ecosystem (Clements and Rohr, 2009).

Many researchers think that the best option to assess the ecological status of water bodies is the use of a tool-box that adds multi-metric indices and ecotoxicological endpoints, especially in aquatic systems that present low biodiversity, such as temporary Mediterranean rivers (Colin et al., 2016; Reyjol et al., 2014; Palma et al., 2016; Van den Broeck et al., 2015; Skoulikidis et al., 2017). This type of strategy will allow a better understanding of the ecosystem functions and dynamics, filling the fragilities of each approach and the gaps between the results from laboratory experiments and field observations (Artigas et al., 2012; Beketov and Liess, 2012).

Considering all these facts, the aim of this study was to evaluate the effectiveness of the use of biological responses, integrating biotic indices and ecotoxicological endpoints, in the detection of pollution induced by agricultural activities in a temporary stream, Brejo of Cagarrão, located in the Mira River Basin, in the South of Portugal.

The selection of Brejo of Cagarrão as a case study was based on the following criteria: (i) it is a southern stream with a temporary hydrological regime; (ii) there is no water quality data for this watercourse; (iii) there are environmental and public health concerns associated with this stream, as it drains directly to Brejo Largo beach; (iv) some local fisherman reported the decrease of the communities of clams and mussels; and (v) it is a watercourse integrated in the Southwest Alentejo and Vicentine Coast Natural Park, a protected region due to its great biodiversity and coastal habitats (Decreto Regulamentar n.° 26/95, 1995).

Furthermore, this initial study is integrated in a research line about the quality, function and dynamic of temporary rivers/streams in Mediterranean areas, that intends to deliver a tool-box, which can be used for responding to the main alterations that influence the ecological status of temporary water streams. This action can be useful to support the risk management strategies of this type of systems, to minimize human influences and ensure ecosystem integrity and human safety.

2. Materials and methods

2.1. Study area

Brejo of Cagarrão is a temporary stream inserted in the Coastal Hydrographic Basin of Mira (Alentejo coast, South of Portugal). According to the Portuguese Water Institute (INAG) (2009), Brejo of Cagarrão is classified as a small river of the South of Portugal (≤100 km^2), which flows into the Atlantic Ocean, at the Brejo Largo Beach.

The Mira Basin presents a drainage area of 1576 km^2, with a lithology mainly constituted by schist, greywacke, and sandstones (85%), sands, little consolidated sandstones and clays (9%), and a slight percentage of metavolcanics (4%) (Mil-Homens et al., 2014).

The climate of the Alentejo coast is Mediterranean, with a strong maritime influence, inducing mild temperatures throughout the year (ranging from 10 to 21 °C) (ARHAlentejo, 2012). During the study period, the clime was characterized by an average atmospheric temperature of 14.5 °C, ranging from 8 °C in January to 21 °C in August (www.snirh.pt, 2010/2011; 2011/2012). The average monthly precipitation for the hydrologic year of 2009/2010 was 53.4 mm (www.snirh.pt, 2008/2009), and for 2010/2011 it was 70.3 mm (www.snirh.pt, 2010/2011), and for the hydrologic year of 2011/2012 it was 29.4 mm (www.snirh.pt, 2011/2012). So, the values of precipitation for the hydrologic year of 2011/2012 were extremely low, comparing with the years before, highlighting the exceptional circumstance of no precipitation in February 2012.

In the riparian vegetation, along the water margins and banks, some degraded communities are evident, probably due to the frequent interventions related to the intense agricultural and livestock activity in the surrounding area. The gallery is practically non-existent and dominated by exotic species, mainly *Acacia sp.*, *Arundo donax*, *Datura stramonium*, as well as by some opportunistic species, like *Rubus ulmifolius* and *Dittrichia viscosa subs Revoluta* (ARHAlentejo, 2012).

The main activity along the basin is the agriculture, representing about 52% of the catchment surrounding area; the main crop is maize, with an area of production of about 21%. Presently the main pressures around the basin are agriculture, aquaculture, mining activity and domestic effluents from the municipalities of Odemira, Zambujeira and Vila Nova de Milfontes (Medeiros et al., 2012).

Two sampling sites were established at Brejo of Cagarrão for the characterization of the water quality status during a period of time of 9 months: site 1, located at the source of Brejo of Cagarrão watercourse (N 37°40′19.90″; W 8°45′37.09″); and site 2, located at the mouth of Brejo of Cagarrão, near Brejo Largo Beach (N 37°40′49.15″; W 8°47′44.48″), with a distance of 4.5 km between sampling sites (see Fig. 1).

2.2. Sampling

Sampling was carried out during the hydrological years of 2010/2011 and 2011/2012, from June 2011 to March 2012. Water and macroinvertebrates were collected on June and September of 2011, and on January and March of 2012. The wet season included the months of January (Jr) and March (Mr) and the dry season included the months of June (Jn) and September (Sp); these periods were defined by the Portuguese Environmental Protection Agency (APA), for the Alentejo region (ARHAlentejo, 2011).

Considering the macroinvertebrates, the INAG sampling protocol for temporary rivers (2008) indicates that the sampling must occur at spring, under continuous flow conditions, when community and habitat diversity are generally considered at a maximum. Despite that, in the present study the macroinvertebrates were sampled during the whole period of the study, to try to correlate the temporal and spatial chemical variability observed in the water with the biotic indices and ecotoxicological endpoints obtained. However, during this study, the dry phase of the stream occurred in March, which is considered the beginning of the spring, making impossible the sampling in this month at the source of the stream.

Sampling collection at each site included: (i) 1 L of surface water on polyethylene (PET) bottles for the analysis of physicochemical support parameters; (ii) 1 L of surface water on amber low-density polyethylene (LDPE) bottles for the analysis of pesticides; (iii) 5 L on PET bottles for ecotoxicological assays. All the samples were collected on the shore, at a depth of 50 cm (when possible) and transported to the laboratory in coolers at 4 °C, where they were preserved and stored, following the requisites for water conservation for each parameter, until the analysis was performed (maximum storage time: 1 week) (APHA, 1998). The bottles for the analysis of pesticides were stored in the dark at −18 °C until analysis. For the water ecotoxicological assays, samples were previously filtered through 0.45 μm membrane filters and stored at −20 °C.

Temperature, pH, dissolved oxygen, and electrical conductivity were measured in situ, using a multiparametric probe YSI 6820 MPS probe®.

2.3. Physicochemical analyses

2.3.1. Water characterization

Water chemical parameters were determined using officially recommended methods of analysis (APHA, 1998), which are displayed in

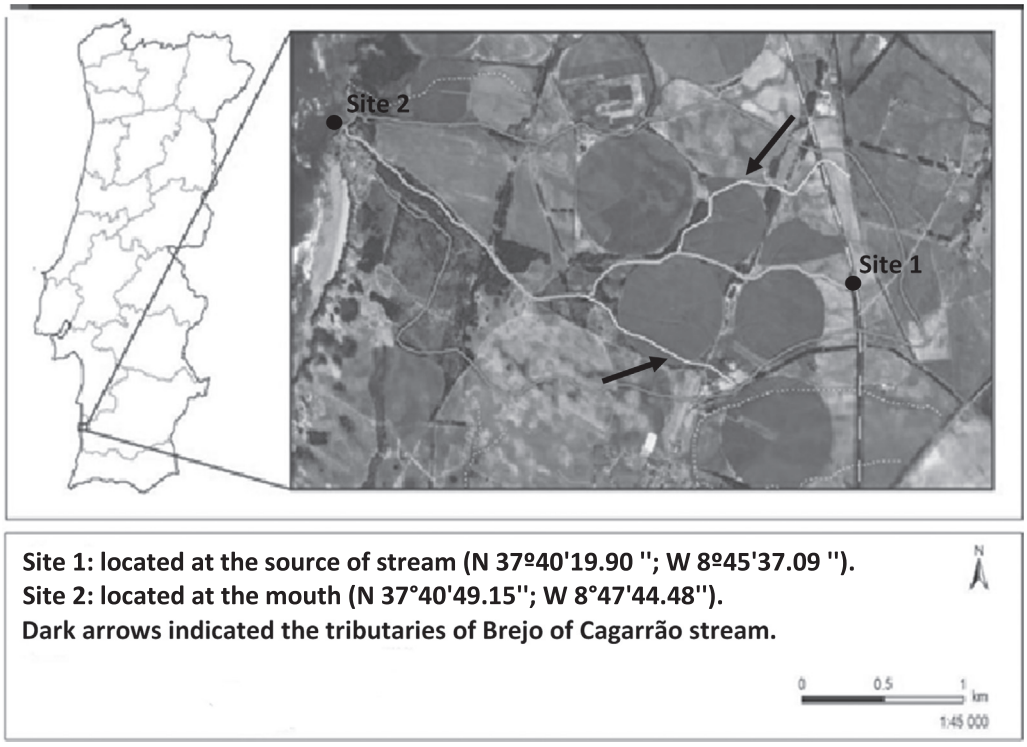

Fig. 1. Map showing the two sampling points at Brejo Cagarrão located at Mira Basin, in the South of Portugal.

Table 1, along with their units, the analytical techniques employed and the respective maximum concentrations, considering the normative of INAG (2009), adapted by the Water Framework Directive (WFD) (ECC, 2000) and the Decreto-Lei n°. 236/98. The selection of the chemical parameters was done bearing in mind the support parameters that must be evaluated for the characterization of the ecological status of rivers (INAG, 2009). Trace elements quantification included Cd, Pb, Cu, Zn, As, Fe, and Mn. However, only As, Fe, and Mn presented temporal and spatial variability in surface water, surpassing the stipulated limit values of the Portuguese Legislation (Decreto-Lei n°. 236/98), which justified their analysis in the study.

2.3.2. Pesticides analysis

A total of 25 target pesticides, representative of different chemical classes and modes of action (herbicides, insecticides and fungicides), were selected to be analysed, considering those included in the list of priority substances from the European Union's water policies (Directive 200/60/EC), the extent of their use, and the suitability of their analysis by means of liquid chromatography-tandem mass spectrometry. This list of compounds comprised triazines ((atrazine, cyanazine, simazine, terbuthylazine and the degradation products deisopropylatrazine (DIA) and desethylatrazine (DEA)), phenylureas (chlortoluron, diuron, isoproturon and linuron), chloroacetanilides (alachlor and metolachlor), anilides (propanil), organophosphorous compounds (diazinon, dimethoate, chlorfenvinphos (CFP), malathion, fenitrothion, and the metabolites fenitrothion oxon ((FOX) and malaoxon (MOX)), thiocarbamates (molinate), and acid compounds ((2,4-dichlorophenoxy) acetic acid (2,4-D), bentazone, (4-chloro-2-methylphenoxy) acetic acid (MCPA) and mecoprop)).

Target analysis of these compounds in water was performed with a fully automated method based on on-line solid phase extraction—liquid chromatography—electrospray—tandem mass spectrometry (SPE-LC-ESI-MS/MS), after previous filtration of the samples and addition of the surrogate standards, as described in Palma et al. (2014a). The analyses were performed with a Prospekt-2 system (Spark Holland, Emmen, The Netherlands) connected in series with a binary HPLC pump Model 1525 and a TQD triple-quadrupole mass spectrometer, both from Waters ((Milford, MA, USA). On-line SPE of the samples (5 mL) was carried out in duplicate using two different disposable polymeric cartridges (Hysphere Resin GP and PLRP-s, both from Spark Holland). LC separation was achieved in a Purospher STAR-RP-18e column (125 × 2 mm, 5 μm) from Merck (Darmstadt, Germany). ESI-MS/MS detection was performed in both positive and negative ionization modes and acquisition under selected reaction monitoring (SRM) conditions recording 2 SRMs per analyte and 1 SRM per surrogate standard. A total of 22 isotopically-labelled compounds were added to the samples for quantification by the isotope dilution method. Limits of detection achieved with this methodology were within 0.03 and 5.2 ng L^{-1}, except in the case of deisoprylatrazine (35 ng L^{-1}), while limits of quantification were below 10 ng L^{-1} in all cases but bentazone (12 ng L^{-1}), fenitrothion (17 ng L^{-1}) and deisoprylatrazine (116 ng L^{-1}). Further details on the experimental conditions and performance of the method can be found in Palma et al. (2014a).

2.4. Ecotoxicological endpoints

The test battery was outlined to integrate assays assessing lethal and sub-lethal responses with representative species of key taxonomic and functional groups. All bioassays performed have largely been used in other ecotoxicological studies and most of them have already been standardized: (i) lethal endpoints were investigated using two crustaceans with different sensitivities, namely, *Daphnia magna* and *Thamnocephalus platyurus*; (ii) bioassays with sublethal endpoints included luminescence inhibition of *Vibrio fischeri* and reproduction assay with *Daphnia magna*. Temperature, pH, dissolved oxygen (DO) and electric conductivity (EC) of the samples were measured and were in accordance with the standard protocols used. A reference test with potassium dichromate ($K_2Cr_2O_7$) was conducted as a positive control. The lethal assays were used for assessing drastic conditions relative to pollution processes while sublethal bioassays, namely those that integrate the whole life-cycle of the organism, have a great ecological relevance.

2.4.1. V. fischeri bioassay (Luminotox®)

Luminotox® was used to evaluate the inhibition of the marine bacteria *V. fischeri* luminescence (NRRL B-11177), according to the protocol "DR LANGE luminescent bacteria test" following ISO 11348-2 (1998). The bacteria were supplied as liquid-dried solution, by Dr. Lange GmbH & Co. KG, Düsseldorf, Germany. Tests were carried out using the following dilutions (100, 50, 25, 12.5, 6.25 and 3.125%, *v*/v). Two replicates per treatment were used. The inhibition of the bacteria natural light emission was measured against a non-toxic control (2% NaCl solution), at a temperature of 15 ± 0.5 °C. For each sample, bioluminescence was measured before and after the desired incubation period (30 min) and EC_{50} (%; the concentration of each sample that reduced 50% of the bacterial luminescence) was determined.

2.4.2. T. platyurus bioassay

The effect of the samples (water and pore-water) on the mortality of *T. platyurus* was evaluated in accordance with the standard operational procedure provided in the THAMNOTOXKIT F™ kit (Persoone, 1999). The concentrations tested were 25, 50, 75, and 100% (*v*/v), using the sample or its dilution with synthetic freshwater (included in the test

Table 1
Water parameters, abbreviations, units, analytical techniques, and maximum limits (Max.) for the establishment of the Good Ecological Status in rivers of short dimensions of the South of Portugal, adapted from Water Framework Directive (ECC, 2000; INAG, 2009).

Parameter	Abbreviation	Units	Analytical technique	Detection limit	Max.
Temperature	T	°C	Temperature probe		–
pH	pH	Sorensen scale	Potentiometry/pH probe		6–9
Dissolved oxygen	DO	%	Oxygen probe		60–120
Electrical conductivity	EC	μS cm^{-1}	Conductometry		–
Chemical oxygen demand	COD	mg L^{-1}	Dichromate technique	1.7	–
Biochemical oxygen demand	BOD_5	mg L^{-1}	Respirometric	1	≤6 mg O_2 L^{-1}
Nitrite	NO_2-N	mg L^{-1}	MAS	0.01	–
Nitrate	NO_3-N	mg L^{-1}	MAS	0.04	≤25 mg NO_3-N L^{-1}
Total nitrogen	TN	mg L^{-1}	MAS	0.0003	–
Ammonium	NH_4-N	mg L^{-1}	MAS	0.01	≤1 mg NH_4-N L^{-1}
Total phosphorus	TP	mg L^{-1}	MAS	0.003	≤0.13 mg TP L^{-1}
Chloride	Cl	mg L^{-1}	MAS	4	200[a]
Iron	Fe	mg L^{-1}	FAAS	0.013	0.30[a]
Manganese	Mn	mg L^{-1}	FAAS	0.001	–
Arsenic	As	mg L^{-1}	ETAAS	0.0012	0.05[a]

MAS - molecular absorption spectrometry; FAAS - flame atomic absorption spectrometry; ETAAS – electrothermal atomic absorption spectrometry. (a) maximum concentrations allowed by Portuguese legislation concerning the water quality for multiple uses, such as treatment for human consumption (Law-Decree No. 236/98).

kit, also used as a non-toxic control). Larvae of shrimp *T. platyurus* (<24 h), obtained by the hatching of cysts, were incubated in 24-well plates, with 1.0 mL of test solution and ten crustaceans per well, using four replicates per treatment, at 25 °C for 24 h in the dark. Animals were not fed during the test. The number of dead shrimps after 24-h contact with each test solution was used as the selected endpoint, and the EC_{50} (%) was calculated.

2.4.3. D. magna bioassays

Daphnids were obtained from continuous cultures maintained in the laboratory in a medium of American Society for Testing and Materials (ASTM) hard water (with a density of 15 individuals per 800 mL; ASTM, 1998) at 20 ± 1 °C and with a 16 h light:8 h dark photoperiod. Daphnids were fed with algae (*Pseudokirchneriella subcapitata*) with a density of 3.0×10^5 cells mL^{-1} $daphnia^{-1}$ (an equivalent carbon content of 2.65 mg C/mL) and organic additive Marinure "25" (Pann Britannica Industries Ltd., Waltham Abbey, UK), an extract from the algae *Ascophyllum nodosum* (Baird et al., 1989), at a concentration of 4.0 mL L^{-1}.

The *D. magna* acute bioassay was performed according to the ISO 6341 (1996) guideline. For each treatment, 20 juveniles (<24 h) between the third and the fifth brood were used. The water samples were diluted with ASTM solution (12.5, 25, 50, 75 and 100% *v*/v). All assays had a negative control with ASTM. Animals were not fed during the test. After 48 h, daphnids were observed for their mobility/death and the EC_{50} (% *v*/v) was determined.

To assess the effects of water samples on the reproduction of daphnids, tests were conducted in accordance with the OCDE *D. magna* reproduction test (OCDE, 1998). <24 h old neonates from the third-brood were exposed to the different dilutions of water samples (25%, 50%, 75%, and 100% v/v) and to the control medium ASTM. Ten replicates per treatment group were used with one daphnid per glass jar, filled with 50 mL of test solution. Test solutions were renewed three times a week and at the same time the organisms were fed with *Pseudokircheneriella subcapitata* (3.0×10^5 cells ml^{-1} $daphnia^{-1}$) and Marinure extract®. These maintenance procedures were like those for the stock cultures. All experiments were conducted for 21 d, in a chamber with a constant temperature, 20 ± 1 °C, and a photoperiod of 16 h light and 8 h dark. During the assay the number of living offspring produced per female was recorded for each broad. After the 21d exposure period, the total number of viable offspring produced by each female was used to estimate the reproduction rate.

2.5. Benthic macroinvertebrates communities

Benthic macroinvertebrates were collected following the proportional habitat sampling protocol (PHS), a multi-habitat procedure based on the collection of six samples of 1 m drag, distributed proportionally by the different types of habitat (gravel, rocks, pebbles, sands, organic materials, aquatic macrophytes) (INAG, 2008). The 50-m-long sampling area was selected to cover the greatest possible diversity of microhabitats, representing 25 m upstream and 25 m downstream of an area of turbulent flow (INAG, 2008). The sampling was performed with a hand net of 25 × 25 cm and a mesh size of 0.5 mm. The hand net method implies that the operator needs to place the net against the current and agitate the substrate to a depth of ca. 10 cm to dislodge the macroinvertebrates to the water column, which are dragged into the network ("kick sampling"). Samples were preserved in situ with 4% (*v*/v) of formaldehyde and transported to the laboratory. Prior to the identification of taxonomic level, the organisms were preserved in 70% ethanol. The organisms were identified under a microscope of 40× magnification (Leica®).

In the present study, the biotic endpoints were selected to allow the analysis of the variability and abundance of macroinvertebrate communities at the ecosystem, namely: single metrics: (i) macroinvertebrate abundance (S); (ii) Shannon-Wiener index (H); (iii) Evenness index (E); (iv) percentage of Ephemeroptera, Plecoptera and Trichoptera (% EPT); and quality indices: (i) Iberian Biological Monitoring Working Party (IBMWP; Alba-Tercedor and Sánchez-Ortega, 1988); (ii) Iberian Average Score Per Taxon (IASPT; Alba-Tercedor and Sánchez-Ortega, 1988); (iii) multi-metric Southern Portuguese Index of Invertebrates (IPtIs); and (iv) Ecological Quality Ratio (EQR) that, according to the intercalibration exercise of the geographic Mediterranean group, should be used to evaluate the ecological state of Portuguese southern rivers based on the macroinvertebrates communities (INAG, 2009).

2.6. Statistics

Water quality data were subjected to descriptive statistics (mean and standard deviation), and the spatial and seasonal variations of the parameters were analysed.

To assess possible associations among variables, a correlation test was performed. Considering the number of samples, and that most data failed the Shapiro-Wilk normality test, correlations between parameters were assessed using the Spearman's rank coefficients, as a non-parametric measure of the correlation between the variables, which is computed over ranked data (Wunderlin et al., 2001). With the Spearman correlations, we intended to determine whether two variables are associated or not, the direction of the association, and whether the association is strong or weak. Furthermore, as we had chemical and biological parameters to correlate, data were normalized to avoid misclassification due to the wide differences in data dimensionality.

The estimation of the single metrics and the quality indices were performed following the equations displayed in Table 2. The $IPtI_S$ values were obtained from the sum of the weighted metrics, which were calculated multiplying the normalized value of the metric (obtained by the quotient between the value calculated for each metric and the corresponding reference value, see Table 2) by the respective weighting factor. The Ecological Quality Ratio (EQR) was obtained dividing the $IPtI_S$ value by the $IPtI_S$ reference value of 0.99 for small southern rivers (INAG, 2009).

For the ecotoxicological endpoints, the EC_{50} (%) for the *V. fischeri* bioluminescence inhibition values were determined using LUMISsoft 4

Table 2
Biotic indices and reference values used to assess the ecological status of Brejo Cagarrão (South of Portugal).

	Equation	Reference value
Single metric		
Abundance (S)		27.00
Ephemera, Plecoptera, Trichoptera Index (EPT) (%)	$EPT = (\Sigma(S_{EPT}) / S) * 100$	10.00
Evenness index (E)	$E = H / lnS$	–
Shanon Wienner index (H)	$H = -\Sigma pi \ln pi$ where $pi = ni/N$	–
Quality indices		
Iberian Bio-Monitoring Working Party index (IBMWP)	$IBMWP = \Sigma SF$	101
Iberian Average Score Per Taxon (IASPT)	IASPT-2 = ((IBMWP/S)-2)	3.29
Multi-metric index		
Southern Portuguese Index of Invertebrates ($IPtI_S$)	$IPtI_S = S * 0.4 + EPT * 0.2 + (IASPT\text{-}2) * 0.2 + Log(\Sigma S_{EPTCD} + 1) * 0.2$	0.99

Where: S_{EPT}: abundance of taxa belonging to the Ephemera, Plecoptera, Trichoptera order; S: number of Taxa; ni: number of individuals of each Taxon; N: number of total individuals; SF: score factor relatively to the pollution sensitivity of each taxa (1 (more resistant) to 10 (more sensitive)), adapted from Alba-Tercedor and Sánchez-Ortega, 1988); S_{EPTCD}: abundance of the individuals belonging to the families Chloroperlidae, Nemouridae, Leuctridae, Leptophlebiidae, Ephemerellidae, Philopotamidae, Limnephilidae, Psychomyiidae, Sericostomatidae, Elmidae, Dryopidae, Athericidae.

Software™. The EC_{50} (%) for the *T. platyurus* and *D. magna* mortality data were determined using the probit analysis (Finney, 1971). Data of reproduction and inhibition growth bioassays were checked for homogeneity of variance by the Kolmogorov–Smirnov test (Sokal and Rohlf, 1995) and, when possible, subjected to one-way analysis of variance (ANOVA). Data, which do not satisfy the assumption for ANOVA, were analysed non-parametrically using Kruskal–Wallis ANOVA by ranks test. Whenever significant differences were found ($p < 0.05$), a post hoc *Dunnett's* test was used to compare treatments with the control, for an alpha value of 0.05 as the significant level (Zar, 1996).

The principal components analysis (PCA) was applied with the objective of determining the main environmental parameters (support parameters and hazardous substances) that account for the variability of the water body status/quality and tried to correlate them with the biotic indices and ecotoxicological endpoints applied. Before the application of multivariate statistical analysis, the data were normalized ($\log(x + 1)$; x = mean value) to avoid misclassification due to the wide differences in data dimensionality (Liu et al., 2003; Simeonov et al., 2003). Statistical analyses were carried out with the software Statistica 6.0.

3. Results and discussion

3.1. Physicochemical supporting parameters

At the present study the dry phase of the stream occurred during the early spring (March 2012). This inflection of the ecosystem hydrological conditions occurred earlier than usual, considering the normal flow patterns observed in temporary rivers/streams in the Mediterranean area (Arenas-Sánchez et al., 2016). Nevertheless, in recent years, in the region of Alentejo (South of Portugal), with a strong influence of the Mediterranean climate, a shortening of the rainy season, with lower precipitation levels, and the corresponding increment of extreme drought periods, has been observed. In fact, in the hydrological year of 2011/2012, during the winter (mainly in December 2011 and January 2012), the rainfall levels were very low, and no precipitation occurred in February 2012 (as already reported; www.snirh.pt, 2011/2012). Hence, these extreme hydrological conditions induced an early cessation of flow in the stream.

At the mouth of the stream, this inflection of the ecosystem did not occur, due to the two tributaries to the Brejo of Cagarrão (see Fig. 1). Thus, in this scenario, and whenever possible, we tried to establish correlations among the chemical dynamics, the biological communities and the ecotoxicological responses, at both stream sampling sites.

The temporal and spatial variability of the most relevant physicochemical parameters that support the biological life of Brejo of Cagarrão is described in Table 3. According to the criteria for the classification of the status of surface water bodies ((INAG, 2009, adapted from WFD (ECC, 2000)), these parameters assess the general status of the watercourse, giving us information about the respective level of oxygenation, state of acidification and nutrients profile.

The results highlight that most of the parameters, except of pH and electric conductivity (EC), express significant temporal and spatial variations during the study, which may be caused by: (i) the hydrologic regime of the stream; (ii) climatic factors; and (iii) point and/or diffuse pollution sources.

Concerning the parameters determined "in situ" (pH and EC), and according to the reference values for small rivers of the South of Portugal (INAG, 2009), Brejo of Cagarrão presented a Good Status at both sampling sites during the study period.

With respect to dissolved oxygen (DO), the results highlight a high temporal and spatial variability of the values obtained. Thus, in the stream source, the DO was always outside the proposed limits for this type of surface water (60–120%) during the flow phase, achieving lower values in July and September 2011 and higher percentages of saturation in January 2012. At the mouth of the stream (site 2), the DO values remained between the limits for the classification of Good Status, though in March 2012 the DO achieved the highest values (117%), near the upper limit. In line with the matrix of Spearman's coefficients correlation (R) (see Table S1), DO displayed a negative correlation with the temperature ($R = -0.80$; $p < 0.05$), which indicates that the temperature was the most important physical factor for the natural variability of the DO in the stream. In fact, the winter low temperatures increase the solubility of oxygen, while in the summer, the temperature increase induces a natural decrease of DO levels (Palma et al., 2016). Furthermore, lower concentrations of DO during the summer may also relate to the decomposition of aquatic plants, particularly at the end of the growing season, and with low stream flow conditions. Another important factor, that may contribute to the DO drop down during the summer period, is the addition of oxygen-demanding organic matter to the stream system (e.g. sewage, agricultural runoff, etc.) (Harvey et al., 2011). Regarding what occurred at the source of the stream, the results point to the increment of pollution processes, such as inflows of untreated or inefficiently treated domestic wastewaters, with large amounts of nutrients discharged to the watercourse, as well as, runoff from agricultural activities, which are the priority activities around the basin.

Table 3
Descriptive statistics (mean ± SD; n = 3) of the water physicochemical supporting parameters, at the two sites (Site 1: source of the stream; Site 2: mouth of the stream), during 2011–2012.

	Brejo of Cagarrão							
	Site 1				Site 2			
	June	September	January	March	June	September	January	March
T (°C)	21.5 ± 0.2	23.6 ± 0.3	9.9 ± 0.1	(a)	23 ± 0.5	25.1 ± 0.2	9.9 ± 0.1	12.3 ± 0.1
pH	7.2 ± 0.6	7.0 ± 0.3	6.9 ± 0.5		7.6 ± 0.2	6.9 ± 0.3	7.2 ± 05	7.7 ± 0.4
EC (μs cm^{-1})	743 ± 53	890 ± 48	625 ± 27		727 ± 38	739 ± 45	666 ± 32	599 ± 51
DO (%)	53 ± 0.8	52 ± 1.0	125 ± 1.0		60 ± 0.6	88 ± 0.9	98 ± 1.0	117 ± 1.1
BOD_5 (mg L^{-1})	25.50 ± 0.71	18.50 ± 0.71	25.50 ± 0.71		7.50 ± 2.12	10.50 ± 0.71	4.0 ± 1.41	<LD
COD (mg L^{-1})	60.80 ± 2.77	61.23 ± 5.17	193.67 ± 2.89		38.40 ± 0.51	35.71 ± 4.76	67.33 ± 2.31	29.90 ± 3.25
TN (mg L^{-1})	37.75 ± 7.27	0.86 ± 0.06	3.27 ± 0.27		0.68 ± 0.20	1.16 ± 0.29	0.72 ± 0.24	0.38 ± 0.03
NH_4-N (mg L^{-1})	29.03 ± 0.13	0.06 ± 0.003	0.59 ± 0.01		0.22 ± 0.01	0.87 ± 0.001	0.061 ± 0.003	0.03 ± 0.005
NO_3-N (mg L^{-1})	25.22 ± 0.89	17.04 ± 0.26	4.93 ± 0.37		7.08 ± 0.18	8.96 ± 0.16	18.67 ± 0.65	2.4 ± 0.03
NO_2-N (mg L^{-1})	1.18 ± 0.10	0.33 ± 0.012	0.26 ± 0.005		0.09 ± 0.010	1.04 ± 0.04	0.12 ± 0.001	0.02 ± 0.002
TP (mg L^{-1})	0.23 ± 0.001	0.17 ± 0.004	0.33 ± 0.005		0.06 ± 0.002	0.15 ± 0.01	0.32 ± 0.03	0.006 ± 0.0001
Cl (mg L^{-1})	128.7 ± 1.11	109.6 ± 3.99	168.2 ± 7.39		130.4 ± 3.99	125.8 ± 1.99	146.9 ± 2.05	143.0 ± 1.93
Fe (mg L^{-1})	0.56 ± 0.05	0.46 ± 0.02	1.99 ± 0.03		0.59 ± 0.01	0.77 ± 0.01	0.72 ± 0.02	0.29 ± 0.01
Mn (mg L^{-1})	0.25 ± 0.01	0.03 ± 0.01	0.16 ± 0.02		0.14 ± 0.01	0.21 ± 0.06	0.02 ± 0.01	0.01 ± 0.001
As (mg L^{-1})	0.008 ± 0.001	0.002 ± 0.0001	0.007 ± 0.001		0.003 ± 0.001	0.002 ± 0.001	0.002 ± 0.001	0.001 ± 0.001

DL: detection limit; DL (BOD_5) = 1.0 mg L^{-1}; DL(COD) = 1.7 mg L^{-1}; DL(TP) = 0.003 mg L^{-1}; DL(NO_3-N) = 0.04 mg L^{-1}; DL(NO_2-N) = 0.01 mg L^{-1}; DL(NH_4-N) = 0.01 mg L^{-1}; DL(Fe) = 0.013 mg L^{-1}; DL(Mn) = 0.001 mg L^{-1}; DL(As) = 0.0012 mg L^{-1}. (a) Results from March 2012 were not presented, because in this period the stream was at its dry phase, without flow.

Biochemical oxygen demand (BOD_5) and chemical oxygen demand (COD), parameters that influence the oxygenation conditions of water bodies, reached very high values at the source of the stream (BOD_5: 18.5–25.5 mg L^{-1}; COD: 60.8–193.7 mg L^{-1}). According to INAG (2009), concentrations of BOD_5 and COD higher than 5 mg L^{-1} and 20 mg L^{-1}, respectively, compromise the essential conditions for the support of biological life, classifying the water as "Less than Good". These results support the above statement about the intensive processes of pollution that occur at this watercourse. In general, at site 2, the amounts of both parameters decreased, being March 2012 the month when they were quantified at the lowest concentrations (BOD_5 < detection limit (LD); COD: 29.9 mg L^{-1}). Generally, similar temporal patterns were observed for the nutrients parameters ((total nitrogen (TN), total phosphorus TP)), with higher amounts at the source of the stream. Thus, the TN achieved very high concentrations (37.75 mg L^{-1}) in June 2011, probably due to the increment of organic matter from the point pollution sources (wastewater discharges from wastewater treatment plants of the municipalities of Zambujeira and Vila Nova de Milfontes), as well as to the excess of biological activity, as reported by other authors (Korkança et al., 2017; Palma et al., 2014b). The highest concentrations of TP occurred in site 1 (stream source: 0.17–0.23 mg L^{-1}). All these values lead to a status classification of this section of the Brejo of Cagarrão as "Less than Good" with respect to ecological conditions. These results suggest that the main focuses of pollution are near the source of the stream, and when during the drying phase, the main contamination processes are not transferred downstream. Further, the positive correlations observed between BOD_5 and TP ($R = 0.77$; $p < 0.05$); BOD_5 and TN ($R = 0.92$; $p < 0.05$); BOD_5 and NH_4-N ($R = 0.79$; $p < 0.05$); BOD_5 and NO_2-N ($R = 0.81$; $p < 0.05$) suggest the same sources of contamination, namely wastes from agriculture and livestock activities, as observed elsewhere for the Guadiana Basin (Palma et al., 2014b).

Concerning the trace elements, and since the normative for the classification of the ecological status of the water bodies (INAG, 2009) does not integrate them, nor the Directive for "good chemical status" (ECC, 2013), we followed the Portuguese legislation regarding water for multiple uses (Decreto-Lei n°. 236/98, 1998). Iron concentrations in the water stream (site 1 and site 2) were very high, with values at site 1 ranging from 0.46 to 1.99 mg L^{-1} and at site 2 between 0.29 and 0.52 mg L^{-1}, always surpassing the legal limit value of 0.1 mg L^{-1}. As for Mn, the concentrations found were lower than the limit value of 0.025 mg L^{-1} only at Site 2 (January and March 2012). The high concentrations for these trace elements were probably the result of diffuse pollution (predominantly from wastewater discharges), and not a result of the lithology of the basin. Several facts support this assumption: (i) the positive significant correlation observed between nutrients (that in the study resulted from undertreated or inefficiently treated wastewater discharges) and trace elements (see Table S1); (ii) the fact that the Mira Basin sediments are mainly constituted by clay and their amounts of organic matter range 0.7–2.0% (Mil-Homens et al., 2014), factors that contribute to the adsorption of the trace elements to the sediments decreasing the processes of resuspension to the water column; and (iii) the fact that the primary trace elements detected in the sediments were Cr (73–104 μg L^{-1}), Ni (42–62 μg L^{-1}) and Co (16–29 μg L^{-1}) resulting, according to the authors, from the weathering of the basic rocks formations and doleritic veins existing in the formations of the volcano-sedimentary complex of the Odemira and Pomarão areas (Mil-Homens et al., 2014), elements that were not detect in the water column.

3.2. Dynamic of pesticides at Brejo of Cagarrão stream

In general, Brejo of Cagarrão stream exhibited moderate concentrations of the target pesticides. Although all samples had pesticides, only five (all herbicides), out of the 25 compounds analysed, were detected, namely, terbuthylazine (triazine), metolachlor (chloroacetanilide), bentazone, MCPA and mecoprop (acid compounds) (see Fig. 2). All five pesticides were detected in all samples. Mecoprop was the herbicide detected at lower concentrations (Site 1: 7.6–8.0 ng L^{-1}; Site 2: 2.1–7.1 ng L^{-1}), while bentazone and MCPA (usually formulated together) showed the largest maximum concentrations: up to 1769 ng L^{-1} of bentazone in Site 1 in January 2012, and up to 580 ng L^{-1} of MCPA in Site 2 in June 2011. None of the pesticides quantified are included in the list of priority substances in the field of water policy (ECC, 2013), however two of them (bentazone and mecoprop) were considered to review for possible identification as priority substances or priority hazardous substances (Directive 2008/105/EC). Nonetheless, all but mecoprop surpassed the reference value of 100 ng L^{-1} set as maximum admissible concentration (MAC) for individual compounds in groundwater (ECC, 2006) and drinking water (ECC, 1998): terbuthylazine and metolachlor (usually formulated together for maize crop application) surpassed this limit in 71% and 42% of the samples, respectively, while bentazone and MCPA exceeded this value only once during the study. It may be worth noting that

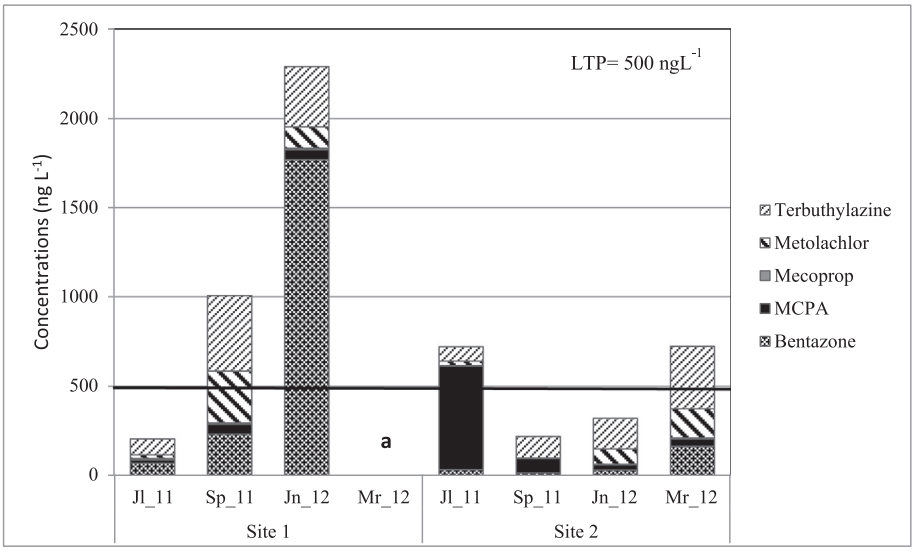

Fig. 2. Concentrations of pesticides (ng L^{-1}) quantified in Brejo do Cagarrão stream, in June 2011 (Jn_11) and September 2011 (Sp_11), and in January 2012 (Jr_12) and March 2012 (Mr_12). (a. Site 1 at March 12, corresponding to the dry phase).

terbuthylazine and metolachlor are included in the list of specific substances presenting a significant risk to the neighboring Spanish surface waters, due to their special toxicity, persistence and bioaccumulation, or the importance of their presence in the Spanish aquatic environment (Real Decreto n°. 817/2015, 2015). The sample with the lowest value of the sum of pesticides (204 ng L^{-1}) was collected at site 1, in June 2011, while the sample exhibiting the largest overall concentration of the pesticides (2291 ng L^{-1}), due mainly to the concentration achieved by bentazone (1769 ng L^{-1}), was collected also from site 1 in January 2012. The reference value of 500 ng L^{-1}, set as the MAC for the sum of pesticides (including metabolites and transformation products), in groundwater (ECC, 2006) and drinking water (ECC, 1998), was surpassed at the source of the stream in the samples from September 2011 and January 2012, and at the mouth of the stream, in the samples from June 2011 and March 2012. These results highlight the fact that, as far as pesticides are concerned, both sections of the stream present different and not correlated patterns of pollution. Contrarywise to what has been observed for the dynamics of the chemical parameters, and even though the pesticides detected are the same (probably because the crops around the two sections are similar, mainly maize crops), the source section may not influence the contamination patterns at the mouth of stream during the dry phase. Furthermore, the non-existence of significant correlations among support chemical parameters and quantified pesticides supports this hypothesis (see Table S1).

3.3. Ecotoxicological assessment

All ecotoxicological tests reported fulfilled the validity requirements established by their respective guidelines.

The short-term bioassays used, with *T. platyurus* and *D. magna*, did not detect toxicity among the samples tested. The relative low sensitivity of the *D. magna* lethality bioassay to surface waters with low pesticide concentrations (lower than the EQS values, ECC, 2013) has already been reported in rivers and heavily modified water bodies (HMWB) by other authors (Ieromina et al., 2014; Palma et al., 2016). In contrast, previous results with the anostracan *T. platyurus* highlighted the sensitivity of the crustacean to detect low levels of pesticides in HMWB, being considered as good alternative to *D. magna*, when integrating primary consumers in toolboxes for acute ecotoxicity screening of surface waters contaminated by pesticides (Palma et al., 2016). The quantification only of pesticides belonging to herbicide classes (triazines, acids and chloroacetanilides) may justify the acute ecotoxicological results observed during the study, once the crustaceans are most sensitive to insecticides and fungicides (Palma et al., 2008; Bunzel et al., 2015).

The bioassay with *V. fischeri* (sublethal effect) detected toxicity after 30 min of exposure to the sample of January 2012 from the Site 1 (source section of the stream), with an EC_{20}(%; *v*/v) of 11.56; [11.19–11.91] (mean values and 95% confidence interval; n = 2). The results of the correlation matrix showed significant positive correlations between the bioluminiscence inhibition of the bacterial *V. fisheri* and the increment of the concentrations of COD ($R = 0.86$; $p < 0.05$), Fe ($R = 0.92$; $p < 0.05$), and bentazone ($R = 0.80$; $p < 0.05$), suggesting that these three parameters are the main responsible for the toxicity observed. Accentuated bioluminescence inhibition with increasing Fe concentrations at water bodies has already been reported elsewhere (Palma et al., 2016).

The life-cycle assessment through the reproduction bioassay with *D. magna* was the most sensitive test, detecting toxicity at Site 1 in June 2011 (one-way ANOVA; $F_{4,45} = 9.68$; $p = 0.0001$), September 2011 (one-way ANOVA; F4,44 = 3.46; $p = 0.01527$), January 2012 (one-way ANOVA; $F_{4,45} = 6.61$; $p < 0.0005$), and at Site 2 in January 2012 (one-way ANOVA; $F_{4,45} = 12.51$; $p < 0.0001$) and in March 2012 (one-way ANOVA; $F_{4,37} = 10.62$; $p = 0.0001$) (see Fig. 3). The responses observed at Site 1 were probably due to the high levels of the potentially toxic metals Fe, Mn and As, jointly with the presence of pesticides, namely terbuthylazine. The correlation with the presence of As and terbuthylazine and the decrease of the *D. magna* reproduction rate has already been reported in other studies (Palma et al., 2010; Palma et al., 2016).

Notwithstanding, in previous studies, it was possible to conclude that the increment of nutrients and organic descriptors may improve the reproductive performance of the crustacean and mask the toxic effect promoted by pesticides (Palma et al., 2016). In the present study, this effect did not occur, once the reproduction rate decreased significantly in the samples with the highest concentrations of COD and BOD_5, probably because organic matter, above a given concentration, can also contribute to a toxic environment. In Site 2, the decrease of juveniles probably happened due to the presence of pesticides, which reached their highest concentrations in March 2012 (723 ng L^{-1}). This result highlights the importance of pesticides in the ecotoxicological responses observed, once in March 2012, when the levels of other chemical parameters and potential toxic metals lowered, due to the dry phase of the stream, and to the levels of pesticides which remained high, the negative effects continued to be observed.

These results emphasize the importance of integrating longer-exposure bioassays, with higher ecological relevance, to assess more thoroughly the ecotoxicity of surface water samples. These samples are, in general, matrices with lower ecotoxicity, more difficult to be detected by short-term exposition.

The results highlight that an ecotoxicological approach, with sensitive species, allow us to link the presence of chemical stressors with the negative effects observed in the ecosystem communities, condition required for the development of specific management actions in waters. Furthermore, the use of ecotoxicological tools can be very useful in the ecological risk assessment of surface waters where reference scenarios are difficult to be established, such as in temporary streams, once most of them occur intermittently due to the extreme climate conditions.

3.4. Macroinvertebrates

To evaluate the structure of the benthic communities at the studied sites, we sampled 1616 individuals belonging to 14 taxa (see Table 4). The dominant groups were Diptera (29.9%) and Coleoptera (29.5%), followed by Ephemeroptera (23.8%), Heteroptera (6.7%), Plecoptera (5.8%) and Odonata (3.4%). The group of Gastropoda represented only 0.4% of the total number of individuals, appearing punctually at Site 1 (June 2011) (see Fig. 4). As expected, in winter, it was impossible to find individuals from Gastropoda, due to the lower abundance of macrophytes, the primary habitat for this group, returning in the spring-summer when habitat conditions are favourable (Trigal et al., 2007). During the study, the abundance was lower than the metrics benchmarks for small southern rivers of Portugal (27.00; INAG, 2009), which is an indicator of the existence of environmental stress conditions (Bio et al., 2011; Trigal et al., 2007). Several authors have reported that the increase in NH_4-N concentration in aquatic ecosystems induces a decrease in the abundance of benthic invertebrates (Versteeg et al., 1999; Blanco and Bécares, 2010). In the present study the concentrations of NH_4-N were elevated mainly in Site 1, which may justify the results observed. In the study, we only observed two of the reference taxa (Chironomidae and Elmidae) reported for temporary streams of South of Portugal with almost no slope (0.7%) and high conductivity (>566 mS/cm) (Feio et al., 2009).

The benthic communities did not present an accentuated temporal and spatial variability, occurring a slight increment of the percentage of the principal taxa during the spring-summer, justified by the continuous flow conditions and by the food availability, which is generally greater in this period (Leitão et al., 2014). Moreover, the principal order presented at Site 1 was Diptera represented solely by the Chironomidae family, and at Site 2 was Ephemeroptera, represented by the Ephemerellidae, Ephemeridae and Oligoneuriidae families. Henceforth, and relatively to the tolerance to pollution, the Site 1 was dominated, in general, by resistant families, whose presence is correlated with low

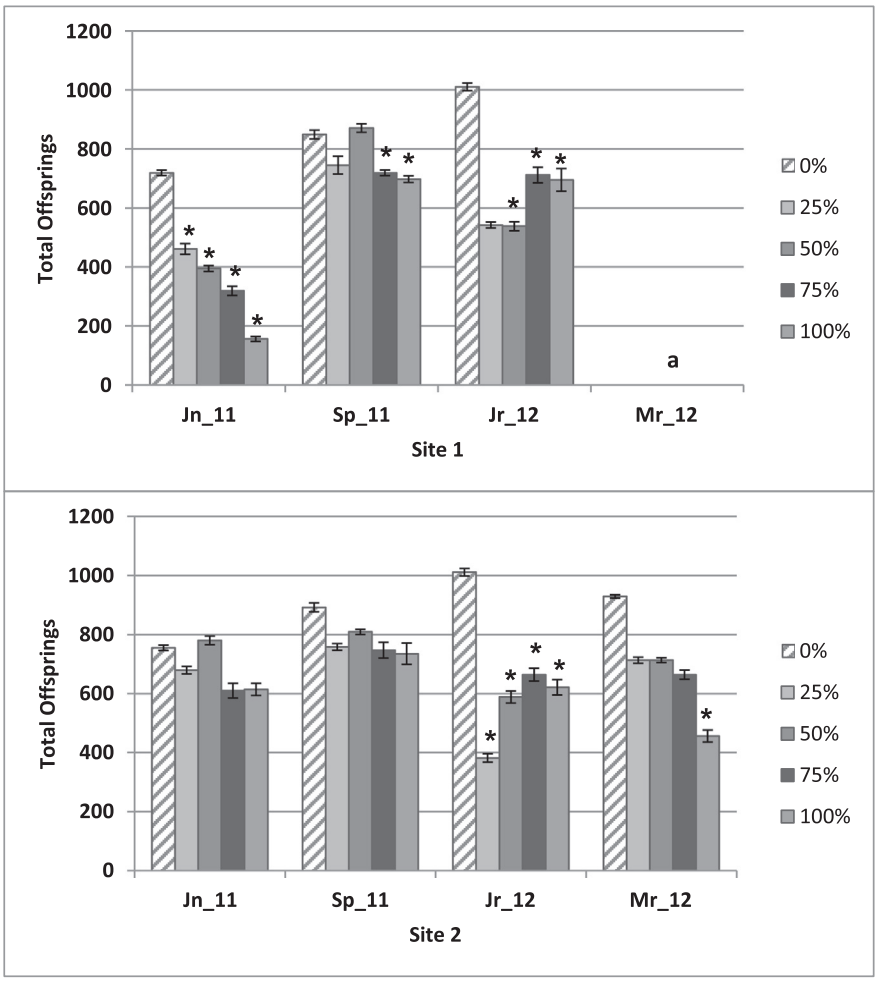

Fig. 3. Total offspring produced during the 21 days of exposure to the surface water samples (25, 50, 75, 100% v/v), at each of the section of the stream, in June 2011 (Jn_11) and September 2011 (Sp_11), and in January 2012 (Jr_12) and March 2012 (Mr_12) ((mean ± standard deviation, n = 10). *$p < 0.05$, Dunnett's test with a control (ASTM hard water)). (a. Site 1 at March 12, corresponding to the dry phase).

concentrations of oxygen, nutrient enrichment and organic pollution (Bio et al., 2011). Contrariwise, Site 2 was dominated by less tolerant families, being, for example, the individuals of Ephemerellidae and Ephemeridae very sensitive to pesticides, with a SPEAR index (Species at Risk index) of 1 (SPEAR = 1, specie at risk; SPEAR = 0, specie at no risk; Liess and von der Ohe, 2005). The EPT index presented values above the reference, correlated with the Taxa of Ephemeroptera and Plecoptera, once the Trichoptera was not observed during the study. Trichoptera, among the three families, is the most sensitive to organic pollution, as well as, to hazardous substances like pesticides; most of the species belonging to this family present a SPEAR index for pesticides of 1 (Liess and von der Ohe, 2005). The macroinvertebrate diversity varied slightly between seasons/months, presenting values considered low in the range of normal index variation. Thus, at Site 1, the Shannon-Wiener index (H) ranged between 1.80 (June 2011) and 2.03 (January 2012) and at Site 2 from 1.52 (January 2012) to 2.20 (September 2011) (see Table 4). This result supports the previous ones reporting the high organic pollution and the presence of pesticides in the stream, once that, in general, the high species richness is correlated with an adequate availability of habitats with food sources and niches to be occupied

Table 4
Ecological endpoints by sample site and month, with the single metrics number of macroinvertebrate taxa and individuals (Ind.), Shannon-Wiener diversity index (H) and Evenness index (E), the quality indices of Iberian Bio-Monitoring Working Party index (IBMWP), and the Iberian Average Score Per Taxon (IASPT-2), and the Ecological Quality Ratio (EQR).

Site	Month	Taxa	Ind.	% EPT	H	E	IASPT-2	IBMWP		EQR	
								Score	Class	Score	Class
1	Jn	12	241	25.0	1.80	0.73	3.64	62	II	0.59	III
	Sp	7	292	14.3	1.61	0.83	2.43	31	IV	0.43	IV
	Jr	10	188	30.0	2.03	0.88	3.90	59	III	0.60	III
	Mr	(a)									
2	Jn	9	185	33.3	1.92	0.87	3.33	48	III	0.54	III
	Sp	11	173	45.5	2.20	0.92	4.18	68	II	0.66	III
	Jr	6	269	16. 7	1.52	0.85	2.67	28	IV	0.42	IV
	Mr	10	262	40.0	1.94	0.84	3.80	58	III	0.62	III

Classes of the (i) IBMWP: >101 considered as Good (I); 100-61 Acceptable (II); 60-36 Doubtful, (III); 35-16 Harmful (IV); and <15 Very Harmful (V) (Alba-Tercedor and Sánchez-Ortega, 1988); and (ii) EQR > 0.95 considered as excellent (I); 0.70-0.95 good (II); 0.47-0.70 reasonable (III); 0.23-0.47 mediocre (IV); and <0.23 bad (V) (INAG, 2009). (a) Results from March 2012 were not presented, because in this period the stream was at its dry phase (without flow).

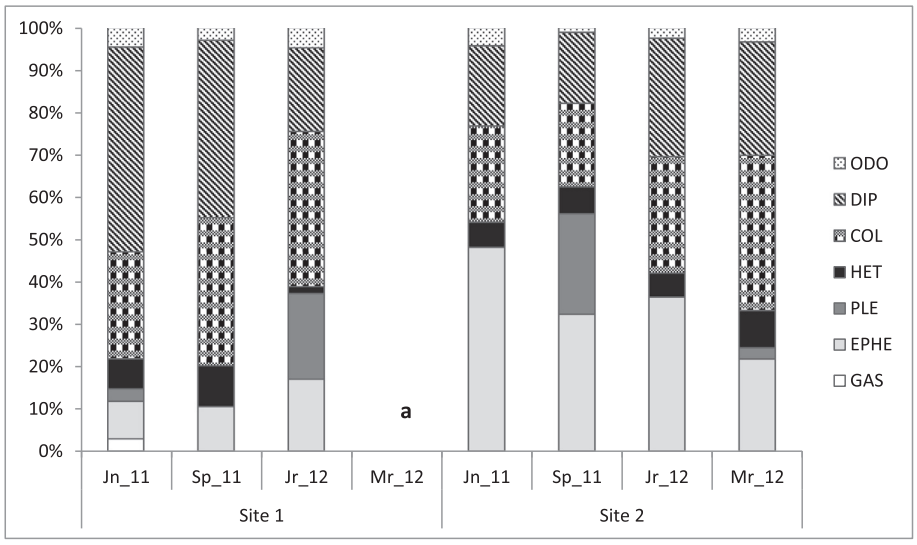

ODO: Odonata; DIP: Diptera; COL: Coleoptera; HET: Heteroptera; PLE: Plecoptera; EPHE: Ephemeroptera; GAS: Gastropoda.

Fig. 4. Distribution of the relative Taxa abundance in both sections of the stream (Site 1 and Site 2), in June 2011 (Jn_11), September 2011 (Sp_11), January 2012 (Jr_12) and March 2012 (Mr_12). (a. Site 1 at March 12, corresponding to the dry phase). ODO: Odonata; DIP: Diptera; COL: Coleoptera; HET: Heteroptera; PLE: Plecoptera; EPHE: Ephemeroptera; GAS: Gastropoda.

and without pollution, supporting the propagation and survival of the aquatic biota (Schäfer et al., 2016). In addition to the low diversity of the benthic organisms, their distribution was uniform for the existing taxonomic groups, since in general, the Evenness index ranged from 0.73 (Site 1 in June 2011) to 0.92 (Site 2 in September 2011). The correlation matrix of Evennes index showed negative correlations with nutrients, namely, TP ($R = -0.84$; $p < 0.05$), KN ($R = -0.77$; $p < 0.05$) and NH_4-N ($R = -0.78$; $p < 0.05$), and with the reproduction inhibition of *D. magna* ($R = -0.81$; $p < 0.05$). Liess and von der Ohe (2005) had already observed negative correlations between abundance of macroinvertebrates and *D. magna* toxicity, at areas strongly contaminated by pesticides.

According to the IBMWP index, a quality index more sensitive to organic pollution than to hazardous substances (García et al., 2014; von der Ohe and Goedkoop, 2013), the ecological status of the water body ranges from acceptable to harmful (Class II–IV; see Table 4). Medeiros et al. (2012), reported similar classifications of watercourses at the Mira estuary. As expected, the IBMWP index, showed strong positive correlations with abundance ($R = 0.95$; $p < 0.05$), Shannon-Wiener index ($R = 0.78$; $p < 0.05$), and EQR (environmental quality ratio) ($R = 0.85$; $p < 0.05$), which denote the consistence between the indices used. The EQR index results of the normalization of the Southern Portuguese Index of Invertebrates, obtained through the sum of the weighting of the remaining indices. This index gives us complete and integrated information about the biotic macroinvertebrates communities, being more sensitive and complete that the IBMWP, and classifying the ecological status of the stream from reasonable to mediocre (class III–IV), during the study.

The Brejo of Cagarrão stream displayed a general gradient of worse to better water quality, from up (Site 1) to downstream (Site 2). This gradient was more marked in chemical support parameters and in pesticides than in ecotoxicological endpoints and biotic indices. This pattern was also observed in other Portuguese rivers and streams, such as Febros (Bio et al., 2011) and Odelouca (Silva, 2012), and in transitional waters, like in the Mira estuary (Leitão et al., 2014).

3.5. Multivariate statistical analysis

PCA allowed the identification of four main components (PCs) using the Kaiser criterion (Kaiser, 1960), which explains 88% of the total variance. PC1 explained 31% of the original data and was correlated principally with nutrients and trace elements. Therefore, PC1 is strongly positively associated with TP, KN, NH_4-N, Mn, As, abundance of taxa (S) and IBMP index; moderately positively related with BOD_5, H diversity index and EQR index; and moderately negatively participated by metoalachlor and total number of individuals (N) (see Fig. 5a). PC2 explained 22% of the variance and was strongly negatively participated by NO_3-N, NO_2-N, and number of total individuals (N), and positively correlated with EPT, H and E metrics. PC3 explained 20% of the total variance and was mainly participated by temperature (negative side), COD, chloride (Cl), bentazone and luminescence inhibition (positive side) (following the Liu et al. (2003) classification: strong correlation (factor score > 0.75); moderate correlation (factor score 0.75–0.5). This PC3 was the only one that correlated the presence of pesticides with ecotoxicological endpoints.

The score of the water samples more influenced by the parameters that explained the two first PCs are represented in Fig. 5b. The samples with worst quality and lower biotic indices were from the source of the stream (Site 1), located at the positive quadrant of PC1 and at the negative quadrant of PC2. Contrarywise, samples collected at Site 2, from March and January, were located at the positive quadrant of PC2, indicating that they were less influenced by COD, nutrients and metolachlor, and on the negative quadrant of PC1 (less influenced by nutrients and BOD_5), which constituted the samples with the highest quality and higher metric indexes.

PCA confirmed the previous results, namely, that the pesticides presented a lower influence in the water quality of the stream than nutrients and potential toxic metals, as well as that the samples with worst quality were from the source of the stream. Further, PCA results also highlight that the variability of metric indices was more influenced by nutrients and potentially toxic metals, and that the ecotoxicological effects were more correlated with pesticides.

4. Conclusions

Temporary streams are dominant freshwater systems in the Mediterranean region, and their number is expected to increase, due to climate change and to the increasing inappropriate use of freshwater resources. So, it is important/ urgent to obtain more information about their hydrological, chemical, and biological behaviour. However,

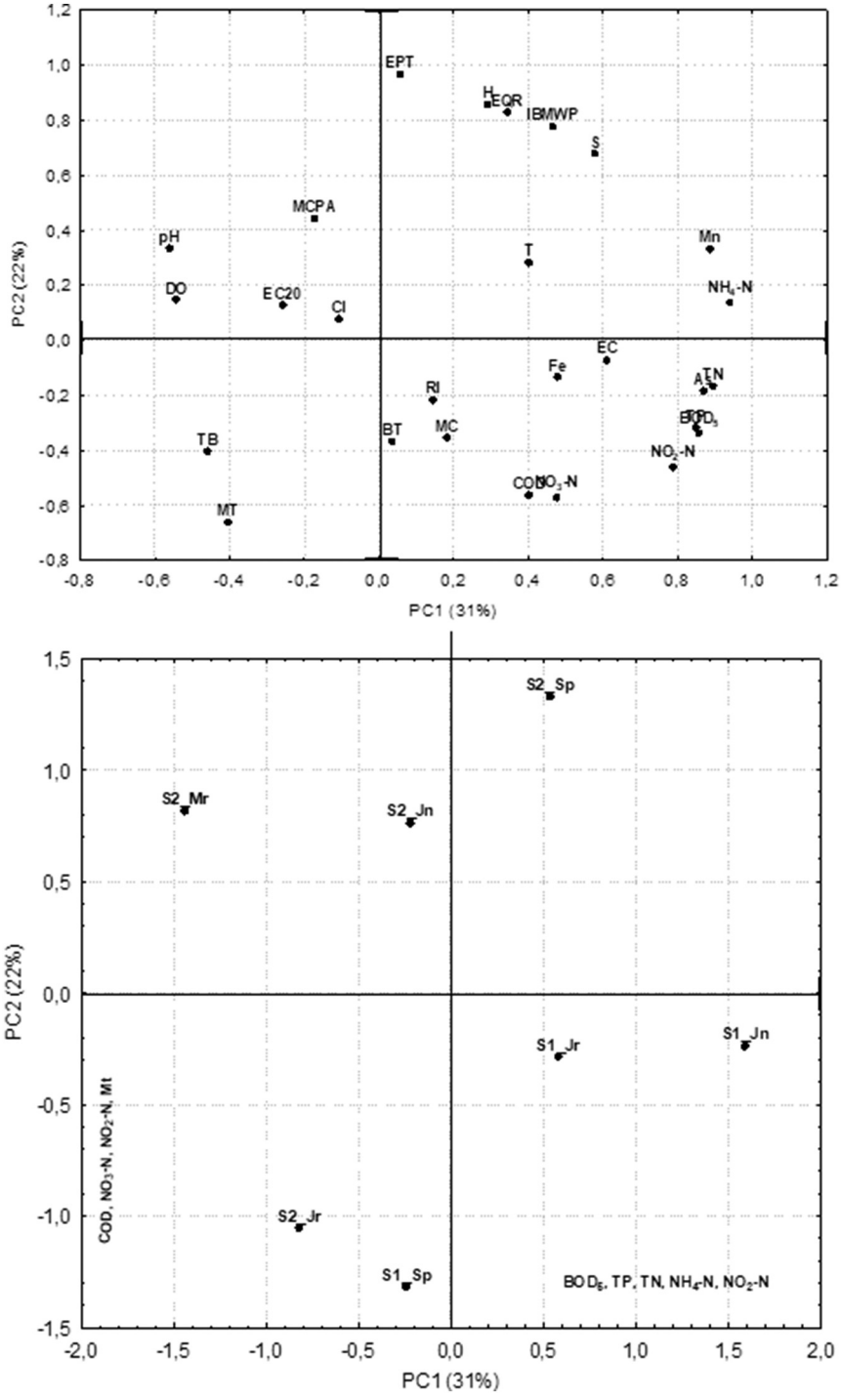

Fig. 5. PCA analysis: (a) the first two axes of the PCA applied to the physicochemical parameters, biotic indices and ecotoxicological endpoints; (b) scores of water samples on the bidimensional plane defined by the first two principle components (PC). TB (Terbutilazine); BT (Bentazone); MT (Metolachlor); MC (mecroprop); IR (Reproduction inhibition of *D. magna*); EC20 (Luminescence inhibition of *V. fisherie* in 20% of the exposure population). Parameters: BOD_5 (Biochemical oxygen demand); COD (Chemical oxygen demand; TP (Total phosphorus); TN (Total nitrogen); NO_2-N (Nitrite); NO_3-N (Nitrate); NH_4-N (Ammonium); Cl (Chloride); Fe (Iron); Mn (Manganese); As (Arsenic); BT (Bentazone); MT (Metolachlor); MCPA ((4-chloro-2-methylphenoxy) acetic acid)); MC (Mecoprop); TB (Terbuthylazine); N (number of total individuals); EPT (Ephemera, Plecoptera, Trichoptera Index); H (Shanon Wienner index); E (Evenness index); IBMWP (Iberian Bio-Monitoring Working Party index); EQR (Ecological Quality Ratio); EC_{20} (20% of *V. fisherie* Luminescence inhibition); RI (Reproduction inhibition_*D. magna*). Site locations: Mouth of the stream: S1_Jn (Site 1_June 2011); S1_Sp (Site 1_September 2011); S1_Jr (Site 1_January 2012); Source of the stream: S2_Jn (Site 2_June 2011); S2_Sp (Site 2_September 2011); S2_Jr (Site 2_January 2012); S2_Mr (Site 2_March 2012).

chemical, and biological assessment of this type of surface water is not an easy task. The unknown and strong variability of hydrological regimes and flows, very dependent on climate conditions, limits the development of sampling plans, complicates the determination of reference sites, and of the best biological parameters for the quality assessment of a specific watercourse. Hence, it is important to increase the number of research studies and results in temporary rivers/streams to decrease the gap of knowledge in this type of systems and help in choosing the best indicators that can be used for their management and restoration.

The results obtained for the assessment of the ecological status of the temporary stream of Brejo of Cagarrão provide evidence of severely

degraded conditions, mainly at the source of the stream, compromising the biodiversity and the respective abundance of species, and classifying this water line with an ecological status lower that good. Furthermore, these results deserve considerable concern, once this stream is in the Southwest Alentejo and Vicentine Coast Natural Park, near Brejo Largo Beach, and may also raise public health issues.

The chemical contamination was principally due to pollution processes located near the source of the stream (intensive agriculture, livestock activities and untreated or insufficient treatment of wastewaters), once the results showed that when the inflection (dry phase) occurs the mouth of the stream presents a better quality. The nutrients and organic matter were the main parameters responsible for the variability of the water quality at the stream.

In general, the multi-metric indices used classified the ecological status of the stream as reasonable to mediocre, being more sensitive to nutrients and organic matter. In the present study, only the sub-lethal ecotoxicological endpoints showed sensitivity to the observed contamination, indicating that, at least during some periods of time, some populations may have been affected and biodiversity compromised. This group of tools was more sensitive to pesticides, than to nutrients or organic matter, although the substances detected belonged only to classes of herbicides and their concentrations were, in general, considered low.

The current results support the complementary use of macroinvertebrate indices and ecotoxicological sub-lethal endpoints in the assessment of ecological status of temporary streams, once they exhibit differential sensitivities, depending on the type of pollutant.

The results highlighted the linearity of the responses among the two groups of biological methodologies. Nevertheless, further studies including more sampling campaigns, the assessment of sediment matrices at the dry phase, and the use of a higher number of bioindicators would be needed, to generalize our findings and to establish thresholds easy to apply and understand in programs of management and restoration of this type of ecosystem.

Supplementary data to this article can be found online at https://doi.org/10.1016/j.scitotenv.2018.03.281.

Acknowledgments

The present research is co-funded by the European Union through the European Regional Development Fund, included in the COMPETE 2020 (Operational Program Competitiveness and Internationalization) through the ICT project (UID/GEO/04683/2013) with the reference POCI-01-0145-FEDER-007690 and also through the ALOP (ALT20-03-0145-FEDER-000004), by the European Union through the EU FP7 project SOLUTIONS (603437), and by the Government of Catalonia (Consolidated Research Groups 2017 SGR 1404 – Water and Soil Quality Unit). It reflects only the author's views. The Community is not liable for any use that may be made of the information contained therein. Merck is acknowledged for the gift of LC columns.

References

Acuña, V., Datry, T., Marshall, J., Barceló, D., Dahm, C.N., Ginebreda, A., McGregor, G., Sabater, S., Tockner, K., Palmer, M.A., 2014. Why should we care about temporary waterways? Science 343, 1080–1081.

Alba-Tercedor, J., Sánchez-Ortega, A., 1988. Un método rápido y simple para evaluar la calidad biológica de las aguas corrientes basado en el de Hellawell (1978). Limnetica 4, 51–56 (in Spanish).

APHA (America Public Health Association), 1998. Standard Methods for the Examination of Water and Wastewater. New York. .

Araújo, R.S., Alves, M.G., Condesso de Melo, M.T., Chrispim, Z.M.P., Mendes, M.P., Silva Júnior, G.C., 2014. Water resource management: a comparative evaluation of Brazil, Rio de Janeiro, the European Union, and Portugal. Sci. Total Environ. 511, 815–828.

Arenas-Sánchez, A., Rico, A., Vighi, M., 2016. Effects of water scarcity and chemical pollution in aquatic ecosystems: state of the art. Sci. Total Environ. 572, 390–403.

ARHAlentejo (Administração da Região Hidrográfica do Alentejo I.P.), 2011. Plano de gestão das bacias hidrográficas integradas nas regiões hidrográficas 6 e 7: Região Hidrográfica 7. Ministério do Ambiente e do Ordenamento do Território. Lisboa (in Portuguese).

ARHAlentejo (Administração da Região Hidrográfica do Alentejo I.P.), 2012. Plano de gestão das bacias hidrográficas integradas nas regiões hidrográficas 6 e 7: Região Hidrográfica 7. Ministério do Ambiente e do Ordenamento do Território. Lisboa (in Portuguese).

Artigas, J., Arts, G., Babut, M., Caracciolo, A.B., Charles, S., Chaumot, A., Combourieu, B., Dahllöf, I., Despréaux, D., Ferrari, B., Fribergi, N., Garric, J., Geffard, O., Gourlay-Francé, C., Hein, M., Hjorth, M., Krauss, M., De Lange, H.J., Lahr, J., Lehtonen, K.K., Lettieri, T., Liess, M., Lofts, S., Mayer, P., Morin, S., Paschke, A., Svendsen, C., Usseglio-Polatera, P., van den Brink, N., Vindimian, E., Williams, R., 2012. Towards a renewed research agenda in ecotoxicology. Environ. Pollut. 160, 201–206.

ASTM, 1998. Standard practice for conducting toxicity tests with fishes, macroinvertebrates and amphibians. Annual Book of ASTM Standards, E729-90. Philadelphia, pp. 271–296.

Baird, D.J., Barber, I., Bradley, M., Calow, P., Soares, A.M.V.M., 1989. The Daphnia bioassay: a critique. Hydrobiologia 188-189, 403–406.

Beketov, M.A., Liess, M., 2012. Ecotoxicology and macroecology and time for integration. Environ. Pollut. 162, 247–254.

Bio, A., Vieira, N., Costa, M.J., Valente, A., 2011. Assessment of habitat and water quality of the Portuguese Febros River and one of its tributaries. Limnetica 30 (1), 103–116.

Blanco, S., Bécares, E., 2010. Are biotic indices sensitive to river toxicants? A comparison of metrics based on diatoms and macro-invertebrates. Chemosphere 79, 18–25.

Bonada, N., Doledec, S., Statzner, B., 2007. Taxonomic and biological trait differences of stream macroinvertebrate communities between Mediterranean and temperate regions: implications for future climatic scenarios. Glob. Chang. Biol. 13 (8), 1658–1671.

Bunzel, K., Schäfer, R.B., Thrän, D., Kattwinkele, M., 2015. Pesticide runoff from energy crops: a threat to aquatic invertebrates? Sci. Total Environ. 537, 187–196.

Calhoun, A.J.K., Mushet, D.M., Bell, K.P., Boixd, D., Fitzsimons, J.A., Isselin-Nondedeu, F., 2017. Temporary wetlands: challenges and solutions to conserving a 'disappearing' ecosystem. Biol. Conserv. 211, 3–11.

Clements, W.H., Rohr, J.R., 2009. Community responses to contaminants: using basic ecological principles to predict ecotoxicological effects. Environ. Toxicol. Chem. 28, 1789–1800.

Colin, N., Porte, C., Fernandes, D., Barata, C., Padrós, F., Carrassón, M., Monroy, M., Cano-Rocabayera, O., de Sostoa, A., Piña, B., Maceda-Veiga, A., 2016. Ecological relevance of biomarkers in monitoring studies of macro-invertebrates and fish in Mediterranean rivers. Sci. Total Environ. 540, 307–323.

Cottarelli, V., Aygen, C., Mura, G., 2010. Fairy shrimps from Asiatic Turkey: redescription of *Chirocephalus tauricus Pesta*, 1921 and descriptions of *Hirocephalus algidus* sp. nov. and Chirocephalus brteki sp. nov. (Crustacea, Branchiopoda, Anostraca). Zootaxa 2528, 29–52.

Damásio, J., Barata, C., Munné, A., Ginebreda, A., Guasch, H., Sabater, S., et al., 2007. Comparing the response of biochemical indicators (biomarkers) and biological indices to diagnose the ecological impact of an oil spillage in a Mediterranean river (NE Catalunya, Spain). Chemosphere 66 (7), 1206–1216.

Decreto Regulamentar n.° 26/95 - Diário da República n.° 219/1995, Série I-B. Ministério do Ambiente e Recursos Naturais. Lisboa.

Decreto-Lei n° 236/98, de 1 Agosto, 1998. Diário da república no. 176/98—I série A. Ministério do Ambiente. Lisboa.

ECC (European Community Comission), 1998. Comission Directive 98/83/EEC of 3 November. Quality of water intended for human consumption. Off. J. Eur. Communities, L330/32 0032–0054.

ECC (European Community Commission), 2000. Common Implementation Strategy for the Water Framework Directive (2000/60/EC). Guidance Document No. 27. Technical Guidance For Deriving Environmental Quality Standards. Technical Report - 2011 – 055.

ECC (European Community Commission), 2006. Decision 2006/118/EC on the protection of groundwater against pollution and deterioration. Off. J. Eur. Communities 19–31 L 372/19.

ECC (European Community Commission), 2013. Decision 2013/39/EC on environmental quality standards in the field of water policy. Off. J. Eur. Communities 1–17 L 226/1.

Feio, M.J., Norris, R.H., Graça, M.A.S., Nichols, S., 2009. Water quality assessment of Portuguese streams: regional or national predictive models? Ecol. Indic. 9, 791–806.

Finney, D.J., 1971. Probit Analysis. Cambridge University Press, Cambridge, DC.

Gallart, F., Prat, N., Garcia-Roger, E.M., Latrón, J., Rieradevall, M., Llorens, P., Barberá, G.G., Brito, D., de Girolamo, A.M., Lo Porto, A., Buffagni, A., Erba, S., Neves, R., Nikolaidis, N.P., Perrin, J.L., Querner, E.P., Quiñonero, J.M., Tournoud, M.G., Tzoraki, O., Skoulikidis, N., Gómez, R., Sánchez-Montoya, M.M., Froebrich, J., 2012. A novel approach to analyzing the regimes of temporary streams inrelation to their controls on the composition and structure of aquatic biota. Hydrol. Earth Syst. Sci. 16, 3165–3182.

Gallart, F., Llorens, P., Latron, J., Cid, N., Rieradevall, M., Prat, N., 2016. Validating alternative methodologies to estimate the regime of temporary rivers when flow data are unavailable. Sci. Total Environ. 565, 1001–1010.

García, L., Pardo, I., Delgado, C., 2014. Macroinvertebrate indicators of ecological status in Mediterranean temporary stream types of the Balearic Islands. Ecol. Indic. 45, 650–663.

Harvey, R., Lye, L., Khan, A., Paterson, R., 2011. The influence of air temperature on water temperature and the concentration of dissolved oxygen in new found land rivers. Canadian Water Resources Journal 36 (2), 171–192.

Ieromina, O., Peijnenburg, W.J.G.M., de Snoo, G.R., Vijver, M.G., 2014. Population responses of *Daphnia magna*, *Chydorus sphaericus* and *Asellus aquaticus* in pesticide contaminated ditches around bulb fields. Environ. Pollut. 192, 196–203.

INAG (Portuguese Water Institute), 2008. Manual para a avaliação biológica da qualidade da água em sistemas fluviais segundo a Directiva Quadro da Água - Protocolo de amostragem e análise para os macroinvertebrados bentónicos. Ministério do Ambiente, do Ordenamento do Território e do Desenvolvimento Regional. Instituto da Água, Lisboa (in Portuguese).

INAG (Portuguese Water Institute), 2009. Critérios para a classificação do estado das massas de água superficiais - rios e albufeiras. Ministério do Ambiente, do Ordenamento do Território e do Desenvolvimento Regional. Instituto da Água, Lisboa (in Portuguese).

ISO 11348-2, 1998. Determination of Inhibitory Effect of Water Samples on the Light Emission of Vibrio Fischeri (Luminescent Bacteria Test). Part 2: Method Using Liquid-dried Bacteria. International Organization for Standardisation, Geneve, Switzerland.

ISO 6341, 1996. Water Quality – Determination of the Inhibition of the Mobility of *Daphnia magna* Straus (Cladocera, Crustacea) - Acute Toxicity Test. International Organization for Standardisation, Geneve, Switzerland.

Kaiser, H.F., 1960. The application of electronic computers to factor analysis. Educ. Psychol. Meas. 20, 141–151. https://doi.org/10.1177/001316446002000116.

Korkança, S.Y., Kayıkçı, S., Korkanç, M., 2017. Evaluation of spatial and temporal water quality in the Akkaya dam watershed (Nigde, Turkey) and management implications. J. Afr. Earth Sci. 129, 481–491.

Leitão, F., Hughes, S.J., Máximo, I., Atanasova, N., Furtado, A., Chícharo, L., 2014. Habitat oriented sampling of macroinvertebrates affects the determination of ecological status in temporary Mediterranean river systems. River Res. Appl. 30, 1233–1247.

Liess, M., von der Ohe, P.C., 2005. Analyzing effects of pesticides on invertebrate communities in streams. Environ. Toxicol. Chem. 24 (4), 954–965.

Liu, C.W., Lin, K.H., Kuo, Y.M., 2003. Application of factor analysis in the assessment of groundwater quality in a Blackfoot disease area in Taiwan. Sci. Total Environ. 313, 77–89.

Medeiros, J.P., Chaves, M.L., Silva, G., Azeda, C., Costa, J.L., Marques, J.C., Costa, M.J., Chainho, P., 2012. Benthic condition in low salinity areas of the Mira estuary (Portugal): lessons learnt from freshwater and marine assessment tools. Ecol. Indic. 19, 79–88.

Mil-Homens, M., Vale, C., Raimundo, J., Pereira, P., Brito, P., Caetano, M., 2014. Major factors influencing the elemental composition of surface estuarine sediments: the case of 15 estuaries in Portugal. Mar. Pollut. Bull. 84, 135–146.

Munné, A., Prat, N., 2009. Use of macroinvertebrate-based multimetric indices for water quality evalution in Spanish Mediterranean rivers: an intercalibration approach with the IBMWP index. Hydrobiologia 628, 203–225.

Muñoz, I., Sabater, S., Barata, C., 2012. Evaluating ecological integrity in multi-stressed rivers: from the currently used biotic indices to newly developed approaches using biofilms and invertebrates. In: Guash, H., Ginebrada, A., Geiszener, A. (Eds.), Emerging and Priority Pollutants in Rivers. The Handbook of Environmental Chemistry Series. Springer, Berlin Heidelberg, pp. 219–241.

Naiman, R.J., Latterell, J.J., Pettit, N.E., Olden, J.D., 2008. Flow variability and the biophysical vitality of river systems. Compt. Rendus Geosci. 340, 629–643.

Nikolaidis, N.P., Demetropoulou, L., Froebrich, J., Jacobs, C., Gallart, F., Prat, N., Lo Porto, A., Campana, C., Papadoulakis, V., Skoulikidis, N., Davy, T., Bidoglio, G., Bouraoui, F., Kirkby, M., Tournoud, M.G., Polesello, S., Barberá, G.G., Cooper, D., Gomez, R., Sánchez-Montoya, M.M., Latron, J., De Girolamo, A.M., Perrin, J.L., 2013. Towards sustainable management of Mediterranean river basins: policy recommendations on management aspects of temporary streams. Water Policy 15, 830–849.

OCDE (Organization for Economic Cooperation and Development), 1998. OCDE 211, *Daphnia magna* Reproduction Test. OCDE, Paris.

von der Ohe, P.C., Goedkoop, W., 2013. Distinguishing the effects of habitat degradation and pesticide stress on benthic invertebrates using stressor-specific metrics. Sci. Total Environ. 444, 480–490.

Palma, P., Palma, V.L., Fernandes, R.M., Soares, A.M.V.M., Barbosa, I.R., 2008. Acute toxicity of atrazine, endosulfan sulphate and chlorpyrifos to *Vibrio fischeri*, *Thamnocephalus platyurus* and *Daphnia magna*, relative to their concentrations in surface waters from the Alentejo region of Portugal. Bull. Environ. Contam. Toxicol. 81, 485–489.

Palma, P., Alvarenga, P., Palma, V., Matos, C., Fernandes, R.M., Soares, A.M.V.M., Barbosa, I.R., 2010. Evaluation of surface water quality using an ecotoxicological approach: a case study of the Alqueva Reservoir (Portugal). Environ. Sci. Pollut. Res. 17, 703–716.

Palma, P., Köck-Schulmeyer, M., Alvarenga, P., Ledo, L., Barbosa, I.R., López de Alda, M., Barceló, D., 2014a. Risk assessment of pesticides detected in surface water of the Alqueva reservoir (Guadiana basin, southern of Portugal). Sci. Total Environ. 488–489, 208–219.

Palma, P., Ledo, L., Soares, S., Barbosa, I.R., Alvarenga, P., 2014b. Spatial and temporal variability of the water and sediments quality in the Alqueva reservoir (Guadiana Basin; southern Portugal). Sci. Total Environ. 470–471, 780–790.

Palma, P., Ledo, L., Alvarenga, P., 2016. Ecotoxicological endpoints, are they useful tools to support risk management strategies in strongly modified water bodies? Sci. Total Environ. 541, 119–129.

Persoone, G., 1999. THAMNOTOXKIT FTM - Crustacean Toxicity Screening Test for Freshwater. Standard Operational Procedure. Belgium.

Petrovic, M., Ginebreda, A., Acuña, V., Batalla, R.J., Elosegi, A., Guasch, H., de Alda, M.L., Marcé, R., Muñoz, I., Navarro-Ortega, A., 2011. Combined scenarios of chemical and ecological quality under water scarcity in Mediterranean rivers. Trac Trends Analytical Chemistry 30 (8), 1269–1278.

Poff, N.L., Allan, J.D., Bain, M.B., Karr, J.R., Prestegaard, K.L., Richter, B.D., et al., 1997. The natural flow regime. Bioscience 47, 769–784.

Real Decreto n° 817/2015, de 11 de septiembre, 2015. Boletín oficial del Estado no. 219/2015 – Sec I. Criterios de seguimiento y evaluación del estado de las aguas superficiales y las normas de calidad ambiental. Ministerio de Agricultura, Alimentación y Medio Ambiente.

Reyjol, Y., Argillier, C., Wendy, Bonne, Borja, A., Buijse, A.D., Cardoso, A.C., Daufresne, M., Kernanf, M., Ferreira, M.T., Poikane, S., Prat, N., Solheim, A.L., Stroffek, S., Usseglio-Polatera, P., Villeneuve, B., van de Bund, W., 2014. Assessing the ecological status in the context of the European Water Framework Directive: where do we go now? Sci. Total Environ. 497–498, 332–344.

Sánchez-Montoya, M.M., Vidal-Abarca, M.R., Puntí, T., Poquet, J.M., Prat, N., Rieradevall, M., Alba-Tercedor, J., Zamora-Muñoz, C., Toro, M., Robles, S., Álvarez, M., Suárez, M.L., 2009. Defining criteria to select reference sites in Mediterranean streams. Hydrobiologia 619, 39–54.

Schäfer, R., Uhn, B., Malaj, E., Onig, A., Gergs, R., 2016. Contribution of organic toxicants to multiple stress in river ecosystems. Freshw. Biol. 61, 2116–2128.

Schinegger, R., Trautwein, C., Melcher, A., Schumutz, S., 2012. Multiple human pressures and their spatial patterns in European running waters. Water and Environment Journal 26, 261–273.

Silva, M.T.F.C., 2012. Macroinvertebrados como bioindicadores da qualidade da água em rios do Sul de Portugal: caso de estudo na Bacia Hidrográfica da Ribeira de Odelouca. Tese de Mestrado em Ecologia e Gestão Ambiental. Faculdade de Ciências, Universidade de Lisboa (in portuguese).

Simeonov, V., Stratis, J.A., Samara, C., Zachariadis, G., Voutsa, D., Anthemidis, A., et al., 2003. Assessment of surface water quality in Northern Greece. Water Res. 37, 4119–4124.

Skoulikidis, Nikolaos T., Sabater, Sergi, Datry, Thibault, Morais, Manuela M., Buffagni, Andrea, Dörflinger, Gerald, Zogaris, Stamatis, Sánchez-Montoya, Maria del Mar, Bonada, Nuria, Kalogianni, Eleni, Rosado, Joana, Vardakas, Leonidas, De Girolamo, Anna Maria, Tockner, Klement, 2017. Non-perennial Mediterranean rivers in Europe: status, pressures, and challenges for research and management. Sci. Total Environ. 577, 1–18.

Sokal, R.R., Rohlf, F.J., 1995. Biometry: The Principles and Practice of Statistics in Biological Research. 3rd Edition. W.H. Freeman and Co., New York.

Stevenson, R.J., Sabater, S., 2010. Understanding effects of global change on river ecosystems: science to support policy in a changing world. Hydrobiologia 657, 3–18.

Trigal, C., Garcia-Criado, F., Alaez, C.F., 2007. Macroinvertebrate communities of mediterranean ponds (North Iberian Plateau): importance of natural and human-induced variability. Freshw. Biol. 52, 2042–2055.

Turner, R.K., Daily, G.C., 2008. The ecosystem services framework and natural capital conservation environmental and resource economics. Environ. Resour. Econ. 39, 25–35.

Van den Broeck, M., Waterkeyn, A., Rhazi, L., Grillas, P., Brendonck, L., 2015. Assessing the ecological integrity of endorheic wetlands, with focus on Mediterranean temporary ponds. Ecol. Indic. 54, 1–11.

Versteeg, D.J., Belanger, S.E., Carr, G.J., 1999. Understanding single-species and model ecosystem sensitivity: data-based comparison. Environ. Toxicol. Chem. 8 (6), 1329–1346.

Wunderlin, D.A., Díaz, M.P., Amé, M.V., Pesce, S.F., Hued, A.C., Bistoni, M.A., 2001. Pattern recognition techniques for the evaluation of spatial and temporal variations in water quality. A case study: Suquía River Basin (Córdoba—Argentina). Water Res. 35 (12), 2881–2894.

Zar, J.H., 1996. Biostatistical Analysis. Prentice-Hall International, Englewood Cliff, USA, DC.